# VOLCANISM IN HAWAII

VOLUME 2

U. S. GEOLOGICAL SURVEY PROFESSIONAL PAPER 1350

DIAMOND JUBILEE (1912–1987)

HVO

HAWAIIAN VOLCANO OBSERVATORY

*Hawaiian Islands*

Cover: Eruption on northeast rift zone of Mauna Loa Volcano, April 3, 1984. View is from cinder cone at 2,775 m (9,100 ft) elevation. Main vent of eruption (right rear) is at 2,900 m (9,500 ft) elevation; flows are moving to the east. Photograph by Katia Krafft, B.P. 5, 68700 Cernay, France.

DIAMOND JUBILEE
(1912–1987)

HAWAIIAN VOLCANO OBSERVATORY

# Volcanism in Hawaii

*Papers to commemorate the 75th anniversary of the founding of the Hawaiian Volcano Observatory*

Overleaf: Slope map of the northern Pacific Ocean, showing prominence of Hawaiian-Emperor volcanic chain (compare with ocean-floor map in front of volume 1). From world slope map by James G. Moore and Robert K. Mark, based on data from National Geophysical Data Tape ETOPO–5, digital relief of the surface of the Earth. Steepness of slope indicated by colors: deep red, >3.4°; red, 2.9°–3.4°; orange, 2.3°–2.9°; yellow, 1.7°–2.3°; green, 1.1°–1.7°; blue, 0.57°–1.1°; purple, <0.57°.

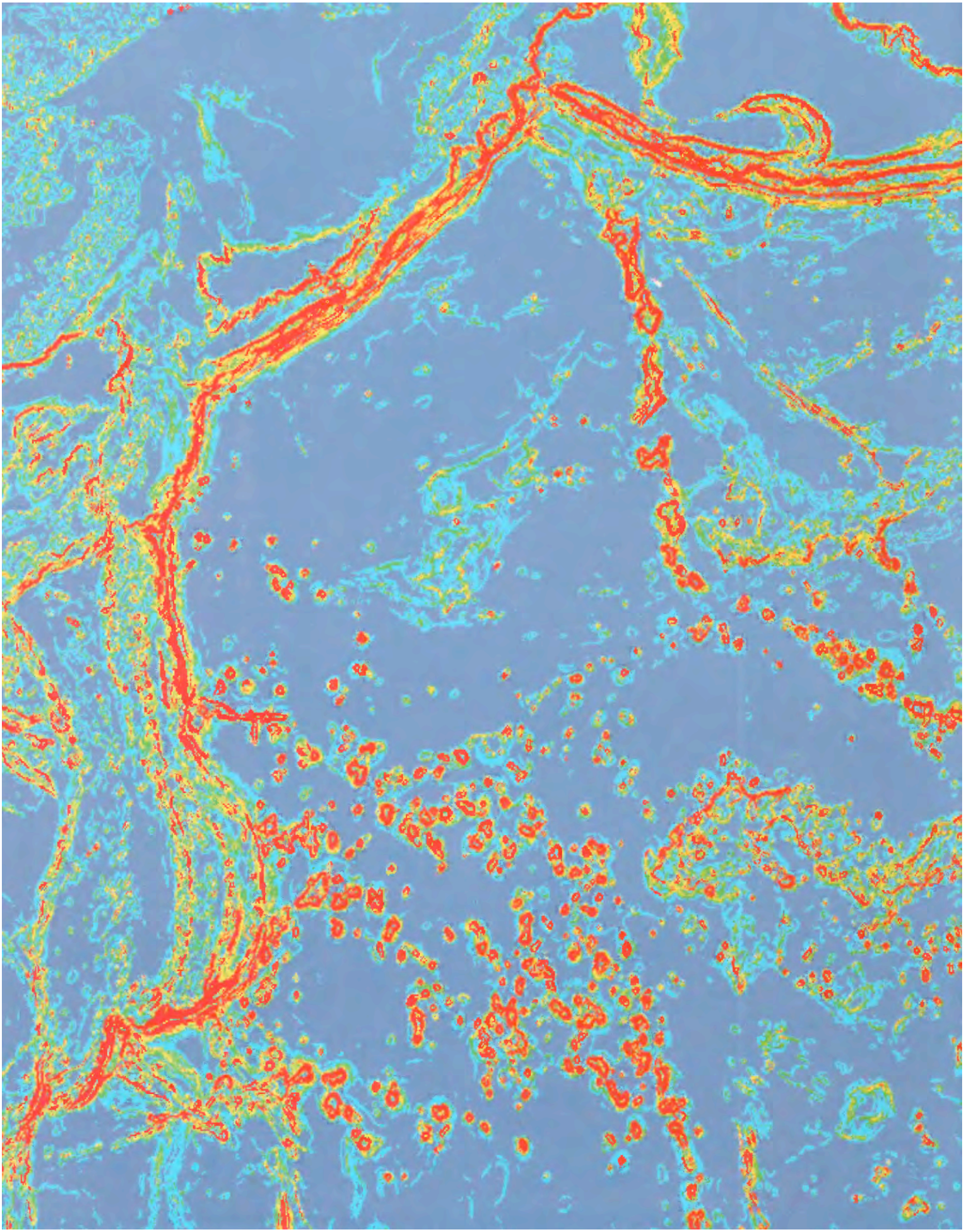

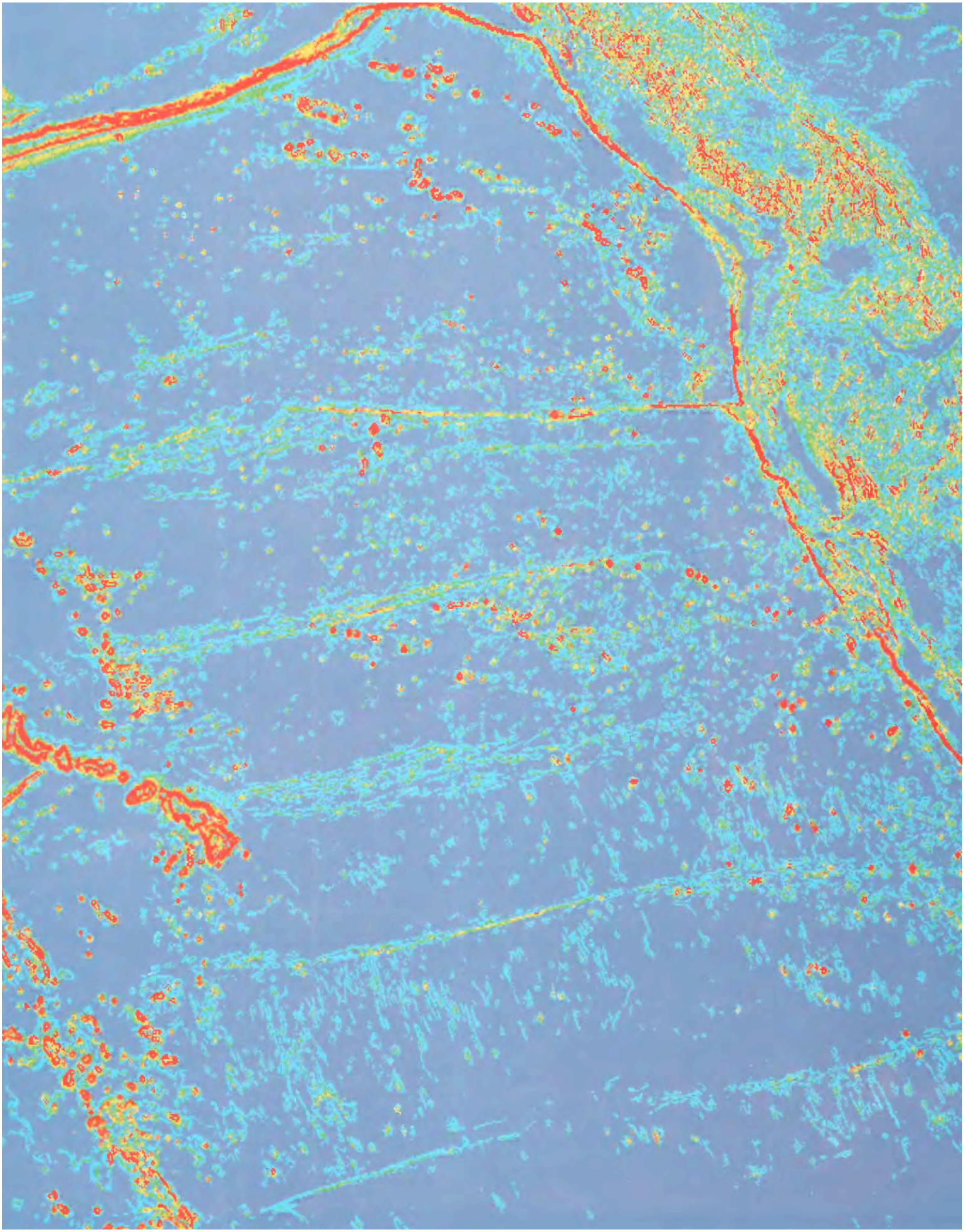

# Volcanism in Hawaii

*Edited by* Robert W. Decker, Thomas L. Wright, *and* Peter H. Stauffer

*Volume 2*

- Structure
- Dynamics
- History of Investigations of Hawaiian Volcanism

U.S. GEOLOGICAL SURVEY PROFESSIONAL PAPER 1350

UNITED STATES GOVERNMENT PRINTING OFFICE, WASHINGTON : 1987

**DEPARTMENT OF THE INTERIOR**

**DONALD PAUL HODEL, *Secretary***

**U.S. GEOLOGICAL SURVEY**

**Dallas L. Peck, *Director***

**Library of Congress Cataloging-in-Publication Data**

Volcanism in Hawaii.

(U.S. Geological Survey Professional Paper 1350)
Contents: v.1. Physiography, tectonics, and submarine geology; Geology of the Island of Hawaii; Petrogenesis and volcanic gases.
v.2. Structure; Dynamics; History of investigations of Hawaiian volcanism.
Supt. of Docs. no.: I 19.16:1350
1. Volcanism—Hawaii. 2. Volcanic ash, tuff, etc.—Hawaii. I. Decker, Robert Wayne, 1927–. II. Wright, Thomas Llewellyn, 1935–.
III. Stauffer, Peter Herman, 1935–. IV. Series: United States. Geological Survey. Professional Paper 1350.
QE524.V65 1987 551.2'2'09969 86–600292

**For sale by the Books and Open-File Reports Section,**
**U.S. Geological Survey, Federal Center, Box 25425, Denver, CO 80225**

# CONTENTS

*VOLUME 1*

PHYSIOGRAPHY, TECTONICS, AND SUBMARINE GEOLOGY

GEOLOGY OF THE ISLAND OF HAWAII

PETROGENESIS AND VOLCANIC GASES

*VOLUME 2*

## STRUCTURE

Chapter 36. Hawaiian volcanic features: A photoglossary *845*
Taeko Jane Takahashi and Jim D. Griggs

37. Geophysical constraints on the structure of Kilauea and Mauna Loa Volcanoes and some implications for seismomagmatic processes *903*
David P. Hill and John J. Zucca

38. Seismic structure and tectonics of Kilauea Volcano *919*
Clifford H. Thurber

39. Aeromagnetic and near-surface electrical expression of the Kilauea and Mauna Loa volcanic rift systems *935*
Vincent J. Flanigan and Carl L. Long

40. Regional self-potential anomalies at Kilauea Volcano *947*
Dallas B. Jackson and James Kauahikaua

41. The dike complex of Koolau Volcano, Oahu: Internal structure of a Hawaiian rift zone *961*
George P.L. Walker

## DYNAMICS

Chapter 42. Dynamics of Hawaiian volcanoes: An overview *997*
Robert W. Decker

43. The seismicity of Kilauea's magma system *1019*
Fred W. Klein, Robert Y. Koyanagi, Jennifer S. Nakata, and Wilfred R. Tanigawa

44. Structural damage and ground failures from the November 16, 1983, Kaoiki earthquake, Island of Hawaii *1187*
Jane M. Buchanan-Banks

Chapter 45. Origin of volcanic tremor in Hawaii
Part I. Data from the Hawaiian Volcano Observatory 1969–1985 *1221*
Robert Y. Koyanagi, Bernard Chouet, and Keiiti Aki
Part II. Theory and discussion *1259*
Bernard Chouet, Robert Y. Koyanagi, and Keiiti Aki

46. A hydraulic model to explain variations in summit tilt rate at Kilauea and Mauna Loa Volcanoes *1281*
John J. Dvorak and Arnold T. Okamura

47. Elastic and inelastic magma storage at Kilauea Volcano *1297*
Daniel J. Johnson

48. Cycling of magma between the summit reservoir and Kilauea Iki lava lake during the 1959 eruption of Kilauea Volcano *1307*
Jerry P. Eaton, Donald H. Richter, and Harold L. Krivoy

49. Tidal effects on Hawaiian volcanism *1337*
Daisuke Shimozuru

50. Geoelectric character of Kilauea Iki lava lake crust *1345*
Lennart A. Anderson

51. Uniqueness of volcanic systems *1357*
Herbert R. Shaw

52. Elasticity and contractancy of Hawaiian olivine tholeiite and its role in the stability and structural evolution of subcaldera magma reservoirs and rift systems *1395*
Michael P. Ryan

53. Origins of blade-like dikes in volcanic rift zones *1449*
Allan M. Rubin and David D. Pollard

54. Heat and mass transport in the east-rift-zone magma conduit of Kilauea Volcano *1471*
Harry C. Hardee

55. Conceptual models of brine evolution in magmatic-hydrothermal systems *1487*
Robert O. Fournier

56. A geochemical model of the Kilauea east rift zone *1507*
Donald Thomas

57. Aa flow dynamics, Mauna Loa 1984 *1527*
Peter W. Lipman and Norman G. Banks

58. Preliminary estimates of the rheological properties of 1984 Mauna Loa lava *1569*
Henry J. Moore

Chapter 59. The role of lava tubes in Hawaiian volcanoes *1589*
Ronald Greeley

## HISTORY OF INVESTIGATIONS OF HAWAIIAN VOLCANISM

Chapter 60. James D. Dana and the origins of Hawaiian volcanology: The U.S. Exploring Expedition in Hawaii, 1840–41 *1607*
Daniel E. Appleman

61. Thomas A. Jaggar, Jr., and the Hawaiian Volcano Observatory *1619*
Russell A. Apple

62. Staff of the Hawaiian Volcano Observatory, 1912–present *1645*
Compiled by Taeko Jane Takahashi and Thomas L. Wright

Guide to pronunciation of Hawaiian words *1663*
Compiled by Taeko Jane Takahashi

Any use of trade names and trademarks in this publication is for descriptive purposes only and does not constitute endorsement by the U.S. Geological Survey.

DIAMOND JUBILEE
(1912—1987)

HVO

HAWAIIAN VOLCANO OBSERVATORY

Volume 2

Oblique aerial photograph of Kilauea caldera, looking north. USGS photograph taken November 1, 1954.

# STRUCTURE

Guided by geological, geophysical, and geochemical observations, the mind's eye attempts to see beneath the Earth's surface. Conceptual models are proposed, tested against the data, and adjusted to fit.

Surface features on the Island of Hawaii are mostly formed by volcanic processes and often buried by subsequent eruptions. Calderas and pit craters collapse and reveal the structures in their walls. Erosion, roadcuts, and quarries expose dike swarms on ancient rift zones. These features and exposures are geologists' windows to the Earth's interior.

Earthquake waves and magnetic and electric fields are shaped by the rocks, pore fluids, and magma bodies through which they pass. When the variations of these geophysical data are inverted, inferred subsurface features emerge.

Using these approaches, the six chapters in this section describe and interpret some of the surface features and subsurface structures of the Islands of Hawaii and Oahu.

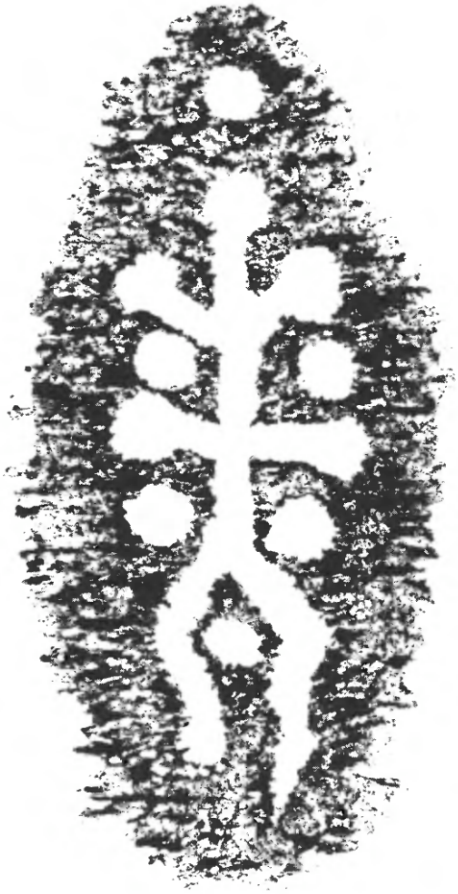

Man and His Family
Hawaiian Petroglyph
Puuloa, Hawaii

# HAWAIIAN VOLCANIC FEATURES: A PHOTOGLOSSARY

*By* Taeko Jane Takahashi *and* Jim D. Griggs

### ABSTRACT

**Selected Hawaiian volcanic features, ranging from shield volcanoes to strands of volcanic glass, are illustrated in 62 photographs. Each feature is defined in a glossary, with a description as to its location, scale, photographer, and date photographed.**

## INTRODUCTION

Type examples of volcanic structures, forms, and textures are represented in this glossary through photographs, arranged alphabetically by the name of the feature shown, that were selected from the archives of the Hawaiian Volcano Observatory. Selections were based on the accessibility of the features' locations and the clarity of the illustrations. The features range in scale from large structures, such as volcanic shields, to textures, such as Pele's hair and tears. For some features (for example, lava flows), photographs taken during and after eruptions give a sense of the changing volcanic landscape.

The descriptions and definitions in this glossary include the location and scale of the feature, the date photographed, and the name of the photographer. Most definitions are from the Glossary of Geology (Bates and Jackson, 1980), and permission to use them has been kindly granted by the American Geological Institute. All photographs were taken by members of the U.S. Geological Survey unless otherwise noted.

More extensive discussions of these and other volcanic features in Hawaii have been published by Stearns and Macdonald (1946), Wentworth and Macdonald (1953), Greeley (1974), Carr and Greeley (1980), and Macdonald and others (1983). A photographic atlas and glossary of volcanic features on a global scale has been published by Green and Short (1971). The photoglossary in this volume provides new illustrations of many features described in the works cited above.

### ACKNOWLEDGMENTS

The authors wish to thank J.P. Lockwood and R.B. Moore for reviewing the photographs and text for this paper. We also thank G.E. Ulrich for his invaluable assistance with definitions of selected features, A.T. Okamura for directing the authors to many of the features, and other staff members of the Hawaiian Volcano Observatory for contributing photographs to this glossary.

## GLOSSARY

The photographs that illustrate this glossary are U.S. Geological Survey photographs unless otherwise indicated. Photographer and date photographed are noted in parentheses. Quoted definitions of features are from Bates and Jackson (1980), except where another source is cited.

## REFERENCES CITED

Bates, R.L., and Jackson, J.A., 1980, Glossary of geology, 2nd ed.: Falls Church, Va., American Geological Institute, 751 p.

Carr, M.H., and Greeley, R., 1980, Volcanic features of Hawaii: a basis for comparison with Mars: Washington, D.C., National Aeronautics and Space Administration, Scientific and Technical Information Branch, 363 p.

Greeley, R., ed., 1974, Guidebook to the Hawaiian Planetology Conference: National Aeronautics and Space Administration, Ames Research Center, University of Santa Clara, and U.S. Geological Survey, 184 p.

Green, J., and Short, N.M., eds., 1971, Volcanic landforms and surface features: a photographic atlas and glossary: New York, Springer-Verlag, 519 p.

Lockwood, J.P., and Williams, I.S., 1978, Lava trees and tree moulds as indicators of lava flow direction: Geological Magazine, v. 115, no. 1, p. 69–74.

Macdonald, G.A., 1972, Volcanoes: Englewood Cliffs, New Jersey, Prentice-Hall, 510 p.

Macdonald, G.A., and Abbott, A.T., 1977, Volcanoes in the sea: The geology of Hawaii: Honolulu, University Press of Hawaii, 441 p.

Macdonald, G.A., Abbott, A.T., and Peterson, F.L., 1983, Volcanoes in the sea: the geology of Hawaii, 2nd ed.: Honolulu, Hawaii, The University of Hawaii Press, 517 p.

Neal, C.A., and Decker, R.W., 1983, Surging of lava flows at Kilauea Volcano, Hawaii: Eos, American Geophysical Union Transactions, v. 64, no. 45, p. 904.

Peck, D.L., 1966, Lava coils of some recent historic flows, Hawaii: U.S. Geological Survey Professional Paper 550–B, p. B148–B151.

Stearns, H.T., and Macdonald, G.A., 1946, Geology and ground-water resources of the Island of Hawaii (Bulletin 9): Honolulu, Hawaii, Hawaii Division of Hydrography and U.S. Geological Survey, 363 p.

Wentworth, C.K., Macdonald, G.A., 1953, Structures and forms of basaltic rocks in Hawaii: a description of the physical features of basaltic rocks and their origin: U.S. Geological Survey Bulletin 994, 98 p.

## Aa

"A Hawaiian term for lava flows typified by a rough, jagged, spinose, clinkery surface." Compare with **pahoehoe.**

Aa flow in Royal Gardens, Kalapana, east rift zone of Kilauea Volcano. The height of the flow front is approximately 2.5 m (April 9, 1983, J.B. Stokes).

## Aa

Detail of aa from Mauna Ulu flow, east rift zone of Kilauea Volcano. The diameter of the coin is 24 mm (June 10, 1985, J.D. Griggs).

## Accretionary lapilli

"More or less spherical masses, mostly between 1 mm and 1 cm in diameter, of cemented ash; the cementation is often weak. Formed by accretion of particles around wet nuclei, e.g., raindrops falling through a cloud of ash" (Macdonald, 1972, p. 133).

Accretionary lapilli from the 1790 eruption, Kau Desert (October 29, 1984, J.P. Lockwood).

## Accretionary lava ball

"A rounded mass, ranging in diameter from a few centimeters to several meters, [carried] on the surface of a lava flow such as aa, or on cinder-cone slopes, [and formed] by the molding of viscous lava around a core of already solidified lava."

Incandescent accretionary lava ball (top) approximately 0.75 m long, Royal Gardens, Kalapana, east rift zone of Kilauea Volcano (July 2, 1983, J.D. Griggs). Accretionary lava ball (bottom) approximately 2.5 m high, formed during the eruption of the prehistoric Keamoku flow from Mauna Loa Volcano, Footprints Trail, Kau Desert (November 24, 1984, T.J. Takahashi).

## Arching fountain

For definition, see **lava fountain**.

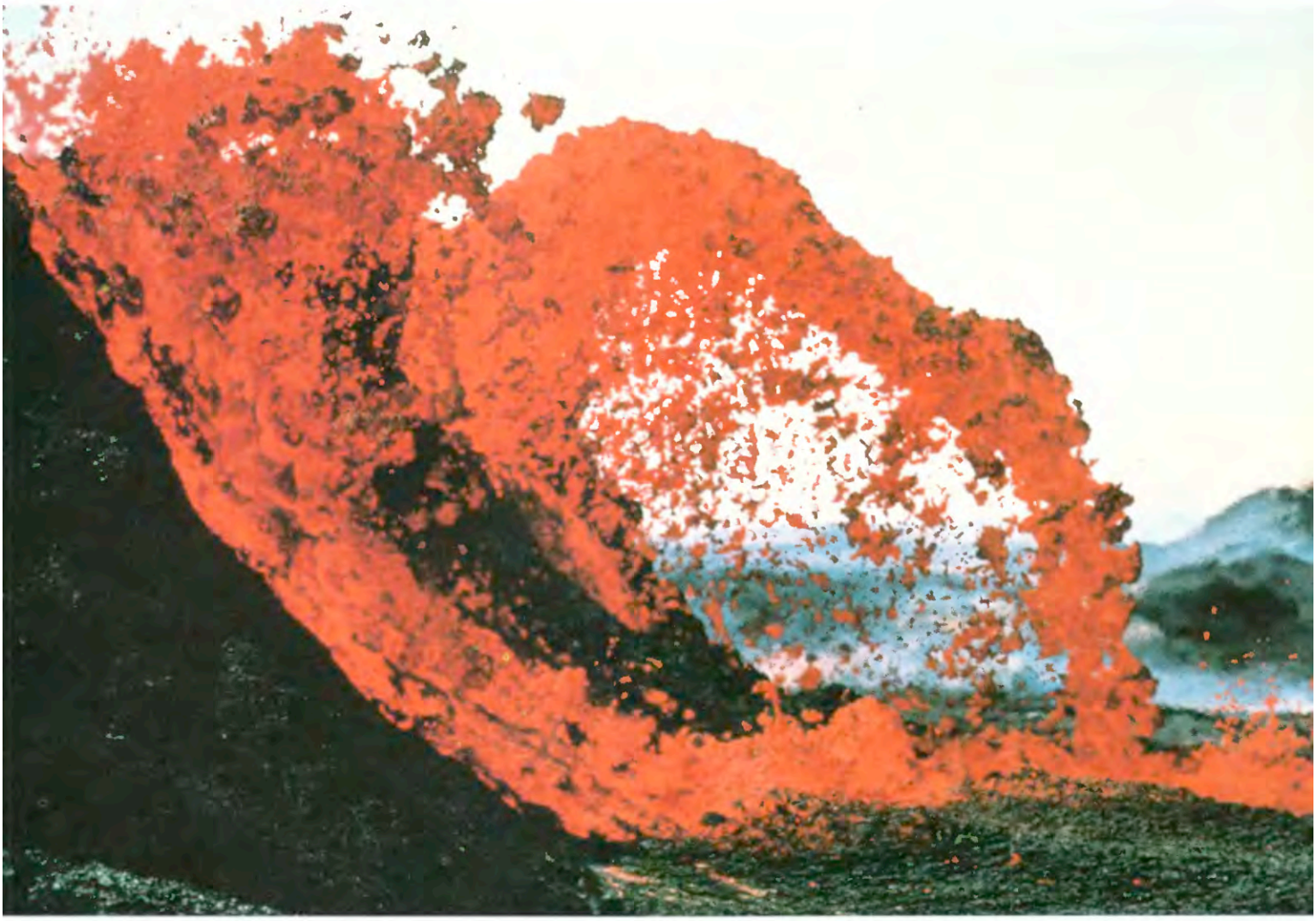

Fountains of the so-called 0740 vents, east rift zone of Kilauea Volcano; the view is to the west-southwest. The approximate height of the fountains is 10–15 m (February 25, 1983, J.D. Griggs).

## Bedded pyroclastic deposits

"* * * nonsedimentary material that exhibits depositional layering, such as the 'bedded deposits' of volcanic tuff alternating with lava in the mantle of a stratovolcano."

Bedded pyroclastic deposits (1790 eruption) visible in the southwest rift zone of Kilauea Volcano. The depth of the exposed area in the photograph is approximately 1.5 m (October 28, 1984, T.J. Takahashi).

## Breach

A break or opening in the rim of a crater. "Breached" is used to describe "a volcanic cone or crater, the rim of which has been broken through by the outpouring lava."

Aerial view of Puu Oo cinder-spatter cone, with breach on the right, east rift zone of Kilauea Volcano; the view is to the northeast (May 12, 1983, E.W. Wolfe).

## Caldera

"A large, basin-shaped volcanic depression, more or less circular *** the diameter of which is many times greater than that of the included vent or vents***."

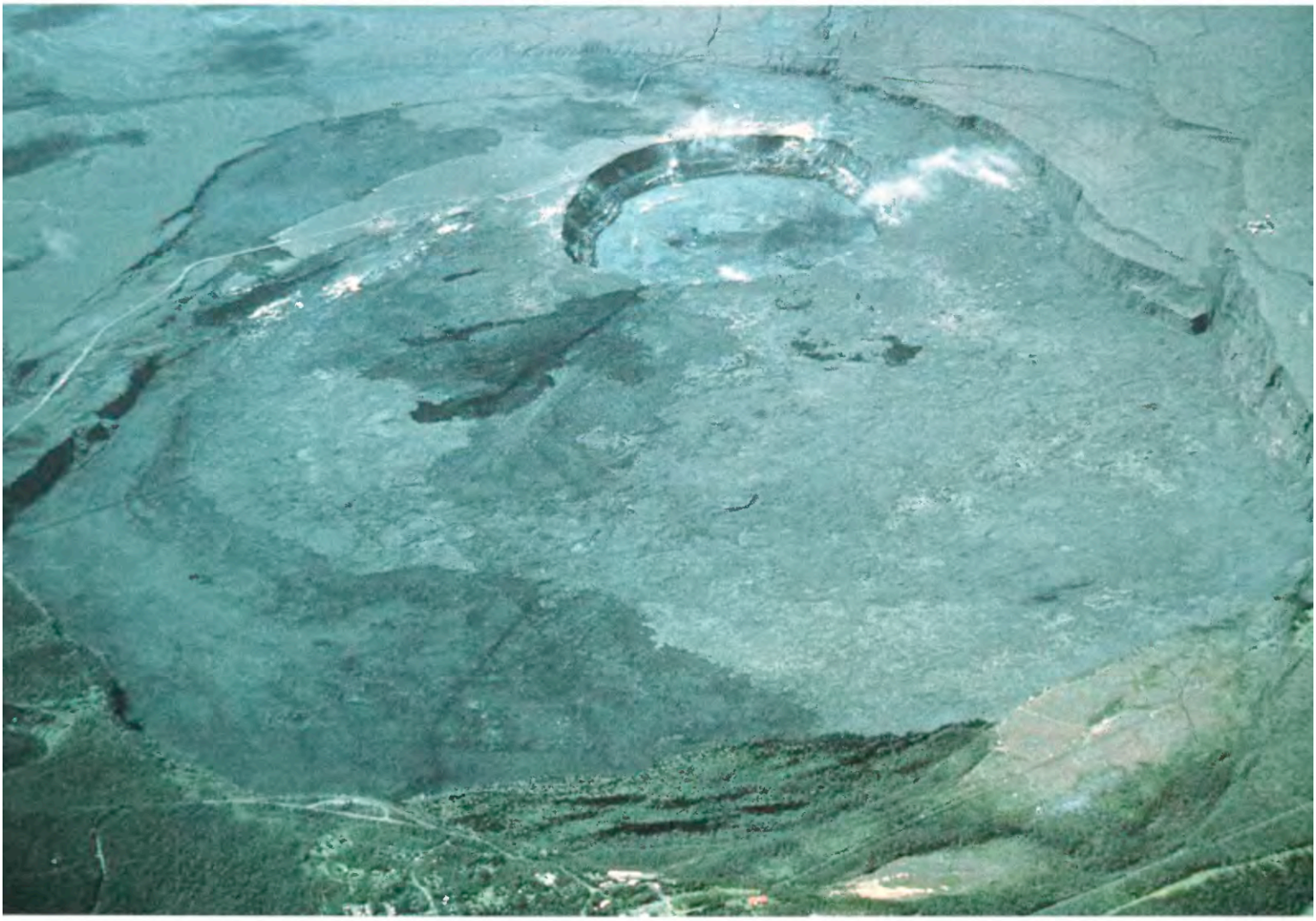

Aerial view of Kilauea Volcano summit caldera; the view is to the southwest. The caldera is 4.5 km by 3 km, and Halemaumau Crater, in the upper center, is 1 km in diameter (January 10, 1985, J.D. Griggs).

## Channel

"A narrow, sinuous flow channel, commonly formed in lava flows."

Aerial view of a flow in a lava channel (top), northeast rift zone of Mauna Loa Volcano; the view is to the south. The direction of the flow is from left to right, and the channel width is approximately 6 m (April 4, 1984, J.D. Griggs). Lava channel wall (bottom), July 1974 flow, Kilauea caldera. The height of the wall is approximately 1.5 m (November 11, 1984, T.J. Takahashi).

## Channel

Lava channel at a low flow level, northeast rift zone of Mauna Loa Volcano. The channel is approximately 1 m wide at the top, widening to more than 2 m below the overhang, and is 2.5 m deep to the flow level (April 4, 1984, M.L. Summers).

## Cinder cone

"A conical hill formed by the accumulation of cinders and other pyroclasts, normally of basaltic or andesitic composition."

Puu ka Pele cinder cone, Humuula Saddle; the view is to the west. This Mauna Kea cone is 95 m in height, and the diameter of the bowl-like depression is 400 m. Hualalai Volcano is in the background (December 1, 1975, J.P. Lockwood).

## Curtain of fire

"A row of coalescing lava fountains along a fissure; a typical feature of a Hawaiian-type eruption" (Macdonald, 1972, p. 214).

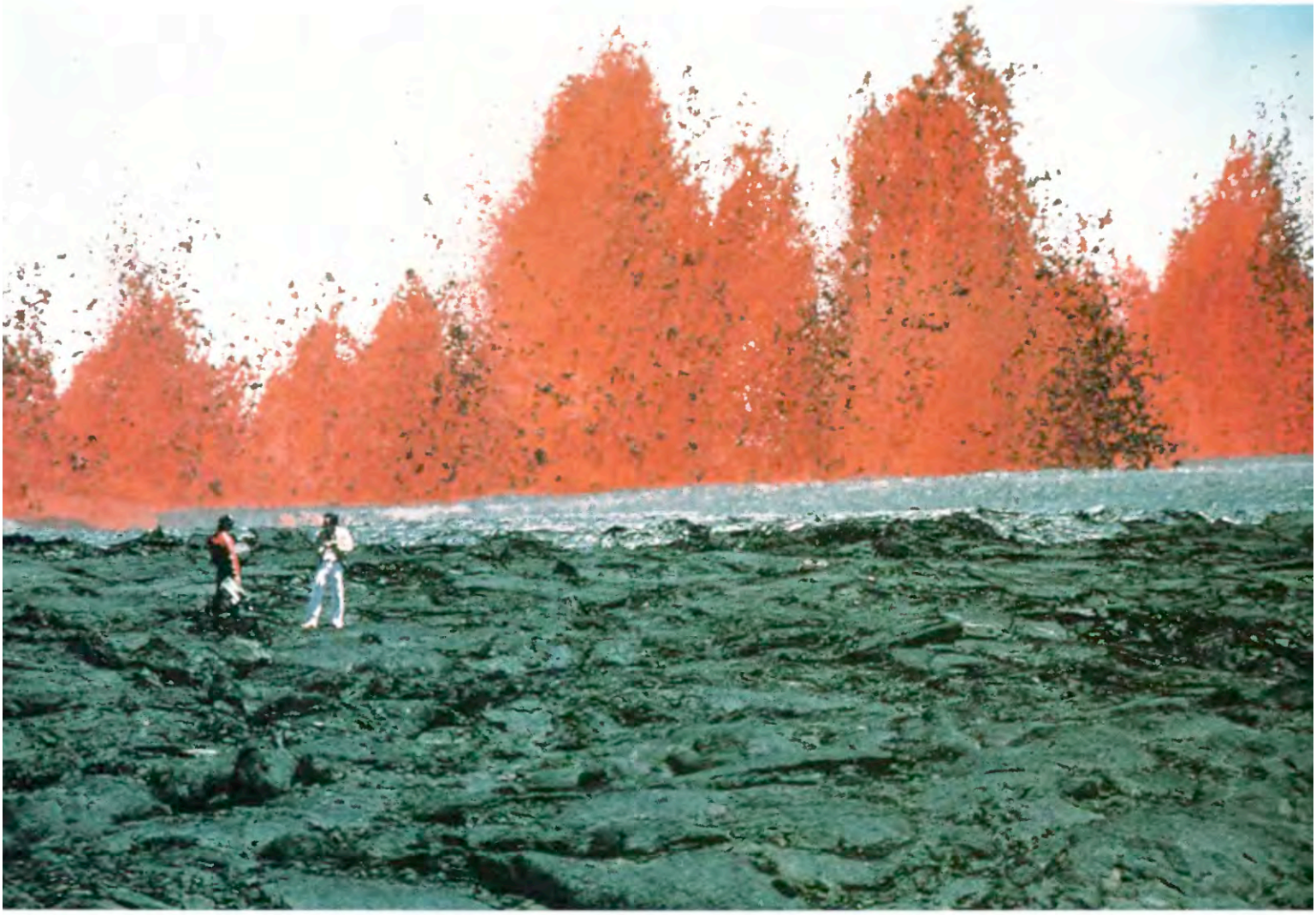

Curtain of fire along the northeast rift zone of Mauna Loa Volcano; the view is to the south. The height of the fountain is approximately 25 m (March 25, 1984, R.B. Moore).

## Dike

"A tabular igneous intrusion that cuts across the bedding or foliation of the country rock."

Dike (1.5 m wide), now mostly covered by 1984 lava drapery, cutting the northeast wall of Lua Poholo, Mauna Loa Volcano (March 1983, J.P. Lockwood).

## Dome fountain

Hemispherically shaped lava fountain that is approximately in equilibrium between the upward pressure of magma from the conduit below and the mass of ponded lava through which the fountain rises. It normally occurs in a low-energy and gas-poor eruptive state and may be several tens of meters high.

Dome fountain formed during the eruption of Mauna Ulu, east rift zone of Kilauea Volcano. The height of the dome is 20 m (October 11, 1969, J.B. Judd).

## Drainback

Lava that returns to the subsurface by flowing into an open fissure, especially lava that, in the late phases of an eruption, reverses its normal direction of movement and flows back into the eruptive fissure that was its vent. It commonly forms dripstone features on the walls of the fissure, showing its downward flow direction.

Drainback into a fissure near the west lip of Aloi Crater, east rift zone of Kilauea Volcano (June 29, 1970, D.A. Swanson).

## Drainback

Congealed drainback into 1971 fissure, Kilauea caldera (October 1964, T.J. Takahashi).

## Echelon

"Said of geologic features that are in an overlapping or staggered arrangement, e.g. faults. Each is relatively short but collectively they form a linear zone, in which the strike of the individual features is oblique to that of the zone as a whole."

Aerial view of fountains along echelon fissures on the northeast rift zone of Mauna Loa Volcano. Pohaku Hanalei cinder-spatter cone is at the upper left (March 25, 1984, J.D. Griggs).

## Fault scarp

"A steep slope or cliff formed directly by movement along a fault and representing the exposed surface of the fault before modification by erosion and weathering."

Aerial view of Puu Kapukapu, south flank of Kilauea Volcano; the view is to the northeast. Maximum height of the scarp is 320 m (June 24, 1971, D.A. Swanson).

## Fumarole

"A vent, usually volcanic, from which gases and vapors are emitted; it is characteristic of a late stage of volcanic activity ***. Fumaroles may occur along a fissure or in apparently chaotic clusters or fields."

Fumarole near Steaming Bluff, summit of Kilauea Volcano; the view is to the west. The vent is approximately 1.5 m wide. Mauna Loa shield is in the background (October 1984, J.D. Griggs, personal collection).

## Fume cloud

"A vaporous cloud of volcanic gases from a body of molten lava."

Fume cloud from the northeast rift zone of Mauna Loa; the view is to the southwest (April 2, 1984, J.D. Griggs).

## Kipuka

"An area surrounded by a lava flow."

Aerial view of kipuka in 1955 flow, east rift zone of Kilauea Volcano. Whitish cast is lichen growing on lava (1977, R.B. Moore).

## Laccolith

"A concordant igneous intrusion with a known or assumed flat floor and a postulated dikelike feeder commonly thought to be beneath its thickest point. It is generally planoconvex in form and roughly circular in plan***."

Aerial view of Uwekahuna Bluff on the north caldera wall (150 m high) at the summit of Kilauea Volcano. The laccolith is the light-colored lenticular area at the base of the caldera wall, along the middle left side of the photograph (September 1977, R.B. Moore).

## Lava bomb

"A pyroclast that was ejected while viscous and received its rounded shape while in flight. It is larger than 64 mm in size, and may be vesicular to hollow inside."

Lava bombs collected from above Hale Pohaku, Mauna Kea Volcano (July 10, 1982, J.P. Lockwood).

## Lava cascade

"A cascade of fluid, incandescent lava, formed when a lava river passes over a cliff or steep part of its course."

Cascade into Aloi Crater, east rift zone of Kilauea Volcano. The approximate height of the cascade is 25 m, and the height of fountain in the background is 30 m (December 30, 1969, D.A. Swanson).

## Lava coils

"Voluted [spiral or scroll-shaped] strips of lava" along a shear zone (Peck, 1966, p. B148).

Lava coils formed during the eruption of Puu Kiai, east rift zone of Kilauea Volcano. Lens cap used for scale is 55 mm in diameter (May 13, 1978, R.B. Moore).

## Lava drapery

A congealed lava cascade (see also **lava cascade**).

Lava drapery over the September 1971 fissures from the eruption in Kilauea caldera. The drapery from the top of the fissure to the fern (center right of photograph) is approximately 1 m (November 11, 1984, T.J. Takahashi).

## Lava fountain

"A jet of incandescent lava, shot into the air as the magma reaches the surface by the hydrostatic pressure on the liquid and the expansion of gas bubbles forming in it. Fountains usually range from about 10 to 100 m in height, but occasionally reach 300 m. They are characteristic of Hawaiian-type eruptions."

Lava fountains of Puu Halulu (formerly known as "1123 vent"), east rift zone of Kilauea Volcano; the view is to the northeast. The approximate height of the fountains is 350 m (April 4, 1983, J.D. Griggs).

## Lava lake

"A lake of molten lava, usually basaltic, in a volcanic crater or depression. The term refers to solidified and partly solidified stages as well as to the molten, active lava lake."

View at night of the west pit of Makaopuhi Crater, east rift zone of Kilauea Volcano. The depth of the crater before the eruption was approximately 310 m, and the depth of the lake during this phase was 42 m (March 3, 1965, D.P. Hill).

View in daylight of the lava lake in the west pit of Makaopuhi Crater, east rift zone of Kilauea Volcano (March 11, 1965, D.L. Peck).

## Lava tree

A sheath of solidified lava, roughly cylindrical in shape, formed when fluid pahoehoe quickly surrounds a living tree and chills against it; when the molten lava drains away, the lava that congealed against the tree stands in relief above the flow surface (Lockwood and Williams, 1978; Wentworth and Macdonald, 1953).

Lava trees formed during the eruption of Puu Kiai, November 1977, east rift zone of Kilauea Volcano. The height of the lava tree in the foreground is approximately 3 m (May 13, 1978, R.B. Moore).

## Lava-tree mold

"A cylindrical hollow in a lava flow formed by the envelopment of a tree by the flow, solidification of the lava in contact with the tree, and disappearance of the tree by burning and subsequent removal of the charcoal and ash. The inside of the mold preserves the surficial features of the tree."

Lava-tree mold (diameter 23 cm, depth 40 cm) formed during the eruption of Kilauea Iki, located along the Devastation Trail, Kilauea Volcano (October 1984, T.J. Takahashi).

## Lava tube

"A hollow space beneath the surface of a solidified lava flow, formed by the withdrawal of molten lava after the formation of the surficial crust."

Thurston Lava Tube, Kilauea Volcano. The height of the tube near the entrance is approximately 4 m (September 7, 1984, T.J. Takahashi).

## Pahoehoe

"A Hawaiian term for a type of basaltic lava flow typified by a smooth, billowy, or ropy surface. Varieties include corded, elephant-hide, entrail, festooned, filamented, sharkskin, shelly, and slab pahoehoe." Compare with **aa**.

Fluid pahoehoe flow (top) on the south-southwest flank of Alae Crater, east rift zone of Kilauea Volcano (December 14, 1972, D.W. Peterson). Detail (bottom) of pahoehoe from Mauna Ulu flow, east rift zone of Kilauea Volcano (October 1984, J.D. Griggs, personal collection).

## Pele's hair

"A natural spun glass formed by blowing-out during quiet fountaining of fluid lava, cascading lava falls, or turbulent flows, sometimes in association with **Pele's tears**. A single strand, with a diameter of less than half a millimeter, may be as long as two meters."

Pele's hair from the eruption of Mauna Ulu, east rift zone of Kilauea Volcano (March 27, 1984, D.W. Peterson).

## Pele's tears

"Small, solidified drops of volcanic glass behind which trail pendants of Pele's hair. They may be tear-shaped, spherical, or nearly cylindrical."

Pele's tears collected from Hilina Pali Road, south flank of Kilauea Volcano, carried westward by wind during the eruption of Mauna Ulu, 1969–74 (November 1984, J.D. Griggs).

## Perched lava pond

An impounded body of pahoehoe lava whose margins consist of chilled lava-flow fronts or spatter ramparts formed earlier in the same or in a previous eruption. The surface of the pond is thus retained at a higher (perched) level one or more meters above the surrounding surface.

Aerial view of the perched lava pond on the north flank of Mauna Ulu satellite shield, east rift zone of Kilauea Volcano; the view is to the south. The diameter of the pond is 130 m (September 1984, T.J. Takahashi).

## Pillow lava

"A general term for those lavas displaying pillow structure and considered to have formed in a subaqueous environment; such lava is usually basaltic or andesitic."

Pillow lava formed where a 3,500-year-old flow poured into the lower Wailuku River, Hilo. Note river conglomerate at the base of the pillows (pick used for scale is 30 cm long) (June 14, 1982, J.P. Lockwood).

## Pit crater

"A crater formed by sinking in of the surface; not primarily a vent for lava" (Macdonald and Abbott, 1977, p. 419).

Aerial view of Makaopuhi Crater on the east rift zone of Kilauea Volcano; the view is to the south. The crater is 1.5 km by 1 km, with a maximum depth of 150 m at the north wall. Flows from the eruption of Mauna Ulu (1969–74) are at the upper right (January 10, 1985, J.D. Griggs).

## Pressure ridge

"An elongate uplift of the congealing crust of a lava flow, probably due to the pressure of underlying still-flowing lava."

Pressure ridge along the western margin of the September 1982 flow, Kilauea caldera. The approximate height of the ridge is 1.5 m (November 1984, T.J. Takahashi).

## Reticulite

"Basaltic pumice; also called 'thread-lace scoria'" (Macdonald and Abbott, 1977, p. 419).

Reticulite collected from Hilina Pali Road, south flank of Kilauea Volcano, blown westward by wind during the eruption of Mauna Ulu, 1969–74 (October 1984, J.D. Griggs).

## Rift zone

"In Hawaii, a zone of volcanic features associated with underlying dike complexes."

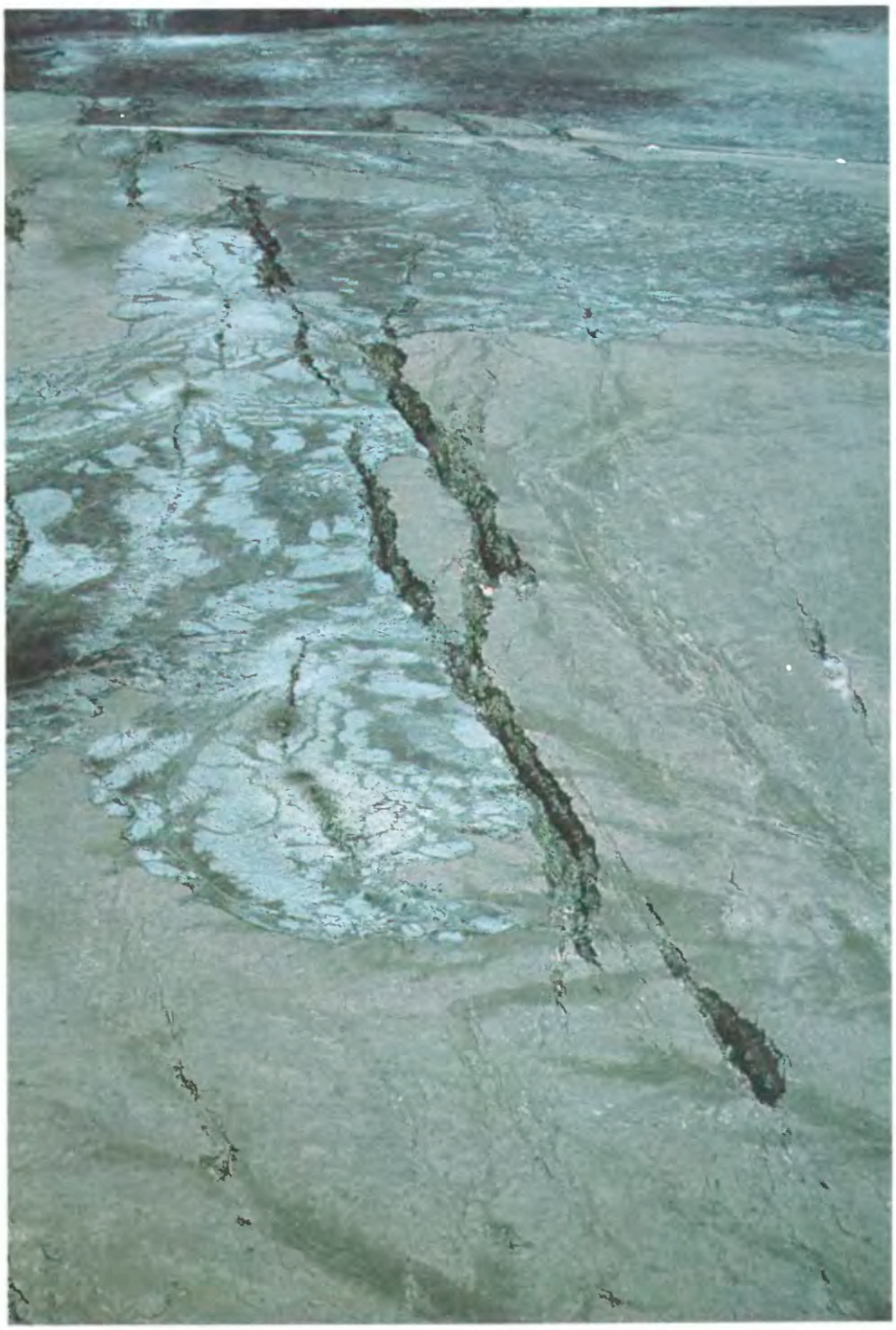

Aerial view of the upper southwest rift zone of Kilauea Volcano; the view is to the east. Crater Rim Drive and Halemaumau Crater are seen across the top of the photo. Darker flows are from the 1971 eruption (March 4, 1985, J.D. Griggs).

## Shield volcano

"A volcano in the shape of a flattened dome, broad and low, built by flows of very fluid basaltic lava***."

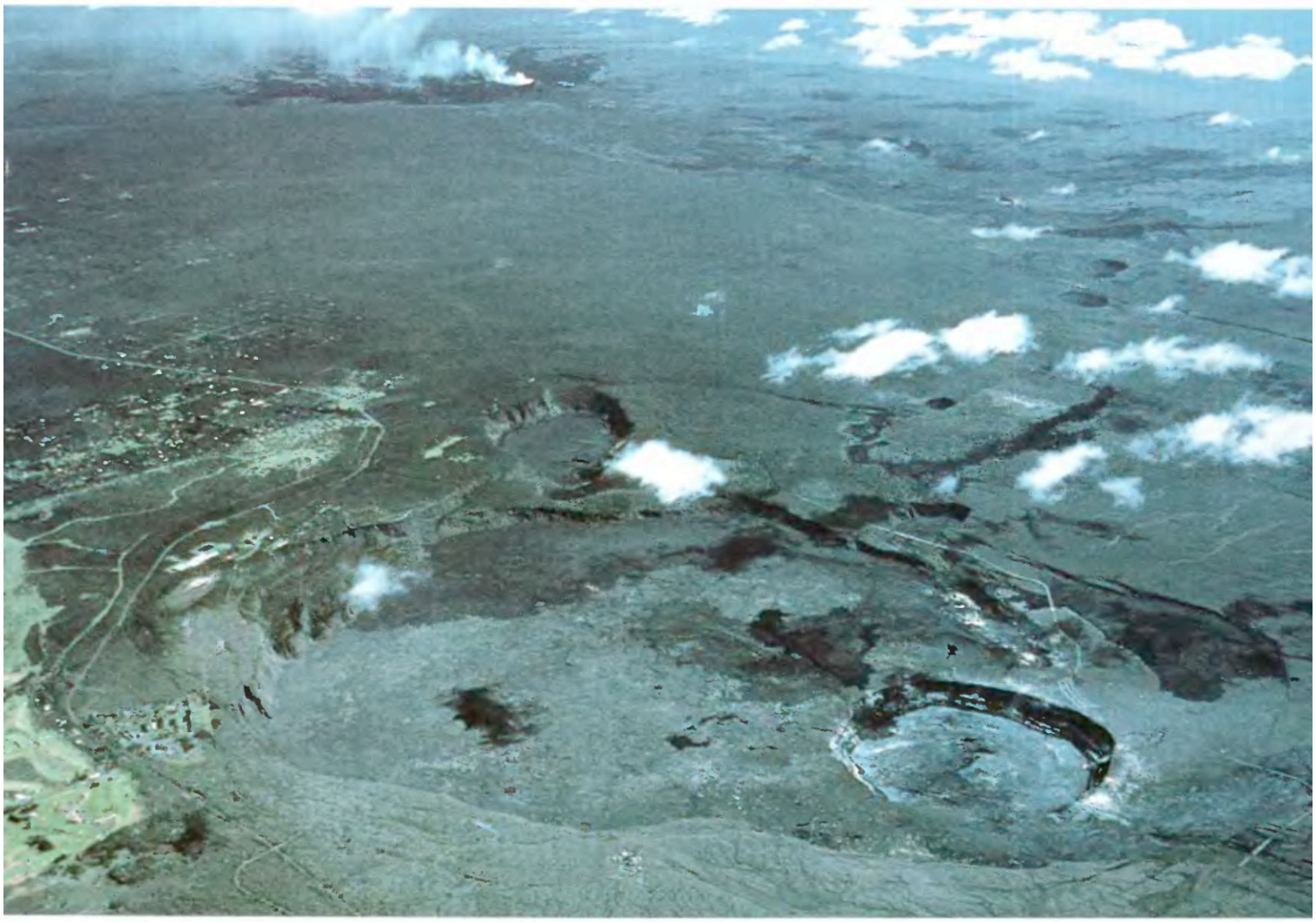

Aerial view of Kilauea Volcano from the summit to the east rift zone, with Puu Oo fuming in the background and Hawaiian Volcano Observatory in the center foreground (January 10, 1985, J.D. Griggs).

## Shield volcano

Aerial view of the summit and the northeast rift zone of Mauna Loa Volcano; the view is to the west-northwest. Darker areas are younger flows; the summit of Hualalai Volcano is in the upper right background (January 10, 1985, J.D. Griggs).

## Skylight

An opening, formed by collapse, in the roof of a lava tube.

Skylight at Mauna Ulu, east rift zone of Kilauea Volcano (May 2, 1983, R.L. Christiansen).

## Solfatara

"A type of fumarole, the gases of which are characteristically sulfurous."

Solfatara on the east rift zone of Kilauea Volcano (May 6, 1983, J.D. Griggs, personal collection).

## Spatter

"An accumulation of very fluid pyroclasts, coating the surface around a vent."

Spatter caught in a tree, west of Hilina Pali, south flank of Kilauea Volcano (May 5, 1973, D.W. Peterson).

## Spatter cone

"A low, steep-sided cone of spatter built up on a fissure or vent; it is usually of basaltic material."

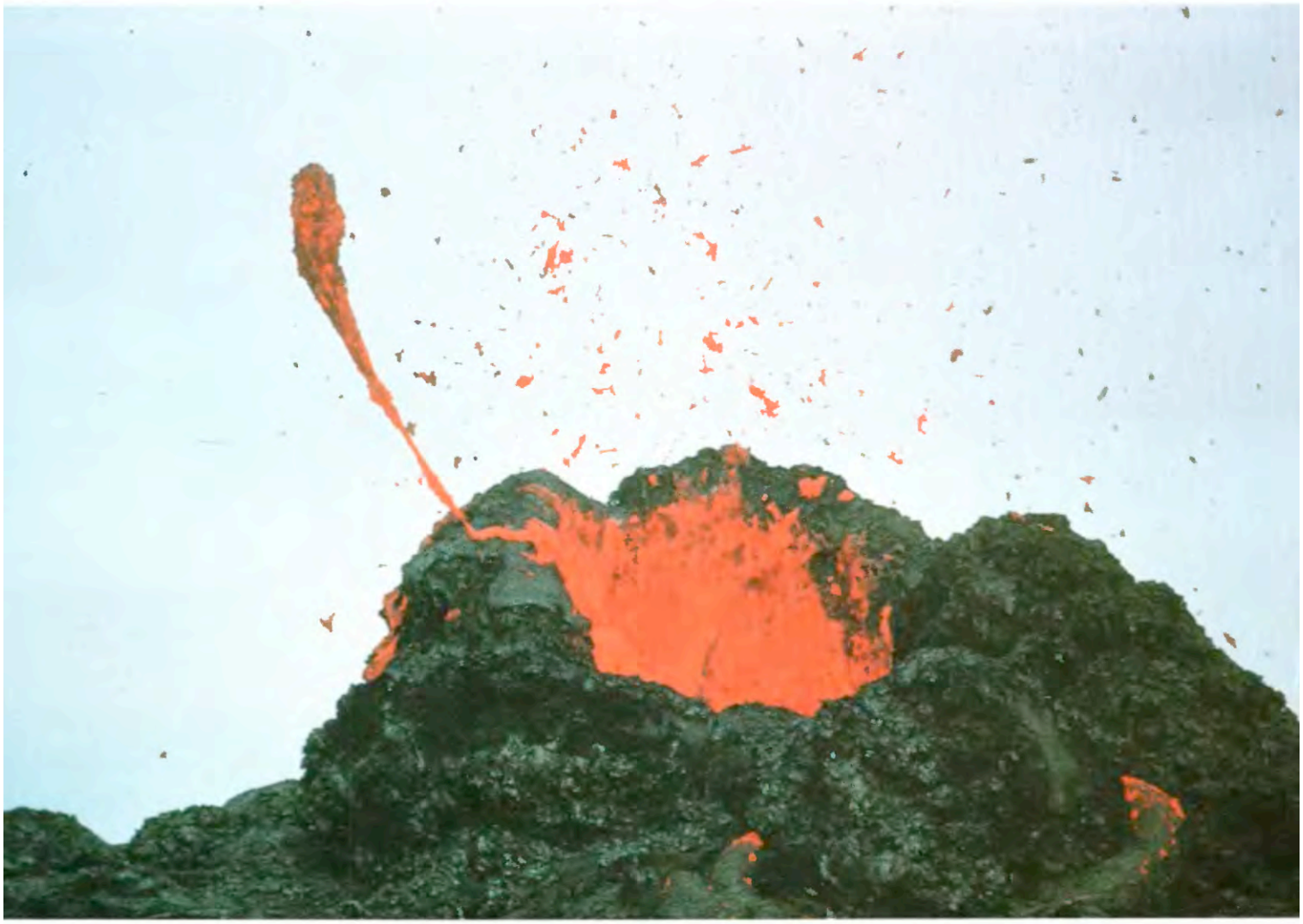

Spatter cone formed during the April 30, 1982, eruption in Kilauea caldera. The approximate diameter of the vent is 2 m (April 30, 1982, T.T. English).

## Spatter rampart

A ridge of congealed pyroclastic material, usually basaltic, built up on a fissure or vent.

View of fountains along a spatter rampart, the principal vents of the 1984 eruption on Mauna Loa Volcano's northeast rift zone, looking northwest (March 26, 1984, J.D. Griggs).

## Spillway

"Overflow channel."

Spillway of Puu Oo cinder-spatter cone on the east rift zone of Kilauea Volcano (spillway is on the northeast side). The height of the cone during this episode was 20–30 m (June 16, 1983, E.W. Wolfe).

## Squeeze-up

"A small extrusion of viscous lava, or toothpaste lava, from a fracture or opening on the solidified surface of a flow, caused by pressure."

Squeeze-up (length 64 cm; width 18 cm) from September 1982 flow, Kilauea caldera (November 25, 1984, T.J. Takahashi).

## Standing wave

"A *** wave, the wave form of which oscillates vertically between two points or nodes, without progressive movement."

Standing waves in lava channel, east rift zone of Kilauea Volcano. The height of the wave is approximately 2–3 m (November 6, 1983, C.A. Neal).

## Step fault

"One of a set of parallel, closely spaced faults over which the total displacement is distributed***."

Aerial view of step faults on the northwest caldera wall at the summit of Kilauea Volcano. Hawaiian Volcano Observatory is at the upper right (January 10, 1985, J.D. Griggs).

## Surge

"A transient increase, of variable duration and magnitude, in the volume flux of a lava flow. Some surges are caused by the sudden release of lava ponded upstream. Surges usually result in the acceleration of the flow front and may produce thin, short-lived breakouts of fluid lava" (Neal and Decker, 1983).

Aa surge, Royal Gardens, Kalapana, east rift zone of Kilauea Volcano. The direction of the flow is from right to left. The height of the glowing area of the surge is approximately 6 m (June 16, 1984, R.W. Decker).

## Tension crack

"A fracture caused by tensile stress" (**Tensile stress**: "A normal stress that tends to cause separation across the plane on which it acts").

The magnitude 6.6 earthquake on November 16, 1983, caused a landslide of sections of the north rim into Kilauea caldera. Tension cracks are at the top of the landslide; the view is to the east from the northeast rim of Kilauea caldera (November 16, 1983, J.D. Griggs).

## Tephra

"A general term for all pyroclastics of a volcano."

Tephra fall (dark material) from Puu Oo, east rift zone of Kilauea Volcano; the view to the east from Puu Kamoamoa (October 5, 1983, J.D. Griggs).

## Tumulus

"A doming or small mound on the crust of a lava flow, caused by pressure due to the difference in rate of flow between the cooler crust and the more fluid lava below. Unlike a *blister* *** it is a solid structure."

Tumulus on Hilina Pali Road, south flank of Kilauea Volcano. The approximate diameter of the base of the tumulus is 10 m (September 23, 1984, J.D. Griggs, personal collection).

## Vent

"The opening at the Earth's surface through which volcanic materials are extruded***."

Aerial view of Puu Oo vent (left) during the period between eruptive episodes, east rift zone of Kilauea Volcano; the view is to the southwest. Note scientists at the edge of the vent, which is 20–25 m wide and approximately 10 m deep to the incandescent area (January 24, 1985, J.D. Griggs). Aerial view of Puu Oo vent (right) at the end of an eruptive episode, east rift zone of Kilauea Volcano; the view is from the north side of the cone (April 22, 1985, J.D. Griggs).

## Xenolith

"A foreign inclusion in an igneous rock."

Lava-encrusted xenoliths collected from Hualalai Volcano. The sample on the left is 14 cm long and that on the right, 10 cm across (November 1984, J.D. Griggs).

# GEOPHYSICAL CONSTRAINTS ON THE STRUCTURE OF KILAUEA AND MAUNA LOA VOLCANOES AND SOME IMPLICATIONS FOR SEISMOMAGMATIC PROCESSES

*By* David P. Hill *and* John J. Zucca[1]

ABSTRACT

**Seismic-refraction and gravity data on and adjacent to Kilauea and Mauna Loa Volcanoes show that the Cretaceous oceanic crust bends downward beneath the load of the volcanic edifice. Dip on the base of the crust (*M*-discontinuity) increases from 3° under the submarine flanks of the volcanoes to 6°–10° under the subaerial flanks; depth to the *M*-discontinuity increases from about 10 km beneath the open ocean to roughly 13 km and 18 km beneath the high, subaerial flanks of Kilauea and Mauna Loa, respectively. This profile of the oceanic crust is consistent with flexural-lithosphere models for flexural response to the load of the volcanoes. *P*-wave velocity structure of the volcano flanks supports the Moore-Fiske model for the volcanic pile, in which an inner wedge of submarine pillow basalt is covered by a mantle of halyoclastics and subaerial basalt flows. Fast *P*-wave traveltimes and positive gravity anomalies over rift zones and summit vent indicate that dense, intrusive cores to these structures form a significant mass-fraction of the volcanic edifice. The triangular shape of these intrusive cores supports the view that the volcanoes grow in part by the spreading of unbuttressed flanks along subhorizontal decoupling surfaces near the base of the volcanic pile in respones to forceful magma intrusion into the rift zones.**

## INTRODUCTION

The internal structure of the Hawaiian volcanoes and the underlying oceanic lithosphere hold important clues to processes governing the growth and contemporary seismomagmatic activity of these massive, midoceanic, basaltic shield volcanoes. Kilauea and Mauna Loa on the Island of Hawaii are of special interest in this regard because, together with Loihi Seamount 55 km south of Kilauea's summit, they are the youngest and most active volcanoes in the Hawaiian-Emperor volcanic chain, and they mark the present position of the Hawaiian hot spot beneath the Pacific plate (see Clague and Dalrymple, chapter 1).

Eaton (1962) first developed a model for the crustal structure of the Island of Hawaii using the traveltimes of *P*-waves recorded on seven seismic stations located at distances of 18–390 km from two magnitude 5 earthquakes that occurred beneath the southeast flank of Kilauea in 1955. His resulting one-dimensional model (velocity varying with depth only) for the average crustal structure of the Island of Hawaii indicated that the volcanoes forming the island rest on a slightly thickened oceanic crust, with the Mohorovicic (*M*) discontinuity at a depth of 14–15 km and with the upper most mantle having a *P*-wave velocity of 8.25 km/s. More recent efforts by Ward and Gregersen (1973), Crosson and Koyanagi (1979), and Klein (1981) to define an average velocity structure for Hawaii in terms of one-dimensional models are based on *P*-waves from a large number of local earthquakes recorded on an increasingly dense seismograph network. These models all place the *M*-discontinuity at depths between 13 and 16 km and indicate an upper mantle velocity of 8.2–8.3 km/s, in general agreement with Eaton's initial model. In these more recent models, however, the average depth to intermediate *P*-wave velocities (6.5–6.8 km/s) is significantly shallower (5–6 km) than the 11 km in Eaton's (1962) model.

An image of the three-dimensional structure of the Hawaiian volcanoes began to come into focus with the gravity survey of Hawaii by Kinoshita and others (1963), the series of seismic-refraction measurements around the island by Ryall and Bennett (1968), Hill (1969), Zucca and Hill (1980), and Zucca and others (1982), and the study of teleseismic *P*-wave delays by Ellsworth and Koyanagi (1977). Results from these experiments indicate that the central vents and rift zones of Kilauea and Mauna Loa are underlain by dense cores of intrusive rocks having high *P*-wave velocities (6.5–7.4 km/s) and reaching to within a few km of the surface; they further indicate that these intrusive cores represent a significant fraction of the volume of the volcanic pile forming the Island of Hawaii.

In this paper we reexamine some of the evidence from seismic-refraction experiments and gravity measurements on the structure of Kilauea and Mauna Loa Volcanoes. We will focus in particular on evidence concerning (1) the relation of the volcanic pile formed by the volcanoes to the underlying Cretaceous oceanic crust (upper lithosphere) and (2) the geometry of the dense intrusive masses forming cores beneath the summit vents and rift zones. We conclude

[1]Lawrence Livermore National Laboratory, Livermore, CA 94550.

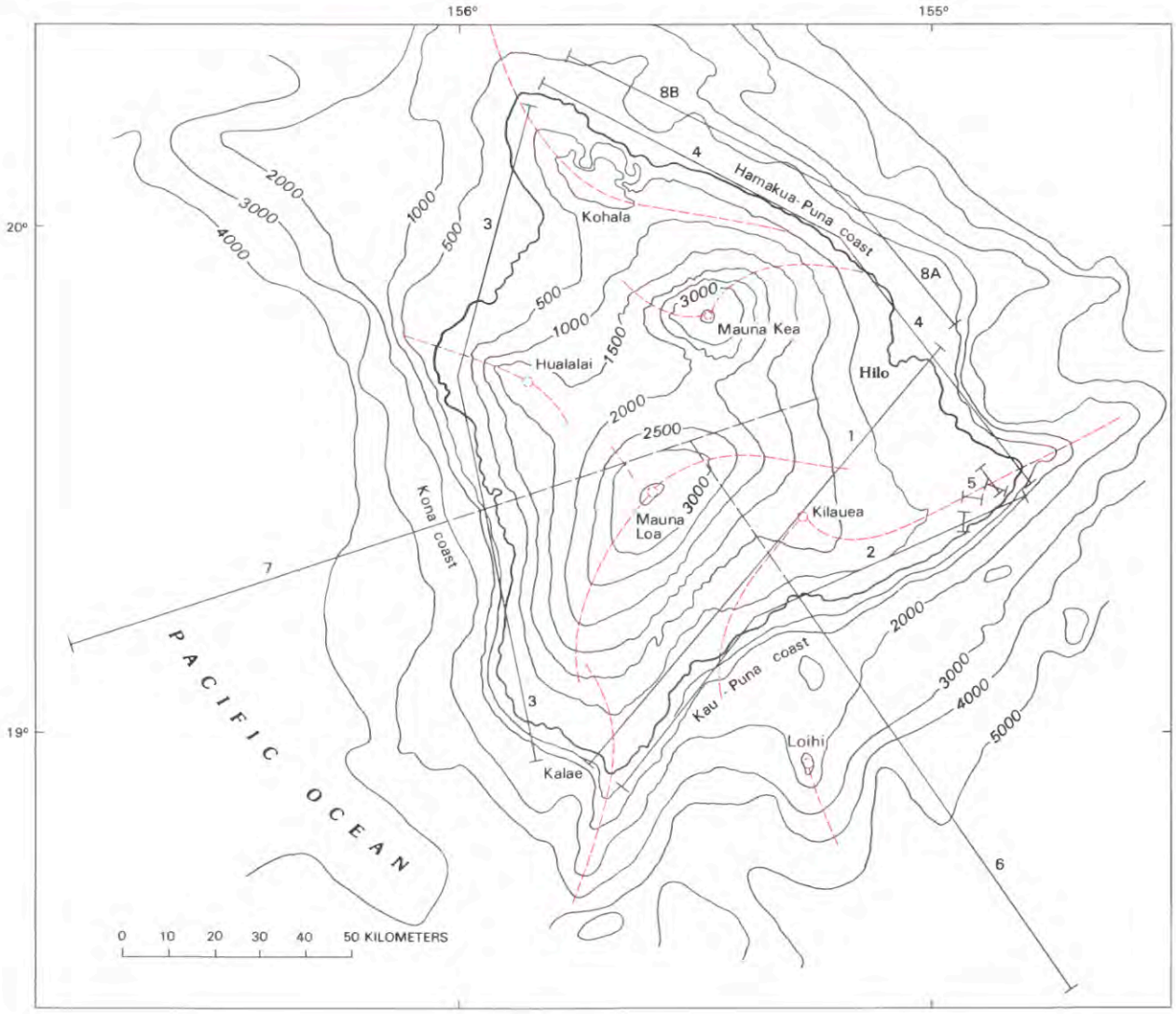


FIGURE 37.1.—The Island of Hawaii showing location of seismic-refraction profiles identified by number: 1, Ryall and Bennett (1968); 2–4, Hill (1969); 5, Broyles and others (1979); 6, Zucca and Hill (1980); 7, Zucca and others (1982); 8A–8B, Pollard and Eaton (1964). Dashed red lines, major rift zones. Elevation and depth contours in meters; contour interval 500 m on land, 1,000 m offshore.

with some thoughts on the significance of these structures for the processes governing the growth of Kilauea and Mauna Loa.

### ACKNOWLEDGMENT

We are grateful to Alan Ryall for providing the traveltime data from the Hilo and Kaloe shot points.

## SEISMIC-REFRACTION PROFILES

The locations of seismic-refraction profiles on and adjacent to the Island of Hawaii are shown in figure 37.1. With the exception of some of the short profiles across Kilauea's east rift zone done by the University of Hawaii (Broyles and others, 1979), all of the profiles were established using offshore shot points and onshore recording arrays. The permanent stations of the Hawaiian Volcano Observatory (HVO) seismic network form a common recording array for all of the profiles, although the number of stations in this array increased for successively later experiments as the HVO network grew with time (see Klein and Koyanagi, 1980). Additional portable stations were used to record the shots at either end of the profile across the summit of Kilauea (Ryall and Bennett, 1968), the series of shots forming the three coastal profiles (Hill, 1969), and the

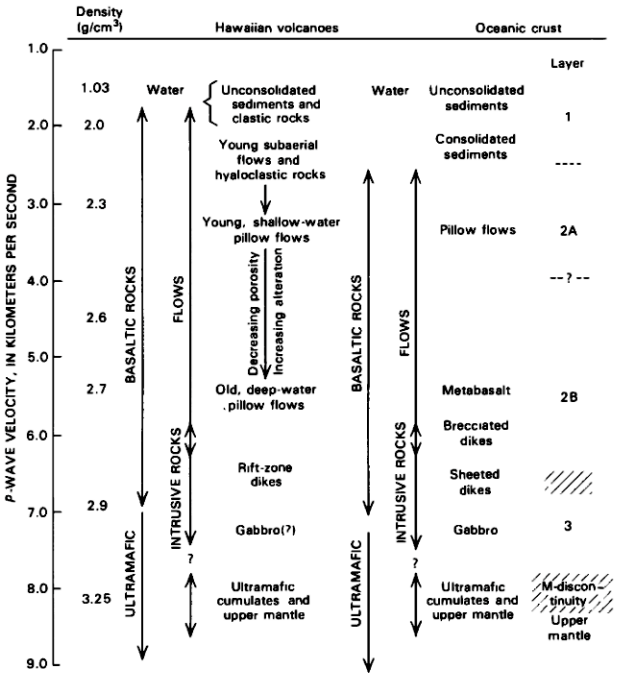


FIGURE 37.2.—Relation between $P$-wave velocity, rock density, and rock type for Hawaiian volcanoes and for oceanic crust. Density is used to compute gravity profiles in figures 37.7 and 37.8 (see Zucca and others, 1982). Moho is the M-discontinuity.

Mauna Loa offshore profile (Zucca and others, 1982). The series of shots perpendicular to the Kau-Puna coast (fig. 37.1, profile 6) were also recorded by two ocean-bottom seismographs deployed along the profile by the University of Hawaii (see Zucca and others, 1979).

These approximately linear seismic-refraction profiles are intrinsically two-dimensional. The internal structure of the volcanoes, however, is dominated by a roughly conical symmetry about the central vents. Profiles that cut obliquely across this dominant structure will be complicated by lateral (out-of-plane) reflections and refractions. Distortion in the interpretation from such out-of-plane ray paths will be more of a problem for coastal profiles than for profiles oriented radial to the central vents.

$P$-wave velocity structure serves as an important guide to subsurface rock types and geologic structure. The association of $P$-wave velocities with the rock types that we used in this paper for Kilauea and Mauna Loa Volcanoes and for the adjacent Cretaceous oceanic crust is illustrated in figure 37.2. This association is based on (1) published values of seismic velocities for rocks compiled by Christensen (1982), (2) petrographic models of the oceanic crust as described by Salisbury and Christensen (1978), and (3) recognition that the Hawaiian volcanoes consist almost entirely of basaltic rocks. Note in particular that $P$-wave velocities ranging from less than 2.0 km/s to more than 6.5 km/s on the Hawaiian volcanoes primarily reflect the wide variation in bulk porosity (bulk density) in rocks having essentially the same basaltic composition. The high bulk porosity in young, subaerial lava flows is produced by clinkery flow tops and bottoms, extensive sets of open fractures, large gas bubbles, and lava tubes; in older, deep-water pillow flows the porosity is reduced by alteration products that largely fill vesicles and cracks, and in basaltic dikes it is limited to small vesicles and intercrystalline cracks with dimensions of micrometers or less.

## VOLCANIC FLANKS AND THE OCEANIC CRUST

The two offshore profiles that extend radially away from the volcanic centers (fig. 37.1, profiles 6, 7) define the base of the oceanic crust (the $M$-discontinuity) from the open ocean to the subaerial flanks of Kilauea and Mauna Loa. Interpretations of these profiles by Zucca and Hill (1980) and Zucca and others (1982), illustrated in figures 37.3 and 37.4, indicate that, beginning 50–60 km from shore, the oceanic crust dips at about 3° beneath the submarine flanks of the volcanoes. The depth to the $M$-discontinuity increases from 10–11 km beneath the unperturbed oceanic crust at distances greater than 50 km from the island to about 13 km under the southeast coast of Kilauea on the Island of Hawaii and 14–15 km under the west coast of Mauna Loa. Zucca and others (1982) inferred that the dip on the base of the crust increases toward the center of the island and is nearly 9° under the west (Kona) coast of Mauna Loa.

Structural details of the unperturbed oceanic crust beyond the submarine flank of Hawaii remain poorly resolved. The Mauna Loa radial profile does not have reversed seismic-refraction coverage, nor does the seaward half of the Kilauea radial profile. The structure for the oceanic crust shown in figures 37.3 and 37.4 is simply a seaward horizontal extension of the structure found for the oceanic crust beneath the distal end of the volcanic wedge in each case. For the Kilauea profile, this structure is based on reversed and overlapping

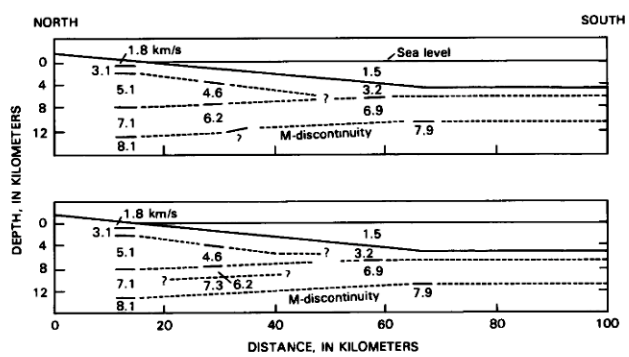


FIGURE 37.3.—$P$-wave velocity structure for the offshore profile perpendicular to the Kau-Puna coast of Kilauea (profile 6 in fig. 37.1). Numbers on profiles indicate $P$-wave velocity in kilometers per second. Upper and lower profiles show alternate interpretations of the traveltime data. Heavy lines and velocities at left (beneath the shoreline) indicate structure along the Kau-Puna coast from Hill (1969). Adopted from Zucca and Hill (1980).

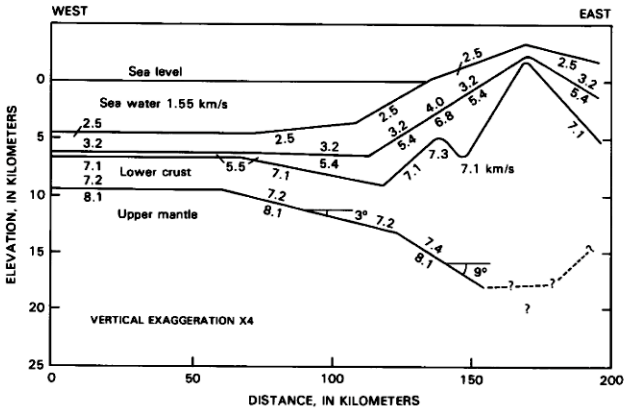


FIGURE 37.4.—*P*-wave velocity structure for the offshore profile perpendicular to the Kona coast of Mauna Loa (profile 7 in fig. 37.1). Inferred dip angle for base of crust shown for two parts of profile; other numbers on profile indicate *P*-wave velocity in kilometers per second. Adopted from Zucca and others (1982).

refraction coverage over the landward half of the profile (Zucca and Hill, 1982); for the Mauna Loa profile, however, it is based only on the overlapping (but unreversed) coverage provided by the array of onshore stations (Zucca and others, 1982). On the basis of the data from these profiles, we can say little more than the following: (1) The oceanic crust south and west of Hawaii is 5–6 km thick, with that west of Mauna Loa being slightly thinner than that southeast of Kilauea; (2) the *P*-wave velocity at the top of layer 2 is approximately 3.0 km/s, and layer 2 appears to be somewhat thicker west of Mauna Loa than it is southeast of Kilauea; and (3) the *P*-wave velocity in layer 3 (the deepest and thickest layer) is approximately 7.0 km/s. These data provide no direct information on the relatively thin sedimentary layer (layer 1) that covers the oceanic crust in the vicinity of the Hawaiian Islands (see Watts and others, 1985).

Our estimate of total thickness for the oceanic crust illustrated in figures 37.3 and 37.4 may be slightly low because the first arrival *P*-wave data did not sample the lower parts of layer 2. In most sections of the oceanic crust, the *P*-wave velocity in layer 2 increases rapidly with depth and averages about 5.6 km/s (see figure 37.2). If the average *P*-wave velocity in layer 2 in the vicinity of Hawaii is closer to 5.6 km/s than the 3.0–3.2 km/s value indicated by our first arrival data, we have underestimated the total crustal thickness by 1.0–1.4 km. In this case, the thickness of the oceanic crust off Hawaii is comparable to the 6.5-km thickness off of Oahu reported by Watts and others (1985).

The 7.9-km/s *P*-wave velocity for the uppermost mantle ($P_n$ velocity) derived from the offshore Kilauea profile (fig. 37.3) is slightly lower than the 8.0- to 8.4-km/s values determined elsewhere beneath the Island of Hawaii and along the Hawaii-Emperor chain (Furumoto and others, 1968; Watts and others, 1985). Because the 7.9-km/s value is based both on reversed traveltime branches over the submarine flank of Kilauea and on clear $P_n$ arrivals over the presumably flat oceanic crust beyond, we feel it is probably reliable. It is also consistent with evidence for anomalously low (by 1–2 percent) *P*-wave velocity in the top 35 km of the upper mantle off the southeast coast of Hawaii found by Ellsworth and Koyanagi (1977) in their three-dimensional inversion of teleseismic *P*-wave residuals recorded on Hawaii.

The wedge of volcanic products that forms the submarine flank of the volcanoes consists of an inner wedge having a *P*-wave velocity ranging from 4.6–5.4 km/s, which rests directly on the Cretaceous oceanic crust. Overlying this inner wedge is a blanket of material 1–3 km thick having a *P*-wave velocity of 3.0–3.2 km/s (see figs. 37.3, 37.4). This *P*-wave velocity structure is consistent with the model proposed by Moore and Fiske (1969) for the substructure of the volcano flanks from their study of dredge samples and ocean-bottom photographs. From the relation between *P*-wave velocities and rock types suggested in figure 37.2 and from the Moore-Fiske model, we infer that the inner wedge consists dominantly of deep-water pillow basalt and the overlying blanket consists dominantly of hyaloclastic rocks (vitric explosion debris, littoral-cone ash, and flow breccia). The shallower part of the 2.8–3.2-km/s layer probably also include young pillow flows and subaerial flows that have been submerged as the crust subsided in response to the growing load of the volcanoes.

Because we cannot distinguish the pillow flows and metabasalt forming layer 2 of the Cretaceous oceanic crust from the pillow flows and clastic rock that form the submarine flanks of the volcanoes on the basis of *P*-wave velocity (fig. 37.2), the position of the distal edge of volcanic debris from Kilauea and Mauna Loa remains ambiguous. The same is true for the position of the boundary between the bottom of the inner wedge of pillow lava and the top of layer 2. Moore (1964) has demonstrated that downslope movement in the form of massive submarine landslides is an important process on the steep submarine flanks of the Hawaiian volcanoes. This raises the possibility that the exceptional thickness of the 3.0-km/s layer in the oceanic crust off the coast of Mauna Loa (fig. 37.4) is due to accumulations of landslide debris extending well beyond the obvious break in slope at the distal end of the volcanic wedge.

The sections of the coastal seismic-refraction profiles interpreted by Hill (1969) that are not adjacent to major rift zones generally support the structural model for the flanks of the volcanoes based on the radial profiles just described (see fig. 37.5). Differences in structure between the coastal and radial profiles near their junction along the central section of the Kau-Puna coast are minor (figs. 37.3, 37.5).

Agreement between layer depths and *P*-wave velocities is not as close, however, for the coastal and radial profiles near their junction along the Kona coast on the west flank of Mauna Loa (see figs. 37.4, 37.5). The problem here probably lies with out-of-plane propagation paths complicating the two-dimensional interpretation of the coastal profile. This profile runs sub-parallel to a pronounced elongate gravity high located just inland of the Kona coast (see fig. 37.5), and it is likely that high *P*-wave velocity in the shallow crust associated with this gravity high provides a lateral, least-time path for seismic waves propagating between sources and receivers along the coast. Accordingly, we are inclined to place more confidence in the structure beneath the coast based on data from the radial profile

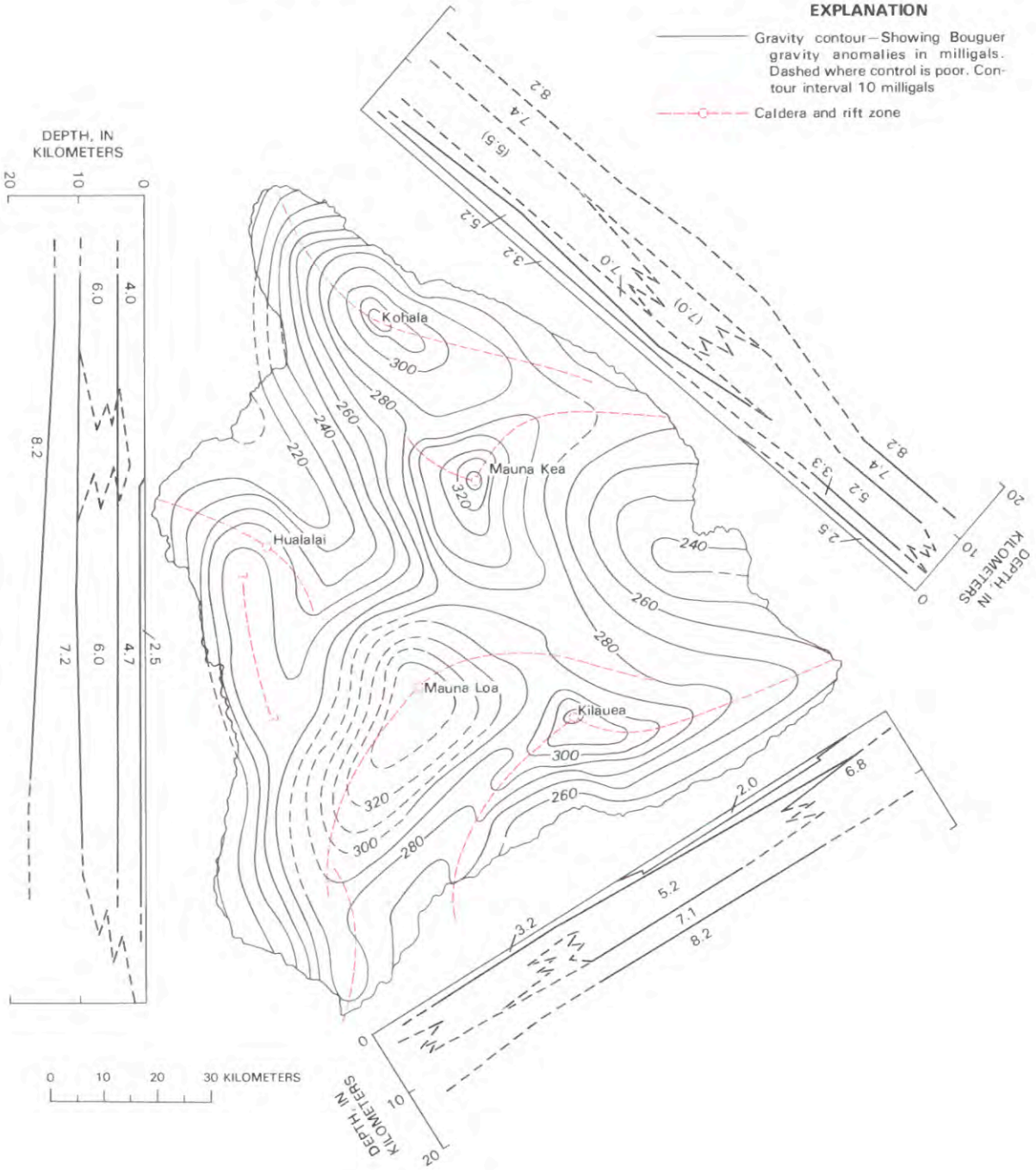


FIGURE 37.5.—Bouguer gravity map of Island of Hawaii (from Kinoshita and others, 1965) and *P*-wave velocity structure for the three coastal profiles (profiles 2–4 in fig. 37.1) around the island (adopted from Hill, 1969). Gravity contours dashed where control is poor; contour interval 10 milligals. Dashed red lines, major rift zones of the volcanoes.

(fig. 37.4) than in that based on the profile along the southern section of the Kona coast (fig. 37.5). In particular, we feel that the crustal thickness directly beneath the Kona coast west of Mauna Loa is closer to the 14 km indicated in figure 37.4 than to the 18 km indicated in figure 37.5 and that the layer depths and $P$-wave velocities for the southern section of the Kona profile in figure 37.5 give a poor image of the structure beneath the coast.

Results from profiles along the Hamakua-Puna coast (Hill, 1969) and from the Hilo-Kalae profile (Ryall and Bennett, 1968) indicate that the base of the crust deepens from about 13 km beneath Hilo to more than 15 km midway between Hilo and Kilauea and then appears to shallow again toward the summit region of Kilauea (figs. 37.1, 37.6). More than 10 km of effusive rocks with an average $P$-wave velocity of 5.3 km/s fill the resulting basin-like depression of the oceanic crust. This thick accumulation of rather porous flows is associated with a distinct gravity low centered just south of Hilo (fig. 37.5). Some of the deeper lava flows in this basin may be from Mauna Kea, but the bulk of the flows were probably fed by vents on Mauna Loa and, to a lesser degree, vents along the east rift zone of Kilauea. The increase in $P$-wave velocity from 3.3 to 5.2 km/s at about 2 km beneath the subaerial surface probably reflects reduced porosity due to alteration and compression; it is not necessarily the boundary between subaerial and pillow flows. Near intrusive cores, in particular, low-grade metamorphism between widely spaced dikes may markedly reduce the bulk porosity (and increase the $P$-wave velocity) in a mass dominated by hyaloclastic rocks and subaerial flows.

## RIFT ZONES

The major rift zones of Kilauea and Mauna Loa are marked by elongate ridges sloping away from the respective summits and by strong, elongate gravity highs closely coincident with the topographic ridges (see figs. 37.1, 37.5). Topographic expression of the rift zones on the older volcanoes of the Island of Hawaii (Mauna Kea, Hualalai, and Kohala) tends to be masked by lava flows from scattered vents that developed in the later evolutionary stages of the volcanoes, but the expression of these older rift zones in the gravity field remains clear. The strong, elongate gravity high extending southward from Hualalai subparallel to the Kona coast, for example, probably defines the location of an ancient rift zone (from Hualalai?) now buried by lava flows from Mauna Loa's actively growing west flank.

As is evident from figures 37.1 and 37.5, seismic-refraction data on the substructure of the rift zones are limited to profiles that either terminate in the vicinity of a rift zone or run subparallel to the axial trend of a rift zone. Taken together, these data provide a patchwork image for the rift-zone substructure. That the rift zones are underlain by rocks with high $P$-wave velocities is indicated by the uniformly early arrival times for $P$-waves propagating along ray paths that penetrate the rift zones. Apparent velocities for first-arrival traveltime curves on profiles that closely parallel rift zones, such as those along the eastern section of the Kau-Puna coast or the northern half of the Hamakua coast (fig. 37.1), are typically 6.5–7.3 km/s (see Hill, 1969, figs. 3, 5, 10). The waves propagating with these high apparent velocities have almost certainly followed laterally refracted ray paths. Nevertheless, reversed traveltime branches limit depths to the high-velocity rocks to no more than 2–5 km. Because of lateral refraction, the apparent depth to the high-velocity rift-zone rocks plotted in the cross sections in figure 37.5 should be regarded as a perpendicular distance (slant depth) between the average surface trace of the seismic-refraction profile and the subsurface flank of the adjacent rift zone. The series of short seismic-refraction profiles across Kilauea's lower east rift zone established by Broyles and others (1979) provides clear evidence that rocks with high $P$-wave velocities beneath the rift zones are at shallow depths. Their results indicate that, along the axis of the rift zone, rocks with $P$-wave velocites of 7.0 km/s lie at depths of only 2.1–2.3 km beneath recent lava flows with $P$-wave velocities averaging about 3.0 km/s.

Available seismic-refraction data provide only loose constraints on the deeper structure of rift zones. In general, it appears that the mass of intrusive rocks forming the high-velocity core of a rift zone broadens with both depth and proximity to the central vent of the volcano. Zucca and Hill (1980), for example, have used the pattern of $P_n$ delays recorded on selected stations of the HVO seismic network from the line of offshore shots southeast of Kilauea, together with average teleseismic residuals at the same stations reported by Ellsworth (1977), in an effort to put constraints on the deeper structure of the rift zones beneath Kilauea. The pattern of $P_n$ and teleseismic delays along a line of stations crossing the central section of the east rift zone indicates that the high-velocity core increases in breadth from about 2 km near the surface to perhaps 13–14 km at depths of 8–9 km, where it merges with the oceanic crust. Based on these sparse data, the sides of the high-velocity rift-zone core have an effective slope of 45°–50° (see Zucca and Hill, 1980, fig. 8). Results from a similar profile crossing the southwest rift zone and extending to the summit of Mauna Loa indicate that there the breadth of the high-velocity core increases more rapidly with depth (effective slope 30°–40°) and the rift-zone core merges with the massive high-velocity core associated with the central vent of Mauna Loa at a depth of 5 km or less (see Zucca and Hill, 1980, fig. 9).

The Bouguer gravity data for the Island of Hawaii (fig. 37.5) also suggest that the dense cores beneath the rift zones broaden with depth (Kinoshita and others, 1963; Broyles and others, 1979). Dense, closely spaced gravity measurements, however, currently stop at the shoreline, where both the topographic and gravity gradients are still quite steep. Until the gravity field is better defined offshore, beyond the steep gradients and the submarine flank of the volcanoes, it is hardly worth attempting to model the gravity field in terms of detailed three-dimensional density structure of the intrusive cores of the volcanoes.

## SUMMIT REGIONS AND CENTRAL CORES

The summits of both Mauna Loa and Kilauea contain large calderas, within which most summit eruptions occur. An elongate conduit system connects the summit vents and subjacent magma chamber located within the edifice of each volcano to magma sources in the upper mantle at depths of 40–60 km (Eaton and Murata,

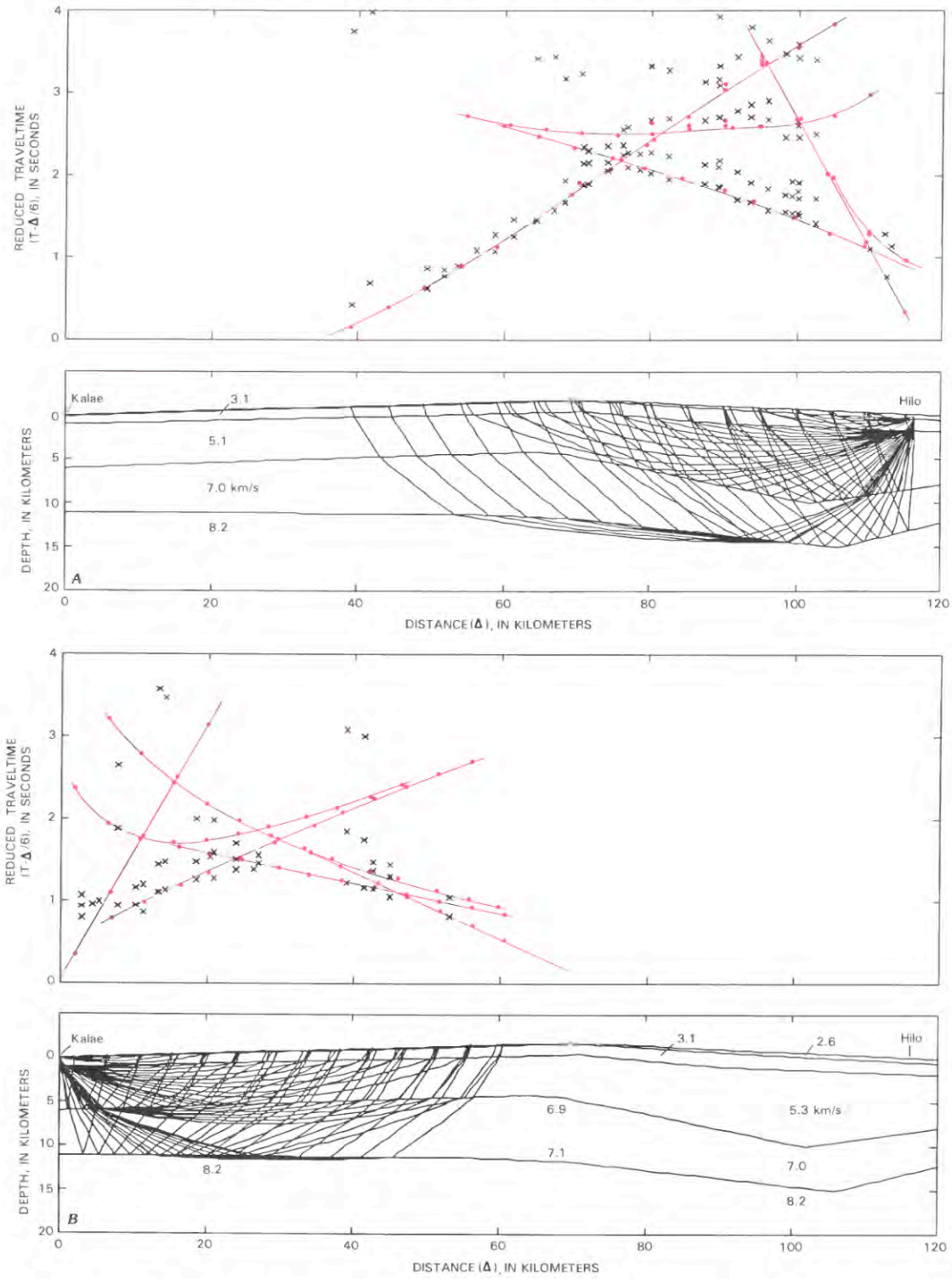


FIGURE 37.6.—Alternate interpretations of the traveltime data for the Hilo-Kalae profile of Ryall and Bennett (1968) across the summit of Kilauea (profile I in fig. 37.1). Interpretations done for shot point at Hilo (***A***) and shot point at Kalae (***B***). Upper diagram in each shows reduced traveltime data (crosses) and the computed traveltime curves ( dots and red lines); traveltimes (T) are reduced by distance (Δ) divided by 6 km/s. Lower diagram in each shows *P*-wave velocity model and ray paths.

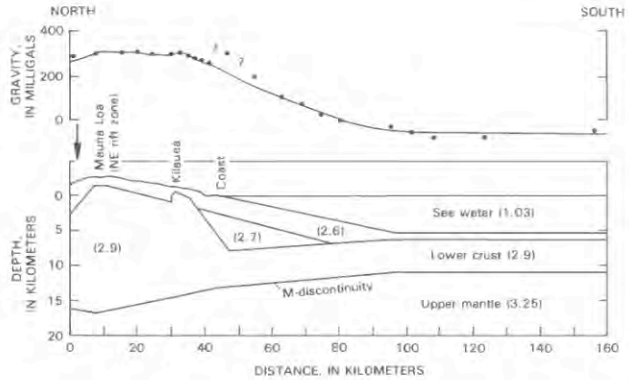


FIGURE 37.7.—Gravity profile and density structure along the offshore Kilauea profile (profile 6 in fig. 37.1) Dots, measured gravity values; gravity curve is that computed from the density model. Figures indicate density of layers in model, in grams per cubic centimeter. Arrow indicates intersection with the profile in figure 37.8. Adapted from Zucca and others (1982).

1960; Ryan and others, 1983). This conduit system forms a vertical axis about which the principal mass of each volcano has accumulated. A core of dense intrusive rock surrounds the conduit system and magma chamber within the summit edifice, producing the positive gravity anomalies over the summit area of each of the volcanoes (compare the topography and gravity fields in figs. 37.1 and 37.5).

The profile established by Ryall and Bennett (1968) between Kalae and Hilo passes immediately northwest of the summit of Kilauea Volcano (fig. 37.1). Although the opposing traveltime curves from the two shotpoints are not reversed (see fig. 37.6), they provide important clues on the deep crustal structure beneath the summit region of Kilauea.

Ryall and Bennett (1968) interpreted the Hilo-Kalae profile in terms of a major northwest-striking, northeast-dipping normal fault beneath the summit of Kilauea that offsets the oceanic crust by nearly 7.5 km and brings the base of the crust to within 10.3 km of the surface beneath the summit (Ryall and Bennett, 1968, fig. 7). We find that the traveltime data can also be fit rather well by a more continuous velocity structure that does not involve offset across a major crustal fault (fig. 37.6). In this structure, we interpret the thickening of a layer of velocity 6.9–7.1 km/s toward the summit region as due to intrusive cores of the southwest rift zone and the central conduit of Kilauea that lie just southeast of the profile where it crosses the summit. An intrusive core associated with the buried end of the Mauna Loa east rift zone may also contribute to the increased thickness of this layer northeast of Kilauea (see figs. 37.1, 37.5).

The profile extending northwest from Kalae runs subparallel to and about 5 km inland from the southeastern half of the Kau-Puna coastal profile (fig. 37.1). Both profiles show a similar structure for the 11 to 13-km-thick crust beneath the coastal flank of Mauna Loa between Kalae and the point where Kilauea's southwest rift zone intersects the coast (figs. 37.5, 37.6). The unreversed traveltime data from the Kalae profile, however, give no indication that the crust thickens significantly toward the summit of Kilauea, a result seemingly at odds with the evidence from the perpendicular profile (fig. 37.3) that the base of the crust dips at about 3° beneath the flank of Kilauea toward the summit region. Whether this apparent discrepancy means that the dip on the base of the crust flattens under the subaerial flank of Kilauea, or, as seems more likely, it reflects the level of uncertainty associated with the interpretation of these unreversed traveltime curves remains to be seen. In any case, the opposing traveltime data along the Hilo-Kalae profile indicate upper mantle $P$-wave velocities at fairly shallow depths (10–11 km below sea level) beneath the summit region of Kilauea. Thurber (chapter 38) finds independent evidence for unusually shallow depths of rocks with 8.0-km/s velocity beneath the summit of Kilauea in his inversion of local earthquake arrival-time data.

Constraints on the structure of the intrusive core beneath Mauna Loa derive from the onshore extensions of the two offshore radial seismic-refraction profiles (figs. 37.1, 37.3, 37.4). The $P$-wave velocity structure in figure 37.4 summarizes results obtained by Zucca and others (1982) from their inversion of the overlapping record sections from each of the nine stations forming the onshore section of the Mauna Loa profile passing just north of the summit. These results indicate that the mass of rocks with $P$-wave velocities of 7.0–7.3 km/s thickens dramatically toward the summit of Mauna Loa, beginning about 10 km west of the present coastline. The thickening occurs as a combination of an increased dip of the $M$-discontinuity and a decreasing depth to rocks with 7.0-km/s velocity toward the summit.

The fairly narrow zone of elevated $P$-wave velocity beneath the coast is consistent with but not required by the seismic-refraction data. A comparable zone of elevated density is required, however, by the elongate gravity high that extends southward along the coast from Hualalai (see fig. 37.5; Zucca and others, 1982). As mentioned in the previous section, this elongate zone of density and velocity probably corresponds to an ancient rift zone buried by the actively growing flank of Mauna Loa.

Unfortunately, none of the record sections on the Mauna Loa profile include waves that bottomed in the lower crust under the summit of Mauna Loa, and we are left with no information on the structure of the lower crust beneath the summit from these seismic-refraction data.

Further constraints on structural models for the Mauna Loa and Kilauea seismic-refraction profiles come from coincident gravity profiles, which Zucca and others (1982) constructed by joining the onshore (complete) Bouguer gravity data of Kinoshita and others (1963) with offshore free-air gravity data compiled by Watts and Talwani (1975). These profiles and their interpretation in terms of the density structure are reproduced in figures 37.7 and 37.8. Zucca and others (1982) modeled the density structure by assuming the relations between velocity and density summarized in figure 37.2 and modifying the layer configurations in the $P$-wave velocity models (figs. 37.3, 37.4) to obtain an acceptable fit between the computed and observed gravity profiles. They used a two-dimensional algorithm for computing the gravity field modified to approximate

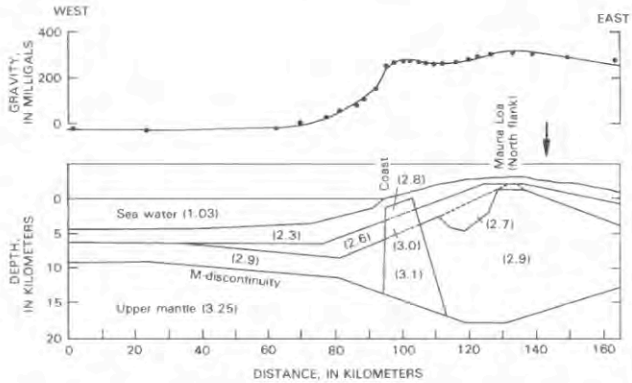


FIGURE 37.8.—Gravity profile and density structure along the offshore Mauna Loa profile (profile 7 in fig. 37.1). Dots, measured gravity values; gravity curve is that computed from the density model. Figures indicate density of layers in model, in grams per cubic centimeter. Arrow indicates intersection with profile in figure 37.7. Adapted from Zucca and others (1982).

the three-dimensional structure of the volcanoes by incorporating an approximate end correction developed by Cady (1977).

The density models in both profiles (figs. 37.7, 37.8) fit the gravity reasonably well, and the boundaries in the density models correspond closely to those in the *P*-wave velocity models of figures 37.3 and 37.4. Taken together, these velocity and density models indicate that the crust beneath Mauna Loa thickens to about 18 km toward the summit region and that the core of dense, high-velocity (intrusive) rocks is the dominant mass (and volume) forming Mauna Loa's central edifice.

## DISCUSSION

### GEOLOGIC SECTIONS

The cross sections in figures 37.9, 37.10, and 37.11 summarize our interpretation of the *P*-wave velocity structure and density structure of Mauna Loa and Kilauea in terms of geologic structures. Two possible geologic interpretations of the velocity structure along the profile crossing the summit of Kilauea from Kalae to Hilo are illustrated in figure 37.9*A*, *B*; a third possibility was shown in Ryall and Bennett (1968, fig. 7). These cross sections are drawn without vertical exaggeration, and the rock types illustrated are keyed to the *P*-wave velocity structure along corresponding seismic-refraction profiles by means of the relations indicated in figure 37.2.

The volcanoes are draped with a surficial blanket as much as 3 km thick that consists of young, subaerial basalt flows, shallow submarine flows, and clastic debris. As described by Moore and Fiske (1969), the submarine portions of this blanket (away from the submarine extensions of rift zones along which pillow flows predominate) consist mostly of clastic debris produced near sea level by the shattering of rapidly quenched lava flows and eruption of ash at littoral cones. Downslope movement in the form of massive submarine landslides carries this clastic debris to the distal ends of the submarine flank and onto the adjacent sections of the Cretaceous oceanic crust (Moore, 1964).

Older submarine pillow flows constitute the dominant effusive product of the volcanoes. These flows were erupted at depths of 100–500 m or more (Moore and Fiske, 1969) and have further submerged with the deflection of the lithosphere in response to the growing load of the volcanoes. Pillow flows probably make up the dominant fraction of the exceptionally thick sequence of effusive rocks in the basin-like depression between the east rift zones of Mauna Loa and Kilauea to the south and the east rift zone of Mauna Kea to the north (fig. 37.9).

The cores of the rift zones and summits of the volcanoes consist of a sequence of densely packed dikes analogous to the sheeted-dike complex forming the uppermost part of layer 3 in the oceanic crust (Salisbury and Christensen, 1978). These intrusive cores, which reach to within 2 km of the surface beneath the summit calderas and rift-zone axes, broaden with depth in a shape that is an exaggerated mimic of the overlying surface topography. The outer boundaries of the intrusive cores are no doubt transitional between altered effusive rocks with widely spaced dikes to a nearly solid mass of intrusive rocks. Walker (chapter 41) finds that, where the dense Koolau dike swarm is exposed on Oahu, most of this transition occurs within a distance of about 1 km. The wave lengths of the *P*-waves refracted by the intrusive rift-zone cores are 0.5–1.0 km for most of our data, and a 1-km-thick transition zone would appear as a relatively sharp boundary to these waves. At the other extreme, a poorly developed intrusive core such as that beneath Kilauea's southwest rift zone may be transitional across its entire width. In any case, though our sampling of the subsurface structure of these intrusive cores is still incomplete, it seems clear that they form an important fraction of the volume of Mauna Loa and Kilauea Volcanoes.

The orientation of the dikes within the intrusive cores reflects the direction of greatest horizontal principal stress at the time of their intrusion (Nakamura, 1977). Within the rift-zone cores, this direction is parallel or subparallel to the rift-zone axis (Fiske and Jackson, 1972). One might expect a more complex configuration of dikes within the summit cores. In the case of Kilauea, it appears as though the complexity in the orientation of more recently emplaced dikes is limited to a relatively small volume surrounding the current position of the central magma chamber beneath the southern margin of the summit caldera. Data from earthquake focal mechanisms (Endo, 1977; Thurber, chapter 38) and the orientation of fissures from recent eruptions (Holcomb, chapter 12) indicate that the stress field of the east rift zone (characterized by an east- to east-northeast-trending greatest horizontal principal stress axis) dominates both the northwest-trending upper east rift zone (see Hill, 1977) and much of the summit caldera. These same data indicate that the stress field of the southwest rift zone (characterized by a northwest trending greatest horizontal principal stress axis) extends only a short distance into the southern part of the summit caldera. The rather abrupt 30°–40° change in the orientation of the greatest horizontal principal stress where the stress fields from the two rift zones intersect coincides closely with the center of inflation for recent eruptive cycles and the current position of the central magma chamber (see Johnson,

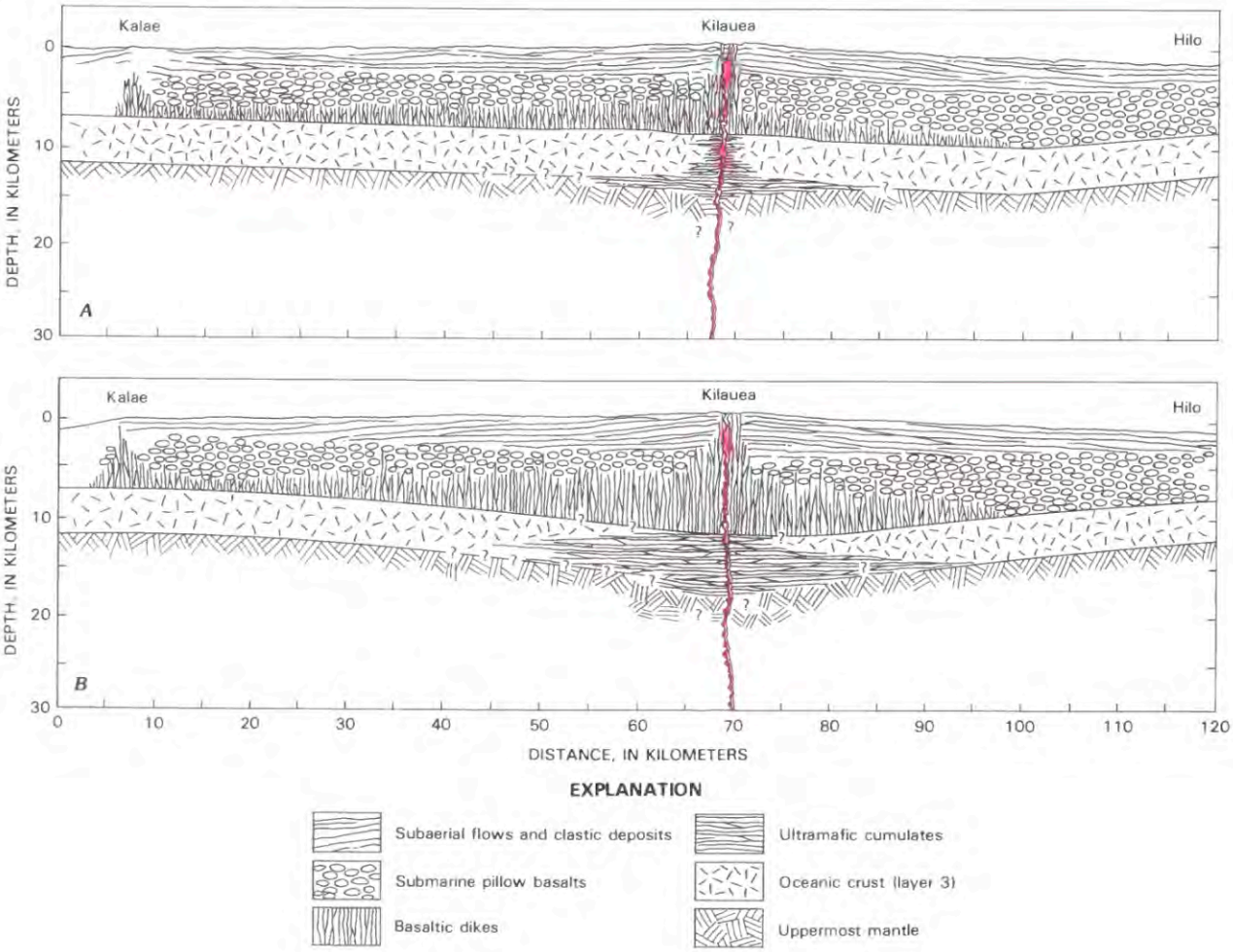


FIGURE 37.9.—Schematic cross sections showing two interpretations of the geologic structure along the Hilo-Kalae profile ( profile 1 in fig. 37.1) based on *P*-wave velocity structure (see figs. 37.3, 37.6, 37.7). Main magma conduit and summit magma chamber indicated in red. The seismic profiles do not pass directly over the summit, and they provide no evidence for the small intrusive cupola included beneath the summit in these sections. ***A***, Interpretation involving little crustal depression and taking high-velocity material at depth beneath Kilauea to be the upper mantle. ***B***, Interpretation involving greater crustal depression and taking high-velocity material at depth beneath Kilauea to be ultramafic cumulate.

chapter 47). The stress field in the summit region may, of course, have had different orientations during earlier stages in the growth of the volcano, and the orientation of older (and deeper) dikes may therefore differ from that of dikes intruded under the influence of the present stress field.

Though dikes appear to be the dominant intrusive form in at least the outer portions of the intrusive cores, sills and somewhat larger, tabular bodies of gabbro are probably also locally important (see, for example, Ryan and others, 1983, p. 1452). Indeed, *P*-wave velocities near 7 km/s strongly suggest the presence of somewhat more mafic rocks such as pyroxene gabbro or olivine gabbro in the intrusive cores; *P*-wave velocities in basaltic (tholeiitic) dikes or sills seldom exceed 6.5 km/s under confining pressures lower than 200–300 MPa (Christensen, 1982). That isolated pockets of magma would be left in the rift zones to form gabbroic bodies seems plausible. The active intrusion of sills is limited to shallow depths in the volcanic edifice, where the overburden pressure forms a vertical least principal stress. It seems likely, for example, that the base of the intrusive cores may consist of a sequence of sills that were intruded below a fairly thin veneer of early pillow basalt on the oceanic crust.

The ultramafic cumulate forming a high-density, high-velocity inner core to the intrusive core of the volcanoes is the most speculative aspect of the structure suggested in figures 37.9 and 37.11. Its existence is consistent with but not required by the seismic-refraction data. Evidence from ultramafic inclusions in erupted basalt, however, indicates that early magma chambers must

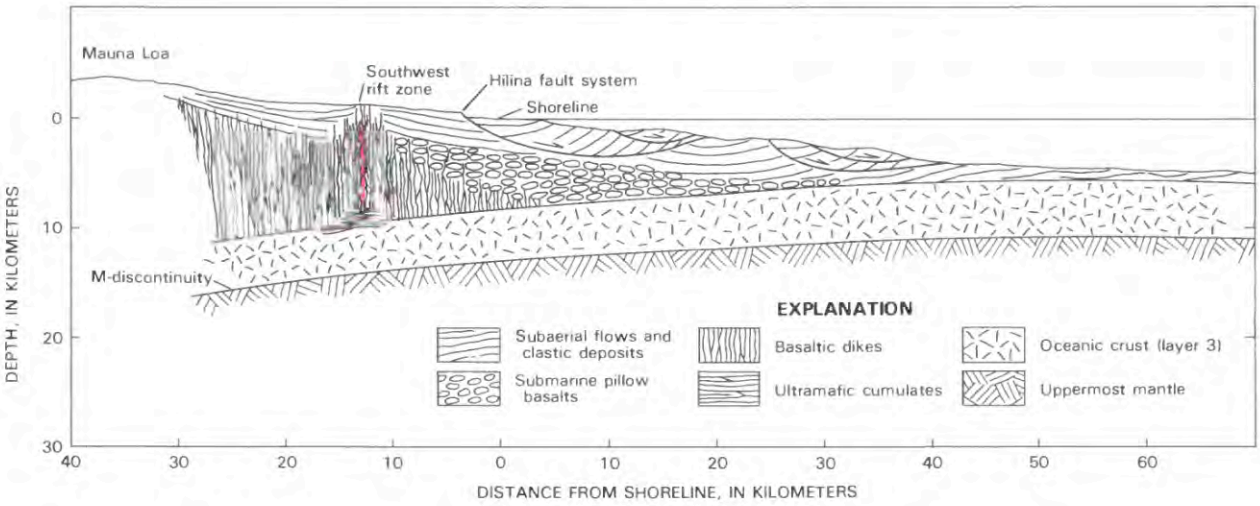


FIGURE 37.10.—Schematic cross section showing inferred geologic structure along the offshore Kilauea profile (profile 6 in fig. 37.1) based on *P*-wave velocity and density models in figures 37.3 and 37.7, respectively. Main magma conduit indicated in red.

have left a trail of residual ultramafic deposits as they migrated upward through the oceanic crust and volcanic pile during the construction of the submarine volcanic edifice (Jackson, 1968). The ultramafic cumulates shown in figure 37.9*A* are limited to a small volume around the central conduit. In this case, the base of the oceanic crust is only about 13 km below sea level under the summit of Kilauea, implying minimal deflection of the lithosphere under the load of Kilauea. In figure 37.9*B*, the ultramafic cumulate forms an extensive mass of sill-like bodies that have disrupted the depressed part of the oceanic crust beneath the summit region of Kilauea. The ultramafic cumulate has mantle-like *P*-wave velocity and its upper surface masquerades as the *M*-discontinuity beneath the summit region. Although we prefer this interpretation (fig. 37.9*B*) because it fits current ideas on the response of the oceanic lithosphere to the loads of the volcanoes, we cannot ignore the simpler interpretation (fig. 37.9*A*) of the Hilo-Kalae velocity structure (fig. 37.6*B*).

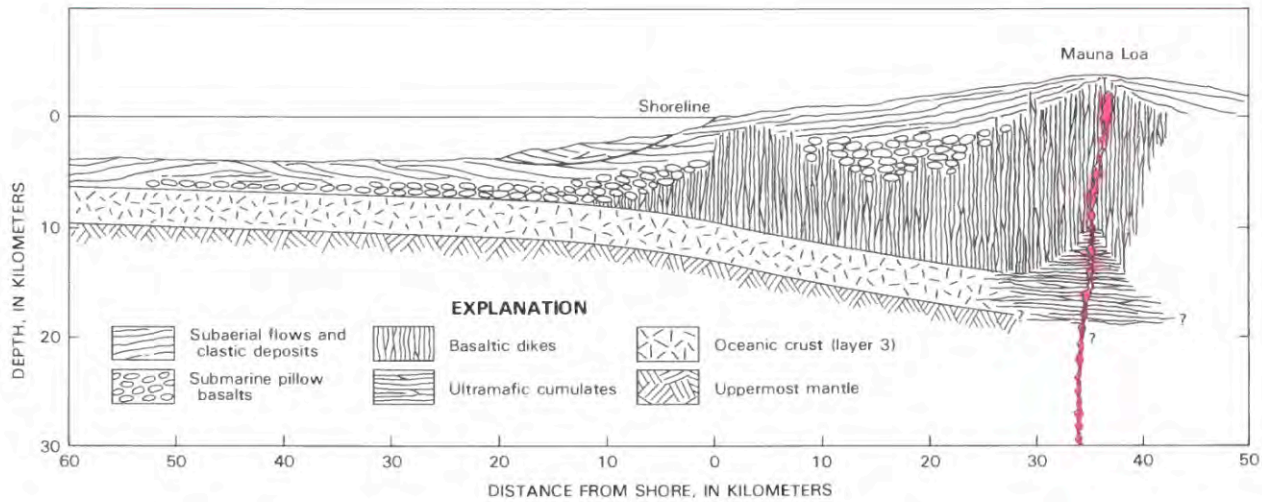


FIGURE 37.11.—Schematic cross section showing inferred geologic structure along the offshore Mauna Loa profile (profile 7 in fig. 37.1) based on *P*-wave velocity and density models in figures 37.4 and 37.8, respectively. Central magma conduit of Mauna Loa Volcano and its summit magma chamber shown in red.

It remains uncertain whether an inner core of ultramafic cumulate extending up to shallow depths under the central vents is an integral part of the Hawaiian volcanoes. The evidence described by Furumoto and others (1968) indicating protrusions of upper mantle $P$-wave velocity (7.7 km/s and above) to shallow depths beneath the center of the eroded core of Koolau Volcano on Oahu and beneath Penguin Banks (a submarine volcanic structure east of Molokai) is consistent with this possibility. Watts and others (1985) describe a body with $P$-wave velocity of 7.4–7.8 km/s as thick as 4 km that underlies the oceanic crust where their multichannel transect crosses the axis of the Hawaii-Emperor chain between Oahu and Molokai. They see no evidence in their data that this subcrustal body extends upward into the axis of the volcanic chain, but their transect does not cross the central vent of a major volcanic edifice.

The evidence for concave-downward curvature on the $M$-discontinuity and the oceanic crust under the subaerial flanks of Mauna Loa supports Walcott's (1970) model for the flexural response of the lithosphere to the load of the volcanoes. Watts and others (1985) find a similar result along the transect between Oahu and Molokai. The evidence for this model at Kilauea, however, is equivocal.

The 8.2-km/s $P$-wave velocity found from the $P_n$ waves propagating in the uppermost mantle under the Island of Hawaii is typical of uppermost mantle elsewhere within the Pacific plate, implying that at least the upper section of the lithosphere beneath Hawaii has undergone little heating from either the Hawaiian hot spot or the narrow conduits that supply magma to the summit reservoirs of Mauna Loa or Kilauea. Immediately southeast of Kilauea, however, and directly over the current position of the hot spot, the $P_n$ velocity is 7.9 km/s (Zucca and Hill, 1980) and the $P$-wave velocity is 8.0–8.1 km/s (1–2 percent low compared to 8.2 km/s) to depths of at least 35 km (Ellsworth and Koyanagi, 1977). Possible explanations for the anomalously low $P_n$ velocity measured on the profile southeast of Hawaii include the following: (1) Anisotropic $P$-wave propagation in uppermost mantle (Zucca and Hill, 1980) similar to that reported by Shor and others (1970) for an area northeast of Oahu; and (2) the presence of a small velocity gradient at the top of the mantle such that $P_n$ apparent velocity recorded at short distances (less than 100 km) would be somewhat lower than that recorded at greater distances (Zucca and others, 1982).

A third possiblility is that the low, lithospheric mantle $P$-wave velocity is related to the hot spot within the underlying asthenosphere. For this to be true, however, the effect must involve mechanical disruption of the upper lithosphere. Thermal conduction alone cannot supply measurable heat to the shallow parts of the lithosphere directly above the hot spot when the relative motion between the lithosphere and the hot spot is on the order of 10 cm/yr as is the case for Hawaii. Mechanical disruption of the lithosphere might be related to the southeastward progression of the flexural front associated with the growing loads of Kilauea and Loihi on the oceanic crust (see Moore, chapter 2). In principle, mechanical disruption of the lithosphere would also allow the rapid transfer of heat into the upper lithosphere by the upward migration of hot fluids from the asthenosphere. Conceivably, the low $P$-wave velocity off the southeast coast of Kilauea represents an early stage in the development of the subcrustal body with velocity of 7.4–7.8 km/s described by Watts and others (1985). Their subcrustal body, however, extends at least 100 km on either side of the ridge axis, and we see no evidence for reduced subcrustal velocity under the flanks of Mauna Loa. At this stage, we do not have adequate data to clearly discriminate between these several possibilities.

## GROWTH OF THE VOLCANIC PILE AND INTRUSIVE CORES

Moore and Fiske (1969) have outlined clearly the events in the growth of the effusive portion of a Hawaiian volcanic edifice: (1) progressive accumulation of pillow basalt flows fed by submarine vents; (2) mantling of the pile of pillow flows by hyaloclastic rocks produced when the vents reach within a few hundred meters of sea level; (3) progressive accumulation of subaerial flows as the central vents emerge above sea level, accompanied by continued production of hyaloclastic rocks where subaerial flows reach the sea; and (4) large-scale submarine slumping that transports the hyaloclastic rocks to the base of the volcanic pile and beyond.

The triangular cross section of the intrusive cores is most readily explained if the rift zones and central vents behave as spreading centers. Indeed, accumulating evidence indicates that spreading plays a central role in the growth of Hawaiian volcanoes. Swanson and others (1976) present a convincing case that the entire south flank of Kilauea Volcano has moved progressively upward and southward over the underlying oceanic crust in response to repeated episodes of forceful magma intrusion into both the summit region and east rift zone. The displacements associated with the magnitude 7.1 Kalapana earthquake of November 29, 1975, which indicate that the south flank of Kilauea moved 2–3 m southward on a low-angle plane at a depth of 8–10 km, add considerable support to this concept (Ando, 1979; Furumoto and Kovach, 1979; Nakamura, 1980).

A series of idealized structural cross sections (fig. 37.12) incorporate the concept suggested by Swanson and others (1976) together with the internal structure of rift zones summarized in figures 37.9–37.11 to illustrate sucessive stages in the growth of a rift zone. In this case the active core of the rift zone (the spreading center) moves away from the buttressed flank and pushes the unbuttressed (mobile) flank ahead of it over the oceanic crust. This process produces an intrusive core that broadens with depth as the progressively older dikes, which were injected into a progressively older and lower edifice, become further displaced from the zone of active intrusion (spreading).

If spreading within the rift-zone core were symmetric (that is, new dikes were nearly always injected midway between the next most recent series of intrusions). the mobile flank would move away from the buttressed flank at twice the rate of the active rift zone (twice the one-sided spreading rate). In the case of Kilauea, at least, it appears that active intrusion preferentially occurs on the side of the mobile flank, producing an asymmetric profile for both the rift-zone core (reflected in the gravity field) and the rift-zone topography (Swanson and others, 1976). In the absence of buttressing, the rift-zone axis would presumably remain stationary with respect to the under-

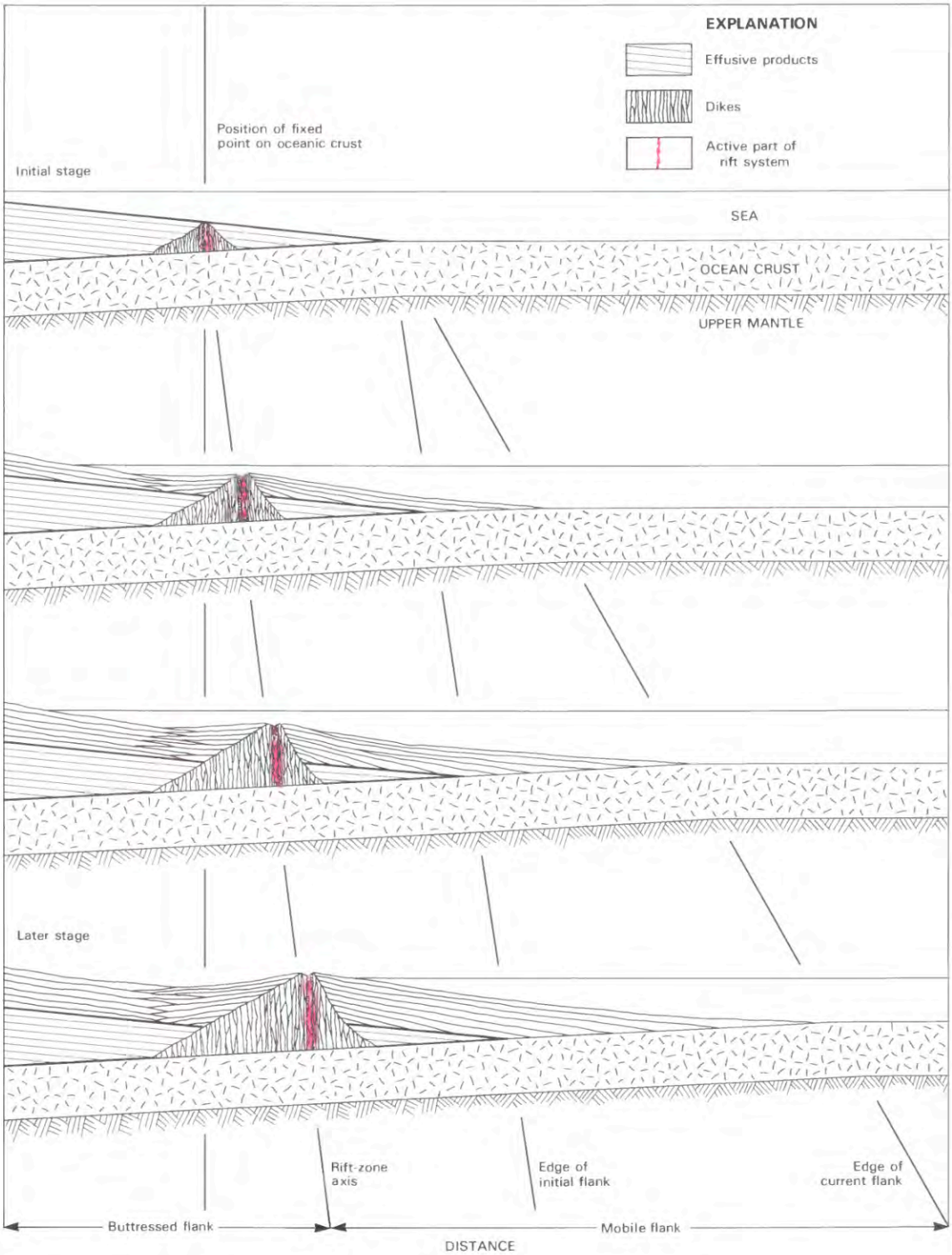


FIGURE 37.12.—Space-time diagram illustrating successive stages in the growth of a rift zone on a volcano's flank. Corresponds approximately to the east rift zone of Kilauea, buttressed on the north (here left) side by the still-growing flank of Mauna Loa. Heavy lines show successive configurations of the initial flank. Decoupling surface assumed to be at top of oceanic crust.

lying oceanic crust and both flanks would move away from the rift-zone spreading center at equal rates, resulting in symmetric topographic and core profiles.

One consequence of this process is that the axis of a rift zone with one buttressed flank will migrate with respect to the more stable position of a summit vent or the axis of a rift zone with two unbuttressed flanks. Indeed, the northward bend in Kilauea's upper east rift zone (see fig. 37.1) probably reflects the southward migration of the east rift zone with respect to the summit vent (Swanson and others, 1976). Similarly, the left-stepping offset in Mauna Loa's southwest rift zone probably reflects the westward migration of the upper part of the rift zone, which is buttressed on the east by Kilauea, with respect to the lower part, which has two unbuttressed flanks (Lipman, 1980).

The location and nature of the decoupling surface (or surfaces) along which the mobile flanks of the rift zones move under this process remains a matter of discussion. We feel that the most likely candidate for this surface is the sedimentary layer of the oceanic crust, as was suggested by Ando (1979), Furomoto and Kovach (1979), Nakamura (1980), and Zucca and Hill (1980). If this layer of abyssal ooze and clay were left more or less intact as the initial flows of pillow basalt were erupted onto the ocean floor, it would form a preexisting weak surface for later displacement between the oceanic crust and the overlying volcanic pile. Swanson and others (1976), however, suggest that decoupling occurs over a zone within the lower section of pillow basalt somewhere near the base of the volcanic pile. Fault plane solutions for the 1975 Kalapana earthquake show slip on a low-angle plane at about the proper depth for the sedimentary layer at the top of the oceanic crust beneath the southeast flank of Kilauea. Furumoto and Kovach (1979) conclude that the fault plane dips about 4° toward the island consistent with the local dip on the top of the oceanic crust. Ando (1979), however, concludes that the fault plane dips about 20° away from the island. Ando's solution is constant with a decoupling surface within the pillow basalt along the lines proposed by Swanson and others (1976). The differences between these two solutions to a large degree reflects the uncertainties involved in determining the dip on the fault plane of a large, shallow earthquake in a region with strong lateral variations in both velocity structure and topography.

We envision that the intrusive core beneath a central vent grows in much the same manner as suggested for the intrusive core within a rift zone. The principal differences are presumably that growth of the summit core would tend to develop with conical symmetry about the central conduit (in contrast to planar symmetry across the rift-zone axis) and the position of the central vent would be anchored by the deep-seated central conduit system. The angles with which rift zones intersect the summit region would no doubt strongly influence the growth pattern within the central core.

Many of the processes occurring at an actively spreading rift zone must be analogous with those occurring at the spreading center of a midocean ridge. In particular, it seems likely that the deeper parts of a rift zone might resemble a small-scale ophiolite sequence complete with pillow basalt, sheeted dikes, gabbroic bodies, and perhaps even layered ultramafic cumulate near the base of the complex. Spreading associated with the Hawaiian volcanoes, however, is a superficial process limited to the volcanic pile on top of the oceanic crust and underlying lithosphere.

## CONCLUSIONS

The seismic-refraction and gravity data reviewed in this paper provide some important clues to the structure of Kilauea and Mauna Loa Volcanoes, but critical details remain blurred. These data make clear that the intrusive cores to the summit regions and rift zones form a significant mass fraction of the volcanic edifice. Reliable estimates of this fraction, however, will require better definition of intrusive core morphology by seismic techniques and by densely spaced gravity measurements over the submarine flanks of the volcanoes. The wedge shape of the intrusive cores supports the idea that spreading plays an important role in the growth of the volcanic edifice. This spreading involves the lateral displacement of unbuttressed flanks over the oceanic crust in response to forceful magma intrusion in rift zones. Understanding the details of this process, however, demands a sharper image of the intrusive-core structure and better constraints on the nature of the decoupling zone between the mobile flanks and the oceanic crust. The profile of the oceanic crust beneath the volcanic pile appears to be consistent with the bending of a fractured lithosphere in response to the load of the pile. Clear delineation of the strongly three-dimensional structure of the deep crust beneath the volcano summits, however, presents a special challenge to high-resolution seismic and gravity techniques.

## REFERENCES CITED

Ando, M., 1979, The Hawaii earthquake of November 29, 1975: low dip angle faulting due to forceful injection of magma: Journal of Geophysical Research, v. 84, p. 7616–7626.

Broyles, M.L., Suyenaga, W., and Furumoto, A.S., 1979, Structure of the lower east rift zone of Kilauea Volcano, Hawaii, from seismic and gravity data: Journal of Volcanology and Geothermal Research, v. 5, p. 317–336.

Cady, J.W., 1977, Calculation of gravity and magnetic anomalies along profiles with end corrections and inverse solutions for density and magnetization: U.S. Geological Survey Open File Report 77–463, 110 p.

Christensen, N.I., 1982, Seismic velocities; *in* Carmichael, R.S. ed., Handbook of physical properties of rocks, v. II: Boca Raton, CRC Press p. 2–228.

Crosson, R.S., and Endo, E.T., 1982, Focal mechanisms and locations of earthquakes in the vicinity of the 1975 Kalapana earthquake aftershock zone 1970–1979: implications for tectonics of the south flank of Kilauea Volcano, Island of Hawaii: Tectonics, v.1, p. 495–542.

Crosson, R.S., and Koyanagi, R.Y., 1979, Seismic velocity structure below the Island of Hawaii from earthquake data: Journal of Geophysical Research, v. 84, p. 2331–2342.

Eaton, J.P., 1962, Crustal structure and volcanism in Hawaii, *in* The Crust of the Pacific Basin: American Geophysical Union Monograph, v. 6, p. 13–29.

Eaton, J.P., and Murata, K.J., 1960, How volcanoes grow: Science, v. 132, p. 925–936.

Ellsworth, W.L., and Koyanagi, R.Y., 1977, Three-dimensional crust and mantle structure of Kilauea Volcano, Hawaii: Journal of Geophysical Research, v. 82, p. 5379–5394.

Endo, E.T., 1971, Focal mechanisms for the May 15–18, 1979, shallow Kilauea earthquake swarm: San Jose, Calif., San Jose State University, M.S. thesis, 165 p.

Fiske, R.S., and Jackson, E.D., 1972, Orientation and growth of Hawaiian volcanic rifts: the effect of regional structure and gravitational stress: Proceedings of the Royal Society of London, Series A, v. 329, p. 299–326.

Furumoto, A.S., and Kovach, R.L., 1979, The Kalapana earthquake of November 29, 1975: an intraplate earthquake and its relation to geothermal processes: Physics of the Earth and Planetary Interiors, v. 18, p. 197–208.

Furumoto, A.S., Wollard, G.P., Campbell, J.F., and Hussong, D.M., 1968, Variations in the thickness of the crust in the Hawaiian Archipelago, *in* Knopoff, L., Drake, C.L., and Hart, P.J., eds., Crust and upper mantle of the Pacific area: Washington D.C., American Geophysical Union, Geophysical Monograph 12, p. 94–111.

Hill, D.P., 1969, Crustal structure of the Island of Hawaii from seismic-refraction measurements: Bulletin of the Seismological Society of America, v. 59, p. 101–130.

——— 1977, A model for earthquake swarms: Journal of Geophysical Research, v. 82, p. 1347–1352.

Jackson, E.D., 1968, The character of the lower crust and upper mantle beneath the Hawaiian Islands: International Geological Congress, v.I, p. 135–150.

Kinoshita, W.K., Krivoy, H.L., Mabey, D.R., and MacDonald, R.R., 1963, Gravity survey of the Island of Hawaii: U.S. Geological Survey Professional Paper 475–C, p. C114–C116.

Klein, F.W., 1981, A linear gradient crustal model for south Hawaii: Bulletin of the Seismological Society of America, v. 71, p. 1503–1510.

Klein, F.W., and Koyanagi, R.Y. 1980, Hawaiian Volcano Observatory seismic network history 1950–1979: U.S. Geological Survey Open File Report 80–302, 84 p.

Lipman, P.W., 1980, The southwest rift zone of Mauna Loa: implications for structural evolution of Hawaiian volcanoes: American Journal of Science, v. 280–A, p. 752–776.

Moore, J.G., 1964, Giant submarine landslides on the Hawaiian ridge: U.S. Geological Survey Professional Paper 501–D, p. D95–D98.

Moore, J.G., and Fiske, R.S., 1969, Volcanic substructure inferred from dredge samples and ocean-bottom photographs, Hawaii: Geological Society of America Bulletin, v. 80, p. 1191–1202.

Nakamura, K., 1977, Volcanoes as possible indicators of tectonic stress orientation—principal and proposal: Journal of Volcanology and Geothermal Research, v. 2, p. 1–16.

——— 1980, Why do long rift zones develop in Hawaiian volcanoes— a possible role of thick oceanic sediments (in Japanese): Bulletin of the Volcanological Society of Japan, v. 25, p. 255–267.

Pollard, D.D., and Eaton, J.P., 1964, Crustal structure of the Island of Hawaii [abs.]: Geological Society of America Special Paper 76, p. 218.

Ryall, A.S., and Bennett, D.L., 1968, Crustal structure of southern Hawaii related to volcanic processes in the upper mantle: Journal Geophysical Research, v. 73, p. 4561–4582.

Ryan, M.P., Blevins, J.Y.K., Okimura, A.T., and Koyanagi, R.Y., 1983, Magma reservoir subsidence mechanics: theoretical summary and application to Kilauea Volcano, Hawaii: Journal of Geophysical Research, v. 88, p. 4147–4181.

Ryan, M.P., Koyanagi, R.Y., and Fiske, R.S., 1981, Modeling the three-dimensional structure of macroscopic magma transport systems: Application to Kilauea Volcano, Hawaii: Journal of Geophysical Research, v. 86, p. 7111, 7129.

Salisbury, M.H., and Christensen, N.I., 1978, The seismic velocity of a traverse through the Bay of Islands ophiolite complex, Newfoundland, an exposure of oceanic crust and upper mantle: Journal of Geophysical Research, v. 83, p. 805–817.

Shor, G.G., Menard, H.W., and Raitt, R.W., 1970, Structure of the Pacific Basin, *in* Maxwell, A.E., ed., The sea; ideas and observations on progress of the seas: Interscience, New York, v. 4, part II, p. 3–27.

Swanson, D.A., Duffield, W.A., and Fiske, R.S., 1976, Displacement of the south flank of the Kilauea Volcano: the result of forceful intrusion of magma into the rift zones: U.S. Geological Survey Professional Paper 963, 39 p.

Walcott, R.I., 1970, Flexure of the lithosphere at Hawaii: Tectonophysics, v. 9, p. 435–446.

Ward, P.L., and Gregersen, S., 1973, Comparison of earthquake locations determined with data from a network of stations and small tripartite arrays on Kilauea Volcano, Hawaii: Bulletin of the Seismological Society of America, v. 63, p. 679–711.

Watts, A.B., and Talwani, M., 1975, Gravity field of the northwest Pacific Ocean basin and its margin, Hawaii and vicinity: Geological Soceity of America MC–9, 6 p.

Watts, A.B., ten Brink, U.S., Buhl, P., and Brocher, T.M., 1985, A multichannel seismic study of lithospheric flecture across the Hawaii Emperor seamount chain: Nature, v. 315, p. 105–111.

Zucca, J.J., and Hill, D.P., 1980, Crustal structure of the southeast flank of Kilauea Volcano, Hawaii, from seismic refraction measurements: Bulletin of the Seismological Society of America, v. 70, p. 1149–1159.

Zucca, J.J., Hill, D.P., and Duennebier, F.K., 1979, A compilation of the data from the 1976 Hawaii seismic refraction experiment: U.S. Geological Survey Open-File Report 79–711, 30 p.

Zucca, J.J, Hill, D.P., and Kovach, R.L., 1982, Crustal structure of Mauna Loa Volcano, Hawaii, from seismic refraction and gravity data: Bulletin of the Seismological Society of America, v. 72, p. 1535–1550.

# SEISMIC STRUCTURE AND TECTONICS OF KILAUEA VOLCANO

*By* Clifford H. Thurber [1]

## ABSTRACT

**Local earthquake data have been used to study the internal structure and tectonics of Kilauea Volcano. A three-dimensional model of Kilauea's seismic velocity structure, determined using simultaneous inversion techniques, reveals features on a scale of one to a few kilometers. The core and rift zones of the volcano are marked by relatively high seismic velocity; a small, shallow, aseismic low-velocity zone beneath the summit coincides with the inferred locus of the summit magma reservoir. High-quality fault plane solutions have been derived for a suite of local earthquakes using this three-dimensional model. The spatial variations in focal mechanisms provide information on the complex tectonics of the volcano; the temporal variations in mechanisms observed for summit-area events may provide clues to help us understand and perhaps predict Kilauea's eruptive behavior.**

## INTRODUCTION

Kilauea Volcano is an excellent natural laboratory for investigating the relations among stress state, seismicity, and magma migration within an active volcano. Seismicity patterns have been used to outline the structure of Kilauea's magma-transport system (Ryan and others, 1981). Earthquake focal mechanisms from the upper east rift zone (UERZ) have been interpreted in terms of a model for magma transport (Hill, 1977). However, magma migration itself is a poorly understood process. Shaw (1980) suggests that seismic data, coordinated with eruption and deformation data, may provide critical tests of hypotheses related to magma transport. It is in this context that a detailed seismotectonic study of Kilauea Volcano has been initiated.

Routinely available local earthquake data, particularly body-wave arrival times and first-motion polarities, can be used as powerful probes of the structure and stress state of the Earth's interior on a local scale. Focal mechanisms derived from first-motion polarities are indicative of the principal stress directions. However the local Earth structure must be known to determine accurately both the source location (the hypocenter) and the direction from which seismic rays leave the source (focal azimuth and takeoff angles). Fortunately, the method of three-dimensional simultaneous inversion of body-wave arrival times is an effective method for determining a detailed model of earth structure on a scale appropriate for the investigation of focal mechanisms (Thurber, 1981). Obviously the velocity model itself also has important bearing on the understanding of the volcano's structure.

Thousands of instrumentally locatable earthquakes occur each year on the Island of Hawaii. These events are thought to be related primarily to the ascent of magma from the mantle, the injection of magma into crustal rift zones, the eruption of lava at the surface, and the mechanical failure of the crust due to volcanic loading. There are two key factors that permit the application of simultaneous inversion and related techniques to the study of volcanic/tectonic processes and of the volcano's internal structure. Firstly, the earthquake activity is broadly distributed laterally and with depth, and the earthquake focal mechanisms vary with location (and perhaps time) according to the nature of the volcanic and tectonic processes causing them. Secondly, the Hawaiian Volcano Observatory (HVO) has been continuously monitoring Kilauea's seismic and magmatic activity for many years, accumulating a substantial catalog of arrival-time data and allowing the possibility of observing temporal variations.

The Island of Hawaii has been the subject of a large number of investigations of crustal and upper-mantle structure (Eaton, 1962; Ryall and Bennett, 1968; Hill, 1969; Ellsworth and Koyanagi, 1977; Broyles and others, 1979; Crosson and Koyanagi, 1979; Zucca and Hill, 1980; Klein, 1981; Zucca and others, 1982) and earthquake focal mechanisms (Endo, 1971; Ando, 1979; Estill, 1979; Furumoto and Kovach, 1979; Unger and Ward, 1979; Crosson and Endo, 1981, 1982; Klein, 1981; Bosher and Duennebier, 1985). Few structure studies modeled laterally heterogeneous Earth structure, and all the focal-mechanism studies adopted simple one-dimensional velocity models for their analyses. Given the strong evidence for laterally varying structure and the somewhat ambiguous results of some of the focal-mechanism studies, a systematic investigation of three-dimensional crustal structure and earthquake source mechanisms is warranted.

## ACKNOWLEDGMENTS

The seismic data used for this study were collected and processed by staff members of the Hawaiian Volcano Observatory. I would especially like to thank Bob Koyanagi, Tom English, Jennifer Nakata, and Will Tanigawa: without their continuing efforts, this study would not have been possible. Reviews by Fred

[1]Department of Earth and Space Sciences, State University of New York, Stony Brook, N.Y. 11794.

Klein and Dave Oppenheimer led to significant improvements in the manuscript. I would like to acknowledge the contributions of Tim Karpin and Sagarika Das to the focal-mechanism study. Thanks are also due to Kei Aki, Bill Ellsworth, Elliot Endo, Bill Prothero, and Donna Eberhart-Phillips for advice and assistance. This paper is based on research supported by National Science Foundation grant EAR 82-06266.

## METHODOLOGY

I use a method for simultaneously determining both the velocity structure of the Earth beneath a seismic network and the hypocenters of a set of local earthquakes. This simultaneous inversion method can be thought of as a generalization of the standard earthquake location procedure (Geiger's method) to include parameters describing the Earth model as unknowns along with the hypocentral parameters. The details of the method have been described in earlier papers (Thurber, 1983, 1984).

Two recent developments have made iterative three-dimensional simultaneous inversion practical. One is parameter separation, introduced independently by Pavlis and Booker (1980), Spencer and Gubbins (1980), and Rodi and others (1980). This is a mathematical device for maintaining a tractable computational problem size even when large numbers of earthquakes are included in the inversion. The second is approximate ray tracing (ART), originally introduced by Thurber and Ellsworth (1980), with variants developed by Thurber (1983) and Thurber and others (1984). These ART methods exploit Fermat's principle of stationarity to derive approximate ray paths and traveltimes in arbitrary velocity structures. The method of Thurber and others (1984) comes closest to being a true ray-tracing method.

One of the most important facets of the crustal-modeling approach is the manner in which the velocity structure is represented or parameterized. The ideal would be to specify the seismic velocity at any point within the volcano, but in practice this is not attainable. As a compromise, a reasonably dense three-dimensional grid of points is defined at which the velocity is to be estimated by the inversion. A simple interpolation function is used for intervening points. In each iteration, the inversion algorithm solves for the fractional change in velocity, using damped least squares. The $F$-test (De Groot, 1975) is used to terminate the iterations. The final velocity values derived by the inversion should represent an average velocity for the volume surrounding each grid point.

Once a three-dimensional model of crustal structure is available, it can be used in a straightforward way for the determination of focal mechanisms. The equivalent of Geiger's method and an appropriate ray-tracing method are used to locate the earthquake in the three-dimensional model, and the focal angles are obtained from the ray paths for the final hypocenter location. This study finds that fault-plane solutions are better constrained and contain fewer inconsistent polarities when a realistic three-dimensional crustal structure is employed.

In order to take best advantage of the distribution of the HVO seismic-network stations and the distribution of seismic activity, an area 20 km by 30 km encompassing Kilauea Volcano was chosen for study (fig. 38.1). The coordinate origin for the study area is at latitude 19° 13.5′ N., longitude 155° 14.0′ W., with the $Y$ axis rotated 28° clockwise from north. The seismic-velocity model of Klein (1981), developed for Kilauea's south flank, was adopted as a reasonable starting model for the inversion. Grid-point spacings of 3–4 km in the $X$ direction and 2–3 km in the $Y$ and $Z$ directions were adopted, reflecting the station density and dispersion of seismicity (figs. 38.1, 38.2). A set of 85 earthquakes from 1980 and 1981 (the years of data originally made available by HVO for this study) was selected for the inversions, on the basis of their having well-constrained epicenters, a large number of observing stations, and (most importantly) at least one station within a focal depth of the epicenter, so that the earthquake depths were well constrained. Arrival times from two man-made explosions near the summit in 1976 were also included.

A composite model for the $P$-wave velocity structure of Kilauea was constructed by averaging the results of a series of inversions for which the grid spacing was kept fixed but the grid as a whole was shifted systematically 1–2 km in the $X$, $Y$, and $Z$ directions. The resulting velocity values varied smoothly among the set of inversion models. Typically, the inversions achieved an 80-percent reduction in the data variance after three or four iterations. Unweighted (RMS) residuals for individual events generally were reduced from about 0.11 to 0.04–0.05 s, close to the estimated reading error for $P$-wave arrival times. Estimated standard errors and model resolution (diagonal elements) for velocity parameters averaged 3 percent (fractional error) and 0.7, respectively. Resolution was poorest for grid points in the deepest layer, on the fringe of the model, and in the near-surface layer not close to a seismic station.

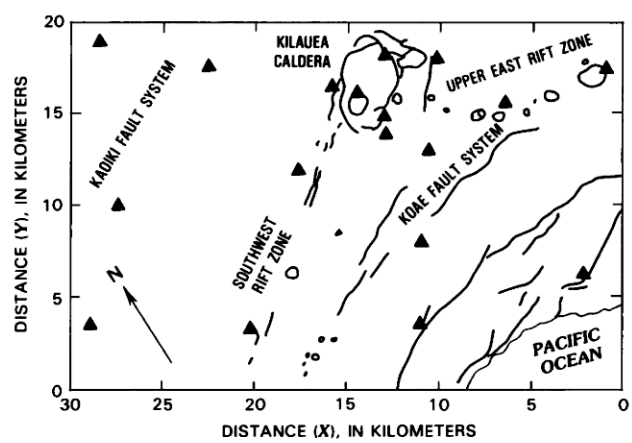


FIGURE 38.1.—Study area on Island of Hawaii, showing principal geologic features and HVO seismic stations (triangles). See figure 38.2 for regional location map. Modified from Thurber (1984, fig. 1), copyright 1984 by American Association for the Advancement of Science.

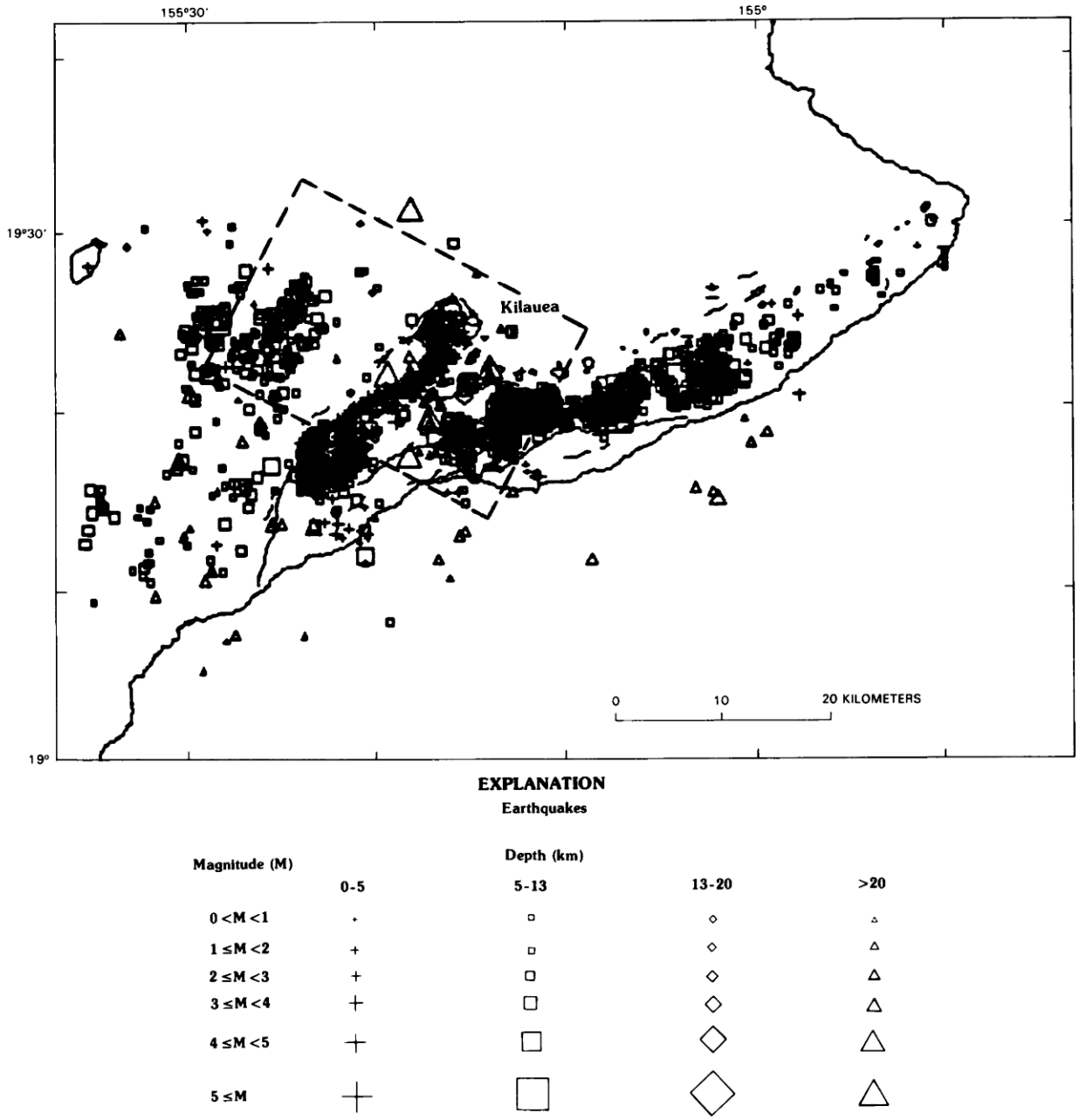


FIGURE 38.2.—Seismicity of southeastern Hawaii for 1981 (Nakata and others, 1982). Dashed lines indicate study area.

## CRUSTAL STRUCTURE

Four grid layers of the composite *P*-wave velocity model are shown in map view in figure 38.3. They are positioned at 1 km above and 2, 5, and 8 km below sea level. In the top layer (fig. 38.3) a velocity high directly beneath the caldera corresponds to the roof of the summit magma complex, and velocity highs also are present along the upper east and southwest rift zones (fig. 38.1). A deeper look into the crust (fig. 38.3), shows a continuation of the velocity highs along the two rift zones to 2 km below sea level. The nonrift areas, particularly the Kaoiki region, have significantly lower seismic velocities.

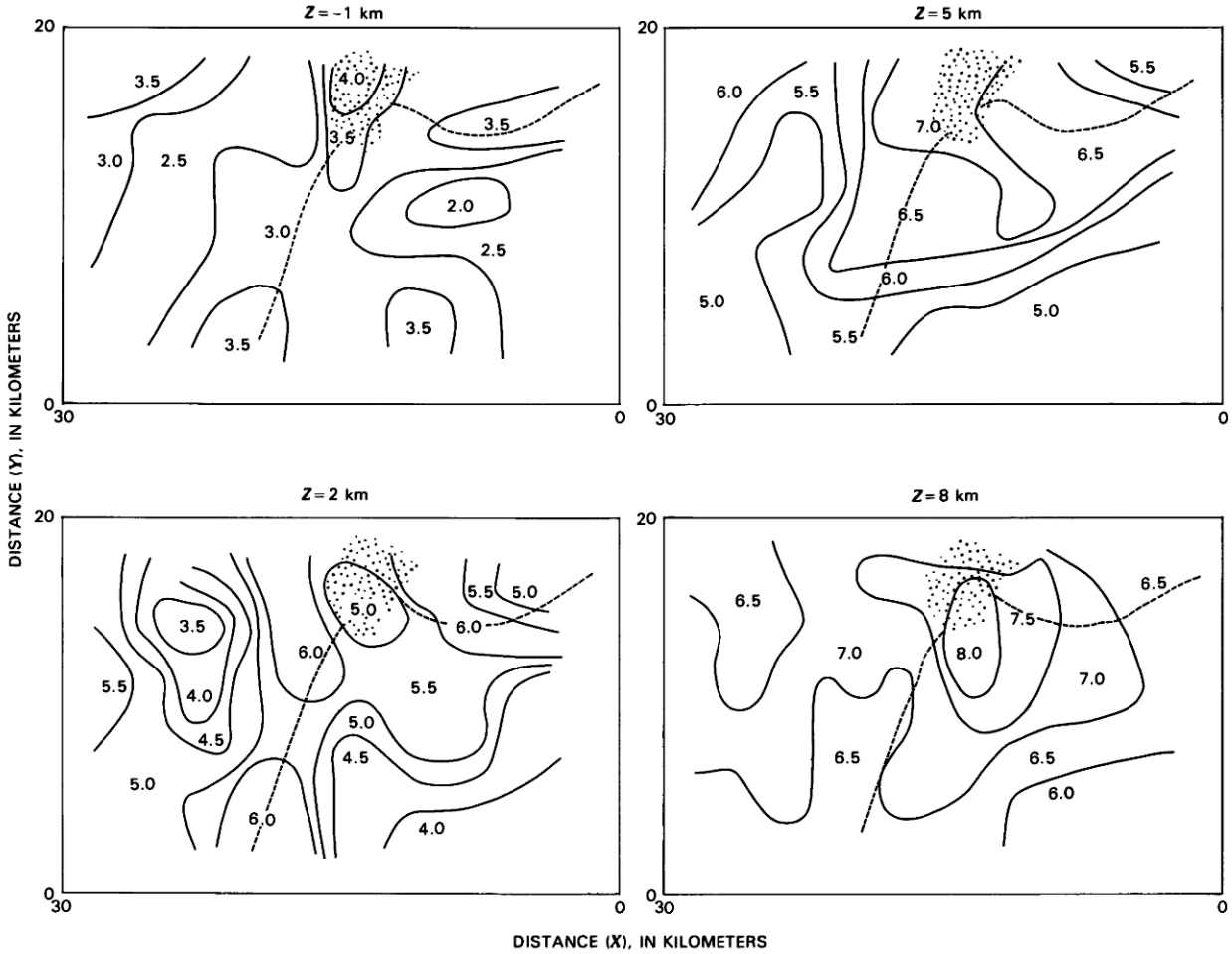


FIGURE 38.3.—Four horizontal slices through composite seismic-velocity model for Kilauea Volcano, positioned at 1 km above and 2, 5, and 8 km below sea level. Velocity is contoured at intervals of 0.5 km/s. Stippling and dotted lines indicate position of caldera and its rift zones, respectively. From Thurber (1984, fig. 2), copyright 1984 by American Association for the Advancement of Science.

Two other important features are apparent at this depth. A high-velocity area along the Koae fault zone indicates the presence of dense, probably competent rock. Recent episodes of intrusive activity in this area have been documented (Swanson and others, 1976), particularly at the northeastern and southwestern boundaries of the fault system, where it intersects the major rift zones. A distinct velocity low is found beneath the caldera, coinciding with the inferred location of Kilauea's summit magma reservoir. Tests with synthetic arrival-time data indicate that the data set is adequate to resolve a small (diameter 2–3 km) low-velocity zone at this point, increasing confidence in the validity of the model results. The actual low-velocity zone could be somewhat smaller, of course, as some degree of smoothing is inherent in the velocity inversion.

At a depth of 5 km (fig. 38.3), the high-velocity core of Kilauea is clearly evident, extending along the UERZ and the southwest rift zone (SWRZ) and intruding into the Koae area. Kaoiki and other nonrift areas continue to exhibit rather low velocities. At 8 km depth (fig. 38.3) the model resolution has become somewhat poor, but the high velocities of the volcano core are still evident, apparently with a slight southward shift from the shallower levels. A similar southward shift with increasing depth is apparent in the estimation of inflation and deflation centers from surface deformation data (Dvorak and others, 1983). Unfortunately, our model does not extend to a sufficient depth to detect the low-velocity layer reported by Crosson and Koyanagi (1979).

These dramatic lateral variations in seismic velocity can be explained in terms of the difference in properties between magma intruded at depth and lava extruded at the surface. As magma nears the surface, the reduction in ambient pressure permits the exsolution of volatiles, creating gas bubbles within the magma. As a result, the

extruded lava is vesicular and has high porosity, low density, and, hence, low seismic velocity. Since the flank areas of Kilauea are constructed predominantly from extruded lava, the low seismic velocities from the inversion are to be expected. In contrast, the rift zones at depth are formed principally from numerous dikes. Except for the very near surface portion of each dike, the intruded magma will not have undergone significant vesiculation. Thus the dikes are probably composed of fairly dense rock with lower porosity and therefore higher seismic velocity.

It is interesting to compare the inversion results with models derived by other seismological techniques. For example, the very high velocity (>8 km/s) at about 8 km depth directly beneath the caldera is consistent with the results of the refraction study of Hill (1969). Rift-zone velocities exceeding 6 km/s at shallow depth have been documented in several refraction studies, and flank velocities on the order of 5 km/s or less are also confirmed (Broyles and others, 1979; Zucca and Hill, 1980; Zucca and others, 1982). Perhaps the most significant comparison is with the teleseismic results of Ellsworth and Koyanagi (1977). The uppermost layer of their model spans the entire depth range of my model, but the correspondence between the results from the two disparate methods is surprisingly strong. The Ellsworth and Koyanagi model displays significantly high seismic velocities beneath Kilauea caldera and its rift zones and also indicates high velocity beneath the Koae area. The Kaoiki and south flank areas are marked by quite low velocities. This agreement strengthens the confidence in both studies.

A rather different comparison can be made between my velocity model and the pattern of seismicity beneath Kilauea caldera. Koyanagi and others (1976) inferred the location of Kilauea's magma chamber from the position of an aseismic zone directly beneath the caldera that spanned a depth range of 2–6 km. However, most evidence favors a smaller, shallow magma reservoir (interconnected sills?) rather than such a large zone of partial melt (Ryan and others, 1983). A nearly east-west cross-section (fig. 38.4) through Kilauea caldera (at $Y=16$ km in figure 38.1) illustrates the association between my model of the velocity structure and the seismicity in the immediate vicinity of the caldera. Earthquakes cluster around the low-velocity zone at shallow depth directly beneath the caldera. An aseismic zone coincides precisely with the zone of low $P$-wave velocity. Thus, the summit magma complex is clearly detectable in the seismic velocity structure of the volcano. The low velocity is most likely due to a combination of elevated temperature and the presence of partial melt and (or) pockets of magma.

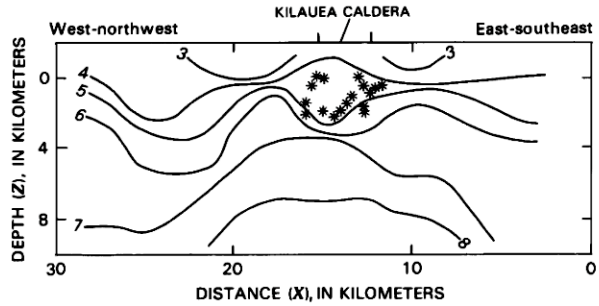


FIGURE 38.4.—Vertical cross section of seismic-velocity model through Kilauea caldera. Section is oriented west-northwest–east-southeast along line $Y=16$ km in figure 38.1. Contours of seismic velocity in kilometers per second. Note association of aseismic region (outlined by earthquake hypocenters indicated by asterisks) with zone of low seismic velocity. For clarity, only shallow earthquakes in immediate vicinity (within 2 km) of caldera are shown. From Thurber (1984, fig. 3), copyright 1984 by American Association for the Advancement of Science.

## EARTHQUAKE RELOCATIONS

Use of a three-dimensional model of the structure of Kilauea has a significant effect on the estimation of earthquake hypocenters (fig. 38.5*A*, *B*). I compare the computed location using the three-dimensional crustal model (3-D) with the HVO catalog location (Tanigawa and others, 1981; Nakata and others, 1982) and also with the location using the one-dimensional starting model (1-D). The 1-D crustal model is essentially the same as the HVO model (Klein, 1981) but does not include the ad-hoc station corrections used in the HVO solutions. One systematic difference is the general shallowing of all hypocenters in the one- and three-dimensional cases relative to the HVO solutions, because of the latter's referral of depths to the ground surface rather than sea level; an additional bias arises from HVO's neglect of station-elevation differences. I also suspect that the relative locations of events are more accurate from my results, as I use a uniform set of stations to locate the entire set of events. In contrast, HVO solutions for a given area are likely to incorporate additional observations from varying sets of stations in the surrounding region, introducing slightly different location biases for each event.

The epicentral shifts of figure 38.5*A* (1-D versus 3-D) indicate the general effect on hypocenters caused by lateral velocity variations, while in figure 38.5*B* (HVO versus 3D) they are indicative of possible location bias in the HVO catalog. The HVO and 3-D locations agree quite well in the UERZ and Kaoiki areas, although there appears to be a slight bias in the northeast Kaoiki region, with the HVO locations displaced 1–2 km southward. The 1-D locations are 1–2 km north of the 3-D locations in both the UERZ and northeast Kaoiki, but they are displaced 2 km eastward in southwest Kaoiki. In comparing the 1-D and 3-D solutions, it appears that accounting for the strong velocity low along the northeast Kaoiki area acts to pull epicenters in that area closer towards Kilauea, whereas the southwest Kaoiki events are pushed away because of the high velocity of the SWRZ. Similarly, the UERZ events are displaced southwards as a result of modeling the high UERZ and summit area velocities.

The comparisons for the summit and upper SWRZ are rather different. Here the 1-D and 3-D locations agree well, but the HVO solutions are displaced 1–2 km southward, most notably for the deeper summit events. This seems to indicate a significant bias in the HVO catalog for this area. Such a bias could have important implications for relating seismicity patterns beneath the summit, and the inferred magma conduit structure, to features visible at the surface (Ryan and others, 1981).

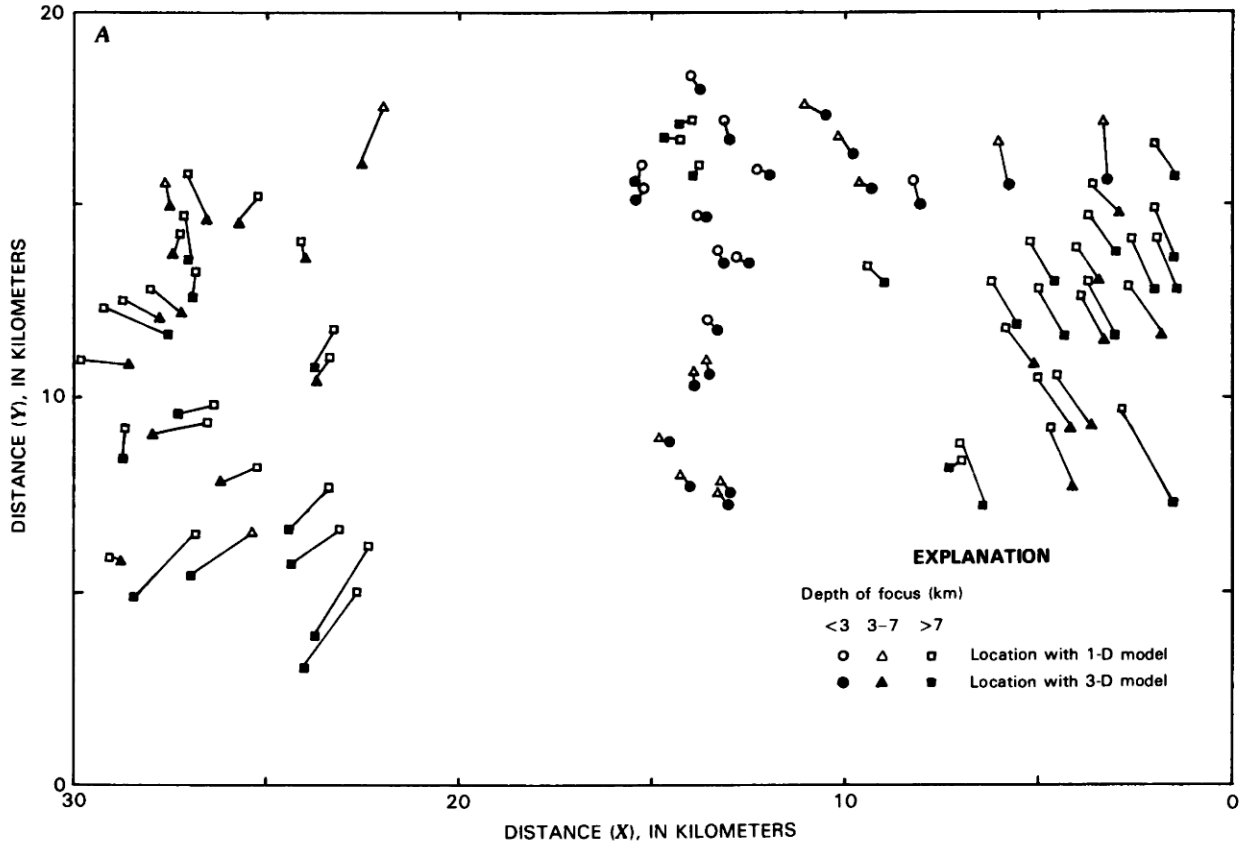


FIGURE 38.5.—Earthquake epicenters in study area relocated using 3-D model in figure 38.3. ***A***, Compared with locations using a 1-D model with no station corrections. ***B***, Compared with HVO catalog locations.

## FINE-SCALE STRUCTURE

To derive a crustal model with significantly better spatial resolution (about 1 km) in a small zone directly beneath Kilauea caldera, I take as a starting point the fairly coarse three-dimensional model for Kilauea's velocity structure described above (which I shall call the regional model). A finer scale velocity grid is imbedded within this regional model, and an inversion is carried out to solve for perturbations to the velocity values on the fine grid only, keeping the values fixed on the coarse grid outside of the imbedded grid. Data from a large number of earthquakes within the imbedded region are included to aid in resolving the detailed structure, in addition to events distributed throughout the regional model.

Such a fine velocity grid, with five nodes by five nodes horizontally by three vertically and a uniform spacing of 1 km, was set up to model the shallow structure of the south caldera area of Kilauea (fig. 38.6). The quality of the fine-scale inversion model was limited by the tight clustering of the available events (from 1980 and 1981), as is clear in figure 38.7*A*. Many events in the south caldera fall within about 100 m of a planar surface 2 km in length and 500 m high dipping 60° to the east; presumably this is either a dike or a normal fault overlying a deflating sill. As a result of this clustering, the resolution of the model is only fair (diagonal elements average 0.4 for the 75 nodes, central nodes closer to 0.7). Nevertheless, consistent results were obtained from a set of inversions, typically achieving an additional 25 to 30 percent variance reduction compared to the regional 3-D model.

Slices through the model from one inversion at depths of 0, 1, and 2 km with respect to sea level are shown in figure 38.7*B–D*. Lateral velocity variations of roughly 1 km/s are present in the model at any given depth. There appear to be two separate zones of low *P*-wave velocity: one lies directly beneath Halemaumau Crater, and the other underlies the Ahua Kamokukolau area. The summit zone corresponds well with the location of the summit reservoir. The velocity low beneath Ahua is at the corner of the grid and therefore is less well resolved, but it may correspond to Ryan and others' (1981) UERZ pipe, which appears to lie about 1 km north of the velocity low. Additional earthquake data from more recent years may allow construction of a more definitive model for the fine-scale structure in this region.

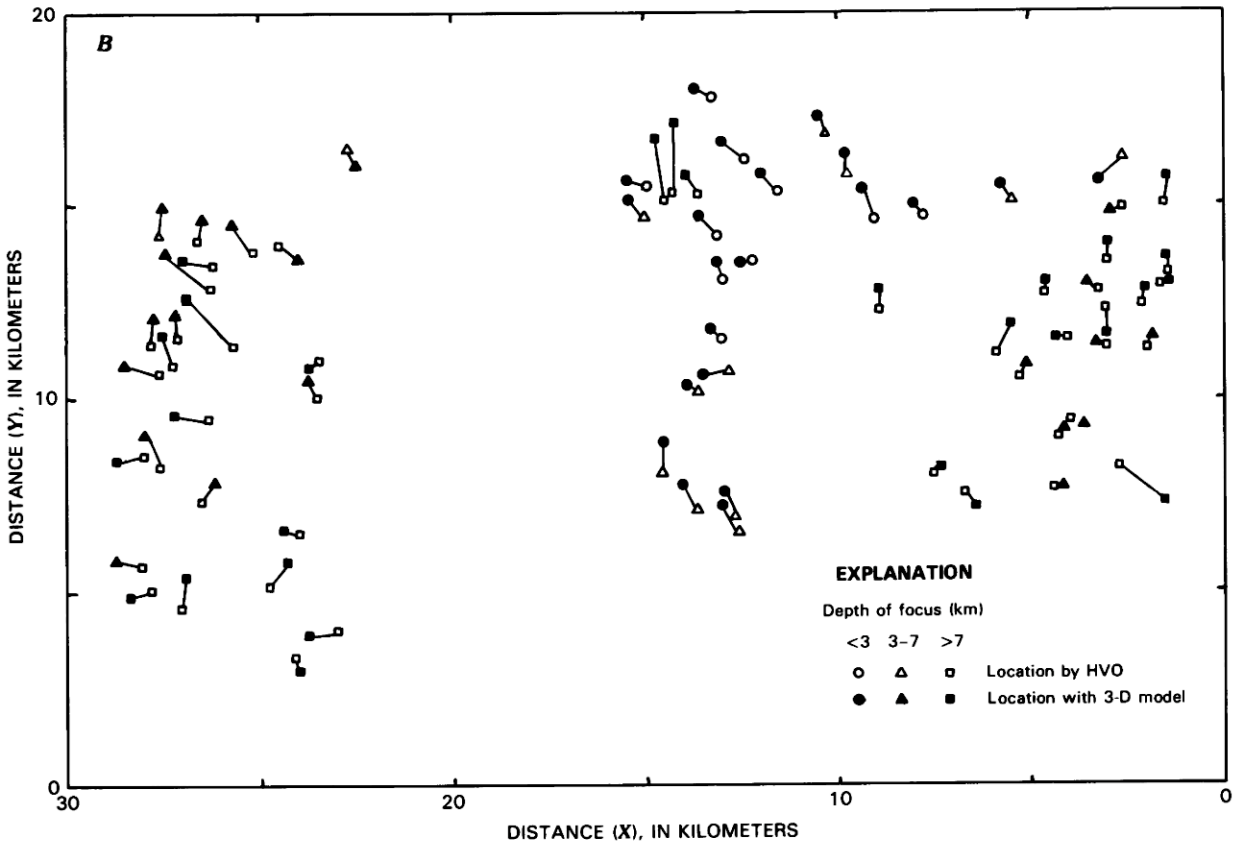


FIGURE 38.5.—Continued.

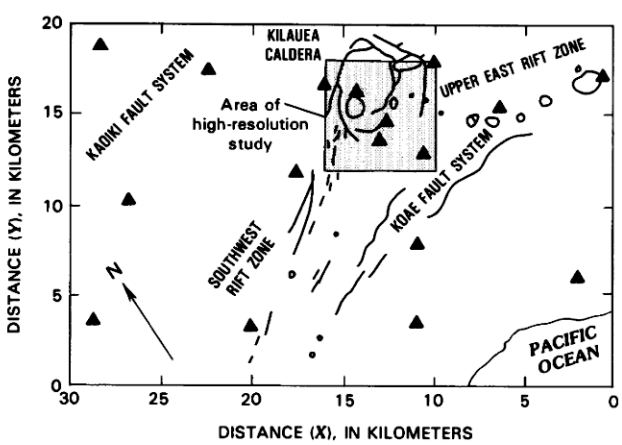


FIGURE 38.6.—Study area near Kilauea caldera (shaded) selected for high-resolution seismic imaging study.

## FOCAL MECHANISMS

The state of stress within Kilauea Volcano arises from a complex interplay among crustal density variations, magma pressure, surface loading, and failure along zones of weakness. Fault-plane solutions of earthquakes are generally indicative of the deviatoric stresses in the earth, so they can be used to explore spatial and temporal variations in stress. Care must be taken in interpreting fault-plane orientations directly in terms of stress, however (Ellsworth, 1982; Gephart and Forsyth, 1984; Michael, 1984).

Using a realistic three-dimensional model for the seismic structure of Kilauea, a detailed study of the source mechanisms of earthquakes in the area has been initiated. The earthquake locations are computed using ray tracing in the three-dimensional model, and the focal angles of the rays for the final locations are taken to construct the fault-plane solutions. In general, markedly improved constraint and increased consistency are found in the 3-D solutions compared to the results obtained for the same events using a one-dimensional crustal model. Some of the more dramatic examples are shown in figure 38.8, but these are not atypical.

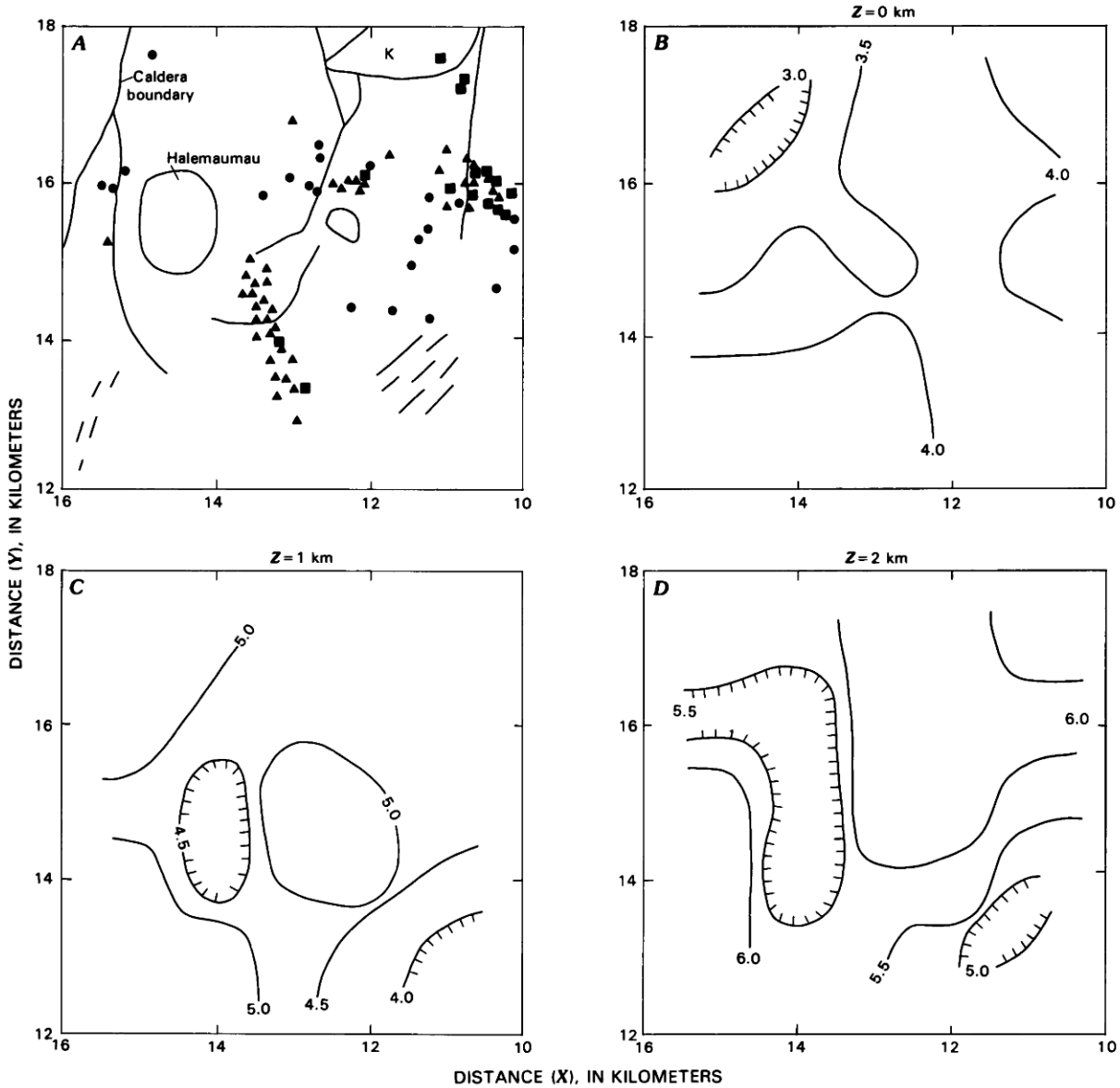


FIGURE 38.7.—Earthquake epicenters and seismic-velocity contours at three levels in high-resolution study area. ***A***, Surface geology and epicenters. Outlines of Kilauea caldera and Halemaumau and Kilauea Iki (K) shown for reference. Faults in lower right are in Ahua area. Focal depths: dots, <1 km; triangles, 1–2 km; squares, 2–3 km. ***B***, Seismic velocities along horizontal slice at sea level. ***C***, Velocities at depth of 1 km below sea level. ***D***, Velocities at depth of 2 km below sea level. Velocity contours in kilometers per second. Hachures indicate closed velocity lows. Two distinct low-velocity zones are evident, although model resolution is only fair.

## SPATIAL VARIATIONS

Sets of earthquake focal mechanisms are first used to explore the tectonics of the major geologic areas surrounding Kilauea caldera: the Kaoiki fault system, the SWRZ, the UERZ, and the Koae fault system. A brief survey of source mechanisms from these regions clearly shows a general relation between the faulting in microearthquakes and the surface expression of the tectonics.

The Kaoiki fault system is thought to be a tectonic boundary between the shields of Kilauea and Mauna Loa. Mechanisms for three small events (magnitudes 2.5–3) are shown in figure 38.9*A*; the earthquake depths ranged from 5 km to 8 km. All three events are almost purely strike slip, presumably right lateral. The microearthquake data suggest east-west compressive stress, in agreement with the mechanism of the November 1983 Kaoiki earthquake of magnitude 6.7 (U.S. Geological Survey, 1983). These observations

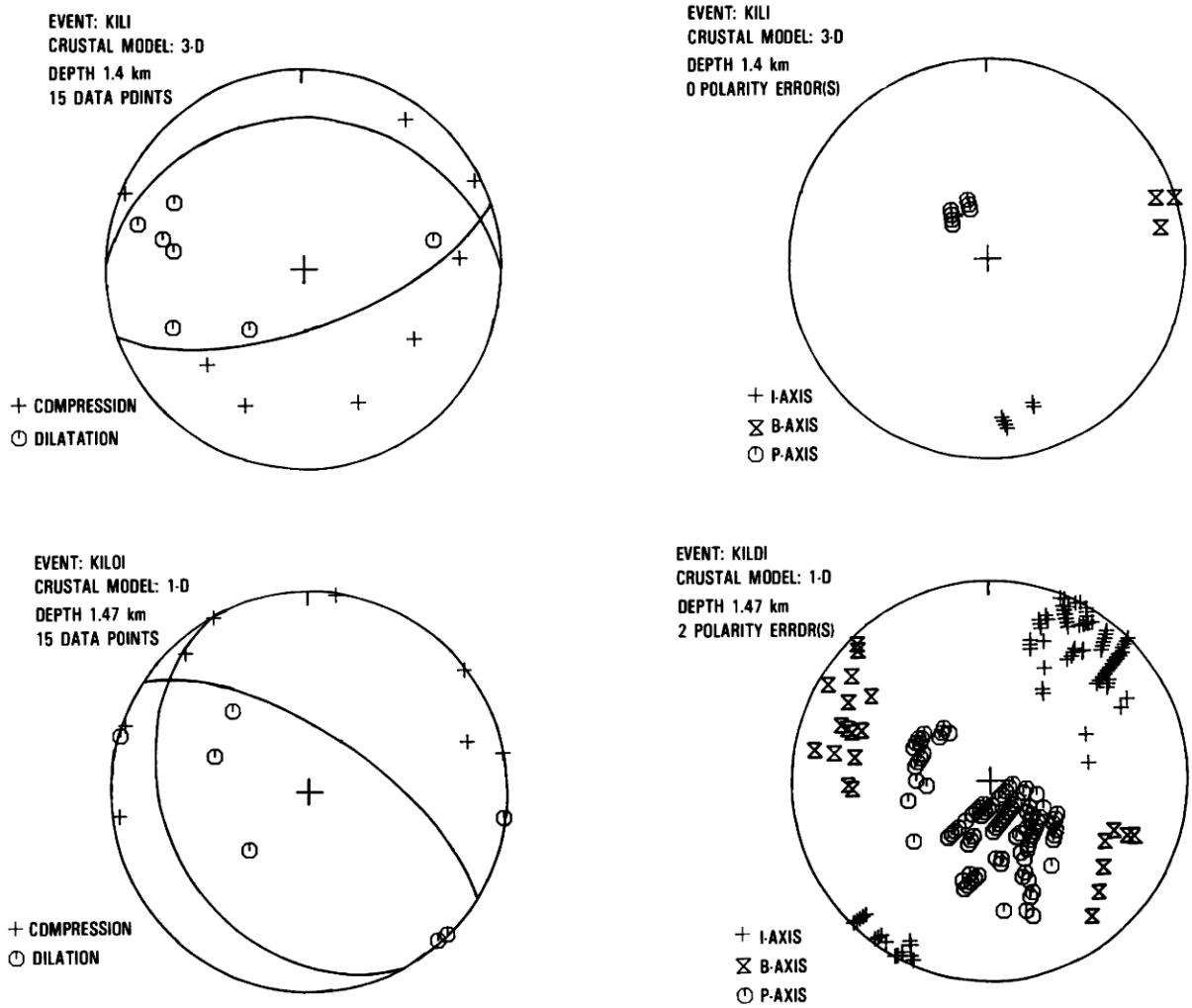


FIGURE 38.8.—Examples of fault plane solutions comparing results using 3-D model (above) to 1-D model (below). Diagrams at left display first motions and reasonable fault-plane solutions; those at right show orientations of permissible maximum, minimum, and intermediate compressive stress axes.

are generally consistent with the notion of stress caused by the nearby growing shields (Endo and others, 1986). Alternatively, it could be thought of as resulting from lateral density variations within Kilauea and Mauna Loa, arising from their dense central cores and in turn producing horizontal stresses oriented radially to their summits. Finally, note that the Kaoiki main shock was located slightly to the northwest and deeper than our events, just off the left side of figure 38.9*A*; if the small events are right lateral, then their northwest-dipping fault plane would dip toward the Kaoiki main shock.

Turning to the SWRZ (fig. 38.9*B*), mechanisms for five 1981 earthquakes of magnitudes 2–3 and depths of 1–3 km are shown. The year 1981 was atypical in that the SWRZ was active and the east rift zone (ERZ) was quiet. With one exception, the mechanisms are clearly consistent with northwest-southeast tension, favorable for intrusive activity on this northeast-southwest rift zone. The discrepant event, number 65, occurred on August 10, 1981, as part of a major intrusive episode, and it may perhaps reflect breaking of an asperity at a bend along the SWRZ.

Along the UERZ (fig. 38.9*C*) is a very clear pattern consistent with east-west compression, permitting intrusion on this east-west rift zone. Five events of magnitude 2–3 and depths of 1–3 km occurred in 1980, when the ERZ was active and the SWRZ was quiet. Except for number 21, all are strike-slip events, but in most cases neither possible fault plane parallels the rift-zone trend, indicating predominance of echelon faulting as suggested by Hill (1977). A similar relation was found by Smith (1984) for a shallow earthquake swarm in Long Valley Caldera, California.

Finally, in the area of the Koae fault system (fig. 38.9*D*) the pattern is as complicated as the surface geology. Five events from

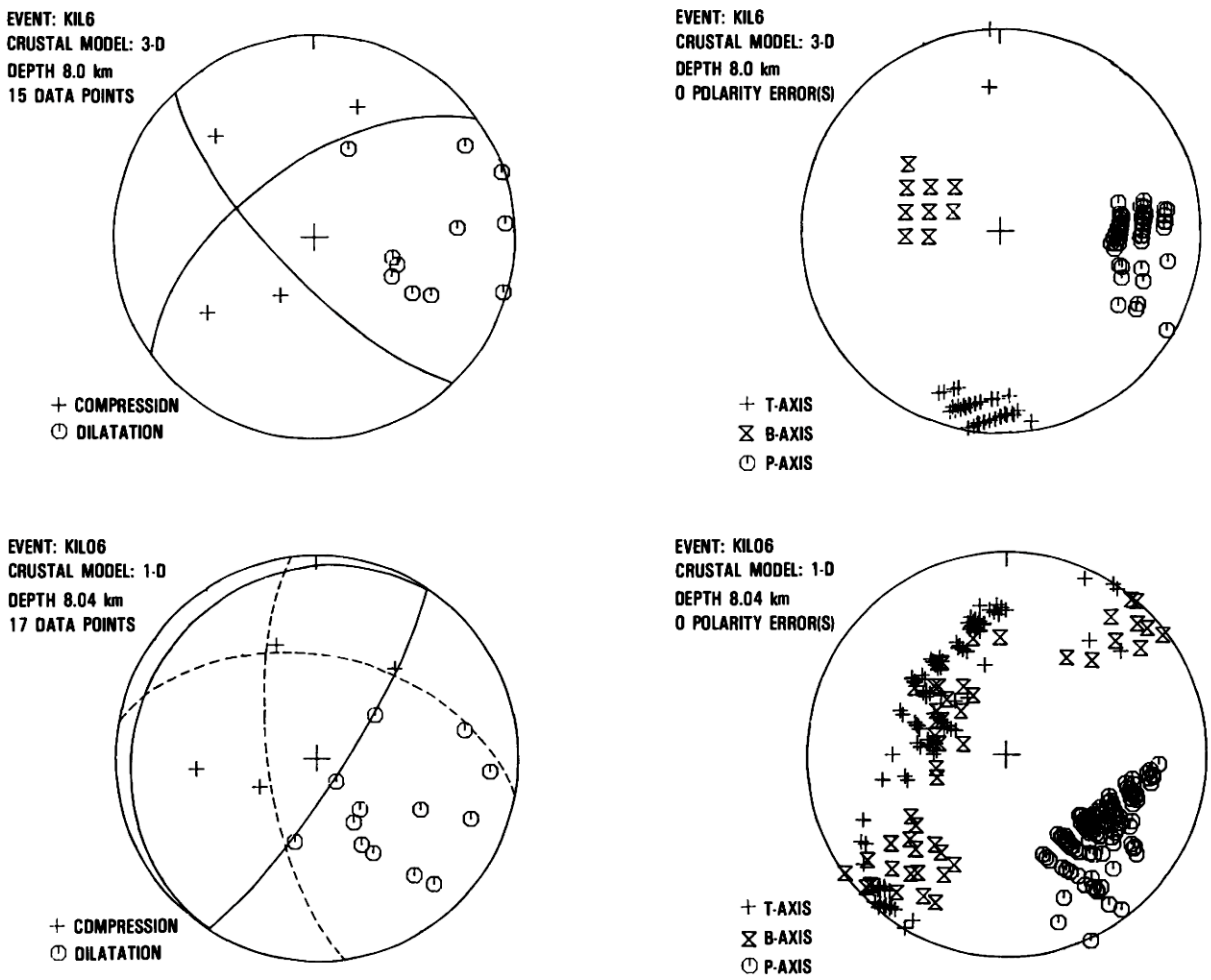


FIGURE 38.8.—Continued.

1980 and 1981 are shown, with magnitudes of 2.5–3 and depths of 4–8 km. Along the eastern section of this area, the earthquakes indicate north-south tension, but those in the western part indicate north-south compression. The eastern events are possibly related more closely to the magma conduit system of the UERZ than to the Koae faults. The western events occurred in 1981, when the SWRZ was experiencing major intrusive activity; the apparent compressive stress south of the SWRZ may be related to this intrusive activity. Mechanisms of events from other years need to be investigated to seek possible temporal variations.

Taken together, these results clearly demonstrate the spatial variability of the stress field surrounding Kilauea Volcano. We suspect these stresses are due in large part to the dramatic lateral density variations present inside the shield, as well as to uneven localized stresses introduced by dike formation. Combining gravity measurements with our model for the seismic velocity structure may enable the direct modeling of these forces.

## TEMPORAL VARIATIONS

For a number of years preceding 1981, Kilauea's eruptive and intrusive activity took place exclusively along the ERZ or at the summit. In 1981, activity shifted abruptly to the SWRZ; subsequently, it has returned to the ERZ. I chose to investigate whether focal mechanisms of summit-area earthquakes might show a shift in fault-plane orientation because of a change in stress orientation related to this shift in direction of magmatic activity. For the ERZ to be active, the hypothesis would predict northwest-southeast compression at the summit, whereas a 90° shift to northeast-southwest compression would be required for the SWRZ to be active. It should be noted, however, that direct inferences of stress orientations cannot be made from earthquake focal mechanisms (MacKenzie, 1969), although efforts have been made recently to formally invert focal-mechanism data for the stress tensor (for

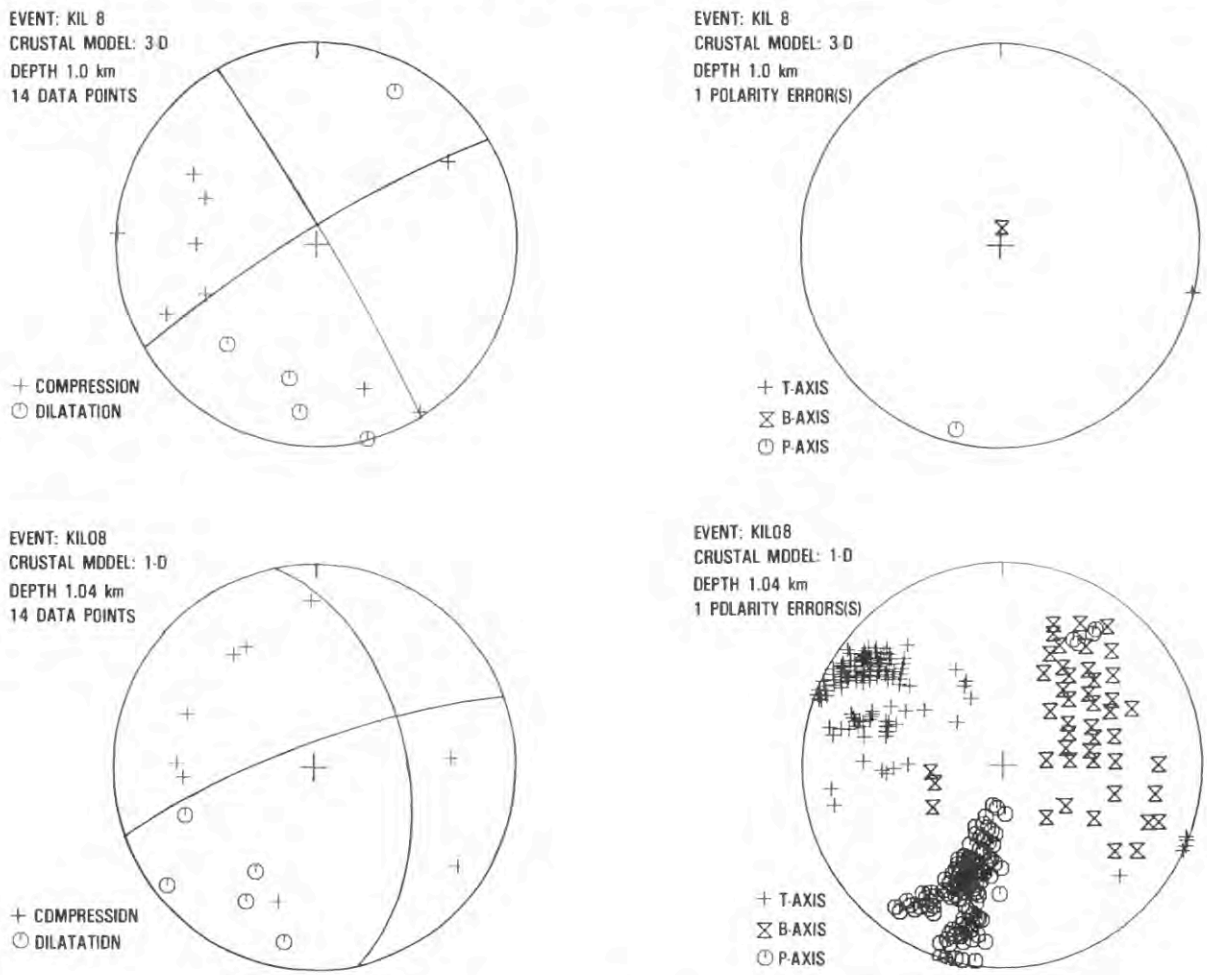


FIGURE 38.8.—Continued.

example, Ellsworth, 1982; Gephart and Forsyth, 1984; Michael, 1984).

Initially, four shallow summit-area earthquakes of magnitude 3 and above were examined (fig. 38.10), one pair from 1980 and a second pair from 1981. These events were the largest and best recorded from the area during this time period. As expected, the 1981 events indicate northeast-southwest compression, and the 1980 events are consistent with northwest-southeast compression. The second 1980 event occurred on December 24, less than one month before the beginning of SWRZ activity. A suite of events encompassing the largest summit earthquakes from January 1981 was therefore selected to seek possible precursory evidence for the impending change in the pattern of magmatic activity.

In order to minimize any confounding effect of spatial variations in stress, only shallow summit earthquakes were examined from two small areas of the caldera (fig. 38.11), all with magnitudes between 2 and 2.5. The range of focal depths was also kept quite small to further reduce the possibility of spatial effects. This series of predominantly strike-slip events, seven along the caldera's southeast rim and four from its west side, indicate a cyclic variation in $P$-axis orientation during January 1–18, with a very sharp change apparent from east-southeast to east-northeast over the last 6 days of the period (fig. 38.12). Unfortunately, no other earthquakes occurred in the vicinity during this time period that were large enough to yield a reliable mechanism.

What are possible causes of this apparent stress reorientation? One possibility would be a rapid change in the rate of magma flow into the summit storage complex. However, the records from tiltmeters around the caldera (fig. 38.13; A.T. Okamura, written commun., 1981) show only minor deviations from a smooth pattern of inflation. The beginning of a major tilt change is evident on January 19, well after the reorientation of the fault-plane solutions is apparent, but before the first SWRZ intrusive episode beginning January 20. Thus this reorientation could have provided early

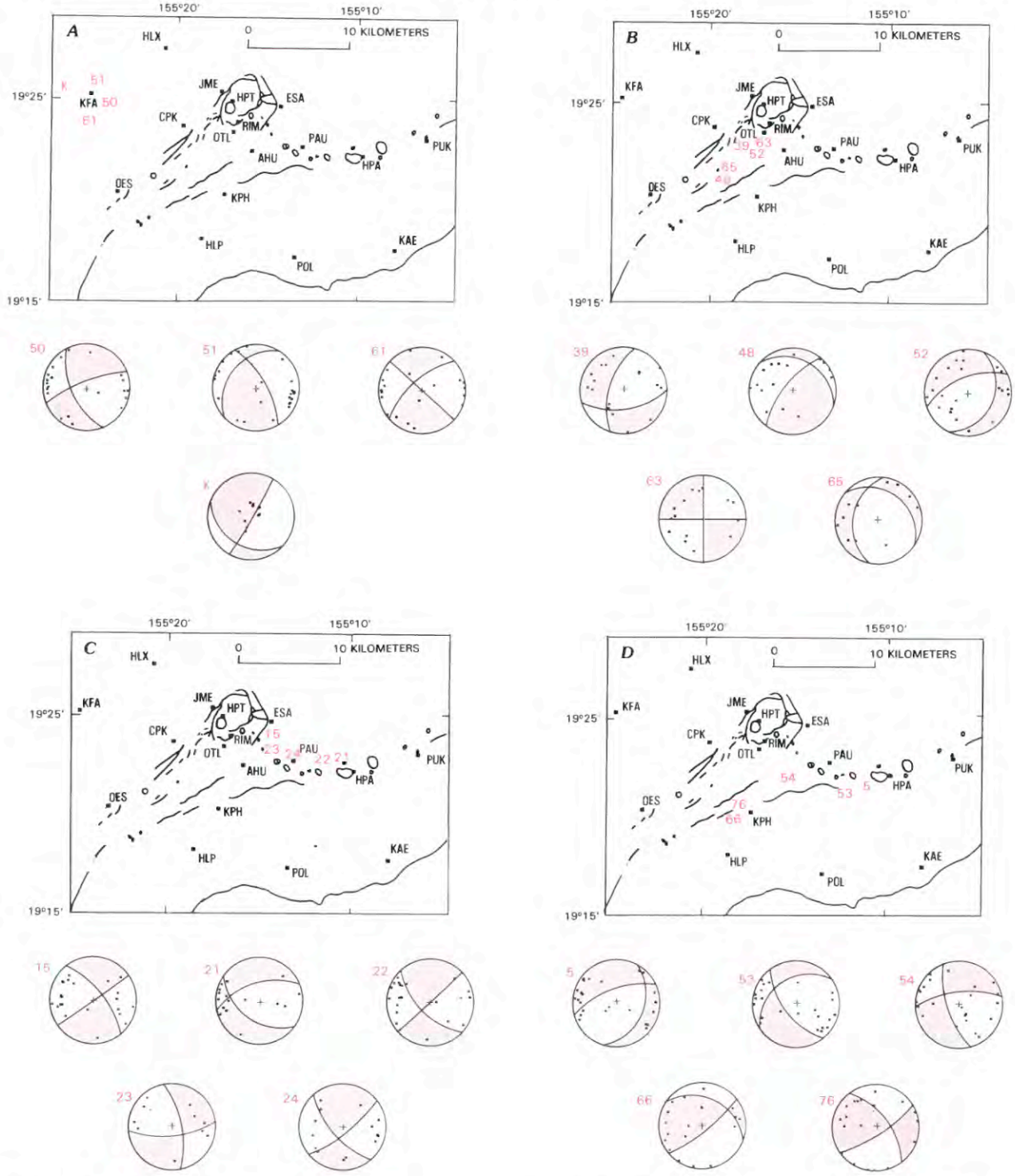


FIGURE 38.9.—Fault-plane solutions for microearthquakes from different sections of study area. Letters refer to HVO seismic stations. ***A***, Kaoiki fault system (including mechanism of 1983 Kaoiki earthquake; U.S. Geological Survey, 1983). ***B***, Southwest rift zone. ***C***, Upper east rift zone. ***D***, Koae fault system.

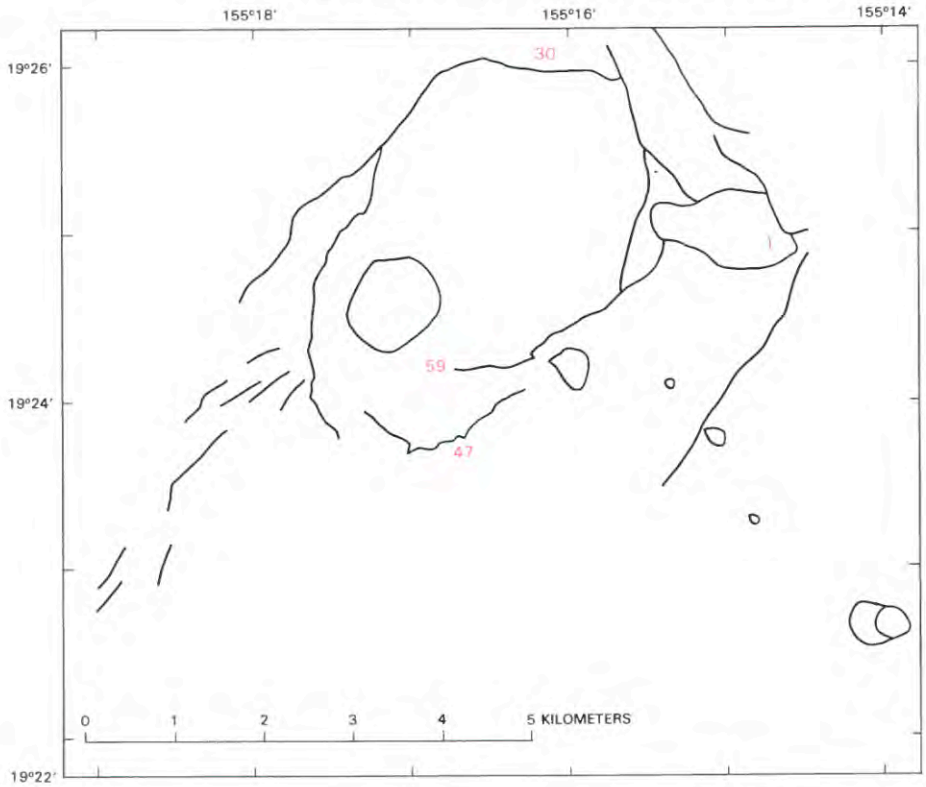


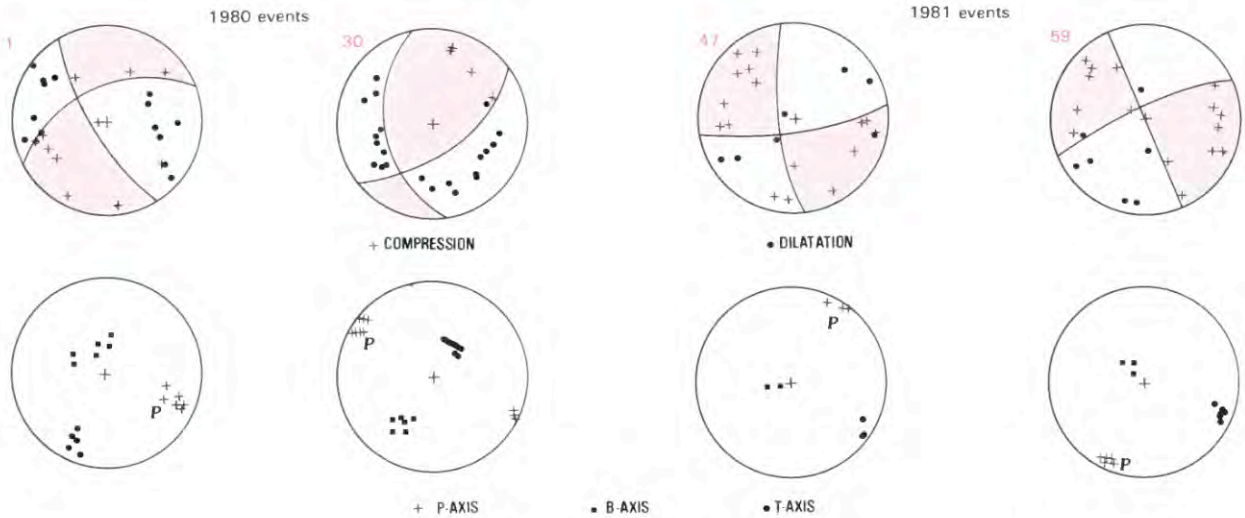


FIGURE 38.10.—Comparison of fault-plane solutions from two caldera-area events in 1980 and two in 1981; differences indicate area-wide change in *P*-axis orientation.

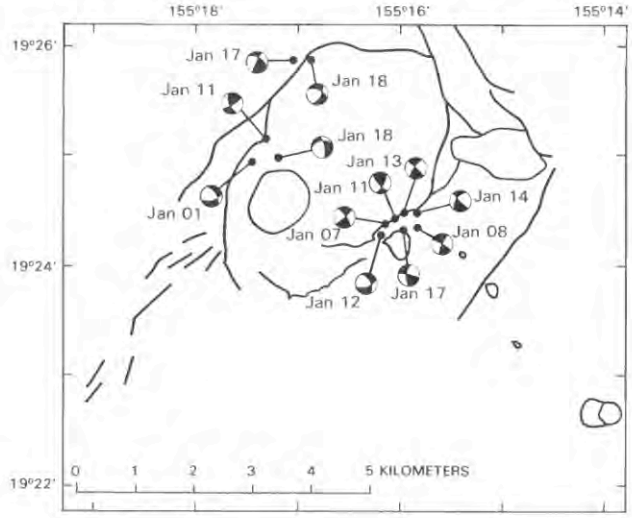


FIGURE 38.11.—Sequence of fault-plane solutions for Kilauea summit earthquakes in two small areas during January 1981 that demonstrates significant temporal variation in faulting orientation (see fig. 38.12).

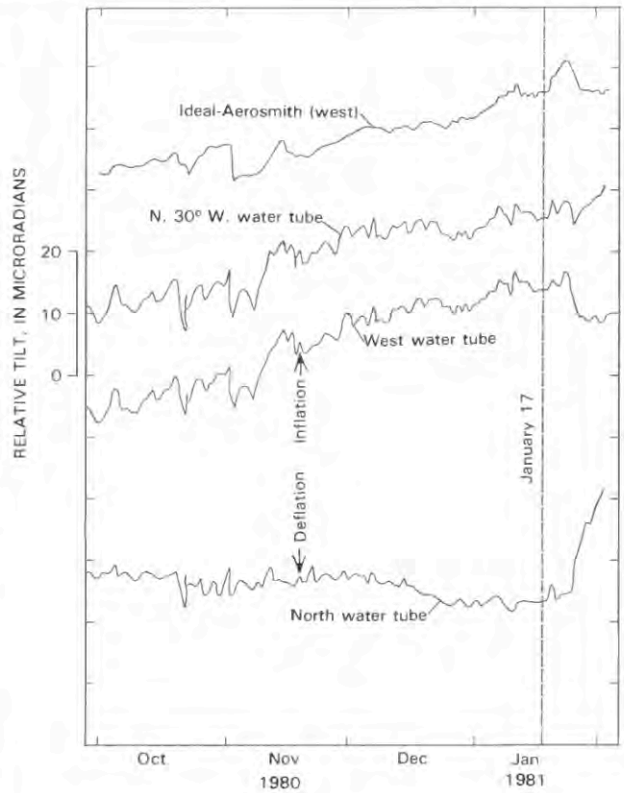


FIGURE 38.13.—Summit tiltmeter records preceding January 1981 southwest rift zone intrusion (A.T. Okamura, unpub. data, 1981), showing no anomalous features before January 17, when earthquake fault-plane solutions had already clearly shown an orientation change.

warning of the impending activity along the SWRZ. This also may be evidence that external forces control the pattern of magma intrusion, rather than the excess pressure of the magma itself.

An extension of this study is necessary to determine the trend of *P*-axis orientation before and after the time period considered. Some questions that need to be addressed include the following: Is this cyclic variation typical or unusual at Kilauea's summit? Are most major intrusions and eruptions preceded by a rapid change in apparent stress reorientation? If so, can this observation be used to help predict eruptions? Planned studies of summit earthquakes for the time period leading up to the 1983 ERZ eruption will seek confirmational evidence.

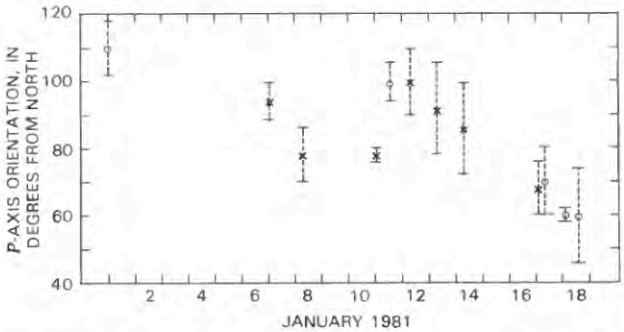


FIGURE 38.12.—Time history of *P*-axis direction (with estimated uncertainties) for focal mechanisms from figure 38.11, showing apparent cyclic variation in faulting orientation from January 1 to January 18, 1981. Crosses and circles indicate events in eastern and western parts of caldera, respectively.

## CONCLUSION AND FUTURE RESEARCH DIRECTIONS

Seismological data clearly are valuable for exploring the structure and dynamics of an active volcano. The vast resource of local earthquake data for Kilauea is just beginning to be tapped; these investigations of volcano structure should be continued and extended both to larger and finer scales. Three-dimensional inversion techniques are perhaps the most promising tool for geophysical imaging of the interior of Kilauea. Fine-scale studies of seismically active areas could be achieved through the deployment of a large network of portable seismographs (for example, PASSCAL), or such an array could be used simultaneously for a larger scale local earthquake and for teleseismic investigation. Detailed focal-mechanism studies should constitute an integral part of the latter type of study.

It seems clear, though, that digital seismic data will hold the key to the analysis of the dynamics of magma transport within the volcano. Earthquake source parameters (moment, dislocation, stress drop, fault area) have already proven useful for the study of Usu Volcano, Japan (Takeo, 1983). Where practical, moment tensor analysis (Wu and Ioannidou, 1985) would provide a means to

explore the relative degrees of shear versus tensile failure (that is, faulting versus magma injection) in local earthquakes associated with magmatic activity. Simply demonstrating the existence of significantly non double-couple events would be of considerable value. A detailed study of an earthquake swarm apparently related to dike formation, like that of 1981, might shed light on the mechanics of magma intrusion. Furthermore, shear-wave attenuation could be used to map the magma conduit system and to search for possible temporal variability. These tasks are difficult but realistic: accomplishing them would make a major contribution toward our understanding of how a volcano works.

## REFERENCES


Ando, M. 1979, The Hawaii earthquake of November 29, 1975: low dip angle faulting due to forceful injection of magma: Journal of Geophysical Research, v. 84, p. 7616–7626.

Bosher, R., and Duennebier, F.K., 1985, Seismicity associated with the Christmas 1965 event at Kilauea Volcano: Journal of Geophysical Research, v. 90, p. 4529–4536.

Broyles, M.L., Suyenaga, W., and Furumoto, A.S., 1979, Structure of the lower east rift zone of Kilauea Volcano, Hawaii, from seismic and gravity data: Journal of Volcanology and Geothermal Research, v. 5, p. 317–336.

Crosson, R.S., and Endo, E.T., 1981, Focal mechanisms of earthquakes related to the 29 November 1975 Kalapana, Hawaii earthquake: the effect of structure models: Bulletin of the Seismological Society of America, v. 71, p. 713–729.

——— 1982, Focal mechanisms and locations of earthquakes in the vicinity of the 1975 Kalapana earthquake aftershock zone 1970–1979: implications for tectonics of the south flank of Kilauea Volcano: Tectonics, v. 1, p. 495–542.

Crosson, R.S., and Koyanagi, R.Y., 1979, Seismic velocity structure below the Island of Hawaii from local earthquake data: Journal of Geophysical Research, v. 84, p. 2331–2342.

DeGroot, M.H, 1975, Probability and statistics: Reading, Mass., Addison-Wesley.

Dvorak, J., Okamura, A., and Dieterich, J.H., 1983, Analysis of surface deformation data, Kilauea Volcano, Hawaii: October 1966 to September 1970: Journal of Geophysical Research, v. 88, p. 9295–9304.

Eaton, J.P., 1962, Crustal structure and volcanism in Hawaii: American Geophysical Union, Geophysical Monograph, v. 6, p. 13–29.

Ellsworth, W.L., 1982, A general theory for determining state of stress in the earth from fault slip measurements: Terra Cognita, v. 2, p. 170–171.

Ellsworth, W.L., and Koyanagi, R.Y, 1977, Three-dimensional crust and mantle structure of Kilauea Volcano, Hawaii: Journal of Geophysical Research, v. 82, p. 5379–5394.

Endo, E.T., 1971, Focal mechanisms for the May 15–18, 1970, shallow Kilauea earthquake swarm: San Jose, Calif., San Jose State University, M.S. thesis.

Endo, E.T., Crosson, R.S., Koyanagi, R.Y., and Nakata, J., (in press), A catalog of earthquake focal mechanisms for the southeast flank of Mauna Loa, 1959–1982: U.S. Geological Survey Open-File Report.

Estill, R.E., 1979, Seismotectonics and velocity structure of the southeastern Hawaiian ridge: Honolulu, University of Hawaii, Ph.D. thesis.

Furumoto, A.S., and Kovach, R.L., 1979, The Kalapana earthquake of November 29, 1975: an intraplate earthquake and its relation to geothermal processes: Physics of the Earth and Planetary Interiors, v. 18, p. 197–208.

Gephart, J.W., and Forsyth, D.W., 1984, An improved method for determining the regional stress tensor using earthquake focal mechanism data: application to the San Fernando earthquake sequence: Journal of Geophysical Research, v. 89, p. 9305–9320.

Hill, D.P., 1969, Crustal structure of the Island of Hawaii from seismic refraction measurements: Bulletin of the Seismological Society of America, v. 59, p. 101–130.

——— 1977, A model for earthquake swarms: Journal of Geophysical Research, v. 82, p. 1347–1352.

Klein, F.W., 1981, A linear gradient crustal model for south Hawaii: Bulletin of the Seismological Society of America, v. 71, p. 1503–1510.

Koyanagi, R.Y., Unger, J.D., Endo, E.T., and Okamura, A.T., 1976, Shallow earthquakes associated with inflation episodes at the summit of Kilauea Volcano, Hawaii: Bulletin Volcanologique, v. 39, p. 621–631.

McKenzie, D.P., 1969, The relation between fault plane solutions for earthquakes and the directions of the principal stresses: Bulletin of the Seismological Society of America, v. 59. p. 591–601.

Michael, A.J., 1984, Determination of stress from slip data: faults and folds: Journal of Geophysical Research, v. 89, p. 11517–11526.

Nakata, J.S., Tanigawa, W.R., and Klein, F.W., 1982, Hawaiian Volcano Observatory Summary 81, part 1, seismic data, January to December 1981: U.S. Geological Survey unpublished report.

Pavlis, G.L., and Booker, J.R., 1980, The mixed discrete-continuous inverse problem: application to the simultaneous determination of earthquake hypocenters and velocity structure: Journal of Geophysical Research, v. 85, p. 4801–4810.

Rodi, W.L., Jordan, T.H., Masso, J.F., and Savino, J.M., 1980, Determination of the three-dimensional structure of eastern Washington from the joint inversion of gravity and earthquake travel-time data: Systems, Science and Software Report SSS-R-80-4516.

Ryall, A., and Bennett, D.L., 1968, Crustal structure of southern Hawaii related to volcanic processes in the upper mantle: Journal of Geophysical Research, v. 73, p. 4561–4582.

Ryan, M.P., Blevins, J.Y.K., Okamura, A.T., and Koyanagi, R.Y., 1983, Magma reservoir subsidence mechanics: theoretical summary and application to Kilauea Volcano, Hawaii: Journal of Geophysical Research, v. 88, p. 4147–4181.

Ryan, M.P., Koyanagi, R.Y., and Fiske, R.S., 1981, Modeling the three-dimensional structure of macroscopic magma transport systems: application to Kilauea Volcano, Hawaii: Journal of Geophysical Research, v. 86, p. 7111–7129.

Shaw, H.R., 1980, The fracture mechanisms of magma transport from the mantle to the surface, *in* Hargraves, R.B., ed., Physics of Magmatic Processes: Princeton, NJ, Princeton University Press.

Smith, A.T., 1984, High-resolution microseismicity study of possible magmatic intrusion in the Long Valley Caldera: U.S. Geological Survey Open-File Report 84–939, p. 527–535.

Spencer, C., and Gubbins, D., 1980, Travel time inversion for simultaneous earthquake location and velocity structure determination in laterally varying media: Geophysical Journal of the Royal Astronomical Society, v. 63, p. 95–116.

Swanson, D.A., Duffield, W.A., and Fiske, R.S., 1976, Displacement of the south flank of Kilauea Volcano: the result of forceful intrusion of magma into the rift zones: U.S. Geological Survey Professional Paper 963.

Takeo, M., 1983, Source mechanisms of Usu Volcano, Japan, earthquakes and their tectonic implications: Physics of the Earth and Planetary Interiors, v. 32, p. 241–264.

Tanigawa, W.R., Nakata, J.S., and Klein, F.W., 1981, Hawaiian Volcano Observatory Summary 80, part 1, seismic data, January to December 1980: U.S. Geological Survey unpublished report.

Thurber, C.H., 1981, Earth structure and earthquake locations in the Coyote Lake area, central California: Cambridge, Massachusetts Institute of Technology, Ph. D. thesis.

——— 1983, Earthquake locations and three-dimensional crustal structure in the Coyote Lake area, central California: Journal of Geophysical Research, v. 78, p. 8226–8236.

——— 1984, Seismic detection of the summit magma complex of Kilauea Volcano, Hawaii: Science, v. 223, p. 165–167.

Thurber, C.H., and Ellsworth, W.L., 1980, Rapid solution of ray tracing problems in heterogeneous media: Bulletin of the Seismological Society of America, v. 70, p. 1137–1148.

Thurber, C.H., Karpin, T., and Um, J.H., 1984, Focal mechanisms of earthquakes at Kilauea Volcano: a detailed study [abs.]: Eos, Transactions of the American Geophysical Union, v. 65, p. 1001.

Unger, J.D., and Ward, P.L., 1979, A large deep Hawaiian earthquake—the

Honomu, Hawaii event of April 26, 1973: Bulletin of the Seismological Society of America, v. 69, p. 1771–1781.

U.S. Geological Survey, 1983, Preliminary determination of epicenters, Nov. 1983.

Wu, F.T., and Ioannidou, E., 1985, Linearized source moment tensor inversion of near-source seismograms [abs.]: Eos, Transactions of the American Geophysical Union, v. 66, p. 315.

Zucca, J.J., and Hill, D.P., 1980, Crustal structure of the southeast flank of Kilauea Volcano, Hawaii, from seismic refraction measurements: Bulletin of the Seismological Society of America, v. 70, p. 1149–1159.

Zucca, J.J., Hill, D.P., and Kovach, R.L., 1982, Crustal structure of Mauna Loa Volcano, Hawaii, from seismic refraction and gravity data: Bulletin of the Seismological Society of America, v. 72, p. 1535–1550.

# AEROMAGNETIC AND NEAR-SURFACE ELECTRICAL EXPRESSION OF THE KILAUEA AND MAUNA LOA VOLCANIC RIFT SYSTEMS

*By* Vincent J. Flanigan *and* Carl L. Long

## ABSTRACT

**Aeromagnetic and electromagnetic data from a draped (90-m terrain clearance) survey of the rift systems extending east and southwest from the summits of Kilauea and Mauna Loa Volcanoes are interpreted to reflect near-surface magnetic and electrical resistivity characteristics of the rift zones. Shallow dike complexes of more intense magnetism than their extrusive equivalents are the main source rocks for the observed magnetic anomalies along the rift zones. Conductive rocks are reflected in the electromagnetic data as apparent resistivity lows. Sharp lateral changes of conductivity are detected as VLF magnetic anomalies and are interpreted to represent relatively narrow, conductive zones over feeder dikes along active parts of the rift zones.**

**The spatial relations of the interpreted magnetic source rocks to observed apparent resistivity and VLF magnetic anomalies are generally consistent with geologic and structural observations. The active part of the east rift zone of Kilauea lies south of the magnetic source rocks in the upper one-third of the east rift zone, reflecting southward movement of Kilauea's south flank. Farther east, beyond Napau Crater, the active part of the east rift zone of Kilauea, as interpreted from VLF magnetic anomalies, lies in the central to northern part of the interpreted magnetic source rocks. This change of spatial relation of the geophysical anomalies is interpreted to reflect structures transverse to the rift zone that are associated with large-scale block slumping of the south flank of Kilauea. Similarly, large-scale block slumping on the west flank of Mauna Loa is reflected by magnetic anomalies east of the active part of the rift zone. A major apparent resistivity and magnetic low transverse to the southwest rift zone of Mauna Loa may reflect the southern boundary of the subaerial Alika slide, which extends 80 km offshore from Mauna Loa's west coast.**

**The buttressing of Mauna Loa by Mauna Kea on the north and Kilauea on the south, as recognized by geophysical data, contributes to the complexity of the Mauna Loa northeast rift zone. The VLF magnetic anomalies defining the active northeast rift zone of Mauna Loa are present only in the upper 10–12 km of the rift, thus indicating that the action of buttress forces limits recent volcanic activity farther east along the rift zone.**

**Two interpretations of an apparent reversely polarized magnetic dipole anomaly over Kapoho Crater are modeled. One model assumes an intrusive body in which the direction of remanent magnetism is nearly opposite to the present magnetic field of the Earth. The other model assumes a nonmagnetic body separating two magnetic dike systems—the northern system related to development of Mauna Loa's northeast rift zone and the southern one related to Kilauea's east rift zone.**

## INTRODUCTION

Mauna Loa and its smaller neighbor, Kilauea, have been studied, and volcanic activity extensively documented for only the relatively brief historical period extending back to the late 19th century. Accumulated evidence from observations of earth scientists has allowed a better understanding of growth, structural complexity, and volcanic activity of these two shield volcanoes. The purpose of this paper is to examine some of the more obvious aeromagnetic and electromagnetic features and show how they complement or augment observations of other earth scientists.

In early 1978 the U.S. Geological Survey (USGS) conducted several airborne surveys that covered large areas of the Island of Hawaii. An aeromagnetic survey of the entire island was flown at a mean terrain clearance of 300 m (Godson and others, 1981). In addition, a low-level (90-m mean terrain clearance) total-field magnetic and very low frequency (VLF) electromagnetic survey was flown over the rift zones extending east and southwest from the summits of Kilauea and Mauna Loa Volcanoes (fig. 39.1; Flanigan and others, 1986a, b). Data from the low-level survey form the basis of this paper.

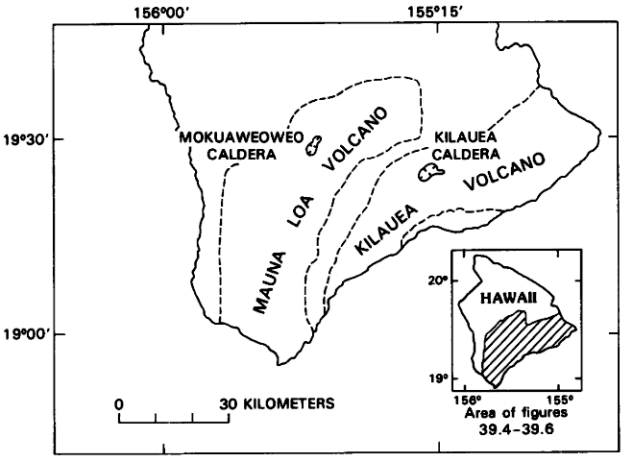


FIGURE 39.1.—Index map of Island of Hawaii, showing boundary (dashed) of airborne electromagnetic-magnetic surveys over Kilauea and Mauna Loa Volcanoes.

Extensive airborne and shipborne magnetic surveys were made over the Hawaiian Ridge in the mid-1960's by Malahoff and Wollard (1966) and Malahoff and McCoy (1967). Most of the data from these earlier magnetic surveys were used with the 1978 data to compile a composite aeromagnetic map of the Hawaiian Islands as part of a cooperative ongoing effort by the Society of Exploration Geophysicists and the USGS to produce gravity and magnetic maps of the United States (Godson and others, 1984).

The low-level airborne survey made by the USGS, primarily designed to record VLF responses, was the first and perhaps only such airborne survey on the Island of Hawaii. The airborne VLF method has proven practical in engineering and geologic applications on the contiguous continental United States and Alaska (Frischknecht, 1971; Hoekstra and others, 1975; Arcone, 1978, 1979).

Extensive ground VLF surveys, along with other electromagnetic methods, have been utilized in geophysical studies mainly in the Kilauea Volcano summit area and parts of the rift zones extending east and southwest from the summit (Zablocki, 1978).

## METHODS

Problems related to aeromagnetic surveying, and in particular over magnetic Hawaiian terrain, are addressed by Malahoff and Wollard (1966). Topographic aeromagnetic anomalies are expected in those areas where the survey aircraft cannot maintain constant terrain clearance. Studies are currently being done in an effort to evaluate and remove terrain effects from aeromagnetic maps (Blakely and Grauch, 1983). Aeromagnetic surveys flown at constant altitude (barometric) or constant terrain clearance (draped) are both subject to some degree of erroneously induced magnetic anomalies due to rugged topography. In fact, terrain effects may be enhanced in magnetic terrane in drape-flown surveys over that of traditional barometric-flown magnetic surveys (Grauch and Campbell, 1984). In the low-level aeromagnetic survey described here the fixed-wing aircraft was successful in maintaining $\pm 30$ m of the nominal survey height, except when the aircraft passed over pit craters and cinder cones.

Theoretical terrain-induced magnetic anomalies were computed for two-dimensional models approximating volcanic cones, craters, and calderas to qualitatively evaluate the observed magnetic anomalies (not shown here). Terrain anomalies, using magnetic susceptibilities of approximately $1.0 \times 10^{-2}$ cgs units, were not over 400 nanoteslas (nT). The most distinguishing feature about the theoretical terrain anomalies is the short wavelength of the anomaly, usually much shorter than the wavelength of many of the observed anomalies. Thus, in an area of abrupt terrain variation, the observed anomaly is a composite magnetic response of the terrain and the magnetic geologic sources.

Hawaiian intrusive rocks, primarily in the form of dikes, have an intensity of remanent magnetization more than 10 times that of the induced magnetization (Decker, 1963; Malahoff and Strange, 1965). It is evident from aeromagnetic data and confirmed by theoretical modeling (Flanigan and others, 1986a) that about the same apparent order of magnitude difference exists between the magnetic properties of intrusive dike systems and lava flows. The reason for this apparent difference of bulk magnetic properties is not clear because the dike rocks are a composite (over time) of the same extrusive rocks comprising the lava flows. The direction of remanent magnetization of lava flows on the Island of Hawaii is essentially the same as the Earth's present field direction. However, remanent magnetization directions on samples of massive basalt flows may not be representative of the overall section. Sequences of exposed Hawaiian lavas (in fault scarps and sea cliffs) are highly porous. L.A. Anderson (oral commun., 1984) says drill core recovery from drill holes in the Kilauea area is about 20 percent, suggesting that the bulk of the section is composed of porous rocks not easily recovered during drilling. We assume that postcooling movement of the lava flows either by tumbling of blocks in breccia envelopes in flows or by postcooling compaction of pahoehoe flows has caused a jumbled assemblage of remanent magnetization directions. The net result would be an apparent lower bulk magnetization of the flow rocks than the intrusive rocks. Induced magnetization would remain unaffected.

Sources of magnetic anomalies are based upon a qualitative interpretation, consistent with the magnetic anomaly shape and approximate orientation of the body with respect to the Earth's magnetic field direction. To illustrate the relative amplitude and anomaly shape that might be expected, an assumed two-dimensional dike representing intrusive rocks of bulk magnetism 10 times greater than the extruded basalt flows was rotated in the Earth's magnetic field, and the theoretical magnetic response calculated (fig. 39.2) at several positions. The magnetic anomaly varies from a symmetrical magnetic high of about 400-nT amplitude, when the dike is oriented parallel to the direction of the Earth's magnetic field (solid line on fig. 39.2), to a dipole anomaly of over 3,000-nT amplitude for a dike oriented about normal to the direction of the Earth's magnetic field (azimuth 90° or 120° on fig. 39.2). Note: for rocks normally polarized—that is, the direction of the remanent magnetism is the same as the Earth's present field direction—the dipole magnetic high is on the south and the low is on the north. For magnetic features oriented normal to the Earth's magnetic field direction, the edges of the magnetic body lie under the apex of the dipole high and low. For magnetic sources oriented parallel to the Earth's magnetic field, the edges of the causative body lie under the point of steepest gradient of the magnetic anomaly. Of course there are any number of cases in between the two extremes mentioned above. Thus, locations for magnetic source rocks based on these qualitative considerations have greater uncertainty in those areas where the strike of the magnetic source rocks is not parallel or normal to the direction of the Earth's present magnetic field.

The theory of radio wave propagation and the measurement of electric and electromagnetic properties of the Earth's near surface has been extensively discussed elsewhere (Wait; 1962; Paal, 1965, 1968; Barringer and McNeil, 1969; Patterson and Ronka, 1971; and Frischknecht, 1973). Details of the electrical and electromagnetic parameters measured by the USGS airborne VLF equipment used to acquire data presented in this paper are given in Flanigan and others (1986b).

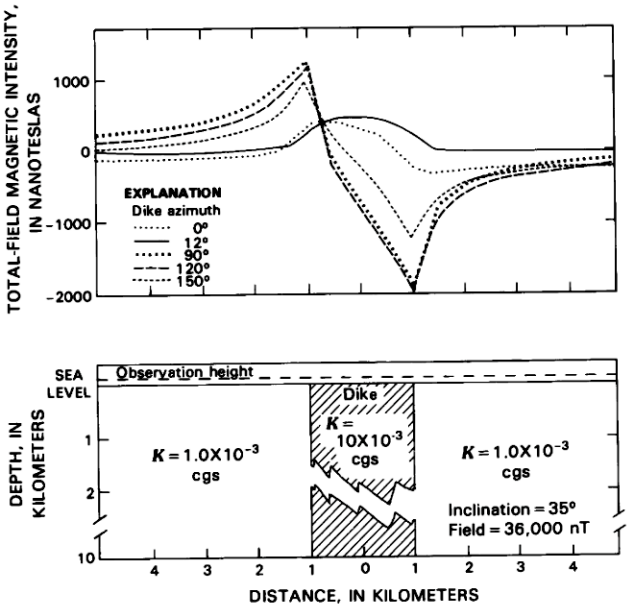


FIGURE 39.2.—Theoretical models of magnetic dike rocks rotated in Earth's magnetic field showing relative amplitude and anomaly shape. Remanent magnetism is considered to be parallel to direction of Earth's present magnetic field. Susceptibilities ($K$) are shown in cgs units.

Briefly, the VLF technique measures the local electric and magnetic characteristics of a vertically polarized groundwave transmitted by one of many VLF communication transmitters located worldwide. The local amplitude of the electric and magnetic fields of the transmitted radiowave is dependent on several factors, such as: transmitted power output, distance between transmitter and receiver site, propagation events in the ionosphere, local topography, and resistivity of the Earth between the transmitter and receiver.

Earth resistivity values are computed from the amplitude ratio of the horizontal electric field to the vertical electric field (wave tilt; Hoekstra and others, 1975). Inasmuch as the Earth resistivities determined by the wave tilt usually are a combined response over a layered earth composed of differing resistivities, they are called apparent resistivities. Wave-tilt apparent resistivities may vary significantly from those determined by ground VLF methods mainly because the airborne and ground methods use different magnetic and electric field components of the transmitted radiowave which are affected differently by the conductivity (inverse of resistivity) and thicknesses of the layered Earth.

The thickness of the upper surface of the Earth that influences the VLF electromagnetic responses, called the skin depth, is related to the surface apparent resistivity and the frequency of the electromagnetic field. The skin depth for rocks of 100 Ω-m apparent resistivity is about 36 m, and for 10,000 Ω-m is about 360 m.

VLF magnetic measurements discussed in this paper are the responses of the measured magnetic field to geologic sources of differing conductivities. The VLF magnetic responses are particularly sensitive to sharp lateral changes of conductivity. In addition, the vertical and horizontal VLF magnetic field components have diagnostic responses to geologic sources, particularly those of high conductivity contrast. To illustrate these diagnostic responses, the real part of the VLF magnetic responses for the horizontal and vertical field components are shown in figure 39.3 over conductive bodies of different widths. The distinctive shape of the VLF magnetic responses over narrow and wide conductive bodies is readily apparent.

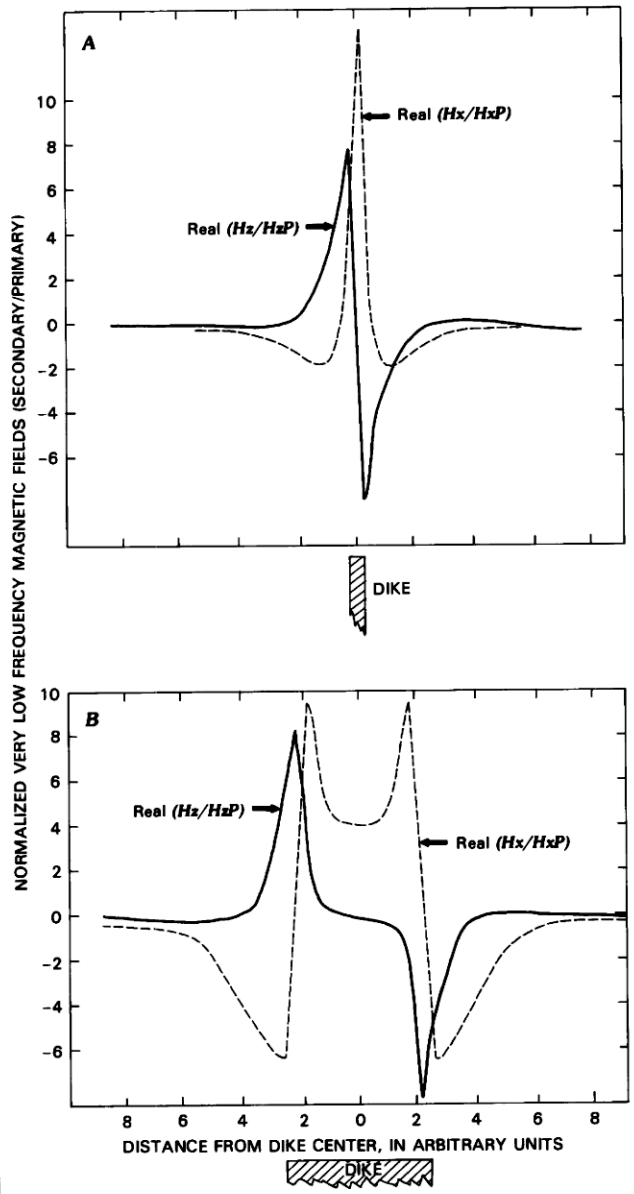


FIGURE 39.3.—VLF magnetic field component response over conductive dikes of 30-m ($A$) and 500-m ($B$) width. Conductivity contrast is 10, that is, a conductive dike of 0.01 mho/m in host of 0.001 mho/m. Horizontal ($Hx$) and vertical ($Hz$) magnetic fields have been normalized to primary ($P$) field components.

Factors affecting the resistivity of basalt over the rift systems of Kilauea and Mauna Loa Volcanoes are important in understanding the VLF data presented in this paper. In nonthermal areas, resistivities of basalt lava flows are $3-20 \times 10^3$ Ω-m (Keller and Rapolla, 1974; Zablocki, 1976). Zablocki (1978) suggests several possible causes for these high resistivities: (1) high permeability of the lava flows resulting in very little water in the zone of aeration above the local water table; (2) resistive pore water in the vadose zone, probably resulting from previous leaching of exchangeable ions from the rock by heavy rainfall; (3) negligible chemical alteration of the flows and surficial ash deposits, thereby maintaining to a minimum the amount of clays in the rock which can contribute to double-layer conductivity in the rock pores (Keller and Frischknecht, 1966).

In contrast to nonthermal areas, areas of recent volcanic activity along the rift systems are often associated with low resistivity (high conductivity) values. Conductive zones associated with magma injected from the summit reservoirs of Kilauea and Mauna Loa are generally relatively narrow, probably because of low thermal conductivity of the basalt, which impedes heat transfer from the injecting magma to the surrounding rocks (Zablocki, 1978). Basalt flows directly over eruptive fissures and related ground cracks become conductive by ascending hot mineralized water or vapor derived from the interaction of ground water with high-temperature magma in the injecting dikes. Large zones of conductive basalt are expected to be developed over magma reservoirs where thermal convection cells have been operative for long periods of time.

Factors other than thermal may also reduce ground resistivities. Thick soils are expected to contribute to lower apparent resistivity values than in areas where overburden is thin or absent. Such soils are widely present in the northwest and northern edges of the Kilauea survey area.

Some apparent resistivity lows along the edges of the survey areas may be an artifact of the automatic gridding program (Webring, 1981), which projects data 2 km beyond the end of real data. Thus, caution should be used when viewing automatically contoured data, particularly near the boundary of the survey area.

### ACKNOWLEDGMENTS

The authors owe much to and acknowledge the contributions of many associates in the U.S. Geological Survey who were instrumental in the original concept of the airborne survey, in particular C.J. Zablocki, John Lockwood, and other scientists of the Hawaiian Volcano Observatory who conceived the project and assisted in the logistics during the actual survey. To the aircraft flight crew, Donald Rohret, electronic technician, and pilot M.G. Steward we extend thanks. To Frank Frischknecht who has led the research and development of the airborne VLF method and provided the authors with many helpful hints and suggestions during the compilation and interpretation of the data we extend a special thanks. Last but not least, we acknowledge the assistance of technicians Mark Sherrard and Pam Mohr who were extremely helpful in the actual compilation of the data. Obviously, responsibility for the validity of the interpretations presented here are the authors' alone.

## MAGNETIC AND ELECTROMAGNETIC FEATURES

### KILAUEA VOLCANO

Numerous magnetic features were delineated over the east and southwest rift zones of Kilauea Volcano. The most prominent magnetic feature on figure 39.4 is associated with the east rift of Kilauea Volcano and consists of linear dipole anomalies, of nearly 2,000-nT amplitude, extending eastward from the summit of Kilauea to within 7 km of the coast, where the dipole anomaly abruptly terminates as a linear feature. East of this termination point, several individual magnetic highs and lows characterize the magnetic expression of the rift zone.

An east-trending series of linear magnetic dipoles, having about one-half the amplitude of the east rift magnetic anomaly, are present 10–12 km farther north. The wavelength of this northernmost linear magnetic anomaly is 6 km, as compared to the east rift magnetic anomaly of about 2 km.

The southwest rift of Kilauea Volcano is characterized by a series of magnetic highs, generally aligned with the eruptive fissures, ground cracks, and scarps of the southwest rift zone, but mostly southeast of the surficial volcanic features.

A north- to northeast-trending belt of magnetic highs, only partially delineated by the low-level survey, is evident along the northwest to north edges of the Kilauea survey area in the more extensive aeromagnetic survey of Godson and others (1981).

The apparent resistivities of near surface (less than 100 m depth) lava flows in the central part of the Kilauea survey area range from under 100 to over 2,500 Ω-m (fig. 39.5). Steep apparent resistivity gradients along the northern edge of the Kilauea survey area are related to powerline interference (see Flanigan and others, 1986b). The steep apparent resistivity gradient along the southern part of the Kilauea survey area, where the survey aircraft flew over the ocean, is the response to the high resistivity contrast between rock and sea water. Several small (less than 1-km diameter) conductive zones are associated with Kilauea caldera and along the active parts of the east rift zone. Three conductive zones (40–250 Ω-m) trend north-northwest from near the seacoast to the east rift of Kilauea. Apparent resistivities of less than 400 Ω-m cover a large area south of Kilauea caldera.

VLF magnetic anomalies associated with zones of comparatively sharp lateral changes of conductivity are also shown on the apparent resistivity map (fig. 39.5). Where the VLF magnetic anomalies were detected by adjacent flightlines, they have been connected to indicate the general trend of the conductor axis. Trends of VLF magnetic anomalies follow volcanic features along the east and southwest rifts of Kilauea, along the southern part of Kilauea caldera, and along east-west conductors in the area south of Kilauea caldera.

Geophysical features discussed above have been combined in a single illustration for ease of discussion (fig. 39.6).

### DISCUSSION OF RESULTS

The spatial relations of the magnetic source rocks to the VLF electromagnetic anomalies along the east rift of Kilauea Volcano is

particularly interesting. The interpreted boundaries of the magnetic source rocks encompass most of the surficial expression of the east rift zone (cones, craters, and cracks) as shown by Stearns and Macdonald (1946). Assuming that the VLF magnetic anomalies are associated with narrow, shallow, abrupt changes of conductivity related to feeder dikes along the east rift, then the currently active zone extends south to at least Napau Crater (fig. 39.6), and generally along the southwest and south edges of the interpreted composite dike system built by earlier injections along the east rift zone (Swanson and others, 1976). East of Napau Crater, the active dike system as defined by the VLF magnetic anomalies (fig. 39.6) changes direction to the northeast and continues eastward along the central and northern part of the interpreted magnetic dike system. The reason for the shift to the central part of the interpreted composite dike system is not readily apparent.

Several indirect lines of evidence suggest a structure zone trending about normal to the east rift that may intersect the rift just east of Napau Crater. A north-northwest zone of conductive lava flows (marked $R_1$, fig. 39.6) intersects the east rift of Kilauea in the area just east of Napau Crater. Rocks are an order of magnitude more conductive than outside of the zone. Assuming the upper 50–60 m of basalt has been altered or contains higher amounts of conductive waters than outside of the zone, then a break in the impervious dikes constraining fluid flow on the southeast side of the rift similar to the reasoning hypothesized by Zablocki (1977, p. 9; Zablocki and Koyanagi, 1979) might be invoked.

Although no surface transverse structure is associated with this conductivity anomaly, several geologic features support this conclusion. Topographic contours within the conductive zone change in direction to the northeast. Fault scarps of the Hilina fault system have an apparent left-lateral offset in this area. Block movement to the southeast on the south flank of Kilauea Volcano, suggested by Fiske and Kinoshita (1969) and well documented by Swanson and others (1976), would allow for such transverse structures, particularly if the south flank is not being forced southward as a contiguous block.

The distribution of 1968–71 earthquakes (Koyanagi and others, 1972) in the south flank of Kilauea has a density pattern that delineates two aseismic zones parallel but offset from the shallow resistivity anomalies $R_1$ and $R_2$ (fig. 39.6). The seismicity is caused

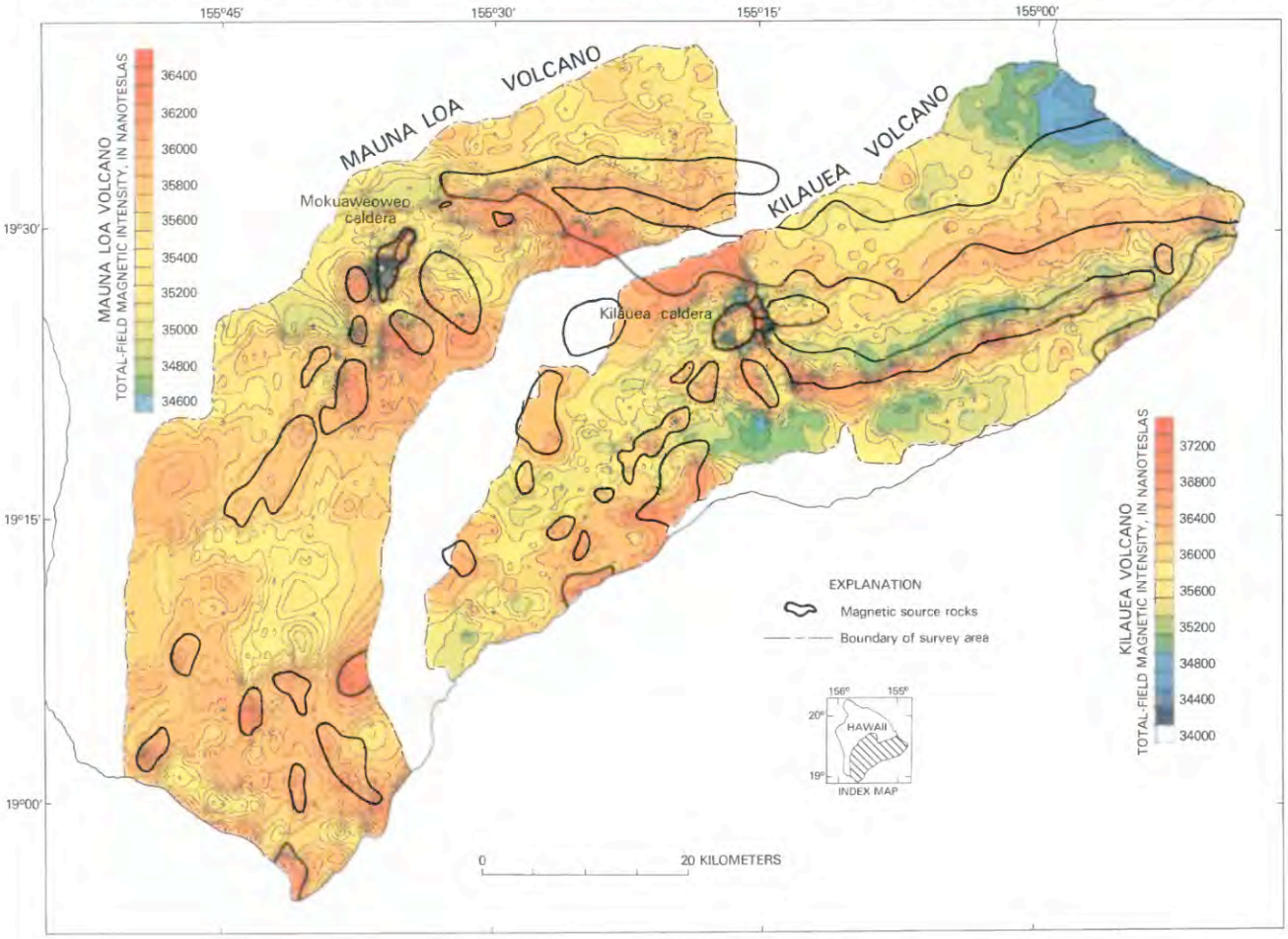


FIGURE 39.4.—Aeromagnetic map of total intensity of Earth's magnetic field over Kilauea and Mauna Loa rift systems.

by volcanic activity in the summit and the rift zones and the subsequent adjustment of the south flank to these stresses (Koyanagi, and others, 1972). If there is differential movement within the south flank, then transverse structures are likely along the edges of the blocks moving seaward from the rift zones. The Kealakakua and Kahuku faults are thought to represent the landward boundaries of sizable terrain subject to large-scale submarine block faulting on Mauna Loa's west flank (Lipman, 1980, fig. 2) analogous to movement of Kilauea's south flank.

Two other zones of conductive rocks, roughly transverse to the east rift were delineated farther east ($R_2$ and $R_3$, fig. 39.6). Conductive zone $R_2$ is situated at another apparent offset (left-lateral) in the currently active part of the rift zone. Here again rocks are considerably more conductive (<160 Ω-m) than the surrounding basalt flows. Though conductive zones $R_1$ and $R_2$ have not been confirmed by ground measurements, independent geophysical work generally confirms the existence of the third transverse conductive zone (Zablocki, 1977). A significant self-potential (SP) anomaly, aligned northwest, was attributed by Zablocki and Koyanagi (1979) to permeable fractures that maintain fluid continuity with a heat source. Numerous warm springs along the downslope beaches and the occurrence of hot (55 °C) brackish water in wells in the conductive area (Macdonald, 1973) support the conclusion that the zone is related to a transverse structure that has offset the rift zone in a left-lateral sense. The linear dipole magnetic anomaly also has a left-lateral offset at this point. A small (300 nT) magnetic low, correlative with a resistivity low, is centered over the Puulenna Crater area, suggesting that Zablocki and Koyanagi's (1979) heat source may still be above the Curie temperature.

An apparent reversely polarized magnetic anomaly is present over the Kapoho Crater area (figs. 39.4, 39.6). The detailed data (fig. 39.7*A*) show a dipole anomaly with a 900-nT low south of a 700-nT high. The apex of the high-low is oriented about 30° counterclockwise to the Earth's present magnetic field direction. If the direction of the remanent magnetic field were exactly opposite the Earth's present magnetic field, the alignment of the dipole anomaly would be in the same direction as the Earth's present magnetic field and the sign of the dipole anomaly would be opposite, that is, with a magnetic high north of the magnetic low. A three-dimensional magnetic anomaly was computed over a cube-shaped body 2.5 km

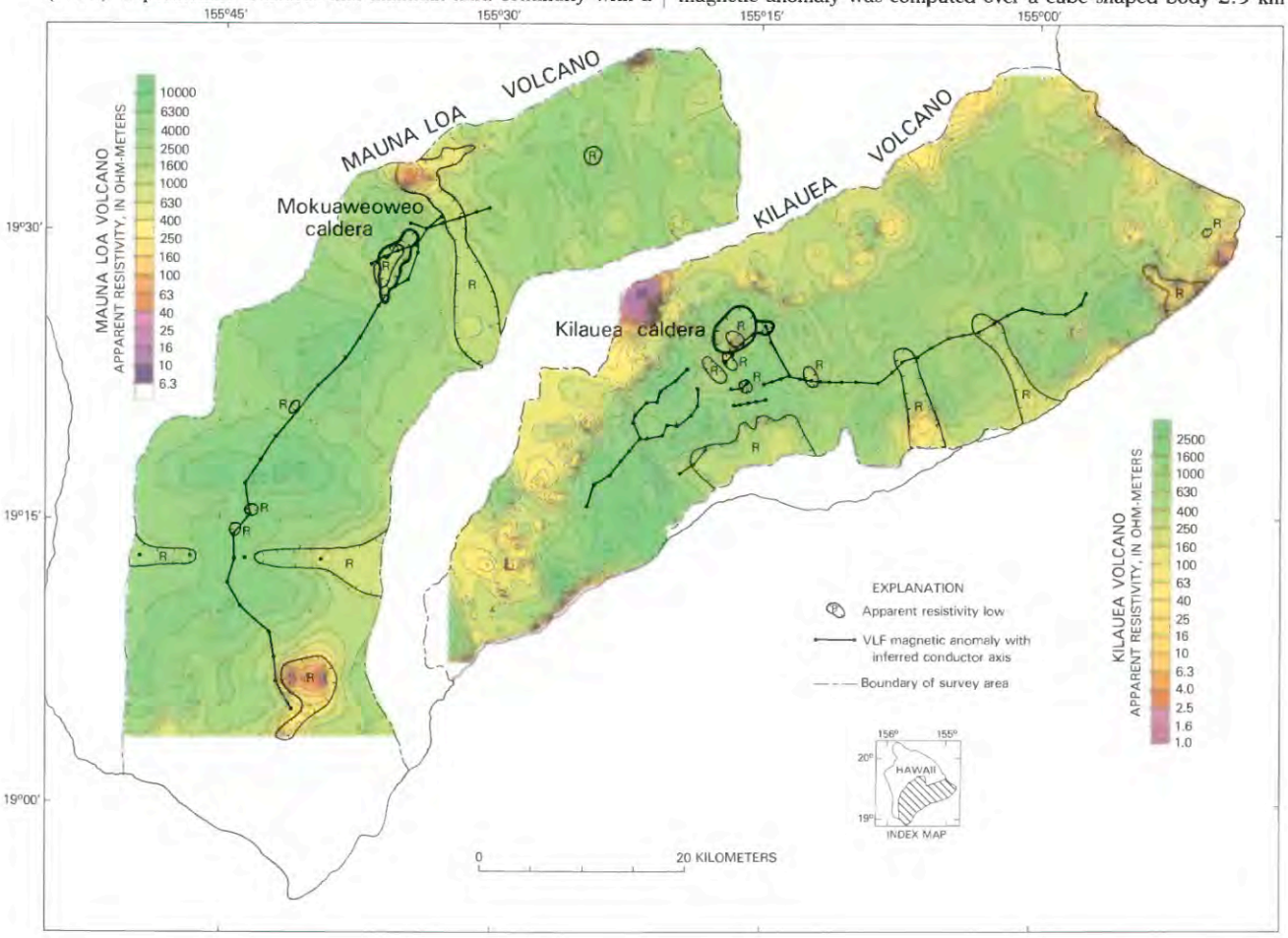


FIGURE 39.5.—Apparent resistivity map and location of VLF magnetic anomalies relative to Kilauea and Mauna Loa rift systems.

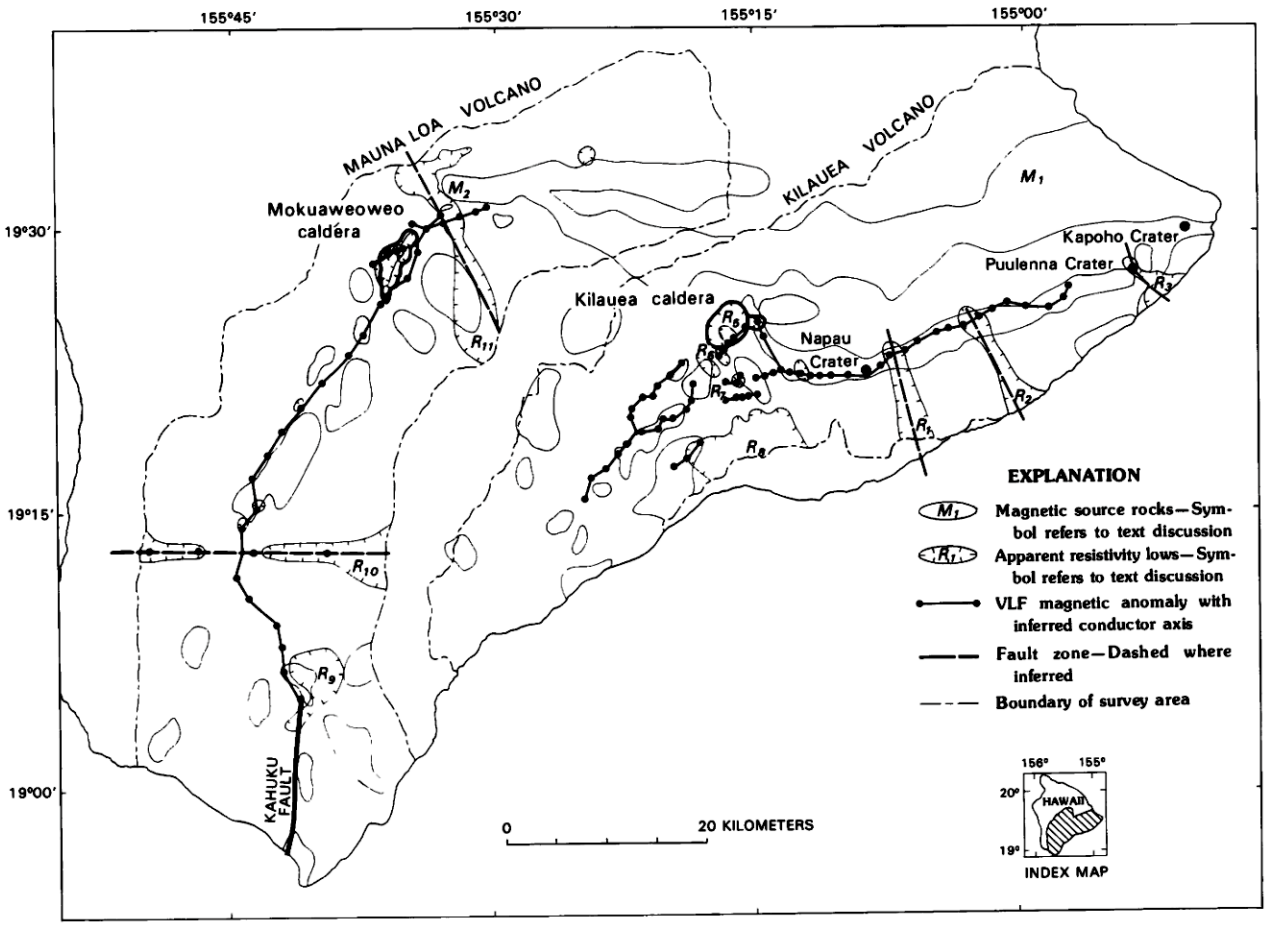


FIGURE 39.6.—Interpretive map of Kilauea and Mauna Loa rift systems, showing magnetic source rock, apparent resistivity anomalies, and VLF magnetic anomalies.

on each side (fig. 39.7*B*; from T.G. Hildenbrand, written commun., 1984). In order to produce a magnetic anomaly that matches the observed data (fig. 39.7*A*) it was necessary to rotate the remanent magnetic direction 30° counterclockwise from the exact opposite of the Earth's present field direction. Thus, one possible explanation to the Kapoho Crater apparently reversed dipole magnetic anomaly is that a body of rock of about 15.6 km$^3$ cooled when the Earth's magnetic field was in a period of reversal. An alternate explanation when considering the magnetic setting of the dipole anomaly is that the magnetic high is part of a broad magnetic high extending eastward from the summit of Mauna Loa ($M_1$, fig. 39.6) and the magnetic low is the magnetic expression of a magma chamber still above the Curie temperature and thus nonmagnetic. Norris (1976), commenting on data from a ground magnetic survey, observed a magnetic high over Kapoho Crater and suggested "that if subsequent measurements were to show a proportionate magnetic low near the south rim, then it could be concluded that there is an anomalously nonmagnetic body beneath Kapoho Crater." To test this theory, a configuration of magnetic bodies was assembled and the magnetic response calculated (M.W. Webring, written commun., 1984). Susceptibilities and vertices describing the body location were allowed to vary in order for the theoretical calculations to best-fit the observed data in a least-squares sense (fig. 39.8). Considering the oversimplification of the theoretical model the calculated data fit the observed data reasonably well. The model represents intrusive dike rocks associated with the east rifts of Mauna Loa and Kilauea separated by a magma chamber all of which have been buried by flows from Kilauea's east rift zone.

Additional geologic and geophysical evidence is necessary to determine which of the two (if either) above possible explanations for the apparent reversed dipole anomaly over Kapoho Crater is the most geologically reasonable. Reversely polarized rocks have not been reported for the Island of Hawaii where they are considered to be younger than the last period of magnetic field reversal, thus suggesting that the first model is unreasonable. We would expect low apparent resistivities caused by alteration of flow rocks lying directly

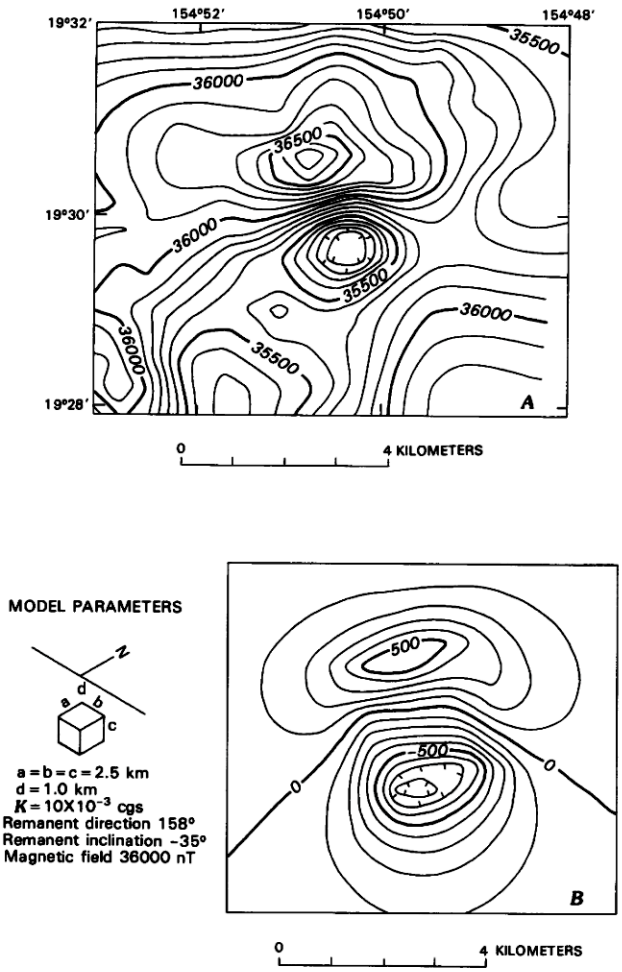


FIGURE 39.7.—Magnetic contour maps of Kapoho Crater. Contour interval is 100 nT. Hachures indicate closed low. ***A***, Observed magnetic anomaly. ***B***, Theoretical magnetic anomaly over assumed magnetic body (from T.G. Hildenbrand, written commun., 1984). Remanent magnetization direction assumed nearly reversed to direction of Earth's present magnetic field.

over the magma chamber as assumed in the second model, and apparent resistivity lows were not observed. However, recent volcanic activity in the Kapoho Crater area may have masked any near-surface apparent resistivity anomalies associated with the inferred underlying magma chamber. Dipole resistivity data presented by Skokan (1974, fig. 29b) indicates that a deep conductivity anomaly may be present in the Kapoho Crater area. This conductivity anomaly may be related to intrusion of sea water or possibly to a very conductive magma body.

Numerous aeromagnetic anomalies are present in the Kilauea Volcano summit area. Terrain-induced magnetic anomalies occur over the abrupt edges of the caldera (Decker, 1963) and are particularly noticeably over Halemaumau and Kilauea Iki Craters. Models (not shown) computed at 90 m above terrain features in the Kilauea summit area have an amplitude of about 150 nT, less than 20 percent of the observed anomalies, suggesting the observed anomaly is a combined aeromagnetic response of topography and geologic magnetic sources. Magnetic source rocks trending north-northwest intersect northeast- east-trending magnetic sources in the summit area.

A simple theoretical model over an assumed 1-km diameter, 4-km deep nonmagnetic magma chamber south of Halemaumau, as suggested by Eaton (1962), would produce an aeromagnetic anomaly of about 100 nT. It is doubtful that one could positively identify the Kilauea summit magma chamber by magnetic modeling because of the presence of magnetic source rocks of unknown configuration

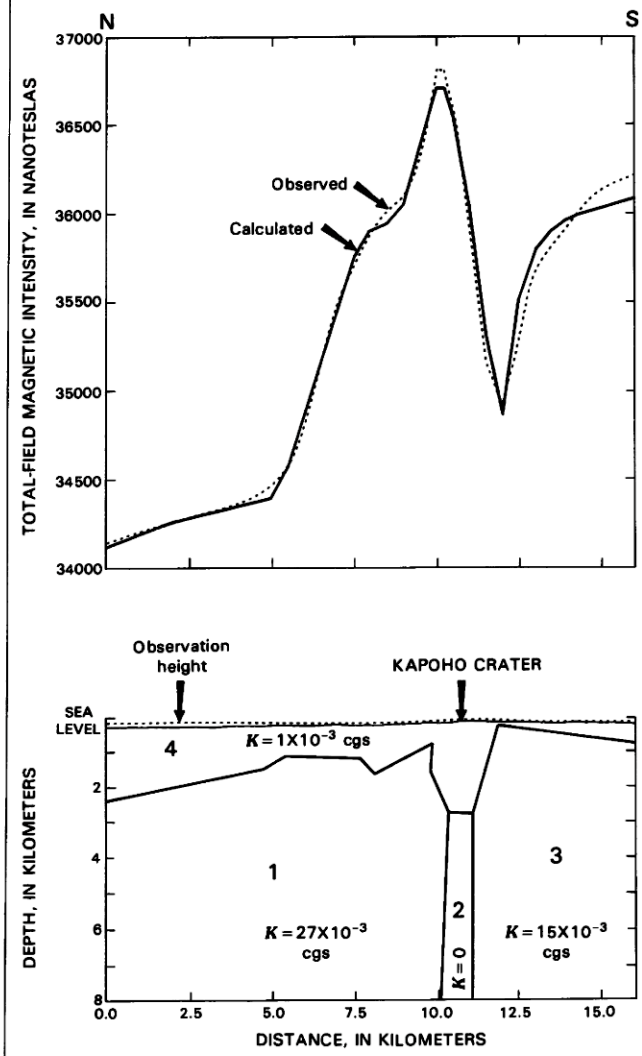


FIGURE 39.8.—Theoretical 2½-dimensional model over Kapoho Crater area assuming intrusive dike rocks to north (body 1) and south (body 3) of Kapoho Crater and nonmagnetic magma chamber (body 2) about 2 km deep beneath flow rocks (body 4). Susceptibilities ($K$) are shown in cgs units.

which are the apparent sources of the bulk of the observed aeromagnetic anomaly.

Apparent resistivity anomalies in the Kilauea summit area are thought to be caused by conductive rocks related to eruptive volcanic features similar to those outlined by Zablocki (1978, fig. 24) in the Sand Spit horst area. The airborne VLF data indicate an apparent resistivity low ($R_5$, fig. 39.6) just southeast of Halemaumau Crater. The airborne VLF magnetic-anomaly locations correspond very closely to Zablocki's VLF tilt and ellipticity measurement across Sand Spit horst. Apparent resistivity low $R_5$ lies north of the VLF magnetic anomaly, suggesting surface rocks are more conductive than to the south. Eaton (1962), by use of tilt measurements, indicates that the pre- and post-eruptive swelling and subsidence of Kilauea point to a magma reservoir just south of Halemaumau Crater. The VLF apparent resistivity data do not reflect directly the magma reservoir, but indirectly indicate increased alteration and (or) conductive hot circulating fluids associated with rock overlying the reservoir.

Other apparent resistivity lows have been delineated in the area southwest of Kilauea caldera ($R_6$, fig. 6). These conductive zones were also detected by surface VLF measurements by Zablocki (1978), who attributed them to conductive anomalies associated to cracks and hot steaming fissures. Apparent resistivity low $R_7$ (fig. 39.6) is thought to be associated with conductive features caused by intrusion into the Koae fault system at its junction with the east rift zone as described by Duffield (1975), and generally confirms ground geophysical observations of Jackson and Sako (1979). A broad apparent resistivity low ($R_8$, fig. 39.6) covers a significant area just north of the Hilina fault scarps south of Kilauea caldera. Gravity subsidence of large blocks of the unbuttressed south flank of Kilauea is largely responsible for the Hilina fault system (Swanson and others, 1976, p. 33). In places the surface of the fault blocks are nearly level or dip gently inland. These gentle slopes suggest the possibility of soils, which would contribute to low apparent resistivities. However, only a thin layer of ash is present in the near-surface rocks that could contribute to low VLF apparent resistivities (D.B. Jackson, written commun., 1985).

VLF magnetic anomalies are associated with many of the apparent resistivity anomalies in the Kilauea summit area (fig. 39.6). Most notable are VLF magnetic anomalies related to the conductive anomalies in the southern part of Kilauea caldera and to the southwest and an east-trending conductive zone parallel to the Koae fault system. Abrupt lateral changes in resistivity contrast are the causes for the VLF magnetic anomalies, and inasmuch as only one anomaly was detected at the edge of the feature they are considered to be narrow features. One would expect to see two VLF magnetic anomalies, one at each edge, of a broad conductive feature that had a sharp lateral resistivity contrast at each edge.

Several VLF magnetic anomalies extend southwest from Kilauea caldera. One of these was briefly ground-checked and thought to be related to a seismic cable extending from the Hawaiian Volcano Observatory. This anomaly was not included on figures 39.5 and 39.6. However, the other long VLF magnetic anomalies shown may have similar sources (J.P. Kauahikaua, written commun., 1984).

## MAUNA LOA VOLCANO

Magnetic data (fig. 39.4) in the Mauna Loa survey area are similar to that recorded over Kilauea Volcano in several ways. The northeast rift of Mauna Loa, like the east rift of Kilauea, is characterized by linear magnetic dipoles ($M_2$, fig. 39.6) extending eastward from several kilometers northeast of Mokuaweoweo caldera; however, the amplitude of the magnetic dipoles is about one-half that of the Kilauea east rift. A southeast-trending linear magnetic dipole intersects the Mauna Loa east rift about 15 km east of the summit and appears to be contiguous with the east-west long-wavelength (6 km) linear magnetic dipole ($M_1$, fig. 39.6) crossing the northern part of the Kilauea survey area. Steep magnetic gradients outline Mokuaweoweo caldera.

The magnetic expression of the Mauna Loa southwest rift, like the Kilauea southwest rift, is composed of discontinuous linear magnetic highs of a few hundred nanoteslas extending southwest from the summit to beyond the southern tip of the island. The magnetic data accurately reflect the prominent westward bulge in the rift zone coincident with the topographic ridge of Mauna Loa's southwest rift zone (Lipman, 1979).

Two conspicuous breaks in the linear magnetic anomalies occur in the Mauna Loa magnetic data: (1) a northwest-trending magnetic low crosses the northeast rift zone at the northeast end of Mokuaweoweo caldera and (2) an east-west magnetic low crosses the southwest rift zone near the apex of the bulge.

Qualitative interpretive lines (fig. 39.4) show the approximate location of intrusive rock considered to be the source of the magnetic anomalies mentioned above.

Apparent resistivities of near-surface rocks in the Mauna Loa survey area range from 16 to over $10^4$ Ω-m (fig. 39.5). Lava flows of highest apparent resistivity are present mainly in the upper one-third of the southwest rift zone. Apparent resistivity lows (<1,000 Ω-m) occur over Mokuaweoweo caldera and in the southern part of the survey area; these lows coincide with the two transverse magnetic breaks mentioned above. VLF magnetic anomalies (fig. 39.5) were detected along the entire length of the southwest rift zone except near the southern tip of the island where powerline interference and an equipment malfunction rendered the VLF data unuseable. Conductive zones produce VLF magnetic anomalies in Mokuaweoweo caldera and along its southeast edge that extends northeast for 10 km or more, beyond which no other VLF magnetic anomalies were seen. Northeast of the caldera, pairs of VLF magnetic anomalies, spaced 1 km or more apart along the flightline, were detected on several flightlines.

## DISCUSSION OF RESULTS

Injection of magma into Hawaiian shield volcanoes, surface eruptions, and subsequent gravitational slumping of the flanks of the volcanoes are important mechanisms for volcano growth (Swanson and others, 1976; Lipman, 1979; Normark, 1979).

The structural complexities and growth of Mauna Loa, like Kilauea Volcano, reflect the interaction of concurrent and past volcanic activity in adjacent volcanoes (Fiske and Jackson, 1972; Lipman, 1980). For example, Mauna Kea Volcano interferes with the unrestricted growth of Mauna Loa by forming a northern buttress. The same is true of Kilauea Volcano, which is buttressed on the northwest by Mauna Loa. Lipman (1979, 1980) postulates that the buttressing effect of Mauna Kea and the growing Kilauea Volcano has affected the recent growth of Mauna Loa: (1) recent volcanic activity along the Mauna Loa northeast rift zone has been limited to the first 20 km from the summit; (2) buttressing of the south flank of Mauna Loa by the growing Kilauea Volcano has limited southeast gravitational slumping of that flank, with the net result that the active part of the Mauna Loa southwest rift zone has migrated to the west; (3) westward migration of the active part of the rift zone accompanied by block slumping to the west accounts for the west bulge in the zone.

The spatial relation of the interpreted magnetic source rocks (dike and dike swarms) and the VLF magnetic data (narrow conductive zones) add weight to Lipman's observations. For instance, VLF magnetic anomalies (fig. 39.6), probably associated with the active part of the Mauna Loa southwest rift zone, follow the fissure vents, spatter cones, and pit craters that are thought to be less than 5,000 yr old. Magnetic source rocks generally lie to the east of the VLF magnetic anomalies, suggesting westward migration of the active part of the rift zone similar to the postulated south to southeast migration of the active rift zone on the upper one-third of Kilauea's east rift zone (Swanson and others, 1976). The eastward offset of the magnetic anomalies in relation to the VLF magnetic anomalies also confirms Lipman's (1980) gravity observations, which generally indicate dense rocks are present east of the surface evidence of recent volcanic activity. The dense rocks are interpreted to be dikes and dike swarms of greater density than the adjacent rocks.

Several small, circular, apparent resistivity lows with associated VLF magnetic anomalies along the active part of the Mauna Loa southwest rift zone are thought to reflect conductive rocks associated with volcanic vents.

Another subcircular apparent resistivity low ($R_9$, fig. 39.6) covers a significantly larger area (30 km$^2$) than the small conductive zones mentioned above. The long axis of apparent resistivity low $R_9$ is aligned roughly north-south and lies just east of Kahuku fault (Lipman, 1980, fig. 1). Aeromagnetic anomalies southeast of apparent resistivity low $R_9$ are aligned northwest-southeast and appear to be a continuation of the southeast structural trend of the rift zone at the lower end of the bulge (fig. 39.6). Apparent resistivity low $R_9$ is thought to be related to the high conductivity of near-surface rocks at the intersection of Kahuku fault and an inferred northwest- to southeast-trending fault zone, possibly the northwest extension of Waiohinu fault (Malahoff and Wollard, 1966). The characteristics of the conductive rock in the inferred fault intersection area are unknown; however, the salinity of intrapore fluids and clay content in the zone may contribute to the low apparent resistivity of the zone. The anomaly also appears to coincide with the 1868 eruption vent. The 1868 eruption was accompanied by movement along the Waiohinu fault, all of which suggest a possible thermal anomaly as the source of the observed resistivity anomaly.

An east-west apparent resistivity low ($R_{10}$, fig. 39.6) cuts across the southwest rift zone a few kilometers north of the apex of the bulge in the rift zone. The east-west trend is along the aircraft flightline direction so the possibility of an equipment-base shift that would contribute to such an apparent resistivity low was considered. The anomaly is considered valid for three reasons: (1) it was detected on three successive flightlines, thus its width (north-south) is at least 3.2 km; (2) the east-west apparent resistivity anomaly is coincident with an east-west aeromagnetic low, as seen on, not only the aeromagnetic data presented here, but also the 300-m flight-height aeromagnetic survey of Godson and others (1981); (3) the high-level (12,000-ft barometric) aeromagnetic data of Malahoff and Wollard (1966) also show a similar break in the magnetic data in this area. Malahoff and Wollard (1966, p. 289) interpret the east-west to southeast magnetic feature to be related to a now-buried ancient volcanic complex lying along an east-west rift zone crossing the Hawaiian Ridge.

Assuming that a deep-seated crustal fracture zone crosses the Mauna Loa southwest rift zone at the apex of the bulge, it has affected the conductivity of the near-surface rocks. The most obvious reason is near-surface water held in by rift-related dikes flows out and downslope along the transverse structure, analogous to transverse structures on Kilauea's east rift zone. Several VLF magnetic anomalies were detected on one flightline crossing the area, indicating that in some places there are rather sharp boundaries of rock of differing resistivity. Though the Malahoff and Wollard aeromagnetic survey was better suited to detect deep magnetic sources, there is apparently some shallow geophysical expression of the same features reflected in the low-level aeromagnetic-electromagnetic data presented here.

The aeromagnetic and electromagnetic data follow an asymmetric bulge in the topographic and geologic expression of the Mauna Loa southwest rift zone, and it seems plausible that the east-west zone just discussed has played some part in the development of this asymmetry. Of course it is obvious that the buttressing effect of Kilauea on the east-southeast flank of Mauna Loa prevents growth of Mauna Loa in the southeast direction, which adequately accounts for the westward migration of the active part of the southwest rift zone, but it does not address the asymmetry seen in the geophysical data. The subaerial Alika slide, a result of oversteeping of Mauna Loa's west flank, (Normark, 1979) extends 80 km off the west coast and may have been controlled on the south by the transverse zone inferred from the geophysical data.

Another zone transverse to the northeast rift of Mauna Loa has a similar geophysical relation to that just discussed; that is, it is a northwest-trending apparent resistivity low ($R_{11}$, fig. 39.6) coincident with an aeromagnetic low and occurs just north of Mokuaweoweo caldera. Here, once again, the high-level aeromagnetic data of Malahoff and Wollard (1966, fig. 13) indicate a northwest-trending magnetic low that crosses Mauna Loa's northeast rift zone in the same area. Many eruptive fissures cut the north flank of Mauna Loa at high angles (Lockwood, 1979) and may be indicative of stresses active during the evolution of Mauna Loa that are also responsible for the aeromagnetic and electromagnetic fea-

tures seen in the near-surface rocks. Here, once again, northeast-trending rift dikes ruptured by a transverse structure may allow near-surface water to flow downslope and are, thus, the cause of the conductive anomaly.

A VLF magnetic anomaly, thought to be associated with eruptive volcanic features, extends about 10 km northeast of Mauna Loa summit (fig. 39.6). The VLF magnetic anomaly defines a conductor axis cutting the northwest-trending apparent resistivity low and generally lies south of magnetic source rocks ($M_2$, fig. 39.6). These relations imply that in the first 10 km northeast from the summit the presently active part of the rift zone has moved south relative to presumably older complex dikes (the source of the aeromagnetic anomalies). Farther to the east no VLF magnetic anomalies were detected, although volcanic cones extend for 25 km or more east of the summit. Perhaps buttressing of the lower part of Mauna Loa's northeast rift zone by Mauna Kea Volcano on the north and Kilauea Volcano on the south has restricted volcanic activity. Or perhaps conductive zones associated with feeder dikes are deeper, having been covered by lava flows occurring at higher elevations, hence are at a depth greater than can be detected by the VLF method. Alternatively, the presence of VLF magnetic anomalies only along the upper (10 km) part of Mauna Loa's northeast rift zone may be more closely related to the presence of greater amounts of conductive electrolytes than occur farther east along the rift zone.

The middle to lower Mauna Loa northeast rift zone is implied to be complex by the distribution of dike swarms interpreted as the aeromagnetic source rocks in area $M_1$ (fig. 39.6). The aeromagnetic expression of the northeast rift zone divides about 15 km from the summit, one fork continuing east, the other, southeast—toward Kilauea Volcano. Whether this southeast fork represents a one-time interconnection between the volcanoes is not known. It is almost certainly an early evolutionary feature of Mauna Loa development because: (1) prehistoric volcanic centers, if they ever existed, are absent along this zone, having been covered by flows from the summit area and (2) the long wavelength of the magnetic anomaly suggests deeper source rocks than associated with the Kilauea east rift zone.

## SUMMARY AND CONCLUSIONS

Linear magnetic dipoles reflect intrusive dikes along the rift zones of Kilauea and Mauna Loa Volcanoes. The linear magnetic anomalies, normally polarized, vary in shape and amplitude according to the orientation of the source rocks with respect to the Earth's present field direction. At least 2 km of southward displacement of Kilauea's south flank is necessary to accommodate the intrusive dike system associated with the Kilauea east rift. The linear magnetic dipole anomaly along the Kilauea east rift zone is terminated on the eastern end of the island by an interpreted structure transverse to the rift zone. The magnetic data suggest a left-lateral offset of about 1.5 km in the rift zone beyond the termination point.

VLF magnetic anomalies are interpreted to reflect zones of conductive rocks of limited horizontal extent, but having relatively sharp lateral boundaries with large conductivity contrasts, and are interpreted as defining the currently active part of the rift zones. Most of the VLF magnetic anomalies are present along eruptive and intrusive volcanic features, thus confirming earlier ground electrical geophysical surveys.

The spatial relation of interpreted magnetic source rocks to the active part of the rift zones are important indicators of the recent evolutionary development of Kilauea and Mauna Loa Volcanoes. In the upper one-third of the Kilauea east rift zone the active part of the rift zone lies along the southern edge of interpreted magnetic source rocks, correlating with independent observations that the south flank of Kilauea is being forceably moved to the south by repeated magma injection from the summit reservoir. Just east of Napau Crater the active part of the Kilauea east rift zone is over the central and northern part of the interpreted intrusive dike system, suggesting controlling factors such as transverse fault zones caused by differential movement of Kilauea's south flank. Large-scale block slumping with accompanying transverse boundary faults of Kilauea's south flank are proposed as a possible explanation for the spatial relation of the active rift zone to early magnetic dike rocks. Rupture of impervious dikes bounding the east rift zone allowing downslope movement of conductive hot-water electrolytes may produce apparent resistivity lows along the postulated transverse boundary faults.

Two explanations for an apparently reversely magnetized magnetic dipole over the Kapoho Crater area are suggested from theoretical magnetic models. One model assumes a 2.5-km cube-shaped body of rock in which the remanent magnetic direction is nearly opposite the Earth's present magnetic field direction. This model has two drawbacks: (1) reversely polarized magnetic rocks have not been reported on the Island of Hawaii; (2) in order to compute a magnetic response of this theoretical model that closely resembles the observed data, the remanent magnetic direction must be rotated about 30° counterclockwise. This rotation infers that either there has been postcooling rotation of that part of the island or that the remanent magnetic field direction was not exactly opposite to the Earth's present magnetic field direction, a condition seldom seen or recognized in magnetic data interpretation. The second model assumes magnetic dike rocks north and south of Kapoho Crater are separated by a nonmagnetic shallow magma chamber. Absence of a resistivity anomaly over the proposed shallow magma chamber may be due to covering by young resistive lava flows.

The effects of concurrent growth of Kilauea and Mauna Loa Volcanoes are reflected in the magnetic and electromagnetic data, most clearly in evidence along Mauna Loa's southwest rift zone. Interpreted source rocks for aeromagnetic anomalies along the upper part of Mauna Loa's southwest rift zone lie east of the active rift zone as defined by VLF magnetic anomalies and are consistent with gravity data and geologic observations indicative of westward migration of the rift zone. An east-west aeromagnetic and apparent resistivity low near the apex of the bulge in the Mauna Loa southwest rift zone is interpreted as offset of water-constraining dikes along the southwest rift by a transverse structure, allowing conductive ground water to flow downslope. The Alika landslide which incorporates a large part of the west flank of Mauna Loa, may have been controlled on the southern boundary by this inferred transverse structure.

A northwest-trending zone just north of Mokuaweoweo caldera, reflected as apparent resistivity and aeromagnetic lows in the airborne data, is interpreted as another transverse structure that has allowed impounded near-surface water to flow downslope.

Many of the conclusions and observations presented here have a reasonable correlation with the observations of other earth scientists, others are highly speculative and hopefully will stimulate future research in understanding the evolutionary development of these two very interesting Hawaiian volcanoes.

## REFERENCES CITED


Arcone, S.A., 1978, Investigation of a VLF airborne resistivity survey conducted in northern Maine: Geophysics, v. 43, p. 1399–1417.

——— 1979, Resolution studies in airborne resistivity surveying at VLF: Geophysics, v. 44, p. 937–946.

Barringer, A.R., and McNeill, J.D., 1969, The radio-phase technique of airborne resistivity mapping: Geophysics, v. 36, p. 1014.

Blakely, R.J., and Grauch, V.J.S., 1983, Magnetic model of crystalline terrane: Geophysics, v. 48, p. 1551–1557.

Decker, R.W., 1963, Magnetic studies on Kilauea Iki lava lake, Hawaii: Bulletin Volcano, v. 26, p. 23–35.

Duffield, W.A., 1975, Structure and origin of the Koae fault system: U.S. Geological Survey Professional Paper 856, 12 p.

Eaton, J.P., 1962, Crustal structure and volcanism in Hawaii: Crust of the Pacific Basin: American Geophysical Union Geophysical Monograph Series, no. 6, p. 13–29.

Fiske, R.S, and Jackson, E.D., 1972, Orientation and growth of Hawaiian volcanic rifts: The effect of regional structure and gravitational stresses: Proceedings, Royal Society of London, Ser. A, v. 329, p. 299–326.

Fiske, R.S., and Kinoshita, W.T., 1969, Rift dilation and seaward displacement of the south flank of Kilauea Volcano, Hawaii, *in* Symposium on volcanoes and their roots, Oxford, England: International Association of Volcanology and Chemistry of the Earth's Interior, p. 53–54.

Flanigan, V.J., Long, C.L., Rohret, D.H., and Mohr, P.J., 1986a, Aeromagnetic map of the rift systems of Kilauea and Mauna Loa Volcanoes, Island of Hawaii, Hawaii: U.S. Geological Survey Miscellaneous Field Investigations Map MF–1845A.

——— 1986b, Apparent resistivity map of the rift systems of Kilauea and Mauna Loa Volcanoes, Island of Hawaii, Hawaii: U.S. Geological Survey Miscellaneous Field Investigations Map MF–1845B.

Frischknecht, F.C., 1971, Results of some airborne VLF surveys in northern Wisconsin: U.S. Geological Survey Open-File Report, 28 p.

——— 1973, Electromagnetic scale model studies of geophysical methods using a plane wave source: Golden, Colo., University of Colorado, Ph.D. thesis.

Godson, R.H., 1984, Composite magnetic anomaly map of the United States, Part B, Alaska and Hawaii: U.S. Geological Survey Geophysical Investigations Map GP–954B, scale 1:2,500,000.

Godson, R.H., Zablocki, C.Z., Pierce, H.A., Frayser, J.B., Mitchell, C.M., and Sneddon, R.A., 1981, Aeromagnetic map of the Island of Hawaii: U.S. Geological Survey Geophysical Investigations Map GP–946, scale 1:250,000.

Grauch, V.J.S., and Campbell, D.L., 1984, Does draping aeromagnetic data reduce terrain induced effects: Geophysics, v. 49, pp. 75–80.

Hoekstra, P., Sellmann, P.V., and Delaney, A., 1975, Ground and airborne resistivity surveys of permafrost near Fairbanks, Alaska: Geophysics, v. 40, p. 641–656.

Jackson, D.B., and Sako, Maurice, 1979, Self-potential mapping on the southwest rift zone of Kilauea Volcano [abs.]: Hawaii Symposium on Intraplate Volcanism and Submarine Volcanism, abstract volume, p 165.

Keller, G.V., and Frischknecht, F.C., 1966, Electrical methods in geophysical prospecting: New York, Pergamon Press, 519 p.

Keller, G.V., and Rapolla, A., 1974, Geoelectric surveys of thermal areas, *in* Civetta, L., Gasparini, P., Luongo, G., and Rapolla, A., eds., Physical Volcanology: Amsterdam, Elsevier, p. 133–-166.

Koyanagi, R.Y., Swanson, D.A., and Endo, E.T., 1972, Distribution of earthquakes related to mobility of the south flank of Kilauea Volcano, Hawaii: U.S. Geological Survey Professional Paper 800–D, p. D89–D97.

Lipman, P.W., 1979, The southwest rift zone of Mauna Loa; implications for structural evolution of Hawaiian volcanoes [abs.]: Hawaii Symposium on Intraplate Volcanism and Submarine Volcanism, abstract volume, p. 169.

——— 1980, The southwest rift zone of Mauna Loa; implications for structural evolution of Hawaiian volcanoes: American Journal of Science, v. 280–A, p. 752–776.

Lockwood, J.P., 1979, Asymmetry of the northwest rift zone of Mauna Loa Volcano, Hawaii, evidence for a mobile south flank [abs.]: Hawaii Symposium on Intraplate Volcanism and Submarine Volcanism, abstract volume, p. 170.

Macdonald, G.A., 1973, Geological prospects for development of geothermal energy in Hawaii: Pacific Science, v. 29, no. 9, p. 209–219.

Malahoff, Alexander, and McCoy, Floyd, 1967, The geologic structure of the Puna submarine ridge, Hawaii: Journal of Geophysical Research, v. 72, no. 2, p. 541–548.

Malahoff, Alexander, and Strange, W.E., 1965, The paleomagnetic significance of aeromagnetic surveys of the Hawaiian Islands: Pacific Science, v. 19, no. 3, p. 390–392.

Malahoff, Alexander, and Wollard, G.P., 1966, Magnetic surveys on the Hawaiian Islands and their geologic implications: Pacific Science, v. 20, p. 265–311.

Normark, W.R., 1979, Regional slump structures on the west flank of Mauna Loa Volcano, Hawaii [abs.]: Hawaii Symposium on Intraplate Volcanism and Submarine Volcanism, abstract volume, p. 172.

Norris, R., 1976, Puna magnetics, *in* The Hawaiian geothermal project initial phase II progress report: University of Hawaii, p. 32–33.

Paal, G., 1965, Ore prospecting based on VLF-radio signals: Geoexploration, v. 3, p. 139–147.

——— 1968, Very low frequency measurements in northern Sweden: Geoexploration, v. 6, p. 141–149.

Patterson, N.R., and Ronka, V., 1971, Five years of surveying with the very low frequency-electromagnetic method: Geoexploration, v. 9, p. 7–26.

Skokan, C.K., 1974, A time-domain electromagnetic survey of the east rift zone, Kilauea Volcano, Hawaii: Golden, Colo., Colorado School of Mines Ph.D. thesis, no. T–1700, 152 p.

Stearns, H.T., and Macdonald, G.A., 1946, Geology and groundwater resources of the Island of Hawaii, territory of Hawaii: Division of Hydrology Bulletin, no. 9, 363 p.

Swanson, D.A., Duffield, W.A., Fiske, R.S., 1976, Displacement of the south flank of Kilauea Volcano; the results of forceful intrusion of magma into the rift zones: U.S. Geological Survey Professional Paper 963, 39 p.

Wait, J.R., 1962, Electromagnetic waves in stratified media: New York, Pergamon Press.

Webring, M.W., 1981, MINC; a gridding program based on minimum curvature: U.S. Geological Survey Open-File Report 81–1224, 12 p.

Zablocki, C.J., 1976, Mapping thermal anomalies on an active volcano by the self-potential method, Kilauea, Hawaii: Proceedings of the 2d United Nations symposium on the Development and Use of Geothermal Resources, San Francisco, California, May 1975, v. 2, p. 1299–1309.

——— 1977, Self-potential studies in east Puna, Hawaii, *in* Geoelectric studies on the east rift, Kilauea Volcano, Hawaii Island: Geothermal Resources Exploration in Hawaii, v. 3, University of Hawaii, HIG–77-15, p. 175–193.

——— 1978, Applications of the VLF induction method for studying some volcanic processes of Kilauea Volcano, Hawaii: Journal of Volcanology and Geothermal Research, p. 155–195.

Zablocki, C.J., and Koyanagi, R.Y., 1979, An anomalous structure in the lower east rift zone of Kilauea Volcano [abs.]: Hawaii Symposium on Intraplate Volcanism and Submarine Volcanism, abstract volume, p. 127.

# REGIONAL SELF-POTENTIAL ANOMALIES AT KILAUEA VOLCANO

*By* Dallas B. Jackson *and* James Kauahikaua


## ABSTRACT

**Self-potentials (SP) at Kilauea Volcano, when referenced to the potential at sea level, appear as a broad, negative bowl-shaped anomaly with smaller wavelength anomalies that are positive-tending, but not necessarily of positive amplitude, superimposed over thermal volcanic features. To a first approximation, the broad-wavelength negative anomaly is inversely correlated with topography. Plots of SP versus topography and (or) vadose-zone thickness determined from vertical electrical soundings show linear, sometimes segmented, correlations along four lengthy SP profiles on Kilauea. The slopes of the correlation lines are used to calculate an apparent water-table elevation along the entire profile. When compared with surface geology and nearby well data, the apparent water table is reasonable. The ground water table is near sea level for most areas south of the middle and lower east rift zone and at the boundary between the southwest rift zone of Kilauea and the southeast flank of Mauna Loa near the coast. By contrast the profiles show that water may be impounded to high elevations within the east rift zone, both east and west of the upper east rift zone, and beneath the summit region. The water table is also elevated beneath the southwest flank of Kilauea.**


## INTRODUCTION

The self-potential or spontaneous-potential (SP) method measures naturally occurring electric-field potentials that exist at the Earth's surface. Extensive potential-field mapping on Kilauea shows there is a direct relation between volcanic structure and SP field distribution at the summit of Kilauea Volcano (Zablocki, 1976). An SP map of the intersection of the lower east rift zone of Kilauea with the coast (Zablocki, 1977) and two new profiles, each referenced to the potential at sea level, show that the regional (that is, the long-wavelength) portion of SP appears strongly correlated with topography. Zablocki suggested that a more meaningful correlation is between SP and vadose-zone thickness. In this paper we will first discuss SP-measurement techniques and possible measurement errors in order to demonstrate that our field measurements genuinely reflect natural Earth potentials. Then we will quantify the relation of SP magnitude to topography and (or) thickness of the vadose zone in an attempt to isolate a cause of regional SP.

## MEASUREMENT TECHNIQUES

The measurement of self-potential is quite simple, requiring only a high-impedance millivoltmeter, nonpolarizing electrodes, and approximately 2 km of insulated single-conductor wire. It is desirable to space reference points as far apart as practical to keep cumulative errors to a minimum, but to make measurements also at smaller intervals between reference points. For example, we commonly make measurements at 100-m intervals, but only move reference points every 1.5 km.

A typical nonpolarizing electrode consists of a bare copper strip immersed in a supersaturated copper-sulfate solution in a porous ceramic cup. The cup has sides wrapped in fiberglass for added strength and can be fabricated with a large bottom surface area to improve electrical contact with the ground.

At Kilauea, it is essential that a very high impedance millivoltmeter be used. The electrical resistance between the electrodes and the earth can easily vary between a few tens of ohms for deeply weathered or altered ash and lava flows to megaohms for dry sand and ash or unweathered lava flows. A millivoltmeter input impedance several orders of magnitude larger than the largest expected electrode resistance insures that errors due to electrode resistance are kept small. We use a very simple system designed by Zablocki (1976) that incorporates an electrometer amplifier ($10^{14}$ ohms impedance) with a filtered input to reject AC signals and a digital display of 1 to 999 mV. The amplifier has an input bias current of only $10^{-14}$ A, an important consideration because large bias currents will polarize the measuring electrodes.

In the field, a reference electrode is established and a second electrode is moved successively to each measurement site. The electrode is positioned by simply placing it on the ground and rotating it to make contact with the soil-moisture layer that is usually present just a few millimeters beneath the surface. Only in rare cases is it necessary to disturb the ground surface by digging to make adequate contact. If a reading is not repeatable to within 1–2 mV or is unstable, we assume that contact resistance is probably very high, and readings are discontinued at that location. In areas where soil texture varies from very coarse ash (commonly well drained and dry) to finer grained ash, the electrical contact may improve at the next reading position and readings are continued. The most common cause of high contact resistance is usually a long period of drought, in which rainfall has been too low to maintain fluid continuity between the ground surface and the film of water that is always present in the vadose zone (unsaturated zone between the ground surface and the water table).

Water is almost never added to the ground surface to improve electrical contact because watering of electrodes can produce extraneous potentials and a complex voltage drift (one exception to this is

described later). A good example of such behavior is shown in Corwin and Hooever (1979). The same considerations do not apply to the surfaces of fresh lava flows. There a moist rag or a sponge pushed into cracks in the flow surface is usually sufficient to lower contact resistance enough to give readings repeatable to within 1–2 mV.

The only exception we have made to the rule of not watering electrodes is on a monitored profile on Mauna Loa Volcano at the 3,400-meter elevation (Lockwood and others, 1985), where rainfall is very low most of the year. Even with a high impedance millivoltmeter, stable readings are normally not possible in this environment. As an experiment, water was added at each position that a reading was to be made, and then the SP drift was observed. After about 2 hours, the initial rapid potential drift (that began at about 10 mV/min) stopped; readings thereafter appeared stable and the profile was measured. A repeat of the profile 24 hours later gave readings that differed by less than 10 mV from the first measurements. Although very time-consuming, watering of electrodes appears to be permissible under these circumstances and may be the only way data can be collected in extremely dry areas.

## POSSIBLE MEASUREMENT ERRORS

Measurement errors related to mapping can be caused by (1) poor electrical contact with the ground surface in extremely dry areas, as discussed above; (2) failure to reoccupy electrode positions exactly when changing references on a traverse; (3) use of electrodes that are polarized; and (4) telluric currents.

### INEXACT REFERENCE ELECTRODE POSITIONING

The failure to reoccupy exact reference-electrode positions can produce measurement errors in areas of anomalous gradients (for example, on the flanks of short-wavelength high-amplitude anomalies). This is a simple error to correct because high gradient areas are easily recognized during data collection and can be avoided as reference locations. Typical closures calculated for a wide variety of grounding conditions have always been less than 10 mV/km. Such errors are insignificant in mapping large potential changes; we are convinced that serious reference-electrode positioning errors can generally be avoided with a bit of care.

### ELECTRODE BIAS

Copper sulfate nonpolarizing electrodes can sometimes drift from a balanced state (zero difference between electrodes) as they age or if they are contaminated. Such offsets can range from common values of 1–10 mV to more than 50 mV in extreme cases. To correct this, readings may be numerically compensated for the polarization by linearly distributing potential differences along a traverse, or matched pairs of electrodes with minimal bias can be selected from a large set of electrodes maintained for mapping.

### TELLURIC CURRENTS

Temporal variations of the Earth's magnetic field induce current flow in the Earth (telluric currents). The fluctuations of the electric field range in duration from milliseconds to centuries and can produce electric-field gradients of several hundred millivolts per kilometer over highly resistive terrain (Keller and Frischknecht, 1966), as is common in the continental interior. However, in an island setting such as Hawaii, where the rocks may also be highly resistive, the telluric currents tend to flow around the island in the conductive ocean water (Klein and Larson, 1978). At Kilauea, tellurics are generally too small (less than 1 mV/km) to be seen while SP readings are being made. Longer term and higher amplitude variations could conceivably introduce errors in SP traverse readings if their rate of change is such that measurable electric-field changes are produced during the time required for successive profile readings (about 4–8 minutes). The magnitude of potentials related to telluric currents is approximately proportional to the length of line on which they are recorded; therefore, the greater the distance between the reference and measuring electrodes the larger will be the error.

There is no way to quantitatively correct for changes related to telluric currents. However, one can attempt to estimate the perturbations and then dismiss them as sources of error if they are small. We estimate that a 1.5-km profile segment should take no longer than 2 hours to sample at 100-m intervals. The best set of published telluric measurements at Kilauea are those by Zablocki (1980) for potentials continuously recorded over 5 months in 1974 on two stationary orthogonal lines near the upper-east-rift-zone (UERZ) profile in figure 40.1. During that study, the largest excursions recorded over a 2-hour period were 25 mV/km. The great majority of such excursions were of about 10 mV/km or less. Therefore, for the worst case, it might be possible to have an error of about 40 mV over the 1.5 km segment. When mapping anomalies with amplitudes of several hundred millivolts, even this worst case would not seriously affect the results.

## GEOLOGIC SP SOURCES

Two source mechanisms seem to be capable of generating large self-potentials. The first mechanism, electrokinetic coupling or streaming potentials, is related to the circulation of fluids through porous rock (Sill, 1983). The second mechanism, thermoelectric coupling, can generate anomalous potentials at the ground surface from thermal gradients near dike-like heat sources (Fitterman, 1983).

### THERMOELECTRIC COUPLING

Rocks are capable of producing an electric potential gradient in response to a thermal gradient. Fitterman (1984) has shown that the necessary conditions for the generation of a thermoelectric SP anomaly are a heat source and a change in the thermoelectric coupling property (ratio of voltage change to temperature change) in the vicinity of the heat source within the earth. Examples of theoretical SP anomalies produced by various heat sources and

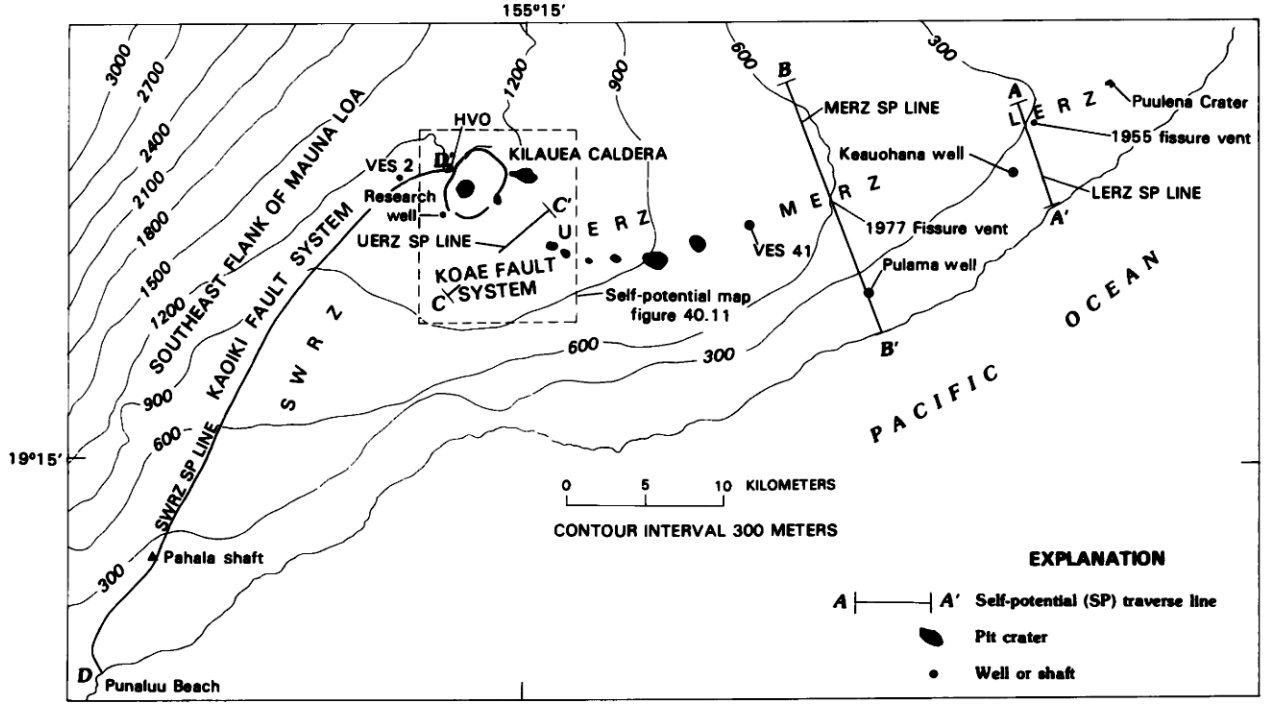


FIGURE 40.1.—Self-potential (SP) lines and major geologic features on Kilauea Volcano. SWRZ, southwest rift zone; UERZ, upper east rift zone; MERZ, middle east rift zone; LERZ, lower east rift zone.

various distributions of thermoelectric coupling property are shown in Fitterman (1978, 1979, 1983, 1984). Typical Earth heat sources in a volcanic terrain are buried magma bodies.

### ELECTROKINETIC COUPLING

Rocks can also be a source of electric potential gradients if subjected to fluid flow within the rock pores. Necessary conditions for production of an electrokinetic SP anomaly are a fluid pressure gradient and a change in the electrokinetic coupling property (ratio of voltage change to pressure change) in the vicinity of the pressure gradient. Sill (1983) models various geometries for point pressure sources (abstract representations of pumping wells or springs) and for fluid which is convecting (Sill, 1982). As a rule, electric potentials become more positive in the direction of flow. In a uniform halfspace with nonzero electrokinetic coupling properties, positive anomalies are produced over a convection cell which is flowing vertically upward at the center and over a point source (such as a pumping well) in which fluid is flowing toward the point source. Electrokinetic causes have been hypothesized for SP anomalies observed in Yellowstone National Park (Zohdy and others, 1973) and Long Valley caldera, California (Anderson and Johnson, 1976).

## SP CORRELATIONS WITH TOPOGRAPHY

A negative correlation between ground elevation (topography) and self-potential has been recognized for many years (Poldini, 1939; Yungul, 1950). Such correlations have been observed in many places, including Adagdak Volcano, Adak Island, Alaska (Corwin and Hoover, 1979), Hualalai Volcano, Hawaii (Jackson and Sako, 1982), and Kilauea Volcano (Zablocki, 1977).

The correlation with topography was initially thought to be due to the flow of nonthermal subsurface water (Poldini, 1939; Yungul, 1950) presumably through an electrokinetic mechanism. More recently, Zablocki (1978) proposed that the vertical descent of meteoric water through the vadose zone to the water table is the source mechanism, implying that SP intensities should actually be correlated to the underlying vadose-zone thickness, not to topography.

SP is clearly correlated with topography where the water table is horizontal near the coast. When both topography (meters) and SP (millivolts) are referenced to sea level and are plotted against one another, linear trends are commonly found which can be described by an equation of the form

$$SP = \text{ground elevation} \times C_e + A,$$

where $C_e$ is the coefficient relating SP and ground elevation and $A$ is the Y-axis intercept. For coastal areas where the water table is horizontal and at sea level, the constant ($A$) is zero. However, more than one value of the coefficient is found even for single SP profiles, indicating that SP is not primarily related to ground elevation but possibly instead to vadose zone thickness.

SP should also be plotted against vadose-zone thickness where data are available, such as vertical electrical (Schlumberger) soundings or drilled wells. Linear trends of the form

$$\text{SP} = \text{vadose zone thickness} \times C_v + A$$

should be sought, where $C_v$ is the constant of proportionality between SP and vadose-zone thickness. The constant, $A$, should be zero in this case. Unfortunately, measurements of vadose-zone thickness are not as common as ground elevation measurements. Only one of the four profiles (UERZ) presented in this paper has enough measurements of vadose-zone thickness available to determine a value for $C_v$. The other profiles have only one or two vadose-zone thickness determinations. For those, the SP correlation with topography was determined at the coast where the water table is almost certainly horizontal and at sea level. Using the value of $C_e$ so derived, which in this case is equivalent to $C_v$, we calculated apparent water-table elevations for the entire profile by means of the equation

$$\text{water-table elevation} = \text{ground elevation} - \text{SP}/C_v.$$

These calculated values were then compared with the few known water-table elevations to test the supposition that regional scale SP is related more directly to vadose-zone thickness than to topography.

Many shorter wavelength SP anomalies may also be related to local vadose-zone thickness variations. For the most part, these anomalies are positive, monopolar, and located over thermal areas. Zablocki (1978, p. 747) proposes that these anomalies "may simply reflect the shallow depths to which cool meteoric water may descend before encountering higher temperature fluids rising above a deeper heat source. Enhancement of the anomalies may result from the ascending water vapor over the thermal area and from a large flux of liquid-phase water diverted laterally downward along the immediate flanks of the thermal zone." These short-wavelength anomalies may also be produced by thermoelectric sources (heat produced by intrusive magma) or electrokinetic sources other than the descent of meteoric water (such as thermal convection of water below the water table).

## SP PROFILES MEASURED ON KILAUEA VOLCANO

The following section describes four SP profiles measured on long traverses over large changes either in elevation and (or) in thickness of the vadose zone.

### MIDDLE EAST RIFT ZONE (MERZ)

A 17-km traverse was run from the ocean up the south flank and across the MERZ to the north flank of the rift (fig. 40.2; see also fig. 40.1). This SP profile has the form of a broad potential low, becoming increasingly more negative relative to sea level as the rift zone is approached. A positive-tending, high-amplitude (about 1,000 mV relative to adjacent levels) SP anomaly about 3–4 km wide is present over the active rift zone. Prominent but narrow positive-tending inflections on the SP profile also mark a fissure associated with a 1977 eruption (10.2 km from the SW. end of the profile at the coast), a 1963 eruptive fissure (10.7 km), and a 1968 fissure (11.5 km) that erupted lava from vents about 1.5 km on either side of the profile.

A zone with a good correlation ($C_e = -1.7$ mV/m) between topography and SP (circles on fig. 40.3) extends approximately 8.2 km from the coast to the northwest beyond the large fault scarps of the steep south flank. We infer from well data (Pulama well) at about the 2.8-km position on the profile that the water table is nearly horizontal and at sea level in this portion of the profile (State of Hawaii Department of Land and Natural Resources, 1970). The linear gradient of $-1.7$ mV/m ends at 8.2 km where the large positive-tending SP anomaly over the active rift begins (fig. 40.2).

At 10.2 km, the potentials rise above the zero reference by about 200 mV for a short distance across the 1977 fissure vent. Similar short-wavelength (<1 km) monopolar features (fig. 40.2) are also associated with the 1963 vent and the 1968 fissure. A fourth short-wavelength anomaly, similar in appearance to those at the 1963 vent and 1968 fissure, occurs on the SP profile between 13 km and 14 km. This feature is not directly associated with any surface feature but is only about 0.5 km beyond the northern limit of a horst-and-graben structure that is probably related to shallow intrusions of prehistoric (before the first recorded MERZ eruption in 1790) age but less than 300 years old (Holcomb, 1980).

Northwest of the rift zone (beyond any surface expression of eruptive features), the SP gradually increases (fig. 40.2). The slope of SP plotted against elevation for this section of the profile is about $-4.4$ mV/m (fig. 40.3), steeper than that measured southeast of the rift zone. Calculations of apparent water-table elevations using the coefficient of $-1.7$ mV/m are shown in figure 40.2.

### LOWER EAST RIFT ZONE (LERZ)

The LERZ SP mapped by Zablocki (1977, fig. 2), has basically the same pattern of potential distribution as the MERZ. All areas not associated with obvious thermal features are more negative than potentials at sea level. Only two areas, one associated with a 1955 fissure vent (fig. 40.4) and the other associated with a prehistoric pit crater, Puulena (located on fig. 40.1; data not shown), are positive relative to sea level (about 50 mV). The one data set that Zablocki (1977, fig. 4) examined for a topographic-SP correlation runs from the ocean to a 1955 fissure vent and has a correlation coefficient ($C_e$) of $-1.8$ mV/m (fig. 40.5). This is comparable to the correlations we have found for other parts of the volcanic edifice where we believe the water table to be nearly horizontal. Using the SP and topographic data from Zablocki's figure 4, we have calculated and plotted the apparent water table along the profile (fig. 40.4).

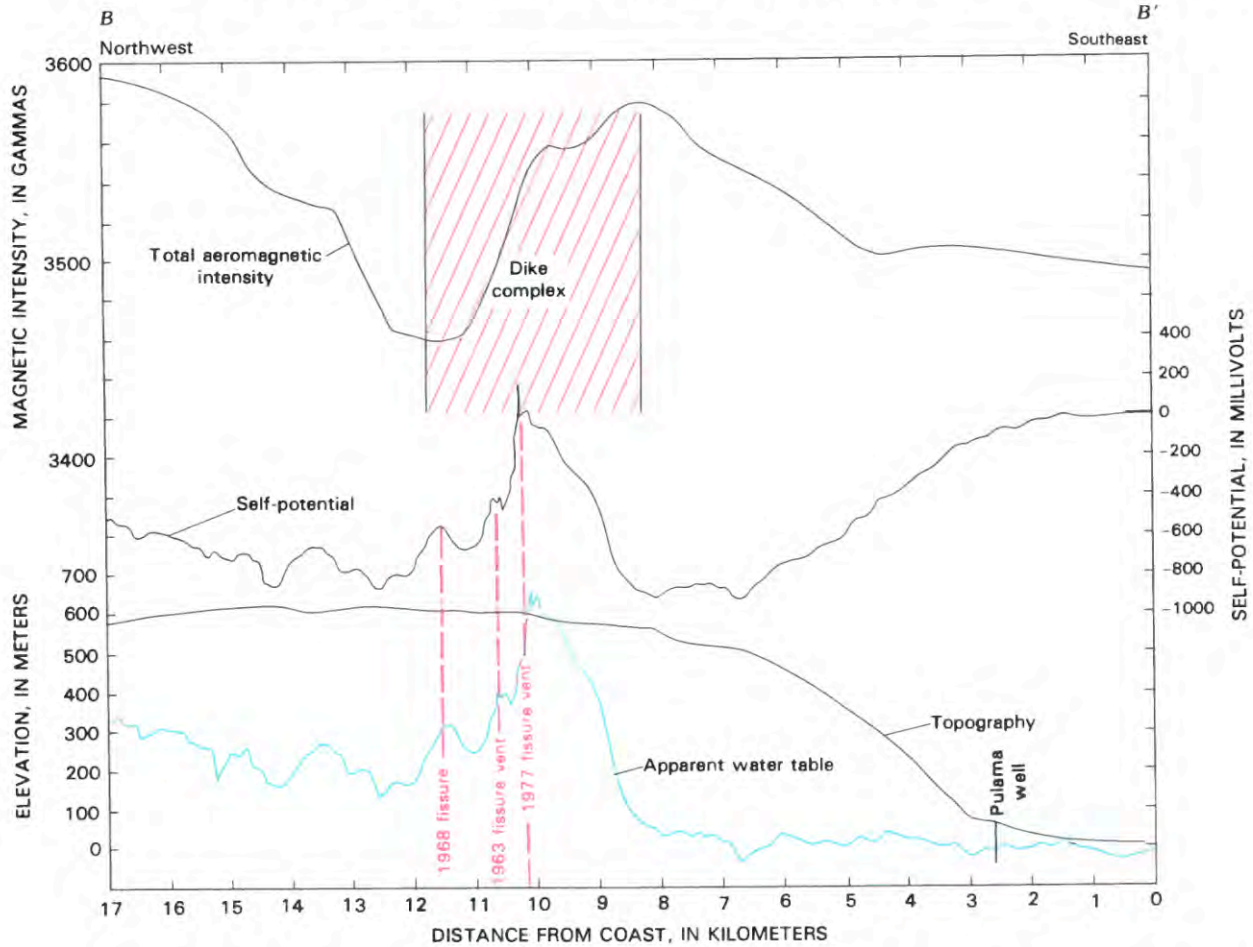


FIGURE 40.2.—Topography, self-potential, apparent water table, and total magnetic intensity (aeromagnetic) for profile B–B′ across the middle east rift zone of Kilauea Volcano. See figure 40.1 for profile location.

## UPPER EAST RIFT ZONE (UERZ)

The SP anomaly over the UERZ (fig. 40.6) has much the same form in cross section as the SP profile across the MERZ in figure 40.2, that is, a major positive anomaly (relative to nearby potentials) flanked by adjacent major potential lows. The UERZ anomalies are correlated with pit craters as far downrift as Pauahi and with fissure vents (not visible at the figure scale) northeast of Pauahi as far east as the right edge of the figure.

A plot of elevation against SP for the UERZ profile (fig. 40.7) shows no clear correlation. Lacking more direct measures of vadose-zone thickness for this profile, we choose to use interpretations from nearby vertical electrical soundings (VES). VES 1, 3, and 17 (fig. 40.8; locations shown in fig. 40.11) show the vadose zone to be 480, 230, and 690 m thick, respectively. These values are plotted with the corresponding SP values in figure 40.7 along with a line showing the determined value of $C_v$, the correlation coefficient of vadose vent thickness to SP, of $-3.6$ mV/m. An apparent water table calculated using this value is shown in figure 40.6.

## SOUTHWEST RIFT ZONE (SWRZ)

An SP profile from ocean to the summit of Kilauea (fig. 40.1, left side) is shown in figure 40.9. This profile is 43 km long and extends from Punaluu Beach on the southwest flank of Kilauea to the Hawaiian Volcano Observatory (HVO) on the northern rim of the caldera at 1,246-m elevation. As in the MERZ profile, potentials become increasingly more negative as elevation increases. The SP at the end point of the profile (HVO) is $-1{,}430$ mV relative to sea level.

The Punaluu-summit profile parallels the SWRZ of Kilauea and the Kaoiki fault zone and runs for its entire length over a

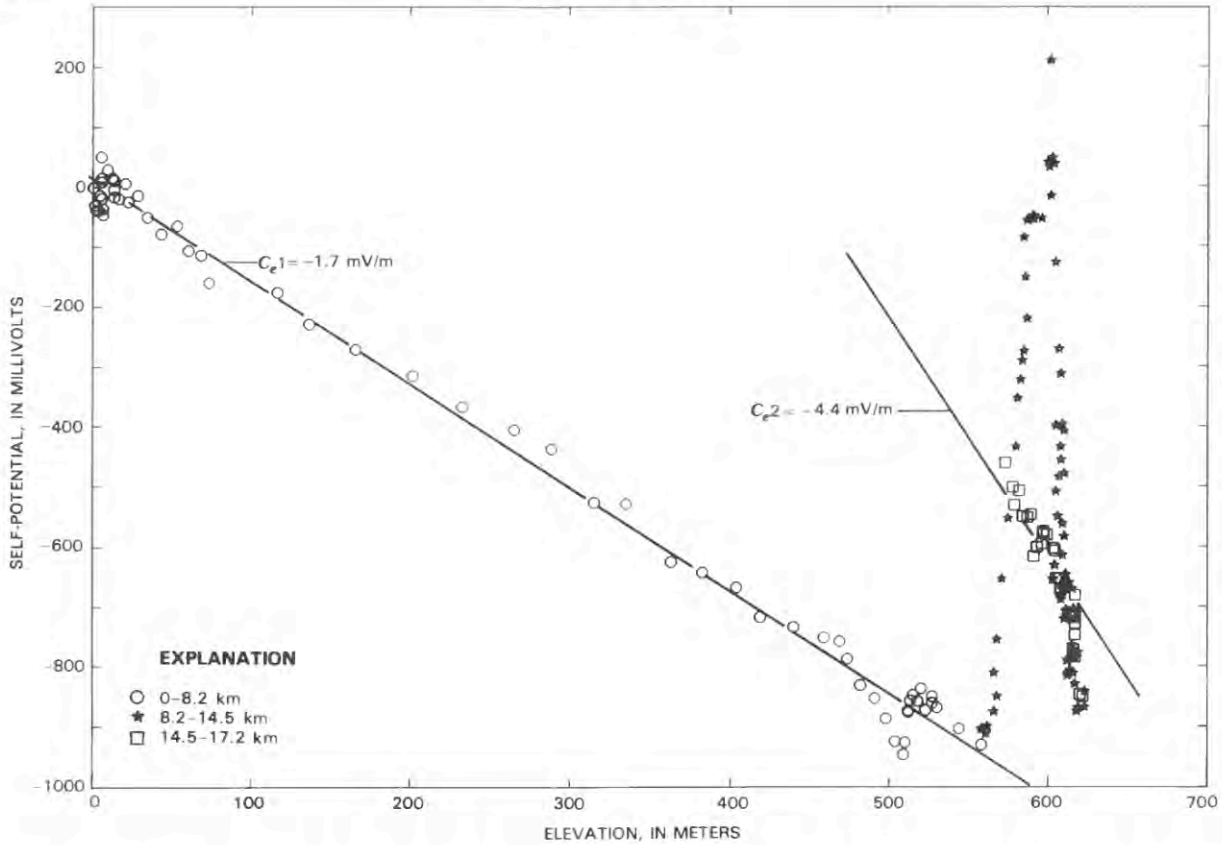


FIGURE 40.3.—Plot of elevation versus self-potential for the 17-km MERZ profile shown in figure 40.2. The lines show linear correlations (graphically determined) between self-potential and elevation with coefficients ($C_e$) of $-1.7$ mV/m and $-4.4$m V/m.

section in which flows from Kilauea and Mauna Loa interfinger. The Kaoiki fault zone extends from just north of Kilauea summit nearly to Pahala, and in places seems to act as a hydrologic barrier between Kilauea and the south flank of Mauna Loa (HVO unpublished electrical sounding data, 1980).

A plot of topography against self potential (fig. 40.10) shows three distinct values of $C_e$ (labeled $C_e1$, $C_e2$, and $C_e3$) increasing in value from the coast toward the summit:

(1) $C_e1$, from the coast to 500-m elevation, about 6 km above the town of Pahala, has a value $-0.6$ mV/m.

(2) $C_e2$, from 500-m elevation to 1,100-m elevation, about 2 km from the summit caldera, has a value of $-1.6$ mV/m; this is approximately the same as observed on both the south flanks of the MERZ ($-1.7$ mV/m) and the LERZ ($-1.8$ mV/m).

(3) $C_e3$, from the 1,100-m elevation to the caldera rim at HVO, has a value of $-3.2$ mV/m.

Apparent water-table values along this profile were calculated three times, once for each of the $C_e$ values determined above. Only those calculated for $C_e2$ and $C_e3$ were hydrologically reasonable (that is, they did not go below sea level); both these apparent water-table plots are shown in figure 40.9.

## DISCUSSION

Three of the four self-potential profiles at Kilauea, one from the summit down the SWRZ, another from the MERZ down the south flank, and a third covering most of the LERZ (Zablocki, 1977), all referenced to sea level, clearly show that the edifice of Kilauea sits within a broad potential low. Within this low, and coinciding with the active elements of the volcano (rift zones, intrusions, pit craters, and fissure vents) are large self-potential highs that, with few exceptions, are nonetheless still negative with respect to sea level.

In each of these three areas, at places where it is reasonable to expect a nearly horizontal water table, ground elevation shows an excellent correlation to self-potential with a coefficient of approximately $-1.7$ mV/m. Along the UERZ profile, a good correlation was found between vadose-zone thickness and SP with a coefficient of $-3.6$ mV/m.

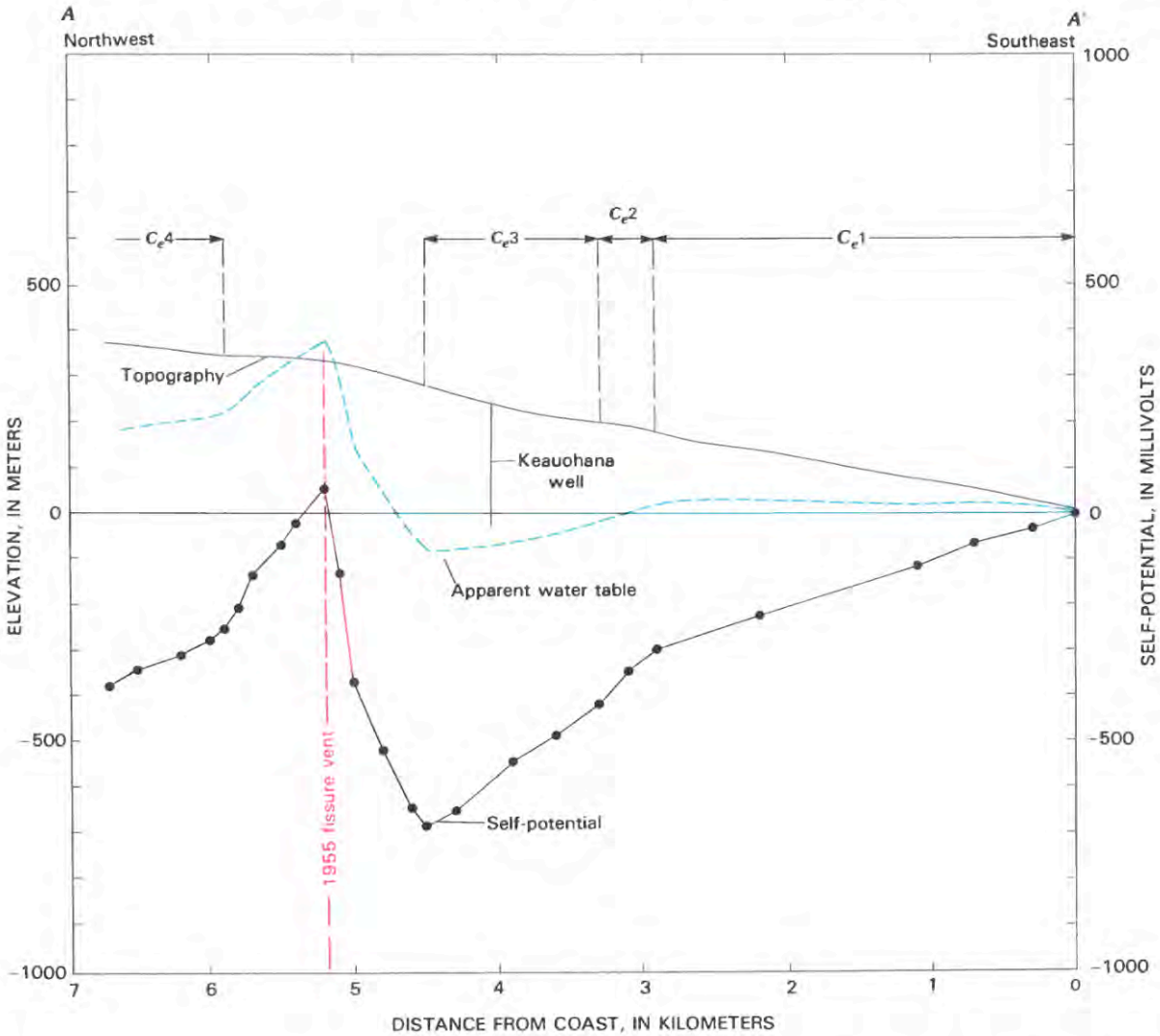


FIGURE 40.4.—Topography, apparent water table, and self-potential for profile A–A′ on the lower east rift zone of Kilauea Volcano. Self-potential and topography digitized from Zablocki (1977, fig. 2). Segments of the profile that correspond to different linear correlations ($C_e1$ through $C_e4$ on fig. 40.5) are shown. See figure 40.1 for profile location.

We believe, along with Zablocki (1978), that the regional pattern of SP is more directly related to the distance to which water can percolate vertically through the vadose zone before reaching the water table than it is to topography. We recognize that our anlaysis is not definitive but only indicative. Inconsistencies can be shown in the correlation of SP to topography, and those inconsistencies indicate a relationship of SP to vadose-zone thickness. The exact mechanism by which the negative potentials are generated is not known, but it is probably related to streaming potentials generated within the vadose zone by water moving downward.

If we suppose a valid relationship between vadose-zone thickness and self-potential, then self-potentials referenced to sea level at known elevations may be converted to apparent water-table depths. Circumstantial evidence that such a conversion is valid would come from any agreement of these apparent water-table elevations with actual determinations (well data and electrical resistivity soundings) at the same sites.

## MIDDLE-EAST-RIFT-ZONE PROFILE

The apparent water-table elevations remain near sea level from the shore inland to the edge of the dike complex and then increase rapidly toward the 1977 eruptive fissure (fig. 40.2). Northwest of the 1977 fissure, apparent water-table elevations decrease to a point

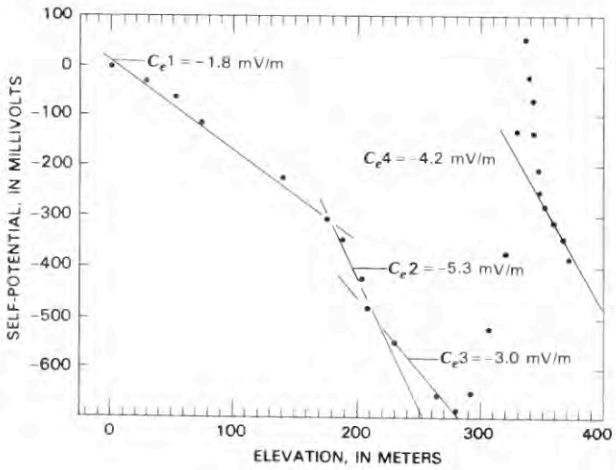


FIGURE 40.5.—Plot of elevation versus self-potential for the LERZ profile shown in figure 40.4. Four linear segments and the values of their correlation coefficients ($C_e1$–$C_e4$) are shown. Correlation lines are graphically determined.

about 14 km from the coast, from where they rise slowly to the end of the profile.

The apparent water-table elevations rise dramatically along the MERZ profile over the portion of the rift underlain by a dike complex. The long-wavelength (about 3 km) high in SP over the dike complex and the shallow apparent water table derived from the SP within this high are best explained as a thinning of the vadose zone caused by impoundment of ground water by dikes within the rift zone. An elevated water table within the rift is confirmed by VES 41 approximately 5 km uprift from the MERZ profile. For VES 41, at 740-m elevation (figs. 40.1 and 40.8), the water table is interpreted to be at 390 m above sea level. Although VES 41 is evidence of elevated water within this structure, its location is too far uprift to allow direct comparison with the MERZ profile.

At 8.2 km from the shore on the profile is the southern boundary of the active rift as indicated by the southernmost occurrence of pyroclastic cones in this area (Holcomb, 1980, p. 167). A low-level total-intensity aeromagnetic profile of the east rift zone (fig. 40.2; see also Flanigan and Long, chapter 39) also shows that the southern margin of the dike complex is about 8.2 km from the coast,

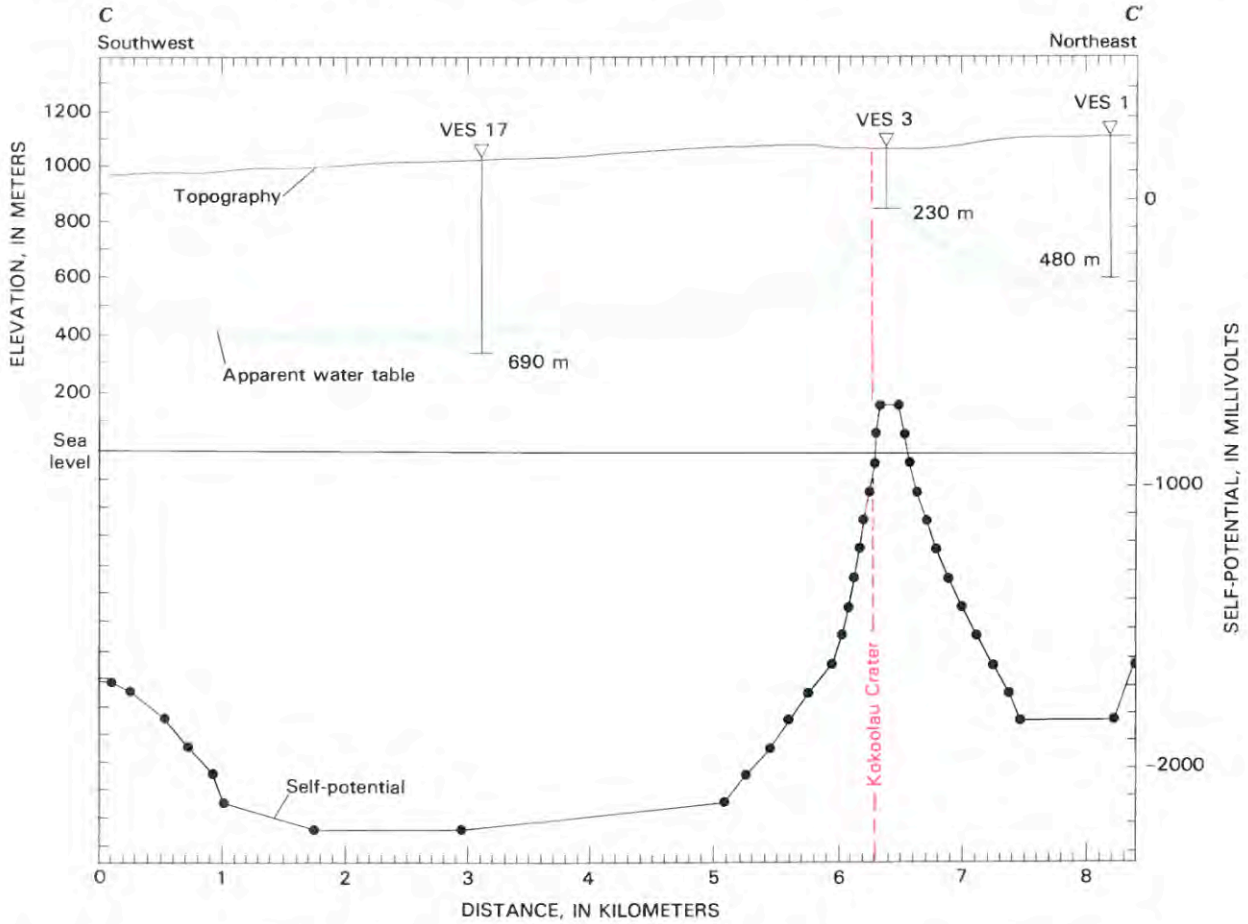


FIGURE 40.6.—Topography, apparent water table, and self-potential for profile C–C′ on the upper east rift zone of Kilauea Volcano. See figures 40.1 and 40.11 for profile location and figure 40.8 for VES interpretations.

and the complex extends to at least the 11.5-km position on the profile. The interpreted dike-complex margins on the aeromagnetic profile correspond to the crest of the aeromagnetic high to the southeast and the trough of the aeromagnetic low to the northwest (fig. 40.2).

The point at which the apparent water table rises above the ground surface (fig. 40.2) coincides with a short-wavelength (<1.5 km) anomaly that is positive relative to sea level and thus cannot be attributed to vadose-zone thinning. Because the short-wavelength anomaly coincides with a fissure vent, it must be caused by a thermoelectric or electrokinetic mechanism (or a combination of both) associated with the subsurface heat source responsible for the fissure. The other short-wavelength anomalies along the profile that are associated with fissure vents may also not be related directly to the vadose zone.

The more gradual decrease of apparent water-table elevation northwest of the 1977 fissure may be the result of a leaky dike system that cannot support the same hydraulic head that is maintained southeast of the fissure. The gradual rise of the apparent water table at the northwest end of the profile may be evidence for high-level impoundment of ground water by an older ERZ dike system or possibly by older dikes related to an aeromagnetic lineation that branches off from the Mauna Loa northeast rift zone 15 km from the summit and parallels the north side of the Kilauea ERZ (Flanigan and Long, chapter 39).

## LOWER-EAST-RIFT-ZONE PROFILE

The apparent water table calculated for the LERZ profile (fig. 40.4) begins at zero elevation at the coast then dips as much as 100 m below sea level (4.5 km inland) in the area immediately southeast of a 1955 fissure vent (at 5.2 km). The Keauohana well located to the south of the rift just off the profile at the 4-km position shows that the water table is about 1 m above sea level (State of Hawaii Department of Land and Natural Resources, 1970), though the apparent water table is about 100 m below sea level. The discrepancy implies that this portion of the profile either is affected by SP mechanisms associated with the 1955 vent more than by vadose-zone variations or that it has a different coefficient for the correlation of vadose-zone thickness and SP.

Northwest of the fissure vent and within the rift, the apparent water table is elevated nearly 200 m above sea level; this is consistent with interpretations of elevated water tables in the middle and upper east rift. Self-potentials associated with the 1955 fissure vent and (or) a changing coefficient, $C_v$, may also bias the apparent water-table depths northwest of the vents, but we do not know how much. A discrepancy is obvious at the position of the fissure vent, where the apparent water table is about 30 m above the ground surface. Here again we believe that these eruptive-vent anomalies, which are generally short wavelength, are due to thermoelectric or electrokinetic phenomena associated with subsurface heat sources.

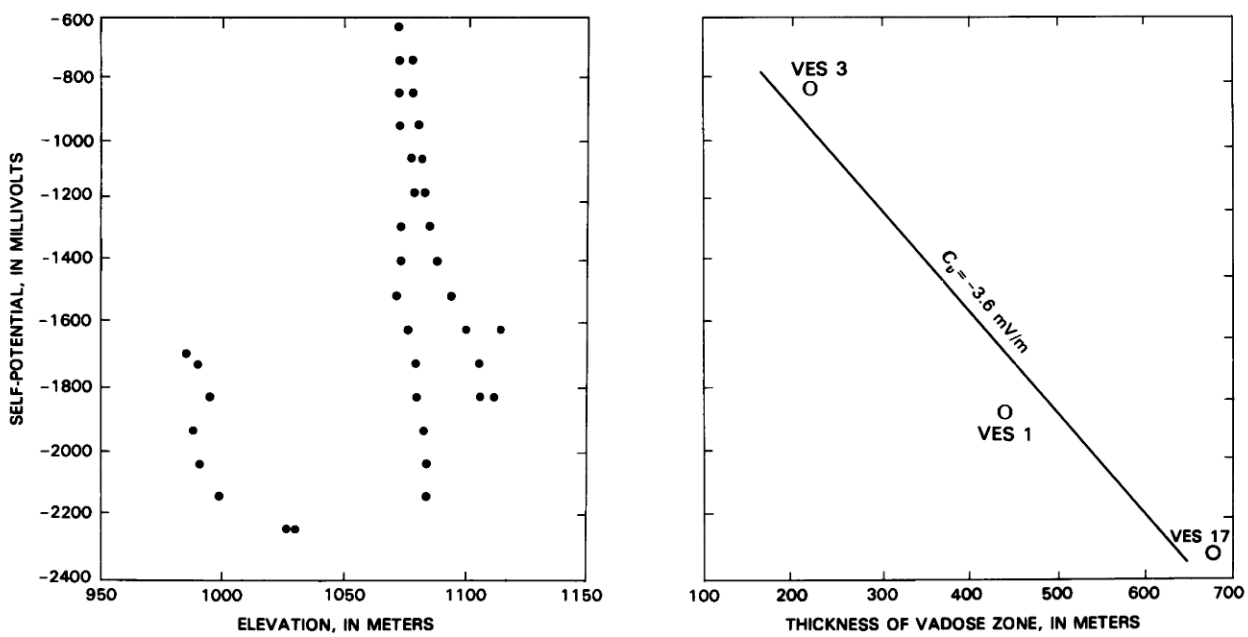


FIGURE 40.7.—Plots of self-potential versus elevation and versus vadose-zone thickness for the UERZ profile shown in figure 40.6. In the latter plot, the correlation of self-potential and vadose zone thickness is derived from VES interpretations discussed in the text. Correlation line is graphically determined.

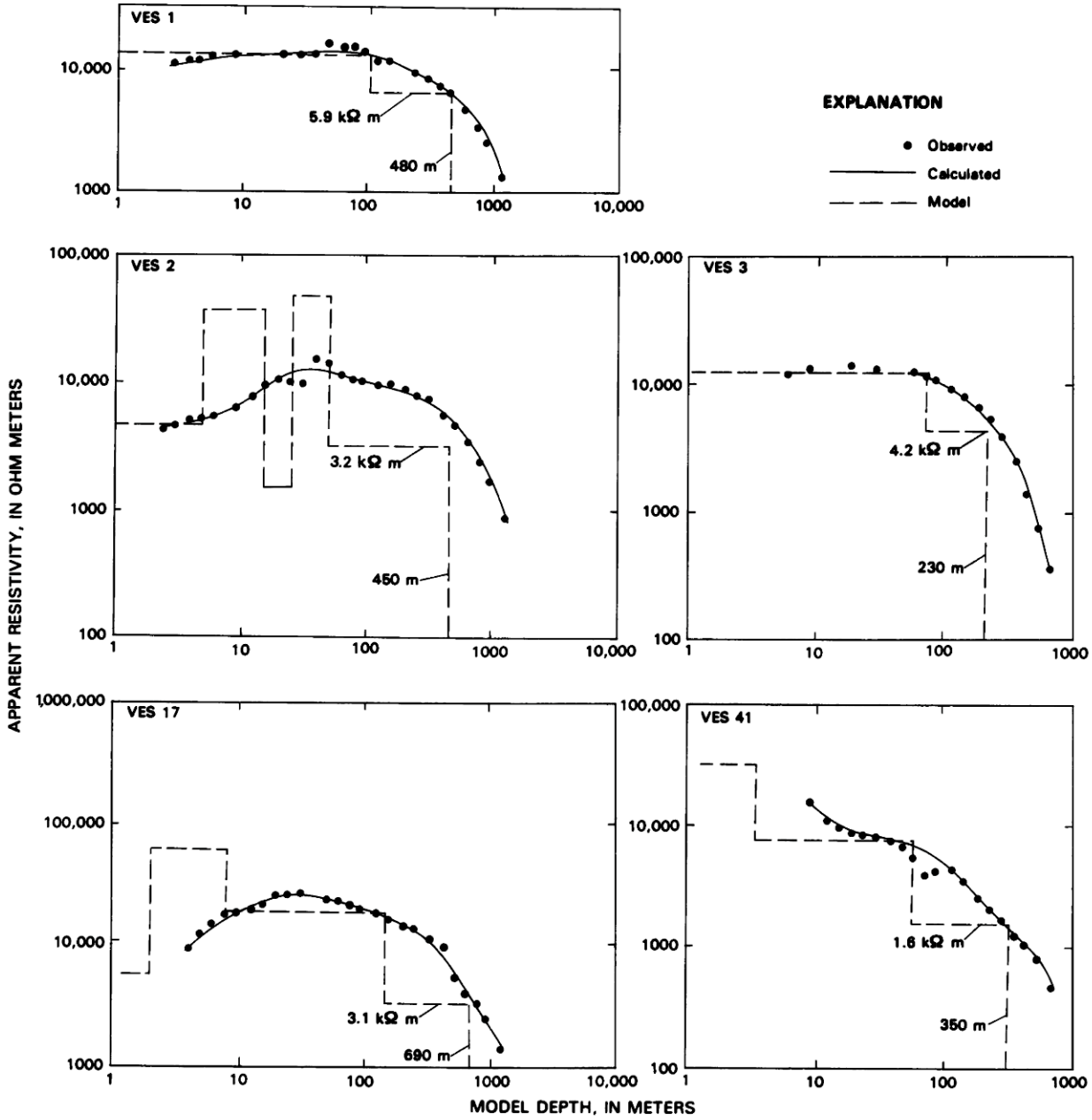


FIGURE 40.8.—Data plots and interpretations for vertical electrical soundings (VES) 1, 2, 3, 17, and 41. See figures 40.1 and 40.11 for locations of soundings. Data for VES 1, 2, and 3 provided by C.J. Zablocki (written commun., 1985).

## UPPER-EAST-RIFT-ZONE PROFILE

The calculations of apparent water table beneath the UERZ profile (fig. 40.6) shows a generally elevated water table, locally even higher beneath the zone of pit craters. This seems reasonable; the water table is elevated about 610 m above sea level in a research well (location shown in fig. 40.1) about 3.5 km north of the profile (Zablocki and others, 1974). These water-table elevations are far too high to represent the basal water-table conditions that one expects to find in Hawaii within permeable volcanic rocks where no lateral barriers such as dikes or fault gouge exist (Stearns, 1966). Therefore, the elevated water table must be impounded by high-angle, water-impermeable structures such as dikes. The presence of high-level water outside of the visible surface expression of the rift

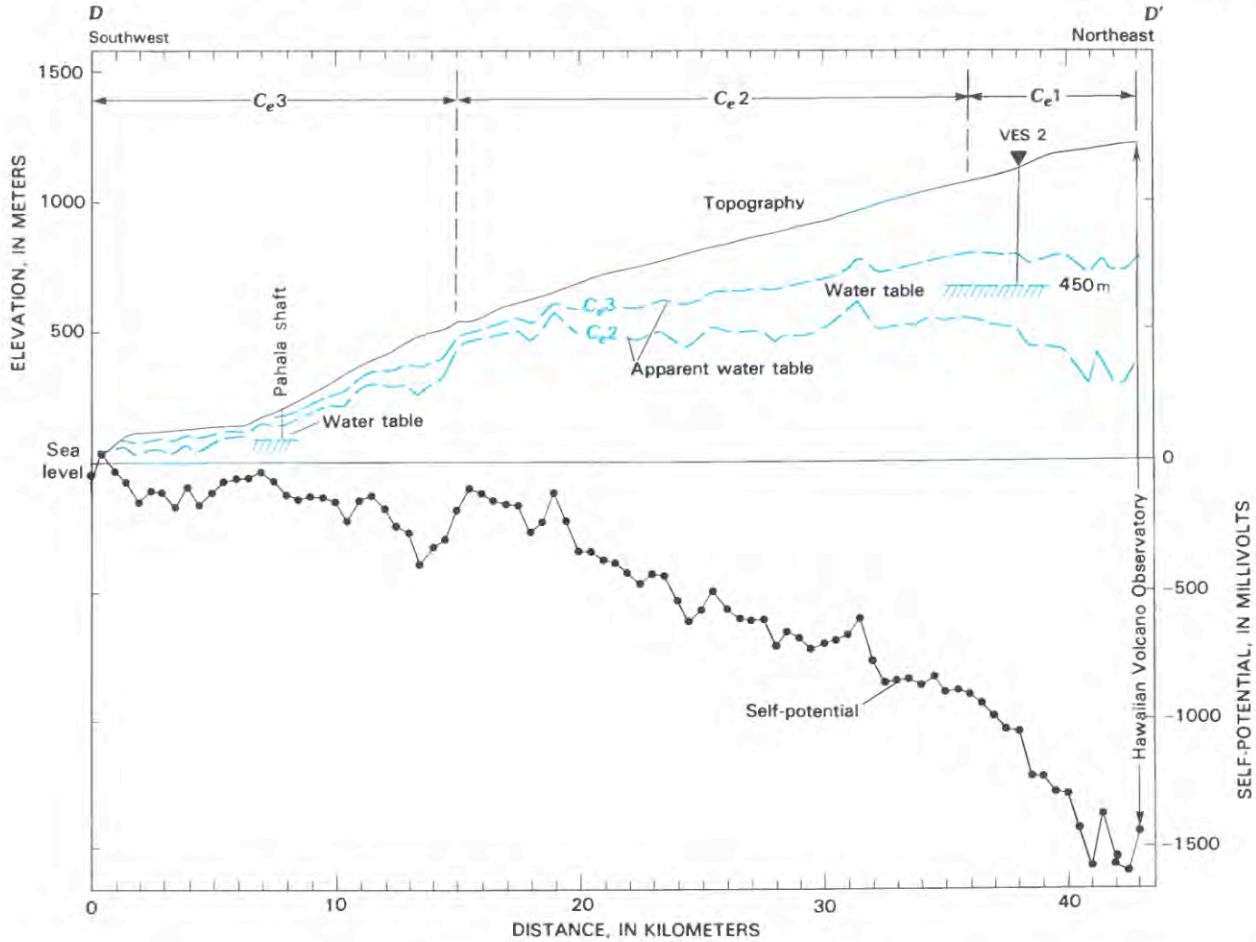


FIGURE 40.9.—Topography, apparent water-table elevations, and self-potential for profile D–D' from Punaluu to the summit (HVO) of Kilauea. An interpretation for VES 2 and the water table in the Pahala shaft are shown for comparison. Segments of the profile that correspond to different linear correlations ($C_e1$ through $C_e3$ in fig. 40.10) are indicated. See figure 40.1 for profile location.

zone indicates either that the rift is broader than its surface expression or that faults exist that may be impeding the lateral flow of water.

VES 1 (fig. 40.8, see fig. 40.11 for location) is just within the aeromagnetic anomaly that delineates the northeast boundary of the dike complex (Flanigan and Long, chapter 39). The fact that no short-wavelength SP anomalies (fig. 40.6) occur northeast of the rift suggests that only the southwest side of the rift (coincident with the UERZ line of pit craters) is still active. The elevated water table on the northeast side of the rift can be satisfactorily explained as caused by impoundment by dikes that are now buried and without surface expression. The position at which the elevated water table becomes basal should be the boundary on the northeast side of the rift-zone anomaly. It follows that the northeast boundary of the rift zone is beyond the SP data that we see in figures 40.6 and 40.11. If so, the wavelength of the SP anomaly should be much broader than indicated in either figure 40.6 or 40.11.

VES 17, southwest of the rift, lies outside of the aeromagnetic expression of the dike complex (Flanigan and Long, chapter 39). However, numerous large normal faults of the Koae fault system (figs. 40.1 and 40.11) probably act as the hydrologic barrier that elevates the water table beneath VES 17. Either gouge on the Koae faults or dikes intruded into the fault planes (in May 1969 for example; see Swanson and others, 1979) from either the SWRZ or the UERZ probably form the actual impermeable part of the hydrologic barrier.

## SOUTHWEST-RIFT-ZONE PROFILE

The plots of apparent water table (fig. 40.9) indicate that an elevated (nonbasal) water table, which dips to the southwest, underlies the profile between the 28-km and 43-km positions. This inference is supported by ground-water studies near the town of Pahala. Ground water beneath the town stands at approximately 72

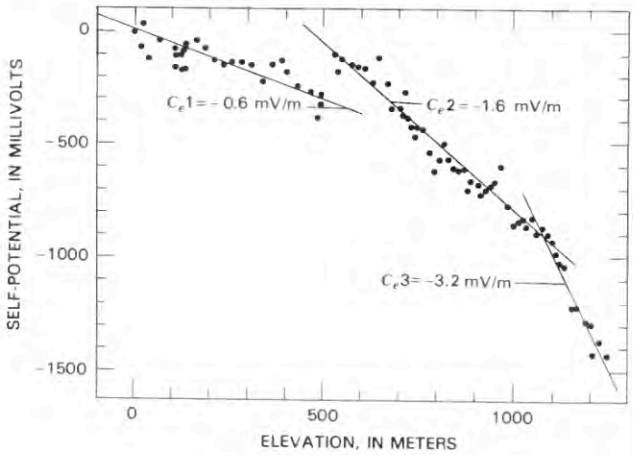


FIGURE 40.10.—Plot of elevation versus self-potential for the 43-km profile shown in figure 40.9. Three gradients, $C_e1$, $C_e2$, and $C_e3$, show the linear correlations between self-potential and elevation for 3 segments of the profile. Correlation lines are graphically determined.

m above sea level (fig. 40.9) in a Maui-type well (Stearns and Macdonald, 1946) and is probably impounded by older dikes of the SWRZ. Evidence from an electrical sounding survey (Hussong and Cox, 1967) in the immediate area around Pahala indicates that the anomalously high water-table elevation extends to at least 1 km northeast of Pahala (the edge of the study area) and along the highway towards Punaluu. This explains the shallow $C_e$ gradient ($C_e1$) for this part of the profile in figure 40.10.

The portion of the profile between 7-km and 28-km positions appears underlain by a nearly horizontal water table that is at an even higher level than that under the seaward part of the profile. A low-resistivity zone beneath VES 2 (figs. 40.8–40.9) at the 5-km position is interpreted to be the top of the water table; it lies at 450-m depth or about midway between the two plotted apparent water tables. The estimation of water table from SP is only approximate, but the qualitative agreement between the apparent water table and data from the Pahala shaft and VES 2 seems meaningful. Additional determinations of actual water-table elevation would allow a more accurate value of the correlation coefficient of SP and vadose-zone thickness ($C_v$) to be chosen.

## CONCLUSIONS

The edifice of Kilauea sits in a broad self-potential low that appears to be related to negative potentials generated by the percolation of ground water through the vadose zone to the underlying water table. Plots of SP against elevation often have more than one linear segment, which indicates that SP is correlated to something other than elevation. Examination of SP plotted against elevation for profiles where water-table elevation is known indicate the SP correlation is really with vadose-zone thickness rather than with elevation. An empirical gradient of about −1.7 mV per meter of elevation above sea level seems to best fit the vadose-zone-related potentials along the MERZ and LERZ profiles. A value of −3.6 mV/m appears better for the UERZ profile. A gradient of either −1.6 or −3.2 mV/m may best fit the SWRZ profile; a choice cannot be made without additional data. The observation that the correlation between vadose-zone thickness and SP is not always constant, even when the water table is at a constant elevation, implies the possible addition of potentials related to deep or broad heat sources or possible variation of the parameters of the presumably electrokinetic generating mechanism.

The self-potential profiles, referenced to sea level, have been used to calculate an apparent water-table configuration. Electrical soundings have confirmed the water-table depth directly at critical places and shown places where potentials unrelated to the thickness of the vadose zone must be taken into account.

At only a few locations on the volcano, related to obvious thermal features, do self-potentials become more positive than potential at sea level. On the basis of that observation we are in partial agreement with Zablocki (1978), who conjectured that all

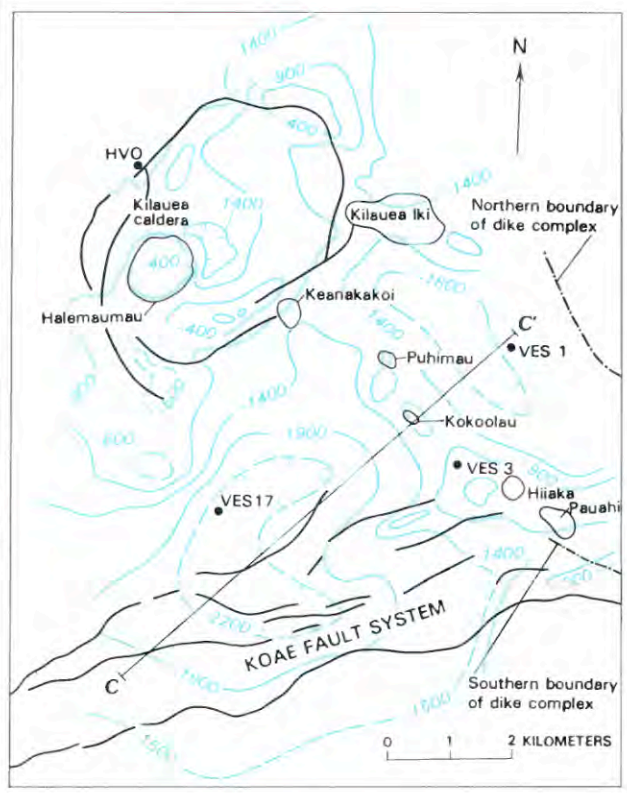


FIGURE 40.11.—Self-potential map of the summit region of Kilauea Volcano (after Zablocki, 1976). Selected contours (blue) show values in millivolts. The potentials are referenced to sea level via the SWRZ profile in figure 40.9. Also shown are the location of profile C–C′ and VES 1, 3, and 17 and main geologic features. The northern and southern boundaries of the dike complex defining the east rift zone derived from aeromagnetic studies (Flanigan and Long, chapter 39).

anomalies on Kilauea reflect the distance that water in the vadose zone descends before encountering higher temperature fluids rising above a deeper heat source. Over the rising fluids the more positive potentials (which might still be negative in relation to sea level) reflect (1) a thinner vadose zone and (2) electrokinetic potentials contributed by the rising fluids. We infer, however, that the primary means by which the vadose zone is thinned is high-level impoundment of ground water by dikes in areas known to be loci of intrusions and eruptions on the volcano. The impoundment results in broad anomalies (>3 km) associated with Kilauea's summit and rift zones. The long-wavelength anomalies are not restricted to currently active thermal features but also appear to reflect older dike systems left behind as the rift systems shifted in position to the south. Shorter wavelength anomalies, superimposed on the longer wavelength anomalies, are probably caused by a combination of thermoelectric and electrokinetic effects associated either with specific, recently active fissure vents or with known areas of recent intrusions.

Use of a variety of geophysical techniques combined with observation of recent volcanic activity can contribute to understanding the geologic history of a volcano. An example of this is the UERZ, which is defined by (1) a zone of pit craters on the currently active rift, (2) a broad SP anomaly that extends about 2 km farther to the northeast, and (3) an aeromagnetic anomaly, which is nearly coincident with the SP anomaly. The lack of any high-amplitude narrow-wavelength features in the zone of broad SP and aeromagnetic anomalies northeast of the active rift is consistent with the lack of volcanic activity in that area. The fact that the water table is elevated in this zone indicates that water is impounded northeast of the line of UERZ pit craters by older dikes of the rift system. A second example can be found in the MERZ profile: a rising apparent water table north of the MERZ can best be explained as dike impoundment of ground water by an older dike system of the ERZ or by a postulated inactive branch of the northeast rift zone of Mauna Loa Volcano.

## REFERENCES CITED


Anderson, L.A., and Johnson, G.R., 1976, Application of the self-potential method to geothermal exploration in Long Valley, California: Journal of Geophysical Research, v. 81, no. 8, p. 1527–1532.

Corwin, R.F., and Hoover, D.B., 1979, The self-potential method in geothermal exploration: Geophysics, v. 44, no. 2, p. 226–245.

Fitterman, D.V., 1978, Electrokinetic and magnetic anomalies associated with dilatant regions in a layered earth: Journal of Geophysical Research, v. 83, p. 5923–5928.

——— 1979, Calculations of self-potential anomalies near vertical contacts: Geophysics, v. 44, p. 195–205.

——— 1983, Modelling of self-potential anomalies near vertical dikes: Geophysics, v. 48, no. 2, p. 171–180.

——— 1984, Thermoelectrical self-potential anomalies and their relationship to the solid angle subtended by the source region: Geophysics, v. 49, p. 165–170.

Holcomb, R.T., 1980, Preliminary geologic map of Kilauea Volcano, Hawaii: U.S. Geological Survey Open-File Report 80–796, 2 sheets, scale 1:50,000.

Hussong, D.M., and Cox, D.C., 1967, Estimation of ground-water configuration near Pahala, Hawaii, using electrical resistivity techniques: Water Resources Research Center, University of Hawaii, Technical Report 17, 35 p.

Jackson, D.B., and Sako, M., 1982, Self potential surveys related to probable geothermal anomalies, Hualalai Volcano, Hawaii: U.S. Geological Survey Open-File Report 82–127, 10 p.

Keller, G.V., and Frischknecht, F.C., 1966, Electrical methods in geophysical prospecting: New York, Pergamon Press, 517 p.

Klein, D.P., and Larson, J.C., 1978, Magnetic induction fields (2–30 cpd) on Hawaii Island and their implications regarding electrical conductivity in the oceanic mantle: Royal Astronomical Society Geophysical Journal, v. 58, no. 53, p. 61–77.

Lockwood, J.P., Banks, N.G., English, T.T., Greenland, P., Jackson, D.B., Johnson, D.J., Koyanagi, R.Y., McGee, K.A., Okamura, A.T., and Rhodes, M.J., 1985, The 1984 eruption of Mauna Loa Volcano, Hawaii: Eos, Transactions of the Americal Geophysical Union, v. 66, no. 16, p. 169–171.

Poldini, E., 1939, Geophysical exploration by spontaneous polarization methods: Mining magazine, v. 60, p. 22–27.

Sill, W.R., 1982, Self-potential effects due to hydrothermal convection-velocity crosscoupling: Earth Sciences Laboratory, University of Utah Research Institute, no. DOE/ID/12079–68, 23 p.

——— 1983, Self potential modeling from primary flow: Geophysics, v. 48, p. 76–86.

State of Hawaii Department of Land and Natural Resources, 1970, An inventory of basic water resources data—Island of Hawaii: Report R34, 188 p.

Stearns, H.T., 1966, Geology of the State of Hawaii: Palo Alto, California, Pacific Books, 266 p.

Stearns H.T., and Macdonald, G.A., 1946, Geology and ground water resources of the Island of Hawaii: Hawaii Division of Hydrography Bulletin 9, 363 p.

Sawnson, D.A., Duffield, W.A., Jackson, D.B., and Peterson, D.W., 1979, Chronological narrative of the 1969–71 Mauna Ulu eruption of Kilauea Volcano, Hawaii: U.S. Geological Survey Professional Paper 1056, 55 p.

Yungul, Sulhi, 1950, Interpretation of spontaneous polarization anomalies caused by spheroidal ore bodies: Geophysics, v. 15, no. 2, p. 237–246.

Zablocki, C.J., 1976, Mapping thermal anomalies on an active volcano by the self-potential method, Kilauea, Hawaii, *in* Proceedings, 2nd United Nations Symposium on the Development and Use of Geothermal Resources, San Francisco, Calif., May 1975, v. 2, p. 1299–1309.

——— 1977, Self-potential studies in East Puna, *in* Geoelectric studies on the east rift, Kilauea Volcano, Hawaii Island: Honolulu, Hawaii Institute of Geophysics, University of Hawaii Technical Report HIG–77–15, p. 175–195.

——— 1978, Streaming potentials resulting from the descent of meteoric water—a possible source mechanism for Kilauean self-potential anomalies: Geothermal Resources Council, Transactions, v. 2, sec. 2, p. 747–748.

——— 1980, Observations from self-potential monitoring studies on Kilauea Volcano, Hawaii (1973–1975): U.S. Geological Survey Open–File Report 80–99, 15 p.

Zablocki, C.J., Tilling, R.I., Peterson, D.W., Christiansen, R.L., Keller, G.V., and Murray, J.C., 1974, A deep research drill hole at the summit of an active volcano, Kilauea, Hawaii: Geophysical Research Letters, v. 1, no. 7, p. 23.

Zohdy, A.A.R., Anderson, L.A., and Muffler, L.J.P., 1973, Resistivity, self-potential and induced polarization surveys of a vapor dominated geothermal system: Geophysics v. 38, no. 6, p. 1130–1144.

# THE DIKE COMPLEX OF KOOLAU VOLCANO, OAHU: INTERNAL STRUCTURE OF A HAWAIIAN RIFT ZONE

*By* George P.L. Walker[1]

## ABSTRACT

**The Koolau dike complex in the deeply eroded lava shield of Koolau Volcano on Oahu is extraordinarily intense and where widest contains an estimated 7,400 subparallel dikes totaling 3–5 km in width. Quantitative study involving measurement of 3,550 dikes reveals that the complex has a non-Gaussian intensity distribution. Dikes generally constitute 50–70 percent of the total rock and form an intensity plateau across the complex, decreasing very rapidly to <5 percent at the edges. A proposed model for formation of the complex envisages the highly mobile tholeiitic magma as being tightly constrained by the zonation of bulk-rock density in the volcanic edifice. This model, applied to the active Hawaiian volcanoes, explains well the marked propensity of magma to stay underground in what is evidently a gravitationally very stable situation. Flow lineations on Koolau dike margins indicate that the magma generally rose obliquely, from two distinct magma supply centers situated 5 km apart and 2–3 km deep. The dikes are systematically nonvertical and form two complementary sets dipping at 65° to 85° in opposite directions, like normal faults in an extensional setting. Predominance of one dip direction over a wide area may indicate an early tendency to seaward creep of the volcano in that area. Stages in the buildup of the complex are marked by increasing proportions of dikes entering multiple clusters, these clusters having the characteristics of a sheeted dike complex. The Koolau Volcano has a wide caldera of downsag type, with probable conventional calderas in the middle. The strong inward decrease in dike concentration is interpreted to mean a general inward increase in subsidence rate, subsidence in the central area exceeding the rate of upward growth of the dike complex. This leads to the concept that subsidence of Hawaiian calderas is caused by the weight of intrusions in an area of lithospheric weakness above a hot spot.**

## INTRODUCTION

Many dikes are exposed where denudation has cut deeply into the older basaltic shield volcanoes of the Hawaiian Islands, and in some volcanoes they are concentrated into well-defined dike complexes. These complexes have long been regarded as the subsurface expression of rift zones such as those in which eruptions on Kilauea and Mauna Loa Volcanoes are concentrated.

A full understanding of active rift zones requires a knowledge of dike complexes, just as surely as understanding the dike complexes depends on knowing how active rift zones develop. The general distribution patterns and characteristics of the dike complexes are well established, but very little detailed information about them is available, and the present study is aimed at documenting one complex more fully than has been attempted before.

Another reason for documenting one of these complexes is that they are very similar to the sheeted dike complexes of the ophiolite suite. This suite is interpreted to form by oceanic crustal spreading along globally extensive spreading zones, whereas the dike complexes of denuded Hawaiian lava shields occur in an intraplate tectonic setting and extend high into the individual volcanic edifices. It is important to have a basis by which they can be compared with sheeted complexes.

One of the most intense and accessible of the Hawaiian dike complexes is that exposed in the core of the Koolau shield volcano on Oahu. Lava of this shield gives K-Ar ages of 2.67–1.83 Ma (McDougall and Aziz-ur-Rahman, 1972; Doell and Dalrymple, 1973). The Koolau Volcano is strongly elongate on a northwest-southeast axis and has a subaerial length of 57 km. The shield surface is well preserved on the lower parts of the interfluves along the southwestern or leeward side, and the shield form may be reconstructed (fig. 41.1) by drawing generalized contours that neglect all the lesser topographic features.

The position of the long axis of the Koolau shield is apparent from curvature of the generalized contours around the northwestern end, and this coincides with the antiform on the two sides of which the lava dips outward in opposite directions. The position is less clear at the southeast end, but the antiform lies between the Mokulua Islands and Makapuu Head, and its approximate position is shown in figure 41.1.

Erosion of the Koolau shield has been concentrated on the northeastern or windward side; between Waikane and Waimanalo, deep embayments cut right across the long axis, and more than half of the original shield has there disappeared. I agree with Moore (1964) in regarding much of the loss as having been accomplished by great landslides. An impressive cliff (the pali), which faces northeast and is as high as 900 m (3,000 ft), marks the headwall of the series of landslide scars.

A strip of low-lying ground 4–8 km wide extends from Waikane to Waimanalo and between the pali and the coast consists mostly of alluvium and reef deposits, but it is transected by

[1]Hawaii Institute of Geophysics, Honolulu, HI 96822.

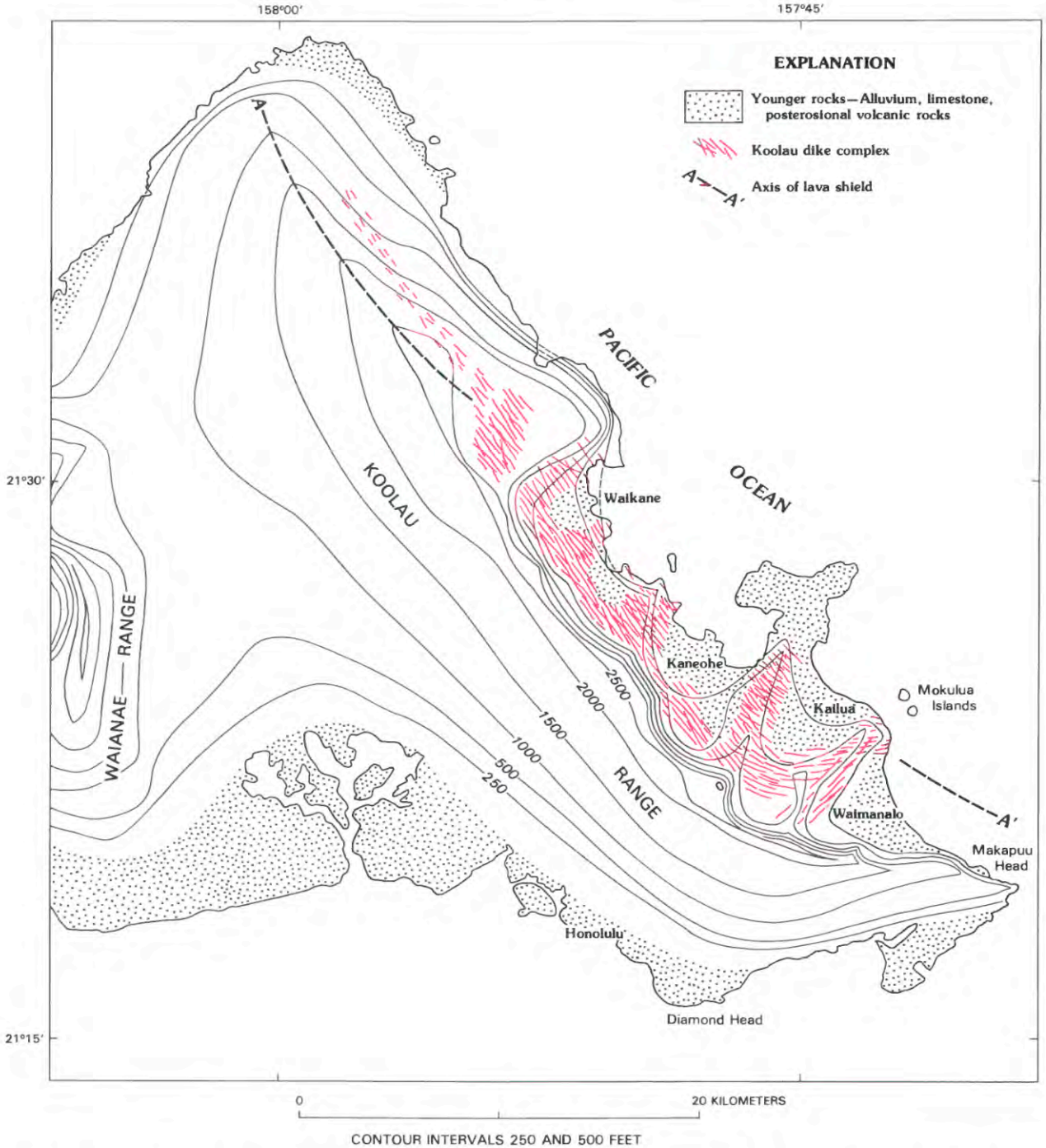


FIGURE 41.1.—Setting of Koolau dike complex on Island of Oahu. Distribution of complex (modified from Stearns, 1939) shown in relation to Koolau lava-shield volcano, form of which is portrayed by generalized topographic contours. Volcano is very strongly elongate northwest-southeast and position of axis is based on generalized contours and opposing dip directions of shield lava.

northeast-trending ridges—possibly these are septa between the landslide scars—where most exposures of the Koolau dike complex are found. Natural exposures tend to be difficult of access and unfavorable for quantitative studies. A notable exception is the two small Mokulua Islands, on which are found the finest known outcrops.

The present study has relied much on artificial exposures. Noteworthy among these are roadcuts in the unfinished H3 Highway, the two large Kapaa quarries, and cuts in new housing subdivisions in the Keolu Hills. The available artificial and natural exposures are thought to be just adequate to reveal the principal features of the Koolau dike complex.

### ACKNOWLEDGMENTS

This research was not funded and was undertaken as a part-time activity to satisfy scientific curiosity, contribute to the geological understanding of Hawaii's volcanism, and complement the fine research done on active volcanoes of Hawaii by personnel of the Hawaiian Volcano Observatory. It was made possible by my employment at the University of Hawaii. I thank Kevin Kennedy for introducing me to the Mokulua Islands, the Manager of Kapaa Quarry for permission to visit, and the U.S. Air Force for permission to visit Bellows Air Force Base. I also acknowledge useful comments by reviewers Paul Delaney, Mary M. Donata and Tom L. Wright, and my wife for her help and forebearance. This paper is Hawaii Institute of Geophysics contribution number 1706.

## PREVIOUS WORK

The distribution of the dike complex and the positions and trends of isolated dikes elsewhere, were clearly shown on the 1:63,360-scale map of Stearns (1939) and described by Stearns and Vaksvik (1935). They distinguished two dike complexes lying alongside one another and having a parallel trend. The former cuts volcanic rocks of the Kailua Volcanic Series (now Kailua Member of the Koolau Basalt) which they interpreted to have accumulated under or close by the caldera of the Koolau shield volcano, whereas the latter cuts shield-building lava of the Koolau Volcanic Series (now Koolau Basalt). Takasaki and others (1969, 1982) accepted the distinction between caldera infill and shield-building lava but regarded the complex as one, and I follow this usage.

Wentworth (1951) applied the term "dike complex" to areas where there are 100 or more dikes per mile, and Takasaki and others (1969) applied it to areas where dikes constitute more than 5 percent of the rock. The latter authors called the zone adjacent to the dike complex, characterized by scattered dikes that constitute less than 1 percent of the rock, the marginal dike swarm, and pointed out (p. 14) that "although the strike of dikes is generally the same in both zones, the dike complex and the marginal dike zone are distinct, and no transition zone intervenes." Dike complex is a useful term for an intense swarm in which the dikes are so narrow, numerous and intertwined that it is not feasible to map individual members.

The important influence of the Koolau dikes on ground-water storage in the Koolau Range led to studies of them by Takasaki and others (1969), Takasaki (1981), and Takasaki and Mink (1982). These authors mapped the dike complex and marginal zone and measured the dike trend and intensity in six water-supply tunnels west of Waikane.

The maps of Stearns (1939), Takasaki and others (1969), and Takasaki and Mink (1982) show clearly the predominant northwest-southeast trend of the dikes, parallel with the longitudinal axis of the Koolau shield. They also show dikes trending in a southwesterly direction from Kailua into the leeward side of the Koolau Range towards Diamond Head; these have been identified as a secondary swarm (the Kaau or southwest rift zone) analogous with the minor rift zones that occur on some active Hawaiian volcanoes.

Few studies have hitherto been made of the dike structures, apart from that by Wentworth and Jones (1940) on jointing and the distribution of amygdules. Among recent workers, Ryan and others (1983) most clearly recognized how important it is to study the dike swarms when seeking to understand rift zones. Walker and Kennedy (in preparation) describe aspects of the dike complex exposed on the Mokulua Islands, and Walker (1986) discussed the origin of the complex in an earlier report on the present study.

## DIKE DISTRIBUTION

The present quantitative study of the Koolau dike complex is based on measurements made at 55 localities in windward Oahu, distributed as shown in figure 41.2 and listed in table 41.1. At each locality the width, trend, and dip of each dike was measured; the dike widths in a measured traverse were also totaled so as to yield the dike intensity, expressed as the percentage of rock composed of dikes, as shown in figure 41.3. Intensity is alternatively expressed as the calculated number of dikes per 100 m of traverse in a direction at right angles to the predominant dike trend, as shown in figure 41.4. The measured traverses totaled 7.4 km in length and contained 3,550 dikes aggregating to 2.6 km in width. Data from these 55 localities are supplemented by data from six water-supply tunnels (Takasaki and others, 1969; Takasaki, 1981).

The dikes very commonly occur in multiple clusters as wide as about 20 m, in which successive subparallel members were injected either along the margins of, or inside, preceding dikes; dikes constitute 100 percent of the width of such a cluster. Screens of country rock occur between clusters. A valid value for the dike intensity is obtained only if the measured traverse includes at least several dike clusters and their intervening screens.

The highest intensity (80–85 percent) occurs on the coast at Heeia (locality 41) and on the Mokulua Islands (localities 19 and 20); a measured 185-m traverse most of the way across the northwestern island recorded 240 dikes totaling 145 m thick. The dike intensity is high, exceeding 40 percent, in a belt of country 3–6 km wide extending northwest from Kailua, but it is not uniformly high over the entire length or width of this belt; in particular it drops to 2 percent in the Kailua caldera, which interrupts the continuity of the complex. The calculated number of dikes per 100 m (fig. 41.4)

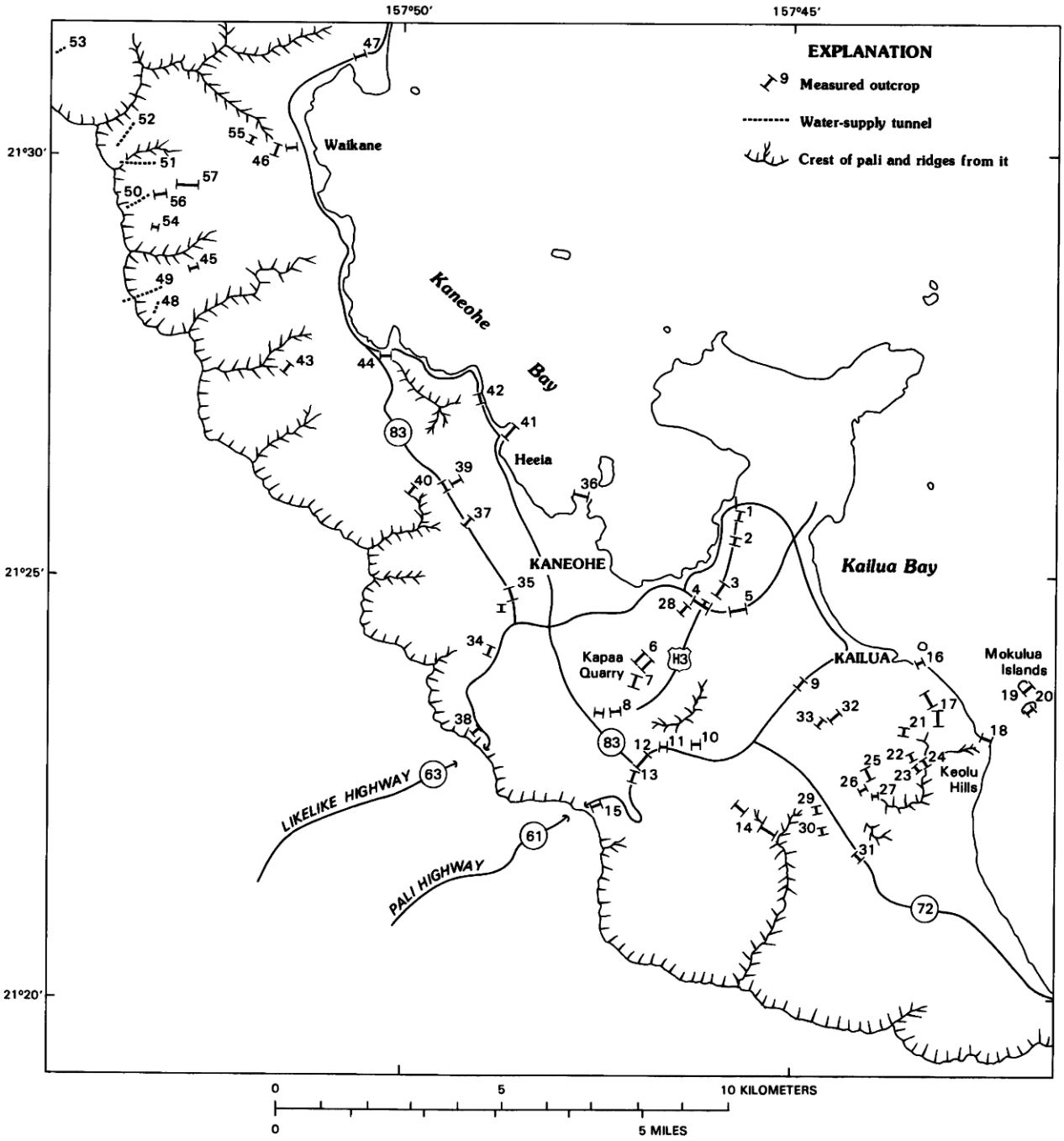


FIGURE 41.2.—Windward side of Oahu showing location of outcrops at which dike complex was studied. Numbers identify outcrops listed in table 41.1. All but outcrops 14, 15, and 38 are less than 240 m (800 ft) above sea level, and most are less than 120 m (400 ft) above sea level.

TABLE 41.1.—*Localities in the Koolau dike complex used for the present study*

[W, deeply weathered outcrop]

| Number | Location and description |
|---|---|
| 1. | Northernmost deep cut in Highway H3. |
| 2. | Middle cuts beside viewpoint on Highway H3. |
| 3. | Southernmost deep cut in the Highway H3 north of the join with Mokapu Saddle Road. |
| 4. | Cuts in Mokapu Saddle Road near the Highway H3 overpass and adjacent cuts. |
| 5. | Cut in Mokapu Saddle Road near Kalaheo High School. |
| 6. | Kapaa Quarry, northeastern of two. |
| 7. | Kapaa Quarry, southwestern of two. |
| 8. | Cuts in Highway H3 between Kapaa Quarry and Kamehameha Highway (W). |
| 9. | Cut in Kailua Road south of its join with Kaelepulu Street. |
| 10. | Cut behind Kailua Drive-in Theatre (W). |
| 11. | Cut in Kalanianaole Road 0.8 km (0.5 mi) northeast of join with Kamehameha Highway (W). |
| 12. | Cut in Kalanianaole Road just northeast from join with Kamehameha Highway (Castle Junction) (W). |
| 13. | Cut in Kalanianaole Road just southwest from join with Kamehameha Highway. |
| 14. | Northwest ridge of Olomana Peak. |
| 15. | Cuts in Old Pali Highway, northeast from pass. |
| 16. | Coast exposures and nearby road cuts, Alala Point. |
| 17. | Northern part of Kaiwa Ridge. |
| 18. | Coast exposures at Wailea Point. |
| 19. | Coast exposures on northwestern Mokulua Island, northwestern of two. |
| 20. | Coast exposures on Mokulua Islands. |
| 21. | Hillside west of Kaiwa Ridge, above Kamahele Place. |
| 22. | Cuts behind subdivision alongside Kuuna Place. |
| 23. | Cuts at north end of Apokula Street. |
| 24. | Cuts on hilltop east of Apokula Street. |
| 25. | Cuts behind subdivision alongside Auwaiku Street. |
| 26. | Cuts west of Auauki Street. |
| 27. | Cuts near hilltop south of Aunauma Street. |
| 28. | Cut in track off Kahinani Way. |
| 29. | Northern section of Old Kalanianaole Road. |
| 30. | Middle section of Old Kalanianaole Road. |
| 31. | Southern end of Old Kalanianaole Road. |
| 32. | Cuts north of Akiohala Place. |
| 33. | Cuts north of Akiohala Street. |
| 34. | Cut on southwest Kahekile Highway 0.8 km (0.5 mi) of join with Likelike Highway (W). |
| 35. | Cuts in and near Kahekile Highway 0.8 km (0.5 mi) north of join with Likelike Highway (W). |
| 36. | Coast exposures and nearby road cuts at Pohakea Point. |
| 37. | Cut in Kahekile Highway 1 km (0.6 mi) northwest of join with Haiku Road (W) and behind subdivision east of Highway (W). |
| 38. | Stream section at foot of Pali just north of Wilson Tunnel. |
| 39. | Cut in Kahekile Highway just southeast of Temple Valley Shopping Center and in fields to east (W). |
| 40. | Cuts in Valley of the Temples Memorial Garden (W). |
| 41. | Coast exposures at Kealohi Point (Heeia State Park) (W in part). |
| 42. | Coast exposures 0.8 km (0.5 mi) northwest of Kealohi Point. |
| 43. | Pit at foot of southeastern spur of Kalahaku Ridge (W). |
| 44. | Cuts in Lulani Street and at join of Kamahameha Highway with Kahekile Highway. |
| 45. | Roadcuts west of Waiahole Camp (W). |
| 46. | Badland and ridge exposures on southeastern side of Puu Pueo Ridge (W). |
| 47. | Cuts in Kamahameha Highway west of Kualoa Park turnoff. |
| [1]48. | Intake tunnel A. |
| [1]49. | Main transmission tunnel R. |
| [1]50. | Uwau tunnel. |
| [1]51. | Waikane 2 tunnel. |
| [1]52. | Waikane 1 tunnel. |
| [1]53. | Kahana tunnel. |
| 54. | Path cuts at head of Waianu Valley. |
| 55. | Badland exposures at southwestern foot of Puu Pueo (W). |
| 56. | Path cuts east of Uwau tunnel. |
| 57. | Path cuts on southern side of interfluve between Waikeekee and Uwau Valleys. |

[1]From Takasaki and others (1969).

is between 50 and 100 over most parts of the complex where the intensity exceeds 40 percent, and reaches 130 in the Mokulua Islands; it drops to less than 10 in the Kailua caldera.

The Koolau dike complex was shown by Stearns (1939) to extend at least 35 km from Kailua in a northwest direction. It is assumed to extend also southeast beyond Waimanalo; exposures deep in the volcano are absent there, however, and all that is seen is a few southwest-trending dikes cutting lavas near the original shield surface on and near Makapuu Head.

The dikes predominantly have a northwest-southeast strike parallel with the longitudinal axis of the Koolau shield (fig. 41.5) and show a high degree of parallelism. Dike swarms elsewhere tend to have a fascicular (that is, cornsheaf-like) or radial arrangement, with at least some degree of divergence away from the volcanic center to which the dikes are related; the Koolau complex is noteworthy for the lack of divergence.

A subsidiary dike complex, well defined but narrower and less intense, trends southwest across the Keolu Hills in the general direction of Diamond Head, and the generalized contours of figure 41.1 show that the volcano bulges out slightly in this direction. This subsidiary complex attains a maximum intensity of about 15 percent at locality 31. Southwest-trending dikes on its extension to the leeward side of the Koolau Range were mapped by Stearns (1939) and Wentworth and Jones (1940).

The center of the Koolau Volcano is considered to be situated in the general area of Kailua, and the two complexes are regarded as the subsurface expression of two rift zones, a main northwest one and a minor southwest one. Note, however, that the pattern is not a simple one of two intersecting orthogonal dike complexes: the western part of the main complex seen in localities 12 and 13 curves around toward the Keolu Hills, where it converges on the minor southwest one. The dike swarm intensity of 80 percent at locality 23 in the Keolu Hills is therefore not simply that of the southwest rift zone.

At localities 23 and 24, where both northwest- and southwest-trending dikes occur, crosscutting relationships indicate that the injection of northwest dikes alternated with that of southwest dikes (fig. 41.6*A*), and similar relationships are seen at locality 4 (fig. 41.6*B*) and elsewhere. This shows that the periods of injection in the two directions overlapped.

This time relationship was not expected: in the model of Fiske and Jackson (1972), dike orientation is controlled by the overall geometry of a Hawaiian volcano and tends to run parallel with the long axis of the edifice. It is difficult to see how the edifice effect by itself could generate dikes alternating in trend along two orthogonal axes.

## DESCRIPTION OF THE DIKES

### WIDTH

Widths were measured on 3,550 dikes of the Koolau complex and are recorded by the histogram, figure 41.7*A*. Dikes range in width from less than 5 cm to 670 cm, and the median width is 53 cm. The arithmetic average width is 73 cm; this is greater than the median because of the contribution made to the total width by the small number of very broad dikes. The dike widths can also be portrayed in a different way, as the percentage of total dike width contributed by each width class (fig. 41.7*B*); 50 percent of the dikes are 60 cm or less wide, but these narrow dikes account for only 20 percent of the total width, and the 20 percent of dikes that are more

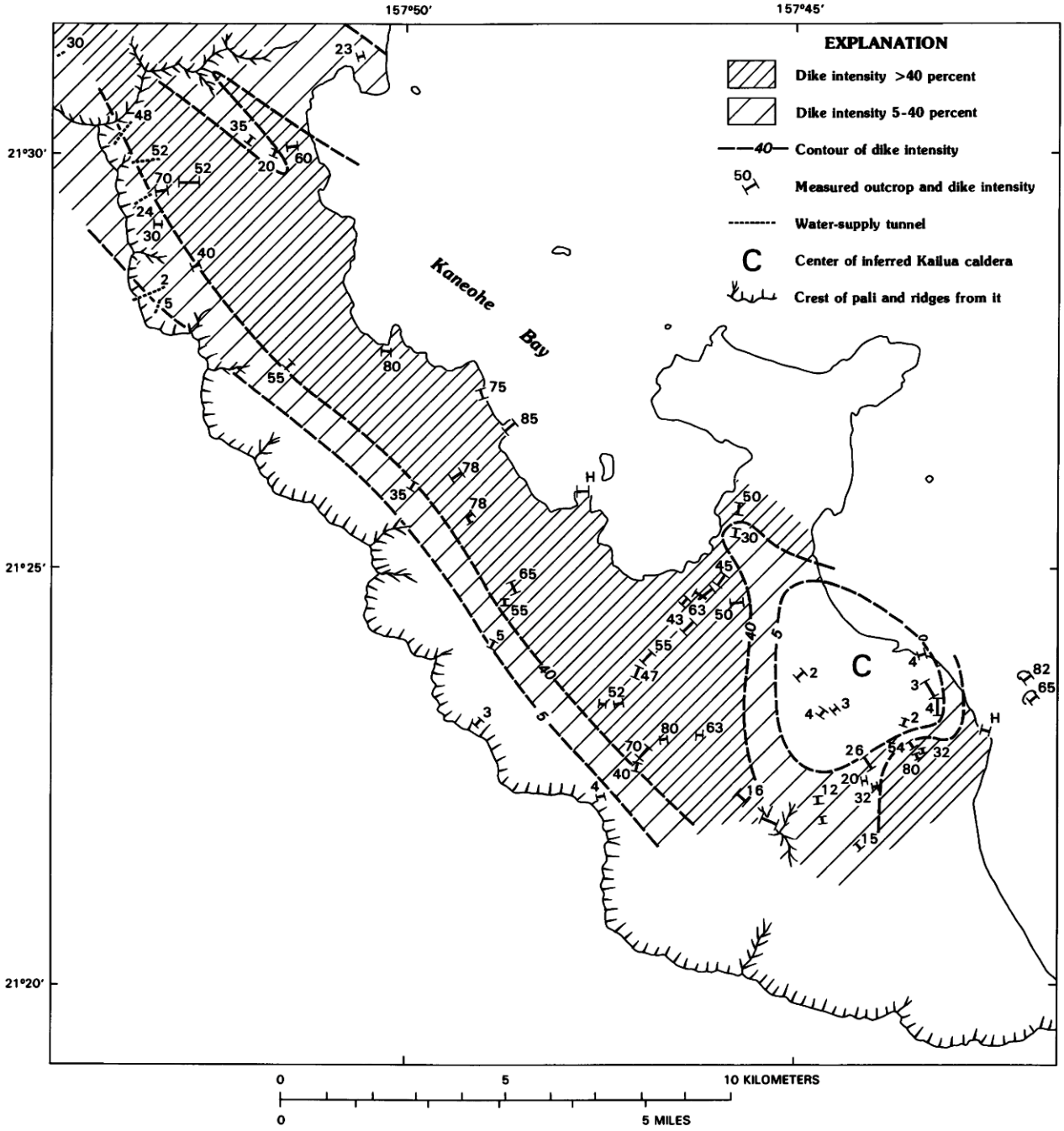


FIGURE 41.3.—Intensity of Koolau dike complex, expressed as percentage of outcrop width occupied by dikes. Close-shaded area is that in which dikes constitute 40 percent or more. Complex attains its maximum width of about 7 km in Kailua area, and narrows significantly toward northwest. The dike intensity is anomalously low in a large area centered on Kailua, interpreted to mark a caldera or caldera cluster. The intensity values at localities 3, 5, and 10 include 30 percent added for early brecciated dikes. H denotes a high intensity, but no measurement obtained.

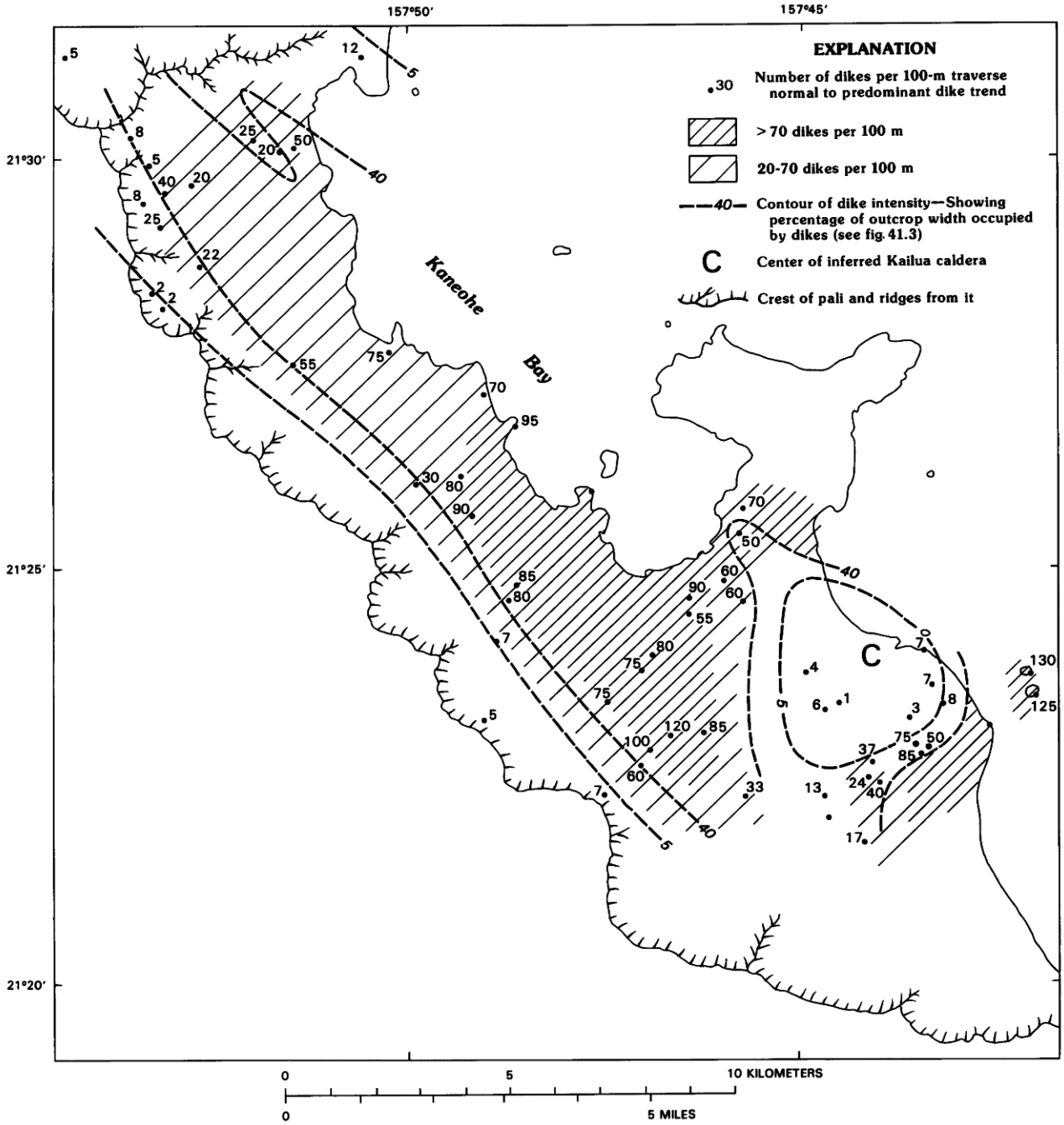


FIGURE 41.4.—Intensity of Koolau dike complex, expressed as number of dikes per 100-m traverse at right angles to predominant dike trend. Intensity contours from figure 41.3 also shown. Highest numbers of dikes (>100) occur where dikes form a high percentage of outcrop and also are narrow.

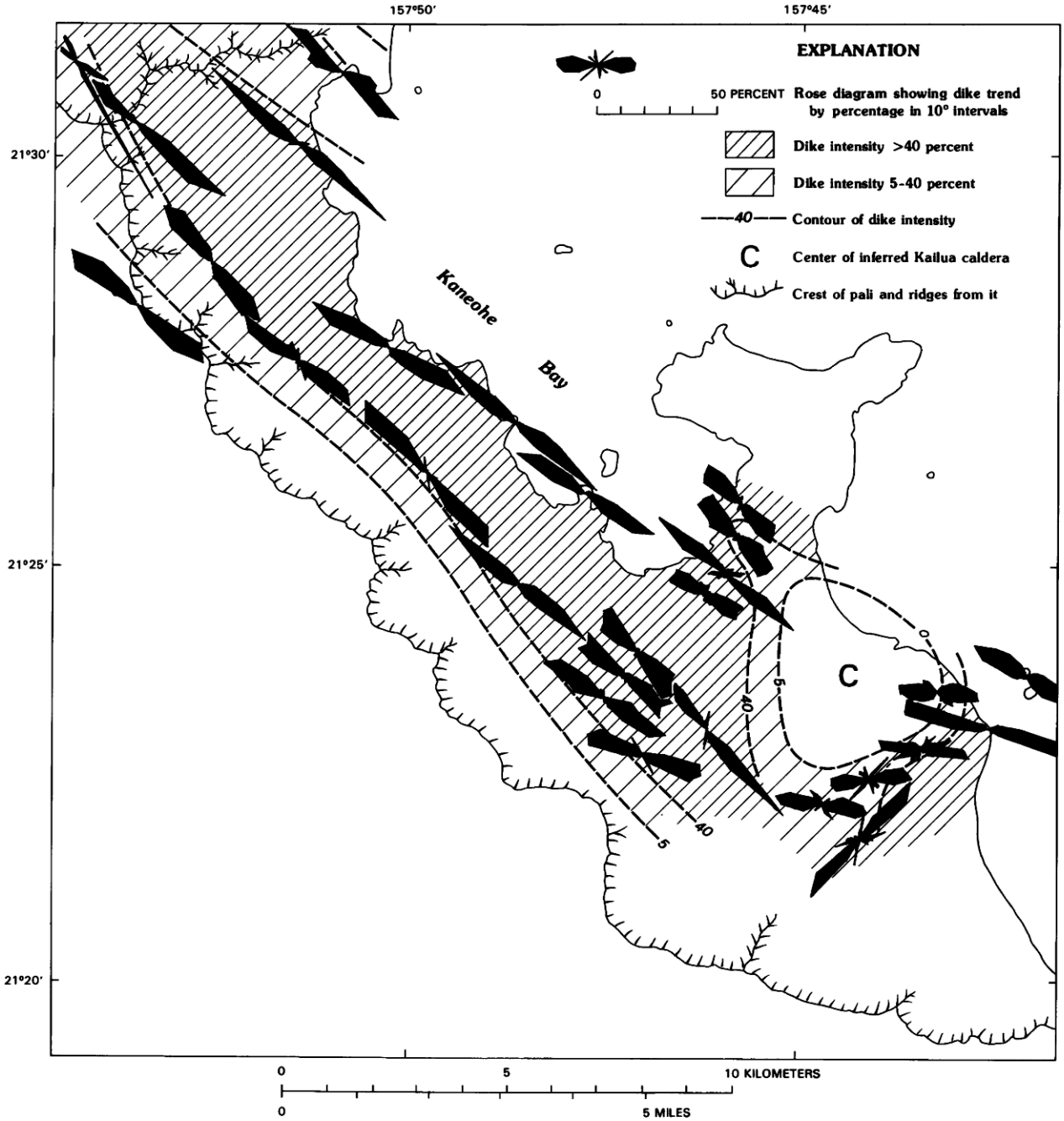


FIGURE 41.5.—Dike trends in Koolau dike complex. Rose diagrams constructed using 10° interval. Pattern is dominated by northwesterly trend: 70 percent of all measured dikes have a trend within 22.5° of N. 50° W. Subordinate but distinct southwest-trending complex occurs in south of area.

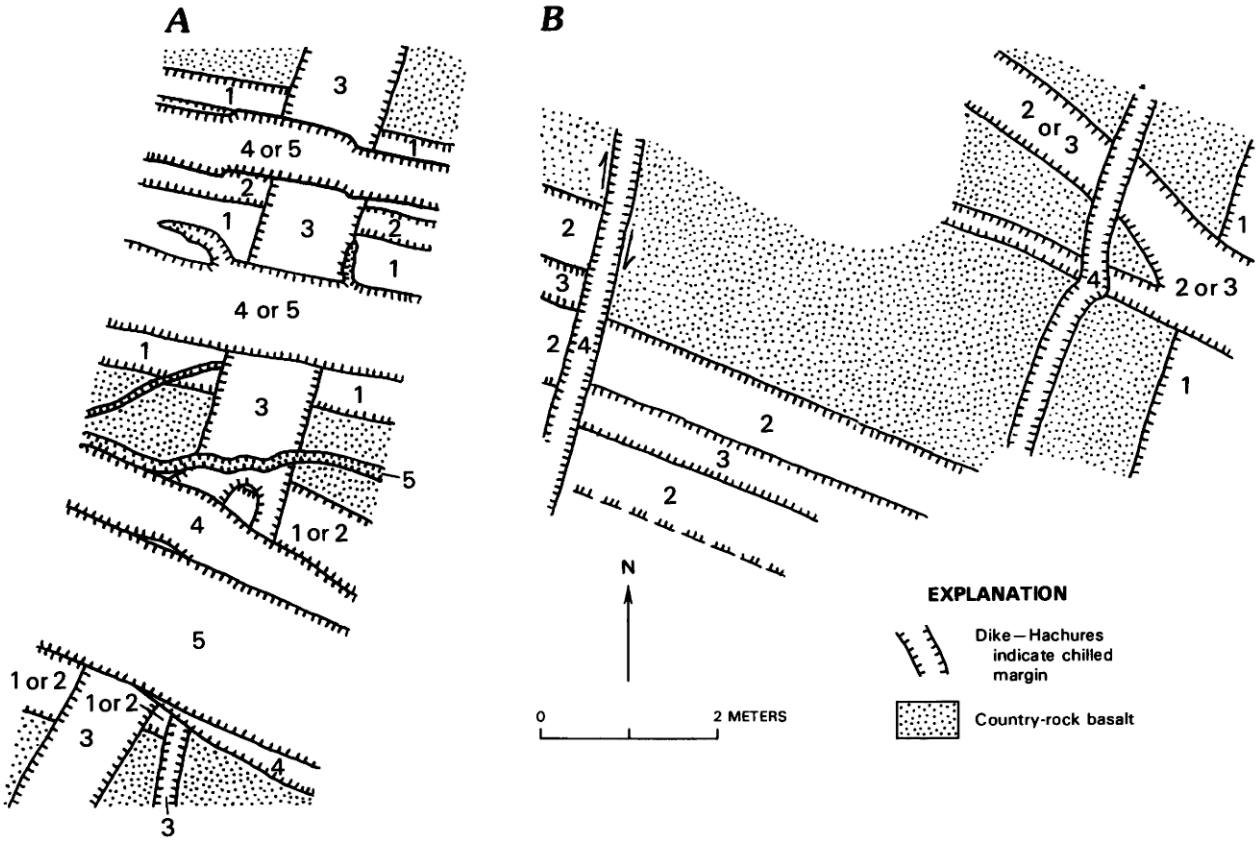


FIGURE 41.6.—Examples of age relationships at outcrops in Koolau dike complex where orthogonal dike intersections occur, shown somewhat schematically. ***A***, At locality 24. West-northwest-trending dikes (1 and 2) are cut by north-northeast-trending dike (3) that is cut by west-northwest-trending dikes (4 and 5). ***B***, Locality 4. North-northeast-trending dike (1) is cut by west-northwest-trending dikes 2 and 3, which are in turn cut by north-northeast trending dike (4). Note that significant fault movement occurred on one of the dikes (4).

than 110 cm wide account for 50 percent of the total width. The distribution in figure 41.7*B* closely approximates a lognormal distribution.

The dike widths of the Koolau complex are compared in figure 41.8 with those of Tertiary basaltic dike swarms in Iceland (Walker, 1959; Gudmundsson, 1984), which occur in the tectonic setting of an oceanic spreading center. The Koolau dikes are on the whole much narrower. This may reflect a generally lower viscosity of the Koolau magma but is at least partly attributable to the close proximity of most of the measured Koolau dikes to their volcanic center. Most of the measured Koolau sections lie within 15 km of the Kailua center, whereas the Icelandic dikes were mostly measured farther than 15 km from the respective volcanic centers to which they are related.

The width of dikes varies in different parts of the Koolau complex; it trebles from the Kailua volcanic center to the Waikane area (figs. 41.9, 41.10). The most obvious reason for this increase in width is that the lateral distance a dike travels from its source is related to its width: broader dikes are more far-ranging, and therefore far from the source the dikes tend all to be wide ones. As discussed in a later section, the trebling of average dike width is accompanied by a decrease to less than one third of the number of dikes present in transects across the complex.

## LITHOLOGY

The Koolau dikes are basalts and diabases and are generally aphyric or have only a small content of phenocrysts. Phenocrysts are of olivine, augite, and plagioclase and are mostly less than 4 mm in size. Some dikes are highly porphyritic; the most common type, several examples of which are seen at localities 1 and 3, has aphyric margins and a central part containing abundant olivine phenocrysts. The abrupt juxtaposition of aphyric and porphyritic rocks is suggestive of the injection of two successive magma fractions. One porphyritic dike at locality 4 contains about 50 percent of platy plagioclase crystals, many exceeding 1 cm in size, decreasing in abundance toward the margins.

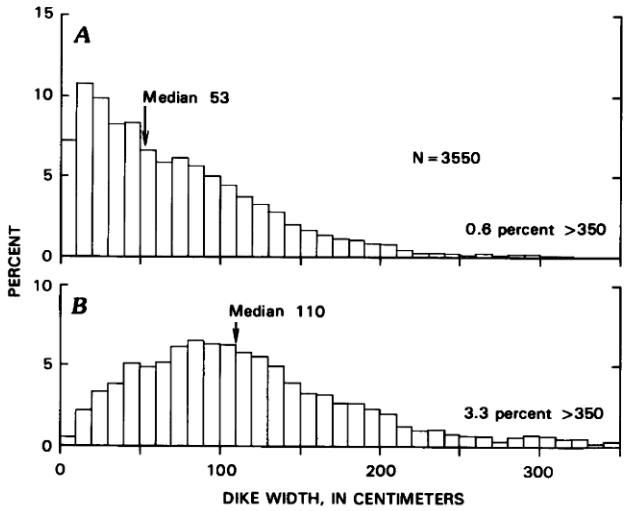


FIGURE 41.7.—Distribution of dike width in Koolau dike complex. N, total number of dikes. ***A***, Histogram of dike widths. Median width is 53 cm, arithmetic average 73 cm. About 90 percent of the dikes are less than 150 cm wide. ***B***, Percentage of total dike width contributed by each width category.

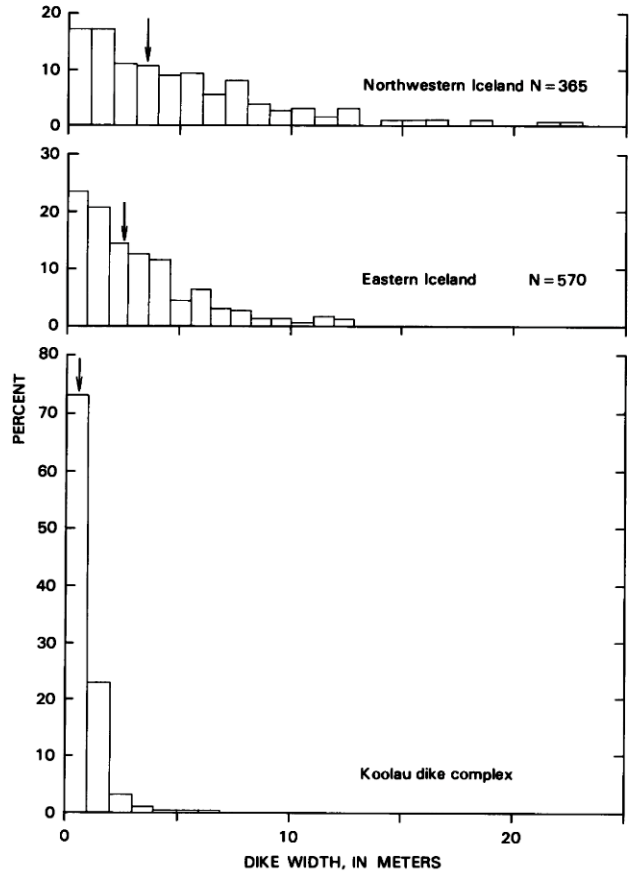


FIGURE 41.8.—Dike widths in Koolau complex compared with Tertiary basaltic dike swarms in eastern Iceland (Walker, 1959) and northwestern Iceland (Gudmundsson, 1984). Arrows indicate median width. Dikes in the Icelandic swarms are significantly wider than those in Koolau complex (median width 5–6 times greater). N, total number of dikes.

The dikes typically have glassy chilled margins and show a gradual steady increase in grain size inward from rim to center. The inner part of the glassy selvage is generally altered to orange palagonite, and this makes the dike margins easy to see. The width of the layer of glassy rock averages about 1 cm but varies from less than 1 cm to about 5 cm. One dike on the shore at locality 41 has glassy margins about 10 cm wide; the glass has varioles scattered through it or concentrated in narrow bands, and the banding is locally folded.

The three main roadcuts in the completed section of Highway H3 (localities 1–3 in figure 41.2 and table 41.1) provide fine exposures of the Koolau dike complex, and close examination of localities 1 and 3 reveals that the complex actually consists of two complexes, as follows: (1) An older complex consisting of highly irregular sheetlike intrusions, many of them amygdaloidal, which lack their own individual sets of cooling joints and have been affected at locality 3 by a pervasive propylitic alteration; and (2) a younger complex consisting of nearly planar dikes, which mostly have a low content of amygdules, possess their own individual sets of prismatic or sheetlike cooling joints normal to their margins, and are less altered.

An outstanding feature of the older dikes is that they are highly irregular, often curved and with outwardly convex protuberances, suggesting that they were intruded into a loose and yielding environment. The best explanation is that these dikes were injected into thin and strongly disjointed lava flows near the land surface of their day and sent off many sheetlike and irregular apophyses into these flows. Near-surface lava in Hawaii is typically transected by a great many cooling joints, vesicle partings, flow-unit boundaries, rubble layers and other planes of weakness, and dikes cutting them are highly irregular. Good examples are seen in the walls of Kilauea caldera and in roadcuts near Makapuu Head in Oahu.

The older dikes are amygdaloidal, often conspicuously so, and this is consistent with their intrusion near the surface. Amygdules tend to increase in size toward the dike center (fig. 41.11*C*), and attain a greater size (commonly exceeding 1 cm) in the wider dikes than in the narrower ones (fig. 41.11*A*). They tend to be concentrated in layers parallel with the dike margins. The amygdules contain zeolites (notably laumontite) and other secondary minerals.

A few older dikes contain pipe amygdules in a zone near the margin. The pipes on either side of a dike form parallel sets, the orientations of which combine growth of the pipes inward from the dike margin and their alignment in the magma flow direction.

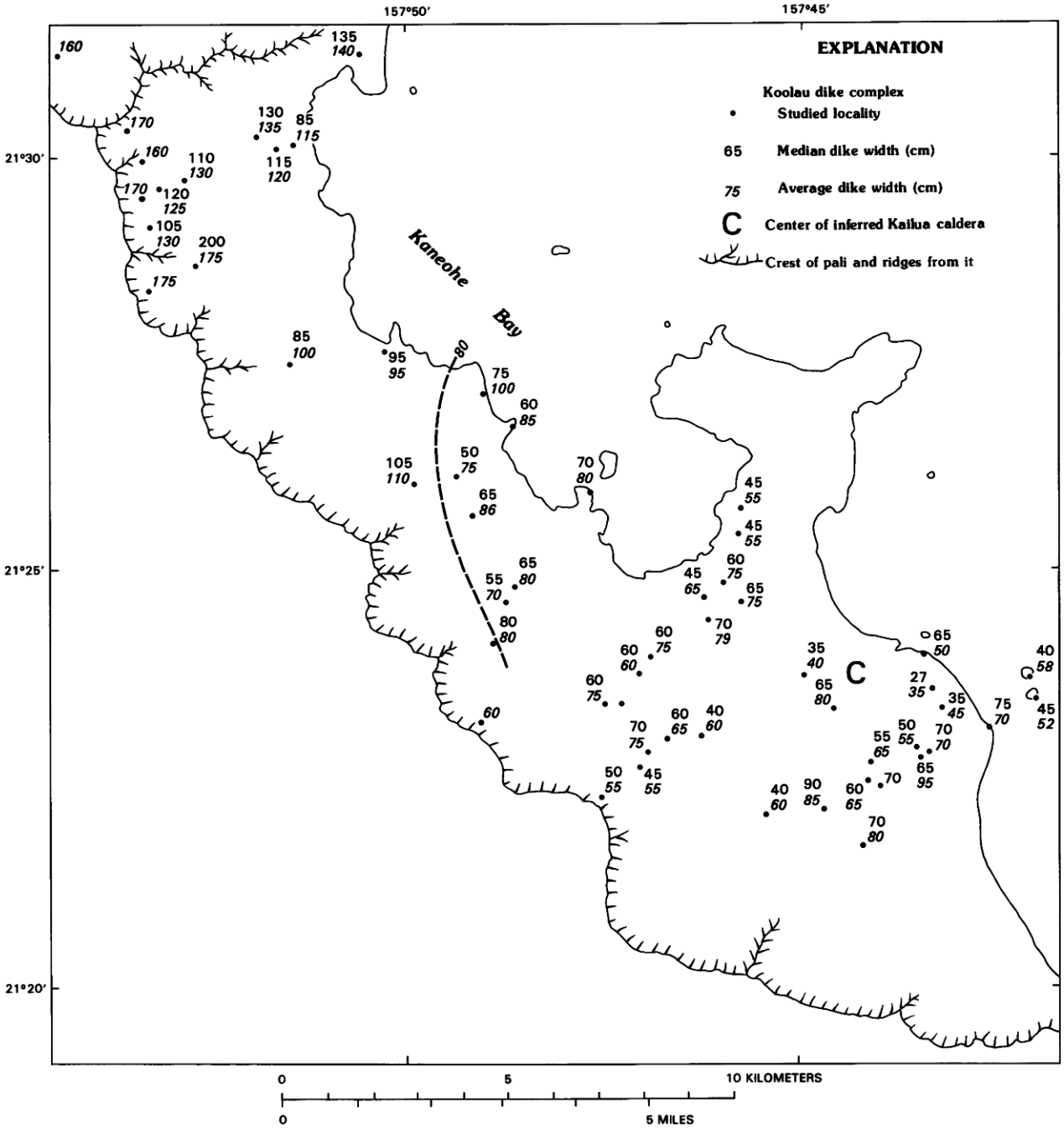


FIGURE 41.9.—Geographic variation of dike width in Koolau complex. Figures give width in centimeters. Arithmetic average width is generally larger than median. Note that lowest values occur in Kailua area, where center of Koolau Volcano was situated, and values tend to increase with increasing distance from center.

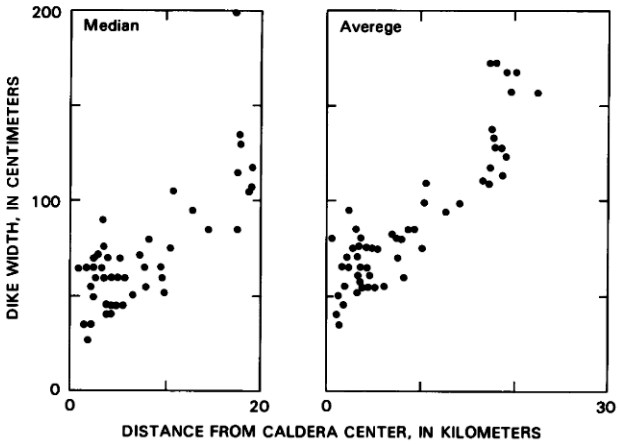


FIGURE 41.10.—Variation in median and average dike widths in Koolau complex with distance from presumed center of Kailua caldera (see figure 41.9 for location). Both median and average widths show a clear tendency to increase with increasing distance.

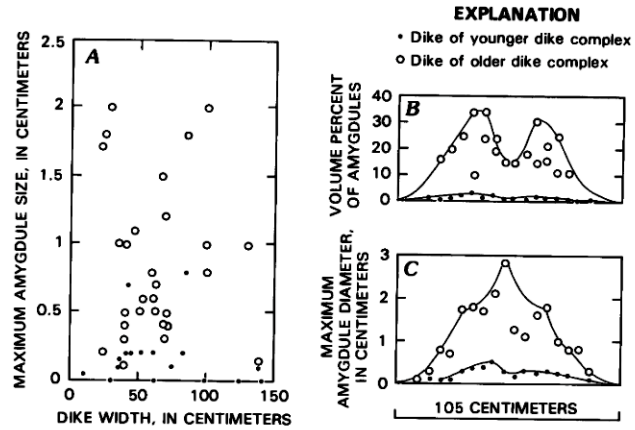


FIGURE 41.11.—Variation of amygdule size and content in dikes of Koolau dike complex. ***A***, Maximum amygdule size versus dike widths for 49 dikes at localities 2, 3, and 4, showing tendency for amygdule size to increase with dike width. ***B***, Profiles showing amygdule content across two dikes at locality 3, a typical member from each of older and younger complexes; each dike is 105 cm wide. ***C***, Profiles showing maximum amygdule size across same two dikes as in *B*.

Another important feature of the older dikes is the presence on them of conspicuous pale green rims 1–2 cm and occasionally as much as 5 cm wide, interpreted to consist of altered glass of a thickness suggestive of quenching in water. The loose and yielding lava pile into which they are interpreted to have been intruded may have contained abundant ground water.

The younger dikes in the roadcuts on Highway H3 tend to possess their own joint sets instead of imposed joint systems such as cut the older dikes. Close-spaced cooling joints normal to the margins are particularly well developed in marginal parts of many dikes. The nearly planar form of the dikes indicates that they were intruded into rigid rocks. The general scarcity and small size of amygdules indicates that the younger dikes were probably intruded under a thick cover.

The observed relations among the dikes in localities 1 and 3 are consistent with the view that the earlier members were intruded in a very shallow setting, near the land surface of their time, into an assemblage of thin and mechanically very weak lava flows with a high water table; the younger members on the other hand were intruded at a much deeper level after a considerable thickness of lava had been added to the Koolau shield volcano. The differences are similar to those that Wentworth and Jones (1940) inferred to be related to different depths of intrusion; at localities 1 and 3, however, dikes intruded thus at different depths are now found side by side at the same level, instead of (as Wentworth and Jones found) at different levels in the shield.

## FLOW LINEATIONS

The chilled edges of many dikes carry a lineation that appears to have been produced by magma flowage through the dike fissure. The flow lines of this lineation generally consist of millimeter-high wrinkles projecting out from the glassy surface of the dike or from planes within the glass selvage. Streaky coloration often also occurs in the outermost few millimeters of glass. Slickensidelike grooves are occasionally seen on a sheet joint a few centimeters inside the dike margin. Pipe vesicles in marginal parts of a few dikes have a parallel orientation neither vertical nor normal to the dike margins but in the flow direction. Spindle-shaped vesicles are also rarely found in the dike margins elongate in the flow direction.

The attitude of the flow lineation has been systematically measured to investigate its utility. Such mapping has rarely been attempted since attention to its potential was drawn by Harker (1904). Flow lineations are common on the Koolau dikes but have been measured on fewer than 10 percent of the dikes examined because they are seen only where a sufficiently broad dike surface is bared and is not so weathered that the outermost few millimeters have been stripped off.

The lineation plunges at an angle that, within a few meters, typically varies over a range of about 50°, as illustrated by figure 41.12. Some of this variation is clearly related to local irregularities in the dike surface as where the flow lines curve around surface bulges.

Wherever possible, measurements of the plunge were made at different points on the same dike, avoiding places where the lineation was strongly curved. The median plunge angle was then determined. In all, measurements were made and the median angle determined on more than 100 dikes.

At some localities, the lineations in most dikes plunge in the same direction, though the angle varies from dike to dike over about 50°, as illustrated by figure 41.13*A*. At such localities the median plunge angle was determined and is plotted on figure 41.14. At other localities the dikes fall into two groups having opposing plunge

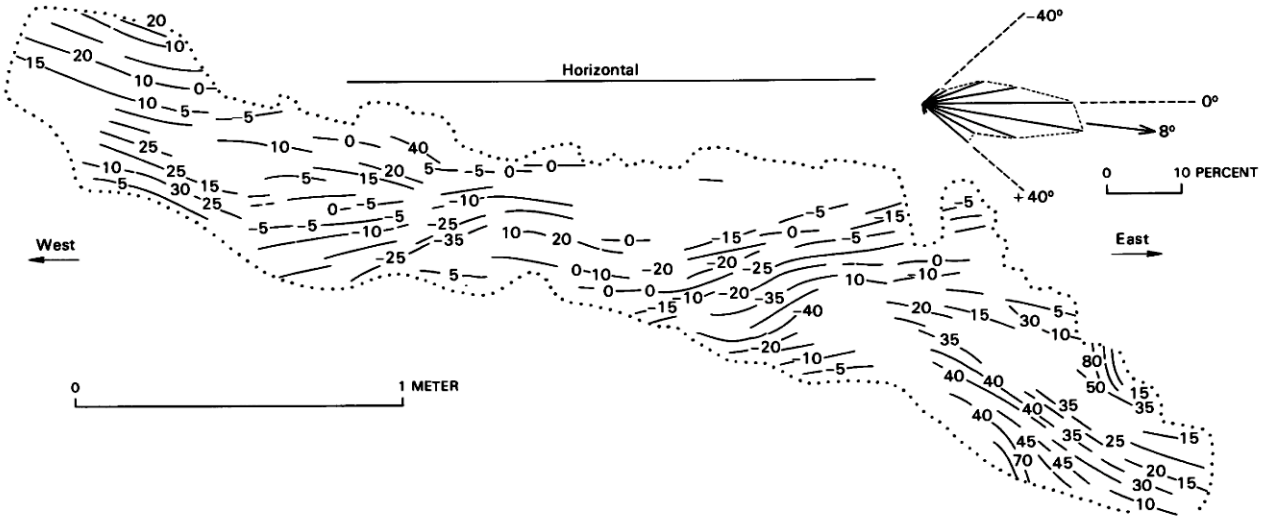


FIGURE 41.12.—Flow lineations on steeply dipping dike surface (area 1.8 m²) in Koolau dike complex (loc. 4). Numbers give measured plunge in degrees measured from horizontal. Inset at upper right: rose diagram showing variation in plunge angle, based on 89 measured values. Median plunge angle is 8° to east; 75 percent of measured values are within about 25° of this angle.

directions, as illustrated by figure 41.13*B*; at these localities the median plunge angle for each group was determined, and both angles were plotted on figure 41.14.

The arrows on figure 41.14 record the predominant directions of the flow lineation at each locality, and the numbers give the median plunge angle. Most of the arrows point toward Kailua or to an area southwest of Kailua, but many point toward Kaneohe Bay.

In interpreting these data it is assumed that the magma rose through each dike fissure, and the arrows that record the predominant plunge directions on figure 41.14 thus point back towards the source regions from which the dike magma came. At least two source regions are indicated, one below Kailua caldera and the other below Kaneohe Bay. The depth at which the plunge lines would intersect is about 2–3 km below sea level.

## DIKE SIDESTEPS

Dike sidesteps are commonly observed in which a dike tapers out and then resumes on a parallel course as much as several meters to one side. In some examples the two sidestep segments are joined by a narrow stringer; in others a connection is presumed to have existed above or to exist below the present erosion surface. Sidesteps are observed on both vertical and horizontal surfaces, but outcrops in the Koolau complex are less favorable for studying the latter. Attention is therefore concentrated on the features of sidesteps seen in vertical sections.

At a sidestep in a dike having the dominant northwesterly trend, the upper segment may step either to the southwest or the northeast side; these are referred to as southwest and northeast sidesteps, respectively. A study was made at several sites to determine if one sidestep direction is particularly favored and whether dike sidesteps have utility in structural studies. Curry and Ferguson (1970) considered the origin of offsets, and Pollard and others (1975) and Delaney and Pollard (1981) investigated the position of offset segments in sheet intrusions relative to the propagation direction. Few studies, however, have attempted to relate dike sidesteps to the overall structure of a rift zone (see Duffield and Nakamura, 1973).

Eight good examples of sidesteps were identified among the younger dikes in locality 3 (fig. 41.15), and it is seen that southwest and northeast sidesteps are roughly equal in number. This is also true at other localities, and thus the sense of sidesteps is probably not determined by any regional pattern.

Closer examination of the dike sidesteps at locality 3 reveals that about half occur where the sidestep dike cuts across an earlier dike and steps across from one to another plane of structural weakness.

I conclude that the dike sidesteps form mostly where the course of a dike trends obliquely across the preexisting grain (the trend of earlier intruded dikes) of a dike complex.

## DIKE INCLINATION

The dikes of the Koolau complex are predominantly steeply dipping (generally 65°–85°) but not vertical. The measured dips are plotted on the histograms of figure 41.16. The reason for this departure from verticality is one of the most intriguing of the problems posed by the complex.

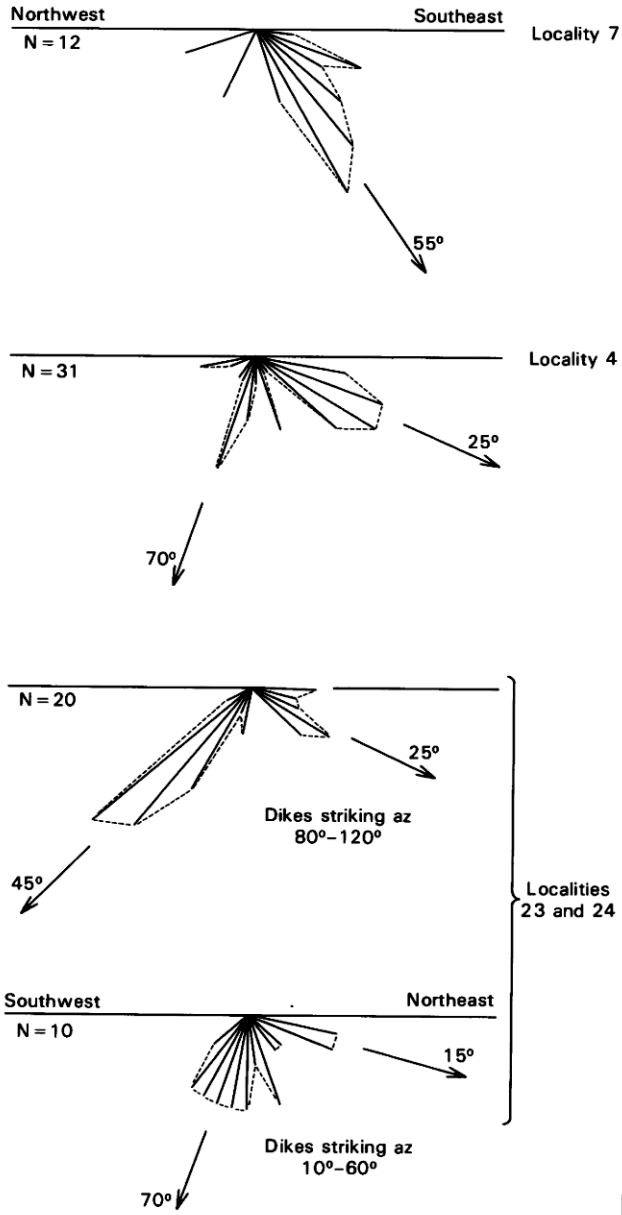


FIGURE 41.13.—Rose diagrams of average plunge of flow lineation measured on dikes at localities 4, 7, 23, and 24. At least one source is deduced for locality 7 and two sources for locality 4; arrows give predominant plunge. N, number of measured dikes.

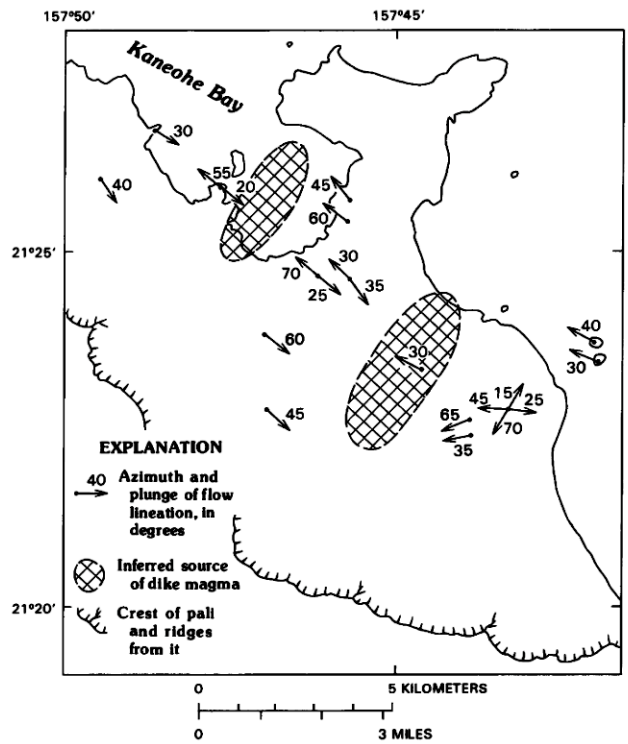


FIGURE 41.14.—Predominant plunge of flow lineation on dikes in Koolau complex. On the assumption that arrows point back to sources from which dike magma came, two sources are inferred, one near Kailua and the other under Kaneohe Bay.

The most common relationship is that the dikes in part of an exposure mostly dip in the same direction and at about the same angle, whereas farther along in the same exposure the dikes mostly dip in the opposite direction. This is clearly shown at locality 12, where the predominant dip direction changes from southwest to northeast several times along the 350-m length of the outcrop. The frequent change in the dip direction is well shown on the Mokulua Islands (localities 19 and 20): there the same cluster of dikes that in one place dips predominantly in one direction may be found to swing over and dip in the opposite direction a short distance along strike or higher up on the same cliff section. There are also many places at locality 12 and on the Mokulua Islands where, though the dikes predominantly dip in one direction, a significant number dip in the opposite direction and intersect to produce a braided pattern.

Individual dikes commonly vary in dip over several tens of degrees in the same outcrop, and it is often difficult to know what to measure. An attempt was generally made to measure the dip of a plane joining the points on each dike at top and bottom of the outcrop. This value for the dip obviously has a different validity depending on whether the outcrop is 1 m or 10 m high. Although the individual dip readings are of varied validity, the collective readings from many dikes at the same locality should define significant trends.

On the whole the dikes dip predominantly outward on either side of the Koolau Volcano (fig. 41.17). This would be in accord with the anticipated dip of normal or listric faults on either side of a high-standing edifice. The axis separating mainly southwest-dipping from mainly northeast-dipping dikes, however, coincides with the axis of the volcano only near Waikane; elsewhere it is strongly

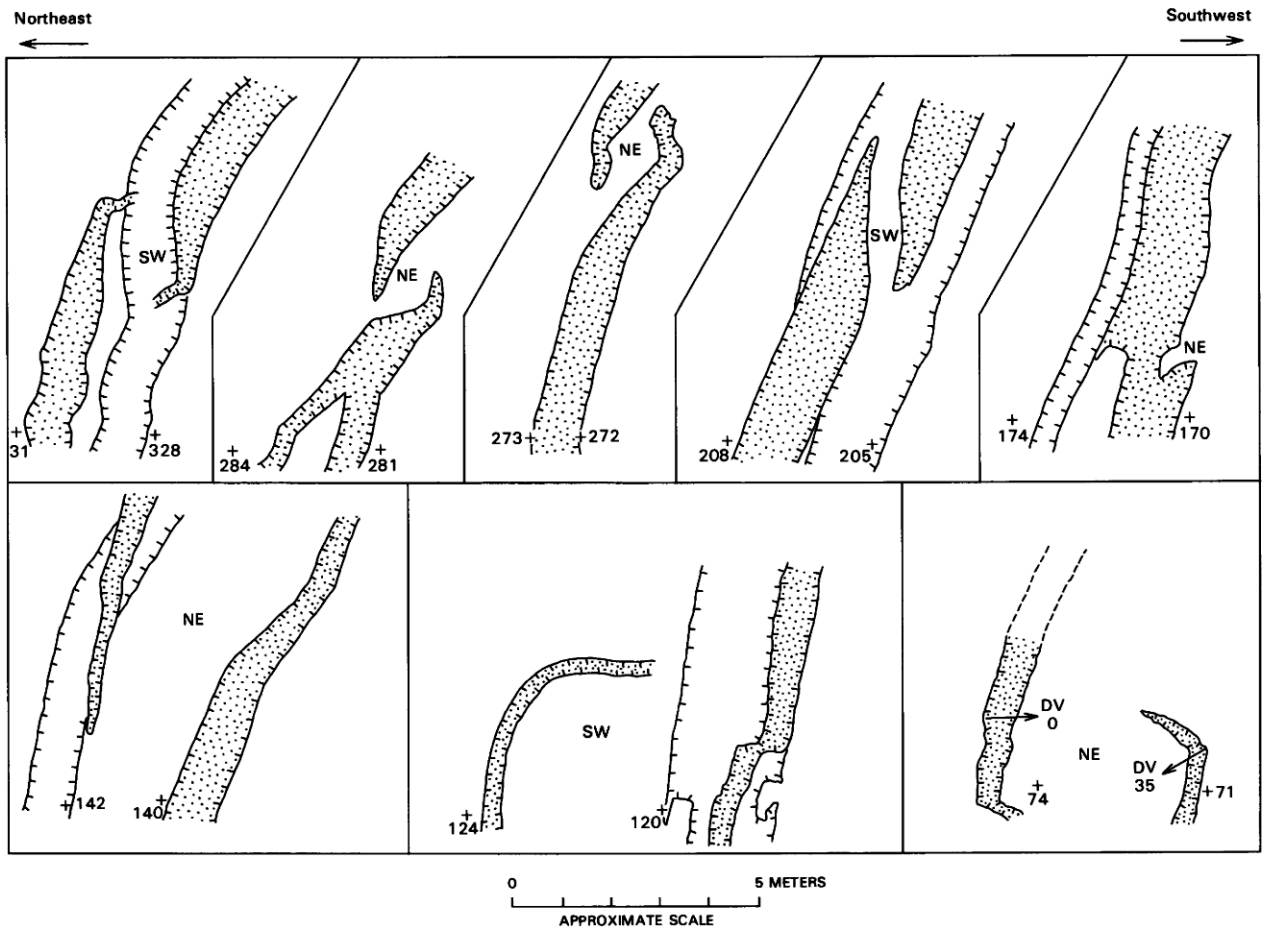


FIGURE 41.15.—Eight examples of dike sidesteps in Koolau complex of roadcut on Highway H3, locality 3. Where dike cuts dike, younger one is stippled. NE, SW, examples in which dike sidesteps upward to northeast and southwest, respectively. Numbers give distance in meters from south end of roadcut. DV, orientation and plunge angle of dilation vector, where known. Hachures indicate chilled margins.

displaced toward the southwest. In the area of locality 15 the part with northeast-dipping dikes embraces the entire width of the complex. This anomalous dip could indicate a weakness of the volcano and a tendency for it to creep northeastward toward the deep ocean in this area.

An older dike complex may be distinguished from a younger one at localities 1–7 as described earlier, and both dip predominantly in the same direction, showing that this weakness of the volcano was manifested early.

A late-manifested consequence of the weakness of the northeastern side of Koolau Volcano was the collapse by landsliding of much of that side (Moore, 1964). It is interesting to note that landsliding extended farthest across the volcano in the same area in which predominantly northeast-dipping dikes extend farthest. This may mean that both are manifestations of the same weakness. Alternatively, the predominance of northeast-dipping dikes in this area may have facilitated the landsliding.

The dip directions and angles of the dikes are apparently unrelated to the dip of the country rock lava; they are instead strikingly similar to those of normal faults developed in a tensional setting, which form complementary sets having opposing dips. The dikes of the Koolau complex may likewise form complementary sets oriented by a stress pattern similar to that which generates normal faults.

In many dike swarms elsewhere in the world the dikes are vertical or approximately so, as documented in Iceland by Gudmundsson (1983, 1984; fig. 41.16*D*). The problem is why the dikes of the Koolau complex systematically depart from verticality.

Dikes are conventionally interpreted to lie in the plane containing the maximum and intermediate principal stress axes and thus at right angles to the minimum principal stress axis (fig. 41.18). On the other hand, in an extensional tectonic setting in which horsts and grabens form, sets of normal faults form on planes oriented at about 20° on either side of the vertical plane that contains the maximum

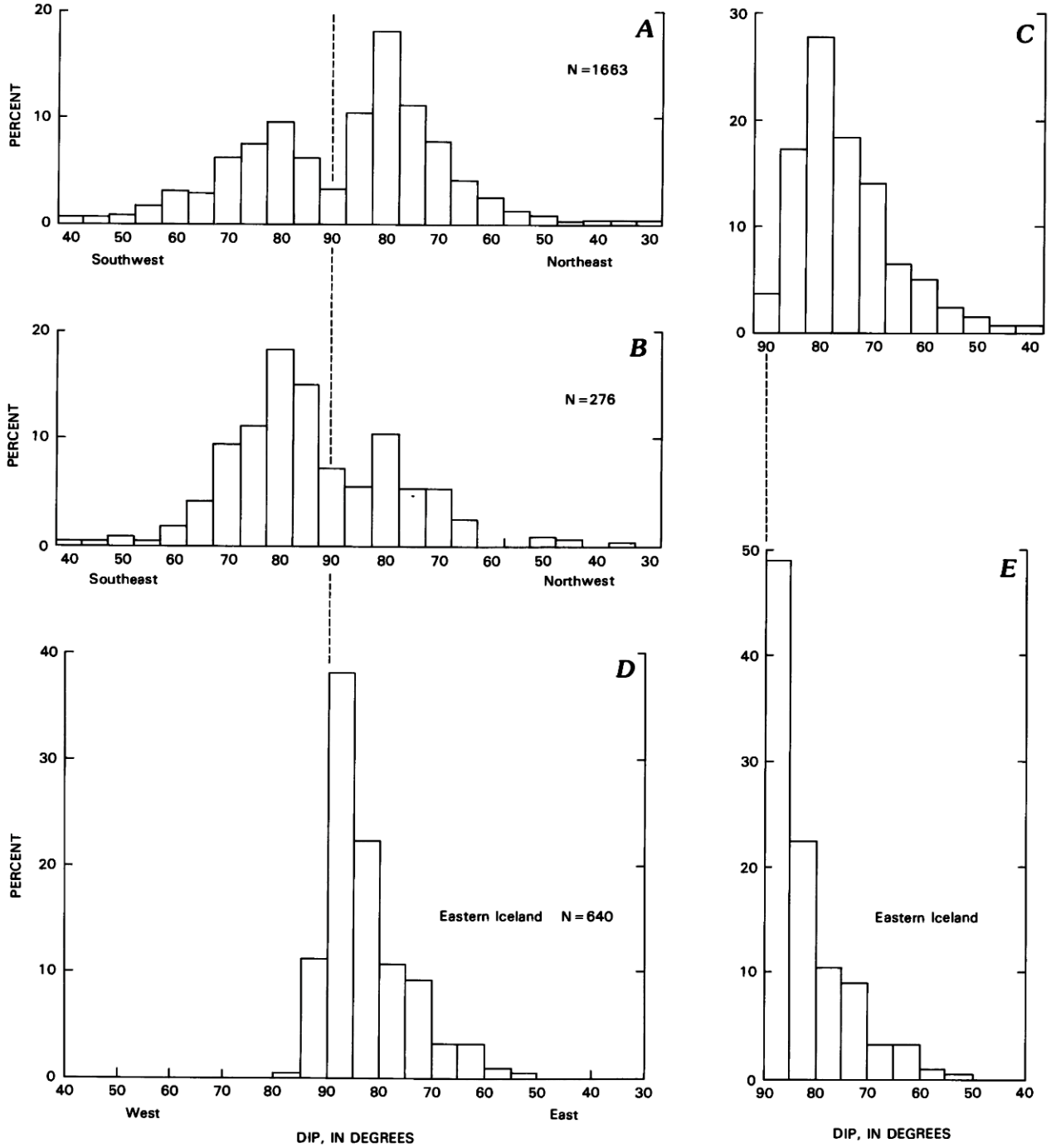


FIGURE 41.16.—Dip angles of dikes in Koolau dike complex and Tertiary dike swarm of eastern Iceland. N, number of dikes in each set. ***A***, Dips of northwest-trending dikes in Koolau dike complex. Note two peaks at 10°–20° on either side of vertical. ***B***, Dips of northeast-trending dikes in Koolau dike complex. Note similar peaks as for northwest-trending dikes. ***C***, Numerical values of dike dips in Koolau dike complex, disregarding both strike direction and dip direction. ***D***, Dips of dikes in Tertiary dike swarm of eastern Iceland (Gudmundsson, 1983); 73 percent are within 10° of vertical (this remains true even after compensation for 5° of later westward tilt). These dips were measured to nearest degree, whereas Koolau dikes are so irregular that their dips were measured to nearest 5°. ***E***, Numerical values of dike dips in Tertiary dike swarm of eastern Iceland, disregarding dip direction.

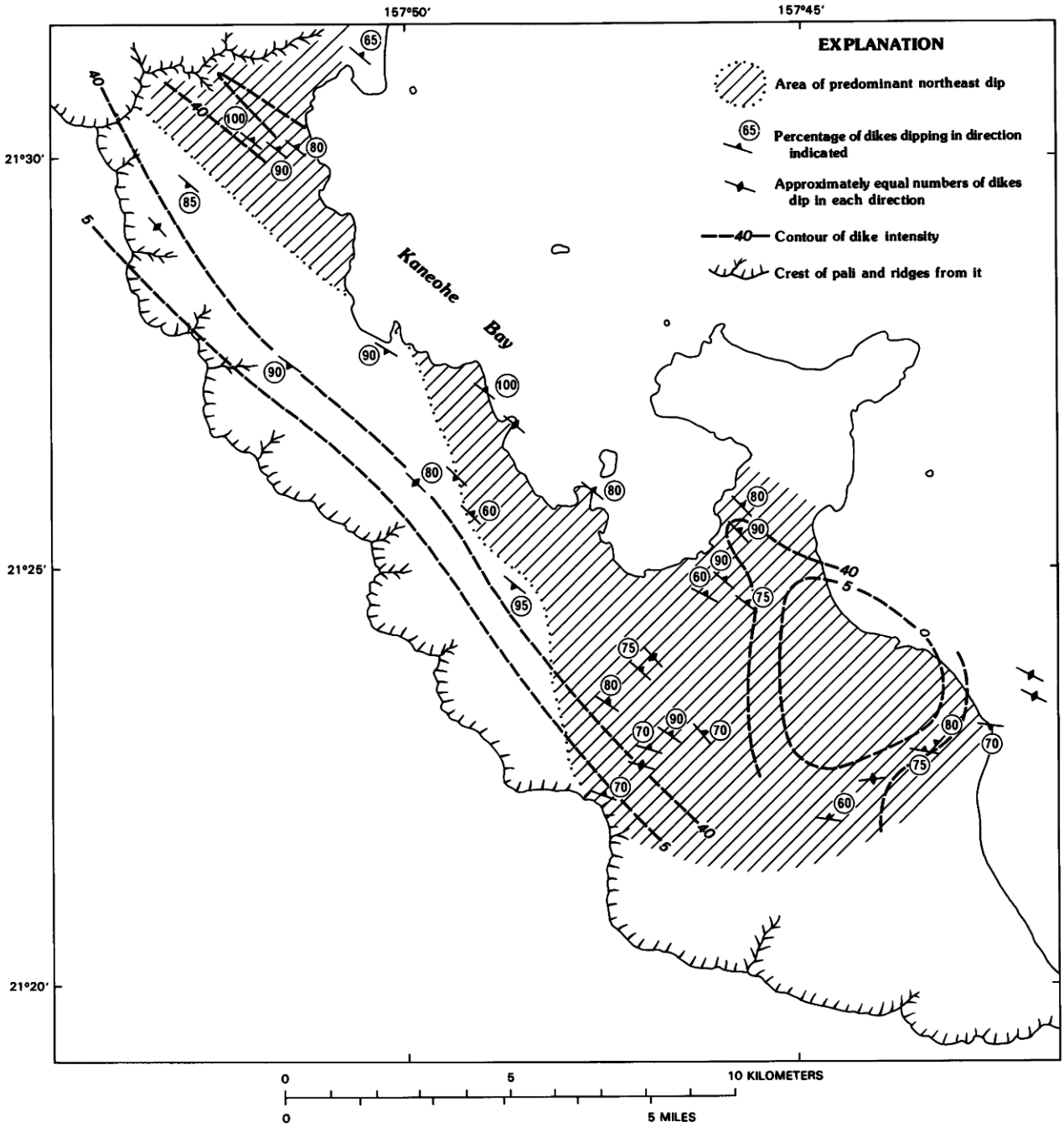


FIGURE 41.17.—Predominant dip directions of dikes in Koolau dike complex. Generally dip is outward on either side of axis of Koolau Volcano. In a large anomalous area, however, predominant northeast dip extends across entire width of complex. Intensity contours from figure 41.3.

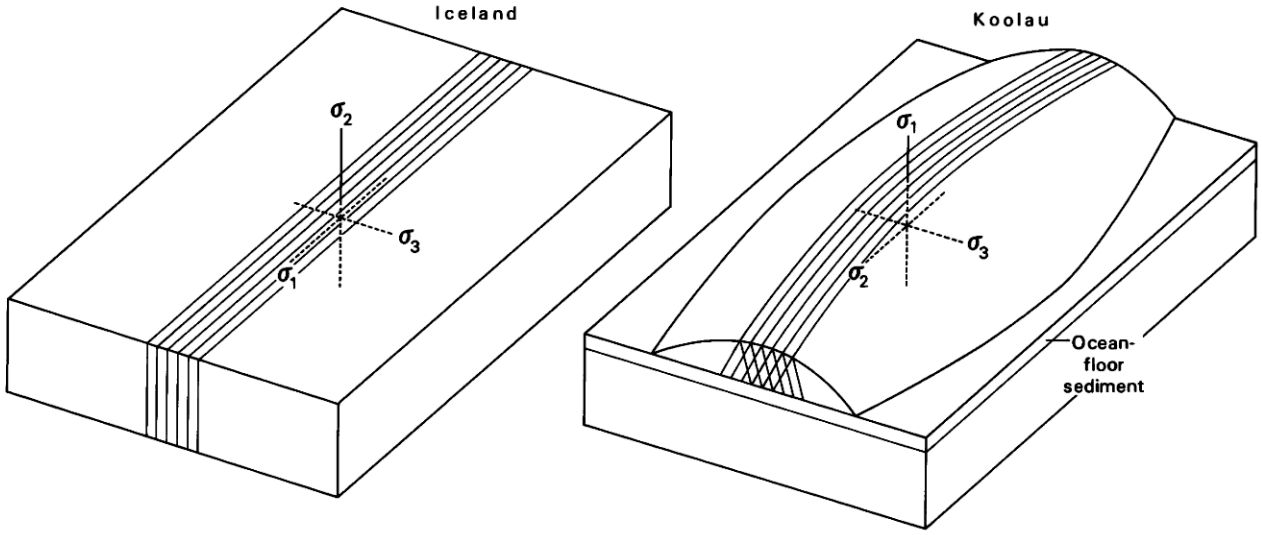


FIGURE 41.18.—Comparison of rift zones in two tectonic settings showing postulated positions of maximum ($\sigma_1$), intermediate ($\sigma_2$), and minimum ($\sigma_3$) stress axes. An oceanic spreading ridge is exemplified by Iceland (see Keith, 1981), which rises 3 km above deep ocean floor in 300–400 km. An intraplate volcanic edifice is exemplified by Koolau Volcano on Oahu, which rises 5 km above deep ocean floor in 60 km. Icelandic rift zone can be regarded as being confined at both ends, and formation of vertical dike fissures is favored. Hawaiian edifice is not confined at sides or ends and is free to move on its underlying layer of ocean-floor sediment (Nakamura, 1980); hence $\sigma_1$ is much greater than $\sigma_2$ and $\sigma_3$ and formation of inclined dike fissures forming two complementary sets is favored.

and intermediate stress axes. Vertical dikes like those in Iceland and complementary sets of faults both form in an extensional setting. How may the vertical orientation of most dikes be reconciled with the nonvertical orientation of normal faults and Koolau dikes?

I propose that the explanation for this is that Hawaiian volcanoes, being high-standing and comparatively steep structures (the Koolau Volcano rises 5 km above the deep ocean floor in 60 km), have a strong tendency to spread laterally (Fiske and Jackson, 1972) and have axes of minimum and intermediate stress both lying in the horizontal plane. The maximum stress axis is vertical and greatly exceeds the other two. In contrast, fissure eruptions in Iceland occur in a setting in which the tendency for gravitationally induced lateral spreading is small (Iceland rises only 3 km above the deep ocean floor in 300–400 km), and under these conditions the maximum stress axis may be horizontally oriented in this direction and if vertical will not be much greater in magnitude than the other two (compare with Keith, 1981). It is postulated that dikes in this situation tend to be vertical.

A possible alternative explanation for the nonverticality of the Koolau dikes is the mechanical anisotropy of a Hawaiian volcanic pile. Ryan and others (1983) pointed out that, though the pile behaves as a mechanical continuum, an elastic solid, the rock is so disjointed in the vertical direction that it lacks mechanical continuity in the horizontal plane. When, for example, horizontal displacement magnitudes are made up of reversible and irreversible components, the restoring forces for the former tend to be either weak or nonexistent. Lateral extension then tends to generate nonvertical fractures. Thus, where a vertical fissure passes up into poorly consolidated ash or sediment, a graben between nonvertical normal faults develops in that deposit; good examples are seen where fissures of Kilauea's southwest rift zone, just outside the caldera rim, transect thick pyroclastic deposits of the 1790 explosive eruption.

Though mechanical anistropy is capable of accounting for the extreme irregularity and nonverticality of the older dikes, it does not readily explain the nonverticality of younger dikes such as are seen cutting well-lithified breccias in locality 3. I conclude therefore that the nonverticality is mainly attributable to the edifice effect—the tendency for lateral spreading in a very high volcanic edifice.

## CONE SHEETS AND SILLS

A small proportion (about 1 percent) of the dikes have a dip of less than 50°, and the possibility that they might be cone sheets (as was suggested by Macdonald and Abbott, 1970) must be considered. The essential attribute of cone sheets is that they dip toward a common focus. When the low-angle sheet intrusions found in the present study are plotted on a map (fig. 41.19), no tendency toward a centripetal dip can be discerned, which lends no support to the idea that they are cone sheets. These dikes are therefore regarded as constituting simply the low-angle tail of a Gaussian distribution.

Only one sill was noted; it is highly irregular, is about 1 m thick, and can be traced for a few tens of meters in a roadcut where the highway climbs the pali at Makapuu Head.

## VERTICAL DISPLACEMENTS CAUSED BY DIKE INJECTION

The injection of vertical dikes does not cause any uplift or subsidence of the country rock apart from that which may result by

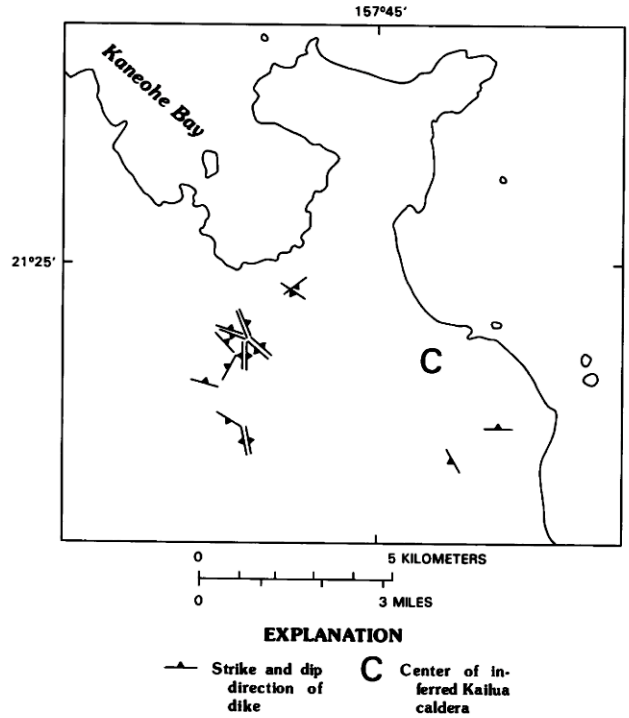


FIGURE 41.19.—Strike and dip direction of 1 percent of dikes in Koolau complex that dip less than 50°. Attitudes show no tendency toward centripetal pattern and thus lend no support to idea that these intrusions are cone sheets.

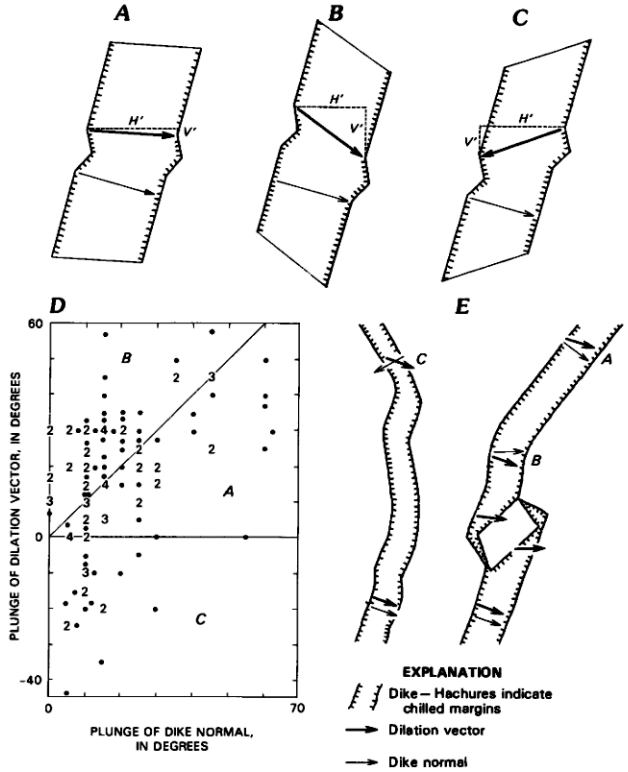


FIGURE 41.20.—Dilation relationships in vertical cross sections of dikes in Koolau dike complex. ***A***, Example of dike in which dilation vector plunges less steeply than dike normal. ***B***, Example of dike in which dilation vector plunges more steeply than dike normal. ***C***, Example of dike in which dilation vector plunges in the opposite direction to dike normal. ***D***, Plunge of dilation vector plotted against plunge of dike normal in sample of 126 dikes from localities 1, 3, 6, 7, and 23. For some dikes dilation vector (given a negative value on the plot) plunges in opposite direction from dike normal, giving a negative value of $V'$. Letters indicate regions exemplified by dikes in *A*, *B*, and *C*. Duplicate values from different measurememts shown by numbers. ***E***, Schematic profiles across two irregular dikes showing how departures of dilation vector from dike normal can be explained by variations in dip of dike. Note variation in plunge of dilation vector at dike sidestep where rotation of block has occurred.

eventual isostatic adjustment: it simply causes a lateral displacement of the country rock. Pollard and others (1983) have shown that injection of a vertical dike that fails to reach the surface does cause uplift, but the amount is very small.

Because the Koolau dikes are, in general, not vertical, their intrusion by simple dilational opening resulted not only in a horizontal dilation but also in a vertical displacement that uplifted the hanging wall relative to the footwall. The component of dilation in the horizontal plane ($H$) exceeds that in the vertical direction ($V$) in dikes dipping at more than 45°, but $V$ approaches $H$ as the dip approaches 45°.

It is generally tacitly assumed that dilational opening of a dike is along the direction normal to the dike. On many of the Koolau dikes it is possible to determine the direction of opening (called here the dilation vector, figure 41.20) by matching features on the two walls of the dike, and it is found that in general this direction does not coincide with the normal to the dike. The components of dilation in the horizontal and vertical directions, referred to as $H'$ and $V'$, respectively, are therefore different from $H$ and $V$. Few studies have hitherto been made on this aspect of dikes; measurements were therefore made to investigate its significance. Outcrops in the Koolau complex are generally not favorable for determining the attitude of the dilation vector in three-dimensional space; measurements were therefore mostly made where dikes are exposed in vertical section. The data are summarized in figure 41.20*D*.

For about half of the measured dikes the dilation vector plunges more steeply than the dike normal, thereby increasing $V'$ (fig. 41.20*B*). For a small proportion of dikes it plunges in the opposite direction from the dike normal (fig. 41.20*C*); $V'$ is then negative, because intrusion of the dike resulted in a subsidence of the hanging wall relative to the footwall.

For each of the measured dikes, $H'$ and $V'$ were calculated, and their average values together with the two values of dike width (measured along the dike normal and along the dilation vector) are summarized in table 41.2.

TABLE 41.2.—*Widths and dilation components of dikes in the Koolau dike complex*

[All measurements in meters; $H$, $H'$, horizontal components; $V$, $V'$, vertical components. $H$, $H'$, $V$, $V'$ in per meter of dike width, $N$]

| | Locality | | | | | | | |
|---|---|---|---|---|---|---|---|---|
| | 1 | 3 | 6 | 7 | 24 | 30 | Total | Average |
| Number of dikes | 21 | 28 | 18 | 37 | 16 | 6 | 126 | -- |
| Measurements along dike normal | | | | | | | | |
| Total dike width, $N$ | 8.08 | 19.76 | 11.27 | 23.20 | 11.58 | 4.90 | 78.79 | 0.625 |
| Average dike width | .385 | .706 | .626 | .627 | .724 | .817 | | |
| $H$ | .891 | .944 | .899 | .911 | .941 | .990 | -- | .925 |
| $V$ | .277 | .277 | .314 | .335 | .275 | .134 | -- | .290 |
| Measurements along dilation vector | | | | | | | | |
| Total dike width | 8.06 | 21.13 | 12.02 | 24.61 | 12.14 | 5.08 | 83.04 | .659 |
| Average dike width | .384 | .755 | .668 | .665 | .759 | .847 | | |
| $H'$ | .914 | .970 | .997 | .921 | .958 | 1.009 | -- | .954 |
| $V'$ | .208 | .278 | .226 | .424 | .274 | .159 | -- | .298 |

It is seen that the average values of $H'$ and $V'$ differ only very slightly from the average values of $H$ and $V$, and the small difference is probably not significant. This, together with the apparently random scatter of points seen in figure 41.20*D*, suggests that the dilation vector varies randomly about the dike normal. An explanation which appears adequately to explain this randomness is illustrated in figure 41.20*E* and is based on the observed irregularity of most dikes in the complex. It is postulated that on average the dilation vector of each dike coincides with the dike normal, but where a dike trend departs from its average trend the dike normal will depart from its dilation-vector direction.

The average values for $H'$ and $V'$ per meter of dike-normal width are 95.4 cm and 29.8 cm respectively. If the measured dikes are representative, injection of the dike complex having a total $H$ of 3.3–4.8 km would involve a total relative uplift or subsidence ($V$) of 1–1.5 km, which is comparable to the height above sea level of the Koolau Volcano and is thus not insignificant. Note that axial uplift has accompanied some recent activity in the east rift zone of Kilauea Volcano (Swanson and others, 1976).

The question then arises whether intrusion of the dike complex has caused any significant net uplift or subsidence. The obvious test is by mapping a distinctive stratigraphic horizon right across the complex, but this does not seem feasible because of generally unfavorable topography in the Koolau Range combined with the relatively uniform lithology of the shield lava; the existence of a large collapse caldera in the area where exposures would otherwise be the most favorable is a further hindrance.

In many older, eroded volcanoes, the floor has been strongly updomed; a good example is the Carlingford Tertiary volcanic center in Ireland. Le Bas (1971) attributed the updoming at Carlingford to the intrusion of a swarm of cone-sheets that, like the Koolau dikes, have a significant $V'$ vector. The evidence is, however, ambiguous, because it is also possible that the updoming was caused by an underlying granophyre pluton.

## THE CALDERA OF THE KOOLAU VOLCANO

Hawaiian active volcanoes have a central caldera from which rift zones radiate like spokes, and the fact that the northwest and southwest dike complexes of the Koolau Volcano radiate from the Kailua area implies that the center of the volcano was located there. There is good evidence for the existence of a caldera in this general area.

Stearns and Vaksvik (1935) distinguished a Kailua Volcanic Series, occupying a circular area 5 km (3 mi) across centered on Kailua, which they interpreted to consist of lava infilling the caldera of the Koolau Volcano. Woollard (1951) and Strange and others (1965) found a major positive gravity anomaly centered on this caldera, and they attributed it to a concealed high-density intrusive pipe underlying the caldera. The postulated intrusion is not exposed. Adams and Furumoto (1965) and Furumoto and others (1965) explored the gravity high by seismic profiling and found high velocity ($v_P$=7.7 km/s) rocks at a depth of less than 2 km beneath the caldera.

Certain coarse breccias on the ridge between Kaneohe and Kailua Bays were interpreted by Stearns and Vaksvik (1935, p. 97) as a caldera infilling "a throat breccia such as exists in the bottom of Halemaumau built up chiefly as talus within a crater or caldera, and [which] appears to mark the main vent of the Koolau volcano." They found that the breccia crops out over nearly 2.5 km$^2$ (1 mi$^2$), reaches 160 m (520 ft) thick, and consists of angular to subangular fragments mostly under 50 cm in size of amygdaloidal basalt of diverse lithologies set in a fine green matrix. Macdonald and Abbott (1970), however, interpreted the breccia to consist probably of mudflows.

New evidence is now available, and in presenting it the distinction is made between evidence for the existence of a caldera, and evidence on the origin of the breccia.

### EVIDENCE FOR A CALDERA

New evidence for the existence of a caldera comes from three roadcuts in Highway H3, in two of which (localities 1 and 3) older, amygdaloidal and altered dikes can be distinguished from younger, massive and fresh dikes. In the third (locality 2), which lies at about the same elevation, no older dikes can be identified, and the dike complex is similar in character and intensity to the younger complex at localities 1 and 3. The country rock at locality 2, moreover, consists of more massive lava.

The most plausible explanation for the differences is that the basalt of locality 2 is younger than the older dike swarm of localities 1 and 3; this is consistent with its being the infilling of a caldera postdating the older complex. A schematic view of these relationships is given in figure 41.21. The massive flows of locality 2 are suggestive of ponding in a depression. The lower dike intensity in locality 2 most likely indicates that the lava flows are younger than those exposed in contiguous areas, and less time was thus available for dikes to cut them. An alternative mechanism, namely downfaulting of these thick lava flows, can explain the lower dike intensity but not the absence of strongly amygdaloidal dikes.

Caldera infill can, thus, be identified here by three criteria:

1. It consists mainly of thick massive lava flows unlike the thin pahoehoe flow units that characterize most of the Koolau lava shield.
2. It has a significantly lower dike intensity than contiguous areas.
3. It may lack strongly amygdaloidal dikes like those of the earlier complex found in sites 1 and 3. This lack presumably indicates rapid infilling of the caldera.

Within a large area centered on Kailua the lava flows have dip directions and amounts that are anomalous and quite different from those of the shield lava; the dip, though variable, is on the whole centripetal and varies in amount from 15° to 30° or rarely as much as 60°, whereas the shield lavas dip at 5° to 15° outward from the shield axis. This large area of centripetal dip is interpreted to be a caldera of the downsagged type (Walker, 1984). No comparable feature has been recognized on the active Hawaiian volcanoes, but it could be concealed beneath young lava.

Important evidence bearing on the downsag caldera comes from the Kapaa Quarry, where the country rock consists of thin pahoehoe lava flows that resemble shield building lava. These flows dip in the contrary direction to the shield lava and at an angle (30° to 60°) that is excessive for shield lava. Some flows moreover contain pipe amygdules, which, it has recently been demonstrated, are good paleoslope indicators. Their presence show that the lava was deposited on a slope of less than 4°. The Kapaa quarry lava must therefore have been tilted at least 30°–60° after being deposited. The amount of subsidence by down-sagging can be estimated to have been about 1 km.

The dike complex that cuts the lava of Kapaa Quarry consists of the usual two complementary sets having opposed dips of 65°–85° (fig. 41.23), and this implies that these dikes were injected after the lava had been more or less fully tilted. The dike complex here built up to its full intensity of more than 50 percent after a major episode of subsidence had occurred. Note that where the country rock has the steepest dip, at the northeast end of the northeast quarry, several intrusions follow the stratification of the lavas. Technically these intrusions are sills, but in relation to the volcanic edifice they are dikes.

The approximate extent of the downsag caldera as determined from dip measurements is shown on figure 41.22; it is greater than that given by the other criteria and is similar to that mapped by Stearns and Vaksvik (1935) as constituting the caldera fill of their Kailua Volcanic Series.

The Kailua caldera as delineated by these several criteria varies greatly in intensity of dike injection, from 1 percent to 50 percent or more. Some variation would of course be anticipated in different parts of the same caldera transected by one or more rift zones, but a more plausible explanation is that two or more calderas of different ages occur, the older being cut by more numerous dikes than the younger. This multiple origin is evidenced by the dike relationships in the Highway H3 roadcuts and is consistent with the fact that the Kailua caldera measures at least 13 by 10 km, which is far greater than the diameter of calderas on Kilauea and Mauna Loa (2.5–4.5 km).

The very low intensity of the dike complex in the inner part of Kailua caldera implies that subsidence there was a very fast or late event relative to formation of the dike complex and considerably exceeded 1 km. Most likely this area of low dike intensity is a conventional caldera nested within a much broader area dominated by downsagging.

## NATURE AND ORIGIN OF THE BRECCIAS

The coarse breccias that make up much of the ridge between Kaneohoe and Kailua Bays and that are well exposed at localities 1, 3, 4, 5, and 10 have long been enigmatic. Important evidence relating to their origin is that much of the breccia consists of dike fragments (fig. 41.24). This leads to a new interpretation, namely that the breccias consist of the older part of the dike complex (together with country-rock basalt screens), which has suffered an extensive and pervasive brecciation.

The evidence for brecciation of a dike complex seems unequivocal because all stages in disruption of dikes are seen:

1. The dike rock is pervasively brecciated but little relative movement of the fragments has occurred: sufficient to generate angular spaces (infilled with secondary minerals) between fragments but not sufficient to break the continuity of the dike, which is contained by chilled margins.
2. The dike as a whole is still continuous, but it is thoroughly brecciated, and relative movement of fragments has caused it to have a jagged shape.
3. The dike is thoroughly brecciated, and relative movement and intermixture of dike fragments with country rock basalt has occurred, but dike fragments remain concentrated in a relatively narrow zone within the breccia, showing that in-place brecciation of a dike has occurred.
4. The dike is totally disrupted, and all continuity is lost; abundant breccia fragments that possess a chilled edge on one side are all that attest to the derivation of much of the breccia from dikes.

All indications are that the breccia formed by a pervasive fragmentation in place of country-rock lava cut by dikes. The degree of brecciation varied apparently in a rather haphazard way, leaving areas, several meters to tens of meters across, of intact lava and dikes enveloped in breccia. These areas pass upwards and laterally into breccia and generally lack any discrete boundaries.

The measured length of chilled dike margin exposed at locality

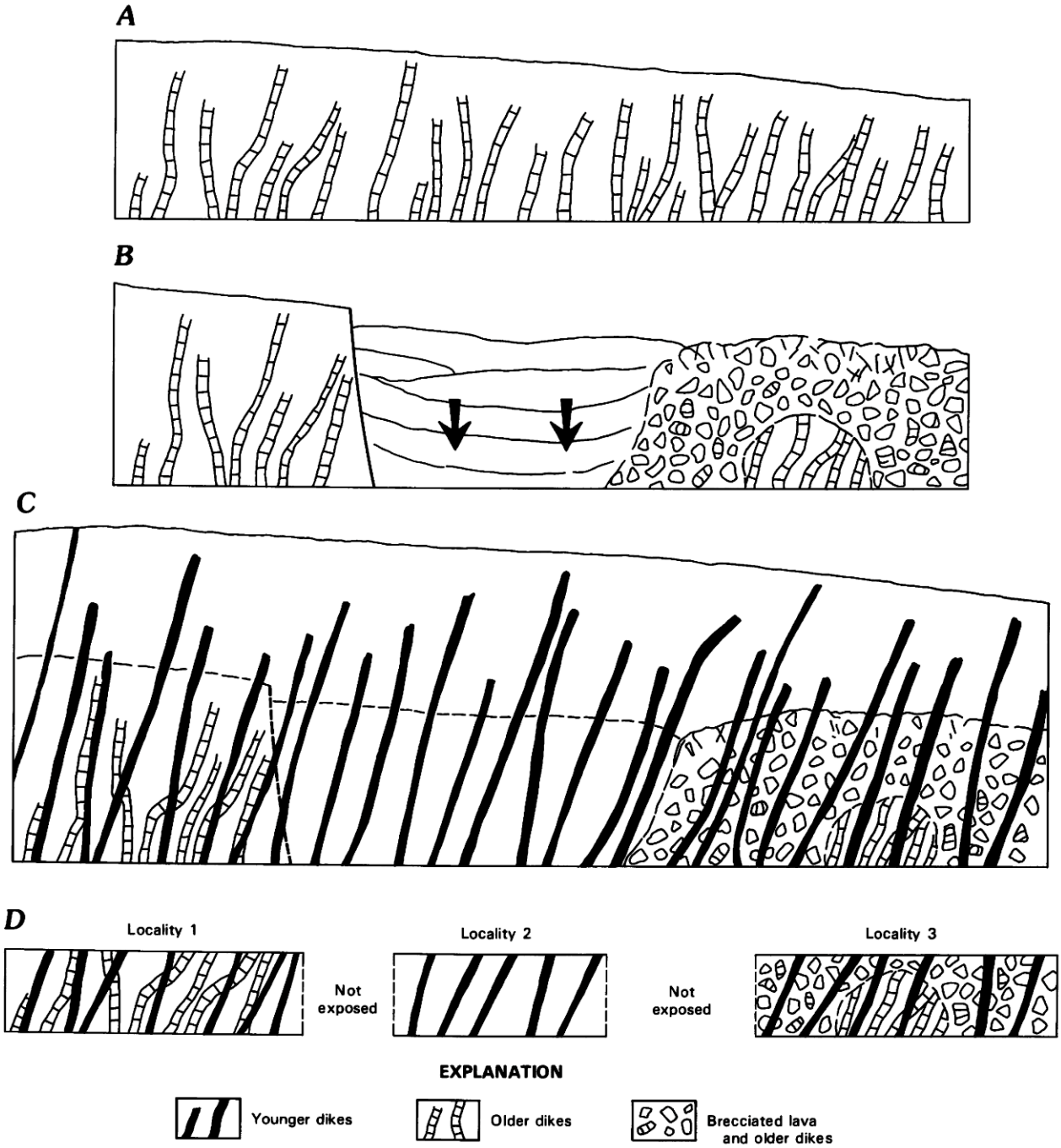


FIGURE 41.21.—Inferred origin of dike relations at localities 1–3. ***A***, Inital intrusion of older dikes. ***B***, Subsequent caldera subsidence (arrows), pervasive brecciation of part of lava and older dikes, and infilling of caldera by thick massive flows. ***C***, Later intrusion of younger dikes. ***D***, Dike relations as presently seen at localities 1–3.

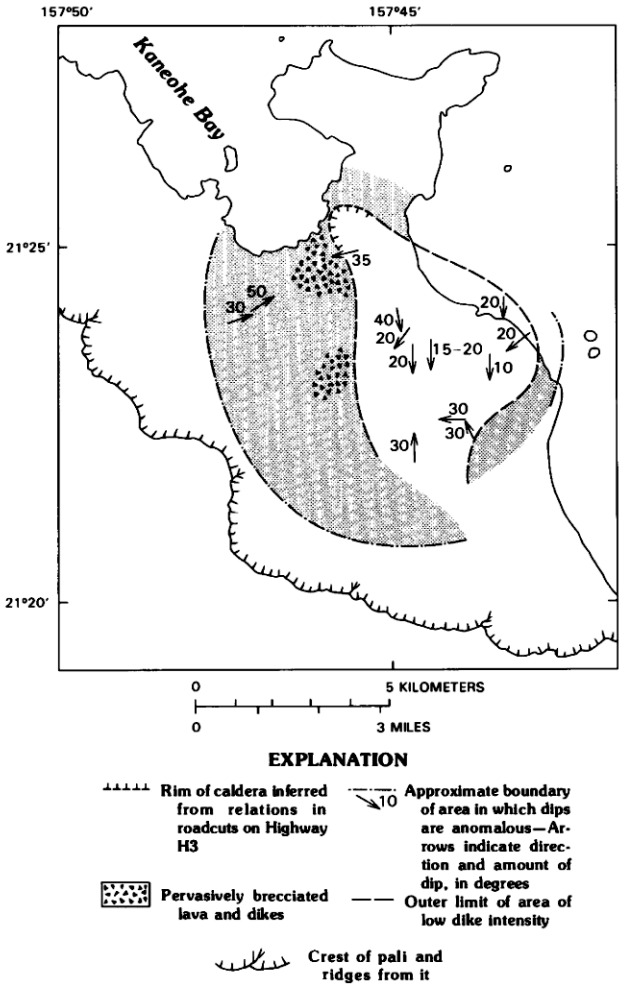


FIGURE 41.22.—Evidence indicating position and extent of caldera complex (shaded) in Kailua area. Area of low dike intensity shown in more detail in figure 41.3; relations in roadcuts on Highway H3 shown in figure 41.21.

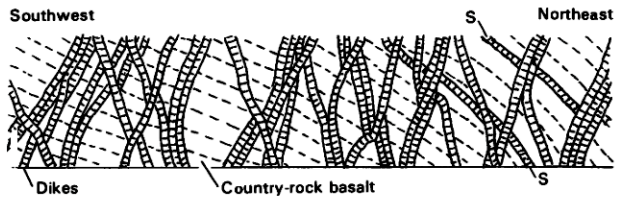


FIGURE 41.23.—Schematic relations at Kapaa Quarry. Strongly tilted lava flows are cut by dike complex in which dikes form two sets; opposing dips of sets are equal in amount, indicating that complex was intruded after lava had been fully tilted. Some dikes (S) cutting steeply inclined lava are conformable and technically sills, but they are better identified as inclined dikes.

3 varies from 0–2.6 m per square meter of rock surface, and the average of 20 measurements is 1.2 m. Where the older dike complex is intact at the same locality and has a local intensity of 100 percent in dike clusters, the measured total length of chilled margin per square meter averages 2.9 m. This is consistent with derivation of the breccia from a moderately intense (about 40 percent) older dike complex cutting lava.

The abundance of dike fragments would be opposed to the idea that the breccia is a kind of talus that accumulated in a crater or caldera: exposures at a level sufficiently high to generate talus on a Hawaiian volcano contain very few dikes. Casadevall and Dzurisin (chapter 14) counted only 18 dikes on the 6.5-km-long western and northern wall of Kilauea caldera, for example. The absence of stratification in the breccia and the way in which dikes show various degrees of in-place brecciation are opposed to an epigene formation for the breccia.

An alternative breccia-forming mechanism is hyaloclastic brecciation of dikes injected into rocks saturated by ground water. There are many places at localities 3–7 and 28 where green rims, presumed to be propylitized glass, are unusually conspicuous and thick, and some hyaloclastic fragmentation has almost certainly occurred. It seems, however, to have been on a small scale. Another alternative mechanism is auto-brecciation of dike injected into dike. What seem to be unequivocal examples of this are found among earlier dikes on the Mokulua Islands and in outcrops west of Waikane, but the brecciation is very localized.

The best explanation is that the bulk of the breccia is of tectonic origin and developed in place at or near the margin of a caldera, where the strain, instead of being confined to discrete fault planes, was distributed over a broad zone. As here envisaged, the stress acted on a pile of lava with a great many planes of weakness of various kinds, cut by a swarm of highly irregular dikes that had been injected into water-saturated rocks and hence were strongly jointed. The stress therefore caused a pervasive brecciation.

Formation of the breccia at localities 3–5 was followed by a metamorphic event that produced a widespread propylitic alteration accompanied by the deposition of laumontite, epidote, calcite and other secondary minerals (Fujishima and Fan, 1977). This event effectively lithified the breccia so that to the younger dikes it behaved as a rigid rock.

## ORIGIN OF CALDERAS OF BASALTIC VOLCANOES

Many large basaltic shield volcanoes possess a caldera. Fine examples occur on oceanic islands such as Grand Comore, the Galapagos, Hawaii, Mauritius, and Reunion; other examples occur in continental-margin settings and include Masaya (Nicaragua) and Osima (Japan). The calderas of basaltic volcanoes differ in six important respects from calderas of volcanoes that have significant amounts of felsic or silicic products:

1. They tend to develop by incremental subsidence events and not consequent on a single major eruption (whether explosive or effusive).
2. Subsidence events are sometimes but not always correlated with eruptive activity.

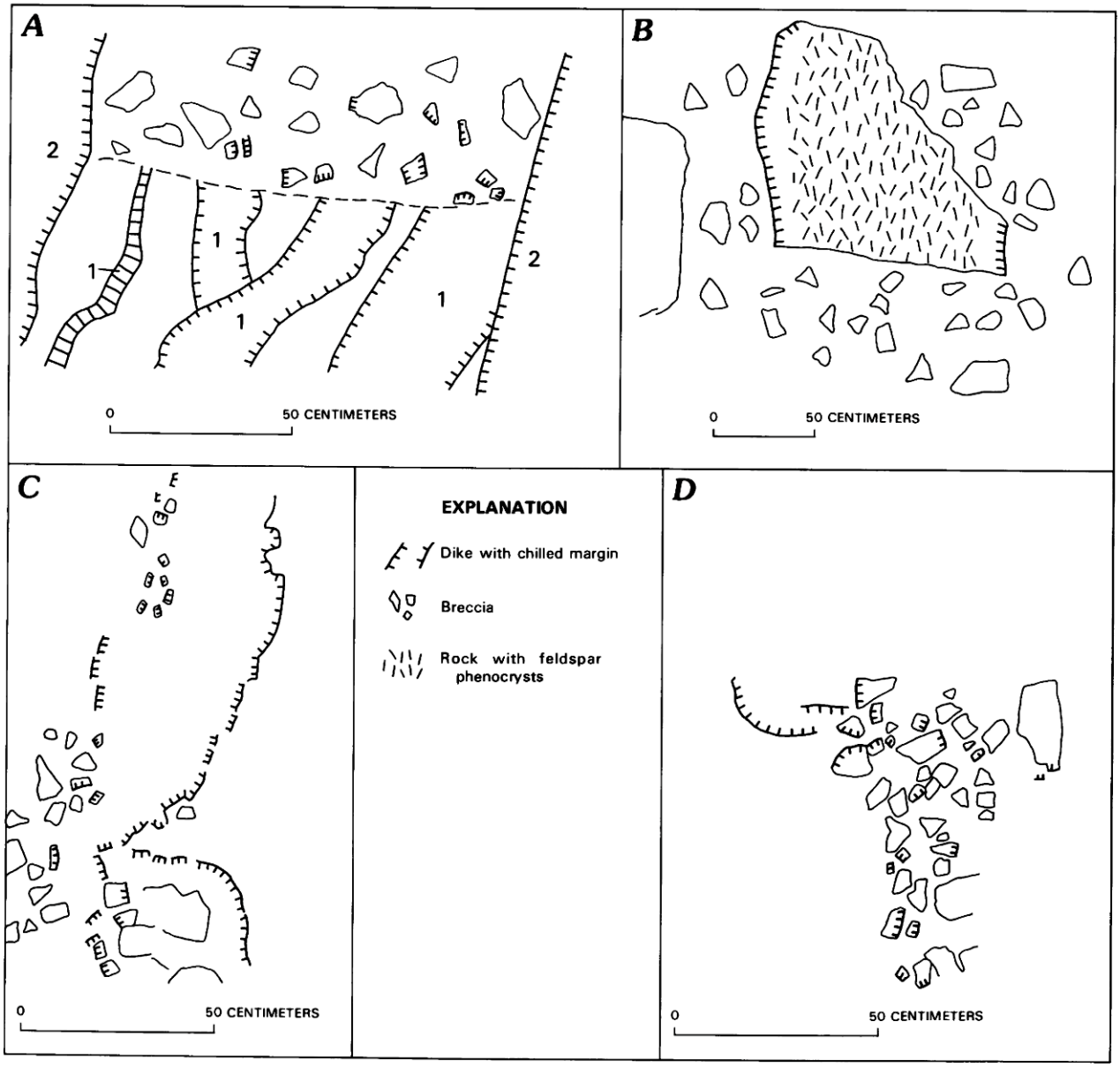


FIGURE 41.24.—Relations shown by breccia at locality 3. ***A***, Group of older dikes (1) terminates abruptly against breccia. Some fragments in breccia originate from dikes and have chilled margin on one side. Younger dikes (2) intruded after breccia had been lithified. ***B***, Intact but isolated fragment of richly feldspar-porphyritic dike. ***C***, Dike with one margin fairly complete but other brecciated and the fragments somewhat dispersed. ***D***, Breccia containing dispersed dike fragments characterized by chilled margins on one side.

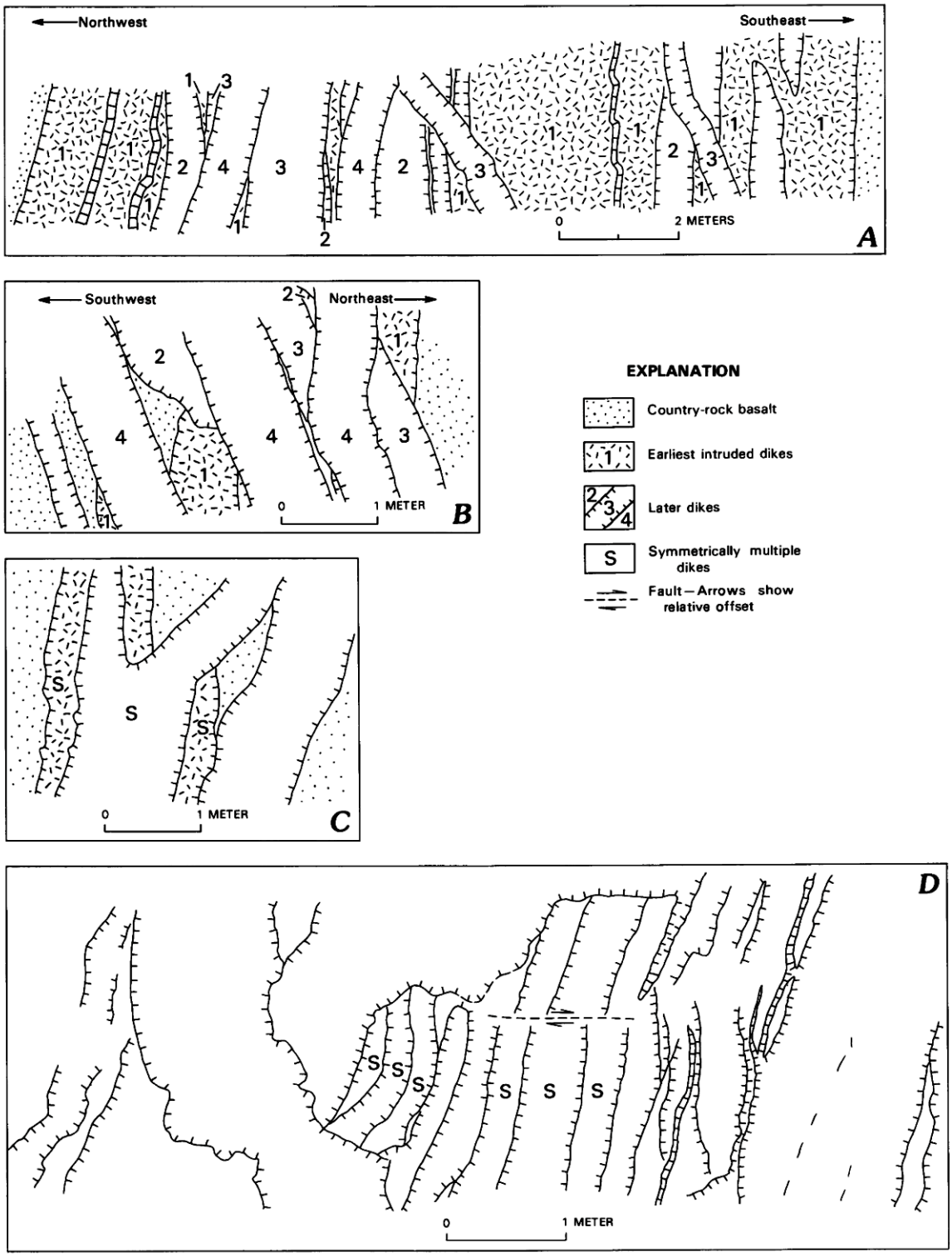


FIGURE 41.25.—Examples of multiple dike clusters. ***A***, Cluster of 14 dikes totaling 13.6 m thick at locality 23. Oldest dike is unusually wide (about 6.4 m) and is split into many screens. Country-rock screen at northwest end of cluster is 16 cm wide; that at southeast end is 330 cm wide. ***B***, Dikes intersecting at acute angle forming braided pattern (locality 5). ***C***, Symmetrically multiple dike (locality 3). ***D***, Part of a cluster of more than 14 dikes (locality 1). Four of the dikes are symmetrically multiple pairs.

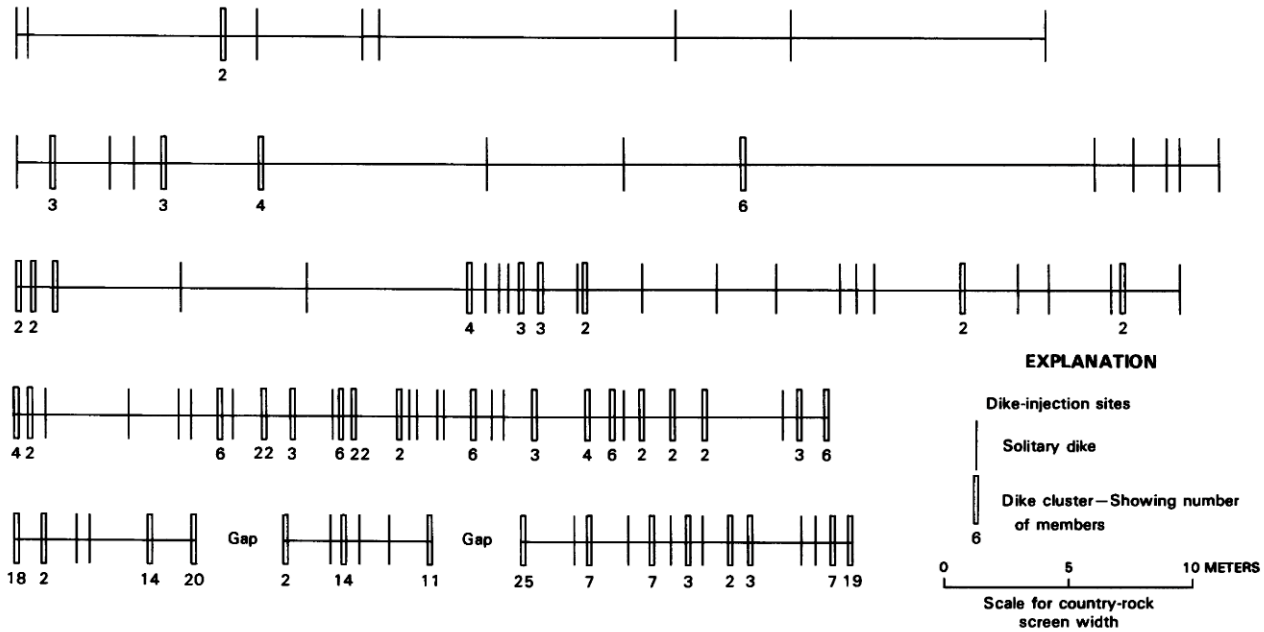


FIGURE 41.26.—Distribution pattern of dikes in representative exposures of Koolau complex (localities 47, 5, 2, 20, and 41, from top down), showing how number of dike-injection sites and multiple dikes vary. As intensity of dike complex increases, so dike spacing decreases and number of dikes in multiple clusters increases. Widths refer only to country-rock screens; dike widths are ignored.

3. They tend to have a complex history of alternating subsidence and partial infilling by lava flows, and significant changes in topography may occur on the more active volcanoes in a period as short as a century. These changes are well documented for Kilauea and Mauna Loa by Macdonald and Abbott (1970).
4. They tend to have a number of more or less concentric fractures on which downdropping has occurred instead of a single bounding fault, and the displacement on these faults tends to increase inwards; Kilauea is a good example. They also are often associated with or contain pit craters.
5. They coincide approximately with positive Bouguer gravity anomalies, in contrast with the negative anomalies shown by calderas associated with felsic and silicic volcanism.
6. They are transected by one or more rift zones along which activity is concentrated; in deeply dissected examples they are seen to be in line with, or are cut by, intense swarms or complexes of dikes and associated intrusions.

I now propose a new concept for the origin of basaltic calderas: that their subsidence is a consequence of the high density of the intrusive complex combined with the reduced strength of the lithosphere above a hot spot, which makes localized downward creep possible. Macdonald (1965) considered but rejected the idea that the calderas were caused by the weight of intrusions because he did not consider the possibility of creep occurring.

The pile of basaltic lava that constitutes much of the edifice of a Hawaiian volcano is estimated to have an overall density of about 2.35 g/cm$^3$ (Kinoshita and others, 1963), whereas a dike complex having >50 percent intensity is likely to be at least 0.35 g/cm$^3$ denser. Large gabbroic and ultramafic intrusions are likely to underlie the caldera and may be as much as 1.0 g/cm$^3$ denser than the lavas. A complex of dikes and associated large intrusions therefore represents a great localized and unevenly distributed load, the cause of the large Bouguer anomalies of the Koolau Volcano (Strange and others, 1965) and the active volcanoes on Hawaii (Kinoshita and others, 1963).

The very low dike intensity in the central part of the Kailua caldera is interpreted to indicate that the subsidence rate there exceeded the buildup rate of the dike complex, whereas in marginal parts of the caldera the reverse applied. This is important evidence in support of the postulated caldera-forming mechanism, in which the subsidence rate should be greatest at the locus of magmatic activity.

## GROWTH MECHANISMS OF THE KOOLAU DIKE COMPLEX

### PREFERENTIAL DIKE PATHWAYS

A large proportion of dikes in the Koolau complex are multiple and occur in parallel clusters, in which most commonly the members lie alongside and in chilled contact with one another without any intervening country-rock screen (fig. 41.25).

These dike clusters indicate that dike margins were structural planes of weakness that offered very favorable pathways guiding later intrusions. This is underscored by the fact that when an intrusion trends obliquely to an earlier dike it commonly changes course and follows the margin of the earlier dike for a space before resuming its oblique trend. The ease with which a dike breaks apart

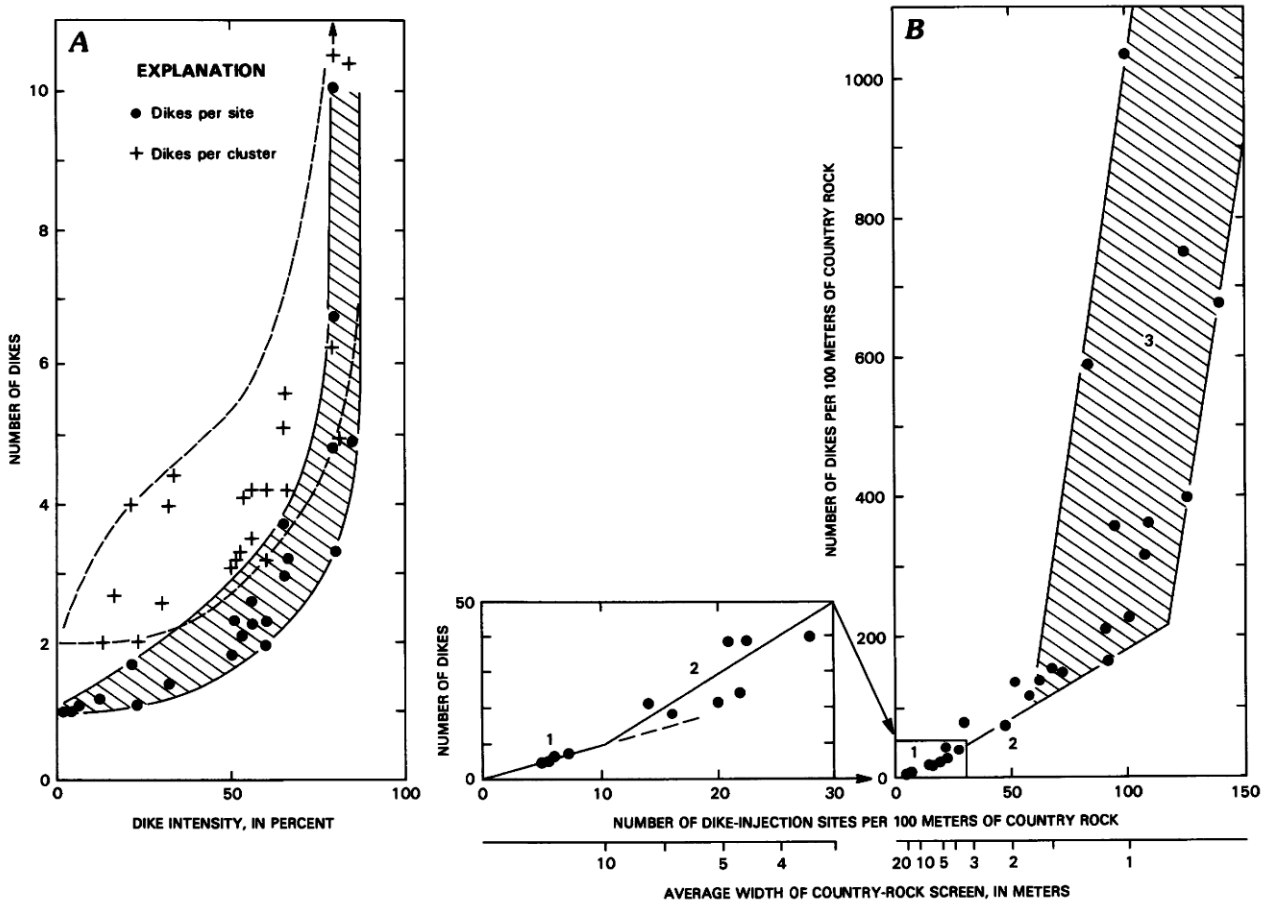


FIGURE 41.27.—Diagrams illustrating build-up of dike complex. ***A***, Plot of number of dikes per site and per cluster against dike intensity of complex. As intensity increases, average numbers of dikes per site and per cluster increase. ***B***, Plot of number of dikes and dike-injection sites per 100 m of country rock. In segment 1, the numbers are comparable. In segment 2, number of dikes increases twice as fast as number of sites, showing that half the dikes are forming multiple clusters. In segment 3, number of dikes increases much faster than number of sites because most of dikes are entering multiple clusters.

from the country rock or from an adjacent dike is clearly evident in any roadcut.

Data on dike spacings from a number of localities covering a wide range of dike intensities (fig. 41.26) form a basis from which to assess the manner in which the dike complex developed. It is assumed that these outcrops record stages in a progressive process, halted at each location by the cessation there of further dike injections. A dike-injection site is defined as a site in which either a solitary dike or a multiple dike cluster occurs.

Two features of the relationships shown in figure 41.26 are portrayed in figure 41.27: the average number of dikes per intrusion site, and per multiple cluster, increases at an increasing rate as the dike intensity increases (fig. 41.27*A*); and the number of dikes rises increasingly rapidly as the number of dike-injection sites per 100 m of country rock increases (or the average country-rock screen width decreases) (fig. 41.27*B*).

The dike-injection pattern has been reconstructed from figure 41.27*B* as follows. The first dikes to be injected all followed independent pathways through the country-rock basalt and subdivided the basalt into screens. In this early stage the number of dikes per unit width of country rock equaled the number of dike-intrusion sites (segment 1 on figure 41.27*B*).

When the average screen width decreased to less than 10 m, a proportion of the dikes began to follow the margins of previously intruded dikes instead of new pathways through the country rock, and the first dike clusters were thus formed.

As the dike-swarm intensity increased, and the average screen width decreased from 10 m to less than 2 m, roughly the same number of dikes followed margins of previously intruded dikes as followed new pathways in the basalt; the total number of dikes then

increased at about twice the rate that the number of dike-injection sites increased (segment 2 of figure 41.27*B*). Because of the strong tendency for dikes to intrude into existing clusters, where planes of weakness were concentrated, the average number of dikes per cluster increased faster than the proportion of clusters to solitary dikes.

With further dike injection, the proportion of dikes following margins of preexisting dikes became very much greater than that following new pathways through the lava (segment 3 of figure 41.27*B*). It is thought that at this stage the average country-rock screen width tended to become stabilized at about 1 m. The screens were pushed farther and farther apart as more dikes were injected into the clusters between them until, in the most intense parts of the complex, narrow screens occur at intervals of tens of meters.

## SYMMETRICALLY MULTIPLE DIKES

A proportion of the dikes in multiple clusters were intruded inside earlier dikes; an example is shown in figure 41.25*A* in which a broad dike is cut by 13 subparallel dikes situated at various distances from its margins. This particular example is unusual because the first dike fused the country rock, to which it is firmly welded, and later dikes hence showed no tendency to follow these margins.

A few dikes are symmetrically multiple, with the youngest intrusion in the middle and the halves of earlier narrow intrusions that have been split up the middle symmetrically disposed on either side (fig. 41.25*C*, *D*). The best examples are seen on the Mokulua Islands, where as many as four successively injected members occur in the same narrow multiple dike. Each member has chilled against the earlier member.

Solitary dikes of the Koolau complex in general lack any visible median parting or plane of weakness such as could direct a later intruded dike. This raises the possibility that the middle of a dike may be a preferred pathway for thermal reasons. The center of a cooling dike remains fluid longest and after solidification remains hot longest. Even if solid, the still-hot center remains mechanically weak. Thus Ryan and Sammis (1981) demonstrated that the value of Young's modulus at 700 °C is 10 percent less than it is at 25 °C.

## HOW MANY DIKES?

An interesting question is the total number of dikes in the Koolau complex. Exposures are too incomplete to permit this to be determined by counting, but they are adequate for a good estimate to be made.

In a transect of the complex just south of Kaneohe Bay the exposed intense part is 6 km wide (fig. 41.3), and the intensity over this width varies from 30 to 63 percent. If the average intensity is 50 percent, dikes would total 3.0 km. In marginal zones on the southwest side and presumably also on the northeast side of the complex, the dike intensity drops from 40 percent to 5 percent in about 1 km. At an average intensity of 15 percent, these two strips would contribute 0.3 km, bringing the total dike width to 3.3 km.

The average width of dikes at different localities in this transect varies from 55 to 75 cm (fig. 41.9). If we take 65 cm as an overall average, this yields a total of about 5,100 dikes in 3.3 km of dike width. This estimate is probably a minimum: if the complex possesses bilateral symmetry about the Koolau lava-shield axis shown on figure 41.1, the full width of the intense part of the complex would have been about 9 km, increasing the total width of dikes to 4.8 km and the number of dikes to 7,400.

Consider now the number of dikes in a transect of the complex at or near Waikane. The intense part of the complex there is 3.5 km wide and has an average intensity of about 45 percent, giving 1.6 km total width of dikes. To this may be added 0.8 km for the low-intensity strips 2 km wide on either side, giving a total dike width of 2.4 km. The average width of dikes at different localities in this transect varies from 115 to 175 cm. If we take 150 cm as an overall average, this yields a total of 1,600 dikes.

The number of dikes in any given transect cannot be equated with the total number of dikes in the complex; estimation of the latter requires a knowledge of the length-width ratio of the dikes, on which no direct information is available. Gudmundsson (1983) assumed a length-width ratio of $10^2$–$10^3$ in eastern Iceland. If we apply this on Oahu, dikes 50 cm wide would have a length of 50–500 m. This is unrealistically short; it is more than an order of magnitude less than the known length of eruptive fissures on Kilauea and Mauna Loa, and seems incompatible with the origin of the dikes by lateral movement outwards from the volcano center.

If it is assumed that the number of dikes decreases linearly from 7,400 in a transect along the south of Kaneohe Bay to 1,600 at Waikane and to zero at the northwest tip of the Koolau Volcano, and that the average dike length is 5 km, then the dikes would number about 30,000.

## DIKES IN THE BUILDUP OF KOOLAU VOLCANO

Koolau Volcano is deeply dissected; the highest point on the Koolau Range is 960 m (3,150 ft) above sea level, and the original shield crest, extrapolated from the generalized contours of figure 41.1 would have been about 1,100 m above present sea level (actual elevation must have been higher, because the edifice has subsided since then) without allowing for the Kailua caldera. Characteristics of the older dikes such as at locality 3 indicate intrusion at a shallow depth, possibly 100 m or less, at an early stage of shield growth; the younger dikes seen in the same outcrop could have been intruded at a depth of 1,000 m or more.

No information exists on what proportion of dikes fed lava flows. No example is known on Oahu of a lava connected with its feeder dike. Recent experience on Kilauea indicates that dike-injection events without lava eruption are more frequent than fissure eruptions (Dzurisin and others, 1984), and even among the latter some (for example, the two caldera eruptions in 1982) erupt only a negligibly small amount of lava. Most of the Koolau dikes are very narrow, and it is likely that few erupted much lava.

The volume ratio of dikes to lava in subaerial parts of the Koolau Volcano is readily estimated after making two assumptions, namely, that the original volcano possessed a bilateral symmetry about its axis (fig. 41.1) and that the intensity of the dike complex decreases linearly upwards. This second assumption was docu-

mented for eastern Iceland by Walker (1974), but has not been demonstrated in the Koolau Range because of the unfavorable topography. All that is known is that the dike intensity in Kapaa Quarry does not measurably decrease through 95 m of elevation increase.

The reconstructed form of the Koolau Volcano and the distribution of dikes in it are shown in a transverse section in figure 41.28. The maximum total width of dikes in a transect is 4.8 km; the derived total dike cross-sectional area is thus about 2.4 $km^2$. The subaerial part of the volcano on the same transect has a cross-sectional area of 13 $km^2$; dikes therefore compose 15–20 percent of the subaerial volume. Intrusions are likely to constitute an increasing proportion at deeper levels.

Mention was made earlier of several localities where dikes of different ages intersect orthogonally; this is not readily explained if dike trends are determined primarily by the overall form of the volcanic edifice. The dike complex has a total dike width of 4.8 km near the caldera, decreasing to zero very rapidly toward the southeast and less rapidly in the opposite direction. These variations in width caused local stresses concentrated near the caldera, where the rate of change was greatest. Such local stresses may have been sufficient to cause the injection of the transverse dikes.

## COMPARISON OF KOOLAU VOLCANO WITH KILAUEA

The active Hawaiian volcano that is most closely similar to Koolau appears to be Kilauea. Both are very strongly elongate structures having a single dominant rift zone intersecting the caldera, and they are comparable in size. The subaerial part of Kilauea is 30 percent higher and 43 percent longer. The bathymetric chart of Oahu shows a marked increase in slope at 500 m off the north tip of Koolau; if this marks the earlier shoreline then Koolau would have been 77 km long and 1,600 m high before subsidence to its present level. These dimensions are almost identical to those of subaerial Kilauea.

Both volcanoes are buttressed on one side by an older volcanic structure, though the Waianae buttress of Koolau is much smaller than the Mauna Loa buttress of Kilauea. Kilauea shows strong seaward creep on the unbuttressed side. Much of the unbuttressed side of the Koolau Volcano has already collapsed, and the predominantly northeast dip of dikes in part of the Koolau complex may be an early manifestation of this process.

The similarity between Koolau and Kilauea extends also to some of the less immediately obvious features, notably the asymmetry of each volcano along its length (fig. 41.29); their calderas do not occupy a central position, because one rift zone is longer and has been built up higher and wider than the other.

The caldera is assumed to mark the effective center of the volcano, below which magma rises from its deep source and then moves to intrusive or eruptive sites. The plunge of flow lineation on the dikes, however, appears to point to two main magma sources in the Koolau Volcano, one below Kailua caldera and the other below Kaneohe Bay. Possibly the bay is occupied by another caldera or by an extension of the Kailua caldera. Alternatively, the position of Kaneohe Bay is analogous with the setting of Mauna Ulu (site of the 1969–74 eruption) on Kilauea. Some of the Mauna Ulu magma may have come up a separate pathway, which branched off from the main Kilauea one (Ryan and others, 1981), and the Kaneohe Bay center may be a similar branch.

The curvature of the Koolau dike complex west of Kailua is reminiscent of the curvature of the Chain of Craters segment of Kilauea's east rift zone. Surface ground fissures along the Chain of Craters form an echelon group in which the individual fissures preserve the main trend of the east rift zone, and it can only be surmised whether these ground fissures overlie a swarm of dikes paralleling the Chain of Craters (as was proposed by Duffield, 1975; some kind of conduit by which lateral magma movement occurs must unquestionably be present along the chain).

In summary, there are such close similarities between Koolau and Kilauea Volcanoes that the main dike complex in the one may be accepted as a close and valid analog to the subsurface region of the east rift zone in the other.

## A MODEL FOR THE FORMATION OF THE KOOLAU DIKE COMPLEX

In a number of respects the Koolau dike complex is unique among described examples of the dike swarms associated with volcanic centers. The nondivergence of the dikes northwestward from the Kailua center shown on figure 41.5 contrasts with the radial or fascicular structure usually found, in which there is at least some degree of divergence away from the volcanic center. The Koolau complex is unusually coherent and the intensity rises inward from less than 5 percent to 50 percent or more in a remarkably short distance and then tends to be fairly uniform at 50–65 percent across its width, unlike the Gaussian intensity distribution found across most described dike swarms. The Koolau complex also reaches a far higher intensity (maximum 85 percent) than most swarms, which peak at 25 percent or less.

A model for the formation of the Koolau complex that explains these unique features and takes account also of the implications of recent magmatic activity on Kilauea Volcano (Walker, 1986) considers that three effects constrain the intrusion of dikes in the complex. One is the edifice effect, which tends to localize dike injection parallel with the long axis of the volcano. A second is the existence of plentiful pathways along margins of existing dikes in the complex. The third is a hydrostatic effect by which magma is able to reach a high crustal level in the relatively high-density environment of the dike complex.

Consider the third effect more closely. The generally high fluidity of Hawaiian tholeiitic magma gives it great freedom to move through the disjointed lava shields, and in these free conditions it comes to move into and become localized in those regions of the volcano in which it is gravitationally most stable. These regions are the marginal zones of the dike complexes, in which the average density of the rocks—a mix of lava flows and 5–50 percent of dikes—is closely comparable with that of weakly vesicular tholeiitic magma (fig. 41.28*B*).

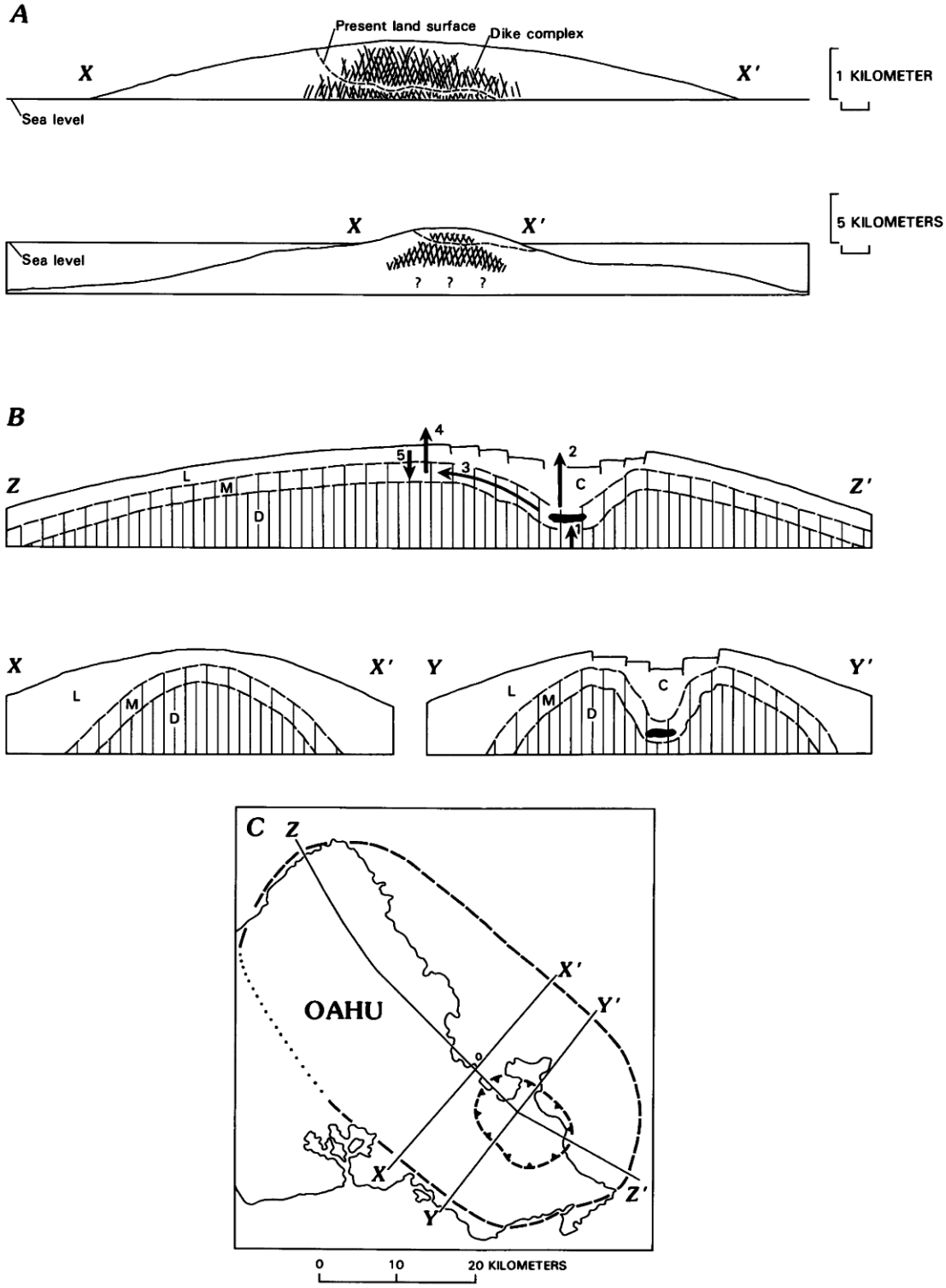
A
Present land surface
Dike complex
X
X'
1 KILOMETER
Sea level
X
X'
5 KILOMETERS
Sea level
? ? ?
B
Z
Z'
L
M
D
C
1
2
3
4
5
X
X'
L
M
D
Y
Y'
L
M
D
C
C
Z
X'
Y'
OAHU
X
Y
Z'
0
10
20 KILOMETERS

It can be surmised that when part of a dike complex has built up to 50–65 percent intensity it becomes denser on average than tholeiitic magma so that magma tends to avoid it; hence an intensity of significantly more than 65 percent is attained only locally.

Because of increased vesiculation, the magma density may then decrease so as to fall below that of the lava, and when this happens the magma rises to the surface. This concept explains well the activity of Kilauea Volcano in recent years, in which dike injection events into the rift zone without lava effusion have occurred repeatedly and the eruptions have been mostly short events characterized by vigorous fire-fountaining. The geyserlike regularity of eruptive phases 4–46 in the 1983–6 activity of Kilauea is also strongly suggestive of a gas-accumulation control. Moreover it has often been observed that after magma has reached the surface and degassed, much of the degassed lava flows back down into fissures and presumably returns to the gravitationally stable zone.

## SUMMARY AND CONCLUSIONS

When I began to study the Koolau dike complex I did not anticipate that it would prove to be in any way unusual, yet a wide range of unexpected features has emerged. Earlier workers were handicapped by a general paucity of good exposures, and the present study was feasible because of many new outcrops generated in the past 10 years. Some unexpected features were revealed only because of the quantitative nature of the present study, made possible by these new outcrops.

The Koolau dike complex is much more intense, and contains five to ten times more dikes, than was previously realized. Indeed, it is the most intense documented example of a dike swarm of volcanic-edifice type, and its 4.8 km of total dike width compares with the 1–2 km of total dike width for Tertiary dike swarms in eastern Iceland (Walker, 1974; Gibson and others, 1966), Scotland (Speight and others, 1982), and the Columbia River basalts (Taubeneck, 1970). If cone sheets are included, then some of the intrusive complexes in Scotland (for example, Mull; Bailey and others, 1924) will have an intensity closely comparable with Koolau.

One of the most intriguing features of the Koolau complex is the nonverticality of the dikes, which form two sets having opposing dips of 65° to 85°. These are interpreted to be complementary sets, closely analogous with normal faults in an extensional environment, and are thought to have resulted when the maximum principal stress direction acted vertically and was much greater in magnitude than the principal stresses acting in the horizontal plane. The nonverticality is a consequence of dike injection into a high-standing volcanic edifice. The dikes tend to dip out from the axis of the Koolau Volcano, but there is a large anomalous area in which the dikes predominantly dip in a contrary direction, toward the northeast. This seems to reflect a tendency, manifested very early in the history of the complex, toward seaward creep in that area; this creep later culminated in the major collapse of that same part of the volcano.

The Koolau complex displays many of the features of a sheeted dike complex, although it occurs in an intraplate setting unlike the sheeted complexes of the ophiolite suite. The sheeted structure resulted because the Koolau dikes showed a pronounced tendency to intrude along the margins of earlier dikes. As the dike-complex intensity increased, so an ever-increasing proportion of dikes utilized such planes, leading to the development of multiple dike clusters tens of meters wide containing tens of members. Some dikes followed a pathway along the middle of an earlier dike, which, when still hot, was a favored site for thermal reasons.

Many dikes possess a flow lineation on their margins, and the measured attitudes point to two main centers, about 5 km apart and situated at 2–3 km below present sea level, from which the dikes are presumed to have risen obliquely into higher parts of the edifice.

Because of their nonverticality, injection of the Koolau dikes involved a significant vertical component of dilation totaling more than 1,000 m. The contribution of this vertical component to the buildup of the Koolau shield is not known; we cannot distinguish absolute uplift of a dike hanging wall from subsidence of a dike footwall.

The Koolau dike complex is much denser than the lava pile and is so intense and concentrated as to represent a great localized load, reflected in the high positive Bouguer anomaly. The unequal bulk-density distribution in the volcano is considered to have had two consequences: one was to channel magma batches into a zone, in marginal parts of the dike complex, in which the magma was gravitationally most stable; the other was to tend to cause differential subsidence where the dike complex was widest and heaviest.

The preferential channeling of magma into a zone at the margins of the dike complex, where the magma density matches the bulk-rock density, is the key mechanism of a proposed model which explains buildup of the dike complex into a remarkably coherent structure having an intensity plateau at a level of 50–65 percent. This mechanism also explains the strong propensity of Hawaiian tholeiitic magma to remain underground, evidenced clearly by the record of the most recent magmatic activity; even when, because of vesiculation, magma does reach the surface, it may then promptly plunge underground again when it loses its gas bubbles.

The tendency for differential subsidence can account for the calderas of Hawaiian volcanoes: I propose that their subsidence is

FIGURE 41.28.—Relation of dike complex to bulk-density zonation and magma pathways of Hawaiian volcanoes. ***A***, Profiles across Koolau lava-shield volcano on two different scales, showing setting of dike complex. ***B***, Schematic profiles across a Hawaiian volcano such as Koolau, showing bulk-density zonation and typical magma pathways. L, lava shield cut by only a few scattered dikes, less dense than nonvesicular tholeiitic magma; M, marginal zone of dike complex, intensity 5–50 percent, into which nonvesicular or weakly vesicular tholeiitic magma tends to be channeled because of matching densities; D, dike complex, intensity >50 percent, denser than nonvesicular or weakly vesicular tholeiitic magma; C, caldera complex; calderas of varying sizes and ages where density zones are strongly depressed; 1, magma residing in a chamber in zone M where it is lowest (in caldera complex). This is gravitationally most stable situation for nonvesicular magma in entire edifice; 2, rapid vesiculation carries a magma batch to the surface, producing caldera (summit) eruption; 3, slow vesiculation carries a magma batch into a rift zone channeled along zone M; 4, vesiculation carries a magma batch to the surface, producing rift-zone eruption; 5, degassed lava returns to zone M. ***C***, Map of Koolau Volcano showing location of profiles in *A* and *B*.

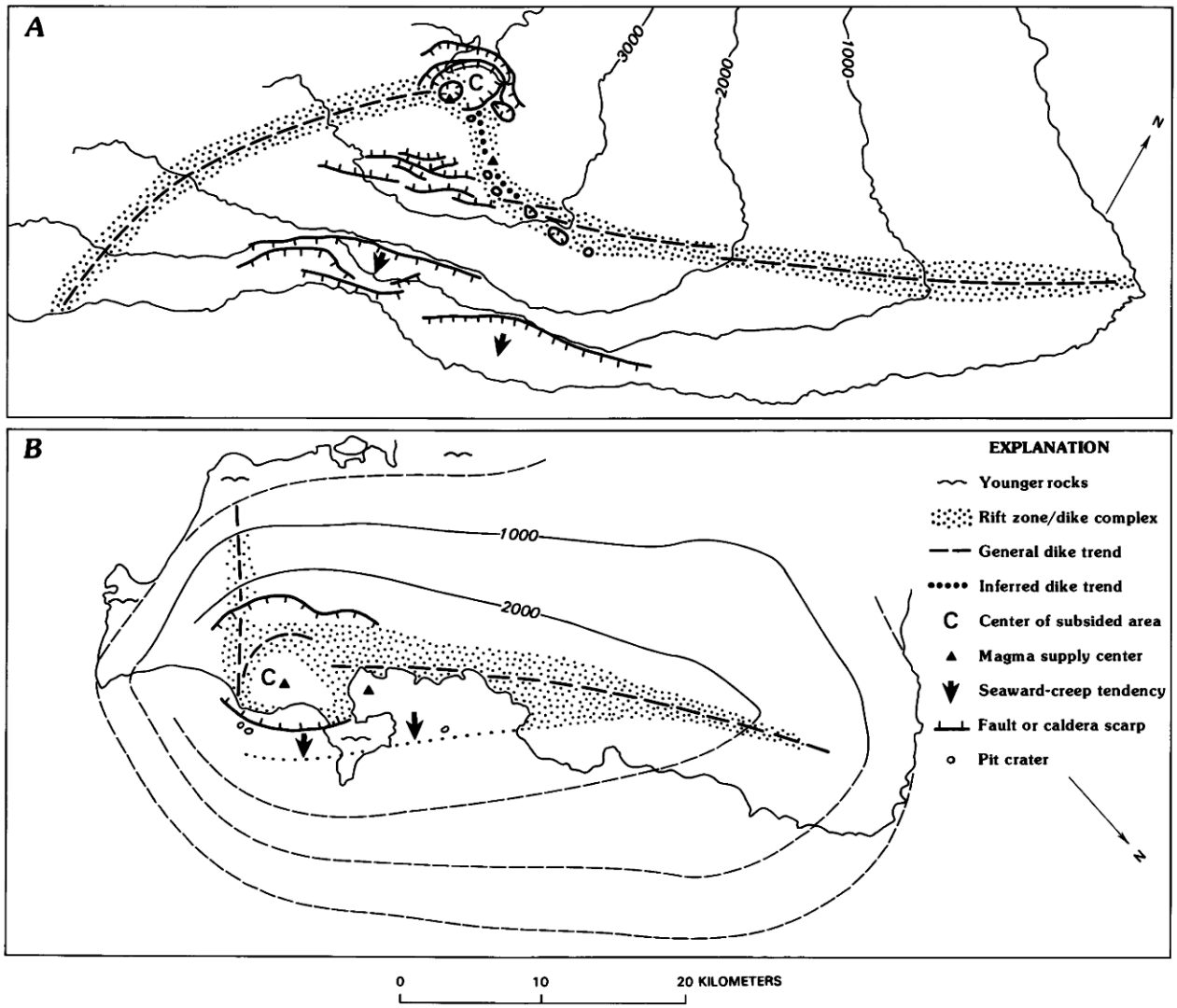


FIGURE 41.29.—Maps of Kilauea and Koolau Volcanoes at same scale. ***A***, Kilauea on the Island of Hawaii. Volcano contour interval 1,000 ft; heights in feet above sea level. ***B***, Koolau Volcano on Island of Oahu. Contours, in feet above present sea level, are generalized from present topography to show original form of volcano; dashed where very uncertain because of deep erosion.

caused by the load of intrusions and is possible because the hot lithosphere above a hot spot is sufficiently weak to permit downward creep of a prism of the dike complex.

The Koolau Volcano has a broad subsidence area that measures at least 10 km by 12 km. In part this is an area of general downsagging, and in part it may consist of discrete down-faulted cauldrons. The Kailua caldera is now exposed at an erosion level 1 km beneath the final top surface of the Koolau Volcano, and variations in the makeup of the caldera rocks can be explained by an imbalance between two processes that operated at different rates. One process was subsidence, which caused high-level rocks having few or no dikes to appear at today's erosion level. The other process was the injection of dikes seeking to rebuild the dike complex to the 50 percent to 65 percent intensity at the same level. In some outer parts of the Kailua caldera where subsidence was caused by downsagging, the rebuilding of the complex was completed. In the middle part of the Kailua caldera, subsidence greatly exceeded the capacity of dike injection to rebuild the complex. It is thought that Kilauea caldera is a good present-day analog, and the magma chamber which is postulated to be situated in the marginal zone of its dike

complex is now 3–5 km deep, maintained at that depth by rapid subsidence.

This mechanism is consistent with features of Hawaiian calderas such as their highly dynamic nature—great changes in caldera geometry can occur within a century—and the fact that the calderas are the locus of dike injections.

## REFERENCES CITED


Adams, W.M., and Furumoto, A.S., 1965, A seismic refraction study of the Koolau volcanic plug: Pacific Science, v. 19, p. 296–305.

Bailey, E.B., Clough, C.T., Wright, W.B., Richey, J.E., and Wilson, G.V., 1924, Tertiary and post-Tertiary geology of Mull, Loch Aline, and Oban: Memoir of the Geological Survey of Scotland.

Currie, K.L., and Ferguson, J., 1970, The mechanism of intrusion of lamprophyre dikes indicated by "offsetting" of dikes: Tectonophysics, v. 9, p. 525–535.

Delaney, P.T., and Pollard, D.D., 1981, Deformation of host rocks and flow of magma during growth of minette dikes and breccia-bearing intrusions near Ship Rock, New Mexico: U.S. Geological Survey Professional Paper 1202, 61 p.

Doell, R.R., and Dalrymple, G.B., 1973, Potassium-argon ages and paleomagnetism of the Waianae and Koolau Volcanic Series: Geological Society of America Bulletin, v. 84, p. 1217–1242.

Duffield, W.A., 1975, Structure and origin of the Koae fault system, Kilauea Volcano, Hawaii: U.S. Geological Survey Professional Paper 856, 12 p.

Duffield, W.A., and Nakamura, K., 1973, A photogeologic method for determining the direction of horizontal dilation from patterns of en echelon fracturing: U.S. Geological Survey Journal of Research, v. 1, p. 283–287.

Dzurisin, D., Koyanagi, R.Y., and English, T.T., 1984, Magma supply and storage at Kilauea Volcano, Hawaii, 1956–1983: Journal of Volcanology and Geothermal Research, v. 21, p. 177–206.

Fiske, R.S., and Jackson, E.D., 1972, Orientation and growth of Hawaiian volcanic rifts: the effect of regional structure and gravitational stress: Proceedings of the Royal Society of London, Series A, v. 329, p. 299–326.

Fujishima, K.Y., and P-F. Fan, 1977, Hydrothermal mineralogy of the Keolu Hills, Oahu, Hawaii: American Mineralogist, v. 62, p. 574–582.

Furumoto, A.S., Thompson, N.J., and Woollard, G.P., 1965, The structure of Koolau Volcano from seismic refraction studies: Pacific Science, v. 19, p. 306–314.

Gibson, I.L., Kinsman, D.J.J., and Walker, G.P.L., 1966, Geology of the Faskrudsfjordur area, eastern Iceland: Visindafelag Islendinga, Reykjavik, Greinar, v. 4, no. 2, 52 p.

Gudmundsson, A., 1983, Form and dimensions of dykes in eastern Iceland: Tectonophysics, v. 95, p. 295–307.

———1984, Tectonic aspect of dykes in northwestern Iceland: Jokull, v. 34, p. 81–96.

Harker, A., 1904, Tertiary igneous rocks of Skye: Memoir of the Geological Survey of Scotland.

Keith, M.L., 1981, Regional mid-ocean stress and a proposed focal mechanism of 'stress-discordant' earthquakes: Geophysical Journal of the Royal Astronomical Society, v. 65, p. 627–644.

Kinoshita, W.T., Krivoy, H.L., Mabey, D.R., and Macdonald, R.R., 1963, Gravity survey of the island of Hawaii: U.S. Geological Survey Professional Paper 475–C, p. 114–116.

Le Bas, M.J., 1971, Cone-sheets as a mechanism of uplift: Geological Magazine, v. 108, p. 373–376.

Macdonald, G.A., 1965, Hawaiian calderas: Pacific Science, v. 19, p. 320–334.

Macdonald, G.A., and Abbott, A.T., 1970, Volcanoes in the sea: Honolulu, University of Hawaii Press, 441 p.

McDougall, I., and Aziz-ur-Rahman, 1972, Age of the Gauss-Matuyama boundary and the Kaena and Mammoth events: Earth and Planetary Science Letters, v. 14, p. 367–380.

Moore, J.G., 1964, Giant submarine landslides on the Hawaiian Ridge: U.S. Geological Survey Professional Paper 501–D, p. 95–98.

Nakamura, K., 1980, Why do long rift zones develop in Hawaiian volcanoes—a possible role of thick oceanic sediments: Bulletin of the Volcanological Society of Japan, v. 25, p. 255–269.

Pollard, D.D., Delaney, P.T., Duffield, W.A., Endo, E.T., and Okamura, A.T., 1983, Surface deformation in volcanic rift zones: Tectonophysics, v. 94, p. 541–584.

Pollard, D.D., Muller, O.H., and Dockstader, D.R., 1975, The form and growth of fingered sheet intrusions: Geological Society of America Bulletin, v. 86, p. 351–363.

Ryan, M.P., Blevins, J.Y.K., Okamura, A.T., and Koyanagi, R.Y., 1983, Magma reservoir subsidence mechanics: theoretical summary and application to Kilauea Volcano, Hawaii: Journal of Geophysical Research, v. 88, p. 4147–4181.

Ryan, M.P., Koyanagi, R.Y., and Fiske, R.S., 1981, Modeling the three-dimensional structure of macroscopic magma transport systems: application to Kilauea Volcano, Hawaii: Journal of Geophysical Research, v. 86, p. 7111-7129.

Ryan, M.P., and Sammis, C.G., 1981, The glass transition in basalt: Journal of Geophysical Research, v. 86, p. 9519–9535.

Speight, J.M., Skelhorn, R.R., Sloan, T., and Knapp, R.J., 1982, The dyke swarms of Scotland, *in* Sutherland, D.S., ed., Igneous rocks of the British Isles: New York, Wiley, p. 449–459.

Stearns, H.T., 1939, Geologic map and guide to the island of Oahu, Hawaii: Territory of Hawaii Division of Hydrography Bulletin 2, 75 p.

Stearns, H.T., and Macdonald, G.A., 1946, Geology and ground-water resources of the Island of Hawaii: Honolulu, Hawaii Division Hydrography Bulletin 9.

Stearns, H.T., and Vaksvik, K.N., 1935, Geology and ground-water resources of the Island of Oahu, Hawaii: Territory of Hawaii Division of Hydrography, Bulletin 1, 479 p.

Strange, W.E., Machesky, L.F., and Woollard, G.P., 1965, A gravity survey of the Island of Oahu, Hawaii: Pacific Science, v. 19, p. 350–353.

Swanson, D.A., Duffield, W.A., and Fiske, R.S., 1976, Displacement of the south flank of Kilauea Volcano: the result of forceful intrusion of magma into the rift zones: U.S. Geological Survey Professional Paper 963, 39 p.

Takasaki, K.J., 1981, Evaluation of major dike-impounded ground-water reservoirs, Island of Oahu: U.S. Geological Survey Open-File Report 81–1119, 146 p.

Takasaki, K.J., Hirashima, G.T., and Lubke, E.R., 1969, Water resources of windward Oahu, Hawaii: U.S. Geological Survey Water-Supply Paper 1894, 119 p.

Takasaki, K.J., and Mink, J.F., 1982, Water resources of southeastern Oahu, Hawaii: U.S. Geological Survey Water Resources Investigations 82–628, 97 p.

Taubeneck, W.H., 1970, Dikes of Columbia River Basalt in northeastern Oregon, western Idaho, and southeastern Washington: Proceedings of the Second Columbia River Basalt Symposium, p. 73–96.

Walker, G.P.L., 1959, Geology of the Reydarfjordur area, eastern Iceland: The Geological Society of London, Quarterly Journal, v. 114, p. 367–393.

———1974, The structure of eastern Iceland, *in* Kristjansson, L., ed., Geodynamics of Iceland and the North Atlantic area: Reidal, Dordrecht, p. 177–188.

———1984, Downsag calderas, ring faults, caldera sizes, and incremental caldera growth: Journal of Geophysical Research, v. 89, p. 8407–8416.

———1986, Koolau dike complex, Oahu: Intensity and origin of a sheeted-dike complex developed high in a Hawaiian volcanic edifice: Geology, v. 14, p. 310–313.

Wentworth, C.K., 1951, Geology and groundwater resources of the Honolulu—Pearl Harbor area, Oahu, Hawaii: Board of Water Supply, Honolulu, Hawaii, 111 p.

Wentworth, C.K., and Jones, A.E., 1940, Intrusive rocks of the Leeward slope of the Koolau Range, Oahu: Journal of Geology, v. 48, p. 975–1006.

Wentworth, C.K., and Winchell, H., 1947, Koolau basalt series, Oahu, Hawaii: Geological Society of America Bulletin, v. 58, p. 49–78.

Woollard, G.P., 1951, A gravity reconnaissance of the Island of Oahu: American Geophysical Union Transactions, v. 32, p. 358–368.

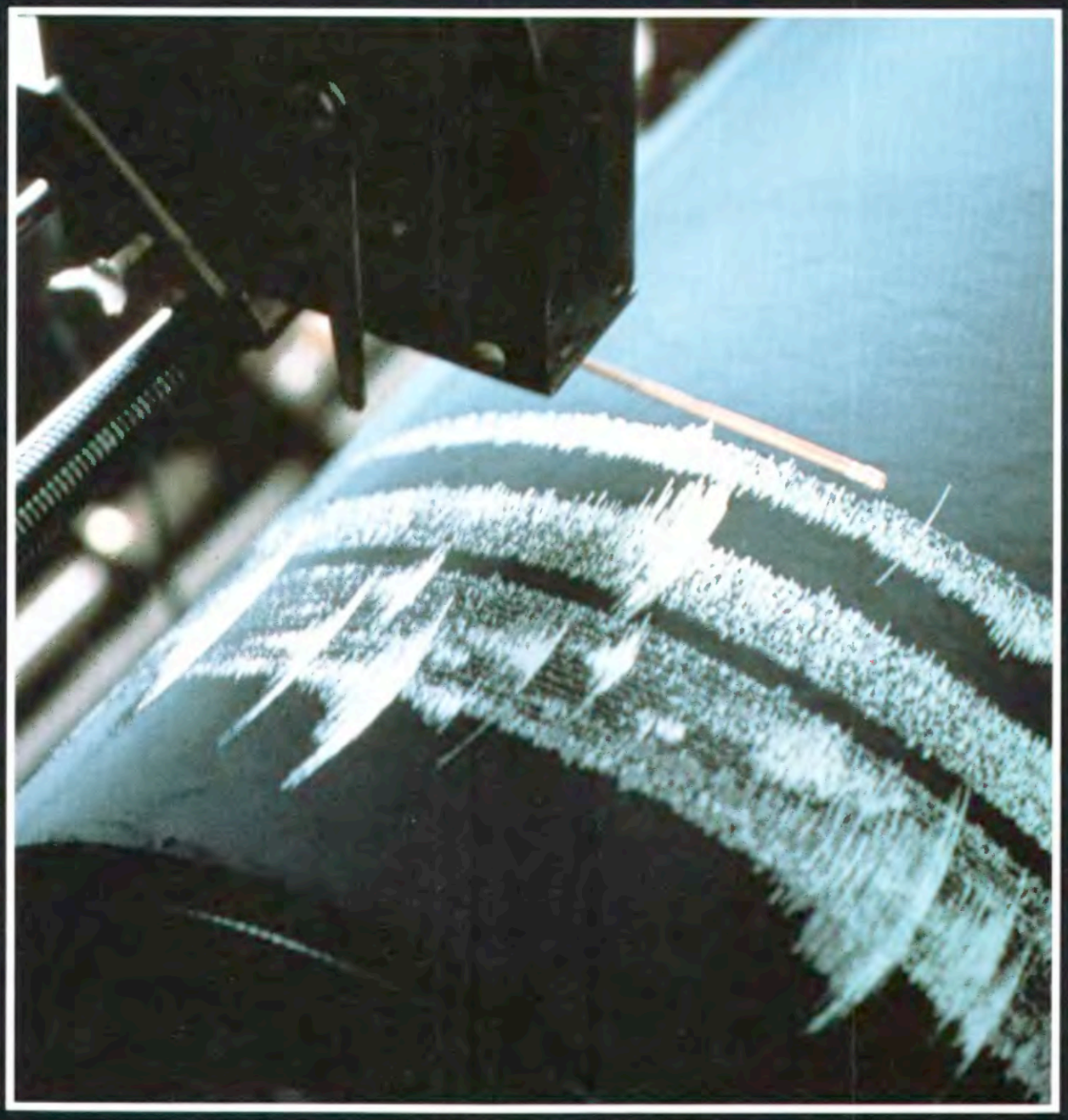

Earthquake swarm and volcanic tremor being recorded on seismograph at Hawaiian Volcano Observatory, November 16, 1979. Photograph by R.W. Decker.

# DYNAMICS

Much of the present research on Hawaiian volcanoes is directed towards understanding how they work. It is appropriate, therefore, that this section on dynamics is the longest in the two volumes on Volcanism in Hawaii.

The eighteen chapters in this section address questions about the physical and chemical dynamics of magma formation, accumulation, ascent, storage, intrusion, and eruption. These questions cannot be investigated in isolation, and many of the papers in the section on petrogenesis and volcanic gases and in that on structure are closely related.

An overview chapter is followed by three chapters on earthquakes and volcanic tremor, four chapters on ground-surface deformation related to magma movements, and one on the geoelectric contrast between the crust and molten core of a lava lake. Chapter 51 points out the resemblance of the cyclical behavior of Hawaiian volcanoes to patterns predicted by attractor dynamics, a new conceptual approach to understanding the interactions in complex systems. The next two chapters delve into the rock mechanics that constrain the physical dynamics of Hawaiian volcanoes, and chapters 54 through 56 consider the thermodynamics and geochemistry of the magmatic-geothermal systems formed on active Hawaiian volcanoes. The last three chapters in this section discuss the flow dynamics of Hawaiian lava.

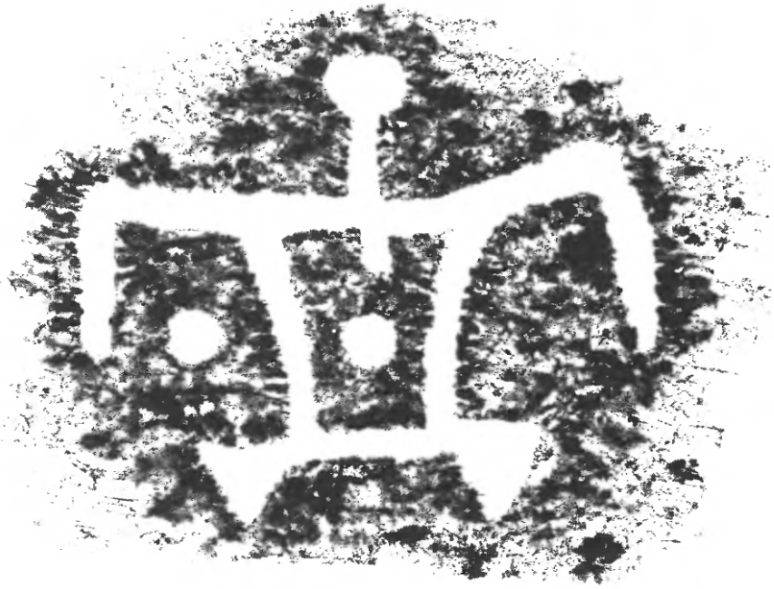

**Turtle**
**Hawaiian Petroglyph**
**Puuloa, Hawaii**

# DYNAMICS OF HAWAIIAN VOLCANOES: AN OVERVIEW

*By* Robert W. Decker

## ABSTRACT

**Eaton and Murata's cross section of Kilauea Volcano, published in 1960 (Science,v. 132), remains the basic model of how Hawaiian volcanoes work. Magma forms by partial melting of mantle rock at depths between 60 and 170 km in a specific area of mantle known as the Hawaiian hot spot. The melt accumulates by migrating through small fractures, or by shear coalescense, into volumes large enough to ascend. The ascensive pressure is caused by the greater density of the rocks surrounding and overlying the magma. Ascent through the lithosphere occurs in discontinuous conduits that are generated by magmafracting. Apparently there are enough of these ascensive conduits so that magma is supplied to a shallow reservoir system 3–7 km beneath the summit caldera at rates that vary by less than an order of magnitude over time scales of months to decades. When the shallow magma reservoir fills to about lithostatic pressure, magmafracting emplaces dikes upward or laterally into the rift zones; those dikes that reach the surface erupt. Eruptions at high-volume rates rapidly reduce the pressure in the shallow magma reservoir and are of brief duration. Long-lived eruptions occur at low-volume rates and are sustained by the resupply of magma from depth. Lava fountains are produced by the rapid expansion of magmatic gases—$H_2O$, $CO_2$, and $SO_2$—at near-surface pressures. Major caldera collapses, sometimes associated with explosive eruptions, occur repeatedly at intervals of a few thousand years. One probable cause of these collapses is intrusion or eruption on the submarine rifts which produce major draindown of the shallow reservoir system. The newly formed volcanic islands subside at exponentially decreasing rates as the Pacific plate moves slowly northwestward past the Hawaiian hot spot.**

## INTRODUCTION

The literature on Hawaiian volcanism contains many descriptions of eruptions, but fewer interpretations of the dynamic processes that form magma and that cause it to ascend and erupt at the surface. Present studies, however, are concentrating on obtaining the necessary surface and subsurface data to compare with inferences from dynamic models of how Hawaiian volcanoes work. Those models, constrained by geological, geophysical, and geochemical data, are beginning to give a glimpse of the complex, hidden processes that occur beneath Kilauea and Mauna Loa Volcanoes. The purpose of this chapter is to synthesize these studies into a comprehensive model of the dynamics of Hawaiian volcanoes, particularly during their stage of vigorous growth.

The earliest recorded speculations on the subsurface structure and dynamics of Hawaiian volcanoes appear in the journal of William Ellis, a Christian missionary from England, who walked around the Island of Hawaii in 1823. While visiting Kilauea caldera, Ellis (1827, p. 171) noted that his Hawaiian guides told him about many eruptions on the flanks of Kilauea "on which occasions they supposed Pele went by a road under ground from her house in the crater to the shore." Present-day interpretations of rift-zone eruptions on the flanks of Kilauea are considerably more detailed, but in essence are the same as this "road under ground" of the native Hawaiians.

Ellis goes on to speculate about the dynamic processes beneath the active lava lakes that he saw in Kilauea caldera (p. 181): "Perforated with innumerable apertures in the shape of craters, the island forms a hollow cone over one vast furnace." This concept has not survived as well as Pele's road.

J.D. Dana (1890, p. 174–175), geologist with the U.S. Exploring Expedition to Hawaii in 1840, was the first to distinguish clearly the more or less steady ascensive force of magma at depth from the rapid fountaining of erupting lava that is caused by the sudden boiling off of gases at near-surface pressures. Dana (1895, p. 303) attributed the ascensive force in the volcano to "1) the expansive action of moisture from the deep-seated source of the lavas; and 2) the gravitational pressure of the contracting crust of the globe, forcing up the lavas* * *." He noted that the top of the Kilauea magma column had risen 360 feet in 6 years. Both of Dana's interpretations are close to, but not quite the same as, present interpretations. These two causes of ascensive force could now be reworded as follows: (1) The expansive action of fluids, particularly $CO_2$, from the deep-seated source of the lava, forming separate phases; and (2) the gravitational pressure of the overlying, heavier crust and upper mantle of the globe, forcing up the lighter lava.

Eaton and Murata (1960) were the first to draw a dynamic cross section of a typical Hawaiian volcano (fig. 42.1). In their model, magma moves upward by density contrast, more or less continuously, through conduits from the top of a source region at 60 km depth to a storage reservoir at a depth of 3–7 km. Intermittent eruptions from the shallow magma reservoir to the surface occur through newly formed fractures breaking upward to the caldera or laterally into the rift zones. The eruption rates from the shallow magma reservoir to the surface are often much higher than the rate of resupply from depth, and thus the eruptions tend to be self-limiting and intermittent. Sometimes low-volume-rate eruptions form active lava lakes in the caldera, presumably sustained by the resupply rate. Such more or less steady-state eruptions can last for months or years. This overall model fits well with the seismic data and observed ground-surface deformation on Kilauea Volcano, and it is still the

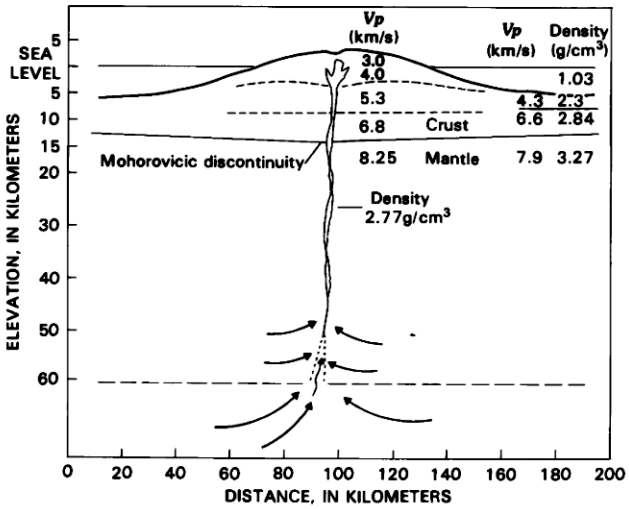


FIGURE 42.1.—Schematic cross section through idealized Hawaiian volcano. Magma from a source about 60 km deep streams up through conduits and collects in shallow reservoir beneath caldera. Occasional discharge of lava from shallow reservoir through dikes that split to surface constitute eruptions. Note slight depression of Mohorovicic discontinuity beneath volcano. $V_p$ is the velocity of seismic $P$-waves. Modified from Eaton and Murata (1960).

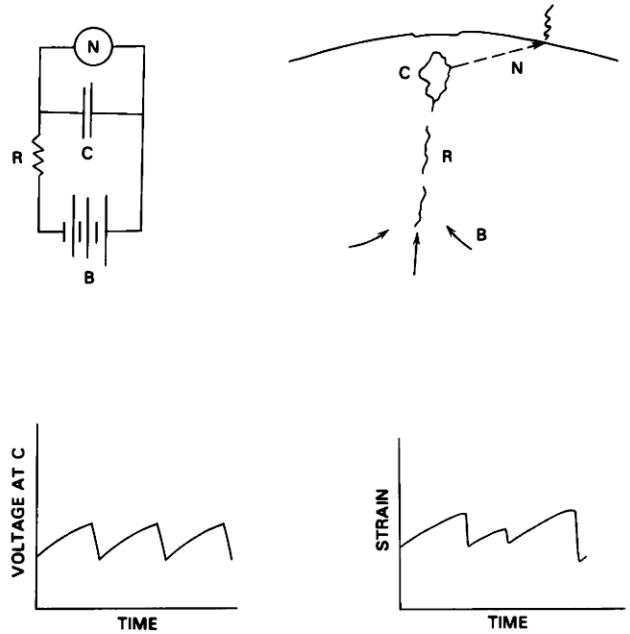


FIGURE 42.2.—Electrical analog of dynamics of Kilauea Volcano. Electrical circuit is a battery (B) charging a condenser (C) through a resistor (R). When voltage across condenser reaches firing voltage of neon bulb (N), bulb winks on until voltage drops below sustaining level. In Kilauea deep ascensive force of magma represents battery, conduits from deep source to shallow magma reservoir form resistor, and shallow magma reservoir is condenser. Dike breaking to surface or intruding a rift zone reduces magma pressure (voltage) and is equivalent to neon bulb. Variation of strain in volcanic edifice is similar to variation of voltage in circuit, but less regular in its cycles.

basic concept of how Hawaiian volcanoes work.

Building on Eaton and Murata's model, Decker (1968) and Shimozuru (1981) have noted that the fluid and fracture dynamics of this model are analogous to the storage and discharge of electricity in a resistance-capacitance (RC) circuit (fig. 42.2). The ascensive pressure is analogous to a battery, the resistance to fluid flow through the system is analogous to a network of electrical resistors—within the battery, between the battery and the condenser, and between the condenser and the surface—and the shallow magma reservoir is analogous to a condenser. If the resistance between the condenser and the surface operates in two modes—almost infinite resistance or very low resistance, as in a neon bulb—then intermittent discharges of the condenser in the electrical model will be analogous to eruptions.

Although this electrical analog model is greatly oversimplified, it has the advantage of allowing thought experiments about what happens when changes occur in the ascensive pressure, the resistance to flow, or the volume of the shallow magma reservoir, either separately or in combination. For example, if the ascensive pressure were doubled, the repose time between eruptions would be halved and long-term lava output would double, but the individual eruptions would have the same volume as before. Increasing the capacity of the shallow magma reservoir would increase the repose time between eruptions, but the eruptions would be of proportionately greater volume. Changing the breakdown strength of the rocks between the shallow magma chamber and the surface—analogous to changing neon bulbs—could change both the repose time between eruptions and the volume of the eruptions. If the values of the various components are computed or assumed, then their quantitative interrelation can be calculated using well-established electrical or hydraulic equations.

Realistic models of the structure and dynamics of Hawaiian volcanoes are strongly dependent on the physical properties of magma and its host rocks. Some of these properties vary greatly, and the numerical values of others are only poorly known. Refined models are therefore dependent on improved knowledge of these physical properties.

Attempting to understand the hidden dynamics of an active volcano calls upon the most eclectic abilities of volcanologists. A valid dynamic model must explain the geologic and eruptive history of the volcano, as well as the seismic, deformational, and electromagnetic changes that occur before, during, and after eruptions. In addition it must explain the composition and changes in composition of the solid, liquid, and gaseous products emitted from the volcano. Besides all this, the model must be consistent with the laws of physics and chemistry and, if possible, satisfy the philosophy of Ockham's Razor—that is, not to be unnecessarily complicated. Such a task clearly requires a team effort. This article is therefore a selected synthesis of the data and interpretations of many students of Hawaiian volcanism.

**ACKNOWLEDGMENTS**

Jerry Eaton, Howard Powers, and Gordon Eaton were my kind hosts and patient teachers while I was a guest investigator at the Hawaiian Volcano Observatory (HVO) in the 1960's and 1970's. Robert Tilling offered me the opportunity of returning to HVO as Scientist in Charge, and my fine colleagues at HVO continued my education during my tenure there from 1979 to 1984. Jerry Eaton, Dan Dzurisin, and Barbara Decker gently but thoroughly reviewed earlier versions of this chapter. My warmest thanks to all these fellow students of volcanoes.

## MAGMA FORMATION

When, where, and how does magma form? There are no clear answers to these questions, but there is no lack of hypotheses. Since volcanism has been a persistent geologic process for billions of years, it seems reasonable to assume that magma has continued to form during most of the Earth's history. A counter argument could be that magma only formed in the early history of the Earth, has always been present within the Earth, and has been released slowly enough to stretch out volcanism for billions of years. This alternative has not been proven wrong, but since most geologic processes work at levels close to equilibrium, it is difficult to accept a process that could be restrained for such enormous periods of time. For this reason it is assumed that magma is forming within the Earth at the present time.

There is reasonably good agreement about where basaltic magma is formed. Yoder (1976) carefully reviewed the geophysical and geochemical evidence and concluded that basaltic magma may be generated in broad regions generally at depths of 50–170 km; in more restricted environments the source of basaltic magma may be as deep as 300–400 km. Eaton and Murata (1960) concluded on the basis of depths of earthquake sources that the magma source region beneath Hawaii has its top at a depth of 60 km, but they were not able to infer how far the source region may extend below this level. Wright's model (1984) for the origin of Hawaiian tholeiite proposes a depth of formation ranging from 60 to 90 km. Recent studies by Anderson and Dziewonski (1984) using seismic tomography indicate an anomalously slow (hot) zone in the Earth's mantle at a depth of 350 km over a broad area south of Hawaii. Mantle flow in this area is apparently upward. At shallower depths in the upper mantle, the anisotropy of Rayleigh wave velocity suggests horizontal flow in a southeastward direction beneath Hawaii. As a working hypothesis, it is assumed that magma is currently being formed beneath Hawaii at some depth interval between 60 and 170 km.

The question of how magma forms is even more complex than when or where it forms. From what rock material is it melted, and what is the source of heat? Yoder (1976) thinks that the best candidate for the parent rock of basaltic liquids is garnet peridotite, a crystalline aggregate of olivine, orthopyroxene, clinopyroxene, and garnet. He accepts this source—tentatively—and lists the following features of garnet peridotite as supportive evidence (Yoder, 1976, p. 42):

(1) Its occurrences are appropriate to deep-seated environments of origin.

(2) Its close compositional relation to meteorites supports a derivation from material accumulated in the primordial Earth.

(3) Partial melts of natural samples at high pressure have basaltic compositions.

(4) The mineral asmblage was found experimentally to be stable at high pressure and temperature.

(5) It has appropriate density and seismic velocity.

Wright (1984) prefers a source rock for Hawaiian tholeiite magma composed of lherzolite, a crystalline aggregate of olivine, orthopyroxene, and clinopyroxene, with some other constituents (amphibole, nephelinite, ilmenite, apatite, and ferrous iron oxide) added from depth.

The source of heat to melt a basaltic liquid from a crystalline rock aggregate must be either internal or external to the rock being melted. If it is external, some thermal process such as conduction, convection, or radiation must transport heat into the source region. If it is internal, the heat must be generated by some process such as radioactive decay or mechanical friction, unless it is heat that is already present in the rock. In the latter case, some other process must be called upon to lower the melting temperature of the basaltic liquids, such as lowering the confining pressure or introducing fluxing elements or compounds into the source region.

The problem is not a lack of possibilities, but too many permutations and combinations to choose among. Yoder (1976, p. 60–61) lists 21 proposed mechanisms to melt rock into magma. Several of these are not tenable for Hawaii; for example, those mechanisms that require subsidence of continental crustal layers of the Earth by 5 km or more (Hess, 1960). Among the more reasonable mechanisms for generating Hawaiian magmas are the following (in alphabetical order by author):

(1) Melting caused by the friction of shear strain released from stored elastic strain energy along a propagating crack (Griggs and Baker, 1969).

(2) Internal radioactive heat production (Joly, 1909).

(3) Conductive heat trapping caused by changes in thermal conductivity with temperature and pressure (McBirney, 1963).

(4) Rise of the source material as a buoyant diapir, thus reducing confining pressure and melting temperature (Ramberg, 1972).

(5) Melting caused by the friction of viscous strain. In this thermal feedback or runaway model, constant shear stress on a crystalline rock at its melting temperature causes small viscous strains that increase the temperature. This temperature increase lowers the viscosity, increases the strain rate, and thus further increases the temperature (Shaw, 1973).

(6) Melting caused by the friction of shear strains associated with tidal energy dissipated in the solid Earth (Shaw, 1970).

(7) Rise of the source region by solid-state convection, thus reducing the confining pressure and melting temperature (Verhoogen, 1954).

(8) Reduction in melting temperature of the basaltic liquids by addition of volatiles ($H_2O$, $CO_2$) to the parent-rock source region (Yoder and Tilley, 1962).

Radioactive uranium, potassium, and thorium isotopes are

apparently ubiquitous in upper-mantle rocks but low in amount. Hawaiian lava exhibits no abnormal content of these radioactive isotopes, so radioactive heating (mechanism 2) does not seem to be a principal cause of the high rate of Hawaiian magma production. However, on a global basis and over tens to hundreds of millions of years, radioactive heat production probably contributes significantly to heating the rocks of the upper mantle to near melting temperatures.

Choosing among the 7 remaining mechanisms to explain Hawaiian magma generation depends in part on tectonic prejudices. Those who favor the hot-spot hypothesis (chapter 1, part I) will probably favor the diapiric rise (4) and (or) volatile transfer (8) mechanisms, while those who favor a propagating fracture may prefer the stored elastic energy release (1) and (or) the conductive heat trap (3) mechanisms. Wright's model (1984) combines a thermal plume to drive up the added chemical elements from depth and thermal feedback to provide the principal heat of melting. It is probably best to say that the melting problem is not resolved at this time. Detailed seismic tomography studies may soon provide more definite evidence on this important but difficult subject of the heat source of Hawaiian magma.

In all the proposed mechanisms for melting crystalline rock to form magma, the enthalpy of melting is about $4.2–5.2 \times 10^5$ J/kg (100–125 cal/g). This heat of fusion has a major buffering effect on the temperature and rate of melting or freezing in the source region, implying that basaltic magmas of similar composition at similar depths of formation are nearly isothermal. At 60-km depth, Hawaiian tholeiite magma has a calculated formation temperature of 1,350–1,400 °C (T.L. Wright, oral commun., 1985). Measured temperatures of erupting Hawaiian lava are in the range of 1,100–1,200 °C.

## MAGMA ACCUMULATION AND ASCENT

Melting a garnet peridotite or lherzolite mantle involves a 10–15 percent volume increase from the crystal aggregate to the basaltic fluid. A change from solid to 30 percent partial melt would thus bring about a 3–5 percent increase in the bulk volume of the rock-liquid mixture.

In experimental studies on crystalline silicate aggregates, the first melt forms films between mineral grains that then unite into a liquid-bonded aggregate—a network of melt coating the mineral grains with a thin film of fluid (Yoder, 1976, p. 164-165). The volume of these molten films can reach 10 percent of the mineral-liquid mixture. As the volume of melt increases, deformation from internal volume expansion and (or) interaction with external stresses takes on an increasingly important role.

Extension fractures perpendicular to the direction of the least compressive stress can form even at mantle depths if the pore-fluid pressure exceeds the tensile strength of the rock. Shaw (1980) found that these conditions are probable in the thermal and stress domains estimated to occur in the asthenosphere beneath Hawaii. His model of melt accumulation and ascent is shown in figure 42.3; in it the accumulation fractures are subhorizontal (sills) if the least compressive stress is vertical, or they are nearly vertical fractures (dikes) if the intermediate compressive stress is vertical. Because of small transient changes in the shear stresses, pore pressures, or gravitational load on this deep region where the three major compressive stresses are nearly but not quite equal, Shaw thinks both of the above conditions will occur and will generate a set of planar melt lenses oriented at 50°–90° to one another, with intersections parallel to the general direction of maximum compressive stress. These intersections are shown schematically in figure 42.3 by the broken horizontal line segments within the asthenosphere. The inferred lenses of melt accumulation would tend to lie both (vertically) in the plane of the cross section and (horizontally) perpendicular to it. Since there is no seismic evidence for major brittle fracturing in the asthenosphere beneath Hawaii, these proposed cracks would have to be small or form slowly.

An alternative way of expressing the fracture-accumulation hypothesis is shearing of the films of melt into progressively larger pockets of molten rock. Shaw (1969, p. 533) refers to the melt fraction as being "kneaded from the crystalline source"; Weertman (1972), on the basis of observed bubble coalescense in deforming glacial ice, believes a similar process may occur during shear creep in partially melted rock. Spera (1980) points out that the rate of melt segregation is governed by the rheology of the rock-liquid mush and by the balance among buoyancy, pressure, and viscous forces. He also notes that he can estimate buoyancy reasonably well and stress gradients to within an order of magnitude, but viscous forces and permeabilities only poorly. Nevertheless, Spera, on the basis of correlation to rigid porous-media systems, estimates that the segregation rate is highly dependent on the melt fraction; in dimensionless terms it would be 6,500 times larger for a 30-percent partial melt than for a 2-percent partial melt.

Whatever the mechanism of melt segregation is beneath Hawaii, it must be rapid enough throughout the source volume to provide about 0.1 $km^3$/yr of magma to Kilauea Volcano for time periods longer than a few decades (Swanson, 1972; Dzurisin and others, 1984) and a roughly similar but less well known amount to Mauna Loa Volcano. Assuming that the source region is approximately cylindrical, as wide as the island (100 km), and 30 km thick, the source volume would be approximately $2.5 \times 10^5$ $km^3$. Using a partial melt of 30–40 percent (Wright and others, 1979; Wright, 1984), the calculated average fraction of the total melt delivered to shallow levels in Hawaii on a yearly basis is only $2–3 \times 10^{-6}$. About $2.5 \times 10^{17}$ J ($6 \times 10^{16}$ cal) of heat of fusion are needed by this slowly evolving source region on a yearly basis to maintain a steady-state supply rate of 0.2 $km^3$/yr. Under the above assumptions, this translates into about $3.2 \times 10^{-5}$ J/$m^3$/s ($7.7 \times 10^{-12}$ cal/$cm^3$/s), an amount of heat nearly $10^3$ times greater than the heat production from radioactivity in an average garnet peridotite. These numbers assume that the melting and segregation processes are spread evenly throughout the source region; it is likely that these processes in fact become more concentrated near the apex of the source region.

The mechanism of the ascent of magma through the more rigid rocks of the lithosphere must be both qualitatively and quantitatively

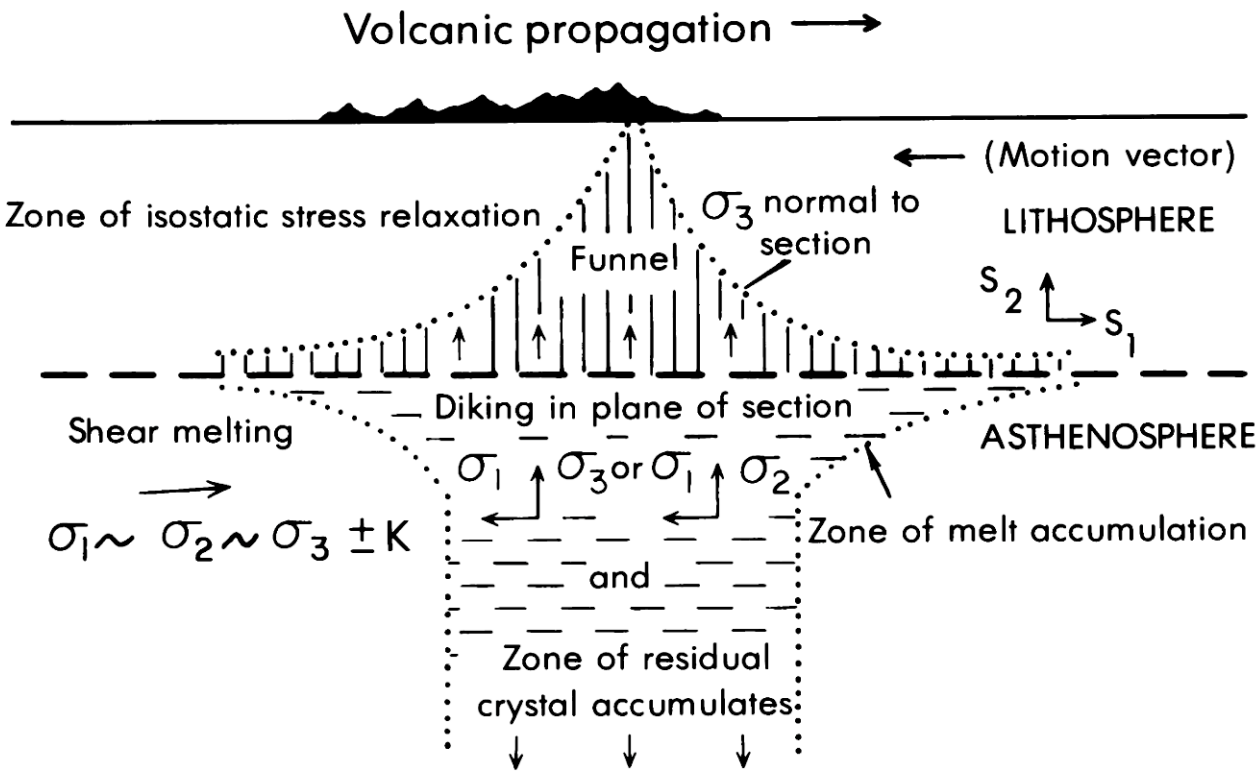


FIGURE 42.3.—Schematic longitudinal section showing stress domains beneath active Hawaiian volcanoes. S, total normal stress acting at a point in rock; σ, effective normal stress acting in rock containing an interconnected fluid phase. Subscripts 1, 2, and 3 refer to maximum, intermediate, and minimum principal stresses, respectively. K, tensile strength. In zone of melt accumulation, fractures would be either nearly vertical in plane of section, or nearly horizontal in plane perpendicular to section. In ascent funnel, fractures would be nearly vertical in plane of section. Modified from Shaw (1980).

different from that of its segregation and ascent in the source region. The tensile strength of the lithospheric host rocks is greater than that in the asthenosphere, although it may become weakened by heating from ascending magma. Deviatoric stresses in the lithosphere may be much greater than in the asthenosphere, and beneath Hawaii the lithosphere is seismically active whereas the asthenosphere is apparently not.

Magma is pushed upward into and through the lithosphere by the pressure gradient caused by gravity acting on the density difference between lighter magma and heavier host rocks. This explanation of the ascensive force was first clearly proposed by Daly (1914, p. 183) who suggested "that magmatic eruption is, in the first instance, a hydrostatic phenomenon." Daly later became even more convinced. His second edition (1933, p. 247) states "The leading cause for the ascent of primary magma, assumed to move up abyssal fissures, is naturally found in the weight of the adjacent crust." Almost no one would now disagree with this explanation of the ascensive force; the origin of the abyssal fissures, however, is much more debatable.

Does Hawaiian magma passively rise through conduits in the lithosphere generated by external stresses, or does it actively generate or help to generate these conduits? Turcotte and Oxburgh (1978) propose that deformation of the Pacific plate in adjustment to thermal and Earth-curvature changes may cause a major propagating intraplate fracture. They suggest that magma leaking up this propagating fracture has progressively formed the Hawaiian volcanic chain. Since Wilson (1963) proposed the hot-spot origin for the Hawaiian Islands, most other researchers believe the melting anomaly is fixed in position and that plate motion over the hot spot causes the age progression of the Hawaiian chain (Dalrymple and others, 1973; McDougall, 1979). Implicit in the hot-spot hypothesis is the idea that magma in sufficient quantities can somehow force itself upwards through the lithosphere. Possibly the stresses proposed by Turcotte and Oxburgh (1978) may assist in this magmafracting process.

The concept that magma can actively fracture its way upward is strengthened by the distribution of earthquake hypocenters beneath Kilauea Volcano (see chapter 43). Over periods of years this earthquake distribution outlines a zone of active fracturing in the lithosphere that is shaped like a steeply dipping inverted funnel reaching generally to a depth of 45 km and occasionally to nearly 60 km (Eaton, 1962). Close association of the earthquakes with the inferred conduit path of the rising magma, rather than with the site of

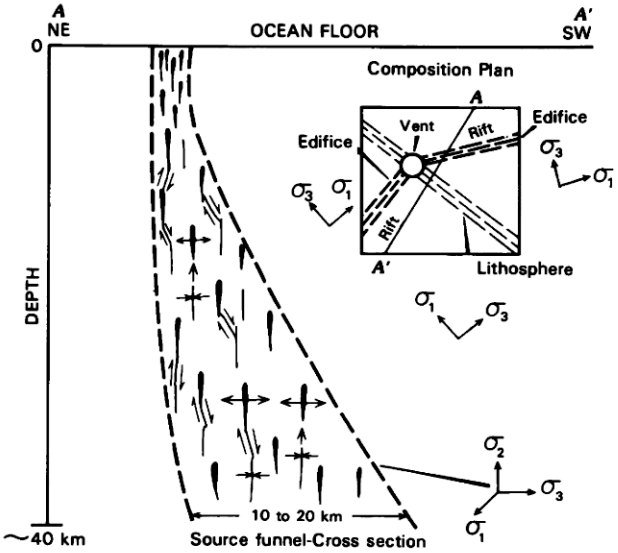


FIGURE 42.4.—Schematic cross section of lithosphere beneath Kilauea Volcano showing magma ascent funnel as region of extensional fractures and magma batches migrating upward from asthenosphere. Inset shows simplified plan of rift zones. Stress orientations and dike orientations have different directions in lithosphere and in edifice of volcano. Symbols have same meaning as in figure 42.3. Modified from Shaw (1980).

the postulated intraplate fracture, indicates that the magma plays an active role in the formation of the conduits.

Shaw (1980) proposes that magma is injected into the lithosphere by a process analogous to hydraulic fracturing of the wall rocks in a borehole by increasing fluid pressure. The normal compressive stresses in the buried host rock can be balanced or exceeded by the magma pressure to produce zero or even negative effective stresses. When these effective stresses equal or exceed the tensile strength of the rock, extensional fractures form perpendicular to the direction of least compressive stress (figure 42.4). Yoder (1976, p. 179) has called this process magmafracting. In this view most of the earthquakes beneath Hawaii are the effect, not the cause, of the transport of magma.

As the vertical dikes of magma shown in figure 42.4 intermittently force their way upward by brittle fracture, they must be resupplied with more magma from the source region, or the trailing edge of the rising dike will close off because of the recovering compressive stresses (Pollard, 1976). Hill (1977) shows that shear stresses will cause the active dike system to become a complicated network of dike-like lenses connected by faults. Movement of magma within one of the dikes will change the local pattern of deviatoric and effective stresses, and this may trigger new fractures or movements on the existing fracture network. Hill uses this model to explain earthquake swarms in Hawaii, and Shaw calls such resulting swarms failure cascades.

Shaw (1980) then inverts the seismic data from Hawaii in order to estimate the volume and magma fraction of the active intrusion zone in the lithosphere located between the deep source region in the asthenosphere and the shallow magma-reservoir system beneath Kilauea Volcano. His calculations suggest that this zone has a volume of about $10^3$ km$^3$ and a melt fraction between $10^{-5}$ and $10^{-4}$ (that is, 0.01–0.1 km$^3$ of magma). For continuity, the 0.1-km$^3$ yearly magma supply to Kilauea would thereby have an average residence time of only a month to a year while rising through this zone. Magma ascent may appear relatively continuous over time spans of months to years, but can be quite variable at time scales of minutes to days. Several batches of lava may be moving upward in independent spurts. Some batches may rise 30 km in a few weeks, while other batches may never reach shallow levels. The varying rate of inflation of the summit region of Kilauea, as measured by continuously recording tiltmeters, supports this model of semicontinuous rise of magma into the shallow reservoir system.

## MAGMA STORAGE

Batches of Hawaiian magma rising through the lithosphere apparently take various paths and various amounts of time in their ascent, but most of the magma supplying Kilauea Volcano during the past several decades has paused in a shallow magma storage system before erupting to the surface.

Mogi (1958), using data from Wilson (1935), first identified the presence and depth of this shallow magma reservoir by analysis of surface uplift and subsidence of the summit and upper flanks of Kilauea. Using elastic-deformation theory he identified two major sites of pressure and (or) volume change in the region beneath Kilauea caldera: one well-defined site at 4 km depth and another less well defined site at 25 km depth. Eaton (1962) rejected the deeper site as an apparent artifact of leveling-rod error in the long survey traverse from Hilo to the summit of Kilauea. Using additional level and tilt data, Eaton confirmed the shallow reservoir system and showed it on his schematic cross section (fig. 42.1) as an irregular vertical cylinder about 4 km wide and at 3–7 km depth beneath the summit of Kilauea.

Patterns of continuously recorded summit tilt over the past two decades (fig. 42.5) indicate that this shallow magma-reservoir system slowly inflates over periods of months to years during the intervals between eruptions and then rapidly deflates over periods of days to weeks during flank eruptions or lateral intrusions into the rift zones. Expansions and contractions of the caldera diameter by as much as a few meters accompany these inflations and deflations.

On many of the inflation cycles shown in figure 42.5, the rise of the summit shows a high rate of inflation immediately after a deflation event. This is followed by an exponentially decreasing rate of inflation, probably caused by the decreasing pressure gradient between the shallow magma-reservoir system and the sources of magma at greater depths and (or) by the increased leakage of magma into parts of the shallow magma reservoir away from the summit as the pressure in the shallow reservior system increases.

Considerable research has been done to attempt to define the depth, shape, and dynamic nature of the shallow magma-reservoir

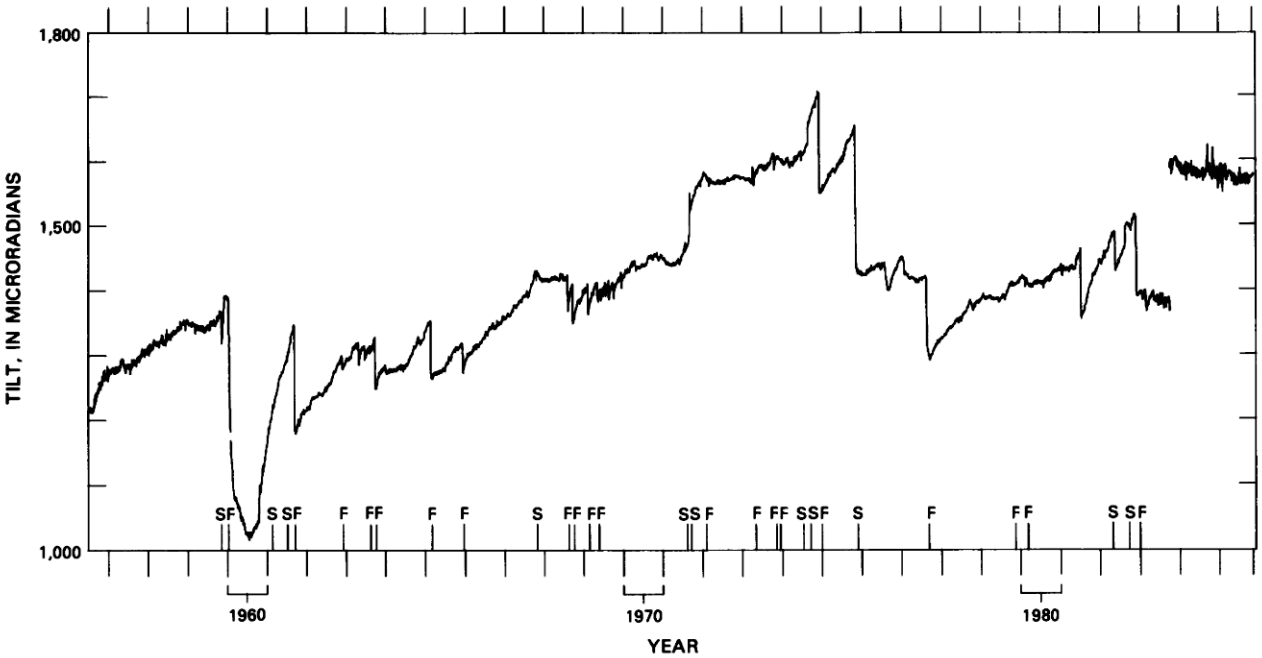


FIGURE 42.5.—Radial tilt at Hawaiian Volcano Observatory (HVO) on northwest rim of Kilauea caldera. Increasing tilt (radially outward) indicates inflation of summit region; decreasing tilt indicates deflation. One hundred microradians (μrad) of tilt at HVO indicates uplift of apex of summit bulge by about 50 cm. Rapid deflation marked by sharp drops in tilt represent volume change of bulge of about $3.3 \times 10^5$/μrad and pressure drop in shallow magma reservoir system of about 90 kPa/μrad. Magma is added slowly to shallow reservoir system from depth between eruptions and is rapidly removed during flank eruptions. Vertical lines indicate eruptions; S, summit eruptions; F, flank eruptions. Offset in tilt record in November 1983 was caused by $M$=6.6 earthquake (see Buchanan-Banks, chapter 44).

system. Geologic evidence from the location and form of Kilauea caldera and the pit craters along the upper east rift zone gives some indication of the subsurface location and lateral extent of the reservoir system. The caldera and pit craters have formed by collapse and thus identify the subsurface regions from which magma has been removed in such large quantities that the deflation cannot be accommodated by elastic or plastic surface deformation. Presumably these large removals occur during major eruptions from the distant submarine portions of the east rift zone. Interpretation of this morphological evidence indicates that the main magma reservoir beneath Kilauea caldera is (or was) roughly elliptical in plan—4 km NE.-SW. by 3 km NW.-SE.—and that about 3 $km^3$ of magma had been removed from the shallow subsurface reservoir to accommodate the volume of the caldera as it appeared in 1823.

The location of the pit craters is evidence that the magma storage system extends (or extended) southeast and then northeast beneath the upper east rift zone at least as far as Napau Crater, 15 km east of the summit caldera. The pit craters range in diameter and volume from 1 km and $77 \times 10^6$ $m^3$ (Makaopuhi before 1965) to 25 m and $90 \times 10^3$ $m^3$ (Devil's Throat); these figures put some limits on the width and volume of previous magma-storage regions beneath the east rift zone. There are only two small but deep pit craters along the southwest rift zone, indicating its subordinate role as a magma-storage region. Duffield and others (1982) conclude that the southwest rift zone breaks primarily because of accumulated movements of the east rift zone and to a lesser degree because of magmatic pressure from the summit reservoir system.

Geodetic data on the changing elevations and displacements of the deforming ground surface above the shallow magma-reservoir system have provided the best evidence on the dynamic nature of these magma storage chambers (Ryan and others, 1983). Detailed leveling of the summit area of Kilauea during an inflation period by Fiske and Kinoshita (1969) shows that the apex of inflation migrates over distances of 1–3 km within or near the caldera (figure 42.6). This shift of the center of inflation indicates that the summit reservoir is a plexus of interconnected storage zones. It can be compared to a Mickey Mouse balloon whose head inflates separately from the ears. Recording tiltmeters near HVO show that this migration of the apex of inflation or deflation during the larger cycles of magma influx and discharge has a repetitive pattern. After a major summit deflation, reinflation begins beneath the northern part of the caldera and then moves southward; during the next major deflation, the northern part of the caldera also subsides first and is quickly followed by the south end subsiding. This implies that the main input and withdrawal conduits for the summit reservoir plexus are on the north side of the general storage zone, which lies mainly beneath the south end of the caldera.

Dvorak and others (1983) analyzed the surface deformation

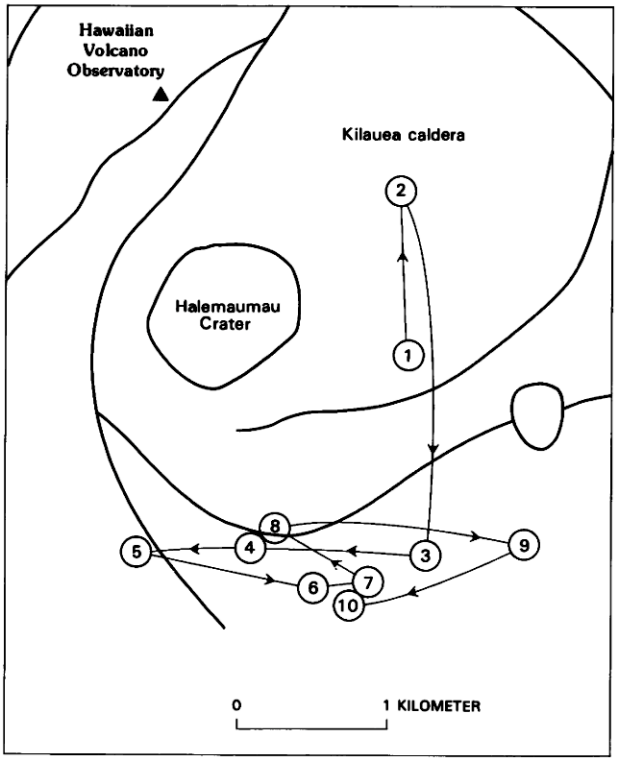


FIGURE 42.6.—Lateral shift of apex of uplift of inflating bulge at summit of Kilauea Volcano, modified from Fiske and Kinoshita (1969). Level surveys demonstrate shifting center of uplift: (1) January–July 1966; (2) July–October 1966; (3) October 1966–January 1967; (4) January–February 1967; (5) during February 1967; (6) February–May 1967; (7) May–June 1967; (8) June–July 1967; (9) July–September 1967; (10) September–October 1967. Position of Hawaiian Volcano Observatory and caldera and crater walls (heavy lines) shown for reference. Total uplift of the 10-km-wide bulge at its apex from January 1966 to October 1967 was approximately 70 cm; summit eruption of Kilauea began in November 1967.

data on Kilauea for the period 1966–1970 by simultaneous inversion of the level, tilt, and horizontal-distance measurements. They determined 32 centers of inflation and deflation, which clustered into two groups, one at the south end of Kilauea caldera at depths from 2–7 km and the other near Makaopuhi Crater on the east rift zone at depths of 3–8 km. Their results show that although the general deformation pattern is apparently elastic, there are departures from ideal elastic behavior. The differences between measured and calculated horizontal displacements indicates that a gradual north-south extension across the summit caldera occurred during 1966–1970.

Changes in gravity as much as a few tenths of a milligal accompany the inflation and deflation of the summit area of Kilauea (Johnson, chapter 47; Dzurisin and others, 1980; Jachens and Eaton, 1980). These changes are more complex than those expected from simple changes in elevation, and they indicate that mass that is not proportional to the volume changes can be both added to and removed from the summit region.

The volume of the shallow magma-reservoir system beneath Kilauea can be estimated by assuming that it is roughly spherical with a diameter similar to the 3.5-km diameter of the caldera. Because the magma-reservoir system is probably a network of magma bodies separated by screens of solid rock, only part of this 22-$km^3$ volume is estimated to be molten rock. A net volume of 11 $km^3$ would be the same as the estimate of magma-reservoir volume made by Wright (1984, p. 3238) on the basis of his summary analysis of the geodetic data.

Earthquake hypocenters also provide important and independent evidence on the shallow magma-reservoir system. Koyanagi and others (1976), on the basis of an aseismic zone largely surrounded by an envelope of seismic sources beneath Kilauea caldera, estimated that the zone of primary summit magma storage has a mean diameter of 3 km and extends from a depth of 3 km to 6 km beneath the surface. Their interpretation is based on the concept that the magma reservoir is too ductile to produce earthquake-generating fractures, whereas the rocks above and around the magma storage zone respond to inflation and deflation of the magma reservoir by brittle fracturing.

Ryan and others (1981) expanded this approach and produced a detailed model of Kilauea's magma-reservoir system from the surface to a depth of 15 km (fig. 42.7). Their model has a primary conduit extending vertically beneath the south end of the caldera, an upper-east-rift-zone pipe extending vertically through depths of 2–6 km beneath the Koae fault zone 1 km southwest of Kokoolau Crater, two horizontal ducts connecting the primary conduit and the pipe at depths of about 2 km and 6 km, and an extension of the upper horizontal duct beneath the east rift zone to the Mauna Ulu eruption site.

The main shallow magma-storage reservoir beneath Kilauea is apparently not completely aseismic. During times of rapid summit collapse and initial reinflation, swarms of peculiar microearthquakes have their apparent source within or very near the margins of the summit magma reservoir. These earthquakes generally have magnitudes less than 1 and have a low-frequency, emergent signal. They are difficult to locate because they are only recorded on a few seismographs near the summit of Kilauea and their onset signals are not clear enough to establish accurate arrival times. These swarms of long-period earthquakes are thought to be related to rapid readjustments among magma pockets within the plexus of the main magma reservoir.

The question of a deeper storage reservoir about 25 km beneath Kilauea remains unresolved. At present, deformation data are not accurate enough to detect small inflations and deflations of a zone that deep. The region at that depth is relatively aseismic, but no envelope of earthquake hypocenters surrounds it. Wright (1971) proposed a region of temporary accumulation of magma at a depth of 20–30 km beneath Kilauea to allow for removal of olivine and pyroxene (fig. 42.8) He called this region the intermediate staging area.

The dynamic nature of the well-established shallow magma-reservoir system beneath Kilauea is currently being investigated from several directions. Epp and others (1983) have shown that there is a

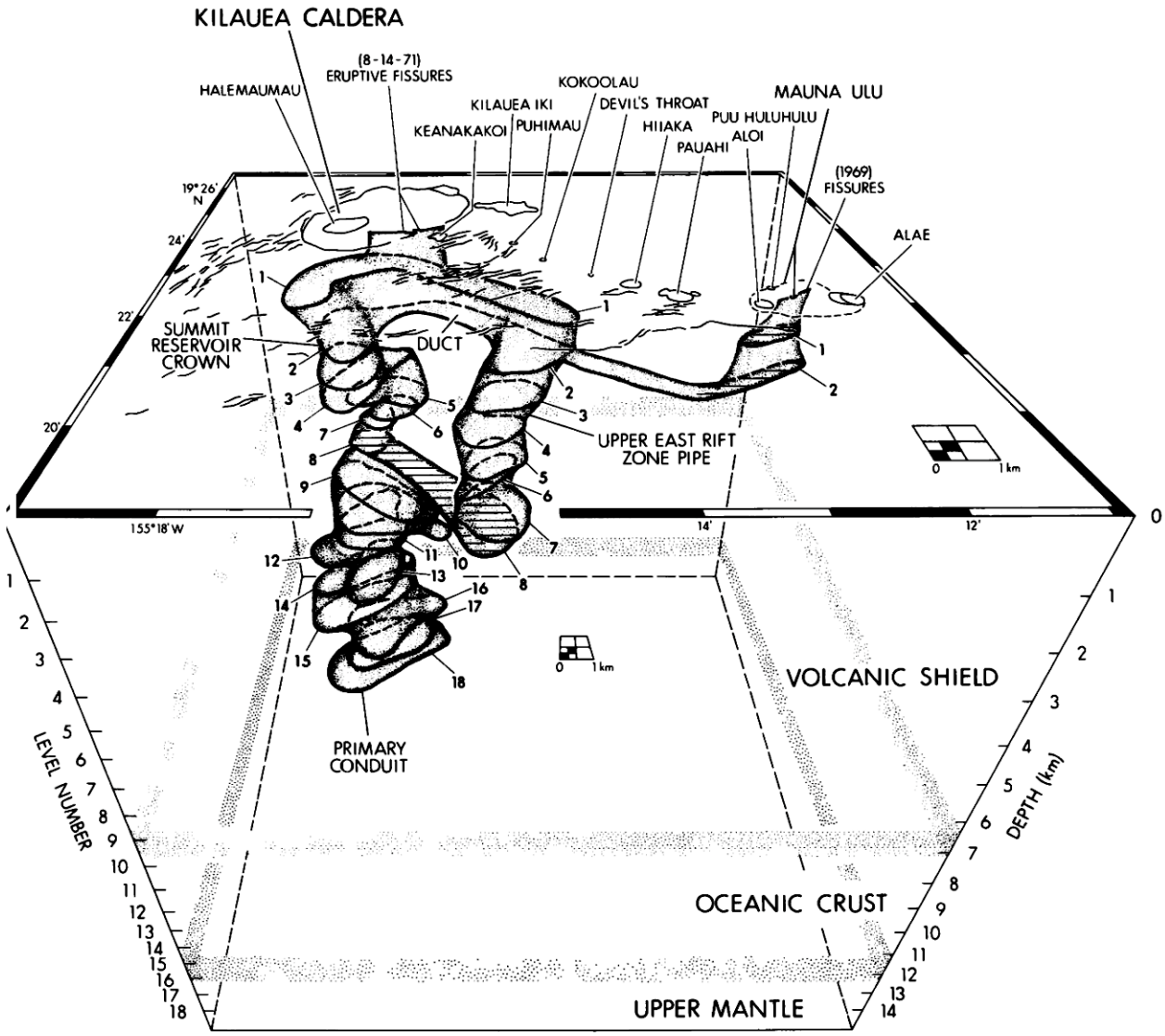


FIGURE 42.7.—Perspective view northward and downward into interior of Kilauea Volcano, from Ryan and others (1981). Magma conduits are defined by zones of earthquake hypocenters that surround them over periods of several years. Numbers on magma conduits represent horizontal sections at depths corresponding to level-number scale on left side.

strong linear correlation between the amount of summit deflation and the elevation of a flank eruption of short duration (fig. 42.9). Summit eruptions involve little or no deflation, whereas low-elevation flank eruptions are accompanied by large deflations. A simple explanation of this relation is that the magma pressure in the reservoir drops until it is balanced by the back pressure from the column of magma in the conduit from the reservoir to the surface. If this is the case, the magma pressure in the reservoir at the end of an eruption is simply the product of the average density of the magma column multiplied by the elevation difference and the gravitational constant. For example, assuming the average density of the magma column is 2.7 g/cm$^3$, the pressure in the magma reservoir 3 km below sea level beneath Kilauea following the eruption at Kapoho (30-m elevation) in 1960 would have been 83 MPa (830 bars); the lowest pressure in the magma reservoir during the past few decades. Since there are no major deflations associated with summit eruptions, there must be little or no pressure drop in the magma reservoir during these eruptions. The pressure of a magma column from the present floor of Kilauea caldera to a depth of 3 km below sea level would be 109 MPa. This difference of 26 MPa (109 minus 83) is the approxi-

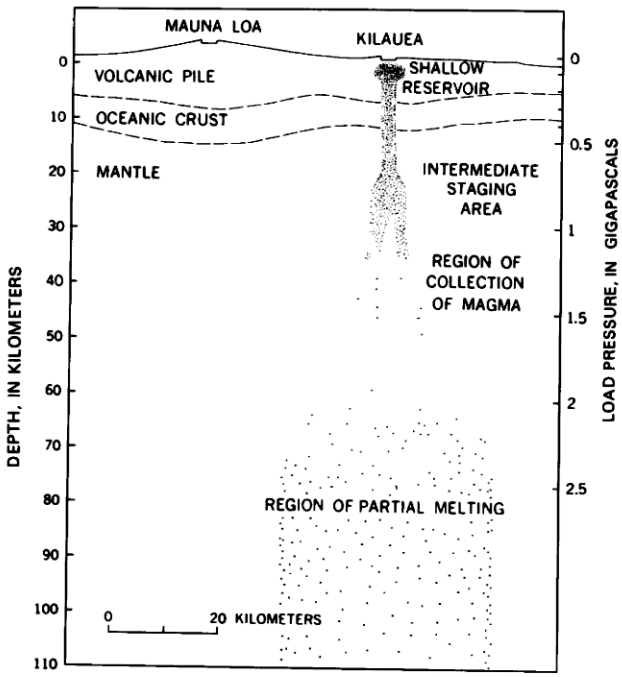


FIGURE 42.8.—Schematic cross section of Kilauea Volcano by Wright (1971) outlining regions of melting, transport, and storage of magma. Fractionation of magma occurs mainly in intermediate staging area and shallow reservoir, but also during its ascent from 60 to 30 km.

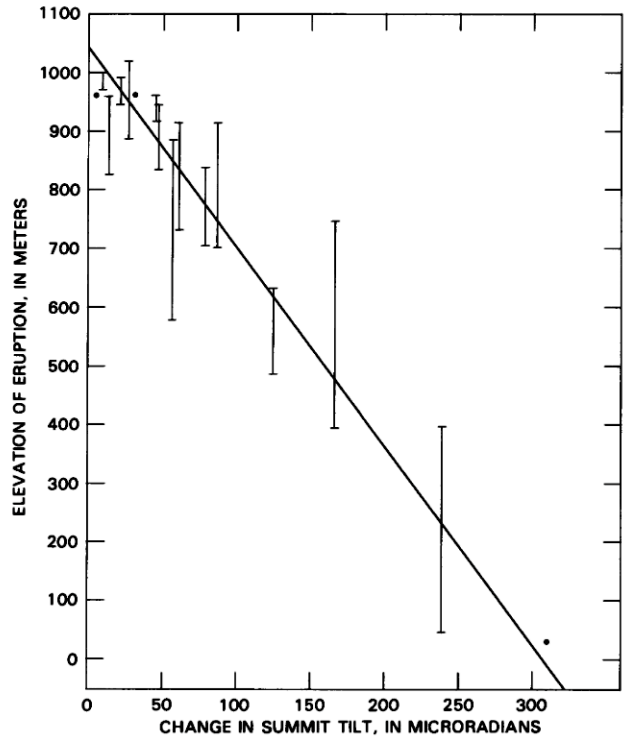


FIGURE 42.9.—Deflation measured by change in radial summit tilt at Kilauea Volcano versus elevation of associated vents during eruptions from 1955–1979. Bars indicate that eruptions occurred from fissures with considerable range in elevation. Linear relation of deflation and vent elevation indicates that pressure drop in summit magma reservoir is closely related to hydraulic head of magma at erupting vent. Modified from Epp and others (1983).

mate maximum range of pressure change in the shallow magma-reservoir system beneath Kilauea during the past few decades. In addition, the pressure change related to the amount of rapid deflation can be estimated from the data of Epp and others as 0.17 MPa (1.7 bars) per centimeter of summit deflation. Davis and others (1973, 1974, 1979) concluded from the absence of any marked piezomagnetic effects related to tilt changes at the summit of Kilauea that the volcano can support no large-scale pattern of shear stresses. They suggested that the rocks surrounding the shallow magma reservoir are of low shear strength and may behave in a plastic manner. Because the summit region of Kilauea probably does not behave in a perfectly elastic manner, particularly over time periods of months to years, slow inflations may represent volume changes more closely than pressure changes in the magma reservoir.

Magmafracting of the host rocks surrounding the magma reservoir appears to take place when the magma pressure reaches or slightly exceeds lithostatic pressure. This indicates low bulk tensile strength in the surrounding rocks.

The residence time for magma storage in the shallow reservoir system beneath Kilauea is easily estimated from the annual supply rate (0.11 $km^3$/yr, Swanson 1972; 0.086 $km^3$/yr, Dzurisin and others, 1984) and the volume of the reservoir system (11 $km^3$, Wright, 1984). The result, 100–120 yr, should be regarded as an average residence time. Some magma may crystallize in remote niches in the reservoir system and never erupt, while other magma batches, such as some of that which supplied the Kilauea Iki eruption in 1959, may spend only a small fraction of the average residence time in the magma reservoir system.

Another dynamic quality of shallow Hawaiian magma-reservoir systems on a vastly different time scale is their apparent ability to migrate upward as the volcano they supply grows in height. The submarine volcano Loihi is assumed to be in a youthful stage of growth, yet already a caldera and rift zones have apparently developed upon it (Klein, 1982a; Malahoff and others, 1982). This implies that it has probably developed a shallow magma-reservoir system. The depth to Loihi's magma reservoir is not known, but the summit area of Loihi is about 1 km below sea level. Mauna Loa Volcano, at the other extreme, has reached a height of 4,169 m, and recent studies by Decker and others (1983) indicate that it has a shallow magma-reservoir system similar to that beneath Kilauea. The source of inflation shown by deformation measurements before the 1984 eruption of Mauna Loa was at a depth of only 3 km beneath the summit. Thus, the top of the magma-reservoir system beneath Mauna Loa is at nearly the same elevation as the ground

surface at the summit of Kilauea. The long-term evolution of Hawaiian volcanoes apparently involves progressive upward remelting, stoping, and (or) shoving aside of the rocks overlying the shallow magma-reservoir systems.

## SHALLOW INTRUSIONS

As the shallow magma-reservoir system slowly inflates with magma added from depth, the increasing pressure and volume puts new stresses on the surrounding rocks. Sometimes the summit deflates slowly or remains level as magma moves almost aseismically into the open magma conduit of the upper and middle east rift zone of Kilauea. These slow intrusions or readjustments of the existing shallow magma-reservoir system involve volume flow rates of 1–10 $m^3/s$. When stresses reach the breaking strength of the host rocks surrounding the magma- reservoir system, fractures occur and a dike or sill is intruded upward or laterally into the shallow, brittle rocks of the volcanic edifice. These rapid intrusions are common at the summit and along the rift zones of Hawaiian volcanoes, and they occur at volume flow rates of $10^2$–$10^3$ $m^3/s$. During 1959–1980, 21 rapid intrusions without eruptions occurred at Kilauea Volcano and 25 other rapid intrusions led to eruptions (Klein, 1982b).

The orientation of rapid, shallow intrusions is controlled by the strength of the rocks and by ambient stresses generated by both internal magma pressure and external gravitational forces. Fiske and Jackson (1972) have shown that the topography of the earlier volcanoes in Hawaii affects the orientation of the rift zones of later forming, adjacent volcanoes (see Peterson and Moore, chapter 7, fig. 7.7). Rift zones form perpendicular to the direction of least compressive stress; once a topographic ridge has formed from numerous dike-fed eruptions along a rift zone, the gravitational slumping of this ridge reinforces the least compressive stress in a direction perpendicular to the ridge. The name Mauna Loa means long mountain, and this great shield volcano is markedly elongated by the gently-sloping ridges along its northeast and southwest rift zones. Kilauea Volcano is younger than Mauna Loa Volcano and inherited the gravitational stress system on the southeast flank of Mauna Loa. Kilauea thus developed a principal east rift zone and subsidiary southwest rift zone.

A typical rapid intrusion into a rift zone of Kilauea Volcano is characterized by a swarm of small earthquakes occurring at rates of 2–4 events per minute that lasts for a few hours to a few days. The sources of these earthquakes are concentrated at 2- to 4-km depths beneath a segment of the rift zone several kilometers long. The hypocenters of the swarm outline a tabular shape a few kilometers high and about 1 km wide. The hypocenters also migrate progressively in time and space, both vertically and along the rift zone, indicating that the intruding fracture is propagating at a velocity of a few hundred to a few thousand meters per hour. The linear trace of intrusions that reach the surface as eruptions, and the eroded rift zones of older Hawaiian volcanoes, indicate that the rapid intrusions are steeply dipping dikes that parallel the rift zones. However, the shapes of the rapidly intruded bodies and the more open magma conduit along the upper and middle east rift zone of Kilauea below a few kilometers depth have not been established. The concentration of earthquake hypocenters at depths of 2–4 km in the seismic swarms associated with rapid intrusions suggests that the intrusion has some sort of axis at that depth.

In addition to their associated earthquakes, rapid intrusions are generally characterized by rapid deformation of the summit area and ground deformation above the intruded region. Volcanic tremor, new gas emissions and electromagnetic field changes also accompany some intrusions.

Rapid intrusions into the summit region of Kilauea Volcano are accompanied by rapid summit inflations, whereas rapid flank intrusions into the rift zones remove magma from the summit region and are accompanied by rapid subsidence of the summit area. Rapid intrusions into the rift zones of Kilauea have typical magma volumes of $10^6$–$10^7$ $m^3$ and they occur at volume rates of $10^2$–$10^3$ $m^3/s$. These typical volumes are associated with subsidence of the summit by 1–15 cm and pressure drops of 0.3–3 MPa in the shallow magma reservoir. An approximate rate of magma supply to a dike intruding the rift zones can be estimated from the tilt record. The radial tilt at HVO on the northwest side of Kilauea caldera has been calibrated as representing about $3.3 \times 10^5$ $m^3$ of subsided volume for each microradian (μrad) of inward tilt (Dzurisin and others, 1984). This is a minimum value for the amount of magma removed because of the unknown values of strength in the rocks surrounding the summit magma reservior and of the bulk compressibility of the reservoir. In addition, one microradian of inward radial tilt at HVO also indicates an approximate vertical subsidence of 5 mm at the apex of the deformation bulge and an approximate pressure drop in the summit magma reservoir of 90 kPa (0.9 bars).

Ground deformation in the area above a rapid intrusion causes rapid excursions and sometimes reversals of tilt vectors on nearby recording tiltmeters. Ground cracking is also common with the larger and shallower intrusions, and new or renewed volcanic-gas fumaroles are sometimes formed along these surface fractures.

When the volume rate of magma intrusion exceeds about 0.5 μrad of summit subsidence per hour (about 50 $m^3/s$), shallow volcanic tremor begins to appear as a background vibration between individual events in the earthquake swarm. Shallow volcanic tremor is a continuous ground vibration with a predominant frequency of 2–5 Hz, and it is associated with shallow subsurface movement and eruption of magma.

Increases in the electrical self-potential anomalies associated with active rift zones and changes in the electrical conductivity of the summit region of Kilauea also occur in association with the larger intrusions. The absence of observable magnetic anomalies associated with rapid subsidence of the summit area of Kilauea has led Davis and others (1974) to postulate a plastic envelope of low-rigidity rock material surrounding the summit magma reservoir.

During 1980 there were five rapid intrusions without eruptions into the east rift zone of Kilauea Volcano (table 42.1). During 1981 the intrusions shifted into Kilauea's southwest rift zone and on August 10–12 a large intrusion affected an 18-km-long segment of that rift. Excellent observations were made on this rapid intrusion, and they are summarized as follows:

TABLE 42.1.—*Rapid intrusions without eruptions into the east rift zone of Kilauea Volcano during 1980*

[*, possible eruption of a few cubic meters of lava; EM, electromagnetic; n.d., not determined]

| Date | Location | Length (km) | Height (km) | Minimum depth (km) | Volume ($m^3 \times 10^6$) | Propagation rate (m/h) | Gases | EM anomalies |
|---|---|---|---|---|---|---|---|---|
| March 2 | Hiiaka | 2 | 2 | 1 | .6 | n.d. | no | no |
| March 10–12* | Mauna Ulu | 5 | 3 | .5 | 5.3 | 200–500 | yes | no |
| August 27–28 | Puhimau | 4 | 3 | .5 | 2.3 | 1,000 | yes | yes |
| October 22 | Mauna Ulu | 2 | 2 | 2 | .6 | n.d. | yes | yes |
| November 2 | Kokoolau | 2 | 2 | 1 | 2.0 | 700 | no | no |

The August 10–12, 1981, event involved at least $4 \times 10^7$ $m^3$ of magma and was the largest rapid intrusion without an eruption of Kilauea Volcano since increased seismic and deformation monitoring began in the late 1950's.

Thousands of small earthquakes occurred in a swarm at rates as high as 3–4 per minute and although most were microearthquakes, a few reached magnitudes of 3.5–3.9. The hypocenters of the earthquakes in the region of the intrusion formed a zone 18 km long, 1–2 km wide, and extending from the surface to 5-km depth beneath the southwest rift zone (see Klein, chapter 43, fig. 43.90). Downrift migration of the earthquake locations indicates an intrusion propagation rate of 2 km/h slowing to 0.5 km/h (fig. 43.90).

Shallow volcanic tremor and rapid summit subsidence at about 10 μrad/h indicate a high-volume rate of intrusion, as much as $10^3$ $m^3/s$. The tilt at HVO totaled 107 μrad of deflation, and an elastic model of the summit level changes indicates $4 \times 10^7$ $m^3$ of subsidence volume. The ratio of the volume rate to the downrift migration rate gives an estimate of the cross sectional area of the intrusion. This area is $2 \times 10^3$ $m^2$, and if the intrusion is a dike 3 km high, then its width is about 0.7 m.

Large horizontal and vertical displacements occurred along the southwest rift zone, indicating major extension across the rift on the order of 1 meter; and a horst-and-graben pattern developed that indicates a shallow dike intrusion parallel to the rift and dipping steeply southeast. New surface cracks parallel to the rift follow the trend of the 1974 eruption vents and continue southwest for several kilometers (fig. 42.10). Much of the new surface cracking involves reactivation of 1974 or older fractures.

Renewed gas emissions and increased temperatures were measured at a fumarole on a newly activated surface crack. Self-potential anomaly changes were measured in the Koae fault system 5 km east of the trend of the seismic swarm; except near the renewed gas vent, no significant self-potential changes occurred over the seismic zone.

During 1982, rapid intrusions causing eruptions occurred twice in the summit area of Kilauea, in April and September. In June 1982 there was another large rapid intrusion without eruption into the southwest rift zone. Activity then switched back to the east rift zone and a major rapid intrusion and eruption occurred there during January 2–3, 1983. That event formed the magma conduit that has erupted through 47 episodes so far (as of June 1986) during the long-lasting 1983–1986 (and continuing) eruption of Kilauea Volcano.

The dike swarms formed by many rapid intrusions over the years tend to wedge apart the volcanic edifice and lead to long-term dynamic evolution of the rift zones.

## RIFT ZONES

The rift zones of Hawaiian volcanoes are "Pele's under ground roads" referred to by Ellis' Hawaiian guides in 1823 (Ellis, 1827). They are persistent zones of weakness in the volcanoes' flanks, resulting from thousands of rapid lateral intrusions. Many of these rapid intrusions also cause eruptions.

The rift zones are not primary conduits that penetrate to magmatic source depths; rather they are secondary features that form from radial pressures generated in the summit reservoirs at depths of

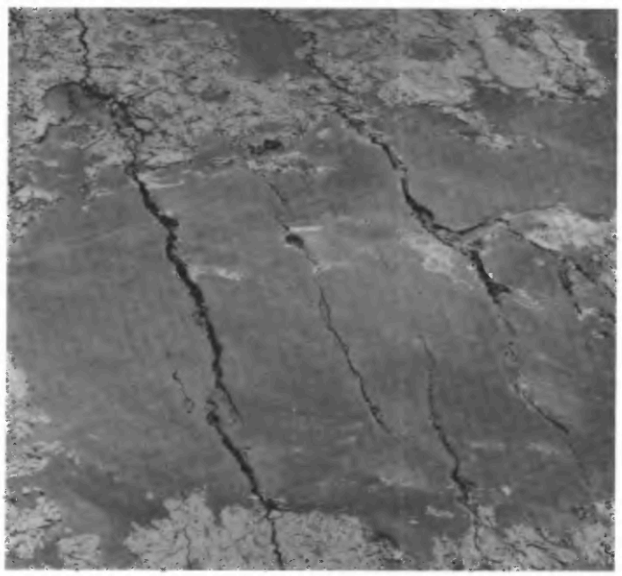

FIGURE 42.10.—Aerial photograph of ground cracks formed during August 10, 1981, intrusion beneath southwest rift zone of Kilauea Volcano. Area here covered by barren lava flows and by reworked volcanic ash from 1790 eruption. Cracks are as much as 1 m wide, and a shallow graben about 20 m wide has formed between principal fractures. Some of these cracks existed before the August 10, 1981 intrusion and were reactivated by the event. U.S. Geological Survey photograph by Norman Banks.

a few kilometers. Earthquake locations along the rifts of Kilauea Volcano indicate that the main dynamic axes of the rifts are about 3 km beneath the surface and that the overall rift zones extend from the surface to a depth of about 8 km below sea level. Because of isostatic subsidence of the Island of Hawaii, 8 km is about the depth of the old Cretaceous sea floor on which the Hawaiian volcanoes formed. It appears that the rift zones penetrate virtually the entire volcanic pile but do not extend down into the underlying oceanic crust.

Fiske and Jackson's (1972) analysis of the evolution and orientation of Hawaiian rift zones is also consistent with the concept that the rift zones are fairly shallow and secondary features compared to the deep magma conduits that supply the summit magma reservoirs. In their view, the rifts are fed by lateral intrusions from the summit magma reservoirs, and their orientations are controlled by the gravitational stresses of the surface topography.

The north-south elongation of the submarine topography and seismicity of Loihi Seamount (Klein, 1982a) indicates that rift zones are generated in the early stages of life of Hawaiian volcanoes, and the major rift systems still active on Hualalai and Haleakala Volcanoes indicate that rift zones persist into the waning stages. Thus, although the rifts are secondary features, they play a major and long-lived role in the structure and dynamics of Hawaiian volcanism.

The rift zones of Kilauea Volcano have been very active during the past few decades, and their dynamic behavior is therefore fairly well known. From 1959 through 1984 there were 20 rapid intrusions into the east rift zone without eruptions and 19 rapid intrusions that resulted in eruptions. During the same period there were 8 rapid intrusions into the southwest rift zone without eruptions and 2 rapid intrusions that resulted in eruptions. Summit activity over this same period consisted of 4 rapid intrusions without eruptions and 12 with eruptions. Eleven of these intrusions beneath the summit area were emplaced between 1966 and 1984.

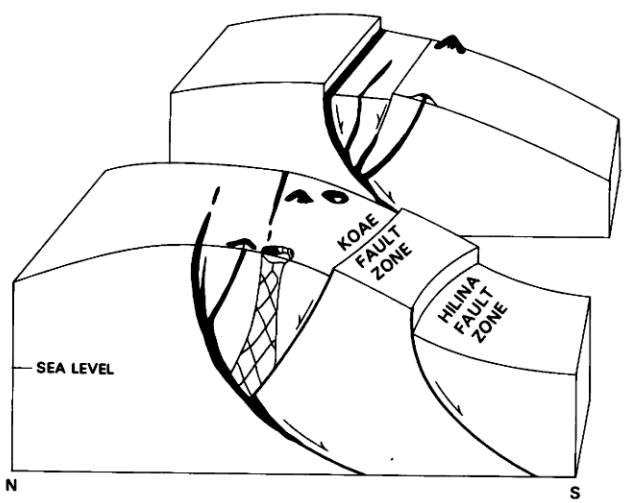


FIGURE 42.11.—Schematic block diagrams of the east rift zone of Kilauea Volcano looking downrift, from Moore and Krivoy (1964). In this interpretation stresses causing rift are largely gravitational, and rift zone dips seaward at depth. Pit craters (cross-hatched example) form by collapse into voids within rift if magma is drained far downrift.

Since each rapid intrusion and eruption involves a dike being injected into the carapace or flank of the volcano, the volcano must widen to accommodate these multiple intrusions. Using an estimate of 0.5 m for an average dike width, we can infer that the summit and upper rift zones of Kilauea Volcano should have widened by 5.5 m over this 19-year period. The actual measured widening of Kilauea caldera, between HVO on the northwest rim and Ahua on the southeast is 4.2 m from 1966 to 1984. There are various possible reasons why the estimate and the corrected measurement differ: the average dike width may be less than 0.5 m; each dike probably extends only part way across the summit area; and there probably is some elastic compression stored in the rocks adjacent to the intruded dikes. Even allowing for these considerations, it is clear that major widening of the summit of Kilauea Volcano perpendicular to its rift zones has occurred in the past few decades.

The widening of the rift zones becomes less downrift because fewer dikes reach long distances from the summit. The fact that some summit eruptions are followed by progressive downrift migration of rapid intrusions and flank eruptions can be explained by this progressive summit wedging effect extending down the rift zones.

Eaton and Murata (1960) suggested that a core of magma in the east rift zone of Kilauea remains molten between some eruptions, and Swanson and others (1976b) discussed this concept more thoroughly on the basis of seismic evidence from 1968 and 1969 eruptions on the east rift zone. Hardee (1982) has shown by theoretical heat-flow calculations that if a sufficient number and volume of intrusions are injected into a region, part of these intrusions will remain molten. He calculated (written commun., 1983) that the recorded intrusions into the east rift zone of Kilauea Volcano should result in a molten conduit from the summit to about 30–40 km downrift. The number and volume of intrusions into the southwest rift zone, however, have not been sufficient to maintain a molten conduit. The evidence for slow intrusions into the east rift zone provided by slow aseismic deflations of the summit and measurable inflation along the east rift zone as far as 32 km from the summit (Dieterich and Decker, 1975; Swanson and others, 1976a) give strong support to Hardee's conclusion.

Moore and Krivoy (1964) were among the first to consider the dynamics of the east rift zone of Kilauea Volcano. They suggested that gravitational slumping was the major factor causing the rift to widen and that magma moved rather passively into the fractures formed in the head of the slumping block (fig. 42.11). Swanson and others (1976a) took the opposite position that magmatic pressure pushed the rift apart and that slumping was the result rather than the cause of the rifting process (fig. 42.12). In a sense they are all correct; the gravitational and magmatic stresses are additive, and together they control the evolution of the rift zone.

Swanson and others (1976a) measured the progressive shortening of survey lines across the Hilina fault system on the south flank of Kilauea Volcano south of the east rift zone. They recognized that

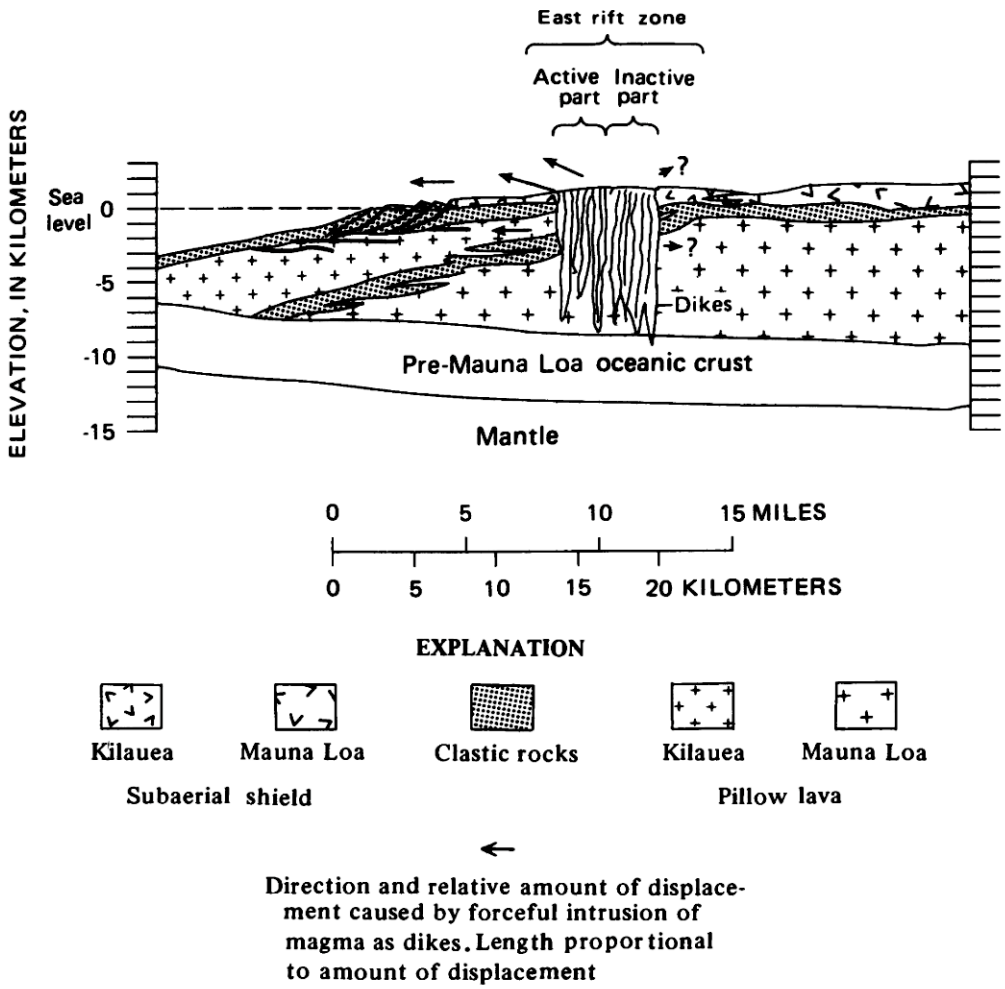


FIGURE 42.12.—Schematic cross section at true scale of east rift zone of Kilauea Volcano looking uprift, from Swanson and others (1976). In this interpretation stresses causing rift arise from forceful injection of magma, and dikes are nearly vertical.

the intrusions and eruptions occurring on the east rift zone in the late 1960's and early 1970's were wedging the rift apart but that much of the widening was being accommodated by compression and uplift of the flanks of the rift zone. They realized that this accumulating strain might be released by sudden failure of the Hilina fault system, and they wrote in 1974 (Swanson and others, 1976a, p. 35): "Some of the data suggest that the Hilina fault system is poised for another episode of subsidence, with only minor additional ground displacement needed to trigger it. Most of the strain acquired since 1965 remains, however, and we anticipate a subsidence (strain-release) event of unknown magnitude in the not too distant future."

Fifteen months later, but before their work was formally published, a magnitude-7.2 earthquake released the pent-up compressive strain in the south flank of Kilauea. Portions of the south coast moved seaward several meters and subsided as much as 3.5 m (Tilling and others, 1976; Lipman and others, 1985). Swanson and others (1976a) had clearly forecast the nature and imminence of that major earthquake.

Analysis of the source mechanism and aftershock pattern for this earthquake (Ando, 1979; Furumoto and Kovach, 1979) indicates that the strain was released by rupture on a nearly horizontal fault about 8–10 km beneath the south flank of Kilauea along 50 km of the coastline and across a region 10–20 km wide, bounded on the north by the east and the southwest rift zones. The slip on the fault was several meters in a seaward direction away from the rift zones (fig. 42.13). The net long-term result of dikes wedging into a rift zone therefore appears to be widening of the rift zone down to a depth of about 8 km, and this widening is accommodated by intermittent movement of the seaward flank of the volcano along a nearly horizontal slip surface close to the old sea floor on which the volcano grew.

More than 3 m of extension occurred on survey lines on the

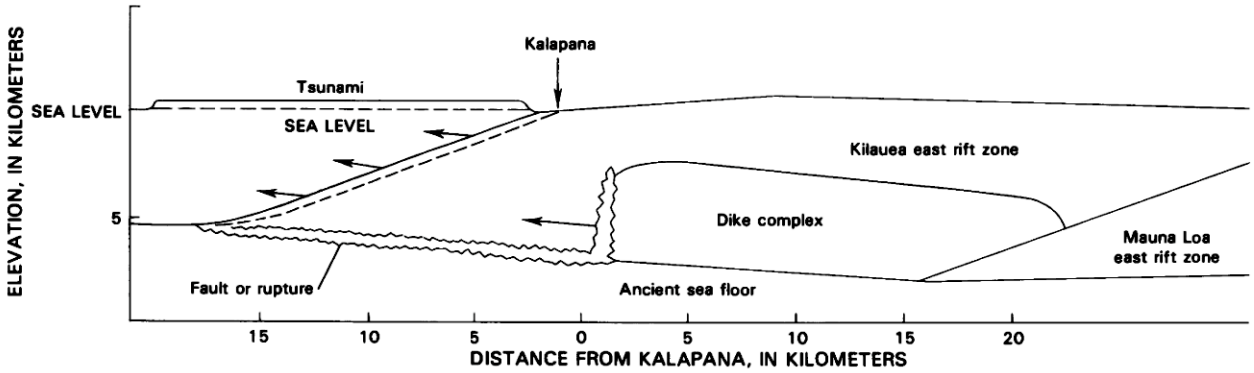


FIGURE 42.13.—Schematic cross section of east rift zone of Kilauea Volcano looking uprift and showing inferred mechanism of 1975 earthquake ($M$=7.2) and tsunami. Dike intrusions (at left side of dike complex) compress adjacent rocks over time. When stress reaches breaking point, unbuttressed flank of rift zone suddenly fails. Modified from Furumoto and Kovach (1979).

south flank of Kilauea Volcano during the period of the major earthquake; figure 42.14 shows changes from 1970 to 1984 in the 8.6-km-long line that extends from the north side of the Hilina fault system to the south coast.

It appears that Hawaiian volcanoes do not only grow upward from successive lava flows piled one upon another, but they also grow sideways by successive intrusions into the summits and rift zones and by intermittent failure of the seaward flanks of the rift zones to accommodate these intrusions. The east rift zone of Kilauea Volcano slopes down gently for 50 km from the summit at 1,200 m to sea level. It continues for another 70 km eastward as a slightly steeper submarine ridge to depths of nearly 5,000 m below sea level (Moore, 1971). Since Epp and others (1983) have shown that eruptions at lower elevations on the rift tend to be more voluminous than single short-lived eruptions high on the rift, it is clear that eruptions must become progressively much rarer at large distances from the summit. This decrease is probably caused by at least two factors: the widening of the rift zone and its wedging effect apparently decrease with distance from the summit; and the molten core in the rift zone also apparently decreases in size and finally disappears with distance from the summit. The very even slope of the ridge along the axis of the east rift zone indicates that the frequency and volumes of eruptions maintain a steady equilibrium over long time spans.

## ERUPTIONS

Most volcanic eruptions in Hawaii are outpourings of incandescent lava from linear or point-source vents. Lava fountains from linear vents are called curtains of fire and reach heights up to about 200 m. Lava fountains from point-source vents reach heights up to about 600 m.

A reduction in the volume rate of eruption or in the gas content reduces the vigor of lava fountaining until incandescent lava simply pours out from the linear or point-source vent. Vents in the bottoms or sides of craters feed active lava lakes that, at low-volume rates of eruption, can remain in eruption for years.

Lava flows fed by the erupting vents move down the slopes of the volcano or pond in topographic depressions. The formation of various lava textures and structures such as aa, pahoehoe, and lava tubes depends upon the complex interaction of the rheological properties of the lava, the volume rate and continuity of the eruption, and the environment and topography over which the flows are moving (Swanson, 1973; Holcomb and others, 1974; Peterson and Swanson, 1974; Peterson and Tilling, 1980). Lava commonly drains back down old surface cracks or even down the active fissures as the eruption wanes.

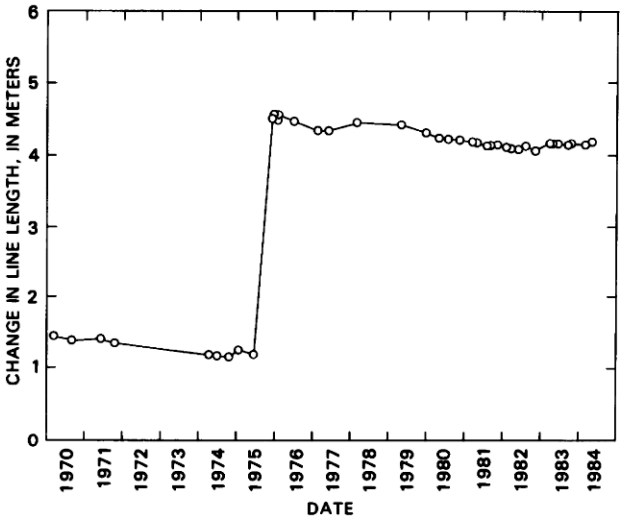


FIGURE 42.14.—Multiple surveys (small circles) of 8.6-km-long line on south flank of upper east rift zone of Kilauea Volcano indicate gradual contraction from 1970 to 1975, sudden extension related to the $M$=7.2 earthquake of November 1975, and renewed gradual contraction since 1975. Surveyed line runs from Goat to Apua Point.

Data on the eruptions of Kilauea and Mauna Loa Volcanoes since 1823 are compiled in Peterson and Moore (chapter 7, tables 7.3, 7.4). The long-lived, low-volume-rate eruptions of active lava lakes in the caldera of Kilauea Volcano that continued with a few interruptions from their first-recorded observation in 1823 until 1924 are not included in table 7.4.

The quality of these data on eruptions becomes, in general, better for more recent times. Continuous scientific observation began in 1912, and aerial observation and helicopter access to remote eruption sites has increased progressively during the past few decades.

Several major changes in the character of eruptions of Kilauea are evident in table 7.3. Between 1823 and 1919, during the century of active lava lakes and slow filling of Kilauea caldera, there was only one confirmed east-rift-zone eruption (in 1840) and one southwest-rift-zone eruption (1868). Beginning in 1919 and culminating with a probable east-rift submarine eruption in 1924, three rift eruptions marked the end of a long period of predominance of summit activity. The 1924 summit eruption, associated with subsidence of more than 400 m in the magma column feeding the active lava lake in Halemaumau Crater, has been the only explosive eruption in Hawaii since written records began in 1823.

From 1924 to 1934, seven small eruptions filled the bottom of the deep Halemaumau Crater formed by subsidence in 1924; from 1934 until 1952 there were no eruptions of Kilauea. This hiatus was ended by two eruptions in Halemaumau Crater in 1952 and 1954, and then a major eruption on the lower east rift zone in 1955 began a still-continuing period (1955–1986) of major eruptive activity on the east rift zone (18 eruptions), the summit (12 eruptions), and the southwest rift zone (2 eruptions).

What constitutes a separate eruption of Kilauea is not always clear. The breakout of an eruption in an entirely new location—not just an extension of a fracture associated with an ongoing rapid intrusion—is one criterion. Another criterion is the occurrence of a seismic swarm at the beginning of an eruption in a familiar location, like Halemaumau Crater. This indicates that a new subsurface fracture has been opened to feed the surface eruption. In long-lived eruptions such as the Mauna Ulu eruption on the upper east rift zone from 1969 to 1974 and the current Puu Oo eruption on the middle east rift zone from 1983 to 1986 (and still continuing), there have been periods of repose between episodes of high lava fountaining or other changes in the character of the eruption phases. However, the same general conduit system appears to be involved throughout these continuing eruptions, and on this basis these distinct episodes or phases are not considered separate eruptions.

Under these limits of definition, the eruption statistics for Kilauea from 1918 through 1984 are as follows: The average time from the beginning of one eruption to the next is 494 days (range is 2 to 6,504 days). The average duration of an eruption is 86 days (range is less than 1 to 1,884 days). The average volume of an eruption is $2.7 \times 10^7$ m$^3$ (range is less than $10^5$ to over $4 \times 10^8$ m$^3$). The average area coverered by an eruption is 4.4 km$^2$ (range is 0.1 to 55.7 km$^2$).

Dzurisin (1980) has compared tidal stresses to the onset times of eruptions of Kilauea and concludes that more eruptions begin near maximum fortnightly tidal stress (new moon and full moon) than would be expected by random chance at the 90-percent confidence level. He ascribes this to the triggering effect of tidal stresses on a system that has almost reached the point of eruption.

Klein (1982b) has investigated the statistical pattern of the eruptions of Kilauea since 1918 and concludes that the overall pattern is largely random, but that some non-random features appear. He finds that summit eruptions tend to cluster, that large-volume eruptions are usually followed by repose times that are longer than average, and that long periods of increased activity of Kilauea—for example during 1960–1979, when the average repose period was only 261 days—are associated with periods of less vigorous activity of Mauna Loa Volcano.

A complete list of known historical Mauna Loa eruptions is presented in table 7.4. Mauna Loa has not had any sustained lava-lake activity during this time period. There is less apparent variation in the pattern of Mauna Loa eruptions than in that of Kilauea eruptions, but the eight summit eruptions of Mauna Loa that occurred between 1870 and 1876 show an unusual clustering of locations and shorter-than-average repose times. In addition, the complete lack of eruptions between 1950 and 1975 was an unusually long repose period for Mauna Loa.

Statistics for Mauna Loa eruptions are as follows: The average time period from the beginning of one eruption to the next is 1,459 days (range is 104 to 9,165 days). The average duration of an eruption is 69 days (range is less than 1 to 547 days). The average volume of an eruption is $1.88 \times 10^8$ m$^3$ (range is $2.7 \times 10^7$ to $6.88 \times 10^8$ m$^3$). The average area covered above sea level by an eruption is 34 km$^2$ (range is 5 to 91 km$^2$).

All historical eruptions of Kilauea and Mauna Loa Volcanoes appear to have started with a rapid intrusion injecting a dike upwards or sideways from some part of the shallow magma reservoir into the summit or flank of the volcano. These rapid intrusions precede the eruptions by minutes to days, and provide important warnings of both the probable imminent occurrence and the probable location of an eruption.

The character of an eruption depends on several factors and is best explained by examples:

The long-lived eruptions of active lava lakes in Kilauea caldera begin with a dike injection into the summit area. Pressure in the shallow magma reservoir is high enough to push magma to the surface, and the resupply rate from depth is sufficient to match the low-volume rate of eruption, which is typically about 3 m$^3$/s. The rift zones are strong enough to withstand magmafracting. These eruptions have become less common as Kilauea caldera has refilled because the higher the magma column, the more pressure there is to fracture the rift zones and thereby lower the magma column. The latest long-lived eruption of an active lava lake occurred in Halemaumau Crater in 1967 and lasted 251 days (Kinoshita and others, 1969).

Short-lived eruptions at the summits and along the rift zones of Kilauea and Mauna Loa Volcanoes are the most numerous. The volume rates of these eruptions are typically 10–200 m$^3$/s; since this

exceeds the resupply rate from depth, pressure rapidly drops in the shallow magma reservoirs. The eruptions stop when the reservoir pressure can no longer push magma to the surface. The latest eruption of this type on Kilauea Volcano occurred in the caldera in September 1982 and lasted 16 hours (Scientific Event Alert Network, 1982). The latest one of this type on Mauna Loa Volcano occurred along the northeast rift zone in March–April 1984 and lasted 21 days (Lockwood and others, chapter 19).

Although long-lived flank eruptions are more unusual, two have occurred on Kilauea Volcano since 1969: the Mauna Ulu eruption on the upper east rift zone from 1969 to 1974 (Tilling and others, chapter 16; Peterson and others, 1976; Swanson and others, 1979), and the Puu Oo eruption on the middle east rift zone from 1983 to 1986 and still continuing (Wolfe and others, chapter 17). These eruptions consist of many episodes from essentially the same vent area. The subsurface magma conduits apparently remain open between eruptive events because the onsets of new episodes are not preceded or accompanied by earthquake swarms. Individual episodes of lava fountaining involve volume flow rates of 50–400 $m^3/s$, but they generally last only about 10–20 hours and produce lava volumes of about $5 \times 10^6$–$15 \times 10^6$ $m^3$. The longer term volume flow rates through several fountaining episodes or during sustained low-volume-rate phases average about 3 $m^3/s$, which is approximately the resupply rate of Kilauea Volcano for the past two decades.

The spectacular lava fountains and curtains of fire that characterize many Hawaiian eruptions are caused almost entirely by the rapid effervescense of gases boiling out of the magma at near-surface pressures and by the geometry of the vents. High-volume-rate eruptions of gas-rich magma in constricted vents produce the highest fountains. Gerlach and Graeber (1985), and Gerlach (written commun., 1985) have determined that magmatic gases of the volume and composition normally occurring in flank eruptions of Kilauea Volcano begin to boil rapidly out of magma at pressures equivalent to depths of only 40–100 m. In addition, as Paul Greenland has noted (written commun., 1984), near-surface pressures will move downward into an open magma column as rapid lava fountaining progressively unloads the upper part of the column, and the actual depth at which sustained effervescense is formed will be deeper than 40–100 m below the surface.

Most Hawaiian eruptions begin with linear vents (curtains of fire). After a few hours or days the fountaining becomes restricted to one or a few principal point-source vents. Apparently zones along the erupting fissure that were wider than average at the start of the eruption become enlarged by melting and erosion, while the narrower zones along the original fissure tend to freeze shut (Delaney and Pollard, 1982).

Once the magma flow supplying a fountaining vent is no longer replenished from depth, the fountaining will cease, and degassed surface lavas ponded near the vent will drain back into the conduit. Drainback in an active lava lake may also occur if the feeder dike is extended or some newly formed dike is generated in the subsurface. Magma in hydraulic communication will move toward the lowest pressure region in the system.

## CALDERA COLLAPSE AND EXPLOSIVE ERUPTIONS

Hawaiian volcanoes have a reputation for producing numerous but relatively harmless eruptions of fluid lava. Explosive eruptions, similar to those at Surtsey Volcano in Iceland in 1963 (Thorarinsson, 1965), were probably common during the transition from submarine to subaerial eruptions in the Hawaiian Islands, but these usually cease after the summit of a volcano grows above sea level. Less than 1 percent of Hawaiian volcanic products above sea level are pyroclastic (Macdonald, 1972, p. 355), and most of these are tephra from high lava fountains. Nevertheless, major explosive eruptions of hydromagmatic and hydrothermal character have occurred in Hawaii. Their occurrence appears to be closely related to episodes of major caldera collapse.

The last major collapse and explosive eruption of Kilauea caldera occurred in 1790 (Swanson and Christiansen, 1973; Christiansen, 1979; Decker and Christiansen, 1984). The caldera was more than twice its present depth when visited by Ellis in 1823 (Ellis, 1827), but its depth and configuration prior to 1790 are not known.

Holcomb's paleomagnetic data (1980) indicate that lava overflows were occurring from the summit region of Kilauea during the period of about 1–0.3 ka, and Ellis' Hawaiian guides told him that "in earlier ages it used to boil up, overflow its banks, and inundate the adjacent country" (Ellis, 1827, p. 171).

A much smaller collapse accompanied by small explosive eruptions occurred at Kilauea in 1924 (Jaggar and Finch, 1924). A nearly full lava lake in Halemaumau Crater drained down more than 400 m as a major intrusion was injected into the lower east rift zone of Kilauea near Kapoho. This intrusion possibly fed an eruption on the submarine extension of the east rift zone, but there was no direct evidence of this.

As the magma column in Halemaumau Crater drained below zones of subsurface water beneath the summit of Kilauea Volcano, the equilibrium between the magma column and subsurface water was destroyed and steam explosions of hydromagmatic and hydrothermal origin issued from the crater (fig. 42.15).

The subsidence in 1924 occurred during February through April, and the multiple steam explosions occurred for 18 days in May. Since magma moves out of the summit reservoir through conduits in the rift zones, the volume rate of magma removal is limited and the process of caldera collapse occurs over periods of weeks to months rather than minutes to hours. In theory there should be time for people to evacuate the summit region of Kilauea in case of future caldera collapses.

Overflows of lava that were erupted from the summit region of Mauna Loa Volcano as recently as 590 years ago as determined by radiocarbon dating (J.P. Lockwood, oral commun., 1985) are beheaded by Mauna Loa caldera. When first mapped in 1841 (Wilkes, 1845), the caldera was 50–100 m deeper than the present surface of ponded lavas. Thus it appears that the present caldera on Mauna Loa is similar in many ways to Kilauea caldera; it formed only a few hundred years ago and has been rapidly refilled with

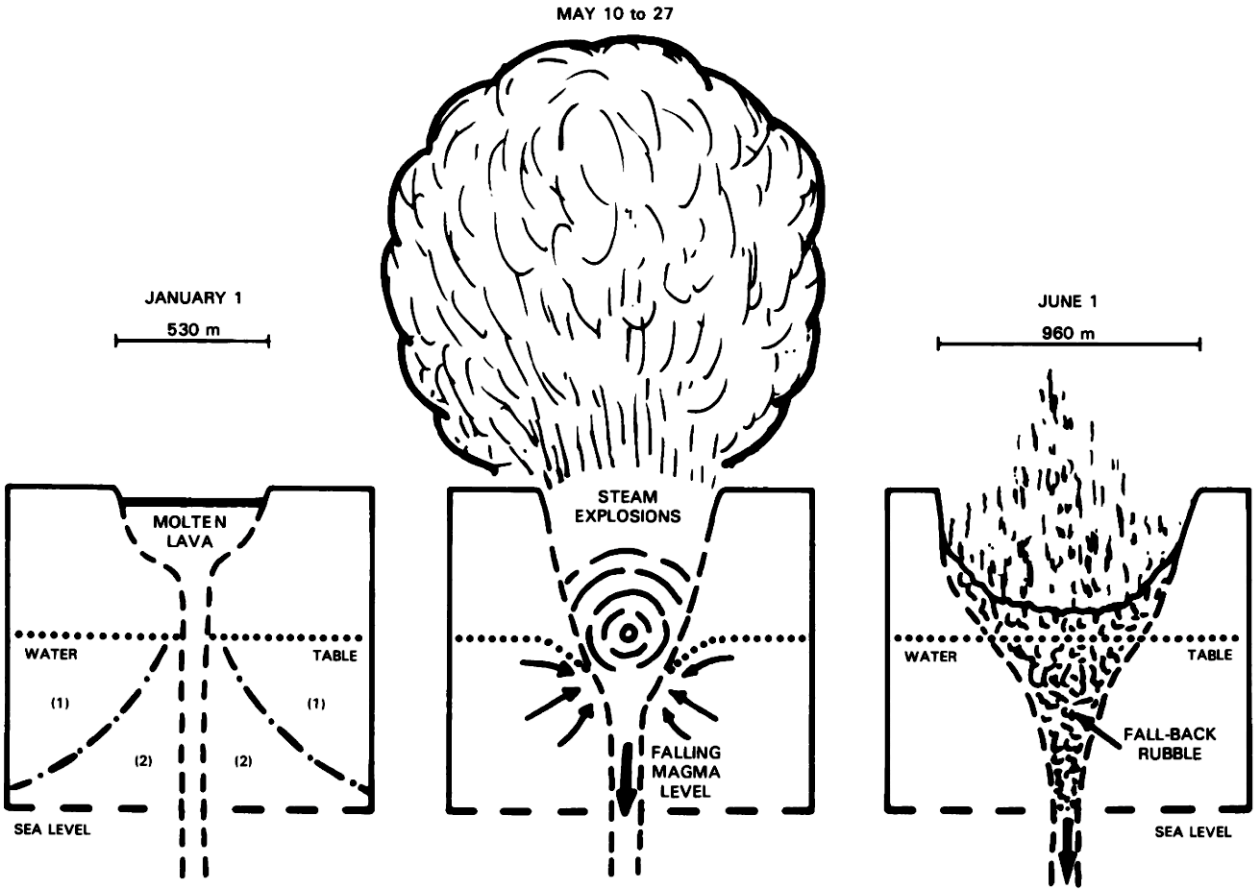


FIGURE 42.15.—Schematic cross sections showing conditions at Halemaumau Crater before, during, and after 1924 explosive eruption. On January 1, one zone of subsurface water (1) is cooler than boiling temperature, and other zone (2) is at boiling temperature for that depth; dash-dot line marks approximate boundary. During May 10–27, as magma column subsides below water table, equilibrium between subsurface water and magma is destroyed, and water from zone 1, rushes into broken hot rocks surrounding subsiding magma column and flashes into steam. Water from zone 2 also flashes into steam as hydrostatic pressures are suddenly reduced. Explosions are multiple because of progressive lowering of the magma column; they stop in late May with exhaustion of thermal energy above the subsided magma column, leaving a collapsed crater. From Decker and Christiansen (1984).

ponded lavas. There are scattered blocks of explosive ejecta on the rim of Mauna Loa caldera, but any explosive eruptions that may have accompanied the caldera collapse were minor compared to the 1790 eruption of Kilauea. This difference in explosive habits of Kilauea and Mauna Loa Volcanoes is probably related to the greater depth from the surface to zones of subsurface water beneath Mauna Loa.

Major caldera collapses of Kilauea Volcano have occurred repeatedly, with an average recurrence time of about 2,000 years (Decker and Christiansen, 1984; Dzurisin and Casadevall, 1986). Refilling the caldera with ponded lavas apparently takes several hundred years. Since both the young submarine volcano Loihi and Kilauea's older neighbor volcano Mauna Loa have calderas, this repeated process of caldera collapse and refilling apparently occurs during most of a Hawaiian volcano's active life span—roughly 0.5–1 m.y. If the caldera recurrence interval of 2,000 years at Kilauea is typical, this indicates that 200–500 generations of major caldera collapse and refilling occur during the evolution of a Hawaiian volcano.

This concept of repeated caldera collapse and refilling, combined with the evidence of progressively upward migration of the shallow magma reservoir systems of Hawaiian volcanoes (fig. 42.16), suggests that some lavas ponded in early calderas may be partly reassimilated into the summit magma-reservoir systems.

## SUBSIDENCE OF THE ISLANDS

Hawaiian volcanoes form a massive load on the lithosphere of the Pacific plate. The great positive gravity anomalies of young Hawaiian volcanoes—as much as 330 mGal Bouguer (Kinoshita, 1965)—indicate that they are not compensated by local roots of less dense rock. As Hawaiian volcanoes form, therefore, they also begin

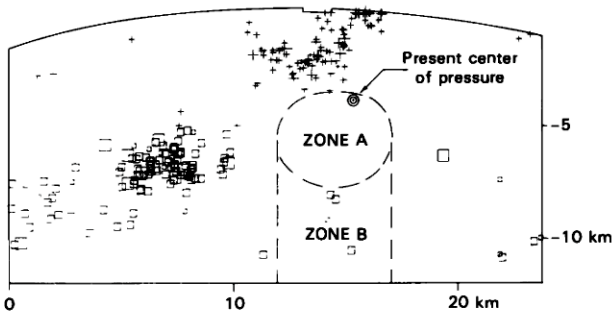


FIGURE 42.16.—Schematic cross section at true scale of inferred magma-reservoir system beneath summit of Mauna Loa Volcano. Zone A is more active region of magma addition and removal. Zone B is more passive; it contains magma and allows magma to move through it, but does not increase or decrease in volume as does zone A. Zone A migrates upward as the volcano grows in height. Pluses and squares represent well-located hypocenters of earthquakes ($M$=2 or greater) that occurred from January 1962 through May 1983 within 2.5 km of the cross-section plane. From Decker and others (1983).

to sink, and this process has been largely completed when the volcano becomes extinct.

Moore (chapter 2) and Moore and Fornari (1984) have determined from tide-gauge and drowned-reef data that the average rate of subsidence of the west shore of the Island of Hawaii is about 2 mm/yr over the past 150,000 yr and that the rate of subsidence has been generally increasing during this time period. The subsidence is apparently more rapid near the center of the island than at the shoreline. Eustatic sea-level changes are superimposed on this general subsidence and complicate the actual change of sea level. For example, the worldwide rise in sea level over the past century added to the subsidence of the Island of Hawaii has caused a rise in sea level at Hilo of about 4 mm/yr during the past few decades. Tide-gauge data at Honolulu reflect a eustatic rise in sea level but do not indicate any measurable subsidence of the Island of Oahu.

Very high sea-level stands reported by Stearns (1978), which imply periods of major uplift following the subsidence of some Hawaiian islands, have recently been interpreted by Moore and Moore (1984) as deposits from giant waves. Present opinion favors general subsidence of the Hawaiian islands rather than some complex oscillating tectonic movements.

Tectonic subsidence probably results from at least four factors: (1) removal of magma from beneath the active volcanoes; (2) elastic compression of the lithosphere nearly as fast as load is added; (3) plastic flow in the lower lithosphere and upper mantle as a result of volcanic load over periods of $10^5$–$10^6$ yr; and (4) the slow thickening of the oceanic lithosphere and its subsidence as it loses heat over periods of $10^7$ to $10^8$ yr (Yoshii and others, 1976). Liu and Kosloff (1978) calculated factors (2) and (3) using an elastic/plastic plate-bending model with laboratory data on rock deformation.

This concept of general subsidence of the Hawaiian Islands has some interesting geologic implications. If any mineral deposits were ever formed by interaction of magma and subsurface water, these deposits would probably not be exposed above sea level by later erosion. In addition, subaerial erosion would in general not expose any Hawaiian volcanic rocks or structures formed below sea level.

## FUTURE RESEARCH DIRECTIONS

As in most geologic problems, our understanding of how Hawaiian volcanoes work decreases with depth below the surface. Nevertheless, there are some research paths that look promising over the next decade or two for providing new insights into the structure and dynamics of Hawaiian volcanoes.

More detailed information on the variations in temperature and kinetics of the Earth's mantle should be forthcoming from worldwide seismic tomography. The deep anomalies beneath the central Pacific, emerging in the present work of Anderson and Dziewonski (1984), should become clearer if a worldwide net of digital seismometers is deployed, particularly at sites on the ocean floor.

Deployment of a few ocean-bottom seismometers around the Island of Hawaii would also greatly improve the capability of the present seismometer network of the Hawaiian Volcano Observatory. Potential specific benefits from this type of research effort include better location of earthquake sources beneath Loihi Seamount, the ability to determine the source functions of deeper earthquakes beneath Hawaii, and the ability to gain more depth and detail for the seismic velocity structure beneath Hawaii.

Volcanic tremor speaks in a language we do not yet clearly understand, but the technology probably exists to translate this babble into meaningful words and sentences. Arrays of portable digital broad-band seismometers are needed to record volcanic tremor in sufficient detail to interpret its source functions. With such data in hand, we may be able to resolve some of the ambiguity in present models of how volcanic tremor is generated.

Recent developments in satellite geodesy suggest that a revolution in the technology of measuring the surface deformation on active and potentially active volcanoes is only a few years away. The ability to measure distance changes between points that are not intervisible, and the potentially great consequent improvements in the quality of far-field data, would make observations possible that cannot now be made with conventional surveying devices. These new observations are essential for testing more complex theoretical models of the size, shape, and depth of subsurface magma bodies. Add to this the great potential savings in surveying time and manpower, and the attractiveness of satellite global positioning systems becomes clear.

The recent successes in observing detailed gravity changes related to activity of Kilauea and Mauna Loa Volcanoes (Johnson, chapter 47; Dzurisin and others, 1980; Jachens and Eaton, 1980), and the fact that these new data indicate important mass changes in the shallow magma-storage systems not quantitatively shown by surface deformation measurements, clearly demonstrate the importance of long-term measurement of gravity changes on the summits and rift zones of Kilauea and Mauna Loa Volcanoes. Recording gravity meters in conjunction with recording tiltmeters would provide the most definitive data on the mass and volume changes in the shallow magma reservoir systems.

Significant changes in the electrical, magnetic, and electromagnetic fields associated with the activity of Kilauea Volcano (Davis and others, 1973; Zablocki, 1976; Dzurisin and others, 1980; Jackson, 1983) indicate that these methods of geophysical research should continue to be pursued vigorously at HVO. Needed most in this research are a comprehensive analysis of the available data and the generation of theoretical models to try to explain the data. This type of effort would define more clearly what types of field observations are most important.

Great progress has been made in the past few years in determining the composition of gases in Hawaiian magma, and in understanding the complex manner in which some of these gases exsolve from the melt and escape to the atmosphere (chapters 27–36; Gerlach and Graeber, 1985) These studies have set the stage for determining the role of volcanic gases in the dynamics of the ascent, the shallow storage and intrusion, and the eruption of magma. Carbon dioxide apparently forms a separate but dense fluid phase at depths as great as 40 km beneath the summits of Hawaiian volcanoes. Studies of the thermodynamic and mechanical behavior of oxygen, carbon, hydrogen, and sulfur in the generation, ascent, shallow storage and intrusion, and eruption of Hawaiian magmas is a research opportunity of great importance.

The destruction of homes and property in the 1983–1985 eruption of Kilauea Volcano, and the threat to Hilo from flows of the 1984 Mauna Loa eruption, make it clear that we need to know more about the mechanical processes of Hawaiian lava flows in order to predict their behavior better. The complex interaction of the volume rate of eruption, the rheological properties of lava, and the topography over which the flows are moving combine to make a challenging research area that needs more study. Careful plans must be made for future experiments. When an eruption begins it is usually too late to start planning.

As a parting note, one area of the dynamics of Hawaiian volcanism that has been almost entirely overlooked is the study of the interaction of magma with subsurface water beneath the summits and rift zones of the active volcanoes. Few direct data are available: only one 1,260-m drill hole into the summit of Kilauea (Keller and others, 1979), and a few geothermal wells on the east rift zone of Kilauea whose data are still largely proprietary. Some resistivity data on the depth to the water table at various places are available. The potential for important new insights into the interaction of magma and ground water awaits a creative hydrogeologist who wants to venture into volcanology.

## REFERENCES CITED


Anderson, D.L., and Dziewonski, A.M., 1984, Seismic tomography: Scientific American, v. 251, no. 4, p. 60–68.

Ando, M., 1979, The Hawaii earthquake of November 29, 1975: Low angle faulting due to forceful injection of magma: Journal of Geophysical Research, v. 84, p. 7616–7626.

Christiansen, R.L., 1979, Explosive eruption of Kilauea Volcano in 1790 [abs.]: Hawaii Symposium on Intraplate Volcanism and Submarine Volcanism, Hilo, Hawaii, Abstract Volume, p. 158.

Dalrymple, G.B., Silver, E.A., and Jackson, E.D., 1973, Origin of the Hawaiian Islands: American Scientist, v. 61, p. 294–308.

Daly, R.A., 1914, Igneous rocks and their origin: New York, McGraw-Hill, 563 p.

——— 1933, Igneous rocks and the depths of the Earth (2nd ed.): New York, McGraw-Hill, 598 p.

Dana, J.D., 1890, Characteristics of volcanoes: New York, Dodd Mead and Co., 399 p.

——— 1895, Manual of geology (4th ed.): New York, American Book Company, 1088 p.

Davis, P.M., Hastie, L.M., and Stacey, F.D., 1974, Stresses within an active volcano—with particular reference to Kilauea: Tectonophysics, v. 22, p. 355–362.

Davis, P.M., Jackson, D.B., Field, J., and Stacey, F.D., 1973, Kilauea Volcano, Hawaii: A search for the volcanomagnetic effect: Science, v. 180, p. 73–74.

Davis, P.M., Stacey, F.D., Zablocki, C.J., and Olson, J.V., 1979, Improved signal discrimination in tectonomagnetism: Discovery of a volcanomagnetic effect at Kilauea, Hawaii: Physics of the Earth and Planetary Interiors, v. 19, p. 331–336.

Decker, R.W., 1968, Kilauea volcanic activity: an electrical analog model [abs.]: Eos, Transactions American Geophysical Union, v. 49, p. 352–353.

Decker, R.W., and Christiansen, R.L., 1984, Explosive eruptions of Kilauea Volcano, Hawaii, *in* Explosive volcanism: Inception, evolution, and hazards: Washington, D.C., National Academy of Science, p. 122–132.

Decker, R.W., Koyanagi, R.Y., Dvorak, J.J., Lockwood, J.P., Okamura, A.T., Yamashita, K.M., and Tanigawa, W.R., 1983, Seismicity and surface deformation of Mauna Loa Volcano, Hawaii: Eos, Transactions of the American Geophysical Union, v. 64, p. 545–547.

Delaney, P.T., and Pollard, D.D., 1982, Solidification of basaltic magma during flow in a dike: American Journal of Science, v. 282, p. 856–885.

Dieterich, J.H., and Decker, R.W., 1975, Finite element modeling of surface deformation associated with volcanism: Journal of Geophysical Research, v. 80, p. 4094–4102.

Duffield, W.A., Christiansen, R.L., Koyanagi, R.Y., and Peterson, D.W., 1982, Storage, migration and eruption of magma at Kilauea Volcano, Hawaii, 1971–1972: Journal of Volcanology and Geothermal Research, v. 13, p. 273–307.

Dvorak, J.J., Okamura, A.T., and Dieterich, J.H., 1983, Analysis of surface deformation data, Kilauea Volcano, Hawaii: October 1966 to September 1970: Journal of Geophysical Research, v. 88, p. 9295–9304.

Dzurisin, D., 1980, Influence of fortnightly earth tides at Kilauea Volcano, Hawaii: Geophysical Research Letters, v. 7, p. 925–928.

Dzurisin, D., Anderson, L.A., Eaton, G.P., Koyanagi, R.Y., Lipman, P.W., Lockwood, J.P., Okamura, R.T., Puniwai, G.S., Sako, M.K., and Yamashita, K.M., 1980, Geophysical observations of Kilauea Volcano, Hawaii, 2. Constraints on the magma supply during November 1975–September 1977: Journal of Volcanology and Geothermal Research, v. 7, p. 241–269.

Dzurisin, D., and Casadevall, T.J., 1986, Stratigraphy and chemistry of Uwekahuna Ash: Product of prehistoric phreatomagmatic eruption at Kilauea Volcano, Hawaii [abs.]: Auckland, N.Z., Abstracts volume, International Volcanological Congress, p. 100.

Dzurisin, D., Koyanagi, R.Y., and English, T.T., 1984, Magma supply and storage at Kilauea Volcano, Hawaii, 1956–1983: Journal of Volcanology and Geothermal Research, v. 21, p. 177–206.

Eaton, J.P., 1962, Crustal structure and volcanism in Hawaii: American Geophysical Union, Geophysical Monograph 6, p. 13–29.

Eaton, J.P., and Murata, K.J., 1960, How volcanoes grow: Science, v. 132, p. 925–938.

Ellis, W., 1827, Journal of William Ellis: London, reprinted 1963 by Advertiser Publishing Co., Honolulu, Hawaii, 342 p.

Epp, D., Decker, R.W., and Okamura, R.T. 1983, Relation of summit deformation to east rift zone eruptions on Kilauea Volcano, Hawaii: Geophysical Research Letters, v. 10, p. 493–496.

Fiske, R.S., and Jackson, E.D., 1972, Orientation and growth of Hawaiian

volcanic rifts: The effect of regional structure and gravitational stresses: Proceedings of the Royal Society of London, Ser. A, v. 329, p. 299–326.

Fiske, R.S., and Kinoshita, W.T., 1969, Inflation of Kilauea Volcano prior to its 1967–1968 eruption: Science, v. 165, p. 341–349.

Furumoto, A.S., and Kovach, R.L., 1979, The Kalapana earthquake of November 29, 1975: An intra-plate earthquake and its relation to geothermal processes: Physics of the Earth and Planetary Interiors, v. 18, p. 197–208.

Gerlach, T.M., and Graeber, E.J., 1985, Volatile budget of Kilauea Volcano: Nature, v. 313, p. 273–277.

Griggs, D.T., and Baker, D.W., 1969, The origin of deep-focus earthquakes, *in* Mark, H., and Fernback, S., eds., Properties of matter under unusual conditions: New York, Interscience Publishers, p. 23–42.

Hardee, H.C., 1982, Incipient magma chamber formation as a result of repetitive intrusions: Bulletin Volcanologique v. 45, p. 41–49.

Hess, H.H., 1960, Stillwater igneous complex, Montana: Geological Society of America Memoir 80, 230 p.

Hill, D.P., 1977, A model for earthquake swarms: Journal of Geophysical Research, v. 82, p. 1347–1352.

Holcomb, R.T., 1980, Preliminary geologic map of Kilauea Volcano, Hawaii: U.S. Geological Survey Open-File Report 80–796, 2 sheets, scale 1:50,000.

Holcomb, R.T., Peterson, D.W., and Tilling, R.I., 1974, Recent landforms at Kilauea Volcano, a selected photographic compilation, *in* Greeley, R., ed., Hawaiian Planetology Conference, NASA TMX 62362, p. 49–86.

Jachens R.C., and Eaton, G.P., 1980, Geophysical observations of Kilauea Volcano, Hawaii, 1. Temporal gravity variations related to the 29 November, 1975, M=7.2 earthquake and associated summit collapse: Journal of Volcanology and Geothermal Research, v. 7, p. 225–240.

Jackson, D.B., Kauahikaua, J., and Zablocki, C.J., 1983, Resistivity monitoring of an active volcano: Application of the controlled-source electromagnetic technique at Kilauea Volcano, Hawaii [abs.]: Eos, Transactions of the American Geophysical Union, v. 64, p. 1072.

Jaggar, T.A., and Finch, R.H., 1924, The explosive eruption of Kilauea in Hawaii: American Journal of Science, Ser. 5, v. 8, p. 353–374.

Joly, J., 1909, Radioactivity and geology: London, Archibald Constable and Co., 287 p.

Keller, G.V., Grose, L.T., Murray, J.C., and Skokan, C.K., 1979, Results of an experimental drill hole at the summit of Kilauea Volcano, Hawaii: Journal of Volcanology and Geothermal Research, v. 5, p. 345–385.

Kinoshita, W.T., 1965, A gravity survey of the Island of Hawaii: Pacific Science, v. 19, p. 339–340.

Kinoshita, W.T., Koyanagi, R.Y., Wright, T.L., and Fiske, R.S., 1969, Kilauea Volcano: The 1967–68 summit eruption: Science, v. 166, p. 459–468.

Klein, F.W., 1982a, Earthquakes at Loihi submarine volcano and the Hawaiian hot spot: Journal of Geophysical Research, v. 87, p. 7719–7726.

——— 1982b, Patterns of historical eruptions at Hawaiian volcanoes: Journal of Volcanology and Geothermal Research, v. 12, p. 1–35.

Koyanagi, R.Y., Unger, J.D., Endo, E.T., and Okamura, A.T., 1976, Shallow earthquakes associated with inflation episodes at the summit of Kilauea Volcano, Hawaii: Bulletin Volcanologique, v. 39, p. 621–631.

Lipman, P.W., Lockwood, J.P., Okamura, R.T., Swanson, D.A., and Yamashita, K. M., 1985, Ground deformation associated with the 1975 magnitude-7.2 earthquake and resulting changes in activity of Kilauea Volcano, Hawaii: U.S. Geological Survey Professional Paper 1276, 45 p.

Liu, H., and Kosloff, D. 1978, Elastic-plastic bending of the lithosphere incorporating rock deformation data, with application to the structure of the Hawaiian Archipelago: Tectonophysics, v. 50, p. 249–274.

Macdonald, G.A., 1972, Volcanoes: Englewood Cliffs, N. J., Prentice-Hall, 510 p.

Malahoff, A., McMurtry, G.M., Wiltshire, J.M., and Yeh, H., 1982, Geology and chemistry of hydrothermal deposits from Loihi, the latest active submarine volcano of the Hawaiian hot spot: Nature, v. 298, p. 234–239.

McBirney, A.R., 1963, Conductivity variations and terrestrial heat-flow distribution: Journal of Geophysical Research, v. 68, p. 6323–6329.

McDougall, I., 1979, Age of shield-building volcanism of Kauai and linear migration of volcanism in the Hawaiian Island chain: Earth and Planetary Science Letters, v. 46, p. 31–42.

Mogi, K., 1958, Relation between the eruptions of various volcanoes and the deformation of the ground surface around them: Tokyo, Bulletin of the Earthquake Research Institute, v. 36, p. 99–134.

Moore, J.G., 1970, Relationship between subsidence and volcanic load, Hawaii: Bulletin Volcanologique, v. 34, p. 562–576.

——— 1971, Bathymetry and geology—East Cape of the Island of Hawaii: U.S. Geological Survey Miscellaneous Geological Investigations Map I–677, Scale 1:62,500.

Moore, J.G., and Fornari, D.J., 1984, Drowned reefs as indicators of the rate of subsidence of the Island of Hawaii: Journal of Geology, v. 92, p. 752–759.

Moore, J.G., and Krivoy, H.L., 1964, The 1962 flank eruption of Kilauea Volcano and structure of the east rift zone: Journal of Geophysical Research, v. 69, p. 2033–2045.

Moore, J.G., and Moore, G.W., 1984, Deposit from a giant wave on the Island of Lanai, Hawaii: Science, v. 226, p. 1312–1315.

Peterson, D.W., Christiansen, R.L., Duffield, W.A., Holcomb, R.T., and Tilling, R.I., 1976, Recent activity of Kilauea Volcano, Hawaii, *in* International Association for Volcanology and Chemistry of Earth's Interior, Symposium on Andean and Antarctic Volcanology Problems, Santiago, Chile, Proceedings, p. 646–656.

Peterson, D.W., and Swanson, D.A., 1974, Observed formation of lava tubes during 1970–71 at Kilauea Volcano, Hawaii: Studies in Speleology, v. 2, p. 209–233.

Peterson, D.W., and Tilling, R.I., 1980, Transition of basaltic lava from pahoehoe to aa, Kilauea Volcano, Hawaii: Field observations and key factors: Journal of Volcanology and Geothermal Research, v. 7, p. 271–293.

Pollard, D.D., 1976, On the form and stability of open fractures in the Earth's crust: Geophysical Research Letters, v. 3, p. 513–516.

Ramberg, H., 1972, Mantle diapirism and its tectonic and magmagenetic consequences: Physics of Earth and Planetary Interiors, v. 5, p. 45–60.

Ryan, M.P., Blevins, J.Y.K., Okamura, A.T., and Koyanagi, R.Y., 1983, Magma reservoir subsidence mechanics: Theoretical summary and application to Kilauea Volcano, Hawaii: Journal of Geophysical Research, v. 88, p. 4147–4181.

Ryan, M.P., Koyanagi, R.Y., and Fiske, R.S., 1981, Modeling the three-dimensional structure of macroscopic magma transport systems: Application to Kilauea Volcano, Hawaii: Journal of Geophysical Research, v. 86, p. 7111–7129.

Scientific Event Alert Network, 1982–1985, Monthly accounts of the activity of Kilauea and Mauna Loa Volcanoes, Hawaii: SEAN Bulletin v. 8-10, no. 1-12, Washington, D.C., Smithsonian Institution.

Shaw, H.R., 1969, Rheology of basalt in the melting range: Journal of Petrology, v. 10, p. 510–535.

——— 1970, Earth tides, global heat flow, and tectonics: Science, v. 168, p. 1084–1087.

——— 1973, Mantle convection and volcanic periodicity in the Pacific; evidence for Hawaii: Geological Society of America Bulletin, v. 84, p. 1505–1526.

——— 1980, The fracture mechanisms of magma transport from the mantle to the surface, *in* Hargraves, R.B., ed., Physics of Magmatic Processes: Princeton, New Jersey, Princeton University Press, p. 201–264.

Shimozuru, D., 1981, Magma reservoir systems inferred from tilt patterns: Bulletin Volcanologique, v. 44-3, p. 499–504.

Spera, F.J., 1980, Aspects of magma transport, *in* Hargraves, R.B., ed., Physics of Magmatic Processes: Princeton, New Jersey, Princeton University Press, p. 265–323.

Stearns, H.T., 1978, Quaternary shorelines in the Hawaiian Islands: Bernice P. Bishop Museum, Bulletin 237, Honolulu, 57 p.

Swanson, D.A., 1972, Magma supply rate at Kilauea Volcano, 1951–1972: Science, v. 175, p. 169–170.

——— 1973, Pahoehoe flows from the 1969–1971 Mauna Ulu eruption, Kilauea Volcano, Hawaii: Geological Society of America Bulletin, v. 84, p. 615–626.

Swanson, D.A., and Christiansen, R.L., 1973, Tragic base surge in 1790 at

Kilauea Volcano: Geology, v. 1, p. 83–86.

Swanson, D.A., Duffield, W.A., and Fiske, R.S., 1976a, Displacement of the south flank of Kilauea Volcano: The result of forceful intrusion of magma into rift zones: U.S. Geological Survey Professional Paper 963, 39 p.

Swanson, D.A., Duffield, W.A., Jackson, D.B., and Peterson, D.W., 1979, Chronological narrative of the 1969–71 Mauna Ulu eruption of Kilauea Volcano, Hawaii: U.S. Geological Survey Professional Paper 1056, 55 p.

Swanson, D.A., Jackson, D.B., Koyanagi, R.Y., and Wright, T.L., 1976b, The February 1969 east rift eruption of Kilauea Volcano, Hawaii: U.S. Geological Survey Professional Paper 891, 30 p.

Thorarinsson, S., 1965, Surtsey: Island born of fire: National Geographic Magazine, v. 127, p. 713–726.

Tilling, R.I., Koyanagi, R.Y., Lipman, P.W., Lockwood, J.P., Moore, J.G., and Swanson, D.A., 1976, Earthquake and related catastrophic events, Island of Hawaii, November 29, 1975: A preliminary report: U.S. Geological Survey Circular 740, 33 p.

Turcotte, D.L., and Oxburgh, E.R., 1978, Intraplate volcanism: Philosophical Transactions Royal Society of London, Ser. A., v. 288, p. 561–579.

Verhoogen, J., 1954, Petrological evidence on temperature distribution in the mantle of the earth: Eos, Transactions of the American Geophysical Union, v. 35, p. 85–92.

Weertman, J., 1972, Coalescence of magma pockets into large pools in the upper mantle: Geological Society of America Bulletin, v. 83, p. 3531–3632.

Wilkes, C., 1845, Narrative of the United States exploring expedition during the years 1838–1842: Philadelphia, v. 4, p. 87–231.

Wilson, J.T., 1963, Continental drift: Scientific American, v. 208, p. 86–100.

Wilson, R.M., 1935, Ground surface movement at Kilauea Volcano, Hawaii: University of Hawaii, Honolulu, Research Publication 10, 56 p.

Wright, T.L., 1971, Chemistry of Kilauea and Mauna Loa lava in space and time: U.S. Geological Survey Professional Paper 735, 40 p.

——— 1984, Origin of Hawaiian tholeiite: a metasomatic model: Journal of Geophysical Research, v. 89, p. 3233–3252.

Wright, T.L., Shaw, H.R., Tilling, R.I., and Fiske, R.S., 1979, Origin of Hawaiian tholeiitic basalt: a quantitative model [abs.]: International Association for Volcanology and Chemistry of the Earth's Interior, Symposium on intraplate volcanism and submarine volcanism, Hilo, Hawaii, July 16–22, 1979, Abstracts Volume, p.

Yoder, H.S., 1976, Generation of basaltic magma: Washington, D.C., National Academy of Sciences, 265 p.

Yoder, H.S., and Tilley, C.E., 1962, Origin of basalt magmas: an experimental study of natural and synthetic rock systems: Journal of Petrology, v. 3, p. 342–532.

Yoshii, T., Kono, T., and Ito, K., 1976, Thickening of the oceanic lithosphere: American Geophysical Union, Monograph 19, p. 423–430.

Zablocki, C.J., 1976, Mapping thermal anomalies on an active volcano by the self-potential method, Kilauea, Hawaii: United Nations Symposium on the development and use of geothermal resources, 2nd San Francisco, Proceedings, v. 2, p. 1299–1309.

# THE SEISMICITY OF KILAUEA'S MAGMA SYSTEM

*By* Fred W. Klein, Robert Y. Koyanagi, Jennifer S. Nakata, *and* Wilfred R. Tanigawa

## ABSTRACT

Earthquake-hypocenter data collected by the Hawaiian Volcano Observatory during 1960–83 provide a wealth of information on the active processes of Kilauea's magma system. The magma conduits produce volcanic earthquakes that occur in episodic swarms often accompanied by tilt changes or eruptions. Tectonic earthquakes in Kilauea's flanks and some parts of the upper mantle occur more continually and are punctuated with mainshock-aftershock sequences. Volcanic earthquakes also have smaller magnitudes, a greater proportion of small events, and frequent association with tremor. Three-dimensional earthquake patterns and separation of volcanic and tectonic seismicity can be visualized in a series of hypocenter depth slices and cross sections. Earthquakes reveal a magma system consisting of a vertical conduit from Kilauea caldera to about 60 km depth, two shallow rift zones radial to the caldera, and a shallow magma reservoir joining these three conduits.

The shallow magma reservoir is an aseismic zone beneath the south edge of Kilauea caldera. The reservoir is surrounded on two sides by intensely active rift conduits centered near 3 km depth, above by a seismically active cap in the caldera mostly between 1 and 2 km depth, and below by the vertical magma conduit having earthquakes as shallow as 7 km. The deformation centers are mostly between 2 and 4 km depth, near the top of the aseismic zone that is between 3 and 7 km depth. Inflation of the reservoir produces earthquakes above and in the adjacent rift conduits by extension in the summit region and slow magma intrusion into the rifts.

The vertical magma conduit, as defined by earthquakes, consists of two parts: a narrow and nearly vertical pipe between 7 and 20 km depth mostly having swarms of volcanic earthquakes, and a zone that widens into a diffuse and south-dipping region between 20 and 60 km depth. Earthquakes in the deeper conduit are larger in magnitude and more continuous in time, as if tectonic in origin. Earthquakes below 40 km depth merge with the Hawaiian hot spot below Kilauea, Loihi and Mauna Loa Volcanoes. Kilauea's deep earthquakes also join a band of seismicity along the island's south coast, which is probably caused by shear stress applied from Kilauea's mobile south flank and by the growing and asymmetrical weight of the Kilauea shield. The number of earthquakes in the vertical conduit dropped dramatically at the time of the $M=7.2$ Kalapana earthquake in 1975. This decrease indicates that conduit earthquakes are partly driven by regional stresses derived from the seaward push of the south flank.

The vertical distribution of conduit earthquakes shows pronounced gaps near depths of 5, 13 and 20 km. The first gap results from the magma reservoir between 3 and 7 km depth, and the 13-km-depth gap is probably bounded by the Moho and the prevolcanic oceanic sediments. The depth of 20 km is also a gap for earthquakes in the surrounding lithosphere, marks the change from volcanic-style earthquakes above to tectonic below, and is probably the zone of the neutral stress axis in the lithosphere bending under the island's weight. The vertical magma conduit thus is similar to a passive, weak zone in the lithosphere that triggers earthquakes mainly driven by regional stresses.

Kilauea's rift zones produce shallow swarms of varied intensity and complexity arising from periods of summit inflation, slow intrusions, and rapid intrusions that may also result in eruptions. Slow intrusions may feed the rifts adjacent to the caldera during inflation, send slow pulses of magma (and hence earthquakes) down the rifts, or be aseismic except at the terminus of the intrusion where magma collects. Much of this paper documents earthquakes from swarms during 1962–84. To examine the dynamics of intrusion and dike formation, computer plots for each swarm are designed to show the position, depth, size and shape of the seismic zone, deflation and seismicity with time, and migration of earthquakes along the rift or vertically.

Rapid intrusions generally begin with earthquakes in a small volume near the main rift conduits at 3 km depth and may spread along the rift and upward. Migration and growth speeds are about 0.1 to 6 km/h. An intrusion often loses upward speed as it approaches the surface, or downrift speed as it nears its terminus. Earthquakes occur at and behind the front of the dike as the conduit widens and the walls compress. Barriers within the rifts, where the conduit is pinched shut or stress is concentrated, often generate clusters of earthquakes and act as places where intrusions start and stop. The most prominent barriers are adjacent to the summit magma reservoir and in the east rift zone below Pauahi Crater and Mauna Ulu, but many are present along both rifts. The Pauahi-Mauna Ulu barrier is important because many intrusions start there and move uprift and downrift, and it also marks a bend in the rift, where it intersects the Koae fault zone. A possible small magma reservoir below Pauahi Crater is recognized by the absence of earthquakes; this reservoir is dammed uprift of the Pauahi-Mauna Ulu barrier.

The most common earthquake migration direction at Kilauea is downrift and is presumably driven by gravity and a pressure gradient along the magma conduit. Upward earthquake migration is visible in many intrusions and reflects ascending magma presumably driven by buoyancy forces. The east rift zone between Kilauea caldera and Mauna Ulu is an anomalous zone of earthquake migration; uprift, downrift and bilateral migration of earthquakes are equally likely. This zone is also unusual in its high degree of activity, its northwest trend oblique to the regional stress, its shallowness of earthquakes, its ability to feed two intrusions simultaneously, and its short 2- to 3-hour interval from the beginning of an intense earthquake

**swarm to the start of an eruption. The upper east rift zone thus seems to be a multitiered and complex honeycomb of conduits. The various directions of earthquake migration in this area may result from a complex pattern of stresses and pressure gradients, or from an uprift-traveling pressure pulse within magma flowing downrift. The latter may have caused the reflection of a downrift earthquake migration off a rift barrier back uprift, as observed in many intrusions.**

**Intrusions occur in larger cycles that alternate between rifts. Intrusions are often grouped in pairs or triplicates within a few weeks of each other—they may retrace the same path or occur adjacent to their predecessors. In addition, four complete cycles of east-rift-zone to southwest-rift-zone shifts, each lasting 3–4 years, occurred during 1968–83. A basic cycle consists of several east-rift-zone intrusions (beginning near Mauna Ulu), a period of inflationary swarms at the summit, a major intrusion usually in the southwest rift, and about one year of no new intrusions before beginning the cycle again. This cycle may be an oscillatory tectonic process involving the south flank. A series of intrusions in one rift apparently helps trigger other intrusions and also compresses the adjacent flank. This compression inhibits additional intrusions and hinges open the other rift until a switch occurs. The Kalapana earthquake in 1975 may have disrupted the basic pattern set by the first two cycles: periods of inflationary swarms did not occur in 1977 and 1980–81, no southwest-rift intrusions occurred in 1977–78, and the switch from the southwest rift zone to the east rift zone in 1982–83 occurred without a pause.**

## INTRODUCTION

Few volcanoes in the world are as seismically active and as extensively monitored as Kilauea has been since 1960. The Hawaiian Volcano Observatory (HVO) has steadily expanded its seismic network and data-processing effort, and routinely analyzes several thousand earthquakes each year. This paper draws heavily on a catalog of about 70,000 earthquakes of all types carefully gathered by the past and present staff of HVO during 1962 through 1983.

Kilauea is a tholeiitic shield volcano, and eruptions occur in the summit caldera or from either the east rift zone (ERZ) or southwest rift zone (SWRZ) (fig. 43.1). The basic model of Kilauea has been refined by HVO through the years, but is not fundamentally changed from that stated by Eaton and Murata (1960) and Eaton (1962). The key feature of the Kilauea model is a magma reservoir beneath the caldera. The basic eruption cycle begins with gradual inflation of the magma reservoir as it fills via feeder conduits from below. The inflation is revealed by a bulge of the ground surface and by an increase of small earthquakes within the caldera. The summit becomes unstable when the barriers holding back the magma give way and magma rapidly intrudes the caldera or the rifts. Formation of vertical dikes appears to be the dominant process in rift-zone intrusion (for example, see Macdonald, 1956; Fiske and Jackson, 1972; Swanson and others, 1976a; Pollard and others, 1983). The intrusion may take a few hours or days and is revealed by a rapid deflation of the summit, inflation or extension above the new dike, an intense earthquake swarm caused by stress surrounding the new dike, harmonic tremor, and an eruption if the dike reaches the surface.

### THE SUMMIT MAGMA RESERVOIR

Deformation data provide the best evidence for the location and depth of the magma reservoir beneath Kilauea caldera. Using tilt data from 1960, Eaton (1962) determined a center of deflation 3–4 km beneath the southern part of the caldera. Fiske and Kinoshita (1969) obtained similar depths and a migrating pattern of uplift deformation centers using leveling data from 1966 and 1967. Dieterich and Decker (1975) used level and trilateration data from 1967 to infer a vertically elongate zone of inflation extending from about 1 to 3 km depth. Ryan and others (1983) modeled several subsidence events as magma withdrawal from a sill-like body. Careful inversions of tilt, level and trilateration data from several inflation and deflation episodes during 1966–70 produced a set of about 26 deformation centers within and just outside of the southern part of the caldera (Dvorak and others, 1983). The deformation centers scattered within a radius of about 2 km from a point 2 km south-southeast of Halemaumau Crater. Depths were mostly between 2 and 4 km, but occasional deformation centers may have been as deep as 7 km. The buried centers of deformation coincide with the seismically defined magma reservoir.

The above papers inferred that the magma reservoir is in fact a honeycomb of interconnected fluid pockets from the many different deformation centers. The top of the reservoir complex is about 2 km beneath the southern part of the caldera, and it extends at least to 4 km depth. The nature of magma storage below 4 km is difficult to determine from deformation measurements, because surface displacements are dominated by the shallowest active parts of the reservoir and because parts of the reservoir below 4 km may be too weak to partake in large elastic changes.

The magma reservoir was delineated seismically and was spatially related to the dynamics of intrusions and earthquake swarms (Koyanagi and others, 1976a, 1976b). Using selected summit earthquakes during 1971–73, they identified several regions: (1) a vertical conduit below about 7 km depth delineated by mostly long-period earthquakes, (2) a region of relatively low seismicity between about 3 and 6 km depth that they interpreted as the magma reservoir, (3) a seismically active cap above the magma reservoir, and (4) two seismic zones that form the uppermost parts of the rift zones adjacent to the reservoir. Their study also related the temporal activity of these regions to the eruption cycle. The cap above the magma reservoir is mainly active during periods of inflation and prior to eruptions and intrusions. The rift zones adjacent to the reservoir are mainly active when magma intrudes the rift zones and deflates the reservoir.

The three-dimensional distribution of hypocenters beneath Kilauea's summit and upper ERZ was clarified by a transparent model and series of perspective figures by Ryan and others (1981). Using the same 1971–73 data as Koyanagi and others (1976a), Ryan and others expanded the discussion of magma storage and transport and identified the same seismic and aseismic regions. In addition, the latter paper identified a vertical pipe below the upper ERZ and inferred a feeder conduit connecting its base with Kilauea's main conduit. The pipe was about 3 km downrift of Kilauea caldera (1 km southwest of Kokoolau) and was defined by

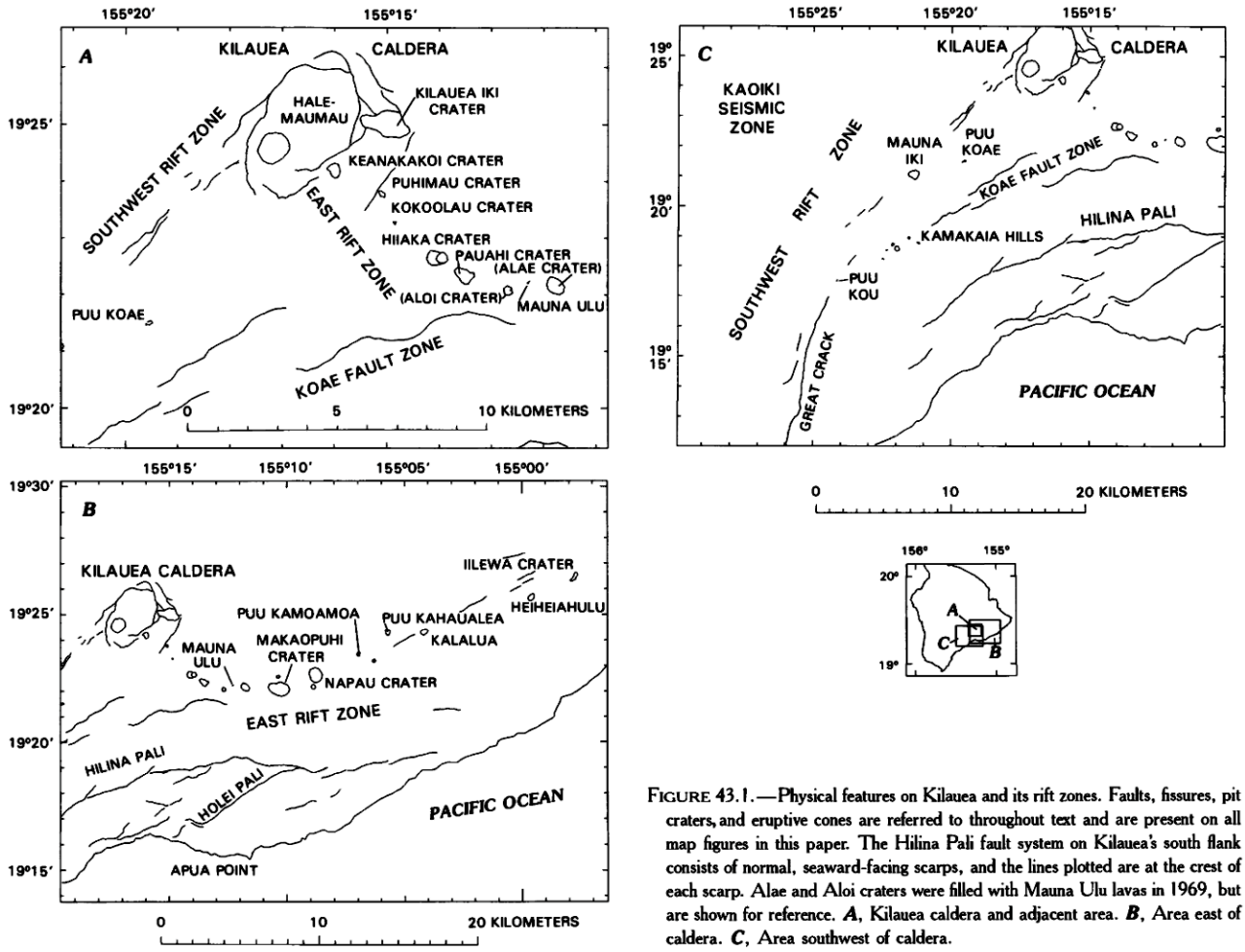


FIGURE 43.1.—Physical features on Kilauea and its rift zones. Faults, fissures, pit craters, and eruptive cones are referred to throughout text and are present on all map figures in this paper. The Hilina Pali fault system on Kilauea's south flank consists of normal, seaward-facing scarps, and the lines plotted are at the crest of each scarp. Alae and Aloi craters were filled with Mauna Ulu lavas in 1969, but are shown for reference. ***A***, Kilauea caldera and adjacent area. ***B***, Area east of caldera. ***C***, Area southwest of caldera.

hypocenters between 1.9 and 5.7 km depth. This ERZ pipe is not visible in the present study, which uses a much expanded and revised data set.

In addition to seismicity, the newer technique of three-dimensional seismic-velocity inversion reveals the presence and location of Kilauea's magma reservoir (Thurber, chapter 38; 1984). The reservoir is recognized as a zone at least 0.5 km/s slower than the surrounding rock, and its position coincides with that obtained from other methods within the resolution of the technique.

## INFERRING MAGMA FROM EARTHQUAKES

Ideally Hawaiian earthquakes could be used to infer the positions and dynamics of magma conduits and storage reservoirs, but several precautions must be heeded when doing this. Most importantly, earthquake generation requires rock that is both stressed and brittle. In addition, rock that already contains fractures or faults is far more likely to be seismically active than an equivalent perfectly homogeneous region. Aseismic regions, however, may be either unstressed, unfractured or hot and ductile. Direct associations, therefore, cannot always be made between seismicity and magma. In addition, pressured magma as a source of stress can generate earthquakes in brittle rock that is adjacent to or intermixed with the magma conduit. Earthquakes may occur on systems of fault planes between echelon tips of active dikes (Hill, 1977). Thus, two possible lines of thought could lead one to infer that magmatic zones are either seismic or aseismic. Thus, other factors such as earthquake time behavior, their relation to deformation measurements and geology must be considered. Relating seismicity to magma is not a simple process, but requires a fabric of related observations and assumptions.

We generally interpret regions of swarm seismicity to be zones of dike intrusion or magma conduits (the rift zones or vertical feeder conduit). An aseismic region adjacent to volcanically related seismicity is either an inferred zone of primary magma storage (the

summit magma reservoir) or a stable block (such as Kilauea's north flank).

Earthquake locations have both systematic and random errors, and give a somewhat blurred view of the magma system. Largely because of a finite number of stations and an inability to perfectly model the true three-dimensional velocity structure, the earthquake location error and hence resolution in the summmit region is typically several hundred meters and sometimes more. Therefore, resolving structures of meters to tens of meters in size is hopeless, although determining and using a three-dimensional velocity model offers some improvement locally (Thurber, chapter 38; Thurber and others, 1984).

All earthquakes in Hawaii are ultimately attributable to volcanism, but several characteristics of seismicity can be used to infer the closeness of its relation to magma. We use the term "volcanic" earthquake for those that are in or immediately adjacent to magma conduits. By "tectonic" earthquake, however, we mean those that are at least one step removed from a magma conduit: although deriving their driving stress from dike intrusion or volcano growth, they may be several kilometers from any magma. Kilauea's volcanic earthquakes occur beneath its mappable rift zones and summit caldera, where they are less than 5 km deep. Volcanic seismicity is also typical of the vertical conduit below the reservoir, which extends to 55–60 km depth. Tectonic seismicity occurs on Kilauea's active flanks, such as south of the rift zones (for example, Koyanagi and others, 1972; Crosson and Endo, 1982), and in the Kaoiki seismic zone between Mauna Loa and Kilauea's SWRZ (for example, Endo and others, 1978; Koyanagi and others, 1984; Endo, 1985). These flank earthquakes typically occur between about 5 and 13 km depth. Location and depth are thus good discriminants of volcanic and tectonic earthquakes.

The time behavior of a sequence, seismic *b*-value, maximum magnitude and association with tremor also are significantly different in volcanic and tectonic earthquake source areas. Volcanic earthquakes at Kilauea typically occur in swarms (a sequence more or less isolated in time and without a single dominating mainshock). The swarm may last for hours or days if it accompanies rapid dike intrusion in the summit or rift zones, or it may be days or weeks long if driven by the gradually inflating magma reservoir. Tectonic earthquakes, however, occur both continuously and in mainshock-aftershock sequences. Mogi (1963) interpreted earthquake swarms as characteristic of concentrated sources of stress and heterogeneous material properties (such as magma conduits and dike swarms), and mainshock-aftershock sequences as typical of more homogeneous regions (such as volcano flanks). Swarms are also typical of geothermal regions. Because intrusions and eruptions generally produce both earthquake swarms and tremor, their frequent association implies that moving magma is a direct cause for both.

In addition to swarm character, volcanic earthquakes on Hawaii have other distinguishing characteristics. As will be discussed later, volcanic events generally show higher seismic *b*-values, which is the slope of the statistical frequency-magnitude distribution. The maximum magnitudes of tectonic events are larger because these regions can sustain higher stress over a larger volume and because the faults or other stressed structures that can slip in a single event are larger than in volcanic earthquake regions. The $M=7.2$ Kalapana earthquake in 1975 (for example, Ando, 1979) ruptured nearly the entire length of Kilauea's south flank. The Kaoiki seismic zone broke with a $M=6.6$ event in 1983 (Koyanagi and others, 1984). By contrast, the largest volcanic events located near Kilauea's magma system are about magnitude 4.

The differing behavior of earthquake sequences in time, the *b*-values and maximum magnitudes of volcanic and tectonic earthquakes are all expressions of the differing regimes in which they occur: the magmatic zones are heterogeneous and highly fractured, and have concentrated sources of stress; the tectonic flanks are more homogeneous in stress and material properties. Kilauea's earthquakes are somewhat analogous to those on plate boundaries on a larger scale around the world: the characteristics of volcanic earthquakes are typical of spreading ridges, and tectonic events bear resemblance to those at transcurrent faults and subduction zones.

Note that many of the differences we infer between volcanic and tectonic earthquakes are statistical or based on a property of a group of events. These methods will of course not work for a single earthquake. No difference may be apparent in individual seismograms between the two event types, but discrimination occurs only after it is located and assigned to a region known to be volcanic or tectonic. One may thus use either location or group behavior to determine the type of a group of events, and only one type of information may be available at a sparsely monitored volcano or one whose magma system has a poor surface expression.

Earthquakes elsewhere in Hawaii are analogous to those at Kilauea. The submarine volcano Loihi generates earthquakes of both types, indicating that it is an active volcano with mobile flanks (Klein, 1982a). Mauna Loa's summit and rifts produce volcanic seismicity (for example, Decker and others, 1983), and tectonic earthquakes are characteristic of its southeast flank to the west of Kilauea. Earthquakes scattered elsewhere around the island appear to be mostly tectonic and may often be generated by deformation of the lithosphere and subsidence of the island under its own weight. Seismicity of Kilauea's vertical conduit below about 25 km depth displays some characteristics of both volcanic and tectonic regimes. At this depth the seismic zone is much wider than those above and may represent a distributed network of magma channels. The broad conduit complex may then experience more uniform stresses associated with lithospheric flexure.

The remainder of this paper will explore some aspects of Kilauea's volcanic earthquakes in space and time. We will begin with a description of the earthquake data and how it is processed. Then we examine the three-dimensional seismicity structure of Kilauea through a series of earthquake depth slices. The physical relations and time histories of the seismic zones seen in the depth slices provides a basis for their classification as volcanic or tectonic. The following sections explore the size and shape of Kilauea's shallow reservoir and vertical magma conduit using maps and cross sections of earthquakes. We then examine the chronology of shallow earthquake swarms in Kilauea's rift zones as one expression of magma flow and storage. This section does contain interpretations of

individual swarms, but casual readers may wish to skip it owing to its length and chronological format. The paper concludes with a summary and discussion of various types of rift swarms and what they reveal of the intrusion process, the structure of the rifts, and large-scale interactions of intrusions with each other.


### ACKNOWLEDGMENTS

The vast amount of earthquake data summarized here is the work of many of the past and present staff of the Hawaiian Volcano Observatory. People whose persistence in the face of boredom contributed to the completeness and continuity of this data set include Karen Meagher, Pat Stevenson, Irene Takayesu, Alvin Tomori and many others. George Kojima's dedication to maintaining and recording the seismic network over the years made it all possible. We are grateful to Elliot Endo and Michael Ryan for their thoughtful reviews, and to Bob Decker for his editorship and determined coaxing to get the manuscript ready for this volume.


## EARTHQUAKE DATA GATHERED BY THE HAWAIIAN VOLCANO OBSERVATORY

A network of high-gain seismometers has operated on Kilauea since the 1950's, and its steady improvement brought an explosion in both quantity and quality of earthquake data. The number and sensitivity of stations, their recording and timing accuracy, and the effort devoted to reading records and locating earthquakes have all greatly improved. The growth of the seismic network operated by HVO is clear from figure 43.2, which shows the station sites operating in 1963, 1973 and 1983. The greater number and improved accuracy of located earthquakes means that small swarms during the 1980's often can be studied in greater detail than larger sequences in the 1960's. The characteristics and growth of the network are documented by Klein and Koyanagi (1980), but we briefly summarize a few milestones here:

1958–60 Network of six Kilauea summit stations centrally recorded at HVO on smoked paper with telemetry by overland wire. Five distant stations independently timed and recorded.

1962–63 Increase in seismic staff (R.Y. Koyanagi) resulted in daily analysis and more earthquakes systematically timed and analyzed. Addition of 3 smoked-paper recorders.

1968–71 Rapid increase in number and sensitivity of stations. Introduction of telemetry by radio and recording on a Develocorder permit a reading precision of 0.10–0.05 s. Additional staff increase.

1974–75 Growth in number of stations, especially on Mauna Loa.

1978–79 Arrival of Eclipse computer at HVO for all seismic processing. Timing precision now 0.01–0.02 s.

1985 Network consists of 50 station sites on the Island of Hawaii. Increased numbers of 3-component stations.

The improvements in the seismic network resulted directly in increases in numbers of Kilauea earthquakes (a smaller magnitude

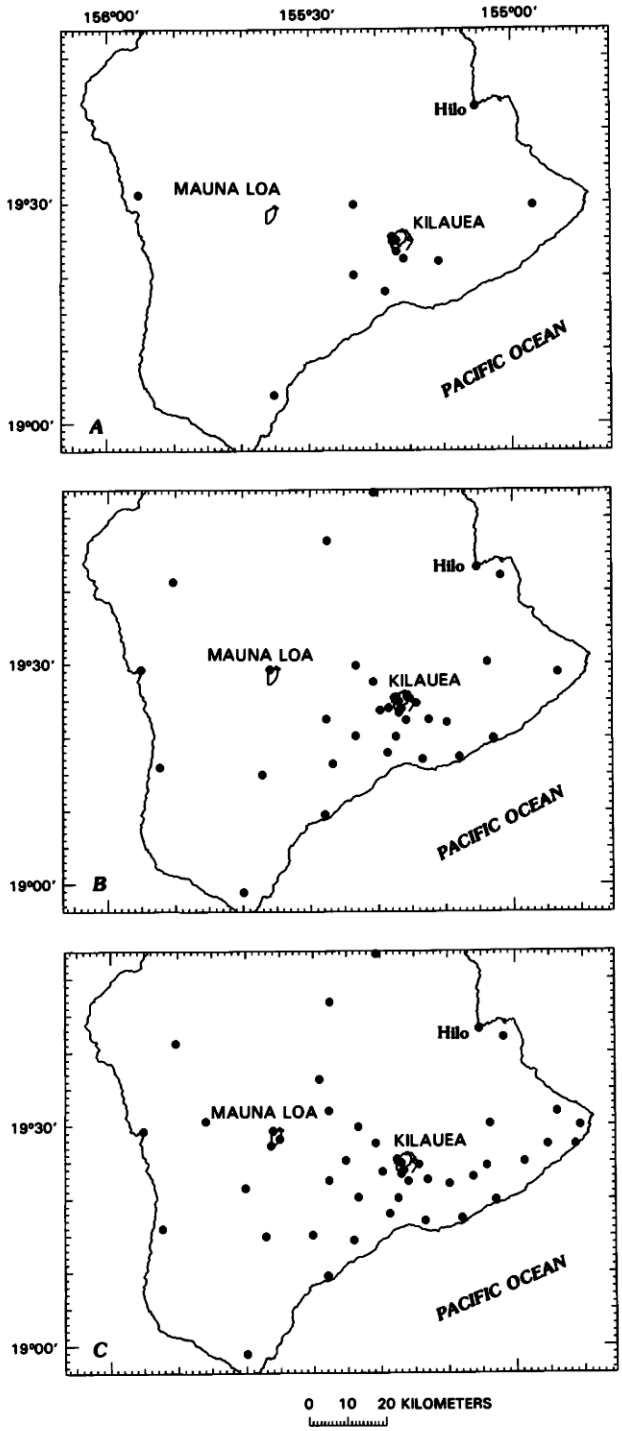


FIGURE 43.2.—Growth and coverage of network of seismic stations operated by the Hawaiian Volcano Observatory. *A*, December 1963, 13 station sites. *B*, December 1973, 34 station sites. *C*, December 1983, 47 station sites. Faults, fissures, and pit craters are as shown in figure 43.1.

above which events are complete) and in the precision of locations. Shallow Kilauea earthquakes in the early 1960's were often only located if larger than about magnitude 2, but the level of completeness in the early 1980's is now about 1. This means roughly a tenfold increase in the number of events with which to study swarms and other features, and smaller magma intrusions can now be identified. The number of seismic stations used for earthquake location by computer was often less than 10 in the 1960's, but was usually more than 20 in the 1980's. The level of completeness of Kilauea events deeper than about 13 km and flank earthquakes more than about 10 km from the caldera has been about magnitude 2 in the 1970's and 1980's. Structures such as magma conduits revealed by earthquakes can now be resolved and associated reasonably well with geologic features. In the early 1960's location and depth errors of 2–5 km meant swarms looked like formless clouds, but errors of 0.5–1 km in the 1980's give swarm clusters internal detail.

All earthquake data presented in this paper have been reprocessed using the same procedures currently used to locate earthquakes at HVO. Thus no bias occurs to the earlier hypocenters other than larger errors resulting from sparser station coverage and poorer timing precision. The earthquake data presented in this paper are more systematically located and slightly more accurate than those used in previous papers (for example, Koyanagi and others, 1976; Ryan and others, 1981). Annual seismic summaries (for example, Nakata and others, 1982) list earthquake hypocenters and other seismic data together with a description of the analysis procedure. The computer program HYPOINVERSE (Klein, 1978) locates all events. A crustal velocity model incorporating linear gradients within velocity layers (Klein, 1981) was used. Earthquake depths determined by this method are referred to the land surface above the hypocenter. In the Kilauea summit region the depth datum is about 1 km above sea level. Both the velocity model and two sets of station corrections were designed to minimize the residuals between observed and calculated arrival times and were derived using numerous earthquakes under south Hawaii. The stations which operated during the year, and their locations and timing corrections are listed in the annual seismic summaries. The space, time and magnitude coordinates of earthquakes are plotted for this paper using the program QPLOT (Klein, 1983).

## A THREE-DIMENSIONAL OVERVIEW OF KILAUEA SEISMICITY

Representing the three-dimensional distribution of earthquakes is difficult on any two-dimensional plot. Klein and Koyanagi (1985) produced a seismicity map of the south side of Hawaii, but depths are only indicated by one of four symbol colors. One of the easiest ways to visualize earthquakes is by depth slices using only a narrow, horizontal layer of events plotted on each map. Depth slices suit Kilauea very well because patterns change with depth and an earthquake's depth is often useful in discriminating it as volcanic or tectonic. The intent of this section is to present an overview; later sections of this paper will explore the magma system in more detail.

A series of depth slices for Kilauea from the surface to 40 km depth is shown in figure 43.3. Because the vertical magma conduit broadens with depth, deeper slices should cover a broader area. Figure 43.4 thus includes the entire south side of Hawaii and covers depths from 20 to 60 km. Figures 43.3 and 43.4 include data from 1970 through 1983. Figure 43.5 duplicates the slices of figure 43.4, but covers the 1960–69 period. The earlier data is plotted separately because it differs somewhat in pattern and is poorer in quality. The layers plotted thicken from 1 km at the surface to 4 km at depth, thus compensating for both spatial patterns that change less rapidly at depth and the slightly larger location errors associated with deeper events. Typical location errors for each depth range are about one-half the cutoffs chosen, which only eliminate the poorest events. Thus, an error in depth could possibly place a given event in an adjacent layer from where it actually occurred. Descriptions of the main features in different depth ranges follow.

### THE SHALLOW CRUST BETWEEN 0 AND 5 KILOMETERS DEPTH

Events in the depth range 0–5 km are mostly volcanic earthquakes at Kilauea's caldera, rift zones and the Koae fault zone. Caldera seismicity extends mainly from 0 to 4 km depth. The aseismic magma reservoir beneath the southern part of the caldera is indistinguishable at this scale. Earthquakes in the northern and central parts of the caldera are most intense between 1 and 3 km depth and thus are mainly in the rocks of the caldera floor capping the summit reservoir. Southern caldera seismicity occurs both above and to the side of the reservoir and thus is active during periods of inflation and during rapid intrusions of dikes connected to the reservoir.

The most active part of the ERZ is between 2 and 4 km depth, at which nearly all of the 25 km of rift just east of the caldera has experienced some seismicity during 1970–83. Most of these earthquakes were produced during rapid intrusions or eruptions. The main ERZ magma conduit is most active at about 3 km depth. Unlike the SWRZ and the rest of the ERZ, the 6 km of ERZ adjacent to the caldera is seismically active nearly to the surface (fig. 43.3*A*). This shallow part of the ERZ may form a secondary conduit system that is intruded repeatedly and is a region brittle and stressed enough to generate earthquakes. This shallow earthquake zone could also be the result of tensile deformation when the main conduit below is intruded.

The SWRZ seismicity also forms a narrow and nearly continuous band. It does not exactly follow the course of the rift at the surface, but heads south from the caldera for about 3 km before bending to the southwest. The center of the ERZ earthquake band is displaced about 0.5 km south of the surface axis of the rift (defined by pit craters and eruptive centers), whereas the SWRZ seismic axis is displaced as much as 2 km south of the surface rift. The buried SWRZ magma conduit active during the last decade thus has no obvious surface expression. The SWRZ probably consists of a 3-km-wide zone of parallel dike systems that are active

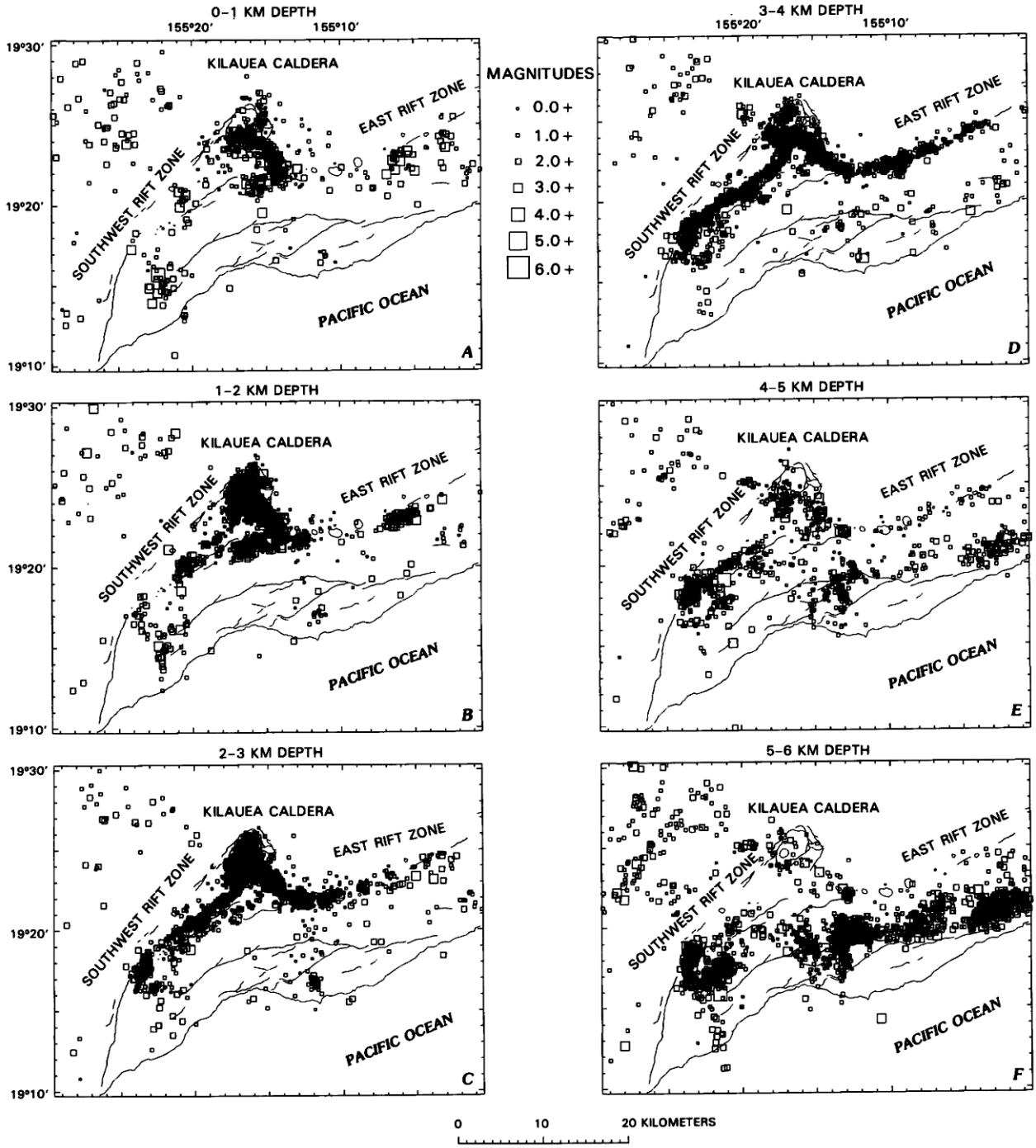


FIGURE 43.3.—Depth slices from 0 to 40 km showing hypocenters of Kilauea earthquakes, 1970–83. Earthquake symbols are squares whose size depends on magnitude. Maximum horizontal error of plotted hypocenters is: ***A–O***, 2 km; ***P–T***, 4 km. Maximum vertical error is: ***A–J***, 2 km; ***K–O***, 3 km; ***P–T***, 5 km. Faults, fissures, and pit craters are as shown in figure 43.1.

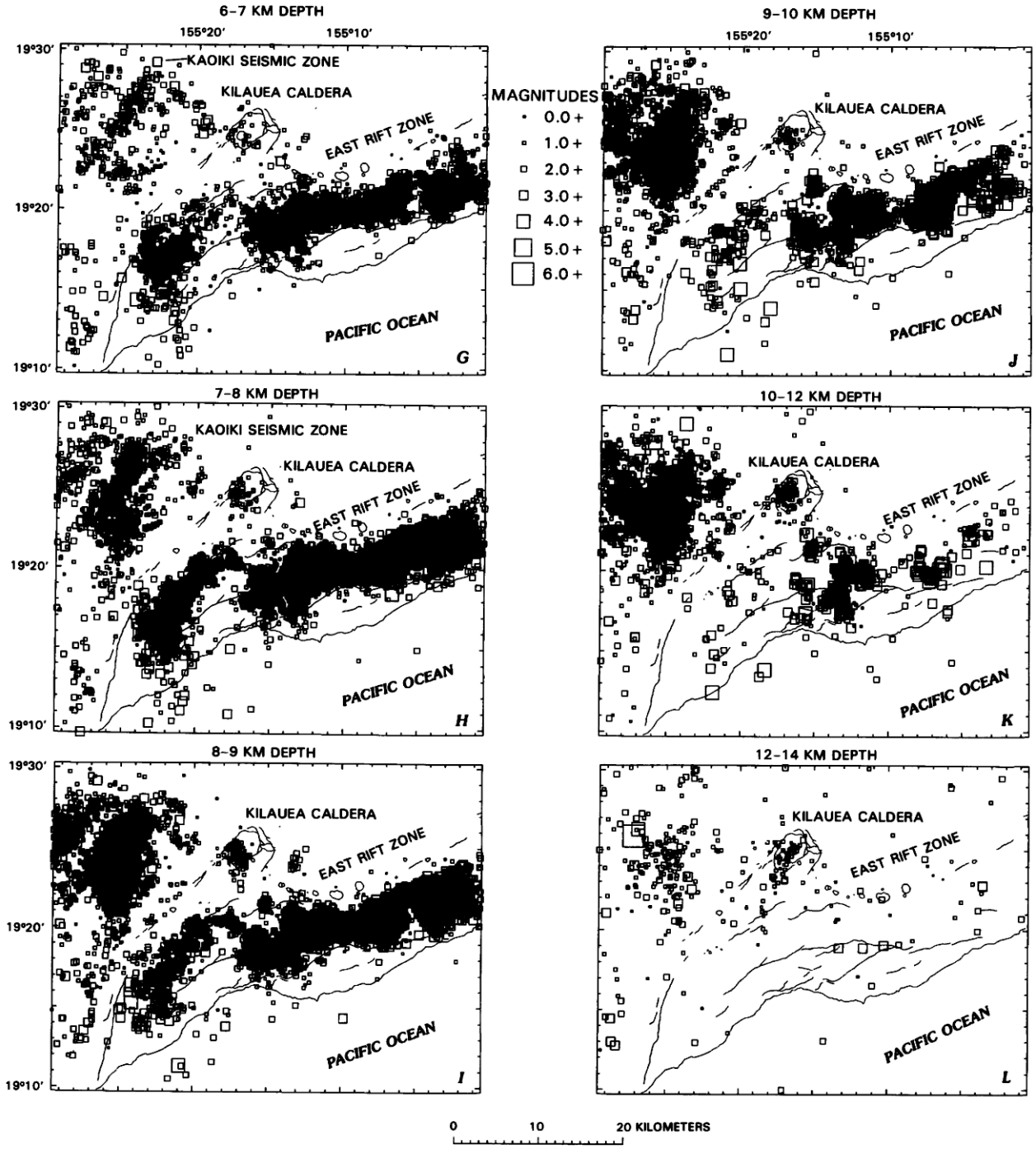


FIGURE 43.3.—Continued.

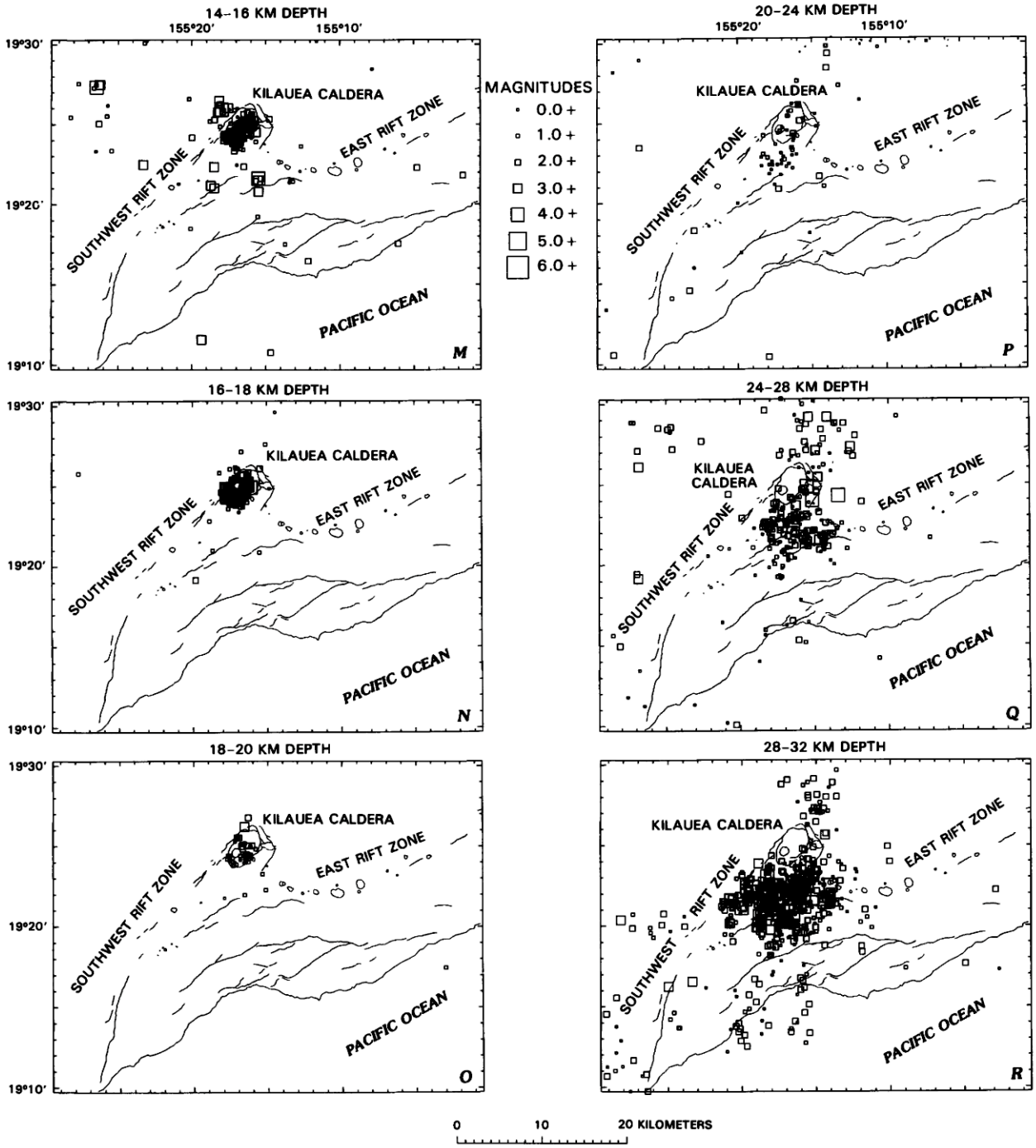


FIGURE 43.3.—Continued.

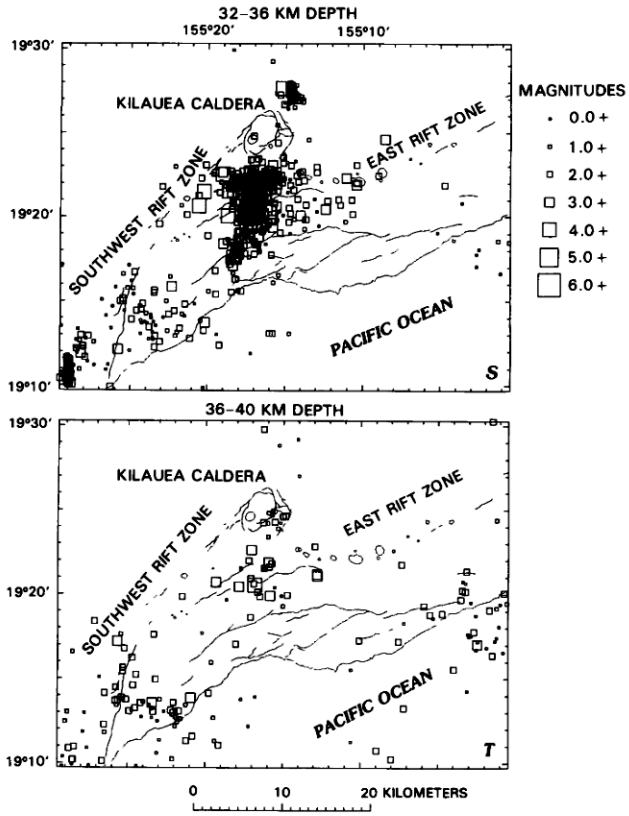


FIGURE 43.3.—Continued.

at various times and that evolve with time. Because the contemporary magma conduits of both the ERZ and SWRZ are south of the established surface features, the vertical dike trajectories must dip southward. The offset of earthquakes and surface geology could be a consequence of southward migration of the rifts with time (Swanson and others, 1976a).

Like the ERZ, the primary conduit of the SWRZ is at about 3 km depth, with seismicity extending for about 1 km above and below. A notable exception is the shallow clump just downrift of Puu Koae (19°20′ N., 155°20.5′ W.; fig. 43.3*A*, *B*). Surface cracks appeared in this area during the August 1981 SWRZ intrusion and were probably caused by a dike branching upward from the main conduit. A similar shallow extension occurs above the ERZ conduit near Mauna Ulu (19°22′ N., 155°12.5′ W.; fig. 43.3*B*). Much of the shallow seismicity near Puu Kamoamoa and Puu Kahaualea (19°23′ N., 155°06′ W.; fig. 43.3*A*, *B*), however, occurred in a series of extended swarms that coincided with inflation of the rift near the earthquake epicenters. The very shallow seismicity thus appears to be over a part of the rift conduit that was accumulating magma and is analogous to the seismic cap over the summit magma reservoir. The rift inflation occurred cyclically and coincided with times of slow summit deflation.

The linear part of the SWRZ active during 1970–83 extends only to the north end of the Great Crack (19°17′ N., 155°25′ W.; figs. 43.1*C*, 43.3*A–E*), where the rift bends to a more southerly trend. The seismicity in this lower southwest rift (LSWR) region is somewhat complex and diffuse. Earthquakes scatter south of the rift over a wide range of depths. Between 0 and 3 km depth this area is active most of the way to the coast, and below 2 km the seismically active rift branches into parallel segments just south of the main rift axis. Unlike the rest of the SWRZ, the LSWR can be intensely active below 4 km depth, and seismicity merges with the region of tectonic earthquakes in Kilauea's south flank. In addition, LSWR earthquakes accompany both the larger SWRZ intrusions and major tectonic events on the south flank, such as the November 1975 Kalapana earthquake. The LSWR thus seems to be a weak but brittle zone extending from 0 to 10 km depth in which activity can be triggered either by intrusions in the SWRZ to the north or by tectonic events to the east.

Other scattered events at 0–4 km depth occur away from the volcanic conduits. The events distributed broadly through the upper part of Kilauea's south flank occurred both as aftershocks of the $M=7.2$ Kalapana earthquake and as induced events associated with larger ERZ intrusions (Dvorak and others, 1985). This area thus responds both to large scale slip in the lower crust (tectonic events) and to compressional stress generated by dike intrusion to the north (volcanic events). The Kaoiki seismic zone also produces some shallow tectonic earthquakes even though most activity lies below 5 km depth. Small isolated clusters of tectonic earthquakes also occur near Apua Point (0–4 km depth) and 4 km west of Kilauea caldera (3–8 km depth).

## TECTONIC EARTHQUAKES BETWEEN 5 AND 14 KILOMETERS DEPTH

The vast majority of Kilauea earthquakes at 5–14 km depth are tectonic events on the south flank and in the Kaoiki seismic zone. The tectonic events plotted in figure 43.3*F–L* are composed of both continuous seismicity and aftershocks of larger earthquakes. The majority of earthquakes on the portion of the Kaoiki seismic zone included in figure 43.3 show right-lateral slip on northeast striking planes (Endo and others, 1978). Lineations of earthquakes also follow this trend. The typical focal mechanism of south-flank events is low-angle faulting with the upper block slipping seaward (Crosson and Endo, 1982). Unlike the Kaoiki seismic zone, no clear alignment of hypocenters on fault planes is apparent, and many slip planes are active.

## THE MAGMA CONDUIT BETWEEN 5 AND 20 KILOMETERS DEPTH

The vertical magma conduit below Kilauea caldera is clearly defined by hypocenters below about 6 km depth. In the depth slices of figure 43.3*G–O*, the seismic conduit is centered below Halemaumau and Kilauea's summit magma reservoir. The shape and size of the seismic conduit varies only slightly with depth, and typically is about 3 km in diameter. The earthquake location errors from both random and systematic sources means that small variations in cross-sectional shape and a precise diameter probably are not significant within about 1 km. It is tempting to interpret the ring of seismicity in figure 43.3*N* surrounding an aseismic magma conduit, but the precision of hypocenter position does not justify the interpretation. The earthquakes represent a zone of deformation in brittle rock surrounding the conduit itself, which is probably much smaller than the seismic zone and may even be multiple. An upper limit to the diameter of the seismically active conduit complex is thus about 3 km. Magnitudes of these events are small and seldom exceed 3.0.

## THE MAGMA CONDUIT BETWEEN 20 AND 40 KILOMETERS DEPTH

The seismicity of the magma conduit changes character in several ways below 20 km: (1) the earthquake zone broadens to about 13 km in diameter (fig. 43.3*R–S*) (2) the seismic pipe plunges southward, unlike its vertical direction above 20 km; (3) the activity is more intense, with more events as large as magnitude 4.5; and (4) events are more continuous in time and generally not in swarms like the seismicity above. Earthquakes in the upper conduit are thus typically volcanic, whereas those between 20 and 40 km are mostly tectonic. The broadening with depth and southward plunge of the seismic conduit were plotted but not interpreted by Koyanagi and Endo (1971).

Inversion of teleseismic *P*-times for lateral velocity variations (Ellsworth and Koyanagi, 1977) showed another change in the conduit that occurs near 20–30 km depth. Although the resolution was limited by the 8-km wavelength, the average velocity is a few percent low directly below and to the south of Kilauea caldera at 28–58 km depth, suggesting a laterally extensive conduit system. Conduit velocities above that depth, however, are several percent higher than their surroundings (Ellsworth and Koyanagi, 1977; Thurber, 1984). These inversion studies also demonstrate high seismic velocities in the upper crust below the rifts, suggesting that a narrow conduit lies within a high-velocity intrusive complex in both the rifts and upper vertical conduit.

The narrow finger of earthquake hypocenters between 5 and 20 km depth is adjacent to the magma conduit and is thus seismically somewhat analogous to the shallow rift zones. The stress causing earthquakes in the upper pipe is thus partly derived from magma pressure within the conduit. The stress driving the earthquakes centered near 30 km depth, however, seems to be more than just that from magma pressure within the conduit complex. The magma conduit apparently passes through the 30-km-deep seismic zone and may have triggered its formation initially. But the size and intensity of the 30-km-deep seismic zone indicate a more regional stress source. Possibilities include flexure of the lithosphere under the gravitational load of the island or response to tractional stress applied from the volcanic edifice. Depletion of mass near this depth could also cause intense local seismicity. The behavior of these earthquakes in time (see next section) provides additional evidence bearing on the cause of these earthquakes.

Kilauea's magma conduit seismicity below 20 km must be examined in the context of a wider seismic region. Figure 43.4 plots depth slices below 20 km and includes deeper earthquakes from Mauna Loa and Loihi Volcanoes. The main seismic root of Kilauea is the prominent feature between 20 and 40 km, but a smaller funnel-shaped zone between 24 and 34 km is recognized just north of the caldera (figs. 43.3*Q–S*, 43.4*B-D*).

## THE MAGMA CONDUIT AND HOT SPOT BELOW 40 KILOMETERS DEPTH

Earthquakes below about 30 km depth mostly occur in a wide band roughly coincident with the south coast of Hawaii (fig. 43.4*C–J*). The deep seismic zone consists partly of dense earthquake clusters (fig. 43.4*F–H*). The small clusters do not extend vertically more than about 8 km, so they cannot clearly be identified with long magma conduits. The clusters may occur at places weakened by past and present magma flow, or simply at points having a high density of fractures. Seismicity concentrates in the triangle with corners at Kilauea, Mauna Loa and Loihi, but also extends to the northeast and southwest. Kilauea loses its narrow seismic root at about 40 km depth in this diffuse cloud. Earthquakes become sparse below about 50 km (fig. 43.4*I–J*) and none are located reliably below 60 km depth.

Earthquakes mark an isolated, narrow conduit beneath Mauna Loa that can be traced between about 28 and 48 km depth (fig. 43.4*C–G*). The earthquakes north of Hilo around 40 km depth are mostly aftershocks of the April 1973 Honomu earthquake (Unger and Ward, 1979).

Most deep earthquakes occur continually, which suggests a relatively uniform stress by analogy with crustal events. A few deep earthquakes are in swarms, which may be associated with pulses of ascending magma. The part of the seismic zone equidistant from Kilauea, Mauna Loa and Loihi is a frequent source of deep harmonic tremor, and magma certainly is present there. Tremor originating in this region can be quantitatively related to Kilauea's magma supply and transport to the shallow reservoir (Aki and Koyanagi, 1981). The coincidence of tremor, of the center of the deep seismic zone, and of the major earthquake cluster shown in figure 43.4*E–G* suggests that the contemporary Hawaiian hot spot is centered there (Klein, 1982a).

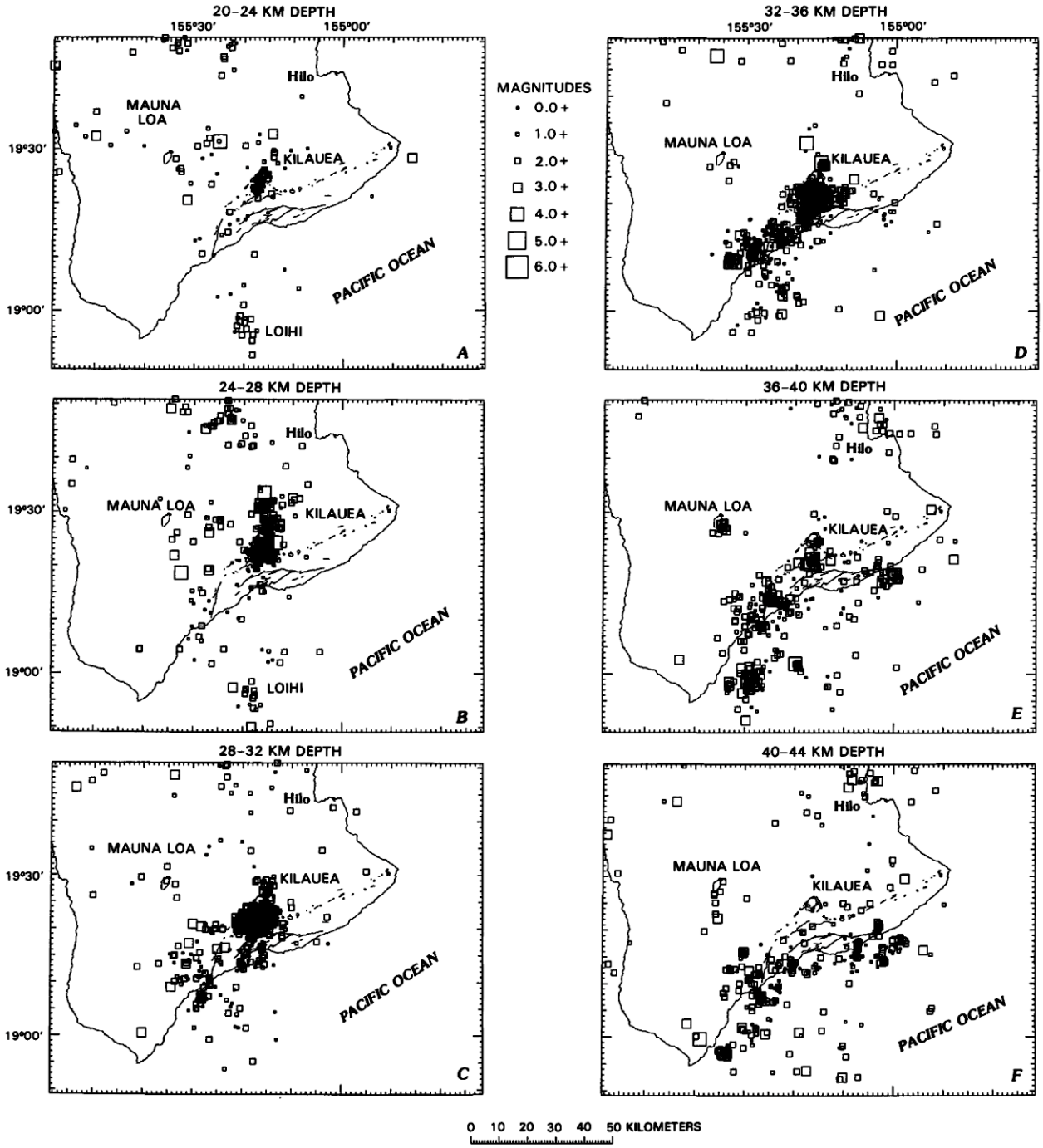


FIGURE 43.4.—Depth slices from 20 to 60 km showing hypocenters of south island earthquakes, 1970–83. Earthquake symbols are squares whose size depends on magnitude. Maximum horizontal and vertical errors for *A–J* are 5 and 7 km, respectively. Note that *J* includes hypocenters to 99 km depth, but those below 60 km are not reliably located. Faults, fissures, and pit craters are as shown in figure 43.1.

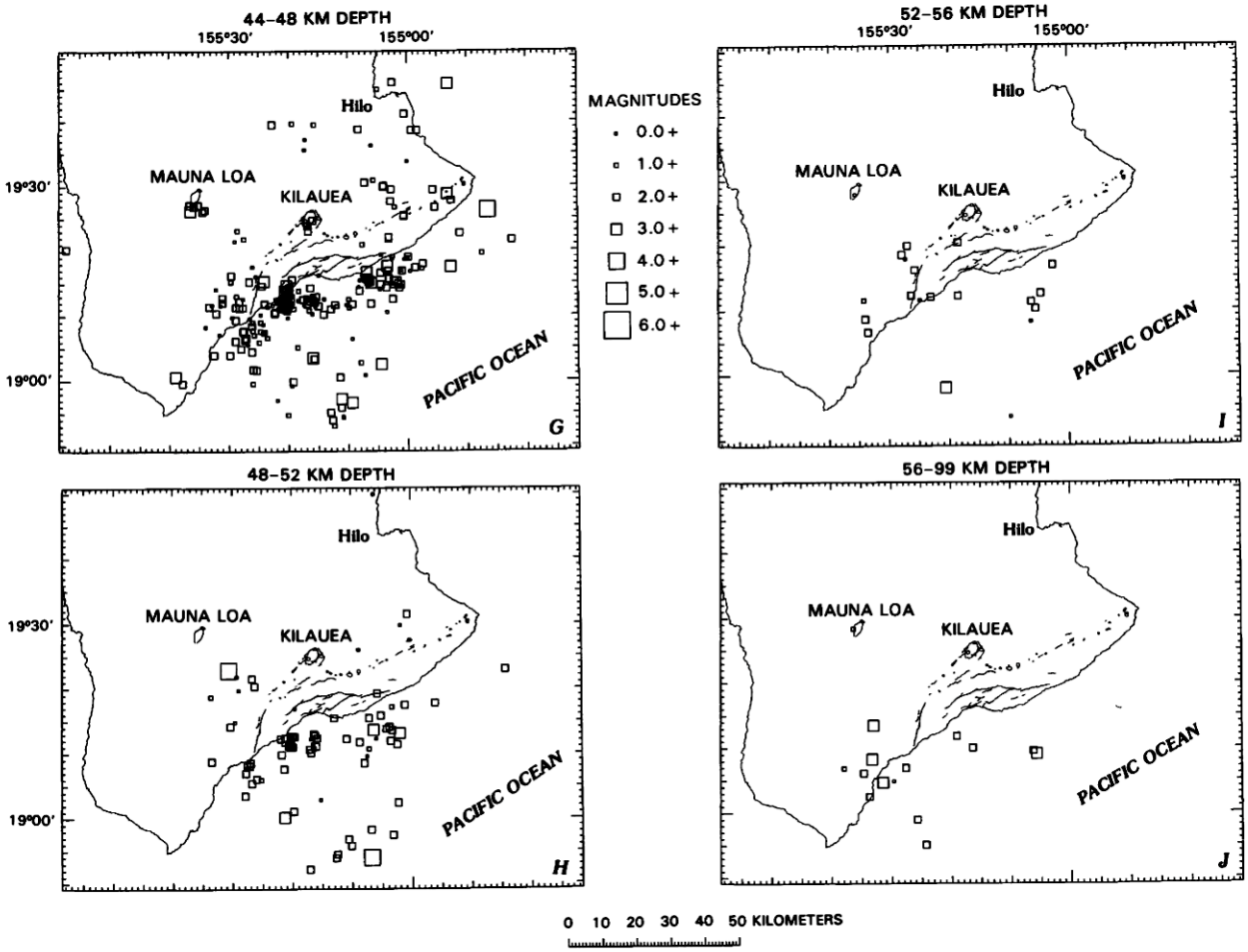


FIGURE 43.4.—Continued.

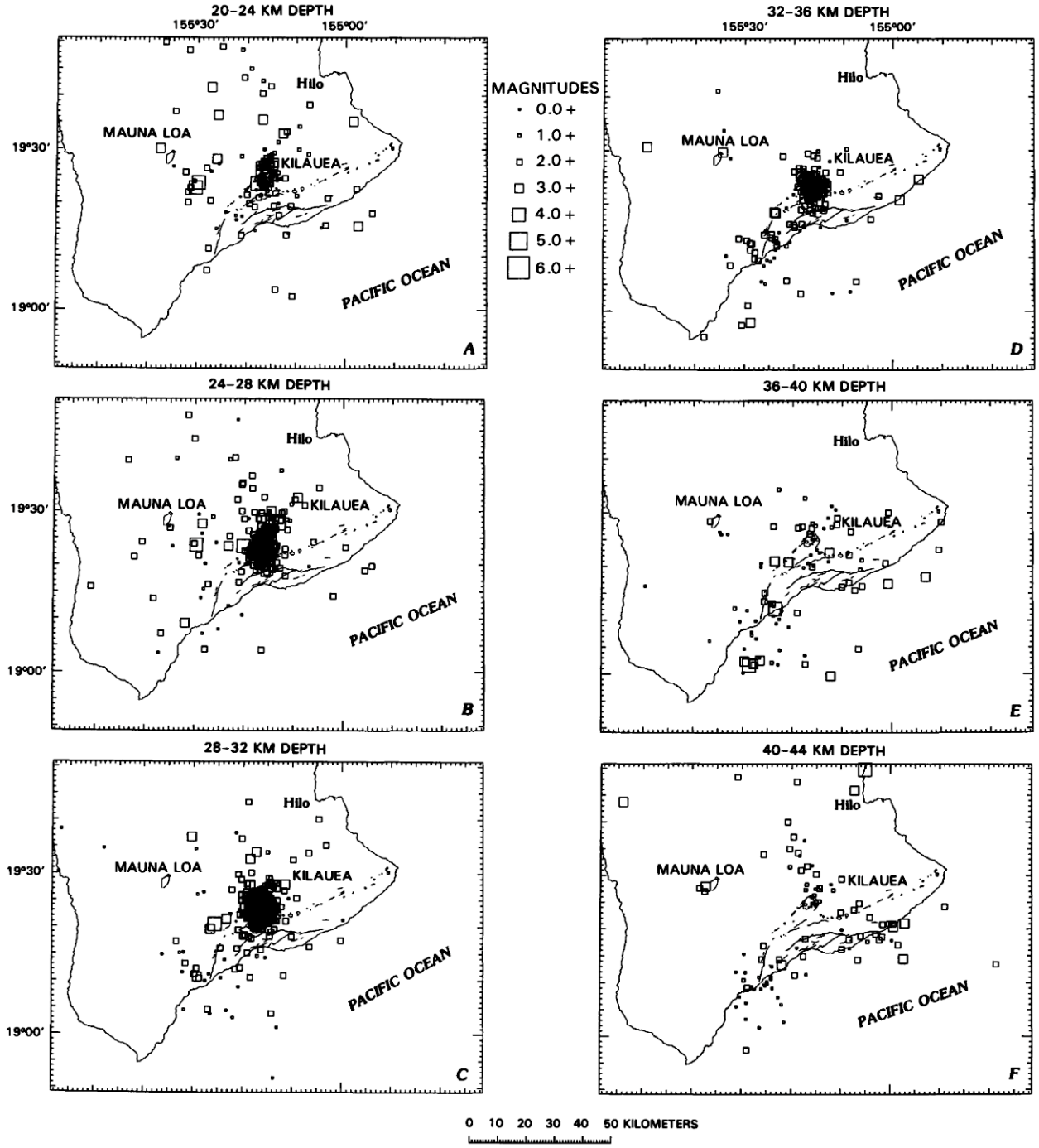


FIGURE 43.5.—Depth slices from 20 to 60 km showing hypocenters of south island earthquakes, 1960–69. Earthquake symbols are squares whose size depends on magnitude. Maximum horizontal and vertical errors for *A–J* are 10 and 15 km, respectively. Note that *J* includes hypocenters to 99 km depths, but those below 60 km are not reliably located. Faults, fissures, and pit craters are as shown in figure 43.1.

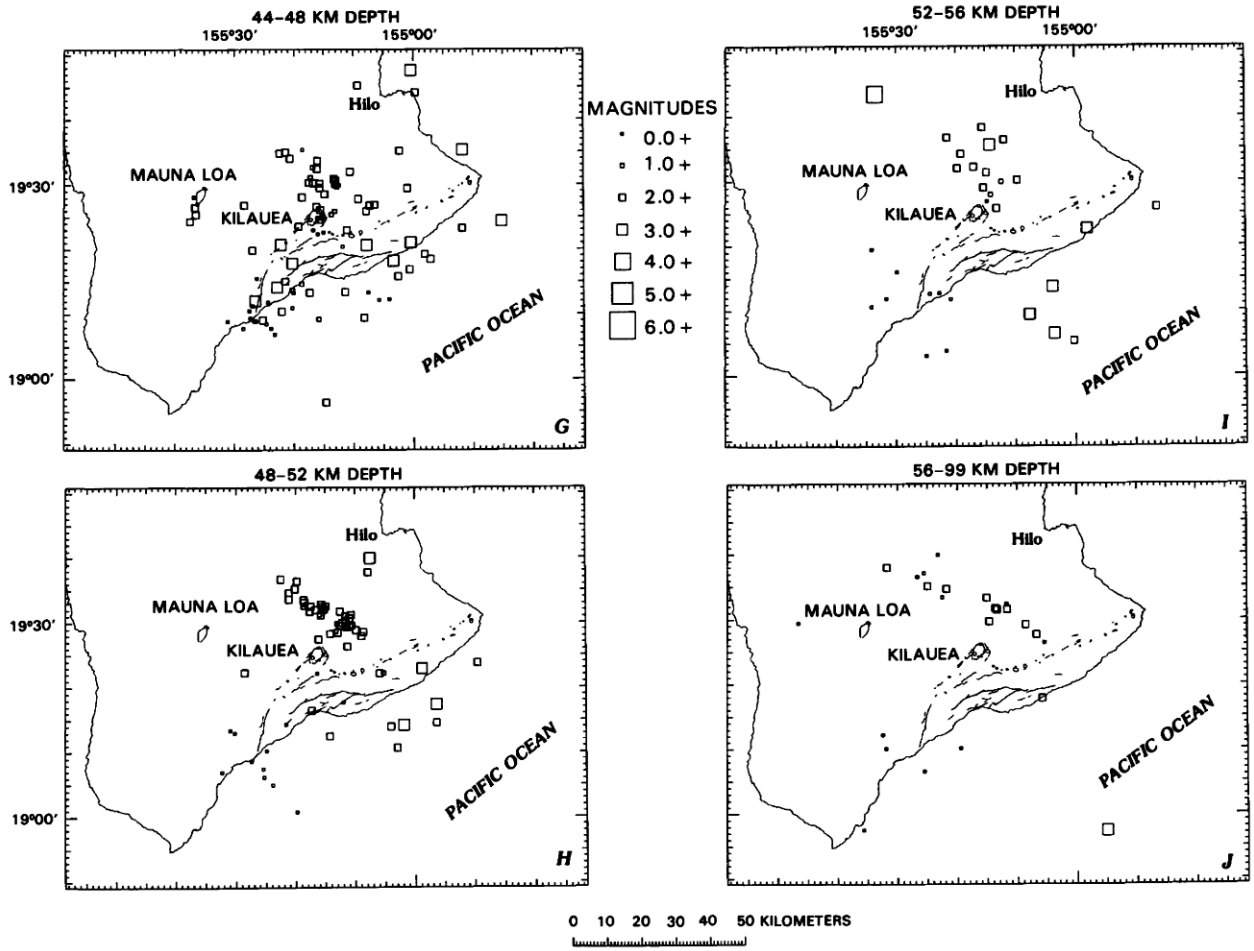


FIGURE 43.5.—Continued.

## THE MECHANISM OF DEEP EARTHQUAKES

The deep seismic band roughly coincides with the mobile and growing south flank of the island. This coincidence suggests that the stress causing the earthquakes is related to the dynamics of the volcanic pile above. In recent decades, the south side of the island has been most active volcanically, seismically and tectonically, and the three phenomena are related. Stress at depth could arise in three main forms: (1) the unbuttressed and mobile south flanks of Kilauea and Mauna Loa exert a lateral shear on the lithosphere as they are pushed seaward by their growing rift zones and gravitational slumping; (2) the added weight of new lava and dikes continually increases the normal gravitational stress on the lithosphere, and its nonuniformity causes earthquakes near the additional load; and (3) the mantle beneath the seismicity is being melted and depleted, and mass from above slumps down along active faults to replenish the lost volume.

The circumstantial evidence favors some combination of shear and normal stress applied from the volcanic pile above as a driving mechanism of Kilauea earthquakes below 13 km. First, the fact that most deep earthquakes do not occur in swarms argues against the close association of earthquakes and partial melting. If widely distributed pockets and conduits of magma were present, then local stress concentrations would result in swarms, as it does in the shallow rift and conduit systems. Seismicity resulting from settling to compensate for much deeper melt depletion would produce continuous seismicity essentially similar to the effects of applying stress from above. The stress and geometry of magma distribution at 20-40 km depth may change with time, as suggested by the absence of earthquakes at this depth prior to 1961, and the fact that some swarms did occur in the early 1960's (Eaton and others, chapter 48).

Second, the time behavior of Kilauea's deep earthquakes (13–60 km) is linked to the stress state of Kilauea's south flank. The rate of Kilauea's deep seismicity dropped markedly at the time of the 1975 Kalapana earthquake (see next section). The effect of the $M=7.2$ earthquake was to relieve compressional stress stored in the mobile south flank by slipping seaward, thus also releasing shear stress that had been applied to the mantle below. The sudden drop of applied stress could have caused the drop in rate of Kilauea's deep earthquakes. The occurrence of the Kalapana earthquake suppressed the seismicity of Kilauea's vertical magma conduit from 6 to 60 km, and its effect on earthquake rates diminished with depth. The Kalapana earthquake, however, had little influence on the deep and broad band of earthquakes along Hawaii's south coast. Apparently the effects of relieving stress in 1975 did not extend beyond Kilauea's immediate vicinity.

Third, the position of the band of earthquakes below 36 km along Hawaii's south coast argues that stress applied from volcanic and tectonic activity is a causative mechanism. Growth of the island's volcanic pile is on the south half of the island, but was primarily under Kilauea during recent decades. Addition of mass is far greater on land north of the band of deep earthquakes than to the south offshore. This differential loading produces a stress gradient under the coastline. The unbuttressed seaward coasts of both Kilauea (Ando, 1979; Crosson and Endo, 1982) and Mauna Loa (for example, the $M=5.6$ and $M=5.4$ Ninole Hills earthquakes of January 21, 1982) are mobile and experience large tectonic earthquakes in which the upper block slips seaward. The stress build-up which causes these earthquakes also exerts a shear on the lithosphere that is greatest along the south flank of the island.

Lithospheric flexure also appears to play a part in the distribution and cause of deep earthquakes. It is a complex problem, with varying shear and normal stresses applied to the top of a rigid lithosphere containing weaker magma conduits. Kilauea's deep seismicity thus seems to result from a combination of tectonic and gravitational stress applied from above, perturbation from its magma conduit, flexure of the lithosphere, and interaction with the Hawaiian hot spot.

## EARTHQUAKES AT 20–60 KILOMETERS DEPTH DURING 1960–69

Earthquakes during 1970–83 are more accurately located and more complete than those before, but earlier events are important because some changes of spatial pattern occur with time. The seismic coverage during 1960–69 was not good for resolving fine details in shallow seismicity, but was adequate for larger patterns of deeper earthquakes. Figure 43.5 plots the same depth slices and map area as figure 43.4, but contains only 1960–69 data.

Kilauea's seismic root above 36 km depth appears the same during both periods (compare fig. 43.4*A–D* with fig. 43.5*A–D*), but differences are obvious in other areas. The band of earthquakes that coincides with the island's south coast was better developed during 1970–83 (fig. 43.4*C–H*). Although the many small earthquake clusters cannot be resolved by the sparser network during 1960–69, the band itself had roughly the same size and shape (fig. 43.5*C–H*). Most Loihi earthquakes occurred during swarms in 1971-72 and 1975 (fig. 43.4*A*, *B*; Klein, 1982a). The absence of Loihi events during 1960–69 is a combination of its inactivity and reduced network sensitivity to distant earthquakes.

The greatest seismicity differences are deeper than 40 km (compare fig. 43.4*F–J* and fig. 43.5*F–J*). The area about 20 km north of Kilauea caldera was very active in 1960, but during 1961–83 the southwest corner of Kilauea was most active. This shift is not a result of changing seismic network geometry, but stems from deep swarms in July and October 1960 that did not recur in the subsequent 23 years. Earthquakes in 1959 similar to those in 1960 were interpreted by Eaton and Murata (1960) as originating from Kilauea's magma conduit. The apparent northwest trend of epicenters in this deep 1960 zone (fig. 43.5*H–J*) is partly real and partly an artifact of the station geometry: this is the direction of poorest control by the stations to the southwest. By looking at only 1960 data one might conclude that Kilauea's main seismic root plunged north rather than southwest as current evidence suggests. No seismic pattern should be considered permanent, and our view of the vertical magma conduit will surely be modified in subsequent decades.

### THE *b*-VALUES OF SHALLOW EARTHQUAKES

The earthquake regions discussed in this "Three-dimensional overview" section differ in their time history, maximum magnitude and a statistical parameter called earthquake *b*-value. The log-number of events is generally a linear function of magnitude when the sample of earthquakes is complete. The constant of proportionality is the *b*-value and usually ranges from about 0.5 to 1.5 (Richter, 1958). Higher *b*-values are often characteristic of volcanic areas and should be typical of regions with lower and heterogenous stress (Mogi, 1962; Wyss, 1973). A detailed survey of *b*-values is beyond the scope of this paper, but preliminary results suggest that *b*-values are higher in Kilauea's volcanic earthquake regions. Earthquake *b*-values were computed for each region shown in figure 43.6 using events shallower than 20 km depth during 1970–79. Major swarms and aftershock sequences were removed, but their inclusion would not significantly change the results. The regions with *b*-values larger than 1.1 include Kilauea's rift zones and parts of the immediately adjacent south flank, Mauna Loa and Loihi: these are volcanic areas where magma presumably produces concentrated stress and larger *b*-values. Lower *b*-values are characteristic of Kilauea's flanks more distant from rift zones. These flank areas apparently can sustain higher and more uniform stresses.

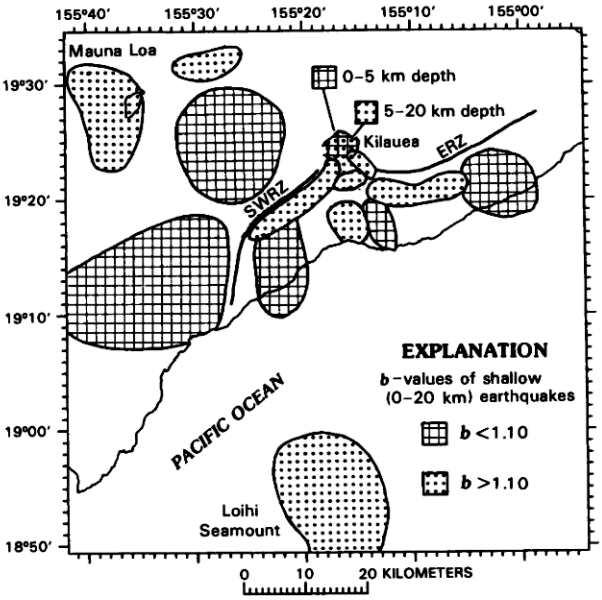


FIGURE 43.6.—Kilauea and part of Mauna Loa, differentiating areas of higher *b*-values (>1.1, dot pattern) from areas of lower *b*-values (<1.1, grid pattern). The *b*-values were only calculated for the regions shown. Earthquake data from 1970 to 1979 were used, but swarms and aftershock sequences were excluded.

## GENERALIZED HISTORY OF KILAUEA EARTHQUAKES

A key discriminant between volcanic and tectonic earthquake regions is whether seismicity occurs in episodic volcanic swarms or combines continual activity with mainshock-aftershock sequences as in tectonic regions. Changes in the rate of earthquake occurrence also indicate times when stress is changing. We divided Kilauea into several regions (fig. 43.7) and plotted the cumulative number of earthquakes versus time for each (fig. 43.8). Only events larger than a particular cutoff magnitude were chosen so that the detection would be complete or at least consistent. For shallow earthquakes at Kilauea, coverage is reasonably complete to magnitude 1 except during the most intense swarm periods. Kilauea's deep and flank events are mostly complete to about magnitude 2, except during times of exceptionally high seismicity, such as aftershocks of the 1975 Kalapana earthquake. For present purposes, it is better to choose a cutoff magnitude low enough to provide sufficient events to characterize an area's behavior, than to choose it high to be sure of an absolutely complete sample above the cutoff magnitude.

### SHALLOW VOLCANIC EARTHQUAKES

The cumulative plots of shallow earthquakes in volcanic areas have a characteristic sawtooth pattern resulting from episodic swarms. For shallow caldera earthquakes (fig. 43.8*A*), the curve for a typical eruption cycle begins as a plateau with few earthquakes following an intrusion and deflation. During reinflation seismicity gradually increases, resulting in an upward curving line. The cycle ends with an upward jump in the graph whose length is the number of events in the swarm larger than magnitude 1. Because figure 43.8*A* includes both caldera and some adjacent rift zone events, we see both the gradually building earthquakes related to inflation (in the caldera and upper rifts) and the rapid swarms (usually in the rift zones). The prominent increase in the rate of seismicity beginning in 1979 appears not to be just an artifact. The lower rate prior to 1979 is not a simple result of incomplete reporting of events larger than magnitude 1 because cumulative curves with magnitude cutoffs larger than 1 show the same increase. The beginning of a new procedure based on computer processing at HVO occurred in 1979, so the apparent increase arises from a combination of changes in event selection and magnitude calculation.

Seismicity of the upper ERZ and middle ERZ (fig. 43.8*B*, *C*) also shows a sawtooth pattern. The background rate is typically low, but is punctuated by short swarms that cause the curve offsets. Many of the larger swarms contributed earthquakes to both ERZ regions and hence to both curves of figure 43.8*B* and *C*. Some immediate aftershocks of the $M=7.2$ Kalapana earthquake contribute to figure 43.8*C*, but this is the only earthquake large enough to have caused aftershocks in this region. During 1979 and 1980, the middle ERZ experienced several cyclic intrusions that occurred too slowly to produce an intense swarm or eruption. Drops in summit tilt and seismicity were coupled with periods of inflation and intermittent earthquakes at shallow depth below the rift.

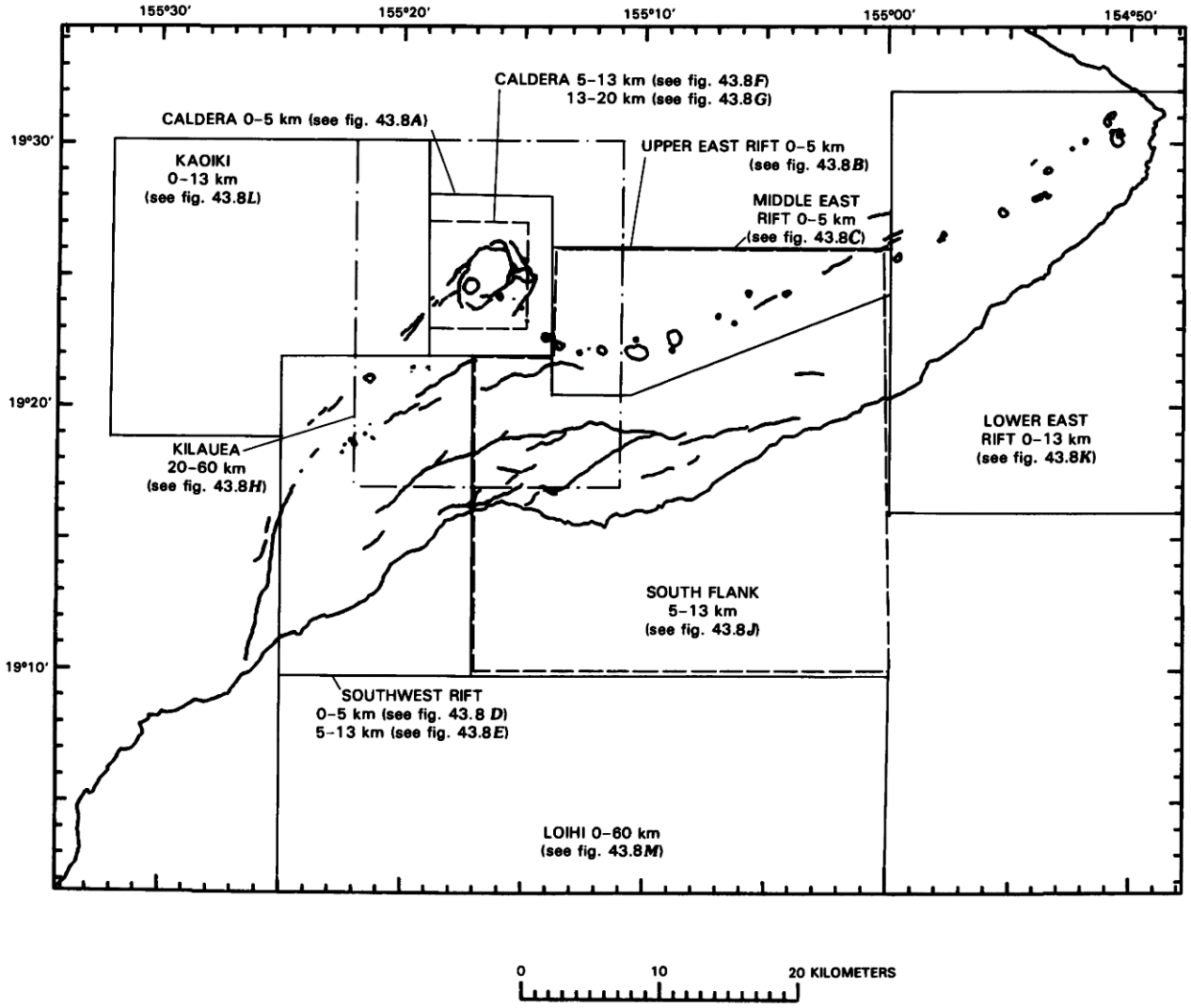


FIGURE 43.7.—Locator map of regions used to select earthquakes for cumulative seismicity curves shown in figure 43.8. Boundaries were chosen to enclose approximately homogeneous seismic regions, but seismicity is certainly not distributed uniformly in each region. Solid lines are used for boundaries that extend up to the surface, dashed lines for regions between 6 and 20 km depth, and a dash-dot line for Kilauea's root below 20 km. The Loihi region between 155° 00′ and 155° 25′ W. longitude extends south (beneath the figure) to 18° 40′ N. latitude.

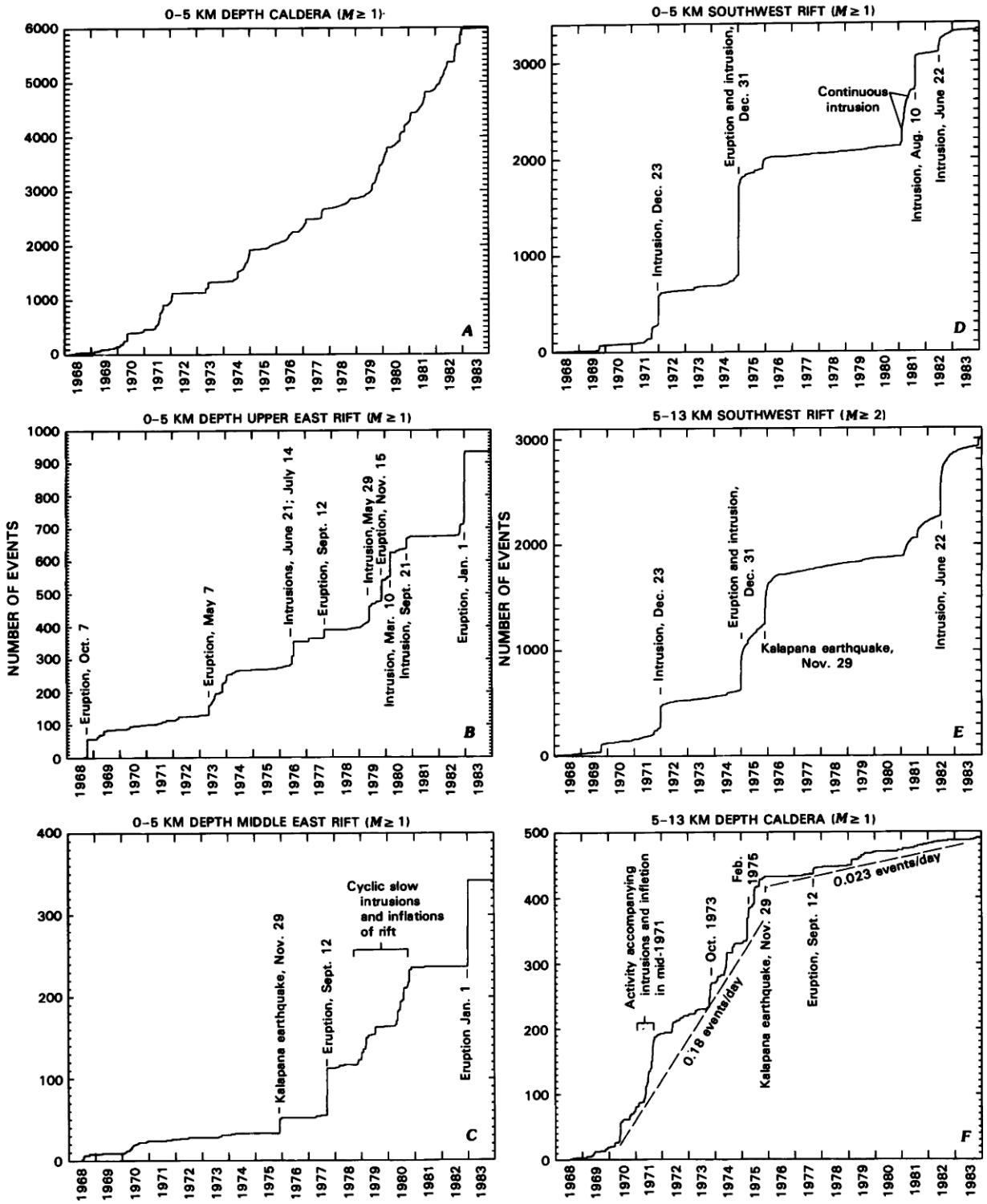


FIGURE 43.8.—Cumulative numbers of earthquakes plotted versus time. ***A–M***, Regions outlined in figure 43.7. The "south island" region of figure 43.8*I* includes the entire area of figure 43.7. Curve shape indicates how episodic or continuous seismicity is. Only events larger than indicated magnitude are included in count, in an attempt to maintain uniform completeness. Apparent increase in activity after 1969 in some areas may be an artifact of network improvements at about that time. Some large earthquakes, eruptions and intrusions are noted. Dashed lines are labeled with their slopes in events per day.

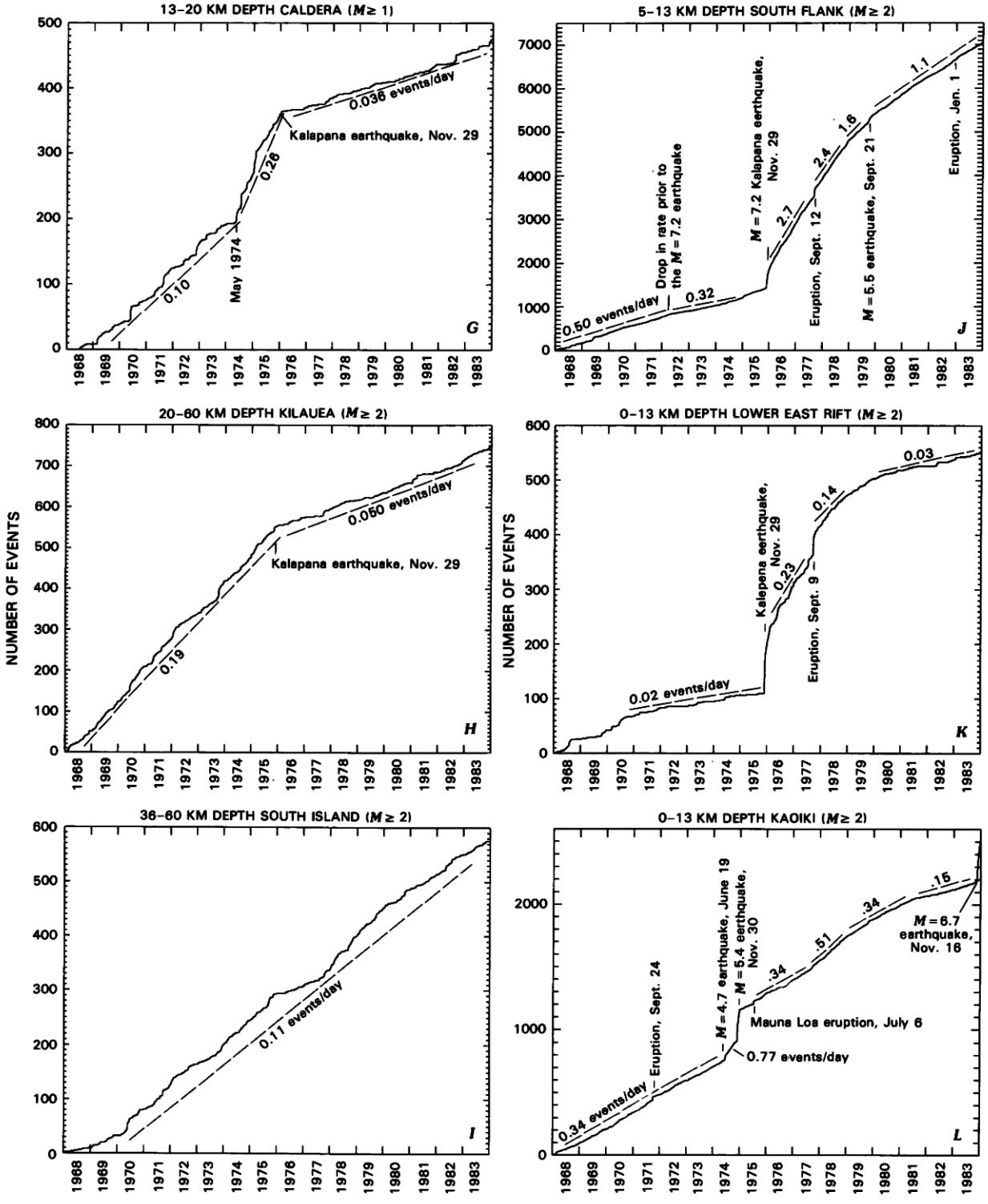


FIGURE 43.8.—Continued.

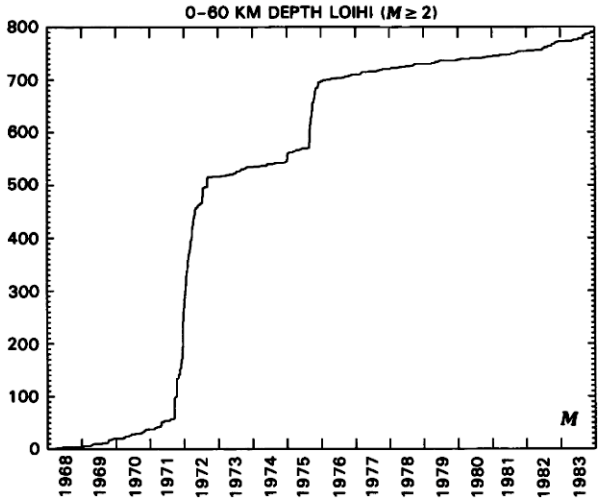


FIGURE 43.8.—Continued.

Shallow SWRZ seismicity (fig. 43.8*D*) is composed mostly of major intrusions in 1971, 1974 and 1981. The pattern is similar to that of the ERZ but with fewer and more seismogenic intrusions. Similar to the ERZ in 1979 and 1980, the SWRZ experienced a prolonged and continuous intrusion in the first half of 1981. This intrusion was marked by continuous but low-level seismicity of 5–10 events of magnitude 1 or larger per day. Summit tilt was nearly constant, suggesting that Kilauea's magma supply was being diverted into the rift without accumulating in the summit reservoir. At 5–13 km depth beneath the same region (fig. 43.8*E*), most earthquakes were in swarms and were south of the rift axis. Note that seismicity following the intrusions of 1974 and 1982 wanes gradually, as expected for tectonic earthquakes within the south flank produced indirectly by stress generated at the rift zone. The region of figure 43.8*E* also includes part of the Kalapana aftershock zone, so both south flank (tectonic) and rift (volcanic) events induce earthquakes here. The seismicity between intrusions in figure 43.8*D* and *E* comes mostly from the region's inclusion of small portions of the constantly active south flank and Kaoiki seismic zones.

## KILAUEA'S MAGMA CONDUIT BELOW 5 KILOMETERS DEPTH

Seismicity rate curves for Kilauea's vertical magma conduit below 5 km depth are shown in figure 43.8*F*–*H*. Most of the events in the upper region (fig. 43.8*F*) occurred in swarms, but deeper activity becomes more continuous in time (fig. 43.8*H*). This change apparently is caused by a shift from volcanic earthquakes and concentrated stress in the shallow system to more uniform stress in the deeper conduit.

Earthquake data prior to 1968 is incomplete, but was not as continuous in time as the 1968–83 period of figure 43.8*G*–*H*. The 30-km-depth source was relatively inactive in the years prior to January 1961 (Eaton and others, chapter 48). In addition, several major swarms from 40–60 km depth occurred in late 1959 and 1960 (Eaton and others, chapter 48). The change from swarms to continuous seismicity may have been associated with the major subsidence of the summit of Kilauea during the 1960 Kapoho eruption, which was twice as large as any subsidence since.

Many swarms at 5–13 km depth (fig. 43.8*F*) occur in the days or weeks following major subsidence of the summit during large intrusions or eruptions. Examples include January–February 1975 and September 1977. The post subsidence swarms often consist of events having a long period seismic signature and are probably related to rapid refilling of the magma reservoir from below. This intermediate-depth seismicity was also high accompanying a series of swarms at the summit during 1971 (Koyanagi and others, 1976a). The summit seismicity was associated with both slow and rapid intrusions into the upper parts of both rifts. Other swarms in figure 43.8*F*, such as October 1973, are not obviously related to shallow volcanic or seismic activity.

The most prominent characteristic of the vertical conduit seismicity (fig. 43.8*F*–*H*) is the sharp drop in rate following the November 1975 Kalapana earthquake. The long-term drop in rate is not the result of masking by Kalapana aftershocks. The aftershocks interfered with the analysis of other earthquakes in two ways: (1) the intense seismicity for several days after the Kalapana earthquake masked most everything on the seismograms; and (2) the magnitude threshold for reading all events was raised to 2.6 for most of 1976 owing to the intense activity.

The drop in earthquake rate after the Kalapana earthquake was most pronounced between 5 and 13 km depth where it dropped by a factor of 8. The earthquake rate fell less for deeper events: there was a factor of 5 decrease between 13 and 20 km, and a factor of 4 below 20 km depth. Because the slip plane of the earthquake was at 10 km depth and displaced the entire block above, its effect on conduit seismicity was greatest in the crust.

As discussed above in the section "The Mechanism of Deep Earthquakes," the Kalapana earthquake relieved stress on both the magma conduit and upper mantle as the south flank moved seaward and expanded. The south flank had been compressed by numerous dike intrusions into the rifts during the century preceding the magnitude-7.2 earthquake (Swanson and others, 1976a). The sudden decompression and slip of the south flank caused the immediate intrusion of about 100 million cubic meters of magma into the ERZ (Dzurisin and others, 1980). The earthquake also triggered a shift in volcanic behavior from mostly eruptions to mostly intrusions, because the reduced stress near the rift accommodated magma below the surface without sufficient pressure to come to the surface and erupt (Klein, 1982b). The 1975 earthquake, however, apparently did not cause a drop in Kilauea's magma supply rate (Dzurisin and others, 1984). The Kalapana earthquake thus relieved stress on Kilauea's shallow magma system, and the rate drop of vertical conduit earthquakes indicates stress relief on the deeper

system as well. A future study of fault-plane solutions and history of vertical conduit earthquakes is planned to help constrain the space and time changes in stress.

The effects of the Kalapana earthquake on volcanic seismicity suggest that the stresses driving rift and vertical conduit earthquakes are slightly different. At depths below 5 km, the earthquake both relieved elastic stress and reduced seismicity in distributions that diminish with depth, thus suggesting that vertical conduit seismicity and tectonic earthquakes on the flanks are driven by interacting regional stresses. The conduit seismicity occurs because this stress is geometrically concentrated around the zone weakened by the presence of magma. In contrast, the Kalapana earthquake had no obvious effect on either the earthquake occurrence rate or intensity of individual swarms in the shallow summit and adjacent ERZ where swarms are frequent (fig. 43.8*A*, *B*). Seismicity was unchanged even though the shallow conduit system should have experienced stress and displacement changes larger than in the deeper conduits. Earthquakes in the shallow conduit system must therefore result more directly from very local stress generated by magma pressure than by regional or tectonic stress. This difference in the local versus regional scale of driving stress is in perfect agreement with the contrast in magnitude, time and space characteristics of shallow and deeper earthquakes.

The magnitude-2 or larger earthquakes below 36 km depth and under the entire south side of the island occur at a nearly constant rate of about 0.11 per day (fig. 43.8*I*). A few of the deepest events directly below Kilauea are plotted in both figure 43.8*H*, *I*, but they are a small percentage and do not dictate the behavior of either plot. The Kalapana earthquake appears to have caused a temporary drop in rate that is probably not real; for much of 1976, aftershocks were so numerous that processing of all smaller events was not completed. The recovery of rate indicates that the Kalapana earthquake had no lasting effect (either real or artificial) on the deepest seismicity. Earthquakes below about 36 km thus depend on the long-term mantle processes discussed earlier, and not on stress or volcanic changes in the crust.

## TECTONIC EARTHQUAKES ON KILAUEA'S SOUTH FLANK

Kilauea's south flank seismicity is nearly continuous (fig. 43.8*J*), unlike the swarms that characterize the adjacent ERZ. Earthquake rates vary as the mechanical state of the flank changes. The 1968–71 period probably represents the most normal time in figure 43.8*J* and has a background rate of 0.50 events per day. The rate for the entire south flank dropped to about 60 percent of its prior value in early 1972. The change was localized to a few areas of the south flank and was interpreted by Wyss and others (1981) as premonitory to the 1975 Kalapana earthquake. The drop in rate presumably resulted from partial stress release adjacent to areas that remained locked and seismically active, but that showed different precursory anomalies.

The November 29, 1975 earthquake caused both immediate aftershocks and a massive seismic excitation of the south flank that persists a decade later. The upward step in figure 43.8*J* is from immediate aftershocks. The step should be larger than plotted because data during December 1975 and most of 1976 is incomplete between magnitudes 2.0 and 2.6. The bending over of the seismicity curve to a constant rate of about 2.7 events per day (which is a reliable value in 1977) signified the end of immediate aftershocks. This immediate aftershock sequence diminished with a time constant of weeks to months, but the value is difficult to determine with the presently incomplete data. For seismicity to continue at a rate about 5 times above background level more than a year following the earthquake is unusual for a magnitude 7.2 event. South-flank seismicity in this extended aftershock sequence is diminishing very slowly, as shown in figure 43.8*J*. The rate of decrease is approximately exponential with a time constant of about 6 years. One possibility for the high south-flank seismicity is simply relaxation of localized stress changes caused by the earthquake, but at an unusually low rate. In addition, the south-flank seismicity is above the nearly horizontal slip plane of the Kalapana earthquake. These aftershocks are thus not simple in the sense of being confined to the mainshock fault plane, and may thus have a more complex history.

Earthquakes in the south flank are ultimately driven by stress applied from repeated intrusions into the ERZ to the north. The largest events, such as September 1977 and January 1983 (fig. 43.8*J*), induce south-flank earthquakes that decrease after a few days or weeks (Dvorak and others, 1985). It is difficult to reconcile the rate of decrease of intrusions (days to weeks) and immediate Kalapana aftershocks (weeks to months) with the prolonged decrease of the extended aftershocks. Additional magma intrudes the rift steadily and between the rapid intrusions at rates difficult to estimate (Dzurisin and others, 1984). Stress was therefore applied incrementally but often to the south flank, at least during the period plotted in figure 43.8*J*. The cause of the extended aftershocks may therefore lie not in response to incremental stress from the Kalapana earthquake, but in a fundamental change in the mechanical behavior of the flank as it responds to stresses applied more or less steadily. For example, the creation of many new fractures by the Kalapana earthquake may shift the flank's response from elastic compression and aseismic creep to seismic slip on new faults. The new faults could then heal or become locked on a several-year time scale and eventually shift the balance back to aseismic deformation. This difficult problem needs more detailed work.

Kilauea's lower ERZ experienced a similar dramatic increase in seismicity at the time of the Kalapana earthquake (fig. 43.8*K*). From a pre-1975 rate of 0.02 events per day for magnitude-2 and larger earthquakes, the rate jumped by an order of magnitude even after the immediate aftershocks decreased. The rate diminished steadily and in the early 1980's was close to the pre-earthquake value. The decay time constant is roughly one-half that of the central south flank to the west. Earthquake swarms related to volcanic processes also occur in this section of rift (Koyanagi and others, 1981), such as in 1970, 1977 and 1982 (fig. 43.8*K*). The earthquakes determining the basic shape of the cumulative event curve, however, are primarily tectonic.

### TECTONIC EARTHQUAKES IN THE KAOIKI SEISMIC ZONE

The Kaoiki seismic zone is the second most active region of tectonic flank earthquakes in Hawaii, and the cumulative curve shows continuous activity punctuated by aftershock sequences (fig. 43.8*L*). A background rate of 0.34 events per day is characteristic of 1968–73 and appears to be typical for the years following the two aftershock sequences of 1974. Between the aftershock sequences of June and November 1974 the rate is nearly constant at 0.77 events per day.

The Kaoiki seismic zone, however, cannot be considered in isolation from Kilauea and Mauna Loa. Mauna Loa's seismic reawakening in 1974 was in preparation for its July 1975 eruption (Koyanagi and others, 1975), and its accompanying inflation added stress to the Kaoiki seismic zone and may have helped trigger the $M=4.7$ (June 19, 1974), $M=5.4$ (Nov. 30, 1974) and $M=4.7$ (Dec. 15, 1974) earthquakes. The November Kaoiki earthquake was followed one month later by a large intrusion into Kilauea's SWRZ. The earthquake probably did not cause the intrusion, but may have caused Kilauea to shift its attention away from the ERZ, where eruptions and intrusions occurred during the previous three years. The strike-slip mechanism of the November 1974 earthquake (Endo and others, 1978) would have relieved confining stress on the SWRZ permitting an easier intrusion path than before. Seismic shaking of Kilauea's magma system may also have changed the magma conduit of least resistance and led to the shift from the ERZ to the SWRZ.

The variations in seismic rate of the Kaoiki seismic zone after 1974 are also significant. The drop in rate in mid-1981 to one-half its former value is readily identifiable and can be interpreted as the onset of seismic quiescence precursory to the November 1983 earthquake (M. Wyss, written commun., 1985). The variations in rate during 1975–80 are real, but it is harder to identify breaks in slope and the three periods of varying seismicity whose rates are indicated in figure 43.8*L*. The origin of the high seismicity of 1977–78 has not been identified.

## SEISMICITY NEAR KILAUEA'S SHALLOW MAGMA RESERVOIR AND RIFT ZONES

Kilauea's summit region produces its most intense seismicity, which is detailed in a series of depth slices only 0.5 km thick in figure 43.9. Several earthquakes per minute can be generated within volumes smaller than a few cubic kilometers during rapid intrusions. Most active are the short sections of the two rifts within about 4 km of the summit caldera (fig. 43.9*E–G*). Events are highly concentrated both in time and space, indicating that the source of stress producing them is nearby, produces large gradients and can change rapidly. The most intense and linearly continuous seismicity is between 2.5 and 3.5 km depth (fig. 43.9*F*, *G*), and the main magma conduits are presumably centered at about 3 km depth.

Most seismicity between intrusions is caused by inflation of the magma reservoir. The reservoir is capped by brittle rock within the caldera, which produces earthquakes when the reservoir inflates. As stated in the previous section, a gradual buildup of caldera earthquakes lasting several days to months often precedes an intense swarm and intrusion. The pre-intrusion activity is not only within the caldera and reservoir cap, but may include slow intrusions of the sections of rift adjacent to the reservoir. Portions of the rifts thus appear at times to be magma-filled and directly connected to the inflating summit reservoir.

### THE SUMMIT MAGMA RESERVOIR

The summit magma reservoir, as defined by a gap in seismicity, is at the intersection of the active conduits of the two rifts. The seismic gap coincides with the geodetic deformation center and is part of a zone of low rigidity (fig. 43.9*F*, *G*). The rift conduits constrain the reservoir's position on its south and east sides near 3 km depth. The clusters of earthquakes in the north-central caldera and just southwest of Halemaumau apparently form other parts of an incomplete ring of brittle deformation surrounding the magma reservoir. Some earthquakes do plot within this region identified with the magma reservoir, however: these may either be slightly mislocated owing to the large lateral and unmodeled velocity gradients, or actually inside brittle slivers within a magma storage complex. All of the limitations of location precision discussed earlier apply here and mean that we cannot resolve detail within this 1- to 2-km-diameter void.

These relations can be seen from a different perspective by examining vertical cross sections taken through the summit magma reservoir. Figure 43.10*A* is a map showing the rectangular areas included in the four sections of figure 43.10*B–E*. The cross sections intersect at summit magma reservoir. Only earthquakes with both horizontal and vertical errors less than 1 km are plotted in figure 43.10, so structures of about this size should be resolvable. This also means that proportionally more earthquakes below about 4 km than above this depth are eliminated from the plots, because errors increase somewhat with depth.

A zone with few or no earthquakes below the caldera contains the magma reservoir complex. The dashed oval in figure 43.10*B–E* is not meant to portray its exact size or shape, but only to sketch the outer limits of sparse seismicity. Its position is constrained by four zones of seismicity: a cap of earthquakes mostly between 1 and 2 km depth directly above the reservoir, the intensely active segments of the ERZ and SWRZ adjacent to the reservoir's upper part near 3 km, and the top of the vertical conduit at a depth of about 7 km.

The reservoir's seismic cap is centered and most intense beneath Halemaumau, but extends across most of Kilauea caldera (fig. 43.10). The greater intensity of seismicity between 1 and 2 km compared to just above is probably a result of its proximity to the source of stress below. The reduced activity above 1 km may also be a result of lessened confining stress on the shallowest fault planes or a concentration of seismicity in very small-magnitude events that are detected but are not locatable with the seismic network. The northern half of the caldera produces events most intensely near 2 km

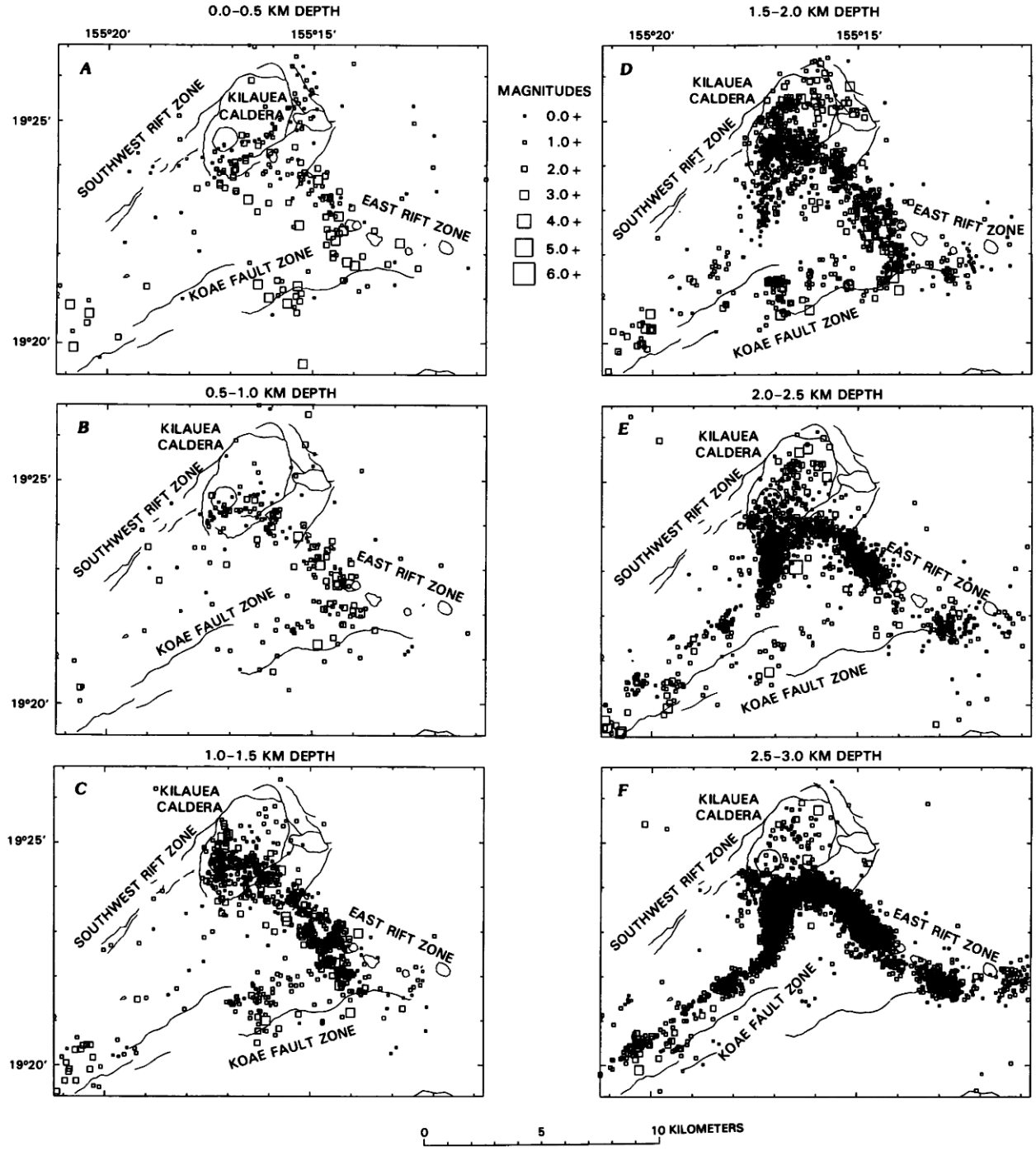


FIGURE 43.9.—Depth slices, 0.5 km thick, of 1970–83 earthquakes near Kilauea caldera between 0 and 5 km depth. Maximum location error of plotted events is 3 km horizontally or vertically. Earthquake symbol size scales with magnitude. Faults, fissures, and pit craters are as shown in figure 43.1.

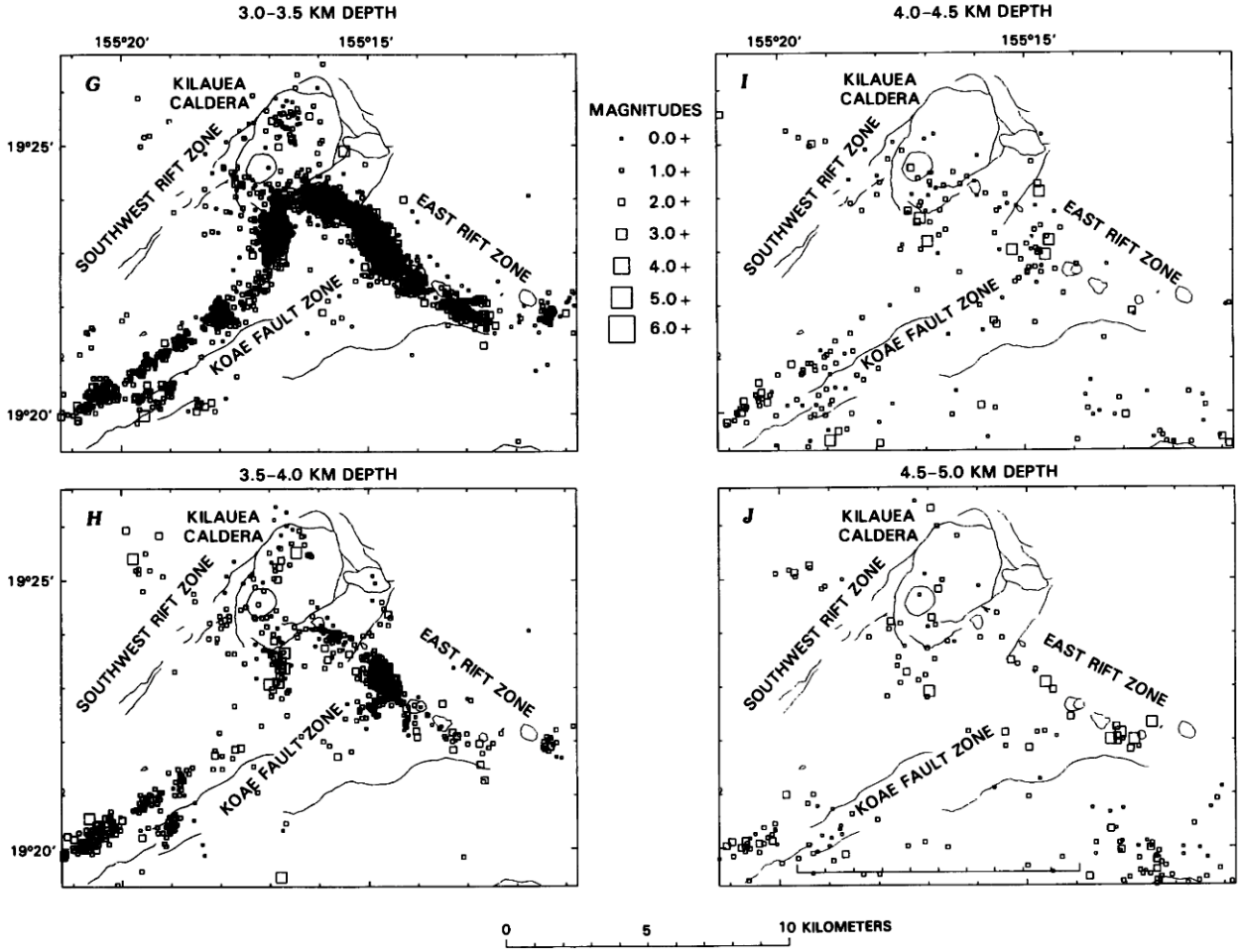


FIGURE 43.9.—Continued.

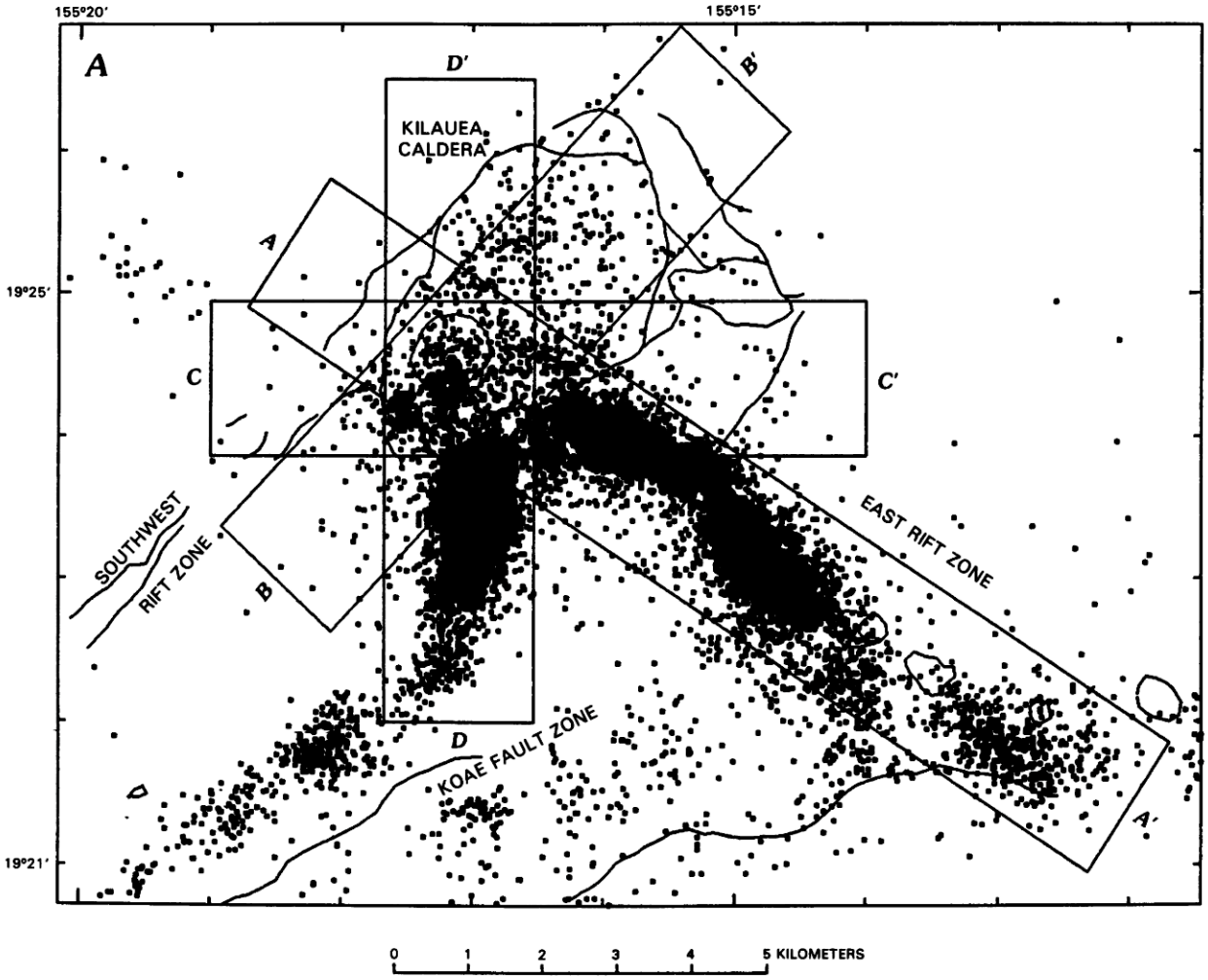


FIGURE 43.10.—Epicenters and hypocenters of shallow 1970–83 earthquakes near Kilauea caldera. ***A***, Epicenter map showing positions of cross sections. Sections cross over buried magma reservoir. Endpoints of sections are labeled with letters keyed to the distance axes of figure 43.10*B–E*. Only earthquakes inside the 2-km-wide rectangular areas of figure 43.10*A* are plotted on figure 43.10*B–E*. ***B–E***, Cross sections of 1970–83 hypocenters. Position of magma reservoir is approximated by dashed oval. Horizontal and vertical errors of all hypocenters plotted is 1 km or less. Datum for sections is ground surface. When comparing earthquake patterns in map and sections note that sections extend to 12 km depth, but map only plots events in upper 5 km for clarity. Faults, fissures, and pit craters are as shown in figure 43.1.

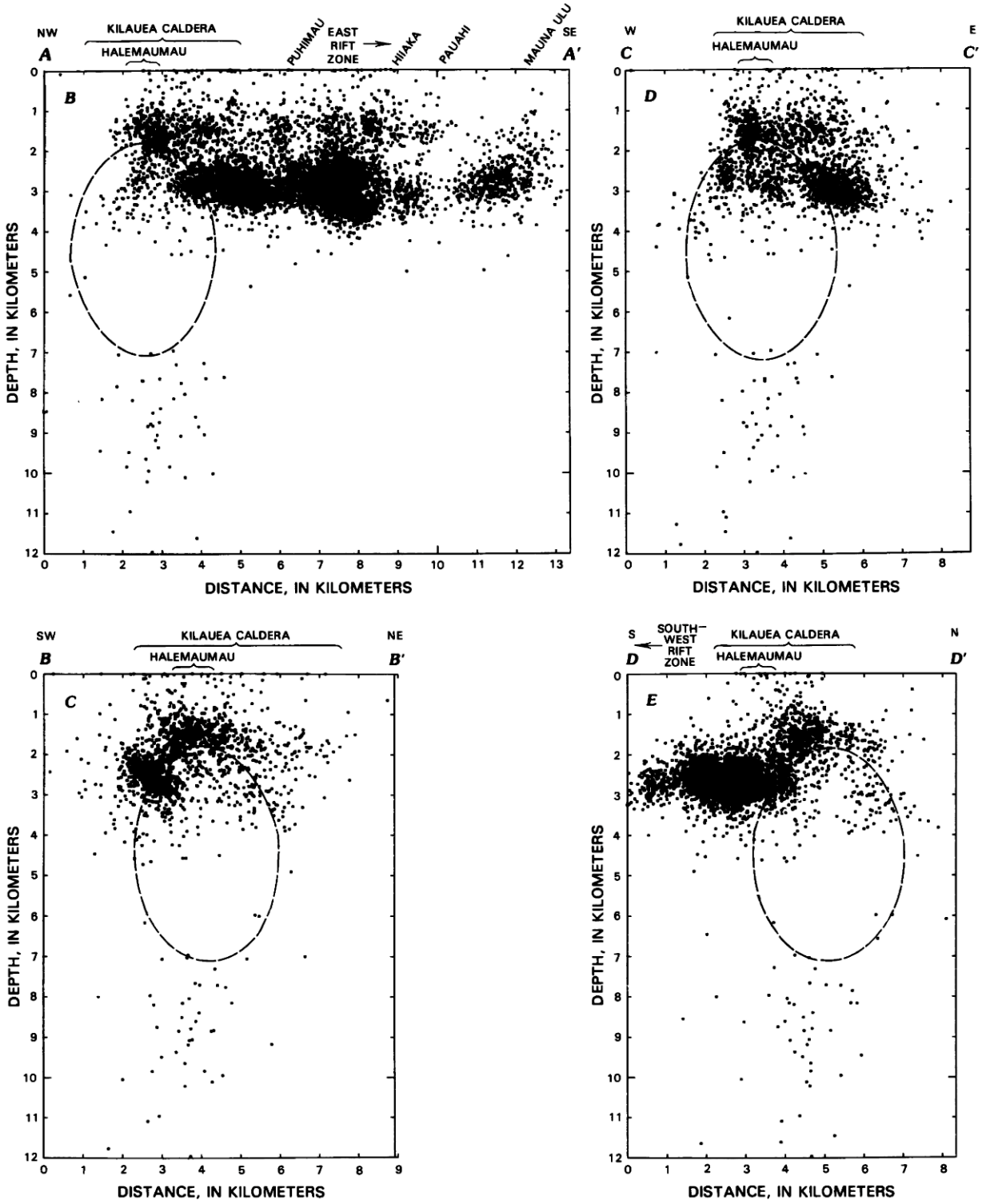


FIGURE 43.10.—Continued.

depth (fig. 43.9*D*, *E*). Most of these earthquakes occur at times of rapid inflation and probably are triggered by lifting and extension of the brittle cap over the magma reservoir. Seismicity above the reservoir also accompanies major and rapid deflations such as in September 1977, August 1981 and January 1983. The band of very shallow events north of Kilauea Iki (fig. 43.9*A*) parallels the caldera rim and appears to be caused by movement on rim faults during periods of inflation.

The upper and lower parts of the magma reservoir behave differently. The buried centers of inflation and deflation of Dvorak and others (1983) are mostly in the upper half of the dashed oval shown in figure 43.10*B*–*E*. These deformation centers are below the base of the seismic cap at 2 km, but above the completely aseismic region between 4.5 and 7 km depth. The upper section of the magma storage complex is thus the active portion: it produces some seismicity, the changes in magma volume near the deformation centers occur there, and it is surrounded by the zones in which seismicity and intrusions occur. The lower section of the reservoir is passive and has low rigidity, however: it is aseismic and seldom supports centers of elastic deformation. Any deformation of the lower half of the reservoir would probably be masked by that in the upper half, to which surface measurements are most sensitive. The reservoir can also be viewed as the upper part of a fluid column whose top level fluctuates with changes in stored magma volume. Variations in level then change the pressure on the confining cap where the seismicity and uplift occur. The magma reservoir is apparently a connected network of liquid and solid segments, as indicated by the limited seismicity and the fact that different centers of deformation are active at different times (Fiske and Kinoshita, 1969; Ryan and others, 1983; Dvorak and others, 1983).

## THE SUMMIT SECTION OF THE EAST RIFT ZONE

Unlike the SWRZ, the ERZ between Halemaumau and Pauahi (fig. 43.1) generates seismicity above its main conduit and essentially to the surface (fig. 43.9*A*–*D*). During the last few decades the ERZ has been more active magmatically than the rest of the rift system. This high magmatic activity may extend the ERZ dike network vertically and stress the upper 2 km to such a degree that it deforms seismically. The shallow seismicity usually occurs at the same times and places as the earthquake swarms in the more intense zone centered at 3 km. There is thus a close seismic and probably magmatic coupling to the main conduit. We interpret the shallow seismicity and patterns of shallow intrusions as evidence of a multitiered and complex honeycomb of magma conduits in the upper ERZ.

Internal structures in the ERZ appear to control seismically active and inactive regions. There is a major cluster of earthquakes about 1 km uprift of Mauna Ulu (fig. 43.10*B*, *C*). The earthquakes that plot below this cluster at 5 to 8 km depth (fig. 43.10*B*) mostly occur just after intrusions and are immediately adjacent to tectonic earthquakes in the south flank. The ERZ bends eastward and the Koae fault zone meets the rift there. This area is thus structurally complex. Migrating swarms (and by inference also propagating dikes) often begin between Pauahi and Mauna Ulu. We interpret this cluster as a barrier or pinched zone that sometimes blocks downrift magma flow at this point. Earthquakes are then generated by the formation or rejuvenation of dikes that break through the barrier.

Just uprift of the Mauna Ulu cluster is a seismically inactive zone beneath Pauahi (fig. 43.10*A*, *B*). A break in continuity of earthquakes is at 3 km depth, and the 1- to 2-km-deep seismicity essentially ends there. This apparently is a low stress or low rigidity zone of relatively unobstructed magma passage. The magma conduit here is possibly very similar to the rest of the ERZ, but for some structural reason such as proximity to the Koae fault zone, it does not accumulate stress to be released seismically. We favor an alternative interpretation of this seismic gap as a small magma storage reservoir within the rift. Magma stored there would be held in place by the barrier just downrift. In addition to times of intrusion, this Pauahi reservoir could easily receive magma during periods of summit inflation when the rift between it and the summit reservoir is seismically active and is slowly being fed magma. This possible magma reservoir will be treated below in the section "Discussion of Rift Zone Intrusions." The total volume of magma stored below Pauahi may be small, but if it is consistently kept hot and low in rigidity, seismic stresses will never accumulate to be released in earthquakes.

## EARTHQUAKE HYPOCENTERS IN THE SOUTHWEST RIFT AND CENTRAL EAST RIFT ZONES

The SWRZ and the ERZ downrift of Mauna Ulu (fig. 43.11) are in some ways simpler than the uprift section of the ERZ: they are less frequently active and have simpler earthquake patterns. Longitudinal cross sections of earthquakes during 1970–83 from both rifts are plotted in figure 43.12. The main magma conduit at about 3 km depth is prominent in each section. The conduits of both rifts plunge from about 2.5 km depth below the surface at their uprift end to about 3.5 km downrift. The apparent 3.7-degree plunge of the ERZ conduit must be added to the 1.3-degree surface slope to give a plunge of about 5 degrees. The SWRZ is somewhat steeper, with apparent and surface slopes of about 5.0 and 1.7 degrees respectively for a total of about 7 degrees. The apparent plunges are probably real, although unmodeled seismic velocity variations are a source of error in the apparent slopes.

The quantity of ERZ earthquakes diminishes with distance from the caldera owing to the reduced frequency and intensity of intrusions. The ERZ conduit cannot be defined seismically farther than 30 km from the caldera. Major intrusions of the SWRZ, however, produce earthquakes in most of the 20 km of rift between the caldera and Puu Kou in a way that does not diminish with distance along the rift.

Considerable rift-zone structure is visible in the sections of figure 43.12. We associate the prominent and persistent clusters of events along both rifts with barriers or blockages of the magma conduit that resist penetration by dikes and produce high stresses during intrusions. The major SWRZ barrier near Puu Kou, for example, has produced an intense cluster of earthquakes and prevented any intrusion from continuing downrift during the period

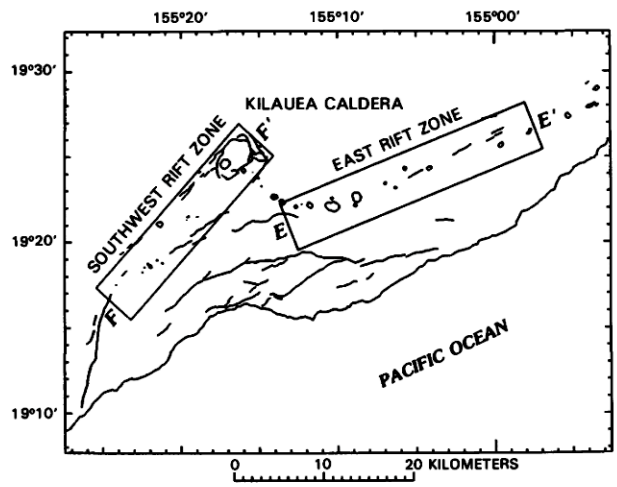


FIGURE 43.11.—Areas included in longitudinal cross sections of rift zones. Only earthquakes within rectangles are plotted in sections. Section *E-E'* is shown in figure 43.12*A* and *F-F'* in figure 43.12*B*. Faults, fissures, and pit craters are as shown in figure 43.1.

of historical observation. This barrier also coincides with a bend in the rift (fig. 43.1*A*). The earthquake gaps between clusters are apparently places of unstressed magma passage, and some may be secondary magma storage pockets. The most prominent gap just northeast of Puu Kamoamoa is such a storage reservoir. This section of rift was geodetically observed to inflate during the slow intrusions of 1978–80. In addition, the earthquakes above the main conduit (0–2 km depth in figure 43.12*A* occurred during these intrusive pulses, much as shallow caldera earthquakes occur above the summit magma reservoir when it inflates.

Earthquakes in Kilauea's flanks are separated from the rift magma conduits in both map position and depth. Most of the events shown deeper than 5 km in figure 43.12 are tectonic earthquakes from the south flank that fall within the cross-section regions. The base of the zone of tectonic earthquakes is near 10 km and is the approximate depth of the prevolcanic layer of ocean sediments on which the mobile south flank slips seaward (for example, Crosson and Endo, 1982). A series of transverse sections, whose positions are shown in figure 43.13, will make this clear. Figures 43.14*A–D* are sections successively downrift along the ERZ. The main magma conduit at 3 km depth and north of the deeper south-flank seismicity is visible in each section. The detailed cross-sectional shape of the magma conduit cannot be determined owing to errors in earthquake hypocenters. The sections uprift of Mauna Ulu (fig. 43.14*A*, *B*) and near Puu Kamoamoa (fig. 43.14*D*) include seismicity above the main conduit. Shallow events plotted at the south end of figure 43.14*A* are in the Koae fault zone. Only the section including Pauahi and Mauna Ulu (fig. 43.14*B*) reveals significant activity beneath the main magma conduit.

The relation between rift and flank seismicity is very similar in the SWRZ. Figures 43.14*E–G* are transverse cross sections successively downrift along the SWRZ (fig. 43.13). The main magma conduit is visible at about 3 km depth in each section, defined largely by the major intrusions of December 1974 and August 1981. The scattered earthquakes northwest of the main conduit near the caldera (fig. 43.14*E*) are partly from the September 1971 intrusion into the northern portion of the SWRZ. The shallow earthquakes southeast of the conduit in the same section are from the west end of the Koae fault zone. The conduit near Mauna Iki (fig. 43.14*F*) splits into two strands. The shallow (0–2 km depth) earthquakes in this area were generated by an apparent upward branch of the dike formed in the August 1981 intrusion, which also produced surface cracks in this area. Considerable seismicity also occurs southeast of the rift near Puu Kou in Kilauea's mobile south flank (fig. 43.14*G*).

The rift and adjacent flank earthquakes are spatially better separated at the ERZ than at the SWRZ (compare fig. 43.14*B–D* with fig. 43.14*F*, *G*). The greater distance of flank events from the ERZ correlates with their greater independence from the times of rift intrusions. Earthquakes adjacent to the SWRZ, however, are more closely coupled to the rift in both time and space. The greater separation of rift and flank earthquakes in the ERZ may also result from the narrowness of the surface expression of the ERZ: the wider SWRZ at the surface may be related to the multiple seismic strands and closely coupled flank earthquakes at depth.

The rift zones below about 5 km depth are mostly aseismic. Rifting must extend to about 10 km depth where the volcanic pile is decoupled from the prevolcanic oceanic crust. The lack of seismicity then means the deep rifts are too hot and too ductile to support earthquakes, and the timing of deep rifting relative to the episodic shallow intrusions is unknown. There are, however, some deep rift earthquakes. The main SWRZ magma conduit downrift of Mauna Iki directly overlies a deeper but somewhat diffuse seismic zone (figs. 43.12*B*, 43.14*F*, *G*). This deep zone was active in the intrusion of June 1982, in which rifting apparently extended downward through the crust. A few hypocenters 5 to 10 km beneath Mauna Ulu in the ERZ (fig. 43.10*B*) are also produced by rifting. These deep ERZ events occurred during and immediately after several shallower swarms and apparently represent a locally brittle zone that responds to intrusions above.

## THE KOAE FAULT ZONE

The Koae fault zone is seismically active, though far less so than either rift zone. The Koae consists of noneruptive fissures and north-facing normal fault scarps and is interpreted as a tear-apart zone linking the ERZ and SWRZ (Duffield, 1975; Unger and Koyanagi, 1979). Nearly all Koae earthquakes occurred during a few short swarms apparently caused by magma intrusions from the ERZ into an otherwise dry fault zone. No recent eruption from the Koae is known, however, and confining stress is probably so low that magma can be accommodated underground without building enough

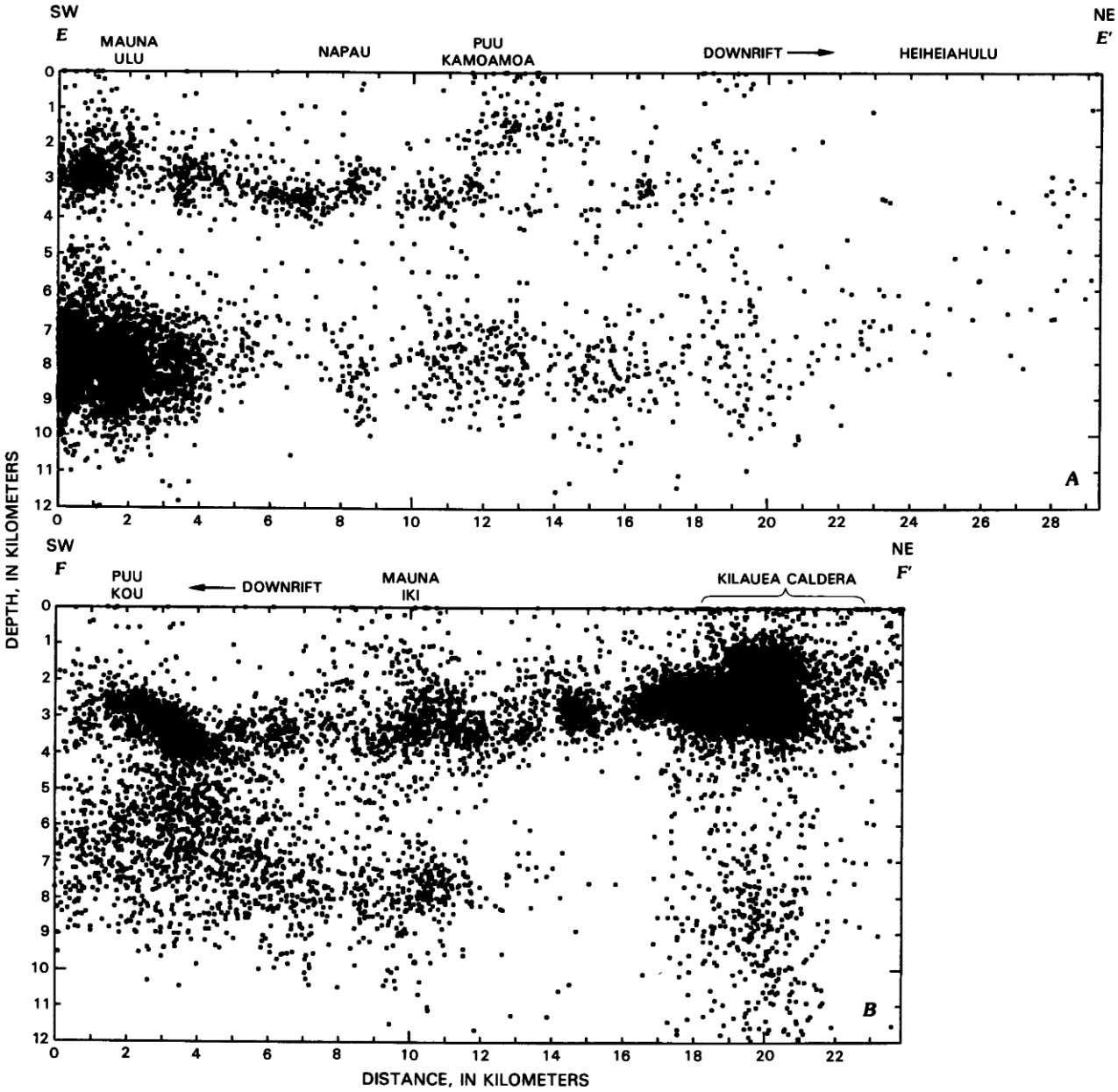


FIGURE 43.12.—Longitudinal cross sections of earthquakes below east rift zone (*A*) and southwest rift zone (*B*). Positions and areas of sections are shown in figure 43.11. Main magma conduits are at about 3 km depth.

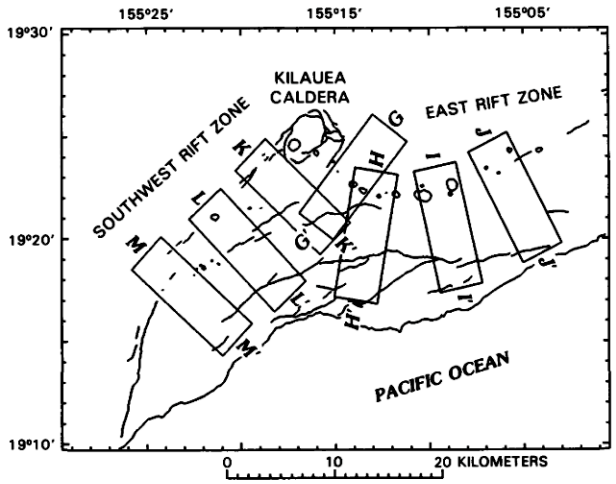


FIGURE 43.13.—Areas included in transverse cross sections of rift zones. Only 1970–83 earthquakes within rectangles are plotted in sections. Sections *G-G'* through *J-J'* are plotted in figure 43.14*A–D*, *K-K'* through *M-M'* in figure 43.14*E–G*. Faults, fissures, and pit craters are as shown in figure 43.1.

hydrostatic pressure to erupt. Earthquakes generally migrate rapidly from east to west as intrusions penetrate the Koae. The immediate source of magma might be the suspected magma reservoir in the adjacent ERZ below Pauahi.

Figure 43.15 shows a map and cross section of shallow Koae earthquakes. The seismicity extends about 6 km from the ERZ in a linear band that underlies the zone of faults and fissures. Earthquake depths are mainly between 1 and 2 km, the same as the shallow seismic conduit system in the uprift part of the ERZ (figs. 43.10*B*, 43.15*B*). The Koae intrusions may thus be related to the shallow ERZ conduit system. The main ERZ conduit at 3 km depth, however, is not seismically expressed in the Koae. The earthquakes below 6 km depth in figure 43.15*B* (not plotted in figure 43.15*A*) are part of the tectonic seismicity in Kilauea's south flank. Very shallow earthquakes are seen in a small area of the SWRZ (fig. 43.9C, *D*, lower left corner). These earthquakes apparently result from an upward-branching dike within the rift zone, which may be influenced by the intersection of the SWRZ magma conduit with the Koae.

## KILAUEA'S VERTICAL MAGMA CONDUIT AND THE PATTERN OF DEEP EARTHQUAKES

Kilauea's magma conduit is clearly recognized in the earthquake depth slices discussed earlier. Although depth slices show the size and position of the conduit at a particular depth very well, variations in seismicity with depth are more easily seen in a vertical cross section. The map positions of three sections are shown in figure 43.16, along with epicenters of earthquakes below 13 km depth. The three sections (fig. 43.17) extend from the surface to 60 km depth and all include the seismically defined magma conduit. Enlargements of the central parts of each section restricted to 0–25 km depth (fig. 43.18) clarify the dense seismicity in the upper part of the conduit. Most plotted earthquakes between 0 and 5 km depth are related to Kilauea's summit and rifts, and those between 5 and 13 km occur mostly under the south flank and Kaoiki seismic zones. The magma conduit earthquakes are most clearly separated from shallow seismicity when viewed from the east (figs. 43.17*A*, 43.18*A*).

An important geometrical feature of the seismicity associated with the conduit is its unevenness with depth. Earthquakes tend to cluster near depths of 9, 16 and 30 km with reduced activity centered near 5, 13 and 20 km (figs. 43.17*A*, 43.18A). Several possible reasons exist for the seismic gaps based on either low rigidity, low stress or a low fracture density relative to the conduit above or below. As has been inferred, the gap at 4–7 km results from the low rigidity of the summit magma reservoir. The possibility of magma storage near 13 or 20 km is much more difficult to determine, however: (1) a deeper reservoir may not accumulate enough magma to swell elastically and deform the surface, but merely transmit magma passively; and (2) it would be difficult to detect because of its greater distance from the surface and because of the much larger deformation from the shallow reservoir. The present gradation from volcanic seismicity in the shallow parts of the conduit to more tectonic earthquakes at depth argues against a deep magma reservoir large enough to influence seismicity.

The gaps in seismicity near 13 and 20 km probably result from differences in lithology or stress within the lithosphere, and not necessarily magma reservoirs. The base of the south flank zone of tectonic earthquakes at about 10 km depth (fig. 43.18*A*) and the basal slip during the 1975 Kalapana earthquake may coincide with the layer of ocean sediments at the base of the Hawaiian volcanic pile (Furumoto and Kovach, 1979; Crosson and Endo, 1982). The depth and landward dip of the oceanic Moho beneath the island's south coast (Hill and Zucca, chapter 37; Zucca and Hill, 1980) if projected, should intersect the vertical magma conduit around 15 km near the base of the seismic gap. The gap in seismicity near 13 km would then roughly coincide with the old oceanic crust and be bounded by the old Moho and sediment layers. The low-rigidity sediment layer could be viewed as a low-stress zone that partially decouples the stresses above and below.

One must consider the interaction between the lithosphere and the whole volcanic system to determine the cause of the very clear absence of earthquakes in the volcanic conduit near 20 km depth. Note that very few events occur at this depth anywhere beneath Kilauea (figs. 43.3*O*, *P*, 43.17). This observation suggests that stresses are low at this depth in the lithosphere beneath Kilauea. The lithosphere beneath Hawaii can be modeled as an elastic plate flexing downward under the weight of the volcanic pile (for example, Watts and Cochran, 1974; Watts and others, 1985). More detailed modeling of the lithosphere as an elastic-plastic plate suggests that its neutral stress axis (relative extension above and compression below) may lie at a depth of about 23 km (Liu and Kosloff, 1978). The

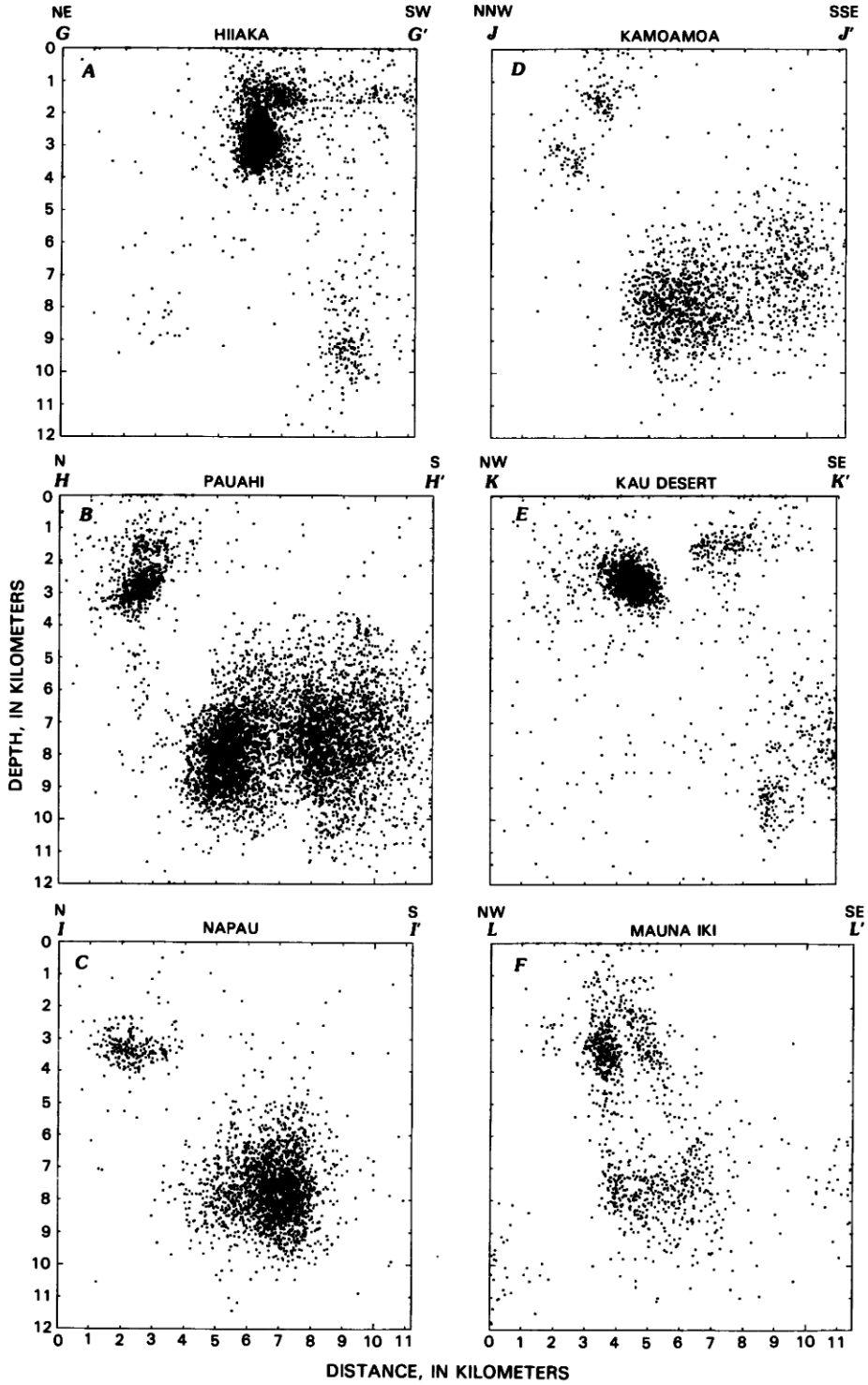


FIGURE 43.14.—Transverse cross sections of earthquakes beneath east rift zone (*A–D*) and southwest rift zone (*E–G*). Positions and areas of sections are shown in figure 43.13. Main magma conduits are at about 3 km depth.

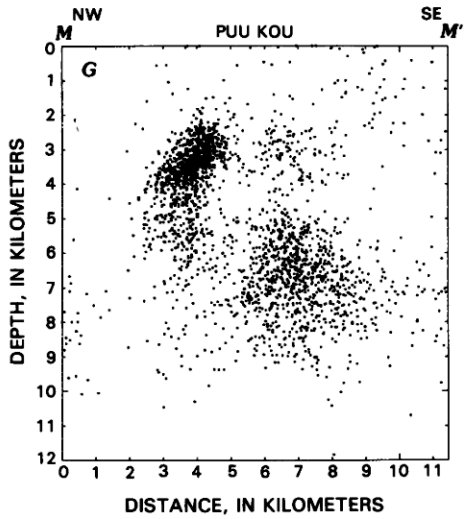


FIGURE 43.14.—Continued.

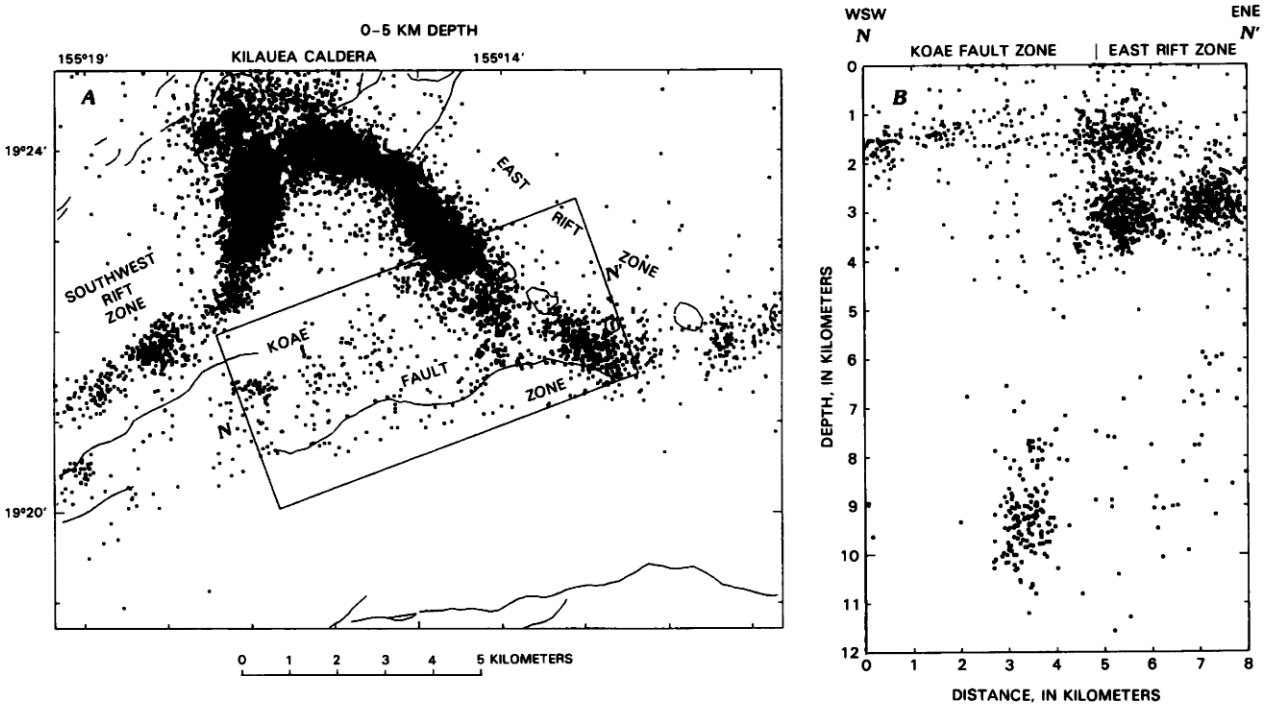


FIGURE 43.15.—Locations of shallow 1970–83 earthquakes south of Kilauea caldera in Koae fault zone. ***A***, Map view showing rectangular area of seismicity plotted in cross section *N-N'*. Faults, fissures, and pit craters are as shown in figure 43.1. ***B***, Cross section *N-N'* showing earthquakes to 12 km depth, but *A* only plots earthquakes to 5 km depth for clarity.

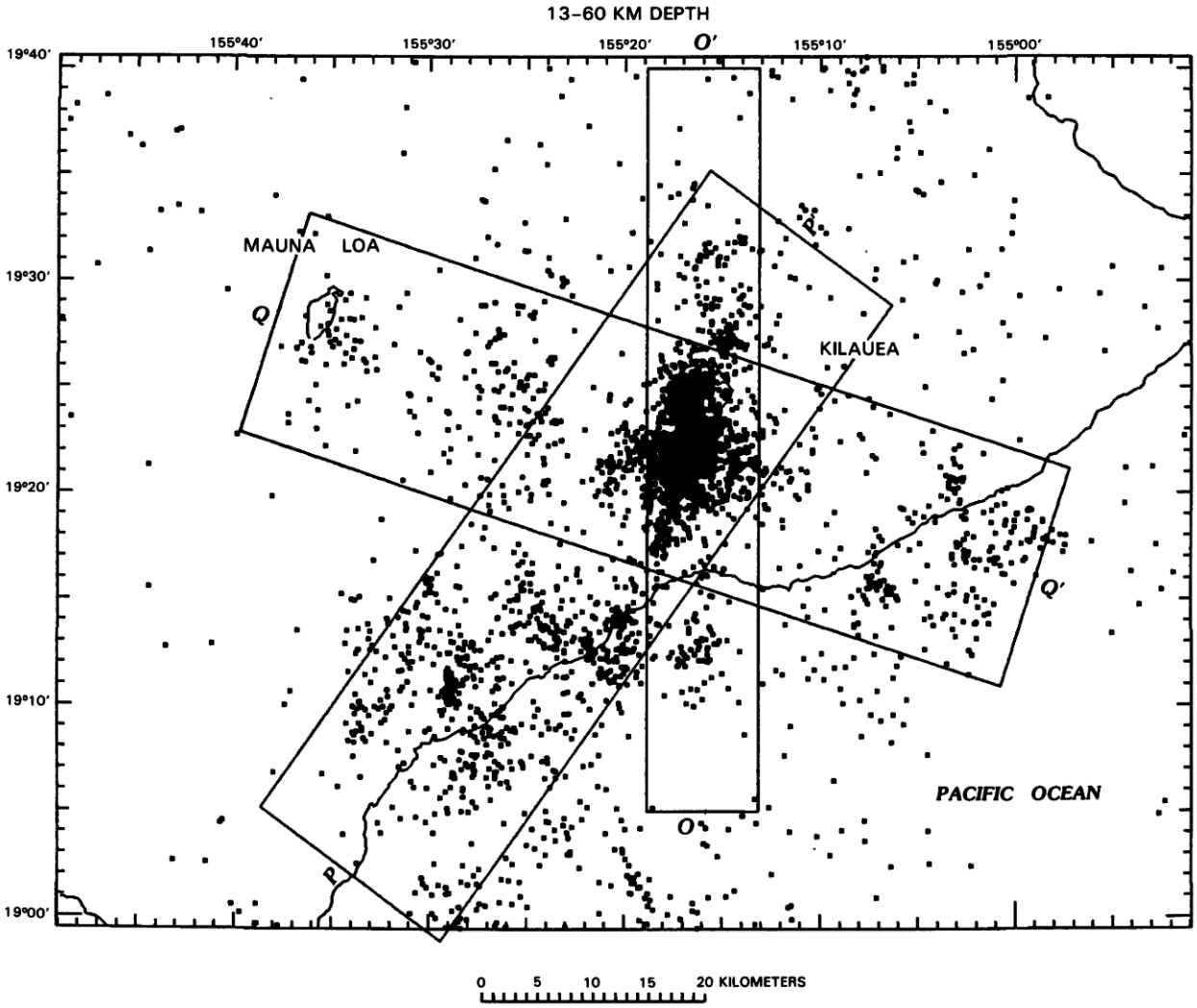


FIGURE 43.16.—Locations of 1970–83 earthquakes from 13–60 km depth beneath south side of Hawaii. Cross sections O-O′ through Q-Q′ are shown at different scales in figures 43.17*A*–*C* and 43.18*A*–*C*. Only earthquakes within rectangular areas are plotted on sections. Although events above 13 km are plotted on sections, they are omitted from map for clarity. All three sections include Kilauea's vertical magma conduit. Faults, fissures, and pit craters are as shown in figure 43.1.

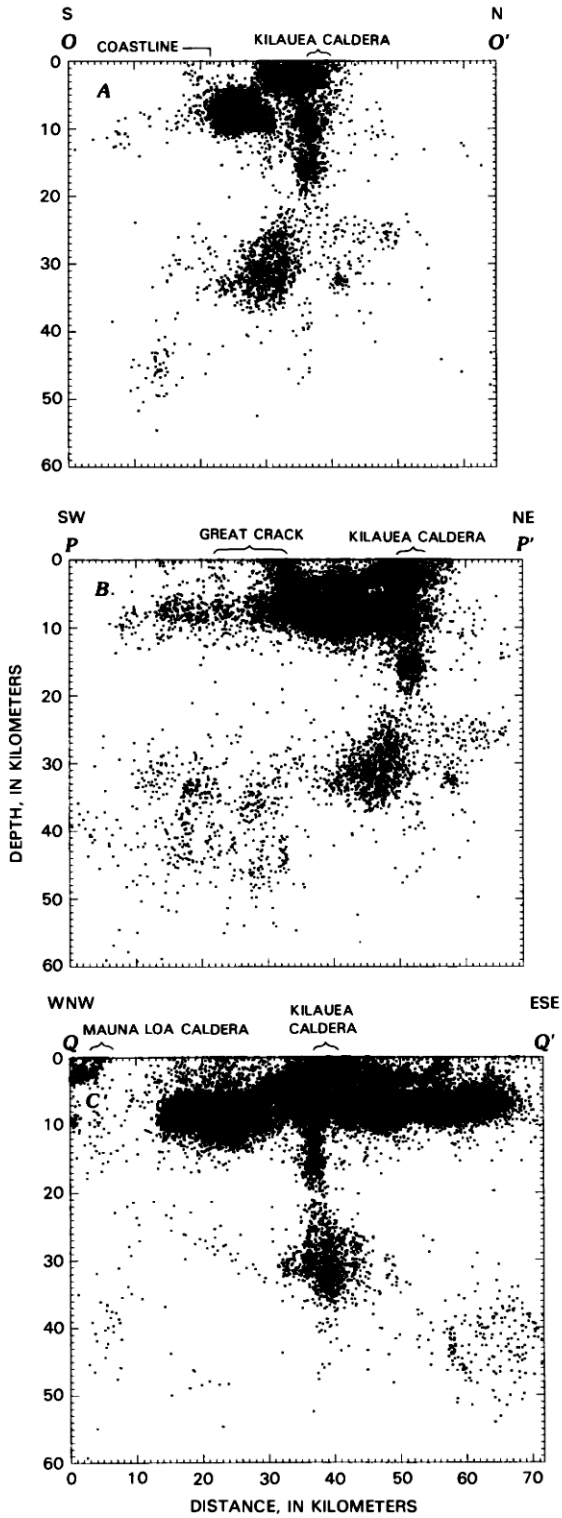


relative absence of earthquakes near 20 km depth thus may mark the lithosphere's neutral stress axis and locally help constrain flexure models. The earthquake gap also means that it is lithospheric stress, and not the magma pressure at this depth, that is the driving stress for these earthquakes. The fault plane solutions of a large set of Kilauea earthquakes deeper than 27 km have compressional axes radial to a point below Hawaii and thus may be oriented by flexure stress below the neutral axis (Elliot Endo, written commun., 1977). The seismic gap at 20 km depth and focal mechanisms of events below that thus suggest that regional stresses arising from lithospheric flexure play a dominant part in Kilauea's deeper seismicity.

The 20-km-depth point not only is a seismic gap, but also marks other differences in earthquake patterns: (1) a change occurs at 20 km from a conduit that is narrow and vertical above and broad and south-plunging below; (2) few events other than near the magma conduit are seen between 13 and 20 km, but earthquakes scatter widely under the south side of Hawaii below 20 km depth; and (3) earthquakes between 13 and 20 km are small and seldom exceed magnitude 2, but those below often exceed magnitude 4. These differences suggest that different lithospheric stresses prevail above and below 20 km. If the neutral stress depth is at 20 km, then the compressive regime below appears to favor earthquake production whereas the relatively extensional conditions above do not generate seismicity except where stresses are perturbed by the magma conduit or active rifts and flanks.

As discussed earlier, the seismically defined magma conduit merges with a diffuse cloud of hypocenters southwest of Kilauea that apparently marks the Hawaiian hot spot at 40–50 km depth. This cloud also lies centrally between Kilauea, Mauna Loa and Loihi, and is commonly a source of volcanic tremor and long-period earthquakes. Kilauea's deepest seismicity and conduit system thus become involved with the diffuse hot spot itself and become difficult to trace.

Not all deep seismicity is as readily interpreted as the major cloud southwest of Kilauea caldera. A smaller but similar cluster is southeast of Kilauea near 40–50 km depth (figs. 43.4*E–H*, 43.17*C*). These earthquakes are tectonic and do not appear to be related to tremor or to another volcano. This earthquake cluster can also be considered a part of the band of seismicity that underlies Hawaii's active south coast. The south coast is where the greatest amount of mass has been added to the island as lava flows and intrusives in recent decades and where seaward slip of the south flank occurs. Shear stress in the deep seismic zone is produced both from asymmetric loading by Kilauea growth to the north and southward motion of the flank driven by intrusive growth of the ERZ. Thus,

FIGURE 43.17—Cross sections through Kilauea taken from the surface to deepest seismicity at 60 km. Events from 1970–83 within areas of rectangles shown on figure 43.16 are projected onto sections. ***A***, Section *O-O'*. ***B***, Section *P-P'*. ***C***, Section *Q-Q'*.

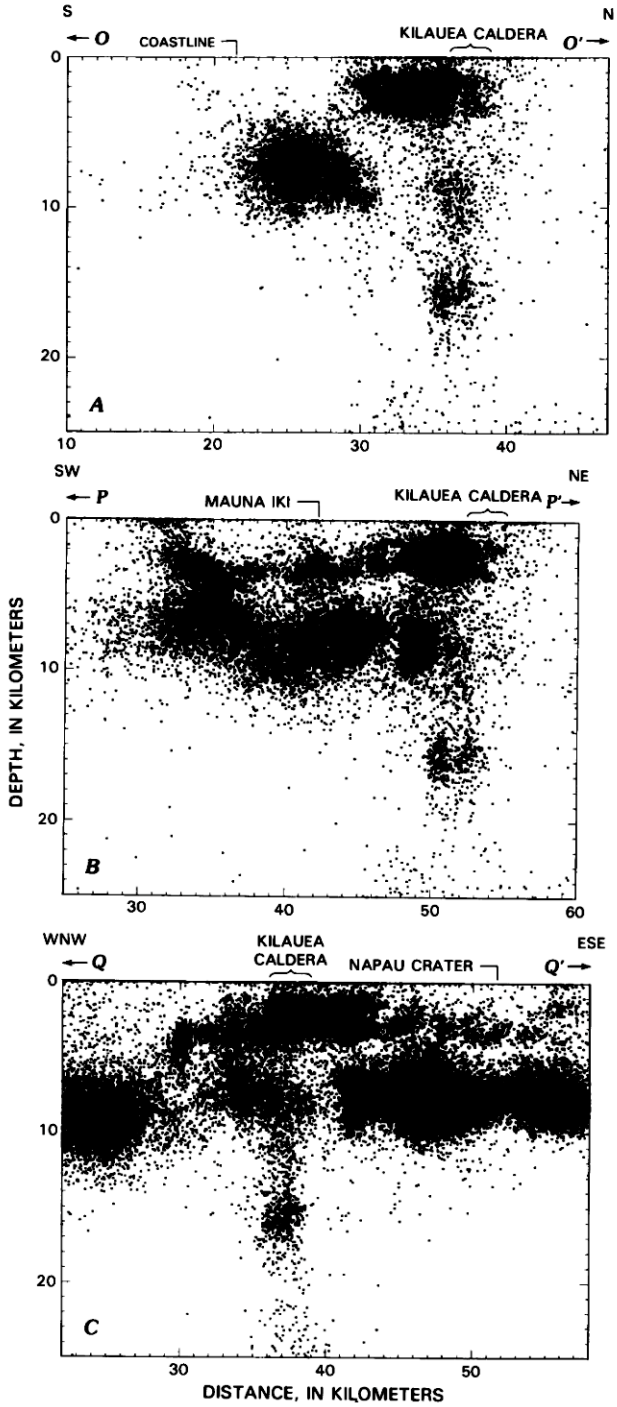


FIGURE 43.18—Enlargements of central portions of cross sections of figure 43.17*A*–*C* showing finer detail in upper part of Kilauea's vertical conduit system. ***A,*** Section *O-O'*. ***B,*** Section *P-P'*. ***C,*** Section *Q-Q'*.

rapid loading and stress on the lithosphere possibly produces this concentration of events. The fact that earthquakes do not diminish smoothly with depth in the mantle means that the distribution of stress and material properties is more complex than for a simple halfspace.

Other noteworthy concentrations of seismicity are: (1) the northward extension of the major cluster at 25 to 35 km beneath Kilauea (fig. 43.17*A*, *B*); (2) a deep seismic root of Mauna Loa Volcano (fig. 43.17*C*)—although far less active than Kilauea's, the Mauna Loa conduit is nearly vertical to a depth of almost 50 km; and (3) a diffuse thread of earthquakes linking Kilauea's conduit at 35 km with Mauna Loa's near 20 km depth (fig. 43.17*C*). Whether this thread represents a magmatic connection between the two volcanoes is not known, but it emphasizes the complex and multizoned web of upper mantle seismicity. Also note that the tectonic events under the south flank (right side of fig. 43.18*C*) extend to about 10 km, but the Kaoiki zone is active to 12–13 km (left side of fig. 43.18*C*). If these boundaries are both controlled by the layer of prevolcanic sediments below the volcanic pile, then it deepens toward the interior of the island as expected from the observed dip of the Moho (Zucca and Hill, 1980).

To make some of the major seismic zones easier to see, we present in figure 43.19 some paired hypocenter plots to view with a pocket stereoscope. The earthquakes plotted were selected to represent each major seismic zone with enough events to define it, but not so many as to obscure other features. Figure 43.19*A* shows most of the island and includes Loihi Submarine Volcano south of the island. Figure 43.19*B*, *C* show boxes including nearly all of Kilauea, the summit of Mauna Loa and part of Loihi. The vertical magma conduit with its southward plunge into the zone of deepest earthquakes is clearly visible. Note the prominent cloud centered near 30 km depth. The shallow earthquakes below the ERZ and their distinct separation from the south flank zone at 6–10 km depth can also be seen. Figure 43.19*D* zooms in for a closer look at the central part of Kilauea and includes earthquakes to a depth of 35 km. Figure 43.19*E* is a close-up of the shallow magma system beneath the caldera to a depth of 18 km. The very active sections of both rift zones are adjacent to the summit magma reservoir. The earthquakes in the foreground between 6 and 10 km depth are tectonic events in the south flank.

We have examined the depth distribution of Kilauea's vertical magma conduit and found three zones of low or no seismicity: the summit magma reservoir causes an absence of earthquakes between 3 and 7 km; the reduced activity near 13 km may be an effect of the buried oceanic crust and sediment layer; and the absence of earthquakes near 20 km depth under all of Kilauea might be associated with the neutral stress level within a lithosphere flexing under the load of the volcanic pile. The vertical conduit thus looks like a passive intruder in the lithosphere: it is a zone weakened by magma in which earthquakes seem to be ultimately driven by regional lithospheric stresses. The low-rigidity conduit both concentrates regional stress and fails more easily than its surroundings. The conduit thus does not need to produce enough magmatic stress to cause earthquakes by itself. If the conduit produced magma pressures much higher than

stress in the adjacent mantle, one would probably see major swarms of volcanic earthquakes and a depth distribution different from its surroundings. The reduction in deep seismicity caused by the stress change during the 1975 Kalapana earthquake also argues for regional rather than magmatic stress as driving the deep earthquakes. A planned examination of earthquake statistics, depth and time history, and earthquake focal solutions will better address the interaction of magma ascent and lithospheric stress.

## THE HISTORY OF KILAUEA'S SHALLOW EARTHQUAKE SWARMS, 1963–83

This section presents a summary of the basic data on two decades of Kilauea's summit and rift-zone earthquake swarms. The emphasis here is on a consistent treatment of basic earthquake patterns, not detailed chronologies. Particular attention will be paid to migration of earthquakes with time as an indicator of magma flow or dike propagation. We will be looking for characteristics common to many swarms and what they reveal of rift-zone dynamics. This section is thus complementary to the traditional treatment of a few well-studied examples. We feel the benefits of this survey approach outweigh the necessary omissions in dealing with so much data.

One benefit of treating two decades of swarms at once is the ability to classify swarms into similar groups, make comparisons and look for simple evolutionary trends. Shallow Kilauea swarms can be loosely divided into fast, intense swarms lasting for a few hours to a couple of days and slow swarms lasting several days to a few weeks. The fast swarms accompany rapid intrusions, which are presumably either the opening of an older magma conduit or the emplacement of a new dike. An eruption occurs if the dike reaches the surface, so nearly all eruptions are accompanied by intrusions and fast swarms. Except for harmonic tremor generated near an erupting vent, intrusions and eruptions are seismically indistinguishable. Summit tilt generally falls rapidly during fast swarms because of the high rate of magma flow. If the eruption or intrusion is within the caldera, however, the superposition of the deformation fields of the deflating reservoir and the nearby dike may cause rapid tilt changes in any direction.

Slow swarms occur between eruptions and intrusions, and are generally related to resupply of magma from depth. The most common slow swarms are within the caldera or immediately adjacent rift zones and result from gradual extension of the caldera during inflation or pressure increase of the magma reservoir. Summit tilt will usually be high and slowly rising during inflationary swarms. Seismicity and tilt levels are often closely correlated, as many examples will show. During some of the intereruption periods, the new magma supply partly or completely flows into a rift zone as a slow intrusion. These slow intrusions are generally accompanied by little or no gain in summit tilt and by a long-lived but low-intensity earthquake swarm in the part of the rift where magma accumulates. These four types of swarms will be referred to as eruptions, intrusions (fast), inflationary swarms and slow intrusions.

Most of the information in this section is contained in a series of figures, one set per swarm. The basic characteristics of all but the smallest swarms will be presented in four types of earthquake plots: map, cross section, hourly number of earthquakes versus time and downrift position versus time. Because most of the larger swarms form linear seismic zones, the distance axis for both cross sections and position versus time plots will be the same and along the appropriate section of rift zone. When different rift segments are active during the same swarm, more than one set of cross section and position versus time plots may be presented. For a particular swarm, all of the distance and depth scales will be the same on the maps and distance axes. The time scales, however, will vary as appropriate to the swarm.

Time on the position versus time plots proceeds from top to bottom. Significant migrations of earthquakes are noted by lines whose slope is the inverse of the migration speed. Solid lines are used where the migration and speed are clearest, dashed lines where the continuity and speed are uncertain, and a small arrow where a general migration is only suggested. Formal errors of the migration speeds cannot be given, but can be judged qualitatively from the scatter of earthquakes in the distance versus time plots used to determine speeds. For eruptions, the eruptive vents are shown for comparison by red lines on maps, cross sections and distance versus time plots. Vent positions are approximate and not plotted accurately. The position versus time history of vents refers only to the eruption start time of the earliest episode. The time histories of vents are particularly approximate and are usually sketched from limited observations like the beginning times of lava emission at only a few places.

The basic data for all swarms are listed in table 43.1, including the time period for each figure. Each of the several cross sections are identified with a set of letters ($T$–$T'$ for the upper ERZ, for example). The endpoints and halfwidths of all sections are listed in table 43.2.

### INTRUSIONS AND ERUPTIONS OF 1963

The seismic network and recording during the early and mid-1960's were not adequate to resolve fine spatial details in the swarms. The 1963 sequences are good examples of swarms whose approximate positions are known, but with no resolvable internal structure. Depth control may also not be adequate for some of the early swarms. Therefore, we cannot assume that events with calculated depths below 5 km are tectonic earthquakes, as is reasonable for most sequences after the late 1960's. Open squares are used in some swarm figures for events between 5 and 13 km depth and may include both tectonic and mislocated swarm earthquakes.

The first swarm for which adequate seismic data exists began on May 9, 1963 (fig. 43.20). This swarm was apparently a SWRZ intrusion, because the shallow swarm cloud is centered at a part of the SWRZ seismically active in later, better located intrusions. Earthquakes began at the time of summit deflation (fig. 43.20*B*), which is typical for earthquakes caused by rapid magma flow. The swarm's location may have been controlled by the intersection of the SWRZ magma conduit and the west end of the Koae fault zone. Ground cracking and inflation were observed in the

TABLE 43.1.—*Data for individual Kilauea swarms during 1963–83*

[The date the main part of the swarm started is not necessarily same date as an accompanying eruption. Event type is classified: Inf, swarm accompanying inflation; SI, slow intrusion; I, intrusion; E, eruption; Defl, caldera swarm accompanying major deflation. Main swarm locations are Cald, caldera; UERZ upper east rift zone; ERZ, east rift zone; USWR, upper southwest rift zone; SWRZ, southwest rift zone; LSWR, lower southwest rift zone; Koae, Koae fault zone. Swarm location may not coincide with eruptive vents. Seismic zone size refers to map view, parentheses imply epicenters are diffuse and poorly located. Query (?) for earthquake migration speed indicates migration appears to have occurred but with a speed too uncertain to measure. Map and cross-section plots include earthquakes from number of days listed. Delay times are between start of swarm beneath a vent and eruption at vent. Tilt changes are at Uwekahuna and are negative for deflation and positive for inflation. Tilt rates are computed at same time(s) as earthquake migration speed(s). Conduit area is obtained by dividing tilt rate by earthquake migration speed (for example see section "Southwest Rift Zone Intrusions and Caldera Eruption, January through August 1981")]

| Figure number | Swarm start date | Swarm type | Swarm location | Swarm duration | Seismic zone size (km) | Downrift speed (km/h) | Uprift speed (km/h) | Upward speed 1-3 km (km/h) | Upward speed 0-1 km (km/h) | Plot duration (days) | Swarm-eruption delay (hours) | Tilt change (mrad) | Tilt rate (mrad/h) | Conduit area (m ) |
|---|---|---|---|---|---|---|---|---|---|---|---|---|---|---|
| 43.20 | May 9 63 | I | SWR | 3 d | (9 by 5) | -- | -- | -- | -- | 8 | -- | -32 | -- | -- |
| 43.21 | Jul 2 63 | I | Koae | 3 d | (6 by 4) | east? | -- | -- | -- | 6 | -- | -20 | -- | -- |
| 43.22 | Aug 21 63 | E | UERZ | 1 h? | -- | -- | -- | -- | -- | 2 | -- | -11 | -- | -- |
| 43.23 | Oct 5 63 | E | ERZ | 3 d | (8 by 3) | -- | -- | -- | -- | 8 | -- | -79 | -- | -- |
| | | | Koae | | (2 by 2) | | | | | | | | | |
| 43.24 | Mar 5 65 | E | ERZ | 3 d | (8 by 4) | -- | -- | -- | -- | 5 | -- | -84 | -- | -- |
| 43.25 | Aug 24 65 | I | ERZ | 1.5 d | (15 by 5) | -- | -- | -- | -- | 8 | -- | -3 | -- | -- |
| 43.26 | Dec 28 65 | E | Koae | 2 d | (5 by 5) | -- | -- | -- | -- | 5 | -- | -45 | -- | -- |
| 43.27 | Nov 5 67 | E | Cald | 1 h? | -- | -- | -- | -- | -- | 3 | -- | -11 | -- | -- |
| 43.28 | Aug 22 68 | E | Koae | 4 h | 2 by 2 | west | -- | -- | -- | 3 | 3 | -54 | -- | -- |
| 43.29 | Oct 7 68 | E | ERZ | 2.5 d | 11 by 2 | 3.4 | -- | -- | -- | 5 | 3 | -60 | -- | -- |
| 43.30 | Feb 18 69 | Inf | Cald | 2.5 d | 1 by 1 | -- | -- | -- | -- | 6 | -- | +11 | -- | -- |
| 43.31 | Feb 22 69 | E | ERZ | 10 h | (11 by 3) | -- | ? | -- | -- | 5 | 5 | -46 | -- | -- |
| 43.32 | Mar 21 69 | I? | UERZ | 2 h | 2 by 2 | -- | 14 | -- | -- | 3 | -- | <3 | -- | -- |
| 43.33 | May 20 69 | Inf? | ERZ | 2.5 d | (8 by 4) | -- | -- | -- | -- | 4 | -- | <3 | -- | -- |
| 43.34 | May 24 69 | E | ERZ | 13 h | 6 by 6 | -- | 4.4 | -- | -- | 6 | 1 | -24 | -- | -- |
| 43.35 | Jul 3 69 | I | UERZ | 18 h | 7 by 3 | 1.3 | 1.4 | -- | -- | 4 | -- | <3 | -- | -- |
| 43.36 | Oct 7 69 | SI | LSWR | 4 d | 7 by 4 | -- | -- | -- | -- | 6 | -- | +5 | -- | -- |
| 43.37 | Nov 3 69 | I | ERZ | 1 h | 1 by 1 | 6 | -- | -- | -- | 3 | -- | -6 | | |
| 43.38 | Dec 22 69 | Inf | USWR | 7 d | 1 by 1 | -- | -- | -- | -- | 8 | -- | +5,-23 | -- | -- |
| 43.39 | Jan 22 70 | I | Cald | 4 h | 2 by 2 | -- | 2.2 | -- | -- | 3 | -- | <3 | -- | -- |
| 43.40 | Feb 3 70 | Inf | UERZ | 8 d | 5 by 1 | .13,.02 | -- | -- | -- | 9 | -- | +3 | -- | -- |
| | | | USWR | | 2 by 1 | .017 | | | | | | | | |
| 43.41 | Mar 17 70 | Inf | USWR | 6 d | 2 by 1 | ? | -- | -- | -- | 7 | -- | +5 | -- | -- |
| 43.42 | Apr 2 70 | Inf | UERZ | 7 d | 2 by 2 | -- | -- | -- | -- | 8 | -- | +6,-10 | -- | -- |
| | | | USWR | | 2 by 2 | | | | | | | | | |
| 43.43 | May 15 70 | I | UERZ | 3 d | 5 by 2 | 4.2 | .13 | -- | -- | 8 | -- | -8 | -- | -- |
| 43.44 | Dec 12 70 | Inf | Cald | 2 d | 5 by 3 | -- | -- | -- | -- | 3 | -- | <3 | -- | -- |
| 43.45 | Dec 22 70 | Inf | Cald | 19 d | 11 by 3 | .02 | (1.3) | -- | -- | 20 | -- | +4 | -- | -- |
| 43.48 | Jun 6 71 | Inf | Cald | 9 d | 3 by 3 | -- | -- | -- | -- | 10 | -- | +2 | -- | -- |
| 43.49 | Jun 11 71 | Inf | USWR | 5 d | 3 by 1 | .35,.05 | -- | -- | -- | 5 | -- | -2 | .01 | 70 |
| 43.50 | Jul 19 71 | Inf | UERZ | 12 d | 2 by 2 | .17,.008 | -- | -- | -- | 12 | -- | +3 | -- | -- |
| | | | USWR | | 3 by 1 | ? | | | | | | | | |
| 43.51 | Aug 8 71 | Inf | UERZ | 7 d | 6 by 1 | .22 | -- | -- | -- | 8 | -- | +12 | -- | -- |
| | | | USWR | | 4 by 1 | .02 | | | | | | | | |
| 43.52 | Aug 14 71 | E | Cald | 12 h | 1 by 1 | -- | -- | -- | -- | 1 | -- | -16 | -- | -- |
| 43.53 | Sep 6 71 | Inf | UERZ | 8 d | 6 by 1 | -- | -- | -- | -- | 8 | -- | +3 | -- | -- |
| | | | USWR | | 4 by 1 | | | | | | | | | |
| 43.54 | Sep 17 71 | Inf | UERZ | 6 d | 3 by 1 | -- | -- | -- | -- | 7 | -- | +5 | -- | -- |
| | | | USWR | | 4 by 1 | ? | | | | | | | | |
| 43.55 | Sep 24 71 | E | SWRZ | 7 d | 13 by 3 | .53,.31 | -- | -- | -- | 7 | 4-18 | +12,-23 | .44 | 280 |
| 43.56 | Dec 23 71 | SI | LSWR | 7 d | 8 by 6 | .29 | -- | -- | -- | 8 | -- | <3 | -- | -- |
| | | | UERZ | | 4 by 1 | | ? | | | | | | | |
| 43.57 | Jan 19 72 | Inf | UERZ | 9 d | 4 by 1 | .08 | .15,.15 | -- | -- | 10 | -- | +5 | -- | -- |
| 43.58 | Feb 1 72 | E | UERZ | 5 d | 2 by 1 | -- | -- | -- | -- | 7 | .5-2 d | <3 | -- | -- |
| 43.59 | May 5 73 | E | Koae | 25 h | 8 by 2 | .36 west | -- | 3 | 1 | 2 | 6 | -23 | 1.7 | 1500 |
| | | | ERZ | | | | 3.6 | | | | | | | |
| 43.60 | Jun 9 73 | I | Koae | 23 h | 3 by 1 | 1.0 west | -- | -- | -- | 1 | -- | -7 | 2.2 | 700 |
| 43.61 | Nov 10 73 | E | UERZ | 16 h | 3 by 1 | ? | -- | 1.6 | ? | 2 | 5 | -25 | -- | -- |
| 43.62 | Mar 24 74 | I | UERZ | 3 h | 1 by 1 | ? | -- | -- | -- | 1 | -- | -2 | -- | -- |
| 43.63 | Jul 19 74 | E | UERZ | 10 h | 3 by 1 | -- | .16 | .55 | .18 | 1 | 2 | -18 | -- | -- |
| 43.64 | Sep 16 74 | Inf,E | USWR | 3 d | 7 by 1 | ? | -- | -- | -- | 4 | -- | +12 | -- | -- |
| 43.66 | Dec 24 74 | Inf | UERZ | 7 d | 4 by 1 | .06 | -- | -- | -- | 7 | -- | +4 | -- | -- |
| | | | USWR | | 3 by 1 | .03 | | | | | | | | |
| 43.67 | Dec 31 74 | E | SWRZ | >14 d | 20 by 2 | 1.3,.67 | ? | -- | -- | 14 | -- | -128 | 5.3 | 1400 |
| | | | USWR | | 3 by 1 | .08 | .17 | 5 | .3 | | 2 | | | |
| 43.68 | Jun 21 76 | I | UERZ | 19 h | 5 by 1 | ? | 1.3 | .5 | -- | 2 | -- | -7 | -- | -- |
| 43.69 | Jul 14 76 | I | UERZ | 17 h | 6 by 1 | ? | ? | .7 | -- | 2 | -- | -13 | -- | -- |
| 43.70 | Jan 22 77 | Inf | UERZ | 26 h | 4 by 1 | .7 | -- | -- | -- | 2 | -- | +2 | -- | -- |
| 43.71 | Feb 8 77 | I | UERZ | 7 h | 4 by 2 | .37 | ? | -- | -- | 2 | -- | -6 | -- | -- |
| 43.72 | Sep 12 77 | E | ERZ | 5.5 d | 17 by 3 | 1.23,.23 | -- | -- | -- | 8 | 11 | -91 | 3.2 | 870 |
| | | | Koae | | 4 by 2 | .09 east | | | | | | | | |
| | | | Cald | | 4 by 4 | | | | | | | | | |
| 43.73 | Sep 27 77 | Defl | Cald | 5 d | 2 by 1 | .01 | -- | -- | -- | 16 | -- | -7 | -- | -- |
| 43.75 | May 29 79 | I | ERZ | 8 h | 5 by 2 | .65 | .67 | 6 | -- | 2 | -- | -3 | -- | -- |
| 43.76 | Aug 12 79 | I | UER | 5 h | 5 by 1 | 1.6 | -- | -- | -- | 5 | -- | -2 | -- | -- |
| 43.77 | Sep 22 79 | Inf | Cald | 3 h | 2 by 2 | -- | -- | -- | -- | 1 | -- | <2 | -- | -- |
| 43.78 | Nov 15 79 | E | UERZ | 21 h | 5 by 2 | 3.8 | 4.0 | 1.2 | .09 | 7 | 11 | -8 | 0.5 | 44 |
| 43.79 | Mar 2 80 | I | UERZ | 4 h | 3 by 2 | -- | ? | -- | -- | 3 | -- | -2 | -- | -- |
| 43.80 | Mar 10 80 | E | ERZ | 30 h | 6 by 2 | ? | 1.8 | 4.3 | -- | 3 | -- | -16 | -- | -- |
| | | | Koae | | | .22 west | | | | | | | | |
| 43.81 | Jul 30 80 | I | UERZ | 1 h | 2 by 1 | 30 | -- | -- | -- | 1 | -- | <2 | -- | -- |
| 43.82 | Aug 27 80 | I | UERZ | 12 h | 5 by 1 | 1.6 | .75 | 3 | 3 | 2 | -- | -9 | 2.6 | 860 |
| 43.83 | Oct 21 80 | I | ERZ | 27 h | 6 by 2 | -- | -- | -- | -- | 3 | -- | <1 | -- | -- |
| 43.83 | Oct 22 80 | I | UERZ | 3 h | 2 by 2 | 2.7 | -- | 2.1 | -- | 3 | -- | -3 | -- | -- |
| 43.84 | Nov 2 80 | I | UERZ | 4 h | 2 by 2 | .7 | ? | ? | ? | 3 | -- | -6 | 2.2 | 740 |
| 43.86 | Jan 20 81 | SI | USWR | 1.2 d | 2 by 1 | -- | .04 | -- | -- | 3 | -- | <3 | -- | -- |
| 43.87 | Jan 24 81 | SI | USWR | 5 d | 4 by 1 | -- | -- | -- | -- | 5 | -- | -5 | -- | -- |
| 43.88 | Feb 9 81 | SI | LSWR | 8 d | 4 by 1 | ? | -- | ? | -- | 8 | -- | -12 | -- | -- |
| 43.89 | Aug 2 81 | SI | USWR | 8 d | 5 by 1 | ? | -- | -- | -- | 8 | -- | -2 | -- | -- |
| 43.90 | Aug 10 81 | I | SWRZ | 3.5 d | 22 by 2 | 2.6,.28 | .14 | .46 | -- | 9 | -- | -107 | 11 | 1500 |
| | | | USWR | | 4 by 1 | 2.6 | 3.5 | | | | | | | |
| 43.91 | Mar 23 82 | I | USWR | 1 h | 2 by 1 | -- | ? | -- | -- | 1 | -- | <2 | -- | -- |
| 43.92 | Apr 30 82 | E | Cald | 4 h | 2 by 2 | -- | 14 | -- | -- | 2 | -- | +5 | -- | -- |
| 43.93 | Jun 22 82 | I | SWRZ | 5 d | 12 by 2 | .2 | -- | ? | -- | 3 | -- | -45 | .83 | 1400 |
| 43.94 | Sep 25 82 | E | UERZ | 1.6 d | 5 by 1 | 1.4 | -- | 1 | 1 | 7 | 2 | +18 | -- | -- |
| | | | USWR | | 2 by 1 | 1.4 | | | | | | | | |
| 43.96 | Dec 9 82 | I | UERZ | 2 d | 5 by 1 | 6.4 | -- | .8 | -- | 3 | -- | -3 | -- | -- |
| 43.97 | Jan 1 83 | E | ERZ | 6 d | 16 by 2 | .62 | .06 | ? | ? | 9 | 21 | -120 | 1 | 540 |
| | | | ERZ | | | .025,.61 | | | | | | | | |

TABLE 43.2.—*Endpoints and widths of cross sections*

[Half-width of each cross section is distance from cross-section plane within which earthquakes are included on plot. Latitude and longitude are given in degrees and minutes]

| Cross Section | Left endpoint | | Right endpoint | | Half-width (km) |
|---|---|---|---|---|---|
| | Latitude | Longitude | Latitude | Longitude | |
| *A-A'* | 19 25.35 | 155 18.4 | 19 21.4 | 155 12.0 | 0.8 |
| *B-B'* | 19 23.0 | 155 18.5 | 19 26.5 | 155 15.0 | 0.8 |
| *C-C'* | 19 24.4 | 155 19.0 | 19 24.4 | 155 14.0 | 0.8 |
| *D-D'* | 19 22.0 | 155 17.1 | 19 26.5 | 155 17.1 | 0.8 |
| *E-E'* | 19 20.9 | 155 13.1 | 19 26.8 | 154 57.5 | 2.7 |
| *F-F'* | 19 16.4 | 155 24.3 | 19 26.0 | 155 15.2 | 2.6 |
| *G-G'* | 19 25.4 | 155 12.1 | 19 20.6 | 155 16.0 | 2.0 |
| *H-H'* | 19 23.3 | 155 12.8 | 19 17.0 | 155 13.9 | 2.0 |
| *I-I'* | 19 23.5 | 155 9.7 | 19 17.6 | 155 8.3 | 2.0 |
| *J-J'* | 19 24.7 | 155 6.9 | 19 19.3 | 155 4.0 | 2.0 |
| *K-K'* | 19 24.1 | 155 19.5 | 19 20.0 | 155 15.0 | 2.0 |
| *L-L'* | 19 21.7 | 155 21.9 | 19 17.2 | 155 17.4 | 2.0 |
| *M-M'* | 19 19.3 | 155 25.0 | 19 15.1 | 155 20.2 | 2.0 |
| *N-N'* | 19 20.9 | 155 17.0 | 19 22.4 | 155 12.7 | 1.7, 2.1 |
| *O-O'* | 19 5.0 | 155 16.0 | 19 40.0 | 155 16.0 | 5.0 |
| *P-P'* | 19 2.0 | 155 34.0 | 19 32.0 | 155 11.0 | 10.0 |
| *Q-Q'* | 19 28.0 | 155 38.0 | 19 16.0 | 154 59.0 | 10.0 |
| *R-R'* | 19 21.0 | 155 18.8 | 19 26.0 | 155 15.9 | 1.6 |
| *S-S'* | 19 20.9 | 155 17.9 | 19 22.4 | 155 12.7 | 1.7, 2.1 |
| *T-T'* | 19 24.8 | 155 17.5 | 19 21.3 | 155 12.0 | 1.3 |
| *U-U'* | 19 23.5 | 155 18.5 | 19 23.5 | 155 2.5 | 4.3 |
| *V-V'* | 19 21.8 | 155 15.2 | 19 22.4 | 155 9.5 | 1.3 |
| *W-W'* | 19 21.3 | 155 16.0 | 19 21.3 | 155 5.8 | 3.8 |
| *X-X'* | 19 22.3 | 155 20.3 | 19 26.6 | 155 14.6 | 1.6 |

Koae, and magma may also have intruded the fault zone (Kinoshita, 1967). Some downrift earthquake migration appears to have occurred (fig. 43.20*D*), but location accuracy is not sufficient to be sure. All subsequent large SWRZ intrusions have shown clear downrift migration of earthquakes.

Another intrusion involving the Koae occurred two months later on July 2, 1963. Earthquakes occurred east of the previous swarm in the central and eastern Koae (fig. 43.21*A*). Many earthquakes were sharply felt and heard as cracking and booming sounds by observers in the epicentral area on July 1 and 2. Ground cracking was also noticed in the epicentral area and was confined to the eastern Koae fault zone. These observations suggest that many hypocenters were shallow and above about 2 km depth. The deflation indicates that magma left the summit reservoir, though the relative amounts of magma emplaced in the ERZ, SWRZ and Koae are uncertain. Two more accurately located and more clearly paired Koae intrusions occurred in May and June 1973. Earthquake migration (and presumably magma flow), however, was westward from the ERZ in the latter intrusions.

Relatively few earthquakes were located during the August and October 1963 ERZ eruptions (figs. 43.22*A*, 43.23*A*). This decrease is more an effect of inadequate instrumentation than failure of the volcano to produce earthquakes. No seismic stations were in this area of the ERZ (fig. 43.2*A*), and the masking of earthquakes by harmonic tremor is a more serious problem on the smoked-paper records then used to measure earthquakes. The recently active Koae experienced earthquakes during the October event (fig. 43.23*A*). Geologic and seismic descriptions are given by Moore and Koyanagi (1969).

## THE ERUPTIONS AND INTRUSION OF 1965 AND 1967

The ERZ eruption of March 5, 1965 (fig. 43.24; Wright and Kinoshita, 1968) and the August 24, 1965 intrusion (fig. 43.25) were both accompanied by swarms with many earthquakes exceeding magnitude 2. As before, seismic-station geometry did not permit accurate locations. Inaccuracy may account for the scattering of earthquakes away from the rift and into the south flank. Shallow south-flank earthquakes are seen accompanying more recent, better recorded ERZ intrusions and eruptions, but only as events clearly secondary to the main swarm beneath the rift. These 1965 earthquakes must be considered poorly located. Earthquakes during the August event apparently migrated eastward at a speed of 12 km/h, but concluding anything more than the possibility of a migration is ruled out by the location inaccuracies.

Seismic data from the ERZ eruption of December 1965 (fig. 43.26) and the caldera eruption that began on November 5, 1967 (fig. 43.27) are incomplete. None of the events in the first 3 days of the December 1965 eruption (and intrusion) were initially timed and located owing to their quantity and intensity. Although the eruption was on the ERZ, earthquakes were generated by an intrusion into the Koae (fig. 43.26*A*). Boscher and Duennebier (1985) timed many small events not plotted here and concluded that the Koae hinged apart in response to stresses in the volcano. The eruption, seismicity and ground cracking in the Koae are described by Fiske and Koyanagi (1968). The migration direction of major ground cracking and earthquakes was westward, as it was for earthquakes in later events combining ERZ eruptions with Koae intrusions. Only two earthquakes accompanying the November 1967 summit eruption were located, owing to the brevity of the swarm prior to the eruption and the intensity of harmonic tremor. The location of the two earthquakes suggests that an intrusion of the adjacent SWRZ initially accompanied the eruption (fig. 43.27*A*). The eruption that episodically continued until July 1968 is documented in detail by Kinoshita and others (1969).

## THE EAST RIFT ERUPTIONS OF 1968 TO MARCH 1969

The period from August 1968 to March 1969 was active for the central ERZ between Hiiaka and Puu Kamoamoa, which experienced three eruptions and one intrusion. The ability to adequately record and locate earthquakes improved markedly during this period. The eruptions of August 22 and October 7, 1968, are fully described by Jackson and others (1975). No earthquakes in the immediate vicinity of the August 1968 eruptive vents were large enough to time and locate, but events did occur to the southwest in the adjacent section of the Koae fault zone (fig. 43.28*A*). The Koae earthquakes anticipated the onset of eruption by about 3 hours and also apparently began an eastward migration of vent opening (fig. 43.28*D*). This eruption was seismically complex, because it began with small and unlocatable earthquakes near Makaopuhi (Jackson and others, 1975) and involved a Koae intrusion at the opposite end of the eruptive zone.

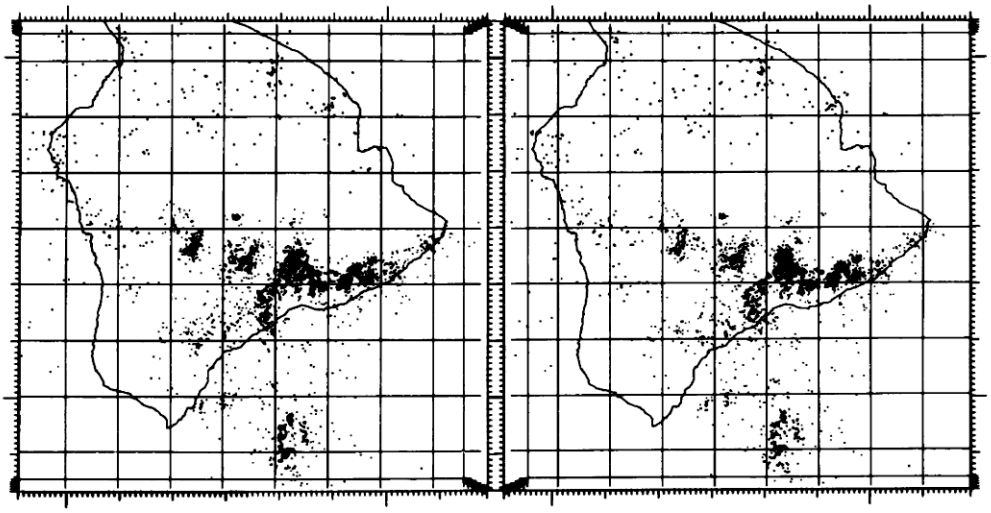

*A*

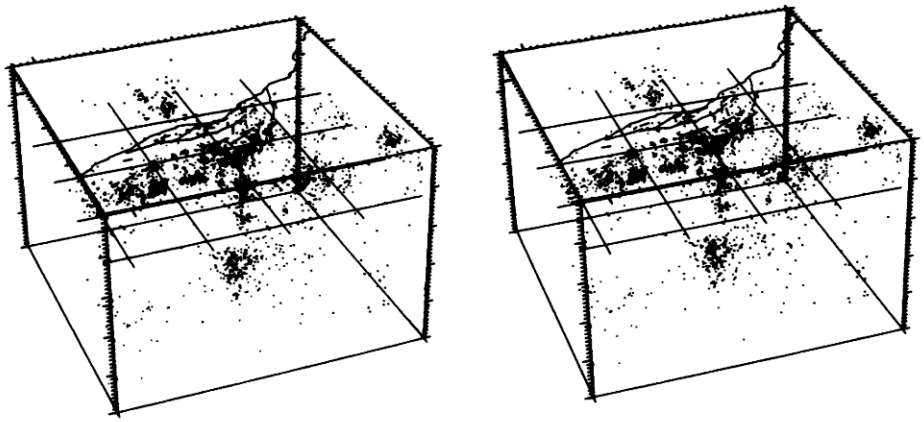

*B*

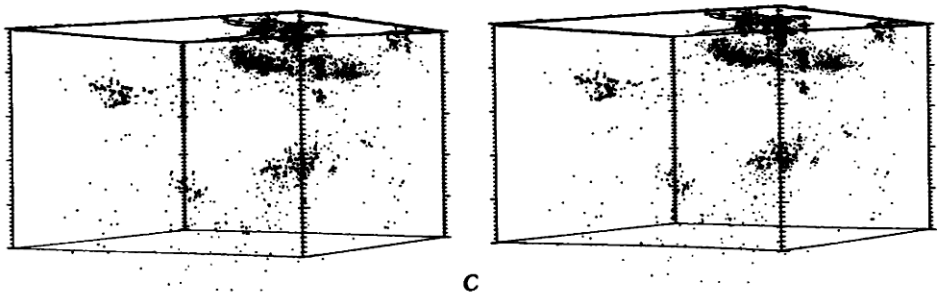

*C*

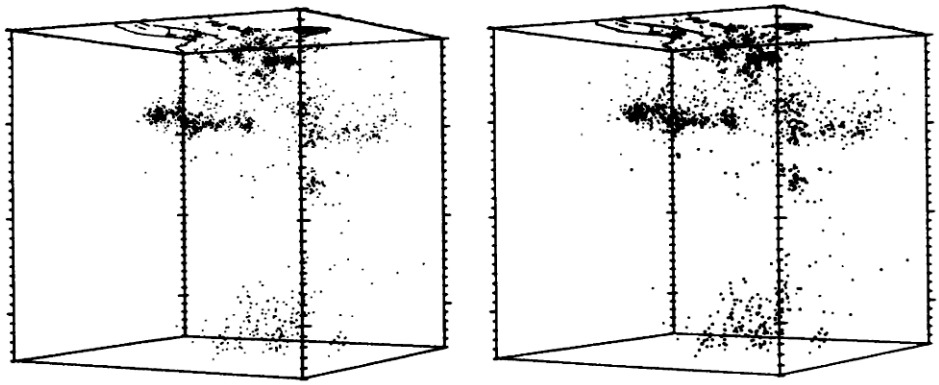

*D*

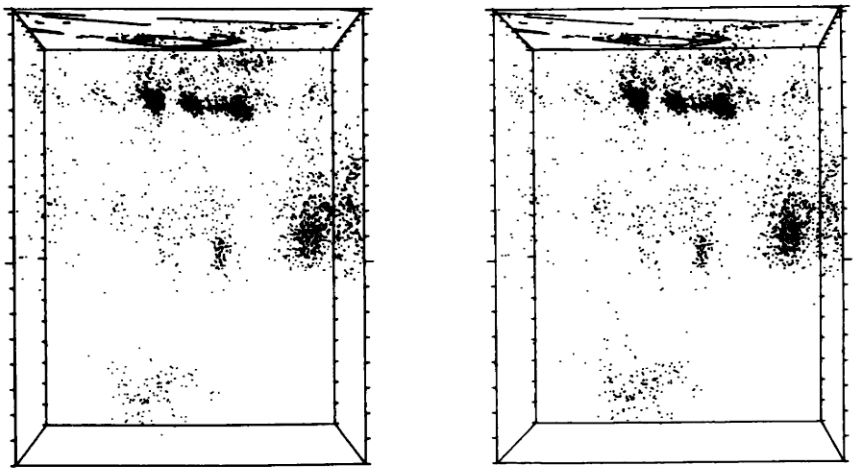

*E*

FIGURE 43.19—Stereopair views of 1970–81 Kilauea earthquakes showing major seismic zones. Tick marks on horizontal axes are plotted every minute of latitude and longitude, and those on depth axes are every kilometer. ***A,*** View from above Hawaii. Loihi Volcano is to south. Coastline is at surface, and grid of lines is at 13 km depth and approximates Moho. ***B,*** Closer view of Kilauea from north. Grid is plotted at 13 km depth near Moho, and box is 50 km high. Most of shallowest seismicity is below rift zones. Tectonic earthquakes below Kilauea's south flank are mostly between 6 and 10 km depth. Vertical magma conduit and major cluster near 30 km are clearly visible. ***C,*** Same box as in *B* viewed from northeast at depth of 25 km. Magma conduit merges with diffuse cloud of seismicity in far lower corner, which marks present Hawaiian hot spot. Earthquakes from Loihi are to left and from Mauna Loa in upper right corner. ***D,*** Closer view of Kilauea from northeast at depth of 17 km. Box is 35 km high. Low seismicity associated with summit magma reservoir is below caldera between about 3 and 7 km. ***E,*** Close-up view of Kilauea summit region from south at a depth of 9 km. Unlike other stereopairs, essentially all available earthquakes are plotted in *E*. Intense seismic zones at 3 km depth are rift conduits that abut magma reservoir behind and beneath them. Foreground events between about 6 and 10 km depth are tectonic earthquakes in south flank.

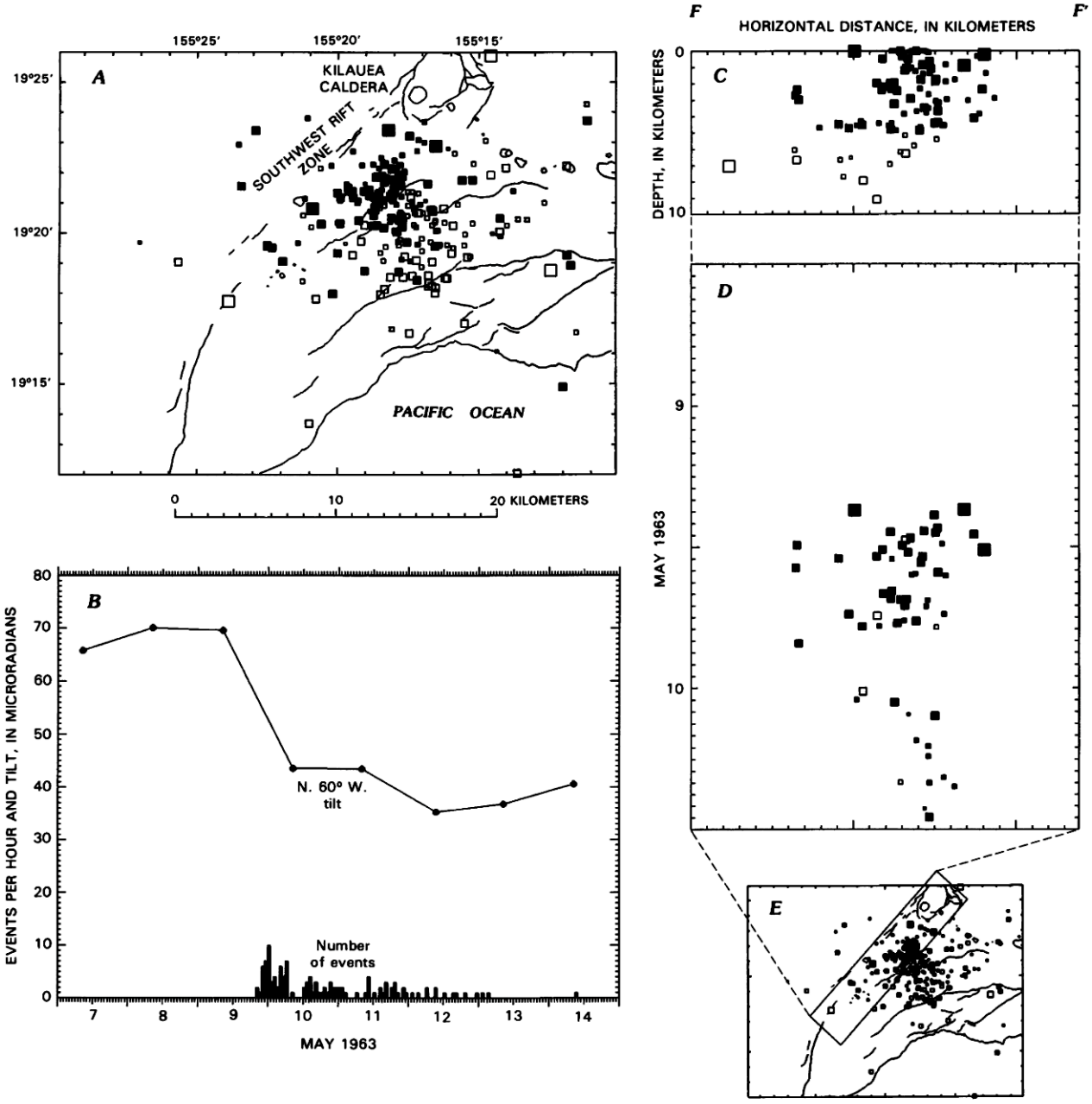


FIGURE 43.20.—Earthquake swarm (and presumed magma intrusion) beginning on May 9, 1963. Only earthquakes that were timed and located are plotted. ***A,*** Map of earthquake epicenters. Solid squares, earthquakes in depth range 0–5 km; open squares, 5–13 km below surface. Faults, fissures,and pit craters are as shown in figure 43.1. ***B,*** Plot of tilt at Uwekahuna and hourly number of earthquakes on same time base. Decreasing tilt values correspond to tilt down to east and south and generally to deflation of summit magma reservoir. Connected points are readings from two-component water-tube tiltmeter rotated to N. 60° W., approximately in line with deformation center. Continuous line, beginning with figure 43.49, is from east-west Ideal Aerosmith tiltmeter. ***C,*** Cross section of hypocenters. End points of cross section and half-width distance from cross section plane are presented in table 43.2. Ticks on horizontal axis at 1-km intervals. Beginning date of earthquakes included in *A* and C is the starting swarm date unless otherwise noted. The number of days included in *A* and C is given as plot duration in table 43.1 and is not necessarily the same as time axis of tilt and seismicity graph. ***D,*** Horizontal position of earthquakes versus time; time increases downward, ticks at hourly intervals. Lateral migration of epicenters is recognized as diagonal bands of points. ***E,*** Rectangular area within which earthquakes are plotted on C and *D*.

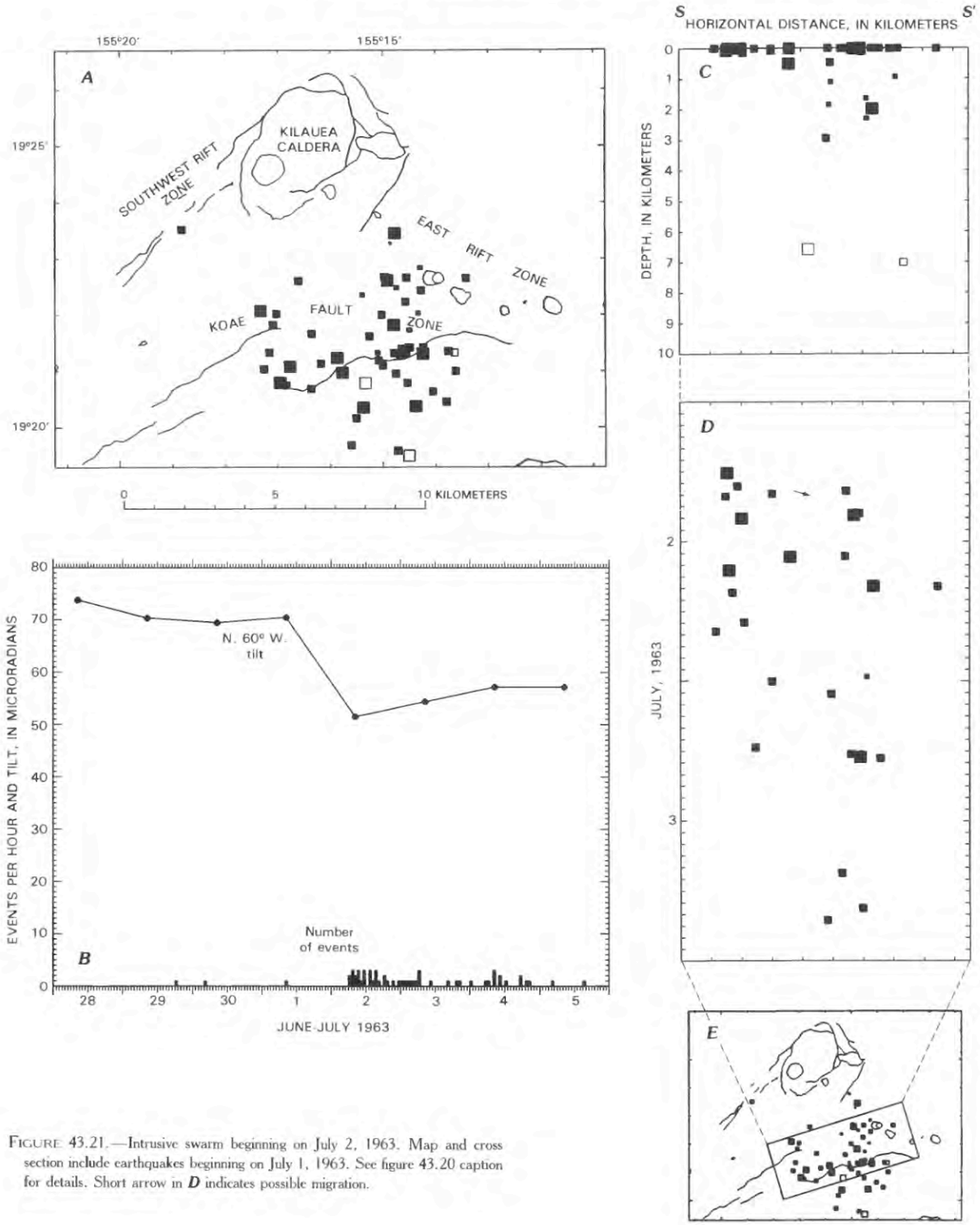


FIGURE 43.21.—Intrusive swarm beginning on July 2, 1963. Map and cross section include earthquakes beginning on July 1, 1963. See figure 43.20 caption for details. Short arrow in ***D*** indicates possible migration.

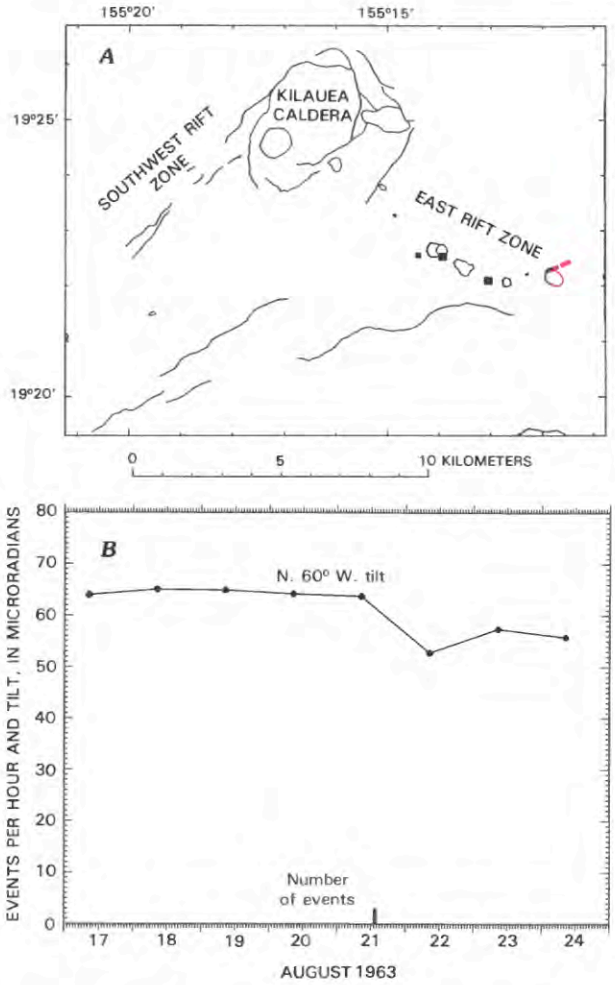


FIGURE 43.22.—Eruptive swarm beginning on August 21, 1963. See figure 43.20 caption for details. Red, eruptive vents.

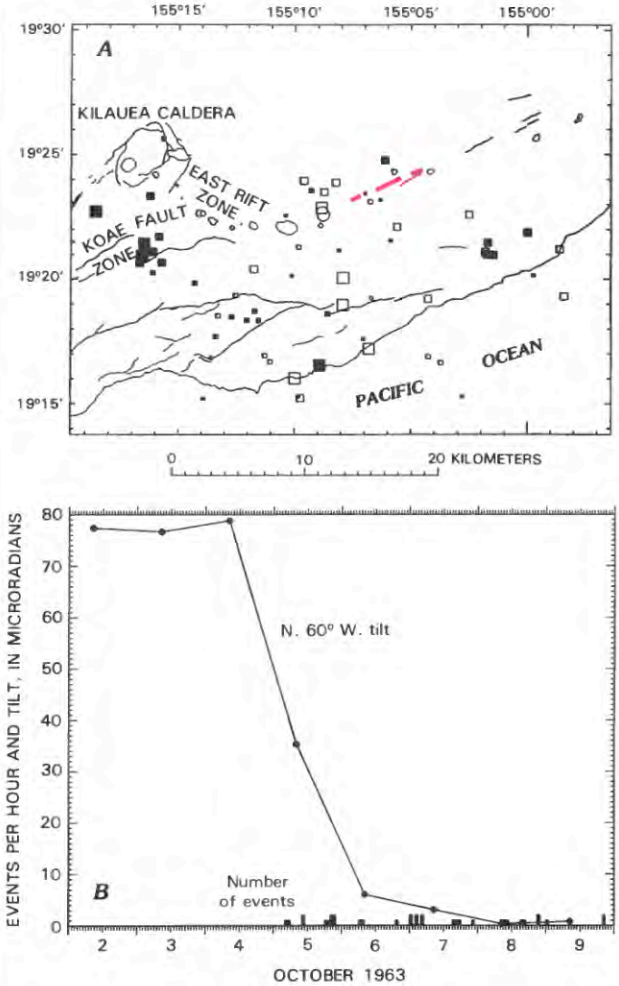


FIGURE 43.23.—Eruptive swarm beginning on October 5, 1963. See figure 43.20 caption for details. Red, eruptive vents.

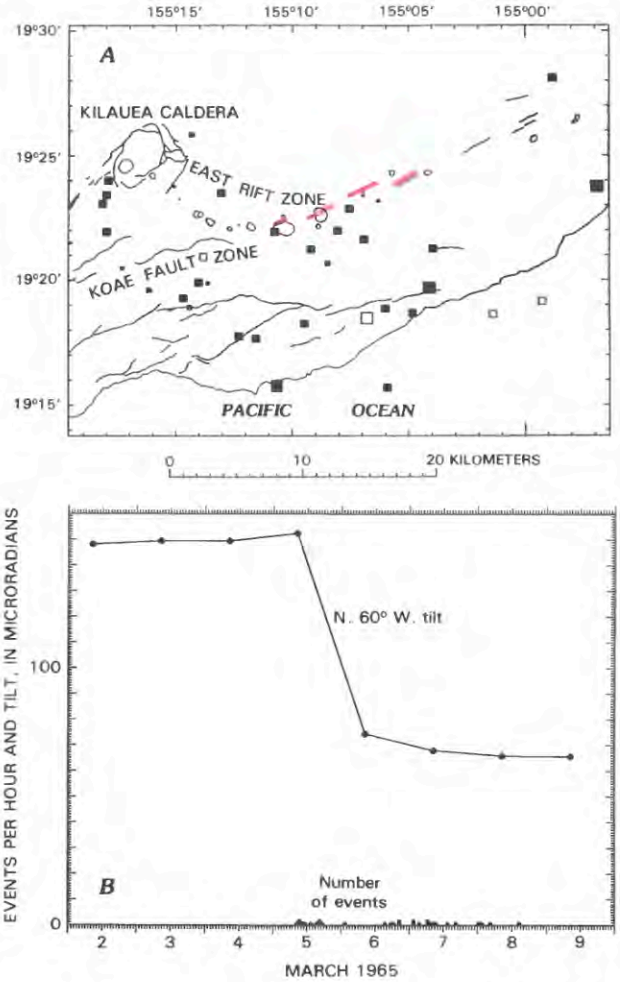


FIGURE 43.24.—Eruptive swarm beginning on March 5, 1965. See figure 43.20 caption for details. Red, eruptive vents.

Earthquakes and volcanism were much more clearly related during the October 1968 eruption. The length and position of the eruptive vents and seismic zone coincide very closely (fig. 43.29*A*). The displacement of the seismic zone slightly south of surface rift and eruptive vents is typical of later ERZ swarms, but may partly be a result of a biased distribution of seismic stations. A clear downrift migration of earthquakes at about 3-4 km/h occurred uprift of Puu Kamoamoa (fig. 43.29*D*). The speed then slowed to about 1 km/h. Eruptive vents opened in the same direction and at comparable speed, and followed the earthquakes in a given place by about 3 hours. The dike thus grew downrift at 1–3 km/h and upward at about 0.6 km/h simultaneously. Passage of magma upward from the main conduit at 3 km depth was essentially aseismic, as seen by the absence of earthquakes within 2 km below the vents (fig. 43.29*C*).

The ERZ eruption of February 22, 1969, is associated with two swarms. The first preceded the eruption by several days and was in the southern part of the caldera (fig. 43.30*A*). It occurred gradually over several days and was concurrent with a premonitory rise in Uwekahuna tilt (fig. 43.30*B*). The earlier swarm was thus caused by summit inflation. This pulse of inflation may have also triggered the eruption by incrementing magma pressure just above a critical level. The eruption itself was immediately preceded by a swarm located mostly south of the ERZ eruptive vents (fig. 43.31*A*). Most of these earthquakes are probably mislocated too far south of the rift zone and vents. The first vents to erupt were near Alae crater, and vents opened rapidly to the east and slowly to the west (Swanson and others, 1976b). In each part of the vent system, earthquakes essentially ceased when the vent began erupting (fig. 43.31*C*). This cessation could result from masking of smaller earthquakes by strong vent-related tremor, by stress and pressure release when the dike reached the surface, or both.

A small swarm lasting less than three hours occurred on March 21, 1969. It was concentrated in a small cluster 1–2 km uprift of the future site of Mauna Ulu and preceded the Mauna Ulu eruption by two months. The March swarm may have been associated with small-scale magma movement in some sense preliminary to the later eruption. Any summit deflation associated with this small intrusion was below the tilt noise level (fig. 43.32*B*). An apparent and very rapid westward migration of epicenters (fig. 43.32*D*) is not well seen since the swarm is so small.

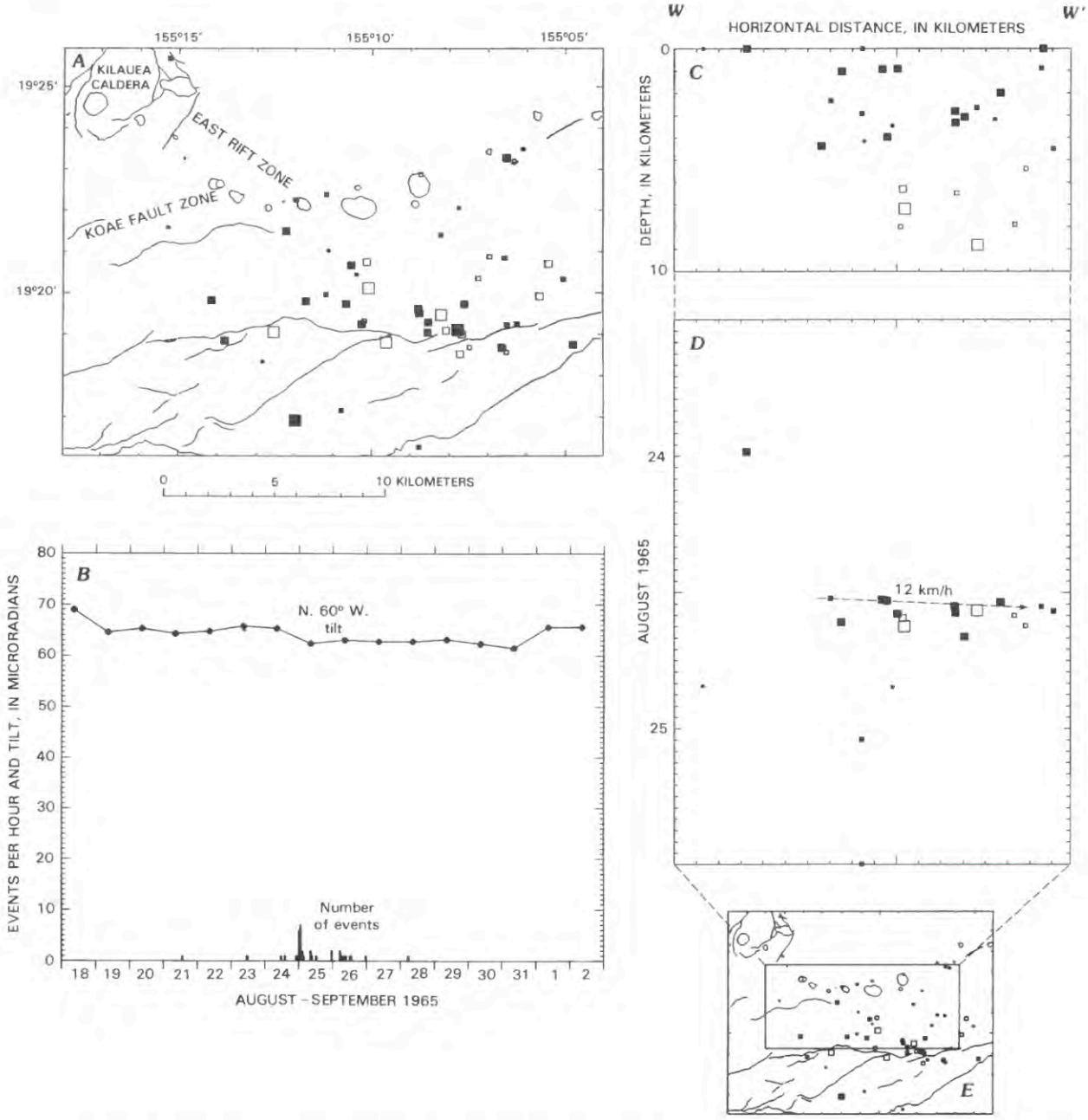


FIGURE 43.25.—Intrusive swarm beginning on August 24, 1965. Map and cross section include earthquakes beginning on August 21, 1965. See figure 43.20 caption for details. Dashed line in ***D***, poorly resolved shift in seismicity.

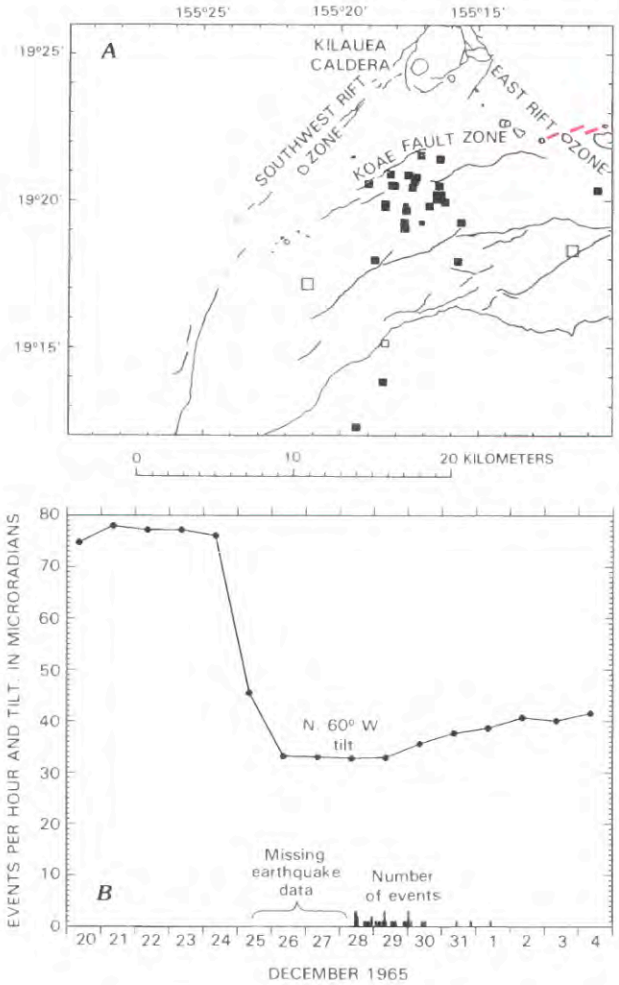


FIGURE 43.26.—Eruptive swarm beginning on December 28, 1965. Map and plot include earthquakes beginning on December 27, 1965. See figure 43.20 caption for details. Red, eruptive vents.

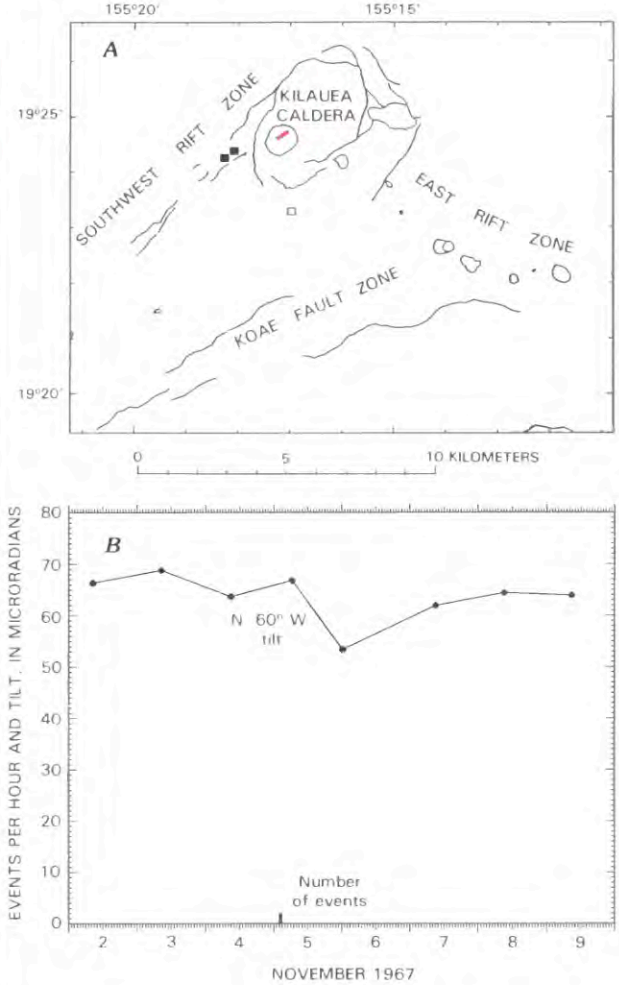


FIGURE 43.27.—Eruptive swarm beginning on November 5, 1967. Map and plot include earthquakes beginning on November 4, 1967. See figure 43.20 caption for details. Red, eruptive vent.

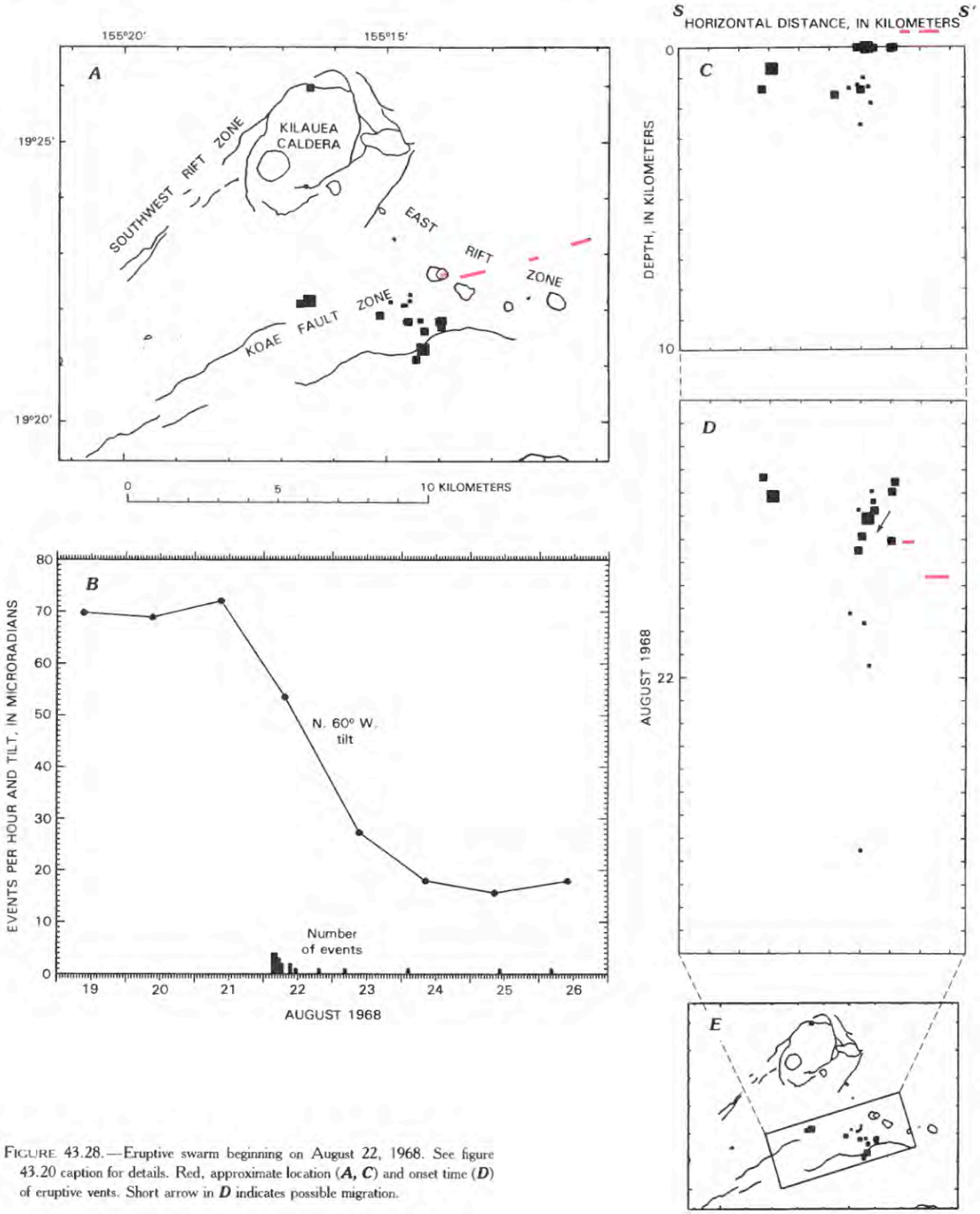


FIGURE 43.28.—Eruptive swarm beginning on August 22, 1968. See figure 43.20 caption for details. Red, approximate location (***A, C***) and onset time (***D***) of eruptive vents. Short arrow in ***D*** indicates possible migration.

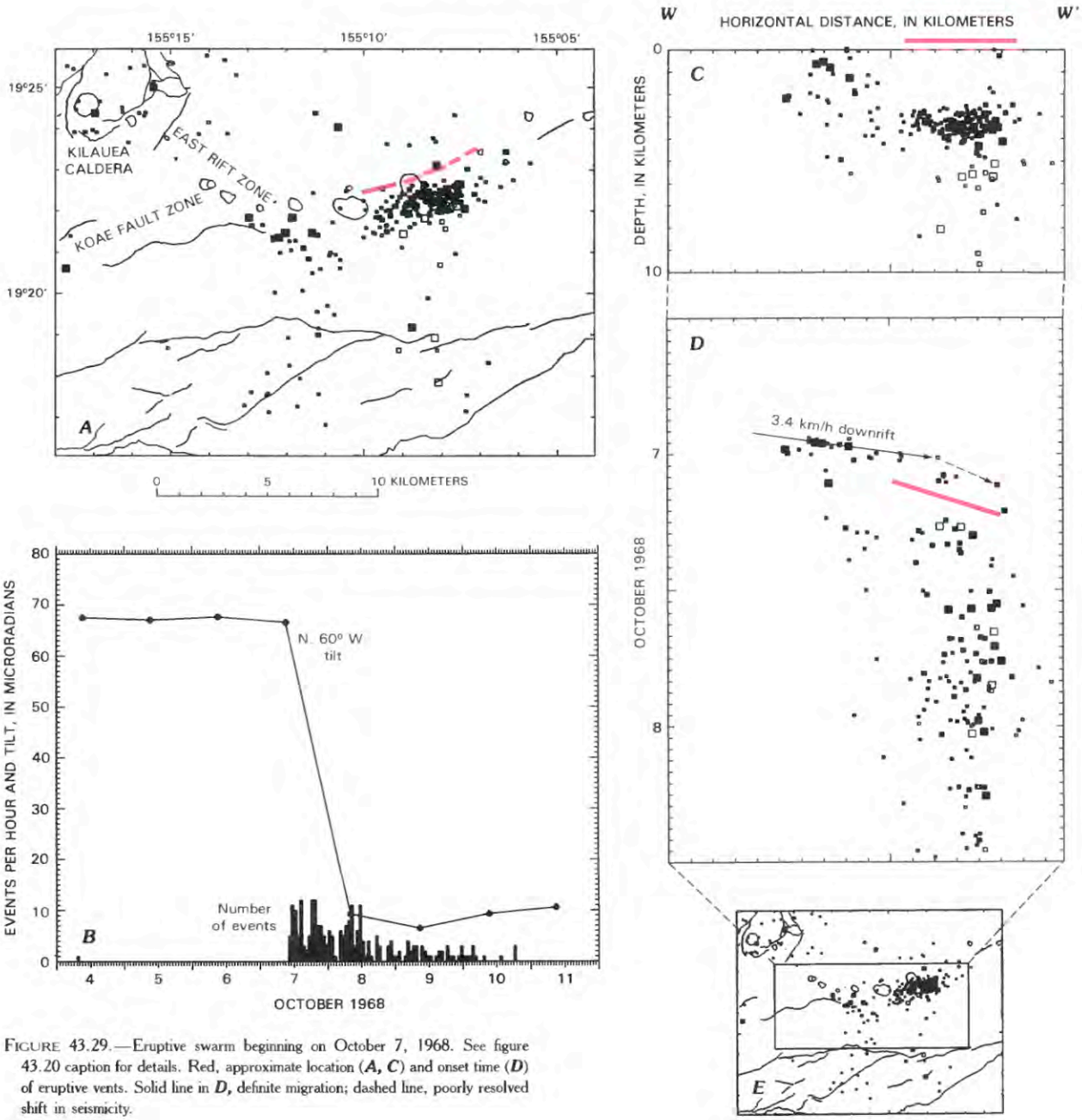


FIGURE 43.29.—Eruptive swarm beginning on October 7, 1968. See figure 43.20 caption for details. Red, approximate location (***A, C***) and onset time (***D***) of eruptive vents. Solid line in ***D***, definite migration; dashed line, poorly resolved shift in seismicity.

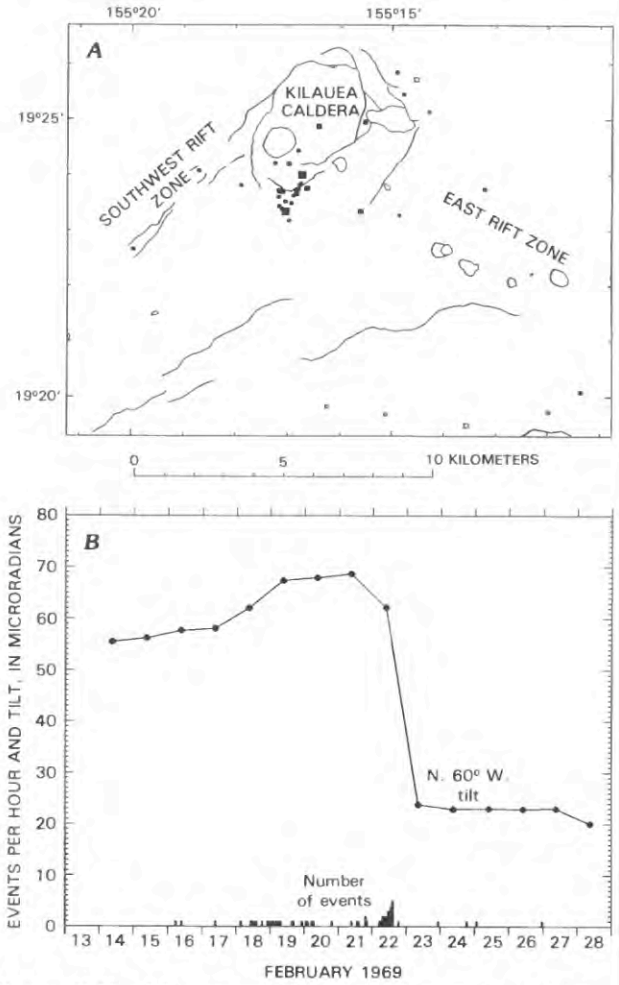


FIGURE 43.30.—Inflationary swarm beginning on February 18, 1969, immediately preceding eruption of February 22. Map and plot include earthquakes beginning on Fegruary 16, 1969. See figure 43.20 caption for details.

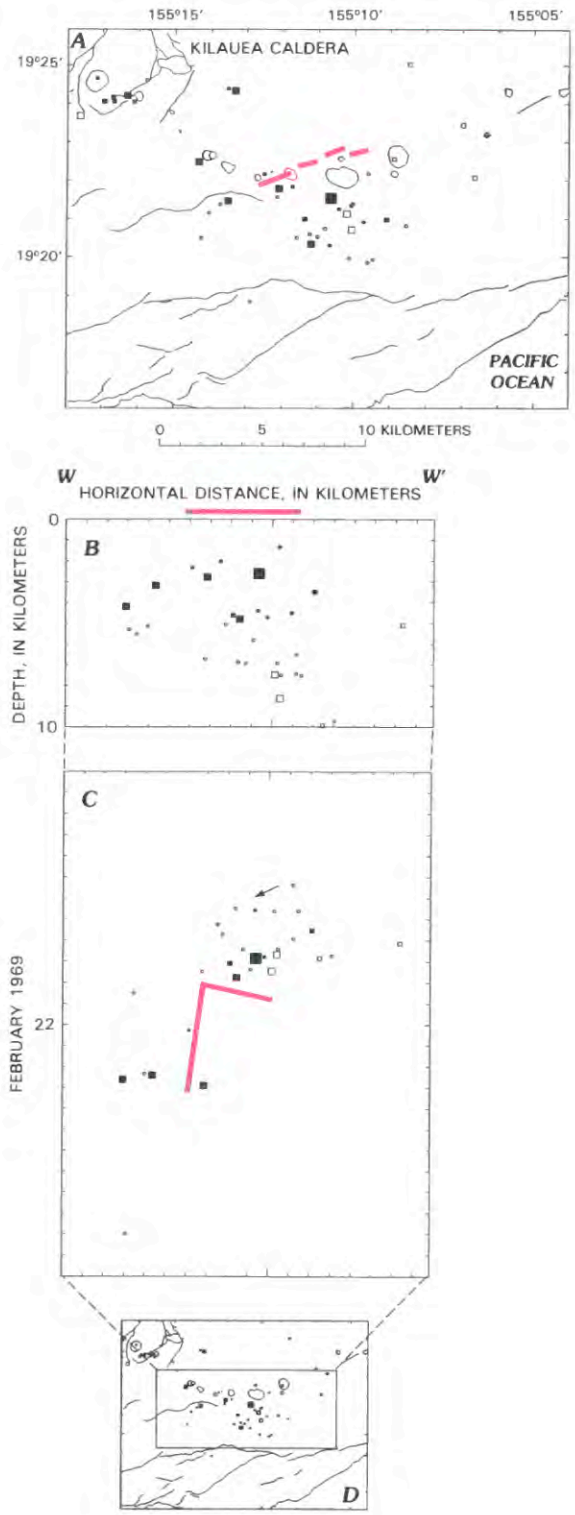


FIGURE 43.31.—Eruptive swarm beginning on February 22, 1969. See figure 43.20 caption for details and figure 43.30*B* for tilt and hourly earthquake rate. Red, approximate location (***A, B***) and onset time (***C***) of eruptive vents. Short arrow in ***C*** indicates possible migration.

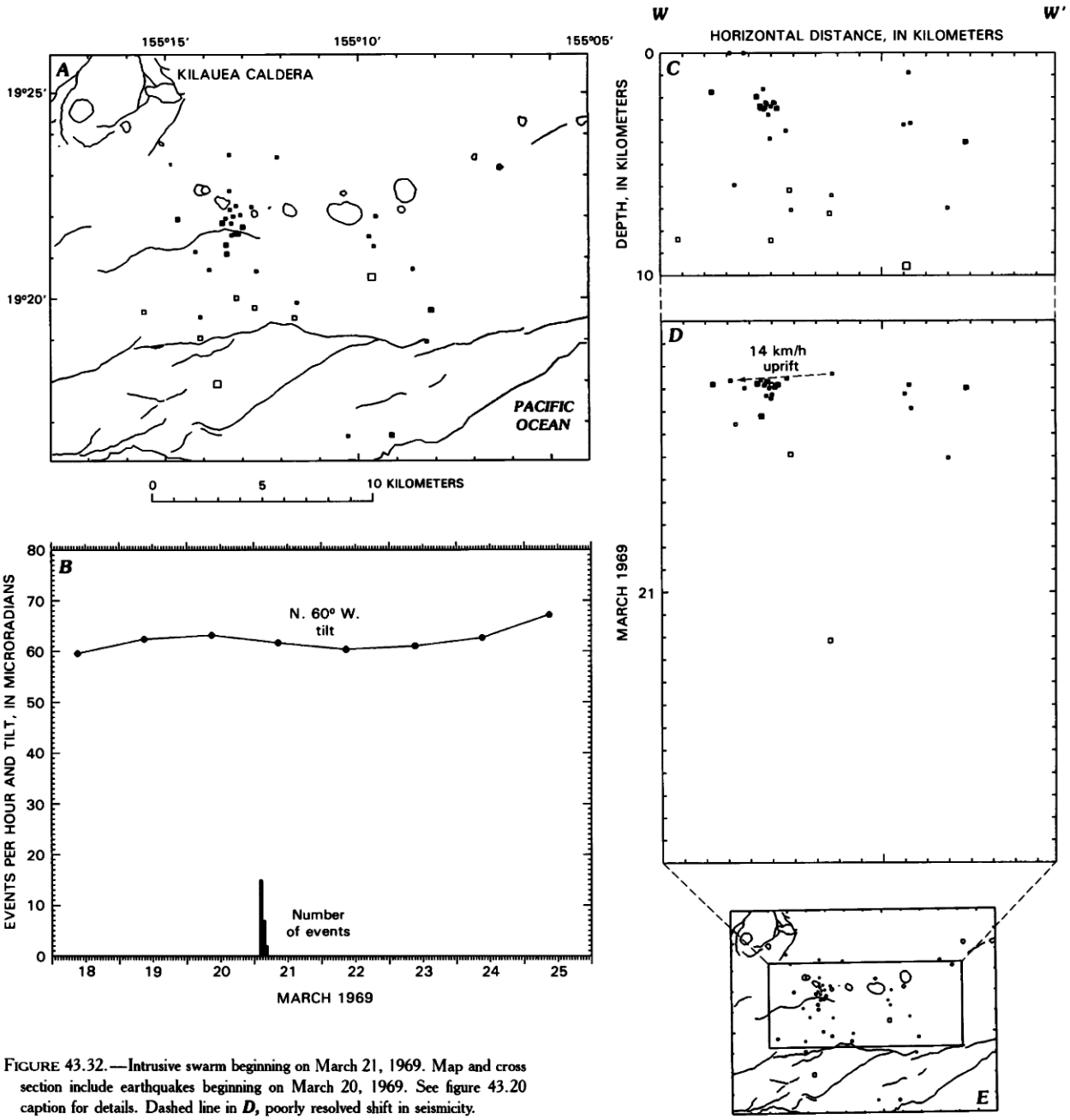


FIGURE 43.32.—Intrusive swarm beginning on March 21, 1969. Map and cross section include earthquakes beginning on March 20, 1969. See figure 43.20 caption for details. Dashed line in *D*, poorly resolved shift in seismicity.

## THE MAY 1969 MAUNA ULU ERUPTION AND INTRUSIONS THROUGH NOVEMBER 1969

Like the February 1969 eruption, the Mauna Ulu eruption commencing on May 24, 1969, was preceded by about three days of low-level seismicity. The pre-Mauna Ulu seismicity, however, appears to emanate from Kilauea's flank south of Makaopuhi and Napau (fig. 43.33*A*). This swarm was very unusual in that it was not in or near the summit caldera and thus not clearly related to inflation prior to the eruption. The shallow earthquakes were in the south flank near the areas active during the March and August 1965 and February 1969 swarms. This precursory swarm was possibly caused by some sort of south-flank instability that triggered the Mauna Ulu eruption. Because later volcanic swarms seen with an improved seismic network have all been located much closer to the ERZ, the May 20–23, 1969 swarm is probably mislocated too far south.

The swarm accompanying the onset of the Mauna Ulu eruption scatters within about 3 km of the eruptive vent (fig. 43.34*A*). These earthquakes are shallower than 4 km and locate very close to the surface in the vent area (fig. 43.34*B*). The intense seismicity began soon after 0300 H.s.t. on May 24 and rapidly migrated westward at an apparent speed of about 4 km/h (fig. 43.34*C*). This event was apparently a minor intrusion into the east end of the Koae fault zone about one hour before magma reached the surface. This intense seismicity ended about the time the eruption began. The vents opened nearly simultaneously in the eastern half of the fissure, but opened gradually westward (Swanson and others, 1979). This westward vent progression can be extrapolated to a later burst of earthquakes southwest of Mauna Ulu (fig. 43.34*C*). A dike or pulse of magma possibly moved westward at about 0.3 km/h into the Koae, extending the initial vent and causing earthquakes before it stopped. During the next several hours, scattered earthquakes occurred at depths between about 6 and 9 km to the southeast of Mauna Ulu (figs. 43.33*D*, 43.34). These events apparently were tectonic and were induced by rifting during the onset of the eruption. They also occurred directly beneath the zone of premonitory earthquakes (compare figs. 43.33*C* and 43.34*B*). The relations between pre-eruption and posteruption south-flank earthquakes and the eruption itself are unclear.

While Mauna Ulu continued with a series of its own eruptive episodes, a sequence of intrusions took place in July, October and November 1969. None coincided with Mauna Ulu eruptive episodes, and Kilauea apparently went about the business of generating intrusions between episodes of supplying Mauna Ulu with magma. The shunting of magma to Mauna Ulu during 1969–71 was the apparent cause of the increased frequency of intrusions relative to eruptions at Kilauea (Klein, 1982b). The ongoing Mauna Ulu eruption may have robbed the other intrusions of the magma supply and pressure they needed to erupt themselves.

The July 3, 1969 intrusion was near Hiiaka on the upper ERZ (fig. 43.35*A*). Earthquakes clearly define an east-west lineation about 7 km long that is oblique to the rift axis. The seismic trend is aligned with the local direction (N. 75° E.) of eruptive vents and fissures, and hence the axis of greatest compressive stress. In this unusual case the shallow stress orientation typical where vents form was also dominant at the 2- to 4-km earthquake depth. The swarm began at the intersection of the seismic lineation and the rift magma conduit. Earthquakes rapidly progressed bilaterally east and west at nearly the same speed of about 1.8 km/h, when projected along the lineation (fig. 43.35*D*). We interpret this event as the intrusion of a new dike whose direction is controlled by regional stress rather than the pre-existing ERZ magma conduit. Only a small volume of magma was intruded, because no detectable summit deflation was recognized (fig. 43.35*B*). The intruded magma had likely all been stored within the ERZ near Hiiaka. The observed earthquake migration speed is very typical of other intrusions that propagate along the axes of the rift zones. The processes of intrusion either parallel or oblique to the rift axis must therefore be fairly similar, although dikes off the rift axis may be thinner and not accommodate or store much magma.

Two other small intrusions also occurred between eruptive phases at Mauna Ulu in October and November 1969. The swarm that began on October 7 lasted for about 4 days and was accompanied by slow inflation then deflation (fig. 43.36*B*). All earthquakes were in the south flank 5 to 8 km southeast of Puu Kou (fig. 43.36*A*). This swarm is thus puzzling because there was no seismicity beneath the SWRZ. As discussed earlier, the October earthquakes were in a region frequently activated by large SWRZ intrusions. The October swarm may thus have resulted from a slow and aseismic SWRZ intrusion or some sort of rifting episode that stressed the south flank and triggered the swarm. The earthquakes are not a tectonic aftershock sequence: their time history is like a volcanic swarm with no mainshock. The swarm is similar to that of February 1981 (see below), which is more obviously a slow intrusion, owing to its location directly beneath the rift, to the larger deflation and to other associated SWRZ intrusions in 1981. We tentatively interpret the October 1969 swarm as resulting from a slow SWRZ intrusion or a related south flank adjustment.

The November 3, 1969 ERZ intrusion was small and lasted less than one hour (fig. 43.37). It was accompanied by a small summit deflation (fig. 43.37*B*) and is thus clearly an intrusion. It occurred beneath Mauna Ulu (fig. 43.37*A*), but did not coincide with a major eruptive episode there (see Swanson and others, 1979). The sparse earthquakes rapidly moved downrift at about 6 km/h (fig. 43.37*D*), though the speed is not well defined. This swarm appears to have accompanied the emplacement of a small dike below Mauna Ulu, rather than a new pulse of magma to Mauna Ulu itself. No significant earthquake swarms or new seismic intrusions accompanied any of the later Mauna Ulu eruptive episodes. The independence of Mauna Ulu eruptions and the many other intrusions emphasizes the fact that the upper ERZ is really a network of distinct magma conduits, different segments of which can be active simultaneously.

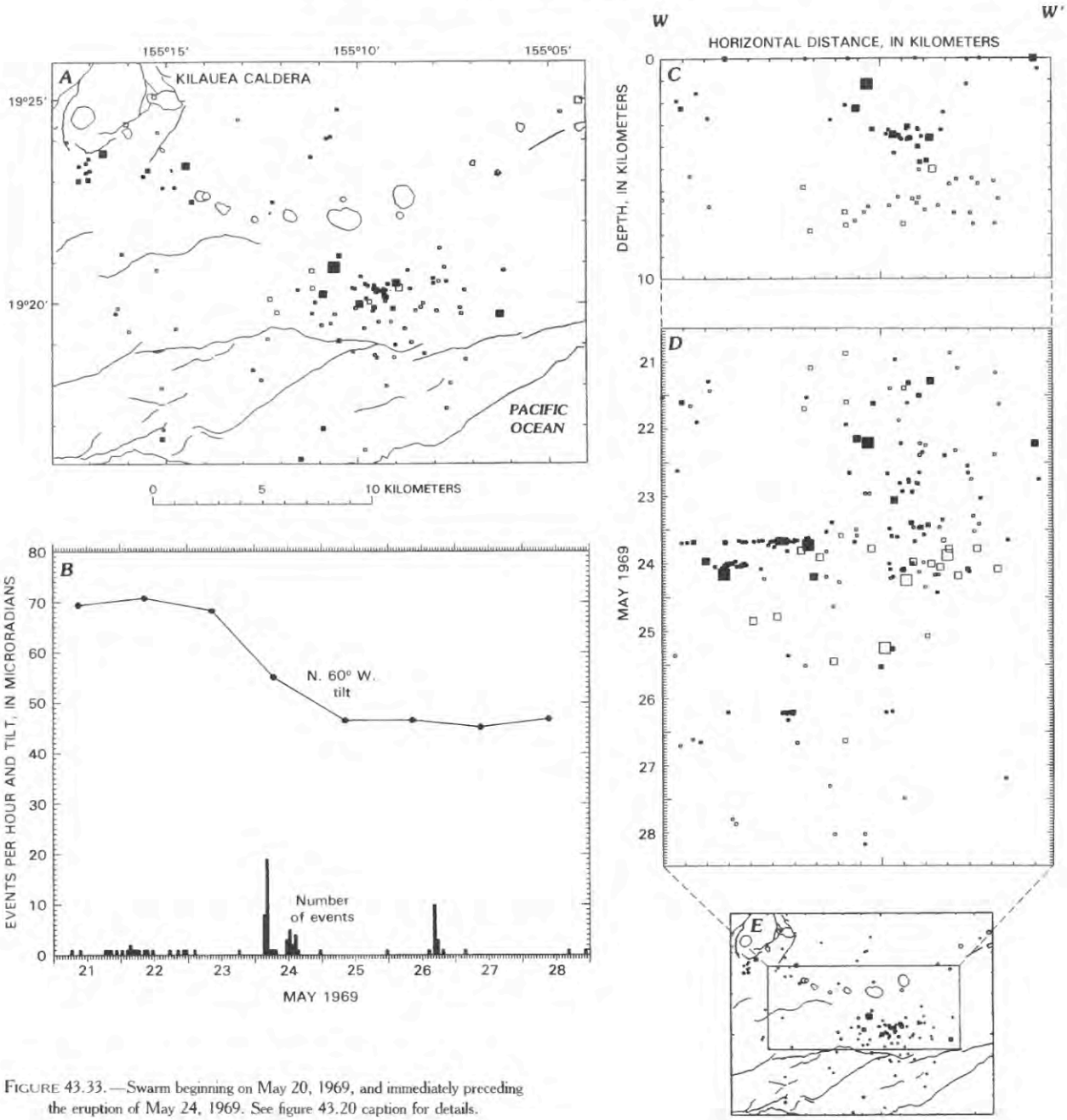


FIGURE 43.33.—Swarm beginning on May 20, 1969, and immediately preceding the eruption of May 24, 1969. See figure 43.20 caption for details.

FIGURE 43.34.—Eruptive swarm beginning on May 24, 1969. See figure 43.20 caption for details, and figure 43.33*B* for tilt and hourly earthquake rate. Red, approximate location (***A, B***) and onset time (***C***) of eruptive vents. Dashed line in ***C***, poorly resolved shift in seismicity.

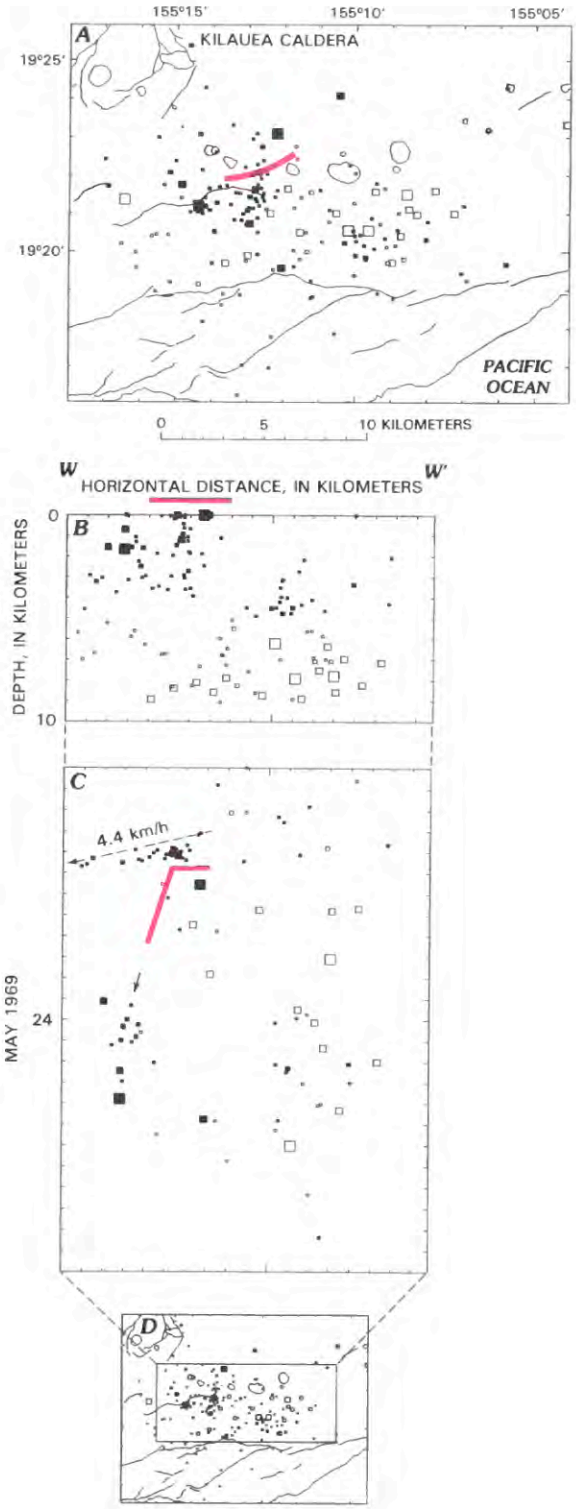

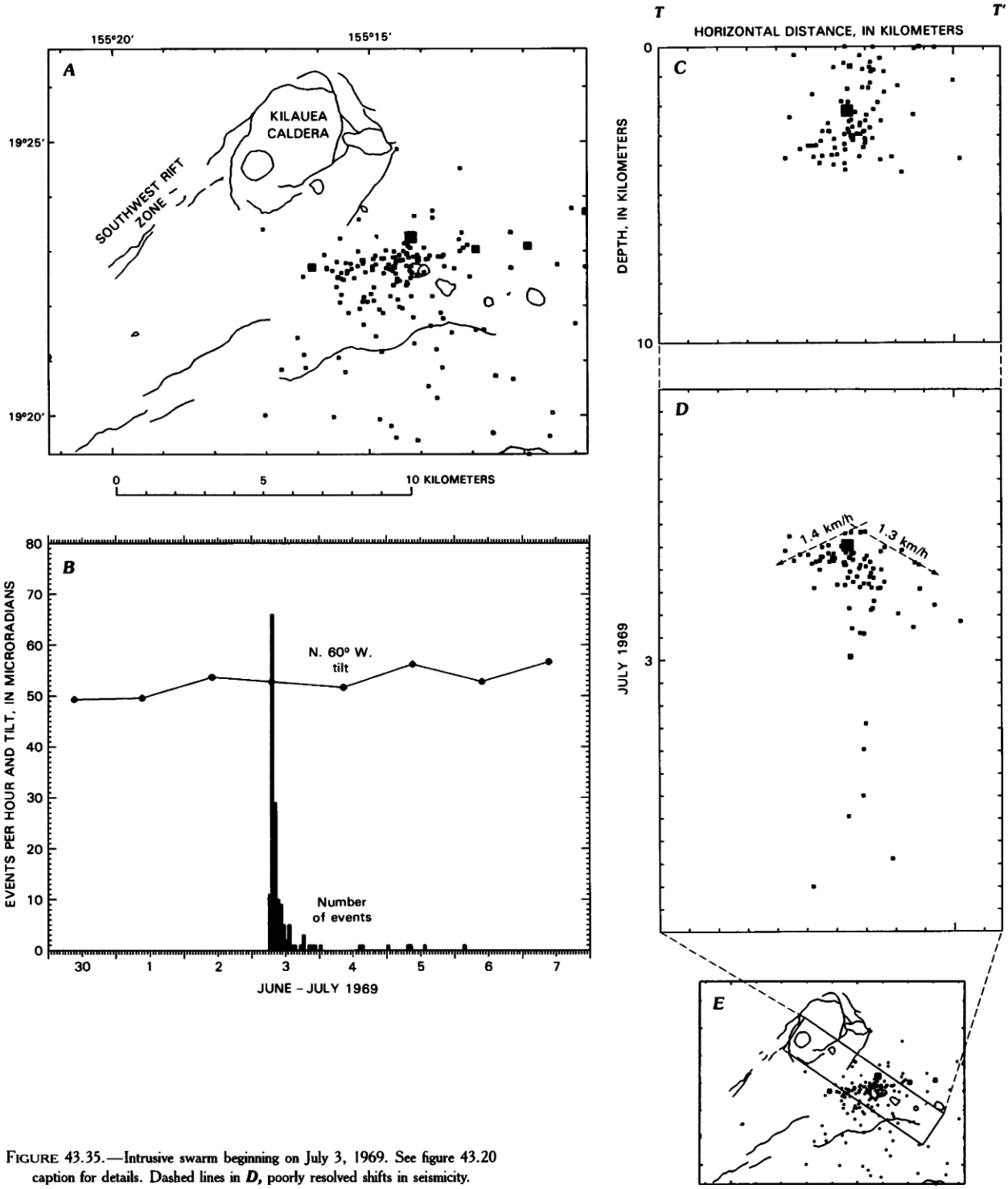


FIGURE 43.35.—Intrusive swarm beginning on July 3, 1969. See figure 43.20 caption for details. Dashed lines in *D*, poorly resolved shifts in seismicity.

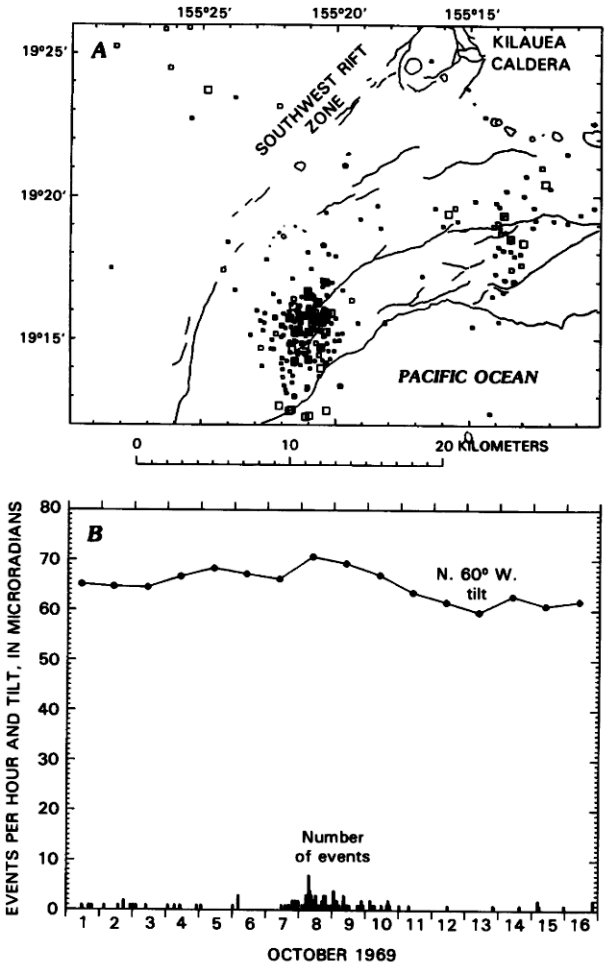


FIGURE 43.36.—Intrusive swarm beginning on October 7, 1969. Map and plot include earthquakes beginning on October 6, 1969. See figure 43.20 caption for details.

## INFLATION-RELATED SWARMS AND INTRUSIONS, DECEMBER 1969 TO DECEMBER 1970

Uwekahuna tilt rose steadily during 1970 and most of 1971 as magma accumulated in the summit reservoir. Mauna Ulu's eruption was waning, so that more magma was available for summit storage. An additional consequence of the summit inflation during this period was a series of slow swarms within and adjacent to the caldera. The fluctuating tilt and seismicity were often well correlated, since both are consequences of inflation. The division of these inflation earthquakes into swarms is somewhat arbitrary, because summit seismicity fluctuated between a few and a few dozen locatable earthquakes per day for long periods. We have identified the most active intervals and called them slow swarms. The period from December 1969 through September 1971 contains 11 such slow swarms that last several days each, but only 4 rapid swarms accompanying intrusions or eruptions.

Many of the inflation-related swarms appear to also involve intrusion of magma into the rifts. As with the rapid swarms, earthquakes during inflation often penetrate into the uppermost sections of rift in addition to the caldera. As discussed earlier, the inflation earthquakes and hence the accumulating magma appear to stop at blockages within the rifts. Earthquakes sometimes migrate along the rift conduits. The migration speed of earthquakes and hence the rate of intrusion is generally much slower than during the intrusions that generate intense swarms. The summit tilt changes slowly during these slow intrusions and may either rise, fall or remain unchanged. The 1970–71 period of inflationary seismicity and slow intrusions occurred when tilt values were much higher than average. Inflation swarms generally begin and end gradually, unlike the sharp onset of most swarms accompanying eruptions and rapid intrusions. These contrasts leave the impression that magma leaks or spills over into the rifts during slow intrusions, but pours through a ruptured barrier during rapid intrusions.

Inflationary swarms began on December 22, 1969 (fig. 43.38), February 3, 1970 (fig. 43.40), March 17 (fig. 43.41), and April 2 (fig. 43.42). In each case, tilt and seismicity were correlatable. Each swarm was limited to 2 or 3 km of the ERZ and SWRZ just outside the caldera. The seismicity apparently reached barriers within the rift conduits that could not be overcome by the slow pace of intruding magma. The Mauna Ulu eruptive episode on December 30 and its rapid deflation abruptly ended all earthquakes (fig. 43.38*B*). The eruption phase itself was aseismic, as were all Mauna Ulu episodes except the first. After the initial swarm, the conduit to Mauna Ulu was mostly open, and no new dike growth or rupture of rock was required. Of these inflationary swarms, only the one on February 3 showed a clear migration of earthquakes. Earthquakes penetrated the SWRZ first (fig. 43.40*G*). The ERZ soon followed with a more rapid migration that soon slowed (fig. 43.40*D*). The final downrift speed was only about 0.02 km/h into both rifts. The slow earthquake migration demonstrated that an intrusion occured even while magma accumulated in the summit reservoir.

Rapid intrusions occurred on January 22 (fig. 43.39) and May 15, 1970 (fig. 43.43). The first was near Keanakakoi, only lasted for three hours, and produced no recognizable deflation (fig. 43.39*B*). Apparently the volume of magma was small, or it merely shifted position such that no tilt change at Uwekahuna resulted. The swarm moved rapidly toward the caldera (fig. 43.39*D*). The May swarm was clearly an ERZ intrusion accompanied by about 9 microradians of deflation (fig. 43.43*A*, *B*; Duffield and others, 1976). Pollard and others (1983) used a profile of surface displacements to constrain an elastic model of deformation surrounding a new dike. They inferred a dike dipping 86° NW., extending between 0.4 and 0.8 km depth, and 80 cm thick. The numerous earthquakes close to the surface (fig. 43.43*C*) emphasize the shallow nature of this event. The initial burst of earthquakes may have moved rapidly downrift from Puhimau at about 4.2 km/h (fig. 43.43*D*). Activity

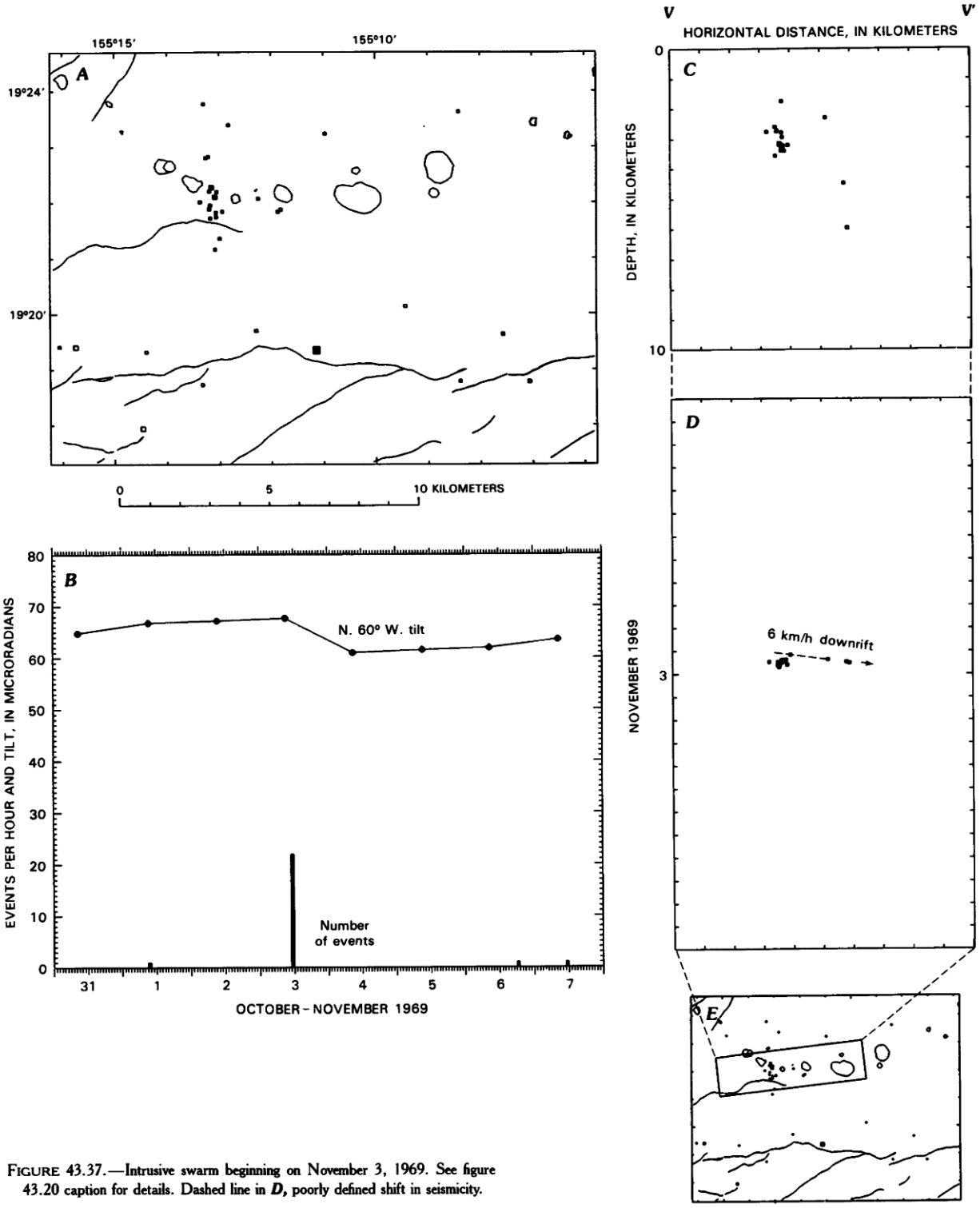


FIGURE 43.37.—Intrusive swarm beginning on November 3, 1969. See figure 43.20 caption for details. Dashed line in *D*, poorly defined shift in seismicity.

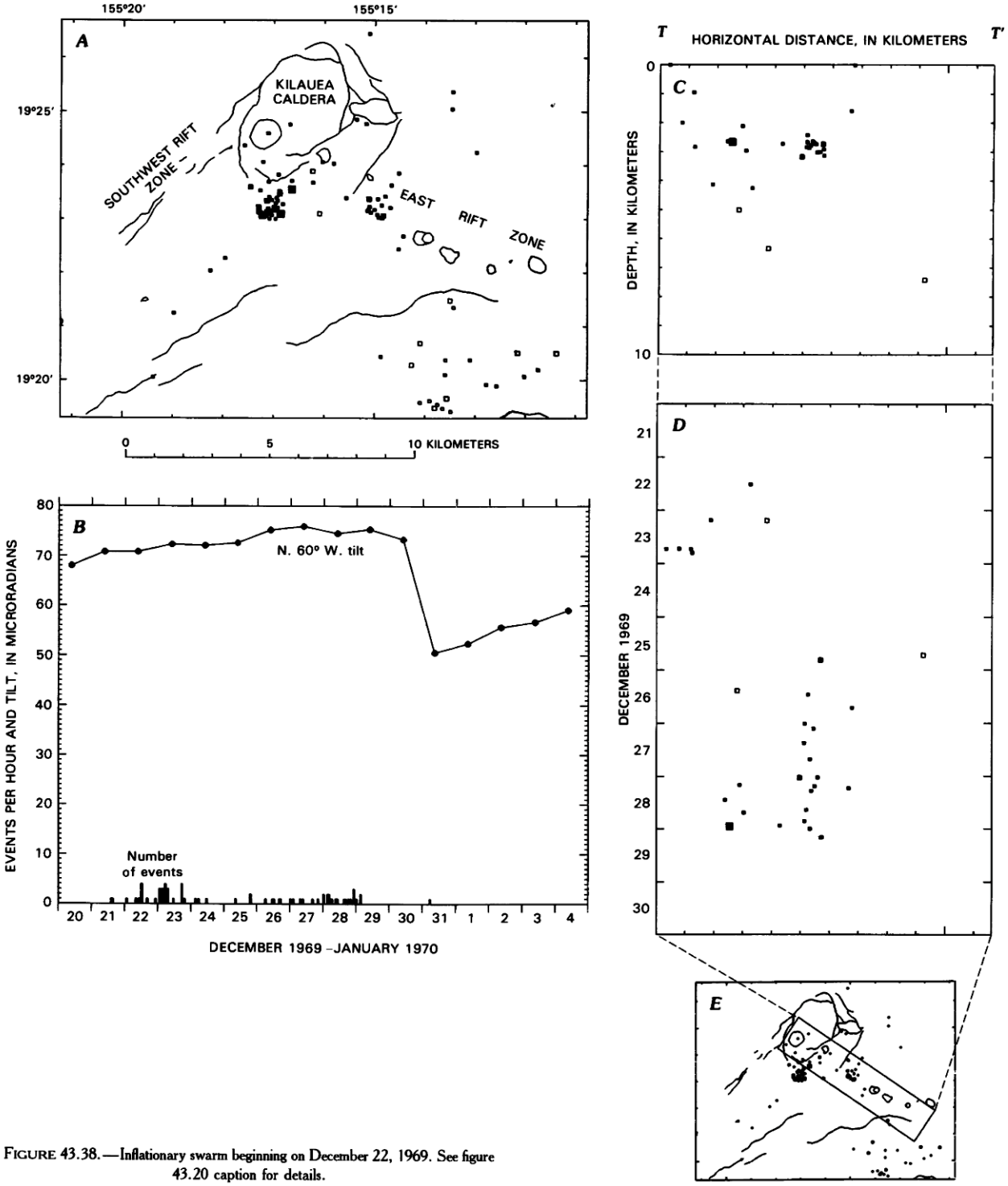


FIGURE 43.38.—Inflationary swarm beginning on December 22, 1969. See figure 43.20 caption for details.

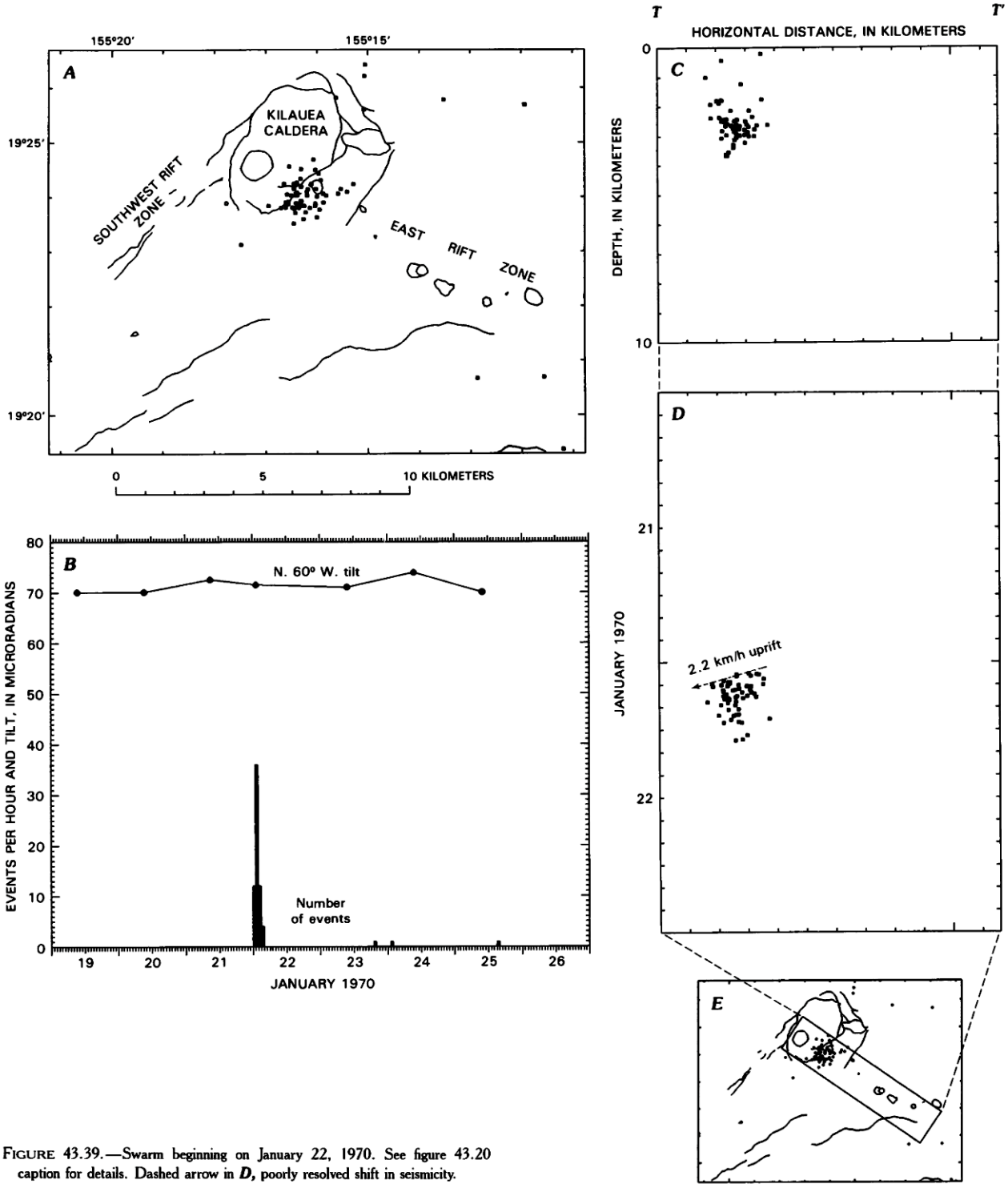


FIGURE 43.39.—Swarm beginning on January 22, 1970. See figure 43.20 caption for details. Dashed arrow in *D*, poorly resolved shift in seismicity.

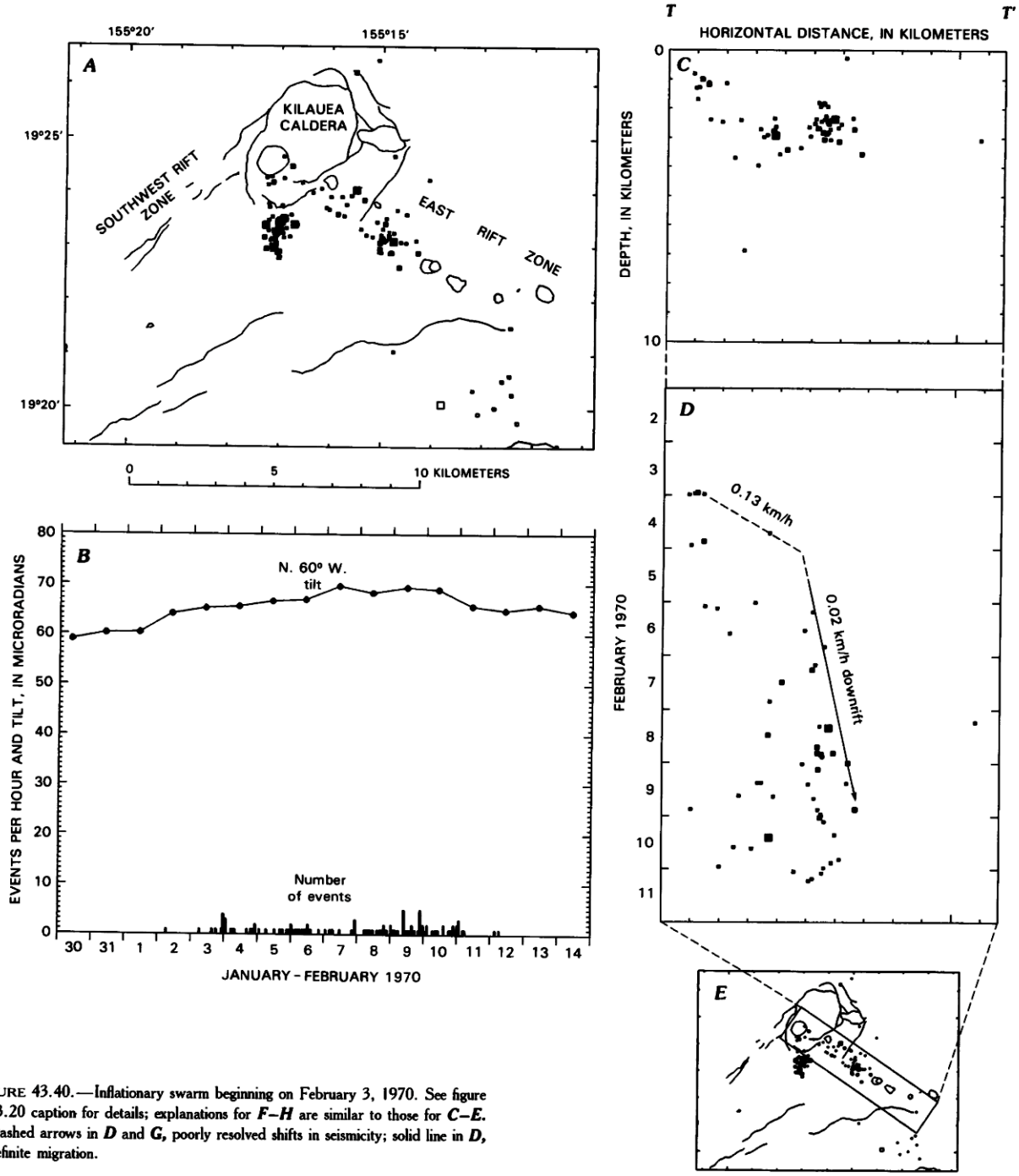


FIGURE 43.40.—Inflationary swarm beginning on February 3, 1970. See figure 43.20 caption for details; explanations for ***F–H*** are similar to those for ***C–E***. Dashed arrows in ***D*** and ***G***, poorly resolved shifts in seismicity; solid line in ***D***, definite migration.

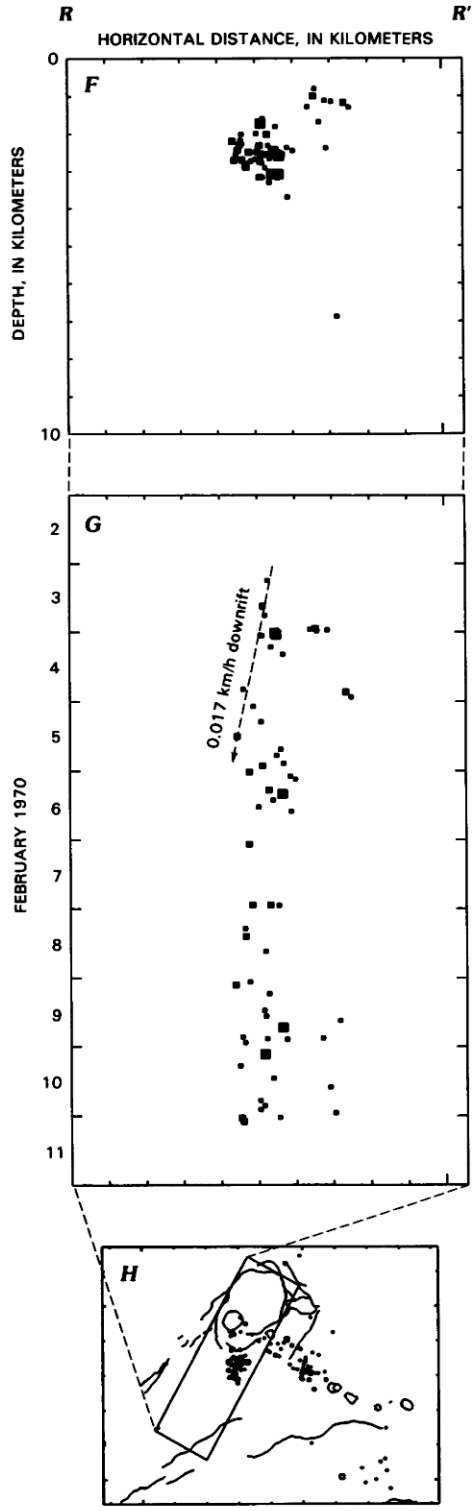


FIGURE 43.40.—Continued.

also moved uprift at about 0.13 km/h and culminated in the second burst about one day later. A few scattered earthquakes near the ERZ between Puu Kamoamoa and Heiheiahulu (fig. 43.43*F*) may have been coincidental.

The inflationary swarms during December 1970 were unlike their predecessors, in that earthquakes occurred throughout the caldera and in particular at its northeast end (figs. 43.44*A* and 43.45*A*). The first swarm began on December 12 as tilt slowly rose and fell synchronously with the earthquakes (fig. 43.44*B*). As tilt rose steadily, the second phase became noticeable on December 22 (fig. 43.45*B*), began in the southwest caldera, and spread rapidly northward into the entire caldera (fig. 43.45*D*). Also note the slow migration and intrusion into the SWRZ at the same 0.2 km/h speed as the February 1970 swarm. The path taken by the December 1970 earthquakes on the northern branch of the SWRZ (fig. 43.45*A*) anticipated the location of the September 24, 1971 eruption.

Another view of these swarms is given by figure 43.46, which superimposes summit tilt and position of earthquakes along the upper ERZ versus time. Figure 43.46*A* plots the entire November 1969 through February 1972 time interval. Figure 43.46*B*–*D* expands the time scale for this period. Moderate inflation and several swarms (3 intrusions and 4 inflationary swarms) with relative seismic quiet between them characterize the period of figure 43.46*B*. As noted above, the slow swarms are generally at the times of the most rapid inflation. The July 1970 to April 1971 period (fig. 43.46*C*) saw no net inflation and relatively low summit seismicity. A nearly continuous eruption at Mauna Ulu tapped most of Kilauea's magma supply during this period. By contrast, the next 10 months (fig. 43.46*D*) saw rapid inflation and considerable caldera and rift seismicity, including 2 eruptions, 2 rapid intrusions, 6 inflationary swarms and a high background of seismicity. This graph illustrates the close correlation between inflation and summit seismicity, and the difficulty of identifying discrete inflationary swarms during such active periods.

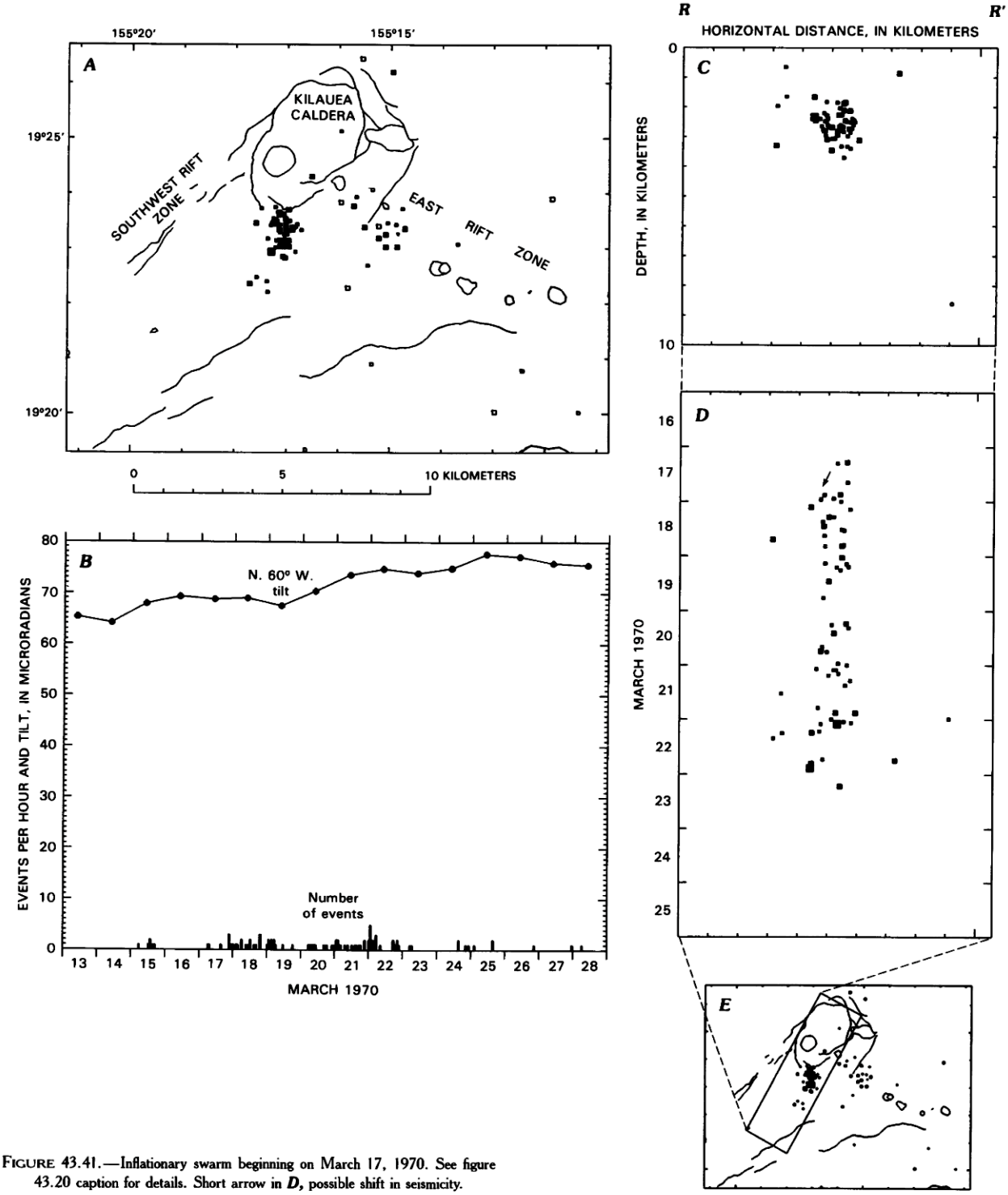


FIGURE 43.41.—Inflationary swarm beginning on March 17, 1970. See figure 43.20 caption for details. Short arrow in *D*, possible shift in seismicity.

## INFLATIONARY SWARMS AND ERUPTIONS, JUNE 1971 THROUGH JANUARY 1972

Rapid inflation and high seismicity returned in the June–September 1971 period (figs. 43.46*D*, 43.47). Earthquakes were primarily close to the caldera, but to a lesser extent within the rift zones. Eight individual swarms from this interval will be discussed below, but there was also a high background of activity.

The activity of early June 1971 continued at a relatively low but continuous level throughout the south caldera and was accompanied by slowly rising tilt (figs. 43.48, 43.49*B*). The June 1–10 seismicity was thus caused by steady inflation. On June 11 the seismicity intensified and concentrated into a small finger that extended south of the caldera (fig. 43.49*A*). Earthquakes migrated southward at a rate that slowed when seismicity crossed the caldera boundary (fig. 43.49*D*). Following the most intense seismicity, continuing but sparse activity began near Mauna Iki (fig. 43.47). The gradual deflation, slow migration, and later downrift seismicity indicate this was a slow intrusion.

Another episode of elevated summit seismicity commenced in July 1971. It was preceded by about one month of increasing activity in the caldera (figs. 43.46*D*, 43.47). The south caldera activity continued, but on July 19 the ERZ near Kokoolau came alive (fig. 43.50*A*). The swarm moved into the ERZ at about 0.17 km/h, but its rate of advance soon slowed considerably to only 8 m/h (0.2 km/d, fig. 43.50*D*). There was also a hint of migration into the SWRZ (fig. 43.50*G*). The HVO staff expected an eruption very soon because of the high tilt and summit seismicity, but with magma apparently leaking into both rift zones, there was no strong indication of where the eruption would be.

The tilt and rate of seismicity were very high prior to the eruption of August 14, 1971 (fig. 43.51*B*). Earthquakes continued in the south caldera and adjacent 3 km of both rifts (fig. 43.51*A*). The summit inflated as simultaneous slow intrusions penetrated into both rifts (fig. 43.51*D*, *G*). What appeared to be moving trends of earthquakes into the ERZ may have been caused by pulses of magma leaking into the rift. The eruption occurred in the southern part of the caldera on August 14 (Duffield and others, 1982). The lack of earthquakes in the hours following the onset of the eruption (fig. 43.51*D*, *G*) was a result of saturation of the seismic network by high tremor. Both tilt and seismicity dropped rapidly, however, indicating that some of the pressure built up during inflation had been relieved. The few earthquakes that could be timed and located after the eruption began were very close to the eruptive vent in the southern part of the caldera (fig. 43.52).

Another prominent episode of inflation and summit seismicity preceded the SWRZ eruption of September 24, 1971. We divided it into two periods beginning on September 6 (fig. 43.53) and on September 17 (fig. 43.54). The distribution of epicenters matched that of the previous inflationary swarms. Thus the August eruption in the caldera did not change the pattern of magma accumulation. Premonitory seismicity did not seem to favor either rift zone for the impending eruption, although there was a suggestion of earthquake migration into the SWRZ (fig. 43.54*G*).

The earthquakes accompanying the September 24 SWRZ eruption did not follow a continuous linear trend below the eruptive fissure (fig. 43.55*A*). Instead, four main clusters of earthquakes occurred along the rift. The first three roughly coincided with the three main zones of eruptive vents, and the fourth was in the south flank adjacent to the intrusion terminus near Puu Kou. We interpret each cluster as a blockage of the rift conduit, which magma forcefully broke through to continue downrift. Earthquakes were triggered as the dike penetrated and wedged apart each barrier. Earthquake clusters and vents would then coincide because the blockages that produced seismicity also diverted the dike upward before the barrier rifted open. Note also that one barrier is directly beneath Mauna Iki (fig. 43.55*A*), which may have been responsible for its formation in 1919–20. This barrier is probably a major one, as it appears to be responsible for much of the seismicity induced adjacent to it on both sides of the rift, including as much as 12 km into the Kaoiki seismic zone (fig. 43.55*A*).

The earthquakes clearly do not form a linear trend that coincides with the main seismic conduit active during 1970–83 (fig. 43.3*C*, *D*). The September 1971 eruption chose a more northwesterly path. Note also that the eruption earthquakes in the south caldera are displaced west of the inflationary swarms prior to the eruption. Thus, two main SWRZ conduits were active during recent decades: the northerly one which was seismically active during the December 1970 inflationary swarm, the September 1971 eruption, and perhaps the November 1967 eruption; and the southerly one, active during the intrusions of December 1974 and August 1981, as well as most periods of inflation. Using deformation data, Duffield and others (1982) concluded that the September 1971 eruption was fed by shallow parts of the summit reservoir, and the observed range of earthquake depths is consistent with this interpenetration (fig. 43.55*B*). The main rift zone conduits, however, tap the summit reservoir at about 3 km depth.

The September 1971 eruptive vents and earthquakes both progressed downrift (fig. 43.55*C*), indicating that both were caused by the same propagating dike. The times of first eruption from the various vent segments and approximate rates of opening of individual fissures from Duffield and others (1982) are plotted with earthquakes in figure 43.55*C*. The apparent downrift movement of vents is about 0.31 km/h. This speed is a little slower than the initial earthquake migration speed of about 0.53 km/h, but a second wave of earthquakes accompanies the progression of migrating vents. Another way to view the slower speed of the vents relative to the initial earthquake wave is that the time delay between passage of earthquakes and the start of eruption at a given place increased with distance down the rift. The delay ranged from 4 hours in the caldera to about 18 hours at the most distant vent. If the first earthquakes at a given spot mark the initial penetration of magma within the main conduit, the time delay of the eruption occurs while magma moves upward from the conduit to the surface. The increase of these delay times may then be a result of the plunge of the conduit to greater depths away from the caldera and the greater upward distance magma had to travel. The pattern of delay times could also be a

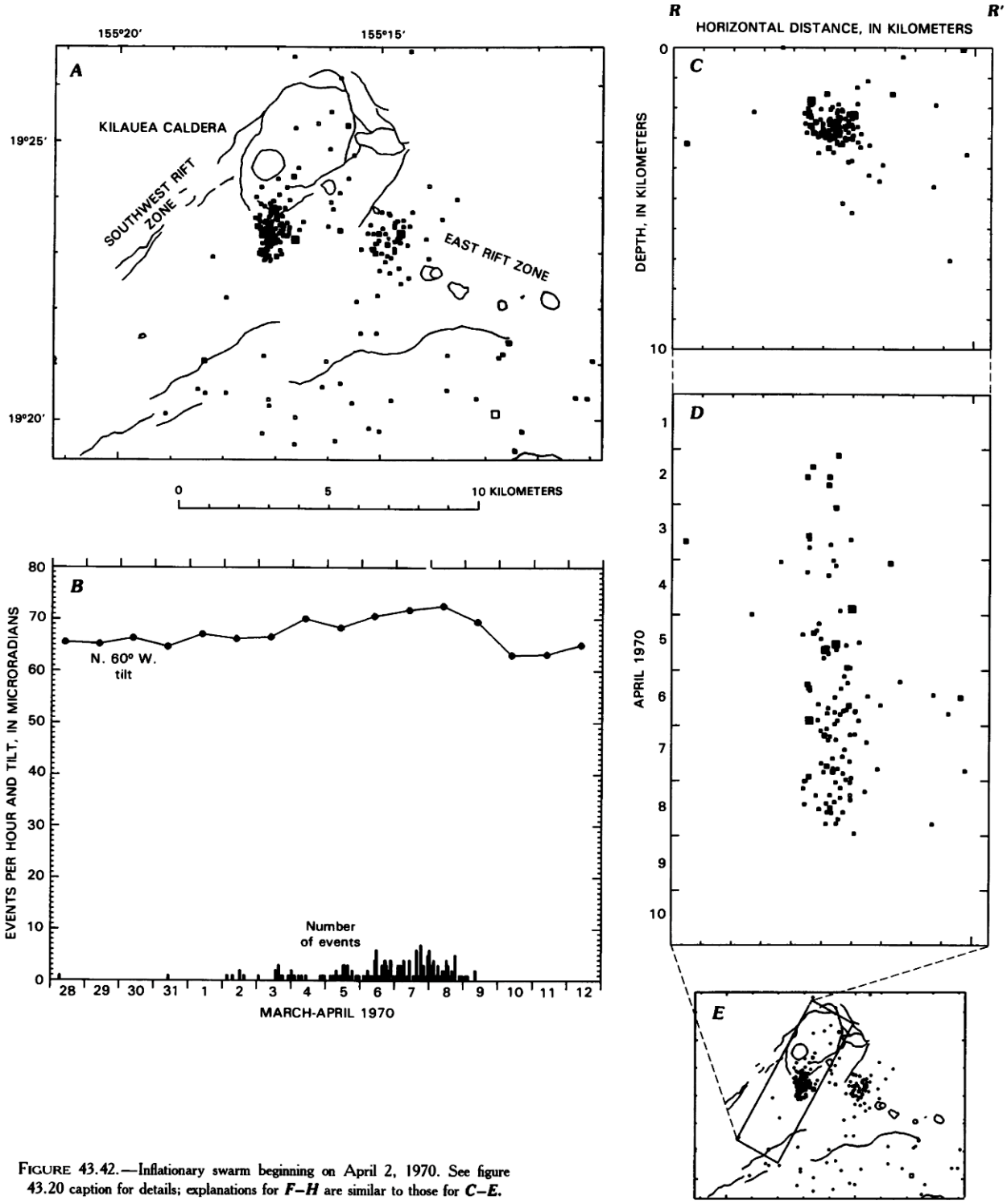


FIGURE 43.42.—Inflationary swarm beginning on April 2, 1970. See figure 43.20 caption for details; explanations for *F–H* are similar to those for *C–E*.

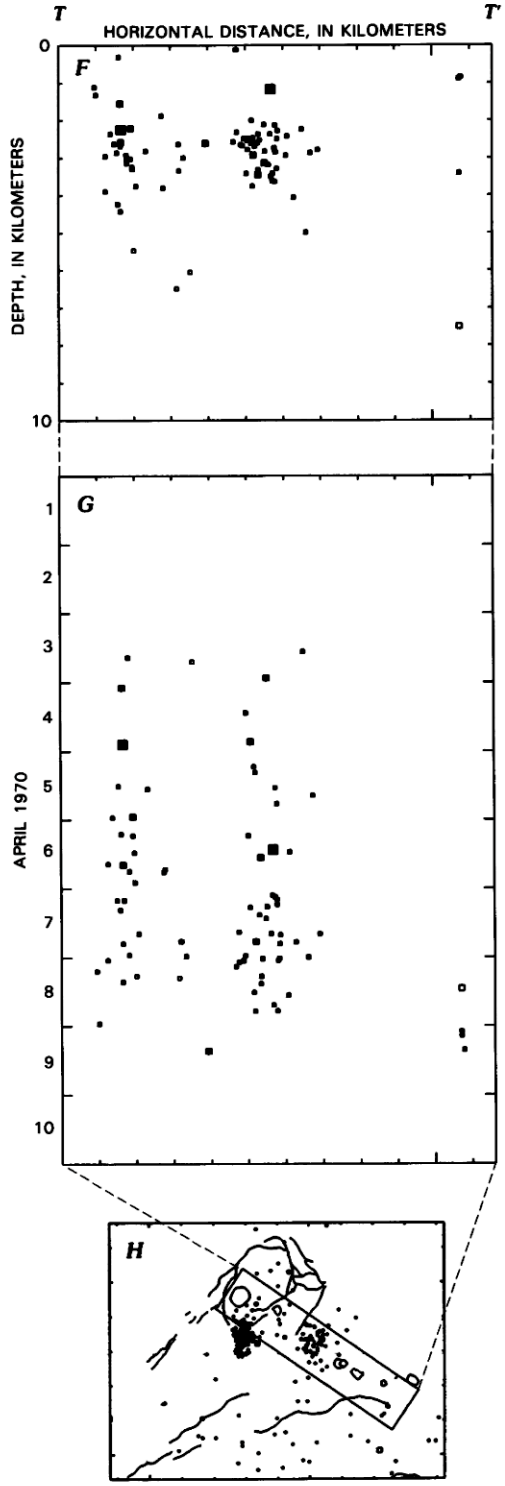


FIGURE 43.42.—Continued.

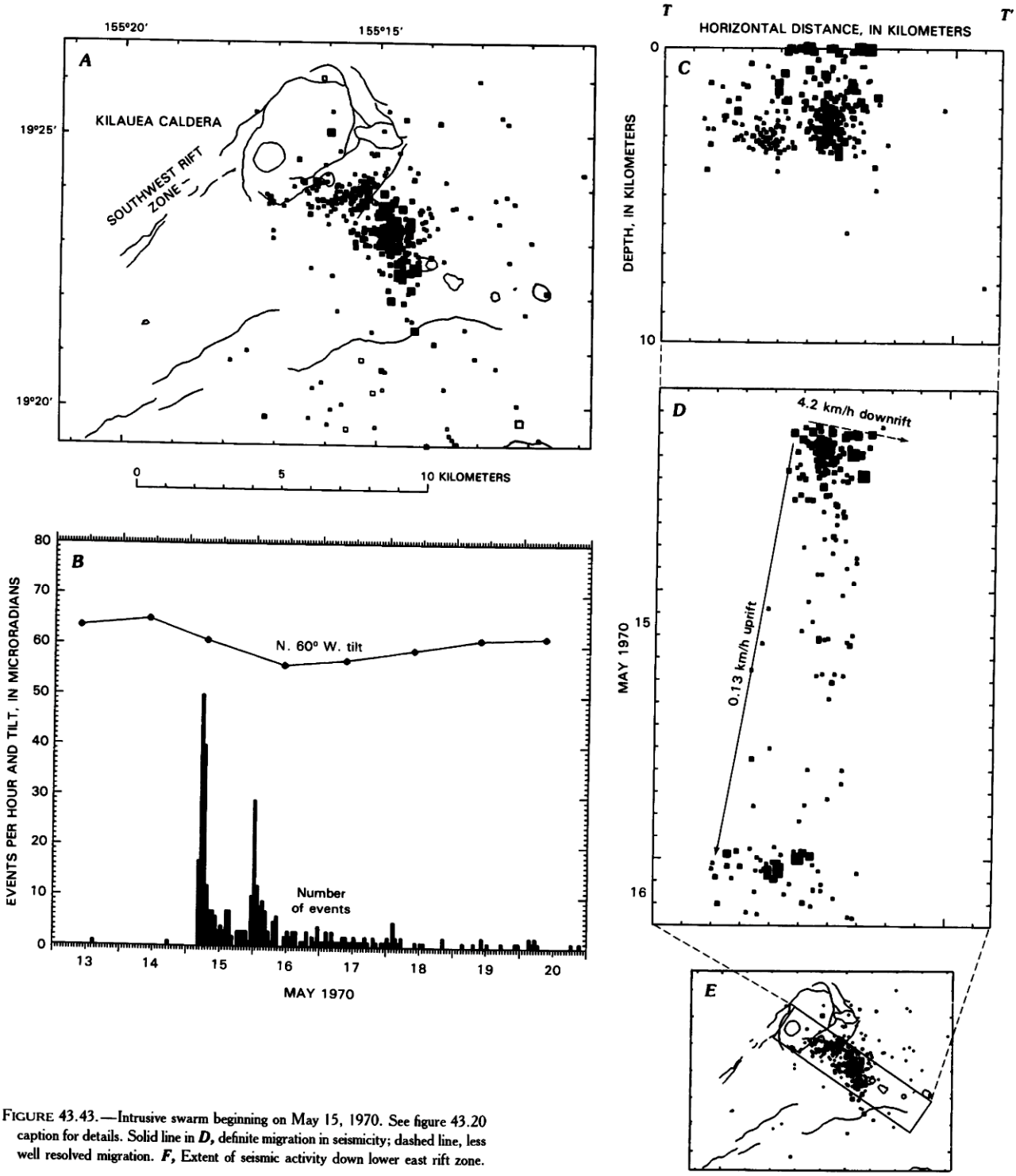


FIGURE 43.43.—Intrusive swarm beginning on May 15, 1970. See figure 43.20 caption for details. Solid line in *D*, definite migration in seismicity; dashed line, less well resolved migration. *F*, Extent of seismic activity down lower east rift zone.

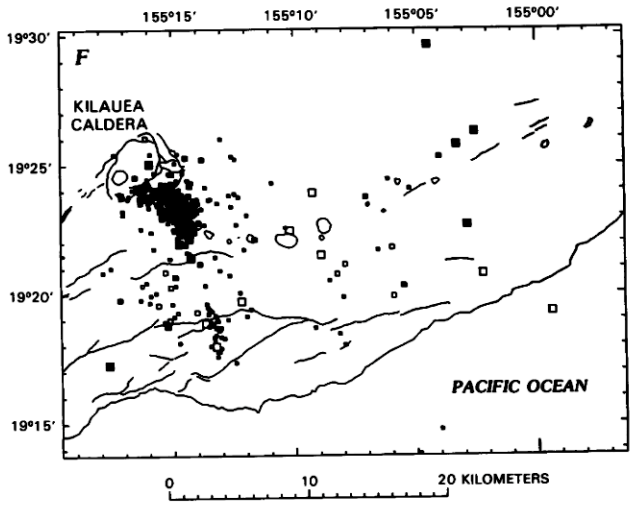


FIGURE 43.43.—Continued.

result of reduced magma pressure and slower upward speed farther down the rift, or a combination of both factors.

The September 1971 eruption is a good example of equating earthquake migration with magma movement and dike propagation. Irregularities in speed do occur, but the leading edge can move at a constant average speed for long segments of the rift. A few scattered earthquakes occur before the magma front passes their location (such as events above the solid line in fig. 43.55*C*). These events are apparently triggered by small stress increases that move ahead of the growing dike at the much faster speed of elastic waves.

Seismicity declined dramatically following the September eruption (figs. 43.46*D*, 43.47). The rift widened by perhaps 1–2 m (Duffield and others, 1982), so a significant volume of magma was intruded from the summit reservoir in addition to that erupted. Tilt and survey line changes around the caldera were dominated by the effects of the dike. Subsidence of the magma reservoir was difficult to document geodetically, although part of the floor of Halemaumau did fall 45 m (Duffield and others, 1982). The drop in seismicity indicates that a drop in magma pressure took place, however, similar to that during caldera subsidence of other eruptions. Kilauea reinflated rapidly after the eruption, and earthquakes increased and gradually penetrated farther into the ERZ (fig. 43.46*D*).

Another SWRZ swarm three months after the September eruption was probably related to it. The swarm began on December 23, 1971, and lasted about 7 days (fig. 43.56B). Most activity was in the south flank adjacent to the terminus of the September intrusion (fig. 43.56*E*). The flank probably received an increment of stress from the recently intruded SWRZ. Some earthquakes did occur uprift (fig. 43.56*A*, *F*) and they preceded the main part of the swarm in a way suggestive of downrift migration (fig. 43.56*H*). Little or no change occurred in summit tilt, however, so apparently magma (or stress) was redistributed within the rift complex without much new magma from the summit. As noted above, considerable newly intruded magma was available within the SWRZ conduit. Seismicity in the ERZ was concurrent with the central SWRZ earthquakes and generally progressed uprift (fig. 43.56*A*, *D*). The seismicity pattern and lack of a tilt change thus do not suggest a replay of the September event, but rather a readjustment of the two rifts and perhaps the south flank.

Kilauea refocused her attention to the ERZ with an inflation-related swarm there in January 1972. As with similar swarms of the previous two years, seismicity and magma only accumulated above the rift blockage near Pauahi (fig. 43.57*A*). The swarm was accompanied by rising tilt (fig. 43.57*B*). The first swarm episode saw events slowly penetrate the rift (fig. 43.57*D* but two periods of uprift migration appeared to characterize the second episode (fig. 43.57*F*). The possible causes of uprift earthquake migration will be discussed in more detail later, but the phenomenon is probably related to the complex system of multiple conduits in the ERZ above Mauna Ulu and their close magmatic communication with the summit reservoir. If the entire uprift part of the ERZ slowly receives and stores magma from the summit supply, then a propagating episode of rifting and accompanying seismicity could go in either direction, because the magma to drive it is present along the whole rift segment. The January swarm was followed by a major eruptive phase at Mauna Ulu on February 4, 1972 (Tilling and others, chapter 16). The eruption was marked by only minor earthquake activity in the Pauahai to Mauna Ulu area and by a halt to the slow inflation (fig. 43.58). The few earthquakes occurred both before and after the eruption, whose onset time was only approximately known due to lack of direct observations (fig. 43.58*D*).

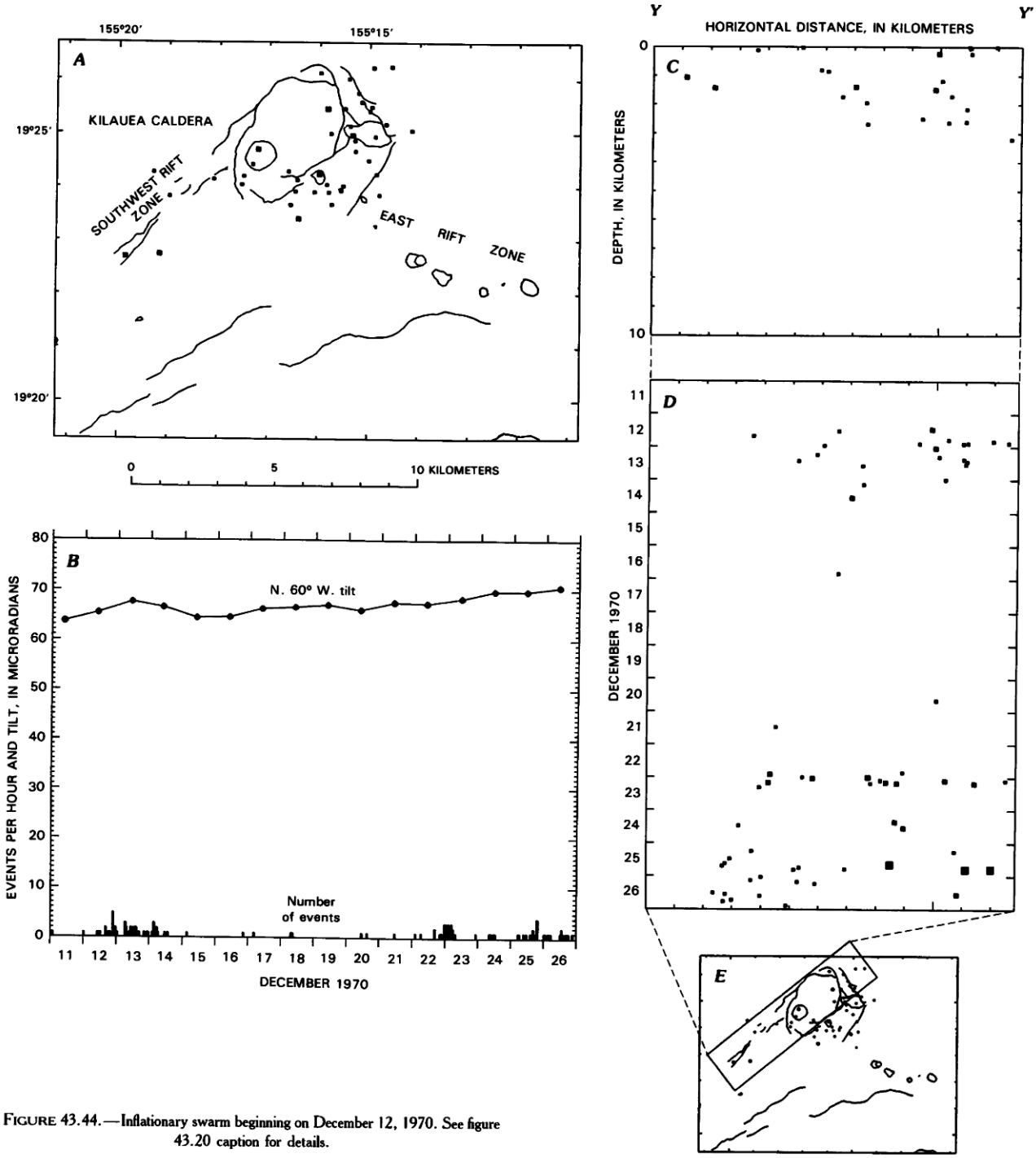


FIGURE 43.44.—Inflationary swarm beginning on December 12, 1970. See figure 43.20 caption for details.

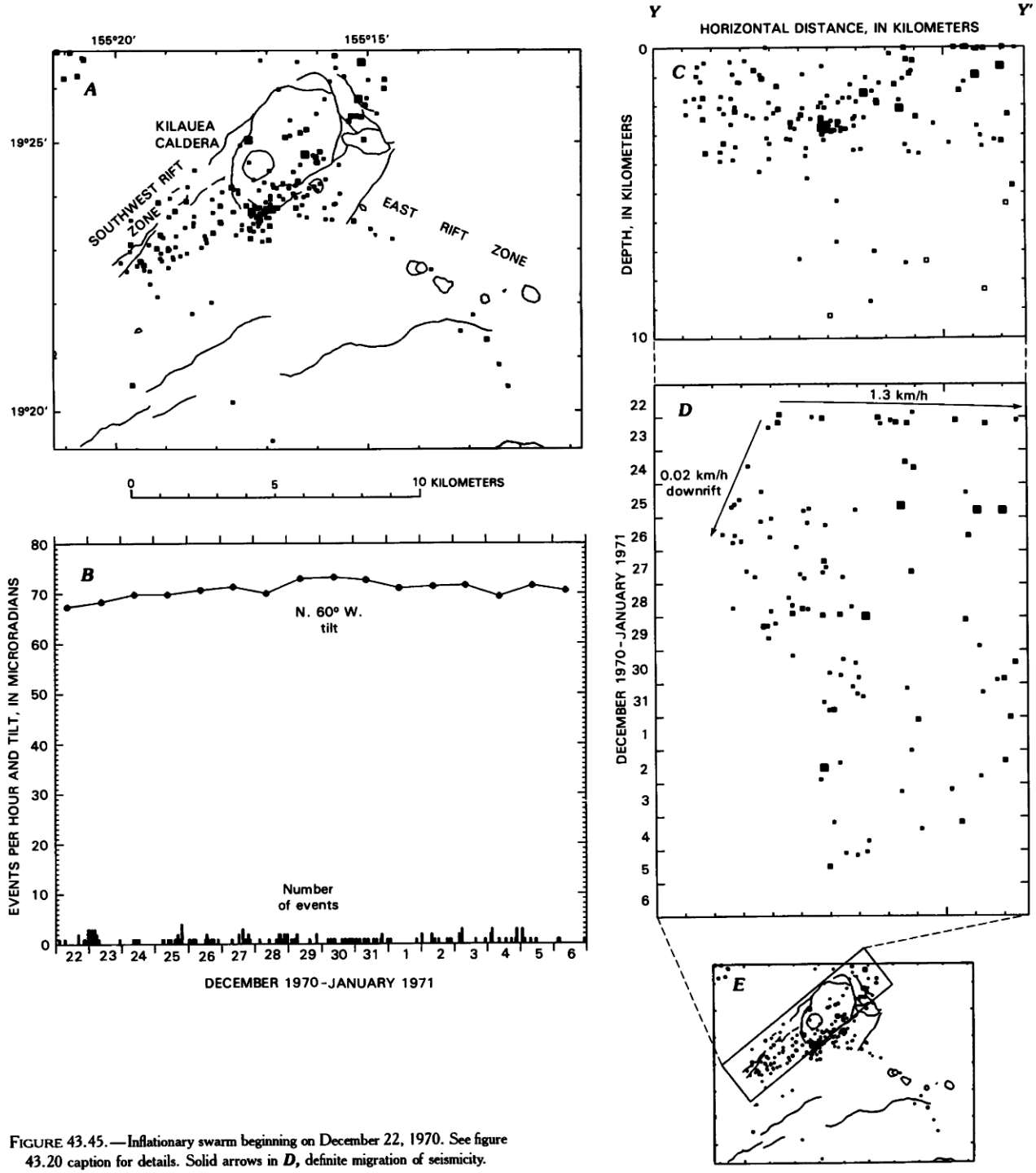


FIGURE 43.45.—Inflationary swarm beginning on December 22, 1970. See figure 43.20 caption for details. Solid arrows in *D*, definite migration of seismicity.

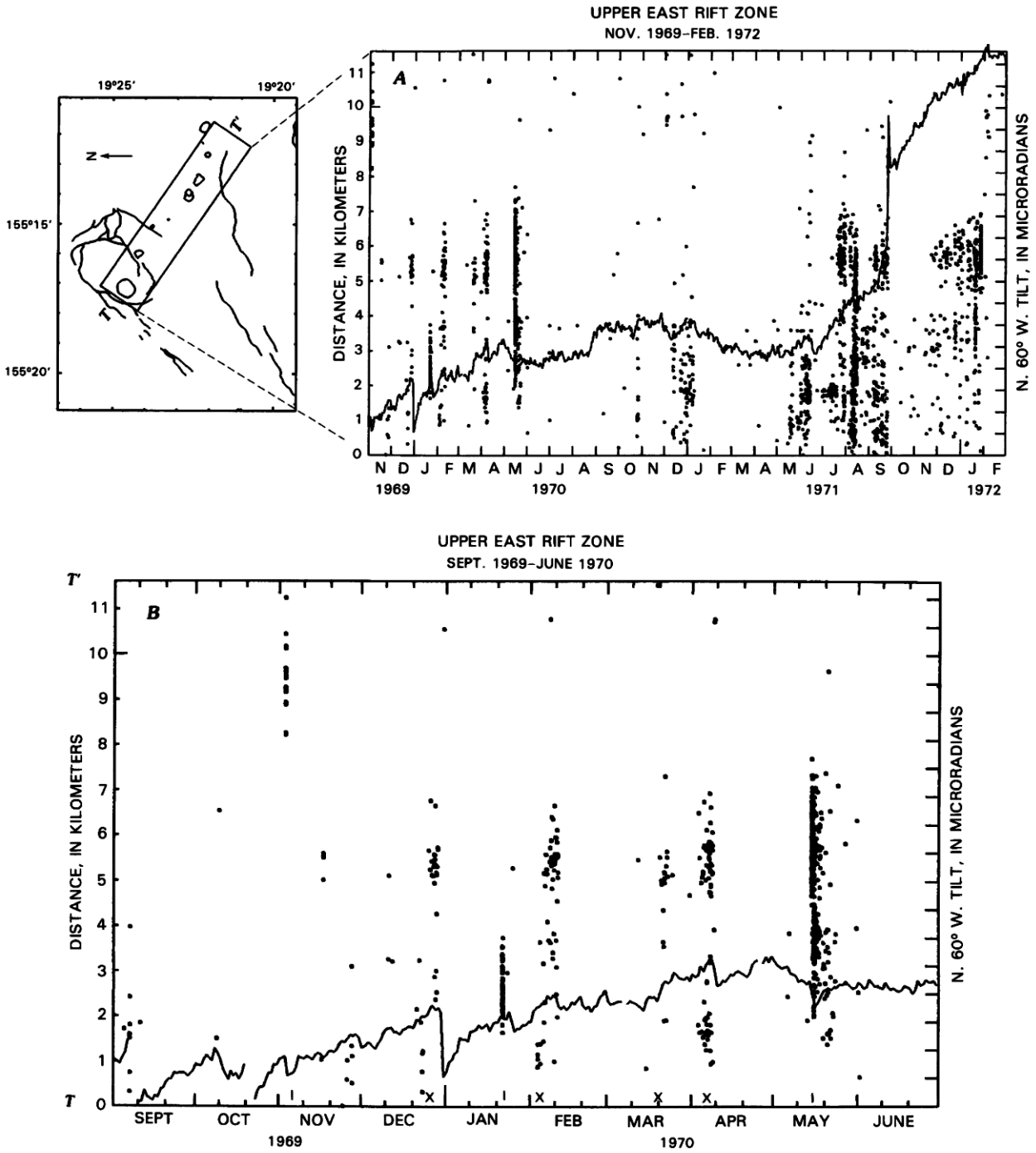


FIGURE 43.46.—Plot of earthquakes along upper east rift zone and N. 60° W. water-tube tilt at Uwekahuna versus time. Tilt axes marked in 10-μrad divisions. All earthquakes shallower than 5 km and within geographic box shown are plotted. Endpoints for $T$–$T'$ are given in table 43.2. ***A,*** Plot for entire 28-month period. ***B–D,*** Same plot as in *A*, but on an expanded time scale. Halemaumau is near endpoint $T$ and Alae crater is near $T'$. Notations along time axis refer to specific swarms detailed in other figures: E, eruption; I, intrusion; X, swarm accompanying inflation.

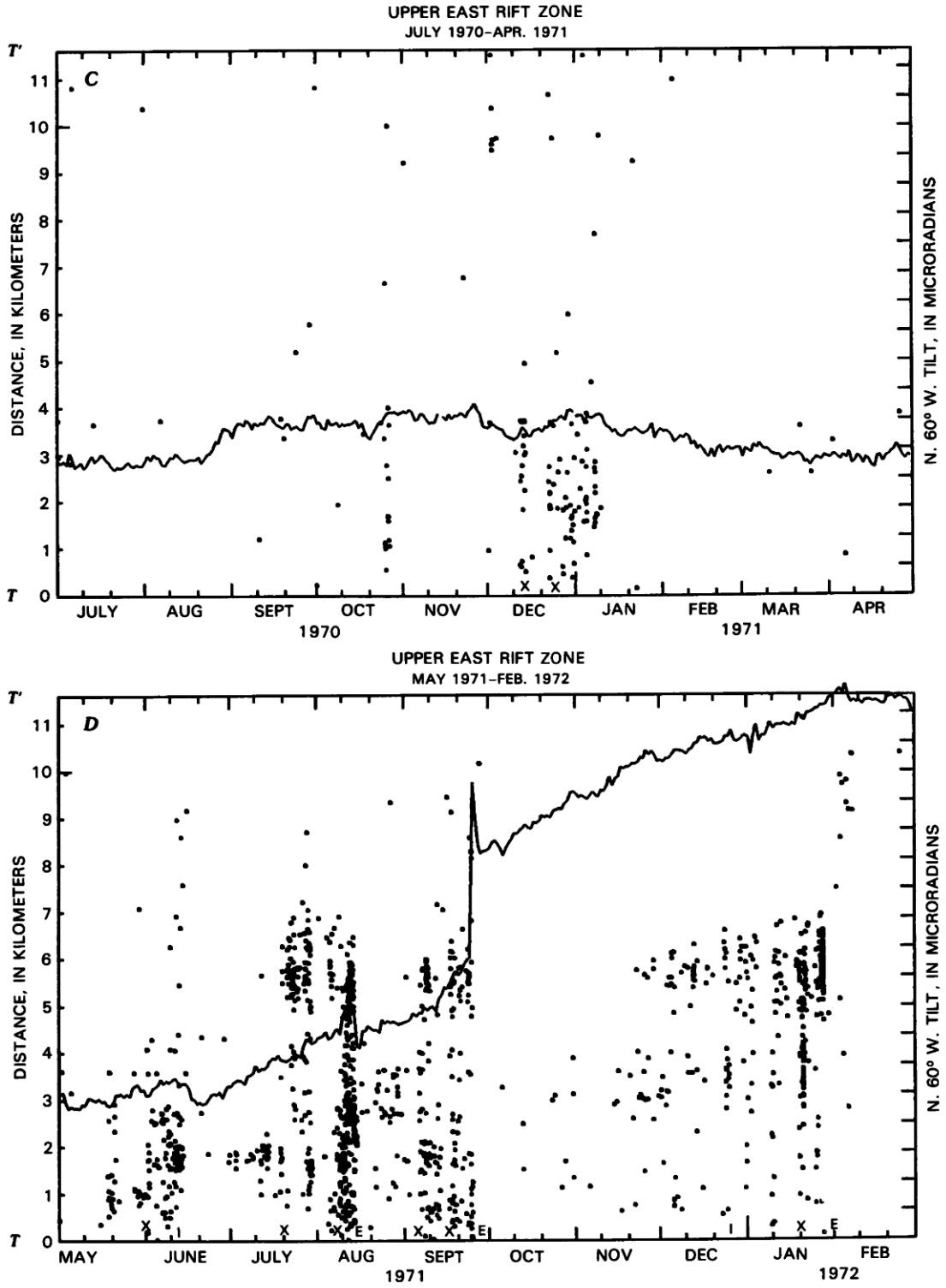


FIGURE 43.46.—Continued.

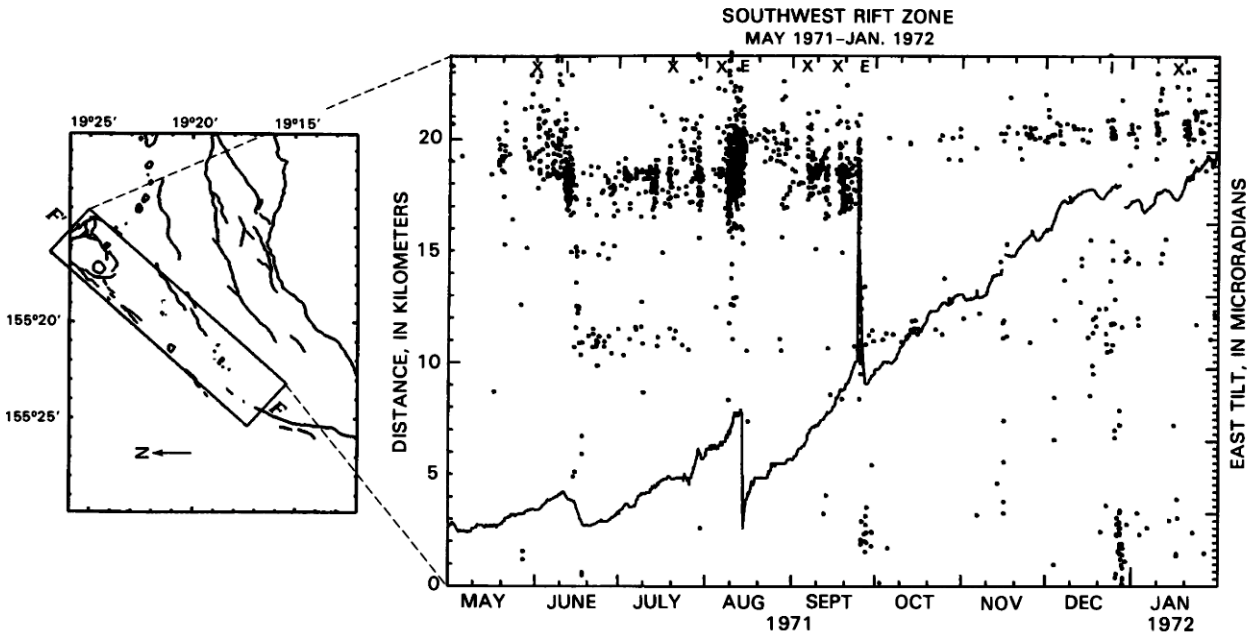


FIGURE 43.47.—Plot of earthquakes along the southwest rift zone and east tilt at Uwekahuna versus time. Endpoints for distance axis $F$–$F'$ are given in table 43.2. Tilt is from east-west Ideal Aerosmith tiltmeter, where east-down tilt is down on plot and generally indicates deflation of summit caldera. Large divisions on tilt scale are 10 μrad. Notations along time axis refer to specific swarms detailed in other figures: E, eruption; I, intrusion; X, swarm accompanying inflation.

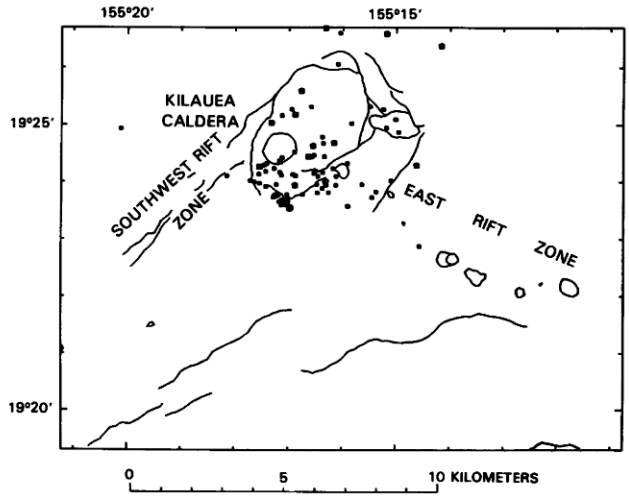


FIGURE 43.48.—Inflationary swarm beginning on June 6, 1971. See figure 43.20 caption for details and figure 43.49$B$ for tilt and hourly earthquake rate.

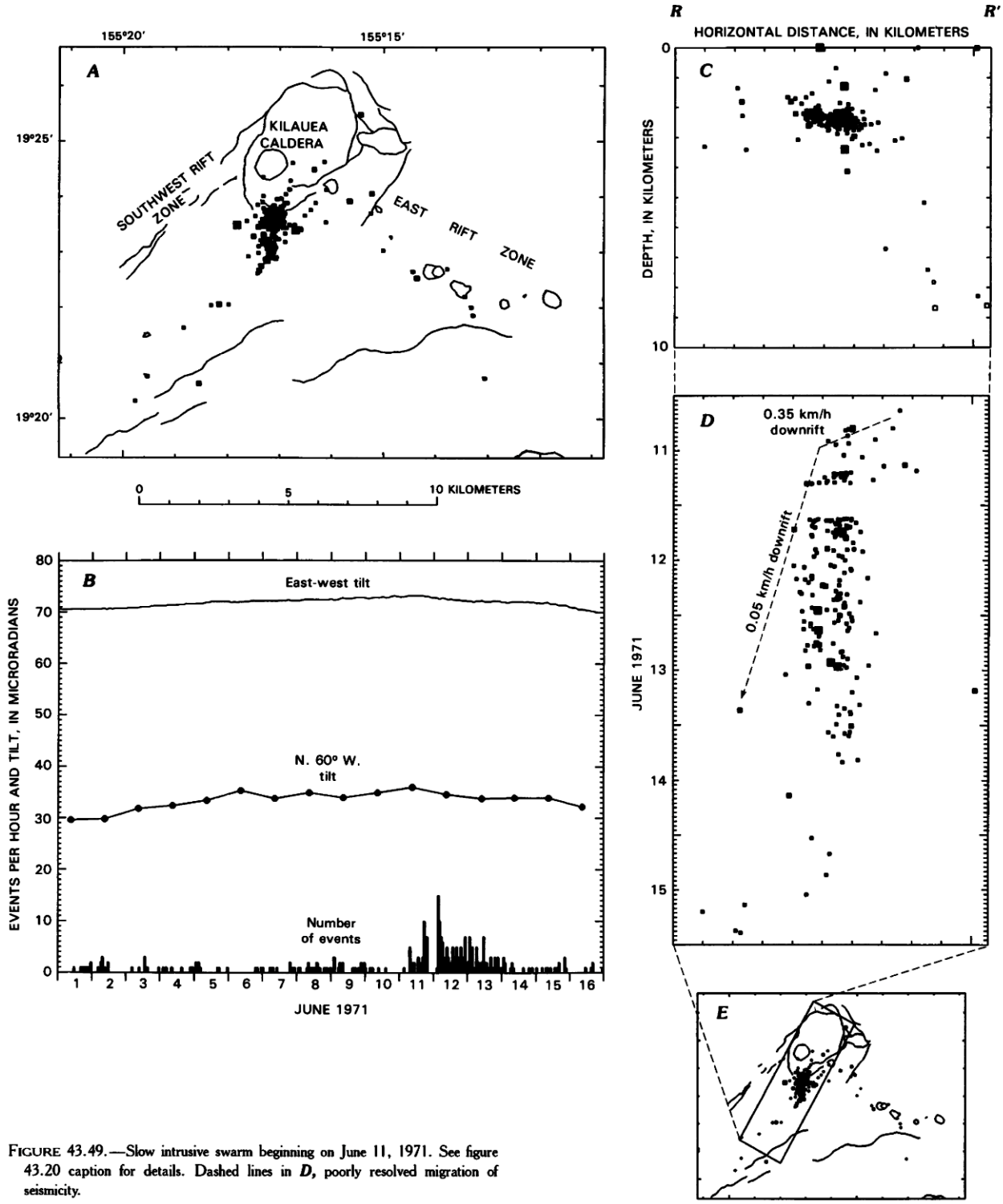


FIGURE 43.49.—Slow intrusive swarm beginning on June 11, 1971. See figure 43.20 caption for details. Dashed lines in *D*, poorly resolved migration of seismicity.

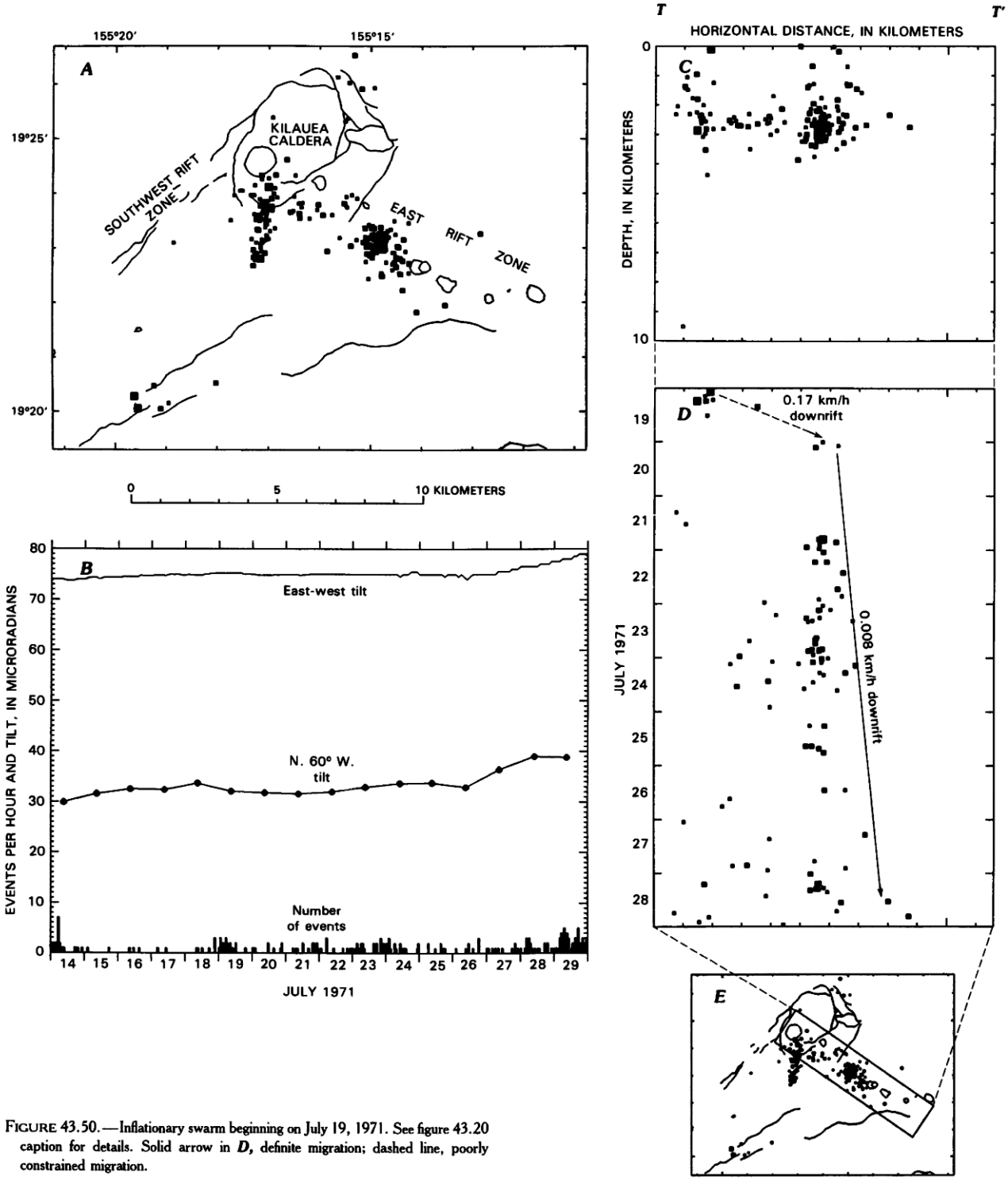


FIGURE 43.50.—Inflationary swarm beginning on July 19, 1971. See figure 43.20 caption for details. Solid arrow in *D*, definite migration; dashed line, poorly constrained migration.

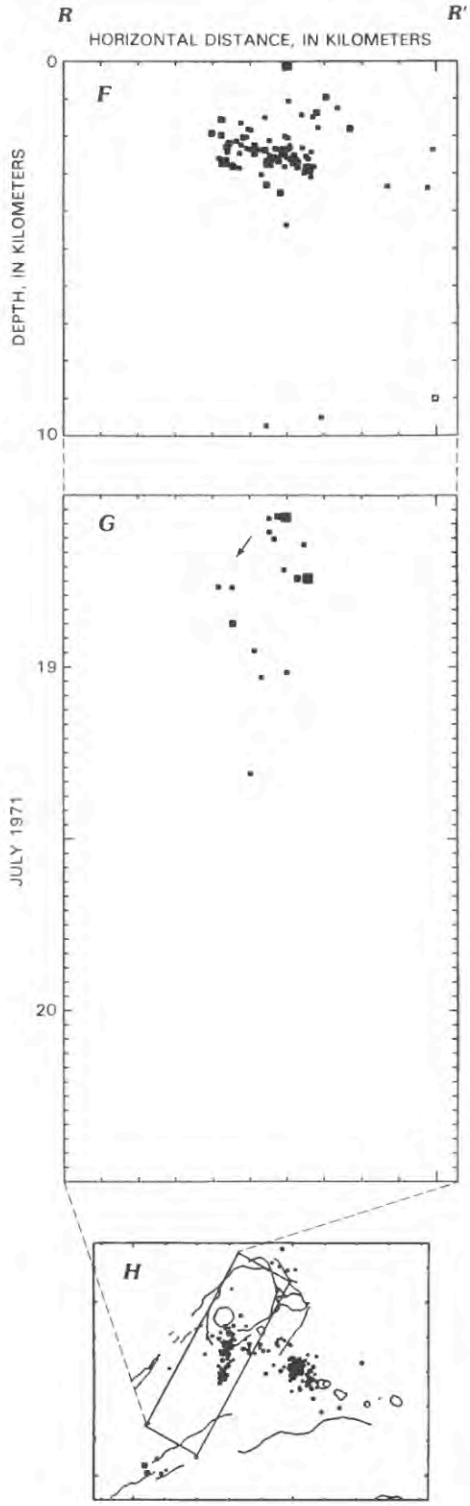


FIGURE 43.50.—Continued.

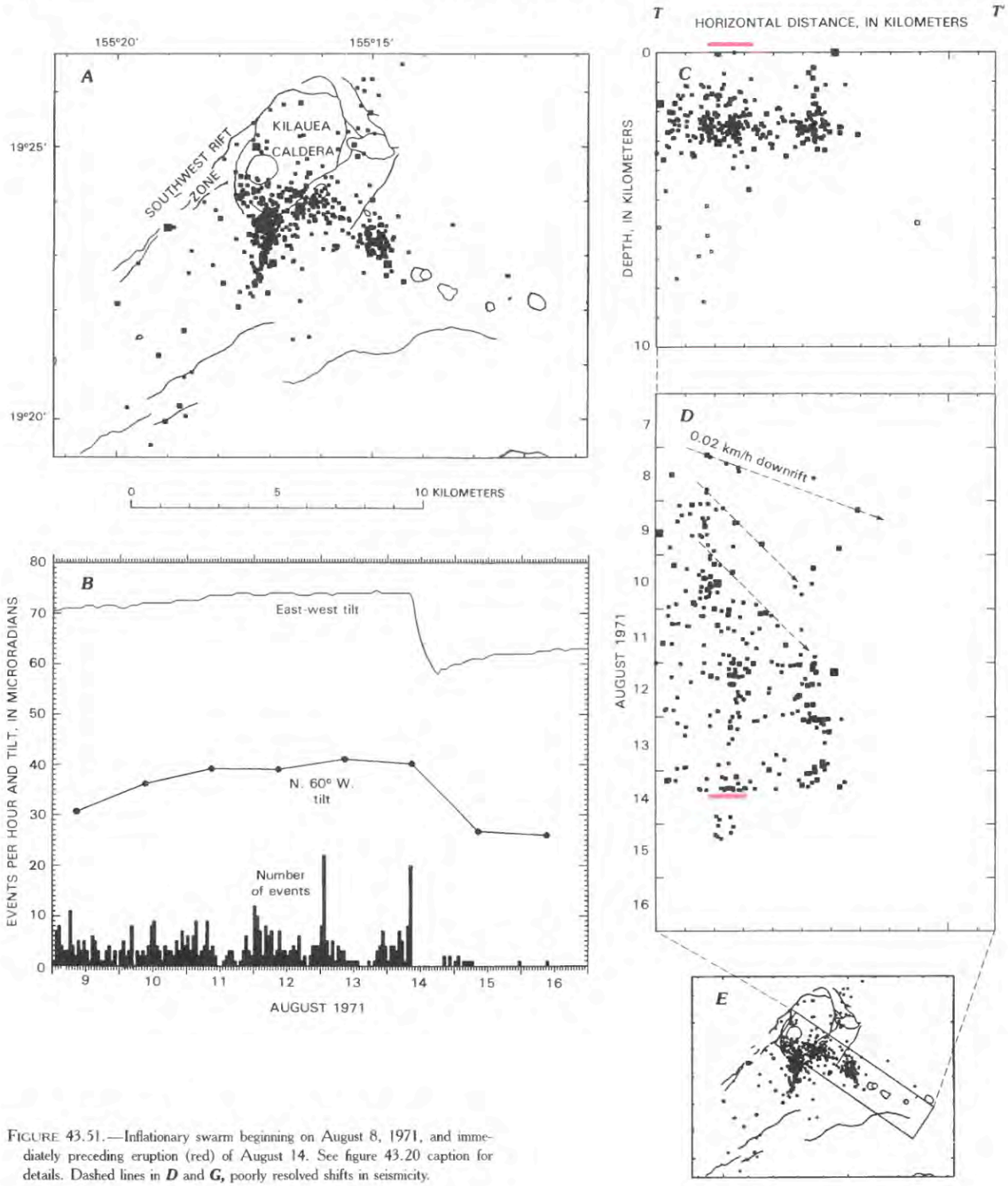


FIGURE 43.51.—Inflationary swarm beginning on August 8, 1971, and immediately preceding eruption (red) of August 14. See figure 43.20 caption for details. Dashed lines in ***D*** and ***G***, poorly resolved shifts in seismicity.

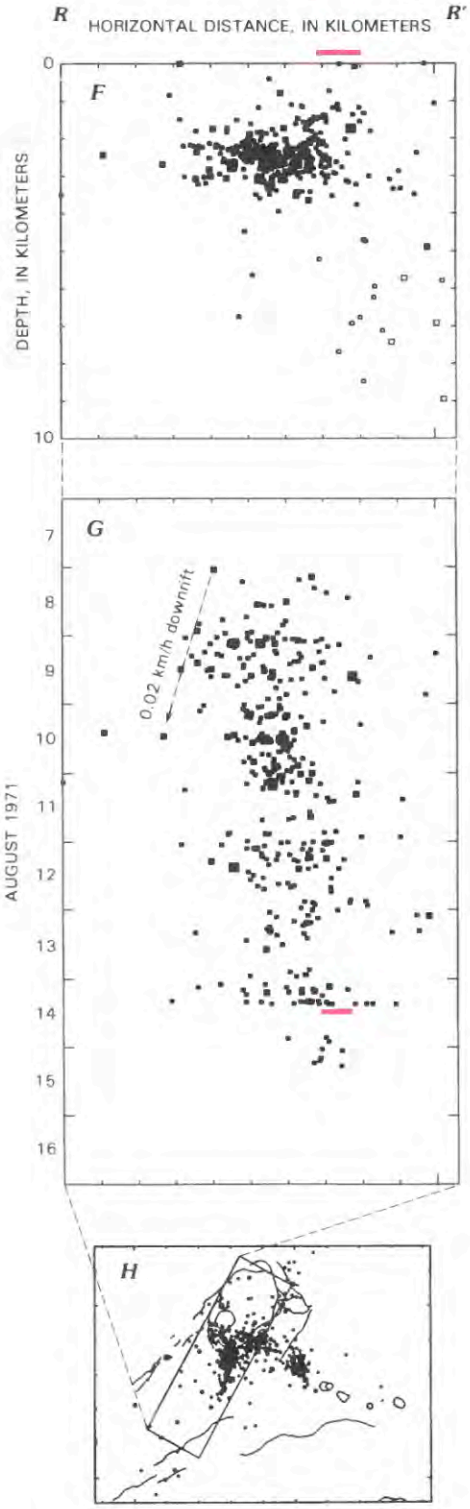


FIGURE 43.51.—Continued.

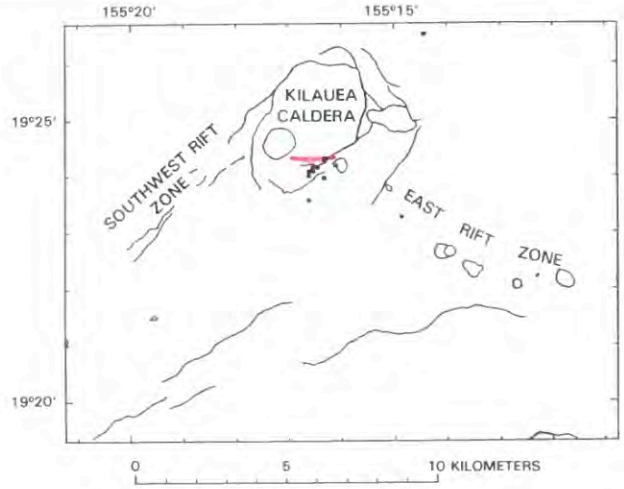


FIGURE 43.52.—Eruptive swarm beginning on August 14, 1971. See figure 43.20 caption for details. Red, location of eruptive vent. See figure 43.51*B* for tilt and earthquake counts, and figure 43.51*D* for relation of eruptive swarm to prior seismicity and onset time of eruptive vent (red).

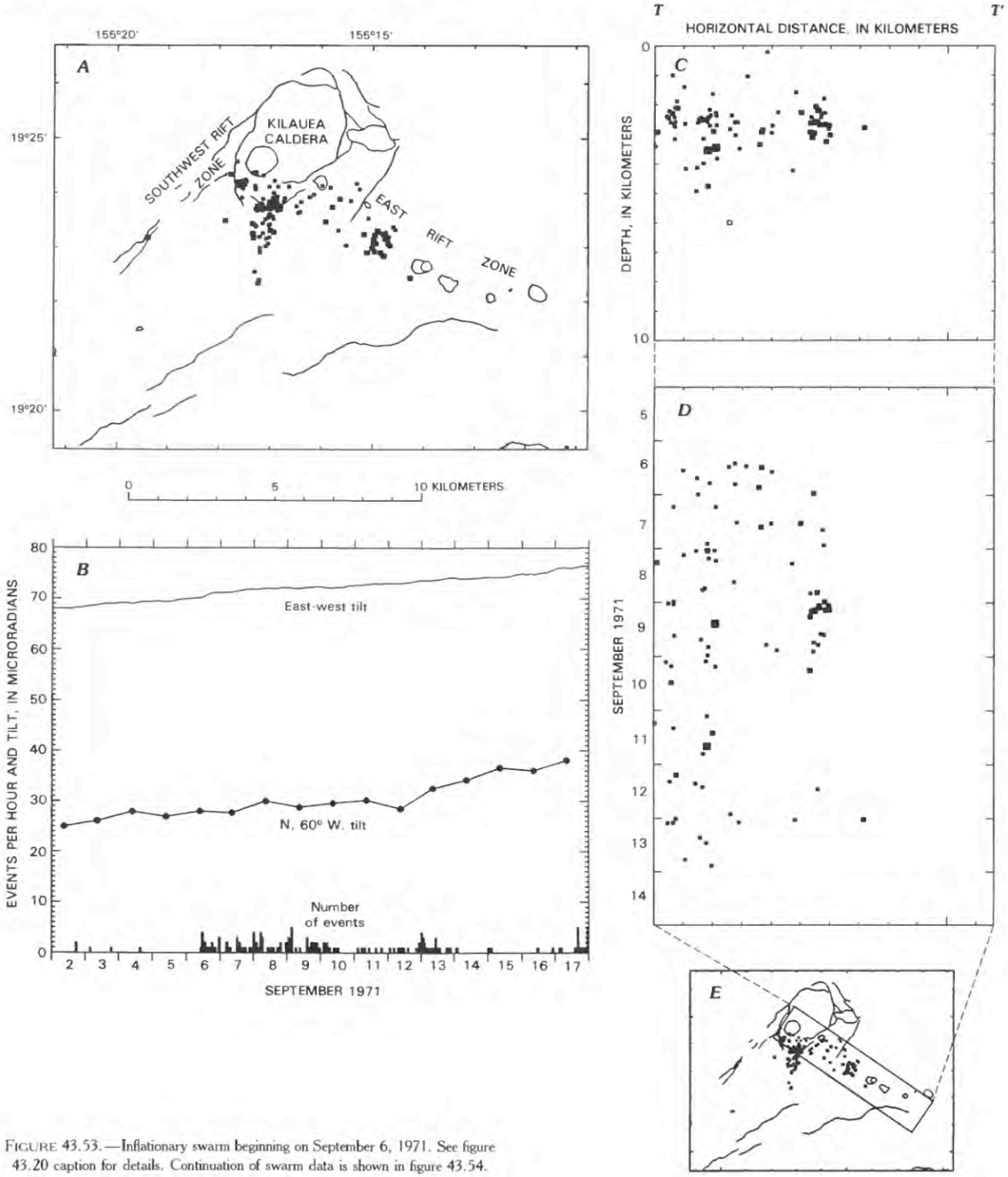


FIGURE 43.53.—Inflationary swarm beginning on September 6, 1971. See figure 43.20 caption for details. Continuation of swarm data is shown in figure 43.54.

## THE MAY AND JUNE 1973 INTRUSIONS OF THE KOAE FAULT ZONE

More than one year after the resumption of Mauna Ulu volcanism, activity shifted briefly to an eruption at Pauahi on May 5, 1973. The eruption was accompanied by an intense swarm in the adjacent Koae fault zone (fig. 43.59*A*; Unger and Koyanagi, 1979). The earthquake swarm formed a linear zone extending westward into the Koae from Pauahi (fig. 43.59*A*), lasted for almost 24 hours, produced may surface cracks and saw rapid deflation of the summit caldera (fig. 43.59*B*). The shift of eruptive activity from Mauna Ulu to Pauahi was possibly related to the magnitude-6.2 Honomu earthquake north of Hilo on April 26, 1973. This earthquake did disturb Kilauea caldera enough to trigger rockfalls and small earthquakes. The May 5, 1973, eruption was immediately preceded by draining of the Mauna Ulu and Alae lava lakes. Therefore, the eruption was likely fed by Mauna Ulu lava or at least diverted its magma supply from under the Pauahi-Mauna Ulu region. The time history of earthquakes supports this inference.

The May 5 swarm began under Mauna Ulu, and seismicity rapidly spread up the ERZ to Hiiaka. The lateral speed of this initial migration was 3.6 km/h (fig. 43.59*G*), which reduces to an apparent 3.2 km/h when foreshortened by looking from the south-southeast (fig. 43.59*D*). This initial migration was also from 2–4 km depth below Mauna Ulu to 0–2 km depth below Hiiaka, as seen on the cross sections (fig. 43.59*C*, *F*). An upward movement of earthquakes thus took place, as is evident on a depth versus time plot (fig. 43.59*I*). The initial vertical rate of 3 km/h slowed to 1 km/h within 1.5 km of the surface. These speeds should be regarded as very approximate, because both lateral and vertical migration occurred simultaneously and because they are defined by only a few earthquakes. The observed eruption time requires that vertical migration slowed near the surface, as might be expected for a dike that of 0.36 km/h westward into the Koae for the next 16 hours (fig. 43.59*D*). Note that earthquakes ceased about 2 km or 6 hours behind their point of inception, so that the point at which earthquakes stopped also migrated into the Koae.

We interpret this swarm as the result of a dike propagating from below Mauna Ulu to Pauahi and then into the Koae fault zone. The dike spread from the active pocket of magma presumably feeding Mauna Ulu. The dike initially found an easy and fast path in the ERZ, probably because of the frequency of intrusions and consequent high temperatures there. The advance of the dike slowed in the noneruptive Koae, however, perhaps because of more rapid cooling of the dike. Cooling could slow the dike either by increasing magma viscosity or by chilling dike margins and constricting flow to a narrower space. The constant speed of advance and continuous earthquake migration without halting or jerky movement are suggestive of viscous flow under relatively uniform stress conditions.

The initial activity at the eruptive vents migrated from east to west at about the same 0.3 km/h speed as the earthquakes (fig. 43.59*D*). As noted with other intrusions, vents opened about 3–6 hours after the initial seismic front passed their location. At a particular vent, the time of eruption coincides with the cessation of earthquakes. Thus the earthquakes are not simply being masked by tremor, because events continued to the west. The start of eruption thus relieves some of the stress that caused the earthquakes, probably at the time the dike reaches its maximum width. We then associate the seismicity with the time and place where the dike is growing in width and under increasing pressure, and the moving point at which earthquakes cease is where the dike has reached its maximum width and magma flow is stable.

With the association of earthquakes and dike growth in mind, a very low confining stress in the Koae explains two observations: (1) the dike widens easily, accommodating all the magma it is given without building enough hydrostatic head to reach the surface and erupt, and (2) the dike encounters little resistance from compressive stress normal to itself, and once opened to a width permitting stable and sustained flow, the dike exerts little stress on its walls so that earthquakes cease. The migration speed and width of the earthquake zone during Koae intrusions would then be determined by the mechanical and thermal properties of magma in a cold, dry crack under relatively little stress.

About one month after the May 5 eruption, a second Koae intrusion occurred (fig. 43.60). The June 9, 1973 intrusion was parallel to and about 1 km north of the prior intrusion, but was only about 3 km long (fig. 43.60*A*). It was also smaller than the May event in the sense of a shorter swarm and smaller deflation (fig. 43.60*B*). This intrusion apparently did not involve Mauna Ulu directly, because it began from a point just uprift of Hiiaka on the ERZ. The migration speed was about 1 km/h (fig. 43.58*D*), three times faster than in May. The pairing of these two Koae intrusions is probably not coincidental, and they probably interacted in some way.

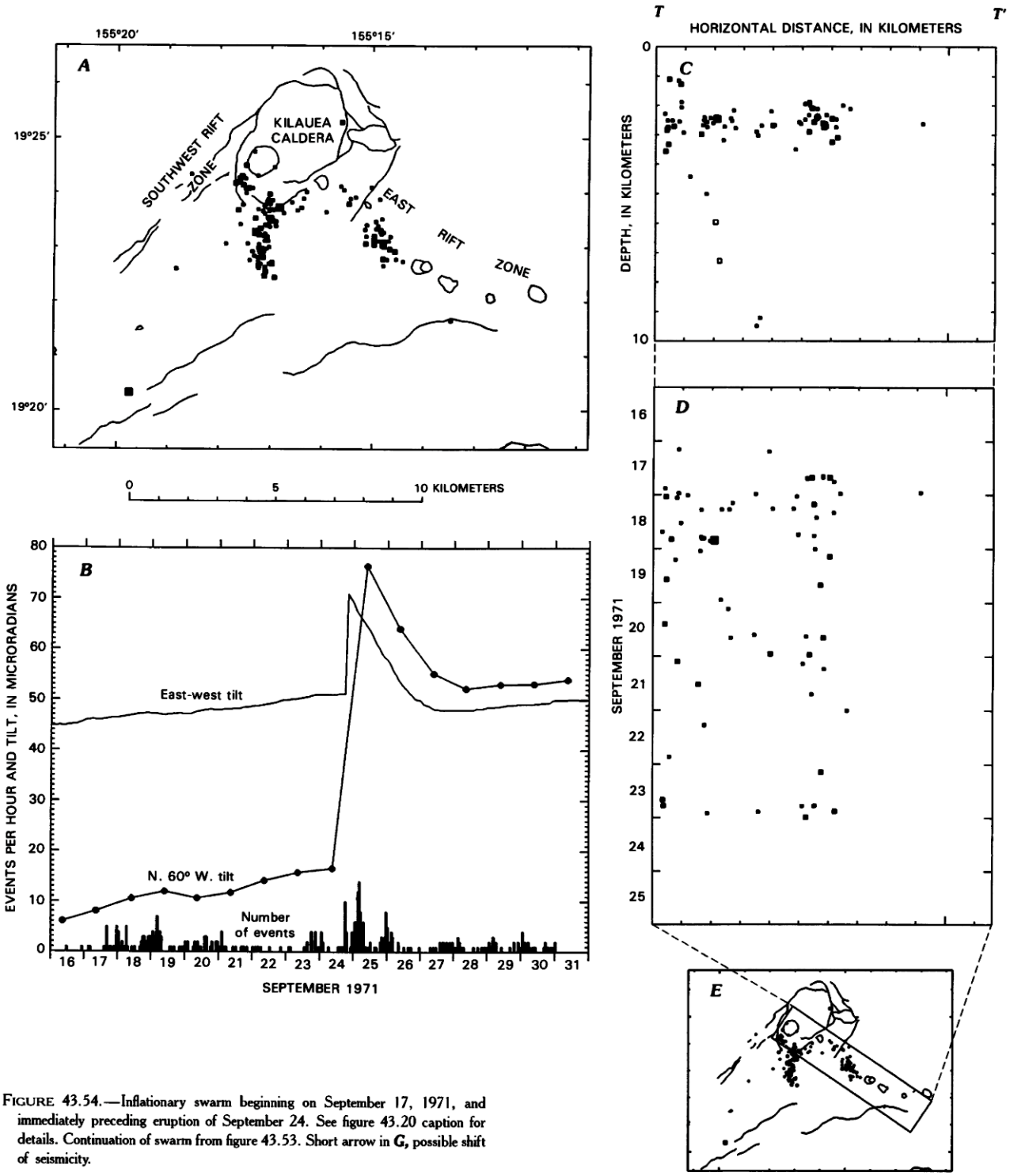


FIGURE 43.54.—Inflationary swarm beginning on September 17, 1971, and immediately preceding eruption of September 24. See figure 43.20 caption for details. Continuation of swarm from figure 43.53. Short arrow in *G*, possible shift of seismicity.

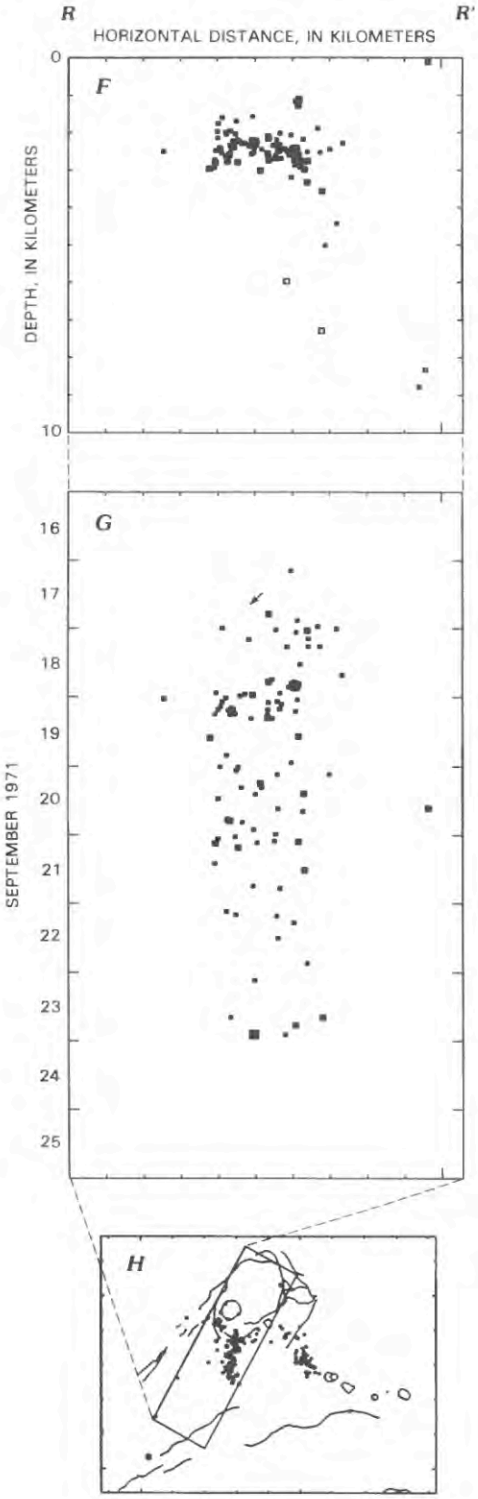


FIGURE 43.54.—Continued.

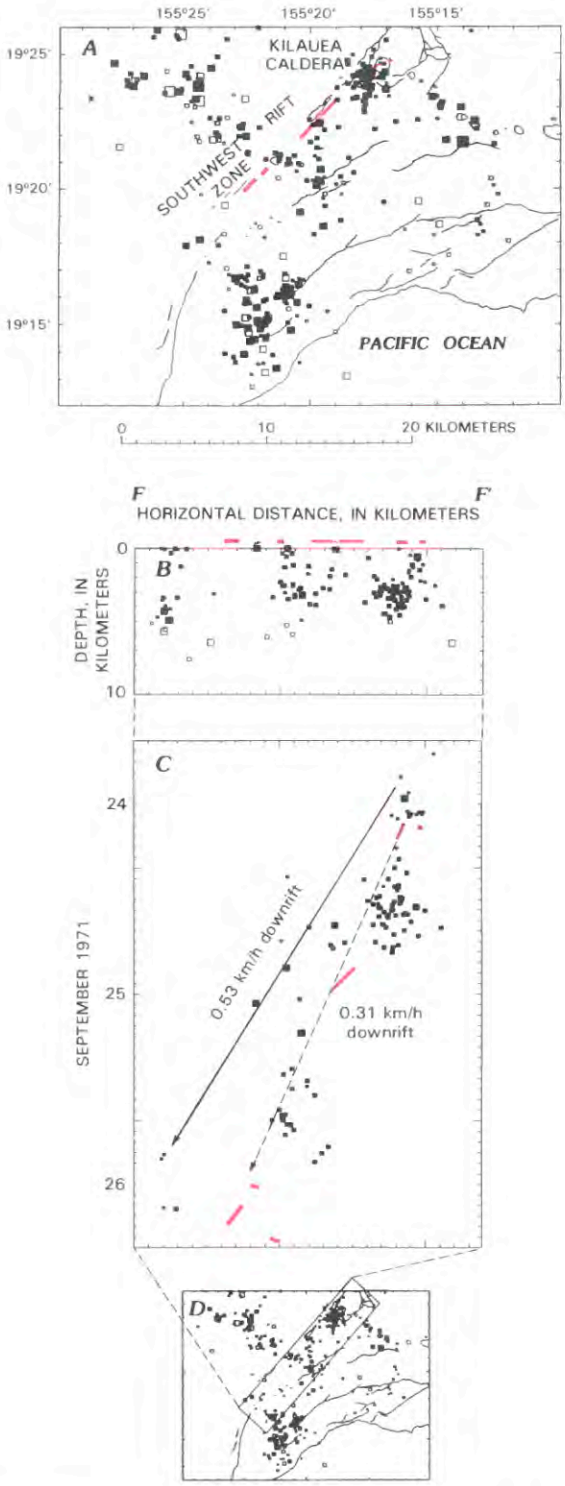


FIGURE 43.55.—Eruptive swarm beginning on September 24, 1971. See figure 43.20 caption for details and figure 43.54 for tilt and earthquake rate. Red, approximate location (***A, B***) and onset time (***C***) of eruptive vents; solid arrow in ***C***, definite migration; dashed arrow, poorly resolved migration of seismicity.

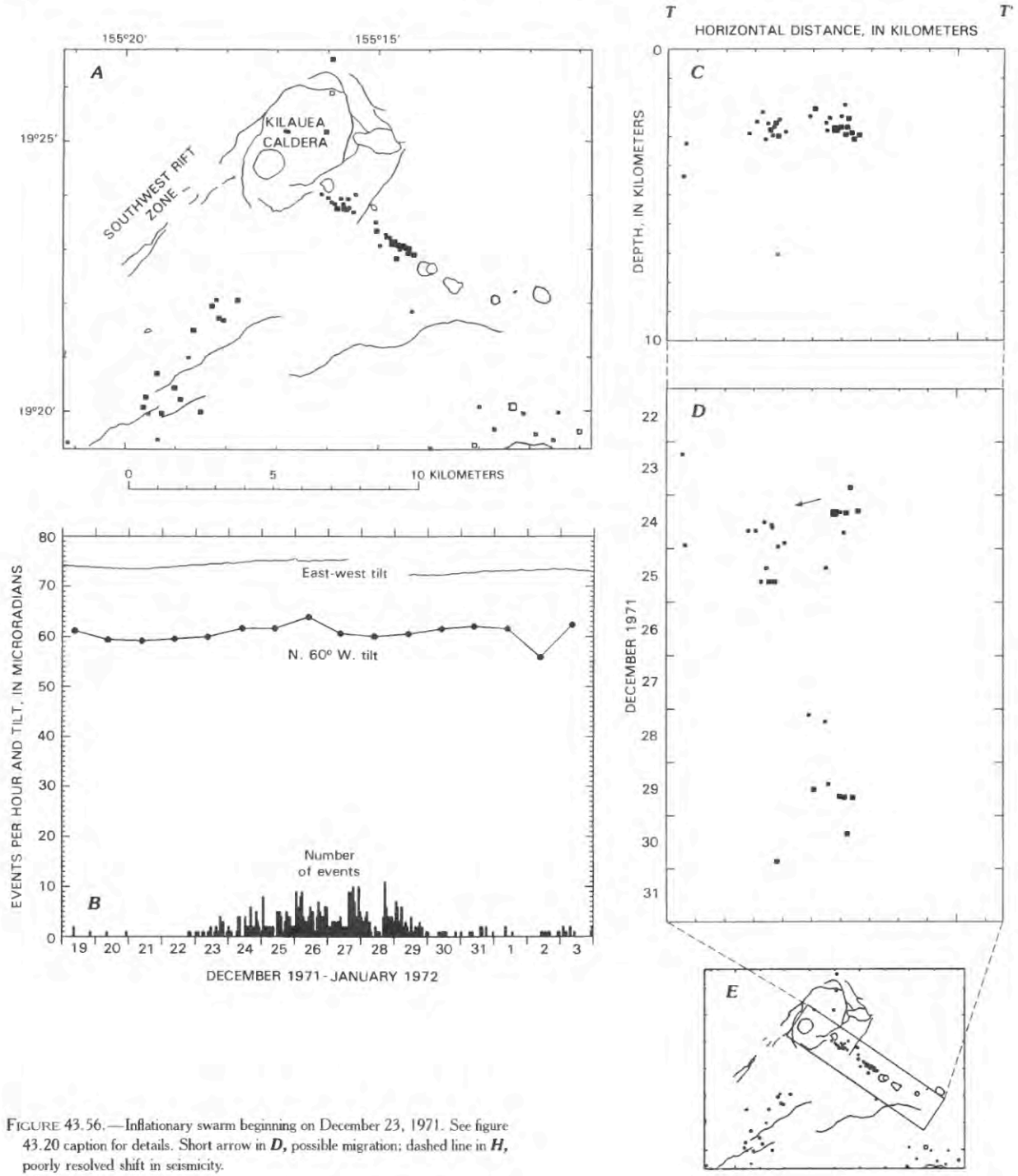


FIGURE 43.56.—Inflationary swarm beginning on December 23, 1971. See figure 43.20 caption for details. Short arrow in ***D***, possible migration; dashed line in ***H***, poorly resolved shift in seismicity.

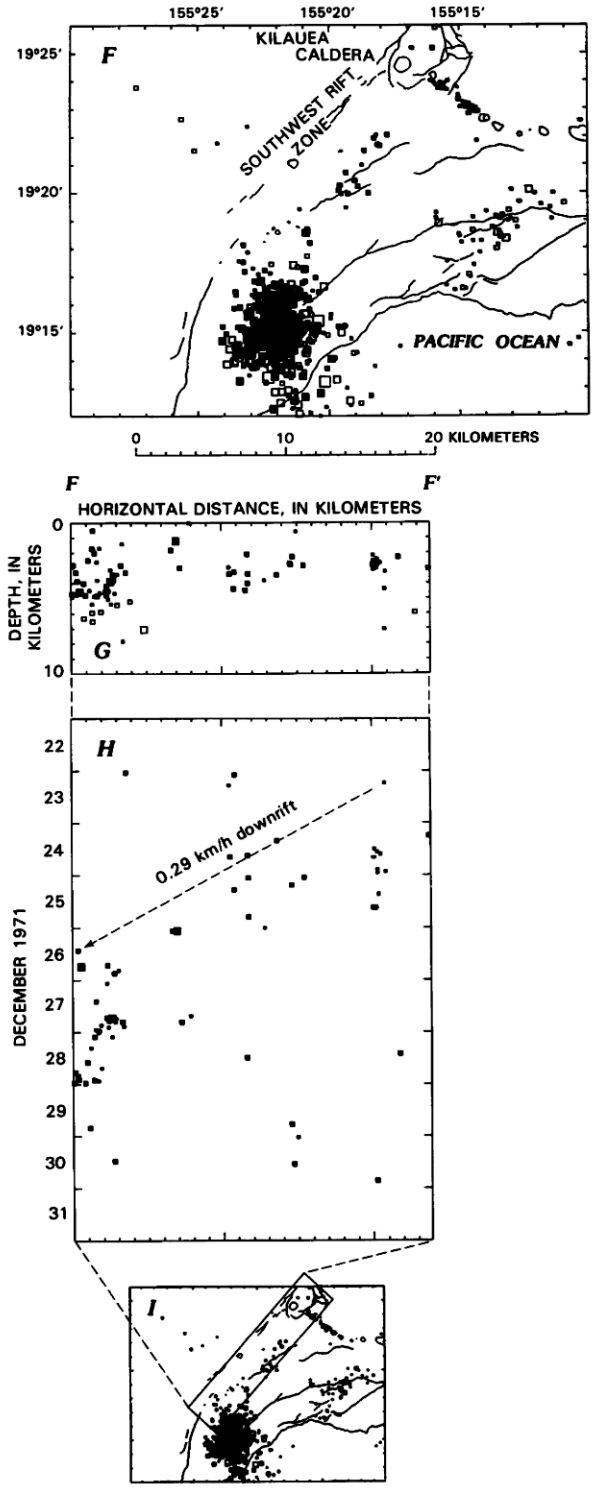


FIGURE 43.56.—Continued.

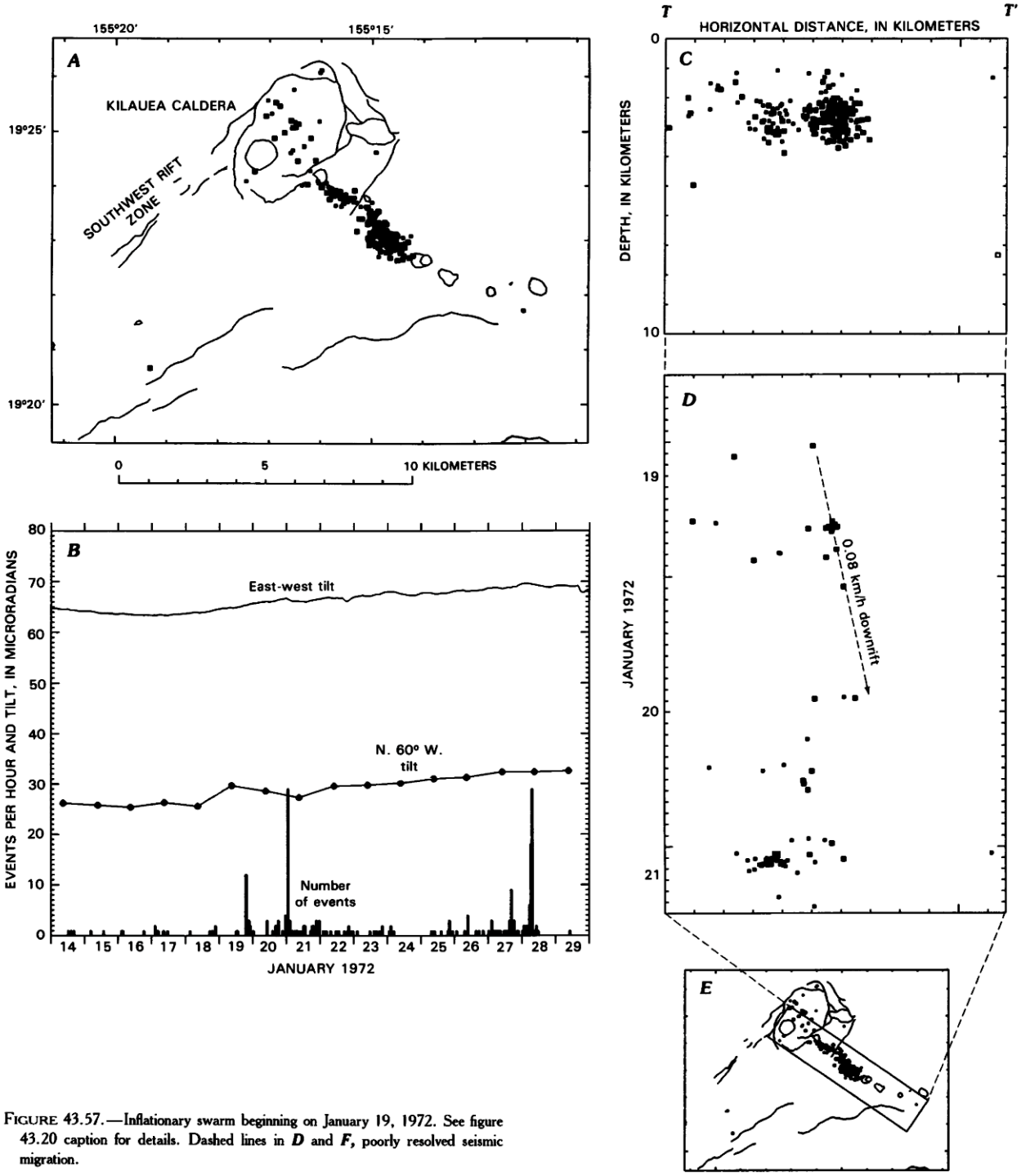


FIGURE 43.57.—Inflationary swarm beginning on January 19, 1972. See figure 43.20 caption for details. Dashed lines in *D* and *F*, poorly resolved seismic migration.

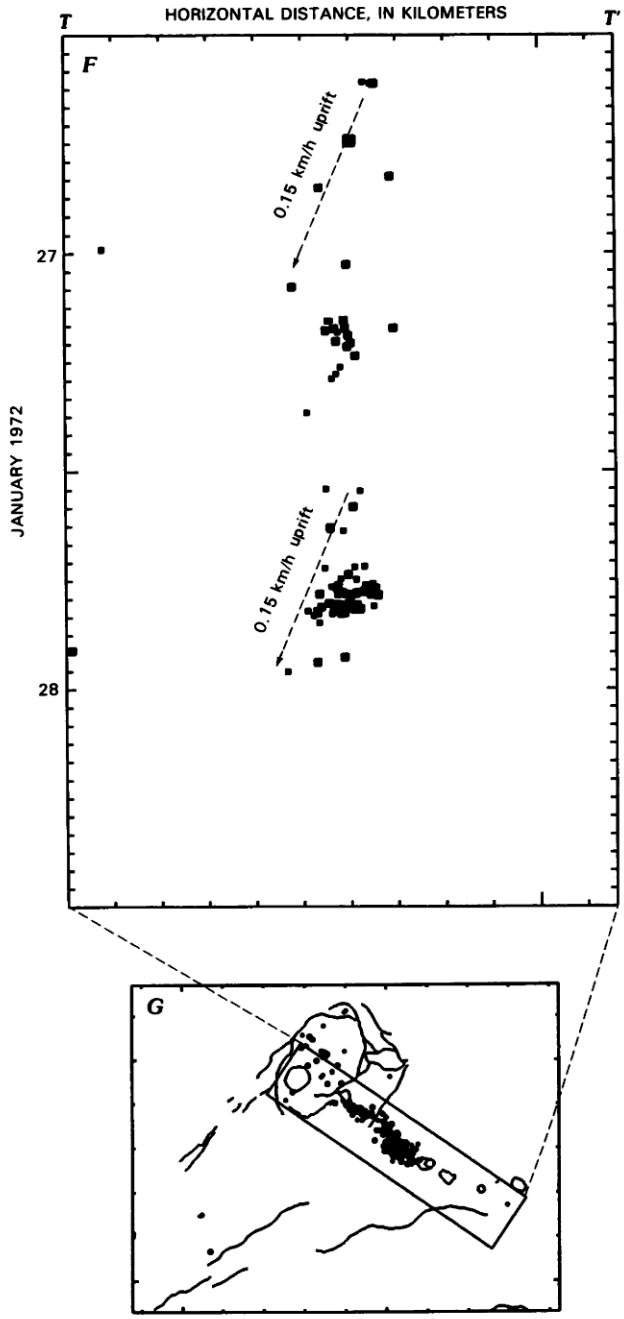


FIGURE 43.57.—Continued.

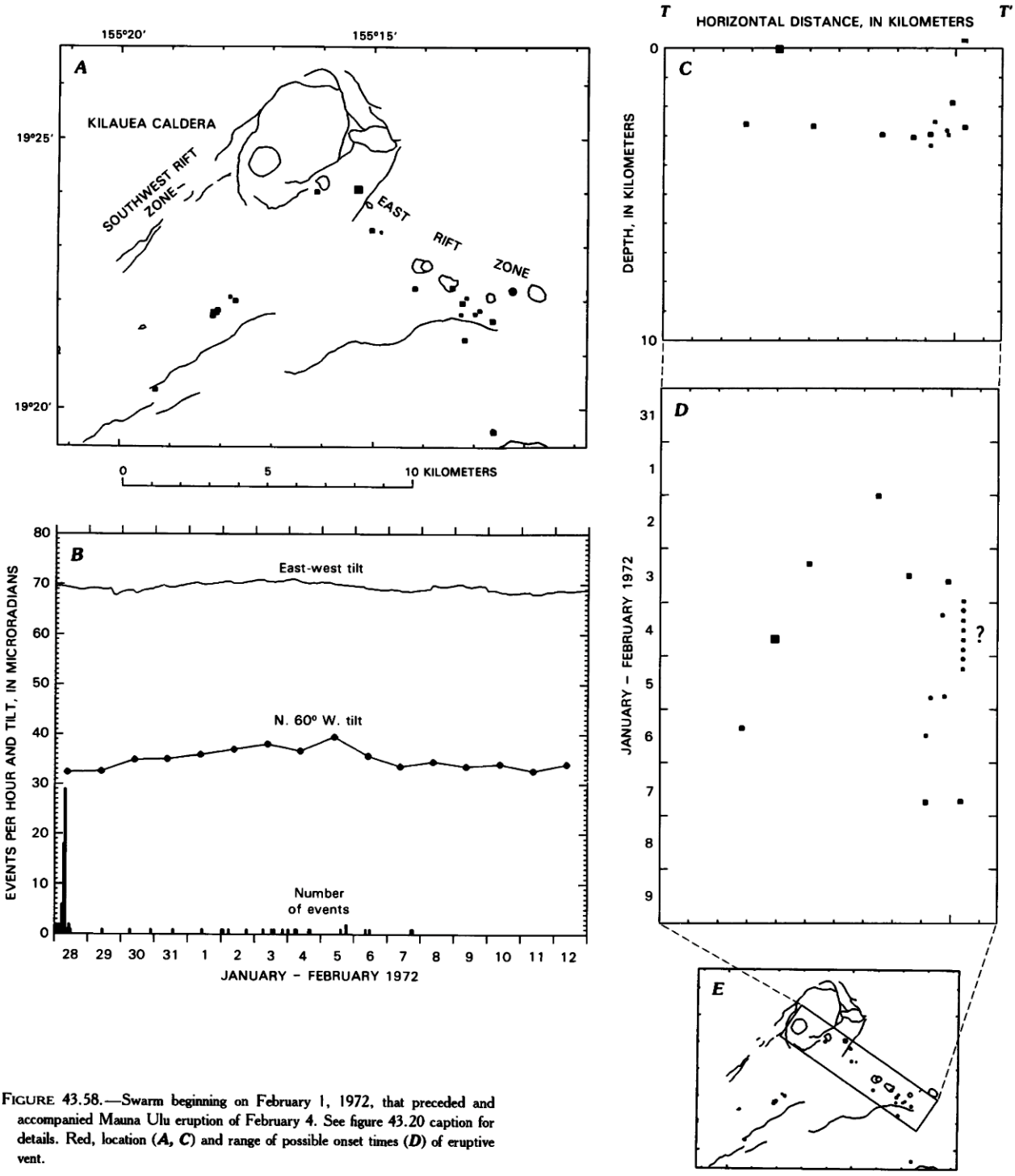


FIGURE 43.58.—Swarm beginning on February 1, 1972, that preceded and accompanied Mauna Ulu eruption of February 4. See figure 43.20 caption for details. Red, location (*A, C*) and range of possible onset times (*D*) of eruptive vent.

## ERUPTIONS AND INTRUSIONS, NOVEMBER 1973 THROUGH SEPTEMBER 1974

The next three swarms took place in the ERZ within 8 km of the caldera. The swarm of November 10–11, 1973, preceded and accompanied an eruption near Pauahi. In addition to the main seismic zone parallel to the rift, a few small events extended to the northeast beneath the eruptive vents (fig. 43.61*A*). The absence of earthquakes in the middle of the swarm (fig. 43.61*B*, *D*) is a result of masking of earthquakes by intense tremor. Uprift earthquake migration is suggested, and fountaining spread both east and west along the vent (fig. 43.61*D*). A definite shallowing of earthquakes, however, preceded the eruption (fig. 43.61*F*). The apparent vertical speed was about 1.6 km/h interrupted by a break of about 3 hours, but this pattern is based only on a few earthquakes. Figure 43.61*E* also shows that the depths of events after the start of the eruption averaged about 2 km shallower than those before.

An earthquake swarm lasting less than three hours occurred on March 24 in the Pauahi-Mauna Ulu section of the ERZ (fig. 43.62*A*). This section is a common place for earthquake swarms to begin, as did 3 of the 4 previous swarms. Three microradians of summit deflation accompanied the swarm, as seen on the Uwekahuna tiltmeter (fig. 43.62*B*). The event was accompanied by harmonic tremor and a short-lived increase of lava and gas production in the ongoing Mauna Ulu eruptive activity. We therefore interpret this event as a minor intrusion in which some sort of localized magma adjustment occurred, thus feeding the Mauna Ulu system. The episode caused a small volume of magma to drain from the summit complex through the aseismic section of rift above Pauahi.

The earthquake swarm immediately preceding the July 19, 1974 eruption was very intense and lasted only 9 hours (fig. 43.63*B*). It was in the same Keanakakoi-Kokoolau region active during the preceding 3 months of inflationary seismicity. The summit deflated about 3 microradians, after which tilt nearly leveled off. A larger and more rapid summit deflation followed at 1030 H.s.t., high amplitude tremor began, and the number of earthquakes that could be timed and located sharply diminished. Magma reached the surface about 2 hours later.

The seismic zone is slightly elongate and extends from about 3.5 km beneath Kokoolau to within 1 km or less of the surface near Puhimau (fig. 43.63*C*). The active zone thus plunges steeply to the southeast. The absence of events between 0 and 1 km depth may result from the poor depth control of the very shallowest earthquakes or from the fact that the low-rigidity and low-stress surface layer may be too weak to generate earthquakes of locatable magnitude.

Earthquakes migrated uprift at a well-determined rate of about 0.16 km/h (fig. 43.63*D*). Earthquakes also moved upward at roughly 0.55 km/h (fig. 43.63*F*), which slowed to about 0.18 km/h within 1 km of the surface, assuming the dike moved at constant speed to the surface. A slowing near the surface is typical of most dikes for which upward movement can be seen The observed migration patterns and vent location are explained by a plunging zone growing first at about 0.6 km/h then 0.24 km/h. This event was apparently a forceful intrusion of a dike leading from the ERZ conduit below Kokoolau up to the surface. The intense seismicity and tilt rate patterns show that rock was initially breaking under high magma pressure and relatively low volume flow. When the dike reached the surface, pressure and seismicity decreased, and flow volume, tremor and tilt rate increased.

The caldera eruption of September 19, 1974, was seismically unlike the others during the year and did not generate an intense earthquake swarm. It was instead preceded by three days of slightly elevated seismicity just south of the caldera under the SWRZ (fig. 43.64*A*) and a slowly inflating caldera (fig. 43.64*B*). The activity of September 16–19 is not distinguishable from other inflationary seismicity during the rest of 1974, although the probability of an eruption is measurably higher when such summit seismicity increases (Klein, 1984).

The pre-eruption earthquakes may have accompanied a slow and low-volume intrusion into the SWRZ. Although the swarm was a weak one, there is a hint of a downrift earthquake migration (fig. 43.64*D*). The absence of an intense swarm indicates that magma came to the surface without having to create a new dike in a high stress environment. When the eruption began, earthquakes abruptly ceased. This relation is expected if magma pressure induces the earthquakes and suddenly drops when flow and pressure are redirected to an active vent.

A pattern of increasing seismicity in the SWRZ during 1974 suggests that the rift participated in Kilauea's continuing inflation and slowly received magma. The seismic and tilt changes can be seen in figure 43.65, which plots earthquake positions and tilt from May 1974 through February 1975. In May and June most earthquakes were confined to the inflating summit area, but the July–December period saw increasing seismicity as far downrift as Mauna Iki. The rapid inflation of September through December produced the highest tilt values yet recorded. Kilauea appeared to be preparing for a SWRZ event, which came in December and dramatically shifted the active area from the upper to the lower SWRZ.

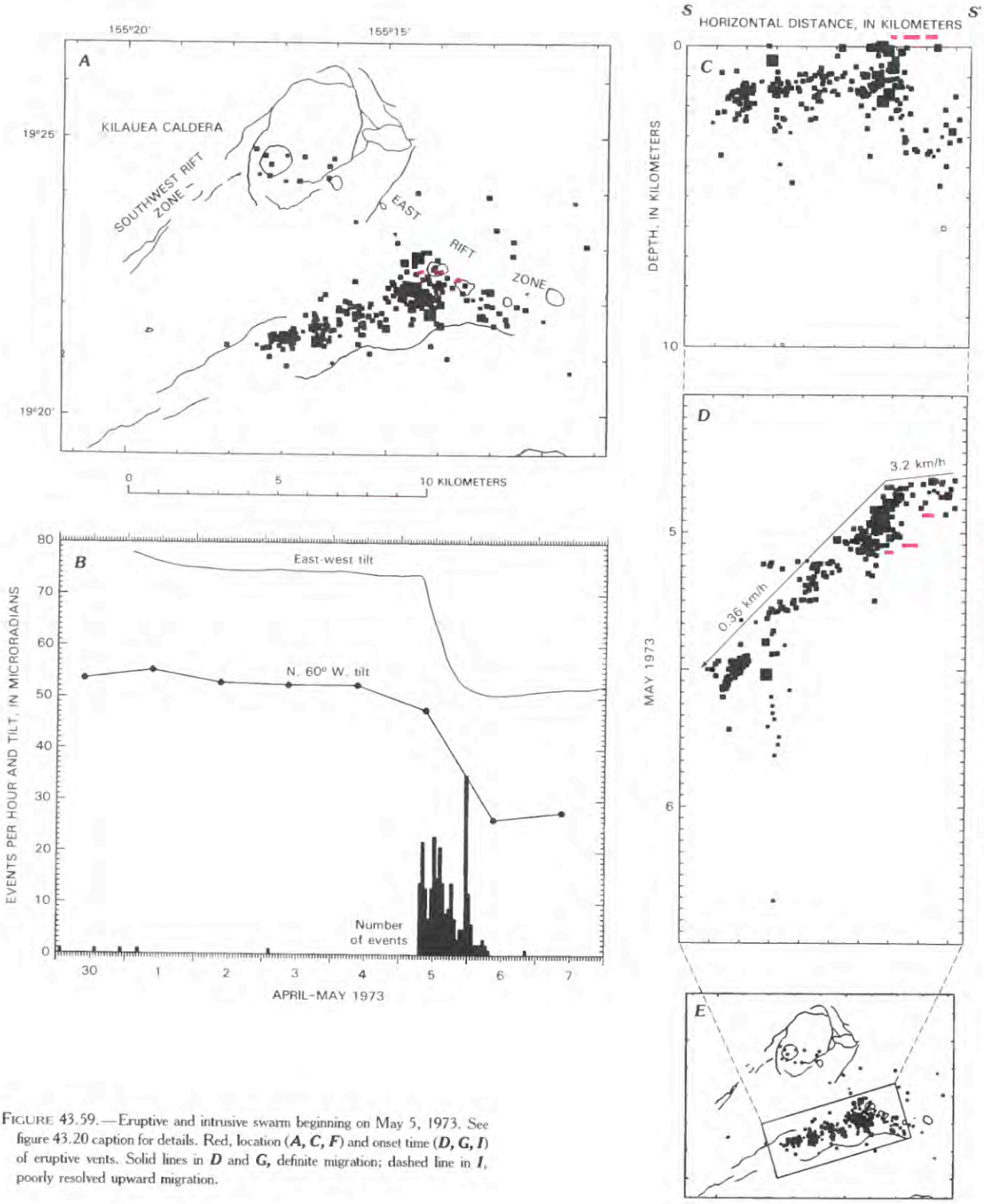


FIGURE 43.59.—Eruptive and intrusive swarm beginning on May 5, 1973. See figure 43.20 caption for details. Red, location (***A, C, F***) and onset time (***D, G, I***) of eruptive vents. Solid lines in ***D*** and ***G***, definite migration; dashed line in ***I***, poorly resolved upward migration.

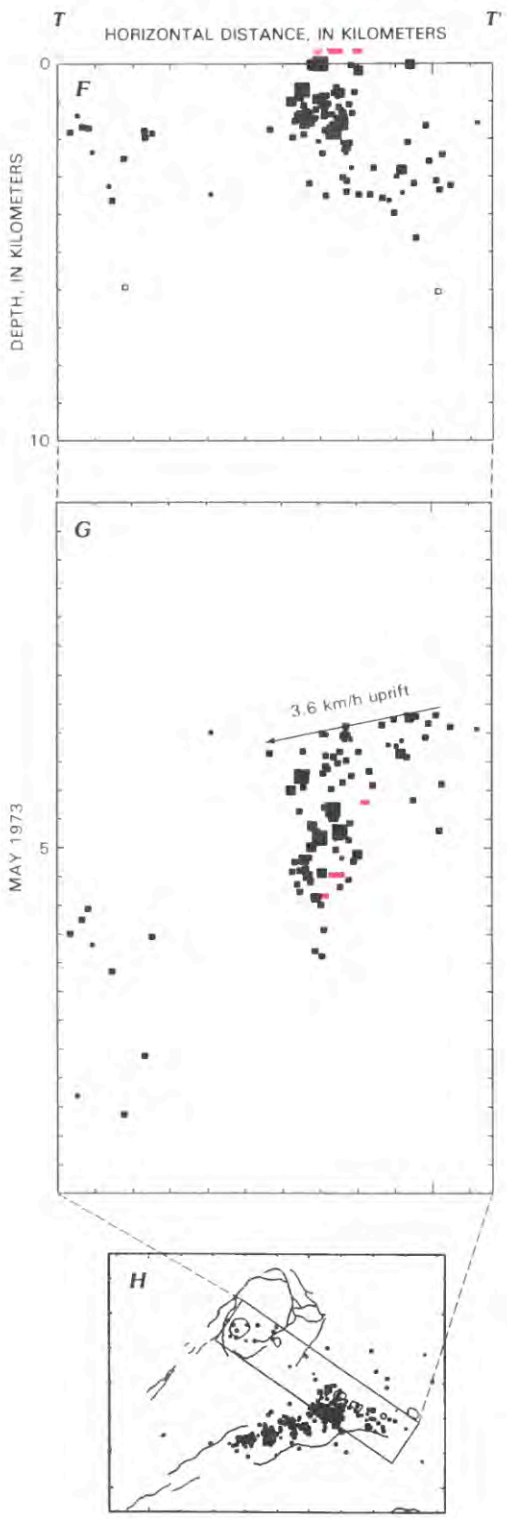


FIGURE 43.59.—Continued.

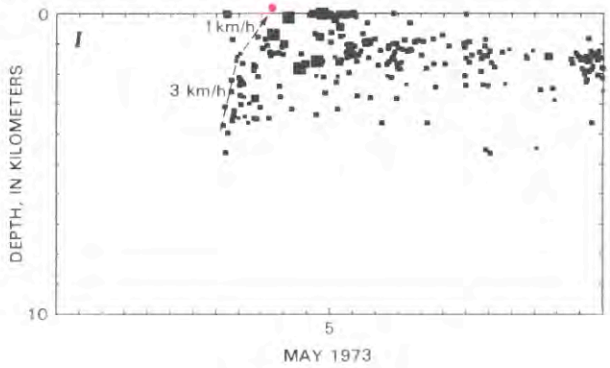


FIGURE 43.59.—Continued.

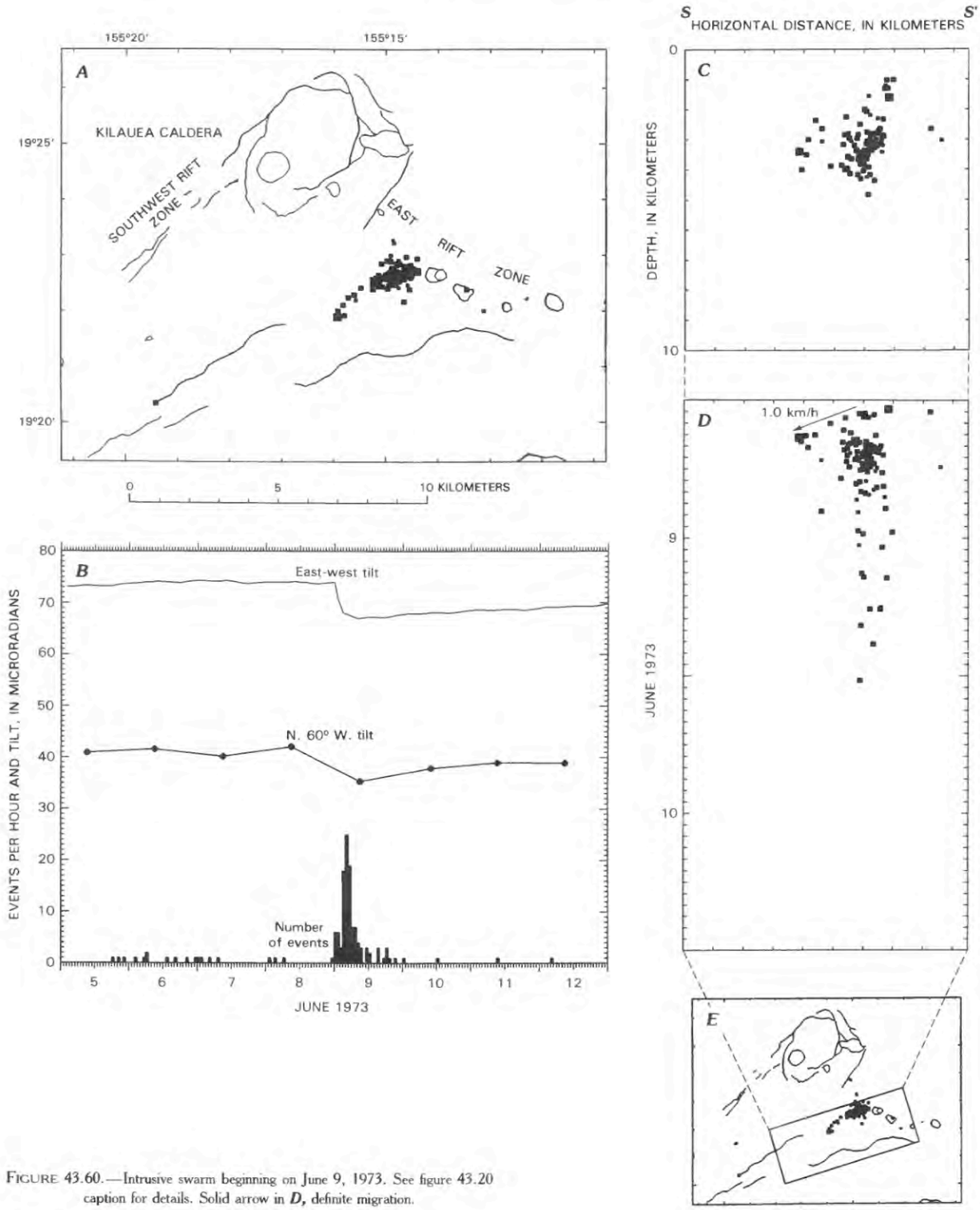


FIGURE 43.60.—Intrusive swarm beginning on June 9, 1973. See figure 43.20 caption for details. Solid arrow in ***D***, definite migration.

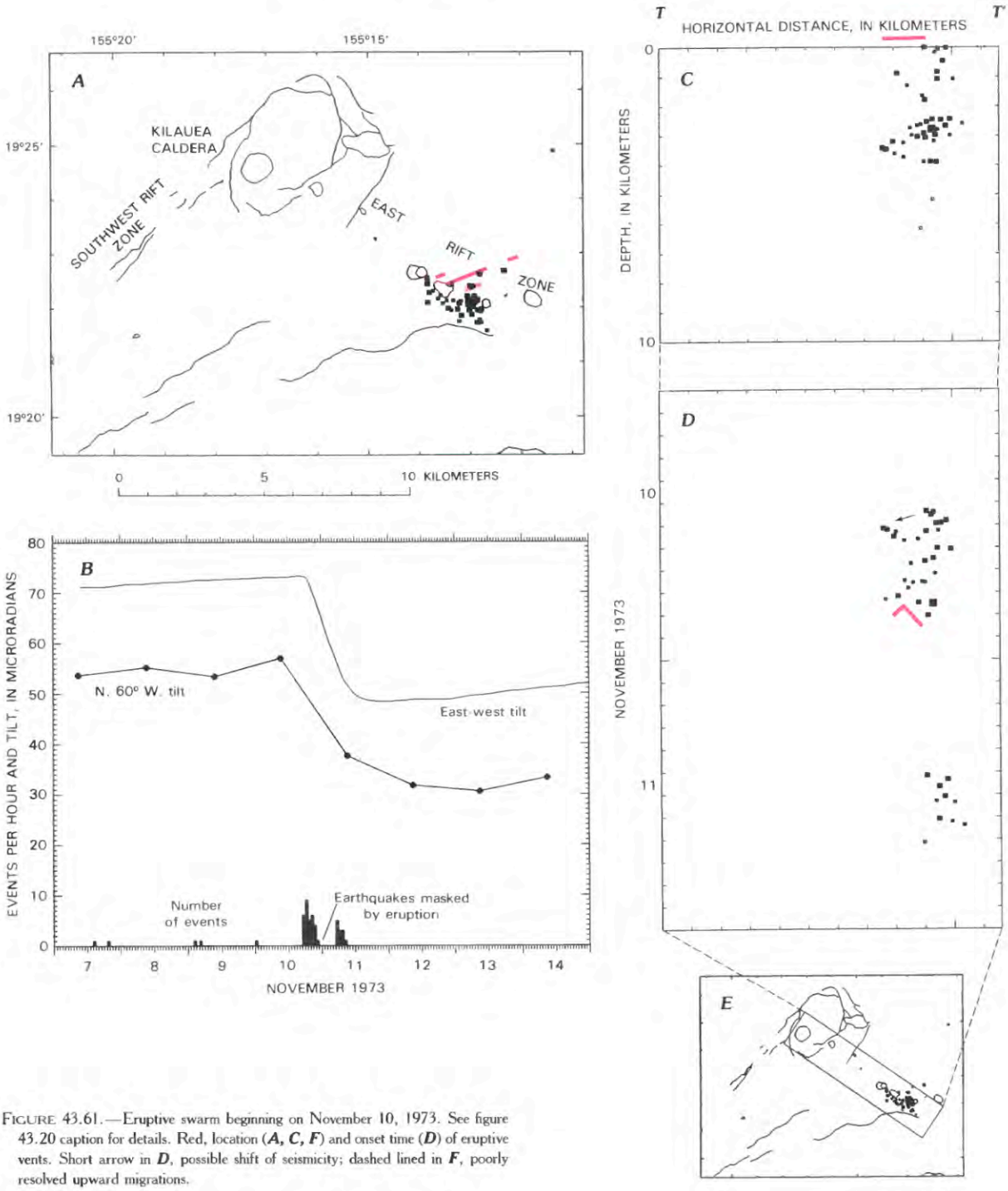


FIGURE 43.61.—Eruptive swarm beginning on November 10, 1973. See figure 43.20 caption for details. Red, location (***A, C, F***) and onset time (***D***) of eruptive vents. Short arrow in ***D***, possible shift of seismicity; dashed lined in ***F***, poorly resolved upward migrations.

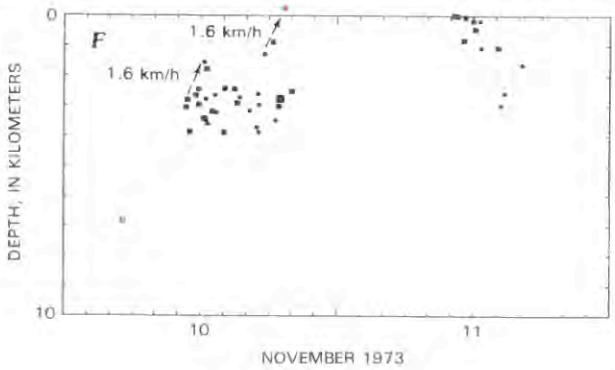


FIGURE 43.61.—Continued.

## THE DECEMBER 1974 SOUTHWEST RIFT ZONE ERUPTION

Summit seismicity in the parts of both rift zones adjacent to the caldera intensified during the week prior to the December 31 eruption (fig. 43.66). Beginning on December 24, this heightened activity apparently migrated very slowly into both rifts at roughly one kilometer per day (fig. 43.66*D*, *G*). These slow intrusions of magma into both rifts simultaneously were another indication of abundant supply in the summit reservoir.

Seismic patterns divide the eruption into two different phases: an intense but short swarm just south of the caldera related to the dike that fed the eruption, and a subsequent intrusion into an additional 18 km of the SWRZ.

The small cluster of earthquakes about 3 km south of Halemaumau occurred beneath the eruptive vent (fig. 43.67*A*). Earthquakes began in the middle of this cloud around 1600 H.s.t. on December 30 (fig. 43.67*D*), and were about 2.5 km deep. The seismic zone slowly grew in size until 0100 H.s.t. on December 31, when it was about 2 km in diameter and the swarm reached maximum intensity. The events then ranged between 1 and 4 km depth. Earthquakes migrated upward at about 5 km/h during this intense period, but the dike grew aseismically upward at about 0.3 km/h during the last 3 hours of its journey to the surface (fig. 43.67*K*). Earthquakes then diminished and tremor intensity grew prior to lava breakout shortly before 0300 H.s.t. As in July, an intense swarm accompanied the lateral and vertical growth of the dike that fed the eruption.

About the time this first swarm reached maximum intensity, additional earthquakes began migrating downrift. The seismically active dike grew about 1.3 km/h for about 14 km, then slowed to one-half that speed as it grew an additional 4 km (fig. 43.67*G*). Earthquakes not only occurred near the shallow rift conduit at 3 km depth, but also well southeast of the rift near the terminus of the new dike (fig. 43.67*B*). The events within Kilauea's mobile south flank are typical of those induced by other large SWRZ intrusions and large tectonic earthquakes. The effects of the intrusion (though probably not magma itself) thus reached at least 10 km from the rift axis.

Compressional stress generated by the new dike acting on a weak zone already close to seismic failure apparently caused the south flank earthquakes, including one of magnitude 5.5. Both rift and flank seismicity lasted for several days after the eruption and deflation ceased (figs. 43.66*B*, 43.67*I*). Thus either magma continued draining down the rift after its source at the summit was cut off, or the whole system displays a relaxation time of several days, or both. The seismic response of the section of rift adjacent to the caldera was rapid, and earthquakes diminished when the dike reached the surface and the pressure dropped. The lower rift, however, accommodates magma pressure by seismic slip and deformation in the mobile south flank, a process that takes several days because of its mechanical lag time (Dvorak and others, 1985).

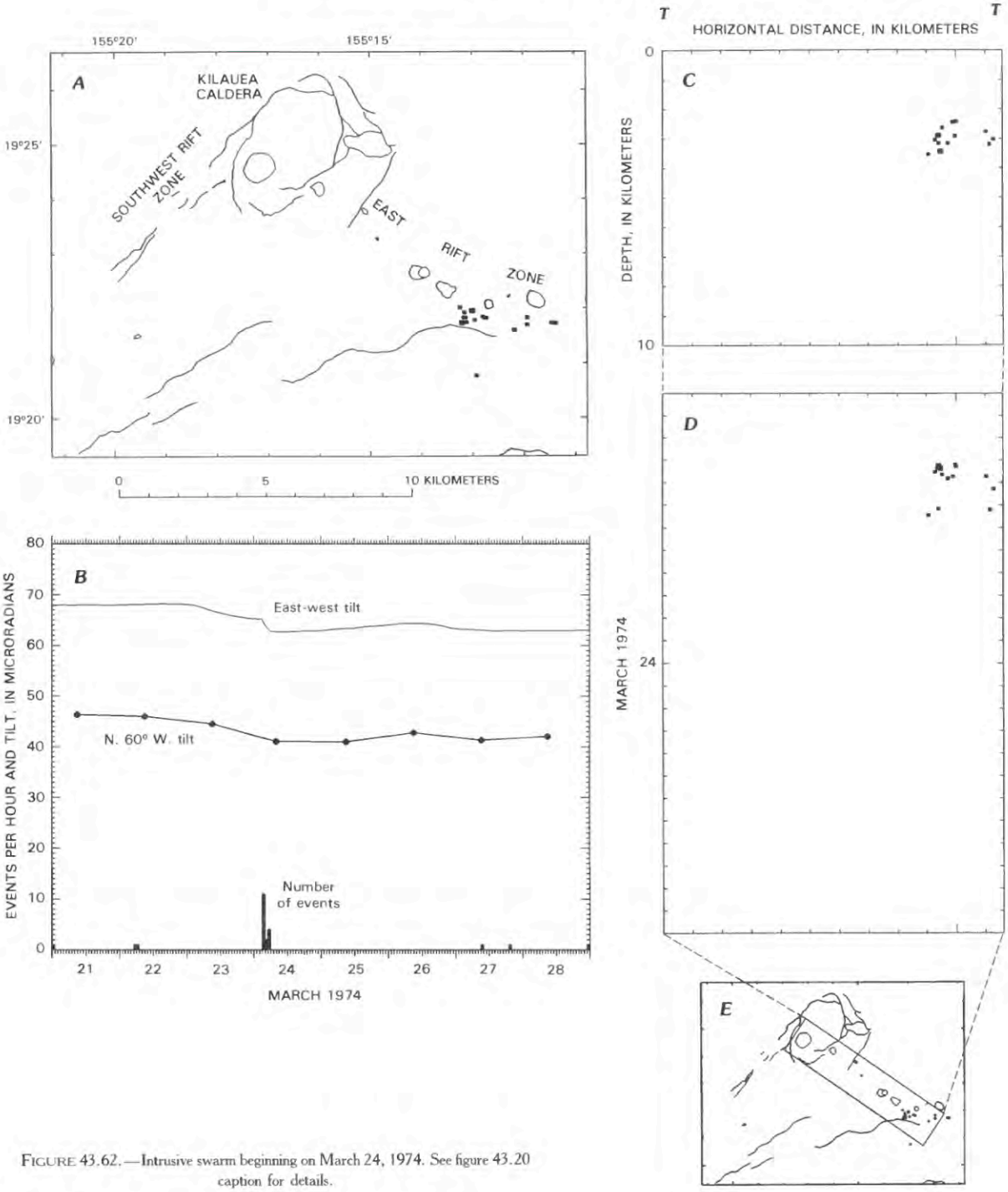


FIGURE 43.62.—Intrusive swarm beginning on March 24, 1974. See figure 43.20 caption for details.

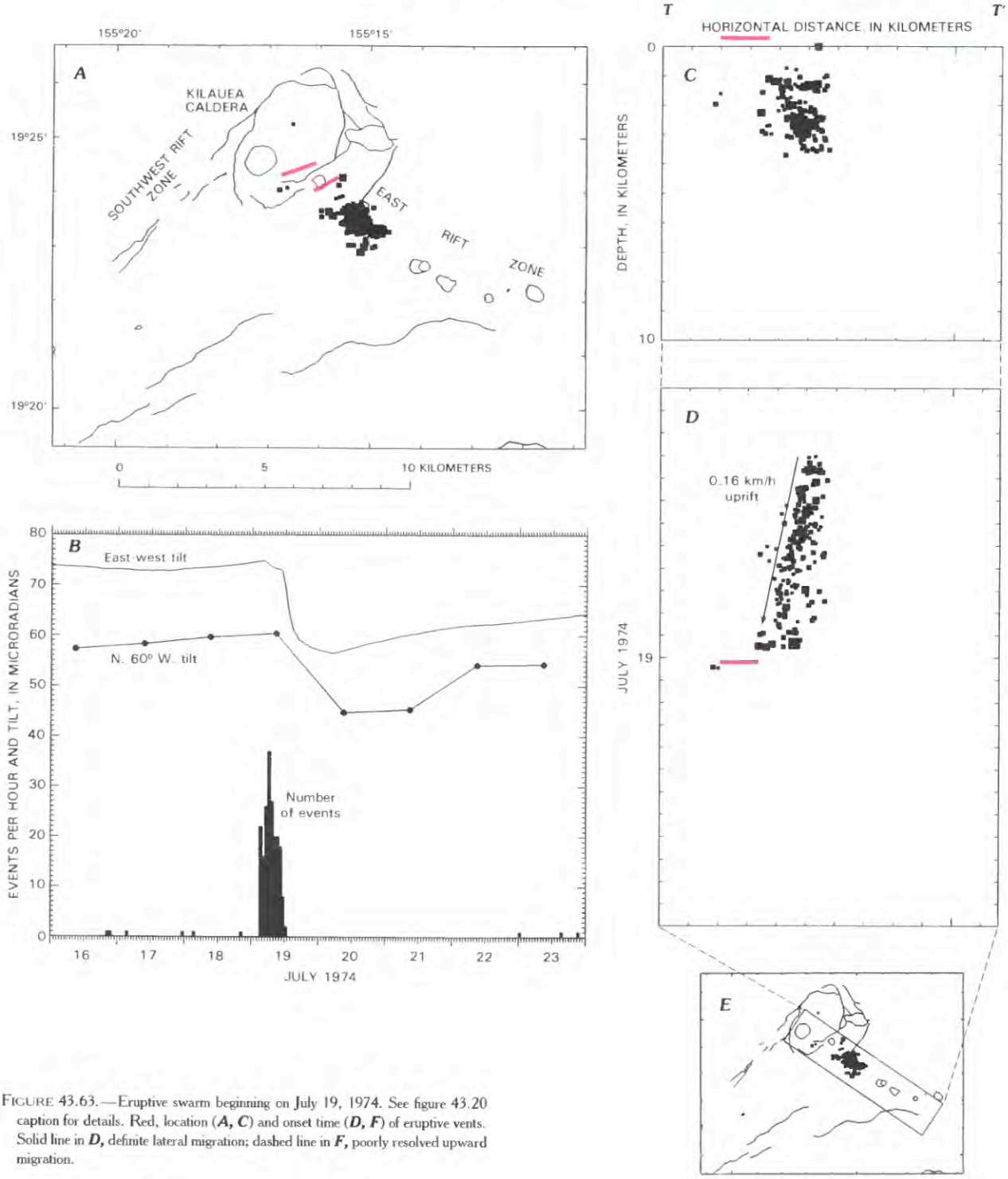


FIGURE 43.63.—Eruptive swarm beginning on July 19, 1974. See figure 43.20 caption for details. Red, location (***A, C***) and onset time (***D, F***) of eruptive vents. Solid line in ***D,*** definite lateral migration; dashed line in ***F,*** poorly resolved upward migration.

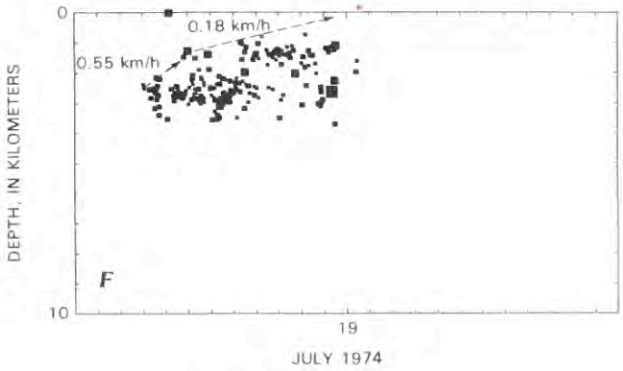


FIGURE 43.63.—Continued.

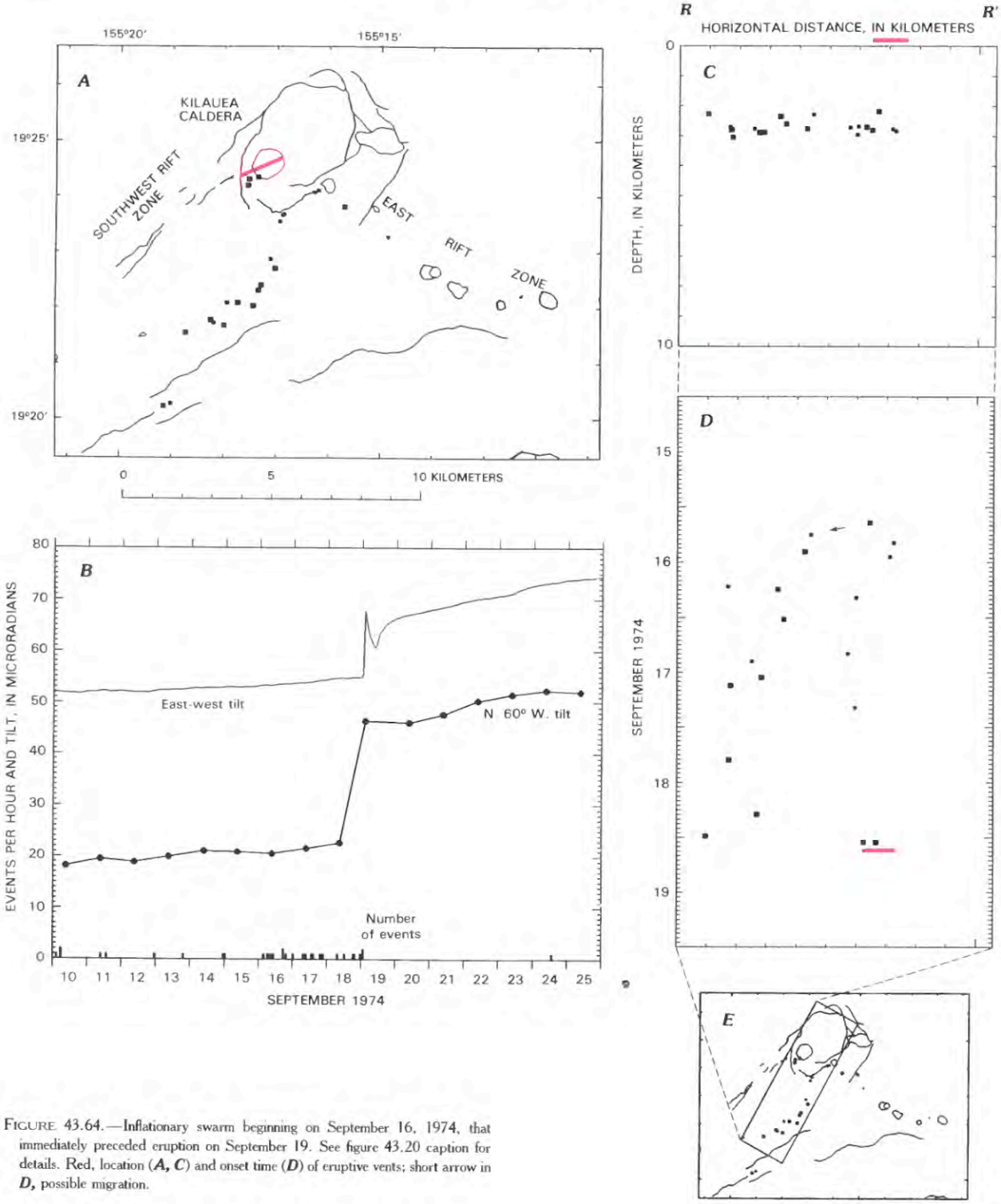


FIGURE 43.64.—Inflationary swarm beginning on September 16, 1974, that immediately preceded eruption on September 19. See figure 43.20 caption for details. Red, location (***A, C***) and onset time (***D***) of eruptive vents; short arrow in ***D,*** possible migration.

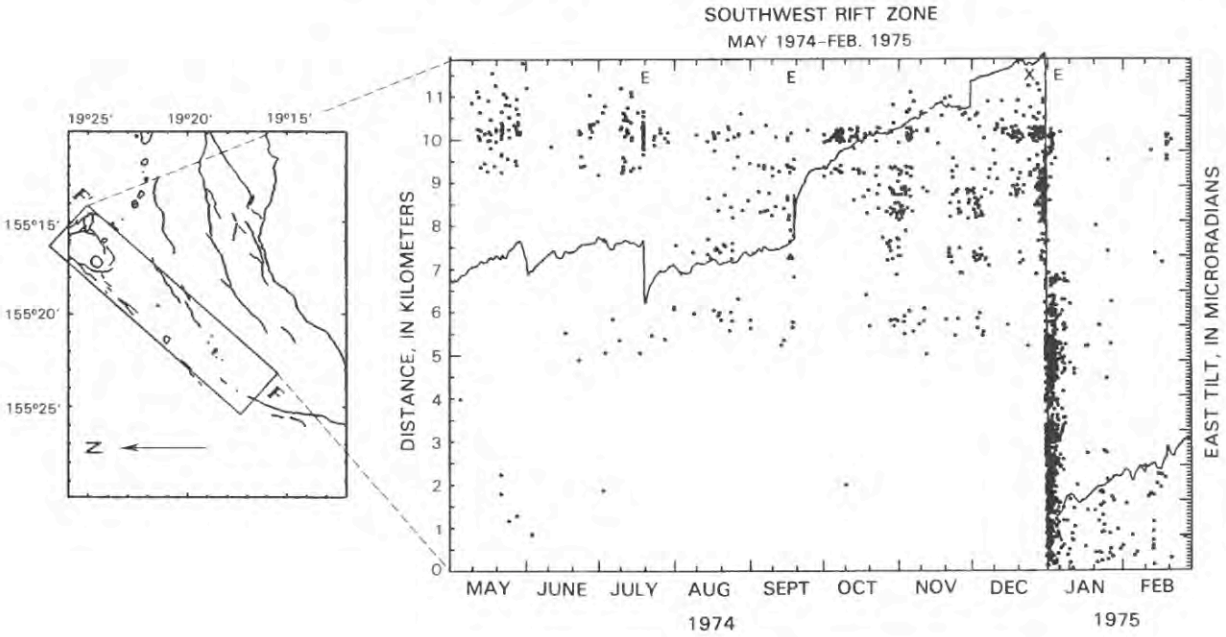


FIGURE 43.65.—Plot of earthquakes along southwest rift zone and east tilt at Uwekahuna versus time. Endpoints for distance axis *F-F'* are given in table 43.2. Tilt is from east-west Ideal Aerosmith tiltmeter, where east-down tilt is down on plot and generally indicates deflation of summit caldera. Notations along time axis refer to specific swarms detailed in other figures: E, eruption; X, swarm accompanying inflation. Small tick marks on tilt scale are 1 μrad.

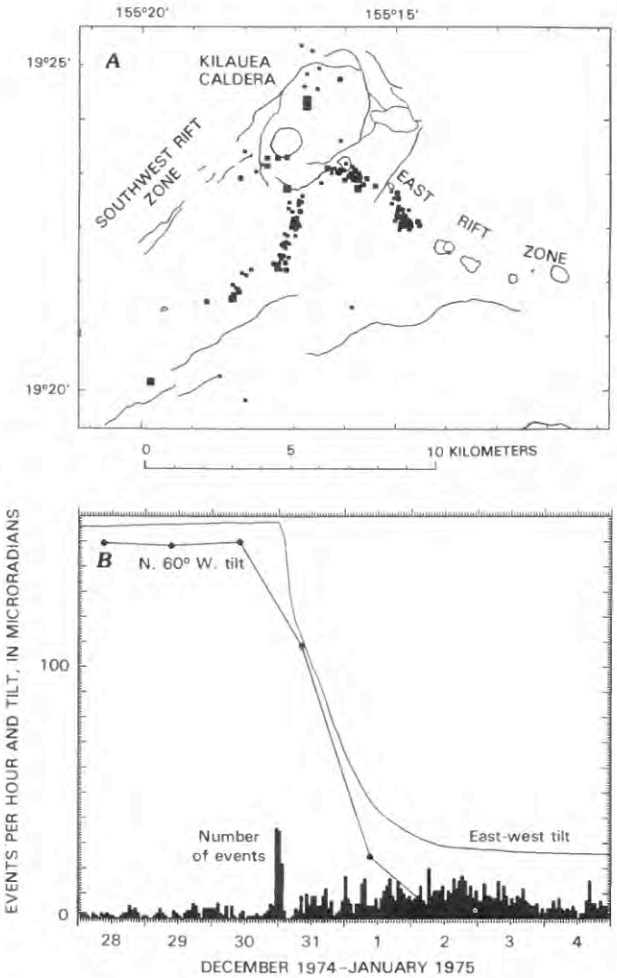


FIGURE 43.66.—Inflationary swarm beginning on December 24, 1974, that immediately preceded the eruption on December 31. See figure 43.20 caption for details. Dashed lines in ***D*** and ***G***, poorly defined migration of seismicity.

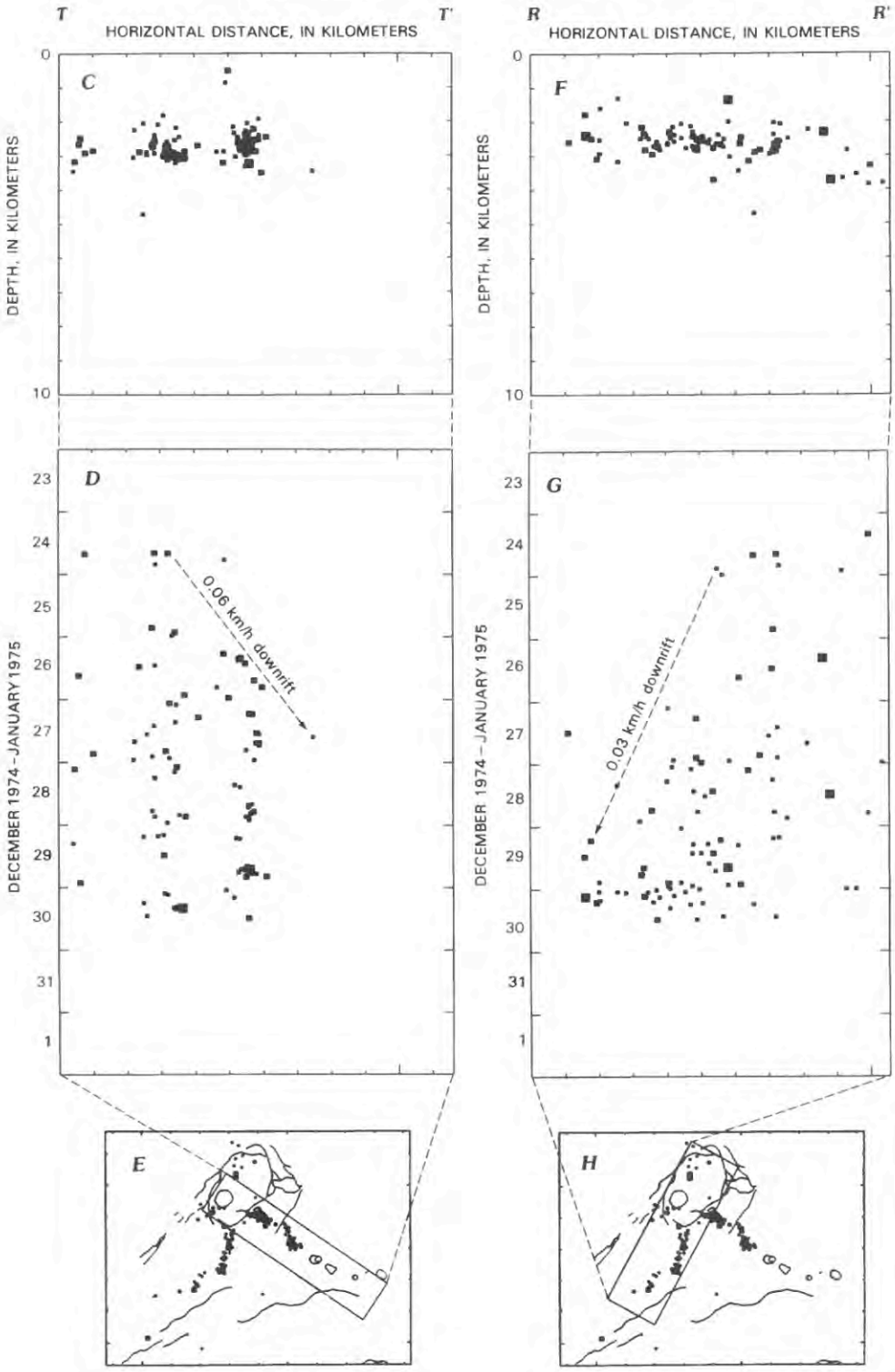


FIGURE 43.66.—Continued.

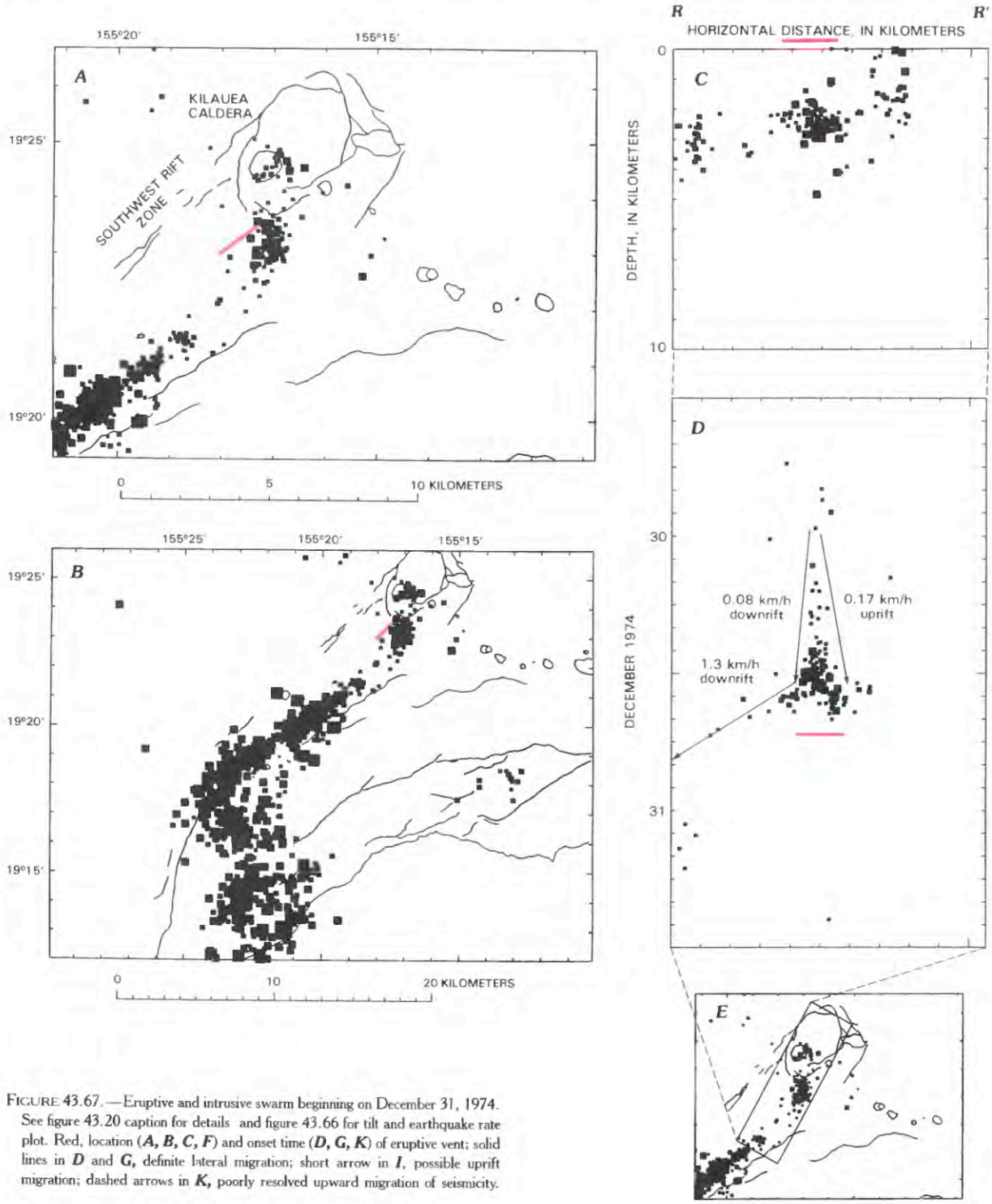


FIGURE 43.67.—Eruptive and intrusive swarm beginning on December 31, 1974. See figure 43.20 caption for details and figure 43.66 for tilt and earthquake rate plot. Red, location (***A, B, C, F***) and onset time (***D, G, K***) of eruptive vent; solid lines in ***D*** and ***G***, definite lateral migration; short arrow in ***I***, possible uprift migration; dashed arrows in ***K***, poorly resolved upward migration of seismicity.

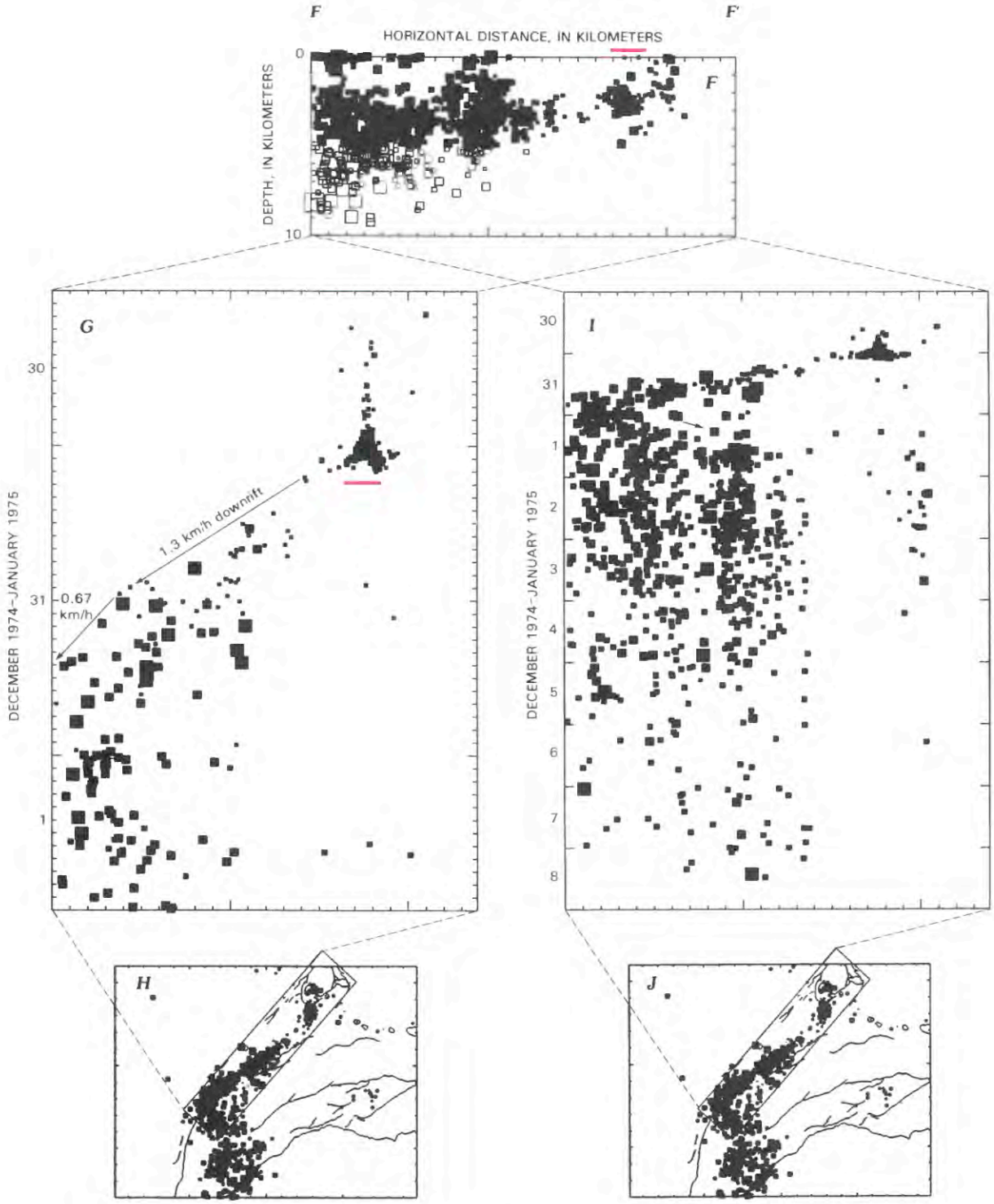


FIGURE 43.67.—Continued.

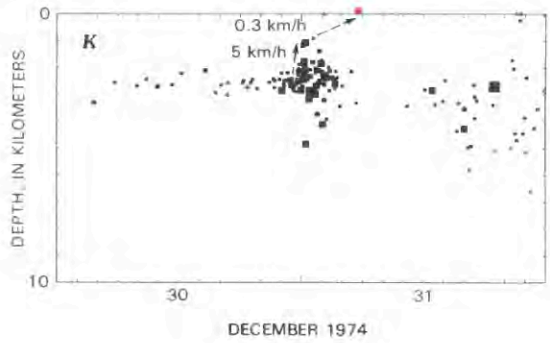


FIGURE 43.67.—Continued.

### 1976-77 EAST RIFT ZONE INTRUSIONS AND ERUPTION

The next major event at Kilauea was the magnitude-7.2 Kalapana earthquake on November 29, 1975. The south flank's accumulated elastic compression was partly released, and it slipped seaward as much as 8 m (Lipman and others, 1985). The ERZ dilated and accommodated roughly 100 million cubic meters of magma as the summit deflated (Dzurisin and others, 1980). A small summit eruption was triggered by the earthquake, but no ERZ eruption occurred and its magma remained below the surface. We do not consider the November 29, 1975 eruption here because of its atypical origin and because any intrusion seismicity was completely masked by the large earthquake and its aftershocks.

A major change in the short-term volcanic behavior of Kilauea resulted from the Kalapana earthquake. Whereas most swarms immediately prior to the earthquake culminated in eruptions, intrusions outnumbered eruptions during 1976–81. This change in behavior is statistically significant and can be attributed to lowered confining stress on the ERZ and its ease of rifting to accommodate new magma without sustaining pressures necessary for it to reach the surface (Ando, 1979; Klein, 1982b). A second change associated with the Kalapana earthquake was a shift of activity from the SWRZ to the ERZ. Following the December 1974 eruption, the SWRZ did not experience another intrusion until 1981.

The ERZ intrusions of June 21 and July 14, 1976, occurred while aftershocks of the Kalapana earthquake continued. The swarms were very similar. Both extended from Kokoolau to Mauna Ulu (figs. 43.68*A*, 43.69*A*). Each swarm lasted less than 24 hours and experienced 10–15 microradians of deflation coincident with the swarm (figs. 43.68*B*, 43.69*B*). Both swarms began between Pauahi and Mauna Ulu and migrated uprift. Migration was more recognizable during the June 21 swarm where the speed was about 1.3 km/h (fig. 43.68*D*). About the time the June earthquakes ceased moving uprift they veered upward to within 1 km of the surface (fig. 43.68*F*). The upward speed was about 0.5 km/h. The July earthquakes also displayed an upward migration (at 0.7 km/h, fig. 43.69*F*). The upward movement in June was between Kokoolau and Hiiaka, but that in July was near the former Aloi Crater.

Both of the 1976 intrusions originated from a point 3 km beneath the surface and just downrift of Pauahi. We interpret the immediate source of these intrusions as a secondary magma pocket below Pauahi. This Pauahi magma reservoir was suggested in an earlier section as the cause of the gap in seismicity below Pauahi, also seen in the 1976 swarms. A barrier containing this reservoir and just downrift of it is then a possible place for magma pressure to initiate earthquake swarms and intrusions. Whatever its cause, a concentration of stress beneath the Pauahi-Mauna Ulu region apparently initiates earthquake swarms that can move along the rift and upward. The magma supplying these intrusions is ultimately from the summit reservoir, but may have been stored within the rift. The summit reservoir must be in close hydraulic communication with the propagating dike, as evidenced by the simultaneity of rift swarm and summit deflation. Intrusions such as these are not simple downrift growth of dikes, and the possible relations of uprift earthquake migration and magma pockets within the rift will be discussed in more detail in the next section.

The ERZ between the caldera and Hiiaka was the site of two brief swarms on January 22 and February 8, 1977. The January swarm began at Keanakakoi, but soon moved to Kokoolau (fig. 43.70*A*, *D*). The fact that the summit did not rapidly deflate, but instead experienced slowly rising tilt (fig. 43.70*B*), and that the swarm's occurrence adjacent to the caldera might lead one to relate this sequence to summit inflation. The brevity of the intense part of the swarm (1 day) and relatively rapid though not precisely determined downrift migration rate (0.7 km/h) were more indicative of a rapid intrusion. This small swarm falls somewhere between the typical event types we have called slow, inflationary swarms and rapid, intrusive swarms.

The January swarm terminated near Kokoolau, where a more intense intrusion began 17 days later on February 8 (fig. 43.71*A*). The February intrusion lasted for about 11 hours and produced a rapid deflation (fig. 43.71*B*). The disturbance spread both uprift and downrift, though the continuity of migration is not well developed (fig. 43.71*D*). The initial 5 earthquakes were followed by an aseismic period, then a more intense episode that coincided with rapid summit deflation. The significant growth in dike volume

thus coincided with the most intense seismicity. At the beginning of the intense part of the swarm, an area of about 3 km by 3 km was active simultaneously (fig. 43.71*A*, *D*), and it did not grow in area. The disturbed zone thus seems to have aseismically enlarged in surface area before it seismically grew in thickness and volume. We therefore generally associate earthquakes primarily with growth of dike thickness and the compression of adjacent brittle rock. The enlargement of the disturbed zone alone does not then generate intense seismicity in these intrusions unless the dike also grows significantly in width.

The early 1977 swarms suggest that an initial low-volume intrusion propagated from the caldera to Kokoolau on January 22, where it encountered a blockage in the magma conduit. The blockage broke on February 8 when a greater magma volume became involved.

The September 1977 swarm and eruption penetrated farther along the ERZ than any other during 1962–83. A detailed eruption chronology is given by Moore and others, (1980). Four disconnected seismic zones were active during the eruption: the southern part of the caldera and central Koae fault zone (fig. 43.72*A*), and the ERZ at Makaopuhi and near Kalalua (fig. 43.72*F*). The deflation of Kilauea summit exceeded 90 microradians and continued for about four days (fig. 43.72*B*). The start of the rapid deflation, the beginning of the swarm in the southern part of the caldera, and four earthquakes south of the former Aloi Crater were all nearly simultaneous (fig. 43.72*D*). Seismicity at Makaopuhi and later at Kalalua shows that the part of the intrusion downrift of Mauna Ulu propagated at 1.2 km/h, then slowed to about 0.23 km/h downrift of Kalalua (fig. 43.72*H*). The absence of earthquakes between the caldera and Aloi and the simultaneity of seismicity at each place indicate that the intrusions of the previous two years left much of the magma conduit open and fluid, and no new dike intrusion or earthquakes were required to transport magma through this area.

The shallow conduit between Makaopuhi and Puu Kamoamoa was aseismic, but deeper earthquakes were induced in the south flank immediately adjacent to the gap in shallow earthquakes (fig. 43.72*F*). This pattern indicates that rifting did occur here, but was probably deeper than elsewhere on the rift. The eruption induced considerable seismicity in the south flank 5–13 km from the vents (fig. 43.69*F*; Dvorak and others, 1985). Considerably more and larger flank earthquakes were induced as a result of the September 1977 eruption than the somewhat similar January 1983 eruption. The induced seismicity is testimony both to the stress caused by the large intrusion and to the sensitivity of the south flank; these earthquakes can be partly considered aftershocks of the Kalapana earthquake less than two years earlier. The south flank was left with residual but local stresses, and these caused both aftershocks and the abundance of seismicity triggered by the 1977 intrusion.

The eruptive vents spanned a length of rift equal to that of the Kalalua seismic zone, but were displaced about 2–3 km downrift from the earthquakes (fig. 43.72*F*). This seismic pattern suggests that the dike intruded at 2–3 km depth and fed the eruption through feeders angled upward and downrift. The vents near Kalalua began erupting 5–10 h after the conduit 2–3 km beneath them became seismically active (fig. 43.72*H*). The time of opening of the easternmost vent was not observed directly, but the end of the uncertain period seems more likely: vent opening would then follow earthquakes as it does elsewhere. The last vent to open (uprift of Kalalua) does not follow the progression, but seems to accompany a new episode of seismic activity.

The earthquakes in the caldera and Koae are related to the large subsidence and deformation in the summit area. Earthquakes in the central Koae began about 12 hours after the intrusion and slowly progressed eastward at about 0.09 km/h (fig. 43.72*K*). This earthquake migration was also upward, owing to the dip of the seismic zone (fig. 43.72*J*). The migration of earthquakes is much slower and of opposite direction to that seen during intrusions of the Koae in 1973, and the seismic zone does not abut either rift. Tectonic movement on Koae faults is thus more likely than an intrusion, because summit subsidence would produce the correct sense of offset on the north-facing fault scarps. The caldera earthquakes began as soon as the intrusion started and slowly diminished during the next 6 days.

Caldera and Koae seismicity resumed on September 27 (fig. 43.73*A*) and accompanied the major eruptive phase that built the Puu Kiai spatter cone. The ERZ was nearly aseismic during this episode. The earthquakes below Halemaumau spread to the south very slowly at about 10 m/h (fig. 43.73*D*) and were apparently caused by the slow deflation. The caldera seismicity during the whole eruption thus generally correlates with deflation rate and is probably caused by compressive stresses in the summit area produced as the caldera contracted. These deflation earthquakes are in a similar location but appear to be the reverse of the slow swarms accompanying summit inflation and extension. The September 1977 eruption, the first following the $M=7.2$ Kalapana earthquake, was thus seismically complex. This complexity arose not only from the length of rift and volume of magma involved, but also from the probable disequilibrium of stresses following the Kalapana earthquake.

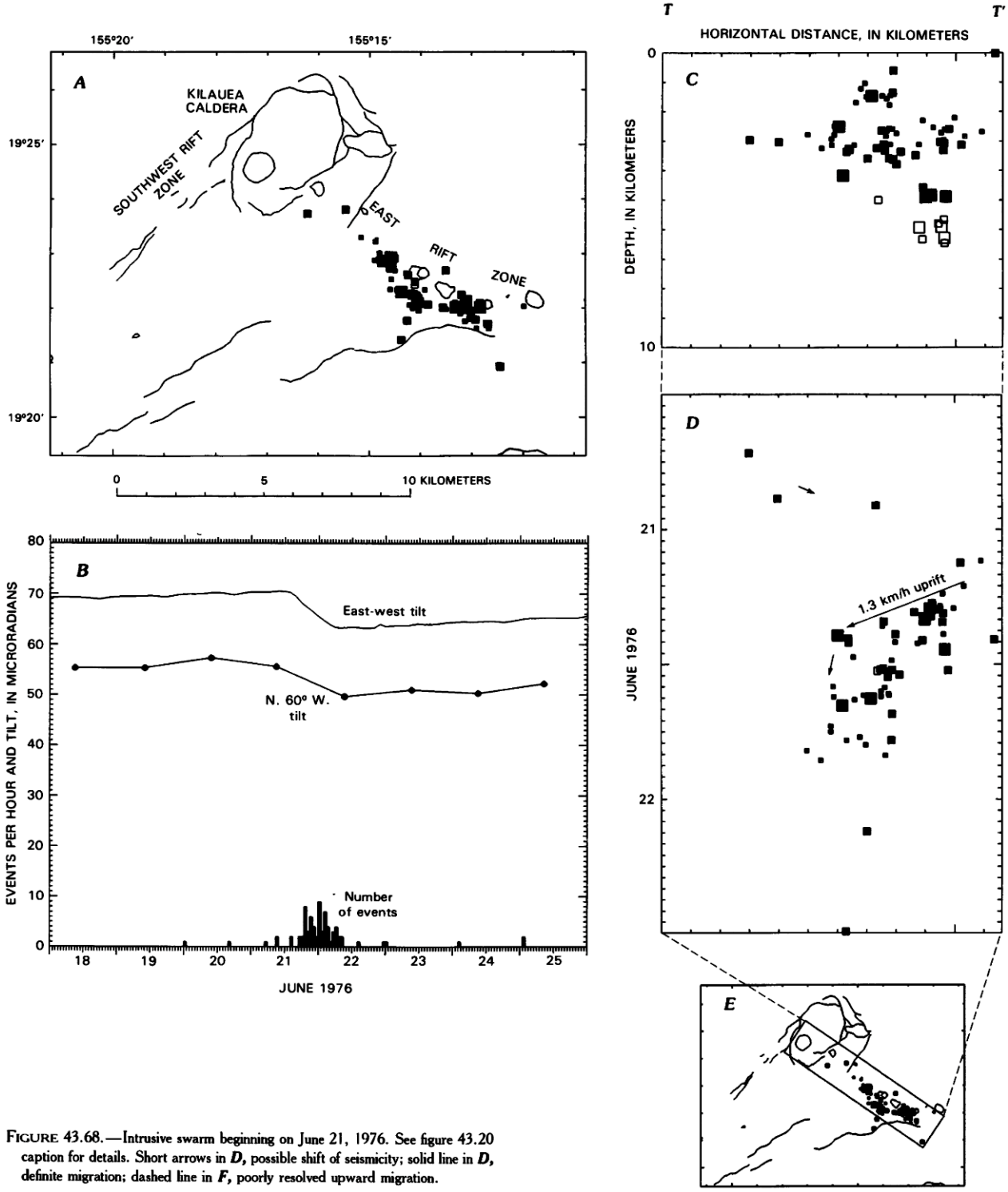


FIGURE 43.68.—Intrusive swarm beginning on June 21, 1976. See figure 43.20 caption for details. Short arrows in *D*, possible shift of seismicity; solid line in *D*, definite migration; dashed line in *F*, poorly resolved upward migration.

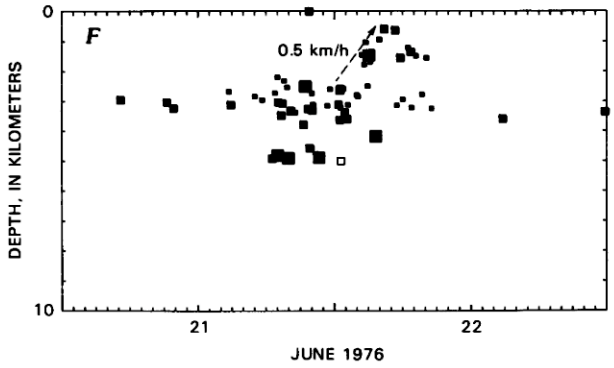


FIGURE 43.68.—Continued.

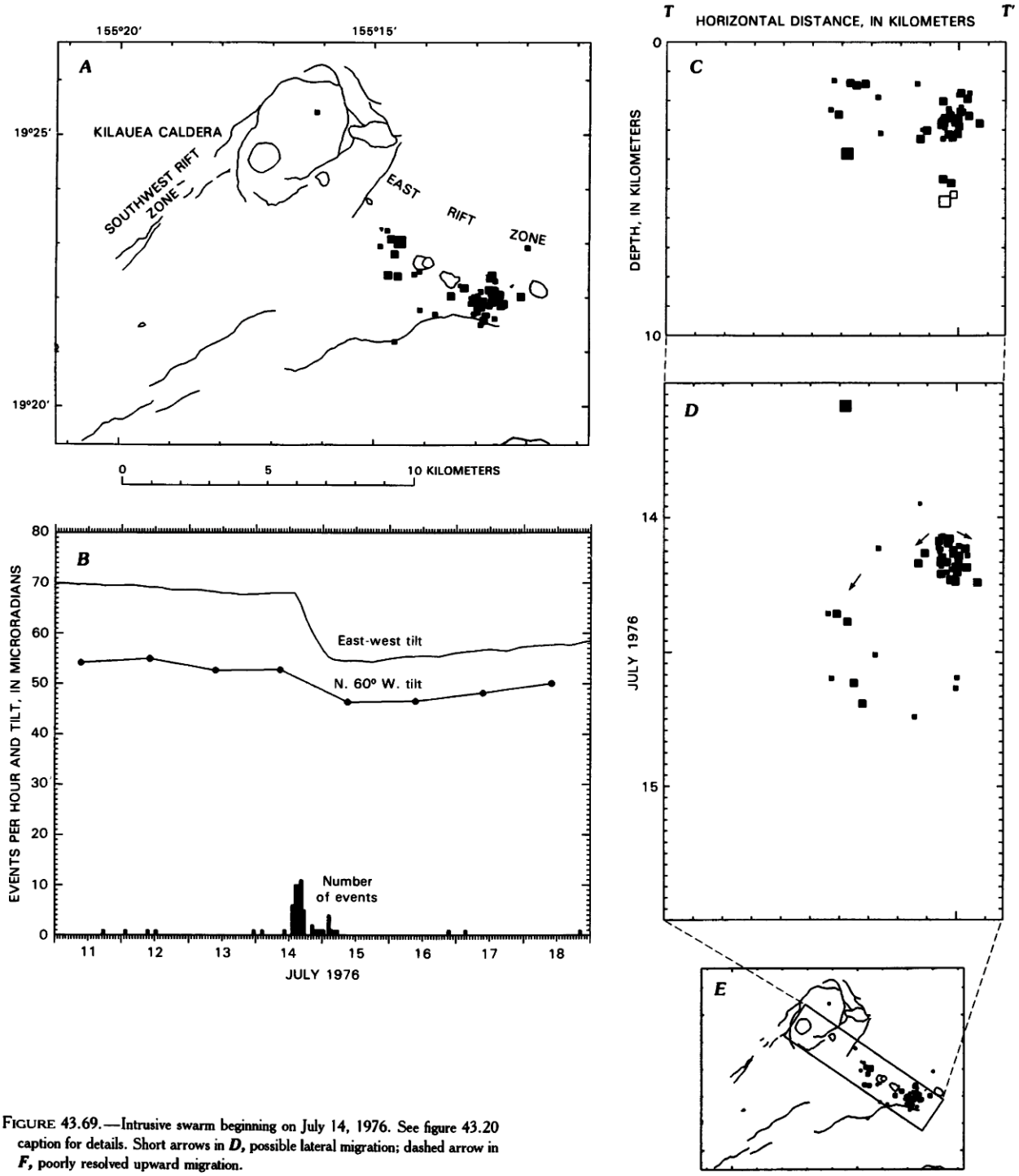


FIGURE 43.69.—Intrusive swarm beginning on July 14, 1976. See figure 43.20 caption for details. Short arrows in *D*, possible lateral migration; dashed arrow in *F*, poorly resolved upward migration.

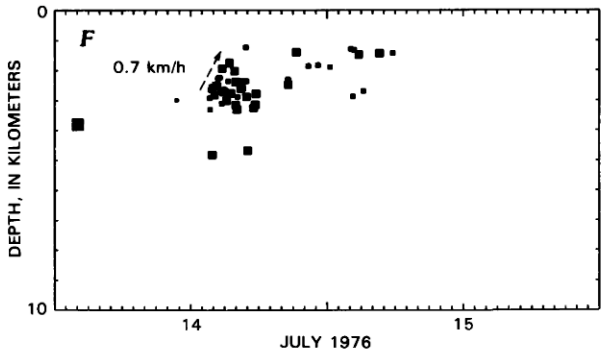


FIGURE 43.69.—Continued.

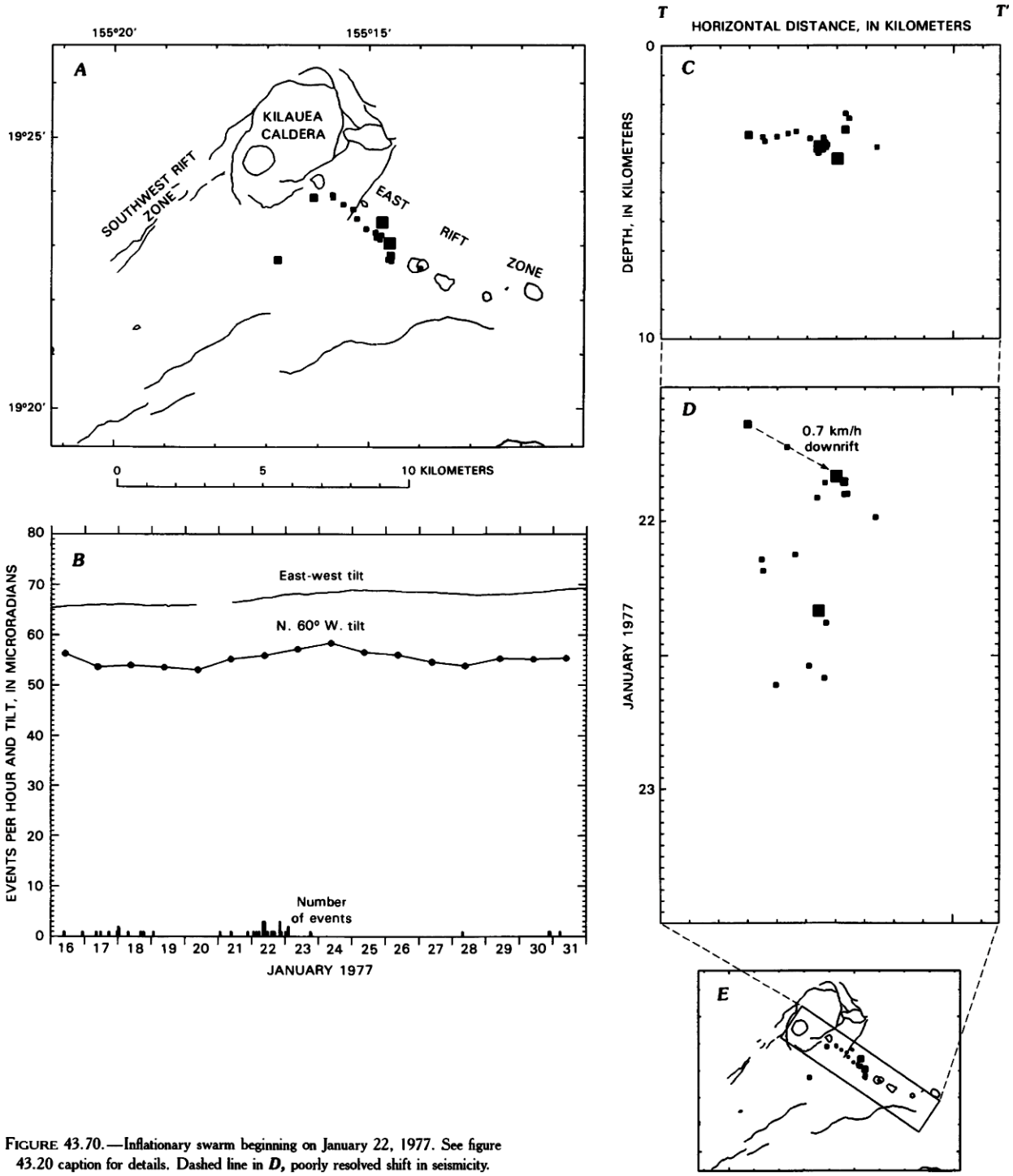


FIGURE 43.70.—Inflationary swarm beginning on January 22, 1977. See figure 43.20 caption for details. Dashed line in *D*, poorly resolved shift in seismicity.

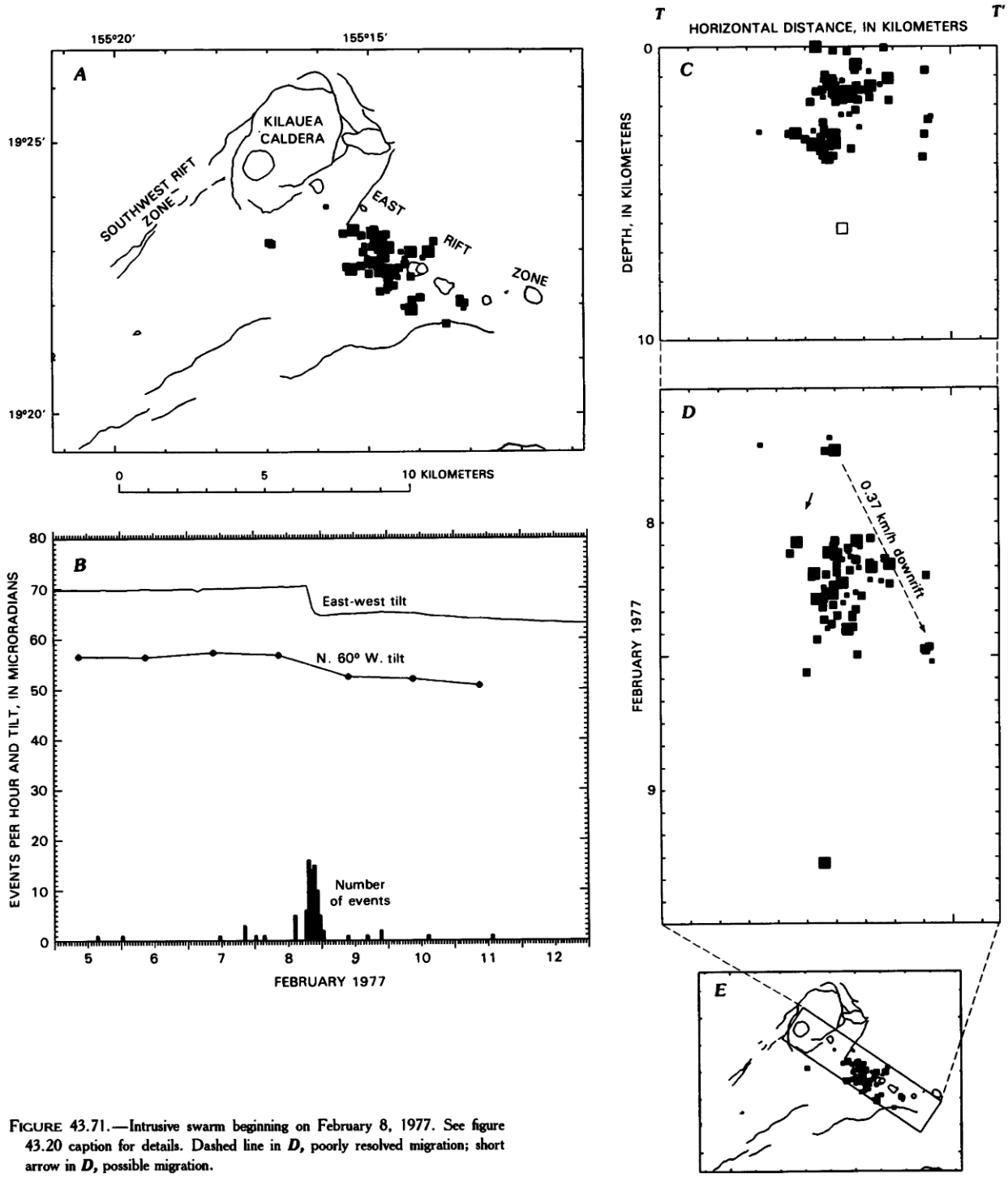


FIGURE 43.71.—Intrusive swarm beginning on February 8, 1977. See figure 43.20 caption for details. Dashed line in *D*, poorly resolved migration; short arrow in *D*, possible migration.

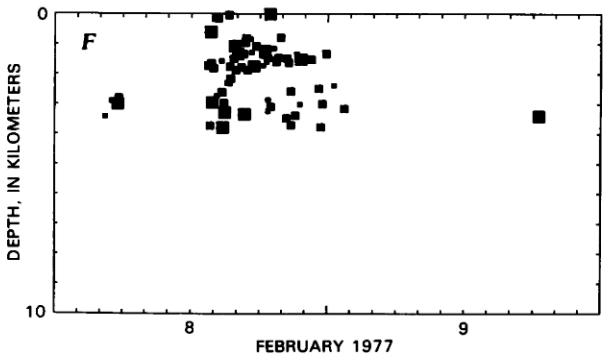


FIGURE 43.71.—Continued.

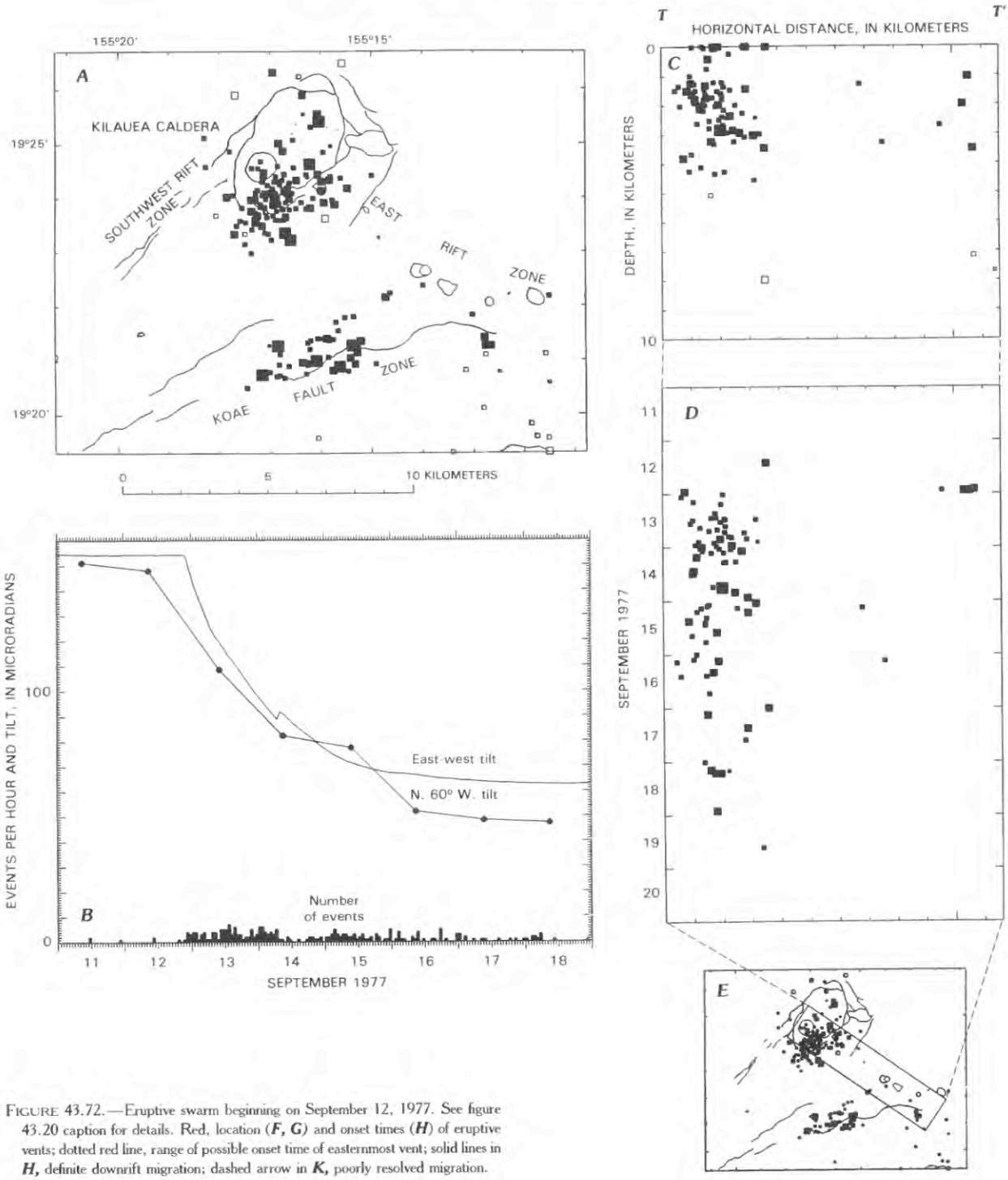


FIGURE 43.72.—Eruptive swarm beginning on September 12, 1977. See figure 43.20 caption for details. Red, location (***F, G***) and onset times (***H***) of eruptive vents; dotted red line, range of possible onset time of easternmost vent; solid lines in ***H,*** definite downrift migration; dashed arrow in ***K,*** poorly resolved migration.

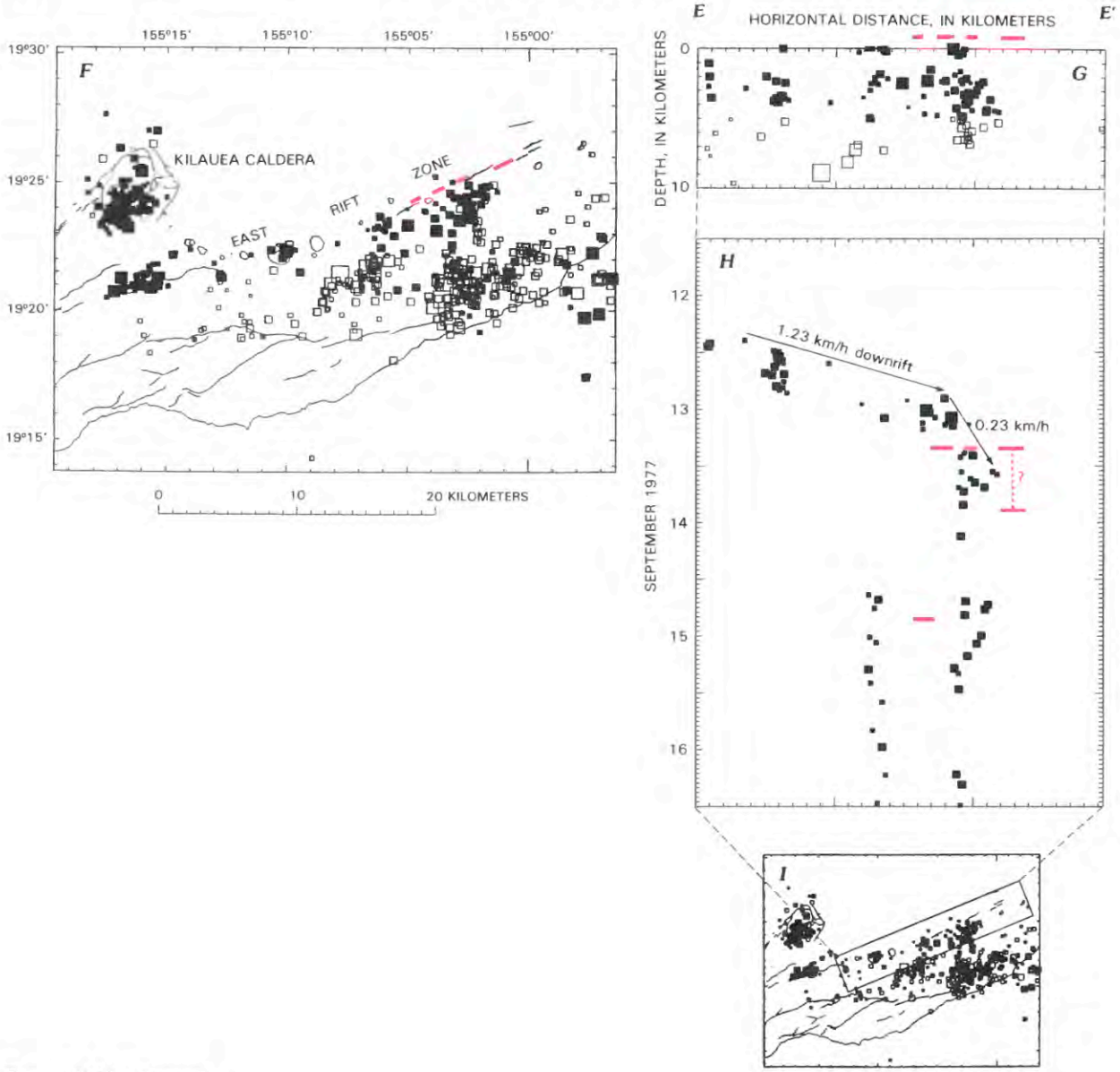


FIGURE 43.72.—Continued.

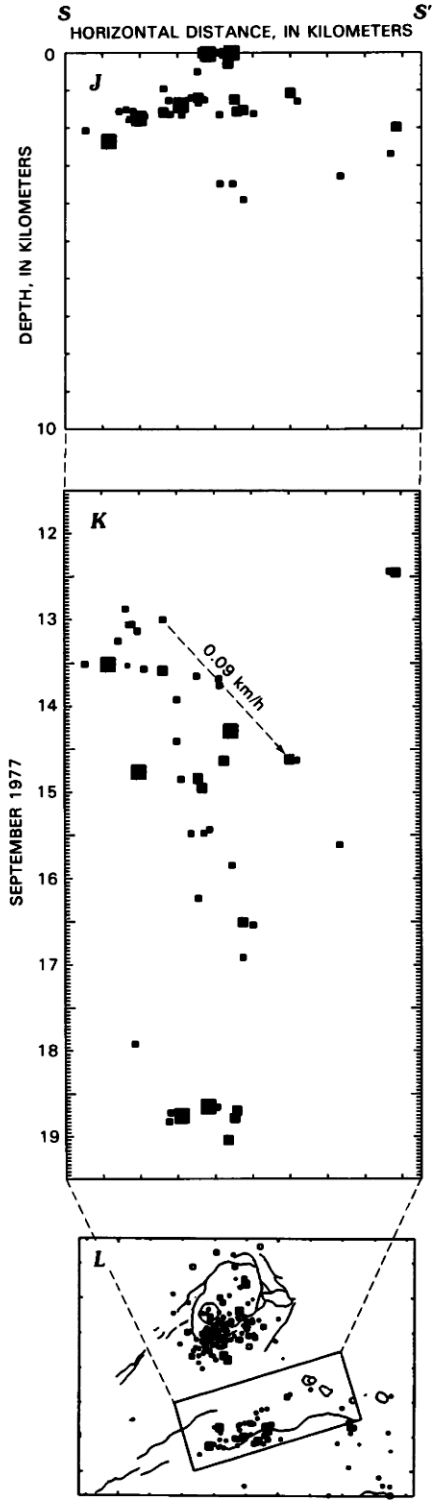


FIGURE 43.72.—Continued.

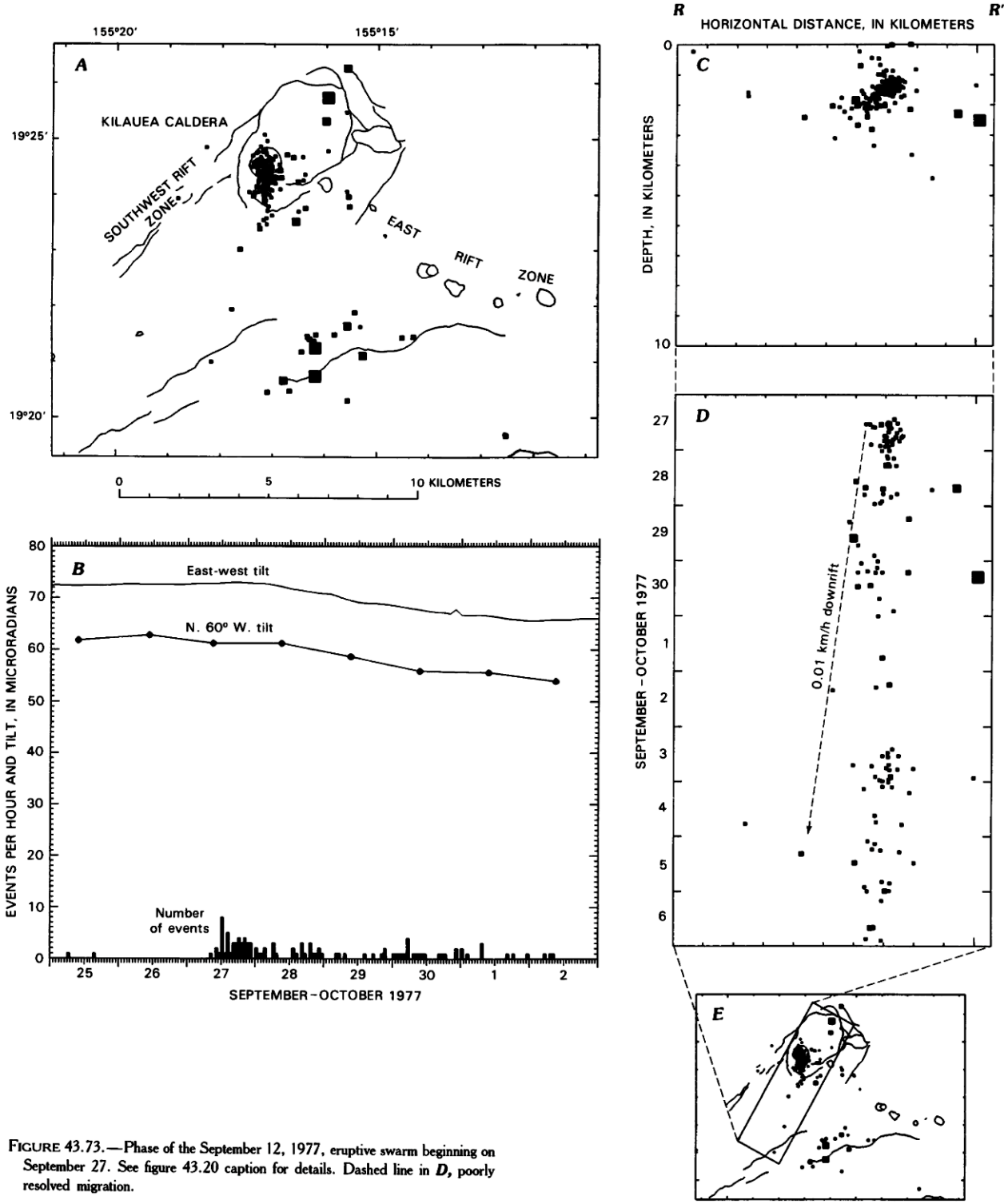


FIGURE 43.73.—Phase of the September 12, 1977, eruptive swarm beginning on September 27. See figure 43.20 caption for details. Dashed line in *D*, poorly resolved migration.

## EAST RIFT INTRUSIONS AND ERUPTION, NOVEMBER 1978 TO NOVEMBER 1979

The ERZ continued to overshadow the SWRZ during 1978–80 with a variety of eruptions and intrusions. An overview of the summit tilt and position of caldera and ERZ seismicity for the November 1978 through November 1980 interval is shown in figure 43.74. Prior to the first intense swarm on May 29, 1979, both tilt and caldera seismicity increased gradually as the summit inflated slowly (fig. 43.74*A*). Episodes of shallow earthquakes in the ERZ near Puu Kamoamoa also appeared during this period. These events were generally in slow swarms lasting several days and coincided with episodes of gradual summit deflation. The Puu Kamoamoa swarms were therefore slow intrusions. Because this activity was most prominent in mid-1980, it will be discussed in more detail below, following the March 1980 intrusions.

The ERZ generated two short but intense intrusive swarms on May 29 and August 12, 1979. Both seismic zones were about 4.5 km long (figs. 43.75*A*, 43.76*A*), but the May swarm was a little larger in terms of maximum magnitudes, swarm duration, and amount of deflation (figs. 43.75*B*, 43.76*B*). The May swarm began under Mauna Ulu and spread simultaneously both uprift to Pauahi and downrift to Makaopuhi (fig. 43.75*D*). It also started at about 3 km depth but spread rapidly both upward and downward (fig. 43.75*F*). The vertical migration speeds of 4–6 km/h were an order of magnitude faster than the lateral speeds of 0.6–0.7 km/h. Since the vertical propagation was much faster than for other intrusions, it may have been by a mechanism other than formation of a new dike, such as transmission of a pressure increase in a still-fluid dike.

A vertical column of earthquakes below 5 km depth was observed after 1200 H.s.t. on May 30, more than 12 hours after the intrusion (fig. 43.75*C*, *D*). The deeper events thus were induced by the intrusion and probably caused by continuation of rifting to depth or a downward moving dike. Growth of the rifts by intrusion must continue to about 10 km depth where the mobile south flank decouples from the pre-Hawaiian sea floor (Crosson and Endo, 1982). The rifting between 5 and 10 km depths is normally aseismic, and its timing is unknown. Only under Mauna Ulu and in the central section of the SWRZ (see the section "The Southwest Rift Zone Intrusions and Caldera Eruption of March through June 1982") are significant numbers of earthquakes below 5 km depth seen during intrusions.

The August 12 intrusion originated near Keanakakoi adjacent to the caldera and moved rapidly downrift at 1.6 km/h (fig. 43.76*D*). The intrusion was centered at 3 km depth and was less than 1 km in vertical extent (fig. 43.76*C*). The swarm continued for a few days in the downrift portion of the intrusion and extended at a very reduced rate (fig. 43.76*F*). This intrusion is one of the clearest examples of a fairly simple but rapid intrusion originating directly from the summit magma reservoir.

Kilauea continued to inflate and seismicity was nearly continuous in the portions of the SWRZ and ERZ immediately adjacent to the caldera (fig. 43.74*B*). A short swarm confined to the southern portion of the caldera (fig. 43.77*A*) punctuated a 30-day period of rapid and nearly continuous inflation. Inflationary swarms are generally not so short and intense. This one may have been associated with some form of dike intrusion caused by the increasing magma pressure, such as the breaking of rock to bridge two chambers of the magma reservoir.

The Pauahi eruption of November 16, 1979, began with a swarm starting abruptly on November 15. Earthquakes eventually engulfed the ERZ from Puhimau to the former Aloi Crater and partly into the Koae fault zone (fig. 43.78*A*). Both the main magma conduit at 3 km depth and the shallow 1- to 2-km depth zone were active (fig. 43.78*C*). The cross section also shows that the shallowest ERZ earthquakes mark a branch of the dike extending upward to Pauahi near the eruptive vents.

The temporal pattern of earthquakes in the November swarm is somewhat complex but shows characteristics common to many intrusions in this part of the ERZ. Earthquakes again underscored the key role played by the hypothesized magma blockage just downrift of Pauahi. The first two earthquakes were uprift of Pauahi. They lie along a front moving at about 3.8 km/h which became seismically intense when it reached Pauahi, and continued for another 1–2 km to the southeast (fig. 43.78*D*). When projected along the Koae fault zone, the same migration appears with a foreshortened speed of 1.5 km/h (fig. 43.78*G*). Earthquakes then moved slowly into the Koae at a decreasing speed. Summit deflation did not coincide with the first earthquakes, but commenced just minutes after the initial seismic front reached Pauahi and the intense seismicity began. This relation shows that the initial downrift migration did not draw much magma from the summit reservoir, but that the coincidence of intense seismicity and deflation implies a close hydraulic communication between the summit reservoir and Pauahi. Earthquakes then migrated back uprift at about the same speed, almost as if some sort of disturbance was reflected from a barrier just downrift of Pauahi.

After the intense seismicity began, the sense of migration was generally uprift: (1) the western boundaries of the seismic zone moved uprift and into the Koae, (2) the eastern boundary of the seismic zone moved uprift at about 0.08 km/h, and (3) the eruptive vents opened westward (fig. 43.78*D*). The possible mechanisms of this uprift migration will be discussed in the section "Discussion of Rift Zone Intrusions." Coincident with the initial uprift movement was an upward migration from 3 km depth that slows and becomes nearly aseismic at a depth of 1 km (fig. 43.78*I*). These patterns reinforce the earlier suggestion of a secondary magma reservoir about 3 km beneath Pauahi and a blockage of the magma conduit just downrift of Pauahi. The initial downrift migration was not strong enough to penetrate the barrier, where a stress concentration triggered a rifting episode fed by summit magma. Even though possibly triggered by a pulse from the summit, the sequence of events culminating in the eruption at Pauahi were initiated at Pauahi.

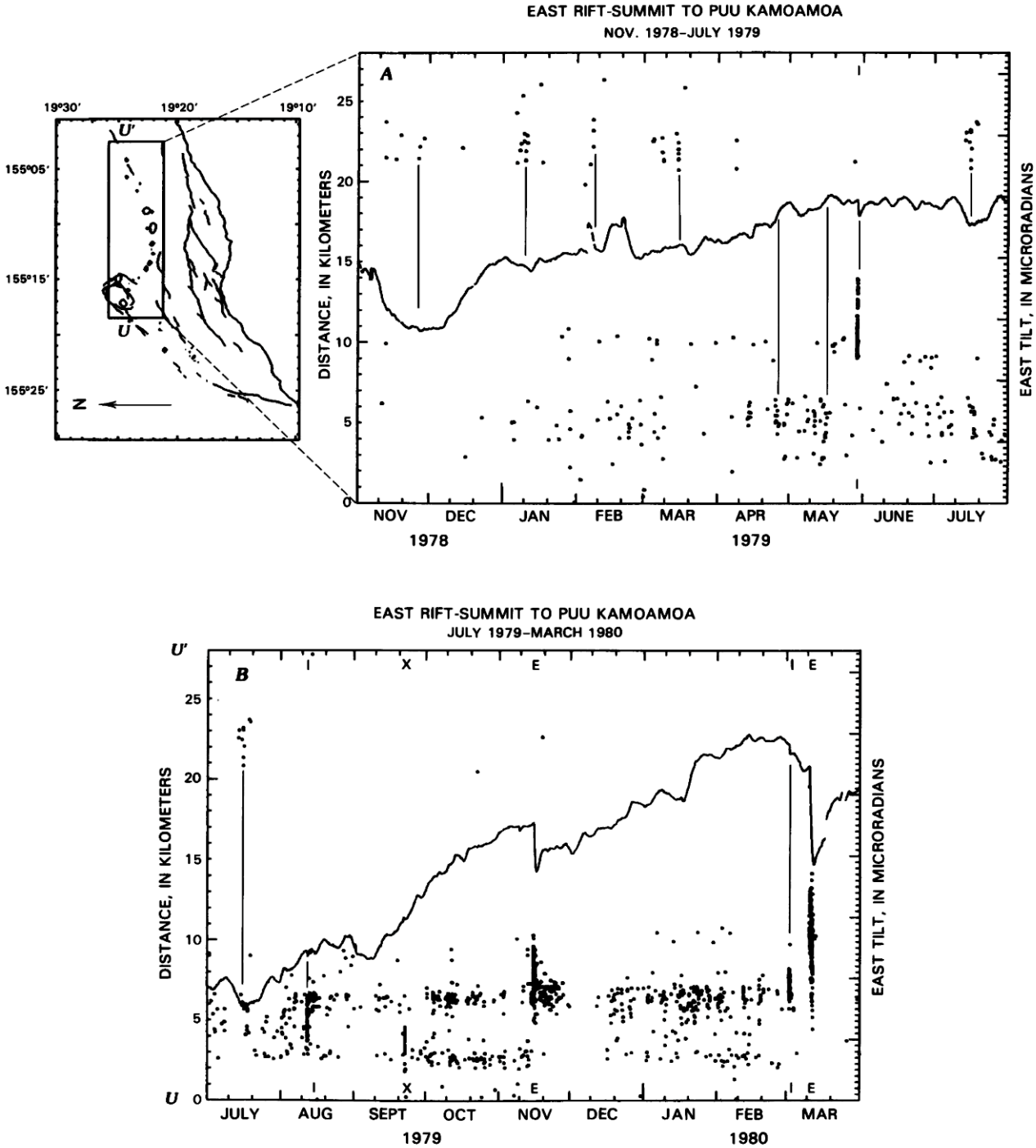


FIGURE 43.74.—Plot of earthquakes along east rift zone and east tilt at Uwekahuna versus time. ***A,*** November 1978 through July 1979. ***B,*** July 1979 through March 1980. ***C,*** March through November 1980. Plot shows changes of position of seismicity with time. Endpoints for distance axis *U-U'* are given in table 43.2. Tilt is from east-west Ideal Aerosmith tiltmeter, where east-down tilt is down on plot and generally indicates deflation of summit caldera. Large divisions on tilt scale are 10 μrad. Notations along time axis refer to specific swarms detailed in other figures: E, eruption; I, intrusion; X, swarm accompanying inflation. Vertical lines connect swarms or concentrations of earthquakes with corresponding changes in tilt. Mid-1980 was a period of oscillating tilt and alternating locations of seismicity corresponding to cyclic slow intrusions of the east rift zone.

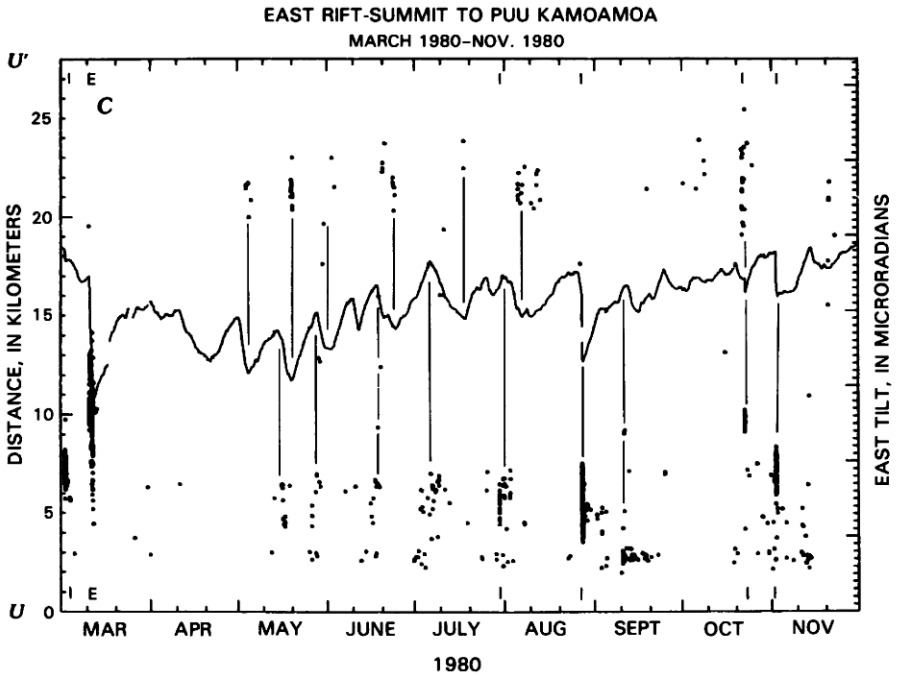


FIGURE 43.74.—Continued.

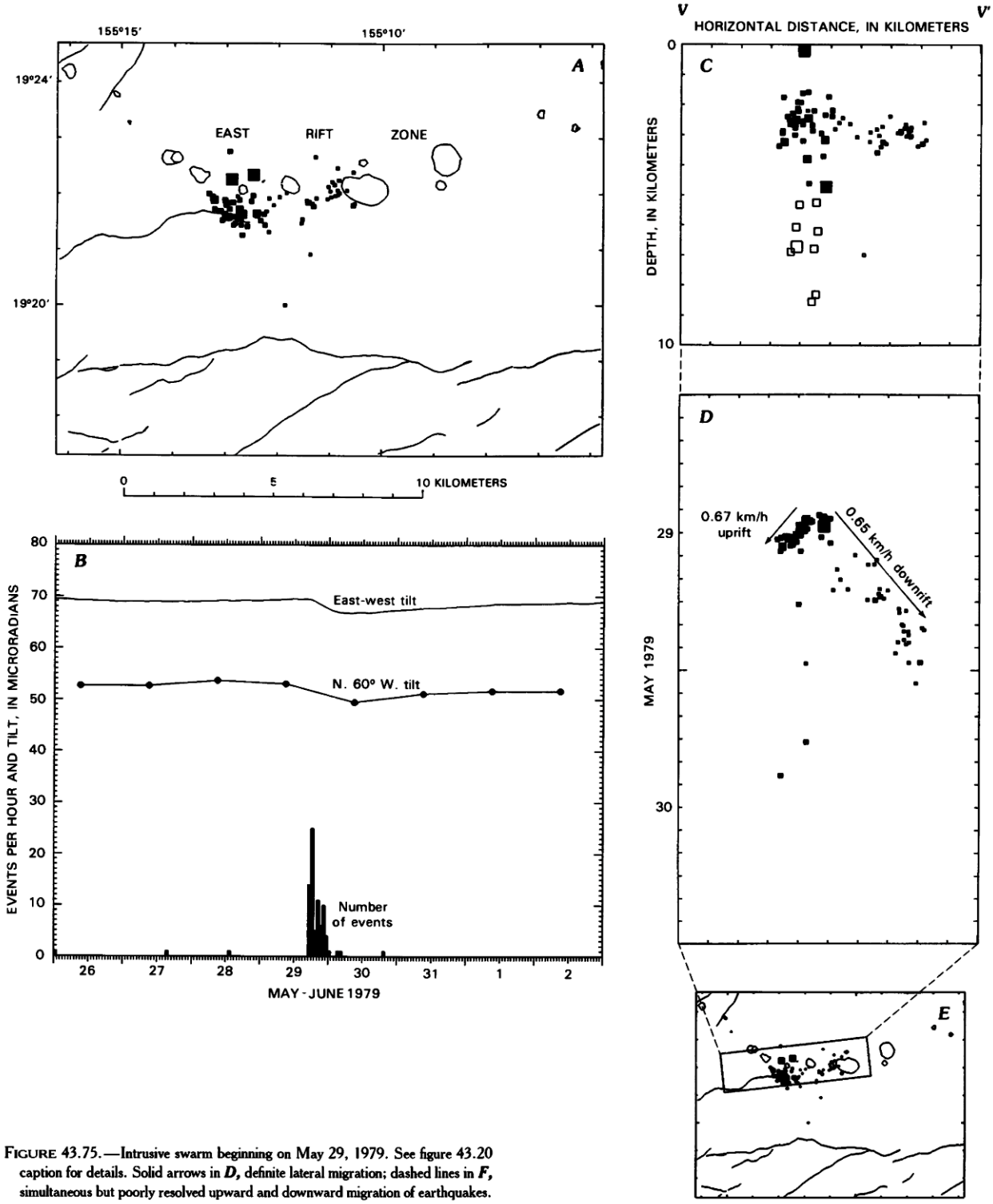


FIGURE 43.75.—Intrusive swarm beginning on May 29, 1979. See figure 43.20 caption for details. Solid arrows in *D*, definite lateral migration; dashed lines in *F*, simultaneous but poorly resolved upward and downward migration of earthquakes.

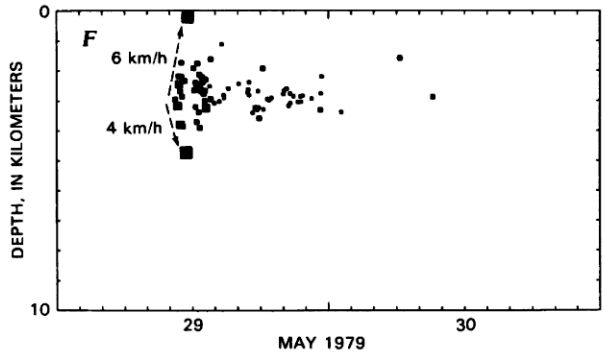


FIGURE 43.75.–Continued.

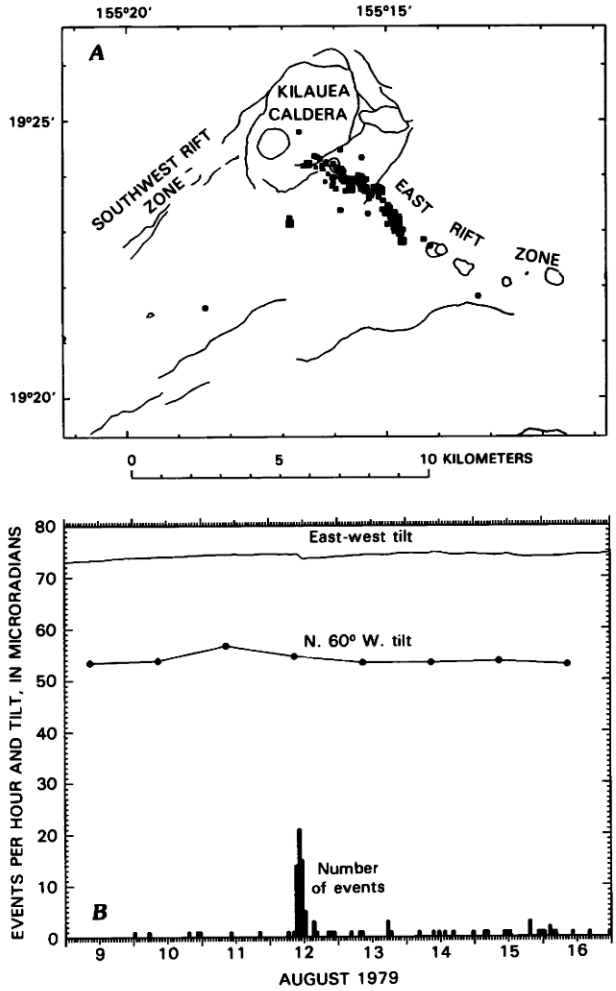


FIGURE 43.76.—Intrusive swarm beginning on August 12, 1979. See figure 43.20 caption for details. Solid line in ***D***, definite migration; short arrows in ***F***, possible additional downrift migration.

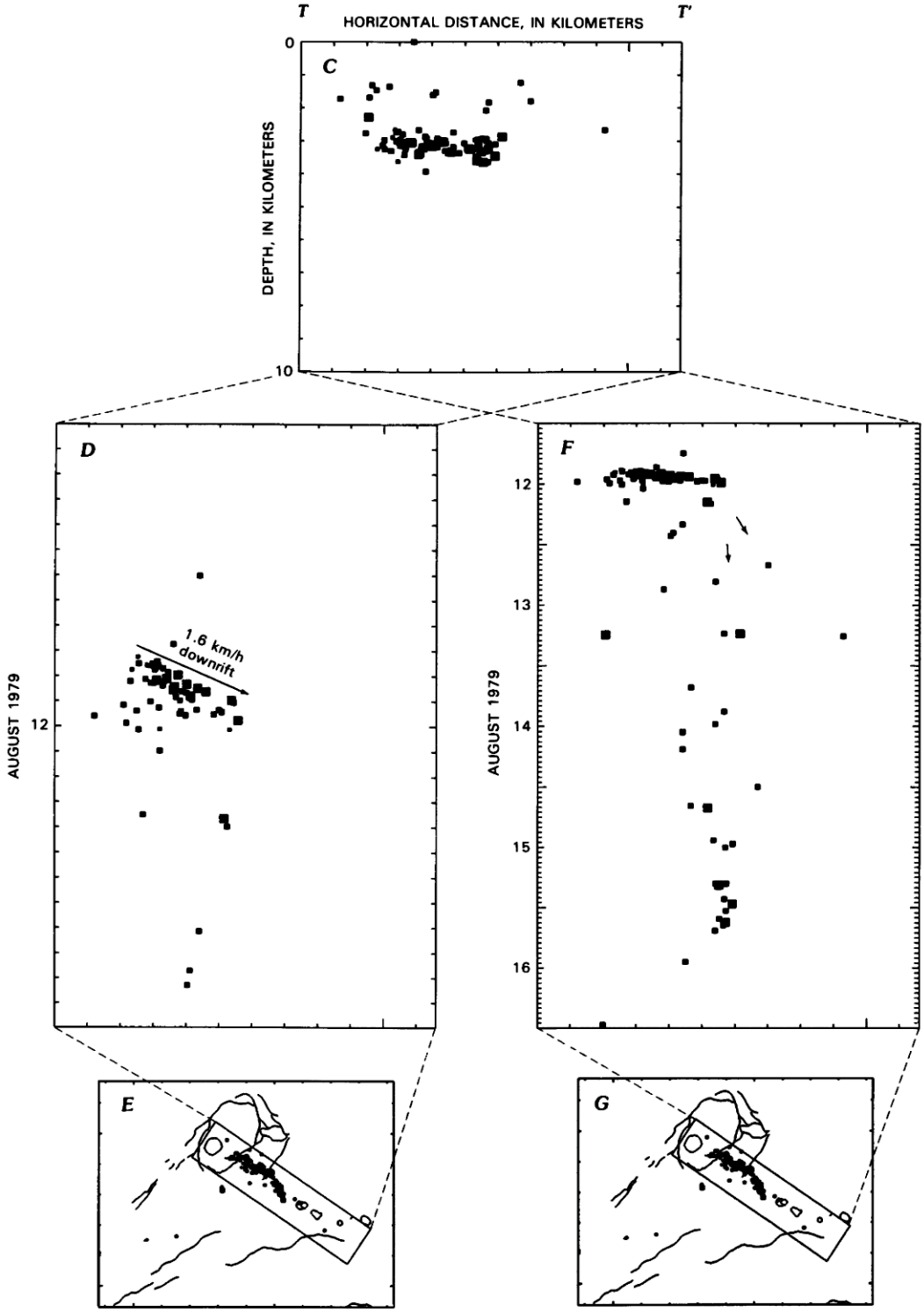


FIGURE 43.76.—Continued.

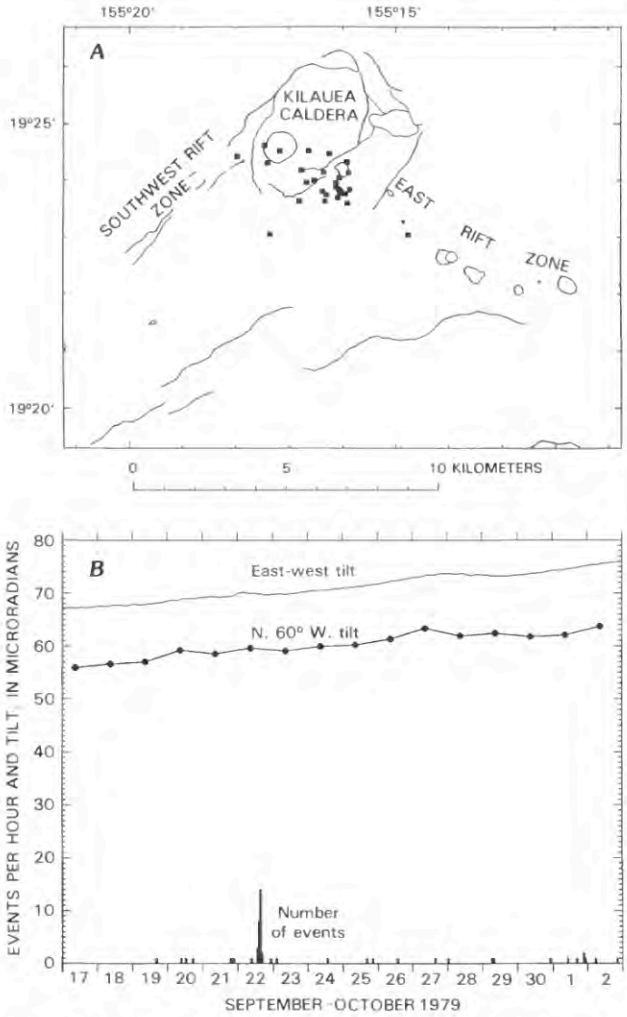


FIGURE 43.77.—Inflationary swarm beginning on September 22, 1979. See figure 43.20 caption for details.

## EAST RIFT ZONE INTRUSIONS OF MARCH 1980

The ERZ was very busy during 1980 and produced six rapid intrusions, one of which was apparently also a very small eruption. A condensed position versus time summary of the summit and ERZ seismicity is plotted in figure 43.74C. The first two intrusions in March and the last four in the last half of 1980 are readily identified by their intense swarms and sudden deflations in the summit tilt record. The other swarms during May through August were cyclic slow intrusions and will be discussed separately below.

The intrusions of March 1980 were only 8 days apart and successively activated adjacent sections of the ERZ. They appear to be causally related. The March 2 earthquakes were from Kokoolau to Pauahi (fig. 43.79*A*), and the March 10 swarm continued downrift from Pauahi nearly to Makaopuhi (fig. 43.80*A*). The March 2 intrusion was shorter in time, less in deflation, more compact spatially, smaller in earthquake magnitude, and less complex than the March 10 event. The March 2 swarm began about 1 km west of Pauahi where it was most active, but earthquakes soon moved uprift (fig. 43.79*D*).

The March 10 intrusion produced a complex earthquake pattern and apparently also erupted a few cubic meters of lava that was not noticed until after the event (Norman Banks, written commun., 1981). The intrusion began under Mauna Ulu, and earthquakes rapidly moved uprift at 1.8 km/h for about 2 km (fig. 43.80*D*) and upward at roughly 4 km/h (fig. 43.80*I*). The next earthquakes were between the former Alae crater and Makaopuhi, and they probably accompanied the tiny eruption. Next, a relatively slow movement of small earthquakes at 0.2 km/h westward along the rift and into the Koae occurred (fig. 43.80*D*, *G*). The halo of small earthquakes in the north and south flanks adjacent to the intrusion also diffused outward at this time. Before the swarm ended, a burst of earthquakes just south of the former Aloi crater moved downrift at 3 km/h in the same place as the first part of the swarm.

Clearly, a complex system of dikes and conduits were magmatically active in March 1980. We favor a scenario similar to the following, though many variations and possibilities may exist. During January and February 1980, Kilauea inflated and the accumulating magma produced earthquakes in the ERZ uprift of Pauahi (fig. 43.74*B*). Magma collected behind a blockage of the conduit, which also forms the uprift side of the magma pocket below Pauahi. The slowly rising magma pressure on the barrier eventually ruptured it, producing the March 2 swarm. This intrusion also drained a small volume of magma from the summit reservoir, which passed through the uppermost section of the ERZ conduit triggering a few earthquakes there.

The summit then deflated slowly and aseismically, sending magma to accumulate behind the next barrier in the conduit near Aloi crater. This second barrier was intruded by a dike on March 10, that moved upward and uprift from a point 3 km beneath Mauna Ulu. The resulting episode of rifting then moved both up and down the ERZ and was fed by summit magma for the 1.5-day duration of the swarm. The rifting and a possible small intrusion also penetrated the Koae fault zone. Magma collected on the uprift side of the Aloi blockage faster than it could pass through and thus triggered a second rupture through it, this time in the downrift direction. The amount of dike widening was significant over much of the length of the intrusion and induced small earthquakes as much as 3 km from the rift. The fact that earthquakes migrated in several directions and at different speeds requires rifting by various processes involving shifting stress and moving magma. This complexity also requires more than a single linear magma conduit, a conclusion reinforced by the range of earthquake depths in cross sections of this area.

The ERZ intrusions and eruptions of August and November 1979 and March 1980 each penetrated farther along the rift (fig. 43.74*B*). They may each have thus opened new sections of the rift conduit and prepared the rift for the passive intrusions of mid-1980.

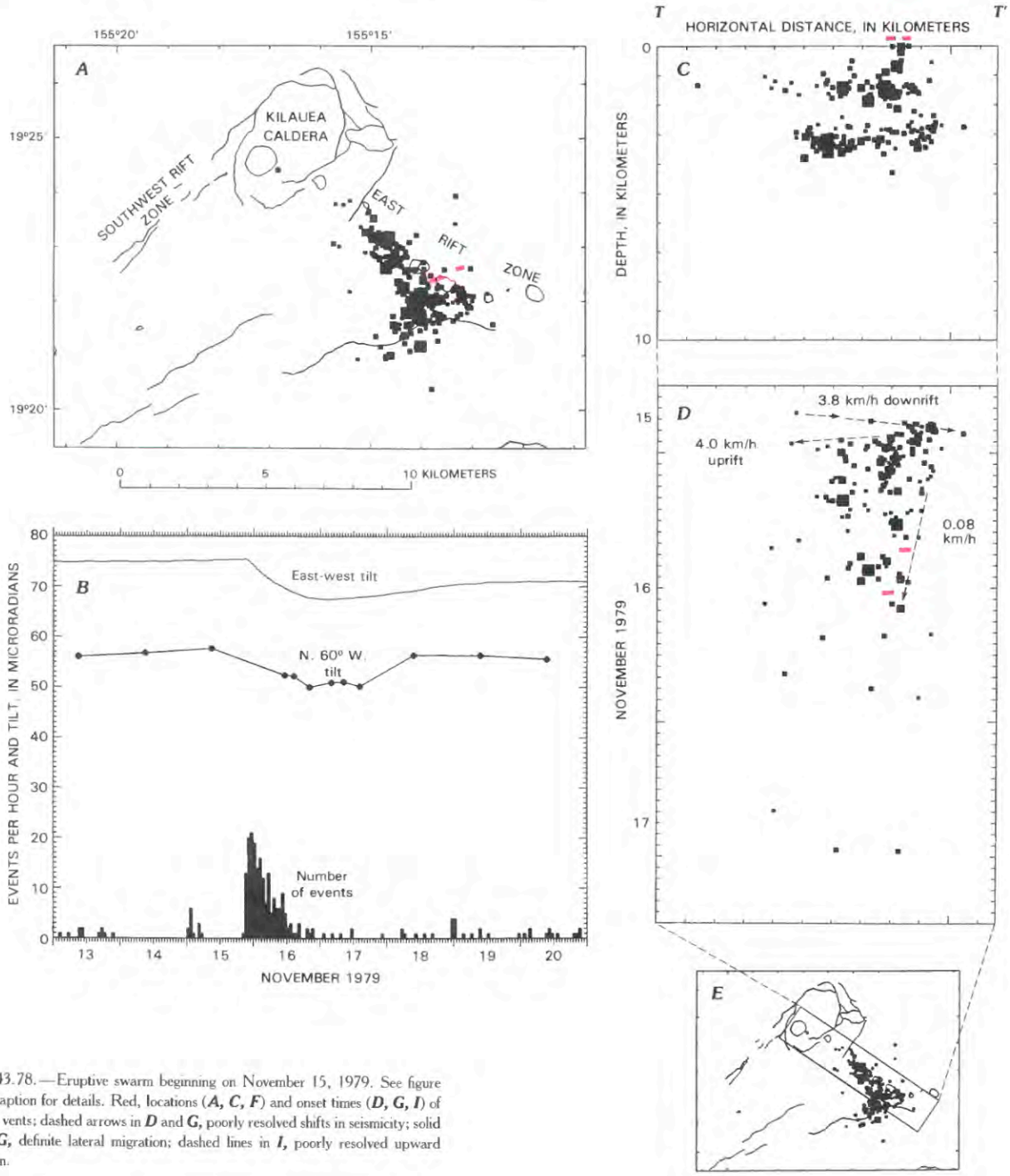


FIGURE 43.78.—Eruptive swarm beginning on November 15, 1979. See figure 43.20 caption for details. Red, locations (***A, C, F***) and onset times (***D, G, I***) of eruptive vents; dashed arrows in ***D*** and ***G***, poorly resolved shifts in seismicity; solid line in ***G***, definite lateral migration; dashed lines in ***I***, poorly resolved upward migration.

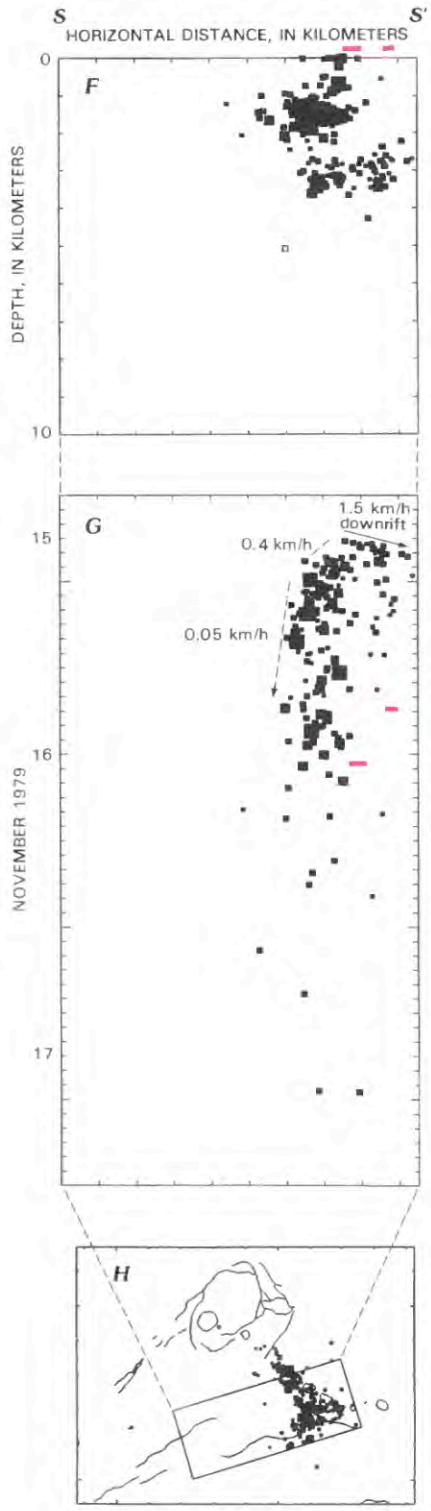


FIGURE 43.78.—Continued.

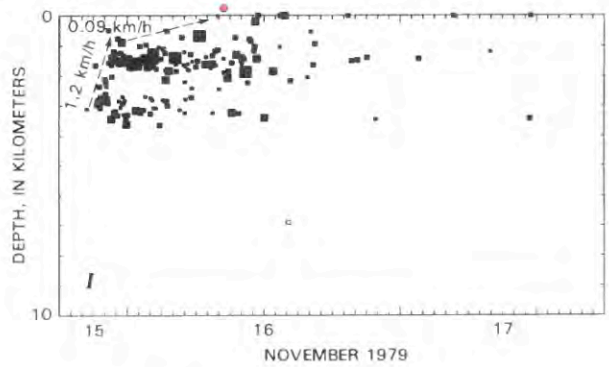


FIGURE 43.78.—Continued.

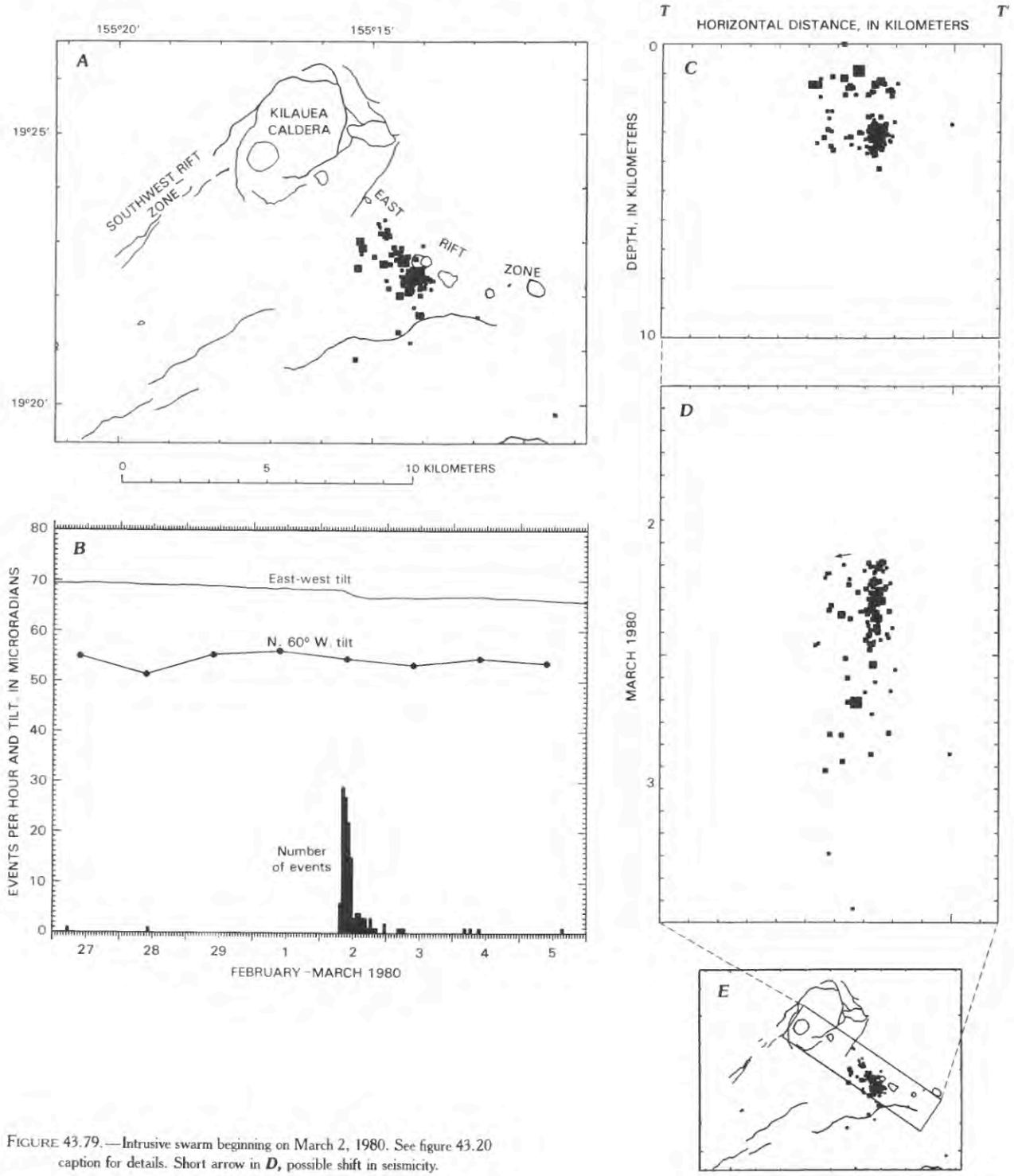


FIGURE 43.79.—Intrusive swarm beginning on March 2, 1980. See figure 43.20 caption for details. Short arrow in ***D***, possible shift in seismicity.

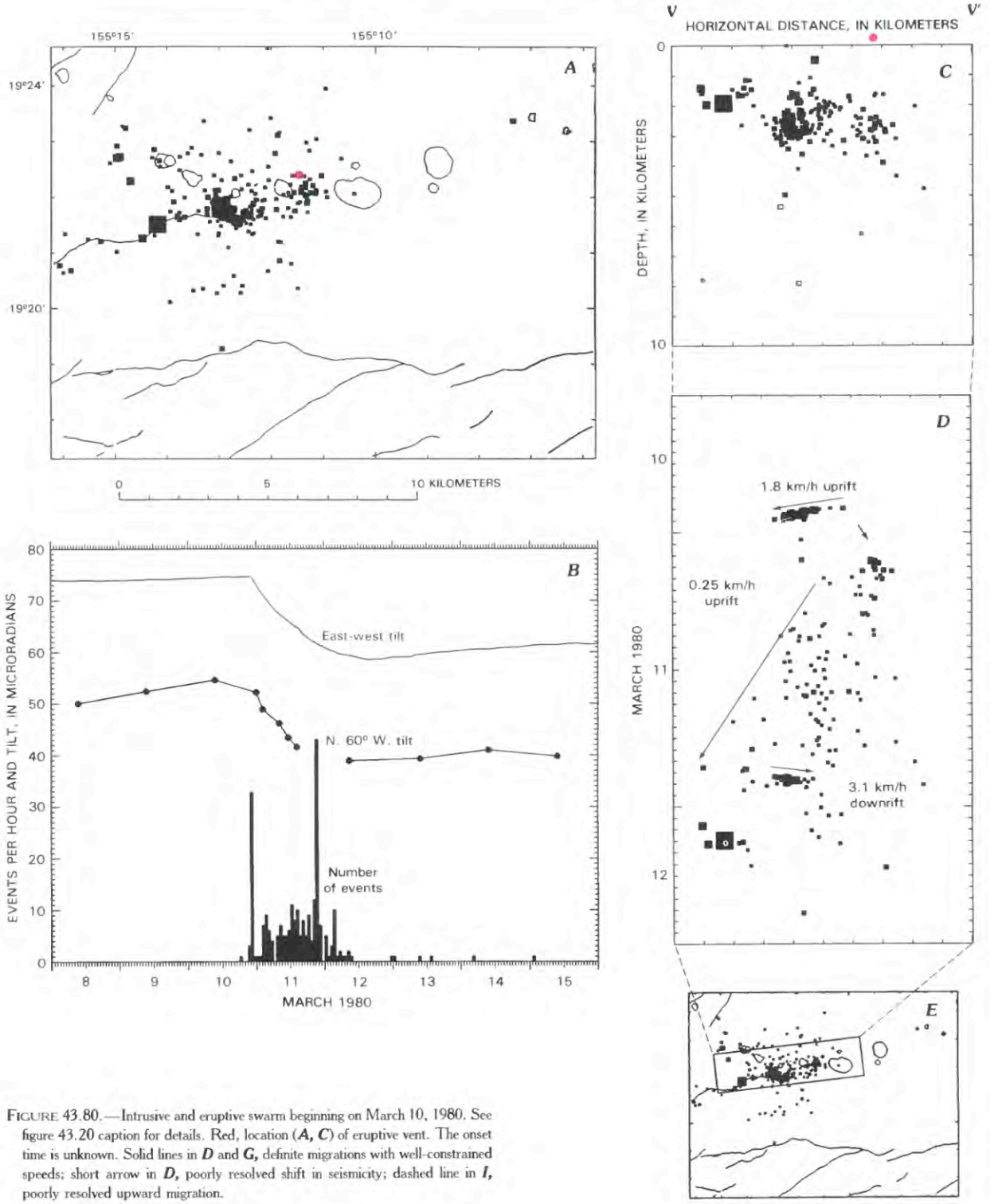


FIGURE 43.80.—Intrusive and eruptive swarm beginning on March 10, 1980. See figure 43.20 caption for details. Red, location (***A, C***) of eruptive vent. The onset time is unknown. Solid lines in ***D*** and ***G***, definite migrations with well-constrained speeds; short arrow in ***D***, poorly resolved shift in seismicity; dashed line in ***I***, poorly resolved upward migration.

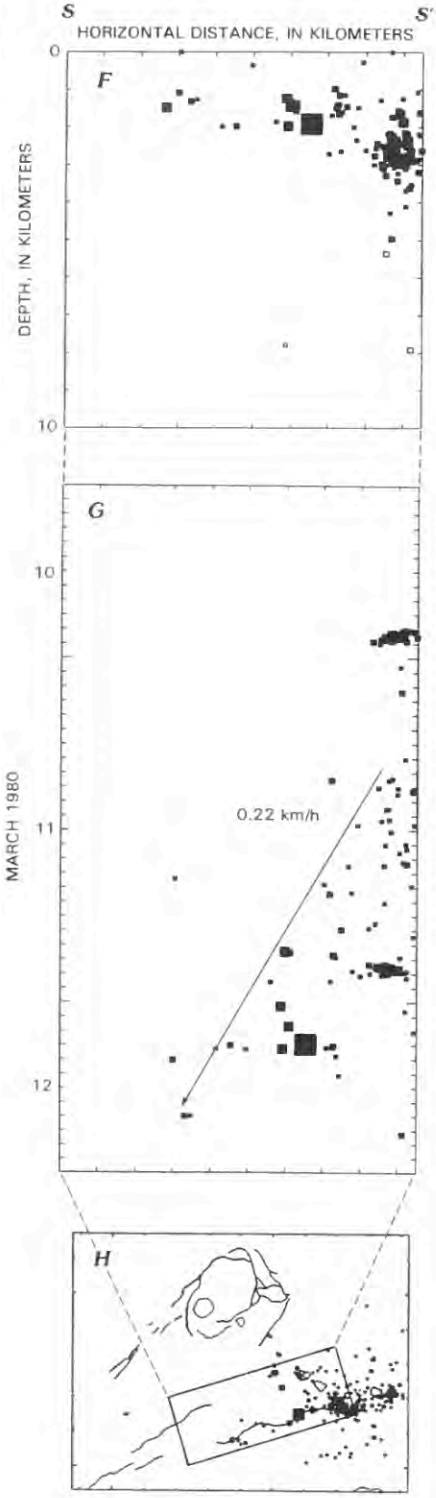


FIGURE 43.80.—Continued.

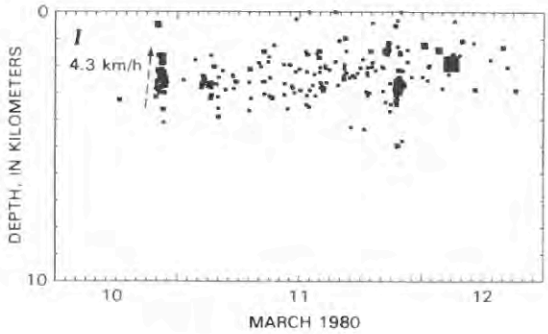


FIGURE 43.80.—Continued.

## CYCLIC EAST RIFT ZONE INTRUSIONS OF MAY–AUGUST 1980

After the March 1980 intrusions, Kilauea began an unusual mode of transferring magma from the summit reservoir to storage in a section of rift near Puu Kamoamoa. The intrusions were cyclic and at intervals more regular than other intrusive swarms. Kilauea inflated gradually for 5–10 days, then deflated at a similar rate for 5–10 days. The accumulating magma in the ERZ during mid-1980 and a similar episode in 1978–79 was measured by outward tilt from a linear zone of inflation (Dzurisin and others, 1984). The largest tilts were near Puu Kamoamoa and Kalalua, close to the shallow earthquakes. Dzurisin and others (1984) attributed the rift and summit tilt patterns to a passive and steady transfer of magma from summit to rift. We add the view that earthquake swarms at both summit and rift are variants of the inflationary swarms cataloged in this paper.

A cyclic pattern of magma transfer and oscillatory tilt may also be characteristic of successive episodes of eruption from the same vent, as during the early phases of the Mauna Ulu eruption in 1969–70 or the episodes of the Puu Oo eruption starting in January 1983. Unlike the symmetrical oscillations of tilt during the 1980 cyclic intrusions, the shape of the tilt curve for eruption phases is one of gradual inflation and sudden deflation. Both phenomena accompany a regular delivery of magma to the ERZ.

The cyclic intrusive pattern can easily be seen from the oscillatory tilt in figure 43.74C. The net gain in tilt during this period was very small. A slow swarm of caldera earthquakes generally coincided with peaks in the tilt, and similar swarms near

Puu Kamoamoa were at tilt minima. These swarms are very similar to but smaller than those accompanying inflation and slow intrusions. Caldera earthquakes signaled an inflated summit and ceased as magma drained downrift. Rift earthquakes were caused by local inflation of the rift and occurred while or just after magma was transferred there from the summit. The epicenters of events at the inflating rift can be seen in figure 43.3*B* as an elongate zone above the main magma conduit. One Puu Kamoamoa swarm (fig. 43.83*A*) occurred one day before another ERZ intrusion.

Similar episodes of shallow ERZ earthquakes near Puu Kamoamoa were observed from November 1978 to July 1979 (fig. 43.74*A*). These slow swarms also were generally at or just before minima in summit tilt. Episodes of summit earthquakes similar to those in 1980 were not apparent during this period, except possibly for earthquakes in April and May 1979 that coincided with brief intervals of rapid inflation (fig. 43.74*A*). The oscillations of tilt and an alternating pattern of earthquake locations did not develop as during the otherwise similar rift inflation of 1980. The rift dilation caused by the 1975 Kalapana earthquake and the ERZ eruption of September 1977 apparently opened most of the ERZ conduit and encouraged the passive magma transfer of 1978–79. Opening of the rift continued with the intrusions and eruptions of August and November 1979 and March 1980. Four additional but rapid ERZ intrusions in the latter half of 1980 apparently disrupted the delicate equilibrium of the magma conduit that permitted the regular cycles of slow intrusion in mid-1980.

## EAST RIFT ZONE INTRUSIONS OF JULY-NOVEMBER 1980

The ERZ intrusions of July, August and October 1980 successively penetrated farther along the rift, as did the intrusions of August and November 1979 and March 1980. The July 30, 1980 swarm lasted only for about one hour and activated only the 2-km section of rift between Keanakakoi and Puhimau (fig. 43.81). No deflation was detected, apparently because only a small volume of magma was transferred. Earthquakes began nearly instantaneously along the zone. The high speed of swarm growth is probably a result of the presumed high temperatures and lower magma viscosity where the rift conduit adjoins the summit reservoir.

The intrusion of August 27, 1980, reached an additional 3 km downrift to Hiiaka (fig. 43.82*A*). The swarm began 3 km below Puhimau where the July intrusion terminated. The initial intense seismicity moved downrift at 1.6 km/h and remained at 3 km depth (fig. 43.82*D*, *F*). As the main dike moved downrift, earthquakes also moved upward and uprift (fig. 43.82*D*). The dike had two horizontal lobes end-to-end at 3 km depth and a connecting vertical lobe (fig. 43.82*C*). Earthquakes propagated outward along each lobe from the initial center of activity. Summit reservoir deflation and the enlargement of all three seismic lobes were simultaneous. The uprift lobe may have fed magma to the dike system in the downrift direction, with earthquake migration opposite to magma flow. The process by which earthquakes can migrate uprift while magma flows downrift may be complex, but not impossible; for example, widening of an already open dike and the consequent earthquakes may begin from the end toward which magma is flowing and move against the flow direction as the dike fills.

The next intrusion on October 21–22, 1980, may actually have been two unrelated but nearly simultaneous events. The swarm beginning on October 21 near Puu Kamoamoa is apparently one of the last of the slow intrusions recurring from 1978 through 1980. The second intrusion occurred one day later and 14 km uprift of Puu Kamoamoa below the former Alae crater (fig. 43.83*A*, *E*). The Puu Kamoamoa swarm happened at a broad minimum in summit tilt typical for these slow intrusions (fig. 43.74*C*). The rapid deflation and more intense seismicity of the Alae swarm were on a much shorter time scale (fig. 43.83*B*, *D*). The second swarm was very compact (1.5-km diameter) and short (3 hours), but movement with time could be resolved. The downrift speed of 2.7 km/h (fig. 43.83*H*) and upward speed of about 2 km/h (fig. 43.83*J*) are consistent with the dip of the main finger of earthquakes seen in cross section (fig. 43.83*G*). The October 22 event appears to be a dike intruded into the rift blockage just downrift of the Pauahi magma pocket. Magma feeding the Puu Kamoamoa inflation probably traveled through a different rift conduit several days earlier, although a local increase in magma pressure could have triggered the second intrusion.

The October intrusion was followed in 11 days by another on November 2, 1980, just 2–3 km uprift (fig. 43.84*A*). The swarm was very intense but lasted only 4 hours. It began just uprift of Hiiaka and expanded downrift at 0.7 km/h (fig. 43.84*D*). Earthquakes also moved uprift, but only for about 1 km. No consistent depth migration can be seen, but earthquakes did spread up and down from 3 km depth (fig. 43.84*F*). Apparently a dike grew outward from a point near the main ERZ magma conduit. This intrusion was the last of a series of ERZ intrusions before Kilauea shifted its magma supply to the SWRZ.

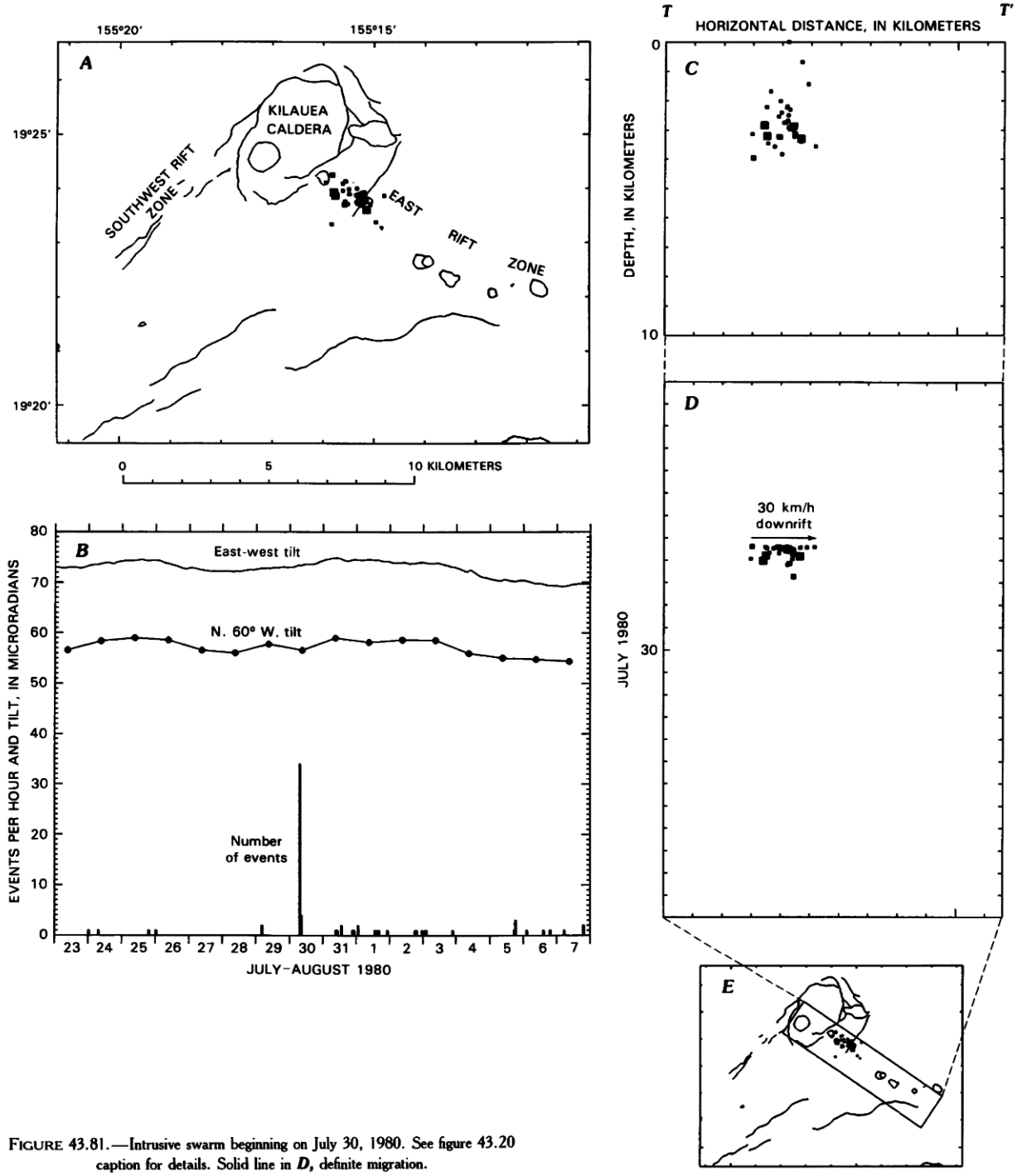


FIGURE 43.81.—Intrusive swarm beginning on July 30, 1980. See figure 43.20 caption for details. Solid line in *D*, definite migration.

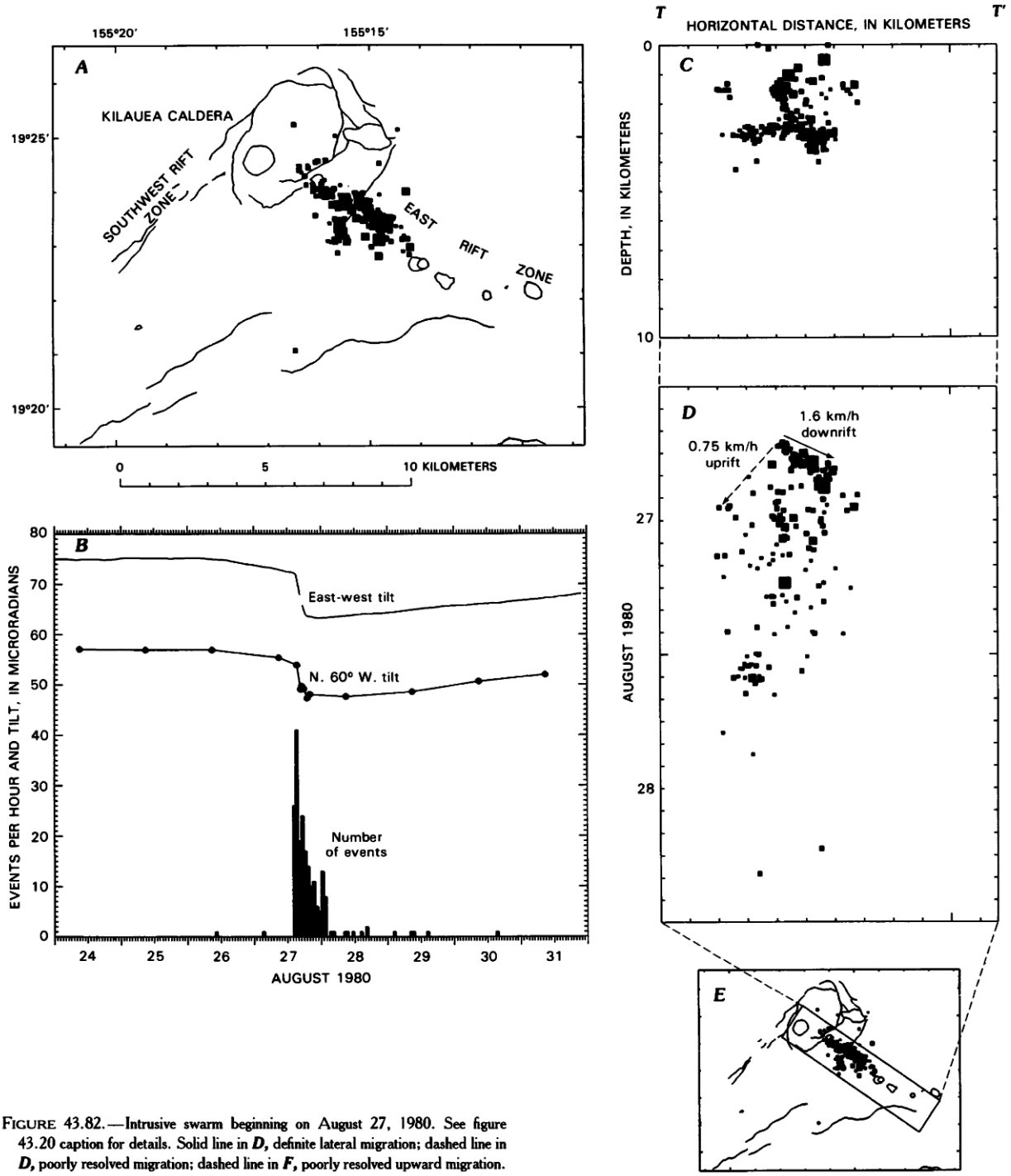


FIGURE 43.82.—Intrusive swarm beginning on August 27, 1980. See figure 43.20 caption for details. Solid line in *D*, definite lateral migration; dashed line in *D*, poorly resolved migration; dashed line in *F*, poorly resolved upward migration.

FIGURE 43.82.—Continued.

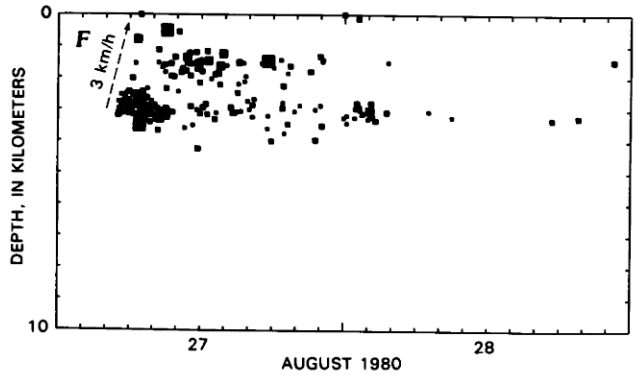


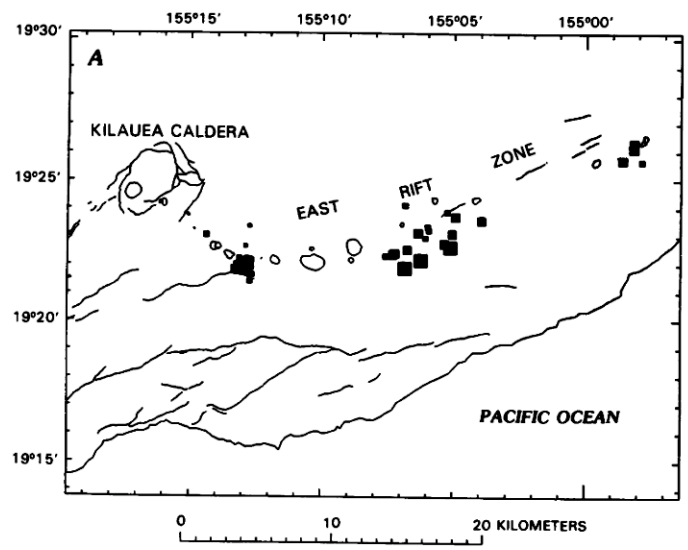


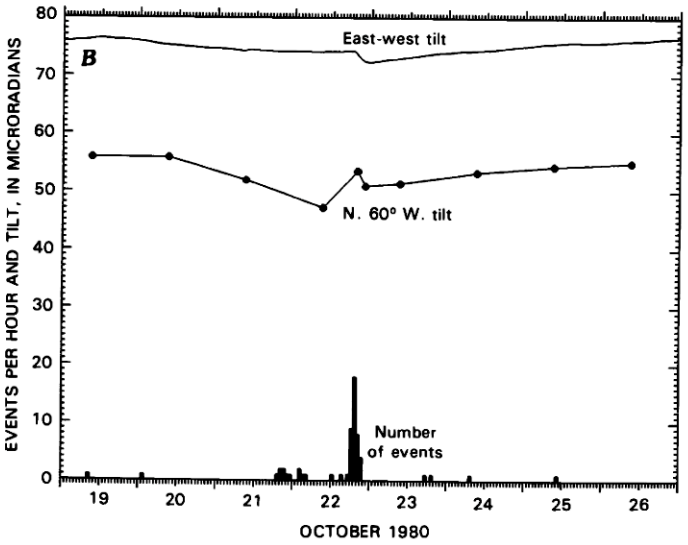


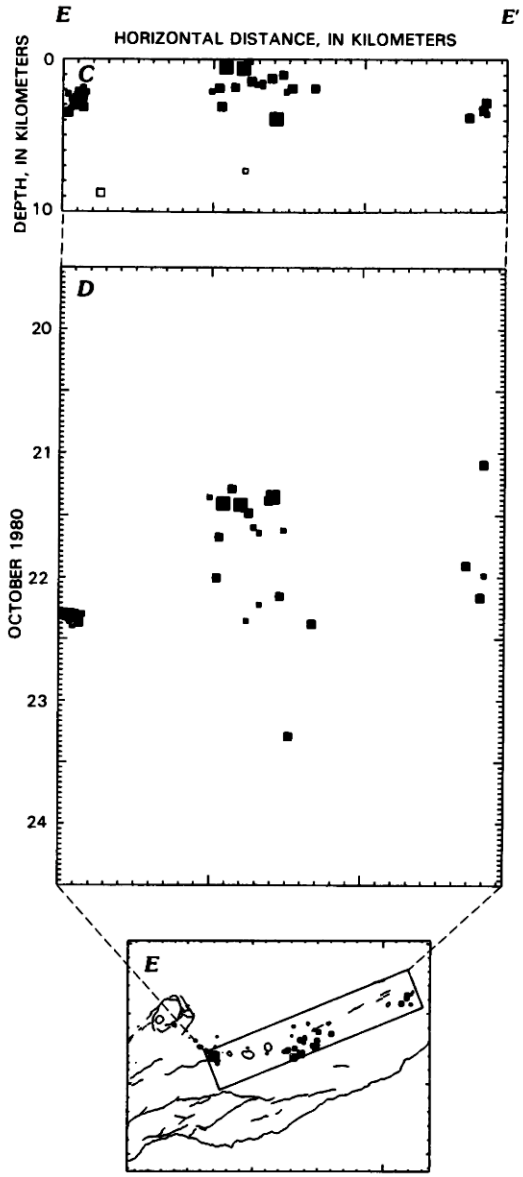


FIGURE 43.83.—Intrusive swarm beginning on October 21, 1980. See figure 43.20 caption for details. Solid line in *H*, definite lateral migration; dashed line in *J*, poorly resolved upward migration.

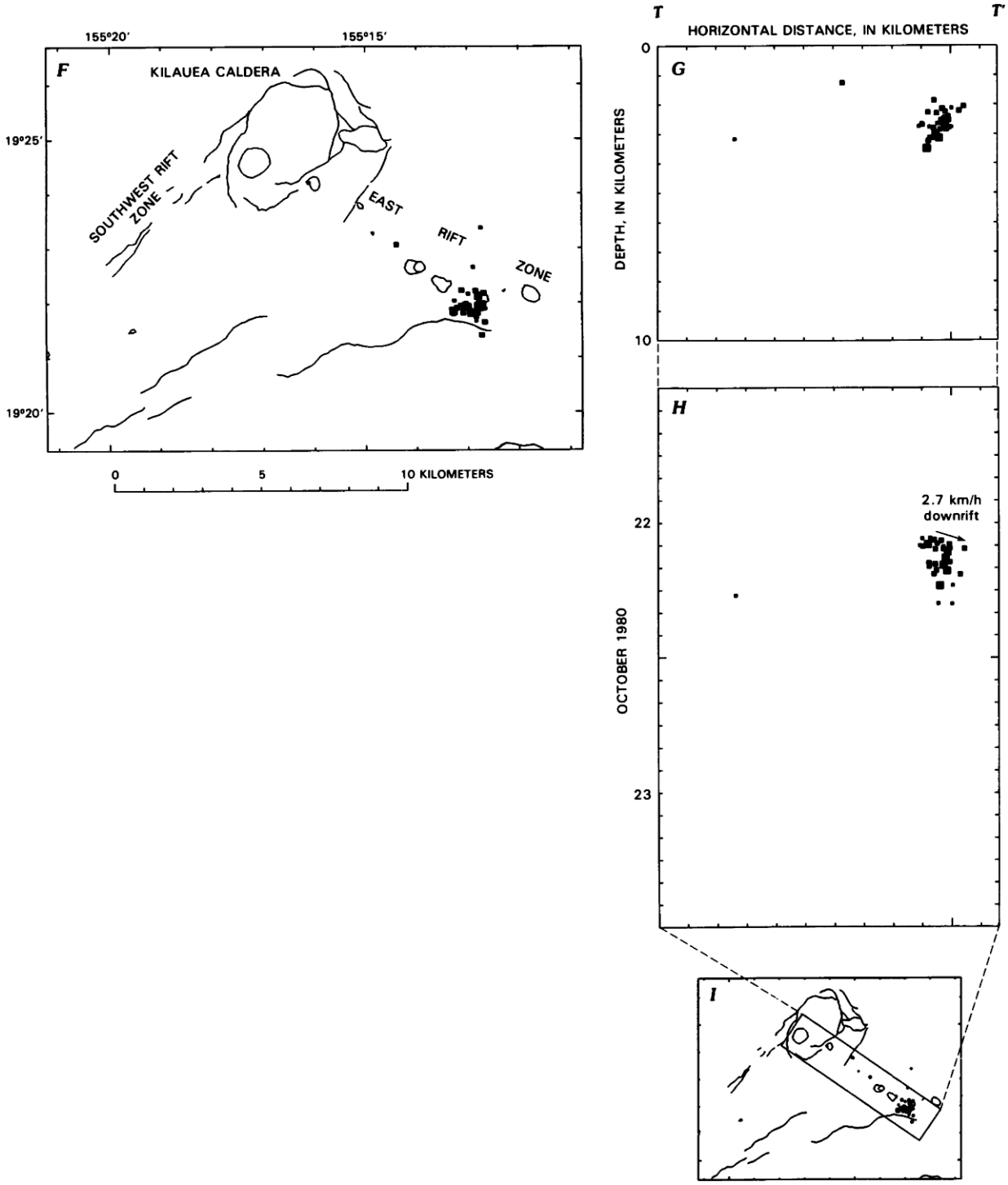


FIGURE 43.83.—Continued.

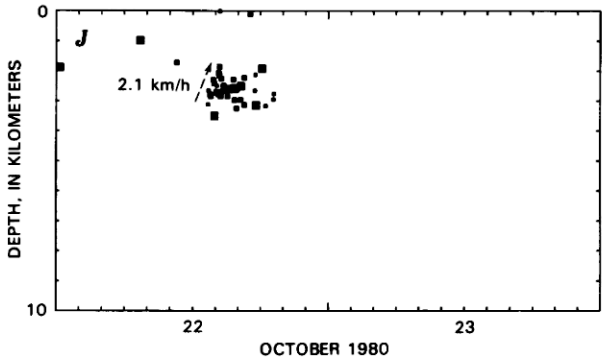


FIGURE 43.83.—Continued.

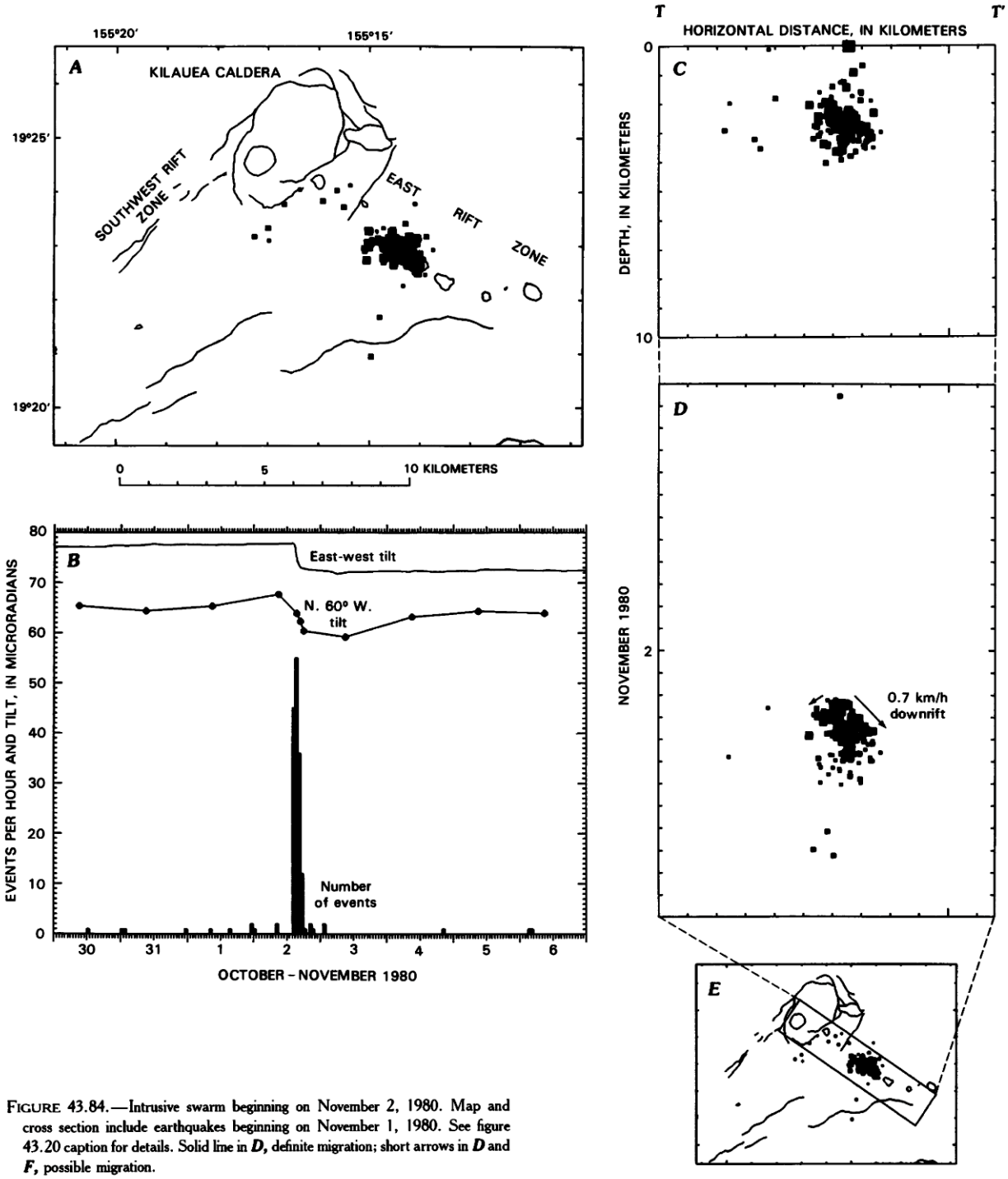


FIGURE 43.84.—Intrusive swarm beginning on November 2, 1980. Map and cross section include earthquakes beginning on November 1, 1980. See figure 43.20 caption for details. Solid line in *D*, definite migration; short arrows in *D* and *F*, possible migration.

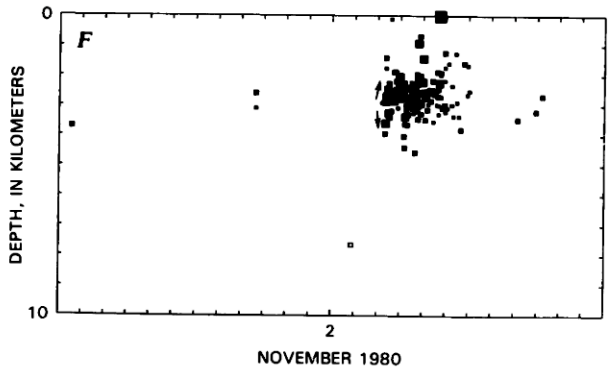


FIGURE 43.84.—Continued.

## SOUTHWEST RIFT ZONE INTRUSIONS AND CALDERA ERUPTION OF JANUARY–AUGUST 1981

From January 1981 to mid-1982, Kilauea focused most of its magmatic activity on the SWRZ. Figure 43.85 summarizes the positions of shallow SWRZ earthquakes and summit tilt during this 18-month period. Three major intrusions occurred; the first penetrated the SWRZ in three progressive steps in January and February 1981, and continued to slowly pass magma into the SWRZ through June. The prolonged nature of this first intrusion did not require a major summit deflation. The other two intrusions in August 1981 and June 1982 followed a more conventional pattern of rapid summit deflation during a brief earthquake swarm, followed by reinflation of the summit reservoir.

The first phase of the January–February intrusion began on January 20, 1981, with a compact swarm in the main SWRZ magma conduit just south of the caldera (fig. 43.86*A*). No measurable deflation accompanied this first phase, and in fact Kilauea was inflating at this time (figs. 43.85*A*, 43.86*B*). Earthquakes did not migrate downrift, but did spread slowly north into the caldera as the seismic zone enlarged (fig. 43.86*D*). This phase was apparently the breaking open of a part of the magma passageway in response to inflation of the summit reservoir, but very little magma volume was actually intruded. Had it not been associated with the subsequent SWRZ intrusion and also produced so many earthquakes in a short period of time, this event may have been mistaken for a typical inflationary swarm.

The intrusion's second phase began on January 24 and demonstrated that a slow intrusion was in progress. Earthquakes now extended an additional 3 km along the rift in a zone including the bend in the magma conduit (fig. 43.87*A*). The deflation and earthquake rates were several times slower than in typical rapid intrusions (fig. 43.86*B*). Earthquakes began almost simultaneously along the seismic zone, which remained uniformly active for 3–4 days (fig. 43.87*C*). This time behavior suggests that a section of the magma conduit filled slowly enough that its expansion was very uniform and without a fast-moving stress concentration such as the tip of a new dike. This pattern is consistent with earlier observations that the sections of rift adjacent to the caldera are often in direct magmatic communication and inflate with the summit reservoir. The January 20 swarm thus accompanied the breaking of a barrier and slow intrusion of the uppermost 5 km of the SWRZ during January 24–27.

The next phase of the intrusion began when magma moved almost aseismically down the SWRZ and generated a swarm near Puu Kou (fig. 43.88*A*). The sparse seismicity between the caldera and terminus of the intrusion seems to result from the low deflation rate (fig. 43.88*B*) and probable accommodation of magma flow through an existing conduit without additional rifting. The intrusion apparently stopped at a blockage of the conduit where the rift axis bends just north of the Great Crack. The main seismic zone tilts upward (fig. 43.88*C*), suggesting that the magma conduit began rising up and over the barrier until it lacked sufficient pressure to overcome it. The slowing expansion of the seismic zone upward and downrift (fig. 43.88*D*, *F*) would also be expected if the dike encountered a dipping barrier.

The unusual nature of the January SWRZ intrusion is underscored by the continuing seismicity along the rift through the first half of 1981. After the initial intrusion in January and February, earthquakes persisted in the Puu Koae, Mauna Iki and Puu Kou areas through June (fig. 43.85*A*). The positions of earthquakes can be related to summit tilt to infer where magma accumulated during this period. The initial major deflation in February caused caldera earthquakes to stop for about two months, but they returned during the very slow reinflation in April. Their numbers increased as tilt rate accelerated in July. The seismicity of the rift was complementary to that in the caldera, and the pattern paints the following picture. In February and March, all of Kilauea's magma supply was directed into the SWRZ: the summit did not inflate and all earthquakes were downrift and caused by the intruded magma. In April, May and June very slight inflation occurred, a partial shift of seismicity back to the caldera was evident, and a fraction of the magma supply remained in the summit reservoir. The intrusion stopped in July, and typical inflation and earthquakes returned to the summit. This period illustrates the coincidence of falling or level tilt and rift seismicity during intrusions, and rising tilt and caldera earthquakes during inflation.

The passage of magma down the SWRZ was somewhat episodic: migrating pulses of earthquakes and hence magma may be discernable (dashed lines in fig. 43.85*A*). The speeds of these pulses ranged from about 0.12 km/hr (3 km/d) to 0.024 km/h (0.6

km/d), which are comparable to the speeds of other slow intrusions discussed in this paper. Kilauea's reinflation during July, combined with the opening and heating of the SWRZ magma conduit during the previous six months, apparently combined to permit the rapid intrusion in August 1981.

Just as before the January 1981 intrusion, earthquakes and magma leaked into the rift as a prelude to the August intrusion. Earthquakes slowly expanded into the SWRZ during July as the summit inflated (fig. 43.85*A*). A pre-intrusion also extended 5 km from the caldera on August 2 (fig. 43.89*A*). This pre-intrusion was scarcely noticed because no increase in earthquake activity or significant deflation was recognized (fig. 43.89*B*), only a shift in epicenters down the SWRZ (fig. 43.89*D*). The slight deflation suggests that some magma did move into the rift, but when this pre-intrusion reached the blockage in the magma conduit 5 km from the caldera, magma backed up and rapid inflation began, triggering the main intrusion on August 10. This pattern is very similar to that in January.

The intrusion on August 10 began with earthquakes just south of the caldera, which rapidly spread both into the caldera and downrift (fig. 43.90*D*). Some of the initial seismicity moved from the rift conduit at 3 km depth back and up over the magma reservoir (fig. 43.90*C*, *D*, *F*). The swarm soon engulfed the SWRZ from Halemaumau to Puu Kou (fig. 43.90*G*). The rapid downrift speed of 2.6 km/h slowed near the Kamakaia Hills by a factor of 10 to only 0.28 km/h (fig. 43.90*I*). The tilt rate slowed dramatically when the dike front reached Puu Kou on August 11 (fig. 43.90*B*). Earthquakes persisted mainly in the Puu Kou and Mauna Iki areas for about 5 days (fig. 43.90*K*). The seismicity near Mauna Iki actually spread back uprift. This uprift migration may have resulted from a wave of back pressure in the conduit produced when the downrift migration stopped. Earthquakes also continued in the caldera for about 5 days and were mostly long-period events associated with the subsidence and adjustment of the reservoir and its feeder conduit.

Many earthquakes were in dense clusters along the rift (fig. 43.90*G*, *H*). We associate these clusters with constrictions and barriers in the magma conduit. The passage of magma at these places thus required either formation of a new dike or the widening of an existing conduit too narrow to accommodate the magma flow. Either process causes earthquakes. Note that the terminus of the pre-intrusion on August 2 about 3 km east of Puu Koae was very active then, but nearly aseismic during the August 10 intrusion (compare fig. 43.89*A* and 43.90*A*). Apparently this area had already rifted open, allowing the main intrusion to pass through aseismically.

Although the intrusion deepened with distance from the caldera, a cluster of earthquakes at only 1 km depth were seen just southwest of Puu Koae (fig. 43.90*H*). These shallow earthquakes were below the surface cracks produced by the intrusion. Both phenomena were apparently the result of an upward-branching dike from the main conduit that did not quite reach the surface. A plane joining the area of surface cracks and the main seismic conduit dips about 80° SE. This dip matches the shape of the seismic conduit in this area seen in cross section (fig. 43.19*E*, *F*) and the dip of the intruded dike deduced from leveling lines crossing the rift (Dvorak and others, 1983).

Comparing the August 1981 intrusion with others in the SWRZ is informative. The August intrusion was much faster and more energetic than the one in January–June, perhaps because the earlier intrusion opened and heated the magma conduit making subsequent intrusions easier. The migration rate in August was double that of the December 1974 intrusion, probably again because of the prior intrusive activity in 1981. Both the 1974 and 1981 intrusions activated the same section of rift, and both produced an apparent reflection from the intrusion terminus of earthquakes migrating back uprift. The 1974 intrusion was about 50 percent larger in magma volume and produced more earthquakes, especially in the flank south of the rift. The reduced flank seismicity in 1981 may have resulted from the intrusion's smaller size, a different distribution of emplaced magma, or release of compressive stress in the flank in 1975 during the intervening Kalapana earthquake.

The geometry of the August 1981 dike can be estimated from the observed rates of deflation and earthquake migration. Using a deflation rate of 11 μrad/h at the time of the 2.6-km/h migration yields a cross-sectional area of $(11/3)/2.6\times1000=1{,}500$ m$^2$. A dike averaging 1.5 km by 1 m is consistent with earthquake migration speed and depth range and with deflation and geodetic observations. Pollard and others (1983) used a profile of surface displacements to constrain an elastic model of deformation surrounding a new dike. They inferred a dike dipping 82° SE., which is consistent with the dip of the seismically defined conduit of figure 43.14*F*. Their solution of a 1-m-thick dike extending from 0.25 to 2.75 km depth fits the surface profile everywhere except the central 3 km over the dike, where inelastic deformation occurred. Their cross-sectional area of 2,500 m$^2$ may include a shallow portion of the rift that grew aseismically and inelastically and that did not participate in the magma flow reflected in our 1,500-m$^2$ area.

The volume of intruded magma in August 1981 was about 35 million cubic meters, using the observed deflation and the value of 0.3 million cubic meters per microradian of Uwekahuna tilt from Dzurisin and others (1984). The August 1981 volume is comparable to that of the January-June intrusion. The tilt was nearly flat for the earlier period, so Kilauea's magma supply rate of about 9 million cubic meters per month (Swanson, 1972; Dzurisin and others, 1980) was mostly supplied to the SWRZ. Thus about 45 million cubic meters was supplied to the rift during the 5 months of the intrusion, but at a rate 100 times slower than in August.

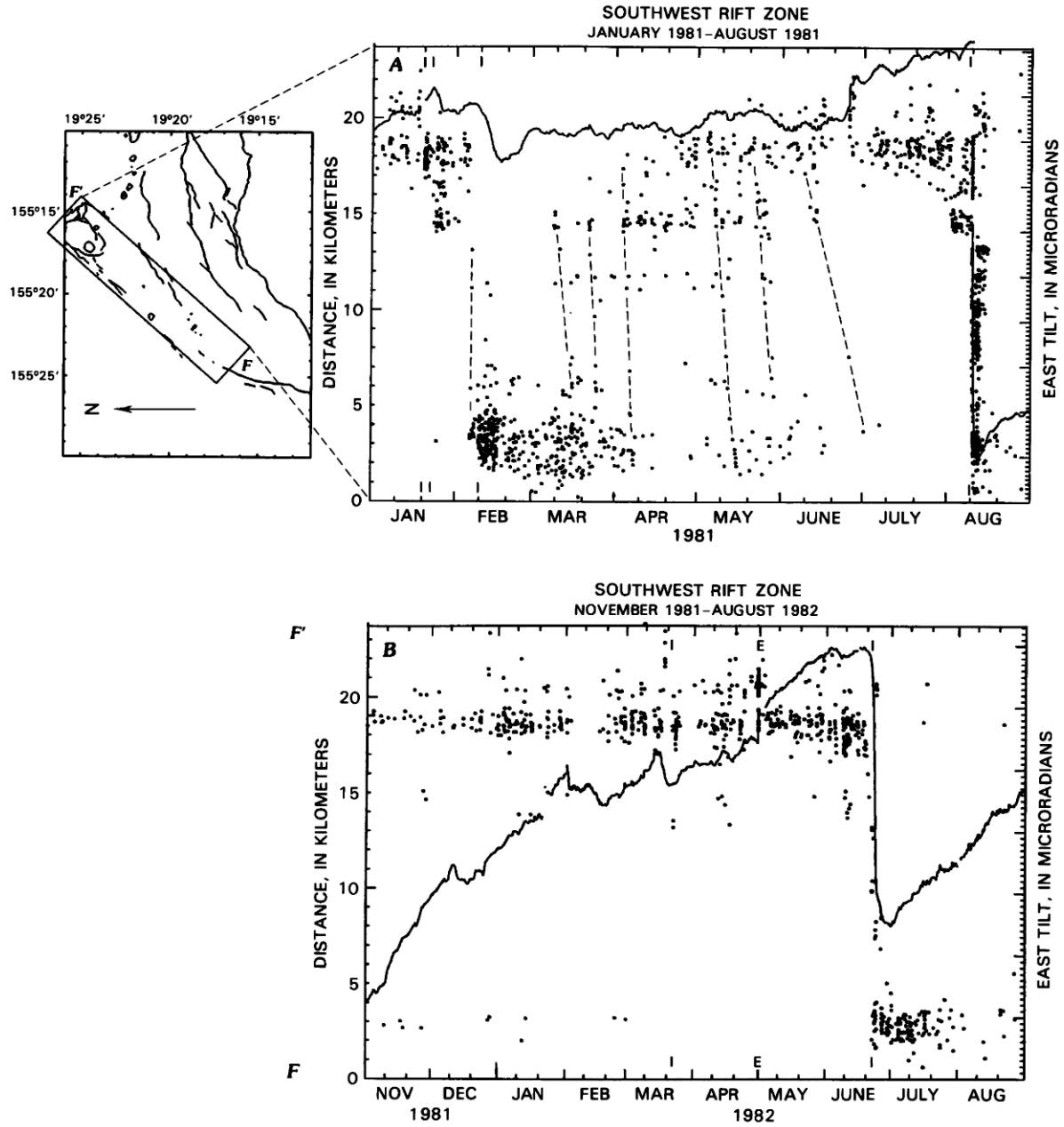


FIGURE 43.85.—Plot of earthquakes along the southwest rift zone and east tilt at Uwekahuna versus time. ***A***, January through August 1981. ***B***, November 1981 through August 1982. September and October 1981 are omitted and were a seismically quiet time of reinflation. All earthquakes shallower than 5 km and within geographic box shown are plotted. Kilauea caldera is at top and Puu Kou is near bottom. Tilt is from Ideal-Aerosmith instrument and down on plot generally indicates deflation of summit caldera. Notations along time axis refer to specific swarms detailed in other figures: E, eruption; I, rapid intrusion. Dashed lines in *A* suggest individual intrusive pulses.

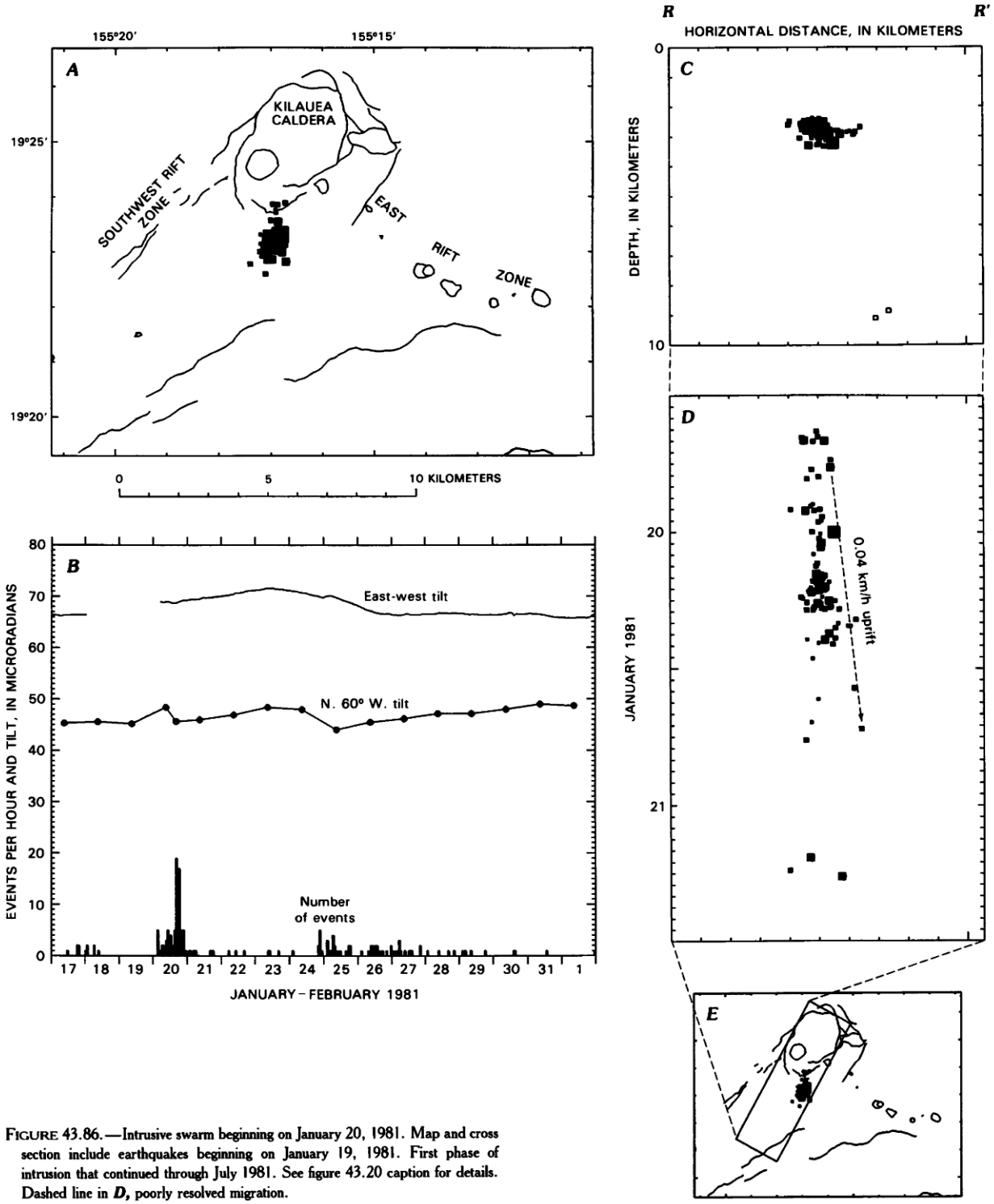


FIGURE 43.86.—Intrusive swarm beginning on January 20, 1981. Map and cross section include earthquakes beginning on January 19, 1981. First phase of intrusion that continued through July 1981. See figure 43.20 caption for details. Dashed line in *D*, poorly resolved migration.

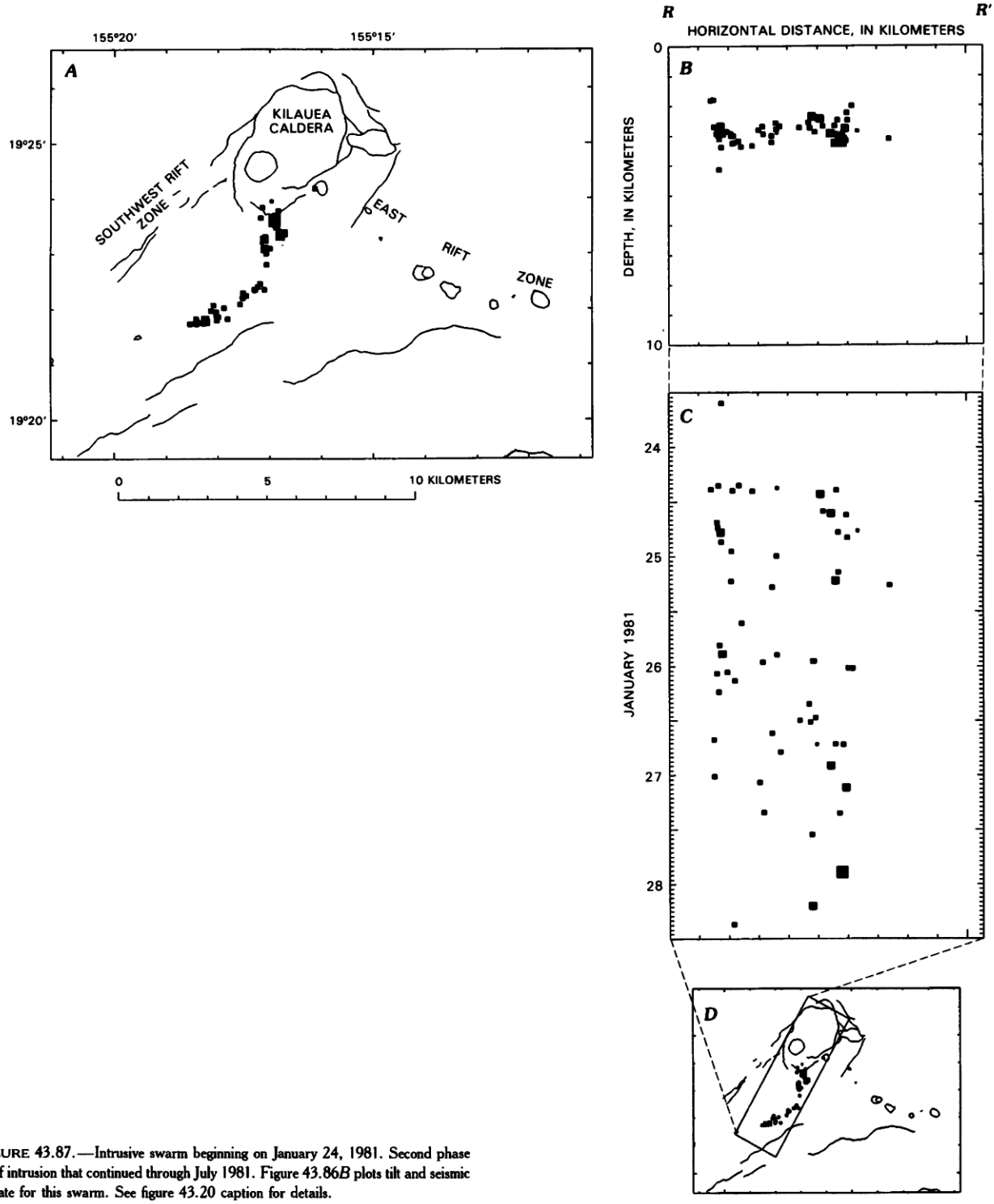


FIGURE 43.87.—Intrusive swarm beginning on January 24, 1981. Second phase of intrusion that continued through July 1981. Figure 43.86*B* plots tilt and seismic rate for this swarm. See figure 43.20 caption for details.

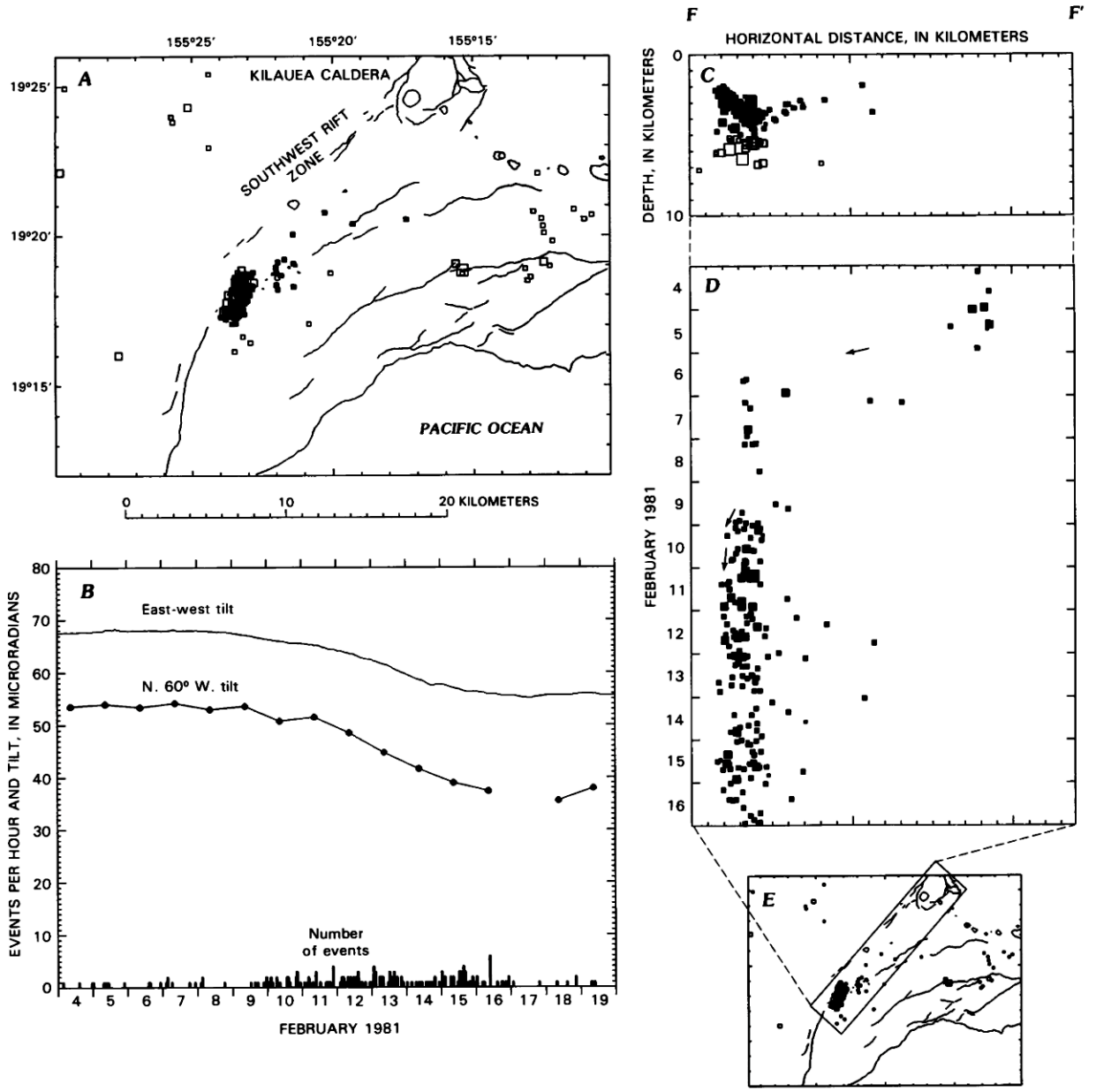


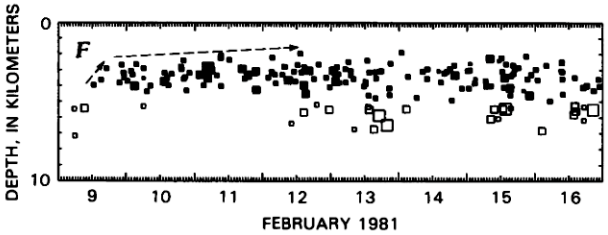


FIGURE 43.88.—Intrusive swarm beginning on February 9, 1981. Largest phase of intrusion during January–July 1981. See figure 43.20 caption for details. Short arrows in *D*, possible shift in seismicity; dashed arrow in *F*, poorly resolved upward migration.

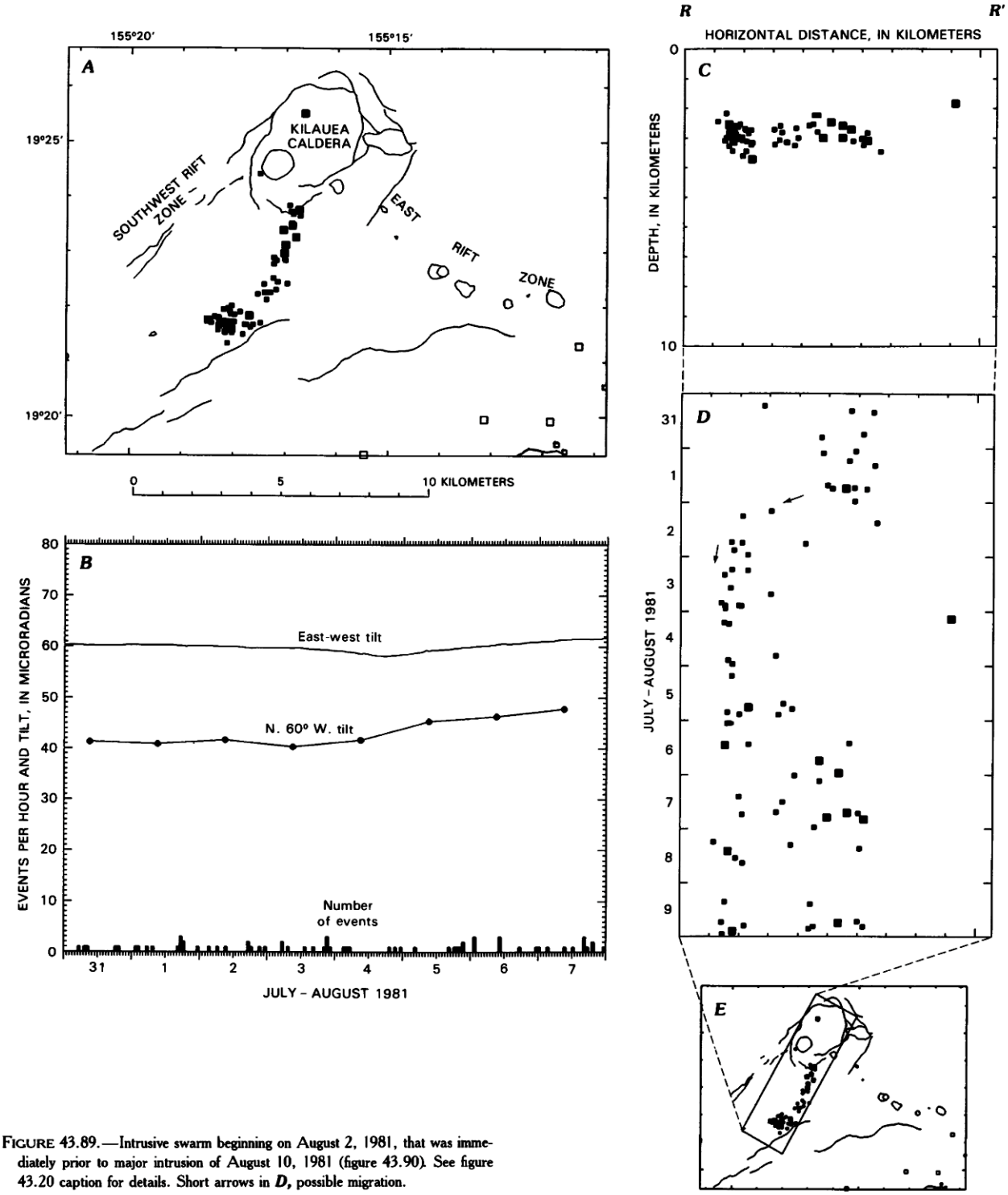


FIGURE 43.89.—Intrusive swarm beginning on August 2, 1981, that was immediately prior to major intrusion of August 10, 1981 (figure 43.90). See figure 43.20 caption for details. Short arrows in *D*, possible migration.

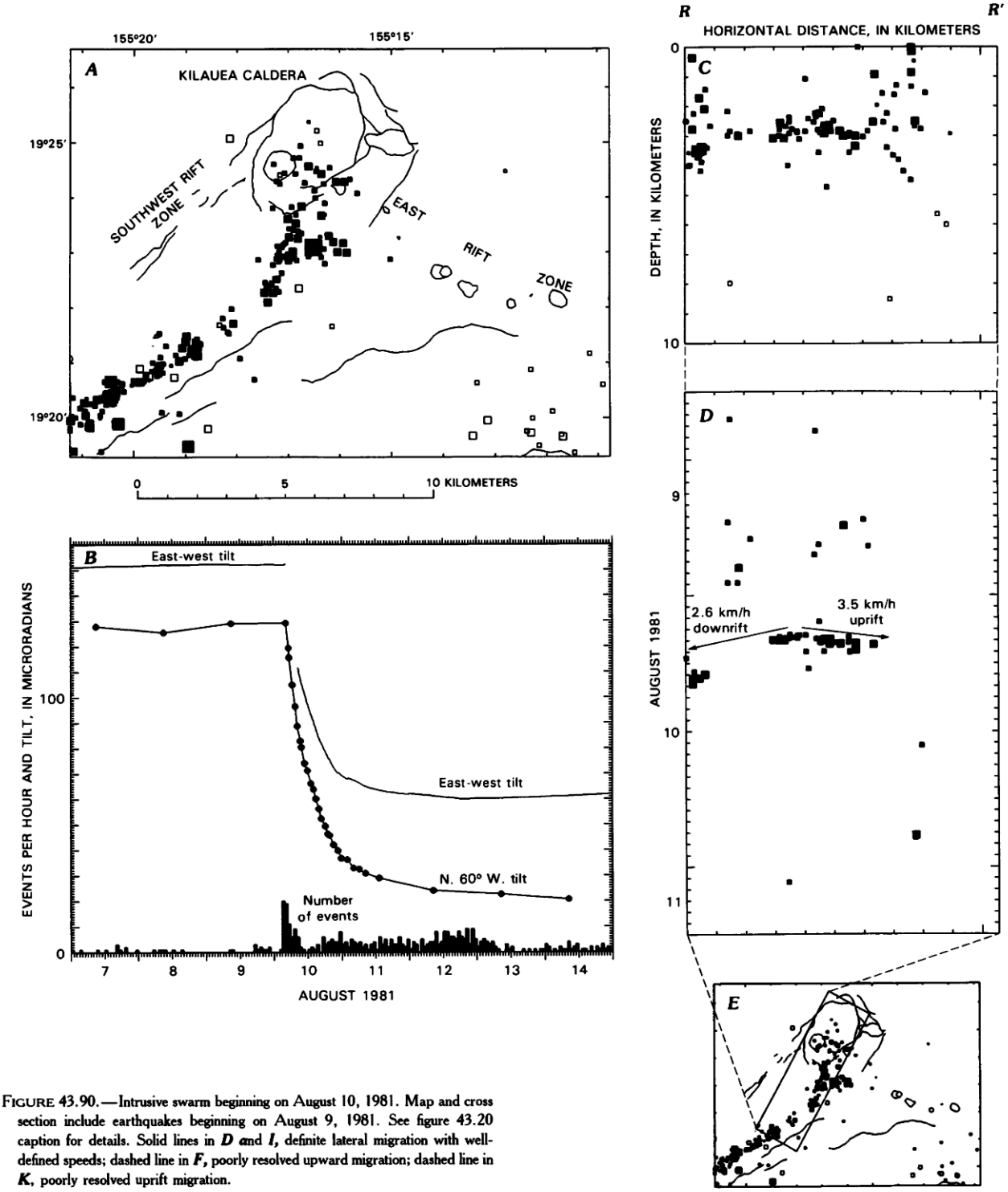


FIGURE 43.90.—Intrusive swarm beginning on August 10, 1981. Map and cross section include earthquakes beginning on August 9, 1981. See figure 43.20 caption for details. Solid lines in *D* and *I*, definite lateral migration with well-defined speeds; dashed line in *F*, poorly resolved upward migration; dashed line in *K*, poorly resolved uprift migration.

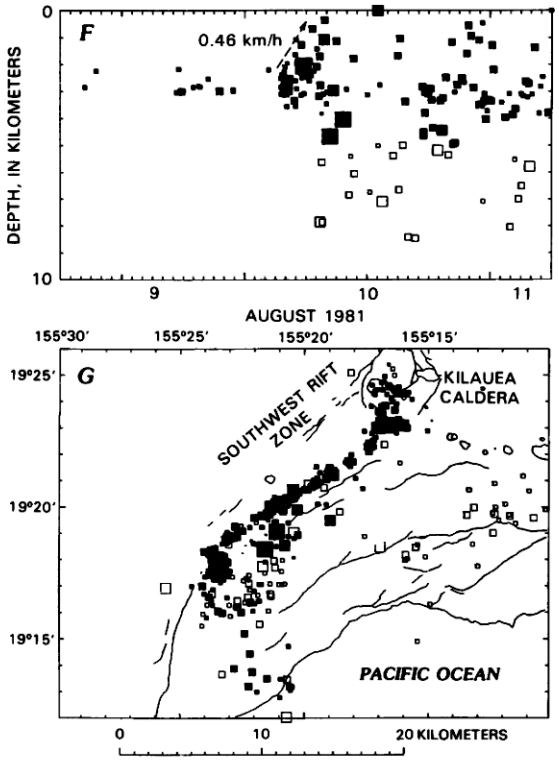


FIGURE 43.90.—Continued.

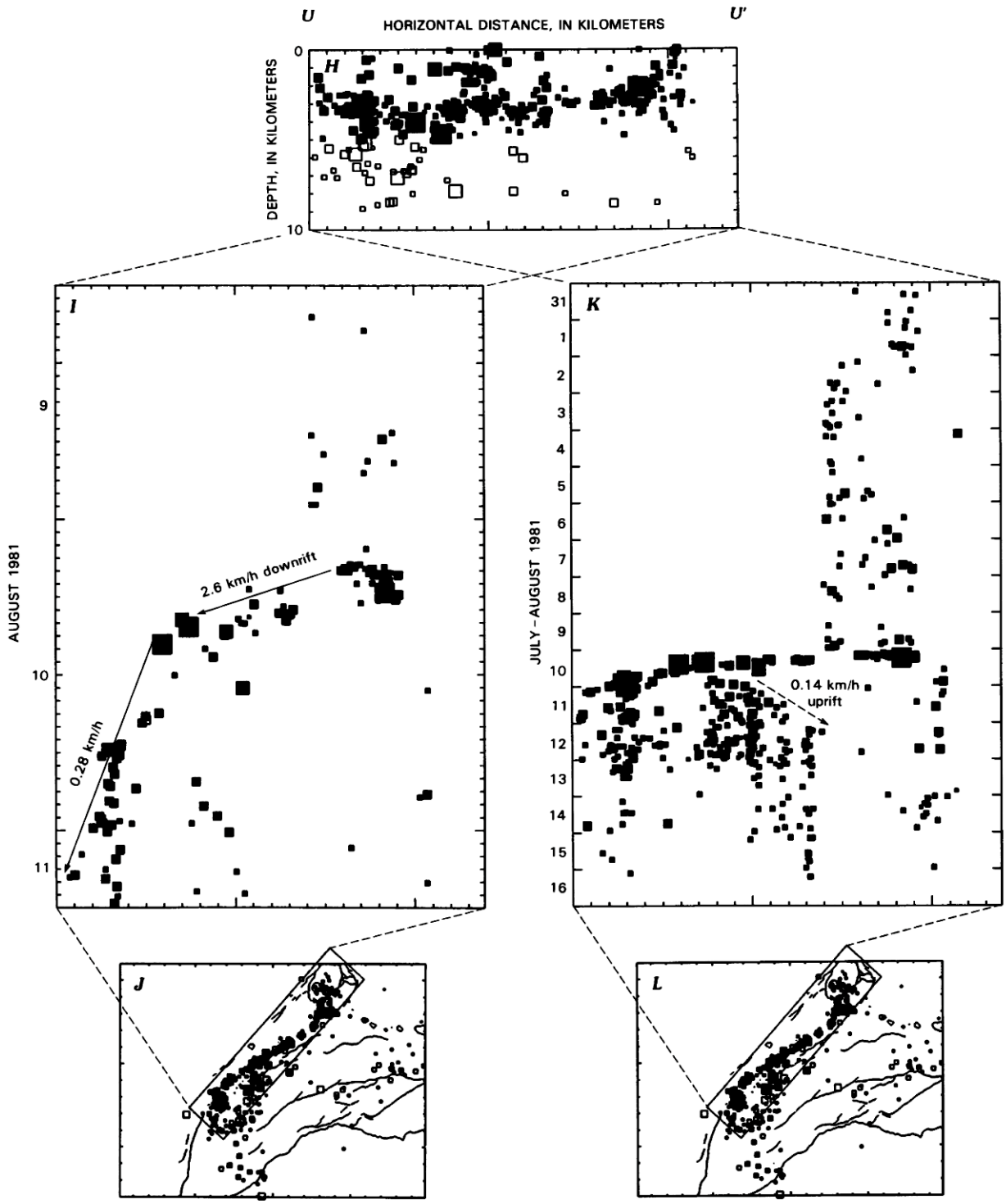


FIGURE 43.90.—Continued.

## THE SOUTHWEST RIFT ZONE INTRUSIONS AND CALDERA ERUPTIONS OF MARCH–JUNE 1982

In the 10 months following the August 1981 intrusion, Kilauea reinflated rapidly and earthquakes in the south and central caldera steadily increased (fig. 43.85). Very little magma appears to have been intruded into the SWRZ, except possibly for three brief periods of slow deflation. The second deflation in February 1982 temporarily halted the caldera seismicity. The third deflation nearly did the same except for a one-hour swarm on March 23. The swarm may have marked a small intrusion just south of the caldera (fig. 43.91*A*), but if so the quantity of magma intruded during the swarm itself was so small it was nearly invisible on the tilt record (fig. 43.91*B*).

Kilauea's reinflation was also punctuated by a brief caldera eruption on April 30, 1982. Earthquakes were located in the central caldera between Keanakakoi and the eruptive vent (fig. 43.92*A*). Earthquake depths primarily 1–2 km beneath the caldera were shallower than the main magma conduit of the adjacent ERZ (fig. 43.92*C*). The seismic zone was therefore above and to the side of the magma reservoir and did not align with the April vents. The earthquakes may thus have surrounded a set of dikes branching upward from the magma reservoir to the ERZ conduit. The redistribution of magma within the summit complex caused a brief tilt step at Uwekahuna (fig. 43.92*B*). The onset of the swarm was nearly instantaneous, but appeared to move very rapidly to the northwest (fig. 43.92*D*). The swarm preceded the eruption by about 2.5 hours, slightly shorter than for typical rift eruptions.

An intrusion in late June 1982 continued the SWRZ activity, but in a pattern very different from the other SWRZ intrusions of the previous 18 months. The June intrusion saw seismicity shift from the summit to the lower SWRZ, as had occurred after the August 1981 intrusion (fig. 43.85). Earthquakes only extended from Puu Koae to Puu Kou, however, and most of the activity was below 6 km depth (fig. 43.93*A*, *C*). The main magma conduit at 3 km depth scarcely produced any earthquakes, in marked contrast to all other SWRZ intrusions. The pattern of summit deflation was also unusual, having begun very gradually and without reaching the high tilt rates typical of the other SWRZ intrusions (fig. 43.93*B*). In addition, earthquakes lagged deflation by 1–2 days. Intrusive earthquakes generally begin at the onset of deflation and correlate closely in time with deflation rate, making this an unusual event.

The rates of deflation and earthquake migration suggest that the same uprift section of the magma conduit was involved in the December 1974, August 1981 and June 1982 intrusions. The observed downrift rate of earthquake migration in 1982 was about 0.2 km/h (fig. 43.93*D*). If the magma front proceeded at the same speed through the aseismic upper 6 km of rift, about 30 hours would have been required, which is close to the observed time delay between the onset of deflation and the first earthquakes seen downrift. We can also repeat the calculation of rift cross-sectional area done for the August intrusion using 0.2 km/h and a deflation rate of 0.83 μrad/h. The result is an area of 1,400 $m^2$ involved in magma flow, which matches the values of 1,500 (1981) and 1,400 (1974) remarkably well.

We interpret the June 1982 intrusion as a relatively passive one into a magma conduit already rifted open by two major intrusions in the previous 1.5 years. The energetic seismicity and rapid deflation characteristic of new dike formation or a highly pressured intrusion were absent. The dike at 3 km depth was aseismic because it was filled with still-liquid magma from the recent intrusions. This older magma could be quietly pushed through the conduit without the wedging apart of wall rock that creates earthquakes. Downrift of Puu Koae, rifting did extend below the shallow conduit to 10 km, which is the approximate depth of the pre-Hawaiian ocean floor. The intrusion probably represents a downward flow of magma within the SWRZ. The event then completed the cycle of SWRZ intrusions by separating the two flanks down to the base of the volcanic pile at which the south flank is decoupled from the lower crust.

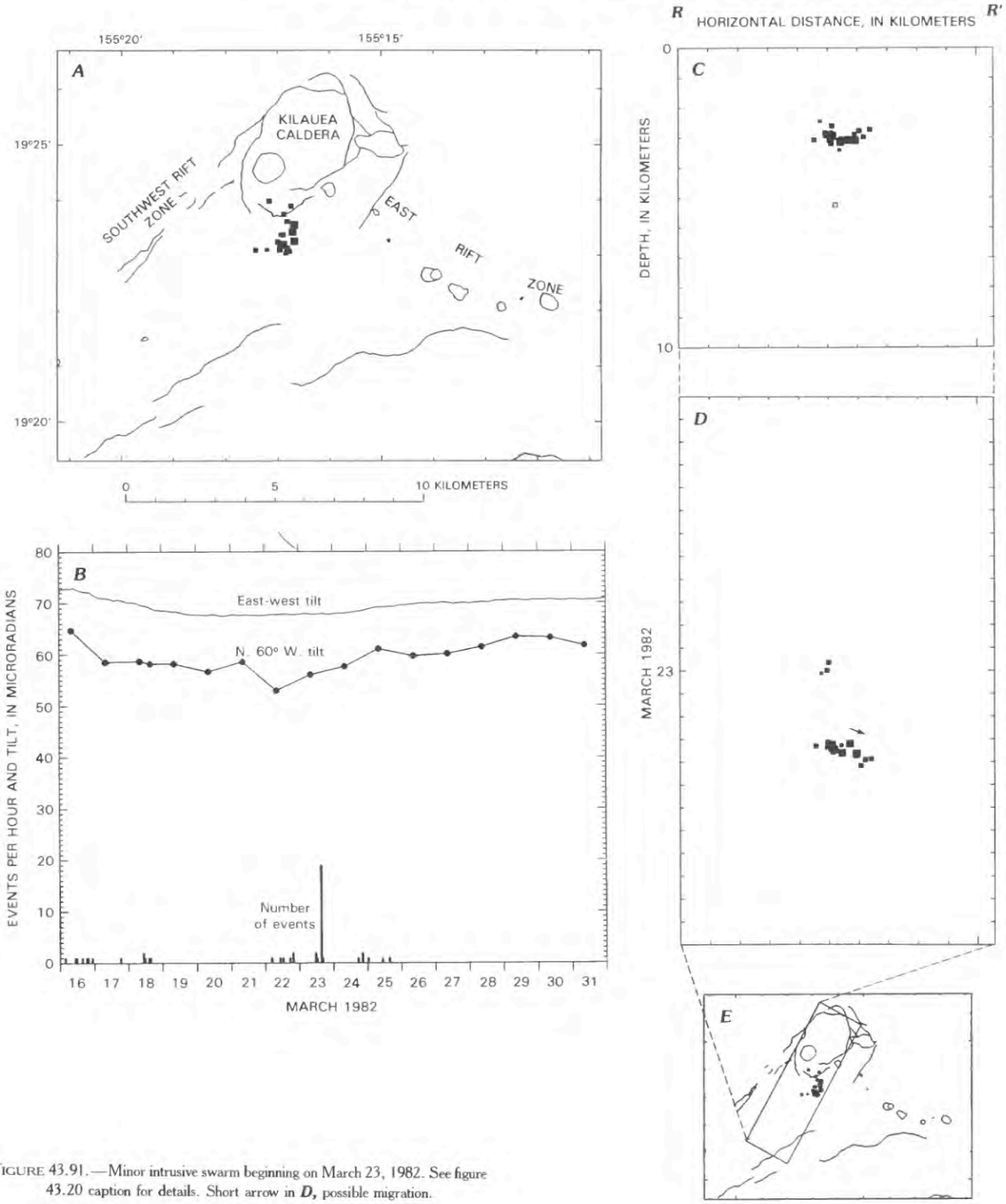


FIGURE 43.91.—Minor intrusive swarm beginning on March 23, 1982. See figure 43.20 caption for details. Short arrow in ***D***, possible migration.

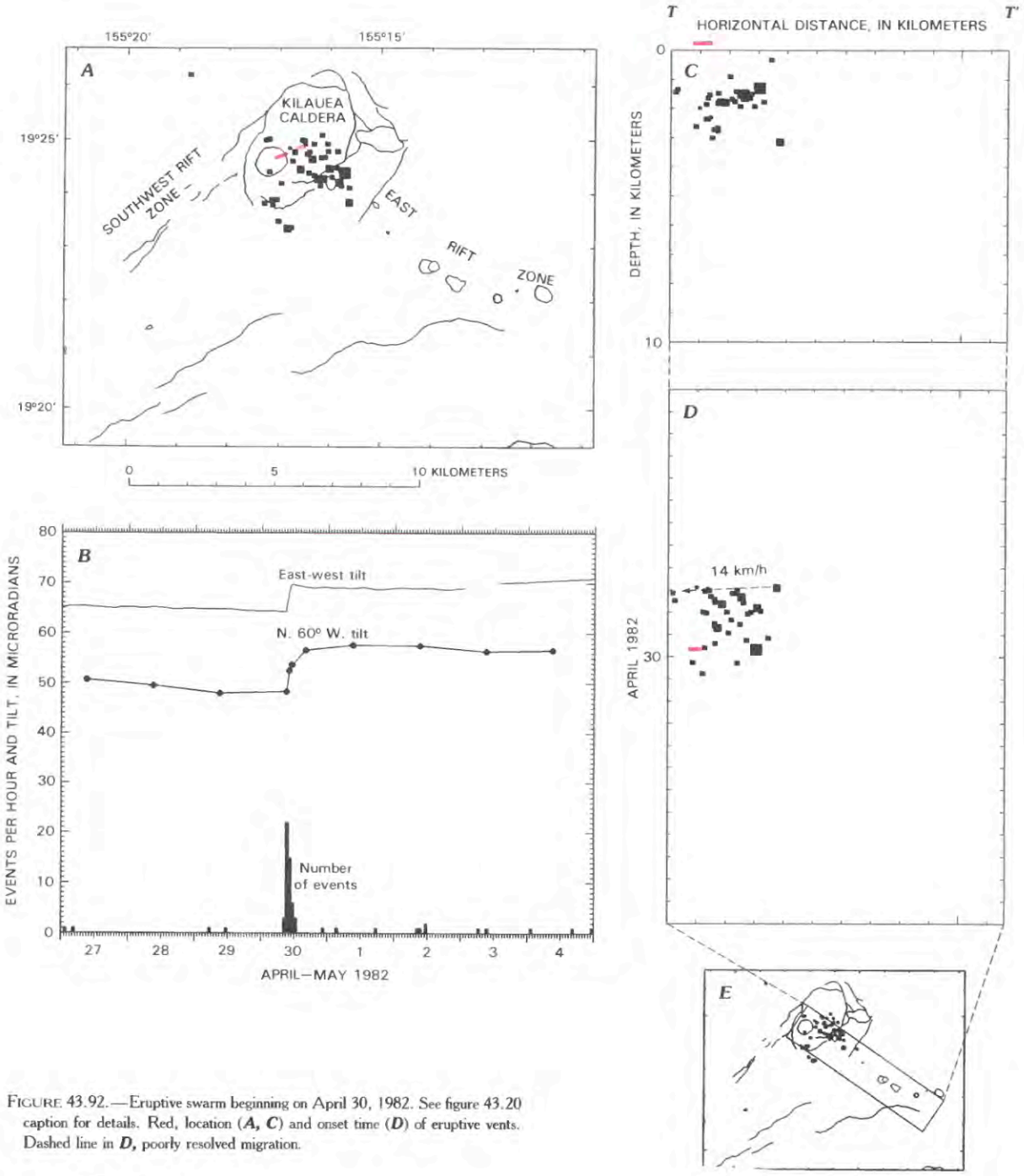


FIGURE 43.92.—Eruptive swarm beginning on April 30, 1982. See figure 43.20 caption for details. Red, location (***A, C***) and onset time (***D***) of eruptive vents. Dashed line in ***D***, poorly resolved migration.

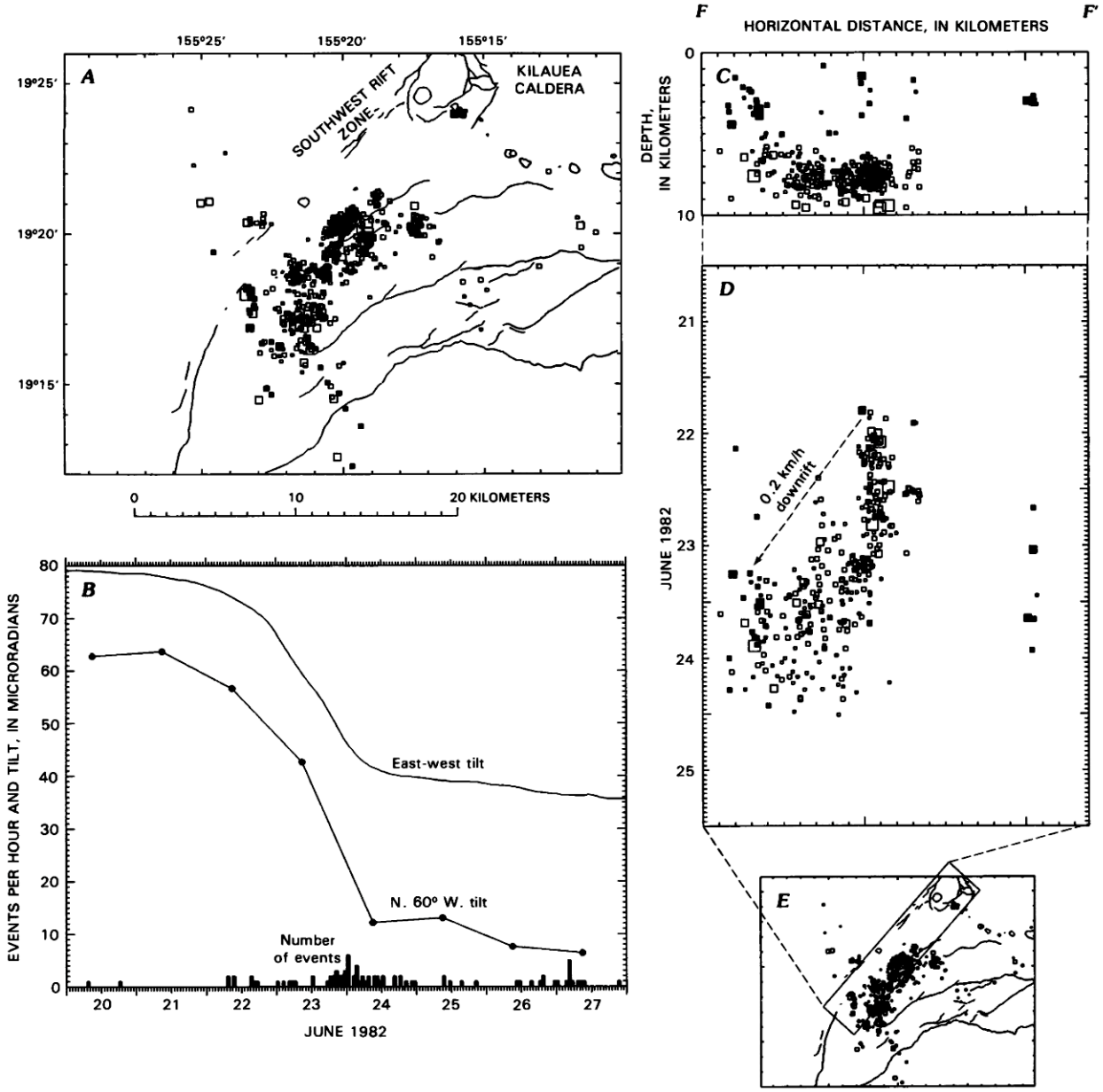


FIGURE 43.93.—Intrusive swarm beginning on June 22, 1982. See figure 43.20 caption for details. Dashed line in *D*, poorly resolved shift of seismicity; short arrows in *F*, possible vertical migration.

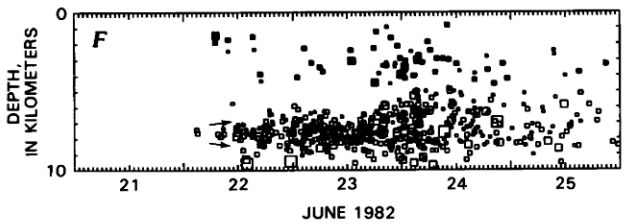

## CALDERA AND EAST RIFT ERUPTIONS OF SEPTEMBER 1982 THROUGH JANUARY 1983

After several SWRZ intrusions, Kilauea began turning her attention back to the ERZ with a caldera eruption on September 25, 1982. The swarm began abruptly and coincided with a rapid step in summit tilt (fig. 43.94*B*). The intrusion affected portions of both the SWRZ and the ERZ adjacent to the caldera (fig. 43.94*A*). Earthquakes began under the area of the eventual vent in the south caldera. Seismicity soon spread to the ERZ and moved into both rifts at a speed of roughly 1.4 km/h for a short time (fig. 43.94*D*, *G*). A larger but slower wave of earthquakes moved into the ERZ about one hour later, presumably triggered by a major pulse of magma. As the intrusion progressed into the rifts, a dike also moved upward at about 1 km/h producing an eruption only about 2 h after the swarm began (fig. 43.94*I*).

When the dike reached the surface, earthquakes in the south caldera abruptly ceased (fig. 43.94*G*). This relation shows that the eruptive and intrusive dikes were hydraulically connected and the erupting dike dropped the magma pressure below the point needed to generate earthquakes. Earthquakes continued in the ERZ, however, which presumably was not as closely connected and did not feel the pressure drop at the time of eruption (fig. 43.94*D*). The sharp decline in seismicity early in the morning of September 26 is partly a result of masking of the seismograms by high tremor and partly of the real cessation of seismicity caused by magmatic pressure release accompanying the eruption. Conversely, the burst of ERZ seismicity following the eruption at about 0900 H.s.t. on September 26 is a result of timing more earthquakes and the apparent diversion of magma from the eruption to intrusion in the ERZ.

The September 1982 caldera eruption appears to have reactivated the ERZ following its quiescence during the series of SWRZ intrusions. This ERZ activity is partly demonstrated by the multiple pulses of magma intruded at the time of the eruption (fig. 43.94*D*). The ERZ also appears to have received magma during a slow and continuous intrusion during the month following the eruption. This slow intrusion is revealed by the flat summit tilt, the continuing seismicity in the Kokoolau area and the general tendency of earthquakes to migrate slowly downrift (fig. 43.95). The migration speed was a very slow 6 m/h (0.14 km/d). It was thus not surprising that the next two magmatic events were in the ERZ.

A rapid intrusion of the ERZ on December 9, 1982, extended from the caldera almost to Hiiaka (fig. 43.96*A*). Earthquakes thus reactivated the same area which was intruded during September and October (fig. 43.95), and the same conduit or dike was likely active at both times. Earthquakes migrated downrift at a rapid 6.4 km/h (fig. 43.96*D*), one thousand times faster than in October. The earlier slow intrusion, as with the SWRZ in 1981, may have prepared and heated the magma conduit and thus enabled the succeeding intrusion to move very rapidly. The high speed of intrusion may also have been aided by its proximity to the magma reservoir and the frequency of intrusion in this section of the ERZ. Coincident with the most intense seismicity, earthquakes migrated upward at about 0.8 km/h (fig. 43.96*F*). The upward movement thus followed the downrift migration by 1–2 hours. Magma apparently was deflected upward by the same blockage in the main conduit that halted both this and the October intrusion between Kokoolau and Hiiaka. The three weeks following the December 9 intrusion saw continuing seismicity in the Kokoolau area (fig. 43.95). After December 19, earthquakes began downrift of Pauahi, suggesting that the ERZ was transferring magma downrift in possible preparation for another event.

The ERZ swarm that began on January 1, 1983, was to lead to a major and long-lived eruption. Earthquakes only accompanied the first few eruption phases in early January, however. All succeeding major eruptive episodes were localized to the Puu Oo vent area, a continuous ERZ magma conduit was kept open by the eruption, and essentially no additional volcanic seismicity and probably no new dikes were created. Because this eruption captured most of Kilauea's magma supply, none was left to produce an eruption or intrusion elsewhere. The January 1983 sequence is thus the last

volcanic swarm in this chronology, which is complete through mid-1985.

The earthquake swarm and other studies of the first part of the eruption are treated in detail by Koyanagi and others (in press) and Wolfe and others (in press). The seismic zone extended 17 km from Makaopuhi to just east of Kalalua (fig. 43.97*A*). Eruptive vents were confined to an 8-km segment from Napau to Puu Kahaualea, so the zone of intrusion was about twice the length of the ERZ experiencing extrusion. Earthquakes were concentrated along the ERZ magma conduit centered at about 2.5 km depth near Makaopuhi, but deepening to 3.5 km beneath Kalalua (fig. 43.97*C*). Most earthquakes are clustered and are probably at highly stressed areas where magma flow is constricted.

Magma was supplied from the summit reservoir for the 7 days of the swarm, but at a slower average rate than during other intrusions of comparable size. The summit tilt curve (fig. 43.97*B*) does not show the typical initially rapid subsidence followed by a gradual leveling off: the deflation rate was instead relatively constant except for pauses on January 3, 4 and 6. Seismicity was roughly correlated with deflation rate, both being higher on January 2, 5 and 7.

Both earthquakes and eruptive vents moved successively downrift and in a complex and protracted pattern, eventually localizing near what was to become Puu Oo. The initial seismicity just uprift of Makaopuhi on January 1 broke downrift at 0.6 km/h on January 2 (fig. 43.97*D*). This first intense seismicity stopped when it reached Napau. The first emission of lava was at Napau about 24 hours after the first earthquakes reached that point. Earthquakes also shallowed with time on January 2 just prior to the first eruption (fig. 43.97*F*). The vent then opened progressively downrift at the same speed as the downrift earthquake migration, stopping near Puu Kamoamoa. The progress of the vent coincided with the cessation of earthquakes at the same point, which thus apparently released the magma pressure that caused the earthquakes. In fact the first phase of the swarm consisted of a zone of earthquakes whose leading and trailing edges both moved downrift at 0.6 km/h (fig. 43.97*D*). The last part of the trailing edge of earthquakes coincided with the start of eruption. Earthquakes at any one point lasted for about 24 hours, which probably represents the time for stress to be released either by the growth of the dike to its full width and height or for magma to reach the surface and relieve pressure.

The next phase of the swarm from noon on January 3 through January 6 was marked by somewhat reduced seismicity that expanded slowly both uprift and downrift from near Puu Kamoamoa (fig. 43.97*D*). Both deflation and the eruption had stopped during the first 2 days of this period. A shallowing of earthquakes preceded the resumption of lava emission at noon on January 5 to the east of Puu Kamoamoa (fig. 43.97*F*). For the last phase of the swarm, earthquakes shifted from uprift of the vents (fig. 43.97*D*). The intrusion then extended an additional 4 km downrift, moving at the same 0.6 km/h speed as the initial intrusion from Makaopuhi to Napau. The intrusion and most earthquakes stopped when the next eruption phase began on the morning of January 7.

The complexity of the swarm in space and time indicates that it was really several successive intrusions that opened the magma conduit from Makaopuhi to the eventual site of the Puu Oo vent. The conduit opened rapidly from Makaopuhi to Puu Kamoamoa, then at about 1/25 the initial speed to the lowermost vent, which was established at about the same time as another rapid but short extension of the dike downrift. When the swarm was less than half over at about 1530 H.s.t. on January 3, the eruption stopped, the number of earthquakes diminished and they began moving back uprift, and the summit tilt had leveled off. Apparently the major downrift flow from summit reservoir to vent was momentarily stopped or blocked, and increasing magma pressure and dike growth moved back uprift. This uprift growth originated at the same hypothesized barrier in the magma conduit that initially prevented the vent from opening farther downrift. A variety of these space and time relations are common to many intrusions and will be summarized and discussed in the next section.

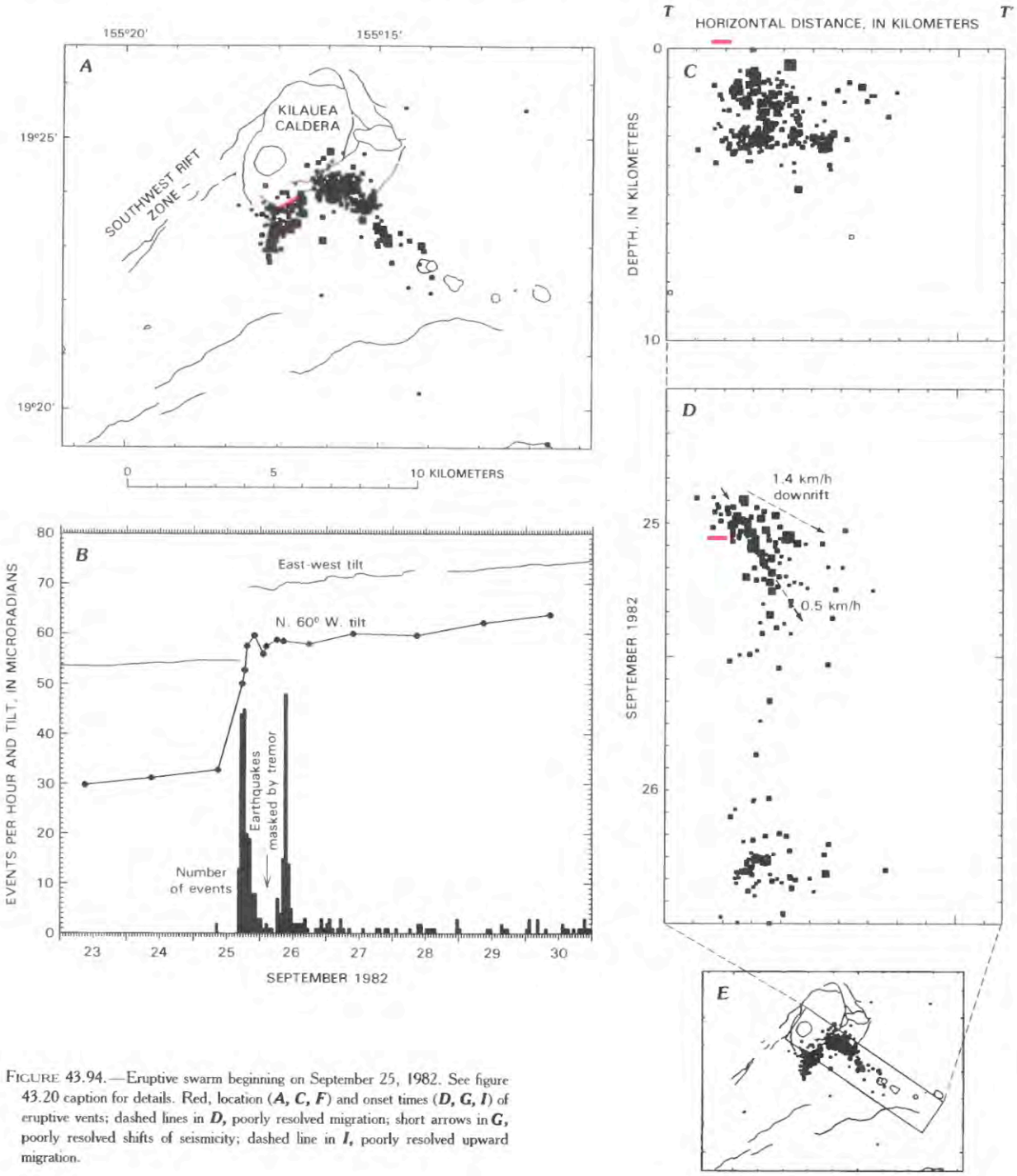


FIGURE 43.94.—Eruptive swarm beginning on September 25, 1982. See figure 43.20 caption for details. Red, location (***A, C, F***) and onset times (***D, G, I***) of eruptive vents; dashed lines in ***D***, poorly resolved migration; short arrows in ***G***, poorly resolved shifts of seismicity; dashed line in ***I***, poorly resolved upward migration.

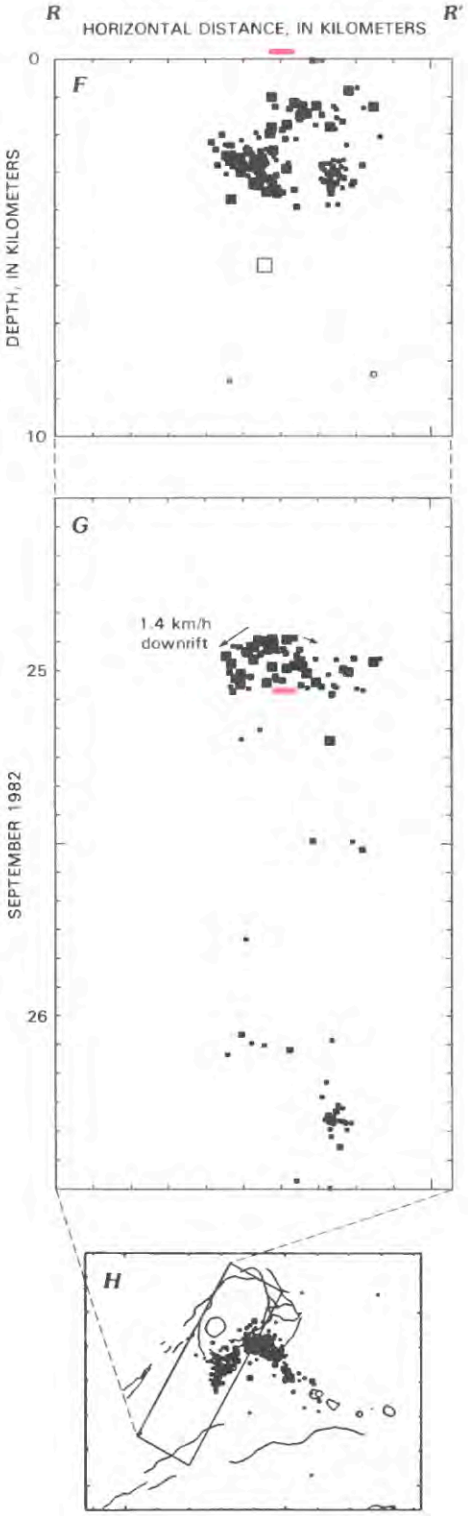


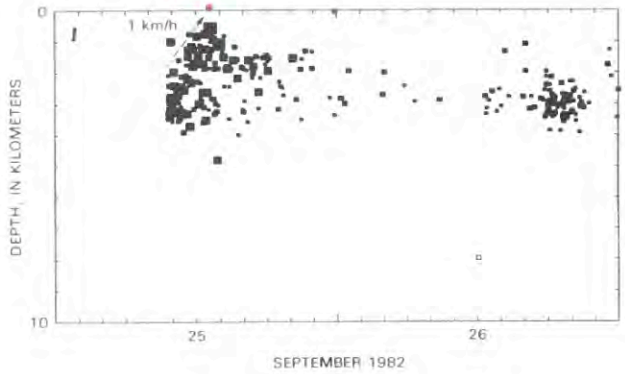


FIGURE 43.94.—Continued.

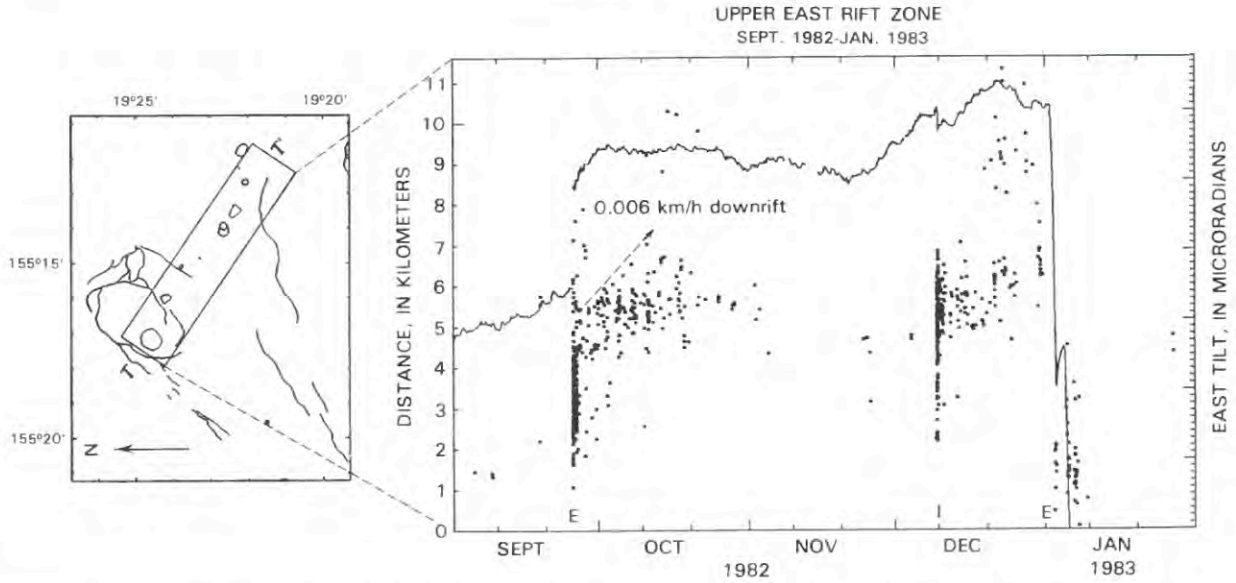


FIGURE 43.95.—Plot of earthquakes along east rift and east tilt at Uwekahuna versus time. All earthquakes shallower than 5 km and within geographic box shown are plotted. Halemaumau is at bottom and Mauna Ulu is near top. Tilt is from Ideal-Aerosmith instrument and down on plot generally indicates deflation of summit caldera. Large divisions on tilt scale are 10 μrad. Notations along time axis refer to specific swarms detailed in other figures: E, eruption; I, rapid intrusion. Dashed line, poorly resolved but very slow migration.

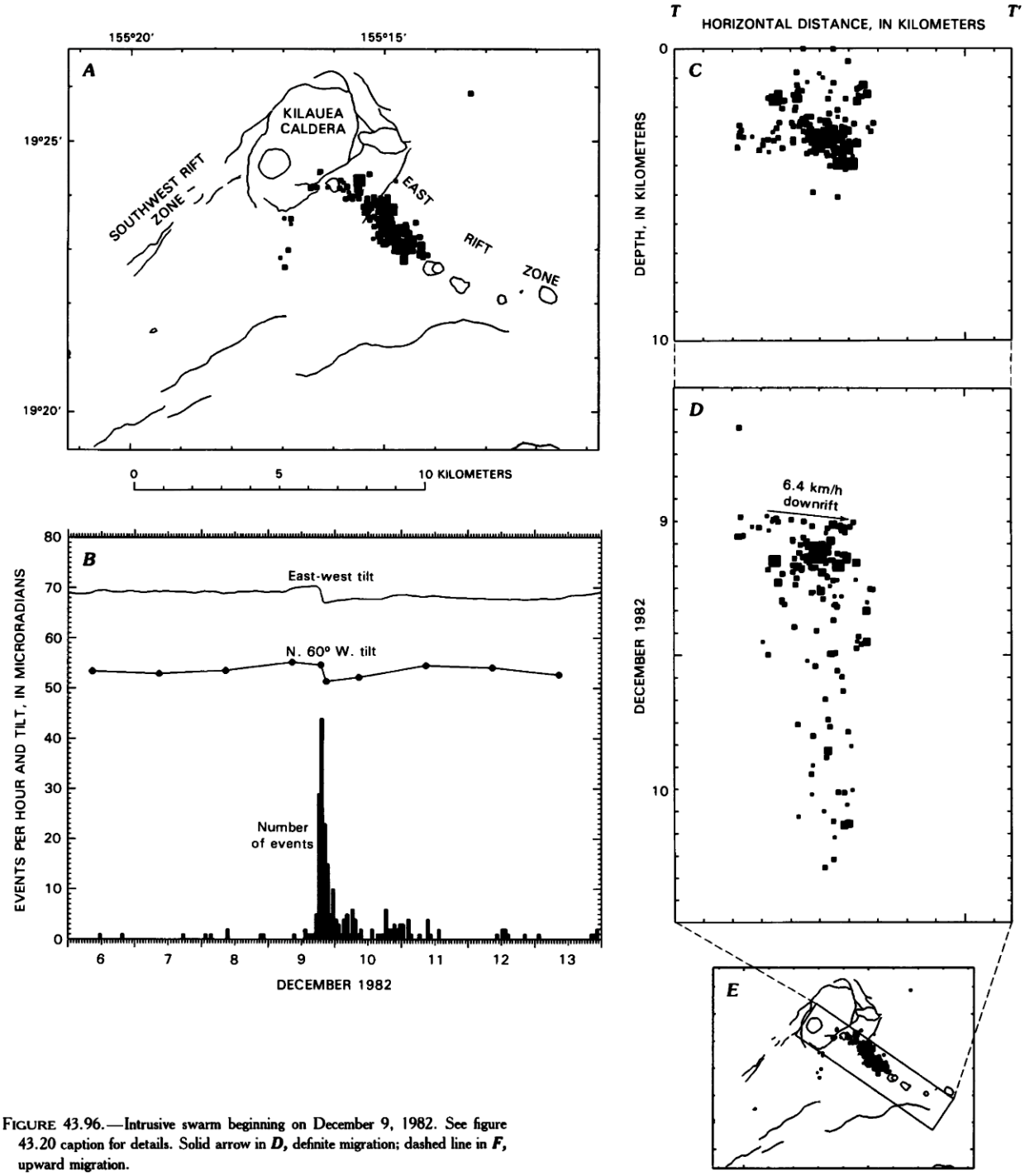


FIGURE 43.96.—Intrusive swarm beginning on December 9, 1982. See figure 43.20 caption for details. Solid arrow in *D*, definite migration; dashed line in *F*, upward migration.

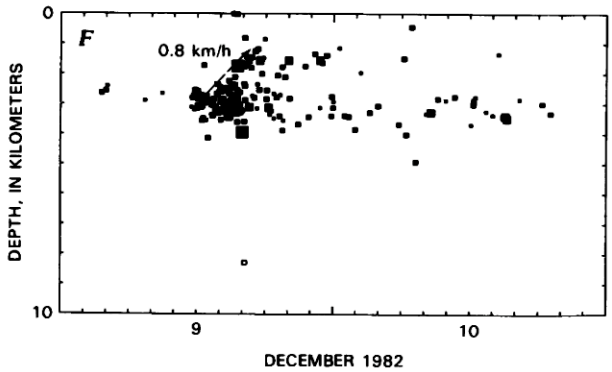


FIGURE 43.96.—Continued.

## DISCUSSION OF RIFT-ZONE INTRUSIONS

This section summarizes and discusses many of the basic seismic patterns seen during intrusions. We will mention processes common to many intrusions and eruptions and discuss their implications for the structure and dynamics of the rifts. We will also point out some relations between different intrusions and how one might affect a later one. Many of these patterns were mentioned in the previous section, but could not be developed in a comparative way because of its chronological format. For detailed descriptions and interpretations of individual swarms, the reader is referred to the previous section. Table 43.1 summarizes the basic data of the individual swarms enumerated in this paper.

Nearly all shallow volcanic earthquakes at Kilauea can be attributed to magma intrusion in some form. We have given different names to different types of swarms based essentially on their location and intensity, but they all result from magma transfer. Swarms accompanying inflation of the summit reservoir are generally of low intensity, in or near the caldera, and are caused by intrusion of the reservoir with magma from below. Slow intrusions may produce a low level of seismicity lasting several days or weeks along the rift zones. Rapid intrusions generally produce an intense, short swarm in the caldera or rift zones and transport magma much faster than Kilauea's magma supply rate. Rapid intrusions either create or enlarge dikes, which produce an eruption if one reaches the surface.

The mechanics of rift intrusions in Hawaii have been treated in many previous studies. Fiske and Jackson (1972) emphasized the large-scale effects of gravitational and edifice stresses on rift-zone development. Dieterich and Decker (1975) and Pollard and others (1983) calculated the deformation and stress field surrounding a dike interacting with the Earth's surface. Duffield and others (1976, 1982) discussed and interpreted deformation measurements for several Kilauea intrusions in terms of forceful magma transport and dike emplacement. Swanson and others (1976a) and Dvorak and others (1985) discussed ERZ intrusions and their effect on deformation of the adjacent south flank. Shaw (1980) treated magma transport and ascent in terms of fracture mechanics in an applied stress field. Nakamura (1980, 1981) discussed the role of decoupling of the volcanic pile at the buried sediment layer in the formation of long rift zones.

### INFLATIONARY SWARMS AND SLOW INTRUSIONS

Most rapid intrusions are preceded by a period of inflation and consequent slowly increasing seismicity at the summit. A period of inflation lasting several weeks may produce intermittent swarms during that period. The level of swarm seismicity may only be a few times that of the background level and is often accompanied by a brief increase in the rate of rising summit tilt. Seismicity and tilt are highly correlated during inflation, and the caldera seismicity generally ends abruptly if rapid deflation feeds an intrusion downrift. Inflationary swarms are thus caused by increasing magma pressure, uplift and extension in the summit region. The rift zones adjacent to the caldera become active in many inflationary swarms and may receive magma in pulses and slow intrusions. Inflationary swarms were most numerous from December 1969 to January 1972 and during 1974 when tilt and caldera inflation reached the highest values sustained in recent years.

Some inflationary swarms occur immediately before rapid intrusions and are precursory in some sense. Notable examples include February 1969 and September 1974. Other inflationary swarms, such as those of January 22, 1977, and January 20, 1981, may be distinct but precede a rapid intrusion by a few days. These paired inflationary and intrusive swarms are not coincidences, because they are typically adjacent in both space and time. Many inflationary swarms represent periods of accelerated inflation, during which the barriers containing the accumulating magma are more likely to break. Many intrusions may thus be triggered by episodes of rapid inflation.

Some seismic precursors to intrusions are not as obvious as inflationary swarms at the summit. A swarm of shallow ERZ and south flank earthquakes preceded the first Mauna Ulu eruption in May 1969. Although the quality of epicenter locations is poor, the precursory swarm was definitely not at the summit. The Mauna Ulu eruption may have thus been triggered by some south flank instability or downrift magma movement. Some rapid intrusions are immediately preceded by an adjacent intrusion that may also be a precursor or trigger. This pattern will be discussed below in the section "Sequential Relations Between Intrusions Along the Rift Zones."

Slow intrusions have been observed along the active segments of both rifts within 20 km of the caldera, and all share several features in common. Summit tilt may slowly rise, fall or stay level, but the rate is never more than a few microradians per day. Typical rapid intrusions, in contrast, deflate the summit at rates of several microradians per hour. The slow intrusion may be aseismic or weakly seismic, or may produce earthquakes only near the terminus of the intrusion where magma accumulates. As with all intrusions,

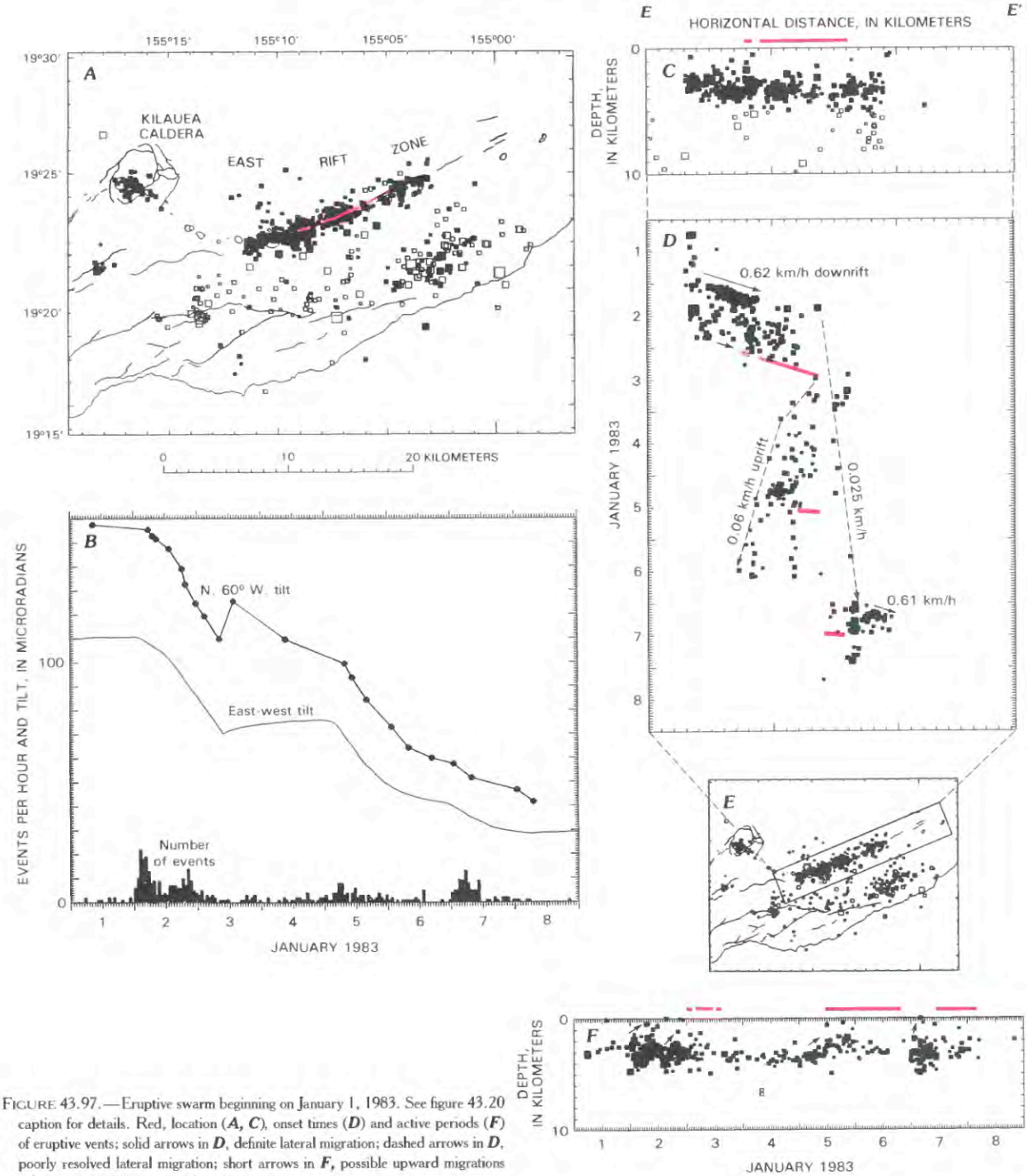


FIGURE 43.97.—Eruptive swarm beginning on January 1, 1983. See figure 43.20 caption for details. Red, location (***A, C***), onset times (***D***) and active periods (***F***) of eruptive vents; solid arrows in ***D***, definite lateral migration; dashed arrows in ***D***, poorly resolved lateral migration; short arrows in ***F***, possible upward migrations culminating in different eruptive phases.

aseismic magma passage is presumed to indicate that the rift conduit is unstressed and in equilibrium, and need not widen to accommodate the magma flow. Completely aseismic intrusions are not considered in this paper, but Dzurisin and others (1984) used downward steps in tilt to account for magma transfer into the rifts. We infer that slow intrusions reveal magma leaking passively into the rifts at a rate comparable to that of its accumulation at the summit.

The most common slow intrusions occur from the summit reservoir during periods of inflation. The distinction between steady accumulation and pulsed flow of magma can often only be made if migrations of earthquakes are visible. Pulses of slowly intruding magma are seen in the intrusions of February and December 1970, June and July 1971, January 1972 and December 1974. Migration speeds are typically 0.01–0.05 km/h, which is 1 to 2 orders of magnitude slower than during rapid intrusions. At these speeds, several days are required for magma to traverse a few kilometers of rift. Some intrusions do not fall neatly into a category: the January 1977 event accompanied a short episode of inflation (as might a slow intrusion), but showed a rapid 0.7 km/h speed typical of a rapid intrusion.

Slow intrusions more than 5 km from the caldera have different characteristics on each rift zone. The SWRZ intrusions of October 1969 and February 1981 each generated earthquakes only near Puu Kou, lasted several days, and were accompanied by gradual deflation. Magma thus moved aseismically down 20 km of rift conduit. Pulses of slowly moving magma similar to ones near the summit triggered seismicity along the SWRZ following the June 1971 intrusion, in the 6 months prior to the December 1974 eruption, and during February–June 1981. The ERZ experienced a series of cyclic slow intrusions during November 1978–July 1979 and May–October 1980. The summit tilt oscillated as discrete pulses of magma were dispatched downrift. Episodes of summit seismicity coincided with peaks in tilt, and very shallow swarms near Puu Kamoamoa close to minima in tilt were caused by accumulating magma downrift. The rift between the caldera and Puu Kamoamoa did not produce migrating earthquakes as magma passed through. The intrusion thus was slow, magma transfer was passive, and seismicity was produced only at places of local inflation.

## SEQUENCE OF EVENTS WITHIN A RAPID INTRUSION

Most intrusions occur in stages, only some of which may be evident during any one event. Larger and longer intrusions often display the most complexity, such as multiple phases and a variety of earthquake migration patterns.

The seismic zone formed by a rapid intrusion nearly always grows in size or shifts location as magma flows through conduits or fills a dike. In the first tens of minutes an intrusion often produces earthquakes in a small volume 1 $km^3$ or less in size. Most intrusive swarms begin from the rift-zone magma conduits (and sometimes the summit reservoir itself) near 3 km depth. When shifts in epicenter locations can be resolved, downrift migration of earthquakes and magma is typical of the SWRZ and the ERZ downrift of Mauna Ulu. The caldera and the ERZ between the caldera and Mauna Ulu are more complex, and swarms may migrate either uprift or downrift with comparable likelihood. A shallowing of earthquakes with time is often observed in swarms where a range of depths can be resolved.

Major intrusions that also produce an eruption often divide into two types of processes, which can be illustrated by the July 1974 eruption. The first phase produced intense seismicity and a moderate deflation rate. Earthquakes migrated laterally (in this case uprift) and also upward from the ERZ magma conduit in a linear fashion toward the vent. We infer a high magma pressure and a growing dike from the intense seismicity, but a relatively low-volume flow from the deflation rate. When the dike reached the surface and the eruption began, tremor and the deflation rate increased dramatically. Earthquakes then ceased, partly because of masking by high tremor on the seismograms and partly because the dike stopped growing. Magma flow through an open-ended dike presumably dropped the magma pressure and did not require a lengthening or widening of the dike. Intense seismicity is therefore associated with a dike that is growing and compressing its walls.

Larger and more complex eruptions may display these seismic dike growth and aseismic magma flow modes simultaneously. If a dike is many kilometers long, eruption from a vertical feeder may start while the dike continues to intrude downrift, as seen in the September 1977 and January 1983 eruptions. Earthquakes at a given place will generally cease when the dike there reaches the surface and magma pressure drops, but seismicity will continue where the dike is still growing. The time between the first earthquakes and eruption at a given location is a measure of the time required for magma to migrate from the conduit at 3 km depth to the surface. This time may be 2–24 hours but is typically 3–6 hours. The deflation rate (and hence the magma volume rate) generally correlates either with the extrusion rate or the intensity of seismicity, depending on the importance of additional dike growth. This correlation of tilt rate and seismicity is easiest to see during large multiphase eruptions such as September 1977 and January 1983.

## THE GEOMETRY AND DYNAMICS OF INTRUSIVE SWARMS

An intrusion may occur either by the fracturing of rock and emplacement of a new dike or by the opening of an older magma conduit. In either case the pressurized expansion of dike width apparently produces earthquakes in the rock near the dike. How much seismicity if any is produced by tensile fracture at the tip of a dike expanding into fresh rock is presently difficult to say. The recurrence of intrusive swarms in the same rift zone suggests that most intrusions propagate along planes of weakness that are the molten cores or boundaries of older dikes. Thus tensile failure at the crack tip is seismically a minor process compared to shear failure in the compressed rock near the dike. This view is consistent with Hill's (1977) earthquake swarm model, in which earthquakes occur on shear planes joining echelon dike segments.

The mechanics of rapid and slow intrusions determine whether a given event is forceful or passive. The compression and seaward displacement of Kilauea's south flank is a result of forceful intrusions

in the rift zones (Swanson and others, 1976a). We believe that the amount of seismicity and to some degree the speed of migration provide the distinction: rapid and seismically intense intrusions are forceful, and slow intrusions with weak seismicity result from a more passive flow of magma.

Patterns of seismic and aseismic migration of intrusions support the concept of earthquake generation adjacent to an expanding dike. Most Kilauea intrusions produce earthquakes for some distance behind its leading edge, not just at its foreward tip. This presumably is the region in which the dike continues to widen after its initial opening. Seismicity then stops at a given place when the dike reaches its full width. Magma-filled conduits are clearly present in the ERZ much of the time, otherwise each intrusion would produce earthquakes along the entire rift between the summit and the intrusion terminus.

Intrusions may alternately migrate both seismically and aseismically. The aseismic migration occurs where the dike is already open and fluid, the adjacent rock is easily and aseismically compressed, or the dike widens only enough to supply magma to its leading tip. One example of aseismic migration through a previously rifted area was seen in the SWRZ intrusions of August 1981. The pre-intrusion of August 2 produced earthquakes out to only 5 km from the caldera before stopping. The main intrusion on August 10 produced no earthquakes where the earlier intrusion stopped because that section was already rifted open. Another type of aseismic dike growth is illustrated by the February 1977 intrusion. An initial and small burst of earthquakes was followed by about 3 hours of seismic quiescence and no deflation. The intense swarm then began simultaneously throughout the seismic zone and was rapidly fed by magma from the deflating summit. We interpret the aseismic period as growth of the dike to its eventual area but only to a small thickness. The dike was then filled at a high volume rate and generated earthquakes as it grew in thickness simultaneously over most of its area.

Earthquakes alone are not adequate to resolve the cross-sectional shape of the conduit, but do constrain its area through which magma flows. The ratio of magma supply rate (deflation rate converted from microradians of summit tilt to magma volume using the value of 0.3 million cubic meters per microradian from Dzurisin and others, 1984) to the earthquake migration rate is equal to the cross-sectional area of the dike. The SWRZ intrusions of December 1974, August 1981 and June 1982 all yield about 1,500 $m^2$ as the effective area of the main SWRZ conduit (table 43.1). Modeling the August 1981 dike as about 1,500 m by 1 m matches an observed leveling profile (Pollard and others, 1983), so these dimensions are consistent with all seismic and deformation data. The cross-sectional area of the northern SWRZ dike active in September 1971, however, is only about 280 $m^2$. The ERZ conduits are also smaller than the main SWRZ conduit and do not exceed 900 $m^2$ (table 43.1).

Intrusions are most efficient at producing earthquakes between 2 and 4 km depth in most of the rift system, which is apparently the depth of the main magma conduits. The uppermost 2 km of the rifts probably lack sufficient confining stress, and slip occurs aseismically. Unseen intrusion probably occurs below 4 km, which may be too hot and ductile to deform seismically. Intrusion in some form extends from the surface to at least 10 km depth where the volcanic pile rests on the pre-Hawaiian sea floor. Intrusive volume is ultimately accommodated by seaward slip of the unbuttressed south flank on its base at about 10 km depth.

When intrusive earthquakes do occur above 2 km depth, they often migrate up from the main conduit and follow an upward-branching dike. Many recent examples of upward earthquake migration are apparent, especially in the ERZ from the caldera to Mauna Ulu. Examples of intrusions whose earthquakes display both an upward branching finger and clear shallowing of hypocenters with time are November 1979 and July, August and October 1980. The SWRZ intrusion of August 1981 also contained a vertical branch that produced shallow earthquakes and a zone of surface cracking.

Earthquakes directly beneath the main conduit are less common, but have been recognized under both rifts. The central SWRZ swarm in June 1982 followed 1.5 years of shallow SWRZ intrusions. The swarm appeared to accompany a downward draining of magma to complete the rifting process to the base of the volcanic pile. The most common place that deeper volcanic earthquakes are seen below the ERZ is in a rootless cluster at 5–7 km depth below Mauna Ulu. Activity there (see fig. 43.3*F*, *G*) was recognized during the intrusions of June 1976, September 1977, May 1979, and to a lesser extent during many others. Earthquakes during the May 1979 intrusion spread both upward and downward and reached 7 km depth the day after the main swarm. Most of the rifting process below 4 km depth is aseismic, and the study of earthquakes cannot determine the degree to which magma is supplied from the main rift conduit above or through a deeper and lateral system directly from Kilauea's vertical magma conduit.

## THE MECHANICS OF EARTHQUAKE MIGRATION

As we have seen many times, migrating earthquakes reveal moving magma and the growth of dikes within the rift zones. Earthquakes mostly originate at or just behind the leading edge of the dike, where it is growing in width. Some earthquakes occur ahead of a smoothly advancing front of seismicity. These may be from (1) irregular or jerky dike motion, (2) a stress increase in front of the dike, or (3) triggering by elastic waves radiated by earlier earthquakes.

The direction of migration is generally downrift, except within the caldera and in the ERZ between the caldera and Mauna Ulu. Magma is supplied at the summit, and both its pressure gradient and downslope gravitational flow transport it primarily in the downrift direction. Note that upward movement by bouyancy requires that magma have at least lithostatic pressure. The observed combinations of upward and downrift magma movement thus require the rift to be in a mixture of lithostatic and sublithostatic stress conditions. Sublithostatic pressure might thus prevail in places where downrift magma movement is rapid, continuous or aseismic. Lithostatic pressure probably prevails near blockages of the rift conduit and places where dikes branch upward to form eruptive vents.

The intrusive patterns for the SWRZ are simpler than for the ERZ. The positions, starting points, migration directions and migration speeds for the earthquake swarms discussed in this paper are summarized in figure 43.98. This distance versus time plot shows what happened where and when. For example, most SWRZ intrusions begin near or just south of the caldera. Within 3 km of Halemaumau, intrusions are about equally likely to migrate into or out of the caldera. The region close to the summit magma reservoir is presumably a complex of conduits that grow as an interconnected network. All intrusions in the SWRZ more than 3 km from the caldera migrate in the downrift direction. The six best observed SWRZ intrusions all reached Puu Kou. Thus, no major barriers capable of stopping an intrusion are present between the south caldera and Puu Kou. The migration speed slowed significantly near the terminus of the major 1974 and 1981 intrusions. This speed decrease could be caused by a drop in temperature or pressure near the end of the intrusion, or the observed upward bend of the seismic conduit over a barrier near Puu Kou.

Intrusions downrift of Mauna Ulu in the ERZ are also relatively simple. For the present discussion we exclude the intrusions of 1963, 1965 and February and May 1969 owing to their diffuse earthquake distributions within the south flank. Each of the seven events that penetrated downrift of Mauna Ulu started within 1 km of that point, and each intruded in the downrift direction. The major September 1977 and January 1983 intrusions slowed with distance from the summit, as did the two largest SWRZ intrusions. Long intrusions apparently cannot sustain a high speed for the entire length of the dike. Unlike the SWRZ, the three ERZ intrusions that passed Makaopuhi each stopped at different places, implying that many barriers capable of stopping intrusions exist in the ERZ. The simplicity of a single, linear magma conduit at 3 km depth appears to exclude complexities such as uprift earthquake migration in the SWRZ and central ERZ.

## BEHAVIOR OF THE EAST RIFT ZONE FROM THE CALDERA TO MAUNA ULU

Intrusions between the caldera and Mauna Ulu in the ERZ are varied and often complex. This section of rift is distinctly different from the rest of the rift system in several ways: (1) intrusions in recent years were much more frequent than elsewhere; (2) the area often partakes in inflation of the summit magma reservoir and may continuously produce earthquakes during these times; (3) it is the only section of Kilauea's rift system that trends north of west and is therefore most oblique to the greatest principal stress, which controls the strikes of individual vents and the majority of the rift system; (4) the Koae fault zone meets the ERZ near Mauna Ulu, tectonically separating this section from the simpler ERZ downrift; (5) the only major intrusion to trend oblique to the rift axis was here in July 1969, and some eruptive vents also obliquely extend several kilometers from the rift; (6) earthquakes near 1–2 km depth are numerous—though the main magma conduit at 3 km depth is typical of the whole rift system; (7) magma may supply two events

FIGURE 43.98.—Diagram of position of swarms and intrusions versus time as documented in this paper. Horizontal scale in ***A*** is in kilometers from center of Halemaumau along the SWRZ (left) and ERZ (right). Solid lines show time and lateral extent of rapid intrusions. Dashed lines, intrusions with diffuse hypocenters; F, swarms in flanks off rift axis; dotted lines, inflationary swarms and slow intrusions; each swarm is labeled with its month and year; solid circles, initiation point of each swarm where earthquakes started; arrowheads and numbers in parentheses, direction, extent, and speed (in kilometers per hour) of earthquake migration. Swarms with a starting point but no arrowhead or speed have speeds that are difficult to measure. ***B***, Similar diagram as *A* for the Koae fault zone.

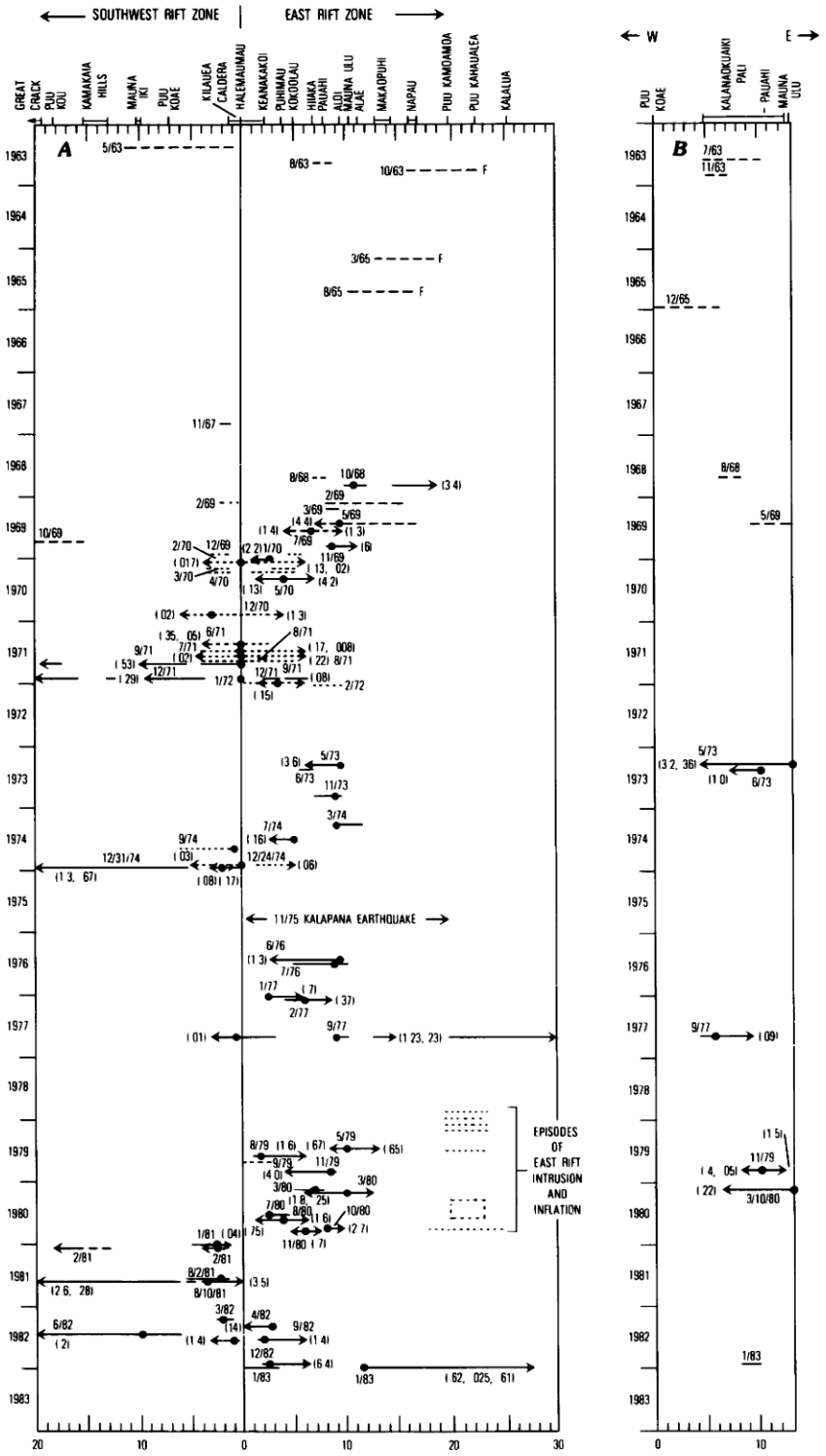
SOUTHWEST RIFT ZONE
EAST RIFT ZONE
GREAT CRACK
PUU KOU
KAMAKAIA HILLS
MAUNA IKI
PUU KOAE
KILAUEA CALDERA
HALEMAUMAU
KEANAKAKOI
PUHIMAU
KOKOOLAU
HIIAKA PAUAHI
ALO MAUNA ULU ALAE
MAKAOPUHI
NAPAU
PUU KAMOAMOA
PUU KAHAUALEA
KALALUA
A
B
W
E
11/75 KALAPANA EARTHQUAKE
EPISODES OF EAST RIFT INTRUSION AND INFLATION
KALANAOKUAIKI PALI
PAUAHI MAUNA ULU

simultaneously, as with the series of eruptions and intrusions during the 1969–74 Mauna Ulu activity or the two intrusions during October 21–22, 1980; (8) intrusions are equally likely to migrate uprift or downrift and sometimes move outward in both directions from their starting points; (9) intrusions may begin and end at several different places, implying a population of significant blockages within the conduit system; (10) the suspected magma reservoir beneath Pauahi is in this section of rift; and (11) the time between the first seismicity and later eruption at the same point is typically 2–3 h, but is at least 5–6 h elsewhere in the rift system. Though many of these differences are probably interrelated and are consequences of the evolution of the ERZ, we will only discuss a few of them in detail. We interpret differences in the seismicity of the ERZ from the caldera to Mauna Ulu as a result of a complex honeycomb of magma conduits, a high frequency of intrusions and the local trend oblique to the rest of the rift system.

The ERZ as a whole has been seismically and volcanically more active than the SWRZ, both historically and prehistorically. This greater activity is recognized by eruption frequency, higher topography, and larger gravity and magnetic anomalies (Duffield and others, 1982). Of the intrusions and eruptions during 1962–83, about 75 percent have been in the ERZ, and about 75 percent of those primarily involved the section uprift of Mauna Ulu.

The extensive seismicity above 2 km depth uprift of Mauna Ulu probably derives from a complex honeycomb of magma conduits and from a response to frequent slow and fast intrusions of the main magma conduit at 3 km depth. Shallow earthquakes may thus be produced in two ways: (1) The direct intrusion of magma into the shallow parts of the interconnected conduit system produces earthquakes near fingers of dikes that branch upward. These vertical intrusions produce upward earthquake migration and may feed an eruption if they reach the surface. (2) The region above the main magma conduit responds mechanically to intrusions below. A fast intrusion produces earthquakes by frequently extending and uplifting a zone that is highly fractured. A slow intrusion generates the same seismic and deformation patterns as a fast intrusion, but is analogous to the shallow seismicity in the caldera above the main magma reservoir. The occurrence of 0- to 2-km seismicity both above the magma reservoir and within the section of rift that can inflate during slow intrusions suggests that extensional stresses applied for long periods play a part in generating the shallow earthquakes.

The misalignment of the rift axis and greatest principal stress may contribute to the complex seismicity of the ERZ between the caldera and Mauna Ulu. Locally, the shallow stress orientation is defined by eruptive fissures in the rifts and faults in the Koae fault zone, which trend east-northeast. Evidence of a similar trend at 3 km depth comes from the intrusion of July 1969, which trended east-northeast and crossed the rift near Hiiaka. Earthquakes migrated east and west from the dike's intersection with the main ERZ magma conduit, which thus fed the intrusion. Regionally, the greatest principal stress is also defined as east-northeast by the remainder of Kilauea's rift system. Most intrusions of the ERZ between the caldera and Mauna Ulu, however, follow the southeast trend of the main magma conduit. The magma conduit is self-sustaining and may have twisted southward with the apparent southward migration of the ERZ (Swanson and others, 1976a). We believe that the rift conduit is now oblique to the greatest principal stress, and this stress direction complicates many of the observed seismic patterns. Stress orientation possibly changes with depth, or the intersecting Koae fault zone perturbs stresses locally. Additional work including focal mechanisms will be required before stress patterns can be adequately discussed.

## UPRIFT EARTHQUAKE MIGRATION

A unique characteristic of the ERZ between the caldera and Mauna Ulu is uprift migration of earthquakes during intrusions. Figures 43.98 and 43.99*B* show that roughly one-half of the migrating intrusions in this section of rift do so in the uprift direction. This observation underscores the fact that intrusions are complex redistributions of magma and stress. Three complicating factors bear on the mechanism of uprift earthquake migration: (1) We interpret the greater vertical extent of earthquakes and the simultaneity of two intrusions or eruptions as indicators of a multitiered honeycomb of magma conduits in the uprift section of the ERZ. (2) Earthquakes appear to be generated by expansion of dike walls under magma pressure. Earthquakes may thus be produced either by rock fracturing near the leading edge of an advancing dike or by a pressure pulse moving within an existing dike. (3) Magma will only flow downward by gravity if confined below hydrostatic pressures, but will flow upward by bouyancy if confined at or above the higher lithostatic pressure. Various intrusion paths are thus possible.

Consider a few examples of how uprift earthquake migration might occur: (1) Over a distance of many kilometers, the magma conduit slopes downward in the downrift direction. Downrift flow might then accompany low stress conditions, and later uprift or bouyant flow might result from high stress conditions. The opening and closing of the connections between conduits in the honeycomb only complicates the possible flow directions. (2) While magma flows downrift, a pulse of pressure causing dike widening and earthquakes might travel uprift. This pulse could occur, for example, after a downrift-moving intrusion reaches a barrier that stops it and creates a back wave of pressure against the flow of magma. Such reversals from downrift to uprift migration accompanied the intrusions of January 1972, December 1974, June 1976, November 1979 and January 1983. (3) The entire intrusion and rifting process may begin at one of the conduit blockages, which serves as a point of stress concentration within the rift. The intrusion may then grow outward from this point in several directions, as did the August 1980 event. The fact that summit deflation begins within minutes of the first intense seismicity argues that a magma storage pocket within the rift, such as suspected at Pauahi, acts only as an initiating stress concentration rather than a major source of magma feeding nearby intrusions. We conclude that the variety of earthquake migration directions in the upper ERZ indicates a complex interaction of varying stresses and pressure gradients on a multiplicity of magma conduits.

## THE STARTING POINTS OF INTRUSIONS

An examination of the places where intrusions begin producing earthquakes reveals likely blockages within the rift conduit where magmatic stresses are concentrated. These blockages probably occur where dikes are squeezed shut or have completely solidified. Magma then accumulates at these barriers, which are the first to break under rising magma pressure. Figure 43.99*A* shows where well-resolved swarms have begun. Five inferred blockages are near the southern part of the caldera, Keanakakoi, Puhimau, Hiiaka and Pauahi-Mauna Ulu. The Keanakakoi zone is adjacent to the summit magma reservoir. The southern part of the caldera initiates nearly all SWRZ intrusions and also surrounds the summit reservoir. These two barriers are the most intuitive, because they regulate inflating magma and are stressed directly by the inflating reservoir. The barriers identified here in seismicity patterns are larger scale versions of the barriers linking dike segments proposed as a source of harmonic tremor (Aki and others, 1977; Aki and Koyanagi, 1981).

The Pauahi-Mauna Ulu barrier, however, initiates more intrusions than any other. The ERZ bends there and meets the Koae fault zone. Structural stresses thus can concentrate in the Pauahi-Mauna Ulu area, where the conduit appears to be frequently pinched closed. Most central ERZ intrusions begin here, and only the January 1983 swarm was observed to begin downrift of this point. Inflationary earthquakes are not recognized downrift of this point, which is the final barrier containing this process. Swanson and others (1976b) proposed a barrier there to account for the pattern of eruption locations during 1965–69 and the absence of any ERZ activity between the August 1965 and August 1968 events. The Pauahi-Mauna Ulu zone was also a major barrier during the June 1976 and November 1979 intrusions: downrift migration of a few earthquakes were immediately followed by a reflected pulse of intense seismicity moving uprift. A wave of magma pressure may have been reflected from this major barrier, which also prevented the intrusion from penetrating farther downrift.

Other barriers within the rifts are recognized by earthquake clusters and by places where intrusive swarms end. Earthquake clusters apparently are caused by barriers having a high stress concentration. The high density and distribution of earthquakes at Puu Kou in the SWRZ implicate it as a major barrier, and it has stopped every intrusion that reached it since at least 1962. Shallow earthquake clusters beneath Mauna Iki (September 1971) and just southwest of Puu Koae (August 1981) also mark significant SWRZ blockages. Another barrier 5 km south of the caldera held the small intrusion of August 2, 1981, before it broke on August 10. Places where the intrusions of September 1977, May 1979, March 1980 and January 1983 started, stopped or paused also suggest five additional barriers in the ERZ. All of these major or suspected barriers are plotted in figure 43.100. The lifetime of these barriers beyond the period of seismic observation is not known.

We summarize the starting points and directions of intrusions in figure 43.99*B*. Triangles point in the approximate directions taken by intrusions, and thin diamonds are used for swarms that spread in both directions from that point. Swarms in the ERZ uprift of Mauna Ulu are about equally likely to spread downrift, uprift, or in both directions. Two such intrusions moved primarily into the Koae. All moving SWRZ intrusions went downrift except for three that started 1.5 km south of the caldera.

The gap between the Hiiaka and Pauahi-Mauna Ulu blockages is a suspected pocket of magma storage within the ERZ conduit. Magma apparently collects behind the major Pauahi-Mauna Ulu barrier. Like the summit magma reservoir, the Pauahi zone is aseismic and is bordered by barriers that initiate intrusions. This magma pocket apparently fed the November 1979 Pauahi eruption with degassed lava (Norm Banks, written commun., 1979), and its existence and proximity are supported by the short 2-hour interval between the first earthquakes and the start of the eruption. Another rift magma reservoir beneath Puu Kamoamoa inflated during the cyclic and slow intrusions of 1978–80. The two ERZ reservoirs and the main summit reservoir are plotted in figure 43.100. A magma reservoir was proposed beneath Makaopuhi by Swanson and others (1976b) and Jackson and others (1975) that may account for the deformation centers reported by Dvorak and others (1983). Seismicity beneath Makaopuhi, however, is not sufficient to resolve a magma reservoir. Other reservoirs are likely present but are not obvious from seismicity patterns. Parts of the rift system between the barriers plotted in figure 43.100 are probably good places to look for reservoirs.

## UPWARD MIGRATION OF EARTHQUAKES

The vertical extent of earthquakes in the ERZ uprift of Mauna Ulu makes upward earthquake migration recognizable and reveals a shallow conduit system. The vertical speed of a dike is generally not as accurate as its lateral speed owing to the greater depth error and narrower depth range of hypocenters, but are observed between 0.1 and 5 km/h (see table 43.1). The retarding effect of gravity may explain why vertical speeds are typically less than lateral speeds. Upward migration is best determined between 3 km depth, where it typically starts, and about 1 km, where the production of earthquakes diminishes as the dike moves upward. The times of eruptions demonstrate that dikes generally slow to a fraction of their initial speed during the last kilometer of their trip to the surface. The persistence of earthquakes below the upward-moving top of a dike shows that typical growth is like a wedge with expansion continuing after the leading edge passes a given point. Clear vertical migration with a slowing near the surface is seen, for example, in the intrusions and eruptions of May and November 1973, July 1974 and November 1979.

Another view of upward movement is provided by the delay time between a dike first reaching a point below an eventual vent (the first earthquakes) and the moment of eruption. This approach is most useful for intrusions where simultaneous migration in several places masks a simple trend on a plot of earthquake depth versus time. Typical delay times are 2–3 h near the caldera and uprift of Mauna Ulu. Short times of dike migration to the surface are reasonable here owing to the vertical extent and shallowness of the conduit system, and the high frequency of intrusive activity. Longer

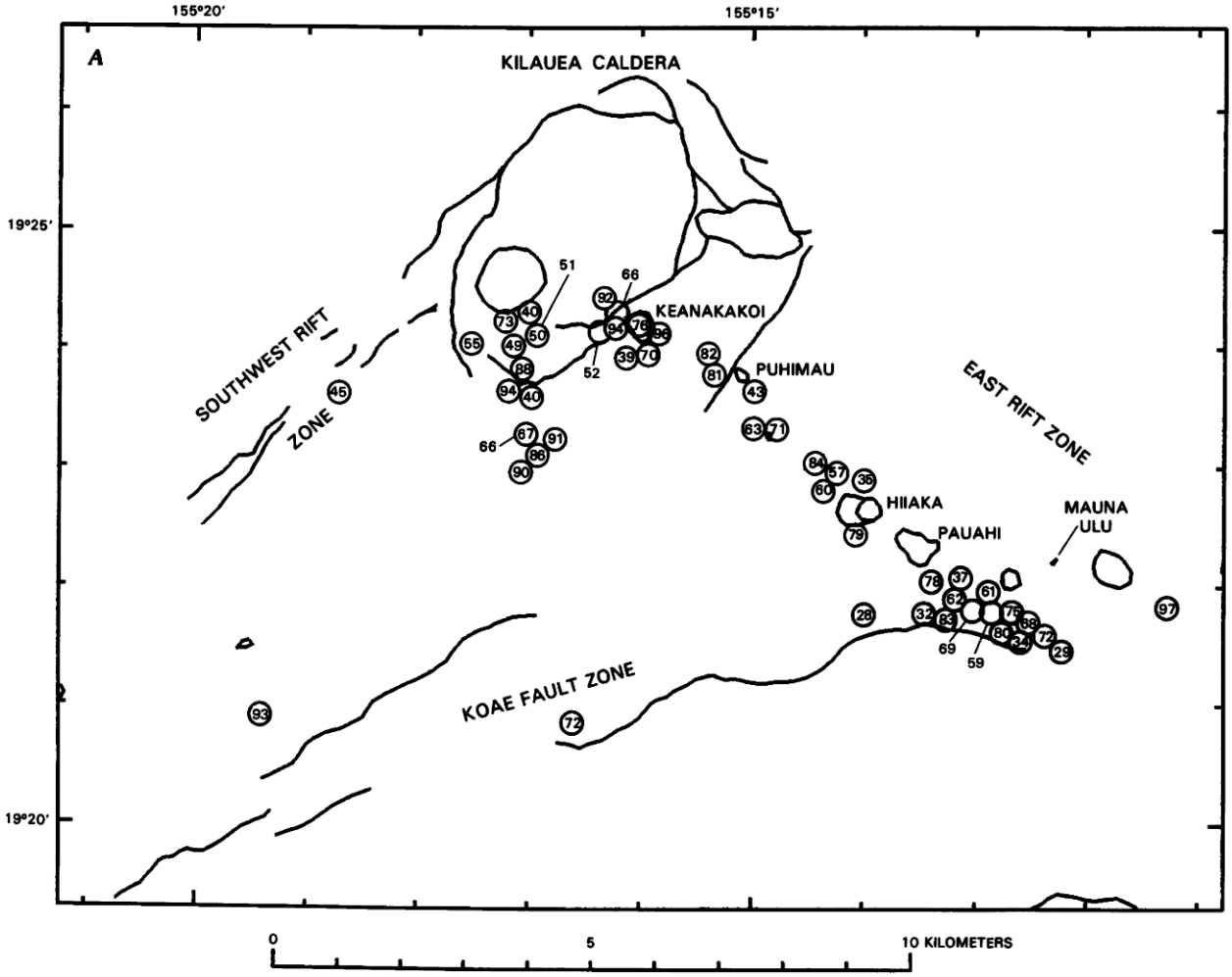


FIGURE 43.99.—Locations of starting points of intrusions. ***A***, Those that can be determined from locations of first earthquakes. Circled numbers are figure numbers and are listed in table 43.1. Starting points cluster into five stress points or rift zone barriers. ***B***, Locations of starting points and directions of intrusions. Thin triangles show general direction of migration (uprift, downrift, or into the Koae fault zone). Thin diamonds indicate earthquakes moved out in both directions.

10- to 12-h delay times are occasionally observed in the caldera-Mauna Ulu area, namely from the December 1974 and November 1979 eruptions, but may be as short as the 1-h delay of the May 1969 Mauna Ulu eruption. The times required for magma to reach the surface characteristically increase with distance from the caldera. A good example is the September 1971 SWRZ eruption, where the delay ranged from about 4 h near the caldera to about 18 h downrift of Mauna Iki. Delays observed in the ERZ are 5 h near Makaopuhi (February 1969), 21 h at Napau (January 1983) and 11 h near Kalalua (September 1977). The infrequency of intrusion, the increased distance from magma conduit to the surface and the reduced magma pressure and temperature downrift presumably all contribute to lengthened transit times of magma to the surface.

## SEQUENTIAL RELATIONS BETWEEN INTRUSIONS ALONG THE RIFT ZONES

Intrusions clearly tend to occur near their predecessors (fig. 43.98), and activity shifts between the ERZ and the SWRZ. For the moment we exclude the 1963–67 period from discussion because of the reduced sensitivity and resolution of the seismic network.

Many intrusions occur in groups of two or three, and may retrace nearly the same path, as in September and December 1971, May and June 1973, June and July 1976, and February and August 1981. In these cases the first intrusion may weaken and heat a conduit for the second. The second intrusion finds an open conduit and may easily push out magma from the previous event rather than

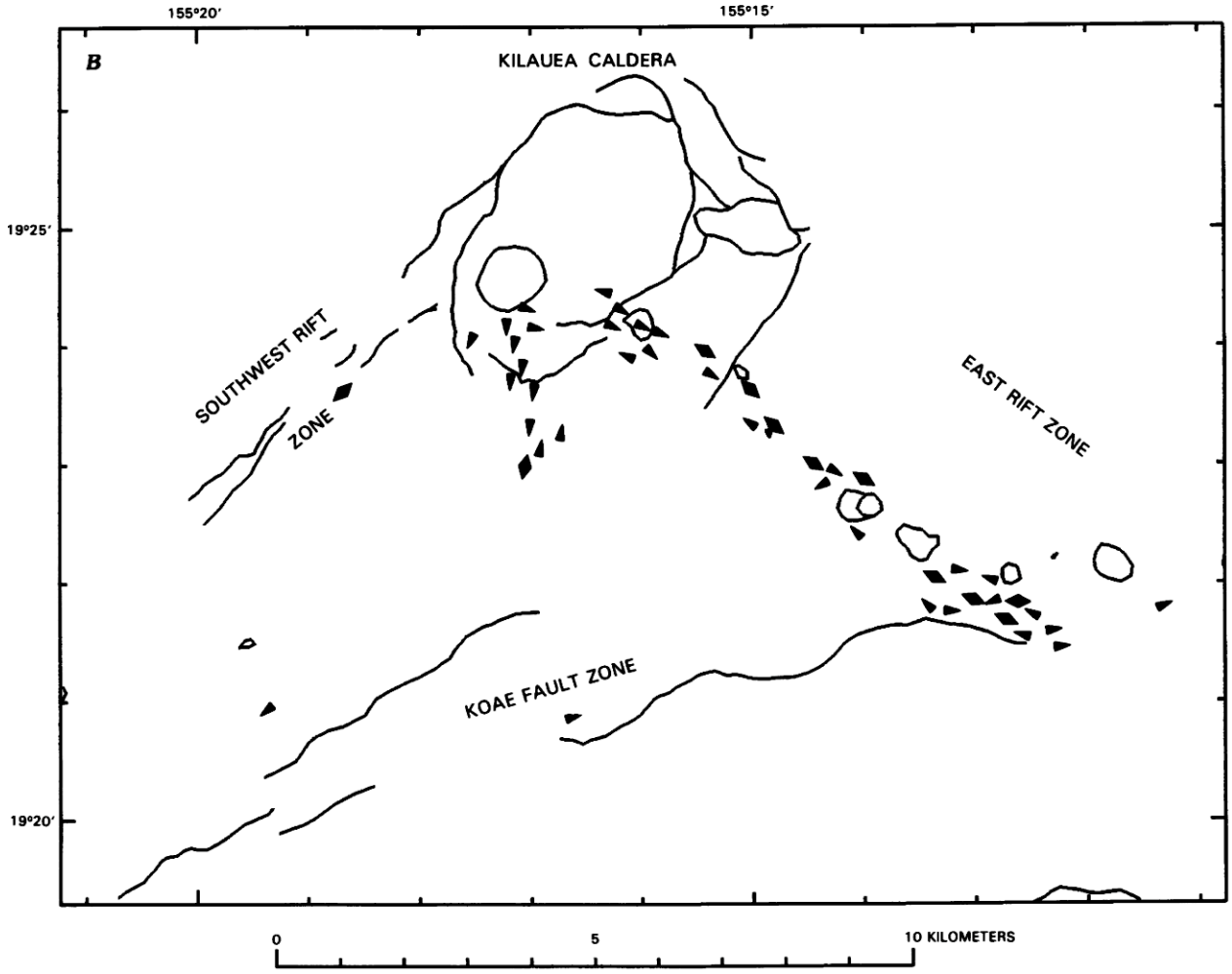


FIGURE 43.99.—Continued.

starting a new one elsewhere. Intrusions may also trigger an adjacent one, as in May, July and November 1969, January and February 1977, May, August and November 1979, March 2 and 10, 1980, July through November 1980, December 1982 and January 1983. These intrusions apparently stressed an adjacent section of rift, which was in turn intruded when magma supply and pressure became sufficient to do so. Alternatively, one intrusion may inhibit a later one if a dike solidifies and increases the compressional stress near it, or locally makes the rift more competent. We prefer the interpretation that a barrier in the magma conduit stops the first intrusion, and this newly stressed barrier becomes the initiation point for the next intrusion.

A shifting pattern of intrusions from the ERZ to the SWRZ and back is also apparent from figure 43.98. Four cycles of activity occurred during the 1968–83 period, each lasting 3–4 yr. The cycle begins in the ERZ with intrusions originating in the general region of Mauna Ulu, noted above as a major stress point of the rift. Subsequent intrusions in the first part of the cycle are mostly in the Kilauea caldera-Mauna Ulu section of the ERZ. As a whole they may migrate uprift, as during 1968–70. In two of the four cycles, this ERZ activity was followed by a period of inflationary swarms and high summit tilt (1970–71 and 1974). The westward progression of activity continued into the SWRZ for three of the four cycles. Kilauea did not activate the SWRZ in 1977–78. The last stage in the cycle is 1–2 years of quiescence. The quiescent stage was omitted in 1982, when intrusions immediately migrated from the SWRZ back to the ERZ. A distorted and probably incomplete fifth cycle may have occurred during 1963–67. A shift from the

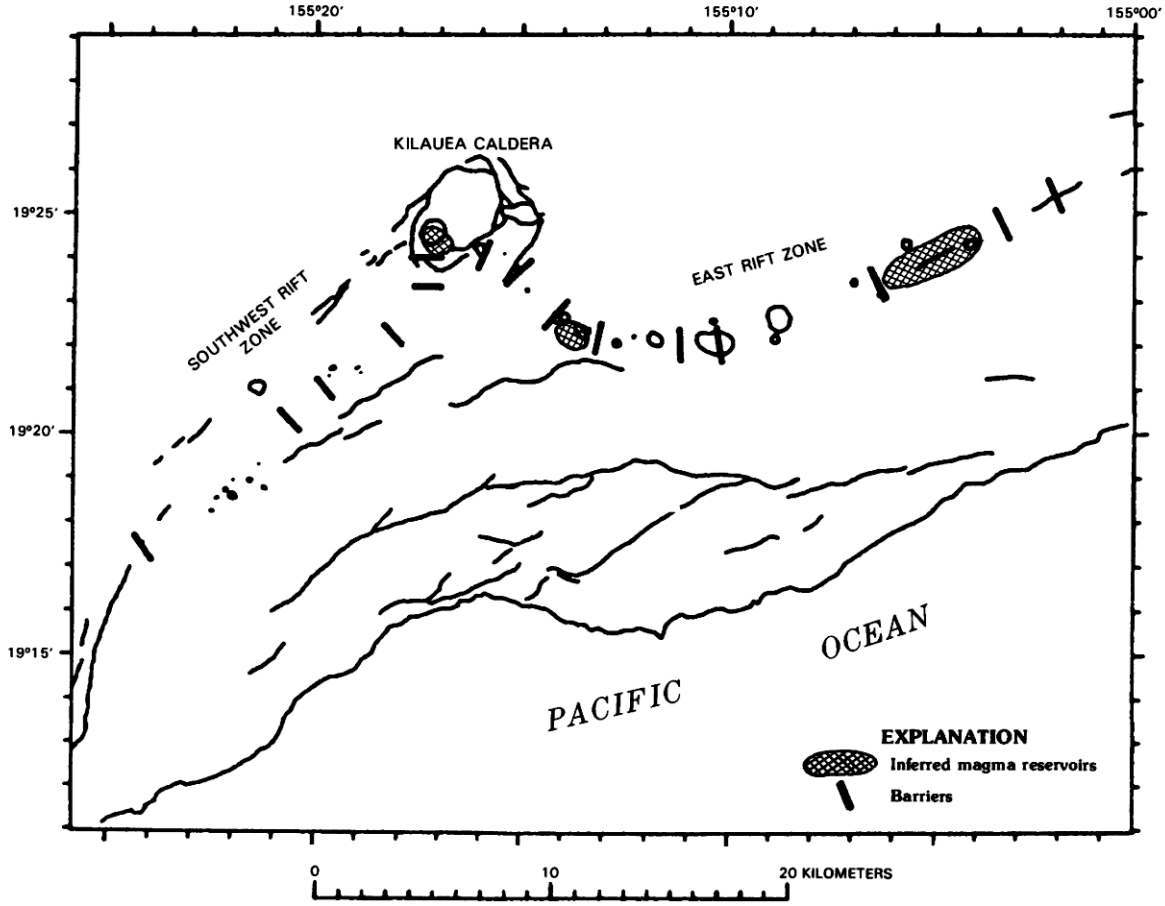


FIGURE 43.100.—Magma reservoirs and barriers within Kilauea caldera and its rift zones. Thick lines transverse to rifts, locations of stress points or barriers within rift zone conduits. Barriers are derived from points at which intrusions frequently start and stop. Three shaded zones mark main magma reservoir beneath caldera and secondary reservoirs in east rift zone inferred from seismicity.

SWRZ to the ERZ occurred in 1963, but without a long pause. Activity moved up the ERZ to the caldera in 1967 but did not then produce a SWRZ intrusion. The overall pattern is then one of intrusions progressing up the ERZ through the summit to the SWRZ, followed by a rest before the cycle starts again.

These large-scale shifts of intrusion location may be aided by the tendency of one intrusion to trigger an adjacent one, but this tendency alone cannot produce such systematic shifts. Some regional and oscillatory tectonic process seems also to be at work. The accumulated compression in the south flank adjacent to one rift may hinge the other rift open, making intrusions there more probable. Once a series of intrusions begins in one rift zone, they tend to trigger each other until compression of the south flank retards intrusion in that rift and favors the other one. Using similar reasoning, Duffield and others (1982) suggested that a combination of south-flank displacement and a deflated Mauna Loa foster SWRZ intrusions by a reduction of compressional stress there.

Completion of rifting downward to the 10-km depth at which the volcanic pile is decoupled from the prevolcanic sea floor may play a part in the cycle. We interpret the 5- to 10-km depth swarm and intrusion of the SWRZ in June 1982 as extension of rifting to depth following the series of shallow 1981 intrusions. A similar but aseismic process may occur after each cycle or half-cycle, possibly during the seismically quiescent interval between cycles.

If changes in regional stress play a part in the intrusion cycle, then large earthquakes within Kilauea's flanks must also interact with the cycle. The $M=7.2$ Kalapana earthquake in November 1975 was by far the largest during this period and caused Kilauea's south

flank to slip seaward as much as 8 m. Surprisingly, the earthquake did not disrupt the cycle in a major way: the SWRZ intrusion of December 1974 was followed in 18 months by resumption of intrusions in the ERZ, as if no earthquake had occurred. The Kalapana earthquake, however, may have caused some significant changes. (1) Intrusions outnumbered eruptions in the six years following the earthquake, but the reverse was true prior to the earthquake (Klein, 1982b). This switch may have resulted from a drop in confining stress on the rifts and the inability of magma to develop sufficient pressure to reach the surface. (2) The cycle following the earthquake was disrupted to the extent that no SWRZ intrusion occurred. The greatest coseismic displacements were in the flank south of the ERZ, which may have favored it as the site of intrusions until the end of the following cycle. (3) The two cycles following the earthquake had no period of inflationary swarms. (4) Two major ERZ eruptions penetrated downrift of Kalalua, but no others had since the 1960 eruption. (5) The cyclic slow intrusions and magma accumulation near Puu Kamoamoa may have been made possible by reduced stress across the ERZ. (6) The shift of intrusions from the SWRZ back to the ERZ in 1982 without a quiescent period shows that the ERZ was in some sense favored for intrusion, as in (2) above. (7) The Puu Oo eruption that started in January 1983 captured all of Kilauea's magma supply and prevented any other eruptions or intrusions. The long-lived Mauna Ulu eruption, however, coexisted with other intrusions. The intervening Kalapana earthquake may have permitted the establishment of a major magma path to the exclusion of others.

Another tectonic change may have been coupled with the shift of intrusive activity from the ERZ to the SWRZ during 1974. Significant earthquakes occurred in the Kaoiki seismic zone on June 19, 1974 ($M=4.8$), November 30, 1974 ($M=5.5$) and December 15, 1974 ($M=4.8$). The mechanism of the events was strike-slip (Endo and others, 1978; Endo, 1985), which acted to relieve compressive stress across the SWRZ and permit an easier intrusion path than before. Shaking from the larger earthquake may also have disturbed the delicately balanced equilibrium of the magma system. The Kaoiki earthquakes may have been triggered by the inflation accompanying the seismic reawakening of Mauna Loa (Koyanagi and others, 1975), which would have acted to increase the shear stress on the ultimate fault plane. Thus, shifts in rift activity could be accomplished through mechanical coupling with Kilauea's flanks. Large earthquakes in the flanks apparently play a part, but aseismic deformation and even Mauna Loa may contribute as well. Seismicity and magma movement at Kilauea are clearly linked in a variety of ways, and earthquakes provide many insights into the dynamics of Kilauea Volcano.

## REFERENCES


Aki, K., Fehler, M., and Das, S., 1977, Source mechanism of volcanic tremor: fluid-driven crack models and their application to the 1963 Kilauea eruption: Journal of Volcanology and Geothermal Research, v. 2, 259-287.

Aki, K., and Koyangi, R.Y., 1981, Deep volcanic tremor and magma ascent mechanism under Kilauea, Hawaii: Journal of Geophysical Research, v. 86, p. 7095-7109.

Ando, M., 1979, The Hawaii earthquake of November 29, 1975: low dip angle faulting due to forceful injection of magma: Journal of Geophysical Research, v. 84, p. 7616-7626.

Bosher, R., and Duennebier, F.K., 1985, Seismicity associated with the Christmas 1965 event at Kilauea Volcano: Journal of Geophysical Research, v. 90, p. 4529-4536.

Crosson, R.S., and Endo, E.T., 1982, Focal mechanisms and locations of earthquakes in the vicinity of the 1975 Kalapana earthquake aftershock zone 1970–1979: implications for tectonics of the south flank of Kilauea Volcano, Island of Hawaii: Tectonics, v. 1, p. 495-542.

Decker, R.W., Koyanagi, R.Y., Dvorak, J.J., Lockwood, J.P., Okamura, A.T., Yamashita, K.M., and Tanigawa, W.R., 1983, Seismicity and surface deformation of Mauna Loa Volcano, Hawaii: Eos, Transactions, American Geophysical Union, v. 64, p. 545-547.

Dieterich, J.H., and Decker, R.W., 1975, Finite element modelling of surface deformation associated with volcanism: Journal of Geophysical Research, v. 80, p. 4094-4102.

Duffield, W.A., 1975, Structure and origin of the Koae fault system, Kilauea Volcano, Hawaii: U.S. Geological Survey Professional Paper 856, 12 p.

Duffield, W.A., Christiansen, R.L., Koyanagi, R.Y., and Peterson, D.W., 1982, Storage, migration and eruption of magma at Kilauea Volcano, Hawaii, 1971–1972: Journal of Volcanology and Geothermal Research, v. 13, p. 273-307.

Duffield, W.A., Jackson, D.B., and Swanson, D.A., 1976, The shallow, forceful intrusion of magma and related ground deformation at Kilauea Volcano, May 15–16, 1970: Bulletin Volcanologique, v. 39, p. 577-597.

Dvorak, J., Okamura, A.T., and Dieterich, J.H., 1983, Analysis of surface deformation data, Kilauea Volcano, Hawaii, October 1966 to September 1970: Journal of Geophysical Research, v. 88, p. 9295-9304.

Dvorak, J.J., Okamura, A.T., English, T.T., Koyanagi, R.Y., Nakata, J.S., Sako, M.K., Tanigawa, W.R., and Yamashita, K.M., 1986, Mechanical response of the south flank of Kilanea Volcano, Hawaii to intrusive events along the rift zones, Tectonophysics, v. 124, p. 193-209.

Dzurisin, D., Anderson, L.A., Eaton, G.P., Koyanagi, R.Y., Lipman, P.W., Lockwood, J.P., Okamura, R.T., Puniwai, G.S., Sako, M.K., and Yamashita, K.M., 1980, Temporal variations in gravity on Kilauea Volcano, Hawaii: implications for the magma budget, November 1975–September 1977: Journal of Volcanology and Geothermal Research, v. 7, p. 241-270.

Dzurisin, D., Koyanagi, R.Y., and English, T.T., 1984, Magma supply and storage at Kilauea Volcano, Hawaii, 1956–1983: Journal of Volcanology and Geothermal Research, v. 21, p. 177-206.

Eaton, J.P., 1962, Crustal structure and volcanism in Hawaii, *in* Crust of the Pacific Basin: American Geophysical Union Monograph no. 6, p. 13-29.

Eaton, J.P., and Murata, K.J., 1960, How volcanoes grow: Science, 132, p. 925.

Ellsworth, W.L., and Koyanagi, R.Y., 1977, Three dimensional crust and mantle structure of Kilauea Volcano, Hawaii: Journal of Geophysical Research, v. 82, p. 5379-5394.

Endo, E.T., 1985, Seismotectonic framework for the southeast flank of Mauna Loa Volcano, Hawaii: Seattle, University of Washington, PhD dissertation, 350 p.

Endo, E.T., Koyanagi, R.Y., and Klein, F.W., 1978, Geologic and seismic evidence for strike-slip faulting between Kilauea and Mauna Loa Volcanoes, Hawaii [abs.]: Seismological Society of America, annual meeting, Sparks, Nevada.

Fiske, R.S., and Jackson, E.D., 1972, Orientation and growth of Hawaiian volcanic rifts: the effect of regional structure and gravitational stresses: Proceedings of Royal Society of London, series A, v. 329, p. 299-326.

Fiske, R.S., Kinoshita, W.T., 1969, Inflation of Kilauea Volcano prior to its 1967–68 eruption: Science, v. 165, p. 341-349.

Fiske, R.S., and Koyanagi, R.Y., 1968, The December 1965 eruption of Kilauea Volcano, Hawaii: U.S. Geological Survey Professional Paper, 607, 21 p.

Furumoto, A.S., and Kovach, R.L., 1979, The Kalapana earthquake of November 29, 1975: an intraplate earthquake and its relation to geothermal processes: Physics of the Earth and Planet Interiors, v. 18, p. 197-208.

Hill, D.P., 1977, A model for earthquake swarms: Journal of Geophysical Research, v. 82, p. 1347-1352.

Jackson, D.B., Swanson, D.A., Koyanagi, R.Y., and Wright, T.L., 1975, The August and October 1968 east rift eruptions of Kilauea Volcano, Hawaii: U.S. Geological Survey Professional Paper 890, 33 p.

Kinoshita, W.T., 1967, May 1963 earthquakes and deformation in the Koae fault zone, Kilauea Volcano, Hawaii: U.S. Geological Survey Professional Paper 575–C, p. C173-C176.

Kinoshita, W.T., Koyanagi, R.Y., Wright, T.L., and Fiske, R.S., 1969, Kilauea Volcano: the 1967–1968 summit eruption: Science, v. 166, p. 459-468.

Klein, F.W., 1978, Hypocenter location program HYPOINVERSE: U.S. Geological Survey Open-File Report 78–694, 113 p.

——— 1981, A linear gradient crustal model for south Hawaii: Bulletin of the Seismological Society of America, v. 71, p. 1503-1510.

——— 1982a, Earthquakes at Loihi submarine volcano, and the Hawaiian hot spot: Journal of Geophysical Research, v. 87, p. 7719-7726.

——— 1982b, Patterns of historical eruptions at Hawaiian volcanoes: Journal of Volcanology and Geothermal Research, v. 12, p. 1-35.

——— 1983, Users guide to QPLOT, an interactive computer plotting program for earthquake and geophysical data: U.S. Geological Survey Open-File Report 83-621, 40 p.

——— 1984, Eruption forecasting at Kilauea Volcano, Hawaii: Journal of Geophysical Research, v. 89, p. 3059-3073.

Klein, F.W., and Koyanagi, R.Y., 1980, Hawaiian volcano observatory seismic network history 1950–79: U.S. Geological Survey Open-File Report 80-302, 84 p.

——— 1985, Earthquake map of south Hawaii 1968–1981: U.S. Geological Survey Miscellaneous Field Investigations Map I–1611, scale, 1:100,000.

Koyanagi, R.Y., and Endo, E.T,, 1971, Hawaiian seismic events during 1969: U.S. Geological Survey Professional Paper 750–C, p. C158-C164.

Koyanagi, R.Y., Endo, E.T., and Ebisu, J.S., 1975, Reawakening of Mauna Loa Volcano, Hawaii: a preliminary evaluation of seismic evidence: Geophysical Research Letters, v. 2, p. 405-408.

Koyanagi, R.Y., Endo, E.T., Tanigawa, W.R., Nakata, J.S., Tomori, A.H., and Tamura, P.N., 1984, Kaoiki, Hawaii earthquake of November 16, 1983: a preliminary compilation of seismographic data at the Hawaiian Volcano Observatory: U.S. Geological Survey Open-File Report 84–798, 6 p.

Koyanagi, R.Y., Endo, E.T., and Ward, P.L., 1976b, Seismic activity on the Island of Hawaii, 1970–1973, *in* The geophysics of the Pacific Ocean basin and its margin: American Geophysical Union Monograph 19, p. 169-173.

Koyanagi, R.Y., Nakata, J.S., and Tanigawa, W.R., 1981, Seismicity of the lower east rift zone of Kilauea Volcano, Hawaii, 1960–1980: U.S. Geological Survey Open-File Report 81–984, 15 p.

Koyanagi, R.Y., Swanson, D.A., and Endo, E.T., 1972, Distribution of earthquakes related to mobility of the south flank of Kilauea Volcano, Hawaii: U.S. Geological Survey Professional Paper 800–D, p. D89-D97.

Koyanagi, R.Y., Tanigawa, W.R., and Nakata, J.S., in press, Seismicity associated with the eruption of Kilauea Volcano from January 1983 to July 1984, *in* Wolfe, E.W., ed., The Puu Oo eruption of Kilauea Volcano, Hawaii: the first 1½ years: U.S. Geological Survey Professional Paper.

Koyanagi, R.Y., Unger, J.D., Endo, E.T., and Okamura, A.T., 1976a, Shallow earthquakes associated with inflation episodes at the summit of Kilauea Volcano, Hawaii: Bulletin Volcanologique, v. 39, p. 621-631.

Liu, H-P., and Kosloff, D., 1978, Elastic-plastic bending of the lithosphere incorporating rock deformation data, with application to the structure of the Hawaiian Archipelago: Tectonophysics, v. 50, p. 249-274.

Lipman, P.W., Lockwood, J.P., Okamura, R.T., Swanson, D.A., and Yamashita, K.M., 1985, Ground deformation associated with the 1975 magnitude-7.2 earthquake and resulting changes in activity of Kilauea Volcano, Hawaii: U.S. Geological Survey Professional Paper 1276, 45 p.

Macdonald, G.A., 1956, The structure of Hawaiian volcanoes, Koninklijk Nederlandsch Geologisch Mijnbouwkundig Gehootschap, v. 16, p. 274-295.

Mogi, K., 1962, Study of the elastic shocks caused by the fracture of heterogeneous materials and its relation to earthquake phenomena: Bulletin of the Earthquake Research Institute of Tokyo University, v. 40, p. 125-173.

——— 1963, Some discussions on aftershocks, foreshocks, and earthquake swarms—the fracture of a semi-infinite body caused by an inner stress origin and its relation to the earthquake phenomena, 3: Bulletin of the Earthquake Research Institute of Tokyo University, v. 41, p. 615-658.

Moore, J.G., and Koyanagi, R.Y., 1969, The October 1963 eruption of Kilauea Volcano, Hawaii: U.S. Geological Survey Professional Paper 614–C, p. C1-C14.

Moore, R.B., Helz, R.T., Dzurisin, D., Eaton, G.P., Koyanagi, R.Y., Lipman, P.W., Lockwood, J.P., and Puniwai, G.S., 1980, The 1977 eruption of Kilauea Volcano, Hawaii: Journal of Volcanology and Geothermal Research, v. 7, p. 189-210.

Nakamura, K., 1980, Why do long rift zones develop in Hawaiian volcanoes: a possible role of thick oceanic sediments (in Japanese with English abstract): Bulletin of the Volcanological Society of Japan, v. 25, no. 4, p. 255-269.

——— 1981, Why do long rift zones develop better in Hawaiian volcanoes: a possible role of thick oceanic sediments: Symposium on Oceanic Volcanism, International Association of Volcanology and Chemistry of the Earth's Interior, Azores University, 1980, Proceedings.

Nakata, J.S., Tanigawa, W.R., Klein, F.W., and Decker, R.W., 1982, Hawaiian Volcano Observatory Summary 81, Seismic data, January to December 1981: U.S. Geological Survey Hawaiian Volcano Observatory, Hawaii National Park.

Pollard, D.D., Delaney, P.T., Duffield, W.A., Endo, E.T., and Okamura, A.T., 1983, Surface deformation in volcanic rift zones: Tectonophysics, v. 94, p. 541-584.

Richter, C.F., 1958, Elementary seismology: W.H. Freeman, San Francisco, 768 p.

Ryan, M.P., Blevins, J.Y.K., Okamura, A.T., and Koyanagi, R.Y., 1983, Magma reservoir subsidence mechanics: theoretical summary and application to Kilauea Volcano, Hawaii: Journal of Geophysical Research, v. 88, p. 4147-4181.

Ryan, M.P., Koyanagi, R.Y., and Fiske, R.S., 1981, Modelling the three-dimensional structure of macroscopic magma transport systems: application to Kilauea Volcano, Hawaii: Journal of Geophysical Research, v. 86, p. 7111-7129.

Shaw, H.R., 1980, The fracture mechanisms of magma transport from the mantle to the surface, *in* Hargraves, R.B., ed., Physics of magmatic processes: Princeton, Princeton University Press, p. 201-264.

Swanson, D.A., 1972, Magma supply rate at Kilauea Volcano, 1952–1971: Science, v. 175, pp. 169-170.

Swanson, D.A., Duffield, W.A., and Fiske, R.S., 1976a, Displacement of the south flank of Kilauea Volcano: the result of forceful intrusion of magma into the rift zones: U.S. Geological Survey Professional Paper 963, 39 p.

Swanson, D.A., Duffield, W.A., Jackson, D.B., and Peterson, D.W., 1979, Chronological narrative of the 1969–71 Mauna Ulu eruption of Kilauea Volcano, Hawaii: U.S. Geological Survey Professional Paper 1056, 55p.

Swanson, D.A., Jackson, D.B., Koyanagi, R.Y., and Wright, T.L., 1976b, The February 1969 east rift eruption of Kilauea Volcano, Hawaii: U.S. Geological Survey Professional Paper 891, 30 p.

Thurber, C.H., Um, J.H., and Das, S., 1983, New ideas in seismic ray tracing and velocity inversion: applications to Kilauea Volcano, Hawaii [abs.]: Eos, Transactions, American Geophysical Union, v. 64, p. 901.

Thurber, C.H., Karpin, T., and Um, J.H., 1984, Focal mechanisms of earthquakes at Kilauea Volcano: a detailed study [abs.]: Eos, Transactions, American Geophysical Union, v. 65, p. 1001.

Thurber, C.H., 1984, Seismic detection of the summit magma complex of Kilauea Volcano, Hawaii: Science, v. 223, p. 165-167.

Unger, J. D., and Koyanagi, R.Y., 1979, Evidence of the effects of shallow magma intrusion on Kilauea Volcano [abs.]: Hawaii Symposium on Intraplate Volcanism and Submarine Volcanism, Hilo, Hawaii, July 1979.

Unger, J.D., and Ward, P.L., 1979, A large, deep Hawaiian earthquake—the Honomu, Hawaii event of April 26, 1973: Bulletin of the Seismological Society of America, v. 69, p. 1771-1781.

Watts, A.B., and Cochran, J.R., 1974, Gravity anomalies and flexure of the lithosphere along the Hawaiian-Emperor Seamount Chain: Geophysical Journal of the Royal Astronomical Society, v. 38, pp. 119-141.

Watts, A.B., ten Brink, U.S., Buhl, P., and Brocher, T.M., 1985, A multichannel seismic study of lithospheric flexure across the Hawaiian-Emperor Seamount Chain: Nature, v. 315, pp. 105-111.

Wolfe, E.W., Neal, C.A., Banks, N.O., Duggan, T., and Ulrich, G., in press. Geologic observations and chronology of the first 20 episodes of the Puu Oo eruption, January 3, 1983 through June 8, 1984, *in* Wolfe, E. W., ed., The Puu Oo eruption of Kilauea Volcano, Hawaii: the first 1½ years: U.S. Geological Survey Professional Paper.

Wright, T.L., and Kinoshita, W.T., 1968, March 1965 eruption of Kilauea Volcano and the formation of Makaopuhi lava lake: Journal of Geophysical Research, v. 73, p. 3181-3205.

Wyss, M., 1973, Towards a physical understanding of the earthquake frequency distribution: Geophysical Journal of the Royal Astronomical Society, v. 31, p. 341.

Wyss, M., Klein, F.W., and Johnston, A.C., 1981, Precursors to the Kalapana $M=7.2$ earthquake: Journal of Geophysical Research, v. 86, p. 3881-3900.

Zucca, J.J., and Hill, D.P., 1980, Crustal structure of the southeast flank of Kilauea volcano, Hawaii, from seismic refraction measurements: Bulletin of the Seismological Society of America, v. 70, p. 1149-1159.

# STRUCTURAL DAMAGE AND GROUND FAILURES FROM THE NOVEMBER 16, 1983, KAOIKI EARTHQUAKE, ISLAND OF HAWAII

*By* Jane M. Buchanan-Banks


## ABSTRACT

**On November 16, 1983, at 0613 (H.s.t.), a magnitude 6.6 earthquake occurred on the Island of Hawaii at a depth of 12 km midway between the active volcanoes of Mauna Loa and Kilauea. The right-lateral strike-slip faulting was probably generated by compressional stresses caused by inflation of the crustal magma reservoirs of both volcanoes. The earthquake shaking was felt for nearly one minute and caused substantial damage to structures in the southeastern part of the island. Landslides occurred on steep slopes throughout the island and, together with cracking of the ground and vibrational settling of subsurface materials, caused temporary closure of some roads. Fortunately, only a few people received minor injuries as a result of the earthquake; this was most likely because it struck at an early hour, when most people were still in bed.**


## INTRODUCTION

At 0613 Hawaii standard time (H.s.t.) on Wednesday, November 16, 1983, most residents of the Island of Hawaii were awakened by a magnitude 6.6 earthquake. The shaking from this earthquake was felt for nearly one minute and caused substantial damage in the southeastern part of the island, throwing houses from foundations, toppling water tanks, and causing electrical power and telephone outages in the epicentral area. Instruments at the U.S. Geological Survey's Hawaiian Volcano Observatory (HVO) were rendered temporarily inoperative. Landslides occurred on the steep caldera and crater walls in Hawaii Volcanoes National Park and on steep slopes elsewhere on the island. These landslides together with ground cracking and failure of subsurface materials made some roads impassable.

Only four or five people were injured in the earthquake and their injuries were slight. This was probably because it occurred at an early hour, when most residents were still in bed. However, financial losses from the earthquake were estimated at $7 million (Harry Kim, Hawaii Civil Defense Director, oral commun., 1983).


### ACKNOWLEDGMENTS

The author gratefully acknowledges the cooperation of the residents of the Volcano Golf and Country Club Subdivision and of Upper Wright Road, Volcano, who, at a time of great personal stress and loss, assisted in the accumulation of damage information, and of J. Barclay Stokes, U.S. Geological Survey (USGS), who took many of the photographs in those communities. Information on the location of the fault trace and on damage in the towns of Pahala, Wood Valley, Kapapala Ranch and parts of Volcano were supplied by Elliot T. Endo, USGS, Vancouver, Washington, who was also kind enough to review the manuscript. Harry Kim, Hawaii Civil Defense Director, Hilo, supplied much of the information on locations of road and structural damage, both public and private, in the Hilo area. I thank David K. Keefer for thorough and thoughtful review of the manuscript. Discussions with Robert Y. Koyanagi and Norman G. Banks provided many helpful insights that contributed to this research.


## THE EARTHQUAKE

The earthquake was located in the Kaoiki region between the centers of Hawaii's most active volcanoes, Mauna Loa and Kilauea, at a depth of nearly 12 km (fig. 44.1). Inflation of the summit regions of both Mauna Loa and Kilauea apparently caused sufficient horizontal compressional stress between the two crustal magma reservoirs to generate the faulting. A *P*-wave first-motion analysis from local seismic data indicates a strike-slip mechanism with a northeast-trending nodal plane (see fig. 44.1, inset); right-lateral motion is preferred on the basis of the pattern of ground cracking from this and previous seismic events in the Kaoiki region (Koyanagi and others, 1984, p. 1). Ground cracking indicating right-lateral faulting included a system of left-stepping echelon extension fractures found at about the 1,900-m elevation on Mauna Loa Road. The fractures were traced 4.5 km to either side of the road. Extension of 20–30 cm was common across the longer fractures (Endo, 1985, p. 67).

Detailed analysis of the mainshock and aftershock sequence, however, did not substantiate a simple strike-slip mechanism. There were several discrepancies: (1) The distribution of aftershocks did not define a fault plane that substantiated the mechanism derived from the mainshock. (2) Most aftershocks occurred at shallower depths than the mainshock. (3) Teleseismic fault-plane solutions from other locations were slightly, but significantly, different (Endo, 1985, p. 186-187, 211-213). To explain these discrepancies Endo suggests that the initial right-lateral strike-slip movement was immediately followed by southeastward low-angle slip of part of the southeast flank of Mauna Loa (Endo, 1985, p. 213-215). Such slip would relieve the compressional stresses in the epicentral area, thereby altering the pattern and depth of the aftershocks, and would account for the differences in teleseismic solutions.

## KAOIKI EARTHQUAKES

Seismic events called Kaoiki earthquakes occur in a region midway between the summits of Mauna Loa and Kilauea Volcanoes. Although the region takes its name from the Kaoiki fault system, a prominant geologic feature on the southeast flank of Mauna Loa, the seismically active area lies more than 5 km northwest of the Kaoiki system. The Kaoiki fault system probably developed as a result of gravitational stresses induced by forceful intrusions of magma along the southwest rift zone of Mauna Loa before Kilauea was large enough to provide a buttress (Swanson and others, 1976, p. 32). Radiocarbon dating of lava flows and stratigraphic relationships along the fault system, however, indicate that the normal faults of the Kaoiki system have been inactive for tens of thousands of years (Lipman and Swenson, 1984).

The Kaoiki region, on the other hand, is an area of constantly high seismicity with hundreds to thousands of earthquakes recorded by nearby seismographs each year. During the past 25 years, three earthquakes of magnitude greater than 5 have occurred in the Kaoiki region (table 44.1); these events were aligned within the seismic zone in a northeast-southwest direction and were separated from each other by about 3 km (Koyanagi and others, 1984, p. 3). This pattern of seismicity could not be related to any known geologic structure until 1976, when surface fissures probably related to the November 1974 Kaoiki earthquake were discovered (Endo, 1985, p. 42). First-motion data compiled by Endo (1985) for crustal earthquakes from 1959 to 1982 at depths less than 16 km beneath the southeast flank of Mauna Loa and nearby areas of Kilauea confirm a fault system trending predominantly northeast-southwest between Mauna Loa and Kilauea. However, the combination of strike-slip and dip-slip solutions from this compilation also imply a complex tectonic region having both compressional and extensional local stresses (Koyanagi and others, 1984, p. 4).

## SEISMIC INTENSITY

The greatest structural damage and abundance of landslides occurred in the epicentral area. Maximum intensity was estimated at VIII to IX (modified Mercalli scale) in parts of Kau and Puna Districts (fig. 44.2). Especially hard hit were the summit area of Kilauea and parts of Hilo. A table of relative intensities for the island was compiled from residents' reports received at the HVO, from information provided by the Hawaii Civil Defense Agency, and from fieldwork (table 44.2; for locations see fig. 44.1).

## DESCRIPTION OF DAMAGE

The fault rupture in the epicentral area occurred in an uninhabited part of the island (fig. 44.1) and therefore caused no direct damage to structures. However, the earthquake shaking damaged more than 350 homes and 35 businesses in the southeastern part of the island (Hawaii Tribune-Herald, 1983). A preliminary survey of public buildings conducted by governmental agencies found minor to moderate damage to two health facilities (one in Hilo, one in south Kona), seven schools (five in Hilo, two in Kau), two libraries (one in Hilo, one in Laupahoehoe), and one church in North Kohala (Hawaii County Civil Defense, written commun., 1983). In addition, there was structural damage to Hilo Hospital, resulting in a reduction in available beds in some units. The new Hilo Hospital under construction at the time of the earthquake was almost undamaged.

In the epicentral area, telephone service, electricity and water supplies were affected (Chiu and others, 1984). Most telephone and electrical services were restored within a few hours. However, residents of the area obtain water from rain-catchment systems; hence the destruction of, and damage to, water tanks and connecting pipes caused great inconvenience and disruption to many people.

### STRUCTURAL DAMAGE

Most houses on the island are single-story wood-frame structures with either post-and-pier (fig. 44.3) or concrete slab foundations. In this earthquake, houses with post-and-pier construction sustained greater structural damage, primarily because of lateral displacement of the piers and consequent decoupling of the piers from the houses. The piers often moved with respect to each other as well as to the ground. Most structures with concrete slab foundations, on the other hand, had little damage, generally limited to hairline cracks through the slabs. However, the degree of shaking damage to loose objects inside houses seemed to have little or no relation to the type of foundation.

#### KAU DISTRICT

##### Ka Lae, Waiohinu, Naalehu, Punaluu and Pahala

There was little structural damage reported from these towns. One house about one mile south of the highway on the Ka Lae Road moved 1.2–1.5 m northward off its foundation (fig. 44.1, locality 1; Vicki and Robert Taylor, oral commun., 1983). The house was supported on cylindrical concrete piers almost 1 m high and about 0.4 m in diameter with a 2.5-cm length of reinforcing steel bar (rebar) protruding through the piers into beams in the subfloor of the house. The rebars penetrated the subflooring when the house landed on them during the ground movement.

##### Wood Valley

Wood Valley is a sparsely populated agricultural community built mostly on an ash deposit and on deposits of landslides induced by the magnitude 7.5–8 1868 earthquake and earlier earthquakes (Brigham, 1869, p. 574-576; Tilling and others, 1976, p. 29-30; fig. 44.1, locality 2; fig. 44.4). Several houses of post-and-pier construction (two built on ash and (or) landslide deposit) moved more than 0.5 m off their foundations toward the southeast at azimuths 105°–155° (fig. 44.4, vectors a, b, c). The 8-cm by 8-cm posts of one house were connected to the foundation piers with 0.5-cm-thick steel plates. The plates were not always on the same side of the posts, and therefore some posts were snapped at the anchor bolts connecting the post to the plate; other posts were relatively

undamaged, but the steel plate was bent at an angle of about 45° (fig. 44.5*A*, *B*). Nearby houses with concrete slab foundations on ash or with post-and-pier foundations on a pahoehoe flow sustained little movement (fig. 44.4, vectors d, e). Greenhouses were moved as much as 0.15 m in a complex pattern toward azimuths anywhere from 67° through 340° (fig. 44.4, vector e). These structures had few central supports or walls, hence the various structural elements may have failed at different times during the shaking, which could account for the range in direction of failure.

The Wood Valley Buddhist Temple had only a few centimeters of displacement with respect to its piers, but the two-story frame dormitory structure situated in the front yard of the temple shifted 0.26 m northeastward (fig. 44.4, vector f). Nearly every headstone in the cemetery was overturned, according to a spokesperson. The pattern of movement was complex: One headstone that had been mortared to a larger base was displaced 0.28 m to the northwest (az 290°), but a similarly constructed headstone fell in a southeasterly direction (az 140°). This divergence in direction of fall may be due to the headstones breaking loose from their mortar at different times during the earthquake shaking. Restoration work was nearly completed when the site was visited eight days after the mainshock, hence no other observations were possible (E.T. Endo, written commun., 1984).

### Kapapala Ranch

The main house shifted 0.18 m downhill toward the south-southeast (fig. 44.1, locality 3; fig. 44.4, vector g) whereas a ranch house (locality 4 on figs. 44.1, 44.6) located 19 km (12 mi) to the northeast, nearer the epicenter, was displaced about 0.8 m northeastward (az 55°) off its foundation piers (fig. 44.7). A water tank about 100 m uphill from the ranch house had a length of PVC pipe, which was originally connected to the body of the tank, trapped underneath it (fig. 44.8). It seems likely that the pipe was severed early in the shaking, fell to the ground, and then rolled beneath the tank as the tank swayed back and forth. Several wooden water tanks located elsewhere on the ranch, one with a 378,500-L (100,000-gal) capacity and nearly full, were leaning precariously and leaking profusely; they were eventually dismantled.

### Volcano Golf and Country Club Subdivision

Most houses in this subdivision were built on a thin pahoehoe flow that overlies an ash deposit at least 0.5 m thick (locality 5 on figs. 44.1, 44.6). At the time of the earthquake, 48 houses had been built or were under construction in the subdivision. Of these, 18 houses with post-and-pier construction were displaced 0.2–1.2 m southwest from their foundations. Only one of the houses had 2.5 cm of reinforcing rebar protruding through the foundation piers into the posts (fig. 44.9). After the earthquake, this house was southwest of its piers, but the posts were not sheared by the rebar nor were most of the rebars bent, suggesting that the house rocked laterally and slid up along the rebars during the earthquake shaking.

Some houses with post-and-pier foundations had attached garages with concrete-slab foundations. In most such cases, the house moved farther than the garage, causing a tearing of the shared wall (figs. 44.10*A*, *B*). In one case, however, the garage was situated on the southwest side of the house (the general direction of movement) and because of its greater rigidity, may have kept the house on its foundation.

Of the 30 other houses in the subdivision, 9 moved on their post-and-pier foundations and suffered minor damage, and the remaining 21 houses, most of which were on concrete slabs, showed no evidence of movement. However, large metal water tanks adjacent to some of these houses showed 5–9 cm of movement north-northeastward. A few fiberglass water tanks had vertical ruptures in their sides wide enough to allow loss of all the water.

There were reports of extensive breakage inside many houses, regardless of foundation type, and of heavier applicances and furniture displaced more than lighter pieces.

### Hawaii Volcanoes National Park

Although no buildings within the national park moved off their foundations, there was extensive interior damage in some buildings (locality 6 on figs. 44.1, 44.6). At the HVO, a concrete foundation slab was cracked in two places but not offset, and work areas were chaotic with toppled equipment and books (fig. 44.11). Some seismic stations were disabled because of damage to the sensors or recorders, while the operating stations were saturated for several hours with signals from ground oscillations. Tiltmeters could not be reset until there was a substantial reduction in the oscillation of the ground. Within the park residential area just south of park headquarters, damage to houses was minor and seemingly arbitrary. Similarly constructed and situated houses differed greatly in the amount of dishevelment of the interiors. There was no damage nor dishevelment to the park headquarters' buildings. Damage to leaking water pipes and valves in the park amounted to $16,000.

At Kilauea Military Camp within the national park boundary, buildings moved but stayed on their foundations. In the Short Stop, a grocery store, bottled foods and beverages were broken and the concrete slab floor, supported on piers about 1 m high, was cracked and vertically offset about 1 cm. The Post Exchange also had breakage of glass items. Concrete slabs and walkways were cracked, and some concrete steps were buckled compressively where they abutted buildings. Service pipes from the water storage tanks to the camp were damaged and had to be replaced (Glenn Higa, Foreman, Engineers' Section, oral commun., 1985). Stone chimneys were cracked but could be repaired.

## PUNA DISTRICT

### Upper Wright Road, Volcano

Damage was severe and affected nearly every structure in this part of Volcano, which is underlain by an ash deposit locally as much as 4.7 m thick (locality 7 on figs. 44.1, 44.6). Patterns of movement were complex and are difficult to interpret; many houses in this part of Volcano are older and have combined post-and-pier and slab construction. Houses were displaced off their post-and-pier

foundations as much as 0.7 m, generally in either a southwesterly or northeasterly direction. One three-story-high wood frame house had recently had its original piers replaced with steel-reinforced concrete piers poured as a single unit (fig. 44.12*A*, *B*). This house was displaced about 0.3 m northeastward (az 35°) of the piers, and the steel rebar had sheared most of the posts that supported the upper story of the house. The use of rebar alone to connect the posts to the foundation proved inadequate. The superstructure of the house appeared to be undamaged.

More water tanks collapsed or were damaged in this community than elsewhere in the epicentral area; others, though undamaged, were moved as much as 0.8 m southeastward (E.T. Endo, written commun., 1984; fig. 44.13). Wooden water tanks were more severely damaged than those made of fiberglass or metal, probably because the former were less rigid. Many of the collapsed tanks were observed by residents to sway back and forth during the period of shaking before their failure. Evidence of a few centimeters of movement of heavier metal tanks could be seen in the soft ground. Connecting pipes were often severed or damaged.

In this largely argicultural community, financial losses resulted from crop damage when the earthquake shaking caused greenhouses to collapse, shook vegetables off plants (fig. 44.14), and caused vibrational settling of loose earth into adjacent furrows, thereby uncovering seeds and seedlings.

## SOUTH HILO DISTRICT

### Hilo

Major structural damage in Hilo occurred in two main areas, shown in figure 44.15 as areas A and B. There was also structural damage at Hilo Hospital, located near a cliff overlooking the Wailuku River (see table 44.2 for details). Minor structural damage, ranging from collapsed rock stairways to cracked rock walls, was common throughout the Hilo area.

Most of the damaged residences in Hilo were built on a thick ash deposit or near the edges of lava flows overlying an ash deposit (fig. 44.1, locality 8; fig. 44.15, area A). Several houses were damaged when they moved downslope off their post-and-pier foundations in response to the earthquake shaking. Others were severely damaged because of the steeper slopes on which they were built (fig. 44.16*A*) or their location alongside unbuttressed slopes such as stream channels. A few houses built across steep slopes were structurally damaged by the shaking (fig. 44.16*B*), although there was no evidence of ground failure. Houses with concrete slab foundations fared better, with only minor hairline cracks in some slabs.

The old part of Hilo, built on an ash deposit locally as thick as 4.7 m (fig. 44.15, area B), was also severely shaken; major structural damage resulted to two buildings (figs. 44.17, 44.18), but most losses were due to breakage of plate-glass windows and damage to goods. A heavy canopy that recently had been installed on a commercial structure fell off during the shaking. It probably had been inadequately connected to the structural elements of the building. A gas station reported the severing of connecting pipes to an underground gasoline-storage tank, causing the loss of some 11,355 L (3,000 gal) of fuel.

## ANALYSIS OF STRUCTURAL DAMAGE

Structural damage was influenced by three main factors: (1) shaking of the ground, (2) lithology of the substrate, and (3) construction practices.

### SHAKING OF THE GROUND

Damage to structures in the epicentral area may have been caused by the prolonged, strong ground shaking of greater than one-tenth the acceleration of gravity (0.1 g) for 8.5 seconds (table 44.3). One exception to this may have been the ranch house at location 4 (fig. 44.1). Because of its nearness to the epicenter, it is likely that the *P* and *S* waves arrived there nearly simultaneously, thus causing greatly enhanced first motion at this locality. The block south of the fault on which the ranch house was located, moved laterally to the southwest, decoupling the piers from the house and leaving the house northeast of its foundation.

In Hilo, the shaking damage in the Kaumana area (fig. 44.15, area A) may have been enhanced by the decoupling effect of a thin lava flow from Mauna Loa Volcano overlying a 3- to 6-m-thick ash deposit and deeply-weathered lava flows from Mauna Kea Volcano. That this type of enhancement could be expected was anticipated by Nielsen and others (1977), Wieczorek and others (1982), and Buchanan-Banks (1983).

### LITHOLOGY OF THE SUBSTRATE

Structural damage appeared to be worse in areas where buildings were constructed on ash deposits 0.5 m or more thick; however, not every area underlain by ash had structural damage to buildings.

The volcanic ash was originally composed of particles of volcanic glass and crystal fragments, but severe weathering resulting from high average annual temperatures and abundant rainfall has altered most of the original constituents (Bates, 1960; Wieczorek and others, 1982; Buchanan-Banks, 1983). The ash has a large amount of clay-size material and a water content as high as 392 percent (weight of water as a percentage of weight of dry sample). Undisturbed deposits are fairly well indurated and resistant to erosion, forming road cuts at angles often steeper than 60°, even greater than the high angle of internal friction of the material (40°–43°). However, the ash has been found to become plastic after repeated passes of heavy equipment but to subsequently harden again after cessation of the vibrational stress (Hirashima, 1948, p. 485). Although the ash deposits were found to have a sensitivity to slope failure classed as medium to very sensitive (Wieczorek and others, 1982, p. 5), no evidence of large-scale slope failures were

found in the Hilo area. The shear wave velocity of the ash was calculated by Nielsen and others (1977, p. 34) to be between 67 to 142 m/s (219 to 467 ft/s) at strain percents of $10^{-1}$–$10^{-3}$ and an undrained shear strength of 136 kg/m$^2$ (300 lb/ft$^2$).

Data on the response of the ground to strong motion from this earthquake was collected and analyzed by the USGS from strong-motion accelerographs scattered throughout the island (Acosta and Maley, unpub. data, 1984; see fig. 44.1 for location of accelerographs and thickness of ash deposits at some recording sites). The amplification of the earthquake waves because of ash deposits is apparent when data from the U.S. Fish and Wildlife accelerograph, located on ash deposits about 3 m thick, and the University of Hawaii, Hilo, accelerograph, located on lava flows, are compared (table 44.3); these two accelerographs are essentially equidistant from the epicenter. The records from the accelerograph situated on ash show peak accelerations that are 5 to 6 times greater than the accelerations recorded on the lava flow, indicating that the amplitude of the earthquake waves was increased in the ash deposits.

In the 1973 Honomu earthquake (for data on this earthquake see table 44.1), similar results were found after analysis of a pseudovelocity response spectrum derived from seismic data from a selected aftershock. A simple response peak was obtained from the spectrum from a seismometer sited on lava about 17 km (11 mi) south of the epicenter, whereas a spectrum from a seismometer on ash (located about 14 km (9 mi) south of the epicenter near the U.S. Fish and Wildlife accelerograph that recorded the 1983 earthquake) showed a complex pattern with at least three periods of high response indicating greater wave amplitude on the ash (Nielson and others, 1977, p. 11-12). Nielsen and others (1977) estimate that the velocity response of the volcanic ash was 5–10 times greater than the response measured on the lava flows. Although the difference in response in 1973 between the ash and lava might be attributed to the closer location of the seismometer on ash deposits to the epicenter, the data are consistent with the 1983 damage pattern.

On the other hand, during the 1975 Kalapana earthquake (for data about this earthquake see table 44.1), data from two seismoscopes at the same locations as the seismometers that recorded the 1973 earthquake do not indicate an increase in velocity response in the ash; the maximum motion of the seismoscope pen was 3.4 cm on the University of Hawaii, Hilo, seismoscope, 43 km (29 mi) from the epicenter, and the seismoscope on ash, 45 km (31 mi) from the epicenter, recorded 3.1 cm displacement (Rojahn and Morrill, 1977, p. 499). It seems likely that the 1975 earthquake did not produce enough energy in a frequency band to cause the ash to respond.

## CONSTRUCTION PRACTICES

Few houses with post-and-pier construction had structural ties between the house, the piers, and the ground, and each element was therefore left free to move with respect to the others. In the few cases where structural ties such as rebar and bracing were used between the house and the piers, they appear to have been too few, flimsy, or poorly connected. Neither rebar nor bracing was adequate when used alone. Houses built across steep breaks in slope or near the edges of unsupported slopes generally sustained structural damage.

## GROUND FAILURES

For several hours after the earthquake, the air at Kilauea's summit was brown with dust from the initial and continuing landslides off the caldera walls and within Halemaumau Crater (fig. 44.19). Hundreds of landslides, of volume generally less than 3,000 m$^3$, occurred within the epicentral area; rock slides, falls, and topples were the dominant types of failure. These failures caused extensive road and trail damage in Hawaii Volcanoes National Park and temporarily closed the major highway around the island. For many kilometers southwest and northeast of the epicentral area, small rock falls, extensional cracks in the ground, and collapsed lava tubes were evident. Slope failures also occurred at Kealakekua Bay, about 50 km from the epicenter, and along the Hamakua Coast, nearly 60 km from the epicenter. The generation of landslides at such distances from an epicenter is in good agreement with the findings of Keefer (1984, fig. 2*A*, *B*) for worldwide data on earthquake-induced landslides. Only small failures occurred in the thick and seismically sensitive ash deposits near Hilo and Pahala.

No fatalities or damage to dwellings resulted from the landslides, but two people were injured in rock falls onto the highway along the Hamakua coast about 25 km north of Hilo.

## KAU DISTRICT

### Hawaii Volcanoes National Park

Most landslides from the earthquake occurred within Hawaii Volcanoes National Park, where the lava flows of Kilauea Volcano form cliffs as much as 120 m high (locality 6 on figs. 44.1, 44.6). These nearly flat-lying lava flows are a few tens of centimeters to a few meters thick, and thin ash beds occur between some of them. The flows are well indurated and fairly young (0.2–1.5 ka), but are extensively cracked and jointed because of rapid cooling and initial deformation (fig. 44.20). Locally the flows are overlain by about 2 m of loosely consolidated tephra deposits from phreatomagmatic eruptions of Kilauea Volcano.

Hiking trails along the northern edge of the caldera between Kilauea Iki Crater and Uwekahuna Bluff were extensively damaged where perhaps as many as 200 rock slides and rock falls removed sections of trails and covered those at lower elevations with landslide debris (fig. 44.20). A few had volumes greater than 3,000 m$^3$. Some vertical cliff faces failed by toppling, when outward-rocking slabs of coherent material failed at the top because of imbalance; the upper parts of such landslides traveled farthest from the slope.

A reconnaissance survey of damage along Crater Rim Drive was conducted immediately after the earthquake. Although the road pavement was extensively cracked throughout its length, only the zones of greatest damage are shown in figure 44.6. Most of the road cracks depicted in this figure were caused by cracking of the ground beneath the road. The road damage included small apparent offsets in both right- and left-lateral senses, major to minor failures of subsurface material, and extensive compressional and extensional cracking, with the most severe damage where the road crosses

fracture systems related to Kilauea caldera (fig. 44.6, sites *a*, *b*, *c*; St. Ours, 1982). All the damage was attributable to the shaking effects of the earthquake.

At the eastern roadway into Kilauea Military Camp (fig. 44.6, site *a*) vibrational compaction of fill caused the road to collapse where a system of earth cracks lies under the road (fig. 44.21). Earlier failures of this type had occurred periodically along the verge of the road at this location, though on a smaller scale and usually induced by drenching rains removing supporting material. Tilling and others (1976, p. 26) describe compressional damage to a roadway near this locale in the 1975 earthquake.

Highway 11 near the northwestern roadway into Kilauea Military Camp (fig. 44.6, site *b*) was closed for several hours because of failure of subsurface material at a circum-caldera fault.

The southwest rift zone of Kilauea lies parallel to the Kaoiki fault system and is characterized by gaping cracks and fissures. Where Crater Rim Drive crosses the 0.5-km-wide zone (fig. 44.6, site *c*), there was both extensional and compressional damage throughout the zone, with an overall extension of about 4 cm (fig. 44.22*A*, *B*).

The roadway cracks at Keanakakoi Crater are subparallel to the west wall of the crater and probably reflect a subsurface zone of fractured rock related to the collapse of the pit crater. The cracks show only small right-lateral offsets and slight upward movement of the northeast side. The viewing overlook had extension cracks approximately 1 cm wide through it, and the rock wall slumped downward and outward toward the crater.

From Keanakakoi Crater, Crater Rim Drive was extensively cracked for 2 km. This earthquake-induced cracking is most likely related to preexisting crack systems in the area (St. Ours, 1982) as well as to settling of uncompacted tephra deposits from the 1959 Kilauea Iki eruption upon which the road was built.

Crater Rim Drive, which is adjacent to Crater Rim Trail between Waldron Ledge and Volcano House, was permanently closed to traffic, and the hiking trail rerouted, because of landslide damage and cracking of the road from vibrational settling of tephra deposits and fill (fig. 44.6, site *d*). This section of road also was badly damaged in the 1975 Kalapana earthquake, when cracks as much as 1 m wide formed parallel to the caldera rim (Tilling and others, 1976, p. 24). The cracks were subsequently filled in and the road repaired; many of the repaired areas failed again in the November 1983 earthquake.

Of the several large landslides that formed on the cliffs, 60–120 m high, along Waldron Ledge, the largest failure was a rock slide with a volume of about 4,600 $m^3$ that occurred at a site that had been identified as an incipient landslide and had been monitored since April 1980 by the USGS (compare fig. 44.23*A*, *B*). Details of this monitoring program are included at the end of this section. At the time of the earthquake, a resident of the park housing area, who ran outside after the severe shaking had ceased, heard a whooshing sound that lasted 15–20 seconds and came from the direction of the caldera. This sound was probably generated by the rapid failure of this slide and others along this section of cliff. Judging from the shape of the headwall scarp, the slide probably began as a block slide and disintegrated as it fell down the cliff face (fig. 44.24*A*, *B*). The debris did not travel far from the base of the cliff.

Major to minor arcuate cracking reflecting subsurface movement of material toward a free face also occurred at several locations along the road, from the park residential area to park headquarters and between the headquarters and Sulphur Banks.

South of Kilauea caldera, the Chain of Craters and Ainahou Ranch Roads (fig. 44.1) were extensively cracked by the shaking, and the road cracks in the Hilina Pali Road originally caused by a large intrusion in March 1980 were reactivated by the earthquake shaking. North of the caldera, damage to Mauna Loa Road was particularly severe and increased toward the epicenter and the zone of surface faulting. Some cracks in the epicentral area showed extension of as much as 5 cm, while others showed evidence of the pavement on either side having been repeatedly compressed (fig. 44.25).

### Monitoring Program at Incipient Waldron Ledge Landslide

Soon after torrential rainstorms in early 1979, a series of cracks appeared in a section of Crater Rim Drive along Waldron Ledge (fig. 44.6, site *d*). These cracks widened in the heavy rains of March 1980. In order to watch for changes that might forecast the failure by landsliding of this part of Crater Rim Drive and Trail, a monitoring program was established by the USGS in April 1980.

Monitor 1 consisted of five nails set out as a quadrilateral centered over the road cracks (fig. 44.26). The distance between the nails was measured with steel tape once a week for the first month, then once a month for the next few months, and thereafter with lessened frequency (table 44.4). Within the first few months, nearly all the lines began showing measurable and cumulative extension, particularly those normal to the cracks (figs. 44.26, lines AE, BC, BD, 44.27*A*). In addition, the cracks had lengthened at both ends, and vertical offsets had become apparent.

To assess the rate of vertical change, a leveling line was added to monitor 1 in November 1980; it consisted of two lengths of rebar driven into bedrock, rebar 1 and Base, in a line northeast of, and off, the landslide (fig. 44.26). The level gun was placed at point 0 between the rebars to check their respective stabilities (fig. 44.26, right center); the gun was then moved to rebar 1 and the rod to each nail of the quadrilateral to measure its elevation.

Monitor 2 was added to the program in April 1981 to measure horizontal movement on cracks not crossed by the quadrilateral (fig. 44.26). Line X′-X was established northwest of the quadrilateral beyond the zone of visible cracking; it extended 23.7 m from X′, a nail in a tree at the caldera edge to X, a nail in the centerline of the road. A second line was established across the quadrilateral and comprised two segments; one segment, line Y′–Z (24.1 m) was measured from Y′, a nail in a tree at the caldera's edge to Z, another nail in a tree northeast of the road, and the second segment, line Y′ to Y.

The monitors were measured frequently until mid- to late

1982. Measurements were discontinued in January 1983 because of the onset of the prolonged east rift eruption of Kilauea Volcano.

### RESULTS OF THE MONITORING PROGRAM

During the period of measurement, all of the monitors normal to the cracks showed lengthening of lines and small vertical offsets indicating that the incipient landslide block was moving slowly outward and downward toward the caldera.

The lines of the quadrilateral were measured 14 times between April 1980 and October 1982 (table 44.4). Cumulative extensions above background level on the lines normal to the cracks (for background level see data for line ED, parallel to the cracks) was detected within a few months of the establishment of monitor 1 (fig. 44.27*A*). Continued documented movement of the incipient landslide block toward the caldera led to a decision by the Superintendent, Hawaii Volcanoes National Park, to close this section of road to traffic in April 1981 (fig. 44.6, site *d*). Although monitoring frequency decreased after the closing of the road, accelerated movement both laterally and vertically can be seen in the data after July 1981. The largest changes in line lengths within the quadrilateral occurred between July 1981 and July 1982 on lines AC, AD, AE, BC and BD, crossing the cracks (table 44.4, fig. 44.27*A*). The largest vertical changes also occurred during the same period when nails C, D, and E (the three on the caldera side of the cracks), moved downward with respect to rebar 1 (table 44.4, fig. 44.27*B*).

Line Y′–Z, which also crossed the cracks curving away from the caldera (see fig. 44.23*A*, *B*, location B) as well as the cracks monitored by the quadrilateral, extended about 7 mm more than the shorter quadrilateral lines, AE and BD, over the period June 1981 to July 1982 (table 44.4, fig. 44.27*C*), suggesting that incipient failure was also developing on the cracks curving away from the caldera.

The monitors were destroyed by landslides caused by ground shaking associated with the November 1983 earthquake. Nails A, B and E of the quadrilateral survived the earthquake but E was on a separated block and could not be reached for measurement. The distance between A and B shortened 0.3 m. Lines X′–X, Y′–Y and Y′–Z, could not be remeasured because the trees on the caldera rim holding the nails, and the section of road where nail Y was located, were gone.

### SOUTH AND NORTH HILO DISTRICTS

Dozens of soil falls and slides of volume about 15 $m^3$ occurred in the ash deposits near Hilo, and at one location along Kaumana Drive there was evidence of minor subsidence (fig. 44.28). Narrow cracks in asphalt were common.

Small (volume <20 $m^3$) rock falls and soil slumps were observed along the highway from Hilo northward to Ookala, where Mauna Kea ash deposits blanket lava flows of the Hamakua Volcanic Series, also from Mauna Kea Volcano (Stearns and Macdonald, 1946, pl. 1). These flows are deeply weathered and have locally produced saprolite consisting of well-rounded to subangular rock remnants in a clayey matrix. The rocks are in large part soft and frequently slide during periods of heavy rain. Six landslides with volumes less than 500 $m^3$ deposited debris on the highway between Maulua Bay and Kaawalii Gulch causing temporary closure of the road (fig. 44.1, locality 9; fig. 44.29). The debris was removed by midday of November 16 and the highway was reopened (Harry Kim, oral commun., 1983).

In mid-January, when fieldwork was conducted north of Hilo, only four of the six landslides could be located. All the observed failures were rock slides from the steep roadcuts and all appeared to have shallow head scarps, 1–2 m deep. Close examination of the landslides was limited because of the busy, narrow road and the steep slopes. Rock slides could be seen in the roadcuts in each of the highway's large horseshoe bends, with the largest slide occurring in Laupahoehoe Gulch (estimated volume 420 $m^3$) from the near-vertical cliff west of the road. During the next heavy rainstorm, material loosened by the earthquake shaking west of the earthquake-induced slope failure in Laupahoehoe Gulch caused another large landslide in this gulch (fig. 44.30). For several months after the earthquake, similar landslides occurred in this location during rainy periods.

The earthquake-induced rock slide in Maulua Gulch (volume about 6 $m^3$) was the one that caused injury to two people travelling in autos. Another rock slide (volume about 36 $m^3$) covered both lanes of the narrow secondary road to Laupahoehoe Point (fig. 44.31) making it impassable for a short time.

Similar ground failures occurred at these locales as a result of the 1975 earthquake (Tilling and others, 1976, table 1) and the 1973 earthquake (Nielsen and others, 1977, p. 15). Rock and soil falls also occurred on the steep wave-cut cliffs just north of Hilo, about 17 km south of the 1973 earthquake epicenter (Nielsen and others, 1977, p. 14).

### KONA DISTRICT

#### KEALAKEKUA BAY

Shortly after the earthquake occurred, a large dust cloud over Kealakekua Bay was reported to the USGS as possible volcanic venting from beneath the bay (fig. 44.1, locality 10). Aerial reconnaissance determined the cause of the cloud as dust from several rock slides off the steep slopes around the bay. Currents of brown, cloudy water were observed from the air to extend about one kilometer from the shore (J.P. Lockwood, written commun., 1983).

Several rock slides at Kealakekua Bay occurred from about the 120-m elevation on the face of a nearly vertical cliff of weathered Mauna Loa lava flows with intercalated thin ash beds (fig. 44.32; Stearns and Macdonald, 1946, pl. 1). This cliff section has been dated as spanning the interval 2–30 ka by charcoal samples collected from beneath lava flows near the top and at the base of the cliff, respectively (J.P. Lockwood, oral commun., 1985). The largest of these rock slides had a volume of about 5,500 $m^3$. The slides could not be examined closely because of the steep slopes, but the head scarps appeared to be fairly shallow (volume <3 m). Several smaller rock falls also occurred from the steeper lower slopes.

## ANALYSIS OF GROUND FAILURES

Ground failures appeared to be influenced by three main factors: (1) proximity to the epicenter, (2) lithology of the substrate, and (3) slope steepness.

### PROXIMITY TO THE EPICENTER

The greatest ground cracking occurred in the epicentral area; most landslides also occurred there, the size and abundance of failures decreasing with distance from the epicenter (fig. 44.33). This localization of ground failures is most probably due to the shallow depth of the earthquake and to the generating mechanism. The strike-slip faulting occurred on a near-vertical fault plane that ruptured the ground surface; the seismic energy released along the fault was thereby transferred to the surface as earthquake waves, and the resulting strong ground shaking in the epicentral area caused abundant ground failures.

### LITHOLOGY OF THE SUBSTRATE

The lava flows from Hawaii's five volcanoes are typically flat lying, forming broad, shield-shaped volcanic edifices. These gentle slopes are locally modified by faulting, collapse features, and erosional processes, each of which can form steep cliffs. The lava flows, extensively cracked and jointed as a result of cooling and initial deformation, vary in their degree of weathering with the age of the deposit, the density of the rock, and the amount of rainfall to which they have been subjected. The thickness of the flows also varies from a few centimeters to several meters, and they are sometimes interbedded with volcanic ash deposits that are locally as much as 9 m thick (Hirashima, 1948, p. 484; Buchanan-Banks, 1983). In some areas the ash units are the surficial deposits. Landslides and small soil slips frequently occur in the ash and, locally, in the underlying materials following heavy rains. The deeply weathered Mauna Kea lava flows are particularly susceptible to failure induced both by saturating rains and by earthquake shaking.

### SLOPE STEEPNESS

Topography was a factor in controlling the location of landslides, and, to a lesser degree, areas of structural damage in the November 1983 earthquake. The largest landslides invariably occurred from the near-vertical cliffs in the epicentral area and from steep slopes elsewhere on the island. Numerous rock falls could be observed along highways where roads were cut through lava flows regardless of the height of the cut. Small soil slumps in ash deposits also occurred where the slope had been steeply cut.

## CONCLUSIONS

The 1983 Kaoiki earthquake provided a unique opportunity to examine earthquake-induced structural damage and ground failures in Hawaii. Although the 1975 Kalapana earthquake had a higher magnitude (*M* 7.2) and hence more seismic energy, its location near the coast allowed some of this energy to be propagated seaward away from the main cultural centers of the island. The inland location of the Kaoiki earthquake, therefore, resulted in greater structural damage (Koyanagi and others, 1984, p. 4).

Damage to structures was greatest in the epicentral area, where the foundations under some houses moved as much as 1.2 m away from the house. Structures with post-and-pier foundations were more severely damaged in this earthquake than those with concrete slab foundations. In some cases, the posts and piers were joined together with steel plates or rebar reinforcement; these houses nonetheless came off their foundations.

Lithology and topography also seemed to affect the location and degree of structural damage. Houses in Wood Valley, Volcano Golf and Country Club Subdivision, Volcano, and Hilo were damaged where ash deposits at or near the surface were at least 0.5 m thick. Houses built across breaks in slope, on uneven terrain, on sloping ground, or near the edges of unsupported embankments sustained greater damage than those on flat ground.

The regional distribution of landslides resembles the overall pattern of seismic intensity, most failures occurring in the epicentral area. The threshold intensity for triggering small rock falls and soil slumps was IV to V (modified Mercalli scale).

The predominant types of landslide generated by this earthquake were shallow rock slides and falls. They most commonly occurred on the steep slopes and were induced by the earthquake shaking.

Virtually all large landslides occurred in extensively cracked and jointed lava flows. Small soil failures and extensional cracks also occurred in the thick ash deposits in the epicentral area and in Hilo.

Because of the relatively sparse population in the epicentral area and the early hour at which the earthquake occurred, there were few injuries from the landslides. However, landslides along the Hamakua coast slightly injured two people and caused closure of the circum-island highway for a few hours until debris was removed. Compactional failure of road fill also closed the circum-island highway in the epicentral area for a few hours.

## REFERENCES

Bates, T.F., 1960, Rock weathering and clay formation in Hawaii: College Station, Pennsylvania State University, Bulletin, College of Mineral Resources, v. 29, no. 8, 4 p.

Brigham, W.T., 1869, The eruption of the Hawaiian Volcanoes, 1868: Boston Society of Natural History, Memoirs, v. 1., p. 564-587.

Buchanan-Banks, J.M., 1983, Reconnaissance map showing thicknesses of volcanic ash deposits in the greater Hilo area, Hawaii: U.S. Geological Survey Miscellaneous Field Studies Map MF–1499, scale 1:24,000.

Buchanan-Banks, J.M., and Lockwood, J.P., 1982, Geological map of the Alenaio-Waipahoehoe Stream area, South Hilo District, Hawaii: U.S. Geological Survey Open-File Report 82–655, map scale 1:24,000.

Chiu, A.N.L., Lum, W.B., Nielsen, N.N., and Koyanagi, R., 1984, Damage survey of the Kaoiki, Hawaii earthquake of November 16, 1983: Earthquake Spectra, v. 1, no. 1, p. 173-182.

Endo, E.T., 1985, Seismotectonic framework for the southeast flank of Mauna Loa: Seattle, University of Washington, PhD. thesis, 253 p.

Hawaii Tribune-Herald, 1983, Quake toll: 350 houses, 35 businesses: Hawaii Tribune-Herald, Friday, December 9, 1983, no. 287, p. 1.

Hirashima, K.B., 1948, Highway experience with thixotropic volcanic clay: Proceedings of the Highway Research Board, v. 28, p. 481- 494.

Keefer, D.K., 1984, Landslides caused by earthquakes: Geological Society of America Bulletin, v. 95, no. 4, p. 406-421.

Koyanagi, R.Y., Endo, E.T., Tanigawa, W.R., Nakata, J.S., Tomori, A.H., and Tamura, P.N., 1984, Kaoiki, Hawaii, earthquake of November 16, 1983: A *preliminary compilation of seismographic data at the Hawaiian* Volcano Observatory: U.S. Geological Survey Open-File Report 84–798, 6 p.

Lipman, P.W., and Swenson, Alan, 1984, Generalized geologic map of the southwest rift zone of Mauna Loa Volcano, Hawaii: U.S. Geological Survey Miscellaneous Investigations Series Map I–1323, scale 1:100,000.

Nielson, N.N., Furumoto, A.S., Lum, Walter, and Morrill, B.J., 1977, The Honomu, Hawaii, earthquake: report of inspection: Washington, D.C., National Academy of Science, 79 p.

Peterson, D.W., 1967, Geologic map of the Kilauea Crater quadrangle, Hawaii: U.S. Geological Survey Geologic Quadrangle Map GQ–667, scale 1:24,000.

Rojahn, Christopher, and Morrill, B.J., 1977, The island of Hawaii earthquakes of November 29, 1975: Strong-motion data and damage reconnaissance report: Seismological Society America Bulletin v. 67, no. 2, p. 493-515.

St. Ours, Patrice, de, 1982, Structural map of the summit area of Kilauea Volcano, Hawaii: U.S. Geological Survey Miscellaneous Field Studies Map MF–1368, scale 1:24,000.

Stearns, H.T., and Clark W.O., 1930, Geology and water resources of the Kau district, Hawaii: U.S. Geological Survey Water Supply Paper 616, 194 p.

Stearns, H.T., and Macdonald, G.A., 1946, Geology and groundwater resources of the Island of Hawaii: Hawaii Division Hydrography Bulletin 9, 363 p.

Swanson, D.A., Duffield, W.A., and Fiske, R.S., 1976, Displacement of the south flank of Kilauea Volcano: The result of forceful intrusion of magma into the rift zones: U.S. Geological Survey Professional Paper 963, 39 p.

Tilling, R.I., Koyanagi, R.Y., Lipman, P.W., Lockwood, J.P., Moore, J.G., and Swanson, D.A., 1976, Earthquake and related catastrophic events, Island *of Hawaii, November 29, 1975: A preliminary report:* U.S. Geological Survey Circular 740, 33 p.

Wieczorek, G.F., Jibson, R.W., Wilson, R.C., and Buchanan-Banks, J.M., 1982, Geotechnical properties of ash deposits near Hilo, Hawaii: U.S. Geological Survey Open-File Report 82–279, 20 p.

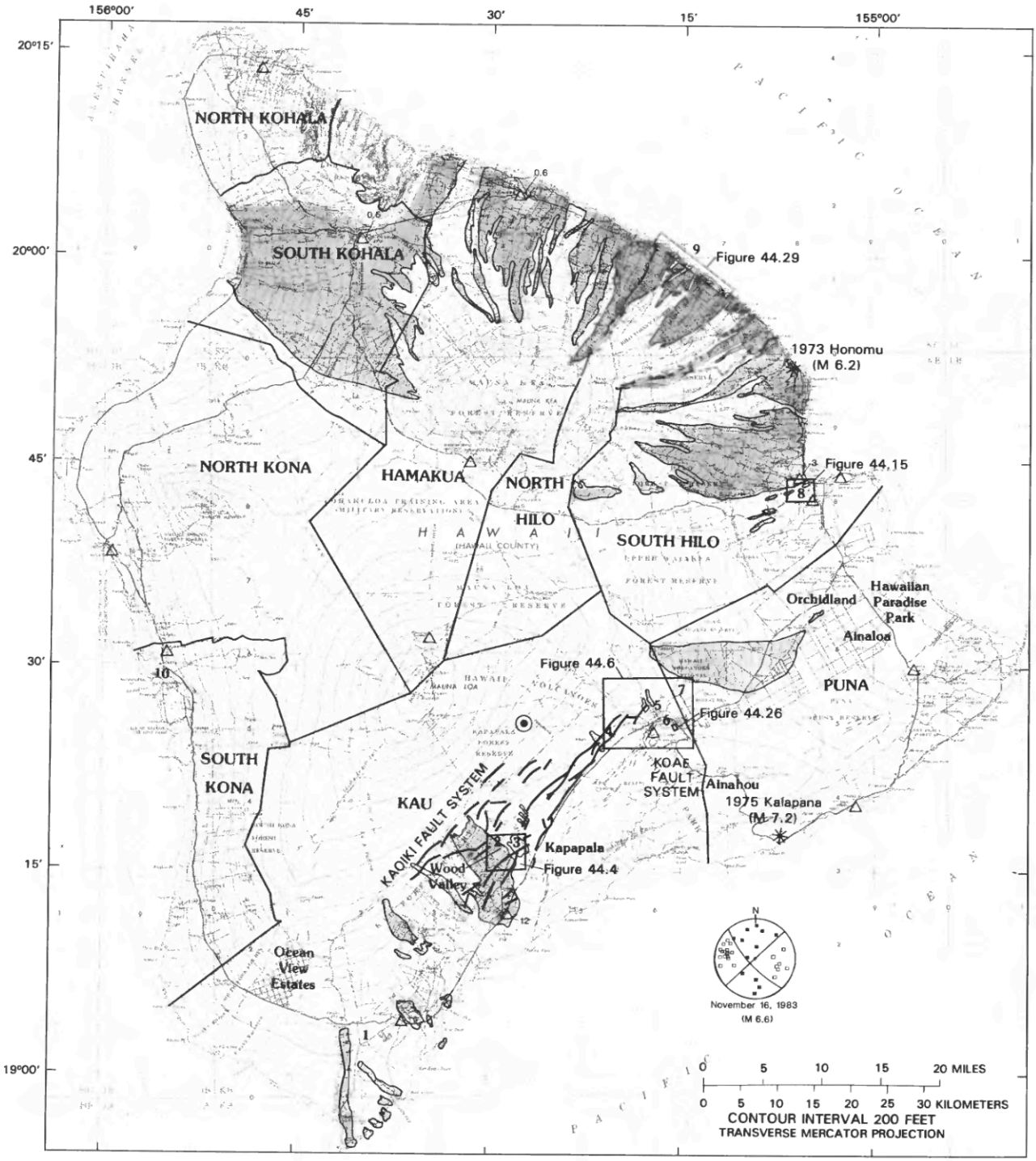


FIGURE 44.1.—The Island of Hawaii showing epicenters of November 16, 1983, Kaoiki earthquake and two earlier damaging earthquakes; also shown are areas of 1983 structural damage and earthquake-related ground failures discussed in text. Additional text figures cited where applicable. Inset shows focal-mechanism solution for 1983 earthquake from Endo (1985, p. 186): *P*-wave first motions plotted on lower hemisphere equal-angle stereograph; open squares, down first motions; solid squares, up first motions. Topography from U.S. Geological Survey Hawaii Island series W532, 1975, 1:250,000.

**EXPLANATION**

**Earthquake epicenters**

**Kaoiki earthquake, November 16, 1983**

**1973 and 1975 earthquakes**

**1 Areas of structural damage or ground failure during 1983 earthquake: 1, Ka Lae Road; 2, Wood Valley; 3, Kapapala Ranch house; 4, Ranch house at east end of Kapapala Ranch; 5, Volcano Golf and Country Club Subdivision and Keauhou Ranch house; 6, Hawaii Volcanoes National Park; 7, Upper Wright Road; 8, Hilo; 9, North Hilo District; 10, Kealekekua Bay**

**Ash deposits**

**Accelerograph location and ash thickness, in meters**

**Fault trace, from Stearns and Macdonald (1946, pl. 1) and Lipman and Swenson (1984)**

**District boundary**

FIGURE 44.1.—Continued.

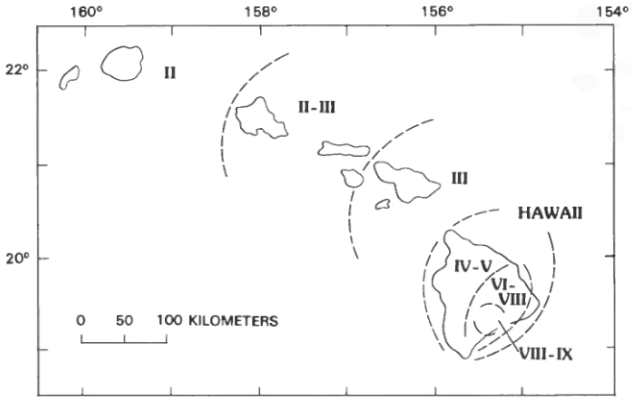


FIGURE 44.2.—Isoseismal map for November 16, 1983, earthquake prepared from observations of damage and felt reports from residents compiled by Hawaii County Civil Defense Agency. Numbers indicate intensity on modified Mercalli scale (from Koyanagi and others, 1984, fig. 3).

FIGURE 44.3.—Post-and-pier house support displaced in November 16, 1983, earthquake. In this type of construction, two concrete blocks form pier and a vertical wooden 10-cm by 10-cm post supports house. Larger block is resting on ground; smaller is placed on top of this and usually not connected to it. Between upper block and post is a termite shield of thin metal. At this locality, both post and upper foundation block have moved several centimeters to right on their respective supports. Dashed line indicates original position of post; arrow shows direction of movement.

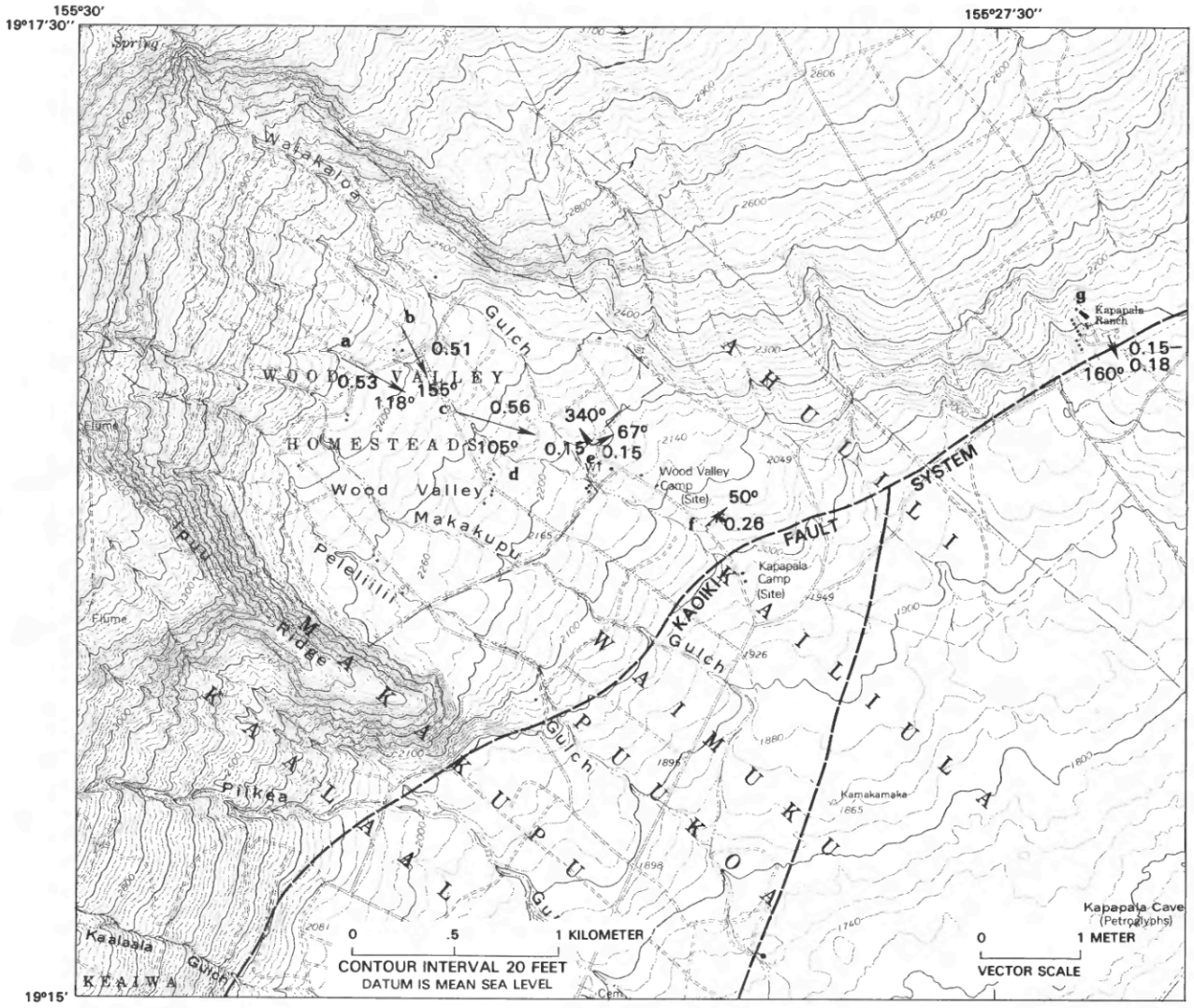


**EXPLANATION**

67° / 0.15 — **Vector showing direction (azimuth) and amount of movement of structure, in meters—Point of observation at base of vector; letter refers to locality described in text**

**Fault, approximately located—Bar and ball on downthrown side**

FIGURE 44.4.—Earthquake-related movement of structures in Wood Valley and western Kapapala Ranch, November 1983 (fig. 44.1, localities 2, 3). Topography from U.S. Geological Survey Wood Valley 7.5-minute quadrangle, 1981, scale 1:24,000. Location of faults from Stearns and Clark (1930, pl. 1) and Lipman and Swenson (1984).

***A*** ***B***

FIGURE 44.5.— Damage to a wood-frame house with post-and-pier construction in Wood Valley (fig. 44.4, locality b). ***A***, Northeast corner post fractured where anchor bolts connected it to 0.5-cm-thick steel plate positioned on southwest side of post (away from the viewer). Concrete foundation block appears to have been poured as single unit around the steel plate. Post also was torn loose from house and from diagonal bracing when ground, pier, and post moved southeastward. ***B***, Northwest corner post with steel plate on south side of post. The 0.5-cm-thick steel plate is bent at 45° angle. Photographs by E.T. Endo.

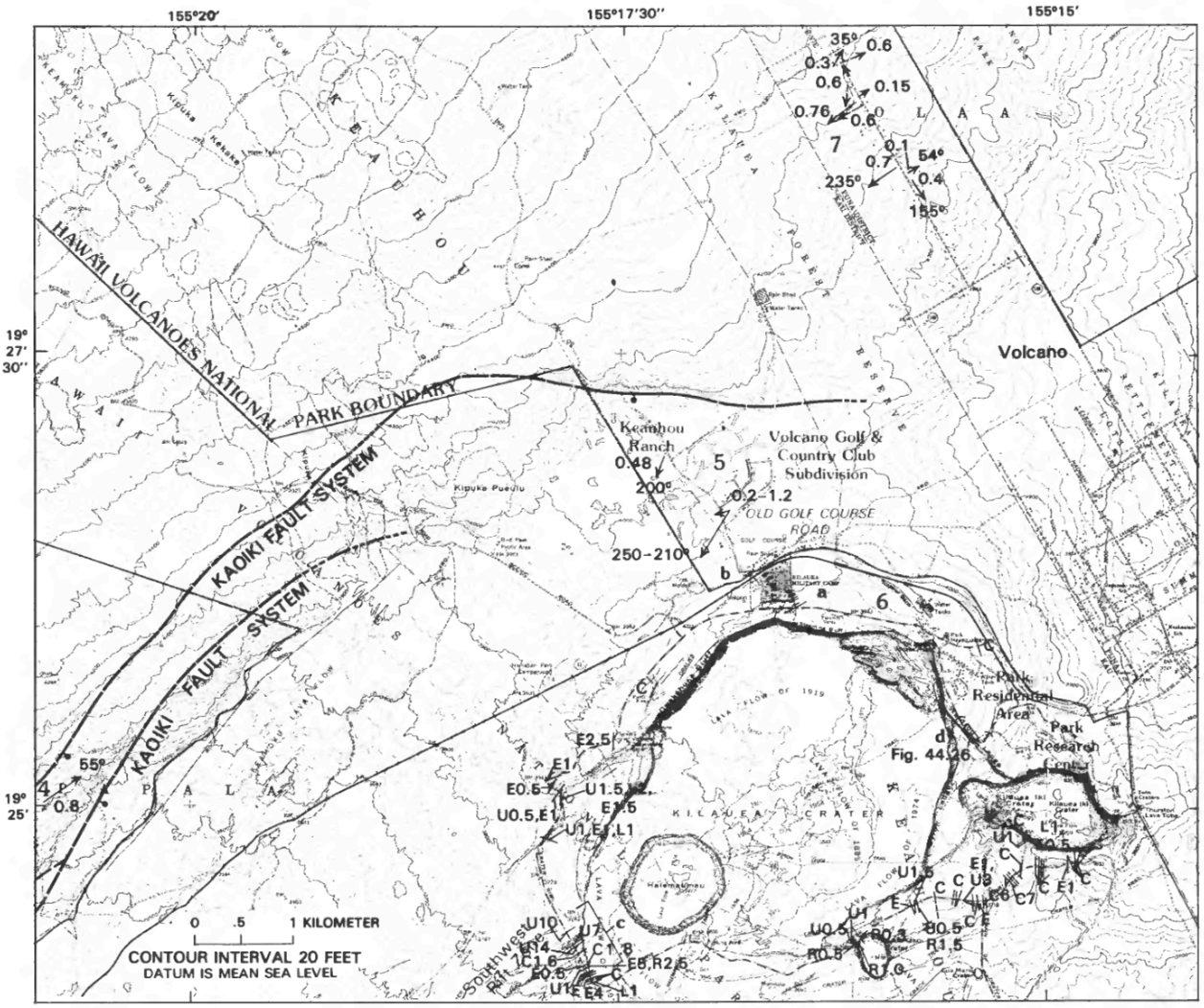


**EXPLANATION**

Kaoiki fault system—Dashed where approximately located; dotted where concealed. Bar and ball on downthrown side. From Peterson (1967)

U0.5 E2 R1 C1.6 — Ground cracks across Crater Rim Drive—Dashed where amount and direction of movement uncertain. Numbers indicate amount of movement, in centimeters. E, extension; C, compression; U, vertical, symbol on upthrown side; R, right lateral; L, left lateral

0.4 0.8 180° 110° — Vectors showing direction (azimuth) and amount of movement of house, in meters—Dashed where direction approximate. Joined vector indicates range in direction of movement. Point of observation at base of vector except for joined vector

0 1 METER VECTOR SCALE

6 — Area of damage—Numbers keyed to figure 44.1

a — Area of severe road damage—Letters refer to localities discussed in text

Part of Crater Rim Drive closed to traffic in April 1981 because of incipient landslide; figure citation refers to text

FIGURE 44.6.—Earthquake damage in epicentral region near Kilauea summit (localities 4–7, fig. 44.1). Some of the worst structural damage occurred in this area. Topography from U.S. Geological Survey Kilauea Crater and Volcano 7.5-minute quadrangles, 1981, scale 1:24,000.

FIGURE 44.7.—House on Kapapala Ranch about 12 km east of epicenter was displaced 0.8 m northeastward during earthquake. Most supporting posts remained vertical, but those used to frame a basement room were tilted. Concrete foundation piers, partly obscured by grass, behind figure in dark jacket. Windows broken during earthquake are covered with plastic. Near clump of trees on hill behind house, small soil slips can be seen and broken branches strew the ground.

FIGURE 44.9.—North corner pier of damaged two-story frame house in Volcano Golf and Country Club Subdivision. Although house is now 1.2 m southwest of its foundation, rebar protruding through piers is still straight. Termite shield from atop pier can be seen on ground. House subfloor was originally 1 m above ground, but most supporting posts collapsed.

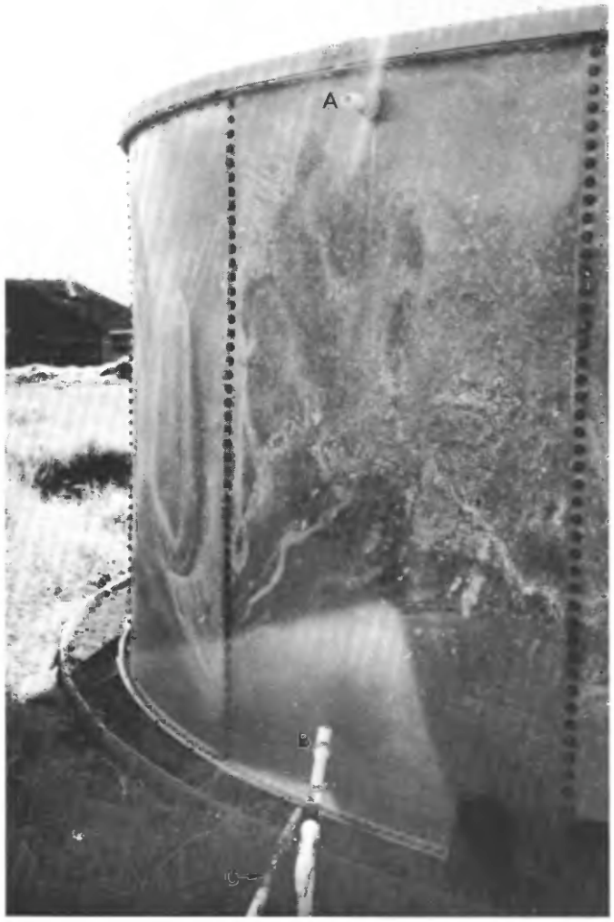


FIGURE 44.8.—Water tank that may have moved as much as 0.12 m southward (to right in photograph) during November 1983 earthquake. The 1.8-m length of pipe that originally extended from A to B now lies under tank at C. First motion apparently snapped pipe, which rolled under tank as tank tilted back and forth.

***A***

***B***

FIGURE 44.10.—Damaged frame house in Volcano Golf and Country Club Subdivision. ***A***, View of attached garage (with concrete foundation) and house (post-and-pier foundation). House moved farther than garage, breaking a 10-cm by 10-cm upright and causing a tear in southwest wall at electric meter. Photograph by R.Y. Hanatani. ***B***, Detailed view of right side of house; to right of drainpipe, a supporting post can be seen resting on ground southwest of pier on which it originally stood. Photograph by J.B. Stokes.

FIGURE 44.11.—Main meeting room and library at Hawaiian Volcano Observatory after 1983 earthquake. Bookcases were torn from back wall and fell onto table; storage cabinets were moved as much as 0.5 m. Preearthquake location of cabinets is documented by dust marks on floor behind and to right of plastic waste bin. Smoked-drum seismographs (obscured by easel) located under windows to right were temporarily out of order because their drive mechanisms jammed. Photograph by J.D. Griggs.

***A***

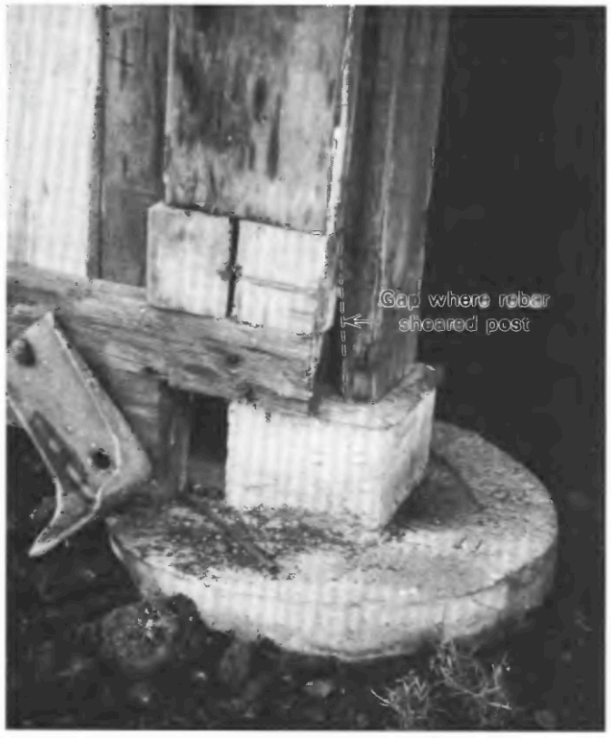


***B***

FIGURE 44.12.—Barnlike three-story-high frame house in Puna District that was moved off its foundation about 0.3 m toward northeast in 1983 earthquake. ***A***, View of house showing position of one of sheared support posts (circled). ***B***, Close-up of footing circled in *A*. The 14-cm by 14-cm wooden post was sheared by rebar that extended from base of footing upward into post as much as 11 cm; most other posts supporting upper story were similarly sheared. House has been replaced on piers.

FIGURE 44.13.—Water tanks in Volcano affected by 1983 earthquake. Most water tanks here were constructed like one standing at right rear. Tank in foreground has collapsed, while other appears little damaged although displaced southwestward 0.7 m. This difference in response to earthquake may be because of a difference in water level in tanks at time of earthquake, or because of a difference in age or condition of tanks. Photograph by E.T. Endo.

FIGURE 44.14.—Greenhouse on Upper Wright Road leaning to southwest after earthquake; view to southeast. Crop loss in this area was severe because of collapse of some greenhouses and uncovering of planted furrows. Crop shown here is tomatoes. Photograph by E.T. Endo.

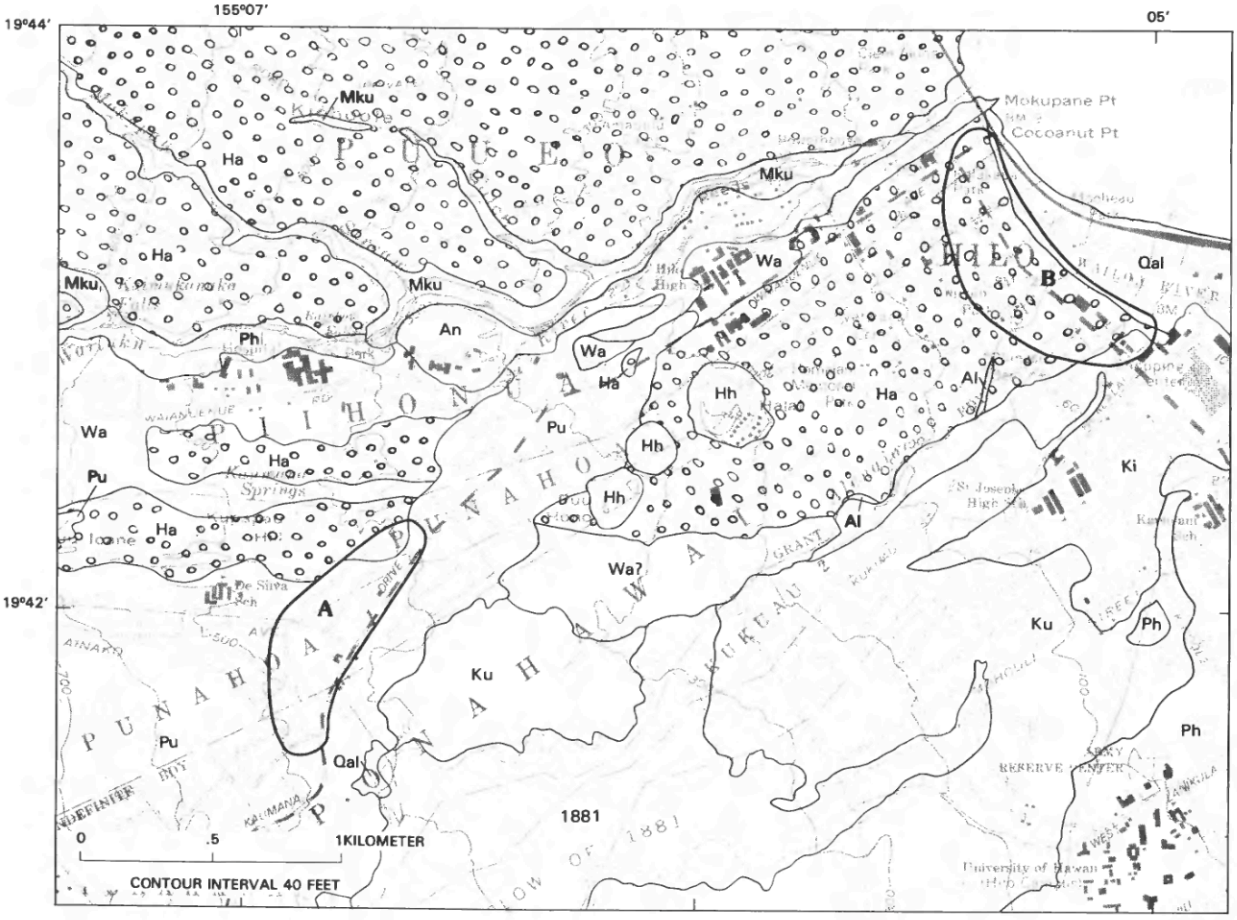


**EXPLANATION**

**A** Area of earthquake damage— Letters refer to discussion in text

**CORRELATION OF MAP UNITS**

| Surficial deposits | | Mauna Loa Volcano | | Mauna Kea Volcano | |
|---|---|---|---|---|---|
| Qal | Quaternary alluvium | 1881 | 1881 pahoehoe | Ha | Homelani ash Age >14.2 ka |
| | | Ku | Kukuau pahoehoe Age ~1.35 ka | Mku | Lavas of Mauna Kea, undivided |
| | | Pu | Punahoa pahoehoe Age ~3.5 ka | | |
| | | Ki | Kinoole aa Age <8.0 ka | | |
| | | Ph | Malaai picrite Age ~9.7 ka | | |
| | | An | Anuenue aa Age ~10.6 ka | | |
| | | Wa | Waianuenue pahoehoe Age ~14.2 ka | | |
| Al | Alenaio Stream picrite Age > 14.2 ka | Hh | Halai Hills spatter Age > 14.2 ka | | |

FIGURE 44.15.—Geologic map of Hilo and vicinity showing areas of structural damage from November 1983 earthquake (fig. 44.1, locality 8). Adapted from Buchanan-Banks and Lockwood (1982). Topography from U.S. Geological Survey Hilo 7.5-minute quadrangle, 1981, scale 1:24,000.

***A***

***B***

FIGURE 44.16.—Damage to houses in South Hilo District. ***A***, Wood braces have been emplaced to prevent second story of this house from moving farther downslope. Broken and twisted drain pipe gives an indication of amount of distortion this house has undergone. ***B***, Living area of this wood-frame house extends across break in slope from street level, marked by vegetation on left, to above four-car garage. Concrete blocks of garage level are broken both through and between blocks. Upper story is warped and has moved toward back of house (toward viewer) and to right. New uprights and cross bracing behind garage doors (not visible in this photograph) have been added to support weight of upper story. Drainpipe has been reattached at street level with rope. A decorative rock wall has collapsed and rocks rolled downhill.

FIGURE 44.17.—Damaged commercial building in old part of Hilo. Side wall separated from main structure, leaving a gap at roof level of about 21 cm.

A B

FIGURE 44.18.—Apartment building in Hilo damaged in November 1983 earthquake. ***A***, View along two-thirds of length of building, which was difficult to photograph because of steep slope down to left. Cracked cinder block can be seen between most of windows of first and second floors; less structural damage was apparent at third floor. Arrow indicates area shown in detail in *C*. ***B***, Detail of damage to a part of first floor not shown in *A*. Along longest and widest crack, smeared texture and flaking paint indicate an old crack that had been repaired and repainted. As a result of earthquake, there is renewed cracking along this feature as well as some new cracks through cinder blocks. This building probably was damaged originally by the 1973 Honomu earthquake and (or) by 1975 Kalapana earthquake. ***C***, Detail of damage indicated by arrow in *A*. Some blocks were broken in such a way that pieces of them protruded from block or spalled off.

C

FIGURE 44.18.—Continued.

FIGURE 44.19.—View of Uwekahuna Bluff in Kilauea caldera, taken from Crater Rim Trail a few hours after November 1983 earthquake. Dust plumes mark rock falls that were still occurring along this section of caldera wall. Hawaiian Volcano Observatory is just out of photograph to right. Photography by J.D. Griggs.

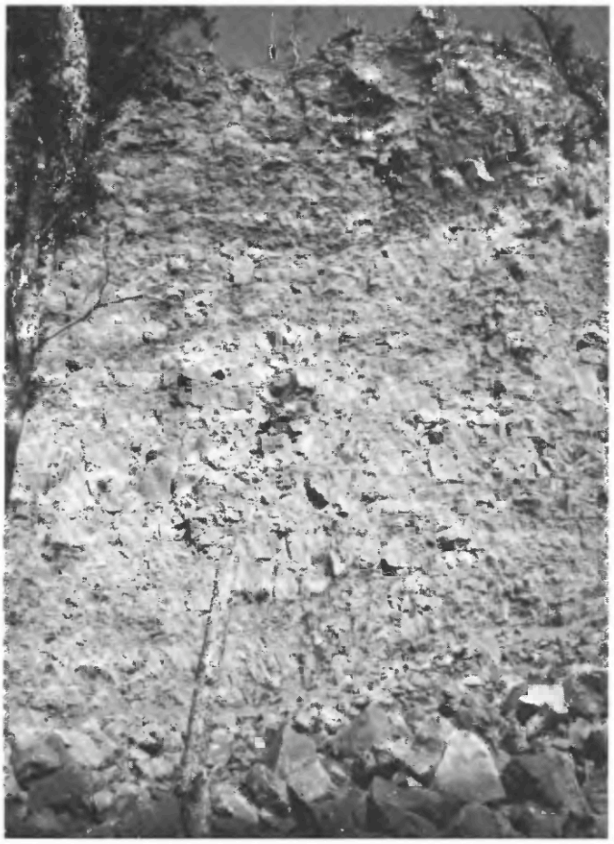

FIGURE 44.20.—Typical section of cliff in Kilauea caldera composed of flows from Kilauea Volcano. View looking up from Halemaumau Trail below Volcano House toward Crater Rim Trail; guardrail (arrow) can be seen suspended over 60-m-high cliff where a rock slide has removed part of trail.

FIGURE 44.21.—Section of Crater Rim Drive at eastern entrance to Kilauea Military Camp that collapsed in November 1983 earthquake along a system of cracks trending at az 60°. Earthquake shaking caused subsurface material to settle, thus undermining road. Note pavement patch from repair of earlier failure at same place.

***A***

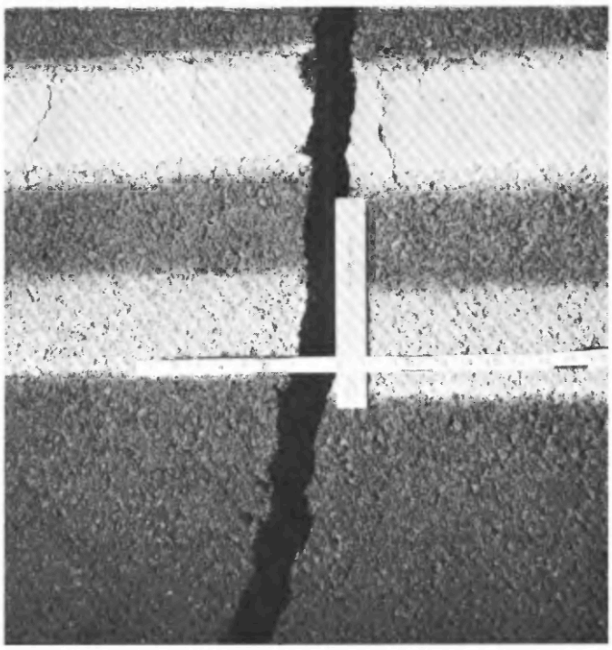

***B***

FIGURE 44.22.—Compressional and extensional features produced by November 1983 earthquake where Crater Rim Drive crosses southwest rift zone of Kilauea Volcano. ***A***, A compressional fold 12 cm high; far end of fold has been collapsed by passage of vehicle. ***B***, An open extension crack 5 cm wide, which shows apparent right-lateral offset of about 2 cm, and vertical offset up to north (left) of about 1 cm.

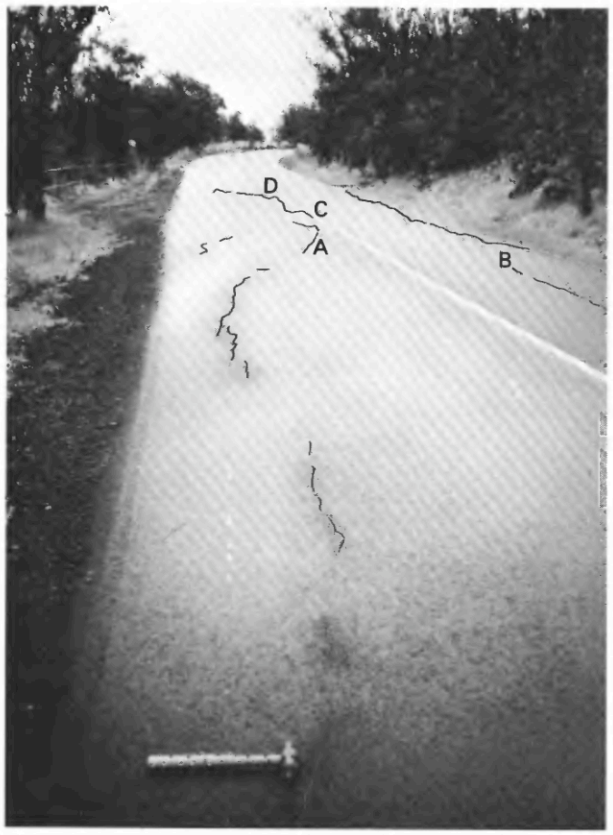


*A*

*B*

FIGURE 44.23.—Ground failure in November 1983 earthquake along Crater Rim Drive between Waldron Ledge Overlook and Research Center turnoff. ***A***, Photograph taken in March 1980, looking northwest, showing road cracks curving toward caldera (left) and outlining incipient landslide (A, C, D). Along the right edge of pavement, additional cracks curving away from caldera (B) mark west side of graben-like depression that runs parallel to roadway for nearly same length as incipient landslide cracks. ***B***, Photograph of same section of road taken in October 1984. Slope failed along preexisting cracks (A, C, D) during earthquake shaking. A graben about 2 m deep by 1–2 m wide has formed along cracks at right side of road (B) and caused trees to tilt.

***A***

***B***

FIGURE 44.24.—Details of failure of Waldron Ledge landslide. Labelled points (A, B, C, D) are same as in figure 44.23. ***A***, View southeast at head scarp of landslide and of parallel graben on other side of road. Headwall scarp was approximately 14 m high and 30 m long; landslide removed 11-m-wide section of road and trail. ***B***, View downward from road of jumbled mass of rock resulting from disintegration of slide block; mass did not travel far from base of cliff.

FIGURE 44.25.—Earthquake-produced crack across road at northwest entrance to Waldron Ledge Overlook. Chips of broken pavement indicate sides of crack were bashed together repeatedly. Photograph by J.B. Stokes.

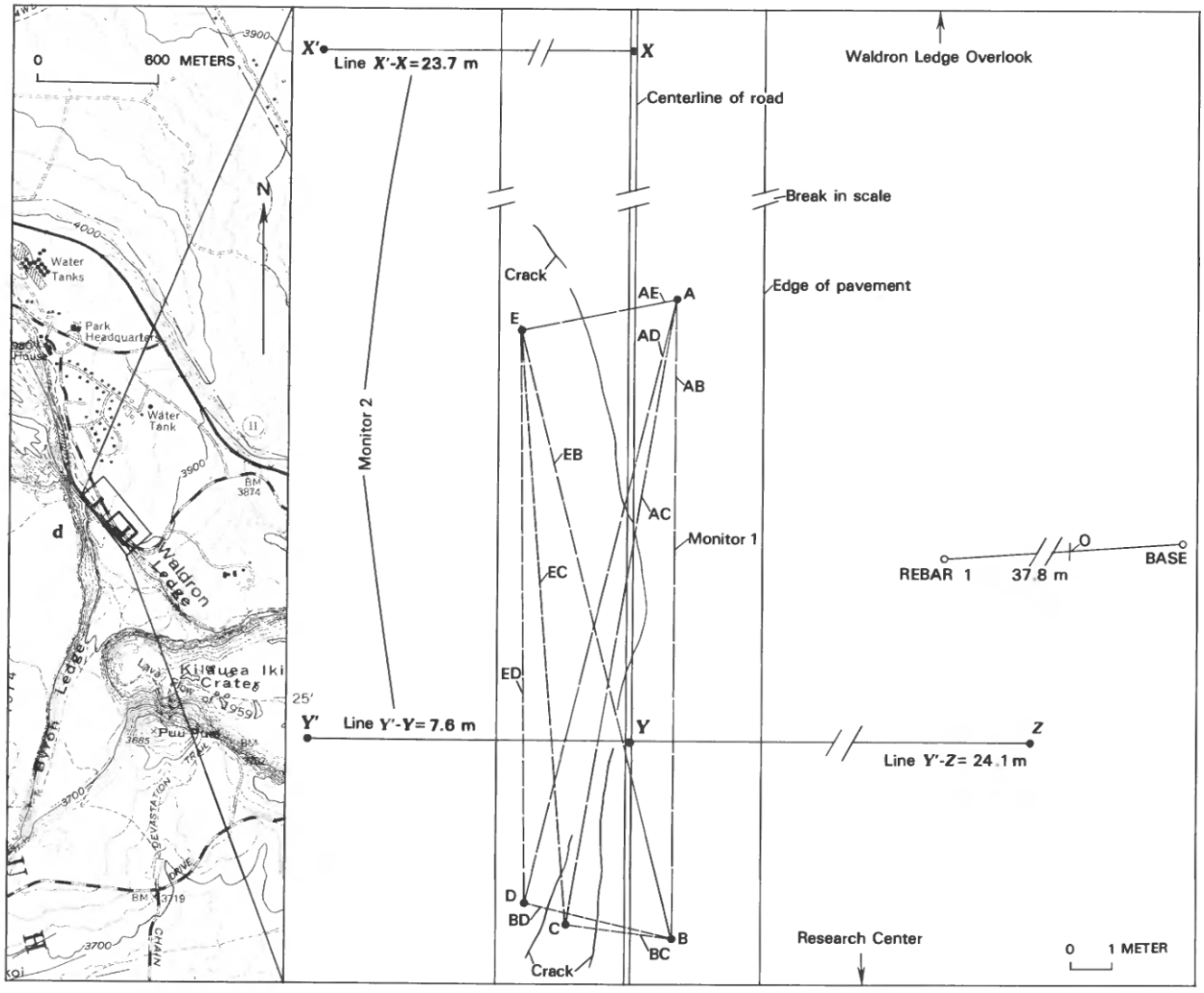


**EXPLANATION**

Monitor 1—
Quadrilateral A-B-C-D-E
Level line from rebar 1 to nails A-B-C-D-E
Monitor 2—
Lines X'-X, Y'-Y, and Y'-Z

Location of Monitor 1
● Nails of quadrilateral and level lines
I Locations of Monitor 2
○ Rebar
d Letter keyed to figure 44.6

FIGURE 44.26.—Location map and plan of monitors established by USGS across series of cracks in Crater Rim Drive near Waldron Ledge. Topography from USGS Kilauea Crater 7.5-minute quadrangle, 1981, scale 1:24,000.

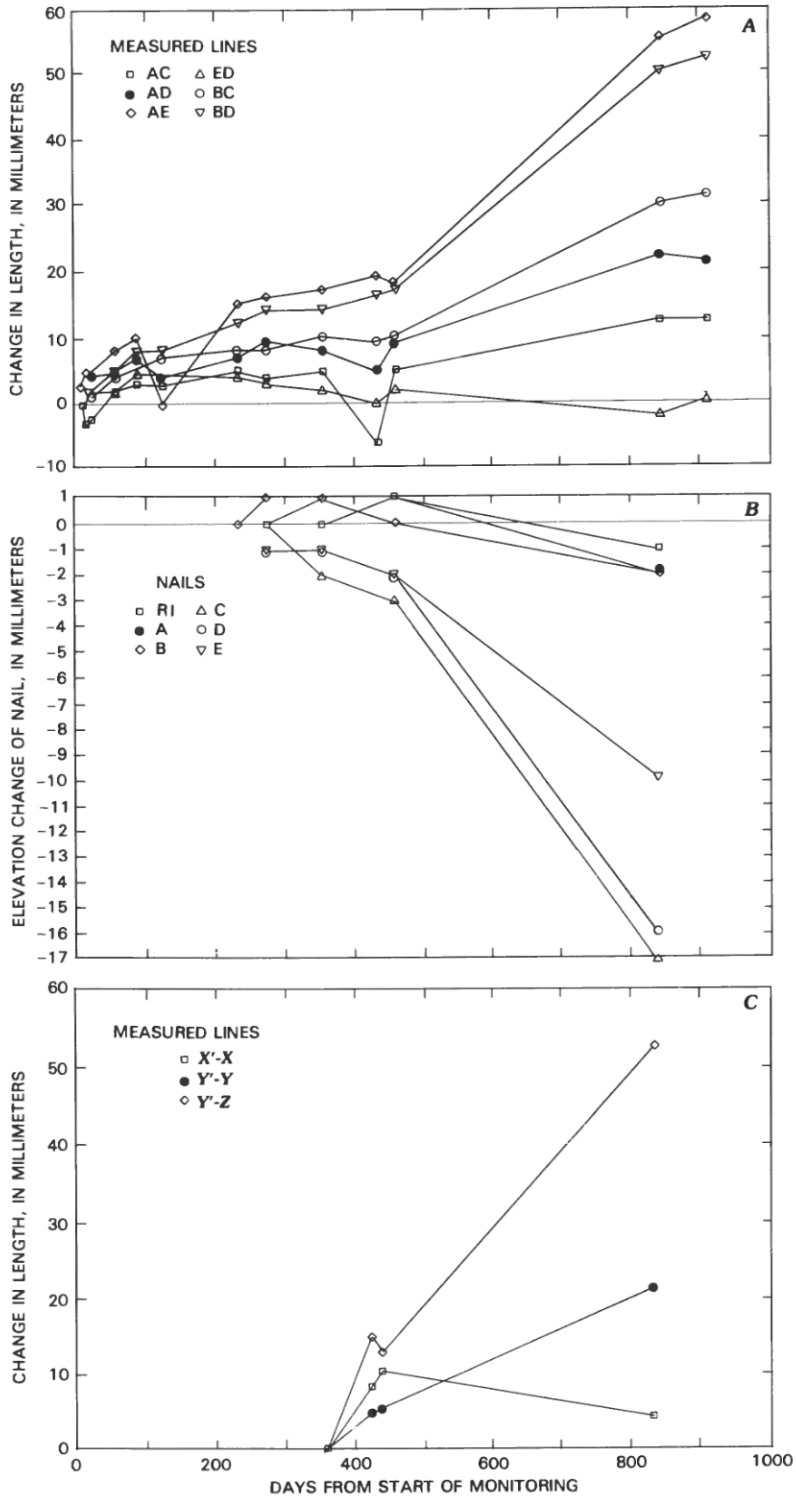


FIGURE 44.27.—Results from monitors established across incipient landslide on Waldron Ledge. ***A***, Changes in line lengths recorded by monitor 1, the quadrilateral. ***B***, Vertical changes recorded by monitor 1 between nails of quadrilateral and rebar 1 (R1). ***C***, Changes in line length recorded by monitor 2, lines measured with steel tape.

FIGURE 44.28.—Arcuate road crack along Kaumana Drive (fig. 44.15, area A) formed in November 1983 earthquake. Ground slopes downward to right. Houses were structurally damaged and water main was broken in area just out of photograph to left.

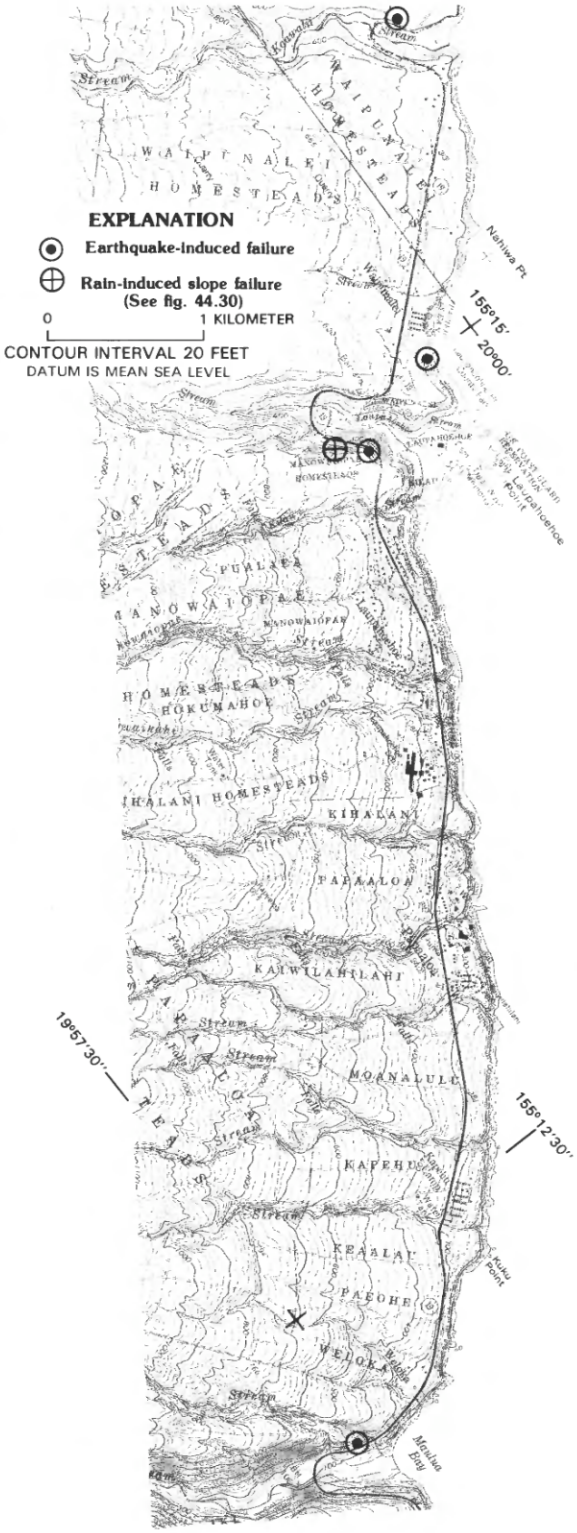


FIGURE 44.29.—Locations of earthquake-induced and subsequent rain-induced slope failures that occurred in North Hilo District between Maulua Bay and Kaawalii Gulch as a result of November 16, 1983, earthquake. Topography from U.S. Geological Survey Keanakolu, Kukaiau, and Papaaloa 7.5-minute quadrangles, 1981, scale 1:24,000.

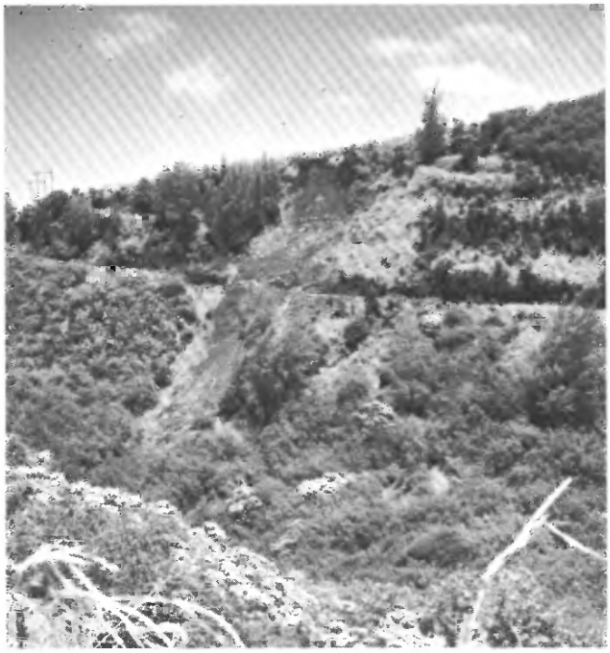

FIGURE 44.30.—Rain-induced slope failure in Laupahoehoe Gulch a few months after November 1983 earthquake. Heavy rains caused earthquake-loosened material to slide. Material below road was pushed over by bulldozer. Light-colored grassy area above road to right of new slide lacks vegetation and indicates that area has been site of landslides in past. At time of earthquake, a smaller rock slide occurred from the nearly vertical cliff just below the power poles (left), and blocked highway for a few hours. Photograph by N.G. Banks.

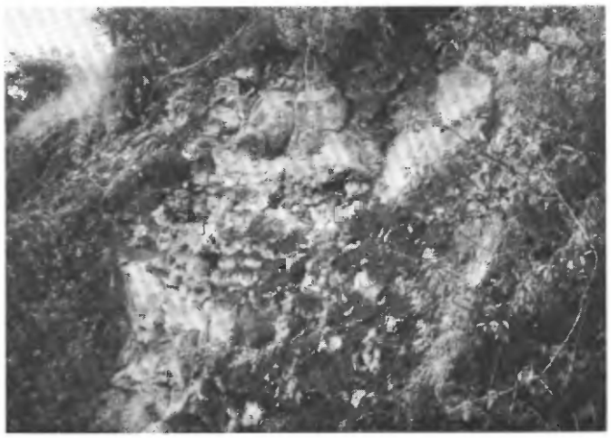

FIGURE 44.31.—Headwall scarp of earthquake-induced rock slide that briefly blocked secondary road to Laupahoehoe Point. It was not possible to picture entire slide in one photograph because of steep cliff bounding road and fact that slide occurred between two curves in road. Lower part of rock slide cannot be seen here; slide was about 1 m deep, 9 m high, and 4 m across (volume about 36 $m^3$). In-place formation of spheroidal boulders of weathering in Mauna Kea lava flows attests to severity of disintegration of these rocks.

FIGURE 44.32.—Narrow chutes (outlined) formed at time of November 1983 earthquake by landslides from steep slopes surrounding Kealakekua Bay, west coast, Island of Hawaii. Rock falls (rf) occurred on lower, steeper slopes. View northwestward.

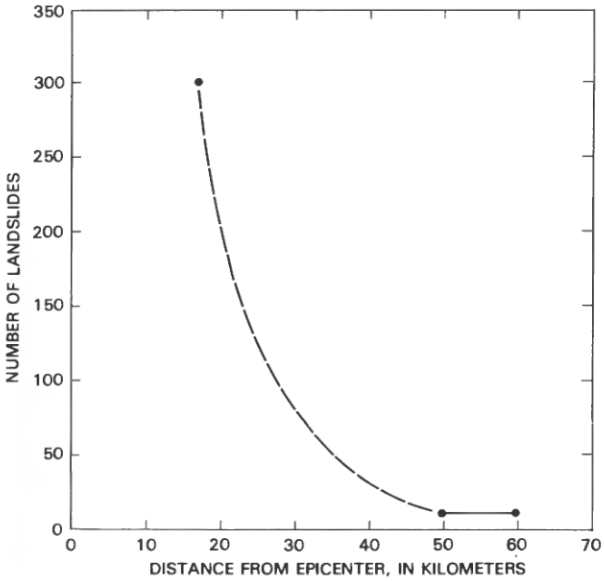


FIGURE 44.33.—Number of landslides caused by November 1983 earthquake in relation to distance from epicenter. Dashed line is estimated interpolation.

TABLE 44.1.—*Selected parameters of damaging earthquakes in Hawaii, 1962–1983*

[Modified from Koyanagi and others, 1984, table 1]

| Date | Location | Magnitude | Energy release ($10^{12}$ J) | Maximum intensity (modified Mercalli) | (location) | Damage (millions) | Depth (km) | Focal mechanism |
|---|---|---|---|---|---|---|---|---|
| June 27, 1962 | Kaoiki | 6.1 | 40 | VI | Volcano | $1.0(?) | 8 | Strike slip |
| April 26, 1973 | Honomu | 6.2 | 60 | VII | Hilo, Hamakua | 5.6 | 48 | Strike slip |
| November 30, 1974 | Kaoiki | 5.5 | 4 | V | Kapapala, Volcano, Hilo | <1 | 6 | Strike slip |
| November 29, 1975 | Kalapana | 7.1 | 2170 | VIII | Hilo, Puna, Volcano | 4.1 | 8 | Low-angle thrust? |
| November 16, 1983 | Kaoiki | 6.6 | 260 | VIII-IX | Volcano, Kapapala, Hilo | 7.0(?) | 12 | Strike slip |

TABLE 44.2.—*Intensity and description of damage at various localities on the Island of Hawaii, November 16, 1983, Kaoiki earthquake (magnitude 6.6)*

| City, town, village | Intensity (modified Mercalli) | Description of damage |
|---|---|---|
| | | **South Hilo District** |
| Hilo | V-VIII | Extensive damage in downtown area. Minor cracks in roads and water pipes, concrete walls and floors, and plaster. Connecting pipes to an underground gasoline storage tank were ruptured. Most public buildings sustained damage to architectural plaster and acoustic-tile ceilings, and had spalling concrete. The public library also had plate glass windows broken. Hilo Hospital suffered structural damage, roofing, and architectural-plaster damage estimated at $250,000. Apartments and business buildings suffered structural and equipment damage. Numerous plate glass windows broke. Shelved items in markets fell or tumbled over. Homeowners reported losses because of houses and garages shifting from foundations; cracked windows, retaining walls, driveways, and concrete house pads; broken windows; water pipes, and water heater fittings; collapse of rock walls and fences; steps torn away from houses; plumbing damage and septic tank cave-ins; doorways, window frames and cupboard doors distorted; chimneys separated from walls; lightweight furniture and table lamps fell over; loose and hanging objects fell and broke. Several people experienced difficulty standing. A driver described his car trying to wander as if it had a flat tire. Another observer described undulating ground waves with crests and troughs approximately 0.3 m high and 0.5 m across. |
| Papaikou | VI | Septic tank caved in; shelves fell from framing; objects fell from high shelves; books and mirrors fell; dishes broke; minor cracks to interior walls. One householder reported damage to interior walls, as well as structural damage to house and cracking of concrete slab in carport. |
| Pepeekeo | VI | Water splashed out of sink. |
| Honomu | VI | Loose objects fell off shelves and broke; dishes and bottles broke; stone walls opened up. |
| | | **Puna District** |
| Hawaiian Paradise Park | V-VII | A few knickknacks tipped or fell; 5 percent of the water in a 75,500-L (20,000-gal) pool was lost through sloshing. There was one report of a destroyed water tank. |
| Orchidland | IV | Many objects on shelves fell. Nothing broke. |
| Ainaloa | | Cupboard doors opened and dishes toppled out; book shelves fell; two support beams for a deck moved 10 cm off blocks. |
| Keaau | VI | House rocked; objects on shelves and in cupboards fell over but few broke. Water sloshed out of catchment tank. |
| Kurtistown | VI | Television, lamp, and statue fell off shelves. Dishes broke and pictures fell off wall. |
| Mountain View | VI-VIII | One house shifted 2 cm on its foundation piers, pulling away from back wall. A resident reported water pipe to toilet broke and fittings to water heater were damaged and leaking; water sloshed in water tank; cupboard doors opened and contents fell out; dishes and lamps broke; bookcases overturned and books were scattered; furniture was moved; loose objects tumbled off shelves. Hand-stacked rock wall collapsed in some places. A driver traveling at about 50 mph uphill on Highway 11 between Mountain View and Glenwood found it impossible to maintain control of the car. It felt as though the car had several flat tires, and he was forced to stop. He observed two other cars coming downhill whose drivers also stopped and got out to examine their cars. |
| Glenwood | VII-VIII | Loose objects fell off shelves; items fell from cupboards and freezer; contents of closets spilled; television overturned and books were dumped off bookshelves; large appliances moved, drywall was cracked in some places; stacked lumber was unstacked; full doughboy water tank moved about 5 cm. |

| | | |
|---|---|---|
| Volcano | VI-VIII | Houses and garages were moved off foundations as much as 1 m. Masonry was broken and house frames cracked. Carports were leaning and a few collapsed. Many water tanks were damaged and some collapsed; others were moved as much as 0.5 m and pipes were broken. Three fireplace chimneys at residential homes collapsed. Ground cracks opened about 2 cm; pavement cracks occurred and small soil slips were observed on steep road cuts. Doors of cabinets and refrigerators opened and contents spilled out; dishes broke; objects fell off shelves; cabinets overturned. Chest drawers opened. Books fell from shelves, and furniture moved. A driver travelling northeast on Wright Road felt as if car had flat tire, then it turned at right angle to the road. He saw the ground undulating. |
| **Kau District** | | |
| Hawaii Volcanoes National Park | VIII | Substantial ground cracking and ground failures resulted in extensive road damage. On Crater Rim Drive damage was severe at Waldron Ledge, Kilauea Military Camp, the Southwest Rift Zone, Keanakakoi Overlook, and Puu Puai. The main highway was damaged at the entrance to Kilauea Military Camp. Ground cracking also occurred on the Chain of Craters, Ainaho, Hilina Pali, and Mauna Loa Roads. Many hiking trails were damaged by slope failures that removed parts of trails and buried other trails. Some instruments at the Hawaiian Volcano Observatory were temporarily out of order and others were damaged; books were tossed from shelves and bookcases fell over; file cabinets shifted. There was some cracking and minor offsetting of concrete foundation slabs. Dishes and loose objects on shelves fell and broke. |
| Volcano Golf and Country Club Subdiv. | IX | Many houses and garages were moved off their foundations towards the southwest. Hairline cracks occurred in concrete slabs. People reported difficulty in standing or walking. Water tanks moved across their gravel beds as much as 5 cm, and some of their roofs were knocked off or damaged; water sloshed out of many tanks; water heaters were moved and the PVC lines to the water tanks were snapped. Refrigerator and cupboard contents were dumped on floors; cabinet drawers opened; books and tools were thrown off shelves; televisions were overturned, and bookcases toppled. Lamps and canned goods fell to the floor. Heavier furniture moved. |
| Old Golf Course Road | VIII | Dishes broke and scattered; books fell off shelves; bookcases overturned; file cases moved; objects thrown out of closet and medicine chest with velocity. An 18,500-L (5,000-gal) water tank that was two-thirds full moved 2.5 cm. |
| Kapapala Ranch | VII-VIII | Main house moved nearly 17 cm off its foundation toward the southest. Hot water tank torn from pipes and thrown over; partially collapsed rock walls. |
| Wood Valley | VII-VIII | A few wood-frame houses moved off their foundations; PVC pipes broken and minor cracks in stucco facing; nearly every headstone in the cemetery overturned. |
| Pahala | VI | In Kau Hospital, bookshelves fell over, ceiling panels dislodged, patients' beds moved as much as 1.5 m, wall clocks dangled by wires and contents of cabinets were displaced. Dishes fell from cupboards and loose objects fell from shelves; pictures and mirrors fell from walls; bookcases, books and shelving fell; tables and floor lamps were broken as well as dishes and an aquarium. Cabinet, refrigerator and freezer doors opened and contents fell out. Appliances and furniture moved as much as 10 cm from original locations and small applicances fell from stands. A few water heaters were knocked over and one was moved about 0.3 m, breaking and connecting pipes. At a store, 75 percent of the merchandise fell from the shelves and was damaged. |
| Naalehu | V | Table lamps, bookshelves, and knickknacks tipped over and dishes broke; television and microwave oven were moved; water splashed out of fish tank; slight leak in water pipe. |

TABLE 44.2.—*Intensity and description of damage at various localities on the Island of Hawaii, November 16, 1983, Kaoiki earthquake (magnitude 6.6)*—Continued

| City, town, village | Intensity (modified Mercalli) | Description of damage |
|---|---|---|
| | | **Kau District (continued)** |
| Ka Lae | V | Part of cliff fell into ocean; a large sand hill subsided; rock walls in north-south direction were damaged. One house was moved about 1.5 m off its foundation. North of the highway, a few water pipes were broken; refrigerator doors opened and contents fell out; loose objects on shelves fell; damage to bookshelves, table lamps, and glassware; stone walls were severely damaged. |
| Ocean View Estates | IV | Cabinets and drawers opened; objects on shelves fell to floor; rocks fell into driveway. |
| | | **South Kona District** |
| Honaunau | V | Rocks tumbled from stone walls; houses shook vigorously; loose objects tumbled from shelves and cupboards, and some broke; bookshelves fell over; filing cabinets moved; a few water pipes were broken. Wave action was observed in a pond and a concrete water tank. Water spilled out of toilet tank. |
| Kealakekua Bay | IV | Landslides from cliff into bay discolored water and caused substantial dust cloud over bay. Rock falls also occurred off slopes into some driveways. Loose objects tumbled from shelves but there was little breakage. |
| Captain Cook | IV | Lamp, vases, bottles and books fell from shelves. |
| | | **South and North Kohala** |
| Hawi, Kapaau, Kamuela | V | Buildings shook, rattling dishes; pictures fell; loose objects fell from shelves; hanging plants swayed. |
| | | **Hamakua** |
| Kukuihaele | V | Houses shook and dishes rattled; a few dishes and loose objects fell from shelves; a stone wall cracked. There was one report of house siding splitting and clocks being damaged. |
| Honokaa | V | Wood-frame buildings shook severely. A few objects fell from shelves; rocks fell from roadcuts. |
| Paauhau | V | Minor damage to objects on shelves. |
| Paauilo | V-VI | Some objects fell off shelves, houses shook. Driver on main highway did not feel quake while driving his truck, but noted rock debris on highway. |
| | | **North Hilo** |
| Laupahoehoe | VI | Landslides from slopes along the circum-island highway and on the road down to the coastal village blocked roads. Buildings swayed, cupboard doors opened and items fell out; loose objects fell from shelves and broke; items inside cabinets fell over. At the school library, ceiling tiles fell, books fell off shelves and scattered, bookcases were loosened from walls. |
| Ninole | VI | Report spoke of wierd rumbling noise accompanied by vigorous rolling and shaking; bottles and pictures fell. |

TABLE 44.3.—*Data from strong-motion accelerographs for November 16, 1983, Kaoiki earthquake*

[Distance is distance of station from epicenter. Components are: L, longitudinal with instrument; V, vertical; T, transverse to instrument; figures by horizontal components are azimuth directions. Slightly modified from Arnold V. Acosta and Richard P. Maley, USGS, Branch of Engineering Seismology and Geology, unpublished table, 1984]

| Station | Latitude, Longitude | Distance (km) | Component | Peak acceleration of gravity | Comments |
|---|---|---|---|---|---|
| Volcano Observatory, Hawaii Volcanoes National Park | 19.423°N. 155.291°W. | 17 | 360°L<br>up V<br>270°T | [1]0.67<br>.21<br>.39 | Greater than 0.1 acceleration of gravity for 8.5 seconds. |
| Wahaula Maintenance Center, Hawaii Volcanoes National Park | 19.329° 155.031° | 45 | 145°L<br>up V<br>055°T | .12<br>.07 | Long period record. 18 Hz superimposed near beginning. |
| Fire Station, Pahoa | 19.498° 154.951° | 53 | 087°L<br>up V<br>357°T | .18<br>.07<br>.11 | |
| Sewage Plant, Hilo | 19.734° 155.050° | 54 | 333°L<br>up V<br>243°T | .10<br>.02<br>.07 | |
| University of Hawaii, Hilo | 19.707° 155.083° | 49 | 085°L<br>up V<br>355°T | .07<br>.04<br>.11 | Dominant sinusoidal response, about 2.8 Hz horizontal. |
| U.S. Fish and Wildlife Office, Hilo | 19.731° 155.100° | 49 | 360°L<br>up V<br>270°T | .40<br>.15<br>.50 | |
| Fire Station, Honokaa | 20.080° 155.465° | 72 | 021°L<br>up V<br>291°T | .25<br>.10<br>.37 | Dominant sinusoidal response, about 8 Hz horizontal. |
| Kahala Police Station, Kapaau | 20.230° 155.801° | 95 | 102°L<br>up V<br>012°T | .07<br>.05<br>.09 | |
| Fire Station, Kamuela | 20.03° 155.66° | 70 | 155°L<br>up V<br>065°T | .13<br>.07<br>.08 | Dominant sinusoidal response, about 7 Hz horizontal. |
| Mauna Kea State Park, Saddle Road | 19.752° 155.530° | 36 | 050°L<br>up V<br>320°T | .17<br>.21<br>.26 | |
| Mauna Loa Observatory, 3,350-m (11,000-ft) elevation, Mauna Loa | 19.539° 155.580° | 18 | 030°L<br>up V<br>300°T | .34<br>.46<br>.58 | V and T peaks were single simultaneous spikes. |
| Fire Station, Kailua-Kona | 19.649° 155.996° | 62 | 312°L<br>up V<br>222°T | .04<br>.01<br>.03 | |
| Kona Hospital, Kealakekua | 19.523° 155.879° | 46 | 346°L<br>up V<br>256°T | .10<br>.07<br>.10 | |
| Kau Baseyard, Waiohinu | 19.070° 155.615° | 43 | 065°L<br>up V<br>335°T | .19<br>.09<br>.17 | |
| Kau Hospital, Pahala | 19.20° 155.47° | 26 | 188°L<br>up V<br>098°T | .59<br>.16<br>.31 | |

[1]A high-frequency peak (raw scaling 0.87 acceleration of gravity) was superimposed on the main pulse. This is believed to be other than ground motion.

TABLE 44.4.—*Length and elevation changes recorded by monitoring programs at head of incipient Waldron Ledge landslide, April 1980 to October 1982*

[Positive length changes represent extension, negative ones, shortening; positive elevation changes represent uplift, negative ones subsidence; --, not measured]

| Measured item | Original measurement (m) | Measured change (mm) | | | | | | | | | | | | | | |
|---|---|---|---|---|---|---|---|---|---|---|---|---|---|---|---|---|
| | | 1980 | | | | | | | 1981 | | | | | 1982 | | |
| | | [1]Apr. 14 | [1]Apr. 21 | [3]Apr. 28 | [3]Jun. 2 | [2]Jul. 3 | [2]Aug. 8 | [2]Nov. 25 | [2]Jan. 5 | [2]Mar. 26 | Jun. 13 | [3]Jun. 27 | [2]Jul. 9 | [3]Jul. 23 | [2]Jul. 26 | [2]Oct. 1 |
| **Length changes in lines of monitor 1 originally measured April 7, 1980** | | | | | | | | | | | | | | | | |
| Line AB | 14.905 | 0 | 0 | 0 | 0 | 4 | 3 | 3 | 2 | 3 | [2]14 | -- | 0 | -- | 6 | -2 |
| Line AC | 15.712 | 0 | -3 | -2 | 2 | 3 | 3 | 5 | 4 | 5 | [2]-6 | -- | 5 | -- | 12 | 12 |
| Line AD | 15.444 | 3 | 0 | 2 | 5 | 7 | 4 | 7 | 9 | 8 | [2]5 | -- | 9 | -- | 22 | 21 |
| Line AE | 3.726 | 3 | 5 | 5 | 8 | 10 | 0 | 15 | 16 | 17 | [2]19 | -- | 18 | -- | 55 | 58 |
| Line EC | 14.102 | 3 | -2 | 2 | 3 | 5 | 3 | 5 | -9 | 2 | [2]-2 | -- | 3 | -- | -3 | -5 |
| Line ED | 13.558 | 3 | 0 | 2 | 2 | 5 | 4 | 4 | 3 | 2 | [2]0 | -- | 2 | -- | -2 | 0 |
| Line EB | 13.885 | 2 | -2 | 2 | 5 | 8 | 3 | 3 | 3 | 2 | [2]-1 | -- | 3 | -- | 2 | 2 |
| Line BC | 2.525 | 2 | 1 | 1 | 4 | 5 | 7 | 8 | 8 | 10 | [2]9 | -- | 10 | -- | 30 | 31 |
| Line BD | 3.651 | 2 | 2 | 4 | 5 | 8 | 8 | 12 | 14 | 14 | [2]16 | -- | 17 | -- | 50 | 52 |
| **Elevation changes, relative to rebar 1, at monitor 1 originally measured November 25, 1980** | | | | | | | | | | | | | | | | |
| Base | 0.234 | -- | -- | -- | -- | -- | -- | -- | 0 | 0 | -- | -- | 1 | -- | -1 | -- |
| Nail A | 1.854 | -- | -- | -- | -- | -- | -- | -- | 0 | 1 | -- | -- | 1 | -- | -2 | -- |
| Nail B | 2.461 | -- | -- | -- | -- | -- | -- | -- | 1 | 1 | -- | -- | 0 | -- | -2 | -- |
| Nail C | 2.487 | -- | -- | -- | -- | -- | -- | -- | 0 | -2 | -- | -- | -3 | -- | -17 | -- |
| Nail D | 2.477 | -- | -- | -- | -- | -- | -- | -- | -1 | -1 | -- | -- | -2 | -- | -16 | -- |
| Nail E | 1.949 | -- | -- | -- | -- | -- | -- | -- | -1 | -1 | -- | -- | -2 | -- | -10 | -- |
| **Length changes in lines of monitor 2 originally measured April 10, 1981** | | | | | | | | | | | | | | | | |
| Line X'-X | | | | | | | | | | | | | | | | |
| Hard pull | 23.764 | -- | -- | -- | -- | -- | -- | -- | -- | -- | [3]6 | 10 | -- | 6 | -- | -- |
| Soft pull | 23.771 | -- | -- | -- | -- | -- | -- | -- | -- | -- | [3]11 | 11 | -- | 3 | -- | -- |
| Line Y'-Y | | | | | | | | | | | | | | | | |
| Hard pull | 7.620 | -- | -- | -- | -- | -- | -- | -- | -- | -- | [3]5 | 0 | -- | 11 | -- | -- |
| Soft pull | 7.623 | -- | -- | -- | -- | -- | -- | -- | -- | -- | [3]5 | 11 | -- | 32 | -- | -- |
| Line Y'-Z | | | | | | | | | | | | | | | | |
| Hard pull | 24.098 | -- | -- | -- | -- | -- | -- | -- | -- | -- | [3]14 | 12 | -- | 52 | -- | -- |
| Soft pull | 24.101 | -- | -- | -- | -- | -- | -- | -- | -- | -- | [3]16 | 14 | -- | 54 | -- | -- |

[1]Measurement by J.M. Buchanan-Banks and R.B. Moore.
[2]Measurement by K.M. Yamashita and M.K. Sako.
[3]Measurement by J.M. Buchanan-Banks and N.G. Banks.

# ORIGIN OF VOLCANIC TREMOR IN HAWAII

## PART I
## Data from the Hawaiian Volcano Observatory 1969–1985

*By* Robert Y. Koyanagi, Bernard Chouet, *and* Keiiti Aki[1]

### ABSTRACT

**Harmonic tremor characterized by an almost constant frequency pattern throughout the duration of its seismic signal is associated with eruptive activity and magma movement in Hawaii. The signal frequency is believed to vary inversely to the length of the generating source, and amplitude varies according to rate of magma movement under confining pressure. The eruption related tremor reflects high-frequency seismic and acoustic disturbance from lava-fountain activity. The amplitude of eruption tremor oscillates at intervals of a few seconds in a temporal pattern resembling that of intense lava fountaining, in which high bursts repeatedly occur seconds apart. This characteristic pattern may be related to pulsating magma movement driven by continual pressure fluctuations. Added to the eruption zone activity, tremor and long-period events that are localized at the summit vary in intensity according to the magnitude and rate of the associated inflation-deflation episodes. Long-period events and tremor are inferred to share a common origin, and selected long-period events with identifiable onset times are locatable using standard earthquake locating techniques. The locations of long-period events may, in turn, be used to identify the source region of tremor beneath Hawaii and to further define depth-time classifications of tremor.**

**The clustered hypocentral distribution of long-period events defines a magma transport system originating from a broad 30-km-wide central complex at depths of 30–60 km. This central complex separates laterally and connects discontinuously to smaller cylindrical conduit zones that rise steeply to the summit regions of Kilauea, Mauna Loa, and Loihi. Gaps occur in tremor activity in some regions expected to be passageways for magma along the lateral rift conduit and at depths of 15–30 km in the vertical plumbing system. These gaps may be low-stress regions that allow quasi-steady flow accompanied by pressure pertubations too small to generate measurable tremor in the normally recorded frequencies of 1–10 Hz.**

## INTRODUCTION

Harmonic tremor, a seismic indicator of magma movement and eruptive activity, has been instrumentally documented at the Hawaiian Volcano Observatory (HVO) since 1912. It is identified on seismograms by a sustained signal that varies within a limited range of frequencies. Its duration is determined by the duration of volcanic eruption or of accelerated magmatic activity within the transport system. At HVO, tremor is classified into three categories of inferred depth on the basis of relative amplitude and areal extent of detection in the seismic network. Tremor is logged in terms of minutes per hour for short episodes and hours per day for longer events. Most of our tremor data is related to activity at Kilauea, since that is where most activity has occurred in the past 20 years and where our network of seismometers is densest. Seismic data collected from such prolonged Kilauea eruptions as the Mauna Ulu sequence in 1969–1974 and the Puu Oo sequence in 1983–1985, and from a significant southwest rift intrusion in August 1981 have provided a comprehensive record of shallow tremor associated with eruptions and intrusions, as well as, tremor associated with the aftermath of eruptive-intrusive activity or during periods of increased magmatic activity within the magma transport system at depth. Tremor near eruptive vents varies in amplitude according to the vigor of eruption. Abrupt changes in tremor amplitude occur simultaneously with changes in lava extrusion rate and fountain intensity, indicating that shallow tremor is dominantly produced at the eruption site. The seismic signal associated with eruption attenuates rapidly with increasing distance from the eruptive vent. Even low-level tremor between major outbreaks often varies in amplitude according to the intensity of lava movement in the vent.

Harmonic tremor that occurred in places or times unrelated to eruptions is presumed to be associated with magma movement at depth. It is commonly localized beneath the Kilauea summit region at crustal depths but spreads to cover a large area beneath the active volcanoes in the south Hawaii region at mantle depths. Episodes of such tremor are often accompanied by increased numbers of long-period events, which have measurable onsets and travel times across the seismic network that fit *P*-wave velocities expected for normal earthquakes. The amplitude and signal duration of the long-period events vary like those of earthquakes, but otherwise their spectra resemble those of tremor in having consistently peaked frequencies

[1]Department of Geological Sciences, University of Southern California, Los Angeles, California 90089-0741.

throughout the coda. Similarity of the distance-attenuation rates for the long-period events and for tremor further implies a common source or origin. If we accept a common origin for long-period events and tremor, then the precise determination of hypocenters for a sufficient number of long-period events accurately constrains the source region for tremor beneath Hawaii. The depth distribution of located long-period events as a function of time provides insight into the dynamic processes involved in the ascent of magma from the mantle through temporary storage and transport in the shallow magma plumbing system to eruptions of lava on the surface.

Koyanagi and others (1976) have shown how swarms of short-period earthquakes outline the upper boundary of the shallow storage system beneath the summit of Kilauea and how a persistent source of long-period events defines the magmatic feeding system below. A region in which few earthquakes occur, located at a depth of 3–6 km, is interpreted to be the storage zone of magma having an expected low rigidity. Since that earlier compilation, expansion of the seismic network and added records of intrusive and eruptive activities have provided more locatable short-period earthquakes and long-period events in the lower magnitude range that occurred episodically during rapid changes in ground tilt at the summit. Thurber (chapter 38), from a study of seismic velocity anomolies using seismic data collected by HVO in recent years, infers a smaller and shallower aseismic zone about 2 km in diameter and located 2–4 km beneath the summit caldera. This zone is surrounded by earthquakes that were relocated using a ray-tracing method in his three-dimensional velocity model. In our recent compilation of data, very small long-period events sometimes accompanied short-period earthquakes during critical stages of inflation before intrusive or eruptive events. More common, however, were those long-period events that followed a significant deflation event; these were shallow events concentrated near the center of deflation.

Swarms of shallow earthquakes and rapid changes in ground tilt during vigorous intrusions of magma are often accompanied by a background of low-amplitude tremor. Upon eruption of lava, the tremor amplitude increases and the frequency of earthquakes decreases. During the eruption, the amplitude of tremor is influenced by lava movement and fountaining at the eruption site and by magma movement within the conduit system near the summit.

Bursts of tremor at intermediate depths beneath Kilauea are occasionally recorded during eruptions, but these usually accompany gradual inflation of the summit. Persistent deep tremor in the mantle beneath south Hawaii has individual episodes that last one-half hour to several hours, and their cumulative reduced displacement as a function of time yields a rate of magma ascent from the mantle (Aki and Koyanagi, 1981). Reduced displacement refers to the source intensity of tremor calculated from seismographically measured ground amplitudes. In our search for the origin of volcanic tremor in Hawaii, we describe its seismic signature in terms of spectral content and amplitude of the ground motion. We consider the spatial and time distribution of tremor in relation to volcanic processes at Kilauea. The source region of tremor and the inferred magma-transport system is outlined from hypocenters of long-period events; the time sequence of these events describes the pattern of magma movement in the transport system. These collections of field observations and instrumental records complement Chouet and others (chapter 45, part II), who discuss the origin of volcanic tremor and outline the evolution of theoretical models. We draw upon those current concepts in organizing our presentation of the data collected at HVO over the past 16 years.

### ACKNOWLEDGMENTS

The authors appreciate the helpful reviews of this paper by Thomas Wright and Elliot Endo. Technical support and corroborating scientific information provided by the staff of HVO are gratefully acknowledged. Wil Tanigawa, Jennifer Nakata, and Sandra Zane assisted in the preparation of essential data plots for our figures. Pauline Tamura and Dorothy Footer prepared type drafts of the manuscript. Jim Griggs made photographic reproductions of seismograms used in our figures.

## SEISMIC INSTRUMENTATION

The U.S. Geological Survey's Hawaiian Volcano Observatory (HVO) maintains a continuously operating network of 50 seismometer stations on the Island of Hawaii (figure 45.1; table 45.1). The system, designed for microearthquake detection, consists primarily of vertical-component stations with a peak magnification of $10^5$ at about 15 Hz (figure 45.2, type 1, based on the Develocorder format). Thirteen are three-component stations with horizontal seismometers of type 1 response, operated at about −12 dB in relation to the vertical component for preferential detection of *S*-waves of local events, or a modified Wood-Anderson response that is flat over a relatively wide range of frequencies for amplitude measurements. With the exception of two stations, signals are continually telemetered to the observatory and recorded on rotating-drum recorders, Develocorder film, and magnetic tape. One station on Maui and one on Oahu provide additional coverage of regional seismicity in the Hawaiian Islands.

The history of HVO seismograph operation was presented in detail by Klein and Koyanagi (1980), and an updated description of station parameters is given by Nakata and others (1984). Information pertaining to the capability and limitations of the HVO seismic net and to the routine processing of data is included in Koyanagi and others (in press).

## DATA PROCESSING

In the day-to-day processing of data, seismic events are classified according to their signatures by comparison with an assemblage of seismograms obtained on rotating drum recorders and two 20-channel Develocorders. The variations from station to station of recorded arrival times, amplitudes, and spectral features provide the basic criteria to classify seismic events into different categories. The procedure for routine processing of the standard seismograms obtained at HVO and the characteristic differences in signature used as the basis for general classification were outlined in a preliminary report (Koyanagi, 1982). Computer processing of seismic data and determination of earthquake hypocenters are based

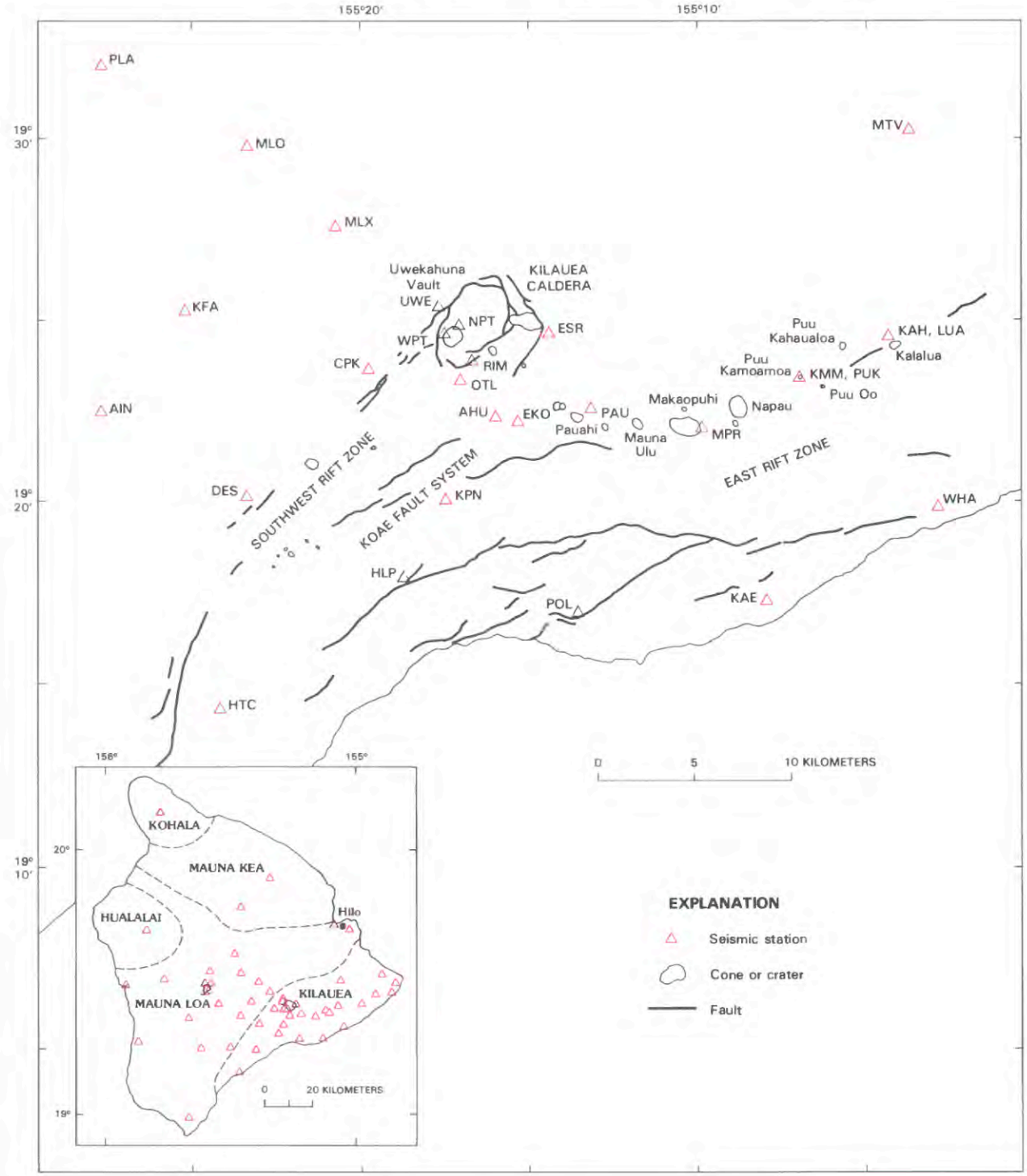


FIGURE 45.1.—Geologic features and seismometer stations in the region around the summit of Kilauea, southeast Hawaii. The seismometer stations are identified by their three-letter codes (see table 45.1). Inset shows all seismometer stations (triangles) operated in 1983 on the Island of Hawaii (Nakata and others, 1984) and the boundaries of the island's five volcanoes.

TABLE 45.1.—*Seismometer stations in Hawaii operated by the U.S. Geological Survey*

[Vertical components are designated by 3-letter codes and horizontal components by 4-letter codes, the last letter of which indicates their orientations, east-west (E) or north-south (N). Operation of stations EKO and WPT was discontinued by 1972. Following minor relocations made due to new lava flows in 1983, station Puu Kamoamoa (PUK) was replaced by Kamoamoa (KMM) and station Kalalua (LUA) was replaced by Kahaualea (KAH)]

| Name | Code | Number of Components | North latitude (deg) | North latitude (min) | West longitude (deg) | West longitude (min) | Elevation (m) |
|---|---|---|---|---|---|---|---|
| Ahua | AHU, AHUE, AHUN | 3 | 19 | 22.40 | 155 | 15.90 | 1,070 |
| Ainapo | AIN, AINE, AINN | 3 | 19 | 22.50 | 155 | 27.62 | 1,524 |
| Captain Cook | CAC | 1 | 19 | 29.29 | 155 | 55.09 | 323 |
| Cone Peak | CPK | 1 | 19 | 23.70 | 155 | 19.70 | 1,038 |
| Dandelion | DAN | 1 | 19 | 21.42 | 155 | 40.04 | 3,003 |
| Desert | DES | 1 | 19 | 20.20 | 155 | 23.30 | 815 |
| East Koae | [1]EKO | 1 | 19 | 22.17 | 155 | 14.99 | 1,009 |
| Escape Road | ESR | 1 | 19 | 24.68 | 155 | 14.33 | 1,177 |
| Hawaiian Beaches | HAB | 1 | 19 | 31.89 | 155 | 53.89 | 92 |
| Hilo | HIL, HIE, HIN | 3 | 19 | 43.20 | 155 | 5.30 | 20 |
| Hilina Pali | HLP | 1 | 19 | 17.96 | 155 | 18.63 | 707 |
| Hale Pohaku | HPU | 1 | 19 | 46.85 | 155 | 27.50 | 3,396 |
| Humuula Sheep Station | HSS | 1 | 19 | 36.31 | 155 | 29.13 | 2,445 |
| Hot Caves | HTC | 1 | 19 | 14.33 | 155 | 24.02 | 361 |
| Hualalai | HUA | 1 | 19 | 41.25 | 155 | 50.32 | 2,189 |
| Heiheiahulu | HUL, HULE, HULN | 3 | 19 | 25.13 | 154 | 58.72 | 369 |
| Kaapuna | KAA | 1 | 19 | 15.98 | 155 | 52.28 | 524 |
| Kaena Point | KAE | 1 | 19 | 17.35 | 155 | 7.95 | 37 |
| Kahaualea | KAH | 1 | 19 | 24.58 | 155 | 4.36 | 625 |
| Kaoiki Faults A | KFA | 1 | 19 | 25.26 | 155 | 25.14 | 1,579 |
| Kaoiki Faults B | KFB | 1 | 19 | 25.26 | 155 | 25.14 | 1,579 |
| Kahuku | KHU | 1 | 19 | 14.9 | 155 | 37.10 | 1,939 |
| Kanekii | KII | 1 | 19 | 30.56 | 155 | 45.90 | 1,841 |
| Keanakolu | KKU | 1 | 19 | 53.39 | 155 | 20.58 | 1,863 |
| Puu Kaliu | KLU | 1 | 19 | 27.48 | 154 | 55.26 | 271 |
| Kamoamoa | KMM, KMME, KMMN | 3 | 19 | 23.47 | 155 | 6.98 | 750 |
| Kohala | KOH, KOHE, KOHN | 3 | 20 | 7.69 | 155 | 46.77 | 1,166 |
| Kipuka Nene | KPN | 1 | 19 | 20.10 | 155 | 17.40 | 924 |
| Kapoho | KPO | 1 | 19 | 30.02 | 154 | 50.51 | 134 |
| Kalalua | [1]LUA | 1 | 19 | 24.55 | 155 | 4.25 | 622 |
| Mauna Loa | MLO, MLOE, MLON | 3 | 19 | 29.80 | 155 | 23.30 | 2,010 |
| Mauna Loa X | MLX | 1 | 19 | 27.60 | 155 | 20.70 | 1,475 |
| Mokuaweoweo | MOK | 1 | 19 | 29.28 | 155 | 35.98 | 4,104 |
| Makaopuhi | MPR | 1 | 19 | 22.07 | 155 | 9.85 | 881 |
| Mountain View | MTV | 1 | 19 | 30.25 | 155 | 3.75 | 409 |
| National Guard | NAG | 1 | 19 | 42.12 | 155 | 1.72 | 18 |
| North Pit | NPT, NPTE, NPTN | 3 | 19 | 24.90 | 155 | 17.00 | 1,115 |
| Outlet | OTL | 1 | 19 | 23.38 | 155 | 16.94 | 1,038 |
| Pauahi | PAU, PAUE, PAUN | 3 | 19 | 22.62 | 155 | 13.10 | 994 |
| Puu Ulaula | PLA | 1 | 19 | 32.00 | 155 | 27.67 | 2,992 |
| Pohoiki | POI | 1 | 19 | 27.42 | 155 | 51.22 | 16 |
| Poliokeawe Pali | POL | 1 | 19 | 17.02 | 155 | 13.47 | 169 |
| Puu Pili | PPL | 1 | 19 | 9.50 | 155 | 27.87 | 35 |
| Puu Kamoamoa | PUK | 1 | 19 | 23.00 | 155 | 6.25 | 704 |
| Rim | RIM | 1 | 19 | 23.90 | 155 | 16.60 | 1,128 |
| South Point | SPT, SPTE, SPTN | 3 | 18 | 58.91 | 155 | 39.92 | 244 |
| Southwest Rift | SWR | 1 | 19 | 27.26 | 155 | 36.30 | 4,048 |
| Trail | TRA | 1 | 19 | 24.91 | 155 | 32.96 | 3,207 |
| Uwekahuna | UEEE, UENN, UEZ, USEE, USZ | 5 | 19 | 25.40 | 155 | 17.60 | 1,240 |
| Wahaula | WHA | 1 | 19 | 19.90 | 155 | 2.92 | 29 |
| Weather Observatory | WOB | 1 | 19 | 32.31 | 155 | 35.01 | 3,396 |
| West Pit | [1]WPT | 1 | 19 | 24.70 | 155 | 17.50 | 1,115 |
| Wilkes Camp | WIL | 1 | 19 | 28.15 | 155 | 35.02 | 4,037 |
| Wood Valley | WOO | 1 | 19 | 15.08 | 155 | 30.12 | 909 |

[1]Not currently in operation.

on the program HYPOINVERSE (Klein, 1978). Graphical representations of the seismic data for this manuscript were mainly prepared on the format prescribed in the plotting program QPLOT (Klein, 1983).

Tremor is identified by its continuous signal of sustained amplitude at frequencies within a limited range. Long-period events are discrete signals having an amplitude envelope like that of normal earthquakes but spectral feature like those of tremor. Frequency content and pattern remain relatively unchanged from start to end of their signals. The frequent occurrence of long-period events together with tremor indicates they share a common source. Distinguishable arrival times of long-period events fit the $P$-wave travel pattern of normal earthquakes and so allow their source to be located. The normal earthquakes termed short-period earthquakes to distinguish

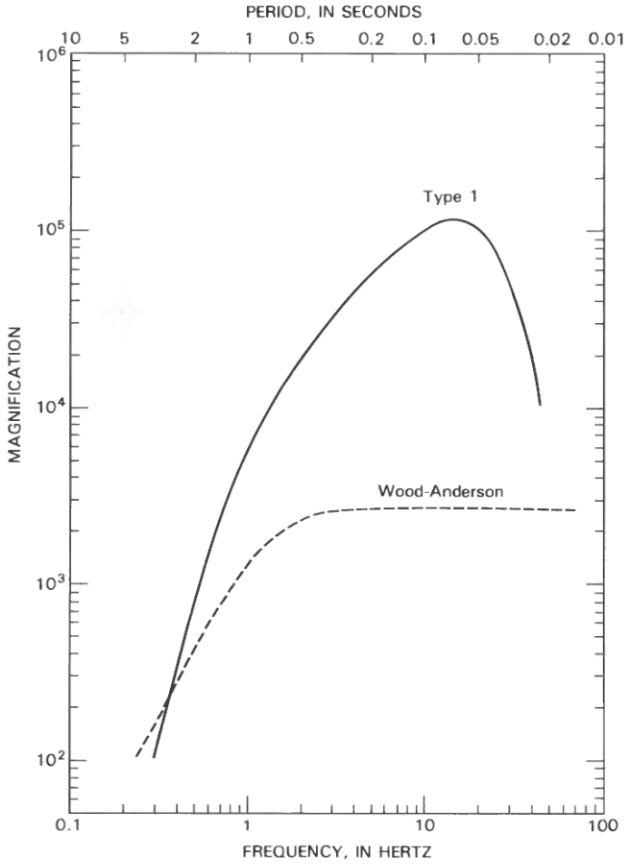


FIGURE 45.2.—Principal system-response curves for short-period seismographs operated by the U.S. Geological Survey in Hawaii. Type 1 curve applies to standard HVO high-gain vertical components on the FM system; Wood-Anderson response applies to the lower-sensitivity horizontal seismometers on 3-component stations. See Nakata and others (1984) for further description of seismic instrumentation and their system-response curves used at HVO.

them from long-period events and tremor have characteristic features, including sharp *P*-wave and *S*-wave onsets and recorded initial frequencies of about 10 Hz that change systematically in time to lower frequencies of less than 1 Hz. Seismograms of the various types of seismic events associated with volcanic activity beneath Kilauea are shown in figure 45.3.

## CASE HISTORY 1: THE MAUNA ULU ERUPTION IN 1969

Background information for activity at Mauna Ulu is from Swanson and others (1979), who provide a narrative account of eruptive activity and cursory summaries of seismic activity and ground deformation.

The Mauna Ulu eruption series was preceded by increased frequency of shallow earthquakes in the summit region several weeks before and a subsequent increase in the number of east-rift earthquakes a week before the pre-eruption seismic swarm. The initial outbreak on May 24, 1969, started within hours of earthquake swarms and weak tremor in the east rift and deflation of the summit. Increased harmonic tremor occurred just before the lava outbreak on the east rift. After a two-week repose, activity renewed with high lava output accompanied by high fountains. A pattern of activity featuring short intervals of intense lava emission alternating with long periods of quiescence persisted until the end of the year, producing 12 pronounced episodes of strong eruption. The intense fountaining episodes accompanied by high-amplitude tremor generally lasted less than a day; they were spaced at intervals varying from several days to more than two months. Between the major episodes, low-amplitude tremor was continuous in the area of the active vents. The repeated pattern of eruption and accompanying sequence of tilt and seismic events is summarized in figure 45.4. The nearness of the eruptive vent to the summit made it difficult to distinguish tremor possibly generated from separate sources along the conduit system during major episodes of eruption. Strong eruption tremor dominated at stations near the eruptive vents, as well as at those in the summit region.

Gradual inflation and an increase in shallow earthquakes at the summit preceded the eruptive outbreaks. Shallow tremor at the eruption vent increased in amplitude simultaneously with the increase in lava output and fountaining. Abrupt onsets and endings of these eruptive episodes were accompanied by equally rapid changes in tremor amplitude. Sustained high rates of summit deflation associated with the major eruptive outbreaks were followed by an increase in very small long-period events and harmonic tremor at the summit.

Harmonic tremor sometimes developed into a fluctuating pattern, in which bursts of higher amplitude lasting 5–10 seconds occurred repeatedly and as frequently as several times per minute (figure 45.5). The activity sometimes decayed to a barely detectable level of continuous tremor, and long-period events with higher amplitude and more definable onset times occurred at wide intervals of many minutes (compare with the samples shown in figure 45.14*E*–*F*).

The areal variation of tremor amplitude is shown in figure 45.6 by 1-min samples of seismograms from temporary stations occupied with a jeep-mounted mobile seismic unit. This survey was made a few hours after a major eruptive episode in order to avoid seismic and acoustic noise from high fountaining and during a time interval when tremor amplitude remained fairly stable so that time difference had minimal effect on station-to-station comparisons. However, the sampling was intended to be soon enough after the eruptive episode to capture the expected stabilizing movement of magma within the conduit system following a major outbreak. The survey was repeated several times after major episodes of lava fountaining. For comparability, the tremor was recorded at the same instrumental gain at each station. Amplitudes read from continuously recording stations near the eruptive vent and in the summit area were used for reference. The comparisons of amplitudes in figures 45.6*A* and 45.6*B* (immediately following and one day after eruptive episode 4, respectively) generally indicate a persistent source at the active vent, and a secondary source at the summit caldera region, which decayed to background after about a day of activity.

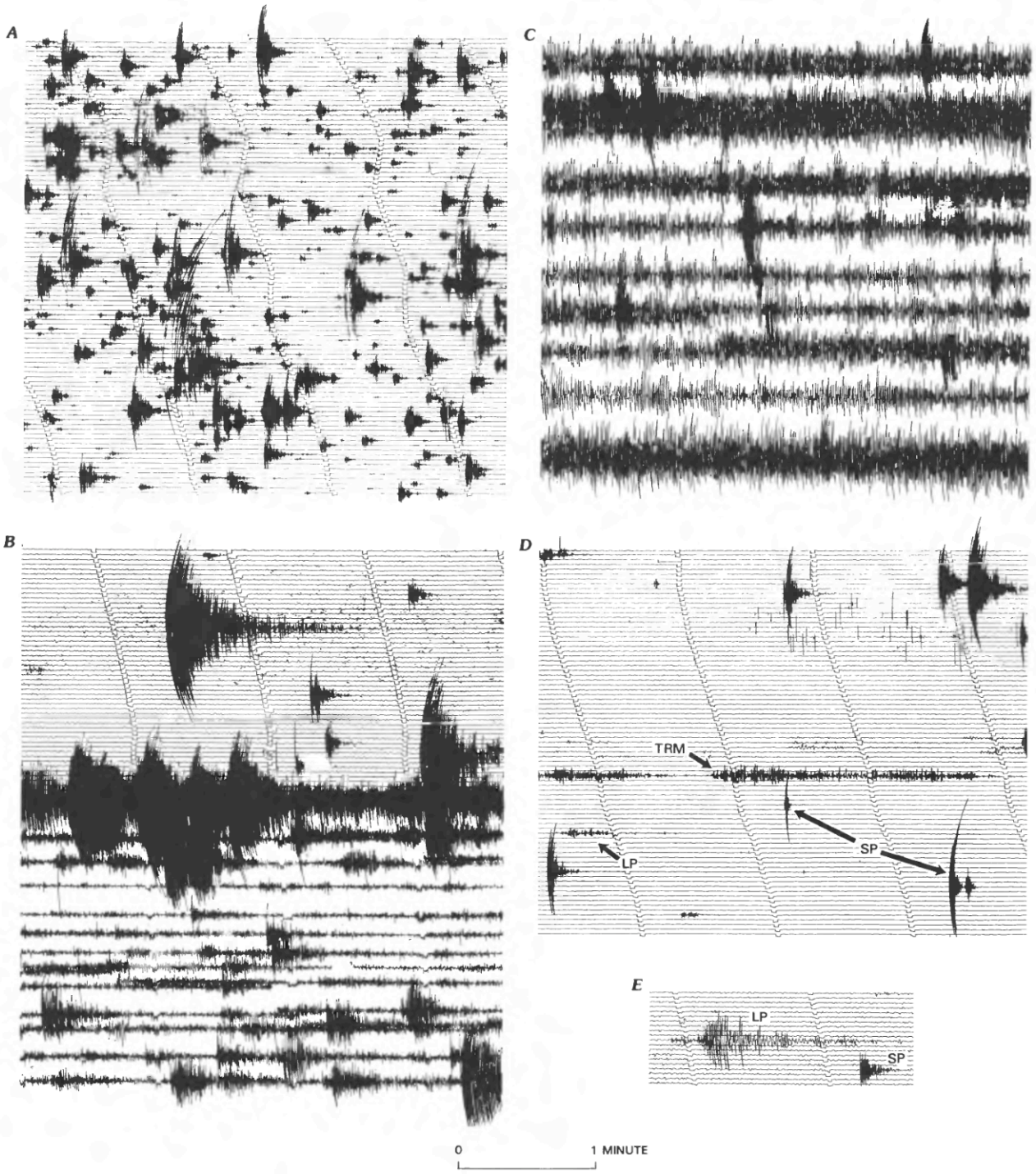


FIGURE 45.3.—Smoked-drum seismograms showing records of earthquakes and volcanic tremor in south Hawaii. ***A***, Swarms of short-period earthquakes. ***B***, Intrusion-related swarms of short-period earthquakes followed by eruption tremor (lower part). ***C***, Continuous harmonic tremor during sustained eruption. ***D***, Short-period earthquakes (SP), long-period event (LP), and intermediate-depth tremor burst (TRM). ***E***, Signatures of a long-period event (LP) and a smaller short-period earthquake (SP).

Between major episodes of lava fountaining, when eruptive activity was limited to varying rates of visible lava movement in the vent (Swanson and others, 1979), the amplitude of harmonic tremor recorded on seismographs within a few km of the vent changed according to the rate of lava movement. An example of time variation in tremor amplitude that correlated with a pattern of lava oscillation in the Mauna Ulu vent is shown in figure 45.7. High and low activity alternated at intervals of a few to many hours.

During other intervals between major outbreaks of lava, low tremor activity showed fairly constant amplitude sustained for many days, or erratic fluctuations with peak amplitudes lasting from less than a minute to many minutes, or cyclic patterns with regular time intervals of amplitude changes. One variety of cyclic oscillation, described as gas piston activity (Swanson, 1971), was defined by tremor of low amplitude for 5–15 minutes during gradual rise of the lava column in the vent, alternating with about one minute of higher amplitude associated with a dramatic collapse of the column and spattering within the vent. The increased seismic signal during collapse of the lava column characteristically has a symmetrical cigar-shaped envelope: amplitude increases gradually, reaches a peak at least several times above the initial background, and finally decreases at a rate comparable to the rate of increase during onset. Signal frequencies at peak amplitudes are 2–5 Hz at a recording distance of about one kilometer from the eruptive vent. The tremor signal is generally local and decreases below background noise a few kilometers from the source vent.

This oscillating pattern of lava and tremor activity, sometimes lasting for many days, was observed again during the Puu Oo eruption. It will be further described in the next section (see figure 45.8*A*).

## CASE HISTORY 2: THE PUU OO ERUPTION IN 1983-1985

The pattern of seismicity from mid-1982 to 1985 and continuing reflects the mechanical process within Kilauea Volcano that developed into a major eruptive sequence in the east rift zone (Koyanagi and others, in press). The geologic and geophysical data pertaining to the sequence of rift intrusions, fissure outbreaks, and eruptive episodes from a centralized vent system for this eruption from 1983 to mid-1984 are summarized by Wolfe and others (chapter 17). From September to December 1982, increase of shallow earthquakes in the summit region during periods of inflationary ground tilt, alternating with downrift-migrating swarms of earthquakes in the east rift zone during deflationary periods, indicated that episodic surges of magma were supplying the conduit system in the rift zone. This episodic activity led to a major intrusive event on January 2, 1983: rapid summit deflation and vigorous downrift migration of shallow earthquakes were sustained for 24 hours and finally resulted in a fissure outbreak in the east rift zone. High-frequency tremor accompanied the pre-eruption swarm of earthquakes in the east rift. The sustained deflation at the summit was accompanied by short-period earthquakes, presumably due to fracturing of the host rocks in response to the withdrawal of magma, and harmonic tremor and long-period events associated with the accelerated magmatic activity.

The onset of eruption was accompanied by a marked increase in east-rift tremor, followed by five days of incremental intrusion earthquakes and outbreak of lava farther downrift. The subsequent history of eruptive activity is given in detail by Wolfe and others (in press).

The early weeks of the Puu Oo eruption were characterized by strong tremor with erratic high-frequency signals from a wide source area. As the pattern of eruption changed from fissure outbreaks to multiple-vent eruption and eventually to repeated lava emissions from a single vent system at Puu Oo, weaker and more continuous harmonic tremor originated near the eruptive vent and corresponded in amplitude to the vigor of eruptive activity. Episodes of high lava fountains accompanied by high-amplitude tremor that usually lasted from less than a day to more than a week occurred at intervals of about one to nine weeks. Between major episodes of eruption, the amplitude of the local tremor varied according to the level of the limited lava activity, which was sometimes visible, at depths of 0–50 m in the vent. The patterns of tremor recorded near the active Puu Oo vent between eruptive episodes are illustrated in figure 45.8. As in the Mauna Ulu eruption, bursts of moderate-amplitude tremor lasting about one minute occurred repeatedly during periods of low-amplitude background tremor lasting 5–15 minutes that characterized gas piston activity (figure 45.8*A*). More sustained episodes consisting of increased amplitude lasting about one-half to nearly one hour alternating with low amplitude lasting about three hours were observed during a repose period in February 1985 (figure 45.8*B*). Seismicity associated with microfracturing caused by structurally and thermally induced adjustments at the vent and under new lava flows is also recorded in figure 45.8. Major episodes of high fountains and lava output were accompanied by increased tremor, whose amplitude exceeded by more than an order of magnitude the continuous background tremor during intervals of subdued eruptive activity. The rapid response of seismic amplitude to changes in lava fountaining and output rate imply that the principal source of tremor is shallow and localized at the eruption site.

Convincing evidence of a deeper tremor source beneath the summit of Kilauea, separated from activity in the eruption region, was the tremor recorded at the North Pit (NPT) station (see table 45.1 for list of stations) following sustained high rates of deflationary tilt at the summit. This relationship of tremor that varied in amplitude and duration according to the rate and magnitude of the deflationary tilt was observed fairly consistently for the successive episodes of the Puu Oo eruption from 1983 to mid-1984, and a reduction of the data indicating this relation is documented by Koyanagi and others (in press). These episodes of summit tremor that accompanied major episodes of the eruption were frequently preceded by increasing rates and amplitudes of discrete long-period events, which peaked into continuous tremor and then decayed gradually back to background, with bursts of long-period events at progressively lower amplitude and wider intervals of time (figure 45.9).

In contrast to both the summit storage zone and the east-rift eruption site, the rift conduit connecting them remained virtually free of detectable harmonic tremor during the repeated major episodes of

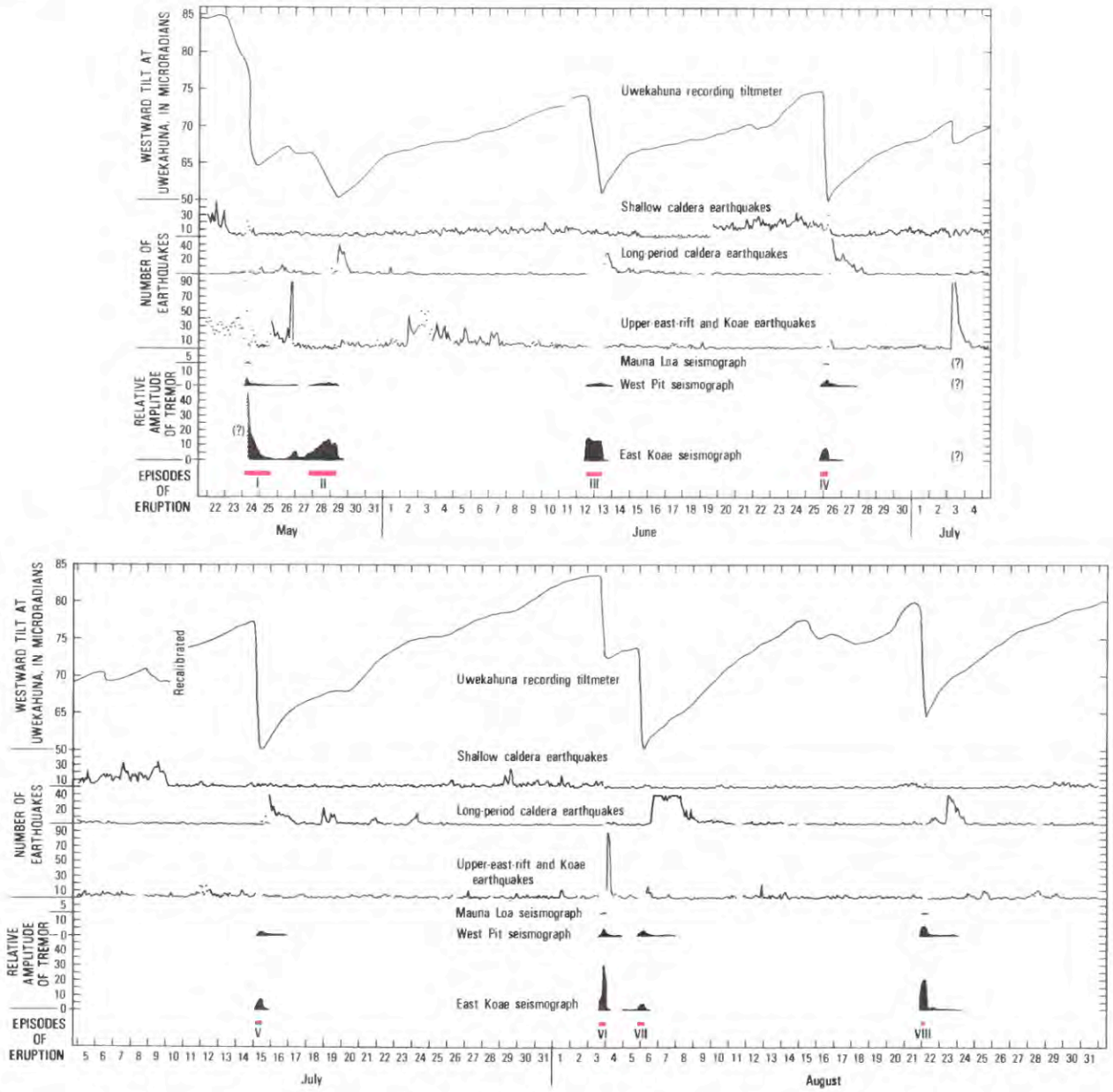


FIGURE 45.4.—Plot of summit tilt, numbers of shallow earthquakes, relative amplitude of tremor, and episodes of eruption for the Mauna Ulu eruption of Kilauea Volcano, May–October 1969. Tilt measurements at 2-hour intervals from the Uwekahuna east-west component tiltmeter near the northwest rim of Kilauea caldera. Earthquake counts at 2-hour intervals from selected local stations, detection threshold estimated at about magnitude 0.1. Amplitude of tremor taken from adjusted hourly readings of smoked-paper records and plotted in relative units above background noise at three stations: Mauna Loa (MLO), 25 km from the eruption site; West Pit (WPT), 11 km from the eruption site; and East Koae (EKO), 5 km from the eruption site. Times of major eruptive episodes indicated by horizontal bars and labeled with their sequence numbers. Data beyond October incomplete and therefore omitted.

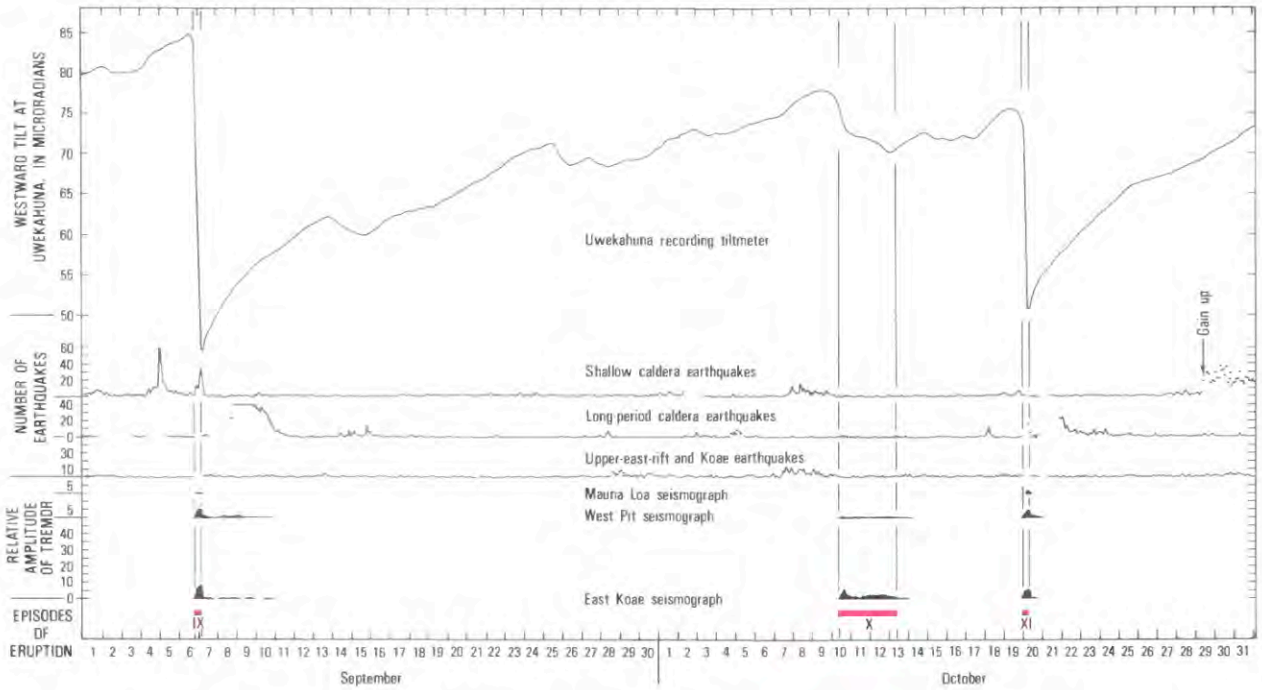


FIGURE 45.4.—Continued.

eruption. From this we infer an absence of barriers in the central part of the lateral conduit system, allowing quasi-steady flow of magma with minimal pressure fluctuations.

A chronological sequence of lava production, increased harmonic tremor in the east rift zone and summit, and ground tilting is outlined in figure 45.10 for one of the vigorous eruptive episodes in the prolonged east rift eruption.

Ground tilt showing rapid deflation during the twenty-fifth eruptive episode in September 1984 (figure 45.10) was measured as the east-west component on a continuously recording tiltmeter located at Uwekahuna vault northwest of the summit deformation center. Deflationary tilt started gradually at about 1400 (H.s.t.) on September 19 and accelerated in rate at 1700. It continued at a high rate until 0600 on September 20 and then gradually declined, ending by about 0900. The deflationary tilt during these 19 hours totaled 15 microradians, and it reached a maximum rate of 1.35 μrad per hour at about 2000 on September 19 (R. Hanatani, written commun.)

Peak-to-peak amplitude of harmonic tremor was measured on Develocorder seismograms from station MPR for east-rift tremor and from station NPT for summit tremor. Ground oscillation in micrometers was reduced from the amplitude measurements averaged for about one minute at each hour and adjusted for instrumental magnification at the recorded frequency and for station corrections. The average period of the east-rift tremor signal recorded at MPR was about 0.5 s, and that of the summit tremor recorded at NPT was about 0.3 s. Station MPR, situated about 6 km west of the eruptive vent, recorded rapid increase and decrease of east-rift tremor at the onset and end of the eruptive episode, with a temporary decrease in the middle. The hourly sampling rate used in figure 45.10 omitted a strong burst of tremor between 1622 and 1633 during the early activity, as well as the exact times of rapid changes at the onset and end of the vigorous fountaining episode. Continuous-record seismograms indicate that east-rift tremor started to increase in amplitude at about 1530 on September 19. The amplitude increased rapidly from about 1600, reached peaks of $0.4 \pm 0.2$ micrometers at about 2300 and 0400 (September 20), and remained variably high until 0532. A rapid decrease accompanied the end of sustained high fountaining at 0532. As is typical of later episodes in prolonged eruptions, there were no precursory swarms of intrusion-related microearthquakes. This may be because the repeated outbreaks created a hydraulically connected magma conduit system free of barriers and affected only by episodic adjustments in the fluid pressure.

Summit tremor and the accompanying long-period events started to increase rapidly at about 2100 on September 19, peaked to about 0.3 micrometers of ground amplitude at 0700 on September 20, and gradually decreased with increasing numbers of distinctive long-period events. Summit tremor decreased to nearly background level by the end of September 21. Summit tremor and summit tilt, both of which are assumed to be measures of magma movement, did not always correlate in their pattern of amplitude

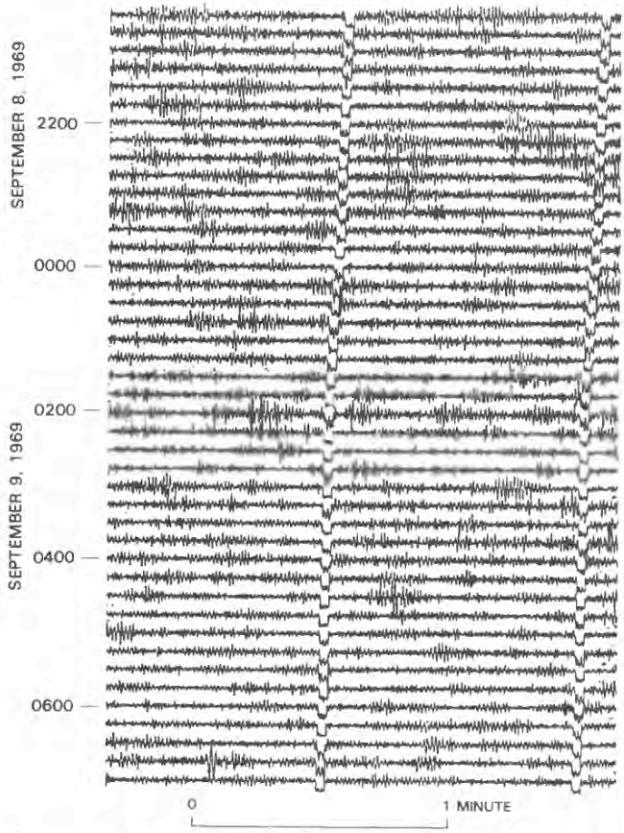


FIGURE 45.5.—Portion of a smoked-drum seismogram from the West Pit station (WPT) in the summit caldera of Kilauea showing local long-period events and weak harmonic tremor. These events were recorded about 1.5 days after episode XI of the Mauna Ulu eruption during a post-deflation period of rapid reinflation of the summit.

changes; the increase, peak, and decay patterns of tremor amplitude generally lagged behind changes in tilt rate by several hours to many hours.

Field observations and time-lapse photographs documented the increased eruption activity that started at about 1604 on September 19. The activity peaked with a fountain height of nearly 500 m and lava extrusion rates estimated at $8 \times 10^5$ $m^3/h$, and ended at about 0532 on September 20. Subsequent measurements of the area and thicknesses of the flows produced indicate an approximate total volume of $11 \times 10^6$ $m^3$ of lava was extruded from, this eruptive episode that lasted 13.5 hours (G. Ulrich, oral commun.).

Tremor associated with high fountaining during vigorous eruption on September 19–20 was high in amplitude near the eruptive vent; its amplitude and dominant frequencies varied at intervals of several seconds. The short-term pattern of amplitude repeatedly changing by nearly half an order of magnitude and frequencies varying from about 2 to 5 Hz was partly influenced by the peaked response of the instrumental system, which increasingly amplified the high frequencies. Otherwise, however, the tremor pattern resembles the oscillating pattern of lava fountaining, in which bursts of high fountain repeatedly occur seconds apart. Summit tremor that accompanies sustained deflation produces a signature with comparable amplitude and spectral features.

Normalized power spectra of tremor recorded during a major episode of the Puu Oo eruption on August 20, 1984, are shown in figure 45.11*A–C* for a station located 1.25 km from the active vent. These spectra were derived from seismograms recorded with a three-component digital seismograph using 1.0-Hz geophones. The results were obtained by computing the spectra for 20-second windows of data and averaging the results of all windows. The spectra are characterized by a series of dominant and subdominant frequencies that vary among the three components of ground motion. As these data were obtained during heavy fountaining activity, they represent the contribution of fountain noise in addition to the excitation of the magmatic conduit.

## CASE HISTORY 3: THE AUGUST 1981 SOUTHWEST-RIFT INTRUSION

On August 10–12, 1981, an intrusion occurred on the southwest rift of Kilauea (Klein and others, chapter 43; Nakata and others, 1982). It was identified by summit-to-rift migration of shallow earthquakes, summit deflation, and rift dilation (A.T. Okamura, oral commun.); increased $CO_2$ gas emission (L.P. Greenland, oral commun.); and geo-electrical anomalies (D.B. Jackson, oral commun.). The intrusion is a significant one in terms of the volume of magma transferred from the summit to the southwest rift, as inferred from the 107 μrad of deflationary ground tilt measured at Uwekahuna station on the northwest rim of the summit caldera.

The progression of seismic events, initiated by an increased number of short-period earthquakes in the summit region, developed into an earthquake swarm and tremor that migrated into the southwest rift zone, followed by long-period events that culminated in continuous harmonic tremor at the summit. This sequence is

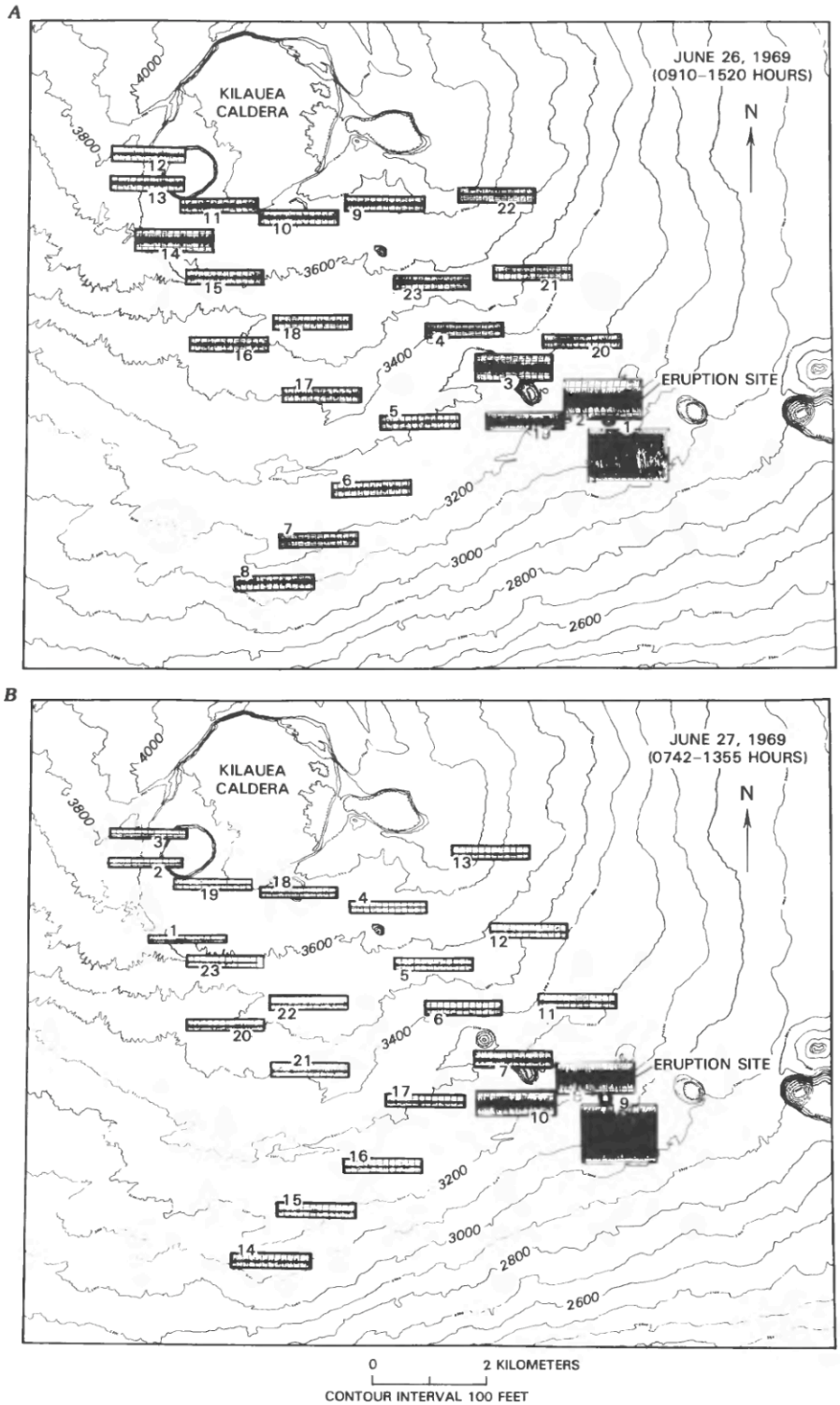


FIGURE 45.6.—Harmonic tremor recorded by portable seismograph following eruptive episode IV of the Mauna Ulu eruption. The numbers indicate the order in which each site was monitored. All seismogram segments are one minute long. ***A***, Immediately after the eruptive episode. Note the moderate-amplitude tremor at the summit stations 11 and 14. ***B***, One day after the eruption. Note that tremor in the summit area (stations 1 and 19 here) has decreased to background noise.

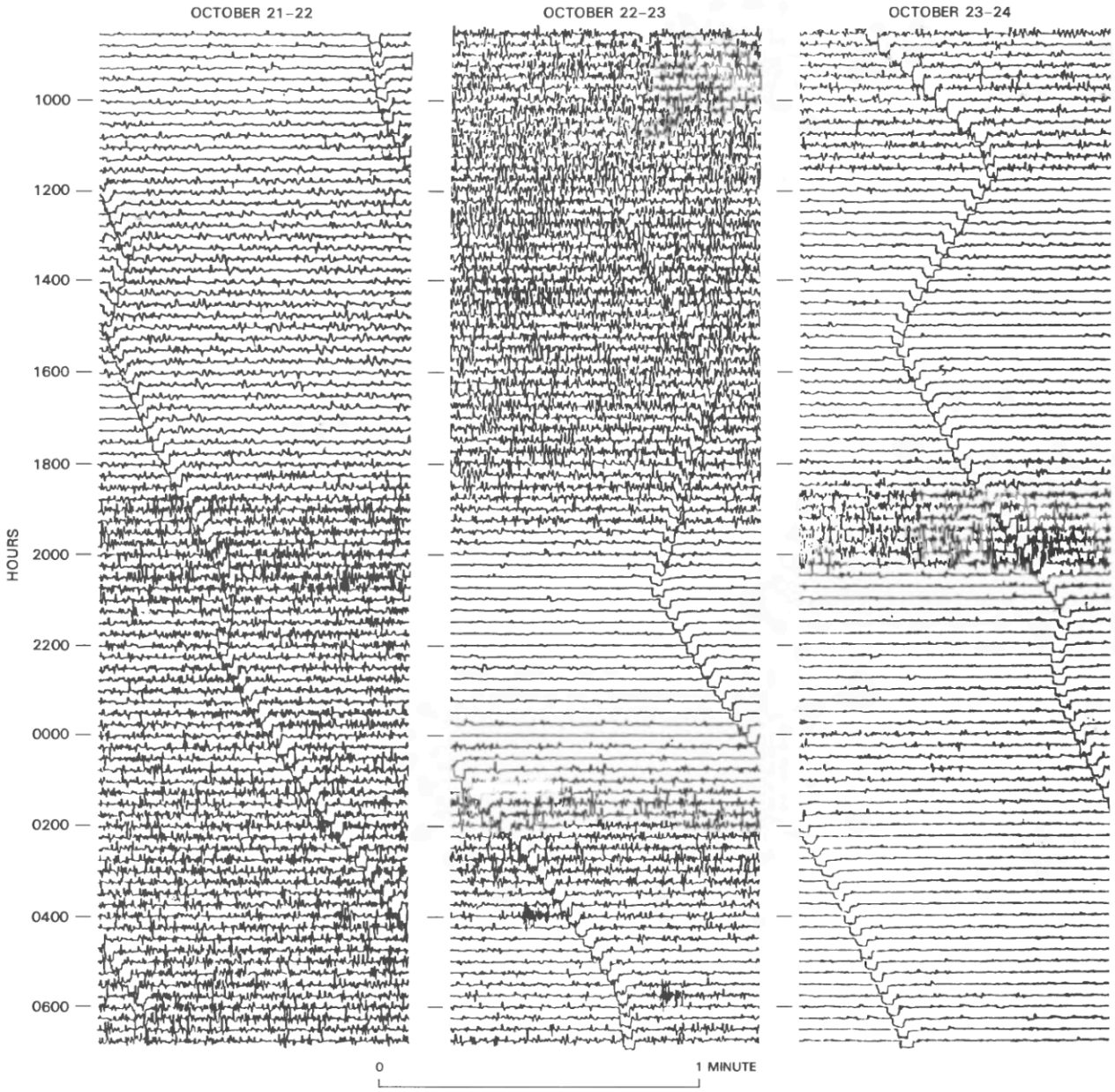


FIGURE 45.7.—Portions of a smoked-paper seismogram from a station (EKO) on the upper east rift zone of Kilauea, 4.5 km from the eruptive vent, that monitored varying amplitudes of low tremor associated with confined lava movement following a major episode of the Mauna Ulu eruption in October 1969. Recording speed and instrumental magnification were kept constant over the entire interval of time.

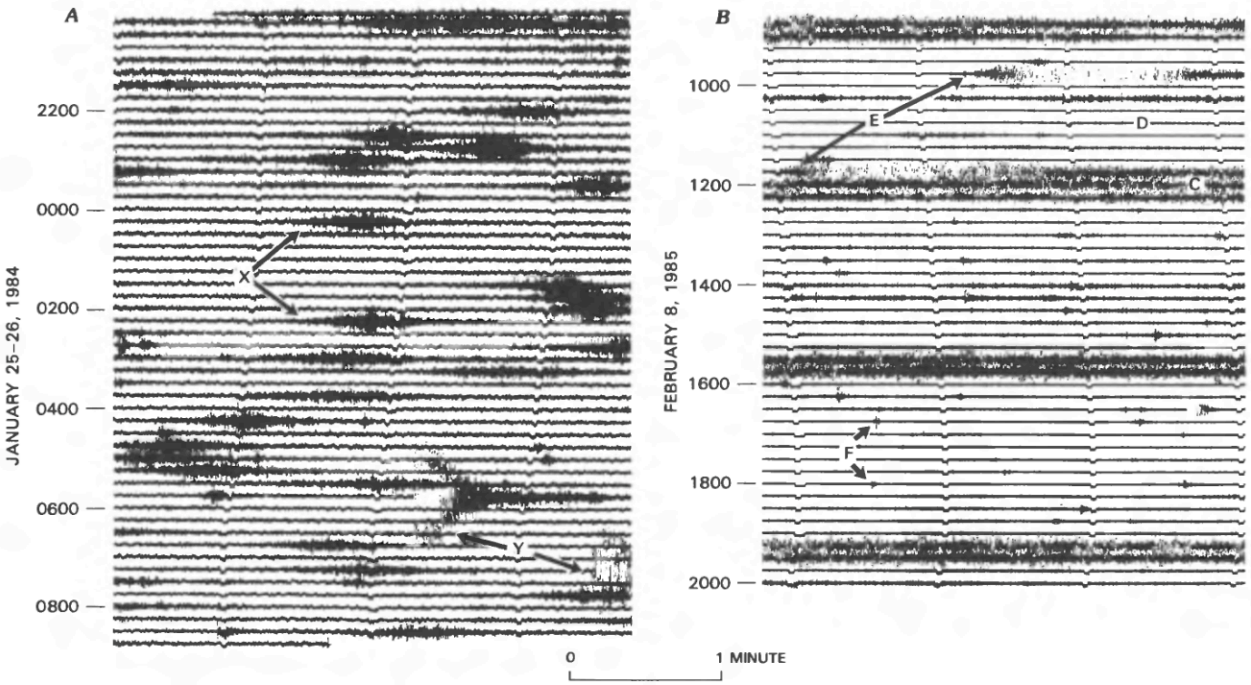


FIGURE 45.8.—Portions of seismograms from revolving-drum recorders at stations on Kilauea Volcano showing various seismic events. ***A***, Record from station PUK, about 1 km west of the eruptive vent Puu Oo showing gas-piston events (X) and south flank earthquakes (Y). ***B***, Record from station KMM showing a cyclic pattern of low tremor at the eruptive vent between the major episodes on February 4 and March 13, 1985, of the Kilauea east-rift eruption. Episodes of high tremor (C) less than an hour in duration repeatedly alternated with several hours of lower amplitude (D) during February 7–11, 1985. Two cigar-shaped events (E) recorded at 0946 and 1145 were signals characteristic of cyclic lava movement, termed gas-piston activity, in the vent. Numerous microshocks (F) associated with thermal contraction cracking on the adjacent new lava flows, degassing explosions, and continual structural adjustments at the vent were conspicuous during times of low-background tremor. Other varieties of repose tremor during the prolonged eruption at Puu Oo are described by Wolfe and others (in press).

clearly seen in the series of smoked-paper seismograms that recorded the changes in seismicity (see figure 45.12).

The high rate of inflationary tilt and frequency of summit earthquakes were interrupted on August 10 by a rapid collapse and simultaneous increase of earthquakes and tremor that propagated into the southwest rift zone. With the onset of deflation and the apparent relaxation of the summit, the number of inflation-related caldera earthquakes decreased. A pattern of southwest-rift inflation complemented the summit deflation and migrating swarm of shallow earthquakes to further indicate summit-to-rift transfer of magmatic pressure. Near the end of the two days of summit collapse and during the early reinflation period starting August 12, a swarm of long-period events was recorded at the summit stations (figure 45.13). These events increased in size until August 14 and then became smaller again. As the number of long-period events decreased, continuous tremor gradually increased and peaked in amplitude on August 15. Subsequently, from August 16 to about August 20, the amplitude of tremor gradually decayed below detection level.

A variety of seismic events were identified on seismograms according to arrival-time patterns, wave frequencies, and amplitude envelopes during the August intrusion (figure 45.14*A–F*). Shallow rift tremor was locally recorded with a broadly variable range of high frequencies, in contrast to intermediate-depth summit tremor, which retained a narrower band of lower frequencies. Rockfalls along the crater walls resulting from the increased instability caused by summit collapse generated strong local high-frequency seismic signals, which rapidly decreased with increasing epicentral distance; at distant stations these events had signatures dominated by low-frequency surface waves. Long-period events had signatures varying from nearly monochromatic, with sharp peaks in frequencies and very gradual beginnings comparable to tremor (figure 45.14*D*), to a wider band of frequencies that sometimes showed sharper onsets (figure 45.14*E–F*). The patterns of amplitude attenuation with distance for long-period events and for the concurrent tremor were similar, indicating a common source region (figure 45.15). Long-period events recorded by arrival times that could be matched for about ten or more stations were read and processed by the same location procedure used for normal earthquakes, from which reasonably accurate locations were obtained. Such long-period events are used in a later section of this chapter to determine the spatial distribution of harmonic tremor sources in Hawaii.

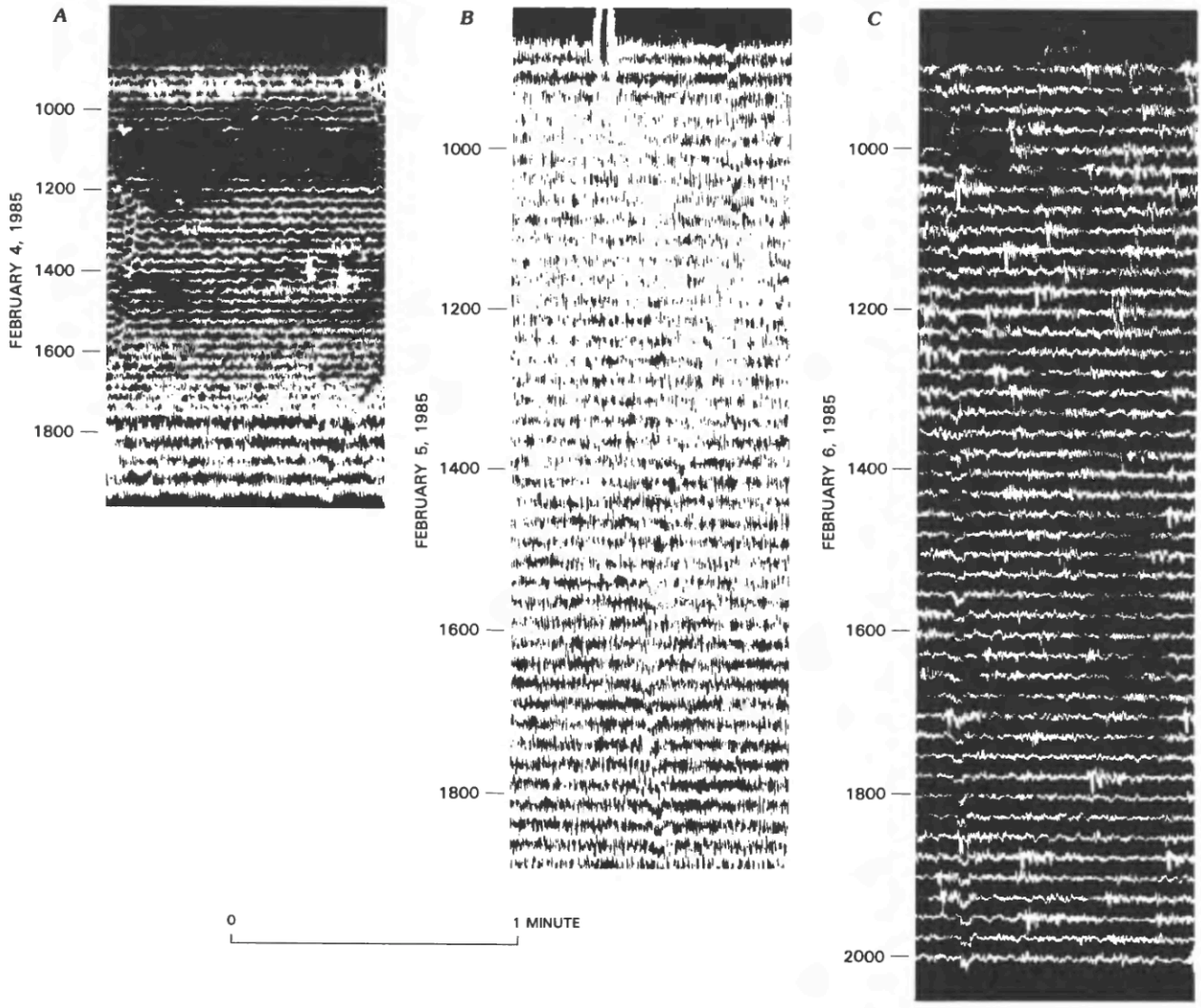


FIGURE 45.9.—Sections of smoked-paper seismograms from station NPT showing the sequence of harmonic tremor and long-period events at the summit following episode 30 of the east-rift eruption on February 4–6, 1985. Recording speed and instrumental magnification were kept constant over the entire time interval. ***A***, Period from 0900 to 1800 on February 4, 1985, shows increasing level of summit tremor from about 1600; the drum rotation interval was subsequently doubled to increase the spacing between seismic traces. ***B***, Period from 0900 to 1900 on February 5, near the peak of activity, shows continuous high tremor. ***C***, The final stage of the activity from 0900 to 2000 on February 6 shows an increased number of discrete long-period events in a decreasing background of continuous tremor. Occasionally, stronger long-period events were recorded widely on the summit network of stations.

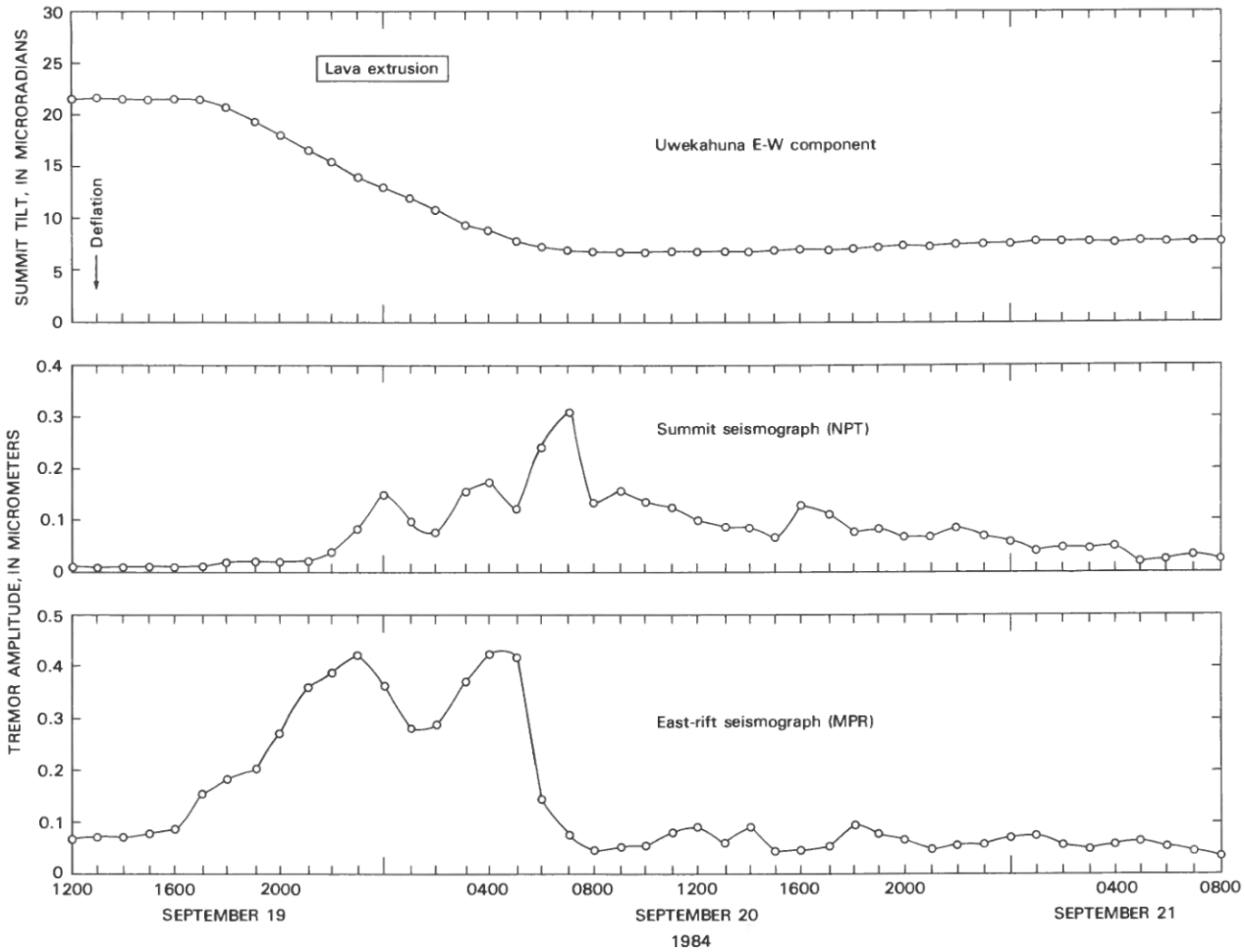


FIGURE 45.10.—Changes in tilt and tremor amplitude during and after episode 25 of the prolonged Kilauea east-rift eruption characterized by high lava production and fountaining. Tremor amplitudes are approximate averages, ±0.2 micrometers. Curves between hourly readings were interpolated.

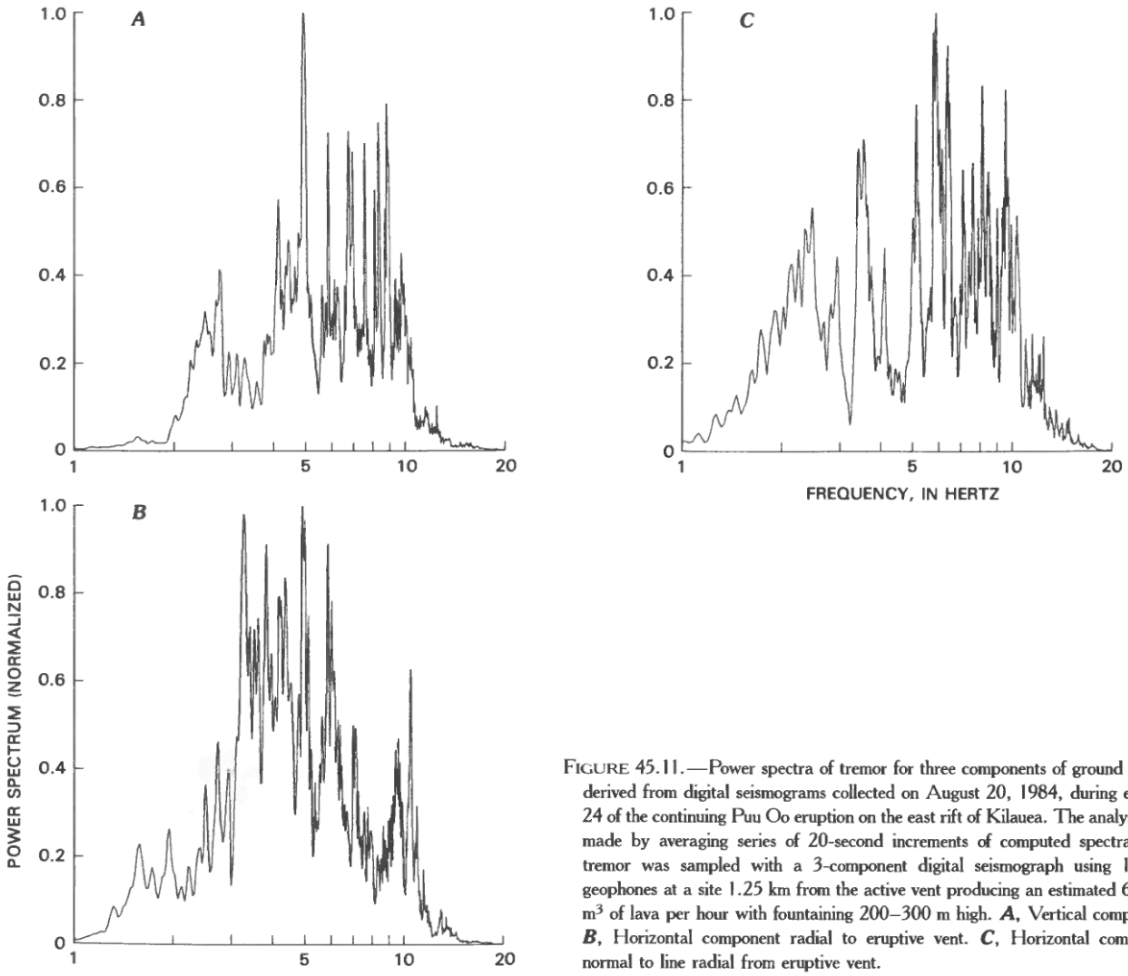


FIGURE 45.11.—Power spectra of tremor for three components of ground motion derived from digital seismograms collected on August 20, 1984, during episode 24 of the continuing Puu Oo eruption on the east rift of Kilauea. The analysis was made by averaging series of 20-second increments of computed spectra. The tremor was sampled with a 3-component digital seismograph using 1.0-Hz geophones at a site 1.25 km from the active vent producing an estimated $6 \times 10^5$ $m^3$ of lava per hour with fountaining 200–300 m high. ***A***, Vertical component. ***B***, Horizontal component radial to eruptive vent. ***C***, Horizontal component normal to line radial from eruptive vent.

FIGURE 45.12.—Seismograms from smoked-drum seismographs showing the sequence of seismic events accompanying the August 1981 magma intrusion in the southwest rift zone of Kilauea. Unless otherwise indicated, recording speed and instrumental magnification were constant over this interval of time. Time advances right and down in all seismograms. ***A***, August 9–10. Left seismogram shows the background of high microearthquake activity preceding the seismic swarm at the onset of magmatic activity as recorded from station AHU in the south summit area. Right seismogram shows the continuing harmonic tremor and microearthquakes recorded at a lowered sensitivity during the peak of the intrusive event at the summit caldera station NPT. ***B***, August 13–14. Left seismogram shows a flurry of long-period earthquakes that followed the moderate collapse of the summit in the late stage of the intrusion as recorded at station NPT. Right seismogram shows the decreasing level of continuing microearthquake activity in the intruded part of the southwest rift zone as recorded by the nearby station DES. ***C***, August 15–19. Left seismogram shows harmonic tremor presumably due to magmatic movement during the adjustment process in the summit storage complex, following a major deflation as recorded locally at the summit station NPT on August 15–16. Right seismogram shows the gradual decay of harmonic tremor as the vigor of magmatic activity subsides at the summit, August 18–19, and occasional tectonic earthquakes as the volcano's south flank responds to the rift dilation.

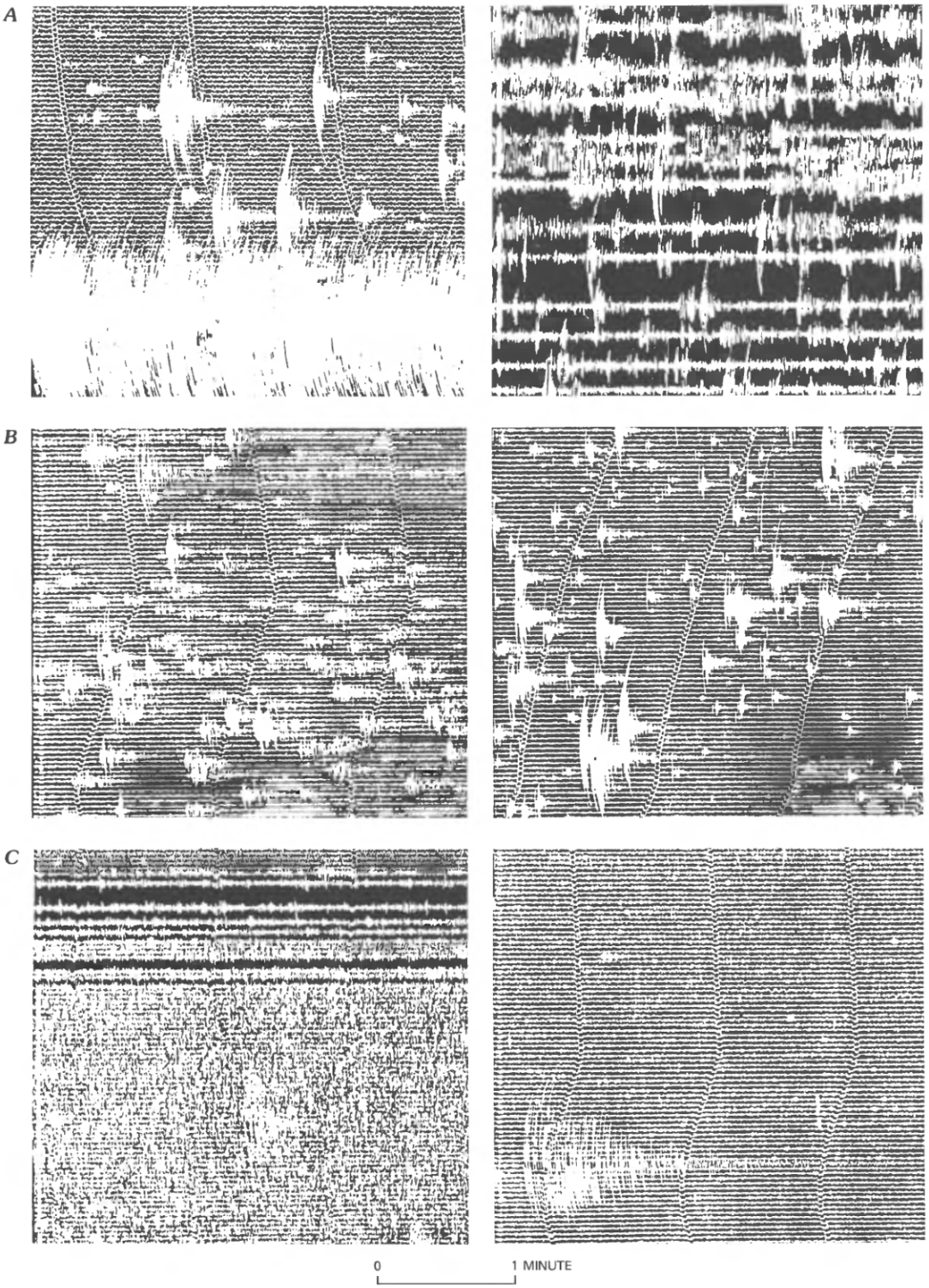
A
B
C
0
1 MINUTE

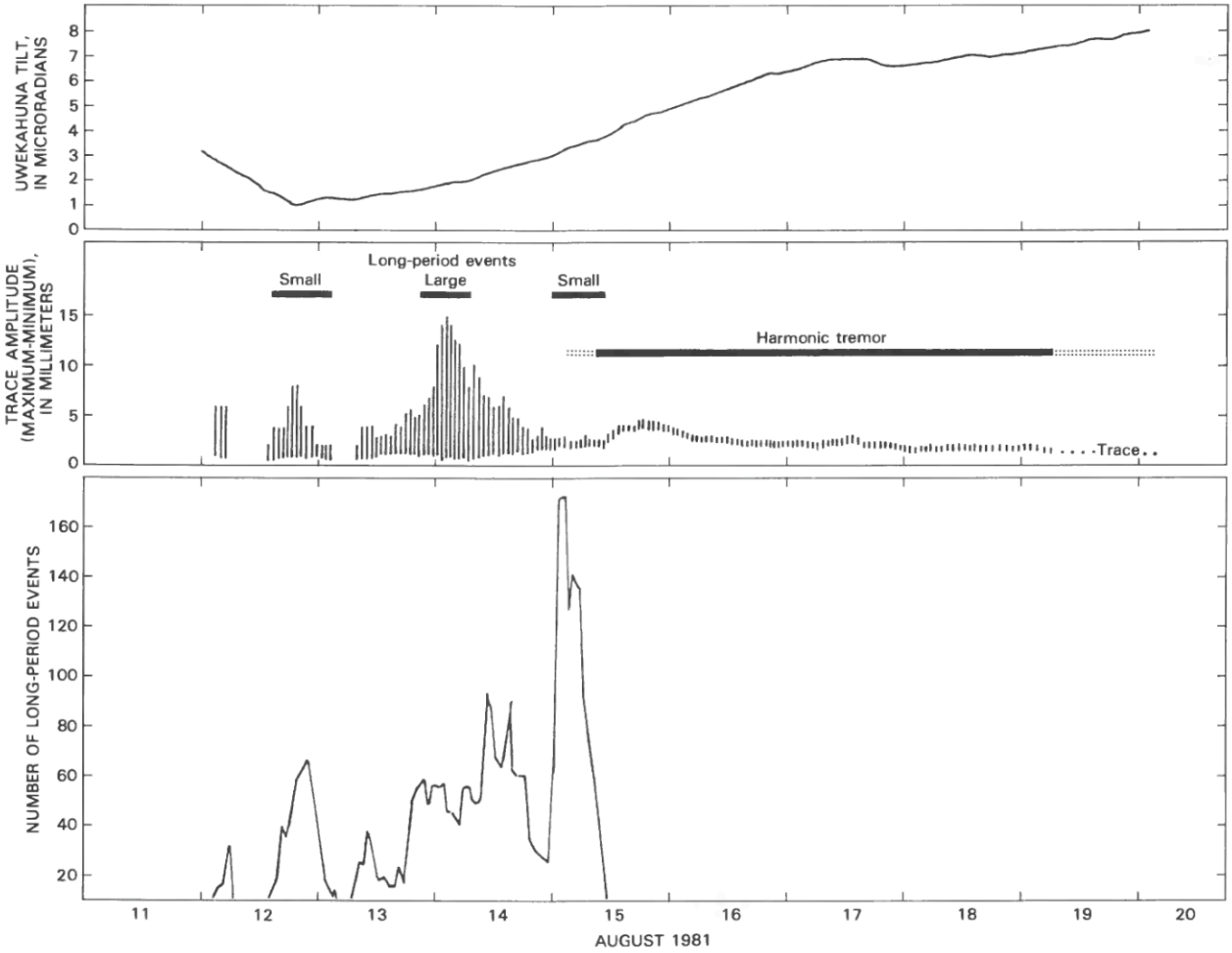


FIGURE 45.13.—Ground tilt, long-period earthquakes, and tremor plotted hourly following and during the later part of the August 1981 intrusion in the east rift zone of Kilauea. In the upper plot, the east-west component of tilt at Uwekahuna indicates reversal and reinflation of the summit following a major collapse. In the middle plot, vertical lines represent the hourly maximum-to-minimum amplitude range from tremor and long-period events read on station NPT at standard gain using Develocorder seismograms magnified 20 times. A wide maximum-minimum range implies large long-period events in a low background of tremor, whereas a narrow range and high minimum amplitude indicate high harmonic tremor with no discernible long-period events. The lower plot shows the hourly number of long-period events (>10 events per hour) recorded at station NPT.

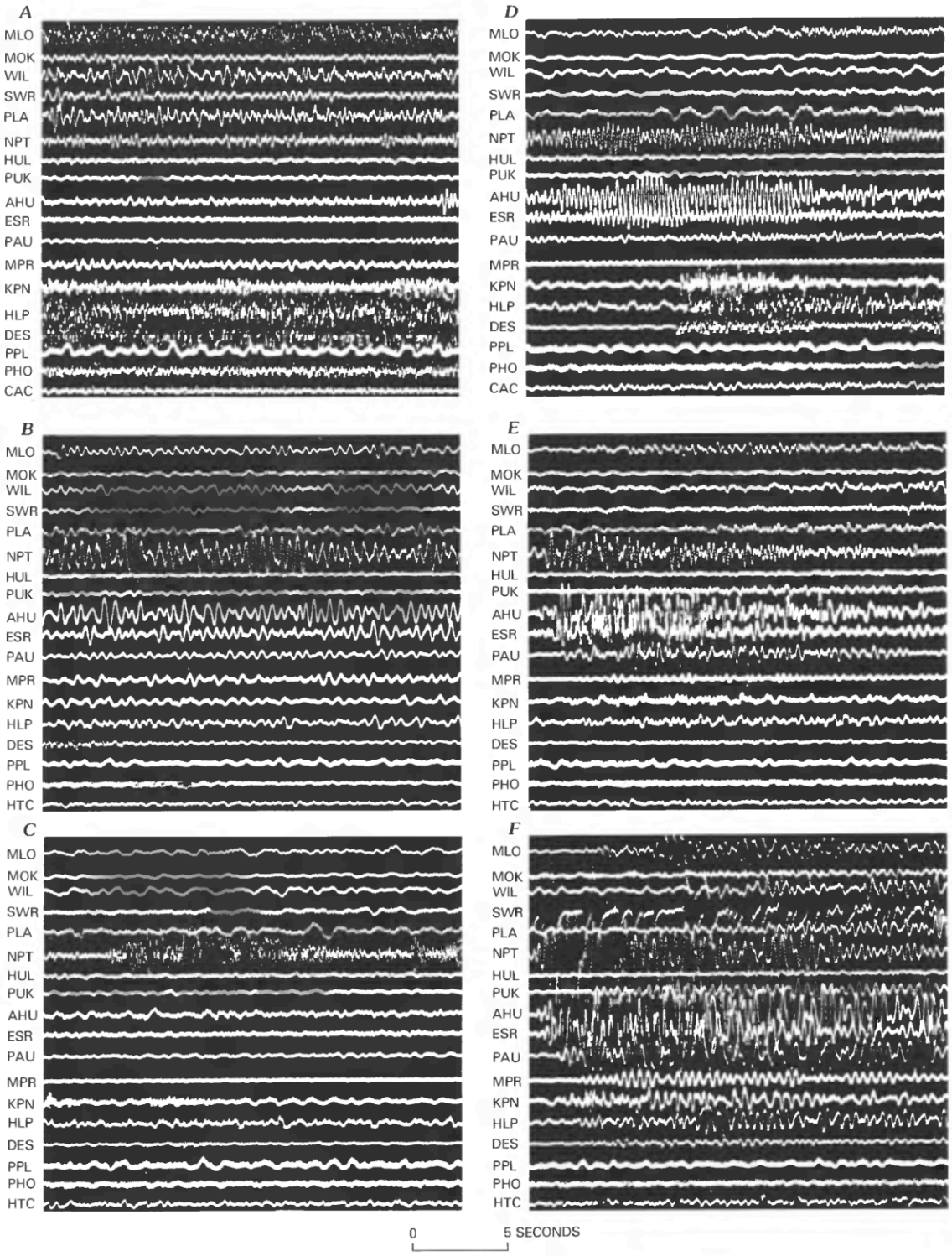


FIGURE 45.14.—Seismograms showing signatures of common events recorded during the August 1981 intrusion on Kilauea's southwest rift zone. ***A***, High-frequency tremor on stations DES and HLP, August 10. ***B***, Intermediate-depth tremor, strong on station NPT and weak on stations AHU, MLO, and ESR, August 15. ***C***, Rockfall on station NPT, August 13. ***D***, Uniform-frequency long-period event on stations NPT, AHU, and ESR and deeper short-period southwest-rift earthquake on stations KPN, HLP, and DES, August 12. ***E***, Long-period event on stations NPT, AHU, ESR, and PAU, August 13. ***F***, Long-period event strong on stations NPT, AHU, ESR, and PAU, August 13.

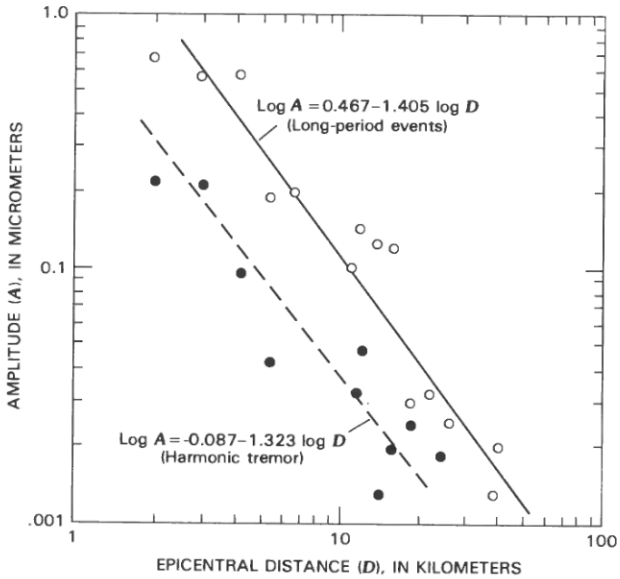


FIGURE 45.15.—Log-log plot of amplitude against epicentral distance for harmonic tremor (dots) and a 4-km-deep long-period earthquake (circles) on Kilauea. Trace amplitudes read at corresponding times at various stations from the summit to 40 km away were reduced to actual ground movement compensated for instrumental magnification at the dominant frequency of the seismic waves. Equations and straight lines are from linear least-squares regression.

The locatable long-period events were concentrated beneath the summit deflation epicenter for the August 1981 event (figure 45.16). This region is notably free of normal short-period earthquakes and has been interpreted to be a shallow storage zone for magma (Koyanagi and others, 1976).

The proportionality of amplitude and signal duration that exists for normal short-period earthquakes also applies generally to long-period events. This provides a means to estimate energy radiation from the long-period events on the basis of their magnitude. Magnitude is calculated for each event by signal duration and amplitude measurements applied in the earthquake-location program HYPOINVERSE (Klein, 1978), and temporal and spatial variation of the size of long-period events may then be examined. Because of the normally elongate signals for long-period events, magnitude determined by duration appear to be generally higher than magnitude determined by amplitude, when calibrated to normal earthquake magnitudes. The narrow range of magnitude and the relative lack of linearity in the magnitude-frequency distribution, to be further discussed later, suggest their source parameters differ from those of normal earthquakes. The long-period events of the August activity processed for locations were limited to a narrow range of magnitude (0.6–1.7), with the largest ones generally occurring during the peak of activity on August 13–14 (figure 45.17).

In a depth-time graph, focal depths of long-period events were persistent at 2–6 km for most of the duration of high activity on August 12–13 (figure 45.18). Depths expanded to a wider range of approximately 1–8 km during the peak of activity in the late hours of August 12 and early hours of August 13.

## CASE HISTORY 4: INTERMITTENT BURSTS OF INTERMEDIATE-DEPTH TREMOR

Intermediate-depth tremor at Kilauea usually occurred in series of short bursts, each a few minutes long, that lasted for a few days to several weeks. It was generally dominated by long-period events, sometimes with measurable onsets, whose signals were best registered on stations within a few tens of kilometers of the summit (figure 45.19). These events sometimes accompanied shallow tremor following deflation at the summit, but more commonly they occurred during periods of inflation not associated with intrusion or eruption.

Locatable long-period events at intermediate depths (7–12 km) beneath the summit region of Kilauea increased in February and

FIGURE 45.16.—Long-period events of August 13–15, 1981, at the summit caldera of Kilauea following the August 1981 intrusion. Crosses designate hypocenters at depths of 0–4.9 km; squares designate those at depths of 5.0 km or deeper. ***A***, Map showing epicenters. The summit caldera, pit craters, and faults are also shown. W–E and N–S are reference centerlines for the following vertical sections *B* and *C*. ***B***, Hypocenters projected onto a vertical west-east section within 3 km on either side of line W–E. ***C***, Hypocenters projected onto a vertical north-south section within 3 km on either side of line N–S.

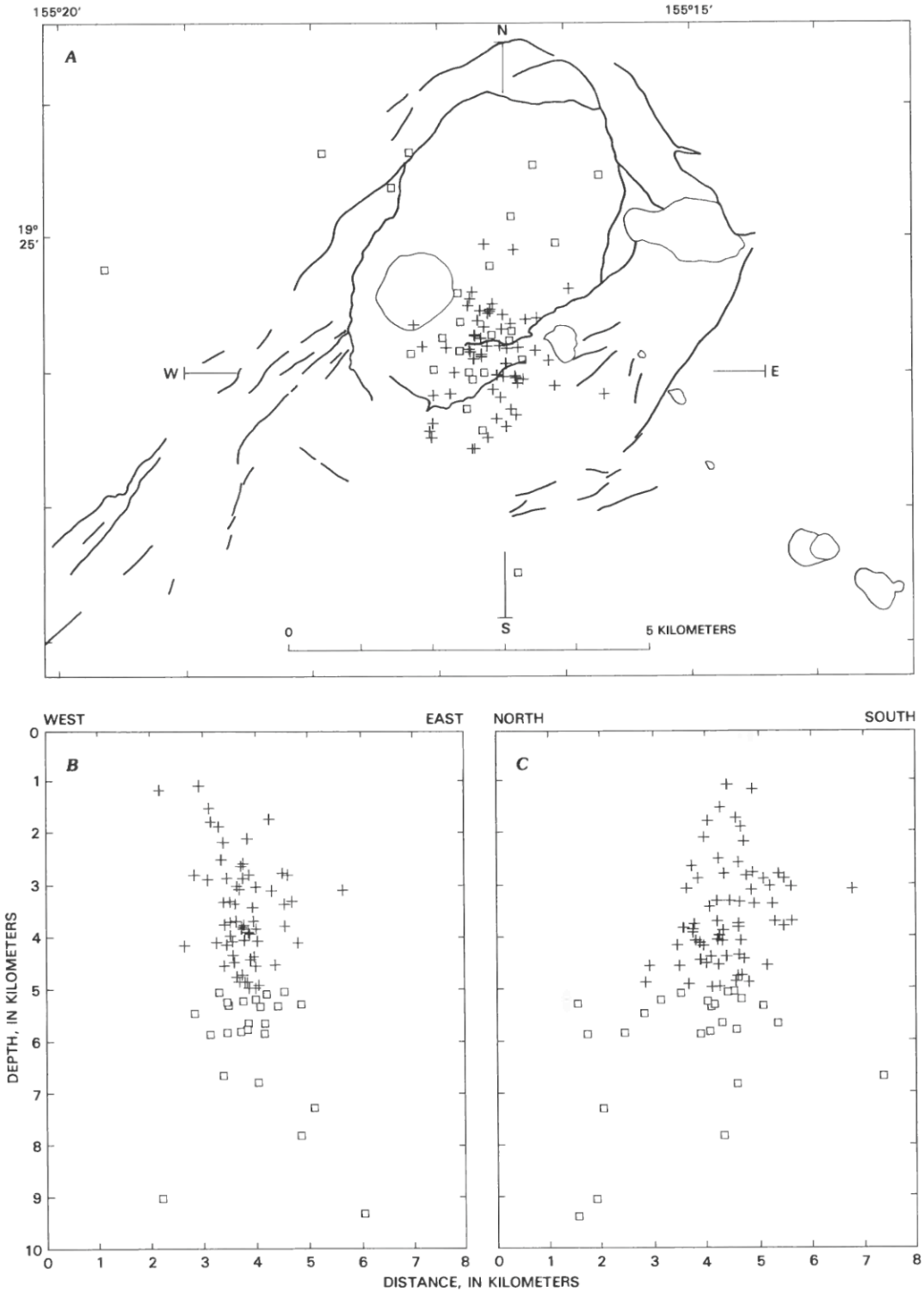
155°20′
155°15′
A
N
19°
25′
W
E
S
0
5 KILOMETERS
WEST
EAST
NORTH
SOUTH
B
C
DEPTH, IN KILOMETERS
DISTANCE, IN KILOMETERS

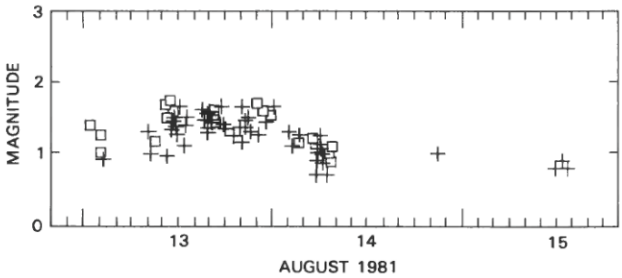


FIGURE 45.17.—Magnitudes of long-period events at the summit caldera of Kilauea (see figure 45.16) following the August 1981 intrusion, plotted against time. Symbols indicate hypocentral depths: crosses, 0–4.9 km; squares, 5.0 km or deeper.

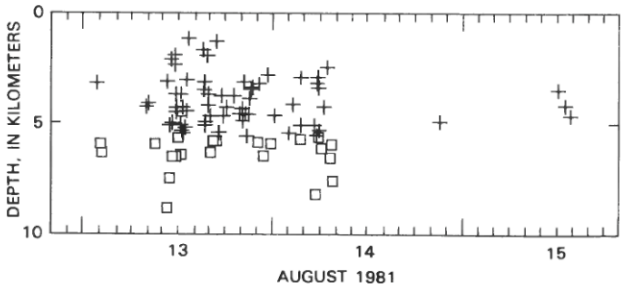


FIGURE 45.18.—Depths of long-period events at the summit caldera of Kilauea (see figure 45.16) following the August 1981 intrusion, plotted against time. Symbols indicate hypocentral depths: crosses, 0–4.9 km; squares, 5.0 km or deeper.

March 1985. They persisted over the following months at intermittently high rates, especially in periods of sustained inflation during the continuing eruption on the middle east rift. Differences in the amplitude envelope and spectral features on seismograms distinguish these long-period events from short-period earthquakes in the shallow summit region and intermediate-depth zone in the south flank (see figure 45.19). The smoked-paper seismogram from the summit station NPT on June 26–27, 1985 (figure 45.19*A*), shows the characteristics of shallow summit earthquakes, intermediate-depth south flank earthquakes, and intermediate-depth long-period events. The signatures of these seismic events are also illustrated on record from station PAU, located on the upper east rift zone about 8 km southeast of station NPT (figure 45.19*A*). The initially sharp onset and the high amplitude that attenuates rapidly with distance for short-period earthquakes contrasts with the uniform spectral features and gradually changing pattern of amplitude for long-period events. Digitized records from an array of stations at various epicentral distances emphasize the differences in the arrival pattern, amplitude envelope, and spectral features between the short-period earthquakes and long-period events (figure 45.19*B–E*).

Over the years, a variety of amplitude patterns and dominant periods have been recorded for different flurries of the intermediate-depth events. The amplitude patterns vary from isolated single bursts to series of multiple bursts. Recorded frequencies vary from monochromatic to fairly erratic. Dominant periods of 0.3–1.0 s are common. Some events possess longer periods of 1.0 s or more. On some occasions, energetic long-period events at intermediate depth beneath the summit were weakly recorded by the nearby recording tiltmeter which normally responds to long-period signals of about 20 s or more. The similarity in the envelope at various frequencies in figure 45.19 indicates a stationary spectral shape throughout the coda, which is characteristic of long-period events and tremor.

Short-period earthquakes and long-period events are routinely separated according to pattern of seismic-wave frequencies read on rotating-drum or Develocorder seismograms. The short-period earthquakes are initiated by sharp beginnings of high frequencies at about 10 Hz, followed by progressively lower frequencies. In contrast, long-period events persist within a limited band throughout the coda.

## CASE HISTORY 5: INTERMITTENT BURSTS OF DEEP TREMOR

Deep tremor and its associated long-period events were described by Aki and Koyanagi (1981). A common source region for the long-period events and tremor is inferred on the basis of the coincidence in their time of occurrence and the similarity in the distance attenuation of their amplitudes across the seismic network; therefore, the hypocenter determinations for the long-period events were used to define the source region for the concurrent tremor. Widely recorded signals for deep long-period events with the earliest arrivals at stations southwest of Kilauea were commonly observed on seismograms (figure 45.20). These events frequently occurred in deep-tremor episodes of variable amplitude that were consistently limited in duration to about one-half to several hours (figure 45.21). Deep tremor contained frequency components up to 10 Hz, which is

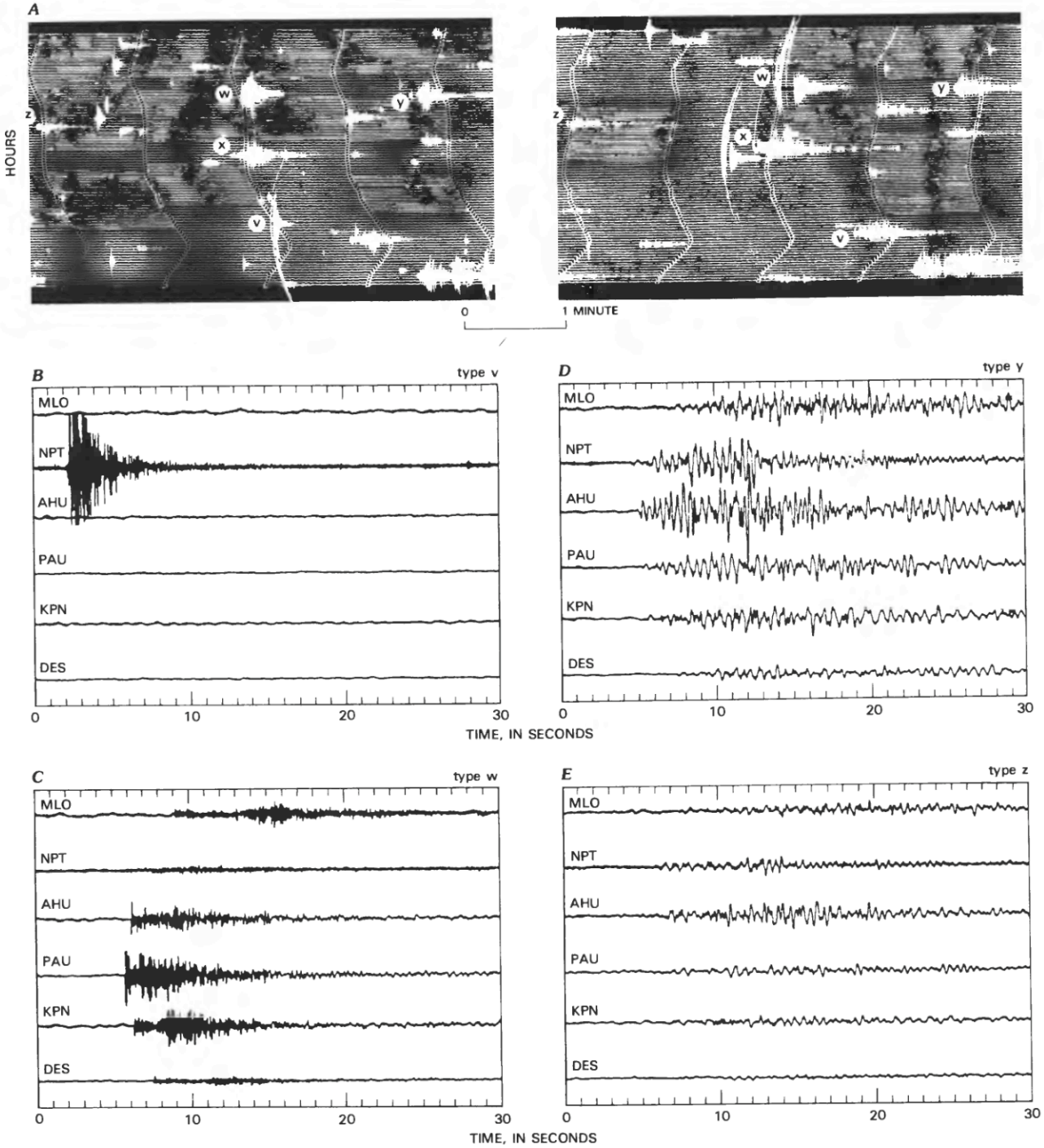


FIGURE 45.19.—Records showing high seismicity during an inflationary trend of the summit about two weeks following eruptive episode 33 in the continuing eruption of the middle east rift zone of Kilauea. The variety of seismic events in the crustal region of Kilauea in the magnitude range of about 0.1 to 1.5 included a shallow summit earthquake less than 5 km in depth (v), a south-flank earthquake at 9 km in depth (w), and long-period events 8–10 km beneath the summit region of Kilauea (x,y,z). ***A***, Portions of smoked-paper seismograms for (left) June 26–27, 1984, from station NPT at the summit of Kilauea and (right) June 26–27, 1984, same time section, from station PAU in the east rift zone 8 km southeast of NPT. Instrumental sensitivity to ground motion between NPT and PAU stations are not identical, but restrictively compatible; relative differences of up to 20 percent should be expected. ***B***, The shallow summit earthquake (v) shown on seismograms from digitized magnetic tape records for an array of six stations. For locations of stations see figure 45.1. Instrumental sensitivity for individual stations was kept constant but differences in magnification from station to station of as much as 20 percent may be present. ***C***, The south-flank earthquake (w). ***D***, The long-period event at 10 km in depth (y). ***E***, The small long-period event at 8 km in depth (z).

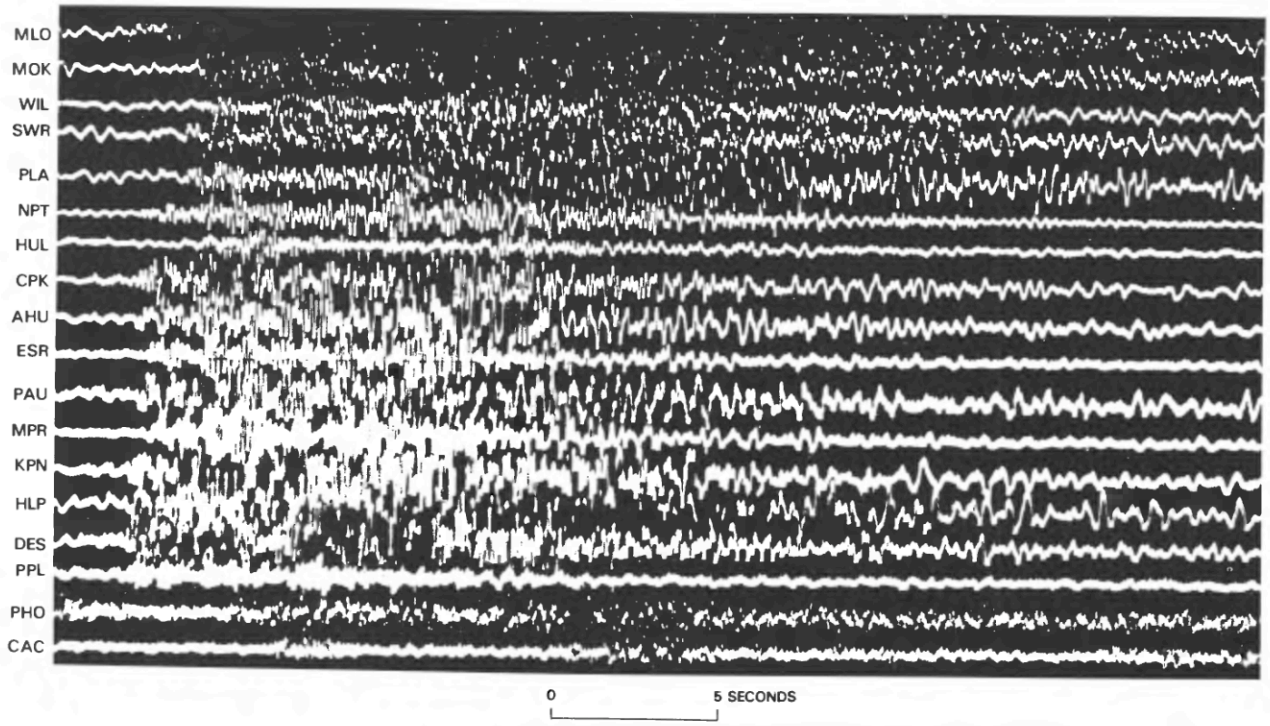


FIGURE 45.20.—Develocorder seismogram of a uniform-frequency long-period event 50 km deep southwest of Kilauea recorded at 0017 (H.s.t.), January 14, 1978. Three-letter codes indicate seismograph stations (see figure 45.1).

slightly higher than those in tremor from shallower sources other than the tremor near eruptions.

## DEPTH CLASSIFICATION OF TREMOR AND COMPARISON WITH LONG-PERIOD EVENTS

In the routine processing of seismic records at HVO, tremor is classified into three depth categories on the basis of the distance-attenuation pattern of amplitude. Episodes of tremor not related in time or space to eruptions and presumed to be caused by magmatic activity vary in their amplitude-attenuation pattern across the network of stations. This variation was used to classify the tremor as shallow, intermediate-depth, and deep tremor. If tremor was related to an eruptive event and its amplitude varied according to the intensity of lava movement, fountaining, and extrusion rate, it was considered to be shallow.

The tremor in the various depth categories was frequently accompanied by short bursts of long-period events with envelopes that resembled those of tectonic earthquakes and spectral features similar to those of the concurrent tremor. These long-period earthquakes often had onset times or identifiable bursts that were measurable to within 0.1 s at a significant number of stations. The arrival times of their onsets are consistent with $P$-wave travel times for local earthquakes in Hawaii, thus permitting standard earthquake-location procedure to be used for hypocenter determination. The compilation of well-located long-period events from 1972–1984 was used to outline the source region of tremor beneath Hawaii.

Normalized amplitudes of clearly recorded and located long-period events, corrected for instrumental magnification and station noise, generally showed an exponential pattern of spatial attenuation rates that decreased with increasing focal depth. Attenuation patterns averaged from several long-period events at approximate mean depths representing our three general depth categories of Kilauea tremor (shallow: less than 5 km; intermediate: 5–15 km; and deep: 30–60 km) were compared with those of the concurrent background of tremor (figure 45.22).

Using the epicentral distances for the long-period events and replacing the normalized amplitude measurements with those of the concurrent harmonic tremor, we found a similar pattern of amplitude attenuation with distance, indicating a common source region. In the attenuation of amplitude with distance, the linear relation between log amplitude and log distance is represented by

$$\log A = x - y \log D,$$

where $A$ is the relative amplitude, $D$ is the epicentral distance in kilometers, and $x$ and $y$ are constants. Values of $y$, the measure of amplitude attenuation, determined for Kilauea tremor decrease with increasing focal depth; they are 1.3–1.4 for shallow tremor, 0.9–1.0 for intermediate-depth tremor, and 0.4–0.5 for deep

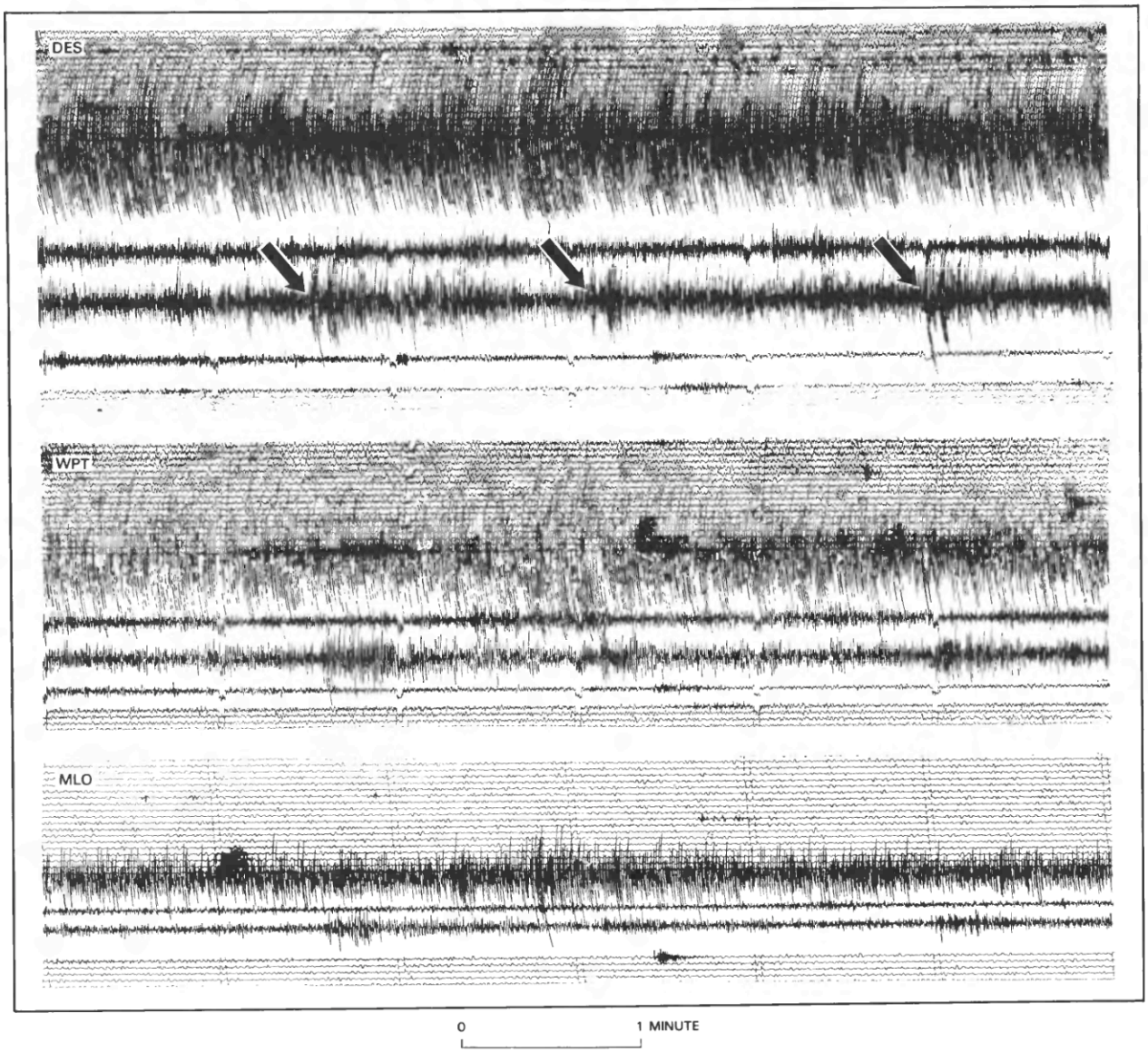


FIGURE 45.21.—Part of a 50-minute burst of tremor and intermittent deep earthquakes on July 22, 1969, recorded on smoke-drum seismograms at the Desert (DES), West Pit (WPT) and Mauna Loa (MLO) stations. The long-period events, defined by abrupt increase in amplitude and higher frequency, are marked by arrows on the Desert seismogram. Average distances from earthquake focus to seismometer are: Desert, 45 km; West Pit, 52 km; and Mauna Loa, 57 km.

tremor. The characteristics and associated volcanic events for the various categories of tremor are summarized in table 45.2.

## HYPOCENTER DETERMINATION OF LONG-PERIOD EVENTS USING STANDARD EARTHQUAKE LOCATION PROCEDURE

Long-period events with reasonably sharp onset times or identifiable episodes that could be matched at 10 or more stations around the epicentral region were selected and read from Develocorder or digitized magnetic-tape seismograms. The arrival times based on *P*-wave velocities were used to process locations using the earthquake-location program HYPOINVERSE (Klein, 1978).

These events were located within the bounds of accuracy expected for earthquakes. The accuracy in terms of horizontal and vertical standard error was reasonably good: most events were located with a precision better than $\pm 5.0$ km and many within $\pm 2.0$ km (figure 45.23). Events located with standard errors less than $\pm 2.0$ km amounted to 96 percent of events shallower than 5

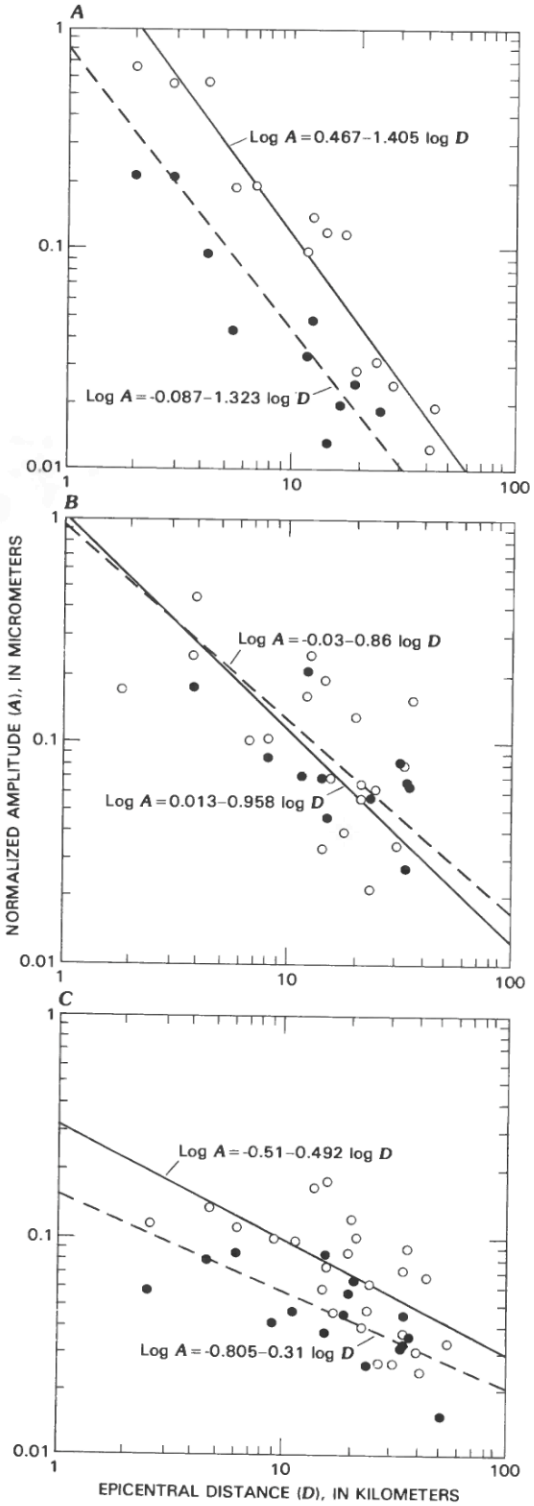


FIGURE 45.22.—Amplitude plotted against epicentral distance for located Kilauea long-period events (circles) at various depths and the tremor (dots) associated with each. The derived linear regression equation is given for each plot; solid lines for long-period events and dashed lines for tremor. Amplitude normalized to remove effects of instrument differences. ***A***, Shallow events (4 km). ***B***, Intermediate-depth events (10 km). ***C***, Deep events (37 km).

km, 62 percent of intermediate-depth events in the depth range of 5–15 km, and 26 percent of deep events at depths of 15–60 km.

Amplitude and signal-duration patterns for long-period events were roughly consistent with those of short-period earthquakes. A comparison of magnitudes derived from signal amplitude ($M_a$) and from signal duration ($M_d$) for shallow, intermediate-depth, and deep long-period events indicates an approximately linear relation (figure 45.24). There is some deviation from linearity toward higher magnitudes, with a tendency for duration magnitude ($M_d$) to be progressively overestimated in the higher magnitude range. This may reflect some inherent differences between long-period events and short-period earthquakes. Source duration differences are expected between short- and long-period events (see Chouet and others, chapter 45, part II). Attenuation rate for long-period events may be lower and the same calibration curve may not apply to both. Controlled by the seismometric coverage and signal clarity, the magnitude thresholds of the located long-period events were generally, less than 0.5 for shallow events, about 1.0 for intermediate-depth events and nearly 1.5 for the deep events.

## TREMOR SOURCE REGION BENEATH HAWAII INFERRED FROM LOCATIONS OF LONG-PERIOD EVENTS FROM 1972 TO 1984

The normal short-period earthquakes between January 1981 and December 1982 were widely spread beneath Kilauea, outlining the regions of rock fracturing caused by intrusive events at the summit and rift zones and the seaward displacement of the south flank (figure 45.25*A*). A view of these events projected onto an east-west profile (figure 45.25*B*) indicates that most of the events were confined in the crust at depths of less than 10 km.

In contrast to the broadly distributed short-period earthquakes defining the tectonic environment beneath Kilauea, long-period events located beneath Kilauea during 1972–1984 with horizontal and vertical standard errors of less than ±2.0 km were concentrated in the summit region (figure 45.26*A*). These hypocenters were projected onto cross sections in an east-west plane (figure 45.26*B*) and in a north-south plane (figure 45.26*C*); they outline a columnar source region separated into two depth concentrations in the crust. The shallow concentration beneath the caldera was centered at depths of about 2–4 km and the deeper one at 6–12 km, leaving a zone of low activity at 4–6 km depth.

On an islandwide scale the long-period events located for 1972–1984 with less than ±5.0-km horizontal and vertical standard errors were concentrated at the summits of Kilauea, Mauna Loa, and Loihi and in a broad region at depth about equal distances

TABLE 45.2.—*Classification of tremor types beneath Kilauea Volcano by depth and area of origin*

[Dominant frequencies are those commonly recorded on HVO network stations, recorded distance is the maximum distance at which tremor type recorded on typical HVO type 1 station]

| Type | Origin | | Associated events | Duration | Amplitude at nearest station (μm) | Dominant frequencies (Hz) | Recorded distance (km) |
|---|---|---|---|---|---|---|---|
| | Depth (km) | Area | | | | | |
| Shallow 1 (strong) | <5 | Rift and summit | Earthquake swarm, summit deflation, high lava fountains, high rate of lava extrusions, degassing during strong intrusions and eruptions | Few to many days | More than 5 at distance about 1 km | 2–10 | About 40 |
| Shallow 2 (weak) | <5 | Rift | Low lava movement, lava spattering, degassing between episodes in prolonged eruptions | Few days to many weeks | Less than 1 at distance of about 1 km | 2–10 | Less than 5 |
| Shallow 3 (weak) | <5 | Summit | Sustained rate of summit deflation, long-period events | Few to many days | Less than 1 at distance of about 1 km | 2–5 | Less than 5 |
| Intermediate | 5–15 | Kilauea | Summit inflation, long-period events | Several minutes to hours in sequences that may last for days | Less than 5 at distance of about 1 km | 1–3 | About 50 |
| Deep | 30–60 | South Hawaii | Long-period events | Less than one to several hours | Less than 1 at distance of about 15 km | 2– 10 | About 100 |

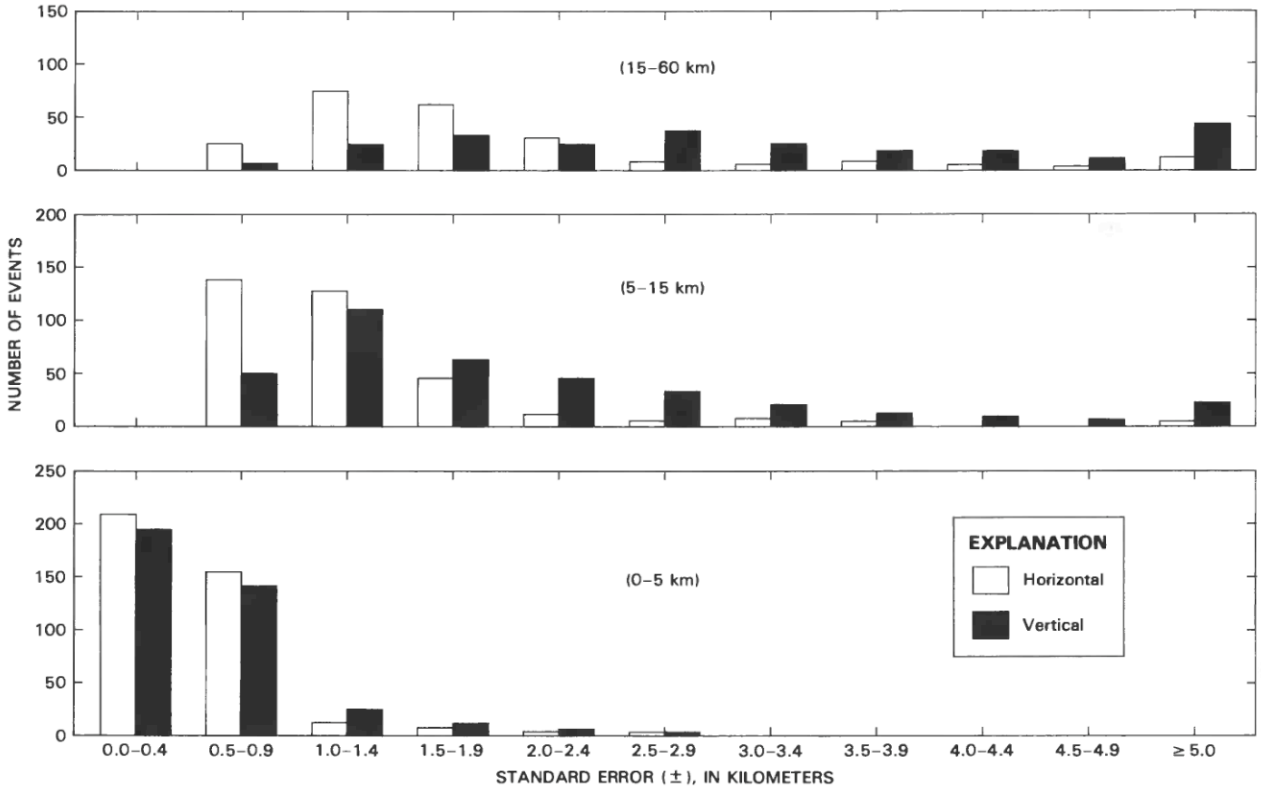


FIGURE 45.23.—Standard errors in the horizontal (white bars) and vertical (black bars) location of long-period events within three depth intervals beneath Hawaii from 1974 to 1984.

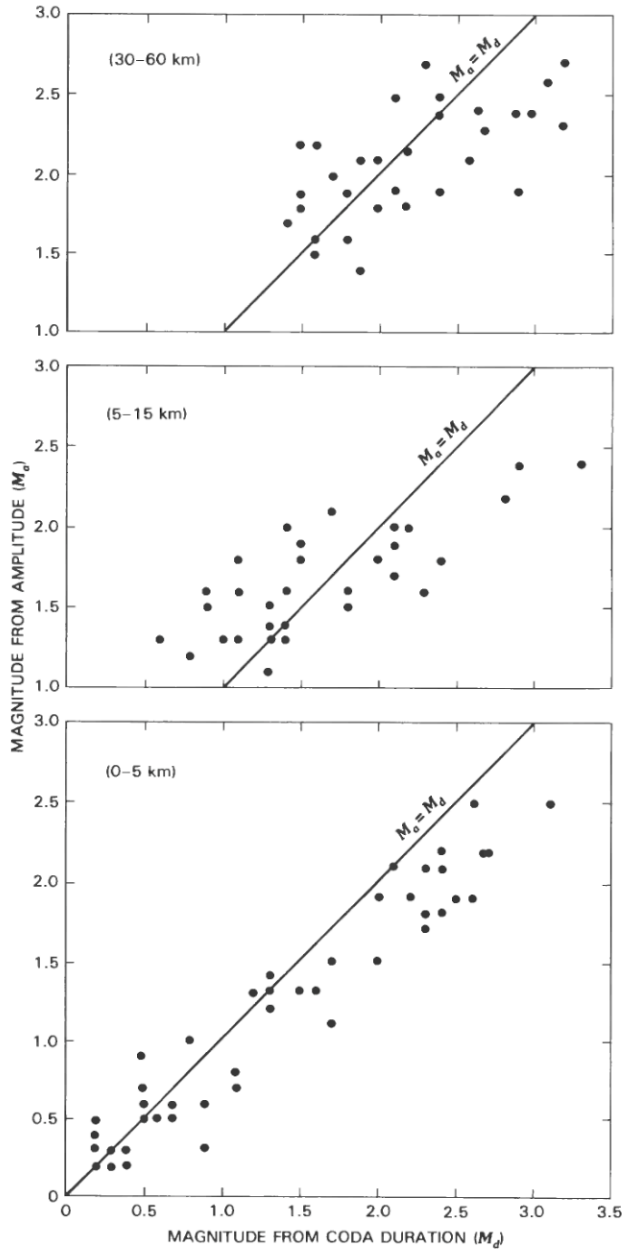


FIGURE 45.24.—Plot of magnitude determined from amplitude ($M_a$) against magnitude determined from coda duration ($M_d$) for long-period events on Kilauea at three depth intervals.

from these three summit localities. The map distributions for various depth intervals of these events beneath the Island of Hawaii are shown in figure 45.27*A–D*. Hypocenters are also shown projected onto the southwest-northeast line w–x from 40 km on either side of it, effectively including the entire seismic zone (figure 45.27*E*) projected onto the same line from a narrower zone 10 km on either side, selectively defining the plumbing system for Kilauea (figure 45.27*F*); and projected onto the northwest-southeast line y–z from a region 40 km on either side of it, showing the alignment of the three dynamic volcanic centers with the deep central system in the mantle.

Circular source regions of nearly equal size, about 5 km in diameter, define the summit of each of the volcanoes. The seismic zone centrally located between the three summit clusters is broader and has width of about 30 km. Cross-sectional profiles outline a columnar distribution from shallow summit regions that discontinuously connect with the deeper central source.

## HISTORY OF TREMOR AND LONG-PERIOD EVENTS FROM 1972 TO 1984

An index to the history of tremor in Hawaii is provided by the daily seismic records at HVO, on which harmonic tremor is routinely identified, separated into three general depth categories, and logged as minutes of tremor per hour (Nakata and others, 1984). Shallow tremor has characterized times of major intrusions and eruptions in addition to sporadic internal activity. Significant bursts of intermediate-depth tremor have generally decreased in recent years, with a background level that typically fluctuates from month to month. Duration of deep tremor was fairly steady throughout 1972–1984, with repeated bursts of activity.

Because the selection of long-period events for the determination of hypocenters was dependent largely on the quiality of their onset times, our compilation may be incomplete in terms of sizes and numbers of events located. Gaps in our file of located long-period events, and inconsistencies between the number of located long-period events and the actual number of events detected are normal discrepancies to be expected. Allowing for such discrepancies, however, our data are sufficiently complete to provide an approximate quantitative base from which to evaluate long-period events according to their spatial distribution over many years and their temporal relation to major volcanic events. By considering the total number of long-period events detected and classified generally according to time and region, temporal gaps in our collection of accurately located long-period events can be filled by estimation.

A compilation of locatable long-period events provides a means to quantify the spatial distribution and magnitude parameters of the tremor-related activity. Depth-time plots of long-period events, with symbol sizes designating magnitudes, show the sporadic nature of shallow activity related to eruptions and to shallow magmatic events and the more dispersed but persistent pattern of deep events (figure 45.28). The magnitudes for the located events were confined to less than about 3.5, with deep events showing a tendency toward larger magnitude. There also appears to be a tendency for activity of deeper events to increase following accelerated shallow activity.

Locatable shallow (depth less than about 5 km) long-period events correlated with major eruptive or intrusive events such as those in December 1974, September 1977, and August 1981 (figure 45.29). The depth-time plots in general indicate that episodic shallow activity is related to significant volcanic events and that deeper events increase over a longer timespan.

The time-relation of long-period events to the inflation-deflation pattern of the summit is plotted on a longer time base in figure 45.30. A marked increase in long-period events, which are usually shallow, followed major collapses. Deeper crustal events appear dispersed during general periods of inflation.

The rates of deep-tremor generation, magma movement in the shallow summit storage system at Kilauea, lava extrusion at Kilauea, and times of significant volcanic events and earthquakes from 1972 to 1984 are compared in figure 45.31.

The time plot of reduced displacement of deep tremor was expanded from Aki and Koyanagi (1981, figure 10), who interpreted reduced displacement in terms of magma flow rate. Tremor readings were made from standard optical-drum seismograms and checked with smoked-drum records. Peak-to-peak amplitudes were measured in 5-min increments and reduced to micrometers of ground movement according to the instrumental response (basically types 3 and 4, see Nakata and others, 1982) for the averaged frequency of the deep tremor. Variations in system response for the predominant range of frequencies of the deep tremor may introduce discrepancies as large as a factor of two in the reduction of absolute amplitude, but they should not affect the relative continuity over the entire period. The instrumental response and analysis procedure emphasized signals in the range of frequencies from about 2 to 10 Hz.

The volume of magma movement in the shallow summit storage system at Kilauea could be estimated from tilt changes on the east-west component continuously monitored from Uwekahuna on the northwest side of Kilauea caldera. An average magma volume to tilt ratio of $0.63 \times 10^6$ $m^3/\mu rad$ was derived from the volumes of lava extruded as extrapolated from field surveys compared with the east-west tilt changes during episodes 2–20 of the Puu Oo eruption in 1983–1984, ratios for individual episodes range in variation by $\pm 0.21 \times 10^6$ $m^3/\mu rad$ (Wolfe and others, chapter 17). The volume of erupted lava was adjusted for 25 percent porosity. In view of the relatively wide variation in volume to tilt ratios observed for the individual eruptive episodes that may be caused by lateral migration of the summit tilt center or magma drainage within the conduit system, as well as the difficulties in measuring extruded lava, we chose a slightly high conversion value of $0.8 \times 10^6$ $m^3$ to use in our calculation in figure 45.31.

Steady long-term trends of deep-tremor production are occasionally interrupted following sustained high rates of lava emission, such as during the Mauna Ulu eruption at Kilauea in 1969–1974 and the continuing Puu Oo eruption in 1983–1984. The increasing rate of deep tremor from late 1983 subsequent to the onset of the Kilauea eruption in January 1983, and then again in 1984 following the start of the major eruption of Mauna Loa in March, indicate that a pressure reduction in the upper conduit system may induce increased buoyancy of the magma along the interconnecting plumbing system, propagating downward to accelerate the feeding rate from the mantle source. The possibility of such a mechanism was recently suggested by Dzurisin and others (1984) and is also consistent with evaluations based on geochemical data (Wright, 1984).

## CONCLUSIONS

Data from study of volcanic tremor in Hawaii justify the following generalizations and inferences.

(1) Harmonic tremor, a seismic signal with relatively constant frequency content and pattern from start to end, is generated and sustained by eruptive activity and magma movement, and its amplitude varies according to its intensity.

(2) Shallow tremor at an eruption site is strongly influenced by flow impact and acoustical noise from high fountains, as well as by the rate of lava extrusion. Eruption tremor is characterized by a peaked spectrum and amplitude variations that alternate at intervals of a few seconds. This pattern generally reflects the activity of intense fountaining in which recurring lava bursts occur at intervals of about 5 s. The continuously fluctuating tremor signal produces a multipeaked spectrum at 1–10 Hz.

(3) Repose periods between major episodes of lava production in prolonged eruptive series, such as the Mauna Ulu and Puu Oo eruptions of Kilauea, are characterized by a nearly continuous background of tremor local to the active vents. The relatively weak tremor varies in amplitude according to the rate and intensity of lava movement and degassing activity within the eruptive vents.

(4) Long-period events are a unique form of seismic event closely associated with harmonic tremor and magmatic activity. A common source for tremor and long-period events is implied by their similarity in spectral features, time of occurrence, and spatial attenuation of amplitude. Long-period events sometimes increase progressively and culminate in continuous tremor, and tremor sometimes decays into episodic bursts evolving into long-period events; tremor may therefore be a collective aggregate of long-period events.

(5) Some long-period events with identifiable onset times are locatable within the accuracy constraints of normal earthquakes. The locations of these events thus outline the source regions of tremor beneath Hawaii. Shallow events are concentrated in epicentral areas about 5 km in diameter centered at the summits of Mauna Loa, Kilauea, and Loihi Volcanoes in expected locations of magma storage. The three centers appear to be connected, though not continuously, to a broader and deeper common source region; together they are inferred to outline the plumbing system beneath Hawaii that supplies magma from a common mantle source to the separate volcanoes. The broad mantle source may be compartmental to explain the chemical differences in the erupted lavas of Kilauea, Mauna Loa, and Loihi, which are believed to have formed within the mantle (Wright, 1984).

(6) The located long-period events provide a quantitative means to classify tremor according to depth and associated volcanic events into (i) shallow rift and summit tremor less than 5 km beneath the eruptive vent; (ii) shallow summit tremor less than 5 km deep associated with deflation episodes at the summit; (iii) intermediate-depth tremor at 5–15 km beneath Kilauea and generally associ-

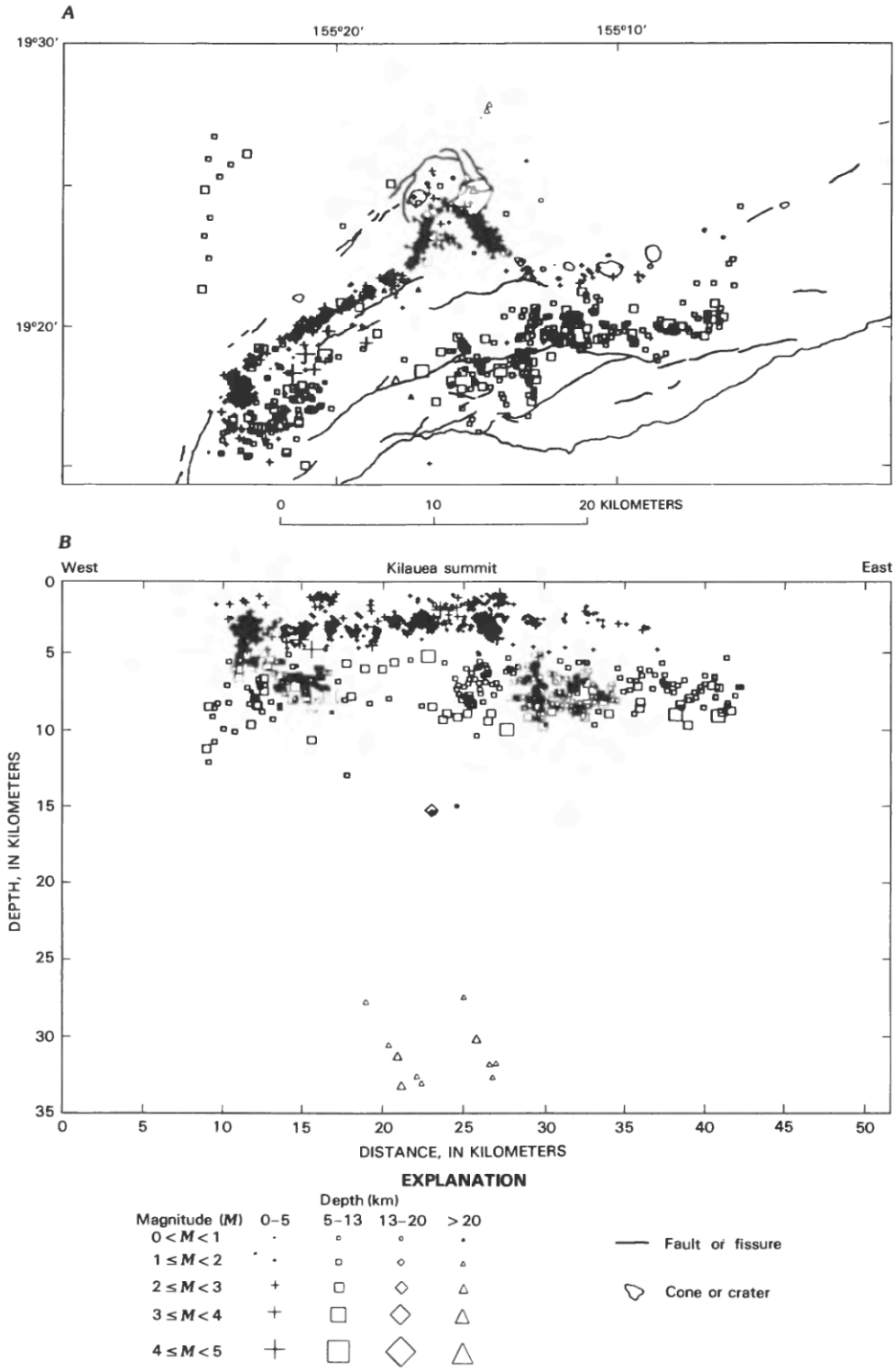


FIGURE 45.25.—Short-period earthquakes in the region of Kilauea caldera, January 1981 to December 1982. Horizontal and vertical standard errors for these events were less than ±2 km. ***A***, Epicentral locations. ***B***, Depth profile of the earthquakes projected onto an east-west plane.

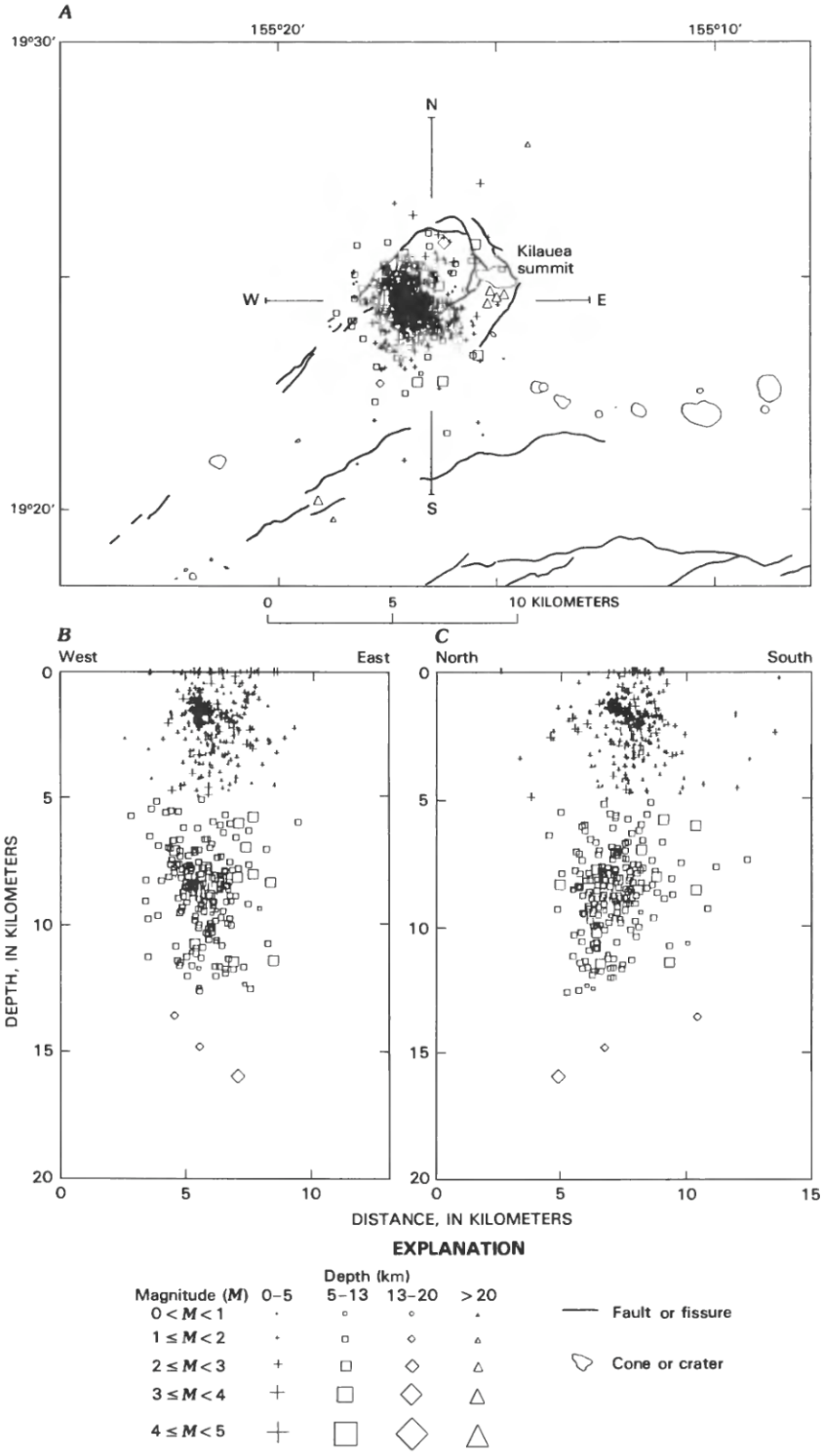


FIGURE 45.26.—Long-period earthquakes 0–20 km beneath Kilauea region from 1972 to 1984. Only events with horizontal and vertical standard errors less than ±2.0 km were plotted. ***A***, Locations of epicenters, and lines of two depth sections W–E and N–S. ***B***, West-east depth section with events projected onto line W–E. ***C***, North-south depth section with events projected onto line N–S.

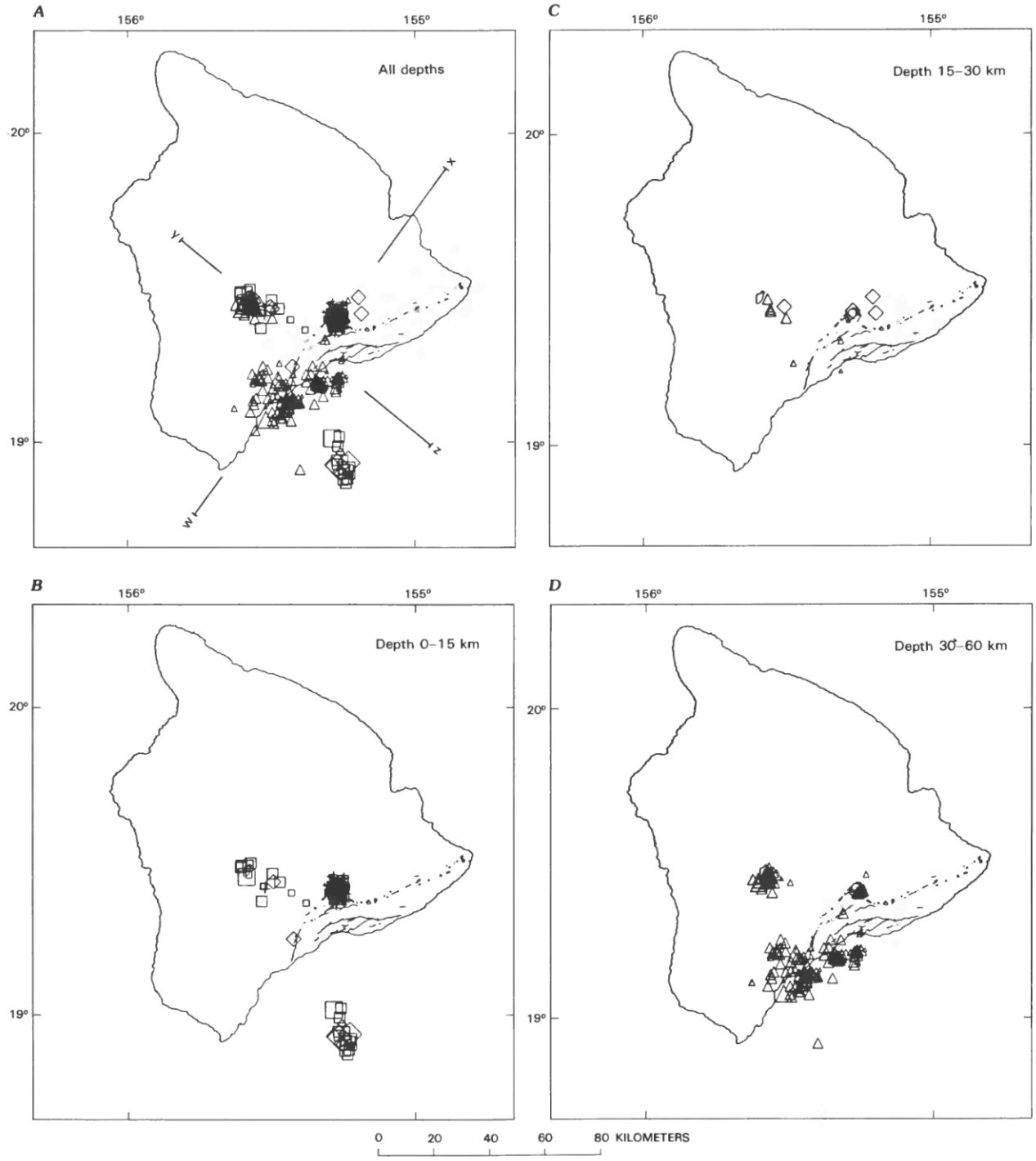


FIGURE 45.27.—Long-period earthquakes beneath the Island of Hawaii region from 1972 to 1984. Only events with horizontal and vertical standard errors less than ±5.0 km were plotted. ***A***, Locations of all epicenters and reference lines for depth sections. ***B***, Locations of epicenters for events at depths 0–15 km. ***C***, Locations of epicenters for events at depths 15–30 km. ***D***, Locations of epicenters for events at depths 30–60 km. ***E***, Southwest-northeast depth section with events projected from a zone 80 km wide onto line w–x. Projected positions of Mauna Loa and Kilauea summit areas are indicated. ***F***, Southwest-northeast depth section with events projected from a zone 20 km wide onto line w–x. Approximate position of Kilauea summit is indicated. ***G***, Northwest-southeast depth section with events projected from a zone 80 km wide onto line y–z. Projected positions of Mauna Loa, Kilauea, and Loihi summit regions are indicated.

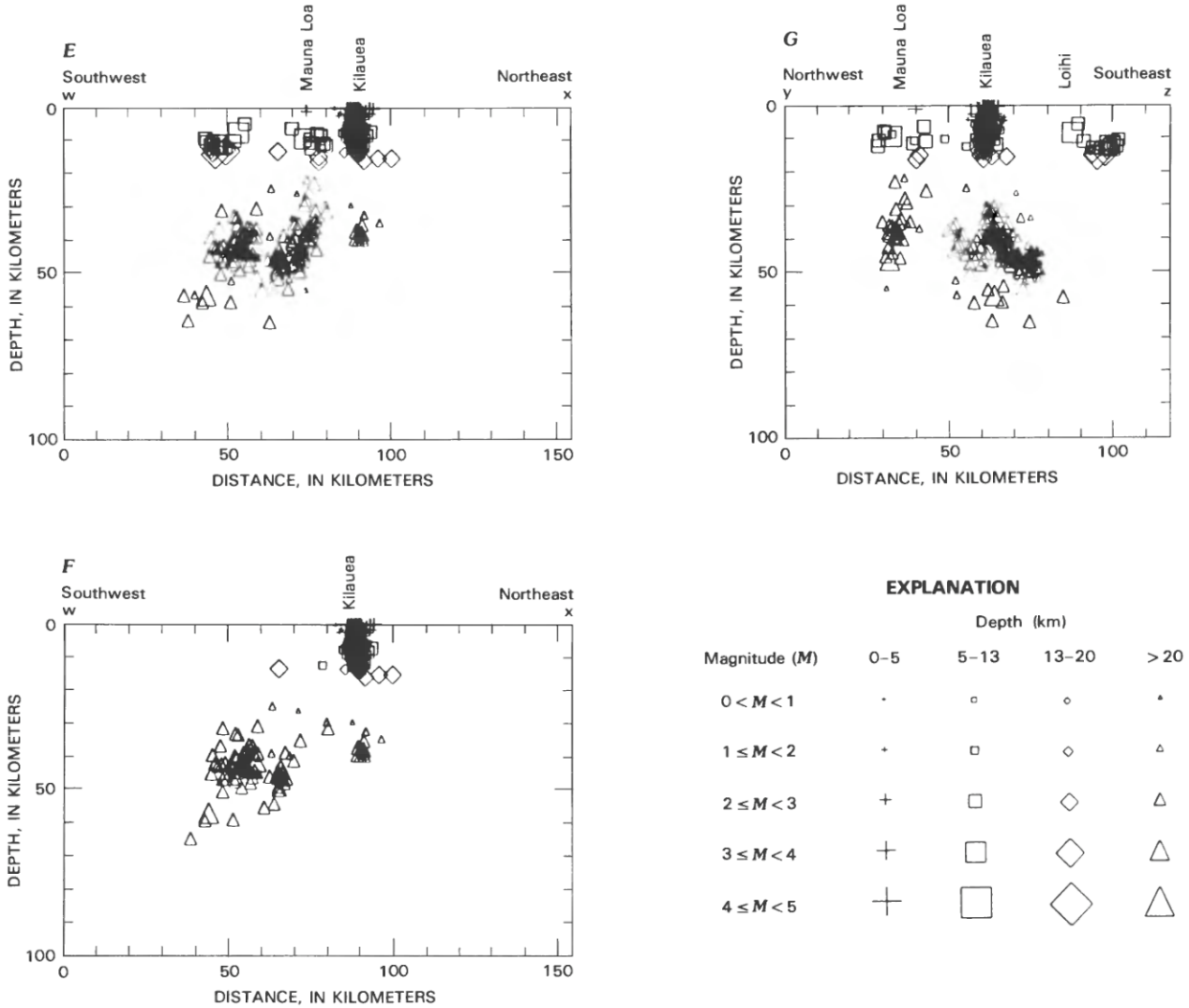


FIGURE 45.27.—Continued.

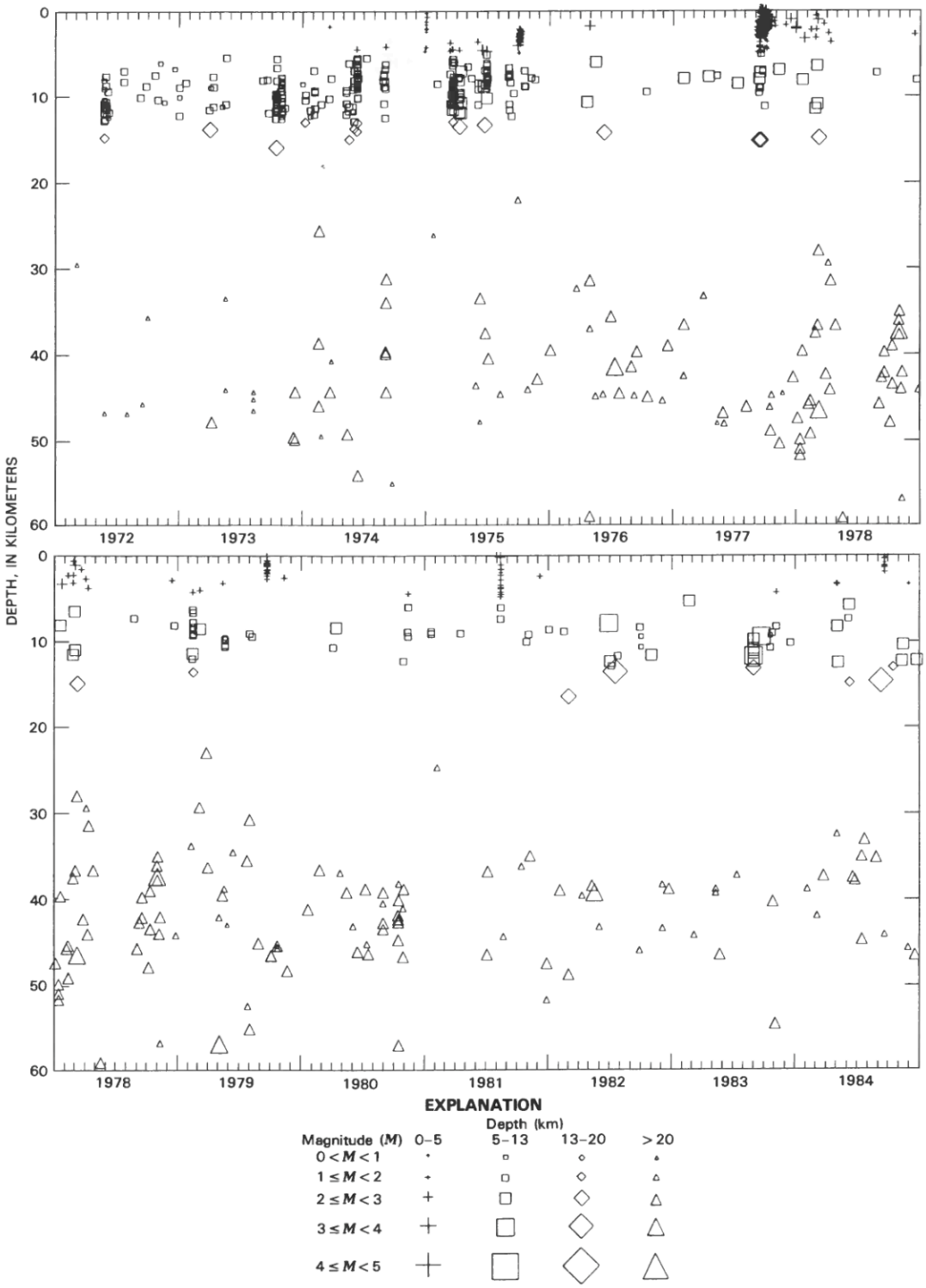


FIGURE 45.28.—Depth-time plot of long-period events 0–60 km beneath Hawaii between north latitudes 18°45′ and 20°20′ and west longitudes 154°40′ and 156°20′ from January 1972 to December 1984. Magnitude ranges are designated by symbol sizes. The selected events were those with horizontal and vertical standard errors of ±5.0 km or less. Data for 1978 repeated where plot is broken.

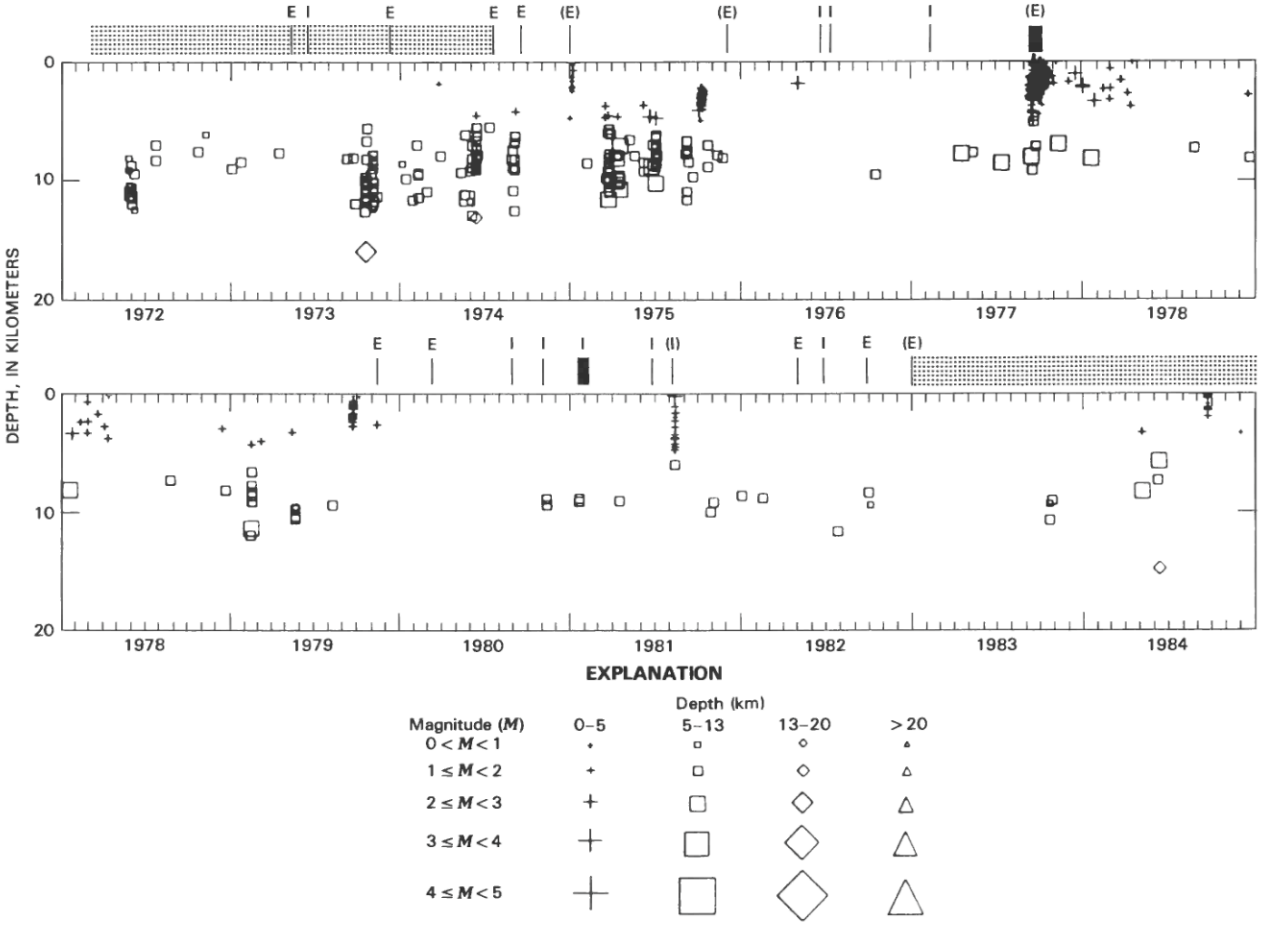


FIGURE 45.29.—Depth-time plot of long-period events 0–20 km beneath the summit region of Kilauea between north latitudes 19°23′ and 19°26′ and west longitudes 155°15′ and 155°18′. Only events with horizontal and vertical standard errors ±2.0 km or less were plotted; therefore the number of events selected is comparably less than in figure 45.28 for the region considered here. Solid bars above plot indicate: (I), magmatic intrusions accompanied by major deflation of the summit, as indicated by more than 100 microradians of east-west tilt measured at Uwekahuna station near the northwest edge of Kilauea caldera; (E), intrusions with subsequent eruptions accompanied by major deflation of the summit; I, intrusions without major deflation but with at least 5 microradians of east-west tilt; E, intrusions with eruption and at least 5 microradians of east-west tilt but without major deflation. Dotted bars above plot indicate prolonged eruptions of repeated episodes at Mauna Ulu (renewed, 1972–1974) and Puu Oo (1983–1984, continuing).

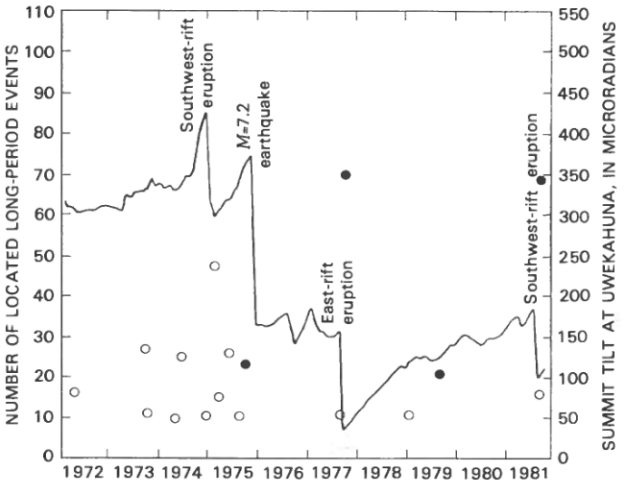


FIGURE 45.30.—Time plot of summit tilt and number of located long-period events of 10 or more per day on Kilauea, 1972–1981. Dots, shallow events (depth less than 5 km), circles, deep crustal events (depth 5–15 km).

ated with inflation at the summit; and (iv) deep tremor at 30–60 km beneath south Hawaii that occurs at a fairly constant rate of reduced displacement, with a subtle increase sometimes following major volcanic events near the surface.

(7) The time-depth distribution of long-period events outlines the dynamic process in the magma transport system. Shallow events are closely associated with observed volcanic events. The activity of progressively deeper events becomes more diffuse but also more persistent over long time intervals. After sustained high rates of shallow intrusions, deep long-period events tend to persist and the rate of reduced displacement of deep harmonic tremor tends to increase. This may be explained by a hydraulically linked system in which a decrease in pressure at shallow depths is propagated to the deeper source and increases the buoyancy of the rising magma.

(8) The source regions of harmonic tremor inferred from the locations of long-period events have a clustered distribution, with gaps along the intermediate and deep parts of the plumbing system. These aseismic regions connecting the seismic sources along the expected magma transport paths may be relatively open, low-stress passages in which magma can maintain a state of quasi-steady flow that does not generate measurable seismic signals.

(9) In the Kilauea region, large numbers of short-period earthquakes reflect the tectonic response to magmatic pressure, and their distribution only broadly encompasses the interconnecting regions of magmatic activity. The spatial distribution of long-period events, on the other hand, outlines a more confined region that presumably represents the actual magma transport system beneath Hawaii.

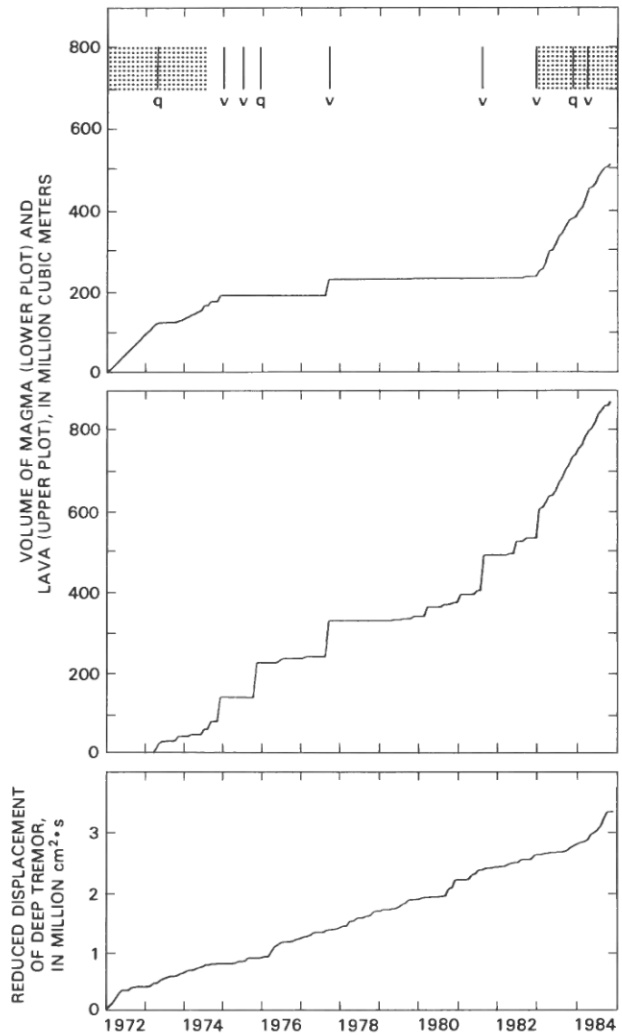


FIGURE 45.31.—Cumulative plots, for period 1972-1984, of reduced displacement of deep tremor, volume of magma removed from the summit storage system of Kilauea (estimated from tilt changes at Uwekahuna), and volume of lava extruded in eruptions on Kilauea Volcano. The plots are derived from monthly totals. Solid vertical bars mark onset times of significant volcanic events with more than an estimated ten million cubic meters of magma withdrawal from the summit storage system at Kilauea and Mauna Loa (v) and times of strong earthquakes of magnitude greater than 6.0 in Hawaii (q). Dotted vertical bars mark prolonged eruptions with frequently repeating episodes of lava output at Kilauea's Mauna Ulu (1972–1974) and Puu Oo (1983–1984).

(10) The temporal and spatial distribution of long-period events usually infer their immediate relation to harmonic tremor and magma movement. In some instances, however, shallow long-period events that develop above the summit reservoir during sustained ground deformation and continued swarms of short-period earthquakes may be the result of attenuation of high frequency signals transmitted through a path of increasingly fractured cap rocks. These are very shallow events within a few km of the surface that often do not lead to eruptions, and because they are typically small and recorded on a limited number of nearby stations, the possibility for a tectonic origin attributed to structural adjustments above the magma body cannot be conclusively excluded.

## REFERENCES


Aki, K., and Koyanagi, R.Y., 1981, Deep volcanic tremor and magma ascent mechanism under Kilauea, Hawaii: Journal of Geophysical Research, v. 86, no. B8, p. 7095–7109.

Dzurisin, D., Koyanagi, R.Y., and English, T.T., 1984, Magma supply and storage at Kilauea Volcano, Hawaii, 1956–1983: Journal of Volcanology and Geothermal Research, v. 21, p. 177–206.

Klein, F.W., 1978, Hypocenter location program HYPOINVERSE, U.S. Geological Survey Open-File Report 78–694, 113 p.

———1983, Users guide to QPLOT, an interactive computer plotting program for earthquake and geophysical data, U.S. Geological Survey Open-File Report 83–621, 45 p.

Klein, F.W., and Koyanagi, R.Y., 1980, Hawaiian Volcano Observatory seismic network history 1950–79: U.S. Geological Survey Open-File Report 80–302, 84 p.

Koyanagi, R.Y., 1982, Procedure for routine analyses and classification of seismic events at the Hawaiian Volcano Observatory, part 1: U.S. Geological Survey Open-File Report 82–1036, 77 p.

Koyanagi, R.Y., Tanigawa, W.R., and Nakata, J.S., in press, Seismicity associated with the eruption of Kilauea Volcano from January 1983 to July 1984, *in* Wolfe, E.W., ed., The Puu Oo eruption of Kilaeua Volcano, Hawaii: the first 1½ years: U.S. Geological Survey Professional Paper.

Koyanagi, R.Y., Unger, J.D., Endo, E.T., and Okamura, A.T., 1976, Shallow earthquakes associated with inflation episodes at the summit of Kilauea Volcano, Hawaii: Proceedings of the Symposium on Andean and Antarctic Volcanology and Chemistry of the Earth's Interior, special series, 11 p.

Nakata, J.S., Tanigawa, W.R., and Klein, F.W., 1982, Hawaiian Volcano Observatory summary 81, part 1: U.S. Geological Survey Preliminary Report, 77 p.

Nakata, J.S., Tomori, A.H., Koyanagi, R.Y., and Tanigawa, W.R., 1984, Hawaiian Volcano Observatory summary 83, seismic data January to December, 1983: U.S. Geological Survey Preliminary Report, 86 p.

Swanson, D.A., Duffield, W.A., Jackson, D.B., and Peterson, D.W., 1979, Chronological narrative of the 1969–71 Mauna Ulu eruption, Kilauea Volcano, Hawaii: U.S. Geological Survey Professional Paper 1056, 55 p.

Swanson, D.A., Jackson, D.B., Duffield, W.A., and Peterson, D.W., 1971, Mauna Ulu eruption, Kilauea Volcano: Geotimes, v. 16, no. 5, p. 12–16.

Wright, T.L., 1984, Origin of Hawaiian tholeiite: a metasomatic model: Journal of Geophysical Research, v. 89, no. B5, p. 3233–3252.

Wolfe, E.W., Neal, C.A., Banks, N.G., and Duggan, T.J., in press, Geologic observations and chronology of eruptive events during the first 20 episodes of the Puu Oo eruption, January 3, 1983, through June 8, 1984, *in* Wolfe, E.W., ed., The Puu Oo eruption of Kilaeua Volcano, Hawaii: the first 1½ years: U.S. Geological Survey Professional Paper.

# ORIGIN OF VOLCANIC TREMOR IN HAWAII

## Part II
## Theory and Discussion

*By* Bernard Chouet, Robert Y. Koyanagi, *and* Keiiti Aki[1]

### ABSTRACT

**Seismic events at Kilauea and other volcanoes suggest that harmonic tremor results from the sustained random occurrence of so-called long-period events. The long-period event can be viewed as the elementary process of tremor and interpreted as the impulse response of the tremor-generating system. Kinematic and dynamic source models are discussed, in which the tremor is generated by the excitation of a fluid-filled conduit triggered by an impulsive pressure transient. In one model, applicable to shallow tremor, a fluid-filled crack is excited into resonance by the brittle failure of rock caused by excess fluid pressure. The crack expands by the incremental extension of its tip or by the opening of a channel allowing the migration of fluid between neighboring cracks. Two types of sources are considered; in the first, the fluid behaves passively as a cushion and there is no acoustic source within the crack. In the second, the crack contains a viscous fluid that supports acoustic wave propagation. The crack behavior depends critically on a parameter called the crack stiffness, $C=(k/\mu)(L/d)$, where $k$ is the bulk modulus of the fluid, $\mu$ the rigidity of the solid, $L$ the crack length, and $d$ the crack thickness. This dimensionless factor characterizes the ability of the crack to vibrate passively; oscillation of the wall is most pronounced when $C$ is zero. For a passive fluid in a crack of stiffness $C=5$, simulating a shallow dike filled with molten basalt, the source duration never exceeds a few cycles. The resulting ground-motion spectrum displays broadband peaks whose dominant frequencies are markedly dependent on location and the component of motion considered.**

**Two time scales characterize the dynamics of the crack when the fluid participates actively in the motion of the source: the duration of brittle failure and the period of acoustic resonance of the fluid-filled crack. The failure of the crack tip has a duration proportional to the distance that the crack propagates. The resonant period is proportional to the length of the crack and varies inversely with the acoustic velocity in the fluid; it is generally much greater than the duration of brittle failure. Source duration depends strongly on fluid viscosity and associated viscous damping at the crack wall. When the fluid viscosity is low, the main mechanism of dissipation of energy is elastic radiation. The radiation loss only weakly affects the long-period motions of the crack, with the result that the fundamental mode of oscillation of the source can be maintained over a considerable length of time, the crack acting then as a high-$Q$ oscillator.**

**Another model, in which the motion of a magmatic pipe is excited by the sudden flashing of ground water to steam as magma intrudes into the phreatic layer, displays similar characteristics. The motion of the source is represented by the excitation of the organ-pipe modes, whose bandwidths are determined from the combined losses due to viscous attenuation in the fluid and elastic radiation in the solid. In a cylindrical magma column, the radiation loss and the loss related to viscous damping are proportional and inversely proportional, respectively, to the square of the pipe radius, indicating that their relative importance depends critically on the geometry of the magma reservoir.**

**A kinematic model of fluid transport to explain deep tremor under Kilauea involves a constant total volume of magma and periodic magmatic injection, the period being proportional to the source length and inversely proportional to the velocity of the magma front. The predicted tremor spectrum is independent of the radiation direction, in agreement with observations. This model yields a simple relationship between the radiated elastic field and magmatic transport: the volume flow rate of magma ($\dot{q}$) is about 20 times the product of the velocity of the compressional wave in the solid ($\alpha$) and the reduced displacement (the RMS displacement corrected for geometrical spreading and instrument magnification).**

**Seismic estimates of the volume of magma transported under Kilauea are consistently and significantly lower than estimates from deformation measurements for both deep and shallow tremor, suggesting that some magma flow occurs without significant pressure fluctuations in zones of undisturbed transport.**

## INTRODUCTION

A successful model for the source of volcanic tremor must account for the mass balance from magmatic transport in addition to the observed seismic wave field. The constraints on the flow, obtained mainly from deformation studies (that is, tilt and geodetic measurements) and surface observations of eruption products, must be compatible with the seismic amplitudes recorded. The model must also be consistent with the eruptive sequence, the spatial distribution of tremor amplitude, and the spectral characteristics and duration of the observed signal. Since harmonic tremor can last for a long time, it is not easy to perform a deterministic analysis of the entire signal. So efforts have been directed toward regarding tremor as a random sequence of shorter individual events that are more

[1] Department of Geological Sciences, University of Southern California, Los Angeles, California 90089-0741.

easily tractable. Recent observations point to the common characteristics shared by volcanic tremor and so-called long-period or low-frequency events. For example, at Ruapehu and Ngauruhoe Volcanoes in New Zealand, Latter (1979) distinguished volcano-tectonic earthquakes occurring in competent rock from low-frequency events associated with weak, low-impedance materials such as gas, magma, or fractured rock; he viewed volcanic tremor as a train of low-frequency events. At Mount Etna, Seidl and others (1981) identified transient seismic events that they termed wave packets. The spectral characteristics of these wave packets are similar to those of tremor and they are probably also low-frequency events. At Mount St. Helens, Fehler (1983) noted a strong similarity between the spectra of long-period events and of volcanic tremor and proposed that a tremor episode is nothing but a sustained sequence of long-period events. A similar conclusion was reached by Malone (1983), who studied a larger set of earthquakes at the same volcano. At Kilauea in Hawaii, long-period events and harmonic tremor show similar spatial distributions of observed amplitudes, share common spectral characteristics, and occur concurrently, implying a common source region (see Koyanagi and others, chapter 45, part I). Other studies pointing out the similarities in the frequency content of tremor and long-period events include Schick and Riuscetti (1973), Dibble (1974), Guerra and others (1976), Riuscetti and others (1977), Capaldi and others (1978) and McNutt (1986).

The evidence thus seems to suggest that volcanic tremor is simply a swarm of long-period events. Although this inference appears similar to the old notion that volcanic tremor is a swarm of Minakami's *b*-type events (see, for example, Minakami, 1974), there is a fundamental difference between these two concepts. In the earlier idea, the spectral characteristic of tremor is attributed to a path effect, while in the other it is viewed as a source effect. The *b*-type events' lack of clear shear arrivals and their spindle-shaped envelope of signal amplitude were attributed by Minakami to the extreme shallowness of the source. A similar idea is shared by many seismologists, who know that seismograms with signatures similar to that of *b*-type earthquakes are often observed for nonvolcanic sources such as explosions or tectonic earthquakes when the wave path is extremely heterogeneous and absorptive, as might be expected in volcanic areas. If volcanic tremor is nothing but a swarm of *b*-type earthquakes, it is logical to conclude that the spectral signature of tremor is also due to the path effect.

This conclusion, however, fails to explain some of the most spectacular observations made on volcanic tremor. Aki and Koyanagi (1981) presented conclusive evidence for the existence of sources of volcanic tremor at depths around 40 km below Kilauea and showed that their spectral characteristics and the temporal change of these characteristics cannot be explained by a path effect. The tremor frequency became lower as the volcanic activity increased, suggesting an increase in the source region and a larger volume of magma involved in the vibration. Temporal changes in the spectra of shallow tremor, which also cannot be explained by path effects, have been reported for various volcanoes including Mount Aso (Kubotera, 1974), Kilauea (Shimozuru and others, 1966), Mount St. Helens (Fehler, 1983), Etna (Schick and others, 1982), and Sakurajima (Kamo and others, 1977). Among these observations, that of *c*-type tremor at Sakurajima by Kamo and others (1977) offers the most convincing evidence. The Fourier spectra of the tremor they studied show many peaks spaced at regular frequency intervals; these can be attributed to the fundamental mode and higher harmonics of a one-dimensional oscillator. A typical one of their tremor episodes starts with the occurrence of shallow earthquakes and ends with a summit eruption. During the episode the frequency of the fundamental mode increases gradually and continuously from 0.5 to 1.3 Hz, and there is a corresponding increase in the frequencies of the higher modes. These observations can be explained by the vibration of magma and gas in a pipe, in which a rise of the magmatic column decreases the volume occupied by the gas and increases the eigenfrequency of vibration.

A shift of the tremor spectrum to higher frequencies during increased volcanic activity was also observed by Schick and others (1982) at Mount Etna, although the shift was probably not continuous in that case, because the various peaks were attributed to different segments of the feeder pipe.

These considerations appear convincing enough for us to reject Minakami's idea and to adopt the working hypothesis that the peaked spectra of volcanic tremor and long-period events are due to source effects. Furthermore, we can consider the long-period event as the basic element of the tremor signal, which means that we can view this event as the impulse response of the tremor-generating system. The standard tools of earthquake seismology can then be used for a quantitative description of this volcanic process. We will review the seismic-source models that have been proposed to account for the observations of tremor and discuss their implications.

**ACKNOWLEDGMENTS**

We are grateful to Bruce Julian and Elliot Endo for their careful reviews of this paper. This work was partially supported by the Department of Energy under contract DE–FG03–85ER13336 (Keiiti Aki).

## A DYNAMIC MODEL FOR SHALLOW TREMOR

The first attempt to tie the seismic signature of tremor to the process of magma transport in a quantitative way was made by Aki and others (1977) for shallow tremor. They proposed three models of a fluid-filled crack driven by excess fluid pressure, in which they related the observed signal to physical parameters of the source while at the same time offering a geometry adequate for mass transport. In these models, magma intrusion can occur either by the incremental extension of a crack tip or by the opening of a channel allowing the migration of magma between neighboring cracks. The sudden extension of the tip or opening of the channel triggers the vibration of the crack wall, from which elastic waves are radiated into the solid. Sustained tremor is obtained by the superposition of many such events occurring randomly in time and depending in their spatial location on the actual path of magma.

To model this process, Aki and others (1977) considered two-dimensional cracks filled with fluid in an unbounded elastic medium

and assumed that the crack thickness was much smaller than the seismic wavelengths of interest. When the crack expands or a channel breaks open, an excess pressure is applied to the newly created crack surface. To calculate the motion of the crack resulting from this sudden local application of pressure, Aki and others (1977) used the finite-difference method with the boundary condition that the normal stress at the crack surface is equal to the pressure of the fluid. In this model, the fluid behaves passively as a cushion, and there is no acoustic pressure source within the fluid. A further simplifying assumption is that the fluid viscosity can be neglected; the fluid then does not support shear waves, and the shear stress vanishes at the crack surface.

An example of the solutions obtained by Aki and others (1977) for the opening of a channel between two cracks of length $L/2$ is given in figure 45.32. These plots show the normal component of particle velocities and displacements obtained at five positions on the surface of the double crack and expressed in dimensionless form in terms of the excess pressure (fluid pressure minus overburden pressure) $\Delta P$, lengths $L$ and $\Delta l$ of the double crack and channel, respectively, as well as of the compressional velocity $\alpha$ and rigidity $\mu$ of the solid. Since the solution is symmetrical about the channel, the opening is depicted for one half of the source only. These results were calculated assuming a Poisson's ratio of 0.25 in the rock matrix and depend critically on a dimensionless parameter, C, called the crack stiffness factor and given by

$$C = \frac{k}{\mu}\frac{L}{d} \qquad (1)$$

where $k$ is the bulk modulus of the fluid and $d$ is the crack thickness. This important parameter characterizes the ability of the crack to vibrate passively. The oscillation of the wall is most pronounced when C is zero.

The value $C=0$ represents a dry (empty) crack, whereas the value $C=5$ is assumed to portray the minimum stiffness for a shallow crack filled with molten basalt. Since the rigidity of rock is practically constant and both $L$ and $d$ are more or less fixed from observations (the first by the predominant period of tremor, the second by the measurements made on rift zones or exposed sections of dikes), the critical assumption underlying the choice of C concerns the bulk modulus of the fluid. The observed ratio $L/d$ being on the order of $10^3$ for Hawaiian dikes, the low stiffness value $C=5$ chosen by Aki and others (1977) implies that the bulk modulus of the liquid is roughly a thousand times lower than the rigidity of the surrounding rock. This can only be achieved through the presence of bubbles within the fluid, and it is postulated that the source of these bubbles may be the drop of pressure induced in the liquid by the sudden opening of the crack faces.

Aki and others (1977) calculated the far-field body waves radiated by a variety of expanding wet and dry cracks and showed that in all cases the resulting seismic motion has a peaked spectrum because of the finite preexisting crack, in contrast to that of earthquake faulting, in which the crack nucleates at a point and expands continuously to its final size (Aki, 1967; Brune, 1970). Several strong peaks are present in the theoretical frequency-wavenumber spectra obtained by Aki and others (1977), but most of the high-frequency peaks are outside the range of seismic radiation, suggesting that high-frequency oscillations may be trapped in the near field of the source. Aki and others (1977) pointed out that these features for a crack vibrating by jerky extension correspond well to observed characteristics of volcanic tremor, such as the existence of spectral peaks, the strong high-frequency oscillations in the immediate vicinity of the eruption site, and the temporal change of peak frequency, which is naturally expected if the crack size changes with time. The idea that the high-frequency vibrations commonly observed near eruptive sites are due to inhomogeneous waves is attractive, but in view of the approximations involved in the calculations of Aki and others (1977), this idea needs further testing. An improved model that includes the details of the viscoelastic field within the fluid is also required to provide further insight into the effects of crack geometry and fluid properties on the characteristics of tremor observed near the source.

The model depicted in figure 45.32 was applied by Aki and others (1977) to the shallow tremor recorded by Shimozuru and others (1966) during the October 5–6, 1963, eruption of Kilauea. This eruption occurred along a 10-km fissure segment in the central part of the east rift zone between Napau Crater and Kalalua. According to Moore and Koyanagi (1969), the episode began at 0306 Hawaiian standard time (H.s.t.) on October 5 with a rapid deflation of the Kilauea summit, followed 10 min later by strong continuous harmonic tremor near the summit and in the upper east rift. The outbreak of lava presumably started at 0525 in Napau Crater (see fig. 45.33*A*), some 15 km east of the summit, when an acoustic shock was heard by local residents. By 0930 the line of vents had extended 5–6 km east-northeast of Napau Crater; beginning slightly before 1400, new outbreaks of lava occurred 5–10 km east of this crater. The eruptive activity ceased shortly before 0630 on October 6, but harmonic tremor continued for many hours thereafter. The total volume of extruded lava was estimated as $8.3 \times 10^6$ m$^3$, while the subsidence of the Kilauea summit is consistent with the withdrawal of nearly four times that amount of magma (about $30 \times 10^6$ m$^3$) and its injection into the east rift.

The data of Shimozuru and others (1966) clearly outline the source region of tremor, delineating a zone of maximum intensity centered near Halemaumau early on October 5 and showing a gradual elongation of this zone into a narrow belt extending into the east rift as the eruption progressed. The sequence of summit subsidence followed by onset of tremor, as well as the geodetic data and the relative amplitude of seismic motion at different stations, strongly suggest that the tremor was caused by a forceful injection of magma migrating progressively eastward into the rift zone. The simultaneous occurrence of tremor near the Kilauea summit and at Makaopuhi Crater, however, does not support the idea that the migration of magma occurred on a single well-defined front. Another argument against the idea of a single crack growing through the 25 km between the Kilauea summit and Kalalua is the lack of shift in the observed tremor frequency. For example, the dominant frequency decreased only slightly from 1.27 Hz to 1.08 Hz between 0600 and 1800 on October 5 at the Kaoiki station, while it increased from 1.19 Hz to 1.37 Hz at Ohale during the same period

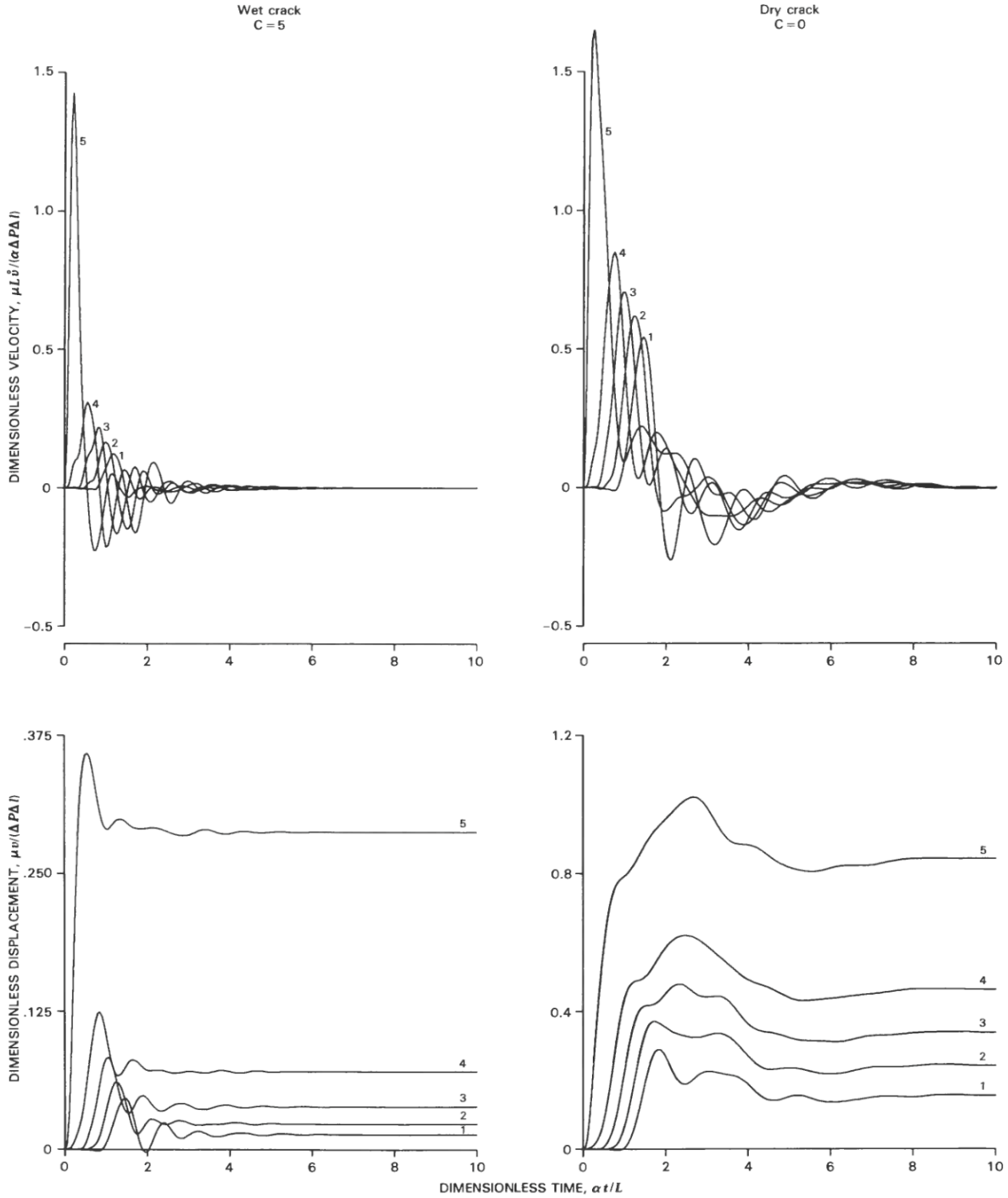


FIGURE 45.32.—Characteristics of the double-crack model of tremor. Normal components of the particle velocities and displacements are plotted as functions of time for different positions on the surface of the double crack opening in the middle. The double crack is 10 grid-intervals long but symmetrical about the middle; therefore only 5 positions are depicted on one-half of the source. Location 5 corresponds to the point of application of the excess pressure $\Delta P$, and location 1 is at the crack tip. The velocities, displacements, and times are given as dimensionless functions of the crack and medium parameters (see text for details).

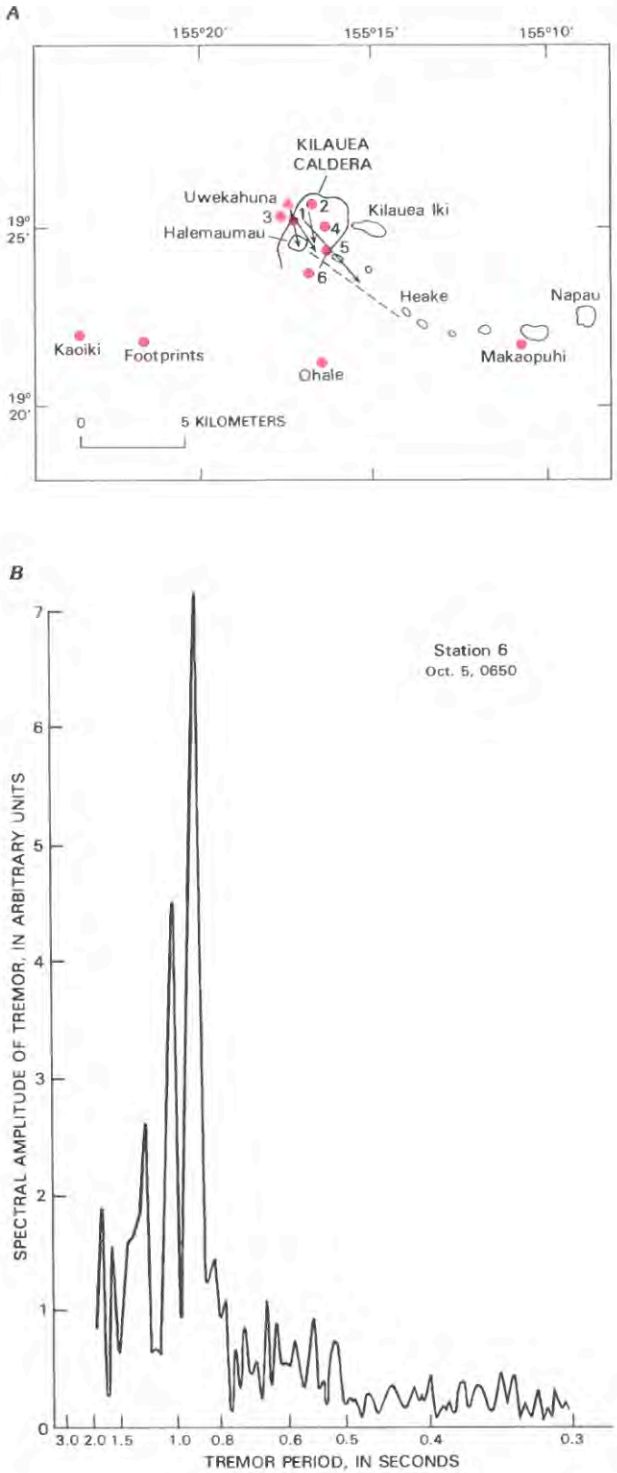


(see figure 45.33*A* for the location of the stations). The decreases of frequency shown by other stations are also too small to be significant. These observations can be explained if one assumes that the rift was still charged with melt from previous episodes of non-eruptive summit collapses and that magma started to move en masse into the rift as the eruption began.

To fit these observations, Aki and others (1977) proposed a transport model that consists of a chain of cracks connected by narrow channels and extending from the summit caldera to the eruption site. In this scheme, the motion of each pair of cracks excited by the opening of the channel linking them constitutes a seismic source and represents an individual long-period event. The tremor signal is then visualized as the sum of the contributions from the ensemble of these sources triggered independently of each other. Using the data of figure 45.32, Aki and others (1977) calculated the elastic radiation at a large distance from the source region, assuming that the channel openings occur randomly at a rate of $n$ events per unit time. For shallow sources with focal depths in the range of 0.1–1 km and for epicentral distances exceeding a few wavelengths from the source, Rayleigh waves dominate the signal on the vertical component of motion. The root-mean-square (RMS) amplitude of Rayleigh waves radiated by an ensemble of shallow tremor sources embedded in a homogeneous half-space is given by

$$\mathrm{RMS}(u^R) = \frac{1}{\beta\mu}\sqrt{\frac{1}{\lambda r}}\,(p + q\sin^2\psi)cL\Delta P\Delta S\sqrt{2n\Delta f} \qquad (2)$$

where $\beta$ is the shear wave velocity, $p$ and $q$ are constants depending on focal depth, $r$ is the epicentral distance, $\psi$ the azimuthal angle, $c$ a constant approximately equal to 0.2 fixed by the source model, $\lambda$ the wavelength, $\Delta S$ the area of the channel, and $\Delta f$ the bandwidth of the dominant spectral peak of tremor. Assuming $\beta \simeq 2$ km/s, $\mu \simeq 3\times10^{11}$ dyne/cm$^2$, and $(p + q\sin^2\psi) \simeq 0.1$, this equation becomes

$$L\Delta P\Delta S\sqrt{2n\Delta f} \simeq 3\times10^{18}\cdot(\text{reduced displacement}), \qquad (3)$$

where the reduced displacement is the RMS displacement corrected for geometrical spreading and instrument magnification. This is given by Fehler (1983):

$$\text{reduced displacement} = \mathrm{RMS}(u^R)\sqrt{\lambda r} = \frac{A}{2\sqrt{2}}\,\frac{\sqrt{\lambda r}}{M}, \qquad (4)$$

FIGURE 45.33.—Some characteristics of tremor recorded at Kilauea Volcano in October 1963. ***A***, Map showing seismic stations (red dots) and pit craters in region of Kilauea caldera and upper east rift zone. Dashed line marks trend of maximum ground amplitude of volcanic tremor developed during the first 14 hours of activity on October 5, 1963. Arrows show azimuth of approach of tremor obtained for individual spectral components recorded with two tripartite arrays of seismographs, one near Uwekahuna (red triangle), the other inside the caldera (stations 1, 2, and 4). ***B***, Sample of tremor spectrum obtained at station 6 at 0650 on October 5. The spectrum shown is for the vertical component of motion and has been corrected for instrument response (from Shimozuru and others, 1966).

where $A$ is the peak-to-peak amplitude of tremor and $M$ is the magnification of the seismograph at the tremor frequency.

Using the vertical displacements observed at Ohale, Foot Prints, and Kaoiki (fig. 45.33*A*), Aki and others (1977) obtained an average reduced displacement of 4 $cm^2$, from which they estimated

$$L\Delta P\Delta S\sqrt{2n\Delta f} \simeq 10^{19} \text{ dyne}\cdot\text{cm/s}. \quad (5)$$

This quantity is termed the seismic moment rate and expresses the intensity of volcanic tremor at its source. The seismic moment for the October eruption, obtained by integration of the moment rate over the entire episode of tremor activity, is about $0.5 \times 10^{24}$ dyne·cm, which is roughly equivalent to a single magnitude 5 earthquake.

The length of the double crack constituting an individual source can easily be derived by comparing the dominant frequency on the synthetic seismograms of figure 45.32 with that observed in the records, yielding $L \simeq 1.2$–$2.6$ km. The continuity of tremor at frequencies near 1 Hz (see, for example, fig. 45.33*B*) further suggests that $n$ (the event occurrence rate) cannot be very different from 1 per second, or else either the signal would become spasmodic or its frequency would be too high. Using the bandwidth $\Delta f \simeq 0.1$ Hz observed by Shimozuru and others (1966), one can easily derive from equation (5) the force $F$ applied by the fluid to open the channel,

$$F = \Delta P\Delta S \simeq 10^{14} \text{ dyne}. \quad (6)$$

The excess magmatic pressure and area over which this pressure is applied cannot be uniquely determined from the seismic data alone in this simple two-dimensional model. To obtain additional constraints on these parameters it is necessary to construct a three-dimensional model of mass transport between the two cracks. Such a model was considered by Chouet (1981), who made a detailed analysis of the motion of the ground in the near field of the tremor source postulated by Aki and others (1977).

## GROUND RESPONSE IN THE NEAR FIELD OF A FLUID-DRIVEN CRACK

Using the discrete wave number method (Bouchon, 1979), Chouet (1981) obtained the ground response in the near field of the opening crack whose source space-time dependence is depicted in figure 45.32. His model, tailored to fit the parameters derived earlier by Aki and others (1977), consists of two vertical cracks with dimensions of 1 km by 1 km separated by a channel as shown by the rectangle in figure 45.34. The space-time history of crack opening depends on the horizontal dimension of the double crack only; the opening is taken to be independent of the vertical coordinate. Thus, the situation considered is that of the opening of a vertical strip bisecting the source; however, as Chouet's model uses the source function obtained for a two-dimensional crack by Aki and others (1977), the effect of the finite vertical dimension of the crack is neglected.

Chouet (1981) calculated the ground motion for a variety of earth structures compatible with the medium under Kilauea as determined by Ryall and Bennett (1968). He considered the motion

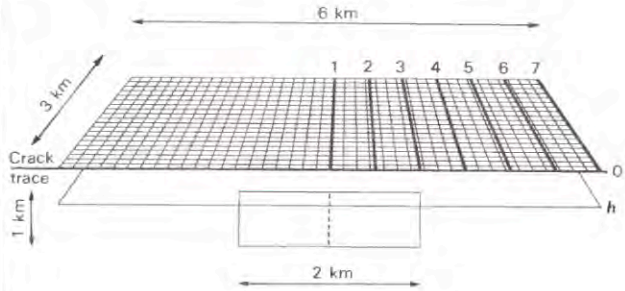


FIGURE 45.34.—Configuration of source, medium, and receivers used in computing ground motion produced by the jerky opening of a channel between two cracks. Source is represented by vertical rectangular plane, 2 km by 1 km; channel is marked by dashed vertical line bisecting the source plane. Ground displacements are computed at 861 locations over an area 3 km by 6 km adjacent to the crack trace. Separation between stations is 0.15 km in both the transverse and longitudinal directions. Heavy lines give positions of seven transverse profiles, spaced 0.5 km apart (see text). Plane at depth $h$ represents bottom of surficial layer used in three of Chouet's case studies.

in an area of 3 km by 6 km adjacent to the crack trace, calculating the displacements at 861 locations spaced every 0.15 km in the directions normal and parallel to the crack plane. The configuration of the source, medium, and receivers is shown in figure 45.34, where each node represents a station and the plane at depth $h$ represents the bottom of a surficial layer used in some of the calculations. In addition, Chouet (1981) made a detailed analysis of the synthetic seismograms obtained at selected stations along seven profiles marked by the heavy lines in the figure. These profiles, spaced 0.5 km apart, are set such that profile 1 bisects the source, and profile 7 is 2 km away from the crack tip.

The basic features of the ground response are displayed in a series of snapshots (fig. 45.35) obtained for the simple case of a fluid-filled crack with stiffness $C = 5$, buried at a depth of 0.5 km in a homogeneous half space with compressional velocity $\alpha = 3$ km/s, shear velocity $\beta = \alpha/\sqrt{3}$ and density $\rho = 2.7$ g/$cm^3$. The snapshots are taken at intervals of 0.25 s, starting 0.25 s after the failure and covering the entire duration of motion for this event. The three components $u$, $v$, and $w$ correspond to the horizontal axis along the crack plane (positive to the right in fig. 45.34), the horizontal axis normal to the crack plane (positive away from the source in fig. 45.34), and the vertical axis (positive upward).

The sequence displayed in figure 45.35 clearly shows the onset of the disturbance and the propagation of the various wave fronts over the area, leaving a pattern close to the static displacements after 3 s. Note that the first motion is compressive everywhere but the static longitudinal and vertical displacements are inward and downward immediately above the source. Note also the behavior of the peak dynamic motion in the time interval 0.5–1.5 s, which shows a pattern similar to the static deformation rather than to the first motion; that is, the maximum displacement of $w$ is negative (downward) immediately above the source, and $u$ is negative to the right of the epicenter and positive to the left of the epicenter. The crack trace

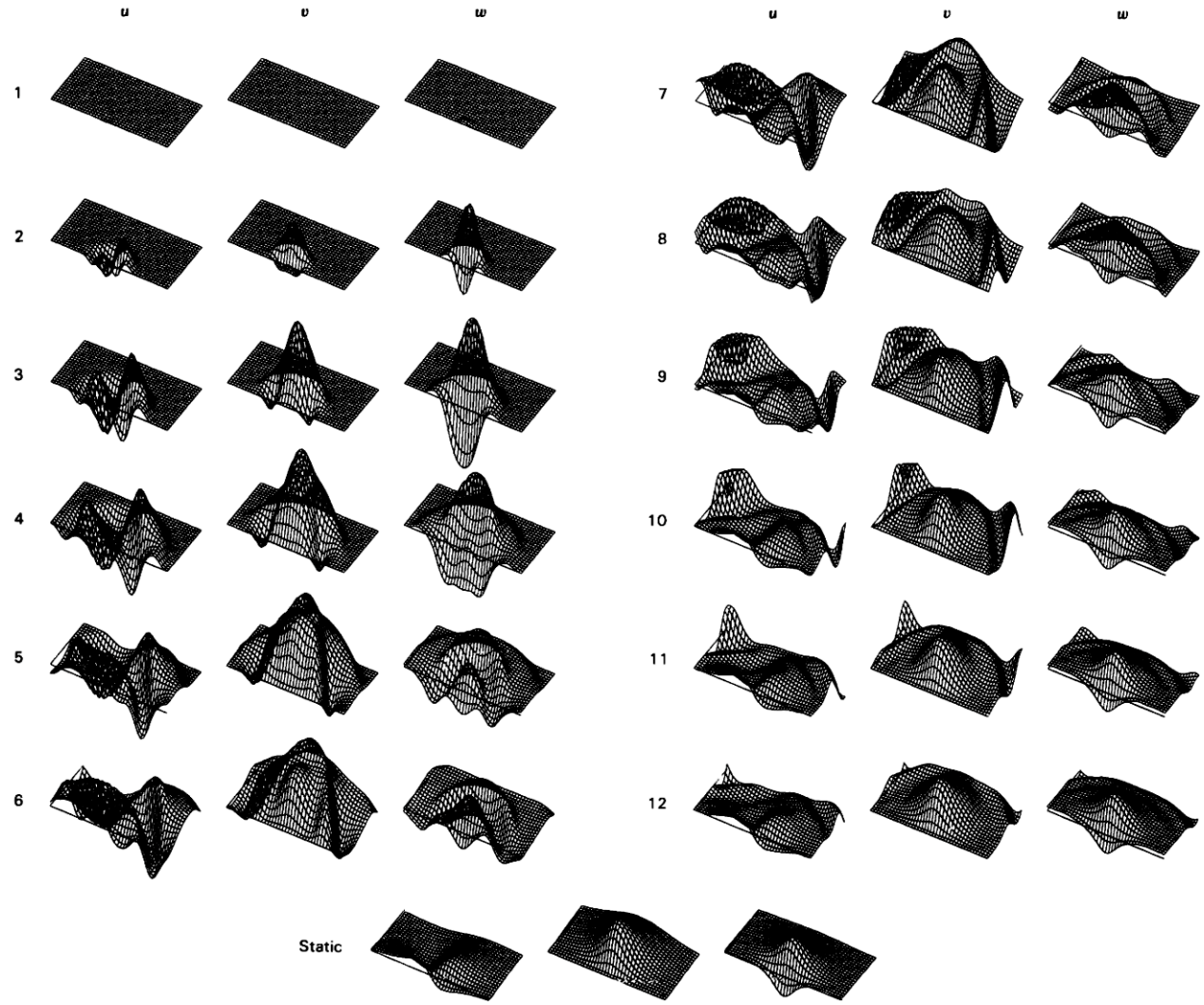


FIGURE 45.35.—Computer-generated snapshots of surface displacements produced by the jerky opening of a double crack in a homogeneous half-space. Depth to the top of the source is 0.5 km. Three components of displacement shown at top: $u$, longitudinal; $v$, transverse; and $w$, vertical. Snapshots are taken every 0.25 s, starting 0.25 s after rupture and covering the first 3 s of the event history. Final static displacement shown at bottom.

and the direction of profile 1 are both nodes for horizontally polarized shear (*SH*) motion because of the antisymmetry of the horizontal displacements about these two lines.

A useful tool in the study of tremor is the representation of the ground response in the frequency domain. This is done in figure 45.36, which displays the spectral amplitude of the ground velocity as a function of frequency and distance along individual profiles. These three-dimensional plots are obtained by sampling the entire record of motion depicted in figure 45.35 over the band of 0–3 Hz. The spectra have a characteristic structure marked by dominant and subdominant peaks at frequencies that depend on the receiver location and on the component of motion being considered. The shift of the dominant spectral peak as a function of receiver location is most pronounced on the horizontal component of velocity normal to the crack plane: the strong peak observed at low frequency eventually vanishes completely, giving place to another peak roughly one octave higher as we move along a line parallel to the crack trace. By comparison, the other two components of motion are much more stable, showing shifts of only 20–30 percent at several locations close to the source. The remarkable variation of the dominant peak observed on the transverse horizontal component reflects the rapid evolution in the composition of the wave field from compressional and shear motions that are purely vertically polarized (*P–SV* motions) along profile 1 to motions that are dominantly *SH* along profile 7. There is no strong evidence in these plots or in other models analyzed by Chouet (1981) that high-frequency energy is predominant near

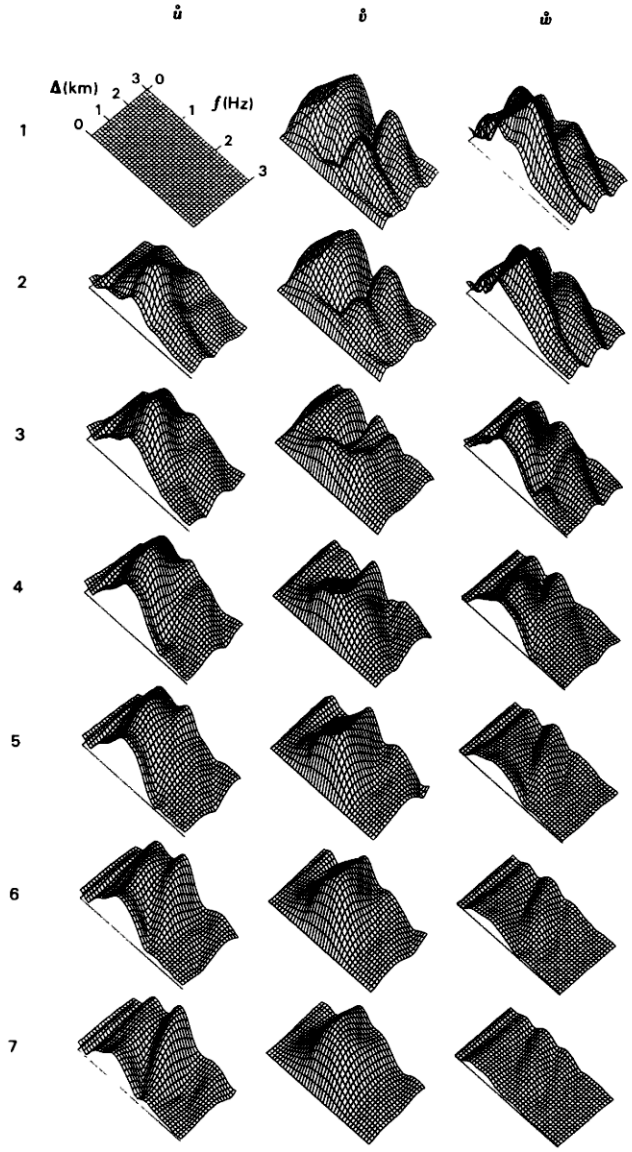


FIGURE 45.36.—Spectra of the three components of ground velocity at 21 stations along 7 profiles of figure 45.34 for a wet crack with stiffness $C=5$ opening in a homogeneous half-space. Profiles are numbered at left; components are indicated at top: $\dot{u}$, longitudinal; $\dot{v}$, transverse; and $\dot{w}$, vertical. Disposition of the plots is given at upper left: Δ, distance along the profile from the crack trace; $f$, frequency. The spectra are representative of the entire 3-s record of motion.

the source. These models, however, do not extend far enough from the crack to allow a meaningful comparison of near- and far-field spectral characteristics in the ground motion; hence they cannot fully resolve the question of the partitioning of elastic energy between radiating and nonradiating fields. The main factor contributing to the complexity of the ground-response spectra in Chouet's models is the structure of the medium. For example, the presence of a layer in the medium can affect the dominant frequency of the signal by two octaves or more on any component of motion.

Synthetic seismograms of the ground displacements are shown in figure 45.37 for the more complex response obtained in a structure that consists of a single surficial layer underlain by a half space. The layer is 0.25 km thick and has the density and compressional and shear velocities ($\rho=2.3$ g/cm$^3$, $\alpha=1.7$ km/s, and $\beta=\alpha/\sqrt{3}$, respectively), appropriate for the unconsolidated volcanic deposits found along the east rift (Ryall and Bennett, 1968; Aki and others, 1977). The parameters of the half space and depth of the source are the same as in the previous model. The displacements are shown for 56 stations located along the 7 profiles given in figure 45.34. There are 8 stations per profile, set at distances from 0 km to 3 km from the crack trace. The synthetics have been normalized by the product $\Delta P \Delta l$, the excess pressure applied in the channel times the length of the channel.

The pattern of radiation is similar to that seen earlier and depicts the evolution of the signal from a rather simple signature close to the source to a complex train of Love and Rayleigh waves, as well as multiply reflected *SH* and *SV* waves at larger ranges. Vertical motion attenuates more rapidly than horizontal motion, with the result that *SH* motion dominates at distances greater than a few source depths. The maximum radiation for this type of motion is in the azimuth bisecting the two nodal lines represented by the crack trace and profile 1. These nodal lines also correspond to maxima in the Rayleigh-wave radiation, the maximum Rayleigh motion being found in the direction of profile 1. Indeed, well-developed Rayleigh waves are conspicuous in the later part of the signal on the vertical component at distances beyond 2 km along this profile. The calculations made by Chouet (1981) indicate that these surface waves dominate the dynamic response at a distance of roughly 9 km, in agreement with the assumption made by Aki and others (1977) in computing the far-field radiation from the source. As observed earlier, the first motion is always a compression. Notice the very small amplitude of this first arrival close to the crack trace, where it is followed by a strong dilatation corresponding to the peak signal amplitude on the vertical and longitudinal components. This dilatational response is predominantly a near-field effect, and its amplitude decreases quickly at larger ranges from the source.

## IMPLICATION OF THE DYNAMIC MODEL FOR MAGMA TRANSPORT

The results depicted in figure 45.37 were applied by Chouet (1981) to the data obtained by Shimozuru and others (1966) at stations 5 and 6 in the near field of the tremor source (see fig. 45.33*A*). From these observations, and assuming the rate of channel opening to be one event per second as considered earlier by Aki and others (1977), he derived the magnitude of the force applied by the fluid $F \simeq 4-12 \times 10^{13}$ dyne, in close agreement with the result derived from the analysis of the data from the Ohale, Foot Prints, and Kaoiki stations. Using the data from figure 45.32, Chouet

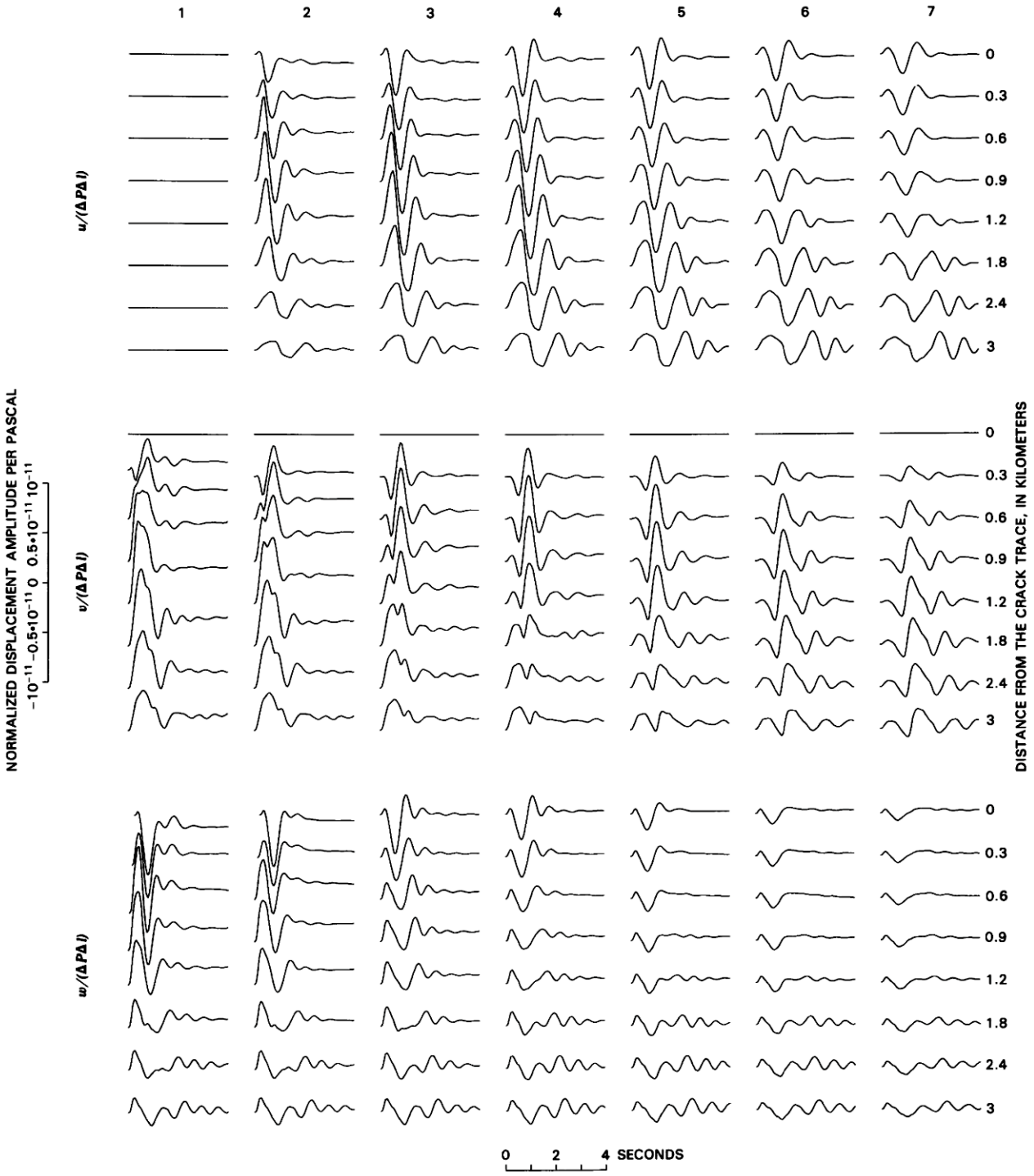


FIGURE 45.37.—Synthetic seismograms of three components of normalized ground displacement at eight stations along each of the seven profiles of figure 45.34 for the case of an opening crack in a half space with a surface layer. The source depth is 0.5 km, and the layer thickness is 0.25 km. For each component of motion marked at the left and for each profile indicated at the top of the figure, records are shown for distances of 0 (top), 0.3, 0.6, 0.9, 1.2, 1.8, 2.4, and 3 km (bottom) from the crack trace. Each record starts with the arrival of the *P* wave and is approximately 4 s long.

(1981) then determined the static channel opening, $\Delta v$, to be about 0.1 mm and the incremental volume of the source, $\Delta V$, to be about 40 $m^3$. From equation 1 he found that the assumed value $C=5$, together with the values $L=2$ km and $\mu=8.1\times10^{10}$ dyne/$cm^2$ that are compatible with the medium parameters, gives the ratio $k/d=2\times10^6$ dyne/$cm^3$. For a crack 0.5 m thick, representative of the average Hawaiian dike (Swanson and others, 1976), this requires a bulk modulus for the fluid of $10^8$ dyne/$cm^2$.

A critical result obtained by Chouet (1981) is the width of the channel opening compatible with the seismic data, which is too small to account for significant mass transfer between the two cracks. This suggests that numerous incremental openings are necessary for fluid flow to take place, and since the total area of the double crack is fixed by the observed frequency of tremor, the only way to accommodate this idea is to assume that the channel does not open over the entire height of the source at once. The assumption that the source space-time function is independent of the vertical crack dimension, which stems from the two-dimensional model of Aki and others (1977), is violated in that case, but the seismic moment estimate itself will not change, because it represents the integral of the opening over the area of the crack, a figure independent of the details of the rupture history. Therefore, the seismic estimate of $\Delta V$ derived above will not change, and the area of the channel cross section will remain the same, although the actual shape of this cross section may be different from the simple model that Chouet (1981) assumed. This, of course, is important from the standpoint of the transport problem, because the amount of fluid migrating between the two cracks is a function of this cross section.

To model the magma-transport process, Chouet (1981) assumed that the excess pressure in the magma-supplying crack is constant and that there is no outflow from the magma-receiving crack. He further assumed that the channel opens at a steady rate of one event per second and used the results from the seismic data to define the rate of increase of its cross-sectional area. Considering a Poiseuille flow, he obtained a model in which the fluid flow increases with the cumulative jerky openings, reaches a peak, and then decreases with the decrease in pressure difference between the two cracks. His result is depicted in figure 45.38 for an assumed excess pressure in the magma-supplying crack of $\Delta P=4$ MPa, a channel length of $\Delta l=0.5$ m, and fluid viscosity of $\eta=10^2$ poise. The loading time in this model is 617 s, or approximately 10 min, and the final opening of the channel is 6.17 cm; the peak volume flow rate through the channel is 929 $m^3/s$, reached 307 s after the onset of loading; the peak flow velocity is 31.5 m/s, reached 278 s into loading; and the total volume of fluid accumulated in the receiving crack during this process is about $0.2\times10^6$ $m^3$.

The subsidence of the Kilauea summit indicates that approximately $2.2\times10^7$ $m^3$ of magma was injected and remained in the east rift during the October eruption. Since the distance between the summit reservoir and Kalalua is about 25 km, a chain of about 25 1-km cracks is required to provide a continuous fluid connection to the erupting fissures. This suggests that the total amount of magma accumulated in the rift by the above process is roughly 25 times $0.2\times10^6$ $m^3$ or $5\times10^6$ $m^3$. Thus there is a significant discrepancy between the seismic estimate of the magmatic intrusion and the estimate from summit deformation. Another difficulty with the above model is the apparent disparity between the observed total duration of the tremor episode, which amounts to about 35 hours, and the duration expected for the model process. For the channel-opening rate of one event per second and loading time of approximately 10 min per crack, the model can satisfactorily explain the 150 min delay observed between the onset of subsidence at the Kilauea summit and the presumed breakout of lava in Napau Crater. The additional distance to Kalalua can perhaps account for another two or three hours of activity, but then one would expect the tremor to stop. Thus, while the postulated failure process may play a significant role in the magmatic transport, it does not easily account for the total balance of fluid transport or the duration of a tremor episode. We shall come back to this problem later.

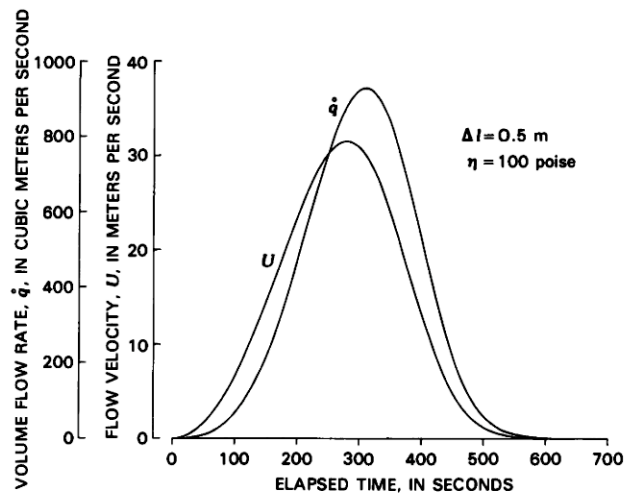


FIGURE 45.38.—Loading characteristics of dike, showing the volume flow rate and flow velocity in the channel separating the two cracks as functions of the time elapsed since onset of channel opening. Channel length ($\Delta l$) and viscosity $\eta$ are indicated.

## A KINEMATIC MODEL FOR DEEP TREMOR

We have seen from the previous model that the basic requirement for a fluid-filled crack to vibrate is for it to have a low stiffness (C) on the order of 1, a condition which can only be satisfied by assigning a value as low as $10^8$ dyne/$cm^2$ to the bulk modulus of magma; this low figure implies that there is a large amount of bubbles in the fluid. Although this requirement may seem reasonable for shallow tremor, it is unlikely to be met at depths of 30–50 km, where the confining pressure exceeds 1 GPa. Furthermore, both near-field spectra calculated by Chouet (1981) and far-field spectra calculated by Aki and others (1977) show a dependence on the radiation direction, at odds with observations made on deep tremor, which show the same period at every station.

In view of these limitations, the dynamic model of Aki and others (1977) cannot be applied to the source of deep tremor under

Kilauea. For such tremor Aki and Koyanagi (1981) proposed a new kinematic model that offers a direct relation between magmatic transport and tremor amplitude and also provides an identical period at every station. Because the high ambient pressure in the source region should prevent the formation of a cavity during any mode of crack vibration, they considered a model of transport in which the total volume of magma remains constant. Their two-dimensional source, depicted at the top of figure 45.39*A*, consists of a pair of cracks of lengths $L/2$ linked by a narrow channel, a situation reminiscent of the earlier model. The channel opens in response to excess pressure buildup in the left crack, allowing magma to migrate rapidly into the crack at the right. The successive snapshots of the source shown in the figure graphically depict the deformation of the two cracks during magma transport. To simulate this process, Aki and Koyanagi (1981) assumed a uniform-displacement model, in which the magma migrates with a constant velocity $a$ and the tensile displacement of the crack walls $\pm\Delta v$ associated with this migration is steplike in character. The far-field radial displacement produced by this kinematic source has a Fourier transform given by

$$u^r(\vec{R},\omega)=\frac{\lambda+2\mu\sin^2\theta}{4\pi\rho\alpha^3R}W\Delta v\frac{1}{i\omega}\cdot \left[\left(1-\exp\left[-i\omega\frac{L}{2}\left(\frac{1}{a}-\frac{\cos\theta}{\alpha}\right)\right]\right)\left(\frac{1}{a}-\frac{\cos\theta}{\alpha}\right)^{-1} -\left(1-\exp\left[-i\omega\frac{L}{2}\left(\frac{1}{a}+\frac{\cos\theta}{\alpha}\right)\right]\right)\left(\frac{1}{a}+\frac{\cos\theta}{\alpha}\right)^{-1}\right], \quad (7)$$

where $\vec{R}$ is the observation point, $R=|\vec{R}|$, $\theta$ is the angle between the direction of magma movement and the direction of the observation point, $W$ the crack width (in the direction perpendicular to the plane of figure 45.39*A*), $\omega$ the frequency, $\rho$ the density, and $\lambda$ the first Lamé elastic modulus.

The pulse shape corresponding to the large bracketed term premultiplied by $1/(i\omega)$ in equation 7 is shown in figure 45.39*B*. The total duration of the signal is $\Delta t=(L/2)[(1/a)+(\cos\theta/\alpha)]$, and the seismic moment of the source is zero because there is no net change of volume. To account for tremor sustained over many cycles, Aki and Koyanagi (1981) arbitrarily assumed that the magmatic injection is a periodic process with a period $T\simeq L/a$. The signal during $T-\Delta t$ was assumed to be zero.

This model offers the following simple relation between the volume flow rate of magma and the observed seismic displacement:

$$\dot{q}=WL\Delta v/(2T)\simeq aW\Delta v/2. \quad (8)$$

For an order-of-magnitude estimate of the magma transport associated with the source of deep tremor, Aki and Koyanagi (1981) assumed that the observed free-surface displacement is composed mainly of $P$ waves. Neglecting anelastic attenuation, they defined the reduced displacement for body waves as

$$\text{reduced displacement}=RMS(u^r)\cdot R=\frac{A}{2\sqrt{2}}\frac{R}{M}, \quad (9)$$

where the root-mean-square amplitude of $P$ waves obtained from equation 7 is

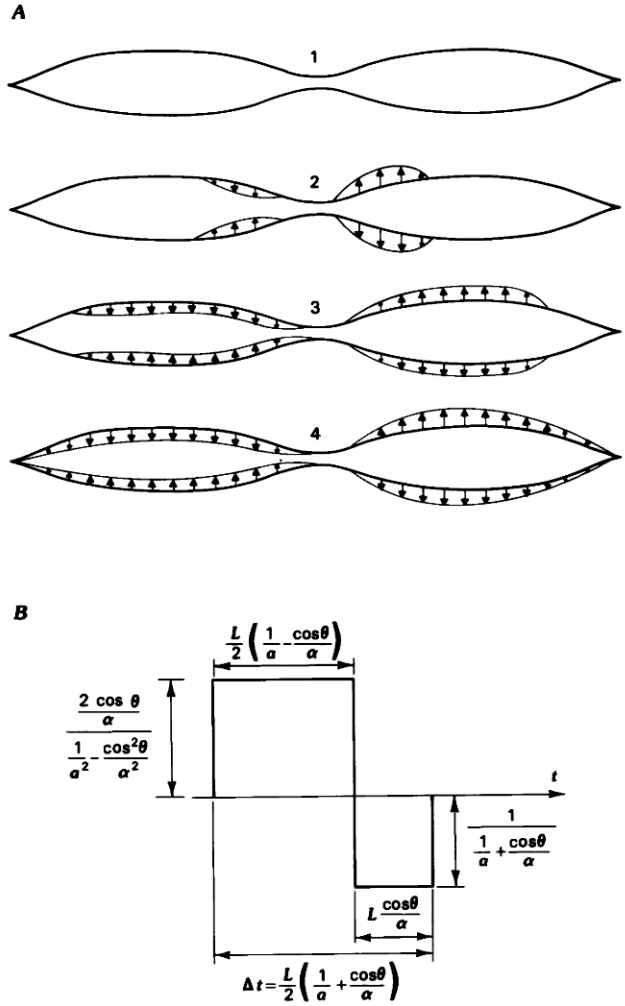


FIGURE 45.39.—Magma transport between two cracks connected by a channel. ***A,*** Schematic view of magma transport from the crack on the left to the crack on the right. Arrows indicate change of crack shape as magma movement spreads over whole crack area. ***B,*** Far-field waveform of $P$ waves radiated from the source represented by this double crack (see text for explanation).

$$\mathrm{RMS}(u^r)=\frac{\lambda+2\mu\sin^2\theta}{4\pi\rho\alpha^3R}W\Delta v\cdot \left(\frac{2\cos\theta}{\alpha}-\frac{L}{T}\right)^{1/2}\left(\frac{1}{a^2}-\frac{\cos^2\theta}{\alpha^2}\right)^{-1/2}, \quad (10)$$

which corresponds to equation 5 of Aki and Koyanagi (1981), corrected for a missing exponent of ½. Assuming $\lambda=\mu$, $\theta=45°$ and $\alpha/a=4$, we obtain from equations 8, 9, and 10

$$\dot{q}\simeq 20\alpha\cdot(\text{reduced displacement}), \quad (11)$$

which, for $\alpha=8$ km/s, gives a flow rate in $cm^3/s$ of $1.6\times10^7$ times the reduced displacement. The reduced displacement is plotted

against the dominant frequency of deep tremor in figure 45.40, which yields the relation that reduced displacement is about $(1/T)^2$, from which one can obtain a quantitative estimate of the flow. For example, tremor with a period around 0.5 s has a reduced displacement of 30 $cm^2$, which corresponds to a flow of $0.5 \times 10^9$ $cm^3/s$ or $5 \times 10^2$ $m^3/s$. The slope of $-1/2$ depicted in this figure can be explained if strong and weak tremor are dynamically similar, or, in other words, if the nondimensional products made of physical parameters are the same for strong and weak tremor. While the observed similarity between large and small earthquakes (Aki, 1972; Kanamori and Anderson, 1975) implies a constant stress drop, independent of earthquake size, the similarity for deep tremor implies a constant excess pressure, independent of crack size. This similarity, however, breaks down for shallow tremor, which is clearly nonfractal (Mandelbrot, 1977), because the period appears fixed, independent of signal amplitude, for a given episode (Shimozuru and others, 1966; Fehler and Chouet, 1982; Fehler, 1983). It is interesting to note that dike widths have a fixed average value for a given area. For example, the average width is 4 m in Iceland, 1.8 m in Scotland, 6 m at the Columbia River (Williams and McBirney, 1979), and 0.5 m at Kilauea (Swanson and others, 1976). Thus, dikes near the surface appear to be nonfractal. The data of figure 45.40, therefore, provide an exceptional observation in support of a trend toward self-similarity for deeper magmatic processes.

Aki and Koyanagi (1981) made a systematic search for deep tremor episodes during the period 1962–1979 using data from stations around Kilauea. These data consist of narrow-band smoked-paper records that predominantly sample the longer-period tremor. Selecting records with duration longer than about 10 min and peak-to-peak ground motion larger than a few hundredths of a micrometer, they tabulated the starting and ending time of each episode, as well as the period and average peak-to-peak amplitude of tremor for every 5-min interval of the seismic trace. From these data they derived the reduced displacement assuming an average distance of 52 km obtained from sources of tremor episodes with known locations. Their results are summarized in table 45.3, and the average yearly duration of tremor with calculated reduced displacement larger than a specified value is shown in figure 45.41. The duration decreases exponentially with increasing displacement, reflecting the predominant length scale sampled by the narrow-band records. These long-period tremors represent the dominant contribution to the observed surface displacements.

To determine the cumulative reduced displacement over the 18-year period, Aki and Koyanagi (1981) took the reduced displacement for each interval, multiplied it by the duration of the interval, and summed over successive episodes cumulatively with time. The result, shown in figure 45.42, indicates a steady accumulation of reduced displacement with time. This plot can easily be converted to cumulative magma flow as a function of time, in which case the left-hand vertical coordinate becomes cumulative magma flow in units of $1.6 \times 10^{13}$ $cm^3$, indicating a total magma flow of $10^{14}$ $cm^3$, or 0.1 $km^3$ in 18 years. This is about 1/20 of the 1.8 $km^3$ expected from Swanson's (1972) estimate of 0.1 $km^3$ per year, and about 1/5 of the erupted lavas as shown on the right hand side of the figure.

The low estimate of magma ascent obtained by Aki and Koyanagi seems to suggest that a significant volume of magma is transported through Kilauea without generating measurable tremor. Although one cannot discount the possibility that part of the magma may be transported in a steady flow that would not generate any tremor at all, a more plausible explanation may be that the pressure fluctuations associated with the unsteadiness of the flow are too small to be observable. To see the implication of this result in terms of the excess magmatic pressure involved at the source, we have to deal with the energetics of the process of tremor generation.

According to Aki (1984), from simple energy conservation we can derive the following relation between the reduced displacement for body waves and the root-mean-square pressure fluctuation, RMS($\Delta$P), applied over the volume $V$ of the source:

$$\mathrm{RMS}(u^r)R = \frac{1}{2\pi}\left(\frac{1}{Q_s}\right)^{1/2}\left(\frac{V}{2f\alpha\rho k}\right)^{1/2}\mathrm{RMS}(\Delta P), \qquad (12)$$

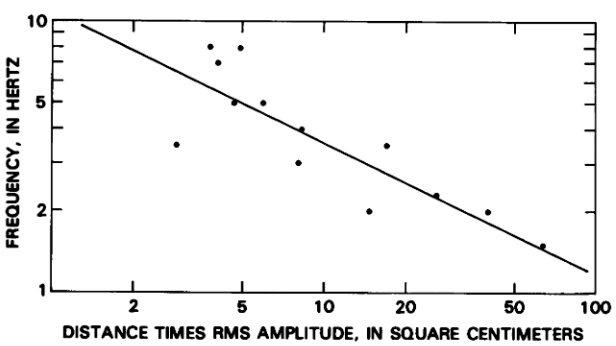


FIGURE 45.40.—Relation between tremor period and reduced displacement for body waves. The slope of $-1/2$ can be explained by the similarity between large and small cracks, implying a constant excess pressure independent of crack size.

TABLE 45.3.—*Duration of tremor at Kilauea per year, 1969–1979*

[After Aki and Koyanagi, 1981; RD, reduced displacement, in $cm^2$]

| Year | Duration of tremor (min) | | | |
|---|---|---|---|---|
| | RD≥5 | RD≥10 | RD≥15 | RD≥20 |
| 1962 | 316 | 164 | 90 | 35 |
| 1963 | 250 | 83 | 43 | 0 |
| 1964 | 516 | 213 | 127 | 85 |
| 1965 | 234 | 93 | 63 | 25 |
| 1966 | 152 | 72 | 27 | 17 |
| 1967 | 312 | 108 | 35 | 25 |
| 1968 | 425 | 241 | 117 | 69 |
| 1969 | 401 | 218 | 126 | 76 |
| 1970 | 438 | 241 | 109 | 61 |
| 1971 | 358 | 189 | 136 | 46 |
| 1972 | 505 | 310 | 141 | 70 |
| 1973 | 305 | 142 | 50 | 25 |
| 1974 | 214 | 80 | 39 | 19 |
| 1975 | 153 | 50 | 7 | 7 |
| 1976 | 352 | 160 | 93 | 62 |
| 1977 | 231 | 77 | 30 | 15 |
| 1978 | 314 | 206 | 137 | 83 |
| 1979 | 267 | 121 | 81 | 36 |
| | 319 | 154 | 81 | 42 |

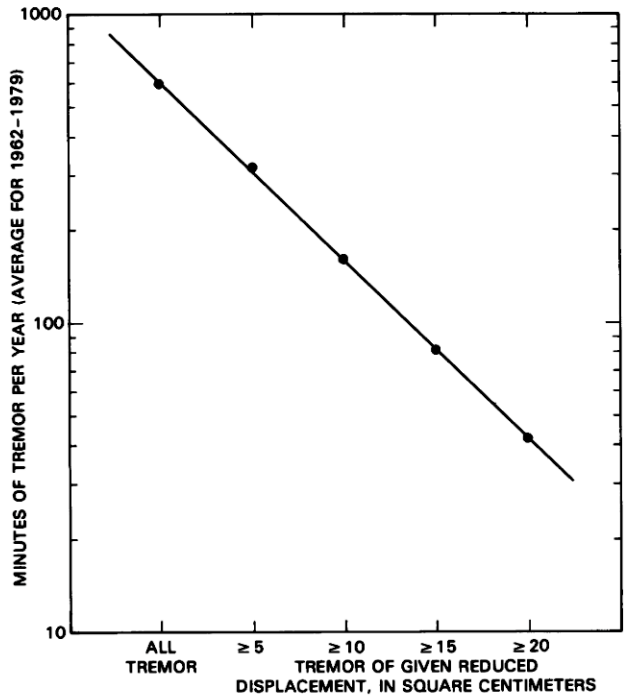


FIGURE 45.41.—Duration of tremor recorded per year with reduced displacements greater than specified values.

where $f$ is the dominant frequency of tremor and $Q_s$ is the quality factor corresponding to the radiation loss. This factor is given by

$$\frac{1}{Q_s} = \frac{1}{Q} - \frac{1}{Q_\eta}, \tag{13}$$

where $Q$ is the apparent quality factor and $Q_\eta$ is the quality factor due to magma viscosity. The apparent quality factor can be measured directly from the observed spectra of tremor as $Q \simeq f/\Delta f$. For Hawaiian tremor, $Q$ is about 10 and the quantity $(1/Q_s)^{1/2}$ is on the order of 0.1. The observed reduced displacements (fig. 45.40) themselves range from 1 to $10^2$ cm$^2$ in the frequency interval 1–10 Hz. Since $f = a/L$ in the above kinematic model, one can obtain $L$ once the velocity of the magma front is known. Assuming $a = 2$ km/s (Aki and Koyanagi, 1981), the observed frequencies correspond to single crack lengths in the range of 0.1–1 km. For a rough order-of-magnitude estimate of the volume of fluid involved at the source, we further assume that the crack is circular and has a thickness on the order of 1 m, from which we obtain $V$ in the range of $10^{10}$–$10^{12}$ cm$^3$. Other parameters in equation 12 that are easily estimated are $\rho \simeq 3$ g/cm$^3$, $\alpha \simeq 8$ km/s and $k \simeq 10^{11}$ dyne/cm$^2$ (assuming no bubbles in magma). This yields RMS($\Delta P$) = $8 \times 10^4$–$2.5 \times 10^5$ Pa, indicating that the minimum root-mean-square pressure fluctuation required at the source to generate observable tremor is on the order of $10^5$ Pa for the case of deep tremor in Hawaii.

The above kinematic model implies an actively participating fluid in the tremor-generation process, and in that sense it is a precursor to the more elaborate models unifying the fluid dynamics and elastodynamics that we discuss in the next section.

## KINEMATIC AND DYNAMIC MODELS WITH ACTIVE FLUID PARTICIPATION

Although the injection model of Aki and others (1977) is in general agreement with various seismic observations, it does not provide a ready explanation for the sharply peaked nature of the tremor spectrum. The observed spectral peaks are, in fact, much narrower than the theoretical peak derived from the model (compare, for example, the bandwidth of the dominant peak of tremor shown in figure 45.33*B* with the synthetic data of figure 45.36). A similar characteristic is displayed by the long-period events of Mount St. Helens (Fehler and Chouet, 1982), which last much longer than the vibrations triggered by the opening channel, a difference that cannot be ascribed to path or station-site effects. In addition, figure 45.36 shows a marked dependence of the spectral characteristics of the tremor model on radiation direction, in contrast to observations, which consistently indicate that the tremor spectrum is only weakly dependent on azimuth. The negligible attenuation with distance displayed in figure 45.37 does not easily fit the observations either.

To resolve these discrepancies, it is necessary to include the fluid as an active element in the vibration of the source. The idea that the excitation of fluid motion plays an important role in the origin of tremor is not new; it actually has been advocated by volcanologists for many years, and several models have recently been proposed (Kamo and others, 1977; St. Lawrence and Qamar, 1979; Wada, 1980, 1981; Ferrick and others, 1982; Ferrick and St. Lawrence, 1984). In these models , however, analysis of the coupling of the fluid motion to the elastic medium surrounding the fluid body has not been sufficiently quantitative for comparison with seismic observations.

Aki and Koyanagi (1981) proposed a kinematic model that includes a simple relationship between the radiated elastic field and magmatic transport, as discussed in the previous section. Recently, Crosson and Bame (1985) considered a purely elastic model, in which a spherical magma chamber buried in a homogeneous isotropic elastic full-space is excited by excess pressure applied over the wall of a small spherical cavity at the center of the chamber. This model is an extension of the cavity model of Blake (1952) and the liquid sphere model of Shima (1958), and it simulates a sudden gas expansion in the magma. The magmatic fluid is treated as an elastic solid with very low rigidity and with damping introduced by adding a complex part to the shear modulus. The simplicity of the model allows a closed-form analytical solution for the radial displacement, which depicts a peaked spectrum and an oscillating decaying seismogram. The fundamental mode is a pure radial mode in which the fluid and solid participate in the motion with phase synchronization. The fundamental frequency becomes insensitive to the size of the magma chamber when both inner and outer radii are greater than a specified value, but depends significantly on the shear velocity of the magma. Thus, the fundamental resonant radial-oscillation mode of this source is dependent on the existence of a compliant gas or

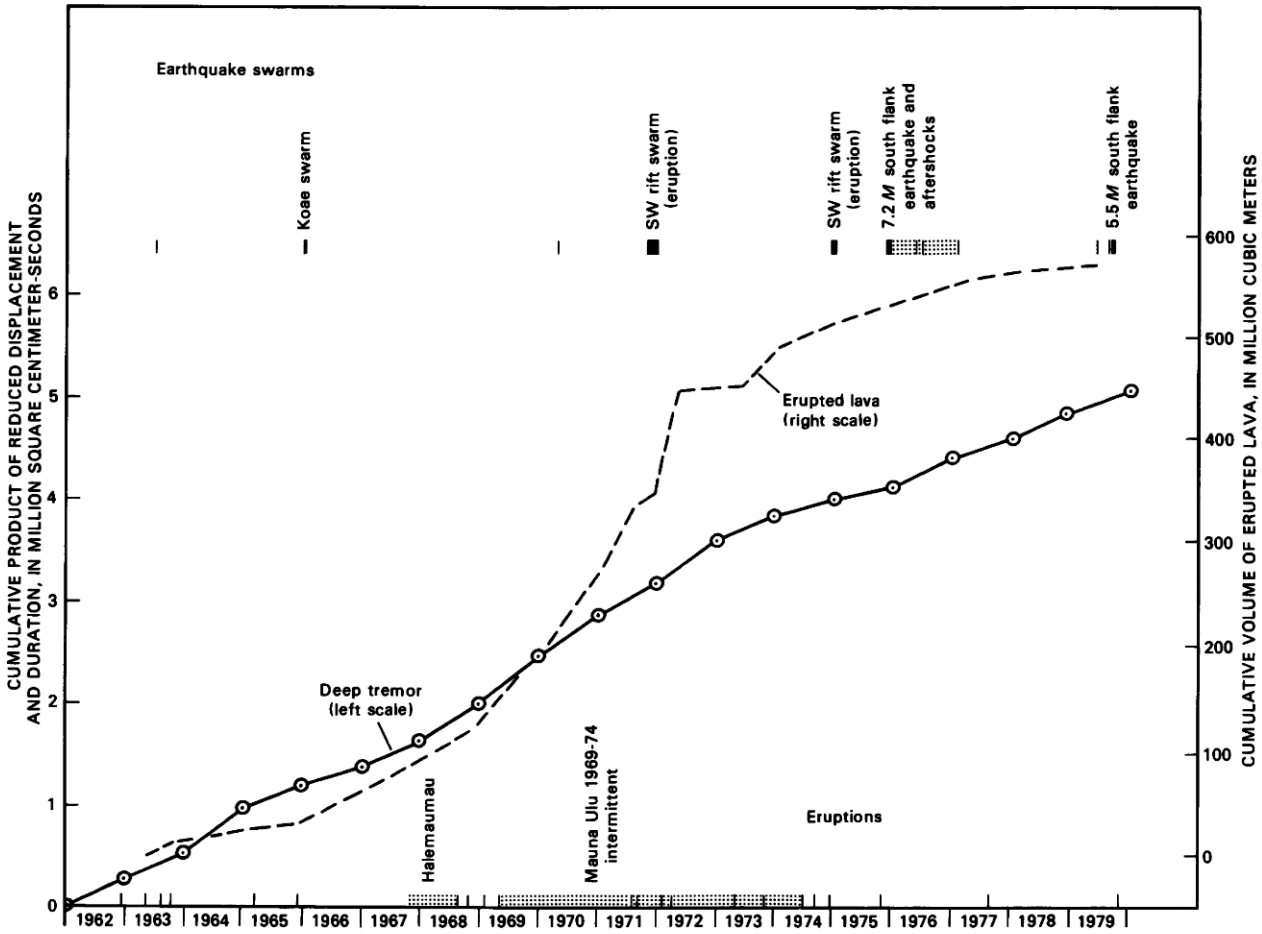


FIGURE 45.42.—Cumulative reduced displacement of deep tremor and cumulative volume of erupted lava at Kilauea, 1962–1979. According to the kinematic model of Aki and Koyanagi (1981), each unit of the vertical coordinate of reduced displacement corresponds to cumulative magma flow of about $16 \times 10^6$ $m^3$. Major earthquake swarms and eruptive activities also shown for comparison. Dotted line at the bottom marks periods of prolonged eruptive activity with frequent episodes of lava output during the Halemaumau and Mauna Ulu eruptions. Dotted pattern at the top marks aftershocks of $M$=7.2 south flank earthquake.

froth region of significant extent inside the magma chamber. This dependence of the excitation on the source stiffness is similar to the results obtained by Aki and others (1977) and Chouet (1981). However, the extreme simplicity of this model's geometry does not allow a realistic approach to the magmatic transport problem. Furthermore, the model does not allow fluid flow, because the equations for the transfer of mass and momentum in the fluid are not specifically considered. The physical nature of effective cavity formation for a gas phase over dimensions of meters, which is required to produce the frequencies observed for long-period events and tremor, also remains an elusive question. Finally, the model does not explain the driving force of tremor and requires a source of pulsation in the gas that is difficult to realize by simple physical means.

An initial attempt at unifying the fluid vibration and seismic radiation in the tremor source was made by Chouet (1985), who considered the motion of a magmatic pipe excited by the sudden flashing of ground water to steam as magma intrudes the phreatic layer. This model, displayed in figure 45.43, consists of a vertical pipe shut at the bottom by a horizontal disk and terminated at the top by a gas-filled hemispherical cavity acting as an explosive trigger. The source of tremor is the acoustic resonance of the fluid-filled conduit triggered by the excess gas pressure; the motion of the source is expressed in terms of the excitation of the well-known organ-pipe modes, while the bandwidth of these modes is determined from the combined losses due to viscous attenuation in the fluid and elastic radiation in the solid. Two assumptions are implicit in this model: first, that the volume of gas is large enough to sustain a pressure

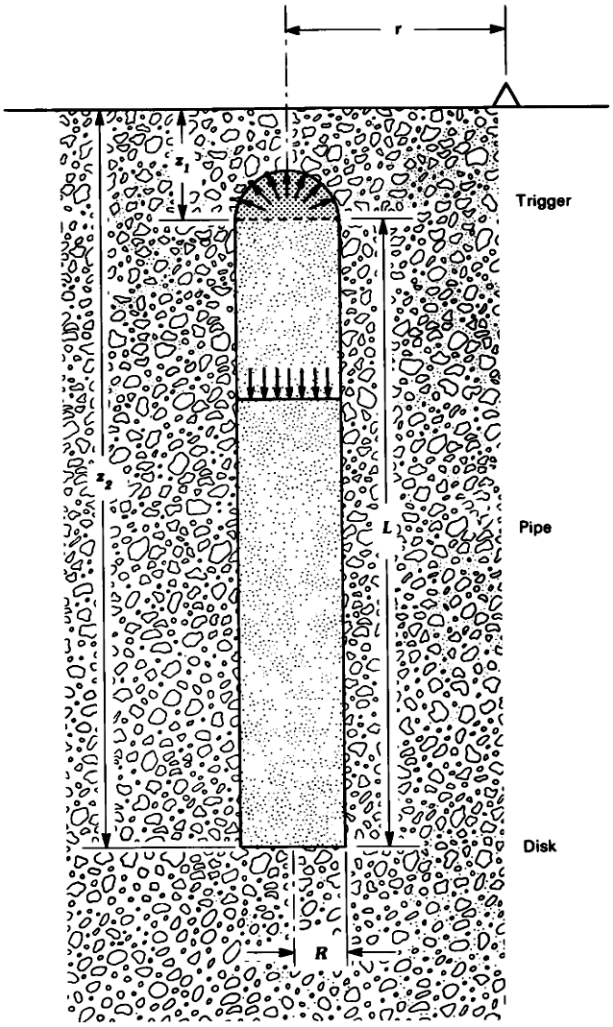


FIGURE 45.43.—Configuration of source, medium, and receiver used in computing ground motion produced by the excitation of a fluid-filled pipe. The composite source consists of a vertical conduit of radius $R$ and length $L$ capped by a hemisphere and shut at the bottom by a horizontal disk at depth $z_2$. Pipe is filled with liquid; hemispherical cap contains gas. Depth to pipe inlet is $z_1$, and receiver is located at epicentral distance $r$.

pulse of sufficient magnitude to generate the observed excitation; second, that the volume of magma is large enough to allow a high-Q vibration. In relation to the magmatic transport problem, this seismic model represents the characteristic scale length of a magmatic conduit between changes in its cross section or direction. The model is thus applicable to long-period events or tremor with a stable dominant frequency. It bears some similarities to the model of Crosson and Bame (1985) in that it incorporates a gas-filled chamber; however, this is done only for the source excitation and does not affect in a fundamental manner the determination of the oscillating frequency as in Crosson and Bame's model.

By restricting his analysis to seismic wavelengths that are large compared to the pipe diameter and demonstrating that the damping of the fluid system due to elastic radiation is trivial at low frequencies, Chouet was able to treat the problem of seismic radiation separately from that of the fluid dynamics, thus considerably simplifying the analysis of tremor generation. The space-time histories of the flow pressure and velocity, derived from the solution of the equations for the conservation of mass and momentum in the fluid, are given in figure 45.44, which also shows the triggering event, a pressure transient of the form $P_0 = \Delta P \exp[\ln(t) - (t/T)]/\exp[\ln(T) - 1]$ applied at the pipe inlet (fig. 45.44*A*). The pertinent source parameters, listed in table 45.4, are taken to be representative of a dacitic magma such as is involved in the current activity at Mount St. Helens.

Examples of the ground response to the excitation of the magmatic pipe, calculated by the discrete-wave-number synthetic method, are shown in figure 45.45 for 18 stations at epicentral distances of 0–10 km. The situation considered is that of a pipe buried at a depth of 50 m in a homogeneous half-space with the compressional velocity $\alpha = 4$ km/s and shear velocity $\beta = \alpha/\sqrt{3}$. The records start with the *P*-arrival from the trigger and cover most of the duration of the ground motion at each location.

The four traces displayed for each station represent, from left to right, the contributions from the trigger source, the pipe source, and the disk source, and the composite source from the superposition of these three elements; the two components of the displacement are identified at the top. No *SH* waves are present in the signal because of the isotropic distribution of the equivalent body forces representing the source in the horizontal plane. Furthermore, no clear shear-wave arrival can be recognized in the ground response, because the contributions of the *SV* waves are completely buried in the complex signature generated by the source.

The first motion due to the trigger and pipe elements is always a compression. That due to the disk, on the other hand, shows up as a dilatation everywhere, as can be expected from the downward orientation of the force applied by the fluid at the bottom of the conduit. As this arrival is delayed with respect to the others by an amount equal to the travel time of the tube wave over the length of the pipe, the onset of the signal from the composite source is always a compression. The trigger and pipe elements dominate the ground response in the immediate vicinity of the source, producing a pulse-like waveform characteristic of the disturbance exciting the source (see fig. 45.44*A*). The contributions of these sources, however, diminishes rapidly with increasing epicentral distance, so that at distances exceeding 250 m the free-surface response effectively reflects the repeated hammering of the fluid at the bottom of the conduit. The resulting motion then evolves into a well-developed harmonic wavetrain dominated by Rayleigh waves at distances greater than 3 km.

The spectral characteristics of the ground response are given in figure 45.46, which displays contour maps of the displacement spectral amplitude versus frequency and epicentral distance. Both components of motion display a maximum amplitude at 0 Hz within

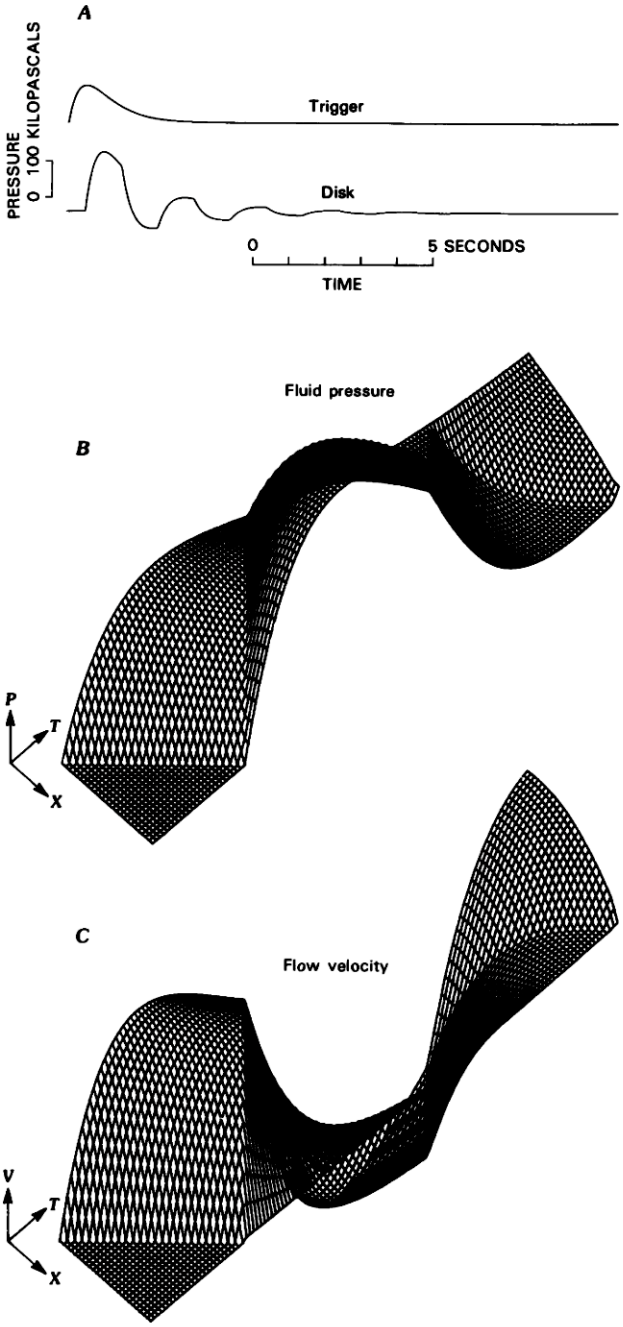


FIGURE 45.44.—Time variation of pressure and flow velocity for the elements of the composite tremor source. ***A,*** Pressure-time functions for the trigger and disk sources. ***B,*** Space-time dependence of the fluid pressure for the pipe source. Peak pressure is 160 kilopascals. ***C,*** Space-time dependence of the flow velocity for the pipe source. Peak velocity is 2.4 cm/s.

TABLE 45.4.—*Source parameters for the pipe model of tremor*

| | |
|---|---|
| Fluid properties | |
| Viscosity | $\eta = 2 \times 10^5$ N·s/m$^2$ ($= 2 \times 10^6$ poise) |
| Density | $\rho = 2.7$ g/cm$^3$ |
| Tube wave velocity | $a = 1.6$ km/s |
| Dimensions of pipe | |
| Radius | $R = 25$ m |
| Length | $L = 800$ m |
| Excess pressure | $\Delta P = 10^5$ Pa ($= 10^6$ dyne/cm$^2$) |
| Rise time of trigger pulse | $T = 0.5$ s |

100 m of the epicenter. Dominant and subdominant peaks are observed at frequencies near 0.5, 1.5, 2.5, and 3.5 Hz, corresponding to the organ-pipe modes of the conduit. As noted in figure 45.45, the fundamental mode of the source is indistinct in the spectra obtained at short distances; in fact, it is not until the range exceeds a few hundred meters that this mode becomes a dominant feature. As for the dominant mode, the higher harmonics are not strongly developed in the epicentral area. The dominant frequency is slightly lower on the vertical component than on the horizontal one, and the vertical spectrum has more variability at higher frequencies than its horizontal counterpart. The spectral peaks are much narrower than those produced by the model of Aki and others (1977). The importance of the fluid viscosity in the shaping of the spectral response in Chouet's model is well demonstrated in figure 45.47 for a station located at a range of 200 m. A lower viscosity produces a more peaked spectrum and amplifies the dominant and subdominant peaks on both components of motion.

The analysis made by Chouet has interesting implications for the radiation and viscous damping losses of the fluid system. For the cylindrical magma column considered, the radiation loss is proportional to the square of the pipe radius, while the loss related to viscous damping is inversely proportional to the same factor. Thus, the relative importance of the two loss mechanisms (see equation 13) is critically dependent on the geometry of the magma reservoir. The relative importance of the pipe and disk elements of the source in shaping the ground response is likewise a function of the conduit cross section. Since the observed $Q$ represents the sum of these losses, a unique measurement of $Q$ from the amplitude decay of long-period events cannot separate the two mechanisms. The radiation loss, however, may be estimated from seismic measurements made in the far field, while the total energy of vibration in the fluid can be determined by the measurement of near-field motion trapped in the vicinity of the oscillating fluid. In fact, the synthetic seismograms of figure 45.45 show that the displacement attributed to the pipe is of the nature of near-field motion, while that due to the disk is of the nature of far-field motion. Changes in the conduit cross section would change the relative contributions of the pipe and disk elements, thus suggesting the possibility of determining the geometry of the source, as well as the radiation loss and in-situ magma viscosity from a comparison of near- and far-field observations.

A further step toward understanding the interaction of the fluid and solid in the tremor source was taken by Chouet and Julian (1985), who extended the original finite-difference crack model of Aki and others (1977) by improving the boundary conditions

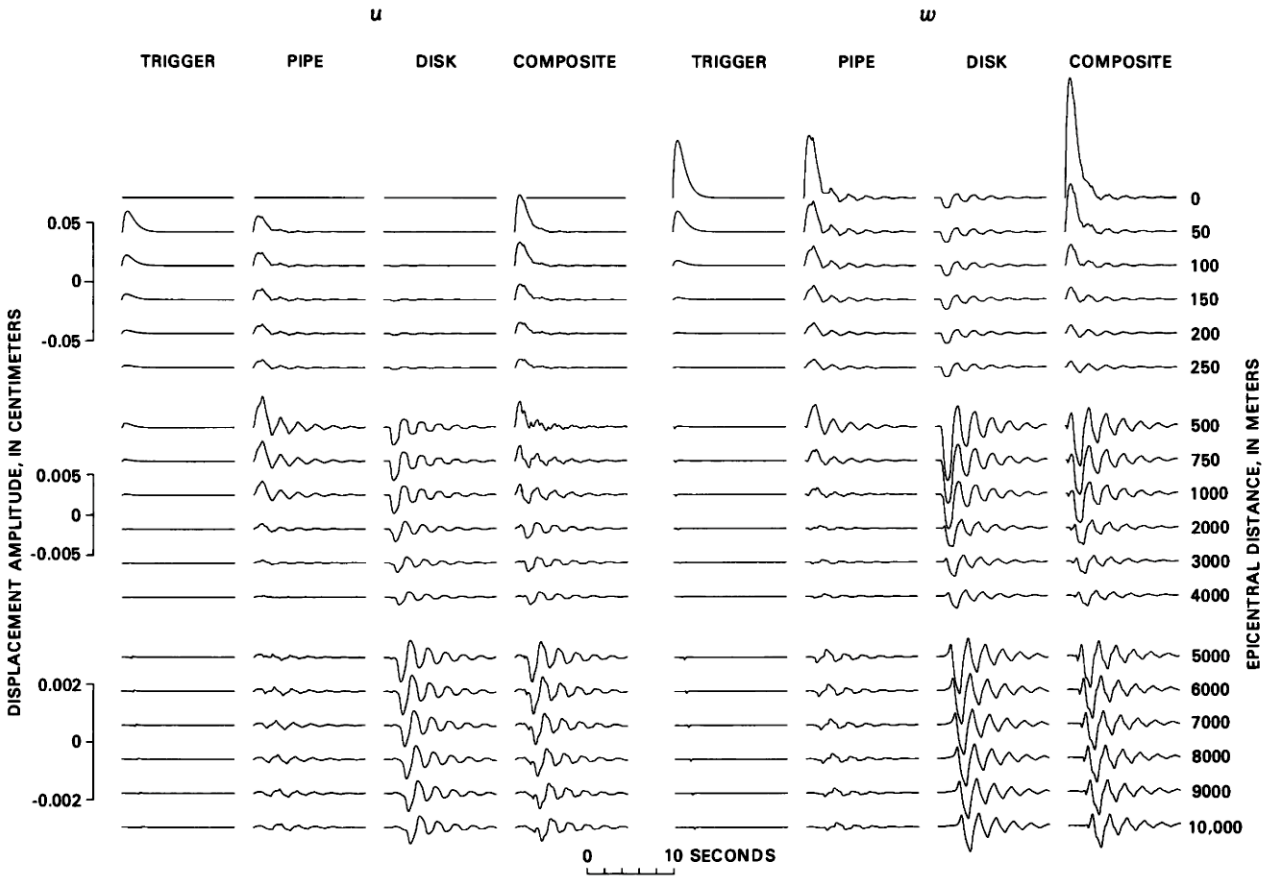


FIGURE 45.45.—Synthetic seismograms of the two components ($u$, horizontal; $w$, vertical) of ground displacement resulting from excitation of a fluid-filled pipe buried in a homogeneous half-space. Depth to pipe inlet is 50 m, and records are shown for 18 stations at increasing epicentral distances. Four sources are represented: the hemispherical cap that triggers the motion of the fluid column; the pipe; the disk shutting off the bottom of the conduit; and the composite source resulting from superposition of these three. Each record starts at a time corresponding to arrival of the $P$-wave from the trigger and lasts 13 s.

applied in the plane of the crack and by coupling the equations for mass and momentum transfer in the fluid to the elastodynamic equations in the solid. As in Aki and others (1977), the model of Chouet and Julian consists of a two-dimensional crack with thickness much smaller than the seismic wavelengths of interest and containing a fluid whose bulk modulus is low because of bubbles. They follow Aki and others (1977) in formulating the initial conditions and assume that the crack tip suddenly propagates by a small increment in response to excess fluid pressure. The area of the crack thus suddenly increases by $\Delta S$ and the dynamic motion of the crack surface triggered by the rupture is considered as the response of the crack to a pressure step of amplitude $\Delta P$ applied over this incremental area. Although the magma has a finite viscosity in this model, the rate of fluid flow into the expanding crack tip is considered to be instantaneously equal to the rate of increase of the crack-tip volume, and the rupture of the crack tip over the area $\Delta S$ is also assumed to be instantaneous. Thus, the rate-limiting effect of the viscosity in the propagation of the fracture is not taken into account, and the details of the coupling between the acoustic and elastic processes at the expanding crack tip are greatly simplified.

The basic features of the solutions obtained by Chouet and Julian (1985) are displayed in figures 45.48–45.50. These examples are given for a Poisson ratio of 0.25 in the solid and for a ratio $k/\mu$ of 0.1. The behavior of the fluid is characterized by three dimensionless parameters, namely the crack stiffness $C=(k/\mu)(L/d)$, seen previously, the viscous damping loss $F=6(\eta/k)(a/d)$, and the velocity ratio $G=\alpha/a$, where $\eta$ is the viscosity and $a$ the acoustic velocity of the fluid.

The normal displacement of the crack surface is shown in figure 45.48 for an increment of the crack tip $\Delta l=L/20$. As in figure 45.32, the variable plotted is a dimensionless combination of the applied pressure step, the crack length, and the rigidity and compressional velocity of the solid. Of particular interest is the direction of the dominant motion following the initial response of the wall at various locations on the crack surface; the initial motion at the expanding tip is an opening, but at other locations the main

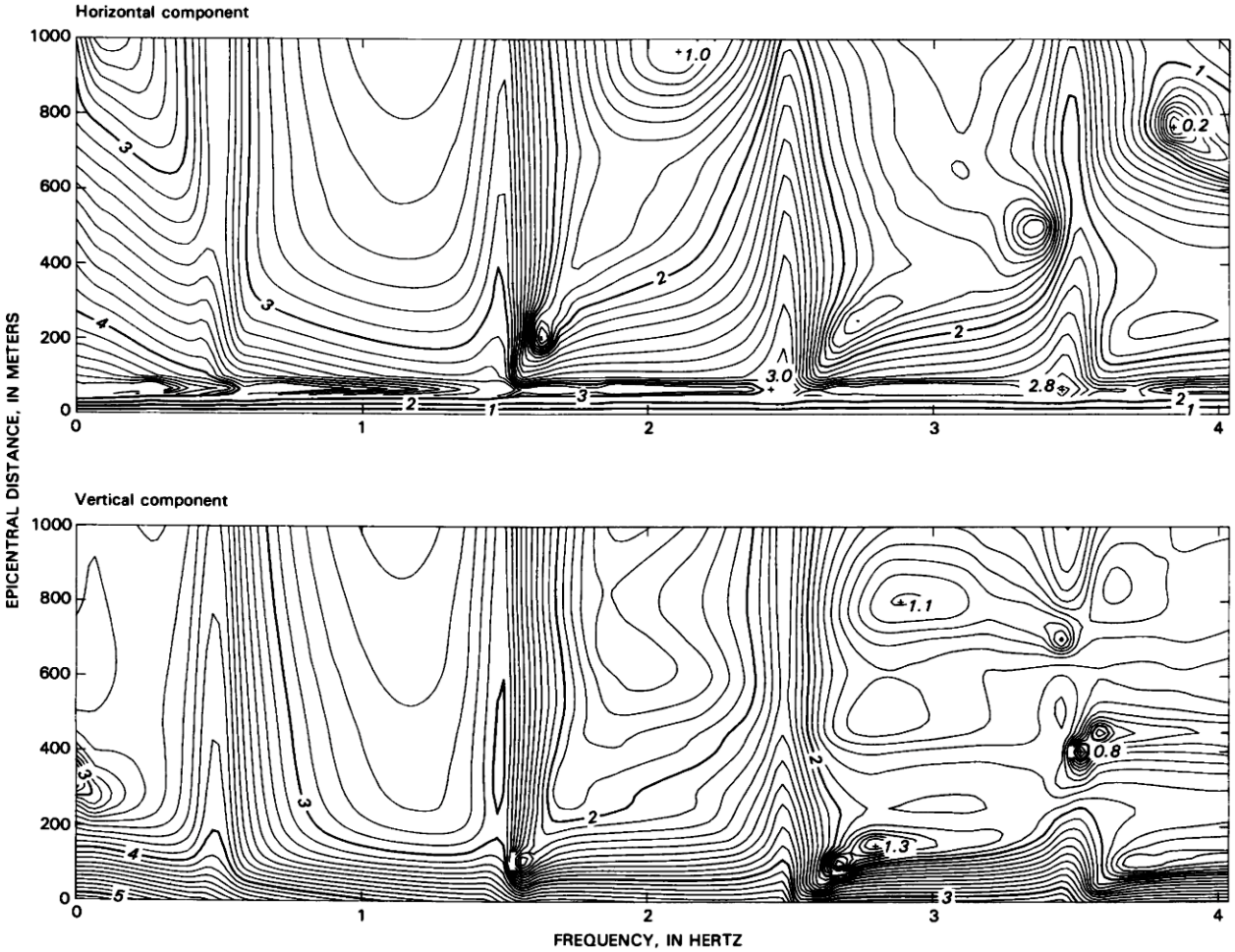


FIGURE 45.46.—Contour maps of the spectral amplitudes of the horizontal and vertical components of ground displacement obtained in the band 0–4 Hz and epicentral range 0–1,000 m for the source model defined in table 45.4. The plots show the logarithm in base 10 of the displacement spectral amplitudes (in cm·s) magnified by a factor of $10^6$. Every tenth contour is labeled.

component of motion clearly shows a partial collapse of the crack walls. This closure occurs because the opening of the crack tip causes a drop in the fluid pressure, which propagates across the crack with a velocity slightly lower than the acoustic velocity because of elastic yielding of the crack faces. This large low-frequency wave has the characteristics of the Stoneley wave observed in fluid-filled boreholes (Biot, 1952; Cheng and Toksöz, 1981) and corresponds to the so-called water-hammer wave in pipes (Wylie and Streeter, 1978).

For a crack containing an inviscid fluid, the only mechanism of energy loss is the radiative loss into the solid. This process is well illustrated in figure 45.48, which shows that the higher frequency components of the wall vibration are quickly damped over the first cycle of flow oscillation. This behavior is at odds with the earlier suggestion of Aki and others (1977) that high-frequency motions are trapped near the source. The problem of high-frequency radiation was not treated in detail by Chouet and Julian and is clearly of a complex nature that depends on the physical parameters of the fluid (see fig. 45.50 and comments below); this question is presently the subject of further investigation. The lower frequencies, on the other hand, are only weakly affected by radiation losses, suggesting that the elastic energy is a trivial part of the available acoustic energy of the fluid at these frequencies and confirming the assumption made earlier by Chouet (1985). The effect of viscosity is shown in figure 45.49 for a fluid characterized by the parameter $F=0.01$ (note that this particular choice for the value of $F$ implies viscosities in the range of $10^4$–$10^6$ poise if we assume $\mu \simeq 10^{11}$ dyne/cm$^2$, $k=0.1\mu$, $a \simeq 10^1$–$10^3$ m/s, and $d \simeq 10^{-1}$–$10^1$m). The factors $C$ and $G$ and the extension $\Delta l$ are the same as in the previous figure, so this plot offers a direct comparison with the result obtained for a

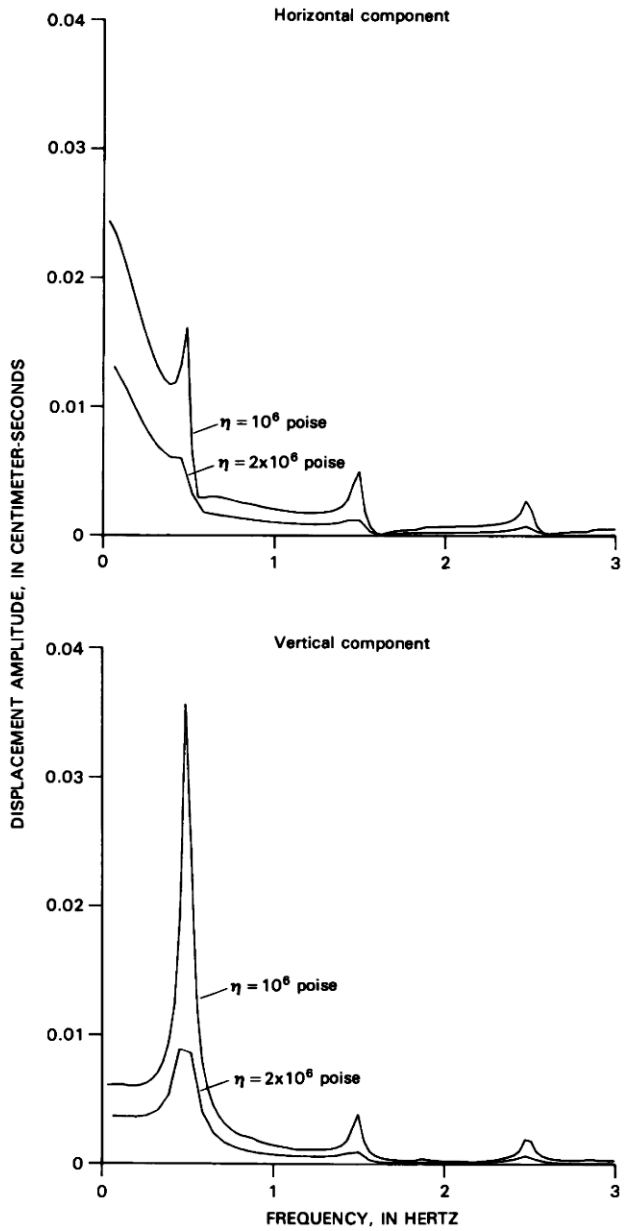


FIGURE 45.47.—Effect of the fluid viscosity on the displacement spectra observed in the band 0–3 Hz at an epicentral range of 200 m. Two values of viscosity are considered; other source parameters are listed in table 45.4.

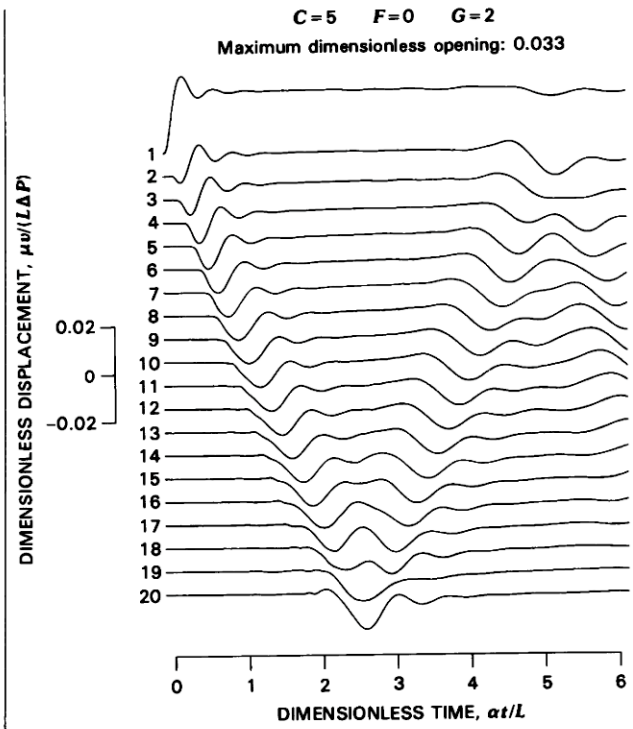


FIGURE 45.48.—Transverse displacement of the crack surface in dimensionless units for a crack 20 grid-intervals long that contains an inviscid fluid and that expands by $\Delta l = L/20$. Crack parameters are listed (see text for details). Traces 1–20 are spaced at 1 grid interval along the crack length.

nonviscous fluid. Viscous dissipation at the crack wall strongly affects the duration of dynamic motion but does not markedly change the shape or period of the signal over the first few cycles of flow oscillation.

The motion of the crack has two time scales: the duration of brittle failure, which is proportional to the length $\Delta l$ that the crack extends, and the period of acoustic resonance of the fluid, which is a function of the length of the crack and the acoustic velocity of the fluid. This is obvious in figures 45.48 and 45.49, when one compares the period of the high-frequency response of the wall associated with the incremental extension to the period of the acoustic cycle; the latter period is usually much longer than the duration of brittle failure.

Finally, the effect of a lower acoustic velocity in the fluid is illustrated in figure 45.50, which displays the normal particle velocity at 160 locations on the surface of a crack extending by $\Delta l = L/160$. The parameter $G$ is set equal to 4, that is, the acoustic velocity in the fluid is one-fourth of the compressional velocity in the solid; the other crack parameters are identical to those used in figure 45.48. The plot depicts the motion of the crack over roughly a quarter of the acoustic cycle, showing three wave fronts propagating over the wall. The first of these wave fronts is a weak $P$ wave which rapidly attenuates away from the expanding tip. Following the $P$ wave, another stronger wavetrain propagates across the crack with a velocity lower than the shear velocity in the solid. These guided waves are similar in nature to the pseudo-Rayleigh waves observed at the solid-fluid interface in a fluid-filled borehole (see, for example, Cheng and Toksöz, 1981). They are highly dispersive, having phase velocities bounded by the shear velocity of the rock at low frequencies and approaching the acoustic velocity of the fluid at higher frequencies. The final front corresponds to the acoustic arrival.

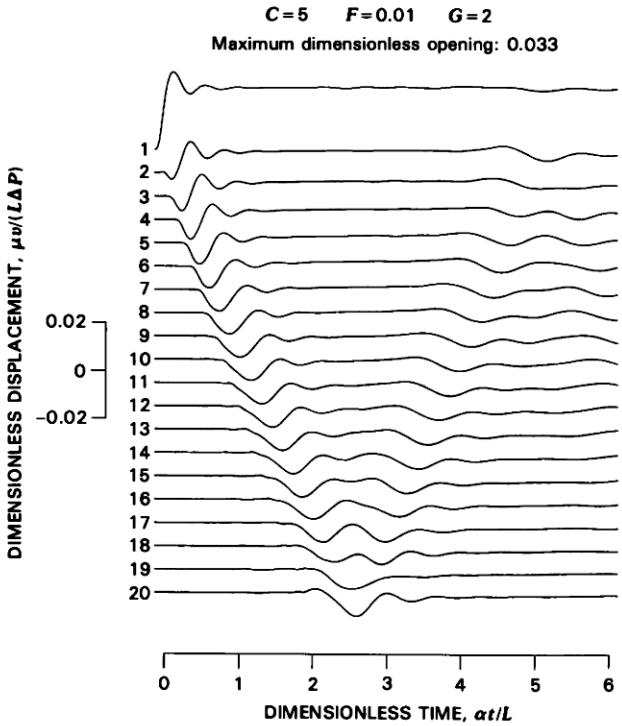


FIGURE 45.49.—Transverse displacement of the crack surface in dimensionless units for a crack 20 grid-intervals long that contains a viscous fluid and that expands by $\Delta l = L/20$. Other than the changed fluid viscosity, the source is the same as that in figure 45.48. Traces 1–20 are spaced at 1 grid interval along the crack length.

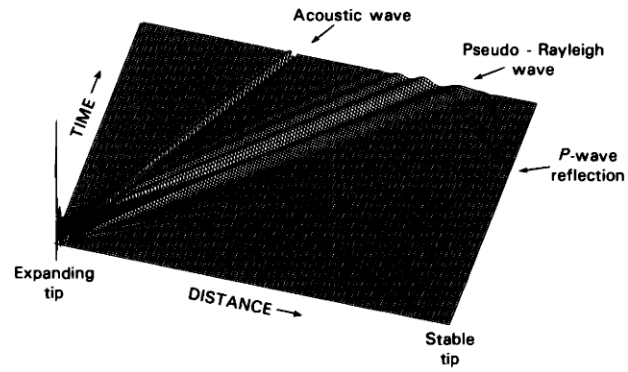


FIGURE 45.50.—Normal component of the particle velocity plotted at 160 locations on the surface of a crack expanding by $\Delta l = L/160$. Crack contains an inviscid fluid and has a stiffness $C = 5$. Acoustic velocity in the fluid is ¼ the compressional velocity in the solid. Note the individual wavefronts labeled and marked by arrows.

In the same configuration of source, medium, and receivers, the ground displacements produced by the expanding crack show a pattern similar to that depicted in figures 45.35 and 45.37 for the opening of a channel. In the present model, however, the duration of motion is essentially controlled by the fluid viscosity and the associated damping at the crack wall. In particular, when the fluid viscosity is low, the vibration of the source at the fundamental mode can persist for a considerable time, with the crack acting then as a high-Q oscillator. The inhomogeneous waves trapped near the liquid-solid interface (see fig. 45.50) produce high-frequency motions that are observed only in the immediate vicinity of the source.

## IMPLICATIONS OF THE MODELS FOR TRANSPORT MECHANISMS

By including the fluid as an active element in our seismic-source model of tremor, we have now established the premise for a unified theory that not only accounts for the driving force in the fluid and the elastic radiation in the solid, but also explains the observed frequency, bandwidth, amplitude, and duration of tremor. When the fluid viscosity is low and the viscous damping is small, the main mechanism of dissipation of energy is through elastic radiation. This radiation loss only weakly affects the low-frequency motion of the source, with the result that the fundamental mode of oscillation of the source can be maintained over a considerable period of time, the source acting then as a high-Q oscillator. This low-frequency signal represents the so-called long-period event, which may be viewed as the impulse response of the tremor generating system. According to this view, sustained harmonic tremor simply results from the superposition of the responses of a volcanic conduit to many individual pressure impulses occurring randomly in time. Various mechanisms can trigger the oscillation of the fluid in the source. Fluid flow in an open vent during active fountaining, rock failure, and thermal and chemical mechanisms are probably all equally plausible triggers. In that sense, the opening of a channel or jerky extension of a crack, as well as the thermal interaction of magma with ground water that we have considered in our models remain highly speculative. Clearly, the identification of the elusive trigger associated with the postulated sequence of long-period events is one of the major challenges facing us in our modeling attempts.

An interesting result stemming from our analysis is the apparent discrepancy between the volume estimates of magma transport obtained from the seismic data and those derived from deformation studies. The seismic estimates were found to be consistently and significantly lower than those obtained from deformation measurements for both deep and shallow tremor, suggesting that magma transport in the lithosphere may be largely aseismic. Although this conclusion is somewhat unfortunate for the seismologist who wants to determine magma flow solely from seismic measurements, it is supported by field observations of shallow tremor made during prolonged eruptions such as those at Halemaumau in 1967 and at Mauna Ulu during 1969–1974, as well as the current activity at Puu Oo. The initial phase of an eruption usually is accompanied by stronger tremor than the later phases, when larger volumes of lavas

are erupted, and some eruptions even occur without measurable tremor. Furthermore, the size of the tremor source region at Kilauea decreases during repeated eruptions at the same location; that is, the tremor becomes restricted to the vent area while the summit area remains active at a lower level. A conspicuous gap in tremor activity appears to develop in the rift zone between the erupting vent and the summit reservoir during a sustained eruption in the east rift. A gap also exists at depths of 15–30 km along the conduit system beneath the summit region. The lack of measurable tremor activity in these regions suggests that there are undisturbed zones of transport where magma flow may occur without significant pressure fluctuations. Indeed, if tremor is generated by unsteady fluid flow, as the evidence gathered so far seems to indicate, then it is easy to relate the absence of tremor to episodes of steady flow. It is possible that strong barriers may become weakened by continued or repeated magma flow, accounting for the disappearence of tremor during an eruption and the absence of tremor at some depths below Kilauea.

Further data are needed on tremor. The deployment of an array of broadband three-component instruments in the active east rift of Kilauea could provide the high-quality data essential for resolution of the basic questions remaining on tremor.

## REFERENCES CITED


Aki, Keiiti, 1967, Scaling law of seismic spectrum: Journal of Geophysical Research, v. 72, p. 1217-1231.

———1972, Earthquake mechanism: Tectonophysics, v. 13, p. 423-446.

———1984, Evidence for magma intrusion during the Mammoth Lakes earthquakes of May 1980 and implications of the absence of volcanic (harmonic) tremor: Journal of Geophysical Research, v. 89, p. 7689-7696.

Aki, Keiiti, Fehler, Michael, and Das, Shamita, 1977, Source mechanism of volcanic tremor: fluid-driven crack models and their application to the 1963 Kilauea eruption: Journal of Volcanology and Geothermal Research, v. 2, p. 259-287.

Aki, Keiiti, and Koyanagi, R.Y., 1981, Deep volcanic tremor and magma ascent mechanism under Kilauea, Hawaii: Journal of Geophysical Research, v. 86, p. 7095-7109.

Biot, M.A., 1952, Propagation of elastic waves in a cylindrical bore containing a fluid: Journal of Applied Physics, v. 23, p. 997-1005.

Blake, F.G., 1952, Spherical wave propagation in solid media: Journal of the Acoustical Society of America, v. 24, p. 211-215.

Bouchon, Michel, 1979, Discrete wave number representation of elastic wave fields in three-space dimensions: Journal of Geophysical Research, v. 84, p. 3609-3614.

———1981, A simple method to calculate Green's functions for elastic layered media: Bulletin of the Seismological Society of America, v. 71, p. 959-971.

Brune, J.N., 1970, Tectonic stress and the spectra of seismic shear waves from earthquakes: Journal of Geophysical Research, v. 75, p. 4997-5009.

Capaldi, G., Guerra, I., Lo Bascio, A., Luongo, G., Pece, R., Rapolla, A., Del Pezzo, E., Martini, M., Ghiara, M.R., Lirer, L., Munno, R., and La Volpe, L., 1978, Stromboli and its 1975 eruption: Bulletin Volcanologique, v. 41, p. 259-285.

Cheng, H.C., and Toksöz, M.N., 1981, Elastic wave propagation in a fluid-filled borehole and synthetic acoustic logs: Geophysics, v. 46, p. 1042-1053.

Chouet, Bernard, 1981, Ground motion in the near field of a fluid-driven crack and its interpretation in the study of shallow volcanic tremor: Journal of Geophysical Research, v. 86, p. 5985-6016.

———1985, Excitation of a buried magmatic pipe: a seismic source model for volcanic tremor: Journal of Geophysical Research, v. 90, p. 1881-1893.

Chouet, Bernard, and Julian, B. R., 1985, Dynamics of an expanding fluid filled crack: Journal of Geophysical Research, v. 90, p. 11187-11198.

Crosson, R.S., and Bame, D.A., 1985, A spherical source model for low frequency volcanic earthquakes: Journal of Geophysical Research, v. 90, p. 10237-10247.

Dibble, R.R., 1974, Volcanic seismology and accompanying activity of Ruapehu Volcano, New Zealand, in Civetta, L., Gasparini, P. Luongo, G., and Rapolla, A., eds., Physical Volcanology: Amsterdam, Elsevier, p. 49-85.

Fehler, Michael, 1983, Observations of volcanic tremor at Mount St. Helens volcano: Journal of Geophysical Research, v. 88, p. 3476-3484.

Fehler, Michael, and Chouet, Bernard, 1982, Operation of a digital seismic network on Mount St. Helens volcano and observations of long-period seismic events that originate under the volcano: Geophysical Research Letters, v. 9, p. 1017-1020.

Ferrick, M.G., Qamar, Anthony, and St. Lawrence, W.F., 1982, Source mechanism of volcanic tremor: Journal of Geophysical Research, v. 87, p. 8675-8683.

Ferrick, M.G., and St.Lawrence, W.F., 1984, Comment on "Observations of volcanic tremor at Mount St. Helens volcano" by Michael Fehler: Journal of Geophysical Research, v. 89, p. 6349-6350.

Guerra, I., Lo Bascio, A., Luongo, G., and Scarpa, Roberto, 1976, Seismic activity accompanying the 1974 eruption of Mt. Etna: Journal of Volcanological and Geothermal Research, v. 1, p. 347-362.

Kamo, K., Furuzawa, T., and Akamatsu, J., 1977, Some natures of volcanic micro-tremors at the Sakurajima Volcano: Bulletin of the Volcanological Society of Japan, v. 22, p. 41-58.

Kanamori, Hiroo, and Anderson, D.L., 1975, Theoretical basis for some empirical relations in seismology: Bulletin of the Seismological Society of America, v. 65, p. 1073-1095.

Kubotera, A., 1974, Volcanic tremors at Aso Volcano, in Civetta, L., Gasparini, P., Luongo, G., and Rapolla, A., eds., Physical Volcanology : Amsterdam, Elsevier, p. 29-47.

Latter, J.H., 1979, Volcanological observations at Tongariro National Park, 2 types and classification of volcanic earthquakes, 1976-1978: New Zealand Department of Science and Industrial Research, Geophysics Division, Wellington Report 150, 60 p.

Malone, S.D., 1983, Volcanic earthquakes: Examples from Mount St. Helens, in Kanamori, H., and Boschi, E., eds., Earthquakes: Observations, Theory and Interpretation ; Amsterdam, Elsevier/North Holland Publishing Co., p. 436-455.

Mandelbrot, B.B., 1977, Fractals, form, chance, and dimension : San Francisco, W.H. Freeman and Co., 365 p.

McNutt, S.R., 1986, Observations and analysis of B-type earthquakes, explosions, and volcanic tremor at Pavlov Volcano, Alaska: Bulletin of the Seismological Society of America, v. 76, p. 153–175.

Minakami, T., 1974, Seismology of volcanoes in Japan, *in* Civetta, L., Gasparini, P., Luongo, G., and Rapolla, A., eds., Physical Volcanology: Amsterdam, Elsevier, p. 1-27.

Moore, J.G., and Koyanagi, R.Y., 1969, The October 1963 eruption of Kilauea Volcano, Hawaii: U.S. Geological Survey Professional Paper 614–C, 13 p.

Riuscetti, M., Schick, R., and Seidl, S., 1977, Spectral parameters of volcanic tremors at Etna: Journal of Volcanological and Geothermal Research, v. 2, p. 289-298.

Ryall, A., and Bennett, D.L., 1968, Crustal structure of southern Hawaii related to volcanic processes in the upper mantle: Journal of Geophysical Research, v. 73, p. 4561-4582.

Sassa, K., 1935, Volcanic micro-tremors and eruption earthquakes: Memoirs of the College of Science, Kyoto Imperial University Series A, v. 18, p. 255-293.

Schick, R., Lombardo, G., and Patane, G., 1982, Volcanic tremors and shocks associated with the eruptions at Etna (Sicily), September 1980: Journal of Volcanology and Geothermal Research, v. 14, p. 261-279.

Schick, R., and Riuscetti, M., 1973, An analysis of volcanic tremors at south Italien volcanoes: Zeitschrift fur Geophysics, v. 39, p. 247-262.

Seidl, D., Schick, R., and Riuscetti, M., 1981, Volcanic tremors at Etna: a model for hydraulic origin: Bulletin Volcanologique , v. 44, p. 43-56.

Shima, M., 1958, On the second volcanic micro-tremor at volcano Aso: Bulletin of the Disaster Prevention Institute of Kyoto University, v. 22, p. 1-6.

Shimozuru, D., Kamo, K., and Kinoshita, W.T., 1966, Volcanic tremor at Kilauea Volcano, Hawaii, during July-December 1963: Bulletin of the Earthquake Research Institute of the University of Tokyo, v. 44, p. 1093-1133.

St. Lawrence, William, and Qamar, Anthony, 1979, Hydraulic transients: a seismic source in volcanoes and glaciers: Science, v. 203, p. 654-656.

Swanson, D.A., 1972, Magma supply rate at Kilauea Volcano, 1952-1971: Science, v. 1975, p. 169-170.

Swanson, D.A., Duffield, W.A., and Fiske, R.S., 1976, Displacement of the south flank of Kilauea Volcano: the result of forceful intrusion of magma into the rift zones: U.S. Geological Survey Professional Paper 963, 39 p.

Wada, T., 1980, Mechanism generating volcanic tremor, I: Bulletin of the Volcanological Society of Japan, v. 25, p. 211-278.

———1981, Mechanism generating volcanic tremor, II: Bulletin of the Volcanological Society of Japan, v. 26, p. 1-8.

Williams, H., and McBirney, A.R., 1979, Volcanology: San Francisco, Freeman, Cooper and Co., 397 p.

Wylie, E.B., and Streeter, V.L., 1978, Fluid transients : New York, McGraw

# A HYDRAULIC MODEL TO EXPLAIN VARIATIONS IN SUMMIT TILT RATE AT KILAUEA AND MAUNA LOA VOLCANOES

*By* John J. Dvorak *and* Arnold T. Okamura


## ABSTRACT

**For a period of several months to a few years preceding eruptive activity, magma accumulates in shallow reservoirs centered 3 to 5 km beneath the summits of Kilauea and Mauna Loa Volcanoes. During flank eruptions, magma movement from the summit reservoir to the rift system is indicated by subsidence of the summit. Progress of the subsidence is monitored by telemetered tiltmeters, by 3-m-long watertube tiltmeters, and by releveling 40-m-long triangles.**

**During large summit-subsidence events at Kilauea, the tilt pattern indicates that the subsidence center may initially migrate 1 to 2 km to the south. Following the initial southward migration, the tilt direction remains constant for the remainder of the subsidence event, suggesting no further horizontal migration of the subsidence center during this period. No variation in tilt direction was measured in the Mauna Loa summit region during the March 25–April 15, 1984, northeast-rift eruption of this volcano.**

**The amount of vertical migration of the subsidence center is estimated from relative tilt rates recorded at different horizontal distances from the subsidence center. During the January 18–May 10, 1960, event at Kilauea, the subsidence center migrated upward 1 km in mid-February 1960. Vertical migration of the March 25–April 15, 1984, summit subsidence at Mauna Loa was less than 0.7 km.**

**During most subsidence events at both Kilauea and Mauna Loa, the tilt curve follows an exponential decay rate. Since 1955, the time constants for the exponential decay in tilt rate at Kilauea have varied from 0.25 days to 21 days; longer time constants are associated with eruptions that occur at greater distances from the summit. An exception to the exponential decay was the January 2–8, 1983, summit subsidence at Kilauea, which consisted of three separate subsidence episodes.**

**We propose a hydraulic model to explain the observed variation in tilt rate recorded during summit-subsidence events. Magma flow rate is assumed proportional to the pressure difference between the summit reservoir and a separate reservoir within the rift system. We further assume that magmatic pressure is linearly related to volumetric strain. On the basis of these assumptions, the magma flow rate and, hence, the summit tilt curve will follow the exponential decay observed during summit subsidences.**


## INTRODUCTION

Frequent periods of eruptive activity at two Hawaiian volcanoes, Kilauea and Mauna Loa (fig. 46.1), make these volcanoes especially well suited for studying the accumulation and movement of magma within the crust. Processes that control the volume and rate of flow of magma within Hawaiian volcanoes may also influence magma migration from the mantle to the surface; so, results derived from monitoring near-surface magma movement at Hawaiian volcanoes should be applicable to magma movement deeper in the crust and upper mantle, at depths too remote for current studies.

Several months to a few years preceding eruptive activity, magma accumulates in shallow reservoirs beneath the summits of both Kilauea and Mauna Loa (Fiske and Kinoshita, 1969; Decker and others, 1983). The accumulation and withdrawal of magma from the summit region produce a pattern of surface displacement that is recorded as change in ground tilt (fig. 46.2). The intersection of tilt vectors locates the average center of uplift or subsidence for the time interval between surveys.

The variation in tilt magnitude as a function of distance from the uplift or subsidence center can be modeled by a single point source embedded in an elastic half-space. The tilt magnitude, $\Phi$, is given by (Eaton, 1962)

$$\Phi = \frac{3V}{2\pi} \frac{dh}{(d^2+h^2)^{5/2}}, \qquad (1)$$

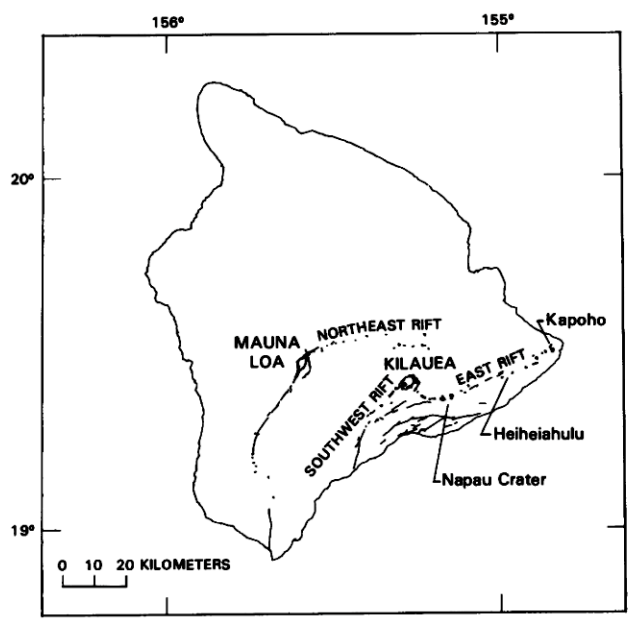


FIGURE 46.1.—Structural features associated with summit regions and rift systems of Mauna Loa and Kilauea on Island of Hawaii. Places along east rift of Kilauea mentioned in text are identified.

where $h$ is the horizontal distance, $d$ is the depth to the source, and $V$ is the volume of elastic uplift. No tilt change is recorded directly above ($h=0$) or at large distances from the point source; the maximum tilt change occurs at $h=d/2$ (fig. 46.3). Comparison of theoretical curves and measured tilt changes show that the summit reservoirs at Kilauea and Mauna Loa are centered 3 to 5 km beneath the summits of both volcanoes (fig. 46.4; table 46.1). A similar depth range to the summit reservoirs has been estimated from level data, using a point-source elastic model, by many earlier investigators (Mogi, 1958; Fiske and Kinoshita, 1969; Decker and others, 1983; Dvorak and others, 1983).

During periods of magma accumulation in the Kilauea summit region, the uplift center usually begins in the central caldera region 1 km northeast of Halemaumau and migrates as much as 2 km south (Fiske and Kinoshita, 1969). A similar migration of the uplift center has not been recognized for Mauna Loa. Magma that accumulates in the summit reservoir may erupt in the summit region or move laterally into either rift system, where it may eventually be erupted. During periods of magma withdrawal from the summit reservoir, the subsidence center may also migrate a few kilometers within the caldera region (Jackson and others, 1975; Swanson and others, 1976).

The accumulation and withdrawal of magma in the Kilauea summit region is easily recorded by making frequent tilt measurements (fig. 46.5*A*). Higher tilt values in figure 46.5 correspond to uplift of the summit region caused by increased magmatic pressure and accumulation of additional magma within the summit reservoir. Prolonged periods of summit uplift are interrupted by much shorter

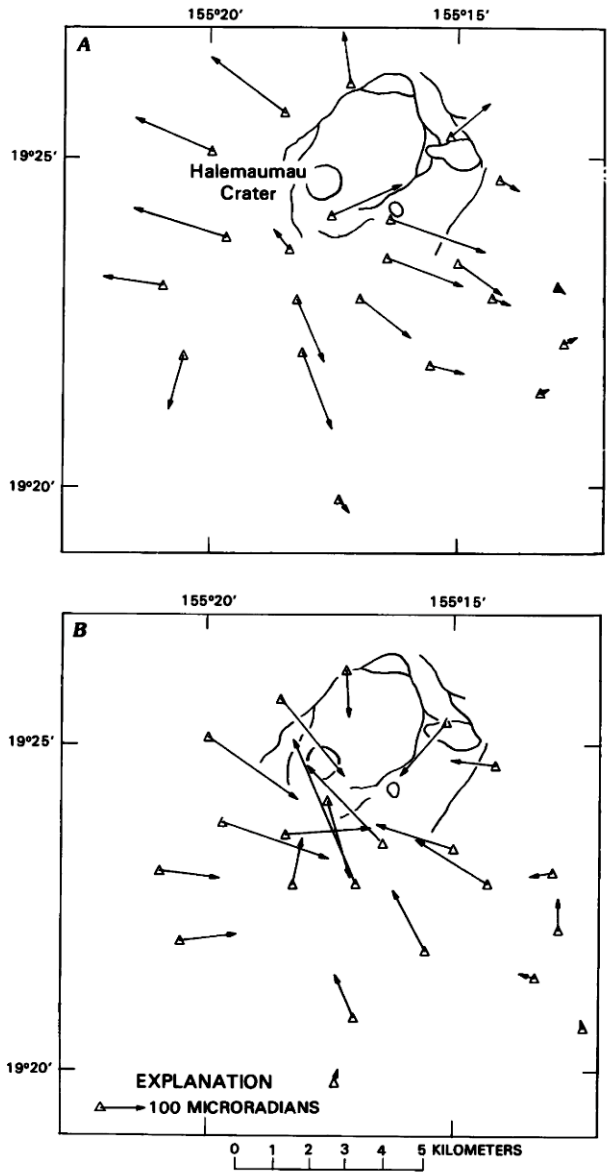


FIGURE 46.2.—Tilt vectors measured in Kilauea summit region. ***A***, Uplift of August 12–14, 1981, to March 3–April 5, 1982. ***B***, Subsidence of September 27–October 14, 1982, to February 2–11, 1983. Vectors were determined by measuring changes in relative elevation along 40-m-long triangles. Station locations, triangles. Tilt vectors point in direction of downward deflection of surface. General radial pattern of tilt vectors indicates that most active part of summit magma reservoir lies beneath southern part of caldera.

TABLE 46.1.—*Point source solutions to Kilauea summit tilt data*

| | August 12–14, 1981 to March 29–April 5, 1982 | September 27–October 14, 1982 to February 7–11, 1983 |
|---|---|---|
| Longitude | 155°17.7′ (±0.36 km) | 155°17.0′ (±0.30 km) |
| Latitude | 19°23.7′ (±0.34 km) | 19°23.8′ (±0.28 km) |
| Depth | 4.31 km (±0.84 km) | 4.38 km (±0.58 km) |
| Volume of elastic uplift or subsidence | $53\times10^6$ m$^3$($\pm26\times10^6$ m$^3$) | $-72\times10^6$ m$^3$($\pm26\times10^6$ m$^3$) |

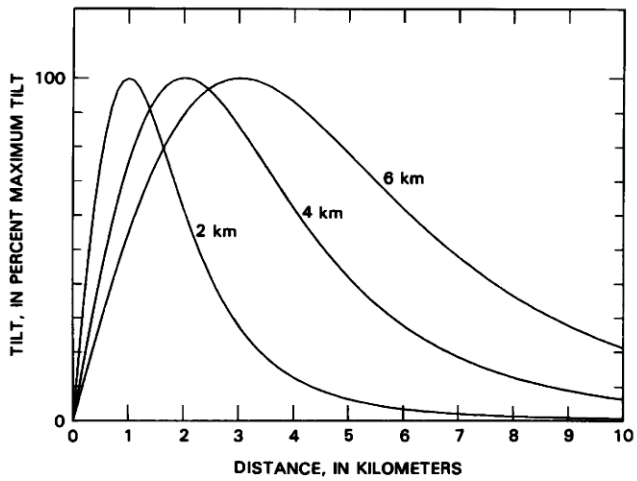


FIGURE 46.3.—Theoretical tilt changes as a function of horizontal distance from a point source embedded in an elastic half-space. Curves, normalized to maximum tilt change, are parametrized by depth to source.

periods of summit subsidence, indicated by sudden decreases in tilt value. These summit-subsidence events are caused by the movement of magma from the summit reservoir to either rift system and are usually associated with eruptive activity along the rift (Eaton and Murata, 1960; Jackson and others, 1975; Swanson and others, 1976). A similar pattern of slow accumulation and rapid withdrawal of magma from the summit reservoir at Mauna Loa is also indicated by summit tilt measurements (fig. 46.5*B*).

We have selected data from 14 subsidence events at Kilauea, indicated by vertical dashed lines in figure 46.5*A*, to determine what factors may control variations in summit tilt rate. Data from the summit subsidence associated with the 1984 Mauna Loa eruption are also included. Based on these data, a simple hydraulic model is proposed to explain magma flow rate in the conduit systems within Kilauea and Mauna Loa.

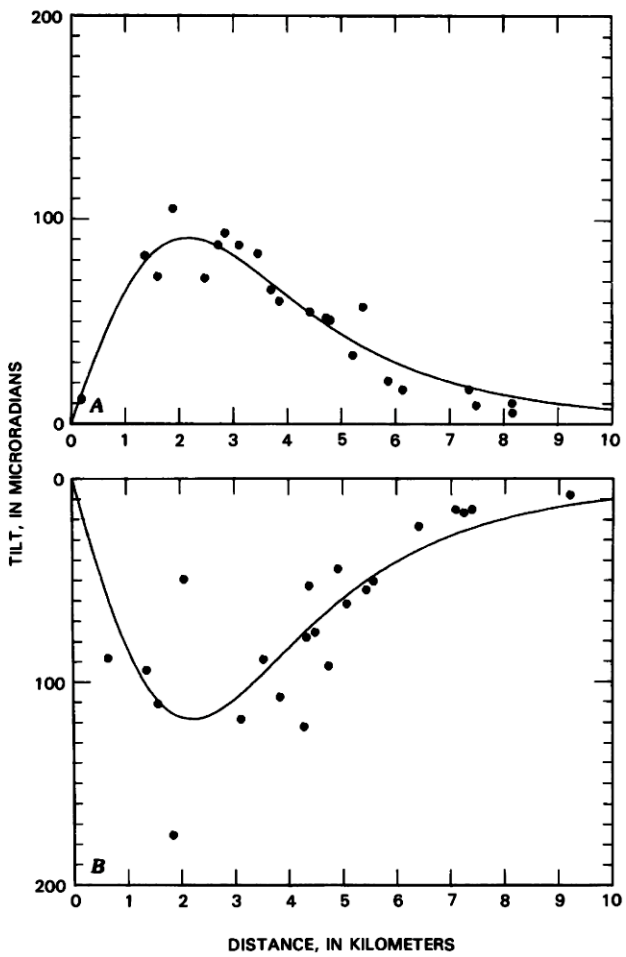


FIGURE 46.4.—Measured changes in radial tilt component and theoretical curves based on a point source embedded in an elastic half-space. ***A***, Uplift. ***B***, Subsidence. Data are same as shown in figure 46.2*A*, *B*. Model parameters are listed in table 46.1.

**ACKNOWLEDGMENTS**

This research has built upon measurements made over the past 30 years by the staff of the Hawaiian Volcano Observatory. R. Decker, J. Dieterich, D. Dzurisin, and T. Wright provided useful comments and suggestions to this manuscript.

## MEASUREMENTS

Tilt measurements were begun in the summit region of Kilauea a few years after the establishment of the Hawaiian Volcano Observatory (HVO) in 1912; however, instruments specifically designed to record tilt changes were not in use until the 1950's. Tilt measurements in the summit region of Mauna Loa were begun 5 months after the July 1975 summit eruption.

Kilauea summit tilt measurements have been made at Uwekahuna since at least 1950 and at Outlet since October 1955 (fig. 46.6*A*). Between 1950 and June 1956, tilt changes at Uwekahuna were recorded by measuring the trace offset from a horizontal-pendulum seismograph. This technique could probably record tilt changes of 10–20 microradians (μrad). In 1955 and 1956, 3-m-long watertube tiltmeters, capable of resolving tilt changes of 2 μrad, were installed at Uwekahuna and Outlet (Eaton, 1959).

Since 1966, a continuously recording, one-component tiltmeter has operated in the Uwekahuna vault. This instrument is a mercury capacitance instrument that records tilt changes along the east-west direction to a sensitivity of 0.1 μrad. In recent years, additional electronic tiltmeters installed in the Kilauea summit region transmit readings at approximately 10-min intervals to a recording system located at HVO.

Tilt measurements in the Mauna Loa summit region (fig. 46.6*B*) are made by the dry-tilt method, which consists of releveling 40-m-long triangles (Yamashita, 1981). The use of 3-m-long wooden rods with permanently installed Invar strips allows tilt changes at MOK (tilt station at Mokuaweoweo) to be measured to 3–4 μrad. At other tilt sites, an accuracy of 8–12 μrad is achieved by the use of 1.5-m-long stainless-steel rods with removable Invar strips.

Repeated tilt measurements at Uwekahuna were made during 14 summit-subsidence events at Kilauea (fig. 46.5*A*) and during the 1984 northeast-rift eruption of Mauna Loa. The beginning dates of summit subsidence and the locations of the related rift intrusion or eruption are given in table 46.2. Parts of the east rift from the summit to Napau Crater, to Heiheiahulu, and to Kapoho are referred to as the upper, middle, and lower east rift, respectively (fig. 46.1). The distance from the summit-subsidence center to the rift eruption is measured along the rift axis to the major lava-producing eruptive vent. For the two events not accompanied by eruptive activity, in August 1981 and June 1982, the distance to the rift intrusion was assumed to correspond to the central region of shallow rift earthquakes. The beginning times and the durations of rift eruptions associated with each subsidence event are also listed in table 46.2. The occurrence of later eruptive phases, which may follow a large summit subsidence and initial eruptive phase, such as

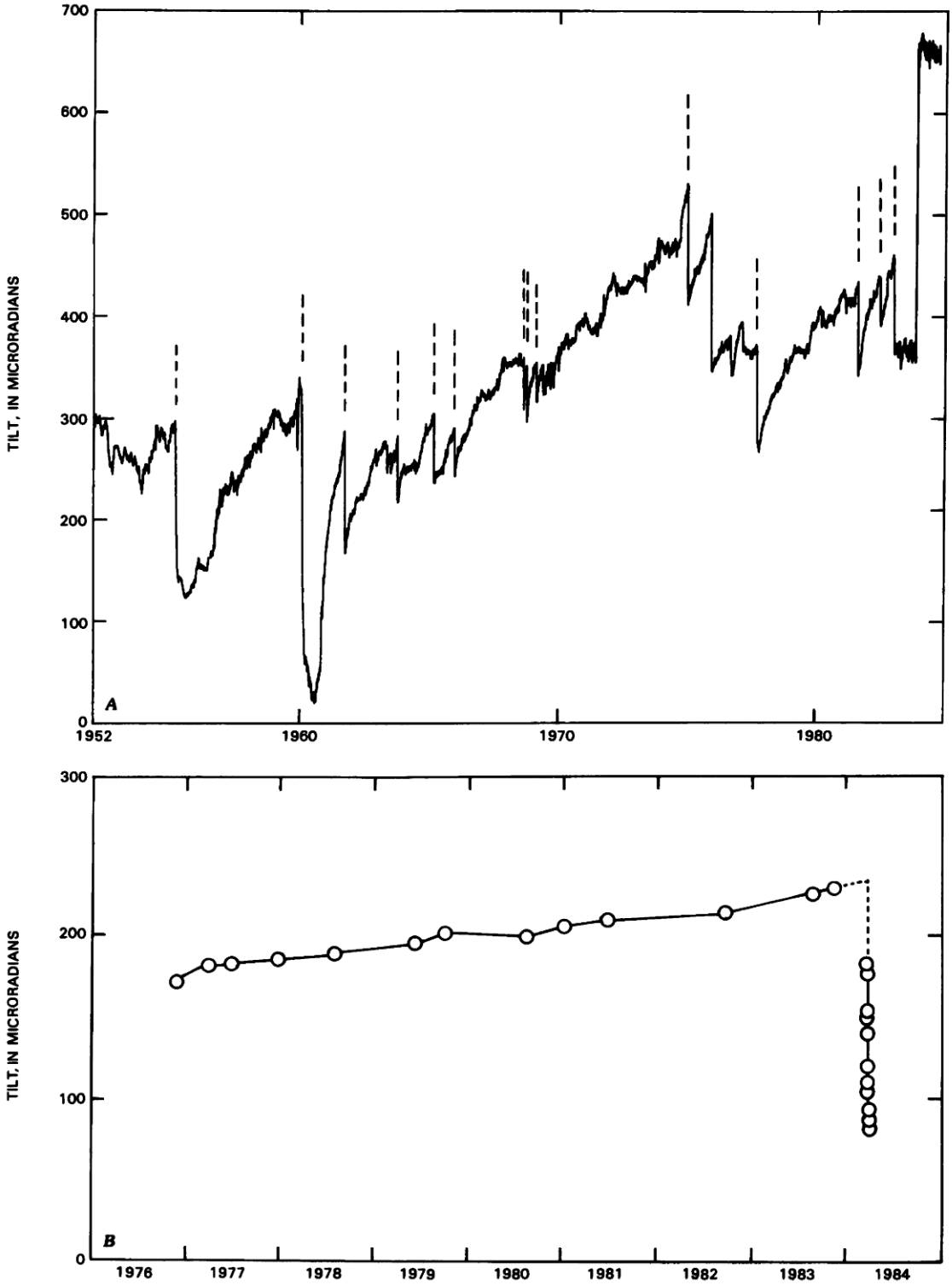


FIGURE 46.5.—Long-term tilt patterns recorded in summit regions of Kilauea and Mauna Loa. A greater tilt value generally corresponds to summit uplift and magma accumulation. ***A***, West-east component of daily tilt recorded in Kilauea summit region at Uwekahuna (see figure 46.6*A* for location). The 300-μrad tilt increase on November 16, 1983, is related to a magnitude 6.5 earthquake located 13 km west-northwest of Uwekahuna. Sudden tilt change probably did not involve magma movement in summit region. Summit subsidences examined in this paper (see table 46.2) are identified by vertical dashed-line segments. ***B***, North-south tilt component recorded in Mauna Loa summit region at MOK (see figure 46.6*B* for location). Sudden tilt decrease in March 1984 corresponds to recent Mauna Loa northeast-rift eruption.

in March–April 1955, September 20–25, 1977, and the succession of eruptive phases that began in February 1983, are not considered in determining eruption duration because these events are associated with smaller, individual summit subsidences.

## HORIZONTAL AND VERTICAL MIGRATION OF SUBSIDENCE CENTERS

Jackson and others (1975) and Swanson and others (1976) noted a horizontal migration of the subsidence center associated with some subsidence events. We show in this section that, though there is a systematic migration, most of the tilt change occurs while the subsidence center is stationary.

Horizontal migration of the subsidence center is indicated by variations in tilt direction, which is determined by examining the amount of north-south and west-east tilt. A constant direction is indicated by a linear relation between north-south and west-east tilt values.

The variation in tilt direction recorded by the Uwekahuna watertube instrument during the December 31, 1974–January 3, 1975, summit subsidence is typical of most events at Kilauea (fig. 46.7). The subsidence center was initially located directly east of Uwekahuna. As the subsidence proceeded, the center migrated southward, indicated by a change in tilt direction at Uwekahuna from east to southeast. The dominant southeastern tilt recorded at Uwekahuna suggests that the subsidence center remained in the same horizontal position throughout most of the subsidence. A second, relatively minor migration of the subsidence center to a position south of Uwekahuna may have occurred near the end of the event.

The net tilt change recorded at Uwekahuna for each subsidence event is listed in table 46.2. Tilt directions listed in this table are for the period following the initial southward migration of the subsidence center. Since 1977, this direction from Uwekahuna has been remarkably constant. The only subsidence that did not display a dominant tilt direction was the February 21–23, 1969, event, which consisted of two different directions equal in tilt change, initially to the southeast and then to the south of Uwekahuna.

The tilt directions at Uwekahuna associated with the August 1981 southwest-rift intrusion and the January 1983 east-rift eruption

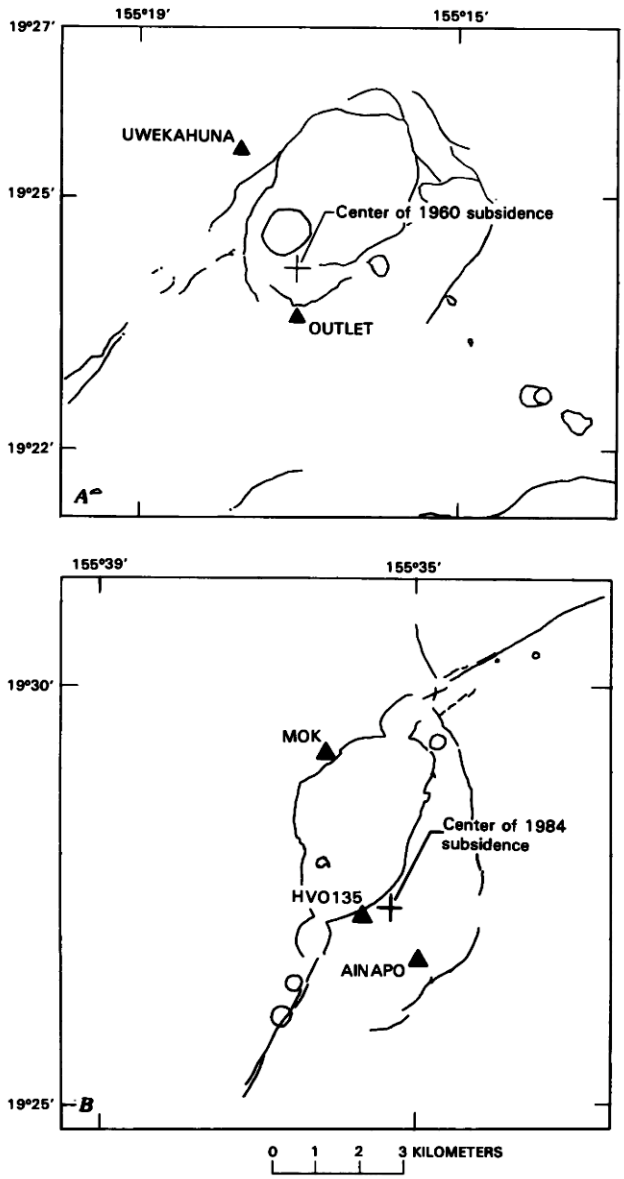


FIGURE 46.6.—Tilt sites (triangles) and subsidence centers. *A*, Kilauea summit region. *B*, Mauna Loa summit region. MOK, tilt station at Mokuaweoweo Crater.

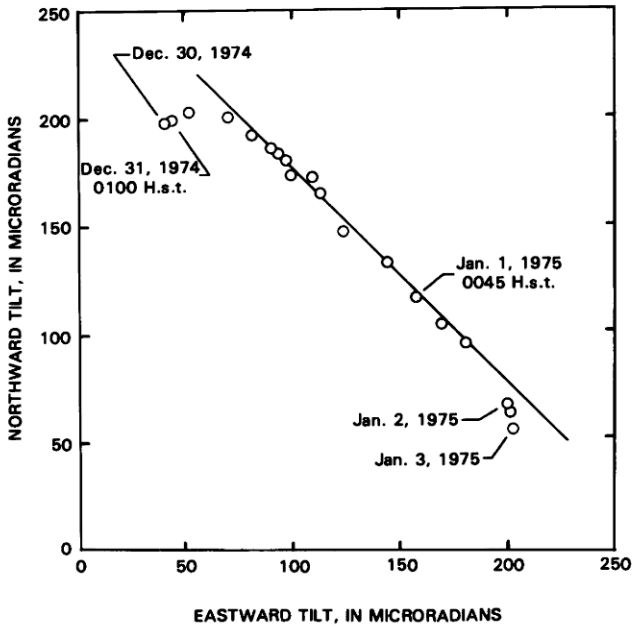


FIGURE 46.7.—Tilt directions measured at Uwekahuna during December 1974 southwest-rift eruption. Linear trend indicates constant tilt direction.

TABLE 46.2.—*Summit subsidence of Hawaiian volcanoes*

[UER, upper east rift; MER, middle east rift; LER, lower east rift; SWR, southwest rift; NER, northeast rift]

| Beginning of summit subsidence | Distance from summit subsidence to rift intrusion (km) | Location of rift intrusion | Eruption: Beginning (Date, hour) | Eruption: Duration (days) | Tilt change (μrad) | Tilt direction | Time constant (days) | References |
|---|---|---|---|---|---|---|---|---|
| | | | **Kilauea** | | | | | |
| 3/7/55 | 37 | LER | 2/28/55 0800 | [1]38 | 192 | S. 57° E. | 16 | Macdonald and Eaton (1964) |
| 1/8/60 | 47 | LER | 1/13/60 1935 | 36 | 345 | S. 60° E. | 21 | Richter and others (1970) |
| 9/21/61 | 32 | UER | 9/22/61 0430 | 3 | 174 | S. 35° E. | 1 | Richter and others (1964) |
| 10/5/63 | 20 | UER | 10/5/63 0306 | 1 | 104 | S. 55° E. | .5 | Moore and Koyanagi (1969) |
| 3/5/65 | 16 | UER | 3/5/65 0921 | 10 | 108 | S. 45° E. | .25 | Wright and others (1968) |
| 12/24/65 | 10 | UER | 12/24/65 2130 | .25 | 60 | S. 85° E. | .25 | Fiske and Koyanagi (1968) |
| 8/22/68 | 6 | UER | 8/22/68 0615 | 5 | 58 | S. 68° E. | .25 | Jackson and others (1975) |
| 10/7/68 | 16 | UER | 10/7/68 1435 | 15 | 78 | S. 65° E. | .25 | Jackson and others (1975) |
| 2/22/69 | 10 | UER | 2/22/69 0950 | 6 | 58 | ([2]) | .25 | Swanson and others (1976) |
| 12/31/74 | 4 | SWR | 12/31/74 0255 | 1 | 219 | S. 44° E. | .75 | ([3]) |
| 9/13/77 | 25 | MER | 9/13/77 1910 | [1]3 | 104 | S. 47° E. | 1.5 | Moore and others (1981) |
| 8/10/81 | 6 | SWR | ([4]) | ([4]) | 103 | S. 47° E. | .5 | ([3]) |
| 6/21/82 | 11 | SWR | ([4]) | ([4]) | 50 | S. 47° E. | 1 | ([3]) |
| 1/2/83 | 25 | MER | 1/3/83 0030 | [1]4 | 149 | S. 47° E. | ([5]) | Dvorak and others (1985) |
| | | | **Mauna Loa** | | | | | |
| 3/25/84 | 18 | NER | 3/25/84 0130 | 20 | -- | -- | 5 | Lockwood and others (1985) |

[1]Duration of initial eruptive phase, later eruptive phases had relatively small tilt changes (all <30 μrad; most <15 μrad) recorded at Uwekahuna.
[2]No dominant tilt direction during the major summit subsidence.
[3]Hawaiian Volcano Observatory, unpublished data.
[4]No eruptive activity associated with these events.
[5]Multiple subsidence event.

were almost identical. Both events began with an eastward-directed tilt and rotated to the southeast (fig. 46.8), similar to the beginning of the 1974 summit subsidence. The tilt directions measured at Uwekahuna during the August 1981 and January 1983 events were identical, suggesting the same subsidence center, even though magma moved into different rift systems. No clear relation exists between location of subsidence center, measured by tilt at Uwekahuna, and movement of magma into either rift system (table 46.2).

A constant tilt direction recorded at a single station does not eliminate the possibility that the subsidence center may migrate radially to that station. Tilt measurements made at two different sites during the January–May 1960 summit subsidence show that at least

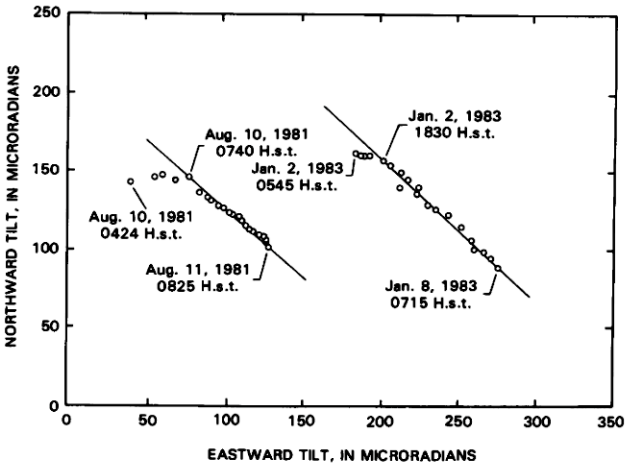


FIGURE 46.8.—Tilt directions measured at Uwekahuna during August 1981 southwest-rift intrusion and January 1983 east-rift eruption.

for this event the subsidence center remained in approximately the same horizontal position (fig. 46.9).

Tilt measurements made at three sites in the Mauna Loa summit region during the March 25–April 15, 1984, northeast-rift eruption showed no horizontal migration of the subsidence center (fig. 46.10). The subsidence center associated with the 1984 Mauna Loa northeast-rift eruption was located 1 km southeast of the rim of the summit caldera Mokuaweoweo (fig. 46.6*B*), a position identical to the uplift center determined from repeated geodetic surveys conducted since 1977 (Decker and others, 1983).

The amount of vertical migration of the subsidence center can be estimated when simultaneous tilt measurements are made at different distances from the subsidence center. The surface displacements produced by magma withdrawal from the summit reservoir are assumed to be adequately represented by a point source embedded in an elastic half-space (Dvorak and others, 1983). The ratio of the magnitude of tilt change ($\Phi_1$ and $\Phi_2$) at different horizontal distances from the subsidence center ($h_1$ and $h_2$) is given by

$$\Phi_1/\Phi_2 = \frac{h_1}{h_2}\,\frac{(d^2+h_2^2)^{5/2}}{d^2+h_1^2}. \qquad (2)$$

If the subsidence center does not migrate horizontally, then changes in the ratio of the magnitude of tilt change are a result of vertical migration. The amount that a small change in depth to the source, $\Delta d$, will change the ratio $\Delta(\Phi_1/\Phi_2)$ is determined by differentiating equation 2:

$$\Delta(\Phi_1/\Phi_2) = 5d\,\frac{\Phi_1}{\Phi_2}\left(\frac{1}{d^2+h_2^2} - \frac{1}{d^2+h_1^2}\right)\Delta d. \qquad (3)$$

For Kilauea, simultaneous tilt measurements were made during the January 18–May 11, 1960, event at Outlet and Uwekahuna

located 1 and 3 km, respectively, from the subsidence center. The ratio of tilt rates between Outlet and Uwekahuna in mid-February is not related to a change in tilt direction (fig. 46.11). The increase in ratio of tilt rates from 0.5 to 0.9 between Outlet and Uwekahuna is consistent with an upward migration of the subsidence center from 4 to 3 km that occurred in mid-February.

Simultaneous tilt measurements made at three different stations in the Mauna Loa summit region during the 1984 northeast-rift eruption showed no apparent change in the ratios of tilt rate (fig. 46.12). The MOK, HVO135, and AINAPO tilt sites are located at horizontal distances of 3.5, 0.5, and 1.5 km, respectively, from the subsidence center (fig. 46.6*B*). Using a value of 4 km for the depth to the source in (3) and noting that the slopes in figure 46.12 do not vary by more than 0.3, data in figure 46.12 indicate that the subsidence center related to the 1984 Mauna Loa eruption did not migrate vertically more the 0.7 km.

## EXPONENTIAL DECAY IN SUMMIT TILT RATE

The summit tilt rate measured during subsidence events usually decreases with time (figs. 46.13–46.15). We have fitted exponential curves to both tilt components recorded during the first 13 Kilauea subsidences listed in table 46.2 and the 1984 Mauna Loa subsidence. For each subsidence event we estimate the magnitude of the north-south and the west-east tilt change, the time constant related to the decay rate, $\tau$, and the beginning time of subsidence.

The time dependence of the summit tilt curves recorded during subsidences of both Kilauea and Mauna Loa is adequately matched by exponential curves, especially when tilt measurements are made by the 3-m-long watertube instrument (fig. 46.13) and by the dry-tilt technique (fig. 46.15). The poorer agreement between measured tilt changes and exponential curves for the March 1955 Kilauea subsidence is probably caused by less precise tilt measurements obtained from the horizontal-pendulum seismograph (fig. 46.14).

The only summit subsidence listed in table 46.2 that significantly departs from an exponential decay is the January 1983 Kilauea subsidence. This subsidence was a multiple event; the summit subsided in three stages over a period of 7 days (fig. 46.16). These three stages correspond to three episodes of downrift earthquake migration, crack opening, and eruption.

The exponential decay in summit tilt rate is reminiscent of a rheological response observed in the laboratory when crustal material is subjected to sudden stress changes, such as may result from the sudden movement of magma. For example, transient creep of crustal material will exhibit an exponential decay in strain rate (Jaeger and Cook, 1969). The time constants for summit subsidences at Kilauea

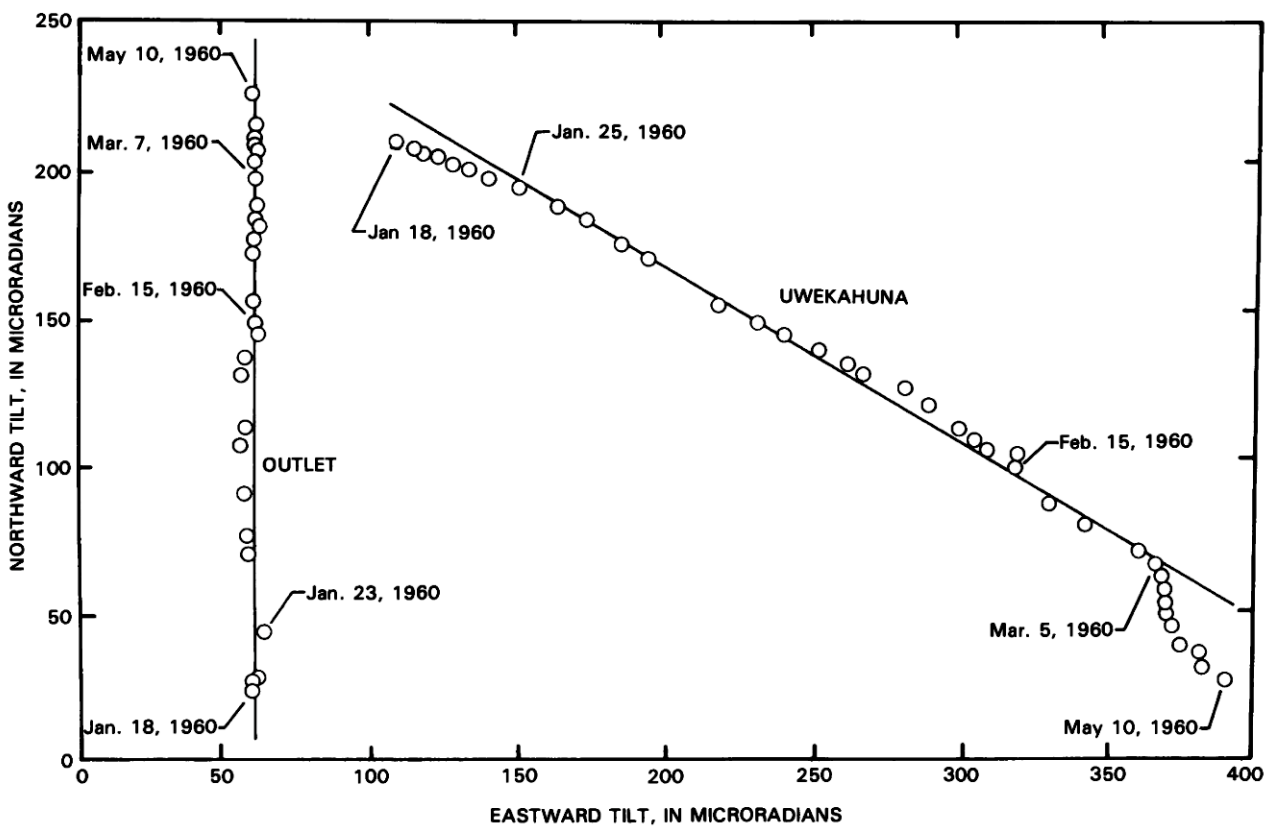


FIGURE 46.9.—Tilt directions measured at Outlet and Uwekahuna during January–May 1960 summit subsidence of Kilauea.

vary by a factor of more than 80. It seems unlikely that transient creep could control summit tilt rates, because rheological properties of the Kilauea summit would also have to vary by a factor of 80.

Along the east rift of Kilauea, the time constant appears to be related to the distance from the summit-subsidence center to the affected part of the rift (fig. 46.17). Longer time constants are associated with eruptions located farther downrift, suggesting that conduit length from the summit reservoir to the eruptive site controls, in part, the summit tilt rate. Time constants related to eruptions along the southwest rift of Kilauea and the northeast rift of Mauna Loa are longer than at comparable distances along the east rift of Kilauea.

Tilt rates recorded during periods of magma accumulation in the summit reservoir from a deeper source may also display an exponential decay. The west-east tilt component at Uwekahuna measured by a continuously recording tiltmeter revealed a cyclic pattern during a recent series of eruptive phases along the middle east rift (fig. 46.18). Beginning in February 1983 and lasting at least two years, the Kilauea summit went through several cycles of gradual uplift and more rapid subsidence. Periods of subsidence were associated with eruptive activity along the middle east rift. The summit tilt curve during noneruptive periods approximately followed an exponential decay curve with a maximum tilt change of 32 μrad. The time constant for summit uplift from February to September 1983 was 40 days, a time constant a factor of 2 greater than the maximum value determined for periods of summit subsidence and rift eruption.

We have argued that migration of the subsidence center and rheology of the volcano are unimportant in explaining summit-subsidence tilt curves. Moreover, an exponential time dependence of tilt rate observed during periods of both magma accumulation and withdrawal suggests that factors that control magma flow rate may be responsible for observed tilt rates.

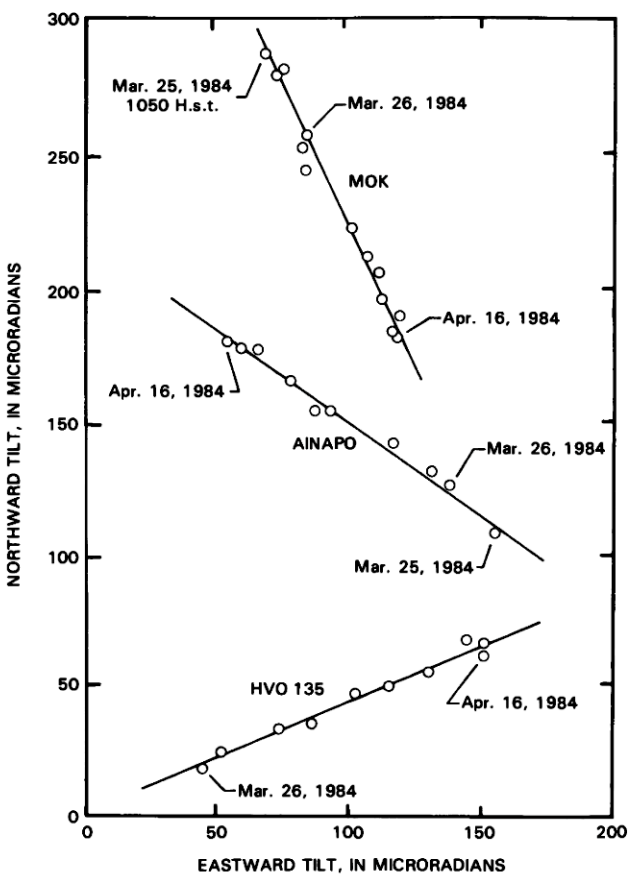


FIGURE 46.10.—Tilt directions measured at MOK, AINAPO, and HVO 135 during March 25–April 15, 1984 summit subsidence of Mauna Loa.

## HYDRAULIC MODEL

We adopt a hydraulic model for magma movement that was originally applied by Machado (1974) to explain decreasing extrusive rates observed at some volcanoes. Magma is stored in reservoirs between the upper mantle and the summit and along the rift systems. Magma moves within a conduit system that connects reservoirs that are under different confining pressures.

The magma flow rate, $Q$, is assumed to be proportional to the pressure change, $\Delta P$, between reservoirs

$$Q=\alpha\Delta P, \tag{4}$$

where the constant of proportionality, $\alpha$, depends on type of fluid flow.

We further assume that magma pressure is linearly related to volumetric strain, $\Delta V/V$,

$$\Delta P=-E\frac{\Delta V}{V}, \tag{5}$$

where $E$ is a constant of proportionality, the bulk modulus of the system. A pressure decrease results in a volume increase. When flow starts, pressure will change according to the equation (Machado, 1974, equation 48)

$$\Delta P=-\frac{E}{V}\left(\Delta V+\int_0^t Q\,dt\right). \tag{6}$$

Substitution of (4) into (6) yields

$$Q=Q_0-\frac{1}{\tau}\int_0^t Q\,dt, \tag{7}$$

where

$$\frac{1}{\tau}=\alpha\frac{E}{V} \tag{8}$$

and

$$Q_0=-\frac{\Delta V}{\tau}. \tag{9}$$

Differentiating (7) gives a simple differential equation for the magma flow rate:

$$\frac{dQ}{dt}+\frac{1}{\tau}Q=0. \tag{10}$$

The solution to the above equation is

$$Q=Q_0e^{-t/\tau}. \tag{11}$$

Several types of fluid flow are based on flow rate proportional to the pressure difference (4). In particular, for laminar fluid flow through a circular pipe of radius $r$, Poiseuille's law gives the constant of proportionality relating flow rate to pressure difference as:

$$\alpha=\frac{\pi}{8\eta}fr^4\left(\frac{\Delta P}{l}\right) \tag{12}$$

where $\eta$ is magma viscosity, $f$ is the frictional-loss factor, and $l$ is the conduit length. The quantity $\Delta P/l$ is the pressure gradient between the two reservoirs. The time constant is given by

$$\tau=\frac{8\eta}{\pi}\frac{\Delta V}{fr^4}\left(\frac{l}{\Delta P}\right). \tag{13}$$

The change in volume, $\Delta V$, is related to the subsidence volume. The time constant increases with conduit length in (13), a relation observed along the east rift of Kilauea (fig. 46.17), though not linearly along the entire rift, as would be expected if $r$, $f$, and $\Delta P$ remained constant.

Equation 13 emphasizes the importance of conduit width on magma flow rate. A 50-percent decrease in conduit width will decrease the flow rate by a factor of 16. Because conduit width probably does not remain constant along the rift system, a time constant derived from the summit tilt curve relates to the minimum constriction along the active part of the conduit.

## INITIAL EARTHQUAKE LOCATIONS AND SHAPE OF THE SUMMIT TILT CURVE

Earthquakes located in the summit region and along the rift zones of Kilauea are probably directly related to the magma conduit system within the volcano (Ryan and others, 1983). The location of the initial earthquake swarm associated with a summit subsidence may indicate where magma movement was initiated. We might expect that earthquake swarms initiated at different locations within the volcano will influence the initial shape of the summit tilt curve.

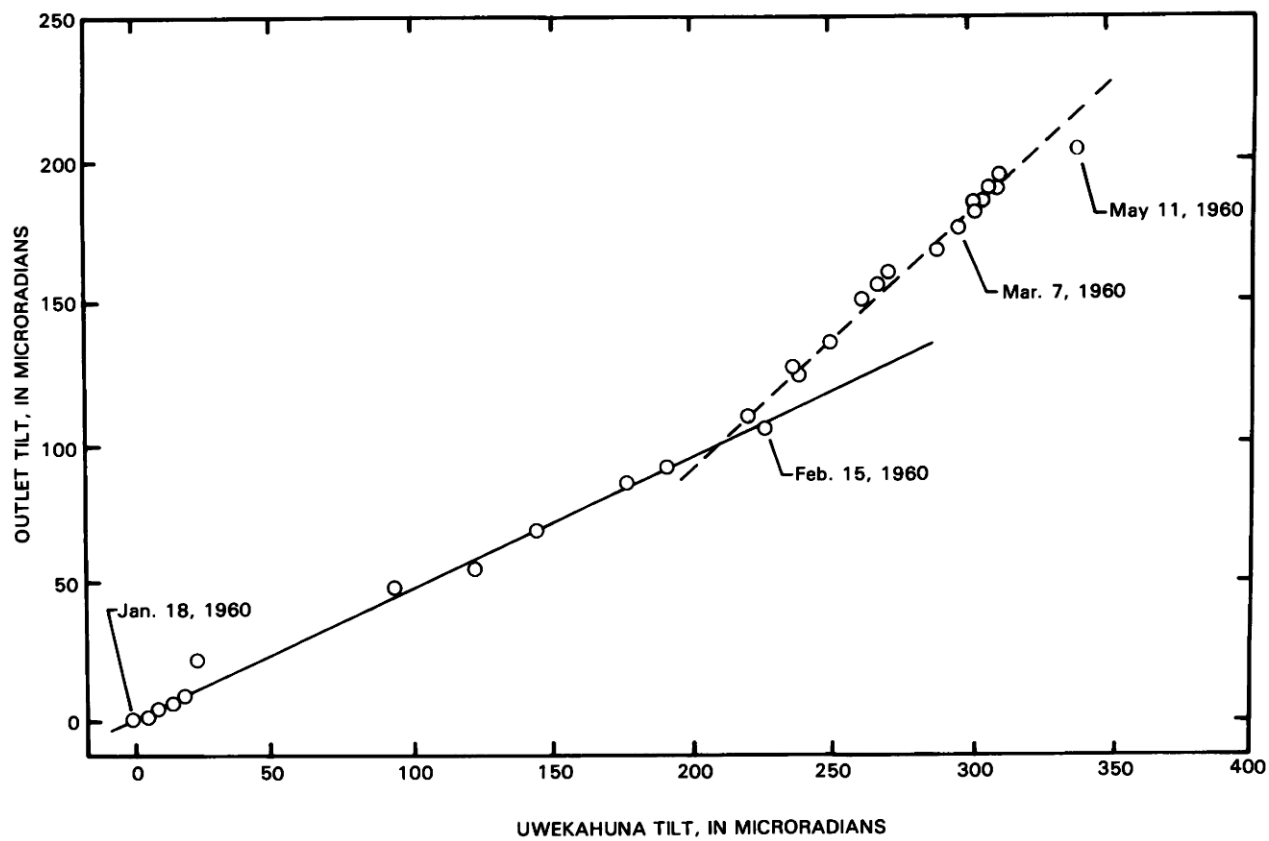


FIGURE 46.11.—Tilt magnitudes recorded at Outlet as a function of tilt magnitudes recorded at Uwekahuna during January–May 1960 summit subsidence of Kilauea.

Increased coverage of the seismic network and advances in seismic processing at HVO have improved hypocenter determinations on the Island of Hawaii (Klein and Koyanagi, 1980). In particular, earthquake swarms occurring at Kilauea over the past decade can be located to within a few kilometers on any part of the volcano with greater resolution in the summit region and along the upper rift systems.

Earthquake hypocenters associated with the onset of summit subsidence and southwest-rift intrusion frequently begin in the south caldera area of Kilauea. For example, earthquake swarms associated with the December 1974 eruption (fig. 46.19*A*) and the August 1981 intrusion (fig. 46.19*B*) began in the south caldera area and migrated along the southwest rift for several hours (Klein and others, chapter 43). The beginning of these two earthquake swarms coincided with an abrupt change in slope of the summit tilt curves (fig. 46.20). On the basis of the location of the initial earthquake swarm and the initial, rapid summit tilt change, we infer that magma movement on December 31, 1974, and on August 10, 1981, was initiated in the summit reservoir.

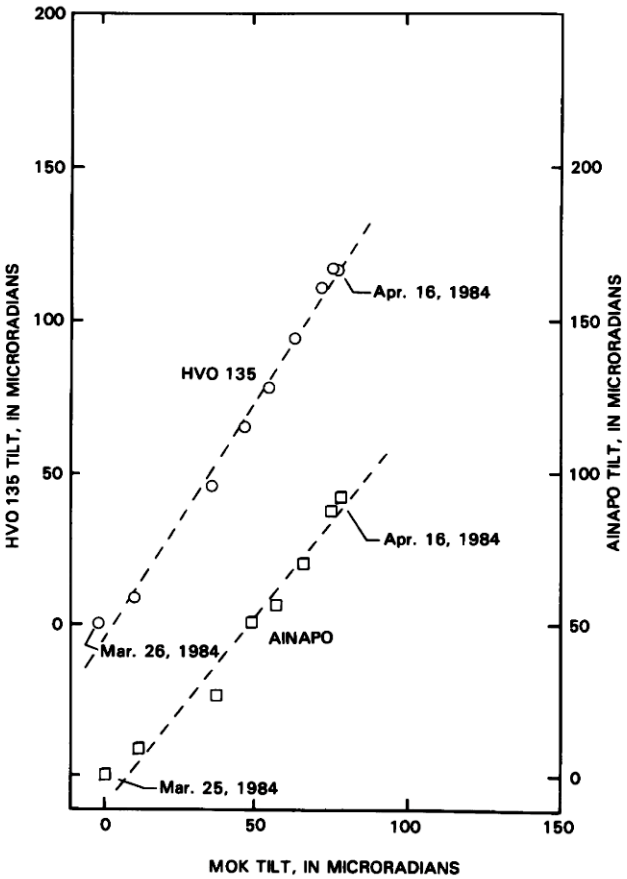


FIGURE 46.12.—Tilt magnitudes recorded at HVO 135 and AINAPO as a function of tilt magnitudes recorded at MOK during March 25–April 14, 1984 summit subsidence of Mauna Loa.

During the two most recent Kilauea subsidences listed in table 46.2, in June 1982 and January 1983, initial earthquake swarms were located along the rift and not in the south caldera area (fig. 46.21). The summit tilt responded gradually for several hours to these two events (fig. 46.22). Along the east rift near the site of the initial earthquake swarm in January 1983, a tiltmeter did record an abrupt change in slope (fig. 46.23). Presumably, initial magma movement was from a reservoir within the southwest rift in June 1982 and within the east rift in January 1983 and not from the summit reservoir. Initial magma flow from the summit reservoir was slower as pressure along the conduit system from the summit to the rift was gradually reduced as magma moved within the rift system.

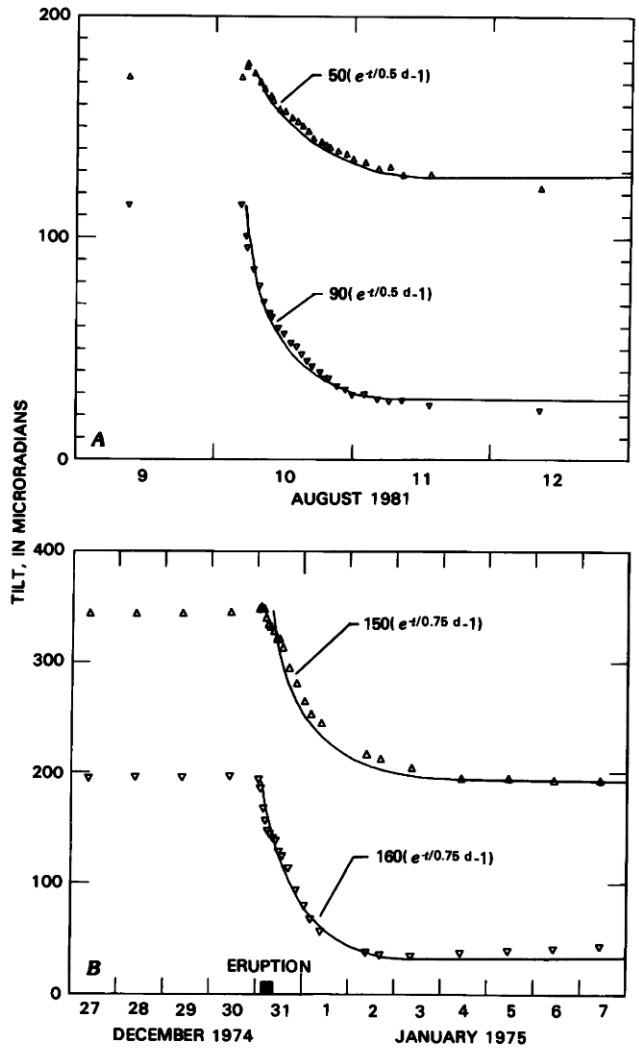


FIGURE 46.13.—Tilt changes recorded by 3-m-long watertube instrument at Uwekahuna. North-south tilt changes, upper curve; west-east tilt changes, lower curve; solid lines, exponential functions empirically fitted to tilt data; numerical constant in each equation is value of total tilt change in microradians. ***A***, August 1981 southwest-rift intrusion. ***B***, December 1974 southwest-rift eruption of Kilauea.

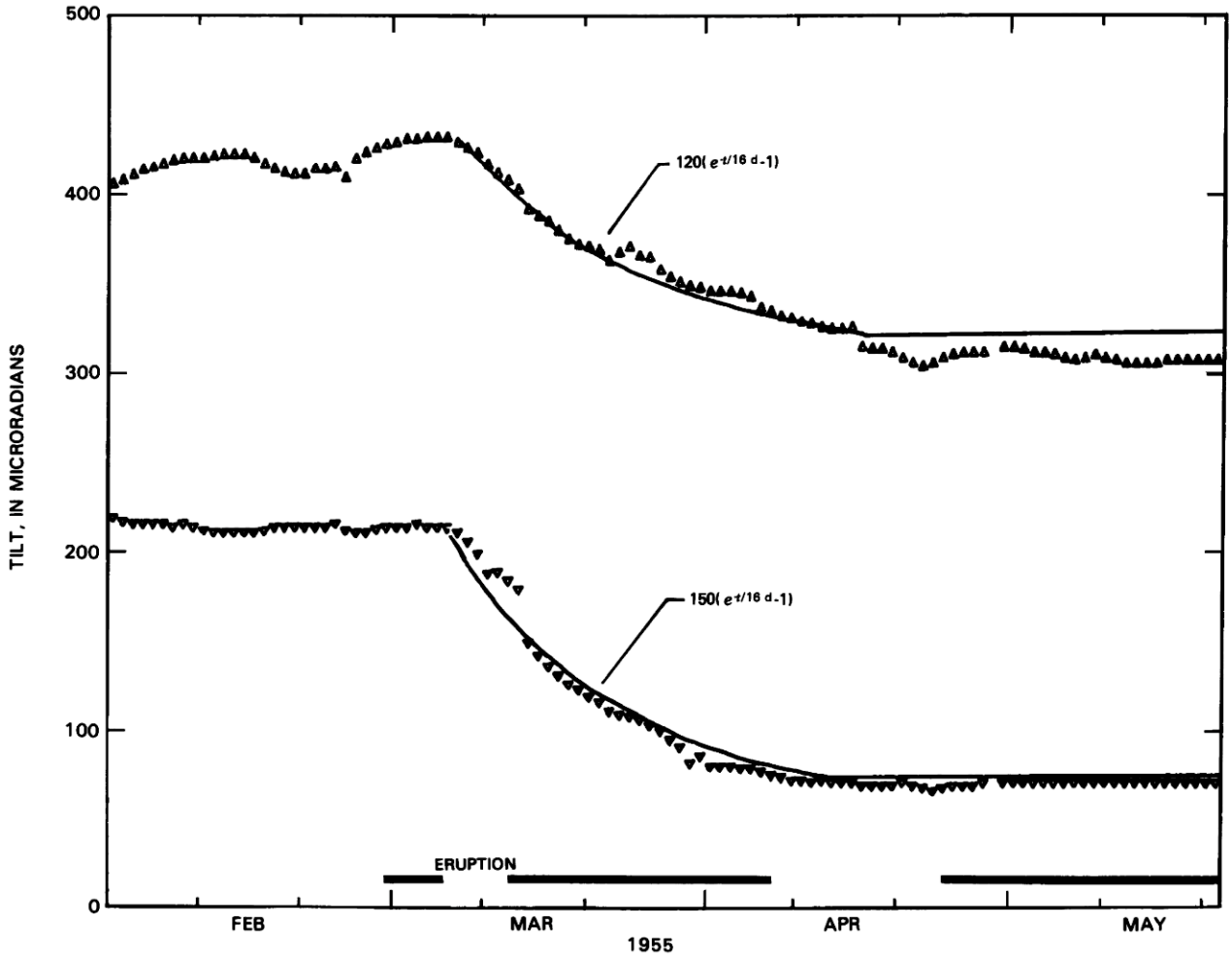


FIGURE 46.14.—Tilt changes recorded by horizontal pendulum seismograph at Uwekahuna during March 1955 lower-east-rift eruption of Kilauea. North-south tilt changes, upper curve; west-east tilt changes, lower curve; solid lines, exponential functions empirically fitted to tilt data; numerical constant in each equation is value of total tilt change in microradians.

A gradual response of summit tilt for 1 to 3 days was also observed after the onset of eruptive activity along the lower east rift in March 1955 and January 1960. Initial earthquake swarms and ground cracking in these two cases began along the rift.

## DISCUSSION

The well-establish relation between summit-subsidence events and rift intrusions and eruptions at Hawaiian volcanoes can be exploited to characterize magma movement within a long conduit system. In particular, we have examined the relation between rate of magma withdrawal from the summit reservoir and the rate and location of rift eruptions. Magma movement from the Kilauea summit reservoir to the east-rift system may be an analog to vertical magma ascent through the upper mantle and crust beneath Hawaiian volcanoes. Therefore, our results may also contribute to understanding how deeper magmatic sources influence eruptive activity at other volcanoes.

Summit tilt measurements at Kilauea and Mauna Loa record magma accumulation and withdrawal from a shallow reservoir. Magma originating in the mantle migrates through the upper mantle and crust and accumulates in the summit reservoir prior to eruption. Horizontal migration of the uplift center at Kilauea suggests that the summit reservoir consists of a plexus of dikes and sills (Fiske and Kinoshita, 1969).

Several lines of evidence indicate that magma also resides in shallow reservoirs along the east rift of Kilauea. The 4- to 5-day delay between the onset of eruptive activity along the lower east rift

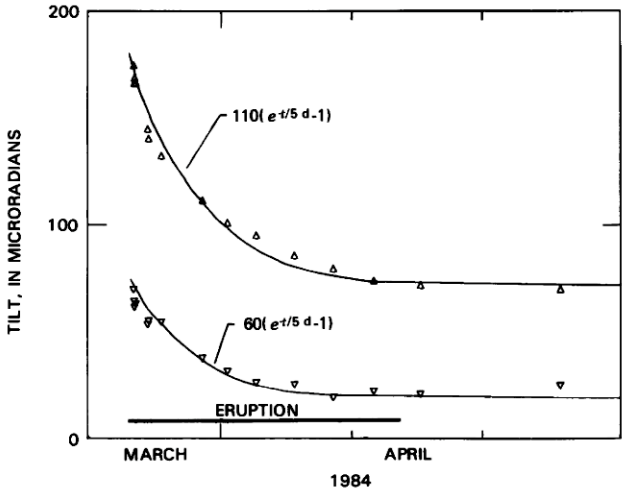


FIGURE 46.15.—Tilt changes recorded by dry-tilt method at MOK during March 25–April 15, 1984, northeast-rift eruption of Mauna Loa. North-south tilt changes, upper curve; west-east tilt changes, lower curve; solid lines, exponential functions empirically fitted to tilt data; numerical constant in each equation is value of total tilt change in microradians.

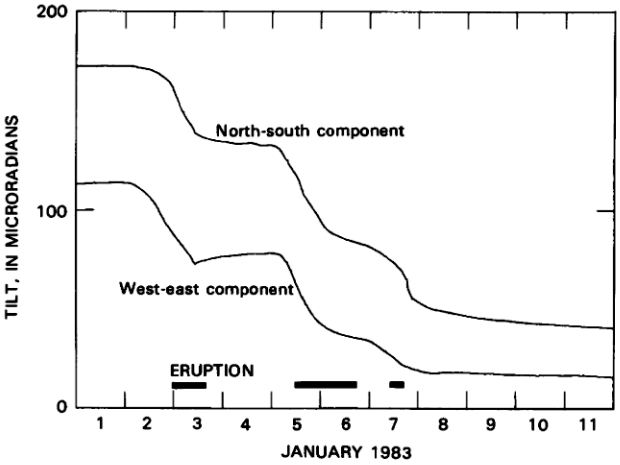


FIGURE 46.16.—Tilt changes recorded by automatic tiltmeter located at Uwekahuna during January 1983 middle-east-rift eruption of Kilauea.

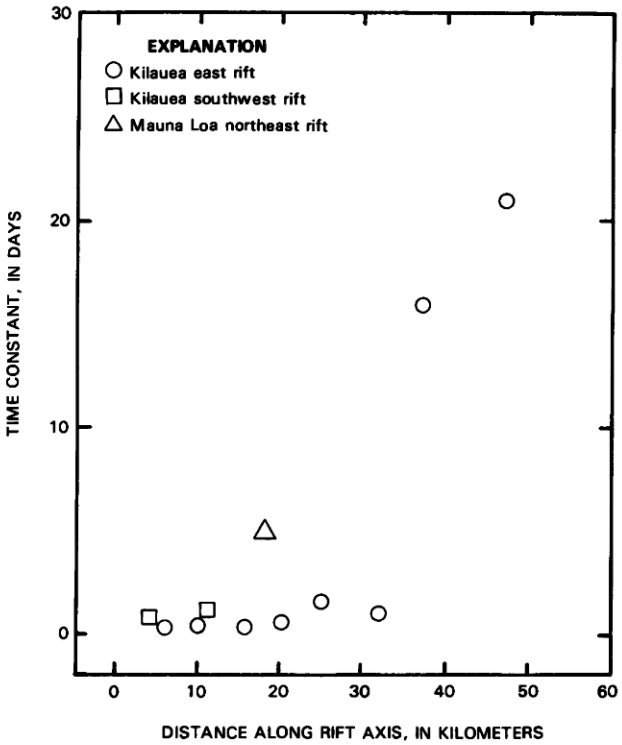


FIGURE 46.17.—Time constants for summit subsidences plotted as a function of distance from subsidence center to rift intrusion or eruption.

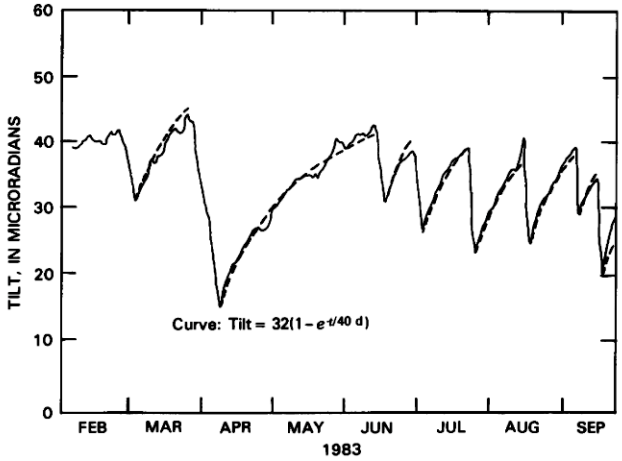


FIGURE 46.18.—West-east tilt changes recorded from February to September 1983 by tiltmeter located at Uwekahuna. Periods of generally increasing tilt values correspond to summit uplift and magma accumulation in Kilauea summit region; periods of rapid decrease in tilt values correspond to magma withdrawal from Kilauea summit region and eruptive activity along middle east rift. Same exponential curve (dashed lines) has been empirically fitted to periods of summit uplift. Exponential curve is for a maximum tilt change of 32 μrad and a time constant of 40 days.

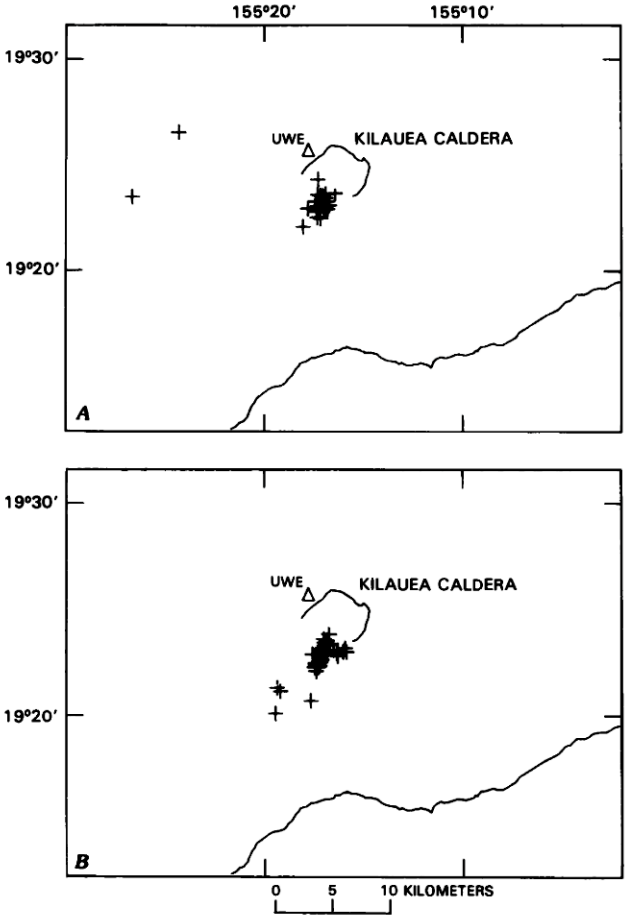


FIGURE 46.19.—Initial earthquake epicenters. UWE, Uwekahuna seismometer station. ***A***, December 31, 1974 (0000–0600 H.s.t.), southwest-rift eruption. ***B***, August 10, 1981 (0300–0600 H.s.t.), southwest-rift intrusion.

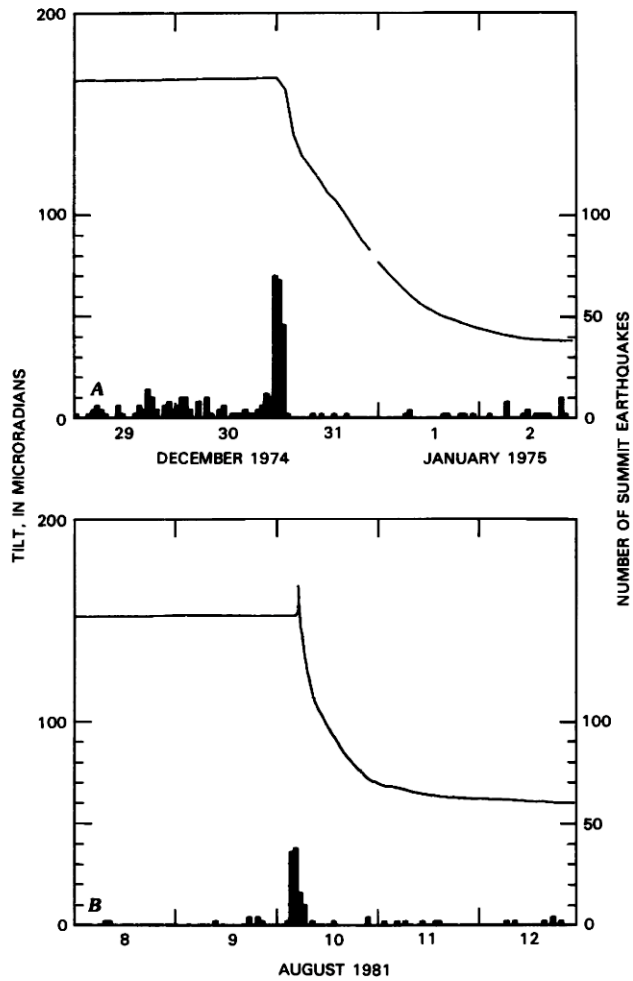


FIGURE 46.20.—West-east tilt curve recorded at Uwekahuna. ***A***, December 1974 southwest-rift eruption. ***B***, August 1981 southwest-rift intrusion. Hourly rate of locatable summit earthquakes is shown by bar graph.

and the onset of summit subsidence in March 1955 and January 1960 led Eaton (1962) to suggest that magma was stored within the rift system. Jackson and others (1975) noted that the volume of summit subsidence at Kilauea exceeds the volume of lava erupted along the rift: some magma withdrawn from the summit remains in the rift system. Differentiated lava initially erupted from the east rift during a new eruptive sequence suggests that rift eruptions are initially fed by magma that has resided for longer periods at shallow levels in the crust than magma erupted in the summit (Wright and others, 1968; Moore, 1983). Finally, geodetic surveys conducted along the east rift of Kilauea have identified centers of uplift presumed to be regions of magma accumulation (Jackson and others, 1975; Swanson and others, 1976; Dzurisin and others, 1984), one persistent center along the upper east rift is centered 2 to 4 km beneath the surface (Dvorak and others, 1983).

Along the east rift of Kilauea, the volume of summit subsidence increases with distance to the rift eruption (Epp and others, 1983). The subsidence rate also increases with distance, though not linearly, along the entire east rift (fig. 46.17). Time constants for summit subsidence range from 0.25 to 1.5 days for southwest- and east-rift eruptions that occur within 35 km of the summit; time constants for lower-east-rift eruptions were considerably longer, from 16 to 21 days. The abrupt increase in time constant for rift eruptions downrift of Heiheiahulu (fig. 46.1) may be caused by constriction of the magma conduit between the middle and the lower parts of the east rift.

The time constant for the 1984 Mauna Loa summit subsidence and northeast-rift eruption is close to the linear trend extrapolated from time constants for the Kilauea lower-east-rift eruptions. This similarity may be related to the several-year interval between rift

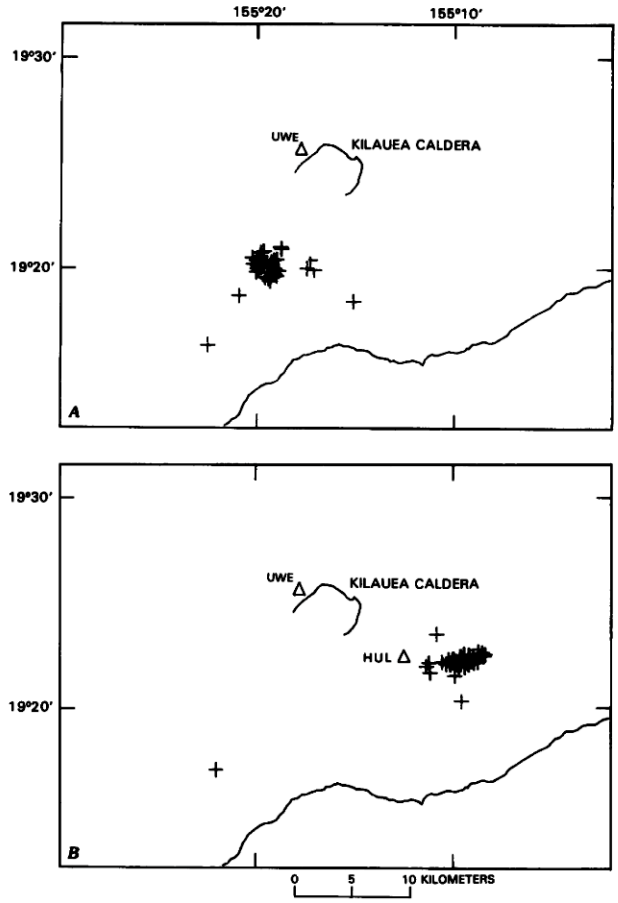


FIGURE 46.21.—Initial earthquake epicenters. Seismometer stations: UWE, Uwekahuna; HUL, Heiheiahulu. *A*, June 22, 1982 (1200–2300 H.s.t.), southwest-rift intrusion. *B*, January 2, 1983 (0000–0600 H.s.t.), east-rift eruption.

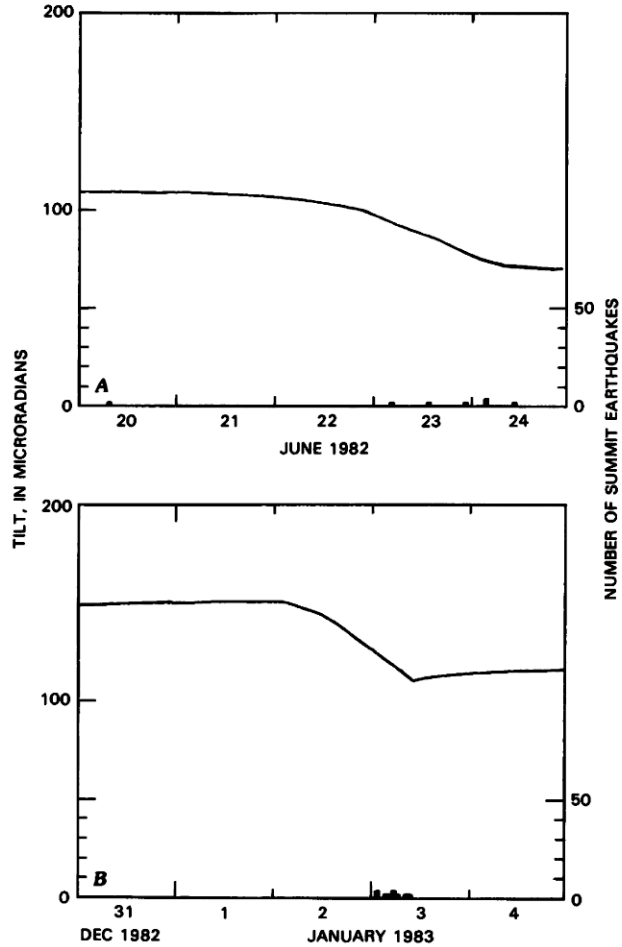


FIGURE 46.22.—West-east tilt curve recorded at Uwekahuna. *A*, June 1982 southwest-rift intrusion. *B*, January 1983 middle-east-rift eruption. Hourly rate of locatable summit earthquakes is shown by bar graph.

intrusions into the lower east rift of Kilauea and the northeast rift of Mauna Loa. By comparison, more frequent episodes of magma movement in the upper east rift result in less flow resistance and, hence, much shorter time constants (Dvorak and Okamura, 1985).

Changes in summit tilt rate recorded during subsidence events usually follow an exponential decay. Periods of magma accumulation in the summit reservoir may also follow an exponential decay in tilt rate, a result previously recognized by Shimozuru (1981), who proposed an electrical analog for the summit magma reservoir.

If we assume that summit tilt changes are related to summit magma accumulation or withdrawal, then the rate of magma accumulation in the summit reservoirs of Kilauea and Mauna Loa may be as much as a factor of 100 less than the rate of magma withdrawal (figs. 46.5, 46.17, 46.18). The different rates of magma accumulation and withdrawal for an eruptive cycle may reflect a basic difference between the vertical conduit feeding the summit reservoir and the horizontal conduit along the rift system. In the context of our model, an increase by a factor of 100 in magma flow rate could correspond to an increase by a factor of 10 in cross-sectional area or of 100 in pressure gradient (equation 13).

If the east rift of Kilauea is an appropriate analog for the vertical conduit beneath Hawaiian volcanoes, then we may have a better understanding of the possible role the upper mantle has on magma supply rate. The 40- to 60-km length of the vertical conduit from the mantle source to the summit, based on maximum earthquake depths beneath Hawaiian volcanoes and on a hydraulic model (Eaton and Murata, 1960), is comparable to the distance from the Kilauea summit to the 1960 lower-east-rift eruption. Because individual magma reservoirs exist along the east rift, magma reservoirs may also be expected to exist along the vertical conduit. Conduit width probably varies with length along both the vertical conduit and the rift system; the conduit width in equation 13 is the width at a constriction that limits the flow rate in the remainder of the conduit.

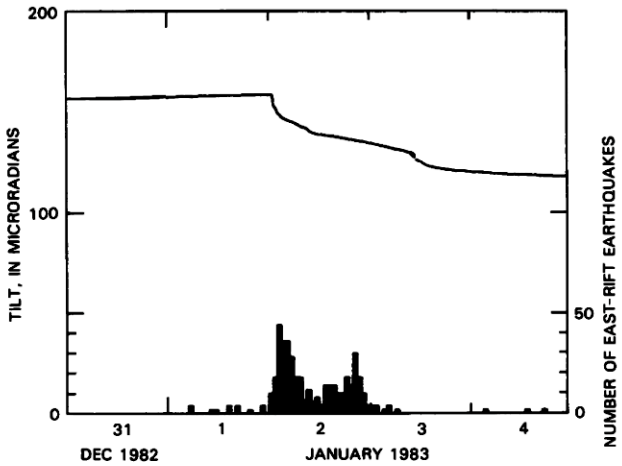


FIGURE 46.23.—West-east tilt curve recorded during early January 1983 along upper east rift (HUL in fig. 46.21*B*). Lower tilt value corresponds to downward deflection to east.

Magma flow may be initiated in a reservoir that lies along the rift system; however, the summit reservoir strongly influences the total volume of magma moved, as evidenced by continued summit subsidence several weeks after the end of eruptive activity in 1955 and 1960. Similarly, magma flow may be initiated in a reservoir within the vertical conduit, although the mantle source region may control the magma flow rate and total volume of magma involved. Recently, Dzurisin and others (1984) have suggested a close link between bursts of deep harmonic tremor, an indicator of magma movement, and magma supply rate to the Kilauea summit. Recognition of a relation between magma volume and flow rate from the Kilauea summit reservoir to east-rift eruptions supports their suggestion.

## SUMMARY

Summit magma reservoirs exist within a few kilometers of the surface at both Kilauea and Mauna Loa. The accumulation and withdrawal of magma in the reservoir is monitored by tilt measurements that can easily be made over periods of a few minutes to several weeks.

Summit tilt curves recorded during subsidence events frequently begin with an abrupt change in slope. The tilt rate is usually greatest at the beginning of the event and steadily decreases with time.

Horizontal or vertical migration of the subsidence center are unimportant in explaining variations in summit tilt rate at Kilauea and Mauna Loa. The summit-subsidence pattern at Kilauea is independent of the rift system involved in magma movement.

Most summit tilt curves associated with subsidence events follow an exponential decay. At Kilauea, the decay time constant has varied by more than a factor of 80, which suggests that rheological properties of the volcano do not control subsidence rate. The rate of magma accumulation in the summit reservoir may also follow an exponential decay.

A simple hydraulic model may explain the observed exponential decay in summit subsidence rate. The model assumes that magma flow rate is proportional to the pressure difference along the magma conduit from the summit reservoir to a second reservoir or eruptive site located along the rift system. Furthermore, magmatic pressure is assumed to be linearly proportional to volumetric strain. One type of fluid flow consistent with these assumptions is laminar flow through a circular pipe.

## REFERENCES

Decker, R.W., Koyanagi, R.Y., Dvorak, J.J., Lockwood, J.P., Okamura, A.T., Yamashita, K.M., and Tanigawa, W.R., 1983, Seismicity and surface deformation of Mauna Loa Volcano, Hawaii: Eos, Transactions of the American Geophysical Union, v. 37, p. 545–547.

Dvorak, J.J., and Okamura, A.T., 1985, Variations in tilt rate and harmonic tremor amplitude during the January–August 1983 east rift eruptions of Kilauea Volcano, Hawaii: Journal of Volcanology and Geothermal Research, v. 25, p. 249–258.

Dvorak, J.J., Okamura, A.T., and Dieterich, J.H., 1983, Analysis of surface deformation data, Kilauea Volcano, Hawaii: October 1966 to September 1970: Journal of Geophysical Research, v. 88, p. 3295–3304.

Dzurisin, D., Koyanagi, R.Y., and English, T.T., 1984, Magma supply and storage at Kilauea Volcano, Hawaii: 1956–1983: Journal of Volcanology and Geothermal Research, v. 21, p. 177–206.

Eaton, J.P., 1959, A portable water-tube tiltmeter: Bulletin of the Seismological Society of America, v. 49, p. 301–316.

———1962, Crustal structure and volcanism in Hawaii, *in* Macdonald, G.A., and Kuno, H., eds., The crust of the Pacific Basin: American Geophysical Union, Geophysical Monograph Series, v. 6, p. 13–29.

Eaton, J.P., and Murata, K.J., 1960, How volcanoes grow: Science, v. 132, p. 925–938.

Epp, D., Decker, R.W., and Okamura, A.T., 1983, Relation of summit deformation to east rift zone eruptions of Kilauea Volcano, Hawaii: Geophysical Research Letters, v. 10, p. 493–496.

Fiske, R.S., and Koyanagi, R.Y., 1968, The December 1965 eruption of Kilauea Volcano, Hawaii: U.S. Geological Survey Professional Paper 607, 21 p.

Fiske, R.S., and Kinoshita, W.R., 1969, Inflation of Kilauea Volcano prior to its 1967–68 eruption: Science, v. 165, p. 341–349.

Jackson, D.B., Swanson, D.A., Koyanagi, R.Y., and Wright, T.L., 1975, The August and October 1968 east rift eruptions of Kilauea Volcano, Hawaii: U.S. Geological Survey Professional Paper 890, 33 p.

Jaeger, J.C., and Cook, N.G.W., 1969, Fundamentals of rock mechanics: London, John Wiley and Sons, Inc.

Klein, F.W., and Koyanagi, R.Y., 1980, Hawaiian Volcano Observatory seismic network history 1950–1979: U.S. Geological Survey Open-File Report 80–302, 84 p.

Lockwood, J.P., Banks, N., English, T.T., Greenland, P., Jackson, D., Johnson, D., Koyanagi, R.Y., Okamura, A.T., and Rhodes, M., 1985, The 1984 eruption of Mauna Loa Volcano, Hawaii: Eos, Transactions of the American Geophysical Union, v. 66, p. 169–171.

Macdonald, G.A., and Eaton, J.P., 1964, Hawaiian volcanoes during 1955: U.S. Geological Survey Bulletin 1171, 170 p.

Machado, F., 1974, The search for magmatic reservoirs, *in* Civetta, L., Gasparini, P., Luongo, G., and Rapolla, A., eds., Physical volcanology, developments in solid earth geophysics, v. 6: Amsterdam, Elsevier, p. 255–273.

Mogi, K., 1958, Relations between the eruptions of various volcanoes and the deformation of the ground surface around them: Bulletin of the Earthquake Research Institute, University of Tokyo, v. 36, p. 99–134.

Moore, J.G., and Koyanagi, R.Y., 1969, The October 1963 eruption of Kilauea Volcano, Hawaii: U.S. Geological Survey Professional Paper 614–C, 13 p.

Moore, R.B., 1983, Distribution of differentiated tholeiitic basalts on the lower east rift zone of Kilauea Volcano, Hawaii: A possible guide to geothermal exploration: Geology, v. 11, p. 136–140.

Moore, R.B., Helz, T.R., Dzurisin, D., and Eaton, G.P., 1981, The 1977 eruption of Kilauea Volcano, Hawaii: Journal of Volcanology and Geothermal Research, v. 7, p. 189–210.

Richter, D.H., Ault, W.U., Eaton, J.P., and Moore, J.G., 1964, The 1961 eruption of Kilauea Volcano, Hawaii: U.S. Geological Survey Professional Paper 474–D, 34 p.

Richter, D.H., Eaton, J.P., Murata, K.J., Ault, W.U., and Krivoy, H.L., 1970, Chronological narrative of the 1959–60 eruption of Kilauea Volcano, Hawaii: U.S. Geological Survey Professional Paper 537–E, 73 p.

Ryan, M.P., Blevins, J.Y.K., Okamura, A.T., and Koyanagi, R.Y., 1983, Magma reservoir subsidence mechanics: theoretical summary and application to Kilauea Volcano, Hawaii: Journal of Geophysical Research, v. 88, p. 4147–4181.

Shimozuru, D., 1981, Magma reservoir system inferred from tilt patterns: Bulletin Volcanologique, v. 44, p. 499–504.

Swanson, D.A., Jackson, D.B., Koyanagi, R.Y., and Wright, T.L., 1976, The February 1969 east rift eruption of Kilauea Volcano, Hawaii: U.S. Geological Survey Professional Paper 891, 30 p.

Wright, T.L., and Fiske, R.S., 1969, Origin of the differentiated and hybrid lavas of Kilauea Volcano, Hawaii: Journal of Petrology, v. 12, p. 1–65.

Wright, T.L., Kinoshita, W.T., and Peck, D.L., 1968, March 1965 eruption of Kilauea Volcano and the formation of Makaopuhi lava lake: Journal of Geophysical Research, v. 73, p. 3181–3205.

Yamashita, K.M., 1981, Dry tilt: a ground deformation monitor as applied to active volcanoes of Hawaii: U.S. Geological Survey Open-File Report 81–523, 21 p.

# ELASTIC AND INELASTIC MAGMA STORAGE AT KILAUEA VOLCANO

*By* Daniel J. Johnson


## ABSTRACT

**Gravity, leveling, and trilateration data recently obtained at Kilauea Volcano indicate that magma is accommodated within the summit reservoir by a combination of elastic magma compression, elastic chamber expansion, and gradual inelastic edifice widening in a south-southeast direction.**

**Elastic (reversible) magma storage is modeled using data from 15 brief summit-deflation episodes in 1984–85 and assuming a spherical geometry for the magma reservoir. Changes in pressure in the reservoir produce the deformation; changes in mass in the reservoir produce the gravity changes. The ratio of residual gravity change (corrected for the free-air effect) to elevation change, measured near the apex of maximum subsidence, averaged $0.28 \pm 0.025$ μGal/mm. If magma density is assumed to be 2.75 g/cm$^3$, the volume of magma withdrawn from the reservoir averaged $2.4 \pm 0.21$ times the associated volume of subsidence. This volume difference is dependent on both the magma bulk modulus (which constrains bulk compression of the reservoir contents) and the edifice shear modulus (which constrains distortion of the surrounding edifice). If deformation is assumed to be from a point dilatational source in an elastic half-space, the observed volume difference implies that the shear modulus of the edifice is $2.0 \pm 0.24$ times the bulk modulus of the magma.**

**Trilateration data show that Kilauea's edifice widens inelastically in time intervals of months to years, primarily in a northwest direction. Over these long time periods, gravity and elevation changes indicate both surface subsidence and mass addition. These observations imply that horizontal extension of Kilauea's edifice decreases lateral support of the fluid magma reservoir, thus lowering the pressure in the reservoir and allowing more magma to be injected without vertical uplift.**

**Increased summit collapse occurred during the November 1975 earthquake, when new reservoir space created by inelastic seaward displacement of the volcano's south flank was not immediately filled by new magma from depth. For 16 months after the earthquake, additional reservoir capacity created by continued edifice dilation was filled with new magma. From January 1984 to July 1985, Kilauea's edifice subsided by 200 mm and widened by as much as 250 mm. No net subsurface mass changes were measured during this period, implying that the subsidence was entirely the result of horizontal extension.**

**A complete magma-budget estimate for Kilauea must therefore consider both elastic and inelastic magma storage. This requires a synthesis of leveling, trilateration, and gravity data.**


## INTRODUCTION

Kilauea Volcano grows by the accumulation of mantle-derived magma that is initially stored in a shallow summit magma reservoir (Eaton and Murata, 1960). The location of this storage region, indicated by an aseismic zone (Koyanagi and others, 1976) and by the inversion of measured surface displacements (Fiske and Kinoshita, 1969; Dvorak and others, 1983), is in a zone below the south rim of the caldera about 3 km in diameter and from 2 to 6 km below the surface. Slow uplift of the volcano's summit over several weeks to a few months is caused by the gradual addition of new magma from a deep source region. Occasional rapid surface subsidence, over periods of hours to days, occurs as magma is withdrawn from the reservoir, either migrating upward or laterally through a conduit system into one of two rift zones (Ryan and others, 1981). Though a part of the mantle-derived magma supply may eventually reach the surface, some magma remains in the summit reservoir and rift systems (Dzurisin and others, 1984).

Previous estimates of magma-volume changes in the subsurface reservoir have been based on geodetic measurements (Duffield and others, 1982; Dvorak and others, 1983; Dzurisin and others, 1984). Because the elastic properties of both magma and volcanic edifice are poorly known, subsurface volume changes cannot be determined from geodetic data alone. Rather, the volume change of the edifice, as determined by integrating vertical displacements measured at the surface, is typically used to approximate the subsurface volume change.

Subsurface volume changes can be estimated more accurately if measurements of changes in both gravity and elevation are available. Gravity and elevation measurements obtained at Kilauea by Jachens and Eaton (1980) and Dzurisin and others (1980) demonstrated that between November 1975 and September 1977 changes in the volume of magma in the reservoir exceeded changes in the volume of the edifice. This was attributed to the effect of void spaces created during periods of magma withdrawal (Jachens and Eaton, 1980), later refilled during periods of magma accumulation (Dzurisin and others, 1980). Gravity studies by Johnsen and others (1980) at Krafla, Iceland, by Sanderson and others (1983) at Mount Etna, Italy, and by Eggers (1983) at Pacaya Volcano, Guatemala, also indicate differences between edifice and subsurface volume changes. Sanderson and others (1983) explained the differences by bulk compression of the magmatic fluid and changes in volume of exsolved gas enabling subsurface magma accumulation to exceed the volume of edifice expansion. Eggers (1983) proposed density changes of about 0.4 g/cm$^3$ in shallow magma bodies caused by changes in the magmatic water content and vesicularity.

A series of gravity observations made in the Kilauea summit region between January 6, 1984, and July 8, 1985, have been

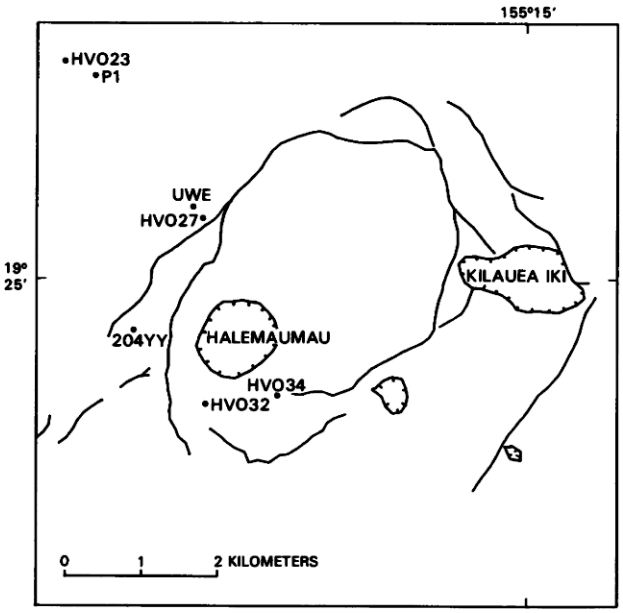


FIGURE 47.1.—Location map of Kilauea summit region showing principal fault scarps and craters, gravity monitoring sites HVO23, P1, HVO27, 204YY, HVO32, and HVO34, and east-west component electronic tiltmeter at Uwekahuna (UWE). Hachures mark inner side of crater walls.

analyzed to determine the empirical relation between magma-volume changes in the summit reservoir and edifice-volume changes as evidenced by surface uplift or subsidence. The short-term relation observed during brief episodes of elastic deflation corresponding to eruptions at the Puu Oo vent along Kilauea's middle east rift zone (Wolfe and others, chapter 17) has been used to estimate the relative elastic properties of the magma reservoir region and the surrounding volcanic edifice. The long-term relation has been used to evaluate the effect of inelastic summit widening on volume changes of the edifice and magma content of the summit reservoir. Results of this study will help improve estimates of the rate of magma supply to Kilauea.

## ACKNOWLEDGMENTS

This study is part of a doctoral dissertation in progress at the Department of Geology and Geophysics of the University of Hawaii. The Hawaiian Volcano Observatory of the U.S. Geological Survey provided logistical support and funds for field expenses. I thank Eduard Berg, Robert Decker, Roger Denlinger, John Dvorak, Daniel Dzurisin, Albert Eggers, Robert Jachens, and Thomas Wright for helpful ideas, suggestions, and assistance given during all phases of this study. I am indebted to Thomas Wright for his continued interest and kind support. He showed this in an exceptional manner by personally doing most of the gravity surveys made after July 1984. This manuscript has benefited from reviews by Edward Brown, John Dvorak, Daniel Dzurisin, Harry Glicken, Robert Jachens, and Michael Ryan.

## DATA

A total of 141 gravity surveys were conducted in the Kilauea summit region between January 6, 1984, and July 16, 1985. Initially, measurements were made at five monitoring sites referenced to a base station (P1) 5 km northwest of the point of maximum vertical movement (from earlier leveling surveys). The monitoring network was reduced to two sites after February 16, 1984, and to one site, HVO34, after July 12, 1984, because data from this site were found to be representative of the others. Only gravity data for HVO34, referenced to P1, are presented in this paper; locations of all measured stations are shown in figure 47.1.

Two LaCoste and Romberg model-G gravimeters, each equipped with galvanometer-assisted readout, were used throughout the study. Measurements were made over two (109 surveys) or three (32 surveys) closed loops between P1 and the network stations. The time to complete each loop, initally 4 h shortened to 1 h as the number of sites was reduced. Gravity readings were corrected for tidal effects (Longman, 1959) using a compliance factor of 1.16. The effects of instrumental drift and residual tide variations were removed by a least-squares solution of a second-order polynomial approximating time-dependent changes in the reading level of each gravimeter. Linear and sinusoidal gravimeter calibration functions were determined from standard calibration loops and applied to all the Kilauea data (table 47.1).

No attempt was made to correct the gravity data for water-table changes. As P1 and HVO34 are only 5 km apart, gravity variations caused by water-table changes are probably similar at both sites and do not affect the relative gravity differences.

Because data from each gravimeter were analyzed separately, agreement between the two gravimeters is a measure of the precision of the observations. A plot of the measurement discrepancy of the two gravimeters at HVO34 versus time is shown in figure 47.2 for surveys done with three loops (triangles) and with two loops (circles). The standard deviation of the intermeter difference for triple-looped surveys is 9.7 μGal and for double-looped surveys is 11.9 μGal. These figures correspond to standard errors of the mean of 3.4 μGal and 4.2 μGal, respectively.

Elevation changes were determined by optical leveling of a line from P1 to HVO34. The surveys were made in only one direction to third-order standards. East-west tilt variations, measured by a continuously recording, 1-m-base, mercury-capacitance tiltmeter at

TABLE 47.1.—*Linear and sine-form calibration functions for LaCoste and Romberg gravimeters G-615 and G-721 as a function of dial reading*

[Linear factor determined by resurveying 6 stations of calibration line established by Jachens and Eaton (1980) on Mauna Kea Volcano. Sine-form calibration functions determined in June 1984 by measuring 25 stations near Palm Desert, California, and comparing results to values obtained by Robert Jachens (written commun., 1984) with LaCoste and Romberg model-D gravimeters. Sine functions were checked and adjusted slightly by comparing values for G-615 and G-721 obtained at Ocean View Estates, Hawaii, in December 1984. c.u., dial reading in counter units; n.d., not detected]

| | Wavelength = 73.33 c.u. | | Wavelength = 36.67 c.u. | | |
|---|---|---|---|---|---|
| Gravimeter | 1/2 amp (μGal) | Phase zero (c.u.) | 1/2 amp (μGal) | Phase zero (c.u.) | Linear factor |
| G-615 ----- | 0.01739 | 2,924.54 | n.d. | n.d. | 1.000573 |
| G-721 ----- | .01415 | 2,996.05 | .02817 | 2,928.51 | 1.000296 |

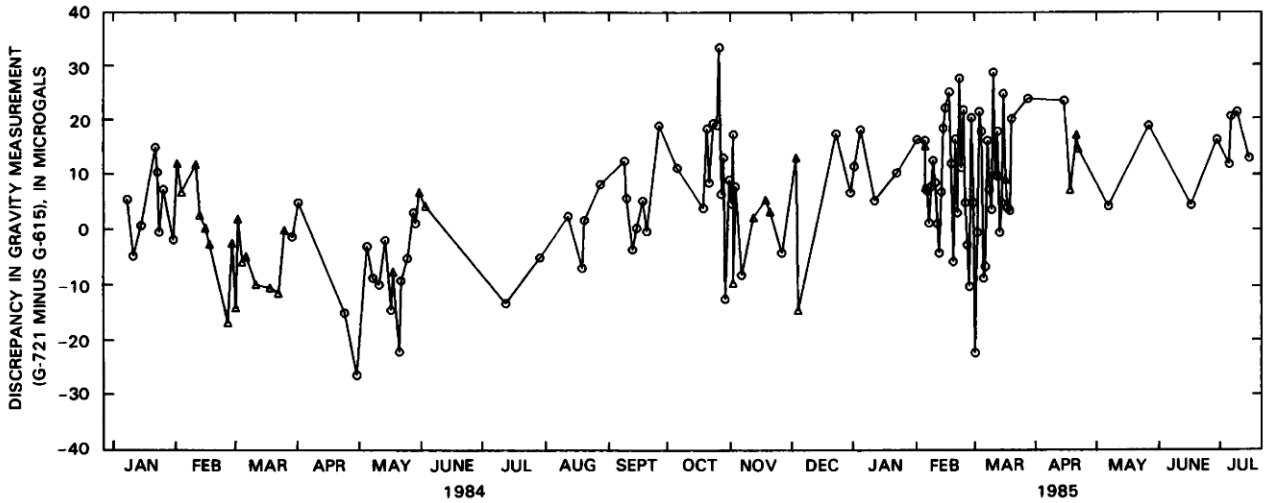


FIGURE 47.2.—Discrepancy between gravity measurements made by gravimeters G–615 and G–721 at site HVO34 plotted as a function of time. Triangles, surveys done with three loops; circles, surveys with two loops.

Uwekahuna (fig. 47.1, UWE), were used to interpolate elevation and edifice-volume changes to values corresponding in time with the gravity surveys. Resurveys of an extensive trilateration network in the summit area of Kilauea in January 1984 and July 1985 provided information on horizontal displacement.

## RESULTS

Observed gravity differences (fig. 47.3C) and elevation differences (fig. 47.3*A*) between HVO34 and P1 and changes in east-west tilt (fig. 47.3*B*) at Uwekahuna have been plotted as a function of time. Episodes of the eruption at Puu Oo are sequentially numbered (fig. 47*B*). Increasing tilt values correspond to inflation of the volcano. Tilt data indicate that activity was characterized by cycles of gradual inflation followed by brief deflation episodes during eruptive pulses at the Puu Oo vent (Wolfe and others, chapter 17). Considering the uncertainty of the gravity observations (3–4 μGal), no systematic short-term gravity changes can be inferred. Apparently the free-air gravity changes caused by cycles of elevation variations are compensated by gravity changes caused by fluctuations in the mass of magma in the reservoir. Superimposed on these eruptive cycles is a net deflation of the summit indicated by a tilt change of −42 μrad and an elevation change of −200 mm. During the same period, the gravity at HVO34 gradually increased by about 65 μGal. These long-term variations follow a free-air relation, implying that there was no net subsurface mass change.

## INTERPRETATION

The gravity data for HVO34 presented in figure 47.3C are corrected for earth tides. The effects of anomalous earth tides, ocean tides, and variations in atmospheric pressure are at least partly removed by the drift correction. The remaining processes that affect the gravity values include (1) accumulation or loss of magma from the reservoir, (2) vertical movement of the observation point in the Earth's gravity field (the free-air effect), and (3) density distribution change in the edifice as a result of deformation. These processes are usually coupled at Kilauea. For example, an intrusion of magma will increase gravity because of its mass, but it will decrease gravity because of the surface uplift that it causes. The gravity effect of (3) for a spherically symmetric source of dilatation is zero, as shown by a numerical analysis (Rundle, 1978) and by an analytical treatment (Walsh and Rice, 1979). The gravity effect of (3) for other source geometries, such as vertical and horizontal cracks, are not zero (Savage, 1984). While other geometries (consistent with the geologic structures seen in ancient volcanoes) have been suggested by Dieterich and Decker (1975) and Ryan and others (1983), the point source approach has been used in this report because of its computational convenience. In considering the gravity data presented here, the assumption was made that the gravity effect of (3) was indeed zero.

Because changes in the magma content of the subsurface reservoir are partly accommodated by slight elastic compression of the total volume of reservoir magma, the density of the reservoir magma can change slightly through time. In this analysis, the phrase magma-volume change indicates a change in the magma content of the reservoir and is expressed using units of volume calculated at a constant, arbitrary density of 2.75 g/cm$^3$. Although the parameter that is actually being measured by gravity is the mass change, conversion to volume change is done here to enable comparison with dense-rock equivalent volumes of lava flows and intrusions reported elsewhere. Another type of subsurface volume change discussed here is changes in the capacity of the reservoir, which refers to changes in the physical dimensions of the reservoir.

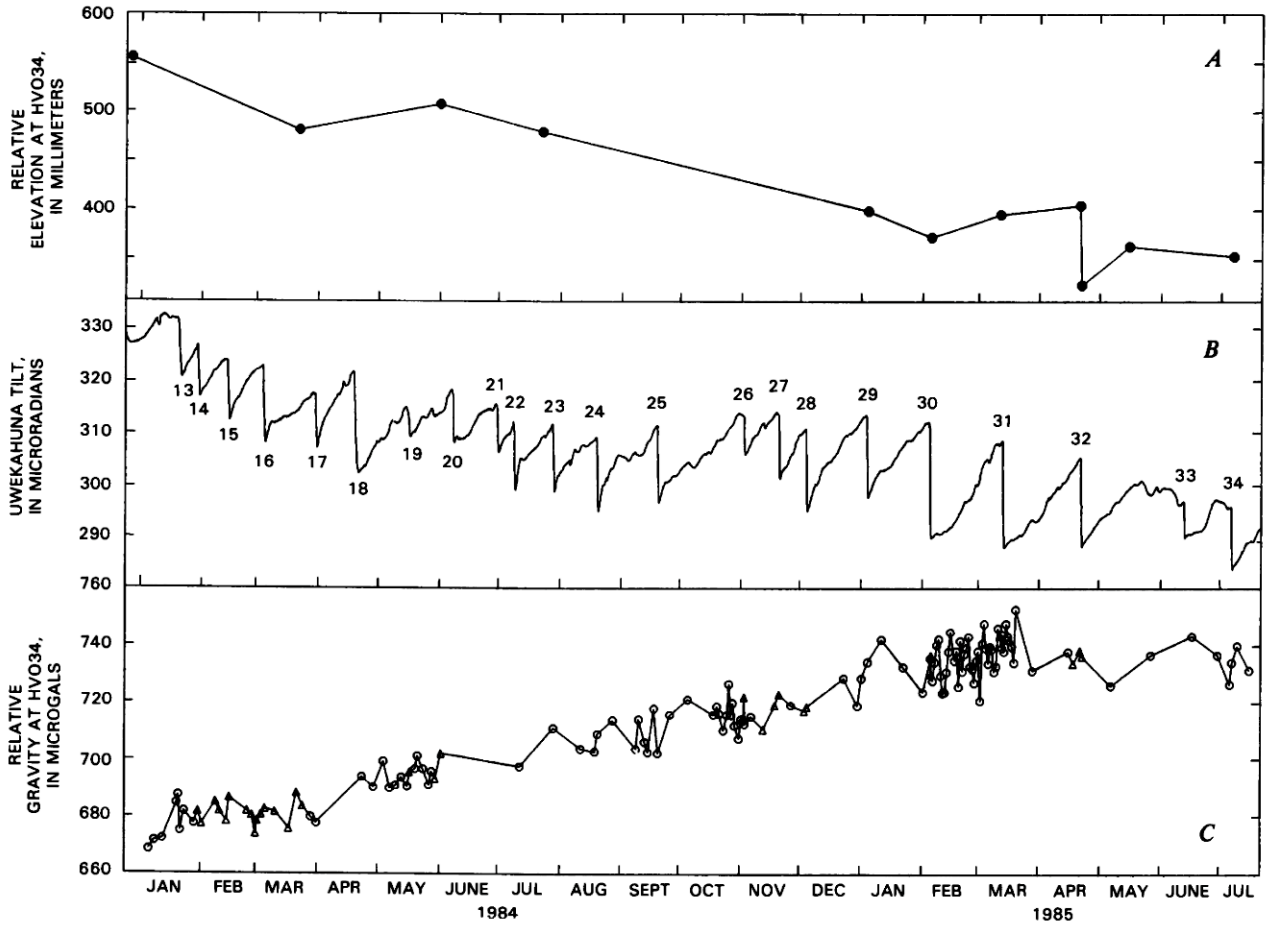


FIGURE 47.3.—Time plots of relative elevation and gravity at HVO34, and east-west tilt at Uwekahuna. ***A***, Relative elevation of site HVO34. ***B***, East-west tilt at Uwekahuna; eruptive episodes at Puu Oo vent indicated by numbers. ***C***, Relative gravity at site HVO34, uncorrected for vertical uplift. Triangles, gravity surveys done with three loops; circles, surveys done with two loops.

## RELATION BETWEEN EDIFICE AND SUBSURFACE VOLUME CHANGES

The ratio of the change in magma volume of the reservoir, $\Delta V_m$, to change in volume of the edifice, $\Delta V_e$, may be estimated from gravity changes, $\Delta g'$, derived from the observed gravity differences, $\Delta g$, by correcting for vertical displacement with a free-air gradient of $-0.3086$ μGal/mm, and from elevation differences, $\Delta h$. The analysis is based on a point dilatational source in an elastic half-space (see, for example Mogi, 1958). The volume change of the edifice was determined by integrating vertical surface displacement. Uplift at the surface is given (Mogi, 1958) by:

$$\Delta h = \frac{3a^3\Delta P}{4\mu_e} \cdot \frac{Z}{(X^2+Z^2)^{3/2}}, \qquad (1)$$

where $a$ is the radius of the source, $\Delta P$ is the pressure change, $\mu_e$ is Lame's constant for the edifice, $Z$ is depth to the source, and $X$ is horizontal distance to the chamber. Integration of equation 1 over the Earth's surface gives an expression for the volume increase of the edifice, $\Delta V_e$:

$$\Delta V_e = \frac{3\pi a^3 \Delta P}{2\mu_e}. \qquad (2)$$

Division of equation 2 by equation 1 and rearrangement yields:

$$\Delta V_e = \frac{2\pi(X^2+Z^2)^{3/2}\Delta h}{Z}. \qquad (3)$$

The mass change of the reservoir was determined next. So that it may be compared with volumes of subsidence and of eruptive products, mass change is expressed in terms of an effective magma-volume change, $\Delta V_m$, using a constant density ρ for the magma.

The graviational attraction of the new magma, approximated by a point mass, is given by:

$$\Delta g = \Delta V_m \gamma \rho \frac{Z}{(X^2+Z^2)^{3/2}}, \quad (4)$$

where $\gamma$ is the universal gravitational constant ($6.67\times10^{-11}$ nm$^2$/kg$^2$) and $\rho$ is the standard magma density. If the location of the dilational source in equation 3 is assumed to be the same as the new magma in equation 4, a combination of equations 3 and 4 yields an expression relating the observed gravity and elevation change to volume changes of the edifice and magma within the reservoir:

$$\frac{\Delta V_m}{\Delta V_e} = \frac{\Delta g'}{\Delta h 2\pi\gamma\rho}. \quad (5)$$

Jachens and Eaton (1980) and Dzurisin and others (1980) found a good spatial correlation between gravity changes and elevation changes at Kilauea; their results are consistent with coincident sources for the gravity changes and the dilatation. This correlation of gravity and elevation changes indicates that in equation 5 the ratio of relative changes at two or more points showing differential changes can be used as validly as the ratio of absolute changes. The present analysis uses relative changes between two points.

Notice that when $\Delta V_m = \Delta V_e$ (that is, when there is no subsurface density change), equation 5 is equivalent to the Bouguer gradient. Furthermore, when $\Delta V_e = 1.5\Delta V_m$ (that is, no magma compression but dilation of the edifice as predicted by the Mogi model with a Poisson's ratio of 0.25), equation 5 plus the free-air gradient is equivalent to theoretical gravity gradients proposed by Dzurisin and others (1980, equation A-11) and Hagiwara (1977, equation 19). In this analysis, the ratio of magma accumulation in the reservoir to surface uplift is considered to be an independent variable. Equation 5 shows that the gravity-change gradient $\Delta g'/\Delta h$ is near 0.08 μGal/mm for an incompressible magma with a density of 2.75 g/cm$^3$ accommodated by edifice expansion. The gradient approaches infinity for magma compressed into an unyielding edifice.

Gravity measurements were made near the beginning and end of 15 summit-deflation events corresponding to eruptive episodes 13–17, 24–32, and 34 at Puu Oo. Because of the brevity of each deflation, these gravity changes should not be influenced by long-term changes (for example, south-flank movement or magma migration unrelated to eruption), but should reflect mass and elevation changes related to simple elastic deflation. The changes in relative gravity at HVO34 and in east-west tilt at Uwekahuna during the monitored deflations are summarized in table 47.2. No real gravity changes ($\Delta g$) significantly larger than the data uncertainty were measured during these events because the gravity data reflect a composite of free-air gravity increases owing to subsidence and gravity decreases, $\Delta g'$, owing to removal of magma.

Elevation changes of HVO34 between gravity surveys were estimated for the period from December 28, 1983, to July 16, 1985, from the calculated relation between elevation of HVO34 and tilt at Uwekahuna. A factor of 5.19 mm/μrad was derived by a least-squares fit to tilt and elevation data (fig. 47.4). Elevation changes during eruptive episode 32 were measured directly by leveling surveys conducted on April 21 and 22, 1985. Table 47.3 summarizes the estimates of $\Delta g'$ (corrected for vertical displacement with a free-air gradient of −0.3086 μGal/mm), $\Delta h$, and the ratio $\Delta V_m/\Delta V_e$ calculated using equation 5. Because virtually no real gravity changes ($\Delta g$) were measured, most of the $\Delta g'$ values shown in table 47.3 result from the free-air correction. These calculations show that the volume of magma lost from the reservoir is 1.2 to 4.5 times (average 2.4±0.21, 1 standard error) greater than the volume of subsidence at the surface during the periods of rapid deflation.

## SUBSURFACE VOLUME CHANGES DURING DEFLATION EVENTS

The empirical relation between volume changes of magma within the summit reservoir and volume changes of the volcanic edifice can be used to estimate the former from measurements of the latter. This means of estimating magma-volume changes at depth is

TABLE 47.2.—*Nominal relative gravity change at HVO34 and tilt changes at Uwekahuna for deflation intervals corresponding to 15 eruptions at Puu Oo, 1984–85*

[Times given are Hawaii standard time; figures for loops give number of closed loops between HVO34 and P1 for each gravity survey. s.e., standard error]

| Eruptive episode | First survey | | | | Second survey | | | | Δg (±1 s.e.) (μGal) | Δ tilt (μrad) |
|---|---|---|---|---|---|---|---|---|---|---|
| | Date | Start time | Duration (h) | Loops | Date | Start time | Duration (h) | Loops | | |
| 13 | Jan. 20, 1984 | 1445 | 4.00 | 2 | Jan. 22, 1984[2] | 0900 | 4.75 | 2 | −4 (5.8) | −10.4 |
| 14 | Jan. 29, 1984 | 1200 | 5.00 | 2 | Jan. 31, 1984[2] | 0800 | 7.50 | 3 | 4 (5.1) | −7.3 |
| 15 | Feb. 14, 1984[1] | 2145 | 4.25 | 3 | Feb. 16, 1984 | 0845 | 6.25 | 3 | 8 (4.4) | −8.9 |
| 16 | Mar. 3, 1984 | 0815 | 6.00 | 3 | Mar. 5, 1984 | 0745 | 6.50 | 3 | 2 (4.4) | −14.1 |
| 17 | Mar. 28, 1984 | 1230 | 3.75 | 2 | Mar. 31, 1984 | 1245 | 3.75 | 2 | −2 (5.8) | −9.5 |
| 24 | Aug. 19, 1984 | 1130 | 2.00 | 2 | Aug. 20, 1984 | 1845 | 2.00 | 2 | 6 (5.8) | −14.1 |
| 25 | Sept. 18, 1984 | 1000 | 1.50 | 2 | Sept. 20, 1984 | 0645 | 1.75 | 2 | −16 (5.8) | −14.4 |
| 26 | Nov. 2, 1984 | 0845 | 1.75 | 2 | Nov. 3, 1984 | 0500 | 2.00 | 2 | −1 (5.8) | −7.5 |
| 27 | Nov. 18, 1984 | 1045 | 3.00 | 3 | Nov. 20, 1984 | 1415 | 2.00 | 3 | 4 (4.4) | −12.5 |
| 28 | Dec. 3, 1984 | 0815 | 2.75 | 3 | Dec. 4, 1984 | 1315 | 3.00 | 3 | 2 (4.4) | −15.6 |
| 29 | Jan. 1, 1985 | 0645 | 1.50 | 2 | Jan. 4, 1985 | 0730 | 1.50 | 2 | 6 (5.8) | −15.2 |
| 30 | Feb. 2, 1985 | 0645 | 1.75 | 2 | Feb. 5, 1985 | 0400 | 2.00 | 2 | 12 (5.8) | −21.5 |
| 31 | Mar. 12, 1985 | 0930 | 2.00 | 3 | Mar. 14, 1985 | 0615 | 1.50 | 2 | 6 (5.1) | −19.9 |
| 32 | Apr. 21, 1985 | 1515 | 2.25 | 3 | Apr. 22, 1985 | 1445 | 4.25 | 6 | −2 (3.8) | −16.9 |
| 34 | July 6, 1985 | 1130 | 1.25 | 2 | July 7, 1985 | 1245 | 1.25 | 2 | 8 (5.8) | −12.2 |

[1]First gravity survey done shortly after onset of deflation.
[2]Second gravity survey done shortly before deflation was complete.

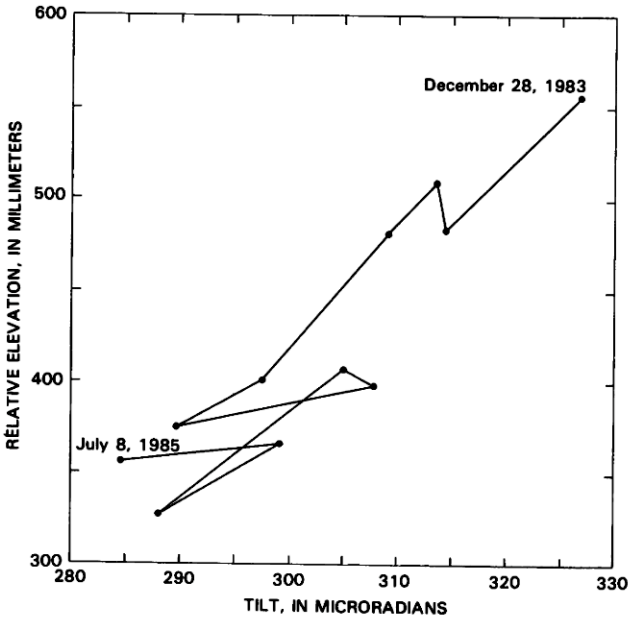


FIGURE 47.4.—Relative elevation of site HVO34 plotted against east-west tilt measured at Uwekahuna between December 28, 1983, and July 8, 1985.

particularly useful for studying intrusions, in which no lava reaches the surface.

The change in volume of the edifice ($\Delta V_e$) was computed by fitting a point-source model (Dvorak and others, 1983) to measured elevation changes for periods when sufficient elevation change and a uniform pattern of surface displacement enabled a stable solution. These periods were: December 28, 1983, to March 22, 1984; July 23, 1984, to January 4, 1985; and April 21 to 22, 1985. The solutions obtained are listed in table 47.4.

Edifice-volume changes (table 47.4) were interpolated to the time of the gravity surveys by means of the continuous record of tilt change at Uwekahuna. From the estimated volume changes of the edifice and the calculated ratios of subsurface-magma to edifice volume change given in table 47.3, the changes of magma volume in the reservoir were calculated. These volume changes are listed in table 47.5, together with estimated lava-flow volumes from the Puu Oo vent for comparison (Wolfe and others, chapter 17; George Ulrich, written commun., 1985).

Absence of significant geodetic change along the rift zones during 1984 and early 1985 indicates that the cumulative volume of lava erupted was equal to the volume of magma drained from the summit reservoir. This inference is supported by the gravity and surface-displacement data. A total of $125 \times 10^6$ m$^3$ of lava was extruded during the monitored eruptive episodes (table 47.5). Corrected for 20 percent (Swanson, 1972) to 25 percent (Wolfe and others, chapter 17) vesicularity, the total volume of lava flows is $94 \times 10^6$–$100 \times 10^6$ m$^3$. For comparison, the cumulative volume of reservoir magma lost during the deflations, based on gravity and geodetic measurements, is an estimated $120 \times 10^6$ m$^3$ (table 47.4).

Gravity and elevation data for eruptive episode 32 were obtained over a timespan of 24 h bracketing the deflation. Because independent calculations of the volume change of the edifice and of the subsurface magma were made from these data, without requiring tiltmeter interpolation, the results for this period provide a good check of the more general procedure. While the edifice subsided by about $6 \times 10^6$ m$^3$ during eruptive episode 32, nearly $18 \times 10^6$ m$^3$ (calculated to 2.75 g/cm$^3$) of magma was removed from the reservoir (table 47.5). This agrees well with the estimated $12 \times 10^6$–$13 \times 10^6$ m$^3$ (table 47.5, corrected for 20–25 percent vesicularity) of lava erupted at Puu Oo.

The general agreement between reservoir magma-volume change and lava output supports the idea of a volume-for-volume link between the summit reservoir and Puu Oo, with magma transfer from summit to rift zone taking place principally during episodes of summit deflation. In other words, during eruptions at Puu Oo, summit magma enters the rift-zone conduit system and forces out an equal volume of rift-zone magma at the Puu Oo vent.

## ELASTIC PROPERTIES OF VOLCANO AND MELT

Data for the ratio of edifice-volume to subsurface magma-volume changes for summit deflations accompanying eruptions of Puu Oo may be used to model the relative strength of the volcanic edifice and the magma-reservoir region. For this purpose, I have derived an expression that relates the ratio of subsurface-magma and edifice-volume changes to the ratio of the rigidity of the edifice, $\mu_e$, and the compressibility of the reservoir melt, $K_m$. Assumptions are that Poisson's ratio for the edifice is 0.25, that the source region can be approximated by a spherical volume of fluid, that the injected magma has a density of 2.75 g/cm$^3$, and that the response of the volcanic edifice and contained fluid to subsurface pressure changes is elastic. Although the source region most likely contains subsolidus rock in addition to a melt phase, the aggregate bulk modulus of the

TABLE 47.3.—*Changes in residual gravity ($\Delta g'$) and elevation ($\Delta h$), ratio between them, and ratio of subsurface ($\Delta V_m$) to edifice volume ($\Delta V_e$) changes for 15 Kilauea deflation episodes, 1984–85*

[Elevation changes interpolated from tilt changes using factor of 5.19 mm/μrad. Subsidence during eruptive episode 32 was determined by leveling surveys before and after period of deflation]

| Eruptive episode | $\Delta g'$ (μGal) | $\Delta h$ (mm) | $\Delta g'/\Delta h$ (μGal/mm) | $\Delta V_m/\Delta V_e$ |
|---|---|---|---|---|
| 13 | −21 | −54 | 0.38 | 3.3 |
| 14 | −8 | −38 | .20 | 1.8 |
| 15 | −6 | −46 | .13 | 1.2 |
| 16 | −20 | −73 | .28 | 2.4 |
| 17 | −17 | −49 | .35 | 3.0 |
| 24 | −16 | −73 | .23 | 2.0 |
| 25 | −39 | −75 | .52 | 4.5 |
| 26 | −13 | −39 | .33 | 2.9 |
| 27 | −16 | −65 | .25 | 2.1 |
| 28 | −23 | −81 | .28 | 2.5 |
| 29 | −18 | −79 | .23 | 2.0 |
| 30 | −22 | −111 | .20 | 1.7 |
| 31 | −26 | −103 | .25 | 2.2 |
| 32 | −27 | −80 | .33 | 2.9 |
| 34 | −11 | −63 | .18 | 1.6 |
| Average | | | | 2.4 |

TABLE 47.4.—*Point-source solutions to level data for selected time intervals in Kilauea summit-area deflation events*

[Uncertainties given are 1 standard error]

| Time interval | Longitude (W.) | Latitude (N.) | Depth (km) | Edifice volume change ($10^6$ $m^3$) | Vertical movement of HVO23 (mm) |
|---|---|---|---|---|---|
| Dec. 28, 1983–Mar. 22, 1984 | 155.2848°(±0.06 km) | 19.4003°(±0.13 km) | 2.92(±0.19) | −4.42(±0.70) | −9(±2) |
| July 23, 1984–Jan. 4, 1985 | 155.2801°(±0.58 km) | 19.4014°(±0.62 km) | 2.46(±0.78) | −3.26(±0.13) | −0.5(±2) |
| Apr. 21, 1985–Apr. 22, 1985 | 155.2753°(±0.30 km) | 19.4101°(±0.11 km) | 2.87(±0.37) | −6.09(±2.04) | −15(±7) |
| Dec. 28, 1983–July 8, 1985 | 155.2822°(±0.13 km) | 19.3960°(±0.26 km) | 3.06(±0.26) | −13.68(±3.38) | −24(±6) |

source region is assumed equal to the bulk modulus of the melt phase. This assumption is valid because the effect of the melt phase is to reduce the aggregate bulk modulus to close to that of melt (Ryan, 1980). First, the change in capacity of the spherical source region was determined. A pressure change within the reservoir displaces the reservoir boundary radially outward. The change in radius, $\Delta a$, of a spherical source region of radius $a$ is given by (Hagiwara, 1977):

$$\Delta a = \frac{a \Delta P}{4\mu_e}. \tag{6}$$

If the radius of the source is large relative to the change in radius, the volume of the the newly added shell, $\Delta V_r$, is approximately:

$$\Delta V_r = \frac{\pi a^3 \Delta P}{\mu_e}. \tag{7}$$

The volume of magma, $\Delta V_c$, accommodated by compression of the fluid within the spherical reservoir region of volume $4\pi a^3/3$ and within the newly added shell of magma, $\Delta V_r$, is dependent on the bulk modulus of the magma, $K_m$:

$$\Delta V_c = \frac{\Delta P}{K_m}\left(\frac{4\pi a^3}{3} + \Delta V_r\right). \tag{8}$$

For simplicity, the relatively small term $\Delta V_r$ in equation 8 can be ignored. The total amount of magma injected is the sum of magma accommodated by enlargement of the reservoir (equation 7) and by compression of the material in the reservoir (equation 8):

$$\Delta V_m = \frac{4}{3}\pi a^3 \Delta P\left(\frac{1}{K_m} + \frac{3}{4\mu_e}\right). \tag{9}$$

The combination of equations 9 and 2 gives:

$$\frac{\Delta V_m}{\Delta V_e} = \frac{8}{9}\cdot\frac{\mu_e}{K_m} + \frac{2}{3}, \tag{10}$$

which can be related directly to the gravity gradient by equation 5.

Some edifice deformation and magma compression are expected during magma injection. Equation 10 shows that, for a given value of $\Delta V_m/\Delta V_e$, a relatively strong edifice implies more magma compression. Conversely, a relatively strong magma implies more edifice deformation. Solution of equation 10, incorporating the average $\Delta V_m/\Delta V_e$ factor of 2.4±0.21 (1 standard error) from the 15 deflations listed in table 47.3, yields $\mu_e = 2.0 \pm 0.24\ K_m$. Additional error stems from uncertainty of the magma density, here assumed to be 2.75 g/cm$^3$.

The effective shear modulus of Kilauea's edifice, $\mu_e$, is difficult to determine independently because Kilauea is built of many vesicular, commonly rubbly lava flows with abundant void space (Ryan and others, 1983). The intrinsic shear modulus of Hawaiian basalt was found by pulse transmission to average 25 GPa (Manghnani and Wollard, 1968) with a range of 4.7–40.5 GPa. Samples with greater porosity had a lower shear modulus. Presence of voids in the volcanic pile results in an effective shear modulus of the volcano that is less than the intrinsic shear modulus of hand samples.

Seismic velocities, and hence rigidity, determined from $P$-wave arrival data from earthquakes and explosions increase with depth and vary laterally (Thurber, chapter 38; Hill and Zucca, chapter 37). This reflects partly the compressive reduction of porosity with increasing depth, and the solidified intrusive zones surrounding the cores of the summit reservoir and rift zones. Any estimate of $\mu_e$ from seismic velocities would be strongly dependent on the depth and horizontal position of the source, and size of the region chosen to represent the edifice.

The bulk modulus of magma, $K_m$, in Kilauea's reservoir should be uniform because the size of the summit magma reservoir is perhaps 1,000 times the yearly magma supply rate (Swanson, 1972), so short-term fluctuations in the gas content and chemical composition of the supplied magma are distributed over a large volume and do not affect the overall bulk modulus. Laboratory

TABLE 47.5.—*Edifice volume change ($\Delta V_e$), subsurface volume change ($\Delta V_m$), and lava flow volume for 12 Kilauea eruptive episodes, 1984–85*

[All figures in millions of cubic meters. Edifice volume changes, from level data inversion, interpolated to time of gravity surveys by tilt variations. Subsurface mass changes, expressed as volume change at standard density of 2.75 g/cm$^3$, estimated using equation 5 and changes of edifice volume, relative gravity, and relative elevation. Measured lava-flow volumes (Wolfe and others, chaper 17; George Ulrich, written commun., 1985) not adjusted for flow porosity]

| Eruptive episode | $\Delta V_e$ | $\Delta V_m$ | *Lava volume* |
|---|---|---|---|
| 13 | −3.7 | −12.3 | 10 |
| 14 | −2.6 | −4.7 | 6 |
| 15 | −3.2 | −3.7 | 8 |
| 16 | −5.1 | −12.3 | 12 |
| 17 | −3.4 | −10.2 | 10 |
| 24 | −4.0 | −7.9 | 12 |
| 25 | −4.0 | −18.2 | 11 |
| 26 | −2.1 | −6.1 | 7 |
| 27 | −3.5 | −7.3 | 8 |
| 28 | −4.4 | −11.0 | 12 |
| 29 | −4.3 | −8.6 | 13 |
| 32 | −6.1 | −17.7 | 16 |
| Total | −46.4 | −120.0 | 125 |

determinations of the bulk modulus made from lava erupted from Kilauea, therefore, should be representative of the bulk modulus of magma in the reservoir. The value of 11.5 GPa determined for $K_m$ of molten Kilauea 1921 olivine tholeiite by Murase and others (1977) was used to calculate the shear modulus of Kilauea's edifice from the relation $\mu_e = (2.0 \pm 0.24) \cdot K_m$ determined above. The value for $\mu_e$ so determined, $23 \pm 3$ GPa, is close to the value for the average shear modulus of Hawaiian basalt given above. Note that this value does not apply to Kilauea's edifice as a whole, but only to the region surrounding the magma reservoir. This is because it was determined by modeling in-place melt-volume changes in the reservoir and resulting surface displacements.

Presence of a $CO_2$ gas phase in the magma would lower the aggregate bulk modulus of the magma. This may not be important for Kilauea, because, as Greenland and others (1985) assert, as $CO_2$ is lost from the magma as soon as it reaches the shallow magma reservoir. However, if some $CO_2$ is retained in the reservoir, then both the magma bulk modulus and the predicted edifice shear modulus would be reduced.

## RELATION BETWEEN LONG-TERM INELASTIC EDIFICE WIDENING AND SUBSURFACE VOLUME CHANGES

The ratio of the long-term change of magma volume within Kilauea's summit reservoir to the edifice volume change between January 6, 1984, and July 16, 1985, may be determined from equation 5 and from the long-term elevation and gravity changes. A gradient of $\Delta g/\Delta h = -0.29$ μGal/mm was determined for the interval by a least-squares fit to the tilt and gravity data, adjusted by the elevation/tilt correlation of 5.19 mm/μrad given above. This is essentially the free-air gradient, so $\Delta g'$ is zero and equation 5 shows that the ratio of $\Delta V_m/\Delta V_e$ is zero. That is, there was no net change in magma storage in the summit reservoir during this interval.

The long-term ratio of volume changes in edifice and subsurface magma is different from that in short-term deflations accompanying Puu Oo eruptions (table 47.3). This implies that different processes affect the volume changes over longer time intervals. Earlier, the short-term deflations of Kilauea were explained using an elastic model, with inflow and outflow of magma accompanied by compression and decompression of the melt. Because short-term and long-term processes occurred concurrently, variations in the physical properties of the magma cannot explain differences in the volume-change ratios. The differences between the long-term and short-term volume changes must then be due to some superimposed long-term process that affects Kilauea's edifice. That process produces subsidence at the surface without a change in the magma content of the reservoir. One possibility is that horizontal spreading of the volcano's summit removes lateral support of the fluid magma reservoir, thereby decreasing the pressure in the reservoir and causing the summit to subside. Horizontal distance measurements at Kilauea have shown that the summit region is prone to widening in a south-southeast direction (Dvorak and others, 1983). This widening was particularly notable during the 1975 magnitude 7.2 earthquake along the south flank and for several months afterward (Lipman and others, 1985).

To investigate the possibility of summit extension during 1984–85, horizontal displacements measured by trilateration surveys conducted on January 16, 1984, and July 16, 1985, were analysed. In order to isolate the pattern of regional displacements in the vicinity of Kilauea's summit from the effects of observed deflation, the contribution of changes in the inflation level of the reservoir (approximated by use of a point source of dilatation determined from leveling data) was subtracted from the observed horizontal displacements. Residual line lengths were then used to compute horizontal displacement vectors (fig. 47.5). South-southeastward movement as great as 250 mm of points located on the south side of Kilauea caldera relative to points to the north show that the caldera widened slightly.

A $\Delta g'/\Delta h$ gradient of 0.138 μGal/mm was measured by Jachens and Eaton (1980) during the subsidence accompanying the November 29, 1975, earthquake and eruption. A value for the $\Delta V_m/V_e$ ratio of 1.2 was calculated from the gravity gradient and equation 5 using an assumed magma density of 2.75 g/cm$^3$. This ratio indicates a greater component of surface collapse following the 1975 eruption, compared to the 1984–85 deflations (table 47.3). This difference results from 1.8 m of south-southeast crosscaldera extension during the November 1975 event (Lipman and others, 1985), in contrast to no measurable extension during the periods of very brief (1–3 d) deflation associated with eruptions in 1984 and 1985. The increased collapse in November 1975 is consistent with horizontal dilation of the edifice and surface subsidence because of the resultant drop in reservoir pressure.

Horizontal extension of Kilauea's edifice lowers the pressure in the magma reservoir; additional magma can be injected without uplifting the surface. In this way the reservoir volume increases by lateral growth. Growth by horizontal spreading and magma intrusion occurs during rift-zone development (Swanson and others, 1976), and it might also apply to the growth of the summit reservoir. Swanson and others (1976) attributed horizontal dilation of the rift zone to forceful injection of magma into dikes. However, at Kilauea's summit area, observation of subsidence concurrent with extension indicates that magma accumulation there is a passive response to dilation. Perhaps the extension of Kilauea's summit that increases the capacity of the reservoir is an indirect response to the forceful dilation of the rift zones that bound the caldera on both the east and west sides.

Net gravity and elevation changes for the 16-mo period following the November 1975 deflation imply mass filling of the reservoir concurrent with subsidence. Dzurisin and others (1980) reported a $\Delta g'/\Delta h$ gradient of $-0.294$ μGal/mm for December 1975 to April 1977, which corresponds to a $\Delta V_m/\Delta V_e$ ratio of $-2.5$ from equation 5, using a magma density of 2.75 g/cm$^3$. This, combined with observed subsidence of the summit area of as much as 180 mm, indicates that the volume of magma in the reservoir actually increased despite the subsidence. The summit region widened by about 0.5 m in a south-southeast direction (Lipman and others, 1985) during this period; that extension created more reservoir space in which additional magma accumulated.

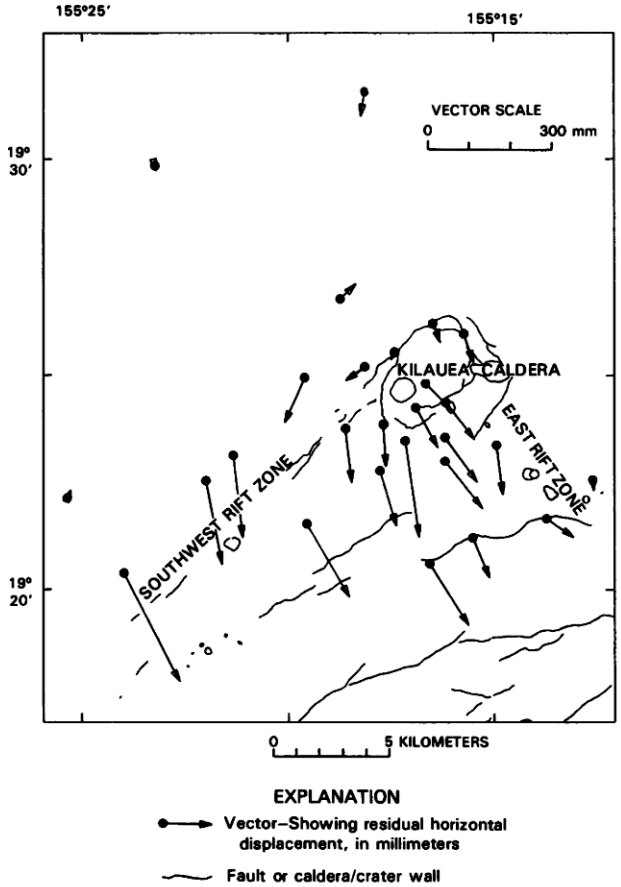


FIGURE 47.5.—Horizontal displacements in the Kilauea summit region determined from line-length changes (January 16, 1984, to July 16, 1985). To remove effects of summit subsidence, computed horizontal displacements based on inversion of level data obtained on December 28, 1983, and July 8, 1985 (table 47.4), were subtracted from measured changes in line lengths between January 16, 1984, and July 16, 1985. Computed residual displacements indicate south-southeastward widening of Kilauea summit area.

## CONCLUSIONS

Gravity and surface-displacement data demonstrate that volume changes of Kilauea's edifice, as determined by integrating vertical displacements, are dependent, not only on the balance between volume of magma supplied from the mantle and volume of magma lost from the reservoir by eruption but also on the volume of summit collapse owing to horizontal extension of the summit region. During times of elastic inflow or outflow of magma from the reservoir, the ratio of subsurface-magma volume change to edifice volume change is $2.4 \pm 0.21$ (1 standard error). This is consistent with expected changes, calculated using a ratio of shear strength of edifice to bulk modulus of magma of $2.0 \pm 0.24$ (1 standard error). On the basis of a laboratory-determined magma bulk modulus of $K_m = 11.5$ GPa, the shear modulus of the edifice is $\mu_e = 23$ GPa. Inelastic horizontal dilation of the edifice in a south-southeast direction increases the capacity of the summit reservoir to accept magma without surface uplift. For the 16-mo period following the November 1975 deflation, additional magma was accommodated by this process. When insufficient magma is supplied to fill space created by summit widening, the pressure in the reservoir drops and the surface subsides as it did during and after the November 1975 earthquake and between January 1984 and February 1985.

## REFERENCES CITED

Dieterich, J.H., and Decker, R.W., 1975, Finite element modeling of surface deformation associated with volcanism: Journal of Geophysical Research, v. 80, p. 4094–4102.

Duffield, W.A., Christiansen, R.L., Koyanagi, R.Y., and Peterson, D.W., 1982, Storage, migration, and eruption of magma at Kilauea Volcano, Hawaii, 1971–1972: Journal of Volcanology and Geothermal Research, v. 13, p. 273–307.

Dvorak, J., Okamura, A., and Dieterich, J.H., 1983, Analysis of surface deformation data, Kilauea Volcano, Hawaii, October 1966 to September 1970: Journal of Geophysical Research, v. 88, p. 9295–9304.

Dzurisin, D., Anderson, L.A., Eaton, G.P., Koyanagi, R.Y., Lipman, P.W., Lockwood, J.P., Okamura, R.T., Puniwai, G.S., Sako, M.K., and Yamashita, K.E., 1980, Geophysical observations of Kilauea Volcano, Hawaii, 2, Constraints on the magma supply during November 1975–September 1977: Journal of Volcanology and Geothermal Research, v. 7, p. 241–269.

Dzurisin, D., Koyanagi, R.Y., and English, T.T., 1984, Magma supply and storage at Kilauea Volcano, Hawaii, 1956–1983: Journal of Volcanology and Geothermal Research, v. 21, p. 177–206.

Eaton, J.P., and Murata, K.J., 1960, How volcanoes grow: Science, v. 132, p. 925–938.

Eggers, A.A., 1983, Temporal gravity and elevation changes at Pacaya Volcano, Guatemala: Journal of Volcanology and Geothermal Research, v. 19, p. 223–237.

Fiske, R.S., and Kinoshita, W.T., 1969, Inflation of Kilauea Volcano prior to its 1967–1968 eruption: Science, v. 165, p. 341–349.

Greenland, L.P., Rose, W.I., and Stokes, J.B., 1985, An estimate of gas emissions and magmatic gas content from Kilauea Volcano: Geochimica et Cosmochimica Acta, v. 49, p. 125–129.

Hagiwara, Y., 1977, The Mogi model as a possible cause of the crustal uplift in the eastern part of Izu Peninsula and the related gravity change: Bulletin of the Earthquake Research Institute, University of Tokyo, v. 52, p. 301–309 (in Japanese).

Jachens, R.C., and Eaton, G.P., 1980, Geophysical observations of Kilauea Volcano, Hawaii, 1, Temporal gravity variations related to the 29 November 1975, $M = 7.2$ earthquake and associated summit collapse: Journal of Volcanology and Geothermal Research, v. 7, p. 225–240.

Johnsen, G.V., Bjornsson, A., and Sigurdsson, S., 1980, Gravity and elevation changes caused by magma movement beneath the Krafla caldera, northeast Iceland: Journal of Geophysics, v. 47, p. 132–140.

Kinoshita, W.T., Krivoy, H.L., Mabey, D.R., and MacDonald, R.R., 1963, Gravity survey of the Island of Hawaii: U.S. Geological Survey Professional Paper 475–C, p. C114–C116.

Koyanagi, R.Y., Unger, J.D., Endo, E.T., and Okamura, A.T., 1976, Shallow earthquakes associated with inflation episodes at the summit of Kilauea Volcano, Hawaii: Bulletin Volcanologique, v. 39, p. 621–631.

Lipman, P.W., Lockwood, J.P., Okamura, R.T., Swanson, D.A., and Yamashita, K.M., 1985, Ground deformation associated with the 1975 magnitude-7.2 earthquake and resulting changes in activity of Kilauea Volcano 1975–1977: U.S. Geological Survey Professional Paper 1276, 45 p.

Longman, I.M., 1959, Formulas for the tidal acceleration of gravity: Journal of Geophysical Research, v. 64, p. 2351–2355.

Manghnani, M.H., and Woollard, G.P., 1968, Elastic wave velocities in Hawaiian rocks at pressures to ten kilobars: American Geophysical Union Geophysical Monograph 12, p. 501–516.

Mogi, K., 1958, Relations of eruptions of various volcanoes and the deformation of the ground surfaces around them: Earthquake Research Institute Journal, Tokyo University, v. 39, p. 99–134.

Murase, T., Kushiro, I., and Fujii, T., 1977, Compressional wave velocity in partially molten peridotite: Annual Report of the Director, Geophysical Laboratory, Carnegie Institution, 1976–1977, p. 414–416.

Rundle, J.B., 1978, Gravity changes and the Palmdale uplift: Geophysical Research Letters, v. 5, p. 41–44.

Ryan, M.P., 1980, Mechanical behavior of magma reservoir envelopes: elasticity of the olivine tholeiite solidus: Bulletin Volcanologique, v. 43-4, p. 743–772.

Ryan, M.P., Blevins, J.Y.K., Okamura, A.T., and Koyanagi, R.Y., 1983, Magma reservoir subsidence mechanics: Theoretical summary and application to Kilauea Volcano, Hawaii: Journal of Geophysical Research, v. 88, p. 4147–4181.

Ryan, M.P., Koyanagi, R.Y., and Fiske, R.S., 1981, Modeling the three-dimensional structure of macroscopic magma transport systems: application to Kilauea Volcano, Hawaii: Journal of Geophysical Research, v. 86, p. 7111–7129.

Sanderson, T.J.O., Berrino, G., Corrado, G., and Grimaldi, M., 1983, Ground deformation and gravity changes accompanying the March 1981 eruption of Mount Etna: Journal of Volcanology and Geothermal Research, v. 16, p. 299–315.

Savage, J.C., 1984, Local gravity anomalies produced by dislocation sources: Journal of Geophysical Research, v. 89, p. 1945–1952.

Swanson, D.A., 1972, Magma supply rate at Kilauea Volcano, 1952–1971: Science, v. 175, p. 169–170.

Swanson, D.A., Duffield, W.A., and Fiske, R.S., 1976, Displacement of the south flank of Kilauea Volcano: The result of forceful intrusion of magma into the rift zones: U.S. Geological Survey Professional Paper 963, 39 p.

Walsh, J.B., and Rice, J.R., 1979, Local changes in gravity resulting from deformation: Journal of Geophysical Research, v. 84, p. 165–170.

# CYCLING OF MAGMA BETWEEN THE SUMMIT RESERVOIR AND KILAUEA IKI LAVA LAKE DURING THE 1959 ERUPTION OF KILAUEA VOLCANO

*By* Jerry P. Eaton, Donald H. Richter, *and* Harold L. Krivoy

## ABSTRACT

**The fortunate combination of observations of deformation of the summit of Kilauea Volcano during the 1959 Kilauea Iki eruption and an accurate log of the eruption of lava into Kilauea Iki lava lake and its subsequent partial withdrawal provides a record of movement of magma into and through the summit reservoir during that eruption. The initial eruption of $30\times10^6$ $m^3$ of lava into Kilauea Iki, with an accompanying 50 $\mu$rad of eastward tilt at Uwekahuna, established a scaling factor relating the change in volume of the summit reservoir to tilting at Uwekahuna. A record of the initial deflation and subsequent reinflation of the summit reservoir was obtained by the liquid-level tiltmeter at Uwekahuna. A good record of episodic eastward tilting during the eruptive stage and westward tilting during the backflow stage of the later phases of the eruption was obtained by analysis of the zero-line deflections of the east-west-component Press-Ewing seismograph. Converted to volumes of deflation and inflation, the tilting associated with eruption of lava into and withdrawal of lava from the lava lake offers a means of determining the net gain or loss of lava in the lake-reservoir system during each phase. Analysis of the interplay between volcanic tremor and the details of the reinflation tilt records permits estimation of the volume of lava that escaped from the summit reservoir during individual backflow episodes.**

**The $30\times10^6$ $m^3$ of lava originally withdrawn from the reservoir was eventually more than replaced by about $60\times10^6$ $m^3$ of lava rising from depth. Of this $60\times10^6$ $m^3$, $40\times10^6$ $m^3$ finally was retained in the reservoir, $8\times10^6$ $m^3$ was added to the lava lake, and about $12\times10^6$ $m^3$ was driven out of the summit reservoir during the late-phase backflow episodes. Lava that erupted into Kilauea Iki from phase 2 onward was material from the reservoir, which was being refilled with new lava from below; this lava was repeatedly erupted from the reservoir and then withdrawn back into it. Overfilling of the reservoir, combined with sharp reinflation pulses during later backflow episodes, drove an estimated $12\times10^6$ $m^3$ of lava out of the reservoir, possibly into the upper end of the east rift zone.**

**The recycling process was made possible by a lava conduit, which remained open after phase 1, that connected a supply of lava in the lake with one in the reservoir. Large-scale vesiculation of lava in the conduit effectively pumped lava from the reservoir up into the lake. Flooding of the vent by devesiculated lake lava quenched the fountain and permitted lake lava to flow back into the reservoir. The process was rekindled repeatedly, after backflow stopped, by the introduction of fresh gas-charged reservoir lava into the conduit, which permitted the vesiculation pump to operate again.**

## INTRODUCTION

The 1959 eruption in Kilauea Iki Crater at the summit of Kilauea Volcano consisted of 16 separate principal phases that poured lava into the bowl-shaped crater from a main vent on the south wall about 90 m above its original floor (Richter and others, 1970). The first phase died out abruptly after the lake surface rose above the level of the vent, leaving a lake 102 m deep and containing $30\times10^6$ $m^3$ of lava ponded in Kilauea Iki. Except for basaltic pumice blown downwind (southwest) from the vent, much of which accumulated on the crater rim above the vent to form a cinder cone, all of the lava erupted was caught in the crater, where its volume could be determined from a simple measurement of the height of the lava lake surface. After each phase, a substantial volume of lava escaped back underground into the main vent or into another somewhat lower vent hidden by the lake nearby. Backflow of lava after cessation of fountaining is not uncommon at Kilauea (for example, the 1954 eruption in Halemaumau; see Macdonald and Eaton, 1957), but the 1959 eruption is the only one for which we have such complete measurements of ground deformation and volumes of eruption and backflow. Except for their smaller volumes of erupted lava and shorter durations, the 15 subsequent principal phases were much like the first. Lava that erupted from the vent collected in the lake, increasing its depth until ponded lava rose above the vent and caused the fountain to die out abruptly. As the lake flooded the base of the fountain, the height of the fountain often oscillated wildly before it was quenched. At the ends of several phases, notably phases 4 and 16, lowering of the lake surface and strong backflow toward the base of the still-active fountain showed that withdrawal of lava from the lake need not await cessation of fountaining. The drainback point appeared to be at or just below the base of the fountain.

Total volumes of lava erupted into and withdrawn from Kilauea Iki during its 16 principal eruptive phases between November 14 and December 19 were $102\times10^6$ $m^3$ and $63\times10^6$ $m^3$, respectively, leaving $38\times10^6$ $m^3$ of lava in the lake at the end of the eruption. Of the $71\times10^6$ $m^3$ of lava poured into the lake after the end of phase 1 fountaining, only $8\times10^6$ $m^3$ remained at the end of the eruption.

What was the fate of the $63 \times 10^6$ $m^3$ of lava that drained back underground from the lava lake? If it returned to its immediate source to be erupted again in later phases, then only about $8 \times 10^6$ $m^3$ of drainback lava must be accounted for (maximum lake volume at end of phase 8 minus final lake volume at end of eruption). The other $56 \times 10^6$ $m^3$ represents the same lava that was erupted many times in small batches and then withdrawn. An important question for this apparently closed lake-reservoir system is: What provided the driving force to erupt the same limited volume of lava over and over again? If the drainback lava escaped from an open lake-reservoir system into another storage zone beneath the summit or into the fluid core of the east rift zone (in preparation for the impending 1960 east-rift eruption), however, then the entire $63 \times 10^6$ $m^3$ must be found.

In addition to the unusual features of the eruption itself, some of which have been outlined above, the 1959 Kilauea Iki eruption was unusual in the range and abundance of geologic and geophysical observations on its progress and effects. There were reasons for this fortunate situation: a new geochemical laboratory had recently been added to the Hawaiian Volcano Observatory (HVO), with an appropriate augmentation of the observatory staff, and the networks of seismometers and tiltmeters around the summit of Kilauea were in the process of being upgraded and expanded in response to lessons learned during the 1954–55 summit and flank eruptions.

Specific measurements that were important for tracking magma as it rose into the volcano from depth, as it was stored temporarily in a shallow summit reservoir, and as it was subsequently erupted into Kilauea Iki Crater and then partially withdrawn include the following:

(1) Seismic network records for (a) locating individual earthquakes and earthquake swarms associated with the eruption and with the expansion of the reservoir before, and its deflation after, the eruption, and (b) the detection and approximate location of the source of volcanic tremor associated with underground movement and eruption of lava;

(2) Measurements of tilting of the Earth's surface around the summit of the volcano as magma moved into or out of the summit reservoir, including: (a) periodic releveling of a network of tilt bases around the summit of the volcano to map the slowly changing pattern of deformation of the entire summit, (b) daily measurement of level changes (tilting) at the Uwekahuna vault (west of Kilauea caldera) and at the Whitney vault (northeast of the caldera), and (c) minute-by-minute monitoring of the rate of tilting and short-term accumulation of tilting at the Uwekahuna vault by analysis of the zero-line drift of the horizontal-component long-period Press-Ewing seismograph;

(3) Systematic observation of the progress of the eruption and periodic measurement of parameters related to the eruption of lava into, and its withdrawal from, the lava lake, including: (a) accurate timing of the beginning and end of eruptive phases, frequent measurement of fountain height, and physical description of the fountain and any unusual phenomena associated with it, (b) periodic measurement of the height of the lava-lake surface, particularly at the end of fountaining and after cessation of drainback, (c) frequent sampling of basaltic pumice thrown out by the fountain and sampling of recently erupted lava from the lake, and (d) measurements of lava fountain temperatures (by optical pyrometer) when conditions at the fountain permitted.

Part of the data covered by item 3 above is from Richter and others (1970), where methods as well as results are described. Data on the volumetric progress of the Kilauea Iki eruption, which form the basis for Richter and others' (1970) figure 2, are presented in table 48.1. The seismic and tilt networks and results have not been treated comprehensively elsewhere, so we shall treat them in detail.

The main purpose of this paper is to present the record of ground-surface deformation at and around the summit of Kilauea that traces the movement of lava within the summit region of the volcano before, during, and after the 1959 eruption and to correlate that record with other measurements and observations carried out during the eruption to answer the question posed above: What was the fate of the $63 \times 10^6$ $m^3$ of lava that drained back underground from the lava lake? A second objective is to analyze the data on tremor amplitude, rate of eruption, fountain height, and recharge of the summit reservoir to discover what they might reveal about the process that caused the repeated eruptions in Kilauea Iki.

We shall begin with explanations of the methods used to measure long-, intermediate-, and short-term tilting at Kilauea and with a brief summary of the seismic network and some of the results obtained from it. Next, we shall trace the course of the eruption to examine the pattern of deformation associated with individual phases and with longer episodes of activity during the eruption. We shall then make a kinematic reconstruction that traces lava into the summit reservoir and through the phases of the Kilauea Iki eruption and that conforms with the observations presented. Finally, we shall examine the relationships among tremor, eruption rate, fountain height, and reservoir recharge quantitatively to develop a better understanding of the mechanics of the eruption.

### ACKNOWLEDGMENTS

The manuscript was reviewed by David P. Hill and Fred Klein, whose many helpful suggestions help to clarify and augment the paper.

## TILT MEASUREMENTS

### TILT BASES

At the time of the 1959 eruption the primary system for measuring deformation of the summit region of Kilauea was a network of 9 permanent tilt bases encircling Kilauea caldera (fig. 48.1) and extending about 10 km south of the caldera. A typical tilt base consists of three concrete piers planted firmly in the ground (on rock if possible) at the vertices of an equilateral triangle about 50 m on a side. Each pier is capped by a brass hub that provides a reference surface and a clamp-down for a precise liquid-level system for measuring height differences between adjacent pairs of piers (Eaton, 1959). The tilt bases are releveled at intervals of 3–6 mo, and changes in the relative heights of the piers reveal any tilting of the base during the interval between measurements. Tilting as small as a few tenths of a microradian (<0.3 μrad) can be detected. The

TABLE 48.1.—*Volumetric progress of the 1959 Kilauea Iki eruption*

[H.s.t., Hawaii standard time; duration is time since last measurement or onset of new eruptive phases; bottom of crater before November 14 at elevation 954 m (3,130 ft) defines zero depth of lava lake; $\Delta V$, change in lake volume since last depth measurement; $V$, volume of lava lake; rate, average rate of lava outpouring since last depth measurement or onset of new eruptive phase]

| Date | Time (H.s.t.) | Duration (h) | Lava lake Depth (m) | Lava lake Area (acres) | Volume of lava $\Delta V$ ($10^6$ m$^3$) | Volume of lava $V$ ($10^6$ m$^3$) | Volume of lava Rate ($10^3$ m$^3$/h) |
|---|---|---|---|---|---|---|---|
| **Phase 1** | | | | | | | |
| Nov. 14 | 2008 | 0 | 0(elev. 954.0) | 37.0 | 0 | 0 | 0 |
| Nov. 15 | 0300 | 7.0 | 1.5 | 37.0 | .2 | .2 | 33 |
| | 1800 | 15.0 | 4.6 | 39.0 | .7 | .5 | 31 |
| Nov. 16 | 1215 | 18.25 | 7.6 | 41.0 | .5 | 1.1 | 25 |
| | 1400 | 1.75 | 8.2 | 41.5 | .1 | 1.2 | 44 |
| Nov. 17 | 1045 | 20.75 | 16.8 | 47 | 1.4 | 2.7 | 70 |
| | 1400 | 3.25 | 18.3 | 48.5 | .3 | 3.0 | 94 |
| | 2030 | 6.5 | 22.0 | 51 | .7 | 3.7 | 106 |
| Nov. 18 | 1200 | 15.5 | 34.1 | 59 | 2.5 | 6.2 | 163 |
| | 2315 | 11.25 | 45.7 | 68 | 2.8 | 9.0 | 252 |
| Nov. 19 | 1150 | 12.5 | 57.9 | 79 | 3.5 | 12.5 | 281 |
| | 2115 | 9.5 | 68.6 | 88 | 3.6 | 16.1 | 378 |
| Nov. 20 | 1210 | 15. | 82.3 | 106 | 5.4 | 21.5 | 357 |
| Nov. 21 | 0930 | 21.25 | 97.5 | 120 | 7.0 | 28.4 | 327 |
| | 1925 | 10.0 | 102.1 | 125 | 2.2 | 30.7 | 222 |
| Nov. 23 | 1000 | [1]38.5 | 100.0 | 123 | −1.1 | 29.6 | −28 |
| **Phase 2** | | | | | | | |
| Nov. 26 | 0100 | 0 | | | | | |
| | 1000 | 9.0 | 102.4 | 125 | 1.1 | 30.7 | 128 |
| | 1635 | 6.6 | 107.0 | 130 | 2.4 | 33.2 | 371 |
| | 1940 | 3.0 | 103.9 | 127 | −1.5 | 31.7 | −510 |
| Nov. 27 | 1230 | 16.75 | [2]97.8 | 121 | −3.0 | 28.7 | −178 |
| **Phase 3** | | | | | | | |
| Nov. 28 | 1645 | 0 | | | | | |
| Nov. 29 | 1500 | 22.25 | 100.9 | 124 | 1.5 | 30.2 | 69 |
| | 2147 | 6.75 | 103.9 | 126 | 1.5 | 31.7 | 226 |
| Dec. 1 | 1500 | 41.25 | [3]100.3 | 123 | −1.8 | 29.9 | −44 |
| **Phase 4** | | | | | | | |
| Dec. 4 | [4]0100 | 0 | | | | | |
| | 2325 | [4]22.5 | 114.3 | 138 | 7.4 | 37.3 | 368 |
| Dec. 5 | 0330 | 4.0 | 117.3 | 142 | 1.7 | 39.0 | 420 |
| | 0630 | 3.0 | 120.4 | 145 | 1.8 | 40.7 | 586 |
| | 0730 | 1.0 | [5]118.0 | 142 | −1.5 | 39.3 | −1453 |
| | 0927 | 2.0 | 120.1 | 145 | 1.2 | 40.5 | 612 |
| | 1155 | 2.5 | 115.5 | 140 | [6]−2.5 | 38.0 | −1009 |
| | 1230 | 0.5 | 114.0 | 137 | −.8 | 37.2 | −1682 |
| Dec. 6 | 1448 | 26.25 | 110.0 | 134 | −2.1 | 35.1 | −79 |
| **Phase 5** | | | | | | | |
| Dec. 6 | 1448 | 0 | | | | | |
| | 2300 | 8.25 | 121.9 | 147 | 6.6 | 41.7 | 797 |
| Dec. 7 | 0023 | 1.4 | 122.8 | 148 | .5 | 42.2 | 382 |
| | 1530 | 15.1 | 114.3 | 138 | −4.7 | 37.5 | −314 |
| **Phase 6** | | | | | | | |
| Dec. 7 | 1530 | 0 | | | | | |
| Dec. 8 | 0245 | 11.25 | 125.9 | 152 | 6.6 | 44.0 | 584 |
| | 0300 | 0.25 | 125.3 | 151 | −.4 | 43.7 | −1529 |
| | 1200 | 9.0 | 118.6 | 143 | −3.7 | 39.9 | −416 |
| **Phase 7** | | | | | | | |
| Dec. 8 | [7]1300 | 0 | | | | | [7](881) |
| | 2012 | 7.25 | 125.3 | 151 | 3.7 | 43.7 | 518 |
| Dec. 9 | 1045 | 14.5 | 118.9 | 143 | −3.6 | 40.1 | −248 |
| Dec. 10 | 1515 | 28.5 | 115.2 | 139 | −2.0 | 38.1 | −70 |
| **Phase 8** | | | | | | | |
| Dec. 10 | [8]1515 | 0 | | | | | [8](746) |
| Dec. 11 | 1048 | [8]19.5 | 126.2 | 153 | 6.2 | 44.3 | 317 |
| | 1130 | 0.75 | 124.7 | 150 | −.9 | 43.3 | −1223 |
| | 1200 | 0.5 | 124.1 | 150 | −.4 | 43.0 | −765 |
| Dec. 12 | 1000 | 22.0 | 116.4 | 141 | −4.2 | 38.8 | −191 |
| Dec. 13 | 0720 | 21.3 | 115.5 | 140 | −.5 | 38.3 | −21 |
| **Phase 9** | | | | | | | |
| Dec. 13 | [9]0508 | 0 | | | | | [9](765) |
| | 1340 | 8.5 | 125.9 | 152 | 5.7 | 44.0 | 674 |
| | 1545 | 2.1 | 120.4 | 145 | −3.1 | 40.9 | −1492 |
| Dec. 14 | 1000 | 18.25 | 112.5 | 136 | −3.8 | 37.1 | −209 |
| **Phase 10** | | | | | | | |
| Dec. 14 | [10]0705 | 0. | | | | | [10](1269) |
| | 1536 | 8.5 | 124.7 | 150 | 6.3 | 43.4 | 746 |
| | 1605 | 0.5 | 123.8 | 149 | [11].5 | 43.0 | 917 |
| Dec. 15 | 0800 | 15.9 | 115.5 | 140 | −4.4 | 38.5 | −279 |
| **Phase 11** | | | | | | | |
| Dec. 15 | 0611 | 0. | | | | | |
| | 0800 | 1.8 | 118.3 | 143 | 1.3 | 39.8 | 722 |
| | 1025 | 2.4 | 123.4 | 149 | 2.7 | 42.5 | 1115 |
| | 1115 | 0.8 | 121.9 | 147 | −.8 | 41.7 | −1051 |
| | 2030 | 9.25 | 116.4 | 141 | −2.6 | 39.4 | −281 |
| **Phase 12** | | | | | | | |
| Dec. 15 | 1930 | 0 | | | | | |
| | 2030 | 1.0 | 118.0 | 142 | .8 | 39.8 | 765 |
| | 2130 | 1.0 | 120.7 | 146 | 1.4 | 41.3 | 1453 |
| Dec. 16 | 1015 | 12.75 | 114.6 | 138 | −3.1 | 38.1 | −246 |
| **Phase 13** | | | | | | | |
| Dec. 16 | 1335 | 0 | | | | | |
| | 1625 | 2.8 | 119.5 | 144 | 2.5 | 40.7 | 901 |
| | 1650 | 0.4 | 120.1 | 143 | .4 | 41.1 | 956 |
| | 1719 | 0.5 | 120.7 | 146 | .3 | 41.4 | 612 |
| Dec. 17 | 0245 | 9.4 | 116.1 | 140 | −2.4 | 38.9 | −260 |
| **Phase 14** | | | | | | | |
| Dec. 17 | 0215 | 0 | | | | | |
| | 0402 | 1.75 | [12]119.8 | 144 | 1.8 | 40.7 | 1048 |
| | 1100 | 7.0 | 118.0 | 142 | −1.0 | 39.8 | −142 |
| **Phase 15** | | | | | | | |
| Dec. 17 | [13]1110 | 0 | | | | | [13](989) |
| | 1532 | 4.4 | 121.3 | 146 | 1.7 | 41.4 | 382 |
| | 1800 | 2.5 | 120.4 | 145 | −.5 | 41.0 | −183 |
| Dec. 18 | 1500 | 21.0 | 115.2 | 139 | −2.8 | 38.2 | −131 |
| **Phase 16** | | | | | | | |
| Dec. 19 | [14]0240 | 0 | | | | | [14](1271) |
| | 0616 | 3.6 | 122.8 | 148 | 4.1 | 42.4 | 1147 |
| | 1115 | 5.0 | 119.5 | 144 | −1.7 | 40.7 | −336 |
| Dec. 20 | 1300 | 25.75 | 114.3 | 138 | −2.7 | 38.0 | −104 |
| **Phase 17** | | | | | | | |
| Dec. 19 Dec. 20 | 2045 to 0800 | 11.25: Slight fountaining activity; no significant output of lava | | | | | |

[1]This subsidence probably occurred during the first few hours of the period.
[2]These figures are approximate. Subsidence of the east pond was 25–30 ft; the smaller west pond subsided 35–45 ft.
[3]These figures are approximate. Subsidence of the east pond was about 7 ft; the smaller west pond subsided irregularly between 15–30 ft.
[4]Strong lava extrusion only during last half of this period. Continuous fountain and tremor after 0320 H.s.t.
[5]Visual estimate of subsidence in pond during eruption.
[6]Volume figures from end of phase 4 through phase 16 take into consideration the volume of the "black ledge."
[7]No appreciable lava output until 1515 on Dec. 8, 1959.
[8]No appreciable lava output until 0230 on Dec. 11, 1959.
[9]No appreciable lava output until 0615 on Dec. 13, 1959.
[10]No appreciable lava output until 1040 on Dec. 14, 1959.
[11]From phase 10 to phase 16 no appreciable volume of lava flowed into the small west pond.
[12]Estimated. Lava level never rose above the "black ledge."
[13]No appreciable lava output until 1350 on Dec. 17, 1959.
[14]No appreciable lava output until 1301 on Dec. 19, 1959.

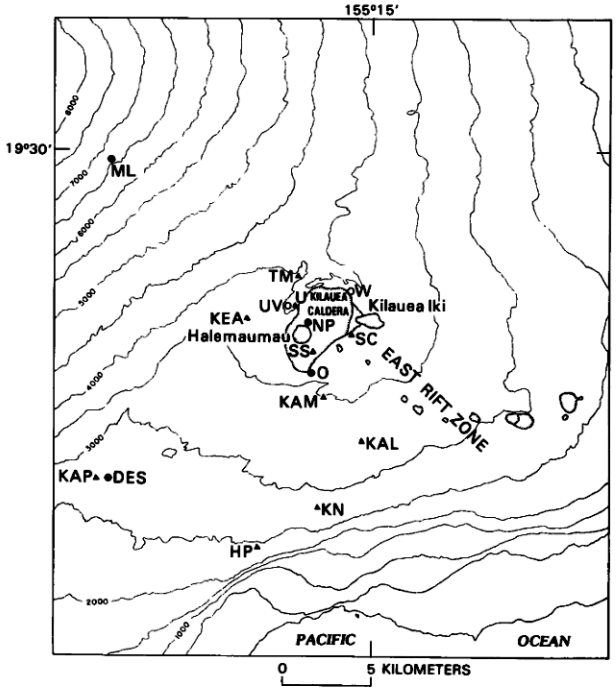


FIGURE 48.1.—Summit of Kilauea Volcano, showing tilt bases as triangles (TM, SC, SS, KEA, KAP, KAM, KAL, KN, HP), tiltmeter vaults as circles (UV and W), telemetered seismographs as dots (ML, DES, NP, O), and geographic localities mentioned in the text. Pit craters are indicated by hachures. Elevation contours in feet.

results are displayed as a map of vectors scaled according to the magnitude of tilt and pointing in the direction of maximum relative subsidence of the ground. Tilt maps for 12 intervals spanning the period February 1959 to November 1960 are shown in figures 48.2 and 48.3.

## WHITNEY VAULT: BOSCH OMORI SEISMOGRAPH

The longest record of tilt measurements on Kilauea Volcano is from the Bosch-Omori horizontal pendulum seismograph at the Whitney vault on the northeast rim of Kilauea caldera. This mechanical seismograph responds to a tilt perpendicular to the seismometer boom by a deflection of the recording point. Systematic tracking of the position of the recording point relative to some standard reference provides a record of ground tilting. Such a measurement was made once a day from 1912 through 1961 (Jaggar and Finch, 1929). This measurement is a relative one and the reference must be reset whenever the instrument is adjusted. Moreover, the Whitney vault has proved to have a very large annual tilt cycle that must be removed before tilting caused by the volcano can be detected (Powers, 1946, 1947). For very large tilts like those associated with the 1959–1960 eruption, however, the signals from this instrument (north-south and east-west components) are much larger than the uncertainties due to the foregoing problems.

## UWEKAHUNA VAULT: LIQUID-LEVEL TILTMETER

The Uwekahuna vault on the west rim of the caldera has proved to be much more stable than the Whitney vault. A liquid-level tiltmeter mounted on the walls of this vault has provided daily readings of tilt since 1956. The daily readings scatter through a range of several microradians, so the measurements are normally reported as weekly averages (Eaton and Fraser, 1958). During periods of strong tilting, such as during the 1959–1960 eruption, the daily scatter in readings is modest compared to the real tilt changes. The daily tilt readings at Uwekahuna and Whitney provide a somewhat noisy time history of tilting at Kilauea caldera that fills in details of tilting between the infrequent resurveys of the tilt bases. Tilt records for these two stations for the interval October 15, 1959, to April 1, 1960, are shown in figure 48.4.

## UWEKAHUNA VAULT: PRESS-EWING SEISMOGRAPH

The most unusual record of tilting at the summit of Kilauea during the 1959 eruption was obtained from the long-period Press-Ewing seismograph in Uwekahuna vault. Part of the tilt response of the instrument is expected and can be calibrated in terms of the operating parameters of the seismograph. Another part of the response was unexpected: it resulted from faulty attachment of the suspension fibers in the galvanometers, which permitted them to detect tilting in the same way as a horizontal pendulum seismograph. This part of the Press-Ewing response is accidental, but it can be calibrated by reference to the liquid-level tiltmeter that was operating in the same vault.

The layout of the Press-Ewing seismometer pendulums and their recording galvanometers, as well as the two components of the Uwekahuna liquid-level tiltmeter, is shown in figure 48.5. The velocity transducer of the Press-Ewing horizontal component seismograph (a coil attached to the mass and moving in the field of a magnet fixed to the frame) produces a signal (output voltage) proportional to the rate at which the coil is moving relative to the fixed magnet. Thus, one obtains a constant output for a constant tilt rate. For tilt rates that change slowly (compared to the 90-s period of the Press-Ewing galvanometer), the displacement of the galvanometer is directly proportional to the output voltage from the seismometer and, hence, to the rate of tilting.

The response of the Press-Ewing seismograph to slow tilting of the ground is thus a displacement of the zero-line trace about which normal shorter period ground movements are recorded. A given seismograph responds to the same component of tilting as it does to displacement. A sharp northward or eastward displacement of the ground produces an upward displacement of the trace on the seismogram (as the HVO instruments are connected), but tilting downward toward the north or east produces a downward displacement of the seismogram trace. From the manufacturer's specifications for the seismometers and galvanometers and for the manner in which

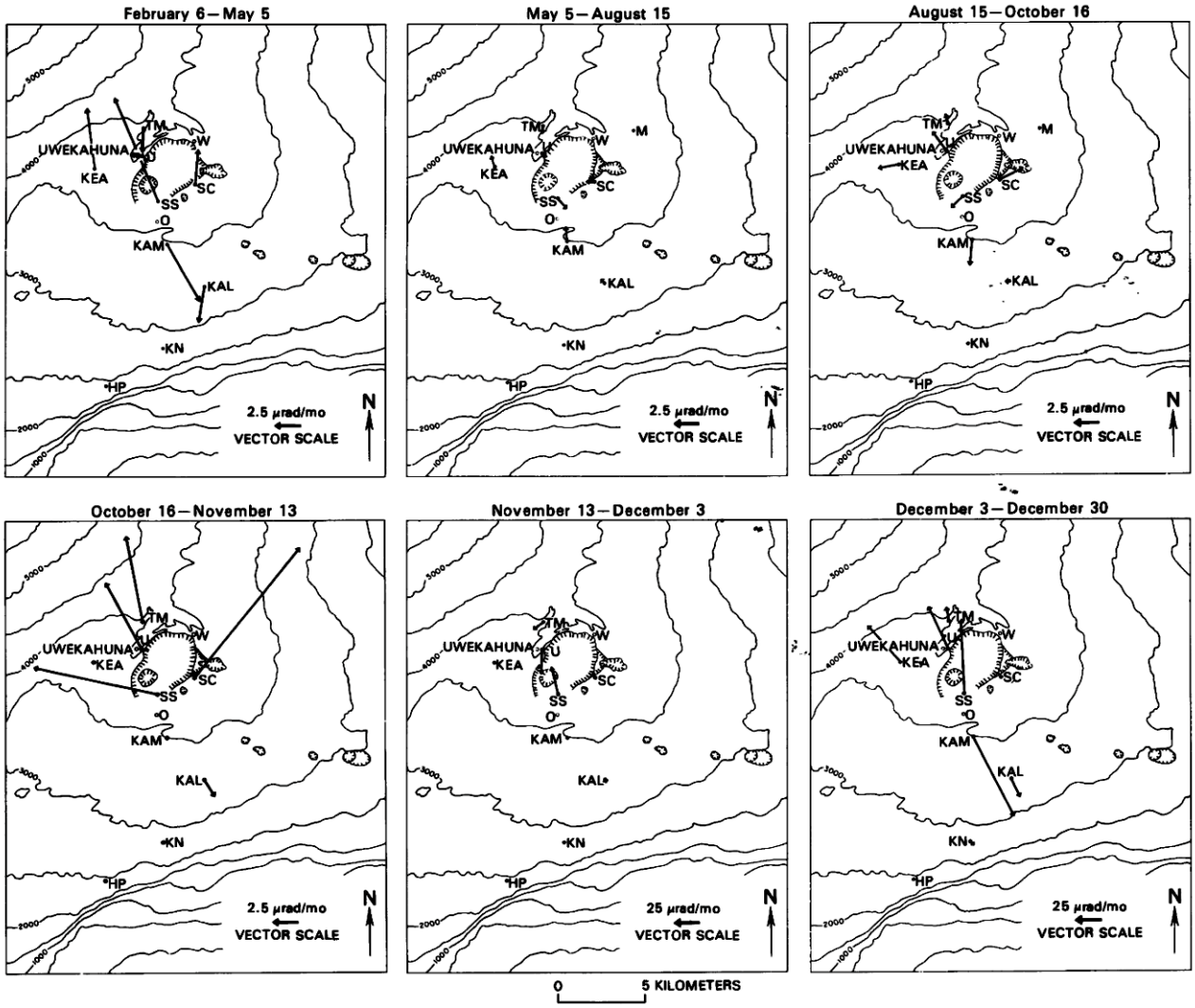


FIGURE 48.2.—Tilt diagrams for summit region for six intervals from February 6, 1959, to December 30, 1959. Tilt vectors point in direction of maximum subsidence of the ground. Note different vector scales used, depending on rate of tilt. For identity of data stations and geographic features, see figure 48.1.

they are set up at Uwekahuna, the theoretical rate-of-tilt sensitivity of both the north-south and east-west Press-Ewing seismographs (neglecting the direct tilt response of the galvanometers) is approximately 0.374 μrad/h per millimeter deflection of the trace.

The principal challenge in using the Press-Ewing seismograms to measure rate of tilt is in establishing an acceptable normal position of the trace from which deflections are to be measured. Surprisingly, however, measuring the position of the ambient zero line to within a fraction of a millimeter even in the presence of 5-mm microseisms is not too difficult. In the plotted results, features that repeat at intervals of 1 h or 1 d (corresponding to one rotation of the drum and to the daily record change, respectively) probably result from errors in the reference base. The east-west Press-Ewing seismogram for December 16–17, 1959, is shown in figure 48.6. Each line across the record is 1 h long. Zero-line excursions associated with the beginning and end of phases 13 and 14 are labeled.

An analysis of the Press-Ewing zero-line deflections from November 8 to December 1 (rapid collapse and recovery associated with the first phase of the eruption) revealed the imperfection in the galvanometers noted above: their coils are suspended in such a manner that the galvanometers, by themselves, act like simple tiltmeters for tilt at right angles to the normals to the galvanometer

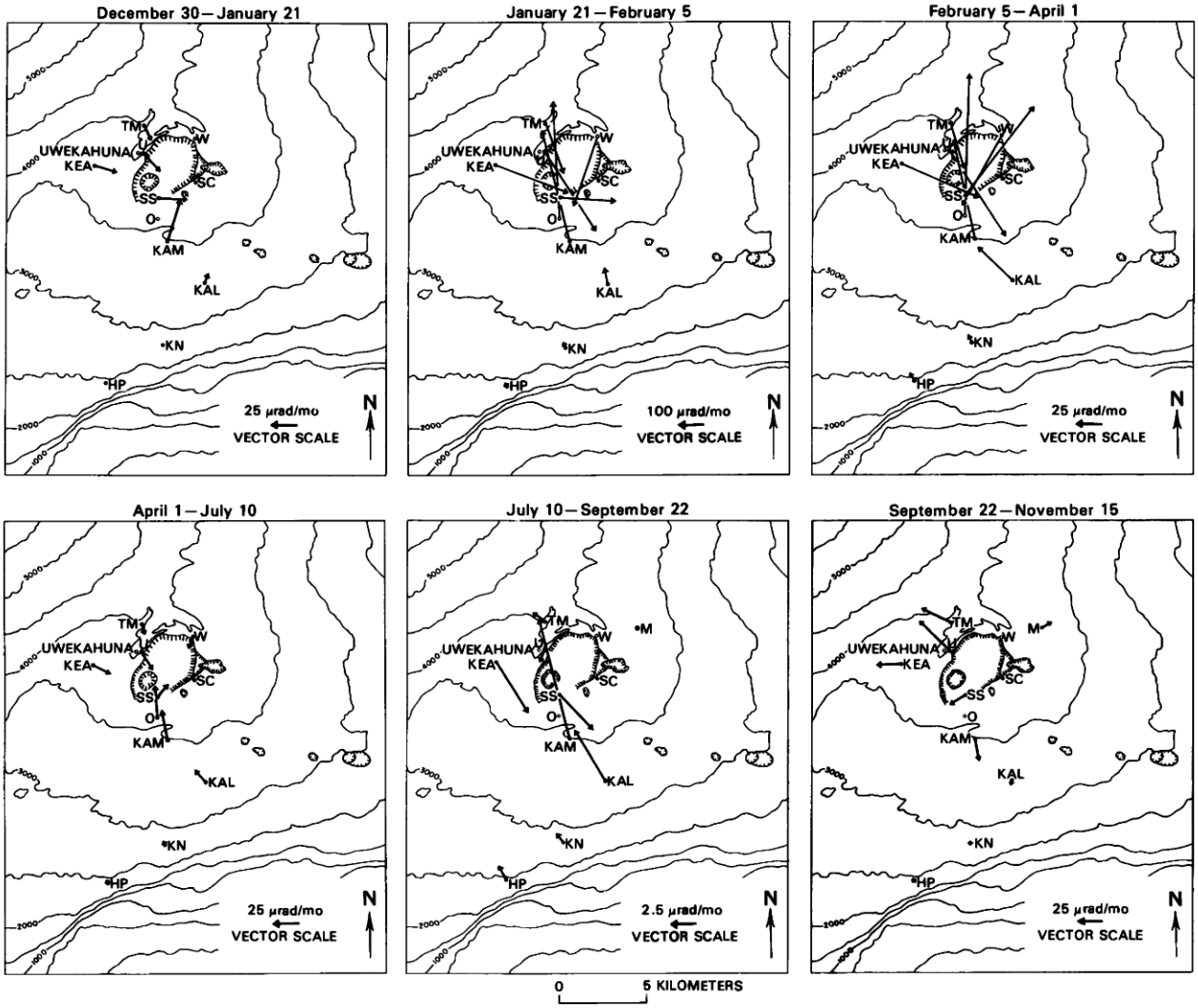


FIGURE 48.3.—Tilt diagrams for summit region for six intervals from December 30, 1959, to November 15, 1960. Tilt vectors point in direction of maximum subsidence of the ground. Note different vector scales used, depending on rate of tilt. For identity of data stations and geographic features see figure 48.1.

mirrors, in our case for tilt in an east-west direction. This effect is small for the east-west galvanometer, so the total seismometer-galvanometer response is dominated by the rate-of-tilt signal from the seismometer. The north-south galvanometer, on the other hand, is quite sensitive to the east-west state of tilt. As seen from Uwekahuna (on the liquid-level tiltmeter, for example) the center of swelling and collapse associated with Kilauea Iki eruptive phases lies almost due east. Thus, the north-south-component seismometer-galvanometer system response is dominated by the galvanometer (which records the east-west state of tilt with moderate sensitivity), the north-south component of tilt and its rate of change being small because of the azimuth to the active region. Large north-south rate-of-tilt deflections detected by the north-south Press-Ewing seismometer were recorded during the preoutbreak swarm on November 14 and during a large tilt transient between phases 4 and 5; moderate ones were recorded as transients when most of the phases stopped abruptly. In these cases the active center appears to have been south of that associated with the eruptions in Kilauea Iki.

In summary, during episodes of tilting associated with the Kilauea Iki eruption, the east-west Press-Ewing instrument measured east-west rate of tilt, and the north-south Press-Ewing instrument measured principally the east-west cumulative tilt at Uwekahuna. This point may be confusing, so it should be noted carefully.

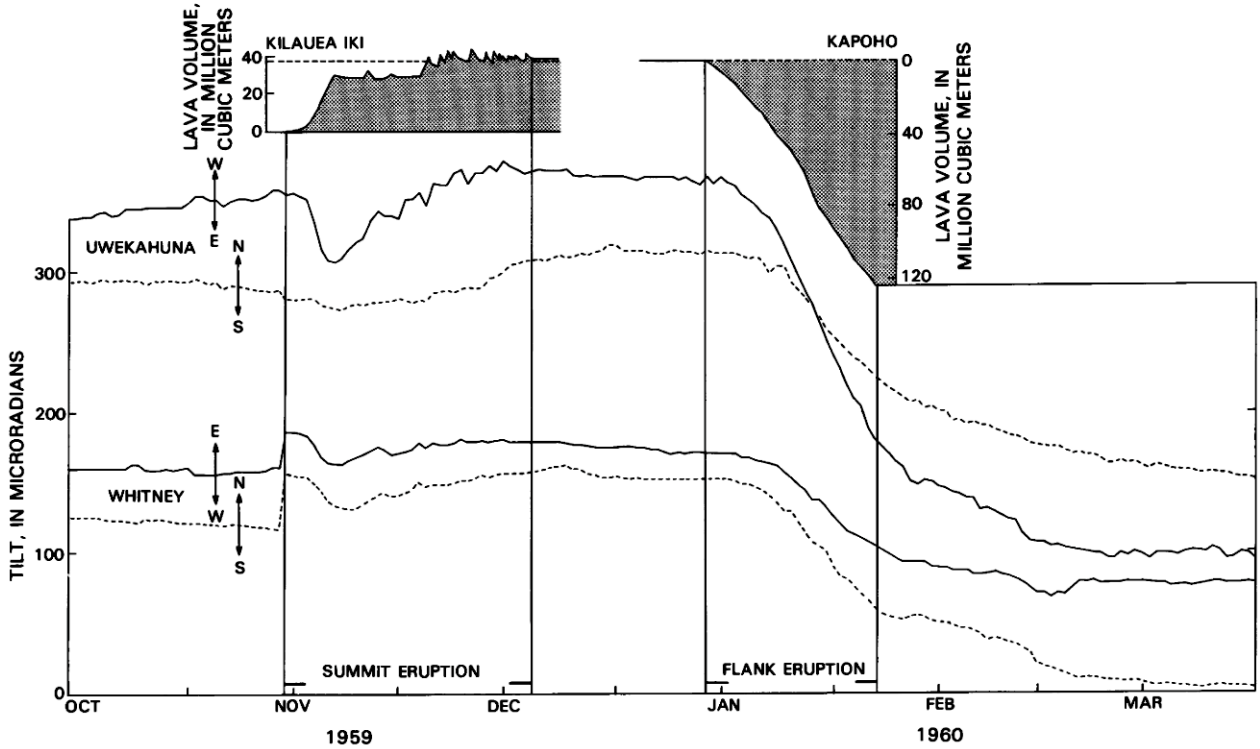


FIGURE 48.4.—Tilt at Uwekahuna and Whitney on Kilauea summit (UV and W of figure 48.1) from October 15, 1959, to April 1, 1960, and volumes of lava in Kilauea Iki Crater erupted during the 1960 eruption from the east rift zone near Kapoho.

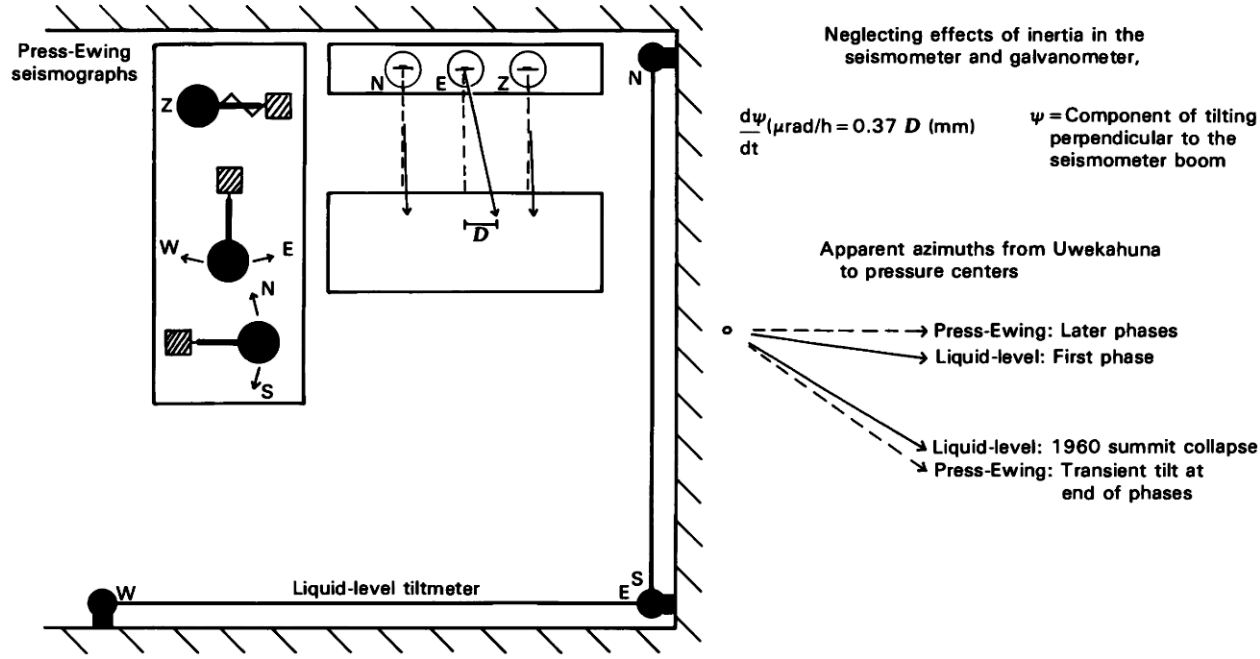


FIGURE 48.5.—Layout of liquid-level tiltmeter and long period Press-Ewing seismographs in Uwekahuna vault. Press-Ewing seismometers are shown at left, and their galvanometers are shown at top of figure. Letters Z, N, and E denote parts of instruments and the components of tilting they record: Z, vertical; N, north-south (N, S); E, east-west (E, W). D, deflection of seismogram trace from normal; $d\psi/dt$, rate of tilting.

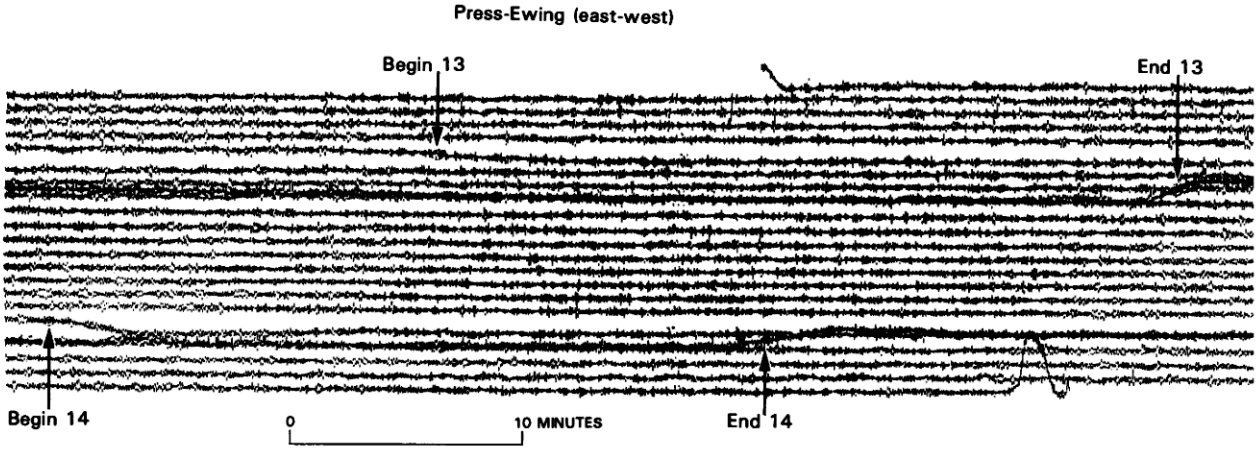


FIGURE 48.6.—Seismogram from east-west Press-Ewing seismograph for December 15–16, 1959, showing shifts in zero line associated with phases 13 and 14 (arrows).

## SEISMIC NETWORK

Before the 1959 eruption a network of sensitive, telemetered, short-period seismographs had been installed around the summit of Kilauea and on the adjacent flank of Mauna Loa to facilitate study of the many earthquakes occurring regularly in that region. The telemetered network was augmented by optically recording seismographs with similar response characteristics that were deployed in a ring around the Island of Hawaii. The combined network provided the means for detecting and locating a variety of seismic manifestations associated with the volcano, including the following:

(1) Individual earthquakes throughout the volcano;

(2) Occasional swarms of small earthquakes marking the opening of dikes around the summit reservoir and in the rift zones;

(3) Volcanic tremor generated by rapid movement of magma within the volcano, particularly during eruptions; and

(4) Swarms of tiny deep earthquakes and associated irregular tremor thought to mark the region from which magma is collected to feed the volcano.

Activity of the last 3 types figure prominently in our analysis of the 1959 eruption.

## OVERVIEW OF THE REGIONAL DEFORMATION OF THE KILAUEA SUMMIT AND DEEP EARTHQUAKE SWARMS ASSOCIATED WITH THE 1959 ERUPTION

### DEFORMATION

The patterns of regional deformation of the Kilauea summit area during the 6 intervals from February 6, 1959, to December 30, 1959, that are shown in figure 48.2 indicate the location and intensity of inflation and deflation in this area before and during the 1959 eruption. The next 6 intervals (fig. 48.3), from December 30, 1959, to November 15, 1960, show the patterns of regional deformation of the summit area during the 1960 Kapoho eruption, the rapid deflation of the summit reservoir accompanying and following the Kapoho eruption, and the onset of rapid reinflation of the summit reservoir in the fall of 1960. The vectors depicting rate of tilting point outward away from centers of inflation and inward toward centers of deflation (fig. 48.3). The lengths of the vectors are scaled according to the rate of tilting. Note the large variation in scale factor from one interval to the next. These plots are shown together for easy comparison, but we shall return to consider them one at a time as the need arises.

A more continuous, but spatially limited, picture of inflation and deflation of the Kilauea summit region is shown in figure 48.4, where the north-south and east-west components of daily tilt measurements at Uwekahuna vault and Whitney vault are compared with the volume of lava ponded in Kilauea Iki and the volume of lava later erupted on the east rift zone near Kapoho in the 1960 eruption. Tilting in response to eruption of lava into Kilauea Iki during phase 1, and its removal from the summit reservoir, is most marked on the Uwekahuna east-west record, where the curve of eastward tilting very closely matches the lava-volume curve. After an initial sharp northeast offset in tilt at Whitney, the curves of both westward and southward tilting also closely match the lava-volume curve. Vectors representing tilting at these two stations during the phase 1 eruption both point into Kilauea caldera; they cross near the center of the caldera, indicating that the lava erupted into Kilauea Iki was removed from beneath Kilauea caldera. Rapid refilling of the depleted reservoir appears to have begun by the time phase 1 ended. Both the east-west and north-south curves at Uwekahuna had recovered approximately to their levels at the start of the phase 1 eruption by the time phase 4 began. As the east-west tilt curve rose still further during the next two weeks, the volume of lava retained in the lake after subsequent eruptive phases (and the height of the lake surface) also increased beyond the $30 \times 10^6$ $m^3$ left by phase 1 in

about the same proportion that the east-west curve rose above its pre-phase 1 level. The movement of the east-west Uwekahuna curve during the later eruptive phases, such as phase 4, suggests eastward tilting while the eruptions were in progress followed by rapid westward tilting when they stopped. However, the once-per-day interval for tilt samples is too large to track individual phases, some of which lasted only a few hours.

A still simpler picture of the swelling and collapse of the Kilauea summit region is shown by a plot of the radial component of tilting at Uwekahuna tilt base relative to the center of collapse near the south rim of Kilauea caldera during and after the 1960 east-rift eruption near Kapoho. Figure 48.7 (adapted from Eaton, 1962) shows this curve for the period 1957–62. The approximate scale for $\Delta V$, volume of the collapse, is based on fitting the tilt changes between January 21–April 1, 1960 (intervals January 21–February 5, 1960, and February 5–April 1, 1960, in fig. 3), to a curve based on Mogi's (1958) theoretical results for change in elevation versus distance for a small spherical source embedded in an elastic half-space (Eaton, 1962, fig. 12).

## DEEP EARTHQUAKE SWARMS

From the early 1950's until the fall of 1960 occasional swarms of small earthquakes, accompanied by a continuous background agitation resembling tremor that waxed and waned during the swarms, were recorded from a source 45–65 km deep beneath the summit of Kilauea and the adjacent flank of Mauna Loa to the north. Until the introduction of the sensitive telemetered seismic net around the summit of Kilauea in 1958, these earthquakes were recorded most clearly on a mechanical horizontal-component seismograph, about 10 km northwest of Kilauea caldera (station ML, figure 48.1, with magnification of about 200). Typically, several hundred events were counted during a swarm, and the location of the swarm, including its depth, was poorly determined. From 1958 onward the detection threshold was lower and the locations were much improved, though still poor by modern standards. The sharpest recordings were obtained at stations 10 km northwest (station ML) or 10 km southwest (station DES) of the caldera (fig. 48.1), which were equipped with high-gain short-period vertical seismographs whose signals were telemetered to Uwekahuna for recording; but the earliest $P$-wave onsets clearly were at Uwekahuna. Swarms recorded by the improved network contained from less than 100 to several thousand individual events, plus many hours of background tremor during the larger swarms. The times of occurrence of nine of these swarms are indicated by arrows along the time axis in figure 48.7, and samples of two swarms are shown in figures 48.8 and 48.9. Between September 1953 and June 1956 (not shown on fig. 48.7) there were 10 additional swarms, but there were none between June 1956 and April 1958.

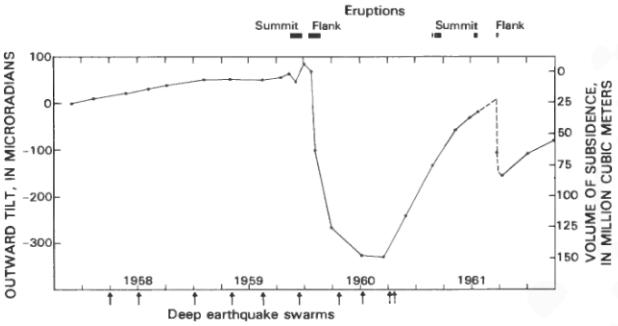


FIGURE 48.7.—Radial component of tilting at Uwekahuna tilt base for 1957–62, relative to 1960 center of subsidence at south edge of Kilauea caldera, showing swelling and subsequent collapse of Kilauea summit. Occurrence times of deep swarms of earthquakes beneath summit of Kilauea and of summit and flank eruptions also indicated.

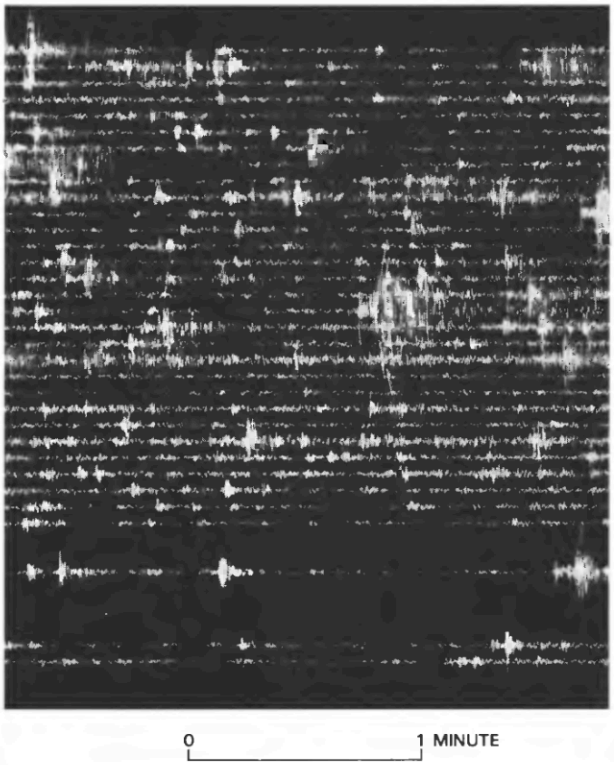


FIGURE 48.8.—Sample of Desert seismogram from August 16, 1959, illustrating swarm of deep earthquakes beneath the summit of Kilauea. Several thousand small earthquakes were accompanied by intervals of continuous tremor.

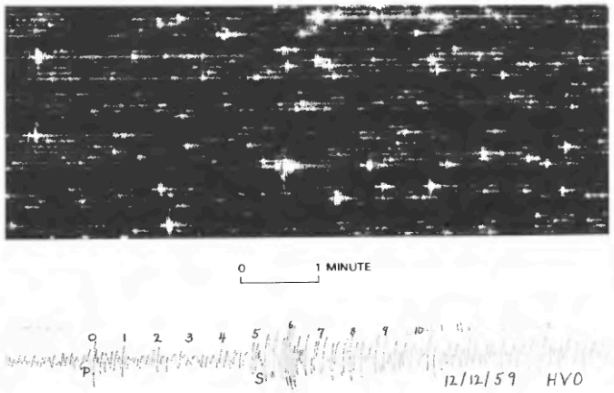


FIGURE 48.9.—Sample of Mauna Loa seismogram of swarm of deep earthquakes on December 11–12, 1959, beneath summit of Kilauea. Large-scale record of a member of this swarm recorded at Uwekahuna is shown at bottom (*P* and *S* arrivals and time in seconds after *P* are indicated).

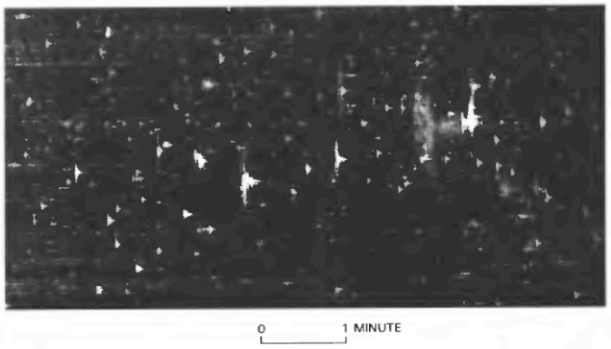


FIGURE 48.10.—North Pit seismogram from November 9–10, 1959, illustrating intense swarm of very small earthquakes that emanated from Kilauea caldera for several months before the 1959 eruption.

## CHRONOLOGY OF TILTING AND EARTHQUAKE SWARMS LEADING UP TO THE 1959 ERUPTION

From November 1957 to May 5, 1959, the summit of Kilauea swelled slowly but steadily (fig. 48.2, 48.7). Deep swarms occurred on April 1, 1958 (weak), July 3–6, 1958 (strong), January 5–6, 1959 (moderate), and May 5, 1959 (very weak). From May 5 to August 15, 1959, the summit subsided very slowly. During August 14–20, 1959, there was a very strong swarm of earthquakes a few kilometers north of Kilauea caldera at a depth of 50–55 km (fig. 48.8). From August 15 to October 16, 1959, swelling of the summit resumed at about the same rate as during 1958.

In mid-September a swarm of tiny very shallow earthquakes began recording on the north Pit seismograph (NP, fig. 48.1) from a source in Kilauea caldera very near the northeast rim of Halemaumau. Initially about 50 per day, the frequency of quakes increased to about 100 per day by the end of September and to about 500 per day during the first week of October. By the first of November earthquakes of this swarm exceeded 1,000 per day, but they were so feeble that they were barely recorded on other seismographs less than 2 km away (fig. 48.10).

Remeasurement of tilting at bases around the caldera in the second week of November revealed that dramatic changes were in progress. The summit was swelling at least three times faster than in previous months (fig. 48.2, interval October 16–November 13, 1959). In midafternoon on November 14, earthquakes emanating from the caldera increased sharply in number and intensity. At frequent intervals during the next 5 h the entire summit region shuddered as earthquakes marked the rending of the crust by the eruptive fissure splitting toward the surface (fig. 48.11). At 2008 (this and all times given in this paper are Hawaii standard time) the lava broke through to the surface in a 900-m-long series of fissures

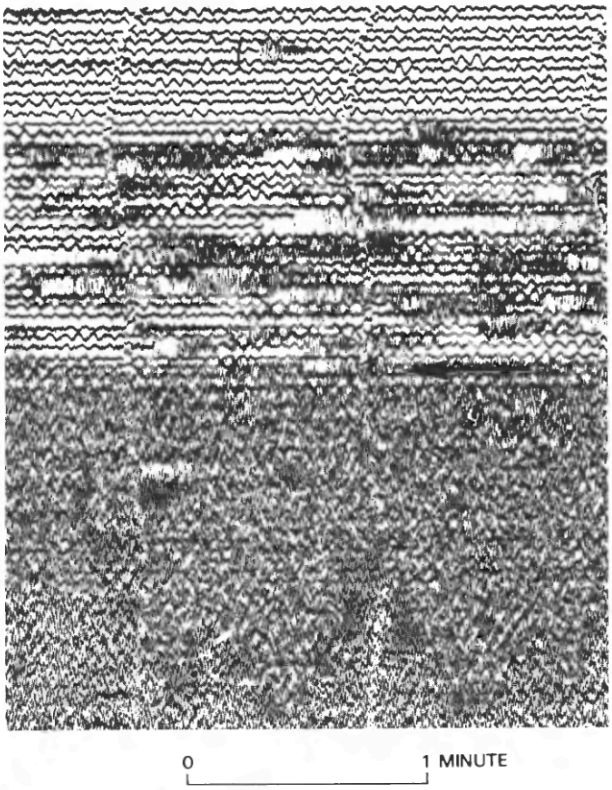


FIGURE 48.11.—Uwekahuna (short-period) seismogram from November 14, 1959, illustrating (upper part) 5-hour-long swarm of earthquakes that preceded the 1959 outbreak. The swarm gave way to strong harmonic tremor when fountaining began (arrow).

about halfway up the 180-m-high south wall of Kilauea Iki Crater, just east of Kilauea caldera. Abruptly the earthquakes stopped, and seismographs around the caldera began to record the strong harmonic tremor characteristic of lava outpouring from Hawaiian volcanoes (fig. 48.11).

Both horizontal components of the Press-Ewing seismograph recorded large excursions of the zero line during the five-hour-long swarm of caldera earthquakes preceding the outbreak of the eruption. Closer examination of the records revealed that the zero lines appeared to be erratic also for the preceding five days. This erratic signal was much stronger, and could be seen earlier, on the east-west than on the north-south component. The deflections of the zero lines from their expected positions were measured from the seismograms for the period 0600 November 6 through 0600 November 15 and the results are plotted in figure 48.12. The activity on the east-west graph before November 9 shows the level of noise (including error of measurement) before the erratic movement of the trace began. On November 9, long-period zero-line shifts began to appear on the east-west component. The disturbance was a distorted sinusoidal oscillation with a period just short of 1 h and a slightly asymmetric appearance: upward peaks (west tilt) were slightly broader than downward peaks (east tilt), and it appeared that the broad upward peaks constituted the zero line away from which the trace moved in brief downward excursions. The amplitude of the disturbance increased and its period decreased (to about 35 min) for several days. From November 12 onward this disturbance, which may be called a tilt storm, was also visible on the north-south component, though its amplitude there was only about one-fourth that of the east-west component. The amplitude of the tilt storm diminished gradually for about one day before the eruption began.

When the caldera swarm suddenly intensified at about 1420 on November 14, both of the Press-Ewing traces deflected abruptly from zero. The southward component of tilting rose rapidly to about 4 μrad/h. It then declined steadily, first to about 0.8 μrad/h by 1700 and then to about 0.2 μrad/h by 2000. The eastward component of tilting was more complex. A strong initial tilting toward the east was replaced after only a few minutes by an equally strong tilting toward the west, which declined rapidly to about 0.5 μrad/h. At 1630 the direction of tilting reversed again, and easterly tilting attained a rate of about 0.9 μrad/h at 1730; after that it decreased steadily to about 0.2 μrad/h by 2000. The complex transient tilting during the outbreak swarm of earthquakes was probably compounded from several effects, including fracturing and propping open of the eruptive fissure and subsidence of the summit owing to escape of lava from the reservoir into the fissure. The tilt storm preceding the outbreak earthquake swarm may have resulted from intermittent escape of lava from the reservoir as it continued to expand before the outbreak.

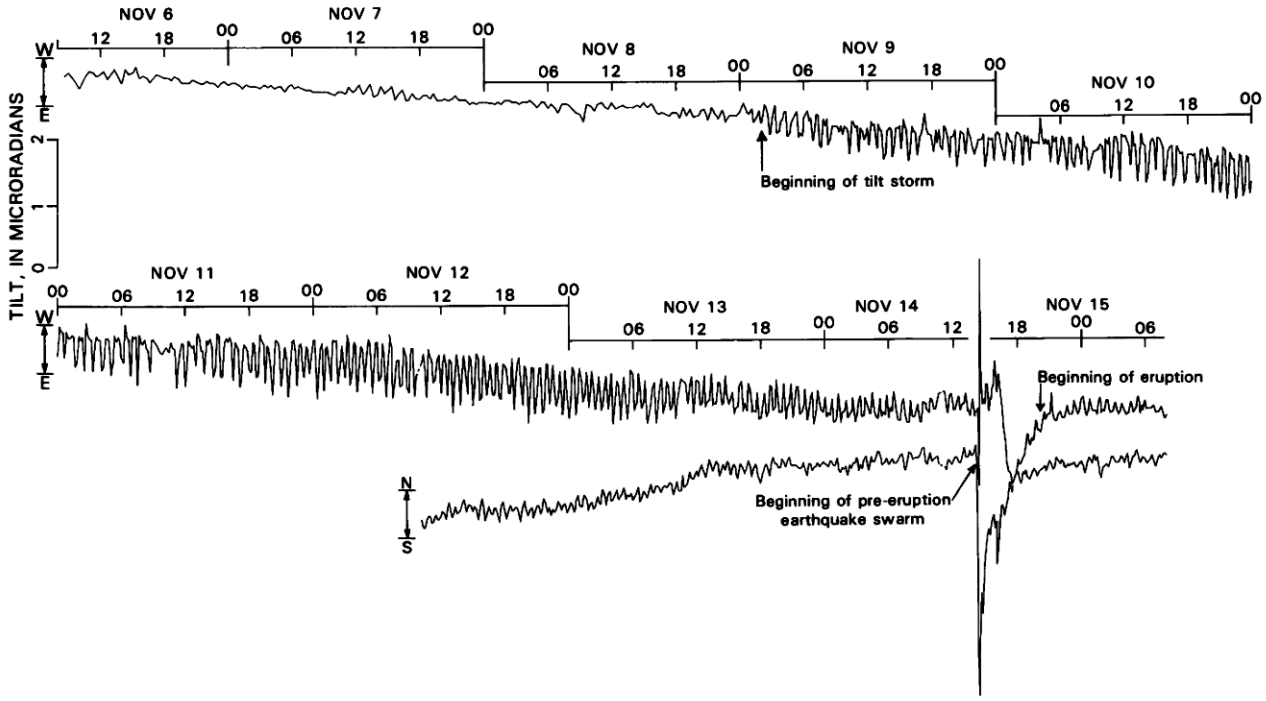


FIGURE 48.12.—Five-day tilt storm and large five-hour tilt excursion recorded by Press-Ewing seismograph before outbreak of 1959 eruption.

## SUMMARY OF SELECTED FEATURES OF THE 1959 ERUPTION

The course of the 1959–60 eruption has been described in detail by Richter and others (1970), and we shall borrow several pictures from that report to illustrate features of the eruption that are related closely to the pattern of summit deformation and the amplitude of tremor that accompanied the eruption. The locations of Kilauea Iki Crater and the 1959 eruption vents relative to Kilauea caldera and other features at the summit of Kilauea are shown in figure 48.13 (Richter and others, 1970, fig. 3). The initial outbreak was in a short line of fountains, about half-way up the south wall of Kilauea Iki, which extended rapidly toward the east and slowly toward the west to form a 900-m-long "curtain of fire" during the first 80 min of the eruption (fig. 48.13, vents A through K). The line of fountains is seen in figure 48.14 at its maximum development from Byron Ledge overlook at 2130 on November 14. Fountaining at the ends of the fissure died out slowly, and fountaining near vent A (fig. 48.14, second group from the right) gradually increased in the following hours. By nightfall on November 15 activity was confined to a single fountain 30–45 m high near the site (vent A) that became the main vent for the rest of the 1959 eruption. The fountain grew slowly in height and lava output until it approached its maximum level late on November 18, when the fountain first exceeded 300 m and the depth of the lake reached 45 m. The fountain and lake are shown in figure 48.15 from Byron Ledge overlook when the fountain was 200 m high and the lake was 52 m deep. Spectacular fountaining and rapid filling of the lake continued unabated until the morning of November 20, when the lake, by then 98 m deep, rose above the level of the vent and began to interfere with the fountain. At 1925 on November 21 the fountain ceased abruptly, leaving a 102-m-deep lake containing $30 \times 10^6$ $m^3$ of lava.

Subsequent phases were similar to the last part of the first phase: large fountains with voluminous outpouring of lava filled the lake until it rose above the vent, and then the fountain died abruptly. The large fountains were accompanied by strong volcanic tremor throughout the summit region (fig. 48.16). When the lake rose above the vent, there was strong interaction between the fountain and the lake (fig. 48.17). Large waves generated at the fountain rolled out over the surface of the fluid lake and played against the north shore, alternately revealing and obscuring an incandescent band at the foot of the wall. Unlike the inconspicuous drainback from the first phase, which was not apparent for many hours after the fountain died, drainback from the later phases began almost immediately and was spectacular (fig. 48.18). The rate of withdrawal of lava during the early part of the drainback stage commonly exceeded the rate of eruption of lava during the previous eruptive stage. The very rapid backflow after cessation of fountaining was generally not accompanied by volcanic tremor, although there was a resurgence of tremor after an initial interval of quiet in many cases, particularly in the latest phases (fig. 48.19). At the end of the summit eruption the lake was 111 m deep and contained about $38 \times 10^6$ $m^3$ of lava (fig. 48.20). The level central part of the lake was surrounded by a black ledge about 15 m high and 15–60 m wide that marked the highest level of the lake at the end of phase 8.

The longest and most productive eruptive period, except for phase 1, was phase 4. It was characterized by unusually quiet outpouring of very hot lava and only moderate fountaining. The mouth of the vent had jumped about 12 m upslope between phases 3 and 4, and the level to which drainback could lower the lake appears to have moved upward a somewhat smaller amount.

During December 12–14, a strong swarm of small earthquakes was recorded from a source 15 km north-northeast of Uwekahuna and 40–45 km deep (fig. 48.9).

## ANALYSIS OF LAVA MOVEMENT DURING INDIVIDUAL PHASES OF THE 1959 ERUPTION

The parameters of tilting, tremor, fountain height, and lava-lake volume measured during the eruption are closely interrelated. Properly understood, these relations should help clarify three important processes underlying the major facets of the eruption: (1) the accumulation of lava in the summit reservoir, (2) the eruption of lava into Kilauea Iki crater and its subsequent partial withdrawal, and (3) the escape of lava from the summit reservoir into a region other than Kilauea Iki.

The character of the phases changed during the eruption. The first phase differed most from the others, and the subsequent phases evolved generally toward more rapid outpouring and withdrawal of lava and toward more complex relationships among backflow into the vent, postfountaining (resurgent) tremor, and reinflation of the summit reservoir. The first phase offers the best opportunity to study the relations between lava-lake volume and cumulative tilting at Uwekahuna (and Whitney). The later phases are more suited to studies of the relation between the rate of east-west tilting, cumulative amount of east-west tilting, eruption rate, fountain height, and tremor amplitude.

The volume of lava in Kilauea Iki, the east-west component of liquid-level tilting at Uwekahuna, the north-south Press-Ewing zero-line drift (east-west cumulative tilting), the east-west Press-Ewing zero-line drift (east-west rate of tilting), fountain height, and tremor amplitude at Outlet (fig. 48.1) have been plotted against time for the first three phases, November 13–30 (fig. 48.21). The shapes of the first three curves (lava-lake volume, daily readings of east-west tilt from the liquid-level tilt meter, and a continuous record of east-west tilt determined from the north-south Press-Ewing zero-line drift) are so similar from start to finish of the first phase (November 14–21) that suitable scaling brings them into very close correspondence. The continuous east-west tilt curve recorded by the north-south Press-Ewing instrument corresponds almost exactly to the daily liquid-level tilt readings, but it gives far more detail of tilt excursions lasting less than one day. The east-west liquid-level tilt curve also corresponds closely to the lava-lake volume curve from the onset of phase 1 until its end. Eruption of $30 \times 10^6$ $m^3$ of lava into the crater was accompanied by about 50 $\mu$rad of eastward tilting.

After an episode of strong tremor with only small fountains during the first day of phase 1, the tremor amplitude diminished markedly. Thereafter, the curves of tremor amplitude and of fountain height are very similar. The rate of lava extrusion built up slowly during phase 1, and any offset of the east-west Press-Ewing zero

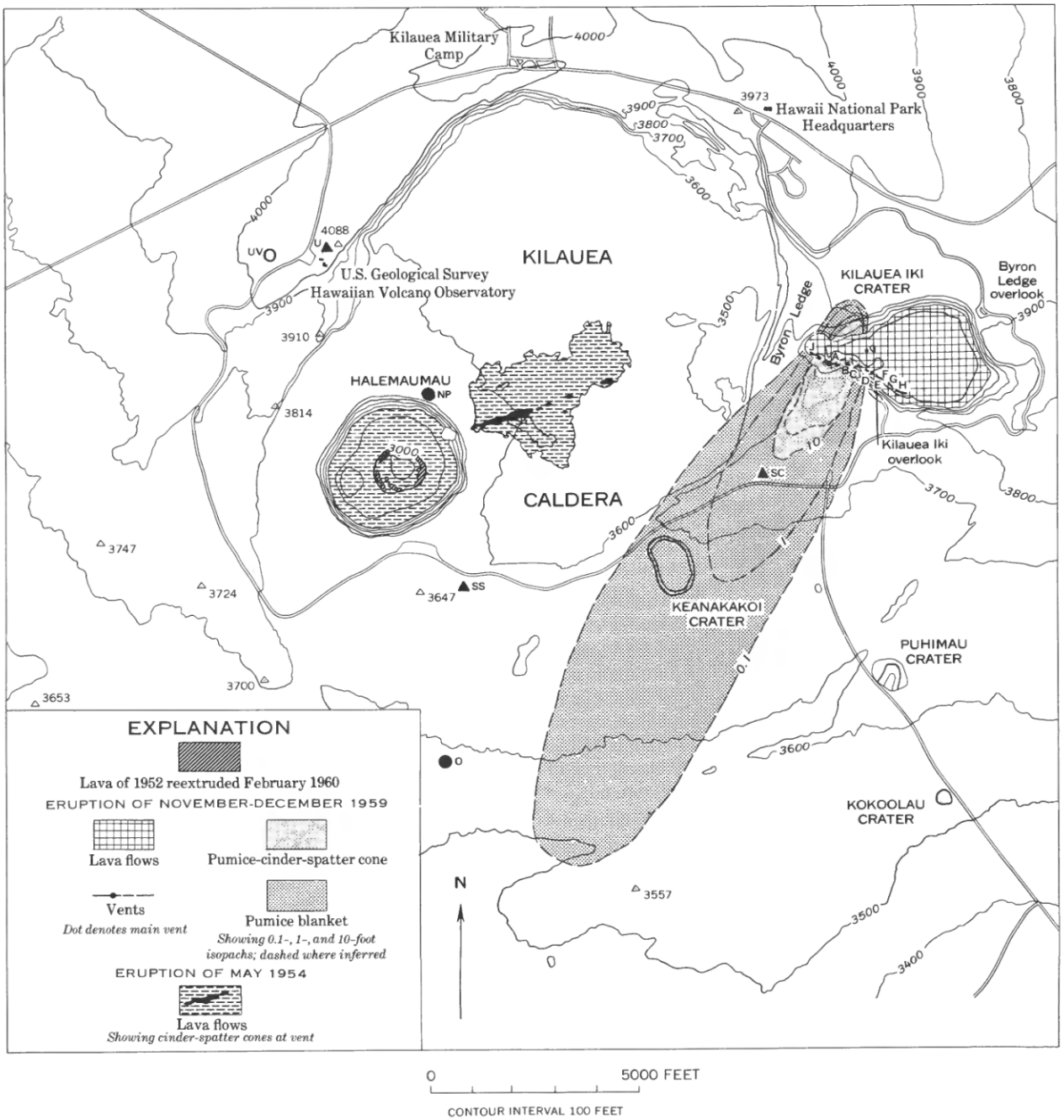


FIGURE 48.13.—Kilauea caldera region, showing relation of 1959 eruption in Kilauea Iki to Kilauea caldera, Halemaumau, east rift zone, and other localities mentioned in text. Modified from Richter and others (1970).

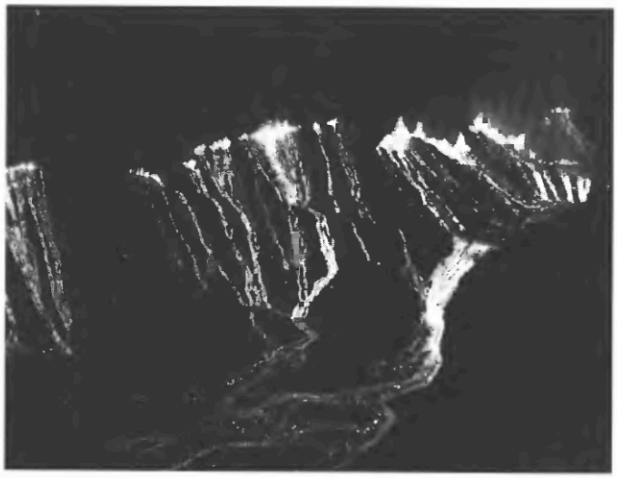

FIGURE 48.14.—Curtain of fire in Kilauea Iki at 2130 on November 14, 1959, 80 min after eruption began, showing maximum development of line of fountains 100 m above floor of crater. View from Byron Ledge overlook.

FIGURE 48.15.—Lava fountain 240 m high at main vent in Kilauea Iki at 0500 on November 19, 1959. Incandescent lava river from fountain is pouring into 50-m-deep lava lake. View from Byron Ledge overlook.

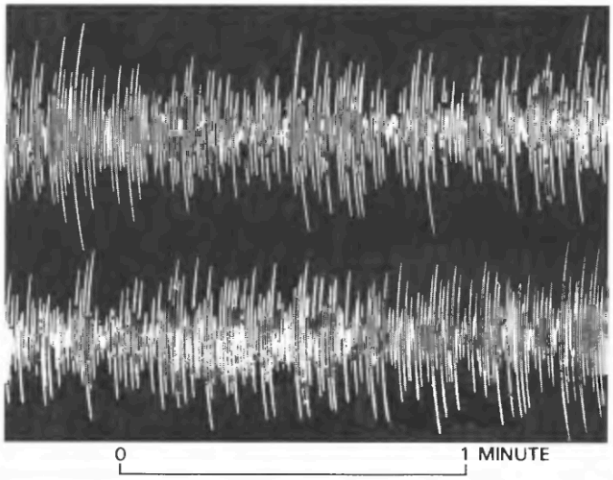


FIGURE 48.16.—Strong harmonic tremor recorded on Outlet seismograph during third phase of the 1959 eruption on November 29.

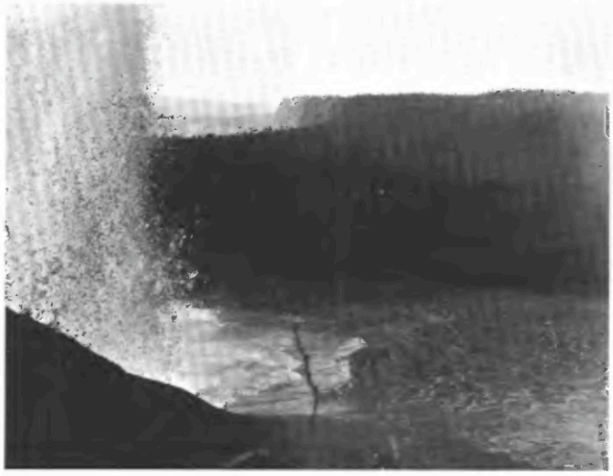

FIGURE 48.17.—Large fountain of phase 10 spurting through edge of lava lake, which has risen above the vent, at 1500 on December 14. Note waves on surface of lake. View from west end of Kilauea Iki overlook.

line resulting from the onset of the eruption would have been masked by the large tilt excursions that immediately preceded the outbreak. Cessation of fountaining was abrupt, however, and a zero-line offset marked the abrupt end of eastward tilting. Withdrawal of lava from the lake was first noticed about 20 h after the fountain died, and the volume of lava that drained back was small. No sharp rebound from eastward to westward tilting was noted at the end of the first phase.

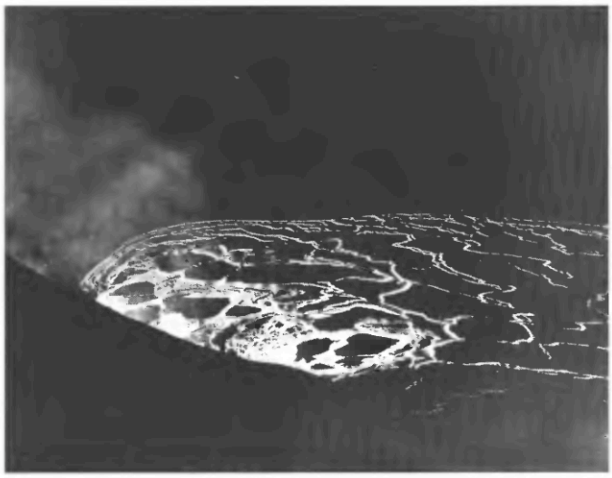

FIGURE 48.18.—Wide stream of lava pouring back into vent at 2200 on December 15, one-half hour after end of phase 12. Huge rafts of solid lake crust, disrupted as backflow stream converges near event, are mixed and swallowed by returning lava. View from top of cone almost directly above vent.

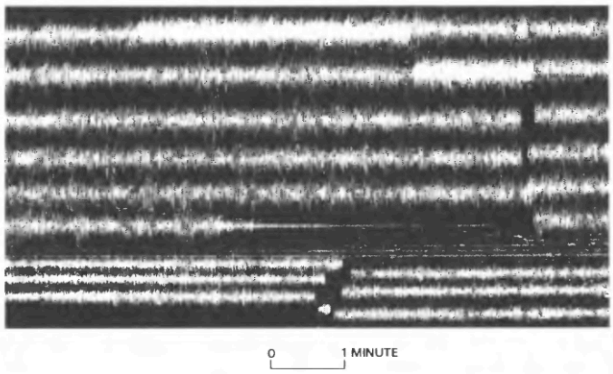


FIGURE 48.19.—Section of Outlet seismogram of December 8, 1959, showing harmonic tremor accompanying phase 7, abrupt dying out of tremor when fountain stopped, and resurgence of tremor during backflow after 50 min of quiet.

For phases 2 and 3, also shown in figure 48.21, the lava-volume changes are small and the east-west tilt changes (both liquid-level and north-south Press-Ewing) are difficult to pick out of the noise. The curves for tremor, fountain height, and rate of east-west tilting (east-west Press-Ewing zero-line offset) are clearly related. At the sharp onset of fountaining, the amplitude of tremor increased suddenly; its amplitude generally followed fountain height throughout each phase. With the onset of fountaining, also, clear eastward tilting began on the east-west rate-of-tilting curve. The shape of the rate-of-tilting curve is similar to those for fountain height and tremor. When the fountain stopped abruptly, tremor amplitude

FIGURE 48.20.—Kilauea Iki lava lake on December 20, 1959, after all activity had ceased. The black ledge, 15–60 m wide and about 15 m high, surrounds entire lake surface. View from Byron Ledge overlook. Photograph by R.T. Haugen, National Park Service.

dropped to zero, and the tilt curve reversed rapidly from moderate eastward tilting to strong westward tilting. The reversal in direction of tilting corresponds closely in time to cessation of fountaining and the immediate onset of strong backflow into the vent. The rate of westward tilting was initially several times greater than the rate of eastward tilting just before the fountain died, but it diminished rapidly during the first few minutes of backflow and then more gradually for several hours until it fell below noise level.

With some variations, the remaining phases were similar to phases 2 and 3. Plots of east-west tilt (north-south Press-Ewing) and east-west rate of tilting (east-west Press-Ewing) for phases 4–16 are shown in fig. 48.22. This figure gives a useful overview of tilting for the rest of the 1959 eruption, but the phases were so short that the relationships discussed for the first three phases are not easily seen. From phase 4 onward, east-west rate of tilting and east-west cumulative tilt at Uwekahuna, fountain height, and tremor amplitude at Outlet are plotted against an expanded time scale in figure 48.23 (phase 4), 48.24, (phases 5–7), 48.25 (phases 8 and 9), 48.26 (phases 10–14), and 48.27 (phases 15 and 16). Isolated episodes of tilting and tremor that were unaccompanied by an eruptive phase occurred between phases 4 and 5 (fig. 48.23) and between phases 15 and 16 (fig. 48.27).

To follow the movement of lava from the summit reservoir to the lake and back again to the reservoir, we need good estimates of the total eastward tilting at Uwekahuna during the eruptive stage and of the total westward tilting during the backflow stage. These tilt totals can then be converted to volumes of lava removed or returned to the reservoir by comparison with the ratio of lava-lake volume to eastward tilting at Uwekahuna recorded during the first phase. Such a conversion assumes that all of the phase 1 lava was mined from the

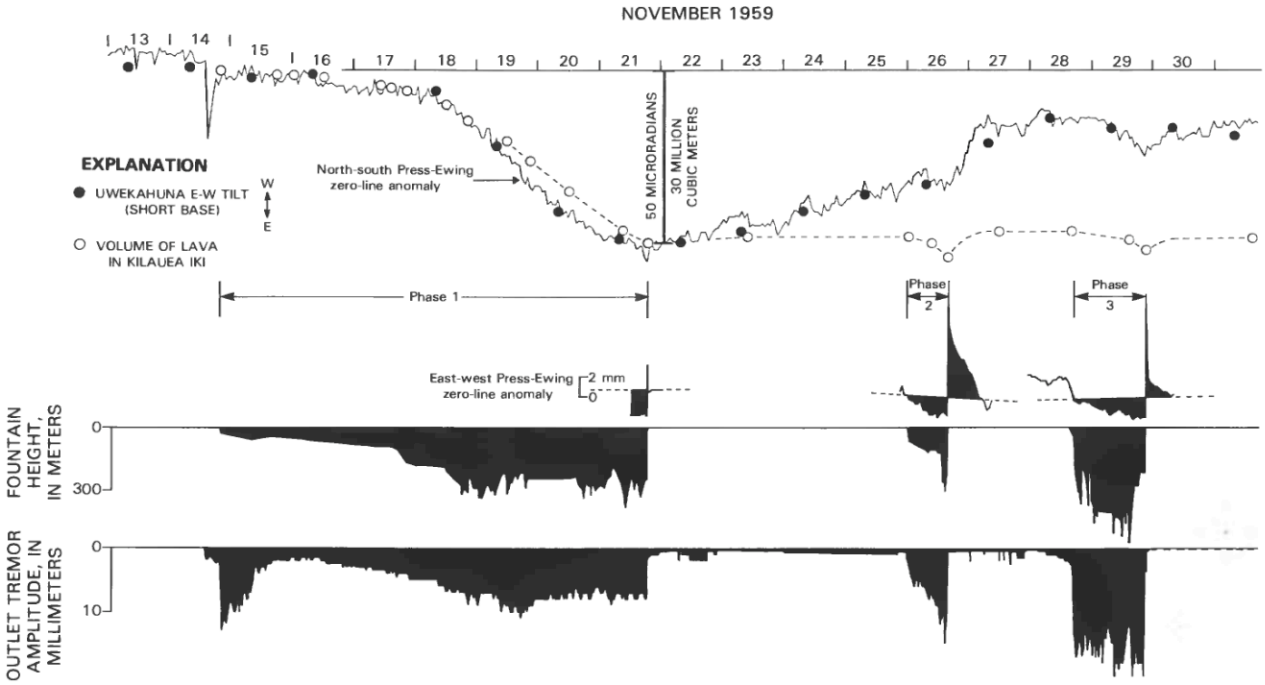


FIGURE 48.21.—Eruption and deformation parameters during first three eruptive phases of 1959 eruption. Volume of lava in Kilauea Iki, east-west component of Uwekahuna liquid-level tiltmeter, and north-south Press-Ewing zero-line anomaly are superposed in upper half of figure; fountain height and tremor amplitude at Outlet station are plotted in lower half. Duration of individual phases indicated.

summit reservoir and that replenishment of the reservoir from the deep source of magma during phase 1 was small compared to the volume of lava erupted. Replenishment during the eruption would lead to the calculated ratio (lava/tilt) being too large. Replenishment would be a less significant factor during very short but voluminous phases, but the estimation of the volume of lava poured into the lake during the later (smaller) phases is relatively less accurate than for the first (larger) phase. The ratio of lava volume to cumulative tilt for phase 1 so calculated is $0.6\times10^6$ m$^3$ per microradian of eastward tilting at Uwekahuna.

An independent estimate of the ratio of the volume of lava removed from the summit reservoir to the change in tilt on the east-west liquid-level tiltmeter at Uwekahuna can be obtained from the summit collapse that accompanied the 1960 flank eruption at Kapoho (fig. 48.4). During the actual outpouring of the estimated $0.12\times10^9$ m$^3$ of lava near Kapoho between January 13 and February 6, the east-west liquid level tiltmeter measured an eastward tilt of 188 μrad, yielding a ratio of $0.65\times10^6$ m$^3$/μrad. The eastward tilting at Uwekahuna did not stop abruptly when the eruption ended but continued until March 10, when the total eastward tilt since January 13 reached 268 μrad, yielding a ratio of $0.45\times10^6$ m$^3$/μrad. Considering the possibility of adding lava to, or withdrawing lava from, storage in the east rift zone itself, the range of values $0.45\times10^6$–$0.65\times10^6$ m$^3$/μrad for the 1960 eruption is in good agreement with the value $0.6\times10^6$ m$^3$/μrad determined from phase 1 of the Kilauea Iki eruption.

To determine the cumulative tilt at Uwekahuna for the eruption and backflow stages of the short later phases, we must depend on the Press-Ewing records. The background noise levels on the north-south and east-west traces are comparable, but the east-west rate-of-tilt signal on the east-west component is much larger than the signal for cumulative east-west tilt on the north-south component; and it appears that the best estimates of cumulative tilting can be obtained by integration of the rate-of-tilt curves. These curves were initially plotted on millimeter cross-section paper, so the integration was performed simply by determining the areas (counting squares) under the rate-of-tilt curves. In some cases uncertainty in the choice of a zero line for the rate-of-tilt curves was a problem. Coupled with the zero-line problem is the fact that rates of backflow less than $0.1\times10^6$ m$^3$/h would probably not be above noise level on the rate of tilt curve.

The two principal means of measuring east-west tilt changes at Uwekahuna, the liquid-level tiltmeter and the integrated east-west Press-Ewing zero-line anomaly, are complementary. With only one measurement per day the liquid-level tiltmeter cannot follow the details of short tilting episodes, but it maintains an absolute record of daily changes. The east-west Press-Ewing zero-line anomaly is measured as a deviation from a zero-line reference that is keyed to

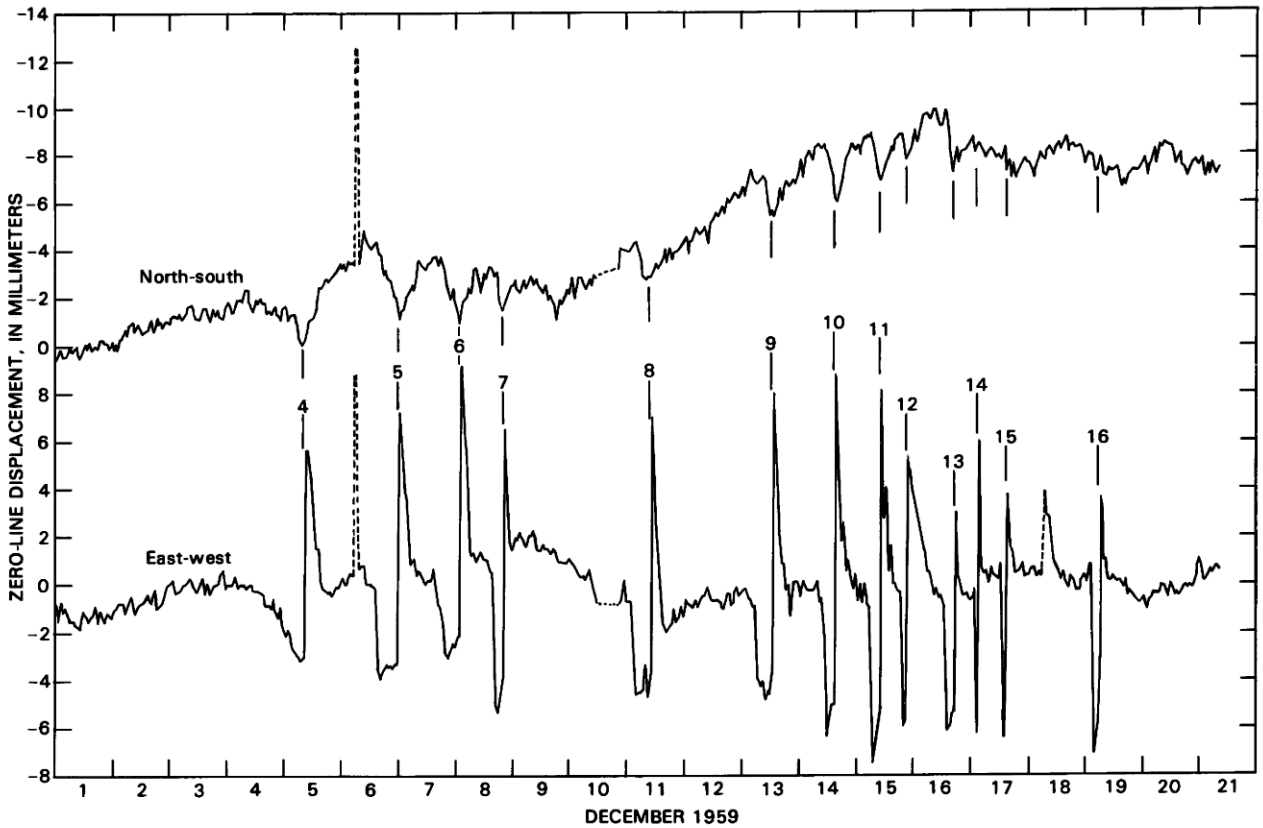


FIGURE 48.22.—Zero-line anomalies from north-south and east-west Press-Ewing seismographs accompanying phases 4–16. Numbers identify ends of individual eruptive phases as shown by abrupt reversals in the east-west zero-line anomaly curve.

what is considered the normal record before and after relatively short anomalous episodes. Thus, it maintains a sensitive record of changes during short episodes of tilting but is blind to slower, underlying, persistent changes like those that can be detected by the liquid-level tiltmeter.

The estimated volumes of lava removed from the summit reservoir during eruptive stages and returned during ensuing back-flow stages are compared (table 48.2) with, respectively, the volumes of lava poured into Kilauea Iki and then withdrawn during the principal phases of the eruption. The volume estimates for the summit reservoir were obtained by multiplying the integrated east-west rate of tilt by $0.6 \times 10^6$ m$^3$/μrad.

Use of this ratio of $0.6 \times 10^6$ m$^3$/μrad (volume of lava erupted during phase 1 divided by tilt change measured on the east-west liquid-level tiltmeter) to convert tilt changes determined from the east-west Press-Ewing zero-line anomaly to equivalent volumes of reservoir lava requires some justification. This justification proceeds in two steps. First, the east-west tilt changes detected by the north-south component Press-Ewing were scaled directly to the east-west tilt changes recorded by the liquid-level tiltmeter during phase 1. Second, the sum of eastward tilt during the fountaining stages of phases 4–16 measured by the north-south Press-Ewing (94.6 μrad) is almost exactly the same as that determined by integration of the east-west Press-Ewing zero-line anomaly (95.1 μrad). The comparison was made on the summed response to phases 4–16 because the Press-Ewing tilt measurements are much more certain for these phases than for phases 1–3.

The curves for fountain height, tremor amplitude at Outlet, and rate of eastward tilting at Uwekahuna were similar in shape during actual outpouring of lava (figs. 48.23–48.27). When fountaining ceased, tremor amplitude abruptly diminished nearly to zero, and eastward tilting abruptly reversed to westward tilting. Cumulative eastward tilt increased steadily during outpouring of lava. When fountaining ceased, brief sharp transients were recorded on both the north-south and east-west Press-Ewings instruments. On the east-west component this transient was a westward pulse of tilting superposed on the crest of the newly reversed tilt curve. On the north-south component it was a sharp northward pulse of tilt (detected by the seismometer, not the galvanometer). After the fountain died in phases 4, 5, and 9, tremor amplitude remained very

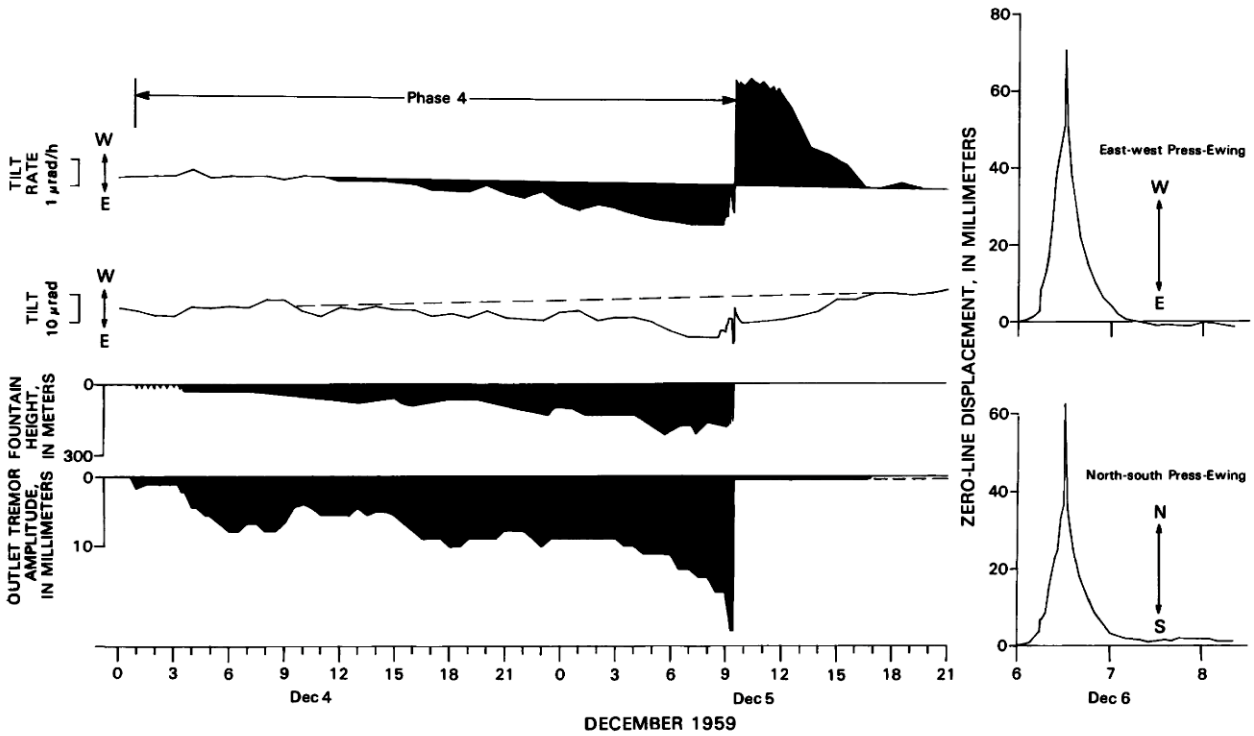


FIGURE 48.23.—East-west rate of tilting, east-west cumulative tilt, fountain height, and Outlet tremor amplitude for phase 4 and for the short but strong tilt excursion between phases 4 and 5.

low for many hours, and the westward tilting accompanying backflow declined steadily from its maximum to the noise level without large offsets or oscillations. Lava backflow rates were large, particularly at the beginning of the backflow stages, when they commonly exceeded the maximum rate of extrusion of lava during the eruptive stage they followed. Yet this rapid backflow was not accompanied by significant tremor. For phases 6–16 (omitting 9) the relationship between westward tilting and tremor was more complex, and it changed with time. After the fountain died and the amplitude of tremor at Outlet decreased abruptly, the tremor revived again after an interval of time that varied from phase to phase: phase 6, 2.5 h; phase 7, 50 min; phase 8, 35 min; phase 10, 1.5 h; phase 11, 50 min; phase 13, 20 min; phases 12, 14, 15, and 16, almost immediately. The renewed onset of tremor (resurgent tremor) was accompanied by a sharp drop in the rate of westward tilting and, presumably, the rate of reinflation of the summit reservoir.

The tremor and east-west rate-of-tilt curves for phases 10 and 11 were unusually complex. After the first resurgence of tremor, the tremor again died out and returned several times, accompanied by matching oscillations in the east-west rate-of-tilt curve. For phase 10, the first three episodes of tremor following cessation of fountaining were accompanied by sharp decreases in the reinflation of the reservoir (westward tilting), but later ones correlated with small increases in the rate of westward tilting. For phase 11 only the first interval of resurgent tremor was accompanied by a sharp drop in reinflation of the summit. Two prominent later episodes of tremor accompanied sharp increases in the rate of westward tilting.

The episode of tremor and tilting unaccompanied by an eruption (phase 15+, table 42.2) between phases 15 and 16 reveals another aspect of the relationship between tremor and tilting. Moderate fluctuating tremor that began abruptly at about 0600 on December 18 was accompanied by matching changes in the east-west rate-of-tilt curve (peaks in the tremor curve correlating with peaks of westward tilting). This behavior lasted for about 3 h. A large increase in tremor amplitude at about 0900 was accompanied by a large increase in rate of westward tilting. Tremor amplitude and westward tilting returned slowly to normal during the next 9 hours. The relationship between tremor and tilting during this episode is the same as that during the later parts of the phases 10 and 11 drainback, but it is opposite to that for the first interval of resurgent tremor for the 10 phases with significant resurgent tremor.

Another episode of very rapid tilting unaccompanied by an eruption took place on December 6 after phase 4. A rapid northwestward excursion began at about 0600. It peaked at 0631 with maximum rates of 26 μrad/h west and 24 μrad/h north, and it had died out by 0715. The net tilting toward the north and west was

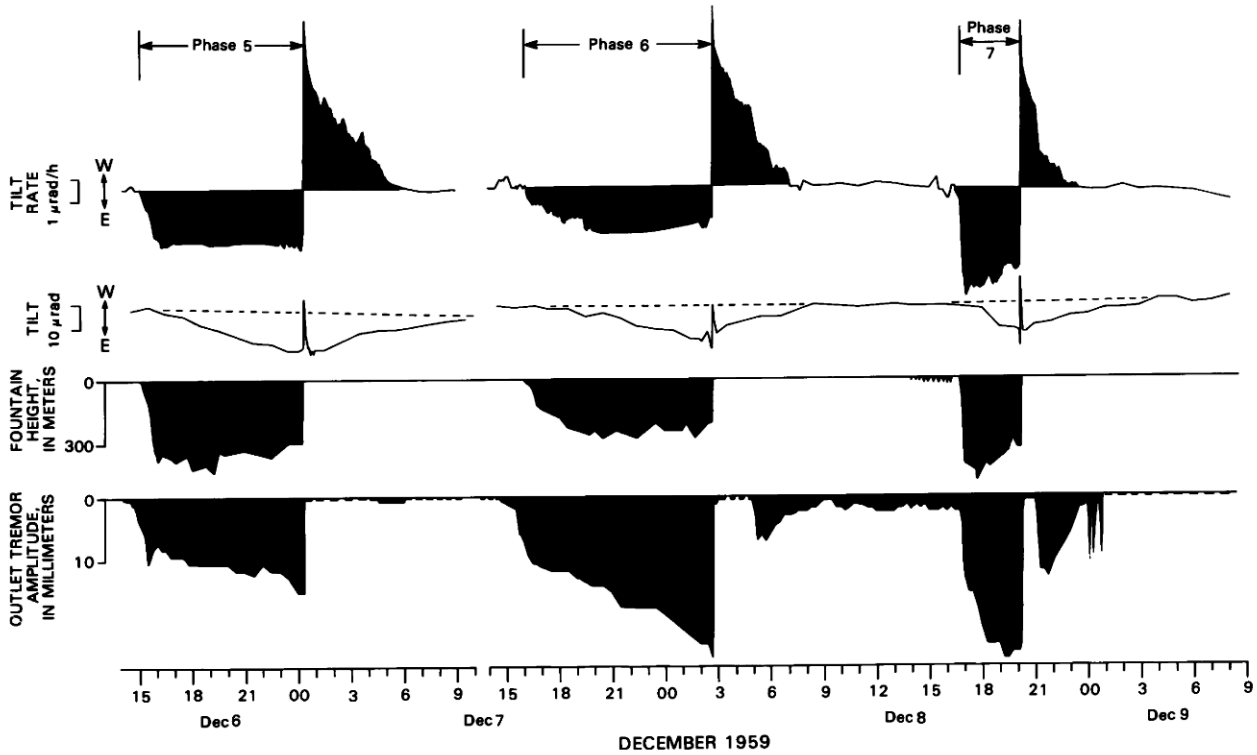


FIGURE 48.24.—East-west rate of tilting, east-west cumulative tilt, fountain height, and Outlet tremor amplitude for phases 5–7.

about 6.6 μrad and 4.8 μrad, respectively. The direction to the center of inflation from Uwekahuna was about az 126°. This azimuth is the same as that for the transient pulses that followed cessation of fountaining in the later phases. Tremor at Outlet remained low during this tilting episode, which was accompanied by a sequence of small earthquakes. At North Pit, inside Kilauea caldera, tremor was strong, and the earthquakes were more numerous and much larger (5–10 times larger amplitude) than at Outlet.

To provide a quantitative basis for discussing the movement of lava at the summit of Kilauea during the 1959 eruption, we have reduced the observations on tilting at Uwekahuna and the corresponding eruption and backflow of lava at Kilauea to tabular form (table 48.2). The state of tilt at the beginning of each eruptive phase (from the Uwekahuna east-west liquid-level tiltmeter) and changes in the east-west component of tilt measured from the Press-Ewing zero-line drift during the deflation and inflation of the summit reservoir that accompanied the eruptive and backflow stages of each phase are shown in columns 2–5. These tilt data are converted to reservoir volume changes and listed in columns 6–8 for comparison with the volumes of lava erupted into Kilauea Iki lava lake (column 9) and then withdrawn from it (column 10).

The best overall summary of the lava budget in the summit reservoir is shown in column 6 of table 48.2, where the volume of lava in the reservoir at the beginning of each phase is compared with that at the end of phase 1 fountaining. At the outbreak of phase 1 the reservoir contained the $30 \times 10^6$ m$^3$ that was poured into the lake during phase 1. Refilling of the reservoir began promptly at the end of phase 1, and it had regained $10.4 \times 10^6$ m$^3$ and $22 \times 10^6$ m$^3$ by the beginning of phases 2 and 3, respectively. At the beginning of phase 4, the entire $30 \times 10^6$ m$^3$ withdrawn during phase 1 had been replenished, presumably by new lava entering the system from below. The reservoir continued to fill steadily, but at a slower rate, until the beginning of phase 8, when at $40.4 \times 10^6$ m$^3$ it had exceeded the phase 1 outbreak level by $9.8 \times 10^6$ m$^3$. The volume of lava in the reservoir at the beginning of subsequent phases fluctuated from a low of $38.5 \times 10^6$ m$^3$ (phases 9 and 15) to a high of $42.8 \times 10^6$ m$^3$ (phases 12 and 14), and at the end of the summit eruption it stood at $40 \times 10^6$ m$^3$.

Net changes in the reservoir volume during deflation (table 48.2, column 7) and inflation (column 8) can be compared with the corresponding volumes of lava erupted into the lake (column 9) and withdrawn from it (column 10). Net changes in the volume of lava in

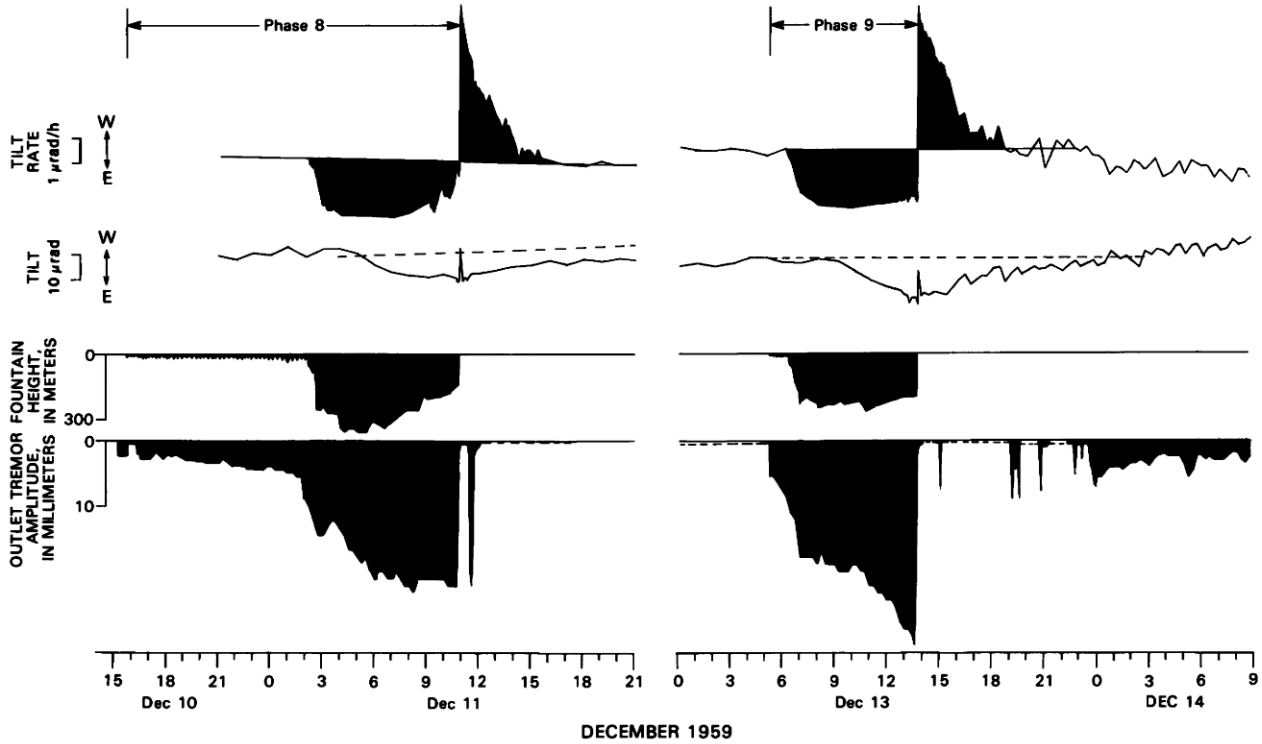


FIGURE 48.25.—East-west rate of tilting, east-west cumulative tilt, fountain height, and Outlet tremor for phases 8 and 9.

the lake-reservoir system during the eruptive stage, during the backflow stage, and during the entirety of each phase can be compared in columns 11, 12, and 13 of table 48.2, respectively. The changes measured during phases 2 and 3 are only poorly determined because of difficulties in establishing appropriate zero-line references for the east-west Press-Ewing instrument. There was a substantial increase in system volume during the first stage of phase 4 and significant increases also during phases 6, 10, and 12. There were substantial losses from the system during phases 7, 8, 9, and 15, principally during the backflow stage. There was a significant loss from the system during phase 13. During phases 5, 11, 14, and 16 the volume of the system showed little change. Phases with large system losses correlate with an overfilled summit reservoir (from phase 7 on), as do the most marked occurrences of resurgent tremor and associated irregularities in the curves of reservoir reinflation during backflow.

## PROPOSED MODEL FOR THE 1959 ERUPTION

On the basis of the data on deformation at the summit of Kilauea and on lava eruption and withdrawal at Kilauea Iki during the 1959 eruption, we have constructed a model to explain the principal mechanical features of the eruption. The model is similar to one proposed by Helz (chapter 25) to explain the characteristics of olivine observed in samples collected at various stages of the eruption and in the lava lake. It is broadly based on the model of the Kilauea plumbing system deduced by Eaton and Murata (1960) and Eaton (1962) from the deformation of the Kilauea summit before, during, and after the 1959–60 eruption of Kilauea.

Following the summit collapse associated with the 1955 east-rift eruption, the Kilauea summit reservoir was slowly refilled by magma moving upward from the source zone 40–60 km deep beneath Kilauea. By early November 1959 the reservoir was sufficiently overpressured that a dike from the reservoir split upward through the enclosing rock and reached the surface inside Kilauea Iki Crater. All of the lava (except cinder and pumice blown away by the wind) accumulated inside the crater.

The initial overpressure required to open the dike to the surface sustained the early part of the first phase of the eruption, when lava flowed upward through the dikelike vent propped open by pressure of the lava. Rapid flow of lava through a section of the dike that was locally wider than average enlarged that section of the dike, forming the stable conduit leading to the main fountain and permitting the rest of the dike to close, either by freezing or because of a drop in the pressure of the lava in the dike. Less constricted passage of lava through the enlarging main-vent conduit relieved the confining pres-

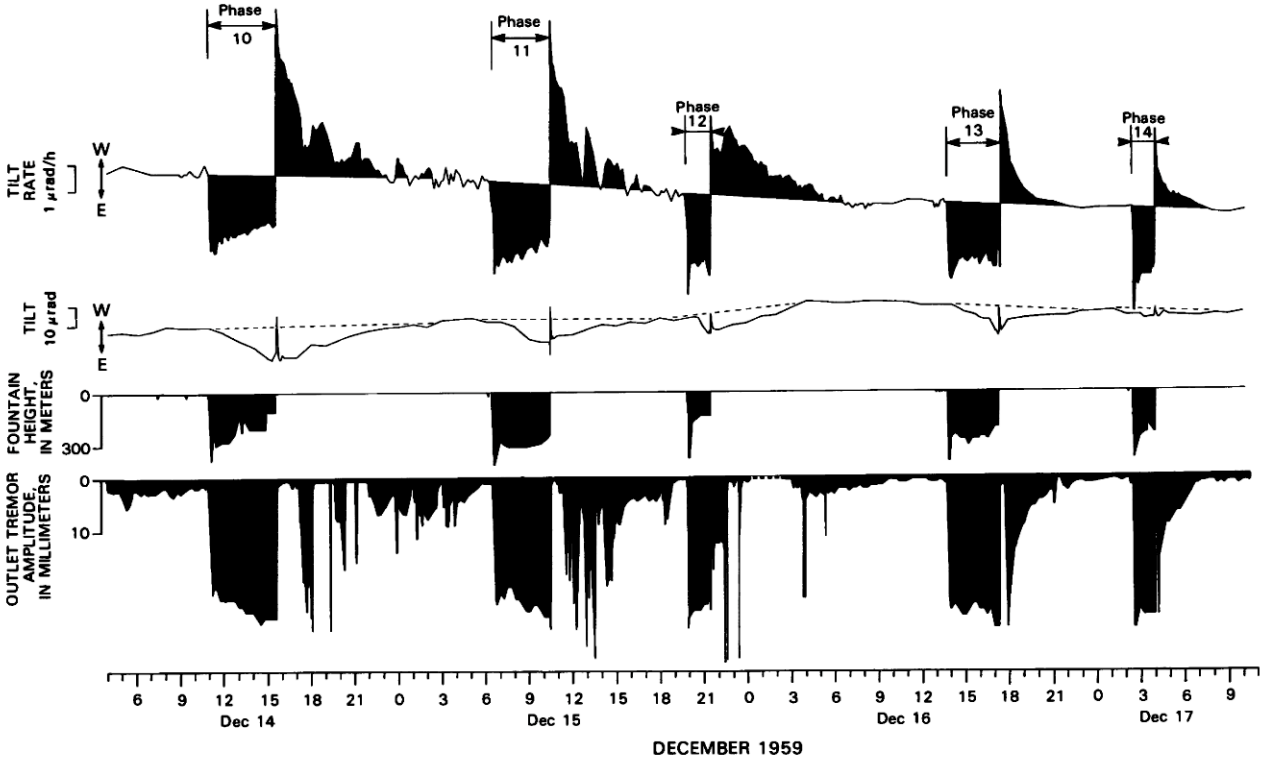


FIGURE 48.26.—East-west rate of tilting, east-west cumulative tilt, fountain height, and Outlet tremor amplitude for phases 10–14.

sure on the rising lava to increasingly greater depths in the conduit, permitting vesiculation and the consequent reduction in the density and viscosity of the lava-gas mixture in the conduit to penetrate to greater depths. This process reduced the average density of the column of lava in the conduit between the reservoir and the vent sufficiently that lava continued to be pumped from the reservoir to the lake even after the reservoir pressure had dropped below the level required to sustain outflow in an unvesiculated conduit. By this process a large volume of lava stored in the reservoir was pumped rapidly to the surface, where it accumulated in Kilauea Iki Crater. When the lava in Kilauea Iki rose significantly above the vent, heavy, degassed lake lava found entry to the conduit, possibly through another opening beside or below the fountaining vent. This inert, heavier lava sufficiently moderated the pumping action of vesiculation in the conduit to cut off the flow of ascending lava entirely, and fountaining stopped abruptly.

During most of phase 1, the rate of inflow of magma to the reservoir remained low. The large drop in reservoir pressure resulting from the rapid transfer of lava from the reservoir to the lake during the last few days of phase 1 led to a substantial increase in the hydraulic potential between the deep supply system and the reservoir, and the rate of inflow from depth therefore increased sharply late in phase 1.

The reservoir began to refill rapidly, and soon the reservoir pressure was again sufficient to raise the lava column, now partially degassed, to the vent in Kilauea Iki. This time overpressure such as required to drive a new dike to the surface was not needed. The flood of new hot magma entering the reservoir from below not only reinflated it but also introduced a supply of gas-rich lava that could help to sustain the vesiculation pump for lifting lava to the lake. The cycle of overfilling the lake, leading to a reversal of the density pump in the conduit, was repeated during phase 2. At the end of phase 2, either because the lake was sufficiently above the vent or because access of lake lava to the conduit was sufficiently less restricted (or both), a substantial volume of degassed lake lava flowed back down the conduit to further reinflate the reservoir. The same pattern was repeated during the subsequent phases of the eruption.

Refilling of the reservoir continued at a rate that was proportional to the hydraulic potential difference between the source at depth and the summit reservoir. As the reservoir was reinflated this potential difference decreased, and so did the rate of lava rising into the reservoir. When the reservoir was refilled to and beyond its state at the outbreak of phase 1, the enclosing rocks were again stressed to near their limits. During the rapid backflow following the later phases, the sudden sharp increase in reservoir pressure induced by the returning lava appears to have opened a temporary passageway,

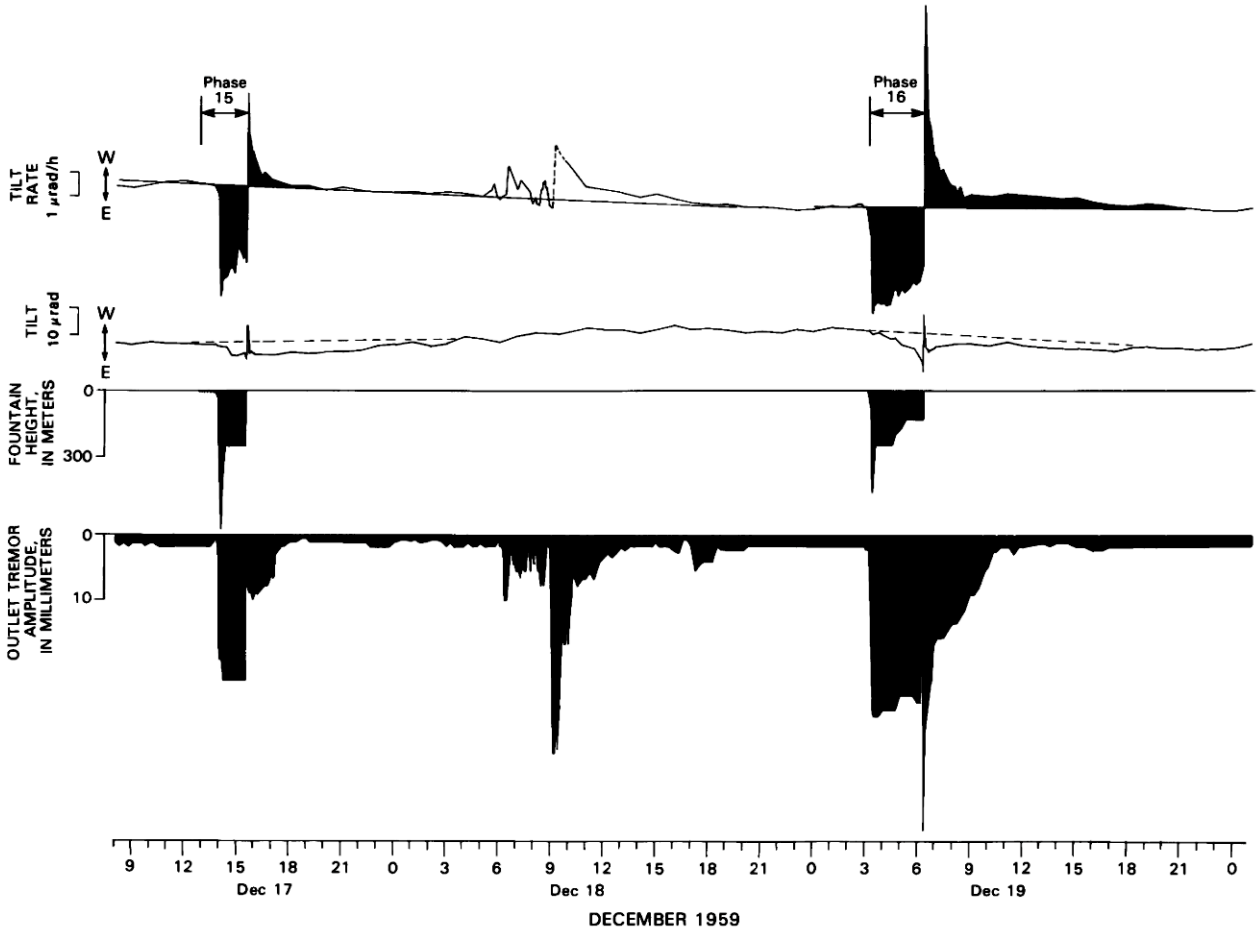


FIGURE 48.27.—East-west rate of tilting, east-west cumulative tilt, fountain height, and Outlet tremor amplitudes for phases 15 and 16 and for episode of tilting and tremor between them.

probably a dikelike zone propped open by excess reservoir pressure, and to have driven some reservoir lava into a nearby zone with lower hydraulic potential, possibly the fluid core of the upper end of the east rift zone.

A summary of the movement of lava into the summit reservoir from depth and out of the summit reservoir into Kilauea Iki lava lake and the east rift zone(?) is given in figure 48.28. The primary withdrawal of lava from the summit reservoir was the $30 \times 10^6$ $m^3$ erupted during the first phase. The outbreak of the eruption depended on the reservoir being overpressured by new lava entering from below. This new, more primitive material may have been included in the initial outbreak, only to be swamped later in phase 1 by larger volumes of lava withdrawn from reservoir storage, as suggested by Helz (chapter 25). The principal system response to the initial deflation of the reservoir was a (somewhat delayed) massive influx of new lava from depth to refill the reservoir, where it presumably was available to mix with lava still retained by the reservoir. Ongoing recharge of the reservoir repeatedly brought the summit reservoir-lava lake system back to a condition that essentially led to a restaging of the last part of the phase 1 eruption: the original conduit and the same vesiculation-pump mechanism that operated during the later part of the phase 1 eruption were utilized over and over again.

Lava draining back from the lake during the early phases was recaptured entirely by the reservoir. During the later phases, however, the reservoir was so full that it could not retain both the new lava that had entered it from below since the last phase and the batch of lava suddenly returned from the lake. Some fraction of the

TABLE 48.2.—*Record of ground tilt at Uwekahuna and volumes of lava erupted into and withdrawn from Kilauea Iki lava lake during the 16 principal phases of the 1959 eruption*

[Data in column 2 from liquid-level tiltmeter; data in column 3 from north-south Press-Ewing instrument; data in columns 4–5 and 7–8 from integrated east-west Press-Ewing instrument; data in column 6 derived from east-west liquid-level tilmeter data; data in columns 2 and 6 are relative to end of phase 1 fountaining]

| | Tilt (μrad) | | | | Lava volume ($10^6$ $m^3$) | | | | | Volume gain or loss ($10^6$ $m^3$) | | |
|---|---|---|---|---|---|---|---|---|---|---|---|---|
| Phase | E-W at start of phase | Deflation episode (eastward) | | Inflation episode (westward) | Reservoir storage relative end phase 1 | Deflation episode | Inflation episode | Erupted into lake | Drainback from lake | First stage of phases (9–7) | Second stage of phases (8–10) | Entire phase |
| 1 | 2 | 3 | 4 | 5 | 6 | 7 | 8 | 9 | 10 | 11 | 12 | 13 |
| 1 | 50 | 50 | -- | -- | 30.6 | -- | -- | 30.6 | 1.1 | -- | -- | (−1.1) |
| 2 | 17 | 5.5 | 4.5 | 21.5 | 10.4 | 2.8 | 13.1 | 3.6 | 4.5 | +0.8 | +8.6 | +9.5 |
| 3 | 36 | 8.1 | 14.0 | 4.7 | 22.0 | 8.6 | 2.8 | 3.2 | 2.0 | −5.4 | +.8 | −4.5 |
| 4 | 50 | 9.6 | 10.2 | 10.2 | 30.6 | 6.3 | 6.3 | 11.5 | 6.3 | +5.2 | .0 | +5.2 |
| 5 | 55 | 10.0 | 9.7 | 7.6 | 33.6 | 6.0 | 4.7 | 6.5 | 4.7 | +.5 | .0 | +.5 |
| 6 | 55 | 8.5 | 9.4 | 7.5 | 33.6 | 5.7 | 4.6 | 6.6 | 3.8 | +.8 | +.8 | +1.6 |
| 7 | 59 | 6.7 | 7.3 | 3.4 | 36.1 | 4.4 | 2.1 | 3.7 | 5.6 | −.7 | −3.5 | −4.2 |
| 8 | 66 | 7.0 | 10.2 | 6.0 | 40.4 | 6.2 | 3.7 | 6.7 | 6.0 | .0 | −2.3 | −2.3 |
| 9 | 63 | 10.4 | 9.3 | 6.5 | 38.5 | 5.7 | 4.0 | 5.7 | 6.9 | .0 | −2.9 | −2.9 |
| 10 | 67 | 9.6 | 8.2 | 9.9 | 41.0 | 5.0 | 6.0 | 6.3 | 4.9 | +1.3 | +1.1 | +2.4 |
| 11 | 65 | 7.0 | 8.5 | 6.8 | 39.8 | 5.2 | 4.1 | 4.7 | 4.1 | −.5 | .0 | −.5 |
| 12 | 70 | 4.8 | 3.4 | 7.8 | 42.8 | 2.1 | 4.7 | 2.2 | 3.1 | +.1 | +1.6 | +1.8 |
| 13 | 70 | 8.1 | 6.4 | 3.0 | 42.8 | 3.9 | 1.8 | 3.2 | 2.4 | −.7 | −.6 | −1.3 |
| 14 | 68 | 2.2 | 3.0 | 1.6 | 41.6 | 1.8 | 1.0 | 1.8 | 1.0 | .0 | .0 | .0 |
| 15 | 63 | 3.3 | 3.1 | 1.1 | 38.5 | 1.9 | .7 | 1.7 | 3.2 | −.2 | −2.5 | −2.8 |
| 16 | 64 | 7.4 | 6.4 | 5.6 | 39.1 | 3.9 | 3.4 | 4.1 | 4.1 | +.2 | −.7 | −.5 |
| End | 65 | | | | | | | | | | | |
| [1]15+ | 63 | -- | -- | 3.9 | 38.5 | -- | 2.4 | -- | -- | -- | 2.4 | +2.4 |

[1]Episode of reservoir inflation without eruption between phases 15 and 16.

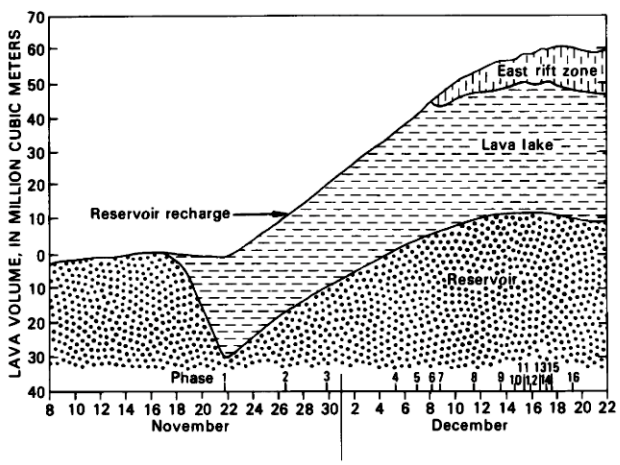


FIGURE 48.28.—Partitioning of lava that was in summit reservoir on November 14 and lava that subsequently recharged it from below between summit reservoir, lava lake, and loss from the reservoir-lake system (to east rift zone?).

returning lava, or a corresponding volume of lava already in the reservoir, was then expelled into the east rift zone (during an episode of resurgent tremor) from the reservoir.

The total volume of lava added to and retained within the summit reservoir after the end of phase 1 fountaining was $40 \times 10^6$ $m^3$. From the gain-loss figures for the individual phases in table 48.1 it appears that some $12 \times 10^6$ $m^3$ of additional lava was added to the reservoir from depth but was then expelled from it during late-phase backflow episodes. An additional $8 \times 10^6$ $m^3$ from the reservoir was added to the lake after phase 1. In summary, it appears that the volume of new lava entering the reservoir after the end of phase 1 was about $60 \times 10^6$ $m^3$, of which $40 \times 10^6$ $m^3$ remained in the reservoir, $8 \times 10^6$ $m^3$ had been transferred to the lava lake, and $12 \times 10^6$ $m^3$ had been driven out of the reservoir, possibly into the east rift zone, by the end of the eruption. Repeated cycling of lava between the reservoir and the lake, with the accompanying turbulence in the upper part of the lava conduit and the fountain, should have been a very effective means of homogenizing the contents of the reservoir. Such cycling of lava also explains the fate of the $63 \times 10^6$ $m^3$ total volume of lava that drained out of the lava lake during the entire eruption.

## RATE OF ERUPTION, FOUNTAIN HEIGHT, AND TREMOR AMPLITUDE

Observations of harmonic tremor generated during various stages of lava outbreak, fountaining, and backflow from the lava lake provide a basis for an analysis of tremor amplitude as a possible function of fountain height, rate of eruption, state of recharge of the summit reservoir, and temperature of the erupting lava (the latter determined by Helz, chapter 25, from glass composition near olivine phenocrysts in air-quenched pumice samples collected during the eruption). The relations among the foregoing parameters are not simple, and they appear to have evolved during the eruption as a whole as well as during the first phase itself. Outlet tremor amplitude, rate of eruption, fountain height, and lava temperature are plotted in figure 48.29*A* versus time for phase 1. In figure 48.29*B*, summit reservoir recharge, Outlet tremor amplitude, rate of eruption, fountain height, and lava temperature are plotted versus eruption phase number. The intensity of eruption changed with time

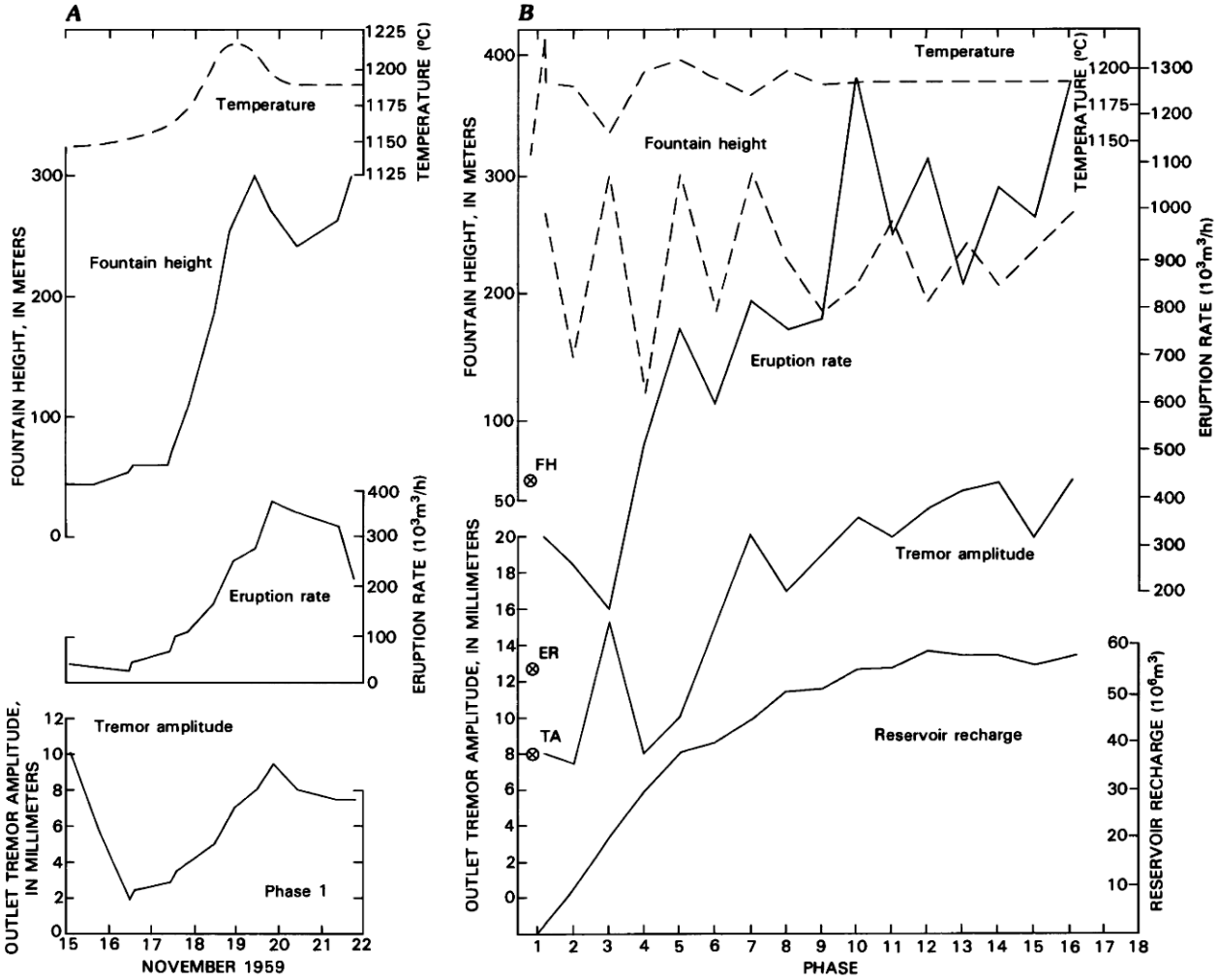


FIGURE 48.29.—Variation of eruption parameters during course of the 1959 Kilauea eruption. ***A***, Tremor amplitude, eruption rate, fountain height, and lava temperature plotted against time for phase 1. ***B***, Reservoir recharge, tremor amplitude, rate of eruption, fountain height, and lava temperature plotted against phase number for phases 1–16. Points for fountain height, eruption rate, and tremor amplitude for the first day of phase 1 are labeled FH, ER, and TA, respectively.

during several phases in addition to phase 1. In order to prepare the simplified plot of parameters versus phase number, values were selected from the parts of phases that seemed best to characterize the phase as a whole. The data plotted in figures 48.29 and 48.30 are also shown in tables 48.3 and 48.4, respectively.

The first few days of phase 1 were very different from the rest of that phase, so two sets of values are plotted. The first set represents the first day; the second set represents the last three days of the fully developed phase 1 eruption. Although tremor amplitude was similar (6–10 mm in the first, 8.5 mm in the second), the contrast between the two sets in other parameters is extreme: $34 \times 10^3$ $m^3/h$ eruption rate, 45-m-high fountain, and 1,145 °C lava temperature for the first versus $340 \times 10^3$ $m^3/h$ eruption rate, 300-m-high fountain, and 1,185–1,215 °C lava temperature for the second. The tremor amplitude remained virtually unchanged despite 7-fold and 10-fold increases in fountain height and rate of eruption, respectively.

During the first few hours of the eruption, lava streamed to the surface through the long thin dike, probably held open by the pressure of the lava, that was opened in response to overfilling the reservoir. Pressure variations in the moving lava interacted with the elastic walls and with lava velocity in the dike and rhythmically distended and contracted the dike as lava moved unsteadily through it. Such a structure is very efficient for generating tremor because of

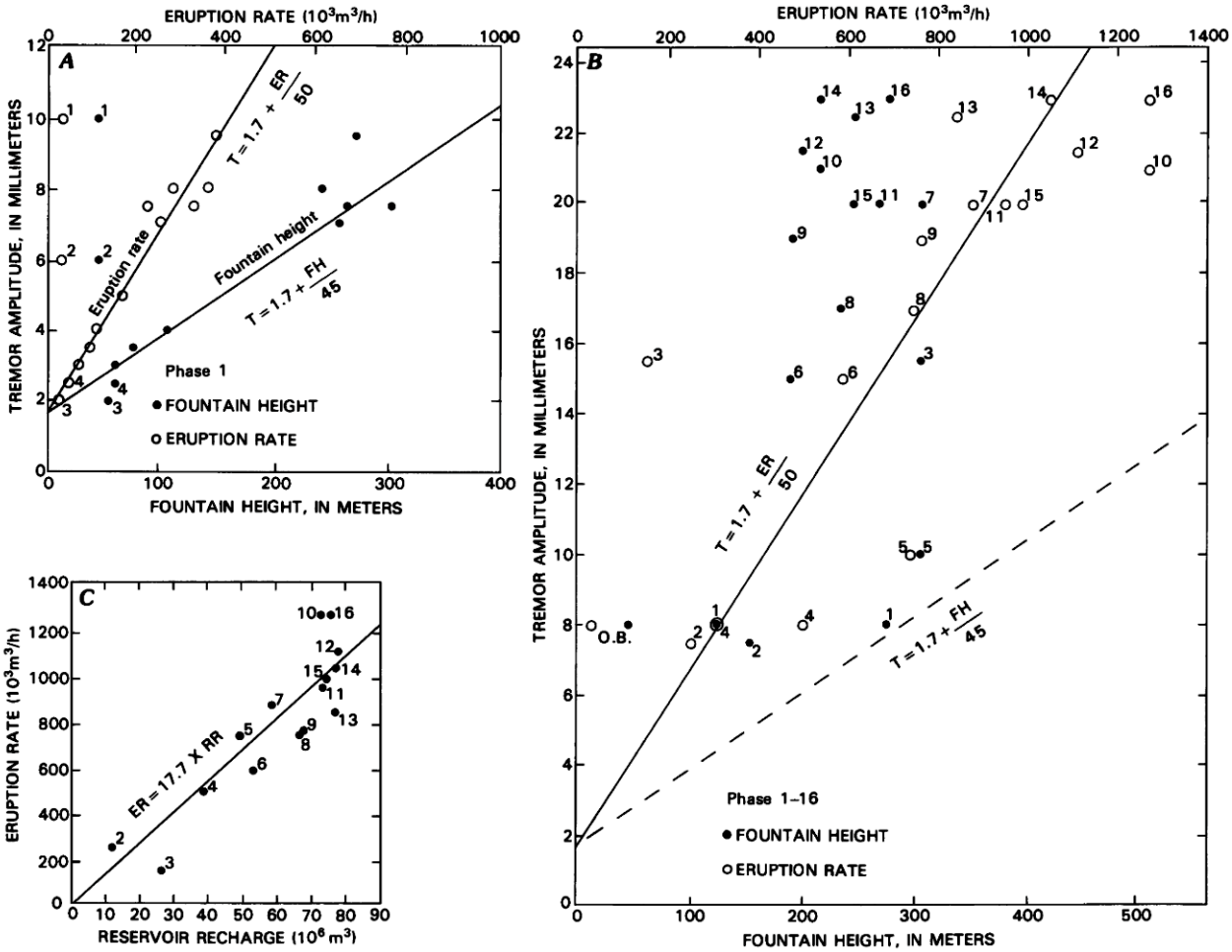


FIGURE 48.30.—Cross plots of eruption parameters for the 1959 Kilauea eruption. Numbers on plot *A* indicate sequence of readings during phase 1 on November 15–16. Numbers on plots *B* and *C* indicate phases. On plot *B*, the earliest data for phase 1 are plotted separately and labeled O.B. ***A***, Tremor amplitude plotted against eruption rate and fountain height for phase 1. ***B***, Tremor amplitude plotted against eruption rate and fountain height for phases 1–16. ***C***, Eruption rate plotted against reservoir recharge for phases 2–16.

its shape: the large surface-area-to-volume ratio of the dike permits good translation of pressure variations in the lava to movement of the walls of the dike.

In the course of the first day, fountaining died out along all of the original fissure except for one small section, where the main fountain gradually grew in height and volume as it took over the function of the dying fountains. The rate of eruption declined only slightly, but the Outlet tremor amplitude dropped from 10 mm to 2 mm (fig. 48.29*A*). After about 36 h, rate of eruption and tremor amplitude both began to rise steadily; and after about 60 h the height of the fountain began a rapid increase, accompanied by further increases in the growth of eruption rate and of tremor amplitude. Plots of tremor amplitude versus fountain height and tremor amplitude versus eruption rate for the first phase of the eruption are shown in figure 48.30*A*. Excluding the first day (points labeled 1 and 2), tremor amplitude is simply related to both eruption rate and fountain height: $T=1.7+ER/50$ and $T=1.7+FH/45$, where $T$ is amplitude of Outlet tremor in millimeters, $ER$ is eruption rate in thousand cubic meters per hour, and $FH$ is fountain height in meters. Points 1 and 2, for the initial stage of phase 1, clearly do not fit with the rest of the data. During the first 36 hours of the eruption it appears that the tremor-generating system evolved from an initial stage dominated by the dike conduit, which produced strong tremor, to a later stage dominated by an open central conduit which was

TABLE 48.3.—*Detailed eruption parameters for phase 1 of the 1959 Kilauea Iki eruption*

[Dates and times are lava-lake depth measurements, from table 48.1; volume rate is average rate of eruption since last measurement of lake depth or onset of new eruptive phase; tremor measured at Outlet; temperatures are quench temperatures of pumice samples collected during the time intervals, from Helz (chapter 25)]

| Date | Time (H.s.t.) | Volume rate ($10^3$ $m^3/h$) | Fountain height (m) | Tremor amplitude (mm) | Temperature (°C) |
|---|---|---|---|---|---|
| Nov. 14 | 2008 | -- | -- | -- | -- |
| Nov. 15 | 0300 | 33 | 46 | 10.0 | 1,144 |
| | 1800 | 31 | 46 | 6.0 | -- |
| Nov. 16 | 1215 | 25 | 55 | 2.0 | -- |
| | 1400 | 44 | 61 | 2.5 | -- |
| Nov. 17 | 1045 | 70 | 61 | 3.0 | -- |
| | 1400 | 94 | 76 | 3.5 | -- |
| | 2030 | 106 | 107 | 4.0 | -- |
| Nov. 18 | 1200 | 163 | 185 | 5.0 | -- |
| | 2315 | 252 | 259 | 7.0 | 1,216 |
| Nov. 19 | 1150 | 281 | 305 | 8.0 | -- |
| | 2115 | 378 | 274 | 9.5 | -- |
| Nov. 20 | 1210 | 357 | 244 | 8.0 | 1,187 |
| Nov. 21 | 0930 | 327 | 267 | 7.5 | -- |
| | 1925 | 222 | 305 | 7.5 | 1,188 |

TABLE 48.4.—*Eruptive parameters characterizing the 16 principal eruptive phases of the 1959 Kilauea Iki eruption*

[Figures for volume rate of eruption, fountain height, and tremor amplitude (measured at Outlet) are averages for the particular phase; temperature is quench temperature of pumice sample collected during phase, from Helz (chapter 25); recharge is volume of lava that entered summit reservoir from depth from end of phase 1 fountaining to onset of current phase]

| Phase | Volume rate ($10^3$ $m^3/h$) | Fountain height (m) | Tremor amplitude (mm) | Temperature (°C) | Recharge ($10^6$ $m^3$) |
|---|---|---|---|---|---|
| 1a | 32 | 46 | 8.0 | 1,142–1,144 | -- |
| 1b | 306 | 274 | 8.0 | 1,187–1,216 | -- |
| 2 | 248 | 152 | 7.5 | 1,185 | 9.4 |
| 3 | 153 | 305 | 15.5 | 1,154 | 20.1 |
| 4 | 497 | 122 | 8.0 | 1,196 | 29.9 |
| 5 | 742 | 305 | 10.0 | 1,205 | 38.1 |
| 6 | 585 | 189 | 15.0 | -- | 40.5 |
| 7 | 879 | 305 | 20.0 | 1,181 | 45.4 |
| 8 | 745 | 232 | 17.0 | 1,197 | 51.4 |
| 9 | 765 | 189 | 19.0 | 1,188 | 52.1 |
| 10 | 1,269 | 213 | 21.0 | 1,189 | 56.2 |
| 11 | 948 | 265 | 20.0 | -- | 56.4 |
| 12 | 1,109 | 198 | 21.5 | -- | 60.0 |
| 13 | 841 | 244 | 22.5 | -- | 59.1 |
| 14 | 1,047 | 213 | 23.0 | -- | 59.2 |
| 15 | 986 | 244 | 20.0 | 1,191 | 57.0 |
| 16 | 1,269 | 274 | 23.0 | 1,190 | 58.6 |
| End | -- | -- | -- | -- | 59.7 |

much less efficient in producing tremor. Thereafter, the eruption increased in intensity, and tremor, rate of eruption, and fountain height all increased proportionally.

The role of lava temperature appears to be important, because the large increases in tremor, rate of eruption, and fountain height appear to coincide with an increase in lava temperature from about 1,145 °C to 1,185–1,215 °C between November 15 and November 18. The exact role of temperature is not clear, however. Higher temperatures certainly are associated with greater fluidity of the lava, but they also mark the lava as being more primitive and less depleted of dissolved gases than cooler lava. The latter attribute may be more important than the former in its effect on the style of eruption.

The evolution of the eruption from phase to phase took a different course from the evolution of phase 1. As the reservoir was recharged with fresh lava after phase 1, tremor amplitude and rate of eruption generally increased from phase to phase, but fountain height was very erratic (fig. 48.29*B*). In an almost regular alternation from one phase to the next, it oscillated between 120–180 m and 270–300 m during the first seven phases. The alternation was slower (2 eruptive phases per half-cycle) and between narrower limits (180–270 m) thereafter. Tremor amplitude is plotted versus eruption rate and fountain height for all 16 phases, in figure 48.30*B*, as it was for phase 1 only in figure 48.30*A*. The lines relating tremor amplitude to rate of eruption and fountain height in the phase 1 plot are repeated in figure 48.30*B*. Although the scatter is somewhat greater here, the data for tremor amplitude versus eruption rate for the 16 phases fit the phase 1 curve very well. The data for tremor amplitude versus fountain height, however, depart widely and systematically from the phase 1 curve. After phase 4, fountain height is restricted to the range 180–300 m, and it appears not to be related to tremor amplitude. The extremely low value for rate of eruption in phase 3 (fig. 48.30*B*) may be explained, at least in part, by the large loss of material blown downwind and away from the lake from the high, very gassy fountain that characterized this phase.

Eruption rate appears to be simply related to reservoir recharge (fig. 48.30*C*) by the relationship $ER = 17.7 \times RR$, where $ER$ is eruption rate in thousand cubic meters per hour and $RR$ is reservoir recharge in million cubic meters. The error in the eruption rate predicted by this relationship for phases 4–16 is less than 25 percent of the measured value in all 13 cases and less than 10 percent in 7 cases. The predicted eruption rates for phases 2 and 3 are 34 percent too small and 133 percent too large, respectively. The discrepancy for phase 3 would be reduced if the volume of lava represented by the pumice blown away from the very gassy fountain (and the lake) during this phase were included.

A change in fountain behavior between the later phases and the earlier phases that is apparent in figure 48.21 and figures 48.23–48.27 deserves special mention. During the early phases the fountain grew steadily in height until it reached a high level that was maintained until the end of the phase. Exceptions to this rule were phase 2, in which the fountain height increased considerably just before it died, and phase 9, in which the fountain declined steadily from a maximum attained early in the phase. Before phase 10, no phase began with a sharp, high pulse of fountaining that declined rapidly to a lower level that then characterized the rest of the phase. From phase 10 through phase 16, however, all phases began with such an initial outburst. This phenomenon was most pronounced in phase 15, in which the outbreak fountain rose briefly to a height of 580 m, about twice the height of fountaining during the rest of the phase.

This change in behavior may reflect a change in composition or amount of gas in the lava of the summit reservoir. Gerlach and Graeber (1985) calculate very different compositions for the gas in the parental magma at depth and in lava stored in the summit

reservoir equilibrated at 2-km depth. They find the concentrations, in weight percent, of the three principal gas components as follows:

| | $H_2O$ | $CO_2$ | $SO_2$ |
|---|---|---|---|
| Parental magma | 0.30 | 0.65 | 0.13 |
| Stored reservoir lava | 0.27 | 0.034 | 0.070 |

At reservoir depths $CO_2$ would have already exsolved from the lava and collected as a separate phase in fluid inclusions, while $H_2O$ would still be dissolved in the lava. At depths of 2–4 km, such low-density $CO_2$ inclusions would constitute 5–10 percent, by volume, of the lava and would reduce its density in approximately the same proportion. In the interval between eruptive phases, gravitative separation of lighter lava rich in $CO_2$ inclusions may have positioned such material near the top of the reservoir for early eruption during the next phase. The $CO_2$ may also be more effective than $H_2O$ in producing rapid vesiculation because it is already exsolved from the lava, whereas $H_2O$ must first diffuse out of the lava into bubbles before those bubbles can expand in response to a drop in confining pressure. After an episode of abnormally vigorous initial fountaining, the eruption would return to normal when the gas-enriched cap of lava in the reservoir was depleted.

The large phase-to-phase variation in fountain height, particularly during the early phases, that is shown in figure 48.30*B* may also result from variations in the composition and abundance of gas from place to place in the mixture in the reservoir of old stored lava and new lava from depth.

## FURTHER DEVELOPMENT OF THE PROPOSED MODEL OF THE 1959 ERUPTION

During the first phase the conduit evolved from a long, thin dike held open by pressure in the lava to a much more stable conduit with a more equidimensional cross section. It remained sufficiently open at the end of phase 1 to admit $1.0 \times 10^6$ m$^3$ backflow from the lake. Descriptions of the onset of all subsequent phases, except the very short phase 14, whose onset is not described (Richter and others 1970), show that the conduit had remained open after the end of the last phase and that a fluid lava column, with large bubbles of gas rising through it and throwing up spatter when they burst, rose slowly to the mouth of the conduit. At the end of these phases lava flowed copiously back into the vent and disappeared underground. These observations strongly suggest that the conduit was an open pipe from the reservoir to the lake, and that the pressure of lava in the reservoir at the base of the conduit was in approximate balance with the weight of lava in the conduit. A slight change in this balance could cause lava to flow out of the reservoir through the pipe to the surface or the reverse.

Following phase 1, which poured about $30 \times 10^6$ m$^3$ of lava into the lake, where it was trapped, new lava from depth streamed up into the reservoir and mixed with the current contents of the reservoir. During subsequent phases some mixture of the older and newer reservoir lava was spewed out into the lake, undergoing intense local mixing in the conduit. Some fraction of the contents of the lake then drained back to the reservoir, with further mixing. As the eruption progressed and more and more lava moved up from depth to recharge the reservoir, its contents gradually took on more of the characteristics of the new lava, including its temperature and charge of dissolved (and exsolved) gases. Reinflation of the reservoir, at least through phase 8 or phase 10, raised the piezometric surface of lava in the reservoir, making onset of the next eruption easier and increasing the pressure drive that would help to sustain it.

As backflow from the last phase ceased, the heavy lake lava occupying the conduit would tend to flow back into the reservoir and be replaced by hotter, lighter lava from the reservoir (if the conduit were not too narrow). This process would be aided by any exsolved $CO_2$ that had come into the chamber with the recharge from depth. When the combination of lighter lava in the conduit and increased reservoir pressure (from further recharge) raised the top of the column sufficiently that it overflowed into the lake, the conditions for starting the next eruption had been met.

Next, consider the factors that might control rate of eruption and fountain height during an eruptive phase once it has started. In the system we have described the rate of eruption should be determined by the balance between the pressure difference driving the eruption and the pressure drop in the conduit resulting from the flow of lava through it. The pressure difference that drives the eruption is primarily a result of vesiculation of lava in the upper part of the conduit, which reduces its density substantially as it flows to the surface. The resulting decrease in weight of lava in the upper part of the conduit is available as a pressure difference to drive lava upward through the conduit. The efficiency of this vesiculation pump will depend on the gas content of the lava, the speed with which it can accumulate in bubbles, and the rate at which the bubbles can escape from the lava. These factors are related to lava temperature to the degree that temperature controls viscosity and is a measure of the proportion of new material from depth in the erupting lava.

The pressure drop owing to movement of lava through the conduit depends primarily on velocity and viscosity (and hence temperature) of the lava and the geometry of the conduit. In the course of the eruption, constrictions in the conduit would have been eroded (melted) away, progressively decreasing the resistance to flow; as the erupting lava was increasingly enriched in new hotter material from depth, its viscosity would have decreased, further reducing resistance to flow.

During an eruption of fairly viscous lava, we should expect a low rate of flow from the reservoir. For a fairly slow ascent of lava in the conduit, the exsolution and separation of gas should be nearly complete and should yield an abundance of gas deep in the conduit to drive the gas-lava mixture above it out of the conduit rapidly, producing a high fountain. During an eruption of less viscous lava, we should expect a high rate of flow from the reservoir. For a rapid ascent of lava in the conduit we may speculate that the short time that lava would spend in the upper, low-pressure part of the conduit would limit the amount of exsolution and, particularly, separation of gas from the lava and would result in a low, voluminous fountain in which the bubbles of gas would still be retained in the lava as it was thrown out of the vent. In the scheme outlined above, low eruption rates and high fountains would correlate with lower than average lava temperatures, and high eruption rates and low fountains would correlate with higher than average lava temperatures. This tendency would be superposed on one of increasingly larger eruption rates

from phase to phase as the conduit was enlarged by continued use and the summit reservoir was refilled by hot, gas-rich lava from depth.

The first part of this pattern appears to have been observed during phase 3 (with its low lava temperature of about 1,155 °C, high fountain, and very low eruption rate) and the ensuing phase 4 (with its high lava temperature of about 1,200 °C, low fountain, and high eruption rate). The second part of the pattern is demonstrated by the relationship between eruption rate and reservoir recharge shown in figure 48.30C.

The apparent linear relation between tremor amplitude and eruption rate in figures 48.29*A* and 48.29*B* supports the view that tremor is generated primarily in the eruption conduit and that its amplitude is proportional to the rate of flow of lava through the conduit. However, tremor accompanying the initial rapid backflow of lava through the conduit when the fountain died was insignificant compared to tremor during fountaining. Thus, the existence of lava fountaining is strongly correlated with strong tremor, but fountain height (the most obvious measure of intensity of fountaining) does not correlate with tremor amplitude during the later phases of the eruption, which produced the strongest tremor. These observations, taken together, suggest that the source of the tremor accompanying the large fountains of the Kilauea Iki eruption was the vesiculation pump mechanism that operated in the upper part of the eruption conduit to lift lava out of the reservoir. Moreover, the amplitude of the tremor is proportional to the volume rate of lava moving through the conduit or, equivalently, to the power consumed in the pumping mechanism to lift the lava.

This tremor-generating mechanism, which operates in a stable open conduit but with rather low efficiency, does not explain the tremor generated during the initial stages of phase 1 nor during episodes of resurgent tremor accompanying backflow from the lake. In both of these cases, it appears that the movement of lava through a dikelike conduit that is being held open by pressure in the moving lava is a more likely mechanism. An important requirement of such a mechanism is that it produce strong tremor as a consequence of the movement of a fairly small volume of lava.

## SUMMARY AND CONCLUSIONS

1. The $30 \times 10^6$ m$^3$ of lava erupted into Kilauea Iki Crater during the first phase of the 1959 eruption was drawn primarily from storage in the summit reservoir. After the outbreak and initial episode of eruption, which were driven by reservoir overpressure, vesiculation in the upper part of the conduit effectively pumped lava from the reservoir up into the lake. During this process the reservoir pressure dropped below that required to hold an unvesiculated column of lava in the conduit up to the level of the vent.

2. When the surface of the lake rose above the level of the vent, heavy degassed lake lava flooded the base of the fountain and poured back into the vent, where it sufficiently inhibited vesiculation in the lava emerging from below that it disabled the vesiculation pump and shut off the eruption. With degassed lake lava in the conduit, the pressure at the base of the conduit exceeded the pressure in the reservoir, and lake lava flowed back into the reservoir. When the lake surface fell below the vent, backflow ceased.

3. The sharp drawdown in reservoir pressure during the final stages of phase 1 led to a sharp increase in the flux of lava into the reservoir from the deep source beneath the volcano. The reservoir inflation rate increased from about $0.3 \times 10^6$ m$^3$/d for the month before the eruption, to about $3 \times 10^6$ m$^3$/d immediately after phase 1. Between the end of phase 1 and the end of the 1959 eruption, about $60 \times 10^6$ m$^3$ of fresh lava entered the reservoir from below.

4. The conduit remained open from the end of phase 1 until the end of the eruption. Increase of pressure in the reinflating reservoir and, possibly, replacement of heavy drainback lava in the conduit by lighter, gas-charged lava from the reservoir raised the lava in the conduit until it rose above the lip of the vent. Vesiculation of the fresh reservoir lava rising in the conduit further reduced the density of lava in the conduit and revitalized the vesiculation pump, turning on the next eruptive phase. When the erupting lava again raised the lake surface sufficiently above the level of the vent, degassed lava from the lake again poured back into the conduit and disabled the vesiculation pump. Cessation of fountaining was again followed by draining of the lake back down to the level of the vent.

5. The process described above was repeated 15 times after phase 1, until the supply to the summit reservoir of fresh lava from below abated. An additional $8 \times 10^6$ m$^3$ of lava was added to the lake, primarily during phase 4, when the mouth of the conduit broke out higher on the south wall of Kilauea Iki about 12 m above the original vent. An estimated $12 \times 10^6$ m$^3$ lava was driven out of the reservoir, probably into the core of the east rift zone, during backflow from the later phases of the eruption. At the end of the eruption the summit reservoir had been refilled with about $40 \times 10^6$ m$^3$ lava to replace the $30 \times 10^6$ m$^3$ that was withdrawn during phase 1. The lava budget of the entire eruption is shown in figure 48.28.

6. Tremor appears to have been generated under two different regimes with very different efficiency. Eruption of lava at even low rates through a long narrow fissure propped open by pressure in the lava produced strong tremor early in phase 1 and, perhaps, during episodes of resurgent tremor accompanying backflow. In the stable conduit that remained open between phases (and was, therefore, not propped open by excess reservoir pressure), tremor was generated with much lower efficiency. In this case, the amplitude of tremor was a linear function of eruption rate during fountaining, but it was much smaller during comparable rates of backflow. Tremor amplitude appears to be independent of fountain height, except during phase 1 when the conduit was being shaped by the flow of lava through it. These observations suggest that tremor in the open conduit was associated with the action of the vesiculation pump that lifted lava from the reservoir to the lake.

7. After the first 3 phases, rate of eruption was proportional to the volume of lava from below that had recharged the summit reservoir. This relation may be a result of the decrease in the work required of the vesiculation pump to move lava from the reservoir to the lake as reservoir pressure increased. It may also be caused by a

progressive change in the ratio in the reservoir of stored reservoir lava to fresh lava from depth.

8. From phase 10 onward, the eruptive phases began with an episode of high fountaining. Fountaining then diminished rapidly to a lower level that was sustained through the rest of the phase. Such behavior might be explained by the accumulation of a light, particularly gas rich batch of lava at the top of the reservoir between phases, which was expelled first during the next phase but was soon depleted. Because $H_2O$ should be completely dissolved in the lava at reservoir depths, it is unlikely that it is the agent for such a process. A far better candidate is $CO_2$. If present in the amount deduced by Gerlach and Graeber (1985), light fluid inclusions of $CO_2$ would constitute 5–10 percent by volume of the parental magma when raised to reservoir depths. The large variation in fountain height, which appears to depend on lava temperature to some extent, might also be explained by a mixture of $CO_2$-depleted stored lava and $CO_2$-rich fresh lava in the reservoir. In the course of the eruption, as the proportion of fresh lava and the mixing of the reservoir contents increased, the range of variation in fountain height and temperature of erupted lava decreased.

## REFERENCES CITED

Eaton, J.P., 1959, A portable water-tube tiltmeter: Bulletin of the Seismological Society of America, v. 39, p. 301–316.

———1962, Crustal structure and volcanism in Hawaii, *in* Macdonald, G.A., and Kuno, Hisashi, eds., The crust of the Pacific Basin: American Geophysical Union Monograph 6, p. 13–29.

Eaton, J.P., and Fraser, G.D., 1958, Hawaiian Volcano Observatory Summary 9, January-March, 1958: U.S. Geological Survey, 8 p.

Eaton, J.P., and Murata, K.J., 1960, How volcanoes grow: Science, v. 132, p. 925–938.

Gerlach, T.M., and Graeber, E.S. 1985, The volatile budget of Kilauea volcano: Nature, v. 313, p. 273–277.

Jaggar, T.A., and Finch, R.H., 1929, Tilt records for thirteen years at the Hawaiian Volcano Observatory: Bulletin of the Seismological Society of America, v. 19, p. 38–50.

Macdonald, G.A., and Eaton, J.P., 1957, Hawaiian Volcanoes during 1954: U.S. Geological Survey Bulletin 1061-B, p. 1–72.

Mogi, K., 1958, Relations between the eruptions of various volcanoes and the deformations of the ground surfaces around them: Bulletin of the Earthquake Research Institute, Tokyo University, v. 36, p. 99–134.

Powers, H.A., 1946, Reanalyzing tilt records at the Hawaiian Volcano Observatory: Volcano Letter 492, p. 1–3.

———1947, Annual tilt pattern at the Hawaiian Volcano Observatory: Volcano Letter 495, p. 1–5.

Richter, D.H., Eaton, J.P., Murata, K.J., Ault, W.U., and Krivoy, H.L., 1970, Chronological narrative of the 1959–60 eruption of Kilauea Volcano, Hawaii: U.S. Geological Survey Professional Paper 537-E, p. E1–E73.

# TIDAL EFFECTS ON HAWAIIAN VOLCANISM

*By* Daisuke Shimozuru[1]


## ABSTRACT

**This paper summarizes earlier work on possible tidal effects at Kilauea Volcano. From a significant test on 52 historical eruptions of Kilauea, Dzurisin inferred that the likelihood of a fortnightly tidal influence is approximately 90 percent. Reanalysis of early work by Jaggar on the fluctuations of the lava-lake level at Halemaumau shows that semidiurnal oscillations during the highest level of the lava-lake activity are well correlated with solid-Earth tides. This tidal fluctuation of the lake level is attributed to cyclic volume change of the magma reservoir caused by tidal strain. Effective volume of the magma reservoir is estimated to be roughly 800 cubic kilometers from the computed cubical dilatation. The effective magma reservoir beneath Kilauea is suspected to be an assemblage of chambers filled with magma rather than a single large chamber.**


## INTRODUCTION

Intracrustal stresses caused by lunisolar attraction, though they are small, have been considered by many workers to influence the occurrence of earthquakes and volcanic eruptions. Many attempts have been made to correlate solid-Earth tides with earthquakes (Hoffmann, 1961; Knopoff, 1964; Simpson, 1967; Ryall and others, 1968; Shlien, 1972; Kayano, 1973; Mauk and Kienle, 1973; Klein, 1976).

Some earthquakes or earthquake swarms show significant correlation with tides. For example, earthquakes on several parts of the world rift system are significantly correlated with the semidiurnal tide. This implies an enhancement of stress on parts of tensional spreading axes. From a global viewpoint, however, significant correlations are not found, and this indicates that most earthquakes are not triggered by specific amplitudes of acceleration of Earth-tide components.

As for volcanic eruptions, it seems also intuitively possible that crustal tidal strain could act as a trigger, provided that the volcano is in a nearly critical state. Chamberlin (1918, p. 231) stated that "Pronounced tidal movement might be expected in the necks of volcanoes if they are connected with large reservoirs of lava below, but if there is any response to tidal strains at all, it is scarcely detectable."

Johnston and Mauk (1972) tested for effects of Earth tides on the major eruptions of Stromboli and found a correlation between eruption times and the modulation envelope of the fortnightly tide. However, there was not a good correlation between eruptions and the phase of diurnal tide. Mauk and Johnston (1973) found similar results for the major eruptions of the world's submarine volcanoes since 1900. Hamilton (1973) demonstrated correlations between worldwide volcanic activity and tidal periods, not only for fortnightly periods, but also for periods as long as 18.6 years. Eggers and Decker (1969) made statistical time-series analyses of worldwide volcanic eruptions and suggested a possible relation with the annual component of Earth-tide cycles.

For Hawaiian volcanoes, the pioneering study of tidal effect was by Jaggar (1924), who observed semidiurnal movement of the level of the liquid lava pool at Halemaumau pit crater. Brown (1925) made Fourier analyses of Jaggar's data and found some evidence of tides with periods of 24 h and 12 h 25 min. More recently, Dzurisin (1980) tested the relation between the well-recorded historical eruptions of Kilauea and the phase of fortnightly tidal cycles. From the point of view of forecasting volcanic eruptions of Kilauea, Klein (1984) concluded, on the basis of Dzurisin's analysis, that the fortnightly tidal modulation is a significant eruption predictor, especially for rift-zone eruptions. Shimozuru (1975) made a detailed analysis of Jaggar's (1924) data on fluctuation of the level of Halemaumau lava lake and found a semidiurnal oscillation correlated with Earth tides when the lake was at its highest levels.

In this article I review the previous investigations of tidal effects on the activity of Kilauea Volcano and attempt to use these data to interpret the character of the magma reservoir system beneath the volcano.

## EARTH TIDES AND VOLCANIC SYSTEMS

For simplicity, volcanoes are here considered to consist of a major magma reservoir and conduits surrounded by solid rock. A volcanic system's response to solid-Earth tides may be different depending on whether the magma reservoir or conduits are filled with magma or not. Furthermore, tidal strain is a function of latitude, as shown in figure 49.1, and so any tidal effects on volcanic activity should be smaller at high latitudes than low latitudes. These two conditions are principal criteria for the evidence for tidal effects on volcanic activity.

Volcanic activities can be categorized into two types. One type is more or less continuous, such as seismic activity including volcanic tremor, lava-lake activity, and long-lasting eruptive events. The other type is discontinuous, such as sporadic eruptions and short-

[1]Physics Department, Tokyo University of Agriculture.

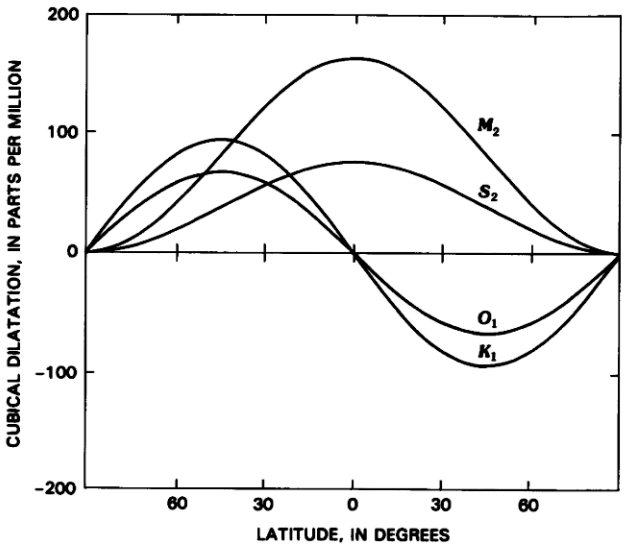


FIGURE 49.1.—Varition of cubical dilatation with latitude due to principal semidiurnal sectorial waves ($M_2$, $S_2$) and principal diurnal tesseral waves ($K_1$, $O_1$).

term seismic swarms. For the latter type, increasing and decreasing pore pressure caused by the movement of lava and gas resulting from tidal strain may act, together with tidal stress, as the triggering mechanism of volcanic earthquakes. These various modes of activity combined with the above mentioned relations make the problem complex. Most investigations to date have been statistical calculations of the possible relation between solid-Earth tides and volcanic activity.

For a more quantitative approach to this problem, we can learn from the tidal fluctuations of water level in deep wells documented by Pekeris (1940) and Richardson (1956). These investigators observed a high tide in the well at the time when the acceleration from the lunisolar attraction was minimal. Pekeris (1940) estimated that a change of water level of 1 cm in a well of 1-m radius could be brought about by cubical dilatation in a water-bearing hemisphere of only 100-m radius. Replacing water with liquid lava, we can apply this to volcanic episodes.

## ROLE OF EARTH TIDES ON ERUPTIONS OF KILAUEA AND MAUNA LOA VOLCANOES—FORTNIGHTLY TIDAL EFFECT

In the light of growing evidence for tidal triggering of volcanic eruptions, Dzurisin (1980) made a statistical study of the onset times of individual eruptions of Kilauea and Mauna Loa in relation to solid-Earth tides. Incorporated in his study were 52 historical eruptions of Kilauea, from 1832 to 1979, and 37 of Mauna Loa, from 1832 to 1972. The beginning of surface lava extrusion was taken as the starting time of each eruption. In light of the results of previous investigations, he concentrated on the influence of the fortnightly tide. Tidal acceleration was computed for the 2-week period centered on each eruption. Examples of the correlation of vertical acceleration of solid-Earth tides and eruptions of Kilauea are shown in figure 49.2. Dzurisin confirmed that eruptions at Kilauea clearly occur preferentially near the fortnightly tidal maxima, with approximately 90 percent likelihood. For Mauna Loa, however, he found that the 37 historical eruptions have been distributed randomly with respect to the fortnightly tide. He inferred that differences in structure or internal plumbing may limit the effectiveness of tidal influences on Mauna Loa. In contrast to the tidal-phase correlation of Kilauea eruptions, Johnston and Mauk (1972) found that eruptions of Stromboli clustered conspicuously about the time of fortnightly tidal minima. This difference in behavior between Kilauea and Stromboli, though they are both basaltic volcanoes, is not understood. Possibly it is related to the difference in tectonic setting.

## TIDAL OSCILLATION OF HALEMAUMAU LAVA LAKE IN 1919—SEMIDIURNAL TIDAL EFFECT

Jaggar (1947, p. 7) stated that the routine of the Hawaiian Volcano Observatory "had been determined by the necessity for

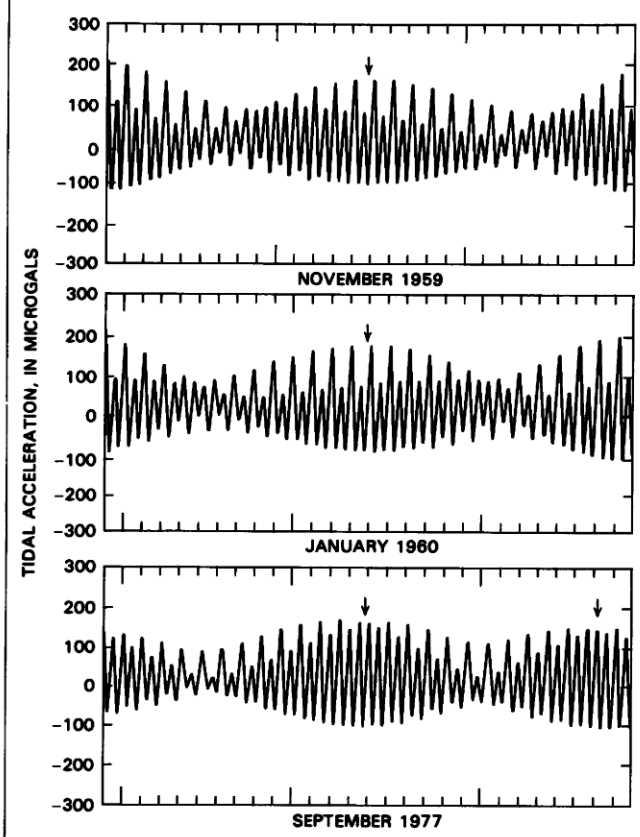


FIGURE 49.2.—Variation of tidal acceleration at Kilauea during time periods in which eruptions occurred. Beginnings of eruptions marked by arrows. After Dzurisin (1980).

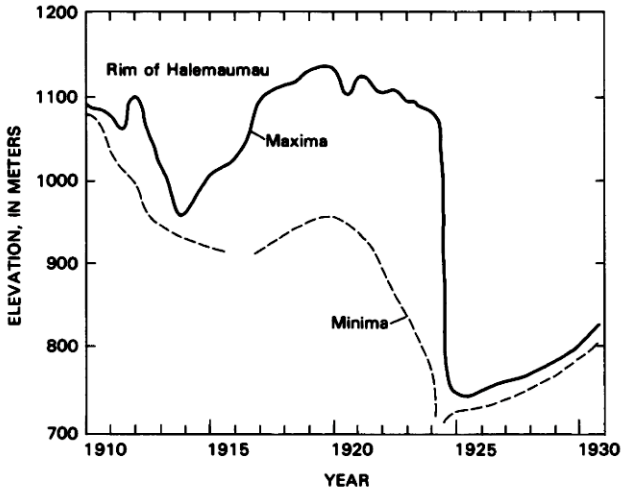


FIGURE 49.3.—Long-term changes in level of Halemaumau lava lake from 1910 to 1930. After Jaggar (1947).

continuous measurement with surveying instruments of the lava pool in Halemaumau pit." The elevation of the surface of the lava lake was measured from 1909 until 1930. Timing of the measurements was arbitrary except during July–August 1919, when the level was highest. A smoothed curve of the level of the lava lake is shown in figure 49.3. The dramatic drop of the level in 1924 was related to magma injection into the east rift zone of Kilauea Volcano and the explosive eruption at Halemaumau.

During the interval of 28 days from July 21 to August 16, 1919, transit measurements of the level of the Halemaumau lava lake were made by Jaggar and his coworkers every 20 minutes. Two points on the edge of the liquid lava lake and two points on the pit floor outside the lava lake were repeatedly measured with reference to a datum station located at the western rim of the crater. The height of the datum station was occasionally checked from the observatory. Brown (1925) made a Fourier analysis of Jaggar's data and found some evidence of tides with periods of the lunar day and lunar half-day, with double amplitudes of about 1 in. His analysis covered the entire measurement interval. However, for a few days near the end of the interval, the liquid lava showed marked oscillations of amplitude 30–60 cm with a period of about 12 h.

While at the Hawaiian Volcano Observatory in 1963 as a member of the Japan-U.S. Cooperative Science Program, I examined Jaggar's data on the level of the Halemaumau lava lake and was very impressed by the detailed measurements. Stimulated by his work, I made an extensive analysis of his data and found that the semidiurnal oscillations during the time of the highest general lake level were in good correlation with the tidal phase (Shimozuru, 1975). This correlation was attributed to squeezing out and drain-back of magma from and to the magma reservoir caused by tidal strain. However, in my previous study there were some uncertain points and a miscalculation. I am therefore revising my analysis of Jaggar's data in order to enhance their scientific value.

## DATA

Assuming they approximately reflect the level change of the entire lava lake, I have adopted the hourly mean values of elevation at the edge of the lava lake from the table in Brown (1925, p. 109). For a 7-h period in the middle of the observation interval, no measurements were made; values were interpolated for this missing time. These data are plotted in figure 49.4 together with the variation of gravitational acceleration caused by tidal forces during the corresponding period. The geographical location was taken as latitude 19.42° N., longitude 155.29° W., and elevation 1,800 m above sea level. Though the level of the lava lake shows in detail a ragged rise and fall, there is a general gradual rise until it reaches its highest level about August 15, 1919.

## METHOD OF ANALYSIS

The data were treated first by a moving-window analysis as shown in figure 49.5. The starting time was taken as 0300 (Hawaiian standard time) on July 23. A significant semidiurnal spectral component at the later stage of the observation period is seen in figure 49.5. This evidence is more clearly shown by the fast Fourier analysis shown in figure 49.6. Over the whole period, there is no significant peak (fig. 49.6, uppermost curve), however, in the later part (August 10–16), a strong peak appears near to the period of the semidiurnal tidal components $M_2$, $S_2$, $N_2$, and $K_2$. The period of the dominant peak is slightly longer than that of the semidiurnal tides; this discrepancy may be partly because the analysis covers such a short period. Considering the difficulties of observation and the limitations resulting from the complex dynamics of the lava lake, particularly the horizontal movement of the liquid lava, I conclude that in the later part of the observation period, a semidiurnal period was evident in the lava lake oscillation.

## CORRELATION WITH SEMIDIURNAL TIDE

Encouraged by this evidence of correlation, I tried to interpret quantitatively the relation of the semidiurnal fluctuation of the lava-lake level to Earth tides. Using the concept of tidal strain causing magma to squeeze out and drain back from and to the magma reservoir, the cubical dilatation was computed for the period from July 20 to August 19, 1919. The cubical dilatation ($\Delta$) at the surface is, if Lame's constants $\lambda$ is equal to $\mu$,

$$\Delta = F(r)\,\frac{W}{rg} = \frac{2}{3}\,(2h-6l)\,\frac{W}{rg},$$

where $W$ is the potential due to tide-generating forces, $r$ is the distance from the point under consideration to the center of the Earth, $g$ is the acceleration of gravity, and $h$ and $l$ are Love's numbers (Melchior, 1966). The world-wide means of $h$ and $l$ are 0.610 and 0.085, respectively. When these values are used in the

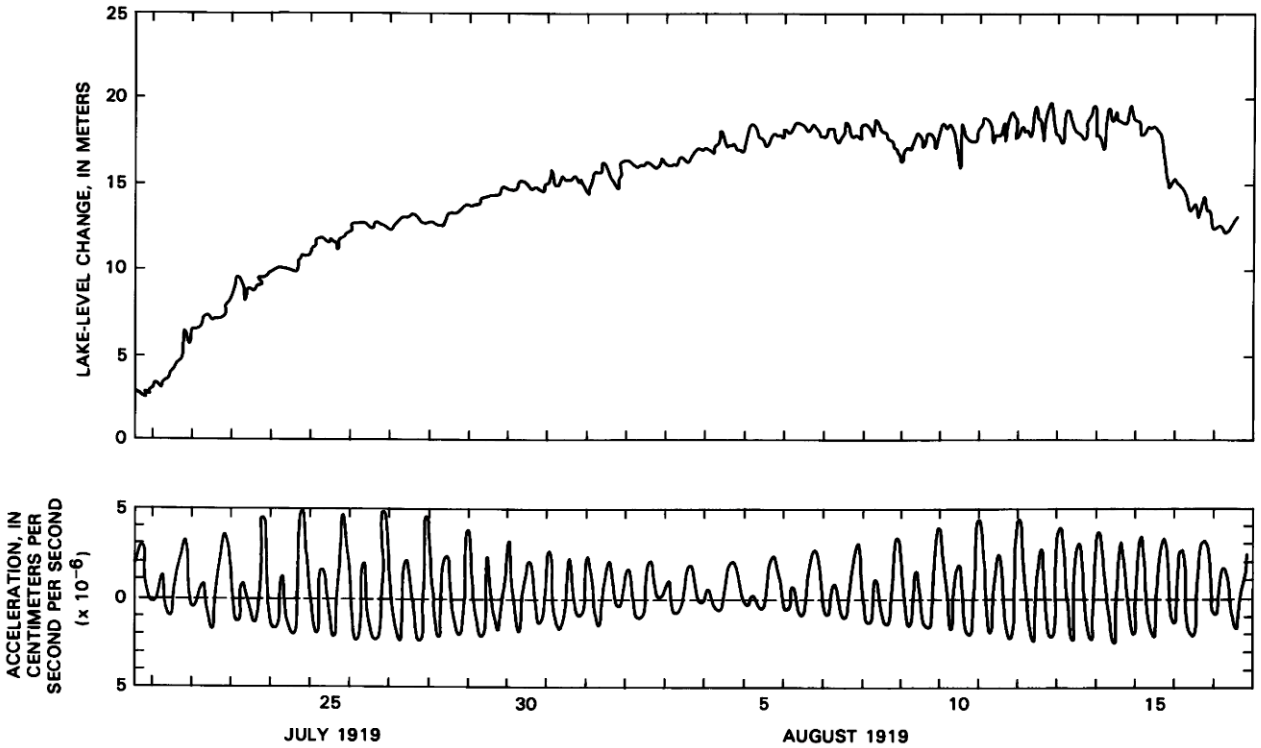


FIGURE 49.4.—Hourly means of level of Halemaumau lava lake and gravitational acceleration due to tide-generating forces during part of 1919. Lake-level data from Brown (1925).

equation, $F(r)$ is 0.47. However, the value of $F(r)$ may be different from the world-wide mean at a hot spot. Cubical dilatation divided by $F(r)$ was computed for the period from August 10–16, 1919, when semidiurnal oscillation of the lava-lake level was dominant. Results are plotted in figure 49.7.

The long-period variation in the original lake-level data was eliminated by Pertzev's method (Pertzev, 1957). The semidiurnal fluctuation of the lake level built up gradually and was mostly pronounced during August 12–14; when the lava lake was at its highest general level. It is interesting to find that the high tide of the lava lake occurs during the time when lunisolar attraction is at a minimum and the low tide occurs when it is at a maximum. A similar relation was also shown by tiltmeter records during the 1968 Halemaumau lava-lake activity (Kinoshita and others, 1969). That eruption started in 1967, and semidiurnal oscillations began to appear in the tilt records during February–March, 1968 (phase 28).

This evidence indicates that magma is transported between the magma reservoir and the lava lake because of semidiurnal dilatational strain. The phase lag of magma transport between the magma reservoir and the lava lake was estimated at 7 minutes, a quantity of time negligible for the present study (Shimozuru, 1975). Phase lag of the oceanic tide is approximately 7 hours at the Island of Hawaii; hence ocean loading had no apparent correlation with the lava-lake fluctuation.

## EFFECTIVE VOLUME OF MAGMA RESERVOIR BENEATH KILAUEA INFERRED FROM TIDAL EFFECT

Using the concepts developed above, we can estimate the effective volume of the magma reservoir during Jaggar's observation period from the following formula:

$$V = dh \cdot A/\Delta,$$

where $dh$ is the change of the lake level, $A$ is the area of the lava lake during the measuring interval, and $\Delta$ is the cubical dilatation. Difficulties arise in estimating the area of the lava lake. Jaggar's sketch map for July 10, 1919 (Jaggar, 1947), is shown in figure 49.8. The lava lake consisted of the main pool in the east and two other pools at the north and southwest. The total area of the lake was estimated at $21.13 \times 10^3$ m$^2$ by tracing the shoreline of the white and lined areas in Jaggar's map (see fig. 49.8). From the difference between the minima and maxima of the lake level ($dh$) during the period August 12–14, we can calculate the volume of magma that

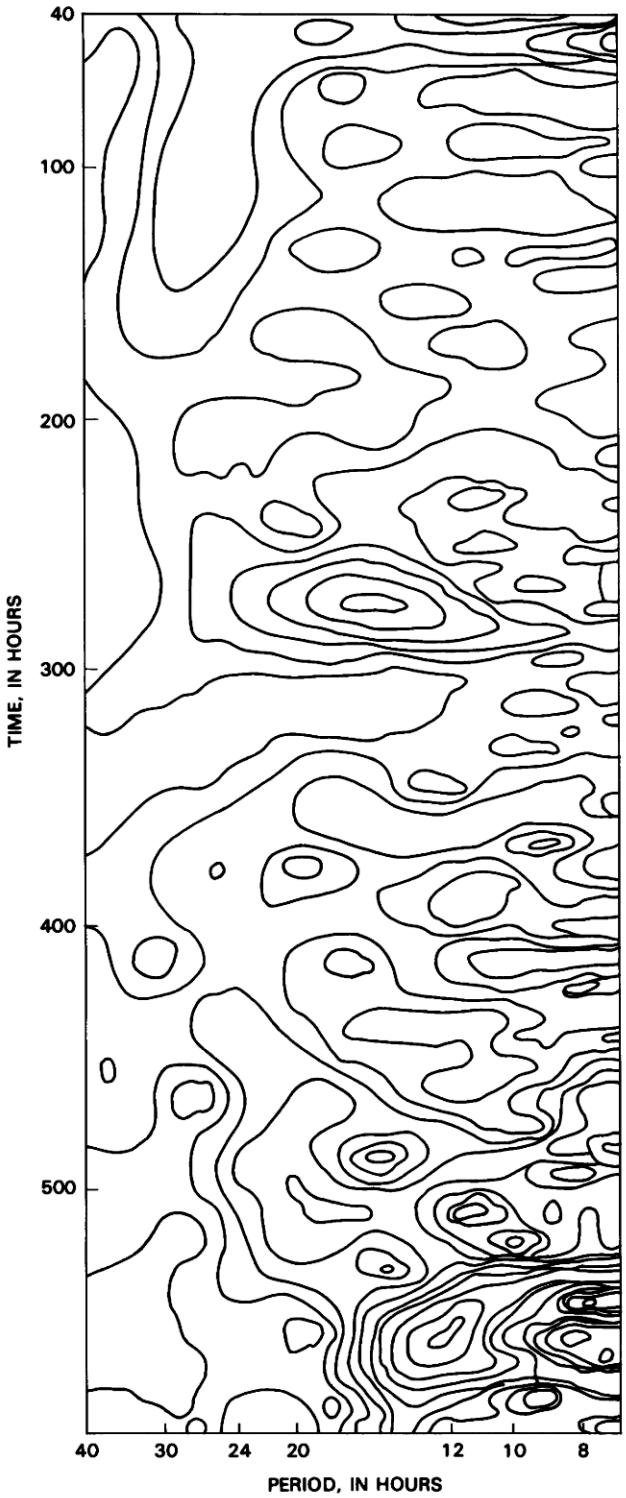


FIGURE 49.5.—Running spectra of fluctuation of height of Halemaumau lava lake during the period from July 21 to August 16, 1919, based on Jaggar's data (Brown, 1925).

squeezed out from the magma reservoir and drained back into it because of semidiurnal tidal strain. If we use the value 0.5 for $F(r)$, then the effective volume of the magma reservoir is roughly 800 $km^3$. On the other hand, Wright (1984, p. 3238) estimated a volume of 11 $km^3$ for Kilauea's shallow magma reservoir on the basis of geodetic data. The effective volume of magma reservoir estimated here is two orders of magnitude larger than that estimated from geodetic data. The reason for this large discrepancy is not clear, however, the calculated volume based on tidal strain may involve not only the shallow magma reservoir, but also involve the entire volume including conduits and plumbing system at the rift zone.

The shape of the magma reservoir beneath Kilauea Volcano is probably complex. Using tilt patterns associated with eruptions, Decker (1968) and Shimozuru (1981) prepared an electric-analog model, a kind of relaxation oscillator. I interpreted the complicated inflation pattern of Kilauea to result from an assembly of a main magma reservoir and several surrounding small reservoirs. The equivalent electric analog is the composite parallel and serial connection of components in a single oscillator. This proposed model of the magma reservoir system is reasonable for interpreting tidal fluctuation of the lava-lake level that appears at the highest general level of the lake and also for explaining the wandering of the uplift center at the summit region of Kilauea (Decker and Kinoshita, 1971, p. 58).

## CONCLUSION

Dzurisin (1980) confirmed that the beginning of surface lava extrusion during 52 historical eruptions of Kilauea occurred preferentially near the fortnightly tidal maxima with approximately 90

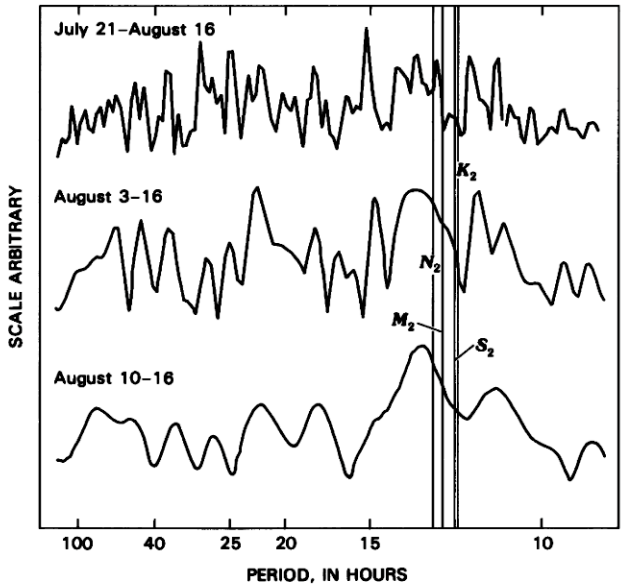


FIGURE 49.6.—Fast Fourier analysis of observed fluctuation in height of Halemaumau lava lake based on Jaggar's (1947) data. Spectra are shown for three different intervals in July–August 1919. Semidiurnal tidal components: $M_2$, $S_2$, $N_2$, $K_2$.

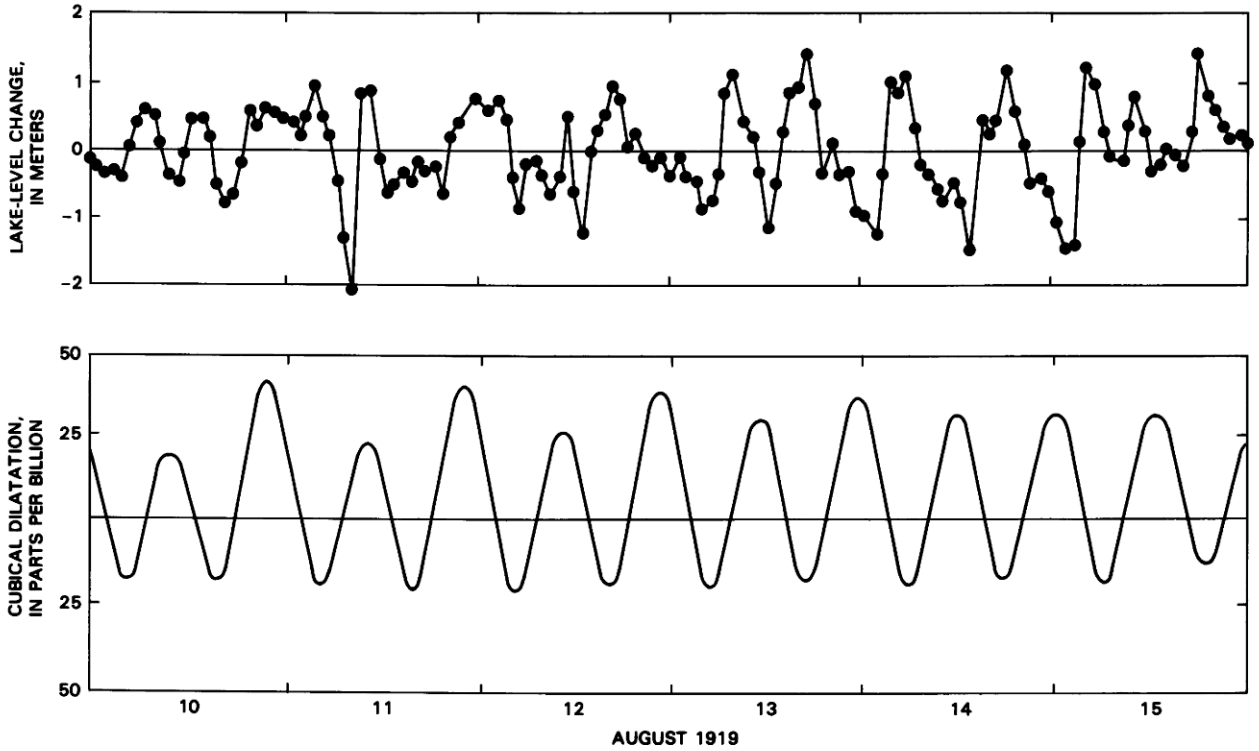


FIGURE 49.7.—Plot of hourly mean of level of Halemaumau lava lake, after filtration of long-term variation, during period August 10–15, 1919, and cubical dilatation ($\Delta/F(r)$) for corresponding interval. Lake-level data from Brown (1925).

percent likelihood. For Mauna Loa, however, he found that 37 historical eruptions began randomly with respect to the fortnightly Earth tide. In earlier work, I analyzed Jaggar's data on the fluctuation of the lava-lake level at Halemaumau in 1919 and found that semidiurnal tidal fluctuations during the highest general lake level correlate well with solid-Earth tides. Using the concept of squeezing out and draining back of magma from and to the magma reservoir caused by tidal strain, I have calculated the concerned volume of magma bodies at roughly 800 $km^3$ in August 1919. The magma reservoir system at Kilauea is suspected to be an assembly of a main magma reservoir and surrounding smaller reservoirs.

## REFERENCES

Brown, E.W., 1925, Tidal oscillations in Halemaumau, the lava pit of Kilauea: American Journal of Science, 5th ser., v. 9, no. 2. p. 95–112.

Chamberlin, T.C., 1918, The Origin of the Earth: Chicago, University of Chicago Press, 231 p.

Decker, R.W., 1968, Kilauea volcanic activity: An electrical analog model: Eos (Transactions of the American Geophysical Union), v. 49, p. 352–353.

Decker, R.W., and Kinoshita. W.T., 1971, Geodetic measurements, *in* The Surveillance and Prediction of Volcanic Activity: Earth Sciences, 8. Unesco, Paris, p. 47–74.

Dzurisin, D., 1980, Influence of fortnightly Earth tides at Kilauea Volcano, Hawaii: Geophysical Research Letters, v. 7, no. 11, p. 925–928.

Eggers, A.A., and Decker, R.W., 1969, Frequency of historic volcanic eruptions [abs.]: Eos (Transactions of the American Geophysical Union), v. 50, p. 343.

Hamilton, W.L., 1973, Tidal cycles of volcanic eruptions: Fortnightly to 19 yearly periods: Journal of Geophysical Research, v. 78, no. 17, p. 3363–3375.

Hoffmann, R.B., 1961, Aftershock-energy release versus tidal effects, Hebgen Lake earthquake, Montana: U.S. Geological Survey Professional Paper 424–C, p. C267–C270.

Jaggar, T.A.. 1924, The lava tide, seasonal tilt, and the volcanic cycle: Pan-Pacific Science Congress, Australia, 1923, Proceedings, v. 2, p. 1369–1375.

———1947, Origin and developments of craters: Geological Society of America Memoir 21, 508 .

Johnston, M.J.S., and Mauk, F.J., 1972, Earth tides and triggering of eruptions from Mt. Stromboli, Italy: Nature, v. 239, p. 266–267.

Kayano, I., 1973, Microearthquake activity in Hiroshima and Shimane Prefectures and surrounding areas, Western Japan: Bulletin of the Earthquake Research Institute, University of Tokyo. v. 26, p. 178–203.

Kinoshita, W.T., and Koyanagi, R.Y., 1969, Kilauea Volcano: The 1967–1968 summit eruption: Science, v. 166, p. 459–468.

Klein, F.W., 1976, Earthquake swarms and semidiurnal solid Earth tide: Geophysical Journal of the Royal Astronomical Society, v. 45, p. 245–295.

———1984, Eruption forecasting at Kilauea Volcano, Hawaii: Journal of Geophysical Research, v. 89, p. 3059–3073.

Knopoff, L., 1964, Earth tides as a triggering mechanism for earthquakes: Bulletin of the Seismological Society of America, v. 54, p. 1865–1870.

Mauk, F.J., and Johnston, M.J.S., 1973, On the triggering of volcanic eruptions by Earth tides: Journal of Geophysical Research. v. 78, p. 3356–3362.

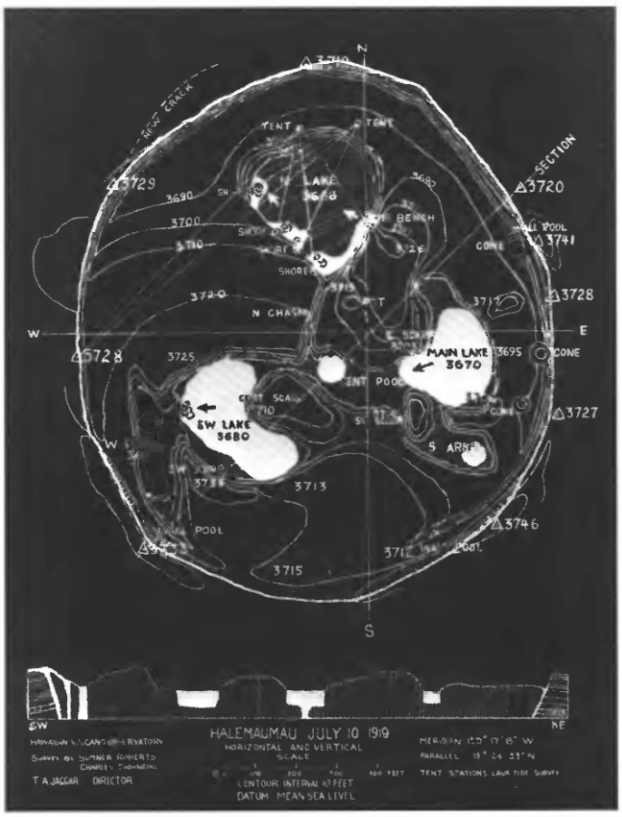


FIGURE 49.8.—Topography and lava pools in Halemaumau pit crater on July 10, 1919. Map originally published in Geological Society of America Memoir 21, (Jaggar, 1947, pl. 79a).

Mauk, F.J., and Kienle, J., 1973, Microearthquakes at St. Augustine Volcano, Alaska, triggered by Earth tides: Science, v. 182, p. 386–389.

Melchior. P., 1966 The Earth Tides: Oxford, Pergamon Press, 609 p.

Pekeris, C.L., 1940, Note on tides in wells: Eos (Transactions of the American Geophysical Union), v. 21, p. 212–213.

Pertzev, B.P., 1957, On the calculation of the drift curve in observation of bodily tides: Marees Terrestres, Bulletin d'Informations, 5. p. 71–72.

Richardson, H.R.M., 1956, Tidal fluctuations of water level observed in wells in East Tennessee: Eos (Transactions of the American Geophysical Union), v. 37, p. 461–462.

Ryall, Alan, VanWormer, J.D., and Jones. A.E., 1968, Triggering of microearthquakes by Earth tides, and other features of the Truckee, California, earthquake sequence of September, 1966: Bulletin of the Seismological Society of America, v. 58, no. 1, p. 215–248.

Shimozuru, Daisuke, 1975, Lava lake oscillations and the magma reservoir beneath a volcano: Bulletin Volcanologique, v. 39, no. 4, p. 570–580.

———1981, Magma reservoir systems inferred from tilt patterns: Bulletin Volcanologique, v. 44, no. 3, p. 499–504.

Shlien, S., 1972, Earthquake-tide correlation: Geophysical Journal of the Royal Astronomical Society, v. 28, p. 27–34.

Simpson, J.F., 1967, Earth tides as a triggering mechanism for earthquakes: Earth and Planetary Science Letters. v. 2, p. 473.

Wright, T.L.. 1984, Origin of Hawaiian tholeiite: A metasomatic model: Journal of Geophysical Research, v. 89, p. 3233–3252.

# GEOELECTRIC CHARACTER OF KILAUEA IKI LAVA LAKE CRUST

*By* Lennart A. Anderson


## ABSTRACT

**Two orthogonal Schlumberger soundings were made in the Kilauea Iki pit crater on the Island of Hawaii to determine the vertical resistivity of the crust overlying a molten lava lens. The data indicate a relatively good conductor in the 6- to 12-m depth interval interposed between two high-resistivity layers. Subsequent borehole resistivity logging disclosed the existence of a second conductive section in the 29- to 34-m depth interval. The upper conductive zone results primarily from the deposition of wet salt precipitates within the vesicles and pore spaces of the basalt, whereas the lower conductive zone results from a sufficient quantity of meteoric water in the liquid phase to reduce the resistivity of the rock. A dry, highly resistive layer separates the lower conductive zone from the melt. Rock-property measurements on borehole core samples indicate that the in-place resistivity of the rock is controlled by environmental factors rather than by compositional or textural variations. Only in those samples from the 6.1- to 6.7-m depth interval are the laboratory resistivity measurements equal to the resistivities measured in the borehole. A scanning electron micrograph of minerals found within the vesicles of the rock sample from the 6.7-m depth revealed evidence of zeolite and clay development in quantities sufficient to reduce the resistivity of the rock by means of surface conduction.**


## INTRODUCTION

In the mid-1970's, the Sandia Corporation, under a Department of Energy grant, began a study of shallow magma reservoirs, with the ultimate objective of determining the feasibility of withdrawing heat from a molten lava body for direct conversion into a useful form of energy (Hermance and Colp, 1982). Kilauea Iki lava lake, on the Island of Hawaii, formed during the summit eruption of November–December 1959, was chosen as the site of the initial study, which consisted of first identifying and subsequently delineating an area of near-surface molten lava through the use of various geophysical methods. Staff members of the U.S. Geological Survey's Hawaiian Volcano Observatory (HVO) on Kilauea were invited to participate in the exploration phase, particularly in the application of electrical measurements to a study of the electrical character of the crust of the lava lake and to the mapping of the lateral configuration of the molten lava lens.

Kilauea Iki is a pit crater, approximately 1.6 km long and 0.8 km wide, situated immediately east of Kilauea caldera (fig. 50.1). Before the November 1959 eruption, the pit crater was 213 m deep at its lowest point and, following termination of volcanic activity, a lava lake 111.3 m deep covered the old floor of the crater (Richter and Moore, 1966). In the ensuing years, cooling and subsequent solidification, which is not as yet complete, has caused the lake surface to subside to a level perhaps as much as 10 m below the initial level.

The first geophysical mapping in Kilauea Iki occurred in April 1961, when electromagnetic profiling and sounding methods were used to identify the boundaries of the molten lava and to determine the thickness of the overlying crust. At that time the 100 °C isotherm was at a depth of less than 1 m below the lake surface, and, despite rainfall in excess of 2.5 m/yr, the meteoric water was rapidly vaporized and none remained in the rock. The resulting resistivity contrast between the dry, solidified lava, about 9 m thick at the time (Richter and Moore, 1966), and the conductive molten lava made interpretation of the field data relatively simple. In 1976, the 100 °C isotherm had descended to a depth of approximately 34 meters below the lake surface, and a perennial cycling of water in the liquid-vapor state had been established in the upper part of the lake crust. As a consequence, the added moisture has altered the upper basalt layers, adding to the complexity of an interpretation involving electromagnetic sensing of the molten lava at depth (Smith and others, 1977).

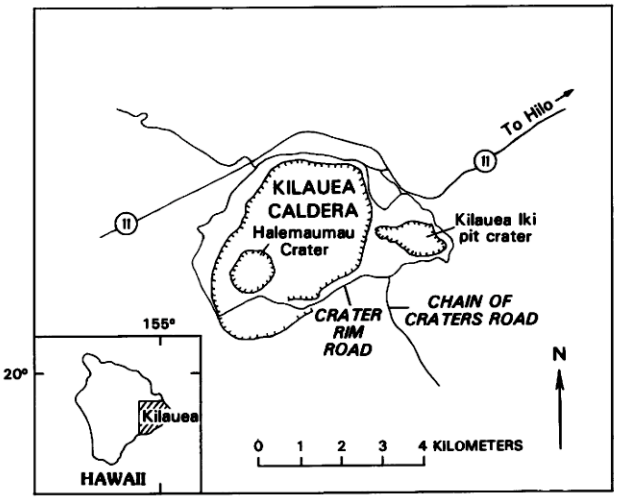


FIGURE 50.1.—Kilauea Volcano showing location of Kilauea Iki pit crater.

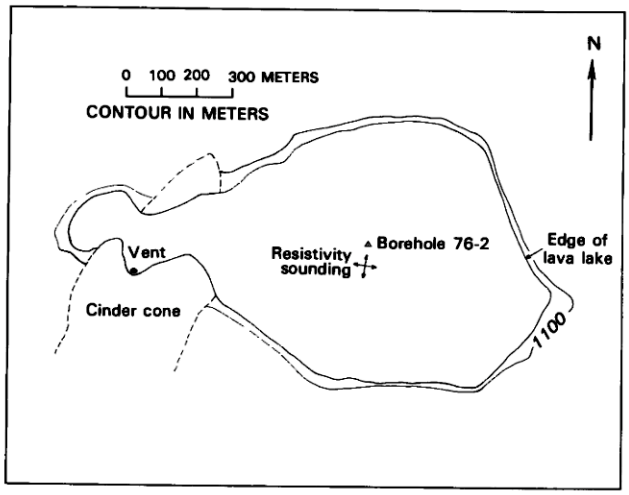


FIGURE 50.2.—Kilauea Iki lava lake showing resistivity sounding and borehole locations.


## ACKNOWLEDGMENTS

I wish to express my gratitude to Neil Fishman, Jim Gude, and Richard Sheppard of the U.S. Geological Survey, Denver, for their contributions to the recognition of the unusual occurrence of zeolites within the crust of the Kilauea Iki lava lake. I am also grateful to John Forbes of the Hawaii Volcano Observatory for his help in constructing the borehole probes used in this investigation.


## SCHLUMBERGER ELECTRICAL SOUNDINGS

To obtain information on the gross distribution of resistivity of the lake crust with increasing depth, two mutually perpendicular Schlumberger electrical soundings were made near the center of the lava lake in April 1976 (fig. 50.2). The sounding curves and their interpretations in the form of geoelectric sections obtained by means of a computer program developed by Zohdy (1974) of the U.S. Geological Survey are presented in figure 50.3. The east-west sounding shown in figure 50.3*A* was expanded along the major axis of the lake. The interpreted geoelectric section indicates the presence of a relative conductor within the 6- to 12-m depth interval interposed between two layers of much higher resistivity. The near-surface layer is essentially dry and hence, resistive, and as the temperature of the lower layer is increased, ground water is excluded from the rock, causing that section to become increasingly resistive with depth.

The effect of lateral variations in resistivity is evident on the sounding curve shown in figure 50.3*B*. The vertical offset in the field data observed at current electrode spacings within the 12- to 16-m depth interval, resulting from repeated measurements at two different potential electrode spacings while maintaining a fixed current

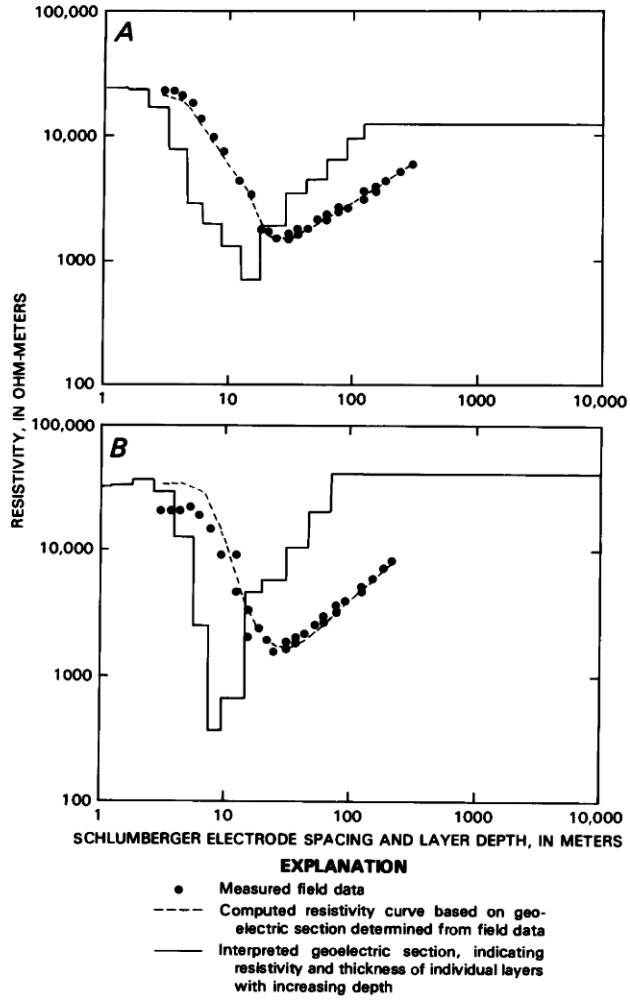


FIGURE 50.3.—Vertical electrical soundings (direct-current resistivity) made by expanding electrode array in (*A*) east-west-direction and (*B*) north-south direction.

electrode spacing, is an indication that the rock resistivity is higher sidewise to the center of the sounding array than at the center of the sounding itself. In Kilauea Iki, the blocklike crustal configuration has produced a network of vertical fractures, some of them visibly open, which tend to interfere with current flow. Following a procedure initiated by Zohdy and others (1973) the curve segment measured at the longest electrode spacings is held fixed in position while the other segments representing shorter electrode spacings are shifted upward or downward to form a continuous curve that can be interpreted in terms of laterally homogeneous media. As the result of an upward shift of the left-hand segment, the surface layer as interpreted from the north-south sounding is appreciably higher than that interpreted from the east-west sounding.

The north-south sounding curve (fig. 50.3*B*) is similar to the

east-west sounding curve in the sense that a shallow conductor is situated between two resistive layers. A fundamental difference exists in that the right-hand branch of the north-south sounding curve rises at a slope of 1, indicating that the resistivity of the lower layer increases abruptly relative to the overlying layer, whereas, the corresponding branch of the east-west curve rises at a slope of less than 1, as if sensing on a zone of gradually increasing resistivity. Neither sounding indicates the presence of an underlying conductive zone.

A problem in interpreting the soundings is to reconcile the nature of the lateral changes in resistivity that produce the slope differences between the right-hand branches of the east-west and north-south sounding curves. Efforts to develop a three-dimensional model representative of the horizontal and vertical resistivity section that may reasonably exist within the lava crust, sufficient to simulate the sounding curves, failed to produce the desired results. The resistivity variations within the lava lake and surrounding environs are highly complex and difficult to reconstruct on the basis of existing data.

## BOREHOLE RESISTIVITY LOGGING

Two boreholes located 61 m north of the direct-current resistivity sounding site were drilled 41 cm apart during August 1976; they penetrated the solid-melt interface at 45.52 m (Colp and Okamura, 1978). When a borehole became available for in-hole resistivity measurements, several design schemes and materials were tested until a suitable probe was eventually assembled made of four sections of quarter-round wood moulding and wiper-type electrodes constructed of welding rod. Although the probe charred badly as the temperature increased in the lower part of the hole, its structural integrity was maintained, allowing measurements to be made until the welding rod lost its resilience and slumped to the extent that mechanical contact with the borehole wall was no longer possible. Resistivity measurements were made as with the normal array using current-potential electrode spacings of 1 and 2 m read at 0.5-m intervals.

The first successful resistivity log was obtained by early December 1976 (fig. 50.4). Resistivities are shown plotted as a function of the depth to the midpoint between the potential and current electrodes. In a general sense, each data set portrays a more complicated geoelectric section than that indicated by the vertical electrical soundings. Instead of two layers of varying resistivity overlying the hot, dry, resistive zone above the molten lava, at least four layers exist. The lowermost, relatively conductive section in the 29- to 34-m depth interval identifies the zone of highest water content where the liquid phase of a two-phase system predominates. Above the wet zone, the moisture is primarily in the vapor phase, resulting in higher resistivities. A second conductive layer exists in the 4- to 12-m depth interval; it has resistivities lower than those measured in the lower conductive zone. Obviously no standing water exists in this upper layer nor is there any reason to suspect a difference in mineralogy sufficient to cause the interval to be less resistive than the main body of solidified lava. The cause of the increased conductivity is believed to be primarily the result of wet salt precipitates forming within the vesicles and pore spaces of the rock as some condensation of the upward-moving wet steam takes place because of a subtle drop in temperature. Temperature measurements made at the time of the December logging survey (fig. 50.4) indicated values slightly less than 100 °C above the 16-m depth, thus verifying that the near-surface zone undergoes some degree of cooling as the result of intermixing with downward-moving rain water. The source of the brine is believed to be a dissolution of magmatic gases within the lower water-saturated layer, portions of which are eventually carried upward within the wet steam. Helz and others (1980) have identified the presence of thenardite—a sodium sulfate salt ($Na_2SO_4$)—within certain intervals of the recovered core. The high-salinity surficial waters coating the rock provide a continuous flow path for electrical current such that the bulk resistivity of the rock is greatly reduced.

In-hole resistivity measurements were repeated in April 1977 with a similar probe at the same electrode spacings as before, the only difference being that the material used for the electrodes was stainless steel rather than welding rod. The character of the resulting data profile is essentially unchanged; however, appreciable changes occurred during the 4-month time period. Among these changes is an overall decrease in the level of resistivity within the entire borehole (fig. 50.5). Apparently the borehole provides an easy escape route for steam, causing an increase in the concentration of salt and possibly the development of clay minerals in the surrounding rock owing to hydrothermal alteration, thereby reducing its bulk resistivity. Another change from the earlier log is an increase in the depth to the lower conductive zone of about 3–4 m during the elapsed 4-month time period. This change is well in excess of the 2.11-m annual solidification rate calculated by Hardee (1980). Possibly the borehole allowed an anomalous quantity of heat to escape, thereby creating a localized deepening of the 100 °C isotherm. In the December 1976 resistivity log (fig. 50.4) the hot, dry zone overlying the molten lava was highly resistive at the depth to which measurement was possible. The April 1977 log (fig. 50.5) indicates this zone to be somewhat less resistive with lower resistivities appearing at greater depth. However, the April log shows an inconsistency in the resistivity correspondence between the 1- and 2-m measurements in the 37- to 39.5-m depth interval. A breakdown in cable insulation may have occurred in the extremely high temperature environment, causing leakage that would produce erroneous resistivity values. Upon removal from the borehole, the probe was checked and found to be intact; however, the probe had cooled considerably once on the surface, so any problem with cable faults relating to thermal expansion may have gone undetected. As with the welding rod, the stainless steel electrodes lost their resilience, making continued contact with the borehole walls impossible. If the contact resistance was high because of the deteriorating condition of the potential electrodes, the measurement may have produced an anomalously low resistivity. Pockets of molten lava could conceivably exist in sufficient quantities in the near-hole environment to produce the low resistivities observed in the dry zone. If the molten lava is nonuniformly distributed, then the bulk

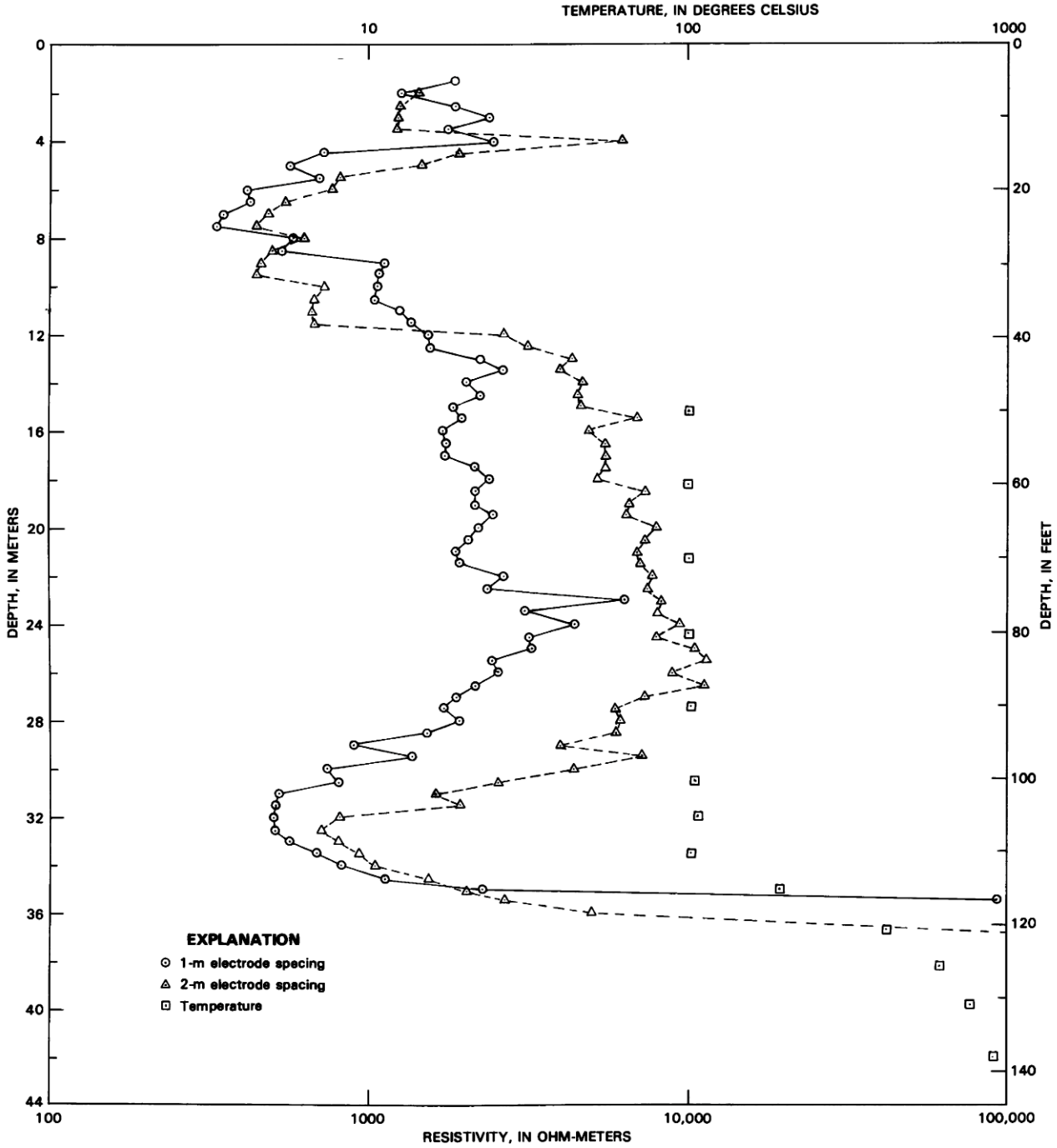


FIGURE 50.4.—Direct-current resistivity and temperature data obtained in Kilauea Iki borehole 76-2 in December 1976.

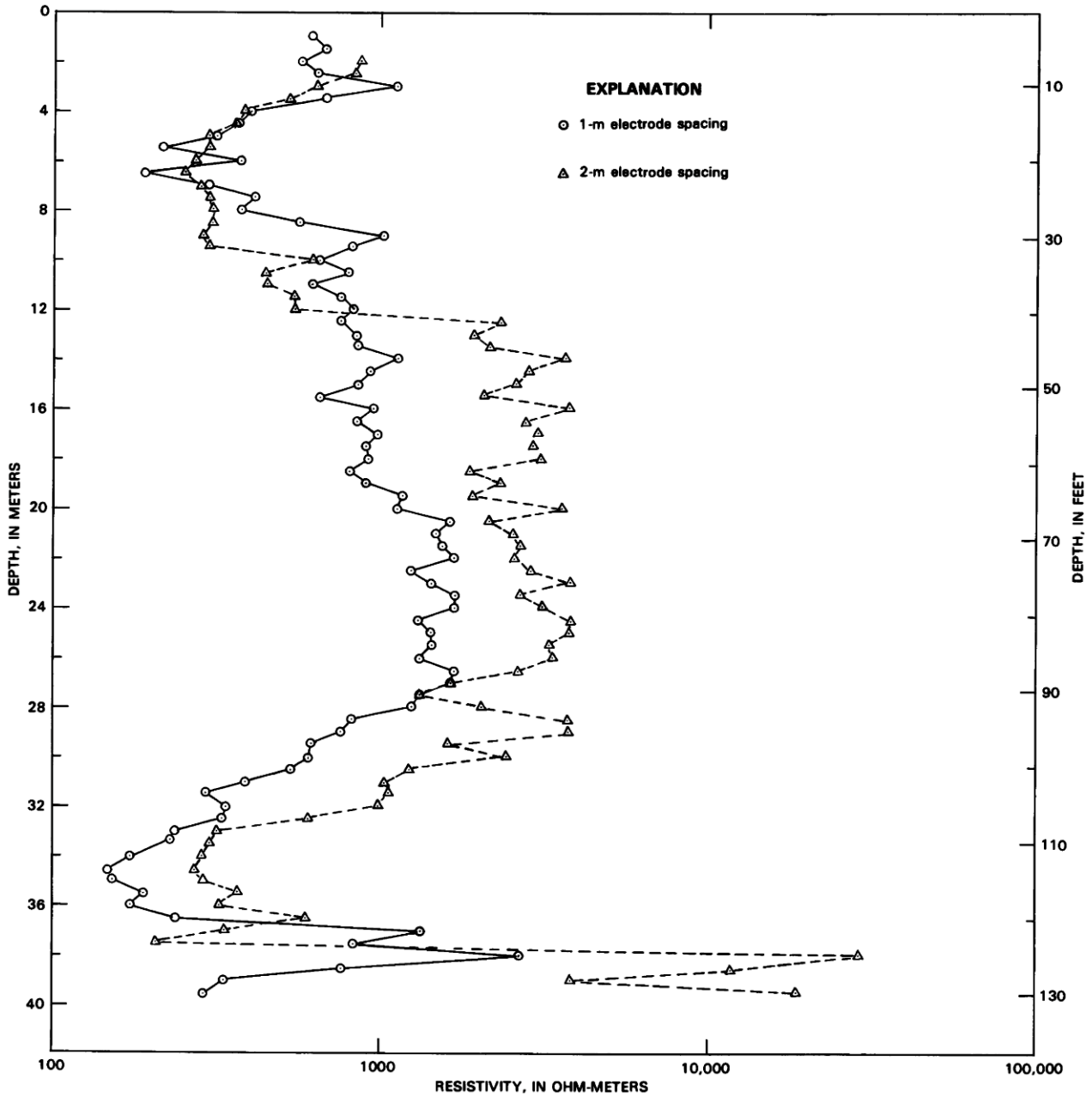


FIGURE 50.5.—Direct-current resistivity data obtained in Kilauea Iki borehole 76-2 in April 1977.

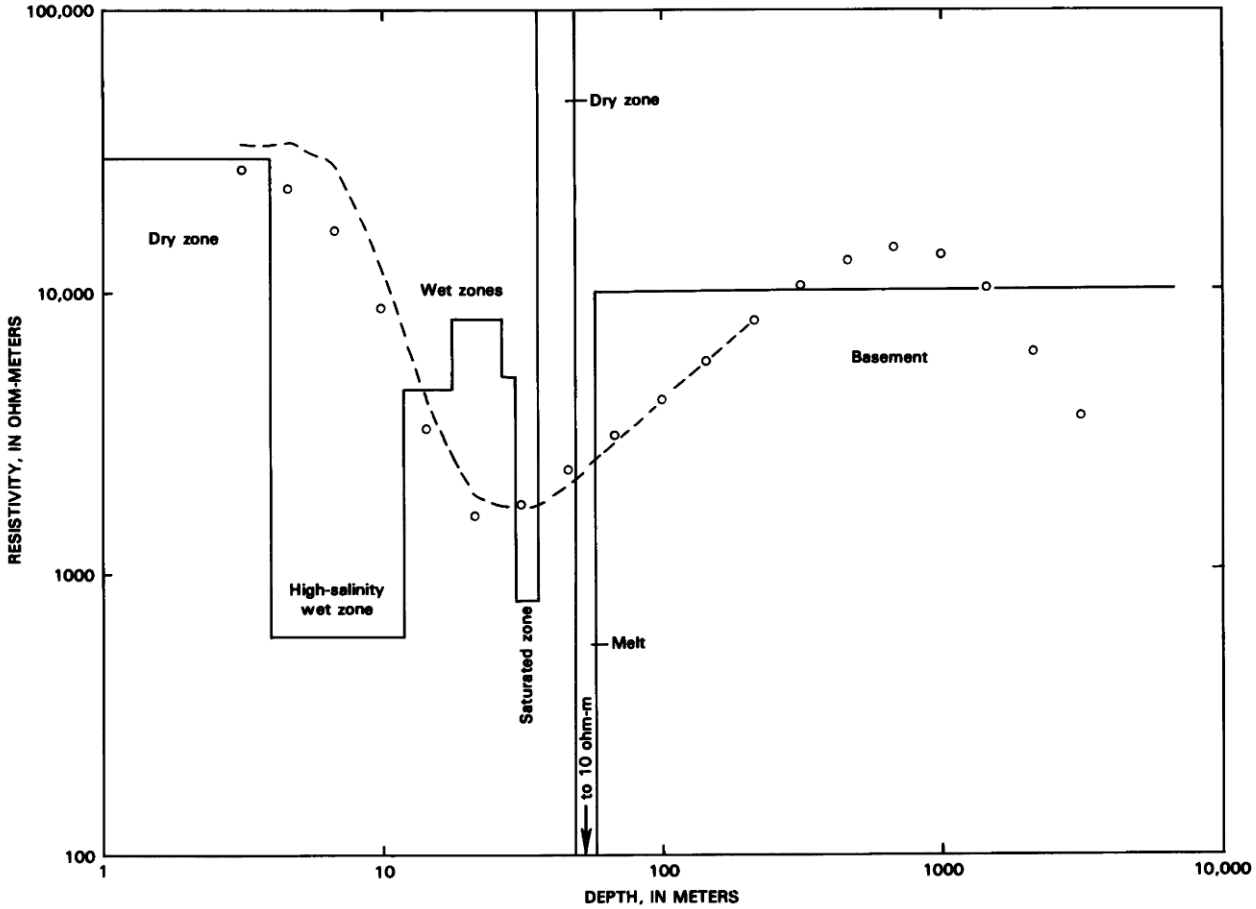


FIGURE 50.6.—Geoelectric section compiled from December 1976 borehole resistivity log obtained at 2-m spacing. Thickness of 100,000 ohm-m section and resistivity of molten lava is inferred from other data. Dashed line, adjusted field curve for north-south resistivity sounding; circles, Schlumberger resistivity values.

resistivity, which is a volume measurement, will differ as a function of electrode spacing. However, intuition suggests that the molten lava would exist in greater abundance with increasing distance from the borehole. The data do not support this notion inasmuch as the resistivities are appreciably higher at the 2-m spacing. A third explanation for the low resistivities near the bottom of the hole may be that the basalt is at a high enough temperature to become ionically conductive. If this were the case the resistivities measured at both electrode spacings would vary in a systematic and uniform manner. Despite the arguments that can be made in support of the validity of the data, the uncertainties are sufficient to judge the resistivity measurements below the 37-m depth to be questionable.

In considering the overall decrease in resistivity of the rock in near proximity to the borehole during the 4-month period between December 1976 and April 1977, it seems likely that the December log may not necessarily be typical of the resistivities of the rock at the time of drilling. As a check on how critical local alteration may have been, a theoretical Schlumberger curve was computed based on layer resistivities and thicknesses derived from the December 1976 2-m log. Because the first resistivity measurement was made at a depth of 2 m, the dry, uppermost part of the surface layer is not represented on the downhole log. Instead, a value of 30,000 ohm-m was selected for the upper 4-m layer.

The computed curve superimposed upon the north-south sounding and the columnar graph showing resistivities and thicknesses selected from the borehole data are shown in figure 50.6. Despite the generalizations made in constructing the model, the fit to the field curve is considered to be satisfactory. To a spacing of 213 m, which is the largest spacing used in the field measurement on the north-south sounding, nine resistivity layers are represented, but from the shape of the sounding curve recognizing more than three is difficult. The existence of the water-bearing conductive zone is obscured by the presence of the underlying hot, dry section arbitrarily assigned a resistivity value of 100,000 ohm-m.

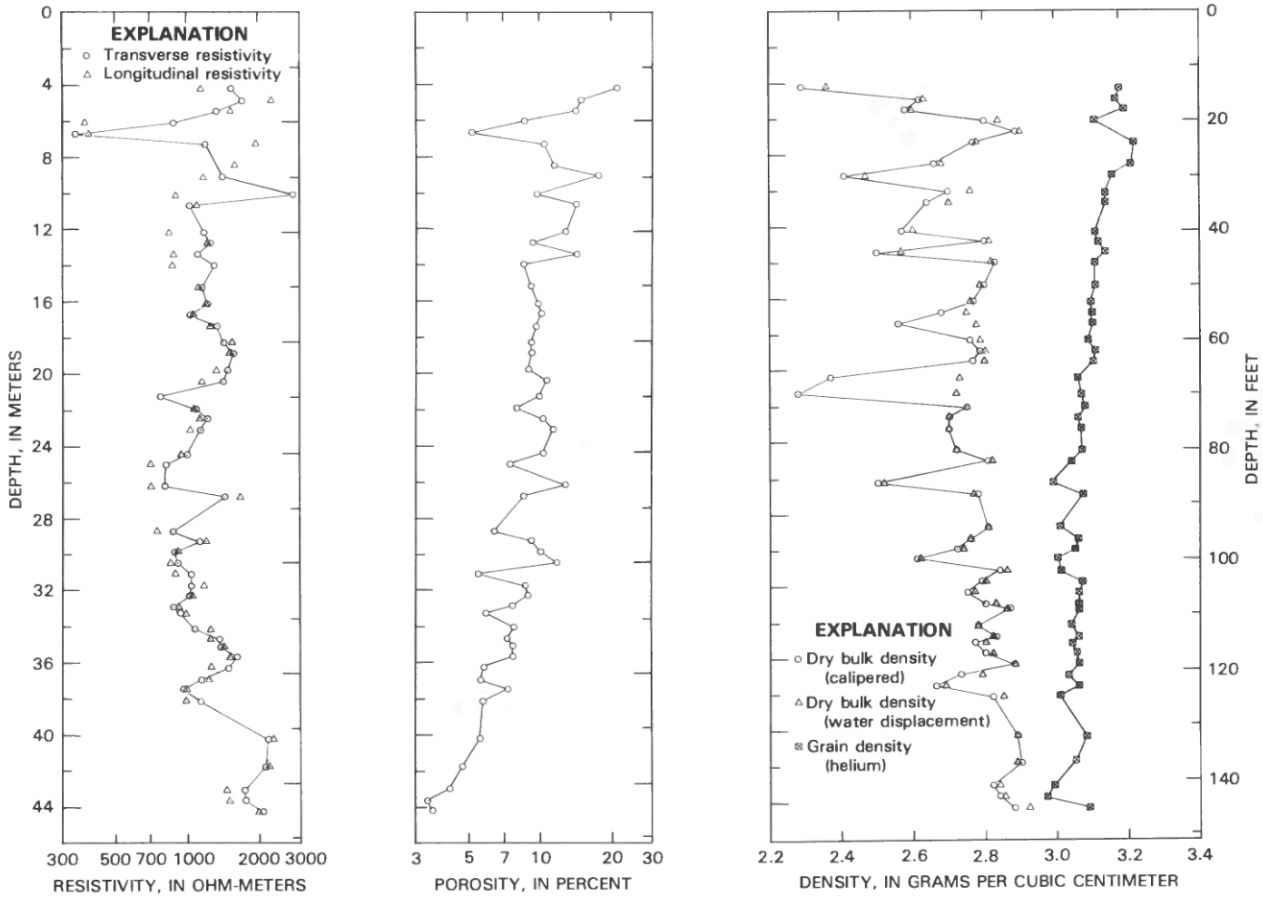


FIGURE 50.7.—Resistivity, porosity, and density values obtained on core samples from Kilauea Iki borehole 76-2.

To determine the half-spacing required to sense on the conductive magma beneath the dry zone the plot was continued by setting constraints on the thicknesses of the layers at depth. According to Hardee (1980) the hot, dry zone has, in recent years, maintained a constant thickness of 12 m. Beyond that knowledge, only estimates can be made of the parameters involving the resistivity and thickness of the molten lava. An indirect measurement of the melt resistivity was made in 1961 (Frischknecht, 1967) and, through curve matching, determined to be precisely 2.09 ohm-m. However, the molten lava was in the early stages of cooling, and subsequent degassing of the lava may have resulted in an increased resistivity requiring that a minimum resistivity of 10 ohm-m be used in order to match the north-south sounding curve. The thickness of the molten section was chosen to be 10 m, underlain by an infinitely thick section of 10,000 ohm-m resistivity. It is apparent from figure 50.6 that a Schlumberger half-spacing in excess of 400 m would be required before the effect of the molten lava becomes evident, and a half-spacing of about 1,000 m is necessary before an actual downturn in apparent resistivity is noted.

## LABORATORY CORE ANALYSIS

To evaluate the causes of the resistivity variations observed in the borehole measurements, 51 core samples were obtained from the 4.27- to 44.21-m depth interval of the 76-2 borehole for laboratory rock-property analysis. Core samples were selected at spacings of 0.61 m, where available, and shaped to an approximate size of 3.33 cm diameter and 3.8 cm length. Samples oriented axially parallel (vertical) to the borehole were used for resistivity, density, and porosity measurements, whereas core samples oriented axially perpendicular (horizontal) to the borehole were only measured for resistivity. Sample resistivities were measured in a four-terminal holder (Parkhomenko, 1967) following core saturation with local tap water. Resistance measurements, made at a frequency of 100 Hz using a high-precision digital resistance meter, were converted to resistivity (in units of ohm-m) from caliper measurements of sample length and diameter.

Procedures for obtaining density and porosity data are those described by Johnson (1979a). Samples in the saturated state were

weighed both in air and suspended in water and reweighed when totally dry. Rock volume was obtained using a water displacement technique discussed in Chleborad and others (1975). From the collective data, dry bulk density, saturated bulk density, and porosity were calculated. A helium pycnometer was used to determine grain density. All measured rock-property values are plotted as a function of depth in figure 50.7.

Resistivities were measured on mutually perpendicular cores cut from the same sample to examine the effect of vesicle alignment on current flow through the sample. Normally, a lava block would be expected to possess uniform electrical properties in that no distinct bedding planes are formed in the cooling process. Examination of the core samples, however, often revealed a distinct alignment of gas bubbles, particularly in the horizontal plane. Should hydrated minerals form within these vesicles their physical continuity would certainly cause an appreciably lower resistivity in one direction than in the other. In virtually all rock types, the transverse resistivity exceeds that of the longitudinal resistivity such that the anisotropy coefficient, defined as the square root of the ratio of transverse to longitudinal resistivity, is greater than 1.0 (Keller and Frischknecht, 1966). With few exceptions, the anisotropy coefficient of the Kilauea Iki basalts is very nearly equal to 1.0, and where it is slightly less than 1.0, the discrepancy may be caused by the fact that the material measured in each sample pair is not quite the same. The plot in figure 50.7 shows the transverse resistivity to be generally greater or equal to the longitudinal resistivity, although obvious exceptions do exist, particularly within the upper conductive zone as defined by the borehole resistivity log.

The environmental conditions in which the borehole and sample measurements were made are obviously so different that the character of the sample resistivity log is totally unlike that of the borehole resistivity logs. The most notable change on the sample plot is in the virtual loss of the conductive zones defined in the borehole log. Dissimilarities in measuring conditions involving factors such as temperature, pore-water levels, and water salinity are considered to be the principal cause of the resistivity differences. Samples from the 6.1- and 6.7-m depths are exceptions producing resistivities equal to those measured in the borehole.

It was anticipated that much of the contained thenardite, identified by Helz and others (1980), would be leached from the rock following the resaturation process. The sample measurements would then be expected to produce resistivities that vary as a function of porosity and mineral content. Grain densities vary only slightly, suggesting a relatively uniform mineral content. Grain densities, however, decrease with depth as a result of higher olivine and pyroxene contents in the upper part of the lava crust. According to Johnson (1979b), high density minerals having high separation temperatures are trapped in the rapidly cooling groundmass, whereas, at depth, where cooling has progressed at a much lower rate, the heavy minerals have had time to settle to the lower levels of the molten lava pool. The grain density values in figure 50.7 indicate the transition to be gradual. Large phenocrysts of olivine can be found in the near-surface lavas, but no evidence of olivine exists in the core taken from the lower lava section. The variation of the heavy mineral content of the basalt, however, would do little to alter the resistivity in the manner shown in figure 50.7.

In the absence of conductive minerals as part of the rock composition, the resistivity of a rock is controlled by porosity, the amount of water within the pore structure, and the salinity of the contained water as predicted by Archie's equation, assuming that electrical conduction is by means of the contained pore waters (Keller and Frischknecht, 1966). An attempt to statistically relate the observed resistivities of the core samples to porosity proved unsuccessful; a least-squares fit to a logarithmic model produced a correlation coefficient of $-0.17$, indicating that other factors also influence the resistivity of the rock.

In an experiment on a Kilauea Iki basalt sample by Olhoeft (1977), a resistivity dependence apart from volume conductance through the pore water was recognized. For resistivity enhancement to occur, alteration products, either in the form of clays or zeolites, must exist within the pore spaces of the rock. Evidence of sparse mineral content was detected within the few vesicles exposed at the surface of the 6.7-m sample. On the premise that the mineral was other than thenardite, a scanning electron micrograph (SEM) was obtained of the mineral (fig. 50.8). That figure shows the wall of the vesicle and tabular crystals of what is thought to be a zeolite. An energy-dispersive X-ray analysis, focusing on the large crystal in the upper left-hand corner of figure 50.8, indicates the mineral to be an aluminosilicate, possibly clinoptilolite or phillipsite based on comparisons of the morphology of zeolite crystals presented in Mumpton and Ormsby (1978).

Further examination of the mineral content of the vesicle revealed what is believed to be clay (montmorillonite?) coating the suspected zeolite (fig. 50.9). The quantity of vug-filling minerals

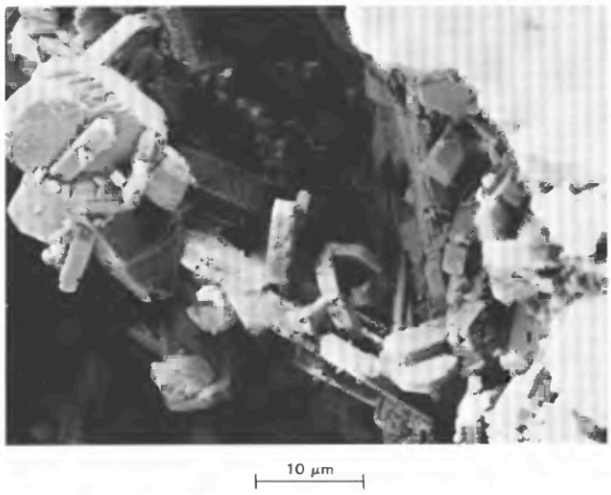


FIGURE 50.8.—Scanning electron micrograph of suspected zeolite mineral found within vesicle of basalt sample from 6.7-m depth of Kilauea Iki lava lake crust.

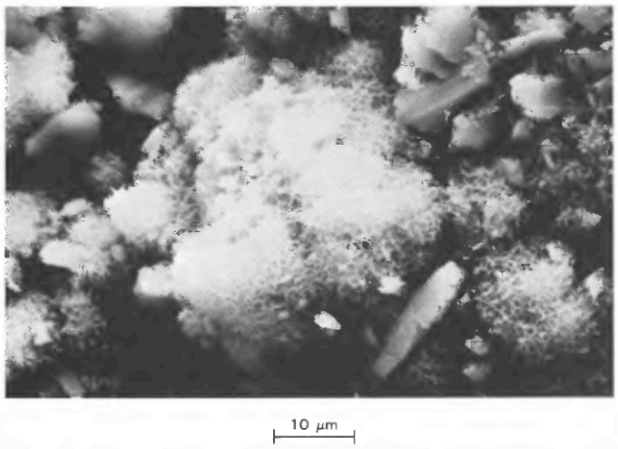


FIGURE 50.9.—Scanning electron micrograph of clay coating on suspected zeolite minerals found within vesicle of basalt sample from 6.7-m depth of Kilauea Iki lava lake crust.

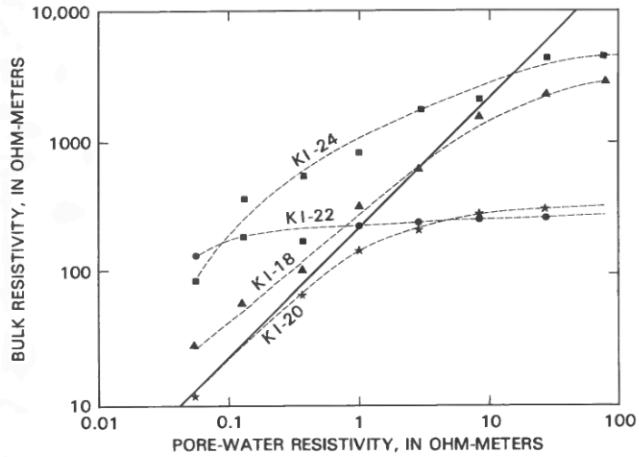


FIGURE 50.11.—Bulk resistivity variation with increasing pore-water resistivity in basalt samples KI-18, KI-20, KI-22, and KI-24, taken from Kilauea Iki lava lake crust at depths of 5.5, 6.1, 6.7, and 7.3 m, respectively. Heavy black line is plot of increasing resistivity as a function of decreasing pore-water conductivity based on Archie's equation.

was, however, insufficient to obtain a positive identification by means of X-ray diffraction.

An SEM of vug-filling minerals, found within the rock covering the surface of the lava lake, is shown in figure 50.10. Although the mineral quantity was adequate for X-ray analysis, the material proved to be an amorphorous mass containing principally silica, aluminum, and potassium. The mineral lining the vug was determined to be opal (R. Sheppard, oral commun., 1984).

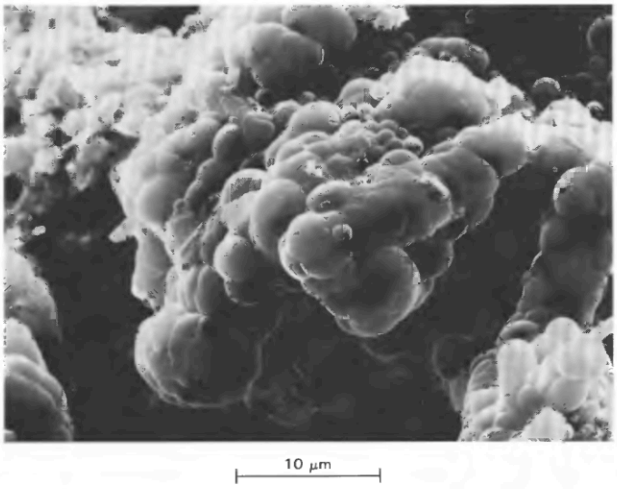


FIGURE 50.10.—Scanning electron micrograph of amorphous mass of silicon, aluminum, and potassium found within vesicles of surface sample of Kilauea Iki basalt. Lining of cavity was determined to be opal (R. Sheppard, oral commun., 1984).

Clays, zeolites, and opal are hydrated minerals and, as such, are capable, by means of surface conduction, of altering the resistivity of the basalt if the minerals exist in sufficient quantities to provide a continuous flow path for electrical current. Surface conduction occurs in certain minerals as the result of an excess ion population within the diffuse layer located on the outer bounds of the electrolyte-solid interface (Keller and Frischknecht, 1966). A thenardite coating on the pore walls of the rock undoubtedly exerts the greatest influence on the in-place resistivity. To determine the extent to which the hydrated minerals contribute to total conduction, resistivities were measured on four samples after progressive saturation with eight KCl solutions of increasing salinity. The core samples are from the 5.49- to 7.32-m depth interval but are labeled in figure 50.11 in units of feet. Figure 50.11 shows the results plotted against increasing pore-water resistivity. Samples KI-20 and KI-22 have similar resistivities when saturated with high-resistivity pore water. As the pore-water resistivity is increased, the resultant decrease in bulk resistivity of the KI-20 sample is dramatic when compared to the relatively small change in the bulk resistivity of the KI-22 sample. The difference in the character of the two resistivity curves is believed to be the result of incomplete invasion of the sequential introduction of the increasingly saline pore water because of the much lower porosity of the KI-22 sample.

The straight line drawn asymptotic to the left hand segment of the curve labeled KI-20 on figure 50.11 is a graph of rock resistivity calculated from Archie's equation using measured values of pore-water resistivity and rock porosity (Keller and Frischknecht, 1966). The departure of the rock resistivity curve from the Archie plot indicates that current flow occurs within the structure of the hydrated

minerals lining the vesicles of the rock as well as through the saturating solution. Although not shown, each sample has an equivalent Archie curve that can be drawn as straight-line projections, illustrating the relative importance of surface conduction in controlling the resistivity of each sample. Surface conduction is most apparent at the higher pore-water resistivities.

Samples KI-20 and KI-22 indicate resistivities most influenced by surface conduction as compared to the bordering samples from the 18- and 24-ft levels. Apparently the conditions for zeolite and clay development are most ideal within a very narrow horizon at the indicated depth interval of the lava crust. From the poor correlation between resistivity and porosity, however, some degree of surface conduction evidently takes place within most samples. Another reason for the lack of correlation is that the original salt content may not have been totally leached from the samples during the resaturation process, thereby causing resistivity variations as a function of differences in pore-water salinity.

## SUMMARY

The geoelectric sections interpreted from Schlumberger soundings made at the center of the lava lake are basically the same, differing only in the thickness of the conductive zone and the value of the bottom-layer resistivity. The difference in the shape of the sounding curves results from lateral resistivity variations whose complexities have not been resolved. Each sounding, however, clearly indicates the presence of a conductive zone at a depth of about 7 m with a thickness of at least 3 m. No evidence of a highly conductive zone at depth representing either the water lens or the molten lava can be seen in the sounding data.

The resistivity logs obtained in the 76-2 borehole verify the existence of a conductive layer within the 4- to 12-m depth interval. In addition, an equally conductive layer was detected below the 28-m depth in a zone overlying the very hot, but dry, layer covering the molten lava at the 45.7-m depth as determined from drilling. The 28- to 35-m depth conductive zone is believed to correspond to a gas-charged hot-water lens that increases gradually in resistivity with decreasing depth as the water vapor/liquid ratios increase. In the central zone the pore spaces of the rock are thought to be filled with wet steam containing ionized molecular particles dissolved from magmatic gases mixing with meteoric waters in the lower conductive zone. Temperatures fall slightly below 100 °C in the upper zone and, coupled with possible pressure release, conditions may be ideally suited for the formation of condensation products within the cavities and pore structure of the rock. Even in substantially undersaturated rock, a wet salt coating, such as made possible by the confirmed presence of thenardite within the lake crust, is sufficient to produce an appreciable decrease in rock resistivity.

The borehole-resistivity log was repeated in April 1977. The notable changes occurring in the 4-month intervening period are the overall decrease in resistivities for the entire penetrated section and a substantial increase in the depth to the lower conductive layer identified as a zone containing hot water. According to Hardee (1980) the established rate of cooling now in progress adds 2.11 m/yr to the thickness of the crust; however, according to the resistivity log, the crust had increased almost 4 m in only a 4-month period. Possibly the two boreholes at this site allow for an anomalously high rate of heat energy release, thereby accelerating crustal development.

It is uncertain as to why the overall resistivity of the rock surrounding the borehole has decreased. The resistivity decrease, however, is believed to be related to the upward migration of the steam phase of meteoric water following a preferential path made possible by the two adjacent drillholes. Perhaps the escaping steam has produced a conductive lining on the borehole walls as a result of alteration in the form of clays and zeolites, thereby causing a decrease in the apparent bulk resistivity measured for the surrounding rock. Based on the fact that thenardite is easily recognized within the cored section, it seems more likely that concentrations of the sodium sulfate salt have been deposited within the vesicles of the basalt in near proximity of the borehole, well in excess of that which is normally formed in the rock, thereby enhancing its conductivity.

Although a borehole may alter the electrical character of the rock in the immediate vicinity of the hole, the geoelectric layering is considered to be representative of that which persists laterally within the lake crust. The fact that the December in-hole resistivity log made at the 2-m spacing could be converted to a sounding curve very similar to that measured at a site 61 m displaced from the borehole provides evidence of the continuity of the geoelectric layering. Some variation in the resistivity of the upper conductive zone may occur as rainfall increases and a certain amount of leaching takes place. However, the salt would be expected to ultimately be redeposited in the 4- to 12-m depth interval where temperature and pressure favor concentration of salts carried upward in the liquid-vapor water system.

Rock-resistivity measurements on core obtained from the 76-2 borehole produce a substantially different pattern from that observed on the in-hole resistivity logs. This difference is not surprising considering the dissimilar environments in which each set of data was taken. However, it was hoped that a sufficient quantity of salt would be retained within the samples in order to verify introduced salt as the principal cause of the anomalously low resistivity measured in the 4- to 12-m depth interval. Apparently the high porosity of most samples allowed the salt to leach out during the resaturation process. The sample from the 6.71-m depth is an exception inasmuch as its laboratory resistivity is very nearly the same as that measured in the drillhole during December 1976 at the 1-m spacing. A scanning electron micrograph of the mineral content within a single vesicle of the 6.71-m sample shows evidence of both zeolite and clay development. Resistivity measurements on samples from the 5.49-, 6.10-, 5.71-, and 7.32-m depths, made while saturated with KCl solutions of increasing salinity, show the effects of surface conduction, apparently as a result of the alteration products lining the pore spaces and vesicles of the samples. Surface conduction is most apparent in the 6.10- and 6.71-m samples, indicating that clays and zeolites are most abundant within a very narrow horizontal interval of the lava crust.

A pictorial representation of the geoelectric layering of the Kilauea Iki lava lake to a depth including the molten lava as it existed

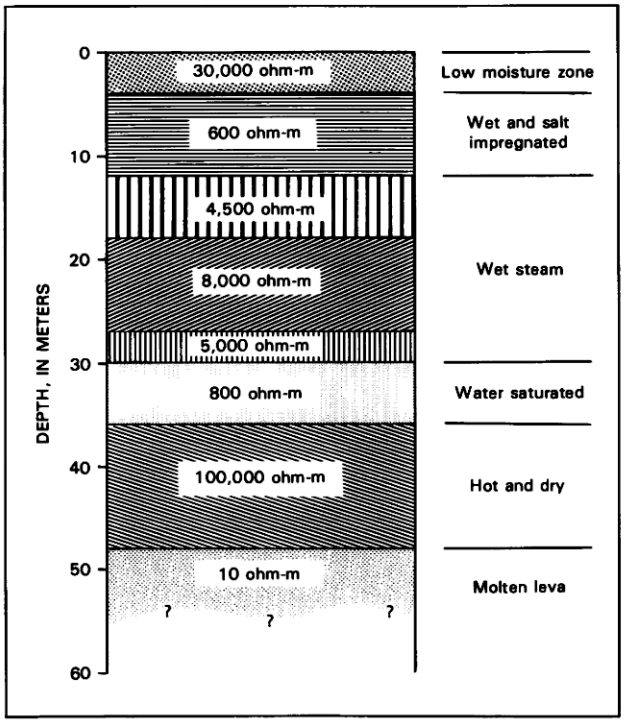


FIGURE 50.12.—Geoelectric layering of Kilauea Iki lava lake crust as determined from December 1976 borehole resistivity log made at 2-m electrode spacing.

in 1977 is shown in figure 50.12. An appreciable thickening of the crust has occurred since that time, most likely adding to the growth of the intermediate zone between the conductive crustal layers and reducing the thickness of the molten lava. From an exploration standpoint the resistivity of both conductive layers within the upper crust is sufficiently low, relative to the surrounding rock, to generate a substantial electromagnetic anomaly. However, if a 600 ohm-m resistivity value is assumed for the entire section overlying the molten lava, at very low frequencies on the order of 20 kHz, the penetrating depth of the primary signal would be more than adequate to sense on the melt. The fact that the resistivity contrast between the solidified and molten lava is at least 60:1 and typically much higher assures that the secondary fields generated by induced eddy currents stem primarily from the molten basalt layer.

## REFERENCES


Chleborad, A.F., Powers, R.S., and Farrow, R.A., 1975, A technique for measuring bulk volume of rock material: Association of Engineering Geologists Bulletin, v. 12, no. 4, p. 307–312.

Colp, J.L., and Okamura, R.T., 1978, Drilling into molten rock at Kilauea Iki: Geothermal Resources Council, Transactions, v. 2, p. 105–108.

Frischknecht, F.C., 1967, Fields about an oscillating magnetic dipole over a two-layer earth, and application to ground and airborne electromagnetic surveys: Quarterly Report of the Colorado School of Mines, v. 62, 326 p.

Hardee, H.C., 1980, Solidification in Kilauea Iki lava lake: Journal of Volcanology and Geothermal Research, v. 7, no. 3/4, p. 211–225.

Helz, R.T., Banks, N.G., Casadevall, T.J., Fiske, R.S., and Moore, R.B., 1980, A catalogue of drill core recovered from Kilauea Iki lava lake from 1967 to 1979: U.S. Geological Survey Open-File Report 80–504.

Hermance, J.F., and Colp, J.L.,. 1982, Kilauea Iki lava lake: Geophysical constraints on its present (1980) physical state: Journal of Volcanology and Geothermal Research, v. 13, p. 31–61.

Johnson, G.R., 1979a, Textural properties, *in* Hunt, G.R., Johnson, G.R., Olhoeft, G.R., Watson, D.E., and Watson, K., Initial report of the petrophysics laboratory: U.S. Geological Survey Circular 789, p. 67–74.

———1979b, Porosity and density of Kilauea Volcano basalts: U.S. Geological Survey Professional Paper 1123 A–D, p. B1–B6.

Keller, G.V., and Frischknecht, F.C., 1966, Electrical methods in geophysical prospecting: New York, Pergamon Press, 517 p.

Mumpton, F.A., and Ormsby, W.C., 1978, Morphology of zeolites in sedimentary rocks by scanning electron microscopy, *in* Sand, L.B., and Mumpton, F.A., eds., Natural zeolites, occurrences, properties, use: New York, Pergamon Press, p. 113–132.

Olhoeft, G.R., 1977, Electrical properties of water saturated basalt. Preliminary results to 506 K (233 °C): U.S. Geological Survey Open-File Report D–77–688.

Parkhomenko, E.I., 1967, Electrical properties of rocks: New York, Plenum Press, 314 p.

Richter, D.H., and Moore, J.G., 1966, Petrology of the Kilauea Iki lava lake, Hawaii: U.S. Geological Survey Professional Paper 537–B, p. B1–B26.

Smith, B.D., Zablocki, C.J., Frischknecht. F.C., and Flanigan, V.J., 1977, Summary of results from electromagnetic and galvanic soundings on Kilauea Iki lava lake, Hawaii: U.S. Geological Survey Open-File Report 77–59.

Zohdy, A.A.R., 1974, A computer program for the automatic interpretation of Schlumberger sounding curves over horizontally layered media: Springfield, Va., NTIS (National Technical Information Service) PB-232 703/AS, 25 p.

Zohdy, A.A.R., Anderson, L.A., and Muffler, L.J.P., 1973, Resistivity, self-potential, and induced polarization surveys of a vapor-dominated geothermal system: Geophysics, v. 38, no. 6, p. 1130–1144.

# UNIQUENESS OF VOLCANIC SYSTEMS

*By* Herbert R. Shaw

## ABSTRACT

**The cyclical behavior of Hawaiian volcanoes resembles patterns predicted on the basis of graphical or numerical attractor dynamics. This is because the recognizable styles of volcanic behavior are outgrowths of contrasts in positive and negative rates of magma transport that control the volumetric states of a growing volcanic edifice. Attractor patterns are likewise the resultants of some specified set of positive-negative rate balances. The distributions of volcanic states (intrusive and extrusive) in space and time constitute sets of complex patterns. Attractor dynamics simulates this complexity. The specification of how unique a given subset of a growth history may be relative to other subsets, or the whole relative to other histories (volcanoes or attractors), involves questions concerning pattern recognition. A totally unique event, pattern, or style of volcanism is one that has never happened before, hence is not recognizable. Volcanism, because it recurs, must represent a hierarchy of simultaneously unique-nonunique patterns. Even though no two growth histories, nor even any two eruptive events, are identical, there are strong resemblances between various volcanic styles that can be classified. Numerical and graphical attractor patterns add insight to such classifications. The problems of discrimination between like and unlike patterns of evolution in volcanic processes are examined on a fourfold basis involving (1) volumes and rates of magma supply and eruption during the evolution of the Hawaiian-Emperor volcanic chain, (2) factors influencing thermomechanical feedback that imply oscillatory changes in conditions of magma generation, storage, and transport, (3) theoretical examples of positive-negative feedback that illustrate methods of constructing attractor diagrams which imply oscillatory and potentially periodic behavior, and (4) comparisons with the observed patterns of Kilauea's volume and rate balances of intrusion and eruption expressed in the same form as the attractor diagrams.**

**These four aspects of volcanic description are mutually consistent. The rate history is dimensionally consistent with thermomechanical feedback processes, and feedback processes imply attractor-like dynamics in which conditions tend to repeat in the neighborhoods of characteristic patterns. Kilauea's eruptions are associated with intrusive inflation-deflation cycles that occur as closed loops in diagrams where present states are plotted against future states of magma supply and supply rates. Large earthquakes like the 1975 Kalapana event seem to occur during characteristic intervals of such loops, at states involving both high intrusive inflation and high inflation rates of both summit and rift storage systems.**

**Volcanic eruptions, intrusive events, and earthquakes are individually unique, but volcanism as a whole is a nonunique process in which repeated combinations of rate balances give rise to categorically similar patterns worldwide. Involutions and convolutions of these common pattern-generating mechanisms are the sources of unpredictable uniqueness. Prediction, therefore, involves locating one sort of cyclical loop, temporally periodic or not, within both larger and smaller contexts of recurring loops. Thus, recognition is the act of predicting several different scales of temporal and spatial action simultaneously. Given sufficiently redundant information, pattern recognition becomes automatic, as in everyday experience, rather than analytic. On this basis, specific attractor-like styles are potentially recognizable on local to global scales of volcanism. Expansion of these ideas to include chemically evolved systems (including silicic cratonic systems) implies that the criteria of pattern recognition also involve information describing chemical rates of change.**

## INTRODUCTION

The purpose of this paper is to examine the general problem of predictability in volcanic processes in terms of the sources of possible periodic and nonperiodic influences. Recurring themes are the issue of scale ratios of relevant properties and processes and the question of self-similarity. As has been my emphasis in other papers, I rely on the documentary history of Hawaiian volcanism to test ideas. In that context, there are two simple tests of self-similarity: first is the extent to which the differing time-scale patterns of day-to-day, historical, and prehistoric activity of the active volcanoes Kilauea and Mauna Loa are distinguishable in regard to the durations and amplitudes of episodic oscillations (whether periodic or nonperiodic). A second test is the degree to which these specific signatures differ from those at the larger scales of the Hawaiian Archipelago, the Hawaiian Ridge, and the Hawaiian-Emperor system as a whole. This paper considers the historical and secular Hawaiian scales quantitatively, explores physical mechanisms that influence the timing of volcanic processes, and points out some conceptual parallels between volcanic phenomena and patterns found in numerical computer experiments in nonlinear dynamics.

The term "nonlinear" is here used loosely to include systems described by equations that are of high order and (or) transcendental, sometimes with nonconstant coefficients, and which involve feedback coupling with other systems, functions, or coefficients. Such a definition is tantamount to saying that the mathematical discussion emphasizes comparisons of patterns without attempting to model sets of descriptive parameters in the form of analytic equations. Undeniably, many basic mechanisms can be described in terms of equations. They are therefore useful in predicting the kinds of mechanisms that may be aspects of a complex system. Such studies are clearly important, even in the absence of any direct applications in forecasting behavior. This is the rationale for including a section on mechanisms of rheological feedback as an important adjunct to studies of pattern recognition (see also Hardee, chapter 54).

The paper consists of five main parts: (1) the remainder of the introduction, which considers some generally relevant concepts from an interdisciplinary perspective; (2) concepts of self-similarity examined in terms of volumetric time-series data for Hawaiian volcanism; (3) rheological concepts of feedback processes; (4) concepts of stationary states expressed from the point of view of mass balance; and (5) Kilauea as a natural example of attractor patterns. Although (5) refers to concepts introduced in (4), the patterns illustrated there do not depend on any theoretical considerations; they are simply plots of the data on Kilauean rate histories recast in a form compatible with attractor patterns and concepts of autocatalytic systems (systems that contain rate-determining steps that catalyze, as well as take part in, subsequent steps in a generally cyclic process; the summit chamber of Kilauea is shown to represent such a controlling step).

I have attempted to make each section of the paper more or less self-contained, so readers who are interested only in specific aspects of the discussion can skip the other parts (if so, however, it may still be helpful to read the introductory and concluding paragraphs in each section). The rheological discussion in (3) is included as an important step in my personal recognition that there is a need for generalized methods of quantitative description of complex processes, as introduced in (4) and (5); otherwise, it can stand alone as an updated commentary on the thermal-feedback processes discussed by Shaw (1969) and as a connection between the present paper and the paper by Hardee (chapter 54).

## PREDICTION AND SELF-SIMILARITY

Concepts of predictability in natural processes are currently undergoing what eventually may be recognized as a revolutionary change or paradigm shift. Traditionally, there have been two major approaches to scientific prediction, based on (1) documentation of a clear dependence on a precisely known and inexorably persistent forcing function and (2) documentation of statistical correlations among complex sets of parameters in the absence of any dominating influence by known forcing functions. The former is often called deterministic forecasting, and the latter probabilistic or stochastic forecasting. Most discussions of natural processes involve some mixture of these methods, because even the most deterministic results involve probabilistic estimates of uncertainties, and probabilistic results usually assume that some aspects of an analysis can be expressed deterministically (for example, patterns of seismicity and ground deformation at an active volcano, even though they may be expressed in terms of probabilistic models, may be determined by known volume changes accompanying the transport of magma; in other instances deformation may be expressed in terms of constant rates of motion determined by the data of plate tectonics).

An example of deterministic forecasting is given by the problem of ocean tides, where the forcing frequency and disturbing potentials are known with high precision and accuracy relative to many other kinds of Earth processes. Examples of probabilistic predictions are given by actuarial tables and some forms of weather forecasting, where results are based on analyses of trends in average behaviors involving numerous complicated, unknown, and (or) chance events. Klein (1982) discusses problems of eruption forecasting at Kilauea with emphasis on probabilistic methods. What is called "chance" often reflects ignorance concerning relevant processes, even though at some level there may be processes that are unknowable by instrumental methods of measurement (for example, the Heisenberg uncertainty). Unless there are such sources of random noise dominating our perceptions of a process, however, the process is potentially knowable from the standpoint of predictable recognition, whether or not it can be described in any specific analytical format.

Numerical forecasting represents the implementation of a scheme to quantify the criteria of recognition, which may simply be a statement of the number of times a given "effect" follows a given "cause." For example, I might get a rash one out of every hundred times I recognize poison ivy, and occasionally I may get a rash when I wasn't aware that I was in its proximity. Obviously, if my criteria of recognition are improved (not only of the leaf itself, but of all the many and subtle ecological indications of its presence), the incidence of rash could be reduced nearly to zero, but I can never be sure I'm infallible. So, if the consequences are bad enough, I am continually motivated to improve my powers of observation.

This example is more complex than it might seem. Its complexity could be demonstrated by attempting a quantitative statistical analysis. The analysis and its forecast of effects might be expressed in terms of numerous and complicated statistical cross-correlations of the factors influencing visibility, individual prowess at classifying plants, numbers of vines per unit area, leaf density and toxicity, humidity, wind direction, allergenic predispositions, and so on, resulting in a statement of numerical probability that I will break out in a rash within varying windows of space and time, expressed in terms of calculated significances within stipulated confidence limits. At least in the case of rashes caused by poison oak, subjective experience in pattern recognition is probably the better method of forecasting risk.

Some of the above distinctions between deterministic and probabilistic methods of prediction can be matters of the relative degrees of resolution in comparing patterns of repetitive processes and their interactions, and this is the aspect with which this paper will be primarily concerned. Hence, the scale dimensions in time and space of those processes responsible for significant effects are an important concern. For example, weather becomes deterministically predictable if we are mainly concerned with seasonal behavior. On the other hand, tidal fluctuations become less and less obviously deterministic the more closely they are examined, to the extent that they may appear essentially probabilistic when they are examined at the level of microsecond variations in the length of day. (This problem is particularly instructive because it involves the interactions of numerous and subtle cyclic phenomena, as do patterns of volcanic cyclicity. In this tidal example, influences involve the dynamics of the solid Earth, oceans, atmosphere, ionosphere, magnetosphere, and solar processes responsible for the solar wind. Clearly, the problem of pattern recognition in such a case is highly interdisciplinary. This paper supports the same conclusion with regard to future advances in the recognition of volcanic patterns that may be describable in deterministic as well as in probabilistic terms.) Basically, then, we

are attempting to evaluate the quantitative relations among natural processes over many different scales of size and time.

One approach to the search for characteristic patterns that may have systematic correlations with other patterns of deterministic origins is to examine similarities in behavior at different scales of observation. If a general process, such as global ocean and atmosphere circulations or global volcanism, shows internally consistent patterns that are indistinguishable at different dimensional scales of behavior, the process is said to have elements of self-similarity. The simplest test for self-similarity is to examine any set of data (such as a map of a geometric pattern or a time series of a varying quantity like wind velocity) over domains of different size and (or) over different durations. If the unlabeled graphs are indistinguishable at different scales, the data are self-similar. In an absolute sense, all variations (such as length, velocity, and energy) would retain the same proportionalities with regard to relative amplitudes, waveforms, and periodicities. A less stringent criterion of self-similarity is that the general ranges of these parameters are statistically indistinguishable, even if there are no point-for-point correspondences of the reduced data. In the latter case the pattern is self-similar from the standpoint of having the same complexity of information content at all scales.

## THE CONCEPT OF FRACTAL GEOMETRY

The idea of self-similarity is sometimes considered to be essentially synonymous with the newly emerging research tool called fractal geometry. Self-similarity is a separate idea, and its documentation depends on the system of measurement by which it is described. A fractal structure, as described below, may or may not be self-similar, as in any other system of measurement. The way in which a fractal measurement is made, however, automatically involves consideration of those conditions that give rise to geometric self-similarity, particularly of the statistical variety, and departures from it (see Mandelbrot, 1982). It is therefore worth considering the general implications of fractal geometry, although the data described in this paper have not been formulated in these terms (the attractor diagrams described later produce structures that are fractal in character, but there I have restricted the discussion to the terminology of attractor theory).

A measure called the fractal dimension represents the relation of pattern lengths to an independent and unchanging (nonmagnified) unit of length as the pattern as a whole is progressively magnified without limit. Mandelbrot (1982, p. 25) calls such a length "the yardstick length," and I think of it as any ruler chosen as the standard of a particular measurement. Equivalently, the fractal dimension is determined by the ratio of the logarithms of the pattern lengths and standard lengths as the latter are changed. Any pattern, whether continuous or discontinuous, can be measured in such a way that it can be described in terms of fractal dimensions. Such patterns can therefore be referred to as fractal structures. If a pattern can be described by a single fractal dimension, it is said to be a self-similar fractal structure.

Evidently many familiar objects (trees, for example) are fractal structures. The idea extends directly to any ramifying patterns, including lava flows and paths of intrusive magma transport. It remains to be demonstrated whether any one or several such objects, or any subset thereof, are self-similar. The idea of a fractal dimension may seem strange because it describes forms that are not limited to the usual topological constructions based on lines, planes, and "solid" geometrical objects like cubes or spheres. That is to say, fractal structures can have fractional dimensions between those of the integers describing Euclidean topologies. Therefore, fractal geometry is very useful as a measure that allows us to expand our abilities to quantitatively classify complex structures showing dendritic, feathery, dusty, and other seemingly irregular forms. In this respect, it sometimes turns out that what is considered very irregular in the traditional geometric sense is actually quite regular and simple from the fractal perspective. This possibility applies to seemingly noisy time-series data as well as to complex spatial patterns. The study of coastline lengths, tracks of Brownian motion, stream-drainage networks, morphologies of fracture sets, and temporal patterns of economic trends are some common applications. Applications to geology are too numerous to mention and have only just begun.

Although fractal geometry is closely related to issues of self-similarity examined in this paper, my principal concern is with the patterns of magma-transport processes in time as they may relate to attractor diagrams. This implies a number of complex dynamic effects not explicitly measured (the distributions of magma transport in both space and time are not adequately sampled to permit a complete discussion of their fractal properties). The fractal concept is, however, implicit to generalizations of the temporal patterns illustrated later and, in principle, can be applied in dimensional contexts that include time and energy as the quantities of measurement.

## APPLICABILITY OF EVOLUTIONARY CONCEPTS TO PATTERNS OF VOLCANISM

A new approach to the study of periodic patterns and complexity in physical processes is arising out of computer studies of the numerical patterns produced by various kinds of recursive algorithms. Numerical recursion refers to some computational scheme (an algorithm)—whether done by hand, graphically, or by computer—wherein repetitive calculations are performed in which the current result, or state, is used to compute the next state, and so on. Except for the initial state, and a set of rules of repetitive computation (which may, for instance, be in the form of a reference equation or a set of "if this, do that" statements), the computation is allowed to guide itself indefinitely. Such programs are sometimes called computational automata, cellular automata, evolutionary strategies, or other names that emphasize the open-ended, self-guiding principle of computation. John von Neumann, famous in the development of computers, influenced terminology and modern computer studies in this area by laying out (in lectures during December 1949 at the University of Illinois) a set of logical criteria by which a machine could reproduce a copy of itself, including a copy of the instructions (these lectures were later completed and published by A.W. Burks; see von Neumann, 1966; Burks, 1970). Resem-

blances to the biological genetic code, which was being discovered almost simultaneously, were noticed later (Judson, 1979, p. 244).

An alternative approach to the development of a system that can reconstruct itself in all details is a computational scheme that is permitted to wander wherever it will without any preconceived goals, subject to a simple set of rules. Such a scheme, invented by John Conway in 1970 (see Poundstone, 1985), is known by the evocative name "Life." Popularized by Martin Gardner in *Scientific American* (his column titled "Mathematical Games"; particularly see issues during the 1970's, or Gardner, 1983), it became the subject of extensive exploration by amateur and professional researchers (and by players of computer games). An extensive description of Life behaviors is given by Poundstone (1985), and a technical note concerning cosmological implications is given by Gosper (1984). A logical extension of computer schemes that would come closer to natural systems is an algorithm that not only reconstructs itself but also invents the rules of evolution, which it subsequently copies, reconstructs, and modifies repeatedly and indefinitely. Because the study of such systems has the potential complexity of natural evolution, a simplifying approach is clearly needed.

The approach taken in this paper is to treat pattern evolution found by means of numerical algorithms in a manner similar to that used in the study of natural systems. I search for resemblances among the results of computer experiments using particular types of recursion algorithms suggested by natural processes, and I look for those properties that have some degree of universality of behavior with natural systems. The recursion strategy I use is derived from concepts of attractor theory, in which a specific governing equation involving aspects of both positive and negative feedback guides the repetitive computation (see May, 1976). Sample computations are discussed later. An important discovery of this approach is that whatever recursive algorithm is used, the resulting numerical patterns generated have some simple properties in common. Among these properties is the observation that numerical patterns (trajectories of plotted points in space and time) often reproduce according to regular geometric progressions in self-similar sets (smaller subsets have the same relative spacings of plotted points as larger subsets; see previous comments on self-similarity). Such patterns are sensitive to the rates of change of a controlling parameter in several different ways: the result may produce one or more stable fixed points (as in the approach to a set of stable thermodynamic equilibrium points, or thermometer readings in a system of steady-state heat flow), or it may produce quasi-periodic, aperiodic, and seemingly chaotic patterns. All of these complex patterns can also be shown to be fractal structures. Some of them are of the fractally self-similar type (sometimes called strange attractors), and these may grow or appear surprisingly out of highly dissipative, random-looking structures (in nature we would describe analogous macroscopic structures as representing states far from equilibrium). In this regard, they are numerical analogs of living systems and of physical devices that do in fact operate far from thermodynamic equilibrium (examples are found in such diverse phenomena as turbulent convection, socioeconomic structures, landform evolution, electronics, laser operation, and many others).

The surprise in the above studies is caused by the complexity of patterns and an inability to follow or to visualize all steps in the evolution, which often takes on an overall form bearing little resemblance to intuition or predictions. In this regard, patterns of numerical evolution have some of the characteristics of natural systems that involve so many different deterministic influences that the resulting behavior looks highly complex and even chaotic. In the numerical context, however, this chaotic behavior is found to contain regions ("windows") of structural simplicity or order. Such substructures are also associated with characteristic temporal periodicities.

Thus, periodicities are produced not only by the deterministic governing algorithm, but also by the evolving autocatalytic properties of repetitive recursion (examples are shown later). Therefore, if natural periodicities are viewed in the same way, there are sources of periodic influences that may be deterministically imposed from outside the system of interest (exogenous forcing functions), and there are others that are generated by the repetitive operation of the system itself (endogenous convergences toward restricted sets of repetitive states). In systems where there are numerous possible forcing functions, it may be difficult to distinguish endogenous from exogenous periodicities, and there may be resonances between some endogenous effects and certain of the exogenous influences (a volcanic example mentioned later is the possible correspondence of self-induced response cycles and tidal cycles). Alternatively, the dynamical context within which the system is described may be expanded so that, in effect, all periodic behavior becomes endogenous. Later I suggest how and why volcanic phenomena show dynamical parallels with patterns generated by numerical algorithms.

I have intentionally avoided using the terms "random" and "nonrandom" in describing patterns in space and (or) in time. The distinction between these terms, as commonly employed, is related to concepts of uniqueness. In my opinion, use of "random" as a descriptor of natural data is unsatisfactory on at least two counts: (1) if a pattern can be recognized, it contains information that already exists in some reproducible form (otherwise, like the unique pattern, it has never been seen before), hence it is nonrandom, and (2) the random state cannot be proven mathematically (a large literature on complexity theory, not cited, concerns the fundamental question of how to quantify departures from this undefinable limit). Statistical tests of randomness really represent comparisons with standardized, hence artificial, concepts of complexity. As such, they are useful ways to classify categories of numerical data. In the process, however, many of the potentially recognizable characteristics of a complex pattern may be lost or overlooked. I contend that natural patterns contain much more usable information than is acknowledged in the application of standard statistical tests as a measure of randomness or nonrandomness.

## ACKNOWLEDGMENTS

I thank Dan Dzurisin for discussions of the magma-supply budget at Kilauea, and for numerous constructive suggestions in the manuscript. I also thank Harry Hardee (Sandia National Laboratories) and Patrick Muffler for constructive reviews, Roy Bailey for discussion of the volcanic patterns at Long Valley, Calif., and Tom

Wright for numerous discussions over the years of Hawaiian volcanism.

## SELF-SIMILARITY IN HAWAIIAN VOLCANISM

Cumulative volumes of volcanic products versus time are shown in figure 51.1 for the Hawaiian-Emperor Chain as a whole and also for the individual volcanic loci during the chain's 74-m.y. history (data from Shaw and others, 1980, table 2). Rates of volcanism from the same data base presented in figure 51.2 include a composite volume rate, rates along loci, and moving-window averages for the overall rate. Notably, the complexity of time series representing volume rates is similar on different spatial and temporal scales; rate episodes look much the same from time to time, and the ranges of rate amplitudes are similar within short as well as within longer intervals of time. If there were no labels on the graphs, therefore, it would be hard to say what general period of time, or what duration in time, a given graph represents; this satisfies the qualitative definition of self-similarity mentioned earlier.

Statistical periodicities at about 12, 6, 3.6, 2.7, and 2 m.y. (fig. 51.3) were found by fast Fourier transform analysis of average volumes per time taken at equal 1-m.y. intervals of time. Similar, but not identical, periodicities are shown by the same sort of analyses for volumes per length along loci, instantaneous volume rates, linear propagation rates, and variations of the azimuths of loci with time, each set of data read at equal 1-m.y. intervals of time. Such periodicities represent averages of a variety of temporal and spatial variations among many different physical processes at the scale of plate tectonics affecting the Hawaiian-Emperor Chain. I do not imply, nor do I believe, that the above periodicities are coherent, and therefore no numerical estimates of statistical significance are assigned. Any statement of confidence limits would be misleading because the global dynamic context indicates that these apparent periodicities involve many different fundamental periods of shorter duration that can combine in numerous complicated ways. The fact that more localized sampling in space and time, to be discussed, also reveals signatures of similar proportional variability is evidence for the composite nature of such time series as those in figures 51.2 and 51.3. Existing data at the scales of observation illustrated are not sufficient to determine the values and possible varieties of fundamental periods.

The shortest resolvable variations in the above records are at time scales of the order $10^5$–$10^6$ years. The next level of extensive information is given by the historical record (<200 years), with variations resolvable at about yearly intervals. At yet finer scales is the three-decade record of modern geophysical measurements at the Hawaiian Volcano Observatory (HVO), with resolution of months to days. Finally, the east rift zone of Kilauea has had almost continuous activity since January 3, 1983, with episodes of fountaining at or near the vicinity of Puu Oo at intervals of about 1–9 weeks (George Ulrich, written commun., 1984).

Unfortunately, there are large jumps in time and size scales between the current local, historical, and Pacific-plate records. Detailed data on rate variations within the time scales of an individual edifice (~$10^5$–$10^6$ yr in duration) or of an individual

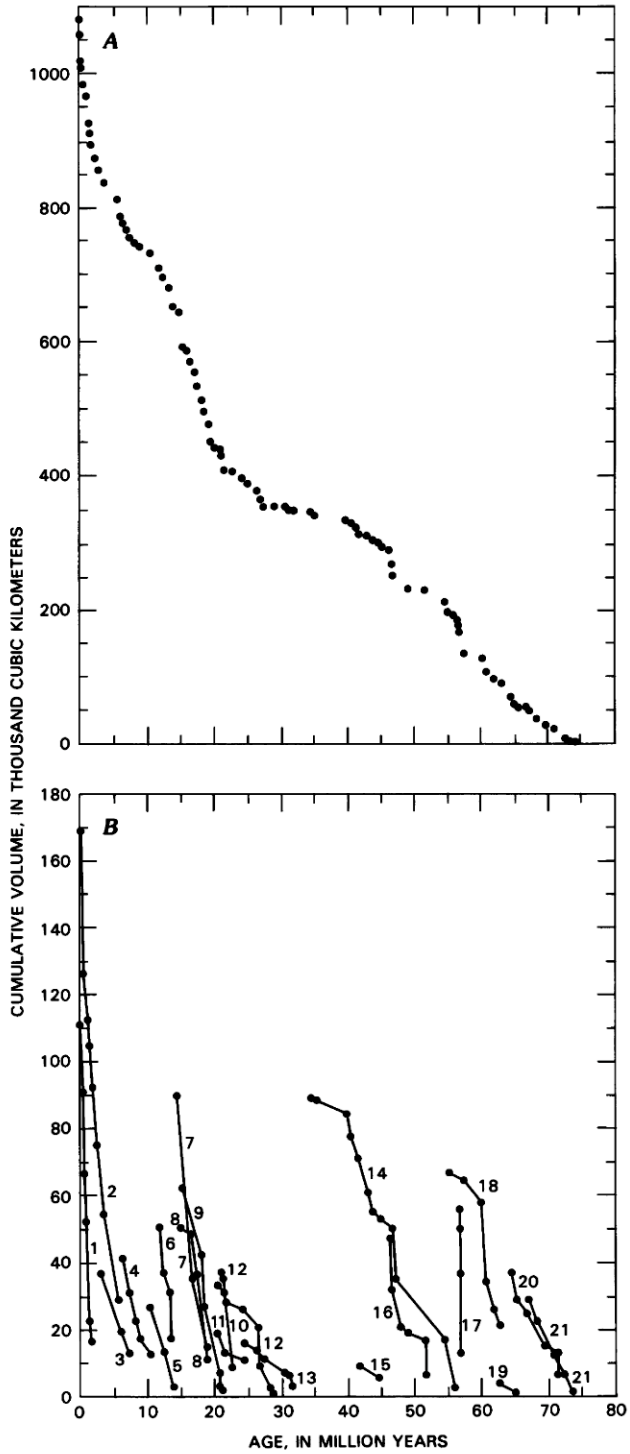


FIGURE 51.1.—Cumulative edifice volume plotted against age for Hawaiian-Emperor Chain. Data from Shaw and others (1980). *A*, Total volume for all volcanic loci. *B*, Cumulative volume for each locus; loci identified by number, see Shaw and others (1980, table 2). Loci numbers 1 and 2 are, respectively, "Kea" and "Loa" trends of Dana (1849).

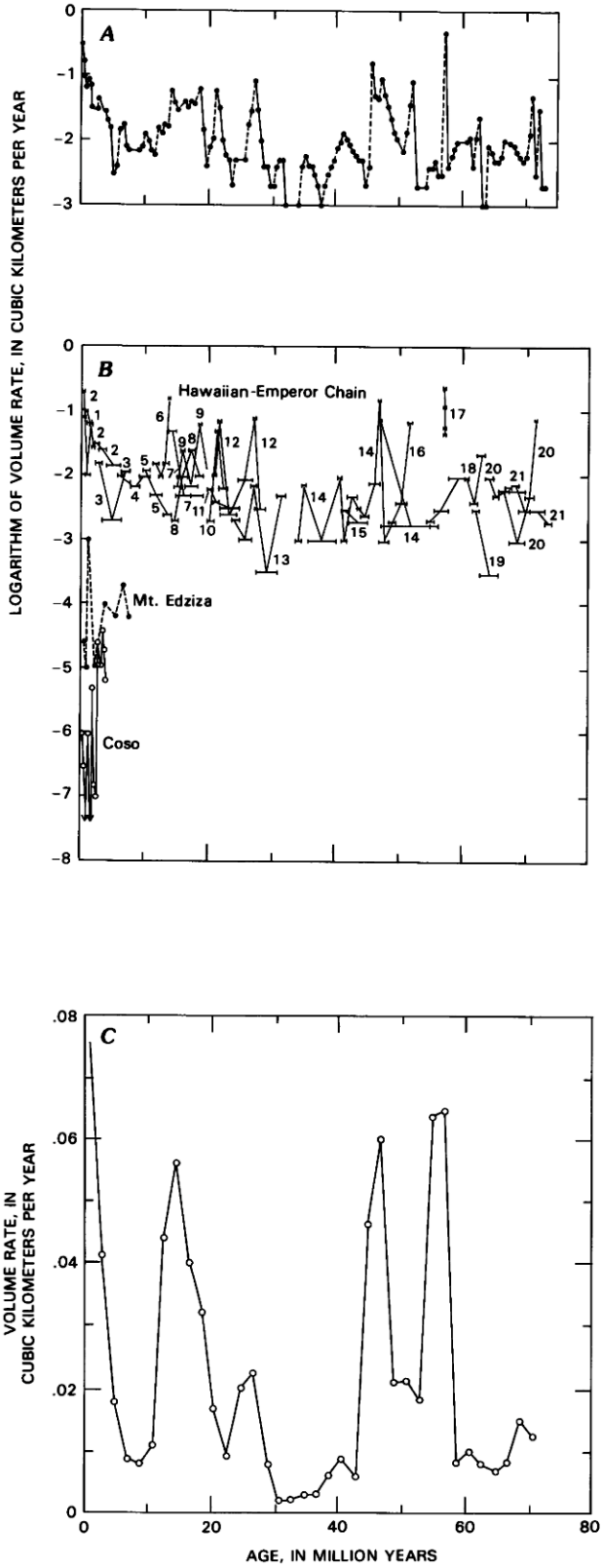


FIGURE 51.2.—Volume rates of volcanic edifice growth for Hawaiian-Emperor Chain. ***A***, Net rates for all loci. ***B***, Rate along each locus (identified by number; see Shaw and others, 1980) and comparative rates for two cratonic silicic systems; Hawaiian-Emperor data are from Shaw and others (1980, table 2); data for Mt. Edziza, British Columbia, from Souther and Hickson (1984); data for Coso Range, California, from Duffield and others (1980). ***C***, Smoothed values of net rates in *A* using a moving average window of 4 m.y. with 2-m.y. shifts. For comparisons of Hawaiian-Emperor and cratonic systems, see Shaw (1985) and discussions of relations among rate, size, and repose time in text (data for Long Valley, California, during latest 2 m.y., from Bailey, written commun., 1984, somewhat exceed rates for Mt. Edziza). For reference, average eruption rate for ash-flow systems is about $10^{-3}$ km³/yr (Smith, 1979), and their intrusive supply rate is about $10^{-2}$ km³/yr (Shaw, 1985).

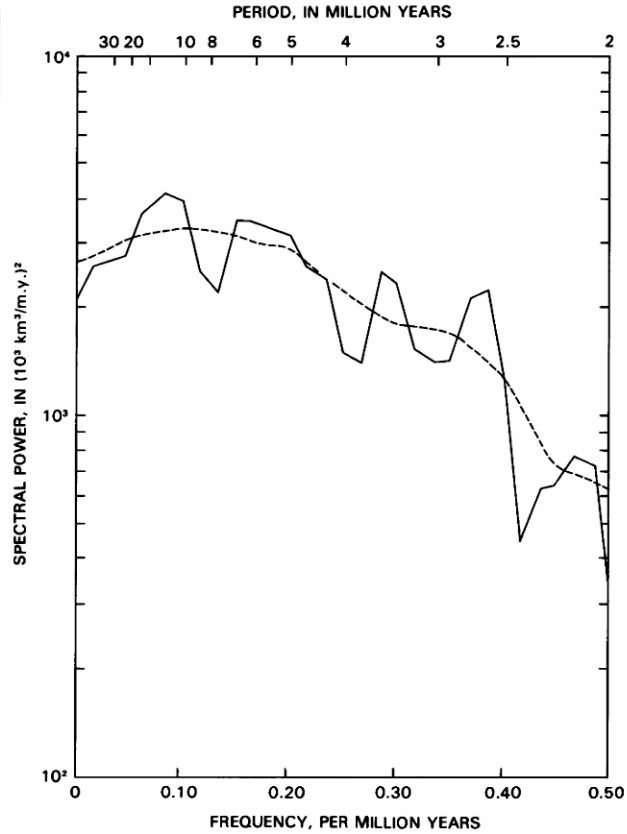


FIGURE 51.3.—Fast Fourier transform analysis of power spectrum for interpolated volumes of volcanic edifices per million years (sampling interval) for Hawaiian-Emperor Chain (Shaw and others, 1980, table 2). Dashed line gives average trend, on which are superimposed localized power maxima (power expressed as square of unit of rate samples). Analysis suggests that maxima may exist near calculated periods 2, 2.7, 3.6, 6, and 12 m.y. with generally increasing power at longer periods, but record is inadequate to demonstrate coherence. Such a trend resembles so-called $1/f$ frequency-dependent spectra that characterize many other kinds of complex time series in nature; see Verveen and Derksen (1968), van der Ziel (1970), and Voss and Clarke (1975).

island (~$10^6$ yr in duration) are unavailable because of the masking effects of younger lava in undissected edifices. Thus, we are dealing with several discontinuous and widely different scale ratios when comparisons are made between data sets describing Hawaiian volcanism in a context that includes both the historical and Pacific-plate records.

Cumulative volumes of lava extruded from Kilauea and Mauna Loa are shown in figure 51.4, together with inferred volumes of the largest deflation episodes of Kilauea (those associated with earthquake activity), as compiled by Klein (1982) from HVO records. The latest data points terminating the records represent estimates for the cumulative eruptive volumes of the 1983–85 east-rift activity and the 1984 Mauna Loa eruption. The approximate mean trends are indicated by dashed lines of slope 0.025 $km^3$/yr drawn subjectively through the data; reference slopes of 0.1 and 0.01 $km^3$/yr are shown for comparison.

The following points of interest are noted in the historical rate behavior of Kilauea and Mauna Loa, as shown in figure 51.4. (1) There is an episodic variation between rates (slopes) of about 0.01 and 0.1 $km^3$/yr for both Kilauea and Mauna Loa. (2) These rate episodes tend to be steplike at intervals of about 10–40 yr rather than scattered uniformly about the mean trend. (3) The mean extrusion rate on the 100-yr scale is near 0.025 $km^3$/yr at both volcanoes (the overall magma-supply rates will be discussed later). (4) The eruption frequency is higher for Kilauea than for Mauna Loa despite similar average rates, underscoring the typically larger eruptions and longer repose times at Mauna Loa (see Klein, 1982). (5) The steplike episodicity of rates resembles the variations in Hawaiian-Emperor rates in figure 51.1*A*, and the similarity in mean eruptive rates for Kilauea and Mauna Loa parallels the long-term similarity of slopes between loci 1 and 2 in figure 51.1*B* (the "Kea" and "Loa" lines of Dana, 1849; see Jackson and others, 1972; Jackson and Shaw, 1975). (6) The intrusive volumes, which are based on the larger deflation episodes listed by Klein (1982, table 1), have episodic trends similar to the eruptive trends, and they have about the same mean slope near 0.025 $km^3$/yr. (7) The slope of the major cumulative intrusive-volume events since about 1960 is less than the slope of eruptive volumes over that time interval, so that eruptive rates intermittently exceed rates of major intrusive volumes; hence, (8) there are decade-long delays in renewed intrusive storage compensating eruptions, and (or) there are components of magma supply that are not recorded by the major intrusive events (evidence described below suggests that the latter factor, acting somewhat like a continually leaking valve, is exceedingly important in the 100-yr scale balances of intrusive and extrusive episodes).

Volumetric variations for Kilauea between 1956 and 1983 are shown in figure 51.5 in more detail, as compiled and interpreted by Dzurisin and others (1984) in terms of magma-supply rates. I intentionally show these data in their units and format to facilitate comparisons of the two discussions and to avoid errors of transcription of the complicated history. This introduces an unavoidable difference in the convention for the orientation of the time axes compared with earlier figures, which were drawn to be compatible with the discussions of time-distance relations given by Shaw and others (1980). Their best estimate of average supply rate during this time (adjusted for vesicle porosity) is about 0.086 $km^3$/yr ($7.2\times10^6$ $m^3$/mo), with episodic deviations over an approximate order of magnitude (uppermost curve in fig. 51.5*A*). They also concluded that, during 1956–83, only 35 percent of the magma supply was extruded and 65 percent was stored in Kilauea's rift zones: 55

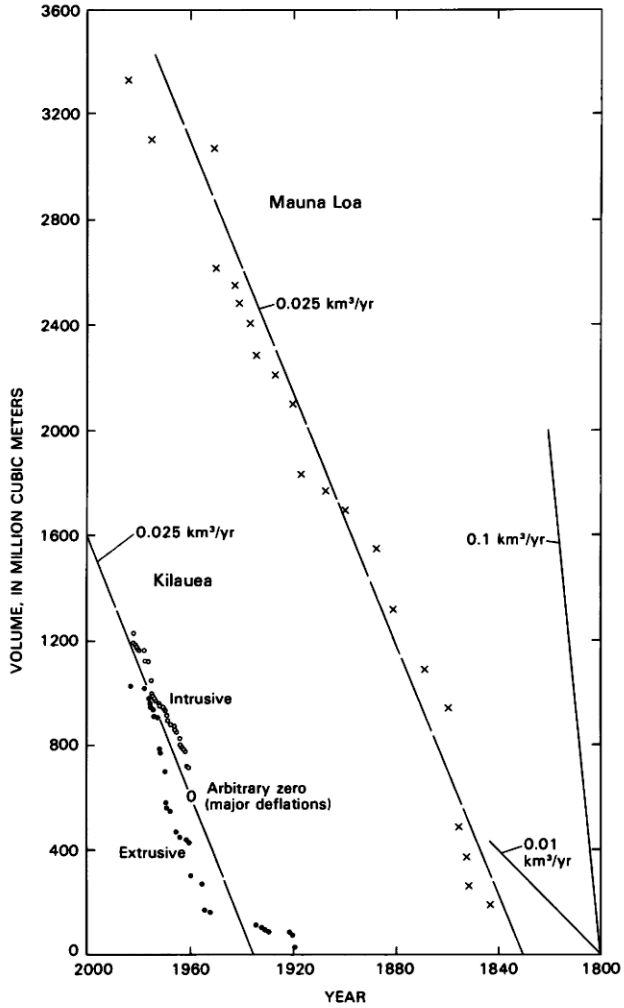


FIGURE 51.4.—Cumulative volumes of erupted lava for Kilauea and Mauna Loa and volumes of major Kilauea intrusive events from Klein (1982, tables 1 and 2); data for Kilauea also given in Dzurisin and others (1984). Intrusive volumes plotted relative to arbitrary initial point on mean trend beginning about 1960. Trend lines (dashed) with slope of 0.025 $km^3$/yr are drawn to indicate rough parallel between average Kilauea and Mauna Loa eruption rates; reference slopes (light solid lines) of 0.1 and 0.01 $km^3$/yr also shown. Although average slopes are not rigorously defined; trends suggest that both Kilauea and Mauna Loa may be expected to continue high eruptive activity (see Wadge, 1982, for comparison of steady-state volcanism in other systems). Mean supply rate for Kilauea is about three times larger than mean eruption rate (Dzurisin and others, 1984); similarity of trends suggests that same relation may also hold for Mauna Loa. Data after 1981 supplied from HVO records: Kilauea (George Ulrich, written commun., 1984); Mauna Loa (Robert Decker, written commun., 1984).

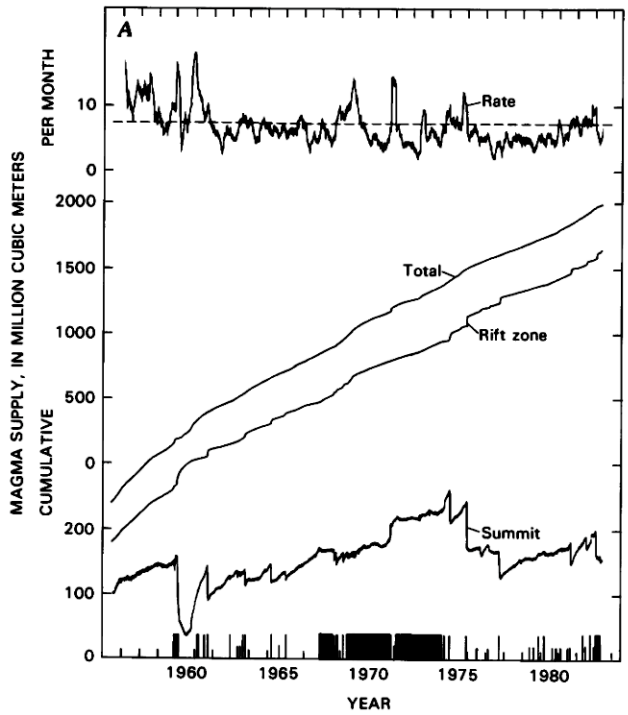


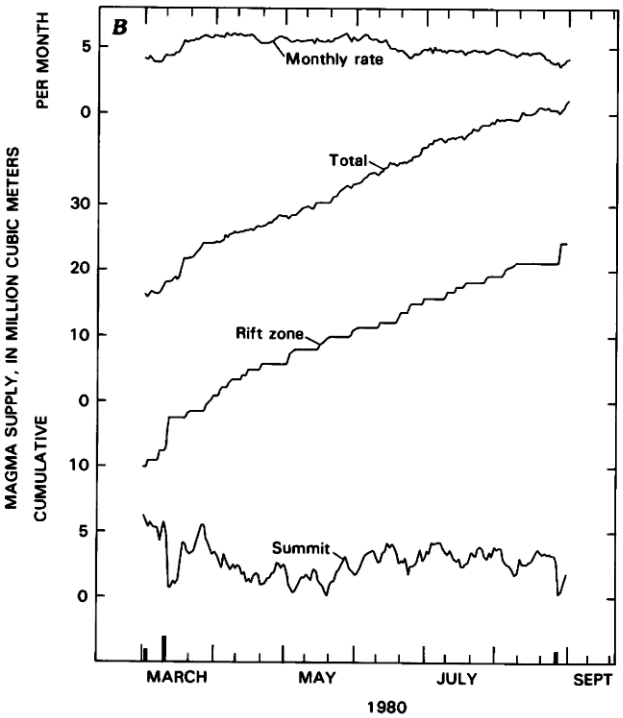


percent in the east rift zone and 10 percent in the southwest rift zone. Thus, their mean extrusive rate for the 1956–83 interval, calculated either from the above percentage of the total or directly from the erupted volume divided by the duration, is about 0.03 $km^3$/yr, in agreement with the average trends in figure 51.4 for the total historical record.

During an approximate 6-month interval of time (fig. 51.5*B*) there was a quasi-steady balance between total rates of magma supply and rates of transport between the summit and rift zones in the absence of eruptions or large intrusive episodes. The average intrusive rate during this time was about $5.0 \times 10^6$ $m^3$/mo, or 0.06 $km^3$/yr. Hence, this period seems to be representative of the 28-year intrusive average (that is, roughly two-thirds of the yearly total of 0.086 $km^3$/yr). Such increments can supply local zones of rift inflation that will become sites of eruption, or they may solidify in situ; the distinction depends on interpretations of deformation data for the east rift zone not considered here.

The fact that Kilauea's extrusive episodes indicated by the volume record of figure 51.4 also transiently equal or exceed the mean supply rate derived by Dzurisin and others (1984) reinforces inference (8) above that either intrusive or extrusive rates may transiently exceed the other for periods of a few years, although overall the average eruption rate is significantly less than the average supply rate. That is to say, the cumulative erupted volume falls far short of the cumulative intrusive volume, at least on the 100-yr scale. This means that intrusion dominates over extrusion in the growth of the volcanic edifice. The overall volumetric rate of growth of the volcanic edifice on the 100-yr scale is about 0.1 $km^3$/yr, which is about three times the average volumetric rate of lava accumulation (about 0.03 $km^3$/yr) and about equal to the long-term rates of edifice growth over the latest $10^6$ years shown by the data in figures 51.1 and 51.2 (also about 0.1 $km^3$/yr).

The cumulative volume of eruption of Kilauea since the beginning of 1983 is shown in figure 51.6. The mean slope of 0.15 $km^3$/yr ($12.7 \times 10^6$ $m^3$/mo), uncorrected for porosity (see below), is consistent with the above inferences concerning discrepancies between intrusive and extrusive rate histories. Even allowing for a reasonable porosity correction (for example, a 15-percent correction, as used by Swanson, 1972, gives 0.13 $km^3$/yr, or $10.8 \times 10^6$ $m^3$/mo), the extrusion rate since the beginning of 1983 (as of this writing, June 1985) is larger than any previous estimates of supply rates and resembles the long-term edifice growth rates for locus 1 in figures 51.1 and 51.2. (Note that the higher rates indicated in fig. 51.2*A* represent the combined growth rates of loci 1 and 2 and of any

FIGURE 51.5.—Record of magma supply for Kilauea, 1957–83 (from Dzurisin and others, 1984), based on continuous records of tilt measurements at Kilauea summit. Vertical bars at bottom of diagrams indicate specific magmatic events: short bars for intrusive events, long bars for eruptions. Estimates of magma supply are independent of measurements of erupted volumes, except as they were used in making tilt calibrations; see Dzurisin and others (1984) for discussion. ***A***, Overall record. ***B***, Record for a six-month period in 1980.

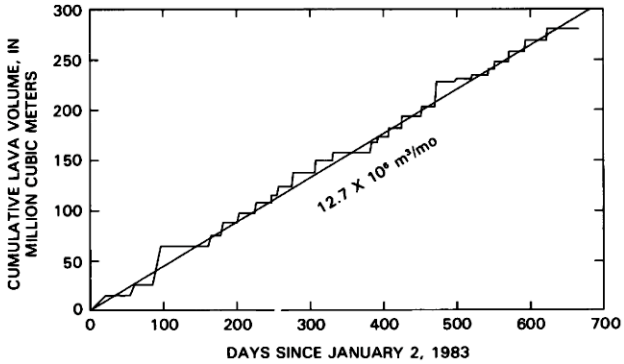


FIGURE 51.6.—Cumulative volume of erupted lava during quasi-continuous east-rift-zone activity of Kilauea (mainly at Puu Oo vent) since January 2, 1983 (George Ulrich, written commun., 1984). Average rate based on gross lava volumes not corrected for porosity. During this time, eruption and supply rates are approximately balanced and roughly equal to long-term Hawaiian-Emperor rates of edifice growth (see fig. 51.7 and discussions in text).

unrecognized loci of new activity. Locus 2, which includes the Hualalai-Mauna Loa-Loihi trend, appears to represent a slightly higher rate history than the Kohala-Mauna Kea-Kilauea trend over the past $10^5$ yr, and this could also be true at the 100-yr scale, judging from the respective slopes in fig. 51.4.)

An interpretation of quasi-steady balances between eruption and supply rates during May–December 1969 was the basis for Swanson's (1972) estimate for the Kilauea magma-supply rate. His estimate of mean extrusion rate, including porosity, was $9.9\times10^6$ $m^3$/mo, compared with $12.7\times10^6$ $m^3$/mo in figure 51.6. He adjusted this rate downward by 15 percent to account for vesicularity, giving $8.4\times10^6$ $m^3$/mo (0.10 $km^3$/yr). This compares with the comparably adjusted value of $10.8\times10^6$ $m^3$/mo in figure 51.6 mentioned above (0.13 $km^3$/yr for the 1983–85 period). Although a mantle-derived magma-supply rate of either 0.10 or 0.13 $km^3$/yr is larger than the 30-yr average of about 0.09 $km^3$/yr calculated by Dzurisin and others (1984), each of these values is consistent with the rate magnitudes of figures 51.1*B* and 51.2*B* in the latest $10^5$ yr or so (see averages in fig. 51.7). If the 30-yr supply rate is typical of longer term averages for Kilauea, then we might expect to see a return to conditions where eruption rates are again lower than intrusive storage rates within future decade-length variations when the current episode of high activity wanes. By this interpretation, the longer the currently high eruption and (or) intrusion rates continue, the longer will be the next interval of subdued activity at Kilauea on the basis of existing patterns. However, if the long-term "Kea" average at Kilauea resembles the "Loa" average (see Shaw and others, 1980), then the 30-yr as well as the 100-yr averages for Kilauean supply rates are less than the potential rates for deep-seated magma generation, and the currently high values of eruption could represent a supply rate that will continue indefinitely. It is important to distinguish between intrusion and extrusion here. Subdued activity, as judged from eruptions, does not necessarily imply a low magma-supply rate, particularly if the intrusion rate is increased relative to the 30-year average because of tectonic adjustments in the structure of the volcanic edifice.

Notice that the mean rate for the large intrusive events in figure 51.4 is approximately in balance with the average extrusive rate (similar slopes). This suggests to me that eruptive events may be associated with preferred sites and paths of storage in the rift systems relative to the more pervasive and seismically quiet intrusive leakage modes (for example, as represented by fig. 51.5*B*). That is, there is a strong correlation between seismicity, the large intrusive pulses, and eruptive pulses. These events, then, seem to be logical candidates for transport rates in which the rate-determining step may be extensional and (or) extensional-shear fracture, according to the mechanisms discussed by Shaw (1980). This, in turn, suggests the possibility that there may be different modes of stress adjustment associated with different intrusive styles, one more localized and directly keyed to eruptions and another more distributed and keyed to the overall changes in edifice growth related to distributed intrusion. The distinction is partly one of time frame, because the overall changes in longer term edifice stresses also must govern the preferred routes of magma transport, according to the principles discussed by Shaw (1980); compare later discussions of figures 51.22 and 51.23. The coseismically more passive (as contrasted with potential for major delayed seismicity) aspects of overall edifice growth must be compensated by the smaller scale intrusive events which are not accounted for in the eruptive volumes (at least on the 100-yr scale), implying that such volumes solidify in place. Otherwise, eventually a very large magma chamber should evolve with comparably larger eruptive events. However, even if the more passive intrusive fractions do not erupt, they contribute to the high-level mass accumulations that affect the larger scale and longer term edifice stresses that, in turn, contribute to the larger and more regional earthquake events, such as the magnitude 7.2 Kalapana earthquake of 1975 (Shaw, 1980). Sites of intrusive magma accumulation and solidification, then, also contribute to edifice stresses, and therefore to frequencies of eruptions and earthquakes, and possibly to catastrophic landslide events that have occurred in the past along the Hawaiian Archipelago.

The various average rates discussed above are summarized in figure 51.7, which also shows the superimposed historical variability of Kilauea and Mauna Loa eruption rates. Although the average of the historical eruption rates for the two volcanoes have been about the same (see fig. 51.4), the minimum rates for Mauna Loa hover near the overall Hawaiian-Emperor average, on the order of 0.01 $km^3$/yr, while the highest rates only occasionally reach the overall 0.3-m.y. rate of 0.18 $km^3$/yr (the value for the "Kea" locus could be lower, depending on how the total volume for Kilauea is reckoned in the 0.3-m.y. average; the 0.3-m.y. average for locus 1 excluding Kilauea is closer to the 1-m.y. average of about 0.08 $km^3$/yr). This suggests that, as with Kilauea, the average edifice growth rates for Mauna Loa (that is, rates indicated by the longer term overall volume rates) are several times the average historical eruptive rates and that large components of undetected magma storage and solidification are also taking place on a large scale in the Mauna Loa

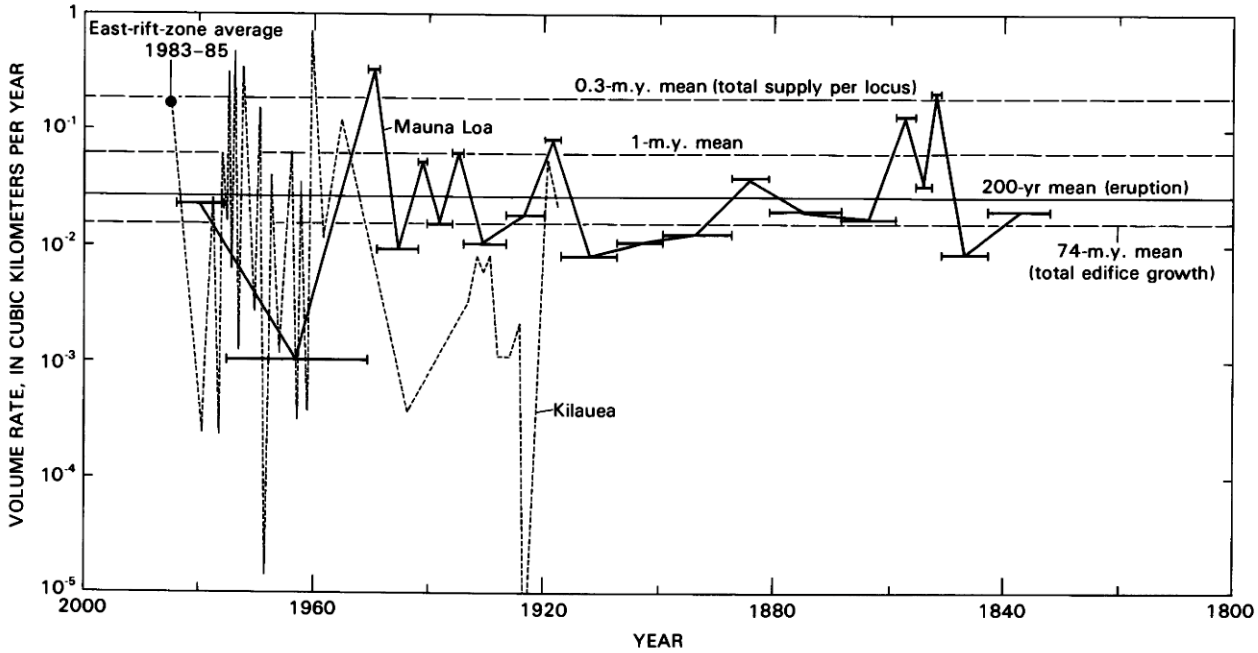


FIGURE 51.7.—Time variation of eruptive activity of Kilauea and Mauna Loa; mean trend from figure 51.4 identified as line labeled "200-yr mean." Average values over different longer term time intervals for Hawaiian-Emperor Chain given by dashed lines, based on data used for figure 51.2*B*. Note that Mauna Loa has oscillated between values near overall average and peak growth rates of Hawaiian-Emperor Chain (about 1 order of magnitude in rate), whereas Kilauea has had much higher frequency oscillations over several orders of magnitude in rate variations (see discussion of relations among rate, size, and repose time in text).

structure. This graph (fig. 51.7) also shows that, despite the same average eruption rates (see fig. 51.4), the fluctuations at Kilauea are of much higher frequencies (since about 1956 the average interval between maxima is about 2 yr for Kilauea compared with an overall average interval of about 20 yr for Mauna Loa) and oscillate over wider ranges of rate amplitudes within the time frame of Mauna Loa repose intervals.

Thus, the temporal variability of events (eruptive and intrusive) seems to relate to their size variability, because the volumes of the higher frequency Kilauea events are typically smaller than the Mauna Loa events (I infer this for the Mauna Loa intrusive events as well, based on the resemblances of extrusive trends in fig. 51.4, but they have not been documented in detail). Present knowledge of the Mauna Loa edifice structure does not allow any rigorous correlation between the periodicity and size/repose-time ratios of Kilauea and Mauna Loa. If repose times were directly proportional to size (that is, the larger the overall edifice volume, the longer the repose times between larger intrusive and extrusive events), Kilauea would be about one-tenth the volume of Mauna Loa (average repose times in fig. 51.7 for Kilauea are about one-tenth those of Mauna Loa). This has some validity on the basis that the overall edifice volume controls the potential magma-storage volume, other factors being equal (neglecting the details of edifice heights and gravitational stress distributions). But according to Shaw and others (1980, table 2) the ratio of the Kilauea to Mauna Loa edifice volume inferred from topography and bathymetry is about one-half, unless much of the volume attributed to Kilauea represents hidden fractions of the Mauna Loa edifice (this possibility is allowed by current knowledge of lava-flow stratigraphy in the region of overlap between Kilauea and Mauna Loa; T. Casadevall, oral commun., 1985; D. Dzurisin, written commun., 1985). The same discrepancy is indicated by a consideration of the relative ages of the Kilauea and Mauna Loa edifices. For example, the estimated age of Mauna Loa given by Shaw and others (1980, table 2) is about $10^5$ yr. Therefore, according to the approximate constancy of both the historical and the 0.3-m.y. average growth rates discussed above, Kilauea's age would be about half that of Mauna Loa, or 50,000 yr, if its volume is also half. So Kilauea's age would be reduced to 10,000 yr and its volume to about a tenth that of Mauna Loa if the argument based on frequency ratios were used.

Another way of looking at the proportionalities between edifice sizes and event frequencies is to consider the possibility that repose times are controlled by the ratio of summit-chamber volumes. The periodicity ratio of 10 to 1 (fig. 51.7) would then suggest that the diameter of the summit chamber of Mauna Loa is a little more than twice the diameter of the Kilauea summit chamber (compare Klein, 1982). Assuming that this ratio of chamber diameters is roughly correct, all the data favor the smaller volume and younger age limits

for Kilauea. There is then a reasonably consistent set of constant ratios of the above parameters between Kilauea and Mauna Loa, respectively, as follows: the ratio of average edifice growth rates is about 1 to 1; the ratios of overall edifice volumes and of summit magma-chamber volumes are both about 1 to 10; the ratio of ages since inception is about 1 to 10; the ratio of repose times between distinguishable eruptive and intrusive events is about 1 to 10; and the volumes per event (both intrusive and extrusive) are in the approximate ratio 1 to 10.

If this interpretation is correct, it suggests an interesting property of volcanic evolution: volcanic systems typically evolve from smaller sizes characterized by higher frequency events to larger sizes characterized by lower frequency events at the same overall average growth rate. A similar inference has been drawn by Smith (1979) and by Shaw (1985) concerning cratonic volcanic systems. In fact, the ratio between the periods of repetitive eruptive events per order of magnitude increase in eruptive volume shown by Smith (1979, fig. 12) is also a factor of 10, as was found above for the ratio of repose times between Mauna Loa and Kilauea eruptions (fig. 51.7). Shaw (1985) demonstrates that this proportionality exists for a roughly constant average rate of intrusive magma supply which, for high-level cratonic systems, is about 0.01 $km^3/yr$; Wadge (1982) discusses other implications of approximately steady-state magma supply in a variety of volcanic systems.

The above proportionalities represent a form of dynamic self-similarity that has some resemblance to fractal self-similarity. That is, if the ratios of event frequencies to average supply rates are decreasing with time as the system as a whole evolves to larger and larger sizes, then there is a great deal more "length" to the time record (more oscillations for the same measure of time) in the smaller systems relative to larger systems (see earlier discussion of fractal length relations). The fact that this tends to occur while the overall rate of magma supply is roughly constant means that the source of the higher frequency oscillations is perpetually present even if it is manifested in eruptive processes having long repose times. This means that on a graph of magma energy fluctuations (as contrasted with a record of erupted volumes of lava) a sufficiently long term record would be very dense with lines (consider the Kilauea record of figure 51.7 extended one thousand years and plotted at the same page size). The analogous map of a coastline length would be so irregular that, somewhat like an ammonite's sutures carried to the extreme, the lines would be essentially area-filling. The area-filling limit for a plane has the fractal dimensional limit of two (it can't be higher unless the map is plotted within a three-dimensional volume); less dense packing gives fractal dimensions between one and two for the coastline problem. By this kind of analogy the simplistic periodicity relation above resembles the fractal limit of two. Such ideas are very important to concepts of what constitutes "live," "dormant," and "extinct" volcanoes, and to the evaluation of possibilities for sudden changes in style (compare Shaw, 1985). The fractal viewpoint considers all such systems equally active but manifesting that activity according to differing "metabolisms" (the suggestive parallel with the relation between sizes and metabolic rates in animals would require a careful assessment of the respective energy budgets in a detail not presently possible).

There is some suggestion of antipathetic alternations of periodic phase between Kilauea and Mauna Loa eruptive activity, as shown in figure 51.7, in that over about 30-yr intervals, when one is at relatively high average rates, the other is at relatively low rates (compare 1920–50 and 1950–80). If this is true, then we might expect increasing eruptive activity at Mauna Loa and decreasing activity at Kilauea within the next few decades (see Klein, 1982). The uncertainty in the ratio of eruptive and intrusive volumes for Mauna Loa, however, precludes rigorous comparisons; we do not have information on the Mauna Loa supply budget that is comparable to the data of Dzurisin and others (1984) for Kilauea. On the time scale of figure 51.1*B*, there are also vague indications of alternating variations between adjacent loci, but during other time intervals adjacent loci appear to be essentially synchronous.

The overall Hawaiian-Emperor curve of cumulative volumes is shown in figure 51.8, scaled down by a factor of $10^6$ in both time and volume and superimposed on the 100-yr scale of Kilauea's eruptive volumes. This comparison demonstrates that a crude scale invariance exists between the growth of lava volume at Kilauea and

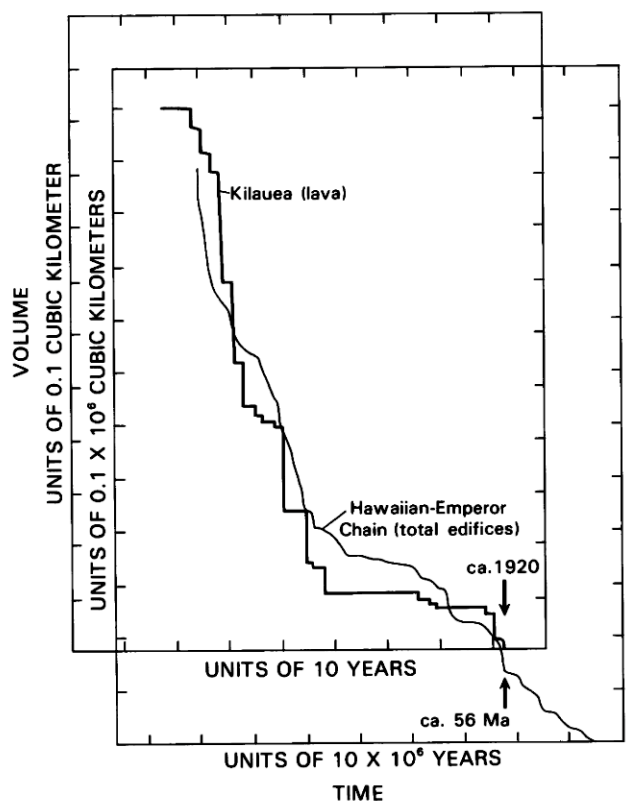


FIGURE 51.8.—Cumulative volumes of Kilauea (lava) and Hawaiian-Emperor Chain (edifice) compared. Composite graph compiled from figures 51.1*A* and 51.4 illustrating crude self-similarity of curves; scale ratio is $10^6$. Origin times for comparison taken at 1920 for Kilauea and about 56 Ma for Hawaiian-Emperor Chain (see text for discussion).

the long-term growth of overall edifice volumes for the chain as a whole. This is interesting because the long-term growth history must include the intrusive volumes within the edifice, which have grown at approximately twice the extrusive growth rate during historical activity (see fig. 51.4 and earlier discussion). Thus, the overall rate of edifice growth on the 100-yr scale (intrusive plus extrusive) should be about three times the extrusive rate if the present pattern existed at all times in the past. That is, if this ratio showed up in the comparative record of figure 51.8, the average slope of the long-term record would be about three times the slope of the cumulative curve of lava volume for Kilauea. Therefore, although the youngest part of the long-term record must at present equal the total supply of both Kilauea and Mauna Loa, the fact that the cumulative curve of edifice growth as a whole over about 56 m.y. essentially parallels the 100-yr extrusive curve suggests that Kilauea's extrusive record may faithfully mimic variations in growth rates of the Hawaiian Ridge. If so, the higher intrusive-rate variations indicated by the 30-yr record of figure 51.5*A* might suggest that similarly large relative rate variations also apply to yet deeper components of intrusive magma-supply rates. This would imply the existence of an intrusive magmatic keel at depths greater than the ocean floor with a volume approximately twice the edifice volume. An alternative is offered by the possibility of a compensating rate of loss of volume related to subsidence; Shaw (1973, p. 1523) shows that possible subsidence rates related to the moving front of volcanic loading could be equivalent to a substantial fraction of the observed magma-supply rate. The distinction is largely one concerning the depth range of intrusive storage in the volcanic edifice and its substructure (compare Shaw, 1980).

In either case, the 3-to-1 proportionality of total supply to extrusive volume, when applied to the edifice as a whole, implies an isostatically hidden root system representing the passively intruded magma in the crust-mantle section underlying the ridge system. By this circumstantial inference the average overall magma-supply rates over long times could be as high as 0.3 $km^3/yr$ beneath individual loci, also implying transient fluctuations of edifice supply rates of comparable magnitudes over short periods of time. Such an interpretation may explain the abrupt terminations of the volumetric records along loci in figure 51.1*B*; that is, the volume records sometimes end while the slopes are still very steep, suggesting that unless magmatic volumes and (or) generation rates in the asthenosphere are suddenly turned off or switched to another locus, the terminations may reflect an increased rate of deep over shallow intrusive storage.

Shaw and others (1980) argued that the total volume of magma supply from the asthenosphere could be about a factor of 2 larger than their tabulated values; the above inference suggests that they may be even larger. J.G. Moore (oral commun., 1985) has also emphasized the need to account for larger isostatically hidden volumes on the basis of studies of the chronological histories of drowned terraces along the Hawaiian Archipelago; volumetric corrections suggested by his data are similar to the above estimates. Also, Watts and others (1985) have performed new seismic profiling studies across the ridge system in the vicinity of Oahu, which suggest the possible existence of a substantial intrusive keel with volumes comparable to the above inferences.

The next section explores the relativity of rate episodes and self-similarity in terms of possible physical mechanisms of feedback, and the subsequent section discusses possibilities for self-induced periodicities. Questions concerning correlations with external forcing functions and issues of possible determinism as contrasted with self-guiding processes in volcanic evolution are considered in a closing section.

## DISSIPATIVE FEEDBACK AS A SOURCE OF PERIODIC RATE VARIATIONS

This section tries to map out in an approximate way some of the factors that influence the variability of magma production and transport. As mentioned in the introduction, the rationale for discussing dynamic and thermomechanical feedback processes is to identify the basis, and the need, for treating magmatic processes as systems of interacting and self-influencing mechanisms of transport that evolve in space and time. This section describes some of the interactions that tend to focus activity within certain ranges of a general dynamical hierarchy that is characterized by the variety of rate signatures discussed in the preceding section. In the subsequent sections, ideas of rate-controlled feedback are explored in a format that attempts to connect physical ideas of feedback with mathematical ideas of feedback according to concepts of attractors and evolutionary strategies previously outlined. The reason for such approaches is to begin to build toward concepts of cyclical magmatectonic processes that have as their natural outcome the patterns of plutonic and volcanic behavior seen in the worldwide record of igneous provinces interacting with analogous cyclical processes of plate tectonics (and possibly also more exogenous influences; see comments at end of introduction).

The approach in this section is based on the thermomechanical relations discussed in Shaw (1969); for consistency, the same sets of physical properties are used here. Since that paper was written, however, several discussions of so-called "thermal feedback," "thermal runaways," and of the effects of variable viscosity, variable rheologies, and other dissipative phenomena in magma transport have appeared in the literature. Hardee (chapter 54) cites some of these studies that are relevant to volcanism and gives calculations demonstrating applications to concepts of magma transport in Kilauea's rift systems.

The present section focuses on comparisons between characteristic times associated with dissipative heating, cooling by thermal conduction, and variations in viscous and elastic states of stress, and on their possible implications for timing of magma transport. The aim is to delineate regimes of behavior without analyzing specific events. It is found that dynamic parameters tend to group naturally around values characteristic of the time and size scales of the observed ranges of volcanic behavior. From the viewpoint of feedback systems, such dimensional correspondences exist because they are produced by a common process of evolution. The association of characteristic dike or conduit dimensions with characteristic variabilities of flow rates is not externally imposed, but occurs as a product of the tendency for balances between competitive thermal, dynamic, and mass-transport phenomena.

The balances between viscous heating and conductive cooling of basaltic magma subjected to a system of shear can be expressed in a nomogram (fig. 51.9). It applies strictly to plane shear with constant forcing, but it also semiquantitatively identifies regimes appropriate to forced flow in tabular conduits. The lines on the nomogram identify half-thicknesses representing approximately equal times for heating by viscous dissipation and cooling by conduction. Higher stresses or lower initial viscosities relative to a given line lead to positive thermal feedback (conditions of thermal "runaway") in the manner illustrated by Gruntfest (1963) and by Shaw (1969, figs. 6–9) and as discussed by Hardee (chapter 54). The lines represent the balance $t_c = t_\infty$, where $t_c$ is a characteristic time for conductive cooling and $t_\infty$ represents the time during which viscous heating would achieve very high temperatures in the absence of heat losses or decreases in shear stress. Table 51.1 summarizes the physical parameters used in the thermomechanical calculations, and

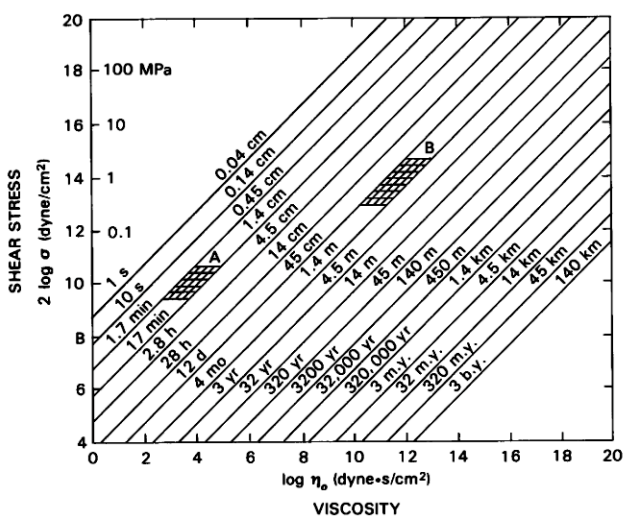


FIGURE 51.9.—Dynamic range of parameters characterizing steady-unsteady thermal-feedback transition defined in terms of equal values of adiabatic viscous-heating time ($t_\infty$) and thermal-diffusion time ($t_c$) for planar shear layers of the indicated half-thicknesses (see tables 51.1 and 51.2 for definitions); diagonal lines represent values of shear stress and initial viscosity for a given slab thickness (and time) that satisfy equality $t_c = t_\infty$, or $t_c/t_\infty = 1$. If $t_c > t_\infty$ thermomechanical instability (or "thermal runaway") is likely; this occurs for values of shear stress and viscosity above and to left of each line for a given half-thickness of shear flow. Because $t_c$ depends only on thickness, each line is associated with a characteristic time, as shown. Two areas identified by crosshatching represent examples of reasonably well delineated conditions for, respectively, (A) laboratory viscometry (Shaw, 1969) and (B) viscous conduit flow on east rift zone of Kilauea (Hardee, chapter 54; Decker, chapter 42); east-rift-zone behavior was plotted on basis of a shear-layer half-thickness on the order of 1 m and an effective shear stress on the order of $10^7$ dyne/cm² (1 MPa). This, in turn, implies an initial viscosity at onset of intermittent shear flow on the order of $10^{11}$–$10^{12}$ dyne·s/cm² ($10^{10}$–$10^{11}$ Pa·s); a compatible crystallinity might be in the neighborhood of 30–40 percent (Shaw, 1969). For additional discussions of thermal feedback, see Shaw (1969) and Hardee (chapter 54).

TABLE 51.1.—*Physical parameters used in analyses*

| Symbol | Name | Unit | Reference values |
|---|---|---|---|
| $\underline{a}$ | Temperature coefficient of viscosity | $K^{-1}$ | $1\times10^{-2}$ (1-phase)<br>$2\times10^{-1}$ (2-phase) |
| $\underline{c}$ | Heat capacity (volumetric) | $erg\cdot cm^{-3}\cdot K^{-1}$ | $3\times10^{7}$ |
| $\underline{c}^*$ | Effective $\underline{c}$ for crystal + liquid | $erg\cdot cm^{-3}\cdot K^{-1}$ | $1\times10^{8}$ |
| $\underline{G}$ | Shear modulus[1] | $dyne\cdot cm^{-2}$ | $\sim10^{11}$ |
| $\underline{k}$ | Thermal conductivity | $erg\cdot sec^{-1}\cdot cm^{-1}\cdot K^{-1}$ | $2\times10^{5}$ |
| $\underline{k}^*$ | Permeability | $cm^2$ | $10^{-11}$ (1 mdarcy) |
| $\underline{\ell}$ | Half-thickness | cm | Variable |
| $\underline{R}$ | Displacement rate | $cm\cdot sec^{-1}$ | Variable |
| $\alpha_p$ | Diffusivity of pressure ($= \underline{k}^*/c\eta^*\beta$) | $cm^2\cdot sec^{-1}$ | $2\times10^{3}$ (water)<br>$2\times10^{-2}$ (melt) |
| $\beta$ | Compressibility | $cm^2\cdot dyne^{-1}$ | $5\times10^{-11}$ |
| $\eta_0$ | Initial viscosity | $dyne\cdot sec\cdot cm^{-2}$ | Assigned (or derived from self-consistent combinations) |
| $\eta^*$ | Pore fluid viscosity | $dyne\cdot sec\cdot cm^{-2}$ | $10^{-3}$ (water)<br>$10^{2}$ (melt) |
| $\epsilon$ | Porosity[2] | fraction | 0.1 |
| $\dot{\epsilon}$ | Shear rate | $sec^{-1}$ | Variable (or assigned, or derived) |
| $\gamma$ | Thermal expansion coefficient of pore fluid | $K^{-1}$ | $\sim10^{-3}$ |
| $\mu$ | Coefficient dynamic friction | — | ~0.5 |
| $\rho$ | Density | $gm\cdot cm^{-3}$ | Variable |
| $\sigma$ | Shear stress | $dyne\cdot cm^{-2}$ | Assigned or derived |

1 The shear modulus is not a constant in mixed media such as magma and partial melt systems. In cases where variable G is possible the symbol G* is used; a range of possibilities for magma is indicated in figure 51.11.

2 The porosity $\epsilon$ appears only in the definition of $\alpha_p$ and is not to be confused with shear rate $\dot{\epsilon}$ which appears in the time-scale ratios of tables 51.2 and 51.3.

table 51.2 identifies the groups of these parameters that define the intrinsic time scales of thermomechanical processes.

The vicinities of the crosshatched areas in figure 51.9 identify conditions resembling those of laboratory viscometry (Shaw, 1969; crosshatched area *A* in fig. 51.9) and the conditions for eruptions along the east rift zone of Kilauea during the 1983–84 activity as analyzed by Hardee (chapter 54; crosshatched area *B* in fig. 51.9). Periodic instabilities are possible at recurrence times of the indicated magnitudes. That is, in the laboratory viscometer, if shear energy were continuously supplied at approximately $10^5$ dyne/cm$^2$ (10 kPa) at a mean viscosity varying from $10^3$ to $10^4$ poise (dyne·s/cm$^2$, or $10^2$–$10^3$ Pa·s), the local values of shear rates and shear stresses would oscillate with an irregular periodicity of about 1–20 min. Similarly, at about $10^7$ dyne/cm$^2$ (1 MPa), the average oscillatory periodicity would be from about one week to a few months for a system of dikelike forced shear flow (rectangular slot or pipe flow) with half-thicknesses on the order of 1 m and an initial static viscosity of $10^{11}$ or $10^{12}$ poise (1–10 GPa·s; roughly one-third crystallized). Such a range suggests one kind of contribution to characteristic recurrence times for repetitive eruptions.

Hardee (chapter 54) shows that equivalent arguments can be expressed in terms of either dissipative heating or nonlinear magma rheology (see Shaw, 1969). The important point for the present discussion is that there are intrinsic properties and dynamical conditions that promote crudely periodic phenomena and under some sets of conditions possibly even regular periodic phenomena.

The relations of figure 51.9 are summarized in figure 51.10 over a range of conditions that span most of those possible in terrestrial shear flows (excluding instantaneous fault-slip, explosive, or impact phenomena). The shaded fields represent broad classes of categorically similar behavior; for example, the shaded field labeled "order of 1 m" corresponds in an order-of-magnitude sense to the approximate monthly variations of the 1983–84 east-rift-zone activity, and the field labeled "5–50 m" corresponds to the historical variability of Kilauea and Mauna Loa with an event frequency in the range 3–300 yr. The large field at the highest viscosities and stress magnitudes spans the ranges of variable activity from the scale of individual volcanic systems (less than one to several million years) to the global scale of propagating volcanic systems and igneous cycles seen throughout Earth's history.

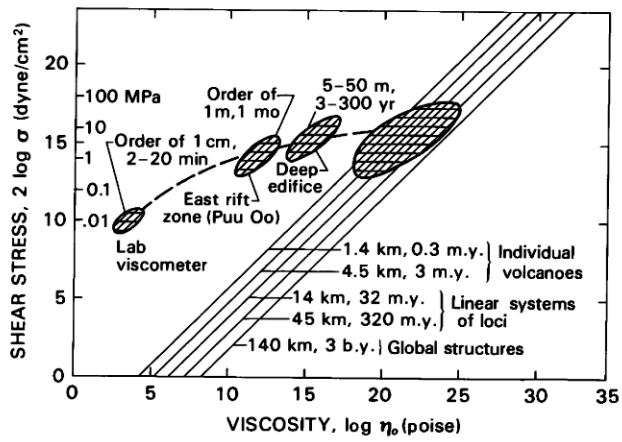


FIGURE 51.10.—Dynamical fields of anticipated oscillatory behavior for self-consistent combinations of shear-layer half-thickness and time according to thermal-feedback relations of figure 51.9 (see tables 51.1 and 51.2). Note that magmatectonic regimes showing intermittent shear-melting instabilities at local to global scales of time and size are characterized by viscosities within liquid-solid range for silicate systems (about 20 orders of magnitude) over a very narrow range of shear stresses (<3 orders of magnitude). Time-thickness pairs selected arbitrarily from geologically reasonable ranges of possibilities. Maximum half-thickness of 140 km would correspond to present-day intermittent shear instabilities in a globally averaged asthenosphere that has evolved over the age of the Earth.

The above scale relations refer only to thermal balances for a given level of continuous forcing, as reflected in the shear-stress magnitude. Therefore, an important measure of variability of the thermal balance, in addition to the time scale of heat transfer, is the time scale of loss and recovery of stress magnitude associated with a given rate of motion. Table 51.1 indicates that a scaling factor for shear stress is given by the ratio of dynamic viscosity ($\eta$) to elastic shear modulus ($G$), or equivalently by the ratio of the shear stress ($\sigma$) to the product of shear rate ($\dot{\varepsilon}$) and elastic shear modulus. This latter ratio is sometimes called the Maxwell or viscoelastic relaxation time.

The physical meaning of stress relaxation can be visualized in terms of the shear rate, which is the ratio of shear displacement per unit time ($R$, in cm/s) to the thickness of the shear layer ($2l$). Thus, the reciprocal $1/\dot{\varepsilon}$ represents the time associated with a 100-percent

TABLE 51.2.—*Time scales based on parameters of table 51.1 for thermomechanical processes*

| Process | Time scale |
|---|---|
| Thermal diffusion[1] | $t_c = \frac{c\ell^2}{k}$ |
| Stress response | $t_s = \frac{2\ell\sigma}{GR}$ or $t_s = \frac{\sigma}{G\dot{\varepsilon}} = \frac{\eta}{G}$ |
| Viscous heating[1] (thermal feedback) | $t_\infty = \frac{2c\ell}{a\sigma R}$ or $t_\infty = \frac{c}{a\sigma\dot{\varepsilon}} = \frac{c\eta_o}{a\sigma^2}$ |
| Pressure "diffusion" | $t_p = \frac{\ell^2}{\alpha_p}$ |
| Thermal pore pressure[1] (Darcian feedback) | $t_d = \frac{c\beta}{\mu\gamma\dot{\varepsilon}_o}$ or $t_d = \frac{2c\beta\ell}{\mu\gamma R_o}$ |

1 The effective heat capacity $c^*$ (and assigning $a = 2\times10^{-1}K^{-1}$) is to be used in evaluating equations for magmatic systems in which there are melting reactions (see Shaw, 1969). A subscript o refers to an assigned constant value of the variable.

shear strain, and the product $(\sigma/G)(1/\dot{\varepsilon})$ is that time normalized by the ratio of viscous to elastic stress components. The smaller the viscous shear stress relative to the elastic modulus, the shorter is the time for either the loss or recovery of stress equilibration across the sheared layer. A very high shear stress at a given displacement rate, hence a given apparent viscosity of the layer, implies a relatively longer time for a large shear disturbance on one side to permeate or diffuse across the layer. For the conditions illustrated in figures 51.9 and 51.10, however, the ratio $\sigma/G$ is less than 1, meaning that the rate of stress equilibration is rapid relative to the time required to achieve unit shear strain in viscous flow. Nevertheless, the ratio must be taken into account because of the potentially unlimited shear strains of viscous flow.

The effect of incorporating the stress response time with the thermal relations of figures 51.9 and 51.10 is illustrated in figure 51.11; the circled points represent the formal identities $t_c = t_s = t_\infty$ (for $t_\infty = t_s$, stress is constant). This means that for conditions that are both above the hachured band (symbolizing elastic responses typical of rocks) and above the 45° lines (where conductive cooling is slow relative to dissipative heating), profound melting instabilities ("runaways") can persist over times longer than those indicated on the diagram or in figures 51.9 and 51.10. For conditions of smaller elastic moduli that may apply to magma (media with a liquid fraction, above an unspecified minimum threshold, have greater compliance in shear), the stress level of this regime would be lowered in proportion to the scale of the effective modulus, $G^\star$, as shown at the right in figure 51.11 (see footnote 1, table 51.1); values of $G^\star$ vary with melt fraction, so numerical values are equivocal. Within regions below the hachured band but still above the 45° lines, thermal instabilities can begin at the indicated stress levels (for example, above about $10^7$ dyne/cm$^2$ or 1 MPa for meter-scale shear couples), but they do not persist over the indicated timespans. That is, within these regions the melting instabilities are intermittent and oscillate according to the stress-recovery times; these relations are generally in accord with stress magnitudes associated with the variations described earlier.

Although the labeling of fluid and solid states on such a diagram is relative and simplistic, oscillatory fluid phenomena, possibly such as cavitating flow and tremor, are associated with low apparent viscosities, whereas shear melting of nearly solid aggregates will occur at the highest viscosities; these observations are also consistent with the great span of time scales of the respective processes (the order of a second or less in cavitating flows, the age of the Earth in mantle-wide shear flows).

The above approach to dynamic regimes can be generalized even more in terms of conditions describing fluid migration, either by percolation as a pore fluid or by percolation as injection pulses associated with extensional fracture events (Lachenbruch, 1980; Shaw, 1980). The analysis parallels that of the thermomechanical balances discussed in Shaw (1969), except that fluid pressure, effective stresses (Shaw, 1980), and fluid mobility are coupled with the thermal responses. An analysis for water as the pore fluid is given in more detail by Lachenbruch (1980) in connection with interpretations of heat-flow and stress variations associated with fault motions. A synopsis of analogous effects is repeated here in terms of ratios of response times, using an approach similar to that of figures 51.9–51.11.

Table 51.3 lists the 10 possible ratios of the time scales given in table 51.2 and gives for each of these ratios (where possible) the relation between the logarithm of shear stress ($\sigma$) and the logarithm of the product $Rl$ of displacement rate ($R$) times half-thickness ($l$) of the shear layer. Equations are written for the condition $t_i/t_j = 1$ ($t_i = t_j$). The quantity $Rl$ is a convenient way to represent deformation rate in viscous systems because it explicitly identifies the roles of both the size of the shear layer and the displacement speed. The coined term "diffusivity of action" is used here for $Rl$ because the product of displacement rate and thickness has the dimensions centimeters squared per second, as in thermal, chemical, or momentum diffusivities (its interpretation, of course, depends on the context considered, for example, faulting or magmatic flow, and the chosen

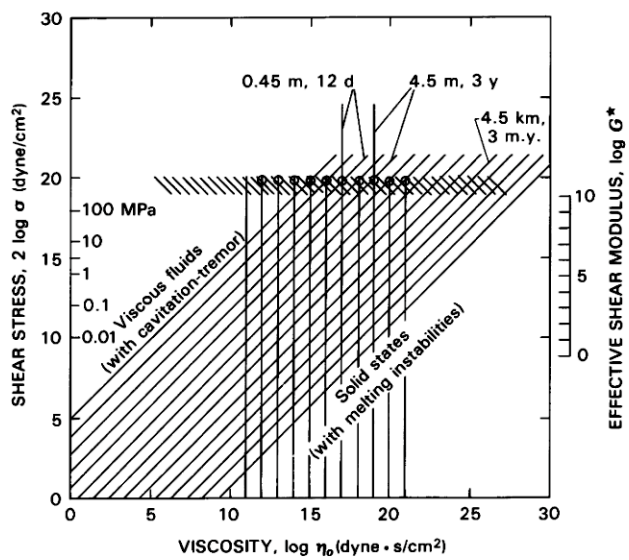


FIGURE 51.11.—Nomogram constructed as in figure 51.9, including stress response times (see table 51.2). Vertical lines represent values of $t_s = \eta/G$; circles represent locus of identities $t_c = t_\infty = t_s$. Also, $t_s > t_\infty$ only above horizontal interval (hachured) for value of shear modulus, $G$, in table 51.1. Hence, stress responses (both relaxation and recovery) of melt-free rocks are rapid relative to thermal-feedback responses at stress levels appropriate to all conditions shown in figures 51.9 and 51.10. Consequently, intermittent thermal instabilities automatically imply, and (or) are implied by, oscillating stress regimes, unless shear modulus is decreased significantly in the molten state (see table 51.1, footnote 1, and text for explanation of effective shear modulus $G^\star$). When that happens, upper stress limit of combined intermittent stress and thermal-feedback regime is lowered and is indicated by scale of log $G^\star$ at right; consequently, thermal instabilities related to melting may occur at effectively constant shear stress under same conditions that permitted intermittent instabilities in solid state (see Shaw, 1969). However, conditions above horizontal limits $t_s = t_\infty$ are artificial in that thermal feedback at constant stress is necessarily transient; thermal-feedback instabilities inevitably alter material states, so that intermittent stress regimes eventually result. Shear melting events may nevertheless be of large magnitude when $t_s > t_\infty$.

TABLE 51.3.—*Reference equations based on possible equalities of pairs of time scales in table 51.2 using values of constants in table 51.1*

[There are 10 possible combinations of the time scales defined in table 51.2; see text for discussion]

| Time-scale ratios | Reference equations[1] | |
|---|---|---|
| | Nonmagmatic (solid + aqueous fluid) | Magmatic (melt + solid) |
| 1. $t_c/t_s$ | $\log \sigma = 12.9 + \log(R\ell)$ | $\log \sigma = 13.4 + \log(R\ell)$ |
| 2. $t_c/t_\infty$ | $\log \sigma = 7.6 - \log(R\ell)$ | $\log \sigma = 6.3 - \log(R\ell)$ |
| 3. $t_c/t_p$ | $3\times10^5$ (constant; $t_c \neq t_p$) | 10 (constant; $t_c \neq t_p$) |
| 4. $t_c/t_d$ | $\log (R_o\ell) = -1.4$ (for all $\sigma$) | $\log (R_o\ell) = -1.4$ (for all $\sigma$) |
| 5. $t_s/t_\infty$ | $\log \sigma = 10.2$ (for all $R\ell$) | $\log \sigma = 9.8$ (for all $R\ell$) |
| 6. $t_s/t_p$ | $\log \sigma = 7.4 + \log(R\ell)$ | $\log \sigma = 12.4 + \log(R\ell)$ |
| 7. $t_s/t_d$ | $\log \sigma = 11.5$ (for all $R\ell$) | $\log \sigma = 12.0$ (for all $R\ell$) |
| 8. $t_\infty/t_p$ | $\log \sigma = 13.1 - \log(R\ell)$ | $\log \sigma = 7.3 - \log(R\ell)$ |
| 9. $t_\infty/t_d$ | $\log \sigma = 9.0$ (for all $R\ell$) | $\log \sigma = 7.7$ (for all $R\ell$) |
| 10. $t_p/t_d$ | $\log (R_o\ell) = 3.5$ (for all $\sigma$) | $\log (R_o\ell) = -0.4$ (for all $\sigma$) |

[1] Equations are based on solving for either $\log \sigma$ or $\log (R\ell)$ under conditions where $t_i = t_j$ is possible (that is, when $t_i/t_j = 1$); this is not possible for $t_c/t_p$ with physical constants of table 51.1.

values of physical parameters in table 51.1, or values considered appropriate to other specific applications).

Among the 10 possible ratios, $t_c/t_p$ is unique in being a constant for the parameters of table 51.1; it represents the comparative decay of a thermal pulse by conduction relative to that of a pressure pulse by pore-fluid flow, neglecting the heat-transfer effect of the flow. In this respect, then, it is a measure of the ease of permeation of fluids away from a thermal disturbance; hence, it also indicates conditions under which advective heat transfer should be important. Clearly, pressure decay is very fast for aqueous pore fluids relative to thermal conduction, but for silicate melt the two are more comparable (depending on melt viscosity, latent heat, and other factors).

Except for $t_c/t_p$, all the other ratios in table 51.3 involve one or both of the quantities $\log \sigma$ and $\log (Rl)$. The equations that involve both terms show that, logarithmically, they are directly proportional, so that their graphs are straight lines with slopes of either $+1$ or $-1$. Equations for which shear stress ($\sigma$) and (or) diffusivity of action ($Rl$) are constants plot as straight lines parallel to either an axis representing $\log \sigma$ or one representing $\log (Rl)$.

Numerical values of these independent variables calculated from the equations of table 51.2, based on the reference parameters of table 51.1, are plotted in figures 51.12 and 51.13. These figures attempt to show how instabilities characterized by the range of time scales in figures 51.9–51.11 can also be expressed as functions of stress and displacement histories. This is not the place to attempt a complete description of the ramifications of such diagrams; their implications address aspects of rock deformation in a manner somewhat similar to the use of thermodynamic-facies concepts in metamorphic petrology. Instead, I focus on the regions of likely periodic variations important to volcanic phenomena, following the approach already discussed in reference to simplified thermal feedback.

The dots in figure 51.12 and the open circles in figure 51.13 mark the invariant intersections of common sets of equations in table 51.3, as listed in figure 51.12. The heavy lines in these figures represent functions based on the variables $t_c$, $t_s$, and $t_\infty$, as in figure 51.11, except for the different choices of independent coordinates. Invariant points $c$ (figure 51.12) and $c'$ (figure 51.13) have the same implications as the circled points in figure 51.11. The hachured triangular regions to the right of $c$ and $c'$ represent conditions of oscillating instabilities limited by the stress-response times, as illustrated in figure 51.11. Figure 51.12 shows the response of a melt-free solid in which the instabilities would take the form of shear fractures rather than melting. If shear melting is allowed, however, the difference between $c$ and $c'$ in figure 51.13 indicates the likely effects of differences in physical properties arising from the inclusion of latent heat and different temperature dependence of viscous activation (see Shaw, 1969).

Points $d$ (fig. 51.12) and $d'$ (fig. 51.13) and the respective regions to their right are related to coupled effects of shear heating, consequent fluid-pressure responses, and tendencies for flow accord-

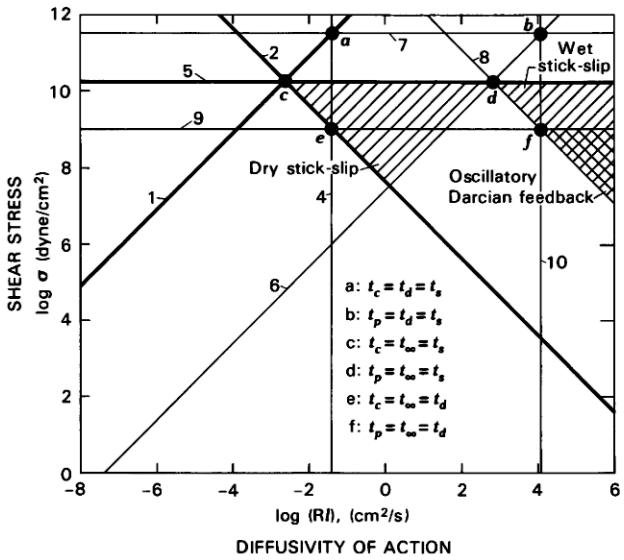


FIGURE 51.12.—All possible dynamic regimes involving thermal feedback, stress oscillations, and aqueous pore-fluid transport according to ratios in table 51.3 based on combining thermomechanical analyses from Shaw (1969) and Lachenbruch (1980). Nodal points labeled *a–f* represent possible invariant identities for variables shear stress, $\sigma$, and what I call "diffusivity of action," $Rl$, where $R$ represents displacement rate of one side of a shear layer relative to other, and $l$ is half-thickness normal to layer. Heavy lines indicate fields delineated by thermal feedback in absence of either melting or pore-fluid transport. Acute angle defined by points *d*, c, and *e* represents conditions where thermal feedback results in endothermic processes of fracture rather than pervasive melting; because such fracture would be activated intermittently, it is labeled the region of "dry stick-slip." Analogous region involving pore-fluid weakening to right of line 8, below line 5, and above line 9 is labeled "wet stick-slip"; it occurs because thermal response is faster than both pore-pressure decay and time for weakening due to pore-pressure response to heating (termed "Darcian feedback"). Below line 9 and to right of line 8, however, Darcian response is faster than both dry thermal response and decay of pore-fluid pressure, hence that region is labeled "oscillatory Darcian feedback"; see Lachenbruch (1980) for a detailed analysis of Darcian regimes appropriate to displacements within fault zones.

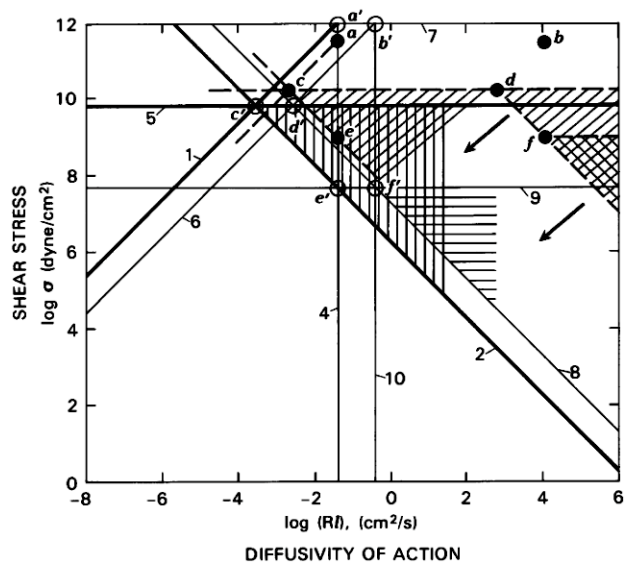


FIGURE 51.13.—Dynamic regimes as shown in figure 51.12 but also including conditions of transport where silicate melt is pore fluid. Dashed lines, unprimed letters, and related shading from figure 51.12; arrows indicate direction in which Darcian regimes shifted when melt is pore fluid. Analogous invariant intersections reflecting properties of solid-melt interactions are indicated by primes (see parameters in table 51.1). In general, fields described in figure 51.12 are telescoped together when melt is pore fluid, and oscillatory Darcian feedback occurs at much lower shear stresses and displacement rates.

ing to Darcy's law in response to the pressure gradient (for details, see Lachenbruch, 1980). Points *f* (fig. 51.12) and *f'* (fig. 51.13) demark the limits of regimes which I will refer to as conditions of "Darcian feedback." This phrase is used in the same context as thermal feedback, in the sense that a tendency for runaway (and eventual changes of state or decreases in effective stress) is countered by a transport rate. The components of negative feedback can be characterized by a thermally coupled pressure diffusivity in the case of Darcian feedback, and a simple thermal diffusivity (which may be an effective value that includes mass transport) in the case of thermal feedback.

In the above terms, the time scale $t_d$ in tables 51.2 and 51.3 represents the time for reduction of frictional resistance owing to Darcian feedback. As such, it represents the relaxation or recovery times for effective stress, hence it also represents conditions of shear failure according to some failure law. A constant value of the coefficient of friction, $\mu$ (see table 51.1), is equivalent to a Coulomb failure law, meaning that there is a constant angle of the failure envelope on a Mohr diagram (see Shaw, 1980, figs. 6 and 7). This point is raised because magmatic extensional fracture, as discussed by Shaw (1980), employs a modified Griffith-Coulomb failure law, implying variable and potentially large values of the ratio of frictional resistance to effective normal stresses, and also implying nonconstant values of increasing dynamic friction ($\mu$) as conditions approach those for pure extensional failure. This point will be reiterated in discussing the shifts of points *c*, *d*, and *f* to points *c'*, *d'*, and *f'* from the conditions for nonmagmatic regimes (fig. 51.12) to those representing magmatic regimes (fig. 51.13).

I attempt to focus the meaning of "dynamic regime" by discussing only the regions in the vicinities of points *c*, *d*, and *f*, or *c'*, *d'*, and *f'* in figures 51.12 and 51.13. In figure 51.12, the region near *c* to the right of line 2 and below line 5 has already been mentioned as identifying oscillatory, thermally coupled shear-failure events (there is no involvement of pore fluid as part of the onset conditions, although melt or pseudotachylite could be a product of failure; if so, the validity of the regime boundaries is modified at the instant of failure). Repetitive failures could be described as episodes of reduced and accelerated displacement rates resembling laboratory

stick-slip. To the right of $d$, below line 5 and above lines 8 and 9 (fig. 51.12), a similar situation occurs, in the sense that the thermal transient ($t_\infty$) is short relative to both the loss of induced pressure ($t_p$) and the Darcian response time ($t_d$), meaning that analogous shear failures would occur in wet rocks for conditions of sufficiently low permeability, high stress (greater than about $10^9$ dyne/cm$^2$ or 100 MPa), and high enough displacement rates (for example, about 1 cm/s for a shear zone 1 m in half-thickness). This regime is labeled "wet stick-slip" in figure 51.12. In figure 51.13, an analogous region to the right of $d'$ is implied with magma as the pore fluid; in this case, the magma-wetted stick-slip regime is nearly superimposed on the dry stick-slip regime, because of the changes in physical properties appropriate to magmatic environments.

Persistence of yet higher displacement rates, however, eventually creates a condition where the pressure-response time is longer than the Darcian response time. At that point, $f$, oscillatory Darcian feedback becomes a possibility; that is, to the right of line 10, but above line 8 and below line 9. This represents the region where Darcian thermal coupling is faster than the loss of induced pressure by flow and also where the Darcian coupling is faster than simple shear heating in the absence of pore fluids. Thus, this region is labeled "oscillatory Darcian feedback" (see labeled area in fig. 51.12; in fig. 51.13 the same area is shown, and an arrow indicates the direction in which this region of oscillatory Darcian feedback is shifted when magma is the pore fluid).

The interpretation of points $c'$, $d'$, and $f'$ in figure 51.13 is parallel to that of $c$, $d$, and $f$ with some qualifications. In particular, if a curved failure envelope, such as that implied by a modified Griffith-Coulomb failure law (Shaw, 1960, fig. 7) applies, the constancy of dynamic friction, $\mu$, does not hold. In the limit of pure extensional failure, the ratio $t_p/t_d$ defining line 10 becomes indeterminate because of this fact; also, the effective permeability is governed by transport related to extensional fracture propagation. The combined effect, however, tends to reduce both the pressure-response time (related to greater ease of flow along dikelike fractures rather than through tortuous pore space) and the modified Darcian response time (because of the increasing dynamic friction associated with an increasing failure angle implied by a Griffith envelope). As a consequence of these offsetting tendencies, the more channelized flow of modified oscillatory Darcian feedback may not differ greatly from that implied by flow in porous media.

The general effect for pore fluids with magmatic properties appears to be to telescope the respective oscillatory fields of figure 51.12 to conditions near point $f'$ in figure 51.13; that is, ordinary thermal feedback in magmatic systems implies the existence of a melt fraction. Hence, the general effect of increased transport brings the oscillatory field to lower stresses and higher diffusivities of action (higher displacement rates for the same values of half-thickness).

Values of shear stress implied by the field limited by point $f'$ and lines 8 and 9 in figure 51.13 are within the range $10^6$–$10^8$ dyne/cm$^2$ (0.1–10 MPa), which is reasonable based on other considerations for natural regimes showing oscillatory behavior (see Decker, chapter 42; Hardee, chapter 54; Shaw, 1980). If we take values of half-thickness ranging from the order of 1 m to 100 km, as in figure 51.10, values of compatible displacement rates, $R$, can be estimated corresponding to log $(Rl)\approx 0$ in figure 51.13. These are, respectively, $10^{-2}$ cm/s (~3 km/yr) and $10^{-7}$ cm/s (3 cm/yr). The former would be associated with mean effective propagation rates of dikelike injections through the lithosphere, and the latter with rates of mantle flow (the actual propagation rates for Hawaiian-Emperor loci, however, vary as much as an order of magnitude relative to mean plate velocity, implying that the local half-thickness of associated asthenospheric flow may vary between about 10 and 100 km; see Shaw, 1973, and Shaw and others, 1980).

An analysis of magma-driven propagation of cracks by Spence and Turcotte (1985) gives a fracture-propagation velocity of 0.5 m/s for a half-thickness of 0.25 m and a fluid pressure of $6.3\times10^8$ dyne/cm$^2$ (63 MPa); this corresponds to a value of log $(Rl)\approx 3$. Although their analysis does not refer to shear-induced extensional fracture, the energy-rate balances resemble those in the field of modified oscillatory Darcian feedback. The examples plotted in figure 51.9 also plot in this general vicinity when they are converted to the independent variables of figure 51.13.

The main conclusion relevant to this paper from the considerations of dynamical time scaling is that repetitive feedback processes involving melting and magma transport as identified in figures 51.12 and 51.13 are likely to occur over a range of self-determined periodicities indicated by the estimates of time in figure 51.10. Feedback interactions of complex processes tend to be self-focusing in that the likely effects converge toward limited ranges of dynamical parameters. Over a long enough time, therefore, the temporal variability and size scales of geometric structures associated with such systems of interactive feedback are not simply imposed by external constraints on geometric states and forcing functions, as in some laboratory experiments, but become artifacts of the dynamical history. Thus, temporal, spatial, and dynamical variability interact repetitively over all the magnitude scales considered. The crude and repetitive self-similarity shown by the volcanic record as portrayed in figures 51.1–51.8 evidently records elements of dynamical similarity that have evolved according to feedback processes. Many different mechanisms exist at each scale of the general feedback process, and much can be learned through inverse reasoning about these mechanisms (and the need for more information concerning them) by considering their conceptual interactions (for example, the mechanisms and properties of magmatic percolation can be viewed in a manner parallel to the hydraulics of pore fluids as described by Lachenbruch, 1980). This generalization does not preclude interactions with external forcing functions, such as extraterrestrial energy influences mentioned later. In the next section I consider a logistical approach to the description of self-induced periodicity.

## STATIONARY STATES AND ENDOGENOUS PERIODICITIES OF ATTRACTION IN THEIR NEIGHBORHOOD

This section, like the previous one, contributes to the idea that there are logical reasons for magmatic systems, and volcanic systems in particular, to be considered as feedback systems subject to the general mathematical principles of recursion outlined in the introduction. In the preceding section, it was found that the repetition of

magmatic processes acts to modify both the dynamic and geometric conditions of localized behavior in a way that leads to focusing of those conditions within limited and characteristic regimes that form a part of a hierarchy of such regimes from the local to global scales. In the present section, the feedback process is viewed as a recursion of characteristic quantities in a way that generates repetitive structures in space and time. The quantities discussed in this section are totally hypothetical, but they can be viewed as sets of data representing imaginary intrusive and (or) volcanic magmatic cycles described in terms of relations between mass, volume, and their rates of change. The purpose is to provide a description in which ideas of dynamic feedback and what may be called "logistical" feedback lead into considerations of the numerical properties of recursion that are treated elsewhere by the theory of attractors (with their implicit relations to fractal self-similarity mentioned earlier).

Whereas the previous section considered conditions consistent with feedback among physical mechanisms, this section considers aspects of logistical processes that are consequences of repetitions involving combinations of net positive-negative feedback rates. That is to say, this section examines the logistics of what I call folded feedback. First, I give working definitions of what I mean by "logistic" and "folded," because both terms are used in a variety of contexts in different disciplines. The usage here is descriptive and does not necessarily correspond to formal definitions found in the literature of economics, biology, mathematics, topology (and catastrophe theory), physics, or other fields.

I use "logistic" to indicate that the method of analysis originates in the logic of numerical sequences (as in the construction of a computer algorithm) and also in the sense of military logistics, where the responsibility entails management of processes affecting aspects of material distributions which support the strategy of operation with or without any absolute knowledge concerning the plan of action. In other words, logistical analysis is the mathematically logical manipulation of quantities, whether they are real or abstract. The quantities can be anything measurable in the sense that there is some kind of unit that can be counted. Depending on the quantities manipulated, the logistical approach in this way resembles the logic of chemical mass balances, physical kinematics, dynamics, and number theory.

"Folded feedback" is shorthand for the net effects of feedback (and feedforward) processes operating in a complex system that contains aspects of both positive (accelerative or regenerative) and negative (decelerative or degenerative) responses. These are the composite processes of the previous section considered to be characteristic of a complex system even in the absence of an ability to dissect, analyze, and describe all mechanisms. The term "feedforward" is sometimes used to describe an input designed to exercise some guiding influence (perhaps via indirect or ancillary information loops) on a following stage of an operation (examples are given by aspects of industrial plant operation or by a satellite-guidance system). It is contrasted with feedback control, which loops output information directly back into the guidance mechanism. Feedforward is subsumed within my meaning of folded feedback and is not subsequently used herein. Thermal and Darcian feedback offer examples of both types of control, depending on the nature of coupling with other processes. Strict thermal feedback in an adiabatic system represents a direct control loop of dissipative output back into the system as an input via the temperature dependence of the stress and shear-rate relations (apparent viscosity). It may be either positive (constant source of shear stress) or negative (constant displacement rate). Thermal feedback also offers a clear demonstration that negative feedback is not necessarily synonymous with stabilizing feedback (see Gruntfest, 1963; Shaw, 1969, p. 531).

The positive and negative aspects of thermal feedback demonstrate some of the general aspects of folded feedback. Folded feedback can be thought of as the combined effects of coupled operations involving a net increase in a quantity followed by a net decrease, for example, an up followed by a down or an in followed by an out. The key idea is that the repetitive action of both kinds of effects as a net consequence of all operative mechanisms, however numerous and complicated they may be, is folded in as an essential aspect of feedback-system operation.

Logistical analyses of biological populations represent examples of folded feedback where there are numerous and complex sets of specific feedback mechanisms. Simpler illustrations are provided by laboratory deformation of elastic solids and viscous liquids. For an elastic solid, it is easy to maintain a constant stress (below the failure stress), whereas the attempt to maintain a constant shearing rate leads eventually to a rising shear stress and failure. Continued shear may then lead to alternating conditions of sticking and slipping along the plane of fracture, with stress oscillations governed by the normal stresses and coefficients of sliding friction (thus conforming to a specific kind of folded feedback). For a liquid, on the other hand, it is usually possible to maintain a constant shearing rate, at least below a critical speed; when one attempts to maintain a constant shearing stress, however, thermal feedback leads to an increasing shear rate. If the layer thickness is large enough, the adiabatic condition is approximated, and the shearing rate is limited only by stress relaxation or by the maximum shearing rate attainable with the instrument, according to the relations already discussed. Because magmatic systems involve both types of behavior and because natural deformation may involve potentially large values of both shear stress and shear rate, conditions tend to oscillate between those approximating constant stress and those approximating constant shear rate, thus implying folded feedback.

These tendencies are schematically summarized in figure 51.14, a type of diagram designed to distinguish between present and future states. The diagonal line at 45° represents those conditions in which the future state of melt concentration is the same as the present state. That is, thermal or mechanical energy is supplied in amounts just sufficient to maintain the status quo. Above the 45° line, each state represents an increase of melt fraction relative to the immediately preceding state; below the line, each state is diminished relative to the immediately preceding state by the combined effects of thermal loss associated with decreased rate of energy dissipation, conduction loss, and melt transport from the region of shear.

The dashed line in figure 51.14 signifies typical paths involving states of increasing melt fraction during episodes of shear melting or intrusive melt transport followed by states of decreasing melt fraction owing to combined effects of stress drop, limitations on shearing rate,

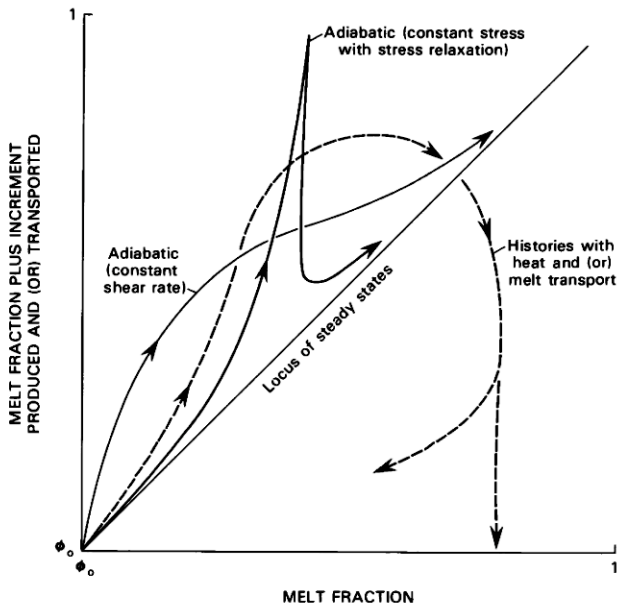


FIGURE 51.14.—Schematic diagram expressing feedback regimes of figures 51.9–51.13 in terms of "future" states plotted against "present" states: ordinate shows values of melt fraction relative to some arbitrary initial value ($\Phi_0$) representing sum of immediately preceding value and amount created or destroyed (for example, by transport loss from system) during specified time increment ($\Phi_0$ not necessarily zero). Each curve is unique, depending on process and on rate and change of rate of that process. Thus, magnitude on ordinate is governed by melting and (or) transport rate. Adiabatic melting without transport is indicated by solid lines, and melting with heat loss and (or) melt transport is indicated by paths resembling dashed lines; if wholesale migration occurs above some critical melt fraction, overall melt concentration may decrease. Steady states, representing thermal balance between melting and solidification and (or) transport, are limited to vicinity of 45° diagonal line. Coupled positive-negative feedback represented by paths like dashed curves is termed in this paper "folded feedback."

melt injection into neighboring domains, and crystallization due to cooling. The foldlike trajectories involving the net effects of positive and negative feedback in figure 51.14 (dashed lines) provide a framework for subsequent diagrams describing the evolution of volcanic volume states. Henceforth, however, the discussion is shifted from dynamics to a logistical description of transport rate.

The strategy of logistical analysis is sketched in figures 51.15–51.18 in terms of the variety of descriptive histories that may be associated with time variation of any general quantity symbolized by the variable $x$. Subsequent diagrams consider the volumetric histories of Hawaiian volcanism expressed in the same way, replacing the symbol $x$ by $V$, using the documentation of transport rates by Dzurisin and others (1984).

Consistent with the approach to magma-supply balances taken by Dzurisin and others (1984), figure 51.15 is based on the idea that any net transport rate of a quantity $x$ can be decomposed into apparent rates of gain and loss, or input and output, both expressed as positive numbers. The net rate, then, apparently is given by the positive (input) rate minus the positive value of the negative (output) rate; the qualifier "apparently" is used because this convention is not free of ambiguities, as will be discussed (possibilities of ambiguity exist in any measurement made up of integrated positive and negative increments, where both are taken as positive numbers, because unless there is absolute knowledge of the exact amount and sign of every relative change, a net increase could result if there is either a greater increase in the positive than the negative term, or a greater decrease in the negative than the positive term; the balance between biologic originations and extinctions over time is a notorious example). Symbols designating positive components of the net rate can be thought of as the rates and amounts of addition or input to some general reservoir of quantity, and symbols designating negative components as the rates and amounts of the output or depletion of that reservoir (also written as a positive number).

An example illustrates that the above convention is a common one. Imagine a fuel tank with an input valve and an output valve, each equipped with a flow gauge calibrated the same way. Each gauge registers a positive reading when input and output flow are occurring simultaneously. Their differences integrated over time give the net change of fuel in the tank. An idealized magma chamber can be thought of in the same way if there is the recognition that the reservoir is of unspecified boundaries and size, and there are no predetermined values for initial and final states; also, input and output paths may be numerous, and flow rates are based on less direct evidence than a fuel gauge. This means that the volumetric states of magma chambers are relative to an arbitrary zero at some defined location and time, as is the case in figures 51.1–51.8.

To assist interpretation of the numerous stages in the construction of figure 51.15, as well as subsequent figures, it should be recognized that not only are the figures drawn approximately (don't look for numerical values to check to better than a few percent), but seemingly contradictory numerical states may be noticed (an example is the quantity "$x_+$" in fig. 51.15*D*; see stepwise description below). An example of materials inventories in commerce indicates how contradictory values can occur in a series of measurements. Consider a wholesale center to be a reservoir of material that is added to by shipments from a factory and subtracted from by shipments to retail outlets. This is the same balance as the fuel tank. Now, however, there are additional degrees of freedom represented by possible returns of items from the wholesaler to the factory and from the retailer to the wholesaler. The count of items received from the factory is a positive number and is either constant or increasing (the running record of items received). But, ignoring the retail transactions for the moment, the input to the reservoir of quantity (the wholesale warehouse) can decrease if more items are returned than received over some interval of time. Obviously the inclusion of this possibility as well as possible returns fom the retailers makes the accounting of inventories a tricky business even in the idealized case. Such transactions, however, are the crux of the logistic diagrams that follow. Ambiguities may be real if records of exchanges are not complete, or they may be apparent ones related to uncertainties in the relative timings of transactions.

The problem of accounting is also a central one from the standpoint that it focuses on the precision of the units of measurement

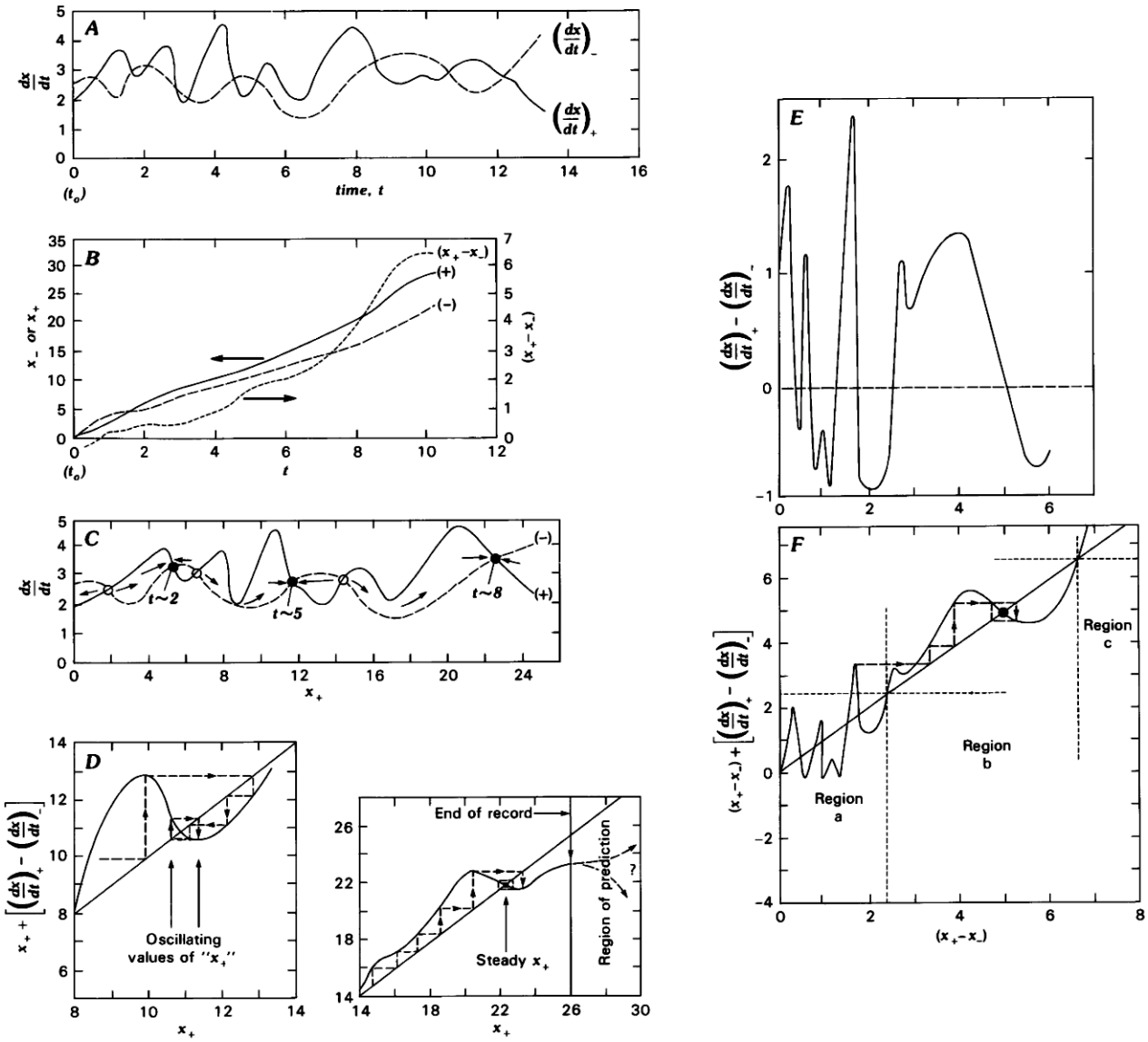


FIGURE 51.15.—Schematic diagrams showing time-variation and $x$-variation of positive and negative rates of change in any extensive quantity $x$. ***A***, Hypothetical information concerning positive and negative rate components of the rate $dx/dt$; used to construct other diagrams. ***B***, Respective integrated positive and negative contributions and net change in $x$. ***C***, Respective values $(dx/dt)_+$ and $(dx/dt)_-$ versus the positive cumulative values of $x_+$ read from $B$ at same values of time in $A$ ($x_-$ or net $x$ could be used on abscissa instead of $x_+$). Dots, values of $x_+$ that tend toward stationary values (convergent arrows), identifying values where there is relatively slow net increase in $x$; circles, points of divergence identifying intervals of relatively rapid net increase in $x$. ***D***, Adjusted future values ("$x_+$") versus present values referred to $x_+$ ($x_-$ or net $x$ could be used as reference; see $F$) calculated from net rates of change $(dx/dt)_+ - (dx/dt)_-$ over a specified unit of time; these two graphs and that in $F$ are analogous to intervals of folded feedback in figure 51.14 (see text for discussion of apparent contradiction between dictated trajectories in $D$ and monotonic curve of $x_+$ in $B$). Dashed trajectories with arrows ($D$, $F$) show arbitrary constructs where projections indicate that future states are defined by present states. That is, among possibilities limited by rate history, if next value is dictated equal to present value, then next value of $x_+$ in graph $D$, or $(x_+ - x_-)$ in graph $F$, is given by horizontal projections from master curve (solid curve representing trend of available states) to diagonal line as locus of intersections of dashed trajectories; along diagonal, next value on abscissa equals immediately preceding ordinate value. Area labeled "region of prediction" in $D$ represents uncertainties associated with possible trends beyond limit of record. ***E***, Net rate plotted versus net values of $x = (x_+ - x_-)$. ***F***, Corresponding loci of available present-future states and corresponding idealized limits of episodic feedback limited by net $x$ and net $x$ plus net rates relative to diagonal line of steady-state net balances (construction as in $D$ for net $x$). Regions refer to different regimes of possible episodic feedback (see figure 51.16 and discussions in text). Prescriptions of future values determined by present values based on logistics of population-dependent biological reproduction (see May, 1976) and concentration-dependent feedback melting. Dashed trajectories in $D$ and $F$ represent idealized histories that may: (1) converge to a fixed value, (2) oscillate over some set of regular intervals around a fixed value, (3) oscillate chaotically in vicinity of fixed value, or (4) diverge to totally different neighborhoods of higher or lower $x$-values.

Types of regions of attraction

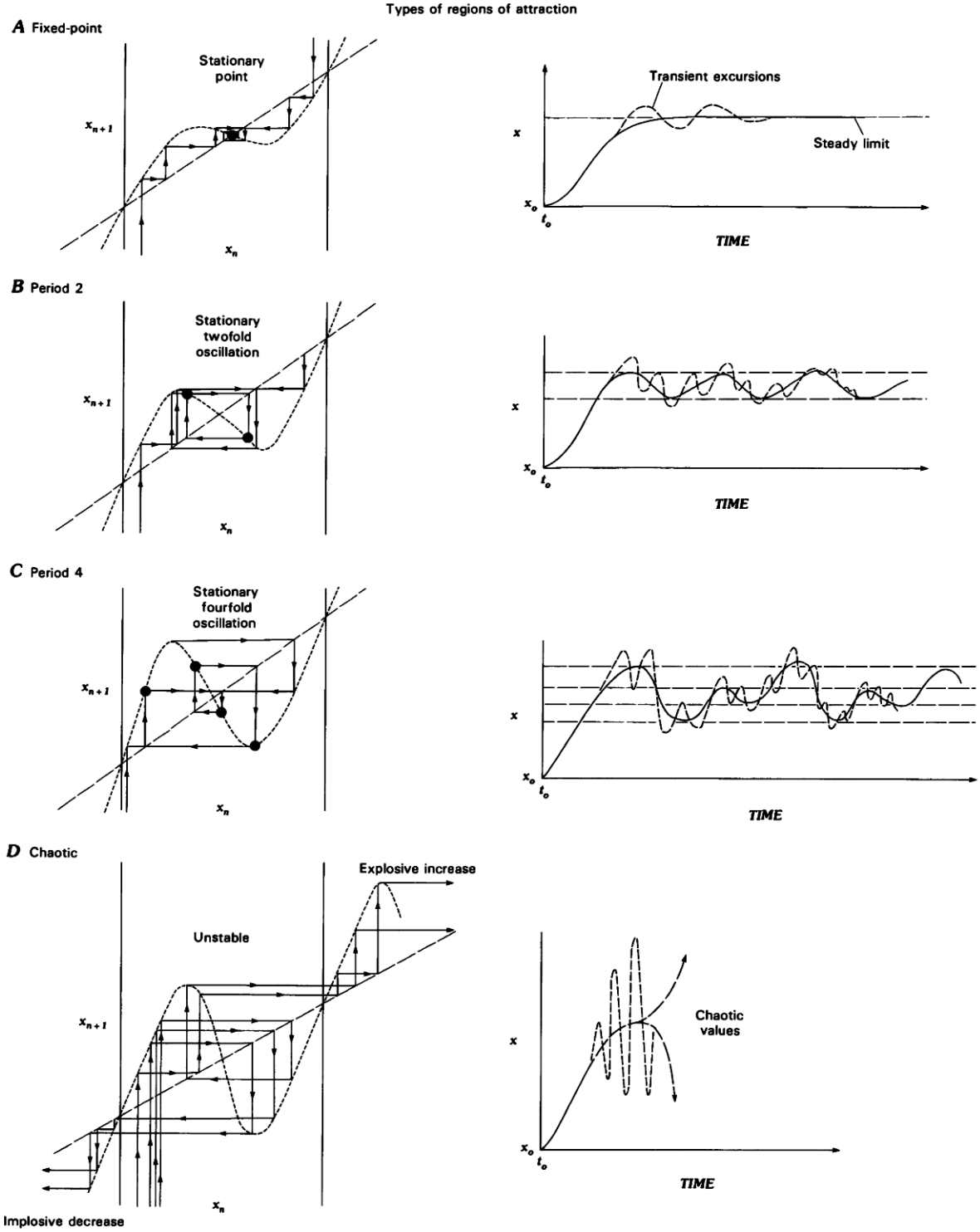

of rate. That is, an input or output record always represents some finite relation between the counts of quantity and time. Notice that the graph in figure 51.15*A* does not specify the units of time. Whatever the choice, there is always a smaller or larger unit possible. Thus, any such curves really represent trends of average readings at an appropriate time scale. The materials inventory above might be taken per day, per week, and so on. At any smaller scale of time the possible measures of rates might be much larger numbers if short-term averages were linearly extrapolated to longer times (for example, if all items are received during one day while the inventory is taken weekly, an extrapolation of the one-day rate overestimates the weekly rate). Inversely, knowledge of longer term averages does not identify the ranges of rates taken over short intervals of time. Examples of this have already been seen in the record of Kilauea's eruption rates (figure 51.7) and in the discussion of fractal self-similarity.

The above kinds of uncertainties are encountered in the later illustrations of magma-supply balances at Kilauea. The budget described by Dzurisin and others (1984) makes the necessary assumption (without it no quantitative inventory could be made) that the inflation of Kilauea's summit documents magma input from deep sources to a near-surface reservoir ("summit reservoir"), and summit deflation documents magma supply to the rift systems from the summit reservoir. In a manner analogous to the uncertainties between the wholesaler-factory and wholesaler-retailer exchanges, this inventory does not explicitly document the possibility of exchanges having more continuous or higher frequency characteristics. For example,

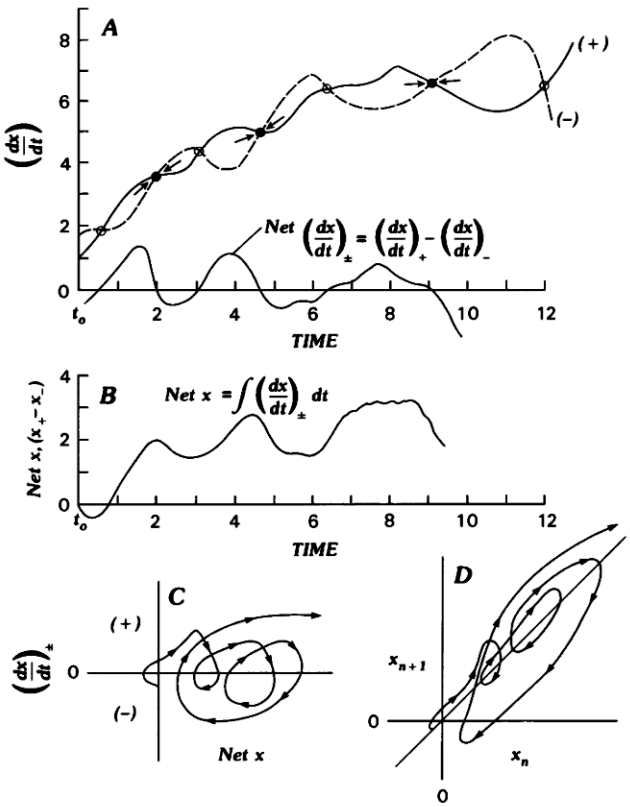


FIGURE 51.16.—Schematic patterns of idealized oscillation relative to possible stationary points (dots) either on or controlled by intersections of locus of steady states (dashed diagonal lines at left) with present-future control curves (dotted lines of present $x_n$ versus future $x_{n+1}$) of available states in an interval of $x$ (vertical light lines). Trajectories of oscillations in present-future values of quantity $x$ shown by solid lines with arrows in left-hand column; corresponding oscillations of $x$-values in time shown in right-hand column (solid lines indicate time-independent limits of stabilized oscillations, dashed lines represent transient or unstable short-term and long-term deviations from time-independent limits). Several regimes of behavior represented, at least two of which are implicit. ***A***, Small positive and negative deviations (folded feedback) occur relative to diagonal locus of steady-state limits, so that trajectories (solid lines with arrows) of feedback events involving neighboring values of $x$ within interval (vertical lines) converge toward point of intersection (dot); this regime implies divergence toward lower values of $x$ if dotted curve is totally below dashed diagonal but crosses it at right-hand vertical limit. ***B***, Curves showing larger excursions in $x_{n+1}$ relative to $x_n$ eventually split away from point of intersection in *A*, which can be thought of as bifurcating or fissioning, creating two continuously or stably repetitive alternations of $x$ on opposite sides of steady-state locus; that is, stationary point in *A* becomes stationary zone or region that contains two stationary points counterbalanced across diagonal locus. Note that angles and slopes not exact, hence scale of $x_{n+1}$ not proportional to $x_n$. If scales 1:1, twofold bifurcation sequence begins when dotted curve exactly perpendicular to dashed diagonal line. ***C***, As folded feedback amplitudes increase, stationary region grows in size and bifurcates or fissions into doubling sequence of counterbalancing stationary points; that is, there is a 4-fold bifurcation that will split to 8-fold, 16-fold, and so on at slightly higher feedback amplitudes. ***D***, At sufficiently high feedback amplitudes, doubling sequence $2^n$ gives way to complex fissioning events that include possibly regular odd-period repeats and irregular or chaotic trajectories, depending on exact amplitudes and curve forms; if this regime occurs totally within vertical lines, stationary region persists (even though it is "fuzzy" and may contain no stationary points); but if amplitude permits excursions of $x_{n+1}$ to exceed vertical limits in $x_n$, eventually all trajectories escape to either larger or smaller values of $x$ (called "sensitive dependence on initial conditions"). Values of $x$ initially very close together (for example, magma concentrations within adjacent sites of a volcanic edifice) may rapidly diverge in opposite directions (that is, one set of trajectories escapes to higher concentrations, the other to lower concentrations). Regions of stationary behavior called "basins of attraction"; term "attractor" stems from patterns of regular to chaotic oscillations within basins.

FIGURE 51.17.—Schematic rate histories and derived curves for situation in which net value of $x$ both increases and decreases with time. ***A***, Schematic curves of rate against time. ***B***, Plot of net $x$ against time, showing both increase and decrease rather than monotonic increase as in figure 51.15*B*. ***C***, Rate plotted against net $x$; note that rate history repeats itself over intervals of $x$ reversals. ***D***, Present states plotted against future states of $x$. Resulting loops of folded feedback here and in figure 51.17*C* repeat themselves in various patterns of tangled and potentially closed loops. Thus, intervals of closure automatically define regions of stationary states that occur within more inclusive intervals of stationary states in a potentially unlimited series of involutions and convolutions. Trajectories describing stepwise feedback, as in figures 51.15 and 51.16, accordingly imply even more localized sets of potential stationary points and regions within a web of available states. In a sense, control curves in *D* resemble cyclical trajectories of stepwise feedback in more monotonic histories, such as those in figures 51.15*D*, *F* and 51.16 (see discussion of rate uncertainties and time scales in text); compare figure 51.18.

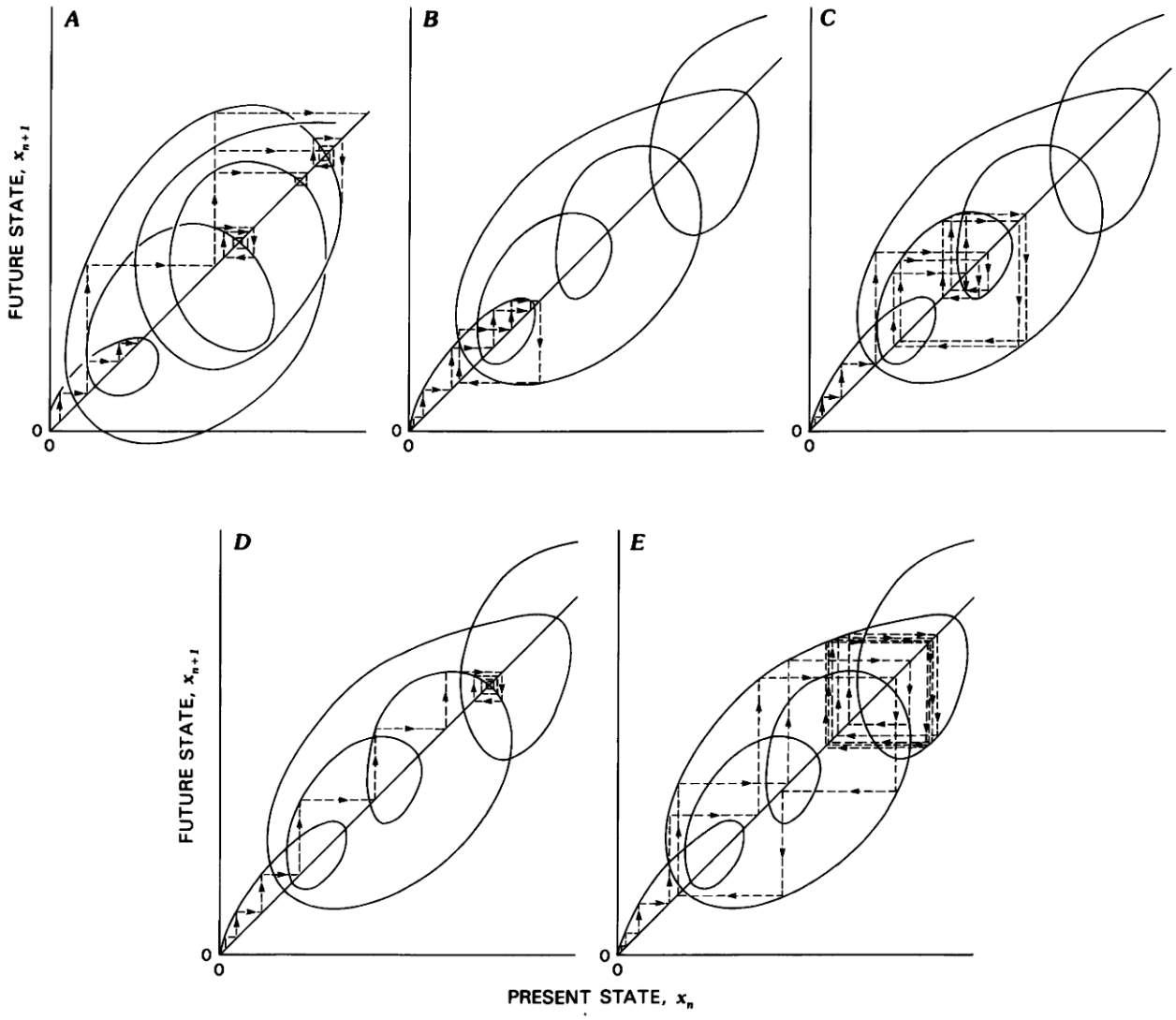


FIGURE 51.18.—Schematic trajectories of feedback steps (dashed lines with arrows) on sets of master control loops (solid curves) conforming to availability of rate histories and $x$-values analogous to figure 51.17. ***A***, Quasi-circular loops with mainly stable attractor intersections along diagonal locus of steady states except at upper right, which is a divergent and possibly chaotic escape trajectory depending on path of master curve beyond interval shown. ***B***, ***C***, ***D***, ***E***, Quasi-elliptical loops elongate in direction of increasing $x$ (because of aspect ratio, feedback events jump across loops and create complex sets of attractor basins of both quasi-steady and chaotic types). No unique solutions for functional relations between $x_{n+1}$ and $x_n$ exist (behavior is both deterministic and probabilistic); feedback trajectories are multivalued and simple or complex over special time intervals (that is, feedback may both circulate near one or several stable states as well as jump about over many different states). A composite of simultaneous trajectories will circulate within central region if master curve closes back to origin from right-hand termination.

any magma that is continually leaking through the summit chamber into a rift system may not show up as an event in the inflation-deflation record (analogous to a blackmarket operation not recorded in a wholesaler's inventory). Also, no explicit accounting is made of any magma increments that may be analogous to material returns. While errors caused by this possibility can be discounted in the intrusive magma balances on physical grounds, they are possible in principle. A magmatic example where they are explicitly included in the budget is given by the data of Eaton and others (chapter 48, tables 48.1–48.3) describing the history of filling of Kilauea Iki lava lake during the 1959 eruption of Kilauea. There, returns from the ponded lava reservoir to the subsurface reservoir were significant, and there were also losses of pyroclastic components during fountaining.

As a consequence of considerations of these kinds, any rate curves such as those in figure 51.15*A* (and especially any that document a natural process) are really very fuzzy lines if viewed at finer scales of resolution. For example, compare figures 51.5, 51.7, and 51.2, in that order, with attention to the relative changes of time and amplitude scales. That is, the time scales increase greatly while the amplitude scales remain similar (see averages over different durations in fig. 51.7; compare fig. 51.8). I will return to a discussion of how such uncertainties relate to an interpretation of hypothetical trajectories of changing quantities in diagrams like figure 51.15.

The schematic rate curves in figure 51.15*A* are drawn arbitrarily to represent the kind of irregular variations seen in the earlier illustrations of volcanic rates (for example, the derived curve of net rate in fig. 51.15*E* qualitatively resembles the Hawaii-Emperor rate curve in fig. 51.2*C*). Figure 51.15*B* shows the approximate values of graphical integrations of areas under the (+) and (−) rate curves in figure 51.15*A*, as well as the integral defined by their difference (the net rate is not shown in fig. 51.15*A*). The input (+) and output (−) rates are plotted against the integrated input ($x_+$) in figure 51.15*C*. This plot is analogous to one showing total magma supply rates and depletion rates (either by eruption or other losses from a chamber) versus total magma supply (fig. 51.5 shows these quantities plotted against time; it is also used subsequently to examine volcanic volumes in a manner like that of fig. 51.15).

Plots of future states against present states for positive or negative net rate increments relative to the total input quantity $x_+$ are shown in figure 51.15*D*; again, the net rate is simply the difference given by the positive (+) curve less the positive (−) curve of figure 51.15*A*. This graph is included to illustrate the implications of applying net rates to the different choices of $x$-values. One might wish to plot the sum of $x_+$ and the net rate against $x_+$ for at least two reasons. (1) It might be desired to see where in the record of input rates there is a tendency for strong depletion effects. (2) The record of output rates might be intermittent and inadequate to permit an integration of $x_-$; hence, the net value of $x$ that ordinarily would be the abscissa of choice is unavailable (that is, it might not be possible to plot fig. 51.15*F*). When the dashed trajectories of present-future states in figure 51.15*D* are constructed, however, a contradiction is encountered. This is shown by the reversal in the directions of trajectories and the implied oscillation in "$x_+$."

According to figure 51.15*B*, $x_+$ is a monotonically increasing function of time; there is no indication that $x_+$ might decrease anywhere. While it is correct that the literal reading of figures 51.15*B* and *C* indicates that such trajectories of recursion imposed artificially in figure 51.15*D* are impossible, the previous discussion of uncertainty indicates that the master rate curves in figure 51.15*A* are average trends of data that have unidentified fluctuations at smaller scales of time. If we were to also allow the possibility that $x_+$ stands for an input quantity that could have components of reversals (analogous to the merchandise returns), then actual reversals in $x_+$ would be possible. Such an effect is equivalent to saying that there are high-frequency fluctuations in at least the (+) rate curve of figure 51.15*C* that extend below zero on the ordinate (that is, the integral must be capable of changing sign locally). The hypothetical trajectories in figure 51.15*D* indicate the magnitudes and locations of where such effects might be looked for in terms of the input record, $x_+$. These results can then be compared with the same vicinities of figure 51.15*C* (dots indicate tendencies for net convergences, or stationary states if plotted against net $x$) to see if there are in fact possibilities for stronger fluctuations. These considerations also explain how a seemingly closed repetition, shown on the left of figure 51.15*D*, can escape to higher values of $x_+$ or net $x$ (see later discussion of basins of attraction and the regions in fig. 51.15*F*). The interval of high variability in Kilauea's eruption record (fig. 51.7) is an example where the record of supply and depletion of the summit chamber is expected to have a highly variable rate history as well. We might suspect complex reversals of flow in such intervals (analogous to drainback; see Eaton and others, chapter 48), although they are also possible in the absence of eruptive phenomena.

The trajectories of recursion in figures 51.15*D* and 51.15*F* symbolize endogenous folded feedback; "endogenous" here refers to the net effects of mechanisms of self-regulation that are dominantly influenced by the way the system has internally evolved, rather than by being dependent on some external system. The crosshatched regions of figures 51.9, 51.10, 51.12, and 51.13 are examples of conditions controlled endogenously, in that the delineated regimes are products of the net effects of several kinds of dynamical feedback intrinsic to the system at different characteristic scales of time and size.

The central idea in figures 51.15*D* and 51.15*F*, and in possible parallels between the logic of repetitive physical processes and the logic of repetitive numerical processes performed graphically or by computer, is the extent to which the quantity portrayed is a product of endogenous folded feedback. That is, if the system states at a given time or quantity ($x_+$, $x_-$, and their differences) are products of preceding states and in turn will in some sense dictate the nature of following states, no matter how intricate the paths may be, then the form and amplitude relations of plots such as figures 51.15*D* and 51.15*F* provide logistical information on how stable or unstable that evolution has been and might become relative to variations in the quantity and in time.

Examples such as the factory-wholesaler-retailer system are instructive in illustrating how oscillations can occur out of attempts to stabilize the inventory and maximize profits. For example, if $x_+$ in figure 51.15*D* represented items from the factory less those returned, then the oscillating behavior of "$x_+$" could be real. The trajectories of recursion might have been designed to provide negative feedback, perhaps because there is limited storage space in the warehouse. The strategy is revealed as a self-defeating one in the particular example at the left in figure 51.15*D*, because until $x_+$ eventually increases, no lasting sale of goods is being made (they are just being carried back and forth between the factory and the wholesale warehouse; implicitly, in this case, returns between the consumer and retailer and the retailer and wholesaler also would have to balance). This kind of oscillation applied to the behavior of a magma chamber would correspond to a condition where magma is pumped in and out through the same source conduit without any evidence of lasting outputs in the form of eruptions or intrusive leaks

(if this kind of behavior existed conspicuously in Kilauea's budget, summit inflation-deflation cycles would occur without eruptions or evidence of magma moving into rift systems). It may also be noted that the transport budget of a geyser basin resembles several aspects of the above kinds of oscillatory transactions.

These and other forms of oscillating material inventories essentially reflect imbalances related to time delays of incremental transport which are intrinsic to nonlinear systems (for example, a large sale of goods triggers a large order from the factory, which may be followed by a large return to the factory if subsequent sales are poorer, and so forth). Although we cannot rule out chance or systematic external influences as a part of the record (for example, thefts of merchandise), we can describe the system in terms of endogenous influences represented by patterns such as those shown in figure 51.15*C* (as another example, if $x$ in fig. 51.15 represented water in an open reservoir, the variations would describe the main features of the material balances, taking into account scale effects as discussed, even if they included the vagaries of rainfall as an input and the chance of external objects falling in).

The relation between positive values of input and output rates versus quantity identifies tendencies for convergence or divergence in the neighborhood of specific values of the quantity. If the positive input is greater than the positive output in some vicinity of the value $x$, the quantity in question is increasing in that vicinity (and implicitly at a given time, or at a given set of times if the pattern is repetitive). Conversely, if the positive output is greater than the input, the quantity is decreasing in that vicinity. Thus, where the rate curves cross, there is either a convergence or a divergence with respect to that value of $x$. Loci of convergence in figure 51.15*C* are identified by the dots with inward-directed arrows, whereas loci of divergence are identified by circles and outward-directed arrows. In a tangible sense, any material states symbolized by the quantity $x$ tend toward the vicinities of the dots relative to any other nearby states. The loci of the circles are avoided, so to speak. In this respect, values of $x$ are "attracted" to the vicinities of convergent rate balances. The circles, therefore, are analogously loci of relative "repulsion" from the standpoint that values of $x$ persist longer in the vicinity of convergent rather than divergent states. Neither type of locus, however, is necessarily an absolute or global center of logistical attraction or repulsion if the net variation of $x$ (as in fig. 51.15*B*, dotted curve) eventually increases beyond the recorded interval. Thus, the set of diagrams in figure 51.15 represents an array of transient states in which are imbedded several quasi-stationary (less transient) attracting states within a set of generally divergent (more transient) states. It may be noted that any system of merchandising that transports goods efficiently and has high sales will have both kinds of states in some optimum balance (barring a factory-outlet system in which goods are made precisely in balance with their consumption at all times).

In computer studies of numerical folded feedback, the incremental paths of convergent circulation just described are often called attractor trajectories. The word "attractor" refers descriptively to the resulting patterns of stable, quasi-stable, or unstable trajectories, much as the terms "cell," "vortex," and others are used in describing fluid motion. The usage stems literally from the circulation of trajectories in the vicinities of stationary loci within a field of numerical possibilities governed by folded feedback. The literature of attractor mathematics is now very extensive, and space does not permit rigorous development. The best introduction I know is given by May (1976); the background of his study is in the biological sciences.

In the present discussion I use the term "attractor" as a shorthand for any patterns represented by the trajectories of present and future states. This is done to distinguish the pattern of trajectories based on numerical recursion from more complete logistical descriptions of all potentially available states represented by loci such as the dots and circles in figure 51.15*C*. In a parallel context, every attractor pattern also implies its converse as a repellor pattern of divergent circulations; generally, these are not shown.

A brief summary of the types of attractor patterns that can be expected in the vicinities of convergent states is given in figure 51.16. The four types of behavior shown are abstracted from an array of classifiable regimes that have been studied numerically by many other workers of diverse backgrounds (assisted by P. Doherty, USGS Computer Division, I have duplicated many of the published results; we have also written algorithms for attractors of higher dimensions, as well as variants of recursive strategies that contain options for evolutionary choices by the program itself along the lines of evolutionary strategies outlined in the introduction). May (1976) gives a concise summary of the possible numerically generated attractor regimes found relative to standard models of folded feedback (feedback curves of analytically explicit forms involving parabolic and exponential functions). The analytic type of feedback equation, however, is less crucial to the attractor pattern than is the range of slope variations in the vicinities of crossing points of the master curve and the reference line, as shown in figure 51.16. The present research has confirmed to my satisfaction that the general concepts of pattern generation by means of computer experiments can be a powerful tool for the exploration of evolutionary strategies in nature.

In figure 51.16 the parallel vertical lines represent the interval of $x$ to be investigated in terms of trajectories of attraction (solid lines with arrows) in the vicinity of a general trend of present-future states (dotted master curves) relative to a line of equal balance of positive and negative feedback (dashed diagonal lines). The large dots again represent stationary or quasi-stationary states, but in this instance such states are those implied by the convergence or divergence of the attractor trajectories themselves, which are generated from the dotted master curve that describes the average trends of states. Stationary states, as fixed points in the graphical context, represent either the intersection of the dotted curve with the diagonal (fig. 51.16*A*) or the intersections of a stable circulation of attractor trajectories as a limit of exactly repetitive paths (fig. 51.16*B*, *C*). Such circulations in dynamics are often called "limit cycles."

One of the major discoveries of computer experiments with numerical feedback is that there is a systematic diversity of limit cycles and other forms of repetitive or nearly repetitive attractor patterns (see, for example, May, 1976). As shown by figure 51.16*C*, the repetitive loop may involve cyclical multiplicities that increase in numbers of stationary states as powers of 2 and that can multiply in that fashion theoretically without limit until a critical

amplitude is exceeded. Actually, it is the combinations of amplitudes and slopes of the dotted curve that determine how many stable states are possible.

One example of divergent paths, shown in figure 51.16*D*, is found when the amplitude and slope attain values that imply both (1) the generation of chaotic (unstable, nonrepetitive) trajectories and (2) the likelihood that at least some trajectories will transcend the boundaries of the $x$-interval. In this diagram there are no stationary states, and two trajectories may begin at almost identical values of $x$ and after one or more circulations spin off, as it were, in totally opposite directions. This is sometimes described as "sensitive dependence on initial conditions."

The statements concerning figure 51.16*D* are qualified in two important respects. (1) Chaotic trajectories lacking any quasi-stationary values can exist between figures 51.16*C* and 51.16*D* for values limited to the interval between the vertical boundary lines; these limits define the region within which a stationary or quasi-stationary attractor pattern can evolve as a distinct, though possibly chaotic, spatial analog of a stationary or quasi-stationary point (within this pattern, discrete odd-period stable attractors are also possible at special values of amplitudes and slopes; they are often called "windows"). (2) If the extrema of the dotted master curve exceed the limits of the intersection with the vertical interval boundaries, and the slope of the master curve at the crossing point with the diagonal is in the neighborhood of $-1$ (perpendicular for equal units on the ordinate and abscissa), some trajectories of stable fixed point and period-doubling sets of attractors may also escape the interval toward either higher or lower values.

The circulatory regions in figure 51.16 are sometimes called "basins of attraction," and the limits just described indicate the tendencies toward either quasi-stationary or unstable behavior of potential attractor patterns relative to these basins. Because the master curve represents a locus of average feedback balances, however, statistical fluctuations around the overall growth trend, as in figure 51.15, imply a net drift toward higher values and what may be termed "leakage" from any particular basin of attraction.

Such leakages of attractor trajectories refer to the numerical persistence of any particular attractor pattern (including fixed points, period-doubling and odd-period stable sets of points, and chaotic regions) and are not to be confused with physical leakage from an actual physical reservoir. Some deliberation of rate balances should show that the concepts of physical leakage relative to attractor leakage are determined by the definitions of positive-negative transport rates relative to some physical locus. That is to say, a leaky basin of attraction could refer to either a progressively filling or emptying mode of an actual physical reservoir. These considerations are the basis for subdividing figure 51.15*F* into three regions: In region *a*, subintervals like those of figure 51.16 might exist even where the overall trend is below the diagonal line; that is, the attractor leakage might be in a negative direction there, whereas it is in the positive direction at the transition to region *b*, and so forth.

The time variations shown at the right in figure 51.16 mimic the above discussion of attractor trajectories. The solid curves show the tendencies toward stable waveforms identified by circulations between stationary or quasi-stationary states. The dashed lines indicate transient trajectories related to deviations from the master curve of average feedback balances. If there is a one-to-one correspondence or a constant proportionality between $x$-values and the timing of the attractor oscillations, then the numerical repetitions of $x$-values are associated with regular time periods of comparable multiplicities; for example, the twofold attractor would have one frequency of oscillation, the fourfold attractor would have a different and phase-shifted frequency of two different amplitudes, and so on.

Because the potential time variations of figure 51.16 are produced by other time variations like those of figure 51.15 that govern the feedback relations of the master curve, it is evident that the overall oscillatory behavior may take place at more than one scale of description in space and time. That is, regular oscillations like those of figure 51.16 may exist at smaller time scales within the irregular oscillations of figure 51.15. By the same token, however, the patterns of figure 51.15 may relate to other scales of variation, which are also describable by relations like those of figure 51.16. Such uncertainties of scale are intrinsic to the behavior of natural open systems and underscore the need to examine rate relations of the sorts just discussed at as many scales of time and size as possible. They are also possible sources of the fractal characteristics and self-similarity in time discussed earlier relative to figures 51.5, 51.7, and 51.8.

These uncertainties of scale are emphasized by figure 51.17, which also draws attention to issues of implicit versus explicit master control curves. This figure is drawn arbitrarily, much like figure 51.15, except that the net rate dips below zero more persistently, rather than being generally positive. As a consequence, the net values of $x$ alternately increase and decrease in magnitudes rather than increasing almost monotonically. Therefore, when the net rate is plotted versus the net quantity, the overall trend loops back on itself over oscillating intervals of $x$. Thus, the stationarity of patterns in certain vicinities of net $x$ is automatically constrained by this alternation, without consideration of possible attractor trajectories of subsidiary oscillations.

It may be asked, however, what happens if figure 51.17*D* is also considered to represent the average path of a master curve that governs more localized tendencies for folded feedback. Each point on the curve implies a feedback influence on a future value, just as before, except that such values are now potentially multivalued; that is to say, there is a considerable redundancy concerning the overall effects on future states. A graphical or computer algorithm derived for single-valued recursions, such as those shown by the trajectories in figure 51.16, could not distinguish between curves except in a specific temporal sequence along the path of the arrows in figure 51.17. Since this path is the average locus of complex variations and may repeat itself again beyond the range of values shown, no unique trajectories of attraction can be specified. Instead, several kinds of attractor patterns may grow and disappear episodically within the time frame of several overall circulations, as rate values oscillate over the repetitive net values of $x$.

Simultaneously evolving trajectories of recurring attractor patterns on a redundantly looping master curve are shown schematically in figure 51.18. Each attractor locus represents one possible unique path of graphical recursions (computer-like repetitions of present-

future value decisions). In figure 51.18*A* most of the loops intersect the diagonal line at slopes permitting fixed-point attractors, except at the upper right, where the trajectories progressively diverge from the crossing point. This may mean that the looping system represents a transient stage of growth toward larger values or that the control loop closes back on the origin. In the latter case, the divergent locus will continually feed attractor trajectories back toward lower values of rates and quantities that will endlessly tend toward the vicinities of the stable attractors.

In figure 51.18*B–E*, however, the slopes of the loops at crossing points are less stabilizing (steeper, or more negative than −1). Fixed-point attractors do not exist, and most trajectories generate twofold or higher order circulations. Because these circulations can interact in many combinations, particular trajectories are sensitive to the starting values and to the parts of the loop that exercise dominant control during any particular history. Thus, if the overall control loop is in any way repetitive (for example, by an intermittent repeat of the same general rate relations or by closure of the outermost loop back to the origin without termination), then many possible combinations may recur for twofold to chaotic attractor patterns that will grow and shift in timing and ranges of $x$ as different parts of the curve exercise their influence.

If the control functions alone were rigorously precise and repetitive, eventually a steady distribution of attractor circulations would evolve. Such a pattern is deterministically predictable in the sense that the structure is generated by combinations of many possible trajectories that lead to the same final states. However, the master curves are fuzzy, as already discussed, or have finite widths because they represent averaging of processes at smaller scales of time and size (for example, a thermal-feedback melting event in polycrystalline aggregate is a composite of many localized events that relate to more localized energy balances). Therefore, there is a continual shifting of trajectories relative to any theoretically exact stable-limit cycles. An expectable consequence of such uncertainties within the context of an overall loop that closes on the origin in figure 51.18 is that attractor patterns will themselves migrate back and forth over an unspecifiably large number of possible configurations. In detail, such a pattern is unpredictable, in that there are intervals of chaotic behavior of individual trajectories. At the same time, however, characteristic regimes of transient twofold and higher order attractors repetitively come and go within the same general ranges of $x$. Thus, even though the overall pattern is unpredictable, there are recurring intervals of subpatterns that show regular temporal periodicities from time to time in a manner like that illustrated in figure 51.16. Unpredictability only refers to the fact that the regularities aren't determined once and for all on the basis of the knowledge symbolized by a master curve that has a finite line width (representing a range of uncertainty in feedback control).

## KILAUEA AS A NATURAL SYSTEM OF RECURRING ATTRACTOR PATTERNS

In this section I attempt to show that many of the generalized styles of attractor circulations discussed in the preceding section actually exist in the circulatory patterns of behavior of Kilauea Volcano. In fact, Kilauea and volcanic systems in general appear to be remarkably good analog computers in terms of demonstrating the effects of repetitive recursions in the vicinities of characteristic basins of attraction. These patterns, however, involve multiple trajectories analogous to the schematic trajectories of figure 51.18. Attractor patterns generated by folded feedback evidently are chaotic if rate amplitudes exceed a critical value (figure 51.16). Furthermore, even the generalized basins of attraction, stable or chaotic, are unpredictable if there is a significant imprecision of rate control in the vicinities of potential stationary states of cyclical control loops (figs. 51.17, 51.18). Nonetheless, the circulatory pattern itself may be predictable, in that it retains a characteristic overall form. Before attempting to summarize the implications concerning general patterns of volcanic evolution, I compare the rate histories of Kilauea's activity with the above schematic examples.

The model of magma supply proposed and documented by Dzurisin and others (1984) provides for the first time a quantitative reference frame for these comparisons. It considers the balances of an overall history of supply between about 1957 and 1983 relative to a distribution between generalized summit and rift loci of storage. Although the erupted volumes are also tabulated in their study, they are not specifically included in the magma-supply budget that refers to intrusive gains to and losses from the summit chamber. In the present discussion of positive-negative rate balances, however, several different combinations among the possible types of data exist; these data include the following categories: (1) Total magma-supply rates, (2) total integrated volumes of magma supply, (3) localized rates of summit supply, (4) localized summit volumes, (5) nonsummit supply rates and volumes (representing rates and volumes of supply to rift systems), and (6) net rates and volumes of stored magma at summit and rift localities, taking into account eruptive losses.

From the previous logistical discussion of positive and negative rate contributions to the history of any net quantity, it is evident that in volcanic systems there are many ambiguities as to relations between the algebraic signs of rates and appropriate loci of accumulation. To simplify the discussion, therefore, the balances will be referred to a generalized summit reservoir and a generalized rift reservoir. A similar approach was used by Dzurisin and others (1980) to estimate the magma-supply rate to Kilauea from November 1975 to September 1977; the longer term budget discussed by Dzurisin and others (1984) is based on analogous considerations. Erupted volumes can be considered to represent possible losses from either reservoir or from their combination. Ignoring the eruptive loss, supply to the generalized rift reservoir can also be considered to represent loss from the potential volumetric states of the generalized summit reservoir. Thus, in figure 51.5 (from Dzurisin and others, 1984) the total supply minus the summit supply (volume or rate) defines the positive supply to the generalized rift reservoir or the loss (negative supply) relative to the hypothetical growth of the generalized summit reservoir.

The above relations are summarized in the form of rate diagrams as in the preceding section; figure 51.19 shows the total supply and eruption rates versus the total volume of supply (fig. 51.19*A*), and also the balances of summit and rift supply, ignoring

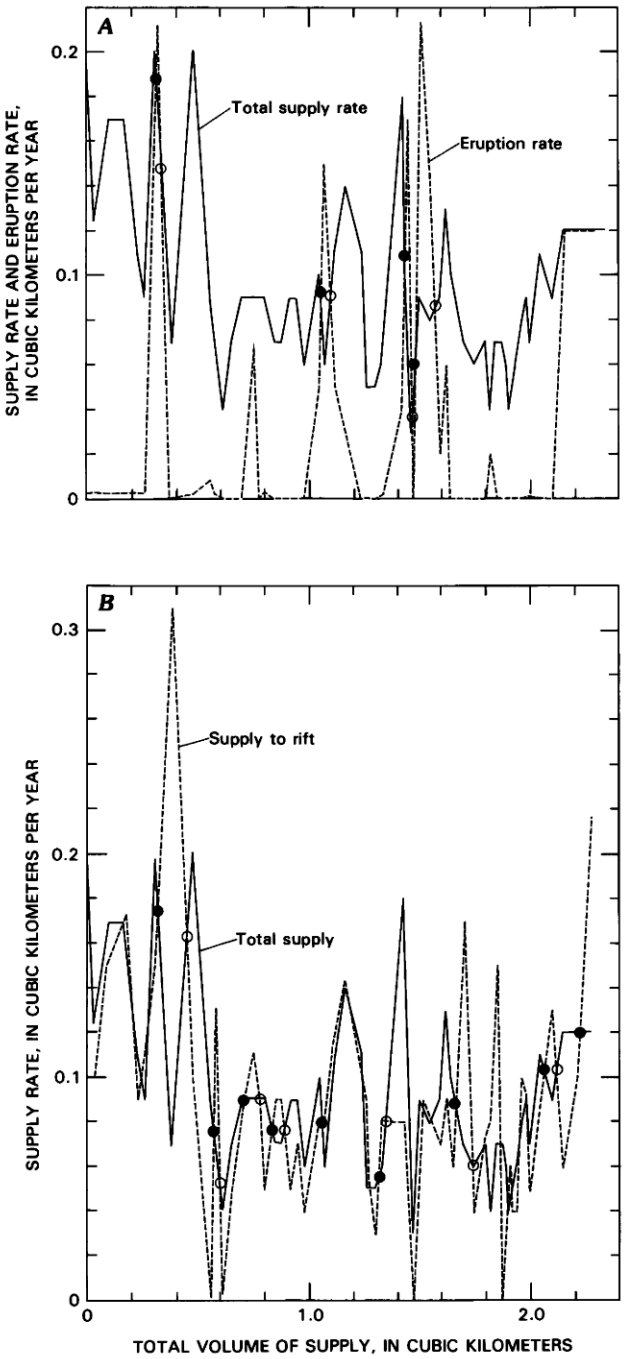


FIGURE 51.19.—Examples of rate histories for behavior of Kilauea since about 1957, based on data in figures 51.4 and 51.5 from Dzurisin and others (1984). Convergent intervals (tendencies toward stationary values) are indicated by dots, and divergent intervals by circles, as in figures 51.15C and 51.17A. ***A***, Total supply rate, corresponding to $(dV/dt)_+$, and eruption rate, corresponding to $(dV/dt)_-$, plotted against total volume of supply with arbitrary zero at beginning of record. ***B***, Total supply rate $(dV/dt)_+$, and supply rate to rift zones (total rate minus summit rate) as $(dV/dt)_-$ plotted against total volume of supply.

eruptions (fig. 51.19*B*). The positions of convergent and divergent tendencies are indicated by dots and circles, as in figures 51.15. Various combinations of rate balances are shown in figures 51.20–51.23, as identified in the captions.

Although the patterns are complicated, there are resemblances in all these diagrams to the hypothetical examples discussed above, as follows. (1) The total and rift supply balances in figure 51.20, and the net-supply-minus-eruption balances of figure 51.21, resemble the patterns in figure 51.15; there is a general history of increasing quantities, with localized circulations related to intervals of large negative rates (eruptive losses). (2) The total and net rates of gain and loss from the summit reservoir, as portrayed in figures 51.22 and 51.23, resemble the cyclical behaviors of figures 51.17 and 51.18, whether or not eruptive losses are taken into account.

These patterns suggest that the generalized rift reservoir behaves as a system of almost monotonically increasing magma storage, with intervals of quasi-stationary states and attractor-like circulations. Eruptive episodes accentuate the stationary states, but they do not control the pattern except over intervals near their occurrences, as in the circulations associated with the negative excursions in figure 51.21. The pattern of overall balances in figure 51.20 is not conspicuously different over times of eruption or noneruption, as shown by the fact that maxima that might be expected to correlate with attractor-like periodicities of gain and loss are not coincident with times of eruption.

The most conspicuous attractor-like behavior is shown by the circulatory states of the generalized summit reservoir. The patterns of repetitive control loops shown in figure 51.22 and 51.23 are analogous to those of figures 51.17 and 51.18, regardless of the way in which the present-future balances are plotted. That is, the patterns seem to oscillate relative to two (or possibly three) general volumetric states, whether they are viewed in terms of total supply rates, net total-minus-rift supply rates, or net total-minus-eruption supply rates.

Perhaps the most informative plots from a pattern-predictive viewpoint are figures 51.22*A* and 51.23, which do not depend on information concerning eruptive volumes; they are determined solely by the volumetric states deduced from summit-tilt data (see Dzurisin and others, 1984). Figure 51.22*A* is hypothetical in the sense that the future states, $V_{n+1}$, are those that would be implied if each increment of total supply actually inflated the chamber by that amount before the next state is encountered (that is, volumes are predicted by extrapolating rates based on short intervals of time). Figure 51.23, on the other hand, more nearly represents the rate increments associated with the actual changes in net volume of the generalized summit chamber as the remaining magma is entering the generalized rift reservoir. The fact that the two patterns are similar suggests that the oscillatory states of the summit reservoir are "controlling" in the logistical sense of figures 51.17 and 51.18.

The summit-reservoir control loop may operate physically somewhat as follows: When the volume of the generalized summit reservoir exceeds some fairly high value, it returns to the vicinity of the stationary state because of higher-than-average rates of loss to the generalized rift reservoir; conversely, when it is at low volumetric states, it returns to higher volumetric levels because of lower-than-

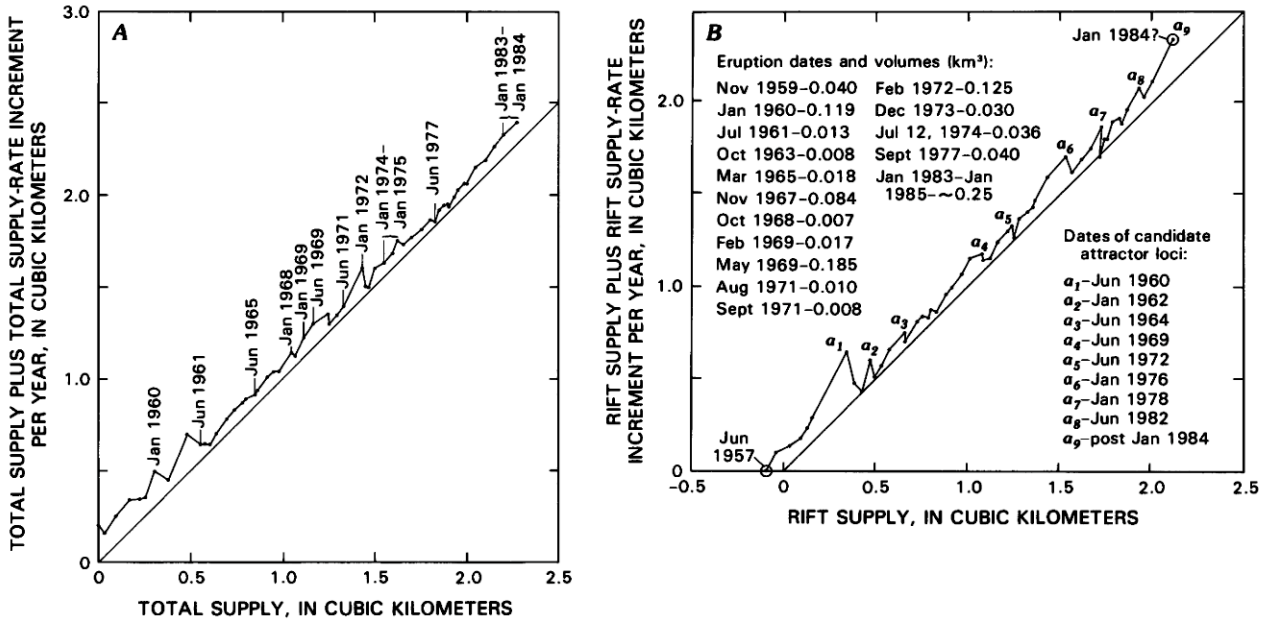


FIGURE 51.20.—Future state, $V_{n+1}$, plotted against present state, $V_n$, for Kilauea magma supply: ***A***, Total supply versus total supply plus total supply-rate increment per year. ***B***, Rift supply versus rift supply plus rift supply-rate increment per year. Data from Dzurisin and others (1984). Rift supply represents total volume of supply minus volume stored in summit chamber, and rift supply rate represents total supply rate minus summit supply rate. Points plotted at 6-month intervals, as indicated in figure 51.20*A*. Potential loci of attraction are suggested with corresponding dates (compare with discussion of fig. 51.15*D* and *F* in text); significant eruptive events are indicated in *B* by date and volume (note progressive intrusive increases despite depletions at indicated times of eruption; see fig. 51.5, and compare fig. 51.21).

average rates of loss to the rift reservoir. These rate excursions do not seem to be dominantly eruption controlled; eruptions occur at times of either higher- or lower-than-average rates of return to the stationary states. That is, if eruptions represented the only rate control, presumably they would occur predominately at times of higher-than-average volumetric states.

Another way of describing the pattern is paraphrased from Dzurisin (written commun., 1985); the statement resembles balances described earlier for the factory-wholesaler-retailer system: An important point is that the summit reservoir tends to buffer the rate of shallow magma supply by adding to the inertia of the magma system. Fluctuations in the rate of magma supply from depth are damped at the surface by the effect of the summit reservoir. When the rate of magma supply from depth is low, eruptions can still be fed by magma stored in the reservoir. When the magma-supply rate is high, eruptions can be avoided by increased subsurface storage.

An addition to this concise summary by Dzurisin is implied by figure 51.23. Whereas eruptions evidently can occur at almost any volumetric stage of the summit chamber, large eruptions occur at times near the locus of stationary states. This fact indicates that the eruption mechanisms themselves may be controlled by the summit-rift reservoir balances. A high net inflation state of the summit reservoir seems to require adjustments by increased net transfer to the rift reservoir from the summit reservoir before optimal conditions for eruption can recur. That is, if the values of magma-supply volume and rate are both too high, the resistance to eruption also seems to increase until summit storage returns toward the stationary states by increased rift storage. If both reservoirs increase together, rift earthquakes may be a more likely outcome than eruption, as suggested by the volumetric excursions during 1974–75 (compare figs. 51.20*B* and 51.22*A*). Conversely, if the summit reservoir is operating at much lower volumes than the stationary states, the eruptive head may be too low to overcome the net viscous dissipation associated with inflation. Consequently, eruptions seem to be most likely at values near those of the stationary states, and perhaps at slightly higher volumes, regardless of the net transport rates. Thus, intrusion is the favored mode of growth of Hawaiian volcanoes. Eruptions are special events that occur when certain preconditions are satisfied—that is, near the stationary states. Such balances also seem to be consistent with the earlier observations on the existence of self-similar relations between system size, chamber size, and repose time (see earlier discussion of fig. 51.7 and the relations between Kilauea and Mauna Loa compared with cratonic eruptive periodicities discussed by Smith, 1979, and Shaw, 1985).

There are many interesting analogies to the above patterns from studies of mechanical systems of forced vibrations with damping. Such systems have been studied extensively, in the form of both physical and numerical experiments. In both types of study, damped

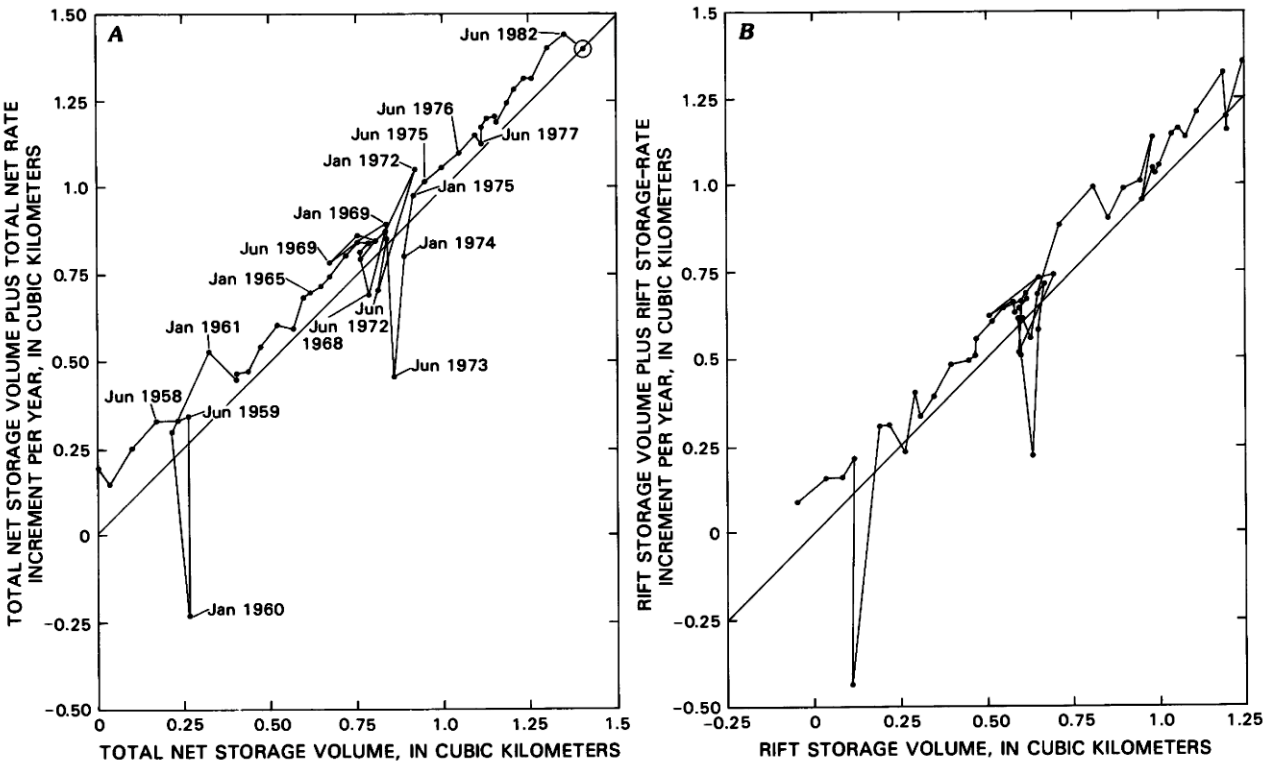


FIGURE 51.21.—Diagrams of future state plotted against present state as in figure 51.20, but taking into account volumes and volume rates of eruption. Eruptions are lumped as representing rift events without regard to location. Points are plotted at 6-month intervals. Strong negative feedback and attractor-like circulations are clearly associated with eruptive events, but these are abrupt excursions that do not control in the sense of forming master control loops. That is, pattern resembles figure 51.20 except for localized circulations. ***A***, Net storage volume (total volume minus erupted volume) versus net volume plus net storage-rate increment per year (total rate minus eruption rate). ***B***, Rift storage volume (rift supply as in fig. 51.20 minus total erupted volume) versus rift storage plus rift storage-rate increment per year (rift supply rate minus eruption rate).

oscillations have been shown to be highly nonlinear and to conform generally to regimes described by mathematical attractors (see Campbell and others, 1985; Shaw, 1984). The physical and numerical forms of behavior of leaky faucets studied by Shaw (1984) show strong resemblances to the descriptions of volcanic behavior. The events of drop formation are analogous to eruptions, and the regimes of overall flow rates supplied at the faucet are analogous to magma supply (except that magma leakage is complicated by many other factors than the setting of a single calibrated valve).

Circulatory patterns and stationary states illustrated in the present paper are analogous to factors influencing oscillations in total rates of leakage in the water-faucet model. At high rates of leakage, drops do not form because flow is continuous; at very low rates of leakage, they do not form because evaporation can keep pace with supply (in the magmatic mode, the analogous process is solidification). The behavior described numerically by Shaw (1984) refers only to the periodicity regimes of drop distributions. These show all the attractor structures mentioned earlier (see fig. 51.16), including stable to chaotic patterns, as documented in terms of the timing between drop-forming events. Eruptions could be illustrated similarly by plotting times between extrusive events. It is evident, from the wide range of extrusive repose intervals, that the eruptive attractor analogous to the faucet attractor is typically much more chaotic. In both cases, however, special regimes of precisely tuned flow can result in stable periodic repetitions. In the faucet model, these regimes can be easily isolated for study. In the volcanic case there is additional feedback among all the other processes mentioned earlier. Therefore, these other systems of oscillation (for example, the oscillation of stress states in the edifice) vitiate any obviously simple interpretation of the possible tuning effects of the faucet model, possibly excepting special intervals of flow (for example, fountaining episodes could represent a subregime in which valvelike control might be sufficiently coordinated that an independent analysis may reveal attractor patterns characteristic of the local process; in this respect there may also be a resemblance to patterns of geyser eruptions described as attractors).

This qualitative explanation of the logistical circulations seems to be in general accord with the earlier discussion of dynamical feedback. That is, the optimal conditions of magma accumulation represent some compromise, between melting and transport, that

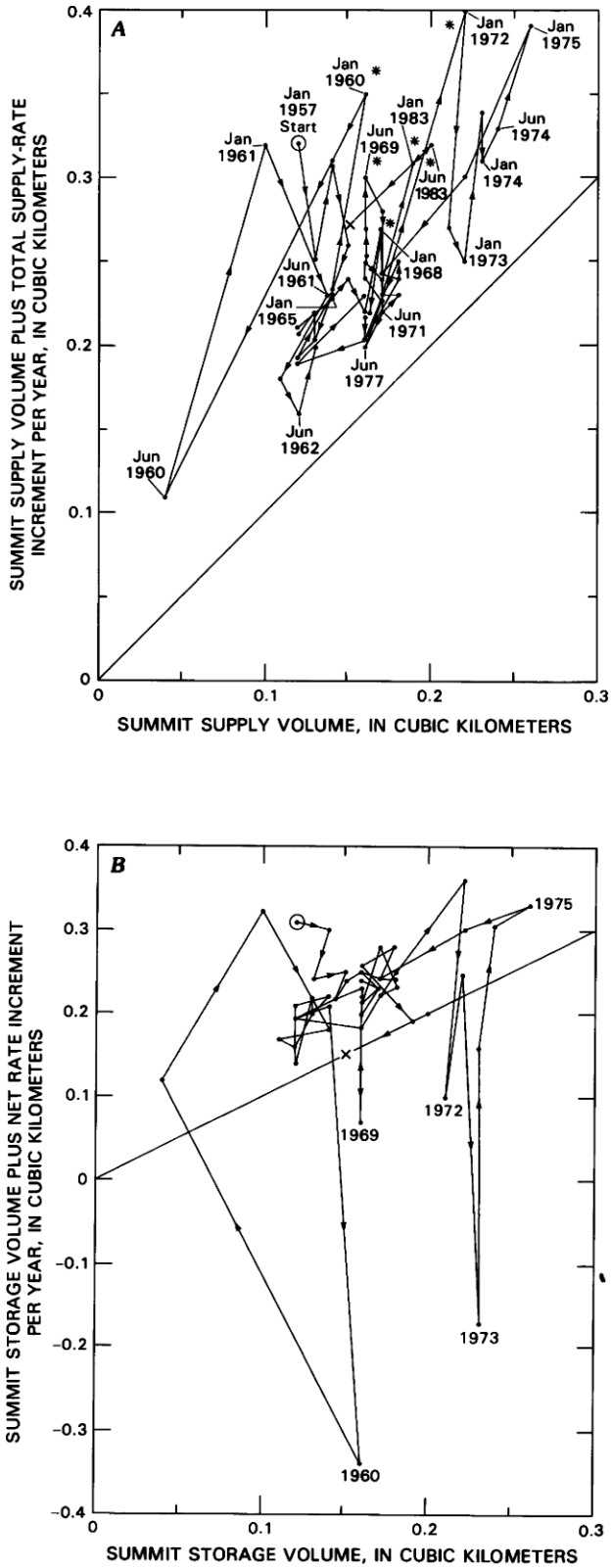


FIGURE 51.22.—Diagrams of future state plotted against present state as in figures 51.20 and 51.21 but based only on volume of supply or storage in summit chamber as defined by Dzurisin and others (1984). Here again, effect of eruption is to superpose large negative feedback events on more general pattern, based on intrusive balances, which circulates in vicinities of two characteristic stationary regions of summit volume, even though future states are expressed in terms of total supply rates (see similar patterns in fig. 51.23 restricted to summit rates). Dates are given for chronological perspective. Major eruptions (of the order 0.1 $km^3$) are indicated by asterisks; they apparently have occurred within a fairly narrow interval of attractor-like circulation, implying that eruption may reflect an intrusive feedback circulation within a characteristic bandwidth of rate-volume relations (see discussion of fig. 51.18). Note that Kalapana earthquake of 1975 occurred during a time of extreme positive divergence from localized circulations, while eruptions occurred in vicinities of median states; both correlate with summit-rift intrusive balances. ***A***, Summit supply volume versus summit supply volume plus total supply-rate increment per year (extrapolated 6-mo rate); this diagram, like figure 51.23, is generated totally on the basis of summit tilt data (see discussion in Dzurisin and others, 1984). ***B***, Summit storage volume versus summit storage volume plus net rate increment (supply minus eruption) per year. Circled point, beginning of record; x, end of record.

compensates oscillations of stress related to flow rates, rates of solidification, and so on (see Hardee, chapter 54). A logistical interpretation of such balances leads to the analogous inference that there are characteristic regimes of oscillatory behavior that may be products of the path of evolution without the intervention of any externally applied forcing frequency. The inclusion of external influences, however, may also be subsumed by the pattern in a way that is then indistinguishable from the endogenous periodicities. Correlations with characteristic frequencies of external signals may be observable only during times when there are reinforcements of the endogenous periodicities or when the external influence is so large that it overrides the previous patterns.

## UNIQUENESS IN PATTERNS OF VOLCANIC EVOLUTION

The words "unique," "pattern," and "evolution" used together raise issues fundamental to prediction as a goal of the natural sciences. I will attempt to summarize a viewpoint concerning their application to volcanology, suggested by the foregoing analysis, as the basis for my concluding comments.

First, I realize after some deliberation, that any rigorous statement concerning this topic is likely to contradict itself before it proceeds very far. Therefore, I limit conclusions to some questioning remarks concerning ways in which the present results may differ from or resemble other viewpoints concerning natural processes. If there is an accepted theory or body of knowledge concerning volcanic evolution (or the meaning of "natural evolution" in general), I do not know where it is stated, so I cannot say that I am commenting on any particular form of conventional wisdom.

Unique means literally "being without a like or equal." That much seems easy, until such questions are asked: How does one know there is no like or equal? Just how much alike do things have to be to be called "like"? What numerical tolerance is applied to

quantitative measures of likeness? What does "equal" mean in any natural context? What are the tolerance limits of numerical equality? (Numerical dynamics makes the latter problem vivid. In some regimes, changes by several digits in the first decimal place of a normalized unit quantity do not change the likeness or equality of a pattern, expressed in terms of periodicity. However, near conditions of critical change between periodicity regimes, such as from period-doubling to chaotic, the likeness of patterns can change drastically with numerical changes at the limit of computer precision. That is to say, in this respect, one part in $10^6$ is a large change, in that periodic equality and likeness are drastically changed. This point is illustrated qualitatively in figure 51.16; see May, 1976, for some numerical examples.)

The word "pattern" can be applied to a crystal structure or to a bomb blast. Can one or the other be said to be either unique or nonunique? "Evolution," at least to some protagonists, implies uniqueness in the sense of a path-dependent process involving so many variables that it seems inconceivable that any given structural stage will ever repeat itself exactly. By this view, natural evolution never has nor ever will construct two identical volcanoes. That is, no complex form, including life, ever evolves in exactly the same way twice in the natural record. Yet, ideas of model building, fabrication, cloning, and even the genetic engineering of arbitrarily designed living forms are now almost commonplace and raise questions such as those mentioned above concerning what is meant by the words "unique," "pattern," and "evolution." Although no fundamental discussion of predictability and forecasting can really avoid such conundrums of science, I will attempt to restrict my conclusions to issues of necessarily rather vague criteria of pattern recognition.

If one were to digitize the coordinates of every piece of shrapnel and debris from every bomb blast in the history of explosives technology, it is highly unlikely that any two lists of numbers would be identical, except for individual or short sequences of numbers which may be similar because of the limits of resolution. Yet people who study such patterns, or patterns of shotgun blasts, can classify different types of shells and explosive materials simply in terms of learned recognitions of pattern morphologies.

Uniqueness in any applied sense of recognition is apparently judged in terms of some, usually unspecified, classification of relative complexity. In that context, the question of forecasting complex behavior is partly one of recognizing a class of complexity as distinct from any other class of complexity (implicitly, this also means that there exists some matrix or background system of states that is simple to some recognizable degree relative to what is called complex). If the recognition of distinguishable complexity is accurate, however, it subsumes the issue of forecasting, because the behavior it is desired to forecast is not separable from the criteria of recognition. One can test this idea by contemplating the recognition of any dangerous animal or of poison ivy. Their recognition and the forecasting of consequences are based on a complex system of evolved information; it is a rare person who would choose to attempt prediction solely on the basis of statistical study of the behavior of the particular specimen or situation confronting him. Yet, that is the way some investigations seem to approach volcano and earthquake hazards. Similar processes are operative even when the species is unknown; behavioral forecasting operates within a context of what is presumed will be a recognizable complexity. That recognition, however, obviously must include its own evolution (the reading of the complexity, the learning of the behavior, and the formulation of the forecast).

These comments may sound familiar to anyone who has spent some time studying the eruptions of Kilauea Volcano, or anyone who has studied the patterns of ocean breakers over a period of variable tides and weather on a particular stretch of beach. The behavior of breaking waves offers a particularly apt comparison to issues of volcanic prediction in the light of patterns studied in this paper.

A breaking wave represents a locus of familiar form and generally predictable action which is constructed in detail by the operation of progressive folded feedback from a more general state of chaotic motion. The trajectories of individual water molecules are statistically turbulent; no individual particle trajectory can be predicted in detail, except in the sense of a generalized involvement in a wave cycle. Yet, at stages of growth just prior to and during the course, say, of a surfer's ride, the waveform is highly familiar and even predictable. From the viewpoint of particle trajectories, no two ocean waves are demonstrably identical, hence each is unique. From the standpoint of recognition and regimes of behavior they are familiar and predictable, hence nonunique, except for the unexpected event (for example, a tsunami).

For ocean breakers, the demarcation between the familiar and the unfamiliar and (or) unexpected event (from a fisherman's or surfer's viewpoint) represents a practical criterion for distinguishing between endogenous and exogenous processes in the sense used earlier in this paper. Yet, on a global basis the general states of ocean circulation are net effects of all such processes. Therefore, the terms endogenous and exogenous, too, are relative to the goals of pattern recognition.

If length permitted, it would be possible to derive a series of logistical diagrams that would describe the relation between, say, water level and time along a stretch of coast during a period of variable barometric pressure (for, example, during the passage of a storm front). Expressed as maps of present versus future heights, such diagrams (as I have drawn them from published storm-wave data) resemble the cyclical control loops outlined in figures 51.17 and 51.18. In this case, however, the meaning of the feedback loops is fairly obvious in terms of the incidence, amplitudes, and repetitive frequency ranges of rising storm waves.

From the logistical viewpoint, figures 51.20–51.23 indicate that the recognizable behaviors of Kilauea Volcano may operate in a fashion somewhat parallel to that of storm fronts and breaking waves. The circulatory excursions of volumetric states relative to quasi-stationary states (for example, figs. 51.22 and 51.23) are analogous to frontogenesis associated with an interval of wave evolution. The implications for long-range forecasting are also parallel. A forecast of wave heights on a given stretch of beach depends critically on a knowledge of frontogenesis on at least a regional scale, as well as on such background information as what are considered normal tidal heights. The familiarity of the resulting local pattern is therefore contingent on a familiarity with other contributing patterns on both smaller and larger scales of time and size. Thus, a forecast on a given scale is ultimately conditioned by

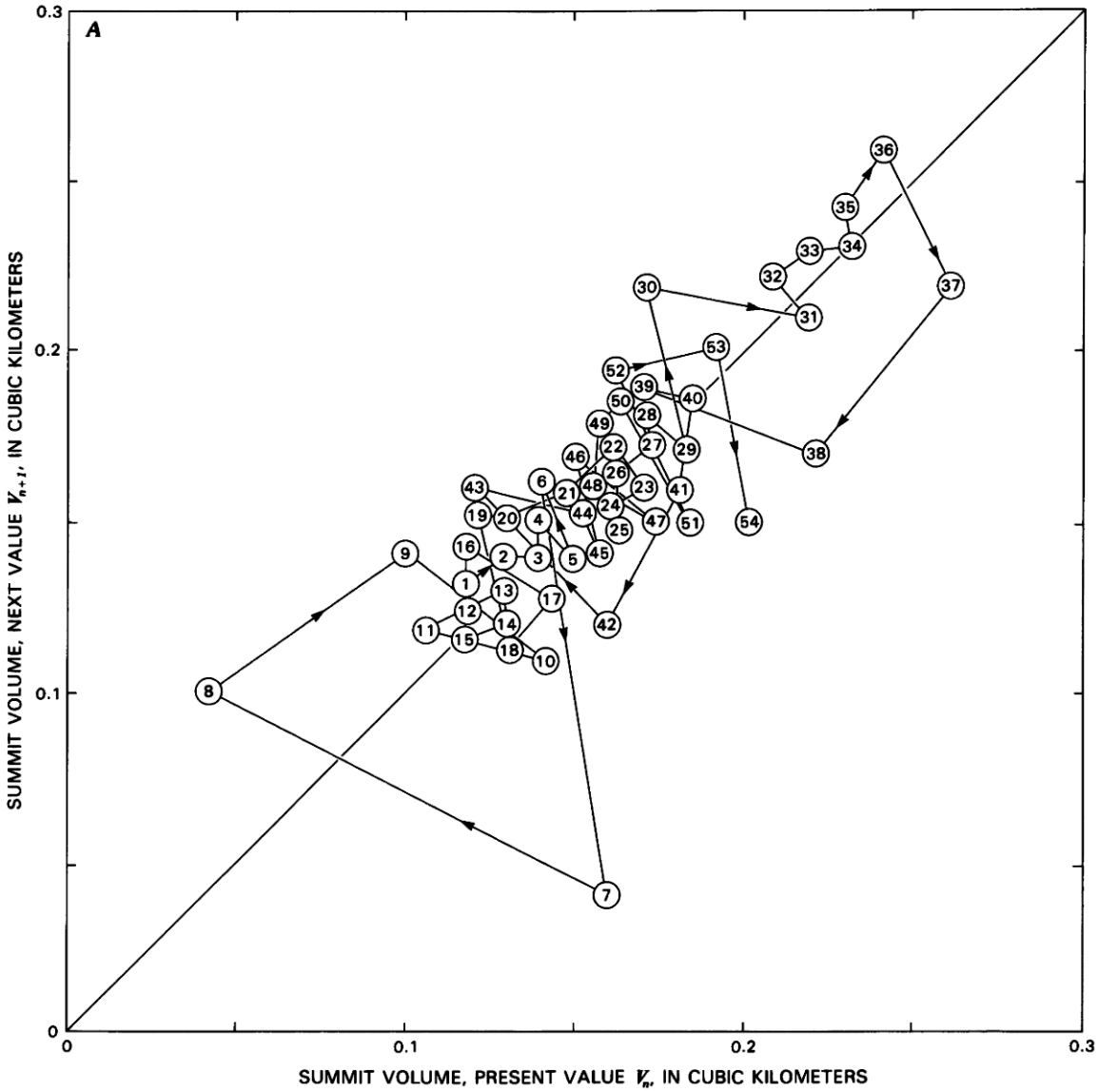


FIGURE 51.23.—Present-future volume states of summit reservoir of Kilauea. Numbers are chronological at half-year intervals beginning with (1) in January 1957. These plots resemble figure 51.22*A*, except that they reflect only summit rate variations rather than total rate variations (that is, they reflect inflation input minus deflation output of summit chamber based on interpretation of tilt data by Dzurisin and others, 1984). Asterisks again mark vicinities of major eruptions, and location of trajectory during time of 1975 earthquake is also indicated. These diagrams and figure 51.22*A* offer an exceedingly simple technique of logistic mapping of future eruption and earthquake patterns based on existing measurements of summit tilt without requiring other information. ***A***, Plot of present value versus next value, based on figure 51.5*A*, in which rate variations are implicit. ***B***, Plot of summit volume versus summit volume plus summit supply-rate increment per year (yearly extrapolation of 6-mo rate shown at each 6-mo interval). This graph amplifies effects of rate amplitudes but illustrates same pattern as in figure 51.23*A*.

both an even more local and a more global forecast; that is to say, the confidence in our recognition of familiarity is conditioned by our confidence in recognizing some more universal pattern of familiarity.

A probabilistic weather forecast evidently represents the measure of nonrecognition of what is, at least potentially, quite familiar. In order to be as candid as possible in the forecast, therefore, it would

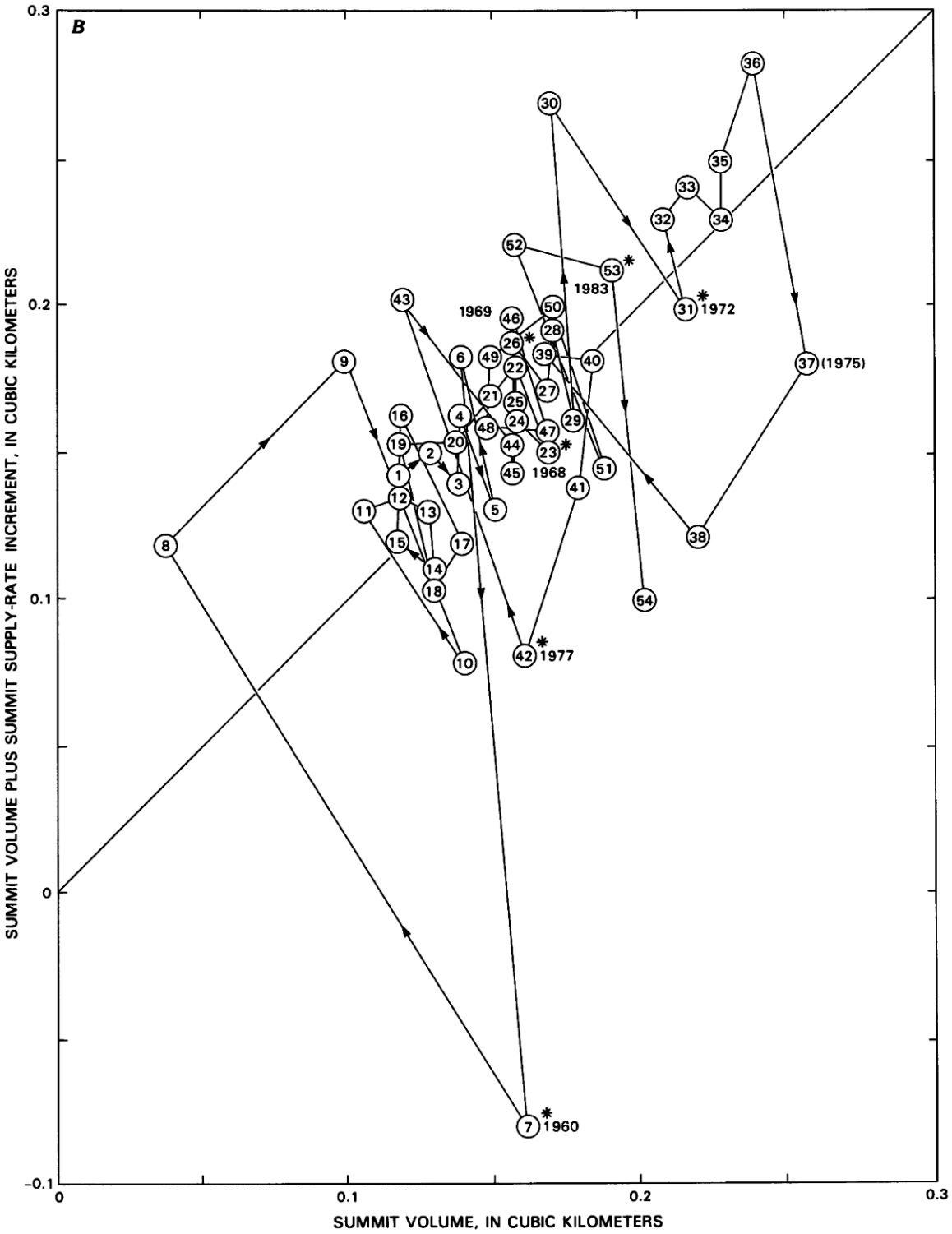


FIGURE 51.23—Continued

have to be concatenated some way according to the possible arrays of logistical folded feedback encompassing the consequences of recognition of all potentially active control loops. The potential diversity and complexity in predicting reasonable variants of diagrams like figures 51.17, 51.18, 51.22, and 51.23 obviously is large. Nevertheless, these alternative histories are integral aspects of the complexity that must be learned if we are to improve the quality of prediction.

The problems of weather forecasting and eruption forecasting are basically little different from everyday processes of pattern recognition. The long timeframe involved in geologic processes and the possibility that there may be future events of unprecedented and hence unrecognizable form, however, are not encompassed by our usual scales of automatic recognition (an example was the May 18, 1980, eruption of Mount St. Helens, Washington; on the other hand, at least several individuals clearly did recognize the potential for that eruption on the basis of familiarity with multiple lines of long-term evidence). The utility of logistical analysis for volcano-hazards forecasting stems from an ability to construct descriptions of folded feedback representing a variety of different scales of volcanic processes. Indications of self-similarity, such as those pointed out earlier in this paper, are important clues to the validity of this approach.

For example, examination of logistical feedback on the scale of monthly variations during the one-year record of figure 51.5*B* also reveals a pattern that shows scaled-down circulations resembling the 28-year pattern of figure 51.23. Another diagram (not shown) is based on the timing of the secular evolution of the Hawaii-Emperor Chain scaled down by a factor of $10^6$. The resulting synthetic record also resembles figure 51.23, suggesting self-similarity in the form of circulations about characteristic stationary states at the larger scale. A literal interpretation of this construction would be that the asthenosphere-lithosphere section has relative properties resembling the interactions of the generalized summit and rift reservoirs. The compatible volume scale of magma in the region of storage, relative to the summit reservoir (that is, $10^6$ times larger), would be on the order of $10^5$ km$^3$, which is appropriate to the size scale of individual islands (closely coordinated groups of volcanic edifices) along the chain.

The logistical approach can be applied as well to positive-negative rate balances during the growth of fractionated magma reservoirs. Preliminary graphical and numerical experiments along these lines suggest that the structures and periodicity scales in time and size of caldera-forming silicic ash-flow systems may behave in principle much like the diagrammatic processes of folded feedback described in this paper. Obviously, the problem is more intricate because of the multiplicity and scale ranges of control loops. In principle, however, conditions of storage, states of fractionation, and eruption represent circulations about nested sets of stationary basins of attraction much like those described in figures 51.15–51.18. The parallels between conditions of charge and discharge (and eruptibility) of a magma chamber with those describing the conditions of the breaking wave apply as well to nested systems of volcanoes. The only differences are in the varieties of timing and size scales of processes analogous to frontogenesis. In silicic cratonic systems, this aspect of the problem also involves variations of supply rate of primitive magma much like the variations shown by the Hawaiian systems (Shaw, 1985). Therefore, in this sense, there are important elements of self-similarity between patterns of oceanic and continental volcanism (also, compare earlier discussions of fig. 51.7 concerning size and repose time relations).

In the global context, logistical methods may be useful in studying correlations of volcanic periodicities with those of external forcing frequencies such as the earth tides. It seems evident from the earlier discussion that endogenous attractor-like periodicities having some regularity are possible in volcanic systems; basaltic systems apparently involve significant variability at the daily to yearly scale as well as at the more secular scales of variations. Analyses by Klein (1976) and by Dzurisin (1980) have confirmed the existence of significant fortnightly tidal correlations with volcanic behavior during certain intervals of time and location. If a crude endogenous periodicity exists in the vicinity of a more regular external (or exogenous) forcing frequency, entrainment of that frequency is likely. By implication, however, this could apply to any of a variety of sources of similar periodic effects (for example, there may be a 27-day solar geomagnetic signal that, according to numerous recent discussions, conceivably becomes involved even in mantle processes by way of momentum coupling between the atmosphere and the solid Earth affecting microsecond fluctuations in the Earth's rotation).

Forecasting terrestrial events evidently implies eventual familiarity with periodic behavior involving a very broad spectrum of cosmological phenomena. Our (at present) low probabilities of accurate geologic forecasting, aside from issues of humanly unknowable hidden variables, can be viewed either as a measure of the uniqueness of terrestrial evolution or as a measure of our reluctance to seek familiarity with a broader context (including major cosmological processes) that will make Earth processes more familiar. If familiarity with processes of change in the Earth is the aim of volcanological research, it will necessarily involve increased familiarity with methods for documenting the evolution and recognition of complex patterns along lines at least analogous to those proposed in this paper. Obviously, these broader goals will require increased emphasis on analysis of interdisciplinary sets of data with an aim toward discovery of common factors in their evolution.

I conclude with some suggestions concerning what might be done within the existing research efforts at the Hawaiian Volcano Observatory to test and (or) to implement the ideas outlined here. There is no doubt in my mind that the methods of documentation and analysis already in progress are of the highest quality and utility for purposes of day-to-day monitoring of hazards potentials. I recommend, however, that these day-to-day records also be plotted in terms of logistic diagrams such as those constructed in this paper. The same approach can be applied to a variety of different scales, ranging from the records of individual episodes of fountaining behavior to long-term studies of the timing patterns in lava-flow stratigraphy. Similar remarks concern the analysis of seismicity and deformation patterns as data accrue. For example, seismic moments can be summed within specified domains, from scales of time and size associated with Kilauea to scales associated with the Hawaiian Archipelago, and their variations plotted in exactly the same format

as the variations in magma supply (see Shaw, 1980). In an analogous way, times between earthquake events and eruptive events (either separately, or in combination) can be plotted at different scales of resolution to create what can be called attractor maps of possible repetitive patterns and trajectories of change. Such an approach is analogous to the method used by Shaw (1984) to document and classify dynamical regimes of nonlinear drop formation in the leaky-faucet experiments mentioned earlier. Also, volume-time data for deformations of the east rift zone of Kilauea could be plotted in much the same way as the summit-tilt data. Trajectories of circulation could be updated incrementally, as are the present plots of summit tilt versus time.

All these additional maps of the dynamical states of the volcano will provide an additional pictorial image and a greater feeling of confidence in describing patterns of waxing and waning activity. In the process, it may become more evident why eruptions, earthquakes, and other events (for example, large-scale landslides), occur where they do in the cycles of repetitive states such as those illustrated in this paper. Needless to say, we are sorely in need of the same sets of data for parallel analyses of Mauna Loa. In view of the current signs of a waxing period of activity there (see figs. 51.4, 51.7), this goal would appear to be of high priority.

Even though the patterns illustrated here would be formally classed in the chaotic regime of attractor dynamics, this does not mean that they have no predictive value. There are clear indications of characteristic patterns of repetition, even if they are not periodically exact. That is to say, prediction, in this sense, stems from an ability to identify multiple sequences of indications of trajectorial trends toward conditions of imminent instability (that is, toward conditions typical of various types of intrusive episodes, eruption, changing edifice-deformation states, or earthquakes). In the chaotic mode, individual sets of trajectories do not repeat themselves exactly, but some composite set of multiple aperiodic trajectories may be diagnostic (that is, a chaotic attractor is very much a recognizable entity, even though any subset of points may be totally unique and mystifying when examined out of context). In principle, the same criteria are automatically activated when we recognize and predict the behavior of any human individual. Prediction is far from infallible, but if I know a person's habits well, it is often obvious what the behavior will be in sufficiently familiar circumstances. The same could be said of predictive abilities concerning traffic flow in a large metropolitan area. Although no individual trajectories of motion are likely to repeat exactly in daily, weekly, monthly, and yearly cycles, most of us who live in such environments can say, even during a nonperiodic episode (that is, patterns within those that clearly correlate with time of day), what will happen next. At that level of familiarity, statistical probabilities are very useful ways to document that what we sense happening is, in truth, likely.

## REFERENCES CITED


Burks, A.W., ed., 1970, Essays on cellular automata: Urbana, Ill., University of Illinois Press.

Campbell, David, Crutchfield, J., Farmer, D., and Jen, E., 1985, Experimental mathematics: The role of computation in nonlinear science: Communications of the ACM (Association for Computing Machinery), v. 28, p. 374–384.

Dana, J.D., 1849, United States Exploring Expedition, during the years 1838, 1839, 1840, 1841, 1842: Geology: Philadelphia, v. 10.

Duffield, W.A., Bacon, C.R., and Dalrymple, G.B., 1980, Late Cenozoic volcanism, geochronology, and structure of the Coso Range, Inyo County, California: Journal of Geophysical Research, v. 85, p. 2381–2404.

Dzurisin, Daniel, 1980, Influence of fortnightly tides at Kilauea Volcano, Hawaii: Geophysical Research Letters, v. 7, p. 925–928.

Dzurisin, Daniel, Anderson, L.A., Eaton, G.P., Koyanagi, R.Y., Lipman, P.W., Lockwood, J.P., Okamura, R.T., Puniwai, G.S., Sako, M.K., and Yamashita, K.M., 1980, Geophysical observations of Kilauea Volcano, Hawaii, 2: Constraints on the magma supply during November 1975–September 1977: Journal of Volcanic and Geothermal Research, v. 7, p. 241–269.

Dzurisin, Daniel, Koyanagi, R.Y., and English, T.T., 1984, Magma supply and storage at Kilauea Volcano, Hawaii, 1956–1983: Journal of Volcanology and Geothermal Research, v. 21, p. 177–206.

Gardner, Martin, 1983, Wheels, life, and other mathematical amusements: San Francisco, W. H. Freeman.

Gosper, R.W., 1984, Exploiting regularities in large cellular spaces, *in* Farmer, D., Toffoli, T., and Wolfram, S., eds., Cellular automata: New York, North-Holland Physics Publishing, p. 75–80.

Gruntfest, I.J., 1963, Thermal feedback in liquid flow; plane shear at constant stress: Transactions of the Society of Rheology, v. 7, p. 195–207.

Jackson, E.D., Silver, E.A., and Dalrymple, G.B., 1972, Hawaiian-Emperor Chain and its relation to Cenozoic circumpacific tectonics: Geological Society of America Bulletin, v. 83, p. 601–617.

Jackson, E.D., and Shaw, H.R., 1975, Stress fields in central portions of the Pacific plate: Delineated in time by linear volcanic chains: Journal of Geophysical Research, v. 180, p. 1861–1874.

Judson, H.F., 1979, The eighth day of creation: New York, Simon and Schuster.

Klein, F.W., 1976, Earthquake swarms and the semidiurnal solid earth tide: Royal Astronomical Society Geophysical Journal, v. 45, p. 245–295.

———1982, Patterns of historical eruptions at Hawaiian volcanoes: Journal of Volcanology and Geothermal Research, v. 12, p. 1–35.

Lachenbruch, A.H., 1980, Frictional heating, fluid pressure, and the resistance to fault motion: Journal of Geophysical Research, v. 85, p. 6097–6112.

Mandelbrot, B.B., 1982, The fractal geometry of nature: San Francisco, W.H. Freeman.

May, R.M., 1976, Simple mathematical models with very complicated dynamics: Nature, v. 261, p. 459–467.

Poundstone, William, 1985, The recursive universe: New York, William Morrow and Co., Inc.

Shaw, H.R., 1969, Rheology of basalt in the melting range: Journal of Petrology, v. 10, p. 510–535.

———1973, Mantle convection and volcanic periodicity in the Pacific: Evidence from Hawaii: Geological Society of America Bulletin, v. 84, p. 1505–1526.

———1980, The fracture mechanisms of magma rise from the mantle to the surface, *in* Hargraves, R.B., ed., Physics of magmatic processes: Princeton, N.J., Princeton University Press, p. 201–264.

———1985, Links between magma-tectonic rate balances, plutonism and volcanism: Journal of Geophysical Research, v. 90, p. 11275–11288.

Shaw, H.R., Jackson, E.D., and Bargar, K.E., 1980, Volcanic periodicity along the Hawaiian-Emperor Chain: American Journal of Science, v. 280–A, p. 667–708.

Shaw, Robert, 1984, The dripping faucet as a model chaotic system: Santa Cruz, Calif., Aerial Press.

Smith, R.L., 1979, Ash-flow magmatism, *in* Chapin, C.E., and Elston, W.E., eds., Ash-flow tuffs: Geological Society of America Special Paper 180, p. 5–27.

Souther, J.G., and Hickson, C.J., 1984, Crustal fractionation of the basalt comendite series of the Mount Edziza volcanic complex, British Columbia: major and trace elements: Journal of Volcanic and Geothermal Research, v. 21, p. 79–106.

Spence, D.A., and Turcotte, D.L., Magma-driven propagation of cracks: Journal of Geophysical Research, v. 90, p. 575–580.

Swanson, D.A., 1972, Magma supply rate at Kilauea Volcano, 1952–1971: Science, v. 175, p. 169–170.

van der Ziel, A., 1970, Noise: Sources, characterization, measurement: Englewood Cliffs, N.J.

Verveen, A.A., and Derksen, H.E., 1968, Fluctuation phenomena in nerve membrane: Institute of Electrical and Electronics Engineering, Proceedings, v. 56, p. 906–916.

von Neumann, John, 1966, Theory of self-reproducing automata (edited and completed by Arthur W. Burks): Urbana, Ill., University of Illinois Press.

Voss, R.F., and Clarke, J., 1975, '1/f noise' in music and speech: Nature, v. 258, p. 317–318.

Wadge, G., 1982, Steady state volcanism: Evidence from eruption histories of polygenetic volcanoes: Journal of Geophysical Research, v. 87, p. 4035–4049.

Watts, A.B., ten Brink, U.S., Buhl, P., and Brocher, T.M., 1985, A multichannel seismic study of lithospheric flexure across the Hawaiian-Emperor seamount chain: Nature, v. 315, p. 105–111.

# ELASTICITY AND CONTRACTANCY OF HAWAIIAN OLIVINE THOLEIITE AND ITS ROLE IN THE STABILITY AND STRUCTURAL EVOLUTION OF SUBCALDERA MAGMA RESERVOIRS AND RIFT SYSTEMS

*By* Michael P. Ryan


## ABSTRACT

Experimental data for the high-temperature elasticity of Hawaiian olivine tholeiite have been evaluated to 1133 K. Young's modulus and the modulus of rigidity demonstrate a linear decrease with increasing temperature. Regression equations developed for replicate runs during flexural resonance have yielded the following relation for the high-temperature Young's modulus: $E(T)=(6.054-0.00083T)\times 10$ GPa. For the rigidity, replicate runs conducted in torsional resonance have yielded the following regression relation: $\mu(T)=(2.615-0.00038T)\times 10$ GPa. Parallel experiments conducted to 973 K have yielded evaluations of the high-temperature expansivity of Hawaiian olivine tholeiite. The linear thermal-expansion coefficients range from $\alpha_L=4.58\times 10^{-6}$ °C$^{-1}$ at 373 K to $\alpha_L=7.93\times 10^{-6}$ °C$^{-1}$ at 973 K. Conducted on the same samples used for the elasticity studies, they have provided a set of internally consistent correction factors for the final evaluations of $E(T)$ and $\mu(T)$. Comparisons of the measured moduli and their temperature derivatives with theoretically predicted values are in good overall agreement. Comparisons of the measured high-temperature thermal expansivities with predictions based on mixing-model computations for basaltic blends of forsterite, augite, and labradorite compare favorably.

A model developed for the high-temperature elasticity of basalt uses the Voigt-Reuss-Hill averaging procedures to provide upper and lower bounds on the aggregate elasticity of basic and ultrabasic rocks. General in nature, it has herein been specialized for basalt. In the general treatment, the composition is variable, ranging from monomineralic aggregates to assemblages with multiple components. The resulting compositional model works directly with the single-crystal properties for each component: molar volumes, adiabatic elastic stiffness and compliance coefficients, and the Voigt and Reuss temperature derivatives for the bulk modulus and rigidity of each mineral phase. The Hill averaging procedure provides a set of median estimates for aggregate elasticity. The parametric contributions of spherical voids (vesicles) and elongate voids (microcracks) that weaken the otherwise pristine solid are incorporated by the self-consistent averaging procedure.

The pressure dependence of elastic-wave velocities for tholeiitic and alkalic basalt, gabbro, periodotite, dunite, and harzburgite is controlled by the progressive closure of microfractures with increasing depth in volcanic systems. For basalt and gabbro, pore-fluid-accessible fracture space is continuously squeezed out as the confining pressures increase within volcanic shields, thus providing a physical background and certain key elements in developing the concept of contractancy in magmatic systems. Combined with geologic observations that bear on the nature of macroscopic fracture networks near the surface of shield volcanoes, the role of contractancy rationalizes: (1) the highly nonlinear confining pressure dependence of compressional and shear wave velocities in intact basaltic rocks; (2) the systematics of $\partial V_p/\partial Z$ for the seismic-velocity profiles for Hawaii, including the low-velocity residuals that characterize the near-surface environment; and (3) the observed in-situ density systematics that characterize the stratigraphy of shield volcanoes, including the frequent observation of their low values at shallow depths. A corollary of the contractant behavior of shield volcanoes is the crossover in the in-situ densities of tholeiitic melt near its liquidus and that of its country-rock environment. This crossover occurs in the nonlinear region of the contractancy curves. In the heart of the crossover is a subregion of neutral buoyancy, where $\rho_{country\ rock}-\rho_{melt}\approx 0$. This behavior rationalizes the long-term stability of tholeiitic magma reservoirs and the frequently observed resting place of intrusives (for example, dikes in rift zones) that lie just beneath the surface of active volcanoes. As Hawaiian volcanoes evolve, they carry their contractancy curves with them. The concept of a contraction profile that has an evolutionary track paralleling the upward growth of the volcanic shield provides the mechanical rationale for the upward climb of subcaldera magma reservoirs as the shield progresses from youth to maturity.


## THE HIGH-TEMPERATURE ELASTICITY OF HAWAIIAN BASALT

### INTRODUCTION

Elastic moduli are essential to the computation of the displacements, strains, and stress distributions that occur in volcanic systems. Provided the level of the applied loading is below the elastic limit, the strains describing the resulting shape changes are recoverable, and load removal returns the body to its original condition. Imposing the idealization that the load application and strain response is independent of direction allows relating the moduli within a generalization of Hooke's law:

$$T_{ij}=\lambda\epsilon_{kk}\delta_{ij}+2\mu\epsilon_{ij}, \qquad (1)$$

where $T_{ij}$ is a symmetric second-order stress tensor, $\epsilon_{kk}$ is a tensor relating volumetric or dilatational strains to the applied loading ($T_{ij}$), $\epsilon_{ij}$ is a second-order tensor that describes the distortional strains that have been generated, $\delta_{ij}$ is the Kronecker delta, and $\lambda$ and $\mu$ are the Lamé elastic constants. The Lamé constants are in turn related to the Young's modulus $E$, the shear modulus $G$, and Poisson's ratio $\nu$ by:

$$\mu = G = \frac{E}{2(1+\nu)} \quad (2)$$

and

$$\lambda = \frac{\nu E}{(1+\nu)(1-2\nu)}; \quad (3)$$

the bulk modulus $K$, relating mean pressure and volumetric strain, is

$$K = \lambda + \tfrac{2}{3}G = \frac{E}{3(1-2\nu)}. \quad (4)$$

Two of these moduli are of particular use in volcanology. They are the Young's modulus and the modulus of rigidity, or the shear modulus. These moduli are the familiar connecting links between uniaxial stress and strain and shear stress and strain. They are indispensable in continuum analyses of the displacement, stress, and strain fields that accompany magmatic intrusion, the subsidence produced by magmatic withdrawal, and numerous related problems concerned with the mechanics and dynamics of active volcanoes. The experimental program has grown out of the author's interest in the fracture mechanics of intact basaltic rocks near their melting point, in low-pressure environments. Accordingly, a series of experiments was undertaken to provide data on the mechanical parameters required for computations related to crack growth near the solidus.

Prior studies of the temperature dependence of the elastic moduli of basalt have been of two types. The first approach focused on the evaluation of compressional- and shear-wave velocities primarily as a function of confining pressure, but taken over a moderate range in temperature. An example of this approach was provided by Hughes and Cross (1951) and Hughes and Maurette (1957), who evaluated compressional-wave velocities ($V_p$) and shear-wave velocities ($V_s$) (from which moduli may be derived) to 600 MPa (6 kbar) and 300 °C. The second approach seeks to determine the temperature dependence in high-temperature environments that cover a significant fraction of the interval from ambient to solidus temperatures. Here, the elastic moduli were of primary interest. Existing work on basalt is limited to the studies of Volarovich and Gurvich (1957), Iida and Kumazawa (1960), and Wingquist (1971). Kern and Richter (1979) extended the earlier temperature limits to 700 °C, in a series of $V_p$ and $V_s$ determinations on altered basalt from the Faroe Islands, with confining pressures to 600 MPa.

The objective of this section is evaluation of the elasticity and expansivity of Hawaiian olivine tholeiite. The primary focus is the evaluation of Young's modulus and the modulus of rigidity, to 1,133 K. Linear thermal-expansion coefficients have been measured in a parallel set of experiments to 973 K.

With respect to the evaluations of the elastic moduli, the present work complements the earlier studies—and is distinct from them—in: (1) combining a theoretical approach for moduli prediction with a parallel experimental program, and using the results of the model predictions to rationalize the compositional and microstructural dependence of elasticity at high temperatures; (2) extending the temperature range from ambient to 1,133 K; (3) focusing on basalt from the Hawaiian province; (4) working with pristine samples that have been unaffected by alteration processes; and (5) refining the resonance approach to incorporate a series of correction factors that properly account for the effects of thermal expansivity.

For the purposes of this report, all rock-unit names are used informally, although some are formal names.

## ACKNOWLEDGMENTS

The collaborative support of Robert Koyanagi is gratefully acknowledged. Fred Klein prepared large-format seismic hypocenter maps. David Popish assisted with the early phases of protracted machine-shop activities. Logistical support by the staff of the Hawaiian Volcano Observatory has contributed in several ways. Particularly helpful have been Thomas Wright, Reginald Okamura, Arnold Okamura, and James Griggs. William F. Brace kindly provided samples of diabase. Ruthie Robertson prepared the typescript with characteristic accuracy and grace. Figures have been prepared with the assistance of Jewel Dixon, Lindel Keaton, Marcia Prins, and Betty Shallcross. Tom Chase kindly loaned marine bathymetry negatives. Thoughtful review comments by Richard C. Bradt, Earl K. Graham, Robert Y. Koyanagi, Manuel Nathenson, Eugene C. Robertson, Roger M. Stewart, and Robert I. Tilling have led to improvements in the manuscript. Portions of the work have been carried out with the support of a Grove Karl Gilbert Fellowship under the auspices of the Geologic Division of the U.S. Geological Survey. Additional support has been provided by the U.S. Department of Energy, Office of Basic Science, under interagency agreement No. DE-AI-1-79RA50294.

## MEASUREMENTS OF THE ELASTIC MODULI OF BASALT

An early consideration in the experimental program dealt with preparing appropriate samples. Sample-selection criteria included (1) an intact lithology that would be representative of volumetrically large portions of Hawaiian shields; (2) individual samples that are pristine; and (3) a sample site that provides for good cross-sectional exposures within the interior of lava flows. These criteria are well satisfied by the Boiling Pots flow units that crop out west of Hilo (fig. 52.1). Details of the sample sites and flow structures in cross section are provided by Ryan and Sammis (1978).

## THE BASALT OF BOILING POTS

### Mineralogy and Petrography

Petrographically, the basalt of Boiling Pots is characterized by phenocrysts and microphenocrysts of olivine, scattered microphenocrysts of hypersthene (almost invariably jacketed with augite), plagioclase, and some augite, set in a very fine grained groundmass of subcalcic augite, pigeonite, magnetite, plagioclase microlites, and dark-amber glass. Textural relations are shown in figure 52.2. Modal analyses (table 52.1) are representative of samples in the experimental evaluations of moduli and expansivity.

Electron-microprobe analyses of the crystalline silicates in the basalt of Boiling Pots were performed with an ETAC Autoprobe. The microprobe was operated at 15-kV accelerating voltage and 0.04-μA current and used a 2.0-μm-diameter focused electron beam. Polished petrographic thin sections were prepared from samples from positions in the basalt blocks adjacent to sample locations for high-temperature elastic moduli and expansivity measurements.

TABLE 52.1.—*Modal mineral abundance in the basalt of Boiling Pots*

[Totals for mineral groups are given in last column; values are in modal percent]

| | | |
|---|---|---|
| Olivine (phenocrysts) | 9.3 | 12.42 |
| Olivine (microphenocrysts) | 3.1 | |
| Hypersthene (augite-jacketed) | 2.8 | |
| Augite (microphenocrysts) | .1 | 32.91 |
| Subcalcic augite + pigeonite (groundmass) | 29.9 | |
| Plagioclase (microphenocrysts) | 1.8 | 37.37 |
| Plagioclase (microlites) | 35.4 | |
| Magnetite (euhedral, groundmass) | 4.3 | |
| Glass (with opaque dustings) | 12.9 | |

*Olivine.*—Olivine is present as subhedral phenocrysts ranging in mean diameter from 2 to 5 mm and as subhedral to anhedral microphenocrysts ranging from 2,000 by 1,300 μm to 520 by 130 μm. Opaque inclusions (chrome-spinel?) are common, while inclusions of amber glass are less common and are in the more poikilitic olivine. Inferred reaction with the melt has corroded crystal faces, and augite rims are present as continuous jackets and as closely spaced neighboring crystals. Transgranular fracture is nearly always present in the larger phenocrysts.

The forsterite content of olivine phenocrysts from the Boiling Pots samples was determined using the X-ray determinative curve of Yoder and Sahama (1957):

$$\text{Fo (in mole percent)} = 4{,}233.91 - 1{,}494.59\ d_{130}$$

where $d_{130}$ refers to the interplanar spacing (in Å) from the (130) reflection. The average of the determinations yielded a composition of $Fo_{90.1}$. The error associated with the determinative curve is 3 to 4 mol percent (Yoder and Sahama, 1957, p. 486). Zoning in olivine microphenocrysts was studied by use of the electron microprobe. Radial microprobe traverses from the center to edge of crystals show relatively magnesian cores and more fayalitic margins. The compositional range covered is $(Mg_{0.86}Fe_{0.14})_2SiO_4$ in the core to $(Mg_{0.78}Fe_{0.22})_2SiO_4$ near the margin. Errors attached to the determination of Mg and Fe are ±1.5 percent and ±2.0 percent, respectively. The combined X-ray analysis and microprobe analyses suggest that the forsterite content of Boiling Pots olivine ranges from $Fo_{90.1}$ in early phenocrysts to $Fo_{78.5}$ as the late olivine crystallized during microphenocryst formation.

*Pyroxenes.*—Augite is present as reaction rims on olivine and hypersthene microphenocrysts and as discrete euhedral to subhedral crystals ranging from about 200 to 100 μm in diameter. Individual microphenocrysts generally are optically homogeneous but may contain minute inclusions of glass. Microprobe analyses of augite microphenocrysts indicate compositions close to $Wo_{36}En_{50}Fs_{14}$.

Hypersthene microphenocrysts are elongate (1,000 by 100 μm) to stubby (75 by 75 μm) and are invariably mottled medium gray under crossed nicols. Euhedral prismatic (100), (010) faces are typically jacketed with augite reaction rims that range in thickness from 10 to 20 μm. Euhedral terminations, however, are rare, and the hypersthene laths have no augitic jacket on the terminations, suggesting breakage during postreaction fluid movement. Crystallographically aligned blebs, stringers, and lamellae of augite commonly are present within the hypersthene host and have the same optical orientation as the external jackets. Approximately aligned poikilitic zones frequently contain opaque-rich glass inclusions. Hypersthene laths that have grown into contiguity with a neighboring olivine microphenocryst may have jackets of augite that not only rim the hypersthene but enclose the olivine as well. In this role, augite has acted as the welding agent in the formation of occasional glomerocrysts.

Electron-microprobe studies of hypersthene microphenocrysts and their jackets of augite were performed using the ETEC Autoprobe. Hypersthene laths are relatively homogeneous with respect to Ca, Mg, and Fe and have internal compositional ranges near $Wo_{3.8-4.1}$, $En_{81.6-82.1}$, and $Fs_{13.9-14.2}$. The composition of the augitic jackets on the prismatic faces is $Wo_{32.8}En_{47.5}Fs_{19.5}$, suggesting that relative to the melt that produced most augite microphenocrysts, depletion in Ca and Mg and enrichment in Fe had taken place by the time augite jacketing occurred.

Pigeonite is present as irregular groundmass crystals that are invariably anhedral. Mean diameters range from 40 to 20 μm, and their diminutive size lets them occupy vacant positions between adjoining plagioclase microlites in the groundmass topology, thus giving the rock fabric an intergranular character.

*Plagioclase.*—Plagioclase is present both as sparse microphenocrysts measuring 400 by 60 μm and as tiny groundmass microlites in the 70- to 40-μm length range, with widths of approximately 20 μm. Twinning follows both the Carlsbad law and albite law, and most microlites have 3 to 8 albite-twin individuals. Plagioclase compositions were determined using the ETEC Autoprobe, where the 2-μm beam diameter permitted analyses to be performed in microlite interiors without including surrounding glass or groundmass clinopyroxene within the excitation volume. The results of microlite analyses span the compositional range $Ab_{27.3-39.0}$, $An_{72.2-60.0}$, $Or_{0.5-0.9}$.

Magnetite is present as discrete euhedral crystals whose equant dimensions are approximately 10 μm. These crystals form a minor groundmass component (4.3 modal percent), and they occupy interstitial positions between adjoining plagioclase microlites in the crystalline groundmass network. Glass is medium to dark amber and is generally heavily dusted with opaque particles. Glass is present as thin films separating subparallel plagioclase microlites and as scattered equant pools and triangular patches. No evidence for devitrification has been found and, with the exception of the associated opaques, the glass is optically homogeneous at all levels of magnification.

Plots of weight percent $K_2O + Na_2O$ versus weight percent $SiO_2$ for the Boiling Pots basalt fall well within the tholeiitic field on an alkali-silica diagram (see, for example, Tilley, 1950; Macdonald and Katsura, 1964). Consistent with a tholeiitic nature, suggested by relations between these oxides, is the common reaction relation between magnesian olivine and their rims of augite.

*Microstructure.*—The three-dimensional microstructure of several Boiling Pots olivine tholeiite samples was examined using a scanning-electron microscope (SEM). This method provided a means of examining: (1) crystal-glass relations between olivine, pyroxene, plagioclase, and the 13-modal-percent interstitial glass; (2) differences in the behavior of glass above and below the glass-transformation temperature, $T_g$; (3) intragranular and intergranular

microfractures and the appropriateness of the assumption of a needle-shape geometry for voids representing microfractures in the elastic microstructural model; and (4) vesicles and vesicle shapes to assess the assumption of spherical voids in the approximation used in the elastic microstructural model.

The study employed a Cambridge Stereoscan (600) scanning-electron microscope with a peak accelerating voltage of 25 kV and a maximum resolution of 250 Å. The electron source was a tungsten-wire filament operated at $10^7$ electrons $s^{-1}$ and was maintained under a vacuum of $10^{-5}$ mm Hg.

The results of the SEM study are as follows:

(1) The glass phase covers practically all matrix crystals with a coat of varying thickness. The only general exceptions to this phase are crystals that are immediately adjacent to vesicles.

(2) Spherical geometry is a fair to good approximation for the shape of most observed vesicles, thus suggesting that the assumption of spherical voids in the elastic microstructural model is appropriate (see section "Modeling the High-Temperature Elasticity of Basalt").

(3) Needle-shaped geometry may be a fair approximation for the shape of many observed microcracks. (This is not always the case, however, as many microcracks have irregular geometries that resemble complexly warped planes.)

*Porosity.*—Most of the porosity in basalt samples may be attributed to spherical or nearly spherical vesicles that, in general, are not interconnected. Another type of porosity occurs in the form of microcracks that are produced as a result of microscopic contraction anisotropy in the fabric of the cooling rock. These microcracks take the form of intracrystalline fractures (especially in olivine microphenocrysts) and intercrystalline fractures along the margins of microlites and surrounding glass.

Because much of the total porosity is of an isolated form, measurement of the absolute porosity was the appropriate approach to assess the overall level of porosity.

The absolute porosity (in percent) may be expressed as

$$\Phi_A = \left(\frac{V_v + V_{mc}}{V_v + V_{mc} + V_{xtl+gl}}\right) \times 100, \qquad (5)$$

*where* $V_v$ is the volume of vesicles, $V_{mc}$ is the volume of microcracks, and $V_{xtl+gl}$ is the volume of the matrix of crystals and glass.

To measure absolute porosity, the bulk (total) volume of a 5.25-cm by 1.25-cm by 0.75-cm sample was measured with a mercury pycnometer. The sample was crushed to 100 mesh with a percussion mortar and pestle. This method effectively released the contribution of the noncommunicating pores and microcracks in the interior of the sample, so that their volume would be added to the total void volume. The volume of the crushed sample was measured using a Russell volumeter, employing kerosene as the working fluid. The difference between the pycnometer and the volumeter measurements is the contribution of vesicle and microcrack volumes to the total (bulk) volume. The measured values are believed to be accurate to ±0.1 percent. Measured absolute porosities ranged from 21.4 to 14.3 percent for combined samples.

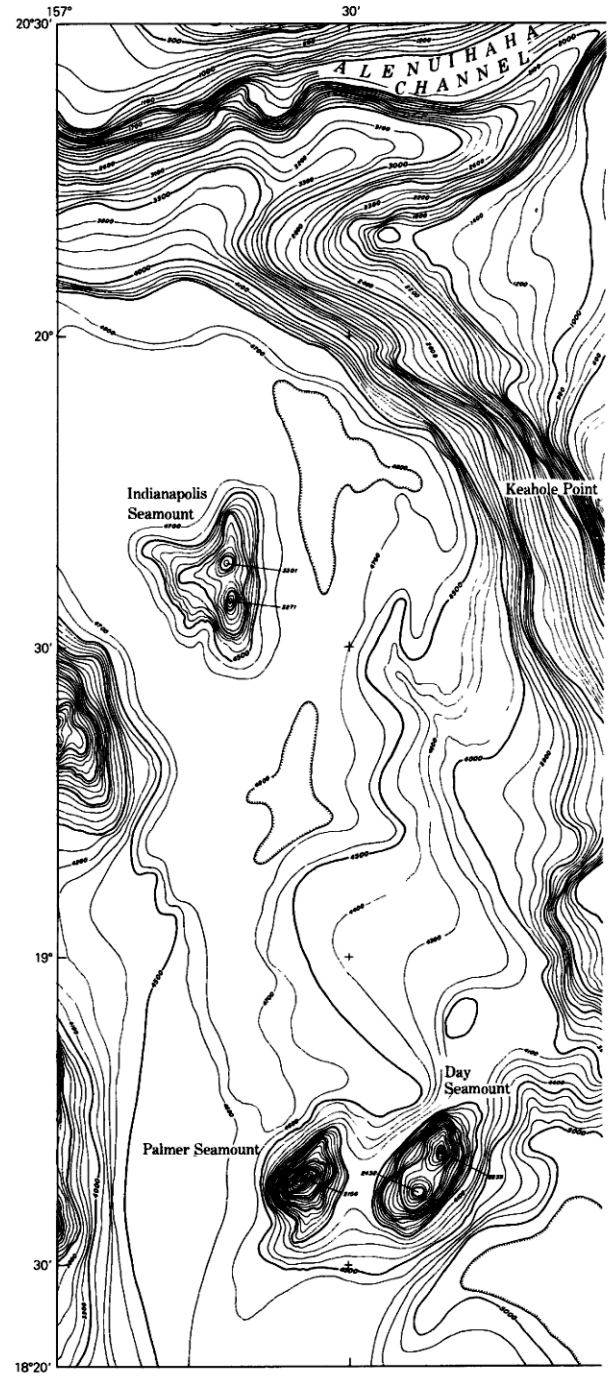


FIGURE 52.1.—Topography of Island of Hawaii, showing summits of principal volcanic shields, Loihi Seamount, and major seamounts of south Hawaii. Surmounting subcaldera magma reservoirs and rift zones of active volcanoes Mauna Loa, Kilauea, and Loihi Seamount is a heavily fractured veneer of country rock characterized by exceptionally low in-situ values of compressional-wave velocity

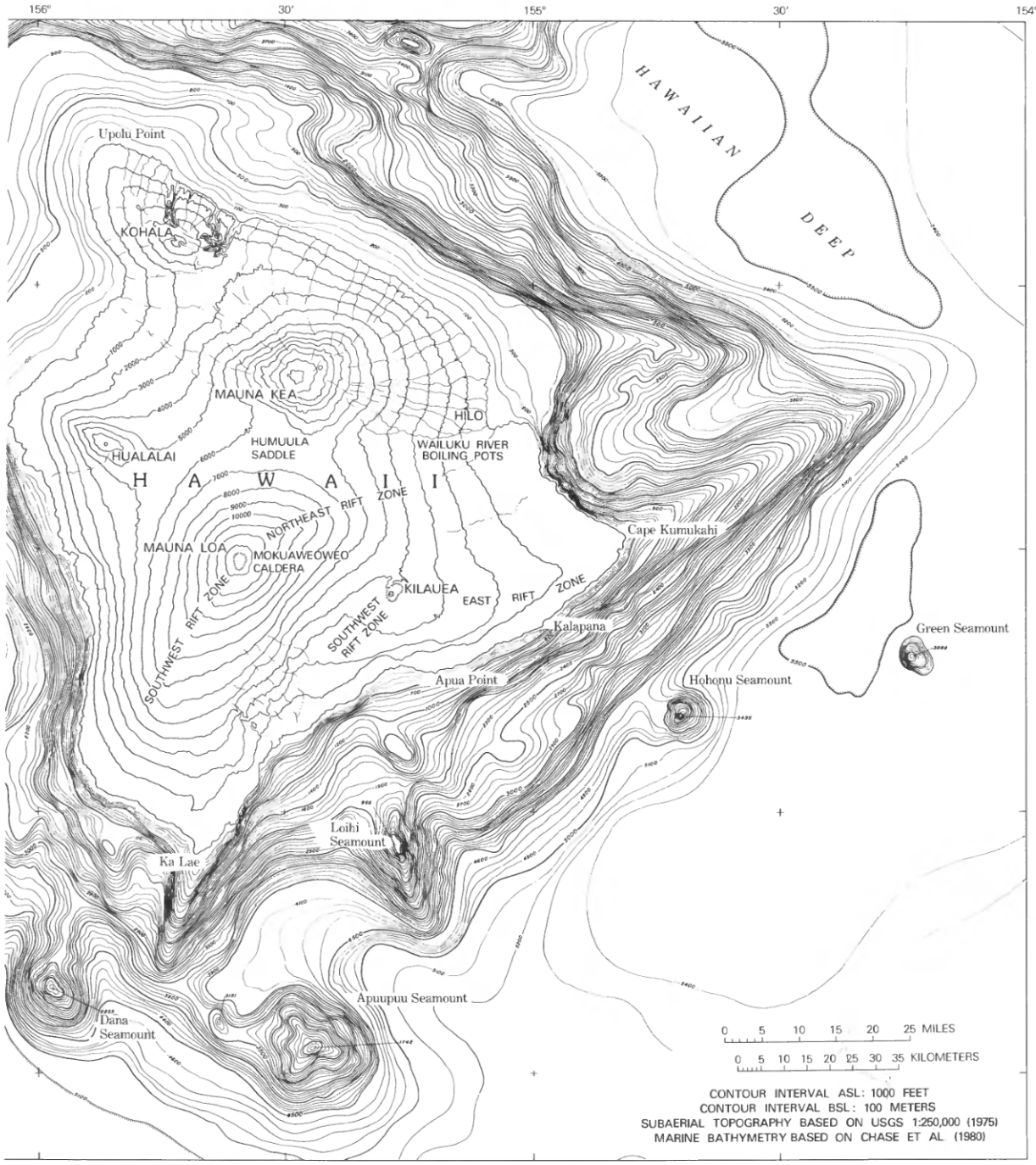


and density. Supersolidus intrusives within magma reservoirs and rift zones of these growing shields are stabilized by crossovers in in-situ density of tholeiitic melt near its liquidus and that of surrounding—and surmounting—country rock. As volcanic centers evolve, they carry their surficial veneer of low-density country rock with them, continuously providing a region of neutral buoyancy for magma within the shield. This, in turn, provides mechanical rationale for upward climb of subcaldera magma reservoirs, as evolving volcano progresses from submarine infancy through subaerial maturity to old age.

## EXPERIMENTAL PROGRAM

The experimental program for the evaluation of elastic moduli employs the dynamic resonance technique developed by Spinner and Tefft (1961) and is based on earlier approaches of Ide (1936) and Förster (1937), who first recognized that controlled mechanical resonance provided a means of measuring the elastic moduli of solids. The computational approach used in evaluating the Young's modulus and shear modulus from the respective flexural and torsional resonant frequencies is based on the presentation in Hasselman (1961).

A Nametre (model 12) acoustic spectrometer was used to induce and record the resonant vibrational frequencies. A schematic diagram of the spectrometer and supporting equipment is shown in figure 52.3. The spectrometer consists of a Hewlett-Packard (3310A) function generator, which produces a sinusoidal output waveform ranging from 0.01 Hz to 100 kHz. Mechanical vibrations were transmitted to the sample by an Astatic commercial cutting head. A second Astatic (x-26) cutting head acted as a pickup transducer. The transducers are composed of quartz crystals, which provide the piezoelectric transmission and reception. Output from the pickup-transducer power amplifier was displayed on a Hewlett-Packard (122A) cathode-ray-tube oscilloscope, which provided a

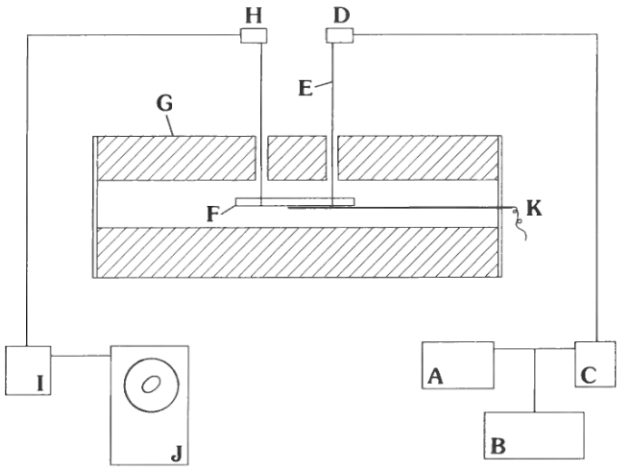


FIGURE 52.3—Schematic diagram of components of assembly for dynamic flexural and torsional resonance measurements at high temperatures: (A) variable-frequency signal generator; (B) digital frequency counter; (C) power amplifier; (D) driving transducer; (E) sample suspension system; (F) sample; (G) Kanthal-wound resistance furnace; (H) pickup transducer; (I) pickup power amplifier; (J) oscilloscope; and (K) platinum-platinum·10 percent rhodium thermocouple.

FIGURE 52.2—Photomicrograph of olivine tholeiite from Boiling Pots. Olivine phenocrysts are surrounded by plagioclase microlites set in a finer grained groundmass of pyroxene microcrysts and intercrystalline glass (heavily dusted with opaques). Under crossed nicols. Field of view is 400 μm by 600 μm.

graphical presentation of vertical-displacement amplitudes in the resonating sample. An associated voltmeter provided the means of maximizing the sample resonance via maximizing the pickup-transducer power-amplifier voltage. Digital readout of the resonant frequency was provided by a Hewlett-Packard (5325B) frequency counter with a range of 5 Hz to 10 MHz and a lower resolution of 0.01 Hz.

Ambient temperature measurements for both the Young's modulus and shear modulus evaluations employed electromagnetic noncontact transducers that induced and picked up vibration in the sample via metal tabs epoxyed to the sample ends.

High-temperature measurements employed an Alumel-wire suspension system connected from the transducers to the sample nodal points. A Satec Systems (Se-17p) Kanthal-wound, horizontally mounted furnace provided the high-temperature environment. Temperatures were maintained with a Thermoelectric (400 series) proportional controller, and a platinum-platinum·10 percent rhodium (Pt-Pt·10Rh) thermocouple.

### Dynamic Young's Modulus at Ambient Temperatures

The Young's modulus ($E$) is evaluated at ambient pressure and temperature by applying equations relating the resonant frequency of the first mode of flexural vibration of an isotropic, homogeneous, elastic prism with a rectangular cross section to the sample mass and shape. Thus,

$$E=\left(\frac{0.94645Cmf^2}{B}\right)\times 10^2 \text{ MPa}, \tag{6}$$

where $E$ is the Young's modulus evaluated at 25 °C, $m$ is the mass (in grams) of the sample, $f$ is the resonant frequency (in hertz) for the first mode of flexural vibration, $B$ is the vertical dimension (in centimeters) of the cross section perpendicular to the direction of vibration, and $C$ is a shape factor given by Hasselman (1961):

$$C=\left(\frac{D}{L}\right)-3\left[1+6.585(1+0.0752\nu+0.8109\nu^2)\left(\frac{D}{L}\right)^2 - \frac{100.083(1+0.2023\nu+2.173\nu^2)\left(\frac{D}{L}\right)^4}{12+76.06(1+0.14081\nu+1.536\nu^2)\left(\frac{D}{L}\right)^2} - 0.86806\left(\frac{D}{L}\right)^4\right], \tag{7}$$

where $D$ is the thickness (in centimeters) of the sample cross section parallel to the direction of vibration, $L$ is the sample length (in centimeters), and $\nu$ is Poisson's ratio.

Samples were prepared by machining 5.00- by 1.25- by 0.65-cm prisms from blocks of basalt that were judged to be homogeneous with respect to the distribution of vesicles and olivine phenocrysts. These rectangular bars were then resin-bonded to steel blocks, and the upper (free) surface ground parallel to the base in an automatic grinding machine. Rotation of the sample and subsequent regrinding assured that the upper and lower surfaces were parallel.

Sample dimensions were measured with a Mitutoyo micrometer, with a stated accuracy of ±0.002 cm. Sample masses were measured using a Mettler electronic balance, with an accuracy of ±0.001 g. Sources of error reside primarily in the measurements of sample geometry (length, width, and height) and sample mass. An additional source of error may result from slight deviations in rectilinearity of the overall geometry. Maximum resolution of resonant frequency on the Hewlett-Packard digital counter was 0.01 Hz; however, resonant frequencies were read to the nearest cycle per second. Table 52.2 summarizes the dynamic Young's modulus at 23 °C in selected samples.

Calibration of the acoustic spectrometer was performed by measurements of the dynamic Young's modulus of fused-silica frequency standards and established a precision of ±0.01 Hz for the fundamental bending mode of resonant vibration.

### Single Crystals and Basaltic Rocks

A preliminary estimate of the modulus defect ($\Delta E/E_o$) produced by the included voids in basalt may be made by combining single-crystal elastic moduli on a weighted-average basis (see fig. 52.4). The Hill-averaged Young's moduli have been computed for each mineral by application of the standard relation of Birch (1960):

$$E_{\text{VRH}}^{\text{XTL}}=\frac{9(K_{\text{VRH}}^{\text{XTL}}\,\mu_{\text{VRH}}^{\text{XTL}})}{3K_{\text{VRH}}^{\text{XTL}}+\mu_{\text{VRH}}^{\text{XTL}}}, \tag{8}$$

where the subscript VRH denotes a Hill-averaged value and the superscript XTL denotes a single-crystal quantity.

Applying the mixing relations for $K_{\text{VRH}}$ and $\mu_{\text{VRH}}$ for a polyphase mixture (see section "Modeling the High-Temperature Elasticity of Basalt"), the Young's modulus for a model basalt composition, $Fo_{100}=0.10$, augite$=0.45$, $An_{56}=0.45$, may be calculated by a second application of the standard relation, where $K_{\text{VRH}}^{\text{MIX}}$ and $\mu_{\text{VRH}}^{\text{MIX}}$ are evaluated at 25 °C and denote the bulk modulus and rigidity for the aggregate:

$$E_{\text{VRH}}^{\text{MIX}}=\frac{9(K_{\text{VRH}}^{\text{MIX}}\,\mu_{\text{VRH}}^{\text{MIX}})}{3K_{\text{VRH}}^{\text{MIX}}+\mu_{\text{VRH}}^{\text{MIX}}}. \tag{9}$$

Employing the bulk modulus ($K$) and rigidity ($\mu$) values $K_{\text{VRH}}=129$ GPa and $\mu_{\text{VRH}}=81.6$ GPa for $Fo_{100}$ (Graham and Barsch, 1969), $K_{\text{VRH}}=95.6$ GPa and $\mu_{\text{VRH}}=57.9$ GPa for augite (Aleksandrov and others, 1964), and $K_{\text{VRH}}=72.0$

TABLE 52.2.—*Ambient-temperature dynamic Young's modulus for basalt of Boiling Pots*

[Young's modulus ($E$) evaluated at 23 °C]

| Sample | $E$ (GPa) | Porosity (percent) |
|---|---|---|
| BP-75-R7 | 74.70 | 14.3 |
| BP-75-R2 | 62.78 | 15.1 |
| BP-75-R4 | 62.60 | 15.6 |
| BP-75-R6 | 60.52 | 15.8 |
| BP-75-R1 | 60.39 | 15.8 |
| BP-75-R5 | 60.06 | 16.8 |
| BP-75-R3 | 55.90 | 17.8 |

GPa and $\mu_{VRH}=34.3$ GPa for $An_{56}$ (Ryzhova, 1964) yield a value of 110.39 GPa.

A comparison between the Young's modulus of this basaltic mixture of single crystals and that of the Boiling Pots olivine tholeiite reveals an appreciable gap of 47 GPa.

This difference in predicted and observed elasticity results from voids (vesicles and microcracks) in the basalt matrix, and so the hachured band in figure 52.4 has accordingly been labeled "defects." It probably, however, represents the maximum effect of microstructure, because the contributions of glass and opaque minerals have not been incorporated.

### Dynamic Elastic Moduli at High Temperatures

Measurements made at high temperatures employed the following additional procedures:

(1) From 25 °C, the set point on the proportional temperature controller was moved up in 25-°C increments. At each increment, a measurement of the flexural or torsional resonant frequency was made.

(2) As the temperature of a sample increases, the flexural (or torsional) frequency at which it absorbs mechanical energy and resonates is continuously lowered.

(3) A uniform sample temperature was provided by blanketing the entire Kanthal resistance furnace with Kaowool spunglass insulation. Care was taken so that filaments of spunglass made no physical contact with the suspension system.

(4) Thermal equilibrium after a 25-°C increment generally required about 1 hour to achieve after the temperature from the thermocouple had matched the set point on the proportional controller. The test of equilibrium was a stationary resonant frequency for a 10- to 15-minute time interval. The overall heating rate from 25 °C to the maximum temperature ($T_{max}$) was 1.1 °C $min^{-1}$.

(5) As temperatures were increased to high levels (in excess of 700 °C), measurements were made until the aperture of the Lissajous figure was no longer a reliable indicator that resonance had been achieved.

(6) Corrections for the effect of thermal expansion were made, using the temperature-dependent linear thermal-expansion coefficients, $\alpha_L(T)$, evaluated at 100 °C increments.

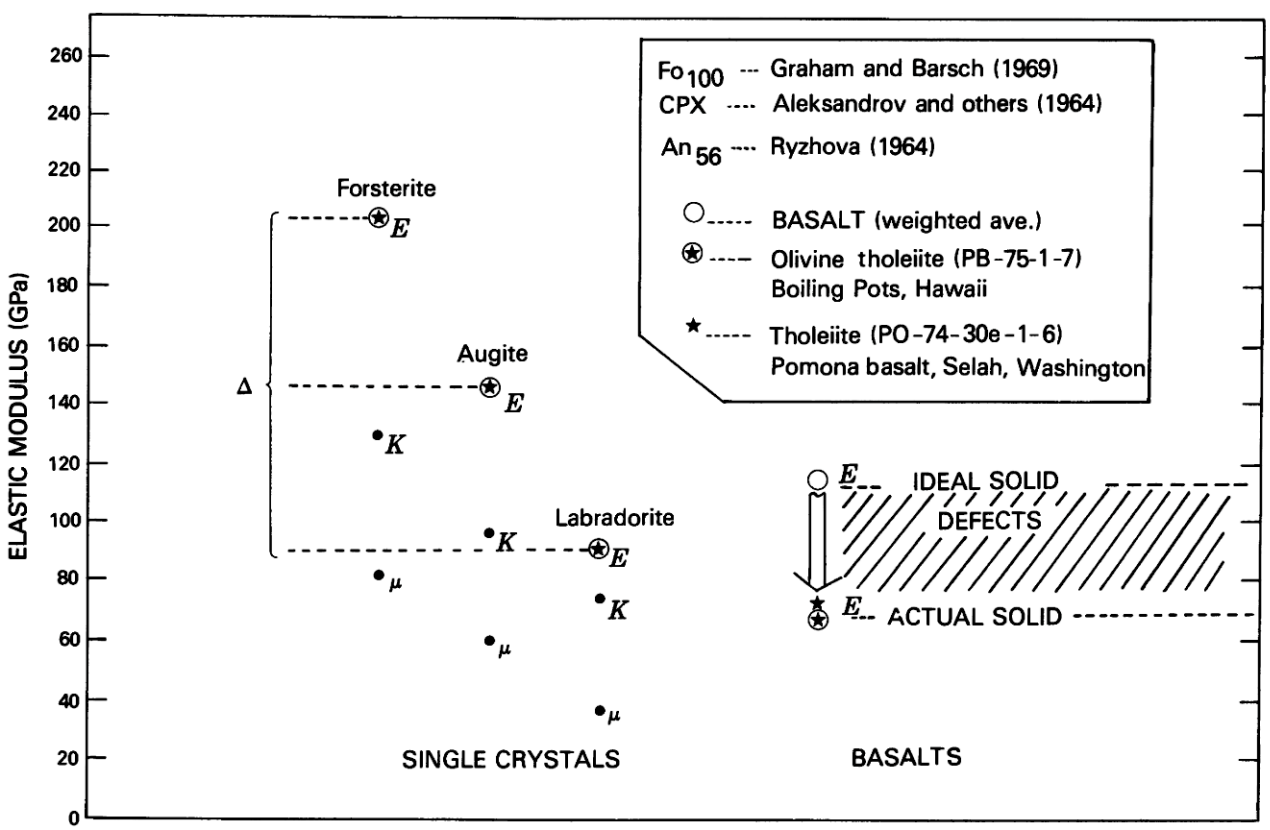


FIGURE 52.4.—Elastic moduli of single-crystal candidates of basalt mineralogy. Young's modulus ($E$) for ideal solid is weighted average of $E$ values for forsterite, augite, and labradorite. Bulk modulus, $K$, rigidity, $\mu$, and Young's modulus, $E$, for forsterite, augite, and labradorite have been included for comparison. Hachured area represents difference between computed composite and measured values for rock and is interpreted as being contribution of defects (vesicles and microcracks) present in rock but not represented in compositional estimate.

(7) Resonant frequencies obtained with the high-temperature Alumel suspension wires at ambient temperature were compared with frequencies obtained with the electromagnetic drive and pickup system.

*Shear modulus.*—Ambient-temperature evaluations of the shear modulus have followed a procedure that is similar to the Young's modulus evaluations. The essential difference requires the transverse excitation of the sample to induce torsional resonant vibrations instead of flexural vibrations.

Evaluations of the high-temperature shear modulus, $\mu$, were made by relating the temperature-dependent torsional resonant frequency to the shear modulus and torsional resonant frequency determined at 25 °C (Hasselman, 1961):

$$\mu(T)=\mu(25)\,\frac{f_T^2}{f_{25}^2}\left[\frac{1}{1+\alpha_l(\Delta T)}\right], \qquad (10)$$

where $\mu(25)$ is the ambient-pressure, 25-°C shear modulus or rigidity, $f_{25}^2$ is the 25 °C torsional resonant frequency, $f_T^2$ is the high-temperature torsional resonant frequency, and $\alpha_L(\Delta T)$ is the temperature-dependent linear thermal-expansion coefficient for basalt, which enters as a correction factor.

Figure 52.5 presents the replicate rigidities and provides a comparison with available data for the high-temperature rigidity of basalt. The values from Wingquist (1971) are for the Dresser basalt, and those from Iida and Kumazawa (1960) are for the 1950 lava of Mihara Volcano (Izu, Oo-Shima, Japan). Table 52.3 lists the rigidity as a function of temperature to 800 °C. The linear-regression relation for $\mu(T)$ from 25 to 700 °C for sample BP-75-R2 is

$$\mu(T)=(2.611-0.00035T)\times 10\ \text{Gpa}, \qquad (11)$$

for sample BP-75-R4

$$\mu(T)=(2.618-0.00042T)\times 10\ \text{GPa}, \qquad (12)$$

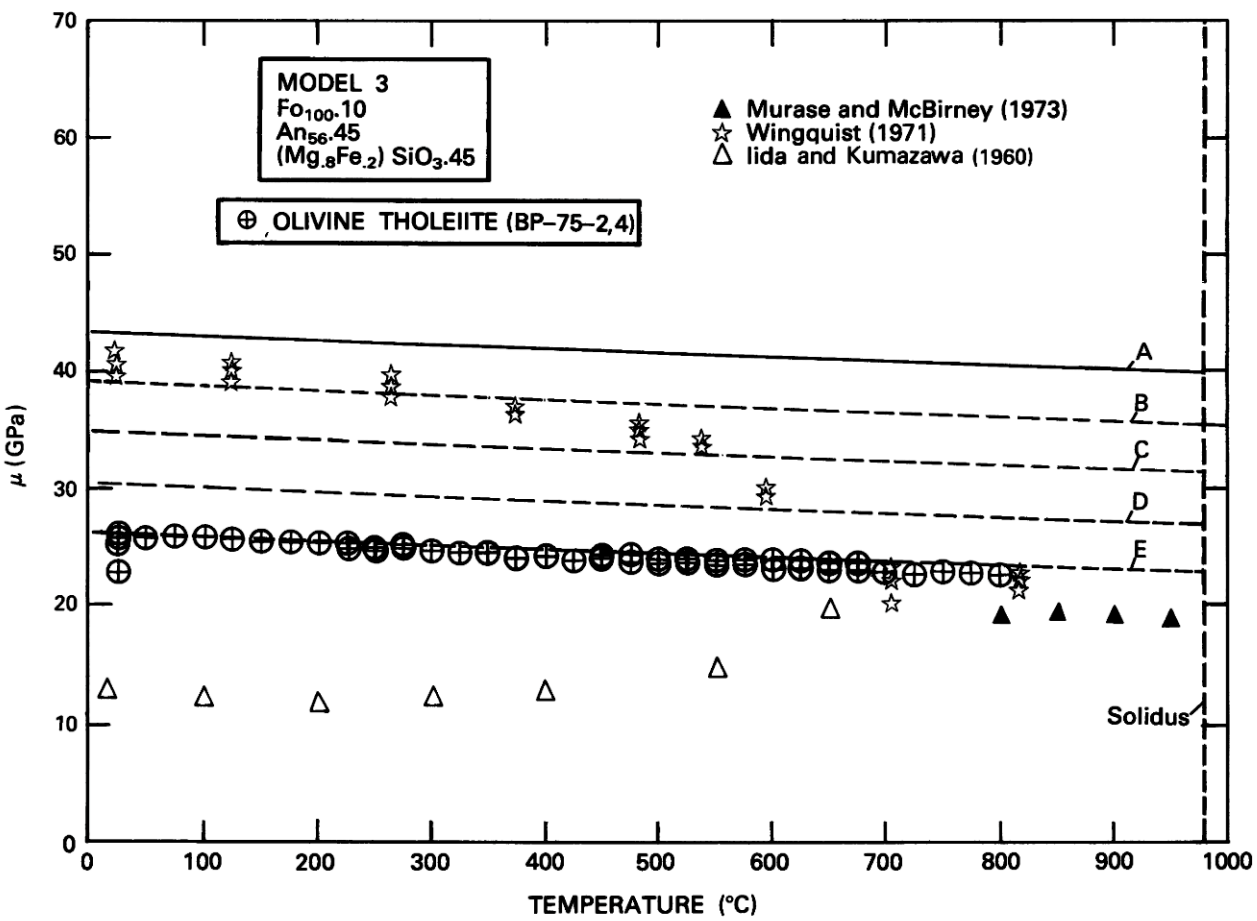


FIGURE 52.5.—High-temperature, ambient-pressure rigidity of Hawaiian olivine tholeiite. Solid line (A) has been computed using V-R-H averaging procedure and a compositional submodel 3 mixture of forsterite, plagioclase, and pyroxene. Computed high-temperature rigidities B, C, D, and E have incorporated progressively higher fractions (5, 10, 15, and 20 percent, respectively) of spherical voids—representing mechanical weakening effects of vesicles. Computed and measured temperature derivatives of $\mu$, $d\mu/dT$, compare favorably.

TABLE 52.3.—*Shear modulus as a function of temperature*

[Sample BP-75-R4(G)]

$$\mu(T)=\underbrace{\mu(25)\left(\frac{F_T^2}{F_{25}^2}\right)}_{A}\underbrace{\left(\frac{1}{1+\alpha_l(\Delta T)}\right)}_{B}$$

| Temperature ($T$) (°C) | A (GPa) | B | $\mu(T)$ (GPa) | $\frac{\mu(T)}{\mu(25)}$ |
|---|---|---|---|---|
| 25 | 26.1 | 1.0000 | 26.1 | 1.00 |
| 50 | 25.9 | .9998 | 25.9 | .99 |
| 75 | 25.8 | .9997 | 25.8 | .99 |
| 100 | 25.7 | .9996 | 25.7 | .98 |
| 125 | 25.6 | .9995 | 25.6 | .98 |
| 150 | 25.6 | .9993 | 25.5 | .98 |
| 175 | 25.5 | .9992 | 25.4 | .97 |
| 200 | 25.4 | .9991 | 25.4 | .97 |
| 225 | 25.3 | .9989 | 25.2 | .96 |
| 250 | 25.2 | .9987 | 25.1 | .96 |
| 275 | 25.1 | .9986 | 25.0 | .96 |
| 300 | 25.0 | .9984 | 24.9 | .95 |
| 325 | 24.8 | .9983 | 24.8 | .95 |
| 350 | 24.7 | .9980 | 24.7 | .94 |
| 375 | 24.6 | .9979 | 24.6 | .94 |
| 400 | 24.5 | .9977 | 24.4 | .93 |
| 425 | 24.3 | .9974 | 24.3 | .93 |
| 450 | 24.3 | .9972 | 24.2 | .92 |
| 475 | 24.2 | .9970 | 24.1 | .92 |
| 500 | 24.0 | .9969 | 24.0 | .91 |
| 525 | 23.9 | .9962 | 23.8 | .91 |
| 550 | 23.8 | .9960 | 23.7 | .90 |
| 575 | 23.7 | .9958 | 23.6 | .90 |
| 600 | 23.6 | .9957 | 23.5 | .90 |
| 625 | 23.6 | .9952 | 23.4 | .90 |
| 650 | 23.5 | .9950 | 23.4 | .89 |
| 675 | 23.5 | .9948 | 23.4 | .89 |
| 700 | 23.4 | .9946 | 23.3 | .89 |
| 725 | 23.3 | .9937 | 23.2 | .89 |
| 750 | 23.2 | .9935 | 23.1 | .88 |
| 775 | 23.1 | .9932 | 23.0 | .88 |
| 800 | 23.0 | .9930 | 22.9 | .87 |

and for the average of samples BP-75-R2 and BP-75-R4

$$\mu(T)=(2.615-0.00038T)\times 10\ \text{GPa}. \qquad (13)$$

Rigidities obtained from the resonant-frequency values and their corresponding predicted values from the linear regression treatment have been compared to 700 °C. The value of the differences between measured and predicted values are the regression residuals. Comparisons of the magnitude of these residuals suggest that a linear temperature dependence for rigidity is appropriate over the interval 25–700 °C. An examination of the sign of the residuals with changes in temperature shows no systematics, either within the data of a single sample or between the pooled data of both samples. The evident linearity in the data is consistent with the behavior expected for a solid that is continuously increasing its volume, and concurs with the behavior in single-crystal studies of forsterite (Graham, 1969; Graham and Barsch, 1969) and bronzite (Frisillo, 1972), as well as in studies of nonsilicates (Jones, 1977) and the formalism of lattice dynamics (Leibfried and Ludwig, 1961).

*Young's Modulus.*—Evaluations of the Young's modulus, $E$, were made by relating the temperature-dependent flexural resonant frequency to the Young's modulus and the flexural resonant frequency determined at 25 °C (Hasselman, 1961):

$$E(T)=E(25)\frac{f_T^2}{f_{25}^2}\left[\frac{1}{1+\alpha_l(\Delta T)}\right], \qquad (14)$$

where $E(25)$ is the ambient-pressure, 25 °C Young's modulus, $f_{25}^2$ is the 25 °C flexural resonant frequency, $f_T^2$ is the high-temperature flexural resonant frequency, and $\alpha_l(\Delta T)$ is the temperature-dependent linear thermal-expansion coefficient for basalt.

The thermal-expansion coefficient $\alpha_l(T)$ that was used to correct the shear moduli is the same one employed here. The Young's modulus of 54.0 GPa and an $E(T)/E(25)$ value of 0.894 for one sample may be compared with values of 54.6 GPa and 0.915 for the replicate, evaluated at their common high-temperature point of 725 °C.

Plots of $E$ versus temperature are presented in figure 52.6 for both samples, and comparisons may be made with the available data for basalt, gabbro, and peridotite. Table 52.4 lists the values of $E(T)$ to 865 °C.

The regression equations for the temperature dependence of the Young's modulus in the Boiling Pots basalt for sample BP-75-R6 is

$$E(T)=(6.059-0.00085T)\times 10\ \text{GPa}, \qquad (15)$$

for sample BP-75-R1

$$E(T)=(6.049-0.00081T)\times 10\ \text{GPa}, \qquad (16)$$

and for the average of samples BP-75-R6 and BP-75-R1

$$E(T)=(6.054-0.00083T)\times 10\ \text{GPa}. \qquad (17)$$

TABLE 52.4.—*Young's modulus as a function of temperature*

[Sample BP-75-R1]

$$E(T)=\underbrace{E(25)\left(\frac{F_T^2}{F_{25}^2}\right)}_{A}\underbrace{\left(\frac{1}{1+\alpha_l(\Delta T)}\right)}_{B}$$

| Temperature ($T$) (°C) | A (GPa) | B | $E(T)$ (GPa) | $\frac{E(T)}{E(25)}$ |
|---|---|---|---|---|
| 25 | 60.4 | 1.0000 | 60.4 | 1.00 |
| 50 | 60.2 | .9998 | 60.2 | .99 |
| 75 | 60.0 | .9997 | 60.0 | .99 |
| 100 | 59.8 | .9996 | 59.7 | .98 |
| 125 | 59.6 | .9995 | 59.5 | .98 |
| 150 | 59.4 | .9993 | 59.3 | .98 |
| 175 | 59.1 | .9992 | 59.0 | .97 |
| 200 | 58.9 | .9991 | 58.8 | .97 |
| 225 | 58.7 | .9989 | 58.6 | .97 |
| 250 | 58.5 | .9987 | 58.4 | .96 |
| 275 | 58.4 | .9986 | 58.3 | .96 |
| 300 | 58.1 | .9984 | 58.1 | .96 |
| 325 | 58.0 | .9983 | 57.9 | .95 |
| 350 | 57.8 | .9980 | 57.7 | .95 |
| 375 | 57.6 | .9979 | 57.5 | .95 |
| 400 | 57.4 | .9977 | 57.3 | .94 |
| 425 | 57.3 | .9974 | 57.2 | .94 |
| 450 | 56.9 | .9972 | 56.7 | .93 |
| 475 | 56.7 | .9970 | 56.6 | .93 |
| 500 | 56.6 | .9969 | 56.4 | .93 |
| 525 | 56.3 | .9962 | 56.1 | .92 |
| 550 | 56.2 | .9960 | 56.0 | .92 |
| 575 | 56.0 | .9958 | 55.8 | .92 |
| 600 | 55.8 | .9957 | 55.5 | .91 |
| 625 | 55.6 | .9952 | 55.3 | .91 |
| 650 | 55.4 | .9950 | 55.1 | .91 |
| 675 | 55.1 | .9948 | 54.8 | .90 |
| 700 | 54.8 | .9946 | 54.5 | .90 |
| 725 | 54.3 | .9937 | 54.0 | .89 |
| 750 | 53.9 | .9935 | 53.6 | .88 |
| 775 | 53.2 | .9932 | 52.8 | .87 |
| 800 | 52.8 | .9930 | 52.4 | .86 |
| 825 | 52.3 | .9928 | 51.9 | .85 |
| 865 | 51.6 | .9924 | 51.2 | .84 |

Inspection of these values reveals that the temperature dependence of the Young's modulus for Hawaiian olivine tholeiite is very nearly linear over the interval 25–700 °C and accords with expectations based on the single-crystal $d(C_{ij})/dT$ for forsterite (Graham, 1969) or bronzite (Frisillo, 1972), or the predictions of lattice dynamics (Leibfried and Ludwig, 1961). Departures in linearity in $E(T)$ have been detected above 700 °C. Examination of the source of this change in slope suggests the presence of the glass transition.

## MEASUREMENTS OF THE THERMAL EXPANSIVITY OF BASALT

An accurate evaluation of the temperature-dependent dynamic Young's modulus and dynamic rigidity requires a correction for the effects of thermal expansion within the resonating sample. Thermal expansivity is itself, however, a function of temperature, as the anharmonic vibrations within crystal lattices and within $SiO_4$ and

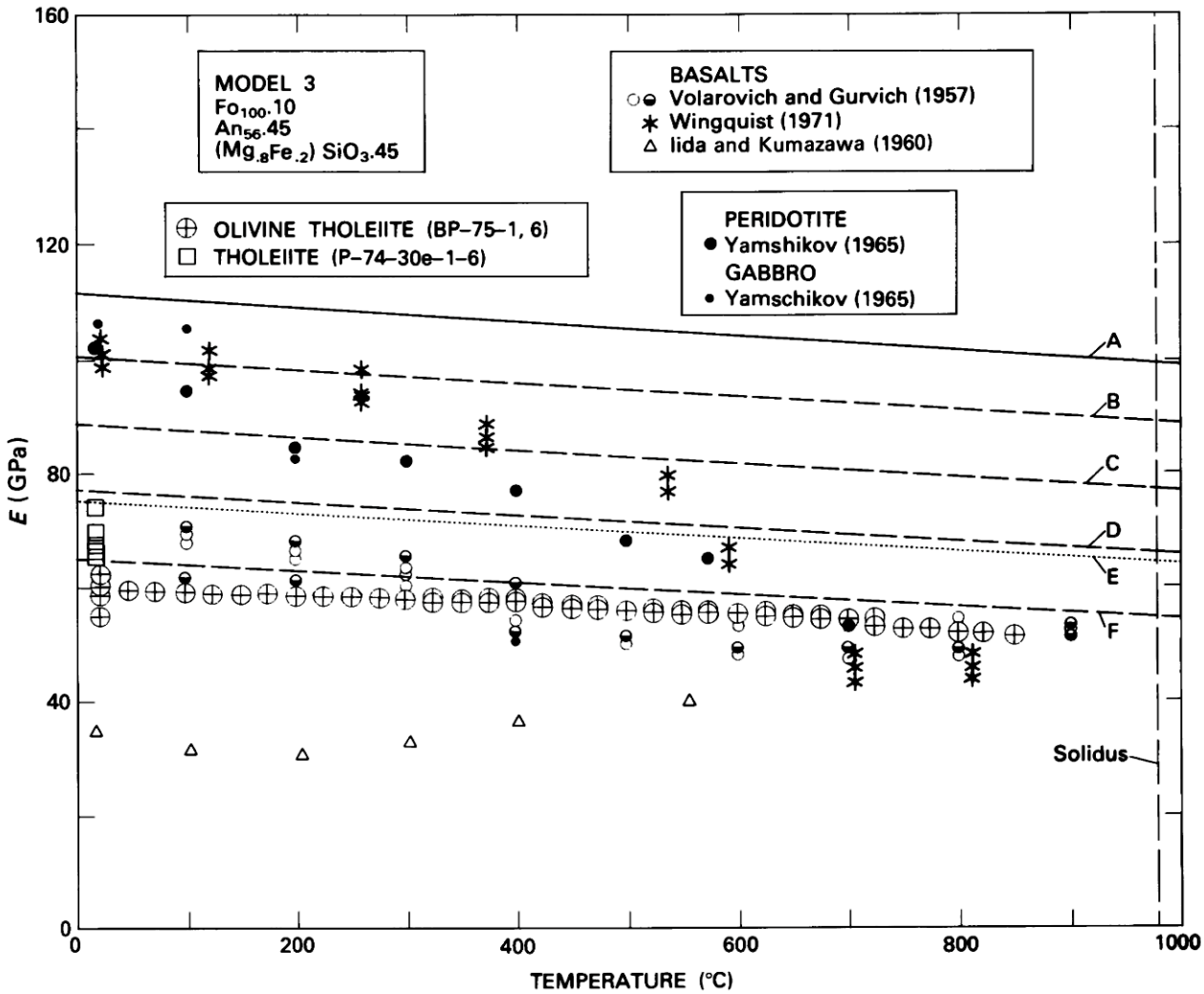


FIGURE 52.6.—High-temperature, ambient-pressure Young's modulus of Hawaiian olivine tholeiite. Available literature data have been included. Squares at 22 °C are data for moduli of Pomona basalt, Selah, Washington. Solid line (A) represents nonflawed computed modulus, without weakening effects of spherical voids (vesicles). Lines B, C, D and F represent progressive increments of 5, 10, 15, and 20 percent voids, respectively. Separation between curves D and E represents addition of 1 volume percent needle-shaped voids, simulating a class of microcracks that occur along crystal junctions. Computed and measured temperature derivatives of $E$, $dE/dT$, compare favorably.

$AlO_4$ tetrahedra in the glass progressively increase in amplitude with temperature.

The objective of this section is to discuss the measurement of linear thermal strain in basalt that will permit the evaluation of linear thermal-expansion coefficients. At the same time, they provide temperature-dependent correction factors that may be applied in the evaluation of the shear modulus and Young's modulus in the same basalt.

Thermal-expansion correction factors were generated by measuring the linear thermal strain by dilatometric methods and by relating incremental changes in longitudinal strain to the change in temperature that produced them. This set of thermal-expansion correction factors covers the temperature range 25–900 °C. The linear expansion coefficients embody within them several expansion components, which involve crystalline and glassy phases in the rock matrix as well as planar voids that heal as temperatures rise (that is, a microstructural component that is temperature dependent).

## EXPERIMENTAL PROCEDURE

High-temperature measurements of thermal expansivity were obtained using an Orton Automatic Recording Dilatometer. A schematic diagram of the dilatometer is shown in figure 52.7; it consists of a 25-cm-diameter by 50-cm-long stainless-steel-clad furnace. An alumina sample holder and pushrod house the sample and transmit sample-length changes to a Daytronic (02B600) linearly variable differential transformer (LVDT). A Daytronic (201B) transducer exciter-demodulator produced a dc millivoltage for a Houston Omnigraphic (HR-100) *x-y* recorder. The *x-y* recorder automatically plotted sample macroscopic strain and temperature during heating (and cooling) cycles.

Samples were prepared by diamond-barrel coring with a 0.40-in.-inner-diameter core barrel. The sample diameter was 1.01 cm, and the sample lengths were $5.08 \pm 0.002$ cm. Sample ends were cut square and then ground flat, using an abrasive wheel and lapping grit normally used in preparing standard petrographic thin sections. One end of the sample was slightly beveled to ensure a single contact point against the alumina pushrod of the LVDT.

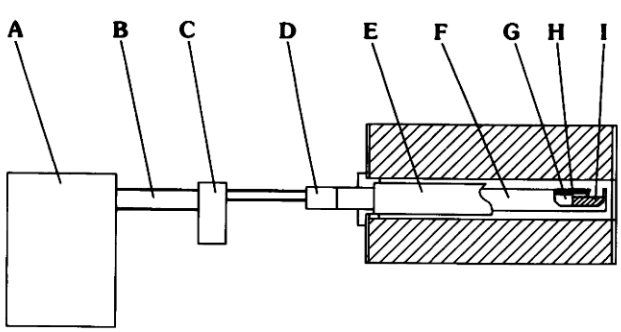


FIGURE 52.7.—Schematic diagram of components in dilatometer assembly used for measurements of linear strain at high temperatures. (A) *x-y* recording unit; (B) thermocouple leads and LVDT leads; (C) transducer exciter-demodulator; (D) linearly variable differential transformer (LVDT); (E) silicon-carbide resistance heating element; (F) alumina sheath; (G) alumina pushrod assembly; (H) platinum-platinum·10 percent rhodium (Pt-Pt·10Rh) thermocouple; (I) sample.

Dilatometer calibration was done using single crystals of α-quartz as comparators.

Linear thermal-expansion coefficients were evaluated from the defining relation

$$\alpha_l = \frac{1}{l_0}\left(\frac{\Delta l}{\Delta T}\right), \tag{18}$$

and volume coefficients taken as

$$\alpha_V \cong 3\alpha_l. \tag{19}$$

Operation of the dilatometer consisted of placing the machined sample in a split-cylinder alumina cradle whose inside diameter was slightly larger than the sample diameter, thus providing horizontal support while minimizing contact friction during expansion. The flat-cut sample end was placed square against the stop block (stationary end of cradle), and the slightly beveled end contacted the center of the pushrod. Temperature measurements were made with a platinum-platinum·10 percent rhodium (Pt-Pt·10Rh) thermocouple. A slight flexure in the thermocouple shank maintained a constant contact between the thermocouple bead and the upper surface of the sample. The millivoltage outputs of the LVDT and the thermocouple were supplied to an *x-y* plotter that provided a continuous record of sample-length changes with changing temperature.

## LINEAR-STRAIN AND THERMAL-EXPANSION COEFFICIENTS

In contrast with the expansivity of samples of basalt from Kilauea Iki lava lake—where $\alpha_v$ values reached $55 \times 10^{-6}$ °C$^{-1}$ above 850 °C—expansion above 700 °C does not have a marked component ascribed to the configurational mobility within the glass. This contrast is attributed to the relatively small volume of glass (13 percent) in the Boiling Pots rocks. Ryan and Sammis (1981) discuss the glass transition in basalt and its mechanical significance in regulating the evolution of the fracture front during thermal-stress-induced cracking.

Table 52.5 contains the mean linear coefficients, $\alpha_l$, for eight replicates and their standard deviation values to 700 °C. Note that variation is highest at low temperatures, lowest at moderate temperatures, and rises again at the 700-°C level. This variation suggests that the progressive closure of randomly oriented microcracks is an important contribution to the aggregate thermal-expansion coefficient below 300 °C and that the minimum variation above 300 °C (but below 700 °C) is reflective of the intrinsic variation in the Boiling Pots basalt expansivity. The larger variation at higher temperatures is interpreted as differences brought about by random differences in the number of olivine phenocrysts from sample to sample. Figure 52.8 illustrates the linear strain produced in basalt samples by controlled heating programs to 925 °C. Figure 52.9 presents the linear and volume thermal-expansion coefficients.

Data on the expansivity of forsterite, augite, and labradorite at 20, 400, and 800 °C (Skinner, 1966) have been employed to form

TABLE 52.5.—*Mean linear thermal-expansion coefficients ($\bar{\alpha}_l$) for basalt of Boiling Pots*

[Mean values determined from samples BP-75-2, BP-75-3, BP-75-4, BP-75-8, BP-75-10, BP-75-11, BP-75-12, BP-75-13]

| Temperature ($T$) (°C) | $\bar{\alpha}_l(\times 10^{-6})$ °C$^{-1}$ | Standard deviation |
|---|---|---|
| 100 | 4.58 | 1.05 |
| 200 | 5.60 | 1.06 |
| 300 | 4.90 | .65 |
| 400 | 6.52 | .75 |
| 500 | 7.01 | .58 |
| 600 | 7.43 | .32 |
| 700 | 7.93 | .821 |

aggregate volume thermal-expansion coefficients for model aggregates by making use of relations for the expansivity of a mixture:

$$\alpha_V = \frac{1}{V}\sum_{i=1}^{n} x_i \nu_i \alpha_i, \tag{20}$$

where $x_i$ is the volume fraction of mineral $i$, $\nu_i$ is the molar volume of mineral $i$, $\alpha_i$ is the expansion coefficent of mineral $i$, and $V$ is the aggregate volume, given by

$$V = \sum_{i=1}^{n} x_i \nu_i.$$

Molar volumes are available in Robie and Waldbaum (1968) and Robie and others (1978). For a model composition of $Fo_{75} = 0.10$, augite $= 0.45$, $An_{64} = 0.45$, $\alpha^l_{20} = 5.07 \times 10^{-6}$ °C$^{-1}$, $\alpha^l_{400} = 6.53 \times 10^{-6}$ °C$^{-1}$, and $\alpha^l_{800} = 8.49 \times 10^{-6}$ °C$^{-1}$, where the subscripts refer to degrees Celsius. Comparison of these

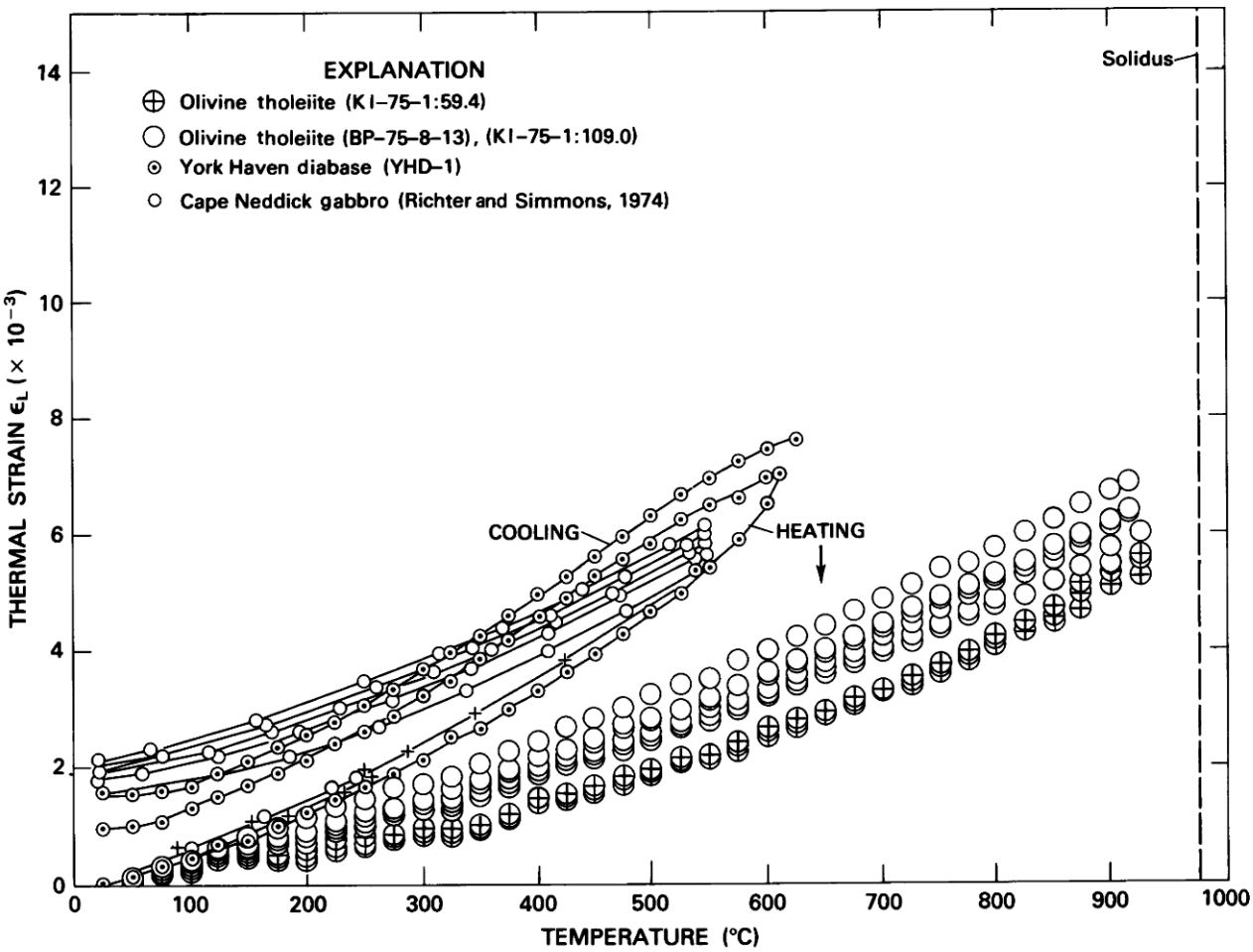


FIGURE 52.8.—Linear strain in olivine tholeiite from Boiling Pots and Kilauea Iki lava lake, Hawaii (open circles from 109-ft level of drill hole KI-75-1 and crossed circles from 59.4-ft level of drill hole KI-75-1). Expansivity has been evaluated from dilatometer measurements made during heating portion of experiment, to minimize contribution of microfractures to $\alpha_l$. Cyclic runs on York Haven diabase have induced a nonrecoverable strain due to microcracking; this data is superposed on results of Richter and Simmons (1974) for comparison. Each successive cooling cycle has opened a new generation of microfractures, as suggested by progressive temperature-thermal strain hysteresis in heating and cooling curves.

values with the $\alpha_l$ values in table 52.5 shows that the expansivity of Boiling Pots rocks climbs in asymptotic fashion to meet the trend of the model composition. For both the rock and model, expansions from 325 to 700 °C are similar, suggesting that a 300-°C temperature excursion is required for preexisting microcracks to close and the full intrinsic expansivity to become dominant. Above 300 °C, the comparison between the predicted and experimental results is excellent.

## CYCLIC EXPANSIVITY AND IRREVERSIBLE THERMAL STRAIN

Experiments have been conducted using cyclic heating and cooling programs, during which the instantaneous sample length has been continuously monitored. These experiments have used the Orton Automatic Recording Dilatometer as configured in the discussion above. In the broadest sense, the experiments have been motivated to develop a qualitative feeling for the ways in which cyclic heating by intrusive bodies (in the near-surface environment) might generate microfractures—of considerable relevance to the discussions in the section "Pressure Dependence of Elasticity in Hawaiian Basalt: Contractancy and Magmatism."

The experiments have been designed to test the following propositions:

(1) For Hawaiian basalt, what are the expansivity effects of cyclic thermal histories?

(2) What proportions of the expansions and contractions are reversible, and how much is irreversible?

(3) What are the mechanical differences in repetitive cycling to the same maximum temperature and in cycling to successively higher temperatures?

(4) Are there essential differences between the cyclic expansivity of porous and nonporous igneous rocks, as exemplified by samples of basalt and diabase?

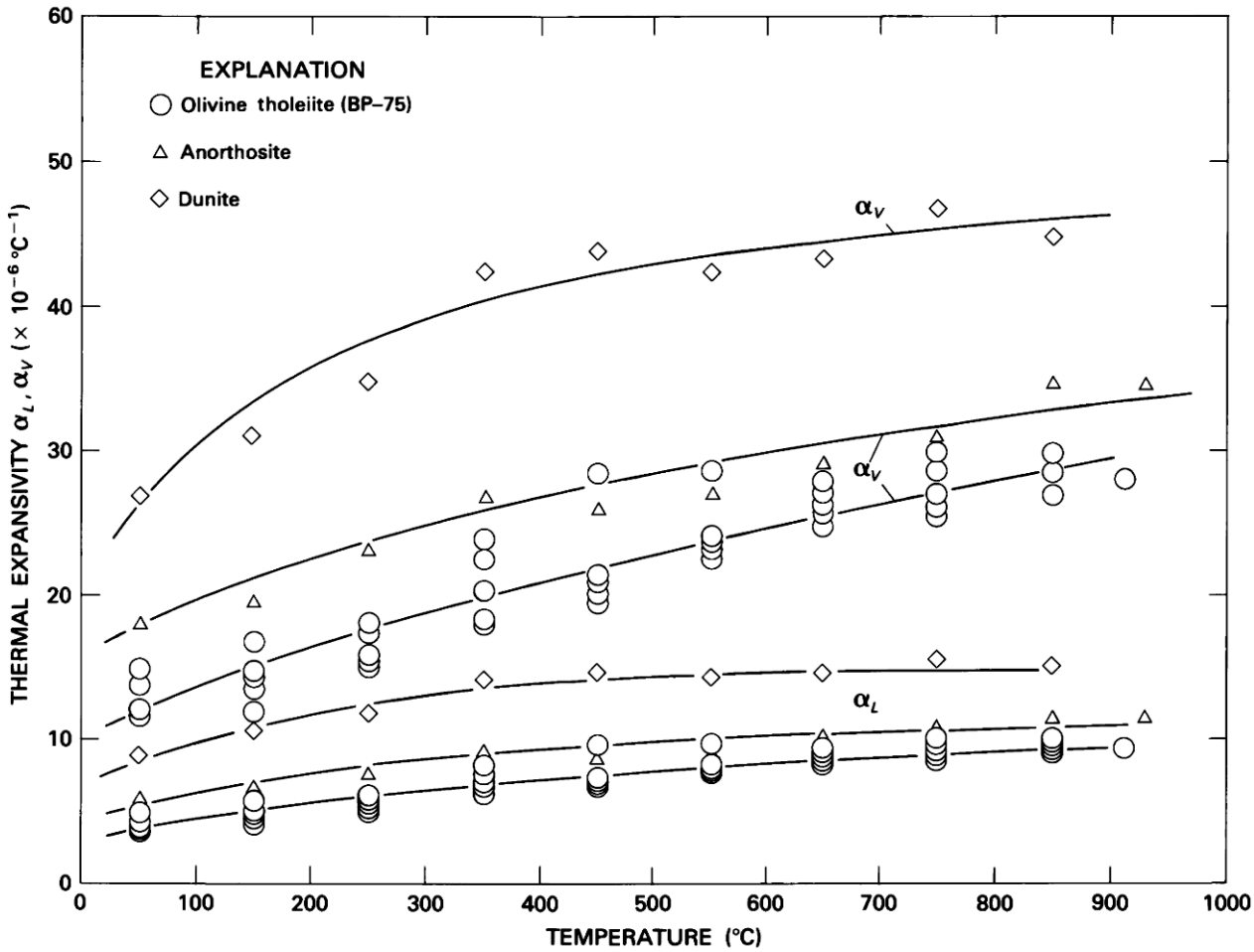


FIGURE 52.9—Linear ($\alpha_L$) and volume ($\alpha_V$) thermal-expansion coefficients for olivine tholeiite from Boiling Pots. Dunite and anorthosite expansivities provide comparisons.

Figure 52.10 illustrates the behavior of basalt during a series of heating and cooling cycles to 950 °C. The experiments were performed on olivine tholeiite from the Boiling Pots with a modal mineralogy as shown in table 52.1 and a porosity level of 15 percent. The heating rate was 3 °C $min^{-1}$, and the cooling rate was determined by the thermal inertia of the furnace at its natural cooling rate. The expansivity-temperature plot has been subdivided into a field of volume increase (as inferred by the sample-length change, in percent) and a field of volume decrease. The line dividing these two fields is the ambient-temperature initial-reference length, $l_0$. The curves show the following features. (1) The cooling portion of a cycle does not retrace the heating portion but lies beneath it, producing a loop that indicates hysteresis in sample volume and irreversible thermal strain. The separation of the curves at ambient temperature is a measure of the nonrecoverable strain induced within a cycle and between cycles. At the conclusion of cycle 1, the irreversible length change is approximately 0.4 percent, for example. (2) Successive cycles to the same maximum temperature (950 °C) accumulate successive increments of irreversible thermal strain. These increments move continuously in the direction of a net contraction in length. The hysteresis in thermal strain produced by temperature increases and the contraction in sample dimensions that accompanies cooling to ambient temperatures suggest thermally induced changes in the microstructure. Compatible with this behavior is the inferred production of microcracks during heating and the densification induced by the rupture of micropore and vesicle-vesicle bridges (microcrack-induced) during cooling and contraction. The experiments suggest that measurements of elastic moduli taken during heating-cooling cycles would similarly display a hysteresis in behavior—producing, for example, values of $K$, $\mu$, and $E$ that would not retrack upon

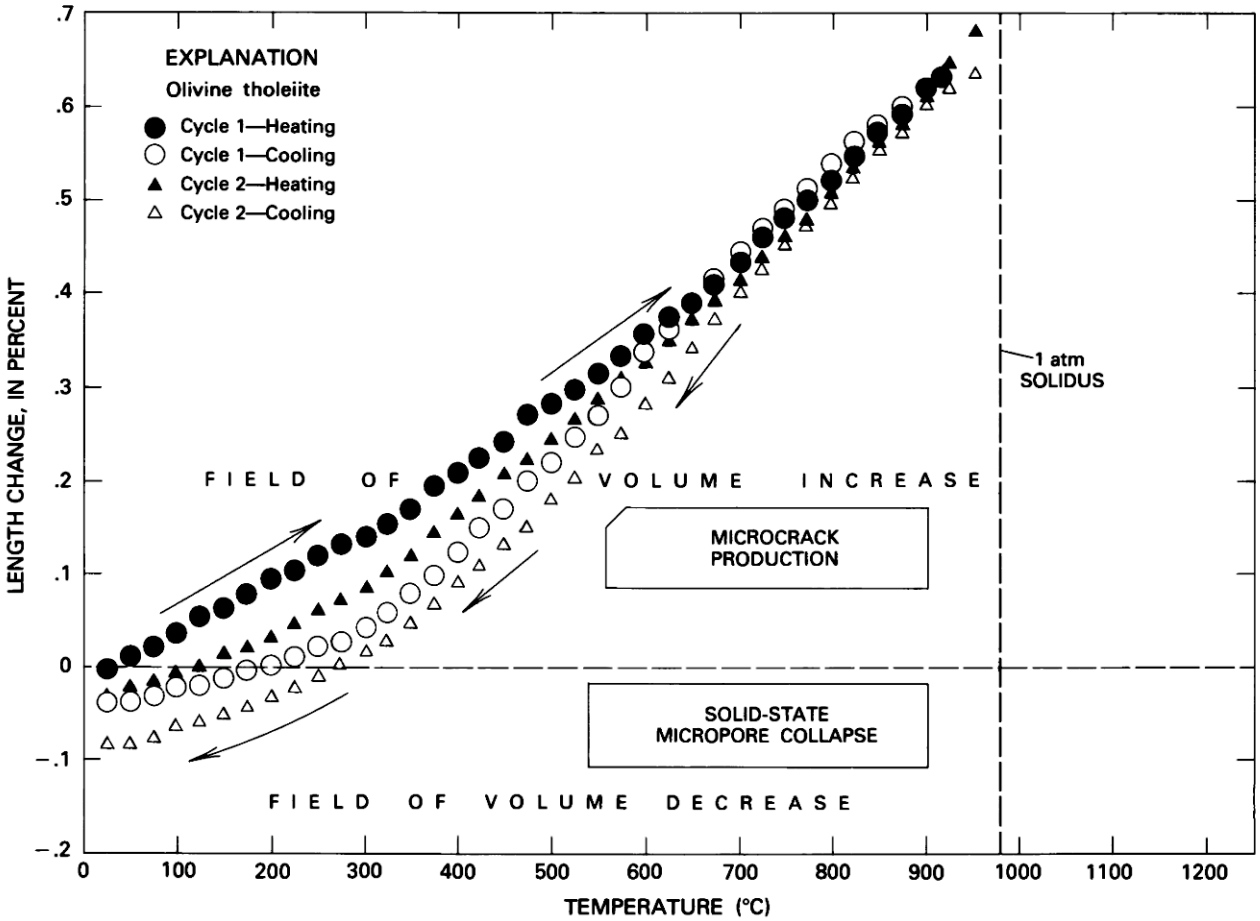


FIGURE 52.10.—Expansivity of Hawaiian olivine tholeiite during cyclic heating and cooling. Solid symbols track change in sample dimensions (length) accompanying heating, whereas open symbols record cooling path within a given cycle. For porous basalt, net effect of cycles to 950 °C, is a reduction in sample length, thus suggesting that microfractures induced during heating have bridged crystal + glass matrix between vesicles, thereby allowing incremental micropore collapse during contraction produced by subsequent cooling portion of a cycle. Contrasting behavior is demonstrated by irreversible length changes produced by microcracking in completely crystalline and nonporous intrusive rocks, as exemplified by diabase in figure 52.11.

cooling those determined during heating. This behavior would qualitatively accord with the results of Ide (1937), who found reductions in the velocity of sound in samples of diabase and norite heated to 700 °C in experiments in which the maximum temperature was raised in successive cycles. Such a program of cyclic elastic-moduli measurements with cooling as well as heating experiments has not been undertaken in this study, and it remains to be determined what, for example, the variance in the Young's modulus or the rigidity induced by, for example, the 0.4-percent change in sample length produced by heating to 950 °C would be after returning the sample to ambient temperature. Note, however, the difference between the net irreversible effects produced in the Ide (1937) samples and those in the olivine tholeiite: the former increasing their dimensions via inferred microcrack production only, and the latter undergoing a decrease in dimension attributed to solid-state densification during micropore collapse. Under confining pressure, we would therefore expect a slight increase in basalt moduli reflecting the sample-volume reduction.

Contrasting with the mechanical behavior exhibited by olivine tholeiite in the heating-cooling cycles is that of diabase, as suggested above. Further evidence of this contrast is provided in figure 52.11, which shows the expansivity of diabase cycled between ambient temperature and 625 °C at a heating rate of 3 °C $min^{-1}$. As before, thermal-strain/temperature hysteresis loops have been induced by the inferred production of microcracks in the sample during heating. But note the very different signature of this hysteresis: the opening of the loops is produced by an irreversible length increase (consistent with inferred lower elastic moduli), as contrasted with a loop opening

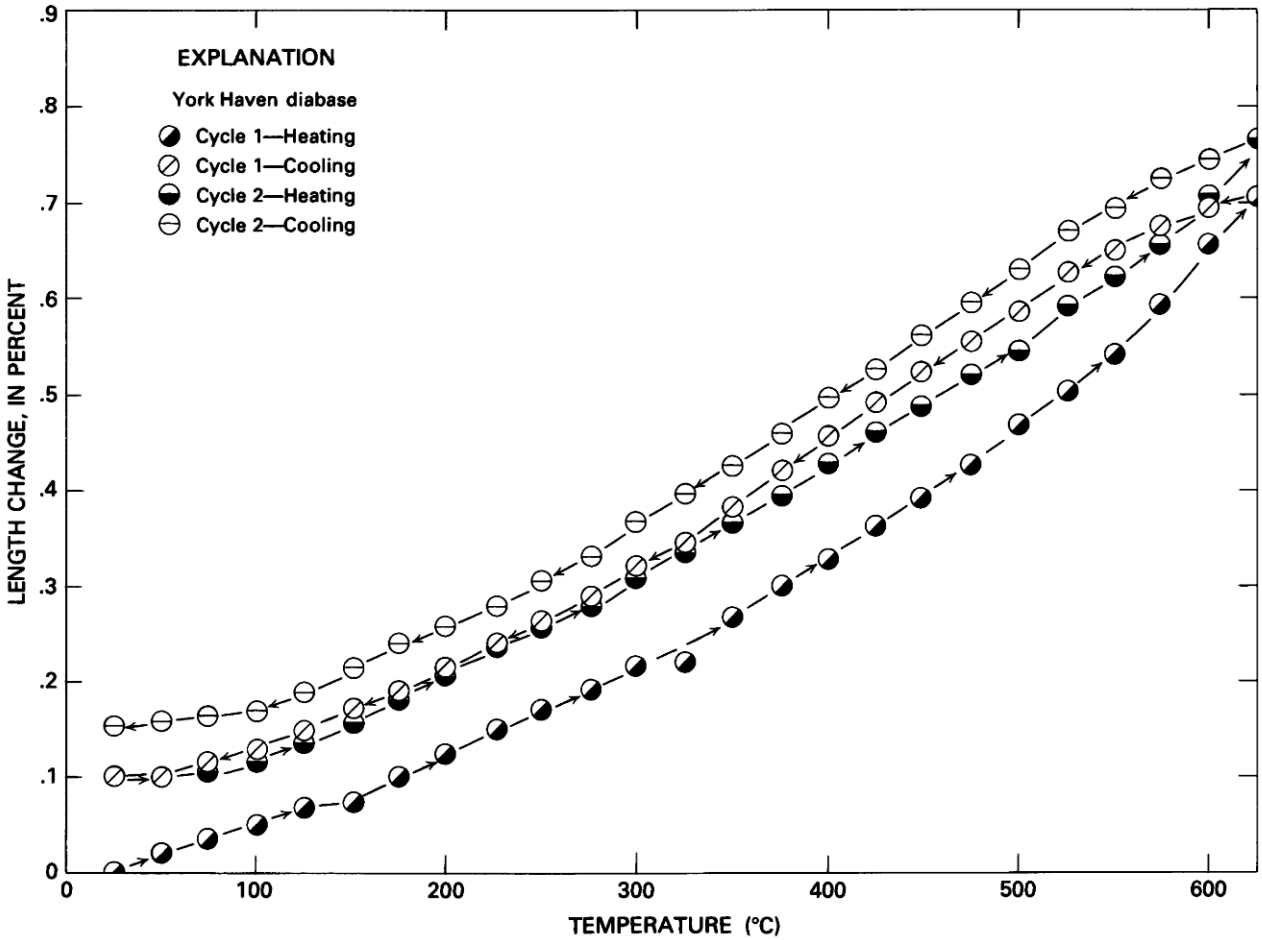


FIGURE 52.11.—Expansivity of diabase during cyclic heating and cooling. Half-filled symbols track change in sample dimensions (length) accompanying heating, whereas open symbols record cooling path within a given cycle. Arrows between data points indicate movement to higher or lower temperatures. For nonporous and holocrystalline intrusives such as diabase, excursions to 625 °C induce microfractures that do not close reversibly upon cooling. Each excursion to high temperatures induces a new generation of microcracks and an additional increment of irreversible dimension change. All cycling is associated with increased sample volume, contrasting with behavior of porous olivine tholeiite (figure 52.10).

induced by length decreases (suggesting higher elastic moduli). Other aspects of the effects of heating-cooling cycles remain qualitatively similar, although the direction in which they move again contrasts with the basalt: successive excursions to high temperature induce progressive increments of irreversible (positive) thermal strain. Thus, sample volumes progressively increase in response to the microstructural changes induced by internal cracking.

Finally, how do the effects of (1) repetitive cycling to the same maximum temperature ($T_{max}$) and (2) cycling to successively higher values of $T_{max}$ differ? Figure 52.12 draws heavily on the work of Richter and Simmons (1974) and adds to that the results of experiments of type (1) and type (2). For the York Haven diabase, raising the $T_{max}$ to 800 °C (from 610 °C) in three successive increments produces three successive generations of new microcracks and, in turn, three distinctly new levels of thermal strain. On the fifth cycle, the $T_{max}$ is maintained at the same level (800 °C), and, by inference, relatively few new microcracks have been generated, producing only a modest increment of irreversible strain. In an experiment of type (1), the same $T_{max}$ is maintained throughout, producing successive generations of new microcracks with progressively smaller populations. This result accords with the results of Richter and Simmons (1974), who found limiting levels of microstructural damage with large numbers of cycles to the same maximum temperature. In turn, this result suggests that a damage threshold exists that is capable of accommodating successive thermal-deformation cycles through internal shock absorbers made up of assemblages of preexisting microcracks. Accommodating higher levels of thermal strain requires the excursion to significantly higher temperatures, initiating a new round of microcrack production. Simply revisiting the same old $T_{max}$ is insufficient to significantly increase this microcrack population.

## MODELING THE HIGH-TEMPERATURE ELASTICITY OF BASALT

In this section, a model for estimating the elastic moduli of basalt is developed. It has been motivated by the desire to construct and apply an approach for computing the ambient and high-temperature moduli, thus providing theoretical guidance for the temperature dependence of the Young's modulus and the rigidity evaluated in the experiments. This modeling therefore forms a complementary companion to the experimental work and has been motivated by the measurements themselves. The primary focus of the modeling is in developing tools for evaluating the temperature dependence of the rigidity ($\mu(T)$) and the Young's modulus ($E(T)$).

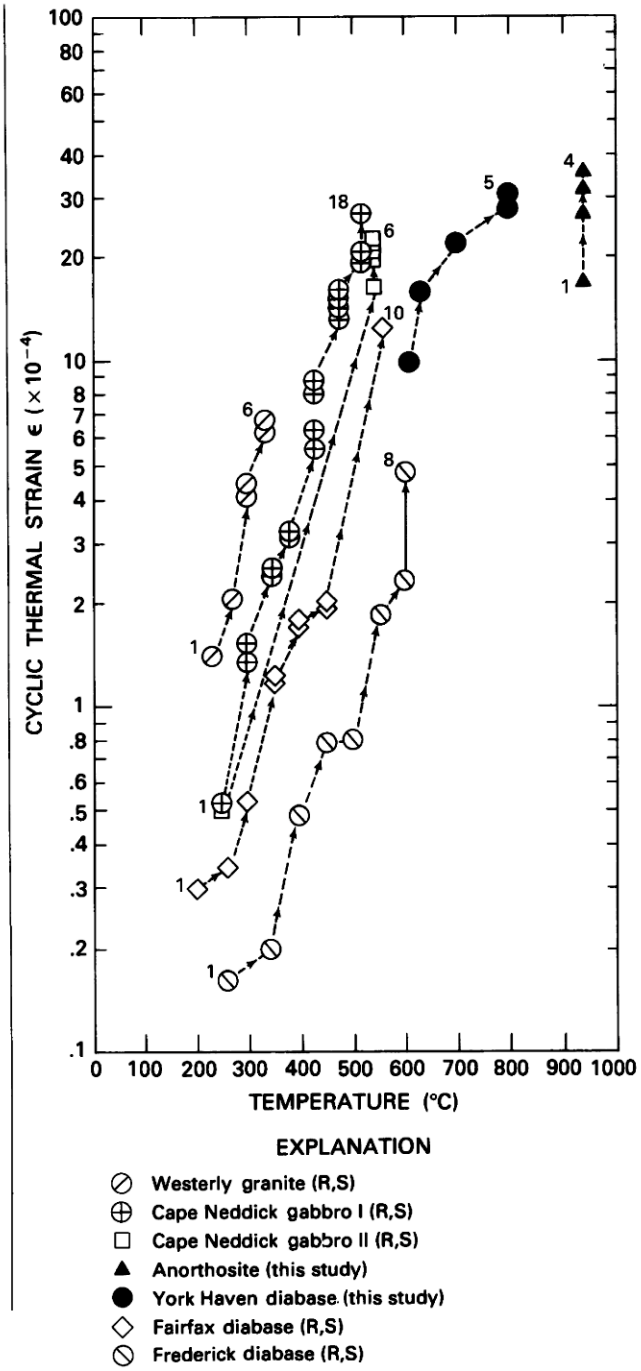


FIGURE 52.12.—Thermal strain-temperature plot of holocrystalline rocks having cyclic heating-cooling thermal histories. Numbers at side of lithologic symbols indicate cycle number within an experimental series; first and last cycle numbers have been labeled. Arrowed pathways indicate temperature (maximum) and correlative thermal strain, through a succession of excursions to high temperatures. For successive cycles to same maximum temperature (symbols line up vertically) relatively small amounts of additional irreversible strain are produced, suggesting diminished production of internal microfractures. Successive excursions to higher levels of temperature (diagonal pathways) induce additional irreversible strain and, by inference, a new generation of thermal microfractures. Samples (Richter and Simmons, 1974) run to maximum temperatures of 600 °C. Experimental comparative runs from the study of Richter and Simmons (1974) are designated (R, S) in the figure explanation.

In the modeling, the temperature range of concern is 25 °C to the solidus for Hawaiian tholeiite (980 ± 5 °C). The rock is assumed to be unconfined, and pressure is not, at this point, a variable. The role of pressure will be discussed in the section "Pressure Dependence of Elasticity in Hawaiian Basalt: Contractancy and Magmatism," with reference to in-situ contractancy.

The model has been divided into two submodels, the first treating compositional effects, and the second one dealing with microstructure. Solids that contain no weakening flaws have elastic properties that are dictated by their composition and their temperature. A compositional model is developed to account for these two contributions to aggregate elasticity. The presence of weakening flaws reduces the moduli that would otherwise result in a pristine solid. A microstructural model has been coupled to the compositional model to account for these effects. Roman numerals have been suffixed to each model to help distinguish one from the other. The compositional model (I) and the microstructural model (II) are shown in figure 52.13.

## COMPOSITIONAL MODEL (I)

### VOIGT, REUSS, AND HILL AVERAGING SCHEMES AND EFFECTIVE ELASTIC MODULI OF A POLYCRYSTALLINE AGGREGATE

The elastic properties of single crystals of olivine (orthorhombic), augite (monoclinic), and plagioclase (triclinic) are functions of direction within the lattice. To construct a compositional model of basalt elasticity by combining single-crystal elastic data, we need a means of averaging the directional moduli over all orientations and thereby producing a solid that is elastically isotropic in a macroscopic sense. Two averaging methods have been used to effect polycrystalline elasticity from single-crystal data, and they provide, through their assumptions, an upper (Voigt, 1928) and a lower (Reuss, 1929) bound to the aggregate elastic moduli.

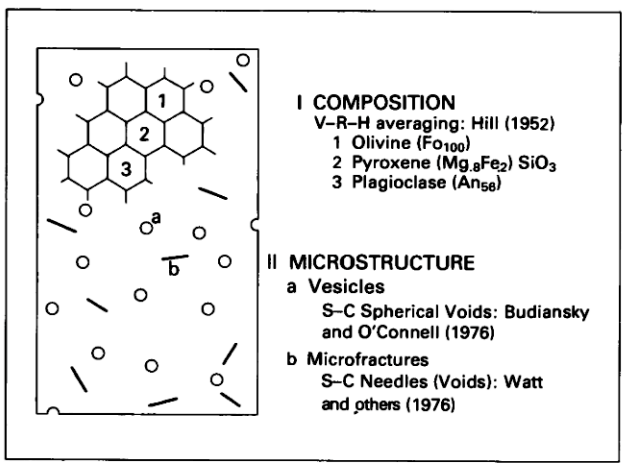


FIGURE 52.13.—Model for high-temperature elasticity of basalt. Compositional submodel I combines contribution of mineral phases (1, 2, 3) to aggregate $K$, $\mu$, and $E$ by combining single-crystal elastic constants in a Voigt-Reuss-Hill averaging scheme for mixtures. Compositional submodel generates magnitude of modulus and predicts overall temperature dependence by combining temperature derivatives for all component phases. Microstructural submodel II incorporates effects of weakening flaws on moduli. Vesicles (a) formed during posteruption degassing of melt are simulated by spherical voids; microfractures (b) formed between crystals during subsolidus cooling are simulated by needle-shaped voids.

Assuming that the strain distribution in a polycrystalline aggregate was uniform and constant, Voigt (1928) derived an effectively isotropic bulk and shear modulus by averaging the single-crystal stiffnesses over all orientations. This approximation, which requires that the microscopic strain in component grains be equal throughout the matrix and equal to the macroscopic strain of the aggregate, results in a disequilibrium of forces between individual crystals. The bulk modulus ($K_V$) of Voigt (1928) is expressed in terms of the single-crystal elastic-stiffness coefficients, $C_{ij}$,

$$K_V = \tfrac{1}{9}[(C_{11}+C_{22}+C_{33})+2(C_{12}+C_{23}+C_{13})], \qquad (24)$$

whereas the rigidity ($\mu_V$) is given by

$$\mu_V = \tfrac{1}{15}[(C_{11}+C_{22}+C_{33})-(C_{12}+C_{23}+C_{13}) +3(C_{44}+C_{55}+C_{66})]. \qquad (25)$$

Assuming that the stress distribution in the aggregate was uniform and constant, Reuss (1929) derived an effectively isotropic bulk and shear modulus by averaging single-crystal compliances over all orientations. This approximation, which requires that the microscopic stresses between component crystals be equal throughout the matrix and equal to the macroscopic stress, produces distorted grains that no longer fit together (that is, compatibility is violated).

The bulk modulus ($K_R$) derived by Reuss (1929) is in turn expressed in terms of the single-crystal elastic-compliance coefficients, $S_{ij}$,

$$\frac{1}{K_R} = [(S_{11}+S_{22}+S_{33})+2(S_{12}+S_{13}+S_{23})], \qquad (26)$$

and the rigidity ($\mu_R$) by

$$\frac{1}{\mu_R} = \tfrac{4}{15}[(S_{11}+S_{22}+S_{33})-(S_{13}+S_{12}+S_{23}) +\tfrac{3}{4}(S_{44}+S_{55}+S_{66})+S_{33}]. \qquad (27)$$

Hill (1952) has demonstrated that the Voigt and Reuss moduli are, in fact, upper and lower bounds on $K$ and $\mu$—a result of the assumptive extremes of constant strain and stress, respectively. Hill suggested that a more appropriate measure of aggregate elasticity would lie between these extremes and proposed using an average of the Voigt and Reuss schemes. This intermediate measure is known as the V-R-H average (or simply the Hill average) and is given by

$$K_{VRH} = \tfrac{1}{2}(K_V+K_R) \qquad (28)$$

and

$$\mu_{VRH} = \tfrac{1}{2}(\mu_V+\mu_R). \qquad (29)$$

The separation between the Voigt and Reuss bounds for an aggregate is thus a measure of the crystal anisotropy within the aggregate, and $K_V = K_R = K$ for an elastic isotropic substance.

## STRUCTURE OF THE COMPOSITIONAL MODEL

The high-temperature bulk modulus and shear modulus for the polyphase mixture, given by Graham and Dobrzykowski (1976), are

$$K(T) = K(25) + \left(\frac{\partial K}{\partial T}\right)\Delta T, \tag{30}$$

and

$$\mu(T) = \mu(25) + \left(\frac{\partial \mu}{\partial T}\right)\Delta T, \tag{31}$$

where $\Delta T = (T - 25)$ in degrees Celsius.

To compute the upper and lower bounds on (30) and (31), the Voigt-averaged and Reuss-averaged moduli for a polyphase mixture are applied.

The upper and lower bounds on the temperature derivatives of the bulk modulus and the shear modulus are computed by applying the appropriate relations for a polyphase mixture.

The Hill-averaged moduli are then evaluated from the averages of the upper and lower bounds for the mixture:

$$K(T)_{\mathrm{VRH}}^{\mathrm{MIX}} = \tfrac{1}{2}[K(T)_V + K(T)_R], \tag{32}$$

and

$$\mu(T)_{\mathrm{VRH}}^{\mathrm{MIX}} = \tfrac{1}{2}[\mu(T)_V + \mu(T)_R]. \tag{33}$$

For an evaluation of the Young's modulus ($E$) at high temperatures, the standard relation (for example, Birch, 1960) is used:

$$E(T)_{\mathrm{VRH}}^{\mathrm{MIX}} = \frac{9K(T)_{\mathrm{VRH}}^{\mathrm{MIX}} \cdot \mu(T)_{\mathrm{VRH}}^{\mathrm{MIX}}}{3K(T)_{\mathrm{VRH}}^{\mathrm{MIX}} + \mu(T)_{\mathrm{VRH}}^{\mathrm{MIX}}}. \tag{34}$$

For high-temperature upper and lower bounds on the Young's modulus, $K(T)_{\mathrm{VRH}}$ and $\mu(T)_{\mathrm{VRH}}$ in (34) are replaced by ($K(T)_V$, $\mu(T)_V$) and ($K(T)_R$, $\mu(T)_R$), respectively.

## COMPOSITIONAL SUBMODELS

The compositional model employs olivine, clinopyroxene, and plagioclase as matrix components. Three compositional submodels have been formed by varying the volume fractions of component minerals. These submodels are referred to as submodel 1, submodel 2 and submodel 3, and their volume fractions are listed in table 52.6.

Submodel 3 was intended to represent an average basalt, whereas submodels 1 and 2 were intended to represent compositional bounds on basalt elasticity by employing relatively pyroxene-rich (hard matrix) and plagioclase rich (soft matrix) mineralogies. It is expected that submodels 1 and 2 would provide upper and lower bounds on aggregate elastic moduli. They enclose the elastic behavior of a submodel 3 aggregate.

TABLE 52.6.—*Compositional submodels for basalt elasticity*

[Values represent volume fractions]

| Component | Submodel 1 | Submodel 2 | Submodel 3 |
|---|---|---|---|
| Olivine $Fo_{100}$ | 0.10 | 0.10 | 0.10 |
| Pyroxene $(Mg_{0.8}Fe_{0.2})SiO_3$ | .60 | .20 | .45 |
| Plagioclase $An_{56}$ | .30 | .70 | .45 |

### OLIVINE

Olivine has been incorporated in the model by using the zero pressure, 298 K elastic stiffness and compliance coefficients of forsterite and the temperature derivatives of the bulk modulus and rigidity as reported by Graham and Barsch (1969) and presented by Graham (1969).

### PYROXENES

The contribution of pyroxene employs the zero-pressure, 298 K data of Ryzhova (1964) for augite. These data permit pyroxene to be included in aggregate moduli calculations for ambient temperature. Temperature derivatives of the elastic coefficients for augite are not available. For high-temperature calculations, the temperature derivatives for the orthopyroxene bronzite, $(Mg_{0.8}Fe_{0.2})SiO_3$, have been used (Frisillo, 1972).

### PLAGIOCLASE

The role of plagioclase in basalt elasticity has been incorporated by employing the results of Aleksandrov and others (1964) as reported for the zero pressure moduli of $An_{56}$ evaluated at 298 K. Data on the temperature dependence of the elastic constants for the plagioclase feldspars is virtually nonexistant. An approximation of this dependence is therefore required. The relatively open structure of α-quartz suggests that the temperature derivatives of the elastic moduli of its framework may approximate the temperature induced changes in the open framework of plagioclase (E.K. Graham, oral commun.). This substitution has been adopted.

The Voigt- and Reuss-averaged bulk and shear moduli for $An_{56}$ based on the Aleksandrov and others (1964) data and reported in Simmons and Wang (1971) are listed in table 52.7.

## MICROSTRUCTURAL MODEL (II)

The primary modulus-reducing agents in a basalt microstructure are vesicles and thermally induced microcracks. Though expressions are provided for incorporating both vesicles and microfractures (where needle shaped), the primary objective has been to simulate the effect of vesicles in weakening the otherwise pristine solid. Thin-section petrography and scanning-electron microscopy has demonstrated that vesicles account for most of the porosity in basalt. Including the mechanical effects of vesicles and microcracks in basalt elasticity has been accomplished by incorporating approximations for the elastic contributions of spherical voids and needle-shaped voids by making use of the self-consistent approximation of Hill (1965) and Budiansky and O'Connell (1976), as presented by Watt and others (1976).

TABLE 52.7.—*Compositional-model input properties and derived interim Voigt and Reuss bulk moduli and rigidities*

[Reference in parentheses]

| Parameter | $Fo_{100}$ | | Augite | | $An_{56}$ | | Units |
|---|---|---|---|---|---|---|---|
| $V_i$ | 43.79 | (2) | 66.09 | (4) | 100.52 | (2) | $cm^3\ mol^{-1}$ |
| $\rho_i$ | 3.221 | (1) | 3.320 | (5) | 2.69 | (7) | $g \cdot cm^{-3}$ |
| $M_i$ | 140.708 | (2) | 216.56 | (4) | 272.44 | (2) | $g \cdot mol^{-1}$ |
| $K_i^V$ | 1,311.9 | (1) | 1,048.0 | (5) | 753 | (7) | kbar |
| $K_i^r$ | 1,268.8 | (1) | 1,021.0 | (5) | 688 | (7) | kbar |
| $\mu_i^v$ | 831.8 | (1) | 754.8 | (5) | 370 | (7) | kbar |
| $\mu_i^r$ | 801.9 | (1) | 738.9 | (5) | 317 | (7) | kbar |
| $\alpha_i^p$ | $24.65\times10^{-6}$ | (1) | $47.7\times10^{-6}$ | (6) | $12\times10^{-6}$ | (8) | $°C^{-1}$ |
| $(dK/dT)_V^i$ | −0.173 | (1) | −0.275 | (3) | −0.10 | (9) | kbar $°C^{-1}$ |
| $(dK/dT)_R^i$ | −0.178 | (1) | −0.261 | (3) | −0.10 | (9) | kbar $°C^{-1}$ |
| $(d\mu/dT)_V$ | −0.134 | (1) | −0.120 | (3) | −0.015 | (9) | kbar $°C^{-1}$ |
| $(d\mu/dT)_R$ | −0.138 | (1) | −0.119 | (3) | −0.015 | (9) | kbar $°C^{-1}$ |

(1) Graham (1969); Graham and Barsch (1969).
(2) Robie and Waldbaum (1968).
(3) Frisillo (1972) values for bronzite.
(4) Robie and Waldbaum (1968) values for diopside.
(5) Aleksandrov and others (1964) data for augite.
(6) Frisillo and Buljan (1972) data for bronzite.
(7) Ryzhova (1964) data for labradorite.
(8) Skinner (1966) data for $An_{95}$ at 20 °C.
(9) V-R-H averaged values for α-quartz from Anderson and others (1968).

## SELF-CONSISTENT TREATMENT

Kröner (1958, 1967) expressed the aggregate moduli of an elastic, isotropic polyphase solid in terms of the individual moduli and individual strains of each component, summed over all included phases and added to the moduli of the matrix. Approximating the strain occurring in an isolated inclusion of the $i^{th}$ material embedded in an infinite (and otherwise homogeneous) elastic matrix subject to pure loading (compressive or shear) at infinity and having the as-yet-to-be-determined elastic constants of the total aggregate led to the first self-consistent approximation.

Budiansky (1965) has combined the Kröner (1958, 1967) approach with the exact results of Eshelby (1957), who demonstrated that the strain state of an inclusion in a matrix sheared at infinity is uniform, to derive coupled, implicit expressions for the effective elastic constants of heterogeneous solids. In the Budiansky approach, the exact Eshelby results are used as estimators of the average shear strain in each phase, which, when coupled to the Kröner aggregate moduli expressions, leads to simultaneous equations for the effective shear and bulk moduli in terms of constituent moduli.

## STRUCTURE OF THE MICROSTRUCTURAL MODEL

For a two-phase aggregate, the self-consistent approximation for the effective modulus Watt and others, 1976) may be expressed as

$$\frac{M^*-M_1}{M_2-M_1}=V_2\left[1+\frac{V_1(M_2-M_1)}{M_1+f}\right]^{-1}, \qquad (35)$$

where $M^*$ is the effective modulus of the total aggregate ($K^*$ or $\mu^*$), $M_1$ is the modulus ($K_1$, $\mu_1$) of the included phase, $M_2$ is the modulus of the matrix ($K_2$, $\mu_2$), $V_1$ is the volume fraction of the included phase, $V_2$ is the volume fraction of the matrix, and $f$ is a function that is dependent on the moduli of the included phase as well as on the effective aggregate moduli (though not necessarily at the same time). The two phases are (1) voids and (2) matrix. Note that the matrix itself is actually polycomponent and polycrystalline.

The approximation for spherical inclusions of the minor phase is given by (35), such that for effective bulk modulus

$$K^*:\quad f=\tfrac{4}{3}\mu^*, \qquad (36)$$

and for effective rigidity

$$\mu^*:\quad f=\frac{\mu^*(9K^*+8\mu^*)}{6(K^*+2\mu^*)}. \qquad (37)$$

In this treatment, the included phase is the vapor phase that occupies spherical vesicles and is described by $K_1=0$; $\mu_1=0$. The finite bulk modulus and rigidity of the matrix is solely a function of the modal percentage of the component mineralogy (that is, submodel 1, 2, or 3).

The expressions for aggregate moduli are coupled (nonseparable) and are solved by an iterative computational procedure. In general, four to five iterations were satisfactory for convergence, and in no case has more than ten iterations been required.

The approximation for needle-shaped inclusions of the minor phase is given by (35), such that for the effective bulk modulus

$$K^*:\quad f=\tfrac{1}{3}\mu_1+\mu^*. \qquad (38)$$

and for the effective rigidity

$$\mu^*:\quad f=\frac{5}{\dfrac{1}{3(K_1+\frac{1}{3}\mu_1+\mu^*)}+\dfrac{2(2\mu_1+\mu^*+G)}{(\mu_1+\mu^*)(\mu_1+G)}}-\mu_1, \qquad (39)$$

where

$$G=\frac{\mu^*(K^*+\frac{1}{3}\mu^*)}{K^*+\frac{7}{3}\mu^*} \qquad (40)$$

and $\mu_1$, $\mu^*$, $K_1$, and $K^*$ have been defined above.

The approximation employs air as the included minor phase that occupies the microcracks that open during cooling, and accordingly, $K_1=0$; $\mu_1=0$.

As in the case for spherical inclusions, the microcrack approximations (needles) are solved iteratively for $K^*$ and $\mu^*$. Convergence rates are comparable to the vesicle approximations.

Flat microcracks have not been explicitly considered, but their incorporation is straightforward (see O'Connell and Budiansky, 1974; Watt and others, 1976).

The results of the combined predictions of the compositional model (I) and microstructural model (II) are presented and discussed below, in light of measured $E(T)$, $\mu(T)$, levels of absolute porosity, and compositional details for Hawaiian basalt.

## ELASTIC MODELS AND ELASTIC MEASUREMENTS

The $\mu(T)_{VRH}$ for compositional submodels 1, 2, and 3 are presented and compared in figure 52.14. Compositional submodel 3 has the mineralogy that most closely resembles an average basalt composition, as contrasted with submodels 1 and 2, and thus

submodel 3 should be compared with the data. The nonporous moduli are given by solid lines of different weight that correspond to the dashed (porous) moduli for the appropriate model. For a given composition, all five curves ($\phi = 0$, 0.05, 0.10, 0.15, and 0.20) are parallel, indicating no computed porosity-temperature interaction. This relation accords with what one would expect, because porosity has been shown to have a negligible effect on thermal expansivity in solids (Coble and Kingery, 1956). The rapid inflexion of the E(T) curves for the data of Wingquist (1971) suggests that dehydration was occurring in the alteration minerals of their samples over the range 500–700 °C. The samples of Murase and McBirney (1973) and Iida and Kumazawa (1960) did not have a reported characterization that permits an evaluation of the reason(s) they do not exhibit a linear temperature dependence.

The $\mu(T)_{VRH}$ for compositional submodel 3 is shown in figure 52.15, and the evaluated rigidities of the Boiling Pots replicates are indicated by the crossed circles. Using an average value of $\phi$ for the entire range of measured porosities gives $\phi = 0.166$. This average is a difference of approximately 3.4 percent porosity based on the magnitude of the predicted and measured ambient-temperature rigidity and the corresponding porosity levels.

The distance between the Voigt- and Reuss-averaged bounds for a nonflawed solid ($K_1$, $\mu_1$, $K_2$, and $\mu_2$ are finite) is a measure of the differences in moduli for the single-crystal components. The

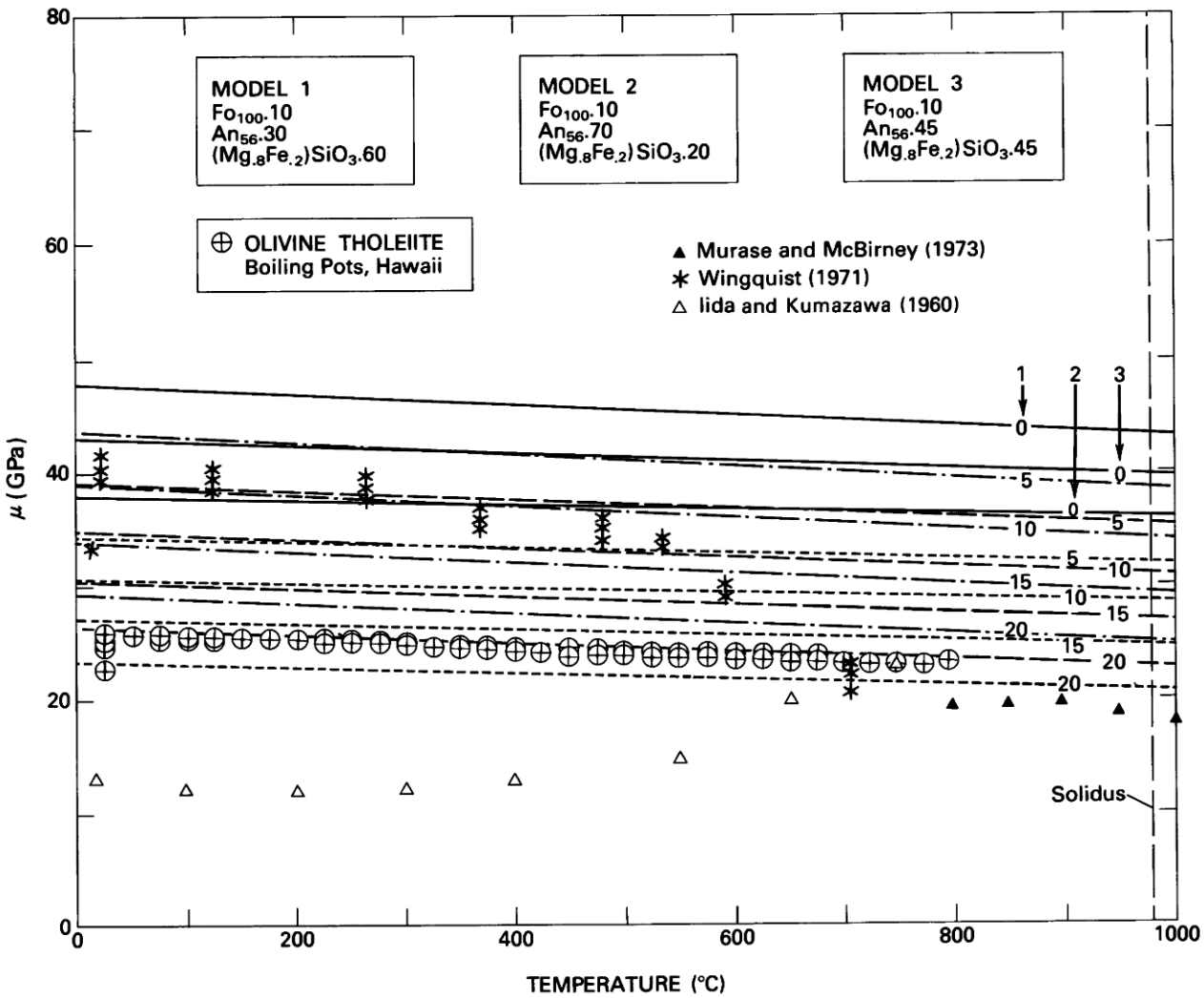


FIGURE 52.14.—Predicted high-temperature, ambient-pressure rigidity for three model basalts (see table 52.6) and rigidity of olivine tholeiite from Boiling Pots. Trends of compositional models without porosity ($\phi = 0$; labeled with 0) are represented by solid lines. Trends of compositional models with varying levels of porosity (labeled 5, 10, 15, 20) are represented by dashed lines for $\phi = 0.05$, $\phi = 0.10$, $\phi = 0.15$, and $\phi = 0.20$ volume fractions of spherical voids, respectively. Bronzite simulates temperature dependence of pyroxenes. Available literature data are included.

V-R-H bounds for the matrix, evaluated at a level of zero porosity, are shown in figure 52.5. This figure illustrates the mineralogical contributions to the model aggregate elasticity.

The Hill-averaged Young's moduli for compositional submodel 3 are presented in figure 52.6 for porosity levels (spherical voids) to $\phi = 0.20$. In addition, the effect of microcracks at dilute concentration are shown (needle-shaped voids) for $\phi = 0.01$. The separation between lines D and E was produced by microcrack additions to an aggregate that already contained 15 percent spherical pores. This addition of microcrack effects produced an additional 1.8-GPa (18-kbar) decrement.

For the temperature-dependent Young's modulus ($E(T)$) replicates evaluated from flexural-frequency measurements of Boiling Pots basalt, the average volume-fraction absolute porosity is $\phi = 0.15$. This value is approximately a 5-percent difference between the porosity value expected, assuming a submodel 3 composition with purely spherical voids, and the determined value.

The temperature dependence of the Hill-averaged bulk modulus, shear modulus, and Young's modulus is presented in table 52.8 for submodel compositions 1, 2, and 3. The highest temperature dependence (largest absolute value) of the moduli on a collective basis is for the pyroxene-rich submodel 1 and is reflective of the relatively large adiabatic temperature derivative of the bulk modulus ($(\partial K/\partial T)^{S}_{VRH}$) value for bronzite ($-26.8$ MPa/ °C) and, in turn, the relatively high volume thermal expansivity of augite ($47.7 \times 10^{-6}$ °C$^{-1}$). Plagioclase-rich submodel 2 shows the lowest

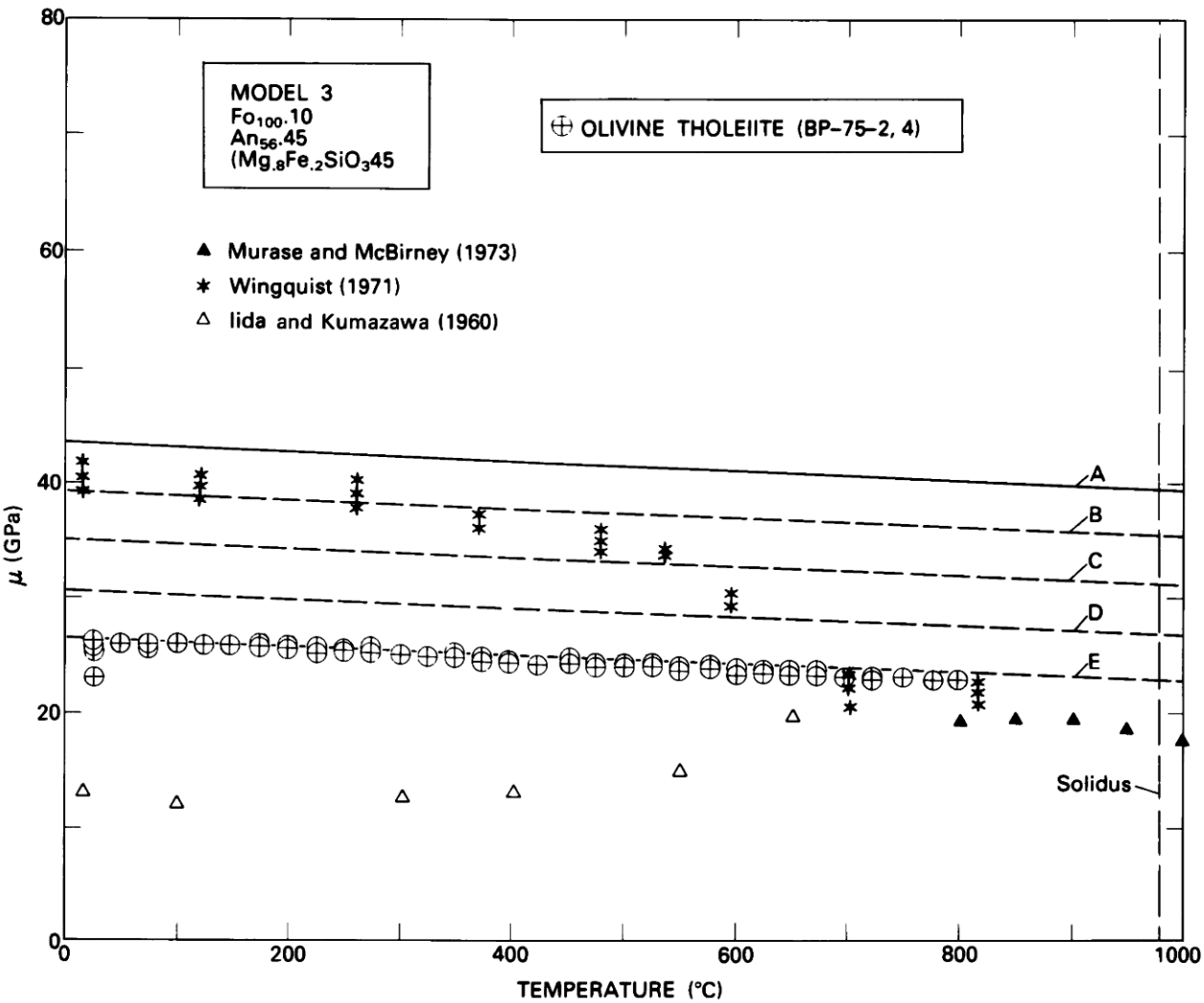


FIGURE 52.15.—Predicted high-temperature, ambient-pressure V-R-H rigidities and matrix Voigt and Reuss bounds on rigidity for compositional submodel 3. Measured rigidity of Boiling Pots olivine tholeiite, crossed circles. Differences between measured and predicted rigidities probably result from iron oxide minerals and intercrystalline glass that have not been incorporated in submodel.

TABLE 52.8.—*Comparison of the temperature dependence of the elastic moduli from the compositional model (I) at $\Phi = 0$ and the measured dynamic rigidity and Young's modulus for olivine tholeiite of Boiling Pots*

| | $(\partial K/\partial T)_{VRH}$ (MPa/°C) | $(\partial \mu/\partial T)_{VRH}$ (MPa/°C) | $(\partial E/\partial T)_{VRH}$ (MPa/°C) |
|---|---|---|---|
| Compositional submodel: | | | |
| 1 | −15.31 | −4.47 | −13.13 |
| 2 | −11.28 | −2.34 | −7.32 |
| 3 | −13.30 | −3.39 | −10.23 |
| Boiling Pots olivine tholeiite measurements | | −3.5(1)<br>−4.2(2)<br>−3.8(3) | −8.5(4)<br>−8.1(5)<br>−8.3(6) |

Sample designation:
(1) BP-75-R2(G)
(2) BP-75-R4(G)
(3) BP-75-R2(G) + R4(G)
(4) BP-75-R6 ..... $\Phi = 0.15$
(5) BP-75-R1 ..... $\Phi = 0.15$
(6) BP-75-R6 + R1 ..... $\Phi = 0.15$

temperature dependence of $K$, $\mu$, and $E$, and the average basalt (submodel 3) lies between 1 and 2 in temperature dependence.

The temperature derivatives for the rigidity and Young's modulus of Hawaiian olivine tholeiite have been generated by the least-squares regression procedure. These derivatives are presented in the lower portion of table 52.8 and may be compared with the model derivatives. In the table, the entries for both $\partial\mu/\partial T$ and $\partial E/\partial T$ of samples BP-75-R2(G), -R4(G), -R6, and -R1 are replicates, whereas the other sample entries are derivatives that were formed via least-squares regression on the averaged-value data set.

Comparison of the model and measured rigidity values in table 52.8 shows that submodel 3 with plagioclase contents of 45–50 percent provides a close approximation to the modulus reduction with temperature of the Boiling Pots olivine tholeiite.

Differences between moduli magnitudes predicted using compositional submodels plus microstructural modeling and those magnitudes evaluated by resonant-frequency measurements are believed to arise from the following sources:

(1) Opaque and glass-filled minor inclusions in olivine, hypersthene, augite, and plagioclase phenocrysts and microphenocrysts;

(2) Groundmass magnetite and opaque-rich groundmass glass pockets that have not been incorporated in the model; and

(3) Subtle differences in the elastic properties of matrix crystals versus model crystals that may arise from (a) compositional zoning and defects in olivine and (or) defects in pyroxene and in labradorite, or (b) unrelieved thermal strains in crystal lattices, induced by posteruption chilling.

For all moduli, the measured values lie between the pyroxene-rich and plagioclase-rich upper and lower values. That is,

$$(\partial\mu/\partial T)_{VRH}^{\text{model 1}} > (\partial\mu/\partial T)_{\text{measured}} > (\partial\mu/\partial T)_{VRH}^{\text{model 2}}$$

and

$$(\partial E/\partial T)_{VRH}^{\text{model 1}} > (\partial E/\partial T)_{\text{measured}} > (\partial E/\partial T)_{VRH}^{\text{model 2}}.$$

These relations hold for both the average of the measured values and for each of the replicates. This bounding behavior of the Hill-averaged models accords with the expected behavior, recalling that the modal abundance of all pyroxene species in the Boiling Pots basalt was 32.9 percent, whereas the total of groundmass and microphenocryst plagioclase content is 37.3 percent and olivine totals 12.4 percent.

## THE PRESSURE DEPENDENCE OF ELASTICITY IN HAWAIIAN BASALT: CONTRACTANCY AND MAGMATISM

This section, which discusses the pressure dependence of elasticity in Hawaiian rocks, complements the discussion of the major sections of this paper on variations in elasticity and expansivity, which are temperature dependent. Focus is placed on the implications these rock properties have for the mechanical controls on magmatic storage regions within active shield volcanoes; both subcaldera reservoirs and their rift systems are considered. Underlying the discussion are the influences of microstructure, microcracks, and composition as previously developed. A major conclusion of this section is that the pressure dependence of elasticity in the rocks of shield volcanoes affects their in-situ behavior in ways that lead naturally to spatial domains of magmatic stability. Ramifications include (1) density crossovers in the in-situ country rock and magma; (2) a rationale that unifies the observed seismic-velocity variations within and beneath Hawaiian shields, experimentally determined rock properties, and the massive dilatancy associated with the free surface of the Earth in regions of active volcanism; and (3) the mechanical rationale for the long-held inference that Hawaiian magma reservoirs move progressively upward during their life cycle.

Studies of the mechanics of magmatic fluids, rock-fluid mixtures, and the deformation accompanying injection and withdrawal with relevance to regions of active volcanism have been approached from six viewpoints: (1) in-situ density contrasts between melt and country rock within mantle and crustal sections (Waff, 1980; Stolper and others, 1981; Grove and Baker, 1983; Herzberg and others, 1983; Sparks and Huppert, 1984), with emphasis on the distribution in and separation from the mantle source region, and the role of fractional crystallization on melt density; (2) wholesale diapiric rise with concurrent decompression melting (Ramberg, 1981); (3) continuum solutions of hydraulic fracture stability and fluid-induced deformation (Weertman, 1971a, b; Johnson and Pollard, 1973; Pollard, 1976; Pollard and Muller, 1976; Weertman and Chang, 1977; Pollard and Holzhausen, 1979; Weertman, 1980; Ryan and others, 1983; Spence and Turcotte, 1985); (4) reviews and syntheses of the effective-stress principle (Shaw, 1980; Gold and Soter, 1985); (5) thermodynamic analyses in combination with the wetting mechanics of basaltic melts (Waff and Bulau, 1979; Bulau and others, 1979; Waff, 1979, 1980); and (6) fluid-dynamic and fluid-static analyses of incompressible single-phase (Shaw and Swanson, 1970; Vogt, 1974; Solomon, 1975; Fedotov, 1977a, b, c), incompressible multiphase (Sleep, 1974; McKenzie, 1984), and compressible multiphase fluids (Wilson and Head, 1981). In a different vein, but of relevance to the following discussion, is the work of Eaton and Murata (1960) and Fiske and Jackson (1972), who respectively computed equilibrium heights expected for

Hawaiian volcanoes and emphasized the importance of gravitational stresses in the development of Hawaiian rift zones.

In its conceptual development, the discussion that follows differs from these studies in the following ways:

(1) The focus of attention on the free surface of the Earth, with particular emphasis on the heterogeneous distribution of material properties, and the nonlinear mechanical behavior exhibited by rocks as the surface is approached;

(2) The evolutionary consequences that derive for magmatic bodies as the Earth's free surface is progressively translated upward—an explicit consideration of the evolutionary track followed by shield volcanoes within a magmatic province, as they mature and age;

(3) An integration of the confining pressure behavior of shield volcanoes, with their geodetic, seismic, density (gravitational), lithologic and structural characteristics, providing guidelines, constraints and tests for internal consistency; and

(4) An exploration of the three-dimensional structure of the resulting contractancy concept, and its implications.

The discussion can be started by posing a series of related questions. What are the controls on the stability of magmatic bodies at depth? What are the roles of open, partially contracted, and fully contracted fractures in these environments? Can the recurring themes of intrusion-eruption and the drainback of lava within rift systems be understood within a context of vertical changes in macroscopic and microscopic fracture closure, as these affect the bulk density of a volcanic shield and interact with the density of magma at depth? The thrust of the discussion then lies in the confining-pressure dependence of the mechanical properties of shield volcanoes. A set of general relations can be developed by the study of well-characterized volcanoes in Hawaii, especially Kilauea and Mauna Loa.

## PHENOMENOLOGY OF CONTRACTANCY

The bulk compressibility of the subsolidus volcanic shield may be expressed as follows:

$$\beta_{VS} = \beta_M + \beta_{MS} + \beta_{PF} + \beta_F, \tag{41}$$

where $\beta_{VS}$ is the volanic-shield compressibility, $\beta_M$ is the mineral phase compressibility, $\beta_{MS}$ is the microstructure compressibility that combines contributions from vesicles and microcracks, $\beta_{PF}$ is the pore-fluid compressibility, and $\beta_F$ is the macroscopic fracture compressibility.

For tholeiitic shield volcanoes, the mineral-phase compressibility is built up from the individual compressibilities of olivine, clinopyroxene, orthopyroxene, and plagioclase, with subordinate contributions from magnetite, ilmenite, and apatite. In general terms, the largely tholeiitic shield will have compressibilities dominated by the volumetrically important mineral species: olivine, clinopyroxene, and plagioclase. The magnitude of this contribution will then scale with the weighted volume fraction of each component.

The total compressibility of large volumes of the shield may now be divided into two contributors: intrinsic and extrinsic. Laboratory studies evaluate the intrinsic contributors, and the separation of single-crystal acoustic-velocity studies and whole-rock studies provides a means of sorting out the crystalline and microstructural contributions. The extrinsic contribution is provided by the large fractures within the shield. These fractures are the dilatant cracks and fissure networks that intersect the free surface of the volcano. They define the bounding planes of rift-zone graben and may be exploited by rising magma during intrusion and eruption sequences. Seismic velocity studies carried out over major segments of a shield then sample the total compressibility. The evaluation of the bulk modulus of portions of the shield then yields a means of recovering the relevant in-situ compressibility—summed for each major contributor above.

Contractancy, in the sense used here, can be viewed as a mechanically opposite effect of dilatancy. It is reflected in the progressive reduction in volume of an element of rock that contains minerals, microcracks, macroscopic joints and fractures, equant pores, and saturating pore fluids, as this conceptual element is subjected to continuously increasing confining pressures. The phenomenon, within the context of magmatic systems, is dominated by the progressive closure of macroscopic fractures and joints, and microscopic fractures with depth. This closure is viewed as a progressive elimination of the extrinsic contributors to bulk compressibility. It is a realization that very nonlinear effects dominate the mechanical behavior of rocks as the surface of the Earth is approached. These effects are well exemplified by the pressure dependence of $V_p$ and $V_s$ in both the laboratory studies and field-derived seismic-velocity profiles. Contractancy may be contrasted with dilatancy, which is an inelastic volume increase under applied loading (Brace and others, 1966; Schock and others, 1973). Such volume increases lead to decreases in the ratio $V_p/V_s$ (Whitcomb and others, 1973; Wyss and Holcomb, 1973) and begin at approximately one-half to two-thirds the fracture strength of the rock.

Evaluations of the compressional and shear wave velocities of rocks, from the transit times of acoustic waves in laboratory samples, provide the means of assessing the microstructural and mineralogical contributions to contractancy. The pressure dependence of $V_p$ for the dominant lithologies of Hawaiian volcanoes is summarized in figures 52.16, 52.17, and 52.18. These lithologic types represent their tholeiitic shields, alkalic and nephelinitic interlayers and caps, intrusive complexes, olivine-rich cumulates, and the mafic and ultramafic rocks of their oceanic crustal and upper-mantle foundations. In each of the figures, the pressure dependence of $V_p$, $\partial V_p/\partial P$, shows the two types of behavior: an early, highly nonlinear dependence extending from 0 to 200 MPa (2 kbar), and a generally linear regime starting at about 200 MPa and extending to higher pressures. Studies of holocrystalline rocks (Todd and Simmons, 1972), as well as of porous lithologies (King, 1966), have attributed this change in wave velocity to the progressive closure of microcracks within the rock matrix. This microfracture closure—or contractancy—produces the early rapid rise in $V_p$ and $V_s$ characteristic of the low-pressure shallow environment. The generally linear change in wave velocity above 200 MPa is produced by the compressibility of the minerals within the matrix.

## CONTRACTANCY WITHIN SHIELD VOLCANOES

Several lines of evidence suggest that the superstructure of Hawaiian shield volcanoes contain dilatant fractures and that these open fractures extend to considerable depths. The evidence includes:

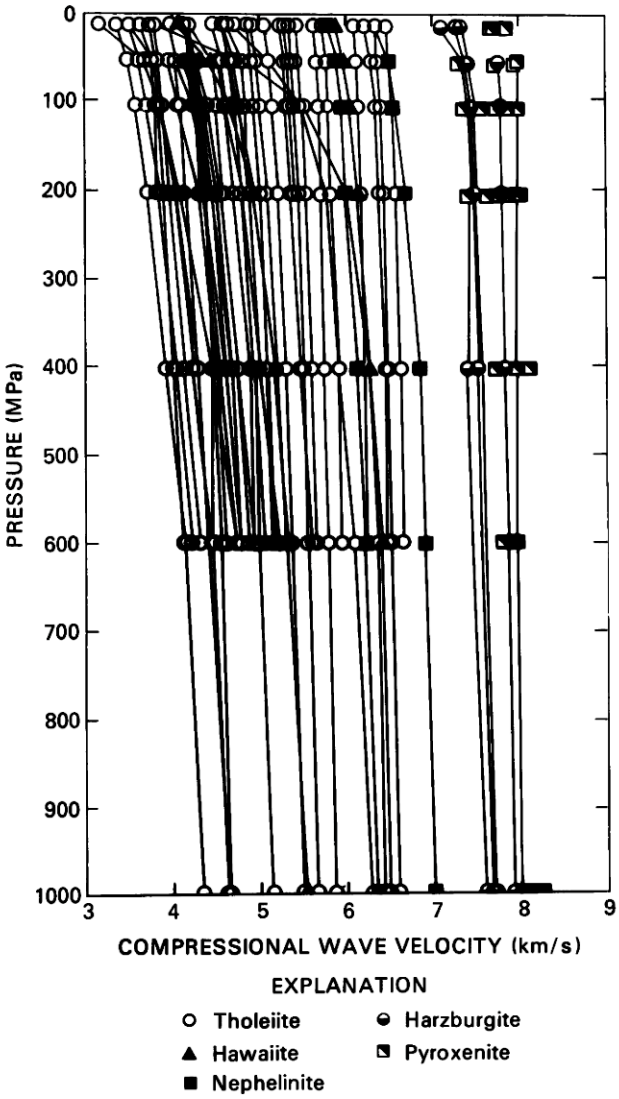


FIGURE 52.16.—Pressure dependence of compressional-wave velocities ($V_p$) in tholeiitic, alkalic, and nephelinitic basalt and in ultramafic lithologies composing upper-mantle underpinnings of Hawaiian volcanoes. Of particular interest is nonlinear behavior of $V_p$ at confining pressures below 200 MPa, which is produced by progressive elimination of microfractures with continued pressure increases. Data compiled from Bajuk and others (1957), Manghnani and Woollard (1968), Christensen and Salisbury (1972, 1973), Christensen (1973, 1976, 1978), Fox and others (1973), Fox and Schreiber (1973), Christensen and others (1974a, b), Schreiber and others (1974), Hyndman (1976), Kroenke and others (1976), and Salisbury and Christensen (1976).

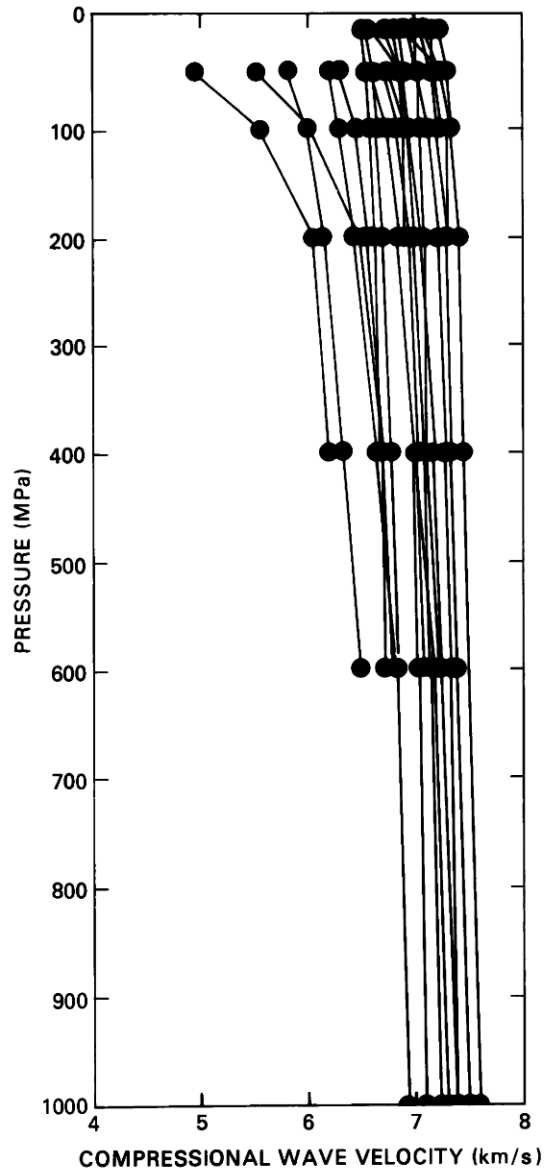


FIGURE 52.17.—Pressure dependence of compressional-wave velocity in gabbro. Distribution of gabbroic xenoliths in vent areas of Hawaiian volcanoes and their resemblance to intrusives exposed in cores and rift zones of dissected volcanoes suggest that gabbros form in a major fraction of magmatic storage region in active portions of system. Marked changes in $\partial V_p/\partial P$ above and below 200 MPa suggest a progressive closure of microfractures in upper regions of volcanic shield, with a transition to mineral compression at $p > 200$ MPa (2 kbar). Data compiled from Schreiber and others (1972), Fox and others (1973), Mizutani and Newbigging (1973), Wang and others (1973), Christensen and others (1975), Hyndman (1976), Kroenke and others (1976), and Christensen (1978).

(1) Gaping cracks in rift systems and summit calderas that have crack opening displacements ranging from tens of centimeters to meters (for example, the Great Crack of Kilauea's southwest rift zone);

(2) Exceptionally low compressional-wave velocities in the upper 2 km of the volcanic pile;

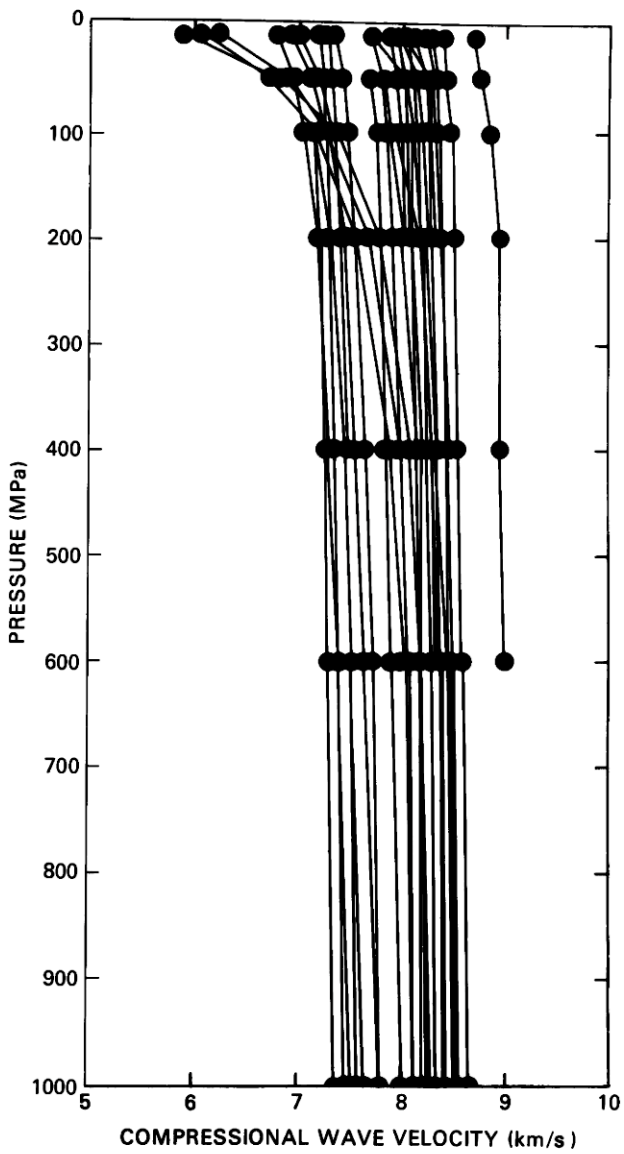


FIGURE 52.18.—Pressure dependence of compressional-wave velocity in dunite. Dunitic xenoliths in alkalic and nephelinitic vent areas suggest relatively widespread occurrence of dunite in upper mantle beneath Hawaii. Additional association is made with refractory mantle-root areas of tholeiitic suite of lavas, as well as a role as cumulates in crustal storage reservoirs during tholeiitic magmatism. In most of these roles, aggregate elastic behavior will lie well within region dominated by mineral compression and structural properties of olivine. For olivine-rich early cumulates that form in storage compartments within a volcanic shield or rift-zone base, nonlinear sections of compressional-wave curves are expected to apply. Data compiled from Hughes and Cross (1951), Bajuk and others (1957), Kanamori and Mizutani (1965), Christensen (1966, 1971), Manghnani and Wollard (1968), Mao and others (1970), Christensen and Ramananantoandro (1971), Babuska (1972), Christensen and Salisbury (1972), and Rao and others (1974).

(3) Exceptionally low in-situ densities in the upper 2 km;

(4) The common observation of massive drainback at the conclusion of an eruptive phase. An archetypical example is the drainback volume of $6 \times 10^6$ m$^3$ for phases of the 1959 Kilauea Iki eruption (Richter and Moore, 1966), and drainback rates as high as $1.5 \times 10^6$ m$^3$ per hour.

(5) Simultaneous eruption and drainback, as exemplified by the 1983 activity at Puu Oo, in Kilauea's east rift zone; and

(6) The long-observed discrepancy between the vertical and horizontal displacement fits to geodetic model predictions. As discussed by Ryan and others (1983), the vertical displacements at Kilauea, for example, are largely reversible, whereas the horizontal components are very weakly reversible. For the upper regions of the shield, rock behavior is elastic in the vertical plane, whereas the horizontal plane contains substantial inelasticity.

The fracture systems within Kilauea caldera, the summit region, and the upper southwest rift zone are shown in figures 52.19 and 52.20.

## ENVIRONMENT AT DEPTH: EFFECTS OF PRESSURE AND TEMPERATURE

Rocks forming the central and basal sections of oceanic shield volcanoes are expected to contain pore fluids. Traveling downward within the subaerial portion of an oceanic volcanic system, we would therefore expect to approach a horizon above which the pore space contains air, volcanic gases, and water vapor and below which the accessible pore space is saturated with $H_2O$. The water would be either fresh or saline, depending on the local configuration of the Ghyben-Herzburg lens. It is relevant then to consider the contractancy of basalt with both dry and $H_2O$-saturated pore space, and its pressure dependence. These curves are presented in figure 52.21*B* for basalt (Christensen and Salisbury, 1975). The characteristically nonlinear $\partial V_p/\partial P$ at pressures less than 200 MPa is well developed—particularly for the dry curve where the accessible porosity is occupied by air. Both sets of curves show an additional effect: there is a pressure window above which (that is, toward higher $P$) the pore space accessible to any second phase—air or $H_2O$—has been squeezed out. For basalt and gabbro, this pressure window corresponds to a transition zone centered at about 200–300 MPa. The figure also contains a series of inset diagrams that depict the progressive elimination of macroscopic and microscopic fracture permeability with progressive increases in confining pressure. The transition zone that coincides with the convergence of the dry and fluid-saturated compression branches is herein referred

to as the compression transition zone. This zone separates the figure into two subregions: a shallow region where the dominant mechanism is the compression of fractures and pore fluids, and a deeper region where further volume reductions are dominated by mineral compression. In constructing the figure, the confining pressures of Christensen and Salisbury (1975) have been converted to depth equivalents, taking into account the density-depth relations for Kilauea presented by Zucca and others (1982).

A summary diagram of data (fig. 52.21*A*) represents the geodetic and seismic constraints on the depth intervals inferred for the position of the summit magma reservoir. These constraints are derived from (1) three-dimensional deformation modeling employing collateral geologic and mechanical property contraints (Ryan and others, 1983); (2) two- and three-dimensional studies of the distribution of magma-reservoir seismicity (Koyanagi and others, 1976; Ryan and others, 1981); (3) geometrically idealized modeling of simply connected sources of pressure or displacement (Mogi, 1958; Deiterich and Decker, 1975); and (4) inversions of summit-tilt, trilateration, and vertical-displacement data, via least-squares regression (Dvorak and others, 1983). The depth interval 2 to 4 km is common to all the inferred ranges and appears to comprise a consensus for the uppermost reaches of the storage region proper. This depth region for magma storage extends to at least 6 km, based on geodetic and seismic evidence.

A comparison of figures 52.21*A* and 52.21*B* suggests that there is a strong correlation between the depths of subcaldera magma storage and the depth intervals that permit the continued dilation of fluid-accessible fractures in basalt. Increases in compression to confining pressure levels in excess of that required to eliminate fracture porosity passes the reference-volume element in figure 52.21*B* below the compression transition zone and into a depth level below the summit storage complex. Note that the curves in figure 52.21*B* describe the microcrack closure behavior for basalt. The addition of macroscopic joint closure has a pressure dependence that is qualitatively similar. Detailed differences between the two arise from the contribution of crack surface topography to joint stiffness

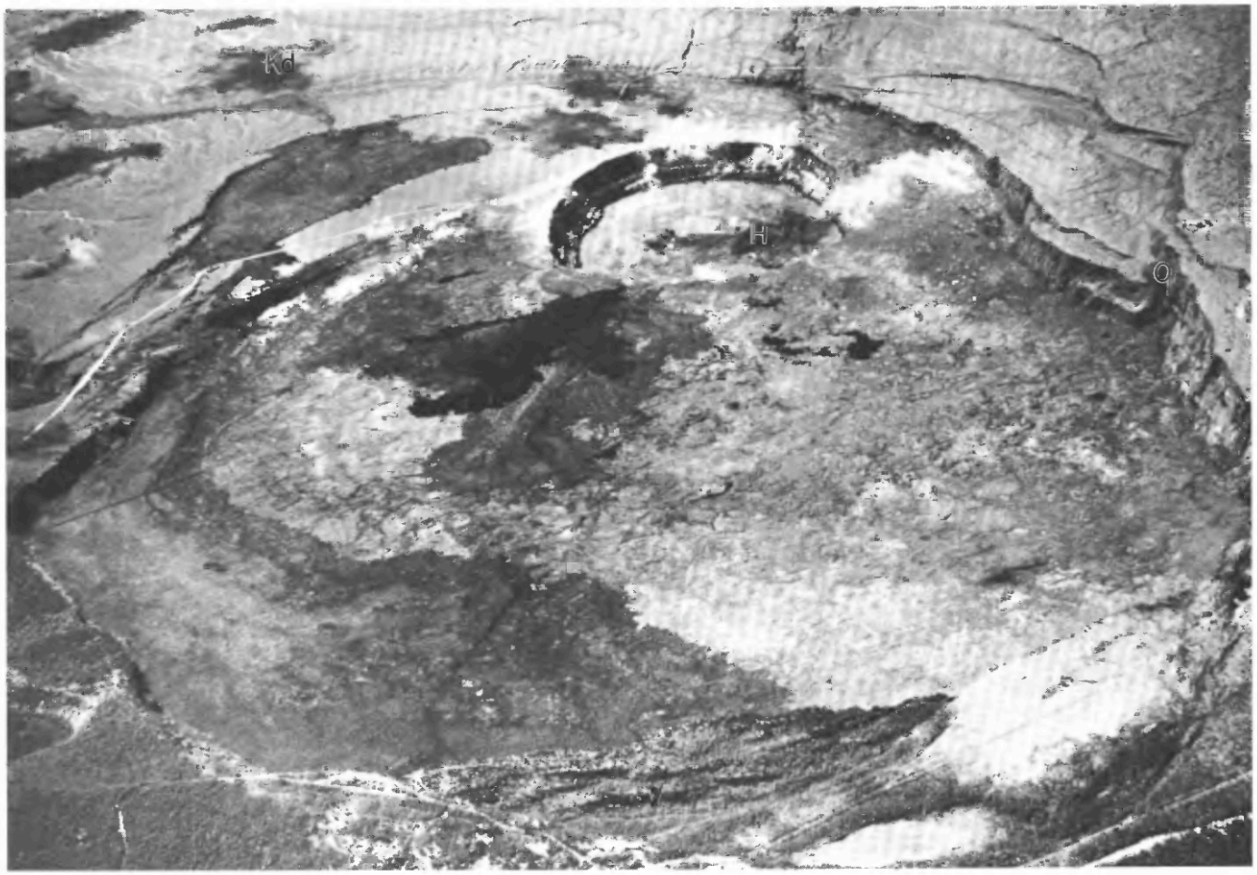


FIGURE 52.19.—Kilauea caldera in west-directed view. Magmatic inflation and deflation centers migrate laterally beneath much of western caldera floor and to south, beyond upper Kau Desert (Kd). Such temporal migration patterns are surface expressions of multiply connected complex of dikes and sills that form summit magma-storage reservoir. They are spatially associated with region of neutral buoyancy. Multiple collapse regions within caldera lie at foot of Volcano House (V). Hawaiian Volcano Observatory (O), and within Halemaumau (H). Photograph by James Griggs.

(Brown and Scholz, 1985). To be noted also is that these curves describe the crack-closure behavior for basalt in the absence of an applied pore pressure—that is, they reflect the inherent crack and rock stiffness itself in maintaining open permeable pathways above the compression transition zone. Applied pore pressures enhance the stability of an open fracture network at depth, as discussed in the next section.

Open fractures provide an environment for laterally extensive magmatic movements in three ways: (1) the obvious intrusion sites provided by dilatant macroscopic fractures; (2) the contributions to neutral buoyancy and magmatic stability produced when the open fracture network is so pervasive that the in-situ rock density is reduced to values equal to (and less than) the in-situ density of melt near its liquidus: and (3) the dilation of microfractures that provide penetration pathways for melt adjacent to advancing crack tips at depth. The wetting properties of basalt near its liquidus (Waff and Bulau, 1979; M. Ryan, unpublished data, 1980) confirm this capability.

The fracture-closure/depth behavior for basalt and gabbro also correlates with the depth extent of Kilauea's rift systems. These depths have been inferred by the position of the bottom of the zone of south-flank seismicity—produced by the inflation of dikes within the southwest and east rift zones. This depth is locally 9–12 km beneath the surface of the volcano. Beneath the east rift zone, this depth is 9–10 km, which is coincident with the 8- to 9-km depth (beneath sea level) inferred from south-flank block kinematics in the study of Crosson and Endo (1982). This region coincides with the transition zone that lies at the base of the field of fracture and pore-fluid compression in figure 52.21*A*. These relations are in harmony with the porposal of Nakamura (1980), who suggested that the mechanically soft sediments of the old ocean floor provided lateral accommodation for the development of long rift zones in Hawaiian shield volcanoes. Indeed, both shield contractancy and lateral slip surfaces in low-modulus sediments may locally work together in regulating the depth extent of rift zones. During continued shield building, however, the keel of the active rift system is expected to rise

FIGURE 52.20.—Junction of southwest rift zone (SWRZ) and Kilauea caldera near Halemaumau (H). Fractures produced on surface record stretch at depth due to increments of dike injection. These fractures produce low in-situ densities and compressional-wave velocities that characterize upper 2 km of shield. In turn, low in-situ densities interact with density of tholeiitic melt near its liquidus to produce region of neutral buoyancy that stabilizes magmatic storage at depth as well as dike emplacement within rift systems. An automobile on caldera rim road (right center) provides scale. Photograph by James Griggs.

above the old oceanic floor and have a depth extent exclusively regulated by the mechanics of volcanic-shield contractancy. A summary of the mechanical relations that have been detailed in figure 52.21*A* and 52.21*B* is provided in figure 52.22.

In addition to the pressure dependence of rock behavior in the vicinity of the magma-storage reservoir, it is of interest to comment on the temperature dependence of basalt elastic moduli near the shallow, low-pressure portions of the reservoir, which can be done by evaluating $E(T)$ and $\mu(T)$ at temperatures approaching the solidus. Applications include estimating the relative contribution(s) of thermal-stress-induced fracture and evaluations of the bending stresses associated with magma-reservoir-roof flexure during inflation-deflation cycling. In evaluating these moduli, three auxilary constraints have been applied: (1) direct temperature-depth measurements beneath the summit of Kilauea; (2) the location of the summit reservoir based on geodetic and seismic studies (discussed above); and (3) eruption and liquidus temperatures determined in summit and near-summit eruptions, and reconstructed in melting experiments on summit compositions. The region of evaluation lies below the upper several hundred meters that characteristically has heavy contributions of macroscopic fractures, leading to the expected low in-situ moduli.

Rotary drilling to 1,262-m depth beneath Kilauea's summit (Zablocki and others, 1974) has provided a temperature-depth profile through the shallow water table to a position below sea level. The stabilized profile shown in figure 52.21*A* has a bottom-hole temperature of 137 °C and suggests an initial thermal gradient of about 370 °C/km. This profile bottom provides a pinning point that is used to hinge a family of thermal gradients, as discussed below.

Temperatures have been measured by optical pyrometry in summit and near-summit lava fountains (for example, Richter and Murata, 1966; Peck and Kinoshita, 1976), and directly in advancing flows and in lava lakes (for example, Wright and Weiblen, 1968; Jackson and others, 1975; Swanson and others, 1976). For many of these measurements, the shrouding effects associated with eruption plumes and the thermal gradients associated with the free surface of active flows suggest that they are generally below true magmatic temperatures. Relations between liquidus temperatures and iron enrichment determined experimentally for samples of Kilauea Iki eruption pumice (Thompson and Tilley, 1969) suggest temperatures in the range 1,225 to 1,188 °C. In addition, Helz and Thornber (1985) present an approach for restoring temperatures measured in lava-lake drill holes to the predrilling in-situ values, based on a glass-based calcium geothermometer. Olivine crystallization in Makaopuhi lava lake (Wright and Weiblen, 1968) has identified a temperature of 1,200 ± 10 °C. Collectively, these studies suggest that the liquidus temperature for Kilauean olivine tholeiite at atmospheric and near-surface pressures lies close to 1,200 °C, and this value has been associated with the subcaldera storage environment in figure 52.21*A*. It is enclosed by a shaded band that encompasses the high temperature end of the illustrated measurement ranges, and extends to 1,210 °C.

From the high-temperature limit of the drill-hole bottom (137 °C) at 1,262 m, four thermal gradients have been constructed to the 2.0-, 2.5-, 3.0- and 3.5-km-depth levels. These gradients are labeled A through D, and they span the range 1,440 to 476 °C/km (fig. 52.21A). They are tied to the 1,200 ± 10-°C low-pressure liquidus for the range of depths appropriate for the "attic" of Kilauea's subcaldera magma reservoir. The span in gradients explicitly recognizes the aggregate uncertainty in both the detailed positioning of the storage region and its temperatures. In this respect, it is prudent to consider a probable range of values. Grouped together, the drill-hole measurements, the liquidus temperature assignments, and the resulting interpolation gradients form a one-dimensional thermal model for the summit section of Kilauea.

From the relations for the temperature dependence of the Young's modulus and the rigidity previously presented and evaluated, working estimates can be made for conditions of low pressure. For the Young's modulus, the relation $E(T)=(6.054-0.00083T)\times 10$ GPa, evaluated along gradient A in figure 52.21*A*, leads to the relation $E(z)_A \approx (6.054-1.195z)\times 10$ GPa, where $z$ is the depth in kilometers. Evaluated along gradient D, the corresponding relation is $E(z)_D \approx (6.054-0.395z)\times 10$ GPa. For the shear modulus, the relation $\mu(T)=(2.615-0.00038T)\times 10$ GPa, leads to $\mu(z)_A \approx (2.615-0.547z)\times 10$ GPa and $\mu(z)_D \approx (2.615-0.181z)\times 10$ GPa. Evaluations made to temperatures approaching the low-pressure solidus suggest that about a 15-percent reduction occurs in both $E$ and $\mu$. Considerations of the high-temperature tensile strengths of basalt (M. Ryan, unpublished data; Ryan and Sammis, 1981), combined with the linear thermal-expansion coefficients described in the section "High-Temperature Elasticity of Hawaiian Basalt" and the relation of thermal stress under plane-strain conditions,

$$\sigma_T = \frac{E\alpha_l(\Delta T)}{1-\nu},$$

suggest that local temperature drops of 50 to 100 °C are sufficient to cause thermal-stress-induced fracture. Hence, moderate falls in temperature that may, for example, be associated with influxes of relatively cool water—produced by tectonic adjustments within the mantling aquifer—may thermally load the rocks above active magma reservoirs to points near failure. This thermal component would then be coupled with the bending stresses that are associated with the flexure of the reservoir roof during inflation-deflation cycling. Together, they produce the seismically active lid on the storage region below. Associated with this recurrent rock fracture would be inferred changes in the fracture network, the mechanics of which are discussed below.

## EFFECTS OF PORE FLUIDS AND JOINT CLOSURE

The curves in figures 52.21*B* and 52.22 illustrate the confining pressure ($P_c$) dependence of compressional-wave velocity for basalt and emphasize the depth dependence of permeable pore-space elimination. The progressive nature of microcrack closure with increasing $P_c$ is also emphasized. It is of interest now to outline the effects expected for macroscopic joint closure and the effect of pore fluids under pressure.

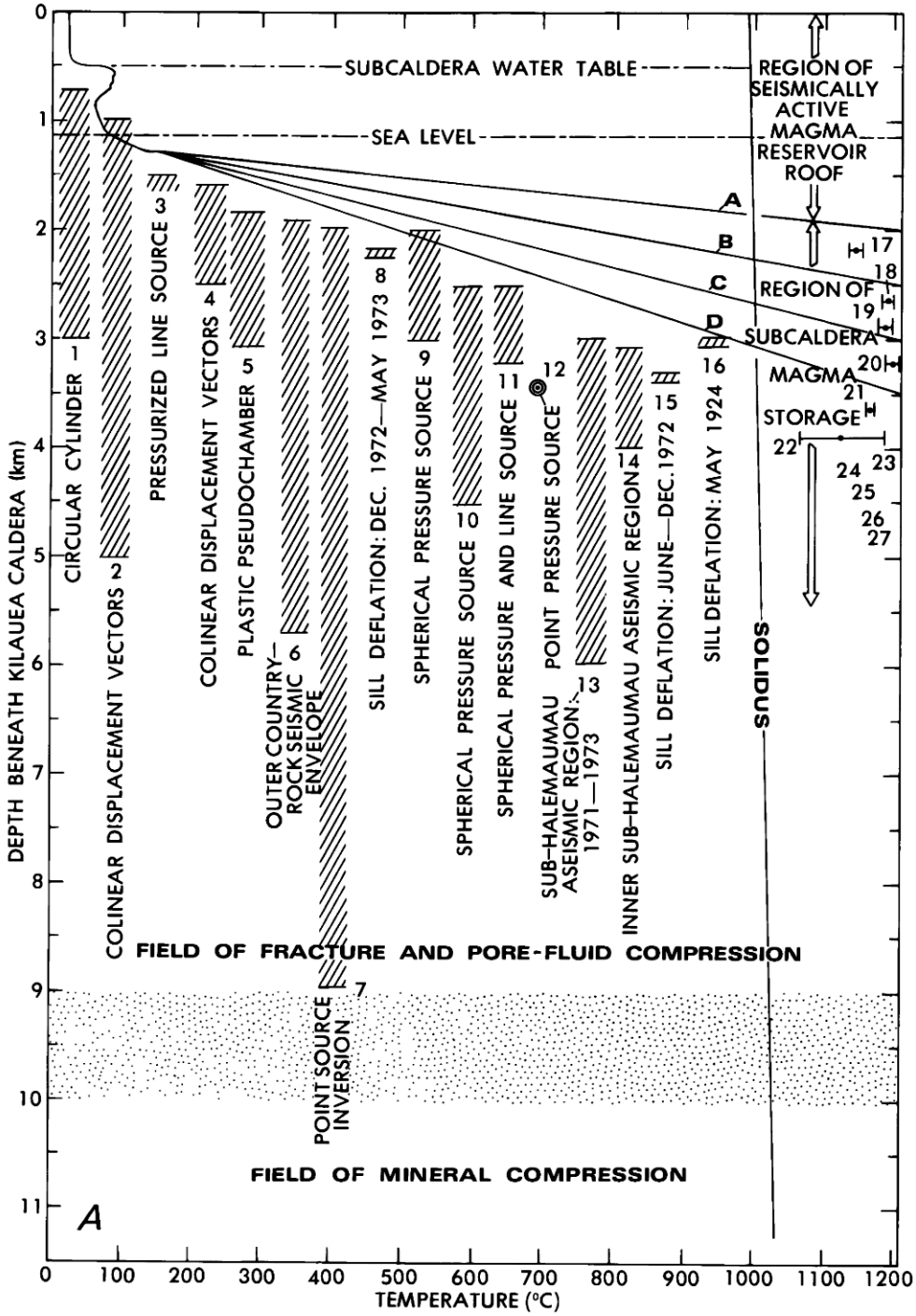


FIGURE 52.21.—Depth relations beneath Kilauea caldera. ***A***, Summary depth distributions of Kilauea's subcaldera magma-storage reservoir and its intrusive components. Depth interval 2–4 km is common to all 16 models and submodels. Added to field is temperature profile beneath summit as measured directly to 1,262 m. Direct temperature measurements in erupted lava, laboratory determinations, and optical pyrometer measurements are given by horizontal bars that cluster near 1,200 °C. They have been assigned to the 2- to 4-km-depth interval, reflecting consensus of geodetic and seismic reservoir models (numbers 1–16). Hachured region that encloses them is intended to suggest a broad-working estimate of a range of in-situ temperatures within this depth interval. Radiating from maximum temperature point at 1,262 m to depth regions along the 1,200-°C margin that

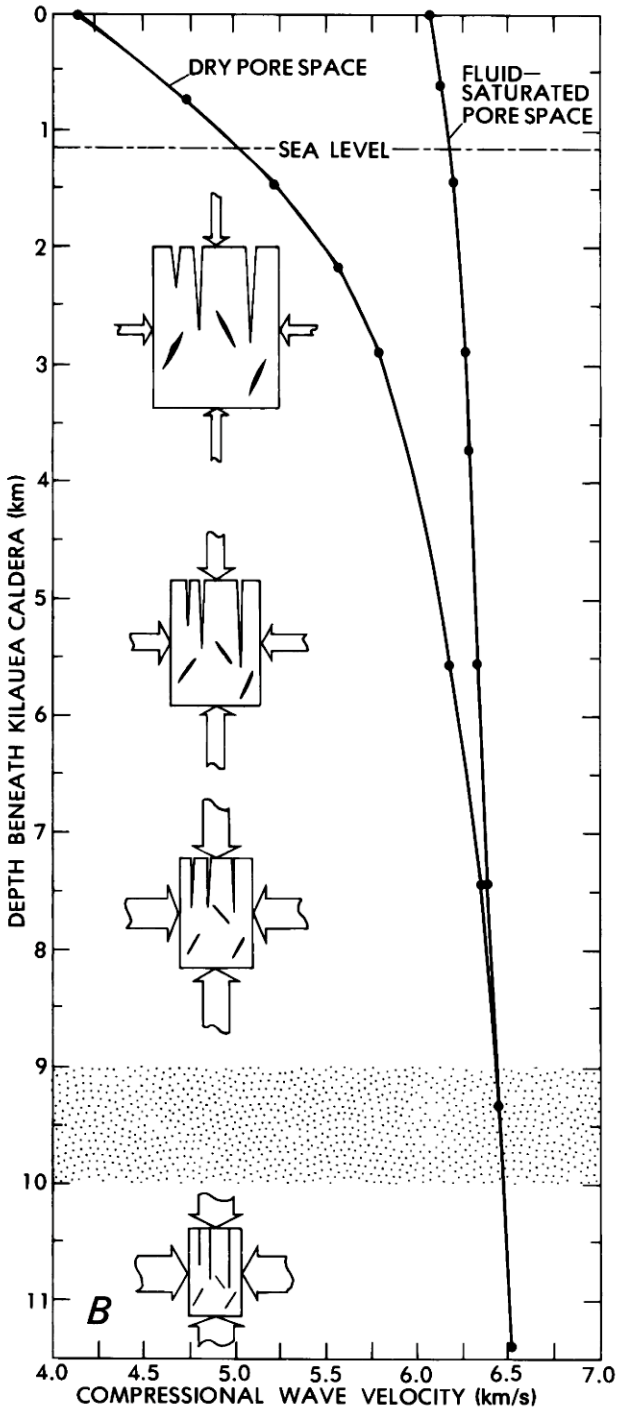


corresponds to upper levels of summit magma storage is a family of four thermal gradients (A–D). They explicitly recognize uncertainty implied by both depth distributions and temperature ranges. Data sources for compilation include (a) Summit temperature-depth profile: Zablocki and others (1974). (b) Solidus: Wright and Okamura (1977); pressure dependence of solidus, $dT_m/dP$: Yoder and Tilley (1962); Hill and Boettcher (1970). (c) Depth of summit magma storage (numbers identify plotted values and ranges): (1) Dieterich and Decker (1975); (2) Duffield and others (1982); (3) Walsh and Decker (1971); (4) Mogi (1958); (5, 7) Jackson and others (1975); (6) Fiske and Kinoshita (1969); (8) Davis and others (1974); (9) Ryan and others (1981); (10) Dvorak and others (1983); (11, 14, 15, 16) Ryan and others (1983); (12) Eaton (1962); (13) Koyanagi and others (1976). (d) Magmatic temperatures (numbers identify plotted measurements): (17) Moore and others (1980); (18, 21) Swanson, Duffield, and Fiske (1976); (19) Jackson and others (1975); (20, 26) Wright and Weiblen (1968); (22) Richter and Murata (1966); (23, 24) Thompson and Tilley (1969); (25) Yoder and Tilley (1962); (27) Wright and Fiske (1971). ***B***, Compressional-wave velocities in dry and $H_2O$-saturated basalt as a function of increasing depth (confining pressures). Congruence of branches at 9-km depth suggests that all $H_2O$-accessible porosity has been squeezed out. Further increases in confining pressure (arrowed pathways) cross through transition region (dot pattern) into field of mineral-compression-dominated volume changes. Inset diagrams depict progressive elimination of microscopic and macroscopic permeability with increasing confining pressure. Data sources for compilation include pressure dependence of compressional-wave velocity from Christensen and Salisbury (1975).

For an orthotropic medium containing three sets of mutually orthogonal joints, the effective compressibility may be expressed as (Amadei and Goodman, 1981):

$$\beta^* = \frac{1}{K^*} = 3\left(\frac{1-2\nu}{E}\right) + \sum_{i=1}^{3} \frac{1}{K_{ni}S_i}, \tag{42}$$

where $\beta^*$ is the effective compressibility, $K^*$ is the effective bulk modulus, $\nu$ is Poisson's ratio, $E$ is the Young's modulus, $K_{ni}$ is the joint stiffness, and $S_i$ is the interjoint spacing.

The nonlinear contribution to compressibility and contractancy arises from the stress-dependent normal fracture (or joint) stiffness. This is a hyperbolic variation in fracture closure with changing normal stress. For dolerite, Bandis and others (1983) have compiled $K_{ni}$ data for joint closure in dolerite. The relevant units are (normal stress component)/(fracture closure), or megapascals per centimeter.

For an unjointed medium, or a medium in which the joint spacing is very large, the volumetric strain may be related to the applied confining pressure ($P_c$) through the elastic moduli:

$$\frac{\Delta V}{V_0} = 3\left(\frac{1-2\nu}{E}\right)P_c. \tag{43}$$

This equation defines volumetric compression in the case of mechanical isotropy, where both flaws and joints are unavailable for closure. The isotropic compression path is plotted in figure 52.23 and is labeled "unjointed media."

Volumetric strain for a jointed media with the potential for pore-pressure ($P_p$) development in the joint network may be expressed as:

$$\frac{\Delta V}{V_0} = (P_c - P_p)\beta^* + 3P_p\left(\frac{1-2\nu}{E}\right). \tag{44}$$

When combined with equation 42, the strain becomes

$$\frac{\Delta V}{V_0} = 3(P_c - P_p)\left(\frac{1-2\nu}{E}\right) + \sum_{i=1}^{3} \frac{1}{K_{ni}S_i} + 3P_p\left(\frac{1-2\nu}{E}\right). \tag{45}$$

The compression paths of jointed media are also plotted on figure 52.23, and the curve for $P_p = 0$ lies to the right of a family of curves that describe contractancy with fluid pressure in the fracture network. The area between the isotropic path and the compression path for $P_p = 0$ has been shaded and represents the expected contractancy range for joint sets whose essentially infinite spacing is tantamount to elastic isotropy, and the suite of curves for the 30-cm joint spacing labeled "jointed media." This area is thought to represent the spectrum of joint spacings relevant to Hawaiian volcanic shields. The jointed media curves generally mimic the nature of the pressure dependence of contractancy as seen in the $V_p$-versus-confining-pressure behavior in figures 52.16 and 52.17, for instances of microfracture closure under laboratory conditions. Particularly well developed is the characteristic form of $\partial(\Delta V/V_0)/\partial P$ at the lowest pressures shown.

Applied pore pressures have three effects. First, increases in fluid pressure force the volumetric-strain curves progressively to the left (fig. 52.23). This effect is expected because pore pressure stabilizes open fractures at depth, preventing less aggregate compression for a given confining pressure. Second, the relative effect of a fixed pore pressure diminishes progressively as the confining pressure is increased. This effect is illustrated by the convergence of

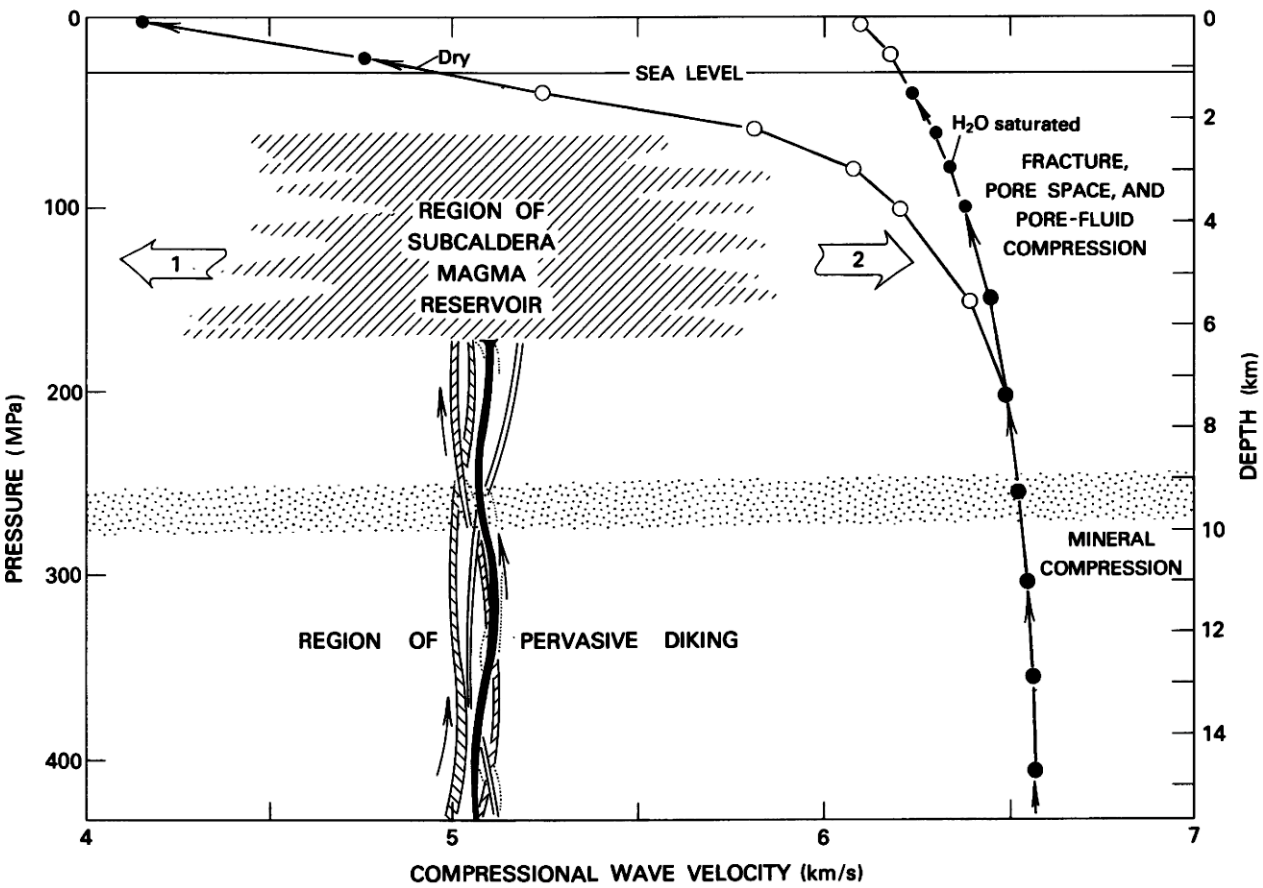


FIGURE 52.22.—Contractancy of basalt in relation to depth distribution of primary magmatic storage within Kilauea. Compressional-wave velocities have been compiled from data of Christensen (1974) and Christensen and Salisbury (1975). Filled and open circles track pathway of $V_p$ as a function of depth and pressure in $H_2O$-saturated and dry environments, corresponding to changes in depth from upper mantle, oceanic crust, volcanic shield, and submarine reference points to subaerial positions. Filled circles correspond to measurements of relevant decompression track for Kilauea. Stippled band represents a contractancy transition zone, above which pore fluids are continuously squeezed out by increasing levels of confining pressure, and below which fluid-accessible porosity has been eliminated. Accordingly, transition zone defines a contractancy map with two subfields: at shallow depths (0–8 km), dominant mechanism is compression of fractures, pore space, and pore fluids; at greater depths (>9 km), dominant mechanism is mineral compression. Stratigraphic extent of magma storage reservoir has been constrained by geodetic and seismic studies and lies mostly in 2.2- to 6-km-depth interval, corresponding to crossruled region. It is coincident with that portion of contractancy field characterized by fluid-accessible fracture space. Horizontally directed arrows (1 and 2) infer lateral injection of magma into adjacent rift zones. Depth extent of these active rift systems is also coincident with that portion of contractancy map that is associated with fluid-accessible fracture space. Beneath transition zone is a region of mineral compression that is stratigraphically associated with pervasive diking linked with vertical magma movements from mantle depths.

the jointed-media curve set with increasing $P_c$. Third, at extremely shallow depths, moderate increases in joint fluid pressure drive the curves from the contraction-dominated field into the dilation field. This effect occurs when fluid pressures exceed the confining pressure.

It is of interest now to look at the ways pore-pressure development in the rock microstructure can influence the contractancy of basalt. Christensen (1984) has studied the effects of confining pressure ($P_c$), pore fluid pressure ($P_p$), and effective pressure ($P_e$), where

$$P_e = P_c - P_p, \tag{46}$$

on the compressional and shear wave velocity in basalt. These effects are summarized in figures 52.24 and 52.25, respectively; they are based on the data of Christensen (1984) and represent adaptations

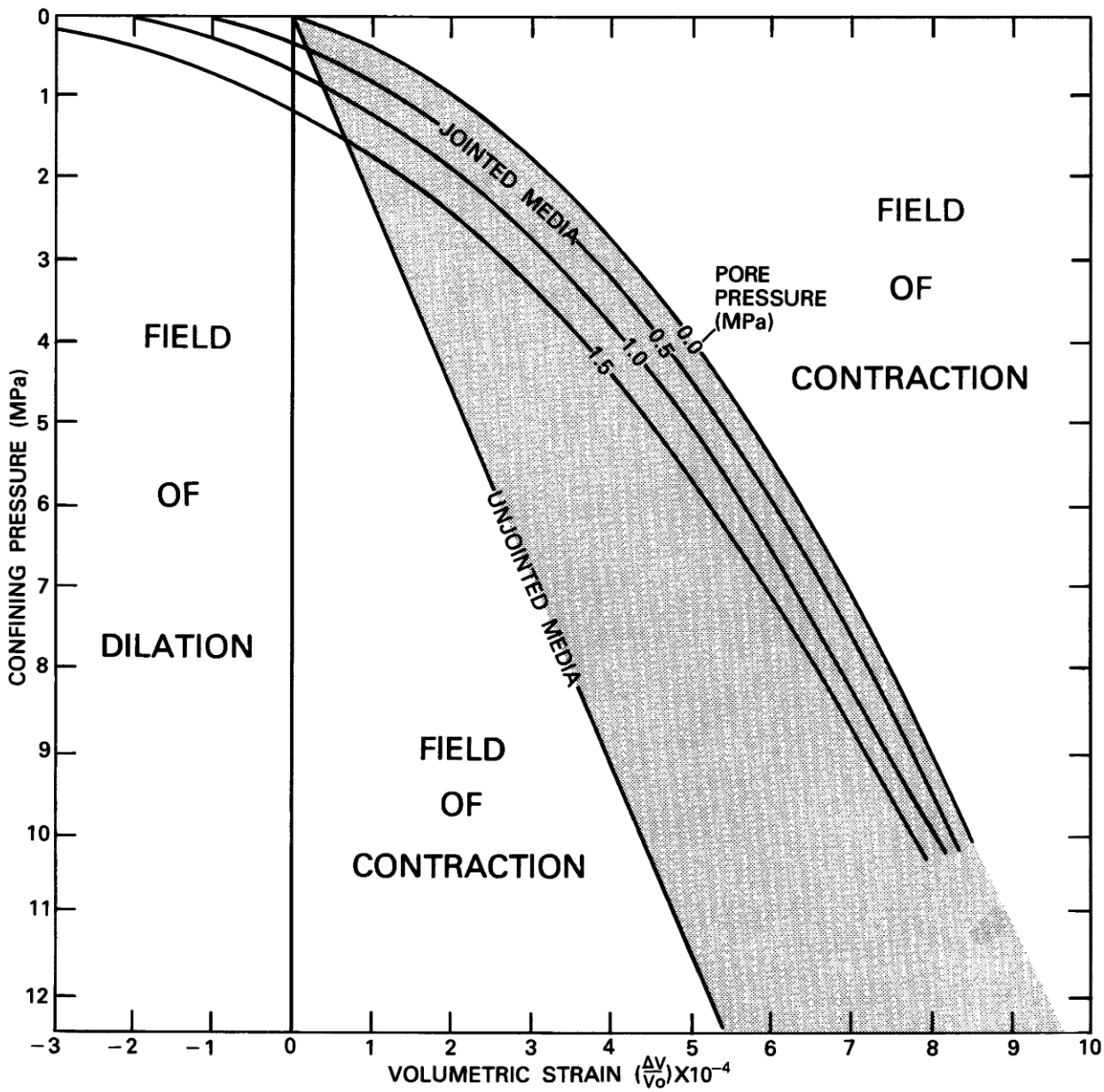


FIGURE 52.23.—Volumetric strain versus confining pressure for unjointed and jointed media with effects of variable pore pressure. Modified from Amadei and Goodman (1981).

of his presentation for reference confining pressures beneath Hawaiian shield volcanoes. In the figures, the familiar nonlinear profile of $\partial V_{p,s}/\partial P$ is produced by the compression of the rock skeleton at zero pore pressure. The hydrostatic reference curve has a fixed low-pressure datum at a depth intermediate between the depth of the summit water table (fig. 52.21*A*) and sea level, for Kilauea as an example. This curve recognizes the temporal and spatial changes in the topography of the intrashield water table and attempts to strike an average. The zero-confining-pressure datum is the volcanic summit. The depth extent encompasses nearly all of the summit magma-reservoir region and most of the rift zones.

The effect of hydrostatic pore pressure shifts the curves to the left, preserving the overall shape of the contractancy profile. Between the $P_p$ = hydrostatic and $P_p = 0$ curves is sandwiched a narrow field where the pore pressure is less than hydrostatic. This field is labeled "C," and it has been shaded in the figures. The pervasive seismicity and rock fracture that characterize the shields of active Hawaiian volcanoes suggest that ambient pore pressures at depth may be inferred to be at or near hydrostatic. To the extent that fluid continuity is maintained by renewed rock fracture, water is expected to be continuously expulsed during the compaction that accompanies volcanic-shield evolution. This general pattern of compaction dewatering should characterize the bulk of the volcanic flanks, where fluid continuity is continuously maintained via the fracture process. For rift-zone environments maintained at near-magmatic temperatures, metamorphism passes through greenschist to amphibolite facies (Liou and others, 1974), and alteration and replacement reactions may be expected to locally close down permeability and promote the development of higher pore-fluid pressures, thus helping, on a local scale, to stabilize open fractures and

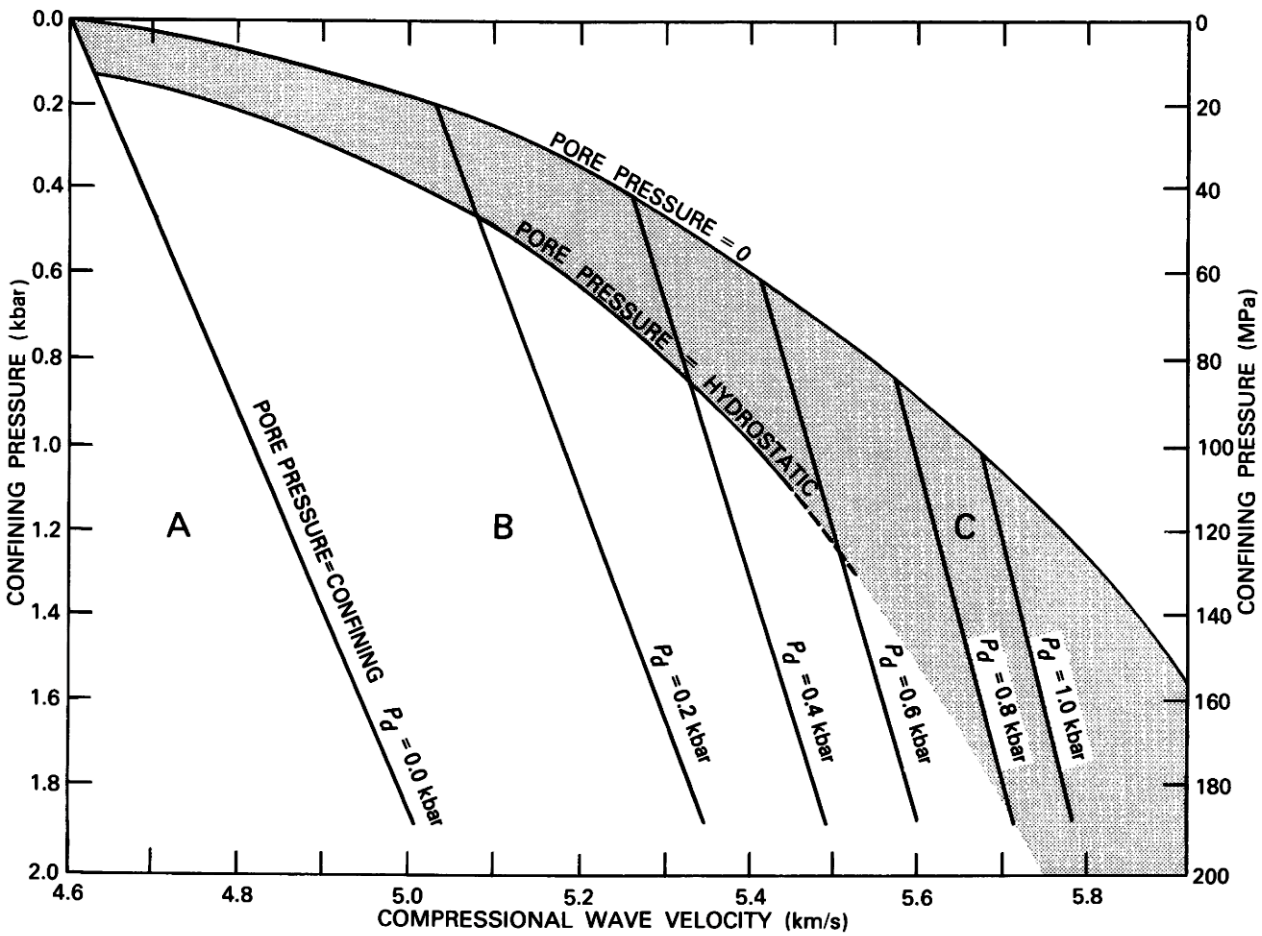


FIGURE 52.24.—Effects of variable pore pressure on compressional-wave velocity in basalt. Fields correspond to mechanically distinct ratios of pore pressure to pressure applied externally to rock skeleton. Field A: pore pressure exceeds external confining pressure; field B: pore pressure is less than confining pressure but greater than hydrostatic; field C: pore pressure is less than hydrostatic. Family of six differential pressure ($P_d$) lines correspond to 20-MPa (0.2 kbar) increments of difference: ($P_{conf} - P_{pore}$). Figure based on data of Christensen (1984).

pores against the confining pressures that would otherwise squeeze them shut. In figures 52.24 and 52.25, the appropriate region is now the B field, where pore pressures are above hydrostatic. For active regions of intrusion and magmatic storage, one may envision a constant competition between the metamorphic reactions tending to promote the sealing that raises pore pressures above hydrostatic, and the reinstatement of permeability by rock fracture and intrusion, returning the pressure to hydrostatic. In-situ $V_p$ and $V_s$ would then repeatedly shift back and forth across the hydrostatic curve, from field C to field B, and then back again as permeability was alternately enhanced and destroyed. The long-term prognosis, however, is the maintenance of near-hydrostatic pressures for those regions of the shield, where fluids are readily available. These regions are expected to be well above the compression transition zone of figures 52.21*A*, 52.21*B*, and 52.22.

## NEAR-SURFACE CONTRACTANCY IN MAGMATIC SYSTEMS

If the dominant mechanism of bulk compression is the continuous elimination of fault, joint, and microfracture porosity in shallow levels of the system, then we should expect to see correlative changes in the density of the volcanic shield with depth, corresponding to increases in confining pressure. The in-situ densities of the volcanic shields of Kilauea and Mauna Loa are plotted in figure 52.26*B*, which is based on the gravity and seismic-refraction surveys of Zucca and others (1982) and the two-dimensional density structure for these volcanoes that resulted from modeling the gravity profile by application of the polygon approach of Talwani and others (1959), with corrections for three-dimensional end effects using the procedure of Cady (1977).

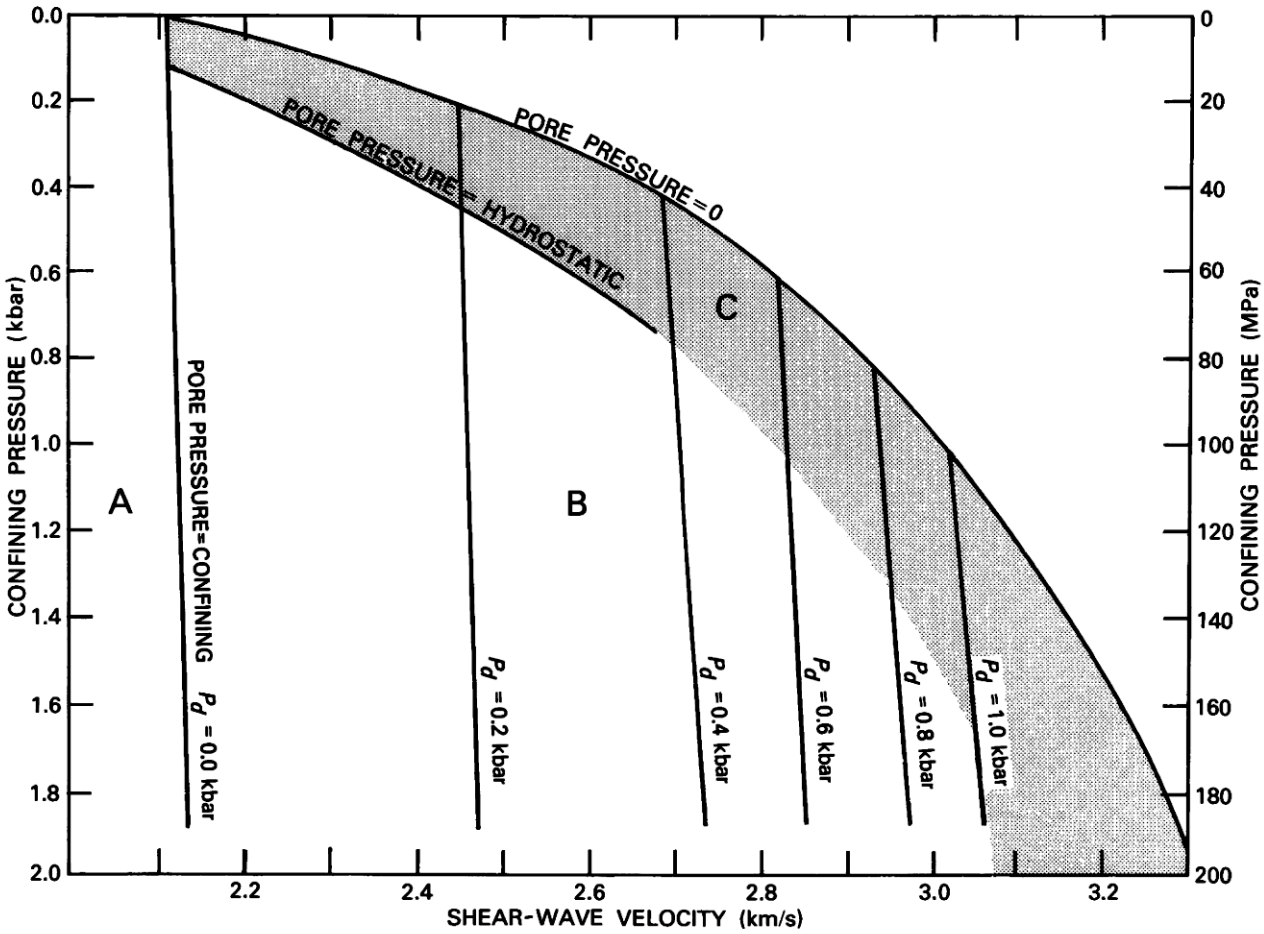


FIGURE 52.25.—Effects of variable pore pressure on shear-wave velocity in basalt. Fields correspond to distinct ratios of pore pressure to externally applied pressure through equivalent lithostatic loading. Field A: pore pressure exceeds external confining pressure; field B: pore pressure is intermediate between confining and hydrostatic; field C: pore pressure is less than hydrostatic. Difference between confining and pore-fluid pressure is differential pressure ($P_d$) of each of six subvertical lines extending from zero-pore-pressure curve. Figure based on data of Christensen (1984).

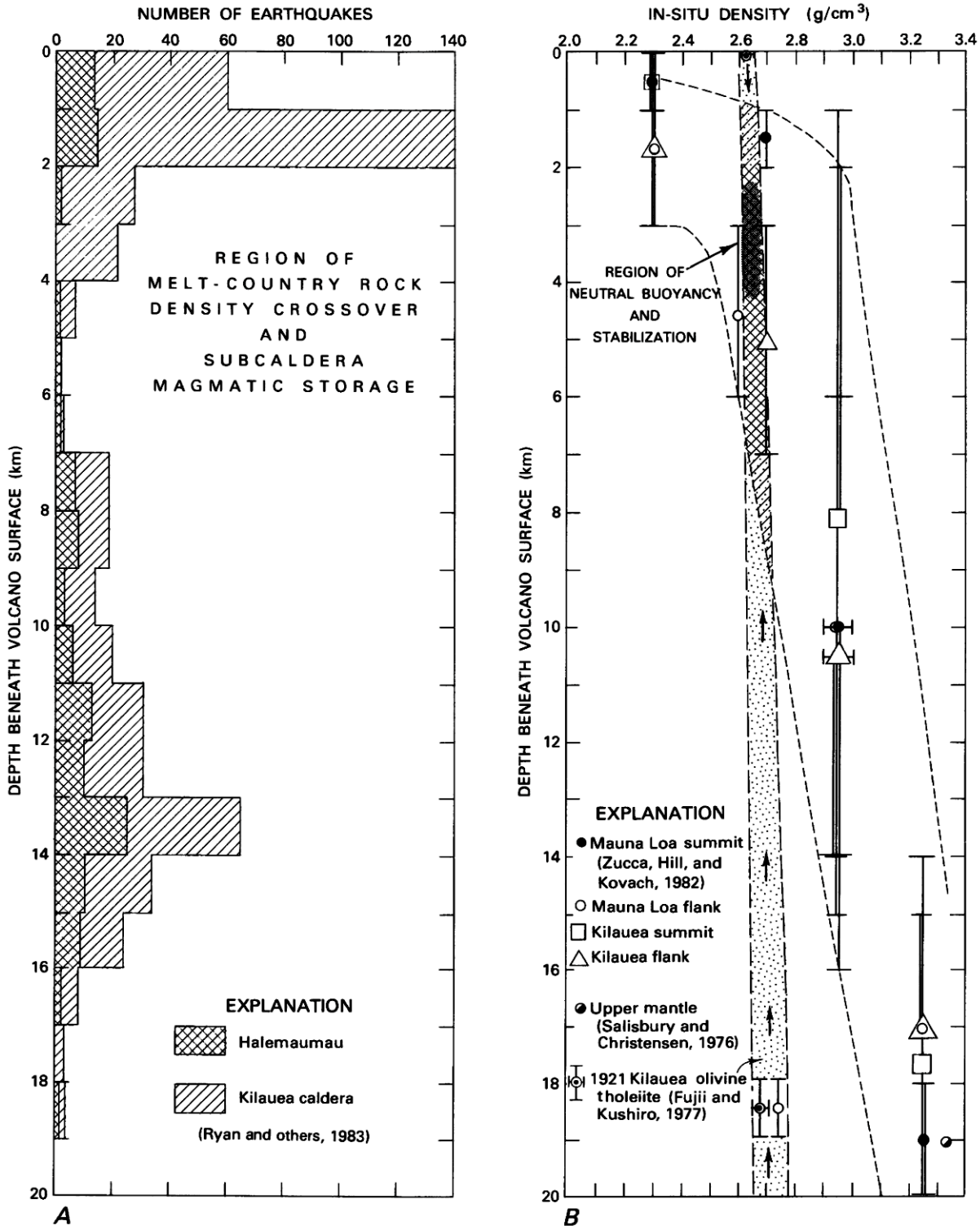
NUMBER OF EARTHQUAKES
0 20 40 60 80 100 120 140
DEPTH BENEATH VOLCANO SURFACE (km)
0 2 4 6 8 10 12 14 16 18 20
REGION OF MELT-COUNTRY ROCK DENSITY CROSSOVER AND SUBCALDERA MAGMATIC STORAGE
EXPLANATION
Halemaumau
Kilauea caldera
(Ryan and others, 1983)
A
IN-SITU DENSITY (g/cm3)
2.0 2.2 2.4 2.6 2.8 3.0 3.2 3.4
REGION OF NEUTRAL BUOYANCY AND STABILIZATION
EXPLANATION
Mauna Loa summit (Zucca, Hill, and Kovach, 1982)
Mauna Loa flank
Kilauea summit
Kilauea flank
Upper mantle (Salisbury and Christensen, 1976)
1921 Kilauea olivine tholeiite (Fujii and Kushiro, 1977)
B

The procedure of Talwani and others (1959) enables bodies of varying geometry and dissimilar density to be assembled into a complex composite. For Kilauea and Mauna Loa, this has enabled Zucca and others (1982) to incorporate the effects of the high-density volcanic rift zones and cores in their inversion procedure. These regions are then embedded in the basaltic flanks of the shields, and the computed gravity profiles matched with the observed profiles. The resulting density structure must then be consistent with the seismic-velocity structure inferred from refraction surveys. In turn, the deduced densities have been required to be consistent with the velocity-density systematics at the appropriate confining pressure. In this report, the results of Zucca and others (1982, figs. 10 and 11) have been used in the following way: for each volcano, two vertical density profiles have been taken from the surface to upper mantle depths—one profile beneath the summit caldera and one profile beneath the flanks (fig. 52.26*B*). The symbols for each profile type are provided in the inset box. Vertical bars delimit the stratigraphic extent of the density along the profile. This combined density and velocity structure for both Kilauea and Mauna Loa is consistent with the velocity-density systematics of basaltic, gabbroic, and ultramafic rocks determined independently at 50 and 100 MPa confining pressures (see Christensen and Salisbury, 1975). Collectively, the density profiles define a nonlinear band of values in in-situ density versus depth space. The nonlinear portion of the density band (as determined by the envelope defined by the total density range along a given profile) occurs over the depth interval 0–7 km. This coincides closely with the nonlinear portion of the experimentally derived contractancy curves for basalt and gabbro (figs. 52.16 and 52.17). It also corresponds very closely with the 0 to 9-km-depth interval required to bring about a convergence of the air-saturated and $H_2O$-saturated branches of the contractancy curve in figure 52.21*B*. Finally, it corresponds closely to the systematics of $\partial V_p/\partial z$ for the seismic-velocity profiles for Hawaii based on the work of Hill (1969), Ward and Gregersen (1973), and Klein (1981), including the low-velocity residuals that lie to the immediate left of the basalt field in figure 52.27. This congruence in depth dependence suggests that several physical states and deduced properties—gravity, density, in-situ seismic velocities and their profiles, and laboratory studies of the pressure dependence of $V_p$ and $V_s$—are all responding to the nonlinear contractancy associated with the Earth's surface. All are marching to the same drummer: the gradual elimination of void space on all scales with increasing depth.

Plotted also on figure 52.26*B* are measured values of the density of the 1921 Kilauea olivine tholeiite as a function of pressure, based on the work of Fujii and Kushiro (1977). The density range plotted at upper-mantle levels incorporates the experimental uncertainties presented in their figure 18 (p. 442) with the range required to reach their calculated density. At ambient pressure, it is determined by the experimental error. This melt-density band has been stippled in the figure. Particularly significant within the context of contractancy and Hawaiian magmatism is the crossover in melt and country-rock densities at low confining pressure. The melt-density band has been hachured within the crossover region, and the centroid of the crossover with respect to the depth range in country-rock density has been shaded.

At upper-mantle depths, the density contrast between melt and country rock will be a measure of the driving pressure through $\Delta\rho Gh$. In this interval, and through the oceanic crust, this density contrast, $\rho_{rock} - \rho_{melt}$, will be positive, with a continuously diminishing magnitude as melt parcels rise within their dikes. This rise is suggested by the upward-directed arrows (fig. 52.26*B*). As the parcel penetrates the oceanic crust and enters the base of the volcanic shield, the surrounding country-rock will be dominated by basalt and gabbro, and the value of the $\Delta\rho$ will approach zero. Further ascent to a depth level within the heart of the crossover region is expected to bring about a match between melt and environment density. This matching or balance region has been labeled the "region of neutral buoyancy and stabilization" in the figure. The chance passage of melt through the region of neutral buoyancy into the country-rock roof of the reservoir reverses the sign of the density contrast, and $\rho_{rock} - \rho_{melt}$ is now negative. Infinitesimal perturbations above the density balance horizon will return the errant melt parcel to the region of neutral buoyancy (downward-directed arrow). This mechanism—the oscillation of melt parcels about a horizon of density balance—provides for the long-term stabilization of subcaldera magma storage. It is a region where the nonlinear contractancy of rock near the Earth's surface has provided an environment where the critical $\Delta\rho \approx 0$. Breaking the balance and producing significant diking within the roof or eruption at the surface requires the wholesale rupture of the edifice via hydraulic-pressure

FIGURE 52.26.—Earthquake abundance and in-situ density as related to depth beneath volcano surface. ***A***, Distribution of earthquakes beneath Kilauea's summit region. Singly ruled histogram corresponds to depth distribution of seismicity within the volume that encompasses entire Kilauea caldera and extends to 20 km beneath caldera floor. Doubly ruled histogram provides depth distribution of seismicity within prismatic volume that encompasses Halemaumau Crater and extends to 20 km. Aseismic region from 2- to 7-km depth is inferred to have differentially high magma-to-rock ratios. Data from Ryan and others (1983). ***B***, In-situ densities of olivine tholeiite near its liquidus, and volcanic shields, oceanic crustal sections, and upper-mantle bases of Mauna Loa and Kilauea. In-situ densities for Mauna Loa and Kilauea are based on seismic-refraction profiling and gravity surveys of Zucca and others (1982), as resolved by inversion modeling of gravity profiles, consistent with velocity-density systematics of basaltic and gabbroic rocks. Region of density crossover is hachured section of melt-density band. Where band coincides with 2- to 7-km-depth region of subcaldera magma storge, it is doubly hachured. Within centroid of crossover region is a darkly shaded subregion of neutral buoyancy. Data for 1921 Kilauea olivine tholeiite from Fujii and Kushiro (1977), and for upper mantle from Salisbury and Christensen (1976).

increase, tectonic kneading of the reservoir from remotely applied tractions or the reinstatement of a positive $\Delta\rho$ via vesiculation of the melt, or a permutation involving a mix of two or more of these contributors. Reduced to its essentials, the contractancy mechanism suggests a fundamental control on the operation and evolution of magmatic systems in the near-surface environment.

What is the correspondence between the density crossover region and the depth interval associated with subcaldera magma storage? For Kilauea, this interval has been constrained by geodetic studies to occupy the range 2 to 9 km, with the suggestion of the subrange 2 to 4 km, as the most frequently retrieved center of deformation (Mogi, 1958; Eaton, 1962; Fiske and Kinoshita, 1969; Walsh and Decker, 1971; Dieterich and Decker, 1975; Jackson and others, 1975; Swanson and others, 1976; Ryan and others, 1983; Dvorak and others, 1983). The total depth range in the density crossover resolved in figure 52.26*B* is 1 to 7 km, with the central region of neutral buoyancy occupying the 2.5- to 4.5-km-depth range. This depth suggests a good correspondence between the zone of melt/country-rock in-situ density equilibration and the center of magmatic storage inferred from geodetic studies.

Studies of the spatial distribution of subcaldera earthquakes at Kilauea provides a collateral line of independent evidence regarding the depth distribution of magma associated with hydraulic fracturing and its three-dimensional topology. Koyanagi and others (1976) have resolved a relatively aseismic zone, with a mean diameter of about 3 km and a depth range from 3 to 6 km, and have associated this zone with the summit storage reservoir. Ryan and others (1981) have resolved the three-dimensional structure of this region for the period April 1, 1971, to December 31, 1973. These results suggest a reservoir floor in the depth range 6 to 7 km, and a storage complex roof at 2 km. The vertical profiles of the seismicity beneath Kilauea caldera and Halemaumau for this same period (Ryan and others, 1983) have been included in figure 52.26*A*. The roof above 2 km is a zone of intense fracturing, forming a seismic lid on the inflating complex beneath. The interval from 2 to 7 km becomes increasingly aseismic with depth and has a quiet zone in the 4- to 7-km range, suggesting differentially high fluid-to-rock ratios. Beneath 7 km, the level of hydraulically induced fracturing increases, suggesting active transport of magma within the dikes of the primary conduit. The interval from 2 to 7 km in figure 52.26*A* can now be compared with

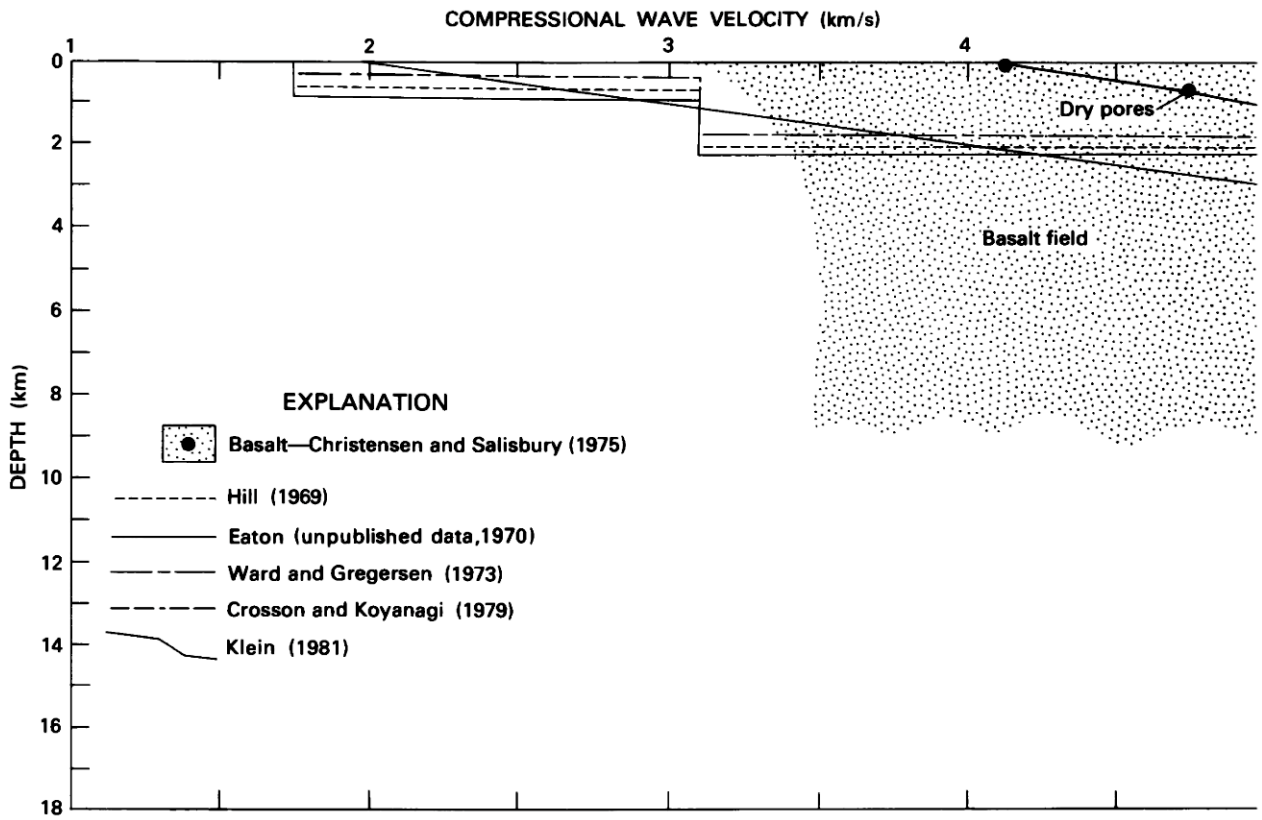


FIGURE 52.27.—Lithologic and seismic compressional wave velocity field beneath Hawaii, with special reference to Kilauea Volcano. Lithologic fields have been compiled from data sets in figures 52.16, 52.17, and 52.18 and references contained therein. Their lateral extents (in $V_P$ space) have been constrained by total ranges in extant compressional wave data as a function of confining pressure. Depth extents of a lithologic field are generally compatible with distribution of seismic velocities with depth, as well as results of gravity surveys and xenolith types in eruptive-vent areas on Hawaii and Oahu. Vertical extent of certain lithologies is expected to be greater than that illustrated, particularly that of gabbro, thus suggesting some overlap between gabbro field and ultramafic fields at upper-mantle

the in-situ melt and country-rock density profiles in figure 52.26*B*. The comparison is striking: there is a 1:1 correspondence between the in-situ density crossover region and the seismically—and geodetically—deduced regions for summit magma storage. Klein and others (1986) resolve the same subcaldera aseismic region. The general relations discussed in this section are summarized in figure 52.28.

## CONTRACTANCY AND THE INTERNAL STRUCTURE OF HAWAIIAN VOLCANOES

The discussion of the pressure dependence of the elastic properties of Hawaiian rocks has been largely one dimensional, because the gravitational-force field drives the compression of rocks and orders its variation with depth. Let us now broaden the focus and look at the role of contractancy as it relates to the three-dimensional structure of the magmatic system. Figure 52.29 is a view of the three-dimensional internal structure of Kilauea to 40 km depth. The map scale is 1:62,500, and the physiographic features of Kilauea's surface include: the fracture system of fault blocks, eruptive fissures, and vents of the southwest rift zone and east rift zone; Kilauea caldera, Halemaumau Crater, and major pit craters within the east rift zone; and the major fault systems of the south flank, including the Hilina, Kalanaokuaiki, and Holei palis. Figure 52.30 is a northward-directed view from a depth of 10 km.

The model has been constructed by applying the following constraints:

(1) Seismicity: following the approach of Ryan and others (1981), the three-dimensional distribution of earthquakes associated with magmatic transport and storage has been resolved by plotting their hypocenters within a transparent volume. The period of the study has been January 1, 1969, to January 1, 1983. Uncertainties in event locations have been constrained to be $\leq 1$ km. From a total data set of about 50,000 earthquakes, approximately 25,000 have passed the selection criteria of a standard error that is 1 km or less. They are events of magnitude 1.5 and above. Hypocenter locations have employed the linear gradient velocity model of Klein (1981), which is shown in this report to be internally consistent with the pressure dependence of rock properties and the lithology of Kilauea (fig. 52.27).

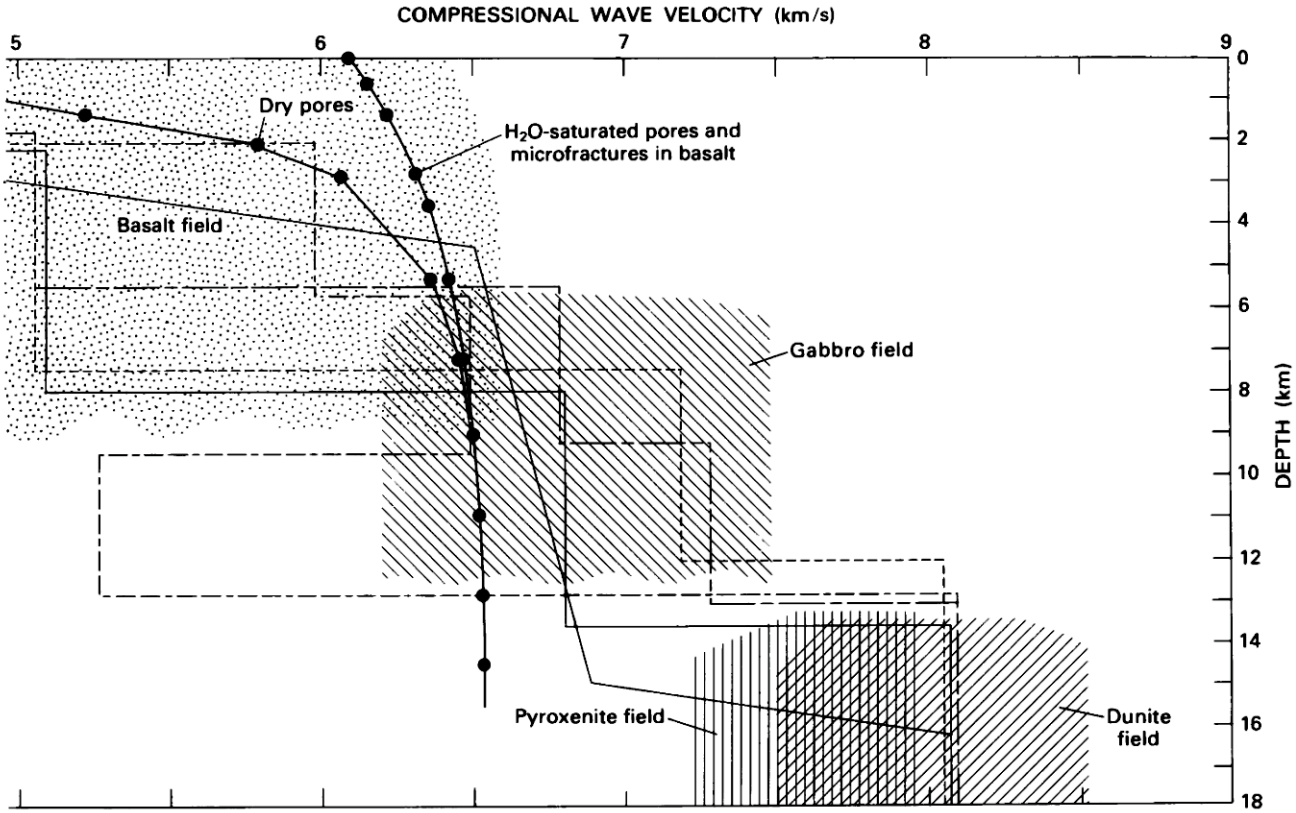


depths, and some additional overlap between gabbro and basalt to within ≈2 km of surface, particularly within core region of volcano. Illustrated field of basalt is constrained laterally by contractancy produced by progressive closure of microfractures and pores with increasing confining pressure. Low seismic velocities outside experimentally determined basalt field suggest contributions from dilatant and partially contracted fracture network associated with free surface of volcano. Base distribution of seismic-velocity profiles has been constructed from profiles of Hill (1969), Eaton (unpublished data, 1970), Ward and Gregersen (1973), and Crosson and Koyanagi (1979) as amended from compilation in Klein (1981).

(2) Geodesy: studies of the deformation associated with rift-zone intrusion have resolved the vertical and horizontal displacement fields generated by the hydraulic inflation of dikes (for example, Jackson and others, 1975; Swanson and others, 1976). These displacement patterns provide essential guidance for the location, strike, and dip of magmatic pressure sources at depth.

(3) Mechanics: the horizontal displacement field for specific intrusive episodes has been modeled for the superstructure of Kilauea at the 1:62,500 scale that corresponds to the model dimensions. The approach uses a finite-element analysis procedure for evaluating the displacement field generated by pressurized discontinuities in an elastic medium. Predicted displacement fields are then examined for consistency with the observed field. Material properties are guided by a combination of in-situ seismic velocities, gravity surveys, and experimental evaluations.

(4) Geology: the distribution of eruptive vents, fissures, and related structures within the rift zones provides collateral constraints on the distribution of magmatic bodies near the surface. Additional guidance is provided by the field study of dikes, sheets, and sills in the dissected shields of ancient Hawaiian volcanoes.

Within the context of this report, the model provides a useful framework for relating the pressure-dependent in-situ properties of the basaltic shield to images of structure and process within and beneath the shield. This framework provides a focal point for applications.

I recognized above that the contractancy of shield volcanoes is influenced by the distribution of faults and fractures in the near surface. Field studies of Kilauea indicate that the fracture networks that influence contractile behavior— and in turn the in-situ $V_p$, $V_s$, and density—are heterogeneously distributed. That is, con-

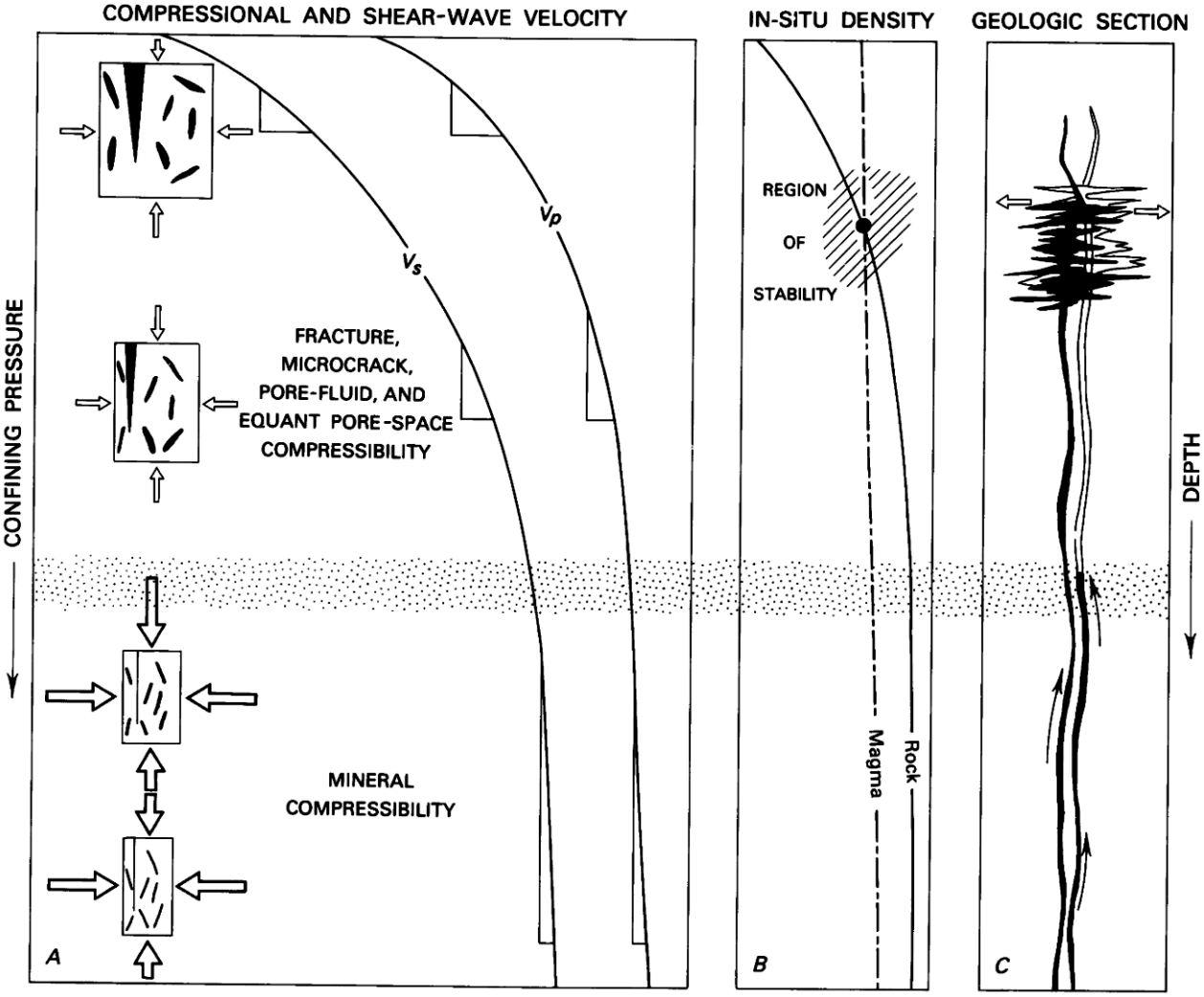


FIGURE 52.28.—*A*, Contributing mechanisms of contractancy in magmatic systems. *B*, Resulting crossover produced in in-situ densities of magma and country rock. *C*, Geologic consequences of a stabilized region with its zone of neutral buoyancy—a subcaldera magma reservoir.

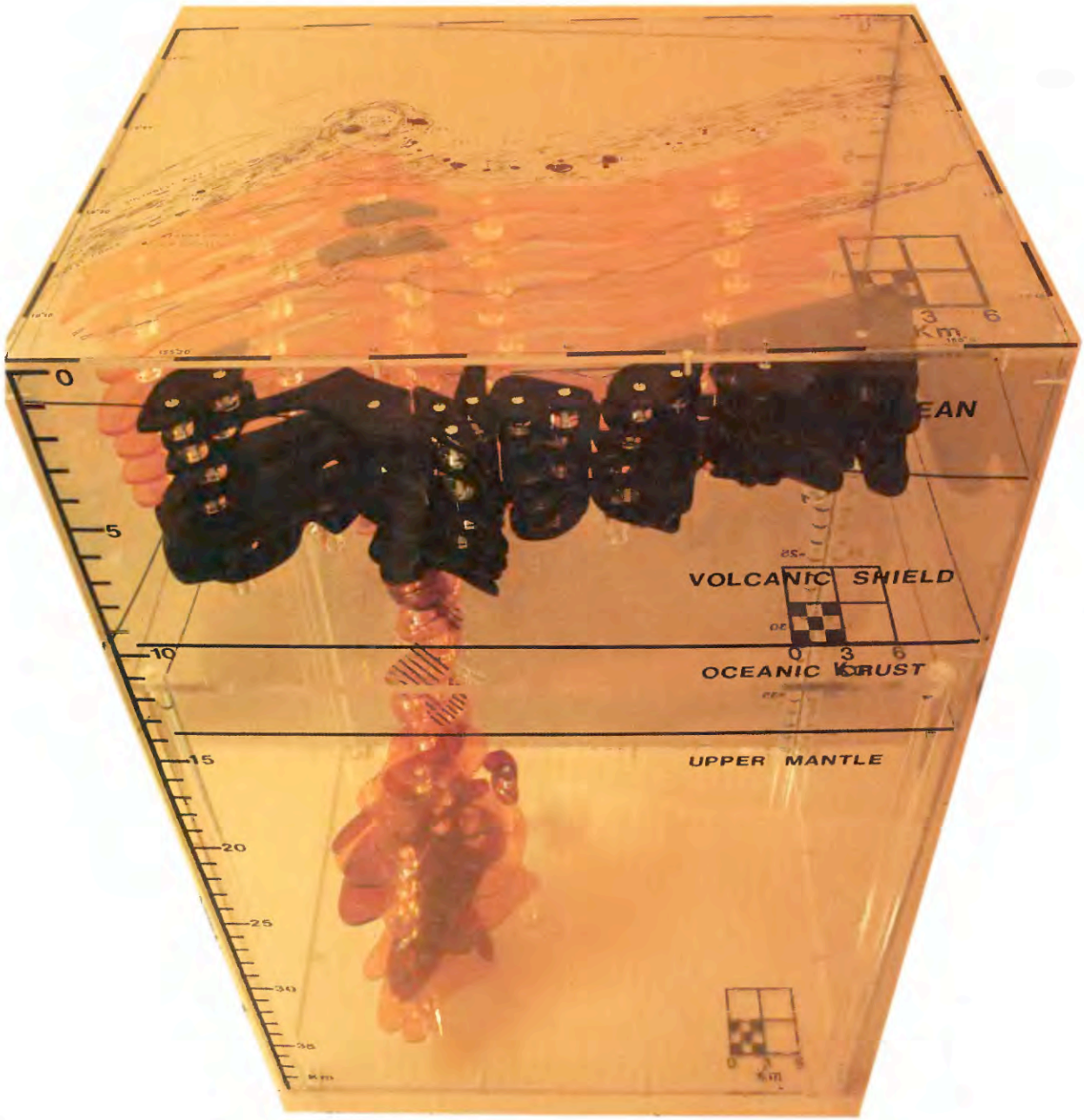


FIGURE 52.29.—Three-dimensional internal structure of Kilauea Volcano, constructed from three-dimensional distribution of earthquakes within and beneath Kilauea, at a map scale of 1:62,500. View orientation is northward, and model extends to 40-km depth. Surface physiography includes fracture systems and eruptive vents of the southwest and east rift zones and Kilauea caldera. Pacific Ocean coastline passes from lower left to middle right. Color coding corresponds to structural elements within the system, as well as temporal variations in hydraulic fracturing associated with magmatic transport from mantle depths. Color-coding format: light to medium amber (within volcanic shield), regions of inferred magmatic movement and storage for period January 1, 1969, to January 1, 1983; maroon, regions of inferred magmatic transport from November 29, 1975, to January 1, 1983; medium amber (within upper mantle), location of magmatic fracture front from January 1, 1969, to November 29, 1975; black, major tectonic blocks within basal levels of volcanic shield, shield-oceanic crust interface, and tectonic blocks of Koae fracture system; hachured amber, levels of low seismic control and uncertainty in geometric constraints. Configuration of major structural subdivisions, including volcanic shield, oceanic crust, and upper-mantle interfaces, is based on work of Hill (1969), Zucca and Hill (1980), and Zucca and others (1982). Vertical scale is 2 times horizontal, allowing an expanded view of geometry of individual level sections.

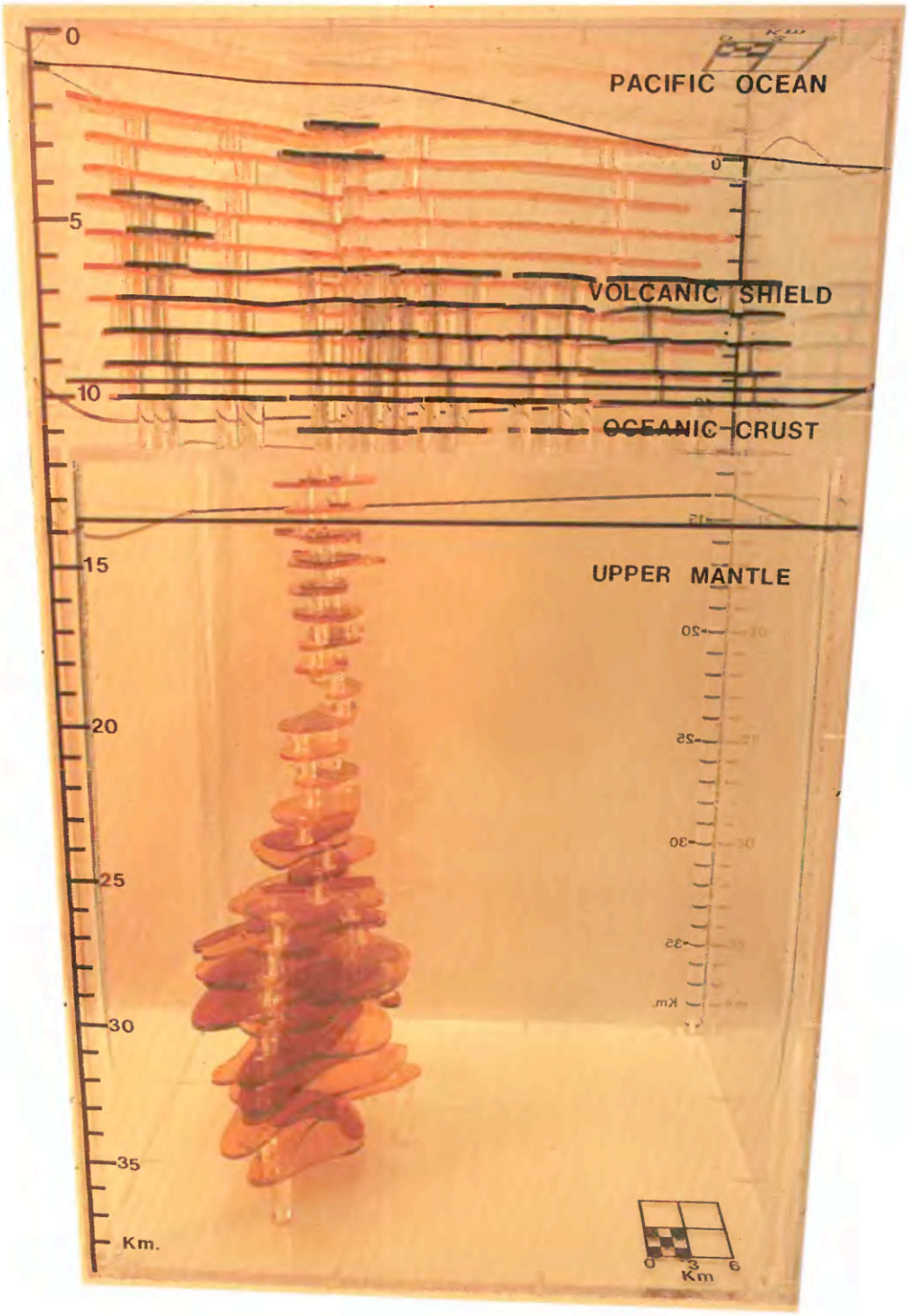
PACIFIC OCEAN
VOLCANIC SHIELD
OCEANIC CRUST
UPPER MANTLE
0
5
10
15
20
25
30
35
Km.
0 3 6
Km

tractancy itself has a three-dimensional structure. It is of interest then to relate these zones of inferred differential rock compression to the three-dimensional structure of the active magmatic system.

The internal structures of the southwest rift zone and east rift zone of Kilauea are resolved in figures 52.29, 52.30, and 52.31. These rift systems appear as medium amber in the figures and extend to the west (left) and east (right), respectively, in these northward-directed views. Their orientation is nearly vertical, and they intersect the surface of the volcano in a region of high fracture density that extends from the "great crack" in the southwest to Heiaheiahulu in the northeast. These fracture systems form in response to the hydraulic inflation of dikes within the rift zones. They record at the surface the differential stretch of rift-zone country rock at depth, as successive intrusive episodes are accommodated. Rift-zone intrusion then produces a zone of differentially contractant (low in-situ $V_p$, $V_s$, and $\rho$) rock above it. It is bounded below by the upper levels of the active dike complex, bounded above by the free surface of the volcano, and elongate along the strike of the rift system. The three-dimensional contractancy structure then mimics the map distribution of the intrusives at depth. Therefore, though rift systems are associated with relatively high densities and seismic velocities at depth, thus reflecting a shift from the velocity structure of the basaltic flanks (fig. 52.16) to the velocities of gabbroic complexes (fig. 52.17), we may expect the thin basaltic veneer of fault blocks above the dike complex to be rather low in in-situ density, $V_p$, and $V_s$ values (for example, the low-velocity residuals in figure 52.27, to the left of the basalt field).

By analogy with the one-dimensional region of neutral buoyancy plotted in figure 52.26*B*, we may now construct an image of the topography of the three-dimensional neutral-buoyancy surface for Kilauea, relating it to the structure of the magmatic system in figures 52.29, 52.30, and 52.31. Such a surface makes up an in-situ isodensity topography for the interior of the volcano. At points on the surface, $\rho_{rock} - \rho_{melt} \approx 0$, and intrusives have reached density equilibrium positions with respect to the surrounding country rock. Consideration of the two-dimensional density structure resolved by Zucca and others (1982) suggests that, in cross-sectional slices orthogonal to the strike of the rift zone, the profile of neutral buoyancy rises from depth within the flanks to near-surface positions above the rift-zone complex, plunging once again to greater depth once the rift zone is crossed. In three dimensions, such a surface resembles an anticlinal fold, with a fold axis that is coaxial with the strike of the rift system, and a fold wavelength that scales with the rift-complex width. The three-dimensional neutral-buoyancy surface for Kilauea may now be visualized with reference to figures 52.29, 52.30, and 52.31. We would expect it to be draped over both the east and southwest rift systems: rising from depth beneath the south flank palis, passing over the axes of the rifts and caldera, and moving to depth once again beneath the stable north flank. From the summit, the fold axis of the neutral buoyancy surface plunges toward the coastline, following at depth the topography of the volcano, along both the southwest and east rift systems.

## MECHANICAL EVOLUTION OF HAWAIIAN SHIELD VOLCANOES

Perhaps the initial suggestion that the summit magma reservoir of Hawaiian shield volcanoes moves progressively upward as the volcano grows was made by Jackson (1968, p. 146), who envisioned:

> A stack of tabular floored chambers representing successive periods of growth [and forming] a cylindrical body of dense rock that could account for the relatively high *P* wave velocities . . . under the summits.

This suggestion was adopted by Hill (1969, fig. 11, p. 129), who incorporated such a sequence in his summary cross section of a generalized Hawaiian volcano. Fiske and Kinoshita (1969, p. 348) concurred with this view:

> If such a reservoir complex has existed throughout much of Kilauea's history, it is reasonable to assume that the reservoir has migrated to progressively higher levels as the volcano grew to its present size. Today's reservoir would, therefore, be underlain by the sites of former reservoirs, and these would probably consist of dense sills and feeder dikes, containing accumulations of olivine.

It remained for Decker and others (1983, p. 547), however, to provide a convincing demonstration that such an evolutionary pattern is a fundamental theme in the development of Hawaiian volcanoes:

> The similarity between the surface-deformation pattern of the summit areas of Mauna Loa and Kilauea volcanoes is striking . . . The similarity of the morphology and evolution of the calderas on Mauna Loa and Kilauea, and the recent discovery of an apparent caldera on Loihi . . . indicate that the filling and collapse of calderas is a long-lasting and common mechanism in the growth of Hawaiian volcanoes. This conclusion implies that the magma storage zone grows upward from the old sea bottom as the volcano gains in elevation.

FIGURE 52.30.—Three-dimensional structure of Kilauea Volcano, in a northward-directed view from a depth of 10 km beneath summit caldera. Submarine topography of volcanic shield is uppermost light-weight line, deepening eastward (right). Black basal sections of south-flank tectonic blocks lie in front of southwest rift zone, caldera section, and east rift zone, progressing from left to right in 6- to 10-km-depth range. Hydraulic inflation of dikes within these rift systems lever blocks incrementally seaward, toward observer. Oceanic crust is isostatically depressed under primary loading of Mauna Loa, with a 3°–4° dip toward island center, based on seismic-refraction surveys of Hill (1969) and Zucca and Hill (1980). This loading produces crustal warping evident in this view. Contraction of volcanic shield takes place in 0- to 8–9-km-depth interval. Above 8 km, contraction is dominated by compression of macroscopic and microscopic fractures, vesicles, and fracture-filling fluids, including magma, sea water, and fresh water. Beneath 9 km, contraction of shield has been completed, and mineral compression is dominant.

The realization that both Mauna Loa and Kilauea possess a ubiquitous thin veneer of surface material of low in-situ density ($\rho \approx 2.3$ g/cm$^3$), combined with an appreciation of the density of tholeiitic melt ($\rho = 2.62$ gm/cm$^3$) at atmospheric pressure, requires a density crossover beneath the surface and poses an additional question. What is the relative position of the subcaldera magma storage reservoir for each of these volcanoes?

Geodetic surveys in the form of horizontal point-to-point distance measurements have been conducted on the summit of Mauna Loa over the period 1977 to 1981 (Decker and others,

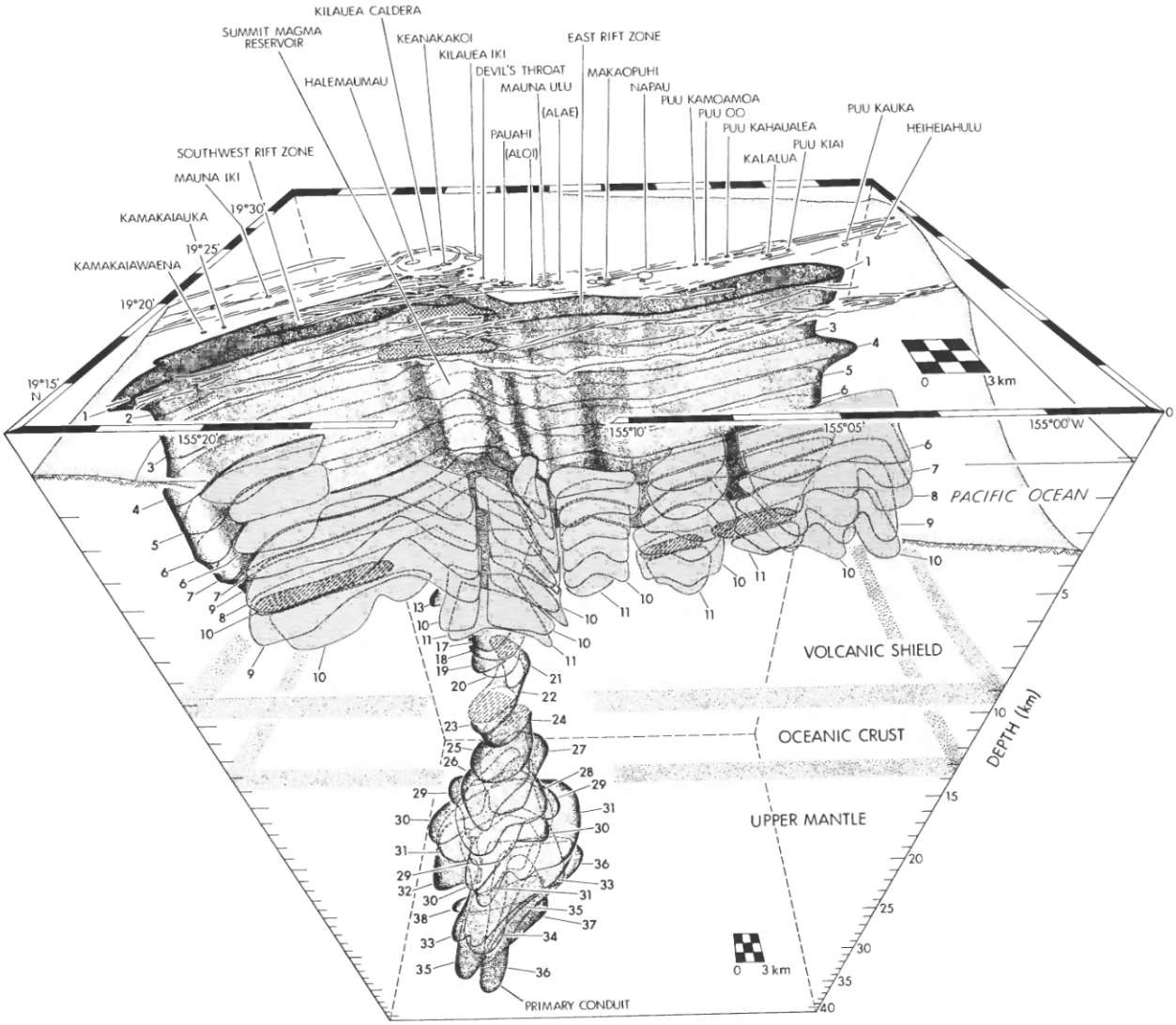


FIGURE 52.31.—Three-dimensional internal structure of Kilauea in a north-directed view from above, as constrained by three-dimensional distribution of earthquakes within and beneath volcano, and analytic mechanics of rift-zone intrusion. Magmatic system within volcanic shield lies to the north (rear) of tectonic blocks of the south flank (even light-gray shading). Influxes of magma within summit reservoir occurs by buoyant rise of melt parcels within primary conduit. Rupture of reservoir wall rock generally occurs at a depth of 3 km beneath caldera floor. This corresponds to region of neutral buoyancy. Dike injection from summit magma reservoir occurs into southwest and east rift zones. During injection process, leading edge of advancing dike propagates along neutral-buoyancy horizon. In general, this lies at a local depth of $\approx 3$ km. Thus, mechanics of lateral dike-injection process are governed by maintenance of a near-constant local depth and neutral-buoyancy principle as pressure increases gained in summit storage are progressively spent. In constructing model, distribution of seismic hypocenters has partially constrained geometric details of rift zones, primary conduit, and south-flank tectonic blocks. Level numbers correspond to individual cross sections. These cross sections are dashed where seismic control is limited. Marine bathymetry has been guided by surveys of Chase and others (1980). Top of magmatic block of rift zone complexes and subcaldera intrusive complex lies at a local depth of 1 km. Between this depth and surface are eruptive fissures and conduits that feed surface activity, such as current eruptive center at Puu Oo. Neutral buoyancy—contractancy-mechanics principle—is viewed as dominant control for producing long rift systems in Hawaiian shield volcanoes. Doubly hachured areas south of caldera are blocks of Koae fracture system.

1983). The inversion of this data set, using the point-source modeling approach of Dvorak and others (1983), suggests an inflation center located at a depth of approximately 3.2 km beneath the caldera floor. Spirit-level tilt measurements taken over the same period suggest, upon inversion, a similar but somewhat shallower depth, 2.6 km (Decker and others, 1983). These surveys defined the geodetic signature of the magmatic pressure increases that led to the outbreak of eruptive activity in March 1984. If we now compare this suggested pressure center with that of its neighbor Kilauea, we see that the depth-below-caldera positions to the summit magma reservoir are remarkably similar: an averaged 2.9 km for Mauna Loa and the range 2–4 km for Kilauea, as discussed earlier. Yet the elevation above sea level for the volcanoes is very different: 4,169 m for Mauna Loa and 1,240 m for Kilauea. The elevation difference in the calderas is then nearly 3 km. Figure 52.32 illustrates the topography of Mauna Loa and Kilauea.

What accounts for this apparently systematic positioning of summit magma storage in these very different volcanoes? Our survey and discussion of the pressure dependence of the in-situ mechanical properties of basaltic and gabbroic rock offer a mechanical rationale. Reduced to its essentials, the contractancy model deals with a dilatant-free surface that is loaded gravitationally. Increases in depth then correspond to increases in lateral confining pressure, as the dilatant fracture space is progressively squeezed shut. A reconsideration of figures 52.21*B* and 52.26*B* suggests that it is the depth below the free-surface reference level that orders the amount of fracture permeability for such dilatant regimes. This reasoning accords well with the role of confining pressure on permeability suggested by Gangi (1978) and Walsh (1981) and implicit in the experiments of Christensen (1974).

A comparison of the relative positioning of subcaldera magma reservoirs in relation to volcanic stature and age turns our attention to

FIGURE 52.32.—Summit caldera of Kilauea (K) in relation to its older neighbor to northwest, Mauna Loa (M). Elevation of Mauna Loa's summit (4,169 m) contrasts with Kilauea's (1,240 m). Similarity in depths of magmatic pressure centers and regions of neutral buoyancy for each volcano (Kilauea, 2–4 km; Mauna Loa, ≈2.9 km) suggests that during evolution of Hawaiian shields, summit reservoir climbs progressively upward. This upward progression is regulated by contractancy of volcanic shield. This mechanism produces increases in confining pressure at fixed reference depths during shield building. Reservoir region may then be viewed as being squeezed upward during maturation process. Hence, shield contractancy has produced a reservoir within Mauna Loa whose upper levels are now at same elevation as Kilauea's summit region (that is, 3 km beneath Mokuaweoweo caldera). Older edifice of Hualalai (H) lies still farther northwest. In foreground is community of Volcano, Hawaii. Photograph by James Griggs.

the south of Kilauea—to Loihi Seamount. Geophysical data in the form of geodetic surveys analogous to those routinely conducted on Kilauea and Mauna Loa are nonexistent, and available seismic data are insufficient to provide the required constraints on the existence and nature of a potential magma-storage region within Loihi's edifice. Bathymetric surveys in the form of sonar mapping and Angus bottom photography have resolved, however, the presence of two radial rift zones and a summit crater complex at an elevation of 980 m below sea level (Malahoff, chapter 6; Malahoff and others, 1982). By analogy with its neighbors to the north, an edifice magma storage capability of modest dimensions may be suggested. Identical conclusions relative to Loihi have been reached by Decker (chapter 42).

The considerations above, coupled with the discussion of the pressure dependence of elasticity and in-situ velocity and density systematics for Hawaiian shield volcanoes, lead naturally to the following proposal for their mechanical evolution. As a shield is formed, the dilatancy produced by diminished lateral constraints within its upper levels produces a contractancy profile. Continued growth and maturation raises the contractancy profile to higher levels, because the origin is always associated with the volcanoes free surface. Stated differently, as a volcano grows, it carries its contractancy profile with it. The upward evolutionary track of contractancy then orders the upward subsurface positioning of the region of neutral buoyancy and the associated magma storage reservoir and its coupled rift systems. This progression, from infancy through middle age to maturity, is illustrated in figure 52.33.

Within a given reservoir, the region of neutral buoyancy will order the positioning of the upper levels of magmatic storage, whereas the basal levels are regulated by the squeezing shut of available fracture permeability. Stated differently, the top of magmatic storage corresponds to the depth level where the compressive

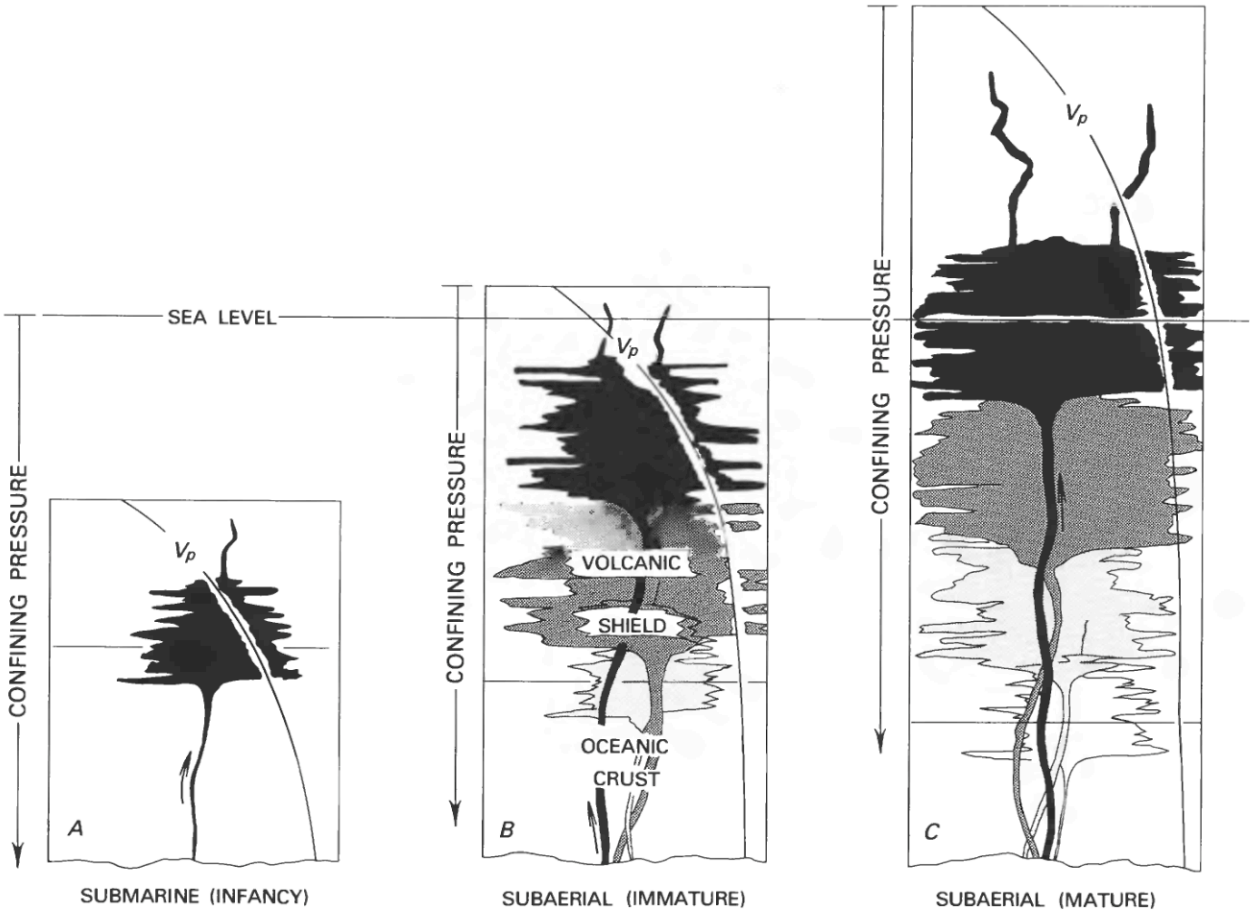


FIGURE 52.33.—Schematic changes in contractancy distribution with depth during growth and evolution of oceanic volcanoes. Volcanic shield-oceanic crust interface is stippled and is isostatically depressed under growing volcanic load. As a volcano grows, it carries its contractancy profile with it. Concomitant changes along this evolutionary track include: (1) progressive upward migration in transition zone that separates fields of fracture and pore-fluid compression above from mineral compression below; and (2) progressive upward migration of zone of neutral buoyancy. These changes provide mechanical rationale for evolutionary climb of subcaldera magma reservoirs in progression from submarine infancy (***A***) through subaerial immaturity (***B***) to subaerial maturity (***C***).

elimination of void space has just begun, and the bottom of the reservoir corresponds to the depth where void-space elimination has been completed. This general correlation is expected to apply to the rift systems as well as the subcaldera reservoir. In light of this relationship, we should expect the summit storage region to be laterally more extensive, with gains in elevation beneath the caldera. In a somewhat crude analogy, the evolving reservoir is lifting itself by its own bootstraps.

## THE NATURE OF THE EVOLUTIONARY TRACK

The integration of in-situ seismic-wave velocities, in-situ densities for country rock and tholeiitic melt near its liquidus, magma-reservoir positions from geodetic and seismic studies, volcanic lithology, and structural geology with laboratory data bearing on the pressure and temperature dependence of elasticity leads to a set of empirical relations that unify the observations. When this type of information is compiled for Mauna Loa, Kilauea, and Loihi Seamount—each in a distinctive phase of its evolutionary progression—a set of further empirical relationships is discovered. These relations, presented below, provide the mechanical linkage between volcanic evolution and in-situ rock behavior. They form the basic correlations and postulates of the contractancy model.

*Relation 1.*—The datum for confining pressure is positioned at the volcanic summit and at the crest of the rift systems. As the volcano grows this datum is progressively raised. In the interior of the volcano, the depth level required to achieve a given confining pressure is simultaneously elevated. During the growth of the shield, the transition zone that separates the relatively shallow field of fracture and pore-fluid compression from the deeper field of mineral compression is therefore progressively elevated. This transition region will have a three-dimensional topography and should be controlled by the stature of the volcanic shield above it. It is expected to be broadly associated with the base of the subcaldera storage complex and the basal section of the rift zones.

*Relation 2.*—The surficial veneer of low in-situ $V_p$, $V_s$, and density is progressively elevated during growth. Formed principally by the macroscopic fracture network in the upper 2 km of the shield, it produces an associated region of density crossover between the country rock and near-liquidus melt. This region of neutral buoyancy provides a mechanically stable environment for the subcaldera storage of magma. Increases in volcanic stature then elevate this region during the maturation process. For Kilauea and Mauna Loa, the geodetically and seismically constrained regions of subcaldera magma storage have a 1:1 correspondence with the region of neutral buoyancy. The stability of intra-rift-zone magmatic storage is expected to adhere to this general principle.

*Relation 3.*—The thickness of the reservoir roof, determined principally by the depth level of the region of neutral buoyancy, is expected to remain roughly constant as growth proceeds. To first order, this approximate constancy in thickness, mean composition, gross crack density per unit volume, and the pressure-temperature ($P,T$) environment suggests broadly comparable volumetric strengths. These relations are compatible with the observation of essentially concurrent and progressive caldera collapse as the edifice evolves.

*Relation 4.*—The progressive and proportional enlargement of the caldera region during shield evolution suggests that the region of neutral buoyancy spreads radially as the shield grows. For Mauna Loa, Kilauea, and Loihi, this spreading is elliptical in plan form, with a major axis that is guided in part by the pervasive influence of the rift systems that originate beneath the caldera.

*Relation 5.*—The progressive closure of macroscopic and microscopic fractures with depth, as well as the continued compression and expulsion of pore fluids, will systematically raise the in-situ values of the bulk modulus ($K$), the shear modulus ($\mu$), and the Young's modulus ($E$). Poisson's ratio ($\nu$) will also vary with depth, because it reflects the ratio of in-situ lateral strains to the axial strains induced by the overburden. These changes track the experimentally determined changes in $V_p$ and $V_s$ with pressure and the in-situ variations of seismic-wave velocities with increasing depth. The progressive closure of fractures with depth will also continuously reduce the amount of bulk anelasticity and simultaneously increase the appropriateness of the continuum assumption employed in mechanical analyses.

*Relation 6.*—During the seamount phase of oceanic shield development, the bottom of the contractancy curve is expected to lie within the oceanic crust. Continued upward growth of the shield will elevate the compression transition zone to the level of oceanic crustal layer one, where the deepest levels of fracture closure will interact with the low-modulus sediments in controlling the base level of active rift systems. This condition describes the current state of Kilauea Volcano. Further increases in volcanic stature will lift the compression-transition-zone above the old oceanic crust and into the base of the volcanic shield itself. This compression-transition-zone elevation characterizes the current status of Mauna Loa Volcano. Thus, contractancy and the pressure dependence of fracture closure regulates the positions of active-rift-system keels during the mature phase of shield evolution.

## SUBMARINE RIFT SYSTEMS AND THE GLOBAL ROLE OF NEUTRAL BUOYANCY

The general association in time and space of rift systems, dike intrusion, dilatant fractures, axial graben, and the neutral buoyancy-contractancy mechanism suggests that this effect may play a fundamental role in the intrusion mechanics and physical evolution of the Earth's oceanic rift systems. Clearly, important differences distinguish Hawaiian rift zones from their counterparts at accretionary plate margins. However, the overall simplicity of the dike-injection process and the primary structures associated with it suggests the following as geologic features of the neutral buoyancy—magma stabilization environment within active rift systems.

(1) Abundant dilatant and deep fissures, aligned parallel with the rift (for example, Ballard and others, 1979; Hey and others, 1985; Renard and others, 1985). Increases in confining pressure with depth will squeeze these fractures shut, increasing the in-situ density and compressional and shear wave velocity. Additional

sealing will be produced by the infilling of sediments and hydrothermal mineralization.

(2) Geomorphic evidence of lava drainback into dilatant fissures (lava-lake terraces, Ballard and others, 1979; and "bathtub" rings, Renard and others, 1985). Large amounts of accessible fracture volume, in turn, suggest significant decreases for in-situ $\rho$, $V_p$, and $V_s$.

(3) Nonlinear increases in compressional-wave velocity in the upper 2 to 3 kilometers within and near the spreading ridge (McClain and Atallah, 1985; Ritzert and Jacoby, 1985; Purdy and Detrick, 1986).

(4) Low aggregate in-situ densities inferred for the upper several hundred meters to 2,000 m.

(5) An axial valley characterized by tensional or downdropped structures.

(6) Gabbroic intrusives that have been emplaced at very shallow depth and subsequently exposed (Fox and others, 1985; Hey and others, 1985).

A consideration of these features prompts the question: What further predictions might the model make? First, a crossover in the in-situ density of basaltic magma and country rock should occur within oceanic rift zones, leading to conditions of neutral buoyancy and mechanical stability. To the extent that a given segment of rift zone was fed from a point source at depth, this would promote the lateral injection of dikes along a shallow horizon of neutral buoyancy. I believe that many sheeted-dike complexes within ancient oceanic crust record the general position of the neutral-buoyancy horizon during their emplacement. A second (and corollary) result is that magmatic eruptions in oceanic rift systems would be appreciably less favored than intrusions. The widespread occurrence of axial grabens suggest a pervasive dike-induced stretch at depth, without the infilling eruptions that would otherwise bury and obliterate these axial valleys. My own field studies on the dynamics of the magma injection-dike formation process in the Gjastykki rift system of the Krafla central volcano, northeastern Iceland, support these inferences. The role of neutral buoyancy in the world's oceanic rift zones is thus a vertically stabilizing one: mechanical equilibrium is achieved between intrusives and their host country rock.

## CONCLUSIONS

Experiments conducted to 1,133 K in flexural and torsional resonance have permitted evaluation of the Young's modulus and the modulus of rigidity for Hawaiian olivine tholeiite. The temperature dependence of elasticity for this rock type is very nearly linear. The explicit temperature dependence from regression treatments of replicate runs for each primary mode of mechanical loading is:

*Young's modulus,*

$$E(T) = (6.054 - 0.00083T) \times 10 \text{ GPa},$$

and *modulus of rigidity,*

$$\mu(T) = (2.615 - 0.00038T) \times 10 \text{ GPa},$$

where $T$ is the temperature in degrees Celsius.

Dilatometric evaluations of linear thermal-expansion coefficients for the same olivine tholeiite yield the value $\alpha_l = 4.58 \times 10^{-6}$ °C$^{-1}$ at 373 K, whereas the expansivity at 973 K is $\alpha_l = 7.93 \times 10^{-6}$ °C$^{-1}$.

The effects of cyclic heating and cooling histories on the thermal expansivity of olivine tholeiite have been studied in experiments conducted to within 30° of the 1-atm solidus—1,223 K. Parallel comparison runs have been made with diabase in companion experiments. For the basalt, cyclic excursions to 1,223 K induce irreversible thermal strain. One cycle is sufficient to achieve this effect, and repeated cycling to the same maximum temperature induces additional increments of irreversible strain. These permanent dimension changes are interpreted as reflecting the production of successive generations of microfractures during successive visits to high temperatures. The behavior of diabase during cyclic heating and cooling is qualitatively similar: thermal-strain hysteresis with continued cycling. The sense of irreversible thermal strain is different, however, for basalt and diabase: contractile and expansive length changes, respectively. This difference suggests a progressive compaction in the basalt, via microcrack-induced micropore collapse, and a progressive opening of the microstructure of the diabase by microfracture only.

A model has been developed for the high-temperature elasticity of basalt that incorporates the compositional and microstructural dependence of the relevant moduli. Specialized for the major mineral phases of tholeiitic basalt in this report, it is general in nature and is applicable to other rock types. Tabulated values of the elastic properties of olivine, clinopyroxene and orthopyroxene, and plagioclase provide a basis for immediate extensions to mafic and ultramafic rock types of relevance to Hawaii.

The model incorporates the following parameters and capabilities:

(1) Compositional: the aggregate may be monomineralic or consist of an assemblage of $n$-multiple phases. There are no conceptual limitations on either the mineralogy or the number of phases. Required input data should be either the directionally dependent elastic stiffness and compliance coefficients or the mineral V-R-H-averaged bulk modulus and rigidity. The ultimate limitations on the number of mineral components reduces to the familiar problem of the availability of reliable input data. The model provides predictions of aggregate bulk ($K$), shear ($\mu$), and Young's ($E$) moduli.

(2) Microstructural: the compositional model is complemented by incorporating the voids and flaws that weaken the solid and lower the moduli. For basalt, these voids are dominated by the vesicles produced during posteruption degassing. Spherical voids approximate the vesicles. Calculations with needle-shaped voids approximate the geometry of certain grain-edge microfractures. Volume fractions within each category are adjustable and may be guided, for example, by petrographic thin-section examination. The model is readily extendable to incorporate flat microfractures.

(3) Thermal: the temperature dependence is incorporated by introducing the temperature derivative for each contributing mineral phase. Specifically required is the temperature dependence for the bulk modulus ($dK/dT$) and the modulus of rigidity($d\mu/dT$). Each

contributes to the aggregate behavior through its weighted average. The model may be extended to incorporate pressure dependence by an application of the V-R-H-averaged pressure derivatives as outlined in Graham and Dobrzykowski (1976).

The effects of pressure on the elasticity of basalt provide a basis for developing the contractancy model of the mechanical behavior of shield volcanoes. The model provides a unifying framework that relates the following physical states and derivative properties: (1) the velocity-confining pressure systematics in laboratory samples for $V_p$ and $V_s$; (2) the in-situ velocity-stratigraphy systematics for seismic profiles beneath the Island of Hawaii; (3) the in-situ density-stratigraphy structure through the Island of Hawaii, as inferred from studies of gravity profiles over summit, rift zone, and flank environments; and (4) the structural geology of Hawaiian shield volcanoes, with particular reference to caldera and rift-zone structure, and their fracture networks.

Additional coherence is suggested by the contractancy model: within Kilauea and Mauna Loa Volcanoes, a crossover occurs between the in-situ density of tholeiitic melt near its liquidus and the in-situ density of the country-rock environment in the subcaldera magma reservoir. The crossover occurs in the nonlinear region of the contractancy profile; that is, at confining pressures that are generally less than 200 MPa (2 kbar). In the core of the density crossover is a region of neutral buoyancy. Here $\rho_{rock} - \rho_{melt} \approx 0$. This mechanism suggests that contractancy provides the fundamental control on the long-term stability of these reservoirs. For Kilauea and Mauna Loa, the geodetically constrained magma-storage reservoirs have a 1:1 coincidence with the density crossover region produced by the contractant shields. This coincidence is produced again in the three-dimensional structure of Kilauea's summit reservoir, as constrained by subcaldera seismicity. In addition, and as a logical consequence, shield contractancy (and derivative in-situ density) provides a mechanism for the frequent observation of intrusives that have come to rest at very shallow depths (for example, dikes in rift systems), as inferred in geodetic-inversion studies and as directly observed in dissected Hawaiian rift systems. Finally, the progressively contractant behavior of Hawaiian shield volcanoes with depth and the attendant in-situ density progression that it implies provide the mechanical rationale for the physical evolution of their subcaldera magma reservoirs as the maturation process continues.

## REFERENCES CITED


Aleksandrov, K.S., Ryzhova, T.V., and Belikov, B.P., 1964, The elastic properties of pyroxenes: Soviet Physics-Crystallography, v. 8, no. 5, p. 589-591.

Amadei, B., and Goodman, R.E., 1981, A 3-D constitutive relation for fractured rock masses, *in* Selvadurai, A.P.S., ed., Mechanics of structured media: Amsterdam, Elsevier, p. 249-268.

Anderson, O.L., Schreiber, E., Liebermann, R.C., and Soga, N., 1968, Some elastic constant data on minerals relevant to geophysics: Review of Geophysics, v. 6, p. 491-524.

Arndt, J., and Häberle, J., 1973, Thermal expansion and glass transition temperatures of synthetic glasses of plagioclase composition: Contributions to Mineralogy and Petrology, v. 39, p. 175-185.

Babuska, V., 1972, Elasticity and anisotropy of dunite and bronzitite: Journal of Geophysical Research, v. 77, p. 6955-6963.

Bajuk, E.I., Valarovich, M.P., Klima, K., Pros, Z., and Vanek, J., 1957, Velocity of longitudinal waves in eclogite and ultrabasic rocks under pressures to 4 kilobars: Studies in Geophysics and Geodesy, v. 11, p. 271.

Ballard, R.D., Holcomb, R.T., and Van Andel, T.H., 1979, The Galapagos rift at 86°N, 3. Sheet flows, collapse pits and lava lakes of the rift valley: Journal of Geophysical Research, v. 84, p. 5407-5422.

Bandis, S.C., Lumsden, A.C., and Barton, N.R., 1983, Fundmentals of rock joint deformation: International Journal of Rock Mechanics and Mining Sciences and Geomechanics Abstracts, v. 20, p. 249-268.

Birch, F., 1960, Velocity of compressional waves in rocks to 10 kilobars, Part I: Journal of Geophysical Research, v. 65, p. 1083.

Brace, W.F., Paulding, B.W., Jr., and Scholz, C.H., 1966, Dilatancy in the fracture of crystalline rocks: Journal of Geophysical Research, v. 71, p. 3939-3956.

Breyer, H., 1930, Über die Elastizität von Gesteinen: Zeitschrift für Geophysik: Heft, v. 2, p. 98-111.

Brown, S.R., and Scholz, C.H., 1985, Closure of random elastic surfaces in contact: Journal of Geophysical Research, v. 90, p. 5531-5545.

Budiansky, B., 1965, On the elastic moduli of some heterogeneous materials: Journal of the Mechanics and Physics of Solids, v. 13, p. 223-227.

Budiansky, B., and O'Connell, R.J., 1976, Elastic moduli of a cracked solid: International Journal of Solids and Structures, v. 12, p. 81-97.

Bulau, J.R., Waff, H.S., and Tyburczy, J.A., 1979, Mechanical and thermodynamic constraints on fluid distribution in partial melts: Journal of Geophysical Research, v. 84, p. 6102-6108.

Cady, J.W., 1977, Calculation of gravity and magnetic anomalies along profiles with end corrections and inverse solutions for density and magnetization: U.S. Geological Survey Open-File Report 77-463, 110 p.

Chase, T.E., Miller, C.P., Seekins, B.A., Normark, W.R., Gutmacher, C.E., Wilde, P., and Young, J.D., 1980, Topography of the southern Hawaiian Islands: U.S. Geological Survey Open-File Map 81–120, 3 pls.

Christensen, N.I., 1966, Elasticity of ultrabasic rocks: Journal of Geophysical Research, v. 71, p. 5921-5931.

———1971, Fabric, seismic anisotropy and tectonic history of the Twin Sisters dunite: Geological Society of America Bulletin, v. 82, p. 1681.

———1973, Compressional and shear wave velocities in basaltic rocks, DSDP leg 16, *in* Van Andel, T.H., Heath, G.R., and others, eds., Initial reports of the Deep Sea Drilling Project: U.S. Government Printing Office, v. 16, p. 647-649.

———1974, The petrologic nature of the lower oceanic crust and upper mantle, *in* Kristjansson, L., ed., Geodynamics of Iceland and the North Atlantic area: Dordrecht, Netherlands, D. Reidel, p. 165-176.

———1976, Seismic velocities, densities and elastic constants of basalts from DSDP leg 35, *in* Hollister, C.D., Craddock, C., and others, eds., Initial reports of the Deep Sea Drilling Project: U.S. Government Printing Office, v. 35, p. 335-337.

———1978, Ophiolites, seismic velocities and oceanic crustal structure: Tectonophysics, v. 47, p. 131-157.

———1984, Pore pressure and oceanic crustal seismic structure: Geophysical Journal of the Royal Astronomical Society, v. 79, p. 411-424.

Christensen, N.I., Carlson, R.L., Salisbury, M.H., and Fountain, D.M., 1975, Elastic wave velocities in volcanic and plutonic rocks recovered on DSDP leg 31, *in* Kraig, D.E., Ingle, J.C., and others, eds., Initial reports of the Deep Sea Drilling Project: U.S. Government Printing Office, v. 31, p. 607-609.

———1974a, Velocities and elastic moduli of volcanic and sedimentary rocks recovered on DSDP leg 25, *in* Simpson, E.S.W., Schlich, R., and others, eds., Initial reports of the Deep Sea Drilling Project: U.S. Government Printing Office, v. 25, p. 357-360.

———1974b, Velocities of compressional and shear waves in DSDP leg 27 basalts, *in* Veevers, J.J., and Heirtzler, J.R., eds., Initial reports of the Deep Sea Drilling Project: U.S. Government Printing Office, v. 27, p. 445-449.

Christensen, N.I., and Ramananantoandro, R., 1971, Elastic moduli and anisotropy of dunite to 10 kilobars: Journal of Geophysical Research, v. 76, p. 4003.

Christensen, N.I., and Salisbury, M.H., 1972, Sea floor spreading, progressive alteration of layer two basalts, and associated changes in seismic velocities: Earth and Planetary Science Letters, v. 15, p. 367-375.

———1973, Velocities, elastic moduli and weathering-age relations for Pacific layer 2 basalts: Earth and Planetary Science Letters, v. 19, p. 461-470.

———1975, Structure and constitution of the lower oceanic crust: Review of Geophysics and Space Physics, v. 13, p. 57-86.

Coble, R.L., and Kingery, W.D., 1956, Effect of porosity on physical properties of sintered alumina: Journal of American Ceramic Society, v. 39, p. 337-385.

Crosson, R.S., and Endo, E.T., 1982, Focal mechanisms and location of earthquakes in the vicinity of the 1975 Kalapana earthquake aftershock zone 1970-1979: Implications for tectonics of the south flank of Kilauea Volcano, Island of Hawaii: Tectonics, v. 1, p. 495-542.

Crosson, R.S., and Koyanagi, R.Y., 1979, Seismic velocity structure below the Island of Hawaii from local earthquake data: Journal of Geophysical Research, v. 84, p. 2331-2342.

Davis, P.M., Hastie, L.M., and Stacey, F.D., 1974, Stresses within an active volcano—with particular reference to Kilauea: Tectonophysics, v. 22, p. 355-362.

Decker, R.W., Koyanagi, R.Y., Dvorak, J.J., Lockwood, J.P., Okamura, A.T., Yamashita, K.M., and Tanigawa, W.R., 1983, Seismicity and surface deformation of Mauna Loa volcano, Hawaii: Eos, v. 64, p. 545-547.

Dieterich, J.H., and Decker, R.W., 1975, Finite element modeling of surface deformation associated with volcanism: Journal of Geophysical Research, v. 80, p. 4094-4102.

Duffield, W.A., Christensen, R.L., Koyanagi, R.Y., and Peterson, D.W., 1982, Storage, migration and eruption of magma at Kilauea Volcano, Hawaii, 1971-1972: Journal of Volcanology and Geothermal Research, v. 13, p. 273-307.

Dvorak, J.J., Okamura, A.T., and Deiterich, J.H., 1983, Analysis of surface deformation data, Kilauea Volcano, Hawaii: October 1966 to September 1970: Journal of Geophysical Research, v. 88, p. 9295-9304.

Eaton, J.P., 1962, Crustal structure and volcanism in Hawaii, *in* Crust of the Pacific Basin: American Geophysical Union Monograph, p. 13-29.

Eaton, J.P., and Murata, K.J., 1960, How volcanoes grow: Science, v. 132, p. 925-938.

Eshelby, J.D., 1957, The determination of the elastic field of an ellipsoidal inclusion and related problems: Proceedings of the Royal Society of London, ser. A, v. 241, p. 376-396.

Fedotov, S.A., 1977a, Geophysical data on deep-seated magmatic activity below Kamchatka and an estimate of the forces that cause the rise of magmas into volcanoes: International Geology Review, v. 19, p. 661-670.

———1977b, Mechanism of deep-seated magmatic activity below island-arc volcanoes and similar structures: International Geology Review, v. 19, p. 671-680.

———1977c, Ascent of basic magmas in the crust and the mechanism of basaltic fissure eruptions: International Geology Review, v. 20, p. 33- 48.

Fiske, R.S., and Jackson, E.D., 1972, Orientation and growth of Hawaiian volcanic rifts: The effect of regional structure and gravitational stresses: Proceedings of the Royal Society of London, ser. A, v. 329, p. 299-326.

Fiske, R.S., and Kinoshita, W.T., 1969, Inflation of Kilauea Volcano prior to its 1967–1968 eruption: Science, v. 165, p. 341-349.

Fornari, D.J., Malahoff, A., and Heezen, B.C., 1978, Volcanic structure of the crest of the Puna ridge, Hawaii: geophysical implications of submarine volcanic terrain: Geological Society of American Bulletin, v. 89, p. 605-616.

Förster, F., 1937, Ein neues Messverfahren zur Bestimmung des Elastizitäts Moduls und der Dämpfung (New method for determination of modulus of elasticity and damping): Zeitschrift für Metallkunde, v. 29, p. 109-115.

Fox, P.J., Moody, R.H., Karson, J.A., Bonatti, E., Kidd, W.S.F., Crane, K., Gallo, D.G., Stroup, J.B., Fornari, D.J., Elthon, D., Hamlyn, P., Casey, J.F., Needham, D., and Sartori, R., 1985, The geology of the oceanographer transform: The transform domain: Marine Geophysical Researches, v. 7, p. 329-358.

Fox, P.J., and Schreiber, E., 1973, Compressional wave velocities in basalt and dolerite samples recovered during leg 15, *in* Edgar, N.T., Saunders, J.B., and others, eds., Initial reports of the Deep Sea Drilling Project: U.S. Government Printing Office, v. 15, p. 1013-1015.

Fox, P.J., Schreiber, E., and Peterson, J.J., 1973, The geology of the Oceanic crust: compressional wave velocities of oceanic rocks: Journal of Geophysical Research, v. 78, p. 5155-5172.

Frisillo, A.L., 1972, The elastic coefficients of bronzite as a function of pressure and temperature: University Park, Pennsylvania State University, Ph.D. thesis.

Frisillo, A.L., and Buljan, S.T., 1972, Linear thermal expansion coefficients of orthopyroxene to 1000 °C: Journal of Geophysical Research, v. 77, p. 7115-7117.

Fujii, T., and Kushiro, I., 1977, Density, viscosity, and compressibility of basaltic liquid at high pressures: Carnegie Institution of Washington Year Book, v. 76, p. 419-424.

Gangi, A.F., 1978, Variation of whole and fractured porous rock permeability with confining pressure: International Journal of Rock Mechanics and Mining Sciences and Geomechanics Abstracts, v. 15, p. 249-257.

Gold, T., and Soter, S., 1985, Fluid ascent through the solid lithosphere and its relation to earthquakes: Pure and Applied Geophysics, v. 122, p. 492-530.

Graham, E.K., 1969, The elastic coefficients of forsterite as a function of pressure and temperature: University Park, Pennsylvania State University, Ph.D. thesis.

Graham, E.K., and Barsch, G., 1969, Elastic constants of single-crystal forsterite as a function of temperature and pressure: Journal of Geophysical Research, v. 74, p. 5949-5960.

Graham, E.K., and Dobrzykowski, D., 1976, Temperatures in the mantle as inferred from simple compositional models: American Mineralogist, v. 61, p. 549-559.

Grove, T.L., and Baker, M.B., 1983, Effects of melt density on magma mixing in calc-alkaline series lavas: Nature, v. 305, p. 416-418.

Hashin, Zvi, 1964, Theory of mechanical behavior of heterogeneous media: Applied Mechanics Reviews, v. 17, p. 1-8.

Hashin, Zvi, and Shtrikman, S., 1962, A variational approach to the theory of the elastic behavior of polycrystals: Journal of Mechanics and Physics in Solids, v. 10, pp. 343-352.

Hassleman, D.P.H., 1961, Tables for the computation of the shear modulus and Young's modulus of elasticity from the resonant frequencies of rectangular prisms: Niagara Falls, N.Y., Applied Research Branch, The Carborundum Co., 17 p.

Hekinian, R., Auzende, J.M., Francheteau, J., Gente, P., Ryan, W.B.F., and Kappel, E.S., 1985, Offset spreading centers near 12°53'N on the East Pacific rise: Submersible observations and composition of the volcanics: Marine Geophysical Researches, v. 7, p. 359-377.

Herzberg, C.T., Fyfe, W.S., and Carr, M.J., 1983, Density constraints on the formation of the continental Moho and crust: Contributions to Mineralogy and Petrology, v. 84, p. 1-5.

Hey, R.N., Sinton, J.M., Atwater, T.M., Christie, D.M., Johnson, H.P., Kleinrock, M.C., Macdonald, K.C., Miller, S.P., Neal, C.A., Searle, R.C., Sleep, N.H., and Yonover, R.N., 1985, Alvin investigation of an oceanic propagatmg rift system, Galapagos 95.5°W: Eos, v. 66, p. 1091.

Hill, D.P., 1969, Crustal structure of the Island of Hawaii from seismic-refraction measurements: Bulletin of the Seismological Society of America, v. 59, p. 101-130.

Hill, R.E.T., and Boettcher, A.L., 1970, Water in the earth's mantle: melting curves of basalt-water and basalt-water-carbon dioxide: Science, v. 167, p. 980-982.

Hill, R.W., 1952, The elastic behavior of a crystalline aggregate: Proceedings of the Royal Society of London, ser. A, v. 65, p. 349-354.

———1965, A self-consistent mechanics of composite materials: Journal of Mechanics and Physics of Solids, v. 13, p. 213-222.

Hughes, D.S., and Cross, J.H., 1951, Elastic wave velocities in rocks at high pressures and temperatures: Geophysics, v. 16, p. 577.

Hughes, D.S., and Maurette, C., 1957, Variation of elastic wave velocities in basic igneous rocks with pressure and temperature: Geophysics, v. 22, p. 23.

Hyndman, R.D., 1976, Seismic velocity measurements of basement rocks from DSDP leg 37, *in* Aumento, F., and Melson, W.G., eds., Initial reports of the Deep Sea Drilling Project: U.S. Government Printing Office, v. 37, p. 373-387.

Ide, J.M., 1936, Some dynamic methods for determination of Young's modulus: Review of Scientific Instruments, v. 6, p. 296.

———1937, The velocity of sound in rocks and glasses as a function of temperature: Journal of Geology, v. 45, p. 689-715.

Iida, K., and Kumazawa, M., 1960, Measurements of elastic wave velocities in

volcanic rocks at high temperatures by means of ultrasonic impulse transmission, Part I: Nagoya University, Journal of Earth Science, v. 7, p. 49-64.

Jackson, D.B., Swanson, D.A., Koyanagi, R.Y., and Wright, T.L., 1975, The August and October 1968 east rift eruptions of Kilauea Volcano, Hawaii: U.S. Geological Survey Professional Paper 890, 33 p.

Jackson, E.D., 1968, The character of the lower crust and upper mantle beneath the Hawaiian Islands: International Geological Congress, 23d, Prague, 1968, v. 1, p. 135-150.

Jackson, E.D., Clague, D.A., Engleman, E., Friesen, W.B., and Norton, D., 1981, Xenoliths in the alkalic basalt flows from Hualalai Volcano, Hawaii: U.S. Geological Survey Open-File Report 81–1031, 33 p.

Jackson, E.D., and Wright, T.L., 1970, Xenoliths in the Honolulu Volcanic Series, Hawaii: Journal of Petrology, v. 11, p. 405-430.

Johnson, A.T., and Pollard, D.D., 1973, Mechanics of growth of some laccolithic intrusions in the Henry Mountains, Utah, I: Tectonophysics, v. 18, p. 261-309.

Jones, L.E.A., 1977, High-temperature elasticity of rutile-structure $MgF_2$: Physics and Chemistry of Minerals, v. 1, p. 179-198.

Kanamori, H., and Mizutani, 1965, Ultrasonic measurements of elastic constants of rocks under high pressures: Bulletin of the Earthquake Research Institute, v. 43, p. 173.

Kern, H., and Rich, A., 1979, Compressional and shear wave velocities at high temperature and confining pressure in basalts from the Faeroe Islands: Tectonophysics, v. 54, p. 231-252.

King, M.S., 1966, Wave velocities in rocks as a function of changes in overburden pressure and pore fluid saturants: Geophysics, v. 31, p. 50-73.

Klein, F.W., 1981, A linear gradient crustal model for south Hawaii: Bulletin of the Seismological Society of America, v. 71, p. 1503-1510.

Koyanagi, R.Y., Unger, J.D., Endo, E.T., and Okamura, A.T., 1976, Shallow earthquakes associated with inflation episodes at the summit of Kilauea Volcano, Hawaii: Bulletin of Volcanology, v. 39, p. 621-631.

Kroenke, L.W., Manghnani, M.H., Rai, C.S., Fryer, P., and Ramananantoandro, R., 1976, Elastic properties of selected ophiolitic rocks from Papua, New Guinea: Nature and composition of oceanic crust and upper mantle, *in* Sutton, G.H., Manghnani, M.H., and Moberly, R., eds., The geophysics of the Pacific Ocean basin and its margins: Washington, American Geophysical Union, v. 19, p. 407.

Kröner, E., 1958, Kontinuumstheorie der Versetzungen und Eigenspannungen: Ergebnisse der Angewandten Mathematik: Springer-Verlag, v. 5.

———1967, Elastic moduli of perfectly disordered composite materials: Journal of the Mechanics and Physics of Solids, v. 15, p. 319-329.

Lambeck, K., and Nakiboglu, S.M., 1980, Seamount loading and stress in the ocean lithosphere: Journal of Geophysical Research, v. 85, p. 6403-6418.

Leibfried, G., and Ludwig, W., 1961, Theory of anharmonic effects in crystals, *in* Seitz, F., and Turnbull, D., eds., Solid State Physics, v. 12: New York, Academic Press, p. 276-444.

Liou, J.G., Kuniyoshi, S., and Ito, K., 1974, Experimental studies of the phase relations between greenschist and amphibolite in a basaltic system: American Journal of Science, v. 274, p. 613-632.

Macdonald, G.A., and Katsura, T., 1964, Chemical composition of Hawaiian lavas: Journal of Petrology, v. 5, p. 82-133.

Malahoff, A., McMurtry, G.M., Wiltshire, J.C., and Yeh, H-W., 1982, Geology and chemistry of hydrothermal deposits from active submarine volcano, Loihi, Hawaii: Nature, v. 298, p. 234-239.

Manghnani, M.H., and Woollard, G.P., 1968, Elastic wave velocities in Hawaiian rocks at pressures to 10 kilobars, *in* Knopoff, L., Drake, C.L., and Hart, P.J., eds., The crust and upper mantle of the Pacific area: American Geophysical Union, v. 12, p. 501-516.

Mao, N.-H., Ito, J., Hays, J.F., Drake, J., and Birch, F., 1970, Composition and elastic constants of hortonolite dunite: Journal of Geophysical Research, v. 75, p. 4071-4076.

McClain, J.S., and Atallah, C.A., 1985, The structure of young oceanic crust near a very fast spreading ridge: Geophysical Research Letters, v. 12, p. 689-692.

McKenzie, D., 1984, The generation and compaction of partially molten rock: Journal of Petrology, v. 25, p. 713-765.

Mizutani, H., and Newbigging, D.F., 1973, Elastic wave velocities of Apollo 14, 15 and 16 rocks: Proceedings of the Fourth Lunar Science Conference, v. 3, p. 2601-2609.

Mogi, K., 1958, Relations between the eruptions of various volcanoes and the deformations of the ground surfaces around them: Bulletin of Earthquake Research Institute, Tokyo University, v. 36, p. 99-134.

Moore, J.G., 1975, Mechanism of formation of pillow lava: American Scientist, v. 63, p. 269-277.

Moore, J.G., and Fiske, R.S., 1969, Volcanic substructure inferred from dredge samples and ocean bottom photographs, Hawaii: Geological Society of America Bulletin, v. 80, p. 1191-1202.

Moore, R.B., Helz, R.T., Dzurisin, D., Eaton, G.P., Koyanagi, R.Y., Lipman, P.W., Lockwood, J.P., and Puniwai, G.P., 1980, The 1977 eruption of Kilauea Volcano, Hawaii: Journal of Volcanology and Geothermal Research, v. 7, p. 189-210.

Murase, T., and McBirney, A.R., 1973, Properties of some common igneous rocks and their melts at high temperatures: Geological Society of America Bulletin, v. 84, p. 3563-3592.

Nakamura, K., 1980, Why do long rift zones develop in Hawaiian volcanos—a possible role of thick oceanic sediments: Bulletin of the Volcanology Society of Japan, v. 25, p. 255-269.

O'Connell, R.J., and Budiansky, B., 1974, Seismic velocities in dry and cracked solids: Journal of Geophysical Research, v. 79, p. 5412-5426.

Peck, D.L., and Kinoshita, W.T., 1976, The eruption of August 1963 and the formation of Alae lava lake, Hawaii: U.S. Geological Survey Professional Paper 935-A, 33 p.

Pollard, D.D., 1976, On the form and stability of open hydraulic fractures in the Earth's crust: Geophysical Research Letters, v. 3, p. 513-516.

Pollard, D.D., and Holzhausen, G., 1979, On the mechanical interaction between a fluid-filled fracture and the Earth's surface: Tectonophysics, v. 53, p. 27-57.

Pollard, D.D., and Muller, O.H., 1976, The effect of gradients in regional stress and magma pressure on the form of sheet intrusions in cross section: Journal of Geophysical Research, v. 81, p. 975-984.

Purdy, G.M., and Detrick, R.S., 1986, Crustal structure of the mid-Atlantic ridge at 23°N seismic refraction studies: Journal of Geophysical Research, v. 91, p. 3729-3762.

Ramberg, H., 1981, Gravity and deformation of the Earth's crust: New York, Academic Press, 452 p.

Rao, M., Ramana, Y.V., and Gogte, B.S., 1974, Dependence of compressional velocity on the mineral chemistry of eclogites: Earth and Planetary Science Letters, v. 23, p. 15-20.

Renard, V., Hekinian, R., Francheteau, J., Ballard, R.D., and Backer, H., 1985. Submersible operations at the axis of the ultra-fast-spreading East Pacific rise (17°30′ to 21°30′S): Earth and Planetary Science Letters, v. 75, p. 339-353.

Reuss, A., 1929, Berechnung der Fleissgrenze von Mischkristallen auf Grund der Plastizitätsbedingung für Einkristalle: Zeitschrift für Angewandte Mathematik und Mechanik, v. 9, p. 49

Richter, D.H., and Simmons, G., 1974, Thermal expansion behavior of igneous rocks: International Journal of Rock Mechanics and Mining Sciences & Geomechanics Abstracts, v. 11, p. 403-411.

Richter, D.H., and Moore, J.G., 1966, Petrology of Kilauea Iki lava lake, Hawaii: U.S. Geological Survey Professional Paper 537–B, 26 p.

Richter, D.H., and Murata, K.J., 1966, Petrography of the lavas of the 1959–60 eruption of Kilauea Volcano, Hawaii: U.S. Geological Survey Professional Paper 537–D, 12 p.

Ritzert, M., and Jacoby, W.R., 1985, On the lithospheric seismic structure of Reykjanes ridge at 62.5°N: Journal of Geophysical Research, v. 90, p. 10117-10128.

Robie, R.A., Hemingway, B., and Fisher, J., 1978, Thermodynamic properties of minerals and related substances at 298.15K and 1 bar ($10^5$ pascals) pressure and at higher temperatures: U.S. Geological Survey Bulletin 1452, 456 p.

Robie, R.A., and Waldbaum, D.R., 1968, Thermodynamic properties of minerals and related substances at 298.15K (25.0°C) and one atmosphere (1.013 bars) pressure and at higher temperatures: U.S. Geological Survey Bulletin 1259,

Ryan, M.P., Blevins J.Y.K., Okamura, A.T., and Koyanagi, R.Y., 1983, Magma reservoir subsidence mechanics: Theoretical summary and application to Kilauea Volcano, Hawaii: Journal of Geophysical Research, v. 88, p. 4147-4181.

Ryan, M.P., Koyanagi, R.Y., and Fiske, R.S., 1981, Modeling the three-dimensional structure of magma transport systems: Application to Kilauea Volcano, Hawaii: Journal of Geophysical Research, v. 86, p. 7111-7129.

Ryan, M.P., and Sammis, C.G., 1978, Cyclic fracture mechanisms in cooling basalt: Geological Society of America Bulletin, v. 89, p. 1295-1308.

———1981, The glass transition in basalt: Journal of Geophysical Research, v. 86, p. 9519-9535.

Ryzhova, T.V., 1964, The elastic properties of plagioclase: Izvestia Geophysics, ser. 7, p. 1049-1051.

Salisbury, M.H., and Christensen, N.I., 1976, Sonic velocities and densities of basalts from the Nazca plate, DSDP leg 34, *in* Yeats, R.S., Hart, S.R., and others, eds., Initial Reports of the Deep Sea Drilling Project: U.S. Government Printing Office, v. 34, p. 543-546.

Schock, R.N., Heard, H.C., and Stephens, D.R., 1973, Stress-strain behavior of a granodiorite and two greywackes on compression to 20 kilobars: Journal of Geophysical Research, v. 78, p. 5922-5941.

Schreiber, E., Fox, P.J., and Peterson, J.J., 1972, Compressional wave velocities in selected samples of gabbro, schist, limestone, anhydrogypsum and halite, *in* Ryan, W.B.F., Hsu, K.J., and others, eds., Initial reports of the Deep Sea Drilling Project: U.S. Government Printing Office, v. 13, p. 595-597.

———1974, Compressional wave velocities in samples recovered from DSDP leg 24, *in* Fisher, R.L., and others, eds., Initial reports of the Deep Sea Drilling Project: U.S. Government Printing Office, v. 24, p. 787-789.

Shaw, H.R., 1980, The fracture mechanisms of magma transport from the mantle to the surface, *in* R.B. Hargraves, ed., Physics of magmatic processes: Princeton, N.J., Princeton University Press, p. 201-264.

Shaw, H.R., and Swanson, D.A., 1970, Eruption and flow rates of flood basalts, *in* Gilmour, E.H., and Stradling, D., eds., Proceedings of the Second Columbia River Basalt Symposium: Cheney, Eastern Washington State College Press.

Simmons, G., and Wang, H., 1971, Single crystal elastic constants and calculated aggregate properties: A handbook (2d ed.): Cambridge, Massachusetts Institute of Technology Press, 370 p.

Skinner, B.J., 1966, Thermal expansion, sec. 6 *of* Clark, S.P., ed., Handbook of physical constants (revised ed.): Geological Society of America Memoir 97, p. 75-96.

Sleep, N.H., 1974, Segregation of magma from a mostly crystalline mush: Geological Society of America Bulletin, v. 85, p. 1225-1232.

Soga, N., and Anderson, O.L., 1967, High-temperature elasticity and expansivity of forsterite and steatite: Journal of the American Ceramic Society, v. 50, p. 239-359.

Solomon, S.C., 1975, Mare volcanism and lunar crustal structure, *in* Proceedings of the Sixth Lunar Science Conference: Elmsford, N.Y., Pergamon Press, p. 2021-2042.

Sparks, R.S.J., and Huppert, H.E., 1984, Density changes during the fractional crystallization of basaltic magmas: Fluid dynamic implications: Contributions to Mineralogy and Petrology, v. 85, p. 300-309.

Spence, D.A., and Turcotte, D.L., 1985, Magma-driven propagation of cracks: Journal of Geophysical Research, v. 90, p. 575-580.

Spinner, S., and Tefft, W.E., 1961, A method for determining mechanical resonance frequencies and for calculating elastic moduli from these frequencies: Proceedings of the American Society of Testing and Materials, p. 1221-1238.

Spudich, P., and Orcutt, J., 1980, A new look at the seismic velocity structure of the oceanic crust: Review of Geophysics and Space Physics, v. 18, p. 627- 645.

Stolper, E., Walker, D., Hager, B.H., and Hays, J.F., 1981, Melt segregation from partially molten source regions: The importance of melt density and source region size: Journal of Geophysical Research, v. 86, p. 6261-6271.

Swanson, D.A., Duffield, W.A., and Fiske, R.S., 1976, Displacement of the south flank of Kilauea Volcano: The result of forceful intrusion of magma into the rift zones: U.S. Geological Survey Professional Paper 963, 39 p.

Swanson, D.A., Jackson, D.B., Koyanagi, R.Y., and Wright, T.L., 1976, The February 1969 rift eruption of Kilauea Volcano, Hawaii: U.S. Geological Survey Professional Paper 891, 30 p.

Talwani, M., Worzel, J.L., and Landisman, M., 1959, Rapid gravity computations for two-dimensional bodies with application to the Mendocino submarine fracture zone: Journal of Geophysical Research, v. 64, p. 49-59.

Thompson, R.N., and Tilley, C.E., 1969, Melting and crystallization relations of Kilauean basalts of Hawaii. The lavas of the 1959-60 Kilauea eruption: Earth and Planetary Science Letters, v. 5, p. 469-477.

Tilley, C.E., 1950, Some aspects of magmatic evolution: Quarterly Journal of the Geological Society of London, v. 106, p. 37-61.

Todd, T., and Simmons, G., 1972, Effect of pore pressure on the velocity of compressional waves in low-porosity rocks: Journal of Geophysical Research, v. 77, p. 3731-3743.

Vogt, P.R., 1974, Volcano height and plate thickness: Earth and Planetary Science Letters, v. 23, p. 337-348.

Voigt, W., 1928, Lehrbuch der Kristallphysik: Leipzig, B.B. Teubner.

Volarovich, M.P., and Gurvich, A.S., 1957, Investigation of dynamic moduli of elasticity for rocks in relation to temperature: Izvestia Akademiya Nauk SSSR. Seriya Geofiziko, no. 4, p. 417-425.

Waff, H.S., 1979, Equilibrium fluid distribution in an ultramafic partial melt under hydrostatic stress conditions: Journal of Geophysical Research, v. 84, p. 6109-6114.

———1980, Effects of the gravitational field on liquid distribution in partial melts within the upper mantle: Journal of Geophysical Research, v. 85, p. 1815-1825.

Waff, H.S., and Bulau, J.R., 1979, Equilibrium fluid distribution in an ultramafic partial melt under hydrostatic stress conditions: Journal of Geophysical Research, v. 84, p. 6109-6114.

Walsh, J.B., 1968, Attenuation in partially melted material: Journal of Geophysical Research, v. 73, p. 2209-2216.

———1969, New analysis of attenuation in partially melted rock: Journal of Geophysical Research, v. 74, p. 4333-4337.

———1981, Effect of pore pressure and confining pressure on fracture permeability: International Journal of Rock Mechanics and Mining Sciences & Geomechanics Abstracts, v. 18, p. 429-435.

Walsh, J.B., and Decker, R.W., 1971, Surface deformation associated with volcanism: Journal of Geophysical Research, v. 76, p. 3291-3302.

Wang, H., Todd, T., Richter, D., and Simmons, G., 1973, Elastic properties of plagioclase aggregates and seismic velocities, *in* The Moon: Proceedings of the Fourth Lunar Science Conference, v. 3, p. 2663-2671.

Ward, P.L., and Gregersen, S., 1973, Comparison of earthquake locations determined with data from a network of stations and small tripartite arrays on Kilauea Volcano, Hawaii: Bulletin of the Seismological Society of America, v. 63, p. 679-711.

Watt, J.P., Davies, G.F., and O'Connell, R.J., 1976, The elastic properties of composite materials: Review of Geophysics and Space Physics, v. 14, p. 541-563.

Weertman, J., 1971a, Theory of water-filled crevasses in glaciers applied to vertical magma transport beneath oceanic ridges: Journal of Geophysical Research, v. 76, p. 1171-1183.

———1971b, Velocity at which liquid-filled cracks move in the earth's crust or in glaciers: Journal of Geophysical Research, v. 76, p. 8544-8553.

———1980, The stopping of a rising, liquid-filled crack in the earth's crust by a freely slipping horizontal joint: Journal of Geophysical Research, v. 85, p. 967-976.

Weertman, J., and Chang, S.P., 1977, Fluid flow through a large vertical crack in the Earth's crust: Journal of Geophysical Research, v. 82, p. 929-932.

Whitcomb, J.H., Garmany, J.D., and Anderson, D.L., 1973, Earthquake prediction: Variation of seismic velocities before the San Fernando earthquake: Science, v. 180, p. 632-635.

Wilson, L., and Head, J.W., 1981, Ascent and eruption of basaltic magma on the Earth and Moon: Journal of Geophysical Research, v. 86, p. 2971-3001.

Wingquist, C.F., 1971, Elastic moduli of rock at elevated temperatures: U.S. Bureau of Mines Report of Investigations 7269.

Wright, T.L., and Fiske, R.S., 1971, Origin of the differentiated and hybrid lavas

of Kilauea Volcano, Hawaii: Journal of Petrology, v. 12, p. 1-65.

Wright, T.L., and Okamura, R.T., 1977, Cooling and crystallization of tholeiitic basalt, 1965 Makaopuhi lava lake, Hawaii: U.S. Geological Survey Professional Paper 1004, 78 p.

Wright, T.L., and Weiblen, P.W., 1968, Mineral composition and paragenesis in tholeiitic basalt from Makaopuhi lava lake, Hawaii [abs.], *in* Abstracts for 1967: Geological Society of America Special Paper 115, p. 242-243.

Wyss, M., and Holcomb, D.J., 1973, Earthquake prediction based on station residuals: Nature, v. 249, p. 139-140.

Yamshikov, V.S., 1965, A study of the temperature dependence of the modulus of elasticity of rocks: Izvestia, Earth Physics Series no. 10, p. 83-87.

Yoder, H.S., and Sahama, H.G., 1957, Olivine x-ray determinative curve: American Mineralogist, v. 42, p. 475-491.

Yoder, H.S., and Tilley, C.E., 1962, Origin of basalt magmas: An experimental study of natural and synthetic rock systems: Journal of Petrology, v. 3, no. 3, p. 342-532.

Zablocki, C.J., Tilling, R.I., Peterson, D.W., Christiansen, R.L., Keller, G.V., and Murray, J.C., 1974, A deep research drill hole at the summit of an active volcano, Kilauea, Hawaii: Geophysical Research Letters, v. 1, p. 323-326.

Zucca, J.J., and Hill, D.P., 1980, Crustal structure of the southeast flank of Kilauea Volcano, Hawaii, from seismic refraction measurements: Bulletin of the Seismological Society of America, v. 70, p. 1149-1159.

Zucca, J.J., Hill, D.P., and Kovach, R.L., 1982, Crustal structure of Mauna Loa Volcano, Hawaii, from seismic refraction and gravity data: Bulletin of the Seismological Society of America, v. 72, p. 1535-1550.

# ORIGINS OF BLADE-LIKE DIKES IN VOLCANIC RIFT ZONES

*By* Allan M. Rubin[1] *and* David D. Pollard[2]

## ABSTRACT

**Seismic and geodetic data have demonstrated that dikes in the rift zones of Kilauea Volcano in Hawaii and Krafla Volcano in Iceland are typically intruded laterally from a central magma reservoir and acquire a blade-like form. A remarkable feature of many such dikes is that they propagate at shallow depths for tens of kilometers without erupting. Using concepts of fracture mechanics, we can specify the conditions necessary for this type of growth. A dike will propagate if the stress-intensity factor at the dike tip exceeds a critical value, known as the fracture toughness of the host rock. An increase in the rift-zone fracture toughness with depth could limit the depth to which dikes extend, but little existing evidence supports this possibility. We find that several geological processes could contribute to a distribution of the stress-intensity factor along the dike perimeter that would promote the development of a blade-like form.**

**Factors influencing the stress intensity along the dike perimeter can be divided into two categories: factors pertaining to the dike geometry, including the dike size, shape, and depth beneath the Earth's surface; and factors pertaining to the distribution of driving pressure (magma pressure minus the remote stress) acting on the dike plane. The pressure within the dike is controlled by magma-reservoir pressure, magma density, presence of vesiculated magma or gas at the dike top, and pressure gradients due to viscous flow. Possible contributors to the remote stress include density stratification of the rift zone, gravitational loading of the volcanic ridge, intrusion of previous dikes, faulting, and plate tectonic forces.**

**Of the geometric factors, both the elongate dike shape and the proximity of the Earth's surface tend to promote upward growth and eruption, rather than continued lateral growth of the dike. Thus a blade-like form must be the result of a driving-pressure distribution that increases the stress-intensity factor at the downrift edge of the dike with respect to that at the dike top and bottom. This can be achieved if the driving pressure is greater at the depth of the dike center than at the dike top or bottom. The vertical pressure variation within a laterally propagating dike is essentially equal to that within a static body of magma. The presence of vesiculated magma in the upper part of the dike enhances upward propagation but has little effect on downward and lateral propagation. Thus the source of the greater driving pressure at the depth of the dike center must be the remote stress; each of the contributors to this stress listed above is a potential source of such a stress distribution.**

**Using the cross-sectional geometry of the August 1981 southwest-rift-zone dike at Kilauea inferred from geodetic data, and assuming a uniform fracture toughness within the rift zone, we estimate the magma pressure and the remote stress at the time of intrusion. The hydrostatic head of the magma was deeper than 50 m below the surface. The excess magma pressure at the dike center was 2.5–10.5 MPa (25–105 bars), and the driving pressure decreased toward the dike top and bottom by about 3–11 MPa/km. If the gradients in the driving pressure toward the dike top and bottom were due only to the local density contrast between the magma and the host rock, they would be about 3 MPa/km. A more precise determination of the driving pressure is not possible without more precise values of the rift-zone fracture toughness and elastic shear modulus. From estimates of the dike thickness, we find that the rift-zone shear modulus is within a factor of 2–3 of 3 GPa. This is in agreement with other inplace determinations of the shear modulus and about an order of magnitude less than laboratory values for intact basalt.**

## INTRODUCTION

Geological studies of eroded Hawaiian and Icelandic volcanoes have documented the importance of shallow dike intrusion as a mechanism of magma transport in these distinct geologic settings. The majority of such dikes are nearly vertical and occur within swarms, or rift zones, that may be more than 100 km long and contain hundreds or thousands of dikes (Walker, chapter 41; Macdonald, 1956; Walker, 1959; Walker, 1963; Fiske and Jackson, 1972; Helgason and Zentilli, 1985). During the last few decades, abundant geological, geochemical, petrological, geophysical, and geodetic data collected from Kilauea and Mauna Loa by scientists at the Hawaiian Volcano Observatory and from Krafla by scientists at the National Energy Authority and the Nordic Volcanological Institute in Iceland have shed considerable light on some of the processes of magma movement and dike emplacement. At both locations, rapid subsidence of the region overlying a shallow magma reservoir is associated with the lateral flow of magma for up to several tens of kilometers into adjacent rift zones. In most cases, this intrusion of magma results in the formation of new dikes, the surface manifestations of which may include observable rift-zone widening and fissure eruptions. The 120-km-long east rift zone of Kilauea, and historical and prehistoric dikes in Iceland that vented nearly 100 km from their sources (Sigurdsson

[1]Department of Geology, Stanford University, Stanford, CA 94305.
[2]Departments of Geology and Applied Earth Sciences, Stanford University, Stanford, CA 94305.

and Sparks, 1978), attest to the extraordinarily extensive form rift-zone dikes can take.

Dikes propagate because the magma pressure within them fractures the rock ahead of the magma front or forces preexisting fractures, such as cooling joints or through-going rift-zone extension cracks, to widen. In either case, this propagation can be interpreted in terms of established principles of fracture mechanics (see, for example, Lawn and Wilshaw, 1975). If the resistance of the host rock to fracture, the magma pressure within the dike, and the remote stress acting perpendicular to the rift zone are known, the directions in which the dike will propagate can be predicted. Alternatively, observations of dike propagation can be used to estimate some of these parameters.

We first summarize the available evidence on dike geometry and emplacement and outline the theoretical model to be used. We then list and analyze the factors governing the horizontal and vertical propagation of basaltic dikes emanating from near-surface magma reservoirs. Using this analysis we estimate the magma pressure and the state of stress in the southwest rift zone at Kilauea for the August 1981 dike intrusion. The model provides a framework for discussion of rift-zone dynamics and possible future research.

### ACKNOWLEDGMENTS

This paper benefited from careful reviews by Paul Delaney, Kieth Evans, Steve Martel, Larry Mastin, Michael Ryan, and Hans Weertman. Paul Davis, Bob Decker, Jim Dieterich, John Dvorak, David Hill, and Fred Klein provided interesting discussions and early versions of some results. We thank John Dvorak, Jack Lockwood, and Arnold Okamura for a kind introduction to Hawaii Volcanoes National Park and the Hawaiian Volcano Observatory. This research was funded in part by a National Science Foundation Graduate Fellowship and NSF grant EAR-8520641.

## CHARACTERIZATION OF THE DIKE-EMPLACEMENT PROCESS

### OBSERVATIONS OF DIKE PROPAGATION AND GEOMETRY

Combined geodetic and seismic data have revealed the presence of a magma chamber or chambers at approximately 2–7 km below the surface at Kilauea, Mauna Loa, and Krafla Volcanoes. During periods of activity these magma chambers inflate slowly, at rates of a few cubic meters per second, over periods of months or years, and deflate rapidly, at rates of 100–1,000 cubic meters per second, for periods of several hours to a few days. Typically, summit subsidence is accompanied by swarms of shallow earthquakes that migrate downrift at velocities of a few tens of centimeters per second (Klein and others, chapter 43; Brandsdottir and Einarsson, 1979). These swarms sweep out tabular zones that are typically 1–2 km wide, a few kilometers high, and as much as several tens of kilometers long. Ground cracking or fissure eruptions may shortly precede or follow the migration of the earthquake swarm beneath a particular site (Hauksson, 1983; F.W. Klein, oral commun., 1985). Deviations from this simple pattern are not, however, uncommon during intrusions into the east rift zone (ERZ) of Kilauea: there some earthquake swarms originate within the rift zone itself, and discontinuous or uprift migration of earthquakes is sometimes observed (Klein and others, chapter 43).

Although the factors controlling the origin and extent of the earthquake swarms are not yet understood, it seems reasonable to use these earthquakes to estimate dike location (Brandsdottir and Einarsson, 1979; Ryan and others, 1981). The approximate boundaries of earthquake swarms associated with a few well-documented intrusions at Kilauea and Krafla are shown on figure 53.1, projected onto cross sections parallel to the rift axes.

Pollard and others (1983) derived a graphical method for estimating the height, depth, dip, and thickness of dikes from surface vertical-deformation data. Although geodetic data are available less frequently than earthquake-source data, their interpretation may improve dike location accuracy considerably. Displacements measured in the rift zones of Kilauea and Krafla yield dike heights and depths consistent with estimates from earthquake-source data. Estimates of dike thickness (0.8–2 m) and of dike dip (within a few degrees of vertical) are both in agreement with observations of eroded rift-zone dikes.

### THEORETICAL CONSTRAINTS ON DIKE STABILITY AND PROPAGATION

In this study dikes are represented as pressurized cracks in an isotropic, homogeneous, linearly elastic half-space. Field observations indicate that dikes are typically nearly planar features. Although the assumptions of isotropy, homogeneity, and elasticity are certainly incorrect in detail (Ryan and others, 1983), we believe the model is appropriate for the physical insight sought here. Geodetic measurements made during the current Puu Oo activity show that rift-zone extension accumulated prior to an eruptive phase is completely recovered following eruption. This indicates that the volcano is capable of elastic behavior over periods of weeks and distances of a few kilometers (Hoffman and others, 1984).

It has been well established theoretically and experimentally that a crack will propagate if the energy available, from work done on the system by the boundary forces (remote stress and magma pressure) and from any release of stored strain energy in the surrounding solid, is sufficient to supply the energy expended in the cracking process (Lawn and Wilshaw, 1975). Though the solid is assumed to be elastic, the theory is sufficiently general that it incorporates inelastic behavior (such as secondary fracturing or local plastic deformation) in a small region around the crack tip. This region is called the process zone.

Another crack propagation criterion, equivalent to the above energy-balance criterion, involves the use of quantities known as stress-intensity factors (Lawn and Wilshaw, 1975). A dilated crack in an elastic material generates stresses in the near-tip region given by

$$\sigma_{ij} = K f_{ij}(\theta)/(2r)^{1/2} \qquad (1)$$

where $\sigma_{ij}$ are components of the stress tensor, $K$ is the mode I (tensile) stress-intensity factor, $r$ is the distance from the crack tip,

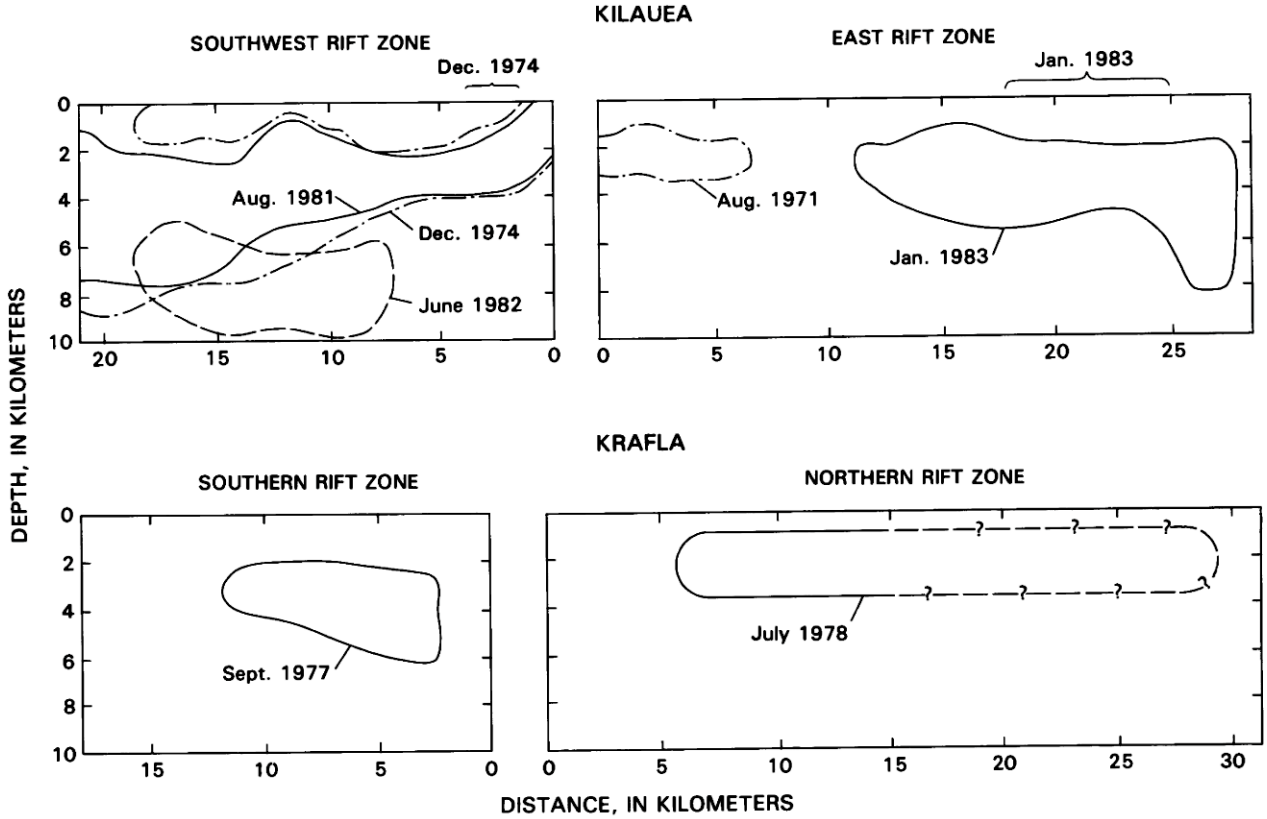


FIGURE 53.1.—Approximate limits of seismic swarms associated with some well-documented dike intrusions at Kilauea and Krafla Volcanoes, projected onto cross sections parallel to the rift axes. The origins for the distance axes are near Halemaumau Crater within the summit caldera at Kilauea and at the center of the caldera at Krafla. Extent of associated eruptive fissures indicated by brackets at the tops of the sections. Note the apparant lack of seismicity, due in part to the low-magnitude filter applied to the data, near the eruption site of the 1983 east-rift-zone intrusion at Kilauea. Data for Kilauea from Klein and others (chapter 43); data for Krafla from Brandsdottir and Einarsson (1979) and Einarsson and Brandsdottir (1979).

and the $f_{ij}(\theta)$ are functions of position around the crack tip (fig. 53.2). (By an alternate convention, this equation would contain an additional factor of $\pi^{-1/2}$, and the value of $K$ would be modified accordingly). $K$ is in general dependent only upon the crack geometry and the distribution of driving pressure $\Delta P$. We consider the driving pressure for dikes to be a function of vertical position $y$: it is equal to the magma pressure $P_m(y)$ minus the remote stress $S(y)$ acting perpendicular to the dike plane:

$$\Delta P(y) = P_m(y) - S(y). \tag{2}$$

A dike will propagate if its stress-intensity factor is greater than a critical value $K_c$, termed the fracture toughness of the rock.[1] A negative value of $K$ indicates that a dike will decrease in length by pinching shut at its tip. A dike is stable if $0 < K < K_c$; that is, the dike will neither increase nor decrease in length (Weertman, 1971).

For dikes following preexisting fractures, as is possible in volcanic rift zones, $K_c$ could be zero. Experimentally determined values of $K_c$ for intact laboratory specimens of basalt at room temperature and pressure lie within the range 1–2 MPa · m$^{1/2}$ (Atkinson, 1984). However, estimates of $K_c$ from studies of dikes exposed in shale (Delaney and Pollard, 1981), made under the assumption that magma had access to the dike tip, are in the range 30–100 MPa · m$^{1/2}$. Examination of dike-parallel joints in sandstone (Delaney and others, in press) suggests that the crack tip process zone associated with propagating basaltic dikes can be

[1]Because crack propagation can proceed much more rapidly than magma flow, it is expected that in actuality $K$ will exceed $K_c$ by only an infinitesimal amount. Physically this may be accomplished by the opening of a low-pressure cavity at the dike tip. The action of the remote compressive stress on this cavity would decrease $K$ to values below that calculated assuming that magma had access to the dike tip. In subsequent calculations of $K$ we assume that magma has access to the dike tip, and interpret a value of $K$ greater than $K_c$ as indicating that propagation will proceed.

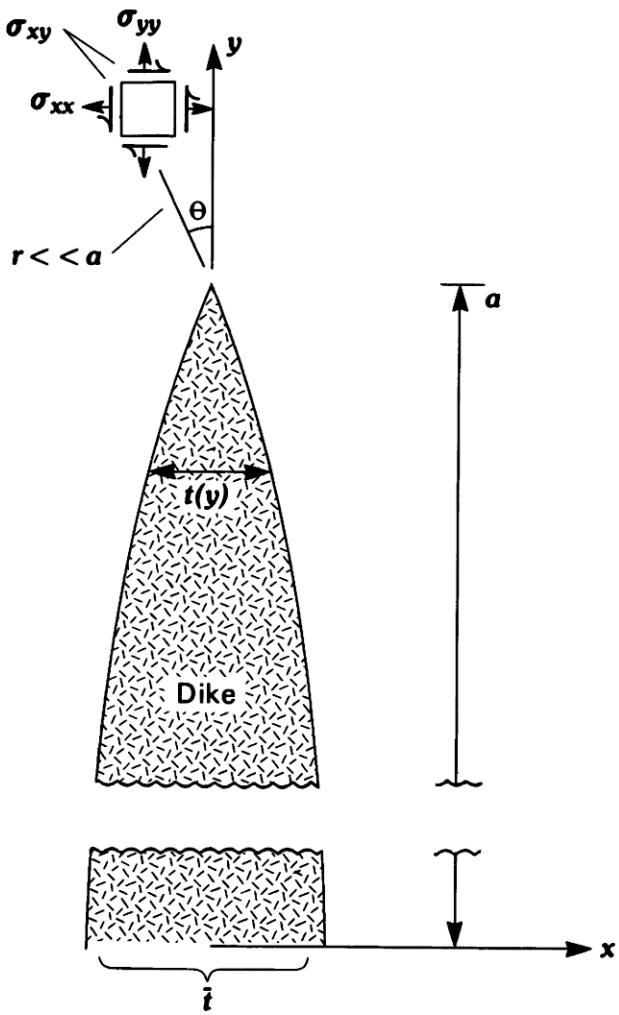


FIGURE 53.2.—Stresses ($\sigma$) in the near-tip region of a crack or dike. The stress is a function of the distance $r$ from the dike tip, the position $\theta$ around the dike tip, and the stress-intensity factor $K$ (eq 1). $a$, dike half-length; $t(y)$, dike thickness at a height $y$ above the dike center; $\bar{t}$, average dike thickness.

larger than that associated with cracks in laboratory specimens, giving larger values of $K_c$. Frictional sliding on fractures near the dike, which is indicated by rift-zone earthquake swarms, is another energy-expending mechanism that would increase $K_c$.

The effects of pressure and temperature on $K_c$ are at present only poorly understood. For dry rock (Schmidt and Huddle, 1977; Winter, 1983) $K_c$ increases with increasing pressure because the added confining pressure inhibits microcracks near the crack tip from opening up and aiding propagation (Atkinson, 1984). When these microcracks are accessible to fluids at presures equal to the confining pressure, for example in experiments on water-saturated sandstone (Winter, 1983), this effect is not apparent. For moderate temperatures, increasing temperature decreases $K_c$ because the energy required for brittle fracture is reduced. Limited experimental determinations indicate that $K_c$ for gabbro decreases by about 30–35 percent from room temperature to 400 °C (Meredith and Atkinson, 1985). At some higher temperature, increased plasticity at the crack tip will cause $K_c$ to increase. Bjornsson (1985) estimates the temperature at 4–5 km depth in Icelandic rift zones to be 500–600 °C. Although more experimental data are needed, we assume these temperatures to be low enough that increased crack-tip plasticity is not a significant factor at the time-scales appropriate for dike intrusion.

Because of sparse high-temperature and high-pressure data, and because of the possible discrepancy between values of $K_c$ appropriate for cracks in laboratory specimens and for dikes in the Earth's crust, we can only restrict the probable range of critical stress-intensity factors to

$$0 > K_c > 100\ \mathrm{MPa} \cdot \mathrm{m}^{1/2}.$$

## THEORETICAL CONSTRAINTS ON DIKE THICKNESS

The length-to-height ratio of typical rift-zone dikes justifies treating them as two-dimensional when calculating dike thickness. For a uniform driving pressure $P_o$, the thickness of the dike at a distance $y$ from its center is given by Pollard and others (1983) as:

$$t = P_o a \frac{(1-\nu)}{\mu} [1-(y/a)^2]^{1/2} \qquad (3)$$

(fig. 53.2), where $a$ is the dike half-height, $\nu$ is Poisson's ratio, and $\mu$ is the elastic shear modulus. The average dike thickness, $\bar{t}$, is about 0.8 times the thickness at the dike center. Equation 3 illustrates the general relation that dike thickness is proportional to dike half-height and driving pressure, and inversely proportional to rock stiffness, $\mu/(1-\nu)$.

Given estimates of the dike thickness-to-height ratio from geodetic data, one can calculate the ratio of driving pressure to rock stiffness. If the rock stiffness is known, one can then estimate the driving pressure. Experimentally determined values of $\nu$ for basalt vary only slightly, generally lying between 0.22 and 0.28 for conditions ranging from room temperature and pressure to those appropriate for depths of several kilometers (Birch, 1966; Ryan and others, 1983). Typical static laboratory values of $\mu$ for basalt are 25–35 GPa (Birch, 1966). However, the shear moduli determined from loading large fractured rock masses in the field are lower than those measured on pristine samples in the laboratory by as much as an order of magnitude (Bieniawski, 1978; Evans, 1982). In actuality the effective shear modulus of the rock mass intruded by dikes probably increases with depth as the rock becomes more competent. From the lack of a significant piezomagnetic anomaly during periods of magma-chamber inflation, Davis (1976) estimates that the effective shear modulus of the summit region of Kilauea is about an order of magnitude less than that of competent basalt. We accept this estimate as a more appropriate average shear modulus for volcanic rift zones than the laboratory value. However, the large uncertainty associated with this figure makes the dike thickness-to-height ratio only a weak constraint on the driving pressure.

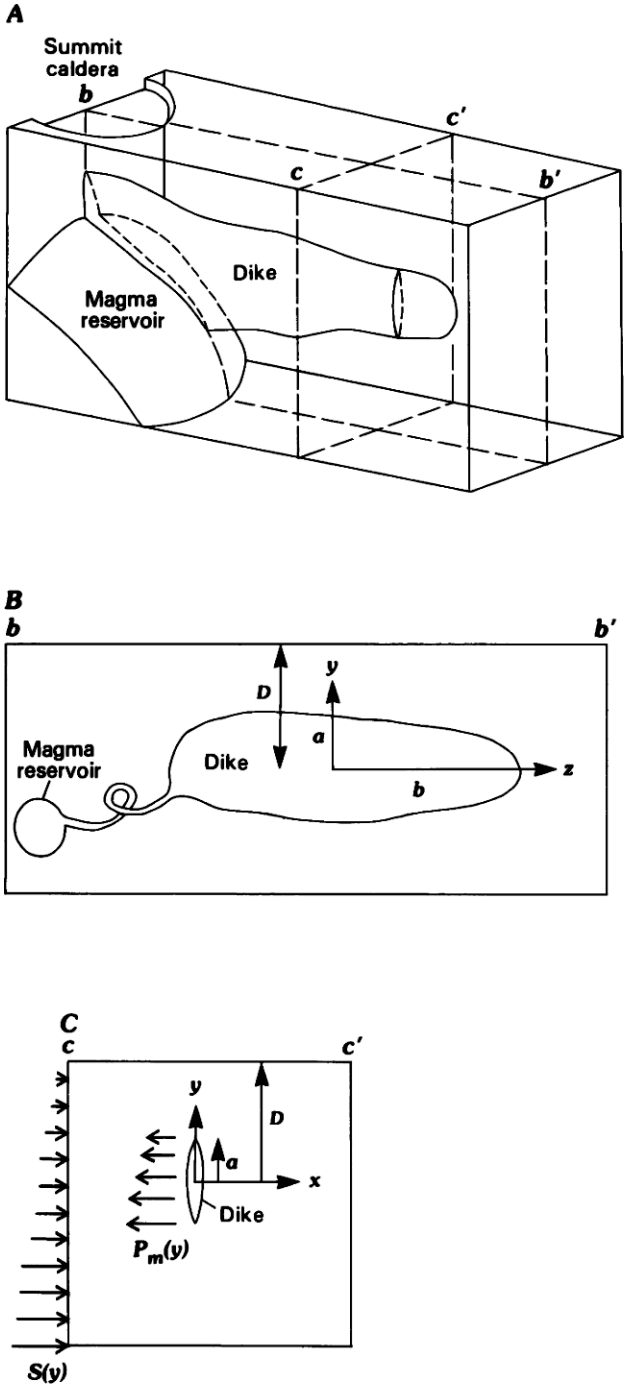


FIGURE 53.3.—Diagrams of a rift-zone dike intruded laterally from a shallow magma reservoir. ***A***, Cartoon sketch of the dike showing general form; planes of sections ***B*** and ***C*** indicated. ***B***, Idealized longitudinal section of the dike, which has a half-height $a$, a half-length $b$, and a depth $D$. The magma reservoir acts as a source of pressure. ***C***, Idealized cross section of the dike. A remote stress $S(y)$ acts perpendicular to the dike plane; a magma pressure $P_m(y)$ acts within the dike.

### PROPAGATION AND STABILITY CRITERIA FOR RIFT-ZONE DIKES

In most cases the region swept out by individual earthquake swarms remains fairly constant in vertical extent and depth as the magma travels great distances laterally. From this observation we infer that the dikes are adopting an approximately equilibrium position in the vertical plane; it is this inference that motivates the analysis which follows. The possibility that some kinetic factor related to magma flow or solidification inhibits dikes from reaching their stable position is considered briefly in the section "Discussion."

The necessary conditions for a dike to have a propagating downrift edge and a stable height are that $K \geq K_c$ at the downrift edge and $K < K_c$ at the top and bottom. These conditions can be met by increasing $K_c$ at the dike top and bottom relative to $K_c$ at the downrift edge, or by decreasing $K$ at the dike top and bottom relative to $K$ at the downrift edge. In what follows we assume a uniform value of $K_c$ throughout the rift zone and examine the factors that could contribute to the required variation in $K$. We infer from the blade-like geometry of typical rift-zone dikes that during downrift propagation sections of the dike top and bottom close to the downrift edge have attained their stable height. This assumption allows us to neglect lateral magma pressure gradients due to both viscous flow and along-strike changes in dike elevation when comparing $K$ at the downrift edge to that at the dike top and bottom.

## FACTORS CONTROLLING DIKE PROPAGATION

A rift-zone dike intrusion is shown in cartoon form in figure 53.3*A*, and our idealizations of the dike to be used for modeling purposes are illustrated in figures 53.3*B* and 53.3*C*. The model dike has a half-height $a$, half-length $b$, and depth $D$. It is embedded in an elastic half-space with uniform shear modulus $\mu$ and fracture toughness $K_c$. The magma reservoir is represented as a source of pressure located at the uprift end of the dike, but is not explicitly accounted for in calculations of $K$, because it is distant from the part of the dike perimeter that is of interest. The magma has a uniform viscosity $\eta$ and a uniform or vertically varying density $\rho_m(y)$. A vertically varying remote stress $S(y)$ acts on the plane of the dike, and a vertically varying magma pressure $P_m(y)$ acts within the dike.

The geologic factors contributing to the stress intensity around the dike can be divided into two categories: those pertaining to the geometry of the dike, and those pertaining to the driving-pressure distribution. The first category includes the dike size, shape, and depth beneath the Earth's surface. The second category can be divided into those factors related to the magma or gas pressure within the dike and those factors related to the remote stresses acting perpendicular to the dike plane. The pressure distribution within the dike body is controlled by the unvesiculated magma density, the presence or absence of vesiculated magma or a separate gas phase, the time-varying magma-reservoir pressure, and pressure loss due to viscous flow. For conceptual purposes, the remote stress acting on the dike plane can be subdivided into two components: the lithostatic load or weight of the rock overburden, including variable density stratification; and any supplementary stresses induced by

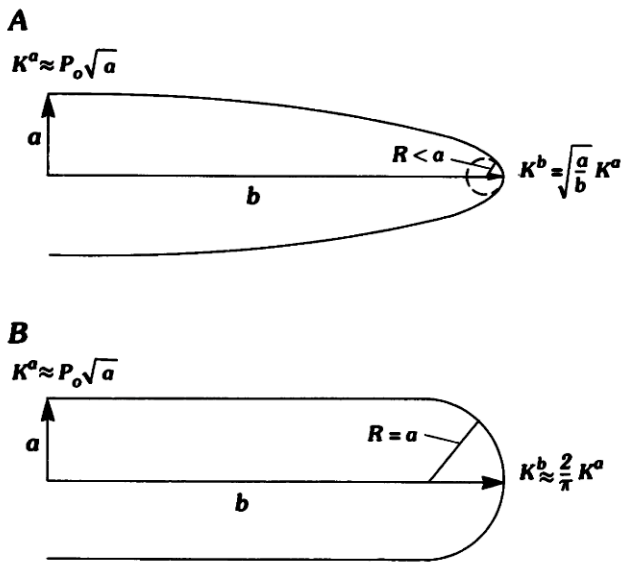


FIGURE 53.4.—Idealized longitudinal sections showing dike geometry. Dikes subject to uniform driving pressure, $P_o$. ***A***, Elliptical dike with half-height $a$ and half-length $b$. The radius of curvature $R$ in the plane of the dike at the downrift edge is less than $a$; as the dike grows laterally, $K^b$ decreases approximately as $\sqrt{a/b}$. ***B***, Dike with a constant half-height $a$ except near its downrift edge, where $R$ is equal to $a$. The larger radius of curvature gives rise to a larger value of $K^b$ than for the ellipse. This idealization is used in this study and is likely to produce an overestimate of $K^b$.

topographic relief, slip along major faults at depth, the intrusion of earlier dikes, or plate-tectonic forces.

## GEOMETRICAL FACTORS

### DIKE SIZE

For a two-dimensional dike of half-height $a$ subjected to a uniform driving pressure $P_o$ (fig. 53.3C, $D=\infty$), the stress-intensity factor at the dike top and bottom is

$$K = P_o\sqrt{a}. \tag{4}$$

This equation illustrates the general result that $K$ is proportional to the square root of the dike half-height. For a propagating dike subject to a uniform, steady driving pressure, $K$ increases with height, so propagation should never cease and eruptions would be inevitable.

### DIKE SHAPE

If the dike is idealized as having an elliptical shape with half-height $a$ and half-length $b$ (fig. 53.4A), the stress-intensity factor around the dike perimeter can be obtained analytically. For a uniform driving pressure the stress intensity at the top or bottom of the dike is given by

$$K^a = \frac{1}{\Phi} P_o\sqrt{a} \tag{5}$$

(Broek, 1982, p. 81), where $\Phi$ is a function of $b/a$ that can be evaluated using tables of elliptic integrals and that approaches unity as $b/a$ becomes large. For $b/a = 3$, $K$ is less than that for an infinitely long dike of height $a$ by only 12 percent.

The ratio of the stress-intensity factor at the tip of the minor axis to that at the tip of the major axis is given by

$$\frac{K^a}{K^b} = \left[\frac{b}{a}\right]^{1/2}. \tag{6}$$

Equation 6 indicates the tendency of such dikes to grow into more equidimensional forms: as the eccentricity of the ellipse increases, the stress-intensity factor at the tip of the minor axis increases with respect to that at the tip of the major axis. For rift zone dikes with $b/a = 10$, the ratio $K^a/K^b$ is about 3. Because $K^a$ for large ratios of $b$ to $a$ does not increase significantly if $a$ remains constant, then equation 6 indicates that $K^b$ actually decreases approximately in proportion to $b^{-1/2}$.

The dependence of $K^a/K^b$ on $b/a$ is in part an artifact of the assumption of ellipticity. In general, the stress intensity at a point on the perimeter of a planar crack is increased by an increase in crack size and by an increase in the in-plane radius of curvature of the crack at that point. If rift-zone dikes are constrained to maintain an elliptical shape and a fixed height, the radius of curvature at the downrift edge of the dike must decrease as the dike grows (fig. 53.4A). The decrease in $K^b$ indicated by equation 6 shows that the effect of decreasing radius of curvature outweighs the effect of increasing crack length. If, on the other hand, the dike front approaches a semicircle of radius $a$ (fig. 53.4B), $K^b$ can be approximated by $K$ for a circular crack of radius $a$ (Paris and Sih, 1965), or

$$K^b \approx \frac{2}{\pi} P_o\sqrt{a} \tag{7}$$

(Broek, 1982, p. 81). In this case the ratio of stress-intensity factors is not very sensitive to dike length and is approximated by

$$\frac{K^a}{K^b} \approx \frac{\pi}{2}. \tag{8}$$

The actual shape of the advancing front of rift-zone dikes is unknown and will depend upon the driving-pressure distribution. In the gelatin experiments of Fiske and Jackson (1972, fig. 6), the fronts of the model dikes were somewhat elliptical. This is the expected shape for driving pressures that are greater at the depth of the dike center than at the top or bottom. We assume that the end of the dike is a semicircle of radius $a$. Given the likelihood of a driving pressure that is greater at the depth of the dike center (see below), and therefore a somewhat elliptical dike end, this approximation is likely to produce a slight overestimate of $K^b$.

### PROXIMITY OF THE EARTH'S SURFACE

The stress-intensity factors at the top ($K^{+a}$) and bottom ($K^{-a}$) of a two-dimensional vertical dike near a horizontal free surface and subject to a uniform driving pressure are plotted as a function of $a/D$ in figure 53.5. The values of $K$ are normalized to their values in an infinite body. The dike intersects the surface when $a/D = 1$. It can be seen that the presence of a free surface increases both $K^{+a}$ and $K^{-a}$, but affects the upper dike tip more. For $a/D < 0.5$, the effect of the free surface becomes negligible, so $K^{+a}$ and $K^{-a}$ approach $K$ for a crack in an infinite body. Shah and Kobayashi (1973) determined the stress-intensity factors around three-dimensional elliptical cracks near a free surface. Their work shows that the two-dimensional approximation is fairly good when $a/b < 0.2$. For all values of $a/D$ and $a/b$, the free surface increases $K^b$ by less than both $K^{+a}$ and $K^{-a}$. The shaded area at the base of figure 53.5 shows the range of increase in $K^b$ due to the free surface for various elliptical shapes. Thus the effect of the free surface on typical rift-zone dikes is to increase $K^{+a}$, and to a lesser extent $K^{-a}$, relative to $K^b$. That is, the surface will tend to cause the dike to increase in its vertical dimension relative to its horizontal dimension, and should enhance eruption rather than downrift propagation.

## MAGMA-PRESSURE DISTRIBUTION

Both the blade-like shape and the shallow depth of rift-zone dikes lead to stress intensities that are higher at the dike top and bottom than at its downrift edge, for uniform applied loads. If the fracture toughness of the host rock is uniform, then the observed propagation of rift-zone dikes dictates that the driving-pressure distribution must increase $K$ at the downrift edge relative to $K$ at the top and bottom to an extent sufficient to overcome these geometric effects. Driving-pressure distributions on vertical sections which would accomplish this are depicted schematically in figure 53.6. In these illustrations lesser excess magma pressure, or even magma underpressure, at the dike top and bottom might ensure that $K^a < K_c$, while the greater excess magma pressure at the downrift edge yields $K^b \geq K_c$. In the following sections we explore the factors governing the magma pressure within the dike. The magma pressure at any point within a dike connected to a magma reservoir is controlled by the pressure at a given point within the reservoir, the elevation of the point within the dike with respect to that point within the reservoir, the magma density, and the pressure drop due to viscous magma flow between the two points.

### MAGMA RESERVOIR PRESSURE

The occurrence of eruptions at the summit of Mauna Loa simultaneous with quiessence in the lava lake at Kilauea 3 km below precludes the existence of an open magmatic conduit from the two volcanoes' reservoirs to a common source region (Williams and McBirney, 1979). We suggest that magma rises through the crust within isolated packets to levels where it is gravitationally stable. Gravity and seismic modeling of Hawaii (Hill and Zucca, chapter 37; Broyles and others, 1979; Zucca and others, 1982) and Iceland (Palmason, 1971) indicate that the bulk crustal density within a few kilometers of the surface is less than that of unvesiculated magma, whereas the density below is greater than that of magma. This provides an explanation for the presence of long-lived magma chambers at 2–7 km depth in Kilauea, Mauna Loa, and Krafla Volcanoes.

The magma-reservoir pressure cannot exceed that required to fracture the reservoir wall or that generated by the injection of magma from depth. However, our knowledge of the reservoir inflation and failure processes is insufficient to use them to calculate an upper bound for the reservoir pressure. We show below that dike behavior can place an upper bound on the magma-reservoir pressure. To estimate a lower bound for the reservoir pressure, we assume that the hydrostatic head of the reservoir is equal to or greater than the weight per unit area of the rock that caps it. Using densities of $2.3 \times 10^3$ kg/m$^3$ for the rock (Zucca and others, 1982) and $2.6 \times 10^3$ kg/m$^3$ for the magma (Fujii and Kushiro, 1977), we calculate hydrostatic heads of 230–350 m beneath the ground surface for reservoir tops 2–3 km deep. In an example to follow we use the more conservative estimate of $-350$ m as a lower bound on the hydrostatic head of the reservoir.

The change in reservoir pressure during a single dike intrusion can also affect dike behavior. If the host rock surrounding the magma chamber behaves elastically, then measured surface displacements above the chamber are proportional to pressure changes within it. Epp and others (1983) point out the linear correlation between summit tilt and vent elevation for ERZ eruptions since 1955 at Kilauea. Decker and others (1983) use this correlation to convert changes in summit tilt into differences in magma-reservoir pressure, by assuming that the hydrostatic head of the reservoir at the cessation of subsidence is controlled by the vent elevation. Using a magma density of $2.8 \times 10^3$ kg/m$^3$, Decker and others calculate a pressure change of 0.085 MPa per mrad of summit tilt. If the magma-reservoir roof behaves to some degree like a piston, the change in reservoir pressure could be less than 0.085 MPa/mrad.

### MAGMA DENSITY

The vertical pressure gradient, $\nabla P_m$, at a given depth, $y$, within a static column of magma is given by

$$\nabla P_m(y) = \rho_m(y) \cdot g, \tag{9}$$

where $\rho_m(y)$ is the magma density at a given depth, and $g$ is the acceleration of gravity, 9.8 m/s$^2$. A typical magma density of $2.6 \times 10^3$ kg/m$^3$ produces a pressure gradient of about 26 MPa/km or 260 bars/km (fig. 53.7A). If the driving pressure simply equals the magma pressure (that is, if $S(y) = 0$), then the stress-intensity factors at the top ($K^{+a}$) and bottom ($K^{-a}$) of the dike are given by

$$K^{+a} = P_o\sqrt{a} - \frac{1}{2}\nabla P_m a^{3/2}, \tag{10a}$$

$$K^{-a} = P_o\sqrt{a} + \frac{1}{2}\nabla P_m a^{3/2}, \tag{10b}$$

where $P_o$ is the excess magma pressure at the dike center. The first

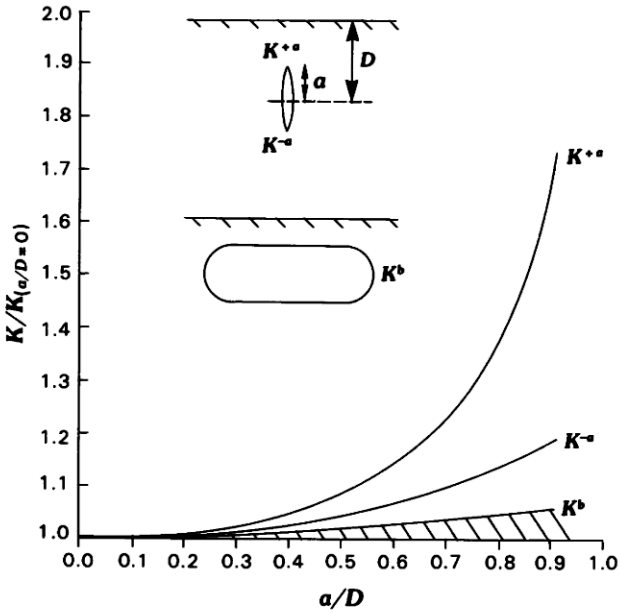


FIGURE 53.5.—Effect of proximity of the Earth's surface on the stress-intensity factors at the top ($K^{+a}$), bottom ($K^{-a}$), and downrift edge ($K^b$) of a dike subjected to a uniform driving pressure. Values of $K$ are normalized to those for a crack in an infinite body. $K^{+a}$ and $K^{-a}$ are calculated for a two-dimensional dike using the method of Pollard and Holzhausen (1979); the range of values for $K^b$ (shaded) was calculated by Shah and Kobayashi (1973) for elliptical cracks with varying ratios of $a/b$. Insets show idealized dike geometry (see fig. 53.3).

term in these equations gives the value of $K$ due to a uniform driving pressure $P_o$ (eq 4), and the second term gives the value of $K$ due to a driving pressure that varies linearly from a value of $-\nabla P_m a$ at $y = +a$ to $\nabla P_m a$ at $y = -a$ (Secor and Pollard, 1975). For a given $P_o$, a decrease in magma density increases $K^{+a}$ and decreases $K^{-a}$, thus promoting upward migration of the dike. If $P_o$ remains unchanged, a change in magma density does not alter $K^b$, because the effect of a change in magma pressure at a height $y$ above the dike center is balanced by an equal and opposite change at $-y$.

## VESICULATION

Vesiculation reduces magma density and thus reduces the magma pressure gradient within a dike. In a dike in which uniformly vesiculated magma rests on unvesiculated magma, the magma pressure above the boundary is increased, relative to a dike in which vesiculation is absent (figure 53.7*B*). The effect of this increase on dike propagation can be assessed through the use of superposition. The driving pressure in a dike with vesiculated magma above a height $y'$ is equal to that in the absence of vesiculation plus that produced by a pressure which increases linearly from a value of zero at $y'$ (fig. 53.8). The gradient of this driving pressure, $\nabla P_v$, is the difference between the pressure gradients within the vesiculated and unvesiculated magma.

The effect of vesiculation on the stress-intensity factor at the dike top, denoted as $K_v^{+a}$, can be evaluated by integrating the effects of point loads (Broek, 1982, p. 78) that give the driving-pressure distribution $\Delta P = \nabla P_v[y - y']$, where $y > y'$ (fig. 53.8). The result is

$$K_v^{+a} = f(y'/a)\nabla P_v a^{3/2}, \tag{11}$$

where $f(y'/a)$ is a function of $y'/a$ that is illustrated in figure 53.9*A* for $y'/a > 0$; that is, for vesiculation originating at or above the dike center.

The effect of the free surface on $K_v^{+a}$ as a function of $y'/a$, for $a/D = 0.86$, is shown in figure 53.9*B*. As $y'/a$ increases, the effect of the free surface diminishes, and for vesiculation occurring near the dike top it can be neglected.

The relations of the stress-intensity factors at the dike bottom, $K_v^{-a}$, and downrift edge, $K_v^b$, due to vesiculation plotted against height of vesiculation, $y'/a$, are shown in figure 53.9*C*. Both stress intensities are normalized by $K_v^{+a}$. When vesiculated magma is present only near the dike top, $K_v^{+a}$ is much greater than either $K_v^{-a}$ or $K_v^b$, and the effect of vesiculation on stress intensities at the dike bottom or downrift edge may be neglected. Thus vesiculation

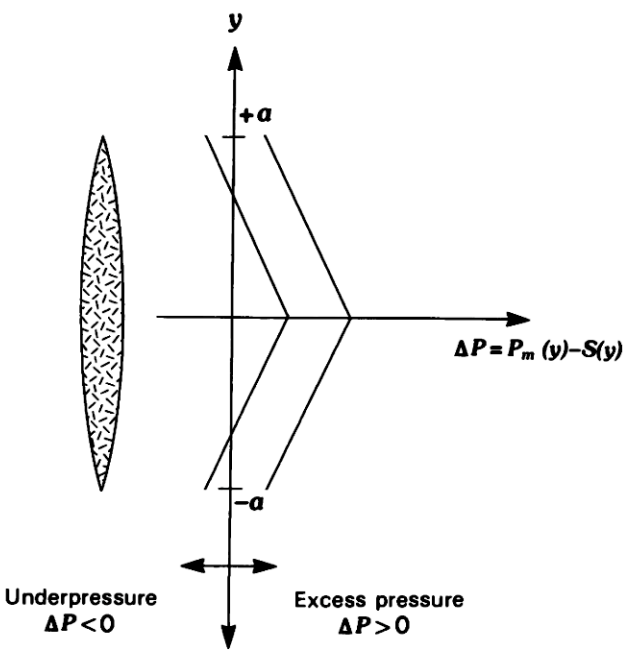


FIGURE 53.6.—Schematic diagram of two possible driving-pressure distributions that would promote the growth of blade-like dikes. If the driving pressure at the dike center is sufficiently greater than at the dike top or bottom, then $K^b > K^a$. For the right-hand curve, there is an excess pressure along the entire dike height. For the left-hand curve, the excess pressure at the dike center is sufficient to keep the dike open for its entire height, even though an underpressure acts locally at the dike top and bottom. $P_m(y)$, magma pressure: $S(y)$, remote stress; $\Delta P$, net driving pressure; $a$, dike half-height.

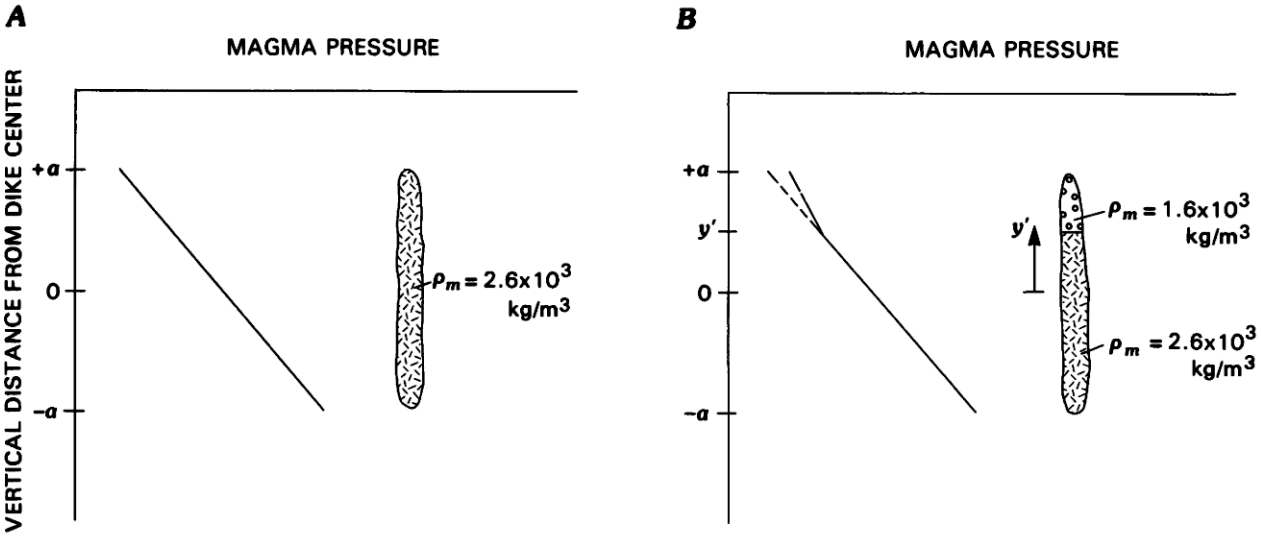


FIGURE 53.7.—Schematic diagram of vertical pressure variation in dikes. ***A***, Pressure in a dike consisting of a static column of magma of density $2.6\times10^3$ kg/m³. ***B***, Pressure in a dike consisting of a static column of magma with a density of $2.6\times10^3$ kg/m³ overlain above a height $y'$ by vesiculated magma with a density of $1.6\times10^3$ kg/m³.

promotes upward growth of the dike, while affecting downward and lateral growth relatively little. Dike thickness is similarly affected relatively little by pressure applied only near the dike top.

## VISCOUS PRESSURE LOSS

The pressure gradients within a dike during flow will deviate from those within a static body of magma. We approximate these pressure gradients by assuming laminar flow of a viscous fluid through a channel of uniform thickness. Following Bird and others (1960, p. 59) we have

$$\nabla \mathbf{P}_{m_i} = -2\frac{V_i\eta}{(t/2)^2}, \qquad (12)$$

where $\nabla \mathbf{P}_{m_i}$ is the magma-pressure gradient minus the gravitational-pressure gradient in the $x_i$ direction, $V_i$ is the velocity of the magma

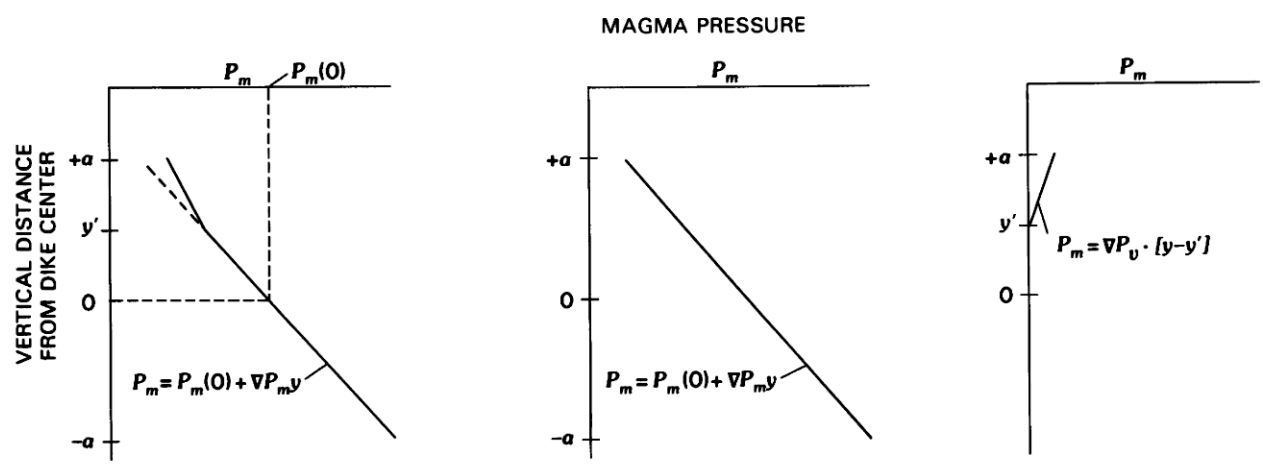


FIGURE 53.8.—The pressure within a dike containing vesiculated magma near its top (graph at left) can be expressed as a sum of the magma pressure in the absence of vesiculation (center) plus a pressure that increases linearly from the point at which vesiculation occurs (right). That pressure gradient, $\nabla P_v$, is equal to the difference in pressure gradients between the vesiculated and unvesiculated magmas.

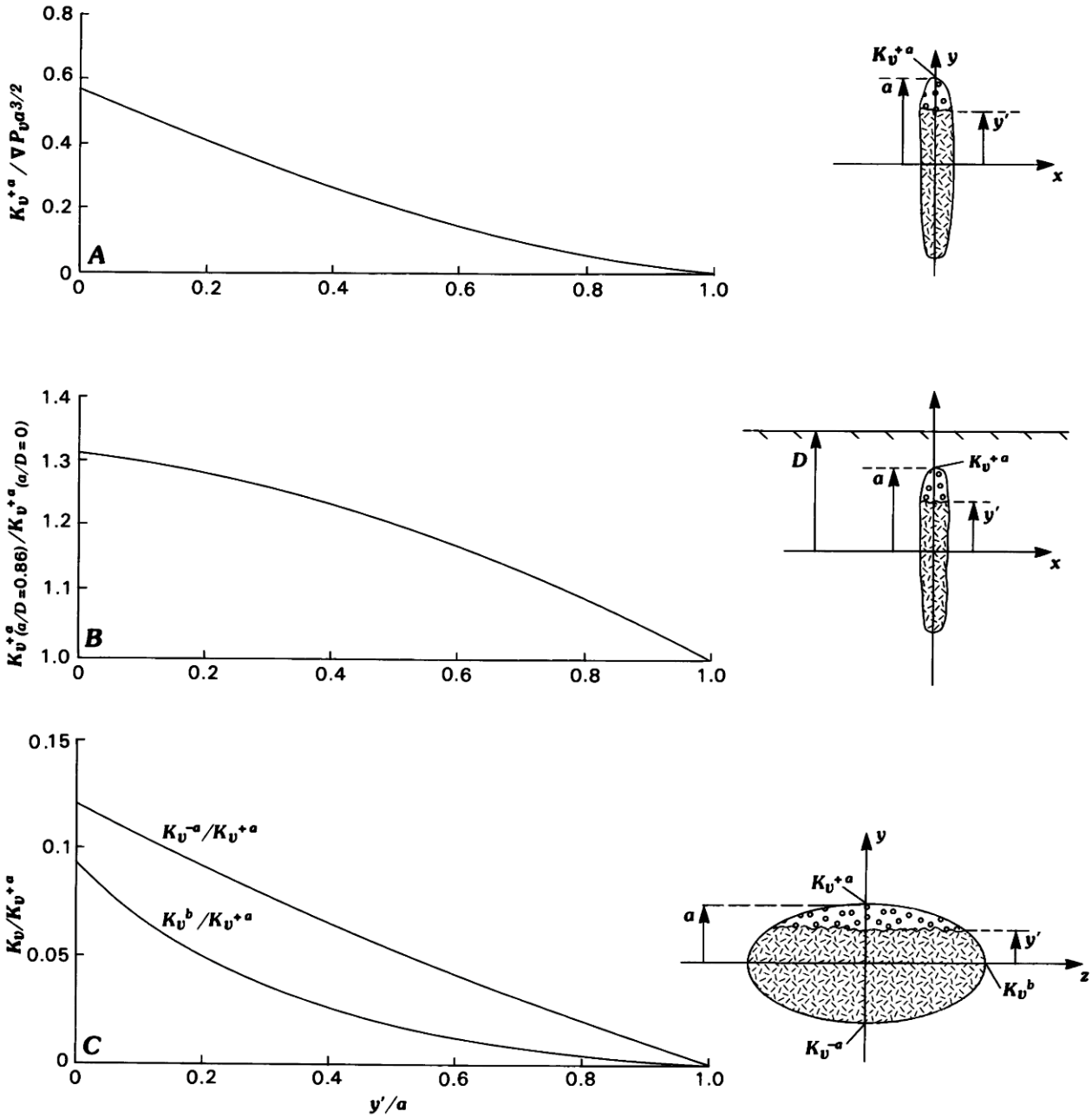


FIGURE 53.9.—Graphs showing effects of vesiculated magma in upper part of a dike. $y'$, height above dike center of base of vesiculated magma; $a$, dike half-height; $D$, depth to dike center. ***A***, Graph of the coefficient $f(y'/a)$ for obtaining the stress-intensity factor at the dike top ($K\pi\pi_v^{+a}$, eq. 11). Note that $K_v^{+a}$ decreases as the extent of vesiculation decreases. ***B***, Effect of the Earth's surface on the stress-intensity factor due to vesiculation at the dike top as a function of $y'/a$ for $a/D = 0.86$. Note that the effect of the free surface diminishes as the size of the vesiculated region decreases, and that for $y'/a > 0.8$ the free surface causes only a 10 percent or less increase in $K_v^{+a}$. ***C***, Stress-intensity factors due to vesiculation at the dike bottom ($K_v^{-a}$) and downrift edge ($K_v^b$) as a function of $y'/a$. Note that the values of $K$ normalized with respect to the stress intensity at the dike top are very small for most values of $y'/a$, so this effect may be neglected.

in the $x_i$ direction in the center of the channel, $\eta$ is the magma viscosity, and $t$ is the channel thickness.

Delaney and Pollard (1981) estimated the upward flow velocity of magma during the initiation of the 1959 Kilauea Iki fissure eruption to be 0.1 m/s. Using a typical magma viscosity of 100 Pa · s and a dike thickness of 1 m, they calculated the driving-pressure gradient for upward magma flow to be 0.05 MPa/km. This is only about 0.2 percent of the pressure gradient due to the weight of a static column of magma with a density of $2.6 \times 10^3$ kg/m$^3$ and about 1 percent of the difference in pressure gradients between a static column of magma and a column of rock with a density of $2.3 \times 10^3$ kg/m$^3$. Vertical flow rates, and therefore vertical pressure gradients due to flow, are likely to be even less for subsurface dikes. Thus we neglect vertical magma flow and relate the vertical magma-pressure gradient only to the magma density, as in figure 53.7.

Although lateral magma-pressure gradients do not enter our model explicitly, they are likely to be important in determining the site of rift-zone fissure eruptions. To estimate these gradients, we take as typical of Kilauea dikes a lateral velocity of 0.5 m/s and a thickness of 1 m (Delaney and Pollard, 1981). From equation 12, this requires a magma-pressure drop of 0.2 MPa/km. By comparison, the slopes of both the east and southwest rift zones of Kilauea are about 25 m/km. If a dike with magma of density $2.6 \times 10^3$ kg/m$^3$ travels at a constant depth within these rift zones, the decrease in elevation would lead to a magma-pressure increase at a fixed depth of about 0.65 MPa/km.

## REMOTE-STRESS DISTRIBUTION

### SOURCES OF THE REMOTE STRESS

Given the nature of the vertical pressure distribution within dikes illustrated in figure 53.7, the source of the nonlinear driving pressure distributions required for the growth of blade-like dikes (fig. 53.6) must arise from variations in the remote stress $S(y)$ acting perpendicular to the dike plane. Several possible mechanisms that could generate the required stress-versus-depth curves at Kilauea are discussed in this section.

#### CRUSTAL DENSITY

Combined seismic and gravity modeling of Kilauea and Mauna Loa indicates that the density within the upper two kilometers of these volcanoes is considerably less than that of unvesiculated magma, and that the density below is considerably greater. The density structure along a section through the Kilauea and Mauna Loa summit regions (Zucca and others, 1982) is shown in figure 53.10. The surface density of $2.3 \times 10^3$ kg/m$^3$ corresponds to an average density for vesiculated lava flows (Kinoshita and others, 1963). The density of $2.9 \times 10^3$ kg/m$^3$ at depth might represent submarine lavas (Moore and Fiske, 1969; Swanson and others, 1976), solidified intrusions (Hill and Zucca, chapter 37), or flows with vesicles now filled with hydrothermal minerals. If the state of stress in the rift zone were lithostatic and the remote horizontal stress were equal to the pressure induced by the overlying column of rock, then $S(y)$ would be of the form depicted in figure 53.6 (fig. 53.11*A*). Assuming a magma density of $2.6 \times 10^3$ kg/m$^3$, the local density contrasts between the magma and the wall rock result in a driving pressure that decreases toward the dike top and bottom at a rate of 3 MPa/km. Interpretation of the density structure of the Icelandic crust (Palmason, 1971) is also consistent with the hypothesis that local density contrast is a sufficient mechanism for the generation of blade-like dikes.

#### GRAVITATIONAL LOADING OF THE VOLCANIC RIDGE

It is commonly assumed that dikes are intruded perpendicular to the local least compressive stress (Anderson, 1938). The numerous parallel dikes and the relative scarcity of sills in eroded Hawaiian rift zones suggests that the stress perpendicular to the rift zone is consistently less compressive than both the vertical stress and the rift-parallel horizontal stress. This implies that some horizontal tensile stress is superimposed on a hydrostatic state of stress. Fiske and Jackson (1972) suggested that the source of this tensile stress is gravity loading of the volcanic edifice. They injected fluid into ridge-shaped gelatin models and produced "dikes" that propagated along the strike of the ridge with a nearly fixed height and depth, raising the possibility that this superimposed stress was not only responsible for dike orientation, but was also of the form necessary to limit their upward and downward growth.

Analyses of the gravitational stresses acting perpendicular to the axial plane of a ridge using numerical methods (McTigue and Mei, 1981) and finite-element models (James Dieterich, written commun., 1985) indicate that the stress is compressive at the surface and decreases or increases only slowly with depth. This generates a stress curve of the form that could prevent the dike top from rising (fig. 53.11*B*). However, the finite-element analysis indicates that the gelatin models were effective in containing the bottom of the propagating dike because of the great vertical exaggeration of the ridge shape and the high Poisson's ratio of gelatin (about 0.49). When realistic slopes and a Poisson's ratio appropriate for rock (about 0.25) are used, the resulting remote stress increases less rapidly than the magma pressure with depth, and barring an increase in $K_c$ with depth, dikes intruded into the rift zone would continue propagating downward and not be trapped within the upper part of the crust (fig. 53.11*B*).

#### PREVIOUSLY INTRUDED DIKES

Following magma solidification, the stresses generated in the rift zone by a dike remain. The compressive stress within the rift zone is increased to values close to the magma pressure near the dike center and decreased near the dike top and bottom (Pollard and Segall, in press). This stress distribution would encourage successive dikes to be emplaced above or below the previous one, or else far to the side (fig. 53.11*C*). Possible examples of dikes that intruded at greater depths than previous dikes include the February 1980 intrusion at Krafla (Bryndis Brandsdottir, oral commun., 1985) and the June 1982 southwest-rift-zone intrusion at Kilauea (fig. 53.1). After several intrusions, $S(y)$ would approach $P_m(y)$

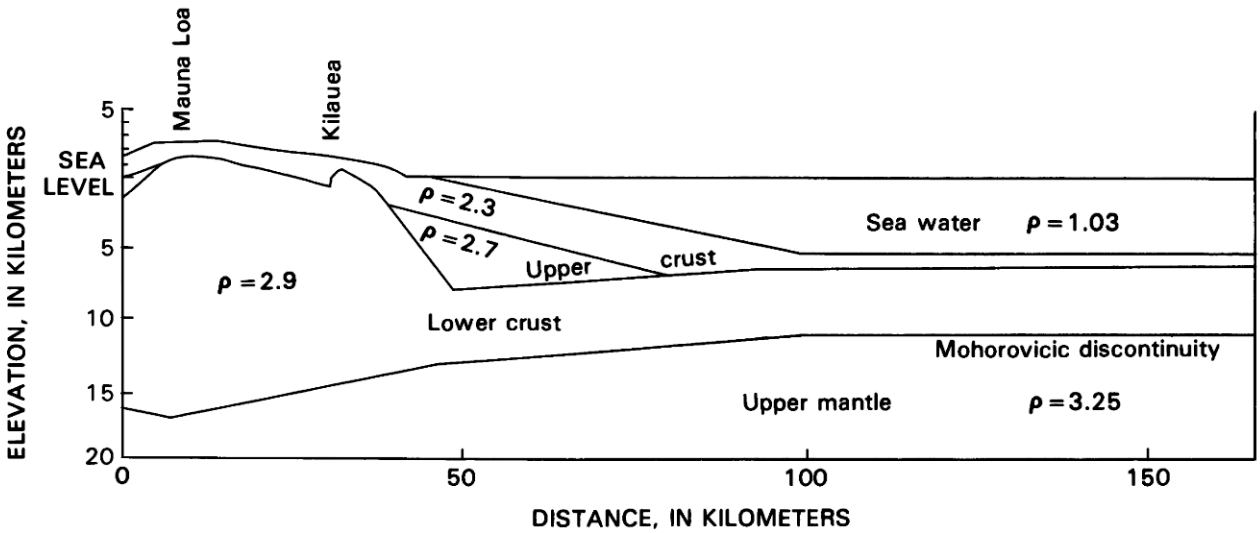


FIGURE 53.10.—Distribution of density (ρ, in $10^3$ kg/m$^3$) in a model section through Kilauea and Mauna Loa Volcanoes (after Zucca and others, 1982). The modeled increase in density from $2.3 \times 10^3$ kg/m$^3$ to $2.9 \times 10^3$ kg/m$^3$ at about 2 km beneath the surface provides a mechanism for confining both magma reservoirs and dikes to shallow depths.

throughout the rift zone, and intrusions would cease unless $P_m(y)$ increased.

### FAULTING

In order for successive dikes to be intruded into the rift zone without the magma pressure increasing monotonically through time, the rift zone must somehow behave inelastically and allow the stresses induced by dike intrusion to relax. One possible mechanism for this relaxation is slip along major faults at depth (Swanson and others, 1976). In 1975 a magnitude-7.2 earthquake occurred near Kalapana on the southeast coast of the Island of Hawaii. This earthquake seemed to have a direct effect on the intrusion-to-extrusion ratio of dikes emanating from the Kilauea magma reservoir (Klein, 1982).

James Dieterich (written commun., 1985) has modeled the stress induced by slip along a segment of a fault whose location and orientation are within the ranges inferred for the Kalapana fault. His results indicate that such motion superimposes tension within the rift zone that reaches a maximum about 3 km below the surface. This yields a driving-pressure distribution of the proper form for stabilizing a dike top and bottom (fig. 53.11*D*). The magnitude of this tension appears to be sufficient for the intrusion of only one or two overlapping dikes of average width before another major earthquake is required. The absence of frequent magnitude-7.2 earthquakes suggests that additional stress-relaxation processes may be active in the rift zone.

## ANALYSIS FOR THE REMOTE STRESS

From the principle of superposition, the driving-pressure distribution $\Delta P(y)$ depicted in figure 53.6 can be represented as the sum of a uniform driving pressure $P_o$ (equal to the excess magma pressure at the dike center) and two linearly varying driving-pressure distributions, each acting over one-half of the dike, which tend to pull the dike walls inward (fig. 53.12). The linear driving-pressure distributions are given by $\Delta P(y) = -\nabla P_u|y|$, $y > 0$, and $\Delta P(y) = -\nabla P_l|y|$, $y < 0$, where $\nabla P_u$ and $\nabla P_l$ are the gradients in the driving pressure acting on the upper and lower halves of the dike, respectively. The stress intensities produced at the top ($K^{+a}$) and bottom ($K^{-a}$) of a two-dimensional dike by these driving pressure distributions can be evaluated by superposing the solutions for cracks subjected to symmetric (Pollard, 1976) and anti-symmetric (Secor and Pollard, 1975) loads. The results are

$$K^{+a} = -\left(\frac{1}{\pi} + \frac{1}{4}\right)\nabla P_u a^{3/2}, \tag{13a}$$

$$K^{-a} = -\left(\frac{1}{\pi} - \frac{1}{4}\right)\nabla P_u a^{3/2}, \tag{13b}$$

for the pressure acting on the upper half of the dike, and

$$K^{+a} = -\left(\frac{1}{\pi} - \frac{1}{4}\right)\nabla P_l a^{3/2}, \tag{13c}$$

$$K^{-a} = -\left(\frac{1}{\pi} + \frac{1}{4}\right)\nabla P_l a^{3/2}, \tag{13d}$$

for the pressure acting on the lower half of the dike. When these equations are combined with equation 4 for a uniform driving pressure $P_o$, the stress-intensity factors for the driving-pressure distribution depicted in figure 53.12*B* are given by

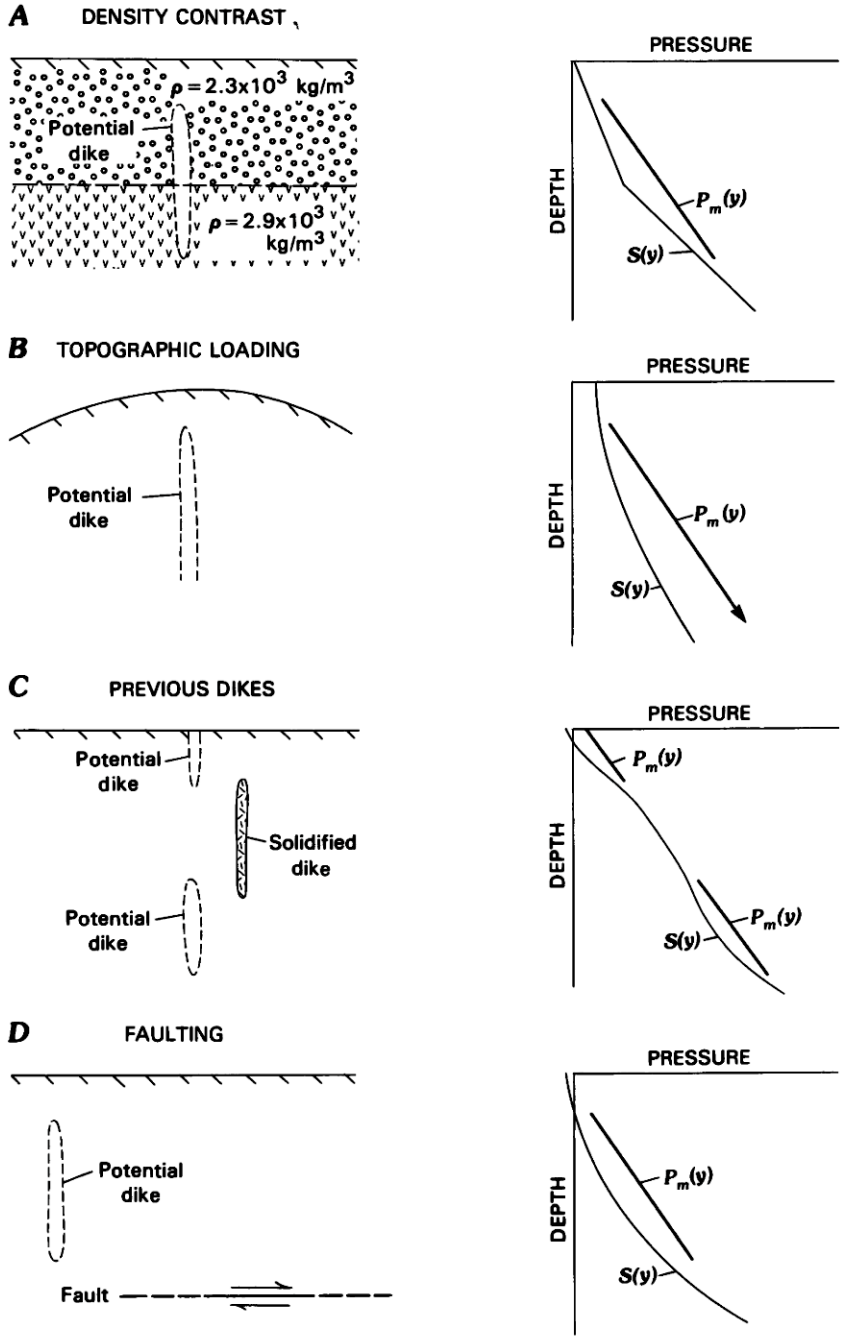


FIGURE 53.11.—Diagrams showing various mechanisms (left) and the resulting remote stress curves (right) possibly acting within a rift zone. Depths of potential dike intrusions shown. $S(y)$, remote stress; $P_m(y)$, magma pressure. ***A***, Lithostatic state of stress in a density-stratified rift zone of the type modeled by Zucca and others (1982). ***B***, Stresses due to topographic loading of the volcanic ridge, from James Dieterich (written commun., 1985). Compressive stress near the surface can prevent the dike top from propagating up, but compressive stress does not increase rapidly enough with depth to prevent the bottom from continuing to propagate down. ***C***, Stresses induced by previous intrusion of dikes. Subsequent dikes would tend to be intruded above, below, or well to the side of earlier ones. ***D***, Stresses generated by motion along a Kalapana-like fault, from James Dieterich (written commun., 1985). The depth of the maximum superimposed tension depends upon the fault dip and the location of slip.

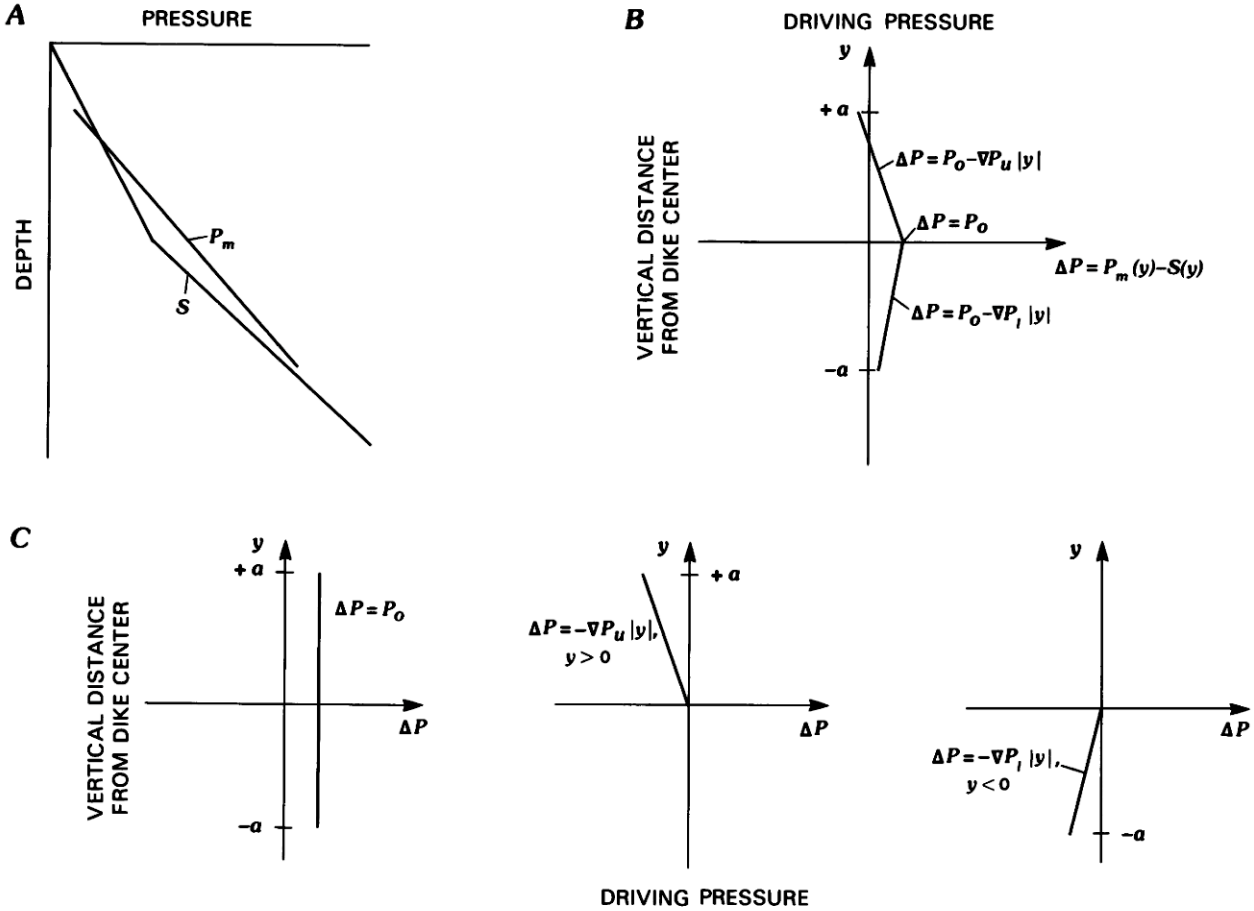


FIGURE 53.12.—Diagrams of stress distributions with depth. ***A***, Remote stress $S$ from idealized density structure (fig. 53.11*A*) and magma pressure $P_m$ caused by static weight of magma (fig. 53.7*A*). ***B***, Distribution of driving pressure $\Delta P(y)$ resulting from $P_m - S$ as depicted in ***A***. ***C***, Driving pressure in ***B*** represented as the sum of a uniform driving pressure (left) equal to the excess pressure acting at the dike center ($P_o$), and two linearly varying driving-pressure distributions ($-\nabla P_u|y|$ and $-\nabla P_l|y|$), acting over the upper and lower halves of the dike (center and right).

$$K^{+a} = P_o\sqrt{a} - \left(\frac{1}{\pi} + \frac{1}{4}\right)\nabla P_u a^{3/2} - \left(\frac{1}{\pi} - \frac{1}{4}\right)\nabla P_l a^{3/2}, \tag{14a}$$

$$K^{-a} = P_o\sqrt{a} - \left(\frac{1}{\pi} - \frac{1}{4}\right)\nabla P_u a^{3/2} - \left(\frac{1}{\pi} + \frac{1}{4}\right)\nabla P_l a^{3/2}. \tag{14b}$$

In a similar fashion, the average dike thickness is found to be

$$\bar{t} = \frac{1-\nu}{\mu}\left(\frac{\pi}{2}P_o a - 0.33\nabla P_u a^2 - 0.33\nabla P_l a^2\right). \tag{15}$$

To estimate $K^b$ at the downrift edge of the dike resulting from a driving-pressure distribution, $\Delta P = -\nabla P|y|$, acting on the upper or lower half of the dike, we calculate $K^b$ for a disc-shaped crack of radius $a$ by integrating the contributions from applied point loads (Tada and others, 1973) giving the distribution $\Delta P = -\nabla P|y|$, $0 < y < a$. The result is

$$K^b = -0.053\nabla P a^{3/2}. \tag{16}$$

The low coefficient illustrates the rather small effect such gradients have on the stress intensity at the downrift edge of the dike. Combining this with (7) for the contribution to $K^b$ from the uniform applied load, we derive

$$K^b = \frac{2}{\pi}P_o\sqrt{a} - 0.053\nabla P_u a^{3/2} - 0.053\nabla P_l a^{3/2} \tag{17}$$

for the driving pressure depicted in figure 53.12*B*.

The effect of the Earth's surface on each of the superposed boundary conditions in figure 53.12 is presented as a function of $a/D$ in figure 53.13*A*. This graph can be thought of as providing correction factors to equation 14 to be used when superposing solutions for particular values of $a/D$. For a given $a/D$, the contribution to $K^{+a}$ or $K^{-a}$ from a particular term in equation 14

should be multiplied by the ordinate of the curve in figure 53.13 corresponding to that term. Because $K^b$ is not very sensitive to $a/D$ (fig. 53.4), its value in an infinite body will be used. An equivalent graph for average dike thickness is presented in figure 53.13*B*.

### SUMMARY OF THE FACTORS AFFECTING DIKE PROPAGATION

We have discussed various parameters that are important to the dike propagation process and, through the calculation of the stress-intensity factors $K^a$ and $K^b$, have analyzed their effects on lateral and vertical propagation. A blade-like dike shape and the presence of the Earth's surface both enhance upward propagation and eruption relative to lateral propagation. Observation of continued subsurface lateral propagation requires the dike driving pressure to be such that it overcomes these geometric effects. A driving pressure that is greater at the dike center than at the dike top and bottom could satisfy this condition. Since the pressure gradient within a column of unvesiculated magma is uniform, and since vesiculation increases the driving pressure only at the dike top, the origin of this driving pressure must be the remote stress. Processes that could contribute to the required remote-stress distribution at Kilauea include density stratification of the rift zone, gravitational loading, previously intruded dikes, and slip along faults.

Equations 14a, 14b, 17, and 15 were developed to calculate the stress-intensity factors at the dike top, bottom, and downrift edge, and the average dike thickness, for a driving pressure that is greatest at the dike center and decreases linearly toward the top and bottom. These equations can be corrected for the effect of the free surface using the graph in figure 53.13. The stress-intensity factor at the dike top (eq 14a) can be modified to include the effects of vesiculation (eq 11), but the effect of the free surface on equation 11, and the effect of vesiculation on equations 14b, 15, and 17 can be neglected. In the following section we show how these equations may be applied to analyze a rift-zone intrusion.

## APPLICATION TO THE INTRUSIVE EVENT OF AUGUST 1981

The above analysis makes it possible to estimate the magma pressure and the horizontal remote-stress distribution acting perpendicular to the rift axis for particular dikes whose geometry is known. We begin by assuming that the magma is unvesiculated, so that the magma pressure variation with depth is given by a line segment of constant slope. We also assume that the remote stress can be adequately represented by two linearly varying line segments (fig. 53.12), each of which acts on one-half of the dike. In general, a dike center is not constrained to be positioned at a kink in the stress distribution. Nevertheless, useful insight into the nature of the driving pressure distribution is obtained by employing this assumption. We assume that $K_c$ is independent of depth, so that $K^{+a} = K^{-a} = K_c$ at the moment the dike ceases to propagate in the vertical direction. Finally, we assume that the shape of the dike determined using geodetic data collected after the cessation of intrusive activity is approximately the shape of the dike when it attained its maximum height.

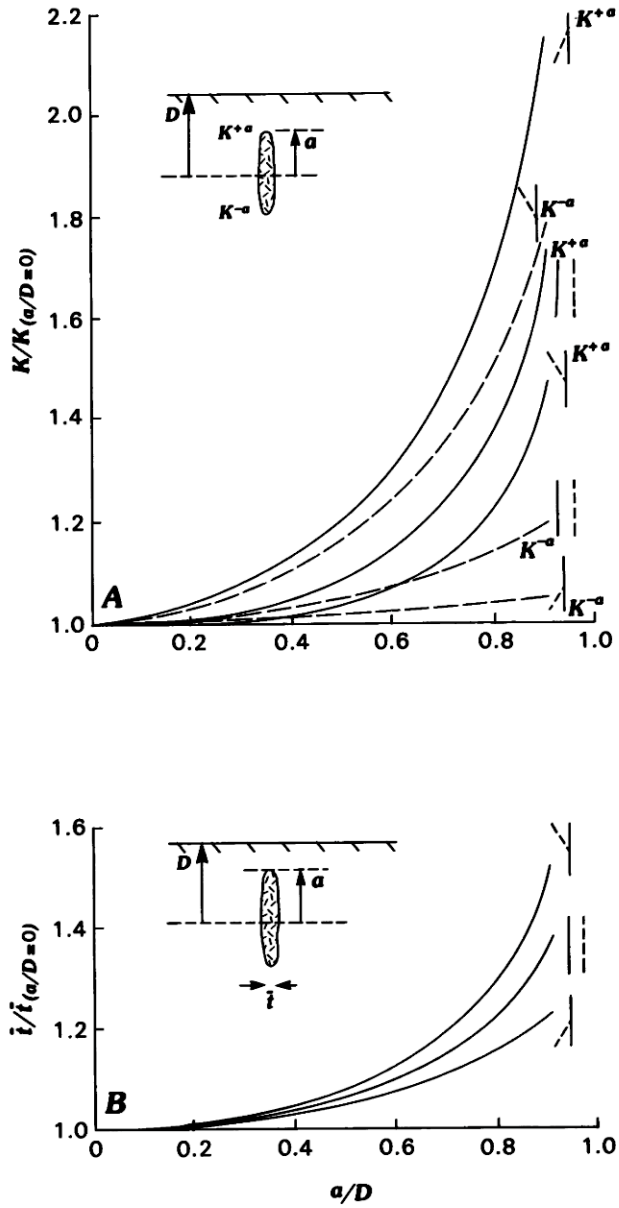


FIGURE 53.13.—Diagrams showing effect of proximity of the Earth's surface on stress-intensity factors and average dike thickness. ***A***, Effect of the Earth's surface on stress-intensity factors at the dike top (solid lines) and bottom (dashed lines) as a function of $a/D$ for components of the driving pressure in fig. 53.12*C*, identified by the schematic diagrams to the right. ***B***, Effect of the Earth's surface on average dike thickness as a function of $a/D$ for components of the driving pressure in fig. 53.12*C*.

In August 1981 a dike approximately 25 km long was intruded into the southwest rift zone of Kilauea (fig. 53.1). From geodetic

data, Pollard and others (1983) estimated a dike half-height of 1.5 km, a depth of 1.75 km, an average thickness of 1.4 meters, and a dip of 82°. Although difficulty was encountered in reproducing the displacement data for the southeast half of the profile using the elastic model, we use these geometric parameters for our analysis. Abundant ground cracks that formed above the dike are good evidence for a shallow dike top; in combination with the large ratio of $a/D$, they indicate that interaction of the dike with the free surface should be included. We ignore the dip of the dike, which alters neither the gradients in driving pressure nor the free-surface correction by more than 1–2 percent.

Using figure 53.13 and a value for $a/D$ of 0.86 to obtain the free-surface correction factors for equations 14 and 15, we have

$$K^{+a} = 1.52P_o\sqrt{a} - 1.31\left(\frac{1}{\pi}+\frac{1}{4}\right)\nabla P_u a^{3/2} - 1.86\left(\frac{1}{\pi}-\frac{1}{4}\right)\nabla P_l a^{3/2}, \quad (18a)$$

$$K^{-a} = 1.17P_o\sqrt{a} - 1.63\left(\frac{1}{\pi}-\frac{1}{4}\right)\nabla P_u a^{3/2} - 1.05\left(\frac{1}{\pi}+\frac{1}{4}\right)\nabla P_l a^{3/2}, \quad (18b)$$

$$\bar{t} = \frac{1-\nu}{\mu}\left(1.29\frac{\pi}{2}P_o a - 1.39(0.33)\,\nabla P_u a^{\,2} - 1.19(0.33)\nabla P_l a^2\right). \quad (19)$$

Setting $K^{+a} = K^{-a}$, we find

$$\nabla P_l a = 1.34\nabla P_u a - 0.74P_o, \quad (20)$$

which we then substitute for $\nabla P_l a$ in equations 17 through 19. To restrict the range of values of $P_o$ and $\nabla P_u$, we first use the requirement that $K^a > 0$. From equation 18a we find

$$P_o > 0.57\nabla P_u a. \quad (21)$$

Next we use the requirement that $K^a < K^b$ for a dike with a stable height but a propagating downrift edge; using equations 17 and 18a, we find

$$P_o < 0.84\nabla P_u a. \quad (22)$$

Limiting remote stress and magma pressure curves for a dike with a half-height of 1,500 m and a depth of 1,750 m are shown in figures 53.14*A* and 53.14*B*. The magma has a density of $2.6\times10^3$ kg/m$^3$ and thus an internal pressure gradient of 26 MPa/km. We specify that the remote stress has a value of zero at the surface. The gradient of the driving pressure acting on the upper half of the dike in figure 53.14*A* is 3 MPa/km, or approximately that generated by the local density contrast between the magma and the wall rock. Modeling by James Dieterich (written commun., 1985) indicates that both gravity loading and slip on a master fault at depth superimpose tensile stresses that increase with depth in the upper few kilometers of the volcano, so 3 MPa/km is likely to be a lower limit for this gradient. The gradient of the driving pressure acting on the upper half of the dike in figure 53.14*B* is 11 MPa/km. We show below that this is an upper limit if the hydrostatic head of the magma is higher than 350 m below the surface. The remote stress acting on the lower half of the dike in figure 53.14 is the average of the relatively narrow range of $\nabla P_l$ obtained from equation 20 and the constraint that $P_o$ be in the range 0.57–0.84 $\nabla P_u a$.

The left-hand magma-pressure curve in figure 53.14*A* corresponds to $P_o = 0.57\,\nabla P_u a$ (eq 21), and the right-hand curve to $P_o = 0.84\,\nabla P_u\, a$ (eq 22). A $P_o$ less than the former would produce a $K^a$ less than zero, in which case the dike could not have propagated to its required height, and a $P_o$ greater than the latter would violate the requirement that $K^a < K^b$. Allowable magma-pressure curves for this value of $\nabla P_u$ therefore lie between the limits indicated. The horizontally exaggerated cross-sectional forms resulting from these two driving-pressure distributions are shown in the upper right of figure 53.14*A*. In figure 53.14*B*, the lower magma-pressure curve has a hydrostatic head beneath the dike top, and so equations 17–19 do not apply. To treat this case, we assume that unvesiculated magma rises to its hydrostatic head and is capped by a near vacuum. We obtain $y'$, calculate $K_v^{+a}$ (eq 11), and include this term in the calculation of $K^{+a}$ (eq 18a). Because of the small effect on $K^{-a}$, $K^b$, and $\bar{t}$, equations 17, 18b, and 19 need not be modified.

The limiting magma-pressure curves in figures 53.14*A* and 53.14*B* require knowledge only of the dike height and depth. In order to restrict the magma-pressure range further, additional constraints are needed. Associated with each magma-pressure curve is a value for $K^a$ and, given a value for the rock stiffness, an average dike thickness. These are indicated in figure 53.14. Magma-pressure curves generating values of $K^a$ equal to those for $K_c$ determined in the laboratory are essentially indistinguishable from those generating a $K^a$ of zero. Note that the right-hand magma-pressure curve in figure 53.14*B* is greater than our upper limit of 100 MPa · m$^{1/2}$. The low values of dike thickness are calculated using laboratory determinations of the shear modulus (30 GPa), and the high values are calculated using estimates of the effective shear modulus from piezomagnetic measurements at Kilauea (3 GPa) (Davis, 1976). Note that the lower values of dike thickness are well below the value of 1.4 m estimated for the 1981 intrusion for each driving-pressure distribution shown.

A summary plot of the driving pressure at the dike center, $P_o$, versus the product of the gradient in driving pressure and the dike half-height, $\nabla P_u a$, is presented in figure 53.15. The wedge-shaped region (red lines) bounded by $P_o = 0.57\ \nabla P_u a$ (eq 21) and $P_o = 0.84\,P_u\, a$ (eq 22) contains all values of $P_o$ and $\nabla P_u\, a$ that are consistent with observed dike-propagation behavior. Points lying below the lower red boundary are unacceptable because the dike could not have propagated to a half-height of 1,500 m, and those lying above the upper red boundary are unacceptable because the dike would have continued propagating vertically and possibly would have erupted. For a given dike height, thickness, and depth, the wedge-shaped region can be contoured for values of the fracture

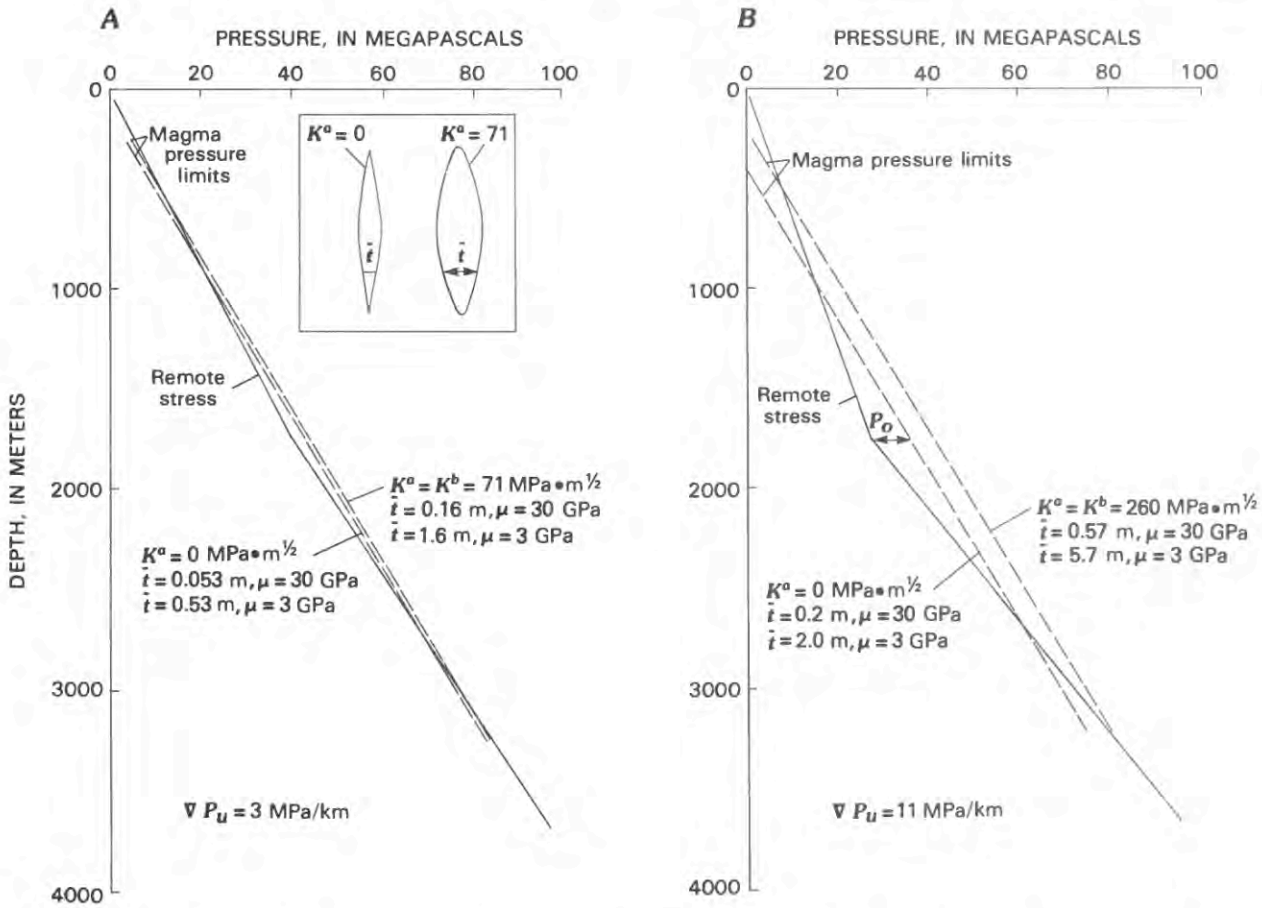


FIGURE 53.14.—Limiting remote-stress and magma-pressure curves for a dike with a height of 1,500 m and a depth of 1,750 m. The magma has a density of $2.6 \times 10^3$ kg/m$^3$. The remote stress is constrained to have a value of zero at the surface. The range of allowable values of $P_o$ is given by the left and right magma pressure curves in each diagram. For any lower $P_o$, $K^a < 0$; for any higher $P_o$, $K^a > K^b$. Each magma-pressure curve is associated with a value of $K^a$, and, given a value for the shear modulus, an average dike thickness. The average dike thicknesses indicated are for shear moduli of 3 and 30 GPa. The higher shear modulus predicts thicknesses too narrow (<1.4 m). ***A***, Curves for $\nabla P_u = 3$ MPa/km. The inset shows the horizontally exaggerated cross-sectional forms of dikes generated by the limiting magma-pressure curves. ***B***, Curves for $\nabla P_u = 11$ MPa/km. $K^a$ for the right-hand curve is greater than our upper limit for $K_c$ of 100 MPa · m$^{1/2}$.

toughness, rock stiffness, and hydrostatic head of the magma column. These contours will be used to further constrain the driving pressure.

Substituting equation 20 into equation 19 and rearranging yields

$$P_o = 0.42 \nabla P_u a + 0.43 \frac{\bar{t}}{a} \frac{\mu}{(1-\nu)}. \qquad (23)$$

Thus contours of the dike thickness-to-height ratio times the rock stiffness are straight lines. For $a = 1{,}500$ m, $\bar{t} = 1.4$ m, and $\nu = 0.25$, these lines become contours of the shear modulus, $\mu$. Contours for values of $\mu$ of 1.5 GPa, 3 GPa, and 6 GPa are shown.

Substituting equation 20 into equation 18a and rearranging yields

$$P_o = 0.57 \nabla P_u a + 0.62 \frac{K^{+a}}{\sqrt{a}}. \qquad (24)$$

Thus contours of $K^{+a}$ divided by the square root of the dike half-height are also straight lines; on figure 53.15, these contours are parallel to the lower boundary of the wedge-shaped region, for which $K^a = 0$. Contours of the lower and upper limits for $K_c$, 0 and 100 MPa · m$^{1/2}$, are shown. If laboratory values ($K_c \approx 1$ MPa · m$^{1/2}$) represent the upper bound, the stress would be constrained to lie near the lower boundary of the wedge-shaped region.

From figure 53.14, one can derive that the magma pressure in the center of the dike is

$$P_m(0) = D(\rho_m g - \nabla P_u) + P_o, \qquad (25)$$

where $D$ is the dike depth and $\rho_m$ is the magma density. The height above the dike center to which a column of unvesiculated magma can be raised is $P_m(0)/\rho_m g$, so the hydrostatic head C is

$$C = -D + \frac{D(\rho_m g - \nabla P_u) + P_o}{\rho_m g}. \qquad (26)$$

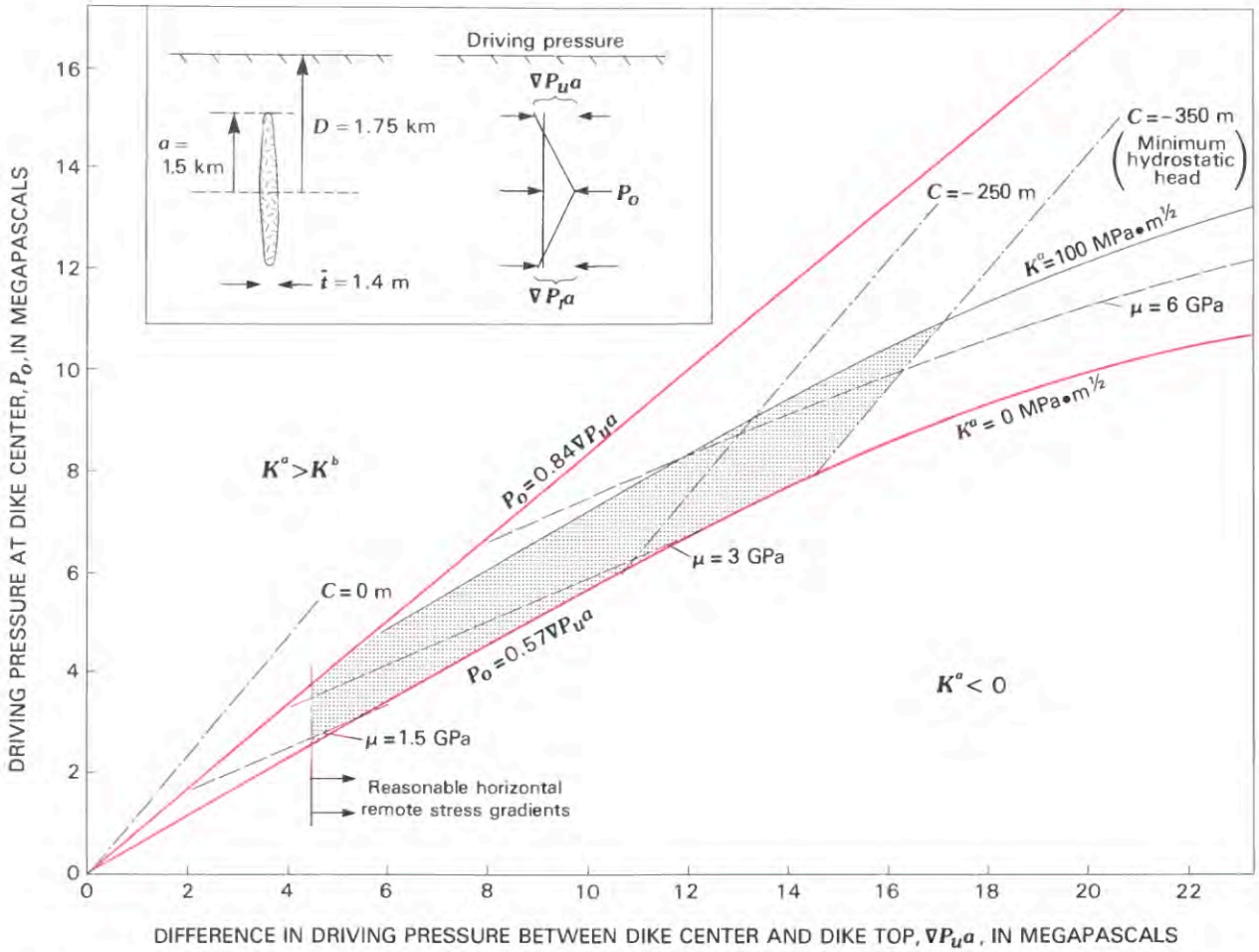


FIGURE 53.15.—Possible values of $P_o$ and $\nabla P_u a$ (wedge-shaped region between red lines) for the August 1981 southwest-rift-zone intrusion at Kilauea, the inferred geometry of which is shown in the inset. Values below the lower red boundary are unacceptable because $K^a < 0$; values above the upper red boundary are unacceptable because values of $K^a$ (eq 24), the hydrostatic head of the magma, C (eq 27), and the shear modulus that would result in an average dike thickness of 1.4 m (eq 23). Values within the stippled region satisfy the requirements that $K^a < K^b$, $0 < K^a < 100$ MPa · m$^{1/2}$, $\nabla P_u \geq 3$ MPa/km, and $C > -350$ m (see text).

Rearranging equation 26, we have

$$P_o = \frac{D}{a} \nabla P_u a + \rho_m g C . \qquad (27)$$

Thus contours of the hydrostatic head are also straight lines on figure 53.15 and have a slope of $D/a$. For $D/a = 1.17$ ($a/D = 0.86$), any dike that has a hydrostatic head above the ground surface (to the left of contour $C = 0$, figure 53.15) fails to satisfy the requirement that $K^a < K^b$. Such a dike would grow in height (increase $\nabla P_u a$ at constant $P_o$ in figure 53.15), and finally erupt.

To the right of the $C = -250$ m contour, the wedge-shaped region has been modified to account for the low-pressure cavity between the top of the magma and the dike tip. Instead of being linear, contours of $\mu$ and $K$ deviate slightly toward lower values of $P_o$. Setting $C > -350$ m, we find that acceptable values of $P_o$ and $\nabla P_u a$ are limited to below about 10.5 MPa and 17 MPa, respectively.

The lower limit on the gradient in driving pressure, $\nabla P_u \geq 3$ MPa/km, becomes $\nabla P_u a \geq 4.5$ MPa for $a = 1{,}500$ m.

The stippled region in figure 53.15 contains all values of $P_o$ and $\nabla P_u a$ satisfying the conditions that $K^a < K^b$, $0 < K^a < 100$ MPa · m$^{1/2}$, $C > -350$ m, and $\nabla P_u \geq 3$ MPa/km. $P_o$, the excess magma pressure at the dike center, lies between about 2.5 and 10.5 MPa. The upper bound of the hydrostatic head, occurring for $\nabla P_u a = 4.5$ MPa and $P_o = 4$ MPa, is about 50 m beneath the surface. $\nabla P_u a$ lies between 4.5 and 17 MPa, corresponding to

values of $\nabla P_u$, the difference between gradients of the magma pressure and the remote stress, of 3–11 MPa/km. This is between 1 and 4 times the difference in pressure gradients due to the density contrast between the magma and the host rock. Thus, the remote stress is bracketed by the curves shown in figures 53.14*A* and 53.14*B*. Without further refinement of the in place values of the rift-zone shear modulus and fracture toughness, it is not possible to determine these parameters more precisely. The limits of the stippled region constrain the effective shear modulus to be within a factor of 2–3 of 3 GPa. By generating diagrams such as figure 53.15 for several intrusions with different dike heights, thicknesses, and ratios of height to depth, it might be possible to constrain the shear modulus still further.

## DISCUSSION

### ASSUMPTION OF A UNIFORM FRACTURE TOUGHNESS

The assumption of a uniform fracture toughness within the rift zone requires that the remote stress and the magma pressure converge with depth over the lower half of the dike ($\nabla P_l > 0$) (fig. 53.14). If $K_c$ increaeses with depth, then $\nabla P_l$ could decrease to values below those indicated. The magma-pressure and remote-stress curves could actually diverge with increasing depth, if the increase in $K_c$ is sufficiently great and its value is much greater than laboratory values. From experimental data it appears that, in the absence of a pervasive pore fluid at a pressure equal to the confining pressure, $K_c$ increases with depth because of increasing pressure. Although its effect is small, increasing temperature will actually decrease $K_c$ with depth, at least to moderate temperatures. There is no evidence to support a rapid increase in $K_c$ at pressures and temperatures corresponding to depths typical of dike bottoms.

A sequence of two dike intrusions into the southern Krafla rift zone in Iceland is instructive in this regard. The first, in September 1977, generated a swarm of earthquakes with focal depths of about 2–5 km (Brandsdottir and Einarsson, 1979), and the second, in February 1980, generated earthquakes with depths of about 4–7 km (Bryndis Brandsdottir, oral commun., 1985). On the assumption that the deeper earthquake swarm is indicative of a deeper dike, this behavior is consistent with the location of the second dike being controlled by the stress field induced by the first (fig. 53.11*C*). In addition it provides evidence that any increase in $K_c$ with depth that might have stabilized the bottom of the earlier dike was not great enough to serve as a barrier to the later dike, and that the bottom of the earlier dike was well within a region capable of sustaining brittle behavior.

If some dikes on the east rift zone of Kilauea bottom within a magma conduit of high temperature and large radius of curvature, then an increase in $K_c$ (because of microplasticity), as well as a decrease in $K$ (because of a large radius of curvature at the dike tip) could result. Such a conduit might serve as an effective barrier to further propagation of the dike bottom.

### OTHER FACTORS THAT MIGHT INFLUENCE DIKE SHAPE

In the preceeding treatment of dike stability, it was assumed that the dike had achieved an equilibrium position in the vertical plane. In the following sections we discuss factors related to magma solidification and flow which could influence dike growth and prevent the dike from reaching such an equilibrium position. Though some of these processes may warrant further study, we explain why they have been neglected in this analysis.

#### MAGMA SOLIDIFICATION

Walker (1974) suggested that low wall-rock temperatures near the Earth's surface could promote magma solidification near the top of a dike and thus prevent eruption. For magma to solidify at approximately the same height as it propagates many kilometers downrift implies that very little heat loss occurs during lateral flow, compared to the heat loss that occurs during upward flow. Following the work of Delaney and Pollard (1982), we estimated the effect of host-rock temperature on the time required for magma solidification during flow in a dike. Even if upward flow occurs entirely adjacent to host rock at the low temperatures appropriate for the dike top, magma originating at a depth of 3 km has less difficulty in flowing to the surface than in flowing 10 km downrift, given a uniform dike thickness and magma flow rate. Under these circumstances, solidification should not be important in stabilizing the dike top. However, if the driving-pressure distribution is such that the dike is thinner in its upper part, and if the resulting magma velocity is less than at depth, the possibility that magma solidification occurs before the dike reaches its stable height cannot be ruled out.

The following observations of dike behavior support our contention that magma solidification, by itself, is unlikely to limit dike height: (1) Fissures that erupt generally permit magma flow to continue for several hours before solidification takes place. (2) Long-term patterns of intrusion and eruption observed at both Kilauea and Krafla (see below) are easily reconciled with evolving magma pressures and remote stresses. The alternative interpretation of this behavior as due to changing susceptibility of the magma to solidification finds no independent support. (3) At least one dike, the February 1980 intrusion into the southern Krafla rift zone, was associated with an earthquake swarm whose top was deeper than 3 km. This depth is below that at which solidification might influence propagation.

#### TWO-DIMENSIONAL MAGMA FLOW

If dike growth in two dimensions is analogous to the pumping of magma at constant pressure into the base of an existing vertical slot in the Earth's crust, then lateral growth will be enhanced relative to upward growth because the pressure gradient available for upward flow is reduced by the static pressure gradient within the overlying column of magma. If this tendency is sufficiently pronounced it could

prevent dikes from reaching their equilibrium height before solidification. To estimate the significance of this effect, we compared the upward and lateral rates of one-dimensional magma flow in a slot, under the conditions of constant pressure at the origin and zero pressure at the advancing magma front. The upward flow rate is not greatly decreased relative to the lateral flow rate until the top of the magma column approaches its hydrostatic head. The hydrostatic head as a limit to the magma column height can be incorporated directly into the analysis of dike stability, as it was for the example of the August 1981 intrusion. A more complete formulation of the one-dimensional dike propagation problem than flow in an existing slot was proposed by Spence and Turcotte (1985). They assumed that the magma wets the dike walls all the way to the tip and coupled the viscous pressure loss within the magma to the elastic dilation of the dike walls. If the remote horizontal compressive stress is constant at a given depth but increases with depth at the same rate as the hydrostatic pressure in the magma column, then vertical and horizontal flow rates would be equal. Although it is not expected that the remote stress and the magma pressure increase identically with depth, the rates of increase are probably close enough that the influence of gravity on the relative vertical and horizontal magma flow rate is minimal. Therefore we feel justified in neglecting the complexities of two-dimensional magma flow in rift-zone dikes as a mechanism for preventing them from attaining their equilibrium height.

### SUBCRITICAL CRACK GROWTH

In a chemically reactive environment, the energy required for a unit increase in crack length, and thus $K_c$, may be decreased. Rates of crack propagation under these conditions are controlled in part by the rate of transport of the reactive species to the crack tip and the kinetics of reaction. Anderson and Grew (1977) suggested that this process, known as subcritical crack growth, might be an important mechanism of dike propagation. However, maximum rates of subcritical crack growth in laboratory rock samples are $10^{-2}$–$10^{-3}$ m/s (Atkinson, 1984), about two orders of magnitude less than observed rates of rift-zone dike propagation. Moreover, these rates decrease by several orders of magnitude for small decreases in $K$. Therefore we have neglected this form of crack growth in our analysis. It is possible that subcritical growth occurs at the top and bottom after a dike has reached a stable height. However, the greatest distance that a typical 1-meter dike could propagate at these rates in the few hours before solidification is only about 100 m.

## POTENTIAL APPLICATIONS OF THE MODEL

### LONG-TERM INTRUSION/EXTRUSION BEHAVIOR

Klein (1982) noted that five of the seven dike intrusions at Kilauea within the 4 years prior to the 1975 Kalapana earthquake resulted in eruptions, whereas only two of the sixteen dike intrusions in the 6 years following the earthquake did so. The two most recent episodes of activity at Krafla, from 1724 to 1729 and from 1975 to the present, began with a series of predominantly subsurface dikes accompanied by either minor eruptions or none, and ended with a series of fissure eruptions emitting successively increasing volumes of magma (Tryggvason, 1983; Saemundsson, 1979). This behavior is consistent with the hypothesis that large earthquakes at Kilauea (Dzurisin and others, 1980; Klein, 1982), and centuries of plate spreading in Iceland (Bjornsson and others, 1979) extend the rift zone and facilitate dike intrusion. The preceding analysis has shown that, independent of the magnitude of the remote tensile stress, a shallow dike with a hydrostatic head above the Earth's surface should erupt. Thus the magma reservoir pressure probably decreased following the 1975 Kalapana earthquake at Kilauea and increased over the course of the activity at Krafla. This conclusion is supported by the record of long-term magma reservoir inflation from 1975–1984 at Krafla (Bjornsson, 1985), and by combined geodetic and gravity data at Kilauea (Johnson, chapter 47). We emphasize that both the remote stress and the magma pressure must be considered in developing models of rift-zone dynamics.

### IMPLICATIONS FOR MAGMA RESERVOIR BEHAVIOR

The August 1981 southwest-rift-zone intrusion at Kilauea resulted in a net summit tilt of −100 mrad, about −50 mrad of which occurred following the passage of the earthquake swarm beneath the geodetic level line. Using the calculation of Decker and others (1983), −50 mrad corresponds to a pressure drop of about 4 MPa, which is a large percentage of the estimated maximum excess pressure of 3–11 MPa within the dike ($P_o$ in figure 53.15). If the rift zone behaves elastically, such a decrease in $P_o$ should be reflected by a decrease in dike thickness and possibly in dike height (if $K^a$ drops below zero) of sufficient magnitude to be measured geodetically. Installation of a line of continuously recording deformation meters perpendicular to the rift zone might allow observations of these changes, which in turn could be used to estimate the change in reservoir pressure.

### ALONG-STRIKE VARIATION OF DIKE GEOMETRY

In addition to magma pressure variation with time, the magma pressure at a given depth within a dike increases with downrift distance because of the slope of the rift zones, and decreases with downrift distance because of viscous pressure loss. The balance between these two factors might be reflected in the locations of fissure eruptions, and in along-strike variations in dike height and thickness that could be measured geodetically. These observations might be useful in further constraining the remote stress field, because the sensitivity of the dike thickness and height to changes in magma pressure are dependent upon the gradient in the driving pressure (fig. 53.16). For example, a dike is more likely to maintain a fairly constant thickness and height for tens of kilometers if the gradients of

the superimposed remote tensile stress acting on the rift zone are large, as in figure 53.16*B*. Thus, it seems likely that data constraining temporal and spatial variations in dike geometry could significantly enhance our understanding of rift-zone dynamics.

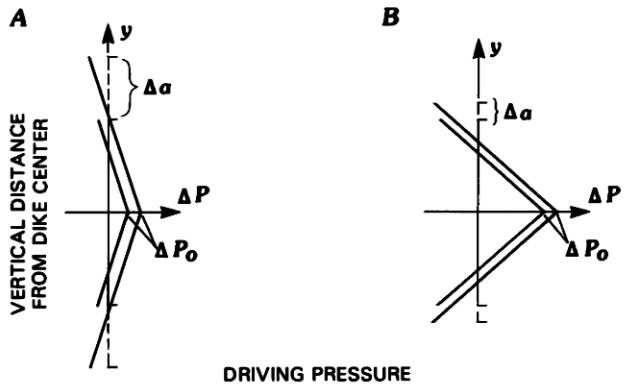


FIGURE 53.16.—Schematic diagrams illustrating the change in dike half-height for a given change in magma pressure. $K_c$ is taken to be zero. ***A***, $P_o = 3$ MPa; ***B***, $P_o = 11$ MPa. For a 2-MPa increase in magma pressure $\Delta P_o$, the dike in ***A*** increases in half-height by a factor of 1.67; that in ***B*** increases by a factor of only 1.18. The dike thicknesses increase as the square of these factors, or by factors of 2.8 and 1.4, respectively.

## REFERENCES CITED


Anderson, E.M., 1938, The dynamics of sheet intrusion: Royal Society of Edinburgh Proceedings, Series B, v. 58, p. 242-251.

Anderson, O.L., and Grew, P.C., 1977, Stress corrosion theory of crack propagation with application to geophysics: Review of Geophysics and Space Physics, v. 15, p. 77-104.

Atkinson, B.K., 1984, Subcritical crack growth in geologic materials: Journal of Geophysical Research, v. 89, p. 4077-4114.

Bieniawski, Z.T., 1978, Determining rock mass deformability: experience from case histories [abs.]: International Journal of Rock Mechanics, Mineral Science and Geomechanics, Abstracts, v. 15, p. 237-247.

Birch, F., 1966, Compressibility; elastic constants, *in* Handbook of Physical Constants: Geological Society of America Memoir 97, p. 97-173.

Bird, R.B., Stewart, W.E., and Lightfoot, E.N., 1960, Transport phenomena: New York, John Wiley & Sons, 780 p.

Bjornsson, A., 1985, Dynamics of crustal rifting in NE Iceland: Journal of Geophysical Research, v. 90, p. 10,151-10,162.

Bjornsson, A., Johnsen, G., Sigurdsson, S., Thorbergsson, G., and Tryggvason, E., 1979, Rifting of the plate boundary in north Iceland 1975–1978: Journal of Geophysical Research, v. 84, p. 3029-3038.

Brandsdottir, B., and Einarsson, P., 1979, Seismic activity associated with the September 1977 deflation of Krafla Volcano in north-eastern Iceland: Journal of Volconology and Geothermal Research, v. 6, p. 197-212.

Broek, D., 1982, Elementary Engineering Fracture Mechanics: Boston, Martinus Nijhoff Publishers, 469 p.

Broyles, M.L., Suyenaga, W., and Furumoto, A.S., 1979, Structure of the lower east rift zone of Kilauea Volcano, Hawaii, from seismic and gravity data: Journal of Volconology and Geothermal Research, v. 5, p. 317-336.

Davis, P.M., 1976, The computed piezomagnetic anomaly field for Kilauea Volcano, Hawaii: Journal of Geomagnetism and Geoelectricity, v. 28, p. 113-122.

Decker, R.W., Okamura, A.T., and Dvorak, J.G., 1983, Pressure changes in the magma reservoir beneath Kilauea Volcano, Hawaii: Eos (American Geophysical Union Transactions), v. 64, p. 901.

Delaney, P., and Pollard, D.D., 1981, Deformation of host rocks and flow of magma during growth of minette dikes and breccia-bearing intrusions near Ship Rock, New Mexico: U.S. Geological Survey Professional Paper 1202, 61 p.

———1982, Solidification of basaltic magma during flow in a dike: American Journal of Science, v. 282, p. 856-885.

Delaney, P.T., Pollard, D.D., Ziony, J.I., and McKee, E.H., in press, Field relations between dikes and joints: emplacement processes and paleostress analysis: Journal of Geophysical Research.

Dzurisin, D., Anderson, L.A., Eaton, G.P., Koyanagi, R.Y., Lipman, P.W., Lockwood, J.P., Okamura, R.T., Puniwai, G.S., Sako, M.K., and Yamashita, K.M., 1980, Geophysical observations of Kilauea Volcano, Hawaii, 2. Constraints on the magma supply during November 1975–September 1977: Journal of Volconology and Geothermal Research, v. 7, p. 241-269.

Einarsson, P., and Brandsdottir, B., 1979, Seismological evidence for lateral magma intrusion during the July 1978 deflation of the Krafla Volcano in NE-Iceland: Journal of Geophysics, v. 47, p. 160-165.

Epp, D., Decker, R.W., and Okamura, A.T., 1983, Relation of summit deformation to east rift zone eruptions on Kilauea Volcano, Hawaii: Geophysical Research Letters, v. 10, p. 493-496.

Evans, K., 1982, Some examples and implications of observed elastic deformations associated with the growth of hydraulic fractures in the Earth, in Zoback, M.D., and Haimson, B.C., eds., Proceedings of Workshop XVII, Hydraulic Fracturing Stress Measurements, U.S. Geological Survey Open-File Report 82–1075, v. 2, p. 661-698.

Fiske, R.S., and Jackson, D.E., 1972, Orientation and growth of Hawaiian volcanic rifts: the effect of regional structure and gravitational stress: Proceedings of the Royal Society of London, Series. A, v. 329, p. 299-326.

Fujii, T., and Kushiro, I., 1977, Density, viscosity, and compressibility of basaltic liquid at high pressures: Carnegie Institution of Washington Yearbook, 1976, p. 419-424.

Hauksson, E., 1983, Episodic rifting and volcanism at Krafla in north Iceland: growth of large ground fissures along the plate boundary: Journal of Geophysical Research, v. 88, p. 626-636.

Helgason, J., and Zentilli, M., 1985, Field characteristics of laterally emplaced dikes: anatomy of an exhumed Miocene dike swarm in Reydarfjordur, eastern Iceland: Tectonophysics, v. 115, p. 247-274.

Hoffman, J.P., Ulrich, G.E., and Chadwick, W.W., 1984, Geodetic measurements on the East Rift Zone, Kilauea Volcano, Hawaii: Eos (American Geophysical Union Transactions), p. 1131.

Kinoshita, W.T., Krivoy, H.L., Mabey, D.R., and MacDonald, R.R., 1963, Gravity survey of the Island of Hawaii: U. S. Geological Survey Professional Paper 475–C, p. C114-C116.

Klein, F.W., 1982, Patterns of historical eruptions at Hawaiian volcanoes: Journal of Volconology and Geothermal Research, v. 12, p. 1-35.

Lawn, B.R., and Wilshaw, T.R., 1975, Fracture of brittle solids: Cambridge, Cambridge University Press, 204 p.

Macdonald, G.A., 1956, The structure of Hawaiian volcanoes: Verchandelingen van het Koninklijke Nederlandsch Geologisch-Mijnbowkundig Genootschap, v. 16, p. 274-295.

McTigue, D.F., and Mei, C.C., 1981, Gravity-induced stresses near topography of small slope: Journal of Geophysical Research, v. 86, p. 9268-9278.

Meredith, P.G., and Atkinson, B.K., 1985, Fracture toughness and subcritical crack growth during high-temperature tensile deformation of Westerly granite and Black gabbro: Physics of the Earth and Planetary Interiors, v. 39, p. 33-51.

Moore, J.G., and Fiske, R.S., 1969, Volcanic substructure inferred from dredge samples and ocean-bottom photographs, Hawaii: Geological Society of America Bulletin, v. 80, p. 1191-1202.

Palmason, G., 1971, Crustal Structure of Iceland from explosion seismology: Societas Scientiarum Islandica, publ. 40, 187 p.

Paris, P.C., and Sih, G.C., 1965, Stress analysis of cracks, fracture toughness testing and its applications, Philadelphia, ASTM, p. 30-81.

Pollard, D.D., 1976, On the form and stability of open hydraulic fractures in the Earth's crust: Geophysical Research Letters, v. 3, p. 513-516.

Pollard, D.D., Delaney, P.T., Duffield, W.A., Endo, E.T., and Okamura, A.T., 1983, Surface deformation in volcanic rift zones: Tectonophysics, v. 94, p. 541-584.

Pollard, D.D., and Holzhausen, G., 1979, On the mechanical interaction between a fluid-filled crack and the Earth's surface: Tectonophysics, v. 53, p. 27-57.

Pollard, D.D., and Segall, P., in press, Theoretical displacements and stresses near fractures in rocks: with applications to faults, joints, veins, dikes, and solution surfaces, in Atkinson, B. K., ed., Rock fracture mechanics: London, Academic Press.

Ryan, M.P., Blevins, J.Y.K., Okamura, A.T., and Koyanagi, R.Y., 1983, Magma reservoir subsidence mechanics: theoretical summary and application to Kilauea Volcano, Hawaii: Journal of Geophysical Research, v. 88, p. 4147-4181.

Ryan, M.P., Koyanagi, R.Y., and Fiske, R.S., 1981, Modeling the three-dimensional structure of macroscopic magma transport systems: application to Kilauea Volcano, Hawaii: Journal of Geophysical Research, v. 86, p. 7111-7129.

Saemundsson, K., 1979, Outline of the geology of Iceland: Jokull, v. 29, p. 7-28.

Schmidt, R.A., and Huddle, C.W., 1977, Effect of confining pressure on fracture toughness of Indiana limestone [abs.]: International Journal of Rock Mechanics and Mining Sciences & Geomechanics Abstracts, v. 14, p. 289-293.

Secor, D.T., and Pollard, D.D., 1975, On the stability of open hydraulic fractures in the Earth's crust: Geophysical Research Letters, v. 2, p. 510-513.

Shah, R.C., and Kobayashi, A.S., 1973, Stress-intensity factors for an elliptical crack approaching the surface of a semi-infinite solid: International Journal of Fracture, v. 9, p. 3-21.

Sigurdsson, H., and Sparks, S.R.J., 1978, Lateral flow within rifted Icelandic crust: Nature, v. 274, p. 126-130.

Spence, D.A., and Turcotte, D.L., 1985, Magma-driven propagation of cracks: Journal of Geophysical Research, ser. B, v. 90, no. 1, p. 575-580.

Swanson, D.A., Duffield, W.A., and Fiske, R.S., 1976, Displacement of the south flank of Kilauea Volcano: the result of forceful intrusion of magma into rift zones: U.S. Geological Survey Professional Paper 963, 39 p.

Tada, H., Paris, P.C., and Irwin, G.R., 1973, The stress analysis of cracks handbook: Hellertown, Pa., Del Research Corp.

Tryggvason, E., 1983, The widening of the Krafla fissure swarm during the 1975–1981 volcano-tectonic episode: Nordic Volcanological Institute Report 8304, 48 p.

Walker, G.P.L., 1959, Geology of the Reydarfjordur area, eastern Iceland: Quarterly Journal of the Geological Society of London, v. 114, p. 367-393.

———1963, The Breiddalur central volcano, eastern Iceland: Quarterly Journal of the Geological Society of London, v. 119, p. 23-63.

———1974, Eruptive mechanisms in Iceland, in Krisjansson, ed., Geodynamics of Iceland and the North Atlantic area: Dordrecht-Holland, D. Reidel, p. 189-201.

Weertman, J., 1971, Theory of water-filled crevasses in glaciers applied to vertical magma transport beneath oceanic ridges: Journal of Geophysical Research, v. 76, p. 1171-1183.

Williams, H., and McBirney, A.R., 1979, Volcanology: San Francisco, Freeman, Cooper, 397 p.

Winter, R.B., 1983, Bruchmechanische Gerteinsuntersuchurgen mit dem Bezung zu Hydraulischen Frac-Versuchen in Tiefbohrungen: Bochum, Ruhr-Universitat, Institut fur Geophysik, Ph. D. dissertation.

Zucca, J.J., Hill, D.P., and Kovach, R.L., 1982, Crustal structure of Mauna Loa Volcano, Hawaii, from seismic refraction and gravity data: Bulletin of the Seismological Society of America, v. 72, p. 1535-1550.

# HEAT AND MASS TRANSPORT IN THE EAST-RIFT-ZONE MAGMA CONDUIT OF KILAUEA VOLCANO

*By* Harry C. Hardee[1]


## ABSTRACT

**The flow of magma in the rift conduit system of Kilauea Volcano is examined by comparing thermal and fluid-flow conduit models with field observations. A repetitive thermal-intrusion model predicts that the conduit will remain relatively open to flow for cyclic intrusion rates above a certain critical level. This agrees well with field observations for the upper east rift zone. This portion of the conduit tends to have aseismic intrusions, implying that fracturing is not required to open the conduit for flow. Observed intrusion rates and times between eruptive cycles for other portions of the Kilauea rift system and for conduits of other volcanoes agree well with the repetitive thermal-intrusion model.**

**Two forced-convection fluid flow models are developed for the Kilauea rift conduit system. One model is based on non-Newtonian rheology effects, and the other on viscous-dissipation effects. Both fluid flow models are compatible with field observations of summit-reservoir pressure changes, intrusive flow rates, eruption temperatures, and eruptive cycles. The nonNewtonian flow model is applicable to conduits on the order of 0.5 m thick or thicker, and this appears to be the situation for the upper portion of the east rift zone. The viscous-dissipation flow model appears to be applicable to thin conduits on the order of 0.5 m or less thick and particularly to those on the order of 0.1 m or less. Thin conduits tend to cool rapidly, and a source of internal heating such as viscous dissipation is needed to keep these conduits open for flow.**


## INTRODUCTION

The model of the magmatic plumbing system of Kilauea Volcano has evolved over the years as that system has been studied by numerous investigators. Magma generated in the upper mantle rises and is stored temporarily in a summit reservoir system at a depth of 2–6 km beneath the summit of the volcano (Duffield and others, 1982). The magma appears to rise from the mantle to the summit-reservoir storage system at a more or less steady volume rate (Swanson, 1972; Dzurisin and others, 1980; Dvorak and others, 1983). As storage in the summit reservoir increases, inflation of the volcano occurs, and eventually sufficient stresses accumulate to cause part of the magma to intrude into a shallow conduit system (Fiske and Jackson, 1972; Ryan and others, 1981). Frequently, intrusion into the conduit system results in the eruption of lava. The shallow magma of the east rift zone exists at a depth of 2–6 km and extends from the summit of Kilauea to a submarine position about 70 km east of Cape Kumukahi (Moore, 1971), a total distance of 120 km. A part of the rift is shown in figure 54.1 in a semiactive stage between eruptive phases during the Kilauea eruption that began in 1983.

Flow or intrusion in the conduit of the east rift zone is an intermittent forced-convection (pressure-driven) process. The seismic models of Ryan and others (1981) suggest that the intrusive flow occurs in a pipelike conduit. Later stress calculations and field observations by Ryan and others (1983), however, indicate that typical conduits may be sill or dike structures with thicknesses on the order of 1 m (0.15–3.38 m). The intermittent intrusions in the east rift zone appear to be of two basic types. Magma movement at large volume rates of 100–1,000 $m^3/s$ are accompanied by shallow seismic swarms and are apparently a result of the formation of new dikes by sudden fracturing (Epp and others, 1983). This process is common in the lower part of the east rift zone and in other areas, such as the southwest rift zone. Slower intrusions at volume rates of 1–10 $m^3/s$ are usually aseismic, implying that the conduit is in an open or nearly open (plastic or near-molten) state and that fracturing is not required for flow to be initiated (Epp and others, 1983). Intrusions of this latter type are common in the upper 20–30 km of the east rift zone nearest to the summit caldera. After an initial slow, aseismic intrusion, additional intrusions may occur at faster rates in later eruptive phases because the conduit remains molten or open and even increases in effective flow area. The slow, aseismic intrusions and the more rapid intrusions in later eruptive phases have been well studied, especially during the recent eruption of Kilauea that began in 1983. Decker and others (1983) have been able to correlate the extensive inflation-deflation records of the 1983–84 eruption phases with volume intrusion rates in the conduit and with estimated dynamic pressure values in the summit reservoir.

This paper concentrates on the low-volume-rate aseismic intrusions that frequently occur in the upper part of the east rift zone. This type of intrusive process repeats through a number of eruptive or intrusive phases, and therefore a large set of observations and data has accumulated. This repetition and the abundant data allow us to learn much about this type of conduit and about conditions in the summit reservoir. A repetitive-intrusion thermal model has been developed which explains how a conduit can remain relatively open to successive intrusions (Hardee, 1982). This model is described and the results applied to intrusion data for Kilauea Volcano. As expected, pressure-driven forced convection is the mechanism that

[1]Geophysics Division 1541, Sandia National Laboratories, Albuquerque, NM.

FIGURE 54.1.—Aerial view (looking southeast) of upper east rift zone of Kilauea Volcano in a semiactive stage between eruptive episodes during 1983–84 eruptive activity. Photograph by R.P. Striker, January 15, 1983.

drives intrusion in the plastic or near-molten conduit. Flow models based on both simple forced convection and forced convection with non-Newtonian-fluid and viscous-dissipation effects are considered. The non-Newtonian convection model is based on earlier work by Shaw and others (1968), who found that Kilauea lava could be modeled as a Bingham-plastic fluid. The viscous-dissipation model builds on the work of Gruntfest (Gruntfest, 1963; Gruntfest and others, 1964) and Shaw (1969), who were the first to introduce the concept of dissipative feedback into igneous petrology. Magma viscosity in the subliquidus temperature range depends on shear stress, shear rate, temperature, time, and previous thermal history. The Bingham-plastic flow model and the viscous-dissipation flow model are simply ways of looking at major magma-viscosity effects one at a time. The models are used to predict conduit size and dynamic pressure in the summit magma reservoir. The models are also used to explain the cyclic nature of eruptive phases. The models correlate well with field observations of the 1983–84 Kilauea eruption episodes.

A few fundamental points need to be emphasized. First, this paper primarily deals with the conduit, 20–30 km long and 2–6 km deep, that carries magma from the summit chamber downrift, where the magma may or may not rise the short remaining distance to a surface vent. To avoid confusion in this paper, the main deep part of the conduit is called the east rift conduit, and the shallow (1 km) final part at the end of the conduit is called the vent conduit. There are several fundamental differences between these two parts of the conduit system. In many intrusions in the east rift zone, eruption does not occur, and the vent conduit does not exist. If an eruption does occur, the vent conduit exists only briefly for that particular eruption. The deeper east-rift conduit has an existence much longer than, and independent of, particular eruptive vents. The east-rift conduit has existed as a fairly open conduit system for several hundred years and will likely exist for many years to come. This paper primarily considers the nature and evolution of the east-rift conduit system on the basis of thermomechanical constraints and balances. Some observations at the erupting vent bear directly on the

nature of the deeper conduit system. Other observations at the erupting vent are important only for processes occurring locally at the vent and are not directly applicable to processes occurring in the deeper east-rift conduit. For instance, at shallow depths in the vicinity of the vent, pressure in the magma is lowered to the point where gases are released. These gases affect geysering at the vent and the viscosity of the magma or lava as it exits the vent. The theoretical models discussed in this paper ignore the effect of such gases because little or no gas is present at the depths (1 km and greater) and corresponding pressures where the east-rift conduit exists.


## ACKNOWLEDGMENTS

This paper benefited greatly from reviews and comments by Terrence M. Gerlach, Robert W. Decker, Edward W. Wolfe, Herbert R. Shaw, and L. Paul Greenland. I would particularly like to thank Ed Wolfe for supplying additional field data on the 1983–84 Kilauea eruptive activity and Herb Shaw for supplying additional background references. This work was supported by the U.S. Department of Energy under contract DE-AC04-76DP00789.


## REPETITIVE-INTRUSION CONDUIT MODEL

Magma intrusions are of two types, as noted earlier. In the first type, the intrusion is an isolated event; repeated or successive pulses of magma through the same conduit are unlikely, although intrusions may occur in nearby regions. This type of intrusive flow occurs in fractures opened by mechanical or tectonic forces. Mechanically controlled intrusions form a majority of magma intrusions and are thoroughly discussed in a recent article by Shaw (1980). The second type of magma intrusion occurs in conduits where repeated injections of magma have left sufficient residual heat to keep the conduit effectively open during the quiescent period between intrusions. The ability of a magma conduit to remain open over a long period of time depends primarily on the average mass rate of magma throughput in the conduit. If the average mass rate of intrusive flow through the conduit exceeds a certain critical value, the conduit remains molten or nearly molten and therefore open to future magma intrusions. This fact was originally recognized from field observations (Smith, 1979; Fedotov, 1981). On the basis of field data, Smith (1979) recognized that a critical magma-eruption rate of about $1\times10^{-3}$ km$^3$/yr was necessary to sustain high-level silicic magma chambers. This can also be interpreted to mean that the critical value of magma intrusion rate through the conduit supplying the magma chamber or erupting vent is also on the order of $1\times10^{-3}$ km$^3$/yr. Fedotov (1981), on the basis of field data, observed a critical magma-intrusion rate on the order of $1\times10^{-3}$ km$^3$/yr for magma conduits feeding volcanic centers in Kamchatka. Theoretical calculations by Shaw (1980) indirectly show that critical magma-intrusion rates on the order of $1\times10^{-3}$ km$^3$/yr or greater are necessary to approach and maintain the liquidus temperature of mafic magma systems.

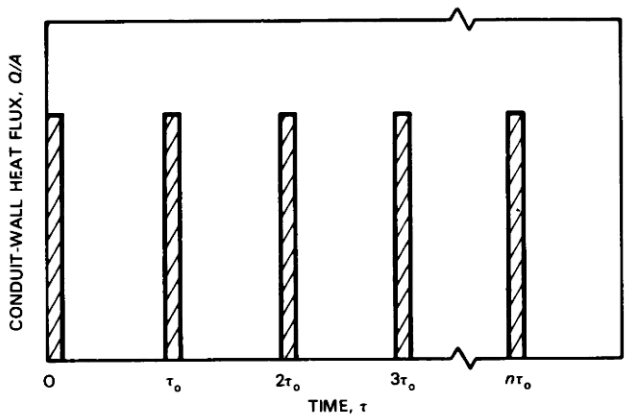


FIGURE 54.2.—Idealized repetitive sequences of thermal pulses used in repetitive-intrusion conduit model.

The critical magma-intrusion rate can be determined theoretically using an idealized conduit-intrusion model (Hardee, 1982). A cylindrical conduit geometry is assumed, which receives periodic intrusions of thermal magnitude $Q$ at time intervals of $\tau_0$. The heat pulses from successive intrusions are idealized as a regular series of heat-flux pulses at the conduit wall (fig. 54.2). The thermal magnitude $Q$ is determined from the latent heat or temperature of the intruding magma. The intruding magma must be at a temperature above the solidus; the conduit wall in contact with molten or flowing magma is, by definition, at the solidus temperature. The difference between these two temperatures is a measure of the energy available to overcome conduction losses at the conduit wall and into the surrounding country rock. The conduit-wall heat flux during an intrusive pulse is simply $Q/A$, where $A$ is the total surface area of the conduit. If a series of heat pulses (fig. 54.2) occur in a conduit, the wall of the conduit will gradually heat up. Even though the conduit cools between successive pulses, it will still be at a temperature above ambient just before the next intrusive pulse. If the value of $Q/A$ and the number of prior intrusive pulses are large enough, the temperature of the conduit wall and any material in the conduit will eventually reach a value on the order of the solidus temperature. At this point the conduit is assumed to be effectively open when the next intrusion occurs. Mechanical fracturing is no longer required to open the conduit for flow in this model. Forces of pressure-driven forced convection are sufficient to initiate flow in the conduit.

The critical condition for flow in an idealized cylindrical conduit with the periodic, pulsed boundary condition illustrated in figure 54.2 was solved by Hardee (1982), using a Laplace transform technique. The Laplace transform technique is well suited for problems in heat conduction with periodic boundary conditions and is uniquely suited to problems involving pulsed (delta function) boundary conditions. The critical magma-intrusion rate in the conduit, $V/\tau_0$, was shown theoretically to be about $1\times10^{-3}$ km$^3$/yr, which is in agreement with related field observations (Smith, 1979; Fedotov, 1981). The critical intrusion condition for the

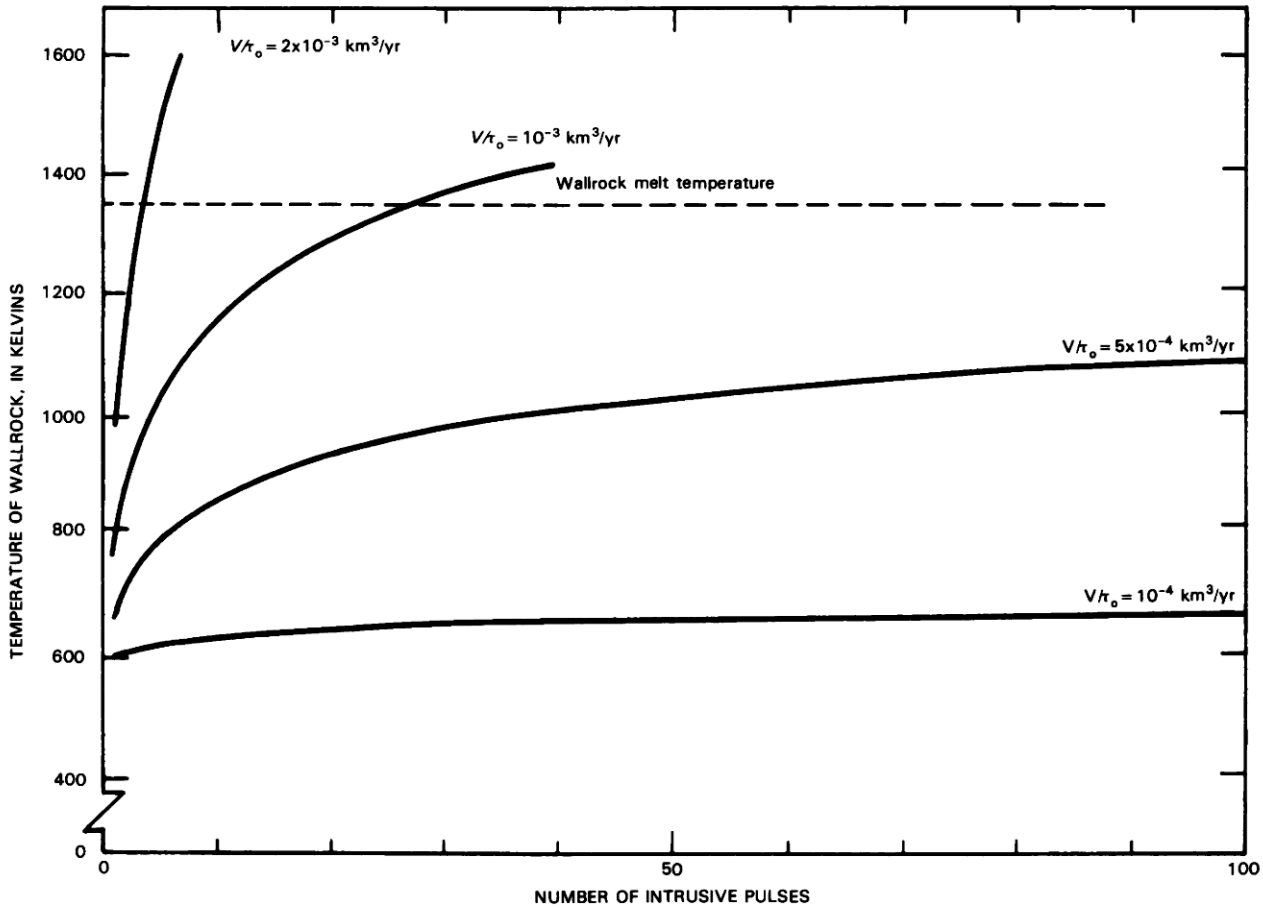


FIGURE 54.3.—Results of repetitive-intrusion model, showing conditions necessary to establish a thermally open conduit. Wallrock temperature rises as a function of increasing number of intrusive pulses; for sufficiently high volume-intrusion rates ($V/\tau_0$), it reaches and stays at or near the melting temperature.

conduit to remain open is a function of the critical magma-intrusion rate and also a function of the length of the conduit and the number of prior intrusive pulses in the conduit (Hardee, 1982). The critical intrusion parameter for a conduit such as the east-rift conduit is

$$\left[(V/\tau_0)1/l\sum_{1}^{m}(1/n)\right]_{\text{critical}} = 3\times10^{-4}\ \text{km}^2/\text{yr} \qquad (1)$$

where $V/\tau_0$ is the volume rate of throughput in the conduit, $m$ is the number of prior intrusive pulses or eruptions in the conduit, $n$ is the variable number of each particular pulse from 1 to $m$, and $l$ is the length of the conduit. Equation 1 is the condition for a conduit to remain effectively open from thermal effects alone. Although this analytical result is for a cylindrical conduit, the critical intrusion parameter is independent of the diameter of the conduit. The initial intrusion obviously requires mechanical fracturing in a weakened zone of country rock to initiate the first flow of magma. Once enough flow in subsequent pulses has occurred such that the critical value of $3\times10^{-4}$ km²/yr is exceeded, the conduit will then remain open from thermal effects alone. Using typical properties for basalt and assuming a typical conduit length, $l=10$ km, Hardee (1982) calculated the temperature of the conduit wall just before the next intrusion as a function of the volume-intrusion rate, $V/\tau_0$, and the number of intrusive pulses. The result (fig. 54.3) indicates that the critical condition for the conduit to remain open is a strong function of the average volume-intrusion rate and a weak function of the number of prior intrusive pulses. For instance, at a volume-intrusion rate, $V/\tau_0$, of $1\times10^{-3}$ km³/yr, the wallrock temperature remains at the melt temperature after about 10 intrusive pulses have occurred. At a volume-intrusion rate of only half this value ($5\times10^{-4}$ km³/yr), the wallrock has not reached the melt temperature even after more than 100 intrusive pulses. Although equation 1 gives a precise expression for the critical conduit condition, figure 54.3 shows that for many typical cases the critical conduit condition is met when the volume-intrusion rate exceeds the value $1\times10^{-3}$ km³/yr. This value is in agreement with the observations of Smith (1979), Shaw (1980), and Fedotov (1981), mentioned earlier.

Equation 1 can be used to compare magma conduit systems at Kilauea. Typical values of the critical conduit-intrusion parameter

TABLE 54.1.—*Intrusion parameters for some magma conduits*

| | Intrusion parameter $\left[(V/\tau_0)(1/l)\sum_1^m(1/n)\right]$ (km²/yr) |
|---|---|
| Kilauea—Upper east rift[1] | $45\times10^{-4}$ |
| Augustine Volcano, Alaska[2] | $40\times10^{-4}$ |
| Mount St. Helens, Washington[3] | $8.1\times10^{-4}$ |
| (critical value) | $3\times10^{-4}$ |
| Kilauea—lower east rift (Puna)[1] | $1.4\times10^{-4}$ |
| Kilauea—southwest rift[1] | $1.1\times10^{-4}$ |

[1]Based on Decker (1983) and Macdonald and Hubbard (1973). Since 1955, upper east rift $V/\tau_0=30\times10^{-3}$ km³/yr, $m=20$, and $l=25$ km. Since 1750, lower east rift $V/\tau_0=3\times10^{-3}$ km³/yr, $m=5$, and $l=50$ km. Since 1823, southwest rift $V/\tau_0=1.1\times10^{-3}$ km³/yr, $m=5$, and $l=25$ km.

[2]Based on Kienle and Swanson (1980). Four major eruptions in last 100 years; typical volume of 0.1 km³; $l=2$ km from depth of first seismicity during last (1976) eruption.

[3]Based on Decker and Decker (1981). Since 1850, $V/\tau_0=4\times10^{-3}$ km³/yr, $l=18$ km, and in the last 4,500 years $m=20$.

for conduits at Kilauea and other sites are listed in table 54.1. The average volume-intrusion rate, $V/\tau_0$, and the number of prior intrusive pulses or eruptions, $m$, are obtained from geologic and historical data. The length of the conduit, $l$, is obtained from seismic data or other estimates of the distance from the magma reservoir to the end of the conduit. Comparing the results in table 54.1 with the critical intrusion factor of $3\times10^{-4}$ km²/yr from equation 1 shows that the upper east rift zone of Kilauea (upper 25 km) and the Augustine and Mount St. Helens volcanic conduits are open conduits in the sense defined earlier, while the lower east rift zone near Puna and the southwest rift zone of Kilauea are normally closed conduits. These latter examples would require mechanical fracturing before intrusive flow could move through the conduit. The repetitive-intrusion model and the result of equation 1 can be applied to different conduits or parts of conduits at the same volcano. The only requirement is that appropriate values of volume-intrusion rate, length of conduit, and number of prior intrusive pulses are used for the particular conduit or part of conduit being studied.

## INTRUSIVE FLOW IN CONDUITS

Intrusive flow in the east-rift conduit of Kilauea can be modeled as simple forced convective flow in a conduit where the flow is driven by pressure in the summit reservoir. Epp and others (1983) and Decker and others (1983) recognized that the intrusive flow in the east-rift conduit was associated with summit deflation, which in turn was related to dynamic pressure changes in the reservoir. Epp and others (1983) noted that the volume of erupted material in many cases was equal to the volume of deflation of the summit reservoir; they further noted that the amount of magma drained from the summit reservoir was related to the elevation of the vent. This again suggests a simple reservoir-controlled, forced-convection type of conduit flow. Decker and others (1983) have made limiting calculations which indicate that dynamic pressure changes in the summit reservoir between 0.09 MPa and 400 MPa have occurred over the last 25 years at Kilauea Volcano. Recent correlations of summit tilt changes with elevations of rift eruption vents indicate pressure changes of 0.085 MPa per μrad of rapid radial summit tilt (Decker and others, 1983). During the 1983–84 eruption episodes at Kilauea, tilt changes on the order of 10 μrad were common; these correspond to dynamic pressure changes on the order of 1 MPa. Dynamic pressure change, as used here, is the pressure change that occurs in the summit reservoir during an eruptive episode (Decker and others, 1983). This pressure is related to the pressure necessary to overcome frictional flow effects during periods of intrusive flow. The dynamic pressure change does not include a hydrostatic component, because the hydrostatic pressure is similar at the beginning and end of an eruptive episode. Hydrostatic is used here in the fluid-mechanics context to mean the static pressure in a liquid (in this case, molten magma).

Simple hydrodynamic flow relations can be used to relate observed flow volumes and flow rates to expected conduit diameters. It is obvious, however, that something more than a simple hydrodynamic conduit model is needed to explain the observed flow. Simple hydrodynamic flow relations alone predict that eruptive episodes such as at Kilauea in 1983–84 would not be observed, but rather a continuous low-level flow would occur at the expected reservoir replenishment rate of $8.5\times10^6$ m³/mo (Swanson, 1972). Instead of a continuous intrusive flow rate of 3.28 m³/s ($8.5\times10^6$ m³/mo), the flow rate in the conduit ranged from 10 to 100 m³/s during periods of eruption and was essentially zero between eruptive episodes. If the flow during eruptive phases were averaged out over a year, it would agree closely with Swanson's estimate of the reservoir replenishment rate of $8.5\times10^6$ m³/mo. An additional mechanism must somehow be included with the simple hydrodynamic flow model in order to explain why intrusive or eruptive episodes occur as isolated, repetitive events rather than as a continuous low-level flow. The analysis in the previous section of this paper explained the condition whereby repetitive intrusive pulses could occur in what I have called an open conduit without mechanical fracturing, but this analysis did not explain what controlled the cyclic nature of the intrusions or eruptive episodes. Since the magma supply rate to the summit reservoir appears to be fairly constant and continuous, the only mechanisms that might explain the observed intermittent intrusive flow in such open conduits are non-Newtonian rheology and viscous dissipation.

## NON-NEWTONIAN FORCED-CONVECTION CONDUIT MODEL

The simplest non-Newtonian flow model for intrusive flow in a magma conduit is a Bingham-plastic flow model, as used by Shaw and others (1968) in their analysis of viscosity measurements at Makaopuhi lava lake. A power-law rheology model also fits the observed viscosity data well for basaltic lava or magma (Hardee and Dunn, 1981); however, the Bingham-plastic model is simpler to use and fully adequate for the first-order calculations that follow. In the Bingham-plastic model, flow does not begin until a certain critical yield stress is exceeded; and once this occurs, the flow is similar to Newtonian flow.

If we consider a cylindrical conduit, the pressure drop in the

conduit from simple hydrodynamic theory for laminar flow is (Vennard, 1956)

$$P = 32\mu l v/D^2, \quad (2)$$

where $P$ is the dynamic or available pressure to drive the intrusive flow, $\mu$ is the average magma viscosity, $l$ is the length of the conduit, $v$ is the average flow velocity of the fluid in the conduit, and $D$ is the diameter of the conduit. For conduits with a noncircular cross section, the concept of an equivalent diameter can be used with this same relation (Chapman, 1967). For geometries such as those of sills or dikes, an expression similar to equation 2 can be developed, or the idea of equivalent diameter can be used. The flow rate $Q$ in the conduit is simply

$$Q = \pi D^2 v/4. \quad (3)$$

In the absence of an internal heating mechanism, such as viscous-dissipation heating, the conduit must be sufficiently large that the fluid does not cool appreciably as it flows through. Otherwise, the magma would cool and solidify in place, thereby shutting off the flow. In the simple forced-convection flow model, the fluid magma leaves the summit reservoir at a temperature (say, 1,413 K) well above that at which the magma is considered virtually solid (1,343 K; see Shaw and others, 1968). By equating the heat lost at the conduit wall to the reduction of sensible heat in the flowing fluid, an expression can be developed for the amount of cooling that occurs in a conduit of length $l$. The heat loss of a fluid to the wall of a circular conduit is

$$q = hA_s(T_b - T_w), \quad (4)$$

where $h$ is the convective heat-transfer coefficient, $A_s$ is the surface area of the conduit, $T_b$ is the bulk temperature of the fluid in the conduit, and $T_w$ is the temperature of the wall (1,343 K). The convective heat-transfer coefficient for fluid flow in a cylindrical conduit (Eckert and Drake, 1959) is

$$hD/k = 3.65, \quad (5)$$

where $k$ is the thermal conductivity of the fluid. Substituting $h$ from equation 5 into equation 4 and noting that $A_s = \pi D\ dl$ for an incremental length $dl$ gives

$$q = 3.65\pi k(T_b - T_w)\ dl. \quad (6)$$

The reduction in sensible heat is the energy lost from the flowing fluid

$$q = -\rho c(\pi D^2/4)v\ dT_b, \quad (7)$$

where $\rho$ is the density of the fluid and $c$ is the specific heat of the fluid. Combining equations 6 and 7 and integrating the result over a conduit length $l$ yields the result

$$T_b - T_w = K\exp[-14.6\alpha l/(D^2 v)], \quad (8)$$

where $\alpha$ is the thermal diffusivity ($\alpha = k/\rho c$) and $K$ is a constant. Assume that when $l = 0$ at the summit reservoir, the bulk temperature of the magma entering the conduit is, as noted earlier, 70 K above the temperature where the magma is virtually solid ($T_b - T_w = 70$). The constant $K$ in equation 8 then becomes 70, and

$$T_b - T_w = 70\exp[-14.6\alpha l/(D^2 v)]. \quad (9)$$

Decker and others (1983) note that the flow in the conduit can be estimated from summit deflation and that this volume is approximately $0.5 \times 10^6$ m$^3$ per $\mu$rad of radial tilt. As an example, episode 2 of the Kilauea eruption that started in 1983 resulted in a summit deflation of 11 $\mu$rad of tilt in 6 days. This corresponds to an intrusive-flow rate of

$$Q = (11/6)(0.5 \times 10^6) = 0.917 \times 10^6 \text{ m}^3/\text{d}$$

or

$$Q = 10.6 \text{ m}^3/\text{s}. \quad (10)$$

Substituting this into equation 3 gives

$$D^2 v = 10.6(4/\pi), \quad (11)$$

and substituting this along with appropriate values for magma properties and an assumed conduit length ($l$) of 20 km into equation 9 gives

$$T_b - T_w = 69.7 \text{ K}. \quad (12)$$

This calculation is interesting in that it shows that the temperature loss as the magma flows the full length of the conduit is only 0.3 K, and this result did not depend on a knowledge of the conduit diameter. A similar result is obtained for a dike. An exact calculation for the dike is not possible because the flow rate $Q$ depends on two geometrical factors: the thickness of the dike ($a$) and the width of the dike ($b$):

$$Q = abv. \quad (13)$$

An approximate calculation for the dike can be obtained by using the concept of equivalent diameter (Chapman, 1967). The equivalent diameter, sometimes called the hydraulic diameter, is an approximating concept used in fluid mechanics for conduits of noncircular cross section. The equivalent diameter, which attempts to preserve the flow area and the viscous shear at the wall, is simply 4 times the cross-sectional flow area divided by the wetted perimeter of the conduit. The equivalent diameter of a circular conduit is equal to the geometrical diameter. For a dike or sill, the equivalent diameter ($D_{eq}$) can be shown to be

$$D_{eq} = 2a. \quad (14)$$

The exact temperature result for a dike or sill, similar to equation 9, can be shown to be

$$T_b - T_w = 70\exp[-7.5\alpha l/(a^2 v)]. \quad (15)$$

With the use of the concept of equivalent diameter from equation 14, an approximate version of equation 15 is

$$T_b - T_w = 70\exp[-30\alpha l/(D_{eq}^2 v)]. \quad (16)$$

Substituting the flow-rate result from equation 11 into equation 16 gives an approximate result for the dike very similar to that for the circular conduit. Specifically, for the 1983–84 Kilauea eruption episodes the temperature loss as the magma flowed in the conduit

was negligible regardless of whether the conduit was a dike or circular conduit.

As noted earlier, Decker and others (1983) estimated pressure changes in the summit reservoir of 0.085 MPa per μrad of rapid, radial summit tilt. Episode 2 of the Kilauea eruption that started in 1983 had a rapid tilt change of 11 μrad during the eruptive phase, and this corresponds to a pressure change of

$$P = 0.085 \times 11 = 0.935 \text{ MPa}. \tag{17}$$

For the current conduit model, we can assume that the pressure driving the forced convective intrusive flow in the conduit is approximately that given by equation 17. The viscosity of the magma can be estimated by using the result of Shaw and others (1968), who found that the viscosity variation with temperature for basaltic lava could be expressed as

$$\mu = (1 \times 10^{-6})\exp(26{,}170/T), \tag{18}$$

where $\mu$ is in SI units (Pa·s) and $T$ is in kelvins. The constant 26,170 in equation 18 is an experimentally determined constant for this lava. At a magma bulk temperature of $T_b = 1{,}413$ K, the viscosity is approximately

$$\mu = 100 \text{ Pa·s}.$$

Substituting this and the estimate of pressure from equation 17 into equation 2 and solving for $v/D^2$ gives

$$v/D^2 = P/(32\mu l) = 0.935 \times 10^6/[32(100)(20 \times 10^3)]$$

or

$$v/D^2 = 0.01461. \tag{19}$$

Equations 11 and 19 are two independent equations in two variables: the flow velocity $v$ and the conduit diameter $D$. Solving these two equations for $v$ and $D$ yields

$$v = 0.444 \text{ m/s} \tag{20}$$

and

$$D = 5.51 \text{ m} \tag{21}$$

for conduit flow during episode 2 of the 1983–84 Kilauea eruptive activity. Values for other episodes of this eruption are listed in table 54.2. These values compare well with observed diameters (4–8 m) of conduit exit holes at eruptive vents such as those shown in figure 54.4. This similarity may be coincidental because flow in the vent conduit, with volatile phases present, is considerably different from flow in the deeper east-rift conduit.

If the conduit were a dike instead of a circular conduit, the dike thickness derived using the approximate result of equation 14 would be

$$a = D/2 = 5.51/2 = 2.76 \text{ m}, \tag{22}$$

and the dike width from equation 13 would then be

$$b = Q/av = 10.6/(2.76 \times 0.444) = 8.67 \text{ m}. \tag{23}$$

Estimates for the dike or sill model for this and other eruptive episodes at Kilauea in 1983–84 are listed in table 54.3.

TABLE 54.2.—*Flow rate, total intruded volume, and estimated velocity and conduit diameter (based on forced-convection flow model) for 1983–84 Kilauea eruptive episodes*

[First values of flow rate based on tilt data; second values in parentheses, supplied by E. W. Wolfe of Hawaiian Volcano Observatory, based on field observations of erupted volumes for episodes 2–15 reduced by 20 percent to account for dense-rock magma equivalent. Conduit diameter values in parentheses correspond to calculated values based on field observations of erupted volume]

| Episode | Flow rate $Q$ ($m^3/s$) | Intruded volume ($10^6$ $m^3$) | Velocity (m/s) | Conduit diameter (m) |
|---|---|---|---|---|
| 2 | 10.6 (15) | 5.50 | 0.444 | 5.51 (6.01) |
| 3 | 13.0 (30) | 9.04 | .629 | 5.12 (6.31) |
| 4 | 15.9 (24) | 5.75 | .556 | 6.03 (6.68) |
| 5 | 19.5 (32) | 5.92 | .624 | 6.31 (7.14) |
| 6 | 31.8 (27) | 8.25 | .942 | 6.56 (6.29) |
| 7 | 42.8 (39) | 8.51 | 1.11 | 7.01 (6.84) |
| 8 | 57.9 (65) | 5.00 | .989 | 8.63 (8.88) |
| 9 | 45.7 (40) | 7.50 | 1.08 | 7.35 (7.10) |
| 10 | 36.0 (52) | 7.00 | .923 | 7.05 (7.73) |
| 11 | 62.1 (62) | 8.84 | 1.36 | 7.64 (7.64) |
| 12 | 56.7 (51) | 6.94 | 1.15 | 7.91 (7.70) |
| 13 | 35.9 (60) | 5.54 | .820 | 7.46 (8.48) |
| 14 | 60.9 (70) | 5.00 | 1.01 | 8.74 (9.05) |
| 15 | 66.6 (94) | 5.75 | 1.14 | 8.63 (9.40) |
| 16 | 55.9 | 4.83 | 1.17 | 8.00 |
| 17 | 57.9 | 5.00 | .990 | 8.63 |
| 18 | 56.4 | 4.88 | 1.36 | 7.26 |
| 19 | 21.2 | 1.83 | .440 | 7.80 |
| 20 | 38.5 | 3.33 | .807 | 7.79 |
| 21 | 35.7 | 3.08 | .747 | 7.80 |
| 22 | 56.8 | 4.91 | 1.13 | 8.00 |
| 23 | 60.2 | 5.20 | 1.15 | 8.16 |
| 24 | 64.5 | 5.57 | 1.26 | 8.08 |
| 25 | 69.4 | 6.00 | 1.33 | 8.16 |

The previous flow calculations for the forced-convection model are valid as long as the temperature drop in the conduit is small (that is, as long as $T_b - T_w$ at the end of the conduit is approximately the same as at the entrance of the conduit). In the calculation for episode 2, this was certainly the case for the flow rate $Q = 10.6$ $m^3/s$. From equation 9, assuming the same magma properties, this temperature condition can be shown to be satisfied as long as the intrusive flow rate is greater than about $Q = 0.5$ $m^3/s$ for a circular conduit. This condition is certainly met for all the eruptive episodes listed in table 54.2. If a dike geometry is assumed, the temperature condition can be shown to be satisfied for the eruptive phases listed in table 54.3 as long as the ratio of dike thickness to dike width ($a/b$) is greater than about 0.025, and this is true for all the episodes listed in table 54.3. In a circular conduit, if the intrusive flow rate $Q$ were very low, the magma would reside in the conduit for a long time and would cool and solidify in the conduit. In a dike, if the ratio $a/b$ were very small, then conduction losses would be large, and the magma would again tend to cool and solidify in the conduit.

Although the previous forced-convection calculations give acceptable values for velocity and conduit size, these calculations do not explain the cyclic nature of the eruptive episodes, with periods of fairly steady intrusive flow separated by quiescent periods with little or no flow. In simple pressure-driven forced convection of Newtonian liquids, we would expect the flow to slow down to the rate at which the summit reservoir is replenished. The flow would continue at this slow rate of 3.28 $m^3/s$ ($8.5 \times 10^6$ $m^3$/mo) and would not shut off between eruptive episodes, as observed. This replenishment flow rate of 3.28 $m^3/s$ is still greater than the minimum value of 0.5 $m^3/s$

FIGURE 54.4.—Eruptive vents during February 1983 eruptive episode at Kilauea Volcano. Photograph by W.C. Luth, February 25, 1983. Highest fountains are spraying about 50 m high.

required to keep the conduit flow from solidifying in place. A possible explanation for the on-off nature of the cyclic eruptive episodes can be found by looking at the non-Newtonian flow properties of magma at temperatures below the liquidus such as occur in the conduit flow process. Shaw and others (1968) observed that Hawaiian basaltic lava at temperatures similar to those seen in the 1983–84 Kilauea eruptive activity behaved much like a Bingham-plastic fluid with a yield stress of 7–12 kg/m$^2$ (700 to 1,200 dyne/cm$^2$). If we assume that a pressure difference large enough to overcome the Bingham yield stress must exist before flow can begin, then this pressure can be estimated and compared with the pressure estimates of Decker and others (1983) used in the previous flow calculations. A simple pressure balance on the conduit is:

$$PA_c = \sigma A_s \tag{24}$$

where $A_c$ is the cross-sectional area of the conduit, $A_s$ is the surface area of the conduit, and $\sigma$ is the Bingham yield stress. For a circular conduit this becomes

$$\pi D^2 P/4 = \pi D l \sigma$$

or

$$P = 4\sigma l/D. \tag{25}$$

For a yield stress of 7 kg/m$^2$, this becomes

TABLE 54.3.—*Estimate of dike size for east-rift conduit (based on forced-convection conduit model) for 1983–84 Kilauea eruptive episodes*

| Episode | Dike thickness (m) | Dike width (m) |
|---|---|---|
| 2 | 2.76 | 8.67 |
| 3 | 2.56 | 8.04 |
| 4 | 3.01 | 9.47 |
| 5 | 3.15 | 9.91 |
| 6 | 3.28 | 10.3 |
| 7 | 3.50 | 11.0 |
| 8 | 4.32 | 13.6 |
| 9 | 3.67 | 11.5 |
| 10 | 3.52 | 11.1 |
| 11 | 3.82 | 12.0 |
| 12 | 3.96 | 12.4 |
| 13 | 3.73 | 11.7 |
| 14 | 4.37 | 13.7 |
| 15 | 4.31 | 13.6 |
| 16 | 4.00 | 12.6 |
| 17 | 4.32 | 13.6 |
| 18 | 3.63 | 11.4 |
| 19 | 3.90 | 12.3 |
| 20 | 3.89 | 12.2 |
| 21 | 3.90 | 12.3 |
| 22 | 4.00 | 12.6 |
| 23 | 4.08 | 12.8 |
| 24 | 4.04 | 12.7 |
| 25 | 4.08 | 12.8 |

$$P=4(7)(20\times10^3)/5.5=0.102\times10^6\ \text{kg/m}^2$$

or

$$P=0.985\ \text{MPa}. \tag{26}$$

Using the upper value for yield stress of 12 kg/m$^2$ results in a predicted pressure of $P=1.69$ MPa. The predicted pressure differential driving the convective flow in the conduit, therefore, ranges from $P=0.985$ MPa to $P=1.69$ MPa. This compares favorably with the estimate of Decker and others (1983), who suggested that this pressure is 0.085 MPa per μrad of rapid radial tilt. Radial tilt changes for the early eruptive episodes in 1983 ranged from 10 to 18 μrad, corresponding to pressures of 0.85 to 1.53 MPa. These pressure estimates using the prediction of Decker and others (1983) agree well with the estimates above, 0.985 to 1.69 MPa, based on the Bingham model of Shaw and others (1968). This agreement supports the idea that the cyclic nature of the Kilauea eruptive episodes in 1983–84 may have been a result of non-Newtonian rheology effects. This calculation also supports the pressure predictions of Decker and others (1983) for the summit reservoir.

The forced-convection flow model can also be applied to other eruptions at Kilauea Volcano. For instance, the 1959–60 eruption was a major one with probably 17 eruptive phases (Richter and Moore, 1966). The conduit length $l$ was probably much shorter than in the 1983–84 eruptive episodes because the eruption site was close to the summit of Kilauea; the 1959–60 conduit length $l$ was probably on the order of 5 km (Peck and others, 1979). The principle effect of this shorter conduit length would be to reduce the time between eruptive episodes. Equation 25 shows that the summit-reservoir pressure necessary to overcome the Bingham-plastic yield stress of magma in the conduit is proportional to conduit length $l$. Since $l$ was much shorter in the 1959–60 eruption, the dynamic pressure needed to overcome the yield stress of the magma was much less. As the summit magma chamber inflated, the necessary pressure level for an eruptive episode would be reached quickly, and the eruptive phases would be expected to repeat on a time period much shorter than the approximate one-month time periods of the 1983–84 eruptive activity. As expected, the eruptive episodes for the 1959–60 eruption repeated on an average interval of about 2 days (Richter and Moore, 1966).

## VISCOUS-DISSIPATION FORCED-CONVECTION CONDUIT MODEL

Viscous dissipation may be an important mechanism in intrusive flow of magma in the rift conduits of Kilauea. Viscous dissipation has been suggested before as a key mechanism in eruptive cycles (Shaw, 1969, 1973; Anderson and Perkins, 1974; Fujii and Uyeda, 1974; Hardee and Larson, 1977; Fujii, 1981). Previous confirmation of the theory has been limited to estimates of runaway temperature and dike thickness for various types of magma. Because of the extensive amount of real-time field observations of conduit flow in the east-rift conduit during the 1983–84 Kilauea activity, it is possible to compare conduit models with a large set of field data, such as eruption temperature of lava, time between successive eruptive episodes, intrusive flow rate, and, in some cases, the conduit exit diameter at the vent.

The energy of viscous dissipation ultimately comes from conversion of pressure energy in the summit reservoir into frictional heat. The pressure in the reservoir overcomes the frictional resistance to flow, and in turn the viscous shear caused by the frictional resistance is converted to heat, which raises the temperature of the fluid. This happens in all cases of simple forced-convective flow in conduits, but usually the heating effect is small. In the case of magmatic intrusions, however, the heating effect can be significant. Without the effect of viscous dissipation, magma would have difficulty flowing in small conduits and thin dikes, and there would be a tendency for the magma to cool and solidify in place. Even where mechanical fracturing occurs and opens the conduit, viscous dissipation is likely to be important in allowing the magma to flow rather than quickly solidify. Since the energy available for viscous heating comes from the pressure or potential energy in the reservoir, field observations of the thermal state of erupting lava can be used to estimate conditions back in the reservoir. Also, it is obvious that the magnitude of the viscous-heating effect is limited ultimately by the pressure or potential energy in the reservoir.

A forced-convection transport model of the east-rift conduit can also be developed in which viscous-dissipation effects are important. Viscous dissipation can affect both the temperature of erupting lava and the cyclic episodes of the eruption. The time required for thermal effects to build to thermal runaway, coupled with the summit-reservoir pressure history, determines the repose period between dissipatively controlled eruptive cycles. The rapid increase of viscosity of the magma as partial crystallization occurs on cooling probably causes the magma to jam up and cease flowing in a reverse type of thermal runaway. Calculations to demonstrate this jam-up phenomenon or reverse thermal runaway are difficult because

the viscosity of the liquid/crystal magma composition at near-solidus temperatures is not well known (Shaw and others, 1968). Such an effect, once started, would rapidly accelerate and cause the flow to shut off suddenly. As pressure in the summit reservoir increased again, a point would be reached at which viscous-dissipation effects would again produce a thermal-runaway situation, and a new eruptive episode would begin. The observed cyclic nature of the eruptive episodes, the observed eruptive temperatures and volumes, and the highly temperature-dependent nature of the magma viscosity are all consistent with a forced-convection magma-conduit model that includes viscous-dissipation effects. The calculations that follow here are for this transport model.

First, the viscous-dissipation thermal-runaway temperature is determined and shown to be consistent with observed eruption temperatures. The pressure drop in the conduit is determined, and this in turn can be related back to the pressure in the summit reservoir. The shape of the conduit is then determined. Next, an approximate calculation shows that the runaway time is of the right order of magnitude in comparison with observed periods of repose between eruptive episodes.

For a cylindrical conduit, the pressure drop in the conduit from simple hydrodynamic theory for laminar flow (equation 2) is (Vennard, 1956) $P=32\mu lv/D^2$, where $P$ is the dynamic or available pressure to drive the intrusive flow, $\mu$ is the average magma viscosity, $l$ is the length of the conduit, and $D$ is the diameter of the conduit. For conduits with a noncircular cross section, the concept of an equivalent diameter can again be used. From the energy equation and the expression for viscous dissipation in cylindrical coordinates (Batchelor, 1970), it can be shown that for steady flow in a conduit where the viscous-dissipation heating in the conduit is in balance with conduction loss at the wall, the temperature of the fluid in the conduit is

$$T_b - T_w = (8/9)\mu v^2/k, \tag{27}$$

where $T_b$ is the average or bulk temperature of the fluid in the conduit, $T_w$ is the temperature of the wall (again, 1,313 K), $v$ is the average flow velocity of the fluid, and $k$ is the thermal conductivity of the fluid. The flow rate $Q$ (equation 3) is $Q=\pi D^2 v/4$. Between eruptions or eruptive episodes, the pressure in the summit reservoir builds in magnitude, and the pressure acts on material in the conduit that is hot but solidified and resistant to flow. The viscosity is high at this point, and the flow velocity is near zero. Flow will begin to occur at an imperceptibly slow rate, producing a small amount of viscous-dissipation heating. Gradually at first and then rapidly, the process will accelerate as viscous heating reduces the viscosity of the fluid. Most of the noticeable activity occurs in the latter part of the thermal-runaway process, giving it the appearance of suddenness. Equations 2 and 18 can be used to calculate the condition under which appreciable flow begins. Once initiated, the flow will tend to persist at the conditions of temperature and velocity in which the viscous heat generation in the fluid is exactly balanced by the conduction loss at the wall. At slower flow rates the fluid will cool too much by conduction loss to the wall, and some of the magma will tend to solidify in place. At higher flow rates the excessive viscous heat generation will produce melting at the walls.

The energy absorbed by latent heat at the wall and the reduced flow velocity as the conduit diameter increases will both tend to restrict the flow and prevent the velocity and temperature from increasing indefinitely. The natural tendency is for the intrusive flow to assume a steady flow condition at the critical temperature at which viscous-heating effects predominate. This critical viscous-dissipation temperature or "runaway" temperature has been studied by Fujii and Uyeda (1974), Hardee and Larson (1977), and others. The runaway temperature, which corresponds roughly with the expected value of the lava-eruption temperature, can be determined by using equations 2, 18, and 27. First, equations 2 and 27 are combined to eliminate $v$:

$$P^2 = (9/8)k(32l/D^2)^2(T_b - T_w)\mu. \tag{28}$$

Assuming a wallrock or melt temperature of 1,343 K (Shaw and others, 1968) for basalt and using equation 18 for viscosity yields:

$$\mu = (1\times10^{-6})\exp[26{,}170/(\Phi+1{,}343)] \tag{29}$$

where $\Phi = T_b - T_w$. Substituting equation 29 into equation 28 gives:

$$P^2 = [(9/8)k(32l/D^2)^2(1\times10^{-6})]\Phi\cdot \exp[26{,}170/(\Phi+1{,}343)]. \tag{30}$$

The condition of thermal runaway occurs when a small change in reservoir pressure $P$ results in a large change in temperature $\Phi$ or, in other words, when $dP/d\Phi=0$. Differentiating equation 30 with respect to $\Phi$, setting $dP/d\Phi=0$ and then solving for $\Phi$ results in

$$[26{,}170\Phi/(\Phi+1{,}343)^2]-1=0$$

or

$$\Phi = 77 \text{ K}. \tag{31}$$

The average temperature of the magma during intrusive flow and the corresponding expected lava-eruption temperature is then

$$T_b = 1{,}343 + 77 = 1{,}420 \text{ K}. \tag{32}$$

This compares well with typical lava-eruption temperatures from measurements such as those shown being made in figure 54.5 near the vent during the 1983–84 eruptive activity of Kilauea (Hardee, 1983).

The dynamic pressure in the reservoir or the pressure driving the flow in the conduit can be determined from equation 2. First, equations 3 and 27 are used to eliminate $D$ and $v$ from equation 2 to give

$$P = 9\pi kl(T_b - T_w)/Q. \tag{33}$$

Substituting the flow rate from equation 10 into equation 33 gives

$$P = 9\pi(2.09)(20\times10^3)(1{,}420-1{,}343)/10.6 = 8.59 \text{ MPa}. \tag{34}$$

This pressure is within the range (0.09–400 MPa) estimated by Decker and others (1983), although it is higher than their estimates

FIGURE 54.5.—Thermal measurements being made in molten lava during February 1983 eruptive episode at Kilauea Volcano. Photograph by W.C. Luth, February 25, 1983.

for dynamic pressure changes in the summit reservoir during Kilauea's 1983–84 activity. The expected flow velocity in the conduit can be found from equation 27:

$$v=[(9/8)k(T_b-T_w)/\mu]^{0.5}. \quad (35)$$

The viscosity to be used in equation 35 is found from equation 18 at the fluid runaway temperature of equation 32:

$$\mu=(1\times10^{-6})\exp(26{,}170/1{,}420)=100\ \text{Pa}\cdot\text{s}. \quad (36)$$

Substituting this and other values into equation 35 gives

$$v=[9(2.09)(1{,}420-1{,}343)/8(100)]^{0.5}=1.33\ \text{m/s} \quad (37)$$

for the average intrusive flow velocity in the conduit during eruptive episode 2. The effective diameter of the conduit can then be found from equation 3:

$$D=(4Q/\pi v)^{0.5}=[4(10.6)/\pi(1.33)]^{0.5}=3.18\ \text{m}. \quad (38)$$

This value compares reasonably well with observed diameters of conduit exit holes, typically around 4–8 m in diameter, at eruptive vents such as those shown in figure 54.4 during the 1983–84 Kilauea activity. The predicted diameter is not too different from the value for the non-Newtonian forced-convection conduit model in the previous section (table 54.4).

TABLE 54.4.—*Comparison of estimated conduit diameter for east-rift conduit during 1983–84 Kilauea eruptive episodes (based on forced-convection conduit model and forced-convection model with viscous dissipation)*

| Episode | Conduit diameter from table 54.2 (m) | Conduit diameter with viscous dissipation (m) |
|---|---|---|
| 2 | 5.51 | 3.18 |
| 3 | 5.12 | 3.52 |
| 4 | 6.03 | 3.90 |
| 5 | 6.31 | 4.32 |
| 6 | 6.56 | 5.52 |
| 7 | 7.01 | 6.40 |
| 8 | 8.63 | 7.44 |
| 9 | 7.35 | 6.61 |
| 10 | 7.05 | 5.87 |
| 11 | 7.64 | 7.71 |
| 12 | 7.91 | 7.36 |
| 13 | 7.46 | 5.86 |
| 14 | 8.74 | 7.63 |
| 15 | 8.63 | 7.98 |
| 16 | 8.00 | 7.31 |
| 17 | 8.63 | 7.44 |
| 18 | 7.26 | 7.34 |
| 19 | 7.80 | 4.50 |
| 20 | 7.79 | 6.07 |
| 21 | 7.80 | 5.84 |
| 22 | 8.00 | 7.37 |
| 23 | 8.16 | 7.59 |
| 24 | 8.08 | 7.85 |
| 25 | 8.16 | 8.14 |

The assumption of laminar flow used in the selection of equation 2 can be checked. The Reynolds number (**R**) for flow in a conduit is

$$\mathbf{R} = vD\rho/\mu. \tag{39}$$

Inserting values of velocity and conduit diameter from equations 37 and 38 gives

$$\mathbf{R} = (1.33)(3.18)(2{,}700)/100 = 113. \tag{40}$$

This value of **R** is well below the critical value of 2,700 for transition to turbulent flow in conduits, and therefore the original assumption of laminar flow in the conduit is valid.

The main portion of the east-rift conduit from the summit reservoir down to the vicinity of the erupting vent may be a tabular dike rather than a circular conduit. Flow equations for the geometry of a dike or sill can be developed that are similar to the previous equations for the circular conduit. Flow in a dike or sill can be modeled as flow between parallel plates. The pressure drop for this flow geometry is (Gebhart, 1961)

$$P = 12\mu lv/a^2, \tag{41}$$

where $a$ is the thickness of the dike. With viscous-dissipation effects considered, the temperature of the fluid flowing in the dike is

$$T_b - T_w = (3/5)\mu v^2/k. \tag{42}$$

Equations 41 and 42 are similar to equations 2 and 27 for the cylindrical conduit model. The volume flow rate in the dike (equation 13) is again $Q = abv$, where $b$ is the width of the dike. If the calculation that led to equation 31 is carried out for the dike geometry using equations 41 and 42, the thermal runaway temperature can be shown to be the same as in equation 31: $\Phi = 77$ K. The different constant in equation 42 does not affect the result for runaway temperature. The flow velocity at runaway is found from equation 42:

$$v = [(5/3)\Phi k/\mu]^{0.5} = [(5/3)(77)(2.09)/100]^{0.5} \tag{44}$$

or

$$v = 1.63 \text{ m/s}. \tag{45}$$

Although velocity and flow rate are known, it is not possible to determine the thickness of the dike or sill from equation 13 because of the additional geometric parameter $b$, the width of the dike, that now occurs in equation 13. In the absence of additional information, the best procedure for dike and sill flow calculations is to use again the concept of equivalent diameter (Chapman, 1967).

Referring to the previous calculation for conduit diameter in equation 38, where the conduit diameter was 3.18 m, and substituting this into equation 14 gives

$$a = D_{eq}/2 = 3.18/2 = 1.59 \text{ m}. \tag{46}$$

This implies that if the flow during episode 2 of the 1983–84 Kilauea activity passed through a dikelike conduit rather than a circular conduit, the dike was on the order of 1.59 m thick, the dynamic pressure was similar to that determined in equation 34, and the flow velocity for the dike was similar to that determined in equation 45, assuming that viscous-dissipation effects were a major factor. The dike thickness in equation 46 is not thin enough for sufficient cooling and solidification to occur to cause the conduit to easily jam up and go into a period of repose. This can be shown by applying equation 8. The value of dike thickness in equation 46, however, is consistent with observations of fossil dikes in Hawaii. The thickness of the dike or conduit in episode 2 of Kilauea's 1983 eruptive activity can be determined using equation 13, the value of dike thickness in equation 46, the flow velocity from equation 45, and a typical value of intrusive flow rate such as that in equation 10:

$$b = Q/(a/v) = 10.6/[(1.59)(1.63)] = 4.09 \text{ m}. \tag{47}$$

Viscous dissipation can explain the intermittent intrusive flow observed in the various eruptive episodes. When a certain critical pressure and temperature (see, for example, equation 32) are reached, flow begins, and the pressure starts to drop. Eventually the flow stops, and magma in the conduit cools. A period of repose then occurs, during which the pressure builds up again, and the magma in the conduit is heated to the runaway condition once more by viscous dissipation. The period of repose or time between eruptive episodes can be determined by a simple calculation in which the viscous-dissipation energy is equated to the increase in internal energy necessary to raise the magma from its solidification temperature back up to its runaway temperature. In the interest of keeping the calculation simple, I assume that the magma and surroundings are hot and near the solidification temperature, as suggested by the earlier analysis leading to equation 1. Conduction losses would then be small during the period of repose between eruptive episodes. This is probably a good assumption; in thermal-runaway problems of this type, the temperature does not increase much until nearly the

moment of thermal runaway (Hardee and others, 1977). The rate of viscous heat dissipation per unit volume in a cylindrical conduit is given by Batchelor (1970) as $(P/l)^2R^2/4\mu$ at any radius $R$. The volume-average viscous heat dissipation for a cylindrical conduit of radius $R$ is found by integrating the local value over the whole volume and is $(P/l)^2R^2/(8\mu)$. The repose time between eruptive episodes (thermal-runaway time) is found by equating the volume-average viscous heat dissipation to the change in internal energy necessary to raise the magma in the conduit from the solidification temperature to the runaway temperature,

$$\rho c \; dT/d\tau = P^2R^2/8\mu l^2, \tag{48}$$

and then integrating this result

$$\int_{1343}^{1420} \exp(26{,}170/T)\; dT = \int_0^{\tau_r} [P^2R^2/(8l^2\rho c \times 10^{-6})]\; d\tau.$$

The integration is performed after making use of the substitution $Z=26{,}170/T$ where $T=1{,}343$ K, $Z_1=26{,}170/1{,}343$, $T_2=1{,}420$ K, and $Z_2=26{,}170/1{,}420$. The solution for the repose time is then

$$\tau_r = [8l^2\rho c \times 10^{-6}/(P^2R^2)]\,[(1/T)\exp(26{,}170/T) - 26{,}170Ei(26{,}170/T)]\Big]_{1343}^{1420}. \tag{49}$$

$Ei(x)$ is the exponential integral function (Mathews and Walker, 1965), which can be evaluated using tabulated values (Gautschi and Cahill, 1965) and equation 49. The expression for the repose time then becomes

$$\tau_r = [8l^2\rho c \times 10^{-6}/(P^2R^2)](1.370 \times 10^{10}). \tag{50}$$

Equations 2 and 27 can be combined to eliminate $v$, and the result can be substituted into equation 50 to eliminate $l^2/P^2$:

$$\tau_r = (1.370 \times 10^4) D^2\rho c/[36k\mu_r(T_b - T_w)]. \tag{51}$$

Substituting into equation 51 the appropriate values and the diameter determined for the conduit in episode 2 gives

$$\tau_r = (1.370 \times 10^4)(3.18)^2(2{,}700)(4{,}186)/[36(2.09)(100)(77)]$$

or

$$\tau_r = 2.70 \times 10^6 \text{ s} = 31.3 \text{ d}. \tag{52}$$

This value of repose time compares well with observed values for the 1983–84 Kilauea eruptive episodes. Repose times for the various episodes listed in table 54.5 were determined either by inflation of the summit or by absence of lava production. A repose period of 41 d based on inflation data or 26 d based on the absence of lava production was observed between the first and second episodes (table 54.5). The average of these two values, 33.5 d, compares well with the estimated value of 31.3 d in equation 52. The repose time of 31.3 d and the average magma-supply estimate of Swanson (1972) imply that each eruptive episode should produce a total magma volume of about $9 \times 10^6$ m$^3$; the observed values in table 54.3 are not far from this, ranging from $5 \times 10^6$ to $9 \times 10^6$ m$^3$.

Equation 51 and the result from equation 52 give an alternative viewpoint to the yield-stress calculations of equations 24–26 for observed cyclic eruptive behavior. Equation 24 is based on the assumption that the non-Newtonian or Bingham yield stress combined with an increasing reservoir pressure is the mechanism behind cyclic eruptive behavior. Equation 51 assumes that viscous dissipation is the mechanism behind cyclic eruptive behavior. Although the agreement of the viscous-dissipation conduit model with observed data is good during early episodes of the eruption, the agreement is not as good in the later episodes. For instance, the observed flow rate, $Q$, increases and the observed repose time, $\tau_r$, decreases in later eruptive episodes (see tables 54.2, 54.5). Substituting conduit diameter, $D$, from equation 3 into equation 51, however, would predict that repose time is proportional to $Q$. Although this may be true in some cases, it is not the pattern of the later episodes of the 1983–84 Kilauea eruptive activity.

The previous analysis has examined how viscous dissipation might be the mechanism responsible for intermittent intrusive flow in the east-rift conduit. As noted earlier, viscous dissipation has been proposed before as the mechanism behind recurring volcanic eruption cycles (Shaw, 1969,1973; Anderson and Perkins, 1974; Fujii and Uyeda, 1974; Hardee and Larson, 1977; and Fujii, 1981). Another interesting possibility is that viscous dissipation may be the mechanism responsible for the fairly constant magma supply to the summit reservoir from the asthenosphere. As mentioned earlier, the summit reservoir appears to be replenished at a rate of 3.28 m$^3$/s (Swanson, 1972). If a conduit from the asthenosphere to the summit reservoir has magma flow due to viscous dissipation at the critical runaway condition, then equations 2, 3, and 27 apply. Fujii and Uyeda (1974) argued that the driving force for magma ascent in the upper mantle or lower crust is buoyancy due to density differences between the country rock and the magma and that this is approximately equal to

$$P/l = 1{,}000 \text{ J/m}^4 \; (100 \text{ dyne/cm}^3). \tag{53}$$

TABLE 54.5.—*Repose times between 1983–84 eruptive episodes of Kilauea*

[Data from Hawaiian Volcano Observatory (HVO) and from E.W. Wolfe]

| Episodes | Repose time ($\tau_r$) Duration of inflation (d) | Repose time ($\tau_r$) Absence of lava production (d) |
|---|---|---|
| 1–2 | 41 | 26.0 |
| 2–3 | 24 | 23.4 |
| 3–4 | 63 | 65.3 |
| 4–5 | 13 | 12.0 |
| 5–6 | 20 | 19.3 |
| 6–7 | 22 | 20.6 |
| 7–8 | 23 | 19.6 |
| 8–9 | 11 | 8.5 |
| 9–10 | 21 | 17.3 |
| 10–11 | 30 | 27.3 |
| 11–12 | 24 | 22.4 |
| 12–13 | 51 | 50.1 |
| 13–14 | 10 | 8.3 |
| 14–15 | 15 | 15.3 |
| Average | 26.3 | 24.0 |

Substituting this pressure gradient and the viscosity (100 Pa·s) at thermal runaway into equation 2 and solving gives

$$D^2/v = 3.2 \text{ m·s}. \quad (54)$$

Substituting this result and the flow velocity at thermal runaway from equation 37 into equation 3 gives

$$Q = (\pi/4)D^2 v = (\pi/4)(3.2)(1.33)^2 = 4.45 \text{ m}^3/\text{s}. \quad (55)$$

This magma-reservoir replenishment rate (4.45 $m^3/s$) compares well with the observed replenishment rate (3.28 $m^3/s$), considering the simplicity of the model and assumptions.

## CONCLUSIONS

The upper part of Kilauea's east-rift conduit (upper 25 km) is relatively open to flow, and intrusions in it are usually aseismic. The lower part of the east-rift conduit is usually closed and requires fracturing to produce intrusions, which are normally associated with seismicity. A repetitive thermal-intrusion model was used to show that the difference between these two types of conduit flow is determined by the average volume-intrusion rate, length of conduit, and, to a lesser extent, the number of previous intrusions in that part of the conduit. Non-Newtonian rheology or viscous-dissipation effects are probably important in determining flow characteristics in the Kilauea conduit system.

A conduit flow model based on forced convective flow of a non-Newtonian (Bingham plastic) liquid is compatible with field observations for the recent 1983–84 Kilauea eruptive activity. Predictions of dynamic pressure based on this model (0.985–1.69 MPa) agree well with the summit pressure estimates (0.85–1.53 MPa) of Decker and others (1983). Predicted effective conduit diameters are on the order of 5–10 m. For the diameters, conduit lengths, and intrusion rates involved in the 1983–84 Kilauea eruptive episodes, the magma does not have time to cool appreciably as it flows the length of the conduit. The temperature of the magma at the vent is therefore probably close to the temperature of the summit reservoir. Although the conduit is circular at the vent, at depth it may have a shape like a dike or sill. The concept of an effective diameter was used to examine conduit shapes such as dikes or sills; predicted dike thicknesses were still large enough that heat loss at the conduit wall would not have been a major factor in the 1983–84 Kilauea activity. The field measurements of Bingham-plastic yield stress of Kilauea basalt (Shaw and others, 1968) were used to explain the cyclic nature of eruptive episodes. The summit magma-reservoir pressure must build sufficiently to overcome the Bingham-plastic yield stress of the magma in the conduit before each eruptive cycle. The resulting calculated pressure changes in the summit reservoir agree closely with pressure-change estimates of Decker and others (1983).

A conduit flow model was also developed in which viscous dissipation effects were included. This conduit model is particularly applicable to thin conduits, on the order of 0.1 m thick or less. Such conduits are sufficiently thin that thermal losses to the conduit wall are important, and an internal heat supply is needed to keep the flowing magma from solidifying rapidly in the conduit. Viscous dissipation is a likely internal heat source for such intrusive flows. The forced-convection flow model with viscous-dissipation effects developed here is compared with field observations. The model predicts lava-eruption temperatures around 1,420 K, and this is in good agreement with field observations. The dynamic pressure driving this intrusive flow is approximately 10 times higher than corresponding pressure predictions for the flow model based on non-Newtonian rheology. The higher pressures occur because pressure is the source of energy for the internal viscous-dissipation heat. Calculation of thermal-runaway time based on the viscous-dissipation flow model predicted times between eruptive episodes on the order of a month for the 1983–84 Kilauea eruptive activity, in agreement with observations. Although the viscous-dissipation flow model gives results that are compatible with field observations, this model predicts effective conduit diameters for the 1983–84 Kilauea activity that are sufficiently large that an internal heat mechanism like viscous dissipation is not needed. This suggests that viscous-dissipation effects may not have been important in the 1983–84 Kilauea eruptive episodes. Viscous-dissipation effects may well be important in other cases of rift intrusions, particularly for rapid intrusions in thin dikes and sills. Viscous dissipation can also be used to explain how the summit reservoir is replenished at a fairly constant rate over long periods of time. Both the non-Newtonian flow model and the viscous-dissipation flow model depend primarily on the unusual rheology of magma. The Bingham-plastic model considers that viscosity depends on shear stress, and the viscous-dissipation model considers that viscosity depends on temperature. Actually, magma viscosity in the subliquidus temperature range depends on shear stress, shear rate, temperature, time, and previous thermal history (Hardee and Dunn, 1981). The Bingham-plastic flow model and the viscous-dissipation flow model are simply ways of looking at major magma-viscosity effects one at a time.

Epp and others (1983) noted that an inverse relation exists between the summit tilt deflation of Kilauea and the elevation of associated eruptive vents. Decker and others (1983) found that this relation indicated a pressure change of 0.085 MPa per μrad of rapid radial summit tilt. By correlating data from near the summit to near sea level, Epp and others (1983) showed that a general relation exists between volume of erupted lava and vent elevation: volume of erupted lava tends to increase with a decrease in elevation. These observations are consistent with the conduit and dike models developed earlier. The dynamic pressure change available to overcome frictional resistance in the conduit was calculated to be about 1.0 MPa (0.985–1.69 MPa). Sufficient pressure must also be available in the summit reservoir to overcome the hydrostatic head from the reservoir up to the vent. The difference in hydrostatic head between summit vents and those near sea level is about 30 MPa (roughly 1 km of liquid magma). The hydrostatic head favors the vents near sea level. The conduit length from the summit reservoir to the vents near sea level is 2 to 3 times longer, and the pressure required to overcome frictional losses is that much greater. However, although this pressure doubles or triples to 2–3 MPa, the 30-MPa

reduction in hydrostatic head more than offsets this. Greater reservoir pressure tends to be available to drive intrusive flows to the lower elevation vents. It is not surprising that the volume of eruption tends to be larger at lower elevation vents.

If pressure favors eruptions at lower elevation vents, the obvious question is, why do most eruptions occur at higher elevation vents? The answer is that thermal effects tend to keep the upper portion of the east rift zone more open to flow (see table 54.1). The lower elevation vents are connected to a portion of the east-rift conduit that is not normally open or available for intrusive flow except at special times when fracturing events or earthquakes have temporarily opened the conduit all the way to vents near sea level.

The east-rift conduit and its eruptions provide valuable data that can be used to construct and test models of intrusive magma flow. Considerably more data are available from east-rift eruptions than are available from other intrusive magmatic processes. Once models of intrusive magmatic flow are tested, it is possible to use them for prediction in other situations where data are meager or absent. It is possible to use the intrusive flow models to predict the thermal-runaway conditions for a shallow magma reservoir that is intersected by a drill hole. These models can also be extended to magma other than basalt. For example, using the data of Piwinskii and Weed (1980), the viscosity for a molten rhyolite sample from Nevada is found to be $\mu=(0.857\times10^{-6})\exp(36{,}194/T)$. This is the same general form of the viscosity function as used earlier in equation 18. When the earlier calculations are repeated using the viscosity function of Piwinskii and Weed (1980), the thermal-runaway times, or times between eruptive episodes, for rhyolite are on the order of hundreds of years or more, depending on the assumptions used for conduit diameter.

## REFERENCES CITED


Anderson, O.L., and Perkins, P.C., 1974, Runaway temperatures in the asthenosphere resulting from viscous heating: Journal of Geophysical Research, v. 79, p. 2136–2138.

Batchelor, G.K., 1970, An introduction to fluid mechanics: Cambridge, U.K., University Press, p. 151–182.

Chapman, A.J., 1967. Heat transfer: New York, Macmillan, p. 338–339.

Decker, R.W., and Decker, B., 1981, The eruptions of Mount St. Helens: Scientific American, v. 244, no. 3, p. 68–80.

Decker, R.W., Okamura, A.T., and Dvorak, J.J., 1983, Pressure changes in the magma reservoir beneath Kilauea Volcano, Hawaii [abs.]: Eos (American Geophysical Union Transactions), v. 64, p. 901.

Dvorak, J.J., Okamura, A.T., and Dieterich, J.H., 1983. Analysis of surface deformation data, Kilauea Volcano, Hawaii, October 1966 to September 1970: Journal of Geophysical Research, v. 88, p. 9295–9304.

Duffield, W.A., Christiansen, R.L., Koyanagi, R.Y., and Peterson, D.W., 1982, Storage, migration, and eruption of magma at Kilauea Volcano, Hawaii, 1971–1972: Journal of Volcanology and Geothermal Research, v. 13, p. 273–307.

Dzurisin, D., Anderson, L.A., Eaton, G.P., Koyanagi, R.Y. Lipman, P.W., Lockwood, J.P., Okamura, R.T., Puniwai, G.S., Sato, M.K., and Yamashita, K.M., 1980, Geophysical observations of Kilauea Volcano, Hawaii, 2. Constraints on the magma supply during November 1975–September 1977: Journal of Volcanology and Geothermal Research, v. 7. p. 241–269.

Eckert, E.R.G., and Drake, R.M., 1959, Heat and mass transfer: New York, McGraw-Hill, p. 190–200.

Epp, D., Decker, R.W., and Okamura, A.T., 1983, Relation of summit deformation to east rift zone eruptions on Kilauea Volcano, Hawaii: Geophysical Research Letters, v. 10, p. 493–496.

Fedotov, S.A., 1981, Magma rates in feeding conduits of different volcanic centers: Journal of Volcanology and Geothermal Research, v. 9, p. 379–394.

Fiske, F.S., and Jackson, E.D., 1972, Orientation and growth of Hawaiian volcanic rifts: the effect of regional structure and gravitational stresses: Royal Society of London Proceedings, v. 329, p. 299–326.

Fujii, N., 1981, A model of magma ascent and eruption sequence for polygenetic volcanoes [abs.]: Tokyo, 1981, International Association of Volcanology and Chemistry of the Earth's Interior, p. 97.

Fujii, N., and Uyeda, S., 1974, Thermal instabilities during flow of magma in volcanic conduits: Journal of Geophysical Research, v. 79, p. 3367–3369.

Gautschi, W., and Cahill, W.F., 1965, Exponential integral and related functions, *in* Handbook of mathematical functions, Abramowitz, M., and Stegun, I.A., eds.: Washington, National Bureau of Standards, p. 227–251.

Gebhart, B., 1961, Heat transfer: New York, McGraw-Hill, p. 137–219.

Gruntfest, I.J., 1963. Thermal feedback in liquid flow; plane shear at constant atress: Transactions of the Society of Rheology, v. 7, p. 195–207.

Gruntfest, I.J., Young, J.P., and Johnson, N.L., 1964, Temperatures generated by the flow of liquids in pipes: Journal of Applied Physics, v. 35, p. 18–22.

Hardee, H.C., 1982, Incipient magma chamber formation as a result of repetitive intrusions: Bulletin Volcanologique, v. 45, no. 1, p. 41–49.

———1983, Heat transfer measurements of the 1983 Kilauea lava flow: Science, v. 222, p. 47–48.

Hardee, H.C., and Dunn, J.C., 1981, Convective heat transfer in magmas near the liquidus: Journal of Volcanology and Geothermal Research, v. 10, p. 195–207.

Hardee, H.C., and Larson, D.W., 1977, Viscous dissipation effects in magma conduits: Journal of Volcanology and Geothermal Research, v. 2, p. 299–308.

Hardee, H.C., Lee, D.O. and Donaldson, A.B., 1977, Predicting the time-to explosion of multidimensional explosives with a constant heat flux boundary condition: Albuquerque, N. Mex., Sandia National Laboratories Report SAND76-0738, 31 p.

Kienle, J., and Swanson, S.E., 1980, Volcanic hazards from future eruptions of Augustine Volcano, Alaska: Fairbanks, University of Alaska, Geophysics Institute Report UAG-R275, 122 p.

MacDonald, G.A., and Hubbard, D.H., 1972, Volcanoes of the national parks in Hawaii: Honolulu, Tongg, 56 p.

Mathews, J. and Walker, R.L., 1965, Mathematical methods of physics: New York, W.A. Benjamin, p. 56–90.

Moore, J.G., 1971, Bathymetry and geology—east cape of the Island of Hawaii: U.S. Geological Survey Miscellaneous Geologic Investigations Map, I–677, scale 1:62,500.

Peck, D.L., Wright, T.L. and Decker, R.W., 1979, The lava lakes of Kilauea: Scientific American, v. 241, no. 4, p. 114–128.

Piwinskii, A.J., and Weed, H.C., 1980, Dynamic viscosity of some silicate melts to 1688 °C under atmospheric pressure: Thermochimica Acta, v. 37, p. 189–195.

Richter, D.H., and Moore, J.G., 1966, Petrology of the Kilauea Iki lava lake Hawaii, The 1959–60 eruption of Kilauea Volcano, Hawaii: U.S. Geological Survey Professional Paper 537–B, p. B1–B26.

Ryan, M.P., Blevins, J.Y.K., Okamura, A.T., and Koyanagi, R.Y., 1983. Magma reservoir subsidence mechanics: Theoretical summary and application to Kilauea Volcano, Hawaii: Journal of Geophysical Research, v. 88, p. 4147–4181.

Ryan, M.P., Koyanagi, R.Y., and Fiske, R.S., 1981, Modeling the three-dimensional structure of macroscopic magma transport systems: Application to Kilauea Volcano, Hawaii: Journal of Geophysical Research, v. 86, p. 7111–7129.

Shaw, H.R., 1969, Rheology of basalt in the melting range: Journal of Petrology, v. 10, p. 510–535.

———1973, Mantle convection and volcanic periodicity in the Pacific: Evidence from Hawaii: Geological Society of America Bulletin, v. 84, p. 1505–1526.

———1980, The fracture mechanisms of magma transport from the mantle to the surface, *in* Hargraves, R.B., ed., Physics of magmatic processes: Princeton, N.J., Princeton University Press, p. 201–264.

Shaw, H.R., Wright, T.L., Peck, D.L., and Okamura, R., 1968, An analysis of field measurements in Makaopuhi lava lake, Hawaii: American Journal of Science, v. 266, p. 225–264.

Smith, R.L., 1979, Ash-flow magmatism, *in* Chapin, C.E., and Elston, W.E., eds., Ash-flow tuffs: Geological Society of America Special Paper 180, p. 5–27.

Swanson, D.A., 1972, Magma supply rates at Kilauea Volcano, 1952–1971: Science, v. 175, p. 169–170.

Vennard, J.K., 1956, Elementary fluid mechanics: New York, John Wiley, p. 188–242.

# CONCEPTUAL MODELS OF BRINE EVOLUTION IN MAGMATIC-HYDROTHERMAL SYSTEMS

*By* Robert O. Fournier

## ABSTRACT

The depth of intrusion of a magmatic body is important in regard to brine evolution and to the type and intensity of hydrothermal alteration that is likely to be associated with that intrusion. At a depth of intrusion of 6–7 km, and in the absence of evaporite deposits somewhere in the section, nonmagmatic water is not likely to be converted to brine unless there are special circumstances, such as repeated magmatic intrusions and repeated fracturing of very hot rock. In contrast, brine is very likely to form from nonmagmatic water where the depth of intrusion comes within about 3–4 km of the surface, and dilute water is heated to above about 400–450 °C.

When pore-fluid pressures are controlled by hydrostatic conditions, magmatic waters will evolve to highly saline brines at depths less than about 10-12 km, irrespective of the initial concentrations of salt and water dissolved in the magma. Dilute hydrothermal fluids of meteoric origin and mixtures of meteoric water and condensed magmatic gas (steam) are likely to form convection systems that float upon the more saline and probably hotter magmatic fluid. Double-diffusive convection is likely to result from the temperature and salinity gradients.

Quasi-plastic flow and mineral deposition generally prevent flow of water at hydrostatic pressure through rock at temperatures above 350–450 °C. However, where there are steep thermal gradients and a relatively rapid rate of change of stress, such as where magma is rapidly injected from a deep environment into a more shallow environment, brittle deformation of rocks may occur at temperatures in excess of 450 °C. Ground water at hydrostatic pressure may flow into and through these fractures and become heated to very high temperatures, possibly flashing in great part to steam with the simultaneous development of a small mass of brine. This situation should persist for only a relatively short time before quasi-plastic flow and mineral deposition limit additional fluid circulation to temperatures below 350–450 °C.

A generalized model is presented for the evolution of a hydrothermal system within an oceanic volcano, such as at Hawaii, in which a slowly rising magma reservoir maintains a depth of about 3–4 km beneath the summit as the volcanic edifice builds upon the sea floor. Significant amounts of highly saline brine are likely to be generated from sea water when the magma reservoir rises to within about 4–5 km of sea level. After a volcanic island forms, fresh water may enter the top of the hydrothermal system and float upon the brine. Sulfides are likely to deposit below sea level within the chloride-rich brine portion of the system, but these deposits are not likely to be exposed during subsequent erosion. With continued growth of the volcano above sea level, temperatures and pressures within the hydrothermal system become appropriate for complete evaporation of pore waters adjacent to the rising magma chamber. Sodium sulfate- and sodium carbonate-rich brines form above sea level where steam condenses and sulfur- and carbon-rich gases react with the country rock.

What is generally thought of as supercritical behavior of a fluid (no phase change upon heating or cooling) occurs only at pressures greater than the hypercritical pressure, a pressure great enough to ensure that the gas phase will retain all the salt that was initially dissolved in the liquid phase at a lower temperature. At hydrostatic conditions the hypercritical point for a dilute water containing about 2,000 mg/kg total dissolved solids would be at about 700 °C at a depth of 4.6 km, and for sea water it would be at about 900 °C at a depth of 12.9 km.

## INTRODUCTION

Studies of fluid inclusions in minerals from fossil hydrothermal systems (Roedder, 1979) show that brines commonly occurred at different times and in different parts of those systems. Descriptions of brine-rich fluid inclusions that formed in hydrothermal systems associated with shallow intrusive rocks are presented in many articles, including Roedder (1971), Nash (1976), Eastoe (1978), Bodnar and Bean (1980), and Reynolds and Bean (1985). Brines may originate in many ways. Connate brines are encountered in many deep sedimentary basins (White, 1965), and the formation of brines by evaporation of closed basin lakes (Langbein, 1961; Hardie and Eugster, 1970; Eugster and Jones, 1979) and the interaction of meteoric water with evaporite deposits (White, 1968) are well documented. Relatively little attention, however, has been given to highly saline brines formed by the interaction of ordinary waters with hot rocks that do not contain evaporites (Bischoff and Pitzer, 1985; Fournier, 1985a). This paper stresses the importance of including information about brine evolution from dilute water, sea water, and magmatic gases in our conceptual models in order to approximate what may happen in natural magmatic-hydrothermal systems. Particular attention will be focused on the important effect that depth of magmatic intrusion has on the generation of highly saline brine from relatively dilute water of meteoric origin and from magmatic gases, and a generalized model will be presented for the evolution of a hydrothermal system within an oceanic volcano, such as at Hawaii.

### ACKNOWLEDGMENTS

The manuscript benefited from thoughtful reviews by P.T. Delaney and J.L. Bischoff. I am particularly indebted to J.L. Bischoff and to K.S. Pitzer for making available to me draft copies

of their manuscripts dealing with experimental and theoretical aspects of the solubility of NaCl in steam. The information that they provided was of great value in deciding which data sets to use in those instances when the experimental data reported by different researchers were in conflict.

## FLUID CIRCULATION AND HEAT TRANSFER IN MAGMATIC-HYDROTHERMAL SYSTEMS

It will be shown subsequently that the attainment of temperatures in excess of about 400 °C is generally a prerequisite for producing brines from dilute to moderately saline waters within convecting hydrothermal systems. Therefore, attention will be focused on the factors that are likely to limit the maximum temperature that is attained by a convecting fluid at hydrostatic pressure.

Models for fluid flow and heat transfer in hydrothermal systems have been discussed by many investigators, including Elder (1965), Bodvarsson and Lowell (1972), Lister (1974, 1980, 1983), Ribando and others (1976), Cheng and Minkowycz (1977), Cathles (1977, 1980, 1983), Norton and Knapp (1977), Norton and Knight (1977), Norton (1978, 1984), Parmentier and Spooner (1978), Torrance and Sheu (1978), Fehn and Cathles (1979), Norton and Taylor (1979), Hartline and Lister (1981), Knapp and Norton (1981), Hardee (1982), and Sleep (1983). One of the most important parameters in these models is permeability, which is generally assumed to have a constant value, or to change uniformly in response to a variable, such as time or temperature. In natural hydrothermal systems permeability is likely to change nonuniformly and even to fluctuate during the life of the system. Processes that tend to increase permeability are faulting (brittle fracture), thermal cracking upon cooling, hydrofracturing, and dissolution of minerals. Processes that tend to decrease permeability are quasi-plastic flow, precipitation of minerals, and thermal expansion of rock. All of these processes must be taken into account in our models.

Several factors influence whether a rock deforms by brittle fracture or quasi-plastic flow, including the inherent strength of the rock, depth of burial (confining pressure), temperature, state of stress, and the rate of loading (rate of change of stress). Brittle, stiff materials are able to accommodate increasingly large stress differences until their strength is exceeded and they fail by fracture. Relatively plastic, compliant materials are unable to accommodate large stresses because they deform in response to relatively small increases in stress difference. As rocks are heated and subjected to greater confining pressure, they tend to exhibit a more ductile response to increased stress difference. The situation is complicated, however, because at a given temperature some materials deform by quasi-plastic flow when the rate of loading is slow and by brittle fracture when the rate of loading is rapid (Lama and Vutukuri, 1978). Thus, a relatively fast rate of change of stress may result in brittle fracture and increased permeability, whereas, at the same temperature, a relatively slow rate of change of stress may lead to quasi-plastic deformation and a decrease in porosity and (or) increase in pore-fluid pressure.

The maximum depths of earthquake foci probably give a good indication of the depth at which quasi-plastic flow limits the downward penetration of ground water above relatively shallow magmatic bodies that are still hot. At Yellowstone National Park, information is available about earthquake focal depths and the maximum temperature likely to be attained by the hydrothermal system that convects to the surface (Fournier and Pitt, 1985). Well-located earthquakes seldom exceed about 4 km depth beneath the Yellowstone caldera but are much deeper outside the caldera. Chemical geothermometers, mixing models, and phase relations in the system $NaCl-H_2O$, indicate that the maximum temperature likely to be attained by the hydrothermal system is 350–430 °C (Fournier and Pitt, 1985). Based on temperature profiles calculated from heat-flow data for several localities in the Western United States and earthquake focal depths at those same locations, Smith and Bruhn (1984) conclude that the temperature at which deformation changes from frictional (brittle fracture) to quasi-plastic flow commonly ranges from about 300–450 °C. Also, self-sealing by precipitation of quartz and other minerals is likely to occur in the temperature range 350–500 °C when solutions are heated at constant pressure (Fournier, 1977, 1983a, 1983b; Sleep, 1983). Thus, permeability reduction by physical and chemical processes becomes increasingly important at temperatures above about 350 °C.

Those rocks situated at depth and in close proximity to a magma probably are at too great a temperature to sustain the large stress differences necessary to induce significant fracturing and faulting. Where fracturing has occurred in rocks at temperatures above about 350–450 °C, quasi-plastic deformation is likely to close those fractures within a relatively short time. Therefore, in most magmatic-hydrothermal systems convecting thermal waters at hydrostatic pressure probably are separated from magma by a region of hot rock that deforms quasi-plastically.

The above considerations lead to a model of a magmatic-hydrothermal system in which thermal energy is transferred mainly by conduction from very hot rock or magma to hydrostatically pressured circulating water. Minor additional heat is transferred by flow of fluids evolved from the crystallizing magma. The schematic depth-temperature profile shown in figure 55.1 represents a situation in which most of the fluid flow is restricted to a few relatively permeable channels, and the base of the convecting hydrothermal system (point B) is above the magmatic body (a simplified representation of real magmatic-hydrothermal systems in which convective flow of heated fluid is likely to occur at the sides as well as the tops of hot intrusive bodies). The temperature gradient for conductive heat flow from magma or hot impermeable rock is shown by line MB. Upward-flowing fluid in the convection system transfers heat relatively efficiently, and eventually temperatures along the flow path may approach an adiabatic profile (from B to A). If the temperature at point B is less than the critical temperature, point C, the adiabatic profile is nearly isothermal (line BA). The upper limit of the nearly isothermal region is set by the boiling-point curve. The position of the boiling-point curve is determined mainly by the location of the water table and the salinity and gas content of the particular fluid in the system.

In summary, quasi-plastic flow and mineral deposition generally prevent flow of water at hydrostatic pressure through rock at temperatures above 350–450 °C. However, where there are steep thermal gradients and a relatively rapid rate of change of stress, such as where magma is rapidly injected from a deep environment into a more shallow environment, brittle deformation of rock may occur at temperatures in excess of about 450 °C. Ground water at hydrostatic pressure may flow into and through these fractures and become heated to very high temperatures, possibly flashing in great part to steam. However, this situation should persist for only a very short time before quasi-plastic flow and mineral deposition limit additional fluid circulation to temperatures below about 450 °C.

## BEHAVIOR OF CHLORIDE-RICH SALINE SOLUTIONS IN HYDROTHERMAL SYSTEMS

The following discussion is based on the experimentally determined behavior at hydrothermal conditions of the system NaCl-$H_2O$ (Keevil, 1942; Ölander and Liander, 1950; Copeland and others, 1952; Sourirajan and Kennedy, 1962; Khaibullin and Borisov, 1966; Hilbert, 1979; Galobardes and others, 1981; Parisod and Plattner, 1981; Gunter and others, 1983; Bodnar and others, 1985; Bischoff and others, in press), NaCl-KCl-$H_2O$ (Ravich and Borovia, 1949), and sea water (Bischoff and Rosenbauer, 1984, 1985; Bischoff and Pitzer, 1985). In related articles (Fournier, 1983b; 1985a), the pressure-temperature-composition relations in the system NaCl-$H_2O$ given by Sourirajan and Kennedy (1962) were used as a basis for constructing a model for the behavior of saline solutions in hydrothermal systems. Results of recent experimental studies (Bischoff and Rosenbauer, 1984, 1985; Bodner and others, 1985; Bischoff and others, in press) and theoretical modeling of the thermodynamics of the behavior of NaCl in steam (Pitzer, 1983; Pitzer and Li, 1984; Pitzer and Pabalan, in press) and in mixtures of $H_2O$ and $CO_2$ (Bowers and Helgeson, 1983) show that the Sourirajan and Kennedy (1962) results for the solubility of NaCl in steam are probably considerably in error at temperatures above 400 °C. For example, the isopleth of 0.4 weight percent NaCl dissolved in steam in pressure-temperature space according to the data of Sourirajan and Kennedy (1962) is compared in figure 55.2 to the same isopleth using the model of Pitzer and Pabalan (in press). Experimental data of Ölander and Liander (1950) are compatible with either isopleth, but the results reported by Bodner and others (1985) clearly favor the Pitzer and Pabalan model. In the remainder of this paper results of the Pitzer and Pabalan (in press) model for the solubility of NaCl in steam will be used.

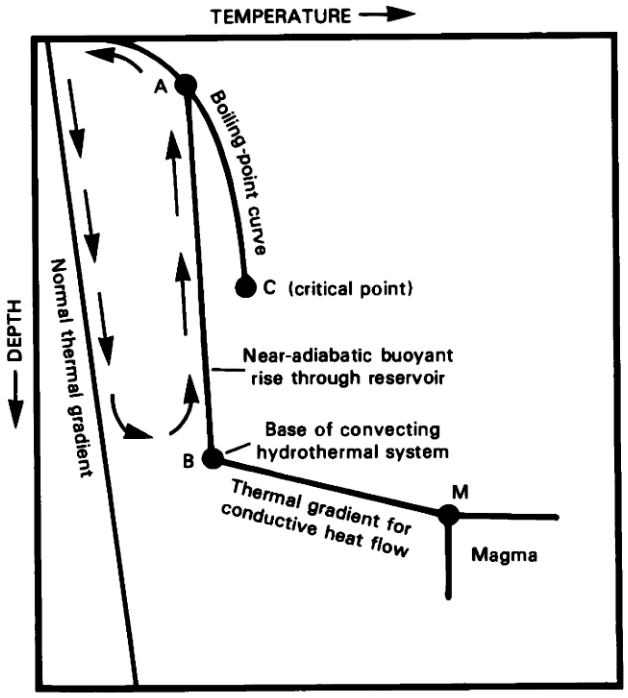


FIGURE 55.1.—Schematic depth-temperature profile for fluid flow (shown by arrows) restricted mainly to a few relatively permeable channels above magmatic heat source. Lettered points are discussed in text.

At a given depth and hydrostatic load (a given pressure) more saline solutions will boil at higher temperatures than less saline solutions, and the critical points of more saline solutions are encountered at higher temperatures and higher pressures (greater depths) than those of less saline solutions. Approximate boiling-point curves, extending to the critical points, for pure water and 10 and 25 weight percent NaCl solutions are shown in figure 55.3. Haas (1971) calculated boiling-point curves for water and various salt solutions of as much as 25 weight percent with an upper temperature limit of 330 °C. His results are slightly different from those shown in figure 55.3 because he assumed that hydrostatic pressure is controlled by the weight of the overlying column of boiling solution, thus correcting for changing density. The boiling-point curves shown in figure 55.3 were calculated with the assumption that the pressure-controlling column of solution has a constant density of 1. This assumption appears to be valid in some presently active hydrothermal systems (Fournier, 1983b). The physical reality appears to be that at given depths, fluid pressures within the hot part of the system are the same as fluid pressures in the surrounding cold part of the system. Lithostatic depths in figure 55.3 and subsequent figures were calculated using an average rock density of 2.5 kg/m$^3$.

Boiling-point curves for hydrostatic conditions are calculated relative to the position of the water table. In many places that water table is far below the Earth's surface. In other places, artesian systems are present in which the pressure-controlling water table is elevated in distant hills or mountains. In still other places, hot springs discharge onto the floors of lakes or the ocean, and boiling-point curves adjust to the overlying column of lake or ocean water. Thus, the 350 °C hot-spring waters discharging on the ocean floor at 21° N. on the East Pacific Rise (Edmond and others, 1979) are below boiling temperature because of their great depth.

The boiling-point curves in figure 55.3 show temperature-depth conditions at which liquids of given salinity will first start to boil. Upflowing solutions start to boil as a result of decompression when the boiling-point curve appropriate for the composition of the particular fluid is first attained. However, as soon as boiling starts, a slight departure from the initial boiling-point curve occurs because of the increase in salinity of the residual solution as boiling progresses. Adiabatic cooling that results from decompression of a relatively dilute solution, starting at temperatures less than the critical temperature, can result in a moderate increase in salinity, but will not result in the generation of a brine. For example, adiabatic decompressional boiling of a dilute solution that results in cooling from 370–100 °C will be accompanied by the conversion of about 64.9 percent of the initial liquid to steam (calculated from data in steam tables of Keenan and others, 1969), and the final residual solution at 100 °C will be about 2.85 times more concentrated in nonvolatile elements than the initial solution.

Isopleths of the solubility of NaCl in aqueous liquids in 10 weight percent increments from 0 to 90 weight percent projected onto a temperature-pressure diagram are shown in figure 55.4. These isopleths are boiling-point curves, but the depth axis is very uncertain because of the previously discussed limitations and the incorporation of significant amounts of salts other than NaCl into natural brines. A liquid-saturation curve (or a total evaporation curve) separates a field of gas plus solid salt (at lower pressures) from a field of gas plus liquid (at higher pressures). For the system NaCl-$H_2O$, the position of this liquid-saturation curve is fixed in temperature-pressure space and is independent of the initial proportion of NaCl and $H_2O$. For aqueous solutions containing mixed salts, the position of the liquid saturation curve in temperature-pressure space will depend on the nature of the salts that are present, and precipitation of some salts will likely take place within the gas plus liquid (brine) field. The short-dashed line in figure 55.4 shows the approximate position of the boundary separating fields of gas plus liquid and gas plus solid when the fluid contains a mixture of NaCl and KCl and the Na/K ratio in that fluid is appropriate for coexisting albite and K-feldspar (Orville, 1963). The salinity of the liquid phases steadily increases with increasing temperature along the liquid saturation curve (the gas + solid + liquid curve), whereas the salinity of the gas phase increases with increasing pressure. At salinities greater than about 30 weight percent the isopleths showing solubilities in the liquid phase originate at the liquid-saturation curve (the three-phase boundary that separates the field of gas plus solid salt from the field of gas plus liquid) and terminate at critical points (shown as dots for solutions with as much as 30 weight percent NaCl). The double-dot-dashed line (fig. 55.4) is the critical curve for the system NaCl-$H_2O$. The positions of all these curves move in temperature-pressure space as other salts are added to the system.

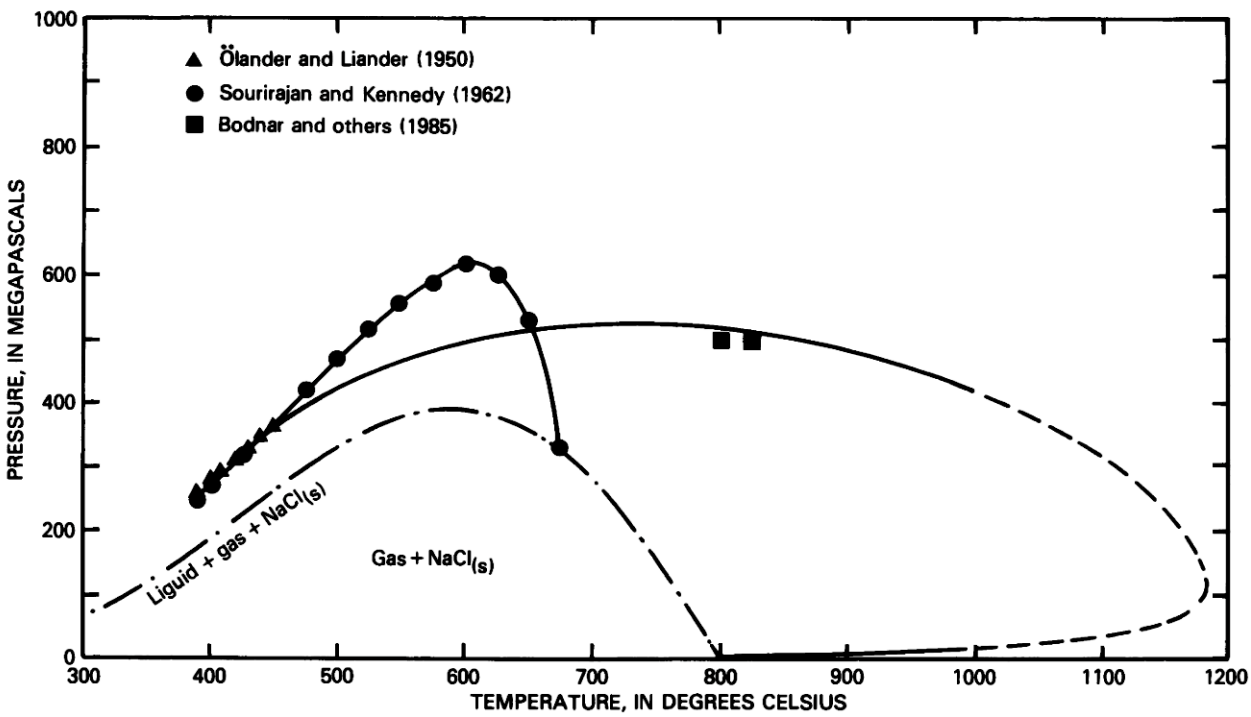


FIGURE 55.2.—Isoplethal pressure-temperature diagram for a vapor-phase composition of 0.4 weight percent NaCl in vapor + liquid region for NaCl-$H_2O$ system. Isopleth is drawn through Sourirajan and Kennedy (1962) data, and a contrasting position for that isopleth is shown using calculated solubilities according to Pitzer and Pabalan model (in press) for temperatures above 600 °C and connected smoothly to experimental data at lower temperatures. Dashed line is projected schematically beyond range of Pitzer and Pabalan model (redrafted from Pitzer and Pabalan, in press).

Boiling-point curves and critical points of solutions show only part of the important information that must be taken into account when modeling magmatic-hydrothermal systems. General phase relations exhibited by any chloride-rich solution of given salinity in temperature-depth space are shown in figure 55.5*A*. The solid line is a boiling-point curve for a solution of given salinity, ending at the critical point, C. Extending to greater depth (higher pressure) and higher temperature from the critical point is what may be thought of as a condensation-point curve for a gas that contains the same concentration of dissolved salt (an isopleth) that the initial liquid contained at subcritical temperatures and pressures. Along the condensation-point curve the gas is in equilibrium with a liquid that is much more saline than the gas, and the salinity of this liquid increases steadily and dramatically going from the critical point, C, through point H to point E. In this discussion, point H is called a "hypercritical" point (Fournier, 1985a). It marks the temperature and pressure at which a fluid of given salinity behaves according to what we normally think of as supercritical behavior; at greater pressures the fluid will not boil or condense upon heating or cooling. To the left of the dotted line that passes through point H the salinity of the gas phase decreases as temperature is increased at constant pressure. In contrast, the salinity of the gas phase increases with increasing temperature at constant pressure to the right of the dotted line.

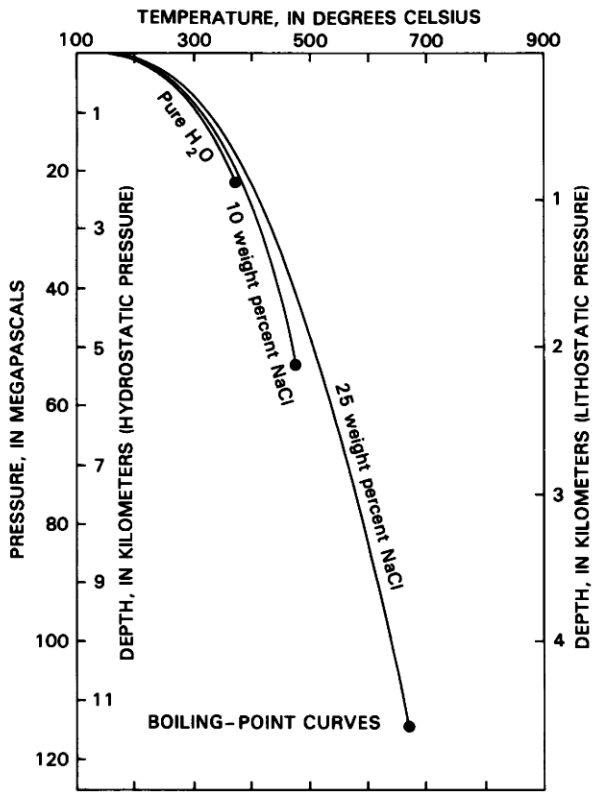


FIGURE 55.3.—Depth-temperature diagram showing approximate positions of boiling-point curves and critical points (dots) for pure water and 10 and 25 weight percent NaCl solutions.

Boiling-point and condensation-point curves are schematically shown in figure 55.5*B* for three compositions of fluid, equivalent to X, Y, and Z weight percent NaCl, such that X<Y<Z. The three boiling-point curves end at their respective critical points, $C_x$, $C_y$, and $C_z$. Gas of composition X is in equilibrium with liquid Y at point m, and liquid Z at point n. At point p gas of composition Y is in equilibrium with liquid Z. In actual water-salt systems, very large increases in salinity are generally required to increase the boiling point a few degrees at constant pressure, as shown in figure 55.4 for solutions up to about 30–40 weight percent dissolved NaCl. Isopleths of solubility of NaCl in steam (condensation-point curves) for salinities as great as 20 weight percent are shown in red in figure 55.6, and in figure 55.7 these isopleths are shown in red superimposed on figure 55.4. As previously noted, a rising fluid that intersects a boiling-point curve would become moderately more saline as a result of decompressional boiling with separation of steam, such as the fluid that follows path A in figure 55.5*A*. In contrast, hot rising fluids that follow a cooling path that is to the high-temperature side of the critical point so that the condensation-point curve is intersected, such as path B in figure 55.5*A*, will undergo a large increase in salinity. This will be discussed more fully later.

In summary, more saline solutions have boiling-point curves at higher temperatures and generally have critical points at much greater depths than less saline solutions. For a solution of given initial salinity, a condensation-point curve extending from the critical point to higher temperatures passes through a pressure maximum (the hypercritical point) and then loops back to intersect the liquid saturation curve at about the melting point of the pure salt (figs. 55.5*A*, 55.5*B*, 55.6, 55.7). The hypercritical point marks the temperature and pressure at which a fluid of given salinity will not boil or condense upon heating or cooling. The depths and temperatures at which these curves would be intersected in natural systems will vary greatly depending upon various hydrologic parameters and the nature of the dissolved salts and partial pressures of dissolved gases.

## GENERATION OF BRINES FROM DILUTE SOLUTIONS

Adiabatic decompression of a liquid, which causes its path in depth-temperature space to intersect the boiling-point curve at a temperature below the critical temperature, is likely to result in only a moderate salinity increase. However, if the cooling path of an ascending fluid brings it into the gas plus liquid field at a temperature greater than the critical temperature, a highly saline solution (brine) will condense from that ascending fluid. The NaCl concentrations of liquids (brines) that will condense from two fluids, one containing 0.2 weight percent NaCl and the other 3.2 weight percent NaCl, that intersect condensation-point curves at various temperatures as a result of decompression are shown in figure 55.8.

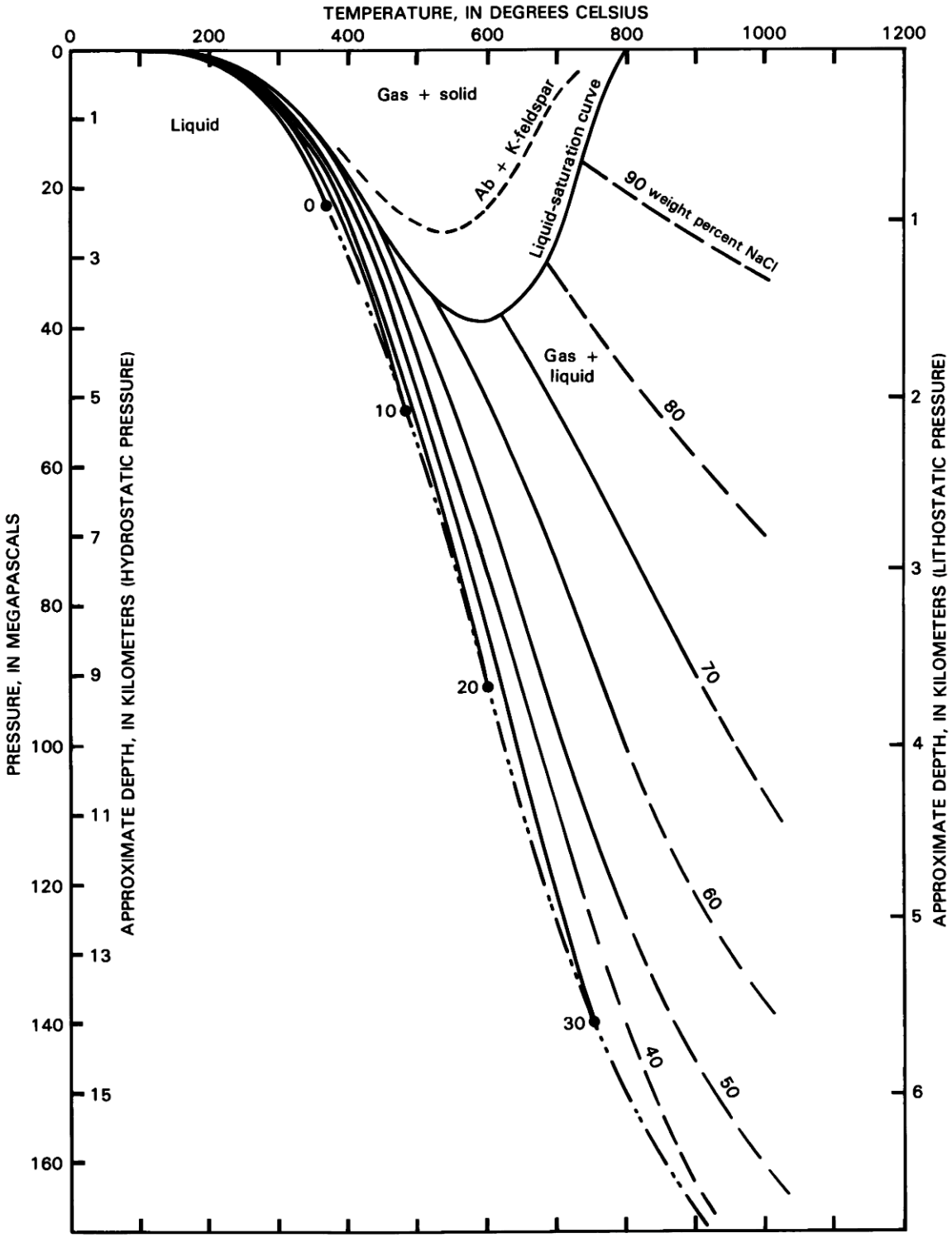


FIGURE 55.4.—Isopleths of solubility of NaCl in water in 10 weight percent increments (boiling-point curves with approximate depths for hydrostatic pressure (fluid density = 1) and lithostatic pressure (rock density = 2.5). Double-dot-dashed line is critical curve. Liquid saturation curve is 3-phase boundary for the system NaCl-$H_2O$, and short-dashed line shows approximate position of liquid saturation curve for system NaCl-KCl-$H_2O$ with Na/K ratios in liquid fixed by base exchange between albite and K-feldspar. Long dashes indicate inferred positions of curves.

A brine containing about 10 weight percent NaCl will condense from the 0.2 weight percent NaCl fluid when the condensation-point curve is intersected at a temperature of about 390 °C, and a 20 weight percent NaCl brine is generated when the condensation-point curve is intersected at about 410 °C (fig. 55.8). However, the mass of brine that forms will be small relative to the mass of coevolving, relatively dilute vapor. Because the brine has a much higher density than that of the initial fluid, the brine might counter-flow downward and accumulate in pockets or near the bottom of the hydrothermal system. Therefore, with prolonged circulation of hot fluid through the system, brine may come to fill the few fractures that are present at the base of the hot part of the convection system, bounded by hot, dilute fluid above and relatively cold water and (or) hot impermeable rock at the sides.

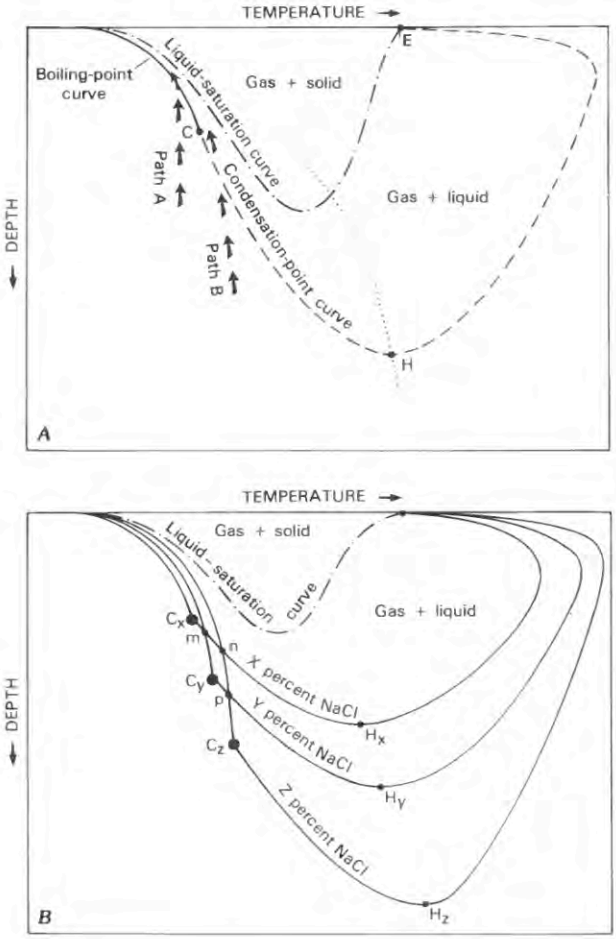


FIGURE 55.5.—Depth-temperature diagrams showing generalized phase relations. ***A***, Chloride-rich aqueous solutions at constant composition. ***B***, Three different compositions, X, Y, and Z, with X<Y<Z. Critical points for respective solutions are at C, $C_x$, $C_y$, and $C_z$, and hypercritical points are at H, $H_x$, $H_y$, and $H_z$. Dotted line and other points are discussed in text.

At given temperatures, less saline brines are generated when sea water intersects the condensation-point curve (fig. 55.8), and the intersection occurs at greater depths than for more dilute solutions. But, a larger proportion of brine is generated from sea water than from the same initial mass of a more dilute solution. The generation of brine by adiabatic decompression of sea water at temperatures above the critical point is nicely shown by Bischoff and Pitzer (1985).

In the above models brines form as a result of decompression, utilizing thermal energy contained in rising, relatively dilute fluids. Dilute fluids also may be converted to brines by prolonged boiling, utilizing thermal energy stored in hot rock to evaporate the waters. One way to accomplish this conversion is to quickly lower the hydrostatic pressure so that the boiling-point curve appropriate for the salinity of the local ground water is shifted to lower temperatures at given depths. This process might occur as a result of sudden draining of a lake or an explosive volcanic eruption. With decreasing hydrostatic pressure at any given depth, as would occur with a drop in the local ground-water table (from L1 to L2 in fig. 55.9), the boiling-point curve would shift (from A to B). Waters that were initially on or to the left of the boiling-point curve A (point C, fig. 55.9) will move into the field of gas (steam). In response to the decrease in hydrostatic pressure, the water will boil vigorously, either to dryness or until the surrounding rock temperature decreases and the salinity of the solution increases to the extent that the ground water (point D, fig. 55.9) lies on a new boiling-point curve (curve E) appropriate for the new pressure, temperature, and salinity. Small amounts of brine that form in this manner could become trapped in fluid inclusions that would give a false impression of the presence of a large convecting brine system. If the permeability of the rock is relatively low, so that the newly formed steam cannot expand and push pore fluids from the rock fast enough to prevent a large pressure increase, and if the resulting steam pressure is greater than the confining pressure, a hydrothermal explosion may occur (Muffler and others, 1971).

In volcanic environments, magma may be injected into wet rocks, causing vigorous boiling and pore-pressure buildup (Delaney, 1982). Boiling, utilizing heat stored in rock, also may occur where newly formed fractures allow water to come into contact with previously hot, dry rock. However, the quantity of brine that forms in this manner may be relatively small, either because little fluid flows through a system with low initial or rapidly decreasing permeability or because a rapid rate of flow of fluid through the system decreases the temperature of the fluid-rock interface to a value that is too low for brine to form. A decrease in temperature at the fluid-rock interface is expected because the formation of steam is likely to consume thermal energy faster than thermal energy can be transferred through rock by conduction. Thermal cracking, however, may cause new fractures to form, allowing the solution to again come into contact with rock hot enough to cause vigorous boiling.

In summary, large amounts of brine are likely to form from dilute solutions only where prolonged circulation occurs through very hot rock. This circulation is likely to occur mainly where there have been multiple injections of magma into already hot rock at moderate to shallow depths (about 2–7 km). The process of generation of

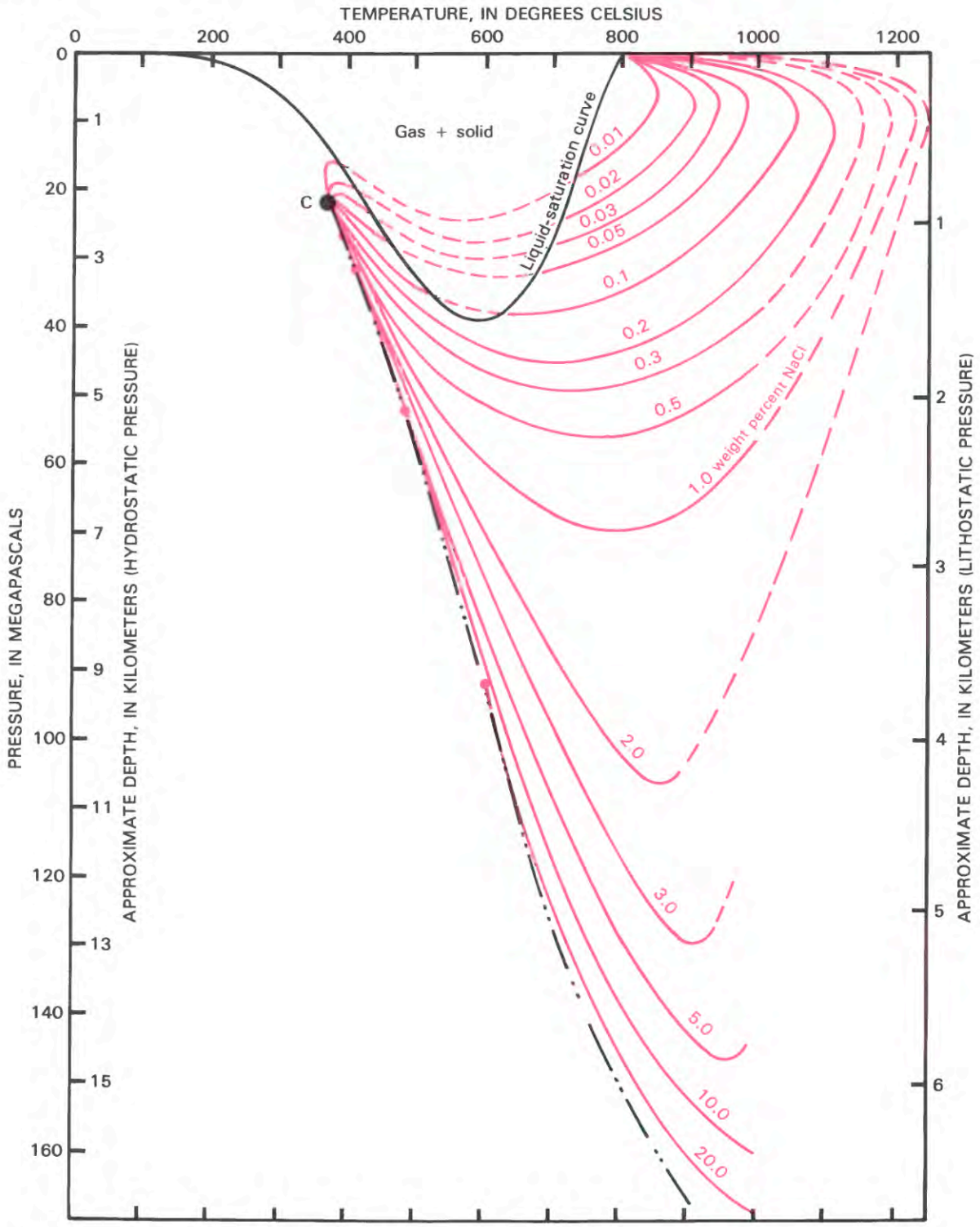


FIGURE 55.6.—Isopleths of solubility of NaCl in steam (red lines) with approximate depths for hydrostatic pressure (fluid density = 1) and for lithostatic pressure (rock density = 2.5). Double-dot-dashed line (black) is critical curve with origin at critical point of pure water (black dot). Critical points of selected salt solutions, red dots. Liquid-saturation curve (black) is 3-phase boundary for system NaCl-$H_2O$.

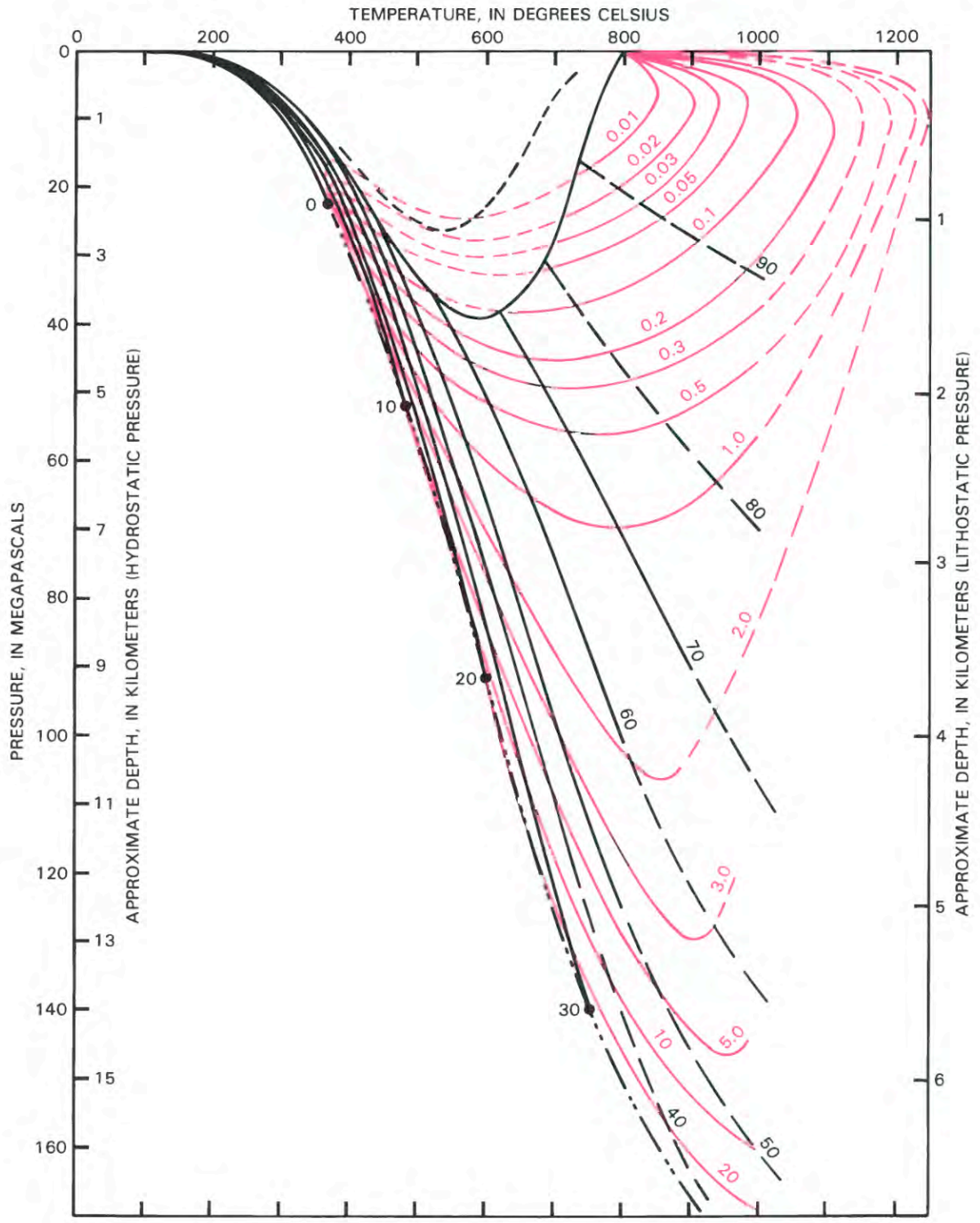


FIGURE 55.7.—Isopleths of solubility of NaCl in steam (red lines, see fig. 55.6) superimposed on isopleths of solubility of NaCl in water (black lines, see fig. 55.4).

hypersaline brines is greatly aided when the initial solution is moderately saline, such as sea water, because a given amount of a fluid that has a greater initial salinity will produce a larger mass ratio of brine to gas than will a less saline fluid.

## BRINE EVOLUTION AND HYDROTHERMAL ALTERATION RELATED TO DEPTH OF MAGMATIC INTRUSION

The depth of intrusion of a magmatic body and the salinity of the ground water that enters the hydrothermal system are important in regard to brine evolution and the type and intensity of hydrothermal alteration that is likely to be associated with that intrusion. These depth-temperature-phase relations will be illustrated by comparing and contrasting a relatively dilute, chloride-rich solution containing 2,000 mg/kg total dissolved solids (TDS) to sea water. Sea water can be modeled by a 3.2 weight percent NaCl solution at high temperatures because most of the sulfate and magnesium precipitate upon heating (Bischoff and Rosenbauer, 1985).

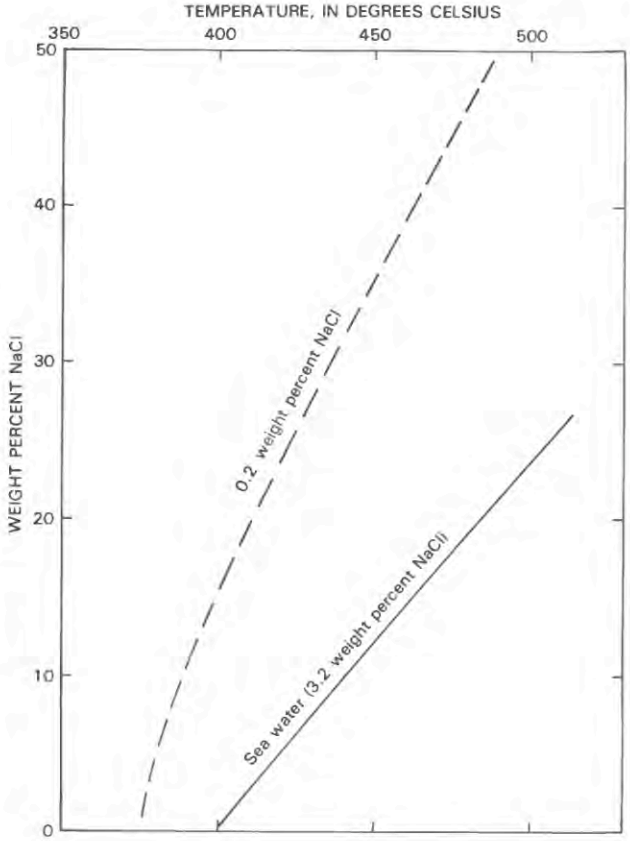


FIGURE 55.8.—Concentrations of NaCl in liquids that will condense from 0.2 weight percent NaCl and 3.2 weight percent NaCl when condensation-point curves are intersected at various temperatures as a result of decompression.

Approximate positions in depth-temperature space of the boiling-point curves, condensation-point curves, critical points ($C_2$ and $C_s$), and hypercritical points ($H_2$ and $H_s$) for the 2,000 mg/kg TDS solution and sea water, respectively, are shown in figure 55.10. The 2,000 mg/kg NaCl solution has a critical point near 375 °C at about 23 MPa and a hypercritical point at about 700 °C at 46 MPa. In contrast, the sea water has a critical point near 405 °C at about 30 MPa and a hypercritical point at about 900 °C at 129 MPa. The dashed parts of the condensation-point curves are beyond the range of experimental data and the Pitzer and Pabalan (in press) model. The position of the saturation curve in figure 55.10 is poorly constrained and is greatly dependent on the relative proportions of cations in the solution. The liquid saturation curve for the binary system NaCl-$H_2O$ is shown by the dot-dashed line, and

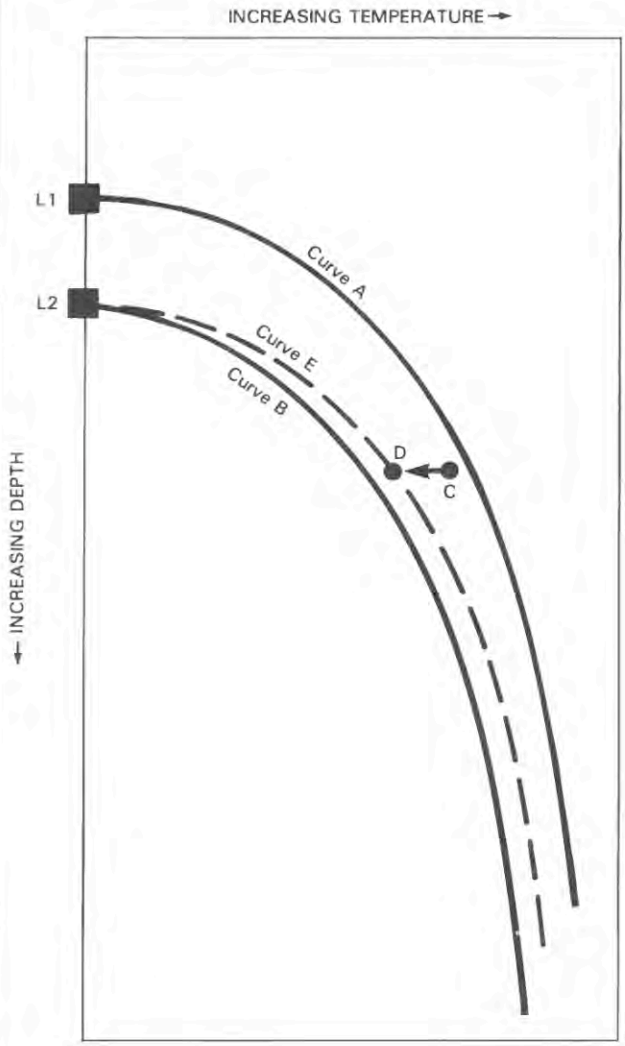


FIGURE 55.9.—Boiling-point curves related to elevation of water table. Lettered points and curves are discussed in text.

the double-dot-dashed line shows the saturation curve for the ternary system NaCl-KCl-$H_2O$ with the Na/K ratio fixed by base exchange between albite and K-feldspar, calculated using the data of Ravich and Borovia (1949) and Orville (1963).

The schematic depth-temperature relations for a relatively early stage of development of a hydrothermal system associated with a body of magma that has been intruded to a depth of 6 km are shown in figure 55.11. The heat source has a temperature of about 800 °C (appropriate for a silicic system). A basaltic heat source could have a temperature well above 1,000 °C. Fluid flow at hydrostatic pressure (shown schematically by arrows in fig. 55.11) is assumed to be controlled by a few well-developed fractures, and temperatures in the convecting hydrothermal system are assumed to be representative of those in the fractures where the maximum rate of fluid flow occurs. The temperature gradient from the heat source to the convecting hydrothermal system is very steep (there has been insufficient time to heat much surrounding rock by conduction), and the hydrothermal system is not well developed. Because the surrounding rock was relatively cool (at a normal or slightly above normal geothermal gradient) prior to the intrusion of the magma, the convecting fluid is in the process of heating the rock adjacent to the channels that control fluid flow, and the rock, in turn, is conducting heat away from the fluid. The maximum fluid temperature of 450 °C, (fig. 55.11) is appropriate for a steady-state situation in which mineral deposition and quasi-plastic deformation have closed off permeability in rocks at higher temperatures. The sudden opening of new fractures adjacent to magma could allow fluid to move into those fractures and become heated to temperatures significantly above 450 °C, resulting in marked fluid expansion. If the expansion of the fluid does not lead to further rupturing of the rock (possibly explosively) and a decrease in fluid pressure thereafter, the expanded 2,000 mg/kg fluid would not undergo a phase change because the pressure at a depth of 5–6 km is greater than the hypercritical pressure; the gas plus brine field would not be entered. In contrast, if flow into new fractures at a depth of 5–6 km allowed sea water to be heated at hydrostatic pressure to temperatures above 450 °C, brine and gas would form as soon as the temperature exceeded about 480 °C (fig. 55.11), and the first brine generated would contain about 19 weight percent NaCl (fig. 55.8).

Given time, a larger portion of rock adjacent to the intrusive becomes heated conductively while the intrusive crystallizes and cools (fig. 55.12). The hydrothermal system heats the rock adjacent to the channels of main fluid flow to the point where the ascending fluids cool mainly by adiabatic decompression, while the fluids in less open channels cool by conduction. The maximum temperature attained by the convecting fluid in figure 55.12 is shown to be less than that in figure 55.11 because mineral deposition and quasi-plastic deformation are assumed to have slowly excluded fluid flow

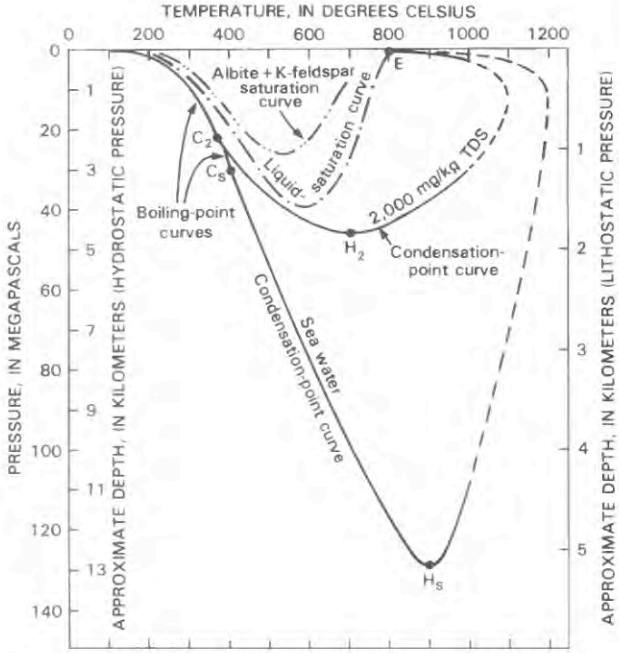


FIGURE 55.10.—Approximate positions in depth-temperature space of boiling-point and condensation-point curves for chloride-rich solution containing 2,000 mg/kg salt (about 0.2 weight percent NaCl) and sea water (about equivalent to 3.2 weight percent NaCl at high temperatures). Critical points are at $C_2$ and $C_s$ and hypercritical points are at $H_2$ and $H_s$, respectively. Liquid-saturation curve and curve labeled Albite + K-feldspar are same as in figure 55.4.

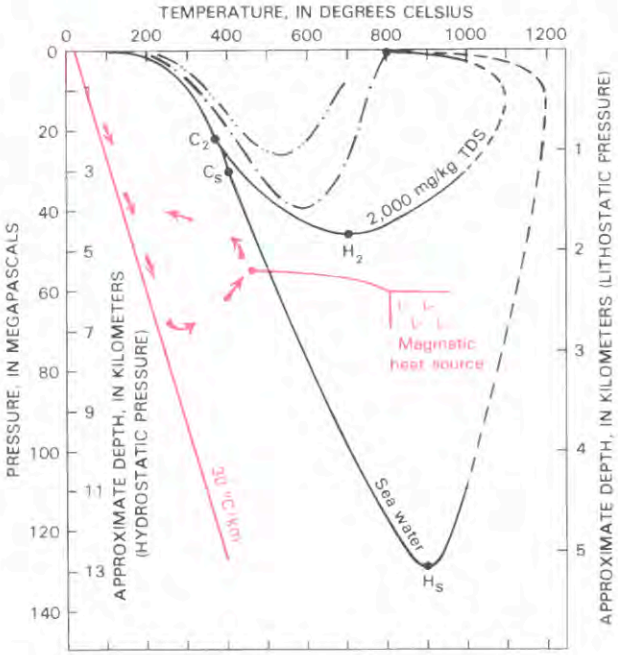


FIGURE 55.11.—Schematic depth-temperature relations (shown in red) for relatively early stage of development of hydrothermal system associated with body of magma that has been intruded to depth of 6 km below water table, superimposed on figure 55.10 (shown in black).

from portions of rock where flow had previously occurred at higher temperatures. In contrast to the situation shown in figure 55.11, renewed fracturing within hot, previously impermeable portions of rock will not result in the formation of brine during inflow of sea water because temperatures are too low for the gas plus brine field to be encountered (figs. 55.8, 55.12).

A situation in which a later magmatic body intrudes an older, partly cooled magmatic body at a depth of about 6 km is shown in figure 55.13. The younger magma injects into rock that was preheated by the previous intrusion, and the hydrothermal system in the vicinity was already well established. Also, in the intrusive process, new fractures are likely to form, allowing fluid to re-enter rock that had previously become essentially impermeable through mineral deposition and slow quasi-plastic deformation. In this situation, as the fluids convect upward there is a good chance that both the dilute solution and sea water would enter the gas plus brine field to the right of their respective critical points (points $C_2$ and $C_s$). In that event, highly saline brines would form by condensation (disproportionation of the initial fluid into a small volume of highly saline liquid and a much larger volume of less saline gas), as previously discussed and shown in figure 55.8. If the relatively dense brine that forms by condensation accumulates in pockets or at the base of the hydrothermal system, important consequences in regard to ore deposition would occur because the chloride-rich brine would scavenge metals from the surrounding rock, and these metals would then be localized and available to combine with sulfur that is released by still-crystallizing magma (Fournier, 1983b).

Intrusions that penetrate to less than about 3–4 km and that attain temperatures above about 400 °C are likely to have associated hydrothermal systems that extend into the field of gas plus liquid, and possibly into the field of gas plus solid salt (fig. 55.14). Within the gas plus solid salt field, acid gases are likely to be generated by the hydrolysis of salts (Fournier, 1985a, 1985b),

$$NaCl + H_2O = NaOH + HCl \quad (1)$$

$$CaSO_4 + 2H_2O = Ca(OH)_2 + H_2SO_4. \quad (2)$$

The hydroxides react with silicates to form a variety of alteration products, including epidote, albite, and chlorite,

$$3CaAl_2Si_2O_8 + Ca(OH) = 2Ca_2Al_3(SiO_4)_3(OH), \quad (3)$$

and

$$2CaAl_2Si_2O_8 + 6MgSiO_3 + NaOH + 4H_2O = NaAlSi_3O_8 + Ca_2Al_3(SiO_4)_3(OH) + Mg_6Si_4O_{10}(OH)_8. \quad (4)$$

The hydrolysis of salts, yielding acidic gases, becomes increasingly important at lower pressures. Therefore, acid alteration is likely to be far more abundant in and around shallow intrusive igneous rocks than deeper intrusive igneous rocks.

Most potassic alteration probably is the result of decreasing temperature that favors the exchange of dissolved K for Na in

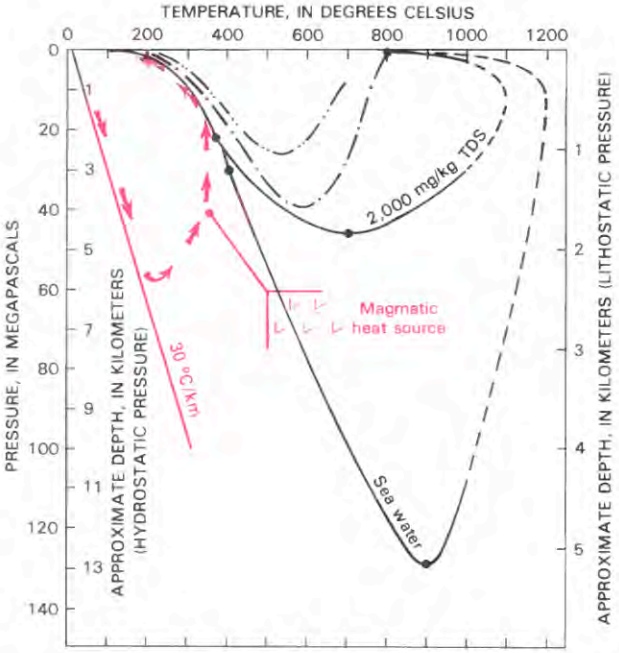


FIGURE 55.12.—Schematic depth-temperature relations (shown in red) for a relatively late stage of development of hydrothermal system associated with body of magma that has been intruded to depth of 6 km below water table, superimposed on figure 55.10 (shown in black).

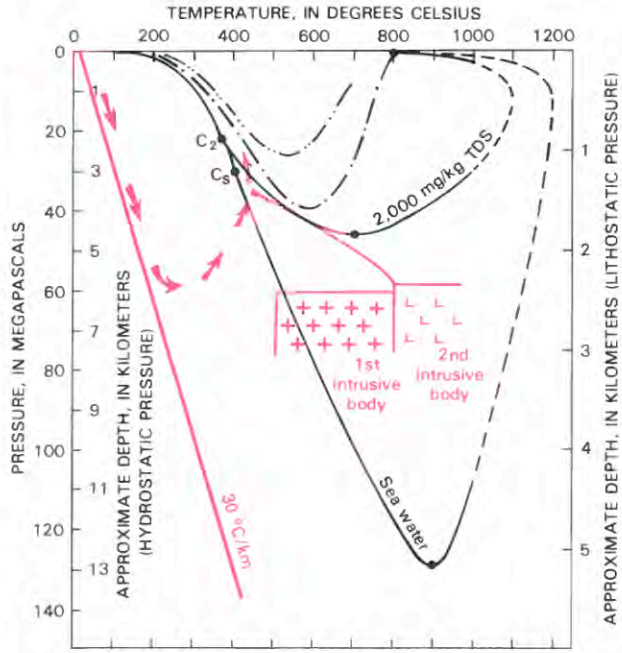


FIGURE 55.13.—Schematic depth-temperature relations (shown in red) for hydrothermal system where there have been multiple injections of magma to depth of about 6 km below water table, superimposed on figure 55.10 (shown in black).

feldspars and micas, so that as the rocks become more potassic, the solution becomes more sodic. However, under some circumstances potassic alteration also may result from a decrease in pressure (Fournier, 1976, 1983b). Within the field of gas plus brine, with decreasing pressure NaCl precipitates from solution before KCl, causing K exchange for Na in albite to maintain the required Na/K ratio in the aqueous solution for chemical equilibrium with the coexisting feldspars. After all the available albite is converted to K-feldspar by base exchange, the solution can become richer in potassium relative to sodium (by continued precipitation of NaCl with decreasing pressure), and the boundary of the gas plus solid region shifts toward lower pressures. Where there is no boiling of liquids or condensation of gas, the hydrothermal alteration products at temperatures of 300–500 °C are likely to be predominantly quartz, albite, K-feldspar, epidote, chlorite, and amphibole, with minimal acid and potassic alteration.

In summary, at a depth of intrusion of 6–7 km, brines are not likely to form by boiling of dilute ground water or by condensation of relatively saline gas unless there are special circumstances, such as repeated magmatic intrusions that preheat the surrounding rock and repeated fracturing of very hot rock that allows convecting water to become heated to temperatures above 450–500 °C. In contrast, brines are very likely to form by boiling of dilute ground water or by condensation of relatively saline gas where the depth of intrusion comes to within about 3 or 4 km of the surface, because the gas plus brine field is entered at a temperature less than 450 °C (fig. 55.14).

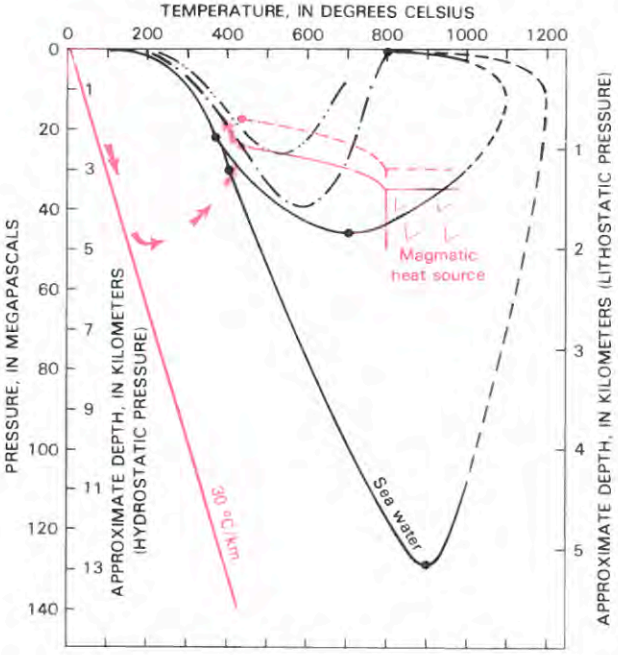


FIGURE 55.14.—Schematic depth-temperature relations (shown in red) for hydrothermal systems where depth of intrusion is within about 3–3.5 km below top of water table, superimposed on figure 55.10 (shown in black). See text for discussion.

The above-mentioned depth ranges are very approximate because of variations of hydrostatic pressure that result from different elevations of the water table, different densities of the fluids, different partial pressures of dissolved gases, different positions of the phase boundaries (shown in figures 55.10–55.14) because of variations in composition of the dissolved salts, and the possible formation of vapor-dominated regions (White and others, 1971) within parts of some hydrothermal systems. Little increase in fluid pressure or temperature is expected from the top to the bottom of a vapor-dominated region, so the relations shown in figures 55.10–55.14 will be displaced downward by the thickness of any vapor-dominated zone. In oceanic volcanic systems that have not formed islands, the depth of intrusion is the depth below sea level and not the depth below the ocean floor.

## HYDROTHERMAL ACTIVITY ASSOCIATED WITH OCEANIC VOLCANOES

Several differences exist between the hydrothermal systems that are likely to develop in and around a continental volcanic center and an oceanic volcanic center. One difference is in the composition and amount of magmatic water that separates from a crystallizing silicic magma compared to a basaltic magma (silicic magmas are richer in water and chloride as shown by their hydrous minerals and quenched glass compositions). More important differences are the greater hydrostatic pressure that will prevail during the early stages of formation of an oceanic hydrothermal system and the fact that the oceanic systems are recharged by an abundant supply of sea water. In contrast, the abundance and composition of recharge water in continental systems is extremely variable.

The hydrothermal systems that develop within volcanic edifices that are built upon the sea floor, such as the Hawaiian Islands, are likely to have complex histories. The old sea floor is about 5 km below sea level near Hawaii. Therefore, extrusion of lava at a new volcanic center on that sea floor brings magma into contact with sea water at a pressure such that brine (equivalent to about 20 weight percent NaCl) plus vapor forms only at temperatures above about 480 °C (figs. 55.8 and 55.10). However, that hot brine is likely to have a density less than about 0.7 kg/m$^3$, which is considerably less than that of the surrounding cold sea water, so both the vapor and the brine will rise and mix with the overlying cold water. Rapid chilling of the surface of the magma and a relatively slow transfer of heat by conduction to the interface with convecting sea water is likely to restrict brine formation to a very short time. Compositionally stratified layers of brine may develop by double-diffusive convection (Huppert and Turner, 1981; Huppert and Sparks, 1984; Vitagliano and others, 1984) in the ocean water above the heat source, but these brine layers are likely to be very transient.

Beneath the sea floor, heating of pore water to temperatures greater than 500–650 °C may occur over a significant period of time where magma is repeatedly injected to relatively shallow levels. Heating sea water to above 500 °C will cause a brine with more than 20 weight percent dissolved salt plus relatively dilute gas to form at a depth of about 0.5 km beneath the sea floor (about 5.5 km beneath the ocean surface, fig. 55.10). At a depth of 4 km beneath the sea

floor (9 km beneath the ocean surface) temperatures in excess of 650 °C are required to form highly saline brine from sea water. The gas component may convect all the way up to the sea floor, cooling, condensing, and mixing with pore water as it rises. The pore water may be sea water or previously condensed gas that contains low to moderate chloride and is rich in carbonate and sulfate, owing to water-rock reactions involving $CO_2$, $SO_2$, and $H_2S$. The brine component will first rise, but then as it cools its density will increase to the point that buoyant upflow will stop. Double-diffusion convection may result in compositionally stratified zones of water above and to the sides of the magmatic heat source. In response to double-diffusion convection, the densities of the hot, saline fluids will adjust and become essentially the same as the densities of the cold, surrounding pore fluids (sea water) at the same depths.

The above scenario assumes that the permeability is great enough that fluid expansion caused by heating of pore water can be accommodated by convective flow of fluid away from the hot part of the system without a hydrothermal explosion (Delaney, 1982), yet low enough that the magma-fluid interface will not be quickly quenched to below 500–650 °C by convecting water. The major factors that limit the amount of brine (greater than 3.2 weight percent NaCl equivalent) that forms are the size, depth, shape, and temperature of the heat source and the total amount and rate of movement of sea water through the system. The rate of movement is likely to slow with time because permeability is decreased by the formation of hydrous alteration products after volcanic glass, by precipitation of sulfate from sea water as it is heated at the inflow part of the system, by precipitation of silica, sulfides, and other minerals at the outflow part of the system, and by quasi-plastic flow of rock at high temperatures.

Decker (chapter 42) noted that the shallow magma chambers beneath Kilauea and Mauna Loa Volcanoes are both at a depth of about 3 km below the respective summits. He concluded that "The long term process of evolution of Hawaiian volcanoes apparently involves progressively upward remelting, stoping, and (or) shoving aside of the rocks which overlie the shallow magma reservoir systems." With the assumption that a 3-km depth to the top of a shallow magma reservoir is approximately maintained from the time a Hawaiian-type volcanic edifice starts to build on the sea floor through the period of island growth, some generalities can be made about the probable associated hydrothermal system.

With the start of volcanic activity the shallow magma chamber would be about 8 km below sea level, and sea water is converted to highly saline brine and gas only at temperatures above about 625 °C at that depth. Very little sea water is likely to become heated to that temperature. As the volcanic pile gets larger and the magma chamber rises, the temperature at which sea water in the vicinity of the magma chamber is converted to highly saline brine and gas decreases, and the likelihood of sea water attaining that temperature increases. The shallowest depth below sea level at which brine will condense from fluid of sea-water salinity is about 3 km at a temperature of about 405 °C (the critical point for a 3.2 weight percent NaCl solution, fig. 55.10). At lower temperatures and pressures the sea water will boil when heated. When the top of the volcanic pile comes close to sea level, the top of the shallow magma chamber may be close enough to the surface (about 3–3.5 km) for portions of the associated hydrothermal system to be heated to the point of complete evaporation (enter the gas plus solid region at temperatures above about 400–450 °C, as shown in fig. 55.14). The evolving gas (steam) will be very rich in acids (chloride as well as sulfur species), but will carry only minor dissolved salt.

The hydrologic situation changes somewhat after a volcanic island emerges from the sea, because meteoric water becomes available to enter the hydrothermal system. Rain water percolates through permeable lava into the ground and, by the Ghyben-Herzberg principle (Bates and Jackson, 1980), forms a lens of fresh water that floats upon saline water (fig. 55.15). In the Hawaiian Islands the head of fresh water above sea level generally increases at a rate of about 0.2 m/km (1 ft/mi) from the shore (Peterson, 1981). However, on the Island of Hawaii, to the east of Kilauea and south of Hilo, the head of fresh water rises at a rate of about 0.8 m/km (Davis and Yamanaga, 1973). When steady-state conditions exist (and volcanic heat is not a factor) the head of fresh water above sea level is balanced by a thickness of fresh water below sea level about 40 times as great (Peterson, 1981). Where volcanic heat is a factor, the position of the fresh water-saline water interface is likely to be considerably different from that predicted on the basis of normal thermal gradients, because the densities of dilute water, sea water,

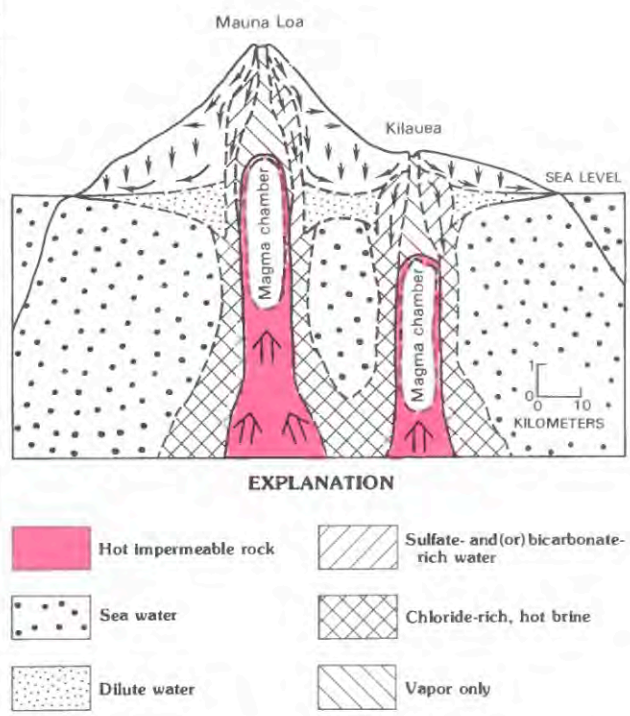


FIGURE 55.15.—Schematic diagram with vertical exaggeration showing shallow magma reservoirs and associated hydrothermal systems beneath Mauna Loa and Kilauea Volcanoes, Hawaii.

and highly saline brine decrease at different rates when heated. Also, hydrothermal alteration that decreases permeability occurs where ground water is heated and cooled. Therefore, the usual assumptions about densities and permeabilities that are made when calculating the elevation and thickness of the Ghyben-Herzberg lens will not be valid. In addition, ground water above shallow magma chambers will likely become rich in sodium sulfate (possibly also rich in bicarbonate) as a result of reactions involving volcanic gases and oxidation of sulfides in the rock. The boundaries between dilute water, sea water, sodium sulfate-rich water, steam, and chloride-rich brine are likely to be complex and transient, changing in response to heating when pulses of magma are injected into shallow reservoirs and when volcanic eruptions occur. Double-diffusive convection (Huppert and Turner, 1981) is likely to occur at these boundaries as a result of sharp thermal and salinity gradients.

Thin and discontinuous bodies of perched water are found within the volcanic edifice above the Ghyben-Herzberg lens, and perched streams flow through lava tubes. For simplicity, discontinuous bodies of perched water are not shown in figure 55.15. In the vicinities of volcanic eruptive centers, bodies of perched ground water may be fed in part from downward percolation of meteoric water and in part from condensation of steam rising from below.

The top of the shallow magma reservoir beneath Kilauea is about 2 km below sea level, and sea water (chemically changed in response to water-rock reactions at high temperatures, and about equivalent in salinity to a 3.2 weight percent NaCl solution) should be present within the volcanic edifice at that depth (fig. 55.15). The depth-temperature range is such that sea water will start to boil at a temperature of about 365 °C in the immediate vicinity of the top of the magma chamber and may even evaporate to dryness (figs. 55.14, 55.15). Within large volcanic edifices gravitational slumping (Fiske and Jackson, 1972) produces tensional stresses that may result in fracturing of rocks at very high temperatures where quasi-plastic flow would normally occur. Therefore, for relatively short, but significant, periods the maximum temperature attained by the convecting hydrothermal system may be considerably above 400–500 °C. Much of the steam that forms by reaction of the hydrothermal system with very hot rock probably will condense above the magma chamber, and the accompanying gases will react with rock, creating a saline solution that is rich in sodium sulfate (and bicarbonate, depending on pH), as previously discussed.

The temperature profile in a well drilled beneath the summit of Kilauea Volcano (Keller and others, 1979) indicates that a water table was encountered 488 m deep (about 600 m above sea level). Whether this is perched water or part of a large, continuous hydrothermal system that underlies the volcano is not known.

The top of the shallow magma reservoir beneath Mauna Loa is about 1 km above sea level, and that reservoir extends above the level of the Ghyben-Herzberg lens of dilute water (fig. 55.15). A hot sodium sulfate-rich brine probably is present between the colder dilute water and the magma reservoir. A vapor-only zone may be present in the upper part of the system where temperatures are too high and pore-fluid pressures are too low for liquid of any composition to exist.

The rift zones on the Island of Hawaii are kept heated by repeated injections of magma that flow laterally from the summit regions (Fiske and Jackson, 1972). The Ghyben-Herzberg lens pinches out near the shoreline, so sea water may come into contact with very hot rock along the rift zone at a relatively low pressure. If the sea water is heated to much higher temperatures than the dilute water in the overlying Ghyben-Herzberg lens, the interface between the two may be depressed considerably below the normal level, and mixing by double-diffusive convection is likely to occur.

In summary, in oceanic volcanic systems, such as at Hawaii, the shallow magma reservoir feeding the eruptions maintains about a 3–4 km depth beneath the summit as the volcanic edifice builds upon the sea floor. The pore spaces in the rocks surrounding the magma reservoir are filled with chemically altered sea water (most of its Mg and $SO_4$ lost by precipitation) that is converted to highly saline brine plus gas when the condensation-point curve is intersected, either by heating or decompression, at temperatures above about 405 °C at depths greater than about 3 km below sea level. At lower temperatures and pressures sea water boils as a result of heating or decompression, but this boiling may progress to dryness in rock that has been heated to a high temperature by magma that has been injected to a relatively shallow level. In the Hawaiian systems the transformation of sea water to highly saline brine may start when the heat source attains a depth of about 12–13 km below sea level, provided (1) hydrostatic pore pressures prevail, (2) the partial pressures of noncondensable gases, such as $CO_2$, are small relative to the total fluid pressure, and (3) the sea water comes in contact with rock that is at a temperature greater than about 800–900 °C (fig. 55.10). These conditions, if attained, are likely to be short lived at 12–13 km. The depth at which sea water may be converted to highly saline brine plus gas by heating is decreased where pore pressures are greater than hydrostatic, and increased by high partial pressures of noncondensable gases. When volcanic activity first appears upon the sea floor, the shallow magma reservoir is likely to be about 8–9 km below sea level, and temperatures in the 600–700 °C range are required to convert sea water to highly saline brine and gas. As the volcanic edifice grows, and the shallow magma reservoir rises, sea water converts to highly saline brine and gas at still lower temperatures. A significant amount of chloride-rich brine may accumulate adjacent to the magma reservoir, especially where repeated episodes of magma injection fracture the adjacent rocks and allow sea water access to very hot rock. Double-diffusive convection occurs at the contacts with colder and less saline waters. Sulfides are likely to deposit within the chloride-rich brine portion of the system below sea level, but these deposits are not likely to be exposed during subsequent erosion because they will always remain below sea level. After the volcano rises above the sea, fresh water enters the top of the hydrothermal system and prevents the buoyant upflow of heated sea water to elevations above sea level. Continuously or episodically thereafter, temperatures may become high enough, and pore pressures low enough to completely evaporate all pore waters near the top of the magma reservoir. Sodium sulfate- and sodium carbonate-rich brines form where steam condenses and sulfur- and carbon-rich gases react with the country rock.

## EVOLUTION OF MAGMATIC FLUIDS

Many investigators have discussed the evolution of aqueous fluids from crystallizing magma, including Morey (1922), Bowen (1933), Emmons (1933), Fenner (1933), Lindgren (1937), Neuman (1948), Burnham (1967, 1979), Fournier (1968, 1972), Holland (1972), Phillips (1973), Norton and Cathles (1973, 1979), Whitney (1975), Cunningham (1978), Henley and McNabb (1978), Eastoe (1982), and Henley and Ellis (1983). Most investigators have assumed that the aqueous phase evolved from crystallizing magma is either a gas or supercritical fluid. Whether this is true or not depends both on the salinity of the magmatic fluid and on the pore pressure of the fluid in the rocks adjacent to the magma. If the permeability of the surrounding rocks is relatively low, the pore-fluid pressure in those rocks may be affected by the thermal effects of the magmatic intrusion (Delaney, 1982) and the rate at which aqueous fluid is expelled from the magma. Therefore, the pore-fluid pressure in the adjacent rocks may range from hydrostatic (or less if a vapor-dominated system is present) to the pressure that will cause hydrofracturing of the rock (a maximum pressure about equal to lithostatic pressure plus the tensile strength of the rock). The adjacent rocks may be outer parts of the magma that have already crystallized.

Chloride is likely to be the dominant anion in most aqueous fluids that evolve from solidifying magmas, although fluoride and boron species may be very important in some places. The total dissolved cations adjust to the available anions so that charges are balanced, and cation ratios are fixed by fluid-rock base exchange reactions. Carbon and sulfur compounds will be present mainly as gaseous species, $CO_2$, $SO_2$, and $H_2S$, at magmatic temperatures and have little influence on the cation-anion balance. Therefore, the salinity of an aqueous fluid that separates from a crystallizing magma depends mainly on the initial concentrations of chloride and water dissolved in the magma, and on how much of that chloride and water are incorporated within minerals that form during the solidification process. Magmas that form by partial fusion of crustal rocks that contain evaporite deposits are likely to have relatively large concentrations of chloride, carbon, and sulfur, and magmas that form by partial fusion of rocks that contain large quantities of hydrous minerals (such as shales) are likely to be relatively rich in water. The average shale contains about 0.15 weight percent chloride (Billings and Williams, 1967) and about 5 weight percent water (Clarke, 1924). Noble and others (1967) analyzed many obsidian glasses that had not been leached by water after solidification and found a maximum concentration of about 0.75 weight percent chloride. It seems reasonable to assume that silicic magmas that form by partial fusion of sediments might contain about 0.1–0.8 weight percent chloride and about 1–5 weight percent water. Then, for magmas initially containing 1 weight percent water that is evolved as a magmatic fluid (little water is tied up in hydrous minerals), the chloride concentration in that fluid could range from about 10–44 weight percent (equivalent to about 16–72 weight percent NaCl). For magmas initially containing 5 weight percent water, the chloride concentration in an evolved aqueous magmatic fluid could range from about 2–14 weight percent (equivalent to about 3–23 weight percent NaCl) if no water were incorporated in hydrous minerals.

The critical curve for the system $NaCl\text{-}H_2O$ is shown in relation to the granite minimum melting curve (Tuttle and Bowen, 1958) in figure 55.16. Two situations are represented in that figure: water pressure equal to lithostatic pressure (in red) and hydrostatic pressure (in black). Where pore-fluid pressures in the adjacent rock are about equal to the lithostatic pressure, aqueous fluids that evolve from silicic magmas that are crystallizing along the granite minimum melting curve should retain their initial salt/water ratios as they cool at depths greater than about 5 km. Where pore-fluid pressures in the adjacent rock are about equal to the hydrostatic pressure, initial salt/water ratios in magmatic fluids are likely to be maintained only at depths greater than about 13 km. A decrease in pore-fluid pressure from lithostatic to hydrostatic would likely cause a magma on the granite minimum melting curve to become supercooled by about 75 °C, with the simultaneous evolution of a highly saline brine and moderately saline to dilute gas.

The position of the granite minimum melting curve is shown in figure 55.17 as it relates to the isopleths of solubility of NaCl in steam and liquid water (fig. 55.7). Point y on the granite minimum melting curve indicates the lowest pressure (with water pressure equal to total pressure) at which the magma can retain 4 weight percent dissolved water (Tuttle and Bowen, 1958). A further

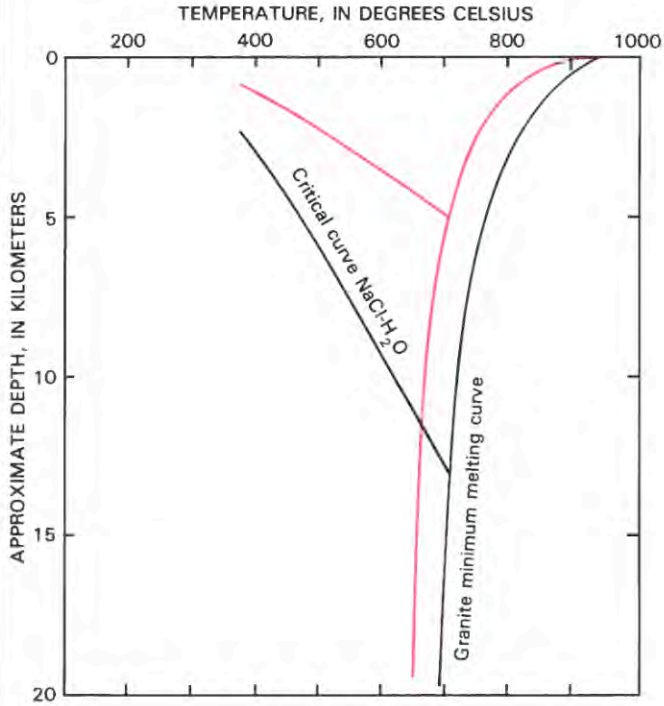


FIGURE 55.16.—Approximate positions of critical curve for system $NaCl\text{-}H_2O$ and of granite minimum melting curve (Tuttle and Bowen, 1958). Red lines, water pressure equal to lithostatic pressure; black lines, hydrostatic pressure.

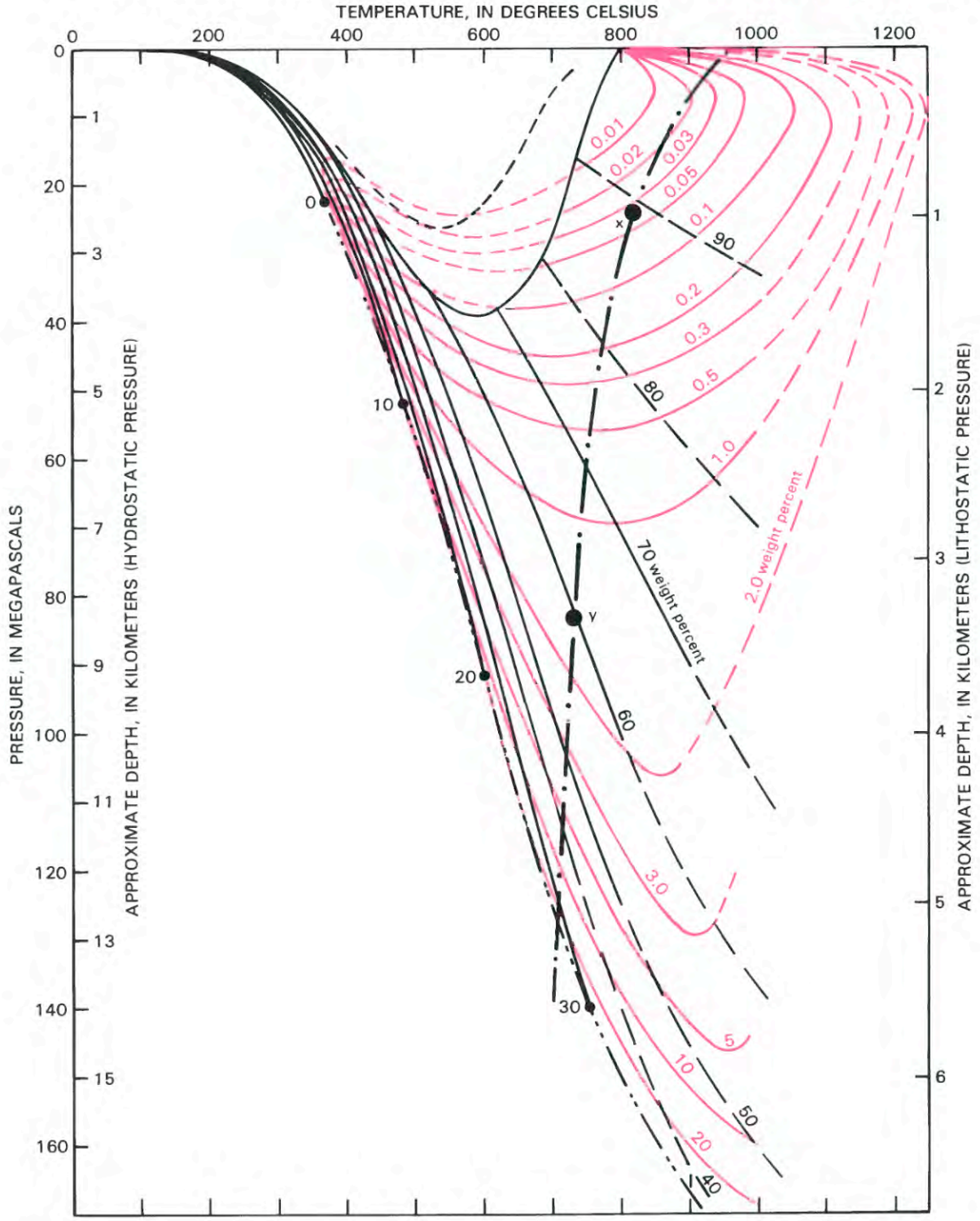


FIGURE 55.17.—Granite minimum melting curve (Tuttle and Bowen, 1958) shown by dot-dashed line, superimposed on figure 55.7. Lettered points are discussed in text.

decrease in pressure would result in evolution of water and an immediate crystallization of the magma. Chloride initially dissolved in the magma will partition strongly into the aqueous phase (Kilinc and Burnham, 1972), and the maximum salt (as NaCl) that the aqueous gas phase can carry is 1–2 weight percent. Point x on the granite minimum melting curve indicates the lowest pressure at which the magma can retain 2 weight percent dissolved water, and the maximum salt that the aqueous gas phase can carry is only about 0.05 weight percent. A much greater solubility of salt in the gas phase at point x would be estimated using the results reported by Sourirajan and Kennedy (1962).

From the foregoing discussion it appears that when pore-fluid pressures are controlled by hydrostatic conditions, magmatic waters are likely to evolve to highly saline brines at depths less than about 10–12 km, irrespective of the initial concentrations of salt and water dissolved in the magma. Dilute hydrothermal fluids of meteoric origin and mixtures of meteoric water and condensed magmatic gas (steam) are likely to form convection systems that float upon the more saline and probably hotter magmatic fluid. Double-diffusive convection is likely to result from the temperature and salinity gradients.

## CONCLUSIONS

Our present knowledge of hydrothermal mineral deposits and active geothermal systems demonstrates the importance of interaction of shallow dilute meteoric water and deeper brines. The highly concentrated brines thus far encountered in active hydrothermal systems are all in environments in which the waters may have interacted with evaporites. Experimental data, however, indicate that highly saline as well as moderately concentrated brines may evolve from a crystallizing magma, depending on the initial water and chloride contents and on the depth of crystallization. Brines may also develop from dilute meteoric water as a result of heating. Heating a solution of given composition to above its critical temperature at a pressure a little above its critical pressure results in its disproportionation into a more concentrated liquid (brine) and a gas. What is generally thought of as supercritical behavior of a fluid occurs only at pressures great enough to ensure that the gas phase will retain all the salt that was initially dissolved in the liquid phase at a lower temperature. As a result of boiling and gas disproportionation, highly saline brines are likely to evolve in and around shallow magmatic intrusions, particularly at depths less than 3 to 4 km. However, a relatively large amount of dilute water must be heated to a very high temperature to produce a small amount of brine. The injection of dilute water into very hot rock is an inefficient way to produce brine because the rock at the liquid interface is chilled rapidly by the colder water and because relatively little water is likely to be involved. Adiabatic decompression of a dilute to moderately saline solution (such as sea water) that is part of a large convection system appears to be a more promising method of producing significant amounts of brine. In a large convecting system heat may be extracted from a large volume of rock, and highly saline brines will form if the decompression path of the fluid brings it into the field of gas plus brine at a temperature a few degrees above the critical temperature. By gravitational settling this brine may accumulate at the base of hydrothermal convection in the few fractures that are present in otherwise impermeable rock. The brines formed by heating and adiabatic decompression of dilute to moderately saline water of meteoric origin (including sea water) will augment brines that result from crystallization and degassing of the magmatic heat source. These hot brines will scavenge metals from the surrounding rock, and the base metals in turn will react with much of the sulfur that is liberated from crystallizing magma. Thus, a base metal ore deposit may form in the brine portion of the system, while the dilute hydrothermal system remains relatively unmineralized with respect to base metals.

## REFERENCES


Bates, R.L., and Jackson, J.A., 1980, Glossary of geology (2d ed.): Falls Church, Va., American Geological Institute, 749 p.

Billings, G.K., and Williams, H.H., 1967, Distribution of chlorine in terrestrial rocks (a discussion): Geochimica et Cosmochimica Acta, v. 31, p. 2247.

Bischoff, J.L., and Pitzer, K.S., 1985, Phase relations and adiabats in boiling seafloor geothermal systems: Earth and Planetary Science Letters, v. 75, p. 327–338.

Bischoff, J.L., and Rosenbauer, R.J., 1984, The critical point and two-phase boundary of seawater, 200°–500°C: Earth and Planetary Science Letters, v. 68, p. 172–180.

———1985, An empirical equation of state for hydrothermal seawater (3.2% NaCl): American Journal of Science, v. 285, p. 725–763.

Bischoff, J.L., Rosenbauer, R.J., and Pitzer, K.S., in press, A note on the system $NaCl-H_2O$: Relations of vapor-liquid near the critical temperature of water and of vapor-liquid-halite from 300° to 500°C: Geochimica et Cosmochimica Acta.

Bodnar, R.J., and Bean, R.E., 1980, Temporal and spatial variations in hydrothermal fluid characteristics during vein filling in preore cover overlying deeply-buried porphyry copper-type mineralization at Red Mountain, Arizona: Economic Geology, v. 75, p. 876–893.

Bodnar, R.J., Burnham, C.W., and Sterner, S.M., 1985, Synthetic fluid inclusions in natural quartz III: Determination of phase equilibrium properties in the system $H_2O$-NaCl to 1000°C and 1500 bars: Geochimica et Cosmochimica Acta, v. 49, p. 1861–1873.

Bodvarsson, G., and Lowell, R.P., 1972, Ocean floor heat flow and circulation of interstitial waters: Journal of Geophysical Research, v. 77, p. 4472–4475.

Bowen, N.L., 1933, The broader story of magmatic differentiation, briefly told, *in* Ore deposits of the western states (Lindgren volume): New York, American Institute of Mining and Metallurgical Engineers, p. 106–128.

Bowers, T.S., and Helgeson, H.C., 1983, Calculation of the thermodynamic and geochemical consequences of nonideal mixing in the system $H_2O$-$CO_2$-NaCl on phase relations in geologic systems: Equation of state for $H_2O$-$CO_2$-NaCl fluids at high pressures and temperatures: Geochimica et Cosmochimica Acta, v. 47, p. 1247–1275.

Burnham, C.W., 1967, Hydrothermal fluids at the magmatic stage, *in* Barnes, H.L., ed., Geochemistry of hydrothermal ore deposits: New York, Holt, Rinehart and Winston, p. 34–76.

———1979, Magmas and hydrothermal fluids, *in* Barnes, H.L., ed., Geochemistry of hydrothermal ore deposits (2d ed.): New York, John Wiley, p. 17–136.

Cathles, L.M., 1977, An analysis of the cooling of intrusives by ground-water convection which includes boiling: Economic Geology, v. 72, no. 5, p. 804–826.

———1980, Fluid flow and genesis of hydrothermal ore deposits: Economic Geology, 75th Anniversary Volume, p. 424–457.

———1983, An analysis of the hydrothermal system responsible for massive sulfide deposition in the Hokuroku Basin of Japan, *in* Ohmoto, H., and Skinner, B.J., eds., The Kuroko and related volcanogenic massive sulfide deposits: Economic Geology, Monograph 5, p. 439–487.

Cheng, P., and Minkowycz, W.J., 1977, Free convection about a vertical flat plate embedded in a porous medium with application to heat transfer from a dike: Journal of Geophysical Research, v. 82, p. 2040–2044.

Clarke, F.W., 1924, The data of geochemistry, 5th ed.: U.S. Geological Survey Bulletin 770, 841 p.

Copeland, C.S., Silverman, J., and Benson, S.W., 1952, The system NaCl-$H_2O$ at supercritical temperatures and pressures: Journal of Chemical Physics, v. 21, p. 12–16.

Cunningham, C.G., 1978, Pressure gradients and boiling as mechanisms for localizing ore in porphyry systems: U.S. Geological Survey Journal of Research, v. 6, no. 6, p. 745–754.

Davis, D.A., and Yamanaga, George, 1973, Water resources summary island of Hawaii: Hawaii Division of Water and Land Development Report R47, 42 p.

Delaney, P.T., 1982, Rapid intrusion of magma into wet rock: Ground water flow due to pore pressure increases: Journal of Geophysical Research, v. 87, p. 7739–7756.

Eastoe, C.J., 1978, A fluid inclusion study of the Panguna porphyry copper deposit, Bougainville, Papua New Guinea: Economic Geology, v. 73, p. 721–748.

———1982, The physics and chemistry of the hydrothermal system in the Panguna porphyry copper deposit, Bougainville, Papua New Guinea: Economic Geology, v. 77, p. 127–153.

Edmond, J.M., Craig, H., Gordon, L.I., and Holland, H.D., 1979, Chemistry of hydrothermal waters at 21°N on the East Pacific Rise[abs.]: Eos (American Geophysical Union Transactions), v. 60, p. 864.

Elder, J.W., 1965, Physical processes in geothermal areas, *in* Terrestrial heat flow: American Geophysical Union Geophysical Monograph 8, p. 211–239.

Emmons, W.H., 1933, On the mechanism of the deposition of certain metalliferous lode systems associated with granitic batholiths, *in* Ore deposits of the western states (Lindgren vol.): New York, American Institute of Mining and Metallurgical Engineers, p. 327–349.

Eugster, H.P., and Jones, B.F., 1979, Behavior of major solutes during closed basin evolution: American Journal of Science, v. 279, p. 609–631.

Fehn, U., and Cathles, L.M., 1979, Hydrothermal convection at slow-spreading mid-ocean ridges: Tectonophysics, v. 55, p. 239– 260.

Fenner, C.N., 1933, Pneumatolytic processes in the formation of minerals and ores, *in* Ore deposits of the western states (Lindgren vol.): American Institute of Mining and Metallurgical Engineers, p. 58–106.

Fiske, R.S., and Jackson, E.D., 1972, Orientation and growth of Hawaiian volcanic rifts: The effect of regional structure and gravitational stress: Proceedings of the Royal Society of London, v. 329, p. 299–326.

Fournier, R.O., 1968, Depths of intrusion and conditions of hydrothermal alteration in porphyry copper deposits [abs.]: Geological Society of America Abstracts with Program, 1968 Annual Meeting, p. 101.

———1972, The importance of depth of crystallization on the character of magmatic fluids [abs.]: International Geological Congress, 24th, Montreal, 1972, sec. 10, p. 214.

———1976, Exchange of $Na^+$ and $K^+$ between water vapor and feldspar phases at high temperature and low vapor pressure: Geochimica et Cosmochimica Acta, v. 40, p. 1553–1561.

———1977, Constraints on the circulation of meteoric water in hydrothermal systems imposed by the solubility of quartz [abs.]: Geological Society of America Abstracts with Program, v. 9, p. 979.

———1983a, Self-sealing and brecciation resulting from quartz deposition within hydrothermal systems: International Symposium on Water-Rock Interaction, 4th, Misasa, Japan, 1983, Extended Abstracts, p. 137–140.

———1983b, Active hydrothermal systems as analogues of fossil systems, *in* Raleigh, C.B., ed., The role of heat in the development of energy and mineral resources in the Basin and Range Province: Geothermal Resources Special Report 13, p. 263–284.

———1985a, Continental scientific drilling to investigate brine evolution and fluid circulation in active hydrothermal systems, *in* Observation of the continental crust through drilling: New York, Springer-Verlag, p. 98–122.

———1985b, Silica minerals as indicators of conditions during gold deposition, *in* Tooker, E.W., ed., Geologic characteristics of sediment- and volcanic-hosted disseminated gold deposits—search for an occurrence model: U.S. Geological Survey Bulletin 1646, p. 15–26.

Fournier, R.O., and Pitt, A.M., 1985, The Yellowstone magmatic-hydrothermal system: International Symposium on Geothermal Energy, Geothermal Resources Council, Hawaii, 1985, International Volume, p. 319–327.

Galobardes, J.F., Van Hare, D.R., and Rogers, L.B., 1981, Solubility of sodium chloride in dry steam: Journal of Chemical Data, v. 26, p. 363–366.

Gunter, W.D., Chow, I-M, and Girsperger, S., 1983, Phase relations in the system NaCl-KCl-$H_2O$ II: Differential thermal analysis of halite liquidus in the NaCl-$H_2O$ binary above 450 °C: Geochimica et Cosmochimica Acta, v. 47, p. 863–873.

Haas, J.L., 1971, Effect of salinity on the maximum thermal gradient of a hydrothermal system at hydrostatic pressure: Economic Geology, v. 66, p. 940–946.

Hardee, H.C., 1982, Permeable convection above magma bodies: Tectonophysics, v. 84, p. 179–195.

Hardie, L.A., and Eugster, H.P., 1970, The evolution of closed-basin brines: Mineralogical Society of America Special Publication 3, p. 273–279.

Hartline, B.K., and Lister, C.R.B., 1981, Topographic forcing of supercritical convection in a porous medium such as the ocean crust: Earth and Planetary Science Letters, v. 55, p. 75–86.

Henley, R.W., and Ellis, A.J., 1983, Geothermal systems ancient and modern: A geochemical review: Earth-Science Reviews, v. 19, 50 p.

Henley, R.W., and McNabb, Alex, 1978, Magmatic vapor plumes and groundwater interaction in porphyry copper emplacement: Economic Geology, v. 73, 19 p.

Hilbert, R., 1979, PVT-Daten von Wasser und von wässrigen Natriumchloride-Lösungen bis 873 K, 4000 Bar und 25 Gewichtsprozent NaCl: Karlsruhe University, Ph.D. Dissertation, 212 p.

Holland, H.D., 1972, Granites, solutions and base metal deposits: Economic Geology, v. 67, p. 281–301.

Huppert, H.E., and Sparks, R.S.J., 1984, Double-diffusive convection due to crystallization in magmas: Annual Review of Earth and Planetary Science, v. 12, p. 11–37.

Huppert, H.E., and Turner, J.S., 1981, Double-diffusion convection: Journal of Fluid Mechanics, v. 106, p. 299–329.

Keenan, J.H., Keys, F.G., Hill, P.G., and Moore, J.G., 1969, Steam tables (international edition—metric units): New York, John Wiley & Sons, 162 p.

Keevil, N.B., 1942 Vapor pressure of aqueous solutions at high temperatures: Journal of the American Chemical Society, v. 64, p. 841–850.

Keller, G.V., Grose, L.T., Murray, J.C., and Skokan, C.K., 1979, Results of an experimental drill hole at the summit of Kilauea Volcano, Hawaii: Journal of Volcanology and Geothermal Research, v. 5, p. 345–385.

Khaibullin, K., and Borisov, N.M., 1966, Experimental investigation of the thermal properties of aqueous and vapor solutions of sodium and potassium chloride at phase equilibrium: Teplofizika Vysokikh Temperature, v. 4, p. 518–523 (English translation, p. 489–494).

Kilinc, I.A., and Burnham, C.W., 1972, Partitioning of chloride between a silicate melt and coexisting aqueous phase from 2 to 8 kilobars: Economic Geology, v. 67, p. 231–235.

Knapp, R.B., and Norton, D., 1981, Preliminary numerical analysis of processes related to magma crystallization and stress evaluation in cooling pluton environments: American Journal of Science, v. 281, p. 35–68.

Lama, R.D., and Vutukuri, V.S., 1978, Handbook on mechanical properties of rocks—testing techniques and results—volume II: Clausthal, Germany, Trans Tech Publications, 484 p.

Langbein, W.B., 1961, Salinity and hydrology of closed lakes: U.S. Geological Survey Professional Paper 412, 20 p.

Lindgren, W., 1937, Succession of minerals and temperatures of formation in ore deposits of magmatic affiliation: American Institute of Mining and Metallurgical Engineers Transactions, v. 126, p. 356–376.

Lister, C.R.B., 1974, On the penetration of water into hot rock: Geophysical Journal of the Royal Astronomical Society, v. 39, p. 465–509.

———1980, Heat flow and hydrothermal circulation: Earth and Planetary Sciences Annual Review, v. 8, p. 95–117.

———1983, The basic physics of water penetration into hot rock, *in* Rona, P.A., Bostrom, K., Laubier, L., and Smith, K.L., Jr., eds., Hydrothermal processes at seafloor spreading centers: New York, Plenum Press, p. 141–168.

Morey, G.W., 1922, The development of pressure in magmas as a result of crystallization: Washington Academy of Science Journal, v. 12, p. 219–230.

Muffler, L.J.P., White, D.E., and Truesdell, A.H., 1971, Hydrothermal explosion craters in Yellowstone National Park: Geological Society of America Bulletin, v. 82, p. 723–740.

Nash, J.T., 1976, Fluid-inclusion petrology—data from porphyry copper deposits and applications to exploration: U.S. Geological Survey Professional Paper 907-D, 16 p.

Neuman, H., 1948, On hydrothermal differentiation: Economic Geology, v. 43, p. 77–83.

Noble, D.C., Smith, V.C., and Peck, L.C., 1967, Loss of halogens from crystallized and glassy silicic volcanic rocks: Geochimica et Cosmochimica Acta, v. 31, p. 215–223.

Norton, Denis, 1978, Sourcelines, source regions, and pathlines for fluid flow in hydrothermal systems related to cooling plutons: Economic Geology, v. 73, p. 21–28.

———1984, Theory of hydrothermal systems: Annual Review of Earth and Planetary Sciences, v. 12, p. 155–177.

Norton, Denis, and Cathles, L.M., 1973, Breccia pipes—products of exsolved vapor from magmas: Economic Geology, v. 68, p. 540–546.

———1979, Thermal aspects of ore deposition, *in* Barnes, H.L., ed., Geochemistry of hydrothermal ore deposits (2d ed.): New York, John Wiley, p. 611–631.

Norton, Denis, and Knapp, R., 1977, Transport phenomena in hydrothermal systems: The nature of porosity: American Journal of Science, v. 277, p. 913–936.

Norton, Denis, and Knight, J., 1977, Transport phenomena in hydrothermal systems: Cooling plutons: American Journal of Science, v. 277, p. 937–981.

Norton, Denis, and Taylor, H.P., 1979, Quantitative simulation of the hydrothermal systems of crystallizing magmas on the basis of transport and oxygen isotope data: An analysis of the Skaergaard intrusion: Journal of Petrology, v. 20, p. 421–486.

Ölander, A., and Liander, H., 1950, The phase diagram of sodium chloride in steam above the critical point: Acta Chemica Scandinavica, v. 4, p. 1437–1445.

Orville, P.M., 1963, Alkali ion exchange between vapor and feldspar phases: American Journal of Science, v. 261, p. 201–237.

Parisod, C.J., and Plattner, E., 1981, Vapor-liquid equilibria of the NaCl-$H_2O$ system in the temperature range 300–440 °C: Journal of Chemical Engineering Data, v. 26, p. 15–20.

Parmentier, E.M., and Spooner, E.T.C., 1978, A theoretical study of hydrothermal convection and the origin of the ophiolitic sulfide ore deposit of Cyprus: Earth and Planetary Science Letter, v. 40, p. 33–44.

Peterson, F.L., 1981, Geologic and hydrologic framework: A history of development, *in* Fujimura, F.N., and Chang, W.B.C., eds., Groundwater in Hawaii, a century of progress: Manoa, University of Hawaii Press, p. 1–13.

Phillips, W.J., 1973, Mechanical effects of retrograde boiling and its probable importance in the formation of some porphyry ore deposits: American Institute of Mining and Metallurgical Engineers Transactions, sec. B, v. 82, p. B90–B98.

Pitzer, K.S., 1983, Thermodynamics of sodium chloride solutions in steam: Journal of Physical Chemistry, v. 87, p. 1120–1125.

Pitzer, K.S., and Li, Y., 1984, Critical phenomena and thermodynamics of dilute aqueous sodium chloride to 823 K: Proceedings of the National Academy of Science, v. 81, p. 1268–1271.

Pitzer, K.S., and Pabalan, R.T., in press, Thermodynamics of NaCl in steam: Geochimica et Cosmochimica Acta.

Ravich, M.I., and Borovia, F.E., 1949, Phase equilibria in ternary water-salt systems at elevated temperatures [in Russian]: Akademiya Nauk SSSR, Institut Obshchei i Neorganicheskoi Izvestiia, Sektor Fiziko Khimicheskogo Analiza, v. 19, p. 69–81.

Reynolds, T.J., and Bean, R.E., 1985, Evolution of hydrothermal fluid characteristics at the Santa Rita, New Mexico, porphyry copper deposit: Economic Geology, v. 80, p. 1328–1347.

Ribando, R.J., Torrance, K.E., and Turcotte, D.L., 1976, Numeric models for hydrothermal circulation in the ocean crust: Journal of Geophysical Research, v. 81, p. 3007–3012.

Roedder, Edwin, 1971, Fluid inclusion studies on the porphyry type deposit at Bingham, Utah, Butte, Montana, and Climax, Colorado: Economic Geology, v. 66, p. 98–120.

———1979, Fluid inclusions as samples of ore fluids, *in* Barnes, H.L., ed., Geochemistry of hydrothermal ore deposits (2d ed.): New York, John Wiley, p. 684–737.

Sleep, N.H., 1983, Hydrothermal convection at ridge axes, *in* Rona, P.R., and Lowell, R.L., eds., Hydrothermal processes at seafloor-spreading centers: New York, Plenum Press, p. 71–82.

Smith, R.B., and Bruhn, R.L., 1984, Interplate extensional tectonics of the eastern Basin-Range: Inferences on structural style from seismic reflection data, regional tectonics, and thermal mechanical models of brittle-ductile deformation: Journal of Geophysical Research, v. 89, p. 5733–5762.

Sourirajan, S., and Kennedy, G.C., 1962, The system $H_2O$-NaCl at elevated temperatures and pressures: American Journal of Science, v. 260, p. 115–141.

Torrance, K.E., and Sheu, J.P., 1978, Heat transfer from plutons undergoing hydrothermal cooling and thermal cracking: Numerical Heat Transfer, v. 1, p. 147–161.

Tuttle, O.F., and Bowen, N.L., 1958, Origin of granite in the light of experimental studies in the system $NaAlSi_3O_8$-$KAlSi_3O_8$-$SiO_2$-$H_2O$: Geological Society America Memoir 74, 153 p.

Vitagliano, P.L., Della Volpe, C., and Vitagliano, V., 1984, Gravitational instabilities in free diffusion boundaries: Journal of Solution Chemistry, v. 13, p. 549–562.

White, D.E., 1965, Saline waters of sedimentary rocks: American Association of Petroleum Geologists Memoir 4, p. 342–366.

———1968, Environments of generation of some base-metal ore deposits: Economic Geology, v. 63, p. 301–335.

White, D.E., Muffler, L.J.P., and Truesdell, A.H., 1971, Vapor-dominated hydrothermal systems compared to hot water systems: Economic Geology, v. 66, p. 75–97.

Whitney, J.A., 1975, Vapor generation in a quartz monzonite magma: A synthetic model with application to porphyry copper deposits: Economic Geology, v. 70, p. 346–358.

# A GEOCHEMICAL MODEL OF THE KILAUEA EAST RIFT ZONE

*By* Donald Thomas


## ABSTRACT

**The east rift zone of Kilauea Volcano is comprised of a northeast- to southwest-trending complex of dikes and fractures extending more than 100 kilometers from the summit caldera to the ocean floor. Geologic, petrologic, and geophysical data indicate that substantial volumes of molten magma are intruded into and stored within the east rift dike complex and that parts of the rift have temperatures exceeding the Curie point of basalt. The shallow ground-water hydrology and chemistry on the lower rift are strongly affected by natural thermal discharge from the rift and indicate a continuous heat loss rate estimated at 291 megawatts of thermal energy. Several deep geothermal wells drilled into the lower rift have confirmed the presence of high temperatures and of an active hydrothermal system associated with the rift. The maximum temperatures encountered in the deep wells approach the critical point of water (374 °C) but show a sharp decline on the southern boundary of the rift. Petrologic studies of drill cuttings from the deep geothermal wells have shown that intermittent, intense hydrothermal alteration has occurred to depths of at least 2.5 km. The alteration phases present indicate that metamorphism reaches the greenschist facies and have strong similarities to alteration suites found in midocean-ridge hydrothermal systems. Chemical data from the deep fluids suggest that the primary source of recharge to the reservoir is meteoric water in the interior of the rift but that saline water is present on the southern boundary. Production data from the deep wells also indicate that accessible parts of the hydrothermal system are capable of producing both dry steam and hot brine. The data that have been gathered to the present indicate that the hydrothermal system associated with the Kilauea east rift zone is actively evolving and has characteristics ranging from low-temperature benign fluids to high-temperature, highly aggressive fluids that may provide both an economically viable geothermal resource and a natural laboratory for the study of ore-forming and geochemical-cycling processes.**


## INTRODUCTION

Exploration for geothermal resources in Hawaii began in 1962 when four shallow wells were drilled into the Kilauea lower east rift zone (LERZ) (fig. 56.1; table 56.1) in an effort to develop a commercial steam resource. Although all four wells encountered above-ambient temperatures, none discovered an economically useful steam or hot-water resource. A second effort to study the deep thermal conditions on the Kilauea east rift zone (ERZ) was initiated in 1972 under funding from the National Science Foundation. This effort culminated in the drilling and completion of the 1,966-meter-deep Hawaii Geothermal Project well A (HGP-A) in 1976. Testing of this well indicated that temperatures of 358 °C were present at the bottom of the hole and that the well was capable of producing approximately 48 tonnes per hour (t/h) of steam and hot water. A geothermal generator facility was installed on this well in 1981 and, as of July 1985, has been in operation for approximately 44 months. Subsequent to the completion and initial testing of HGP-A, six privately financed deep exploration wells have been drilled into the LERZ. The data that have been obtained from the deep exploratory drilling into the rift and from the long-term discharge of HGP-A have now provided us with sufficient information to develop a preliminary model of the hydrothermal system associated with the ERZ.


## ACKNOWLEDGMENTS

The research results reported here have been made possible only through the capable assistance and willing cooperation of numerous very able individuals. Field and laboratory assistance by M. Dahlstrom, C. Fraley, D. Mills, J. McCullough, B. Taylor, L. Bergknut, E. DeCarlo, K.E. Cuff, M.E. Cox, R. Mitiguy, and R. Kochy is gratefully acknowledged. The cooperation and assistance of the Hawaii Geothermal Project staff—J. Shupe, P. Yuen, and L. Lopez—and Hawaii Electric Light Company—N. Oss, F. Kennedy, N. Uchida, and G. Jenkins—have been instrumental in allowing this research to be conducted. Thanks also are due to C. Zablocki, D. Jackson, R. Moore, A. Truesdell, and C.E. Helsley for helpful discussion during the evolution of this model. A special notice of appreciation is also due to Barnwell Geothermal Corporation and Geothermex Inc. for allowing access to their data and providing samples from their wells.

Funding for this work has come principally from the U.S. Department of Energy and the State of Hawaii Department of Planning and Economic Development with additional funding from Hawaiian Electric Industries and the Electric Power Research Institute.

The assistance of L. Kajiwara in drafting and of C. Koyanagi in manuscript preparation is gratefully acknowledged.

Hawaii Institute of Geophysics Contribution No. 1702.


## GEOLOGIC SETTING

The east rift zone, a major structural feature of Kilauea Volcano, extends from the summit caldera in an easterly direction for approximately 50 km, where it enters the ocean and continues as a

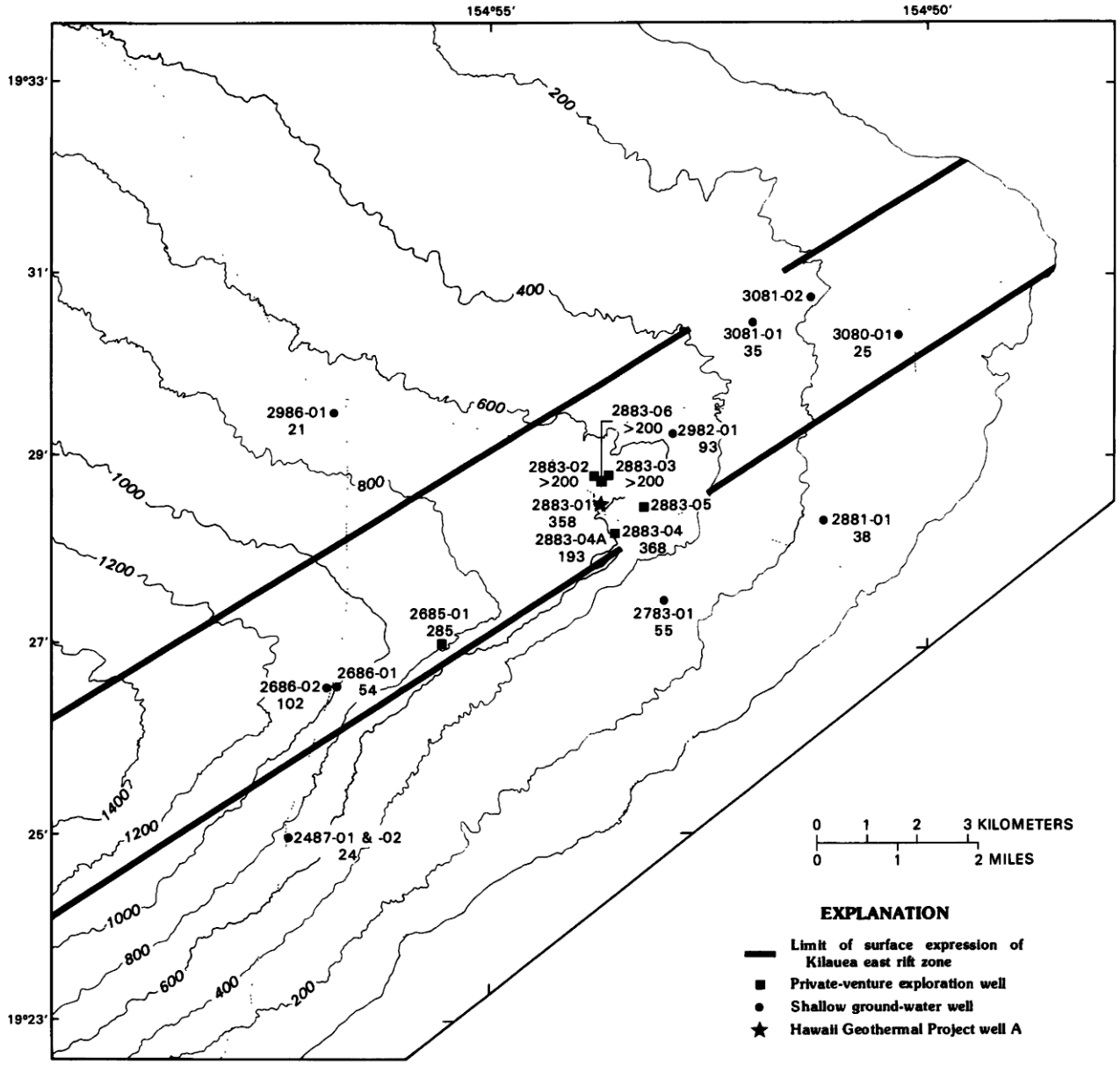


FIGURE 56.1.—Kilauea lower east rift zone showing locations of ground-water and geothermal exploration wells. Well-identification numbers and temperature (in degrees Celsius), if known, are given next to symbols. Dashed lines represent roads.

submarine ridge for another 50–60 km. Geologic mapping on Kilauea and studies of eroded rift systems on the older islands of the Hawaiian Chain indicate that the structure of the rift is composed of hundreds to thousands of near-vertical thin tabular dikes interspersed with highly fractured country rock (Macdonald and Abbott, 1970). The trend of the individual dikes parallels the strike of the rift, and the dip angles of both the fractures and dikes typically deviate by only a few degrees from vertical (Macdonald and Abbott, 1970).

The mechanism responsible for the formation of the ERZ is believed to be the forceful intrusion of magma from the summit magma reservoir into the rift system at depths of 3–6 km beneath the summit (Fiske and Jackson, 1972). The occurrence of these intrusive events, typically indicated by seismic and deformation changes both at the summit and in the area of an intrusion, may result in a surface eruption or in the formation of a subsurface dike. Although the rate of magma intrusion in the rift zone is not well known, theoretical studies have inferred deposition rates as high as

TABLE 56.1.—*Characteristics of geothermal exploration wells drilled on the Kilauea east rift zone*

| Well | Name | Depth (meters) | Bottom temperature (°C) | Comments |
|---|---|---|---|---|
| 2685-01 | Ashida-1 | 2,530 | 326 | Insufficient permeability to sustain production; suspended. |
| 2686-01 | Geothermal-1 | 54.3 | 54 | Drilled 1962, did not reach water table; abandoned. |
| 2686-02 | Geothermal-2 | 169.5 | 102 | Drilled in 1962, did not reach water table; abandoned. |
| 2883-01 | HGP-A | 1,967 | 358 | Sustained production of 50 t/h of brine and steam. |
| 2883-02 | Kapoho State 1 | 2,222 | 339 | Production rate of 32.7 t/h was achieved during short test; operation suspended. |
| 2883-03 | Kapoho State 2 | 2,440 | 342 | Production rate of 15 t/h was achieved during short test; operation suspended. |
| 2883-04 | Lanipuna-1 | 2,557 | >363 | High salinity at intermediate depth and temperature, low permeability at depth; abandoned. |
| 2883-04A | Lanipuna-1 | 1,920 | 149 | Drilled as a slant hole off of 2983-02, maximum temperature of 193 °C with temperature turnover; abandoned. |
| 2883-05 | Lanipuna-6 | | | Very productive low-temperature aquifer encountered at 1,370-m depth. |
| 2883-06 | Kapoho State 1A | 2,000 | 300 | Drilled in 1984; short-duration testing produced self-sustaining flow; production rate and subsurface temperature data are presently proprietary. |
| 2982-01 | Geothermal-3 | 210 | 93 | Drilled in 1962; reached water table but insufficient temperature for production; abandoned. |
| 3081-01 | Geothermal-4 | 88.4 | 43 | Drilled in 1962; insufficient temperature for production; abandoned and now plugged. |

$3 \times 10^6$ m$^3$/mo following the *M*-7.5 earthquake that occurred on the ERZ in 1975 (Dzurisin, 1981). Other studies of surface features such as pit craters (Macdonald and Abbott, 1970; Holcomb, 1980), and of petrologic characteristics of rift eruptions (Swanson and others, 1976; Moore, 1983) indicate that intrusive bodies remain molten for extended periods and may act as subsidiary magma chambers to surface eruptions occurring long after their initial intrusion into the rift zone.

Numerous geophysical studies tend to confirm this interpretation. The total-intensity aeromagnetic map of the rift zone prepared by Godson and others (1981) indicates a clear magnetic signature along the entire length of the rift. This magnetic signature has been interpreted as indicating the presence of temperatures in excess of the Curie temperature of basalt at an estimated depth of 2–3 km (D. Jackson, oral commun., 1985). Controlled-source resistivity surveys on the upper rift have also indicated low subsurface resistivities at depths of 2–5 km, which have been interpreted to be thermal fluids or molten magma bodies (Kauahikaua and others, 1979; Kauahikaua, 1981). More recent very low frequency (VLF) surveys over the ERZ (Flannigan and Long, chapter 39) have similarly identified magnetic and resistivity anomalies that have been inferred to delineate the currently active part of the rift zone and, in some places, molten magma stored in the rift. Although the presence of molten intrusives on the LERZ has not been unequivocally demonstrated, resistivity (Keller and others, 1977; Kauahikaua and others, 1980; Kauahikaua, 1981), self-potential (Zablocki, 1976, 1977), and deep drilling results (Shupe and others, 1978; Yuen and others, 1978; Thomas, 1982) have indicated the presence of high-temperature water.

Although the surface expression of the rift zone is only about 3–4 km wide, some studies suggest that it may be much broader in the subsurface. Swanson and others (1976) analyzed deformation and seismic data for the ERZ and proposed that the focus of active intrusion and eruption on the rift zone has migrated southward with time. Their model considers the north flank of Kilauea to be essentially fixed due to the buttressing effect of Mauna Loa to the north, but that the steep submarine slope to the south of the rift is more mobile and is readily displaced by the forceful intrusion of magma into the rift. The sharp bend in the upper rift is interpreted to be the result of the southward migration of the rift and, on this basis, a subsurface dike complex on the upper rift could approach 10 km in width. Although this width has not been confirmed, interpretations of gravity data by Swanson and others (1976) and gravity and magnetic data by Furumoto (1978) are consistent with a broad subsurface dike complex.

In summary, the structure of the ERZ consists of a broad complex of steeply dipping dikes and fractures extending in a northeasterly direction from the summit caldera for a distance of more than 100 km to the ocean floor. The available geophysical data indicate that the maximum temperatures present at depth in the interior of the rift are in excess of the Curie point. However, the very high permeability of subaerial and shallow submarine extrusive lava is likely to allow rapid hydrothermal circulation and high heat loss rates in the shallow subsurface; hence, only very young intrusives are expected to be significantly above ambient temperatures at depths of less than 1–2 km.

## SURFACE HYDROLOGY AND CHEMISTRY

The near-surface hydrology of the ERZ is characterized by very high recharge rates and rapid subsurface ground-water flow. Rainfall rates exceed 2.5 m/yr over most of the ERZ, and the very high permeabilities of the surface volcanic rocks allow nearly 100 percent of the rainfall to penetrate to basal aquifers (Davis and

TABLE 56.2.—*Chemical data from shallow ground-water wells on the lower east rift zone*

| Well | Name | Temperature (°C) | pH | Chemical contents (parts per million) Na | K | Ca | Mg | Cl | $SO_4$ | $SiO_2$ | Tritium age[1] (yr) | Na-K-Ca temperature (°C) | $^2SiO_2$ temperature (°C) | $^3SiO_2$ temperature (°C) |
|---|---|---|---|---|---|---|---|---|---|---|---|---|---|---|
| 2487-01 | Keauohana | 20.8 | 7.05 | 95.1 | 12.4 | 15.4 | 5.1 | 160 | 28.6 | 44.5 | 18 | 149 | 66.1 | 96.5 |
| 2783-01 | Malamaki | 52.2 | 7.45 | 3,333 | 218 | 293 | 295 | 5,380 | 598 | 100.7 | 15.6 | 149 | 111 | 137.5 |
| 2881-01 | Allison | 37.8 | 7.35 | 1,188 | 68 | 84 | 102 | 2,042 | 69.2 | 24.1 | 12.9 | 122 | 39 | 70.6 |
| 2982-01 | Geothermal 3 | 93 | 6.85 | 2,572 | 378 | 194 | 122 | 4,645 | 314 | 96.6 | 10.3 | 257 | 108 | 135 |
| 2986-01 | Pahoa | 23.3 | 6.65 | 16.7 | 9.3 | 4.5 | 3.1 | 4.93 | 27.3 | 50 | 10.6 | 310 | 72 | 102 |
| 3080-02 | Kapoho | 22.1 | 7.1 | 127 | 15 | 65.6 | 35.2 | 174 | 328 | 53.6 | 10.5 | 124 | 75 | 105 |
| 3081-02 | Airstrip | 33.5 | 7.75 | 241 | 28 | 37.6 | 27.4 | 364 | 211 | 71.3 | 11.1 | 154 | 91 | 119 |

[1]Kroopnick and others, 1978.
[2]Chalcedony.
[3]Quartz conductive cooling.

Yamanaga, 1968). Ground-water transmissivities are typically $5 \times 10^4$ darcies (Mink, 1977; Druecker and Fan, 1976) and hence ground-water residence times, as indicated by tritium dating (table 56.2), are typically less than 10–20 years (Kroopnick and others, 1978); discharge of basal fresh water in coastal springs has been estimated at 88–131 $m^3/s$ (Stearns and Macdonald, 1946; Davis and Yamanaga, 1968; Macdonald and others, 1983).

The temperatures and chemical compositions of ground water on the LERZ (table 56.2) span a broad range and suggest that recharge to the basal ground water in this region is received from several very different reservoirs. Four candidate sources could be anticipated in the region: cold, fresh meteoric recharge; cold sea water; hydrothermal fluids of meteoric origin; and hydrothermally modified sea water. The most convenient tracers that can distinguish these possible reservoirs are temperature, chloride-ion concentration, and the chloride-ion:magnesium-ion ratio. Above-ambient ground-water temperatures are clearly indicative of hydrothermal recharge; chloride-ion concentrations permit the identification of fluids of sea-water origin; and, because magnesium has been found to be heavily depleted by hydrothermal processes (Bischoff and Seyfried, 1978; Cox and Thomas, 1979), the chloride:magnesium ratio is able to provide a qualitative indication of the degree of hydrothermal modification undergone by fresh or saline water independent of the measured temperature. A plot of chloride-ion concentration versus temperature and versus chloride:magnesium ratio (fig. 56.2) provides an indication of the relative contributions of the various candidate source fluids to the ground water in the LERZ. Endmember compositions for the candidate sources are plotted for comparison: fresh water is represented by data from well 2986-01, located north of the rift; cold saline fluid by sea water; hydrothermal-meteoric recharge by the early, low-chloride fluids encountered at HGP-A; saline hydrothermal fluids by the fluid compositions found in high-temperature sea water-basalt experiments (Cl:Mg ratio; Seyfried and Bischoff, 1981) and at midocean-ridge hydrothermal systems (temperature).

The distribution of the data points on figure 56.2 suggests the following observations: (1) Chloride concentrations show a broad variation ranging from near fresh-water chloride to almost 30 percent sea-water chloride. (2) The chloride concentrations show a modest correlation with temperature: higher temperature ground water generally has a higher chloride concentration. (3) The degree of alteration of the thermal fluids, as indicated by the Cl:Mg ratio, generally varies and is well below that found in HGP-A or in high-temperature sea water-basalt experiments. (4) The Cl:Mg ratio is not well correlated with either temperature or chloride concentration: well 2982-01 shows a high temperature and high chloride concentration and a moderately depleted magnesium concentration (relative to sea water), well 2783-01 shows intermediate temperatures, high chloride, and only minor magnesium depletion, and well 2487-01 shows a low temperature and low chloride concentration but a significant magnesium depletion. These observations suggest that meteoric recharge is the predominant source for ground water in the region. However, sea water that has undergone varying degrees of hydrothermal alteration contributes as much as 30 percent

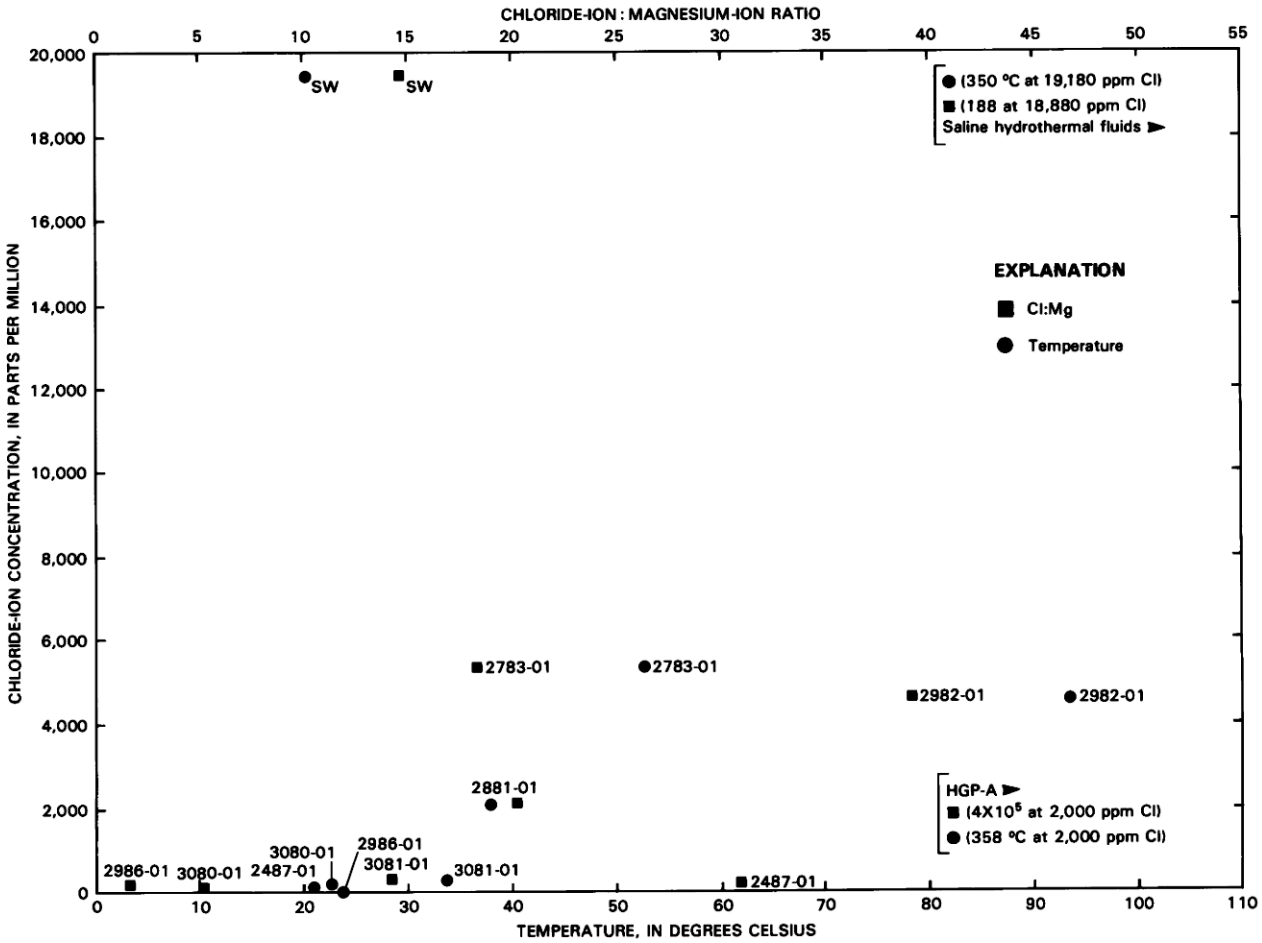


FIGURE 56.2.—Chloride-ion concentration versus temperature and versus chloride:magnesium ion ratio in shallow ground-water wells on lower east rift zone. Wells are identified by number (see fig. 56.1). Data from well 2986-01 represent fresh water; HGP-A data represent hydrothermal-meteoric recharge from early, low-chloride-ion fluids from HGP-A; saline-hydrothermal-fluid data represent high-temperature sea water-basalt experiments (Cl:Mg ratio) and midocean-ridge hydrothermal systems (temperature); SW, sea water.

of the recharge to the basal lens. The role of high-temperature, heavily modified, fresh and saline water in the basal aquifers is not as clearly defined. The chemistry of well 2487-01 could be modeled as a mixture of fresh ground water with a small addition of low-salinity, heavily altered hydrothermal fluid. The low temperatures suggest that the contribution from the latter source is, however, very small.

As many as four source fluids appear to have an influence on the ground-water temperatures and chemical compositions on the LERZ:meteoric recharge; cold, relatively unaltered sea water; higher temperature altered sea water; and low-salinity, heavily altered hydrothermal fluid.

The mixing of these multiple-source fluids in the shallow ground-water aquifers renders any attempt to apply chemical geothermometers highly suspect. Temperatures calculated using the Na-K-Ca geothermometer (Fournier and Truesdell, 1973; Fournier, 1981) are generally correlated with measured temperatures (table 56.2) although the correlation is far from uniform. The silica geothermometer (Fournier and Potter, 1982) similarly yields varying apparent temperatures that, although generally correlated with measured temperatures, do not yield significant insight into the deeper reservoir.

The rate of convective discharge of the thermal energy from the interior of the rift can be crudely estimated using the data from the shallow wells and assuming that: (1) the mean ground-water temperature of the aquifer south of the northern boundary of the ERZ and east of well 2487-01 is the average of that found in wells 2783-01, 2881-01, 3081-01, and 2982-01; and (2) the rate of freshwater recharge is equivalent to the average rainfall rate in this area. Using these assumptions, the mean ground-water temperature is calculated to be about 54 °C. The average rainfall rate is approx-

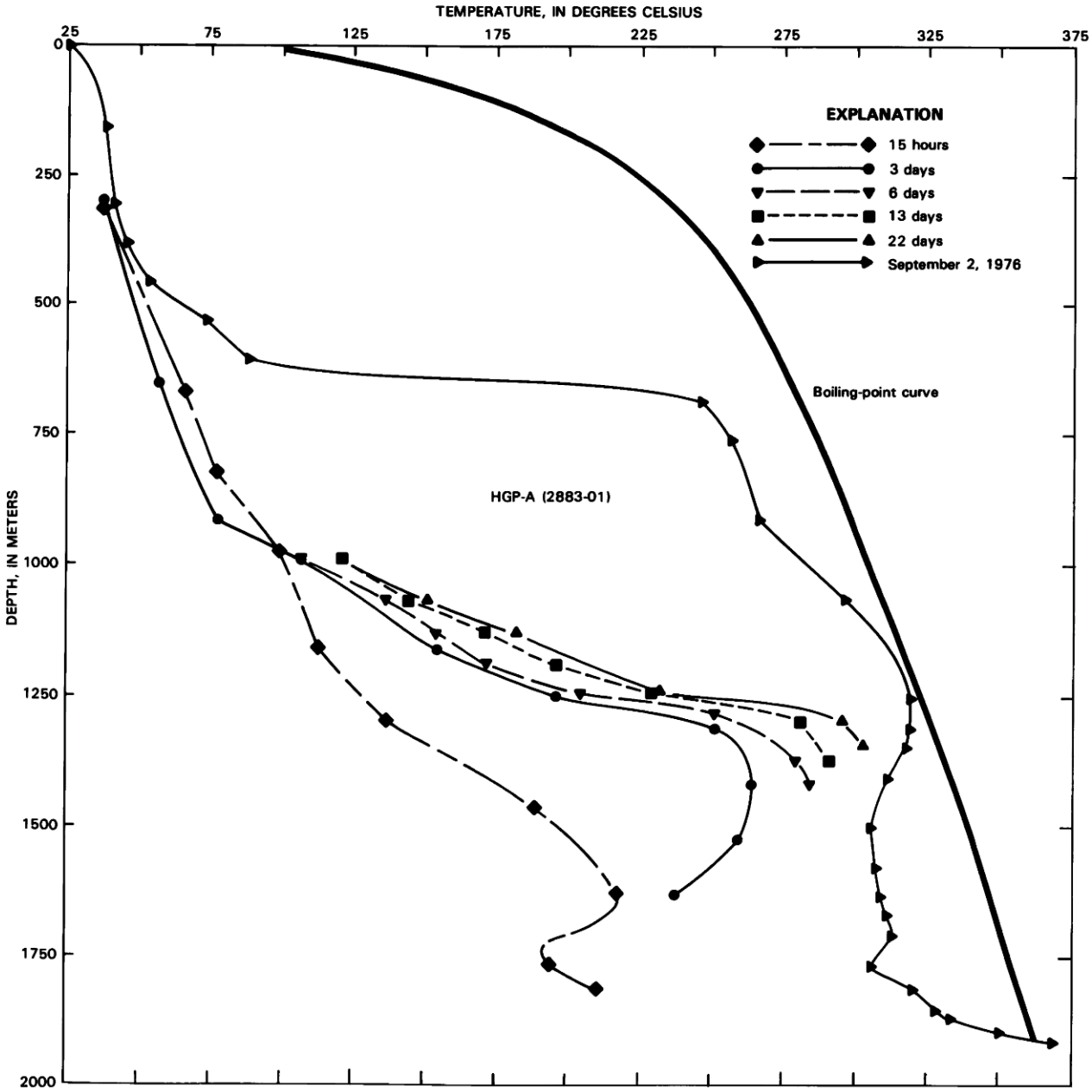


FIGURE 56.3.—Downhole temperatures measured in well 2883-01, HGP-A geothermal well. Individual curves reflect downhole temperature measurements made at specified times after mud circulation in well was suspended. Profile for 9/2/76 was measured with water in borehole.

imately 2.5 m/yr and the area of interest is approximately $25 \times 10^6$ $m^2$; thus, the total fresh-water recharge is approximately $62.5 \times 10^6$ $m^3$/yr. Hence the total thermal discharge in this limited region is estimated to be a minimum of $2.19 \times 10^{12}$ kcal/yr or approximately 291 megawatts of thermal energy continuously. If this heat loss rate is extrapolated over the subaerial rift zone, 50 km of rift zone versus 10 km in the area of the thermal discharge, the heat loss would be approximately 1,455 thermal megawatts. The magma intrusive rate estimated by Dzurisin (1981) at $3 \times 10^6$ $m^3$/mo would bring an estimated 2,800 thermal megawatts into the rift zone. In light of the approximations made and the very short timespans considered, these values are in remarkably close agreement and may be interpreted to

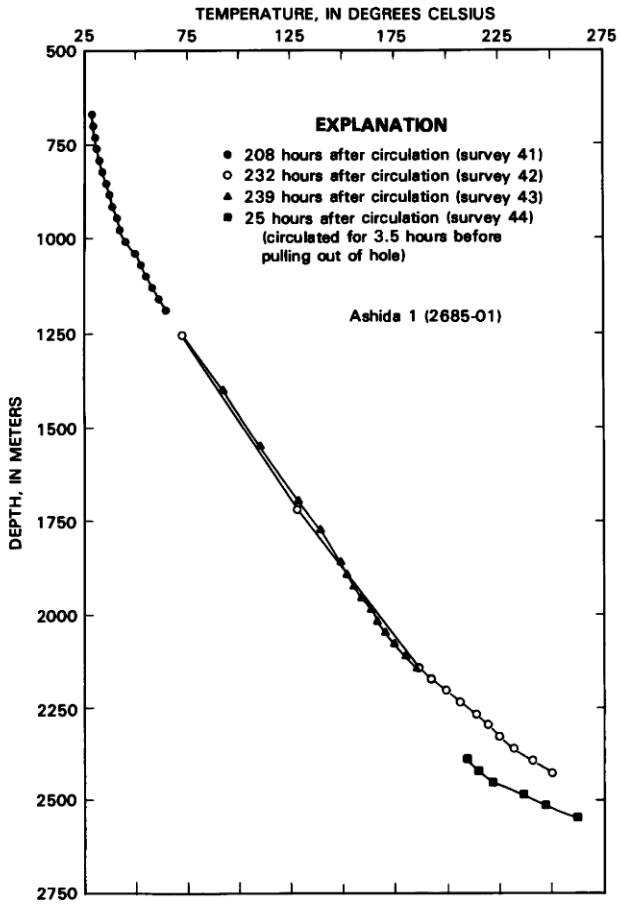


FIGURE 56.4.—Downhole temperatures measured in well 2685-01, Ashida 1.

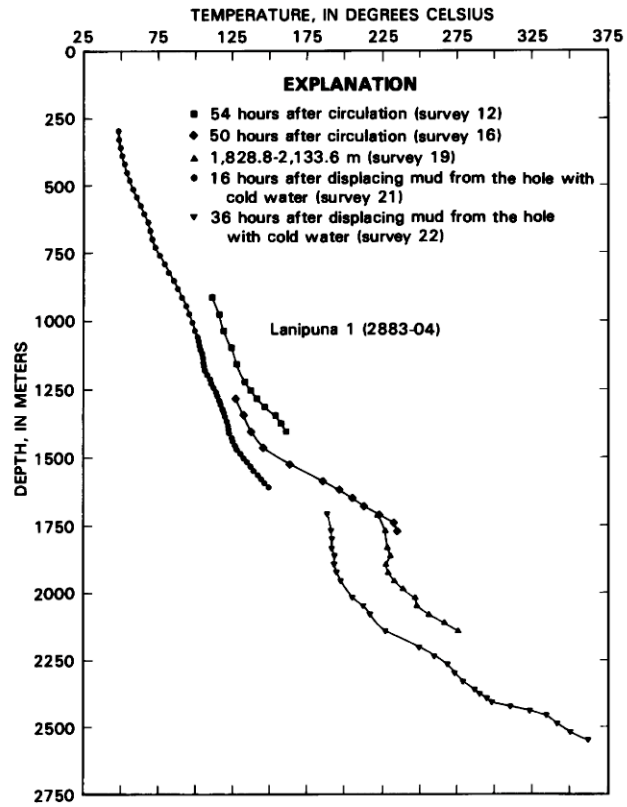


FIGURE 56.5.—Downhole temperatures measured in well 2883-04, Lanipuna 1.

indicate that the rates of convective heat loss to the shallow hydrologic system nearly balances the heat recharge from magmatic processes. If this interpretation is correct, it would in turn suggest that the residual heat present in a rift zone after cessation of intrusive activity would decrease very rapidly.

## DEEP HYDROLOGY

The HGP-A well, completed in 1976, was the first deep research well drilled into the ERZ; seven privately funded deep wells have been completed subsequent to HGP-A in an effort to further define the geothermal resource discovered by this well. HGP-A was funded by several public and private agencies (the U.S. Department of Energy, National Science Foundation, State of Hawaii, County of Hawaii, and Hawaiian Electric Company), and hence more data for this well is publicly available than for the privately financed exploration wells. However, sufficient data has been released to allow us to permit limited extrapolation of the HGP-A data to other parts of the ERZ.

## THERMAL CHARACTERISTICS

The available data from all the deep geothermal wells presently drilled in the LERZ are presented in table 56.1. All but two of the wells recently drilled penetrated to a depth of 2,000 m. The maximum temperatures encountered in each well were substantially above the normal geothermal gradient found in Hawaii. However, clear differences are present in the maximum temperatures encountered in each well, and examination of the temperature profiles is especially revealing. The temperature profiles used for each well must be interpreted carefully however: temperatures measured immediately after drilling and mud circulation cease are likely to be below equilibrium temperatures, whereas those measured after mud has been cleared from the hole may be affected by water circulation within the wellbore. The conditions under which the profiles were taken, if known, are noted.

The well profiles (figs. 56.3–56.6) generally show a shallow zone of moderate temperature over the first 500–1,000 m of the well. The moderate and relatively uniform temperatures in this interval reflect high meteoric recharge rates and rapid ground-water circulation and mixing in the very permeable subaerial and shallow submarine basalts. Underlying this zone is an interval of gradually

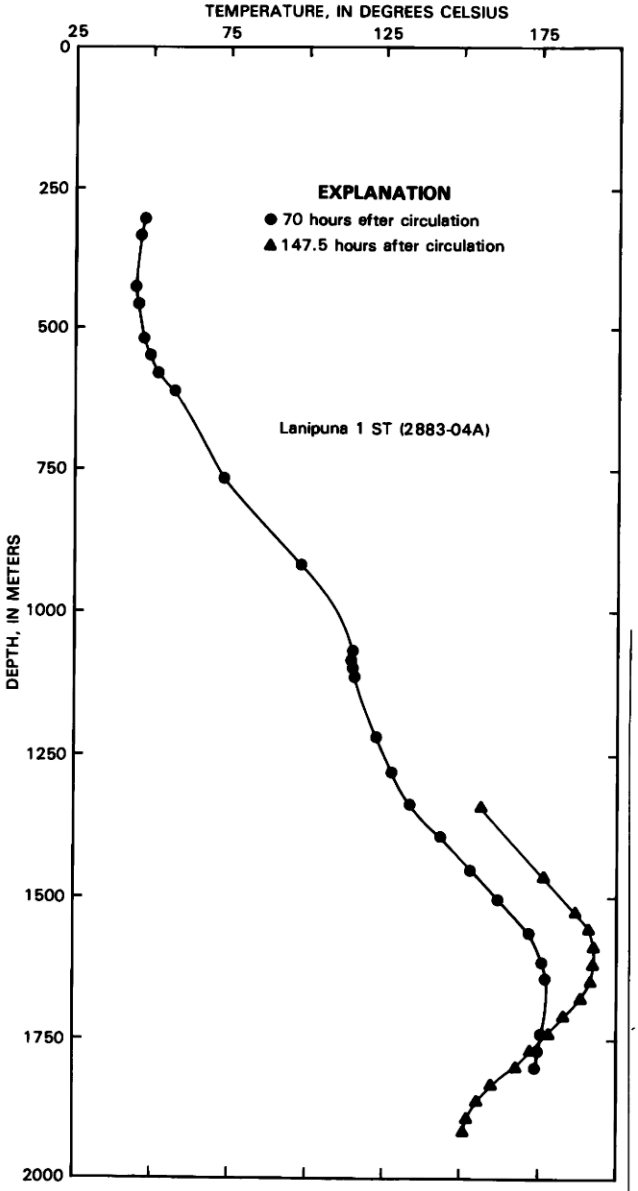


FIGURE 56.6.—Downhole temperatures measured in well 2883-04A, Lanipuna 1 side track.

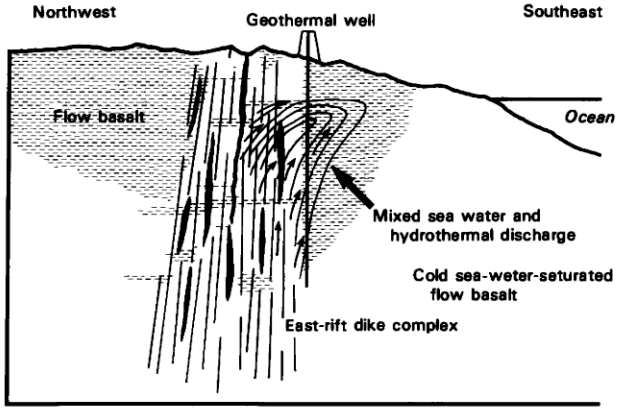


FIGURE 56.7.—Conceptual cross section of lower rift showing fluid circulation across rift zone. Thermal waters, exiting rift toward southeast, form a tongue of hot water overlying colder fluids below. Drilling on southern edge of rift would initially encounter thermal fluids at shallow depths, but at greater depths would reenter lower temperature aquifers.

increasing temperature, possibly representing a conductive temperature gradient, that indicates the decline in basalt permeability and a reduction in the rate of hydrothermal circulation. Below the conductive region, the temperature gradient may steepen and approach a curve corresponding to the temperature of steam-saturated water under hydrostatic pressure (the boiling curve). The conformance to the boiling curve suggests that the thermodynamic conditions in the deep reservoir are controlled by hydrostatic pressure and not by physical barriers, such as a reservoir cap rock. There are, however, exceptions to this general trend. The data from wells 2883-04A and 2883-05 show a distinct temperature turnover in the lower portions of both holes. The location of these wells on the southern boundary of the rift suggests that the wells may have passed through a reservoir outflow zone and penetrated into colder aquifers below (fig. 56.7). This interpretation leads to the speculation that the fractures and intrusives on the southern edge of the ERZ dip toward the north. If the rift structure had a southward dip, deeper drilling in this location would be anticipated to penetrate toward higher temperature intrusives.

A comparison of the temperature distribution among the wells and their relative locations shows that the maximum temperatures encountered are very site specific. For example, well 2883-04 encountered a bottom-hole temperature of >368 °C, the highest temperature reported for the LERZ wells, but a redrill of this well (2883-04A), completed as a slant-hole offset, encountered maximum temperatures of only 193 °C with a bottom-hole temperature reversal (figs. 56.5 and 56.6). The bottom of the redrill is less than 500 m from the bottom of its original straight configuration and from HGP-A, yet its peak temperature is more than 160 °C below the maximum temperatures encountered in either well. The temperatures encountered along the southern boundary of the ERZ vary greatly and may be strongly influenced by local hydrologic conditions. Although fewer wells have been drilled on the interior of the ERZ, the reported temperature information indicates somewhat more consistency than is found on its edge (Iovanitti and D'Olier, 1984).

## PETROLOGY

The petrology of the rocks encountered in the deep exploration wells has not as yet been analyzed in detail. HGP-A was the only well from which cores were taken and hence is the only well for which bulk rock analyses can be done. However, analyses of the cuttings that have been released from the other wells (Barnwell

Geothermal Corp., unpublished data, 1985) are very informative as to the type of alteration present. The wells for which preliminary analyses are available include HGP-A, 2685-01, 2883-04, 2883-04A, and 2883-05; although analyses have been completed for wells 2883-02 and 2883-03, the data have not been released, and a second analysis is currently underway for archived samples from well 2883-02.

Samples of the cuttings from all of the wells indicate the presence of basalt throughout the section. The morphology of the basalt ranges from highly vesicular in the shallow subsurface to dense, nonvesicular pillow lava and dike rocks at depth. Hyaloclastites, palagonitized ash, and hematite were found at depths of 500–800 m below ground level and approximately 300–500 m below the current sea level (Stone, 1977; Barnwell Geothermal Corp., unpublished data, 1985). The morphology and oxidation of the basalt may indicate the approximate location of sea level at the time of extrusion of the lava. Rock textures range from aphyric glass, associated with chill margins or pillow lava, to olivine-phyric and plagioclase-phyric lavas.

The alteration mineralogy found in the individual wells follows a relatively consistent pattern. The shallow parts of the wells are typified by mild low-temperature alteration and deposition products such as montmorillonite clays, anhydrite, and calcite (Stone, 1977; Stone and Fan, 1978; Waibel, 1983). As the depths and temperatures increase, the degree of alteration generally increases as does the grade of metamorphism. Trends in the mineral suites show incipient alteration at intermediate temperatures that increases to total replacement of parent minerals by chlorite and lesser amounts of accessory products such as albite or, at the highest temperatures, epidote (figs. 56.8–56.11). In addition to the above, other alteration products found throughout the geologic section include calcite, anhydrite, zeolites, quartz, pyrite, and magnetite. Despite these general trends, the degree of alteration is by no means continuous throughout the section. Alteration is intermittent, and the extent of alteration at a given depth and temperature varies greatly, thus implying that the alteration process is highly dependent upon the access of (saline?) fluids to the interior of the rift. This intermittent alteration in turn suggests that, whereas temperature is the primary controlling factor in the alteration of the basalt, fracture permeability and fluid circulation within the rift are also major factors.

The depths of the various alteration minerals are significant to the model of hydrothermal circulation within the ERZ. As noted above, anhydrite is distributed throughout the cuttings from some wells and is apparently confined to only a few depth intervals in others. The retrograde solubility of anhydrite and the presence of relatively high concentrations of calcium and sulfate in sea water suggest that anhydrite is being deposited from sea water circulating within the ERZ. Laboratory studies of sea water-basalt reactions have shown that calcium sulfate is removed from sea water as anhydrite (Mottl and Holland, 1978; Mottl and Seyfried, 1980; Seyfried and Mottl, 1982) and that nearly quantitative removal of calcium occurs before temperatures reach 225 °C. The presence of anhydrite in both the low-temperature and the higher temperature parts of the rift could be accounted for by either of two possible

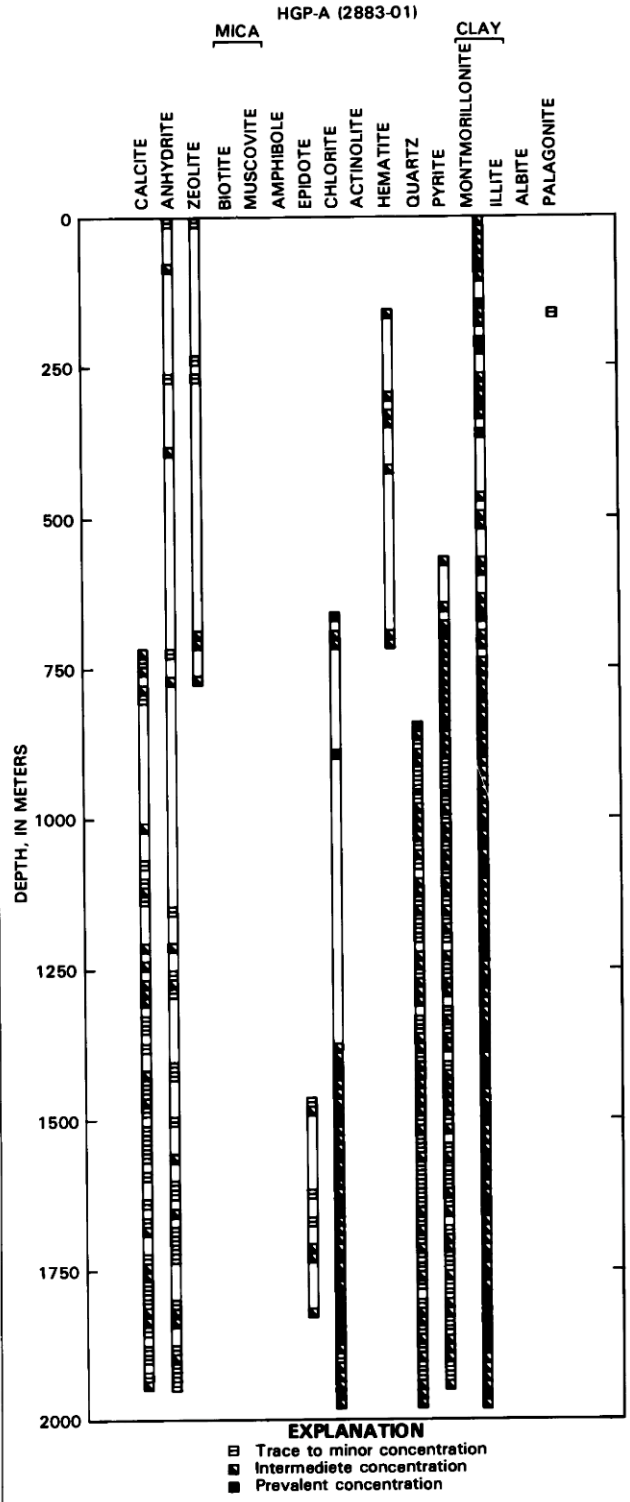


FIGURE 56.8.—Alteration mineral suites encountered with depth in HGP-A. (From Columbia Geosciences, unpublished data, 1983.)

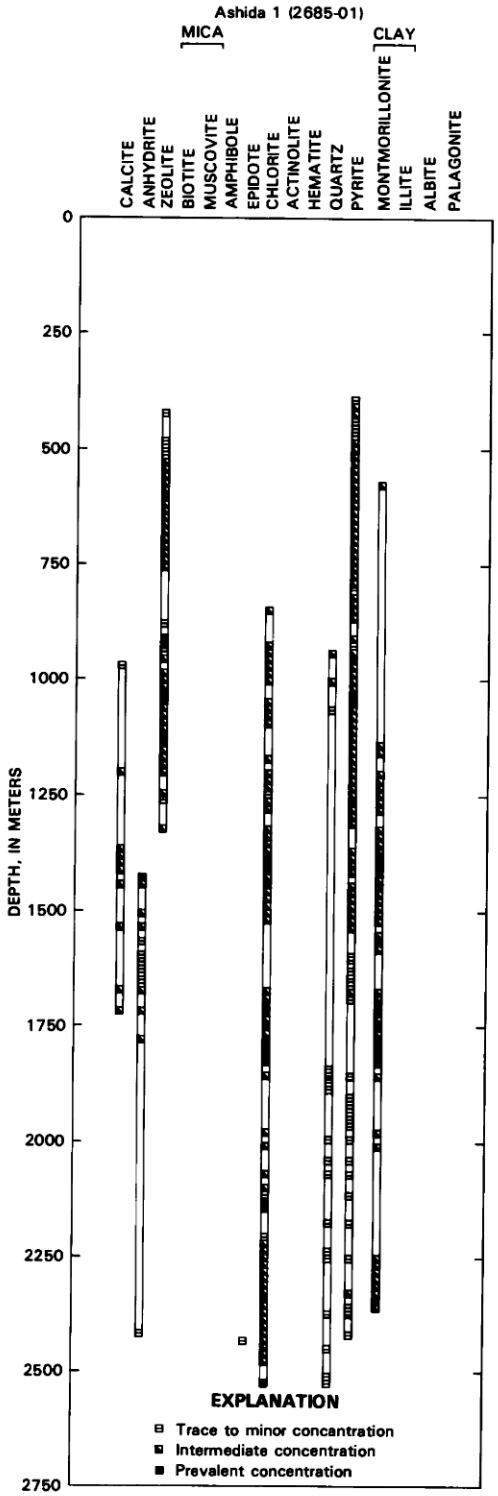


FIGURE 56.9.—Alteration mineral suites encountered with depth in well 2685-01. (From Barnwell Geothermal Corp., unpublished data, 1985.)

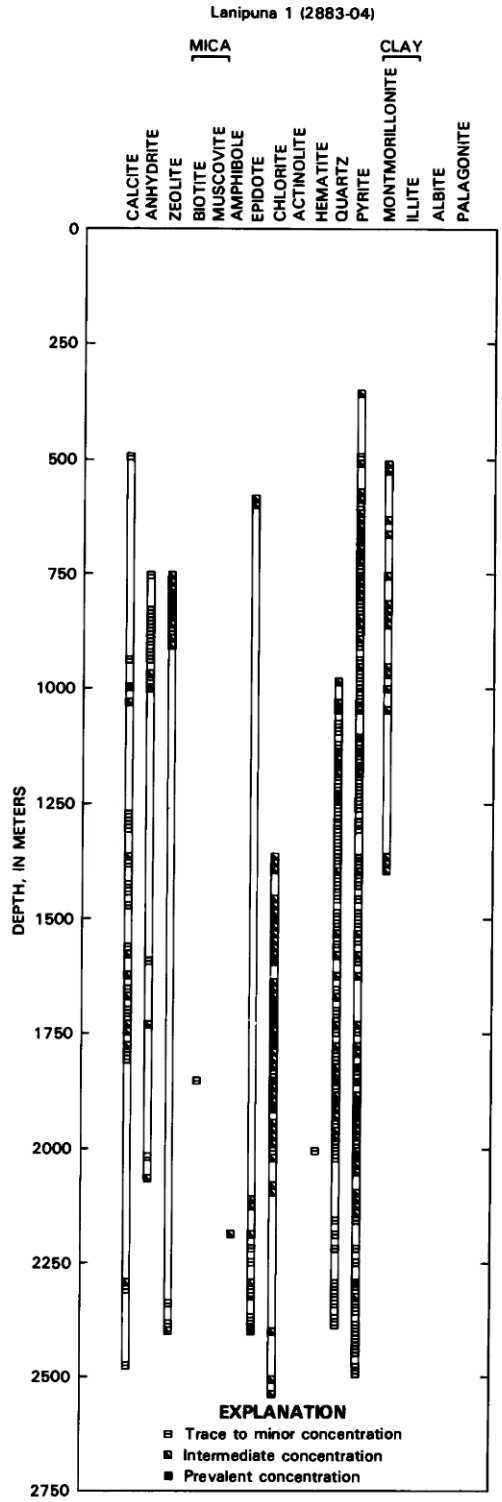


FIGURE 56.10.—Alteration mineral suites encounterd in well 2883-04. (From Barnwell Geothermal Corp., unpublished data, 1985.)

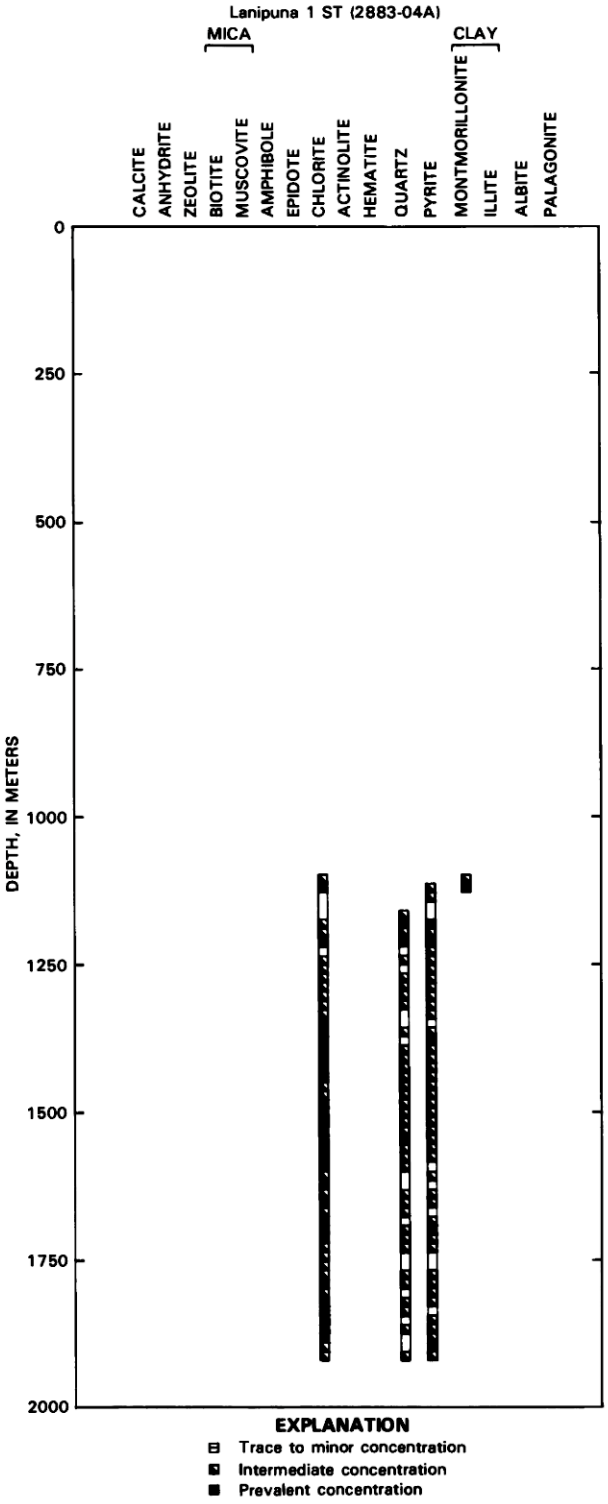


FIGURE 56.11.—Alteration mineral suites encountered in well 2883-04A. (From Barnwell Geothermal Corp., unpublished data, 1985.)

mechanisms: (1) anhydrite precipitation continues at higher temperatures as calcium is mobilized from the basalt matrix by hydrothermal alteration; (2) the part of the rift penetrated by these wells has undergone a complex history of heating and cooling associated with successive episodes of magmatic intrusions and subsequent cooling by hydrothermal circulation.

Pyrite and quartz are present throughout virtually the entire section below sea level. Due to the low temperatures and low metamorphic grades present in the shallow parts of the wells, the fluids precipitating these minerals probably did not originate at the depths of deposition, and hence they represent deposition from cooling hydrothermal fluids discharged from deeper within the rift.

Minerals found in the altered parts of the deep wells are quite similar to those found in sea water-dominated hydrothermal systems such as Reykjanes (Tomasson and Kristmannsdottir, 1972; Kristmannsdottir, 1976), in dredge samples from sea-floor spreading centers (Humphris and Thompson, 1978), and in laboratory studies of sea water-basalt reactions at high temperature (Mottl and Seyfried, 1980; Seyfried and Mottl, 1982). Clearly, the primary agent responsible for the alteration mineral suite observed is the intrusion of sea water into the interior of the ERZ. However, because the grade and intensity of hydrothermal alteration in each well varies with depth, the intermittent highly altered zones in the reservoir are interpreted to be the result of fracture-mediated intrusion of sea water into the interior of the rift.

## PRODUCTION CHARACTERISTICS

The production characteristics of the individual wells have varied over a broad range. HGP-A initially produced a mixed-phase flow comprised of approximately 50 percent steam and 50 percent liquid, at approximately 45,000 kg/h. Discharge rates increased slightly during testing and, at the beginning of production for the HGP-A generator facility, amounted to approximately 50,000 kg/h. The steam:brine ratio is a function of wellhead pressure and, at the operating pressure of the facility, is approximately 57 percent liquid and 43 percent steam at a pressure of 1,200 kPa. Production from the well showed a gradual decline over the first 40 months of operation of the generator facility amounting to about 10–15 percent of its total output. However, during a 48-hour period on the fortieth month, wellhead pressures and production rates increased by slightly more than was lost during the prior forty months. The change occurred in distinct steps that were not accompanied by any seismic activity and hence were probably the result of a change in the wellhole, such as the elimination of an obstruction. This interpretation suggests that the total production from HGP-A may be limited by the borehole diameter rather than by the inherent productivity of the reservoir.

Analysis of the changes that have occurred in the production chemistry indicates that HGP-A is producing from two separate reservoirs having very different characteristics. The liquid or brine phase is apparently produced from an intermediate-depth reservoir having a temperature of approximately 260–280 °C, whereas dry-steam production is occurring from near the bottom of the well.

TABLE 56.3.—*Summary of HGP-A liquid-phase chemistry*

| Date | Depth/ pressure | Chemical contents (parts per million) Na | K | Ca | Mg | Cl | $SO_4$ | $SiO_2$ | Na-K-Ca[1] temperature (°C) | Quartz[2] temperature (°C) | Water:rock ratio ([3]) | ([4]) |
|---|---|---|---|---|---|---|---|---|---|---|---|---|
| 12/2/76 | 1,300 m | 480 | 85 | 17.3 | 0.7 | 920 | -- | 740 | 262 | 290 | 3.2 | 0.71 |
| 2/9/77 | 103 kPa | 720 | 135 | 30.1 | .1 | 1,610 | -- | -- | 219 | | 3.7 | .81 |
| 4/22/77 | 103 kPa | 1,480 | 277 | 72.2 | .1 | 3,190 | -- | -- | 298 | | 3.5 | .77 |
| 1/16/80 | 910 kPa | 1,520 | 224 | 33.9 | .01 | 2,593 | 69 | 832 | 278 | 303 | 3.5 | .78 |
| 6/12/81 | 103 kPa | 900 | 200 | 25.5 | .008 | 2,065 | -- | 1,198 | 336 | 296 | 3.1 | .67 |
| 9/4/81 | 1,200 kPa | 1,890 | 295 | 66.5 | .029 | 3,622 | -- | 860 | 281 | 307 | 3.8 | .84 |
| 12/11/81 | 103 kPa | 1,590 | 300 | 33 | .012 | 2,763 | -- | 1,004 | 332 | 280 | 2.6 | .58 |
| 6/7/82 | 1,170 kPa | 3,120 | 525 | 122.5 | .051 | 5,667 | -- | 803 | 309 | 299 | 3.2 | .71 |
| 11/16/82 | 1,170 kPa | 3,940 | 650 | 217 | .104 | 7,029 | -- | 829 | 301 | 303 | 3.2 | .71 |
| 5/4/83 | 1,170 kPa | 4,220 | 675 | 270 | .152 | 7,965 | -- | 805 | 292 | 300 | 3.6 | .80 |
| 12/5/83 | 1,100 kPa | 4,650 | 763 | 319 | .210 | 8,827 | 24 | 825 | 298 | 303 | 3.5 | .77 |
| 6/26/84 | 1,100 kPa | 4,840 | 773 | 489 | .25 | 8,900 | 15 | 885 | 282 | 310 | 3.5 | .77 |
| 11/28/84 | 1,100 kPa | 5,420 | 733 | 399 | .20 | 9,514 | 4.5 | 913 | 265 | 314 | 4.12 | .91 |

[1]Fournier, 1981.
[2]Fournier and Potter, 1982.
[3]Water to rock ratio based on original sea-water potassium concentration of 399 ppm and Kilauea tholeiite average concentration of 4,500 ppm, and a potassium removal efficiency of 100 percent.
[4]As above but using an extraction efficiency of 22 percent (Seyfried and others, 1984).

The production characteristics of the other geothermal wells on the LERZ have not been as well characterized as that from HGP-A; however, the data available indicate widely divergent discharge patterns. Short-duration production tests conducted on three wells north of HGP-A (2883-02, 2883-03, 2883-06) have clearly confirmed the presence of dry-steam production from the LERZ reservoir: two of these wells initially produced a mixed phase of steam and water that changed to dry steam over a period of a few hours (Iovanitti and D'Olier, 1984). The production rates from the first two wells were reported to be 15 t/h and 33 t/h, respectively; however, the duration of the tests conducted and the presence of debris in the hole suggest that these are neither equilibrium nor representative flow rates. (This third well, 2883-06, was also productive; however, the engineering data are presently confidential.)

In contrast to the wells located north of HGP-A, three of the wells drilled on the southern boundary of the rift (2883-04, 2883-04A, and 2685-01) were unable to sustain production at all. Although permeable zones, as indicated by drilling-mud-loss records, were encountered in these wells, the available records indicate that the permeable zones were much more limited south of the rift than at HGP-A or in the wells more interior to the rift. The fourth well, 2883-05, encountered an extremely permeable fracture at a depth of approximately 1,600 m that did not have sufficient temperature to sustain production.

## RESERVOIR CHEMISTRY

The HGP-A well is the only deep well in the LERZ for which a significant number of samples have been analyzed, and hence the data set from HGP-A yields the most complete picture of the chemical processes underway in the hydrothermal system associated with the ERZ. The limited data set available from the other wells is, however, consistent with the model derived from HGP-A.

The composition of the fluids produced by HGP-A during its production life has shown complex changes during each period of discharge and between periods of discharge. Samples obtained from downhole samplers and from production fluids taken immediately after well completion showed very low dissolved solids concentrations (table 56.3); chloride levels generally ranged from about 1,000 mg/kg to 2,000 mg/kg whereas the total-solids content was approximately 3,000 mg/kg to 5,000 mg/kg. Subsequent samples of discharge fluids showed an increase in the salinities during each well test but a slight reduction in chloride concentrations between tests. The rate of increase during the first production tests was relatively rapid; initial chloride concentrations of approximately 1,000 mg/kg in the liquid phase increased to more than 2,000 mg/kg after steam production (flashing) began and continue to increase throughout the period of discharge. The longest test period, prior to the installation of the generator facility, spanned 1,000 hours; the chloride concentration in the brine at the conclusion of that test was approximately 3,200 mg/kg.

Downhole sampling during the preliminary testing provided chemical data indicating that production was occurring from at least three aquifers: one at a depth of approximately 700 m produced cold saline water; a second at a depth of approximately 1,500 m produced low-salinity fluids; and a third at a depth of approximately 1,900 m produced low- to intermediate-salinity fluids (Kroopnick and others, 1978). Although a subsequent recasing program sealed off the cold, high-salinity aquifer, continuous discharge of fluids from HGP-A between 1983 and 1985 continued to generate substantial increase in salinity (fig. 56.12); by the end of 1985 after four years of continuous production, the chloride concentrations reached a level of approximately 10,000 mg/kg.

The other major dissolved solids present in the brine phase include sodium, potassium, calcium, and silica. The concentrations of all but the latter have shown increases similar, although not

identical, to those observed for chloride (table 56.3). Silica concentrations in the brine have shown little if any verifiable change beyond those associated with changes in the power plant operating conditions.

In contrast to the evolution of the brine chemistry, the gases present in the steam phase have shown very modest variations. Although the gas-chemistry data obtained from HGP-A during the preliminary well testing are suspect due to analytical and sampling difficulties, the data indicate that the major gases, $CO_2$ and $H_2S$, were present at concentrations of less than 1 percent by weight of the steam. Subsequent analyses, conducted during power plant operations, determined that the concentrations of the major gases were approximately as follows: $CO_2$, 1,250 mg/kg; $H_2S$, 950 mg/kg; $N_2$, 130 mg/kg; $H_2$, 12 mg/kg; and $CH_4$, 1 mg/kg. Changes in the gas concentrations were observed during the initiation of well flow that correspond to stabilization of the reservoir in response to production, but subsequently they declined at a very modest rate during the three and one-half years of power plant operations. The gas concentrations currently amount to: $CO_2$, 1,150 mg/kg; $H_2S$, 850 mg/kg; $N_2$, 120 mg/kg; and $H_2$, 12 mg/kg.

Although the chemistry data available from the other privately financed geothermal wells is quite limited, the following information has been made available: Wells 2883-04 and 2883-04A, located on the southern boundary of the rift zone, encountered fluids having salinities approximately equivalent to sea water in the permeable, intermediate-temperature parts of the holes. Due to inadequate permeability at depth, these wells were unable to produce steam or a high-temperature mixed phase. Wells 2883-02 and 2883-03, north of HGP-A, produced fluids having dissolved-solids concentrations of a few thousand milligrams per kilogram to near the solids saturation point, depending upon the wellhead pressures and steam qualities during the production tests. Reported total gas concentrations were approximately 2,000 mg/kg of which 1,100 mg/kg

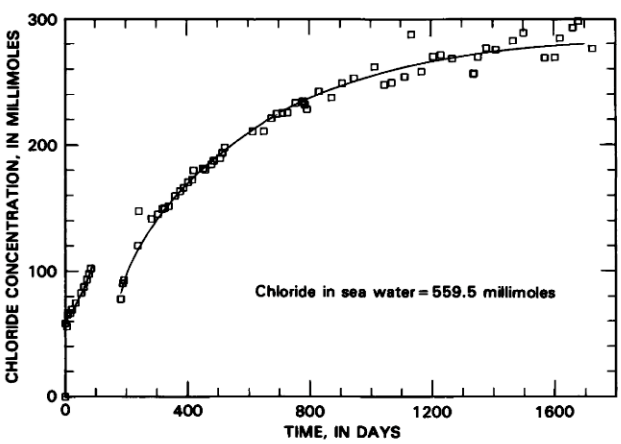


FIGURE 56.12.—Chloride concentrations in brine phase from HGP-A versus duration of production. The interval from day 84 to day 183 represents a period from September 4, 1981, to December 11, 1981 when flow from the well was suspended.

was $H_2S$ (Iovanitti and D'Olier, 1984). Testing of the private exploration wells indicated that multiple production zones were encountered in all wells, and hence the precise source for the fluids are known only to the extent that they are derived from a depth greater than the casing depth of the wells or about 1,100 m below sea level.

## DISCUSSION OF CHEMICAL DATA

One of the most striking aspects of the fluid chemistry data from HGP-A is the very low salinities encountered at depth immediately after well completion. This result was not anticipated, and the presence of fresh water at depth was initially attributed to the presence of drilling fluids lost to the deep production aquifers. However, analysis of tritium levels present in surface waters used for drilling and those from the reservoir (Kroopnick and others, 1978) conclusively demonstrated that the early reservoir fluids were not contaminated by recent surface water. Subsequent analyses conducted after an extended flow test of the well reconfirmed the absence of significant tritium activity in the reservoir fluids (Thomas, 1980).

Because of the density difference between fresh and saline water, the Ghyben-Herzberg model, typically used to describe ground-water hydrology in an island environment predicts that a fresh-water lens should be found floating above sea water in the basal aquifers. The thickness of this lens is dependent upon rainfall recharge rates and the effective permeability of the basal aquifers; in the vicinity of HGP-A, a lens thickness of approximately 70 m would be predicted. However, the presence of a heat source in the ERZ invalidates one of the major assumptions of the Ghyben-Herzberg model: that a density difference exists between fresh and saline water. With a heat source present in the ERZ, sea water entering the hydrothermal system and heated to reservoir temperatures will have a density less than that of cold fresh water. Thus, cold rainfall recharge can enter the ERZ from above and displace warmer, less dense saline water entering the ERZ laterally. This factor alone probably cannot account for the exceptionally low salinities observed at depth in the reservoir: cold saline water should exert a higher hydrostatic pressure on the reservoir than cold fresh water if the hydraulic head heights and permeabilities of the respective infiltration pathways are equal. Hence, other factors may play a key role in the near exclusion of sea water from the deep hydrothermal reservoir. As discussed above, the rift consists of near-vertical tabular dikes and fractures trending in an east-west direction. Hydrologic studies (Stearns and Macdonald, 1946; Takasaki, 1978; Macdonald and others, 1983) have shown that the permeability of intrusive materials may be several orders of magnitude lower than normal country rock, and therefore, the permeability of the rift zone transverse to its strike should be very much lower than the surrounding rocks outside the dike complex. The presence of fractures parallel to the intrusives serves to further increase the permeability of intervening extrusive rocks within the dike complex. Hence, the structure of the ERZ increases the naturally existing east-west and vertical permeability to fresh-water recharge to the rift but inhibits the entry of sea water from the south due to the lower transverse permeability of the dike system.

A third factor that may play a role in the exclusion of sea water from the ERZ is the reaction sequence undergone by sea water when it is heated to reservoir temperatures. Extensive studies conducted on sea-water chemistry at elevated temperatures (Bischoff and Dickson, 1975; Mottl and Holland, 1978; Bischoff and Seyfried, 1980; Seyfried and Mottl, 1982; Pohl and Liou, 1983) have demonstrated that, when sea water is heated in the presence of basalt, a number of reactions occur that can substantially alter the chemical composition of the sea water and the mineral suites present in the rock. Most pertinent to the present analysis are the findings that: (1) the retrograde solubility product of calcium and sulfate ions in sea water result in anhydrite deposition (Mottl and Seyfried, 1980), and (2) reactions at temperatures of 300 °C result in the devitrification of basalt glass and the breakdown of the common basalt minerals and result in the deposition of smectites, chlorite, wairakite, and other alteration products. One sea water-basalt experiment (Pohl and Liou, 1983) was conducted in a flow-through cell that reportedly became plugged due to alteration mineral deposition in less than 48 hours. Similar reactions occurring in the natural sea water-basalt hydrothermal system on the ERZ may result in a sequence of fracture-induced permeability and subsequent sealing by deposition of alteration minerals along the southern (seaward) boundary of the rift. The presence of anhydrite, deposited as a vein-filling mineral, and of intermittent zones of intensely altered but low-permeability basalt in the cuttings from the deep geothermal wells on the LERZ tend to further substantiate this process. Thus the initial absence of sea water in the reservoir fluids encountered by HGP-A can be accounted for by the inhibition of sea-water recharge into the high-temperature part of the rift by permeability barriers imposed by the dike complex, self-sealing by alteration mineral deposition from hydrothermally heated sea water, and the more rapid recharge of cold meteoric water along highly permeable vertical fractures within the rift.

The increasing trend of dissolved solids in the fluid phase produced by HGP-A was initially interpreted to indicate that fluid withdrawal from a single-phase low-salinity aquifer had generated an expanding zone of boiling around the borehole (Thomas and Sakai, 1983). This model postulated that migration of the boiling front into the reservoir led to a progressively steam-depleted (and solids-enriched) residual brine phase entering the borehole. However, this model also required a progressive decline in the relative volume of brine to steam as the boiling front advanced into the reservoir. The more than fivefold increase in dissolved solids in the HGP-A brines, however, have not been accompanied by a similar decrease in the brine:steam ratio. Hence, the single-production-zone model has been abandoned in favor of a multiple-production hypothesis in which at least two separate production zones are supplying fluids to the well: one aquifer supplying a higher temperature steam phase and a second supplying intermediate-temperature brine and steam.

Other data supporting this model include the gas concentrations present in the HGP-A steam and the reported production characteristics of other wells in the LERZ. As noted above, the concentrations of noncondensable gases present in the HGP-A steam have changed only slightly during the production history of the well. A single production zone undergoing progressive boiling should show a rapid decline in the noncondensable gas concentration present in the steam due to the strong partitioning of the dissolved gases in the steam phase. The near constancy of the gas concentrations in the steam phase thus substantiate multiple, independent production aquifers. Further support for the production of brine and steam from separate aquifers in HGP-A comes from the production characteristics of wells 2883-02 and 2883-03. Both wells are drilled and cased to greater depths than HGP-A and both produced a single-phase steam flow within hours of the beginning of their flow tests. Thus the reservoir on the LERZ is clearly capable of producing dry steam. The absence of a brine phase in the more recently completed wells is attributed to their having been cased to greater depths than HGP-A and thus having excluded lower temperature production aquifers.

The steam-production zone present in HGP-A and other wells on the LERZ is not, however, identical to the more classic dry-steam reservoirs found at The Geysers, California, and Larderello, Italy. The latter have lower equilibrium temperatures and are significantly underpressured: the pressure within the steam zone is less than hydrostatic pressure at equivalent depths, indicating that porosity within the reservoir is filled with a low-density two-phase fluid probably consisting of steam and liquid water (Fournier, 1981). The reservoir temperatures in the deeper parts of the ERZ have generally been much higher than those found at The Geysers and at Larderello and, in the high-temperature wells, follow the boiling temperature versus hydrostatic pressure curve with depth. Wellhole-circulation and wellhead-pressure patterns during shut-in (when there is no well discharge at the surface) indicate that reservoir pressures are sufficient to maintain circulation from deeper permeable zones to shallow discharge points in the uncased parts of the roles. Even though dry-steam production is occurring from the deep reservoir, a single-phase fluid is believed to be present at depth that, because of the high temperature and low permeability in the reservoir, boils entirely to steam prior to entry into the wellhole.

The increased salinity of the liquid phase produced by HGP-A is believed to be the result of sea-water intrusion into the reservoir. No other source of chloride ion of sufficient magnitude to account for the observed changes exists in the Hawaiian environment (evaporites, sediment basins, and so forth) and the sodium:chloride ratio in the fluids is nearly identical to that for sea water (fig. 56.13). However, comparison of the chemical composition of the brines with that of sea water indicates that a substantial modification of the sea-water chemistry has occurred: potassium and calcium have been heavily enriched, whereas magnesium and sulfate have been heavily depleted (table 56.3; figs. 56.14–56.16). These chemical alterations are virtually identical to those observed in laboratory sea water-basalt reaction studies and in fluids discharged from mid-ocean-ridge hydrothermal systems. In very general terms (for more detailed discussion see, Mottl and Seyfried, 1980; Reed, 1982; Seyfried and Mottl, 1982; Mottl, 1983), the sequence of reactions found to occur in hydrothermal sea water is characterized by an initial loss of calcium ion to the deposition of anhydrite, the removal

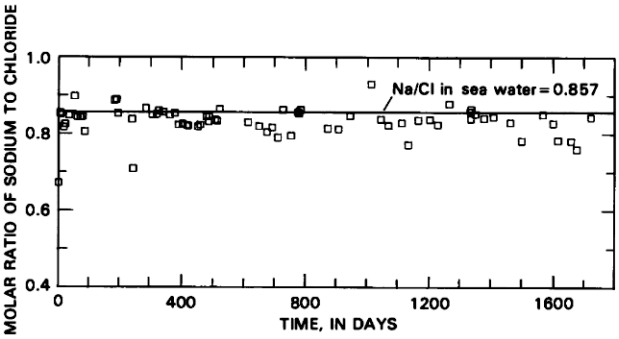


FIGURE 56.13.—Sodium-ion to chloride-ion ratio in HGP-A brines versus duration of production. Straight line represents sodium-ion to chloride-ion ratio in sea water.

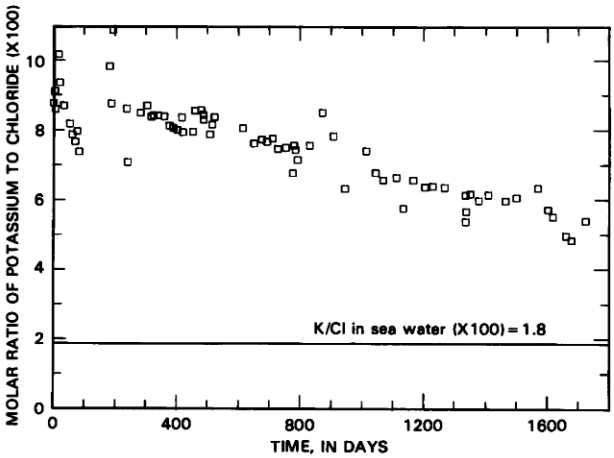


FIGURE 56.14.—Potassium-ion to chloride-ion ratio in HGP-A brines versus duration of production. Straight line represents potassium to chloride ratio in sea water.

of magnesium ion to the formation of magnesium oxysulfate ($MgO \cdot nMgSO_4 \cdot (n-2)H_2O$; Bischoff and Seyfried, 1978), a radical decline in pH, and an increase in the sea-water buffering capacity due to the presence of weak acids such as $HCO_3^-$, $HSO_4^-$, and $HCl^0$, and of $MgOH^+$, a weak base. These chemical changes occur progressively over a temperature of approximately 70–350 °C and are independent of sea water-basalt reactions. When sea water is heated in the presence of basalt, the increased hydrogen-ion concentration and buffering ability of the fluid drives numerous reactions that proceed only very slowly or not at all at lower temperatures and include the alteration of residual glass and primary calcic and sodic mineral suites to smectites, mixed layer clays, and chlorite. These reactions result in the removal of potassium and lithium from basalt, exchange of calcium for the magnesium lost from sea water, and under some conditions, depletion of sodium from sea water.

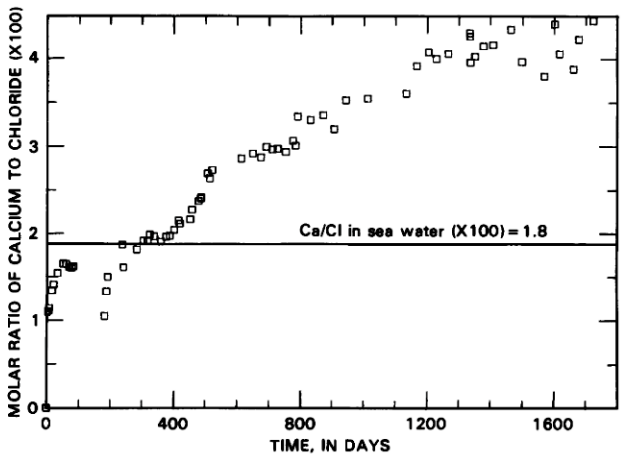


FIGURE 56.15.—Calcium-ion to chloride-ion ratio in HGP-A brines versus duration of continuous production. Straight line represents calcium to chloride-ion ratio in sea water.

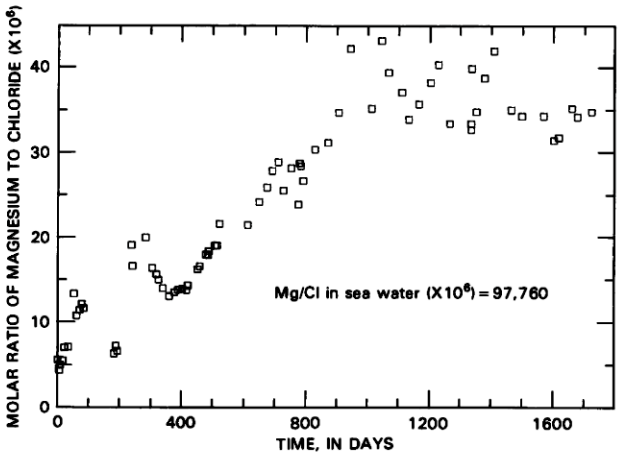


FIGURE 56.16.—Magnesium-ion to chloride-ion ratio in HGP-A brines versus duration of continuous production. Magnesium to chloride ratio in sea water is a factor of approximately 20,000 above that in HGP-A brine and is not plotted.

The hydrolysis of the primary silicates to the alteration-mineral assemblage buffers the pH of the sea water-basalt system at approximately 6.8 as long as primary minerals are available to exchange Ca for $H^+$ released by the loss of $Mg(OH)_2$. However, under sea water-dominated conditions, when the total magnesium available from sea water exceeds the potassium and calcium present in the basalt, pH will be buffered in the range of 2–3 depending upon temperature. This condition has been found to occur at sea water:rock ratios of approximately 50 and above (Mottl and Seyfried, 1980).

The alteration mineral suite typically generated by these reactions includes: zeolite, montmorillonite, illite, anhydrite, magnetite, pyrite, quartz, chlorite, epidote, actinolite (Mottl and Seyfried, 1980; Reed, 1982; Seyfried and Mottl, 1982). The conditions under which an individual mineral species is generated or is stable depends upon kinetics, temperature, and water:rock (W:R) ratios. Although a detailed discussion of the theoretical modeling of mineral stability (Helgeson and others, 1981; Reed, 1982, 1983; Reed and Spycher, 1984) is beyond the scope of the present discussion, the most pertinent findings of these studies to the present analysis are that: high temperatures and low W:R ratios favor epidote, actinolite, and pyrite deposition; high W:R ratios favor chlorite deposition; and cooling hydrothermal fluids precipitate pyrite and, at low W:R ratios, magnetite.

The current depletions of magnesium and sulfate and enrichments of lithium, potassium, and calcium in the fluids at HGP-A are consistent with the theoretical and experimental studies of the sea water-basalt system. The evolution of the chemical composition with time, from the initial production chemistry to the present, further indicates that the apparent W:R ratio has changed during the 4-yr discharge of HGP-A. Calculation of this ratio, using the potassium-ion enrichment of the sea-water component suggests that it was initially substantially less than 1 and that the present ratio approaches 2. A plot of the relative proportions of the three ions most sensitive to the W:R ratio further demonstrates its evolution with time (fig. 56.17). The trends evident in the changing ion ratios suggest an increasing calcium and magnesium concentration relative to potassium. Comparison of the trend in the brine chemistry with laboratory-derived data suggests that, as the sea water:rock ratios evolve, calcium ion will initially predominate at W:R ratios of approximately 10 and, as the ratio increases, magnesium will begin to displace calcium as the major component. More importantly, as the magnesium and W:R ratio increases, the pH will begin to decline due to the depletion of calcium from the reservoir rock (Mottl and Seyfried, 1980; Seyfried and Mottl, 1982). As the pH declines, the reservoir fluids will become far more aggressive and begin to mobilize higher concentrations of transition elements such as iron, lead, zinc, and tin.

A second aspect of the changing brine chemistry is the apparent change in reservoir temperatures that can be calculated. The reservoir temperatures calculated using the Na-K-Ca geothermometer initially indicated a temperature of approximately 300 °C; the silica geothermometer when corrected for steam loss (Fournier and Potter, 1982) yielded a temperature of 305 °C, in good agreement with the Na-K-Ca geothermometer. Na-K-Ca temperatures calculated using later chemical data from HGP-A have shown a decline in the calculated temperatures to approximately 250 °C (table 56.3). Silica, however, does not show a similar temperature change. The declining temperature calculated from the Na-K-Ca concentrations are interpreted to reflect the intrusion of lower temperature sea water into the intermediate-temperature aquifer tapped by HGP-A; the apparent discrepancy between the Na-K-Ca and silica temperatures is the result of the more rapid equilibration of silica to reservoir temperatures in the intruding fluids.

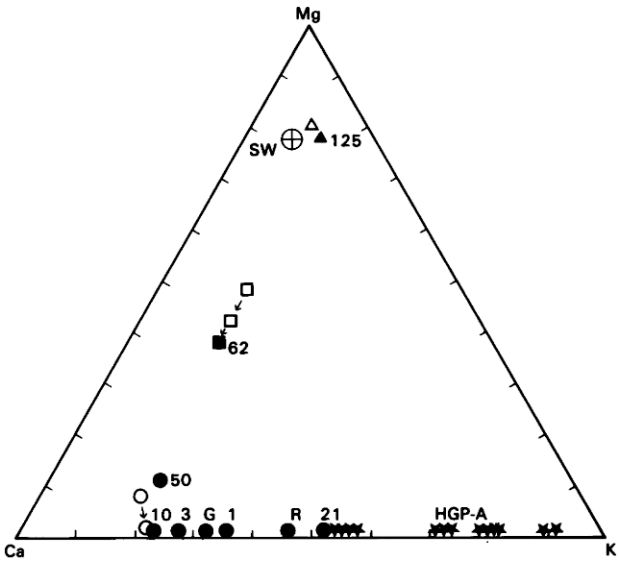


FIGURE 56.17.—Relative potassium-, calcium-, and magnesium-ion concentrations in: HGP-A geothermal brines (filled stars); hydrothermal vent fluids from 21° N., on East Pacific Rise (21) and Galapagos (G); Reykjanes geothermal system (R); liquid phase of high-temperature sea water-basalt experiments at water:rock ratios of 1, 3, 10, 50, 62, and 125 (labeled 1, 3, 10, 50, 62, and 125, respectively); and sea water (SW). Open symbols represent nonequilibrium compositions at noted water:rock ratios. HGP-A fluid chemistry has evolved from a relatively potassium-rich composition to an increasingly calcium-rich solution and is now approaching relative ion concentrations of fluids at 21° N.

The interpretation of the chemistry of the noncondensable gases in the HGP-A discharge is not as straightforward as that for the water chemistry, because two aquifers, having different gas concentrations, are supplying steam to the total flow in the well. Any attempt to partition the gases between the two production zones must rely on equilibrium calculations that will be dependent upon reservoir temperatures. A second aspect of the gas data that inhibits equilibrium calculations is that a significant proportion of the carbon dioxide present in the noncondensable gases is derived from surface sources and there is insufficient isotopic data to clearly differentiate the contributions from the available sources of carbon: sea water, ground water, and magmatic water.

In spite of these problems, several tentative interpretations of the gas chemistry can be offered. Comparison of the gas concentrations found in the steam at HGP-A with those found in laboratory sea water-basalt experiments tends to substantiate the W:R ratios inferred from the brine chemistry. Although mixing of the gas phase from the two production zones does not allow us to apportion the amount of gas from each, $H_2S$ concentrations present in the total discharge (water plus steam) suggest that the average W:R ratio is well below 1 (Seyfried and Mottl, 1982). The decline in gas concentrations, although relatively minor, may further indicate that production of the reservoir is bringing about an increase in the effective W:R ratios. An alternative explanation of the decline in gas

concentrations may, however, be that the boiling front in the deeper reservoir has stabilized, yielding a constant steam:gas ratio.

Another noteworthy aspect of the gas produced by HGP-A is that a significant proportion of atmospheric carbon is present in the carbon dioxide: carbon-14 activities determined for the $CO_2$ have yielded apparent ages ranging from about 9–13 ka, or approximately 20 percent of modern carbon activities. Thus, at least 20 percent, or approximately 200 mg/kg of the 1,100 mg/kg of $CO_2$ in the steam phase is made up of surface carbon. This estimate is a minimum and presumes that the circulation rate in the rift is very short; a fluid residence time of 5,000 years would increase the proportion of atmospheric carbon to nearly 40 percent of the total. The source of this carbon is unclear; ground water typically contains $CO_2$ concentrations of only 10–20 ppm (U.S. Geological Survey, 1977) and, although sea water has a much higher concentration of $CO_2$, its relatively modest concentration in the reservoir fluids limits its contribution to approximately 20–30 mg/kg. The decline in $CO_2$ concentration during the period of increasing salinity has been accompanied by a slightly increased apparent age of the $CO_2$, and hence a sea-water source for the young carbon is not consistent with the observed trends in age and salinity. At present, no clear explanation is known for the carbon-14 data; it can only be stated that atmospheric carbon comprises a significant proportion of the $CO_2$ in the geothermal reservoir and that the fluid circulation time within the system is not more than 10,000 to 13,000 years.

The $CO_2$:$H_2S$ ratio in the noncondensable gases in HGP-A is much lower than that found in most other geothermal systems where carbon dioxide predominates the noncondensable gases and is usually present at a concentration more than 2–5 times higher than $H_2S$. In the HGP-A fluids they are approximately equal when one considers the atmospheric contribution to the total $CO_2$. Two mechanisms can be proposed to account for the unusual $CO_2$:$H_2S$ ratio found at HGP-A. The first is associated with the high-temperature reactions occurring in a sea water-basalt system: sea-water sulfate, at high temperature, oxidizes the reduced iron present in basalt to generate hematite and reduced sulfur by the reaction $8FeO + SO_4^{2-} \rightarrow 4Fe_2O_3 + S^{2-}$.

The high concentration of hematite identified in the intensely altered zones in HGP-A and other wells (Stone, 1977; Barnwell Geothermal Corp., unpublished data, 1985) are consistent with this model, but the relatively low concentration of sea water initially found in the HGP-A fluids suggests that this mechanism could supply only a modest amount of the sulfide found in the reservoir fluids.

The second mechanism that may account for the anomalous $CO_2$:$H_2S$ ratio is that the magmas intruded into the ERZ may be depleted in magmatic carbon. Studies conducted by Gerlach and Graeber (1985) suggest that magma held in the summit magma chamber at Kilauea is preferentially degassed of the more-insoluble volatiles such as helium and carbon dioxide and that the magma later erupted from (and presumably intruded into) the ERZ shows a depletion of carbon relative to sulfur. Hence the low carbon to sulfur ratios observed in the geothermal fluids may be reflecting the C:S ratio present in the dike complex on the ERZ. Which of these mechanisms is ultimately responsible for the unusual C:S ratio in the HGP-A fluids cannot be determined at present; however, sulfur isotopic data currently being gathered may provide further insight into this question.

Although interpretation of the gas chemistry in terms of reservoir temperature is hindered by the mixing of the discharge from two production zones, a very crude estimate of the maximum and minimum temperatures indicated by the gas data can be obtained using the methane gas geothermometer of d'Amore and others (1982) and Nehring and d'Amore (1984) and making the assumptions that: (1) all of the gas present is associated with the deep steam-production zone; or (2) the well discharge is produced from a single aquifer. The gas compositions associated with these assumptions correspond to the gas concentration in the steam phase alone and that in the total discharge respectively and yield temperatures of 380 °C for the former and 350 °C for the latter. Both of these calculated temperatures are well above the Na-K-Ca and $SiO_2$ temperatures calculated for the brine phase, but are within the range of measured downhole temperatures in HGP-A and other nearby wells (358–368 °C). The modest change in the gas concentrations present in the HGP-A discharge do not yield an appreciable change in the gas geothermometry temperatures, indicating that production of steam from the deeper part of HGP-A has not been substantially affected by the intrusion of lower temperature fluids.

The few data available from the private exploration wells do not allow any definite conclusions to be drawn; however, the information available substantiates the interpretation of the HGP-A data. The salinity of the fluids in wells along the southern boundary of the rift tend to confirm the inferred structural control of the rift system over the fluid salinity in this hydrothermal system. The similarity of the gas concentrations present in the dry-steam wells and in HGP-A suggests that the majority of the noncondensable gas produced by HGP-A is coming from the deeper steam zone and, hence, the calculated gas geothermometer temperatures for the steam phase may more accurately reflect deep reservoir temperatures than does the calculation using the gas concentrations in the total discharge.

## SYNTHESIS

The data that are presently available, although far from sufficient to allow a complete understanding of the hydrothermal system associated with the ERZ, provide at least preliminary constraints on a model of this unique geothermal reservoir. The physical dimensions of the hydrothermal system are defined by the location and age of intrusive bodies within the ERZ. The southern boundary apparently corresponds to the southernmost extent of recent eruptive features; temperature inversions in two wells drilled on this boundary demonstrate at least a localized temperature decline toward the south. The northern extent of the dike system is suggested by both geologic mapping and by geophysical models to be several kilometers north of the currently active part ofthe ERZ. However, due to heat loss with time, the temperatures present in the older parts of the ERZ probably will be much lower than those within the

currently active areas. Aeromagnetic data are in agreement with this model and suggest that temperatures in excess of the Curie point (560 °C) are present beneath the southern part of the ERZ but are lower to the north and south of the currently active rift.

The low salinities found in the deep reservoir fluids at HGP-A suggest that sea water is effectively excluded from the interior of the ERZ and that the overall hydrology within the reservoir is controlled by the rift-zone structure. Fluid flow within the ERZ is governed by the near-vertical tabular dikes comprising the rift and its associated fracture system, which trend in a northeast-southwest direction. The fractures effectively channel fresh meteoric water along the ERZ and to depth in the hydrothermal system, whereas the impermeable dike system and chemical self-sealing serve to inhibit intrusion of saline water from the south. Fresh water entering the ERZ in the upper elevations of the Kilauea flank penetrate to depth, are heated within the dike complex, and are discharged at the lower elevation eastern end of the subaerial part of the rift zone. The discharge of hydrothermal fluids in this region is confirmed by surface resistivity data, by ground-water temperature and chemistry data, and by the chemistry of the hydrothermal-alteration products found in the deep wells drilled into the LERZ.

The boundary between the meteorically derived hydrothermal fluids within the ERZ and saline fluids south of the ERZ is indicated to be quite sharp by the deep drilling data obtained on the LERZ: HGP-A had an initial chloride concentration of approximately 1,000 mg/kg and a bottom-hole temperature of 358 °C. The Lanipuna 1 sidetrack well, 2883-04A, located less than 500 m south of HGP-A, had an initial chloride content of about 19,000 mg/kg and a bottom-hole temperature of 149 °C.

The chemistry of the fluids circulating within the ERZ zone is strongly controlled by fracturing in the reservoir. Data from drill cuttings indicate that extreme alteration of basalt occurs intermittently down the geologic column and the alteration mineral suite is clearly generated from sea water-basalt reactions. Thus, access of sea water to the hydrothermal system does occur; laboratory and field studies of sea water-basalt reactions have demonstrated that W:R ratios can strongly influence both the salinity and the pH of the hydrothermal fluids, and therefore in those parts of the reservoir where sea water is present at high W:R ratios, the pH of the fluids may be much lower (and more aggressive) than those currently found in the interior of the ERZ.

## CONCLUSION

A young, actively evolving hydrothermal system is associated with the Kilauea east rift zone. Its physical characteristics range from near-surface ambient conditions to temperatures and pressures approaching the critical point of water. Its chemistry varies from low-salinity, near-neutral fluids to strongly acid, highly aggressive saline fluids. Further study of this system will not only provide further insight into the geothermal conditions present in this reservoir, it may also add to the understanding of chemical cycling in other land-based and submarine hydrothermal systems.

## REFERENCES


Bischoff, J.L., and Dickson, F.W., 1975, Seawater-basalt interaction at 200 °C and 500 bars: Implications for origin of seafloor heavy metal deposits and regulation of seawater chemistry: Earth and Planetary Science Letters, v. 25, p. 385-397.

Bischoff, J.L., and Seyfried, W.E., 1978, Hydrothermal chemistry of seawater from 25 ° to 350 °C: American Journal of Science, v. 278, no. 6, p. 838-860.

Cox, M.E., and Thomas, D.M., 1979, Cl/Mg ratio of Hawaiian groundwaters as a regional geothermal indicator in Hawaii: Hawaii Institute of Geophysics Technical Report, HIG-79-9, 51 p.

D'Amore, F., Celati, R., and Calore, C., 1982, Fluid geochemistry applications in reservoir engineering (vapor dominated systems): Stanford University, Proceedings of the Eighth Workshop on Geothermal Reservoir Engineering, Dec. 1982, p. 295-307.

Davis, D.A., and Yamanaga, G., 1968, Preliminary report on the water resources of the Hilo-Puna area, Hawaii: Circular C45, State of Hawaii, Honolulu, Division of Water and Land Development, Department of Land and Natural Resources, State of Hawaii, 124 p.

Druecker, M., and Fan, P.F., 1976, Hydrology and chemistry of groundwater in Puna, Hawaii: Ground Water, v. 14, no. 5, p. 328- 338.

Duffield, W.A., Christiansen, R.L., Koyanagi, R.Y., and Peterson, D.W., 1982, Storage, migration, and eruption of magma at Kilauea Volcano, Hawaii, 1971–1972: Journal of Volcanology and Geothermal Research, v. 13, p. 273-307.

Dzurisin, D., 1981, Changed magma budget since 1975 at Kilauea Volcano, Hawaii: Eos, Transactions, American Geophysical Union, v. 62, no. 45, p. 1071.

Fiske, R.S., and Jackson, E.D., 1972, Orientation and growth of Hawaiian volcanic rifts: the effect of regional structure and gravitational stresses: Proceedings of the Royal Society of London, Series A, v. 329, p. 299-326.

Fournier, R.O., 1981, Application of water geochemistry to geothermal exploration and reservoir engineering, *in* Ryback, L., and Muffler, L.J.P., eds., Geothermal systems, principals and case histories: p. 109-144.

Fournier, R.O., and Potter, R.W., II, 1982, A revised and expanded silica (quartz) geothermometer: Geothermal Resources Bulletin, v. 11, no. 10, p. 3-12.

Fournier, R.O., and Rowe, J.J., 1966, Estimation of underground temperatures from the silica content of water from hot springs and wet steam wells: American Journal of Science, v. 264, p. 685-697.

Fournier, R.O., and Truesdell, A.H., 1973, An empirical Na-K-Ca geothermometer for natural waters: Geochimica et Cosmochimica Acta, v. 37, no. 5, p. 1255-1275.

Furumoto, A.S., 1978, Nature of the magma conduit under the east rift zone of Kilauea Volcano, Hawaii: Bulletin Volcanologique, v. 41, no. 4, p. 435-453.

Gerlach, T., and Graeber, E.J., 1985, Volatile budget of Kilauea Volcano: Nature, v. 313, p. 273-277.

Godson, R.H., Zablockie, C.J., Pierce, H.A., Frayser, J.B., Mitchell, C.M., and Sneddon, R.A., 1981, Aeromagnetic map of the island of Hawaii: U.S. Geological Survey Geophysical Investigation Map GP–946, 1 sheet, scale 1:250,000.

Helgeson, H.C., Kirkham, D.H., and Flowers, G.C., 1981, Theoretical prediction of the thermodynamic behavior of aqueous electrolytes at high pressures and temperatures: IV. Calculation of activity coefficients, osmotic coefficients, and apparent molal and standard and relative partial molal properties to 600 °C and 5 kb: American Journal of Science, v. 281, no. 10, p. 1249-1516.

Holcomb, R.T., 1980, Preliminary geologic map of Kilauea Volcano, Hawaii: U.S. Geological Survey Open-File Report 80–796, 2 sheets, scale 1:50,000.

Humphris, S.E., and Thompson, G., 1978, Hydrothermal alteration of oceanic basalts by seawater: Geochimica et Cosmochimica Acta, v. 42, p. 107-125.

Iovanitti, J.L., and D'Olier, W.L., 1984, Preliminary results of drilling and testing in the Puna Geothermal System, Hawaii: Stanford University, Proceedings of the Tenth Workshop on Geothermal Reservoir Engineering, December 1984.

Kauahikaua, J.P., 1981, Interpretation of time-domain electromagnetic soundings in

the east-rift geothermal area of Kilauea Volcano, Hawaii: U.S. Geological Survey Open-File Report 81–979, 25 p.

Kauahikaua, J.P., Mattice, M.D., and Jackson, D.B., 1980, Mise-a-la-masse mapping of the HGP-A geothermal reservoir, Hawaii: Geothermal: Energy For the Eighties, Geothermal Research Council Transactions, v. 4, p. 65-68.

Kauahikaua, J.P., Zablockie, C.J., and Jackson, D.B., 1979, Controlled source electromagnetic mapping at the summit of Kilauea Volcano, Hawaii: Eos, Transactions, American Geophysical Union, v. 60, no. 46, p. 811-812.

Keller, G.V., Skokan, C.K., Skokan, J.J., Daniels, J., Kauahikaua, J.P., Klein, D.P., and Zablocki, C.J., 1977, Geoelectric studies on the east rift, Kilauea Volcano, Hawaii Island: Hawaii Institute of Geophysics Technical Report HIG 77-15.

Kristmannsdottir, H., 1976, Hydrothermal alteration of basaltic rocks in Icelandic Geothermal areas, *in* Proceedings of Second United Nations Symposium on the Development and Use of Geothermal Resources, San Francisco, Calif.: Washington, U.S. Government Printing Office, v. 1, p. 441-445.

Kroopnick, P.M., Lau, L.S., Buddemeier, R.W., Thomas, D.M., Lau, L.S., and Bills, D., 1978, Hydrology and geochemistry of a Hawaiian geothermal system: HGP-A. Hawaii Institute of Geophysics Technical Report HIG-78-6, 64 p.

Macdonald, G.A., Abbott, A.B., and Peterson, F., 1983, Volcanoes in the sea: The geology of Hawaii: Honolulu, University of Hawaii Press, 517 p.

Mink, J.F., 1977, Handbook—Index of Hawaii groundwater and resources data, v. 1: Honolulu, University of Hawaii, Water Resources Research Center, Technical Report No. 113, 96 p.

Moore, R.B., 1983, Distribution of differentiated tholeiitic basalts on the lower east rift zone of Kilauea Volcano, Hawaii: A possible guide to geothermal exploration: Geology, v. 11, no. 3, p. 136-140.

Mottl, M.J., 1983, Metabasalts, axial hot springs, and the structure of hydrothermal systems at mid-ocean ridges: Geological Society of American Bulletin, v. 94, p. 161-180.

Mottl, M.J., and Holland, H.D., 1978, Chemical exchange during hydrothermal alteration of basalt by seawater—I: Experimental results for major and minor components of seawater: Geochimica et Cosmochimica Acta, v. 42, p. 1103-1115.

Mottl, M.J., and Seyfried, W.E., 1980, Subseafloor hydrothermal systems: rock-vs. seawater-dominated, *in* Rona, P.A., and Lowell, R.P., eds., Seafloor spreading centers: Hydrothermal Systems: Stroudsberg, Pa., Dowden, Hutchinson and Ross, Inc., 424 p.

Nehring, N.L., and D'Amore, F., 1984, Gas chemistry and thermometry of the Cerro Prieto, Mexico, geothermal field: Geothermics, v. 13, p. 75-89.

Pohl, D.C., and Liou, J.G., 1983, Flow-through reaction of basalt glass and seawater at 300° and 200 °C, 250 bars pressure [abs.]: Misasa, Japan, Fourth International Symposium on Water-Rock Interaction, Aug. 29–Sept. 3, 1983, p. 389-392.

Reed, M.H., 1982, Calculations of multicomponent chemical equilibria and reaction processes in systems involving minerals, gases, and an aqueous phase: Geochimica et Cosmochimica Acta, v. 46, p. 513-528.

——— 1983, Seawater-basalt reaction and the origin of greenstones and related ore deposits: Economic Geology, v. 78, p. 466-485.

Reed, M.H., and Spycher, N., 1983, Calculated pH at high temperature in hydrothermal waters with applications to geothermometry: Misasa, Japan, Fourth International Symposium on Water-Rock Interaction, Aug. 29–Sept. 3, 1983, p. 401-404.

——— 1984, Calculation of pH and mineral equilibria in hydrothermal waters with applicaton to geothermometry and studies of boiling and dilution: Geochimica et Cosmochimica Acta, v. 48, p. 1479-1492.

Seyfried, W.E., Jr., and Bischoff, J.L., 1981, Experimental seawater-basalt interaction at 300 °C, 500 bars, chemical exchange, secondary mineral formation and implications for the transport of heavy metals: Geochimica et Cosmochimica Acta, v. 45, p. 135-147.

Seyfried, W.E., and Mottl, M.J., 1982, Hydrothermal alteration of basalt by seawater under seawater-dominated conditions: Geochimica et Cosmochimica Acta, v. 46, p. 985-1002.

Shupe, J.W., Helsley, C.E., and Yuen, P.C., 1978, The Hawaii geothermal project: Summary report for phases I, II, and III: U.S. Department of Energy Report SAIV-1093-T6.

Stearns, H.T., and Macdonald, G.A., 1946, Geology and groundwater resources of the Island of Hawaii: Honolulu, Hawaii Division of Hydrography, Bulletin B9, 363 p.

Stone, C., 1977, Chemistry, petrography, and hydrothermal alteration of basalts from HGP-A, Kilauea, Honolulu, University of Hawaii, M.S. Thesis No. 1477, 84 p.

Stone, C., and Fan, P.F., 1978, Hydrothermal alteration of basalts from Hawaii Geothermal Project Well-A Kilauea, Hawaii: Geology, v. 6, p. 401-404.

Swanson, D.A., Duffield, W.A., and Fiske, R.S., 1976, Displacement of the south flank of Kilauea Volcano: The result of forceful intrusion of magma into the rift zones: U.S. Geological Survey Professional Paper 963, 39 p.

Takasaki, K.J., 1978, Summary appraisals of the nation's groundwater resources—Hawaii Region: U.S. Geological Survey Professional Paper 813–M, 175 p.

Thomas, D.M., 1980, Water and gas chemistry from the HGP-A geothermal well: January 1980 flow test: Geothermal Resources Council Transactions, v. 4, p. 181-184.

——— 1982, A geochemical case history of the HGP-A well 1976-1982, *in* Proceedings of the Pacific geothermal conference 1982 incorporating the 4th New Zealand geothermal workshop: Auckland, N.Z., University of Auckland Geothermal Institute, p. 273-278.

Thomas, D.M., and Sakai, H., 1983, Chemical and isotopic studies of the HGP-A geothermal well [abs.]: Misasa, Japan, Fourth International Symposium on Water-Rock Interaction, Aug. 29–Sept. 3, 1983, p. 479-482.

Tomasson, J., and Kristmannsdottir, H., 1972, High temperature alteration minerals and thermal brines, Reykjanes, Iceland: Contribution to Mineralogy and Petrology, v. 36, p. 123-134.

U.S. Geological Survey, 1977, Water resources data for Hawaii and other Pacific areas: Water year 1977, v. 10: U.S. Geological Survey Water-Data Report HI-77-1, 348 p.

Waibel, A., 1983, A review of the hydrothermal mineralogy of Hawaii Geothermal Project Well-A, Kilauea, Hawaii: Geothermal Resources Council Transactions, v. 7, p. 205-209.

Yuen, P.C., Chen, B.H., Kihara, D.H., Seki, A.S., and Takahashi, P.K., 1978, The Hawaii geothermal project: HGP-A and reservoir engineering: Honolulu, University of Hawaii, Hawaii Geothermal Project internal report, 96 p.

Zablocki, C.J., 1976, Mapping thermal anomalies on an active volcano by the self-potential method, Kilauea, Hawaii: Second U.N. Symposium on the Development and Use of Geothermal Resources, Proceedings, v. 2, p. 1299-1309.

———1977, Self-potential studies in east Puna, Hawaii, *in* Geoelectric studies on the east rift, Kilauea Volcano, Hawaii Island: Hawaii Institute of Geophysics Technical Report HIG-77-15, p. 175-195.

# AA FLOW DYNAMICS, MAUNA LOA 1984

*By* Peter W. Lipman *and* Norman G. Banks


## ABSTRACT

**The March 25–April 14, 1984, northeast-rift eruption of Mauna Loa Volcano, Hawaii, provided an exceptional opportunity to study development of a large basaltic aa flow system for several weeks. The major flow reached 27 km from its source vent within a few days of start of the eruption, and, fed at a rate of about $10^6$ $m^3/h$, developed an initially simple geographic zonation in aa textural types and flow morphology. Decreases in eruption rate during the first few days, to about $0.4 \times 10^6$ $m^3/h$, triggered a channel blockage and breakout to generate a second major flow on March 29. Without further major changes in vent output from March 30 through April 7, the flow evolved from a single narrow tongue with an efficient channel, which delivered virtually the entire vent output to within 1 km of the toe, to an uprift-migrating stagnating channel system characterized by blockages, ponding, and complexly branching overflows. Lava production again began to decline after April 7, and the rate of upflow stagnation accelerated.**

**A major cause of the stagnation was breakdown in the hydraulic efficiency of the channel. Floating channel debris (lava boats), created by collapse of portions of the channel banks, formed dams at channel constrictions and caused ponding, overflows, and lateral breakouts that robbed the lower flow of much of its lava supply. Upflow stagnation was basically due to increasing viscosity and yield strength of the channel lava, caused by progressive degassing, formation of pasty surface clots, incorporation of channel debris, and ultimately by growth of microphenocrysts in lava stored uprift from the vent.**

**During the eruption, microphenocryst contents of erupted lava increased by nearly two orders of magnitude, from less than 0.5 percent to 30 percent, without concurrent change in either bulk magma composition or eruption temperature ($1,140 \pm 3$ °C). The microphenocrysts have skeletal morphologies typical of undercooling. The increase in microphenocryst content with time was paralleled by a decrease in emission of sulfur and other gases and a decline in lava eruption rate. Growth of the microphenocrysts is interpreted as crystallization from magma that was undercooled 20–30 °C below its liquidus. The undercooling proabably resulted from separation and release of volatiles as the magma moved from the primary high-level magma reservoir at a depth of 3–5 km below the summit caldera to the 2,900-m elevation at the eruption site 12 km down the northeast rift zone. Analogous increases in microphenocryst content and accompanying uprift stagnation of lava flows have occurred during several earlier historic eruptions from Mauna Loa rift zones.**


## INTRODUCTION

The eruption of March 25–April 14, 1984, from the northeast rift zone of Mauna Loa Volcano, Hawaii, provided an exceptional opportunity to observe the development of a major basaltic aa flow system, fed by a high-volume eruption for several weeks. Similarly large aa flows were last erupted on Mauna Loa from the southwest rift zone in 1950 (Finch and Macdonald, 1953), before the availability of helicopters, efficient radio communications, abundant high-quality chemical data, devices for accurate temperature measurements, and other recent technological advances in monitoring techniques. In contrast, recent aa flows from nearby Kilauea Volcano (Moore and others, 1980; Ulrich and others, 1984) lasted only a few days, were fed at rates an order of magnitude smaller than the 1984 Mauna Loa activity, and generally were inaccessible to observers except in vent areas and at toes of flows (midzones are in heavily vegetated areas lacking helicopter landing points). Detailed recent observations of flow dynamics at other volcanoes, notably Etna in Sicily and Arenal in Costa Rica (Sparks and others, 1976; Wadge, 1978; Borgia and others, 1983; Cigolini and others, 1984), also involved small short-lived flows.

At Mauna Loa in 1984, we were able to observe the evolution, over a three-week period, of a complex aa flow system that achieved a maximum length of 27 km. Initial motivation for these observations was to monitor advance of the flow toward the city of Hilo (fig. 57.1*A*). As the flow terminus stagnated and hazard concerns diminished, we became increasingly intrigued by the opportunities to observe complex changes in channel efficiency related to changing parameters of lava temperature, density, gas content, petrography, and eruption rate.

Eruption rates were as high as $2.9 \times 10^6$ $m^3/h$ during the first six hours of the eruption, stabilized at $0.5 \times 10^6$–$1 \times 10^6$ $m^3/h$ for the next 12 days, and slowly diminished thereafter. Total eruptive volume was approximately $220 \times 10^6$ $m^3$. Sizeable pahoehoe flows formed only during the first day of the eruption and within a few kilometers of the vent; the remainder of the flow system consisted of aa. Especially instructive were variations in channel discharge with increasing distance from the vent during periods of steady-state lava production, variations in behavior at the flow toe as a function of slope and magma supply, development and evolution of the aa channels, and variations in density, yield strength, and viscosity of the lava as functions of time and distance from the vent. The main 1984 aa flow evolved (without major change in magma discharge at the vent) from a simple narrow tongue with an efficient channel that delivered virtually the entire lava supply to within 1 km of the toe, to an uprift-stagnating channel system with levees, blockages, ponding, and complexly branching overflows.


### ACKNOWLEDGMENTS

Our channel observations would not have been feasible without the skillful assistance of helicopter pilots Bill Lacy Jr., Ken Ellard,

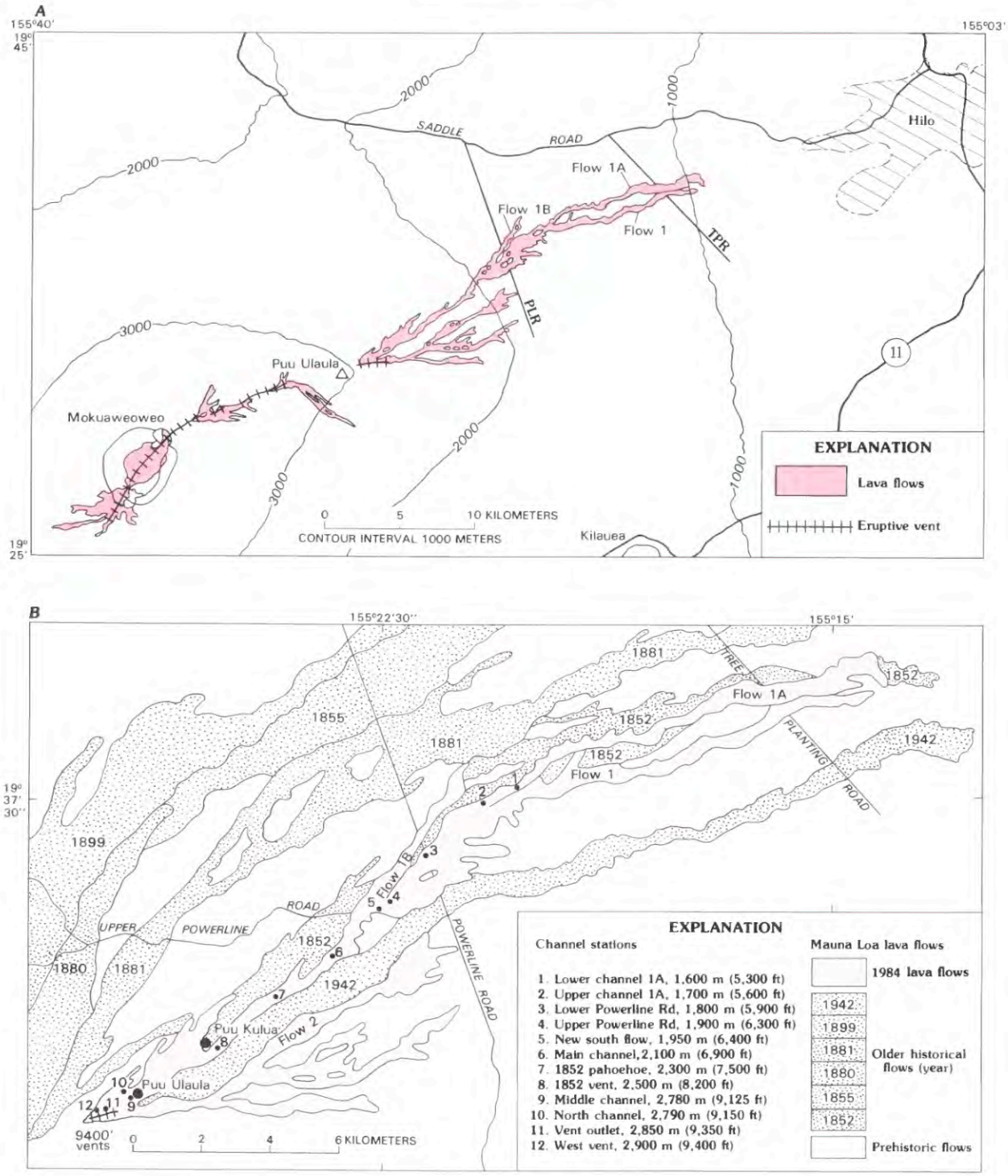


FIGURE 57.1.—Extent of lava flows from the 1984 Mauna Loa eruption. ***A***, Distribution of all 1984 flows with respect to city of Hilo (modified from Lockwood and others, 1985). All lava in the summit caldera (Mokuaweoweo) and adjacent upper parts of the northeast and southwest rift zones was erupted during the first day of the eruption (March 25). PLR, Powerline Road; TPR, Tree-planting Road. ***B***, Distribution of lava flows from the 2,900-m vent system that was active from the afternoon of March 25 until the end of the eruption on April 15. Earlier historical flows (1852, 1855, 1881, 1942) resulted from similar eruptions along the northeast rift zone. Channel stations are measurement sites for observations reported in table 57.3.

Tom Haupmann, and Ed Spencer. We also thank our many colleagues, from the USGS and academia, who assisted with the channel measurements and provided additional observations on the 1984 eruption: especially J. Buchanan-Banks, D. Clague, J. Fink, J.P. Lockwood, H.J. Moore, R.B. Moore, T. Neal, M. Rhodes, and E. Wolfe. Thoughtful reviews of earlier versions of this paper by H.J. Moore, D.A. Swanson, and G.E. Ulrich are greatly appreciated.

## CHRONOLOGIC NARRATIVE

The general evolution of the 1984 Mauna Loa eruption is described elsewhere (Lockwood and others, 1985), and only the features most relevent to development of the aa flows are summarized here. The eruption began at about 0100 (all times are in Hawaii standard time) on March 25, following a nine-year repose after the 1975 summit eruption (Lockwood and others, 1976). Gradually increasing levels of seismicity and ground deformation in the previous several years had led to a forecast of increased probability of a Mauna Loa eruption in 1984–85 (Decker and others, 1983), but few precursors were evident in the days immediately preceding the 1984 outbreak.

Initial activity on March 25 broke out in the summit caldera (Mokuaweoweo) and the uppermost southwest rift zone; after about 0400, activity migrated into the upper northeast rift zone and diminished in the summit area. During that day, vents from the 3,500-m level of the northeast rift zone fed a lava flow that extended about 5 km down the southeast flank (fig. 57.1*A*). At about 1630 on March 25, new fissure vents opened at elevations of 2,800–2,900 m; they became the sites of all lava production for the remainder of the eruption (fig. 57.1*B*). By March 26, activity along the new lower fissures had become concentrated at four areas of fountaining and growth of spatter ramparts, informally designated vents 1–4, and had generated four flows that spread rapidly downslope to the east (fig. 57.2*A*) The three southerly flows (flows 2–4) stagnated by March 27, as lava production diminished from the more easterly vents (2–4), while a relatively constant volume of lava was maintained in the more northerly flow 1. Continued slow oozing of lava at the site of vent 4, accompanied by little or no fountaining, gradually built a broad lava shield 150 m high in late March and early April.

This paper considers primarily the evolution of flow 1 and its channel system, which were active from March 25 to April 13. By March 29, flow 1 had reached the 1,100-m level, 25 km from its source vent, as a relatively simple narrow flow fed by a well-developed central channel 20–50 m wide that extended to within 1–2 km of the flow front (figs. 57.2*B*, *C*, 57.3). In the early morning of March 29, a blockage and overflow at the 1,800-m level took most of the supply away from the lower reaches of flow 1 and generated a new tongue farther north (flow 1A). Flow 1 stagnated 27 km from its source at about 870-m elevation.

Flow 1A reached about 900-m elevation by April 5, when a major overflow—again at the 1,800-m level—cut off most of its supply and created a new fast-moving flow (1B) north of 1A. During April 5–8, repeated blockages and overflows prevented sustained lava supply to any organized flow below the 1,850-m level. On April 7, lava production at the vent and in the upper channel began to diminish, increasing the rate of uprift stagnation along upper parts of the flow. Lava production continued to decline, accompanied by stagnation of lower reaches of the flow system, and by April 10 no active flow toes extended below 2,450 m. By April 13, the lowest active flow toe was at 2,750 m, only about 2 km from the vent. All lava production at the vent ceased late on April 14.

Decreases in rate of lava production were paralleled by declines in volume of gas emissions. Rates of sulfur dioxide production decreased especially rapidly during the first week of the eruption (Casadevall and others, 1984). Gas emissions were intense from fissures at 3,000–3,500 m along the rift zone throughout the eruption, and as lava production began to decline at the 2,900-m vents, visible gas emission from the higher fissures began to exceed that from the active lava vents.

## FLOW TYPES

Both aa and pahoehoe flow types encompass much variation in lava textures (Wentworth and Macdonald, 1953; Macdonald 1972) that can provide information on the kinematics of flow and on lava rheology (Swanson, 1973; Peterson and Tilling, 1980). During the 1984 Mauna Loa eruption, distinctive aa flow types tended to develop as functions of distance from the vent, steepness of terrain, and mechanism of the flow advance. Some of these lava types have not previously been described or interpreted in terms of emplacement kinematics. Lava from the 1984 Mauna Loa eruption includes most of the pahoehoe types recognized on Kilauea (Swanson, 1973), transitional lava between pahoehoe and aa, and diverse aa types—slabby, clotted, spiney, scoriaceous, clinkery, and blocky. These flow types could also be identified within lava channels on the basis of textures developing on the surface crust. General relations among the flow types in the 1984 eruption are summarized here; detailed features of a few are discussed in later sections, where their origin is closely tied to evolution of other flow features such as flow toes, channels, and levees.

### PAHOEHOE

Typical fountain-fed shelly pahoehoe formed in the vent area, at 2,850–2,900-m elevation early during the eruption, but extended as pahoehoe for only about 2 km, to about the level of Puu 9,146 (2,790 m) before changing to aa—probably within less than two hours after the source vents opened. As soon as a channel was well established to this level, virtually all lower lava fronts advanced as aa. The limited extent of pahoehoe may reflect the steeper slopes of this sector of the rift zone (4°–6°), the viscous character of the 1984 lava, or some additional process. Where able to flow slowly (less than 10–15 km/h), lava in the developed channel of flow 1 was capable of generating pahoehoe down to at least the 2,400-m level, about 5 km from the vent, as shown by small pahoehoe overflows during the first hours of the eruption. After March 26, however, the channel delivered lava so efficiently to lower reaches of the flow that no lava front advanced as pahoehoe until the last days of the

*A*

FIGURE 57.2.—Active flow front and channels, 1984 Mauna Loa eruption. ***A***, Rapidly advancing toe of flow 1 at 2030 H.s.t. on March 25, about 2 hours after initiation of lower vents. Toe is at about 2,400-m elevation, advancing at estimated 2 m/s. Photograph by R.B. Moore. ***B***, View uprift toward 2,900-m vents on March 27. Flow 1 channel is on right; smaller channels feed flows 2 and 3 on left. ***C***, Flow 1 toe at 1,350-m elevation, looking downrift on March 27. Channel is well developed and about 50 m wide; it extends to within 1 km of flow toe, marked by smoke from burning forest.

eruption, when blockages and disruption of the channel again permitted pahoehoe overflows from the channel within 1–2 km of the vents.

## TRANSITIONAL LAVA

Because the transition from pahoehoe to aa occurred within the confined channel of flow 1 during much of the eruption, we had ample opportunities to observe this change from a helicopter and from observation stations along channel levees. Our observations on the 1984 lava are in accord with the interpretations of Macdonald (1953) and Peterson and Tilling (1980) that the transition from pahoehoe to aa involves the relation between viscosity and rate of internal disturbance due to flowage (shear strain). If flow mechanics (flow volume, flow dimensions, slope, momentum) impel pahoehoe to continue to move and deform after it has become highly viscous, the lava will change to aa if the critical relation has already been approached. Approach to this critical condition can be recognized when the flow surface is littered with solid and semisolid blebs and blocks that disrupt flow streamlines in the channel.

## AA TYPES

Different aa lava types reflect interrelated aspects of magma rheology, gas content, terrain effects, and flow rates. Lava viscosity and yield strength generally increase downstream because of decreased gas content, decreased average bulk temperature of the flow, increased crystallization of microphenocrysts, and incorporation or formation of solids, as discussed later (also see Moore, chapter 58). The net effect is to trigger successive irreversible changes in aa texture, similar to those accompanying the pahoehoe-aa transition.

*B*

*C*

FIGURE 57.2—Continued.

## SLABBY AA

In the 1984 Mauna Loa eruption, aa flows nearest the transition from pahoehoe tended to form slabby aa (also called slabby pahoehoe), which consists simply of pahoehoe crust completely disrupted in slabs by flowage at a rate too great for the crust to accommodate the shear strain plastically (fig. 57.4*A*). Slabby aa was well developed in the advancing terminus of flow 1 at elevations of 2,450–2,600 m, about 3–5 km from the vent.

## SCORIACEOUS AA

Farther downflow, where the lava was slightly denser and more viscous, the surface of the channel no longer maintained a smooth pahoehoe surface crust. Instead, it developed scattered lumps or clots of relatively cool scoriaceous lava, separated by more fluid incandescent lava retaining crude pahoehoe character (fig. 57.4*B*). When overflows or breakouts of such scoriaceous aa occurred fairly slowly, and flow fronts advanced no faster than 1–2 m/min, this lava type retained its clotted texture as it cooled. The frothy clots consisted of red-brown oxidized scoria masses 5–30 cm across, set in dark gray smoother less vesicular lava having a thin poorly developed glassy surface. When overflow rates were more rapid, as in a sudden sheet-flow breakout through a breached levee, the entire surface of the resulting flow disaggregated into scoriaceous lumps, and the surface of the resulting deposit consists of loose oxidized scoria lumps totally covering the dense interior of the aa flow. This lava type has at times been called spiney aa (Macdonald and Abbott, 1970, p. 26) because of the jagged irregular surfaces of the scoria lumps. The front of flow 1 during its advance on March 25–26 was dominantly scoriaceous aa between elevations of about 2,450 and 1,850 m, at distances of 5–12 km from the vent.

## CLINKERY AA

Even farther downflow, the active lava surface in the channel consisted largely of cooled clots of relatively dense lava that ground against each other while riding on top of the more fluid lava core in

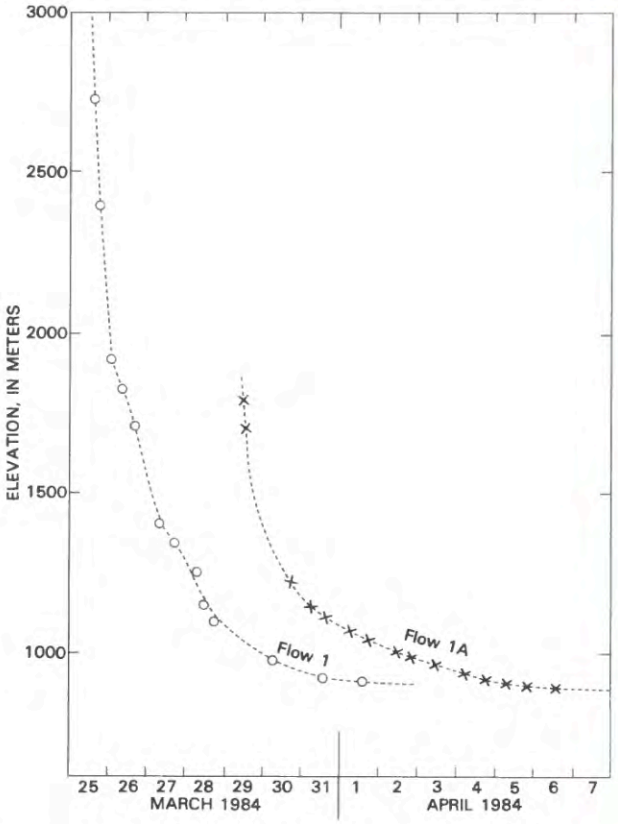


FIGURE 57.3.—Change in elevation of lava-flow toes during 1984 Mauna Loa eruption.

*A*

*B*

*C*

FIGURE 57.4.—Aa lava types observed on April 3, 1984. ***A***, Slabby aa at 2,500-m elevation, overlying spatter from the 1852 vent. Active channel is visible at upper left (arrow). Radio at lower right is 20 cm long (excluding antenna). ***B***, Scoriaceous aa flow top at 1,800-m elevation. Scoria blocks are uniformly small in size, averaging about 10 cm in diameter. Smoother crust between clusters of scoriaceous aa marks points of late stretching of the flow surface and upwelling of degassed lava. ***C***, Blocky aa, at 1,600-m elevation. Tripod and figures at right are on stable marginal levee. Center of flow, at left edge of photograph, contains a broad weakly developed aa channel. Site is near the downflow gradation from the transitional to the dispersed flowage zone (see fig. 57.5).

the channel. Breakouts and overflows of this material formed dark gray clinkery aa, which contrasts with the scoriaceous aa in having angular rather than scoriaceous surfaces, and in being darker in color, less oxidized, and less vesicular. During early advance of flow 1 and the later flow 1A, the gradual transition from scoriaceous to clinkerly aa occurred at elevations of 1,850–1,700 m, about 12–15 km from the vent.

## BLOCKY AA

Along the lower reaches of flow 1, below about 1,500-m elevation and more than about 20 km from the vent, the lava largely solidified beneath a rubble cover of dense dark gray blocky aa (fig. 57.4C). Blocky aa is similar to the so-called block lava characteristic of many andesitic flows (Macdonald, 1972), although surfaces of the aa blocks are less smooth because of vesiculation. Some resulting blocks are as large as several meters across. This material was rafted farther downflow on viscous but still fluid underlying material, mixed with more scoriaceous clinkers and lumps carried from higher in the channel, and finally deposited along the toe or margins of the flow as heterogeneous rubble.

## AA FLOWAGE ZONES

Early development of the 1984 aa flows (especially flow 1 during March 26–29) displayed systematic variations in structure and morphology from vent to toe—in addition to the aa textural types just summarized—that can be described in terms of four zones: flow toe, lower dispersed flowage, transitional channel, and upper stabilized channel (fig. 57.5). Subsequent development of blockages, ponds, and overflows of lava complexly overprinted this simple initial aa flow zonation, but each of the relatively ephemeral blockage-overflow lobes tended to show a similar zonation.

### FLOW TOE

Early in the eruption, most features of the aa flow system were established within a few kilometers of the flow toe during its advance. Upper well-channelized parts of the flow were stable and changed little, as virtually all lava moved efficiently down the channel to the toe area. The character of the flow toe varied mainly as a function of slope of the local land surface and distance of the toe from the stabilized channel.

Near the vent, on steeper slopes, and where the channel was well established close to a flow toe, fluid lava was delivered efficiently to the flow toe. The result was a rapidly moving broad flow front, consisting of scoriaceous or slabby aa, only 1–3 m high and with a nearly flat upper surface (figs. 57.2*A*, 57.6*A*). Such rapidly moving fronts exposed the liquid core of the aa flow as a bright orange band along the entire flow front; the flow advanced by outwelling of the fluid core, which then crusted over, brecciated, and overrode its front. This process produced a poorly developed basal breccia, because the brecciated upper surface moved more slowly than the center of the flow advanced. Such flow fronts tended to form scoriaceous or clinkery aa. Observed velocities at these flow fronts varied from 50 m/h to as much as 5 km/h. This type of flow front was observed during early stages of breakouts from the main channel where relatively fluid ponded lava was released as sheet flows, even late in the eruption (fig. 57.6*A*). Similar features probably were dominant during the early rapid advance of flow 1 on March 25–26.

In contrast, on gentler slopes, at sites more distant from the vent, and where a broader zone of dispersed flow occurred below the channelized flow, the flow toe moved more slowly, was higher and more irregular in profile, and consisted of denser blockier lava (fig. 57.6*B*). Little or no fluid material was visible at the flow front, and the steep high front advanced by spalling of dense blocks and slabs, largely from the breccia layer riding on top of the advancing flow. Fine granular to dusty material, resulting from abrasion of aa blocks, was a significant constituent at the flow toe. Velocities at this type of flow front varied from a maximum of 50 m/h to stagnation. Such flow characterized the fronts of flow 1 and flow 1A during their slow advance below about 1,350 m elevation.

### ZONE OF DISPERSED FLOW

Behind the advancing toe of the 1984 lava was a zone in which movement was dispersed across much of the flow width and a central channel was poorly developed or absent. During rapid advance of flow 1 early in the eruption, the zone of dispersed flow was relatively short; on March 27 this zone extended only about 1 km up from the toe at the 1,350-m level (figs. 57.2*B*, 57.7). As the eruption progressed, the flow toe became more sluggish, and the zone of dispersed flowage extended as much as 5–10 km up the flow. Observations in this zone were sparse, because the lava was still hot and unstable, and surface features were difficult to observe from terrain adjacent to the flow. Movement at the upper surface of the flow tended to occur along discrete shears, between which ridges of blocky aa moved fairly coherently. Near the toe, the most rapidly moving central part of the flow consisted of blocky aa showing little or no incandescence; farther upstream, the center of the flow was more incandescent and graded into a defined central channel containing visible fluid lava. Flow velocities increased gradually from

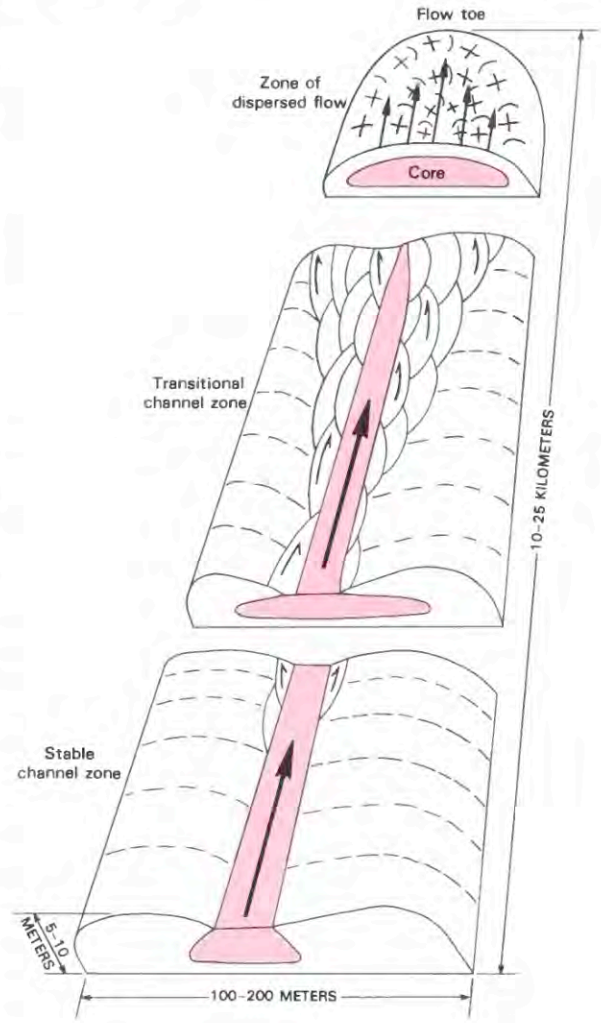


FIGURE 57.5.—Diagram showing contrasting structural features of aa channel zones.

*A*

*B*

FIGURE 57.6.—Aa flow fronts. ***A***, Fast-moving front of flow 1B, characterized by low toe (1–3 m) and exposed fluid core. Note lava boat (arrow) being rafted toward flow front. April 5, at 1,800-m elevation. ***B***, Slow moving front of flow 1A, characterized by higher toe (10–15 m) and rubbly incandescent front. A minimum temperature measured at flow front (not in fluid core) at this site was 1,086 °C (table 57.1). March 31, at 1,150-m elevation.

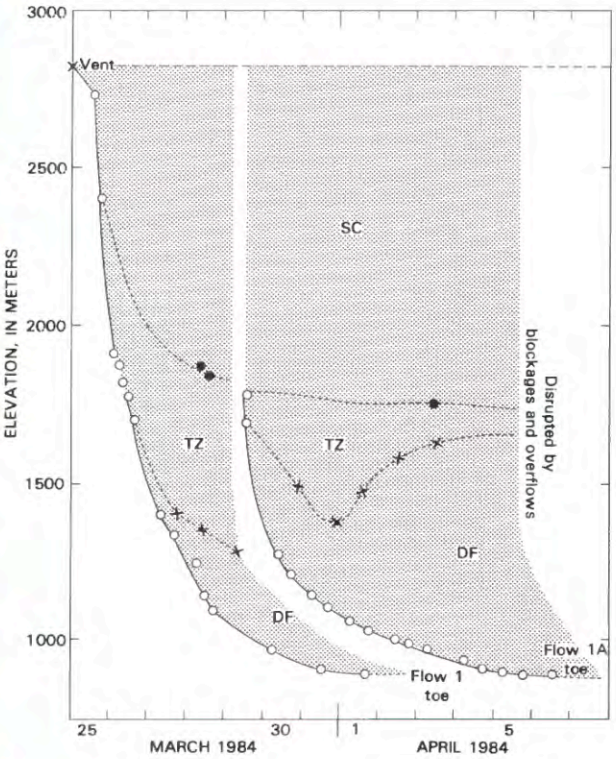


FIGURE 57.7.—Distribution of channel zones in relation to time and elevation, 1984 Mauna Loa lava flows. SC, stable-channel zone; TZ, transition zone; DF, zone of distributed flow. Circle, position of flow toe; x, DF-TZ transition; dots, TZ-SC transition.

the margin to the interior of the flow. Axial velocities were as much as several kilometers per hour; more typically, they were a few hundred meters per hour. Cross-sectional profiles through this zone of the flow are typically convex upward for slow-moving flows but nearly flat for rapidly advancing flows. At times, when a fast-moving flow crossed a steep slope, the channelized center of the flow could break through the more dispersed and sluggish lower part of the flow, delivering fluid lava to a flow front that had previously been more sluggish.

## TRANSITIONAL CHANNEL ZONE

The transition between zones of dispersed flowage and the stabilized channel was marked by the presence of a distinct channel containing incandescent clinkery aa, bounded by blocky or clinkery lava a few tens of meters wide that was still capable of deforming and moving slowly (figs. 57.5, 57.8*A*). These marginal areas consisted of multiple ridges or lenses of blocky lava, bounded by discrete shears (fig. 57.8*B*); they continued downstream into similar features in the zone of dispersed flow. The active channel in the transition zone was generally wider than in the stable channel zone. Toward the zone of dispersed flow, the active channel again decreased in

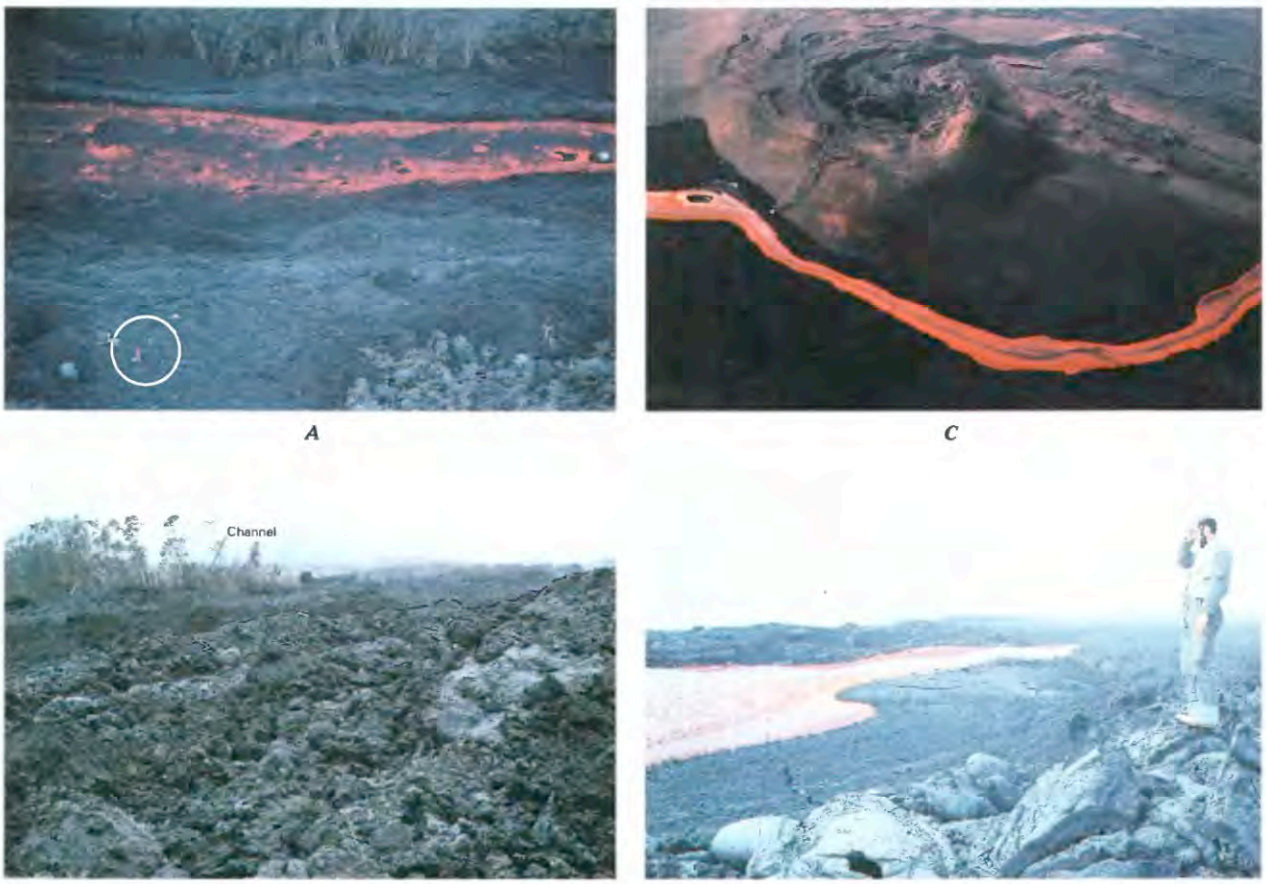


FIGURE 57.8.—Features of stable-channel and transition zones, 1984 Mauna Loa flows. ***A***, Aerial view of channel in transition zone at channel station 1, 1,600-m elevation. Active incandescent channel, about 24 m wide and flowing at 3.4 km/h (table 57.3, no. 1), is flanked by marginal shears in blocky aa moving at only a few meters per minute. Lava balls and other solidified debris are abundant on channel surface. Persons (circled) are standing on stable marginal levee. Photograph taken March 31. ***B***, Shear lenses adjacent to channel margin in transition zone at station 1, 1,600 m. Near ridge at right is stable early formed marginal levee; three shear lenses are present (boundaries marked by dashed lines), and weakly developed aa channel is visible at upper left. Photograph taken April 2. ***C***, Aerial view of stable channel zone at 2,500 m. Channel has been well established since first day of eruption. Dark band in center channel marks maximum velocity zone (19–20 km/h; table 57.3, no. 43–44). Vent of 1852 eruption is in upper part of photograph; channel station 8 is at far right. Photograph by J.D. Griggs, March 30. ***D***, Stable channel zone at station 8, 2,500 m. Man stands on original overflow levee; margin of channel has crusted over, although lava continues to flow beneath thin crust. Photograph taken April 2.

width as the number of marginal shear lenses increased. Individual shear ridges or lenses were several meters wide and traceable longitudinally for tens of meters. Measured flow velocities in the central channel of this zone were as much as 25–50 m/min (2–3 km/h); typical velocities in the marginal shear lenses were 1–3 m/min, with maxiumum velocities accompanying passage of lava surges in the central channel.

In addition to longitudinal movement, the belts of shear ridges inflated and subsided as much as several meters vertically in response to changes in lava levels in the channel. The combined vertical and longitudinal motions indicate that the belts of shear ridges were underlain by fluid lava hydraulically connected to the active channel. In comparison with the zone of dispersed flowage, the fluid core of the flow in the transitional-channel zone was more restricted but still covered a broader area than that of the channel. Audible creaking noises, reflecting hydraulic adjustments of the crust over marginal portions of the core, accompanied passage of lava surges in the adjacent channel. The presence of a sluggish fluid core beyond the margins of the channel 9 days after channel stablilization was documented during leveling toward the channel on April 4, at the 1,900-m monitoring station: 29 m from the active channel, the elevation decreased 10 cm as the lava level in the channel dropped in response to passage of a surge.

Early in the eruption, when flow 1 and then flow 1A were advancing rapidly, the transition zone was broad. On March 28, it extended from within 1–2 km of the flow 1 toe (then at the 1,200-m level) to above the 1,850-m level (fig. 57.7), about 10 km up the flow. Later, as advance of flow 1 and then flow 1A slowed, the zone

of dispersed flow extended 5–10 km up from the toe of flow 1A, but the zone of stablized channel flow began to encroach downslope on the transition zone. By April 3, the transition zone on flow 1A had decreased to a length of 3–4 km, from about 1,750 to 1,600-m elevation.

### STABILIZED CHANNEL ZONE

As the lava lens adjacent to the active channel cooled and marginal deformation of the flow ceased, all movement became concentrated in the central channel, producing a stable geometry in upper reaches of the flow (fig. 57.8*C*, *D*). Above about 2,450 m, where flow 1 had advanced rapidly as a sheet only a few meters thick during March 25–26, the channel appears to have stabilized rapidly, and there is little evidence for ephemeral development of a transition zone. In contrast, the segment from about 2,450–1,850 m elevation, although part of the stable channel zone by March 28, contains structures (broad central depression, inward-facing sags and ridges, and open cracks parallel to the channel) that indicate that this segment passed through a transition zone earlier during the eruption. By March 28–29, just before the breakout of flow 1A, the lower margin of the stable-channel zone was at about 1,850–1,900 m, below channel observation station 4 at 1,900 m and above station 3 along the Powerline Road at 1,800 m (fig. 57.1*B*). By April 3, the flow 1A channel had stabilized at the breakout area at about 1,800 m, but it never stabilized below about 1,750 m. After flow 1B and related breakouts at the 2,100-m level on April 5 had pirated the lava supply from lower parts of the previously stable channel zone, successively higher segments of the channel were abandoned or covered by lava from breakouts higher along the distributary system.

## CHANNEL EVOLUTION

A notable feature of the 1984 eruption was evolution of the main flows and associated channels from a simple long and narrow flow to a more complex geometry, largely as a result of breakdown in the efficiency of the lava channel. A key feature in this evolution was the formation of lava boats by rafting away of unstable portions of the lava channel. The lava boats caused blockages and ponding at downstream constrictions in the lava channel.

### INITIAL CHANNEL DEVELOPMENT

Lava channels formed in all 1984 Mauna Loa aa lobes more than a few hundred meters long, in response to the transverse velocity gradient across the flow near its toe, and by upflow stabilization of the flanks of the flow (figs. 57.5, 57.9). The position of the lowest well-defined channel coincided approximately with the diffuse boundary between the transition zone and the zone of dispersed flow. The first indication of this boundary was an upflow change in the cross-sectional flow profile, from convex upward near the toe (fig. 57.9*A*, *B*), to a broad rounded M-shaped profile upflow (fig. 57.9*C*). This change resulted from draining of lava toward the flow toe, with the greatest velocity in the central trough. Higher in the transition zone, the flow velocity of the axial zone increased further (fig. 57.10), and the velocity gradient between the rapidly moving central area and the stagnating margins became greater and eventually abrupt. This change confined a progressively greater volume of faster moving lava to a smaller channel cross section in an upstream direction. The surface of the central area became more incandescent and finally consisted dominantly of fluid lava (fig. 57.9*C*, *D*)

The geometry of the channel appeared to be sensitively related to other parts of the flow, especially in its lower reaches where the channel remained in dynamic interaction with the associated lava lens that extended as much as tens of meters beneath more stable flanks of the flow. The upper 10 km of the 1984 aa channel—above about 1,850-m elevation—remained stable for 8–10 days after its formation (fig. 57.7), but the lower reaches that never became part of the stable channel zone were sensitive to subtle changes in eruptive volume and lava properties. These changes produced floating debris in the lava channel that eventually caused blockages, ponding, and overflows of lava. This depleted the lava supply to lower channel reaches, and both the blockages and flow progressively stagnated upslope.

### LAVA BOATS

Floating debris of solidified lava was conspicuous in lower reaches of the channel as early as March 27, when channel observations were first undertaken more than a few kilometers from the vent. Large rounded lava masses found on consolidated surfaces

FIGURE 57.9.—Development of the aa channel and levees during the 1984 Mauna Loa eruption. ***A***, Initial aa sheet flow; near toe in zone of dispersed flow. ***B***, Mature aa sheet flow. Zone of dispersed flow; flow has spread laterally and inflated as supply of lava increases. ***C***, Transition zone, showing incipient development of a channel and the rounded M-shaped profile. Solid line indicates flow level at early stage of high lava supply; dashed line indicates lower flow level at later stage, when lava is draining efficiently downflow to zone of dispersed flow and central channel is becoming established. A peripheral zone of sluggish flow has developed along the margins and bottom through degassing, drag, and cooling. The flow has spread and the early levees have grown by overflows and lateral bulldozing during periods of high lava supply. Marginal shear ridges are active above the areas of sluggish flow. ***D***, Development of stable channel. Zone of sluggish flow has developed a more stable solidified crust, beneath which a plastic lava core remains, and erosion may have deepened the axial zone of sluggish flow, thereby deepening the channel and permitting higher flow rates. Also shown are overflow levees adjacent to the narrower deeper channel. ***E***, Mature channel in zone of stable flow. Lateral restriction of channel through inward migration of the zones of solidification and sluggish flow is counterbalanced by continued growth of overflow levees and perhaps by further erosion at the bottom of the channel. ***F***, Alternative types of levees for stage shown in *D*, showing development of structural levees. 1: Similar to *D*, but without development of overflow levee. 2: Uplift and buckling of the early channel crust during period of high lava supply. ***G***, Alternative types of levees for stage shown in *E*, showing concurrent development of overflow and deformation levees. 1: Overflow levee growing adjacent to earlier deformation levee, over regenerated channel crust. 2: Both levees bulldozed laterally during periods of high lava supply, overturning the earlier deformation levee (see fig. 57.16*B*).

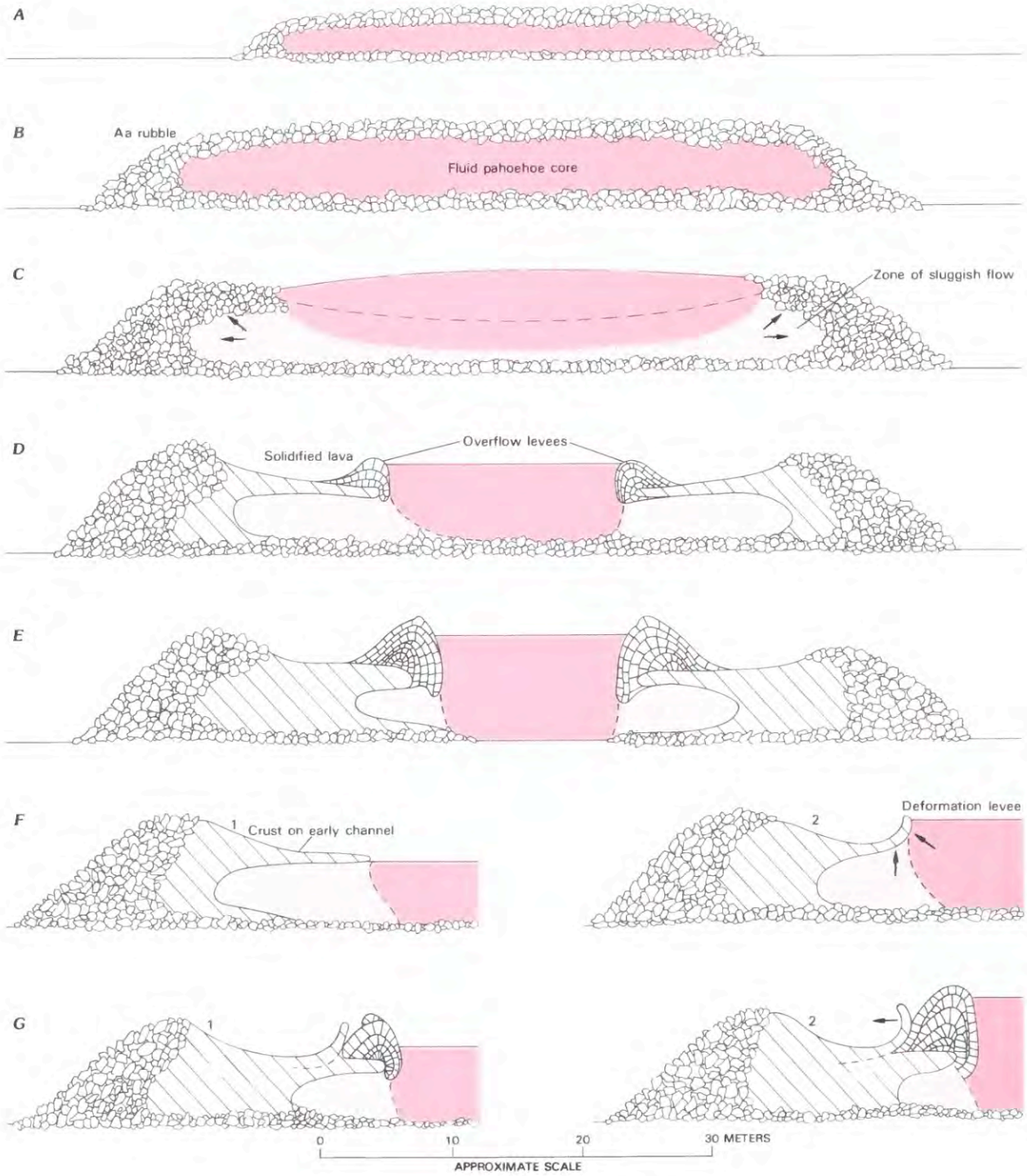
A
B
Aa rubble
Fluid pahoehoe core
C
Zone of sluggish flow
D
Solidified lava
Overflow levees
E
F
1
Crust on early channel
2
Deformation levee
G
1
2
0
10
20
30 METERS
APPROXIMATE SCALE

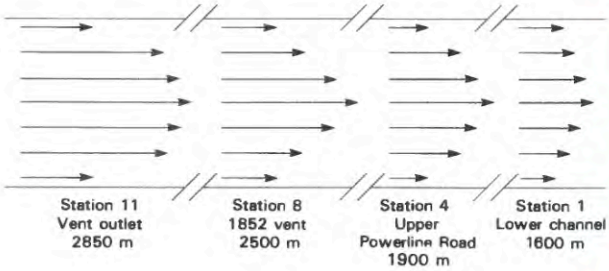


FIGURE 57.10.—Diagrammatic representation (plan view) of across-flow variation in flow velocity, channel of flow 1–1A. Station locations shown on figure 57.1*B*.

of aa flows have been called accretionary lava balls and interpreted as having formed "by the rolling up of viscous lava around some fragment of solidified lava as a center, in much the same way as a snowball rolling downhill" (Wentworth and Macdonald, 1953, p. 64). During the 1984 eruption, we referred to such features as lava boats, to emphasize their origin by caving and rafting within the active lava channel (fig. 57.11*A*), rather than by rolling on the clinkery surface in lower reaches of the flow.

Lava boats and more irregular small debris were observed to form by caving of unstable overhanging channel banks and walls, especially when the level of lava in the channel dropped and so reduced support for the bank (fig. 57.11*B*). Caving and rafting of the channel banks was aided by the presence of still-plastic lava under the channel margins (fig. 57.9), particularly adjacent to marginal shears in the transition zone. In the zone of stabilized flow, some overhangs also originated as partial roofs of incipient lava tubes. Major collapse events along the channel banks were marked by dust clouds and by subsequent increase in the number of lava boats downstream.

Lava boats also formed along the inside banks of meanders, where flowing lava in the channel applied drag and compression and opened tension cracks in the adjacent bank (fig. 57.12) Continued pressure by the moving lava then rafted fragments of the bank into the channel to form lava boats. Such formation of the lava boats tended to straighten the channel with time, in contrast to processes in rivers of water, which erode on the outsides of meanders and deposit sediment on the insides. The first channels in the early aa (fig. 57.9*C*) had meanders because the flow followed irregularities in the pre-eruption topography behind the toe. In addition, the flow advanced as a thin sheet in which the ratio of friction to mass was high (fig. 57.9*A*); the toe of the flow tended to inflate (fig. 57.9*B*), because the upflow channel delivered lava faster than it could be distributed by flow advance or spreading. As a result, the incipient channels initially developed a somewhat disorganized geometry as flow directions and velocities changed in response to changing rates and locations of advance of the toe. Later, as the channel deepened and narrowed (fig. 57.9*C*, *D*), the flow rate increased, and some

*A*

*B*

*C*

FIGURE 57.11.—Lava boats. ***A***, Lava boat floating in full channel during small surge. Channel is confined behind small overflow levee of scoriaceous aa. Photograph taken March 29, at 1,900-m elevation (compare with figure 57.16*B*, taken 7 days later at same site). ***B***, Formation of lava boats by collapse of overhanging levee wall into channel during low stand of lava; small satellitic northern channel. Photograph taken April 9, at 2,800-m elevation. ***C***, Flow front, showing 2-m-diameter lava boat (outlined with dashed line) being pushed ahead by advancing flow. Photograph taken April 6, at 1,700-m elevation.

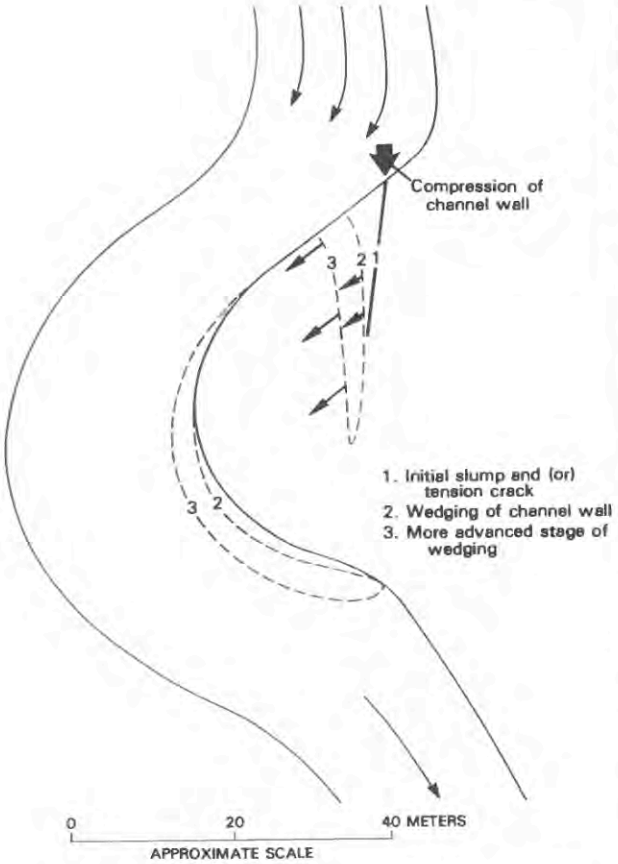


FIGURE 57.12.—Diagrammatic sketch (map view) of origin of lava boats by wedging and slumping from inside bank of channel meander in the stable-channel zone.

early meanders became inefficient for delivery of the lava to the flow front. Such channels tended to straighten through spalling of the inside walls of curves.

The elongate wedges of channel-bank and levee material thus formed floated downstream as lava boats that gradually broke into more equant shapes. Frequently, they disintegrated into equant pieces when they grounded on the channel floor or jammed against the downstream channel walls and adjacent boats. As the boats rolled and bobbed in the channel, they also accreted a lava sheath.

In the zone of dispersed flow below the active channel, the lava boats were rafted along the upper surface of the flow, in conveyer-belt fashion toward the flow front. In this zone, blocks on the flow surface tended to be carried passively downslope, with little differential movement. Thus no additional lava was accreted to the lava boats below the active channel. Frequently, lava boats several meters in diameter were rafted all the way to the flow front and pushed ahead by the advancing flow (fig. 57.11C).

Lava boats were rare in upper reaches of the channel, within about 5 km of the vent, especially during the first half of the eruption, reflecting the more stable channel configuration in this area. In the channel within 200–300 m of the vent, rapidly flowing lava splashing against the channel banks at a curve occasionally stoped large blocks from the bank. Lava boats became progressively more abundant downflow and also with increasing age of the channel.

The lava boats were useful indicators of channel velocities and minimum depths (table 57.2; app. 57.2); they also played a key role in channel evolution by causing blockages and dams in the channel. The largest lava boats were 6–7 m across and extended 2–3 m above the channel surface. Several kinds of observations suggest that they typically projected at least this distance below the channel surface, providing a minimum estimate of channel depth: (1) Most lava boats rafted to the lava surface low on the flow are subequant in shape. (2) Rarely, large lava boats would hang up on the channel floor and roll over, exposing their full geometry. Even during low channel levels, 2–3 m below maximum, large lava boats would commonly float freely—suggesting typical channel depths of 4–6 m. (3) Because the density of lava in the channel is low—about 0.5 g/cm$^3$ at the vent to 1.5–2.5 g/cm$^3$ in lower reaches (discussed later; also see fig. 57.20)—typical channel-bank debris (density 1.0–2.0 g/cm$^3$) is only slightly less dense than the channel lava, and the resulting lava boat could not rise buoyantly more than about one-half its diameter. As the channel lava degassed, cooled, and became more dense downchannel, accompanying lava boats probably gradually emerged higher. Lava boats that originated by caving of unstable banks from lower channel reaches (transition zone) would also be denser than boats derived from higher stretches of the channel. Within a few kilometers of the vent, most lava of the channel walls was more dense than the fluffy lava in the channel; caved fragments of channel banks probably sank rather than floated, and formed saltating blocks along the channel bottom. Only rare rafted fragments from the low-density agglutinated spatter ramparts could float in the channel lava close to the vent.

## BLOCKAGES AND PONDING

Accumulation of lava boats and debris from surface crusts in channel constrictions (fig. 57.13A) caused blockages and ponding of the main channel and produced major changes in the character of the aa flow during early April. Small ephemeral blockages formed at a few channel constrictions in middle and lower reaches of the flow as early as March 27, but the first significant lava dams were not observed in well-developed reaches of the main channel until March 29. During the following week, blockages increased in size and number, and they gradually formed higher along the main channel (fig. 57.14). Overflows from long-lived ponds occurred both to the sides and over the tops of blockages (fig 57.13*B*). When overflow was sustained at one side of a dam that held, a branch flow could be generated. Most branch breakouts advanced at first as sheet flows; if the overflow was maintained, erosion of the flanking levee permitted the flow rate in the branch to increase, a channel to develop, and a stabilized branch flow to form.

By the morning of March 29, a major blockage at the 1,800-m level was able to divert the entire lava supply of flow 1 northward

A B

FIGURE 57.13.—Blockages and surges in lava channels, 1984 Mauna Loa eruption. ***A***, Aerial view of developing blockage along constricted sector of flow channel. Upchannel pond has relatively cool scoriaceous surface; hotter interior lava is draining downchannel from below blockage. Light-colored lava along right margin is 1852 pahoehoe. About 1,800-m level, March 31. ***B***, Aerial view of surge overflow at blockage site, looking upchannel. About 1,650-m elevation, March 31.

to form flow 1A. Many smaller blockages in the next few days caused overflows at this same general elevation. By April 4, blockages were occurring as high as 1,950 m, and on April 5 a large blockage at about 2,050 ft caused a major surge and overflow to form flow 1B. On April 6–7, repeated blockages and overflows at the 2,000–2,100-m level prevented sustained feeding of any flow system below 1,850 m. By April 8, blockages were causing many overflows at elevations as high as 2,300 m), and blockages and overflows extended back almost to the vent during the next two days.

Most debris blockages reduced, but did not stop, downchannel flow; typically, little glowing lava was visible at the surface in the constricted sector of the channel, but fluid lava would continue to flow or at least ooze out at the lower end of the constriction. The amount of lava ponded by a blockage could be large relative to the upslope channel volume; blockages and ponding promoted construction of overflow levees that in turn could be enlarged by spreading of the levees and overflow of the entrapped ponded lava. The largest ponds, at the 1,800-m and 2,050-m levels, were as much as 100 m wide, 10 m deep, and 500 m long; periodic abrupt release of much of the ponded lava could significantly modify the downstream flow regime.

A dynamic relation was established early between blockages and formation of lava boats: generation of a cluster of lava boats by failure of the channel bank provided material to cause a blockage at a downstream constriction, and in turn formation of such a blockage would lower the channel level farther downstream, causing additional failure of the channel bank and generation of more lava boats. As a corollary, when the channel level was low and few lava boats or other debris were evident in the channel, blockages and ponding could be inferred to be occurring upchannel. Both straightening of meanders and small fluctuations in channel level, perhaps initially related to short-term variations in rate of lava production at the vent, were thus capable of generating blockages farther downchannel. The intensity of such perturbations increased during the first two weeks of the eruption, even though the rate of lava production at the vent remained roughly constant, at least from March 30 to April 7.

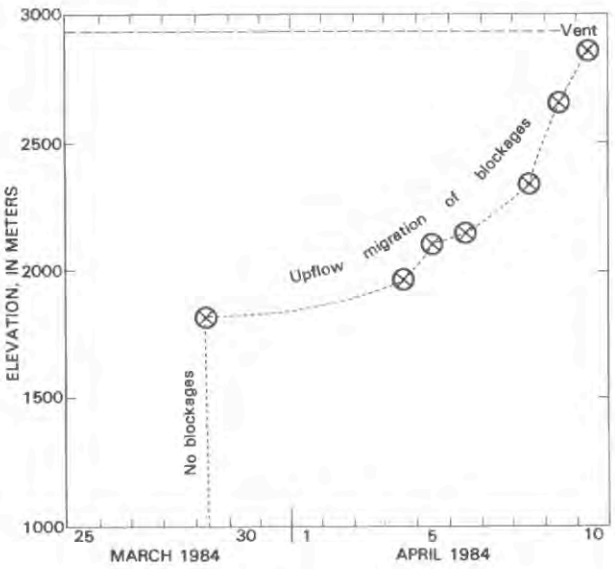


FIGURE 57.14.—Elevations of highest overflow-producing blockages (circled crosses) in main flow channel of 1984 Mauna Loa eruption.

## SURGES AND OVERFLOWS

Lava that ponded behind channel blockages eventually escaped, either by overflowing the channel banks as the pond level rose or by breaking through the blockage to generate lava surges downchannel. Small blockages commonly failed when the weight of the ponded lava exceeded the strength of the obstruction. At first, the dam would begin to creep downchannel, at increasing rates. Within several minutes, flow rates would increase from a few meters per minute to a few meters per second. Then the lava pond would break through a low or weak area to form a surge of lava down the channel. At times, this occurred in such volume that the released lava could not be contained in the channel below the dam (fig. 57.15). At other times, the rising impounded lava would lift and float the jammed debris over the constriction to form an overflow surge. When the volume of the breakout was reduced by overflows to an amount containable within the channel, the excess lava progressed down the flow as a channel surge.

Where the pond was confined behind high overflow levees, the weight of the pond could bulldoze the flank of the levee aside, widening the channel or causing failure of the levee. Failure of the levees, at times observed to open like a giant barn door, could abruptly release a large volume of lava along the flank of the flow rather than directly downchannel. Such lateral breakouts could generate major new lava tongues, such as flows 1A and 1B. In such breakouts large blocks of levee material were rafted downslope embedded in the overflow lava. Much of the volume of the eruption was dissipated in this way after March 29, causing slowing and stagnation of the flow terminus.

In lower reaches of the channel (transition zone), surges caused fluctuations of several meters in channel level; they also affected the height and rate of deformation of the marginal shear lenses adjacent to the channel. Increased marginal deformation during a surge was accompanied by creaking and crunching noises. The marginal shear areas rose during passage of a surge and subsided afterward, demonstrating that the zone of shearing was underlain by fluid lava hydraulically connected to the channel.

Flow velocities in the channel commonly increased during a surge, especially where the channel gradient was fairly uniform. Where the gradient flattened below a cascade, however, the effect of a surge was mainly to increase the lava level, with little or no increase in velocity. Many surges carried abundant debris from the causative blockage as a raft that spanned much of the channel and moved more slowly than the underlying lava. The cooler and more rigid rafted material tended to increase the bulk viscosity of the lava and drag along the marginal levees; these interactions raised the level of flow within the channel and decreased the velocity of the lava. A few minutes after passage of a surge, exceptionally fluid lava that had been stored in the interior of the blockage pond typically arrived in the channel; flow velocities increased, and the previous channel gradients were restored.

## LEVEES

Marginal levees are common features of aa flows and are closely related to channel evolution (Hulme, 1974). At Mauna Loa in 1984, several types of levees formed that are broadly similar to those described for small short-lived aa flows on Mount Etna (Sparks and others, 1976). At Mauna Loa, however, levee growth varied notably with time and with position along the flow.

### EARLY LEVEES

Early levees on Mauna Loa are represented by the broad topographically high rubbly flanks of the aa flow (fig. 57.9C: high points on the M-shaped profile) that were left behind in the zone of dispersed flow as the central zone of highest velocity flow drained downslope to form an incipient channel (fig. 57.5). In many places, lateral spreading of the flow tended to displace and cause outward avalanching of aa rubble along the early formed levees (fig. 57.9C). Thus, the early Mauna Loa levees seem transitional between the features that Sparks and others (1976) called initial levees and rubble levees. Nested lateral levees also tended to form rapidly at Mauna Loa, inside of the early lateral levees, as the center of the flow thinned and movement became concentrated along an incipient channel. In comparison with initial levees of aa flows on Etna, such early lateral levees on Mauna Loa aa flows were morphologically more complex, broader relative to channel width, had high points farther from the channel banks, and formed over a period of hours to days rather than within minutes of passage of the flow front. These differences seemingly reflect the larger size and longer movement history of the Mauna Loa flows. In addition, on Mauna Loa the flowing lava between the levees rapidly developed a concave-upward profile because of draining of the liquid flow core downslope and probably also because of effects of preexisting topography (fig.

*A*

FIGURE 57.15.—Channel overflows. ***A***, Begining of overflow at about 2,800-m level, at 1800 April 10. Blockage has broken, permitting ponded lava to spread downslope and overflow the channel. ***B***, Photograph taken about 5 minutes after that in *A*. Upper part of overflow has stagnated and lava is draining back into original channel; on lower slopes surge continues to flood and overflow channel.

57.9C) In contrast, profiles of flows on Etna (and also those modeled by Hulme, 1974), which are confined within marginal levees, are convex upward. On both volcanoes, formation of early levees appears related to the yield strength of the lava.

The early levees that formed at Mauna Loa were gradually modified by later processes of composite levee growth, mainly involving channel overflow and deformation of already formed levees. These processes produced complex levee structures somewhat similar to those described on Etna—accretionary, rubble, and overflow levees (Sparks and others, 1976)—although larger and more notably composite in origin. All levee growth on Mauna Loa flows, after a central channel was established, was caused by variations in channel level related to blockages and surges.

## OVERFLOW LEVEES

The most common levee-building process was overflow of the channel banks during passage of surges. During vigorous surges, discrete small aa or pahoehoe flows spread laterally to produce overflow levees (figs. 57.16*A*, 57.9*D*, *E*) of the sort diagramed but not observed by Sparks and his associates. Weaker surges that completely filled the channel without overflowing caused scoriaceous or clinkery aa to accumulate along the channel margins, producing rapid growth in levee height by processes somewhat similar to the so-called accretionary levees described on Etna. Overflow and accretionary levee-building processes were thus intergradational, even during a single surge event. At Mauna Loa, levees formed by these

*B*

FIGURE 57.15—Continued.

surge-overflow processes had depositional slopes of no more than 10°–15°, in contrast to slopes of 50°–85° reported at Etna.

## DEFORMATION LEVEES

An important process, which steepened overflow levees at Mauna Loa, was outward displacement of overflow levees pushed by the increasingly deep lava confined in the channel. By this mechanism, overflow levees with initial surface features of small lava flows were converted into angle-of-repose rubble ridges, which stood as much as 6–8 m above the original channel level (fig. 57.9*E*). At times, slabs of scoriaceous pahoehoe several meters across, derived from the crust of the channel lava, were tilted and overturned during upwelling of channel lava associated with surges (fig. 57.9*F*). These features are best described as deformation levees, although somewhat related in process and resultant appearance to the so-called rubble levees described near the toes of Etna flow fronts (Sparks and others, 1976). Deformation of a levee was commonly recognizable at a distance by rising dust clouds, as aa debris ground together and cascaded down the flank of the levee (fig. 57.16*B*). Such outward expansion was frequent during passage of surges, when channel levels were high, and was commonly accompanied by channel overflows, producing composite levee morphologies. The outward displacement of levees also caused fracturing, and at times lava from the interior of the channel oozed out along the base of the rubble levees. This process sometimes led to catastrophic failure of a levee flank, formation of a new lateral breakout, and draining of the lava ponded behind the levee.

Overflow and deformation levees did not form during early advance of the Mauna Loa flows; they constitute a distinct aspect of later evolution associated with blockages and ponding in the channel. Development of such levee features could provide a useful criterion to distinguish between long-lived and short-lived prehistoric aa flows.

## ACCRETED LEVEES

Distinctive additional levee types, observed in the transition zone of the Mauna Loa flow system, are best termed accreted levees

*A*

*B*

FIGURE 57.16.—Lava levees, 1984 Mauna Loa eruption. ***A***, Overflow levee: channel level is low between surges. Slow overflows have produced shiny pahoehoe on levee flanks. Photographed on April 10, at about 2,800-m elevation. ***B***, Deformation levee: weight of perched lava channel is causing restraining levee to spread laterally, as indicated by dust clouds rising from blocks cascading down steepening levee flank. Result is angle-of-repose outer slopes of levees (see fig. 57.9*G*). Photographed on April 4, at 1,900-m elevation.

although different in origin and appearance from the accretionary levees of Sparks and others (1976). In the transition zone, characterized by a developing channel flanked by slowly moving lens-shaped ridges of aa rubble bounded by discrete shear zones (fig. 57.5), the initial levees were widened and enlarged by accretion of laterally moving rubble ridges. The ridges moved fairly rapidly during surges in the adjacent channel; during low stands of the channel, motion of the lateral ridges slowed, and some marginal ridges would accrete to stable flanking rubble levees. In many respects, this process provides a small-scale analog of plate-tectonic accretion of tectono-stratigraphic terranes (Jones and others, 1982). Some accreted levees originated as transverse pressure ridges near the flow toe, which were then deformed by continued flowage into U-shaped ridges (in plan view). These ridges subsequently were breached by continued movement within the center of the flow, and the limbs of the "U" became moving levees parallel to the channel margins (fig. 57.17).

### POSTERUPTION CHANNEL PROFILES

During the eruption, channel depths were estimated mainly by reference to the half diameters of large lava boats (table 57.2). Once, we attempted to measure channel depths directly by dropping 5-m iron bars, stabilized vertically with streamers, from a helicopter. The channel center was difficult to hit by this technique, however, because radiative heat from the channel required a flight height of 100–200 m. Similarly, suitable locations for launching bars 2–3 m long in javelin fashion from high levees were rare, and such attempts failed to penetrate to the channel bottom.

After eruptive activity ceased, we measured profiles across the evacuated channels of flow 1, flow 1A, and the north flow at sites that had drained rapidly because of upflow beheading (fig. 57.18). Most profiles were at or near the flow-rate monitoring stations (fig. 57.1*B*), and some channel sites appeared unmodified except for draining of lava since our last monitoring measurements. Where the monitoring station had been modified by ponding or overflows, we profiled a nearby channel site that appeared representative of the geometry during the eruption. The posteruption channel profiles showed that most of the earlier depth estimates were 20–30 percent low, probably because the lava boats would first shoal on anomalously shallow reaches of the channel. Although the channel profiles improved our estimates of volume rates of flow, the measured depths are only minima because of residual ponded lava and rubble from caving levees. In addition, the profiles are of mature channels; channel geometry in earlier stages are inferred from observed changes in levee height and channel width during the eruption.

In addition to improving the volume calculations, the profiles show that the mature channel had (1) a remarkably uniform depth, about 6 m, from the vent to 17 km downflow; (2) a gradually increasing width downflow, especially within the transition zone (fig. 57.18*M*); and (3) an approximately rectangular shape. The bottoms of many channel profiles are near the projected pre-1984 surface, in agreement with the inference that still plastic parts of the initial flow material are eroded during deepening and narrowing of the maturing flow channel (fig. 57.9).

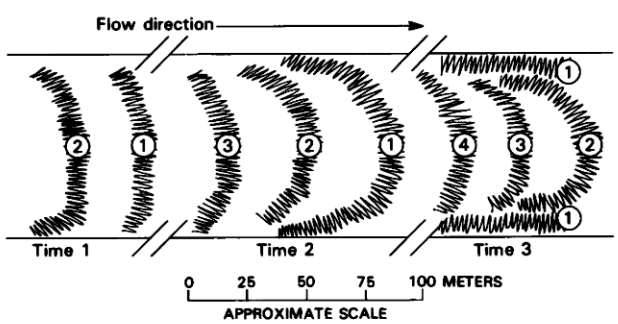


FIGURE 57.17.—Diagrammatic sketch (plan view) of formation, deformation, and accretion of pressure ridges to form accreted levees. Solid lines, margins of channel. Numbers identify individual sequentially formed pressure ridges.

## TEMPERATURE AND DENSITY VARIATIONS OF LAVA

Key parameters in interpreting the evolution of the 1984 lava and channels are variations in lava temperatures and densities in relation to eruption duration, distance from vent, and lava type (table 57.1; fig. 57.19). Temperature determinations on the lavas were considered especially important for evaluating the hazard potential early in the eruption, because an increase in temperature might indicate the arrival of a more fluid magma batch from below the summit area.

### LAVA TEMPERATURES

Temperatures were measured both directly by thermocouple probes inserted into accessible fluid lava and more remotely with a HOTSHOT 2-color infrared pyrometer aimed at active fountains or at brightly incandescant lava in standing waves in channels. Agreement among results by the two techniques was commonly within 5 °C when conditions were optimal. Some low measurments, deemed nonrepresentative and not plotted in figure 57.19, resulted from failure of the thermocouple to reach equilibrium before breakage of the probe tip, or from HOTSHOT measurement of fountains when the view included obstructing fume or cooler peripheral fallback material. Some equilibrium thermocouple measurements, which were lower than other values obtained from the same site, are thought to have inadvertently sampled cooler marginal lava. Details of measuring techniques and instrumental limitations are summarized in appendix 57.1.

The interpreted best measurements indicate that lava temperatures within a few hundred meters of the vents at about 2,850 m remained within the narrow range of 1,140 ± 3 °C throughout the eruption, varying little more than measurement uncertainties (fig. 57.19*A*). Temperatures measured on the most fluid lava at channel sites as much as 10 km downslope were only slightly cooler, in the

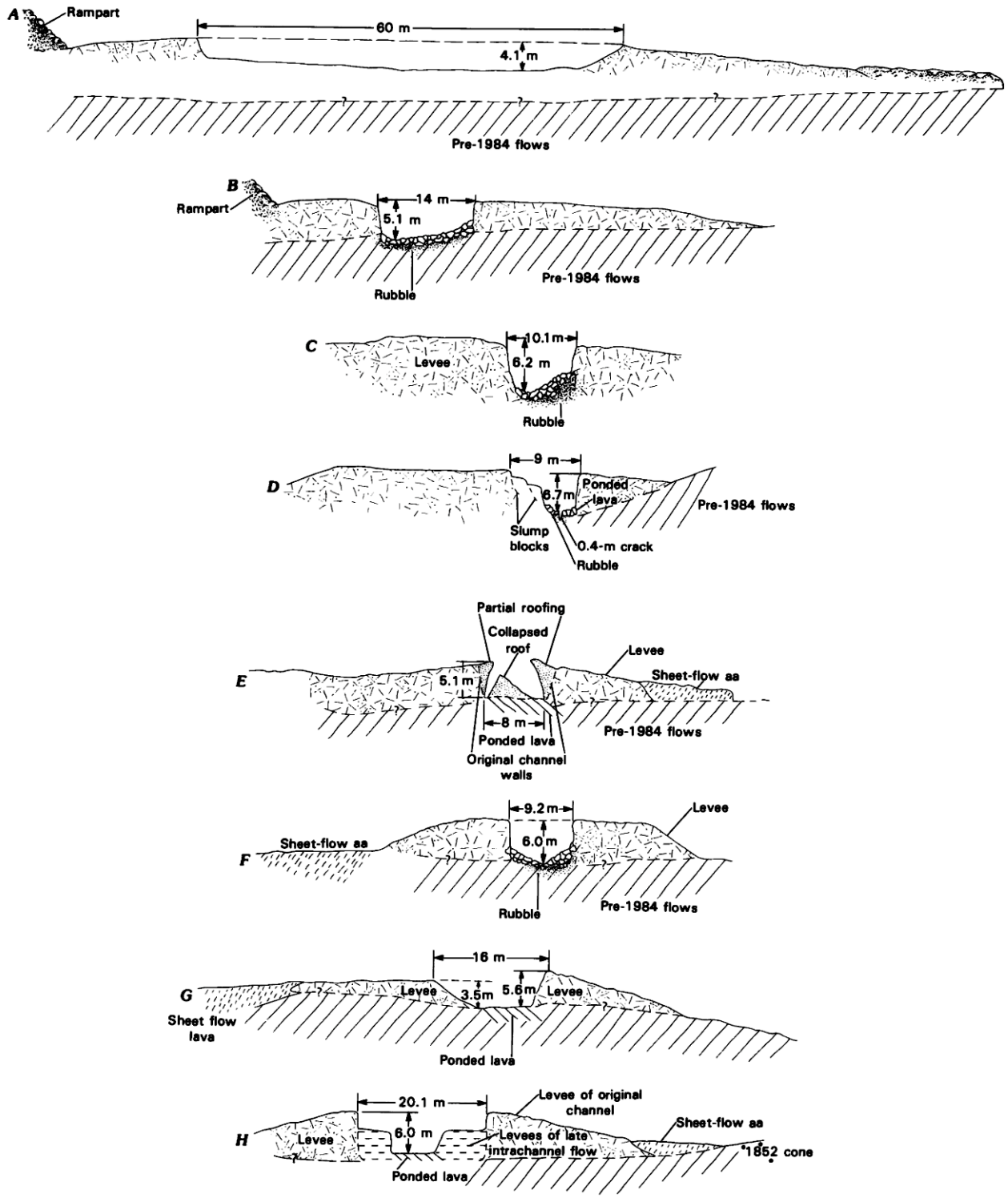
A
Rampart
60 m
4.1 m
Pre-1984 flows
B
Rampart
14 m
5.1 m
Rubble
Pre-1984 flows
C
Levee
10.1 m
6.2 m
Rubble
D
9 m
6.7 m
Ponded lava
Pre-1984 flows
Slump blocks
0.4-m crack
Rubble
E
Partial roofing
Collapsed roof
Levee
Sheet-flow aa
5.1 m
8 m
Ponded lava
Original channel walls
Pre-1984 flows
F
Sheet-flow aa
9.2 m
6.0 m
Levee
Rubble
Pre-1984 flows
G
16 m
Levee
3.5m
5.6m
Levee
Sheet flow lava
Ponded lava
H
20.1 m
Levee of original channel
Sheet-flow aa
Levee
6.0 m
Levees of late intrachannel flow
1852 cone
Ponded lava

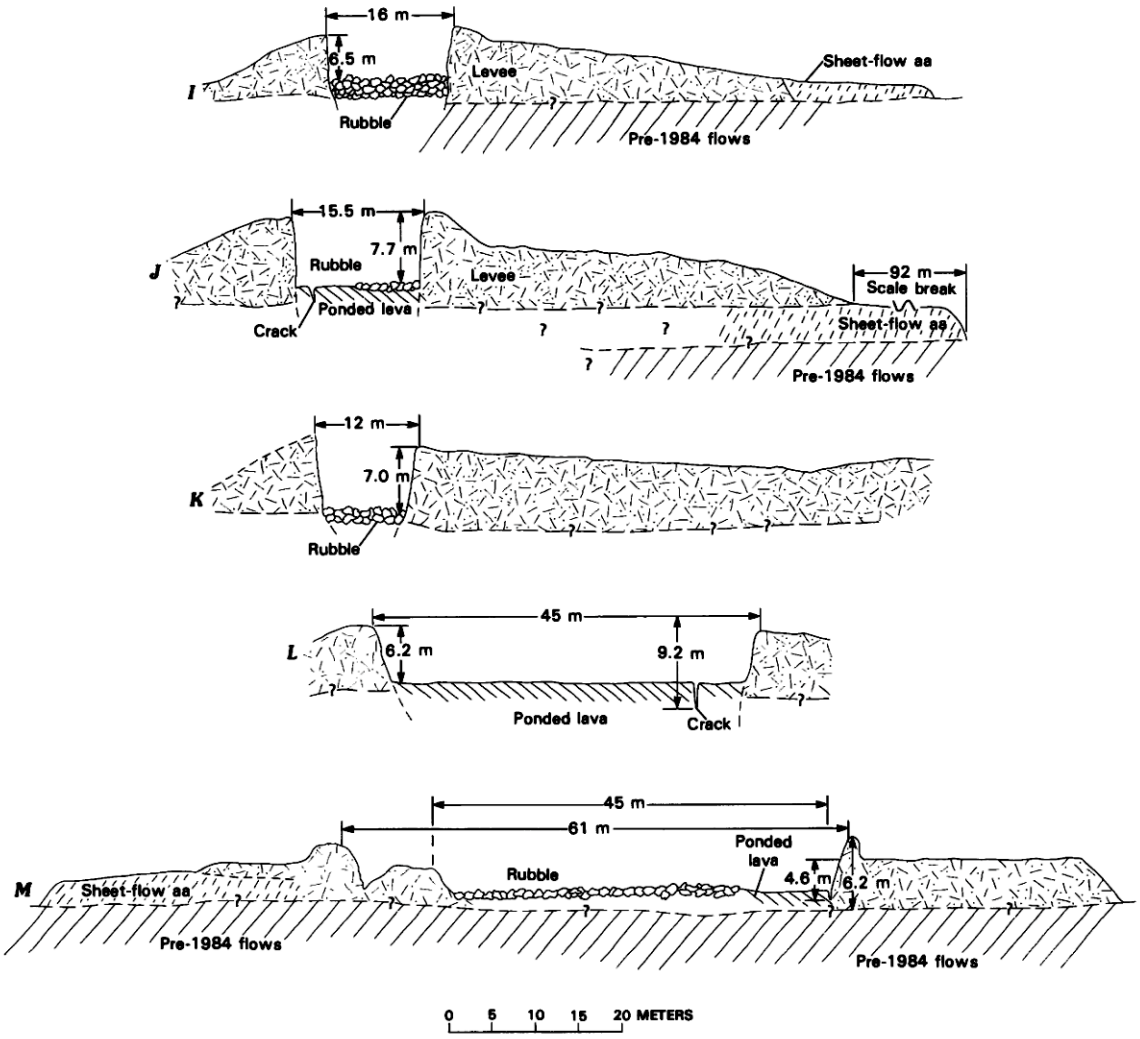


FIGURE 57.18.—Posteruption profiles (no vertical exaggeration) across channels of the 1984 Mauna Loa flows. Locations of channel stations shown on figure 57.1*B*. ***A***, Channel at about 2,900 m, 100 m downflow from westernmost vent, that was abandoned just after initial stabilization on about April 10. ***B***, Channel station 12, at about 2,900 m; mature stage of north channel, adjacent to vent rampart. ***C***, North flow, at 2,850-m elevation, 70 m from vent outlet. ***D***, Channel of north flow at 2,800-m elevation, approximately north of vent 2. ***E***, Channel station 10, at 2,720-m elevation; north flow, near monitor station. About 1 km from vent. ***F***, Channel at 2,710-m elevation, flow 1. About 2.5 km from vent. ***G***, Channel at 2,550-m elevation, flow 1; probably a channel formed after April 8. About 3.5 km from vent. ***H***, Channel station 8; 2,540-m elevation, flow 1; pre-April 8 channel, just above monitor station. About 4 km from vent. ***I***, Channel station 7, 2,200-m elevation, flow 1; pre-April 8 channel, near monitor station. About 6.5 km from vent. ***J***, Channel station 4, 1,950-m elevation, flow 1; pre-April 8 channel, near monitor station. About 10.5 km from vent. ***K***, Channel station 3, 1,800-m elevation, flow 1; pre-April 8 channel, near monitor station. About 12 km from vent. ***L***, Channel at 1,800-m elevation, flow 1; pond below channel station 3. About 12.5 km from vent. ***M***, Channel station 1, 1,600-m elevation, flow 1A; pre-April 8 channel, near monitor station. About 15 km from vent.

TABLE 57.1.—*Lava temperature and density, 1984 Mauna Loa eruption*

[Days, time in days from beginning of eruption; distance, distance from vent]

| Location | Date (mo/d) | Time (H.s.t.) | Days | Elevation (m) | Distance (km) | Temperature (°C) | Code[1] | Density (g/cm³) | Sample | Comments |
|---|---|---|---|---|---|---|---|---|---|---|
| 3,500-m vents | 3/25 | 1015 | 0.37 | 3,500 | 0.01 | 1,073 | T 1 B I | 0.85 | NER-7 | Channel at vent; couldn't probe below surface; poor reading. |
| SE. flow, terminus | 3/25 | 1540 | .59 | 2,670 | 6.6 | 1,128 | T 2 B E | 2.23 | NER-1F | Aa flow front; imbedded 2 m in soft core; stable 15 min. |
| Flow 1 | 3/25 | -- | .70 | 2,560 | 3.6 | -- | | 1.29 | 4/18NB1 | Aa, core of sheetwash flow. |
| Vent 1, middle | 3/26 | 0828 | 1.29 | 2,910 | .0 | 1,125 | H P | -- | -- | Fountain; tripod rest, 50 m distance. |
| Do. | 3/26 | 0854 | 1.31 | 2,910 | .0 | 1,145 | H G | -- | -- | Fountain; tripod rest, 50 m distance; stable 1,144–1,145 °C. |
| Vent 1, east end | 3/26 | 1058 | 1.40 | 2,890 | .0 | 1,103 | T 1 B F | 1.08 | NER-12/2 | 1-m-thick spatter-fed flow; failed tip several tries. |
| Do. | 3/26 | 1324 | 1.50 | 2,890 | .0 | 1,146 | H G | 1.20 | NER-12/3 | Fountain, tripod at 20 m; stable 1,134–1,146 °C, observer 1. |
| Do. | 3/26 | 1340 | 1.51 | 2,890 | .0 | 1,147 | H G | -- | -- | Fountain, tripod at 20 m; stable 1,134–1,146 °C, observer 2. |
| Flow 3 | 3/26 | 1420 | 1.54 | 2,860 | .0 | 1,131 | T 1 B E | 1.19 | NER-12/13 | Pahoehoe overflow from main channel; stable 2 min. |
| Flow 1 | 3/26 | 1600 | 1.61 | 2,760 | 1.5 | 1,139 | T 1 B G | 1.18 | NER-12/4 | Directly in main channel; stable several minutes. |
| Vent 1, east end | 3/26 | 1613 | 1.62 | 2,890 | .0 | -- | | .92 | NER-12/14 | Spatter. |
| Flow 1 | 3/26 | 1730 | 1.67 | 1,880 | 11.7 | 1,131 | T 2 B E | 1.77 | NER-12/5 | Overflow 30 m from channel; stagnating when measured. |
| Vent 1, main vent | 3/27 | -- | 2.50 | 2,890 | .15 | -- | | .60 | NB1ML84 | Cooled shelly pahoehoe overflow from main channel. |
| Vent 1, middle vent | 3/27 | 1421 | 2.54 | 2,910 | .01 | 1,131 | T 1 B E | .83 | NER-12/12 | Spatter-fed flow; 60 cm thick; stable 0.5 min. |
| Vent 1, main vent | 3/27 | 1435 | 2.55 | 2,500 | .0 | 1,139 | H G | -- | -- | Fountain, tripod rest; 10–15 m distance; stable 1,135–1,139 °C. |
| Do. | 3/27 | 1545 | 2.60 | 2,890 | .0 | 1,139 | H G | -- | -- | Do. |
| Do. | 3/27 | 2016 | 2.79 | 2,890 | .01 | 1,131 | T 1 B E | .98 | NER-12/15 | Spatter-fed flow; 1 m thick; stable 0.5 min. |
| Do. | 3/27 | 2035 | 2.80 | 2,890 | .0 | 1,140 | H G | 1.12 | NER-12/16 | Fountain, tripod rest; 10–15 m distance; stable 1,135–1,140 °C. |
| Do. | 3/27 | 2350 | 2.93 | 2,890 | .02 | 1,135 | T 1 B G | 1.36 | NER-12/17 | Tube, directly from vent; stable 3 min. |
| Do. | 3/28 | 0610 | 3.20 | 2,890 | .02 | 1,137 | T 1 B G | .92 | NER-12/18 | Do. |
| Vent 4 | 3/28 | 0835 | 3.30 | 2,810 | .05 | 1,128 | T 1 B E | .92 | NER-12/10 | Tube emitted directly from vent pond; stable. |
| Do. | 3/28 | 1241 | 3.47 | 2,810 | .0 | 1,131 | T 1 B E | -- | NER-12/20 | Do. |
| Do. | 3/28 | 1610 | 3.61 | 2,810 | .05 | 1,128 | T 1 B E | -- | NER-12/21 | Do. |
| Flow 1A | 3/29 | 1300 | 4.50 | 1,610 | 16.50 | -- | | 2.6 | -- | Core of aa flow. |
| Vent 4 | 3/29 | 1755 | 4.69 | 2,810 | .0 | 1,136 | T 1 B G | 1.19 | NER-12/23 | Top of west hornito; 2 times; stable 3 and 2 min. |
| Do. | 3/30 | 0656 | 5.23 | 2,810 | .0 | 1,130 | T 1 B E | -- | NER-12/24 | Tube emitted directly from vent pond; stable. |
| Do. | 3/30 | 0840 | 5.30 | 2,810 | .0 | 1,135 | T 1 B G | 1.84 | NER-12/25 | Top of west hornito; stable 3 min. |
| Flow 1A | 3/30 | 1230 | 5.46 | 1,370 | 20.4 | 1,103 | T 2 B F | -- | -- | Horizontal into lobe terminus; >20 cm penetration, poor. |
| Do. | 3/30 | 1420 | 5.54 | 1,750 | 14.2 | 1,126 | T 2 B E | -- | NER-12/28 | Slabby pahoehoe overflow 30 m from channel; flow stangnant. |
| Vent 4 | 3/30 | 1647 | 5.64 | 2,810 | .0 | 1,136 | T 1 C G | 1.02 | NER-12/26 | Short tubed flow from west hornito; stable 5 min. |
| Flow 1A | 3/31 | 0712 | 6.21 | 1,150 | 24.5 | 1,086 | T 2 B F | -- | -- | Flow terminus; >30 cm penetration; poor reading. |
| Do. | 3/31 | 1056 | 6.40 | 1,610 | 16.5 | 1,125 | T 2 B F | -- | -- | Overflow 3 m from active main channel; aborted before stable. |
| Do. | 3/31 | 1250 | 6.48 | 1,950 | 10.2 | 1,133 | T 1 B G | 1.22 | NER-12/29 | Tube, branch of main channel. |
| Vent 4 | 3/31 | 1556 | 6.60 | 2,810 | .0 | 1,132 | T 1 B E | -- | -- | Short tubed flow from west hornito; stable 5 min. |
| Do. | 3/31 | 1630 | 6.64 | 2,810 | .0 | 1,133 | T 1 B E | 1.01 | NER-12/30 | Do. |
| Do. | 4/01 | 1154 | 7.44 | 2,810 | .0 | 1,129 | T 1 B E | -- | NER-12/31 | Tube emitted directly from vent pond; stable. |
| Vent 1, main vent | 4/02 | 1000 | 8.36 | 2,890 | .03 | 1,135 | T 1 B E | 1.20 | NER-12/32 | Tube emitted directly from vent; stable 4 min. |
| Do. | 4/02 | 1047 | 8.39 | 2,890 | .00 | -- | | .79 | NEW-12/32 | Spatter. |
| Vent channel | 4/02 | 1155 | 8.44 | 2,860 | .15 | 1,137 | H G | -- | -- | Underside of standing wave; 15 m distance; tripod rest, stable. |
| Vent 1, main vent | 4/02 | 1645 | 8.64 | 2,890 | .07 | 1,136 | T 1 B G | 1.10 | NER-12/34 | Tube emitted directly from vent; stable 2 min. |
| Do. | 4/02 | 1715 | 8.66 | 2,890 | .00 | -- | | .70 | NER-12/35 | Spatter. |
| Do. | 4/03 | 1012 | 9.37 | 2,890 | .12 | 1,133 | T 1 B E | -- | NER-12/36 | Tube emitted directly from vent; stable. |
| Do. | 4/03 | 1230 | 9.54 | 2,890 | .12 | 1,140 | T 1 B G | -- | NER-12/37 | Do. |
| Do. | 4/03 | 1417 | 9.54 | 2,890 | .12 | 1,138 | T 1 B G | -- | NER-12/38 | Do. |
| Do. | 4/04 | 0830 | 10.10 | 2,890 | .03 | 1,141 | T 1 B G | 2.40 | NER-12/40 | Tube emitted directly from vent; stable 5 min. |
| Do. | 4/04 | 0915 | 10.33 | 2,890 | .0 | -- | | .51 | NER-12/41 | Tube emitted directly from vent. |
| Do. | 4/04 | 1545 | 10.60 | 2,890 | .12 | 1,139 | T 1 B G | 1.41 | NER-12/39 | Tube emitted directly from vent; stable. |
| Do. | 4/04 | 1550 | 10.60 | 2,890 | .05 | 1,140 | T 1 B G | 1.54 | NER-12/42 | Tube emitted directly from vent; stable 5 min. |
| Do. | 4/05 | 1230 | 11.46 | 2,890 | .3 | 1,139 | T 1 B G | -- | NER-12/43 | Tube emitted directly from vent. |
| Vent 4 | 4/06 | 0945 | 12.35 | 2,810 | .02 | 1,131 | T 1 B E | .82 | NER-12/45 | Tube emitted directly from western hornito; stable 2 min. |
| Do. | 4/06 | 1000 | 12.36 | 2,810 | .0 | -- | | 1.00 | NER-12/46 | Spatter from western hornito. |
| 1852 vent station | 4/06 | 1220 | 12.45 | 2,500 | 4.0 | 1,128 | T 1 B I | 1.15 | NER-12/47 | Directly in main channel; never stable. |
| Flow 1A | 4/06 | 1430 | 12.55 | 1,940 | 11.0 | 1,133 | T 2 B G | 1.72 | NER-12/48 | Aa overflow from main channel; 2 m thick; stable 5 min. |
| Vent 4 | 4/06 | 1630 | 12.63 | 2,810 | .02 | 1,140 | T 1 B G | .80 | NER-12/49 | Tube emitted directly from western hornito; stable 2 min. |
| Flow 1 | 4/07 | -- | 13.5 | 2,240 | 6.8 | -- | | 2.57 | 4/18NB3 | Cooled aa levee material. |
| Vent 1, main vent | 4/07 | 1405 | 13.53 | 2,890 | .3 | 1,142 | T 1 B G | 1.83 | NER-12/44 | Tube emitted directly from vent; stable. |
| Do. | 4/07 | 1053 | 13.39 | 2,890 | .1 | 1,140 | T 1 B G | .89 | NER-12/50 | Do. |
| Vent 4 | 4/07 | 1650 | 13.64 | 2,810 | .10 | 1,124 | T 1 B E | 1.15 | NER-12/51 | Do. |
| Do. | 4/07 | 1730 | 13.67 | 2,810 | .1 | 1,121 | T 1 B F | -- | NER-12/52 | Tube emitted directly from vent pond; stable. |
| 1852 vent station | 4/08 | 1026 | 14.38 | 2,500 | 4.0 | 1,100 | T 1 B F | .99 | NER-12/53 | Directly in main channel; never stable. |
| Vent channel | 4/08 | 1145 | 14.43 | 2,880 | .15 | -- | | .53 | NER-12/54 | Pahoehoe overflow from main channel. |
| Flow 1 | 4/08 | 1306 | 14.49 | 2,230 | 6.0 | -- | | 1.25 | NER-12/57 | Overflow from main channel. |
| Do. | 4/08 | -- | 14.5 | 1,980 | 10.2 | -- | | 2.31 | 4/18NB4 | Cooled lava ponded in beheaded channel. |
| North flow | 4/08 | 1445 | 14.56 | 2,930 | 2.5 | 1,123 | T 1 B F | -- | NER-12/58 | Overflow from channel, never stable. |
| North flow vent | 4/08 | 1515 | 14.58 | 2,910 | .15 | 1,122 | T 1 B F | .69 | NER-12/55 | Pahoehoe overflow from main channel; never stable. |
| North flow | 4/08 | 1530 | 14.59 | 2,930 | .1 | -- | | .38 | NER-12/56 | Scoop sample from channel. |
| North flow vent | 4/08 | 1620 | 14.62 | 2,910 | .20 | 1,126 | T 1 B E | -- | | Paheohoe overflow from main channel; stable 2 min. |
| Flow 1 | 4/09 | -- | 15.5 | 2,550 | 3.3 | — | | 1.43 | 4/18NB2 | Cooled lava ponded in beheaded channel. |
| North flow channel | 4/11 | 0850 | 17.31 | 2,930 | .0 | -- | | .51 | NER-12/60 | Spatter, stable. |
| Do. | 4/11 | 1500 | 17.57 | 2,930 | .0 | -- | | .33 | NER-12/62 | Spatter. |
| Do. | 4/11 | 0850 | 17.31 | 2,930 | .0 | -- | | .51 | NER-12/60 | Spatter, stable. |
| Do. | 4/11 | 1500 | 17.57 | 2,930 | .0 | -- | | .33 | NER-12/62 | Spatter. |
| Do. | 4/11 | 1610 | 17.61 | 2,930 | .04 | 1,087 | T 1 B I | .54 | NER-12/63 | Scoop sample from channel; never stable. |
| Vent 9,146 station | 4/11 | 1700 | 17.65 | 2,700 | 2.6 | 1,125 | T 1 B E | -- | | Pahoehoe overflow from main channel; stable 2 min. |

TABLE 57.1.—*Lava temperature and density, 1984 Mauna Loa eruption—Continued.*

| Location | Date (mo/d) | Time (H.s.t.) | Days | Elevation (m) | Distance (km) | Temperature (°C) | Code[1] | Density (g/cm³) | Sample | Comments |
|---|---|---|---|---|---|---|---|---|---|---|
| Do. | 4/11 | 1710 | 17.66 | 2,700 | 2.6 | 1,106 | T 2 B F | -- | | Aa overflow from main channel, stable 2 min. |
| Vent 1, main vent | 4/13 | 0935 | 19.34 | 2,890 | .20 | 1,102 | T 1 B F | .73 | NER-12/64 | Directly in main channel; never stable. |
| Do. | 4/13 | 1008 | 19.36 | 2,890 | .10 | 1,132 | T 1 B E | 2.12 | NER-12/61 | Tube emitted directly from vent; never stable. |
| Vent 1, west vents | 4/13 | 1142 | 19.42 | 2,930 | .03 | 1,125 | H P | -- | | Fountain; hand held; 20 m distance over channel; poor reading. |
| North flow | 4/13 | 1215 | 19.45 | 2,900 | .16 | 1,137 | T 1 B G | .83 | NER-12/65 | Tube from ponded channel; stable 2 min. |
| Vent 4 | 4/13 | 1550 | 19.60 | 2,810 | .01 | 1,121 | T 1 B I | .57 | NER-12/xx | Tube emitted directly from vent. |
| North flow channel | 4/14 | 0945 | 20.35 | 2,930 | .15 | 1,122 | T 1 B I | .89 | NER-12/66 | Overflow from channel; never stable. |

[1]Meaning of code symbols:
1, Thermocouple measurement, small-gauge (1.5-mm-diameter) wire.
2, Thermocouple measurement, large-gauge (6-mm-diameter) wire.
B, Thermocouple wires exposed to lava.
G, Grounded thermocouple; wires sheathed with INCONEL stainless steel.
E, Thermocouple measurement; stable temperature in equilibrium with lava but in geologically unfavorable site (thin flow, stored lava, and so on).
F, Failed thermocouple measurement; probe broken before equilibrium temperature achieved.
G, Good measurement; stable temperature in a geologically good site (thermocouple), or with good atmospheric conditions (HOTSHOT).
H, Measurement by two-color HOTSHOT infrared pyrometer.
I, Thermocouple became sheathed with a lava icicle before equilibrium temperature was achieved.
P, HOTSHOT measurement under poor atmospheric conditions.
T, Thermocouple measurement.

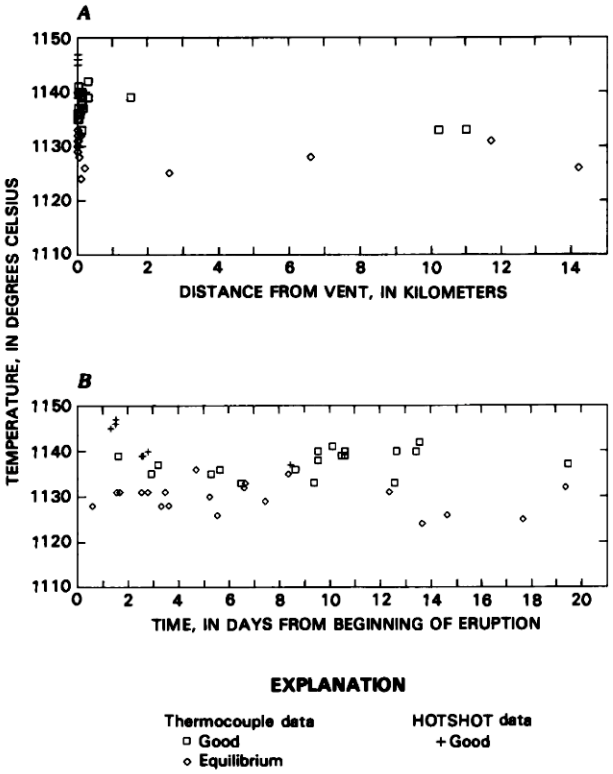


FIGURE 57.19.—Measured lava temperature in 1984 Mauna Loa eruption. Includes all good or equilibrium data, thermocouple and HOTSHOT techniques. Good values are from superior sites, as ranked on geologic criteria; equilibrium thermocouple data are stable results from less favorable sites. Temperature data are from table 57.1; measurement techniques and limitations are described in appendix 1. ***A***, Temperature plotted against distance from eruptive vent; values by the same technique are at most about 5 °C higher at the vent than downchannel. ***B***, Temperature plotted against time: no sigificant variation is evident.

range of 1,135 ± 5 °C. Most of the infrared-pyrometer temperatures for fountains were a few degrees hotter than the best near-vent lava temperatures.

Temperatures from small-volume shield-building lava of the lowest vent (4), at 2,785-m elevation, at times approached 1,140 °C but typically were 5–10 °C cooler. These temperatures are thought to be lower because some vent 4 lava was fed through a lava tube from vent 3, a few hundred meters uprift. The presence of tube-fed lava in this shield was initially inferred from the low to non-existent fountains at vent 4, lower temperature and higher density of spatter and lava from vent 4 compared to those of vent 1 (the main upper vent), and development of a lava tube from vent 3 along the north edge of vent 4 during the first few days of activity. Presence of a lava tube during later vent 4 activity was confirmed by its collapse at the end of the eruption on April 14.

Temperatures obtained at vent 1 are believed to approximate the eruption temperature, as indicated by the consistent results by both measurement methods and the lack of variation during the 20 days of the eruption (fig. 57.19*B*). The vent temperatures for the 1984 Mauna Loa eruption are similar to temperatures measured by the same techniques during recent Kilauea eruptions in which aa flows were dominant (1,135–1,145 °C; Ulrich and others, 1984). These eruption temperatures are 20–30 °C below the expected one-atmosphere liquidus temperature of the lava, as indicated by experimental determinations for other Hawaiian tholeiite (Yoder and Tilley, 1962).

Temperatures of the Mauna Loa flows are about the same as those from most thermocouple measurements for Kilauea eruptions over the past 30 years. Higher temperatures reported for Kilauea lavas and fountains are optical pyrometer measurements that were corrected upward for atmospheric absorption (Alt and others, 1961; Wright and others, 1968), except for the temperatures of 1,500–1,165 °C measured by Swanson (1973) through skylights in lava tubes of pahoehoe from Mauna Ulu. More data are needed to evaluate whether higher eruption temperatures are associated with

long-traveled tube-fed pahoehoe flows, such as have characterized many prehistoric Mauna Loa eruptions.

## LAVA DENSITIES

Vesicularity of the 1984 lava was noted in the field to decrease downchannel, as discussed in connection with the variations in lava types. Near the vent outlet, channel lava was fluffy near-reticulite that had the consistency of whipped egg white; downflow, it became dense blocky lava, containing only the scattered irregular vesicles typical of consolidated aa (Macdonald, 1972, p. 70). Density measurements on samples collected at temperature sites confirm a downflow increase in density (fig. 57.20), particularly for samples collected during a single day, and also indicate a gradual decrease in density of vent material during the eruption (fig. 57.21).

The increase in density of lava with distance from the vent (fig. 57.20*A*) is striking, when differing lava types are distinguished. At the vent, the densest values are largely for degassed pahoehoe oozed out from small tubes near the base of the spatter ramparts or from the quietly effusive vent 4 (fig. 57.20*A*, triangles). In contrast, quenched spatter and frothy lava dipped from the channel have densities as low as 0.35 g/cm$^3$, indicating about 85 percent porosity. Downchannel, samples from the incandescent cores of aa flow fronts are denser than those from rapidly quenched channel overflows (typically scoriaceous aa) or samples taken directly from the channel. These changes in density must relate to degassing and kneading out of vesicles in the lava as it flowed downchannel. Significant gas emission from the channel lava was evident in the field; $SO_2$ levels were so high that manned observations were rarely feasible downwind of the channel. The downchannel density changes probably contributed significantly to the decreased downchannel lava volumes measured in the 1984 channel system, as discussed later.

In addition to density changes with distance from the vent, the density of spatter sampled at the vent decreased fairly systematically during the eruption, from 1.0–1.2 g/cm$^3$ early in the activity at the 2,900-m vents to about 0.5 g/cm$^3$ late in the eruption (fig. 57.21*A*). We interpret this trend as reflecting an increasing ratio of gas to magma in the fountains as discharge rate declined during the eruption. Temporal changes in density of channel or overflow samples were more subdued, presumably because such effects were masked by large concurrent effects of downchannel degassing (fig. 57.21*B*).

The long-term decrease in spatter density is in accord with the observed inverse correlation between fountain height and channel level at the vent, which involved fluctuations over intervals of a few tens of minutes to a few hours (fig. 57.22). At the times of higher fountains, which yielded the least dense and most gas-rich spatter—at times approaching reticulite—the channel level dropped, indicating a decrease in bulk eruption rate of lava. Alternatively, more gas may have been exsolved and kneaded out during the high-fountain phases, producing denser channel lava and lower channel levels without a decrease in discharge. Similar general effects have been noted at several eruptions of Kilauea, in which high wispy fountaining (maximum gas release) occurs as lava production declines just before the end of the eruption (Swanson and others, 1979; Moore and others, 1980).

## RELATION OF LAVA TEMPERATURE, VESICULARITY, AND VISCOSITY

The temperature measurements and other observations on Mauna Loa lava bear significantly on interpretations that the pahoehoe-aa transition reflects increased viscosity related to gradual downflow cooling in open channels (Swanson, 1973; Peterson and Tilling, 1980). At Mauna Loa, lava temperatures varied little for 10 km downstream from the vent (fig. 57.19*A*). Downflow temperatures have been similarly stable in aa at Kilauea Volcano (fig. 57.23). Bulk aa temperatures were presumably lower downflow than near the vent, because the ratio of fluid melt to pasty clots and solid debris decreased down the active channel. Some process, however, maintained the temperature of the fluid portion of the aa, and the bulk aa viscosity increased independently of the limited temperature variations in the fluid part of the channel fill.

High temperatures in the aa were partly sustained by heat of crystallization, as indicated by a downflow increase in microlite population (see next section). Frictional deformation of the melt (Shaw, 1969, p. 532) may also have been significant. Lava in the channel had the consistency of reticulite near the vent, and even 20 km from the vent it contained 30 volume percent vesicles. The melt fraction was present in the form of vesicle walls that deformed as the lava degassed and flowed turbulently downchannel. Flexing of bubble walls (during flowage, turbulent mixing, and buoyant rise of gas), supplemented by friction along margins and shear planes within the channel, is thought to have contributed significant heat to maintain high temperatures in the channel lava.

Given that temperatures in the fluid-melt component were stable and that the slope gradient and flow velocity decreased downflow, what produced the observed increase in viscosity and initiated the downflow transition to aa? On April 2, the apparent viscosity in the channel near the vent was about $10^2$ Pa·s; at 1,950 m, pahoehoe channel fill had an apparent viscosity of $10^3$ Pa·s; and at 1,600 m, the apparent viscosity of aa channel fill was about $10^5$ Pa·s, as determined by relations between flow velocity, channel gradient, and channel depth (Moore, chapter 58). The observed increase in both microlite content and solid debris downflow must have increased the viscosity of the silicate fraction (Shaw, 1969, fig. 2). In addition, the viscosity increases appear closely related to density increases in the channel lava (fig. 57.20). The density increases require an attendant decrease in gas and vesicle content of the channel lava and increased thickness of vesicle walls. Decreased vesicularity has been shown experimentally to increase the viscosity of lava (Murase, 1962; Shaw and others, 1968). Thus, even at constant melt viscosity, the *bulk* viscosity of the channel lava would increase without changes in temperature or microlite population. Thicker vesicle walls would also increase resistance to flexing of the melt, reduce associated deformational heating, and eventually allow a negative heat budget.

High gas content and thin vesicle walls may, in part, also account for the low viscosity and high fluidity of pahoehoe.

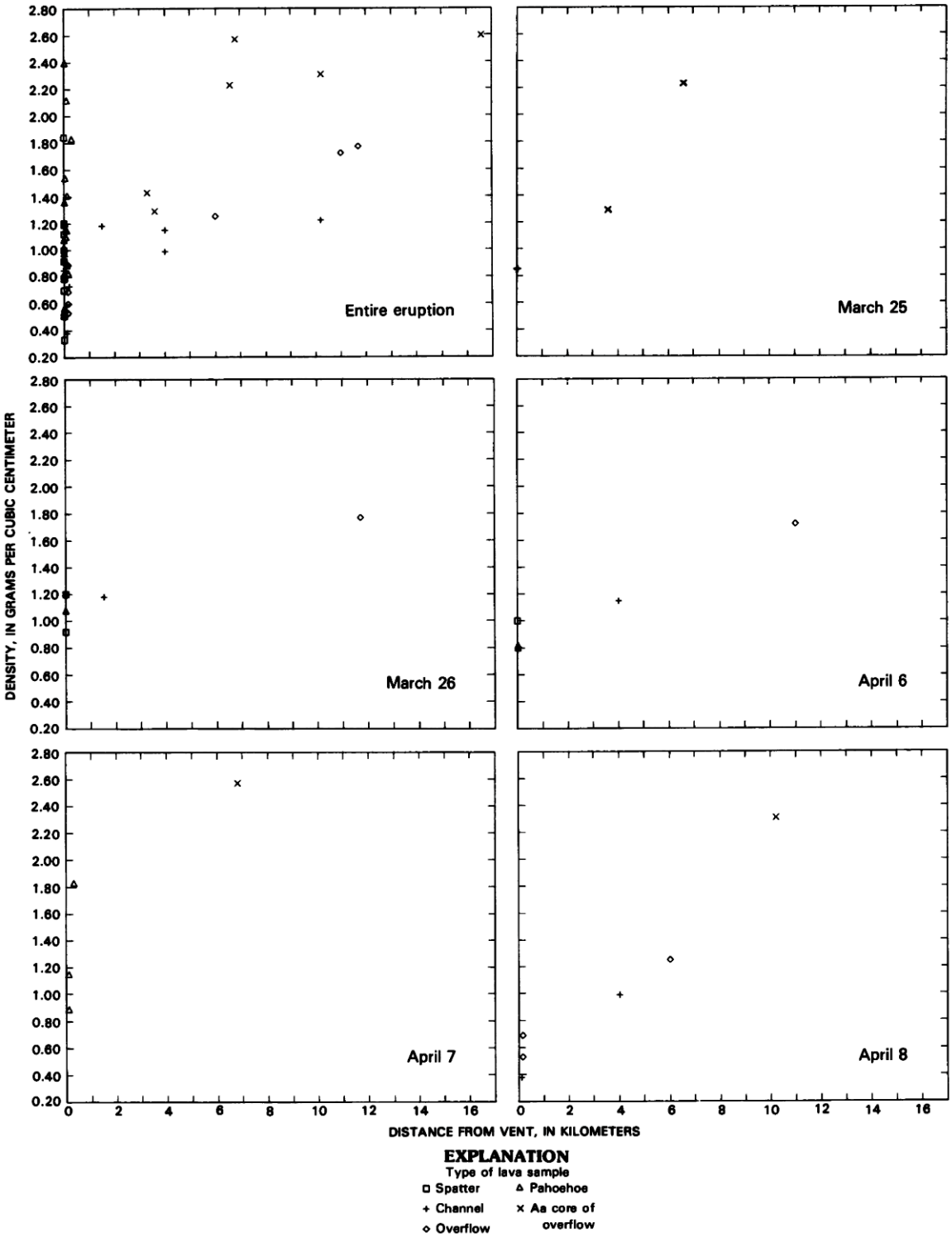


FIGURE 57.20.—Measured lava density plotted against distance from the vent, 1984 Mauna Loa eruption. Data, shown for individual dates as well as for entire eruption, are from table 57.1. All samples were collected hot and quenched in water. Density was determined by weighing a measured cube, sawn from the interior of sample, that had been dried at 20 °C.

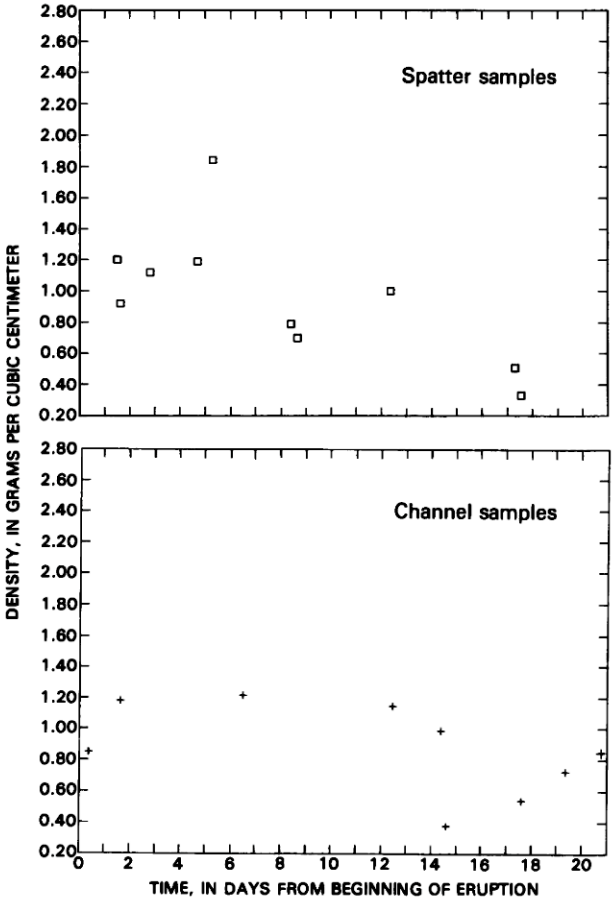


FIGURE 57.21.—Measured lava density of spatter samples and channel samples plotted against time. Data are from table 57.1.

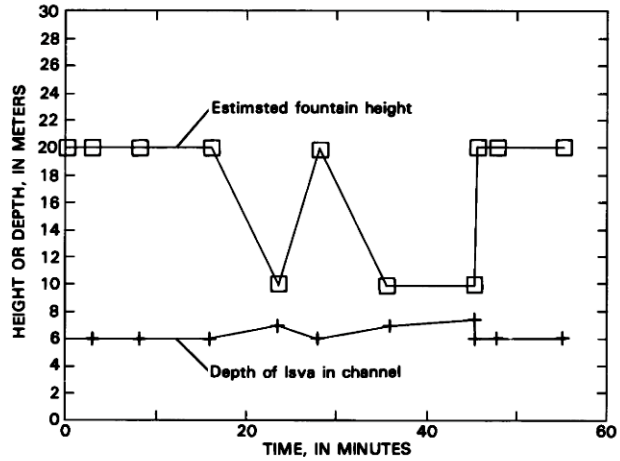


FIGURE 57.22.—Variation of lava level in channel versus height of the fountains at the main vent. Data obtained around 1200 on April 2, 1984. Fountain heights were visually estimated by reference to surveyed height of spatter rampart.

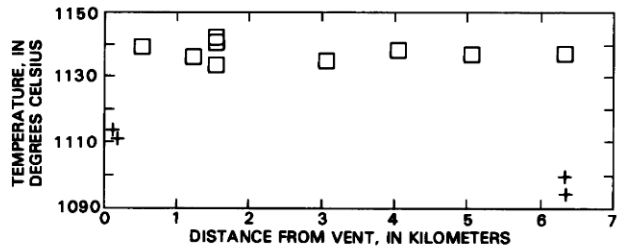


FIGURE 57.23.—Temperature plotted against distance of travel for Kilauea aa flows from the 1983–84 east-rift-zone eruptions. Plus, sample from phase 9, southeast flow; square, sample from phase 16, southeast flow.

Pahoehoe is more vesicular than aa, and retarded degassing in lava tubes may delay the transition to aa, along with the insulating role of the tube (Swanson, 1973). During the Mauna Loa eruption, pahoehoe in tubes flowed at velocities only about 20 percent slower than in open channels. The tubes formed along channels where flow was laminar and flow rates were fairly low and steady or decreasing. In high-volume channels, incipient roofs of tubes were continually broken up and rafted away. Slower flow in the tubes was promoted by lower eruptive volume and by drag against the roof. The slow flow rate appears to have favored less turbulent flow; it thus retarded stretching and breaking of vesicles, maintaining a lower bulk viscosity. The higher vesicle population also may have (1) allowed more rapid flexing of the vesicle walls, (2) generated deformational heating farther from the vent, and (3) combined with the insulating properties of the tube (Swanson, 1973), retarded formation of pasty clots and delayed viscosity increases.

Observations during temperature measurements (see app. 57.1) demonstrate an interrelation between vesicularity and viscosity. A lava sheath invariably formed on even the small-gauge thermocouple if the pahoehoe was moving more than about 0.5 km/h and lava was allowed to flow past the thermocouple tip. The observer could stop growth of the lava sheath by walking the tip downflow with the lava at velocities up to about 3 km/h. At higher flow velocities, the temperature measurements invariably terminated with a thermocouple sheathed in lava. The sheaths were denser than the channel fill and had the consistency of thick taffy, similar to lava from cores of aa flows much farther from the vent, where inserting a probe required more effort.

Two observations suggest that the lava sheath resulted from breakage of vesicle walls and adherence of the viscous melt, rather than from freezing of the melt against the probe. First, the size and growth rate of the lava sheath correlated with velocity of the flowing

lava: the faster the flowage past the thermocouple, the larger were the lava sheaths. Second, thermocouples were carefully preheated prior to insertion, particularly when measuring flowing lava, yet probes in flowing lava accumulated a sheath while those in motionless lava did not. We infer that the thermocouple stretches and breaks the gas bubbles in moving lava, increasing the bulk viscosity of the adjacent melt and making additional melt available to adhere to the probe. The growing surface area exerts additional drag on adjacent melt, hastens bubble breakage, and causes faster accumulation of melt on the sheath.

## LAVA CRYSTALLINITY

Increases in crystallinity affected flow rheology of the 1984 lava both over time at the vents and during flow down the lava channel. Three discrete textural populations of crystals are present: (1) sparse resorbed phenocrysts or xenocrysts of magnesian olivine as much as 5 mm in diameter; (2) dusty microlites less than 0.01 mm in size; and (3) microphenocrysts of augite, plagioclase, and olivine commonly 0.05–1.0 mm in length.

The sparse olivine phenocrysts everywhere are less than 0.5 percent of the lava, did not vary in abundance significantly during the eruption, and are interpreted as disequilibrium crystals that were present in the summit magma reservoir before eruption. Microlites are absent in vent spatter and become increasingly abundant in quenched downchannel samples; they record late groundmass crystallization of the lava as it flowed down the channel. Such surface crystallization of channel lava is probably largely responsible for the observed progression of flowage zones (fig. 57.5), but it seems to have occurred uniformly throughout the eruption. In contrast, the content of microphenocrysts in quenched spatter increased strikingly during the eruption, from less than 0.5 percent of the lava during initial summit activity to as much as 30 percent during the waning eruptive phases (figs. 57.24, 57.25*A*). Microphenocryst size increased concurrently with abundance (fig. 57.25*B*), although the precision of measurement is lower. Microphenocryst size and abundance increased rapidly during the first few days of the eruption, slowed during the subsequent two weeks, and increased slightly again late in the eruption (fig. 57.25). Large changes occurred within a few hours after beginning of the eruption on March 25, as the vents migrated from the summit region downrift to the 2,900-m level, but the abundance and size of microphenocrysts continued to increase after the main vent site stabilized. These changes occurred in the lava before its eruption, as documented by quenched spatter samples, although the same microphenocryst populations are readily recognized in downchannel samples despite additional crystallization of microlites during surface flowage.

During these changes, bulk major-oxide compositions remained constant virtually within analytical uncertainty (table 57.2; Lockwood and others, 1985). This compositionally uniform 1984 lava is in marked contrast to lava erupted during Kilauea rift activity (Wright and Fiske, 1971; Garcia and others, 1984) but is typical for Mauna Loa rift eruptions (Rhodes, 1983).

Most microphenocrysts in the 1984 Mauna Loa lava occur as skeletal, intergrown, and radiating blades and plates (fig. 57.24), including elongate, cored, and swallow-tailed shapes that are typical of rapid crystallization from undercooled liquids (Walker and others, 1976; Lofgren, 1981). Such undercooled textures are especially prevalent in the phenocryst-poor lava of early eruptive phases; late eruptive phases have textures indicative of more prolonged equilibrium crystallization. We attribute the growth of microphenocrysts characterized by undercooled textures largely to separation of a gas phase during the eruption, not to a decrease in magma temperatures.

Observed eruptive temperatures remained constant at $1,140 \pm 3$ °C (fig. 57.19*B*), which is 20–30 °C below calculated liquidus temperatures for most phases at one atmosphere (olivine 1,186 °C, plagioclase 1,169 °C, and clinopyroxene 1,146 °C, all $\pm 15$ °C; method of Nielson and Dungan, 1983). The observed lava temperatures would approximately coincide with the liquidus if the pre-eruptive magma contained about one percent volatile content (Yoder and Tilley, 1962). A pre-eruptive volatile content of about 0.5 percent has been calculated from gas data for tholeiitic basalt from Kilauea Volcano (Greenland and others, 1985), and about one percent volatiles is the estimated average for tholeiitic basalt in general (Haggarty, 1981).

The virtual absence of microphenocrysts in much of the lava erupted early on March 25, followed by increases in the number and size of microphenocrysts (figs. 57.24, 57.25), suggests that the magma reservoir below the summit was initially sufficiently pressurized by volatiles to lower the liquidus temperature to about 1,140 °C, thereby inhibiting crystallization. With depressurization of the magmatic system beginning at onset of the eruption, separation of gas undercooled the magma without actually lowering the observed lava temperatures, thereby inititiating precipitation of microphenocrysts. Degassing at the summit began at onset of the eruption and was later focused at the 3,550-m level, uprift of the active lava vents (Casadevall and others, 1984).

Even slight undercooling can have profound effects on the nucleation and growth rates of crystals. At 20–30 °C of undercooling, crystals in basaltic melts can grow to sizes of 1 mm within periods as brief as a few hours (Kirkpatrick, 1976, 1977). The only alternative to growth of microphenocrysts during the eruption—a zoned pre-eruption magma chamber—seems less able to account for the compositional uniformity of the erupted lava or its undercooled quench textures.

The volatile loss needed to initiate crystallization may have been small. Before eruption, basaltic magmas in the shallow reservoirs beneath the summits of Mauna Loa and Kilauea are believed to contain <0.2 percent $CO_2$, 0.2–0.3 percent $H_2O$, and 0.1 percent S (Moore, 1965; Greenland and others, 1985; Greenland and others, in press). Because of their relative solubilities, S and $CO_2$, but not $H_2O$, would have separated from the magma during transit from the summit reservoir down the rift zone to just below the vent. If the rift magma was under lithostatic confining pressures, $H_2O$ may have saturated and begun to separate only at depths as shallow as 100–200 m below the surface. Although confining pressures within the upper kilometer of the fractured rift zones of Hawaiian volcanoes are unlikely to be purely lithostatic, and may at times approach atmospheric, these relations nevertheless cast doubt on the ability of $H_2O$ loss alone to account for the undercooling and crystallization of the 1984 magma. High flow rates of the rift magma, efficient degassing, and rapid crystallization would be

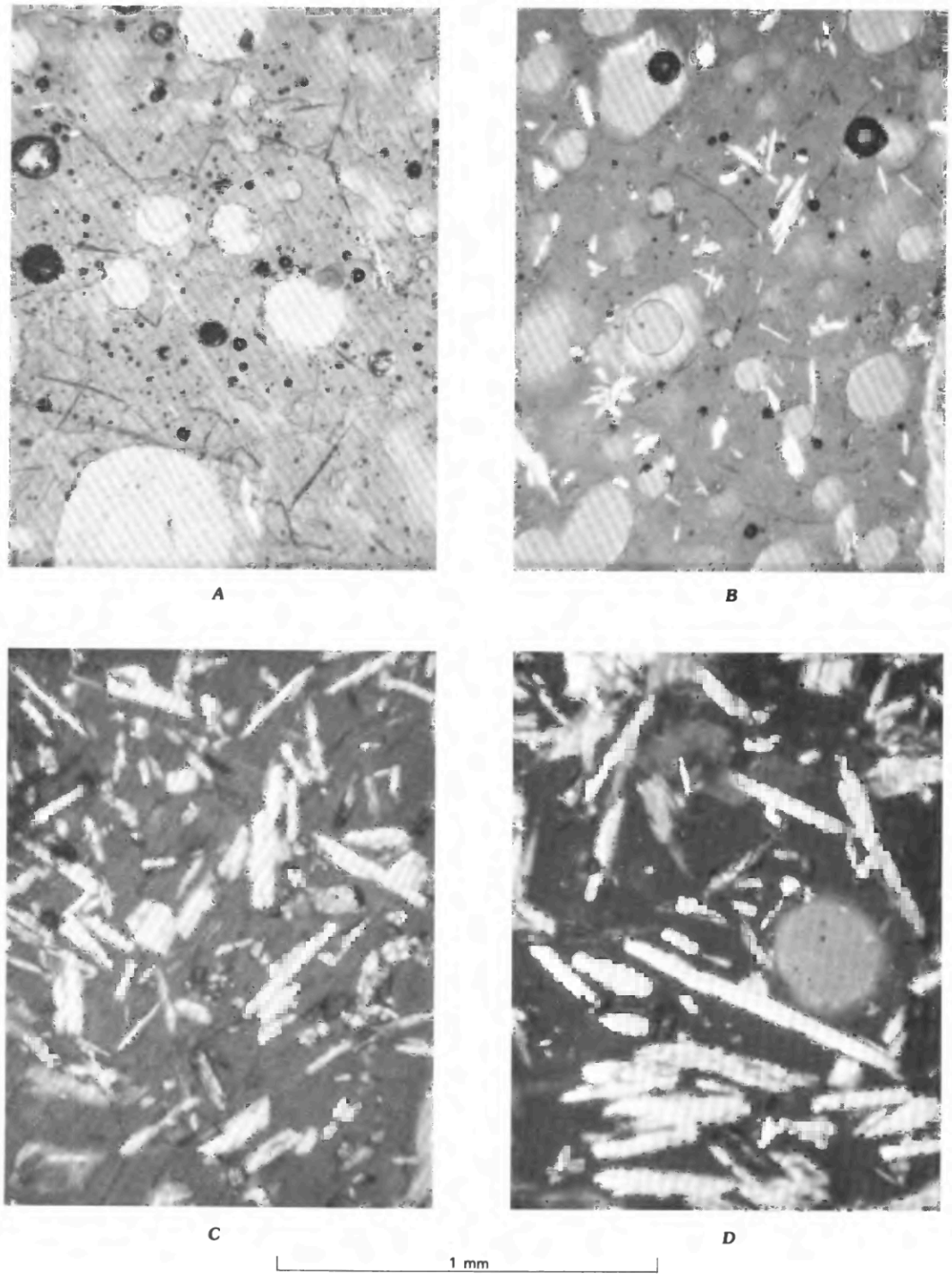


FIGURE 57.24.—Photomicrographs (plane light) of representative samples of 1984 Mauna Loa lava, showing progressive increase in size and abundance of microphenocrysts with time. Microphenocrysts are clear rectangles; circular features are gas bubbles (vesicles). ***A***, Sampled at about 0145 (H.s.t.) on March 25. Spatter from northeast side of 1949 cone, at 4,040 m. Sample MOK–1; 0.4 percent phenocrysts, 0.05 mm in average length. ***B***, Sampled at about 0515 on March 25. Spatter from upper northeast rift zone, at 3,650 m. Sample NER 5; 3.5 percent phenocrysts, 0.1 mm in average length. ***C***, Sampled at about 1750 on March 29. Pahoehoe from perched pond at 2,820 m. Sample NER 12/23; 21 percent phenocrysts, 0.3 mm in average length. ***D***, Sampled at about 0945 on April 14. Channel overflow near 2,870-m vent. Sample NER 12/66; 29.5 percent phenocrysts; 0.6 mm in average length.

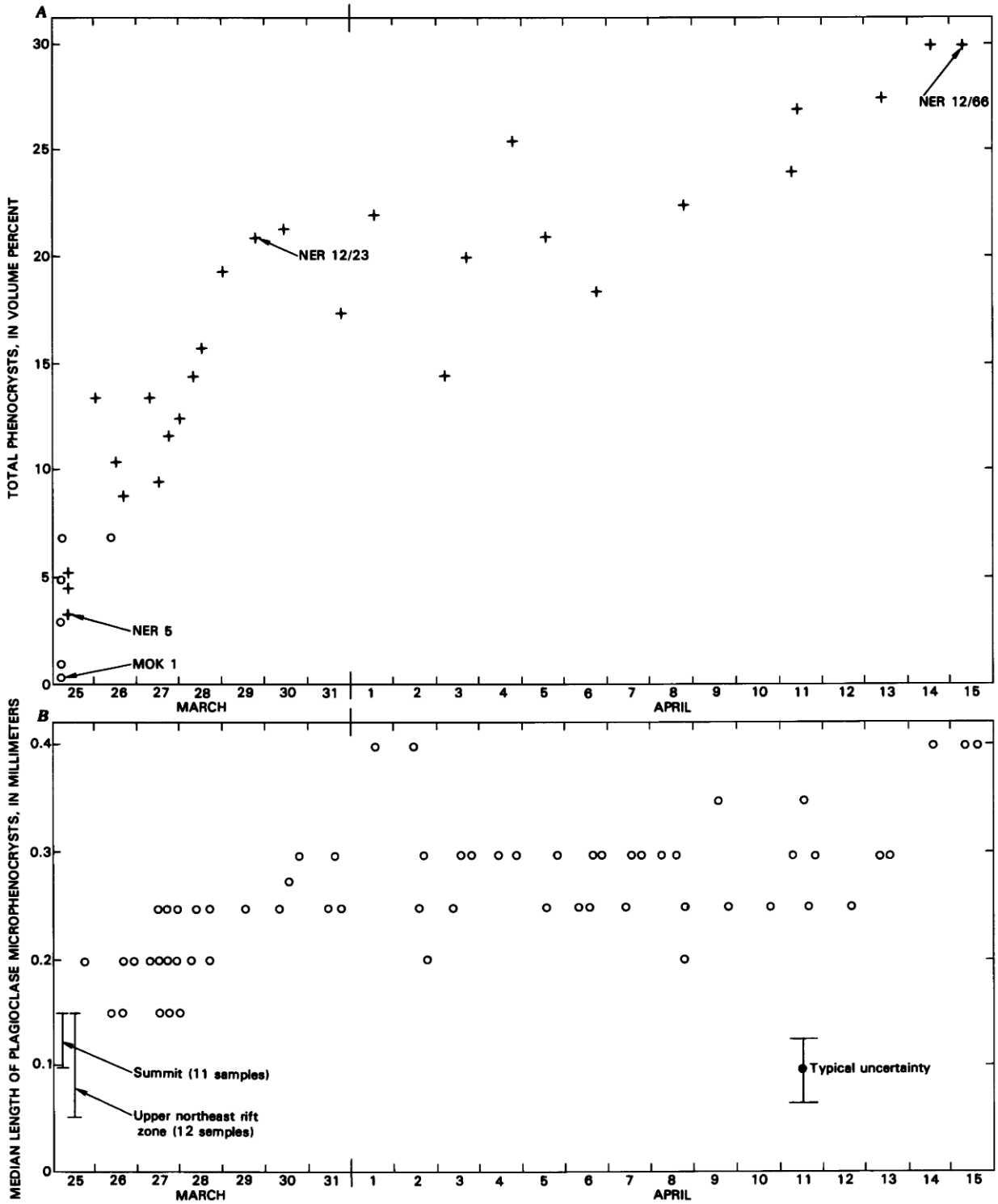


FIGURE 57.25.—Changes in abundance and size of microphenocrysts during 1984 eruption. Samples illustrated in figure 57.24 are identified. ***A***, Changes in abundance of microphenocrysts. Plus, data from petrographic point-counting of thin sections; dots, visual estimates of March 25–26 samples containing only sparse small microphenocrysts (less than 0.15 mm in average length). Values are believed accurate to within 10 percent; a major cause of uncertainty is in estimating areas of microphenocrysts smaller in diameter than the thickness of the thin section (0.03 mm). All samples are quenched glassy spatter or channel overflow. About one-half the originally collected samples of spatter were too vesicular to measure. ***B***, Changes in size of microphenocrysts. Median lengths of plagioclase microphenocrysts (about one-half the maximum length) were estimated visually from thin sections, by reference to a calibrated scale in the microscope ocular.

TABLE 57.2.—*Major-element composition of the 1984 Mauna Loa lava, from X-ray fluorescence analyses*

[Individual samples, selected to be representative, are described in table 57.1 and illustrated in figure 57.24. All values are in weight percent. Total iron listed as $Fe_2O_3$. Uncertainty of averages is plus or minus one standard deviation. Data provided by J.M. Rhodes; see Lipman and others, 1985]

| Date | March 25 | | March 29 | April 14 | Entire eruption |
|---|---|---|---|---|---|
| Time | 0145 | 0515 | 1750 | 0945 | Average of 61 samples |
| Sample | MOK-1 | NER-5 | NER-12/23 | NER-12/66 | |
| $SiO_2$ | 51.51 | 51.56 | 51.71 | 51.27 | 51.54±.24 |
| $TiO_2$ | 2.08 | 2.09 | 2.08 | 2.10 | 2.08±.02 |
| $Al_2O_3$ | 13.75 | 13.69 | 13.69 | 13.60 | 13.65±.07 |
| $Fe_2O_3$ | 12.08 | 12.11 | 12.17 | 12.08 | 12.07±.06 |
| MnO | .17 | .18 | .17 | .19 | .18±.01 |
| MgO | 6.73 | 6.65 | 6.76 | 6.81 | 6.73±.08 |
| CaO | 10.57 | 10.55 | 10.57 | 10.43 | 10.50±.06 |
| $Na_2O$ | 2.56 | 2.42 | 2.56 | 2.45 | 2.54±.11 |
| $K_2O$ | .385 | .383 | .391 | .381 | .385±.009 |
| $P_2O_5$ | .24 | .25 | .26 | .24 | .24±.01 |
| TOTAL | 100.13 | 99.87 | 100.38 | 99.55 | 99.92±.37 |

required, even if the pressure on upper parts of the rift conduit were atmospheric. Alternatively, the major loss of S, beginning at the summit reservoir, may have played a significant role in initiating crystallization. Unfortunately, few experimental data are currently available to permit evaluation of the role of small amounts of S on liquidus temperatures of basaltic magma.

## RELATIONS OF CHANNEL VELOCITY, VOLUME, AND TIME

After the first three days of the eruption, as the vent geometry stabilized at the 2,900-m level and lava moved rapidly toward Hilo, we began establishing monitoring stations along the lava channel to permit repeated observations. At first, a primary need was to determine rates of lava movement downchannel for purposes of hazard evaluation; later, we focused more broadly on processes of channel evolution. For the first few days, limited helicopter support and poor weather confined observations to ground-accessible localities, and only a single observation point could be visited per day. Later in the eruption, working in two parties, we occupied as many as 4–6 stations per day. A total of 69 data sets are available for channel stations (table 57.3).

At each station, channel dimensions were determined, flow velocities measured, and morphologic observations made on the character of the flow, including photography. The resulting record of channel processes provides much of the basis for this paper. Complexities attendant to working on an erupting volcano caused some variations and problems in quality of the observations, as detailed in appendix 57.2. Total error in the channel-volume measurements, due mainly to uncertainties about channel depth, may be as large as 25 percent, but changes in channel volume at any station are believed accurate to about 10 percent, because the channel geometry tended to remain similar during the eruption or to deepen by measureable amounts through increase in levee height, especially for stations within the stabilized-channel zone.

Episodic short-term variations in channel volume, over periods of a few minutes to a few hours, were conspicuous in lower parts of the channel (transition zone), where surges could cause ephemeral channel-volume variations of as much as 50 percent; all plotted data are for observations made between obvious surges. Large short-term volume changes were also noted in stations near the vent, where fluctuations in fountain height related to varying gas release were associated with frequent changes in measured volume of 5–15 percent, occasionally as much as 40 percent. As noted earlier, some of these observed near-vent volume variations mainly reflect varying gas content and lava density, rather than true fluctuations in magma production rate (fig. 57.22). Several stations at mid-distance downchannel yielded volume variations of less than 5 percent when measured repeatedly over periods of several hours while larger fluctuations were being observed at the vent. Apparently, the short-term near-vent fluctuation tended to be smoothed out by downchannel flowage.

The most obvious feature of the channel data is a progressive decrease in channel discharge with lower elevation for any time during the eruption (fig. 57.26). In early April, discharges of $3.5\times10^6$–$5\times10^6$ $m^3/h$ were measured at the vent outlet, in comparision to discharges of only about $1.5\times10^6$ $m^3/hr$ at 2,500-m elevation 5 km downchannel, and $0.5\times10^6$ $m^3/hr$ at 1,900-m elevation 15 km from the vent. This decrease in discharge is interpreted as reflecting volume decrease of the lava due largely to volatile loss, because no overflows were occurring at this time along the intervening channel. The decrease in channel discharge downslope is paralleled by as much as a several-fold downslope increase in the density of quenched samples collected along the channel (fig. 57.20). These density changes alone can account for the changes in discharge, within sampling and measurement uncertainties.

A major feature of the eruption, documented from the channel stations, was a nearly constant rate of magma production during the middle part of the eruption, from March 31, when enough channel stations first became available, through April 6 (fig. 57.26). The steady state of activity during this interval is documented by 9 occupations of channel station 8 (1852 vent, 2,500-m elevation), which yielded channel discharges of $1.55\pm0.05\times10^6$ $m^3/h$, and by 10 occupations of several sites at station 4 (Upper Powerline area, 1,920–1,935 m), which yielded discharges in the range $0.40$–$0.55\times10^6$ $m^3/h$. Both these stations were within the stable-channel zone. The upper one (1852 vent) changed little during this time interval, except for partial crusting of the channel margins by pahoehoe scum (fig. 57.8*D*). Somewhat more variable discharges from the Upper Powerline sites are probably due to greater surge activity and levee building (figs. 57.9, 57.11*A*, 57.16*B*).

Before March 31, eruption rates at the 2,900-m vents had appeared roughly constant to observers, but several lines of evidence now demonstrate that eruption rates decreased during the first few days of the eruption. The first indication of such a decline came from early measurements of lava volumes reaching the channel stations at 1,800–1,900 m. Key evidence is from two channel stations established on March 28–29, which show higher discharges than observed at these elevations later during the eruption (fig. 57.26). The discharge measured for the 1,800-m station (Lower Powerline)

on March 28 is somewhat uncertain, because it depends on an aerial estimate of channel width under adverse weather conditions. Even if it is in error by one-third—the maximum that seems plausible—the resulting discharge ($0.8 \times 10^6$ $m^3/h$) would still be twice that subsequently measured below 1,850 m.

No quantitative data are available for lava production at the vent before April 2, but repeated photography of the upper channel area document a major decline in channel flow levels between March 26 and 31 (fig. 57.27) that was not recognized by qualitative monitoring in the first few days of the eruption. Decreasing eruption rates early in the eruption are also indicated by analysis of lava areas and volumes, as discussed later.

In early April, the highest channel blockages and overflows were at about 1,850-m elevation (fig. 57.14), and the various Upper Powerline stations at 1,920–1,935 m show nearly constant volumes of flow. In contrast, the stations at 1,600–1,700 m show declines of about 50 percent in flow discharge between March 31 and April 4 (fig. 57.26), reflecting increasing loss of lava from the channel by blockages and overflows. By April 5, lava was no longer reaching any major channel below 1,850 m.

On April 6, a possible small decrease in discharge was measured at the 2,500-m station, which had yielded essentially constant results for the previous week, and by April 9 the channel was inactive to this level (fig. 57.26). This large change in channel discharge reflects the beginning of a further gradual decrease in eruptive rate at the main vent, from several million cubic meters per hour on April 6 to only a few hundred thousand cubic meters per hour by April 9 (fig. 57.28). Some of the decrease was taken up by new channels emanating from smaller uprift vents of the 2,900-m cluster, which robbed the main vent of part of its lava supply. Channels from the reopened uprift vents were north of flow 1 and initially carried as much as $0.5 \times 10^6$ $m^3/h$ (density about 0.5 $g/cm^3$), about as much as flow 1.

Lava production continued to decline after April 9 and amounted to only about $0.1 \times 10^6$ $m^3/h$ on April 13, the last full day of vent activity.

## DISCUSSION

During the three-week eruption in 1984, the Mauna Loa aa flow and its distributary channel system underwent a complex morphologic evolution related to several intertwined changes in lava properties. These include decreases in eruptive volume; increased groundmass crystallization of the magma before venting; changes in effective viscosity and yield strength of the lava; degassing in the rift magma chamber, at the vent, and downchannel, which resulted in density increases of the lava; and probable physical maturation of the distributary channel itself. The dominant effects appear to have been (1) sympathetically increasing microphenocryst content, viscosity, and loss of gases from the pre-eruption magma reservoir and rift conduits; (2) constant lava composition and temperature; and (3) decreasing volume and average density of erupted material (fig. 57.29).

The eruption rate was nearly constant from March 30 to April 7 but declined drastically after April 7 (fig. 57.26). Major decreases also occurred early in the eruption, as indicated by (1) the high lava discharges measured at the two channel stations occupied on March 28–29, in comparison with results at similar elevations later during the eruption (fig 57.26); (2) the cessation of eruptive activity at the lower vents that fed flows 2–4 on March 25–27; and (3) interpreted rates of lava erupted per hour, based on the area covered as well as on the channel-station data (table 57.4).

Total volume of the erupted flows has been estimated at $220 \times 10^6$ $m^3$, based on mapped area of coverage and measured flow thickness (J.P. Lockwood, written commun., 1984). If the steady discharge rate determined from channel measurements between March 30 and April 6, about $0.4 \times 10^6$ $m^3/h$ of relatively degassed channel lava at 1,900 m, is extrapolated back to initiation of the eruption, there is a shortfall of about 25 percent in volume ($60 \times 10^6$ $m^3$). In contrast, the eruption rate for the early summit activity on March 25, as determined by area covered, was about $2.8 \times 10^6$ $m^3/h$, and rates for the first two days of activity from the 2,900-m vents were about $10^6$ $m^3/h$ (table 57.3). If the eruption rate further decreased from $10^6$ $m^3/h$ to $0.4 \times 10^6$–$0.5 \times 10^6$ $m^3/h$ during March 28–30, as indicated by the channel measurements (fig. 57.26), then the cumulative volume subsequently determined from the channel measurements ($224 \times 10^6$ $m^3$, fig. 57.30) agrees reasonably well with the volume of $217 \times 10^6$ $m^3$ based on mapped area and flow thickness.

Decreases in eruption rate over time, which characterize many basaltic eruptions, have been inferred to relate to such factors as the release of elastic-strain energy from magma stored in the subvolcanic reservoir, availability of magma from depth during the eruption, and conduit evolution from dike to plug geometry (Wadge, 1981). An additional factor that appears to have been important in the 1984 Mauna Loa eruption, and perhaps for some others, is a change in magma rheology related to increasing crystal content of the erupted lava.

The increase in microphenocryst size and abundance (fig. 57.25) was roughly opposite to the decline in eruption rate (fig. 57.30). The resulting increase in magma viscosity (Shaw, 1969) was probably a major cause of termination of the eruption, as well as the pattern of uprift channel stagnation. At about 1,140 °C, the apparent viscosity of theoleiitic basalt containing an equilibrium crystal assemblage (about 25 volume percent) has been shown by field and laboratory measurements on Hawaiian basalt (Shaw, 1969, fig. 2; Shaw and others, 1968) to be approximately one order of magnitude greater than an undercooled Newtonian liquid lacking crystals. The changes in rheology, interpreted to have occurred largely in the pre-eruption magma chamber and rift conduits of Mauna Loa, are broadly similar to effects on the rheology of basaltic lava inferred to result from degassing during eruption and downslope flowage (Sparks and Pinkerton, 1978).

Such major decreases in eruptive rate in late March, if correctly interpreted, could explain the stagnation of flow 1 on March 30, but they do not account for the cessation of rapid advance and beginning of stagnation of flow 1*A* during the interval March 30–April 6. During this interval, both the eruption rate at the vent and transport in the channel system above about 1,850-m elevation remained constant, as indicated by the channel station data

TABLE 57.3.—*Dimensions and characteristics of lava channels and their changes with time, 1984 Mauna Loa eruption*

[Locations of channel stations on figure 57.1*B*. Distance, spacing of measuring points along channel bank. Depths estimated; see text for details. PWL, Peter W. Lipman; NGB, Norman G. Banks]

| Measurement | Date (mo/d) | Hour (H.s.t.) | Condition | Distance (m) | Time (s) | Velocity (m/s) | Width (m) | Depth (m) | Flow rate ($10^6$ $m^3/h$) | Comments |
|---|---|---|---|---|---|---|---|---|---|---|
| **Station 1: Lower channel 1A, elevation 1,600 m** | | | | | | | | | | |
| 1 | 3/31 | 1130 | stable | 18 | 19 | 0.95 | 24 | 5 | 0.410 | Conspicuous marginal shears, with velocities about 1 m/min, next to central well-defined channel. Channel velocities slow during surges which contain more viscous material. Maximum velocities occur just after surges. Gradient about 3°. Measured by PWL, NGB, and J. Fink. |
| 2 | 3/31 | 1200 | surge | 18 | 22 | .82 | 24 | 5 | .355 | |
| 3 | 4/01 | 1200 | -- | 18 | 28 | .64 | 35 | 5 | .405 | Channel less defined than on 3/31, more choked with viscous debris. Although relatively steep gradient (about 5°) has migrated about 50 m downstream, adjacent to measurement site, velocities have still slowed. Because channel zone seems wider, flow rates have changed less than velocities. Measured by PWL and E. Wolfe. |
| 4 | 4/01 | 1300 | -- | 18 | 30 | .60 | 35 | 5 | .385 | |
| 5 | 4/02 | 1200 | full | 15 | 60 | .25 | 40 | 6 | .215 | Channel less well defined than on 4/01, and choked with rubble; velocities much slowed. Measured by PWL, J. Fink, and H. Moore. |
| 6 | 4/02 | 1230 | low | 15 | 110 | .14 | 40 | 6 | .120 | |
| 7 | 4/03 | 1520 | slow | 25 | 140 | .18 | 52 | 5 | .170 | New station; old one unusable because of inboard levees. Top of active channel varies, 3 m below to 1 m above levees. Gradient 4.5°. Measured by NGB. |
| 8 | 4/03 | 1550 | normal | 25 | 80 | .31 | 52 | 5 | .290 | |
| 9 | 4/03 | 1645 | surge | 25 | 90 | .28 | 52 | 7 | .364 | |
| 10 | 4/04 | 1350 | -- | 25 | 163 | .15 | 50 | 5 | .138 | Measured by NGB. |
| **Station 2: Upper channel 1A, elevation 1,700 m** | | | | | | | | | | |
| 11 | 4/03 | 1430 | stable | 15 | 45 | .33 | 50 | 5 | .295 | Measured by PWL, J. Fink, and H. Moore. |
| 12 | 4/03 | 1530 | surge | 15 | 30 | .50 | 50 | 5 | .450 | |
| 13 | 4/04 | 1345 | stable | 15 | 45 | .3 | 25 | 5 | .150 | Sensitive to release of ponded lava at 1,800-m blockage. Surge provides upper limit in flow rate; estimates for stable periods likely to be more meaningful. Gradient about 4°. Measured by PWL, T. Neal, and H. Moore. |
| 14 | 4/04 | 1430 | stable | 15 | 40 | .4 | 25 | 5 | .170 | |
| 15 | 4/04 | 1500 | surge | 15 | 25 | .6 | 25 | 5 | .270 | |
| **Station 3: Lower Powerline Road (flow 1, south side), elevation 1,800 m** | | | | | | | | | | |
| 16 | 3/28 | 1310–1335 | | 73 | 84 | 0.87 | 75 | 5 | 1.20 | Depth fluctuations of as much as 2–3 m in 5 min, associated with surges; channel in two branches—only southern strand measured; channel broad, measured by visual aerial comparison with distance between power poles. Channel gradient about 2.5°. Measured by PWL and D. Clague. |
| 17 | 3/28 | 1535–1605 | | 73 | 80 | .91 | 75 | 5 | 1.25 | |
| **Station 3: Lower Powerline Road (flow 1B), elevation 1,800 m** | | | | | | | | | | |
| 18 | 4/06 | 1400 | -- | 25 | 210 | 0.12 | 25 | 4 | 0.043 | The channel flow slowed, and its upper surface subsided as we made these measurements. When checked an hour later, the head of flow 1B was captured by other overflows, and its channel was drained and empty. Gradient: 2.5°. Measured by PWL and T. Neal. |
| **Station 4: Upper Powerline Road (site 1), elevation 1,900 m** | | | | | | | | | | |
| 19 | 3/29 | 1300 | blocks | 30.2 | 25 | 1.20 | 13 | 6 | 0.335 | Channel is within a gentle stretch related to large overflows and temporary ponding; probably deep as result. Higher velocities in center channel tend to push blocks to sides; more consistent measurements of maximum velocities obtained from small fragments in center channel. Channel gradient about 2.5°. Measured by PWL and E. Wolfe. |
| 20 | 3/29 | 1400 | fragments | 30.2 | 18 | 2.75 | 13 | 6 | .470 | |
| 21 | 3/31 | 1430 | stable | 30.2 | 23 | 1.3 | 13 | 6 | .365 | All measurements on small fast-moving fragments in center channel; lower level at 22 (about 1 m below levees) because of slightly higher gradient after drainage of ponded blockage downchannel. Gradient about 2.5°. Measured by PWL, NGB, and J. Fink. |
| 22 | 3/31 | 1530 | low | 30.2 | 18 | 1.7 | 13 | 6 | .470 | |
| 23 | 4/01 | 0830 | stable | 30.2 | 18 | 1.7 | 13 | 6 | .470 | Channel is sluggish and viscous; shear and pressure ridges are weakly developed on nearly stagnant channel sides. Measured by PWL and E. Wolf. |
| 24 | 4/01 | 0930 | blockage | 30.2 | 19.5 | 1.6 | 13 | 6 | .435 | |
| 25 | 4/02 | 1700 | -- | 30.2 | 31 | 1.0 | 15 | 7 | .370 | Levees have increased in height about 2 m and largely obscure view of the channel: could only measure large boats during high stand of channel. Measured by PWL, J. Fink, and H. Moore. |
| 26 | 4/03 | 1000 | -- | 30.2 | 32.1 | .94 | 18.3 | 7 | .431 | Levee height is 2.3 m above top of old ponded broad aa channel. Surge caused spreading of levee by 1 m in 15 min. Measured by NGB. |
| **Station 4: Upper Powerline Road (site 2), elevation 1,930 m** | | | | | | | | | | |
| 27 | 4/02 | 1600 | -- | 20 | 9.5 | 2.1 | 14 | 4 | 0.455 | New site, above upper cascade. Gradient about 3.5°. Measured by PWL, J. Fink, and H. Moore. |
| 28 | 4/03 | 1320 | -- | 20 | 12.6 | 1.6 | 14 | 5 | .399 | Measured by NGB. |
| **Station 4: Upper Powerline Road (site 2A), elevation 1,930 m** | | | | | | | | | | |
| 29 | 4/04 | 1200 | -- | 23 | 12.3 | 1.9 | 15 | 5 | 0.500 | Measured lava boats; low gradient due to blockages at head of middle cascade. Measured by PWL, T. Neal, and H. Moore. |
| **Station 4: Upper Powerline Road (site 3), elevation 1,900 m** | | | | | | | | | | |
| 30 | 4/04 | 1120 | boats | 20 | 7.5 | 2.7 | 15 | 4 | 0.580 | Boats are sparse; channel level is 0.5–1 m below recent levee overflows. Gradient about 3°. Measured by PWL, T. Neal, and H. Moore. |
| 31 | 4/04 | 1130 | fragments | 20 | 8.1 | 2.5 | 15 | 4 | .530 | |
| 32 | 4/04 | 1140 | fragments, surge | 20 | 7.2 | 2.8 | 15 | 4 | .600 | |
| 33 | 4/05 | 1100 | -- | 20 | 9 | 2.2 | 20 | 4 | .640 | Little change since yesterday. Channel low and boats sparse, indicative of pond and surge forming upchannel. Measured by PWL and H. Moore. |

TABLE 57.3.—*Dimensions and characteristics of lava channels and their changes with time, 1984 Mauna Loa eruption—Continued.*

| Measurement | Date (mo/d) | Hour (H.s.t.) | Condition | Distance (m) | Time (s) | Velocity (m/s) | Width (m) | Depth (m) | Flow rate ($10^6$ $m^3/h$) | Comments |
|---|---|---|---|---|---|---|---|---|---|---|
| **Station 4: Upper Powerline Road (site 4, flow 1B), elevation 1,900 m** | | | | | | | | | | |
| 34 | 4/06 | 1100 | -- | 24 | 14.9 | 1.6 | 30 | 3 | 0.520 | New station, on uppermost gentle reach of flow 1B, just below breakout area. Channel here appeared broad and shallow, and its depth was confirmed later in day when the channel was drained and empty. Gradient 3°. Measured by PWL and T. Neal. |
| 35 | 4/06 | 1130 | -- | 24 | 14.9 | 1.6 | 30 | 3 | .520 | |
| **Station 5: New south flow (flow 1C), elevation 1,950 m** | | | | | | | | | | |
| 36 | 4/07 | 1000 | -- | 15 | 10 | 1.5 | 10 | 5 | 270 | Station is on channel carrying bulk of lava, just below currently most active ponding and breakout area at about 2,000 m. Gradient about 2.5°. Measured by PWL and H. Moore. |
| 37 | 4/07 | 1545 | -- | 15 | 16 | 1.1 | 10 | 5 | .190 | Many surges: difficult to make an average measurement, but clearly lower than this morning. Presumably, decrease reflects many overflow diversions. Measured by PWL and H. Moore. |
| **Station 6: Main channel of flow 1, elevation 2,100 m** | | | | | | | | | | |
| 38 | 4/07 | 1100 | dropping | 20 | 11 | 1.8 | 22 | 5 | 0.720 | Stable channel, currently just above highest ponding area. Measured by PWL and H. Moore. |
| 39 | 4/07 | 1120 | after surge | 20 | 10 | 2.0 | 22 | 5 | .790 | |
| **Station 7: 1852 pahoehoe, elevation 2,300 m** | | | | | | | | | | |
| 40 | 4/04 | 1630 | -- | 20 | 4.7 | 4.23 | 15 | 5 | 1.15 | Above highest area of blockages, levee building, and overflows. Gradient about 4.5°. Measured by PWL, T. Neal, and H. Moore. |
| 41 | 4/08 | 1250 | -- | 20 | 12.8 | 1.65 | 15 | 5 | .424 | Measured by NGB. |
| 42 | 4/08 | 1310 | -- | 20 | 6.5 | 3.1 | 15 | 5 | .835 | |
| **Station 8: 1852 vent, elevation 2,500 m** | | | | | | | | | | |
| 43 | 4/02 | 0900 | site A | 45 | 8.1 | 5.6 | 20 | 4 | 1.60 | Measured velocities on small fragments in center channel. Gradient at site A is 6°; at site B, 4.5–5°. Measured by PWL, J. Buchanan-Banks, J. Fink, and H. Moore. |
| 44 | 4/02 | 0930 | site B | 40 | 7.6 | 5.3 | 20 | 4 | 1.50 | |
| 45 | 4/03 | 0900 | site A | 45 | 8.7 | 5.2 | 20 | 4 | 1.50 | No change evident. Measured by PWL, J. Fink, and H. Moore. |
| 46 | 4/03 | 0920 | site B | 40 | 7.7 | 5.3 | 20 | 4 | 1.50 | |
| 47 | 4/03 | 1630 | site B | 40 | 7.5 | 5.3 | 20 | 4 | 1.54 | No change since morning, despite reported 50 percent increase in production rate at vent. Measured by PWL and J. Fink. |
| 48 | 4/04 | 0800 | site B | 40 | 7.5 | 5.3 | 20 | 4 | 1.55 | No significant change. Measured by PWL, T. Neal, and J. Fink. |
| 49 | 4/05 | 1415 | site B | 40 | 7.3 | 5.5 | 20 | 4 | 1.60 | No change since previous day. Measured by PWL and H. Moore. |
| 50 | 4/06 | 1100 | site B | 40 | 7.6 | 5.3 | 20 | 4 | 1.50 | Surface channel actually only 10.3 m wide, because of crusting of margins. Measured by NGB. |
| 51 | 4/06 | 1550 | site B | 40 | 7.6 | 5.3 | 20 | 4 | 1.50 | No change, although level of channel at vent reported down 1 m. Measured by PWL and T. Neal. |
| 52 | 4/07 | 1625 | site B | 40 | 7.5 | 5.3 | 18 | 4 | 1.40 | Apparent slight decrease, from decreased estimated width of channel caused by crusting, but lava probably continues to flow slowly under crust. Measured by PWL and H. Moore. |
| 53 | 4/08 | 0930 | site B | 40 | 14.2 | 2.8 | 9.2 | 4 | .375 | Surface is much grayer and has more scum than on 4/6. Volume is only about half as great. Gradient 3.5°. Measured by NGB. |
| **Station 9: Middle channel, elevation 2,780 m** | | | | | | | | | | |
| 54 | 4/09 | 1300 | -- | 15 | 15 | 1.0 | 15 | 4 | 0.215 | Broad shallow sheet-flow channel, the middle of three currently active around the west side of vent at 2,790 m (Puu 9,146). Measured by PWL and M. Rhodes. |
| **Station 10: North channel, elevation 2,790 m** | | | | | | | | | | |
| 55 | 4/09 | 1600 | -- | 22 | 30 | 0.73 | 8 | 5 | 0.105 | Narow channel, mostly well below levees. For visibility, had to measure during high channel flow. Measured by PWL and M. Rhodes. |
| 56 | 4/10 | 1200 | -- | 20 | 20 | 1 | 8 | 4 | .100 | Estimated velocity; channel on average 1–2 m lower than yesterday. Measured by PWL. |
| 57 | 4/11 | 1215 | -- | 15 | 10.1 | 1.5 | 12 | 3 | .190 | Measured by NGB. |
| 58 | 4/12 | 1200 | steady | 16 | 25 | .64 | 6 | 4 | .055 | Just upslope from station of previous day, which is now jammed by an overflow. Measured by PWL and R. Fodor. |
| 59 | 4/12 | 1215 | surge | 16 | 14 | 1.1 | 6 | 5 | .125 | |
| **Station 11: Vent outlet, elevation 2,850 m** | | | | | | | | | | |
| 60 | 4/02 | 1130 | -- | 30 | 1.7 | 17.8 | 21.5 | 3 | 4.50 | Gradient is 6.5°; lava is fluffy; about 70 percent has bubbles. Measured by NGB. |
| 61 | 4/04 | 1030 | -- | 30 | 2.0 | 15 | 21 | 3 | 3.40 | Flow rate is $1.5\times10^6$ $m^3/h$ less than on 4/02. There is an antithetic relation between fountain height and channel level; at highest fountaining, channel flow rate is $5.2\times10^6$ $m^3/h$. Measured by NGB. |
| 62 | 4/06 | 0900 | -- | 30 | 2 | 15 | 20 | 3 | 3.5 | Channel appears unchanged from 4/04; velocity estimated by NGB. |
| 63 | 4/08 | 1145 | -- | 30 | 4.65 | 6.45 | 21.5 | 3 | 1.50 | Surface is grayer, but lava may be even fluffier than earlier. Flow rate half that of 2 days ago. Measured by NGB. |
| 64 | 4/08 | 1600 | -- | 20 | 10 | 2 | 30 | 3 | .650 | Channel much slower than in morning. Velocity estimated by NGB. |
| 65 | 4/09 | 1040 | -- | 40 | 17 | 2.4 | 5 | 3 | .125 | Channel contains viscous ropy pahoehoe. Measured by PWL and M. Rhodes. |
| 66 | 4/09 | 1130 | higher | 40 | 12.5 | 3.2 | 5 | 4 | .230 | |
| **Station 12: West vent, elevation 2,900 m** | | | | | | | | | | |
| 67 | 4/08 | 1620 | -- | -- | -- | 2 | 30 | 2 | 0.430 | Velocity estimated by NGB. |
| 68 | 4/12 | 1400 | -- | 20 | 10.5 | 1.9 | 5 | 5 | .170 | Station is about 100 m downchannel from active vents. Lava is fluffy, like cotton candy. Degassed flow rate probably about $30\times10^3$–$40\times10^3$ $m^3/h$. Gradient about 3°. Measured by PWL and J. Lockwood. |
| 69 | 4/13 | 1400 | -- | 20 | 16 | 1.25 | 5 | 5 | .110 | Channel flow is steeper but slower than yesterday, even though measured at high fountain level. Gradient 4.5°. Measured by PWL and NGB. |

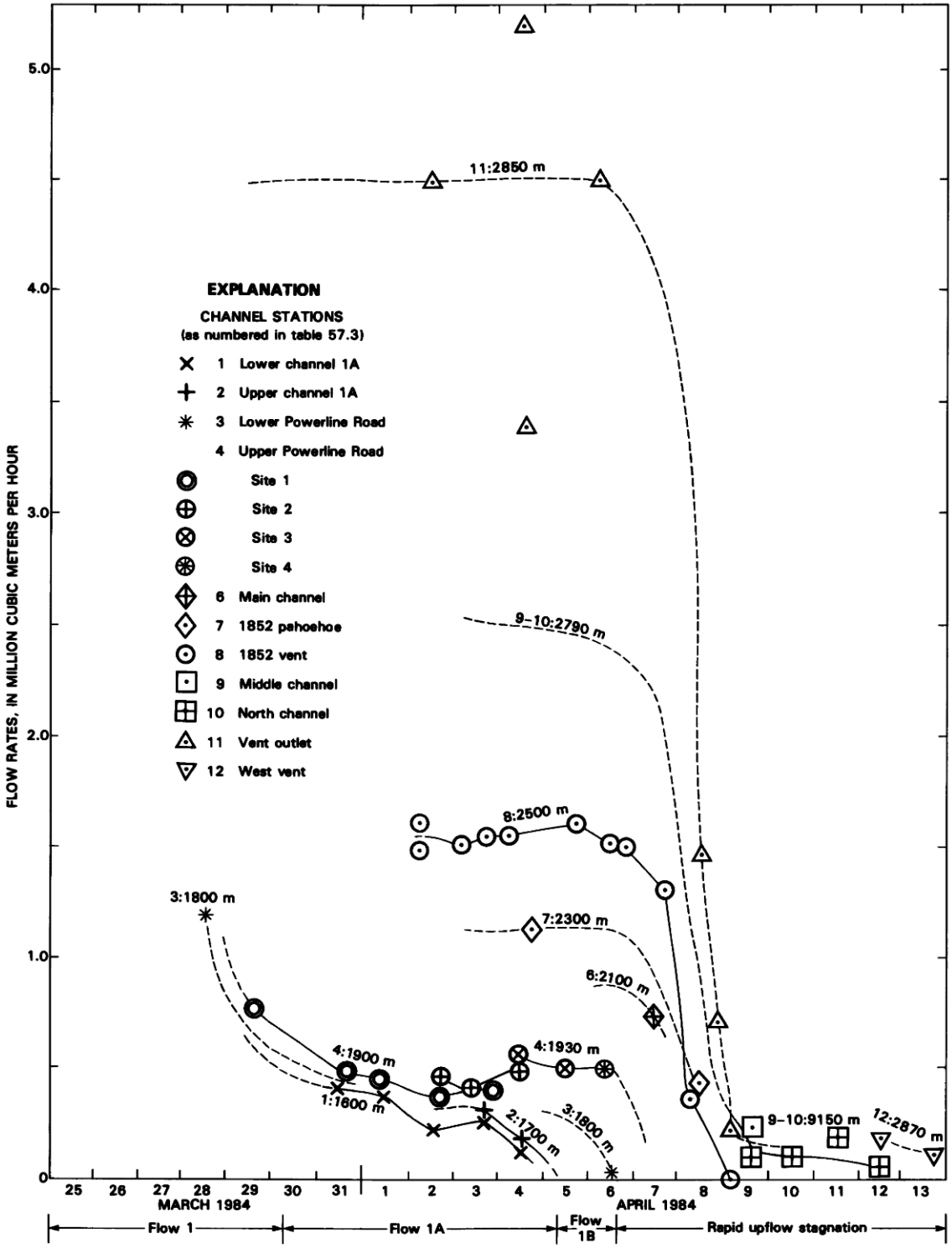


FIGURE 57.26.—Changes in channel discharge with time, 1984 Mauna Loa eruption as measured at channel stations (identified by number; see table 57.3). Solid lines connect repeated observations at individual sites; dashed lines are interpreted trends for discharges based on data at other stations and qualitative observations of channel evolution.

(fig. 57.26). Additional factors came into play during this time interval to cause stagnation of the flow and channel system, and these factors may also have had a role in the early stagnation of flow 1 before March 30.

Lava temperatures at the vent remained nearly constant throughout the eruption, as did temperatures of the most fluid parts of the downchannel flows (fig. 57.19). The latter is thought to have resulted from the heat of microlite crystallization and from thermal feedback associated with deformation of the silicate melt fraction during downchannel flow. Despite the uniform eruptive temperature and chemical composition, the proportion of solid and pasty material (reflecting greater groundmass crystallization) gradually increased in lower reaches of the channel system, raising both the bulk viscosity and the yield strength of the lava. Even in the zones of stabilized and transitional flow, increased downflow sluggishness in the channel indicated progressive increase in viscosity of the fluid matrix between the solid and pasty material. These downchannel effects must have been caused by changes in some intrinsic property of the lava other than decreasing temperature. Decreased gas content and increased groundmass microlite crystalization seem the most likely candidates, as discussed earlier in this paper and as previously suggested for basaltic flows in general by Sparks and Pinkerton (1978).

We infer that decreased gas content played a large role, because fluidity of the flow appears to be at least in part related to the ease of deformation of the silicate liquid that constitutes the vesicle walls. The 80–90 percent decrease in vesicularity of lava in the channel from the vent to the zone of dispersed flow and the accompanying proportional increase in vesicle wall thickness of the silicate melt may have increased the bulk viscosity by several hundred percent.

The greater numbers of microlites downflow must also have increased the effective viscosity of the channel fill, much in the manner that the increased microphenocryst population in the erupted lava raised the viscosity of the lava at the vent. Degassing and crystallization influenced the viscosity and thus the behavior of the lava in differing ways. Degassing of the lava flexed the silicate liquid to produce thermal feedback, adiabatically cooled the lava, and increased the proportion of viscous silicate liquid present. Crystallization heated the lava but also increased its bulk viscosity. The combination of these effects apparently reduced the rate of flow at the vent, delayed temperature decreases downflow and probably also in the lava conduit, produced the conditions required for the pahoehoe-aa transition, and ultimately contributed to the maturation and stagnation of flows during the Mauna Loa eruption.

A further process possibly contributing to stagnation of the flow system was maturation of the channel structures with time. Solidification and increasingly brittle behavior of the channel banks, deepening of the channels by levee growth and possibly by erosion of the channel floor, and crusting over of channel margins and eddies are among the unidirectional processes that could have helped destabilize the channel system during the course of the eruption, regardless of changes at the vent. Such maturation processes could have caused greater formation of channel debris, initially triggered by small fluctuations in vent eruption rate, that led to increasingly larger debris blockages, overflows, and surges downchannel.

Deviations from simple correlations between length of lava flows and eruption rate (Walker, 1973), which have been demonstrated for Hawaiian flows (Malin, 1980), may largely result from the superimposed effects of variable vesiculation, density, undercooling, and crystallinity of the lava. Increased undercooling and crystallinity, decreased vesicularity, and associated increased density would all promote higher effective bulk viscosity and yield strength in basaltic flows, causing transitions from pahoehoe to aa and reducing the length of flows at any constant eruption rate. In contrast, long-lived eruption at liquidus temperature would promote transportation of pahoehoe in lava tubes, permitting lava flows to travel farther. The rheology of lava erupted as gas-rich foam (reticulite, in the case of Hawaiian basalt) that deflates during emplacement will be markedly different from that of degassed lava; such contrasts may extend to highly silicic compositions (Eichelberger and Westrich, 1984). Proposed simple correlations of viscosity and yield strength of lavas with chemical parameters such as silica content (Hulme, 1974) are also imperfect (Moore and others, 1978), perhaps in large part because of the complicating factors just listed.

Finally, it should be noted that the evolution of the 1984 flow system was similar in volume, duration, and eruptive style to several previous historical (since the mid-19th century) rift eruptions of Mauna Loa. Field and photogeologic examination indicates that patterns of upslope stagnation of the distributary channel system characterized many of these earlier events, including the 1852 and 1942 flows that are adjacent to the 1984 flows. Sparse petrographic data indicate that other major historical rift flows (1843, 1926, 1935, 1942, 1950; northeast rift samples collected by J.P. Lockwood and G. Lockwood) also show trends of increasing content of microphenocrysts during the eruption. Similar observations for prolonged summit eruptions, such as those of 1940 or 1949, would be particularly significant because they could permit distinction between the effects of depressurization of the summit reservoir and degassing along the rift conduits. Additional studies of the relations between eruption style, flow evolution, and lava crystallinity of earlier Mauna Loa eruptions are in progress.

More extensive observations are needed on the interrelations between gas content, crystallinity, eruption temperature, and viscosity of erupting basaltic lava. Changes in lava discharge rate, temperature, density, bulk chemistry, and abundance of microphenocrysts were key determinable parameters for the 1984 eruption that should be monitored closely in future activity. Such studies may answer some remaining questions: does lava temperature commonly remain constant during long-lived eruptions, even during periods of declining discharge? Does density of spatter typically decrease during an eruption? Does the development of lava tubes and long-traveled pahoehoe during prolonged eruptions require eruption temperatures near the one-atmosphere liquidus, or at least retardation of major degassing and attendant undercooling before eruption? If eruptions of undercooled lava, marked by increasing microphenocryst populations, can be shown to generate aa flows close to the vent, observations of lava temperature and crystallinity can have important implications for assessing volcanic hazards during early phases of major basaltic eruptions.

*A*

*B*

FIGURE 57.27.—Upper channel system of flow 1, as viewed from vent at 2,790 m (Puu 9,146 ft), approximately 4 km from the active vent at 2,900-m elevation. ***A***, At 0900 on March 26. Channel banks of flow 1 are full or overflowing; small bright specks to right of active channel are areas of still-glowing lava that indicate a large overflow within the previous hour. Small channel of flow 2, fed by low fountains, is visible at upper left. Discharge (normalized to density 2.0 g/cm$^3$) estimated at $1.0 \times 10^6$–$1.5 \times 10^6$ m$^3$/h. ***B***, At 1600 on March 31. Lava confined completely within channel banks; several forks of the channel and intervening islands have emerged. Despite lower channel level, compared to 5 days earlier, fountain height is higher, probably reflecting a higher proportion of exsolved gases. Discharge (normalized to density 2.0 g/cm$^3$) estimated at $0.5 \times 10^6$–$0.6 \times 10^6$ m$^3$/h. Prominent spatter ramparts in left distance mark vents for flows 2–4; these grew rapidly early in the eruption but were inactive after March 27.

*A*

*B*

FIGURE 57.28.—Changes in fountain height and lava production, as seen from vent outlet (channel station 11) during 1984 Mauna Loa eruption. ***A***, April 2: Vent fountains about 40 m high, well above the spatter rampart. Fluffy channel lava was moving at about 60 km/h, with a discharge rate of about $4.5 \times 10^6$ $m^3/h$ (table 57.3, no. 60). In contrast to the lower portions of the stable-channel zone (see figs. 57.8C, 57.10), a broad central part of the channel is moving with plug flow. Velocity gradients are confined to within a few meters of the channel bank. ***B***, April 8, at 1145 h: Vent fountains only 5–10 m high, no longer visible above the spatter rampart. Velocity of the channel lava has declined to about 23 km/h, and the discharge rate is about $1.5 \times 10^6$ $m^3/h$ (table 57.3, no. 63); later in the afternoon of April 8, discharge declined by an additional 50 percent. Nevertheless, the level of lava in the channel remains nearly as high as when the eruption rate was several times greater. Note that the highest part of the channel levee visible on April 2 has caved into the channel, presumably to form lava boats.

TABLE 57.4.—*Estimated daily lava production rates and cumulative volumes, 1984 Mauna Loa eruption*

| Date (mo/d) | Rate ($10^6$ m³/h) | volume ($10^6$ m³) | Cumulative volume ($10^6$ m³) | Note |
|---|---|---|---|---|
| 3/25 | 2.8×6 h | 25×2/3 | 16.7 | 1 |
| 3/25 | .7×8 h | 5.8 | 22.5 | 1 |
| 3/25 | 1.1×8 h | 8.9 | 31.4 | 2 |
| 3/26 | 1.1 | 26.1 | 57.5 | 2 |
| 3/27 | 1.1 | 26.1 | 83.6 | 2 |
| 3/28 | 1.1–1.2 | 26.1 | 109.7 | 3 |
| 3/29 | .75 | 18.0 | 127.7 | 4 |
| 3/30 | .5 | 12.0 | 139.7 | 3 |
| 3/31 | .4 | 9.6 | 149.3 | 3 |
| 4/1 | .4 | 9.6 | 158.9 | 3 |
| 4/2 | .4 | 9.6 | 168.5 | 3 |
| 4/3 | .4 | 9.6 | 178.1 | 3 |
| 4/4 | .4 | 9.6 | 187.7 | 3 |
| 4/5 | .4 | 9.6 | 197.3 | 3 |
| 4/6 | .4 | 9.6 | 206.9 | 3 |
| 4/7 | .3 (1.2) | 7.2 | 214.1 | 5 |
| 4/8 | .16 (.65) | 3.6 | 217.7 | 5 |
| 4/9 | .10 (.40) | 2.4 | 220.1 | 5 |
| 4/10 | .07 (.28) | 1.7 | 221.8 | 5 |
| 4/11 | .05 (.20) | 1.2 | 223.0 | 5 |
| 4/12 | .04 (.17) | .7 | 223.7 | 5 |
| 4/13 | .02 (.08) | .5 | 224.2 | 5 |
| 4/14 | .00 | .0 | 224.2 | 6 |

1. Hourly production rates for early eruptions from summit (0130–0730, 3/25) and upper rift zone (0900–1700, 3/25) determined by area and thickness measurements (J.P. Lockwood, written commun., 1984). Summit lava is mostly shelly pahoehoe (estimated average density, 1.5 g/cm³), so volume is reduced by a third to make comparable to volume estimates for later eruptive phases (estimated average density, 2.0 g/cm³).
2. Hourly production rate for first 48 h of eruption from 2,900-m vent area (1600 3/25 to 1600 3/27), determined by area and thickness estimates, based on field observations by the authors. Data permit a decay in eruption rate, as alternative to constant rate, during this interval.
3. Production rate determined from channel measurements at 1,800 to 1,900-m stations (table 57.3). Estimated average density, 2.0 g/cm³.
4. Production rate interpolated between rates for previous and subsequent days.
5. Production rate determined from channel measurements at 2,500 to 2,850-m stations (table 57.3). Estimated average density, 0.5 g/cm³; accordingly, observed discharges (in parentheses) are reduced by three-quarters to make comparable to other measurements.
6. End of eruption.

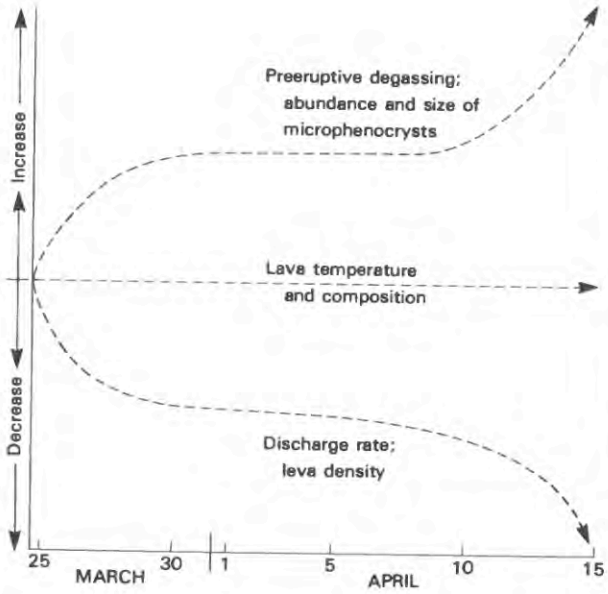


FIGURE 57.29.—Diagram illustrating interdependent time relations between eruptive volume, microphenocryst content, lava composition, eruption temperature, amount of degassing, and lava density during 1984 Mauna Loa eruption.

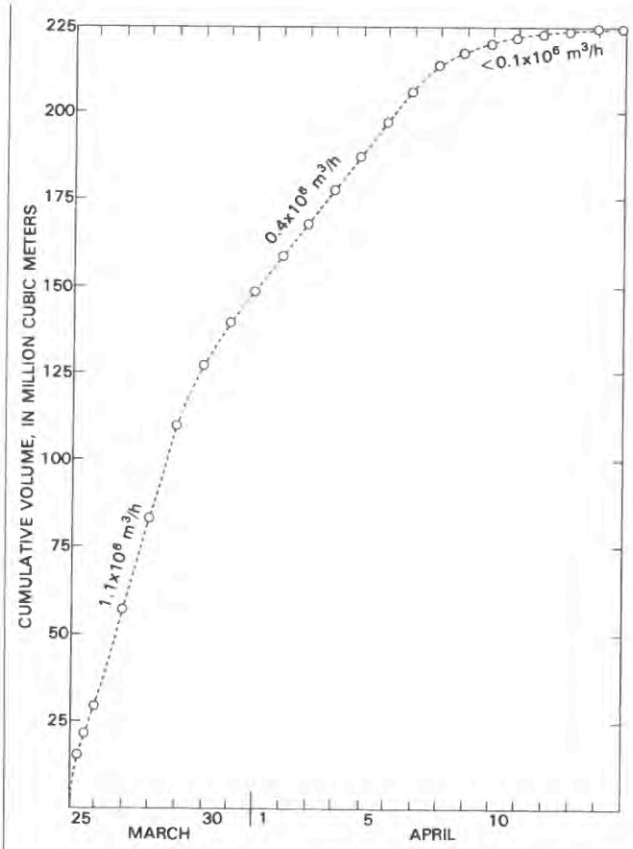


FIGURE 57.30.—Interpreted cumulative volume of erupted lava in 1984 Mauna Loa eruption plotted against time. Data from table 57.4.

## REFERENCES

Alt, W.U., Eaton, J.P., and Richter, D.H., 1961, Lava temperatures in the 1959 Kilauea eruption and cooling lake: Geological Society of America Bulletin, v. 72, p. 791–794.

Banks, N.G., and Hoblitt, R.P., 1981, Summary of temperature studies of 1980 deposits, *in* Lipman, P.W., and Mullineaux, D.R., eds., The 1980 eruptions of Mount St. Helens, Washington: U.S. Geological Survey Professional Paper 1250, p. 295–313.

Borgia, A., Linneman, S., Spenser, D., Morales, L.D., and Andre, J.B., 1983, Dynamics of lava flow fronts, Arenal Volcano, Costa Rica: Journal of Volcanology and Geothermal Research, v. 19, p. 303–330.

Casadevall, T., Krueger, A., and Stokes, B., 1984, The volcanic plume from the 1984 eruption of Mauna Loa, Hawaii [abs.]: Eos, Transactions of the American Geophysical Union, v. 65, p. 1133.

Cigolini, C., Borgia, A., and Casertano, L., 1984, Intra-crater activity, aa-block lava, and flow dynamics, Arenal Volcano, Costa Rica: Journal of Volcanology and Geothermal Research, v. 20, p. 155–176.

Decker, R.W., Koyanagi, R.Y., Dvorak, J.J., Lockwood, J.P., Okamura, A.T., Yamashita, K.M., and Tanigawa, W.R., 1983, Seismicity and surface deformation of Mauna Loa Volcano, Hawaii: Eos, v. 64, p. 545–547.

Eichelberger, J.C., and Westrich, H.R., 1984, Degassing of magma in an obsidian flow and inferred degassing behavior at depth, *in* Active tectonic and magmatic process beneath Long Valley caldera, eastern California: U.S. Geological Survey Open-File Report 84–939, p. 147–150.

Finch, R.H., and Macdonald, G.A., 1953, Hawaiian volcanoes during 1950: U.S. Geological Survey Bulletin 996–B, 89 p.

Garcia, M.O, Byers, C.D., Wolfe, E.W., and Rhodes, J.M., 1984, Chemistry and mineralogy of lavas from the continuing eruption of Kilauea Volcano, Hawaii [abs.]: Eos, v. 65, p. 1130.

Greenland, L.P., Okamura, A., and Stokes, J.B., in press, Constraints on the mechanics of eruption of Puu Oo, *in* Wolfe, E.W., ed., The Puu Oo eruption of Kilauea Volcano, Hawaii: the first 1-1/2 years: U.S. Geological Survery Professional Paper.

Greenland, L.P., Rose, W.I., and Stokes, J.B., 1985, An estimate of gas emissions and magmatic gas content from Kilauea Volcano: Geochemica et Cosmochimica Acta, v. 49, p. 125–129.

Haggarty, S.E., 1981, Volatiles in planetary basalts: hydrogen, carbon, and sulfur gas species, *in* Basaltic volcanism on the terrestrial planets: New York, Pergamon Press, Basaltic Volcanism Study Project, p. 385–398.

Hulme, G., 1974, The interpretation of lava flow morphology: Geophysical Journal of the Royal Astronomical Society, v. 39, p. 361–383.

Jones, D.L., Silberling, N.J., Gilbert, W., and Coney, P., 1982, Character, distribution, and tectonic significance of accretionary terranes in the Central Alaska Range: Journal of Geophysical Research, v. 87, p. 3709–3717.

Kirkpatrick, R.J., 1976, Toward a kinetic model for the crystallization of magma bodies: Journal of Geophysical Research, v. 81, p. 2565–2571.

——— 1977, Nucleation and growth of plagioclase in the Hawaiian lava lakes Makaopuhi and Alae: Geological Society of America Bulletin, v. 88, p. 78–84.

Lipman, P.W., Banks, N.G., and Rhodes, J.M., 1985, Gas-release induced crystallization of 1984 Mauna Loa magma, Hawaii, and effects on lava rheology: Nature, v. 317, p. 604–607.

Lockwood, J.P., Banks, N.G., English, T.T., Greenland, L.P., Jackson, D.B., Johnson, D.J., Koyanagi, R.Y., McKee, K.A., Okamura, A.T., and Rhodes, J.M., 1985, The 1984 eruption of Mauna Loa Volcano, Hawaii: Eos, v. 65, p. 169–171.

Lockwood, J.P., Koyanagi, R.Y., Tilling, R.I., Holcomb, R.T., and Peterson, D.W., 1976, Mauna Loa threatening: Geotimes, v. 21, p. 12–15.

Lofgren, G.E., 1981, Comparative petrography and cooling rates, *in* Basaltic volcanism on the terrestrial planets: New York, Pergamon Press, Basaltic Volcanism Study Project, p. 364–370.

Macdonald, G.A., 1953, Pahoehoe, aa, and block lava: American Journal of Science, v. 251, p. 169–191.

——— 1972, Volcanoes, Englewood Cliffs, New Jersey, Prentice Hall Inc., 510 p.

Macdonald, G.A., and Abbott, A.T., 1970, Volcanoes in the Sea: Honolulu, University of Hawaii Press, 441 p.

Malin, M.C., 1980, Lengths of Hawaiian lava flows: Geology, v. 8, p. 306–308.

Moore, H.J., Arthur, D.W.G., and Schaber, G.G., 1978, An estimate of the yield strength of flows on the Earth, Mars, and Moon: Lunar and Planetary Science Conference, 9th, Proceedings, p. 3351–3378.

Moore, J.G., 1965, Petrology of deep-sea basalt near Hawaii: American Journal of Science, v. 263, p. 40–52.

Moore, R.B., Dzurisin, D., Eaton, G.P., Koyanagi, R.Y., Lipman, P.W., and Lockwood, J.P., 1980, Preliminary report on the 1977 eruption of Kilauea Volcano, Hawaii: Journal of Volcanology and Geothermal Research, v. 7, p. 189–210.

Murase, T., 1962, Viscosity and related properties of volcanic rocks at 800° to 1400°C.: Hokkaido University, Journal of the Faculty of Science, Ser. 7, v. 1, p. 487–584.

Neal, C.A., Duggan, T.A., Wolfe, E.W., and Brandt, T.L., in press, Lava samples, temperatures and compositions; Puu Oo eruption of Kilauea Volcano, Hawaii, phases 1–20, *in* Wolfe, E.W., The Puu Oo eruption of Kilauea Volcano, Hawaii: the first 1-1/2 years: U.S. Geological Survey Professional Paper.

Nielsen, R.L., and Dungan, M.A., 1983, Low pressure mineral-melt equilibria in natural anhydrous mafic systems: Contributions to Mineralogy and Petrology, v. 84, p. 310–326.

Peterson, D.W., and Tilling, R.I., 1980, Transition of basaltic lava from pahoehoe to aa, Kilauea Volcano Hawaii: field observations and key factors: Journal of Volcanology and Geothermal Research, v. 7, p. 271–293.

Rhodes, J.M., 1983, Homogeneity of lava flows: chemical data for historic Mauna Loa eruptions: Journal of Geophysical Research, v. 88 (supplement), p. A869–A879.

Shaw, H.R., 1969, Rheology of basalt in the melting range: Journal of Petrology, v. 10, p. 510–535.

Shaw, H.R., Wright, T.L., Peck, D.L., and Okamura, R., 1968, The viscosity of basaltic magma: an analysis of field measurements in Makaopuhi lava lake, Hawaii: American Journal of Science, v. 266, p. 225–264.

Sparks, R.S.J., and Pinkerton, H., 1978, The effect of degassing on the rheology of basaltic lava: Nature, v. 276, p. 385–386.

Sparks, R.S.J., Pinkerton, H., and Hulme, G., 1976, Classification and formation of lava levees on Mount Etna, Sicily: Geology, v. 4, p. 269–271.

Swanson, D.A., 1973, Pahoehoe flows from the 1969–1971 Mauna Ulu eruption, Kilauea Volcano, Hawaii: Geological Society of America Bulletin, v. 84, p. 615–626.

Swanson, D.A., Duffield, W.A., Jackson, D.B., and Peterson, D.W., 1979, Chronological narrative of the 1969–71 Mauna Ulu eruption of Kilauea Volcano, Hawaii: U.S. Geological Survey Professional Paper 1056, 55 p.

Ulrich, G.E., Wolfe, E.W., Hoffman, J.P., and Neal, C.A., 1984, Continuing eruption of east rift zone, Kilauea Volcano, Hawaii [abs.]: Eos, v. 65, p. 1130.

Wadge, G., 1978, Effusion rate and the shape of aa lava flow-fields on Mount Etna: Geology, v. 6, p. 503–506.

——— 1981, The variations of magma discharge during basaltic eruptions: Journal of Volcanology and Geothermal Research, v. 11, p. 139–168.

Walker, D.R., Kirkpatrick, R.J., Longhi, J., and Hays, J.F., 1976, Crystallization history and origin of lunar picritic basalt 12002: phase equilibrium, cooling rate studies, and physical properties of the parent magma: Geological Society of America Bulletin, v. 87, p. 646–656.

Walker, G.P.L., 1973, Length of lava flows: Philosophical Transactions of the Royal Society of London, v. A274, p. 107–118.

Wentworth, C.K., and Macdonald, G.A., 1953, Structures and forms of basaltic rocks in Hawaii: U.S. Geological Survey Bulletin 994, 98 p.

Wright, T.L., and Fiske, R.S., 1971, Origin of the differentiated and hybrid lavas of Kilauea Volcano, Hawaii: Journal of Petrology, v. 12, p. 1–65.

Wright, T.L., Kinoshita, W.T., and Peck, D.L., 1968, March 1965 eruption of Kilauea Volcano and the formation of Makaopuhi lava lake: Journal of Geophysical Research, v. 73, p. 3181–3205.

Yoder, H.S., and Tilley, C.E., 1962, Origin of basalt magmas: an experimental approach: Journal of Petrology, v. 3, p. 342–532.

## APPENDIX 57.1

### LAVA-TEMPERATURE AND DENSITY MEASUREMENTS

The temperatures in table 57.1 were measured by direct insertion of thermocouples into lava (code T, table 57.1) and by two-color infrared pyrometer readings of fountains or noncrusted fast-flowing lava (code H). Similar equipment has been used to measure temperatures of varied volcanic products (Banks and Hoblitt, 1981; Neal and others, in press). Samples for density and other petrologic studies were collected at many of the sites where temperatures were measured.

#### THERMOCOUPLE EQUIPMENT

Several configurations of commercial thermocouples were used, in which chromel-alumel wires imbedded in MgO were sheathed with and grounded to Inconel high-temperature stainless steel. Grounded thermocouples, which respond 3–5 times faster than ungrounded versions, have proved to be durable and resistant to thermal and mechanical fatigue as well as corrosion under difficult field conditions.

For slow-moving pahoehoe, small-gauge thermocouples (1.5-mm sheath diameter, 3–10 m long; code I in table 57.1) were preferred because of their small thermal mass. Temperatures obtained with such thermocouples were within 5–10 °C of equilibrium with the melt in 1–2 minutes and completed equilibration within the next 2–3 minutes. Where rigidity was required to insert the thermocouple into lava, the thermocouple was wound around a light steel rod, so that the thermocouple tip extended 20–30 cm beyond the rod.

For moving pahoehoe or dense aa, the small-gauge wire usually proved too flexible to insert, and heavier-gauge thermocouples were required. For these situations, 6-mm-diameter Inconel-sheathed thermocouples (code 2, table 57.1) provided excellent results. Response times with the heavy-gauge wire were longer, taking 3–5 minutes to approach within 5 °C of the melt temperature and up to 10 minutes for full equilibration.

Thermal and mechanical stress often caused failure of the thermocouple tips after several insertions, particularly for the small-gauge type. When this happened, 3–6 cm of the faulty end were cut off, and the thermocouple wires were exposed with wire strippers and twisted together. The repaired thermocouple could then be immersed directly in melt to obtain additional temperatures. The double advantage of the exposed tip was an extended life for the thermocouple and a response time about 5 times faster. Calibration of sheathed and bare thermocouple wires in the field and in a test kiln indicated no systematic differences. Code B in table 57.1 indicates that the thermocouple tip was directly exposed to the lava; code C measurements were with a fully clad and grounded thermocouple tip.

Thermocouple voltages were converted to temperatures using direct reading digital voltmeters that were compensated electronically (cold junction). Five meters from two manufacturers were used. The meters were periodically checked against precise millivolt calibrators, which themselves were periodically tested against a laboratory millivolt meter. The meters consistently agreed within ±1 °C of the temperature indicated by the calibrators, as did temperatures obtained by two or more meters sequentially attached to a single thermocouple which had been implanted and equilibrated in lava or a test kiln (see also Banks and Hoblitt, 1981). An exception was a meter, which previously gave good numbers, that was exposed inadvertantly to intense radiation during a measurement; this meter read +4 °C high when next calibrated, and data gathered in the interim were accordingly corrected.

## FIELD TECHNIQUES

Observers and thermocouple meters were shielded from the intense radiative heat of the lava by use of a commercial aluminized heat suit (fig. 57.6*B*) or a sheet of aluminum roofing that was fitted with a handle to avoid contact with the metal. Although both shielding techniques were at times used simultaneously, the sheeting was preferred because of increased body ventilation, mobility, and superior visibility and hearing afforded the observers. At an open lava channel or aa front, the heat suit was frequently the only adequate protection.

Techniques in pahoehoe melts were similar in most situations. After preheating the small-gauge thermocouple tip to 700–900 °C for several seconds, it was inserted slowly to a depth of 10–20 cm in an area of melt where no crust had formed. Undesirable growth of a lava icicle or sheath, particularly a problem with the large-gauge thermocouple, could be minimized by working the tip back and forth during slow insertion.

Generally, two people worked together: one person would immerse and maneuver the thermocouple, attempting to avoid hitting any developing crust that might damage or break the wire, and the other would watch for approaching lava, read the meter, and frequently hold the protective shield. Temperatures were read aloud, and as equilibrium was approached and the thermocouple stabilized, a single reading was recorded.

Most temperatures of aa flows were measured with the 6-mm-diameter thermocouples because of their superior rigidity and resistance to breakage. The probe was clamped to an iron rod 4–6 m long, with 20–30 cm extending beyond the rod, preheated to lessen the thermal shock, and pushed into a brightly incandescent part of an advancing flow front. Depending on the viscosity of the melt and the thickness of the chilled aa rind, the probe might readily penetrate the fluid core of the flow. At times, the observer had to lean full weight against the rod in order to force penetration. In most cases, the probe was gradually enveloped by the advancing flow to depths of 2–6 meters. Acceptable penetration and a stable temperature reading generally took 15–30 minutes, and most probes were not recovered. Temperatures were monitored at a safe distance from the rolling incandescent boulders typical of advancing aa fronts, by using an extension cord to the meter.

## THE TWO-COLOR INFRARED PYROMETER

Temperatures of the fountains and fast-flowing, uncrusted lava near the vent were measured by a hand-held two-color, infrared pyrometer (HOTSHOT). The two colors allow instant direct calculation of emissivities, thereby yielding relatively accurate temperatures for the radiating body. The instrument has interchangeable lenses, and to narrow the field of view, we used a telephoto lens and an almost-closed aperature. This gave a field of view only a few centimeters across at 5 m and less than 1 $m^2$ at 30 m distance. The subject and the light-emitting diode display are viewed simultaneously through the eyepiece, and the instrument has an internal reference calibrator, used to adjust for drift before and after each shot.

The HOTSHOT produced stable fountain temperatures that were similar or slightly above the best thermocouple measurements in near-vent flows. Several precautions were required to obtain accurate temperatures: (1) the instrument was immobilized through ground-bracing or use of a tripod; (2) the area viewed was kept small, to eliminate inclusion of sky or crusted spatter falling in front of the active fountains; (3) little or no cooling lava could be between the subject and the instrument; and (4) measurements were avoided over distances greater than 30–40 m. Item (1) is necessary to minimize fluctuations in the readings. Item (2) is to prevent the two detectors from reading separate subjects, which causes calculation of erroneously high or low emissivities. Items (3) and (4) are precautions because certain gasses, probably water vapor, cause different absorption of the two infrared wavelengths. Empirically, we found that unrealistically high numbers result from long shots or shots over degassing lava.

## CLASSIFICATION OF THE DATA

Several criteria were used to classify the quality of thermocouple and HOTSHOT temperature data (table 57.1). Code I (icicle) indicates that the thermocouple tip acquired an insulating sheath of lava before stabilizing at the actual lava temperature. These measurements were marked by unstable temperatures that peaked 10–100 °C below other temperatures at the same or a similar locality, and by the icicle growth on the thermocouple when withdrawn. Code F (failed) indicates that the thermocouple tip failed at the indicated temperature without stabilizing, or that penetration into the melt was poor. Code P (poor) indicates that nonideal atmospheric conditions or fluctuating values occurred during a HOTSHOT measurement. Code E (equilibrium) indicates that a stable temperature in equilibrium with the lava was obtained, but that geologic conditions suggested that the lava had cooled relative to temperatures at the vent or main channel. Spatter-fed flows, thin rapidly cooling overflows from lava rivers, and lava held in prolonged storage in lava tubes consistently produced temperatures 5–10 °C below those obtained in obviously superior geological settings. Code G (good) indicates measurements that we consider superior by virtue of

temperature stablility, condition of the probe or path of sight, and quality of the geologic location. Confidence in the G-coded measurements grew as identical temperatures within ±3 °C were obtained at the same locations day after day, both at the vents and down the main channel.

G-coded thermocouple measurements were made either in slow-moving pahoehoe that was insulated from the atmosphere or in aa where the probe tip penetrated into the fluid core and remained stable for 5–20 minutes. Ideal situations were pahoehoe toes fed by lava tubes that tunneled directly through the spatter rampart. The best situations for determining downflow lava temperatures were active pahoehoe fronts or margins, oozes through cracks in accretionary levees at the edges of the main channel, lava tubes fed by and near the channel, thick aa overflows near the channel, and the fluid cores of aa fronts.

### SAMPLING AND DENSITY DETERMINATIONS

Several types of samples were collected to study changes in chemistry, mineralogy, texture, and density of the melt during the eruption. Many samples were collected concurrently with temperature measurements. Samples from the channels, channel overflows, and pahoehoe were collected on a hammer or scoop, and were immediately quenched in water to stop growth of gas bubbles and devitrification. Spatter samples were watched in flight, picked up upon landing, and water quenched. Samples labeled "core" (fig. 57.21, 57.22) were from interiors of aa flows. Some were collected from thermocouple tips or hammers and quenched, but a few were collected after they had cooled naturally.

To obtain densities, the samples were diced to cubic or near-cubic form, measured, dried at 20 °C, and weighed.

## APPENDIX 57.2

### OBSERVATION METHODS AT CHANNEL STATIONS

Many interpretations in this paper, especially those related to lava volumes, are based on quantitative measurements at the channel stations (table 57.2, fig. 57.1*B*). These measurements, though relatively straightforward, involve some assumptions and complications that require further explanation.

The initial purpose of the stations was to permit replicate measurement of channel velocities and volumes along lower reaches of the flow to document any changes in rates at which lava was moving toward Hilo. It was thought that more meaningful results could be obtained downchannel than close to the vent, where channel velocities were high and channel volumes were more influenced by short-term fluctuations in vent activity. Observations on lava flow and channel morphology were a supplemental benefit.

Sites for channel stations were chosen along relatively straight channel reaches of uniform gradient, in order to minimize perturbating effects of local channel geometry. At each station, one or more distances for timing velocities, typically 15–30 m in length, was measured and flagged close to the channel bank, along with sighting points located farther back and perpendicular to the channel. Most lava-velocity measurements were thus made by two observers at these sighting points, timing the motion of identifiable channel material along the measured course. Multiple measurements were made, typically 5–10, until consistent results were obtained. Anomalously slow values, mostly related to material that deviated from center channel, were discarded. The others were averaged; the range of values was typically less than 10 percent. At lower channel stations affected by lava surges, some measurements were made during surges, but plotted values (fig. 57.26) were determined during seemingly representative intervening periods. Helicopter-transport logistics commonly permitted or required several hours of observation at each station.

Most such measurements were made on lava boats and large readily identifiable blocks of floating debris near center channel, but at some stations (especially along upper channel reaches where velocities were high), the lava boats traveled more slowly than small pasty debris on the lava surface. In addition, the lava boats tended to migrate from the highest velocity zone in center channel into slower moving marginal zones (fig. 57.10). At such stations (for example, 1852 vent), a single observer had to make the entire measurement from one sighting point, in order to follow difficult-to-identify channel fragments. Accordingly, a diagonal sighting point was established, aimed at center channel on line with the lower observer point. This procedure empirically yielded consistent results, even though inherently more prone to measurement error because of unfavorable geometry for comparing velocities of lava fragments that deviated slightly from center channel.

Within a kilometer of the vent, the cross-flow velocity gradient again became abrupt at the channel edges (fig. 57.10, station 11), but there were relatively few lava boats for timing velocities. In these areas, the channel lava was essentially foam, and we measured velocities by throwing in a piece of levee lava (which sank) and timing the velocity of the resulting dimple in the lava surface.

While surface channel velocities were thus measurable with considerable precision, translation of such values into lava volumes required determination of cross-sectional channel geometry values which involve greater uncertainties. Channel breadth was measured directly at the station by use of an optical rangefinder, if heat shimmer did not interfere, or was estimated from a hovering helicopter by reference to the surveyed distances along the channel bank. Channel depth could be estimated by (1) constraints of pre-eruption topography, (2) limits indicated by the size of the largest lava boats, and (3) profiles of drained channels after cessation of the eruption (fig. 57.18). Factor (1) provided broad constraints, especially for upper channel stations where total flow thickness appeared to be only about 4–6 m, but local irregularity in surface topography precluded detailed estimates based on overall flow thickness. Observation that some large lava boats grounded and rolled (2), especially at low channel levels between surges, provided key channel depth data for some stations. Examination of drained channels after the end of the eruption (3) provided minimum depth estimates for some stations; interpretation of such values was complicated by incomplete draining, by burial of some stations during stagnation of the flow system, and by changes in channel geometry during the eruption. Possible sedimentation and erosion of the channel floor are recognized problems of lava flow evolution, to which we can add little. Channel overflows and levee growth more than doubled the flow thickness at several stations during the eruption.

Beyond such measurements and estimates of the channel cross-sectional geometry, additional uncertainties involve variations in velocity laterally and vertically in the channel, as well as protrusion of the lava lens beneath the channel banks in the transition zone (fig. 57.5). Lateral velocity gradients on the channel surface, noted above, were especially prevalent in the stable channel zone, where fivefold velocity gradients from center channel to margins were common. Intricate eddies and even reverse flow, analogous to any high-energy water stream, were also common. Surface gradients were more modest downchannel (transition zone), where plug flow commonly characterized most of the active channel and only a narrow marginal zone a few meters wide was characterized by a strong velocity gradient. In addition, poorly understood vertical velocity gradients, with velocity decreasing downward in the channel, are demonstrated by the commonly slower velocities measured for lava boats with sizable keels, in comparison with smaller surface debris on the channel surface. Finally, the process of kneading out gas bubbles, as lava flowed downchannel, may well have been increasingly effective with depth in the channel, producing a vertical density zonation in the lava channel. All these complications contribute to uncertainties in the lava-volume measurements that are difficult to resolve quantitatively.

# PRELIMINARY ESTIMATES OF THE RHEOLOGICAL PROPERTIES OF 1984 MAUNA LOA LAVA

*By* Henry J. Moore


## ABSTRACT

**During April 2–3, 1984, the visual characteristics of the lava of Mauna Loa changed dramatically along the length of the flow that was fed from vents near 2,850-m (9,350-ft) elevation. In the upper reaches, 2,500-m (8,200-ft) elevation and 3 km from the vents, the flow was composed of sparse clinkers and cinders in a matrix of incandescent lava and was confined within a channel 20 m across. The flow appeared to be laminar and more or less steady, with a velocity of about 5.3 m/s at its center. Concentration and mean size of solid to incandescent objects carried along by the flow increased downstream. In the lower reaches, at 1,620-m (5,300-ft) elevation and 15 km from the vents, the flow looked like a slowly moving mass of debris confined within rubbly levees; the debris included warm to incandescent fragments that were block size and smaller along with molten lava and incandescent globs or clots. Movement of the flow occurred by displacement of discrete, intact units with boundaries that paralleled the crests of the rubbly levees at the margins of the flow. Flow appeared to be laminar but unsteady, with surges and ebbs. Typical flow velocities were in the range of 0.1–0.3 m/s.**

**Apparent viscosity of the lava on a given day increased along the length of the flow and with time at some locations. On April 2, it was about $10^2$ Pa·s ($10^3$ poise) at the vents, $10^3$ Pa·s ($10^4$ poise) 3 km from the vents, $10^5$ Pa·s ($10^6$ poise) 15 km from the vents, and probably near $10^7$ Pa·s ($10^8$ poise) at the toe of one flow. Apparent viscosity at the vents increased from about $10^2$ Pa·s on April 2 to $2\times10^3$ Pa·s on April 13. These values compare favorably with field and laboratory data on viscosity of basalt at the same temperatures and with similar stresses and rates of shear as the Mauna Loa lava.**

**Rheology of the lava probably varied along the length of the flow and with time. It could have been a Newtonian fluid near the vents, a Bingham fluid 3 km from the vents, and a pseudoplastic fluid farther from the vents. Other models of fluids may also apply.**

**Volume flow rate in the channel at the vents on April 3 was near $1.5\times10^6$–$2.0\times10^6$ m³/h, about 12 times larger than that 15 km from the vents. With certain assumptions, an approximation of conservation of mass along the length of the flow requires that the density of lava flowing from the vents was 220 kg/m³ and implies a mass flow rate near $0.33\times10^9$–$0.44\times10^9$ kg/h. If these masses were deposited as lava with an average density of 2,200 kg/m³, the volume flow rate would appear to be $0.15\times10^6$–$0.20\times10^6$ m³/h.**


## INTRODUCTION

This paper estimates the rheological properties of the lava during the 1984 eruption of Mauna Loa Volcano in Hawaii and applies the results to the problems of volume and mass flow rates along the flow on one day. The derived rheological properties are based on visual observations while the flow was in progress; time and resources have permitted only partial analysis of the available data. Time-lapse photography and motion pictures of the eruption should be reviewed and analyzed in future rheological studies.

The 1984 eruption of Mauna Loa began at 0126 Hawaii standard time (H.s.t.) on March 25 and ended late on April 15 (Lockwood and others, 1984a, 1985). Initially, lava fountains issued from eruption fissures in the southwest corner of the summit caldera (Mokuaweoweo), but within a few hours eruptions from fissures migrated down the southwest rift zone, northeastward across Mokuaweoweo, and down the upper northeast rift zone (Lockwood and others, 1984b, 1985). Later on March 25, lava began pouring sequentially down the northeast rift zone from separate, isolated vents above eruption fissures. At about 1630 H.s.t. on March 25, lava was issuing from fissure vents at 2,830–2,900-m (9,300–9,500-ft) elevations that became the principal sources of lava for the remainder of the eruption (Lipman and Banks, chapter 57; fig. 58.1). Three southerly flow lobes fed by these vents stagnated by March 27, but the fourth (flow 1) was fed at a fairly constant volume flow rate ($\sim1.5\times10^6$ m³/h). Large flow rates were sustained from March 30 to April 7; after April 7 flow rates declined. Flow 1 advanced rapidly as a narrow aa sheet to the 910-m (3,000-ft) level, 25 km from the vents, and a lava channel had formed within the sheet by March 29. On March 29, a breakout or channel overflow near the 1,740-m (5,700-ft) level cut off the supply of lava to flow 1 so that it moved only about another kilometer in about a day and then stopped. Lava of this breakout gave rise to flow 1A which advanced rapidly along a course subparallel to and north of flow 1; advance of flow 1A gradually decreased until April 5, when it stopped about 27 km from the vents. A series of overflows that progressed upstream beginning April 3 reduced the lava supply to flow 1A and culminated in a major breakout at the 1,980-m (6,500-ft) level around noon on April 5. This major breakout cut off the lava supply to flow 1A and produced flow 1B, which flowed toward the northeast. Repeated channel blockages and overflows continued progressively upstream from April 5 to 8. On April 7, lava production at the vent began to dwindle; subsequently the flow system stagnated and vent activity ceased.

Flow 1, initially a narrow aa sheet flow, lenticular in profile, evolved into a flow system with three zones: (1) a channel zone within the sheet flow and below the vents, (2) a transition zone, and (3) a

dispersed-flow zone led by the advancing toe (Lipman and Banks, chapter 57). On March 28, just before the breakout of flow 1A, a stable channel zone extended from the vents about 11 km down to about the 1,830-m (6,000-ft) level; the transition zone extended 10 km down to within 1 or 2 km of the toe, then at the 1,220-m (4,000-ft) level, and the dispersed-flow zone made up the remainder. By April 3, the channel zone extended down to the 1,770-m (5,800-ft) level, the transition zone of flow 1A extended 3–4 km down to the 1,580-m (5,200-ft) level, and the dispersed-flow zone extended down to the toe of flow 1A at the 1,010-m (3,300- ft) level about 26 km from the vents. Significant blockages and obstructions of flow in the channel were observed on March 29. Such blockages and obstructions, which ponded the lava, increased in size and number upstream toward the vents with time. Overflows of lava caused by the blockages and obstructions created lava dams, levees, and elevated lava ponds along the channel zone. Minor failures of blockages in the lava dams produced increased flowage from the ponds and surging and ebbing flow downstream. Larger failures in the lava dams caused larger surges of lava, which overflowed the levees and produced small flows along the channel edges. Major failures caused major surges and breakouts or overflows of large volumes of lava. Such major overflows gave rise to flow 1A on March 29 and flow 1B on April 5. Subsequently, repeated blockages and overflows occurred progressively upstream.

Lava temperature at the vents was $1,140 \pm 3$ °C throughout the eruption, and that of the most fluid lava at channel stations as far as 10 km from the vents was in the range of $1,135 \pm 5$ °C (Lipman and Banks, chapter 57). Reported temperatures of the most fluid lava in the channel beyond about 12 km from the vents were 1,086–1,126 °C (flow 1A at elevations of 1,750–1,150 m; see Lipman and Banks, chapter 57). Bulk temperatures at the various channel stations and at lower elevations may have been lower than this, because there were coherent glowing blocks and solidified fragments in the flows. Bulk density of the flowing lava varied greatly and ranged from 330–2,600 kg/m$^3$ (0.33–2.6 g/cm$^3$); density tended to increase with distance from the vents (Lipman and Banks, chapter 57). Finally, the concentration of microphenocrysts in the lava increased with time at the vents and with distance from the vents (Lipman and Banks, chapter 57).

Subsequent sections of this paper will (1) describe the author's observations; (2) discuss the flow models and equations used to estimate the rheological properties of the flows, volume flow rates, and mass flow rates; (3) present the results; (4) discuss the results; and (5) list the conclusions.


### ACKNOWLEDGMENTS

Robert Decker, Scientist in Charge, and John P. Lockwood of the Hawaiian Volcano Observatory were instrumental in making arrangements for the author to witness the eruption and observe "redrock" for the very first time. Cordial hospitality and assistance were provided by the staff of the Hawaiian Volcano Observatory. Jack Lockwood, Peter Lipman, Norman Banks, and Christina Neal allowed this tyro to accompany them in the field with exemplary tolerance and patience. Helicopter pilots Bill Lacey, Jr., Tom Haupman, Ed Spencer, and Ken Ellard safely delivered the author to and from flows. Work was partly funded by NASA contract W–15–462.


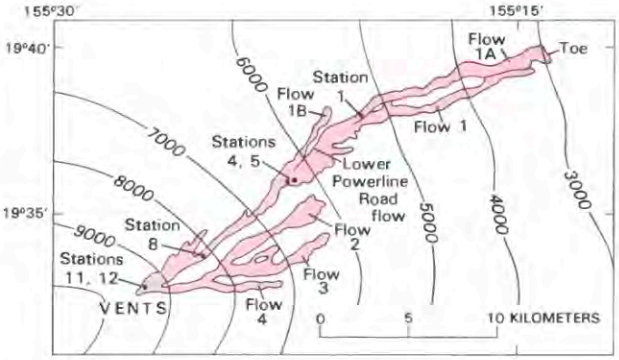


FIGURE 58.1.—Sketch map of the 1984 Mauna Loa lava flows showing stations referred to in text. Contour interval is 1,000 feet.

## OBSERVATIONS

Observations of the author for three localities (fig. 58.1) along the flow for the period April 2 through April 7 are described and discussed below. These localities are (see Lipman and Banks, chapter 57): (a) station 8, vent of 1852, 2,500 m (8,200 ft), 3 km from the vents; (b) stations 4 and 5, 1,920–1,950 m (6,300–6,400 ft), about 9 km from the vents; and (c) station 1, 1,620 m (5,300 ft), about 15 km from the vents. The first two localities were in the stable channel zone, and the third in the transition zone. Also included are the author's description of an advancing, unconfined, wide flow from an overflow and Hawaiian Volcano Observatory staff reports on the toe of flow 1A. These two flows correspond to dispersed flow.

### STATION 8, APRIL 2–7

The flow appeared to be a mass of cinders and clinkers imbedded in a matrix of incandescent lava estimated to be 4 m deep and confined within a channel 20 m across (fig. 58.2). A few floating silvery, meter-size blocks were carried along by the flow. Flow appeared to be laminar and nonturbulent. The central portion of the flow, about 1 m wide, moved as a plug-like unit of silvery to light gray crusty material in a matrix of incandescent lava (fig. 58.3). Between the plug-like center and the margins, bands of red incandescent lava and small cinders and clinkers were aligned parallel to the channel edges. Velocity decreased from about 5.3 m/s near the center to zero at the channel edge (fig. 58.3). The meter-size and smaller blocks did not rotate around horizontal axes and those near

FIGURE 58.2.—Lava in channel at station 8 on April 5. Channel is about 20 m wide; flow surface is composed of very light gray cinders and clinkers set in a matrix of reddish-orange lava; flow from right to left. Foreground is aa of sheet flow.

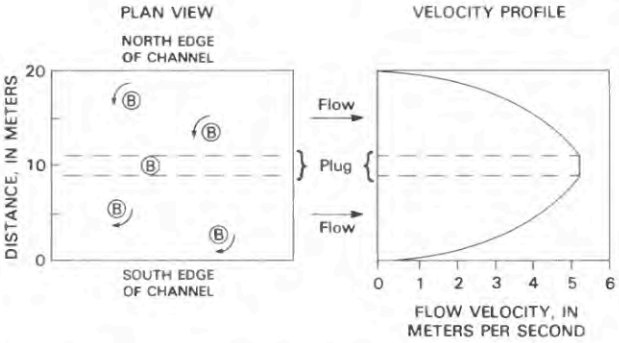


FIGURE 58.3.—Diagrammatic plan view and velocity profile for lava channel at station 8. In plan view, one-meter-wide plug moves as unit with uniform velocity. Blocks (B) north of plug rotate counterclockwise around vertical axes; blocks south of plug rotate clockwise around vertical axes; blocks in plug do not rotate. Velocity profile shows velocity of lava increases smoothly from zero at channel edge to 5.3 m/s in the plug.

the center did not rotate around vertical axes. Between the center and the margin, the blocks rotated around vertical axes. Rotation was counterclockwise on the north side of the channel and clockwise on the south side; the lava was moving from the west toward the east. The flow was remarkably quiet, but it did make faint shushing and swishing sounds. Volume flow rates obtained by multiplying the

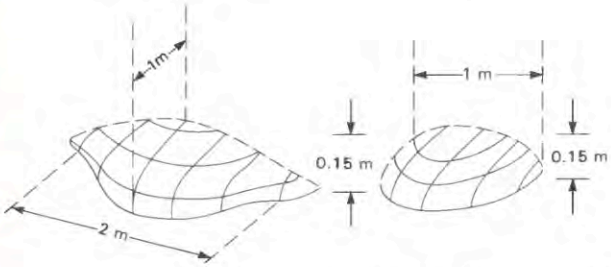


FIGURE 58.4.—Diagram illustrating two solidified overflow lobes at margin of channel at station 8. Lines are form lines.

center velocity, channel width, and estimated flow depth were of the order of $1.5 \times 10^6$ m$^3$/h (Lipman and Banks, chapter 57).

Two silvery lobes, interpreted to be recent overflows, were observed at the channel edge (fig. 58.4). They were estimated to be 0.15 m thick and 1–2 m wide; heat and the possible instability of the channel edge prevented direct measurements or sampling. These lobes are used later to estimate the yield strength of the lava, on the assumption that they represent solidified lava from the channel.

Postflow measurements indicate that the channel is 20 m wide and 6 m deep (Lipman and Banks, chapter 57, fig. 57.18, profile H). The estimated depth of flow was 4 m because the lava surface was 2 m below the channel lip during the eruption. The local slope derived from a 1:24,000-scale map is 5.6°.

## STATIONS 4 AND 5, APRIL 3–7

Characteristics of the flow channels at these stations were diverse. The lava was confined within channels formed by high levees interspersed with sections reminiscent of station 8. In the high, leveed sections, topographic gradients were somewhat reduced. Upstream, lava flowed rapidly into the high, leveed part from channels with low overflow levees. Downstream, the levees, composed chiefly of rubble, increased in height and caused ponding of the lava, which spilled over the downstream side in a lava fall.

On April 3 near station 4 at an elevation of 1,920 m (6,300 ft), lava was flowing in a high, leveed channel with velocity as great as 1.2 m/s during surges and 0.8 m/s during ebbs. The levee was about 2.3 m high. Visible lava within the channel was composed of dark cinders and clinkers and incandescent clots set in a matrix of incandescent lava (fig. 58.5). Concentrations of the cinders and clinkers were larger than at station 8, and incandescent clots were not evident at station 8. Along the margin of the levee, the channel surface was crusted and stranded blocks were present (fig. 58.6*A*). During surges, rising lava would arch upward, and the marginal crusts and stranded blocks would sympathetically tilt upward and outward (fig. 58.6*B*). Surges were accompanied by small outward displacements of the levees and the avalanching of debris down the levee flanks. During peak surges the lava spilled over and onto the crust and stranded blocks (figs. 58.5*A* and 58.6*C*). During ebbs,

*A*

*B*

FIGURE 58.5.—Flow of 1984 Mauna Loa lava in high, rubbly, leveed channels. ***A***, Station 4 on April 3. Lava from center during surge is overflowing material in channel at margin. Note dark, partly cooled lava. Channel is about 14 m wide. ***B***, Station 6 on April 7. Typical flow in leveed channel during ebb. Note the structure and blocky appearance of incandescent clots. Channel is about 22 m wide.

the crust and blocks would become level as the lava subsided. Upstream, lava was flowing in a channel 14 m wide at 1.6 m/s. Here and elsewhere, swishing and shushing noises generated by the flowing lava were evident and more pronounced than those at station 8. The next day (April 4), the height of the rubbly levee had increased to 5 m. Upstream near the 1,935-m (6,350-ft) elevation, lava velocity was near 2 m/s; but the velocity varied somewhat because of surges and ebbs. On the morning of April 7 at station 5 at 1,950-m (6,400 ft), lava was flowing in the channel at 1.5 m/s; later in the day, lava overflowed the debris-choked leveed channel upstream and substantially reduced the input of the lava (fig. 58.6*D*, 58.7*A*). Lava from breakouts (fig. 58.7), or sudden releases of semi-ponded lavas, produced immense surges that overflowed the rubbly levees and formed a thin sheet over the levees and beyond to some distance from the levee crest; exceptionally large breakouts (fig. 58.7*B*) produced sustained flows such as flow 1B. Flow appeared to be laminar and nonturbulent during surges, ebbs, and even breakouts. Distal lobes of a breakout sheet that probably occurred on April 6 were 0.3–0.75 m thick and 3–4 m wide (fig. 58.8). The thickness and width of these lobes are used later to estimate a yield strength for lava that flowed in the channel here.

Volume flow rates for the lava during April 2–5 were estimated to be in the range of $0.37 \times 10^6$–$0.60\ 10^6$ $m^3/h$ (Lipman and Banks, chapter 57).

### STATION 1, APRIL 3

The flow at this station appeared in general to be a hummocky mass of slowly moving debris, rubble, and blocks confined within a rubbly, leveed channel 57 m wide and estimated to be 6 m deep (fig. 58.9). Mounds and blocklike incandescent units, partly to completely veneered by darker, cooler debris, rode along the top of the hummocky surface; at times, spallation of dark and incandescent debris would further expose their incandescent cores. Elsewhere, local exposures of incandescent lava beneath and intermingled with debris were common. The flow was unsteady, but not turbulent. Surges with velocity as great as 0.36 m/s were accompanied by increase in the height of the flow by a few meters; ebbs with velocity near 0.18 m/s were accompanied by decrease in the height of the flow by a few meters. Movement occurred by shearing between intact units along surfaces with traces that paralleled the channel edge (fig. 58.10). At intermediate velocities and thicknesses, the central part of the flow moved as a plug-like unit with little internal relative motion; the units immediately flanking the center moved at a slower velocity and, similarly, with little internal motion; and so on to the channel edges, where the velocity of the outermost units was very small to zero. As the flow surged and thickened, the velocity of the central unit increased and the relative velocities between the units decreased until, at peak velocity, almost the entire width between the levees had the same velocity. Estimates of the flowing width during two surges were 45 and 52 m. Surges were accompanied by crunching noises due to the grinding action between and within the intact units; the rubble levees were displaced outward and debris rolled down the levee flanks. As the flow ebbed and thinned, the velocity of the center unit decreased and that of the other units decreased sequentially outward from the center. Such ebbs were accompanied by a substantial decrease in noise; the levees ceased to move, and debris ceased to roll down their flanks. Further thinning would cause motion of the units to cease progressively from the channel edge toward the center. During one ebb, the entire flow briefly stopped. A visual estimate of the thickness at the center when that part ceased to move was 3 m.

Volume flow rates estimated during the eruption on April 3 were $0.15 \times 10^6$ to $0.45 \times 10^6$ $m^3/h$ (Lipman and Banks, chapter 57).

Post-eruption profiles of the channel suggest that it was 57 m wide and 8 m deep below the levee crest; a 2-m-thick layer of basalt occupied the channel floor (Lipman and Banks, chapter 57, fig. 57.18, profile M). The local slope derived from a 1:24,000-scale topographic map is 3.3°.

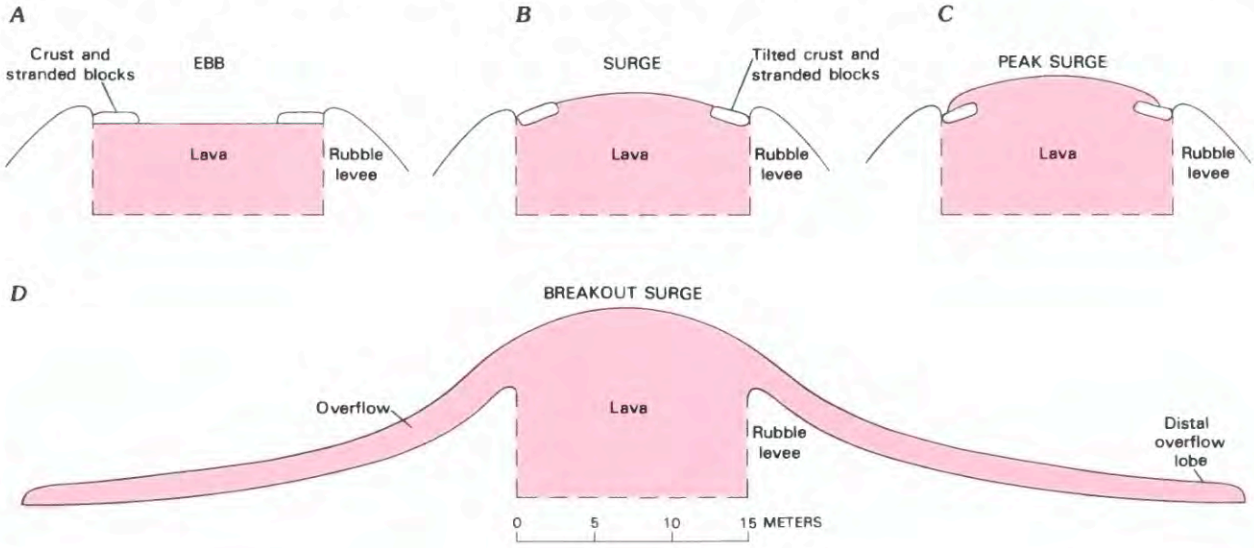


FIGURE 58.6.—Diagrammatic profiles of lava in channel with high, rubbly levees at station 4 on April 3 (*A*–C) and station 5 on April 7 (*D*). ***A***, During ebb flow, marginal crusts, stranded blocks, and lava are nearly level. ***B***, During surge flow, lava arches upward and marginal crust and stranded blocks tilt upward and outward. ***C***, During peak surge, lava overflows tilted marginal crust and blocks. ***D***, During breakout surge, lava spills over rubble levees and flows down levee flanks and onto surrounding surfaces, producing a deposit with lobate margins.

## LOWER POWERLINE ROAD FLOW, APRIL 5

A wide unconfined flow 2–3 m thick, from a previous breakout, advanced eastward at a rate near 0.03 m/s on a slope of 3.6°. The flow was composed of an upper unit of blocks, clinkers, and cinders overlying incandescent molten lava (fig. 58.11). The flow advanced in caterpillar-tractor style (Krauskopf, 1948): debris of the top layer moved faster than the underlying lava so that it avalanched down the advancing front and was overridden by the molten lower part (fig. 58.12*A*). The flow made crunching noises similar to those at station 1 and the avalanching debris made

*A* *B*

FIGURE 58.7.—Breakout surges near stations 4 and 5. ***A***, Breakout surge of April 7 from ponded lava upstream of station 5. Dark horizon to right is near crest of channel levee. Lava spills over levee near huge glob of incandescent lava that is moving toward the right. Overflows like this one produce layers with lobate margins on the flanks of the leveed channels. ***B***, Breakout near station 4 on April 5. Note reddish-orange glowing lava overflowing levee and flowing down levee flank at left middle. Protrusions on center skyline are large (approx. 8-m) blocks carried along the leveed channel by lava flowing toward the left. Glowing lava in foreground and at right is part of breakout that produced flow 1B.

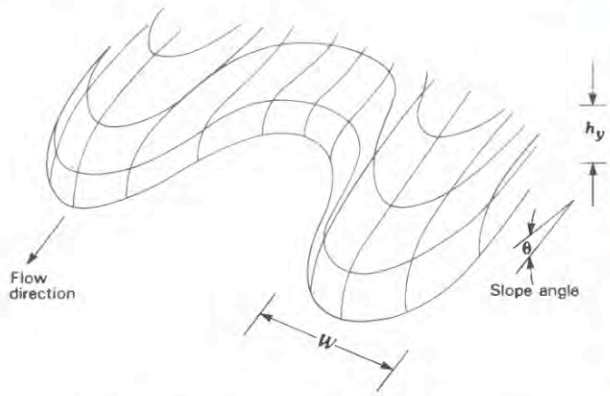


FIGURE 58.8.—Diagram of lobes at margin of overflow sheet from breakout surge on April 6 near station 5. Parameters indicated are lobe width (W), lobe thickness ($h_y$), and slope angle (θ).

FIGURE 58.9.—Surging flow at station 1 on April 3. Flow is composed chiefly of blocks, clinkers, and cinders and is moving from right to left. Spalling of debris from one block has exposed its reddish-orange molten core; some incandescent lava is also visible in ridge just below block. Immediate foreground is rubble levee; flow obscures levee on opposite side of channel. Large block at crest of flow is about 2 m across.

clinking, thunking sounds. In most places the base of the molten lava was in contact with debris, but locally with preflow surfaces. Where exposed, the molten lava at the front of the flow was smoothly curved and showed subtle rounded protrusions here and there (fig. 58.12*B*). At the very base, it curved back upon itself, indicating that molten lava was overriding molten lava and that the velocity at the base of the flow was zero; debris in the process of being overridden was stationary. Large expanses of the upper surface moved downstream as intact units with little internal relative movement, although there was movement between the various intact units. In plan view the front was lobate, and each lobe tended to follow local rilles. The entire flow advanced down a broad, shallow valley.

### FLOW 1A, APRIL 2–3

Although the toe of flow 1A could not be visited because of the dense vegetation there, it was estimated from the air to be 9 m thick and 762 m (2,500 ft) wide, and to be moving at 26 m/h on April 2 and 12 m/h on April 3. The local slope derived from a 1:24,000-scale topographic map is 3.65°. Crude estimates obtained by multiplying the thickness, width, and rate of advance indicate volume flow rates of $0.18 \times 10^6$ m$^3$/h on April 2 and $0.08 \times 10^6$ m$^3$/h on April 3. For an assumed density of 2,400 kg/m$^3$ (2.4 g/cm$^3$), the mass flow rates are $0.43 \times 10^9$ kg/h on April 2 and $0.20 \times 10^9$ kg/h on April 3.

## MODELS AND EQUATIONS

### MODELS

In the calculations below, the Mauna Loa lava flows are treated as Newtonian and Bingham fluids flowing in semi-elliptical channels and as wide, unconfined flows; flow is laminar. The implications of possible pseudoplastic flow are also considered.

A Newtonian fluid is characterized by a viscosity (fig. 58.13). Here, the stresses are always proportional to the rate of shear. At high temperature, dense molten lava is a Newtonian fluid with a viscosity that is a function of composition and temperature (Shaw, 1969, 1972).

In contrast to a Newtonian fluid, a Bingham fluid is characterized by a yield strength in addition to a viscosity (fig. 58.13). The concept of a Bingham fluid was developed to account for the rheological behavior of paints flowing in circular pipes (Bingham, 1922) and later applied with success to the flow of slurries in pipes (Caldwell and Babbitt, 1941; Smith, 1960; Valentyik, 1972). Bingham (1922) suggested that his concept might apply to the flowage of some natural fluids such as lava. Subsequently, numerous authors have attempted to apply Bingham's fluid model to lava flows (Hulme, 1974; Moore and Schaber, 1975; Borgia and others, 1983; Cigolini and others, 1984), debris flows (Johnson, 1970; Fink and others, 1981), and landslips. Bingham-fluid concepts have been invoked by Kilburn (1981) to account for the irreversible transition of pahoehoe to aa (Macdonald, 1953) as described by Peterson and Tilling (1980). There is, however, a general lack of data on yield strengths and Bingham viscosities; such measurements are represented by the pioneering work of Shaw and others (1968) and subsequent works (Sparks and others, 1976; Cigolini and others, 1984).

A pseudoplastic fluid is different from both the Newtonian and Bingham fluids (fig. 58.13). Stresses on the pseudoplastic fluid produce rates of shear that vary according to a power law, and there is no single value of viscosity. Experimental data indicate that basalt at 1,120–1,125 °C behaves like a pseudoplastic fluid when stresses are less than about $16 \times 10^3$ Pa and shear rates are less than 5 s$^{-1}$ (Shaw, 1969).

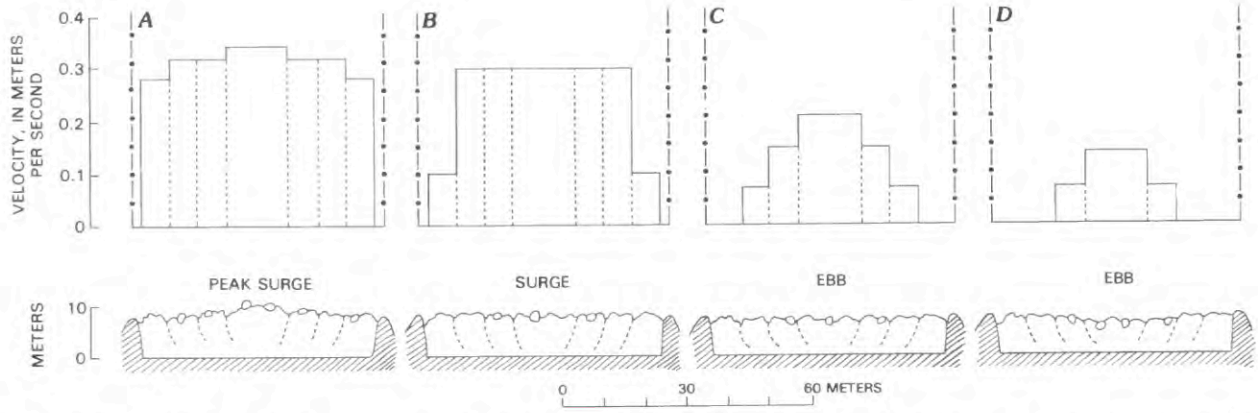


FIGURE 58.10.—Velocity profiles and diagrammatic cross sections of the unsteady flow of lava at station 1 on April 3. Dot-dash lines on velocity profiles represent crests of levees; dashed and solid lines outline discrete intact units of moving surface. Cross sections show upper surface of flow; dashed lines represent postulated unit boundaries (which may actually be vertical). ***A***, During peak surge, surface of flow moves as discrete, intact units with velocities as great as 0.34 m/s; parts of center of flow are a few meters higher than levee crest. ***B***, During surge, entire central 45 m of surface moves with a velocity near 0.3 m/s; velocities of units near edge are much less; surface of flow is about same elevation as levee crest but irregular. ***C***, During ebb, a central unit moves as a plug with a velocity near 0.2 m/s; velocity decreases outward toward levee and that of units at edges is zero; elevation of surface of flow drops below elevation of levees. ***D***, With further ebbing, central unit moves with a velocity near 0.15 m/s; next adjacent unit is slower; other units have stopped; surface of flow sags downward toward center.

## APPARENT VISCOSITY

In an ideal Newtonian fluid, the viscosity is constant, and miniscule stresses produce miniscule rates of shear. In an ideal Bingham fluid, the viscosity is constant, but the rate of shear is zero when the stresses are less than the yield strength (fig. 58.13). Apparent viscosity, which is calculated in the same way as the Newtonian viscosity, is a strong function of the rate of shear for the

FIGURE 58.11.—Flow at Lower Powerline Road on April 5. Flow is about 3 m thick and advancing at a rate near 0.03 m/s. Upper surface is composed chiefly of debris; underlying reddish-orange layer of incandescent lava is locally exposed along front.

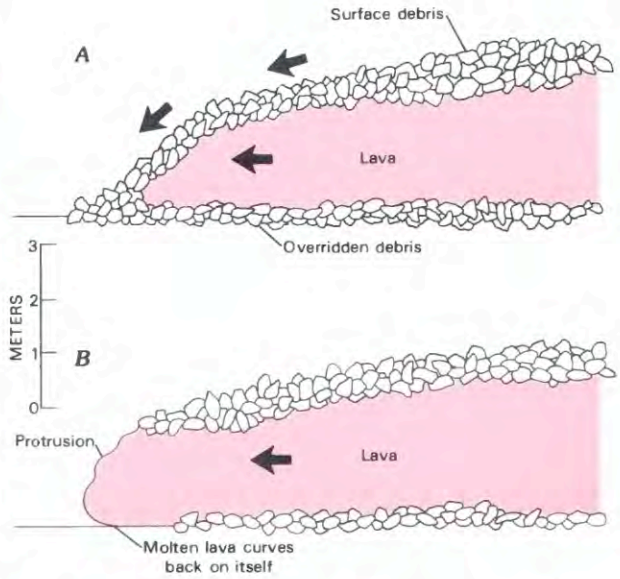


FIGURE 58.12.—Diagrammatic profiles of flow at Lower Powerline Road on April 5. ***A***, The flow is typical aa, with an upper surface of debris overlying molten, incandescent lava. Upper surface moves as a unit with greater speed than underlying layer so that debris avalanches and falls down front and is then overridden by flow. ***B***, Surface of molten lava. Where surface of molten lava is exposed at the front, it is smoothly curved, with some rounded protrusions, and curves back upon itself at the base.

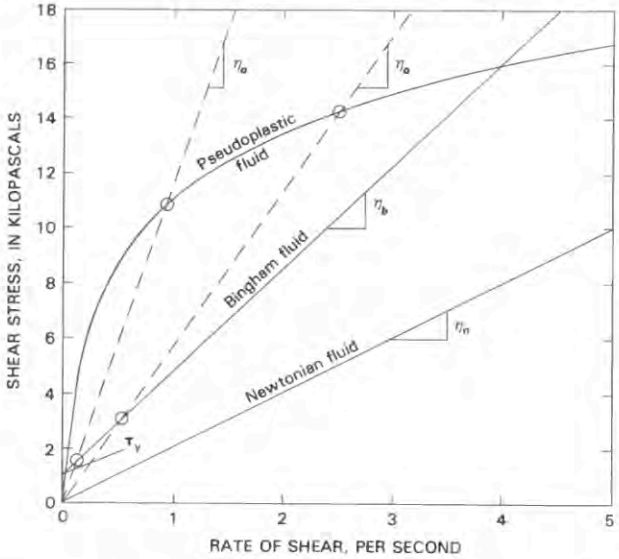


FIGURE 58.13.—Relation between shear stress and rate of shear for Newtonian, Bingham, and pseudoplastic fluids. Newtonian fluid is represented by straight line passing through origin; slope of line ($\eta_n$) is the viscosity. Bingham fluid has a yield strength and a viscosity; shear stress on Bingham fluid must exceed the yield strength ($\tau_y$) to produce a rate of shear greater than zero; slope of line ($\eta_b$) is the Bingham viscosity. Pseudoplastic fluid is represented by curved line; rate of shear is approximately a function of shear stress raised to some power. Apparent viscosity ($\eta_a$) assumes a Newtonian fluid and varies with the rate of shear for Bingham and pseudoplastic fluids. As depicted, viscosity of Newtonian fluid is $2 \times 10^3$ Pa·s. Viscosity and yield strength of Bingham fluid are $3.8 \times 10^3$ Pa·s and $10^3$ Pa, respectively. Pseudoplastic fluid is similar to basalt at 1,125 °C (Shaw, 1969).

Bingham fluid. It varies from large values at small rates of shear to values that approach the Bingham viscosity at very large rates of shear. Similarly, apparent viscosity calculated for a pseudoplastic fluid varies from large values at small rates of shear to smaller values at larger rates of shear. The term "apparent viscosity" is applied to calculations for any fluid when the fluid is assumed to be Newtonian (see, for example, Shaw, 1969).

## PLUGS AND SLABS

As a consequence of the yield strength, the central and upper parts of Bingham fluids flowing in the laminar regime move as plugs in channels and as slabs in wide, unconfined flows (Johnson, 1970). Dimensions of the plugs and slabs depend on the stresses acting on the fluid, the yield strength, and the shape and size of the channel or wide flow. The velocity distribution from the margins of a flow in a semi-elliptical channel to the central plug, or from the base of the wide flow, is the same as the normal velocity distribution for laminar flow of a Newtonian fluid; velocity increases from zero at the margin or base of the flow to the velocity of the plug or slab at its edge. For a Newtonian fluid, the dimensions of the plug or slab are zero.

## EQUATIONS

The yield strength of a Bingham fluid may be estimated from the dimensions of the flow at rest and the plug or slab dimensions when the fluid is flowing. Viscosity for both Newtonian and Bingham fluids may be estimated from the observed velocity. Additional parameters required for these estimates include the acceleration of gravity, fluid density, slope angle or topographic gradient, and channel or flow dimensions. Equations used for these estimates are described below.

### YIELD STRENGTH

Yield strength ($\tau_y$) can be estimated from the rest thickness ($h_y$) of a wide, unconfined Bingham fluid that has stopped. The stress acting on this flow ($\tau$), which is driven by gravity, is given by:

$$\tau = \rho g h \sin \theta \tag{1}$$

where $\rho$ is the density of the flow, $g$ is the acceleration of gravity, $h$ is the distance below the surface of the flow, and $\sin \theta$ is the topographic gradient ($\theta$ is the slope angle measured at a characteristic flow surface). The stress at the base of the flow ($\tau_b$) is obtained when $h$ is equal to the thickness of the flow during flow ($H$). The stress at the base of the slab, which is equal to the yield strength ($\tau_y$), is obtained when $h$ is equal to the thickness of the slab ($h_y$). A wide, unconfined flow comes to rest when the shear stress ($\tau$) is less than the yield strength at all depths. This may occur because the flow thins or the yield strength increases. Because $\tau$ is a maximum at the base of the flow,

$$\tau_y = \rho g h_y \sin \theta \tag{2}$$

where $\tau_y$ is the yield strength of the flow and $h_y$ is the slab thickness or rest thickness of the flow.

Yield strength can be estimated from flow lobes at rest because the viscosity is no longer important and the flow may therefore be treated as a plastic. According to Orowan (1949), the yield strength of a plastic body can be obtained from the relation:

$$\tau_y = \rho g h_y^2 / W \tag{3}$$

where $W$ is the width of the lobe.

Yield strength may also be estimated from the dimensions of the plug of a Bingham fluid flowing in a channel. For a flow driven by gravity in a semi-elliptical channel, Johnson (1970) obtains the relations:

$$\tau_y = \rho g a_y \sin \theta / [(A/B)^2 + 1] \tag{4}$$

and

$$\tau_y = \rho g b_y \sin \theta / [(B/A)^2 + 1] \tag{5}$$

where $a_y$ is the half-width of the plug, $b_y$ is the thickness of the plug, $A$ is the half-width of the channel or flow, and $B$ is the depth of flow in the channel center.

### VISCOSITY

Viscosity of the Mauna Loa lava can be calculated because the velocity of the flowing lava at the centers of channels ($V_o$) and the channel width were measured and good estimates of flow depth were obtained during the eruption (Lipman and Banks, chapter 57). Viscosity ($\eta$) is calculated using an equation for laminar flow in semi-elliptical channels (after Johnson, 1970):

$$\eta = (\rho g \sin \theta / V_o)\{B^2/2[(B/A)^2+1] + [(B/A)^2+1][\tau_y/\rho g \sin \theta]^2/2 - \tau_y B/\rho g \sin \theta\} \quad (6)$$

where $B$ is the depth of flow in the channel center and $A$ is the half-width of channel or flow.

The application of equation 6 needs some discussion; profiles of channels obtained after the eruption indicate that most of them were more or less rectangular (Lipman and Banks, chapter 57, fig. 57.18, table 57.2), whereas equation 6 assumes that the channels are semi-ellipses; the semi-ellipses are inscribed in the rectangular channels and defined by the depth of flow and the half-width of the channel or flow. Additionally, the lava is treated as both a Newtonian and a Bingham fluid in later calculations. When $B/A$ is zero, equation 6 yields the correct expression for laminar flow of a Bingham fluid in an infinitely wide channel or as a wide, unconfined flow. When both $B/A$ and the yield strength ($\tau_y$) are equal to zero, equation 6 yields the correct expression for laminar flow of a Newtonian fluid in an infinitely wide channel or as a wide, unconfined flow. Similarly, when $B/A$ is one, equation 6 yields the correct expression for laminar flow of a Bingham fluid in a semicircular channel. When $B/A$ is one and the yield strength is zero ($\tau_y$), equation 6 yields the correct expression for laminar flow of a Newtonian fluid in a semicircular channel. Intuitively, it seems probable that apparent viscosity calculated for rectangular channels would be reasonably close to that calculated with equation 6. Viscosity of a Newtonian fluid assuming an infinitely wide channel with a depth of $B$ is twice as large as that assuming a semicircular channel with a radius of $B$ because $B/A$ ranges from zero to one; these two conditions should bracket the rectangular channels in most cases (see, for example, Lipman and Banks, chapter 57). For a Bingham fluid, the yield strength results in dead zones (no motion) at the bottom corners of rectangular channels (Johnson, 1970); semi-elliptical channels may therefore be reasonable approximations. Finally, Johnson (1970, p. 505) states that equation 6 may be applied to flows in rectangular and triangular channels with sufficient accuracy for most purposes. Thus, the preliminary viscosities calculated below are believed to be reasonable estimates; but subsequent studies should employ theories for flow in rectangular channels.

### AVERAGE VELOCITY

Average velocity is lower than plug or slab velocity to a varied degree that depends on the yield strength, viscosity, stress, and channel or flow geometry. For flow of a uniformly thick Bingham fluid in very wide channels or as wide flows, the average velocity is given by

$$\overline{V} = (H^2 \rho g \sin \theta / 3\eta)[1 - (3/2)(\tau_y/\tau_b) + (1/2)(\tau_y/\tau_b)^3]. \quad (7)$$

For a Newtonian fluid ($\tau_y = 0$), equations 6 and 7 show that the average velocity is two-thirds the velocity at the surface. For flow of a Bingham fluid in semicircular channels, the average velocity is given by

$$\overline{V} = (R^2 \rho g \sin \theta / 8\eta)[1 - (4/3)(\tau_y/\tau_b) + (1/3)(\tau_y/\tau_b)^4]. \quad (8)$$

For a Newtonian fluid ($\tau_y = 0$), equations 6 and 8 show that the average velocity is one-half the velocity at the channel center.

An explicit equation for average velocity in an elliptical channel is not available to the author at this time. For this reason, estimates were made of the lower and upper bounds for the average velocity. The lower and upper bound estimates use the fact that the average velocity of flow between the plug and margin of a circular channel is between one-half and two-thirds of the velocity of the plug; the average velocity of flow between the slab and base of a wide, unconfined flow is two-thirds the velocity of the slab.

### MASS AND VOLUME FLOW RATES

Volume flow rate is the product of the average velocity and the flow cross-sectional area. Mass flow rate is the product of flow density and volume flow rate. Here, the assumption of semi-elliptical channels may affect the results somewhat because the area of the semi-ellipse inscribed in a rectangular channel is 0.79 times the area of the rectangle. Thus, the volume and mass flow rates for a Newtonian fluid flowing through a semi-elliptical area is 0.39–0.52 times the volume and mass flow rates calculated by multiplying the center velocity and a rectangular area. These factors are less for a Bingham fluid in a variable way that depends on the size of the plug.

### CRITERIA FOR LAMINAR FLOW

The use of the equations above assume laminar flow; the modified Reynolds number ($\mathbf{R}_m$) must therefore be sufficiently low. For wide flows (Moore and Schaber, 1975),

$$\mathbf{R}_m = 2/[(\eta/\rho \overline{V} H) + (\tau_y/2\rho \overline{V}^2)] \quad (9)$$

where $H$ is the thickness of the flow; and for flows in semicircular channels (Smith, 1960),

$$\mathbf{R}_m = 2/[\eta/\rho \overline{V} R) + (\tau_y/4\rho \overline{V}^2)] \quad (10)$$

where $R$ is the radius of the channel. Similar expressions for elliptical channels are not available at this time, but the above equations should give reasonable estimates of whether a flow is either laminar or turbulent.

## RESULTS

### DATA USED

In the calculations of apparent viscosity, I have used in all cases the flow velocities, channel widths, and flow depths reported by

TABLE 58.1.—*Densities used to calculate apparent viscosity, Bingham viscosity, yield strength, volume flow rate, and mass flow rate*

[Slope angles listed were used in calculations of apparent viscosity. See Lipman and Banks (chapter 57) for dates, times, sample numbers, sample densities, and sample descriptions]

| Station | Elevation (m) | Elevation (ft) | Density ($kg/m^3$) | Slope angle (degrees) | Date (mo/d/yr) | Time (H.s.t.) | Sample | Density ($kg/m^3$) | Sample Description |
|---|---|---|---|---|---|---|---|---|---|
| 1 | 1620 | 5300 | 2400 | 3.3 | 3/25/84 | 1540 | NER-1F | 2230 | Core of aa flow. |
| | | | | | 3/29/84 | 1300 | ------ | 2600 | Core of aa flow. |
| 2 | 1710 | 5600 | 2200 | 4.0 | | | | | |
| 3 | 1800 | 5900 | 2000 | 2.5 | | | | | |
| 3 | 1800 | 5900 | 1700 | 2.5 | | | | | |
| 4 | 1920 | 6300 | 1700 | 2.5 | | | | | |
| 4 | 1935 | 6350 | 1700 | 3.5 | 4/06/84 | 1430 | NER-12/48 | 1720 | Overflow from main channel. |
| 4 | 1920 | 6300 | 1700 | 3.0 | | | | | |
| 5 | 1950 | 6400 | 1700 | 2.5 | | | | | |
| 6 | 2100 | 6900 | 1700 | 4.0 | | | | | |
| 7 | 2290 | 7500 | 1300 | 4.5 | 4/08/84 | 1306 | NER-12/57 | 1250 | Overflow from main channel. |
| 8 | 2500 | 8200 | 1000 | 6.0 | 4/06/84 | 1220 | NER-12/47 | 1150 | From main channel. |
| 8 | 2500 | 8200 | 1000 | 5.0 | 4/08/84 | 1026 | NER-12/53 | 990 | From main channel. |
| 11 | 2850 | 9350 | 530 | 6.5 | 4/08/84 | 1145 | NER-12/54 | 530 | Overflow from main channel. |
| 12 | 2870 | 9400 | 530 | 3.0 | | | | | |
| 12 | 2870 | 9400 | 530 | 4.5 | | | | | |

Lipman and Banks (chapter 57). Values for one case (station 11, vent, April 8, 1600 H.s.t.) appear to yield a spurious result, which is graphically reported but omitted from the discussion below. Slope angles also come from the same source, with the exceptions of station 1, which was 3.3° instead of 3°, and station 6 (April 7), for which the author obtained 4°. No slope angles are reported for stations 9 and 10. Flow densities employed are listed in table 58.1 and were selected by the author from values reported by Lipman and Banks (chapter 57). The acceleration of gravity is taken as 9.8 $m/s^2$. According to unpublished Hawaiian Volcano Observatory staff reports, flow 1A advanced at a rate of $7.2\times10^{-3}$ m/s on April 2 and $3.4\times10^{-3}$ m/s on April 3; given a thickness of 9 m, equation 7 yields apparent viscosities near $5.6\times10^6$ Pa·s (April 2) and $12\times10^6$ Pa·s (April 3). Calculated apparent viscosities are reported graphically (fig. 58.14) and described below.

## APPARENT VISCOSITY

There are two general trends in the magnitude of the apparent viscosity (fig. 58.14). First, apparent viscosity increases dramatically along the length of the flow on a given day. On April 2, for example, apparent viscosities were: (1) $1.4\times10^2$ Pa·s at the vent (station 11); (2) $1.0\times10^3$–$1.3\times10^3$ Pa·s 3 km from the vent at station 8; (3) $3.0\times10^3$–$9.5\times10^3$ Pa·s 9 km from the vent at station 4; (4) $0.9\times10^5$–$1.6\times10^5$ Pa·s 15 km from the vent at station 1; and (5) $5.6\times10^6$ Pa·s 26 km from the vent at the toe of flow 1A. Second, apparent viscosity at some stations increases with time. In the vent area, for example, apparent viscosities were $1.4\times10^2$–$1.6\times10^2$ Pa·s (station 11) and more or less constant from April 2 through April 6, but they increased to $2.7\times10^2$–$4.5\times10^2$ Pa·s (stations 11 and 12) on April 8 and 9 (excluding one value for April 8 that is assumed to be spurious); they climbed to $0.9\times10^3$ and $1.4\times10^3$ Pa·s (station 12) on April 12 and 13, respectively. At the 1,620-m (5,300-ft) level (station 1) apparent viscosity increased from about $1.6\times10^4$ Pa·s on March 31 to $0.5\times10^5$–$1.5\times10^5$ Pa·s on April 2, 3, and 4. At some stations, such as station 4, the behavior of the apparent viscosity is mystifying. At 1,920 m (6,300 ft), it was $3\times10^3$–$6\times10^3$ Pa·s on March 29 and by April 2 had increased to $9.5\times10^3$ Pa·s. Upstream, at 1,935 m (6,350 ft), the apparent viscosity on April 2 was $3\times10^3$ Pa·s, fully one-third of that downstream. The magnitudes of the calculated apparent viscosity will be compared with experimental data on basalt, and factors that may account for them will be discussed later.

## BINGHAM LAVA

Three idealized stations and flow conditions are used below to examine the effects of a Bingham fluid on the lava rheology and consider volume and mass flow rates on a given day. These idealized conditions correspond to conditions on April 3 at (1) station 8, (2) station 4, and (3) station 1. The idealized channel and flow conditions (tables 58.2, 58.3, and 58.5) are slightly changed from those used in the calculations of apparent viscosities and listed in Lipman and Banks (chapter 57); the latter are given in tables 58.2, 58.3, and 58.5 as observations and estimates. Some of the calculations test a proposed equation relating viscosity and yield strength

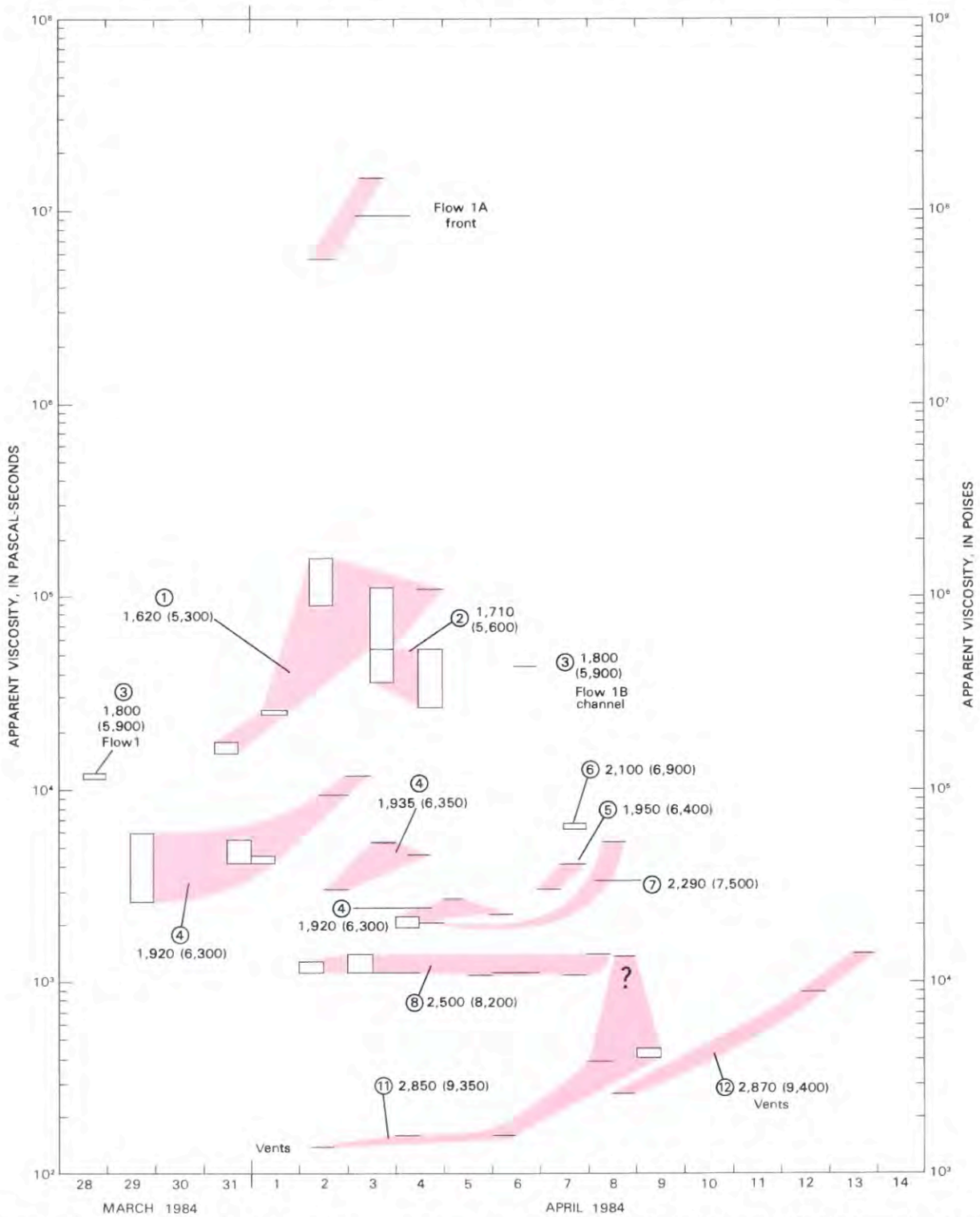


FIGURE 58.14.—Apparent viscosity of Mauna Loa lava at various stations from March 28 through April 13. Graphs of data connected by shaded areas indicate the same station or locality on different days. Station numbers circled from Lipman and Banks (chapter 57, table 57.3). Figures give elevation in meters (elevation in feet in parentheses). One determination for April 8 (queried) is probably spurious. Note that (1) apparent viscosity increases greatly from higher to lower elevations or with distance from vent on any given day from March 31 through April 8 and (2) apparent viscosity increases with time at the vents and at many of the stations downstream of the vents.

TABLE 58.2.—*Observations and calculations for idealized station 8 on April 3*

[Station is at 1852 vent, 2,500 m (8,200 ft) elevation]

| Speed at center, $\underline{V}$ (m/s) | Flow depth, $\underline{B}$ (m) | Channel width, $2\underline{A}$ (m) | Volume flow rate, $\underline{Q}$ ($10^6 m^3/h$) | Mass flow rate, $\underline{M}$ ($10^9 kg/h$) | Yield strength, $\tau_y$ (Pa) | Viscosity, $\eta$ Pa·s | Assumed density, $\rho$ ($kg/m^3$) | Slope angle, $\theta$ (degrees) |
|---|---|---|---|---|---|---|---|---|
| | | | Observations and estimates | | | | | |
| 5.3 | 4 | 20 | 1.5 | 1.5 | — | — | 1000 | 5.0 |
| | | | Calculations | | | | | |
| 5.3 | 4 | 20 | 0.6-0.8 | 0.6-0.8 | [1]0 | 1244 | 1000 | 5.6 |
| 5.3 | 4 | 20 | 0.6-0.8 | 0.6-0.8 | [2]66 | 1195 | 1000 | 5.6 |
| 5.3 | 4 | 20 | 0.6-0.8 | 0.6-0.8 | [3]221 | 1083 | 1000 | 5.6 |
| 5.3 | 4 | 20 | 0.6-0.8 | 0.6-0.8 | [4]150 | 1134 | 1000 | 5.6 |

[1]Yield strength set to zero in equation 6; viscosity is apparent viscosity.
[2]Yield strength calculated from half-width of plug (0.5 m) (eq. 4); viscosity from equation 6.
[3]Yield strength calculated from rest widths and heights of flow lobes at channel edge (eq. 3); viscosity from equation 6.
[4]Yield strength adjusted until velocity of plug was satisfied with a viscosity from equation of Moore (1982), calculated plug width is 2.3 m.

TABLE 58.3.—*Observations and calculations for sections at idealized station 4 on April 3*

[Station is at 1,920–1,935 m (6,300-6,350 ft) elevation]

| Speed at center, $\underline{V}$ (m/s) | Flow depth, $\underline{B}$ (m) | Channel width, $2\underline{A}$ (m) | Volume flow rate, $\underline{Q}$ ($10^6 m^3/h$) | Mass flow rate, $\underline{M}$ ($10^9 kg/h$) | Yield strength, $\tau_y$ (Pa) | Viscosity, $\eta$ Pa·s | Assumed density, $\rho$ ($kg/m^3$) | Slope angle, $\theta$ (degrees) |
|---|---|---|---|---|---|---|---|---|
| | | | Observations and estimates | | | | | |
| 0.94 | 7 | 18.3 | 0.43 | 0.74 | — | — | 1700 | 2.5 |
| 1.6 | 5 | 14 | 0.40 | 0.69 | — | — | 1700 | 3.5 |
| | | | Calculations, lower section | | | | | |
| 1.0 | 6 | 18 | 0.15-0.20 | 0.26-0.34 | [1]0 | 7245 | 1700 | 2.0 |
| 1.0 | 6 | 18 | 0.17-0.22 | 0.29-0.37 | [2]684 | 3723 | 1700 | 2.0 |
| 1.0 | 6 | 18 | 0.21-0.24 | 0.35-0.41 | [3]1185 | 1880 | 1700 | 2.0 |
| 1.0 | 6 | 18 | 0.18-0.22 | 0.31-0.38 | [3]891 | 2885 | 1700 | 2.0 |
| | | | Calculations, upper section | | | | | |
| 1.6 | 5 | 14 | 0.16-0.21 | 0.27-0.36 | [1]0 | 5637 | 1700 | 3.75 |
| 1.6 | 5 | 14 | 0.17-0.22 | 0.28-0.37 | [2]684 | 3702 | 1700 | 3.75 |
| 1.6 | 5 | 14 | 0.18-0.23 | 0.31-0.39 | [2]1185 | 2542 | 1700 | 3.75 |
| 1.6 | 5 | 14 | 0.17-0.22 | 0.30-0.38 | [3]970 | 3014 | 1700 | 3.75 |

[1]Yield strength set to zero in equation 6; viscosity is apparent viscosity.
[2]Yield strength calculated from dimensions of flow lobes (eqs. 2, 3); viscosity from equation 6.
[3]Yield strength adjusted until velocity of plug was satisfied with viscosity from equation of Moore (1982); dimensions required for plug are 2.2 m by 10.0 m and 2.6 by 5.2 m.

TABLE 58.4.—*Dimensions, slopes, and yield strength of overflow lobes at station 5*

[ Overflows probably occurred late on April 6]

| Lobe | Width, $\underline{W}$ (m) | Thickness, $\underline{t}$ Range (m) | Thickness, $\underline{t}$ Average (m) | Slope angle, $\theta$ (degrees) | Yield Strength, $\tau_y$ from equation 2 (Pa) | Yield Strength, $\tau_y$ from equation 3 (Pa) |
|---|---|---|---|---|---|---|
| 1 | 3 | 0.45–0.60 | 0.53 | 5.5 | 846 | 1531 |
| 2 | 4 | 0.60–0.75 | 0.68 | 1–2.5 (1.75) | 346 | 1898 |
| 3 | 3 | 0.45 | 0.45 | 6 | 784 | 1125 |
| 4 | 4 | 0.60–0.75 | 0.68 | 4 | 790 | 1926 |
| 5 | 4 | 0.30–0.45 | 0.38 | 6 | 662 | 601 |
| 6 | 4.5 | 0.30–0.45 | 0.38 | 3 | 331 | 535 |
| 7 | 3 | 0.35 | 0.35 | 10 | 1013 | 680 |
| 8 | -- | 0.60 | 0.60 | 4 | 698 | -- |
| | | | | | Average 684 | Average 1185 |

(Moore, 1982); others deal with a wide, unconfined flow and a channel flow at the vent, although the channel flow is not treated as Bingham fluid. The results are plotted in figure 58.15, from which it can be seen that Bingham viscosity and yield strength exhibit striking increases along the length of the flow; yield strength increases about 10–34 times from station 8 to station 1, and Bingham viscosity increases about 70–80 times.

## STATION 8

The parameters used for this station (table 58.2) are identical to those used for the calculation of apparent viscosity except for a slope of 5.6° instead of 5° or 6°.

Yield strength for the lava at this location is on the order of $10^2$ Pa (table 58.2). Two methods were used in preparing the estimates. In the first method, the half-width of the plug observed by the author (0.5 m), inserted in equation 4, gives a result of 66 Pa. In the second, the height (0.15 m) and width (1.0 m) of the lobes at the channel edge (fig. 58.7), inserted in equation 3 give a result of 221 Pa; if the lobe width is taken as 2.0 m instead of 1.0 m, the yield strength becomes 110 Pa. The larger yield strength requires a plug 3.4 m across instead of the observed 1.0 m.

Bingham viscosity does not differ significantly from the apparent viscosity of $1.2\times10^3$ Pa·s. For the largest yield strength the viscosity is about $1.1\times10^3$ Pa·s. Finally, the observed 5.3 m/s velocity of the plug can be obtained when the yield strength and viscosity, derived from the proposed equation of Moore (1982), are 150 Pa and $1.1\times10^3$ Pa·s, respectively; the calculated plug width is 2.3 m.

It should be noted that the calculated modified Reynolds numbers, which are in all cases 29 or less, are in agreement with the observed laminar character of the flow. The results are plotted in figure 58.15.

## STATION 4

The actual channel and flow conditions at this station were rather complicated, some sections having high, rubbly levees and others low to nonexistent overflow levees. For the idealization of this station, three noteworthy changes in particular were made from those used to calculate apparent viscosity: (1) the slope for the lower section with high, rubbly levees was changed from 2.5° to 2.0°; (2) the flow depth of the lower section was changed from 7 m to 6 m; and (3) the slope of the upper section with low to nonexistent levees was changed from 3.5° to 3.75° (table 58.3). These changes were made in order to satisfy the requirement of conservation of mass and still have the same Bingham fluid properties in two adjacent sections.

Yield strength for this station is probably near $10^3$ Pa. Average values for yield strength calculated with equations 2 and 3 and dimensions of lobes at the margin of an overflow sheet are 684 and 1,185 Pa, respectively (table 58.4). There is some uncertainty in correlation because the overflow producing the sheet probably occurred on April 6, not April 3.

Apparent viscosities required to account for the 1.0 m/s and 1.6 m/s velocities in the idealized lower and upper sections are $7.6\times10^3$ Pa·s and $5.6\times10^3$ Pa·s, respectively; the mass flow

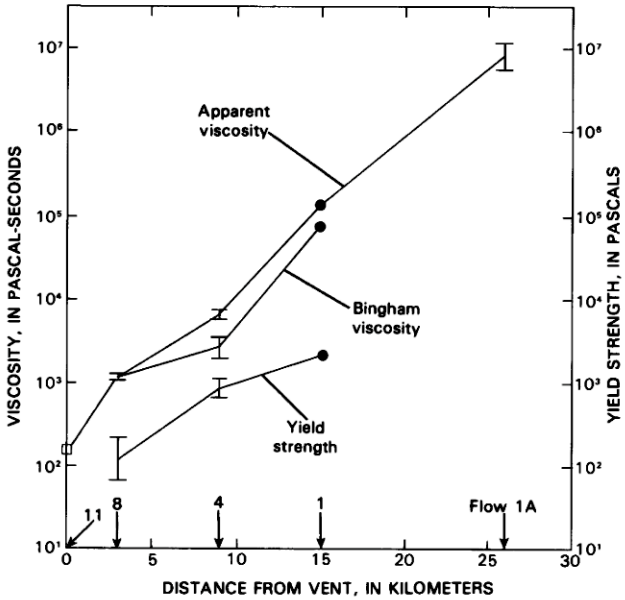


FIGURE 58.15.—Apparent viscosity, Bingham viscosity, and yield strength as a function of distance from vents on April 3. Numbers and arrows on abscissa indicate stations and their distances from vents. Note that Bingham viscosity shows increase in magnitude comparable to that of apparent viscosity. Value for station 11 (open square) is from text; values for station 1(dots) are from table 58.5; vertical lines for stations 8 and 4 show range of values from tables 58.2 and 58.3; vertical line for flow 1A shows range of values from text.

rates are substantially the same (table 58.3). A Bingham fluid with a yield strength near 680 Pa and a viscosity near $3.7 \times 10^3$ Pa·s would conserve mass and provide the same rheology for the lava at the two adjacent sections. Calculations using the larger yield strength of 1,185 Pa do not yield the same viscosity, but the two values are close. Finally, values of yield strength and viscosity from Moore's (1982) equation that satisfy the velocity in equation 6 are reasonably close both to one another and to the values derived from equations 2 and 3.

It should be noted that modified Reynolds numbers, which are less than 11 in all cases, are in agreement with the observed laminar character of the flow. Results are plotted in figure 58.15.

## STATION 1

A simple Bingham fluid cannot account for the flow at this station because it does not explain the occurrence of a number of discrete, intact flow units between the center plug and the channel margin, the velocity gradient of the flow units across the channel increases with ebbing and with lower center velocity, and the Bingham model has nothing to say about nonsteady flow. In one set of calculations that employ a constant channel width, the width of the plug becomes greater than the width of the channel with thinning of the flow. Such a condition would seem to require faulting or shearing of the plug, which could result in a number of discrete, intact flow units and variable yield conditions. In any event, however, the Bingham model will be applied with the intention of illustrating the problem.

Channel dimensions and flow velocities employed below are different from those used for the calculation of apparent viscosity (table 58.5). The channel width and depth are taken as 57 m and 8 m, respectively, on the basis of the profile measured after the eruption. For the nominal conditions, a velocity of 0.3 m/s is paired with a flow depth of 8 m and a plug width of 45 m; these values are consistent with the author's impressions of the flow on April 3. The slope is taken as 3.3°. Subsequent calculations predict the velocity at the center of flow with varying flow depths using (A) a model with a fixed channel width (57 m) but varying flow depth, and (B) a model that assumes effective channel width varies directly with flow depth.

A yield strength of 2,225 Pa is used in the calculations (table 58.5). This value was obtained using equation 4 and the nominal conditions mentioned above; it is reasonably close to the 2,700 Pa obtained using a rest thickness of 2 m estimated from the lava on the channel floor in the postflow profile.

An apparent viscosity of $1.34 \times 10^5$ Pa·s is obtained for the nominal conditions of flow mentioned above (table 58.5); this is only 21 percent higher than the largest apparent viscosity obtained previously for April 3 (fig. 58.14). Incorporation of a yield strength of 2,225 Pa in equation 6 gives a Bingham viscosity of near $81 \times 10^3$ Pa·s (fig. 58.15). This viscosity is 17 times larger than the one predicted by Moore's (1982) equation. Modified Reynolds numbers for all flow calculations, which are discussed below, are less than 1 and consistent with laminar flow.

Calculations for model A (table 58.5) predict some of the salient aspects of the surging and ebbing flow and plug widths that become larger than the channel width with ebbing flow. At the nominal flow condition, the central 45 m of the flow moves as a plug with a velocity of 0.3 m/s. During a surge, the flow thickens to 9 m and the central 36 m of the flow moves as a plug with a velocity of 0.39 m/s. When the flow ebbs, the flow thins to 7 m and the central part of the flow moves as a plug with a velocity of 0.22 m/s. Here, the plug is about the same width as the channel so that some sort of interference of flow and disruption of the plug might be expected. With further thinning to 6 m, the predicted speed of the flow is 0.15 m/s, and the plug will no longer fit in the channel.

In model B, reasonable plug velocities are obtained by varying the yield strength during surging and redefining the channel dimensions during ebbs. For example, if the yield strength increases to 3,200 Pa because of increased friction by loading during a 9.3-m-thick surge, the velocity of the 49-m-wide plug is 0.34 m/s. If the channel is redefined to be 7 m deep and 42 m wide and the yield strength returns to 2,225 Pa, the velocity of the 33-m plug in the fluid-filled channel is 0.2 m/s. Narrower, shallower filled channels have smaller plug velocities, and the plugs do not reach the channel margins.

## WIDE, UNCONFINED FLOWS

There is no information from which to estimate the yield strength and Bingham viscosity for the Lower Powerline Road flow

TABLE 58.5.— *Observations and calculations using two models for idealized station 1 on April 3*

[Station is in lower channel of flow 1A at 1,620 m (5,200 ft) elevation. For explanation of models see text]

| Speed at center, $\underline{V}$ (m/s) | Flow depth, $\underline{B}$ (m) | Channel width, $2\underline{A}$ (m) | Volume flow rate, $\underline{Q}$ ($10^6 m^3/h$) | Mass flow rate, $\underline{M}$ ($10^9 kg/h$) | Yield strength, $\tau_y$ (Pa) | Viscosity, $\eta$ Pa·s | Assumed density, $\rho$ ($kg/m^3$) | Slope angle, $\theta$ (degrees) | Dimensions of plug, $\underline{b}$, $2\underline{a}$ (m) |
|---|---|---|---|---|---|---|---|---|---|
| | | | | Observations and estimates | | | | | |
| 0.38 | 6 | 52 | 0.43 | 1.0 | — | — | 2400 | 3.0 | — |
| 0.3 | 6 | 52 | 0.34 | 0.82 | — | — | 2400 | 3.0 | — |
| 0.2 | 6 | 52 | 0.23 | 0.54 | — | — | 2400 | 3.0 | — |
| | | | | Calculation of apparent viscosity | | | | | |
| 0.3 | 8 | 57 | 0.19–0.26 | 0.46–0.62 | [1]0 | 133,800 | 2400 | 3.3 | 0.0, 0.0 |
| | | | | Calculations using model A | | | | | |
| 0.3 | 8 | 57 | 0.23–0.28 | 0.54–0.67 | [2]2225 | 81,110 | 2400 | 3.3 | 1.8, 45.0 |
| 0.39 | 9 | 57 | 0.32–0.40 | 0.77–0.97 | 2225 | 81,110 | 2400 | 3.3 | 1.8, 36.2 |
| 0.22 | 7 | 57 | 0.15–0.18 | 0.34–0.44 | 2225 | 81,110 | 2400 | 3.3 | 1.7, 57.8 |
| 0.15 | 6 | 57 | 0.09–0.11 | 0.23–0.28 | 2225 | 81,110 | 2400 | 3.3 | 1.7, 77.4 |
| | | | | Calculations using model B | | | | | |
| 0.34 | 9.3 | 57 | 0.31–0.38 | 0.75–0.91 | [3]3200 | 81,110 | 2400 | 3.3 | 2.6, 49.1 |
| 0.3 | 8 | 57 | 0.23–0.28 | 0.55–0.67 | [2]2225 | 81,110 | 2400 | 3.3 | 1.8, 45.0 |
| 0.2 | 7 | 42 | 0.10–0.12 | 0.24–0.30 | 2225 | 81,110 | 2400 | 3.3 | 1.8, 32.9 |
| 0.13 | 6 | 35 | 0.05–0.06 | 0.12–0.14 | 2225 | 81,110 | 2400 | 3.3 | 1.8, 31.2 |
| 0.001 | 4 | 10 | --- | 0.02 | 2225 | 81,110 | 2400 | 3.3 | 2.7, 8.4 |

[1]Yield strength set to zero in equation 6; viscosity is apparent viscosity.
[2]Yield strength calculated from half-width of plug (taken as 45 m) (eq. 4); viscosity from equation 6.
[3]Yield strength assumed to increase with load during surge; viscosity same as in (2) above.

on April 5. If the flow, 3 m thick, had the same properties as those at station 1 ($\tau_y = 2{,}225$ Pa, $\eta = 81 \times 10^3$ Pa·s), it would advance at a rate near 0.02 m/s and its rest thickness would be 1.5 m.

### STATION 11

In order to consider volume and mass flow rates along the length of the flow on April 3, average values for April 2 and 4 must be used. On April 2, the lava was flowing in a channel 21.5 m wide with a flow depth of 3 m at 17.8 m/s; on April 4, the lava was flowing in a channel 21 m wide with a flow depth of 3 m at 15 m/s (Lipman and Banks, chapter 57). Volume flow rates from the average of these conditions are $3.8 \times 10^6$ $m^3/h$ for a rectangular flow at uniform velocity and $1.5 \times 10^6$–$2.0 \times 10^6$ $m^3/h$ for laminar flow in a semi-elliptical channel. Mass flow rates are $2.0 \times 10^9$ kg/h for a rectangular flow and $0.8 \times 10^9$–$1.1 \times 10^9$ kg/h for flow in a semi-elliptical channel. Apparent viscosities on the two days were near $0.15 \times 10^3$ Pa·s, and modified Reynolds numbers were less than 300 and indicate laminar flow.

## VOLUME AND MASS FLOW RATES

This section presents calculated volume and mass flow rates for April 3 along the length of the flow (fig. 58.16) from the vent to the toe. In these calculations, I have used the parameters for the idealized stations (tables 58.2, 58.3, and 58.5), the estimates for the vent given in the previous section, and approximate calculations for the toe. Because of the surging, ebbing flow at station 1, average volume and mass flow rates are difficult to estimate; for purposes of illustration, volume and mass flow rates are taken as those corresponding to velocities of 0.2 and 0.22 m/s in table 58.5. A small overflow upstream of station 1 on the morning of April 3 does not apparently affect the results because the magnitude of changes is much the same as on April 2.

Volume flow rates appear to decrease by about one order of magnitude from the vent to station 1, beyond which estimates are so uncertain that a decrease may or may not be present (fig. 58.16*A*). The volume flow rates calculated for a rectangular flow with uniform velocity are $3.8 \times 10^6$ $m^3/h$ at the vent, $1.5 \times 10^6$ $m^3/h$ at station 8,

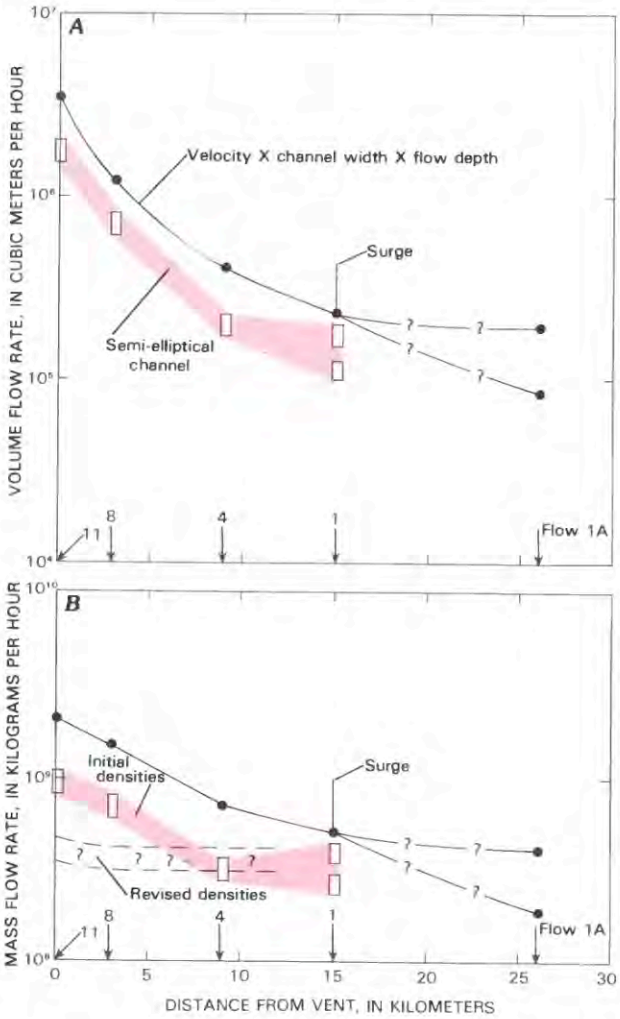


FIGURE 58.16.—Volume and mass flow rates of Mauna Loa lava on April 3, 1984. Numbers and arrows on abscissae indicate stations and their distances from the vents. Rates indicated by boxes calculated assuming semi-elliptical channels; rates indicated by dots calculated assuming rectangular flow cross sections; see text and tables 58.2, 58.3, and 58.5. ***A***, Volume flow rate: note the decrease by a factor of 12 from the vent to station 1, 15 km from the vent. ***B***, Mass flow rate: note the decrease by a factor near 3 from the vents to station 4, 9 km from the vent (using densities initially assumed in calculations of apparent viscosity). Band with question marks represents approximate mass flow rate calculated using revised densities that conserve mass.

$0.42 \times 10^6$ m³/h at station 4, and $0.23 \times 10^6$ m³/h at station 1. Thus, volume flow rates are about 16 times larger at the vent than they are at station 1. The volume flow rates calculated for Newtonian (at the vent) and Bingham fluids in a semi-elliptical channel are $1.5 \times 10^6$–$2.0 \times 10^6$ m³/h at the vent, $0.6 \times 10^6$–$0.8 \times 10^6$ m³/h at station 8, $0.17 \times 10^6$–$0.22 \times 10^6$ m³/h at station 4, and $0.10 \times 10^6$–$0.18 \times 10^6$ m³/h for station 1. The volume flow rate under these conditions is thus about 9 times larger at the vent than at station 4.

Mass flow rates also decrease with distance from the vent (fig. 58.16*B*). Mass flow rates at the vent are about 3 times larger than they are at station 4. For the rectangular flow with uniform velocity, mass flow rates are $2 \times 10^9$ kg/h at the vent and $0.7 \times 10^9$ kg/h at station 4; for reasons stated earlier these values are probably too large by a factor of about 2. For the semi-elliptical channel, mass flow rates are $0.8 \times 10^9$–$1.1 \times 10^9$ kg/h at the vent and $0.28 \times 10^9$–$0.37 \times 10^9$ kg/h at station 4; beyond station 4, no mass flow changes are required by the data. Thus there appears to be a mass flow of $0.5 \times 10^9$–$0.7 \times 10^9$ kg/h that needs to be accounted for in the semi-elliptical channel calculations. This is discussed later.

## DISCUSSION

### APPARENT VISCOSITY

The magnitudes of the apparent viscosity calculated for the Mauna Loa lava are reasonable when compared with experimental data (Shaw, 1969). For example, graphic interpolation of instrument viscosities between 1,150 °C and 1,130–1,135 °C (Shaw, 1969, fig. 1, table 2) suggests that the viscosity of Hawaiian basalt at 1,140 °C should be near 300–400 Pa·s. This is comparable in magnitude to the viscosity calculated for lava at the vents from April 2 through the morning of April 8, which is 140–380 Pa·s. The somewhat lower values for the Mauna Loa lava may be because it was frothy; this could reduce the apparent viscosity (Shaw and others, 1968). Because maximum shear stresses decrease with time at the vents from about $1.6 \times 10^3$ Pa on April 2 through April 8 to about 500–700 Pa on April 12, the frothy lava at the vents might be expected to have apparent viscosity that increases (see, for example, Shaw and others, 1968, fig. 14). The apparent viscosity for station 8 (fig. 58.17), which is $1.1 \times 10^3$–$1.4 \times 10^3$ Pa·s, is reasonably close to the instrument viscosity ($\sim 10^3$ Pa·s) and to the high value of the Bingham viscosity ($0.75 \times 10^3$ Pa·s) measured in Makaopuhi lava at 1,130–1,135 °C (Shaw and others, 1968). Magnitudes of the apparent viscosity at stations 4 and 5 (1,920 to 1,950-m elevation) and its erratic behavior between adjacent sites and stations on the same day (fig. 58.17) might be accounted for if the lava were frothy and cooler than 1,135 °C so that it behaved somewhat like basalt at 1,125 °C and small, but variable, shear rates. Rough estimates of maximum shear stresses and shear rates for the lava at stations 4 and 5 vary within the ranges $1.8 \times 10^3$–$3.5 \times 10^3$ Pa and 1.4–0.3 $s^{-1}$, respectively (fig. 58.17). According to Shaw (1969), instrument apparent viscosity at 1,125 °C is variable and decreases with stress up to $16 \times 10^3$ Pa and shear rates as high as 5 $s^{-1}$. Judging from Shaw (1969, fig. 1, inset), apparent viscosity of basalt at 1,125 °C increases from about $10 \times 10^3$ Pa·s at a shear rate of 1 $s^{-1}$ to about $70 \times 10^3$ Pa·s at a shear rate of 0.05 $s^{-1}$. Thus, if the stations 4 and 5 lava was a few degrees hotter than 1,125 °C and the bubbles affected the lava, the calculated apparent viscosities ($1.9 \times 10^3$–$12 \times 10^3$ Pa·s) are entirely reasonable. Local variations in bubble content, temperature, stress, and rate of shear could produce or contribute to the mystify-

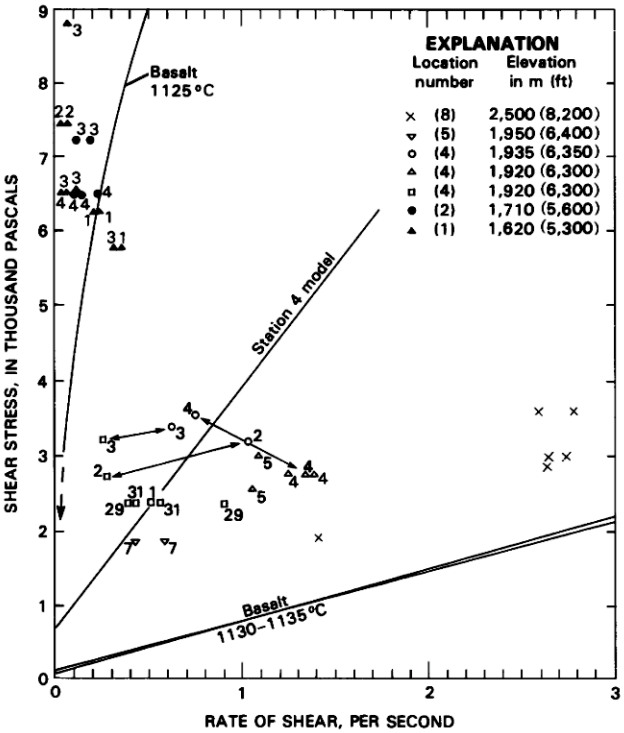


FIGURE 58.17.—Relation between approximate maximum shear stress and rate of shear for 1984 Mauna Loa lava at five stations. Lines labeled 1,130–1,135 °C correspond to data on basalt of Shaw and others (1968); curved line labeled 1,125 °C corresponds to experimental data on basalt at that temperature (Shaw, 1969). Line station 4 model is for Bingham fluid with yield strength of 680 Pa and viscosity of $3.7 \times 10^3$ Pa·s. Note that this diagram fits within inset of figure 14 of Shaw (1969) but that ordinate and abscissa are interchanged. Numbers by plotted points refer to day of month in interval March 29 to April 7; arrowed lines connect data points at different sites on the same day at station 4.

ing variations of the apparent viscosity with time and place. Increase in the volume fraction of solids in the lava, which is known to increase apparent viscosity (see, for example, Shaw, 1969; Moore and Schaber, 1975), is an added variable. For the lower reaches of the flow at stations 1 and 2, where temperatures were near 1,125 °C, maximum stress (fig. 58.17) is about $5.7 \times 10^3$–$9 \times 10^3$ Pa, shear rate about 0.4–0.08 $s^{-1}$, and apparent viscosity $15 \times 10^3$–$160 \times 10^3$ Pa·s. Here, the instrument apparent viscosity of approximately $10 \times 10^3$–$70 \times 10^3$ Pa·s at 1,125 °C (see, for example, Shaw, 1969, fig. 1, inset) is in good agreement with the apparent viscosity obtained for the stations 1 and 2 lava. Apparent viscosity calculated for the toe area of flow 1A, where it must eventually reach infinity, is plausible. Walker (1967) assumes that the flow of Etna lava virtually stops when the velocity is $10^{-4}$ m/s and then calculates that its apparent viscosity is $10^8$–$10^{10}$ Pa·s. If flow 1A was advancing at a rate of $10^{-4}$ m/s and its thickness was unchanged, it would have an apparent viscosity of $0.4 \times 10^9$ Pa·s.

## A BINGHAM LAVA

The principal reasons for considering that the Mauna Loa lava might behave as a Bingham fluid are the rheological studies of Makaopuhi lava lake (Shaw and others, 1968), observations of the flow in progress that indicate the centers of the flows move as plugs, and studies of other volcanic flows (for example, Cigolini and others, 1984). Both the yield strength and Bingham viscosity derived for the idealized station 8 at 2,500-m (8,200-ft) elevation are quite comparable in magnitude to those obtained for the Makaopuhi lava lake at similar temperatures (Shaw and others, 1968). For the lava lake, yield strength was 70–120 Pa, quite comparable to the 66–220 Pa obtained at station 8. Similarly, the Bingham viscosity for the lava lake, $0.65 \times 10^3$–$0.75 \times 10^3$ Pa·s, is quite comparable to the $1.1 \times 10^3$–$1.2 \times 10^3$ Pa·s obtained at station 8. For the idealized station 4, it was shown that a Bingham fluid with one set of properties could conserve mass in two adjacent sections of the same channel with different gradients and dimensions.

As noted previously, a simple Bingham model will not account for the flow at station 1. Some aspects of the model fit the observations. In particular, the upper parts of the flow moved as slabs or pluglike units. Because the model predicts that the width of the plug becomes larger than the channel, faulting and disruption of a Bingham plug into separate intact units could occur. In this case, the yield conditions could vary as a function of angle of internal friction, cohesion, and other factors (Johnson, 1970).

Parts of the Mauna Loa flow may have behaved as a Bingham fluid; but they were heterogeneous in comparison with paints and slurries. For example, the Bingham model predicts the observed slablike motion of the upper layer of wide flows and provides a mechanism for stopping the flow when it thins to its rest thickness. However, the upper slablike parts of the wide, unconfined flows are composed of blocks, clinkers, and cinders, whereas the underlying parts are composed of incandescent, molten lava. Elsewhere, the heterogeneous character of the flow is evident. At station 8, visual observations indicate the presence of the central plug required for a Bingham fluid, but the surface of the flow was clearly heterogeneous. The characteristics of the lava at depth are unknown. At lower elevations near stations 4 and 5, concentrations of fragments in the incandescent lava were larger, the fragments were darker, and the fragments were larger than at station 8; in contrast with station 8, incandescent lumps or plastic clots were evident and abundant. The flow at station 1 looked like a debris flow with warm to incandescent blocks, clinkers, and cinders, large globs or plastic clots, and local exposures of incandescent lava beneath the debris. Although the discrete, intact flow units show that the flow had some strength, and pluglike motion occurred, the Bingham model does not predict a number of intact flow units.

## WHICH MODEL?

It is entirely possible that the Mauna Loa lava obeyed different flow laws at different places and times (see, for example, Shaw, 1969). The lava may have been a Newtonian fluid at the vents, a

Bingham fluid at station 8, and a pseudoplastic fluid or some other kind of fluid in the lower reaches. Concentrations of debris, incandescent blocks and fragments, and plastic clots were so large in the lower reaches of the flow on April 2 and 3 that models of the flow movements might require incorporation of concepts such as cohesion, angle of internal friction, and pore fluids.

The information necessary to establish the appropriate flow models may be embodied in existing time-lapse photography and motion pictures of the flow in progress. If satisfactory velocity profiles of the flowing lava can be obtained from the photography, they can be used to infer the rheological properties of the flow (Johnson, 1970). A velocity profile for an apparently well behaved flow confined in a leveed channel at Arenal (Cigolini and others, 1984) illustrates how such velocity profiles can be used. For the Arenal flow, the lava-filled channel was 30 m wide and 10 m deep. The slope was 30°. The central 18 m of the flow moved as a plug with a velocity of $6 \times 10^{-3}$ m/s; velocity decreased from the plug to zero at the flow margins. Using the half-width of the plug and a density of 2,700 kg/m$^3$ in equation 4, the yield strength comes out to be $37 \times 10^3$ Pa, which is reasonably close to the value of $79 \times 10^3$ Pa obtained by Cigolini and others (1984) using equation 2. Equation 6 gives a Bingham viscosity of $27 \times 10^6$ Pa·s which is essentially the same as an independently measured value of $24 \times 10^6$ Pa·s for unit c of the Arenal flow at 1,075 °C (Cigolini and others, 1984).

## VISCOSITY AND LAVA CHARACTERISTICS

The principal causes of the changes in viscosity and yield strength are related to changes in temperature, gas and bubble contents, concentration of solids, and plastic clots. The major changes at the vents are probably related to changes in gas and bubble contents and concentration of solids because the vent lava at 1,140 °C was frothy and had about 14–21 percent volume concentration of microphenocrysts on April 2–3; by April 13 it was still frothy and the concentration of microphenocrysts was about 27 percent (Lipman and Banks, chapter 57). A 13 percent change in microphenocryst concentration at this temperature would probably increase viscosity by a factor of 2 or so (Shaw, 1969; Moore and Schaber, 1975). Apparent viscosity of the frothy lava at the vents increased by a factor of 10 from April 2 to April 13 (fig. 58.14) with a concomitant decrease in shear stress from about $1.6 \times 10^3$ Pa to $0.5 \times 10^3$–$0.7 \times 10^3$ Pa; it is possible that the apparent viscosity increased because the lava was also frothy (see, for example, Shaw and others, 1968, fig. 14). A similar increase could result if the lava was a Bingham or pseudoplastic fluid because both stress and rate of shear declined from April 2 to April 13.

In order to account for three orders of magnitude increase in apparent viscosity from the vent to station 1 on April 2, 3, or 4 (fig. 58.14) by microphenocrysts alone, the volume concentration would have to increase something like 20 percent (see, for example, Shaw, 1969) to 50 percent (see, for example, Moore and Schaber, 1975) above the initial 14–21 percent. The concentration of phenocrysts increased along the length of the flow, but values are not reported (Lipman and Banks, chapter 57). Solids other than crystals that were incorporated in the lava probably contributed to the increase in apparent viscosity by analogy with slurries (Smith, 1960) and debris flows (Johnson, 1970). The fluid contained warm, solid debris, hot incandescent blocks and fragments, and molten globs or plastic clots, all set in a matrix of hotter, more fluid lava. Both the mean size and the concentrations of these objects increased along the length of the flow in a manner correlative with the increase in magnitude of the apparent viscosity. Such a correlation implies that concentrations of all kinds of objects in the flow might affect the rheology in ways analogous to the effects of solids in slurries and debris flows.

## VOLUME AND MASS FLOW RATE

The conservation of mass in a complicated system such as the Mauna Loa eruption is difficult to establish because gases evolve from the lava and enter the atmosphere, lava overflows channels or becomes ponded, and there may be other sinks. In addition, the observations and data employed may contain errors. In the mass-flow calculations (fig. 58.16*B*), the density employed is the most likely factor that could lead to errors. In order to have a constant mass flow with volume flows of $1.5 \times 10^6$–$2.0 \times 10^6$ m$^3$/h through a semi-elliptical channel at the vent and roughly $0.13 \times 10^6$–$0.16 \times 10^6$ m$^3$/h through a semi-elliptical channel 15 km from the vent at station 1, the density of the lava must change by a factor near 12. If the density of the lava at station 1 is taken as 2,600 kg/m$^3$ (the largest value for station 1 given in Lipman and Banks, chapter 57), the density of the lava in the channel at the vent would have to be about 220 kg/m$^3$ instead of the 530 kg/m$^3$ employed in the "initial densities" mass-flow calculation (fig. 58.16*B*). Correspondingly changed densities for the other stations would be about 530 kg/m$^3$ (station 8) and 1,900 kg/m$^3$ (station 4). It is unlikely that the measured lava velocities and channel widths and the estimated flow depths could lead to a factor of 12 difference in mass flow rates between the vent and station 1 because each of these three values would have to be low by a factor of nearly 2.3 at station 1 (or high by a factor of 0.44 at the vent) or low by a factor of 1.5 at station 1 and high by a factor of 0.67 at station 11 (vent). The change in mass flow rate of $0.5 \times 10^9$–$0.7 \times 10^9$ kg/h from the vent to station 4 on April 3 is much too large to be accounted for by the masses involved in overflows, ponding, and gas emissions.

The changes in density indicated above would reduce the apparent viscosities calculated earlier by factors of 0.4 for the vents (stations 11 and 12) and 0.5 for station 8; Bingham viscosity, most values of yield strength, and maximum stress (but not rate of shear) would be reduced by one-half for station 8. Changes for stations 4 and 1 would be less than 11 percent.

Changes in densities along the length of the flow also have implications for volume flow rates calculated from the areal extent and thickness of the lava after an eruption (Walker, 1973; Malin, 1980). For example, if the volume flow rate observed at the vent during the eruption is $2 \times 10^6$ m$^3$/h (560 m$^3$/s) and the density of the hot, gas-charged lava is 220 kg/m$^3$, the mass flow rate is $0.44 \times 10^9$

kg/h. If the gases exolve and the lava is deposited with an average density of 2,200 kg/m$^3$, the volume flow rate would appear to be $0.2 \times 10^6$ m$^3$/h (56 m$^3$/s), one order of magnitude smaller than the value observed at the vent. A similar conclusion is reached (Moore, 1982) when volume flow rates in channels of the 1942 Mauna Loa eruption (Macdonald, 1943; Finch and Macdonald, 1953) are compared with posteruption volume flow rates (Walker, 1973; Malin, 1980).

## CONCLUSIONS

1. From April 2 to April 3, the physical appearance, behavior, and velocity of the Mauna Loa lava varied dramatically along the length of the flow. In the upper reaches, 3 km from the vents at station 8, the flow appeared to be a mass of sparse cinders and clinkers imbedded in a matrix of more fluid incandescent lava. Flow appeared to be laminar and was steady with a velocity of 5.3 m/s at the channel center. At stations 4 and 5, 9 km from the vents, the visible flow in the channel was composed of abundant dark cinders and clinkers and incandescent clots in a matrix of more fluid incandescent lava; flow was confined in channels with high levees in some places. Flow appeared to be laminar but was unsteady with small surges and ebbs. Velocity was near 1–2 m/s at the channel center. At station 1, 15 km from the vents, the flow was a hummocky mass of slowly moving debris, rubble, and blocks in a matrix of more incandescent lava confined within a rubbly leveed channel. Part of the debris and rubble and some of the blocks were incandescent but coherent. Flow appeared to be laminar but was unsteady with large surges and ebbs. Velocity varied from about 0.3 m/s during surges to about 0.1 m/s during ebbs.

2. Apparent viscosity calculated for the lava increased along the length of the flow, in parallel with physical appearance. On April 2, apparent viscosity increased from about 100 Pa·s at the vents to about $0.1 \times 10^6$ Pa·s, 15 km from the vents. Apparent viscosity also increased with time at the vents from about 100 Pa·s on April 2 to $10^3$ Pa·s on April 12 and 13. Similar increases occurred elsewhere in the lower reaches of the flow. Like the apparent viscosity, viscosity and yield strength calculated for a Bingham fluid on April 3 increased dramatically from $10^3$ Pa·s and $0.1 \times 10^3$ Pa at station 8, 3 km from the vents, to $80 \times 10^3$ Pa·s and $2 \times 10^3$ Pa at station 1, 15 km from the vents. These values compare well with laboratory data on viscosity of basalt with similar temperature, stress, and shear rate. The increase in viscosity is probably related to the increase in concentration of solids and plastic clots, reduction in gas and bubble contents, decrease of temperature, and decreases in stress and shear rate.

3. The rheology of the lava probably varied along the length of the flow. It may have been a Newtonian fluid near the vents, a Bingham fluid 3 km from the vents, and a pseudoplastic fluid at larger distances from the vents. Other kinds of fluids not considered here may also apply. Existing time-lapse photography and motion pictures of the flow in progress should be reviewed and studied because they may contain information about the appropriate flow rheology.

4. Volume flow rates obtained by multiplying the maximum velocity at the channel center, the channel width, and the depth of flow are probably too large by a factor of nearly 2 because the average velocity of a flow is less than the velocity at the channel center. Mass flow rates would be affected in a similar manner. On April 3, volume flow rates at the vent were near $1.5 \times 10^6$–$2.0 \times 10^6$ m$^3$/h. Volume flow rates decreased with distance from the vents. Most of this decrease is due to increases in the density of the lava with distance from the vents. In order to approximate the conservation of mass along the length of the flow on April 3, the density of the lava flowing from the vent would have to be near 220 kg/m$^3$, which implies a mass flow rate of $0.33 \times 10^9$–$0.44 \times 10^9$ kg/h. Lava deposited at these rates with an average density of 2,200 kg/m$^3$ would appear to have a volume flow rate of $0.15 \times 10^6$–$0.20 \times 10^6$ m$^3$/h.

## REFERENCES CITED


Bingham, E.C., 1922, Fluidity and Plasticity, New York, McGraw-Hill, 440 p.

Borgia, Andrea, Linneman, Scott, Spencer, Daniel, Morales, L.D., and Andre, J.B., 1983, Dynamics of lava flow fronts, Arenal Volcano, Costa Rica: Journal of Volcanology and Geothermal Research, v. 19, p. 303-329.

Caldwell, D.H., and Babbitt, H.E., 1941, Flow of muds, sludges, and suspensions in circular pipe: Industrial and Engineering Chemistry, v. 33, no. 2, p. 249-256.

Cigolini, Corrado, Borgia, Andrea, and Casertano, Lorenzo, 1984, Intra-crater activity, aa-block lava, viscosity, and flow dynamics: Arenal Volcano, Costa Rica: Journal of Volcanology and Geothermal Research, v. 20, p. 155-176.

Finch, R.H., and Macdonald, G.A., 1953, Hawaiian volcanoes during 1950: U.S. Geological Survey Bulletin 996–B, 89 p.

Fink, J.H., Malin, M.C., D'Alli, R.E., and Greeley, Ronald, 1981, Rheological properties of mudflows associated with the spring 1980 eruptions of Mount St. Helens volcano, Washington: Geophysical Research Letters, v. 8, no. 1, p. 43-46.

Hulme, Geoffrey, 1974, The interpretation of lava flow morphology: Geophysical Journal of the Royal Astronomical Society, v. 39, p. 361-383.

Johnson, A.M., 1970, Physical Processes in Geology: San Francisco, Freeman, Cooper and Co., 577 p.

Kilburn, C.R.J., 1981, Pahoehoe and aa lavas: discussion and continuation of the model of Peterson and Tilling: Journal of Volcanology and Geothermal Research, v. 11, p. 373-382.

Krauskopf, K.B., 1948, Lava movement at Paricutin Volcano, Mexico: Geological Society of America Bulletin, v. 59, p. 1267-1284.

Lockwood, J.P., Banks, N.G., English, T.T., Greenland, L.P., Jackson, D.B., Johnson, D.J., Koyanagi, R.Y., McGee, K.A., Okamura, A.T., and Rhodes, J.M., 1985, The 1984 eruption of Mauna Loa Volcano, Hawaii: Eos, Transactions, American Geophysical Union, v. 66. no. 16, p. 169-171.

Lockwood, J.P., Decker, R.W., Jackson, D.B., Koyanagi, R.Y., Okamura, A.T., and Johnson, D.J., 1984a, The 1984 eruption of Mauna Loa, Hawaii: Eos, Transactions, American Geophysical Union, v. 65, no. 45, p. 1137.

Lockwood, J.P., Rhodes, J.M., Garcia, Michael, Casadevall, Tom, Krueger, Arlin, and Matson, Michael, 1984b, Mauna Loa Volcano, Hawaii: Eos, Transactions, American Geophysical Union, v. 65, no. 18, p. 339.

Macdonald, G.A., 1943, The 1942 eruption of Mauna Loa, Hawaii: American Journal of Science, v. 241, p. 241-256.

———1953, Pahoehoe, aa, and block lava: American Journal of Science, v. 251, p. 169-191.

Malin, M.C., 1980, Lengths of Hawaiian lava flows: Geology, v. 8, p. 306-308.

Moore, H.J., 1982, A geological evaluation of proposed lava diversion barriers for the NOAA Mauna Loa Observatory, Mauna Loa Volcano, Hawaii, and

some recommendations: U.S. Geological Survey Open-File Report 82–314, 17 p.

Moore, H.J., and Schaber, G.G., 1975, An estimate of the yield strength of the Imbrium flows: Proceedings of the Lunar Science Conference, 6th, Houston, TX, March 17–21, 1975, p. 101-118.

Orowan, E., 1949, Remark from joint meeting of British Glaciological Society, British Rheologists' Club, and Institute of Metals: Journal of Glaciology, v. 1, no. 5, p. 231-240.

Peterson, D.W., and Tilling, R.I., 1980, Transition of basaltic lava from pahoehoe to aa, Kilauea Volcano, Hawaii: field observations and key factors: Journal of Volcanology and Geothermal Research, v. 7, p. 271- 293.

Shaw, H.R., 1969, Rheology of basalt in the melting range: Journal of Petrology, v. 3, no. 3, p. 510-535.

———1972, Viscosities of magmatic silicate liquids: an empirical method of prediction: American Journal of Science, v. 272, p. 870-893.

Shaw, H.R., Wright, T.L., Peck, D.L., and Okamura, R., 1968, The viscosity of basaltic magma: an analysis of field measurements in Makaopuhi lava lake, Hawaii: American Journal of Science, v. 266, p. 225-264.

Smith, R.W., 1960, Flow of limestone and clay slurries in pipelines: Transactions, American Institute of Mining, Metallurgical, and Petroleum Engineers, v. 217, p. 258-265.

Sparks, R.S.J., Pinkerton, H., and Hulme, Geoffrey, 1976, Classification and formation of lava levees on Mount Etna, Sicily: Geology, v. 4, p. 269- 271.

Valentyik, Laszlo, 1972, Rheological properties of heavy media suspensions stabilized by polymers: Transactions, American Institute of Mining, Metallurgical, and Petroleum Engineers, v. 252, p. 99-105.

Walker, G.P.L., 1967, Thickness and viscosity of Etnean lavas: Nature, v. 213, p. 484-485.

———1973, Lengths of lava flows: Philosophical Transactions of the Royal Society of London, Series A., v. 274, p. 107-118.

# THE ROLE OF LAVA TUBES IN HAWAIIAN VOLCANOES

*By* Ronald Greeley[1]


## ABSTRACT

**Lava tubes develop from eruptions that typically involve: (1) moderate rates of effusion, (2) durations greater than one or two days, and (3) effusion of fluid lava (for example, pahoehoe) that has not been greatly degassed. Although some fountain-fed lava and aa flows can form lava tubes, such occurrences are rare in Hawaii. Lava tubes feed flows: (1) directly from the vent (acting as extensions of the conduit), (2) from various holding reservoirs (for example, lava ponds, lava lakes, filled pit craters), and (3) from flows on the flanks of volcanoes. Historical flows of greatest length in Hawaii were emplaced primarily via lava tubes, and many subaqueous flows involve lava tubes. Sustained flow of lava in tubes appears capable of erosion into preflow terrain. Photogeological analyses suggest that at least 30 percent of the flows (by area) on Mauna Loa, 58 percent of the flows on Kilauea, and 18 percent of the flows on Mount Etna were at least partly emplaced via tubes.**


## INTRODUCTION

Lava tubes have been mentioned frequently in the literature on volcanology in Hawaii. From his visit to Hawaii in the 19th century, Dutton (1884) wrote "Probably no great eruption takes place without the formation of several such tunnels ***. There are literally thousands of these tunnels throughout the mass of Mauna Loa ***. So numerous are these caverns that it seems as if they must form some appreciable part of the entire volume of the mountain."

This paper reviews mechanics of lava tube formation, considers their role in various aspects of eruptions in Hawaii (including the emplacement of lava flows), and assesses their occurrence in Mauna Loa and Kilauea Volcanoes (fig. 59.1). Three sources of data were employed in this study: (1) previous descriptions of active eruptions involving lava tubes, (2) photogeologic studies of channels and lava tubes and the associated flows on Mauna Loa and Kilauea, and (3) field observations of active and inactive flows.

In the last two or more decades, new insight has been gained about Hawaiian lava tubes. This insight has been the consequence of several factors, including an increased interest in the morphology of volcanoes in general and the eruptions of Mauna Ulu in particular. Lava tubes were common in many of the Mauna Ulu flows (Wood, 1981) and their formation was readily observed (Greeley, 1971a, 1972a; Cruikshank and Wood, 1972; Peterson and Swanson, 1974). The eruption was relatively accessible, which, combined with frequent aerial photography, resulted in an unparalleled data set on the initiation and evolution of lava tubes and their associated flows.

Numerous studies of lava tubes have been made in areas outside Hawaii, including Mount Etna (Guest and others, 1980), Mount St. Helens (Greeley and Hyde, 1972), and New Mexico (Hatheway and Herring, 1970). From these studies and those in Hawaii, lava tubes clearly reflect a particular style of volcanism and are the primary means for the spread of some types of lava flows.

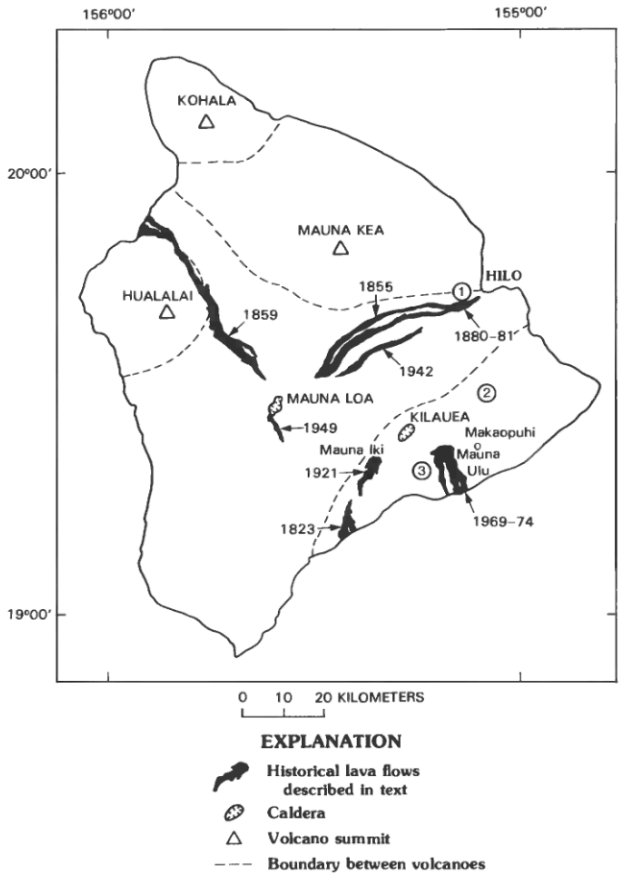


FIGURE 59.1.—Location map of some historical lava flows on Island of Hawaii, showing dates of flows and areas described in text: 1, Kaumana cave; 2, Kazamura cave; 3, Ainahou Ranch cave.

[1]Department of Geology, Arizona State University, Tempe, AZ 85287.

Thus, analysis of prehistorical lava tubes can provide insight into eruption processes and the flows in which they occur.

The term "lava tube" may be defined as the conduit beneath the surface of solidified lava through which molten lava flows. "Lava channels," however, contain nonroofed rivers of lava that frequently develop surface crusts. Many (if not most) lava tubes develop from the roofing of lava channels. For discussion here, the distinction between channels and tubes is made in regard to the roof crust; so long as the crust remains mobile and free-floating on the active flow, the structure is regarded as a channel; sections in which the crust is continuous across the active flow and fixed to the immobile parts of the flow are considered lava tubes. Thus, even if the roof collapses when the flow drains, the feature is considered to be a lava tube. This distinction is important for considerations of heat loss and lava flow emplacement.

### ACKNOWLEDGMENTS

This manuscript benefited greatly from discussions with John Guest of the University of London and from detailed reviews provided by D.W. Peterson and R. Holcomb of the U.S. Geological Survey, for which I am grateful. I thank G. Beardmore and E. Wohl for their assistance in compiling data for the presence of lava tubes and channels on Kilauea and Mount Etna Volcanoes. M. Lovas and the Thermo- and Gas-Dynamics Division of NASA–Ames Research Center are acknowledged for running the samples from the Mount St. Helens lava tube. I also wish to express my appreciation to the staff and members of the Hawaiian Volcano Observatory for the hospitality and logistical support extended during various trips to Hawaii.

This work was supported by the Office of Planetary Geology, National Aeronautics and Space Administration.

## LAVA TUBE FORMATION

Various mechanisms of lava tube formation have been proposed and some have been confirmed by observations of active tubes—primarily in Hawaii.

### CHANNEL-ROOFING

The most frequently observed mode of lava-tube formation involves roofing of lava channels. Roofing can occur in any of several ways, most of which appear to be partly related to the rate of flow and rheology of the lava. Where flow is sluggish to moderate ($\leq$1–3 m/s) a crust may extend from the channel sides, meet near the middle of the active flow, thicken, and form a roof. Aerial views of this mode of formation show a medial bright zone (uncrusted lava) that closes like a zipper as roofing progresses along the flow (fig. 59.2).

Where channelized flow is more vigorous the crustal slabs are often torn free from the sides and are rafted downflow. Crustal slabs may also develop on the moving surface of the lava river. Analysis of photographs taken during the Mauna Ulu eruption shows that more than 50 percent of channel surfaces are commonly covered by these crustal slabs. As they are rafted down the flow, stresses may fracture the slabs into pieces like a jigsaw puzzle. Their shapes permit the slabs to fit together well and allow the slabs to turn meander bends (fig. 59.3). At channel constrictions, however, the rafted slabs may jam together, fuse, and form a tube roof.

FIGURE 59.2.—Aerial view of lava channel in process of roofing by formation of crust along channel margins; closure is occurring down middle of flow; bright area is unroofed; trees are about 12 m high. View is east. Photograph of Mauna Ulu eruption, August 1970.

At moderate rates of flow (2–5 m/s), overflow of the channel banks by lava—as may occur during surges—often builds levees that grow upward and inward until they join (Holcomb and others, 1974). At still higher rates of channelized flow, splashing of lava along the channel also can produce levees of spatter that reach up and over the flow and merge to form a roof. This roofing mechanism commonly occurs where flows pass over steep gradients, as observed during Mauna Ulu eruptions in the filling of Alae Crater (Greeley, 1971a) and as flows crossed Hilina Pali (Holcomb and others, 1974; Swanson and others, 1979). Similarly, Jaggar (1921) described flow within Halemaumau in which lava "shot down the slope like a sluiceway" and roofed over to form a tube. However, such features may be short-lived. Jaggar noted that within one hour, surges of lava alternately destroyed and replaced the roof.

### DEVELOPMENT OF TUBES VIA LAVA TOES

Some lava tubes form without involving a channel phase. Relatively slow-moving pahoehoe flows involve repeated budding of lava toes that can be several meters across at the flow front and along the flow margins. Depending upon poorly understood circumstances, but often involving topographic channeling, the budding and subsequent flow direction may localize, forming a primary conduit within the flow that develops as a lava tube. This mechanism was described by Wentworth and Macdonald (1953, p. 43) in which toes of lava broke free from the flow margin. The skin of the toes is plastic and stretches as the toe elongates. A crust quickly thickens to form a rigid shell, but continued flow exerts sufficient

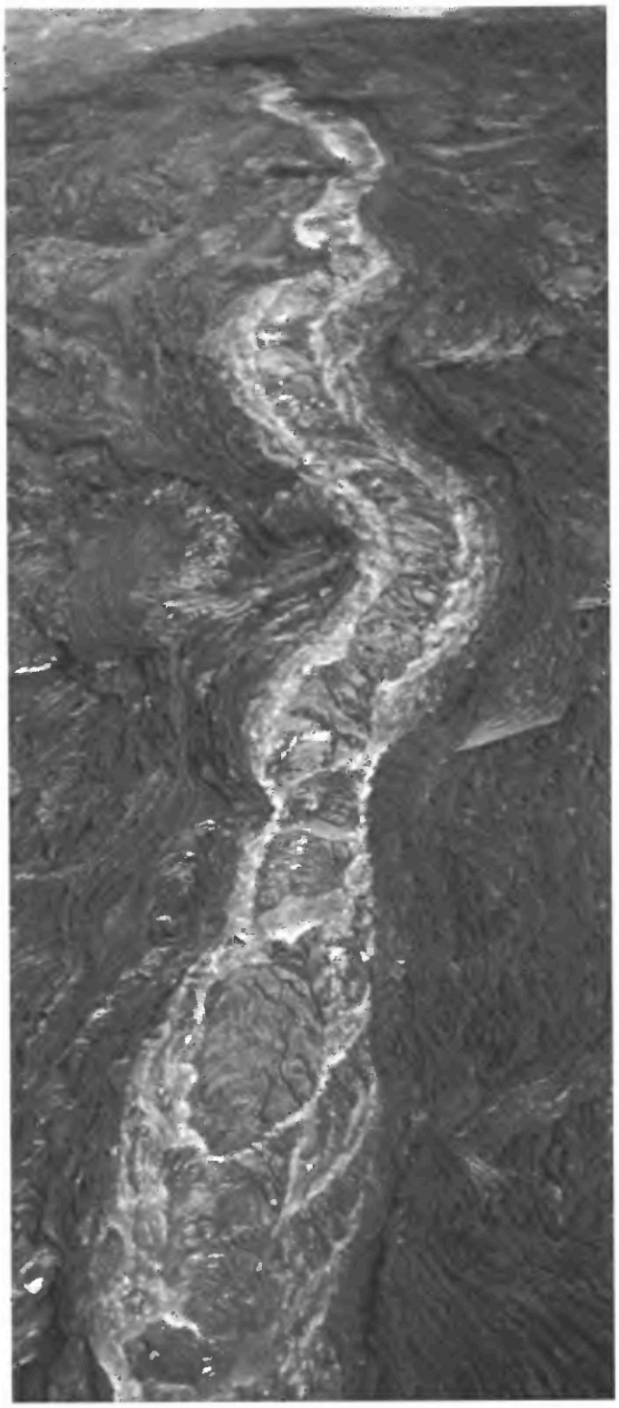

FIGURE 59.3.—Aerial view of channel (approximately 10 m wide) with rafted slabs of crust. Photograph of Mauna Ulu eruption, August 1970.

pressure to rupture the crust to produce a new toe. Repeated outbursts produce multiple toes, fed by an evolving lava tube.

This style of lava tube formation is invoked to explain complex networks of small lava tubes (fig. 59.4). In principle, it may also operate on larger scales. Many of the tubes formed by this mechanism, both large and small, may drain incompletely (or not at all) upon cessation of eruption. Some vast fields of hummocky pahoehoe are emplaced by such tubes and are termed "tube-fed pahoehoe" by Swanson (1973).

## THE LAYERED-LAVA MECHANISM

From study of lava tubes principally in Australia, Ollier and Brown (1965) proposed that internal shearing within lava flows allowed conduits to develop between the shear zones. The conduits then evolved into lava tubes. Horizontal partings observed in some pahoehoe flows, along with features indicative of shear, are consistent with the concept on a small scale (<1 m), but evidence for this mode of formation for large lava tubes is absent in Hawaii (Peterson and Swanson, 1974).

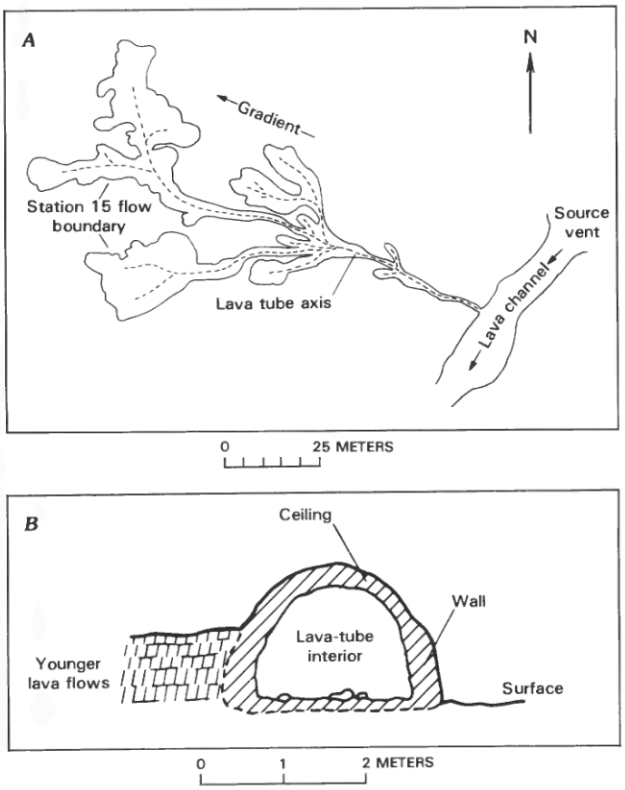


FIGURE 59.4.—Diagram based on plane-table survey of a small lava-tube network in California (south of Medicine Lake, Siskiyou County). ***A***, Distributary system of branches and toes. Nearly all branches contain hollow tubes (from Greeley, 1971b). ***B***, Simplified cross section of tube.

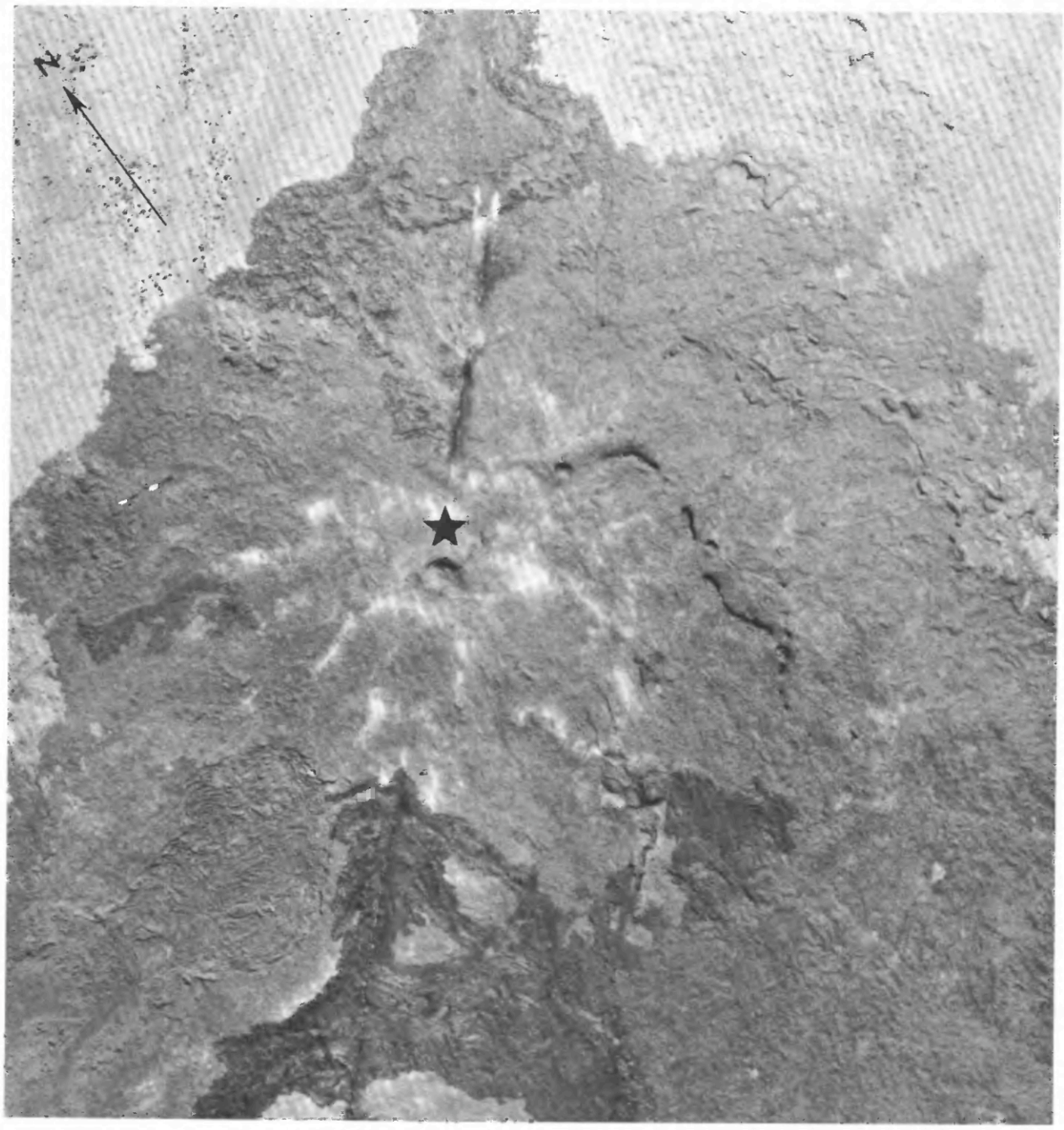


FIGURE 59.5.—Vertical aerial view of summit area of Mauna Iki; star marks summit pit crater; lava tube shown in figure 59.6 is southeast of summit area; area shown is about 1.5 km by 1.5 km. North is toward upper left. Photograph by R.M. Towill Corp., Honolulu.

## ROLE OF LAVA TUBES IN FLOW EMPLACEMENT

Lava tubes are involved in many aspects of Hawaiian eruptions and can transport and emplace flows in various environments, including subaqueous settings. Observations of active flows in Hawaii (Greeley, 1971a; Peterson and Swanson, 1974; Holcomb, 1980) and on Mount Etna (Guest and others, 1980) in which lava tubes developed indicate that the eruptions had been occurring for more than one or two days before tube formation was initiated. Evidently, in order for tubes to form—either via channel-roofing or

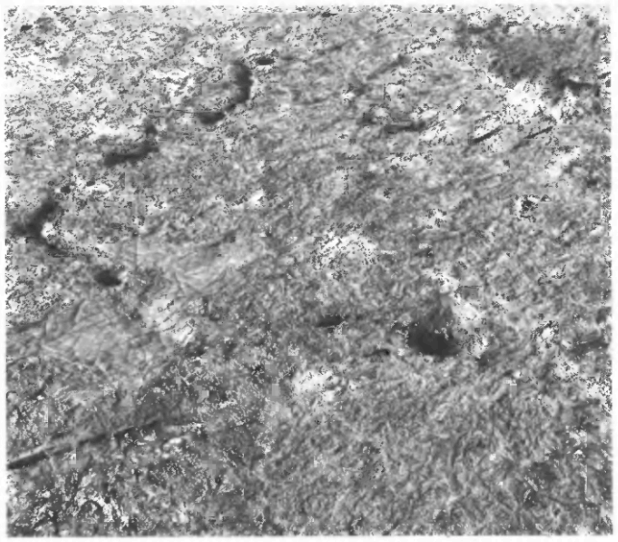

FIGURE 59.6.—Oblique aerial view across Mauna Iki summit area, showing collapses (skylights) that mark presence of lava tubes. View is south. Photograph taken summer 1974.

through advancing toes—effusion must be relatively stable for some minimal time, as discussed by Holcomb (1980). This stability is especially true for tubes formed in aa flows. Thus, it is rare for tubes to develop during the initial stages of eruption when the position of vents and flows are not fixed and the rate of effusion and fountaining are highly erratic.

## NEAR-VENT ACTIVITY

Many eruptions involve multiple vents that may be interconnected by lava tubes. Jaggar (1921, p. 21) described this type of activity within the Halemaumau pit crater of Kilauea. In 1921, the crater consisted of multiple ponds and the lava rose and fell somewhat independently in each pond, although Jaggar also noted that active lava tunnels could be traced between some of the ponds. Sometimes, wall segments containing tunnels were exposed and showed that flows passed from one pond to another.

Although lava tubes rarely develop during the initial phases of eruption, tubes may form at or near the vent within a short time from onset of eruption. For example, the 1949 summit eruption of Mauna Loa (Macdonald and Orr, 1950) involved high-volume fountaining of lava that collected in a pool and fed several lava channels. Within a few days of the initial eruption, some of the channels had roofed over and were the main conduits for lava flowing southeast from the vent area.

Part of Mauna Iki, on the southwest rift of Kilauea, was constructed by flows spread via lava tubes issuing from the vent area (fig. 59.5). As described by Jaggar (1947, p. 142), three lava pools developed over the site that eventually grew to be the low shield volcano Mauna Iki. Effusion of lava resulted in repeated overspilling from the pools; some of the spillovers formed channels and tubes oriented radially to the growing summit. Some of the tubes carried lava directly from the vent area more than 7 km to the distal part of the shield. By the fall of 1920 the eruption ceased, and as the lava drained, large (~15 m in diameter) lava tubes (fig. 59.6) were exposed as connecting the summit craters. Thus, tubes not only provided intercommunication between the summit pools, but also emplaced some of the lava that formed the upper flows of the small shield volcano.

## TUBES DEVELOPED ALONG RIFT STRUCTURES

Eruptions in Hawaii commonly occur along the rift zones of the major volcanoes, and fractures and open fissures can serve as channelways for flows. This activity is especially evident along the southwest rift zone of Mauna Loa. Lava flowing within the channelways may develop roofs by the same mechanisms described for open channels and form lava tubes within the rift (fig. 59.7). The term "rift-tubes" was suggested by Finch (1946) as describing passageways developed along fissures and rift zones as part of the magma conduit. He noted that many eruptions on the rift zones of Kilauea were preceded by a sinking of the lava column in Halemaumau pit crater and suggested a connection via such tubes. These connections are more properly considered part of the intrusive dike-feeding system of the volcano and are not included in considerations of lava tubes developed from flows.

## LAVA TUBES RELATED TO LAVA LAKES

Lava tubes are often involved in both the draining and filling of lava lakes. Entrances to lava tubes are frequently seen in walls of vents (fig. 59.8) and these tubes are often reactivated by subsequent eruptions. Some tubes may partly drain lakes, but become blocked or do not reemerge at the surface. For example, Jaggar (1947, p. 432) described a lava tube about 4 m high and 6 m wide in the wall of Halemaumau. In 1917, lava rose in the crater to the level of the tube, and for several hours lava poured into the tube. No outlet was obvious, and Jaggar suggested that the tube was filled to produce a sinuous cylinder of intrusive rock. Filled tubes of this sort when seen in cross section may show radial joint patterns, described by Waters (1960) for features in the Columbia Plateau basalts as war bonnet patterns, which he considered as filled tubes.

The best documented interaction of lava tubes and lava lakes is the sequence of repeated filling and draining observed for Alae Crater (fig. 59.9) during the Mauna Ulu eruptions (Swanson and others, 1972; Swanson and Peterson, 1972). Beginning in May 1969, lava from Mauna Ulu intermittently spilled into Alae Crater, filling it nearly to overflowing by August. Repeated spillover resulted in accretion of lava that raised the crater rim by several meters. A lava tube developed within the overflows and by late October a

FIGURE 59.7.—Oblique aerial view toward summit of Mauna Loa along southwest rift zone; dark holes in foreground mark presence of tube formed along rift segments; outflows from some skylights have produced local flows. Photograph taken August 1970.

master drainage system fed a series of pahoehoe flows a few hundred meters southeast of the crater (Swanson and others, 1972). Eventually, however, drainage through the tube(s) ceased, possibly because of clogging by solidified lava or blocking of their entrance by subsiding lava-lake crust.

By the summer of 1970, the Mauna Ulu vents fed flows downslope in several directions. In early August, two prominent vents (fig. 59.9, vents 1 and 3) fed lava into Alae lake through open

FIGURE 59.8.—View of lava tube ~1 m wide in wall of summit crater of Mauna Ulu. Such tubes may be reactivated as lava rises within vent and spills into tube. Photograph taken August 1971.

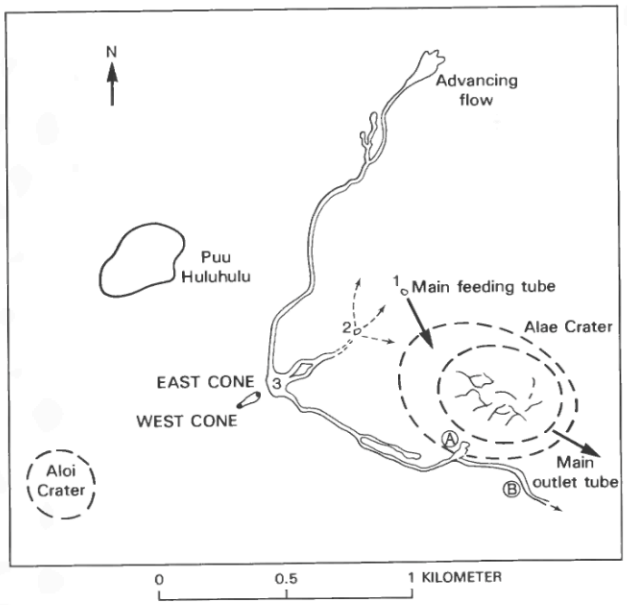


FIGURE 59.9.—Sketch map showing Mauna Ulu activity on August 8, 1970. Primary effusion was from vents 1 and 3, with flows from vent 1 entering Alae lava lake via a feeding tube. By afternoon, drainage of Alae Crater was taking place through an outlet tube to southeast. Southeast flow from vent 3 was via an open channel that initially (A) spilled onto crust of Alae lava lake; channel bypassed crater (B); dashed lines indicate preflow crater outline for Alae and Aloi.

channels (Greeley, 1971a), most of which emptied beneath the crust of the lava lake. One channel, however, appeared to form a tube that spread across the surface of the lake and fed small flows (fig. 59.10). Within one day, channels from the Mauna Ulu vents had nearly completely roofed over and continued to pour lava into Alae lake. However, a new channel had developed in flows from a newly reactivated vent on the fissure. Although the channel initially emptied on the lake crust, later in the same day (August 8, 1970), it bypassed the lake on the west side and fed flows to the southeast (fig. 59.9, A and B).

August 8 marked the beginning of the second episode of drainage of Alae lava lake. Aerial observations at about 0900 showed tube-fed flows that emptied into the lake. Sometime between these observations and midafternoon, drainage of the lake began, which resulted in subsidence of the lake crust by several meters (Greeley, 1971a). The subsidence formed a ring of tensional fractures in the lake crust (concentric to the former crater rim) and resulted in a series of pressure ridges as the crust slid inward toward the center of the ring (fig. 59.10). Swanson and others (1972) suggest that the lava tube that previously drained the lake was reactivated, perhaps as a consequence of increased pressure beneath the lake crust resulting from infilling. They suggest that the tube was 21–22 m below the surface and about 2–3 m above the preeruption level of the southeast crater rim. Subsidence of the lava lake crust continued for several days, after which the inflow was about equal to outflow via lava tubes. Lava emerged from the main outflow tube several kilometers downflow and fed a series of slow-moving pahoehoe flows. Over the next many months, tubes continued to carry lava from Mauna Ulu vents into the holding reservoir of the Alae lava lake, and then to feed lava to the flows spreading downslope to the south.

## EMPLACEMENT OF LONG FLOWS VIA TUBES

The factors governing the lengths of lava flows have been of considerable interest to volcanologists and planetologists. With the discovery of extremely long flows on other planets (>1,000 km on the Moon and Mars), several assessments have been made of the viscosity, effusion rate, volume of lava erupted, and other parameters that might affect flow length (Walker, 1973). Many of these studies, however, have ignored the role of lava tubes, or given the matter only cursory attention. From his study of flows in Hawaii, Malin (1980) suggested that cross-sectional area, effusion rate, and volume of lava erupted were all important and that no single factor seemed more important. He also noted that tube-fed flows appeared to advance farther, all other factors held equal.

In some respects lava tubes act as extensions of the magma-feeding conduit. Because tubes are well insulated, little heat is lost and the lava can remain mobile longer than for nonchannelized flows or unroofed channels. Swanson (1973) measured a decrease in

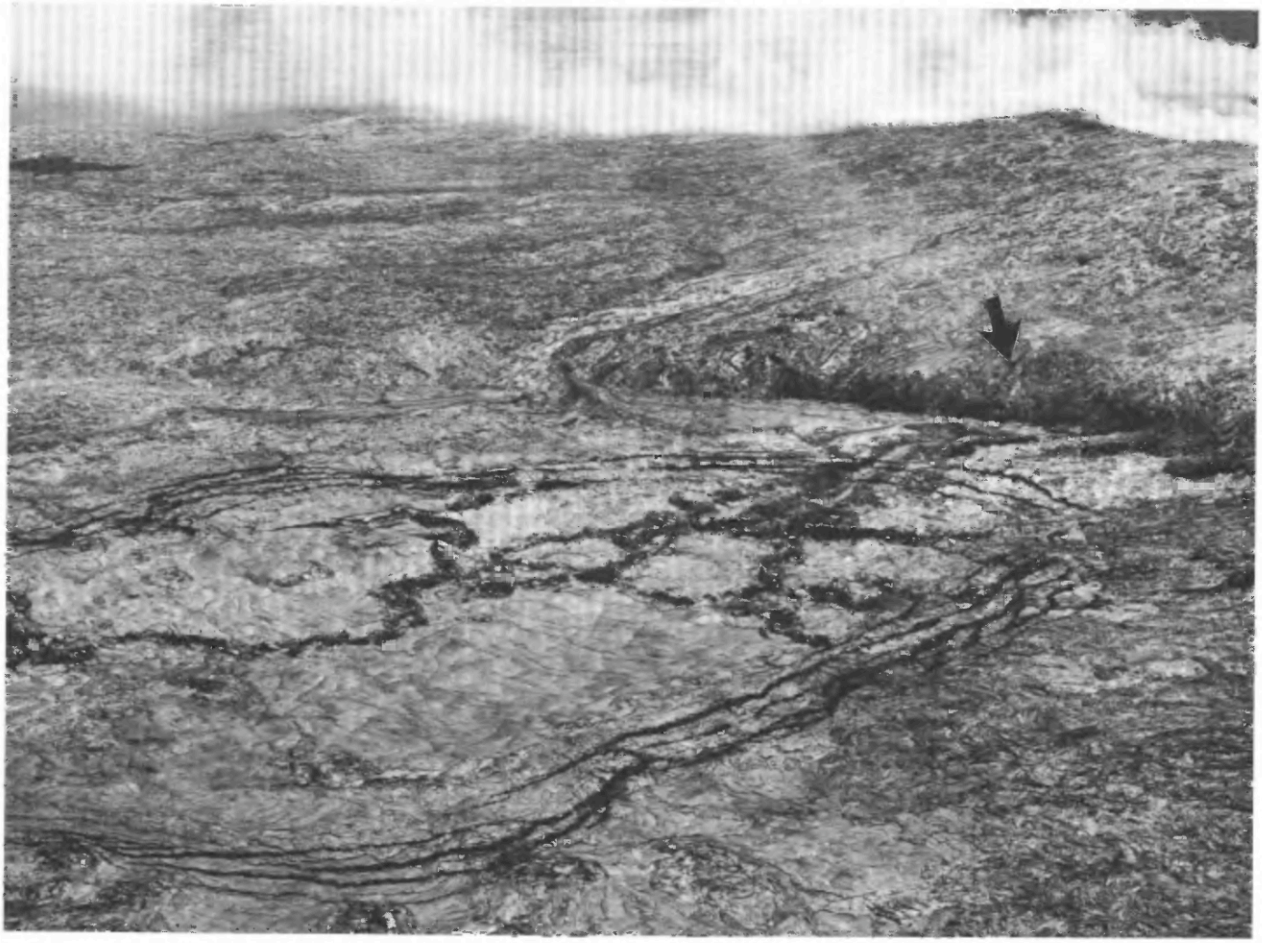

FIGURE 59.10.—Oblique aerial view across Alae lava lake taken in afternoon of August 9, 1970, after drainage of lake had begun via lava tube(s), showing concentric ring fractures and pressure ridges. Arrow marks small flows that spilled into lake from vents 1 (right side) and 3 (left side) and formed small tubes on lake crust. View is west. Photograph taken August 1970.

temperature of only 1–2 °C per kilometer for flow through a lava tube fed by eruption of Mauna Ulu. Even channel flow can be effective in heat retention if a thin crust is present. For example, the crust shown in figure 59.3 covers more than 55 percent of the active flow in the channel.

Two of the longest historical flows in Hawaii (fig. 59.1), the 1859 and the 1880–81 flows (both of Mauna Loa), were emplaced primarily through lava tubes. The 1859 flow erupted at the 3,355-m level and flowed more than 52 km to the sea (Stearns and Macdonald, 1946). The eruption lasted 7 months and extruded about $440 \times 10^6$ $m^3$ of lava (Macdonald and others, 1983, table 3.1). A complex lava tube system—in some places tube segments are more than 12 m across—can be traced through a series of collapsed sections visible in many sections of the flow. In some sections the tube exhibits complex anastomosing and vertically stacked branches, indicative of repeated eruptive surges and emplacement of multiple flow units (Greeley, 1972b).

The 1880–81 flow was erupted on the northeast rift zone of Mauna Loa (Baldwin, 1953) at about 3,325 m elevation. Lava issued quietly from an elongate fissure for 280 days and eventually reached nearly to the outskirts of Hilo. Except for some short aa flows, most of the lava was pahoehoe fed through a 40-km-long lava-tube system. Baldwin (1953) described the flow as follows: "At the advancing front the lava seems to come out of its tunnel and flow in an open red river of fire as much as several hundred feet long. This then appears to clog up and cool on top, and the lava pushes out in great and small lobes, piling one over the other and eventually forming a new tunnel underneath for the molten lava. The latter will then again break out and go through the same process as before." Kaumana cave is a section of this tube near Saddle Road a few

kilometers from Hilo and is open to the public (Greeley, 1974).

The 1880–81 flow can be contrasted with the 1855 Mauna Loa flow, which it parallels for some of its length. Both the 1880–81 and the 1855 flows advanced slowly at a rate of only a few tens or hundreds of meters per day on the middle and lower slopes (Macdonald, 1958). However, the 1855 eruption lasted 450 days and involved vigorous fire fountaining. Most of the flow was aa and did not form tubes. Even though the duration of the eruption was greater than the 1880–81 eruption (Macdonald and others, 1983, table 3.1), the flow is much shorter. Evidently, the fountaining caused outgassing of the magma such that the lava was dominantly aa, and lava tubes were not able to form.

During prolonged eruptions, lava tubes—once established—may be reactivated. Interiors of cooled tubes show evidence of multiple flow, including multiple linings of the walls and flows that only partly drained from the tube. As shown in figure 59.11, surface flows near the summit of Mauna Iki spilled into a tube system; similarly, the copious flows of the 1823 Keaiwa eruption of Kilauea (Stearns, 1926) emptied into an older tube at about 220 m elevation. In most cases, flow does not reemerge at the surface, but evidently blocks or fills the tubes. Occasionally, however, flows will intersect older lava tubes, drain into them, and reemerge in another place. For example, Macdonald (1943) described the 1942 flow of Mauna Loa as erupting at the 2,800-m level; lava also issued quietly 5 km downslope at the 2,380-m level, and Macdonald speculated that lava entered an old lava tube that intersected the eruption fissure higher up the mountain.

Emergence of lava from tubes—both primary tubes and reactivated systems—can produce flows and surface features different from the surrounding lava. Patches of seemingly anomalous pahoehoe set within aa flows (fig. 59.12) possibly can be emplaced through lava tubes. Similarly, tubes intially established in pahoehoe may transport subsequent flows of different properties. Macdonald and Orr (1950) noted that during the 1949 eruption of Mauna Loa, sluggish aa flows were fed by earlier formed lava tubes in the summit area.

Pressure of lava backed up within a tube may inflate the roof into small domes or may rupture the roof. Skylights—formed by collapse of roof sections—often became rootless vents and produced local flows (fig. 59.7) during surges that spilled lava from the tube.

FIGURE 59.11.—View of flows near summit of Mauna Iki that spilled into ~15-m-diameter skylight of lava tube. Photograph taken August 1970.

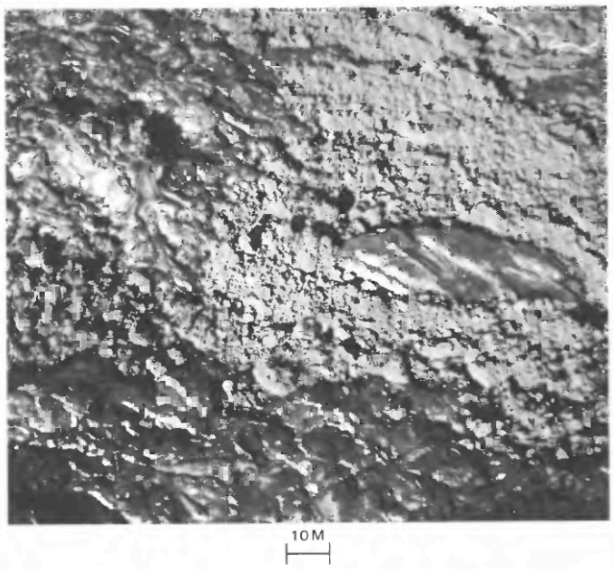


FIGURE 59.12.—Low oblique aerial view of patch of pahoehoe lava (smooth, shiny material) set within aa flow. Pahoehoe flow was possibly emplaced through lava tube. Photograph taken August 1970.

## TALUS-AND-LAVA CONES

Lava flows often spill over steep cliffs and form features termed by Holcomb and others (1974) as "talus-and-lava cones." In observing flows that filled Makaopuhi Crater in 1972, they noted that some larger streams of lava cascaded over the crater rim onto the apex of these talus cones and developed lava tubes that transported flows over the cone and onto the crater floor. Some tubes extended from the crater rim to the apex of the cone, as well as through the cone. As observed by Swanson (1973), pahoehoe flows passing over such steep slopes ordinarily evolve to aa; however, development of tubes enables the flows to remain as pahoehoe.

## LAVA DELTAS AND SUBAQUEOUS FLOW EMPLACEMENT

Many historical flows have reached the sea, and the addition of land through the accumulation of lava has been observed often (Peterson, 1976). The role of lava tubes, however, was not appreciated until the underwater observations by Moore and others (1973) for active flows erupted from Mauna Ulu. They noted a sequence of seaward extension of the advancing lava that began with flows spilling over the seacliff. As the hot lava poured into the sea water, it was quenched and fragmented into glassy sands and rubble that was further churned by wave action. This material accumulated to

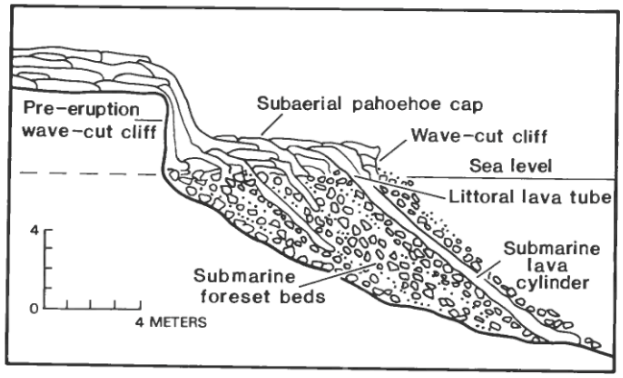


FIGURE 59.13.—Cross section of flows and delta built by Mauna Ulu lava entering the sea (from Peterson, 1976, which was modified from Moore and others, 1973).

produce foreset volcaniclastic deposits as an expanding lava delta (fig. 59.13). Some of the flows were fed by lava tubes; smaller tubes extended as pahoehoe toes that also were quenched and fragmented, whereas some larger tube systems moved forward rapidly enough to maintain coherence through the wave zone and established submarine lava flows. Peterson (1976) termed these "littoral lava tubes" and noted that their formation by abrupt quenching distinguishes them from tubes formed in subaerial environments. Once established, the submarine lava tubes fed complex, anastomosing networks of flow lobes that advanced as budding toes of lava.

Through alternation of volcaniclastic accumulation and tube-fed emplacement, the Mauna Ulu flows built a 470,000-$m^2$ delta to a depth exceeding 70 m. Moore and others (1973) note that many prehistorical flows from Kilauea display similar morphologies and suggest that the sequence they observed may be typical for many of the flows reaching the sea. Since their observations, dives by deep-sea submersibles around Hawaii (Fornari and others, 1980) and in areas of active sea-floor spreading in both the Atlantic and Pacific Oceans have led to the discovery of numerous submarine lava flows, many of which were emplaced via lava tubes (Heirtzler and Bryan, 1975). Thus, just as the emplacement of subaerial lava flows may be facilitated by lava tubes, substantial submarine lava may also involve flow through tubes.

## EROSION BY LAVA TUBES

Several lines of evidence suggest that flow within lava tubes is capable of both downcutting and lateral erosion. Detailed mapping of lava tubes in Hawaii (Wood, 1981), in California (Greeley and Baer, 1971), and in basalt flows of Mount St. Helens shows the crosscutting relations of the flows and tubes to the preflow terrain (fig. 59.14). Wood noted that the thin wall of the Ainahou Ranch cave of Kilauea collapsed into the tube and exposed an older aa flow that he suggested had been eroded by the tube. In California and at Mount St. Helens, the preflow rocks are distinctive from the basalt flows and were easily recognized. In the Mount St. Helens tubes, pieces of preflow rocks—some as large as one meter across—were carried by lava down the tube and are further evidence of mechanical erosion (Greeley and Hyde, 1972). Blocks of solidified lava are also observed in Hawaii in open lava channels; Finch and Macdonald (1950) reported that blocks as large as 6 m high and nearly 10 m long were carried by lava in channel flow during the June 1950 eruption of Mauna Loa. Although these blocks were probably not from preflow lava, they indicate the capacity of flowing lava to transport large masses of solidified lava, and large blocks possibly are also often carried within lava tubes in Hawaii.

Erosion by melting or partial melting is more difficult to document. However, in one section of the Mount St. Helens tubes (Greeley and Hyde, 1972), a block of dacite from the preflow

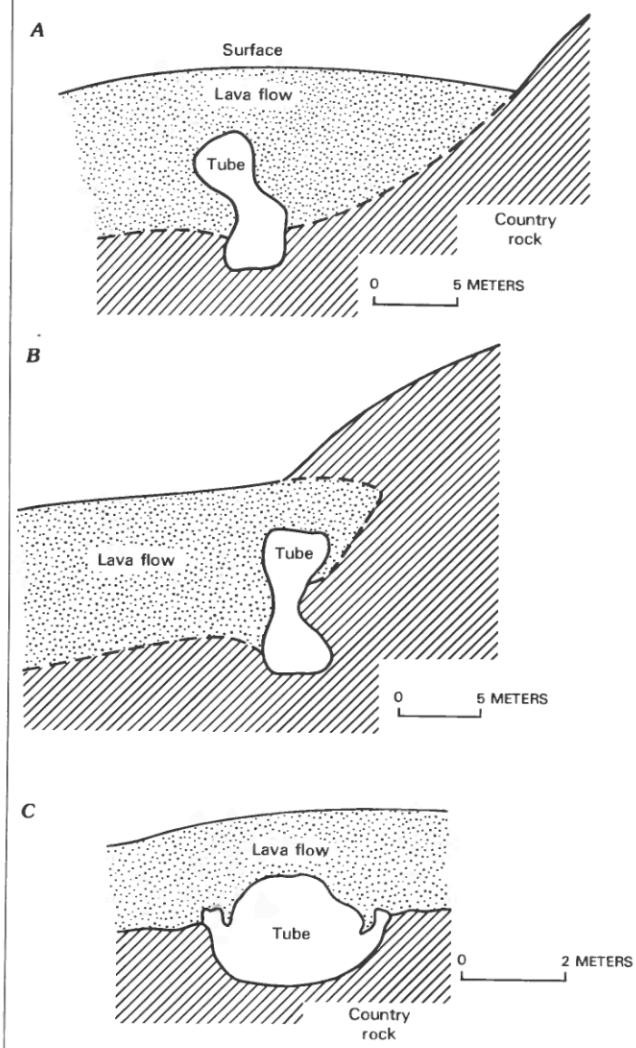


FIGURE 59.14.—Cross sections generated from surveys showing probable erosion by flow within a lava tube. ***A***, ***B***, Ape cave in Mount St. Helens (Wash.) basalt flows (from Greeley and Hyde, 1972). ***C***, Ainahou Ranch tube, Kilauea (surface of lava flow shown schematically, from Wood, 1981).

terrain was heated above the melting temperature for some of the minerals and flowed into the tube through a wall collapse and dripped onto the floor of the tube. Samples taken from the block were heated in a laboratory furnace at temperatures of 1,000 °C, 1,100 °C, 1,150 °C, 1,200 °C, 1,250 °C and 1,300 °C. After one hour, only the samples heated above 1,200 °C showed signs of melting, and it is assumed that a comparable temperature was reached when the lava tube was active. Thus, erosion by partial melting may also have contributed to entrenchment of the tube.

The examples cited above involved preflow rocks that were mostly unconsolidated and of a lower melting temperature than basalt. However, erosion of basalt by lava-tube flow may also occur, as proposed by Carr (1974) from theoretical models and suggested by Peterson and Swanson (1974) from observations of Mauna Ulu flows. Although direct evidence was absent, Peterson and Swanson inferred that the gradual lowering of the flow level in a Mauna Ulu tube (observed through a skylight) reflected downcutting. They noted that the rate of effusion and the rate of flow through the tube was constant and that the lowering of the flow level could not, therefore, be simply a diminution of flow volume.

It is not known if temperatures above melting for basalt are sustained in lava tubes. Several measurements, however, show that high temperatures do occur within tubes as a consequence of burning gases. Macdonald and Eaton (1964) noted during the 1955 eruption in East Puna that temperatures at the flow front for freshly exposed lava were 930–970 °C, but that blue flames were also visible within grottos where temperatures were measured at 1,025 °C. The flames and high temperatures were attributed to burning of gases generated from vegetation buried by the flow. Similarly, Jaggar (1947) described blue flames observed through cracks in a lava-tube roof formed in the Postal Rift flow of 1919 on the floor of Kilauea caldera. This gas probably was not generated from vegetation, but rather was magmatic gas. Cruikshank and others (1973) observed the burning of hydrogen at Mauna Ulu vents and measured temperatures well above the melting point for basalt. The conclusion is that temperatures can be reached within lava tubes that are sufficiently high to melt or at least soften the basalt, but it is not known if widespread melting of preflow rock occurs.

## LAVA TUBE ABUNDANCES

In an attempt to determine the relative importance of lava tubes in the evolution of Hawaiian volcanoes, the abundance of lava tubes and associated flows was assessed for Mauna Loa and Kilauea. For comparison, a similar analysis was made for Mount Etna, Sicily. Although the methods of data collection were somewhat different for the cases studied (making comparisons less than ideal), the results demonstrate that for some basaltic volcanoes—especially in Hawaii—lava tubes play a key role in the volcanic history.

### MAUNA LOA

Lava flows and associated tubes and channels were mapped on aerial photographs for sparsely vegetated parts of the shield (Greeley and others, 1976), representing summit, flank, and rift areas (fig. 59.15). Using 81 aerial photographs (U.S. Department of Agriculture, 1:20,000), about 15 percent of the shield was mapped on stereoscopic photographs and an additional 10 percent was mapped with monoscopic images; thus, about one-quarter of the areal extent of the volcano was analyzed. Lava tubes were identified by the presence of collapsed skylights, but because uncollapsed tubes could not be seen on aerial photographs, the value given for lava-tube frequency is a lower limit. Moreover, only exposed flows were examined. Thus, units buried by younger flows, those below sea level, and those covered by heavy vegetation are excluded.

For each photograph, a map was prepared that delineated the flow units and the presence or absence of lava tubes and channels. Three types of flow units were delineated: (1) those containing predominantly lava tubes, (2) those containing predominantly lava channels, and (3) those lacking tubes or channels. Areas for each flow unit were determined using a planimeter. Limited field work and comparison with maps (for example, Macdonald, 1971) provided additional data; ground checking of the photogeology was done for flows intersected by roads on the west flank of Mauna Loa and in the Saddle area.

The data were compiled on the basis of the percentage of the flows by area that were at least partly emplaced via lava tubes. The results show that 30 percent of the area is covered by flows spread at least partly via lava tubes. If channels are included in the analysis the percentage rises to 83 percent.

### KILAUEA

Some of the longest uncollapsed known lava tubes in Hawaii are within Kilauea lava. For example, the Kazumura cave on the northeast flank has been mapped for more than 11.7 km and is only one of several large tubes in the area (Wood, 1981). Ainahou Ranch cave, in a flow on the southern flank of Kilauea, is more than 7 km long. To determine the frequency of lava tubes for Kilauea, data for Kilauea were compiled from mapping by Holcomb (1976, 1980), who noted the presence of lava channels and tubes and classified flows by age, morphologic assemblage (for example, small lava shield), and morphologic-lithologic type (for example, tube-fed pahoehoe). Holcomb's mapping is based on aerial photographs, supplemented with data from field work by himself and Wood (1981).

Holcomb's map for Kilauea shows both flow boundaries and the trace of lava tubes. Areas for the flows containing lava tubes were found to represent 58 percent of the surface area for Kilauea. It should be noted that some of Holcomb's tube-fed flows were excluded from this analysis, as only those flows in which he indicated the presence of tubes were employed.

### MOUNT ETNA

The presence of lava tubes in flows on Mount Etna was determined from data in Brunelli and Scammacca (1975) and Bella

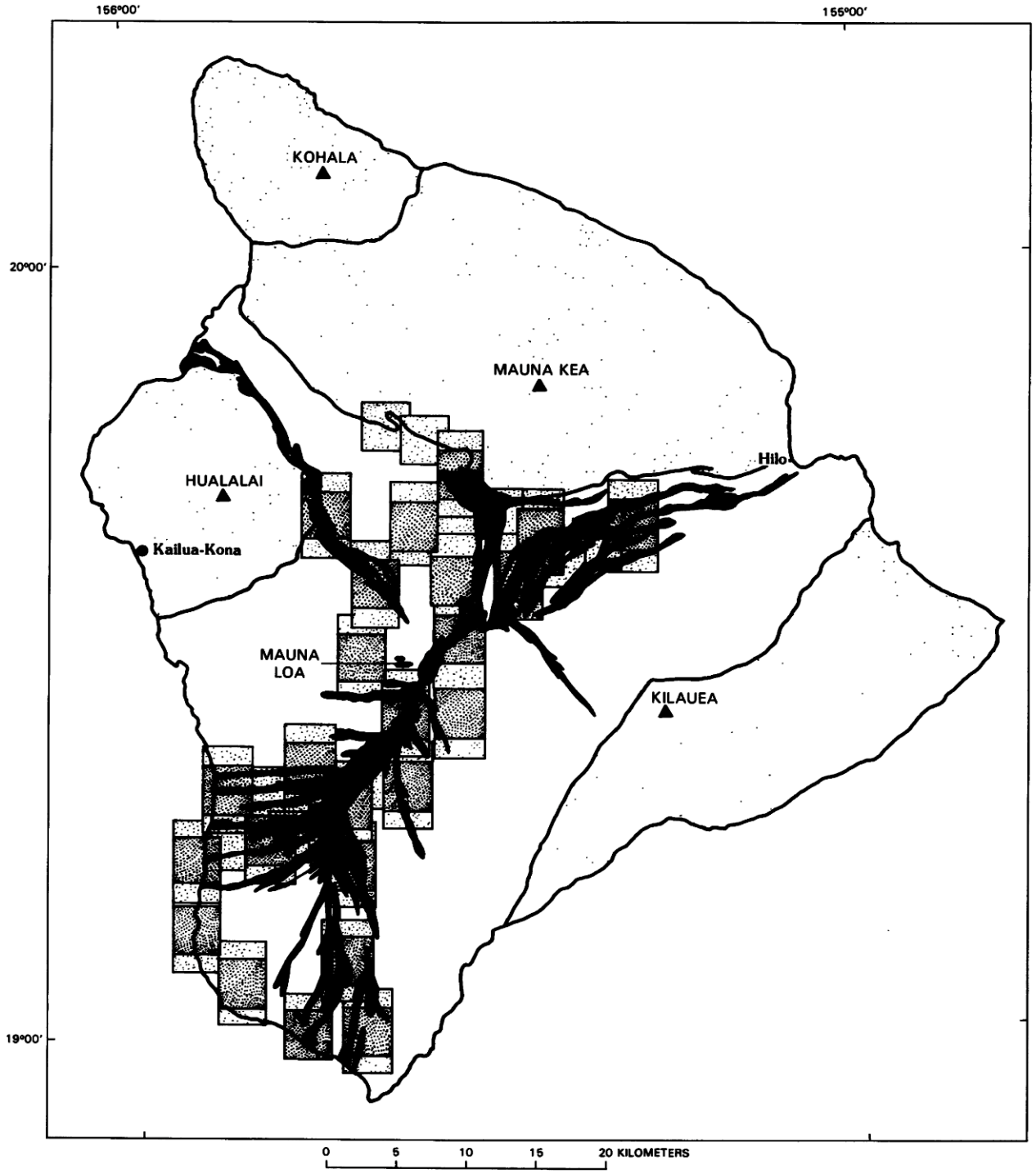


FIGURE 59.15.—Sketch map showing areas of Mauna Loa analyzed for lava tubes; rectangles outline aerial photographs studied; heavy stipple indicates stereoscopic coverage. Solid black, historical flows.

and others (1982), and supplemented by photogeologic study, limited field work, and discussions with members of a speleological organization in Catania, members of which routinely search for and map lava tubes on the volcano. Locations of lava tubes (longer than 100 m) from these sources were plotted on the geologic map of Mount Etna (Romano and others, 1979) and treated statistically like the Hawaiian volcanoes. Of the total surface area of Mount Etna flows, 18 percent was emplaced at least partly via lava tubes.

## DISCUSSION

Studies of active and inactive flows show that lava tubes are involved in many aspects of Hawaiian eruptions. Rarely are either tubes or channels produced in the early phase of eruption, regardless of flow type (aa, pahoehoe, or others). Thus, short duration eruptions (that is, less than one or two days) seldom produce lava tubes (Holcomb, 1980). The often-stated comment that lava tubes form nearly exclusively in pahoehoe flows appears to be correct, although some tubes are documented in aa flows (Wentworth and Macdonald, 1953). Guest and others (1980) note that tubes are often found in aa flows near vents on Mount Etna formed from long-duration eruptions. Not all pahoehoe flows develop lava tubes, however, and factors other than the rheology must be involved. These factors are at least partly related to the style of eruption, especially in regard to the vigor, rate, and duration. Highly vigorous eruptions, as reflected by fire fountaining, cause rapid changes in flow regime and lack well-defined channels to evolve to tubes. In addition, fire fountaining may degas the lava rapidly (Swanson and Fabbi, 1973), producing aa flows, most of which are too viscous to form roofs, or producing degassed pahoehoe which may not become channelized.

High rates of effusion, exemplified by the 1823 flow of Kilauea, may spread out rapidly as sheets and fail to become channelized. Moreover, high effusion is often associated with fissure vents in which the zone of eruption shifts along the fissure; as such, there is not a focused flow of sufficient duration for channels and tubes to develop. Thus, the presence of lava tubes (Holcomb, 1980, chapter 3) reflects a style of volcanism involving moderate rates of effusion and durations typically greater than one or two days, and eruption of relatively fluid lava (for example, pahoehoe) that has not greatly degassed.

Lava tubes may transport lava between vents, along rift zones, and directly from vents to flow fronts. They are effective conduits for the emplacement of the longest flows on Hawaii and play a critical role in the submarine extension of many flows. Although not well documented in Hawaii, erosion by both thermal (melting) and mechanical (plucking) means appear to take place by flow within some tubes.

Analysis of Mauna Loa, Kilauea, and Mount Etna volcanoes shows that lava tubes were involved in the emplacement of one-fifth or more of the flows exposed at the surface. Differences in the percentages for the three volcanoes studied may reflect differences in data analysis or may represent differences in evolution or stage of development. Nonetheless, their high occurrence in all cases demonstrates that lava tubes emplace many of the flows in the evolution of basaltic volcanoes.

## REFERENCES CITED


Baldwin, E.D., 1953, Notes on the 1880–81 lava flow from Mauna Loa: The Volcano Letter, no. 520, April–June, p. 1–3.

Bella, V., Brunelli, F., Cariola, A., and Scammacca, B., 1982, Grotte vulcaniche di Sicilia, notizie catastali: Secondo contributo, Bollettino Accademia Gioenia di Scienze Naturali, v. 15, p. 229–292.

Brunelli, F., and Scammacca, B., 1975, Grotte Vulcaniche di Sicilia: Club Alpino Italiano, Sezione dell'Etna, Gruppo Grotte Cantania, 54 p.

Carr, M.H., 1974, The role of lava erosion in the formation of lunar rilles and martian channels: Icarus, v. 22, p. 1–23.

Cruikshank, D.P., Morrison, D., and Lennon, K., 1973, Volcanic gases: Hydrogen burning at Kilauea Volcano, Hawaii: Science, v. 182, p. 277–279.

Cruikshank, D.P., and Wood, C.A., 1972, Lunar rilles and Hawaiian volcanic features: Possible analogues: The Moon, v. 3, p. 412–447.

Dutton, C.A., 1884, Hawaiian volcanoes: U.S. Geological Survey, Fourth Annual Report, 1883, p. 75–219.

Finch, R.H., 1946, The Puna rift of Kilauea: The Volcano Letter, no. 493, p. 1–2.

Finch, R.H., and Macdonald, G.A., 1950, The June 1950 eruption of Mauna Loa: The Volcano Letter, no. 508, p. 1–11.

Fornari, D.J., Lockwood, J.P., Lipman, P.W., Rawson, M., and Malahoff, A., 1980, Submarine volcanic features west of Kealakekua Bay, Hawaii: Journal of Volcanology and Geothermal Research, v. 7, p. 323–337.

Greeley, R., 1971a, Observations of actively forming lava tubes and associated structures, Hawaii: Modern Geology, v. 2, p. 207–223.

———1971b, Geology and morphology of selected lava tubes in the vicinity of Bend, Oregon: State of Oregon, Department of Geology and Mineral Industries Bulletin 71, 47 p.

———1972a, Additional observations of actively forming lava tubes and associated structures, Hawaii: Modern Geology, v. 3, p. 157–160.

———1972b, Formation of multiple lava tubes [abs.]: Eos, Transactions of the American Geophysical Union, v. 53, p. 276.

———1974, Kaumana lava tube, *in* Greeley, R., ed., Geological Guide to the Island of Hawaii: National Aeronautics and Space Administration CR 152416, p. 233–238.

Greeley, R., and Baer, R., 1971, Hambone, California and its magnificent lava tubes—preliminary report [abs.]: Geological Society of America Abstracts with Program, v. 3, no. 2, p. 128.

Greeley, R., and Hyde, J.H., 1972, Lava tubes of the Cave Basalt, Mount St. Helens, Washington: Geological Society of America Bulletin, v. 83, p. 2397–2418.

Greeley, R., Wilbur, C., and Storm, D., 1976, Frequency distribution of lava tubes and channels on Mauna Loa Volcano, Hawaii [abs.]: Geological Society of America Abstracts with Programs, v. 8, p. 892.

Guest, J.E., Underwood, J.R., and Greeley, R., 1980, Role of lava tubes in flows for the Observatory Vent, 1971 eruption on Mount Etna: Geology Magazine, v. 117, p. 601–606.

Hatheway, A.W., and Herring, A.K., 1970, Bandera lava tubes of New Mexico, and lunar implications: Tucson, Arizona University Lunar and Planetary Laboratory Communications, v. 8, p. 298–327.

Heirtzler, J.R., and Bryan, W.B., 1975, The floor of the mid-Atlantic Rift: Scientific American, v. 273, p. 78–90.

Holcomb, R.T., 1976, Preliminary map showing products of eruptions, 1962–1974, from the upper east rift zone of Kilauea Volcano, Hawaii: U.S. Geological Survey Miscellaneous Field Investigation Map MF–811, scale 1:24,000.

———1980, Kilauea Volcano, Hawaii: Chronology and morphology of the surficial lava flows; Stanford, Calif., Stanford University, Ph.D. thesis, 321 p.

Holcomb, R.T., Peterson, D.W., and Tilling, R.I., 1974, Recent landforms at Kilauea Volcano, a selected photographic compilation, *in* Greeley, R., ed., Hawaiian Planetology Conference: National Aeronautics and Space Administration TMX 62362, p. 49–86.

Jaggar, T.A., 1921, Volcanic conditions in February: Monthly Bulletin Hawaiian Volcano Observatory, v. 9, p. 21–39.

———1947, Origin and development of craters: Geological Society of America Memoirs, v. 21, 508 p.

Macdonald, G.A., 1943, The 1942 eruption of Mauna Loa, Hawaii: American Journal of Science, v. 241, p. 241–256.

———1958, Barriers to protect Hilo from lava flows: Pacific Science, v. 12, p. 258–277.

———1971, Geological map of the Kipuka Pakekake quadrangle, Hawaii: U.S. Geological Survey Geologic Investigations Map GQ–957, scale 1:24,000.

Macdonald, G.A., Abbott, A.T., and Peterson, F.L., 1983, Volcanoes in the Sea: Honolulu, University of Hawaii Press, 517 p.

Macdonald, G.A., and Eaton, J.P., 1964, Hawaiian volcanoes during 1955: U.S. Geological Survey Bulletin 1171, 170 p.

Macdonald, G.A., and Orr, J.B., 1950, The 1949 summit eruption of Mauna Loa, Hawaii: U.S. Geological Survey Bulletin 974–A, 31 p.

Malin, M.C., 1980, Lengths of Hawaiian lava flows: Geology, v. 8, p. 306–308.

Moore, J.G., Phillips, R.L., Grigg, R.W., Peterson, D.W., and Swanson, D.A., 1973, Flow of lava into the sea, 1969–1971, Kilauea Volcano, Hawaii: Geological Society of America Bulletin, v. 84, p. 537–546.

Ollier, C.D., and Brown, J.P., 1965, Lava caves of Victoria: Bulletin of Volcanology, v. 28, p. 215–229.

Peterson, D.W., 1976, Processes of volcanic island growth, Kilauea Volcano, Hawaii, 1969–1973: International Association of Volcanology and Chemistry of the Earth's Interior, Symposium on Andean and Antarctic Volcanology Problems, Proceedings, p. 172–189.

Peterson, D.W., and Swanson, D.A., 1974, Observed formation of lava tubes during 1970–1971 at Kilauea Volcano, Hawaii: Studies in Speleology, v. 2, p. 209–222.

Romano, R., Sturiale, C., and Lentini, F., 1979, Carta Geologica del Monte Etna, (1:50,000), C.N.R. Istituto Internazionale di Vulcanologia, Catania.

Stearns, H.T., 1926, The Keaiwa or 1823 lava flow from Kilauea Volcano, Hawaii: Journal of Geology, v. 34, p. 336–351.

Stearns, H.T., and Macdonald, G.A., 1946, Geology and ground-water resources of the Island of Hawaii: Hawaii Division of Hydrography Bulletin, v. 9, 363 p.

Swanson, D.A., 1973, Pahoehoe flows from the 1969–1971 Mauna Ulu eruption, Kilauea Volcano, Hawaii: Geological Society of America Bulletin, v. 84, p. 615–626.

Swanson, D.A., Duffield, W.A., Jackson, D.B., and Peterson, D.W., 1972, The complex filling of Alae Crater, Kilauea Volcano, Hawaii: Bulletin of Volcanology, v. 36, p. 105–126.

———1979, Chronological narrative of the 1969–1971 Mauna Ulu eruption of Kilauea Volcano, Hawaii: U.S. Geological Survey Professional Paper 1056, 55 p.

Swanson, D.A., and Fabbi, B.P., 1973, Loss of volatiles during fountaining and flowage of basaltic lava at Kilauea Volcano, Hawaii: Journal of Research, U.S. Geological Survey, v. 1, p. 649–658.

Swanson, D.A., and Peterson, D.W., 1972, Partial draining and crustal subsidence of Alae lava lake, Kilauea Volcano, Hawaii, in Geological Survey research 1972: U.S. Geological Survey Professional Paper 800–C, p. C1–C14.

Walker, G.P.L., 1973, Lengths of lava flows: Philosophical Transactions of the Royal Society of London, Series A, v. 274, p. 107–118.

Waters, A.C., 1960, Determining direction of flow in basalts: American Journal of Science, v. 258–A, p. 350–366.

Wentworth, C.K., and Macdonald, G.A., 1953, Structures and forms of basaltic rocks in Hawaii: U.S. Geological Survey Bulletin, v. 994, 98 p.

Wood, C., 1981, Exploration and geology of some lava tube caves on the Hawaiian volcanoes: Transactions of the British Cave Research Association, v. 8, p. 111–129.

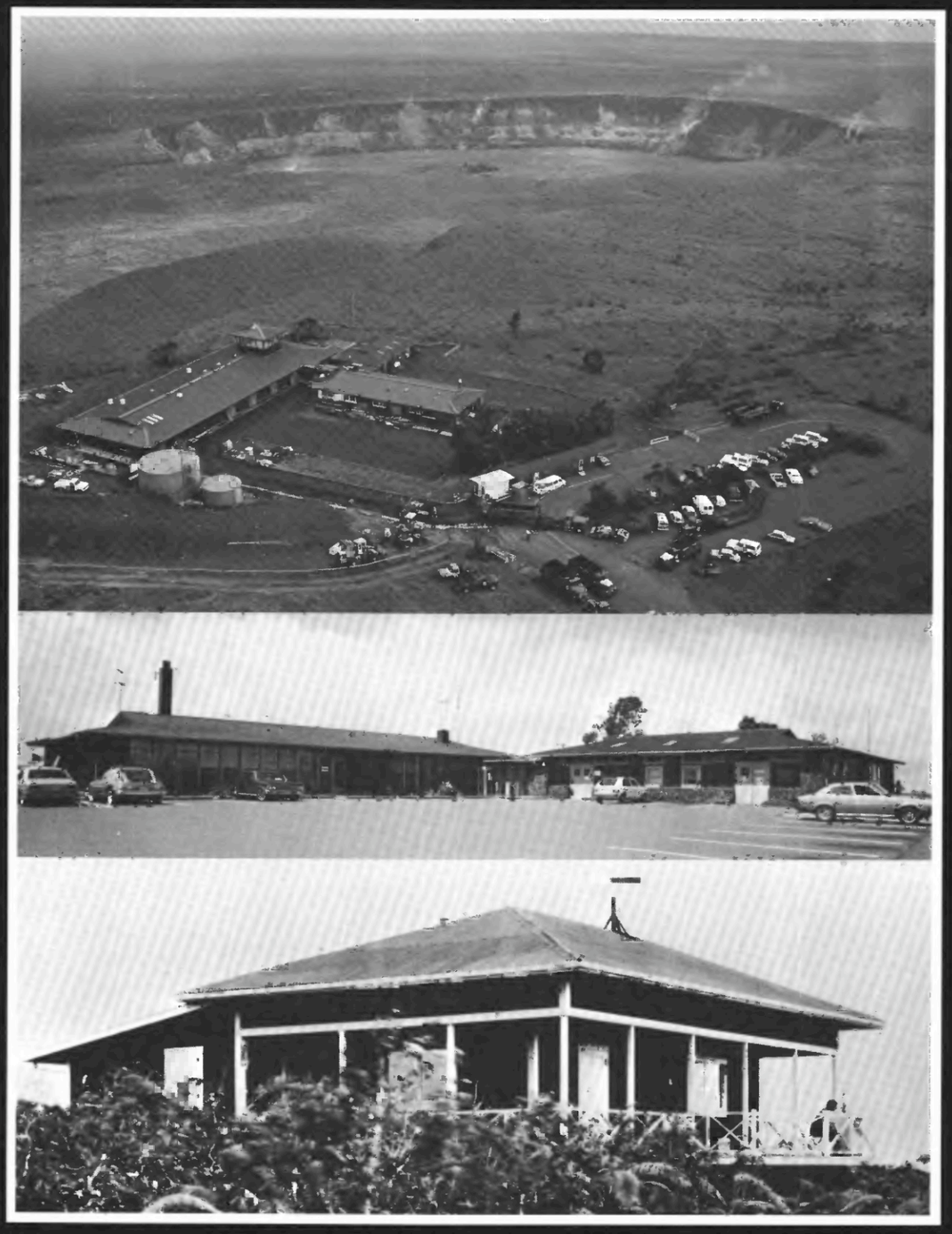

Evolution of Hawaiian Volcano Observatory facilities. Bottom: Original HVO main building on north rim of Kilauea caldera. Photograph by T.A. Jagger, 1913. Center: HVO facilities on Uwekahuna Bluff, about 1979. Top: Oblique aerial view of HVO in April 1986. New building (completed 1986) is at left, Halemaumau Crater in background.

# HISTORY OF INVESTIGATIONS OF HAWAIIAN VOLCANISM

This section could as well have introduced the present work on Hawaiian volcanism as concluded it. Its three chapters deal with some of the earliest known published works on Hawaiian volcanoes and with the background and development of the Hawaiian Volcano Observatory.

Chapter 60 examines the contributions of James Dwight Dana and the U.S. Exploring Expedition of 1840-41. That expedition, which focused on the Pacific Ocean, where most of Earth's active volcanoes reside, greatly advanced the study of volcanoes, and Hawaiian volcanology may be said to have begun with Dana, the expedition's geologist.

The following chapter chronicles the colorful history of the Hawaiian Volcano Observatory, beginning with the digging of the foundation for its first building in 1912. It recounts the dominating role of Thomas A. Jaggar in the early years of HVO and the variety of pioneering and experimental researches done during that time. Instruments and equipment were often designed and built at the Observatory and then field tested in "trial-by-fire" fashion.

The final chapter is a chronological listing of the staff of HVO since its beginning. It tells some of the social history of the Observatory and shows how the staff has grown—fairly slowly, considering the evolution of volcano-monitoring techniques and the corresponding increase in data. Compiling the list generated fond memories of the mechanical and early electronic ages at HVO, when gathering data was simpler and the pace more leisurely than in the present age of computers and telemetry. Some staff from those earlier times are still at HVO, giving continuity to changes in techniques, to the eyewitness record of volcanic events, and to the anecdotal record of the people who created and sustained the Hawaiian Volcano Observatory.

Ceremonial Figure
Hawaiian Petroglyph
Nuuanu, Oahu

# JAMES D. DANA AND THE ORIGINS OF HAWAIIAN VOLCANOLOGY: THE U.S. EXPLORING EXPEDITION IN HAWAII, 1840–41

*By* Daniel E. Appleman[1]

*The Hawaiian * * * group is consequently the key to Polynesian Geology.—J.D. Dana, 1849*


## ABSTRACT

**Scientists and naval officers of the U.S. Exploring Expedition of 1838–42 performed the first systematic volcanologic and geologic research in the Hawaiian Islands. During their 6-month stay they surveyed and mapped Kilauea and Mauna Loa Volcanoes during a period when Kilauea was in continuous summit eruption. James D. Dana, the expedition geologist, made pioneering contributions in characterizing the development and eruptive style of Hawaiian volcanoes and in interpreting the geology of Kauai, Oahu, Maui, and Hawaii. He correctly deduced the age progression in the Hawaiian group based on degree of erosion, and he used his work in Hawaii as the basis for interpreting the regional geology of the Pacific. Dana's monumental geology report, published in 1849, constitutes a virtual textbook of Hawaiian volcanology and geology.**


## INTRODUCTION

On September 20, 1840, the U.S. Exploring Expedition, Lt. Charles Wilkes commanding, arrived in the Hawaiian Islands. Modeled after the great European scientific expeditions of Cook and Malaspina, the "Ex. Ex." was charged with mapping and charting little-known regions of the Pacific and Southern Oceans, advancing the diplomatic and commercial interests of the United States, and performing scientific exploration. Although it was an operation of the U.S. Navy, the expedition carried a corps of civilian scientists, who were responsible for the natural-history investigations. Indeed, much of the impetus for the expedition had come from American scientists, anxious to join their European colleagues in exploring the natural wonders of the globe.

By the time it reached Hawaii the expedition was 2 years old. In those years the voyagers had sailed the coasts of South America and Tierra del Fuego, had made two forays into Antarctic waters, and had demonstrated the existence of the Antarctic Continent. They had visited Australia and New Zealand and explored many of the island groups of the South Pacific. Now, after four difficult and dangerous months spent mapping and collecting in the Fiji Islands, they were looking forward to a peaceful stay in the civilization of Hawaii. Here they would refit the ships after their long months at sea. Meanwhile they would investigate the natural history of this land of active volcanoes, one of the prime scientific objectives of the expedition.


## ACKNOWLEDGMENTS

Various members of the Smithsonian Institution staff contributed to the preparation of this paper. I would especially like to thank my colleague Tom Simkin for many helpful discussions. Carolyn Margolis provided invaluable assistance in obtaining illustrations, Chip Clark made high-quality prints for figures 60.1, 60.2, and 60.7, and Lynnetta Jones performed yeoman service in typing the manuscript.


## THE SCIENTISTS

The scientific corps of the Exploring Expedition consisted of nine men, expert in various aspects of zoology, botany, philology, and geology. Foremost among them was James Dwight Dana, later to become one of the giants of American geology. Dana was only 27 years old in 1840, but he was already well known as the author of the "System of Mineralogy," published in 1837. Dana received his excellent scientific training at Yale College, thanks to the extraordinary school of natural science established by Benjamin Silliman. Here he acquired a consuming interest in geology and mineralogy, and an intensely professional approach to scientific research that was unusual at that period.

Upon graduation from Yale in 1833, Dana was unable to find an academic position in natural science and so signed up as mathematics instructor aboard the U.S. Navy ship *Delaware* for service in the Mediterranean. During the 16-month cruise he ascended the volcano Vesuvius, then in an active phase, and recorded detailed geologic observations. He sent these back to Professor Silliman, who promptly published them in the American

[1]Department of Mineral Sciences, Smithsonian Institution, Washington, D.C. 20560.

Journal of Science (Dana, 1835). Dana's observations on Vesuvius, made just before an eruption in 1834, seem to constitute the first description of an active volcano by an American geologist. Thus began Dana's lifelong love affair with volcanoes: he was, indeed, the first American volcanologist.

Although Dana was principally responsible for the geological department of the expedition, other members of the scientific corps contributed significantly to the geological studies of the Hawaiian Islands. Charles Pickering, a zoologist originally trained as a medical doctor, did superb geologic field work. Joseph Drayton, an expert scientific illustrator, made careful measurements and drawings of the great craters. And Titian Peale, a zoologist who was a member of the famous family of American artists, made the paintings and sketches which show so well the appearance of Kilauea in 1840.

Numerous geologic observations were also made by the naval officers, especially Commander Charles Wilkes. Wilkes had been chosen to lead the expedition largely because of his scientific background (Stanton, 1975). He personally directed the surveying and mapping, as well as the geophysical, meteorological, and hydrographic studies, and felt qualified equally with the scientists to describe and interpret the geological phenomena.

To follow the geologic investigations of Dana and the other scientists in the islands, it is necessary to understand the logistics by which the expedition operated. The scientists were distributed between two of the expedition's four ships: the flagship *Vincennes*, under Commander Wilkes, and the *Peacock*, under Captain Hudson. Dana and Peale were on the *Peacock*, Pickering and Drayton on the *Vincennes*. The *Vincennes* arrived in Honolulu on September 24, 1840, and the *Peacock* on September 30. After several weeks of socializing and field work on Oahu, Dana, Pickering, Peale, and most of the other scientists were ferried over to Kauai on October 25 on the tender *Flying Fish*, the expedition's smallest ship. They spent six days exploring Kauai, returning to Oahu on November 3.

Wilkes planned next to proceed to the Island of Hawaii himself in the *Vincennes*. There he proposed to spend several months erecting an observatory on the summit of Mauna Loa, and observing the active volcanoes. Meanwhile he had ordered the *Peacock* to return to the South Seas to finish charting in the Samoan, Gilbert, and Marshall Islands. The various ships would rendezvous at the end of April at the mouth of the Columbia River in Oregon Territory.

Thus Pickering, the zoologist, would spend two months on the volcanoes of Hawaii, while Dana, the geologist, would examine more coral islands and empty ocean. Fortunately repairs to both ships took longer than expected, and Wilkes allowed Dana, Peale, and the others from the *Peacock* to take the tender from Oahu to Hawaii. They landed on the west coast at Kealakekua Bay on November 14, crossed the island in less than a week, and returned to Honolulu by the 28th. It is clear that Wilkes felt he personally must make the important observations on Hawaii. Furthermore, he saw no need to switch Dana's assignment, since to him the scientists were more or less interchangeable—he called them all "naturalists."

The *Peacock*, with Dana aboard, left for the South Seas on December 2; the *Vincennes*, with Wilkes, Pickering, and Drayton, arrived in Hilo on December 9. During the next 2 months the indefatigable Pickering climbed both Mauna Loa and Mauna Kea and made three visits to Kilauea. On February 15, 1841, Pickering and Drayton left the Island of Hawaii to spend a month exploring Maui, where they were joined by Wilkes on March 6. On March 19 the whole party returned to Oahu, and on April 5 the *Vincennes* departed for the Oregon Territory.

## ORIGINAL SOURCES

The principal publication on the geological work of the expedition in Hawaii is volume 10 of the reports of the U.S. Exploring Expedition: "Geology" (Dana, 1849). In this volume Dana brings together the results of all the expedition scientists and data from many other investigators, to create what is almost a textbook of Hawaiian geology and volcanology. Except where otherwise stated, all references to Dana's work in the present paper are from this volume.

Another valuable source is the unpublished journal of Charles Pickering (Pickering, 1840–41), reporting in detail the observations summarized by Dana (1849). Dana's field notebooks in the Yale University Library contain much of the raw data used in his report. Volume 4 of the narrative of the Exploring Expedition (Wilkes, 1844) contains Wilkes' own account of the expedition's visit to Hawaii, drawn from the journals of all of the expedition's officers and scientists.

## KILAUEA

The appearance of Kilauea caldera in late 1840 is well shown in the expedition map (fig. 60.1) and in the drawing by Drayton (fig. 60.2), made with the help of a camera lucida from the northwest rim near the western end of Steaming Bluff. The outer walls were 198 m high at their highest point, Uwekahuna Bluff. Below them was the Black Ledge, the outer rim of the former caldera floor; 183–610 m wide, it encircled the entire caldera. Within the Black Ledge, the inner pit was 104 m deep and approximately 3.6 km long by 1.2 km wide. The partly isolated basin at the southwest end of the inner pit corresponded to the present location of Halemaumau (figs. 60.3*A*, 60.3*B*). By comparison, the outer walls in 1981 were about 145 m high at Uwekahuna, and Halemaumau, the only present-day vestige of the inner pit, was about 79 m deep. Except for the shallower floor, the general features of the outer walls shown by Drayton are still readily recognizable.

Dana attempted to reconstruct the history of changes within the caldera from the sporadic accounts of visitors, starting in 1823, when it looked much as in late 1840. By early 1832 the entire caldera was filled to within about 185 m of the top with "solid lava" (Martin, 1979), burying the Black Ledge. Later in 1832 the central portion of the caldera floor collapsed, and the Black Ledge appeared again. By 1839, continued summit eruptions had refilled the basin, once more burying the Black Ledge. During the great flank eruption of May–June 1840 the central portion sank yet again, leaving the caldera as the expedition found it. This pattern of

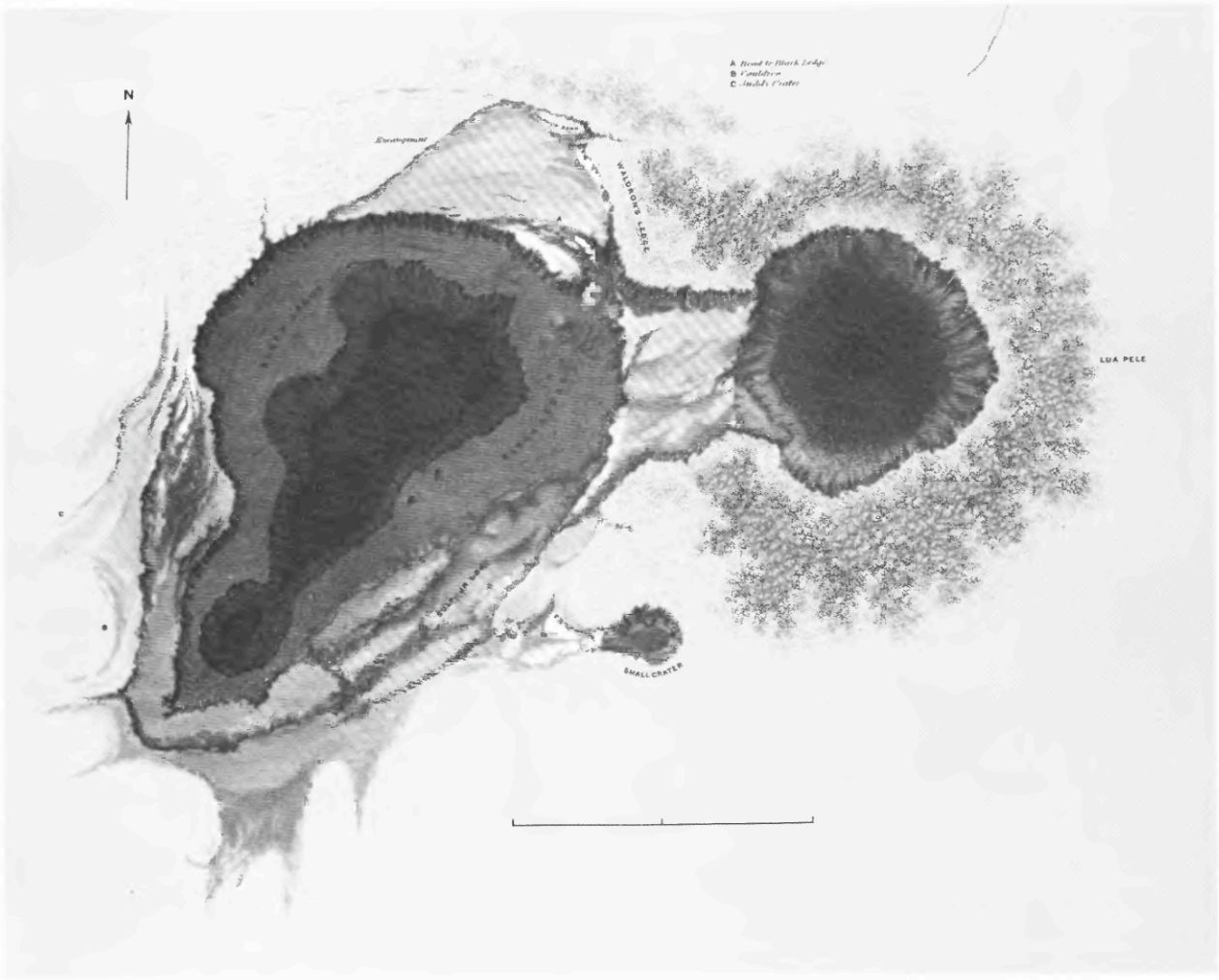


FIGURE 60.1.—Map of the crater of Kilauea made by the U.S. Exploring Expedition, 1841 (from Wilkes, 1844, v. 4, p. 177). North is at top; scale bar represents 8,000 ft.

changes was to be repeated with variations for several decades, until the Black Ledge disappeared for good around 1886 when the caldera floor reached a level close to what we see today (Dana, 1890).

When Dana visited Kilauea in late November 1840, the inner basin contained three lava lakes in continual eruption. The largest was in the present location of Halemaumau; two smaller lakes were on the western and eastern sides of the basin (fig. 60.4). Dana described in meticulous detail the character of these summit eruptions: the lava fountains, the currents within the lakes, the various driblet cones and other constructional features, the sequence of activity. He was particularly impressed with the "remarkable fluidity of the lavas" (Dana, 1849, p. 178); he observed the formation of Pele's hair as a particularly striking phenomenon depending on this fluidity.

Although Dana was allowed to spend only one day at Kilauea, he was able to draw on Pickering's and Wilkes' accounts of its behavior over a three-month period. Pickering in particular records the rapid changes occurring within the inner pit; only Halemaumau remained in constant eruption, though undergoing dramatic changes in level (Pickering, 1840–41).

## THE ERUPTION OF 1840

The Exploring Expedition scientists were lucky in the timing of their visit. Not only was Kilauea in continuous summit eruption, but its greatest flank eruption of historical times had just taken place: the east-rift eruption of May–June 1840 (Macdonald and others, 1983). Dana visited the still-steaming flow where it had entered the sea at Nanawale, destroying the village and throwing up large littoral cones. Pickering spent several days tracing the course of the

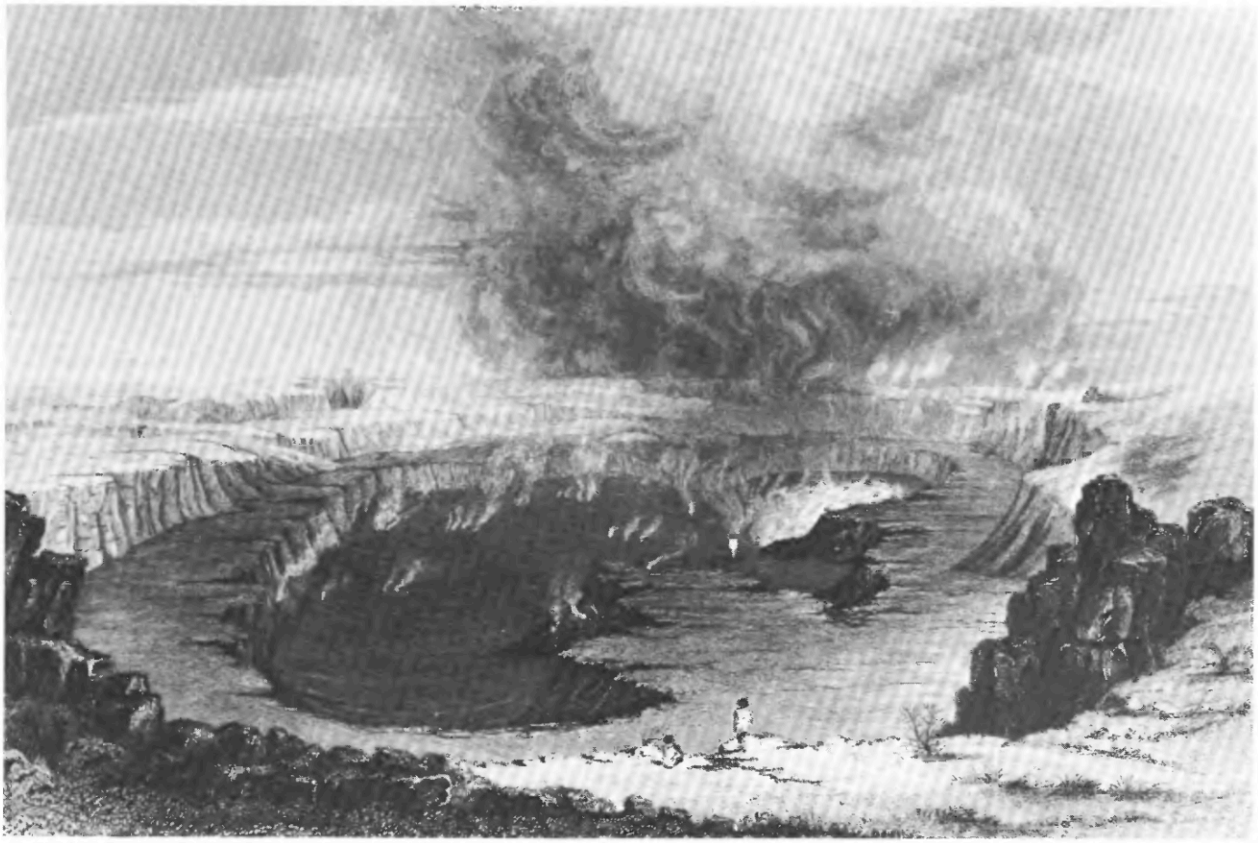

FIGURE 60.2.—"View of crater Kilauea" by Joseph Drayton (from Wilkes, 1844, v. 4, p. 134). View looking south from western end of Steaming Bluff. Kilauea Iki Crater is visible to left of center; constricted part of inner pit at far end is present location of Halemaumau.

eruption and describing its thickness and extent; he, Drayton, and Wilkes produced a map of the 1840 flows that appears in the narrative of the expedition (Wilkes, 1844, v. 4).

The 1840 eruption had a great influence on Dana's thinking; it became in his writings the type example of a flank eruption. The conjunction of this eruption with the collapse of the inner pit of the summit caldera led Dana to conclude that the two events were cause and effect. From the map area and thickness he estimated the volume of lava represented by the flows, obtaining a value of $170 \times 10^6$ m$^3$. Macdonald and others (1983) give an estimate of $205 \times 10^6$ m$^3$ for this eruption. Dana compared the volume of the flows with the volume of the subsidence in the caldera, estimated at $436 \times 10^6$ m$^3$; the difference he attributed to the part of the flows below sea level and to filling of fissures.

The 1840 eruption emphasized to Dana the importance of the rift zones as loci of flank eruptions. He described the southwest rift zone briefly and the east rift zone at length, basing his account on Pickering's detailed field study. Pickering had crossed the rift from Pahoa to Kaimu, followed the coast to Kamoamoa, and ascended near the Kalapana Trail to Makaopuhi Crater. From Puu Huluhulu he mapped the major pit craters, and he observed the evidence of the progress of the 1840 eruption as it migrated down the rift from its beginnings in Alae (Pickering, 1840–41).

## CALDERAS, PIT CRATERS, AND COLLAPSE

From his observations at Kilauea Dana acquired a profound sense of the importance of collapse in volcanic edifices. The subsidence of the inner pit during the 1840 eruption was to him a model for the formation of the summit caldera. The pit craters of the east rift zone he likewise associated with collapse following injection of magma along the rift. The whole idea of withdrawal of magma followed by subsidence of the edifice became central to his thinking, and ultimately it led him to explain correctly the great Krakatau eruption of 1883 as involving explosive eruptions of liquid lava as volcanic ash followed by collapse of the volcano into the space left empty by the discharge (Dana, 1888).

## MAUNA LOA AND "LAVA DOMES"

During his brief stay on Hawaii, Dana traveled around the southern flank of Mauna Loa from Kealakekua Bay to Kilauea,

more or less along the line of the present Highway 11. Most of his information about Mauna Loa, however, came from Pickering and the naval officers, who ascended the mountain and mapped and explored the summit. Besides describing the summit caldera and associated pit craters, Pickering noted the rift zones, especially the northeast rift. Dana also included in his 1849 report a detailed account furnished by Rev. Titus Coan of the large 1843 eruption from this rift zone, during which some flows may have been more than 40 km long.

Mauna Loa was Dana's type example of a basaltic shield volcano, just as Kilauea was his model for the eruptive style that created such volcanoes, which he termed "lava domes." He described at length how so broad a dome could be built by a combination of summit and flank eruptions such as he had observed. Dana also contrasted the quiet eruptive style of these volcanoes with the more violent eruptions of volcanoes like Vesuvius, which resulted in steep cones. He attributed the quiet style to the extreme fluidity of the basaltic lava, which he could not, however, satisfactorily explain.

Dana recognized the lava of Kilauea as typical of shield-forming eruptions, and tried to understand the difference between pahoehoe and aa. He observed that pahoehoe flows could change to aa as they traveled away from the vent; thus the two could not differ in composition. All he could suggest in explanation, however, was that cessation of flow followed by renewed motion created the clinkery aa.

Finally, Dana used the Mauna Loa-Kilauea system as an example of what he called the isolation of the lava conduits. The occurence of an eruption near the summit of Mauna Loa or high on the rim of the Kilauea caldera, without disturbance of the active lava lakes, he interpreted as evidence for many entirely separate conduits, connected only at great depth.

## VOLCANIC CONES

Besides "lava domes" (basaltic shields) and their associated pit craters, Dana recognized two other types of volcanic edifice in Hawaii: these he called "cinder cones" and "tufa cones" (tuff cones). He correctly described the origin of cinder cones as "the result of ejections of the melted lava to such heights that it falls in showers of dry cooled scoria, cinders, or ashes" (Dana, 1849, p. 354). He realized that the hundreds of such cones visible on Mauna Loa and Kilauea were relatively minor features, mostly formed where continued fountaining had occurred along rifts, but that they became more important in the later stages of a volcano's eruptive history, as on the summit of Mauna Kea.

The tufa cones were best described by Dana on Oahu, where he spent most of his time in the islands. After studying the magnificent cones of Diamond Head and Koko Head (fig. 60.5) he accurately ascribed their origin to explosive eruption through water or wet rocks, which chilled and fragmented the lava into smaller particles than the cinder and scoria of the drier cinder cones. He also noted their asymmetry due to eruption during trade winds and their layers dipping inward and outward. Dana also classified as tufa cones what are now called littoral cones, such as the Nanawale sand hills. Though he knew these had formed where the 1840 flows entered the sea, he thought the lava had erupted from a rift beneath the sea floor, and thus he wondered at the lack of a central crater.

## THE ERUPTION OF 1790

When the expedition visited Kilauea, the devastation to the south of the caldera from the great explosive eruption 50 years before was still very obvious: it is clearly shown in Peale's painting "Volcano of 'Kaluea Pele' as seen from the side of Mauna Loa, looking S.E., Nov. 21, 1840" (fig. 60.6). Dana reprinted the account recorded by a missionary from eyewitnesses to the blast, which killed a large party of Hawaiian warriors. Later Dana (1888) explained such rare explosive eruptions as the result of ground water penetrating to the molten lava, deep within the volcano, and flashing into steam—which with some modifications, is not too far from modern interpretations (Decker and Christiansen, 1984). He also convinced himself that explosive eruptions were indeed rare events in Hawaiian volcanoes like Kilauea, because he observed no pyroclastic deposits exposed in the caldera walls or in dissected shields on Oahu or Maui, which he visited in 1887.

## THE ASCENT OF MAUNA LOA

No account of the Exploring Expedition in Hawaii can fail to mention Commander Wilkes' proudest scientific achievement: the establishment of a geophysical observatory atop 4,169-m (13,679-ft) Mauna Loa. True to his plans, he led to the summit a party of 16 expedition members and 200 Hawaiian porters, laden with scientific instruments, food, and supplies. It was not a pleasant place in midwinter: water froze in the tents in the daytime, and the wind was violent and seemed incessant. Here the men spent three arduous weeks making meteorological, gravity, and magnetic measurements (Borthwick, 1965) and mapping the summit region and Mokuaweoweo caldera.

The expedition called their camp "Pendulum Peak" after the most cumbersome of their instruments. They had to erect massive stone walls to protect both instruments and men from the biting winds, which destroyed some of the more delicate barometers despite their best efforts. The ruins of these walls are visible today on the summit—a tangible remainder of the first U.S. Government-sponsored geophysical observatory in the Hawaiian Islands.

Wilkes' measurements were meant to be published as volume 24, "Physics," of the reports of the expedition, but this volume never appeared. Much of the data is preserved in the U.S. National Archives, and the magnetic results were published almost a century later by Ennis (1934). The meteorological results are also discussed by Ramage (1978), who points out that Wilkes came close to discovering the trade-wind inversion.

## OAHU AND KAUAI

Dana correctly discerned that Oahu was composed of two deeply eroded shield volcanoes and Kauai of a single eroded edifice.

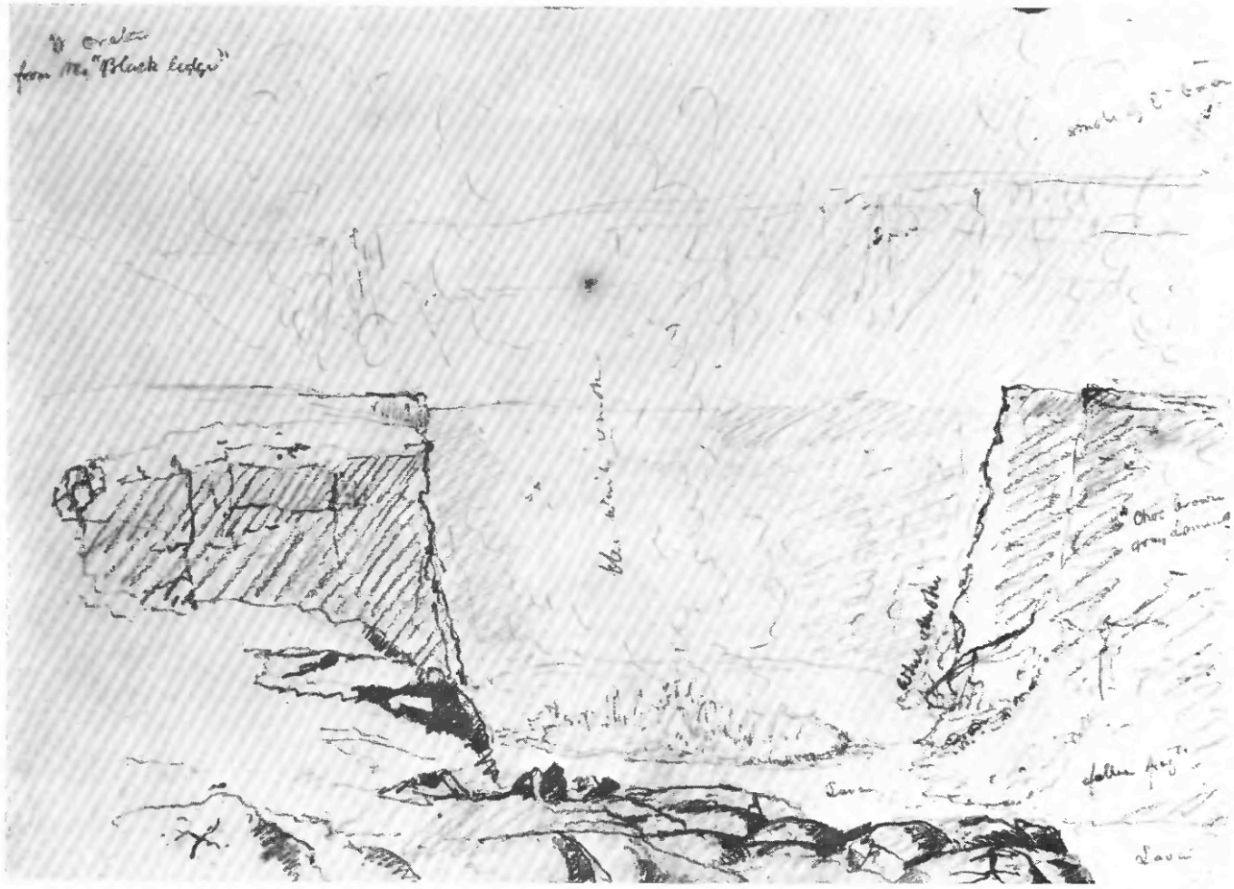

*A*

FIGURE 60.3.—Sketch and painting of western inner pit of Kilauea caldera by T.R. Peale. Courtesy American Museum of Natural History. ***A***, Sketch of "W. crater from the 'Black Ledge,'" drawn in 1840. View is of constricted part of inner pit at present location of Halemaumau, showing active lava lake. The artist has made notes to assist him in making the final painting. ***B***, Oil painting "West crater 'Kaluea Pele' from the Black Ledge'" dated November 1840. Painting presumably based on the sketch (*A*) done on the spot.

He noted that the outer flanks of the volcanoes were composed largely of thin-layered flows, but that toward the center the flows became much thicker and the layering in places disappeared altogether. Drawing on his knowledge of Kilauea, Dana attributed this to the inferred presence of thick lava bodies representing lava lake fill within the caldera region. This is roughly the interpretation of modern workers (Macdonald and others, 1960; Stearns and Vaksvik, 1935). Dana had noted the same phenomenon on Tahiti. On both Kauai and Oahu he identified posterosional eruptive phases that built prominent cinder and tuff cones (fig. 60.7). These are parts of what were later defined as the Koloa Volcanic Series (currently called the Koloa Volcanics) on Kauai by Macdonald and others (1960) and the Honolulu Volcanic Series (currently called the Honolulu Volcanics) on Oahu by Stearns and Vaksvik (1935); for a review of stratigraphic nomenclature, see Langenheim and Clague (chapter 1, part II). For Oahu Dana even made a kind of colored geologic map delineating shield volcanoes, the Honolulu Volcanics cones, coral reef, upraised coral-reef rock, and coral-sand rock (Dana, 1849).

Dana realized that the eastern half of the Koolau shield volcano of Oahu was missing, truncated by the Pali. He did not believe that this type of destruction could be caused by wave or stream erosion alone and attributed it to a rupture of the dome, with the eastern half sliding into the sea. "The portion of the great volcano cut off at the rupture has disappeared beneath the ocean" (Dana, 1849, p. 259). This view is very close to the landslide hypothesis advanced by Moore (1964) for the Koolau shield and more recently supported by Holcomb (1983). Dana believed the same mechanism was responsible for the Napali coast of Kauai and possibly for other apparent truncations.

*B*

FIGURE 60.3.—Continued.

Dana also pointed out that the eastern precipice of Niihau cuts off the eastern portion of that shield; this has been attributed to faulting, rather than wave erosion alone, by Macdonald and others (1983). If this portion of the shield is restored, then Niihau and Kauai lie on a line nearly perpendicular to the trend of the main islands. This statement has been misread by Macdonald and others (1983), who state that Dana said that Niihau represents the northwest edge of Kauai, shifted laterally by faulting; he did not.

## PETROLOGY

Dana distinguished two main groups of lava types in the Hawaiian Islands: those in which feldspar was not dominant, which he termed basalt, and those with dominant feldspar, which he called variously clinkstone, trachyte, syenite, or merely feldspathic. He thought that the feldspathic varieties tended to occur near the centers of the mountains, because that was where the expedition scientists reported them. This misconception may have arisen because, with no geologic mapping, Dana was unaware of the capping of the original shield basalt by later, more differentiated postcaldera lava on Mauna Kea, Haleakala, and other shields (Stearns and Macdonald, 1942).

Pickering and Dana also observed the varied distribution of olivine; they especially noted that abundant large crystals were present in the 1840 flow erupted at low altitude, while summit lava erupted almost simultaneously contained little or no visible olivine (Macdonald, 1944). Dana speculated at length on possible mechanisms for differentiation, rejected the idea proposed by Darwin (1844) for differentiation by crystallization and gravity separation, and came to no clear conclusion. He did, however, suggest the

FIGURE 60.4.—"Sketch of Kilauea Pele, island of Hawaii" by T.R. Peale. Sketch shows main (Halemaumau) lava lake in background and (presumably) westernmost of two smaller lava lakes, observed by Dana, in foreground. Sketch was used by Peale as basis for an oil painting of a night scene of crater. Courtesy of American Museum of Natural History.

possibility of portions of lava being separated within the flanks of the volcano from the main body before differentiation. The evolution of magma compositions with time in the life cycle of a volcano was only indirectly hinted at.

It is clear that Dana was trying to distance himself as much as possible from the Wernerian concept, then only 60 years old, that particular rocks were only formed at particular times in the Earth's history. "If the elements are at hand," he wrote, "it requires only different circumstances as regards pressure, heat, and slowness of cooling, to form any igneous rock the world contains." Thus, in "a basaltic mountain with a feldspathic center***we are not compelled to suppose the feldspathic interior to have formed first or last" (Dana, 1849, p. 377–378).

## SUBSIDENCE, ELEVATION, AND CORALS

One of Dana's major contributions in the geology report was the confirmation and expansion of Darwin's subsidence theory of the origin of coral atolls (Darwin, 1842). Based on the expedition's observations of hundreds of islands in the South Pacific, Dana proposed that as oceanic volcanoes become extinct, fringing coral reefs form around them. The volcanic edifices then gradually subside, but the corals grow upward fast enough to keep pace with the subsidence, forming first barrier reefs around the volcano's sinking summits and finally atolls with no central volcanic peak. His data led Dana to conclude that the subsidence in the Pacific was on a very large scale, related to global tectonism. In the Hawaiian Chain, Dana saw this progression from still-active Hawaii with practically no reefs, through Oahu and Kauai with extensive fringing reefs, to the northwestern islands that are all coral, indicating greatest subsidence at the western extremity.

Dana found no such global pattern in evidences of major elevation. He observed many reefs elevated a few meters, but only scattered, apparently random instances where uplift of 75 m or more could be demonstrated, such as at Metia Island in the Tuamotus. In the Hawaiian Islands, Dana reported elevation of 7–9 m on Oahu,

FIGURE 60.5.—Sketch of "Diamond Hill and Punchbowl seen from SSE" from Dana's field notebook "New Zealand, Tonga to Feejees, Sandwich Islands," Dana Family Papers, Box 6, Folder 134, Yale University Library. Dana recognized these tuff cones as much younger than the shield volcanoes and observed greater erosion of Diamond Head compared to Koko Crater, as shown by truncation of internal structure.

but both he and his colleague J.P. Couthouy were extremely skeptical of reports of coral at 65–70 m on Maui and Molokai. Recent work by Moore and Moore (1984) suggests that these coral-bearing gravels, like others on Lanai, were deposited by a giant landslide-triggered sea wave, and there is no evidence for such a high stand of the sea. Dana, of course, did not in 1840 know about the Pleistocene eustatic changes in sea level responsible for the lower reef-rock terraces.

Recent work, summarized by Scott and Rotondo (1983), indicates that the regional Pacific subsidence delineated by Dana is largely from the sinking of the Pacific plate as it moves away from the spreading centers and cools; this is a truly global effect. Instances of large elevation, such as Metia, on the other hand, are probably local in origin, thus bearing out Dana's conclusions.

## EROSION, AGE PROGRESSION, AND ISLAND CHAINS

Perhaps the best known of Dana's contributions to Hawaiian geology was his recognition of a systematic age progression within the chain of islands. He took Mauna Loa as the type of a still-active, virtually uneroded shield volcano. Mauna Kea was clearly a very similar shield, but it was no longer active. Its eastern side, exposed to the trade winds, was beginning to be heavily gullied, while its protected western side was nearly untouched: proof of stream erosion working since the volcano became extinct. Thus, Dana reasoned, the degree to which a shield volcano was eroded was a measure of the time elapsed since it had become effectively extinct.

Applying this reasoning, he worked out the following sequence of extinction (from oldest to youngest): Kauai, Waianae, West Maui, Koolau, Mauna Kea, Haleakala, and finally Mauna Loa. He was misled to some degree on the older islands by his failure to recognize renewed massive posterosional volcanism, which masked the old eroded topography. On Haleakala, Pickering had described well the unique aspects of Haleakala Crater; he almost always referred to it as a "valley" and pointedly mentioned the very youthful appearance of the lava flows within it (Pickering, 1840–41). Dana, who did not visit Maui during the expedition, interpreted the crater as having formed by fissuring during the last great eruptions; the modern view of its origin by stream erosion did not occur to him (Stearns and Macdonald, 1942). He held to his view even after

FIGURE 60.6.—Painting of "Volcano of 'Kaluea Pele' as seen from the side of 'Mauna Loa', looking S.E. Nov. 21, 1840" by T.R. Peale. Peale crossed the island from Kealakekua Bay by Ahua Umi Heiau, around north side of Mauna Loa at elevation of about 3,000 m and down to Kilauea. Rare silverswords (lower right corner) are now extinct in this area. Courtesy American Musuem of Natural History.

visiting Haleakala in 1887.

The most severe limitation on Dana's concept was his insistence that the geologic evidence showed only an age progression of extinction of the Hawaiian volcanoes, not one of formation. "From Kauai to Mauna Loa all may have thus simultaneously commenced their ejections, and have continued in operation during the same epoch till one after another became extinct***. No facts can be pointed to, which render it even probable that Hawaii is of more recent origin than Kauai, though more recent in its latest eruptions" (Dana, 1849, p. 280). This overly rigorous interpretation of the geologic evidence forced Dana to adopt a static model for origin of the volcanoes by rupture of fissures, which must become wider toward the southeast. Dana's colleague J.P. Couthouy, the expedition conchologist, was more daring. He wrote to Dana, "The foregoing observations are applied to the course of volcanic action at the islands taken separately, with a view to show that it has been sucessive in each, from the western to the southeastern extremity of the group, and the possibility that they were also forced up in regular succession by the subterranean fire. The phenomena they present seem to point to such an origin***" (Dana, 1849, p. 283). Dana never did accept the idea of sequential origin (Dana, 1890).

As others had before him, Dana described the parallel orientation of many Pacific island chains, but he did this at a level of detailed analysis not previously attempted and with a much larger data base. He suggested that the Society Islands showed the same age progression as the Hawaiian Chain, and he clearly implied this was a general trend in chains parallel to Hawaii, although he lacked sufficient data to confirm this. The Samoan Chain, also parallel to the Hawaiian, he considered to have a reverse progression. Recent studies (Natland, 1980; Natland and Turner, 1985) show that the Samoan shield volcanoes do conform to the Hawaiian age progression, but that the older islands to the northwest have been subjected to voluminous posterosional volcanism, possibly related to bending of the Pacific plate.

Dana devoted many pages to painstaking description of the arrangement of the islands. He noted that the 15 Hawaiian volcanoes which he identified actually lie along two parallel trends, and that this same phenomenon was present in other chains (Jarrard and

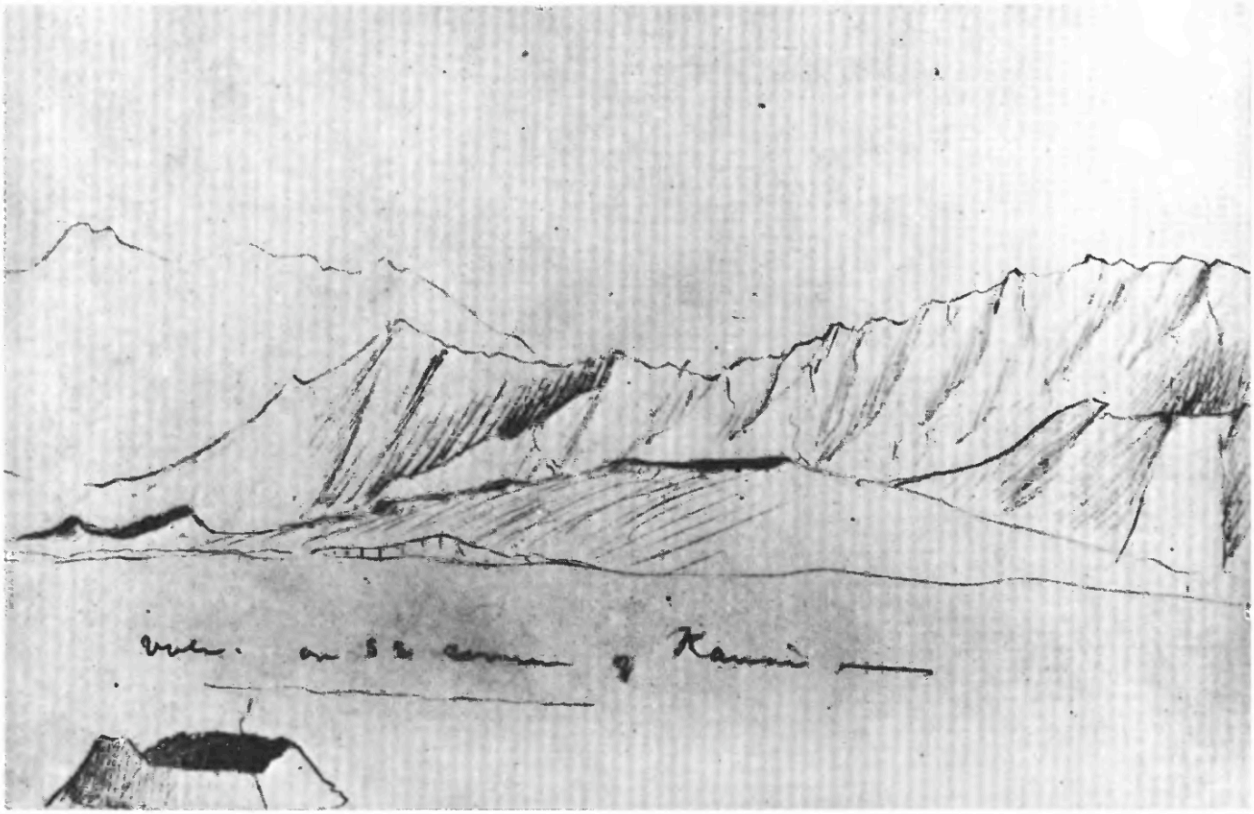

FIGURE 60.7.—Sketch of "View on SE corner of Kauai" from Dana's field notebook "New Zealand, Tonga to Feejees, Sandwich Islands," Dana Family Papers, Box 6, Folder 134, Yale University Library. Dana noted that Hoary Head Range (background) appeared anomalous in terms of shield volcano structure; modern workers have identified it as massive lavas formed in the only flank calderas known on Hawaiian volcanoes (Macdonald and others, 1983). Cones (foreground) are Koloa Volcanics.

Clague, 1977). Dana showed that the "linear chains" were actually broken up into shorter segments arranged in echelon fashion along the trend, and he attempted to relate their geometry to an oceanwide or even global fracture pattern. Some modern workers (for example, Jackson and Shaw, 1975) agree with his observations and propose that the pattern is related to stress in the Pacific plate, an idea to which Dana would certainly have been sympathetic.

Dana's work on linear island chains in the Pacific was clearly of great importance in the development of modern plate-tectonic theory, especially as the direct forerunner of the various hot-spot hypotheses (Wilson, 1963a, b; Morgan, 1972a, b). The difficulties of age interpretation that plagued Dana have not all disappeared with modern dating techniques (Jarrard and Clague, 1977; Jackson and others, 1980). A final example of Dana's acumen in this regard: By extrapolating from observed levels of activity, he calculated (somewhat apologetically) the time required to build the subaerial portion of Mauna Loa as 400,000 years, a figure not far out of line with many modern radiometric measurements on shield volcanoes (Macdonald and others, 1983).

## CONCLUSIONS

The geological investigations of the U.S. Exploring Expedition in Hawaii constitute the beginnings of modern volcanology and geology in the islands. Unlike the episodic and often anecdotal scientific reports of previous visitors, Dana's geology report attempted to be as precise, quantitative, and complete as possible. The careful surveys by Wilkes and his officers of Kilauea and Mokuaweoweo calderas, and their maps of the volcanoes, provided the first accurate base for measurement of future changes.

Dana recognized the great importance of Kilauea and Mauna Loa as a natural laboratory of volcanology, and for the rest of his long life he tried to keep a systematic account of eruptions and changes in the volcanoes (Dana, 1890). Although a semi-invalid, he returned to Hawaii in 1887 at the age of 74 to revisit Kilauea, this time without the restrictions of a naval expedition, before writing his book "Characteristics of Volcanoes" (Dana, 1890). His ideas on volcanoes changed surprisingly little over the years, however, and remained heavily influenced by his work during the Exploring

Expedition. These ideas, disseminated through Dana's highly popular textbooks and prolific writing of technical papers, were in turn influential in the development of geologic thought in the last half of the 19th century. In a very real sense Dana can be considered the spiritual godfather of the Hawaiian Volcano Observatory, which from its inception has continued the tradition of Hawaiian volcanology that he had begun so many years earlier (Jagger, 1947, abstract).

## REFERENCES CITED


Borthwick, D.E., 1965, Outfitting the United States Exploring Expedition: Lieutenant Charles Wilkes' European assignment, August–November, 1836: Proceedings of the American Philosophical Society, v. 109, no. 3, p. 159–172.

Dana, J.D., 1835, On the condition of Vesuvius in July, 1834: American Journal of Science, v. 27, p. 281–288.

——— 1849, Geology: United States Exploring Expedition: Philadelphia, C. Sherman, v. 10, 756 p.

——— 1888, History of the changes in the Mt. Loa craters: American Journal of Science, ser. 3, v. 36, no. 212, p. 81–112.

——— 1890, Characteristics of volcanoes: New York, Dodd, Mead and Co., 399 p.

Darwin, C., 1842, The structure and distribution of coral reefs: London, Smith, Elder and Co., 214 p.

——— 1844, Geological observations on the volcanic islands, visited during the voyage of H.M.S. *Beagle*: London, Smith, Elder and Co., 175 p.

Decker, R.W., and Christiansen, R.L., 1984, Explosive eruption of Kilauea Volcano, Hawaii, *in* Boyd, F.R., Jr., ed., Explosive volcanism: Inception, evolution, and hazards: Washington, National Academy Press, p. 122–132.

Ennis, C.C., 1934, Magnetic results of the United States Exploring Expedition, 1838–1842, Lieutenant Charles Wilkes, Commander: Terrestrial Magnetism and Atmospheric Electricity, v. 39, no. 2, p. 91–101.

Holcomb, R.T., 1983, East Molokai Volcano was halved by giant landslide [abs.]: Geological Society of America Abstracts with Programs, v. 15, no. 6, p. 597.

Jackson, E.D., Koisumi, I., and others, 1980, Initial reports of the Deep-Sea Drilling Project, vol. 55: Washington, U.S. Government Printing Office, 868 p.

Jackson, E.D., and Shaw, H.R., 1975, Stress fields in central portions of the Pacific plate: delineated in time by linear volcanic chains: Journal of Geophysical Research, v. 80, no. 14, p. 1861–1874.

Jaggar, T.A., 1947, Origin and development of craters: Geological Society of America Memoir 21, 508 p.

Jarrard, R.D., and Clague, D.A., 1977, Implications of Pacific island and seamount ages for the origin of volcanic chains: Reviews of Geophysics and Space Physics, v. 15, no. 1, p. 57–76.

Macdonald, G.A., 1944, The 1840 eruption and crystal differentiation in the Kilauean magma column: American Journal of Science, v. 242, no. 4, p. 177–189.

Macdonald, G.A., Abbott, A.T., and Peterson, F.L., 1983, Volcanoes in the sea (2d ed.): Honolulu, University of Hawaii Press, 517 p.

Macdonald, G.A., Davis, D.A., and Cox, D.C., 1960, Geology and ground-water resources of the Island of Kauai, Hawaii: Hawaii Division of Hydrography, Bulletin 13, 212 p.

Martin, M.G., ed., 1979, The Lymans of Hilo (revised ed.): Hilo, Lyman House Memorial Museum, 224 p.

Moore, J.G., 1964, Giant submarine landslides on the Hawaiian Ridge, *in* Geological Survey research, 1964: U.S. Geological Survey Professional Paper 501–D, p. D95–D98.

Moore, J.G., and Moore, G.W., 1984, Deposit from a giant wave on the Island of Lanai, Hawaii: Science, v. 226, no. 4680, p. 1312–1315.

Morgan, W.J., 1972a, Plate motions and deep mantle convection: Geological Society of America Memoir 132, p. 7–22.

——— 1972b, Deep mantle convection plumes and plate motions: American Association of Petroleum Geologists Bulletin 56, p. 203–213.

Natland, J.H., 1980, The progression of volcanism in the Samoan linear volcanic chain: American Journal of Science, v. 280-A, p. 709–735.

Natland, J.H., and Turner, D.L., 1985, Age progression and petrologic development of Samoan shield volcanoes: evidence from K/Ar ages, lava compositions, and mineral studies, *in* Brocher, T.M., ed., Geological investigations of the northern Melanesian borderland; Circum-Pacific Council for Energy and Mineral Resources Earth Science Series, v. 3: Tulsa, Oklahoma, American Association of Petroleum Geologists, p. 147–180.

Pickering, C., 1840–41, Journal kept while on the United States Exploring Expedition (unpublished manuscript), v. 4, p. 129–219; v. 5, p. 1–27: Boston, Massachusetts Historical Society.

Ramage, C.S., 1978, The United States Exploring Expedition on Mauna Loa, *in* Miller, J., ed., Mauna Loa Observatory, a 20th Anniversary Report: Boulder, Colorado, U.S. Department of Commerce, p. 2–9.

Scott, G.A.J., and Rotondo, G.M., 1983, A model for the development of types of atolls and volcanic islands on the Pacific lithospheric plate: Atoll Research Bulletin, v. 260, p. 1–33.

Stanton, W., 1975, The great United States Exploring Expedition of 1838–1842: Berkeley, University of California Press, 433 p.

Stearns, H.T., and Macdonald, G.A., 1942, Geology and ground-water resources of the Island of Maui, Hawaii: Hawaii Division of Hydrography Bulletin 7, 344 p.

Stearns, H.T., and Vaksvik, K.N., 1935, Geology and ground-water resources of the Island of Oahu, Hawaii: Hawaii Division of Hydrography Bulletin 1, 479 p.

Wilkes, C., 1844, Narrative of the United States Exploring Expedition during the years 1838, 1839, 1840, 1841, 1842: Philadelphia, C. Sherman, 5 v.

Wilson, J.T., 1963a, A possible origin of the Hawaiian Islands: Canadian Journal of Physics, v. 41, p. 863–870.

——— 1963b, Evidence from islands on the spreading of ocean floors: Nature, v. 197, p. 536–538.

# THOMAS A. JAGGAR, JR., AND THE HAWAIIAN VOLCANO OBSERVATORY

*By* Russell A. Apple[1]


## ABSTRACT

**The digging of a cellar excavation on the north rim of Kilauea caldera in February 1912 marked the beginning of permanent facilities for what was to become the Hawaiian Volcano Observatory (HVO). The Observatory was largely the creation of Thomas A. Jaggar (1871–1953), then a Massachusetts Institute of Technology (M.I.T.) professor, who recognized the advantages, for the study of volcanism, of onsite facilities at an active volcano. Jaggar's efforts to establish an observatory at Kilauea were enthusiastically supported by Lorrin A. Thurston (1858–1931), a prominent Honolulu lawyer and businessman, who organized private support for Jaggar and HVO that continued into the 1940's. Initial support also came from M.I.T. and the University of Hawaii, and HVO was later successively sponsored by the U.S. Weather Bureau (1919–24), the U.S. Geological Survey (1924–35), the National Park Service (1935–47), and (since 1947) again the USGS.**

**The original HVO building, with a seismograph vault in its cellar, was in use until the early 1940's, when the Observatory was able to occupy a new building 200 m back from the caldera rim. In 1948 HVO moved to a building at the top of Uwekahuna Bluff on the northwest rim of Kilauea caldera; a new and larger building there was completed in 1986.**

**Under Jaggar's directorship (1912–40), HVO pioneered in seismological and other studies of volcanic processes. Seismographs were important instruments from the beginning of the Observatory, and HVO staff made numerous modifications to adapt them to the study of local volcanic seismicity. Jaggar even developed a rugged portable seismograph for use in outlying areas by amateur assistants. Early experiments in measuring the temperature of liquid lava were more educational than successful; the same can be said of the 1922 drilling program of four holes in and around Kilauea caldera. To support the drilling, HVO staff developed a modified touring car fitted with double wheels. For exploration around the coasts, an amphibious vehicle was designed and constructed.**

**Jaggar's campaign to obtain facilities at the top of Mauna Loa Volcano and a road leading to them was never entirely successful, but it has been made unnecessary by the advent of helicopters. Observation of the destruction of property by a lava flow in the 1926 eruption of Mauna Loa led to HVO-guided efforts to divert or stop flows threatening Hilo in 1935 and 1942 and to plans (never realized) for a set of permanent barriers. Concern for protection of lives and property also led to studies of tsunamis; in 1933 HVO used seismograms to predict (accurately) the arrival of a tsunami from a distant earthquake, and people in low-lying areas of Hawaii were for the first time successfully warned in advance. Such efforts reflected Jaggar's concern for not only the advance of science but also its application to the benefit of society.**

**Over its first 75 years, HVO has contributed much to the growing science of volcanology; for this a large debt is owed to the character and qualities of Thomas A. Jaggar.**


## INTRODUCTION

A hole was to be dug—by hand. Wooden stakes marked the corners of a rectangle about 7.3 m (24 ft) long by 6.7 m (22 ft) wide only about 6 m (20 ft) from the clifflike rim of Kilauea caldera on the Island of Hawaii. It was February 16, 1912, and the foundation to be dug was for Thomas A. Jaggar's volcano observation post, precursor of the Hawaiian Volcano Observatory (HVO).

The diggers were prisoners of the Territory of Hawaii, sentenced to a term of hard labor (HVO record book for 1912; Duncan, 1961). Jaggar was not above using free labor, prison or otherwise, to help stretch his limited funds. Their prison camp was nearby at what is now Kilauea Military Camp in Hawaii Volcanoes National Park.

The prisoners dug through almost six feet of volcanic ash and pumice to a layer of thick pahoehoe lava—a firm base for the concrete piers on which seismometers would be anchored. Plans and elevations for the piers had been hand drawn by Professor F. Omori at the Seismological Institute, Imperial University, Tokyo, Japan, and mailed two years before to Jaggar at the Massachusetts Institute of Technology. Omori also shipped to Jaggar, care of the Territorial Division of Forestry in Honolulu, "An Omori-type Horizontal Tromometer (a seismometer) (magnification = 120–200), and a seismograph for the observation of ordinary earthquakes" (Omori, 1910). These instruments were paid for and on hand in their crates as the prisoners dug.

Soon on hand at the crater rim were carpenters and workmen of the Hilo branch of H. Hackfeld and Company, Ltd., one of Hawaii's "Big Five" companies that controlled virtually all economy in the Islands—Hackfeld later became AMFAC, a multi-billion-dollar conglomerate (Weiner, 1982). Jaggar had contracted with Hackfeld for the forms and concrete work for the seismometer vault, and for the wooden structures that were to stand over and adjacent to the vault—the rimside facilities of the Hawaiian Volcano Observatory. The prime contract was for $1,785 and included a redwood tank for water storage. An additional $300 also went to Hackfeld for extra water-storage tanks (Jaggar, 1917a). Hackfeld executives

[1]U.S. National Park Service, retired.

and the directors of the other "Big Five" corporations were personally helping to sponsor the volcano observatory.

When British explorer Captain James Cook "discovered" Hawaii in 1778, Hawaiians had been living on some of the islands for as long as 1,300 years and had developed a complex, affluent Polynesian civilization. By 1795, when the various chiefdoms and islands were united to form the Kingdom of Hawaii, regular contact with Westerners had changed forever Hawaiians' environment and their way of life. However, with volcanism such an obvious presence in these growing islands, one part of the ancient Hawaiian religion that was kept—and still survives today—is the belief in the Hawaiian goddess of volcanoes, Pele.

Hawaiians believed that the goddess and her supernatural associates often entered into the political and social affairs of men. Pele could take human form, sometimes as a beautiful girl, sometimes as an old hag. Any female stranger could be the goddess. Pele was a major deity who had to be properly propitiated—she took offense easily—because in her anger she caused earthquakes and volcanic eruptions, and she personally directed the course of her lava flows.

Hawaiians believed that the summit caldera of Kilauea Volcano was the home of Pele, her family, and associates, but those deities also had "houses" elsewhere on the Islands of Hawaii and Maui that they could visit at will; these houses include the tops of mountains and all craters, cones, and hills. Pele required special behavior from humans in the vicinity of any of her houses, especially within a radius of 10 km (6 mi) or less from Kilauea caldera, and she expected tribute.

When high chiefs or other people failed to submit proper tribute, insulted Pele, her family, or her priests, or behaved improperly in Pele's domain, then the volcanic deities expressed their anger. They either flooded Kilauea caldera with lava and violently ejected it through the air over the countryside, or they took a subterranean passage to one of their "houses" near the land and homes of those who had offended and, using that house as a base of operations, proceeded to punish the offenders by, at a minimum, covering some of their land with fresh lava (Ellis, 1827; Menzies, 1920). Pele stamped her foot enough times before and between episodes of visible volcanism to remind people of her power and presence; each stamp caused an earthquake. Pele could also call down lightning and cause thunder to roll across the sky.

In 1893, the Kingdom of Hawaii was overthrown by non-Hawaiian businessmen. Five years later in 1898, during the Spanish-American War, the United States annexed Hawaii; the Islands thus became "American soil." This was one of the factors that led to the establishment of an American-sponsored volcano observatory on the rim of Kilauea Volcano (Apple, 1982; Apple and Apple, 1979a; Daws, 1968; Kuykendall, 1967).

During the nineteenth century, while the Hawaiians were being introduced to the ways of Western civilization, Hawaiian volcanoes were described in letters, reports, logs, journals, sketches, notes, and books, published in various places and some distributed worldwide. First made famous because Captain Cook was killed there, the Island of Hawaii now added another world-renowned distinction: active volcanoes. Principal fame focused on Kilauea, which appeared to be comparatively benign. Kilauea had an apparent constancy of activity within its vast summit caldera and, in contrast to some European volcanoes, was not known to wipe out villages or cast glowing fragments of lava down upon hillsides devoted to viniculture. At Kilauea, according to reports, volcanism stayed put inside a crater. While the general public was getting armchair thrills from travel writers, some scientists were also becoming aware of, and visiting, the Big Island (table 61.1).

The scientists listed in table 61.1 did not always agree. First there was the continuing, friendly controversy in the *American Journal of Science and Arts* ("Silliman's Journal") between Rev. Titus Coan, a Hilo man who hiked to and described almost every flank eruption of Mauna Loa between 1843 and 1880, and J.D. Dana, one of the journal's editors and a famous geologist, who didn't always believe the testimony of the eyewitness. For instance, after Dana published Reverend Coan's graphic and detailed description of the source and flows of Mauna Loa's 1843 eruption, Dana followed with "Mr. Coan speaks of the lavas as flowing from an orifice in a broad stream down the mountain. It is probable that fissures opening to the fires below were continued at intervals along the course of the eruption, and that these afforded accession to the fiery flood. Any internal force sufficient to break through the sides of a mountain like Mauna Loa, must necessarily produce a linear fissure or a series of fissures, and not a single tunnel-like opening." (Dana, 1852, p. 256; see also Dana, 1850; T. Coan, 1871, 1882; L. Coan, 1884.)

Arguments such as this could only be resolved by volcanologists doing the observing, but they served to publicize the need for further study. The Coan-Dana controversy helped raise questions that needed to be answered about volcanoes, thus helping pave the way for such institutions as the Hawaiian Volcano Observatory.

When a hotel on the rim of Kilauea caldera became a permanent facility in 1866, its series of guest registers became a repository of reports and observations by the guests, an almost daily record (by observers who varied from the scientist to the joker) of earthquakes felt and unfelt and of volcanism seen and unseen on Kilauea and Mauna Loa. Both Brigham (1909) and Hitchcock

TABLE 61.1.—*Some sources for early descriptions of the volcanoes of Hawaii*

| | Name or type of observer | Sponsor, if any | Reference |
|---|---|---|---|
| 1825 | Lord Byron party | England | Byron, 1826 |
| 1834 | Botanist | London Horticultural Society | Douglass, 1834, 1919 |
| 1834 | Captains Parker and Chase | | Kelley, 1841 |
| 1837 | Geologist | ——— | Strzelecki, 1838, 1845 |
| 1839 | Scientist | ——— | Lowenstern, 1841 |
| 1839 | Ship's captain | ——— | |
| Shepherd, 1840 | | | |
| 1840 | U.S. Exploring Expedition | U.S. Government | Wilkes, 1845 |
| 1840 | Geologist | U.S. Exploring Expedition | Dana, 1849 |
| 1846 | Professor | ——— | Lyman, 1851 |
| 1859 | Geologist | ——— | Green, 1887 |
| 1868 | Kilauea historian | Harvard University | Brigham, 1868, 1869 |
| 1873 | Travel Writer | ——— | Bird, 1875 |
| 1880 | Kilauea historian | Bishop Museum | Brigham, 1909 |
| 1882 | Geologist | U.S. Geological Survey | Dutton, 1884 |
| 1883 | Geologist | Dartmouth College | Hitchcock, 1911 |
| 1887 | Geologist | Yale University | Dana, 1890 |
| 1909 | Geologist | Massachusetts Institute of Technology | Daly, 1911 |

(1911) mined the more reliable reports from the Volcano House guest registers, quoting them along with observations from their own visits and reports from many additional sources to yield histories of both volcanoes, comprehensive up to their dates of publication.

Brigham, a scientist who once taught botany at Harvard and also practiced law in Boston, was by 1898 the Director of the Bernice Pauahi Bishop Museum in Honolulu. Hitchcock was a geologist, a member of a prominent Hilo family, and by 1909 was retired as Emeritus Professor of Geology at Dartmouth College. Both Brigham and Hitchcock kept up with the comings and goings of scientists interested in the Big Island volcanoes.

Brigham (1909, p. 216) notes that in the spring of 1909 the "well-known professors in the Massachusetts Institute of Technology, T.A. Jaggar, Jr., and R.A. Daly," visited Kilauea, and that Jaggar and Daly were "interested in the establishment of a permanent observatory at Kilauea, a result so ardently hoped for many years and frequently referred to in these pages."

Hitchcock (1911, p. 306) applauds Brigham's recommendation that a "permanent scientific observatory be established at Kilauea, where notes may be taken with the best instruments, of earthquakes, the diurnal changes of the dome of Halemaumau, the temperatures of the molten lava and steam jets, the analysis of ejecta and spectroscopic investigations."

While arguments on behalf of more formal scientific investigations in Hawaii were being presented, the public had been well prepared by press reports of devastating earthquakes and volcanic eruptions around the world, especially the eruption of Mont Pelé in 1902 and the San Francisco earthquake in 1906.

In the hope that science could close the gaps in geological knowledge and learn to predict earthquakes and eruptions, some New Englanders were willing for humanitarian reasons to finance foreign trips and support work abroad for scientists. For instance, the Springfield (Massachusetts) Volcanic Research Society supported, at least in part, the travels and studies of Frank A. Perret, an electrical engineer and inventor turned volcanologist who became well known for his studies at Vesuvius, Etna, and Stromboli. The Springfield society also helped support Perret's 1911 work at Kilauea (Wentworth and Powers, 1962; Macdonald, 1972).

It was in this climate of opinion that the trustees of the estates of Edward and Caroline Whitney gave to the Massachusetts Institute of Technology the sum of $25,000 for a memorial fund; the principal and interest were to be expended at M.I.T.'s discretion for research or teaching in geophysics, especially seismology, "with a view to the protection of human life and property" (Jaggar, 1917a). Investigations in Hawaii were recommended. The Whitney fund was deeded to M.I.T. by the trustees on July 1, 1909, and three years later a group of twelve other New Englanders supplied M.I.T. with supplemental funds for geophysical research in Hawaii (Jaggar, 1917a).

Even before the Whitney gift, M.I.T. had been searching for a suitable site for full-time, resident study of volcanoes and earthquakes. Professor Thomas A. Jaggar, Jr., had investigated sites in Italy, the Caribbean, and Alaska. At private expense, both Jaggar and Professor Daly visited Kilauea in 1909. Jaggar went on to Japan; Daly stayed to study the action in Kilauea caldera (Daly, 1911). In Japan, Jaggar investigated two volcanoes in eruption and studied the Japanese seismometer network, then the world's most advanced. He became a lifelong friend of Professor F. Omori, famed Japanese seismologist.

After what he termed "mature deliberation," Jaggar chose Kilauea for M.I.T.'s volcano observatory. He gave M.I.T. eight reasons for his choice: (1) Kilauea was the safest known volcano in the world; (2) Kilauea and Mauna Loa were isolated, more than 3,000 km (2,000 mi) away from complications other volcanic centers might impose; (3) Kilauea was reasonably accessible—it could be reached by a 50-km (30-mi) road from Hilo harbor or a day's sail from Honolulu; (4) the central Pacific was good for recording distant earthquakes and was served by good transportation east or west; (5) the climate was uniform, with air clear enough for astronomy; (6) small earthquakes were frequent and easily studied; (7) hot and cold underground waters were available for both agricultural and scientific purposes; (8) "The territory is American, and these volcanoes are famous in the history of science for their remarkably liquid lavas and nearly continuous activity" (Jaggar, 1917a, p. 2).

Jaggar stopped in Honolulu twice in 1909; obviously aware of funds to be forthcoming from the Whitney Fund and sure of support from M.I.T. for an observatory at Kilauea, he sought added patronage in Honolulu. Jaggar gave lectures and met with the Chamber of Commerce, the Bishop Museum, and key businessmen. Guiding him through the interlocking directorships of the Hawaiian business community and introducing him into its parallel island society network was Honolulu businessman Lorrin A. Thurston, who headed, among other things, the Hawaiian Promotion Committee, forerunner of the Hawaii Visitors Bureau. Thurston and Jaggar became close friends.

## JAGGAR AND THURSTON: BACKGROUND

Thomas Augustus Jaggar (1871–1953) was born in Philadelphia, Pennsylvania, son of an Episcopal Bishop. He obtained three geology degrees from Harvard (A.B., A.M., and Ph.D.), studied in Munich and Heidelberg, and then began teaching at Harvard. Jaggar was one of the scientists sent by the U.S. Government in 1902 to investigate the volcanic disasters at Soufrière and Mont Pelé. His experiences there led him to devote his career to active volcanoes and related geophysics. In 1906, already a much-published, respected, well-known geologist, writer, and lecturer, he became head of M.I.T.'s department of geology. Jaggar saw the need for full-time, on-site study of volcanoes. He had long deplored that to date, especially in America, it was only after news of an eruption was received that geologists rushed from academic centers to study volcanism. There was generally no trained observer there beforehand, and scientists from afar often arrived after the eruption was over. There was then only one volcano observatory in the world, that at Vesuvius established in 1847. Jaggar thought America needed one (Jaggar, 1910; Macdonald, 1972; Bullard, 1975; Day, 1984).

Lorrin Andrews Thurston (1858–1931) was born in Honolulu, grandson of one of the pioneer missionaries from New

England. He studied law at Columbia University and became a member of the Honolulu bar. In the Kingdom of Hawaii, Thurston served in both elected and appointed positions, but he was a leader in the revolution (January 17, 1893) that overthrew Queen Liliuokalani and ended the native monarchy. The very next day Thurston sailed from Honolulu for Washington, D.C., to serve the "Provisional Government," which he helped establish, as envoy extraordinary and minister plenipotentiary. He stayed for two years and paved the way for annexation of Hawaii by the United States in 1898. In his business life he developed sugar plantations and railroads, brought the first electric street cars to Honolulu, and was the major stockholder in the Volcano House on the rim of Kilauea caldera. Being a volcano buff, he often visited Kilauea and frequently brought officials and delegations from the United States to see the volcano from the porch of his Volcano House. In 1900, Thurston became publisher of the *Pacific Commercial Advertiser*, a Honolulu daily newspaper (still today under the management of a descendant). Not only did he promote a volcano observatory for Kilauea, but he also wished to make Kilauea a U.S. national park (Day, 1984). Thurston had a powerful influence because of his family connections and the many positions he held, and his support for HVO in its early years was invaluable.

### ACKNOWLEDGMENTS

This historical sketch is the product not only of a search of the literature but also of numerous discussions, conversations, and interviews with volcanologists, staff of HVO, and others with knowledge of the subject. In particular, I wish to thank R.W. Decker, R.V. Koyanagi, B.J. Loucks, and Reginald Okamura for freely sharing their experiences and knowledge of HVO history. I am grateful to R.W. Decker and T.L. Wright for helpful reviews of the paper and to Barbara Decker and P.H. Stauffer for helping to put this manuscript into its final form.

## BEGINNINGS OF THE OBSERVATORY

In 1909 Jaggar proposed to prospective financial supporters in Honolulu an observatory program. Its purposes were listed as follows: (1) To establish "on the brink of the Volcano of Kilauea" buildings for instruments, laboratory, offices, and record storage; (2) to provide a room for a local museum; (3) to welcome advanced students for special work; (4) to establish a network of stations, some manned by volunteer observers, to study tides, soundings, earthquakes, and coastal movements; (5) to mount expeditions to other volcanic and earthquake belts for comparative studies; (6) to conduct research in gravity, magnetism, and latitude variations; (7) to initiate geological surveys; all of these with their "main object * * * humanitarian—earthquake prediction and methods of protecting life and property on the basis of sound scientific achievement" (Jaggar, 1917a, p. 2–3).

Thurston's Honolulu connections in 1909 pledged $3,450 a year for five years to help M.I.T. sponsor the observatory. M.I.T. officials did not think this was sufficient. In Honolulu, the plan was shelved. Jaggar and Daly returned to teaching at M.I.T., but they continued planning for a Kilauea observatory.

The Whitney Fund became available to M.I.T. in July 1909. Part was spent in 1909 and 1910 to secure (from the Werkstätte für Präzisions-Mechanik, Strassburg, Germany) a pair of Bosch-Omori seismometers (Bosch, 1910) and to order through Professor Omori in Tokyo the three Omori-designed seismometers made by Kyo-iku-hin Seizo Kaisha (Educational Appliance Company) (Omori, 1910).

Also in 1910, M.I.T. spent some Whitney Fund money to have Leeds and Northrup, Baltimore, Maryland, construct "special resistance thermometers," designed to take the temperature of liquid lava in the so-called perpetual lake at Kilauea. Part of the fund also helped send the temperature-taking Perret-Shepherd expedition to Kilauea in 1911. Personal and teaching concerns kept both Jaggar and Daly in Boston in 1910 and 1911 (Jaggar, 1917a).

The Leeds and Northrup thermometers were each about 3 m (10 ft) long, with platinum coils inside protected by tubes of iron, nickel, and quartz. The job of measuring the temperature of the lava lake was seen by scientists in Boston and Baltimore to be something like sticking an iron rod into a pot of boiling tar. Readings were to be taken "on shore" through electric wires connected to the thermometer.

A cable system was designed and manufactured on the East Coast of the United States by the Lidgerwood Company and paid for by Whitney funds. Its job was to take a thermometer out over the lake of molten lava, lower it into the bubbling lava, hold it there while readings were taken, lift it out, and return it to shore. By the time the cable system arrived, the diameter of the lava lake in Halemaumau had so enlarged that the system did not fit and had to be modified. Six men were needed to operate the trolley that rode out on the cable and lowered the thermometer. F.A. Perret and E.S. Shepherd (from the Geophysical Laboratory of the Carnegie Institution in Washington, D.C.) had no funds to hire laborers. Work could only be done when enough volunteers showed up. The project dragged out over a month's time, while Pele's hair collected on the main cable and restricted trolley movement. The wires that pulled the trolley back and forth disintegrated and had to be replaced for each experiment. Over the course of the month, cable anchors and cables were weakened from constant exposure to steam and acid vapors. When work was under way, fumes often were so thick that the men at the winch could not see the thermometer. Signals were relayed around the rim of the lava lake to tell winchmen to reel in or out. In the thick of it all was chief volunteer Lorrin Andrews Thurston, who also recruited the other volunteers.

On July 30, 1911, after two thermometers had already been lost in the lake without readings, with the last thermometer mounted on the trolley and time running out for the disintegrating cable fittings, the last chance was at hand. Only three volunteers, including Thurston, showed up. Thurston put his family to work. Thurston himself handled the reel that lowered the thermometer; his wife Harriet held the cable tight on the drum; son Lorrin shifted coils; and daughter Margaret stood on the rim in heavy sulfur fumes to relay signals (from Perret down in the pit by the lake's edge) with a flag—signals that came to her father at the reel, to Shepherd

standing by the meter, and to volunteers Emery and Ferris at the winch.

Before Pele swallowed the last thermometer, Shepherd got a reading of 1,000 C (1,832 F) from two feet under the surface of the lava lake. Shepherd himself suggested that future temperature readings be done with optical pyrometers, for "No mechanical system can long withstand the strain and abuse which Pele applies to any foreign object which invades her private lake" (quoted in Jaggar, 1917a, p. 47–50).

Perret, a meticulous observer and maker of notes, wrote reports not only on the progress of taking Pele's temperature, but also on volcanic phenomena generally. His first report covered almost a month and a half of scientific work and observations; the next five covered a week each (see Jaggar, 1917a, p. 35–46). He also wrote four scientific papers (Perret, 1913a, b, c, d).

Thurston now had hands-on involvement helping scientists begin to investigate his favorite volcano, and he had published weekly a series of six authentic reports about Kilauea in his daily Honolulu *Advertiser*. In 1911 Thurston revived the 1909 subscription list, hoping to get his Honolulu friends and business associates to up the ante sufficiently high that M.I.T. would move its observatory plans off the drawing board and onto the rim of Kilauea caldera.

At a luncheon hosted by Thurston on October 5, 1911, the guests—obviously primed and ready—formed the Hawaiian Volcano Research Association—the famed HVRA. An unpaid executive committee of five were to be elected annually. This founding meeting of the HVRA adopted a motto: *Ne plus haustae aut obrutae urbes* (No more shall the cities be destroyed) (Macdonald, 1953).

Thurston chaired the executive committee, which was quickly endorsed by the Honolulu Chamber of Commerce to raise funds from among its members. Thurston served with Albert F. Judd (representing the trustees of the Bishop Museum), John W. Gilmore (president, College—later University—of Hawaii), James A. Kennedy (of Interisland Steam Navigation Co.), and Clarence H. Cooke (of Charles M. Cooke, Ltd). The pledge was for $5,000 a year for five years, starting January 1, 1912. Treasurer Cooke and his associates of C.M. Cooke, Ltd., guaranteed the full amount in the event of failure of any individual subscribers to pay.

Negotiation by the HVRA executive committee with M.I.T. resulted in the assignment of Jaggar, as M.I.T. professor, to Hawaii as of January 1, 1912. HVRA was to sponsor and operate the Hawaiian Volcano Observatory. M.I.T. became an HVRA subscriber (indeed, the largest) for five years, using the income from the Whitney Fund and payments from 12 other New Englanders to its Seismological Fund. M.I.T. ran HVO's scientific affairs through Jaggar, who obviously received a deep delegation of authority, and granted use of its name and publishing facilities for that five-year period. In December 1911, Jaggar was granted leave of absence from his deanship and teaching duties at M.I.T to continue at Kilauea the work of recording the volcanic activity along the lines started by Perret.

Jaggar arrived in Honolulu and met with the HVRA executive committee on January 9, 1912, and then proceeded to the Volcano House on the rim of Kilauea caldera to go to work as the director of the Hawaiian Volcano Observatory on January 17, 1912. On January 18, using data collected from the Volcano House guest registers and other sources, he renewed the weekly reports to Thurston's *Advertiser*. Although Jaggar had married Helen Kline in 1903 and the couple had two children, Helen did not accompany Jaggar to accept his post as director of the Hawaiian Volcano Observatory in 1911, and a divorce followed. In 1917 Jaggar married a coworker at HVO, Isabel P. Maydwell; she was his wife, assistant, and companion for the rest of his life.

On January 19, Demosthenes Lycurgus, representing Thurston's Volcano House Company, went with Jaggar to Hilo to visit the merchants and leading citizens. Their mission was to raise funds to build a laboratory on the rim of Kilauea caldera for use by representatives of M.I.T. engaged in volcanologic research (Jaggar, 1917a). The $1,785 the merchants and private citizens of Hilo subscribed resulted in the contract with the Hilo Branch of H. Hackfeld & Company, Ltd., to build the forms and pour the concrete for what was soon to be called the Whitney Laboratory of Seismology and to build above the vault a building for the Hawaiian Volcano Observatory. In essence, the merchants of Hilo provided funds for these initial rimside facilities; the HVRA, with heavy reliance on M.I.T., promised operating funds for the first five years. Until the new facilities were built, Jaggar's first home and office at Kilauea were in the Volcano House.

## PIONEERING, 1912–1953

Halemaumau—the circular pit within Kilauea caldera—contained an active lava lake about 65 percent of the time from 1823 to 1924. The lake rose and fell and sometimes overflowed onto the main caldera floor. This rare volcanic feature made Kilauea a tourist destination as well as an attraction to scientists. Two hotels, the Volcano House (1866–present) and the Crater Hotel (1911–21), provided accommodations. By 1911, roads had replaced foot and horseback trails to connect Kilauea's summit area with Hilo 50 km (30 mi) away. The altitude of Kilauea's summit, 1,200 m (4,000 ft) above sea level, created a cool climate and made it an attractive place to visit. Part of Kilauea caldera and part of its rim area were owned by the estate of Bernice Pauahi Bishop, a princess and the last survivor of the royal Kamehameha line. The Volcano House leased its extensive lands on the rim of Kilauea caldera from the Bishop estate, and in 1912, with the estate's permission, it subleased to the Hawaiian Volcano Research Association a site on the rim for the Hawaiian Volcano Observatory.

Suggestions that the Kilauea summit area become a national park began appearing in the Volcano House guest register and in newspapers in Hawaii as early as 1903. When Thurston escorted Congressional parties and Federal officials to his Volcano House to show them the boiling lava in Halemaumau, he promoted both a national park and an observatory. In December 1915, Jaggar was commissioned by the HVRA and M.I.T. to appeal to Congress to take over HVO as a permanent governmental institution and establish under the Weather Bureau a division of volcano observatories and also to help with the national park bill then pending. Jaggar

failed in 1916 to acquire an independent Federal sponsorship for the observatory, but he did succeed with the national park, which became the surrogate sponsor.

The hearing in Washington (February 3, 1916) covered subjects ranging from volcanology to Hawaiian folklore; the Jaggar bill for a Hawaii National Park was reported favorably out of committee, passed by both Houses of Congress, and signed into law by President Wilson on August 1, 1916. Thurston had primed those Congressmen who visited the Islands; Jaggar in Washington had convinced many of the rest. (Congress changed the name to Hawaii Volcanoes National Park in 1961, by which time much additional land had been added). As the National Park Service took up resident management and acquired the land with existing leases and subleases, it became, among other things, the landlord for the Volcano House and HVO (Apple, 1954).

In the absence of Government sponsorship, HVO's founding organization, the privately financed HVRA, continued its support of volcano research well into the 1940's. It employed seismograph observers who worked in detached cellars, such as in Hilo and Kona, and others on research fellowships. It supplied or paid for shops, machine tools, instruments, laboratories, stationery, supplies, expeditions, books, boats, specialists, vehicles, and machines, thus making possible pathbreaking investigations that could not have been so readily attacked under Government alone, owing to the restrictions that control Government funds. The HVRA also published volcano notes from many lands, the weekly reports from Kilauea, Lassen Observatory notes from California, reviews of volcanologic books, and popular statements of the technical works in progress.

In general, after the National Park was created, the Federal Government paid the salaries of the permanent staff, while the HVRA supplied all buildings, much of the equipment and facilities, and services such as publications. The buildings and equipment, for instance, were owned by HVRA and leased to the sponsoring Federal agency. As HVRA support phased out in the late 1940's, HVO came more fully under Federal appropriations and control. By the early 1950's, ownership of all HVRA buildings and chattels had been transferred to the Federal Government.

Publications over the decades listed HVO sponsoring organizations as the Massachusetts Institute of Technology, the Hawaiian Volcano Research Association, the University of Hawaii, the U.S. Weather Bureau, the National Park Service, and the U.S. Geological Survey, in various combinations. Sponsoring organizations of HVO are shown in the following table:

| *Organization* | *Period of sponsoring* |
|---|---|
| Massachussets Institute of Technology | 1911–1917 |
| Hawaiian Volcano Research Association | 1912–1940's |
| University of Hawaii | 1912–1942 |
| U.S. Weather Bureau | 1919–1924 |
| U.S. Geological Survey | 1924–1935 |
| National Park Service | 1935–1947 |
| U.S. Geological Survey | 1947–present |

The USGS has sponsored HVO twice. In 1926, Congress established within the USGS a Section of Volcanology, with Jaggar in charge. Jaggar quickly instituted new stations and staff in California and Alaska. Contraction followed within a few years because of the economic depression. Looking back almost two decades later, Jaggar reminisced as follows: "First it was a splurge of high water mark in appropriations with work in Lassen and Alaska and Hawaii and a maximum staff. There was a navy trip to Tin Can Island and all sorts of cooperation public and private. Then came the big bust in 1932 and an 83 percent cut but we kept Hawaiian volcanology alive and there were immense accumulations to study and publish, and typewriter paper is cheap. The Hawaii business men [HVRA] came to the rescue and never faltered" (T.A. Jaggar, unpublished notes, copy in personal collection of J.P. Lockwood).

Geologist Howard A. Powers, who joined the HVO staff in 1929, also recalled that period of boom and bust. Powers received his Ph.D. from Harvard in 1929 and went to Washington to try to get sworn into the USGS there, "but they said that I would have to be sworn in at the Observatory. (Cagey—that way I had to pay my own way to Hawaii.) * * * The staff at that time was T.A. Jaggar, Richmond Hodges, accounting clerk; and two local men not civil service—Yasunaka, general handyman and husband of Jaggar's maid, and Tai On Au (a local Chinese who had graduated in machine shop from the Hilo Boarding School). The next two years were affluent—we picked up Austin Jones, graduate seismologist from Berkeley, Ed Wingate, a top-notch Topographer to take on problems of starting useful tilt recording. Then the huge cut for fiscal 1933. I was transferred to the USGS Ground Water Branch, Ed Wingate was transferred to USNPS as Superintendent of Hawaii National Park, Tai On Au was released, Austin Jones was kept on as Seismologist, Yasunaka continued his job, and Richmond Hodges transferred to the office of Headquarters, Hawaii National Park" (H.A. Powers, written commun., 1985).

## BUILDINGS AND FACILITIES

### TECHNOLOGY STATION (1911–1918)

In July 1911, Perret selected a site on the eastern rim of Halemaumau that commanded a view of the entire lava lake; there he built a small frame building he called "Technology Station," a place name used in many early datelines of HVO weekly bulletins to the press. Perret lived in this cabin from July 24 through September 17, 1911. By mid-August, Perret noted that vapors from the vent had formed acid, which had consumed the zinc coating of the galvanized iron roof. His field assignment finished, Perret left the cabin and Hawaii.

Jaggar came on duty in January 1912 and discovered that the Technology Station had been vandalized the month before. He believed it was vulnerable because it stood close to the parking area at the end of the road. Jaggar had the cabin torn down and rebuilt, enlarged, and surrounded by a picket fence, at a different site a few yards back from the north rim. There it was used for the storage of

instruments, as a seismometer station, and as an observation camp. By early February the cabin contained a rectangular concrete platform, which protruded through the board floor and soon held a seismometer.

In June 1918, laborers tore down Technology Station and rebuilt it again on the north rim of Kilauea caldera, where it joined other HVO buildings lining the rim. There the cabin was repaired and repainted to become a staff residence; it served until all the HVO facilities along the north rim were razed in 1940.

## INSTRUMENT HOUSES

Jaggar reported that in 1912 an additional hut was constructed wholly without iron for possible magnetic work on the verge of Halemaumau, to allow sheltered direct instrument observation of the lava. Seismologist H.O. Wood described the hut as "at the very edge of the northern rim of Halemaumau" (Wood, 1913, p. 16). If the hut was still standing in 1924, it must have been destroyed by the enlargement of Halemaumau that accompanied a series of steam explosions that year.

In addition, over the years at least four cellars were excavated or constructed on the floor of Kilauea near Halemaumau to house instruments for the detection of earthquakes, ground tilt, or both. Hawaii Volcanoes National Park maintains a list of buildings with assigned numbers; the four known cellars are buildings number 136, 255, 308, and 309. Building 309, the "East Vault" near Halemaumau, was constructed in 1959 and razed in 1973. Three other cellars were built by the Civilian Conservation Corps (CCC) about 1932 as stone-wall pits. The "West Pit" was buried under a lava flow in September 1971; this flow also partially covered the cellar called "Outlet," about 1 km south of Halemaumau. That left only the "North Pit" on the floor of Kilauea caldera with working instruments inside.

## WHITNEY LABORATORY OF SEISMOLOGY (1912–PRESENT)

The hole those prisoners dug on the north rim of Kilauea caldera (fig. 61.1) in 1912, through six feet of volcanic ash, resulted in "a basement room, eighteen feet square, with piers and floor of concrete, reposing upon the upper surface of the basalt, and high walls of concrete. This [basement beneath what became the main HVO building] is the Whitney Laboratory of Seismology. A constant emanation of hot steam from cracks in contact with the concrete walls keeps this room at a fairly uniform temperature and thus improves it for the purposes of seismology" (Wood, 1913, p. 16).

Jaggar was a true pioneer volcanologist; he made mistakes in locating and designing the Whitney vault, but he and his staff lived with their mistakes and tried to overcome them. They made their problems and progress known through their published writings, and early HVO mistakes helped others avoid similar ones when they built vaults elsewhere.

In the Whitney vault as first built, thick reinforced-concrete walls went up to ground level, about 1.7 m (5.5 ft) above the concrete floor. From ground level to the ceiling, glass panels were fixed in wooden frames to admit natural light. When the sun shone, the temperature rose sharply. Because of temperature variations, neither Jaggar nor Wood trusted the records made by the seismometers.

Not only were the temperature swings too great, but stray breezes also blew recording arms to make confusing marks on smoked drums, and dust seeped in around the windows, mixed with oil, and gummed up delicate mechanisms. Some of these problems were solved when the windows and frames were covered with boards and battens and sealed with coats of paint. This made the cellar dark day and night. Battery-operated lights served until 1921, when HVO acquired its first electric generator.

An earthquake in October 1913 opened a crack in the north wall of the Whitney vault. Water seeped from it onto the floor until the crack was repaired and sealed (the concrete floor of the Whitney vault contained no drain).

Being a basement vault with a building above also created problems. Even in calm weather, movements of the building were recorded by the seismometers in the vault below. Winter Kona storms swept high winds from the south across Kilauea caldera, hitting with full force against the north rim and causing such rocking and trembling of the building above as to mask the records on the seismograms. In the winter of 1915–16, gale-force winds stripped the sheets of corrugated iron from the roof of the building. Rain water in the offices above poured into the vault to wash away the seismograms on their drums, flood the floor, and soak the instruments. Repairs took weeks.

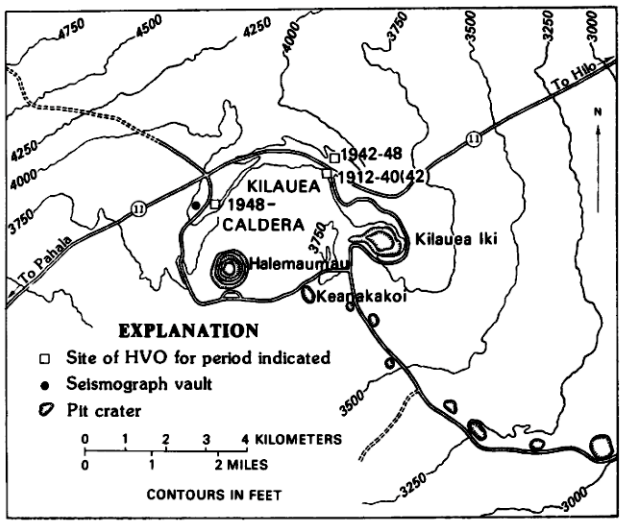


FIGURE 61.1.—Successive sites of main facilities of Hawaiian Volcano Observatory around rim of Kilauea caldera. From 1940, when original buildings were razed, until 1942, when the Observatory was able to occupy Building 41 (newly vacated by the Army), HVO staff and equipment were scattered in various buildings near the original site and elsewhere.

The Whitney vault's location 20 feet from a cliff face also imposed special problems. Cliff-face rocks expanded and contracted, from heating and cooling, sun or shadow, wetting or drying, and all such movements were recorded. Whenever high winds pressed or let up against the face, it was recorded by the seismometers, sometimes masking data about tilting of the ground caused by underground lava movements.

Then, on December 19, 1921, the nearby Volcano House began to run a Fairbanks-Morse engine to power a generator for the first electric lights at Kilauea. Variations in the engine speed as well as the exact times of starting and stopping were duly recorded by seismometers in the Whitney vault until, months later, the exhaust was directed away from a steam crack and into the air. Apparently HVO's own generating plant never caused any such problems.

Whitney vault seismometers over the years recorded much of the truck and automobile traffic that passed on the nearby road. Seismologists quickly learned to separate natural events from the local man-caused ones, but all must have wondered how much the vibrations caused by man obfuscated the records.

Except for changes in the concrete piers as instruments came and went, there was no basic change in the Whitney vault until early 1941 (fig. 61.2). In that year, the building above was dismantled, and a reinforced-concrete slab was poured by the Civilian Conservation Corps (CCC) to become the vault's new roof. The slab was covered with 45 cm (18 in.) of topsoil. The isolation (from the building above) and insulation (from the ambient air) resulted in a nearly constant temperature around 35 °C (95 °F), and the daily variation seldom exceeded 0.5 °C (1 °F).

Two other unfortunate vault characteristics persisted, however. One was that quick body movements often caused recording arms to move because of the air currents generated. Another was the oppressive warmth caused by the natural steam heat. Scientists through the active life of the vault (1912–1963) bundled up in wooly sweaters, scarfs, and raincoats to walk to the vault through the chilling rains and fog at 1,200-m (4,000-ft) altitude and then peeled down to undershirts when they entered the vault to attend the instruments.

The Whitney Laboratory of Seismology went out of active service in 1963 and is, since July 24, 1974, a property in the National Register of Historic Places, complete with some of the original instruments. Part of its nomination to the Register reads: "The Whitney Seismograph Vault, built in 1912, represents the beginnings of the continuous and resident study by American scientists of the earth's volcanic and seismic activity at Kilauea and Mauna Loa volcanoes. The Hawaiian Volcano Observatory, a U.S. Government facility since 1919, used the vault from 1912 through 1963 when more sophisticated instrumentation made the seismometers and tiltmeters it was designed to house obsolete" (U.S. Department of the Interior, 1973).

## OTHER EARLY FACILITIES

Original facilities in 1912 included water-storage tanks, a stable (complete with horse), and a garage. Added over the years were at least one staff residence (1918), a shop and electric plant (1922), an archives building used for storage of records, with corrugated-iron walls and roof to reduce the fire hazard (1922); a chemistry laboratory (complete with chemist O.H. Emerson) (1922, 1923); a new machine shop (complete with instrument maker F.Y. Boyrie) (1927); and additional water tanks, garages, and various sheds, outbuildings, and shacks. After 1922, a drill tower also stood along the rim. The view from its top is shown in figure 61.3. All these were built with HVRA funds. Except for the Whitney vault, all rimside buildings and facilities were razed in 1940.

Also built in 1912, standing above the Whitney Laboratory, with the ceiling of the vault part of the floor, was the main HVO building—a "substantial, wood frame structure containing a photographic darkroom; a workshop and storage room; a large, well-lighted room for drafting, study, routine work, etc.; a room designed for the storage and exhibit of collections, photographs, seismograms, maps, etc., and the accommodation of visiting workers; and an office room for the Director" (Wood, 1913, p. 16). The "large, well-lighted room" is shown in figure 61.4.

A covered porch on two sides permitted views, weather obliging, of the volcanoes Kilauea, Mauna Loa, and Mauna Kea. On the Kilauea caldera side, set so its top could be used from the porch, was a concrete pyramid with an elevation bench mark. The flat top served as a mount for a Theodolite or a camera. A photograph of Halemaumau lava lake was taken daily, and a vertical-angle shot to a bench mark on Halemaumau's rim was also recorded if weather permitted.

The main Observatory building was razed in 1940. Now only the concrete post remains; it, like the nearby Whitney vault, is a property in the National Register of Historic Places. Also in 1940, on February 11, the main Volcano House burned to the ground, and it was this, in fact, that led to the relocating of the HVO facilities. The two-story hotel, built in 1891, had been enlarged in 1921 (see fig. 61.3). Owner-manager "Uncle George" Lycurgus left immediately after the hotel burned down for Washington, D.C., to confer with the many friends in Government whom he had entertained over the years in his hotel at Kilauea. In effect, Uncle George called in his chips.

Lycurgus' Washington conferences resulted in five proposals: (1) The site for a new Volcano House was to be near the old site on the north rim of Kilauea, where HVO facilities had stood since 1912; (2) all HVO structures (except the Whitney vault) on the north rim were to be razed to make room for the hotel; (3) the new hotel building was to be constructed with Lycurgus funds; (4) the Volcano House operating contract would be renewed, with Lycurgus continuing as National Park concessioner but with a different fee structure; and (5) a new building would be built with Federal funds, well back from the rim, to house the Hawaiian Volcano Observatory and provide a place where Park naturalists could meet the public. Such a new HVO building had been in the talking stage since at least 1938.

This proposed HVO building was assigned the number 41 by the National Park Service and labeled the "Volcano Observatory

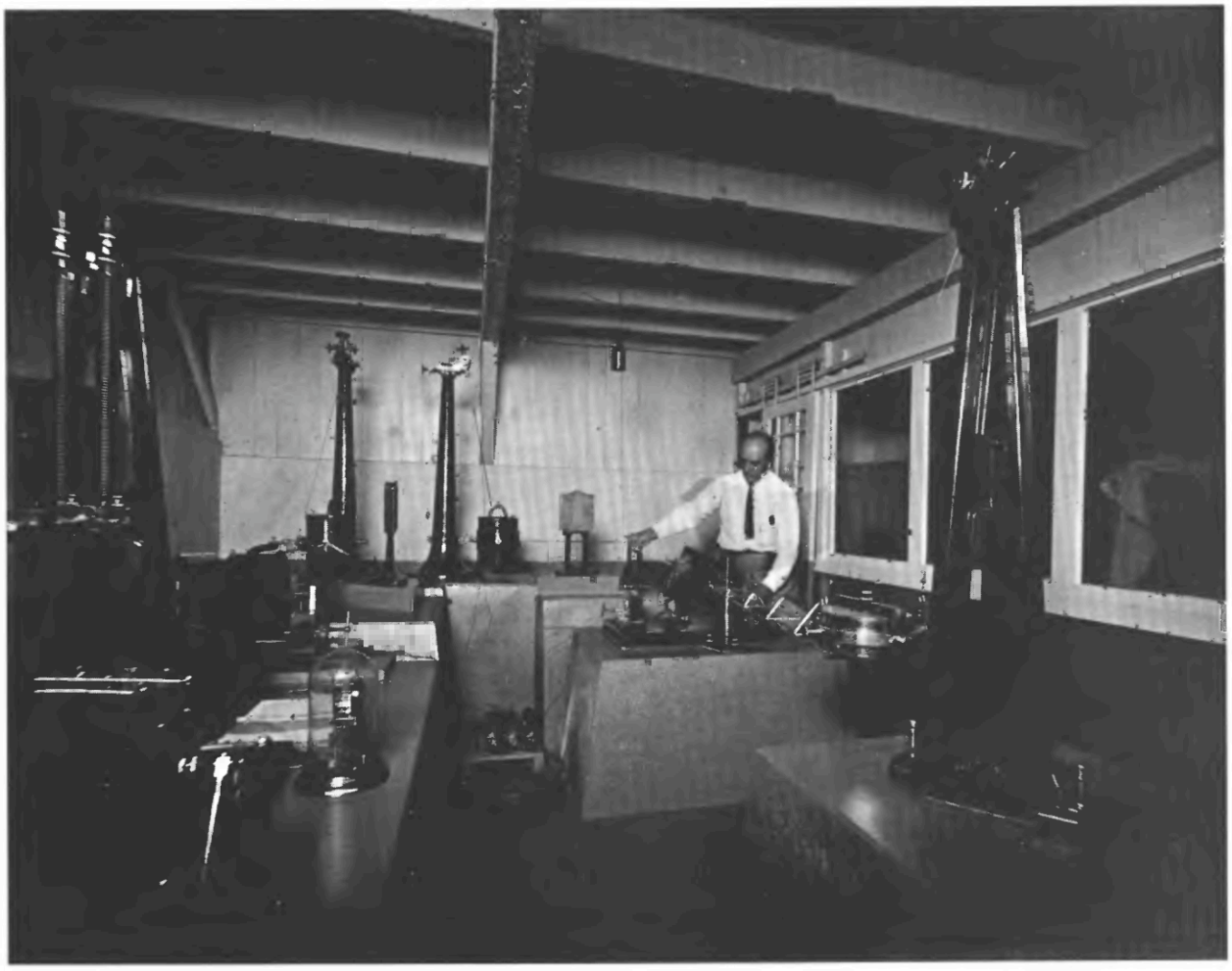

FIGURE 61.2.—T.A. Jaggar in Whitney Laboratory of Seismology, 1913. Stairs from HVO Main Building above come down to right of glass partition. Invited spectators stood behind the glass and were not admitted into instrument room. Jaggar is handling smoked drum that records east-west Earth movements detected by Omori seismometer designed for teleseisms. Two piers against far wall held two-component Bosch-Omori seismometer. Double springs in left foreground are part of self-starting Omori "Ordinary," a three-component seismometer. Photograph courtesy of the Bishop Museum (negative CPBM 58815).

and Naturalist Building." Plans were quickly initiated and whisked through the National Park bureaucracy, and the CCC began construction as soon as the plans were received.

The new Volcano House opened for business in November 1941, an elapsed time of 21 months since the fire. During that time the first four of the five points above were accomplished, and the fifth (Building 41) was almost completed. Inserted in the cornerstone of the "Kilauea Volcano House" and dated July 20, 1941, was a memorandum by Jaggar which said in part: "Under the hotel lobby is a drilled 4-inch well sixty feet deep where drilling experiments were made in 1922, one of about thirty wells for measuring temperatures. The line of observatory houses was strung out exactly where the hotel now stands. The U.S. National Park Service now is erecting a larger laboratory under R.H. Finch. The records are being duplicated at the University of Hawaii, where Jaggar is now research associate in geophysics. It is appropriate that the actual gazing upon crater fires from the old Observatory site should hereafter be the privilege of volcano hotel guests."

### BUILDING 41 (1940–PRESENT)

Workers from the CCC began construction of the "Volcano Observatory and Naturalist Building" 180 m (600 ft) in from the rim of Kilauea caldera (see fig. 61.1) in 1940. Delays were experienced, but by March 1942 Building 41 was almost complete.

By that time, a vertical-component seismometer had been installed and tested in Building 41's basement seismograph vault. The building also had a fireproof room for storage of HVO records

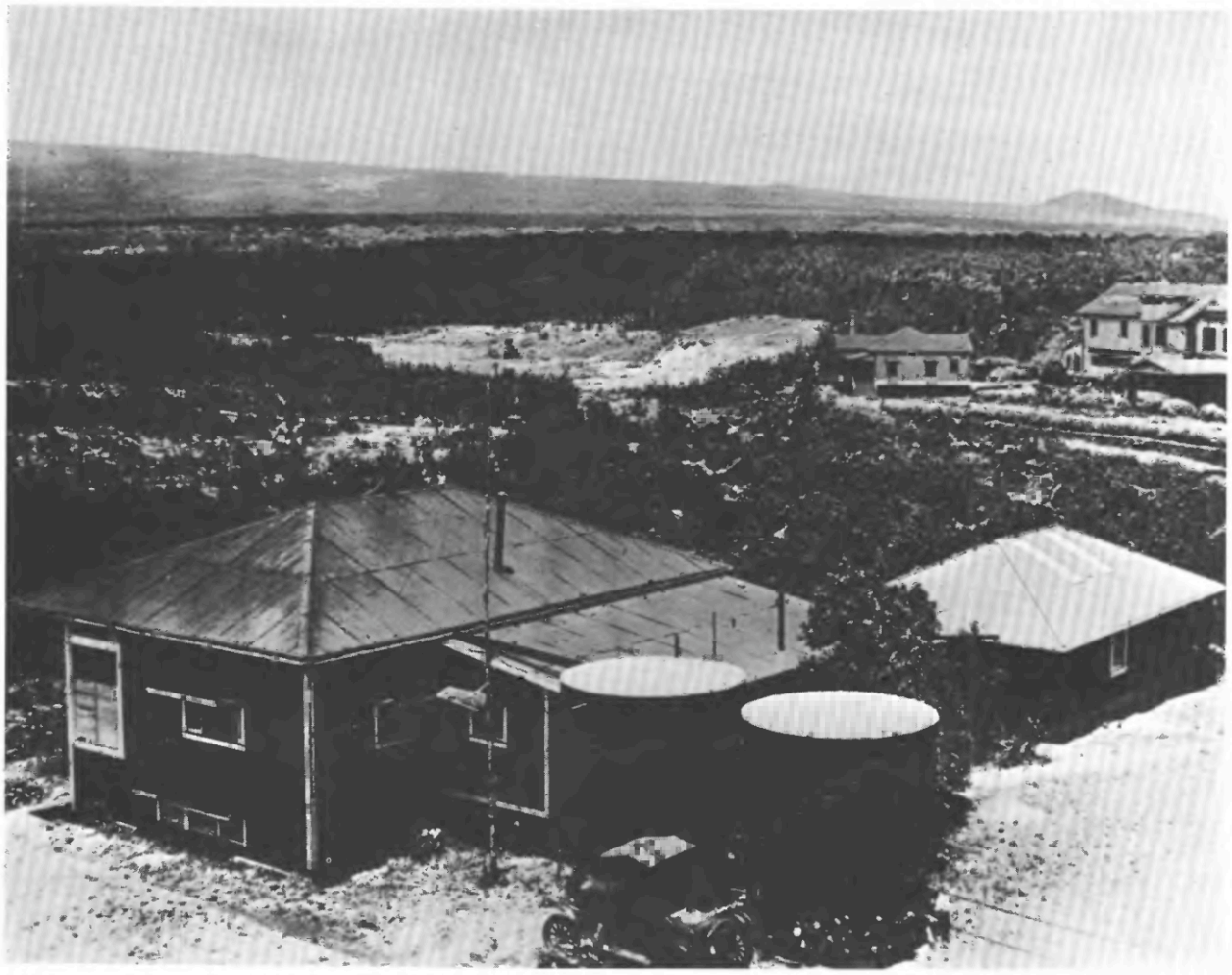

FIGURE 61.3.—Hawaiian Volcano Observatory (foreground) at its first site on north rim of Kilauea caldera (see fig. 61.1). Main observatory building is at left, the Whitney vault in its celler. To right is the machine shop. In right background is Volcano House Hotel, which burned down in 1940. The unknown cameraman climbed a 30-ft drill tower, probably in the late 1920's, to take this picture, facing away from Kilauea Crater.

and what was considered ample office, machine shop, drafting, and library space. Its seismograph cellar was about 195 m (640 ft) from the north cliff of Kilauea caldera. Only slight diurnal and seasonal temperature variations were anticipated, because this vault and basement (unlike the earlier Whitney vault) butted against only a few steam cracks.

Like the Whitney Laboratory, Building 41's seismometer vault also had a building topside. The so-called "second vault" kept its temperature at about an even 29 °C (85 °F), but because Building 41 swayed back and forth in response to above-ground daily temperature variations, ground-tilt data collected in the vault proved to be unreliable. Building 41's vault was as close to the through road (60 m [200 ft] away) as was the Whitney vault, and its records also were marred by the frequent passing of heavy trucks. HVO seismologists maintained only the vertical-component seismometer and a tiltmeter under Building 41, and kept the Whitney vault instruments in operation.

When the HVO rimside buildings were vacated in 1940, records, gear, supplies, machines, furniture, and other chattels had been stored in various places in the national park, including the CCC camp on the rim of Kilauea Iki. As the basement of Building 41 became available—while carpenters finished the floor above—some of the stored items were moved in.

Martial law, which came to Hawaii with World War II, was in effect in 1942, and the U.S. Army commandeered Building 41 as soon as it was completed. It became the Island Military Headquarters—a convenience more to the officers and men stationed there (because of the nearby Kilauea Military Camp) than to the rest of

FIGURE 61.4.—T.A. Jaggar, at work in the "large, well-lighted room for drafting, study, routine work, etc. * * *" in main building of Hawaiian Volcano Observatory, November 1, 1916. Photographer unknown.

the military and to civilians who had business with an Island Headquarters. By October 1942, Island Headquarters was ordered to move to Hilo so as to be close to population center, port, and military and communication facilities. The U.S. Army returned Building 41 to the National Park Service with not so much as a "thank you."

Army occupation of Building 41 had not greatly inconvenienced National Park management, but it certainly continued the delay in providing HVO with its own operating facility. Park Headquarters, which until 1932 had been in a cottage on the rim along with the HVO buildings, occupied a new headquarters building 30 m (100 ft) back from the rim and handy to the road from Hilo. Because of its location, it had escaped the 1940 razing and had then played host to the HVO staff, who crowded into the headquarters building with the park staff. (This headquarters building is now a detached annex of Volcano House.)

With the Army out, HVO occupied Building 41 from October 1942 to September 1948, when HVO was evicted from Building 41 and moved to the building HVRA had built in 1927 at Uwekahuna, on the west rim of Kilauea caldera. At that time, Building 41 became Park Headquarters. Now, greatly modified and enlarged, it serves both as Park Headquarters and Kilauea Visitor Center.

In 1931, two new members were added to HVO's professional staff. Two two-story buildings were acquired by HVRA to house them and add badly needed storage space. Years before, the two buildings had housed employees of the Volcano House; one was known as the "Japanese boarding house," and the other as the "Stage Station." The Stage Station (NPS Building 39) was razed in 1956; the Japanese boarding house (Building 40) was razed in 1959. After he retired in 1940, Jaggar maintained an office in the upper story of Building 40. I interviewed him there several times

and, after his death, sorted, classified, and shipped his office papers to be added to the Jaggar Collection in the Archives of the University of Hawaii, Manoa.

Sometime in the 1920's, a residence for Jaggar was built by him (or the HVRA) on the north rim of Kilauea. This residence (Building 78) was razed in 1956, along with its garage and maid's quarters (Building 77). The former maid's quarters were assigned at times to visiting USGS personnel in the late 1940's and early 1950's; they were handy to the 1941 Volcano House hotel, where meals were available.

### BUILDING 131 AT UWEKAHUNA (1927–PRESENT)

From the very beginning in 1912, volcano visitors often asked questions of HVO staff members they met in the field or found in HVO buildings. When Hawaii National Park came into existence, uniformed personnel began to assume the public-contact work. In 1926, the businessmen of the HVRA raised $20,000 to build an information center on the west rim of Kilauea caldera, to be staffed by park naturalists, which would keep the increasing numbers of visitors away from HVO and its staff. Ground was broken for the new building on February 22, 1927. The site selected was the actual summit of Kilauea, on top of Uwekahuna Bluff (see fig. 61.1). The main building was built of iron and concrete, with stone cornerposts; a large terrace was enclosed by rough stone and fitted with stone benches.

In April 1927 the new building at Uwekahuna was turned over to the Secretary of the Interior and the Director of the National Park Service, which designated it as Building 131. From 1927 to 1948, park naturalists met the public, gave talks, and were headquartered in this building at Uwekahuna. Its view of Kilauea caldera is excellent, and, weather obliging, the view is equally good of Mauna Loa. Park interpreters and park visitors found the facility an ideal place for orientation to local geography and volcanology. Over time, as the numbers of its visitors grew, the "National Park Museum and Lecture Hall" was lengthened and widened, with architecture that matched the original building.

On December 28, 1947, the Hawaiian Volcano Observatory was transferred within the Department of the Interior from the National Park Service to the United States Geological Survey—the second time the USGS was host agency. In 1948 HVO was moved to Building 131 at Uwekahuna, and NPS offices and public services were then consolidated in Building 41 on the north rim.

In preparation for the move, the Uwekahuna Seismograph Vault (Building 135) was built in 1948 in a location well back from the Uwekahuna cliff face and road and far from any building that could move in sun or wind. The cellar is $3.6 \times 6$ m ($12 \times 20$ ft), and a small entranceway serves as an airlock and processing room. The roof is a reinforced-concrete slab covered with about 45 cm (18 in.) of volcanic ash. This vault continues in service.

To receive HVO, the National Park Service in 1948 remodeled Building 131. The former movie hall was converted into offices and machine shop, and most of the exhibit floor became offices and laboratories. HVO moved in during the fall of 1948.

At the time of the move in 1948, it was pointed out by volcanologist R.H. Finch, then the Director of HVO, that Uwekahuna had been the first site selected by Jaggar for the Observatory in 1912 but was given up on account of the scarcity of water and its relative inaccessibility at the time.

### NEW BUILDING AT UWEKAHUNA (1985–PRESENT)

In May 1985, construction of a new facility for HVO began at Uwekahuna. This new building was completed and occupied a year later. Building 131 was renovated and returned to the National Park Service as an interpretation facility named the Jaggar museum. Thus, the original vision of the HVRA of a center combining ongoing scientific studies and interpretation of those studies to the public is, after 75 years, finally realized in a fully modern facility.

## PUBLICATIONS AND DOCUMENTS

Much of the most reliable data about the history of the Hawaiian Volcano Observatory is contained in its publications. Two publication series had long runs, covering the period from before the 1912 start through and beyond the pioneering period. These were the Bulletin and the Volcano Letter.

Jaggar once, in his annual address as Director of HVO (Jaggar, 1917b), characterized "the proper work of volcanic recording" with two words—permanency and extension. Permanency depended on continued financial support. Publication was the method of keeping informed the 150 members (in 1916) of the HVRA, whose membership provided the guaranteed $5,000 a year of local support. Extension was also seen to be a purpose of publication—to interest scientists and governments overseas in sponsoring permanent volcano observatories.

The vehicle that served both roles of "permanency" and "extension" was the weekly report of volcanic activity prepared by the HVO staff. Taking their cue from the 6 popular weekly reports filed with the press in 1911 by Perret, Jaggar and others wrote another 1,249 weekly press reports, many labeled as bulletins. They constitute an uninterrupted series from January 18, 1912, through December 29, 1935. The last weekly press report, numbered 1,249, was published in the Volcano Letter (no. 430) in December 1935.

The weekly Bulletin was a regular feature in the *Pacific Commercial Advertiser* (now the Honolulu *Advertiser*). By arrangement with the Bishop Museum (Jaggar, 1917a), a carbon copy of each typewritten report was sent to that Honolulu institution. Soon a second carbon went to the Hilo *Tribune-Herald*. Appearance of HVO's weekly reports in two newspapers served to inform islanders and tourists about volcanic activity at Kilauea and Mauna Loa, and it kept the observatory in the public eye.

Reprints in leaflet form of the weekly press reports in the *Advertiser* were mailed by HVRA from Honolulu from 1912 through July 1, 1914, to the 150 or so members of the HVRA and

to 200 or more institutions and individuals worldwide on the HVRA's exchange list. Beginning in August 1914, the weekly reports of each month were combined into a monthly before being mailed by HVRA; this practice continued through July 1929. Over the years, while there were some issues without any special back page, the published and mailed leaflet bulletins generally carried informational back pages of ten different designs (Apple, 1985).

The other regular and long-running publication of HVO was the Volcano Letter, which was printed and mailed weekly beginning the first week of January 1925, apparently to the same subscription list as the bulletins. The Hawaiian Volcano Observatory thus had for the years 1925–1929 both a weekly and a monthly publication. In 1930 the two were combined; the weekly press bulletins became a part of the Volcano Letter. The Volcano Letter ceased being a weekly and became a monthly with the June 1932 issue. It went quarterly in 1939, and was finally discontinued in 1955.

The Bulletin and Volcano Letter usually carried the bylines of the scientists involved in their writing. Both often contained illustrations, including photographic halftone plates. The Bulletin dealt mostly with day-to-day raw data, while the Letter was the vehicle for more digested data, summaries, conclusions, reviews, news, predictions, opinions, and project status reports, not only in Hawaii but worldwide.

Over the years there were other serial publications for short times—monthly, quarterly, semiannual, and annual reports, as well as special publications.

The Volcano Letter was published first by the HVRA and then by the University of Hawaii. USGS publications continued the record of observations after the Volcano Letter was discontinued.

Additional information on the history of HVO is in the original holographs and manuscripts at the Bishop Museum, Honolulu, the first archival repository. These include Kilauea record books, by months and years (from 1912 on); folders full of notes, by years; photographic albums and photographic negatives; guest books; carbon copies of weekly reports; and copies of early bulletins.

The University Archives, University of Hawaii, Manoa, has HVRA files and records, the personal papers of Jaggar, some HVO material, and related sources. It was the second archival repository.

The third repository is the University of Hawaii, Hilo. Its Mo'okini Library has a continuing file, by years, starting before 1912, of copies of non-HVO-sponsored publications by Jaggar and others of the HVO staff, copies of the Bulletin and Volcano Letter, HVO special publications, documents sent in recent years for safekeeping, and my own collection of holographic material (Apple collection), prepared over the years and used in this history. Some material is also available in the HVO library for reference use by the staff.

Bulletin and Volcano Letter deadlines over the pioneering years did not keep the professional staff from making numerous professional contributions to scientific journals and periodicals published by others. Bibliographies of contributions by staff members of the Hawaiian Volcano Observatory contain copious entries.

## VOLCANO EXPERIMENTS

The comparatively easy access at Kilauea to a variety of ongoing volcanic activities stimulated and encouraged experiments, ranging from the serious scientific to the decidedly frivolous. Visitors from America and Europe fried eggs in pans that rested on moving lava flows, learned how to thrust their cigarettes and Cuban cigars into hot cracks to light them (nonsmokers lit ends of sticks in the same cracks), embedded coins in small pieces of pasty rock, and scorched the edges of postcards on hot lava before the cards were mailed home. The Volcano House supplied eggs, pans, and postcards, as well as the guide who kept hotel guests safe while performing these feats in or near Halemaumau. The guide, Alex Lancaster, probably wound up each trip into Kilauea caldera with one pocket full of tips and another full of Cuban cigars—until Jaggar put him on the Observatory's payroll as janitor, guide, and general roustabout. Lancaster's experiences close to Kilauea's flowing and fountaining lava made him a good hand for Jaggar.

Lorrin Thurston helped Jaggar to take temperatures, sample gases, and measure depths. On January 11, 1917, Thurston and his assistants helped Jaggar thrust a length of galvanized-iron pipe through the solid crust of the lava lake to take a temperature reading 1 m (3 ft) down. At the end of the pipe was a metal cylinder that contained six cones of fusible clays which melted at temperatures in a range from 900 to 1,150 °C (fig. 61.5). After the end of the pipe had been held in place for six minutes, the crew withdrew the pipe, with difficulty. Softened by heat, the pipe had bent sharply at the point where it pierced the crust, and its end was weighted with the pasty lava that clung to it. None of the clay cones had melted, and Jaggar concluded that the temperature 1 m down was lower than 900 °C. In view of more recent data, this seems unlikely. Probably the clay samples did not reach equilibrium temperatures.

Then Thurston wanted to try an experiment. He had lugged two large pieces of ohia wood out to Halemaumau to toss into the lava lake to see what would happen. Jaggar duly recorded the results for posterity (Jaggar, 1917c): Both logs burned after sinking below the surface. There were abundant yellow flames and puffs of smoke that ballooned the surface crust a bit.

In 1925, Jaggar conceived a plan to bore holes, 3 m (10 ft) deep and 300 m (1,000 ft) apart at corners of equilateral triangles, on the floors of Kilauea caldera, Kilauea Iki Crater, and Keanakakoi Crater, as well as on the surfaces surrounding them. Temperatures at the bottoms of the holes were to be taken, so that isothermal lines could be drawn on a map of the region. The holes would then be sealed so that periodic rechecks could detect changes in the temperature of the bedrock.

In preparation, J.C. Bean, USGS topographic engineer, surveyed the borehole network from December 1925 through May 1926. An air-driven hammer drill, air compressor, truck, some "tested thermometers," a high-speed camera, and some up-to-date surveying instruments were acquired for the project. Drilling got underway in 1926 but was discontinued during the winter of 1927–28 after 30 holes had been drilled. Results were apparently inconclusive or disappointing; no results were ever published.

FIGURE 61.5.—Preparing to measure temperature of lava, January 11, 1917, floor of Halemaumau Crater. L.A. Thurston stands behind Jaggar, who holds pipe to be inserted into lava lake. Cylinder at end holds six Seegar cones of fusible clay. Others, from left to right, are Norton Twigg-Smith, Joe Monez, and Alex Lancaster. Note log of ohia at Thurston's feet, ready for his experiment. Photograph by Horace Johnson.

In retrospect, the 1925–28 project can be considered pioneering, but the real pioneering was an earlier drilling in 1922, described in the various monthly issues of the HVO Bulletin for that year. John Brooks Henderson of Washington, D.C., gave Jaggar $3,000 to begin boring experiments. Local gifts from Hawaii raised the total to $8,000. Honolulu driller A.H. Hobart was hired to use an impact or "churn" drill for three months; HVO was to supply the water needed for the drill and to transport all supplies to the drill sites. By April 1922, HVO had evolved the world's first dune buggy—a Ford touring car modified, as described by Jaggar (1922a, p. 32), by "doubling each rear wheel and fitting a pair of wide non-skid pneumatic tires to each doublet; this gave to each rear driving roller eight inches of grooved rubber traction surface, including a small air space between each pair of wheels. The double wheels were made by bolting two ordinary wheels together with a wooden disc between. A rear axle planetary gear system was added, giving three extra low gear ratios in addition to the usual two forward speeds and one reverse. All unnecessary weight of fenders, steps and doors was removed, and at rear end of car was placed a drawbar and shackle and an extra heavy spring. This converted the car into a general utility vehicle for use both as tractor and conveyance for men and supplies, devised to travel over any ordinary rough lava or on the surface of deep gravels where a common truck would dig in and be stalled."

This vehicle hauled supplies and men over sand, gravel, and billowy pahoehoe lava (fig. 61.6). A new Caterpillar tractor was also tried on lava and then modified to front-wheel steering. Rubber tires went on its rear wheels. It was used as a stationary engine to drive a generator and as a tractor to haul water barrels on sleds to drillsites.

FIGURE 61.6.—Hawaiian Volcano Observatory's modified Ford automobile hauling water for drilling operators on floor of Kilauea caldera, July 21, 1922. Vehicle was stripped of unnecessary weight and fitted with additional low gears, drawbar, and double rear wheels. Photograph by T.A. Jaggar, courtesy of the Bishop Museum (negative 94119).

Boring began May 1, 1922. Hole 1 was at the east corner of Sulphur Bank. The nearby Volcano House supplied water from its tanks, transported in barrels lashed to sleds hauled by the tractor. Casings and tools were skidded to Sulphur Bank behind the touring car.

A kerosene engine powered the rig to deliver 40–50 strokes per minute to a blunt-chisel bit of 6-in. diameter. The bit was turned by hand; water was supplied to the hole also by hand—about 10½ gallons per foot. A bucket was used occasionally to clean the hole bottom. Burlap sacking was wound around the mouth of the well to protect the drillers and machine from hot acid fumes. Eventually a wooden plug was devised for the wellhead that let the cable through but kept most of the fumes in. The cable and other steel parts were frequently painted with crude petroleum to protect them from the fumes.

The temperature was taken by a maximum thermometer lowered the 7 m (22 ft) to the bottom of Hole 1 and exposed five minutes; it read 96 °C. This reading was later checked by an Alumel-Chromel thermoelement and potentiometer and checked again with another maximum thermometer of a different make.

The churn-drill rig was moved about 45 m (140 ft) to start Hole 2, also at Sulphur Bank. Drilling started June 1, 1922, with heavy steaming from the hole. Troubles with the boring limited downward progress to five days out of ten. At 6 m (20 ft) the hole was cased, and the bit diameter reduced from 8 to 7 in. Another reduction to 6 in. and casing came at 12.8 m (42 ft), but the tools became wedged and broke a camshaft and gear wheel. The field forge failed to heat and temper the steel bits properly—they had to be sent to a sugar-plantation forge at Mountain View, 30 km (19 mi) away. At 13 m (43 ft) steam greatly increased, and at 15.2 m

(50 ft) "all sludge and water disappeared in an east-west crack across bottom of hole" (Jaggar, 1922b, p. 64). The hole was complete at a depth of 15.2 m (50 ft) on June 12, 1922. Hole 2's temperature was also about 96 °C. Pipe of 7-in. diameter was set in concrete to protrude a few inches and covered with a screw cap. "In a few weeks the inner surfaces of the iron were black with sulphide; and free sulphur crystals formed" (Jaggar, 1922b, p. 64). A shed of corrugated-iron sheets was built over Hole 2's wellhead; stacked rocks now cover it.

On August 22, 1922, Eugene T. Allen of the Geophysical Laboratory in Washington tested the gases of Hole 2 and was impressed that drill holes acted like natural fumaroles to serve as vents for escaping gases.

Hole 3 was near the center of Kilauea caldera's floor on the 1894 lava flow and in line with the 1920 Kau Desert rift. To make it possible to deliver water, rig, casings, supplies, and drillers, off-duty soldiers from Kilauea Military Camp were hired for four days to beat a rough track from the end of the road near Halemaumau to the drillsite. Meteorologist R.H. Finch, Jaggar's assistant, saw to it that the soldiers made a track over which the modified touring car and tractor could pass, albeit slowly. Hole 3 was drilled to 24 m (79 ft), and the temperature at the bottom was 69 °C.

Because churn-drill holes sometimes went crooked, tools stuck, and bits dulled rapidly, Jaggar wanted to try a rotary-drill rig. One was surplus to the needs of the Hutchinson Sugar Company, and HVO purchased it on June 22, 1922. It was a Davis Calyx "shot" Drill, model BF4, capable of boring a hole of 4-in. diameter to a depth of 300 m (1,000 ft). As it dug, the tube rotated and made a core; in practice, however, the lava rock fragmented, and satisfactory cores were rare and short.

Hole 4 was on the grounds of the Observatory, along the north rim of Kilauea (fig. 61.7). A drill tower 12 m (38 ft) high was part of the package purchased and was assembled on the rim. A shed, with an opening through the roof for the cables, was built about its base to shelter the drillers.

Water in quantity was required for this drill—241 gallons per foot of progress—and the water-storage facilities of HVO were needed to supply it. As drilling proceeded, voids and openings between layers of lava were met that caused frequent loss of water pressure. These hydraulic problems had been solved by October 1922, however, and a depth of 20 m (65 ft) was reached. Bottom temperature was 97 °C. Hole 4 was the well referred to by Jaggar in 1941 as being beneath the lobby of the new Volcano House. The capping of this hole in November 1922 ended HVO's first pioneer efforts at scientific drilling.

## MAUNA LOA

T.A. Jaggar did not confine his efforts to Kilauea; he had a sustained interest in the equally active volcano of Mauna Loa and spent much time and energy attempting to obtain improved access to it. The following account is mainly compiled from various issues of the HVO Bulletin from the years 1913–17, 1920, and 1922.

FIGURE 61.7.—Rotary drill and its tower on grounds of Hawaiian Volcano Observatory during earliest HVO drilling program in August 1922. Photograph by T.A. Jaggar, courtesy of the Bishop Museum (negative 94121).

### ACCESS ROUTES AND FACILITIES

In late November 1914, during a summit eruption of Mauna Loa, Jaggar attempted to view the lava fountains but failed. His mounted expedition was driven back by a severe wind and snow storm near the summit; they were even forced to abandon the camp equipment. From that time on, Jaggar advocated a shelter on the summit for men and horses and for the safe storage of instruments. To reach the summit, Jaggar wanted at least a horse trail (a road for vehicles would be better) from HVO headquarters at Kilauea. This meant the trail or road would ascend the northeast rift of Mauna Loa; overnight facilities would be needed along the trail. Early in 1915, Jaggar told the HVRA that Mauna Loa was a desert waste without water. Expeditions to the summit were exhausting, and animals employed frequently had their legs cut by the rough lava; consequently, ranchers would not rent good animals. There was no shelter on the summit, little water, no feed, violent winds, and low temperatures. It cost several hundred dollars to make a trip to the summit, and one generally had to return before any real scientific work could be done.

Through 1916, the Ainapo Trail over jagged aa and thin-crusted pahoehoe lava fields was the customary route to the summit of Mauna Loa (Apple, 1973). Until horses and mules became cheap and plentiful, an arduous hike of several days' duration up this trail was the most practical way to the summit. Most of the trail lay on the Kapapala Ranch, and Kapapala cowboys were hired as guides and packers. The Ainapo was about 54 km (34 mi) long and rose from 600 m (2,000 ft) to 4,000 m (13,000 ft) above sea level. The lower trailhead was the village of Kapapala. It was by way of the Ainapo Trail that Jaggar first visited the summit caldera in September 1913.

The surface of the Ainapo Trail was rugged, and it was not maintained for either men or mounts. Jaggar wanted a "simple route to the summit" to give scientists and the public access; with Thurston's help, he got the U.S. Army to build one in the fall of 1915.

Seismologist H.O. Wood, guide Alex Lancaster, and J.F. Haworth made a preliminary survey of a trail from Kilauea up the northeast flank of Mauna Loa to the summit in August 1915. Jaggar, Thurston, and a Lt. Philoon, 25th Infantry, U.S. Army, checked it in September. Thurston and his friends had received the approval of the departmental commander for the U.S. Army to build the trail Jaggar wanted. The HVRA put up a 5,000-gallon water tank near HVO headquarters to support the Army trail builders, and transported several smaller water tanks up the flank to a camp near timberline, soon called Camp Bates after Capt. Bates, a civil engineering officer. Thirty soldiers, under Lt. Philoon, arrived on October 15, 1915; they were followed two days later by others.

This trail up the northeast flank of Mauna Loa, called the Mauna Loa Trail, was completed in December 1915, and the soldiers were back at Schofield Barracks on Oahu for Christmas. The costs of round-trip transportation for the soldiers by ship, rental of pack animals, and purchase of materials for two buildings were all borne by the HVRA. When Jaggar prepared his proposal for a Hawaii National Park in Washington, D.C., early in 1916, he already had his trail between the summits of Kilauea and Mauna Loa Volcanoes. He hoped to upgrade it to make it suitable for trucks, and he foresaw perpetual Federal maintenance of the route. His bill, when it became law, authorized a strip of land between the summits for such a road, to be surveyed and given legal boundaries at a later date.

When the trail was built in 1915, horses and mules could go as far as Puu Ulaula (Red Hill), a cinder cone at elevation 3,000 m (10,000 ft). As part of the project, the soldiers built a 10-man overnight cabin and a 12-horse stable at Puu Ulaula, 10 hiking miles from the summit. The army cabin, still in use, is called the Red Hill rest house.

HVO hand labor filled cracks with chunks of lava and generally prepared the trail above Puu Ulaula for mounts. The first riding horses and pack mules reached the summit with Jaggar and his assistant Ruy H. Finch on June 29, 1920. Because there were no stable facilities for the animals, the guides, packer, and animals were sent back to the rest house. Jaggar and Finch stayed at the summit; "Jaggar's Cave" received its first use that night. (In the same week the first tourists reached the summit over the Mauna Loa Trail; HVRA charged each member a dollar a night at the Red Hill shelter.) In 1930, National Park crews improved the trail for horses.

Until a summit shelter was built by the National Park Service in 1934, hikers and riders were forced to camp in "Jaggar's Cave," a crack in the lava roofed over with corrugated-metal sheets. It was near another crack where water, frozen in winter, accumulated.

Since 1915, in an incremental process, lower portions of the trail have been widened and improved for vehicles. In 1936, the CCC built the last increment, the road from Bird Park to near the site of Camp Bates at elevation 2,025 m (6,650 ft), to permit scientists access by small truck to a seismograph vault near that elevation. The road has since been paved. Most hikers to the summit today start their hike at the upper end of this road.

All during his HVO directorship (1912–1940), Jaggar pressured for a vehicular road from Kilauea up the northeast flank to the summit of Mauna Loa. He wanted the 1915 Army trail improved to allow easy and quick access by HVO vehicles for studies at the summit. Although the National Park Service established boundaries and acquired the strip of land within which the road could be built, it has consistently rejected the concept of a vehicular road to the summit of Mauna Loa. This rejection has been sustained over time, in spite of pressures from Jaggar and Thurston and at times from the Territorial Legislature and the Hawaii County Board of Supervisors. As a result, the road has never been built; the advent of helicopters may now have made moot the question of such a road.

Jaggar's Cave, the 1915 cabin, and the 1915 trail have been declared eligible for listing in the National Register of Historic Places (U.S Department of the Interior, 1973). All are still in use, although the trail has had to be rebuilt in places because of damage from earthquakes and lava flows.

## THE 1926 ERUPTION

Mauna Loa's recognized eruptive pattern is a summit eruption followed—within hours, days, or months—by a flank eruption. In 1926 there was a brief summit eruption, followed by 14 days of eruption on the southwest rift zone. A flow from this rift zone passed through a South Kona forest, crossed the main road on April 16, and pooled behind the coastal village of Hoopuloa. Between 0400 and 0900 H.s.t. on April 18, the flow buried the village, wharf, and harbor and entered the ocean. This was HVO's first real experience with property destruction by a lava flow. The following account was compiled from Apple and Apple (1979b), Finch (1926), Jaggar (1926a, b), MacDonald and Hubbard (1982), and unpublished sources.

Edward G. Wingate, USGS topographical engineer, was mapping the summit of Mauna Loa in 1926, changing campsites as the work progressed. On April 10 his camp was along the 3,475-m (11,400-ft) elevation, well into the desolate upland above the Kau District. An earthquake wakened the campers about 0145; as they drifted back to sleep, a further series of quakes had them sitting up, talking, and wondering. About 0330 Wingate braved the cold and

wind; with a blanket wrapped around him, he went outside and stood bathed in reddish light.

From his camp Wingate had a wonderful view of smoke columns lighted by the glow from below. They reached the flows about 0630. With his crew, Wingate mapped lava fountains, moving flows, steaming vents, and spewing cones.

The packer who kept Wingate's camps supplied with water, food, and firewood had spent the night on the trail on his way down to pick up another load; he reached the Ainapo trailhead midafternoon on April 11. More than supplies awaited him—there was an HVO expedition demanding guide service to Wingate's camp. This was the first news of the eruption for the packer. The expedition consisted of Jaggar, topographer J.C. Beam, cook H. Yasunaka, and packers John Kama and Joe Kaipaloa.

After a night at Ainapo, and with three additional pack animals borrowed from Kapapala Ranch, the expedition started up toward Wingate's camp. By midafternoon they reached the camp, which Jaggar described as a primitive affair consisting of three tents and a cook shelter on the rough lava fields. The cook shelter was bolstered with stone walls to protect against wind, but all the tents had to be tacked down to the pahoehoe lava with spike nails.

For three days the HVO party surveyed the sources of the eruption; then they descended and moved into Kona District, where roads, houses, and other property were threatened by the flows. Wingate and his crew stayed behind. Much of the area already mapped was under fresh lava, and there was a lot of remapping to do.

On April 16, Tom Jaggar scratched marks about a foot apart across the rutted, gravel road (the only road) between the Kona and Kau Districts. A lava flow was approaching, and Jaggar wanted to measure the flow's speed as it crossed the road. Perhaps a hundred people were waiting around the Hoopuloa Church, on the uphill side of the road, and at the Kanaana house opposite, on the downhill side of the road. They had seen and heard the flow, 4.5–6 m (15–20 ft) high and more than 150 m (500 ft) wide, as it moved through the forest uphill. When it neared the road, people who lived on the Kona side of the flow moved off to the north, and those who lived on the Kau side moved to the south, so they could go home after the road was closed.

Jaggar recorded that it reached the uphill, inland side of the road at 1222 at an estimated speed of about 2 m/min (7 ft/min); within two minutes the road was crossed. Jaggar and his assistant, H.S. Palmer, stayed on the Kau side. Soon Robinson MacWayne, Honomalino Ranch proprieter, supplied horses, ranch hands, and guide service through coastal Milolii to Hoopuloa. Jaggar and Palmer set up camp in the Hoopuloa store. Jaggar noted that the Chinese proprietor had swept the building spotlessly clean after removing his stock of goods and furniture. Both the store and the adjacent wharf lay directly in the track of the oncoming lava front. Groups of people were huddled along the stone walls back of the village, watching the glowing, crunching, relentless wall of fire behind, but watching it at leisure, without excitement, and with great weariness because the main event had been postponed. All had come to see the lava enter the sea, but it was still several hundred feet away.

Those watching parked their cars on the Kona side of Hoopuloa. One enterprising youth used his small truck to haul water from the Hoopuloa tanks to Milolii, the end of the road. When the flow reached the sea, he and his truck were cut off; he later took his truck apart and transported it piece by piece by outrigger canoe to the road on the Kona side of Hoopuloa.

At about 0300 H.s.t. April 18, the flow rode over the stone walls behind the village and started burning outhouses. Pigs heard squealing in a pen were released. Destruction of the village was gradual and complete. As soon as lava began falling into the sea, steam shot up in jets. Hundreds of dead fish floated along the edge of the turbulent water that spread out from the contact area of hot rock and cold ocean. Hawaiians from Milolii came in their canoes and gathered the dead fish for salting and preserving. Jaggar collected some dead, floating fish and noted that they were perfectly fresh and in no sense cooked.

### CONTROLLING LAVA FLOWS

Many observers have noted that barriers, both natural and manmade, can sometimes stop, divert, or delay the forward movement of a lava front. The worried people of Hilo in 1881 first considered the use of explosives to stop a flow that threatened their port and homes; this is the earliest recorded suggestion for such action in Hawaii (Lockwood and Torgerson, 1980). The concept of using explosives to modify the forward motion of a lava flow was advocated by the HVRA's Thurston in his newspaper in 1929. Tom Jaggar and Ruy Finch of HVO were actively involved in using explosives in the form of aerial bombs on moving lava flows that threatened Hilo in 1935 and 1942, respectively. Bombing the upper reaches of a lava tube feeding a Mauna Loa pahoehoe flow in 1935 is credited with slowing or stopping the advance of the distal end; the 1942 bombing breached the levee of an aa flow and was also partly successful in slowing the flow's advance (Bolt and others, 1975).

In 1937 Jaggar proposed construction of a comprehensive set of embankments, 5–6 m high, to divert Mauna Loa lava flows from Hilo town and its harbor; the embankments would have had a total length of about 20 km (including 11 km in a single wall around the south side of the town) and were projected to cost about $800,000 (Jaggar, 1937). These barriers have yet to be built, though experience elsewhere shows that they could be effective (Bolt and others, 1975). Jaggar's interest in controlling lava flows to protect property continued long after his retirement from HVO (see Jaggar, 1945).

## THE *OHIKI* AND OTHER EXPERIMENTS

Ohiki is the Hawaiian word for sand crab; honukai means sea turtle. In 1928, when the National Geographic Society joined with the USGS to sponsor an expedition with Jaggar in charge to map, photograph, and survey in the Aleutians around Pavlof Volcano, the Society supplied an amphibious boat, to which Jaggar gave the name *Honukai*. It was a twin-screw steel amphibian, built in Chicago by the Powell Mobile-Boat Corp. In the 650 km along the coast of Alaska from Shumagin Islands to King Cove, the expedition did not even have to pump up the tires. The *Honukai's*

numerous excessively low gears even enabled them to drive up to the snowline and bring out the heavy fur and bones of a bear that Jaggar had shot on the snowy volcano, Mount Dana. Jaggar brought the *Honukai* back to Hawaii with him and based it in Kona.

In preparation for this expedition, the HVO machine shop built a wooden amphibious boat around a "low-geared small motor car with balloon tires," that Jaggar had used over tundra and beach of the Alaskan Peninsula in 1927 (Jaggar, 1927). Inlets, rivers, and rocks were obstacles that made Jaggar mentally design modifications of the car into a "car-skiff."

The land and sea trials of this preliminary vessel, the *Ohiki* (fig. 61.8), took place in the spring of 1928 (Wilson, 1928). She first took to the sea at Ninole Cove in the Kau District, and she quickly revealed the need for additional work.

After modifications (freeboard raised, length slightly increased, paddle-wheels enlarged, a winch and cable mounted in bow, 5-horsepower outboard motor added), an extended trip was made along the west coast of the Island of Hawaii to make beach and sea tests. Thurston went along as a passenger and publicity man; Mrs. Jaggar served as stewardess. The car with the boat body excited all the roadside children of Kona with delight.

Jaggar's *Ohiki* made a speed of about 6 km/h (4 mi/h) in water with the combined power of paddle wheels and outboard motor; it weighed 1,700 kg (3,800 lb), was 7 m (22 ft) long, and had a 1.5-m (5-ft) beam and an overall width of 2.1 m (7 ft) at the paddle boxes. It made more than 30 km/h (20 mi/h) over highways. As a result of his experiences and design work with the *Ohiki* and the *Honukai*, Jaggar was later able to help the U.S. Army with the design of amphibious vehicles for World War II, and he received in 1945 the Franklin L. Burr Prize of the National Geographic Society for this work.

Many other experiments were generated by HVO, though some were mostly conducted by others (see Jaggar, 1956). They included studies of the rehabilitation of lava and lava soils by organisms such as lichens; classification of the lava soils of the Kona District on the Island of Hawaii for their suitability for coffee tree cultivation; and installation of tide gauges at Hilo. College-credit courses in volcanology were given over many summers, especially for Island teachers. The widths of selected cracks, especially near Halemaumau, were measured periodically to record any changes. Topographic mapping of the Island of Hawaii and, by 1932, of almost the whole Territory of Hawaii was supported. By 1924, several triangulation and leveling projects had proved the elevation and distention of Kilauea caldera. As early as 1912, private industry (the Dictaphone Corp.) was trying out microphones in attempts to record the true sounds of a volcano in eruption.

## SEISMOLOGY

The history of seismology at HVO begins in 1912 with the completion of the Whitney vault. After two decades of pioneering, Jaggar was amply aware that seismometry on an active volcano is quite different from that at a station that studies mainly distant earthquakes.

### INSTRUMENTS

Instrumentation provided a challenge from the beginning. The story of the evolution of seismic instruments at HVO is documented in Curtis (1913), Jaggar and Romberg (1918), Apple (1978), and various issues of HVO's own publications, the Monthly Bulletin and Volcano Letter. The following account is synthesized and condensed from these sources.

Seismologist H.O. Wood reported for duty June 13, 1912, and he had the crated instruments from Japan installed on their "concrete tables" by July 2—installed, but not necessarily performing properly. These instruments were: (1) a sensitive Omori tromometer, designed for the registration of earthquake motion proceeding from a distant origin; (2) a less-sensitive Omori tromometer, designed for the registration of weak or moderate shocks of local origin; and (3) an ordinary Omori seismometer that started itself upon detecting a strong shock and that registered three components of motion, east-west, north-south, and vertical. The more sensitive tromometer arrived missing the north-south component; it was therefore mounted in such a way as to measure and register the component of earth motion in the east-west direction. Both tromometers had smoked drums and timing capability with marks every one minute. The ordinary Omori was set up so that when earth motion was strong enough to activate its starting device, the smoked drum revolved rapidly and marks were made every one-half second. This instrument could also be set to ring an alarm bell when it started.

Heavy horizontal pendulums detected horizontal earth motions, and a "floating" weight suspended by two balanced helical springs detected, in theory at least, the component of earth motion in the vertical direction. Time marks were made by an electromagnet operated by the brief closing of an electric circuit. Wood had all three instruments operating by August 1912, but all had, sometimes separately and sometimes simultaneously over the years, periods of nonoperation when work was done in the Whitney vault or on the instruments.

Of these three seismometers, the first to leave the Whitney vault was the less sensitive Omori. It was moved to the Technology Station at Halemaumau in February 1913 and later was apparently dismantled for parts. The three-component self-starter never really worked properly, even after it was rebuilt in 1918, renamed "Domesticus," put on full-time duty, and its vertical detection apparatus removed.

The most sensitive Omori seismometer was rebuilt into an optical recorder and given a corner mount in 1918 in the hope that it would detect both north-south and east-west teleseismic motion with its single boom. In 1923 it was retired. After retirement, this and all seismometers were cannibalized for parts to make or repair other instruments in the HVO machine shop.

During their service, the seismometers were modified and changed by the HVO staff to try to make them more suitable for use on the rim of Kilauea caldera—to be more responsive to local short-period earthquakes, volcanic tremor, and the extraordinary ground tiltings. These were the three distinctively Hawaiian geophysical phenomena Jaggar had identified by 1918. Jaggar noted that the

FIGURE 61.8.—Amphibious vehicle *Ohiki* leaving for extensive shakedown cruise and field test around the Island of Hawaii by water and road, February 1928. While T.A. Jaggar poses, his wife Isabel (cruise stewardess) peeps around stern. Paddle wheel can be seen behind Jaggar's right shoulder. It will be installed before vehicle takes to water in Kona. Building in background is HVO machine shop, built in 1927. Photographer unknown.

mechanical imperfections of standard instruments, designed for cheapness and convenience of operating and ill-adapted to such special problems, combined to yield only mediocre results. Dr. Arnold Romberg was hired by HVRA for the summer of 1918 to rebuild and otherwise improve the two original seismometers still in the Whitney vault and to do some work on the Bosch-Omori seismometer that had been acquired in 1913. Romberg also made at least two new one-component seismometers for installation in cellars to be established by HVRA in Hilo and Kealakekua. As Romberg worked, Jaggar noted with satisfaction that small improvements had been made over experiments by Milne, Galitzin, and others and that already the difficulties of friction, magnification, damping, opening the record, and time marking had been partially overcome.

The two-component Bosch-Omori seismometer, purchased from the Whitney Fund, had finally arrived from Germany by April 1913. Wood noted that in order to permit the construction of foundations and the work of installing the Bosch-Omori, a 100-kg tromometer, the seismographs in operation had to be partially dismounted temporarily. The new instrument was mechanically and dynamically superior to those hitherto in use there, and it was expected that a larger proportion of teleseismic records would be written, as well as more precise records of local shocks.

Trial runs of the new Bosch-Omori's east-west and north-south components were made on April 30, 1913; a feeble teleseism was registered, as well as strong volcanic vibrations. Adjustments were completed on May 8, 1913, for the final trial runs. From that time on through 1953, the Bosch-Omori seismometer was the main reliable, basic geophysical instrument of HVO.

Fine tunings of the Bosch-Omori never ended and were required after almost every unhinging caused by a strong earthquake. Modifications and upgradings were intermittent: steel wire replaced silk fibers to suspend the weights; oil damping baths were added, adjusted, redesigned, and readjusted; friction reduction was tried; new hinges were designed and manufactured; magnifications were lowered and raised; different levers, recording pens, and pins were tried; timing devices were improved; better drum-smoking devices were found; Dr. Romberg modified linkages and levers in 1918 so that one smoked drum recorded what two drums did originally; and one of the piers was rotated 7.5° to permit its boom to swing closer to a true east-west line.

In 1948, the Bosch-Omori seismograph in the Whitney Laboratory had a period of 7.7 seconds and a magnification of about 115 times the earth movement. It gave satisfactory records of short-period local earthquakes and of the ground tilt. This standard was the goal always attempted and sometimes met over the decades. Credit goes to the HVO staff for the daily attention they gave to the Bosch-Omori. One or more of the staff came day or night, storm or sunshine, workday or weekend, whenever a felt earthquake or home alarm signaled a potential dismantling.

Whitney vault's Bosch-Omori was the workhorse of the first four decades of the Hawaiian Volano Observatory, 1913 to 1953. HVO staff habit, respect, and momentum kept the Bosch-Omori seismometer operating in the Whitney Laboratory of Seismology for ten years after mechanical seismometers became technologically obsolete. The Bosch-Omori's last official smoked seismogram was removed, shellacked, and read on February 1, 1963, ending a daily series begun 50 years before.

Since the standard commercial seismometers had been tried and found wanting for the detection of short-period earthquakes, volcanic tremor, and ground tiltings, HVO turned its talents to designing and building special-purpose instruments. The most successful of these was the Hawaiian-type seismograph, in service worldwide by 1928. Briefly, it consisted of two horizontal components at right angles, each having a mass as much as about 100 kg (225 lb) consisting of a 69-cm (27-in.) length of pipe of 20-cm (8-in.) diameter, filled with sand. It was hinged above and below with short links of piano wire, had a free period of about 7 seconds, and was damped with light aluminum vanes dipping in oil near the outer end of the boom, giving it a lever magnification of about 130. Time was marked by an electromagnet recording on a smoked drum with paper speed of about 3.2 cm (1.25 in.) per minute. Both components recorded on the same drum, and a drum would run 24 hours without need of a change. The pair was designed for wall mounting, one on each side of a corner, with the mounting so arranged that the assemblies at the ends of the booms could record on the single drum. The only pier needed for the Hawaiian-type seismometer was one to hold the recording drum.

Pairs of Hawaiian-type seismometers were built in the HVO machine shop and supplied to Kodiak, Alaska (1927); Hilo, Hawaii (1927); the U.S. Coast and Geodetic Survey for testing and eventual placement at Sitka, Alaska (1927); Kealakekua, Hawaii (1928); Lassen National Park, California (1928); and Dutch Harbor, Alaska (1928). One design specification met by the Hawaiian-type seismograph was convenience of operation for the semiprofessionals hired by HVRA, USGS, or the Coast and Geodetic Survey at the more remote stations.

By 1929, although so far defeated in the search for a mechanical seismometer that would record the vertical component of seismic motion, staff at HVO continued experimenting. A vertical-component instrument to match the two-component Hawaiian-type already in use was especially desired. HVO seismologists wanted to measure the angle of emergence of earthquake waves at the station and believed this vertical angle would help furnish data on the depth of origin of the quake. By 1930, the HVO machine shop had built a vertical-component seismograph, with the heavy mass hung on spiral springs and temperature compensation provided by small springs. This instrument evolved after a variety of spring arrangements were tried, and it was installed in the Whitney vault. Its performance was never up to expectation, and it was the only seismometer installed under Building 41 in 1941. When that vault was abandoned by HVO in 1948, this instrument appears to have joined those in the bin to be cannibalized.

Recognizing that seismometers took the continuing care of specialists, Jaggar searched for instruments of simple enough design to be "put in the hands of amateurs" (Jaggar, 1932, p. 3). His first "shock recorder," designed in 1928, did record separate east-west and north-south motions, but it "also recorded the motion of rats, kittens, chickens, cockroaches and spiders" (Jaggar, 1931). This was redesigned so that it consisted of two wall-mounted inverted pendulums to be set up in a corner of a room and did not require a

pier. Three pairs of these were set up around Halemaumau. The first field test in the hands of "amateurs" came during the earthquake swarm in 1929 under Hualalai Volcano in Kona. A shock recorder pair was installed at Puu Waawaa Ranch on the slopes of Hualalai. Mr. Hinds the ranch owner and his family learned how to twirl the two daily recording discs over the smoking chimney of a kerosene lantern until each disc was coated an even brown. They also wound the clocks used in making the time marks.

It was this model of shock recorder that Jaggar took with him on the U.S. Navy expedition to Niuafo'ou Island (Tin Can Mail Island) in 1930 and left there with the Tongans. When earthquakes suddenly became a problem in 1930 in New Zealand, Jaggar hurriedly dispatched one such instrument in response to a plea from the New Zealand government. HVRA promised to supply eight more as soon as they could be manufactured, while in New Zealand machinists copied the one Jaggar sent.

By 1937, Jaggar had a new version of his shock recorder. What it gained in simplicity, it lost in sensitivity. It no longer separated arrival times of earthquake waves but registered only maximum intensity. Each instrument depended on a small mercury cup and was called an annunciator-type shock recorder. It showed a number from 1 to 6, depending on the intensity of the earthquake. Once a number became visible, the annunciator had to be reset.

Only two of the new design were on hand when an urgent request was made in 1938 to ship as many as possible on a Coast Guard cutter leaving almost immediately to supply colonists sponsored by the U.S. Government on tiny South Pacific Islands.

H.H. Waesche, a geologist at HVO, went aboard the cutter *Roger B. Taney* to install the two which were portable and could be set up in a few minutes with only a screwdriver and a pair of pliers. No smoked paper was needed; each instrument needed only a solid base and checking every hour or so. The colonists, all young Hawaiian men, would do the checking and report observations through the mail pouch. One recorder was set to read in an east-west direction on Canton Island, and the other to read north-south motions on Jarvis Island.

It was not necessary to wait for a natural earthquake to arrive to test seismometers and shock recorders built in the HVO machine shop; artificial earthquakes of known intensity and duration were created. HVO's earthquake machine, an oscillating table, was designed and built in 1928 in the machine shop by R.M. Wilson, HVO topographic engineer. It consisted of a massive, 365-km (800-lb) concrete slab resting on steel rollers. Instruments to be tested were mounted on the slab. Levers connected the rollers to the chuck of a nearby lathe; amplitude was governed by varying the radius of a crank in the lever train, and a range of periods could be provided by changing the speed of the lathe. Seismologists believed the oscillating table could simulate in part the ground motions of a variety of local earthquakes.

While seismometers were still being tailormade at Kilauea for local earthquakes, HVO acquired a shiny, new, compact, three-component Imamura seismometer from Japan for display to the visiting public in the building at Uwekahuna. All three components recorded on a single smoked drum. Although cars in the Uwekahuna parking lot, crowds moving about the museum floor, people clapping in the projection hall, and the range of daily temperatures in the building all confused the record, Park Naturalists believed that a working seismometer, no matter how befuddled its record, was a worthwhile exhibit and fit in with their lecture content. The Imamura instrument, with its magnification of as much as 50 times, was abandoned when HVO occupied the Uwekahuna building in 1948.

Seismographs are still the principal geophysical instruments at HVO. The electronic amplification and radio-telemetered signals of the current models would be startling to Jaggar's experiences, but not to his dreams.

## TRAVELTIMES OF EARTHQUAKE WAVES

A principal goal of seismological studies at HVO from their beginning has been to determine where earthquakes occur beneath the volcanic edifices. For this purpose the inference of traveltimes for earthquake waves is critical, and much has been learned from the successive attempts to interpret those traveltimes in Hawaii. The story of this evolution has been told in Jones (1935) and in various issues of HVO's Weekly Report and Volcano Letter. The following account has been gleaned from these sources.

In May 1915, HVO seismologist H.O. Wood reported that he had determined the distances of origin for 411 of the 604 local earthquakes registered in the first two and one-half years of operation of the Whitney Laboratory of Seismology. Wood used a table by Zeissig to determine these distances; for clock time he used a chronometer lent by the Territorial Surveyor, corrected by solar observations with a transit borrowed from the College of Hawaii.

The tables of Zeissig, in use then at most seismographic observatories, were designed for large earthquakes many hundreds of miles away. In 1925 HVO Seismologist R.H. Finch reported that HVO had found other tables by Omori, published in the Bulletin of the Imperial Earthquake Investigation Committee of Japan, to be more satisfactory. Omori's values came in fractions of a mile and thus helped in determining earthquake origins only a few kilometers (2–3 mi) away. That Omori's tables were better than the Zeissig table for very local earthquakes was shown by the good agreement between computed and actual distances of felt earthquakes whose approximate locations were known.

By 1925 Finch had in the Whitney cellar a Howard pendulum clock, corrected by radio signals originating from Pearl Harbor. There was a flurry of speculation in 1927 when it was noted that this clock, after being consistently late by 0.08 second per day (s/d), went to a consistent 0.66 s/d and then to a consistent 1.71 s/d. The speculation was that its pendulum might be sensibly indicating changes in the value of gravity; elevations had changed by amounts on the order of 1 m in 1924, and magma movement below might be involved.

In 1931, HVO Seismologist A.E. Jones found that the Omori traveltimes did not completely agree with the seismic facts in Hawaii. He developed a traveltime-distance graph for Hawaii, and by using $S-P$-wave intervals he showed "how to locate Hawaiian local earthquakes without the necessity of accurate time checks on all the master clocks of the several seismograph stations on Hawaii" (Jones,

1935, p. 59).

Trying to keep the scattered stations of the seismic network on the same time was given up by 1937. Most attention had gone to the station at Kealakekua. The line between Kealakekua and Kilauea passed practically through the middle of the great mass of Mauna Loa, and the stations were about equidistant from its center. In 1926, HVO's R.M. Wilson complained that, while the time at the Whitney vault was corrected by radio, the instrument tender at Kealakekua got his time—often more than a minute in error—over the telephone from the Kona switchboard operator. A radio set was supplied to the Kealakekua station in 1926 to receive time signals from the U.S. Naval radio station NPM at Pearl Harbor. A key beside the set, wired into the station clock, was depressed the instant the time signal was received; this recorded a mark on the current seismogram along with the one-minute marks made by the station clock. A measurement between the two marks on the seismogram revealed the correction necessary. It was believed this system recorded the time to within one-half second or better.

By 1939 H.H. Waesche, HVO geologist, had tied together for time control the seismograph stations around Kilauea summit, as well as the one on Mauna Loa at the end of the truck road. The Howard clock in the Whitney vault sent minute and hour signals of sufficient strength to operate relays controlling the electromagnets that lifted the recording needles on the drums. The connecting links between the stations and the clock were the existing National Park telephone trunklines, not connected to the commercial system. Waesche worked out all the circuitry and procured or made the parts to make the system operate. After some troubleshooting, the time signals did not interfere with telephone service in the Park.

Today, seismograph time signals accurate to a few thousandths of a second arrive by satellite. Tom Jaggar would be pleased.

## SCALES OF EARTHQUAKE INTENSITY

"Just as four pounds of sugar ought to be four times as big as one pound, so a number four earthquake should be four times as big as number one. Herein lies the difficulty" (Jaggar, 1929).

When Perret lived in his cabin near Halemaumau for six weeks in 1911, part of his working time was spent with his seismoscope. His views through its eyepiece showed the ground to be continually in motion. Accordingly Perret devised a scale based on the seismicity for the day; five on a scale of 10 was an average day.

H.O. Wood as charter HVO seismologist in 1912 used the Rossi-Forel scale of intensity, but also used phrases such as "this [earthquake] manifested an intensity of little more than 1/20th of that of the minimum shock perceptible to the senses."

In his report for the week ending December 19, 1912, Jaggar adopted for HVO the Cancani scale, which soon appeared on the back page of the printed weekly bulletins and stayed there through 1920. Inside, however, the text often used the Rossi-Forel scale by name, and a Cancani reference is hard to find. By the 1920's, R.H. Finch was using the Rossi-Forel to rate an earthquake recorded in the Hilea (Kau) cellar, and was rating the same quake as recorded in the Whitney vault as "slight" or "feeble."

HVO's R.M. Wilson used Volcano Letter no. 124 in May 1927 to describe the Rossi-Forel scale and explain how HVO graded its earthquakes in terms of acceleration from "feeble" through "alarming." Jaggar took most of Volcano Letter no. 223 in April 1929 to explain the Rossi-Forel, Cancani, and Mercalli scales, the last of which he abridged to show human effects. Jaggar concluded: "In the writer's tests, and Professor Mercalli among Italian peasants evidently had similar experience, ignorant persons in city or country can understand a human scale. They usually distort or exaggerate physical effects on masonry, water, trees, chimneys, etc., because they have no training in measured or judicial statement" (Jaggar, 1929).

Because he believed in the use of a human scale to grade earthquakes, Jaggar borrowed from Japan its postcard reporting system. Preaddressed and franked, with a form to be filled in and signed on the back, postcards were widely supplied to residents on all parts of the Island of Hawaii starting in 1932. People were to fill out and mail cards whenever they experienced a felt earthquake.

In keeping with the seismicity concept brought to Hawaii by Perret, charts and graphs of seismicity curves over various periods and for various purposes were prepared as early as 1920 and regularly by the 1930's. Seismologists at HVO developed for their own use in Hawaii the Hawaiian Volcano Observatory Scale, whose grades were "Tremor, Very Feeble, Feeble, Slight, Moderate, and Strong" (Jones, 1932). It was based on the double amplitude of motion on the Bosch-Omori seismograph and carried a description of the noninstrumental effects ("a human scale"). Its grades were eventually cross-referenced to the Rossi-Forel and modified Mercalli scales.

## TSUNAMIS

Coastal areas in the Hawaiian Islands are vulnerable to seismic seawaves (tsunamis) generated by major earthquakes anywhere in the Pacific Ocean. The tsunami of 1933 demonstrated that seismology could be used to predict the advent of such a wave and therefore to give warning to people in threatened areas. The story of that occasion, in which HVO staff prevented possible loss of life, has been told in the Honolulu *Advertiser* for March 14, 1933, and in Jaggar (1933).

Capt. Robert V. Woods, a retired ship's master who was the HVRA employee at Kealakekua, Kona, operated the seismograph vault there in the cellar of his house. Woods was more than a technician who changed drums and did routine maintenance H.s.t. his instruments. He had learned from the HVO seismologists how to determine the distance and origin of an earthquake from the arrival times of its different waves.

Woods was in his basement vault at 0700 H.s.t. March 2, 1933, getting ready to change drums, when he noticed his seismometer begin to record the arrival of a distant earthquake. The time between arrivals of the first and second different waves was about ten minutes. Woods calculated the distance at about 6,320 km (3,950 mi) and put the origin at the west edge of the Tuscarora Deep, east of Japan.

Meanwhile, in the Whitney vault on the other side of the Island, HVO seismologist Austin E. Jones saw the earthquake arrive on the Bosch-Omori instrument. He also calculated an origin point off Japan.

Over the telephone Woods and Jones agreed that such a quake could generate a tsunami in the Pacific Ocean that would travel at about 720 km/h (450 mi/h) and arrive at the Island of Hawaii about 8.5 h after the earthquake.

Jones notified the Hilo harbormaster at about 1000 to look for a tsunami at about 1530 local time; Woods also notified American factors at the small Kona ports of Kailua and Napoopoo.

Noon radio newscasts in Hawaii featured a Japanese disaster in Iwate Province from both an earthquake and a tsunami, confirming the potential of a tsunami reaching the Island of Hawaii.

People at Napoopoo, recalling tsunamis of 1893 and 1923, removed all cargo stored on the wharf and adjacent warehouses. Other Kona coastal settlements evacuated people but not property to any great extent. Tidal surges in Kona began at about 1520 and continued for hours. They began with a recession that left the sea bottom bare at Napoopoo, Kailua, Keauhou, and even at Kaalualu near Ka Lae (South Point).

On the seventh surge at Napoopoo, water receded vertically 2.5 m (8 ft) and then rose 3 m (9.5 ft). Up and down the Kona coast, rock walls were knocked over and scattered in low-lying areas. Boats were unmoored and capsized, houses flooded, lumber displaced and scattered, and property was washed out to sea. Cars left parked were flooded and some of their motors damaged by sand.

At Hilo, the sampan fleet moved out to anchorages in the harbor. Waves began to arrive at 1536, with an up-and-down motion of as much as 1 m (3 ft). There was no property damage.

No lives were lost in Hawaii during the 1933 tsunami, thanks to the warnings issued by the Hawaiian Volcano Observatory. This appears to have been the first time that a tsunami was predicted through interpretation of seismograms—a forerunner by decades of the Pacific-wide tsunami-alert system now in place.

## TILT

Tilting of the slopes of a volcanic edifice is now a well-known indicator of changes in subsurface magma volume and therefore a key to predicting eruptions. Study of such tilt was pioneered at HVO (see Jaggar and Finch, 1929), and records and discussions of tilt at Kilauea appeared in the various HVO publications from their earliest years.

Seismologist Wood first noticed pronounced ground tilt soon after he set up the Bosch-Omori instruments in 1913. Systematic recording and study of daily and seasonal tilt changes and their relation to Kilauea and Mauna Loa began in 1917 and became important in volcanic research. Over HVO's pioneer period, there were three basic methods of measuring tilt: leveling, use of clinoscopes, and computation from seismograms. Leveling was expensive and time consuming but was performed intermittently with transits and spirit levels. Some precise runs were made up from sea level, and local level lines extended 300 m (1,000 ft) or more. Clinoscopes were in full use by 1932. But the standard was the reliable Bosch-Omori seismograms, which could be used to compute the tilt of the instrument's pendulums in relation to the floor of the Whitney cellar. Such computations were done almost daily from 1913 through 1963 (see Romberg, 1919). In 1940, Waesche believed that the Bosch-Omori piers were capable of detecting a 6-mm (0.25-in.) change in the end of a straight line 16 km (10 mi) long (0.3 microradian in modern terminology).

The clinoscope was a heavy, ring-shaped weight hung by a piano wire from a tripod 2.1 m (7 ft) high. The weight dipped into a bath of automobile oil for damping, and a boom came vertically upward from the space in the middle of the weight. At the top of the boom was a sharp point; this point nearly reached a horizontal circular card that was ruled in points of the compass and in concentric circles. The center of the card was placed precisely above the point at the start of each day, and the point's migration away from the center 24 hours later would indicate both direction and angular amount of change. HVO clinoscopes magnified the amount of change about 50 times.

By 1932, clinoscopes were installed at the corners of an equilateral triangle whose center was the center of Halemaumau. Two of these were in cellars, and the third was enclosed within a glass case in a hut. The frequent earthquakes beneath Kilauea, however, played havoc with the reliability of the readings, as did temperature changes. Staff at HVO hoped to redesign the clinoscopes to make them entirely earthquake proof and to allow readings to be made through a microscope. The HVO "wish list" included a ring of clinoscopes around the summit craters of both Mauna Loa and Kilauea and others at various distances away on the highways out from Kilauea.

Today, that wish has largely come true, but not with clinoscopes. Electronic tiltmeters, sensitive to 0.1 microradian, are installed at several locations on Kilauea and Mauna Loa; they radio their signals directly to recorders at HVO.

## SCIENCE AND THE PUBLIC

> "The by-products of the popularity of our volcanoes [have included] * * * science guiding the police, the ranchers to safety, and the public to sight-seeing through ten lava crises. All of these things we have seen grow up during the last twenty-five years" (Jaggar, 1936, p. 4).

Volcanoes affect human communities, and the work of a volcanologist comes almost inevitably to involve questions of public policy and public safety. Jaggar had watched the 1926 Hoopuloa lava flow block a major highway and destroy a village, and he had directed the dropping of aerial bombs on a 1942 lava flow threatening Hilo. He retired (in 1940) before any more major eruptions seriously threatened human life or destroyed property. In his work, Jaggar had dealt principally with those people who held responsible positions in the local community and in major organizations like governments, academia, and publishing. He was gracious and great with ranch managers, but he did not easily exchange banter with cowboys. Islanders respected this volcanologist but did not call him friendly.

However, as a pioneering and visionary scientist, Jaggar had few peers. In his 1941 "cornerstone message" (Jaggar, 1941), he predicted: "The laboratories will be disseminated as underground earthquake-instrument cellars, underground temperature measuring wells, electrically controlled measurement stations reporting to a central office, and extended automatic and auto-metric facilities sending wired or wireless messages of underground and overground happenings on Mauna Loa. A volcano observatory must see or measure the whole volcano inside and out with all of science to help. The lesson of a third of a century has been to learn to look underground at the inner earth."

As of the time of writing of this historical summary, the Hawaiian Volcano Observatory has achieved much that Jaggar foretold. Fifty-one seismic stations radio information to the Observatory, where earthquake epicenters are located by computer within minutes after an event takes place. Electronic tiltmeters also telemeter data to HVO to give an instant report of the ground movement at various points on the active volcanoes. Other geophysical techniques have been added to these. The geochemical program that began with the early collections of volcanic gas at Halemaumau has gone on to calculate a total volcanic-gas budget for Kilauea. The Hawaiian Volcano Observatory and other institutions worldwide have made great strides in understanding how volcanoes work. This knowledge is being translated into forecasts of volcanic behavior that will reduce loss of life and property.

The volcanological community and the Hawaiian Volcano Observatory owe Thomas A. Jaggar, Jr., a debt of thanks for his vision, his dedication, and his persistence during hard times. Through those qualities he contributed much to the present vigor of volcanology. They are the lessons that must be relearned by every generation.

## REFERENCES CITED


Apple, R.A., 1954, A history of the land acquisition for Hawaii National Park to December 31, 1950: Honolulu, University of Hawaii, M.A. thesis, 158 p.

———1973, Mountain trails: The Ainapo and Mauna Loa: Honolulu, National Park Service, 26 p.

———1978, Physical history outline, Hawaiian Volcano Observatory: Honolulu, National Park Service, holograph, Hilo, Apple collection, Mo'okini Library, University of Hawaii.

———1982, The discoverers of Hawaii: Honolulu Star-Bulletin, October 8, p. A-14.

———1985, Outline of Hawaiian Volcano Observatory publication history with sample bulletin back pages: holograph, Hilo, Apple collection, Mo'okini Library, University of Hawaii.

Apple, R.A., and Apple, Peg, 1979a, Land, Lili'uokalani and annexation: Honolulu, Topgallant Press, 146 p.

———1979b, Mapping Mauna Loa's summit, watching 1926 eruption: Tales of Old Hawaii columns, Honolulu Star-Bulletin, July 13, August 24.

Bird, Isabella, 1966, Six months in the Sandwich Islands: Honolulu, University of Hawaii Press, 278 p.

Bolt, B.A., Horn, W.L., Macdonald, G.A., and Scott, R.F., 1975, Geologic hazards: New York, Springer-Verlag, 330 p.

Bosch, J.A., 1910, Katalog Nr. 22, Seismische Apparate-Instrumente: Strassburg, Werkstätte für Präzisions-Mechanik, 16 p.

Brigham, W.T., 1868, Notes on the volcanoes of the Hawaiian Islands: Memoirs of the Boston Society of Natural History, v. 2, pt. 3, 126 p.

———1869, Notes on the eruption of the Hawaiian volcanoes, 1868: Memoirs of the Boston Society of Natural History, supplement to v. 1, pt. 4, p. 23.

———1909, The volcanoes of Kilauea and Mauna Loa: Honolulu, B.P. Bishop Museum Memoir, v. 2, no. 4, 222 p.

Bullard, F.M., 1975, Thomas Augustus Jaggar, Jr., ms prepared for supplement five (1951–1955) of Dictionary of American Biography: Hilo, Apple collection, Mo'okini Library, University of Hawaii.

Byron, G.A., 1826, Voyage of HMS Blonde, Graham, M., compiler: London, John Murray, 271 p.

Coan, Lydia, 1884, Titus Coan, a memorial: Chicago, Revell, 220 p.

Coan, Titus, 1871, An island of fire: Scribner's Monthly, v. 2, no. 6, p. 56–57.

———1882, Life in Hawaii, an autobiographical sketch of mission life and labors: New York, Anson D.F. Randolph, 402 p.

Curtis, G.C., 1913, Work going on at Kilauea volcano: Science, v. 38, no. 976, p. 355–358.

Daly, R.A., 1911, The nature of volcanic action: Proceedings of the American Academy of Arts and Sciences, v. 47, p. 47–122.

Dana, J.D., 1849, Geology, *in* Wilkes, Charles, U.S. Exploring Expedition during the years 1838–1842, v. 10: Philadelphia, C. Sherman.

———1850, On the volcanic eruption of Hawaii: American Journal of Science and Arts, ser. 2, v. 10, no. 29, p. 235–244.

———1852, Note on the eruption of Mauna Loa: American Journal of Science and Arts, ser. 2, v. 14, no. 14, p. 79–80.

———1890, Characteristics of volcanoes, with contributions of facts and principles from the Hawaiian Islands: New York, Dodd, Mead, 399 p.

Daws, Gavan, 1968, Shoal of time, a history of the Hawaiian Islands: New York, Macmillan, 494 p.

Day, A.G., 1984, History makers of Hawaii, a biographical dictionary: Honolulu, Mutual, 174 p.

Douglas, David, 1834, Extract of a letter to Captain Sabine: Journal of the Royal Geographical Society, v. 4, p. 333–344.

———1919, Botantist at Hawaii (Wilson, W.F., ed.): Honolulu, W.F. Wilson, 212 p.

Duncan, George, 1961, Account of an automobile trip in 1909 around the Island of Hawaii, *in* Apple, R.A., 1965, Trails: From steppingstones to kerbstones, Hawaiian archeology: Honolulu, B.P. Bishop Museum Special Publication 53, 63 p.

Dutton, C.E., 1884, Hawaiian volcanoes: U.S. Geological Survey Annual Report, 4, p. 75–219.

Ellis, William, 1827, Narrative of a tour through Hawaii (2nd ed.), London, H. Fisher, Son, and P. Jackson, 480 p.

Finch, R.H., 1926, The April 10, 1926 outbreak of Mauna Loa: Volcano Letter, no. 68.

Green, W.L., 1887, Vestiges of the molten globe, part 2, the Earth's special features and volcanic phenomena: Honolulu, Hawaiian Gazette, 337 p.

Hitchcock, C.H., 1911, Hawaii and its volcanoes, 2nd ed. with supplement: Honolulu, Hawaiian Gazette, 314 p.

Jaggar, T.A., 1910, Lecture by Thomas A. Jaggar, Jr., to the Society of Arts: Massachusetts Institute of Technology Society of Arts Bulletin, February, p. 1–6.

———1917a, Report of the Hawaiian Volcano Observatory of the Massachusetts Institute of Technology and the Hawaii Volcano Research Association (dated January–March 1912 on cover): Cambridge, Massachusetts Institute of Technology Society of Arts, 74 p.

———1917b, Annual address of the director, the results of six years of work, August 23: Hawaiian Volcano Observatory Bulletin, v. 5, no. 8, p. 81–88.

———1917c, (Summary for the week ending January 13, 1917): Hawaiian Volcano Observatory Bulletin, v. 5, no. 1, p. 4–7.

———1922a, Preparations for boring experiments: Monthly Bulletin of the Hawaiian Volcano Observatory, v. 10, no. 4, p. 32–33.

———1922b, Progress of boring experiments: Monthly Bulletin of the Hawaiian Volcano Observatory, v. 10, no. 6, p. 63–68.

———1926a, Progress 1926 Mauna Loa eruption: Volcano Letter, no. 69.

———1926b, Decline of Mauna Loa eruption: Volcano Letter, no. 70.

———1927, A wheeled boat for volcano exploration: Volcano Letter, no. 156.

———1929, Earthquake intensity scales: Volcano Letter, no. 223.

———1931, Improved Jaggar shock-recorder: Volcano Letter, no. 352, p. 2.
———1932, Progress of Hawaiian volcano research: Volcano Letter, no. 383, p. 1–4.
———1933, Tsunami or earthquake tidal wave March 2, 1933: Volcano Letter, no. 397, p. 1–2.
———1936, The influence of volcanic research in Hawaii: Volcano Letter, no. 434, p. 4–5.
———1937, Protection of Hilo from coming lava flows: Volcano Letter, no. 443, p. 1–8.
———1938, Dr. Jaggar outlines needs for volcano research here (headline): Honolulu Advertiser, March 30, p. 1.
———1941, Kilauea volcano observing (carbon copy of typescript paper inserted in cornerstone, Kilauea Volcano House, July 20): Hilo, Apple collection, Mo'okini Library, University of Hawaii.
———1945, Protection of harbors from lava flows: American Journal of Science, v. 243-A, p. 333–351.
———1956, My experiments with volcanoes: Honolulu, Hawaii Volcano Research Association.
Jaggar, T.A., and Finch, R.H., 1929, Tilt records for thirteen years at the Hawaiian Volcano Observatory: Seismological Society of America Bulletin, v. 19, no. 1, p. 38–51.
Jaggar, T.A., and Romberg, Arnold, 1918, An experiment in teleseismic registration: Seismological Society of America Bulletin, v. 8, no. 2-3, p. 88–89.
Jones, A.E., 1932, A chart of Kilauea seismicity: Volcano Letter, no. 371, p. 1–3.
———1935, Hawaiian travel times: Seismological Society of America Bulletin, v. 25, no. 1, p. 33–61.
Kelley, E.G., 1841, Remarks on the geological features of the island of Owyhee or Hawaii: American Journal of Science and Arts, no. 40, p.117–122.
Kuykendall, R.S., 1967, The Hawaiian kingdom, v. 3, 1874–1893: Honolulu, University of Hawaii Press, 764 p.
Lockwood, J.P., and Torgerson, F.A., 1980, Diversion of lava flows by aerial bombing—lessons from Mauna Loa volcano, Hawaii: Bulletin Volcanologique, v. 43, p. 727–741.
Löwenstern, M.J., 1842, On pyramid at Remedios, with a route from Mexico to Mazatlan, and ascent of Mauna Loa: Journal of the Royal Geographical Society, v. 10, p. 100–107.
Lyman, C.S., 1851, On the recent condition of Kilauea: American Journal of Science and Arts, ser. 2, v. 12, p. 75–80.
Macdonald, G.A., 1953, Thomas Augustus Jaggar: Volcano Letter, no. 519, p. 1–4.
———1972, Volcanoes: Englewood Cliffs, New Jersey, Prentice-Hall, 510 p.
Macdonald, G.A., and Hubbard, D.H., 1982, Volcanoes of the national parks in Hawaii (8th ed.): Honolulu, Hawaii Natural History Association, 64 p.
Menzies, Archibald, 1920, Hawaii nei 128 years ago, Wilson, W.F., ed.: Honolulu, W.F. Wilson, 199 p.
Omori, F., 1910, letter, Seismological Institute, Imperial University, Tokyo, Japan, to Professor T.A. Jaggar, Massachusetts Institute of Technology, Cambridge, July 12, with sketches: original in files of Hawaii Volcano Observatory.
Perret, F.A., 1913a, The lava fountains of Kilauea: American Journal of Science, ser. 4, v. 35, no. 206, p. 139–148.
———1913b, Subsidence phenomena at Kilauea in the summer of 1911: American Journal of Science, ser. 4, v. 35, no. 209, p. 469–476.
———1913c, Some Kilauea ejectamenta: American Journal of Science, ser. 4, v. 35, no. 210, p. 611–618.
———1913d, Volcanic research at Kilauea in the summer of 1911: American Journal of Science, ser. 4, v. 36, no. 215, p. 475–488.
Powers, Sidney, 1915, Hawaii's great volcanoes and the study of them: Bulletin of the American Geographical Society, v. 47, p. 577–583.
Romberg, Arnold, 19, Theory of a non-tilt seismograph: Seismological Society of America Bulletin, v. 9, no. 4, p. 135–139.
Shepherd, John, 1840, Ascent of the volcano Kilauea on Hawaii in November 1839: Athenaeum, no. 681.
Strzelecki, Paul de, 1838, as quoted in Hawaiian Spectator, April 1838, p. 98–101.
U.S. Department of Interior, 1973, National Park Service, National Register of Historic Places, nomination forms, Whitney Seismograph Vault, May 30, Mauna Loa Trail, August 9.
Weiner, F.B., 1982, German sugar's sticky fingers: Hawaiian Journal of History, v. 16, p. 15–47.
Wentworth, C.A., and Powers, H.A., 1962, The Hawaiian Volcano Observatory Fiftieth Anniversary, unpublished ms: Hilo, Apple collection, Mo'okini Library, University of Hawaii.
Wilkes, Charles, 1845, Narrative of the U.S. Exploring Expedition during the years 1838–1842, v. 4: Philadelphia, Lea and Blanchard, 539 p.
Wilson, R.M., 1928, The Ohiki: Monthly Bulletin of the Hawaiian Volcano Observatory, v. 16, no. 4, p. 29–30.
Wood, H.O., 1913, Hawaiian Volcano Observatory: Seismological Society of America Bulletin, v. 3, no. 1, p. 14–19.

# STAFF OF THE HAWAIIAN VOLCANO OBSERVATORY, 1912–PRESENT

*Compiled by* Taeko Jane Takahashi *and* Thomas L. Wright

## INTRODUCTION

Through Thomas A. Jaggar's vision, enthusiasm, and hard work, the Hawaiian Volcano Observatory (HVO) was founded in 1912. HVO's international stature today is largely due to the remarkable cast of characters who worked with him—and who followed after him—during the past 75 years. The men and women of HVO have, over the years, not only continued his work but also refined and expanded the study of volcanoes in ways that even Thomas Jaggar would scarcely have believed.

This chapter lists persons who have worked at HVO, in the order of their appearance on the scene. We made the arbitrary decision to limit the list to those whose appointments lasted one year or more, as indicated on annual budget submissions. We have identified the large number of student appointments by the program under which they were hired: Minority Program in the Earth Sciences (MPES), Federal Junior Fellowship (FJF), and Stay-in-School (SIS). Where possible, we obtained information directly from the persons listed, including for each the years worked at HVO, the position(s) while there, principal work since leaving HVO, and a current address where available. Of particular interest is the information people have given on their work and experience since leaving the observatory. It is evident from this list that HVO has been a leader in the international exchange of ideas and techniques in volcanology.

This list does not tell the whole story, as there are some persons whom we were unable to contact. It also does not include the hundreds of Guest Investigators who have spent time at HVO—some for just a few days and some whose research on Hawaiian volcanism has been ongoing. Their exchange of ideas and information has been vital to the observatory. Also not listed are the names of the many volunteers whose assistance to the staff in untold hours of effort, during and between eruptions, has been immeasurable.

We illustrate this HVO staff history with chronologic montages of Directors and Scientists In Charge (fig. 62.1) and of HVO fieldwork (fig. 62.2). Together they make a silent commentary on dress and field techniques of the past 75 years.

We acknowledge the cooperation of all who responded to the requests for information, and are indebted to those who provided leads to others who are deceased or retired. For an alphabetical listing of the HVO staff giving their places in the chronological sequence, see appendix 62.1.

## CHRONOLOGICAL LIST OF HAWAIIAN VOLCANO OBSERVATORY STAFF

**Thomas A. Jaggar**
Founder of HVO
January 1912–July 1940; Director
Since HVO: Retired from USGS in 1940. Research associate in geophysics at the University of Hawaii
Volcano experience: Martinique, Italy (Vesuvius), Aleutian Islands, Lassen Peak, Japan, Costa Rica, New Zealand, Niuafoou Island
Died January 1953

**Harry O. Wood**
1912–1917; Seismologist

**Alex Lancaster**
1912–1928; Field assistant and guide
Died 1941

**Sidney Powers**
1915–1916; Geologist

**Isabel Maydwell Jaggar**
1917–1940; Secretary (wife of Thomas Jaggar)
Died May 1964

**Kesaburo Suga**
1918–1924; Assistant

**Allen Akim-Seu**
1919–1921; Assistant

**Ruy H. Finch**
August 1919–September 1926; Seismologist
July 1940–January 1951; Director
Since HVO: Retired from USGS in 1951
Volcano experience: Java, Aleutian Islands, Italy, New Zealand, Lassen Peak (Cascades Volcano Observatory)
Died March 1957

**Oliver H. Emerson**
1923–1926; Chemist
Died circa 1970

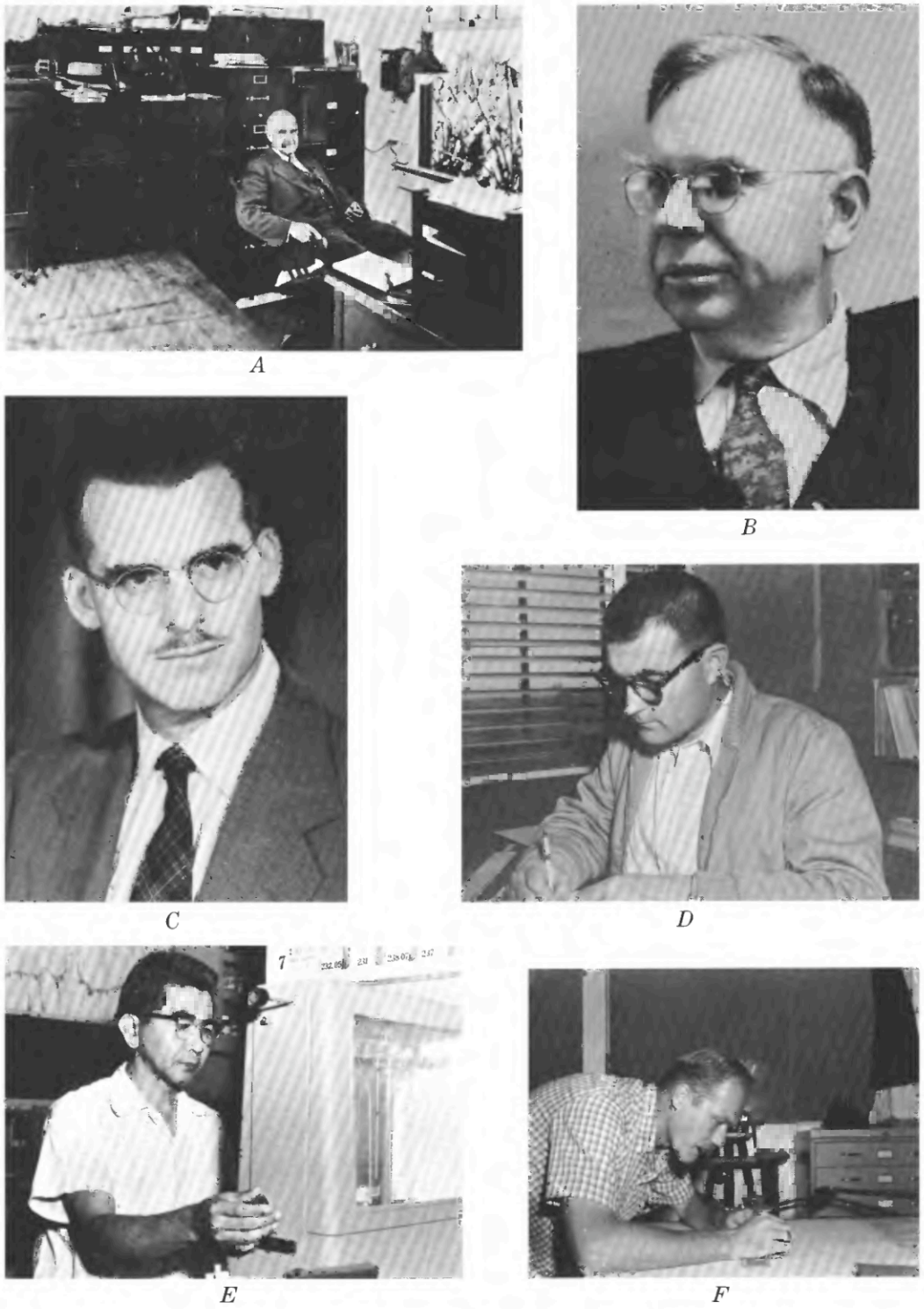


FIGURE 62.1.—Directors (***A–C***) and Scientists In Charge (***D–M***) of the Hawaiian Volcano Observatory during its first 75 years and their periods of service in those posts. All photographs from HVO archives. ***A***, Thomas A. Jaggar, 1912–40. ***B***, Ruy H. Finch, 1940–51. ***C***, Gordon A. Macdonald, 1951–56. ***D***, Jerry P. Eaton, 1956–58, 1960–61. ***E***, Kiguma J. Murata, 1958–60. ***F***, Donald H. Richter, 1961–62. ***G***, James G. Moore, 1962–64. ***H***, Howard A. Powers, 1964–70. ***I***, Donald W. Peterson, 1970–75, 1978–79. ***J***, Robert I. Tilling, 1975–76. ***K***, Gordon P. Eaton, 1976–78. ***L***, Robert W. Decker, 1979–84. ***M***, Thomas L. Wright, 1984–

*G*

*H*

*I*

*J*

*K*

*L*

*M*

FIGURE 62.1.—Continued.

FIGURE 62.2.—Volcanological work of Hawaiian Volcano Observatory staff. All photographs from HVO archives. ***A***, Sounding depth of lava in active lava tube, 1973. ***B***, Operating long-range geodimeter on Mauna Kea, 1973. ***C***, Drilling to liquid lava in Kilauea Iki, 1975. ***D***, Making gravity measurements, 1980's. ***E***, Guiding visitors at Halemaumau, before 1928. ***F***, Reading water-tube tiltmeter, 1971. ***G***, Making self-potential measurements southwest of Halemaumau, 1985. ***H***, Preparing for SCUBA dive from Kealakomo lava delta to observe lava flow beneath the sea, 1971. ***I***, Measuring $SO_2$ from Puu Oo, using correlation spectrometer, 1984. ***J***, Measuring width of cracks on Kilauea's east rift zone, 1985. ***K***, Reading horizontal distance changes, using short-range geodimeter, 1983. ***L***, Estimating lava temperatures with infrared optical pyrometer, 1972. ***M***, Taking gas samples uprift from Puu Oo, 1983. ***N***, Estimating depth of Mauna Ulu lava lake with rangefinder, early 1970's. ***O***, Using portable seismometer near Alae vent, 1972. ***P***, Using thermocouple to measure temperature at Mauna Loa lava river, 1984. ***Q***, Leveling to measure vertical ground deformation at Puu Oo, 1986. ***R***, Retreating from aa flow at the Royal Gardens, Kalapana, 1983.

*J*

*K*

*L*

*M*

*N*

*O*

*P*

*Q*

*R*

FIGURE 62.2.—Continued.

**Hideichi Yasunaka**
1924–1940; Assistant

**Gilbert H. Nakaji**
1925– ; Assistant

**Tai-on Au**
1926–1933; Machinist

**Richmond B. Hodges**
1926–1933; Accounting clerk

**H.S. Palmer**
1926– ; Assistant

**Ronald M. Wilson**
1926–1928; Topographic and geodetic engineer

**F.Y. Boyrie**
1927–1928; Instrument maker

**Howard A. Powers**
July 1929–June 1932; Geologist, petrologist
December 1945–December 1948; Geologist, petrologist
January 1964–August 1970; Scientist In Charge
Retired from USGS in 1970.
Volcano experience: Aleutian Islands; ancient volcanism in Idaho, Wyoming, New Mexico, eastern Washington, and Oregon.
Address: Pohai Nani, Apt. 715
45–090 Namoku Street
Kaneohe, HI 96744

**Edward G. Wingate**
1931–1933; Topographer
Since HVO: 1933–1946, Superintendent of Hawaii Volcanoes National Park
Died March 1975

**Austin E. Jones**
1931–1935; Seismologist
Died June 1985

**Hugh H. Waesche**
1935–1941; Geologist

**S. Sato**
1936–1940; Librarian

**A. Okuda**
1936–1938; Mechanic

**Paul Ernest Shultz**
1940–1941; Geologist
Address: 105 Temebec Circle
Sonoma, CA 95476

**Burton J. Loucks**
1940–1942, 1945–1965; Instrument maker
Retired from USGS in August 1969
Address: 449 Croisan Creek Road
South Salem, OR 97302

**Peter Malo**
1942–1943; Assistant

**Guy Omer**
1943–1946; Assistant

**Gordon A. Macdonald**
September 1948–January 1951; Geologist
January 1951–January 1956; Director
Since HVO: 1956–1957, USGS, Cascade volcanism; 1957–1978, Chairman, Department of Geology, University of Hawaii and Hawaii Institute of Geophysics
Volcano experience: Philippines, Mexico, Italy, American Samoa, Lassen Peak
Died June 1978

**Ruth Loucks**
1948–1950; Secretary
Address: 449 Croisan Creek Rd.
South Salem, OR 97302

**Catherine Hjort**
1950– ; Secretary

**John C. Forbes**
December 1950–April 1983; Physical science technician, equipment maintenance and fabrication, fieldwork
Retired from USGS in 1983 (continues to work for HVO on contract for weekend seismic-record changing)
Address: P.O. Box 74
Volcano, HI 96785

**LaVieve G. Forbes**
1950–1952; Clerk-typist and librarian
Address: P.O. Box 74
Volcano, HI 96785

**Chester K. Wentworth**
1951–1962; Geologist
Retired from USGS in 1962
Died January 1969

**Elizabeth (Betty) E. Johnston**
November 1952–April 1955; Administrative secretary
Since HVO: Volunteer at Hawaii Volcanoes National Park
Address: P.O. Box 787
Volcano, HI 96785

**Jerry P. Eaton**
1953–1956, 1959; Geophysicist
1956–1958, 1960–1961; Scientist In Charge
Since HVO: Earthquake Prediction Program, USGS, Menlo Park, Calif.
Volcano experience: Seismic monitoring in Alaska, Cascade Range, and Central America
Address: U.S. Geological Survey
345 Middlefield Road, MS 977
Menlo Park, CA 94025

**Akira Yamamoto**
1955–1983; Administrative clerk and physical science aide
Since HVO: Retired from USGS in 1983 (continues to work for HVO on contract for weekend seismic-record changing)
Address: U.S. Geological Survey
Hawaiian Volcano Observatory
P.O. Box 51
Hawaii National Park, HI 96718

**George D. Fraser**
July 1956–July 1959; Geologist
Since HVO: USGS, Hebgen Lake earthquake investigation; Conservation Division—coal, phosphate
Retired from USGS in June 1979
Volcano experience: Aleutian Islands, Yellowstone National Park
Address: Rt. 4, Treehaven, Box 2
Cle Elum, WA 98922

**Wayne U. Ault**
1957–1962; Geochemist
Since HVO: Research scientist at Isotopes, Inc.; college and university teaching
Address: 595 Watson St.
Memphis, TN 38111

**William Henry Francis**
1957–1980; Shop and field assistant
Retired from USGS in 1980
Address: Box 603
Pahala, HI 96777

**Kiguma Jack Murata**
July 1958–June 1960; Scientist In Charge and geochemist
Since HVO: Studying diagenetic minerals in Tertiary sedimentary rocks of California, and distribution of zeolites in lavas of the Paraná Basin, Brazil
Retired from USGS in 1978
Volcano experience: Costa Rica (Irazú), Mount St. Helens
Address: 919 Ninth Avenue
Sacramento, CA 95818

**Reggie T. Okamura**
1958–1977; Physical science technician (geology)
1978–present; Chief of Operations
Address: U.S. Geological Survey
Hawaiian Volcano Observatory
P.O. Box 51
Hawaii National Park, HI 96718

**George Kojima**
December 1958–present; Electronics technician
Volcano experience: Indonesia, Northern Marianas (Pagan)
Address: U.S. Geological Survey
Hawaiian Volcano Observatory
P.O. Box 51
Hawaii National Park, HI 96718

**Donald H. Richter**
July 1959–June 1961; Geologist
June 1961–July 1962; Scientist In Charge
Since HVO: Geologic studies in Alaska, both with the State of Alaska (1963–1967) and the USGS (1967 to present)
Volcano experience: Alaska (Wrangell Mountains) and the Alaskan Peninsula
Address: P.O. Box 79
Winston, New Mexico

**Harold L. Krivoy**
1959–1963; Seismologist
Since HVO: Solid Earth geophysics, astrogeophysics, marine geophysics, oil and gas. Since leaving USGS: Exploration geophysics in oil and gas
Address: 1700 Richland Drive
Richardson, TX 75081

**Richard R. McDonald**
1960–1961; Geophysicist
Since HVO: U.S. Navy, presently holds rank of Captain
Volcano experience: Aleutians
Address: 16017 Malcolm Drive
Laurel, MD 20707

**Gilbert Dakujaku**
1961–1962; Geologic field assistant
Since HVO: Optometrist and Manager, Hilo Optical Co.
Address: 315 Kinoole St.
Hilo, HI 96720

**Arnold T. Okamura**
August 1961–present; Geologist (deformation studies)
Volcano experience: Indonesia, Mount St. Helens, Ruiz (Colombia)
Address: U.S. Geological Survey
Hawaiian Volcano Observatory
P.O. Box 51
Hawaii National Park, HI 96718

**Robert Y. Koyanagi**
September 1961–present; Seismologist
Volcano experience: Indonesia, Northern Marianas (Pagan)
Address: U.S. Geological Survey
Hawaiian Volcano Observatory
P.O. Box 51
Hawaii National Park, HI 96718

**James G. Moore**
September 1961–July 1962; Geologist
July 1962–January 1964; Scientist In Charge
Since HVO: USGS, Menlo Park, continued work in Hawaii (especially offshore) and the Sierra Nevada
Volcano experience: Philippines (Taal and Mayon), Sicily (Etna), Iceland (Heimey and Surtsey), Mount St. Helens. Also marine volcanoes: Loihi, Mid-Atlantic Ridge, Gorda Ridge, Revillagigedo Islands
Address: U.S. Geological Survey
345 Middlefield Road, MS 910
Menlo Park, CA 94025

**Alan S. Ryall, Jr.**
December 1962–December 1963; Seismologist
Since HVO: Director, University of Nevada Seismological Lab (1964–1976 and 1978–85); Program Manager, Defense Advanced Research Projects Agency, Nuclear Monitoring Research Office (1976–78), Director of Research, Center for Seismic Studies (1985–present)
Volcano experience: Long Valley caldera, tectonic/magmatic activity
Address: Center for Seismic Studies
1300 N. 17th St., Suite 1450
Arlington, VA 22209

**Nathaniel D. Sherrill**
January 1963–November 1963; Electronic instrument maker
Since HVO: USGS, Menlo Park, engineer in the Branch of Isotope Geology, designing and building instruments
Address: U.S. Geological Survey
345 Middlefield Road, MS 937
Menlo Park, CA 94025

**Elliott T. Endo**
January 1963–December 1965; Geologic field assistant
August 1974–August 1975; Geophysicist (seismology)
Since HVO: 1983–present, Seismologist, Cascades Volcano Observatory,
Volcano experience: Indonesia, Alaska, Cascades, Central America
Address: U.S. Geological Survey
Cascades Volcano Observatory
5400 MacArthur Blvd.
Vancouver, WA 98661

**Dallas L. Peck**
June 1963–August 1965; Geologist
Since HVO: Menlo Park, Calif., Washington, D.C., and Reston, Va. Study of granitic and metavolcanic rocks of the Sierra Nevada batholith. Fifteen years of science administration, including Chief Geologist and Director, USGS
Volcano experience: Cenozoic volcanic rocks of the Cascade Range, Oregon, and Mesozoic metavolcanic rocks of the Sierra Nevada, California
Address: U.S. Geological Survey
National Center, MS 101
12201 Sunrise Valley Drive
Reston, VA 22092

**Willie T. Kinoshita**
June 1963–July 1968; Geophysicist
Since HVO: 1968–1980, Office of Earthquake Studies, Crustal Strain Project; 1980–1984, Deputy Scientist In Charge, Cascades Volcano Observatory
Retired from USGS in 1984
Volcano experience: Galápagos (Fernandina), Guadeloupe, Mount St. Helens
Address: 6901 NE. 159th St.
Vancouver, WA 98665

**David P. Hill**
February 1964–August 1966; Seismologist
Since HVO: USGS, Menlo Park; 1978–1982, Chief, Seismology Branch; seismotectonics and crustal structure, Pacific Coast States; 1984–present, Chief scientist, Long Valley caldera-Mono Craters area
Volcano experience: Long Valley caldera, Italy (Phlegraean Fields caldera)
Address: U.S. Geological Survey
345 Middlefield Road, MS 977
Menlo Park, CA 94025

**Thomas L. Wright**
February 1964–August 1969; Geologist
June 1984–present; Scientist In Charge
Volcano experience: Mapping and petrogenetic study of the Columbia River Basalt Group
Address: U.S. Geological Survey
Hawaiian Volcano Observatory
P.O. Box 51
Hawaii National Park, HI 96718

**Yukie Kimura Endo**
September 1964–November 1966; Clerk-typist
Since HVO: Homemaker
Address: 7604 N.E. 14th Street
Vancouver, WA 98664

**Richard S. Fiske**
October 1965–March 1968; Geologist
Since HVO: Study of ancient volcanic rocks preserved in roof pendants of the Sierra Nevada batholith; 10 years of science administration, including Director of the National Museum of Natural History, Washington, D.C.
Volcano experience: Eastern Caribbean (Guadaloupe, St. Vincent, Montserrat)

Address: Department of Mineral Sciences–NHB 106
Smithsonian Institution
Washington, DC 20560

**Jeffrey Judd**
1966–1985 (intermittent); Geologic field assistant
Since HVO: Henry Opukahaia School
Address: P.O. Box 99
Hawaii National Park, HI 96718

**Kenneth M. Yamashita**
1966–1967; Geologic field assistant
1975–1984; Deformation specialist
Since HVO: 1969–1974, USGS, Menlo Park (crustal strain project); 1984–present, Cascades Volcano Observatory (monitoring magnetic changes at Mount St. Helens, running precise level surveys at Newberry Crater and Yellowstone caldera)
Volcano experience: Indonesia, Montserrat and St. Vincent, Cascades, Yellowstone
Address: U.S. Geological Survey
Cascades Volcano Observatory
5400 MacArthur Blvd.
Vancouver, WA 98661

**Maurice K. Sako**
1967–present; Physical science technician (deformation studies)
Volcano experience: Northern Marianas (Pagan), Philippines (Mayon, Bulusan, and Taal)
Address: U.S. Geological Survey
Hawaiian Volcano Observatory
P.O. Box 51
Hawaii National Park, HI 96718

**Marie S. Onouye**
1967–1980; Administrative clerk
Since HVO: Operating family business (Volcano Store)
Address: P.O. Box 458
Kurtistown, HI 96761

**Donald A. Swanson**
March 1968–July 1971; Geologist (deformation studies)
Since HVO: Geologic study of the Columbia River Basalt Group; study of growth of Mount St. Helens dacite dome; geologic map of Goat Rocks Wilderness
Volcano experience: New Zealand, La Soufrière, St. Vincent, Italy (Vulcano), Cascade Range, Colombia (Ruiz)
Address: U.S. Geological Survey
Cascades Volcano Observatory
5400 MacArthur Blvd.
Vancouver, WA 98661

**Dallas B. Jackson**
June 1968–July 1971, June 1978–present; Geophysicist (electrical studies)
Volcano experience: Pagan (Marianas), Réunion (Indian Ocean)
Address: U.S. Geological Survey
Hawaiian Volcano Observatory
P.O. Box 51
Hawaii National Park, HI 96718

**Cary Arakaki**
1968–1971; Geophysical assistant
Since HVO: Carpenter
Address: 270 Mohala Place
Hilo, HI 96720

**Robert Mitchell**
1968– ; Geophysical assistant
Since HVO: Geophysicist (Ph.D. in seismology), oil-well exploration

**Steven Takeguchi**
May 1968–May 1969; Geophysical assistant
Since HVO: Construction Representative, U.S. Army Corps of Engineers
Honolulu, Hawaii
Address: 98–260 Ualo St.
Aiea, HI 96701

**Wendell A. Duffield**
1969–1972; Geologist
Since HVO: USGS, Menlo Park and Flagstaff; studies of quaternary volcanic rocks, with emphasis on geothermal energy and volcanic hazards
Volcano experience: Mexico (El Chichón), Réunion, Iceland, Azores, Jordan (quaternary basalts), Honduras, Coso volcanic field and Warner Mountains (California), Massif Centrale (France)
Address: U.S. Geological Survey
2255 North Gemini Drive
Flagstaff, AZ 86001

**Donald W. Peterson**
August 1970–January 1975; Scientist In Charge
January 1975–July 1975; Geologist
October 1978–January 1979, Interim Scientist In Charge
Since HVO: 1975–1980, Tertiary volcanic rocks in Arizona; 1980–1985, Scientist In Charge, Cascades Volcano Observatory; 1985–present, Geologist at CVO; special assignments overseas; Tertiary volcanic rocks in Arizona
Volcano experience: Mount St. Helens, Indonesia
Address: U.S. Geological Survey
345 Middlefield Road, MS 910
Menlo Park, CA 94025

**Kenneth T. Honma**
1970–present; Electronics technician
Volcano experience: Indonesia (Galunggung and Merapi), Northern Marianas (Pagan), Mount St. Helens
Address: U.S. Geological Survey
Hawaiian Volcano Observatory
P.O. Box 51
Hawaii National Park, HI 96718

**John D. Unger**
July 1971–July 1974; Seismologist
Since HVO: Reflection seismology to investigate seismotectonic structures in the Eastern United States; deep-crustal reflection seismology to study the history and structure of the northern Appalachians in southern Quebec and northern Maine
Volcano experience: Cascade Range
Address: U.S. Geological Survey
National Center, MS 922
12201 Sunrise Valley Drive
Reston, VA 22092

**Robert L. Christiansen**
September 1971–September 1973; Geologist
Since HVO: Research at Yellowstone, Mount Shasta, Lassen Peak, Mount St. Helens; Coordinator of Geothermal Research Program, 1976–1979
Volcano experience: Yellowstone, Cascade Range, Central America, and old volcanoes in the Great Basin
Address: U.S. Geological Survey
345 Middlefield Road, MS 910
Menlo Park, CA 94025

**Robin Holcomb**
September 1971–December 1975; Geologic field assistant
Since HVO: Studying geomorphology of basaltic flows; dating of Holocene basalt flows using paleomagnetic variation; eruption patterns along subaerial and submarine rift zones; geologist, Cascades Volcano Observatory (growth of lava dome at Mount St. Helens)
Volcano experience: Idaho, Cascade Range, San Francisco volcanic field (Arizona), Pinacate volcanic field (Sonora), Galápagos submarine rift zone, Juan de Fuca submarine rift zone, Iceland, Java
Address: U.S. Geological Survey
Cascades Volcano Observatory
5400 MacArthur Blvd.
Vancouver, WA 98661

**Charles Zablocki**
June 1972–August 1975; Geophysicist
Since HVO: Mineral/geothermal exploration (Arizona, Hawaii), administration (USGS, Reston, Va.), mineral exploration (Saudi Arabia)
Retired from USGS in 1985
Address: 22557 Meadowview Rd.
Morrison, CO 80465

**Robert I. Tilling**
July 1972–February 1975; Geologist (petrology and geochemistry)
February 1975–September 1976; Scientist In Charge
Since HVO: 1976–1981, Chief, Office of Geochemistry and Geophysics, and coordinator of USGS Volcano Hazards Program; 1981–present, research on Hawaiian volcanoes
Volcano experience: Mexico (El Chichón), Indonesia (Merapi and Galunggung)
Address: U.S. Geological Survey
National Center, MS 906
12201 Sunrise Valley Drive
Reston, VA 22092

**John P. Lockwood**
January 1974–August 1978; Geologist
Since HVO: August 1978–present, Project Chief, Geologic History of Mauna Loa Volcano (Mauna Loa eruptive history, lava-diversion studies)
Volcano experience: Indonesia (Galunggung and Gamalama), Italy (Etna), Colombia (Ruiz)
Address: U.S. Geological Survey
Hawaiian Volcano Observatory
P.O. Box 51
Hawaii National Park, HI 96718

**Jennifer Nakata**
1974–present; Physical science technician (seismology)
Volcano experience: Mount St. Helens
Address: U.S. Geological Survey
Hawaiian Volcano Observatory
P.O. Box 51
Hawaii National Park, HI 96718

**Gary S. Puniwai**
1974–present; Electronics technician
Volcano experience: Rabaul (Papua New Guinea), Coso Range (California)
Address: U.S. Geological Survey
Hawaiian Volcano Observatory
P.O. Box 51
Hawaii National Park, HI 96718

**Loren Akaka**
1974–1975; Physical science aide (MPES)
Since HVO: Carpenter
Address: Middle Keei Rd.
Captain Cook, Kona, HI 96704

**Lani Eugenio**
1974–1975; Physical science aide (MPES)
Since HVO: Founded nursery school for Kohala community; homemaker
Address: P.O. Box 871
Kapaau, HI 96755

**Kawailele'ohi'ilawe (Charles) Perez**
1974–1975; Physical science aide (MPES)
Since HVO: Graduate in law, People's College of Law, Los Angeles, CA
Address: 445 Todd Ave.
Hilo, HI 96720

**J. Bruce Finlayson**
August 1974–July 1975; Geochemist
Since HVO: Geothermal exploration
Address: Department of Scientific and Industrial Research
Chemistry Division
c/o Ministry of Works
Private Bag
Taupo, New Zealand

**Timothy (Tim) Anicas**
1975–1976(?); Physical science aide (MPES)
Since HVO: Student, Oregon State University
Died August 29, 1979

**Alberta Doria (Allen)**
1975–1976; Physical science aide (MPES)
Since HVO: Teacher; secretary, legal firm in Seattle
Address: 11840–26th Ave. South
Apt. 316, Bldg. 2
Seattle, WA 98168

**Leona Ferreira (Lee)**
1975–1976; Physical science aide (MPES)
Since HVO: Architectural draftsperson in Arizona
Address: 1102 West Peoria Ave., No. 8
Phoenix, AZ 85029

**Frederick Guidry**
1975–1976; Physical science aide (MPES)

**Sidney Kini**
1975–1976; Physical science aide (MPES)
Since HVO: Taro farmer, Waipio Valley

**Darrell Takabayashi**
1975–1976; Physical science aide (MPES)
Since HVO: Physician

**Anne Thompson**
1975–1976; Physical science aide (MPES)

**Lennart A. Anderson**
August 1975–October 1977; Geophysicist
Since HVO: Petrophysics; Nevada Test Site—Nuclear Waste Site Investigations
Address: U.S. Geological Survey
Denver Federal Center, MS 964
Denver, CO 80225

**Erwin McPherson, Jr.**
August 1975–August 1977; Electronics technician, seismic network
Since HVO: Seismology instrumentation for University of Utah
Volcano experience: Yellowstone and Snake River Plain
Address: Box 81171
Salt Lake City, UT 84108

**Peter W. Lipman**
1975–1977; Geologist
Since HVO: Geologic mapping and petrologic studies of the roots of ash-flow calderas, especially the Questa magmatic system, northern New Mexico
Volcano experience: Mount St. Helens, Japan, Western United States
Address: U.S. Geological Survey, MS 913
Box 25046, Federal Center
Denver, CO 80225

**Gordon P. Eaton**
1976–1978; Scientist In Charge
Since HVO: Associate Chief Geologist; Provost, Texas A&M University; President, University of Iowa
Volcano experience: Fossil volcanic systems in California, Wyoming, and New Mexico
Address: University of Iowa
Office of the President
Iowa City, IA 52242

**Jack E. Harris**
March 1976–September 1982; Field assistant
Since HVO: Surveying
Address: P.O. Box 171
Volcano, HI 96788

**Kamuela Chun**
1976–1977; Physical science aide (MPES)
Since HVO: Coordinator, Alu Like (Native American) program; Kumuhula (teacher of the hula)
Address: 681 Manono St.
Hilo, HI 96720

**Annmarie Cullen**
1976–1977; Physical science aide (MPES)

**Onlino Lawrence**
1976–1978; Physical science aide (MPES)
Since HVO: Working for government of Micronesia

**Lani Maa**
1976–1977; Physical science aide (MPES)
Since HVO: Student, William S. Richardson School of Law, University of Hawaii at Manoa

**J.D. (Jim) Griggs**
1976–present; Photographer
Address: U.S. Geological Survey
Hawaiian Volcano Observatory
P.O. Box 51
Hawaii National Park, HI 96718

**Dan Dzurisin**
December 1976–May 1981; Geophysicist
Since HVO: Cascades Volcano Observatory (volcano monitoring/eruption forecasting using electronic tiltmeters; geophysical surveys including SP, VLF, and magnetic-field intensity); Project Chief—physical processes in large silicic systems (leveling and trilateration surveys at Yellowstone; fieldwork to determine prehistoric deformation)
Volcano experience: Indonesia, Papua New Guinea, Italy (Phlegraean Fields)
Address: U.S. Geological Survey
Cascades Volcano Observatory
5400 MacArthur Blvd.
Vancouver, WA 98661

**Deissery Cabudol**
1977–1979; Physical science aide (MPES)

**Jewell Imada**
1977–1978; Physical science aide (MPES)
Since HVO: Graduate (Ph.D. in hydrology), University of Hawaii at Manoa
Address: 3006 N. Murray Ave.
Milwaukee, WI 53211

**Virginia M. Barba (Johnson)**
April 1977–June 1978, May 1979–February 1980; Geologic field assistant (MPES)
Since HVO: Branch of Seismology, USGS, Menlo Park; Cascades Volcano Observatory
Volcano Experience: Mount St. Helens
Address: U.S. Geological Survey
Cascades Volcano Observatory
5400 MacArthur Blvd.
Vancouver, WA 98661

**Richard B. Moore**
August 1977–October 1980; Geologist
Since HVO: Project Chief—Geology and petrology of Hualalai Volcano, Hawaii (geologic mapping of Hualalai Volcano and part of the east rift zone of Kilauea Volcano)
Volcano experience: Western San Juan Mountains (Colorado), San Francisco volcanic field (Arizona), São Miguel (Azores)
Address: U.S. Geological Survey
Hawaiian Volcano Observatory
P.O. Box 51
Hawaii National Park, HI 96718

**Gail Hill**
October 1977–July 1979; Clerk-typist
Since HVO: Two years as clerk-typist at Redwood National Park, Crescent City, Calif.; presently Office Manager for Cuyahoga Valley Line Steam Railroad
Address: 1660 10th Street
Cuyahoga Falls, OH 44221

**Ronald Y. Hanatani**
November 1977–July 1978; Geologic field assistant
December 1983–present; Geologist (deformation studies)
Volcano experience: Yellowstone caldera
Address: U.S. Geological Survey
Hawaiian Volcano Observatory
P.O. Box 51
Hawaii National Park, HI 96718

**Irene Takayesu (Tengan)**
1977–1979, 1980–1981; Physical science aide
Since HVO: Student, University of Hawaii at Hilo

**Alex N. Bittenbinder**
April 1978–November 1979; Computer specialist
Since HVO: President, NEWT, Inc. (Network seismology systems and consulting)
Address: 3206 16th Ave. W., Suite B
Seattle, WA 98119

**Steven Anicas**
1978–1979; Physical science aide (MPES)
Since HVO: Data Processing Manager at Realty Investment Co., Ltd., Hilo
Address: RR 2, P.O. Box 2309
Pahoa, HI 96778

**Kevin Eugene Cuff**
1978–1979; Physical science aide (MPES)

**Roch Dancil**
1978–1979; Physical science aide (MPES)

**Randy Kama**
1978–1979; Physical science aide (MPES)

**Duk Ho Kim**
1978–1979; Physical science aide (MPES)

**Alfred P. Lerma, Jr.**
1978–1979; Physical science aide (MPES)

**Bryan Mamaclay**
1978–1979; Physical science aide (MPES)

**Jolson H. Nakamura**
1978–1979; Physical science aide (MPES)
Since HVO: Disc jockey at radio station KWXX
Address: 121 Banyan Drive, Apt. 250
Hilo, HI 96720

**Darci-Lynn Malia Pitman**
1978–1979; Physical science aide (MPES)

**Rodolfo Riingen**
1978–1979; Physical science aide (MPES)
Since HVO: U.S. Navy

**William Moniz Viveiros**
1978–1979; Physical science aide (MPES)
Since HVO: Fireman, Hawaii County Fire Department
Address: 229 Desha Ave.
Hilo, HI 96720

**Tom J. Casadevall**
June 1978–January 1981; Geochemist
Since HVO: 1981–1985, Cascades Volcano Observatory, staff Geochemist; 1985–present, Volcanological Survey of Indonesia, advisory volcanologist
Volcano experience: Sicily (Etna), Iceland (Krafla), Argentina, Ecuador, Mexico, Guatemala, El Salvador, Costa Rica, Indonesia
Address: U.S. Geological Survey
USAID, Box 4, Jakarta
APO San Francisco, CA 96356

**Craig C. Crissinger**
1978–1986; Geophysical field assistant
Address: P.O. Box 250
Volcano, HI 96785

**Thomas T. English**
August 1978–present; Computer specialist (manages HVO computer system)
Address: U.S. Geological Survey
Hawaiian Volcano Observatory
P.O. Box 51
Hawaii National Park, HI 96718

**Norman G. Banks**
August 1978–October 1983; Geologist
Since HVO: 1983–1985, Project Chief, Geology of southwest rift of Kilauea; 1985–present, Project Chief, Volcano Crisis Assistance Team
Volcano experience: Indonesia (Merapi, Kelut, Tankuban Prahu), Marianas (Pagan), Papua New Guinea (Rabaul), Philippines (Mayon, Bulusan), Colombia (Ruiz)
Address: U.S. Geological Survey
Cascades Volcano Observatory
5400 MacArthur Blvd.
Vancouver, WA 98661

**Robert K. Cessaro**
August 1978–August 1980; Geophysical instrumentation specialist
Since HVO: Research geophysicist for GeoPac, Inc.; completing Ph.D. in Marine Geology and Geophysics, University of Hawaii
Address: Hawaii Institute of Geophysics
Marine Geology and Geophysics
2525 Correa Road
Honolulu, HI 96822

**Fred W. Klein**
October 1978–September 1982; Seismologist
Since HVO: Hawaiian seismic-studies project at USGS, Menlo Park, analyzing seismicity patterns at Kilauea
Volcano Experience: Seismic studies in Iceland and at Lassen Volcanic National Park
Address: U.S. Geological Survey
345 Middlefield Rd, MS 977
Menlo Park, CA 94025

**Ellen Scandalis Klein**
October 1978–September 1982; Physical science aide and administrative clerk
Since HVO: Completing a degree in Recreation and Leisure Studies program at San Jose State University, San Jose, Calif.
Address: 515 Magdalena Ave.
Los Altos, CA 94022

**Robert W. Decker**
January 1979–April 1984; Scientist In Charge
Since HVO: Coordinating plans and publications for HVO Diamond Jubilee
Volcano experience: Katmai, Mount St. Helens, Indonesia, Iceland, Central America, Colombia (Ruiz)
Address: U.S. Geological Survey
345 Middlefield Road, MS 910
Menlo Park, CA 94025

**Bruce T. Furukawa**
January 1979–October 1980; Electronics technician
Since HVO: Cascades Volcano Observatory
Volcano experience: Mount St. Helens
Address: U.S. Geological Survey
Cascades Volcano Observatory
5400 MacArthur Blvd.
Vancouver, WA 98661

**Wilfred (Wil) Tanigawa**
February 1979–present; Physical science technician (seismology)
Address: U.S. Geological Survey
Hawaiian Volcano Observatory
P.O. Box 51
Hawaii National Park, HI 96718

**Dorothy Footer**
April 1979–June 1986; Secretary
Resigned from USGS in 1986

**Reginald H. Bishaw**
1979–1980; Physical science aide (MPES)
Since HVO: Line worker, Hawaiian Telephone Co., Kona
Address: P.O. Box 1086
Kailua-Kona, HI 96745

**John Costales, Jr.**
1979–1980; Physical science aide (MPES)
Since HVO: Department of Social Services, Maui
Address: 599 Hana Highway
Paia, Maui, HI 96779

**Stephanie A. Garcia**
1979–1980; Physical science aide (MPES)

**Darren P. Gomez**
1979–1980; Physical science aide (MPES)

**Herman U. Hofschneider**
1979–1980; Physical science aide (MPES)

**Jeffrey N. Kahakua**
1979–1980; Physical science aide (MPES)

**Rocco Kaheiki**
1979–1980; Physical science aide (MPES)
Since HVO: Mason's helper, Puna

**Daniel K. Kawaiaea, Jr.**
1979–1980; Physical science aide (MPES)
Since HVO: Park Ranger, Puukohola National Historic Site
Address: P.O. Box 262
Kapaau, HI 96755

**Dwayne S. (Steve) Lerma**
1979–1980; Physical science aide (MPES)
Since HVO: Graduate of William S. Richardson School of Law, University of Hawaii at Manoa

**Andrew Louis**
1979–1980; Physical science aide (MPES)
Since HVO: Teacher, Hookena Elementary School, Kona
Address: P.O. Box 163
Honaunau, HI 96726

**Moses A. Nelson**
1979–1980; Physical science aide (MPES)

**Roanne W. Nip**
1979–1980; Physical science aide (MPES)

**Darryl J. Oliveira**
1979–1980; Physical science aide (MPES)

**Gregory L. Tim Sing**
1979–1980; Physical science aide (MPES)
Since HVO: Technician, Audio-Visual Dept., Modern Camera Center, Hilo
Address: 400 Makalika St.
Hilo, HI 96720

**Marian M. Kagimoto**
October 1979–present; Administrative clerk
Address: U.S. Geological Survey
Hawaiian Volcano Observatory
P.O. Box 51
Hawaii National Park, HI 96718

**Taeko Jane Takahashi**
October 1979–present; Library-photo archive technician
Address: U.S. Geological Survey
Hawaiian Volcano Observatory
P.O. Box 51
Hawaii National Park, HI 96718

**Alvin H. Tomori**
October 1979–present; Physical science technician (seismology)
Address: U.S. Geological Survey
Hawaiian Volcano Observatory
P.O. Box 51
Hawaii National Park, HI 96718

**L. Paul Greenland**
1979–1986; Geochemist, volcanic gases
Retired from USGS in August 1986
Address: U.S. Geological Survey
Hawaiian Volcano Observatory
P.O. Box 51
Hawaii National Park, HI 96718

**Kari Anna Basa**
1980–1982; Physical science aide (MPES)
Since HVO: Missionary work in Paraguay, South America
Address: Hermana Kari Basa
Casilla de Correo 818
Asunción, Paraguay

**Erik Kalani Flores**
1980–1982; Physical science aide (MPES)

**Gary Honzaki**
May 1980–present; Physical science technician (seismology)
Address: U.S. Geological Survey
Hawaiian Volcano Observatory
P.O. Box 51
Hawaii National Park, HI 96718

**Lurline Kahapea**
1980–1981(?); Physical science aide (MPES)

**Robert Rathburn**
May 1980–July 1985; Geologic field assistant (MPES)
Since HVO: M.S. in computer programming (May 1985); computer programmer
Address: 5308 Olapa St.
Honolulu, HI 96821

**Charles F. Sasan**
1980–1981(?); Physical science aide (MPES)

**Joseph (Joe) Sterling**
1980–1982; Physical science aide (MPES)
Since HVO: Substitute teacher and musician
Address: Ainaloa, HI

**Frank A. Trusdell**
1980–1983; Geologic field assistant (MPES)
Since HVO: mapping on R. Moore's project, geology and petrology of Hualalai Volcano, Hawaii; geology student mapping Pahoa North quadrangle as part of master's thesis, University of Hawaii at Manoa
Address: U.S. Geological Survey
Hawaiian Volcano Observatory
P.O. Box 51
Hawaii National Park, HI 96718

**Toni J. Duggan**
January 1981–June 1984; Geologic field assistant
Since HVO: Graduate school, University of New Mexico, and Smithsonian Global Volcanism Program
Address: 13323 Schwenger Place
Herndon, VA 22070

**Roxanne M. Adams**
1981–1982(?); Physical science aide (MPES)
Since HVO: Student, University of Hawaii at Hilo

**Dari-Layne P. Aiwohi**
1981–1982; Physical science aide (MPES)

**Mark K. Duvachelle**
1981–1982; Physical science aide (MPES)

**Richline P. Fong**
1981–1982(?); Physical science aide (MPES)

**Monica LeeLoy**
1981–1983; Physical science aide (MPES)
Since HVO: Teacher, law student
Address: 696 Railroad Ave., A15
Hilo, HI 96822

**Darryl K. Lindsey**
1981–1983; Physical science aide (MPES)

**Kathy Velesco**
1981–1982(?); Physical science aide (MPES)

**Joan M. Yoshioka**
1981–1984; Physical science aide (FJF)
Since HVO: Graduate student in botany, University of Hawaii at Manoa
Address: 84 Ainako Ave.
Hilo, HI 96720

**John J. Dvorak**
June 1981–August 1985; Geophysicist (deformation studies)
Since HVO: Working through AID/Naples to implement monitoring at Pozzuoli in southern Italy
Volcano experience: Java (Indonesia), Mount St. Helens, Italy
Address: U.S. Agency for International Development
American Consulate General
Box 18, FPO New York 09521-0002

**Pauline Tamura**
July 1981–present; Physical science aide (seismology) (FJF)
Address: U.S. Geological Survey
Hawaiian Volcano Observatory
P.O. Box 51
Hawaii National Park, HI 96718

**Allan J. Largo**
September 1981–present; Electronics technician
Address: U.S. Geological Survey
Hawaiian Volcano Observatory
P.O. Box 51
Hawaii National Park, HI 96718

**Barry Stokes**
February 1982–present; Physical science technician (geochemistry)
Address: U.S. Geological Survey
Hawaiian Volcano Observatory
P.O. Box 51
Hawaii National Park, HI 96718

**Edward W. Wolfe**
March 1982–June 1984; Geologist
June 1984–present; Project Chief, 1:100,000-scale geologic map of the Island of Hawaii
Volcano experience: Arizona (San Francisco volcanic field), Washington
Address: U.S. Geological Survey
Hawaiian Volcano Observatory
P.O. Box 51
Hawaii National Park, HI 96718

**M. Candy Hoopii**
1982–1983; Physical science aide (MPES)
Since HVO: Park Interpreter, Hawaii Natural History Association, Hawaii Volcanoes National Park
Address: 466 Desha Ave.
Hilo, HI 96720

**Ian B. LeeLoy**
1982–1983; Physical science aide (MPES)
Since HVO: U.S. Air Force
Address: 509 Brookdale Drive
Alamogordo, NM 88313

**Hannah Kihalani Springer**
May 1982–May 1984; Physical science aide (MPES)
Since HVO: Continued education in anthropology and geography at University of Hawaii at Hilo; park interpretation for Hawaii Natural History Association; volunteer with Interpretation and Maintainence Divisions at Puu Kohola National Historic Site; technical writing for the County of Hawaii Planning Department
Address: P.O. Box 663
Volcano, HI 96785

**Lois-Ann Yamanaka**
1982–1984; Physical science aide
Since HVO: Graduate study in secondary school teaching at University of Hawaii at Manoa, teaching English at Kalakaua Intermediate School, Honolulu
Address: 2140 10th Ave., Apt. 203
Honolulu, HI 96816

**Sandra Zane**
June 1982–present; Physical science aide (seismology) (MPES)
Address: U.S. Geological Survey
Hawaiian Volcano Observatory
P.O. Box 51
Hawaii National Park, HI 96718

**George Kaipo Ah Chong, Jr.**
1983–1985; Physical science aide (MPES)
Since HVO: Farmer; bartender, Volcano Golf and Country Club
Address: 206A Chong St.
Hilo, HI 96720

**John (Keone) P. Ah Chong**
May 1983–1986; Field assistant (deformation studies) (MPES)
Since HVO: Farmer
Address: 206A Chong St.
Hilo, HI 96720

**Lesly Keolanui Brown**
1983–1984; Physical science aide (MPES)
Since HVO: Homemaker
Address: Volcano, HI 96785

**Charlotte M. Forbes**
May 1983–present; Physical science aide (geochemistry) (MPES)
Address: P.O. Box 97
Volcano, HI 96785

**David William Heltz**
1983–1984; Physical science aide (MPES)
Since HVO: Waiter, Volcano House Hotel
Address: Volcano. HI 96785

**Brian C. Moniz**
May 1983–July 1985; Physical science aide (MPES)
Since HVO: Welding and diesel mechanic
Address: 147 West Kent Drive
Chandler, AZ 85224

**Del D. Trusdell**
1983–1984; Physical science aide (MPES)
Since HVO: Machinist-welder
Address: 2505 Lai Rd.
Honolulu, HI 96816

**Christina Neal**
June 1983–May 1984; Geologic field assistant
May 1984–June 1984; Geologist
Since HVO: June 1984–present; 1:100,000-scale geologic map of the Island of Hawaii; geology of the southwest rift zone of Kilauea
Volcano experience: Mount St. Helens, Katmai, Galápagos spreading center (submarine)
Address: U.S. Geological Survey
Hawaiian Volcano Observator
P.O. Box 51
Hawaii National Park, HI 96718

**David N. Little**
December 1983–present; Electronics and computer assistant (SIS)
Since HVO: Department of Geology, University of Hawaii at Manoa (student)
Address: U.S. Geological Survey
Hawaiian Volcano Observatory
P.O. Box 51
Hawaii National Park, HI 96718

**Terry J. Ignacio**
May 1984–present; Physical science aide (MPES)
Address: U.S. Geological Survey
Hawaiian Volcano Observatory
P.O. Box 51
Hawaii National Park, HI 96718

**Kent Kikuchi**
1984–1986; Physical science aide (MPES)
Since HVO: Student in pharmacology at Washington State University, Pullman.
Address: 65 Hiluhilu St.
Hilo, HI 96720

**George E. Ulrich**
June 1984–present; Geologist
Volcano experience: San Francisco volcanic field, Arizona, and late Tertiary volcanic rocks along Mogollon Rim
Address: U.S. Geological Survey
Hawaiian Volcano Observatory
P.O. Box 51
Hawaii National Park, HI 96718

**John P. Hoffman**
June 1984–September 1985; Physical science technician
Since HVO: Graduate student, University of Hawaii, working on evolution of Puu Oo's plumbing system
Address: Hawaii Institute of Geophysics
University of Hawaii
2525 Correa Road
Honolulu, HI 96822

**C. Christina Heliker**
August 1984–present; Geologist
Volcano experience: Mount St. Helens
Address: U.S. Geological Survey
Hawaiian Volcano Observatory
P.O. Box 51
Hawaii National Park, HI 96718

**Lu Setnicka**
December 1984–present; Administrative clerk
Address: U.S. Geological Survey
Hawaiian Volcano Observatory
P.O. Box 51
Hawaii National Park, HI 96718

**Carl Arakaki**
1985–present; Physical science aide (electronics) (MPES)
Address: 270 Mohala Place
Hilo, HI 96720

**Renee Lehualani Ellorda**
May 1985–present; Physical science aide (electronics) (MPES)
Address: 320 Iliahi St., Apt. 1
Hilo, HI 96720

**Lureen K. Helliangao**
June 1985–present; Physical science aide (MPES)
Address: 1292 Haihai St.
Hilo, HI 96720

**Jason Takayama**
1985–1986; Physical science aide (electronics) (MPES)

**Nicole Torres**
1985–present; Physical science aide (FJF)
Address: P.O. Box 433
Pahala, HI 96777

**Laurie Roberts**
1986–present; Physical science aide (MPES)
Address: 15-613 Kahakai Blvd.
Pahoa, HI 96778

**Marcie Vicente**
1986–present; Receptionist (MPES)
Address: P.O. Box 4174
Hilo, HI 96720

## APPENDIX 62.1

### ALPHABETICAL LIST OF HAWAIIAN VOLCANO OBSERVATORY STAFF

Following each name in this list is the year in which that person joined the staff of the observatory. The list can therefore be used to find the entry for a particular person in the main body of the chapter, which is organized chronologically according to those dates.

Adams, R.—1981
Ah Chong, G.K.—1983
Ah Chong, J.P.—1983
Aiwohi, D.-L.P.—1981
Akaka, L.—1974
Akim-Seu, A.—1919
Anderson, L.A.—1975
Anicas, S.—1978
Anicas, T.—1975
Arakaki, C.H.—1985
Arakaki, C.—1968
Au, T.-O.—1926
Ault, W.U.—1957
Banks, N.G.—1978
Barba (Johnson), V.M.—1977
Basa, K.A.—1980
Bishaw, R.H.—1979
Bittenbinder, A.N.—1978
Boyrie, F.Y.—1927
Brown, L.K.—1983
Cabudol, D.—1977
Casadevall, T.J.—1978
Cessaro, R.K.—1978
Chun, K.—1976
Christiansen, R.L.—1971
Costales, J., Jr.—1979
Crissinger, C.C.—1978
Cuff, K.E.—1978
Cullen, A.—1976
Dakujaku, G.—1961
Dancil, R.—1978
Decker, R.W.—1979
Doria (Allen), A.—1975
Duffield, W.A.—1969
Duggan, T.J.—1981
Duvachelle, M.K.—1981
Dvorak, J.J.—1981
Dzurisin, D.—1976
Eaton, G.P.—1976
Eaton, J.P.—1953
Ellorda, R.L.—1985
Emerson, O.H.—1923
Endo, E.T.—1963
Endo, Y.K.—1964
English, T.T.—1978
Eugenio, L.—1974
Ferreira (Lee), L.—1975
Finch, R.H.—1919
Finlayson, J.B.—1974
Fiske, R.S.—1965
Flores, E.K.—1980
Fong, R.P.—1981
Footer, D.C.—1979
Forbes, C.M.—1983
Forbes, J.C.—1950
Forbes, L.G.—1950
Francis, W.H.—1957
Fraser, G.D.—1956
Furukawa, B.T.—1979
Garcia, S.—1979

Gomez, D.P.—1979
Greenland, L.P.—1979
Griggs, J.D.—1976
Guidry, F.—1975
Hanatani, R.Y.—1977
Harris, J.E.—1976
Heliker, C.C.—1984
Helliangao, L.K.—1985
Heltz, D.W.—1983
Hill, D.P.—1964
Hill, G.—1977
Hjort, C.—1950
Hodges, R.B.—1926
Hoffman, J.P.—1984
Hofschneider, H.U.—1979
Holcomb, R.T.—1971
Honma, K.T.—1970
Honzaki, G.Y.—1980
Hoopii, M.K.—1982
Ignacio, T.J.—1984
Imada, J.—1977
Jackson, D.B.—1968
Jaggar, I.M.—1917
Jaggar, T.A.—1912
Johnston, E.E.—1952
Jones, A.E.—1931
Judd, J.—1966
Kagimoto, M.M.—1979
Kahakua, J.N.—1979
Kahapea, L.—1980
Kaheiki, R.—1979
Kama, R.—1978
Kawaiaea, D.K., Jr.—1979
Kikuchi, K.—1984
Kim, D.H.—1978
Kini, S.—1975
Kinoshita, W.T.—1963
Klein, E.S.—1978
Klein, F.W.—1978
Kojima, G.—1958
Koyanagi, R.Y.—1961
Krivoy, H.L.—1959
Lancaster, A.—1912
Largo, A.J.—1981
Lawrence, O.—1976
LeeLoy, I.B.—1982
LeeLoy, M.—1982
Lerma, A.P.—1978
Lerma, D.S.—1979
Lindsey, D.K.—1981
Lipman, P.W.—1975
Little, D.N.—1983
Lockwood, J.P.—1974
Loucks, B.J.—1940
Loucks, R.—1948
Louis, A.—1979
Maa, L.—1976
Macdonald, G.A.—1948
Malo, P.—1942
Mamaclay, B.—1978
McDonald, R.R.—1960
McPherson, E., Jr.—1975
Mitchell, R.—1968
Moniz, B.C.—1983
Moore, J.G.—1961
Moore, R.B.—1977
Murata, K.J.—1958
Nakaji, G.H.—1925
Nakamura, J.H.—1978
Nakata, J.S.—1974
Neal, C.—1983
Nelson, M.A.—1979
Nip, R.—1979
Okamura, A.T.—1961
Okamura, R.T.—1958
Okuda, A.—1936
Oliveira, D.J.—1979
Omer, G.—1943
Onouye, M.S.—1967
Palmer, H.S.—1926
Peck, D.L.—1963
Perez, K.—1974
Peterson, D.W.—1970
Pitman, D.L.M.—1978
Powers, H.A.—1929
Powers, S.—1915
Puniwai, G.S.—1974
Rathburn, R.—1980
Richter, D.H.—1959
Riingen, R.—1978
Roberts, L.—1986
Ryall, A.S., Jr.—1962
Sako, M.K.—1967
Sasan, C.F.—1980
Sato, S.—1936
Setnicka, L.M.—1984
Sherrill, N.D.—1963
Shultz, P.E.—1940
Springer, H.K.—1982
Sterling, J.—1980
Stokes, B.—1982
Suga, K.—1918
Swanson, D.A.—1968
Takabayashi, D.—1975
Takahashi, T.J.—1979
Takayama, J.—1985
Takayesu (Tengan), I.—1977
Takeguchi, S.—1968
Tamura, P.—1981
Tanigawa, W.—1979
Thompson, A.—1975
Tim Sing, G.L.—1979
Tilling, R.I.—1972
Tomori, A.H.—1979
Torres, N.M.—1985
Trusdell, D.D.—1983
Trusdell, F.A.—1980
Ulrich, G.E.—1984
Unger, J.D.—1971
Velesco, K.—1981
Vicente, M.—1986
Viveiros, W.M.—1978
Waesche, H.H.—1935
Wentworth, C.K.—1951
Wilson, R.M.—1926
Wingate, E.G.—1931
Wolfe, E.W.—1982
Wood, H.O.—1912
Wright, T.L.—1964
Yamamoto, A.—1955
Yamanaka, L.A.—1982
Yamashita, K.M.—1966
Yasunaka, H.—1924
Yoshioka, J.M.—1981
Zablocki, C.J.—1972
Zane, S.—1982

# GUIDE TO PRONUNCIATION OF HAWAIIAN WORDS

Compiled by Taeko Jane Takahashi

## INTRODUCTION

The following compilation is an alphabetic listing and guide to pronunciation of the Hawaiian words used in Professional Paper 1350. The diacritical marks used are the glottal stop (‘), known in Hawaiian as the ‘okina or ‘u‘ina, and the macron (¯); these are the marks used in Pukui and others (1974), Pukui and Elbert (1977), Armstrong (1973), and on topographic maps of the U.S. Geological Survey. Words whose pronunciation is uncertain are marked with an asterisk in the second column. Words not in the references listed above but whose pronunciation has been validated by a local Hawaiian-language expert are indicated by a dagger (†) in the second column. Where pronunciation differs with reference to a particular locality or to the inflection of people within that locality, a second pronunciation is given.

## PRONUNCIATION

Pukui and Elbert (1977) give the following guide to Hawaiian pronunciation:

**Consonants**

**p** and **k** are pronounced as in English, but with less aspiration.
**h**, **l**, **m**, and **n** are pronounced about the same as in English.
**w** after **i** and **e** is pronounced like **v**, after **u** and **o** like **w**, and initially and after **a** like **v** or **w**.
‘ A glottal stop is similar to the sound between the *oh*'s in the English *oh-oh*.

**Vowels**

**Unstressed**

**a** like **a** in above
**e** like **e** in bet
**i** like **y** in city
**o** like **o** in sole
**u** like **oo** in moon
} but without offglides

**Stressed**

**a, ā** like **a** in far
**e** like **e** in bet
**ē** like **ay** in play
**i, ī** like **ee** in see
**o, ō** like **o** in sole
**u, ū** like **oo** in moon
} but without offglides; vowels marked with macrons are somewhat longer than other vowels

**Rising diphthongs**

**ei, eu, oi, ou, ai, ae, ao, au** Always stressed on the first member, but the two members are not so closely joined as in English.

**Stress (or Accent)**

*On all vowels marked with macrons*: **ā, ē, ī, ō, ū.**
Otherwise on the next-to-last syllable and alternating preceding syllables or words, except that words containing five syllables without macrons are stressed on the first and fourth syllables. Final stress in a word (‘) is usually louder than the preceding stress or stresses (‘): hále, maká‘u, hòlohólo, ‘èlemakúle.

## LIST OF WORDS

| *Word* | *Pronunciation* |
|---|---|
| Aa | ‘A‘ā |
| Ahi | Ahi |
| Ahu a Umi | Ahu a ‘Umi; †‘Ahu a ‘Umi |
| Ahua Kamokukolau | Āhua Kamokukōlau; †‘Āhua Kamokukōlau |
| Ailaau | ‘Ailā‘au |
| Ainahou | ‘Āinahou |
| Ainaloa | ‘Āinaloa |
| Ainaola | ‘Āinaola |
| Ainaole | †‘Āinaole; †Āina‘ole |
| Ainapo | ‘Āinapō |
| Akea | †Ākea |
| Akihi | ‘Akihi |
| Akiohala | ‘Akiohala |
| Akolea | ‘Ākōlea |
| Alae | ‘Alae |
| Alala | ‘Alalā |
| Alaloa | Alaloa |
| Alapai | Alapa‘i |
| Alauawa | †Alauawa |
| Alenaio | †Alenaio |
| Alenuihaha | ‘Alenuihāhā |
| Alii | Ali‘i |
| Alika | ‘Ālika |
| Aloi | ‘Ālo‘i |
| Anahulu | Anahulu |
| Apokula | †Apokula; †‘Apokula |
| Apua | ‘Āpua |
| Apuupuu | ‘Āpu‘u‘pu‘u |
| Auauki | ‘Au‘aukī |
| Aulepe | A‘ulepe |
| Enuhe | ‘Enuhe |
| Haena | Hā‘ena |
| Haihai | Ha‘iha‘i |

| *Word* | *Pronunciation* |
|---|---|
| Haiku | Ha'ikū |
| Hainoa | Hainoa; †Hāinoa |
| Hakuma | Hākuma |
| Hala | Hala |
| Halalii | Halāli'i |
| Halape | Halapē |
| Halawa | Hālawa |
| Hale | Hale |
| Haleakala | Haleakalā |
| Halekamahina | Halekamahina |
| Halemanu | Halemanu |
| Halemaumau | Halema'uma'u |
| Halulu | Halulu |
| Hamakua | Hāmākua |
| Hana | Hāna |
| Hanalei | Hanalei |
| Hanauma | Hanauma |
| Hanawi | Hanawī |
| Hapaimanu | †Hāpaimanu |
| Hapuu | Hāpu'u |
| Hau Kea | †Hau Kea |
| Hauoki | †Hau'oki |
| Haupu | Hā'upu |
| Hawaii | Hawai'i |
| Hawi | Hāwī |
| Heeia | He'eia |
| Heiau | Heiau |
| Heiheiahulu | Heiheiahulu |
| Hiiaka | Hi'iaka |
| Hilea | Hīlea |
| Hilina | Hilina |
| Hilo | Hilo |
| Hionamoa | Hi'onamoa |
| Hoaka | Hoaka; †Hō'aka |
| Hoakalei | Hoakalei |
| Holei | Hōlei |
| Homelani | Homelani |
| Honalo | Honalo |
| Honaunau | Hōnaunau |
| Honokaa | Honoka'a |
| Honokahau | Honokāhau |
| Honokane Nui | Honokane Nui |
| Honolua | Honolua |
| Honolulu | Honolulu |
| Honomanu | Honomanū; †Honomanu |
| Honomu | Honomū |
| Honuaula | Honua'ula; †Hōnua'ula |
| Honuapo | Honu'apo |
| Honukai | †Honukai |
| Hoopuloa | Ho'ōpūloa |
| Hopukani | †Hopukani |
| Hou | Hou |
| Hualalai | Hualālai |
| Huehue | Hu'ehu'e |
| Huluhulu | Huluhulu |
| Humuula | Humu'ula |
| Iao | 'Īao |
| Iilewa | 'Ī'ilewa; †I'ilewa |
| Iiwi | 'Ī'iwi |
| Ikaaka | *Ika'aka |
| Iki | Iki |
| Ilio | 'Īlio |
| Io | 'Io |
| Kaaha | Ka'aha |

| *Word* | *Pronunciation* |
|---|---|
| Kaala | Ka'ala |
| Kaalaala | Ka'ala'ala |
| Kaalaiki | Ka'alāiki |
| Kaalualu | Ka'alu'alu |
| Kaapuna | Ka'apuna |
| Kaau | Ka'au |
| Kaawaloa | Ka'awaloa |
| Kaelepulu | Ka'elepulu |
| Kaena | Ka'ena |
| Kaeo | Ka'eo |
| Kaeokulani | †Ka'eokūlani |
| Kahaluu | Kahalu'u |
| Kahana | Kahana |
| Kahaualea | Kahauale'a |
| Kahauloa | †Kahauloa |
| Kahawai | Kahawai |
| Kahe | Kahe |
| Kahekili | Kahekili |
| Kahele | Kāhele |
| Kahiliku | Kāhilikū |
| Kahililoa | Kāhililoa |
| Kahoama | Kahoama; †Kahō'ama |
| Kaholo | Kaholo |
| Ka-Holua-o-Kahawali | Ka-Hōlua-o-Kahawali |
| Kahoolawe | Kaho'olawe |
| Kahue | Kahue; †Kahu'e |
| Kahuku | Kahuku |
| Kahukupoko | Kahukupoko |
| Kahului | Kahului |
| Kahuwai | Kahuwai; †Kahūwai |
| Kailua | Kailua |
| Kaiwa | Ka'iwa |
| Kaka | Kākā |
| Ka Lae | Ka Lae |
| Ka Lae Apuki | Ka Lae 'Apuki |
| Kalahaku | Kalahaku; †Kalāhaku |
| Kalaheo | Kalāheo |
| Kalaieha | Kala'i'ehā |
| Kalama | Kalama |
| Kalana | †Kalana |
| Kalanianaole | Kalaniana'ole |
| Kalea | †Kalea |
| Kalihi | Kalihi |
| Kaluaiki | †Kaluaiki |
| Kamaileunu | Kamaile'unu |
| Kamaili | Kama'ili |
| Kamakaia | Kamakai'a |
| Kamakaiauka | †Kamakaiauka |
| Kamakaiawaena | †Kamakaiawaena |
| Kamalo | Kamalō |
| Kamanaiki | Kamanaiki |
| Kamapuaa | Kamapua'a |
| Kamehame | Kamehame |
| Kamehameha | Kamehameha |
| Kamoamoa | Kamoamoa |
| Kamohio | Kamōhio |
| Kamooalii | Kamo'oali'i |
| Kamuela | Kamuela |
| Kanaha | Kanahā |
| Kanahaha | Kanahāhā |
| Kanapou | Kanapou |
| Kane Nui o Hamo | Kāne Nui o Hamo |
| Kanenelu | Kanenelu |
| Kaneohe | Kāne'ohe |

| *Word* | *Pronunciation* |
|---|---|
| Kaniku | Kanikū |
| Kaohikaipu | Kāohikaipu; Kāʻohikaipu |
| Kaoiki | Kaʻōiki |
| Kaone | Kaʻone; †Kaone |
| Kapaa | Kapaʻa |
| Kapaau | Kapaʻau |
| Kapapala | Kapāpala |
| Kapaula | Kapāʻula |
| Kapukapu | Kapukapu |
| Kauhuhuula | Kauhuhuʻula |
| Kauka | *Kauka |
| Kaumalapau | Kaumalapau |
| Kaumana | Kaūmana; †Kaʻumāna |
| Kauna | Kaunā; †Kauna |
| Kaunakakai | Kaunakakai |
| Kaupo | Kaupō |
| Kaupulehu | Kaʻūpūlehu |
| Kawaihoa | Kawaihoa |
| Kawaikini | Kawaikini |
| Ke a Poomoku | Ke ʻā Poʻomoku |
| Kea | Kea |
| Keaau | Keaʻau |
| Keahole | Keāhole |
| Keaiwa | Keaīwa; †Keaʻīwa |
| Kealaikahiki | Kealaikahiki |
| Kealakekua | Kealakekua |
| Kealohi | Kealohi |
| Keamuku | Keʻāmuku |
| Keana Bihopa | Keana Bihopa |
| Keanae | Keʻanae |
| Keanakakoi | Keanakākoʻi |
| Keanakolu | Keanakolu |
| Keanapapa | Keʻānapapa |
| Keaoi | Keaoi; †Keaʻoi |
| Keauhou | Keauhou |
| Keauohana | Keauʻohana |
| Keawakapu | Keawakapu |
| Keawanui | Keawanui |
| Keawewai | Keawewai |
| Kekake | Kēkake |
| Kemole | Kemole |
| Keokeo | Keʻokeʻo |
| Keolu | Keolu |
| Keone | Keone |
| Keopu | Keōpū |
| Ki | Kī |
| Kiai | Kiaʻi |
| Kiholo | Kīholo |
| Kilauea | Kīlauea |
| Kinau | Kīnaʻu |
| Kinikini | Kinikini |
| Kinoole | Kinoʻole |
| Kipapa | Kīpapa |
| Kipuka | Kīpuka |
| Koa | †Koa |
| Koae | Koaʻe |
| Kokoolau | Kokoʻolau |
| Kolekole | Kolekole |
| Koli | *Koli |
| Kolono | Kolono |
| Komohana | Komohana |
| Kona | Kona |
| Koolau | Koʻolau |
| Kou | Kou |
| Kuakini | Kuakini |
| Kualoa | Kualoa |
| Kuanene | Kuanēnē |
| Kuee | Kūʻeʻē |
| Kukae | Kūkae |
| Kukaiau | Kūkaʻiau |
| Kukalauula | Kūkalauʻula |
| Kukuau | Kūkūau |
| Kukui | Kukui |
| Kukuihaele | Kukuihaele |
| Kula | Kula |
| Kulai | Kulaʻi |
| Kulani | Kūlani |
| Kulua | Kūlua |
| Kumukoa | Kumukoʻa |
| Kumukahi | Kumukahi |
| Kupanaha | Kupanaha; †Kūpanaha |
| Kupapau | Kupapaʻu |
| Kupono | Kūpono |
| Lae Apuki | Lae ʻApuki |
| Lahaina | Lahaina |
| Laina | Laina |
| Lalaau | Lalaʻau |
| Lanai | Lānaʻi |
| Lani Puna | Lani Puna |
| Lauiole | Lauiole |
| Laupahoehoe | Laupāhoehoe |
| Lehua | Lehua |
| Leilani | Leilani |
| Lihue | Līhuʻe |
| Likelike | Likelike |
| Liliuokalani | Liliʻuokalani |
| Liloa [or Riroa] | Līloa |
| Loihi | Lōʻihi |
| Lokuana | †Lokuana |
| Lua Hou | Lua Hou |
| Lua Manu | Lua Manu |
| Lua Poholo | Lua Poholo |
| Luakaha | Luakaha |
| Lualualei | Lualualei |
| Luamakani | Luamakani |
| Maalaea | Māʻalaea; †Maʻalaea |
| Mahaua | †Mahaua |
| Mahuka | Mahuka |
| Makaha | Mākaha |
| Makahanu | Makahanu |
| Makai | Makai |
| Makaino | †Makaʻino |
| Makalapa | Makalapa |
| Makalawena | Makalawena |
| Makalii | Makaliʻi |
| Makamakaole | Makamakaʻole |
| Makanaka | Mākanaka |
| Makaopuhi | Makaopuhi |
| Makapipi | Makapipi |
| Makapuu | Makapuʻu |
| Makaukiu | Makaʻukiu |
| Makawao | Makawao |
| Makaweli | Makaweli |
| Makuku | Mākūkū |
| Makuu | Makuʻu |
| Malaai | Mālaʻai |
| Malama Ki | Malama Kī; †Mālama Kī |
| Maliikakani | †Māliʻikakani |

| *Word* | *Pronunciation* |
|---|---|
| Mamalahoa | Māmalahoa |
| Manana | Mānana |
| Manele | Mānele |
| Maniania | Māniania |
| Manoa | Mānoa |
| Manuka | Manukā |
| Maui | Maui |
| Mauka | Mauka |
| Maulua | Maulua |
| Mauna Iki | Mauna Iki |
| Mauna Kea | Mauna Kea |
| Mauna Kuwale | Mauna Kūwale |
| Mauna Loa | Mauna Loa |
| Mauna Ulu | Mauna Ulu |
| Maunaiu | Mauna'iu |
| Maunalei | Maunalei |
| Maunawili | Maunawili |
| Mauu Mae | Mau'u Mae |
| Melia | †Melia |
| Moana Hauae | †Moana Haua'e |
| Moanuiahea | Moanuiahea |
| Moaula | Moa'ula |
| Moiliili | Mō'ili'ili |
| Mokapu | Mōkapu |
| Mokolea | Mōkōlea |
| Moku Manu | Mokumanu |
| Mokuaweoweo | Moku'āweoweo |
| Mokuhooniki | Mokuho'oniki |
| Mokulua | Mokulua |
| Mokuone | Mokuone |
| Molokai | Moloka'i |
| Moo | Mo'o |
| Moolelo | Mo'olelo |
| Na Manu a Haalou | Na Manu a Ha'alou; Nāmanuaha'alo'u |
| Na Puu o na Elemakule | Nā Pu'u o nā 'Elemākule |
| Naalehu | Nā'ālehu |
| Nahiku | Nāhiku |
| Naiomamane | †Naiomāmane |
| Naliikakani | Nāli'ikakani |
| Nanahu | †Nānahu |
| Nanawale | Nānāwale |
| Napali | Nāpali |
| Napau | Nāpau |
| Napoopoo | Nāpo'op'o |
| Nawahine | Nāwāhine |
| Nene | Nēnē |
| Neneakolu | †Nēnē'akolu |
| Nihoa | Nihoa |
| Niihau | Ni'ihau |
| Ninole | Nīnole |
| Nuuanu | Nu'uanu |
| Oahu | O'ahu |
| Ohaikea | 'Ōhaikea |
| Ohale | Ohale |
| Ohelo | 'Ōhelo |
| Ohia-lehua | 'Ōhi'a-lehua |
| Ohiki | 'Ōhiki |
| Olaa | 'Ōla'a |
| Olokele | Olokele |
| Olomana | Olomana |
| Oo | 'Ō'ō |
| Ookala | 'O'ōkala; †'Ō'ōkala |
| Opihikao | 'Opihikao |
| Opihinehe | 'Opihinehe |

| *Word* | *Pronunciation* |
|---|---|
| Paakea | Pa'akea |
| Paauau | Pā'au'au |
| Paauhau | Pā'auhau |
| Paauilo | Pa'auilo |
| Pahala | Pāhala |
| Pahoa | Pāhoa |
| Pahoehoe | Pāhoehoe |
| Pakekake | Pakēkāke |
| Palani | Palani |
| Palawai | Pālāwai |
| Palehua | Palehua |
| Pali Kapu o Keoua | Pali Kapu o Keōua |
| Palikea | Palikea |
| Palikilo | Palikilo |
| Palima | Pālima |
| Panaewa | Pana'ewa |
| Paniau | Pānī'au |
| Papa | Pāpā |
| Papaa | Pāpa'a |
| Papaaloa | Pāpa'aloa |
| Papaikou | Pāpa'ikou |
| Papalehau | Papalehau; †Pāpalehau |
| Papau | †Pāpa'u |
| Pauahi | Pauahi |
| Paupau | Pa'upa'u |
| Pauwalu | Pauwalu |
| Pawai | Pāwai |
| Pele | Pele |
| Peleliilii | Peleli'ili'i |
| Pepeekeo | Pepe'ekeo |
| Piihonua | Pi'ihonua |
| Piinaau | Pi'ina'au |
| Pilau | Pilau |
| Pili | Pili |
| Pohakaa | †Pohāka'a |
| Pohakea | Pōhākea |
| Pohaku | Pōhaku |
| Pohakuloa | Pōhakuloa |
| Pohakupule | Pōhakupule |
| Pohina | †Pōhina |
| Pohoiki | Pohoiki |
| Poliahu | Poli'ahu |
| Poliokeawe | Poliokeawe |
| Pololu | Pololū |
| Pomaikai | Pōmaika'i |
| Ponahawai | Pōnahawai |
| Ponohohoa | Ponohohoa |
| Poomau | Po'omau |
| Puai | Pua'i |
| Puaialua | Pua'i'ālua |
| Pualaa | Pū'āla'a |
| Puea | Pu'e'a |
| Puehu | Puehu |
| Puhimau | Puhimau |
| Pulama | Pūlama |
| Puna | Puna |
| Punahoa | Punahoa |
| Punaloa | †Punaloa |
| Punaluu | Punalu'u |
| Puou | Pū'ou |
| Puueo | Pu'u'eo |
| Puulena | Pu'ulena |
| Puuloa | Pu'uloa |
| Uka | Uka |

| *Word* | *Pronunciation* |
|---|---|
| Ulaula | ʻUlaʻula |
| Ulekuwale Pueo | Ulekūwale Pueo |
| Uluhe | Uluhe |
| Ulupau | Ulupaʻu |
| Uo | ʻUo |
| Uwekahuna | Uwēkahuna |
| Waa | Waʻa |
| Waawaa | Waʻawaʻa |
| Waha Pele | Waha Pele |
| Wahaula | Wahaʻula |
| Waiaha | Waiʻaha |
| Waiaka | Waiʻaka |
| Waiahole | Waiāhole |
| Waiakea | Waiākea |
| Waialae | Waiʻalae |
| Waianae | Waiʻanae |
| Waianu | Waianu |
| Waianuenue | Waiānuenue |
| Waiapele | Waiapele |
| Waiau | Waiau; †Waiʻau |
| Waihu | Waihū |
| Waikahalulu | Waikahalulu |
| Waikane | Waikāne |
| Waikeekee | Waikeʻekeʻe |
| Wailea | Wailea |
| Wailuanui | Wailuanui |
| Wailuku | Wailuku |
| Waimanalo | Waimānalo |
| Waimanu | Waimanu |
| Waimea | Waimea |
| Waiohinu | Waiohinu |
| Waiokamilo | Waiokamilo |
| Waipahoehoe | Waipahoehoe |
| Waipio | Waipiʻo |
| Waipuku | Waipuku |
| Waiwelawela | Waiwelawela |
| Wekiu | Wēkiu |

## REFERENCES CITED

Armstrong, R.W., ed., 1973, Atlas of Hawaii: Honolulu, University Press of Hawaii, 222 p.

Pukui, M.K., and Elbert, S.H., 1977, Hawaiian dictionary: Honolulu, University Press of Hawaii, 590 p.

Pukui, M.K., Elbert, S.H., and Mookini, E.T., 1974, Place names of Hawaii: Honolulu, University of Hawaii Press, 289 p.

## ADDENDUM

| *Word* | *Pronunciation* |
|---|---|
| Kau | Kaʻū |
| Puu | Puʻu |

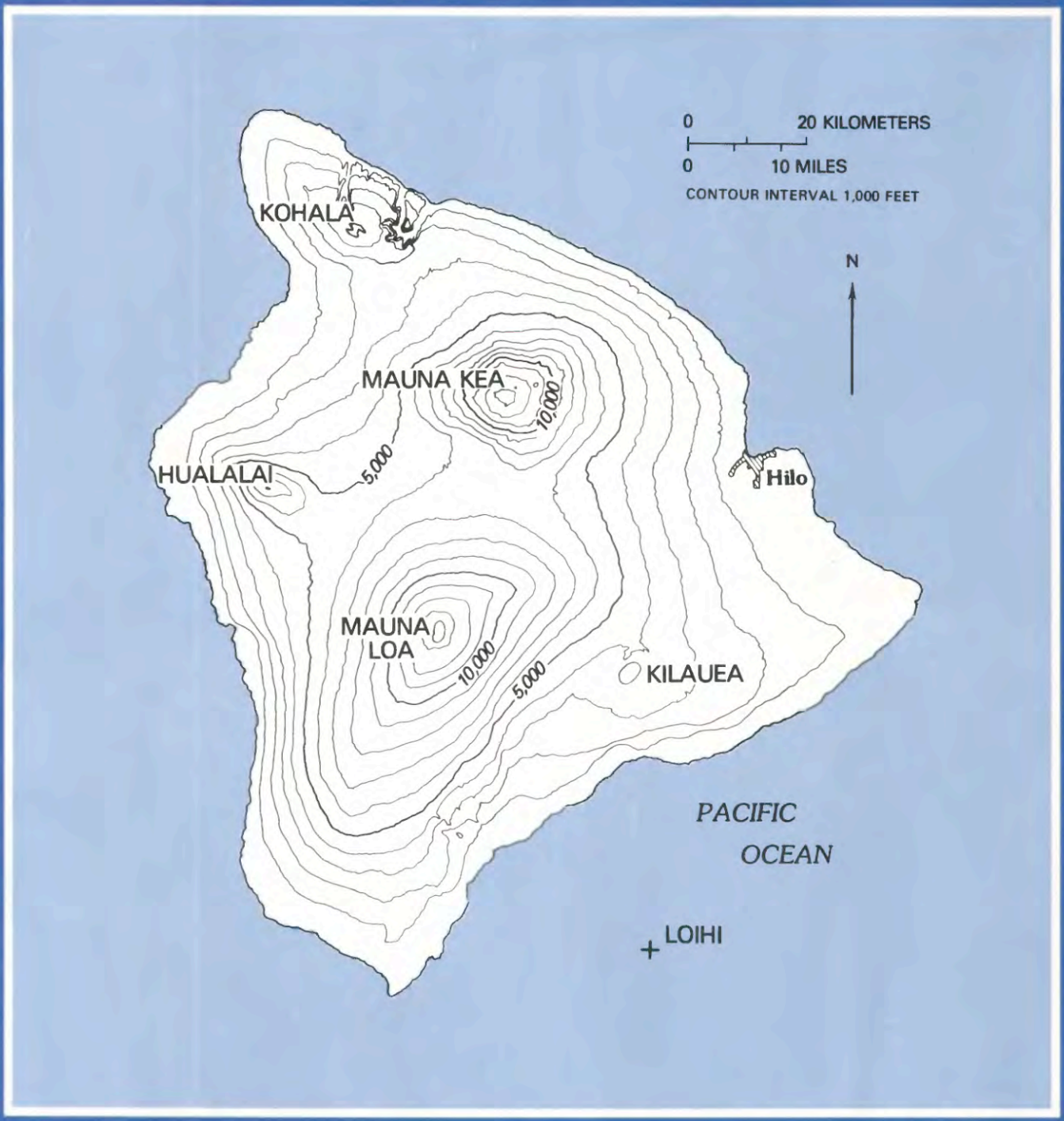


*Island of Hawaii*

U.S. DEPARTMENT OF THE INTERIOR

March 3, 1849